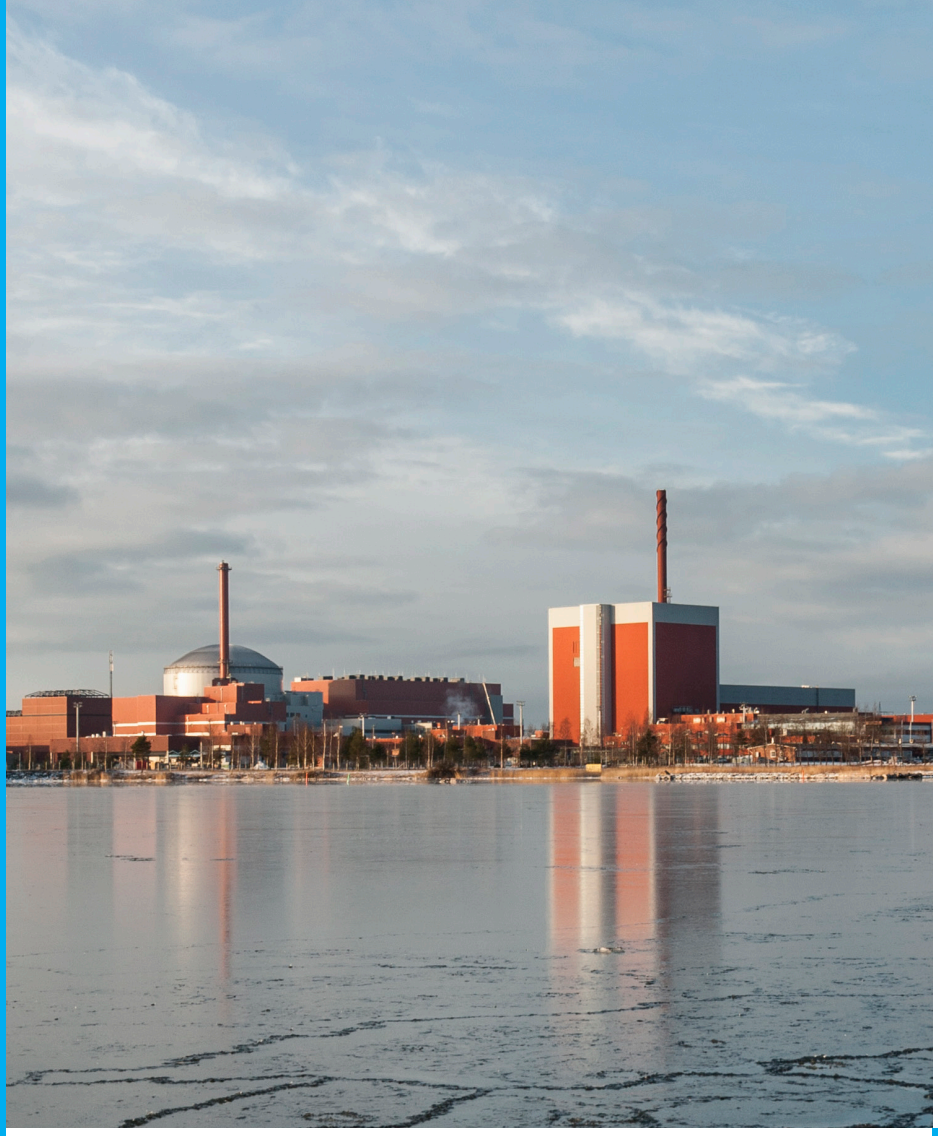

TECHNOLOGY • RESEARCH HIGHLIGHTS • VISIONS • SCIENCE
216

ISSCWR-7 2015

7th International Symposium on Supercritical Water-Cooled Reactors

15th–18th March 2015, Radisson Blu Royal Hotel, Helsinki, Finland

VTT

VTT TECHNOLOGY 216

ISSCWR-7 2015
7th International Symposium on Supercritical Water-Cooled Reactors

15th–18th March 2015
Radisson Blu Royal Hotel
Helsinki, Finland

Sami Penttilä (Ed.)

ISBN 978-951-38-8289-1 (USB flash drive)
ISBN 978-951-38-8290-7 (URL: http://www.vttresearch.com/impact/publications)

VTT Technology 216

ISSN-L 2242-1211
ISSN 2242-122X (Online)

JULKAISIJA – UTGIVARE – PUBLISHER

Teknologian tutkimuskeskus VTT Oy
PL 1000 (Tekniikantie 4 A, Espoo)
02044 VTT
Puh. 020 722 111, faksi 020 722 7001

Teknologiska forskningscentralen VTT Ab
PB 1000 (Teknikvägen 4 A, Esbo)
FI-02044 VTT
Tfn +358 20 722 111, telefax +358 20 722 7001

VTT Technical Research Centre of Finland Ltd
P.O. Box 1000 (Tekniikantie 4 A, Espoo)
FI-02044 VTT, Finland
Tel. +358 20 722 111, fax +358 20 722 7001

Cover picture: TVO

Preface

The 7th International Symposium on Supercritical Water-Cooled Reactors (ISSCWR7) was held in Helsinki, Finland, 15th to 18th March, 2015. This biannual Symposium was hosted by VTT Technical Research Centre of Finland Ltd in co-operation with the Finnish Network for Generation Four Nuclear Energy Systems (GEN4FIN), the International Atomic Energy Agency (IAEA), the Generation IV International Forum (GIF) and the Canadian Nuclear Society (CNS).

This symposium provided a forum for discussion of advancements and issues, sharing information and technology transfer, and establishing future collaborations on research and development for supercritical water-cooled reactors (SCWR) between international research organizations.

Over the last ten years there has been a great interest internationally to develop innovative SCWR concepts. This reactor concept was chosen as a part of the GIF portfolio in 2001 and is being actively investigated in countries like Canada, China, EU, Japan and Russia. The main reasons for this interest are the higher thermal efficiency (44–48%) compared to present Light Water-cooled Reactors (LWRs), improved economic competitiveness, and enhanced safety.

One of the main advantages of the SCWR over other Gen IV concepts is that the system is an evolution from existing LWR technology. Unlike other Gen IV concepts, there is already extensive worldwide experience in the construction and operation of LWRs, and in the construction and operation of fossil-fired supercritical water power plants. Most proposed SCWR concepts are direct cycle concepts that benefit from a higher thermal efficiency and simplified system configuration, as recirculation pumps, pressurizers, steam generators, steam separators and dryers are not needed. In addition, the possibility of using a fast neutron spectrum will increase fuel cycle sustainability.

Because SCWRs will operate under temperature and pressure conditions exceeding the current experience with LWRs, and because of the unique properties of supercritical water as a coolant, some major challenges remain to be solved. As a consequence some of the key areas of interest associated with the development of SCWR systems were chosen as topics of interest at ISSCWR7:

- Reactor core, neutronics and fuel designs
- Materials, chemistry and corrosion
- Thermal-hydraulics and safety analysis
- Balance of plant

We would like to thank all authors, reviewers and organisers for their valuable work in order to make this event successful. All financial and other contributions from each supporting organisation are gratefully acknowledged.

Sami Penttilä

Chair of technical program committee of ISSCWR7

Espoo, Finland, 15th March, 2015

The 7th International Symposium on Supercritical Water-Cooled Reactors
ISSCWR-7
15-18 March 2015, Helsinki, Finland

ISSCWR7-2001

Performance of CVD and Plasma Spray Coated Stainless Steel 310 in Supercritical Water

Xiao Huang*[1], Q Yang[2], Teymoor Mohammadi[1] and Dave Guzonas[3]

[1] Mechanical and Aerospace Engineering Department
Carleton University
1125 Colonel By Dr, Ottawa, ON, Canada, K1S 5B6
*Corresponding author: Xiao.huang@carleton.ca
(613) 520 2600
[2] National Research Council Canada, Ottawa, ON, Canada, K1A 0R6
[3] Atomic Energy of Canada Limited, Chalk River, ON, Canada

Abstract

In this study, aluminized and NiCrAlY plasma sprayed AISI 310 stainless steel samples were tested in supercritical water (SCW) at 500°C. The microstructure after SCW exposure was analyzed using SEM, EDS and XRD. Weight measurements were taken before and after exposure to provide quantitative comparison of the two coatings on the 310 base metal. The results showed that aluminized and bare 310 stainless steel experienced similar weight gain, in the range of 0.02 to 0.08 mg/cm^2 after 1550 hours. Aluminized sample had a slight weight decrease as exposure progressed. Oxide formation, in the forms of Al_2O_3 and $(Fe,Cr)_2O_3$, was found on the aluminized surface along with surface cracking after 1550 hour testing in SCW. NiCrAlY coated 310, however, had the most but consistent weight increase and oxide formation (mainly Al_2O_3) on the surface. Based on the results from this study, the aluminized coating has limitations in providing surface protection due to surface cracking and weight loss. The NiCrAlY plasma sprayed coating with alumina formation on the surface has the potential to provide long term surface protection to the substrate material in SCW.

1.0 Introduction

Safer and more sustainable Generation IV nuclear reactors are being developed to ensure nuclear energy's long term expansion and contribution to the world's energy security. The Supercritical Water Reactor (SCWR) is one of the six systems selected by the Generation IV International Forum (GIF); it uses water above its critical point condition (i.e., 374 ^{o}C and 22.1 MPa) as the coolant [1]. As shown in Figure 1, the peak operating temperature for the proposed SCWR is at least 2 times higher than that of the Pressurized Water Reactors (PWRs) and Boiling Water Reactors (BWRs). Using supercritical water (SCW) as the coolant eliminates the need for steam generators, coolant recirculation pumps, pressurizer, steam generators and separators and dryers, thus making the system more compact and simplified [1]. Due to the much higher operating temperature, SCWRs will have higher thermal efficiencies (as high as 48%) than current water-cooled reactors (about 33%) [2,3]. In the Canadian SCWR concept, 336 vertical fuel channels are used in the core. A high pressure inlet plenum feeds water into the core at a temperature of 350 °C. The fuel channel outlets are connected to an outlet plenum, instead of feeder pipes, with water temperature of 625 °C. The outlet plenum connects to a high-pressure turbine in a direct cycle as shown in Figure 2 [4].

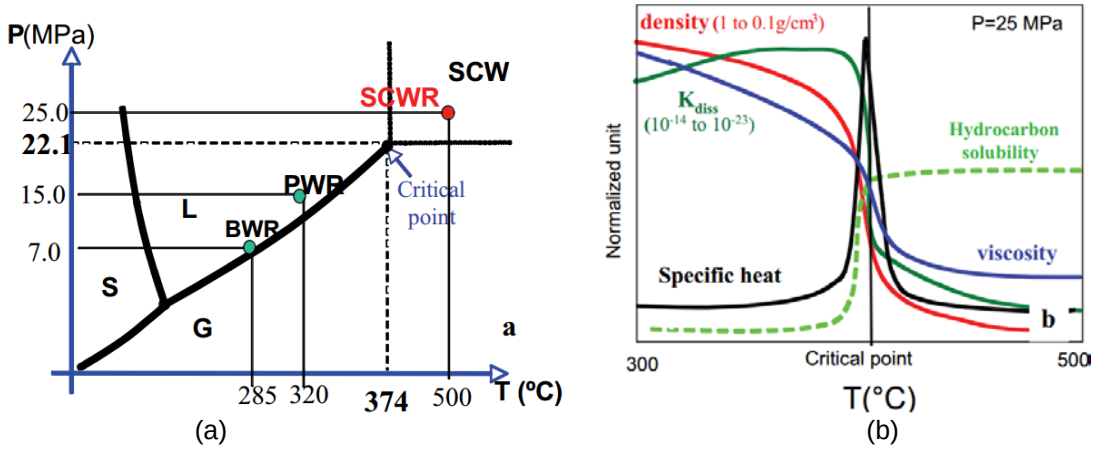

Figure 1. (a) Pressure-temperature regime of SCWR operation compared to that for current BWRs and PWRs, and (b) change in water properties around the critical point [5].

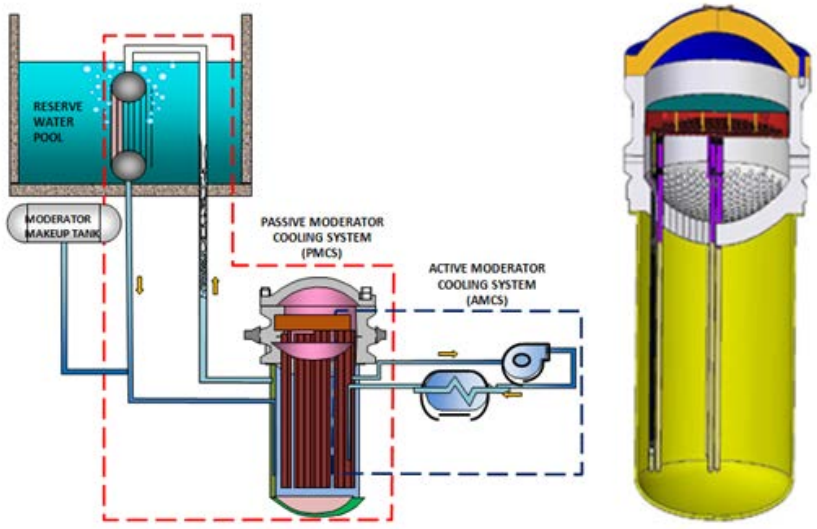

Figure 2. Schematic diagram illustrating Canadian SCWR design [4].

One of the major challenges in developing such reactors is to select suitable materials for in-core components. The conditions in the SCWR core combine high temperature and high pressure with irradiation. Materials chosen for in-core components must be resistant to general corrosion and stress corrosion cracking (SCC), have acceptable dimensional stability under irradiation, be resistant to irradiation creep , and possess acceptable ductility, toughness, and creep rupture strength [2,6,7].
The primary candidate materials for the fuel cladding of the Canadian SCWR include high-strength austenitic steels and nickel-based alloys. Exposure of austenitic stainless alloys 304, 310 and 316 to SCW containing 8 ppm dissolved oxygen resulted in modest weight gains (< 0.9 mg/cm^2) at temperatures up to 550 °C for 500 h. After oxide removal, the weight loss was found to be the least for 310 [5]. Most results on austenitic stainless steels tested in SCW reveal that the surface oxides usually are of a two- or three-layer structure, with the outer layer generally consisting of magnetite and an inner layer that is rich in chromium, either an iron chromium spinel phase or an iron chromium oxide with the corundum structure. An intermediate layer is also present between the inner layer and the base metal and appears to consist of base metal that is supersaturated with oxygen [8].

One possible solution to the problem of reduced component lifetime is to apply anticorrosion coatings to these components [9]. Alumina-based oxide scales are known to mitigate many types of corrosion found in SCW conditions such as SCC, pitting and general corrosion [10]. It has been reported that the addition of Al to stainless steels can increase the high temperature oxidation resistance [11]. To enhance the corrosion and oxidation resistance of the cast stainless steel CF8C-plus, a diffusion aluminide coating was applied. Testing in 10% H_2O at 800°C showed that the Al-rich coating was effective in providing oxidation and corrosion resistance to the substrate via the formation of an alumina scale [13,14,15]. CVD iron-aluminide (Fe-13, 15 and 20 at.% Al) coated T91 and 304L specimens also exhibited excellent performance in water vapour at 700°C as compared to uncoated specimens, which were severely attacked [14]. Iron aluminide coatings, applied by a slurry process [16,17] on ferritic stainless steel steam turbine components, also demonstrated improved steam-oxidation resistance at 650°C. However, depletion of Al from the coating due to Al diffusion into the substrate commonly occurs on exposure to temperatures near or greater than 650 °C.

To improve the oxidation resistance of 310 stainless steel, surface coatings via CVD diffusion and plasma spraying overlay process were examined in this study. Aluminide diffusional coatings are typically fabricated by chemical vapour deposition (CVD) of Al and other alloying elements (e.g. Ni, Cr and Si). Aluminide coatings are often brittle and have much higher ductile-to-brittle transition temperatures (DBTT) than MCrAlY overlay coatings [18]. However, they have a significant application advantage over overlay coatings in that they can be applied to non-line-of-sight locations. In addition, CVD diffusional coatings are often thinner (30 to 50 μm) than MCrAlY overlays [19]. Aluminization of stainless steels by employing a pack cementation process involves the use of aluminum, alumina and ammonium chloride powders as the raw pack materials. The amount of Al introduced and the associated change in microstructure depend upon raw materials composition, temperature, time and atmosphere. MCrAlY (M = Ni, NiCo, CoNi, or Fe) overlay coatings rely on the formation of a dense, adherent and renewable alumina and/or chromia film (via oxidation of aluminum and chromium in the coating) to provide oxidation resistance [20]. The aluminum content in commercial MCrAlY coatings typically varies between 3 and 24 wt.%, with the average being around 10 wt.%. When Al is combined with Cr, a synergistic effect can result in which less Al is required to form a dense Al_2O_3 layer. The MCrAlY coatings, comprised of β aluminide (NiAl) or Ni_3Al embedded in more ductile γ-Ni(Fe,Co) solid solution, are less brittle than aluminide coatings. They can be deposited by either thermal spray (TS) or vapour deposition techniques [21], namely physical vapour deposition (PVD) or chemical vapour deposition (CVD). Plasma spraying (PS) is a more flexible coating process that allows the composition of the coatings to be easily varied. The typical microstructure of a MCrAlY plasma-sprayed coating contains “splat” interfaces parallel to the substrate surface [21]. The surface finish of PS coatings is rougher than that of PVD or CVD coatings. Both PS and PVD processes are classified as line-of-sight process and therefore not applicable to parts with small internal passages. The CVD process, on the other hand, has the capability of coating non-line-of-sight locations and is a batch process in which a large number of parts can be coated at the same time. In this study the corrosion behaviour and microstructure changes of CVD- and plasma spray-coated 310 in SCW were evaluated. More details of the CVD process will be provided in the following section.

2.0 Materials and Experimental Procedures

Stainless steel 310 bars of 10 mm in diameter were cast by Sophisticated Alloy (PA, USA) with the composition shown in Table 1. The alloy bars were HIPped and heat treated to homogenize the microstructure. Disks of 3 mm and 10 mm in thickness were cut from the alloy bar using a diamond wheel and faced with lath. All samples were then ground with 600 grit SiC abrasive paper before further processing. The 3 mm thick disks were tested in the as-received and CVD coated conditions while the 10 mm thick disks were plasma spray coated with NiCrAlY.

Table 1. Chemical composition (in wt.%) of 310 stainless steel.

	Fe	Cr	Ni	Mn	Si	C
Actual 310 cast	Bal.	24.92	20.16	1.53	1.50	0.09
Specification	Bal.	24.0-26.0	19.0-22.0	2.00 max	1.50 max	0.25 C Max, 0.045 P, 0.03 S

The CVD process was carried out in a tube furnace (Model STT-1600C-4-12 by Sentro Tech Corporation, USA) using the pack cementation technique. After running a number of developmental tests with different process parameters, a final aluminizing test was performed at 1050 ^{o}C for 4 hours [15]. The pack mixture used for the aluminizing processes contained pure Al powder as the aluminium source, NH_4Cl as the activator, and alumina powder as the inert filler. The pack composition is shown in Table 2. In order to protect the powder mixture from oxidation before the coating process started, argon gas was used to initially purge the furnace tube for 30 minutes and was then continuously flowed throughout the tube during the CVD process. Before the purging and heating cycle was started, 310 samples, entirely buried within pack in alumina crucibles and covered with an alumina lid, were inserted into the tube furnace. After the pack cementation process, the pack was allowed to cool in the furnace to room temperature. When the samples were removed from the furnace, they were cleaned with a soft brush to remove loose powder and further cleaned in soapy water ultrasonically.

Table 2. Pack mixture and parameters used for the CVD process.

Sample Code		310-5, -6
Al in Powder Pack	wt.%	7.5
	Targeted weight (g)	6
	Actual weight (g)	6.05
NH_4Cl	wt.%	2
	Targeted weight (g)	1.6
	Actual weight (g)	1.62
Al_2O_3	wt.%	90.5
	Targeted weight (g)	72.4
	Actual weight (g)	72.49
Total Weight	Targeted weight (g)	80
	Actual weight (g)	80.16
Temperature (^{o}C)		1050
Time (min.)		240

To deposit the NiCrAlY coating on all surfaces of the cylindrical samples, the samples were sand blasted to attain a clean and rough surface using No. 46 grit alumina abrasive (ALODUR) for about 3 minutes. A jig was designed to hold the samples so that all surfaces could be coated through 5 consecutive runs (two passes for the two flat surfaces and three for the circumferential surface). A Mettech Axial III plasma spray system, manufactured by Northwest Mettech Corporation (Vancouver, Canada), was used to coat the samples in this study. The coating powder composition and plasma spray parameters are given in Table 3 and Table 4, respectively.

Table 3. Powder Used For Plasma Spraying.

Coating	Powder Trade Name	Composition (wt.%)	Powder Size Distribution (μm)	Manufacturer
NiCrAlY	Ni-164-2	22% Cr, 10% Al, 1% Y, Bal. Ni	-75 /+45	Praxair

Table 4. Gas Composition and Spray Parameters for Plasma Spraying (NiCrAlY)

Argon (%)	65	Total Flow Rate (slm*)	230
Hydrogen (%)	25	Powder Feed Rate (g/m)	50
Nitrogen (%)	10	Nozzle Size (in)	3/8
Carrier Gas Flow Rate (slm)	12	Plasma Gun to Substrate distance (mm)	150
Current (A)	251	Duration of Single Coating Run (sec.)	45
Voltage (V)	144	Total Number of Runs	5

*standard litre per minute.

Table 5. 310 Stainless Steel Samples Condition.

Sample ID	Disc Thickness (mm)	Coating Condition	Test Condition
310-1	3	Bare	Reference Sample (not tested in SCW)
310-2	3	Bare	SCW
310-3	3	Bare	SCW
310-5	3	Aluminized (7.5% Al)	SCW
310-6	3	Aluminized (7.5% Al)	SCW
310-8	11	NiCrAlY Sprayed	SCW
310-9	10	NiCrAlY Sprayed	SCW

Seven samples were used in this study and their identification numbers are summarized in Table 5. Before the SCW test, all samples were first cleaned in a soap solution and then acetone for 30 minutes in an ultrasonic bath (BRANSON Ultrasonic Cleaners Model 2510). Samples were baked in an electric oven at 200 °C before initial weighing. To hang samples in the autoclave holder, 1/8" holes were drilled into the samples. The samples were hung from the alumina arms of a customized 316 stainless steel tree (Figure 3), which was placed on a ceramic disc inside the pressure vessel in order to prevent contact with the vessel. Alumina spacers were placed between the specimens to prevent them from contacting each other. The SCW test was carried out in a Parr 4650 autoclave. A vacuum was created in the vessel before injecting a calculated amount of de-aerated water into the vessel to give the desired pressure at the test temperature. The dissolved oxygen (DO) content in water was measured using Oxygen Chemets K-7512 test kit (1-12 mg/L DO) and K-7501 (0-1 mg/L DO). At the end of each test, the pH and DO were measured again. The values of pH and DO before and after SCW test are summarized in Table 6.

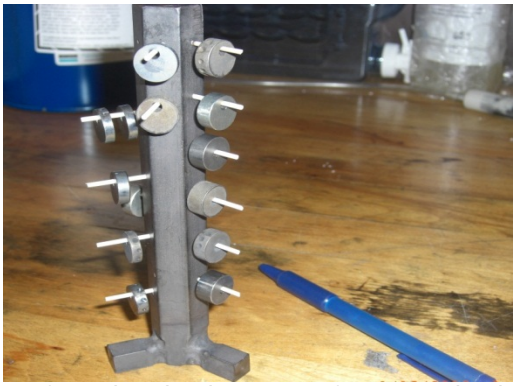

Figure 3. The samples were hung from the alumina arms of a customized 316 stainless steel tree before being placed into the SCW autoclave.

Table 6. SCW Test Parameters.

Test Period	Temp (°C)	Pressure Start/End (MPa)	Total Test Time (hrs)	DO Level Start/End (ppm)	pH Value Start/End
Period 1	500	26.20/22.54	386	0.8/0.9	7/5
Period 2	500	29.32/22.07	501	0.8/0.9	7/5
Period 3	500	28.92/22.10	668	0.9/1.0	7/5

The pressure in the autoclave reduced continuously during the SCW test during minor leakages. As such, the autoclave was recharged by adding more water periodically as soon as the pressure dropped to 22 MPa. Weight measurements of samples were taken during each recharging. Before weighing the samples after each test period, the samples were ultrasonically cleaned consecutively in soap solution and Dow Corning OS-2 silicone cleaner (Hexamethyldisiloxane/Octamethyltrisiloxane) for 15 minutes to remove possible contamination, then (SEM was used to verify the removal of Si-containing substance on the surface) dried at 200 ^{o}C in an oven for 2 hours and then placed in the autoclave again.

The surface morphology and the cross-sectional microstructure were examined using scanning electron microscopy (SEM). The composition of the aluminized layer was analyzed with energy dispersive spectroscopy (EDS). The surface oxide phases formed after the SCW test were identified using an X-ray diffractometer (Bruker D8 Powder). During XRD analysis, a Co K_{α} radiation x-ray source was used with an applied voltage and current of 35 kV and 40 mA, respectively. All tests were carried out within a 2θ range of 40-100 degrees (θ is the angle between the incident x-ray beam and the horizontal surface of the sample).

3.0 Results and Discussion

3.1 Sample Weight Change

After each test period, samples were weighed using an Acculab scale (accuracy of +/- 0.1 mg) and the result of the averaged weight changes are provided in Table 7. The variation of the weight change per unit area in SCW as a function of exposure time is shown in Figure 4. As shown here, the weight change for bare 310 is very small after 1555 hours and increases only slightly over time. The observed weight change of the 310 is consistent with values reported in the literature [22]. The aluminized 310 gained a little more weight than the bare 310, suggesting more oxide formation on the surface, but the weight change decreased over time, an indication of possible oxide dissolution or spallation. The NiCrAlY-coated 310 sample exhibited the most weight gain, almost 100 times greater than the other two types of samples. To further validate this observation, two standalone NiCrAlY coating samples (without substrate), ground to 600 grit, were tested for a longer period. The results (Figure 5) confirmed that the weight change of plasma-sprayed NiCrAlY was in the range of few mg/cm^2, although surface grinding reduced the weight gain by about 3 times. The reason for such large weight gain of NiCrAlY will be further discussed in the following section. Although the weight change of NiCrAlY is quite large, as shown in Figure 5, it has a trend of constant weight gain (any indication of weight loss is a concern for nuclear application) in a parabolic mode.

Table 7. The Net Weight Changes of the Samples (mg/cm^2)

	Average weight change (mg/cm^2)		
Sample	386 h	887 h	1555 h
310-bare	0.02	0.02	0.04
310-Aluminized	0.08	0.06	0.05
310-NiCrAlY coated	5.02	6.38	6.50

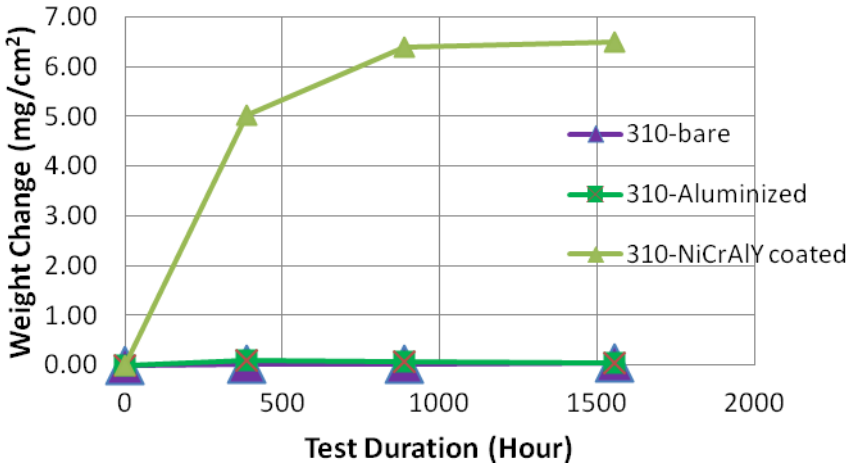

Figure 4. Weight change as a function of exposure time in SCW.

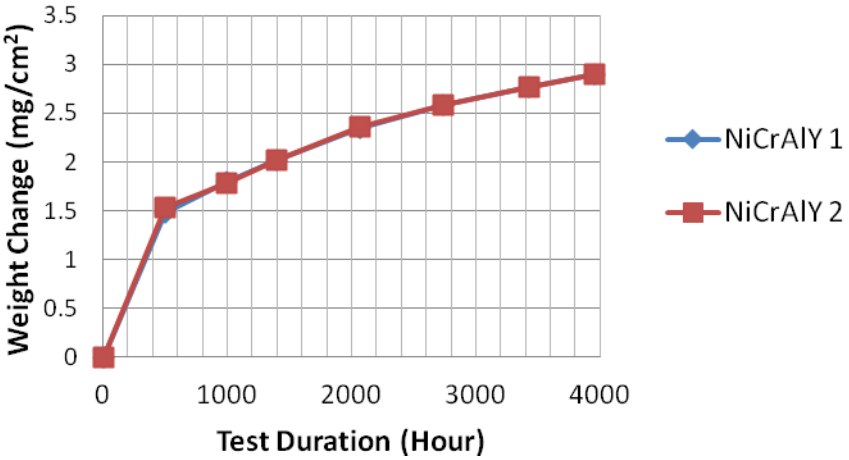

Figure 5. Weight change of standalone plasma-sprayed NiCrAlY (600 grit finish) in SCW.

3.2 Microstructure analysis of as-coated samples

3.2.1 Cross-section analysis of aluminized 310

SEM and EDS analyses were carried out on cross sections of aluminized 310 sample. Figure 6 displays the SEM image in the as-polished condition. Three distinct layers (from left to right) are seen: CVD coating layer (about 60 µm), intermediate diffusion layer (57 µm) and substrate. EDS analysis results from these different layers (Figure 6) show a high concentration of Al in the coating and diffusion layer and high Cr concentration in the substrate. Based on the measured at.% of Al and Ni in the coating, the formation of a (Fe,Ni)Al phase is expected. The diffusion layer has a two-phase structure, likely $(Fe,Ni)_3Al$ in a γ-matrix.

Table 8. EDS composition analysis results of aluminized 310 (at.%).

Elements	O	Al	Si	Cr	Mn	Fe	Ni
Coating	7.0	38.0	1.0	12.2	1.1	28.0	12.7
Diffusion layer	0.0	7.7	3.9	28.0	1.7	46.4	12.4
Substrate	0.0	2.4	3.2	26.9	1.5	48.8	17.2

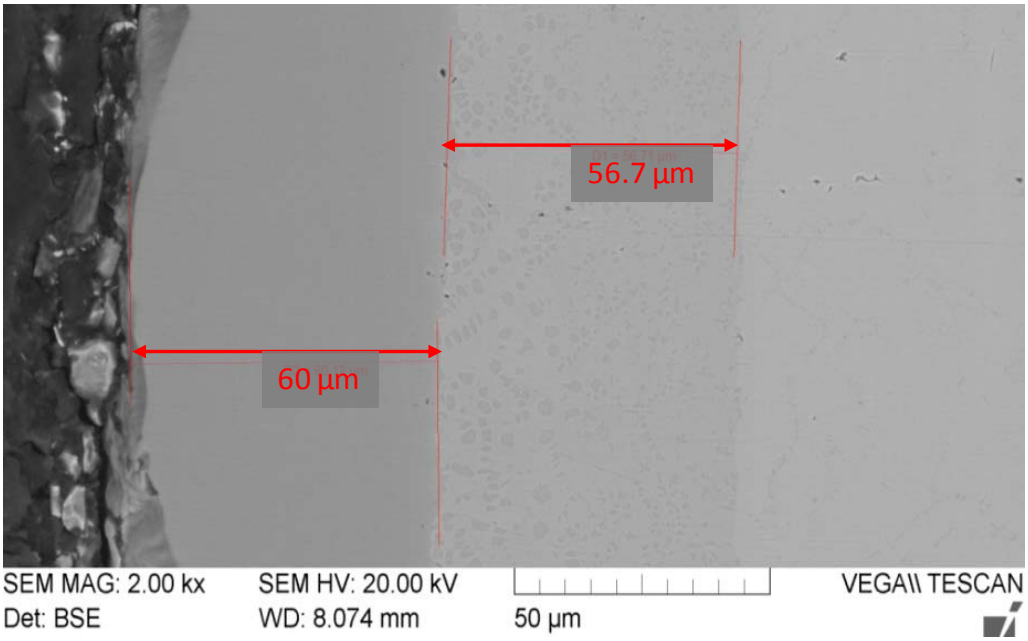

Figure 6. Cross section of aluminized 310.

3.2.2 Plasma sprayed sample

The plasma-sprayed 310 sample shows a laminar NiCrAlY coating structure with thickness of about 250 µm (Figure 7(a)). The coating surface is quite rough and has the typical plasma sprayed lamella structure. The interface is free of cracks or voids. The composition of the NiCrAlY coating varies from point to point. As such a line scan was used to determine the composition of the coating (Figure 7(b)). The Al concentration in the coating was about 30 at.%, and the Cr concentration was about 20 at.%, slightly lower than that in the 310 substrate (26 at.%). Some elemental dilution has occurred during the plasma spray process.

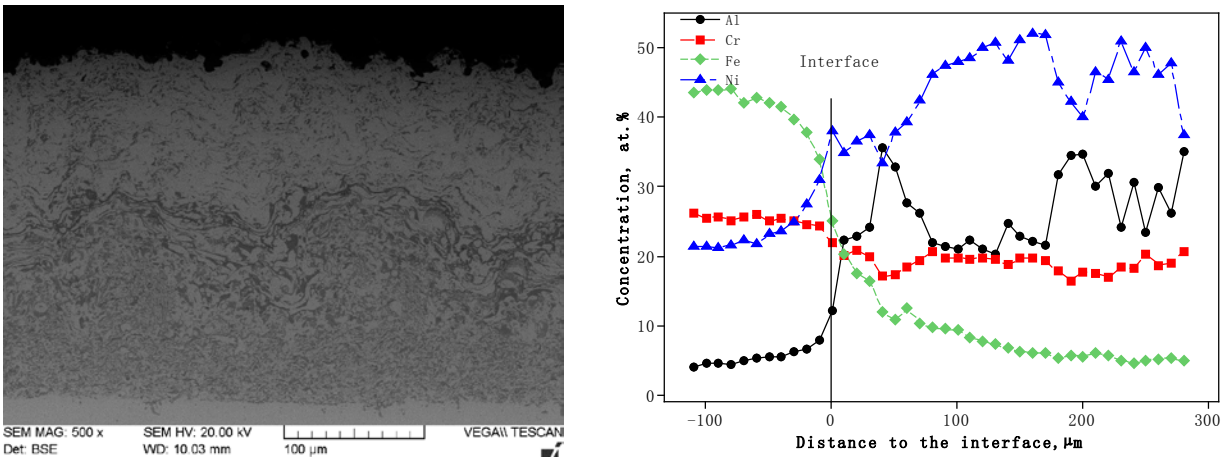

Figure 7. SEM image of NiCrAlY-coated 310 sample (a) and EDS line scan results (b).

3.3 SEM Analysis of Samples after SCW Testing

3.3.1 310 Sample

After 1555 hours of testing in SCW the bare 310 sample (Figure 8(a)) still retained some of the grinding marks left from the surface preparation process. Under high magnification, two different types of phases appear to have formed: lighter areas with small crystals (A) and islands with grey phase (B) (Figure 8(b)). The EDS analysis results (Figure 8(c) and (d)) show elevated levels of oxygen in both areas, thus confirming that oxidation occurred on the surface. In the bright area (A), the presence of Fe, Cr and O suggests the formation of Fe-Cr or Fe-oxide [23] while the presence of primarily Cr and O in area (B) indicates Cr-oxide formation. The formation of an Fe-Cr spinel phase oxide is commonly observed on stainless steels exposed to SCW; the XRD spectrum (Figure 9) and composition measured from the grey phase (B) suggest the possible presence of a $FeCr_2O_4$ spinel phase on the surface, in addition to the presence of austenite peaks from the 310 substrate.

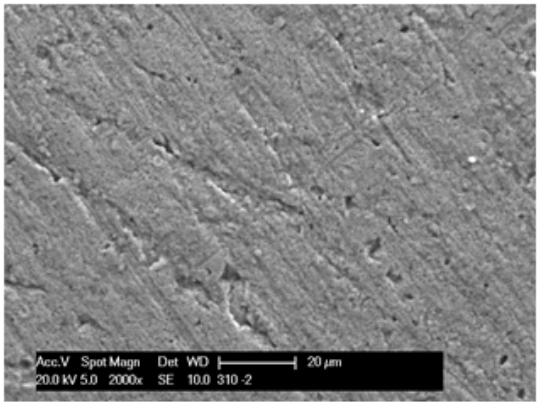

(a)

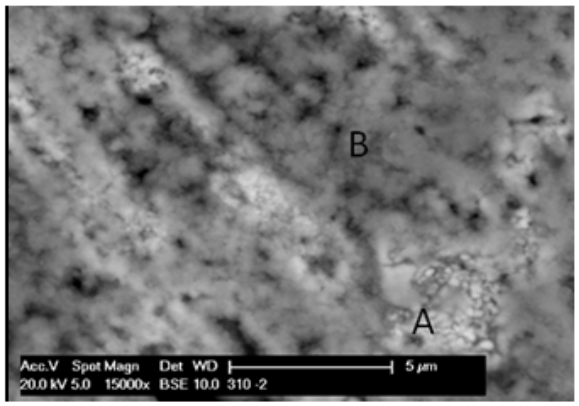

(b)

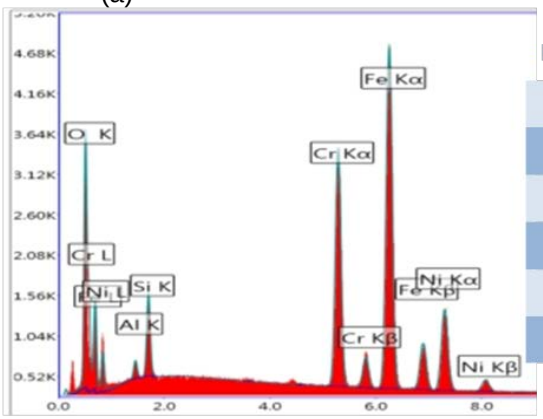

Element	Weight %	Atomic %
O K	10.87	28.79
AlK	0.91	1.44
SiK	3.16	4.77
CrK	19.26	15.7
FeK	48.24	36.62
NiK	17.56	12.68

(c) EDS analysis of area A in (b)

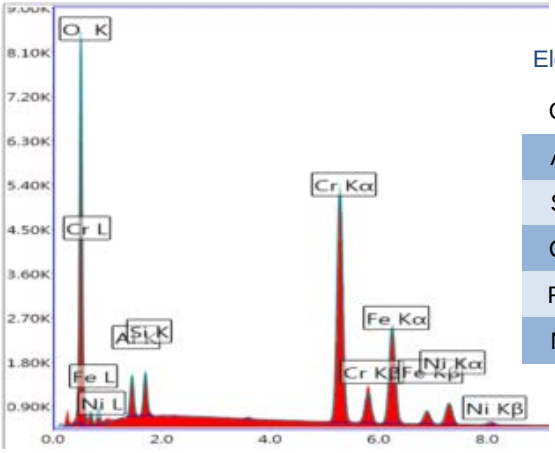

Element	Weight %	Atomic %
O K	25.12	51.35
AlK	3.07	3.72
SiK	2.61	3.05
CrK	36.51	22.97
FeK	24.84	14.55
NiK	7.84	4.37

(d) EDS analysis of area B in (b).

Figure 8. SEM image of bare 310 sample after 1555 hr SCW testing (a) 2000x, (b) 15000x, (c) and (d) EDS analysis result for areas A and B in (b).

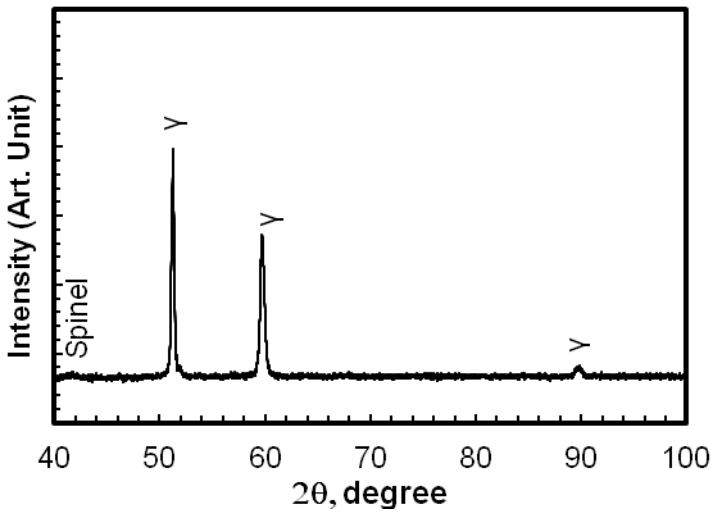

Figure 9. XRD spectrum of bare 310 after SCW testing.

3.3.2 Aluminized 310

The surface of the aluminized sample after 1555 hours exposure in SCW is shown in Figure 10. Some embedded particles (black in the BSE) were identified as alumina from the pack cementation process. The surface film contained Al, Fe, Cr and O. The SCW exposure may have resulted in some Al-oxide formation due to the high Al content in the coating. As the weight gain for aluminized 310 is greater than that of the bare 310, it is likely that more oxidation occurred for this sample. However, a slight weight loss was observed as the test progressed (Table 7), suggesting oxide dissolution or spallation. It is also possible that the embedded alumina particles were gradually dislodged from the surface during SCW testing leading to the weight loss. XRD analysis indicates oxide formation (Al_2O_3 and $(Fe,Cr)_2O_3$ in Figure11) and the presence of (Fe,Ni)Al [24] on the surface of the aluminized coating. Multiple cracks were also observed on the surface of all aluminized samples after 1555 hours of SCW exposure. The occurrence of surface cracking is related to both the brittle nature of the aluminide coating and the heating and cooling cycles during SCW test, which created thermal stresses.

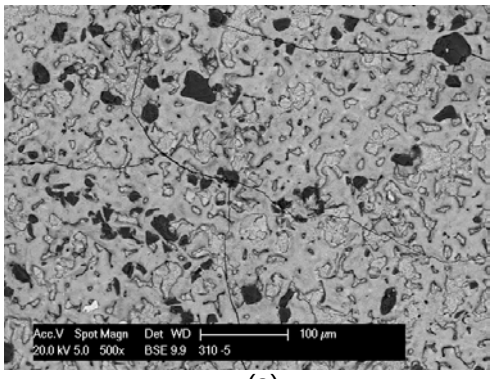

(a)

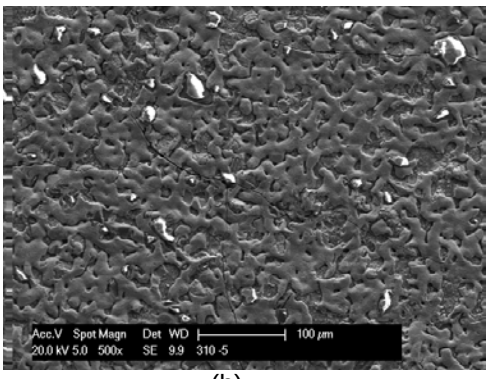

(b)

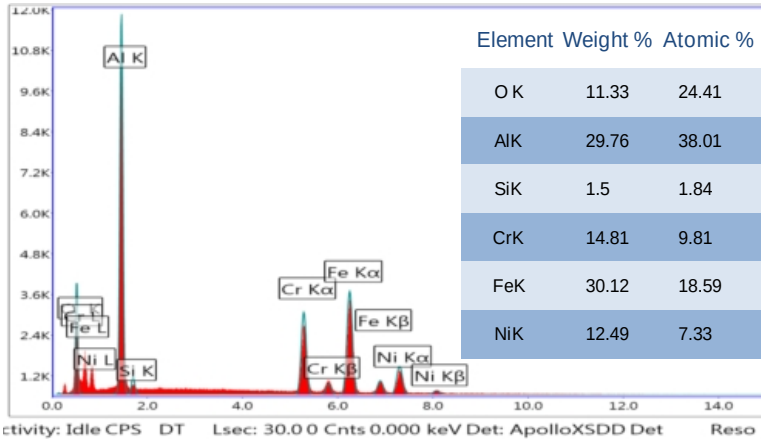

(c)

Figure 10. SEM images (a and b) of aluminized 310 sample after 1555 hr SCW testing and EDS analysis results (c).

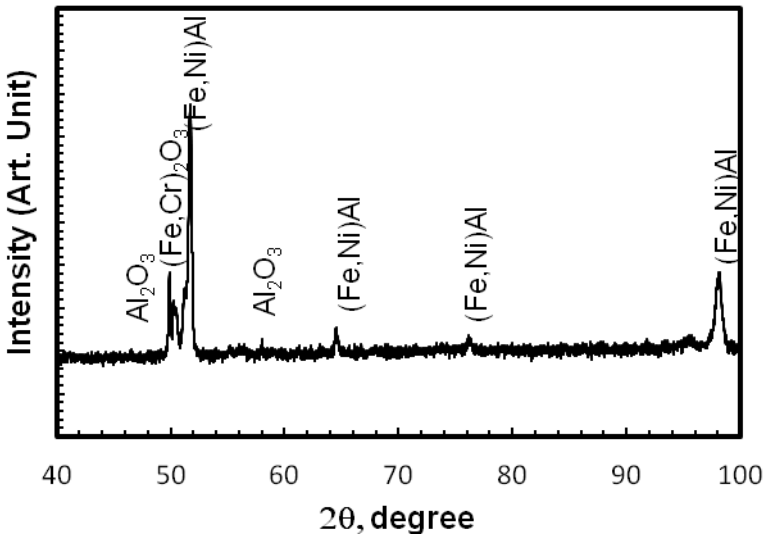

Figure 11. XRD spectrum of aluminized 310 after SCW test.

3.3.3 NiCrAlY Coated 310 Stainless Steels

The surface of the NiCrAlY-coated 310 had an uneven appearance, typical of plasma sprayed coatings. After exposure for 1555 hours in SCW, there were no changes to the surface morphology. As shown in Figure 12, the melted and semi-melted NiCrAlY droplets (from the plasma spray process) are clearly seen. NiCrAlY-coated 310 gained the most weight with respect to aluminized and bare 310 during SCW test. The large apparent surface area and the presence of oxide-forming elements in the coating (Al and Ni) are possible reasons for the large weight gain. Although only qualitative, EDS area analysis of the surface (Figure 12c) shows an elevated amount of oxygen suggesting oxidation during SCW test. The types of oxide formed on the surface are further delineated by XRD analysis (Figure 13). There likely exist spinel and alumina on the surface, in addition to γ+Ni_3Al phases [25] from the NiCrAlY coating structure.

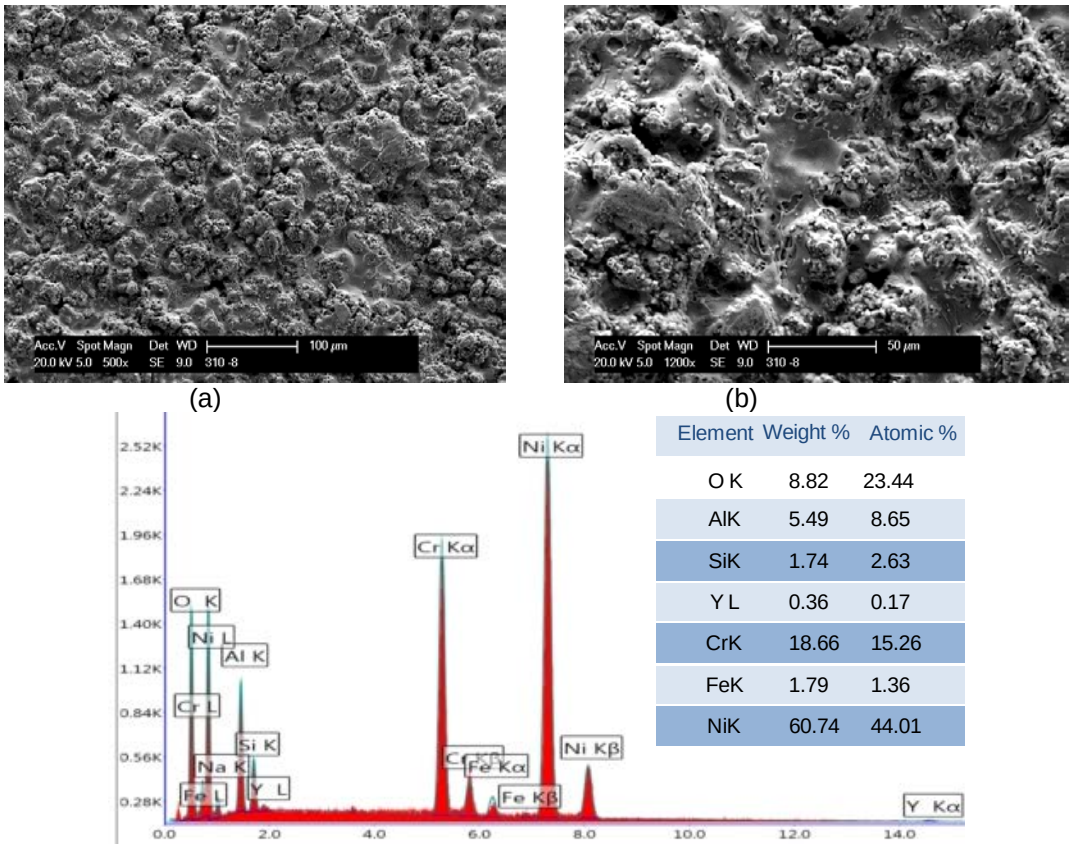

Figure 12. SEM images of NiCrAlY coated 310 sample after 1555 h SCW testing (a) 500x and (b) 1200x and EDS analysis result (c).

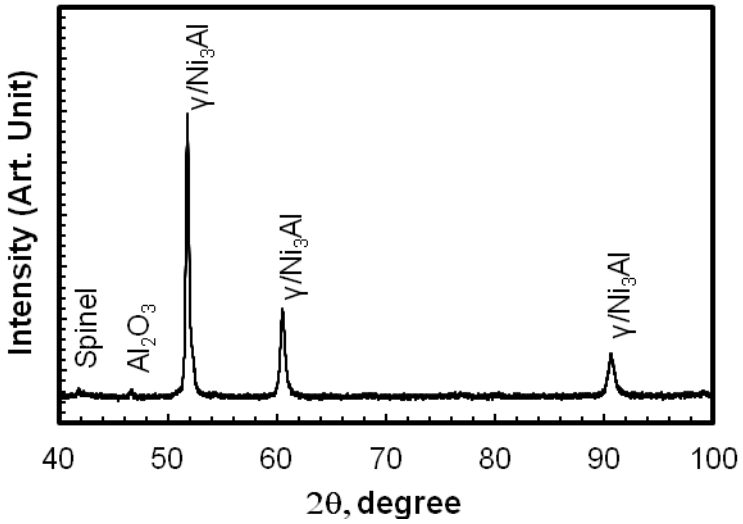

Figure 13. XRD spectrum of NiCrAlY coated 310 after SCW test.

4.0 Conclusion

In this study, aluminized and plasma sprayed 310 samples were tested in SCW for a total of 1555 hours. The weight change measurements showed that both bare and aluminized 310 stainless steel experienced very little weight gain, with the aluminized sample experiencing slight weight reduction after initial stage.

Surface cracking was observed on the aluminized sample due to the brittle nature of the intermetallic compound (NiAl) in the aluminized layer. NiCrAlY-coated 310 showed the most weight gain, likely due to the increased surface area of plasma sprayed coatings. Post-coating heat treatment will be needed to reduce the Al content and the brittleness of the aluminized coating. Also, surface machining (to reduce the exposed surface area) and heat treatment (to consolidate the microstructure) will help improve the performance of plasma-sprayed coatings in an SCW environment.

4.0 Acknowledgment

Funding to the Canada Gen-IV National Program was provided by Natural Resources Canada through the Office of Energy Research and Development, Atomic Energy of Canada Limited, and Natural Sciences and Engineering Research Council of Canada.

References

1. J. Bouchard and R. Bennett, Nuclear Plant Journal, 2008, vol. 26, no. 5, pp. 1-2.
2. J. Buongiorno, Philip E. MacDonald., "Supercritical Water Reactor (SCWR)," Idaho National Engineering and Environmental Laboratory, 2003.
3. H. Khartabil, "SCWR: OVERVIEW," in GIF Symposium, Paris (France) , September 2009.
4. L. Leung, Phase-II NSERC/NRCan/AECL Gen-IV Energy, Technologies Program Kick-Off Meeting, Saskatoon, Canada, June 14, 2012.
5. G. S. Was, S. Teysseyre, "Challenges and Recent Progress in Corrosion and stress Corrosion cracking of Alloys for Supercritical Water Reactor Core Components," in Proceedings of the 12th International Conference on Environmental Degradation of Materials in Nuclear Power System Water Reactors, 2005.
6. J. Kaneda, S. Kasahara, J. Kuniya, F. Kano, N. Saito, A. Shioiri, T. Shibayama, and H. Takahashi, "General Corrosion roperties of Titanium Based Alloys for the Fuel Claddings in the Supercritical Water-Cooled Reactor," in 12th International Conference on Environmental Degradation of Materials in Nuclear Power System – Water Reactors, Salt Lake City, Utah, 2005.
7. C. O. A. Olsson and D. Landolt, Electrochimica Acta, vol. 48, pp. 1093-1104, 2003.
8. D.A. Guzonas, J.S. Wills, G.A. McRae, S. Sullivan, K. Chu, K. Heaslip, M. Stone, "Corrosion-Resistant Coatings for Use in a Supercritical Water CANDU Reactor," in 12th International Conference on Environmental Degradation of Materials in Nuclear Power System – Water Reactors, Salt Lake City, Utah, 2005.
9. P. Kritzer, The Journal of Supercritical Fluids, ELSEVIER, 2004, vol. 39, pp. 1-29.
10. Wen-Ta Tsai and Kuo-En Huang, Thin Solid Films, 2000, vol. 366, pp. 164 - 168.
11. S. C. Tjong, Surface and Coatings Technology, 1987, vol. 30, pp. 207 - 214.
12. D. Kumar, et al., NACE International, Corrosion 2011, Houston, Texas, Paper No. 11197.
13. Y. Zhang, B.A. Pint, J.A. Haynes and P.F. Tortorelli, Oxid. Met., 2004, Vol. 62 (112), 103-120.
14. D. K. Das, V. Singh, S. V. Joshi, Metallurgical and Materials Transactions, 1998, vol. 29A, pp. 2173-2188.
15. F. J. Peres and S. Castaneda, Materials and Corrosion, Vol. 59 (5), pp. 409-413, 2008.
16. A. Aguero, R. Muelas, M. Gutierrez, R. Van Vulpen, S. Osgerby and J.P. Banks, Surf. Coat. Technol., 2007, Vol.201, 6253-6260.
17. J. R. Davis, Nickel, Cobalt and Their Alloys; ASM Speciality Handbook, p. 288 (2000).
18. E. Lang, Coatings for High Temperature Applications, Applied Science Publishers, pp. 270-272 (1983).
19. D. R. Clarke, M. Oechsner, N. P. Padture, Vol. 37 (10), pp. 891-941 (2012).
20. R. C. Pennefather, D. H. Boone, Int. J. Pres. Ves. & Piping, 1996, Vol. 66, pp. 351-358.
21. J. R. Davis, Handbook of Thermal Spray Technology, ASM Thermal Spray Society, ASM International (2004).
22. J. Kaneda, S. Kasahara, J. Kuniya, K. Moriya, F. Kano, N. Saito, A. Shioiri,T. Shibayama, H. Takahashi, General Corrosion Properties of Titanium Based Alloys for The Fuel Claddings in The Supercritical Water-Cooled Reactor, Proceedings of The 12th International Conference On

Environmental Degradation of Materials in Nuclear Power System – Water Reactors , TMS (The Minerals, Metals & Materials Society), 2005, pp.1409-1418.
23. J. Bischoff, A. Motta, C. Eichfeld, R. Comstock, G. Cao and T. Allend, J. of Nuclear Materials, 2012, in press.
24. Z. Yu, D.D. Hass, and H.N.G. Wadley, Materials Science and Engineering A. 2005, vol. 394, pp.43–52.
25. D.R.G. Achar, R. Munoz-Arroyo, L. Singheiser, W.J. Quadakkers, Surface and Coatings Technology, 2004, Vol. 187 (2–3), pp. 272–283.

ISSCWR7-2002

LOCA/LOECC analysis for Canadian-SCWR

Pan WU, Jianqiang SHAN, Junli GOU*, Bin ZHANG, Bo ZHANG, Henan WANG
Xi'an Jiaotong University
Xi'an, Shaanxi, China
029-82663769, junligou@mail.xjtu.edu.cn

Abstract

A two-dimensional thermal conduction model including a radiation heat transfer model has been incorporated in the safety analysis code SCTRAN for SCWR to evaluate radiation heat transfer for this paper. The verification of the radiation model in the SCTRAN code is carried out through code-to-code comparison with CATHENA. Comparison of result shows that the modification of SCTRAN has been successful and that the calculation accuracy is acceptable. Then SCTRAN is applied to analyse a loss of coolant accident with loss of the emergency core cooling system (LOCA/LOECC) of a Canadian-SCWR to verify that it is a "no core melt" concept. The results demonstrate that the Canadian-SCWR has the potential to accomplish the object of "NO-CORE-MELT" under LOCA/LOECC.

1. Introduction

The Canadian-SCWR is a pressure-tube type Supercritical Reactor(SCWR), which is promising to satisfy all the major GIF goals on enhanced safety, sustainability, economics, and proliferation resistance[1]. It applies supercritical light water as coolant and subcritical heavy water as moderator. The high efficiency channel (HEC) design is employed to increase the inherent safety of the Canadian SCWR. The HEC channel has the potential to help the reactor to achieve "no-core-melt" under postulated accident scenarios with a loss of emergency core cooling system (LOCA/LOECC), because the radiation heat transfer inside the HEC and the passive heat rejection through the insulator into the low-temperature moderator can remove the decay heat. A safety analysis is required to demonstrate the feasibility for the continuously updated Canadian-SCWR concept. As LOCA/LOECC leads to the total loss of core coolant and to the most serious accident results, its safety analysis is an important reference for evaluating the inherent safety of the Canadian-SCWR.

Simulations for evaluating and optimizing the thermal performance of the Canadian-SCWR following LOCA/LOECC have been previously performed by AECL utilizing a CANFLEX bundle[2]. The transient simulation was carried out with an assumed decay power variation. The effects of insulator properties and moderator temperature on the fuel cladding temperature were analyzed. The results show that the Canadian-SCWR has the potential to significantly reduce the possibility of core damage frequency. Shan et al. (2011) from Xi'an Jiaotong University performed sub-channel analyses with the ATHAS code and radiation heat transfer analyses with the CATHENA code of a 54-element Canadian-SCWR bundle[3]. The sub-channel analysis results show that the maximum fuel cladding temperatures at BOC and EOC are 761^{o}C and 808^{o}C respectively. The radiation heat transfer calculation was carried at different decay power level and the results indicate that the pressure tube with 54-element fuel bundle can remove about 2% of the rated power to the moderator through radiation heat transfer. Additionally, Licht and Xu (2012) from AECL provided some updated simulation results and analyses of a 78-element Canadian-SCWR bundle in the process of LOCA/LOECC[4] studies. The results demonstrate that, with a non-porous insulator, the fuel

sheath temperature remains below the melting temperature for less than 3% of the rated power. Some other suggestions on the further research were also proposed. Besides the above mentioned papers, only few research studies about “no-core-melt” assessment of the Canadian-SCWR have been published.

The former analyses of the Canadian-SCWR mainly focus on radiation heat transfer and ignore the effect of natural convection during LOCA/LOECC. Up to now, the transition process from supercritical pressure to subcritical pressure has not been simulated in these analyses. Thus, another system code for SCWR, SCTRAN, is introduced to simulate LOCA/LOECC accidents as described in this paper. SCTRAN is able to simulate most accidents for SCWR including LOCA[5]. As described in this paper, a two-dimensional heat conduction model and a radiation heat transfer model are incorporated into SCTRAN. Using this version of SCTRAN, a thermal-hydraulic simulation of the Canadian-SCWR is performed based on the latest conceptual design utilizing a 64-element fuel bundle. An analysis of a LOCA/LOECC accident scenario is carried out including the effects of radiation and convection in the HEC.

2. Modification of SCTRAN

SCTRAN is a safety analysis code developed by Xi’an Jiaotong University, which can be applied to simulate the accidents at both subcritical and supercritical pressures. A homogenous model and a four-equation dynamic slip model are implemented into the code as optional modes for subcritical pressure condition. Its ability to carry out the safety analysis for SCWRs has been verified[5]. SCTRAN has been applied to analyze the accident consequences of Chinese pressure vessel type concepts, such as CSR1000[6], CGNPC SCWR[5].

In order to simulate radiation heat transfer inside the HEC of the Canadian-SCWR, a radiation heat transfer model should be incorporated into SCTRAN. The fuel pin absorbs different amount of radiation heat from different directions, which further results in a prominent circumferential heat conduction in the fuel pin. Therefore, the original one-dimensional heat conduction model in code SCTRAN should be updated to a two-dimensional one.

2.1 Development of two-dimensional heat conduction model

The differential equation of heat conduction with an internal heat source is shown as below:

$$\rho c_p \frac{\partial T}{\partial t} = \nabla \cdot \left[\lambda \nabla T \right] + S \tag{1}$$

The first term at the right side of the equation is the energy variation with space while the last term stands for the heat source in the heat structure.

In two dimensional polar coordinates, the conduction equation can be rewritten as:

$$\rho c_p \frac{\partial T}{\partial t} = \frac{1}{r}\frac{\partial}{\partial r}(\lambda \cdot r \frac{\partial T}{\partial r}) + \frac{1}{r^2}\frac{\partial}{\partial \varphi}(\lambda \frac{\partial T}{\partial \varphi}) + S \tag{2}$$

In order to reduce the calculation iterations and to reach the envisaged calculation accuracy simultaneously, the fuel rod is divided into four sectors in circumferential direction. The mesh layout for two-dimensional heat conduction is shown in Fig. 1. Points P，N，S，W，E represent the nodes needing temperature calculation. The material properties and temperatures in a half mesh interval are assumed to be constants over a time interval. For the control volume of point P, which is shadowed in Fig. 1, the internal energy increase equals to the inner heat source plus the heat conducted from the surrounding control volumes. Thus the discrete form of equation (2) can be given by

$$\left(\rho c_p\right)_p \frac{(r_n + r_s)}{2} \frac{\Delta r \Delta\theta}{\Delta t}\left(T_p - T_p^0\right) = \left(\frac{r_n \lambda_n (T_N - T_p)}{(\delta r)_n} - \frac{r_s \lambda_s (T_P - T_S)}{(\delta r)_s} \right) \Delta\theta + \left(\frac{\lambda_e (T_E - T_p)}{(\delta\theta)_e \, r_e} - \frac{\lambda_w (T_P - T_W)}{(\delta\theta)_w \, r_w} \right) \Delta r + S\Delta V \tag{3}$$

The left part of the equation represents the internal energy increase of the control volume P. The first term on the right side of the equation is the heat conducted from point N and S. The second term is the heat conducted from point E and W while the last term denotes the inner heat source.

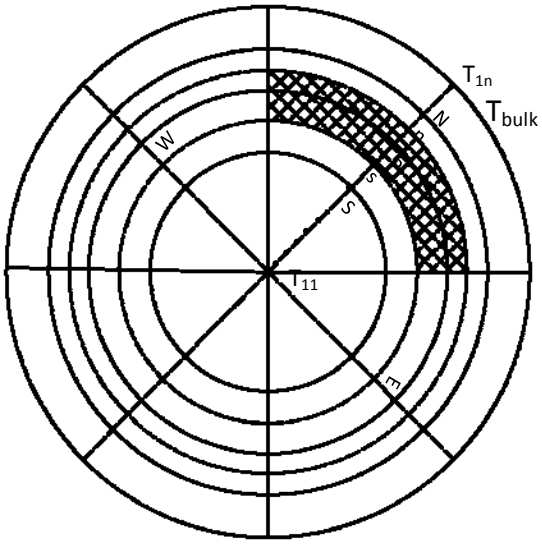

Fig. 1 Mesh layout of the heat structure

Equation (3) can be simplified into the following form:

$$a_P T_P = a_E T_E + a_W T_W + a_N T_N + a_S T_S + b \tag{4}$$

Every node in the mesh layout owns a same heat conduction equation as equation (4). There are five unknown node temperatures in each equation. Simultaneously solving the temperature equations of all nodes will be absolutely time consuming. In consideration of saving the computer memory and calculation time, the conduction equations will be solved sector by sector. The node temperatures in one radial sector are solved together assuming that the node properties of the west and east sectors apply the values from the last iteration:

$$a_P T_P^{(n)} = a_N T_N^{(n)} + a_S T_S^{(n)} + a_E T_E^{(n-1)} + a_W T_W^{(n-1)} + b \tag{5}$$

The equation (5) has only three unknown parameters and can be solved by Tridiagonal Matrix Algorithm(TDMA) with the corresponding boundary conditions[7].

2.2 Development of radiation heat transfer model

The radiation heat transfer will be one of the boundary conditions for the heat conduction solution. The radiation heat transfer inside the HEC is highly related to the fuel configuration. The cross section of the current design of HEC channel is illustrated in Fig. 2. The outer surface of the central channel, the surfaces of the fuel rods in the inner and outer rings, and the inner surface of the liner tube make up a radiation enclosure. The method of solving radiation heat transfer adopted by RELAP5 is referred in the present paper[8]. The following assumptions are made,

1. Radiation heat transfer between different elevations is ignored.
2. All surfaces in the system are diffusive and grey;
3. Calculation results show that the radiation exchange between water steam and fuel surface will not produce a big effect on the result of LOCA/LOECC. Thus, the coolant in the pressure tube neither emits nor absorbs radiant thermal energy;
4. Reflectance from a surface is independent of the reflected direction and the radiation frequency.

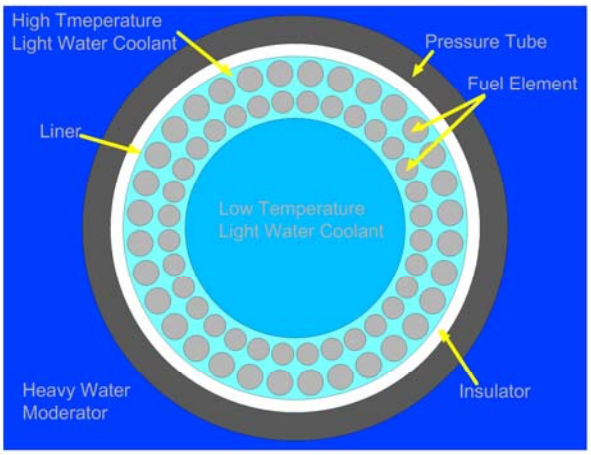

Fig. 2 Cross-section of the high efficiency channel (HEC) [14]

2.2.1 Net radiation heat flux

The radiosity of a surface is the radiant energy flux leaving a surface (i.e., the emitted energy flux plus the reflected energy flux). The energy balance for the i-th surface is:

$$R_i = \varepsilon_i \sigma T_i^4 + \eta_i \sum_{j=1}^{n} R_j \frac{A_j}{A_i} F_{ji} \tag{6}$$

With considering the energy conservation law, the area of surface *i* times the view factor from surface *i* to surface *j* equals the area of surface *j* times the view factor from *j* to *i*:

$$A_i F_{ij} = A_j F_{ji} \tag{7}$$

Substituting equation (7) into equation (6), the following equation is achieved:

$$R_i = \varepsilon_i \sigma T_i^4 + \eta_i \sum_{j=1}^{n} R_j F_{ij} \tag{8}$$

The net heat flux at surface *i*, Q_i, is the difference between the radiosity of surface *i* and radi osity throwing to surface *i* from all surfaces, and it's given by:

$$Q_i = R_i - \sum_{j=1}^{n} R_j F_{ij} \tag{9}$$

Combining equation (8) and equation (9), the net heat flux of surface *i* is expressed by

$$Q_i = \frac{\varepsilon_i}{\eta_i} (\sigma T_i^4 - R_i) \tag{10}$$

In equation (10), the reflectivity η_i and emissivity ε_i are the basic physical properties of surface *i*. According to the conservation of energy, the value sum of the reflectivity and emissivity for a sector equals to 1. In the calculation, the surface temperature of the previous time step is applied, and therefore, the radiosity is calculated explicitly.

2.2.2 Radiosity solution

On the basis of equation (8), the radiosity of all the surfaces can be calculated by the following equations:

$$\begin{cases} i=1:(1-\eta_1 F_{11})R_1+(0-\eta_1 F_{12})R_2+(0-\eta_1 F_{13})R_3\cdots(0-\eta_1 F_{1n})R_{\mathrm{n}}=\sigma\cdot\varepsilon_1 T_1^4 \\ i=2:(0-\eta_2 F_{21})R_1+(1-\eta_2 F_{22})R_2+(0-\eta_2 F_{23})R_3\cdots(0-\eta_2 F_{2n})R_{\mathrm{n}}=\sigma\cdot\varepsilon_2 T_2^4 \\ \quad\vdots \\ i=i:(0-\eta_i F_{i1})R_1+(0-\eta_i F_{i2})R_2\cdots(1-\eta_i F_{ii})R_i\cdots(0-\eta_i F_{in})R_{\mathrm{n}}=\sigma\cdot\varepsilon_i T_i^4 \\ \quad\vdots \\ i=n:(0-\eta_n F_{n1})R_1+(0-\eta_n F_{n2})R_2+(0-\eta_n F_{n3})R_3\cdots(1-\eta_n F_{nn})R_{\mathrm{n}}=\sigma\cdot\varepsilon_n T_n^4 \end{cases} \tag{11}$$

The surface emissivity is regarded as constant. With the view factor of each surface calculated by the GEOFAC code[9], the radiosity matrix can be solved. The detailed distribution of the sector surface in a 64-element fuel bundle can refer to Fig. 3. After that, the net radiation heat flux can be obtained through the equation (11).

2.3 Heat conduction solution considering the effect of radiation and convection

The net heat flux created by radiation and convective heat transfer is used as the boundary condition of the two-dimensional heat conduction equation,

$$-\lambda\left.\frac{\partial T}{\partial r}\right|_{\mathrm{i}}=h_{\mathrm{i}}(T_{\mathrm{i}}-T_{sk})+Q_i \tag{12}$$

The radiation heat flux Q_i in equation (12) is also a function of surface temperature. The bulk-fluid temperature for all the sectors in an enclosure is assumed to be the same. The natural convection heat transfer coefficient inside the HEC is calculated by Churchill-Chu correlation[10]. The forced convection heat transfer in the HEC is mainly calculated by the Dittus-Boelter correlation[11] at subcritical pressure and by the Jackson correlation[12] at supercritical pressure in the process of LOCA/LOECC. In order to simplify the solution, the surface temperatures at the previous time step are adopted to compute the radiation heat flux explicitly and therefore the iteration solution of the radiation heat flux is avoided.

3. Verification of SCTRAN radiation heat transfer model

Due to the lack of experimental data, the verification of the radiation heat transfer model was carried out by code to code comparison with the Canadian system code CATHENA. CATHENA is a one-dimensional, two-fluid thermal-hydraulic computer code[9]. It includes one-dimensional and two-dimensional heat conduction models (GENHTP). Its ability to evaluate the radiation heat transfer has been validated by Lei and Goodman[13].

The 64-element Canadian-SCWR bundle was selected to be the analysis object of the verification. The HEC cross-section is shown in Fig. 2. The bundle power was set to be 9.34MW, while the inner fuel pins occupied 44% and outer fuel pins occupied the remaining 56% of the power, respectively. The moderator outside the pressure tube was of constant temperature of 80 ^{o}C and the heat transfer coefficient between moderator and pressure tube was 1000W/(m^2•K). Three steady-state cases with different decay heat levels (2%, 3% and 4% of the rated power) were simulated by SCTRAN and CATHENA, respectively. In the simulations, the decay heat was transferred from the fuel rod to the inner surface of the pressure tube only by radiation heat transfer. Each sector in the HEC was marked by a number as shown in Fig. 3.

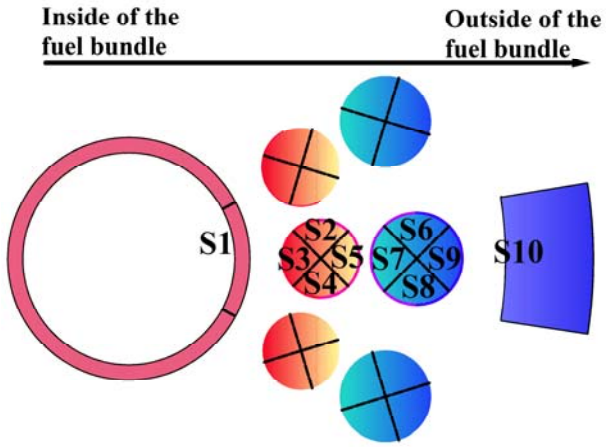

Fig. 3 Numbering of the HEC surfaces

Table 1 lists predicted surface temperatures at various sectors and power levels to illustrate the magnitude of the deviations between these two codes. The maximum absolute deviation in predicted surface temperatures between the SCTRAN and the CATHENA code is 7.7°C (or 1.1% relative deviation) at Surface S7. The results show that the newly developed two-dimensional heat conduction model and the radiation heat transfer model as well as their solution schemes for SCTRAN are valid, and the calculation accuracy can be guaranteed.

Table 1 Surface temperatures of the HEC channel at different power levels calculated by SCTRAN and CATHENA

	Surface	% of Rated Power				Surface	% of Rated Power		
		2	3	4			2	3	4
SCTRAN	S1	1085.0°C	1256.1°C	1398.1°C		S6	962.2°C	1113.6°C	1242.3°C
CATHENA		1080°C	1250°C	1393°C			960°C	1112°C	1241°C
Deviation		5.0 °C	6.1 °C	5.1 °C			2.2 °C	1.6 °C	1.3 °C
SCTRAN	S2	1084.9°C	1253.6°C	1393.7°C		S7	1013.1°C	1182.7°C	1325.4°C
CATHENA		1080°C	1249°C	1389°C			1006°C	1175°C	1318°C
Deviation		4.9 °C	4.6 °C	4.7 °C			7.1°C	**7.7°C**	7.4 °C
SCTRAN	S3	1099.0°C	1272.7°C	1416.6°C		S8	962.2°C	1113.6°C	1242.3°C
CATHENA		1093°C	1266°C	1411°C			960°C	1112°C	1241°C
Deviation		6.0 °C	6.7 °C	5.6 °C			2.2 °C	1.6 °C	1.3 °C
SCTRAN	S4	1084.9°C	1253.6°C	1393.7°C		S9	904.7°C	1034.4°C	1145.4°C
CATHENA		1080°C	1249°C	1389°C			909°C	1040°C	1151°C
Deviation		4.9°C	4.6 °C	4.7 °C			-4.3°C	-5.6 °C	-5.6 °C
SCTRAN	S5	1064.7°C	1226.9°C	1362.4°C		S10	366.8°C	514.2°C	664.9°C
CATHENA		1062°C	1224°C	1359°C			371°C	519°C	670°C
Deviation		2.7 °C	2.9 °C	3.4 °C			-4.2 °C	-4.8 °C	-5.1 °C

4. Safety analysis of LOCA/LOECC

The ability to maintain core components below the melting temperatures during a postulated accident is referred to as the “no-core-melt” concept and is an important safety goal for the

Canadian-SCWR. The accident of LOCA with a loss of ECCS was simulated with the modified SCTRAN to evaluate whether the Canadian-SCWR has the potential to achieve the goal of “no-core-melt”.

4.1 Introduction of Canadian-SCWR

The conceptual Canadian-SCWR design possesses a modular design that separates the coolant from the moderator, as in the current CANDU reactors. The reactor core consists of 336 fuel channels, each housing a 5-m long fuel assembly. It is designed to generate 2,540 MW of thermal power or about 1,200 MW of electric power. In the current conceptual design, as shown in Fig. 4, light water coolant enters the inlet plenum. From there, it flows downwards the central flow tube of the channel. Near the bottom of the channel, the coolant exits the central flow tube, flows upwards to pass through the fuel elements (fuel assembly), and finally arrives at the outlet plenum. From the outlet plenum, the high-temperature and high-pressure coolant is directly fed to the high pressure turbine. The cylindrical vessel houses the relatively low-pressure and low-temperature heavy water moderator. The main parameters of the Canadian-SCWR are listed in Table 2.

Table 2 Main parameters of Canadian-SCWR [14]

Core pressure (MPa)	25
Thermal/Electrical power(MW)	2540/1200
Efficiency (%)	45~50
Inlet/outlet temperatures (°C)	350/625
Fuel channel number	336
Fuel bundle type	64-element
Neutron spectrum/reactor type	Thermal/pressure-tube
Coolant	light water
Moderator	heavy water
Main coolant flowrate(kg/s)	1254
Active core height(m)	5.0
Cladding material	Stain steel(SS310)

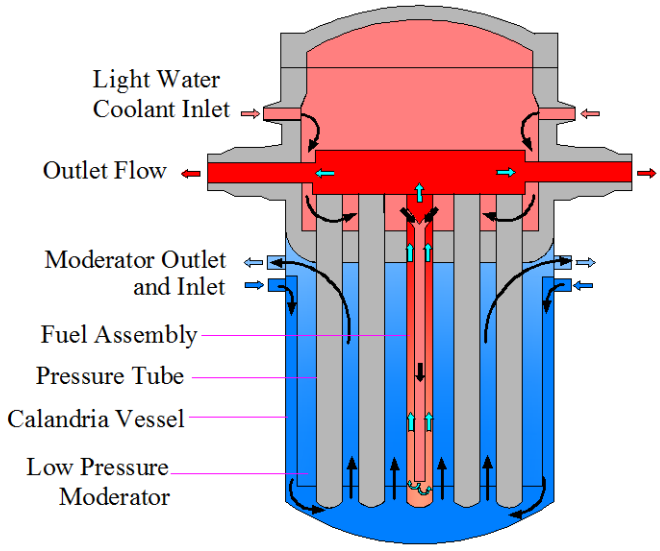

Fig. 4 Schematic of Conceptual Canadian SCWR Core[14]

A high efficiency channel (HEC) is adopted for the Canadian-SCWR conceptual design. The HEC design consists of a pressure tube, an outer liner tube, an insulator and an inner liner tube. The pressure tube is surrounded by heavy water moderator. One of the potential advantages of using the HEC is that in the unlikely event of a LOCA with a coincident loss-of-emergency core cooling, the heat in the fuel will be transferred by thermal radiation to the

liner tube and then conducted to the moderator through the insulator. The 64-element fuel bundle with two concentric rings is equipped inside the pressure tube.

4.2 SCTRAN model

The idealized SCTRAN model of the Canadian-SCWR was developed based on the current conceptual design. In order to get a more accurate simulation with considering the effect of the radial power distribution, the 336 channels in the reactor core are divided into five groups, which are denoted as LP, AP, MP, HP and HHP[14]. In the axial direction, the fuel assembly and the coolant channel are divided into 10 control volumes. The allocation of control volumes is listed below:

- Control volumes 1~10 and 11~20 represent the central flow tube and the fuel assembly, respectively, in the LP channel group;
- Control volumes 21~30 and 31~40 represent the central flow tube and the fuel assembly, respectively, in the AP channel group;
- Control volumes 41~50 and 51~60 represent the central flow tube and the fuel assembly, respectively, in the MP channel group;
- Control volumes 61~70 and 71~80 represent the central flow tube and the fuel assembly, respectively, in the HP channel group; and
- Control volumes 81~90 and 91~100 represent the central flow tube and the fuel assembly, respectively, in the HHP channel.

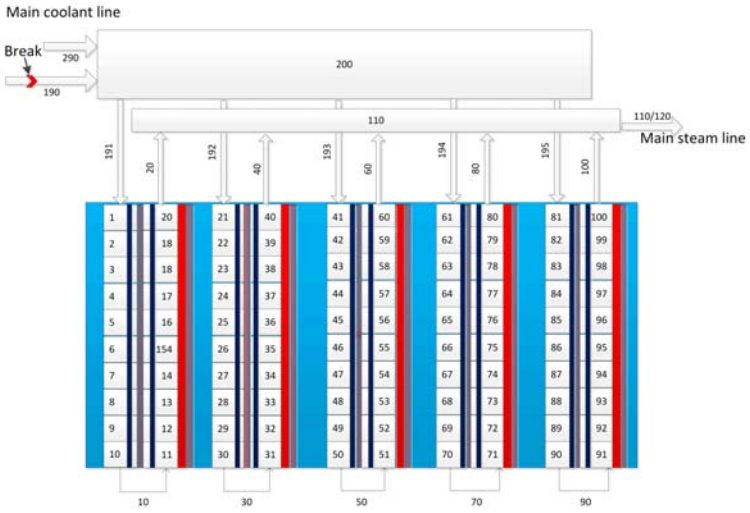

Fig. 5 SCTRAN idealization of Canadian-SCWR concept

Heat exchange between the central channel and the coolant channel is also taken into consideration. A time dependent junction with temperature of 350 ^{o}C and flowrate of 1254 kg/s, as well as a time dependent volume with temperature of 625 ^{o}C and pressure of 25 MPa, are set as the boundary conditions of the main coolant line and main steam line respectively. The moderator cooling system contains an active and a passive moderator cooling system. In the accident conditions, only the passive moderator cooling system is used[15]. The passive moderator cooling system (PMCS) is simulated by volume 800(the blue rectangle), which is shown in Fig. 5, serving as the ultimate heat sink. The passive moderator cooling system will be activated automatically during transients. Thus, the moderator temperature is assumed to be kept at 80^{o}C and a constant heat transfer coefficient of 1000W/($m^2 \cdot K$) between the moderator and the pressure tube is applied[3], which indicates that the moderator removes the core heat through natural convection. There is no active system preparing for the Canadian-SCWR system when LOCA/LOECC occurs. The moderator system is assumed to stay intact during the whole process. Turbine stop valves are installed on the main steam lines, which are tripped by the “power scram” signal.

Besides these assumptions, other initial conditions and assumptions are taken as listed here:

- The reactivity feedback in the core is neglected in both steady and accident simulations;
- The emissivity of the central rod, fuel sheath and liner tube is 0.8;
- The natural convection heat transfer coefficient inside the HEC is calculated by the Churchill-Chu correlation[10];
- Referring to the ASM specialty handbook for stainless steel[17], the melting temperature of SS310 is 1400~1450°C. Thus, the temperature of 1400°C is regarded as the melting temperature of the fuel cladding.
- Due to the radiation heat transfer effect, each fuel sheath has four sector temperatures. The maximum sector temperature is applied to describe the surface temperature variation.

4.3 Results of LOCA/LOECC analyses

The reactor core is anticipated to lose most of its coolant inventory rapidly and suffer from deteriorated cooling conditions when the postulated LOCA event occurs. With a simultaneous loss of the ECC system, the heat in the fuel could only be removed through natural convection to the high temperature steam and through thermal radiation exchange between cladding surfaces and the liner tube of the insulator in the Canadian SCWR fuel-channel concept. The natural convection is the main heat transfer mode at low cladding temperature, and the radiation heat transfer plays the dominant role with increasing cladding temperature (which is anticipated to escalate rapidly after the initiation of the event). The current analysis postulates the double-ended break event at the cold leg, which is the most severe LOCA event.

4.3.1 Decay Power Variation

Fig. 6 illustrates the decay heat variation referring to results of Pencer et al.[16].

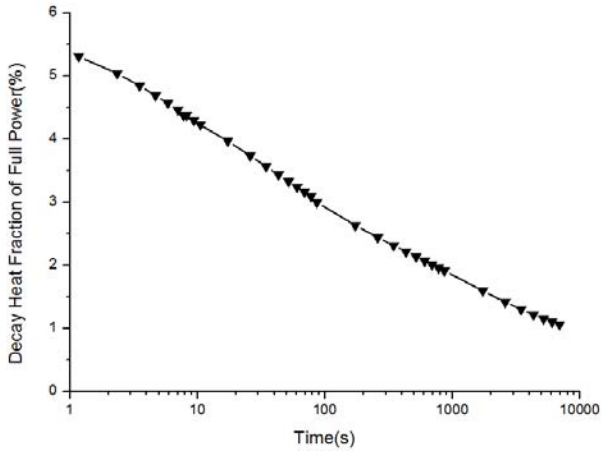

Fig. 6. Decay heat variation with time for 55 MWd/kg burnup fuel [16].

4.3.2 Simulation Results

In the simulation, the break of the cold leg occurs at 0.5s. The control rods are inserted at 1s resulting in a reduction in core power. At the same time, the turbine stop valve is closed. The coolant flowrate from the main coolant pump is maintained in the first 10s and is assumed to decrease to zero within 5s (the duration depends on the pump inertia, which is not specified in the conceptual phase).

Fig. 7 shows variations of the core pressure and the coolant flowrate through the break. When the break occurs, a large amount of coolant is drained out through the break with

critical velocity. The core pressure decreases quickly to a subcritical level because of the loss of coolant. In the first 10s, the main coolant line injects coolant; most of the coolant is directed to the break. The high temperature coolant in the outlet plenum flows in the reverse direction through the channels into the inlet plenum and is drained out through the break. After 15s, the core pressure is close to atmospheric and the break coolant flowrate decreases to a low level. At this time, the coolant inventory in the core is greatly reduced. Fig. 8 illustrates variations of the coolant inventory in the outlet plenum and the inlet plenum. The coolant inventory in the inlet plenum is much larger than the one in the outlet plenum. It is drained out at a much faster rate than the inventory in the outlet plenum due to the location of the break.

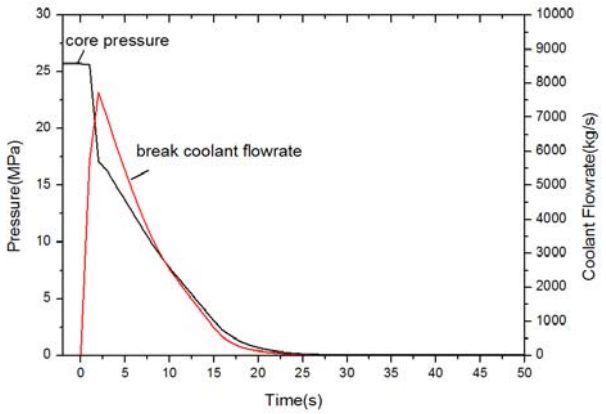

Fig. 7. Variation of core pressure and break coolant flowrate in the first 50s of the postulated LOCA/LOECC event.

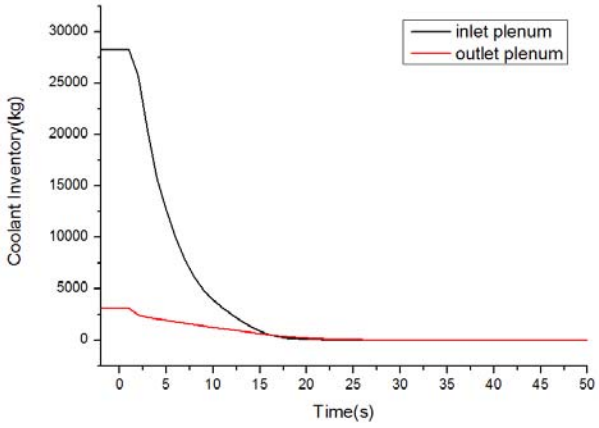

Fig. 8. Coolant inventory change in the inlet and outlet plenums in the first 50s of the postulated LOCA/LOECC event.

Fig. 9 illustrates the coolant flowrate variation in various groups of power channels during the first 50s of the event. The coolant flowrate of HHP channel is included in Fig. 10. The break located in the cold leg has led to flow reversal in each group of channels. A large amount of high-temperature coolant (at about 625^{o}C) in the outlet plenum flows through the fuel channels, reducing the effectiveness of heat transfer.

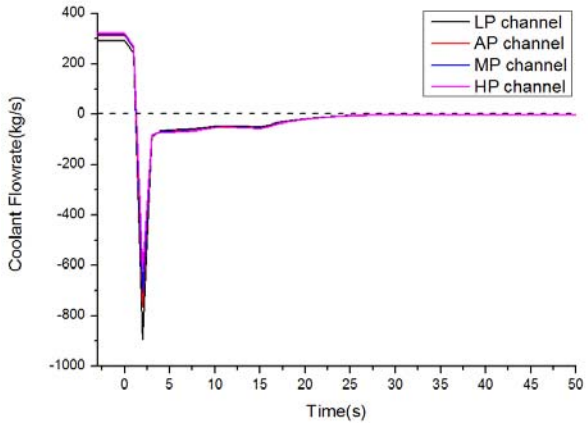

Fig. 9. Coolant flowrate variation in each group of channels in first 50s of the postulated LOCA/LOECC event.

Fig. 10 illustrates variations of the maximum cladding surface temperatures (MCSTs) and the fuel power in the inner and outer rings, as well as the coolant flowrate in the highest power channel during the first 50s of the event. The coolant temperature at the inlet plenum decreases due to isenthalpic expansion when the break occurs. This has led to a drop in MCSTs in the rods of both the inner and outer rings in the beginning. After that, the coolant of high temperature from the outlet plenum flows through the core and the reverse coolant flow rate decreases quickly due to the changing pressure difference between the core and the atmosphere. Thus, the MCSTs increase rapidly and reach a peak at around 6s. At the peak, the MCSTs are 1120°C for rods in the outer ring and 1063°C for rods in the inner ring. Beyond the peak, the MCSTs decrease with the reversed flow stabilized and the decay heat of the fuels staying at a low level. At 15s, the MCSTs in the inner-ring and outer-ring rods start to increase again as the reverse coolant flow rate decreases. Fig. 11 compares the fraction of radiation heat transfer between rings of the fuel assembly in the HHP channel during the first 50s. Heat transfer by radiation is a small contribution in the beginning of the event but it rapidly becomes dominant as the event progresses. When the coolant flow rate becomes very small, most of the heat removal from the cladding relies on radiation heat transfer in the rods of both rings. The radiation fraction of inner ring and outer ring in the HHP channel is 94.5% and 98.7% respectively after 30s.

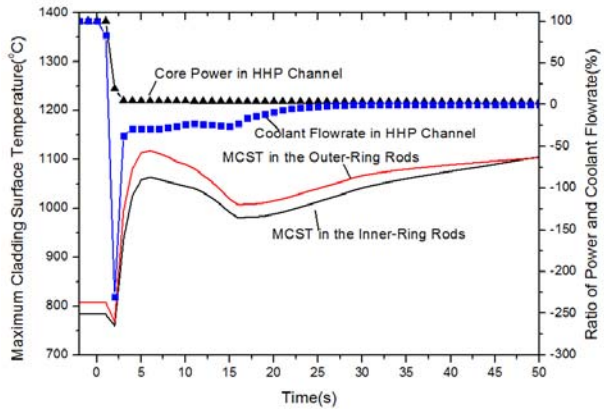

Fig. 10. Variations of surface temperatures, fuel power and coolant flowrate in the HHP channel during the first 50s of the postulated LOCA/LOECC event.

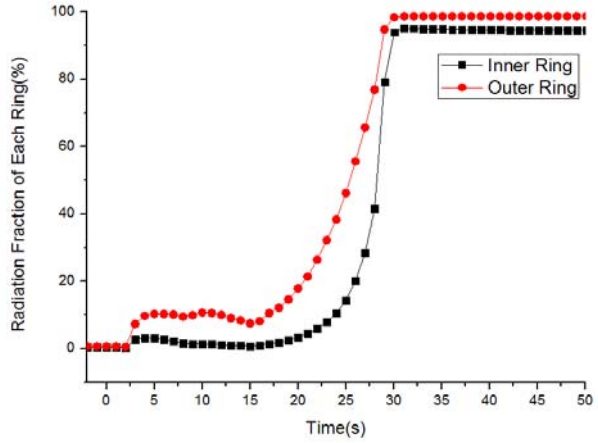

Fig. 11. Comparison of the fraction of radiation heat transfer between rings of the fuel assembly in the highest power channel.

Fig. 12 shows surface-temperature variations at various components in the HHP channel beyond the first 50s of the event. After the first peak at 5s, the MCSTs for the inner-ring and outer-ring rods increase gradually to the second (higher) peak of 1278°C and 1192°C, respectively, at about 240s, beyond which the MCSTs for the inner-ring and outer-ring rods decrease, reflecting the reduction in decay heat within the fuel. There is limited heat removal capacity from the central flow tube (mainly conduction and natural circulation). The surface temperature of the central flow tube increases rapidly and approaches the MCST for the inner-ring rods with a peak at about 240s, beyond which the surface temperature of the central flow tube also decreases with time. Inner-surface temperatures of the liner tube and the outer-surface temperatures of the pressure tube decrease gradually, mainly due to the effective heat removal from the pressure tube to the moderator, after the initiation of the event.

Fig. 13 compares the power generated from decay heat and power removed through radiation and natural convection from the fuel cladding for rods in the HHP channel. The escalation of MCST for rods in both rings is attributed to the low power removal, compared to the power generation, over the 15s to 240s duration. Beyond 240s, the power removal is consistently larger than the power generation leading to a gradual reduction in MCST.

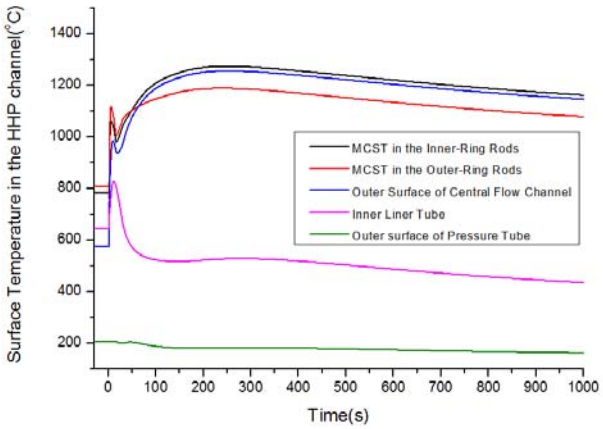

Fig. 12. Variation of surface temperatures in various components of HHP channel group over the duration of 1000s of the postulated LOCA/LOECC event.

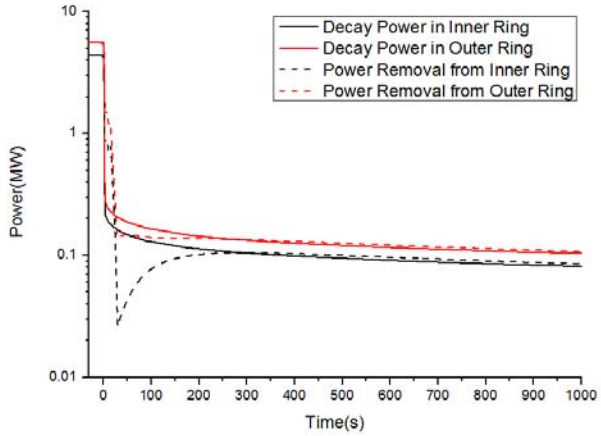

Fig. 13. Comparison of power removal and power generation in rods of the HHP channel.

Fig. 14 compares the predicted MCSTs for all channel groups, which follow a similar trend over the duration of the analysis. As indicated previously, the HHP channel has the highest power resulting in the highest MCSTs in both inner-ring and outer-ring rods. With the reduction in power fraction in other channel groups, the MCST decreases accordingly.

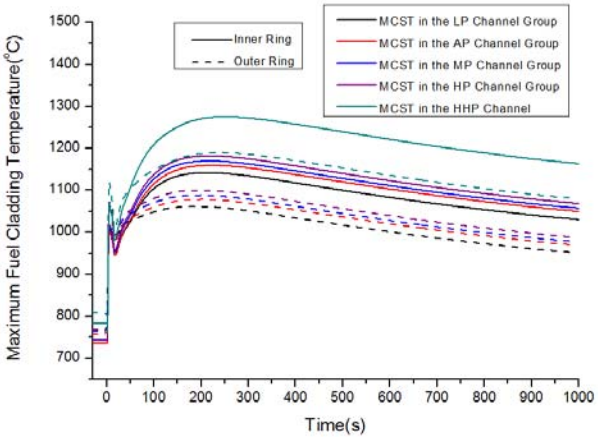

Fig. 14. Comparison of MCST predictions for all channel groups.

In summary, the decay heat of the Canadian SCWR fuel assembly can be removed effectively through radiation and natural convection during the postulated LOCA/LOECC event. Owing to the configuration of the fuel assembly, the predicted MCST is higher for rods in the inner ring than those in the outer ring. This is attributed to the effectiveness of radiation heat transfer from the outer-ring rods to the inner liner tube and subsequently through conduction to the moderator and convection to the ultimate heat sink. The predicted MCST for inner-rings and outer-ring rods are 1278°C and 1192°C. On the other hand, heat removal from the central flow tube relies mainly on natural convection and hence is not as effectiveness (leading to high predicted MCST). Nevertheless, the predicted MCST for inner-ring rods of 1278°C remains lower than the melting temperature of the modified stainless steel SS310 at 1400°C.

5. Conclusion

This paper focuses on the assessment of the inherent safety of 64-element Canadian-SCWR. A two-dimensional heat conduction model and a radiation heat transfer model are developed and incorporated successfully into SCTRAN. Meanwhile, the validity of the newly developed models for SCTRAN is verified by CATHENA, which is a system code developed by AECL.

A SCTRAN idealization of the Canadian-SCWR conceptual design has been developed. Using the SCTRAN idealization developed for Canadian-SCWR, a simulation of the steady-state thermal-hydraulic conditions is performed. During LOCA/LOECC, with total loss of core coolant inventory, radiation heat exchange among sheaths and natural convection of the high-temperature steam can remove a certain amount of core decay heat. On the basis of conservative assumption, the maximum fuel sheath temperatures in the inner and outer rings of the HHP group are 1278ºC and 1192°C, respectively, which are lower than the melting point of the cladding material. The simulation results show that the Canadian SCWR is capable of achieving the design object of “No-Core-Melt” under LOCA/LOECC.

Acknowledgments

The authors appreciate the support of Laurence K.H. Leung from AECL, Feng Jia and Zhang Guomin from Xi’an Jiaotong University.

References

[1] Leung L.K.H., (2010), Thermalhydraulics and Safety Programs in Support of the CANDU SCWR Design, Proceedings of the International Conference on Nuclear Engineering, ICONE18, Xi'an, China.

[2] Vasic A., Khartabil H.F., (2005), Passive Cooling of the CANDU SCWR Fuel at LOCA / LOECC Conditions, Proceedings of GLOBAL. Atomic Energy Society of Japan, Tsukuba, Japan.

[3] Shan J., Jiang Y., Leung L.K.H., (2011), Subchannel and Radiation Heat Transfer Analysis of 54-Element CANDU-SCWR Bundle, ISSCWR-5, Vancouver, British Columbia, Canada.

[4] Licht J., Xu R., (2012), Preliminary No-core Melt Assessment for the High Efficiency Channel Preconceptual Design, The 3rd China-Canada Joint Workshop on Supercritical-Water-Cooled Reactors, CCSC-2012, Xi'an, China.

[5] Wu P., Gou J., Shan J., Jiang Y., Yang J., Zhang B., (2013), Safety analysis code SCTRAN development for SCWR and its application to CGNPC SCWR. Annals of Nuclear Energy 56, 122-135.

[6] Wu P., Gou J., Shan J., Zhang B., Li X., (2014), Preliminary safety evaluation for CSR1000 with passive safety system. Annals of Nuclear Energy 65, 390-401.

[7] Yang S., Tao W., (2006), Heat Transfer. Higher Education Press.

[8] The RELAP5 Code Development Team, (1995), RELAP5/MOD3 Code Manual.

[9] The CATHENA Code Development Team, (2005), CATHENA MOD-3.5d Theory Manual.

[10] Churchill S.W., Chu H.H.S., (1975), Correlating equations for laminar and turbulent free convection from a vertical plate. International Journal of Heat and Mass Transfer 18, 1323-1329.

[11] Dittus F. W. and Boelter L. M. K., Heat Transfer in Automobile Radiators of the Tubular Type University of Ca1ifornia Pub1ications in Engineering, 2, 443-461, 1930.

[12] Hall, W.B., Jackson, J.D., 1971. Heat transfer near the critical point. Adv. Heat Transfer, 1–86.

[13] Lei Q.M., Goodman T.M., (1996), Validation of radiation heat transfer in CATHENA, International Conference on Simulation Methods in Nuclear Engineering, Montreal, Canada.

[14] Wang D.F., Wang S., (2013), A CATHENA MODEL OF THE CANADIAN SCWR

CONCEPT FOR SAFETY ANALYSIS, ISSCWR-6, Shenzhen, Guangdong, China.
[15] Novog D., McGee G., (2012), SAFETY CONCEPTS AND SYSTEMS OF THE CANADIAN SCWR, CCSC-2012, Xi'an, Shaanxi, China.
[16] Pencer J., McDonald M., Anghel V., (2014), Parameters for transient response modeling for the Canadian SCWR, The 19th Pacific Basin Nuclear Conference (PBNC 2014), Hyatt Regency Hotel, Vancouver, British Columbia, Canada.
[17] Davis J.R., (1994), Stainless Steels. ASM International.

ISSCWR7-2003

Direct Numerical Simulation of Heated Turbulent Pipe Flow at Supercritical Pressure

Xu Chu, Eckart Laurien

Institute of Nuclear Technology and Energy Systems
Pfaffenwaldring 31, 70569 Stuttgart, Germany
+49 711 685-60480, xu.chu@ike.uni-stuttgart.de

Abstract

Direct numerical simulation of supercritical carbon dioxide flow in a heated circular pipe L=45 D at a pressure of 8 MPa is developed with the open-source CFD program OpenFOAM in the present study. First, the method is verified with DNS studies of other authors. Then, a turbulent pipe flow with an inlet Reynolds number of Re_0=5400 is simulated with three different assumptions about gravity: (A) gravity neglected, (B) upward, (C) downward flow. In all cases the wall temperature rises from below to above the pseudo-critical temperature, where strong fluid-property variations occur. In the upward flow, heat transfer deterioration has been captured, which leads to a peak followed by the recovery in the wall temperature. The mean flow and turbulence statistic show clearly the influence of variable thermo-physical properties and buoyancy to the flow turbulence. The insight observation of the turbulence in the DNS of this work could help to develop new turbulence models for applications in the future.

1. Introduction

For fluids at supercritical pressure, the phase change from liquid to gas does not exist. When the fluid temperature increases from below to above pseudo-critical temperature (T_{pc}) during an isobaric process, density, thermal conductivity and dynamic viscosity decrease rapidly, while the specific heat at constant pressure shows a peak in a very narrow temperature range (Figure 1). These strong variations in their properties make supercritical fluid useful in many industrial applications, such as extraction, cleaning and refrigerant in air-conditioning and refrigerating systems [B6].

The first work about heat transfer at supercritical pressures started as early as the 1930s. At the end of the 1950s and the beginning of the 1960s, some studies investigated the possibility of using supercritical fluids as coolants in nuclear reactors, which was abandoned for almost 30 years after that, but it then came back to the table in the 1990s [B24]. The Supercritical Water-Cooled Reactor is considered as a Generation IV reactor concept, which directly uses supercritical water as the working fluid, has attracted much attention since the 1990s because of its high efficiency, compact size, and reduced complexity [B8]. However, deteriorated heat transfer has been found for heated flows with fluid at supercritical pressure, which has been proven by experimental studies [B5, B14, B15, B25]. In these works, the heat transfer deterioration has been investigated under different flow conditions: mass flow rate, heat flux, pipe geometry, flow directions etc.. Several comprehensive reviews on the topic of heat transfer to fluids at super-critical pressure have been given by Petukhov (1970), Hall (1971), Jackson & Hall (1979), Polyakov (1991), and more recently by Pioro et al. (2004), Yoo, Jung Yul (2013)

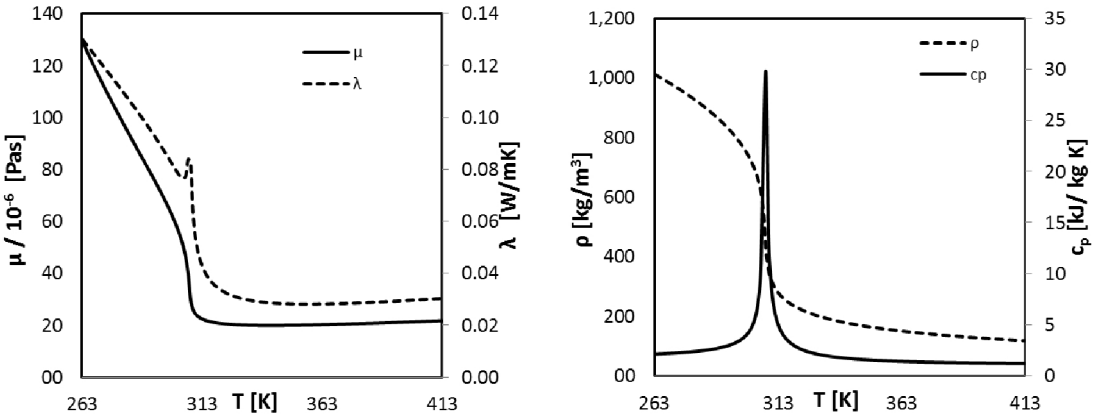

Figure 1: Variation of thermo-physical properties of carbon dioxide based on temperature at P_0 = 80, μ and c_p, λ and ρ

Besides experiments, numerical approaches using CFD code also have been carried out to study heat transfer of fluid at supercritical pressure. Turbulence modelling using different two-equation models is the common method for a first approach in most of the early studies. He et al. [B10] did a comprehensive investigation of Low-Reynolds turbulence models (Launder and Sharma (LS), Chien (CH), a k–x model by Wilcox (WI), and some more recent models: Myoung and Kasagi (MK), Yang and Shih (YS) and Abe, Kondoh and Nagano (AKN), the k–e–v2–f model of Behnia, Parneix and Durbin (V2F)) using an in-house code. He claims that, Low-Reynolds number turbulence models, whose damping functions are based on variables readily responding to buoyancy and flow acceleration (e.g. LS, YS and AKN), significantly over-predict flow laminarization and therefore heat transfer deterioration. Between all tested models, the V2F turbulence model, which incorporates also some near-wall turbulence anisotropy as well as non-local pressure-strain effects, produces the best prediction. Other RANS simulations have been carried out by Cheng [B7], Paloko and Anglart [B22], Yang [B28]. Results from these works suggest that, even in some cases, simulations have good agreement with experiments, but in general the current RANS turbulent models are not reliable for solving heat transfer problem of supercritical fluid. Under that situation, modifying exisisting Low-Re turbulence models or even developing new models seem to be a new solution, which has been already attempted by Mohseni and Bazargan [B16]. They found that the formulation of the viscous-sub layer plays an important role for the turbulent supercritical heat transfer. The conventionel turbulence models tend to overpredict the thickness of this viscous-sub layer. Based on the Low-Re k-epsilon turbulence model, he modified its dampfing function to control the thickness of the buffer layer.

Recently, Large Eddy Simulation is considered as an option besides RANS turbulence models. Because it resolves large scales of the flow field its solution is believed to yield better fidelity than RANS methods, and unlike Direct Numerical Simulation (DNS), the computational cost of LES is affordable for applications with higher Re, which means a direct validation with experimental data may be possible. Kunik [B12] tested different sub-grid scale models using DNS data for validation. The wall temperature along the pipe varies with different sub-grid models, where the dynamic one-equation sub-grid model shows better agreement with DNS than others. Niceno and Sharabi [B18] accomplished a large eddy simulation for supercritical-water pipe flow, in which they successfully made a direct validation with experimental data. As the reason of cartesian coordinate code, they simulate a plane channel with the same hydraulic diameter as the original cylindrical pipe (projection method) and a pipe length of 160 diameters to compare with experimental results. The trend of wall temperature deterioration and recovery has been described, but the difference is still evident. Besides that, they also show the mean value for first- and second order moments.

Bae et al. [B3, B4] investigated the turbulent heat transfer of supercritical fluid with direct numerical simulation at Re_0=5400 for a circular pipe and Re_0=9000 for an annular channel. For circular pipe flow, several cases with different diameters (1mm, 2mm and 3mm), different wall heat fluxes and flow directions have been performed and compared. The mean velocity profiles shows a significant M-shape in the upward cases. Further investigations of the turbulence statistics indicate that $\overline{\rho U_x'' U_r''}$, $\overline{\rho U_x'' h''}$ and $\overline{\rho U_r'' h''}$ are significantly affected by buoyancy. In the later work in 2008, they observed the invalidation of the law of the wall using the Van-Driest transform in the cases with variable properties, while the law still works for cases with constant properties. He concluded that, with low level of Reynolds shear stress in the inertial sub-layer, turbulence cannot be self-sustaining so that the logarithmic velocity profile cannot be realized. With the visualization of instantaneous iso-density surfaces from DNS and experimental visualization of the flows [B26], they compared the similarity of phenomenon of supercritical heat transfer and the normal phase change at subcritical pressure. The data from their works offers a reference for some RANS and LES simulation later ([B10, B12]).

As seen from the above discussion, although the turbulent heat transfer of supercritical fluid has been studied since long time, there are still gaps to be filled. Especially nowadays it is possible to use DNS/LES methods to investigate this phenomenon. Through this study, it is aimed to use OpenFOAM to develop DNS of turbulent heat transfer of supercritical fluid on Re_0=5400, verify the method with other DNS studies, and analyse the turbulence data. Moreover, it is planned to make a direct comparison between DNS and experiment results at higher Reynolds numbers in the future.

2. Mathematic Models

In the present work, heated supercritical pipe flow is simulated by full Navier-Stokes equations in a cartesian coordinate system with the low-Mach-number assumption, with which the acoustic interactions and compressibility effects are eliminated from the full compressible Navier–Stokes equations (Eqn.1, Eqn.2 and Eqn.3). Without considering the compressibility, we can determine all thermodynamic state variables, such as density, enthalpy, dynamic viscosity and thermo conductivity, as a function of enthalpy (Eqn.4), independently of the hydrodynamic pressure variations. The property data are obtained from NIST web chemistry book. [B1]

$$\frac{\partial(\rho)}{\partial t} + \frac{\partial(\rho U_j)}{\partial x_j} = 0 \qquad \text{Eqn. 1}$$

$$\frac{\partial(\rho U_i)}{\partial t} + \frac{\partial(\rho U_i U_j)}{\partial x_j} = -\frac{\partial P}{\partial x_i} + \frac{\partial}{x_j}\left(\mu\left(\frac{\partial U_i}{\partial x_j} + \frac{\partial U_j}{\partial x_i}\right)\right) \pm \rho g \delta_{i1} \qquad \text{Eqn. 2}$$

$$\frac{\partial(\rho h)}{\partial t} + \frac{\partial(\rho U_j h)}{\partial x_j} = \frac{\partial}{\partial x_j}\left(k\frac{\partial T}{\partial x_j}\right) \qquad \text{Eqn. 3}$$

$$h = h(P_0, T), T = T(P_0, h), \rho = \rho(P_0, T), \mu = \mu(P_0, T), k = k(P_0, T), C_p = C_p(P_0, T) \qquad \text{Eqn. 4}$$

Figure 2 shows the integration domain of heated pipe flow in the simulations. An inflow generator with periodic boundary condition generates fully developed turbulent flow at constant temperature (301.15 K) for the heated pipe as inlet velocity. The main pipe begins with a 3 diameter buffer length without heat flux on the wall. In order to capture the wall temperature change along axial direction, the heated pipe has a length of 45 diameters with constant heat

flux on the wall. The outlet boundary condition for the velocity is the convective boundary condition from Orlanki [B2, B21], as seen in Eqn.5. ϕ could be any scalar variable or the velocity vector, U_c is the convective velocity of the outflow. The inlet Reynolds number, which based on the inlet bulk velocity, inlet temperature is 5400 in all three cases.

$$\frac{\partial(\phi)}{\partial t}+U_c\frac{\partial(\phi)}{\partial x}=0 \qquad \text{Eqn. 5}$$

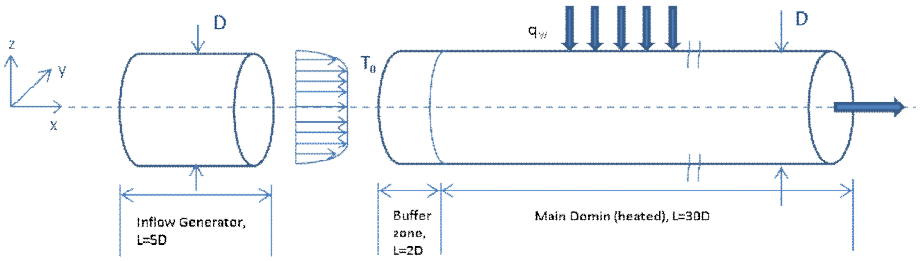

Figure 2: Schematic of the flow region and boundary conditions

3. Numerical Method

3.1 Open Source CFD Solver OpenFOAM

The numerical model has been solved using the open source program OpenFOAM 2.2.2 [B19], which is a finite volume CFD code written in C++. OpenFOAM offers standard solvers for different physical problems and the flexibility to edit and create new solvers and functions at the same time.

In the present study, the Navier-Stokes equations are solved using a second order collocated grid. The velocity-pressure coupling is handled with the PIMPLE Algorithm [B19]. The temporal discretization is solved with second-order implicit backward differencing scheme, while the upwind three-point interpolation QUICK [B13] is used for the convection term in the energy equation to reduce oscillations due to sharp gradients, which is also used for other DNS/LES turbulent heat transfer simulations of supercritical fluids [B3, B17, B18].

3.2 Simulation Conditions

An O-grid mesh, which consists of 5 blocks with 12900 mesh points, 30X30 in the central block and 30X100 in other four blocks, is generated in the y-z plane for the pipe geometry, corresponding radial and circumferential directions. Converted from Cartesian coordinates to cylindrical coordinates respectively, the inflow generator has a mesh resolution of $115 \times 120 \times 256$ along the radial (r), circumferential (θ) and axial direction (z). For the heated main pipe, the mesh resolution is $115 \times 120 \times 2304$. A uniform grid spacing is used in the axial direction, while the radial grid is refined close to the wall, which corresponds to a dimensionless grid resolution of $0.16(wall) < \Delta r^+ < 1.84(center)$, $\Delta\theta^+ \approx 9.6$ and $\Delta z^+ = 7.64$ in wall units, based on a constant temperature at the inlet. One forced convection case (case A) and two mixed convection cases (case B and case C) will be presented here in the study (Table 1). The difference is that case B is an upward flow and case C is a downward flow.

Table 1: Simulation cases

Case	Type	Direction	P (MPa)	D (mm)	Re_0	T_0 (K)	q_w (kW/m2)
A	Forced	-	8	2	5400	301.15	15.44
B	Mixed	Up	8	2	5400	301.15	15.44
C	Mixed	Down	8	2	5400	301.15	15.44

3.3 Verification

Until now, there are still limited DNS studies with OpenFOAM [B11]. It is necessary to verify the fidelity of this code for DNS uses. For this reason, Verifications with DNS turbulent pipe flow without heat transfer and DNS turbulent heat transfer cases with supercritical flow are demonstrated here. All cases base on Re_0=5400. The pipe flow without heat transfer is verified with DNS studies, which has been validated with experiments. [B9, B27]. The turbulent pipe flow with supercritical heat transfer has been carried out by J.H. Bae in 2005, the verification target is upward mixed convection flow case C [B3].

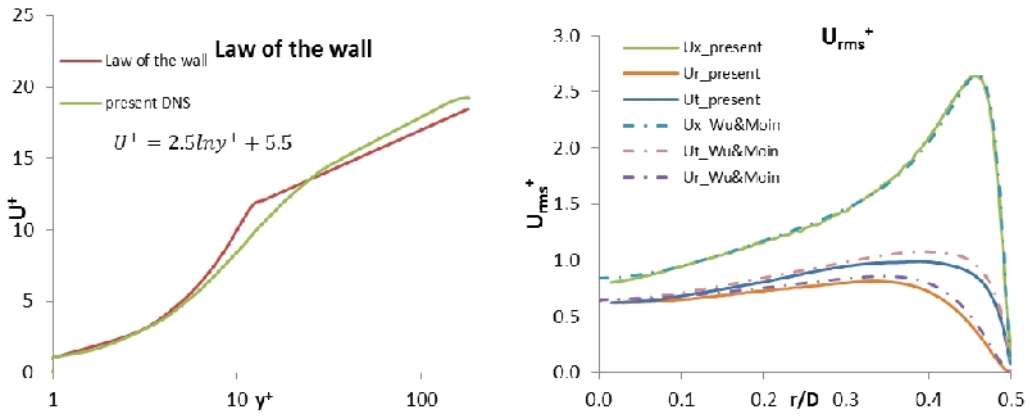

Figure 3: Fully developed turbulent inflow condition at Re_0=5400: left: Mean velocity profile right: root-mean-square velocity fluctuations, solid line: present DNS; dash line: Wu & Moin

In the turbulent pipe flow without heat transfer, the mean velocity distribution shows reasonably good agreement with law of the wall (left picture of Figure 5), while the root-mean-square velocity fluctuations (right picture of Figure 5) show also fairly good agreement, especially in the axial direction, but slightly difference in radial and circumferential directions, which may be an indiction for a low resolution DNS, such as the DNS of [B9] see [B27].

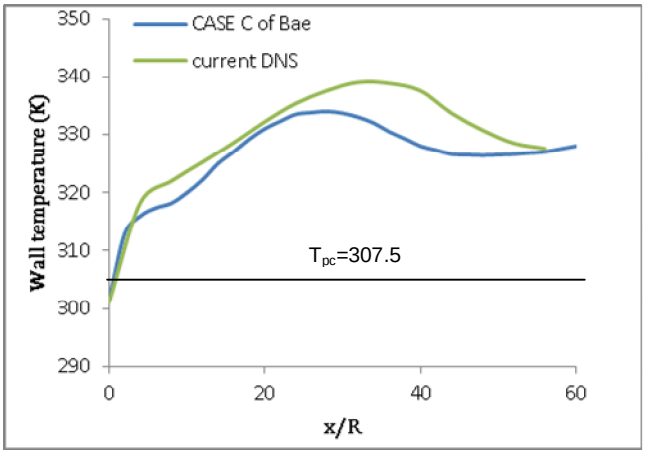

Figure 6: Verification with DNS supercritical heat transfer case from Bae [B3]

In the verification with CASE C from Bae's simulation, the wall temperature shows similar tendency, which means both wall temperature deterioration and recovery have been shown. But slight differences can be identified, which could be stem from different codes, mesh resolutions or thermo-physical properties of different chemical library (NIST vs. PROPATH).

4. Results and Discussion

In the flow statistics below, we define the mean quantities in Favre- (Eqn.5) and Reynolds averaging (Eqn.6). Velocity components and enthalpy are Favre averaged, whereas pressure, density and transport properties are Reynolds averaged.

$$\tilde{\varphi} = \frac{\overline{\rho\varphi}}{\overline{\rho}}, \varphi'' = \varphi - \tilde{\varphi} \qquad \text{Eqn. 5}$$

$$\varphi' = \varphi - \overline{\varphi} \qquad \text{Eqn. 6}$$

4.1 Mean Flow Statistics

The investigation begins with the mean wall temperature statistics in the stream-wise direction.

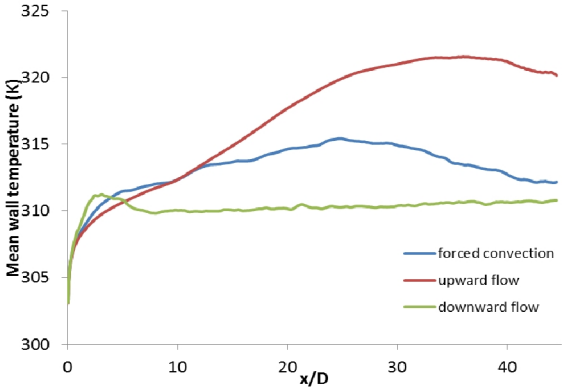

Figure 7: mean wall temperature

The wall temperature deterioration and recovery can be identiefied through this quantities. The mean wall temperatures of the three cases show different trends even with identical inlet mass flux and heat flux at the wall (Figure 7). The wall temperature of the downward flow (C) rises monotonically after a first small peak not far from the pipe inlet, which is similar as the result of of Bae [B3] with twice the wall heat flux. The increase of wall temperature in upward flow (B) is much stronger, and decreases downstream of about x=40D. The range of the wall temperature in the forced convection flow (A) is located between the upward and downward flow. Interestingly, a wall temperature peak could be also identified at about x=25D even in the forced convection case without buoyancy. In the forced convection cases with smaller pipe diameter and shorter pipe (Bae [B3] and Nemati [B17]), this has not been observed.

Figure 8 shows the mean temperature distribution in radial direction at x=0D, 10D, 20D, 30D, 40D. In upward flow (B), the temperature rises significantly in the near wall zone. Before the wall temperature reaches the peak (about x=40D), the increase of fluid temperature on the pipe centreline is minimal, which means a weakened radial heat transport. Downstream of that, the core temperature rises with a wall temperature recovery. In the downward flow, the temperature rise in the near wall zone is relatively mild, but the core temperature is higher than that of upward flow, which means a larger heat flux from the wall to the bulk. For the supercritical fluid, the property variation is significant, as shown in the density field in Figure 8.The density drops fast near the heated wall, and also the specific heat capacity reaches its maximum not far from the wall.

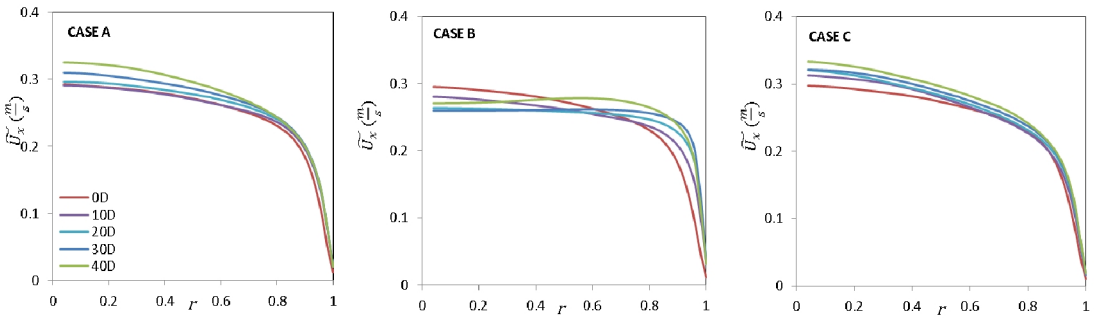

Figure 8: stream-wise mean velocity

Due to the wall heat flux the fluid temperature in the near wall region rises, which corresponds to a lower density (Figure 10). In the upward flow, the buoyancy accelerates flows near the wall, and forms an M-shape stream-wise velocity profile. The stream-wise velocity profile turns to the M-shape progressively along the pipe. In the downward flow, in which thermal expansion has an opposed direction to the flow, buoyancy decelerates the flow near the wall. The influence of buoyancy causes this distortion of mean flow and is denoted as ‘external’ effect or ‘indirect’ effect by Petukhov, while ‘structural’ effect means the direct influence on turbulence [B23].

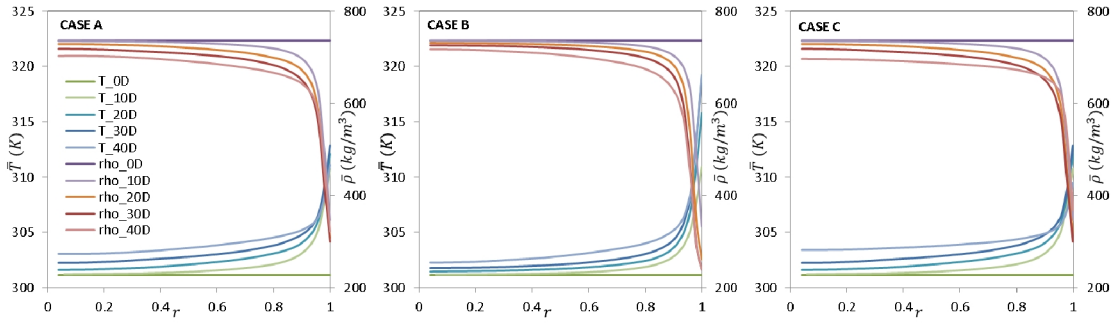

Figure 10: mean temperature and density

4.2 Turbulence statistics

The turbulent kinetic energy (TKE) per unit volume $\overline{\rho U_i'' U_i''}$ is the sum of the three Reynolds-stress components and indicates the intensity of turbulence (Figure 12). The downward flow, where $g(\partial P/\partial x) < 0$, is referred to as 'unstable' in terms of the density stratification: buoyancy delivers a positive contribution to the turbulence and therefore, the TKE of downward flow (C) increases monotonically along the flow direction. For upward flow (B), (stable density case, $g(\partial P/\partial x) > 0$), buoyancy has a negative effect of turbulence at first and then turns to positive. This influence is demonstrated in the TKE of case B. In the forced convection flow case A, when the mean wall temperature increases, the TKE goes down, which means the turbulence intensity is depressed even without the influence of buoyancy. But as for the turbulent kinetic energy, it is clear that turbulence intensity is largely impacted by buoyancy (cases B and C) than the variable properties and thermal expansion (case A).

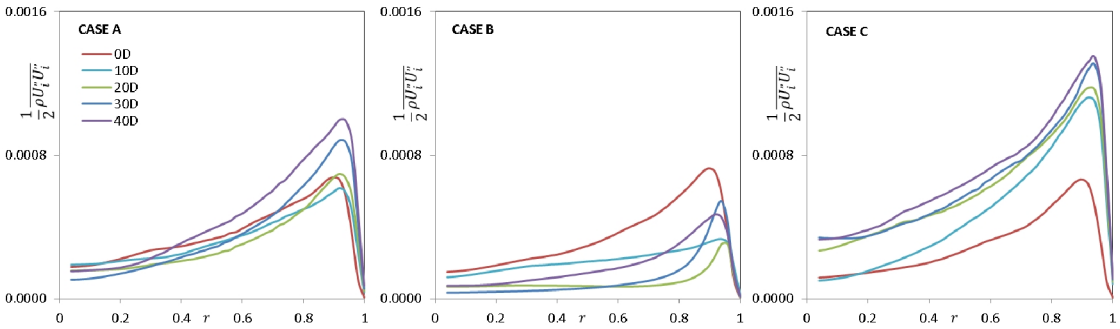

Figure 12: TKE per unit volume $\overline{\rho U_i'' U_i''}$

In Figure 13, profiles of the Reynolds shear stress $\overline{\rho U_x'' U_r''}$ are presented. The forced convective heat transfer case (A) shows similar peak value in all locations, but small depression could still be found at 10D and 20D, where the wall temperature rises. After that, at location 30D and 40D, it rises over the value at the beginning 0D. In the upwards flow case B, $\overline{\rho U_x'' U_r''}$ is strongly influenced by buoyancy, it falls down to almost zero at 30D, where strong turbulent heat transfer deterioration detected, and turn to negative at 40D. On the other side, the downward flow case C has a monotonically increasing Reynolds shear stress due to the positive effect of buoyancy to turbulence.

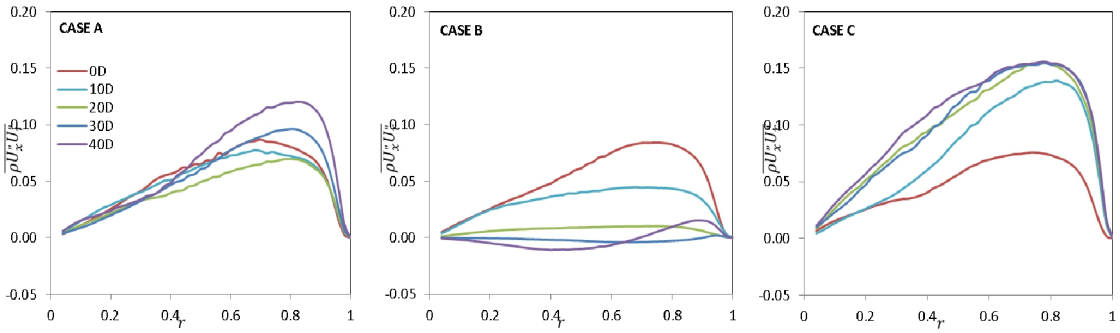

Figure 13: stream-wise Reynolds shear stress $\overline{\rho U_x'' U_r''}$

The stream-wise turbulent heat flux $\overline{\rho U_x'' h''}$, which is directly influenced by buoyancy, shows different distribution in the three cases (Figure 14: stream-wise turbulent heat flux $\overline{\rho U_x'' h''}$). In cases A and C, they have the same sign and similar magnitudes. On the other hand, $\overline{\rho U_x'' h''}$ in case B turns to be positive at 10D downstream of the inlet. The radial turbulent heat flux $\overline{\rho U_r'' h''}$ is not directly connected with buoyancy, and therefore, it does not show a clear difference in sign and magnitude between the three cases like $\overline{\rho U_x'' h''}$. But it could still help to explain the radial temperature distribution in Figure 15. Case B, at 10D, 20D and 30D, $\overline{\rho U_r'' h''}$ shows a relatively low value, which means the heat transfer from wall to bulk is depressed, which means heat transfer deterioration becomes stronger and the wall temperature rises. At 40D, where the wall temperature recovery happens, $\overline{\rho U_r'' h''}$ increases.

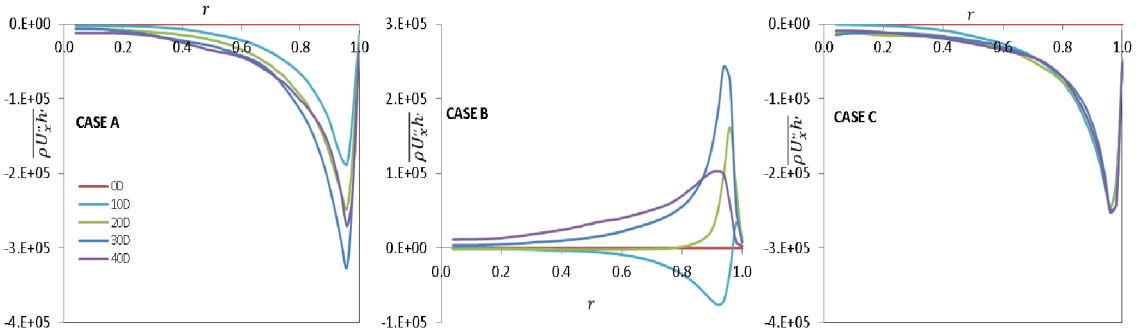

Figure 14: stream-wise turbulent heat flux $\overline{\rho U_x'' h''}$

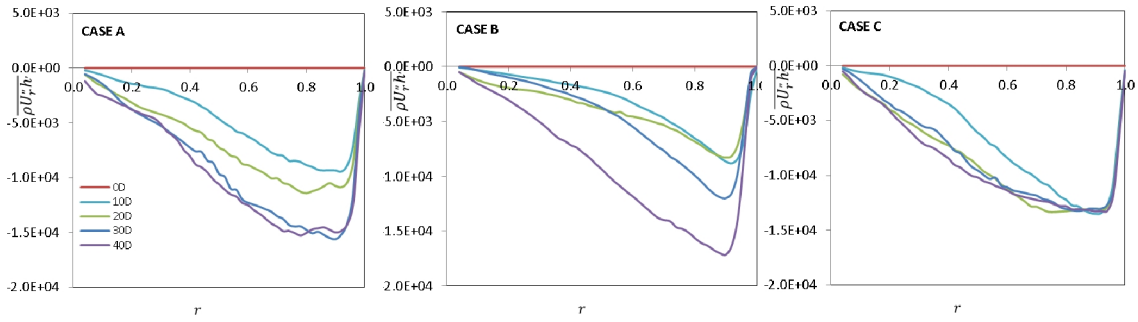

Figure 15: radial turbulent heat flux $\overline{\rho U_r'' h''}$

5. Conclusions

Direct numerical simulation of supercritical carbon dioxide flow in heated circular pipe L=45 D at a pressure of 8 MPa is developed with the open source CFD program OpenFOAM in the present study. The turbulent pipe flow has an inlet Reynolds number of Re_0=5400. The method

using OpenFOAM has been verified with results other DNS studies and shows good agreement. The wall temperature rises from below to above the pseudo-critical temperature, where very strong fluid-property variations are involved. In forced convection flow and the upward mixed convection flow, heat transfer deterioration, which leads to peak wall temperature, followed by a recovery of the wall temperature has been captured. In the forced convection case, the variable thermo-physical properties and thermal expansion could lead to a depression and recovery of turbulence. But the change is relatively mild compared with that of mixed convection. Furthermore, the buoyancy could have a strong influence to turbulence and turbulent heat transfer, which could be proved by the results of Reynolds shear stress and turbulent heat flux. This turbulence statistic in the DNS may aid in the development of new turbulence models for applications in the future.

6. Bibliography

[B1] Thermophysical Properties of Fluid Systems. http://webbook.nist.gov/chemistry/fluid/.

[B2] Ahn, J., Lee, J. H., Jang, S. J., and Sung, H. J., "Direct numerical simulations of fully developed turbulent pipe flows for Reτ=180, 544 and 934," *International Journal of Heat and Fluid Flow*, vol. 44, pp. 222–228, 2013.

[B3] Bae, J. H., Yoo, J. Y., and Choi, H., "Direct numerical simulation of turbulent supercritical flows with heat transfer," *Physics of Fluids*, vol. 17, no. 10, p. 105104, 2005.

[B4] Bae, J. H., Yoo, J. Y., and McEligot, D. M., "Direct numerical simulation of heated CO[sub 2] flows at supercritical pressure in a vertical annulus at Re=8900," *Physics of Fluids*, vol. 20, no. 5, p. 55108, 2008.

[B5] Bae, Y.-Y. and Kim, H.-Y., "Convective heat transfer to CO2 at a supercritical pressure flowing vertically upward in tubes and an annular channel," *Experimental Thermal and Fluid Science*, vol. 33, no. 2, pp. 329–339, 2009.

[B6] Brunner, G., "Applications of Supercritical Fluids," *Annu. Rev. Chem. Biomol. Eng.*, vol. 1, no. 1, pp. 321–342, 2010.

[B7] Cheng, X., Kuang, B., and Yang, Y. H., "Numerical analysis of heat transfer in supercritical water cooled flow channels," *Nuclear Engineering and Design*, vol. 237, no. 3, pp. 240–252, 2007.

[B8] Dostal, V., Driscoll, M. J., and Hejzlar, P., "A Supercritical Carbon Dioxide Cycle for Next Generation Nuclear Reactors," 2004.

[B9] EGGELS, J. G. M., UNGER, F., WEISS, M. H., WESTERWEEL, J., ADRIAN, R. J., FRIEDRICH, R., and NIEUWSTADT, F. T. M., "Fully developed turbulent pipe flow: a comparison between direct numerical simulation and experiment," *journal of fluid mechanics*, 1994.

[B10] He, S., Kim, W. S., and Bae, J. H., "Assessment of performance of turbulence models in predicting supercritical pressure heat transfer in a vertical tube," *International Journal of Heat and Mass Transfer*, vol. 51, no. 19–20, pp. 4659–4675, 2008.

[B11] Komen, E., Shams, A., Camilo, L., and Koren, B., "Quasi-DNS capabilities of OpenFOAM for different mesh types," *Computers & Fluids*, vol. 96, pp. 87–104, 2014.

[B12] Kunik, C., "CFD-Simulationen turbulenter konvektiver Strömungen bei überkritischen Drücken," 2012.

[B13] Leonard, B. P., "A stable and accurate convective modelling procedure based on quadratic upstream interpolation," *Computer Methods in Applied Mechanics and Engineering*, vol. 19, no. 1, pp. 59–98, 1979. http://dx.doi.org/10.1016/0045-7825(79)90034-3.

[B14] Li, Z.-H., Jiang, P.-X., Zhao, C.-R., and Zhang, Y., “Experimental investigation of convection heat transfer of CO2 at supercritical pressures in a vertical circular tube,” *Experimental Thermal and Fluid Science*, vol. 34, no. 8, pp. 1162–1171, 2010.

[B15] Licht, J., Anderson, M., and Corradini, M., “Heat transfer to water at supercritical pressures in a circular and square annular flow geometry,” *International Journal of Heat and Fluid Flow*, vol. 29, no. 1, pp. 156–166, 2008.

[B16] Mohseni, M. and Bazargan, M., “Modification of low Reynolds number k–ε turbulence models for applications in supercritical fluid flows,” *International Journal of Thermal Sciences*, vol. 51, pp. 51–62, 2012.

[B17] Nemati, H., Patel, A., Bendiks Jan Boersma, and Pecnik, R., “Mean statistics of a heated turbulent pipe flow at supercritical pressure,” *International Journal of Heat and Mass Transfer*, 2014.

[B18] Ničeno, B. and Sharabi, M., “Large eddy simulation of turbulent heat transfer at supercritical pressures,” *Nuclear Engineering and Design*, vol. 261, pp. 44–55, 2013.

[B19] OpenFOAM Foundation, *OpenFOAM User Guide*, 2013. http://foam.sourceforge.net/docs/Guides-a4/UserGuide.pdf.

[B20] Orgogozo, L., Renon, N., Soulaine, C., Hénon, F., Tomer, S. K., Labat, D., Pokrovsky, O. S., Sekhar, M., Ababou, R., and Quintard, M., “An open source massively parallel solver for Richards equation: Mechanistic modelling of water fluxes at the watershed scale,” *Computer Physics Communications*, vol. 185, no. 12, pp. 3358–3371, 2014.

[B21] Orlanski, I., “A simple boundary condition for unbounded hyperbolic flows,” *Journal of Computational Physics*, vol. 21, no. 3, pp. 251–269, 1976.

[B22] Palko, D. and Anglart, H., “Theoretical and Numerical Study of Heat Transfer Deterioration in High Performance Light Water Reactor,” *Science and Technology of Nuclear Installations*, vol. 2008, no. 2, pp. 1–5, 2008.

[B23] Petukhov, B. S., Polyakov, A. F., and Launder, B. E., *Heat transfer in turbulent mixed convection:* Hemisphere Pub. Corp, 1988. http://books.google.de/books?id=LBuhFzyF8CAC.

[B24] Pioro, I. L., Khartabil, H. F., and Duffey, R. B., “Heat transfer to supercritical fluids flowing in channels—empirical correlations (survey),” *Nuclear Engineering and Design*, vol. 230, no. 1–3, pp. 69–91, 2004.

[B25] Shiralkar, B. S. and Griffith, P., “The deterioration in heat transfer to fluids at supercritical pressure and high heat fluxes,” 1968.

[B26] Tamba, J., Takahashi, T., Ohara, T., and Aihara, T., “Transition from boiling to free convection in supercritical fluid,” *Experimental Thermal and Fluid Science*, vol. 17, no. 3, pp. 248–255, 1998.

[B27] WU, X. and Moin, P., “A direct numerical simulation study on the mean velocity characteristics in turbulent pipe flow,” *J. Fluid Mech.*, vol. 608, 2008.

[B28] Yang, J., Oka, Y., Ishiwatari, Y., Liu, J., and Yoo, J., “Numerical investigation of heat transfer in upward flows of supercritical water in circular tubes and tight fuel rod bundles,” *Nuclear Engineering and Design*, vol. 237, no. 4, pp. 420–430, 2007.

ISSCWR7-#2004

Implicit Model Equations for Hydraulic Resistance and Heat Transfer including Wall Roughness

Eckart Laurien

University of Stuttgart / Institute of Nuclear Technology and Energy Systems
Pfaffenwaldring 31, D-70569 Stuttgart, Germany
+49 711 685 62415, Laurien@ike.uni-stuttgart.de

Abstract

Heat transfer to water at super-critical pressure within the core of a Super-Critical Water Reactor must be predicted accurately in order to ensure safe design of the reactor and prevent overheating of the fuel cladding. In previous work [1] we have demonstrated, that the wall shear stress and the wall temperature can be computed in a coupled way by a finite-difference method taking the wall roughness into account. In the present paper the classical two-layer model, consisting only of a laminar sub-layer and a turbulent wall layer, is extended towards the same task. A set of implicit algebraic equations for the wall shear stress and the wall temperature is derived. It is consistent with the well-established Colebrook equation for rough pipes, which is included as a limiting case for constant properties. The accuracy of the prediction for strongly heated pipe flow is tested by comparison to experiments [2] with super-critical water. The high accuracy and the generality of [1] is not achieved, but with the help of correction factors the two-layer model has a potential for improved predictions of the hydraulic resistance and the heat transfer of pipe and channel flows at supercritical pressure.

1. Introduction

The prediction of the cladding temperature within the cooling channels of a super-critical water-cooled nuclear reactor is essential for its design and safety analysis. A concept of this reactor has been investigated in [3]. Various methods to predict the heat transfer and the hydraulic resistance have been developed, e.g. correlations of experimental data [4,5], the look-up table [6,7], one-dimensional theory [1,8] and multi-dimensional computational fluid dynamics [9,10,11]. However, there is still need for an improvement and for the development of accurate and reliable prediction methods.

If the flow in a pipe or channel can be regarded as ‘quasi-fully’ developed one-dimensional theory can be applied. Using this theory we have demonstrated in [1] by comparison to various experiments of flows in circular pipes, that the roughness height of the pipe wall should be taken into account. A key aspect of the computation is the simultaneous solution of the momentum and the energy equations. As a result of the momentum equation the wall shear stress is obtained, as a result of the energy equation we get the wall temperature. Since all properties of the fluid are functions of the temperature, an iteration of the implicit equation system must be performed.

As a simple method of theoretical analysis is the two-layer model. It has been developed for constant-property flows [12,13] and an extension to non-constant property flows has been attempted in [14]. In the framework of this theory it is assumed, that the turbulent pipe flow consists of two-layers: (i) the turbulent 'wall layer', and (ii) the 'laminar sub-layer'. This model has been applied successfully to derive often-used fluid-dynamic formulas such as the logarithmic law of the wall for the velocity and the temperature. Key parameters in this theory are the thickness of the laminar sub-layers for the velocity and the temperature.

In this paper, an attempt is made to generalize the two-layer model to non-constant property flows. First, the theory for the hydraulic resistance and the heat transfer for rough walls under the assumption of constant properties is repeated. Then, the theory is extended to conditions of non-constant fluid properties such as water at super-critical pressure.

2. Theory for Constant Properties

2.1 Friction coefficient for a Rough Wall

A well-established equation to determine the Darcy friction coefficient c_f for a constant-property flow in a pipe with a rough wall is the Colebrook equation [15, 16] for turbulent pipe flow. The diameter of the pipe is denoted by $D = 2R$, the radius by R, the density ρ, the dynamic viscosity μ and the dimensional roughness of the pipe surface ε. The implicit Colebrook equation reads

$$\frac{1}{\sqrt{c_f}} = -2\log_{10}\left(\frac{\varepsilon/D}{3.7} + \frac{2.51}{\mathrm{Re}\sqrt{c_f}}\right) \quad \text{with} \quad \mathrm{Re} = \frac{\rho\, u_m\, D}{\mu} \quad ; \quad c_f = \frac{4\,\tau_w}{\frac{\rho}{2}u_m^2} \quad . \tag{1}$$

In the definition of the Reynolds number Re, the density ρ, the mean velocity u_m and the dynamic viscosity μ appear. The definition of the friction coefficient c_f is based on the wall shear stress τ_w. Eq. (1) contains empirical coefficients, which were fitted to experiments.

2.2 Wall Units

In the theory of turbulent flows the wall distance $0 < y < R$ is used as a coordinate and non-dimensional 'wall units' (denoted by the upper index '+') are defined [12]. The dimensional downstream velocity component $\bar{u}$ and the dimensional wall distance y are expressed by a non-dimensional wall distance y^+ and an non-dimensional velocity

$$u^+ = \frac{\bar{u}}{u_\tau} \quad \text{and} \quad y^+ = \frac{\rho\, y\, u_\tau}{\mu} \quad , \tag{2}$$

with the 'friction velocity'

$$u_\tau = \sqrt{\frac{\tau_w}{\rho}} = \sqrt{\frac{c_f \cdot \rho/8\, u_m^2}{\rho}} = \sqrt{\frac{c_f}{8}}\, u_m \quad . \tag{3}$$

Using these 'wall units' we define some additional useful quantities, namely the friction Reynolds number Re_τ and the non-dimensional pipe radius R^+:

$$\mathrm{Re}_\tau = \frac{\rho\, D\, u_\tau}{\mu} = \sqrt{\frac{c_f}{8}}\,\mathrm{Re} \quad ; \quad R^+ = \frac{\rho\, R\, u_\tau}{\mu}\frac{D}{2R} = \frac{\mathrm{Re}_\tau}{2} \quad . \tag{4}$$

2.3 The Velocity Law of the Wall for a Rough Pipe

Let us generalize the definition of the the standard logarithmic law of the wall (with the von Karman constant κ) to derive a law of the wall for rough pipes:

$$u^+ = \frac{1}{\kappa}\ln y^+ + C^+ \quad ; \quad C^+ = A - \frac{1}{\kappa}\ln\left(1+\frac{\varepsilon^+}{B}\right) \quad . \tag{5}$$

The constants A and B must be determined from the Colebrook equation (1). The mean velocity, or the friction coefficient, respectively, can be obtained by an integration of eq. (5) over the pipe cross section:

$$u_m = u_\tau\sqrt{\frac{8}{c_f}} = \frac{u_\tau}{\pi\, R^{+2}}\int_0^{R^+}\left(\frac{1}{\kappa}\ln y^+ + C^+\right)2\pi\left(R^+ - y^+\right)dy^+ \quad . \tag{6}$$

This equation can be re-arranged into

$$\frac{1}{\sqrt{c_f}} = \frac{2\pi}{\sqrt{8}\,\pi\, R^{+2}}\int_0^{R^+}\left(\frac{R^+}{\kappa}\ln y^+ + C^+R^+ - \frac{y^+}{\kappa}\ln y^+ - C^+y^+\right)\; dy^+ \quad . \tag{7}$$

Then, the integration is performed (use integral no. 471 of [17]):

$$\frac{1}{\sqrt{c_f}} = \frac{2}{\sqrt{8}\,R^{+2}}\left[\frac{R^+y^+}{\kappa}\ln y^+ - \frac{R^+y^+}{\kappa} + C^+R^+y^+ - \frac{y^{+2}}{2\kappa}\ln y^+ + \frac{y^{+2}}{4\kappa} - \frac{C^+}{2}y^{+2}\right]_0^{R^+} . \tag{8}$$

Next, we insert the upper and lower limits of the integration. Further re-arrangement yields

$$\frac{1}{\sqrt{c_f}} = \frac{1}{\sqrt{8}}\left[\frac{\ln R^+}{\kappa} - \frac{3}{2\kappa} + C^+\right] \quad . \tag{9}$$

Now, eq. (5) is inserted

$$\frac{1}{\sqrt{c_f}} = \frac{1}{\sqrt{8}\,\kappa}\left[\ln R^+ - \frac{3}{2} + A\kappa - \ln\left(1+\frac{\varepsilon^+}{B}\right)\right] \quad ; \quad \varepsilon^+ = \frac{\varepsilon}{D}2R^+ \tag{10}$$

and re-arranged. The natural logarithm is converted into a logarithm with respect to base 10 and the R^+ is replaced by the Reynolds number due to eq. (4):

$$\frac{1}{\sqrt{c_f}} = -\frac{1}{\sqrt{8}\,\kappa\log_{10}e}\log_{10}\left[\frac{2\sqrt{8}}{e^{-1.5+A\kappa}\,\mathrm{Re}\sqrt{c_f}} + \frac{2\,\varepsilon}{BDe^{-1.5+A\kappa}}\right] \quad . \tag{11}$$

With κ=0.4 we get

$$\frac{1}{\sqrt{8}\,\kappa\log_{10}e} = 2.0352 \approx 2 \quad ; \quad \frac{2\sqrt{8}}{e^{-1.5+A\kappa}} = 2.51 \quad ; \quad \frac{2}{Be^{-1.5+A\kappa}} = \frac{1}{3.7} \tag{12}$$

This is consistent with the Colebrook equation if $A = 5.7814$ and $B = 3.2835$. The logarithmic law of a rough wall becomes

$$u^+ = \frac{1}{\kappa}\ln y^+ + 5.78 - \frac{1}{\kappa}\ln\left(1+\frac{\varepsilon^+}{3.28}\right) \quad . \tag{13}$$

Under the assumption of constant viscosity in the laminar sub-layer is the linear velocity profile $u^+ = y^+$ is valid. Both profiles are depicted in figure 1 for various values of the roughness parameter. The edge of the viscous sub-layer (index *vs*) y^+_{vs} can be obtained from:

$$y^+_{vs} = \frac{1}{\kappa}\ln y^+_{vs} + 5.78 - \frac{1}{\kappa}\ln\left(1+\frac{\varepsilon^+}{3.28}\right) \quad . \tag{14}$$

The equation can be solved by iteration, see results in figure 2. We have approximated this curve as a function of ε^+ by

$$y_{vs}^+ \approx 11.6 \cdot e^{-0.046\varepsilon^+} \quad . \tag{15}$$

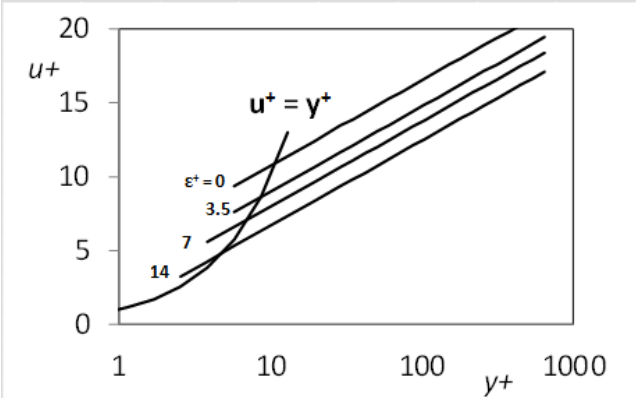

Figure 1: Velocity profile in wall units for a smooth wall and with wall roughness ε in wall units, constant properties

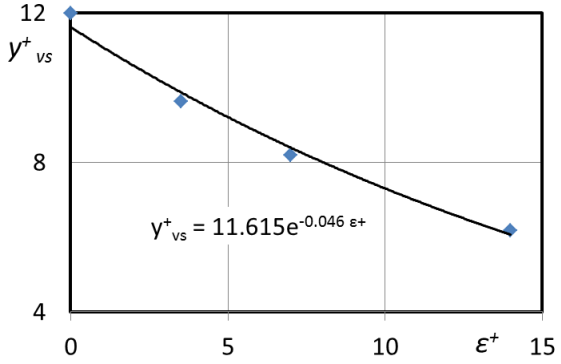

Figure 2: Full line: curve fit of the iterative solution (symbols) of eq. (15) vs. the non-dimensional roughness ε^+

Note, that the term 'viscous sub-layer' (index *vs*) refers to the 'laminar sub-layer' of the velocity, the thickness of the laminar sub-layer of the temperature profile ('conducting sub-layer', index *cs*) may be different, see below.

2.4 The Temperature Law of the Wall

From integration of the non-dimensional heat conduction equation with constant q_w follows

$$\frac{d\,\overline{T}}{d\,y} = -\frac{q_w}{\lambda + \lambda_T} \tag{16}$$

with the average temperature $\overline{T}$, the molecular conductivity λ and the eddy conductivity λ_T. Further integration from the wall to an arbitrary position *y* yields

$$\int_{T_W}^{\overline{T}} d\overline{T} = \overline{T} - T_W = -q_w \int_0^y \frac{1}{\lambda + \lambda_T} dy \quad . \tag{17}$$

Now, a non-dimensional temperature in wall units

$$T^+ = \frac{(T_W - \overline{T})\,u_\tau}{q_W / \rho\, c_p} \tag{18}$$

is introduced and eq. (17) is expressed as

$$T^+(y^+) = \int_0^{y^+} \left[\frac{1}{\mathrm{Pr}} + \frac{\lambda_T}{\mu \cdot c} \right]^{-1} dy^+ \quad \text{with} \quad \mathrm{Pr}_T = \frac{\mu_T \cdot c_p}{\lambda_T} \quad , \tag{19}$$

the turbulent Prandtl number. In the framework of the two-layer model the integral is split into two parts: the first part extends over the conducting sub-layer where the eddy conductivity λ_T is neglected, the second extends over the the turbulent wall-layer where the molecular conductivity λ, represented by the Prandtl number *Pr*, is neglected. The split position is the edge of the conducting

sub-layer y_{cs}^+ . Thus, we get the non-dimensional temperature T^+ as a function of the non-dimensional wall distance

$$T^+(y^+) = \int_0^{y_{cs}^+} \mathrm{Pr}\, dy^+ + \int_{y_{cs}^+}^{y^+} \frac{\mathrm{Pr}_T}{\kappa \cdot y^+} dy^+ \quad . \tag{20}$$

An often used choice [12,13,18] for y_{cs}^+ is

$$y_{cs}^+ = \frac{y_{vs}^+}{\mathrm{Pr}^{1/3}} \quad . \tag{21}$$

As the molecular Prandtl number *Pr* is constant, the first integral of eq. (20) is evaluated for any position $y^+ < y_{cs}^+$ within the conducting sub-layer as

$$T^+(y^+) = \int_0^{y^+} \mathrm{Pr}\, dy^+ = \mathrm{Pr} \cdot \int_0^{y^+} dy^+ = \mathrm{Pr}\, y^+ \quad . \tag{22}$$

For a position $y^+ > y_{cs}^+$ within the turbulent wall-layer both integrals of eq. (20) must be evaluated and we get the 'beta'-function $\beta(\mathrm{Pr}, \varepsilon^+)$

$$T^+(y^+) = \frac{\mathrm{Pr}_T}{\kappa} \ln y^+ + \underbrace{\mathrm{Pr}\, y_{cs}^+ - \frac{\mathrm{Pr}_T}{\kappa} \ln y_{cs}^+}_{\beta(\mathrm{Pr}, \varepsilon+)} \quad . \tag{23}$$

This equation is used with Pr_T =0.85 and κ = 0.4. The heat transfer coefficient can be determined with the assumption that the centreline (index cl) temperature is a good approximation for the bulk temperature

$$\alpha = \frac{q_w}{T_w - T_b} \approx \frac{q_w}{T_w - T_{cl}} = \frac{u_\tau \cdot \rho \cdot c}{T^+_{(y^+ = R^+)}} \quad . \tag{24}$$

In order to compare this theory with other correlations it is useful to express the heat transfer coefficient by a Nusselt number:

$$Nu = \frac{\alpha \cdot 2R}{\lambda} = \frac{\sqrt{c_f/8}\, \mathrm{Re}\, \mathrm{Pr}}{\frac{\mathrm{Pr}_T}{\kappa} \ln R^+ + \beta(\mathrm{Pr}, \varepsilon^+)} \quad . \tag{25}$$

2.5 Comparison to Gnielinski's Correlation

For a smooth wall the results of eq. (25) are compared to Gnielinski's correlation [15], see figure 3 in the range 2300 < Re < 100000 and 1 < Pr < 20. Except for a small region at low *Re* the agreement is good.

The friction factor for a rough wall in the range of interest is given by eq. (1). It depends both on the Reynolds number Re and the relative wall roughness eps/D (often referred to as the 'transitional' range). We can now insert numerical values into eq. (25) and demonstrate the influence of the roughness on the Nusselt number, figure 4. Roughness becomes important only, if for Re > 20000. At lower Reynolds numbers the effect of wall roughness is negligible.

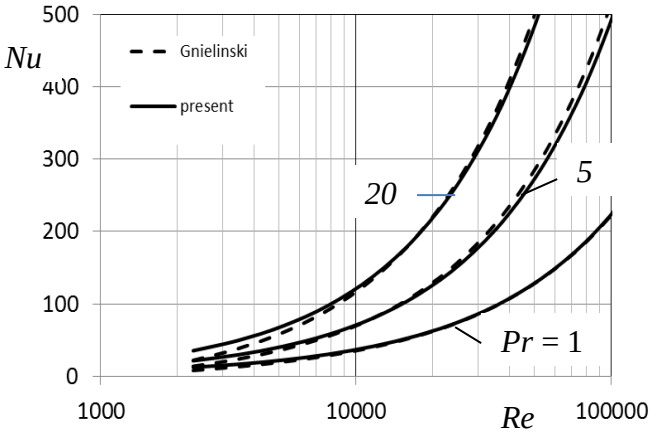

Figure 3: Comparison of the present work *Nu(Re)* from eq. (25), smooth, with Gnielinski's correlation

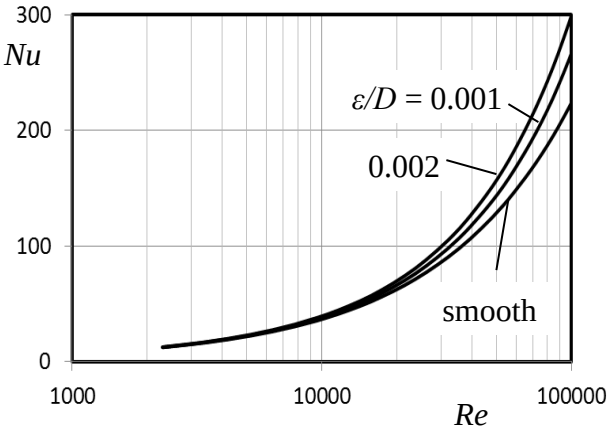

Figure 4: Nu(Re) of the present work eq.(25) for *Pr* =1, smooth and rough wall

3. Theory for Non-Constant Properties

3.1 Friction

The law of the wall eq. (13) does not contain any of the fluid properties. It only describes the effect of turbulence and is valid for fluid with both constant or non-constant properties. For the definition of wall units, however, a choice must be made about the reference quantities. Here, we choose the quantities at the wall (index *w*). Then the wall units are

$$u^{+w} = \frac{\bar{u}}{u_{\tau w}} \quad \text{and} \quad y^{+w} = \frac{\rho_w \, y \, u_{\tau w}}{\mu_w} \quad \text{with} \quad u_{\tau w} = \sqrt{\frac{\tau_w}{\rho_w}} \quad . \tag{26}$$

The friction coefficient, however, is still defined with the bulk density. For the friction velocity we get

$$u_{\tau w} = \sqrt{\frac{c_f \cdot \rho_b / 8 \, u_m^2}{\rho_w}} = \sqrt{\frac{c_f}{8}} \sqrt{\frac{\rho_b}{\rho_w}} u_m \quad . \tag{27}$$

The non-dimensional pipe radius becomes

$$R^{+w} = \frac{\rho_w \, R \, u_{\tau w}}{\mu_w} \frac{D}{2R} = \frac{\sqrt{c_f}}{2\sqrt{8}} \sqrt{\frac{\rho_b}{\rho_w}} \, \mathrm{Re}_w \quad \text{with} \quad \mathrm{Re}_w = \frac{\rho_w \, u_m \, D}{\mu_w} \quad . \tag{28}$$

With these definitions the derivation of the Colebrook equation can be repeated, resulting in the same equation only with the wall Reynolds number Re_w and a modified friction coefficient, denoted as c_f':

$$\frac{1}{\sqrt{c_f'}} = -2 \log_{10} \left(\frac{\varepsilon / D}{3.7} + \frac{2.51}{\mathrm{Re}_w \sqrt{c_f'}} \right) \quad \text{with} \quad c_f' = \frac{\rho_b}{\rho_w} c_f \quad . \tag{29}$$

In the practical calculations an explicit equation [19], which approximates eq. (1) and (29) with good accuracy, has been used. The wall shear stress can be calculated from

$$\tau_w = \frac{c_f}{8} \rho_b u_m^2 \quad . \tag{30}$$

3.2 Heat Transfer

The wall temperature is determined by the bulk temperature T_b and the temperature increase ΔT_{turb} across the turbulent wall layer and ΔT_{cs} the laminar, conducting sub-layer

$$T_W = T_b + \Delta T_{turb} + \Delta T_{cs} = T_{cs} + \Delta T_{cs} \quad . \tag{31}$$

Again, the choice of scaling must be made. The turbulent wall layer extends from the outer edge of the conduction sub-layer to the pipe centre. Therefore, for this layer the bulk quantities are representative. In non-dimensional units it becomes:

$$\Delta T_{turb}^{+b} = \frac{\Delta T_{turb}\, u_{\tau b}}{q_W / \rho_b\, c_b} \qquad \text{with} \quad u_{\tau b} = \sqrt{\frac{\tau_w}{\rho_b}} \quad . \tag{32}$$

However, for the conducting sub-layer the wall quantities are representative:

$$\Delta T_{cs}^{+} = \frac{\Delta T_{cs}\, u_{\tau w}}{q_W / \rho_w\, c_w} \qquad \text{with} \quad u_{\tau w} = \sqrt{\frac{\tau_w}{\rho_w}} \quad . \tag{33}$$

Both relations (32, 33) are based on the same wall shear stress. The non-dimensional temperature increase across the turbulent layer is

$$\Delta T_{turb}^{+b} = \int_{y_{cs}^{+}}^{R^{+}} \frac{\mathrm{Pr}_T}{\kappa \cdot y^{+b}}\, dy^{+} = \frac{\mathrm{Pr}_T}{\kappa}\left(\ln R^{+b} - \ln y_{cs}^{+b}\right) \quad . \tag{34}$$

Under the assumption that $y_{cs}^{+} \approx y_{vs}^{+}$ (the deviation is small) this expression does not depend on the fluid properties and can be used for variable properties. The non-dimensional temperature increase across the conduction sub-layer is

$$\Delta T_{cs}^{+w} = \int_{0}^{y_{cs}^{+w}} \mathrm{Pr}\, dy^{+} \approx \mathrm{Pr}_w\, y_{cs}^{+w} = \mathrm{Pr}_w^{2/3}\, y_{vs}^{+w} \quad . \tag{35}$$

The temperature at the edge of the conducting sub-layer is denoted with T_{cs}. It depends on the fluid properties, because the Prandtl number *Pr* is a function of the temperature and the edge of the conduction sub-layer depends on *Pr*. A modification of this approach to make it agree better to experiments is discussed below.

3.3 Comparison to the One-Dimensional Theory [1]

Fully coupled calculations (with ε =2.5 μm as in [1]), including the calculation of the wall temperature, were made for the parameters of the Yamagata experiment (see inset of figure 5) and compared to the theoretical data of [1], because for the wall shear stress no experimental data are available. The agreement is poor (not shown).

However, with the modification of eq. (30) by

$$\tau_w = \frac{c_f}{8}\, \rho_b u_m^2 \left(\frac{\mu_b}{\mu_w}\right)^{0.9} \tag{36}$$

By this correction factor the agreement is improved, see figure 5. The factor is necessary, because the viscosity at the wall, used in eq. (28) to determine the wall Reynolds number, does not physically represent the viscosity over the entire viscous sub-layer. It only represents its minimum value, corresponding to the highest temperature within this sub-layer.

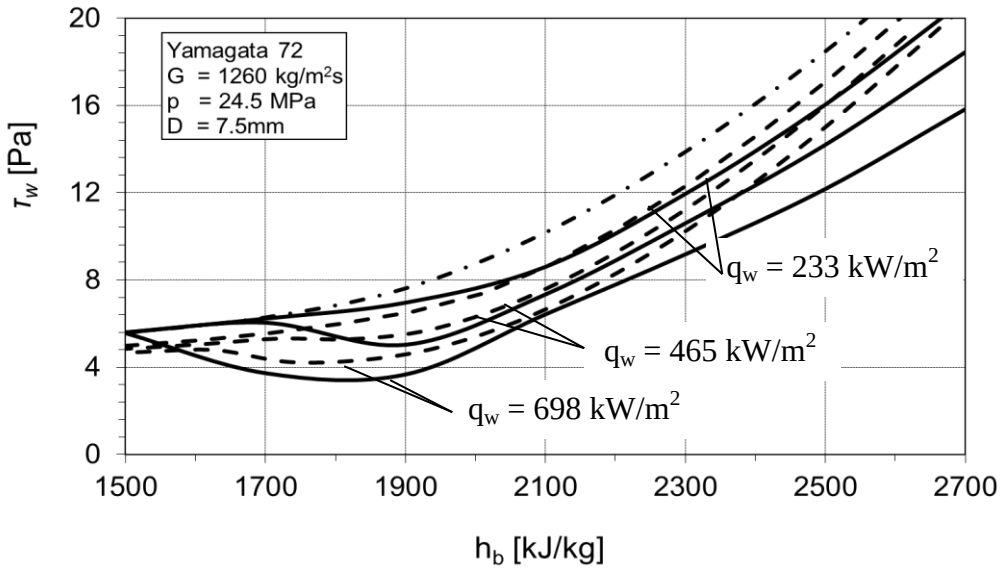

Figure 5: Wall shear stress using eq. (36) for the experimental parameters of [2]. dotdashed line: constant properties (no heating), full lines: present work, dashed lines: results from [1] for the same q_w

4. Comparison to Experiments

Test calculations were made to compare the predictions of eq. (35) and (36) with the wall temperature measurements [2]. The agreement is poor. This is mainly to the fact, that a single temperature (the wall temperature) cannot represent the behaviour of the flow in the viscous/conducting sub-layer, because the temperature and all fluid properties undergo drastic changes across this layer. Eq.(39) is modified with the ratio of the heat conductivity for bulk (index b) and wall (index w) temperature with an exponent:

$$\Delta T_{cs}^{+w} = \mathrm{Pr}_w^{2/3}\, y_{vs}^{+w} \left(\frac{\lambda_b}{\lambda_{cs}} \right)^{0.6} \tag{37}$$

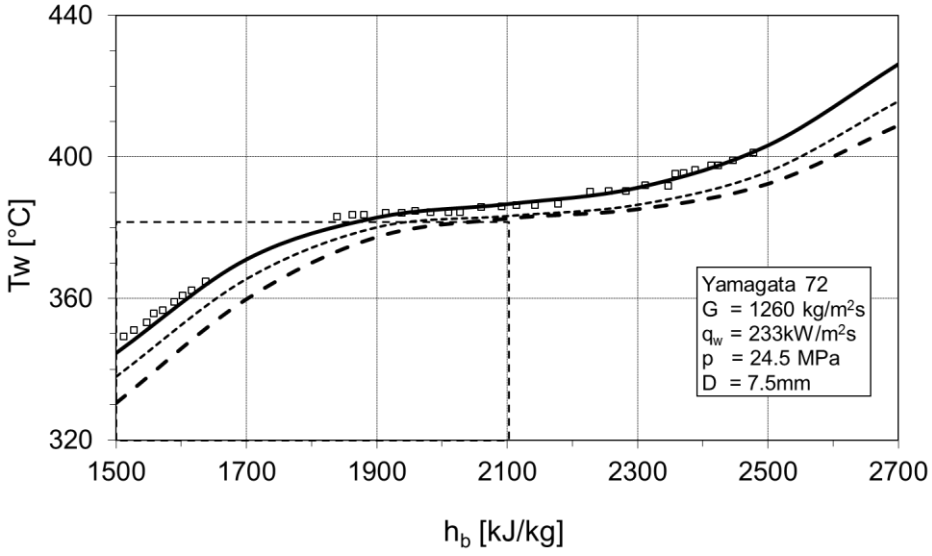

Figure 6: Symbols: T_w of the experiments [2], large dashes: bulk temperature, small dashes: T_{cs}, full line T_w of the present work, q_w = 233 kW/m2

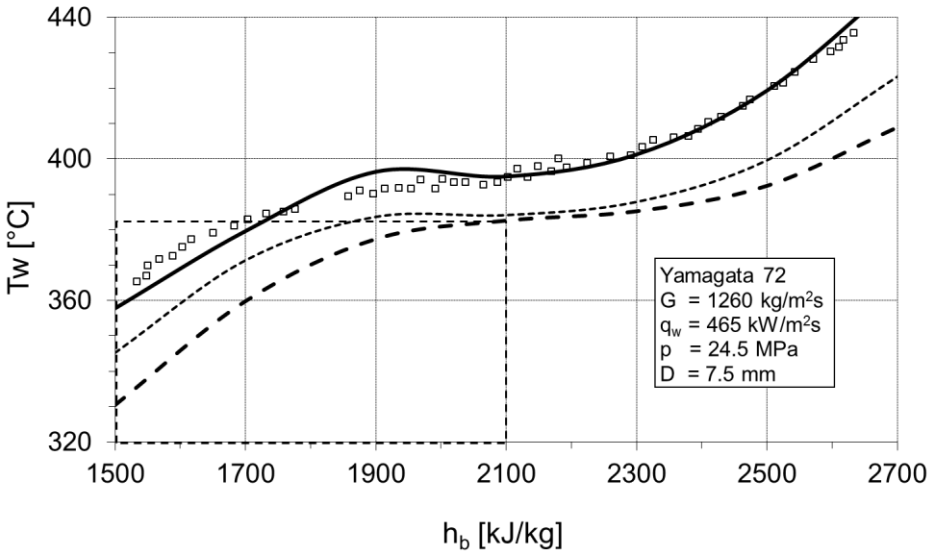

Figure 7: Symbols: T_w of the experiments [2], large dashes: bulk temperature, small dashes: T_{cs}, full line T_w of the present work, q_w = 465 kW/m2

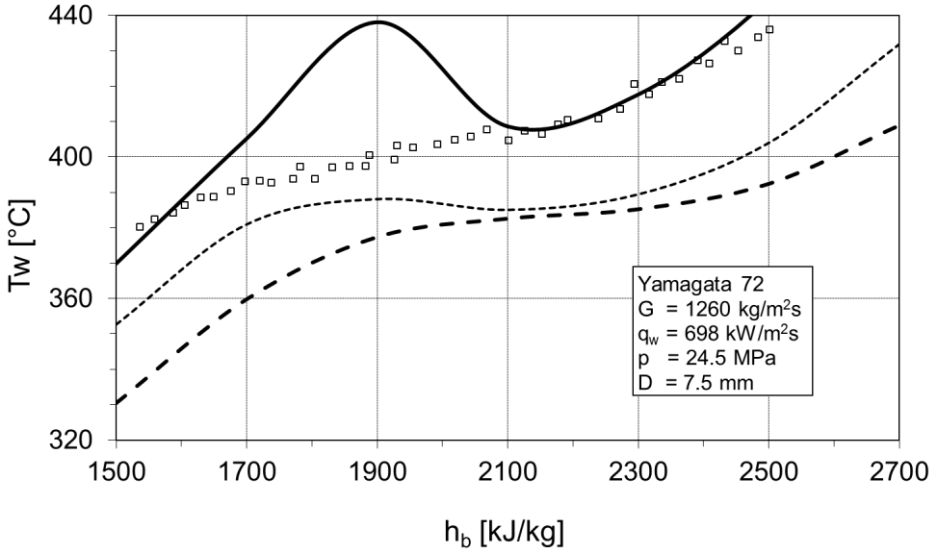

Figure 8: Symbols: T_w of the experiments [2], large dashes: bulk temperature, small dashes: T_{cs}, full line T_w of the present work, q_w = 698 kW/m2

The two cases in figures 6 and 7 are well approximated. The high heat transfer case of figure 8, however, our results exhibit a heat transfer deterioration, which is not observed in the experimental data [2]. Also, deterioration did not occur in [1] for this case. The present deterioration is due to the temperature increase within the conduction sub-layer. It is closely related to the drop in the wall shear stress in the respective temperature range depicted in figure 5, but this effect is predicted as larger than in the experiments. Further adjustment of the correction factors is necessary.

We are aware, that this method of using correction factors does not lead to a universal prediction. The method is applied here only as a first attempt of a generalization of the two-layer theory. Models can only be improved based on a better understanding of the flow physics of the deterioration process.

5. Conclusion

The two-layer theory has been employed to derive a system of model equations for the wall shear stress and the wall temperature of heated pipe flow with a rough wall. For variable properties this system is implicit and must be solved by iteration. The flow in the pipe is represented by two layers, the laminar sub-layer and the turbulent wall layer, each represented by a single temperature (wall and bulk). A distinction between a 'viscous' laminar sub-layer for the velocity and a 'conducting' laminar sub-layer for the temperature is made. It appears, however, that this representation is not sufficient for high heating rates when within the conducting sub-layer a drastic temperature drop exists, resulting in a poor agreement to experiments (not shown). The agreement is improved by introduction of correction factors, which account for this near-wall property variation. These factors, however, may not be universal, because they are not based on the physical understanding on the flow.

The two-layer model provides a suitable basis for further development, because it is able to include wall roughness.

References

1. E. LAURIEN: Semi-Analytic Prediction of Hydraulic Resistance and Heat Transfer for Pipe Flows of Water at Supercritical Pressure, Proc. Int. Conf. Advances on Nuclear Power Plants, ICAPP'12, Chicago, USA, June 24-28, 2012

2. K. YAMAGATA, K. NISHIKAWA, S. HASEGAWA, I. FUJII, and S. YOSHIDA: Forced Convective Heat Transfer to Supercritical Water Flowing in Tubes: Int. J. Heat Mass Transfer 15, 2575-2593 (1972)

3. T. SCHULENBERG, J. STARFLINGER, P. MARSAULT, D. BITTERMANN, C, MARACZY, E. LAURIEN, J.A. LYCKLAMA a NIEJEHOLT, H. ANGLART, M. ANDRE-ANI, M. RUZICKOWA, and A. TOIVONEN: European supercritical water cooled reactor, Nuclear Engineering and Design 241, 3505-3513 (2011)

4. I.L. PIORO, H.F. KHARTABIL and R.B. DUFFEY: Heat Transfer to Supercritical Fluids flowing in Channels - Empirical Correlations (Survey), Nuclear Engineering and Design 230, 2006, 69-91

5. J. A. LYCKLAMA A NIJEHOLT, D.C. VISSER, E. LAURIEN, H. ANGLART, and L. CHANDRA: Development of a Heat Transfer Correlation for the HPLWR Fuel Assembly my means of CFD Analyses, 5th Int. Symp. SCWR (ISSCWR-4) Vancouver, CA, March 13-16, 2011

6. M. F. LÖWENBERG, E. LAURIEN, A. CLASS, and T. SCHULENBERG: Supercritical water heat transfer in vertical tubes: a look-up table, Progress in Nuclear Energy 50, 532-538 (2008)

7. H. ZAHLAN, D.C. GROENEVELD and S. TAVOULARIS: Derivation of a look-up table for trans-critical heat transfer for water-cooled tubes, Proc. Nureth-14, Sept. 25-30, 2011, Toronto, Canada

8. E. LAURIEN, Prediction of Hydraulic Resistance and Heat Transfer of Super-Critical Watar Pipe Flows with Wall Roughness, Workshop on Heat Transfer at Supercritical Pressure in Nuclear Reactors and Solar Energy Systems, Manchester, UK, June 30 – July 1st, 2014

9. S. HE, W.S. KIM, and J.H. BAE: Assessment of Performance of Turbulence Models in Predicting Supercritical Pressure Heat Transfer in Vertical Tube, Int. J. Heat Mass Transfer 51, 4659 – 4675 (2008)

10. Y. ZHU: Numerical Investigation of the Flow and Heat Transfer within the Core Cooling Channel of a Supercritical Water Reactor, Dissertation University of Stuttgart, IKE-8-122 (2010)

11. A. KISS, E. LAURIEN, A. ASZODI, and Y. ZHU: Numerical Simulation on a HPLWR Fuel Assembly Flow with One Revolution of Wrapped Wire Spacers, Kerntechnik 75, p. 148-157 (2010)

12. W. KAYS, M. CRAWFORD, and B. WEIGAND: Convective Heat and Mass Transfer, McGraw-Hill, New York, International Edition 2005

13. H. D. BEHR and K. STEPHAN: Heat and Mass Transfer, Springer, Berlin, Heidelberg (1998)

14. B.S. PETUKHOV: Heat Transfer and Friction in Turbulent Pipe Flow with Variable properties, Advances in Heat Transfer 6, 1970, 503-563

15. C.F. COLEBROOK: Turbulent Flow in Pipes with particular reference to the transition region between smooth and rough pipe Larws, 1939

16. L.F. MOODY and L.J. PRINCETON: Friction Factors for Pipe Flows, Transactions of the ASME (1944), 671-684

17. I.N. BRONSTEIN und K.A. SEMENDJAJEW: Taschenbuch der Mathematik, 25. Auflage, Teubner, Stuttgart, Leipzig, 1991

18. B.A. KADER: Temperature and Concentration Profiles in Fully Turbulent Boundary Layers, Int. J. Heat and Mass Transfer 24, 1541-1544 (1981)

19. A. AVCI and I. KARAGOZ: A Novel Explicit Equation for Friction Factor for Smooth and Rough Pipes, Journal of Fluid Engineering 131, 061203 (2009)

ISSCWR7-2005

SCC tests in SCW at 550°C on two heats of 316L

Aki Toivonen[1], Sami Penttilä[1] and Radek Novotny[2]
[1]VTT Technical Research Centre of Finland
Kemistintie 3, Espoo, Finland
Telephone +358 505941587, Email aki.toivonen@vtt.fi
[2]Joint Research Centre, Institute for Energy and Transport
Westerduinveg 3, 1755LE Petten, Netherlands

Abstract

A number of SSRT tests were performed in order to determine best behaving stainless steel for fuel cladding for supercritical water at 550°C with regards to SCC resistance. The materials were limited to austenitic stainless steels which have a code case for reactor internal applications and have a relatively good general corrosion resistance in supercritical water below 550°C. The initial results indicated that SS 316L has good enough SCC resistance, but further tests on another heat of 316L showed adverse results. The former heat showed no SCC whereas the latter heat showed very high SCC susceptibility in as-received (mill-annealed) condition, shot peened condition and in as-received condition with a TIG weld in the middle of the gauge section of the SSRT specimen. Further electrochemical testing of the degree of sensitisation revealed that the heat giving good enough SCC resistance in SSRT test was also partially sensitised.

1. Introduction

SCWR has been considered as an option for future light water reactors by the Generation IV International Forum (GIF). In an SCWR, a direct once through steam cycle where neither steam generators nor steam separators and dryers are required. Steam turbines and re-heaters could also be smaller than in present reactors generating the same net electricity. This could be achieved through higher steam enthalpy in an SCWR than in conventional LWRs [1].

A European SCWR called HPLWR (High Performance Light Water Reactor) was designed within Euratom funded projects HPLWR (2000-2002) and HPLWR Phase 2 (2006-2010). With regards to construction materials, fuel cladding was recognised to remain a problem. No materials that would simultaneously have a code case for in-core applications and clearly fulfil the needed general corrosion and stress corrosion resistances, creep strength, mechanical properties at 550-650°C and have low enough neutron capture cross-section were available. Candidate materials that are close to fulfil the above mentioned properties are some austenitic stainless steels. The best Zr-alloys used in present day reactors are limited to lower temperatures due to fast oxidation. Some experimental zirconium alloys, e.g. Zr-Fe-Cr, have shown better oxidation resistance and are better than F/M steels but worse than austenitic stainless steels at 500°C [1-2]. On the other hand, the core outlet temperature in HPLWR is 500°C and the peak cladding temperature 630°C [1]. The estimated cladding temperature is too high for the Zr-alloys and F/M steels. A possible approach to overcome the cladding temperature problem is that the HPLWR could be developed in steps from lower temperature to

the envisaged core outlet temperature of 500°C. This would decrease also the peak cladding temperature to 500-550°C.

As the next step, it has been proposed to carry out a fuel qualification test of a small scale fuel assembly in a research reactor under typical prototype conditions. Design and licensing of an experimental facility for the fuel qualification test, including the small scale fuel assembly, the required coolant loop with supercritical water and safety and auxiliary systems, is the scope of the project "Supercritical Water Reactor - Fuel Qualification Test" (SCWR-FQT) [3].

Within the SCWR-FQT project, material tests have been performed at temperatures of 500°C and 550°C. General corrosion and stress corrosion specimens have been exposed in pure supercritical water with low oxygen content (150 ppb) and high oxygen content (2000 ppb). High oxygen content has shown a negative impact on general corrosion performance of the materials but no significant effect of oxygen levels on the stress corrosion susceptibility was observed. Based on the results of general corrosion tests as well as SSRT (Slow Strain Rate Test), stainless steel 316L was chosen as the fuel cladding material for the planned fuel qualification test. The maximum reasonable duration of the test is foreseen to be around 6 months [3].

As only material from one heat of cross rolled type 316L steel plate was studied in the initial phase of the SCWR-FQT project, supplementary tests were performed on specimens prepared from 316 L stainless steel tube that has its dimensions close to the dimensions of the foreseen fuel cladding. The tube outside diameter is 5/16" (~7.94 mm) and wall thickness 0.020" (~0.51 mm). The purpose of the supplementary tests was to verify that the manufacturing process (tube vs. plate) does not influence the SCC susceptibility.

2. Experimental

2.1 Test material and specimens

The test materials were 316L plate supplied by Solomon's Metalen B.V. and 316L tube supplied by Tokio Seimitsukan Co. Ltd. The plate was (cross-) rolled and annealed and the tube was cold drawn, annealed and pickled. The chemical compositions are shown in table 1. The grain sizes in both of the heats are in the range of 40-50 µm (~ASTM # 6).

Table 1. Chemical compositions of the two studied 316L heats.

	C	Si	Mn	P	S	Ni	Cr	Mo
Plate	0.022	0.65	1.86	0.03	0.001	10.12	16.6	2.06
Tube	0.024	0.45	1.26	0.033	0.001	12.06	16.3	2.06

The specimens were flat tensile type SSRT specimen. Two specimens were prepared from the 316L plate and six from the tube. The specimens were polished with #600 emery paper after cutting. Two of the tube specimens were cut from a tube that had a circumferential TIG weld in it. 316L filler metal was used for the TIG weld. Two of the four specimens cut from the tube without the weld remained in the mill-annealed condition and two specimens were shot peened prior to the tests in SCW. The specimen geometries and cutting plans are shown in Figure 1.

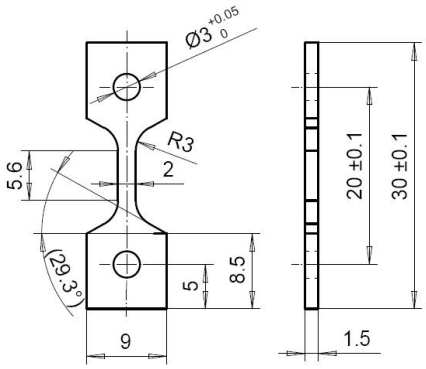

a)

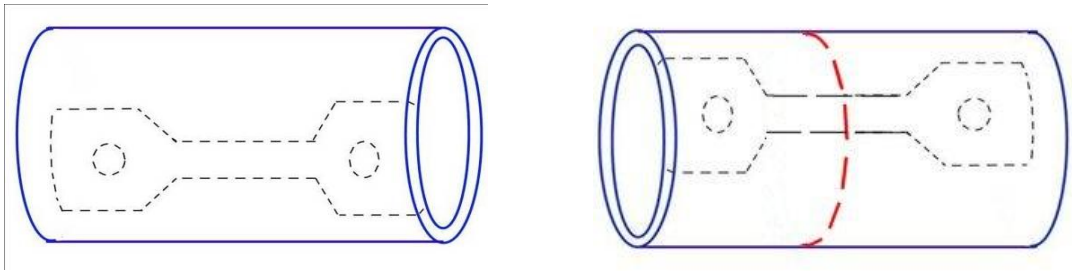

b)

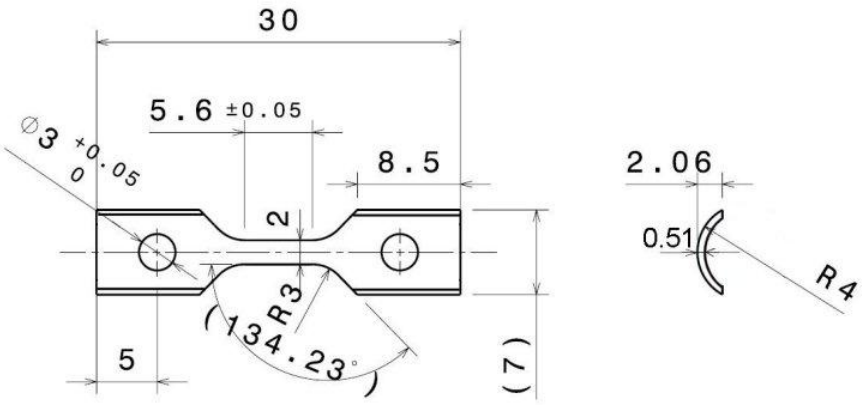

c)

Figure 1. Dimensions of the 316L plate specimens a), cutting scheme of the as-received and welded tube specimens b) (red dashed line indicates the location of the TIG weld in the tube) and dimensions and shape of the 316L tube specimen c).

2.2 Test procedures and environment

The specimens were loaded with a nominal strain rate of 1e-7 1/s until failure. The tests were performed in SCW at 550°C/250 bar with 125 ppb O_2 and in air at 550°C at ~1 bar overpressure.

After the SSRT experiments, the samples were examined using an SEM in order to characterize the cracking mode on the fracture and the gauge surfaces. Double Loop EPR (Electrochemical Potentiokinetic Reactivation) tests according to EN ISO 12732 [4] were performed in order to determine level of thermal sensitisation.

.

2.3 Test loop and autoclave

The specimens were exposed to high temperature water in a supercritical autoclave, which was connected to a recirculation water loop, Figure 2.

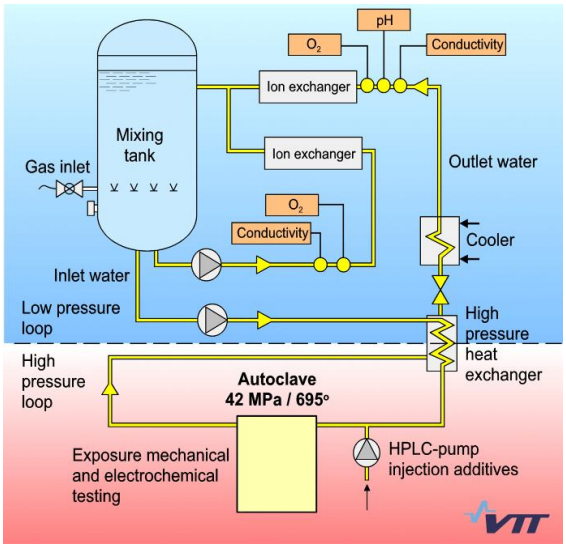

Figure 2. A schematic presentation of the SCW testing system at VTT.

The system consists of low and high pressure water recirculation loops in addition to the materials testing autoclave. The high pressure loop consists of a high pressure pump, a heat exchanger and a pre-heater. The water returning from the autoclave flows through the heat exchanger and a cooler. The maximum working temperature and pressure of the system is 700°C and 42 MPa, respectively. The high pressure loop is pressurised using a diaphragm pump and a back pressure regulator. The maximum flow rate of the high pressure loop is about 85 ml/min. The used flow rate was ~5 ml/min. The applied flow rate was limited by the high test temperatures together with the heating capacities of the autoclave and the pre-heater. The main construction material of the loop is 316L and the autoclave is mainly constructed of Nimonic 80A. Specimens were loaded in the autoclave using stepper motor controlled materials testing device.

3. Results and discussion

The SSRT stress vs. strain curves measured in air on the thin walled tube and the plate materials are shown in Figure 3. The yield strengths of the as-received and the welded tube material are in the same range as that of the plate material. However, the elongations to failure are larger and also the tensile strengths. No notable differences can be seen between the as-received and the welded tube specimens.

Yield and tensile strengths of the shot-peened tube specimen are much higher than those of the other specimens. Also, the elongation to failure has decreased to less than half of those of the other specimens. These changes follow from the strain hardening caused by the shot-peening process. The fracture surfaces of all specimens are fully ductile with related dimpled structure. The failure location of the welded tube specimen is in the middle of the TIG weld. The fracture surfaces of the tube specimens are shown in Figure 4.

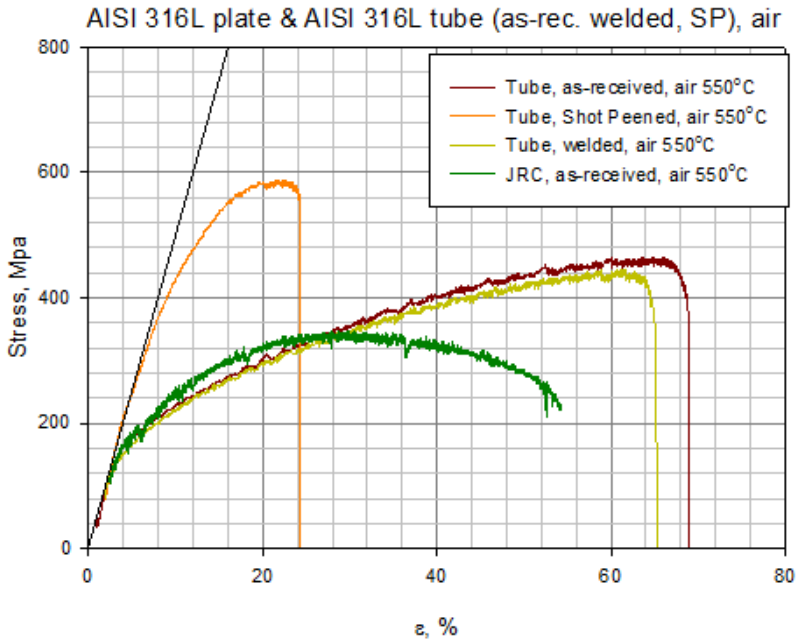

Figure 3. SSRT curves measured in air at 550°C on specimens cut from ~8*0.5 mm 316L tube in as-received (+polished), shot-peened, and welded conditions together with the SSRT curve of the specimen cut from the 316L plate (marked as JRC).

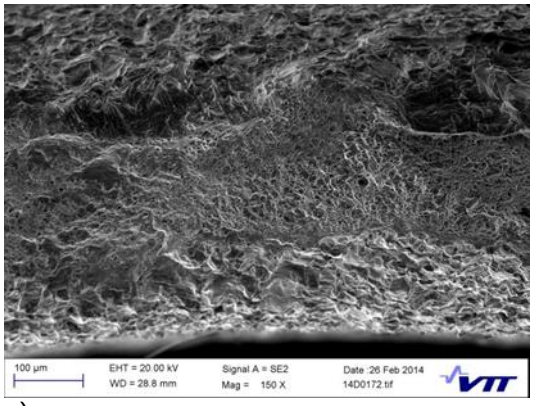

a)

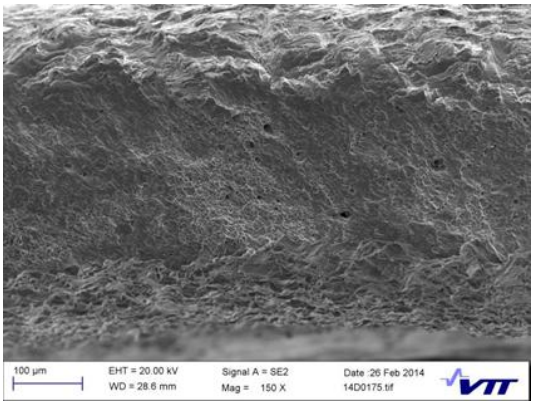

b)

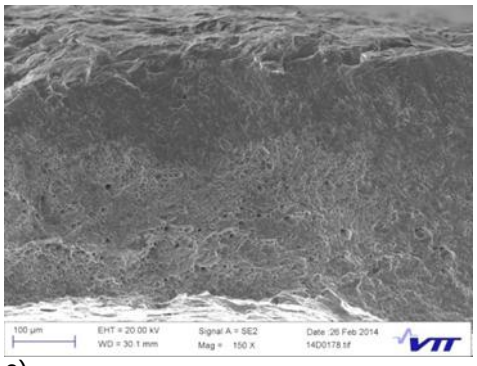

c)

Figure 4. Fully ductile fracture surfaces of specimens cut from the ~8*0.5 mm 316L tube after the SSRT test in air at 550°C. As-received specimen a), welded specimen (fracture in the middle of the weld) b) and shot peened specimen c).

A very notable decrease in mechanical performance caused by the environment can be seen in the maximum stresses and elongations to failure in all of the specimens cut from the ~8*0.5 mm tube. However, no notable change can be seen in the yield stress, maximum stress or elongation to failure in the case of the specimen cut from the plate, Figure 5. The decrease in the values of the tube specimens is related to the change in the failure mechanism: a considerable amount of intergranular cracking was seen on the fracture surfaces of the tube specimens, Figure 6. The fracture surface of the plate specimen after the test in SCW was ductile. Yield strengths (Rp1.0%), ultimate tensile strengths and strains to failure are shown in Table 2. Due to the high compliance of the loading train (thin and long pull rod, specimen attachment pins, etc.), the yield strength is a rough estimate and the strain to failure is the plastic component of the specimen gauge section strain, i.e. the values in Table 2 can not be taken as real tensile properties but as a rough means to compare the behaviour of the different material conditions.

It was expected that the two heats of mill-annealed 316L steel would behave in a similar manner in SSRT tests in SCW. Both heats have rather similar mechanical properties in air (except the specimen hardened by shot-peening), similar chemical compositions (slightly more Ni in the tube), similar grain sizes and are both annealed after cold drawing or cross rolling.

The Double Loop EPR test results give an indication of the underlying reasons for the different behaviour of the two heats (Table 3): the specimens exposed to SCW have Ir/Ip (catodic/anodic current peaks during the polarisation loop) ratios of 0.04 (plate) and 0.049 (tube). According to the standard EN ISO 12732, the ratios below 0.01 indicate that the material is not sensitised, 0.01-0.05 indicates it is slightly sensitised and >0.05 indicates that it is sensitised [4]. The Ir/Ip

ratio of the fresh tube is below 0.01. Cathodic current peak could not be distinguished from the polarisation curve. No fresh samples were available from the plate.

Although it seems that the critical degree of sensitization for intergranular cracking in the specific SSRT test/test environment combination is between the Ir/Ip ratios of 0.04 and 0.049, the reason for the different degree of sensitisation is not very clear. Although low carbon austenitic stainless steels are generally considered resistant to sensitisation, long exposures to high temperature can result in carbide growth/sensitisation in the grain boundaries in them. The sensitisation typically takes place faster the higher the carbon content. However, the carbon contents of the tested two heats are close to each other and the less sensitised heat was exposed to SCW at 550^{o}C for a considerably longer time (i.e. ~1500 h vs. ~500 h).

Several issues have been recognised to affect the sensitivity to intergranular stress corrosion cracking or degree of sensitisation (DOS). All of them are not linked to grain boundary carbide growth.

-Parvathavarthini et al. [6] propose that Grain boundary engineering in order to produce lower effective grain boundary energy (EGBE) lowers the tendency to sensitisation. EGBE is a combined factor of several aspects of the nature of the grain boundary.

-According to Parvathavarthini et al. [7], the limit of carbon content with which a steel is not susceptible to sensitization is closely connected to the presence of other alloying elements like chromium, molybdenum, nickel, nitrogen, manganese, boron, silicon as well as titanium and niobium in stabilized steels. Chromium has a pronounced effect on the passivation characteristics of stainless steel. With higher chromium contents, time to reach the resistance limit of chromium depletion at the grain boundaries is shifted to longer time. Alloys with higher chromium contents will be more resistant to sensitization.

-Oh et al. [8] report that their DL-EPR test results indicate that cold work (CW) levels up to 20% enhance sensitization while 40% CW suppresses sensitization at all aging times. Also, the increase in the nitrogen content at the similar carbon content accelerated the sensitization at CW levels below 20%.

-Deformation type during production (e.g. cross rolling of a plate vs. cold drawing of a tube) results in different microstructures. Nezakat et al. [9] report that rolling mode in their tests had a direct effect on the deformation texture of the remaining austenite. Unidirectional rolling resulted in Brass, Goss and γ-fibre textures, whereas cross-rolling formed mainly Brass texture in deformed austenite after 90% reduction in thickness.

-The effect of grain size on the intergranular corrosion susceptibility of 316L stainless steel was investigated by Li et al. [10]. Both DL-EPR tests and microstructure inspections of 316L with different grain sizes showed that the susceptibiltity to intergranular corrosion decreased with increasing grain size. Li et al. [10] suggest that increasing grain size to an optimum level could be an effective way to increase the intergranular corrosion resistance, but on the other hand, it is a big challenge to improve corrosion resistance without losing good mechanical properties resulting from small grain size.

-Terada et al. [11] reported DL-EPR test results of 316L(N) steel creep tested at the temperature of 600^{o}C for 7500 h and for 85000 h. The DL-EPR tests showed clear sensitisation to intergranular corrosion. However, they did not observe $M_{23}C_6$ carbides at grain boundaries. Instead, they attribute the sensitisation to intergranular corrosion to intermetallic phases (mainly sigma phase).

At the present stage, the underlying reason for the different behaviour of the two heats tested here is not clear. The microstructures of the steels in as-received (mill-annealed) conditions as

well as after the exposure to SCW should be studied more closely before any comparisons to the results of the above mentioned authors can be done. A closer look into the microstructures is planned.

Based on the fact that the mill-annealed tube was sensitised during the exposure, it is not surprising that the shot-peened specimen also failed by intergranular fracture. Shot-peening was performed in order to simultaneously increase the yield strength of the steel and also to decrease its oxidation rate which both would be beneficial to SCWR fuel cladding. The oxidation rate of austenitic stainless steels has been observed to decrease by surface cold work [12]. Cold work also increases the yield strength but at the same time increases the risk of SCC. In this case, the increased risk could not be distinguished due to the susceptibility already present in the mill-annealed (+exposure to SCW) condition.

The weld specimen failed in the middle of the weld. The fracture mechanism was intergranular/interdendritic. The strain to failure and also the yield and tensile strengths were very similar to those of the mill-annealed specimen, i.e. apparently the degree of sensitisation was similar as or higher than the degree of sensitisation in the base metal. Typically, in sensitised stainless steels, stress corrosion initiates and propagates in the heat affected zone (HAZ) of the weld due to thermal sensitisation resulting from the heat input of the welding process. Apparently the welding process did not result in excess sensitisation of the HAZ in this case.

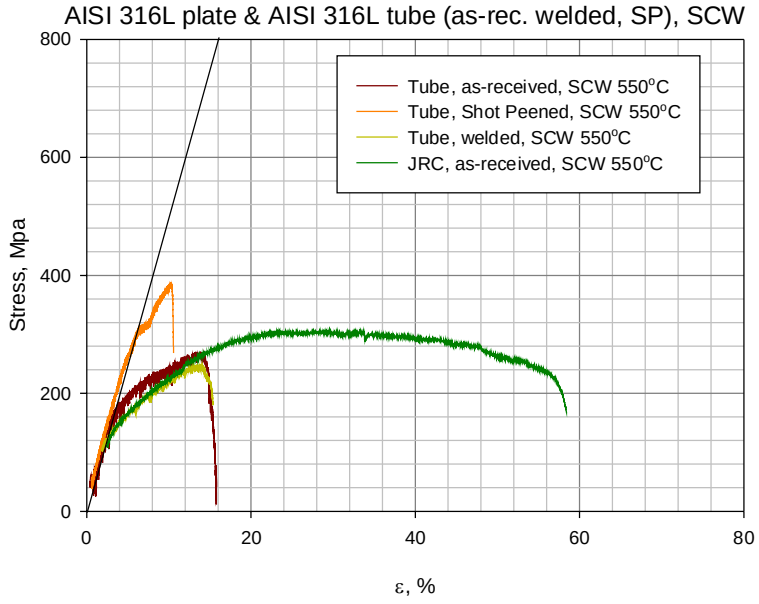

Figure 5. SSRT curves measured in SCW at 550°C on specimens cut from ~8*0.5 mm 316L tube in as-received (+polished), shot-peened, and welded conditions together with the SSRT curve of the specimen cut from the 316L plate.

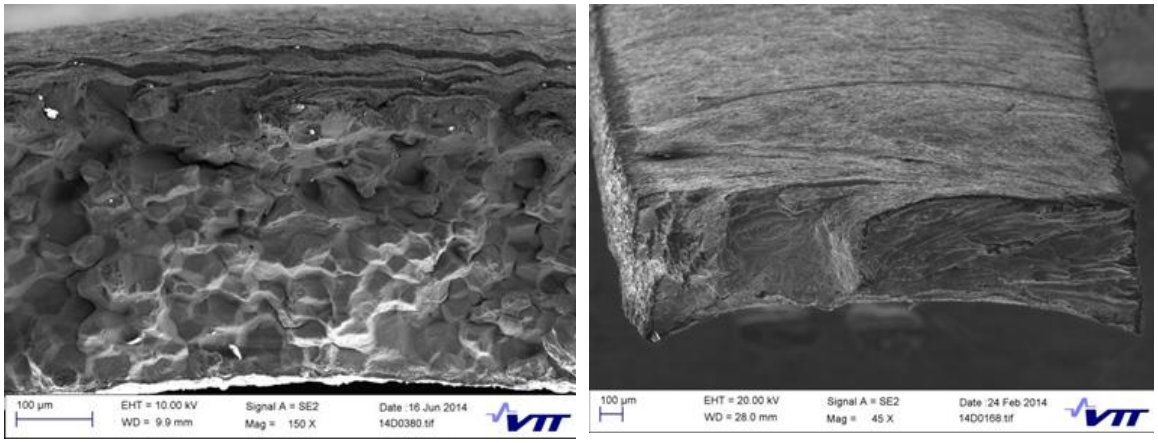

a) b)

Figure 6. Fracture surfaces of specimens cut from the ~8*0.5 mm 316L tube after the SSRT test in SCW at 550°C. As-received specimen a) has almost fully intergranular failure, and welded specimen (fracture in the middle of the weld) b) has mostly intergranular/interdendritic failure.

Table 2. Yield strengths (Rp1.0%), ultimate tensile strengths (Rm) and plastic strains to failure (Ap) of the two 316L heats.

Material	Environment	Rp1.0%, MPa	Rm, MPa	Ap, %	Fracture mode
Plate	Air	170	340	49	Ductile
Plate	SCW	155	300	55	Ductile
Tube, mill-annealed	Air	170	460	61	Ductile
Tube, mill-annealed	SCW	180	265	16	Intergranular
Tube, welded	Air	160	440	58	Ductile
Tube, welded	SCW	145	245	12	Intergranular/ interdendritic
Tube, shot-peened	Air	310	580	12	Ductile
Tube, shot-peened	SCW	305	380	5	Intergranular

Table 3. Double loop EPR test results of the two heats in mill-annealed condition before and/or after the exposure to SCW at 550°C.

Material	Ir, µ A	Ip, µ A	Ir/Ip
Plate, exposed	330	8200	0.040
Plate, ref	NA	NA	NA
Tube, exposed	490	10 000	0.049
Tube, ref	<100 *	10 300	<0.01

*No clear reactivation peak

4. Conclusions

At least some austenitic stainless steel 316L heats become sensitised at 550^{o}C in supercritical water in a very short time. A clear difference was observed in the rate of the sensitisation between two different heats although the underlying reasons for the different rates are not clear. Several factors affecting the sensitisation behaviour have been presented in literature. None of those factors can be directly attributed to the behaviour differences of the steels studied in this work, at least not without a closer look at the microstructures.

Precaution is needed if un-stabilised austenitic stainless steels like 316L are used at this temperature (550^{o}) even for rather short times. It's suggested that any 316L heat used as fuel cladding in SCW should be fully characterised and thermally aged (at the same temperature or above) and tested before it is accepted.

References

1. T. Schulenberg, J. Starflinger, P. Marsault, D. Bittermann, C. Maráczy, E. Laurien, J.A. Lycklama à Nijeholt, H. Anglart, M. Andreani, M. Ruzickova, A. Toivonen, Nuclear Engineering and Design 241 (2011) 3505–3513

2. C. Sun, R. Hui, W. Qu, S. Yick, Corrosion Science 51 (2009) 2508–2523

3. A.T. Motta, A. Yilmazbayhan, M.J. Gomes da Silva, R.J. Comstock, G.S. Was, J.T. Busby, E. Gartner, Q. Peng, Y.H. Jeong, J. Y. Park, Journal of Nuclear Materials 371 (2007) 61–75

4. M. Ruzickova, T. Schulenberg, D.C. Visser, R. Novotny, A. Kiss, C. Maraczy, A. Toivonen, Progress in Nuclear Energy 77 (2014) 381-389

5. Electrochemical potentiokinetic reactivation measurement using double loop method, EN ISO 12732, 2008

6. N. Parvathavarthini, S. Mulki, R.K. Dayal, I. Samajdar, K.V. Mani, B. Raj, Corrosion Science 51 (2009) 2144–2150

7. N. Parvathavarthini, R.K. Dayal, Journal of Nuclear Materials 305 (2002) 209–219

8. Y.J. Oh, J.H. Hong, Journal of Nuclear Materials 278 (2000) 242-250

9. M. Nezakat, H. Akhiani, M. Hoseini, J. Szpunar, Materials Characterization 98 (2014) 10–17

10. S-X. Li, Y-N. He, S-R. Yu, P-Y. Zhang, Corrosion Science 66 (2013) 211–216

11. M. Terada, D.M. Escriba, I. Costa, E. Materna-Morris, A.F. Padilha, Materials Characterization 59 (2008) 663–668

12. S. Penttilä, A. Toivonen, J. Li, W. Zheng, R. Novotny, Journal of Supercritical Fluids 81 (2013) 157–163

ISSCWR7-2006

Combined effect of irradiation and temperature on the mechanical strength of Inconel 800H and AISI 310 alloys for in-core components of a GEN-IV SCWR

Robert J. Klassen and Heygaan Rajakumar

Department of Mechanical and Materials Engineering,
University of Western Ontario
1151 Richmond Street
London, Ontario, Canada, N6A 3K7
Tel: 519-661-2111 extension 88323
Email: rjklasse@uwo.ca

Abstract

The Canadian Gen-IV SuperCritical Water Reactor (SCWR) concept has in-core components that will be exposed to very high levels of neutron flux and temperature. It is therefore important to understand the effect of concurrent irradiation hardening and thermal annealing on the mechanical properties of the materials used for these components. We present here the results of indentation hardness tests performed on two alloys, Inconel 800H and AISI 310, which are being considered as candidate high-temperature in-core materials for the Canadian Gen-IV SCWR. The alloys were irradiated with 8 MeV Fe^{4+} ions to invoke various levels of crystallographic damage, up to 15 displacements per atom (dpa), to simulate neutron irradiation damage. The ion irradiated samples were then subjected to isothermal annealing for various lengths of time at 400^{o}C and 500^{o}C to induce thermal recovery of the irradiation damage.

The indentation hardness of both alloys increased very rapidly, by 20 to 40%, with relatively small levels of ion irradiation corresponding to about 1 dpa and followed a power-law dependence upon dpa over the range of irradiation damage up to 15 dpa. The ion-irradiation hardening in both alloys recovered rapidly with annealing at 400^{o}C and 500^{o}C and the time t_c for complete recovery of the irradiation damage increased with dpa according and the same power-law function for $t_c(dpa)$ applied for both alloys.

Our findings suggest that in the case of high-temperature in-core applications typical of those being proposed for some in-core components in Canada's proposed Gen. IV SCWR, both AISI 310 and Inconel 800H alloys will undergo significant irradiation hardening as a result of low levels of neutron irradiation damage however this hardening effect will be concurrently negated by even more rapid thermal recovery of the irradiation damage due to the elevated in-core temperature.

1. Introduction

A primary challenge associated with the Canadian proposed Gen. IV pressure tube type SCWR is the selection of suitable alloys for the nuclear fuel cladding and pressure tube liner components [1-2]. The alloys must be capable of enduring high levels of neutron irradiation in supercritical water at temperature up to about 750^{o}C. Two alloys that are currently being studied for this application are AISI 310 and Inconel 800H. To date little is known of the effect of prolonged high-temperature neutron irradiation on the mechanical properties of these materials.

It is well known that neutron irradiation has a significant hardening effect on crystalline material and this is the result of the generation of neutron-induced crystal defects in the material [3]. The effect of neutron irradiation on the hardening of common nuclear materials, such as iron- and zirconium-based alloys, is now quite well characterized over the 250 to 350^{o}C temperature range typical of current water-cooled reactors. The rate of neutron irradiation hardening above this temperature will, presumably, be affected by faster rates of thermal recovery of the irradiation damage however this has yet to be quantified experimentally.

Studies of the effect of neutron irradiation hardening have traditionally been done by direct in-core exposure of test samples followed by mechanical testing in radiation shielded facilities. These tests are very time consuming and expensive. Recently there is increased use of high energy (E > 1MeV) self-similar ion irradiation to invoke irradiation hardening at a rate that is orders of magnitude faster than in-reactor neutron irradiation [4-8]. The depth of penetration of high energy heavy ions into a crystalline solids is only several micrometers; therefore, the use of ion irradiation to simulate neutron irradiation hardening must be accompanied with a nano-mechanical testing technique capable of sampling the hardness of this small region.

This paper reports some results from our study of the effect of high energy Fe^{4+} irradiation on the hardness of the AISI 310 and Inconel 800H alloys under temperature conditions of 400 and 500^{o}C. We approach this problem by: i) measuring the rate of increase in hardness as a function of ion irradiation damage, and then ii) measuring the rate of decrease of hardness due to thermal recovery of the ion-induced damage. To this end, we perform room temperature indentation hardness tests on both alloys exposed to various levels of Fe^{4+} irradiation and then expose these samples to isothermal heating, at 400 and 500^{o}C, for various lengths of time to measure the rate of recovery of the indentation hardness. This research is part of a larger study to assess the suitability of these alloys for use as high temperature fuel cladding and pressure tube liner material in the proposed Canadian Gen. IV pressure tube type SCWR.

2. Procedure

2.1 Test Material

The chemical composition of the AISI 310 and Inconel 800H alloys is given in Table 1. Polished surfaces, 12.7mm x 12.7mm, were prepared from each material by conventional mechanical grinding and polishing techniques. The final polishing step was performed with an aqueous suspension of 0.05 μm Al_2O_3 abrasive particles. The polished samples were then annealed for 20 minutes in a protective atmosphere at 1000^{o}C to remove residual cold-work from the grinding/polishing steps. The annealed samples were then lightly polished with the 0.05 μm Al_2O_3 suspension to remove any surface oxidation resulting from annealing. The etched microstructure of the alloys is shown in Figure 1 and consists of large equiaxed grains of 50 to 100 μm diameter.

2.2 Ion irradiation

The polished unetched samples were irradiated with 8.0 MeV Fe^{4+} ions at the Tandetron Ion Accelerator facility at the University of Western Ontario (http://www.isw.physics.uwo.ca/). The samples were masked such that different regions of the polished surface received different levels of ion dosage. The SRIM software (http://www.srim.org/) was used to calculate the ion penetration depth (Figure 2). The ion dosage necessary to invoke specific levels of irradiation damage, in units of displacements per atom (dpa), was calculated from the number of ion-induced atom displacements calculated by SRIM using the Kinchin-Pease model. Regions of the AISI 310 samples were exposed to ion dosage levels corresponding to 0.01 to 10 dpa while regions of the Inconel 800H samples were irradiated to levels from 0.10 to 15 dpa (Table 2).

2.3 Indentation hardness tests

Multiple indentation hardness tests were performed on each dpa region of the ion-irradiated samples. The tests were performed with a diamond Berkovich indenter at a constant ratio of indentation loading rate/load, $\dot{F}/F = 0.05$. Multiple partial unloadings were performed during each indentation test to allow determination of the indentation hardness at various indentation depths. The plastic indentation depth *h* was calculated using the Doerner-Nix equation [9]. The indentation hardness *H* was calculated as

$$H = \frac{F}{A(h)} \tag{1}$$

Where *A(h)* is a high-order polynomial shape function describing the dependence of the projected indentation contact area *A* upon the indentation depth *h*. The function *A(h)* was determined from calibration tests performed, during this study, by indentation of fused silica.

The indented ion-irradiated samples were then annealed at 400 and 500°C for various lengths of time from 1 to 100 minutes (Table 2). The annealing was performed in an electrical resistance tube furnace containing an argon atmosphere. The samples were removed from the furnace after each annealing time and multiple indentation hardness measurements were performed using the method described above. Approximately ten indentations, each containing nine partial unloading, were performed at each of the 86 test conditions shown in Table 2.

Table 1. Chemical composition, in weight percent, of the two alloys in this study.

	C	Al	Si	P	S	Ti	Cr	Mn	Fe	Ni	Cu	Mo
AISI 310	0.08	-	0.75	0.05	0.03	-	25.00	2.00	50.35	20.50	0.50	0.75
Inconel 800H	0.08	1.40	1.00	0.05	0.02	1.40	21.00	1.50	39.50	33.00	0.75	-

Table 2. Conditions of irradiation damage (dpa), annealing temperature, and annealing time at which indentation hardness tests were performed on the AISI 310 (●) and Inconel 800H (■) samples.

		400°C anneal (minutes)				500°C anneal (minutes)			
Irradiation damage (dpa)	**As-irradiated**	**1**	**2**	**10**	**100**	**1**	**10**	**50**	**100**
0	●, ■	●, ■	●, ■	●, ■	●, ■	●, ■	●, ■	●, ■	●, ■
0.01	●, ■					●, ■	●, ■	●, ■	●, ■
0.1	●, ■	●	●	●	●	●, ■	●, ■	●, ■	●, ■
0.5	●	●	●	●	●				
1	●, ■	●	●	●	●	●, ■	●, ■	●, ■	●, ■
2	●	●	●	●	●				
4	●	●	●	●	●				
8	●	●	●	●	●				
10	●, ■					●, ■	●, ■	●, ■	●, ■
15	■	■	■	■	■				

Figure 1. Micrographs of the etched surfaces of the AISI 310 (left) and the Inconel 800H (right).

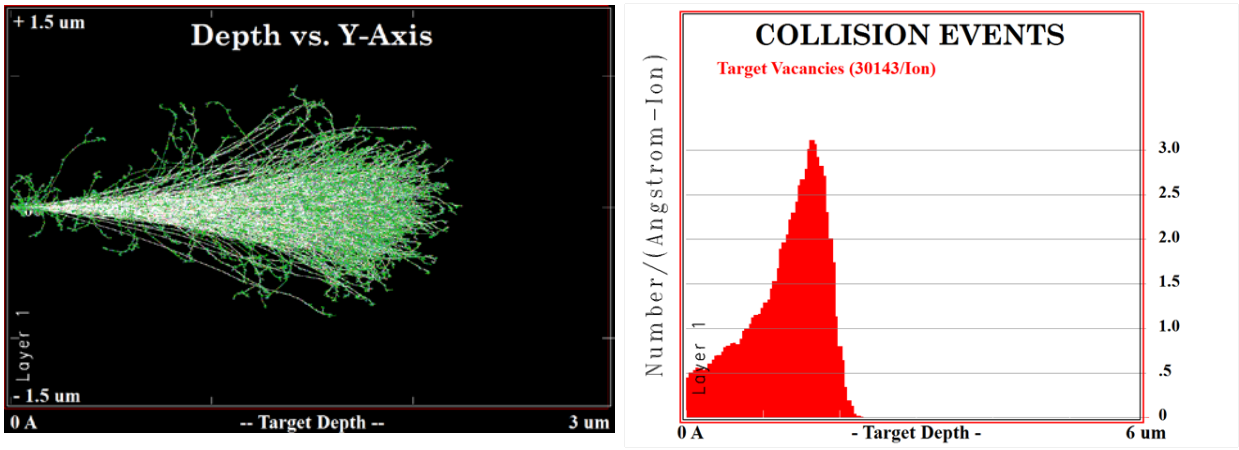

Figure 2. SRIM simulation of the penetration of 8.0 MeV Fe^{4+} ions into the AISI 310 alloy: (a) The simulated ion trajectories. (b) The calculated number of ion/atom collisions per Angstrom travelled by the ion as a function of penetration depth. The maximum ion irradiation damage occurs at a depth between 1 and 2μm.

3. Results and Discussion

3.1 Effect of ion irradiation on the indentation hardness

Figure 3 shows indentation force versus depth curves for the AISI 310 alloy in the non-irradiated and the ion-irradiated (8 dpa) conditions. The material clearly becomes hardened as a result of ion irradiation. The hardness of both the AISI 310 and Inconel 800H alloys displayed an indentation depth effect with higher hardness when the indentation depth was small (Figure 4). This is consistent with the well known indentation depth dependence of hardness that is generally observed for ductile materials and reflects the increased "geometrically necessary" dislocation density in the plastic zone around the shallow indentations of depth less than about 1 μm [10].

Although the ion irradiated material displayed higher hardness than the non-irradiated material at all indentation depths, the increase in hardness was greatest for indentations of depth less than about 500 nm (Figure 4). This is likely due to the geometry of the test system as shown in Figure 5. Since the hardness reflects the average stress necessary to invoke plastic strain in a finite volume beneath the indenter, only indentations of depth less than that in which the plastic zone does not extend significantly beyond the ion penetration depth will reflect the true effect of irradiation damage on the hardness.

Johnson proposed the following equation for the radius *c* of a hemi-spherical plastic zone beneath a conical indenter of flank angle β and width *a* (Figure 5)

$$\frac{c}{a}=\left[\frac{E^{*}\tan\beta}{6\sigma_{y}(1-\upsilon)}+\frac{2}{3}\left(\frac{1-2\upsilon}{1-\upsilon}\right)\right]^{\frac{1}{3}} \tag{2}$$

where σ_y is the flow stress and ν is the Poisson's ratio of the indented material while E* is the reduced elastic modulus of the indenter/substrate system [11]. Substituting into this equation values representative of our test material and indenter: β = 20°, ν = 0.36, E* = 184GPa, and $\sigma_{y(irradiated)} \approx H_{irradiated}/3$ [12] where $H_{irrad.} \approx$ 4.0GPa we find that radius *c* of the plastic zone is about 1.15, 2.31, and 4.61μm for indentation depths *h* of 100, 200, and 400nm respectively. This relation, *c = 11.5h*, is very close to the *c = 12h* calculated, using elastic-plastic finite element analyses, for pyramidal indentations of the same geometry as that used in this study [13, 14]. Since the calculated depth of the ion-irradiation hardening in our study is slightly more than 2 μm, and based upon the analysis above, we will assess the effect of ion-irradiation on the hardness by considering the hardness data from indentation depths of 200 and 400nm.

The average non-irradiated indentation hardness, at depths of 200 and 400nm, was 3.6 and 3.1GPa for the AISI 310 and 4.1 and 3.7GPa for the Inconel 800H alloys. Figure 6 shows the effect of increasing Fe^{4+} ion irradiation damage, in units of dpa, on the average hardness of both alloys. The average indentation hardness was determined from multiple, about ten, indentations at each indentation depth, 200nm and 400nm, and each dpa level. The scatter in the data in Figure 6 indicates the variability in the hardness arising primarily as a result of surface roughness.

The following power-law functions for hardness *H*, in units of GPa, were obtained by fitting to the data in Figure 6(a) for the 200nm indentations.

$$H_{200nm\,\mathrm{AISI\,310}}=3.6+1.6(dpa)^{0.09} \tag{3}$$

$$H_{200nm\,\mathrm{Inconel\,800H}}=4.1+2.5(dpa)^{0.02} \tag{4}$$

One can see that the two alloys show very similar irradiation hardening characteristics with rapidly increasing hardness after small amounts of irradiation damage such that *H* increases by 20 to 40% after about 1.0 dpa of irradiation damage. These hardness values, and the extent of irradiation hardening at low dpa levels, are very consistent with previously reported findings for the ion irradiated AISI 316 alloy [15].

3.2 Effect of annealing on recovery of ion irradiation hardening

Figure 7 indicates how the average room-temperature indentation hardness *H*, for 200nm deep indentations, decreases as a function of annealing time, *t*, at 400°C. The hardness displays a logarithmic dependence upon annealing time. Curves of $H = H_{0dpa} + At^n$ were fit to the data for each dpa level and these equations were used to determine the time t_c required for complete recovery of the irradiation damage, i.e. the annealing time needed for H = H_{0dpa}.

Figure 8 depicts a logarithmic plot of t_c versus dpa for data obtained from tests performed, primarily at annealing temperature of 400°C followed by room temperature indentation, of 200nm and 400nm depth, on the AISI 310 and the Inconel 800H alloys. Linear regression analysis of the data indicate the following functional relationship between t_c (minutes) and irradiation damage (dpa)

$$t_c=574(dpa)^{1.26} \tag{4}$$

The data suggest that the rate of thermal recovery of ion-induced crystallographic damage follows a single trend for both alloys and both indentation depths.

Included in Figure 8 are data from 400nm depth hardness tests performed on the AISI 310 alloy at 500°C. These data lie on the same trend as the 400°C data indicating that the rate of irradiation damage recovery is not significantly greater, within the precision limits of our measurement techniques, at 500°C than at 400°C.

The time for complete recovery of irradiation damage at 400°C and 500°C is quite short for these alloy. For example, Equation (4) predicts that 1dpa of irradiation damage, which is in the order of magnitude of the annual accumulated irradiation damage of in-core components such as fuel cladding, is recovered in about 10 hours at 400°C or 500°C.

It should be noted that we observed some oxidation on the surfaces of both alloys when annealed at 500°C and this affected the 200nm depth hardness measurements. The amount of oxidation was greater on the Inconel 800H than on the AISI 310 alloy and, in both materials, the heavily ion irradiated regions displayed less oxidation than the non-irradiated regions. The effect of ion irradiation on the oxidation rate of these alloys is currently being investigated.

Conclusions

In this study we performed 8.0 Mev Fe^{4+} ion irradiation, to damage levels up to 15 dpa, followed by isothermal annealing at 400°C and 500°C to assess for the AISI 310 and Inconel 800H alloys: i) the dependence of indentation hardness upon ion irradiation induced crystal damage and ii) the thermal recovery rate of the irradiation damage.

The average indentation hardness of both alloys increased very rapidly, by about 20 to 40%, with relatively small levels of ion irradiation corresponding to about 1 dpa. Our measured average hardness of the non-irradiated and the ion-irradiated material is similar, both in magnitude and dependence upon irradiation damage, to what was previously reported for similar alloys [15]. Similar power-law functions of H(dpa) were determined for both alloys indicating that their hardness displayed similar dependence upon irradiation damage.

We observed that the ion-irradiation hardening in both alloys recovered rapidly with annealing at 400°C and 500°C. Differences in the rate of recovery with annealing temperature from 400°C to 500°C could not be detected. The time t_c for complete recovery of the irradiation damage was found to increase with the level of dpa and a power-law function of t_c(dpa) was obtained that predicted t_c for both alloys at 400°C and for AISI 310 alloy at 500°C.

Our findings suggest that in the case of high-temperature in-core applications typical of those being proposed for fuel cladding and pressure tube liners in Canada's Gen-IV SCWR, both AISI 310 and Inconel 800H alloys will undergo at least 20% increase in hardness as a result of low levels of neutron irradiation damage typical of what could be expected within one year in core. This increase will however be negated by very rapid concurrent thermal recovery. Our data suggest that the recovery rate is sufficiently rapid that no net irradiation hardening will occur. We are currently continuing our studies to more accurately quantify the rates of irradiation hardening and thermal recovery in these alloys.

An important other factor that will affect the actual rate of irradiation hardening and thermal recovery in these alloys is the rate of hardening resulting from accumulated hydrogen and helium transmutation products. We are currently expanding our study to implant samples of AISI 310 and Inconel 800H with various levels of helium to assess the resulting hardening and the rate at which the He-induced hardening recovers, if at all, with isothermal annealing.

In our study we observed some oxidation on the surfaces of both alloys when annealed at 500°C. The amount of surface oxidation was greater on the Inconel 800H than on the AISI 310 and, in both materials, the heavily ion irradiated regions displayed less oxidation than the non-irradiated regions. This effect is currently being investigated further.

Acknowledgements

The authors wish to acknowledge the financial support for this research from the Canadian federal government through a Collaborative Research and Development grant involving two departments: the Natural Science and Engineering Research Council (NSERC) and the Natural Resources Canada (NRCan). The technical assistance of Mr. Jack Hendriks at the Tandetron Ion Accelerator facilities at the University of Western Ontario (London, Ontario, Canada) is also gratefully acknowledged. We wish to thank Ms. Maisaa Tawfeeq for providing the optical micrograph of the Inconel 800H alloy (Fig. 6). Finally, the many helpful discussions concerning the findings of this study with members of the Canadian Gen. IV Materials Research group, coordinated by Dr. David Guzonas, are also gratefully acknowledged.

References

1. H.F. Khartabil, R.B. Duffey, N. Spinks, W. Diamond; “The pressure-tube concept of Generation IV supercritical water-cooled reactor (SCWR): overview and status”, proceedings of ICAPP ’05, Seoul, Korea, May 15-19, 2005, Paper 5564.
2. U.S. DOE Nuclear Energy Research Advisory Committee and the Generation IV International Forum; “A Technology Roadmap for Generation IV Nuclear Energy Systems” GIF-002-00, December 2002.
3. S.M. Bruemmer, E.P. Simonen, P.M. Scott, P.L. Andersen, G.S. Was, J.L. Nelson, Journal of Nuclear Materials, 274(1999) pg. 299.
4. R. Dutton, C.S. Lim, Canadian Metallurgical Quarterly, 25(1986) pg. 169.
5. D.Radjabov, Vacuum, 42(1991) pg. 163.
6. I.G. Romanov, I.N. Tsariova, Vacuum, 68(2003) pg. 213.
7. N. Li, M.S. Martin, O. Anderoglu, A. Misra, L. Shao, H. Wang, X. Zhang, Journal of Applied Physics, 105(2009) pg.123522.
8. P. Hosemann, Y. Dai, E. Stergar, H. Leitner, E. Olivas, A.T. Nelson, S.A. Maloy, Experimental Mechanics, 55(2011) pg. 1095.
9. M.F. Doerner, W.D. Nix, Journal of Materials Research, 1(1986) pg.601.
10. W.D. Nix, H. Gao, Journal of Mechanics and Physics of Solids. 46(1998) pg.411.
11. K.L. Johnson; “Contact Mechanics”, Cambridge Press, Cambridge, United Kingdom, (1985) pg. 153-184.
12. D. Tabor, “The Hardness of Metals”, Clarendon Press, Oxford, UK (1951). pp. 44 – 83.
13. Y. Murakami, M. Itokazu, Int. J. Solids Structures 34(1997) pg. 4005.
14. P.-L. Larsson, A. E. Giannakopoulos, E. Soderlund, D. J. Rowcliffe, R. Vestergaard, Int. J. Solids Structures 33(1996) pg.221.
15. J.D. Hunn, E.H. Lee, T.S. Byun, L.K. Mansur, J. of Nuclear Materials, 282(2000) pg.131.

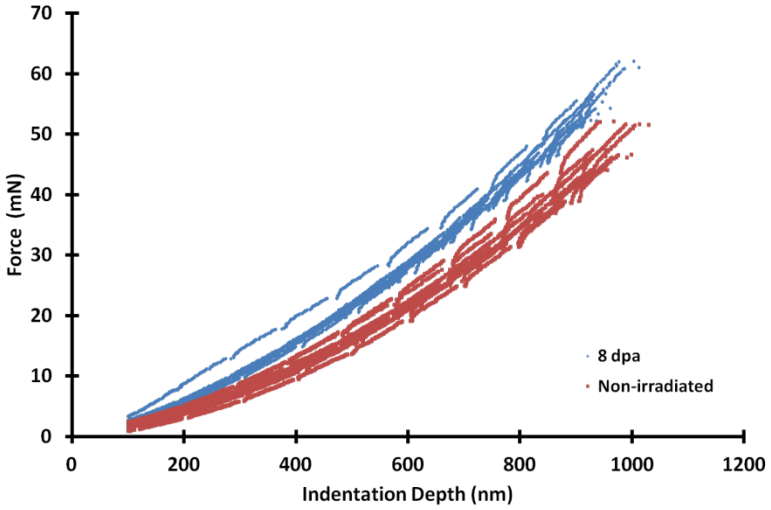

Figure 3. Indentation force versus depth from multiple tests performed on the AISI 310 alloy in the non-irradiated and the ion-irradiated (8 dpa) conditions. The data from the partial unloading were removed from this graph to display more clearly the force-depth trend.

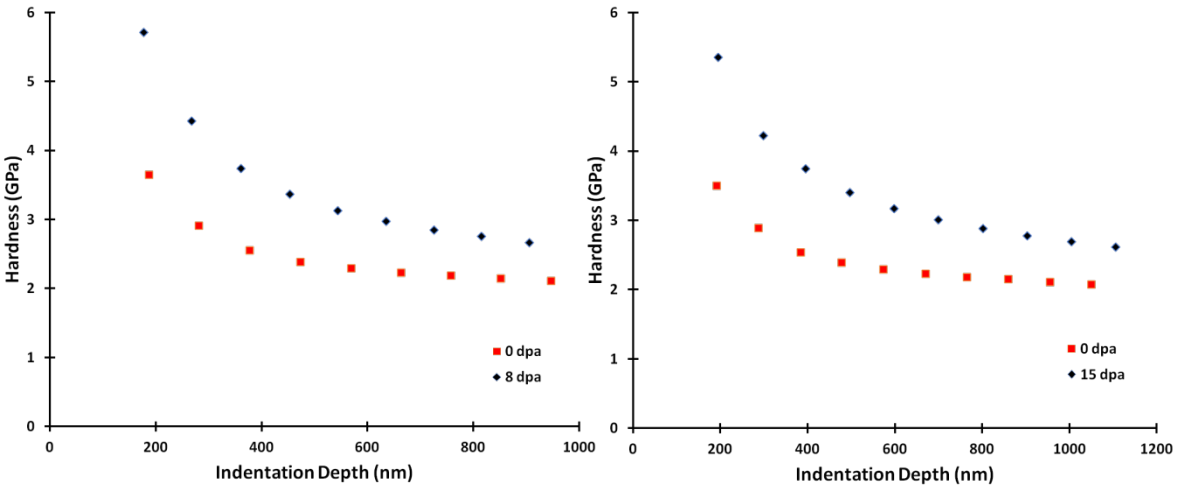

Figure 4. Indentation hardness versus depth for: (a) the AISI 310 alloy in the non-irradiated and the ion-irradiated (8 dpa) conditions and (b) the Inconel 800H alloy in the non-irradiated and the ion-irradiated (15 dpa) conditions. Each series of data was obtained from a single indentation test involving multiple unloading; therefore, the data points do not represent the average hardness values for any indentation depth. Average hardness values are shown in Figure 6.

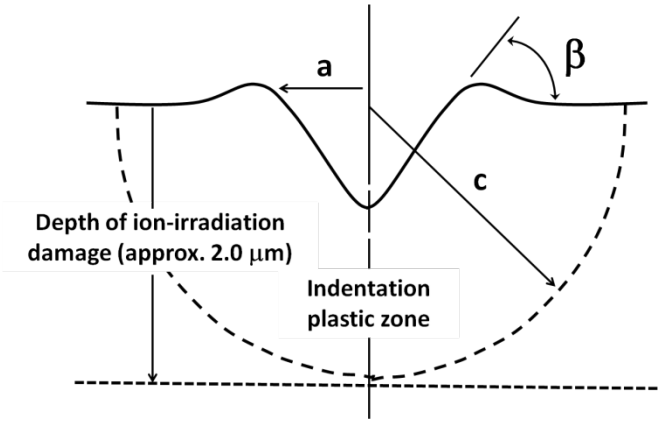

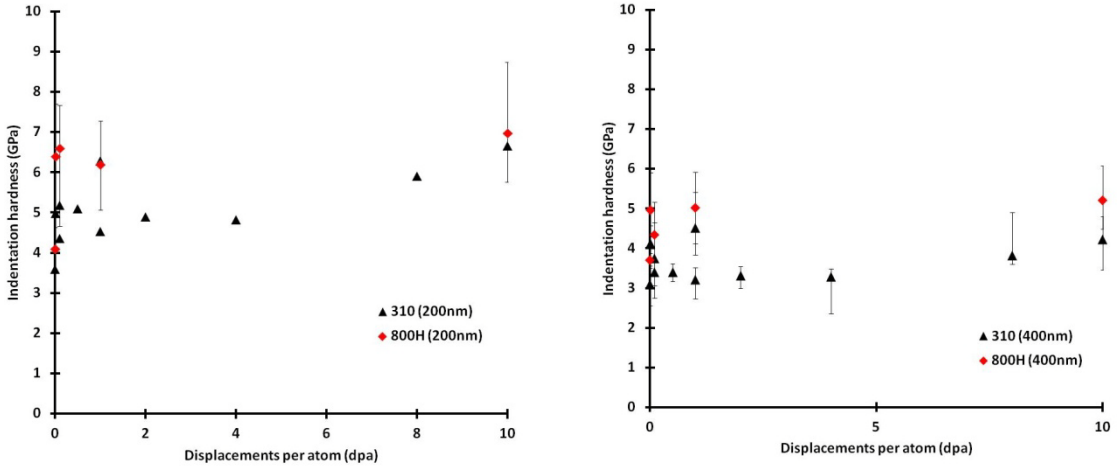

Figure 5. Schematic illustration of an indentation and its associated hemispherical plastic zone of radius c. In our study, the indentations must be made at a small enough depth that c is less than the ion irradiation depth.

(a) **(b)**

Figure 6. Average indentation hardness versus Fe^{4+} ion irradiation damage for the AISI 310 and Inconel 800H alloys. The 200nm deep indentations (a) show increased hardness compared to the 400nm deep indentations (b) because of the indentation depth dependence of the hardness shown in Figure 4 and discussed in Section 3.1.

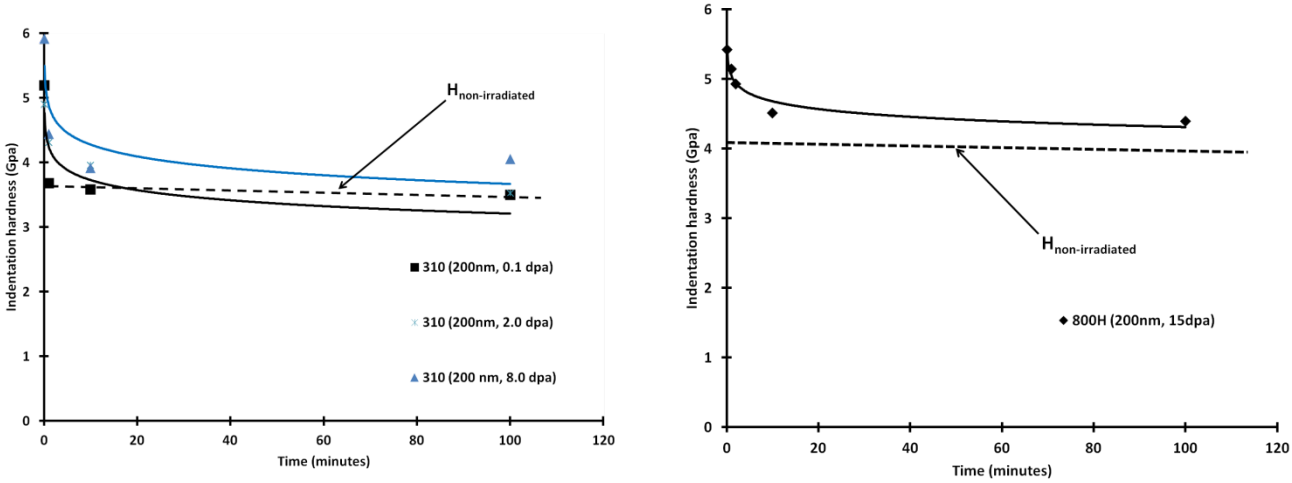

(a) (b)

Figure 7. Average indentation hardness, for indentation depth of 200 nm, versus 400°C annealing time for (a) AISI 310 and (b) Inconel 800H samples. The solid curves indicated power-law functions of time that were fitted to the data and were used to calculate the critical time t_c for complete recovery of the irradiation hardening.

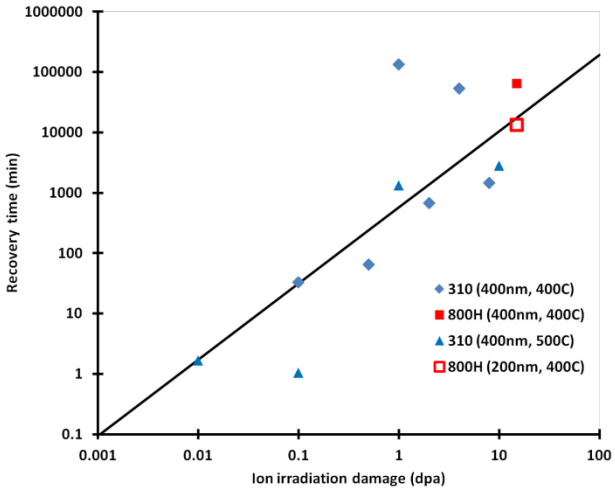

Figure 8. Time t_c required to completely recover the irradiation hardness, by annealing at 400^{o}C or 500^{o}C, of the AISI 310 and Inconel 800H alloys versus dpa.

ISSCWR7- 2007

CFD Investigation of Supercritical Water Flow and Heat Transfer in a Rod Bundle with Grid Spacers

Malwina Gradecka
Warsaw University of Technology
Nowowiejska 21/25, 00-665 Warsaw, Poland
+48 739212603, mgradec@itc.pw.edu.pl

Roman Thiele, Henryk Anglart
Royal Institute of Technology, KTH
Roslagstullsbacken 21, 106 91 Stockholm, Sweden
+46 8 5537 8887, romant@kth.se, henryk@kth.se

Abstract

This paper presents steady state CFD simulation approach to supercritical water flow and heat transfer in a rod bundle with grid spacers. The current model was developed using the ANSYS Workbench 15.0 software (CFX solver) and first applied to supercritical water flow and heat transfer in circular tubes. The predicted wall temperature was in good agreement with the measured data. Next, a similar approach was used to investigate three dimensional vertical upward flow of water at supercritical pressure of about 25 MPa in a rod bundle with grid spacers. This work aimed into understanding thermal and hydrodynamic behaviour of fluid flow in complex geometry at specified boundary conditions. The modelled geometry consisted of a 1.5 m heated section in the rod bundle, a 0.2 m non-heated inlet section and five grid spacers. The computational mesh was prepared using two cell types. The sections of the rods with spacers were meshed using tetrahedral cells due to the complex geometry of the spacer, whereas sections without spacers were meshed with hexahedral cells resulting in a total of 28 million cells. Three different sets of experimental conditions were investigated in this study: a non-heated case and two heated cases. The non-heated case, A1, is calculated in order to extract the pressure drop across the rod bundle. For cases B1 and B2 a heat flux is applied on surface of the rods causing a rise in fluid temperature along the bundle. While the temperature of the fluid increases along with the flow heat deterioration effects can be present near the heated surface. Output from both B cases is temperature at pre-selected locations on the rods surfaces

Nomenclature

A – surface area [m^2]

c_p – specific heat at constant pressure [kJ/kgK]

D_h – Hydraulic diameter [m]

h – heat transfer coefficient [W/m^2K]

i – enthalpy [J]

k – thermal conductivity [W/mK]

Nu – Nusselt number

p/d – pitch to diameter ratio

ρ – density [kg/m^3]

SUBSCRIPTS

b – bulk

pc – pseudo-critical

w – wall

1. Introduction

The Supercritical water reactor (SCWR) is one of the IV generation designs which are currently under development. As this type of reactor introduces unique features/advantages into the branch of LWR's operational parameters, there is a need to model behaviour of such reactor. Once water parameters reach pseudo-critical values extensive variation of fluid properties occurs resulting in a rapid heat transfer enhancement or deterioration effect. These effects are hard to predict and CFD modelling of supercritical water still needs to be developed and validated. This study undertakes modelling of heat transfer in a rod bundle with grid spacers at three different sets of conditions. The conditions selected for the study are drawn from an experiment performed by Misawa [1]. This work aims at understanding thermal and hydrodynamic behaviour of fluid flow in complex geometry at specified boundary conditions. Three different sets of experimental conditions were investigated in this study: a non-heated case and two heated cases. The non-heated case, A1, is calculated in order to extract the pressure drop across the rod bundle. For cases B1 and B2 a heat flux is applied on the surface of the rods causing a rise in fluid temperature along the bundle. While the temperature of the fluid increases along with the flow, the heat deterioration effects can be present near the heated surface.

Various works carried out by [2] and [3] computed wall temperatures and local Nusselt numbers for different experimental flows with the supercritical water. The chosen flows included normal and deteriorated heat transfer in upwards flowing configurations [4]-[6]. Both studies used ANSYS CFX as their computational tool and found that the low-Reynolds number k-ω-SST turbulence model is capable of predicting the normal heat transfer, as is expected in case B1 of the current study. For the deteriorated heat transfer, as expected for case B2 due to the larger wall heat flux, k-ω-SST is capable of predicting the deteriorated heat transfer and the resulting peak in the wall temperature, however, caution needs to be applied. The results are highly dependent on the choice of the grid and care must be taken that all computational nodes, especially the ones close to the point of deterioration, comply with the condition of $y^+<1$. This assures that the buoyancy forces responsible for the heat transfer deterioration are well captured. Figure 1 shows computational results in comparison to experimental result for two different flow configurations. Both cases use the supercritical water flow in a pipe. Different inlet conditions and wall heat flux conditions apply. While the case by Ackerman [8] employs a low heat flux and a high mass flux, the case by Ornatskij et al. [9] corresponds to a high heat flux and a low mass flux. On the left-hand side of Figure 1 one can see results for the Ackerman case which exhibits the normal heat transfer. The usage of ANSYS CFX together with k-ω-SST shows to be a suitable tool to reproduce the wall temperatures. On the right-hand side in the same figure, results for the deteriorated heat transfer are shown. The calculations use a setup which is similar to the one used in the current study, the low-Reynolds number k-ω-SST turbulence model with $y^+<1$. Even though some problems with recovery after heat transfer

deterioration is visible, the result show acceptable prediction concerning the location and the magnitude of the peak wall temperatures.

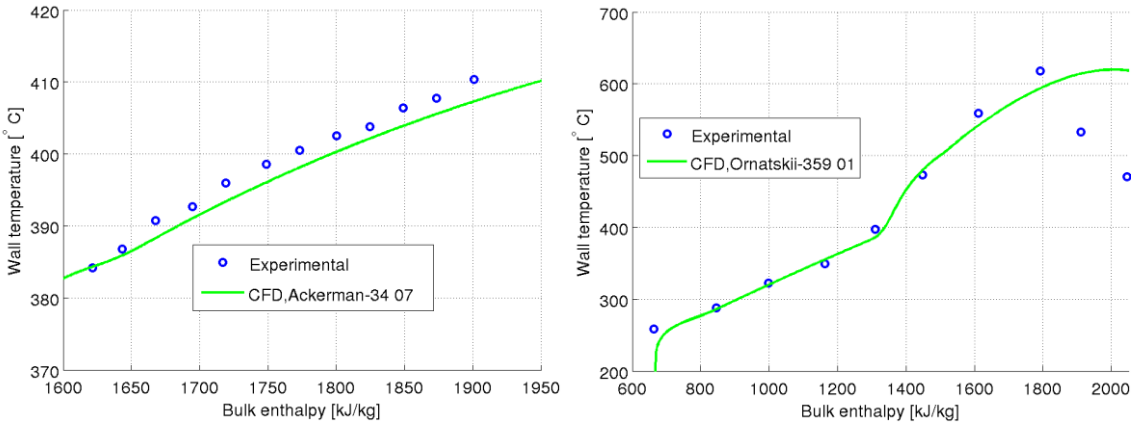

Figure 1 Comparison of experimental work and CFX computations with k-ω-SST model. Left: Calculations carried out by Jaromin [7] for experiments by Akerman [8]. Right: Comparison between ANSYS CFX and experiments by Ornatskij et al. [9].

2. Materials and methods

In this study two types of tools were used. First a numerical CFD model for flow in rod bundles was developed and calculated. The results from the numerical model were then compared to selected heat transfer correlations. A three dimensional, steady state simulation was conducted using ANSYS Workbench 15.0 software with CFX solver. Turbulent flow was modeled applying the shear stress transport turbulence model with the automatic wall function (assuming the turbulent Prandtl number 0.9).

2.1 Geometry

The geometry used in this study was in agreement with the blind benchmark study initiated by the Gen-IV International Forum. The modelled geometry consists of a 1.5 m heated section of a 7-rod bundle, a 0.2 m non-heated inlet section and five spacers. The unheated inlet section was added to account for the inlets effects. The rod bundle consists of seven rods with an outer diameter of 8 mm. The spacers are of hexagonal structure with three spacing fins in every of the seven hexagons. The modelled domain presented in this study represents just the water volume without solid parts of the bundle such as spacers or rods. The heating rods volume, insulation and cladding were not modelled and replaced with a heat flux boundary condition at the rod surface. Solid boundaries are introduced as no-slip, smooth walls. Detailed design of a bundle including spacer is presented in Figure 2. The cross section area used for calculations is $A=0.000192\ m^2$ which is consistent with the experiment [1]. Corresponding equivalent hydraulic diameter is $D_h=0.002757$ m.

2.2 Mesh

The numerical mesh was prepared using the meshing module of Workbench 15. Since a large scale geometry was investigated it was necessary to optimize computational time and reduce the number of mesh cells. To accommodate this, the computational mesh was prepared using two cell types. Sections of the rods with spacers were meshed using tetrahedral cells due to complex geometry of a spacer, whereas sections with only rods were meshed with a purely hexahedral mesh [10].

To assure accurate resolution in near wall regions, surfaces of the rods and spacers were inflated with 3 prism layers. To maintain wall distance y+ approaching 1, it was determined that the first layer thickness for applied flow conditions should be 5×10^{-6} m. The computational mesh created as described consisted of 28 million cells and it is shown in Figure 3.

2.3 Boundary conditions and investigated cases

Three sets of boundary conditions were applied to model cases which represent pseudo-critical conditions for water. Steady state boundary conditions were applied as shown in Table 1, where walls are modelled as smooth and adiabatic unless stated otherwise (does not apply to heated rods in case B1 and B2). The inlet uses a constant mass flow condition with magnitudes specified in Table 1. The working fluid first passes through the additional inlet section (non-heated in every case) and then through the first spacer enters the heated section of the bundle, continuing to pass through all following spacers.

Case A1 is designed to investigate the pressure drop across the rod bundle. In this case the lowest inlet temperature – 297.35 K and the highest flow rate – 26.33 kg/min are applied. Case A1 is a non-heated case, thus all rod surfaces are adiabatic.

The inlet temperature for case B1 is higher and is equal to 353.58 K. However, the temperature does not rise above the pseudo-critical point.

As B1 is a heated case, a constant heat flux is applied in the following manner. The rods are subdivided into three groups: group 1 – rod A, group 2 – rod B, D and F, group 3 – rod C, E and G. The central rod heat flux is lower than for the surrounding rods for this case.

In case B2 the highest inlet temperature is applied with the flow rate comparable to case B1. Unlike to case B1 the heat flux applied at all the rods is approximately equal.

Table 1 Boundary conditions for case A, B1 and B2.

Case No.	Fluid	Inlet temp. [K]	Inlet pressure [MPa]	Flow rate [kg/min]	Heater A [kW]	Heater B, D, F [kW]	Heater C, E, G [kW]
A1	Supercritical water	297.35	25.00	26.33	-	-	-
B1		353.58	24.98	16.69	19.67	22.51	22.52
B2		519.58	25.03	16.52	34.14	34.08	34.13

3. Preliminary Results

The study presented in this paper contains results of CFD model for postulated conditions as well as predictions obtained from analytical correlations for volume averaged parameters for case B1 and B2. Results are presented in the following sub-chapters.

3.1 CFD

The three cases described in the previous sections were examined in this study. In case A only the pressure drop along the rod bundle is of importance. In case B1 and B2 various heat flux values are applied on the rods' surfaces causing an increase in fluid temperature along the bundle. While the temperature of the fluid rises in the flow direction, it can approach or pass the pseudo-critical point at 25 MPa and 658.01 K [11] where heat deterioration effects can be present near the heated surface. Results for each case are presented in the following subsections.

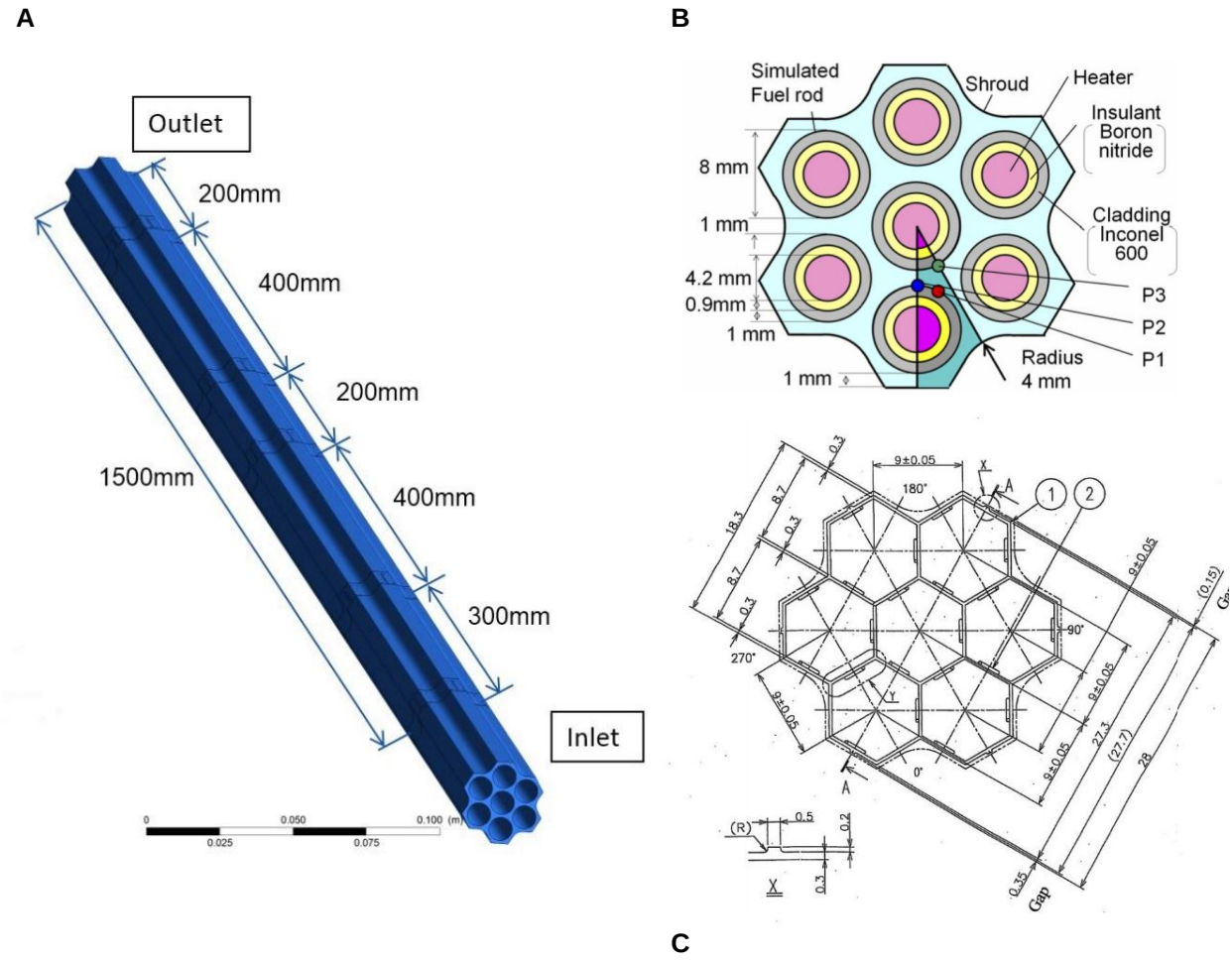

Figure 2 Geometry of the rod bundle and the spacer details; A - full 7-rod bundle domain; B - non-simplified geometry of the bundle; C - spacer design.

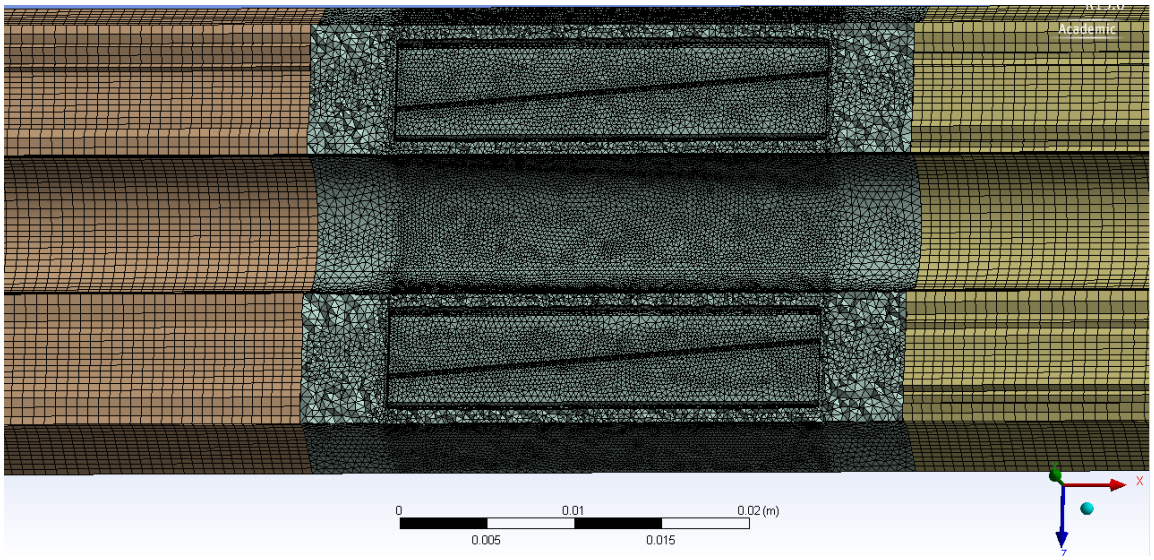

Figure 3 Computational mesh in the XZ plane.

3.1.1 Case A

As this is a non-heated case temperatures do not vary in the flow. The velocity field corresponds to the turbulent flow. The spacers introduce additional distortions of the flow, causing the flow of different sub-channels to interact. The obtained pressure drop in the bundle is 67.6 kPa. The influence of the spacers on pressure variation can be clearly seen at the Figure 4.

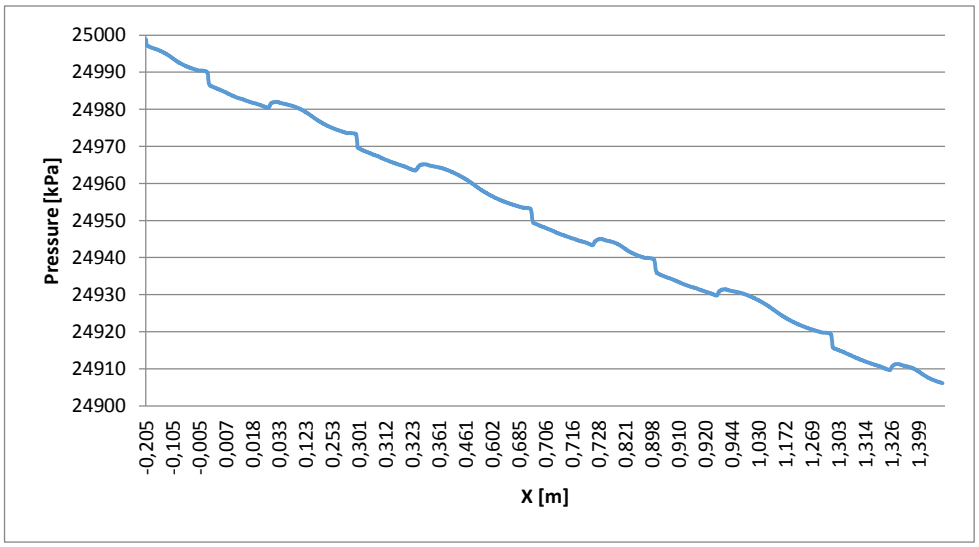

Figure 4 Pressure variation along the bundle

3.1.2 Case B1

Case B1 exhibits condition of the flow where the water temperature rises gradually but does not approach the pseudo-critical temperature of 658.01 K.

The temperature field across the bundle can be examined at the YZ cross-section of the model in Figure 5. It can be seen that the highest temperature can be found around the rod A as well as heat bridges are visible in the gaps between the rods. Overall, temperature of the water rises from 353 K to about 530 K (Figure 5 B). Formation of several hot spots can be seen, especially at the end of spacing fins (at the spacer – Figure 6 B). Due to a local stagnation of the flow, lower amount of heat is transferred from the surface of the rod to the water. The maximum temperature of 554 K is reached at the exit of the rod bundle as it is visible in Figure 6 A. This hot spot is located on D rod surface in a vicinity of rod A.

The flow in the bundle is turbulent with velocities varying between 1 and 2 m/s (Figure 5 A). However some stagnation can be seen in the boundary layer of the shroud. The velocity field visible in the YZ cross-section indicates that the highest velocity areas are located in the space between groups of three neighbouring rods, and it can reach over 2 m/s. Similar but lower velocity triangular-like areas are located in the vicinity of the shroud however with lower velocity of about 1.7-1.9 m/s.

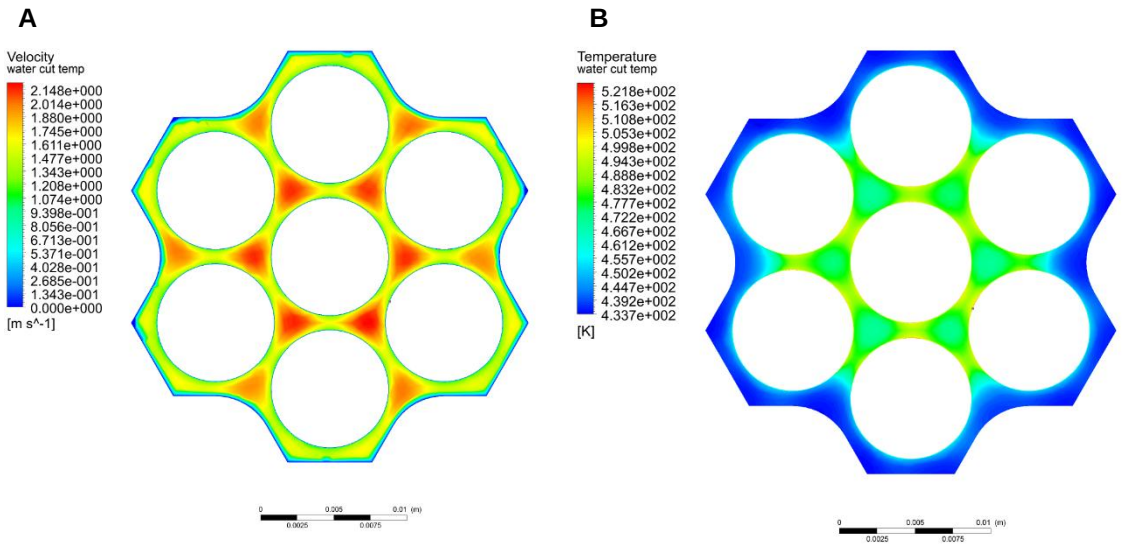

Figure 5 YZ plane at x= 1.1431 m; A - velocity contour; B - temperature contour.

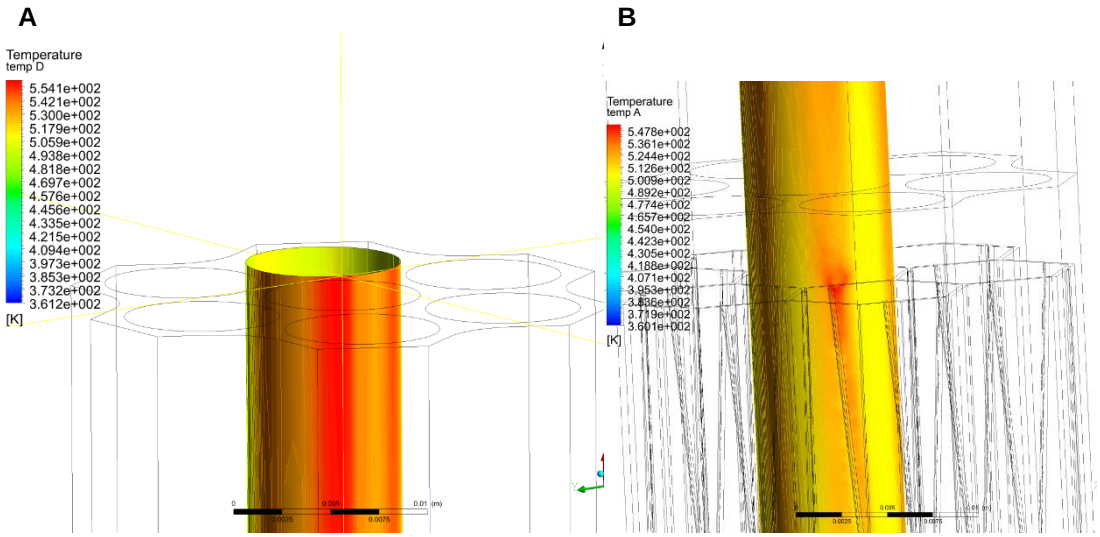

Figure 6 Temperature at the rods surface; A - the hottest point at D rod; B – hot spot at A rod at the 5th spacer.

3.1.3 Case B2

Case B2 represents flow with a significantly higher inlet temperature than both previous cases. The temperature of the water in the bundle rises from 519 K to about 770 K at the bundle outlet.

In the YZ cross-section in the vicinity of a spacer the temperature varies from 600 K to 700 K with a distribution similar to case B1 (Figure 7 B). However case B2 shows greater gradient of temperature across the bundle.

In the same cross-section velocity filed is shaped differently than in the previous case. Here it can be seen that higher speed areas are formed exclusively around rod A, and the velocity magnitudes increase up to 3.6 m/s. In other areas the velocity magnitude varies from 1.8 m/s to 2.7 m/s (Figure 7 A). Velocity increase is caused by a rise in water temperature and consequential decrease of water density due to heat transfer from surfaces of the rods.

Further upward as the temperature of the water rises, the gradients of the temperature and the velocity become non-uniform. In ZX cross-section through the 5th spacer a large difference

in the velocity is noted. The fluid with velocity of 3.5 m/s before the spacer accelerates to over 5.2 m/s at the spacer exit in vicinity of rod A (Figure 8 A). In the spacer itself differences in radial direction of up to 1 m/s can be noticed, decreasing with growing distance from A rod. Additionally, the spacer seams to not affect the water temperature unless in direct contact with the spacer (Figure 8 B). The hottest point in the bundle is located several centimeters downstream of the outlet section, in the last water section. Unlike in case B1 it is placed at rod D where the temperature reaches 945 K.

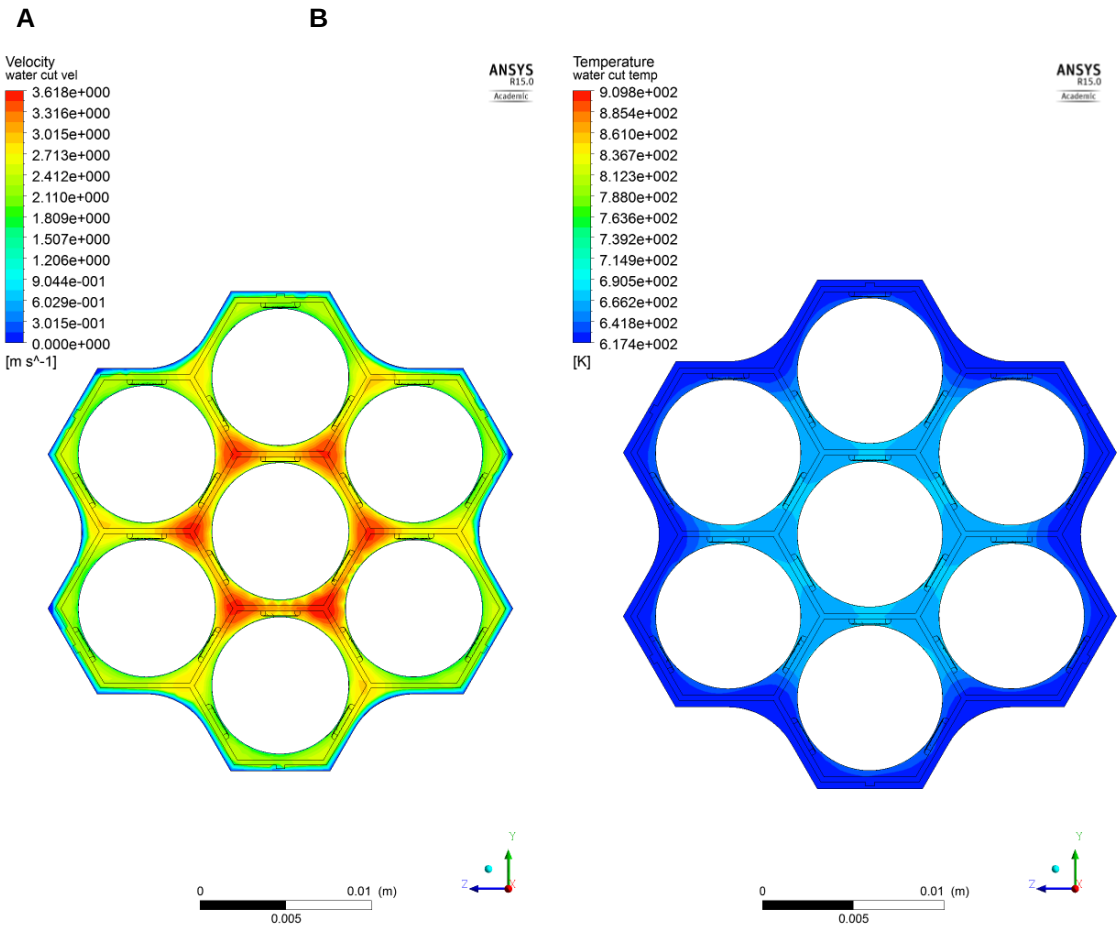

Figure 7 YZ plane at x= 1.1431 m; A – velocity contour; B – temperature contour.

The deteriorated heat transfer can be seen before the 5th spacer and before the section outlet. The effect is local and it decays along the flow. Figure 9 A and B show the areas suspected of DHT, stripe-like areas with significantly higher temperatures than surrounding surface can be distinguished with temperature gradient of up to 200 K between adjacent “stripes”. As the shape of areas suspected of DHT is not anticipated, it is discussed in the next section.

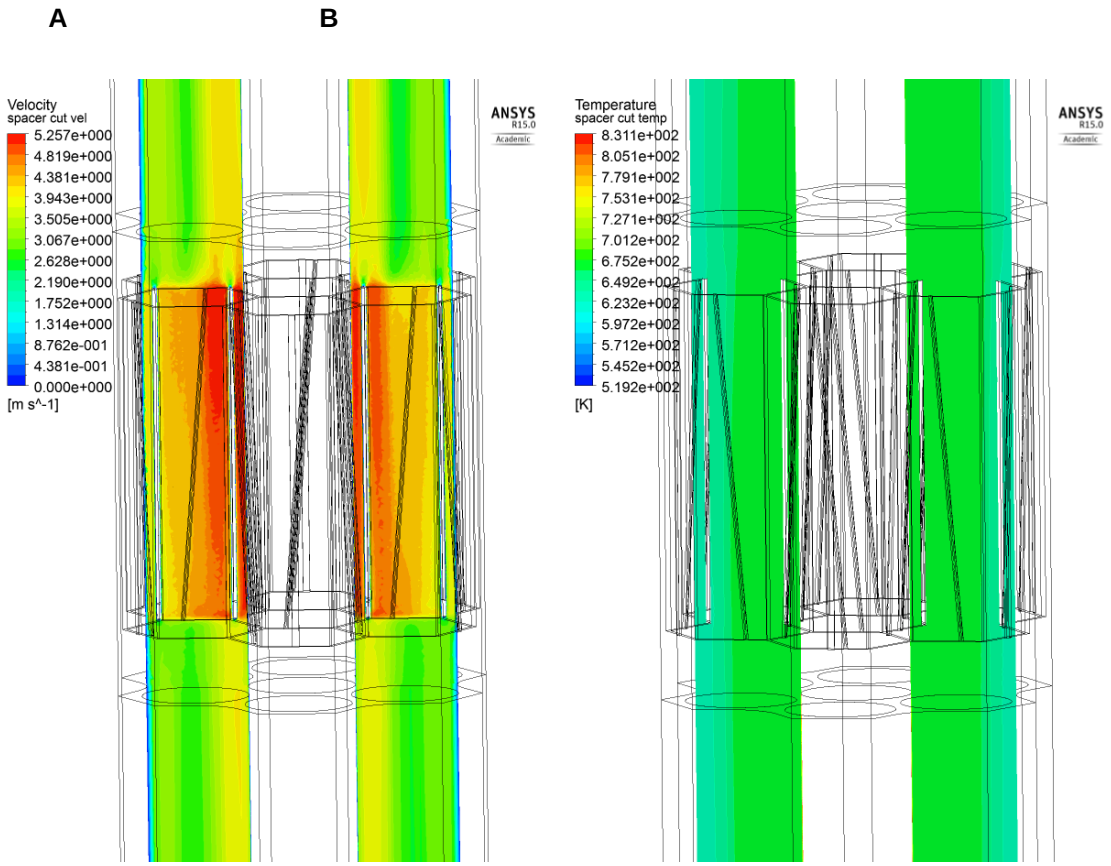

Figure 8 ZX plane at y= 0.0004 m, view of 5th spacer closest to the outlet; A – velocity contour; B – temperature contour.

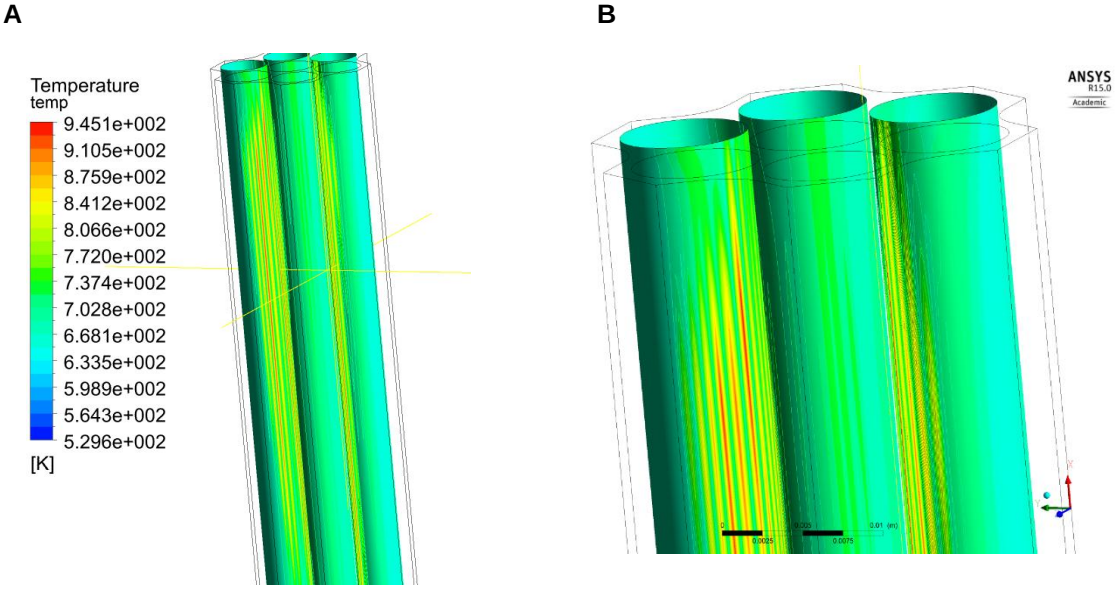

Figure 9 DHT visible at water section near outlet; A – Hot spot location; B – detailed view of DHT.

To illustrate influence of DHT occurring in this case plot of the maximum cladding temperature has been presented in figure 10 as function of height. The curve exhibits effect of

spacers at temperature distribution introducing a cool down after each spacer. Additionally two areas with occurrence of DHT are present in top part of the bundle.

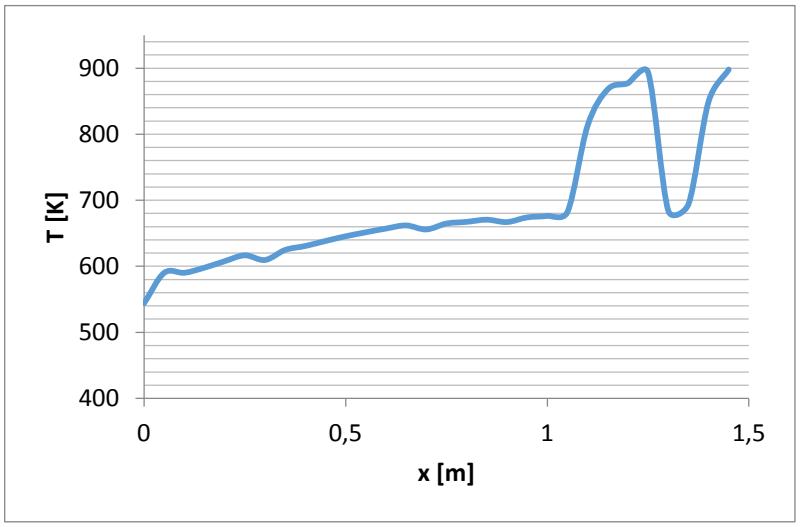

Figure 10 Maximum rod surface temperature as function of height for case B2

3.2 Empirical correlations

To calculate the heat transfer coefficient (HTC) equation (1) was used with various correlations for the Nusselt number. For the purpose of this calculation the average bulk temperature was computed from an empirical model to obtain the water properties.

$$h = \frac{Nu \cdot k}{D_h} \tag{1}$$

Here h – heat transfer coefficient, k – thermal conductivity of water, D_h – hydraulic diameter of the channel.

The data used for calculations are summarized in Table 2, whereas additional fluid properties were obtained for corresponding temperatures and pressures from NIST databases [12].

Table 2 Averaged properties for B1 and B2.

Property	**Case B1**	**Case B2**
Averaged bulk temperature	412.8 K	519.2 K
Averaged wall temperature	453 K	634 K
Pressure	24.98 MPa	25.03 MPa
Re_{in} number	11000	35000
Pr_{in} number	2.18	0.81

In literature many empirical correlations for heat transfer in a pipe can be found. Probably the most recognized one is the Dittus-Boelter (DB) correlation with a wide range of use and simple combination of Prandtl and Reynolds numbers. However its application is limited to the pipe flow and it does not account for other shape flow effects. The Dittus-Boelter correlation is applicable for $Re>10^4$ and $0.7<Pr<100$, and is given as follows:

$$Nu = 0.023 Re^{0.8} Pr^{0.4} \tag{2}$$

The next group of correlations accommodate other geometrical arrangements such as rod bundles with triangular and square lattices. As the arrangement of the rod bundle used for the experiment is most analogous to the triangular lattice, the corresponding coefficients were used. Three correlations were applied, introduced respectively by Ushakov, Weissman and Markoczy [11]. The Ushakov correlation is applicable for $5x10^3<Re<5x10^5$ and for $0.7<Pr<20$. The Ushakov correlation is more complicated than the previously introduced Dittues-Boelter correlation and introduces the pitch to diameter ratio *p/d*:

$$Nu = \left(0.0165 + 0.02\left(1 - \frac{0.91}{\left(\frac{p}{d}\right)^2}\right)\left(\frac{p}{d}\right)^{0.15}\right) Re^{0.8} Pr^{0.4} \quad (3)$$

The Weissman correlation uses a similar approach as the Dittus-Boelter correlation; however, instead of a constant coefficient of 0.023, Weissman introduces a parameter C which is a numerical combination of the pitch-to-diameter ratio and constant coefficients. The correlation is applicable for $1.1<p/d<1.5$.

$$Nu = CRe^{0.8} Pr^{1/3} \quad (4)$$

Where for the triangular lattice coefficient C is formulated as:

$$C = 0.026\left(\frac{p}{d}\right) - 0.006 \quad (5)$$

The last of the correlations accounting for the rod bundle effects considered in this paper is the Markoczy correlation. It is considerably more complicated than the other correlations presented here, but it can still be computed in a straightforward manner. Markoczy introduces an additional factor B, a mathematical combination of the pitch-to-diameter ratio as well as it relates the Nusselt number of the rod bundle to the Nusselt number based on the Dittus-Boelter correlation. Markoczy correlation is applicable for $3x10^3<Re<10^6$, $0.66<Pr<5$ and $1.02<p/d<2.5$ and is given as follows,

$$\frac{Nu_{bundle}}{Nu_{DB}} = 1 + 0.91Re^{-0.1} Pr^{0.4}\left(1 - 2e^{-B}\right) \quad (6)$$

Where for the triangular lattice coefficient B is given as:

$$B = \frac{2\sqrt{3}}{\pi}\left(\frac{p}{d}\right)^2 \quad (7)$$

Pseudo-critical flow conditions can exhibit phenomena such as the heat transfer deterioration or enhancement effects, which need to be addressed in the Nusselt number correlations. One of the correlations which accounts for heat transfer alteration at pseudo-critical conditions is the Jackson correlation. As some of the previously-described correlations it is applicable to pipes. However, new parameters describe density and heat capacity at constant pressure of the fluid for the bulk and at the heated wall. Jackson introduces a modified heat capacity coefficient as:

$$c_p = \frac{i_w - i}{T_w - T_b} \quad (8)$$

With the modified average heat capacity factor (as shown in Eq. (8)), the Jackson correlation is as follows:

$$Nu = 0.0183Re^{0.82} Pr^{0.5}\left(\frac{\rho_w}{\rho_b}\right)^{0.3}\left(\frac{c_p}{c_{pb}}\right)^n \quad (9)$$

Where for $T_b < T_w < T_{pc}$,the coefficient n is equal to 0.4.

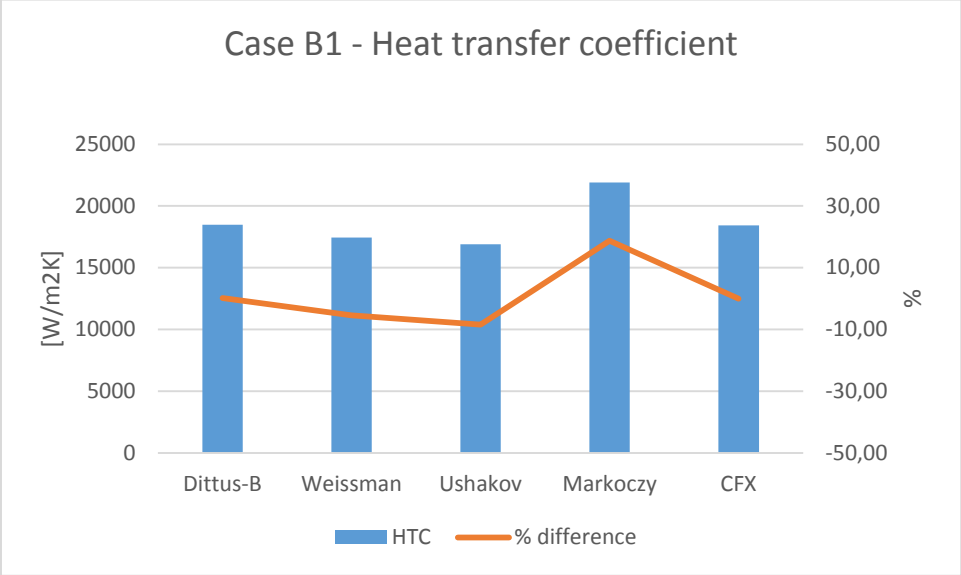

Figure 11 HTC calculated in CFX and via correlations for case B1.

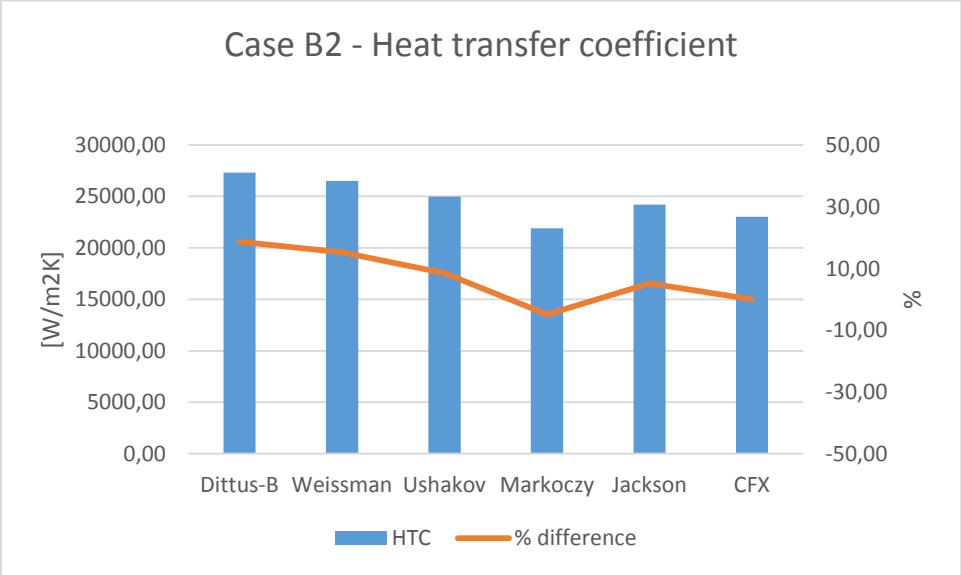

Figure 12 HTC calculated in CFX and via correlations for case B2.

The heat transfer coefficient (HTC) for cases B1 and B2 was extracted from CFX calculations as well as calculated through equation (1) where the Nusselt number was obtained from various empirical correlations (presented at Figure 11 and Figure 12). The CFX value has been extracted as a simple volume average of the wall heat transfer coefficient from the full domain (including/excluding non-heated section). It has been found that for case B1 where the temperature of the water does not reach the pseudo-critical point the Markoczy correlations performs worst in comparison to CFX results. Results of the Markoczy correlation are off by 18 % from CFX values. HTC values calculated in B2 case are in general agreement with what was obtained from numerical modeling in CFX. However, between the correlations the Dittus-Boelter places within maximum difference of 18% from CFX value. However, for Jackson correlation which account for the heat transfer deterioration/enhancement the HTC value is off by only 5 %.

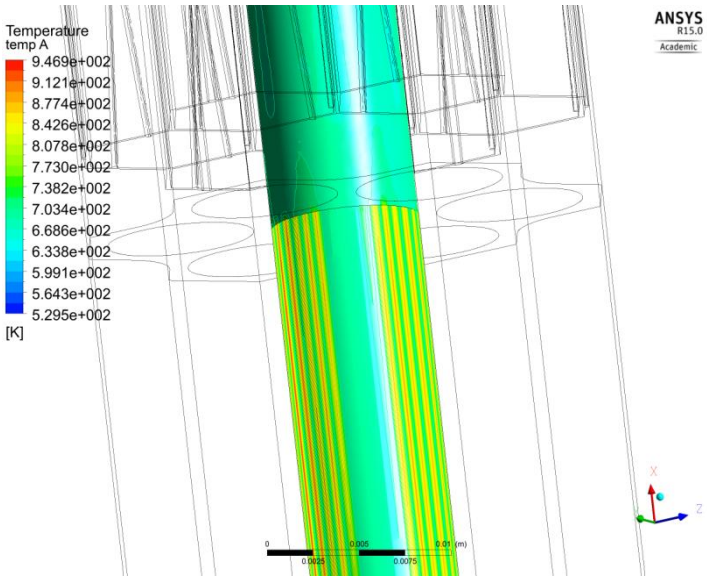

Figure 13. Temperature profile inconsistency at the mesh connection.

3.3 Discussion

A certain level of inconsistency in temperature profiles at mesh connection between structured and unstructured mesh can be seen in Figure 13. When the water temperature reaches pseudo-critical conditions, stripe shaped temperature contours are formed in areas of the structural mesh. It is anticipated that the peculiar shape is a result the of elongated cell shape in Z-direction and it is recommended to recalculate this case with a modified mesh.

4. Conclusions

An approach to modelling of supercritical water flow and heat transfer in a rod bundle with grid spacers in agreements to the blind benchmark study initiated by the Gen-IV International Forum is presented. Values obtained for the HTC from the numerical model are compared to several empirical correlations. The results are show that the different correlations are in general agreement with the CFD calculations within a maximum deviation of ±18% (DB correlation), which is within the accuracy of such correlations. A case with heat transfer deterioration is presented in case B2, where this phenomenon is present in the last section of the heated domain, easily visible due to the local rapid wall temperature increase.

It is recommended to recalculate the case B2 with a modified mesh, because it seems that strongly elongated cells can deteriorate the computational accuracy.

References

[1] Misawa, Takeharu; Nakatsuka, Toru; Yoshida, Hiroyuki; Takase, Kazuyuki (Japan Atomic Energy Agency, Tokai, Ibaraki (Japan)); Ezato, Koichiro; Seki, Yohji; Dairaku, Masayuki; Suzuki, Satoshi; Enoeda, Mikio (Japan Atomic Energy Agency, Naka Fusion Institute, Naka, Ibaraki (Japan)), Heat Transfer Experiments and Numerical Analysis of Supercritical Pressure Water in Seven-rod Test Bundle, NURETH-13: Proceedings of the 13th International Topical Meeting on Nuclear Reactor Thermal hydraulics.

[2] D. Palko and H. Anglart, “Theoretical and Numerical Study of Heat Transfer Deterioration in High Performance Light Water Reactor,” Sci. Technol. Nucl. Install., vol. 2008, pp. 1–5, 2008.

[3] M. Jaromin and H. Anglart, “A numerical study of heat transfer to supercritical water flowing upward in vertical tubes under normal and deteriorated conditions,” Nucl. Eng. Des., vol. 264, pp. 61–70, Nov. 2013.

[4] A. P. Ornatskij, L. F. Glushchenko, and S. I. Kalachev, “Heat transfer with rising and falling flows of water in tubes of small diameter at supercritical pressures,” Therm. Eng., vol. 18, no. 5, pp. 137–141, 1971.

[5] L. F. Glushchenko, S. I. Kalachev, and O. F. Gandzyuk, “Determining the conditions of existence of deteriorated heat transfer at supercritical pressures of the medium,” Teploenergetika, vol. 19, no. 2, pp. 69–72, 1972.

[6] M. E. Shitsman, “Impairment of the heat transmission at supercritical pressures,” High Temp (Engl. Transl.), vol. 1, no. 2, pp. 267–275, 1963.

[7] Jaromin, M. (2012). Theoretical and Computational Study on the Onset of Heat Transfer Deterioration in Supercritical Water. KTH, Reactor Technology.

[8] Ackerman, J. W. (1970). Pseudoboiling Heat Transfer to Supercritical Pressure Water in Smooth and Ribbed Tubes. Journal of Heat Transfer, 92(3), 490. doi:10.1115/1.3449698

[9] Ornatskij, A. P., Glushchenko, L. F., & Kalachev, S. I. (1971). Heat transfer with rising and falling flows of water in tubes of small diameter at supercritical pressures. Thermal Engineering, 18(5), 137–141.

[10] CFX User’s guide.

[11] H. Anglart, Applied Reactor Technology, Institute of Heat Engineering Warsaw University of Technology 2013, pp. 115 – 122.

[12] E.W. Lemmon, M.O. McLinden and D.G. Friend, "Thermophysical Properties of Fluid Systems" in NIST Chemistry WebBook, NIST Standard Reference Database Number 69, Eds. P.J. Linstrom and W.G. Mallard, National Institute of Standards and Technology, Gaithersburg MD, 20899, http://webbook.nist.gov, (retrieved November 28, 2014).

ISSCWR7-2008

Natural Circulation Experiment of Flow and Heat Transfer with Supercritical Water in Parallel Channels

Yuzhou Chen, Chunsheng Yang, Minfu Zhao , Keming Bi, Kaiwen Du
China Institute of Atomic Energy
Beijing China
Tel：8610-69357901, Email：chenyz@ciae.ac.cn

Abstract

An experiment of natural circulation of supercritical water in parallel channels was performed with inner diameter of 7.98 mm and heated length of 1.3 m, covering the ranges of pressure of 24.7 – 25.5 MPa and the heat flux of up to 1.9 MW/m^2. At the outlet water temperature of around 325 ℃ the flow exhibited some instability. When it was higher than around 360 ℃ the flow rate increased in one channel and decreased in another one, until the outlet water temperature reached to the pseudo-critical point. The experiment with single heated channel was also performed for comparison. The measurements on heat transfer coefficients were compared with the calculations by Bishop's, Jackson's and Yamagata's correlations, showing different agreements for different conditions. The experimental results on flow rates were compared with the calculations by system code RELAP5/MOD3.3, but some errors were observed in the code.

1. Introduction

Natural circulation will be encountered at normal and accident conditions of a supercritical water cooled reactor, and the flow and heat transfer behavior will be important to the reactor safety [1,2]. Since 1950's, for improving the thermal efficiency in the design of supercritical thermal power plants the heat transfer characteristics have been studied actively over the world [3-6]. In recent years the supercritical water-cooled reactor has been selected as a candidate for generation IV nuclear power system and these investigations have been extended further [7-12].

In the region of supercritical pressure the properties vary significantly, and they have great influences on the flow and heat transfer. In general, the supercritical experimental studies were based on different geometries and flow conditions, and the empiric correlations of heat transfer coefficients were the modified Dittus-Boelter ones with different forms.

In natural circulation the flow rate is lower and the instability could occur. It is recognized to have two types of flow instabilities: a static one and a dynamic one. The former is determined by the static internal pressure drop vs. flow characteristic of the system, and it could occur at the maximum of flow rate. The latter is determined by the density-wave and thermal oscillations. So far, the theoretical studies of natural circulation indicated the effects of the pressure, the core height, the inlet and outlet resistances and the power distribution on the flow instability [13-24]. The experimental investigations were mostly performed with helium, Frion-114 and CO_2 [25-26]. In recent years, some experiments of forced convection were performed with supercritical water [27, 28]. For natural circulation, an experiment was performed using Freon R23 to study the

coupled thermo-hydraulic-neutronic feedback on the stability in HPLWR [29]. In this experiment an artificial neutronic feedback was used based on the average measured density and a thermo-hydraulic mode was used with a time constant, and an instability zone was found. With supercritical water the natural circulation experiments were also performed in diameters of 4.62, 7.98 and 10.89 mm to study the flow and heat transfer behaviour at constant power [30-32]. In the present investigation a natural circulation experiment of supercritical water in parallel channels is performed to show the flow and heat transfer behaviour. For comparison, an experiment with single heated channel is also performed.

2. Experimental Facility and Procedure

Figure1 shows the schematic diagram of experimental facility. It is a vertical rectangular loop with length×height of 3.62×2.76 m. At a vertical side the parallel channels are located. An annular heat exchanger is at the top side with the hot water flowed in the tube and the cooling water in the annulus. The inner diameter of primary system, except of parallel channels, is 16 mm, including all the junctions and branches. In the second side of annulus the diameters are 25×20 (D2×D1) mm. The cooling water is introduced to it, and then discharged to the atmosphere.

In the parallel channels the Inconel-625 tubes are used with the inner diameters of 7.98 mm and outer diameter of 9.6 mm with heated lengths of 1.3 m. The total lengths are 2.1 m. The outer surface temperatures of the test sections are measured by sheathed thermocouples of 1.0 mm in diameter at locations of 0.7, 0.9 and 1.1 m from the beginnings of heating. At each location three thermocouples are installed at the outer surface. The inlet and outlet water temperatures of each channel are also measured by thermocouples. The test sections are insulated by silicon fiber, in which an electrical heating wire is wrapped to compensate the heat lose by controlling the temperature in the insulation close to the outer surface temperature of heated tube. The test section is heated by a DC supply with capacity of 70 V×6750 A. The pressure is kept by a three-head piston pump. For comparison with parallel channels, a single channel, indicated by the dotted line, is removed and the other parts of the loop are remained.

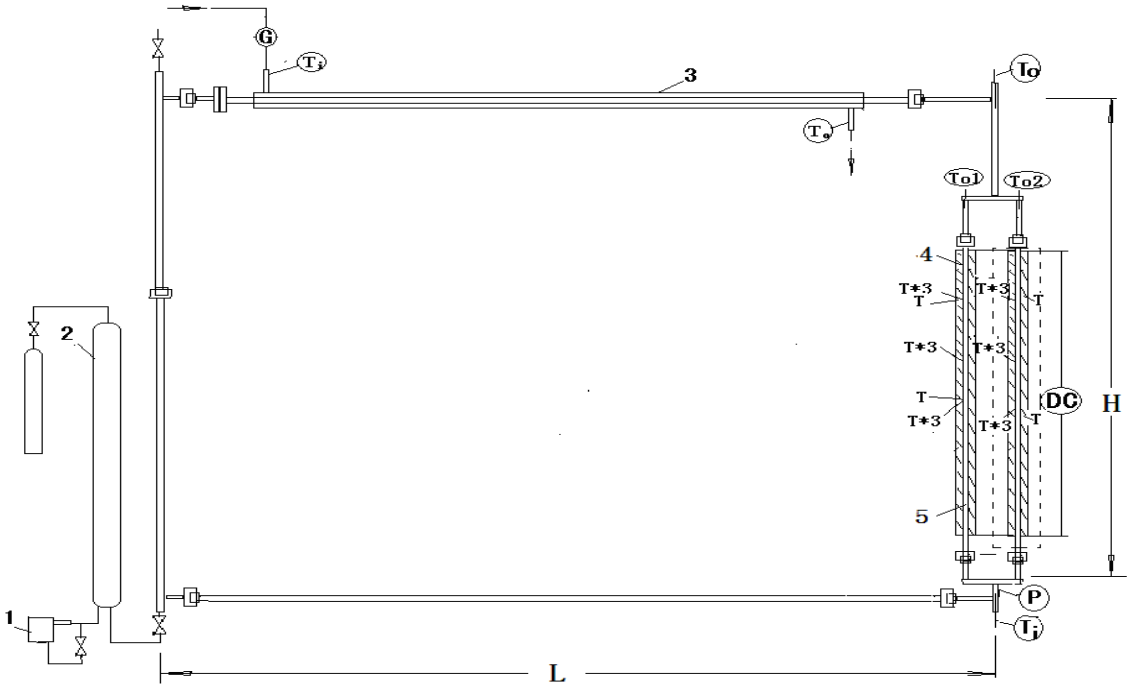

Figure 1 The Schematic diagram of natural circulation loop
(1. piston pump, 2. pressurizer, 3. heat exchanger, 4. thermal insulation, 5. heated test section)

The flow rate at each channel is determined by the heat balance of test section. It is accurate at stable condition because the temperature difference between the inlet and outlet of heated tube is generally larger than 100 K. In the ealier experiment a flowmeter was installed at the bottom side to measure the flow rate [2]. At stable condition the same results were usually obtained by these two methods. However, the measurement range by the flowmeter is limited, and at low flow it is difficult to have accurate results. Furthermore, at flow instability condition both the mass flowrate and the volumetric flowrate are not the same for each location, and the flowmeter can't give accurate result. Therefore, in the latter experiments the flow rate was determined only by the heat balance. At the oscillation condition this method tends to give an average flow rate basically, except for very strong instability, as seen latter.

The major measurement parameters include the inlet and outlet water temperatures and the outer surface temperatures by K-type thermocouples, the inlet pressure by a pressure transducer (DCY1151), the current and voltage across the test section. At the secondary side the inlet and outlet water temperatures are measured by thermocouples and the flow rate by a turbine flowmeter. All these parameters are recorded by a data acquisition system throughout the experiment with frequency of 1 s.

In the primary side the coolant was de-ironed water. During the experiment the primary pressure was kept constant basically, and the flow rate for the secondary side of heat exchanger was not adjusted. The test started with 0 kW and proceeded with increased power of small step by step. At each step the power was kept constant for enough time to reach a stable condition.

2. Experimental Results

Figure 2 shows the experimental results for the inlet and outlet water temperatures of heated tubes with heat flux. As seen, at first the water temperature increases smoothly with heat flux increasing. When the heat flux reaches to 1.12 MW/m^2, the outlet water temperature jumps from about 325℃ to 360 ℃. After that a little oscillations of the wall temperatures and the outlet water temperatures are observed. When the heat flux exceeds 1.38 MW/m^2, in one channel the outlet water temperature increases to nearly the pseudo-critical point, while in another one it decreases. They exhibit a stronge oscillation, accompanying with a sound. When the heat flux exceeds about 1.6 MW/m^2 the outlet water temperatures of two channels reach to nearly the pseudo-critical point.

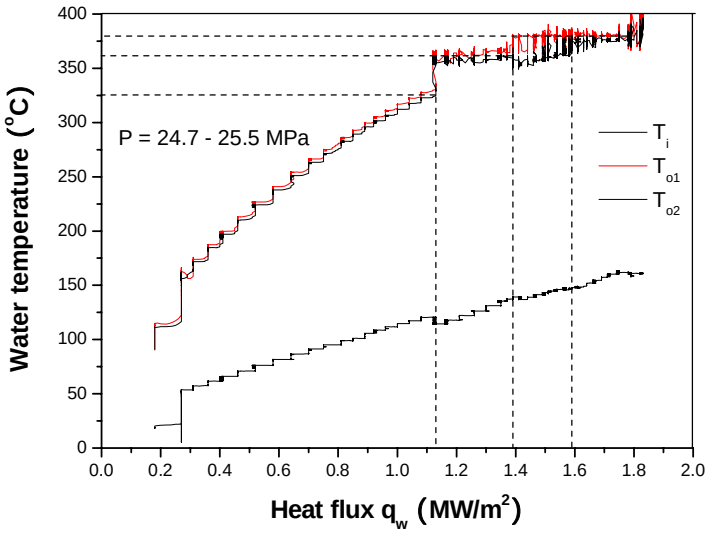

Figure 2 Variations of the inlet and outlet water temperature with heat flux

With heat conduction equation the inner wall temperatures are obtained from the measured outer surface temperature. Figure 3 and 4 show the variations of the inner wall temperatures with heat fluxes for the same channel and different locations, and figure 5 shows the heat

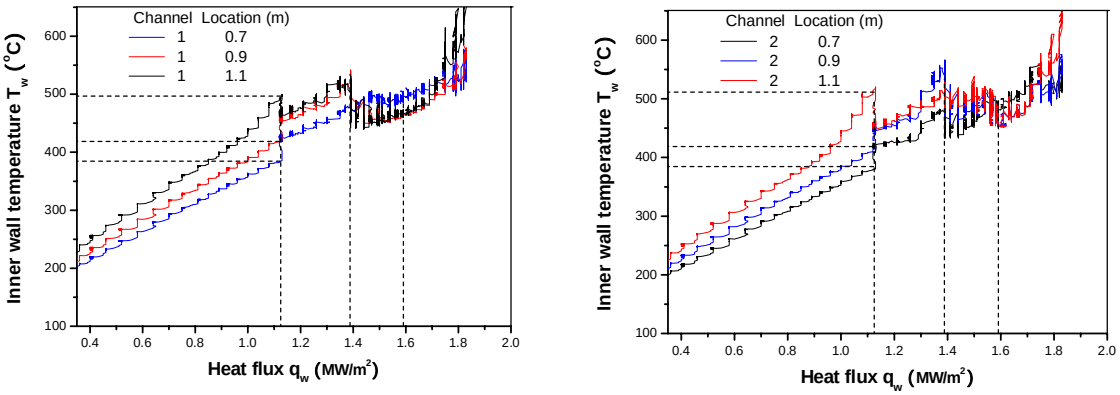

(a) (b)

Figure 3 Variations of the wall temperatures with heat fluxes for different locations ((a) channel 1, (b) channel 2)

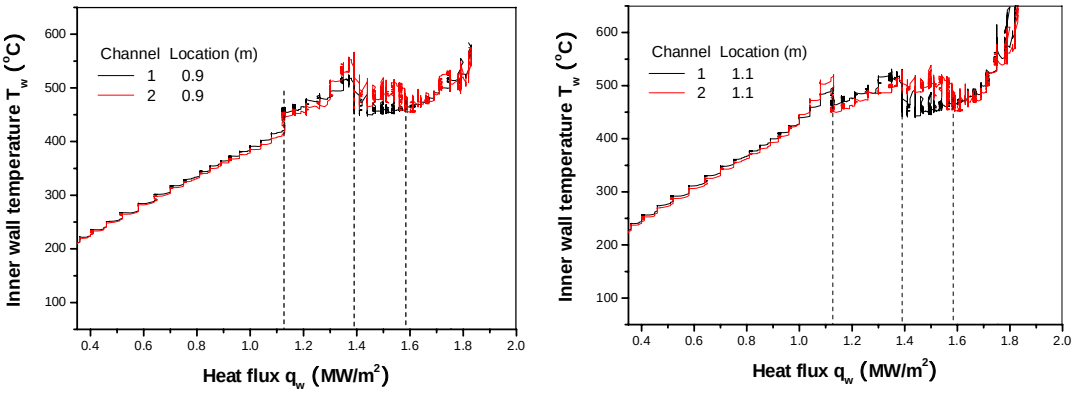

(a) (b)

Figure 4 Variations of the wall temperatures with heat fluxes for different channels ((a) Z = 0.9 m, (b) Z = 1.1 m)

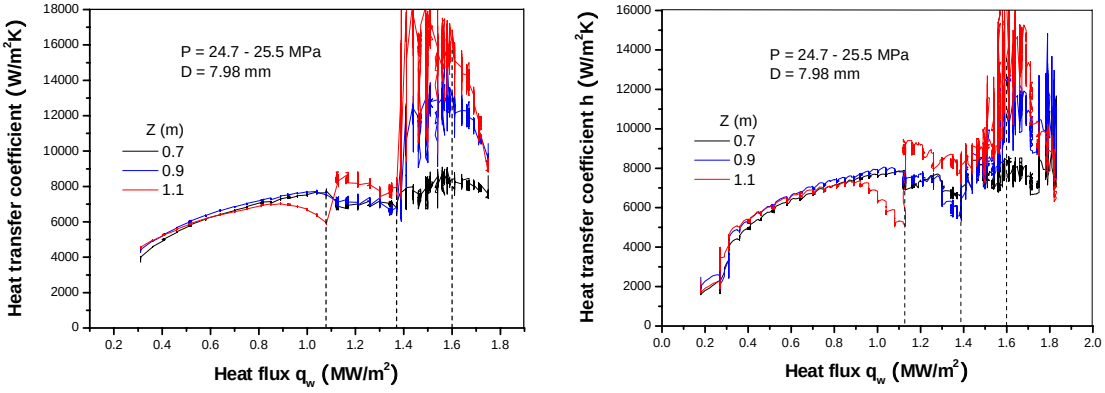

(a) (b)

Figure 5 Variations of heat transfer coefficients with heat fluxes for different channels ((a) channel 1, (b) channel 2)

transfer coefficients with heat fluxes for different channels at the same location. At first, the wall temperatures increase from location 1 to 3, and the heat transfer coefficients increase with heat flux increasing. At heat flux of about 0.9 MW/m^2, the inner wall temperature of location 3 reaches to the pseudo-critical point, then it increases faster to about 500 ℃, associated with a decrease in the heat transfer coefficient. This is apparently caused by the gas-like film created on the surface. For heat flux of higher than 1.12 MW/m^2 the heat transfer coefficient turns to increase, indicating the transition of gas film from laminar to turbulent state. In two channels the wall temperatures exhibit the same behavior basically, thogth a little difference is observed due probably to small differences in the geometry. After the heat flux exceeds 1.38 MW/m^2 the heat transfer coefficient increases substantially. Until about 1.6 MW/m^2 the outlet water temperatures in both channels reach to the pseudo-critical point.

From heat balance equation the flow rates are evaluated, as shown in figure 6. For lower heat flux the mass flux increases as heat flux increasing. At heat flux of 1.12 MW/m^2 the mass flux jumps from 750 to 625 kg/m^{2}s as the outlet water temperature increases from 325 to 355 ℃. Then it increases faster with heat flux increasing further. It is noted that at heat flux of less than 1.12 MW/m^2 the oscillations of the inlet and outlet water temperatures are less then 1.0 ℃ at a constant power supply. While at heat flux of 1.12 to 1.38 MW//m^2 some oscillation of the outlet water temperature is observed with the maximum of ± 4 ℃. For heat flux of larger than 1.38 MW/m^2 the maximum oscillation of the outlet water temperature is ± 7 ℃. This can lead to an uncertainty of flow rate of about ±3%. For heat flux of larger than 1.38 MW/m^2 the flow rate increases in one channel and decreases in another channel. At heat flux of about 1.6 MW/m^2 when the outlet water temperatures reach to the pseudo-critical point, the flow rates in both channels reach to the same values.

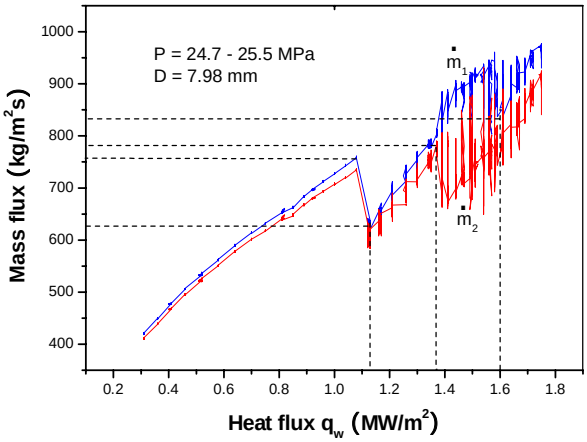

Figure 6 Variations of the mass fluxes with heat fluxes in parallel channels

For comparison with single heated channel, a channel is removed while another one is remained. The experimental results of the water temperatures and the wall temperatures are shown in figure 7, and the mass flux is shown in figure 8. As can be seen, the mass flux increases as heat flux increasing until a maximum of 860 kg/m^{2}s reaches at the outlet water temperature of 305 ℃ and heat flux of 1.28 MW/m^2. Then it decreases to 620 kg/m^{2}s when the outlet water temperature jumps to 358 ℃. This behavior is similar with the parallel channels, though the water temperature and the heat flux are not the same, because the total heating power is different. In the present experiment the parallel channels is divited by the branch, and therefore the flow resistance is increased. When the water temperature increases to more than 300℃, the flow resistantce increases greatly. Therefore the mass flux decreases to maintain the driving force increase smoothly. This behavior is not observed in the early natural circulation experiment with rectangular loop because of a simple loop [30-32].

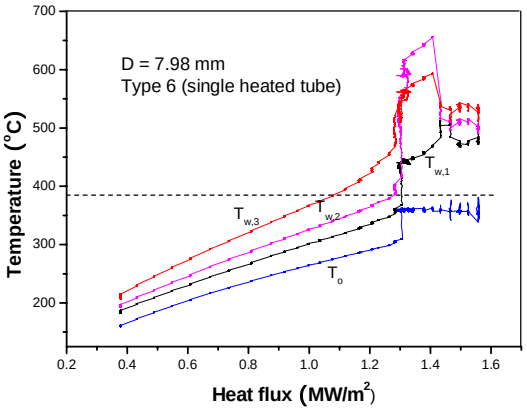

(a)

Figure 7 Variations of outlet water temperature and the wall temperatures with heat flux for single heated channel

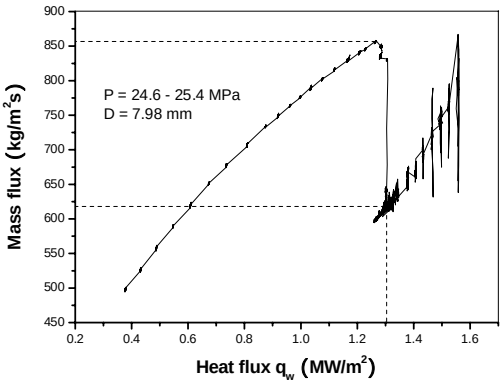

(b)

Figure 8 Variation of mass flux with heat flux for single heated channel

,

4. Calculations by existing correlations

Severous supercritical correlations were published in literature, e.g. the Bishop's correlation, the Jackson's correlation, the Yamagata's correlation and etc. In this paragraph the experimental results of heat transfer coefficients for heat flux less than 1.38 MW/m^2 are compared with the predictions by these correlations. At these conditions the two channels have nearly the same flow rate and the flow instabilities are not very strong.

(1) Bishop et al. correlation [3]:

$$Nu_{\mathrm{b}} = 0.0069 Re_{\mathrm{b}}^{0.9} \overline{Pr}^{0.66} \left(\frac{\rho_{\mathrm{w}}}{\rho_{\mathrm{b}}}\right)^{0.43} \left(1+\frac{2.4D}{x}\right),$$

where,

$$\overline{Pr} = \frac{h_{\mathrm{w}} - h_{\mathrm{b}}}{T_{\mathrm{w}} - T_{\mathrm{b}}} \frac{\mu_{\mathrm{b}}}{\kappa_{\mathrm{b}}}.$$

(2) Jackson correlation [12]:

$$Nu_{\mathrm{b}} = 0.0183 Re_{\mathrm{b}}^{0.82} Pr_{\mathrm{b}}^{0.5} \left(\frac{\rho_{\mathrm{w}}}{\rho_{\mathrm{b}}}\right)^{0.3} \left(\frac{\overline{c_p}}{c_{p\mathrm{b}}}\right)^{n}$$

with

$$n = \begin{cases} 0.4 & T_{\mathrm{w}}/T_{\mathrm{pc}} \le 1, \text{or} T_{\mathrm{b}}/T_{\mathrm{pc}} \ge 1.2 \\ 0.4 + 0.2(T_{\mathrm{w}}/T_{\mathrm{pc}} - 1) & T_{\mathrm{b}} < T_{\mathrm{pc}} < T_{\mathrm{w}} \\ 0.4 + 0.2(T_{\mathrm{w}}/T_{\mathrm{pc}} - 1)[1 - 5(T_{\mathrm{b}}/T_{\mathrm{pc}} - 1)] & 1 \le T_{\mathrm{b}}/T_{\mathrm{pc}} \le 1.2 \end{cases}$$

and

$$\overline{c_p} = \frac{h_{\mathrm{w}} - h_{\mathrm{b}}}{T_{\mathrm{w}} - T_{\mathrm{b}}}.$$

(3) Yamagata et al. correlation [5]:

$$Nu_{\mathrm{b}} = 0.0135 Re_{\mathrm{b}}^{0.85} Pr_{\mathrm{b}}^{0.8} F_{\mathrm{c}},$$

where,

$$F_c = \begin{cases} 1.0 & E > 1 \\ 0.67\, Pr_{pc}^{-0.05} (\bar{c}_p / c_{pb})^{n_1} & 0 \le E \le 1 \\ (\bar{c}_p / c_{pb})^{n_2} & E < 0 \end{cases}$$

with

$$n_1 = -0.77(1 + 1/\mathrm{Pr}_{pc}) + 1.49,$$
$$n_2 = 1.44(1 + 1/\mathrm{Pr}_{pc}) - 0.53$$

and

$$E = \frac{T_{pc} - T_b}{T_w - T_b}.$$

The experimental results of wall temperatures are compared with the calculations by these three correlations at the measured flow rates, as shown in figure 9. Before the dynamic instability (heat flux less than 1.12 MW/m^2 and Reynolds number of less than 50000, 57000 and 64000 for locarion of 0.7, 0.9 and 1.1 m), the Bishop's correlations gives very good prediction. After that the correlation underpredicts the Nuccelt number by 10 - 40%. The Jackson's correlation gives the predictions within ± 20%, and the Yamagata's correlation overpredicts the results mostly within 0 - 40%. It appears that at the experimental condition the calculation of Bishop's correlation is lower than the Jackson correlation by 10 - 20%, while the Yamagata's correlation is higher than the Jackson correlation by 10 - 15%.

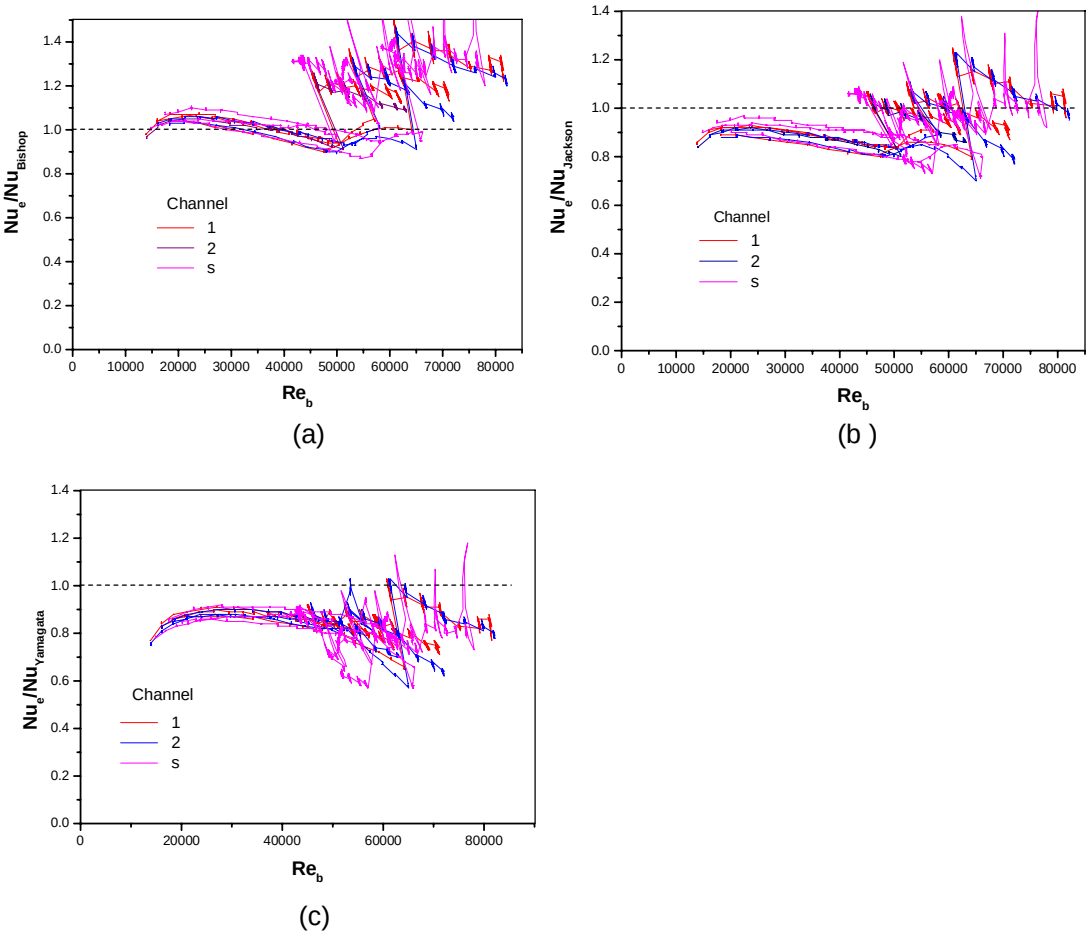

Figure 9 Comparison of the calculations of existing correlations with experimental results ((a) Bishop's correlation, (b) Jackson's correlation (c) Yamagata's correlation)

5. Calculations by RELAP5/MOD3.3

The primary natural circulation system is divided by several Volumes as: 12 for each parallel channel with heating length by 10 and upstream and downstream lengths by 1 respectively, 10 for the primary side and secondary side of heat exchanger respectively, 3 for the downward side and 3 for the lower horizontal side. The pressure is simulated by a Time Dependent Volume. All the elbows are simulated by Junctions with flow energy loss coefficient of 0.5. The branches at the parallel channels are also simulated by flow energy loss coefficient of 0.5. The secondary side is simulated by a Time Dependent Volume for constant pressure and temperature and a Time Dependent Junction for the constant flow rate, as experiment.

The differences between the experimental results and the code calculations are found to relate with the initial conditions, indicating the errors in the code. It is observed that in the code the dynamic viscosity, internal energy, specific heat, density are nearly the same as the values in IAPWS-IF97, except of the values near the pseudo-critical temperature, because in the code the physical properties are provided by the general tables, which are not accurate near the pseudo-critical point. However, the thermal conductivity has some difference with the IAPWS-IF97, as shown in fiqure 10. Furthermore, at transient conditions the thermal conductivity and the dynamic viscosity are the same with the initial values, but they don't vary with the transients of pressure and temperature, and thus, the prandtl number is different from the real one.

In the subcritical region there are no these problems. However in the supercritical region it causes a faired calculation. Actually, many standard problems were performed under the organization by IAEA and EU, like the SPE-1 to 4, ISP-26, 27 and 50. Great differences were observed between different users, and were thought to be caused by both the models and the user's effect. By using accurate physical propertied the flow rate can be predicted properly for the present conditions. But the flow instability can't be predicted because the flow resistance is difficult to measure accuratly and is not available at present. The heat transfer coefficients are also not predicted by the code, because the Dittus-Boelter correlation used in this code is also not suitable for the present supercritical condition.

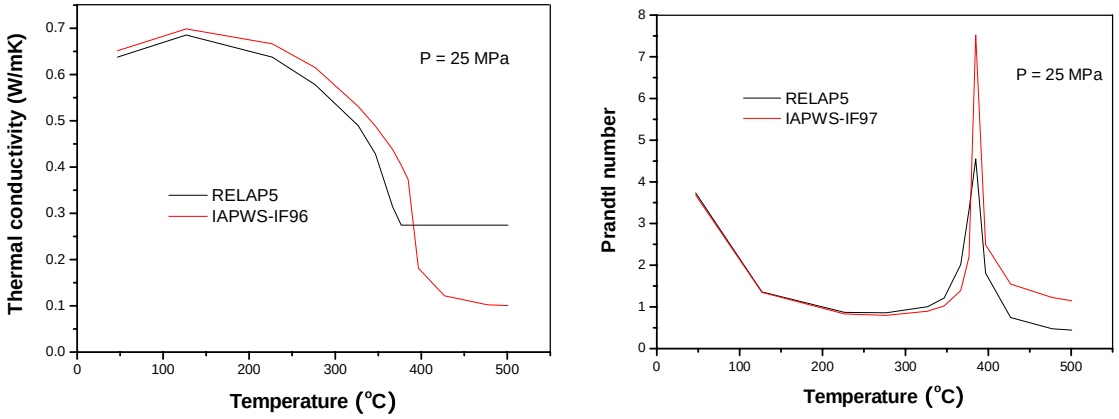

Figure 10 Comparison of the physical properties between RELAP5/MOD3.3 and IAPWS-IF-97 ((a) thermal conductivity, (b) Prandtl number)

6. Conclusions

A natural circulation experiment of supercritical water was performed with parallel and single heated channels to study the flow and heat transfer behavior. At present conditions the following conclusions were achieved.

- At the outlet water temperature reaches to around 360℃ the flow exhibits a strong dynamic instability, accompanying a sound. As power increases further, in one channel the flow rate increases and in another one it decreases. At the outlet water temperatures reach to the pseudo-critical point the flow rates reach to the same values.

- the Bishop's correlation agrees well with the experimental results for lower heat flux, and at dynamic instability it underpredicts the heat transfer coefficient slightly. The Jackson's correlation can predict the present experimental results within ± 20%. The Yamagata's correlation gives slightly an overprediction of the heat transfer coefficient, while it is better for higher flow.

- The system code RELAP5/MOD3.3 has a small error in physical properties for supercritical region and can't be used at this condition.

6. Acknowledgment

The present experiment was supported by International Science and Technology Cooperation Program of China (Grand No. 2012DFG61030). It is also supported by the International Atomic Energy Agency Coordinated Research Project (No. 18341).

References

1. D. Saha and J. Clevelend, Natural Circulation in Nuclear Reactor Systems, *Science and Technology in Nuclear Installations*, Volume 2008, Hindawi Publishing Corporatio (2008).

2. IAEA-TECDOC-1746, Heat Transfer Behavior and Thermohydraulics Code Testing for Supercritical Water Cooled Reactors (SCWRs), 2014

3. Bishop A, Sandberg R, Tong L. Forced convection heat transfer to water at near-critical temperatures and supercritical pressures. *WCAP-2056*, (1964)
.
4. SWENSON, H.S., CARVER, J.R. and KAKARALA, C.R., Heat transfer to supercritical water in smooth-bore tubes, *A.S.M.E. Journal of Heat Transfer, V.87 (4), 477 – 484 (*1965)
.
5. Yamagata K, Nishigawa K, Hasegawa S, Fuju T, Yoshida S. Forced convective heat transfer to supercritical water flowing in tubes. International Journal of Heat *and* Mass Transfer, , **15**(12): 2575–2593 (1972)

6. WATTS, M.J. and CHOU, C.T., Mixed convection heat transfer to supercritical pressure water, Proc. 7th International Heat Transfer Conference, Munich, Paper MC16, Vol. 3, 495-500, 1982

7. PIORO, I. and MOKRY, S., Heat transfer to fluids at supercritical pressures, Chapter in Heat Transfer – Theoretical Analysis, Experimental Investigations and Industrial Systems, Edited by A. Belmiloudi INTECH, Rijeka, Croatia, pp481-504, 2011.

8. ZAHLAN, H., GROENEVELD, D.C., TAVOULARIS, S., MOKRY, S. and PIORO, I., assessment of supercritical heat transfer prediction methods, the 5th Int. Sym. SCWR (ISSCWR-5), Vancouver, British Columbia, Canada, March 13-16, 2011, 20 pages.

9. MOKRY, S., GOSPODINOV, YE., PIORO, I. and Kirillov, P., Supercritical water heat-transfer correlation for vertical bare tubes, Proceedings of the 17th International

Conference on Nuclear Engineering ICONE-17, Brussels, Belgium, July 12-16, Paper # 76010, 2009, 8 pages.

10. CHENG, X. YANG, Y.H. and HUANG, S.F., A simple heat transfer correlation for SC fluid flow in circular tubes, NURETH-13, Kanazawa City, Ishikawa Prefecture, Japan, September 27-October 2, 2009.

11. BAE, Y. Y. and KIM, H. Y., Convective heat transfer to CO2 at a supercritical pressure flowing vertically upward in tubes and an annular channel, Exp. Therm. Fluid Sci. Vol. 33, No. 2, pp. 329-339, 2009.

12. Jackson J D. Consideration of the heat transfer properties of supercritical pressure water in convection with the cooling of advanced nuclear reactors. In: Proceedings of *the 13th Pacific Basin Nuclear Conference*, Shenzhen, China, (2002).

13.. Ambrosini, W., On the analogies in the dynamic behaviour of heated channels with boiling and supercritical fluids, *Nuclear Engineering and Design*, **237 (**11**)** 1164-1174, (2007).

14. Sharma, M., Pilkhwal, D.S., Vijayan, P.K., Saha, D., Sinha, R.K., Steady state and linear stability analysis of a supercritical water natural circulation loop, *Nuclear Engineering and Design* **240** 588–597 (2010).

15.. Chatoogoon, V., Stability of supercritical fluid flow in a single-channel natural-convection loop. *Int. J. Heat Mass Trans*. **44**, 1963–1972 (2001).

16.. Jain R. and Corrandini M.L., A linear stability analysis for natural-circulation loops under supercritical conditions, *Nuclear Technology*, **155**, 312-323 (2006).

17. Jain, P.K., Rizwan-uddin, 2008, Numerical analysis of supercritical flow instabilities in a natural circulation loop, *Nuclear Engineering and Design* **238** 1947–1957 (2008).

18.. Lomperski, S., Cho, D., Jain, R., Corradini, M.L.,. Stability of a natural circulation loop with a fluid heated through the thermodynamic pseudocritical point. In: *Proceedings of ICAPP'04*, Pittsburgh, PA, USA, June 13–17, Paper 4268 (2004).

19.. Sharabi, M.B., Ambrosini, W., He, S.**,** 2008, "Prediction of unstable behaviour in a heated channel with water at supercritical pressure by CFD models" *Annals of Nuclear Energy,* **35** 767–782 (2008).

20.. Yi, T.T., Koshizuka, S., Oka, Y.,. A linear stability analysis of supercritical water reactors, (I) thermal–hydraulic stability. *Journal of Nuclear Science and Technology* **41**, 1166–1175 (2004).

21. Ambrosini, W., 2011, Assessment of flow stability boundaries in a heated channel with different fluids at supercritical pressure, *Annals of Nuclear Energy* **38,** 615–627 (2011).

22. Xi, Xi, Zejun Xiaom Xiao Yan, Ting Xiongn Yanping Huang, Numerical Simulation of the Flow Instability between Two Heated Parallel Channels with Supercritical Water, Annals of Nuclear Energy, 64(2014) 57-66

23. Yali Su, Jian Feng, Hao Zhao, Wenxi Tian, Guanghui Su, Suizheng Qiu, Theoretical Study on the Flow Instability of Supercritical Water in the Parallel Channels, Progress in Nuclear Energy, 68(2013) 168-176

24. Ting Xiong, Xiao Yan, Shanfang Huang, Junchong Yu, Yanping Huang, Modeling and Analysis of Supercritical Flow Instability in Parallel channels, Int. J. of Heat and Mass Transfer, 57(2013) 549-557

25. Swapnalee, B.T., Vijayan, P.K., Sharma, M., Pilkhwal, D.S., 2012, Steady state flow and static instability of supercritical natural circulation loops, *J. Nuclear Engineering and Design*, **245**, 99-112 (2012).

26.. Rohde, M., Marcel, C.P., T'Joen, C., Class, A.G., van der Hagen, T.H.J.J., 2011, Downscaling a supercritical water loop for experimental studies on system stability, International *Journal of Heat and Mass Transfer* **54** 65–74 (2011)

27. T. Xiong, X. Yan, Z.J. Xiao, Y.L. Li, Y.P. Huang, J.C. Yu., Experimental Study on Flow Instability in Parallel Channels with Supercritical Water, Ann. Nucl. Energy 48 (2012) 60-67

28. Chen Yuzhou, Yang Chunsheng, Zhao Minfu, Bi Keming, Du Kaiwen, Forced Convective Heat Transfer Experiment of Supercritical Water in Different Diameters of Tubes, J. Energy and Power Engineering, V.8 (2014) N.9 1495-1504

29. C. T'Joen and M. Rohde, Experimental study of the coupled thermo-hydraulic-Neutronic Stability of a natural circulation HPLWR, J. Nuclear Engineering and Design, 242 (2012) 221-232

30. Chen Yuzhou Zhao Minfu, Yang Chunsheng, Bi Keming, Du Kaiwen, An Experimental Study of Heat Transfer in Natural Circulation of Supercritical Water, Proc. of *NUTHOS-9*, N9P0049, Taiwan, (2012).

31. Chen Y., Zhao M., Yang C., Bi K. and Du K., An Experiment on Flow and Heat Transfer Characteristics in Natural Circulation of Supercritical Water, 2012, CCSC-2012, Xian, China

32. Chen Y., Zhao M., Yang C., Bi K. and Du K., Experiment of Heat Transfer of Supercritical Water in Natural Circulation with Different Diameters of Heated Tubes, Shenzhen, China, 2013, ISSCWR6-13097

ISSCWR7-2009

Construction of a Test Facility for Experimental Investigations of Flow and Heat Transfer with Supercritical CO_2

Wolfgang Flaig, Rainer Mertz, Jörg Starflinger
Institute of Nuclear Technology and Energy Systems
Pfaffenwaldring 31, 70569 Stuttgart, Germany
+49 711 685-62454, wolfgang.flaig@ike.uni-stuttgart.de

Abstract

Supercritical fluids show great potential as future coolants for nuclear reactors or thermal power plants. Compared to subcritical condition, supercritical fluids show advantages in the heat transfer due to its thermodynamic properties near the critical point. This can lead to the development of more compact and more efficient components, e.g. heat exchangers and compressors. But operating a heat exchanger near the critical (i.e. the pseudo-critical) point of a working fluid incurs the risk of triggering Deteriorated Heat Transfer (DHT). Because there is still lack of information about this phenomenon, experimental investigations will be carried out at the Institute of Nuclear Technology and Energy Systems (IKE), University of Stuttgart.
For the experimental investigations supercritical carbon dioxide (CO_2) with its moderate critical parameters T = 30.98 °C and p = 7.38 MPa is an appropriate substitute fluid for supercritical water.

A multipurpose facility will be build up for various experimental investigations on supercritical CO_2. It is now under construction. It consists of a closed loop, in which CO_2 is compressed to supercritical state and delivered to the test section. The test sections itself can be exchanged for various investigations. After the test section, the CO_2 pressure will be reduced and stored as liquid in pressure tanks, from where it is evaporated and compressed again.

The test facility is designed to carry out experimental investigations with mass flows up to 0.111 kg/s, pressures up to 13 MPa and temperatures up to 150 °C. The first subject of interest will be the study of the thermal behavior of a Printed Circuit Heat Exchanger (PCHE) using supercritical CO_2 as working fluid close to its critical point. Pressure drop and heat transfer experiments will be carried out as a start for fundamental investigations of heat transfer in mini-channels.

This publication contains a description and the layout of the test facility and of the first test section.

1. Introduction

1.1 Motivation

The critical point of Carbon dioxide (CO_2) is at p = 7.38 MPa and T = 30.98 °C [1]. These moderate parameters compared to other working fluids like water (e. g. p = 22.12 MPa, T = 374.12) enables the use of CO_2 as a substitute fluid easier to handle in current research work.
Similar to all other supercritical fluids, near its critical point CO_2 shows a significant change in its thermophysical properties. Passing the pseudo-critical point with increasing temperature leads to a massive increase of the isobaric heat capacity and the decrease of the dynamic viscosity. Furthermore, the heat conduction coefficient and the density remain on liquid-like values at first and then drop down after passing the pseudo-critical point. This progression of the properties leads to a high Prandtl Number near the critical point. This high Prandtl Number in turn causes a significant peak in the Nusselt Number respectively the heat transfer coefficient. This leads to high potential as working fluid in heat transfer near the critical point.
Fig. 1 shows the temperature-dependent progression of the heat transfer coefficient for CO_2, calculated with the Nusselt correlation (Eq.1) for turbulent pipe flow by Dittus-Boelter [2].

$$Nu = 0.023\, Re^{0.8}\, Pr^{0.4} \qquad (1)$$

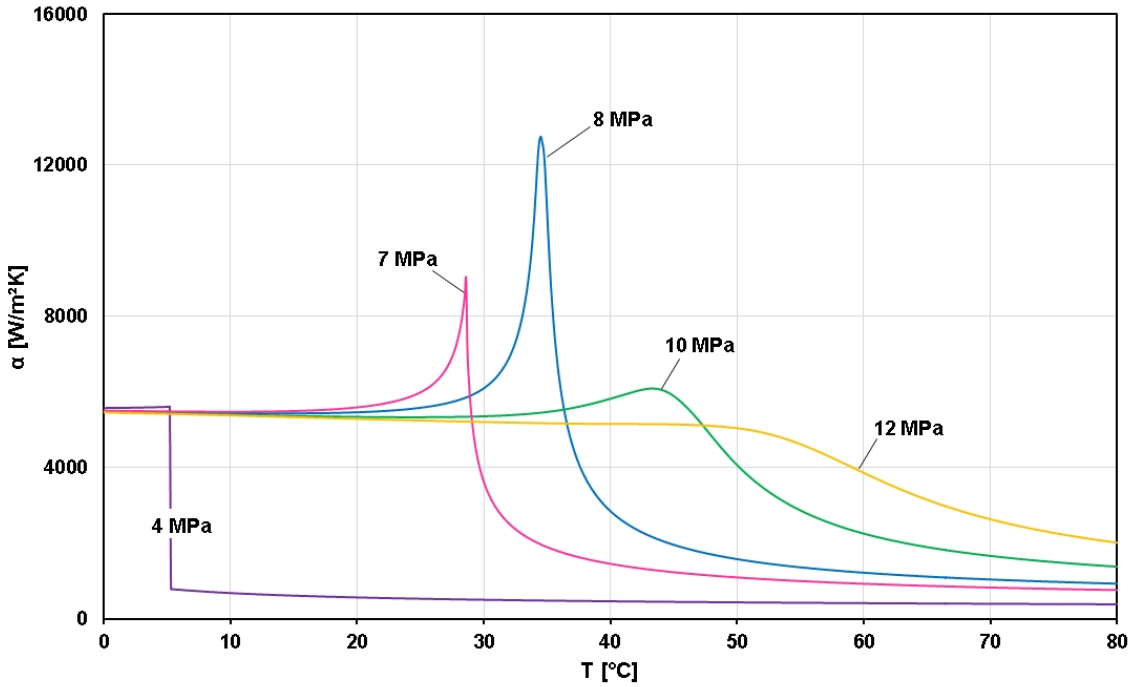

Figure 1: Calculated temperature-dependant heat transfer coefficient.

Pipe and channel flow under supercritical condition with intensively heated walls are influenced by the significant change of fluid properties, e.g. density, viscosity, thermal conductivity. In the range of higher heat flux densities combined with lower mass flow densities, the heat transfer depends intensively and non-linear on heat flux, mass flow and other operation parameters. This may trigger an unexpected and severe raise of the wall temperature, called Detoriated Heat Transfer (DHT). The reasons for these phenomena are not well known yet and they are only understood qualitatively [3-6]. A serious prediction of DHT is not possible until now.
Supercritical CO_2 flow with heat transfer has become of great interest lately, because it is suitable as working fluid in right- and left-handed low-temperature cycles. Dostal [7] showed the possibility to realise these cycles with high efficiency and economic capital costs, if efficient and

compact heat exchangers are applied. But for the dimensioning of compact heat exchangers it is necessary to know the heat transfer mechanisms and to have quantitative predictions of the necessary heat transfer. For these reasons investigations in three scientific fields have been established at IKE, which are involved in fundamental research of supercritical fluids, with focus on supercritical CO_2.
In the first scientific field research on Passive Safety-Systems for Nuclear Reactors is underway. Such a safety system is based on supercritical CO_2-Brayton cycle that is able to transform the nuclear decay heat in electric power and to release the waste heat to the environment [8]. The components of this passive safety-system need to be tested and numerical models for existing simulation programs have to be improved. The necessary programs are partly developed at IKE, but there is still lack of experimental validated models. In this context Printed Circuit Heat Exchanger (PCHE) as special type of compact heat exchanger are of great interest [9]. The technology seems very promising, particularly if supercritical CO_2 is used, because high heat transfer power is achievable, both on the pseudo-evaporation side and the pseudo-condensation side [10, 11].
The second scientific field deals with Thermofluid-Dynamics and especially with the theoretical modelling of complex multi-dimensional flow, heat transfer and mixing, especially fluid flow at supercritical pressure. Origin of these issues was the core dimensioning of a High Performance Light-water Reactor (HPLWR) [12]. This reactor type is working with supercritical pressures up to 25 MPa. Emphasis of the research was the modelling of the turbulent flow and heat transfer in the cooling channels, which show unusual and non-linear behavior due to the severe temperature-dependence of the properties of a supercritical fluid.
Because of the immense costs for experimental investigations with supercritical water, caused by the high critical pressure of 25 MPa, the verification of the models has to be carried out with supercritical CO_2 as a reasonable substitute. Therefore, a third group works on the experimental validation of the numerical models using appropriate experimental set-ups, for nuclear applications as well as for non-nuclear.

1.2 Multi-Purpose Facility SCARLETT

At IKE, a multipurpose test facility, named **SCARLETT** – **S**upercritical **Car**bon dioxide **L**oop at IK**E** Stu**TT**gart, for the investigation of supercritical CO_2 is currently under construction. This facility is intended to enable various experiments for fundamental research and applied science with supercritical CO_2. Separate test sections, which can be exchanged easily as main part of the facility, provide a great variety of experimental investigations. The emphasis of the investigations will be on the validation of numerical flow simulations with supercritical fluids and the gathering of experimental data for simulations about passive safety systems in nuclear reactors. It is also foreseen to transfer the acquired knowledge from nuclear technology to non-nuclear fields, e.g. application of low-temperature heat transfer, waste heat utilization, renewable energy sources and refrigeration engineering.

Planned investigations are:
- Heat transfer in passive safety systems based on supercritical CO_2 as working fluid.
- Qualification and optimization of compact heat exchangers and other components for low-temperature cycles with supercritical CO_2 as working fluid.
- Upgrade of existing, non-invasive measurement methods for supercritical fluids.
- Experimental investigations for validation of DNS and Large-Eddy-Simulations of turbulent heat transfer in heated and cooled pipes with and without wall roughness under supercritical pressure.
- Mixing of CO_2 flows with different temperatures and densities.

2. Experimental Set-up

2.1 Predesign and dimensioning

The layout data of the supercritical recompression cycle according to Dostal [7] are used as guideline for the testing facility. The high-pressure side is working with an operation pressure of 20 MPa. But under these conditions CO_2 shows a gas like flow far away from the critical point and is not of interest for investigations about the special heat transfer phenomena. The low-pressure side in this cycle works with a pressure of 7.7 MPa and in a temperature range from 32 to 69 °C for the precooler, respectively 69 to 157 °C for the low-temperature recuperator. These conditions are near to the critical point and the base for future investigations. For a downscaled 1 MW cycle the mass flow is calculated to 11.9 kg/s. After the comparison of a typical compact heat exchanger from the company HEATRIC with a prototype, which can be used at IKE, the necessary mass flow has to be about 0.122 kg/s for the precooler and 0.027 kg/s for the low temperature recuperator. This prototype allows the investigation of 30 - 40 channels per layer on a basis of 220 mm x 220 mm. This means a progress compared to the investigations of Corradini [13], who tested nine parallel channels.
In contrast to other CO_2 facilities the CO_2 mass flow will not be compressed to supercritical pressure by a gear-pump or a membrane-piston-pump. Instead, a piston compressor used by commercial stationary refrigerating plant is applied, which is able to handle a mass flow of about 0.111 kg/s. This type of compressor limits the maximum reachable pressure to 13 MPa. In the SCARLETT facility, it shall be possible to investigate several layers of a compact heat exchanger, which makes an appropriate value of the mass flow more import than a high pressure level. Hence, in the first stage of expansion, a maximum pressure of 13 MPa is sufficient. All other components are designed for a maximum pressure of 20 MPa, so that in a second stage of expansion a more powerful compressor can be implemented which is able to provide higher pressure.
The compressor outlet temperature of about 140°C makes it necessary to cool down the ejected mass flow massively to ensure the lower planned testing temperatures. Therefore, high thermal power has to be dissipated, which makes an adequate cooling system necessary.
The current operating parameters according to the facility design are shown in Table 1.

Table 1: Operating parameters

Parameter	Sign	Value	Unit
Mass flow	$\dot{m}$	0,013 – 0,111	kg/s
Temperature	T	5,0 – 150,0	°C
Pressure	p	7.5 – 13.0	MPa
Inner Pipe Diameter	d_i	10,1	mm
Cooling Power	P_{cool}	20 - 50	kW
Electrical Power	P_{el}	130	kW
Volume Pressure Vessel	V_{PV}	0,072	m³

The power class of the planned facility fits to the international network of existing research cycles with supercritical CO_2. There are cycles for fundamental research with lower mass flow but similar pressure level [11, 14, 15]. There is a CO_2-cycle at the University of Wisconsin in Madison for investigations on compact heat exchangers [16]. The maximum pressure of this cycle is higher (13 vs. 20 MPa) but the mass flow is lower in return (0.111 vs. 0.015 kg/s). Furthermore, SCARLETT is smaller than the large component cycles which are promoted by the US Department of Energy (DOE) [17]. The cycle at the Bhaba Atomic Research Centre, Mumbai, is of interest regarding natural convection investigations with supercritical CO_2 [18].

Comparisons between this cycle and SCARLETT concerning the development of passive safety-systems are possible.

2.2 Facility Design

The technical purpose of SCARLETT is to provide supercritical CO_2 at defined temperatures and pressures to different test sections. This allows the realization of investigations in many different technical fields.

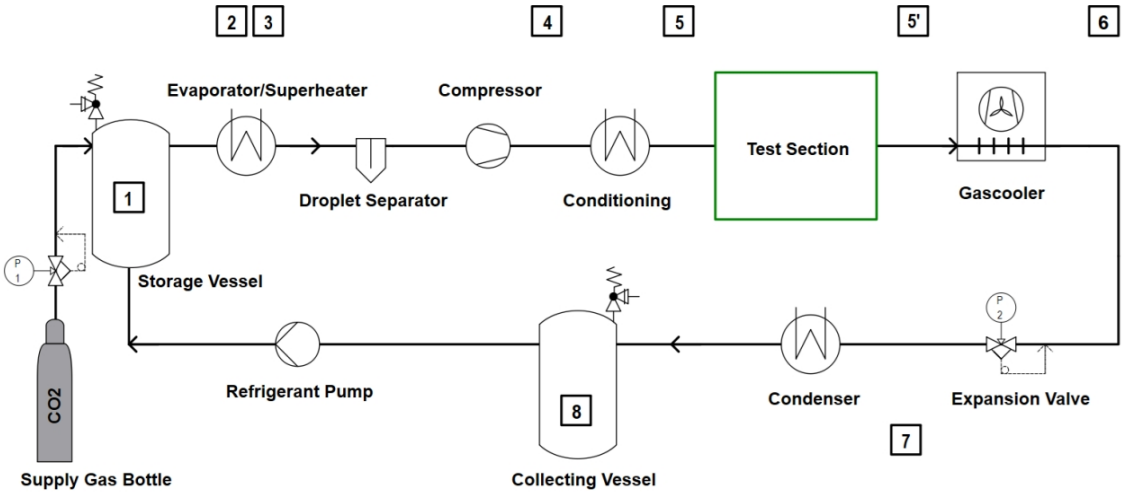

Figure 2: Scheme of the CO_2-loop.

Therefore, the facility is designed as a closed loop, in which CO_2 is circulating continuously. If the facility is off-state, the CO_2 is stored as liquid in two pressure vessels, the storage vessel and the collecting vessel. The storage vessel can be refilled by CO_2 gas (standpipe) bottles. During operation the CO_2 passes through a left-handed thermodynamic cycle, which is shown in Fig. 3. First it flows to an electrical heated evaporator in which it will be completely isobaric evaporated and isobaric overheated for about 10 K to ensure a minimum of remaining liquid droplets in the CO_2 gas flow. After passing a droplet separator, for eliminating the last liquid droplets and to prevent the compressor from damages by liquid strike, the CO_2 will be surged by a piston-compressor and compressed to supercritical pressure and temperature. After the compressor, the supercritical CO_2 will flow through a heat exchanger where it is either cooled or heated to the desired testing temperature (so called conditioning). Then, the supercritical CO_2 will enter the test section, in which the experiments will be carried out. Because of the various conceivable investigations in the test section, it is illustrated as black box in Fig. 2, which shows the scheme of complete the CO_2 loop. After leaving the test section with uncertain conditions the CO_2 is cooled to ambient temperature in a forced-ventilation gas cooler that is installed outside the laboratory building. Now, an expansion valve will reduce the CO_2 pressure in an isenthalpic process to subcritical conditions in the wet steam area. Afterwards the CO_2 will be fully isobaric condensed in a plate heat exchanger and flows into the collecting vessel. A refrigerating pump between both pressure vessels will deliver the liquid CO_2 back to the storage vessel and the loop will be closed. The thermodynamic cycle of the testing facility is plotted in Fig.3 by a log-p-h-diagram.

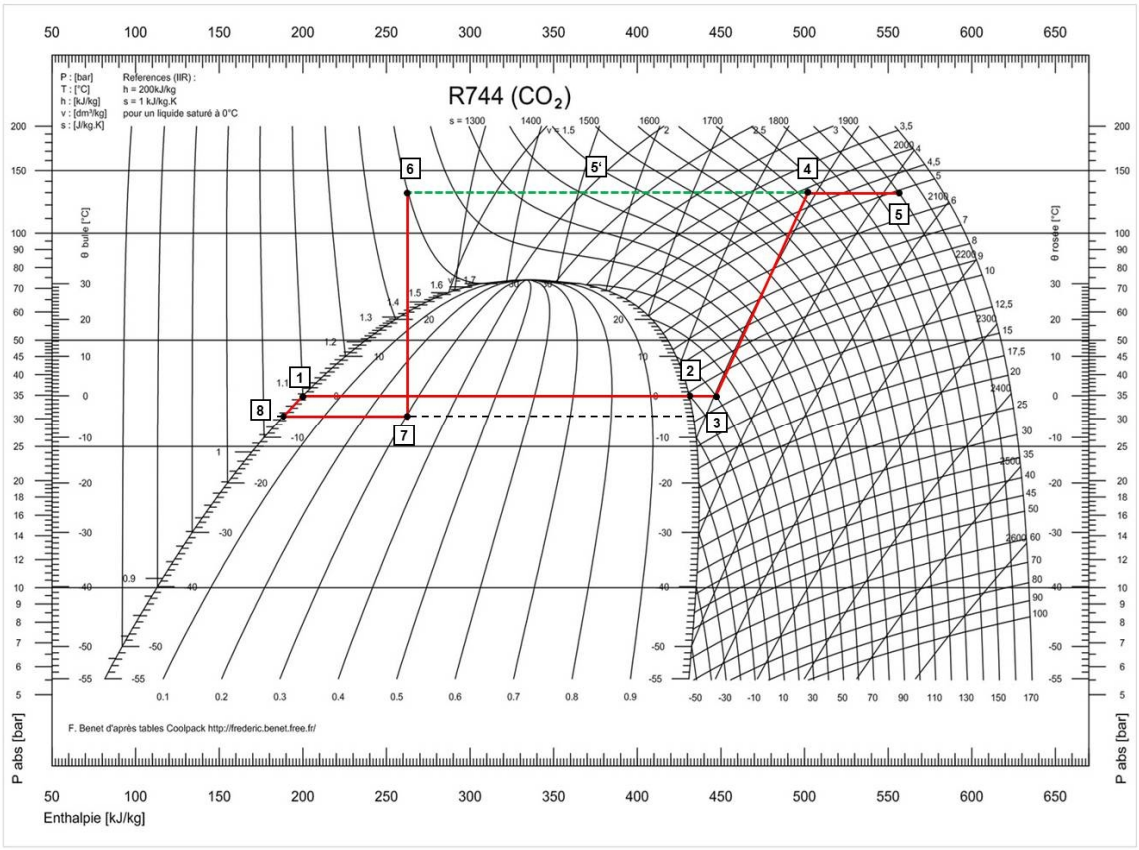

Figure 3: Log-p-h-diagram of the CO_2-loop.

The thermodynamic condition of the CO_2 in each component of the facility, including the exchanged thermal power is shown in Tab.2.

Table 2: Thermodynamic state of the CO_2.

Point	Component	Outlet Temperature	Outlet Pressure	Thermal Power
1	Storage Vessel	5,0 °C	3.97 MPa	-
2	Evaporator	5,0 °C	3.97 MPa	27 kW
3	Superheater	15,0 °C	3.97 MPa	2 kW
4	Compressor	110 °C	13.0 MPa	-
5	Conditioning	5…150 °C	13.0 MPa	8 - 36 kW
5’	Test Section	5…150 °C	13.0 MPa	x
6	Gas cooler	38 °C	13.0 MPa	34 kW
7	Expansion Valve	2.3 °C	3.71 MPa	-
8	Condenser	2.3 °C	3.71 MPa	10 kW
9	Collecting Vessel	2.3 °C	3.71 MPa	-
10	Refrigerant Pump	5 °C	3.97 MPa	-

Fig. 4 shows a CAD-sketch of the CO_2 facility SCARLETT including peripheral components and the laboratory and in Fig. 5 the detailed piping and instrumentation diagram of the facility is presented.

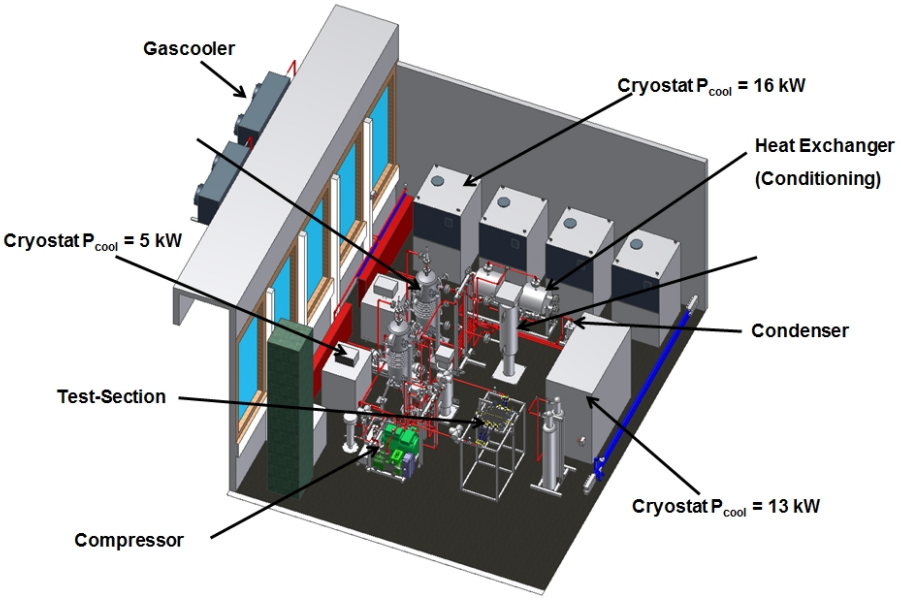

Figure 4: CAD-sketch of the CO_2-testing-facility.

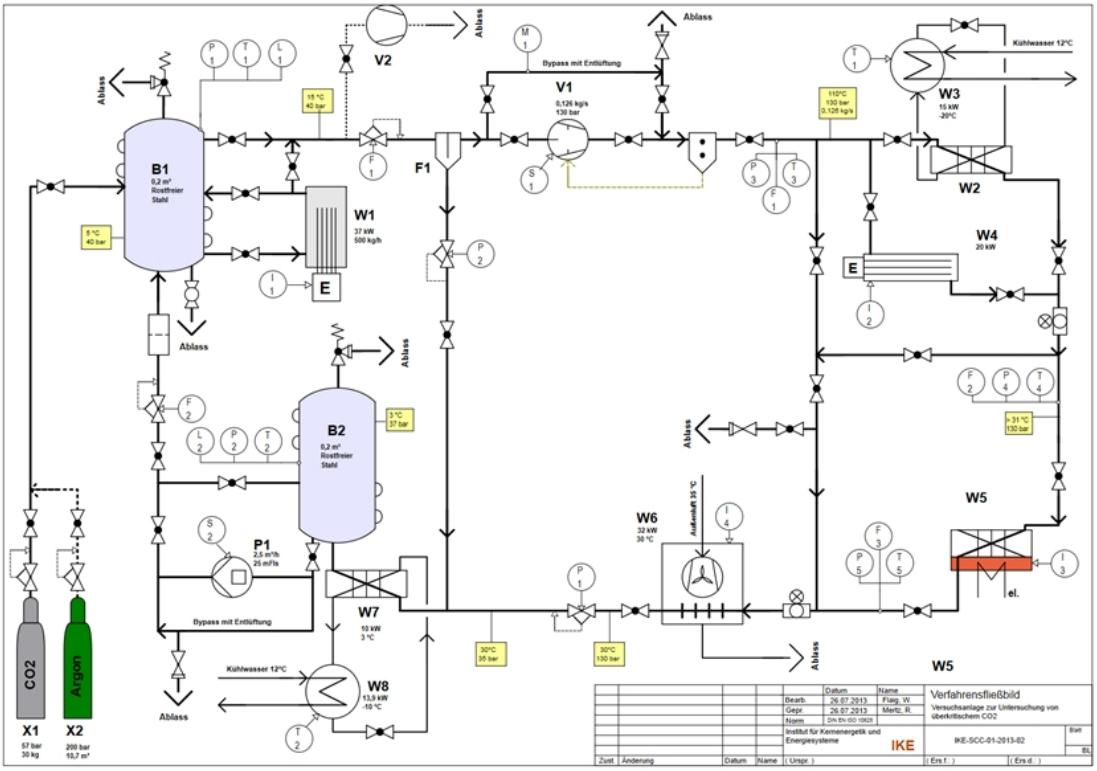

Figure 5: Piping and instrumentation diagram.

2.3 Measurement techniques

For controlling and surveillance of the test facility, several measurement instruments are available. All sensors are connected to an Agilent data acquisition system, which allows sending and receiving data. Tab. 3 gives an overview of the applied measurements instruments and their measuring range, respectively their accuracy.

Table 3: Installed measurement instruments.

Parameter	Device	Range	Accuracy
Mass flow	Coriolis flow meter	0.013 – 0.130 kg/s	0.5 %
Temperature	Pt-100 resistance thermometer	-20 – 200 °C	0.15 K + 0.002 • [t]
Pressure	Piezo-resistive pressure transmitter	0 – 30 MPa	0.15 %
Liquid level	Differential pressure transmitter	200 – 1000 mm	0.075 %

Besides the described measurement devices, an observation window will be installed to enable the application of optical measurements.

2.4 Safety installations

The threshold limit value (TLV) of CO_2 at working place is 5000 ppm, defined for German workplaces by the German Government at TRGS 900. CO_2 is toxic for humans in concentration higher than 5 % of the breathing air. Furthermore, the high pressure in the facility can be a safety risk in the case of a failure of single components.
However, to ensure best possible safety for employees in the CO_2-laboratory, there are several arrangements, which will be implemented for the operation of the facility:

- Gas detection devices to warn in of a dangerous concentration of CO_2.
- Installation of an exhaust extraction system to remain a low level of CO_2 concentration in the air.
- Inhabitancy in the CO_2-laboratory during operation is not permitted. Instead the laboratory will be controlled from an adjacent laboratory by a video system.
- The complete facility is constructed according to the European Pressure Equipment Directive (guideline 97/23/EG) and will be verified by Technical Control Board (TÜV).

3. Test Sections

3.1 Printed Circuit Heat Exchanger (PCHE)

A subject of current research work at IKE is a retrofittable passive decay heat removal system for boiling water reactors (BWR). This system is based on a turbo-compressor-system with supercritical CO_2 as working fluid. Thus the decay heat of the primary circuit is transferred to the CO_2 system via a Printed Circuit Heat Exchanger (PCHE). The CO_2 system converts the decay heat by a Brayton Cycle into electricity and low-temperature waste heat, which can be emitted to the ambient [8]. The CO_2 system is analysed with ATHLET, a thermal-hydraulic system code [8] . The sketch of the described system is shown in Fig. 5.

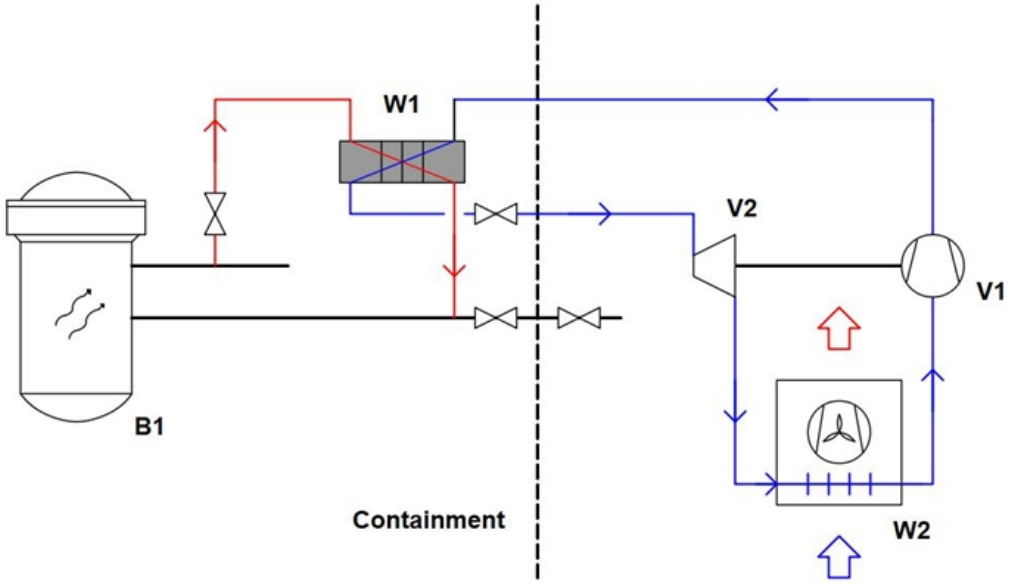

Figure 5: CO_2 based turbo-compressor-system for decay heat removal.

The PCHE works as condenser for the steam on the primary circuit. With the use of supercritical CO_2 on the secondary side it is possible to realise an extremely compact PCHE with a surface to volume ratio of about 500 m²/m³ [8]. The high compactness allows the uncomplicated installation of the PCHE in existing reactor buildings. An example of a PCHE design is shown in Fig. 6.

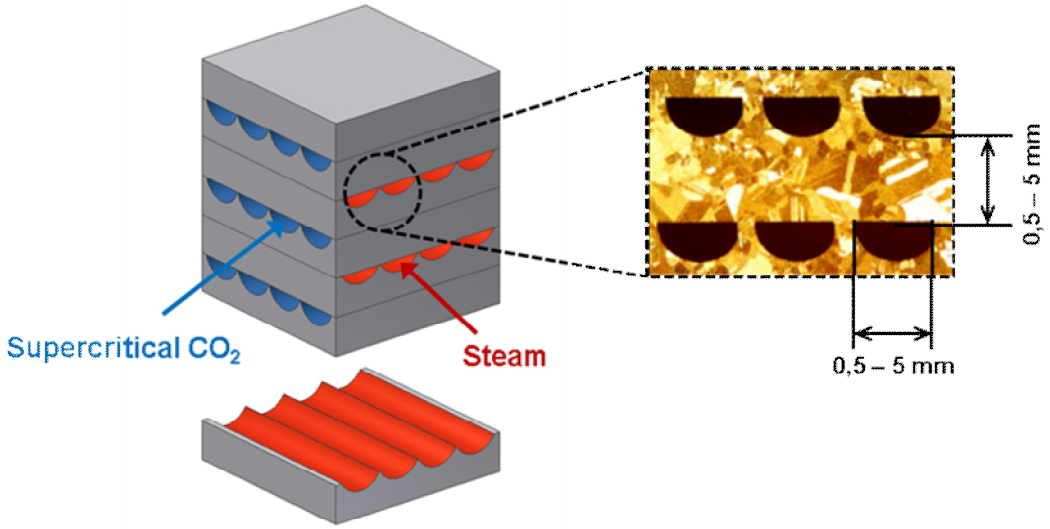

Figure 6: Example for a PCHE-condenser of the decay heat removal system.

Further advantages of a PCHE are the usage in wide temperature ranges (-200 to 900 °C) and for high pressure (up to 60 MPa) and the possibility to work with liquids, gases and two-phase-mixtures. A PCHE can be manufactured by etching flow channels (typical 0.5 to 5.0 mm hydraulic diameter) into single plates and then assembling these single plates by diffusion bonding. This process creates a connection on molecular level. The layer boundary vanishes, which leads to high solidity, respectively high pressure resistance.
The dimensions and operating parameters of the PCHE, which was investigated numerically for the decay heat removal system from Venker [8], are shown in Tab. 4.

Table 4: Parameters of the PCHE [8].

Parameter	Value	Unit
Predicted Heat Flux	60	MW
Heat flux density	100	kW/m²
Mass flow	165	kg/s
Mass flow density	515	kg/m²s
Hydraulic diameter	1.1	mm
Channels per plate	200	-
Basic area	650 x 650	mm
Surface area	600	m²
Volume	1.2	m³
Inlet temperature	67	°C
Inlet pressure	17.5	MPa

This PCHE was dimensioned and analyzed with ATHLET showing promising simulation results as functional unit within the complete CO_2 system. But this analysis has some uncertainties, regarding the actual possible transferable heat flux density, the calculation of the Nusselt Number and the exclusion of DHT. It is necessary to validate these results with experimental data.
Therefore, a test section was developed to investigate one downscaled pair of plates on the CO_2 side. The maximum basic area is due to the dimension of the welding machine 220 x 220 mm, which makes it necessary to mill in about 60 channels (compared to 650 x 650 mm with 200 channels). A sketch of this test section is shown in Fig. 7.

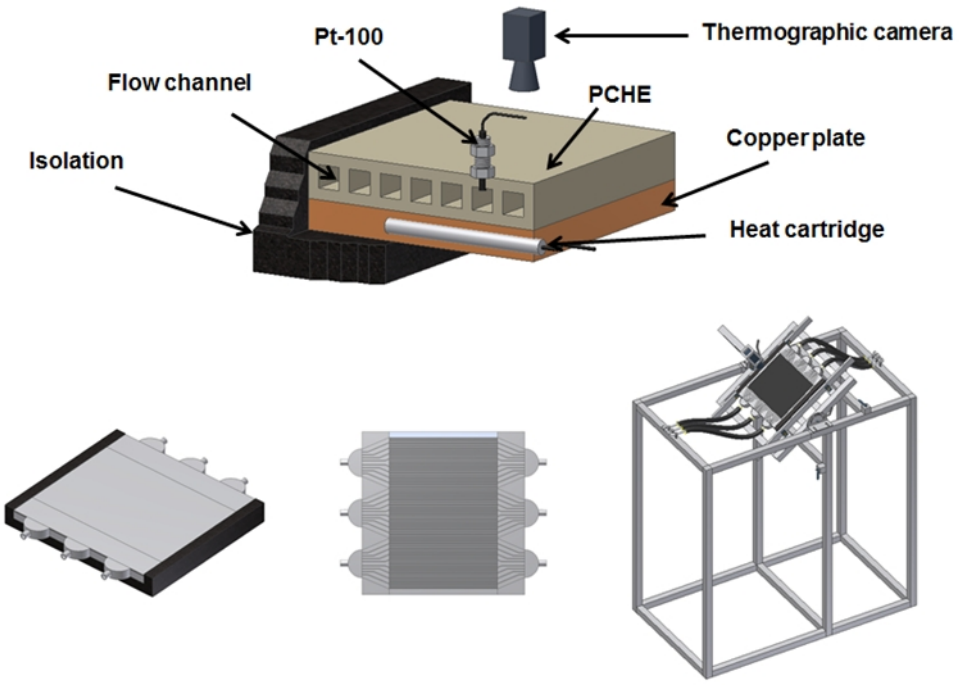

Figure 7: CAD-sketch of the PCHE test section.

The hot primary steam side is imitated by a plate made of copper with installed heating cartridges. The high thermal conductivity of copper (λ = 380 W/m K) leads to uniform distribution of the heat and to a constant temperature over the surface, similar to the thermal condition in flow channels with phase-changing fluid. For the CO_2 side one plate of the PCHE is used, which will be diffusion-bonded to the copper plate to create one consistent unit of a heat exchanger that resists high pressure. The test section will be instrumented with Pt-100 and pressure transmitter to gather wall temperature and pressure loss. A thermography camera will be used to detect the temperature distribution over the surface of the test section. The measurement data will be evaluated to calculate wall overheating, heat transfer coefficient, heat flux density and the onset of DHT.
It will be of interest to vary the parameters mass-flow, heat flux density and inlet temperature to gain knowledge about the achievable thermal power under different operating conditions and the risk of triggering DHT at the same time. For experimental conditions mass flow was chosen to be between 0.02 and 0.07 kg/s, inlet temperature in the range of 15 °C to 45 °C, pressure between 7 MPa and 10 MPa and heat flux between 1 kW to 12 kW.

3.2 Heated vertical/horizontal pipe

In 2010, an IAEA-ENEL meeting [19] showed that there is still a lack of knowledge about turbulent flow with heat transfer, especially in combination with high wall heat flux density under pressure near the critical point and within a temperature range, where the pseudocritical temperature is between wall temperature and bulk temperature. Up to now, it is not possible to derive correlations, laws of similarity and turbulence models without comprehension about phenomena of turbulence, hydrostatic buoyancy, wall roughness and further parameter of influence. Chu et al. [20] started a research project with the goal to gain basic knowledge about the turbulence in intensive heated pipe flow with variable properties in the range of high Prandtl Numbers. A DNS simulation with the software OpenFoam will be performed using supercritical CO_2 as working fluid. An experimental set-up is necessary to validate the results of the theoretical investigations. A scheme of this set-up will be built and will be integrated in the IKE test facility in 2015.
Supercritical CO_2 flows through a 3000 mm long pipe, whose wall is heated directly by electrical power supply. Wall temperature is measured by Pt-100. Bulk temperature can be calculated by enthalpy balance with knowledge of mass flow, heat flux density and wall temperature. This allows the reproduction and comparison of the experiments of Bae [21] and Pioro [22].

4. Summary

A multipurpose test facility for supercritical CO_2 is under construction at IKE. Variable test sections, which can be exchanges easily, will allow various experiments for fundamental and applied research, especially on the field of the validation of numerical models for passive reactor safety systems and turbulent flow with heat transfer. The testing facility is designed as closed loop which delivers a CO_2 mass flow up to 0.111 kg/s to the test section under a maximum pressure of 13 MPa. The testing temperature can be set from 5 to 150 °C. Depending on this test temperature, the transferred thermal power of the facility can raise up to 50 kW. The compression to supercritical condition will be carried out by a piston compressor. A first test section will be manufactured to investigate the thermal behaviour of a PCHE, which is an element of passive decay heat removal system for BWR. For this purpose a downscaled pair of plates is flowed through by supercritical CO_2 whereas the hot side is electrical heated.

Acknowledgment

This work was supported by a grant from the Ministry of Science, Research and the Arts of Baden-Württemberg (Az: 32-7533.-8-112/81) to Wolfgang Flaig.

References

1. VDI-Wärmeatlas, Springer Verlag Berlin Heidelberg, 2013
2. F.W. Dittus, L.M.K. Boelter: Heat transfer in automobile radiators of tubular type. Univ. of California Publ. of Eng. 2, 443 – 461 (1930).
3. M.E.Shitsman: Impairment of the transmission at supercritical pressures, Teplofizika Vysokih Temperature, Vol.1 No.2, p.237-244 (1963).
4. B.S. Shiralkar and P. Griffith: Deterioration Heat Transfer to Fluids at Supercritical Pressure and High Fluxes, Journal of Heat Transfer, 27-36 (1969).
5. J.D. Jackson, W.B. Hall: Forced convection Heat transfer to fluids at supercritical pressure, Turbulent forced convection in channels and bundles, Hemisphere Publishing Corporation, 563-611 (1979).
6. V.G. Razumovskiy, A.P. Ornatskiy, Y.M. Mayevskiy: Local Heat Transfer and Hydraulic Behavior in Turbulent Channel Flow of Water at Supercritical Pressure, Heat Transfer-Sov. Res. 22, 91-102 (1990).
7. V. Dostal, M.J. Driscoll, P. Heijzlar: A supercritical Carbon Dioxide Cycle for Next generation Nuclear Reactors, MIT-ANP-TR-100 (2004).
8. J. Venker, D. von Lavante, M. Buck, D. Gitzel, J. Starflinger: Concept of a Passive Cooling System to Retrofit Existing Boiling Water Reactors, Proceedings of the 2013 International Congress on Advances in Nuclear Power Plants, ICAPP 2013, Jeju Island, Korea (2013).
9. N. Tsuzuki, Y. Kato, T. Ishiduka: High-Performance Printed Circuit Heat Exchanger, Applied Thermal Engineering 27, 1702-1707 (2007).
10. S. Pitla, E.A. Groll, S. Ramadhyani: New Correlation to Predict the Heat Transfer Coefficient during In-Tube Cooling of Turbulent Supercritical CO_2, Int. Journal of Refrigeration 25, 887-895 (2002).
11. S.H. Yoon, J.H. Kim, Y.W. Hwang, M.S. Kim, K. Min, Y. Kim: Heat Transfer and Pressure drop Characteristics during the In-Tube Cooling process of Carbon Dioxide in the Supercritical Region, Int. Journal of Refrigeration 26, 857-864 (2003).
12. K. Fischer, T. Schulenberg, E. Laurien: Design of a supercritical water-cooled reactor with a three-pass core arrangement, Nuclear Engineering and Design 239, 800-812 (2009).
13. M. Corradini: Supercritical Flow and Heat Transfer in Advanced Reactors, Proc. 14th In. Topical Meeting on Nuclear Reactor Thermal Hydraulics, NURETH-14, Sept. 25-30, Toronto, Canada (2011).
14. J.H. Song, H.Y. Kim, H. Kim, Y.Y. Bae.: Heat transfer characteristics of a supercritical fluid flow in a vertical pipe, J. of Supercritical Fluids 44, S.164–171 (2008).
15. P. C. Simões, J. Fernandes, J.P. Mota.: Dynamic model of a supercritical carbon dioxide heat exchanger, J. of Supercritical Fluids 35, S.167-173 (2005).
16. M. D. Carlson, A., Kruizenga, M. Anderson, M. Corradini.: Measurements of Heat Transfer and Pressure Drop Characteristics of Supercritical Carbon Dioxide Flowing in Zig-Zag Printed Circuit Heat Exchanger Channels, Supercritical CO_2 Power Cycle Symposium, Boulder, Colorado, 24.-25. May 2011.
17. S.A. Wright, P. S. Pickard, Bob Fuller.:"S-CO_2 Heated Un-Recuperated Brayton Cycle Development and Test Results" Sandia National Laboratories and Barber Nichols April 29,30 2009, RPI, New York.
18. B.T. Swapnalee, P.K. Vijayan, M. Sharma, D.S. Pilkhwal.: Steady state flow and static instability of supercritical natural circulation loops, Nuclear Engineering and Design S.99-112 (2012).
19. IAEA-ENEL Technical Meeting on "Heat Transfer, Thermal Hydraulics, and System Design for Supercritical Water-Cooled Reactors", Pisa, Italy July 5-8, 2010
20. Xu Chu and E. Laurien: Direct Numerical Simulation of Heated Turbulent Pipe Flow at Supercritical Pressure, 7th Int. Symp. on Supercritical Water-Cooled Reactors (ISSCWR-7), Helsinki, Finland, March 15-18, 2015.
21. Y.Y.Bae, H.Y. Kim: Convective heat transfer to CO2 at a supercritical pressure flowing vertically upward in tubes and an annular channel, Experimental Thermal and Fluid Science 33 (2009) 329-339.
22. I. Pioro, R. Duffey. Heat Transfer and Hydraulic Resistance at Supercritical Pressuresin Power Engineering Applications. ASME, Press, New York, NY, USA, 2007

ISSCWR7-2011

CFD prediction of heat transfer in rod bundles with water at supercritical pressure

Andrea Pucciarelli, Walter Ambrosini
Università di Pisa, Dipartimento di Ingegneria Civile e Industriale
Largo Lucio Lazzarino2, 56126 Pisa, Italy, Tel.+39-050-2218073, Fax +39-050-2218065
Email: andrea.pucciarelli@yahoo.it, walter.ambrosini@ing.unipi.it

Abstract

The paper further explores the application of CFD codes for the study of the heat transfer phenomena involved when working with fluids at supercritical pressure; bundle analysis is here considered in particular. As for previous simulations performed by the Authors considering heat transfer deterioration inside heated tubes, this application points out the limited capabilities of the most commonly used RANS models when approaching the heat transfer deterioration phenomenon. It must be noted that some of the considered experimental conditions, which are very close to the pseudo-critical temperature, represent at the same time one of the most challenging situations for the CFD codes and a very common situation if SCWRs will be developed.

Improvements of the currently available turbulence models are then needed. The paper analyses the most likely causes of the observed insufficient quality of the obtained predictions. In addition to compare the measured and calculated wall temperature trends, the effect of the presence of the spacer grids on the turbulent flow is considered. Spacers are in fact very important in order to assure the structural stability of fuel, though they also affect the flow, generally improving the turbulence conditions in their neighbourhood and slightly impairing it in the downstream region. A comparison between predictions performed including or not the spacers is also performed.

1. Introduction

The Supercritical Water Cooled Reactor (SCWR) currently represents a viable possibility of development of the existing LWRs in the frame of the Generation Four International Forum. The advantages of developing such a reactor are an improved economy and energy efficiency and a simpler plant layout. Gaining advantages also implies overcoming hard challenges; in this paper some of the ones related to thermal-hydraulic predictions are discussed.

The interest of researchers for Supercritical fluids started in the seventies, as demonstrated by several experimental campaigns performed at that time [**1-2-3-4**] regarding heat transfer in circular pipes; however, the interest in supercritical fluids then decreased. Experimental data restarted to be collected with renewed interest in the last two decades [**5-6-7**], considering different fluids and geometries, aiming at improving the predictions by CFD codes of the phenomena involved in the heat transfer to supercritical fluids. Activities [**8-9-10-11-12**] were also performed at the University of Pisa in order to evaluate the capabilities of the different modelling techniques in the application to supercritical fluids; interesting results were found but the obtained values often are inaccurate and reproduce the experimental data only from a qualitative point of view. Broad information about the behaviour of the various models in the

case of circular tubes was obtained, suggesting to perform simulations with more complicated geometries. In fact, evaluating heat transfer in simple geometries is surely important, but better information on the viability of the development of SCWRs could be obtained analysing operating conditions much closer to the ones that should really occur in the future reactor core.
Experimental campaigns analysing heat transfer to supercritical fluids in rod bundles were performed all around the world obtaining interesting suggestions concerning the bundle geometries and the effect of the spacer grids on the fluid flow. In this respect, the paper considers two different sets of experimental data: the one by Zhao, et al. (2013) [**13**] consisting in a four-rod bundle in trans-psuedocritical conditions, and the one used for the "International Benchmark: Supercritical flow in a 7-rod Bundle" [**14-15**], which considers a lower fluid temperature. The objective of the present work is to reproduce the selected experimental conditions by CFD codes in order to evaluate their capabilities in analysing the involved heat transfer phenomena in conditions similar to those in a postulated design. An analysis of the quality of the obtained predictions is performed in the present paper trying to define guidelines for future studies and simple procedures to be considered when dealing with bundle analysis.

2. Considered Experimental Data Sets

As already anticipated in the previous section, two data sets were considered in the present work; the 7-rod bundle geometry was used in the frame of a benchmark exercise [**16**], while the 4-rod bundle one was used for validation. The experimental conditions and the geometry information regarding the two sets are shortly summarised below.

2.1 7-rod Bundle geometry and boundary conditions

This set of data was used in the frame of the "International Benchmark: Supercritical Flow in a 7-rod bundle" organized by the Generation IV International Forum (GIF). Three experimental conditions were considered but in the present work only the two heated cases will be analysed. The adopted geometry and the considered computational domain are reported in Figure 1. **Table 1** shows the experimental conditions, while **Figure 1** and **Figure 2** present the geometry of the channel and of the spacers, together with the considered computational domain.

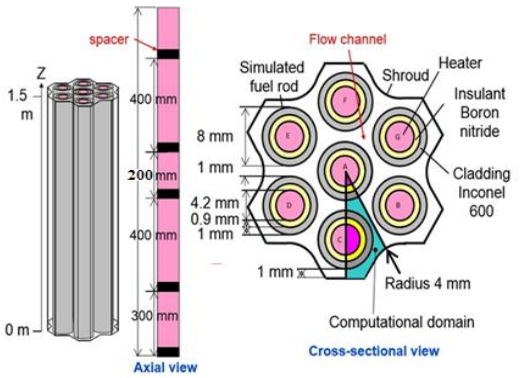

Figure 1. Proposed geometry and considered computational domain, taken from the documentation provided by the Benchmark proposing organization [**16**].

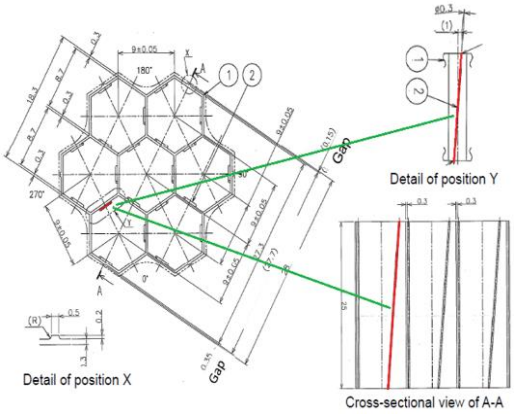

Figure 2. Spacer geometry, taken from the documentation provided by the Benchmark proposing organization [**16**]

Table 1. Considered operating conditions.

Case	Reference Pressure [MPa]	Inlet Temperature [K]	Mass flow rate [kg/m^{2}s]	Supplied Power [kW]		
				Rod A	Rod B,D,F	Rod C,E.G
B1	24.98	353.58	1447.56	19.67	22.51	22.52
B2	25.03	519.58	1432.97	34.14	34.08	34.13

In particular, Figure 2 shows the adopted spacer configuration. It must be remarked that the little support rods highlighted in red were not considered during our calculations, because of mesh gridding problems and because they required the simulation of the whole domain. In fact, by neglecting the support rods and taking advantage of the various symmetry planes, it was possible to perform the simulations considering just 1/12 of the whole domain, saving computational effort. The problem of the computational effort was in fact very challenging; operating with a single four processor computer, the domain had to be divided axially into five parts which were analysed one by one starting from the upstream ones and then assembled together. While the introduced simplifications could have impaired the quality of the obtained results, they actually turned out to be plausible and relatively accurate in front of the experimental data provided at the end of the Benchmark.

2.2 4-rod Bundle geometry and boundary conditions

The addressed experimental data were collected using the SWAMUP facility at the Shanghai Jiao Tong University (SJTU) and presented at the ISSCWR-6 Meeting [**13**]. These experimental conditions were harder to be simulated if compared to the ones of the above Benchmark exercise, because of their trans-pseudo-critical nature, resulting in large property changes. Two operating conditions were considered in the present paper. The geometries of the two cases, though similar, are not exactly the same: some reference information is reported in **Figure 3**, while the corresponding experimental conditions are reported in **Table 2**.

One fourth (1/4) of the whole domain was considered in the analysis taking advantage of the symmetry planes. The only considerable departure of the considered geometry with respect to the real one is related to the distance between the rods and the spacers at the four contact points: because of meshing problems the rod-spacer gap had to be enlarged to about 0.25 mm; this assumption was considered of little importance for the obtained results.

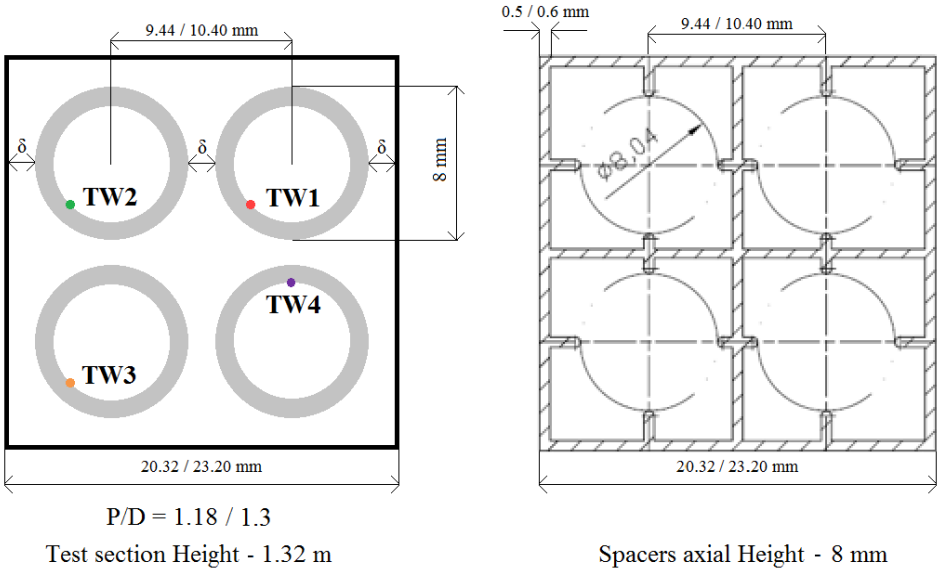

Figure 3, Geometry of the problem and particular of the spacers shape, documentation provided by the Authors of the paper Zhao, M., et al., (2013) [**13**].

Table 2. Considered operating conditions.

Case	P/D	Pressure [MPa]	Inlet Temperature [°C]	Mass flow rate [kg/m^{2}s]	Heat Flux [kW/m^2]
1	1.3	26.01	348.2	456.5	455.4
2	1.18	26.07	342.2	1472.1	785.6

3. Results

The CD-adapco STAR-CCM+ code (Version 7.04.006) [**17**] was used for performing all the calculations; k-ε and k-ω turbulence models were used in association with the Low y^+ wall treatment. As already pointed out in previous works [**18**], these two kinds of turbulence models tend to behave in a different way: the k-ε models usually tend to overestimate the wall temperature measurements, while the k-ω ones often underestimate the experimental data.

This feature was used when approaching the cases of the considered Benchmark as the experimental data were not provided at the time when the calculations were performed. The concept at the basis of the "Squeeze Theorem", regarding the bounding of a function, was borrowed; it was then assumed that the experimental data might lay between the results obtained using a k-ε model (upper bound) and the ones obtained using a k-ω one (lower bound). As a further implication, the idea was postulated that if k-ε and k-ω models returned similar results, the obtained values should have been considered plausible and assumed close to the experimental data. Different Low-Reynolds turbulence models were considered when performing the simulations; in the present work, the results obtained adopting two of them, the AKN (1994) [**19**] and the SST k-ω (1994) [**20**], will be shown, as they are representative enough of the obtained results. The values obtained using these two models were used as the bounds of the ranges where the experimental data should stay and then compared with the provided measured values. **Figure 4** shows the comparison between the experimental data and the obtained ranges for Case B1; the position of the thermocouples is shown as well.

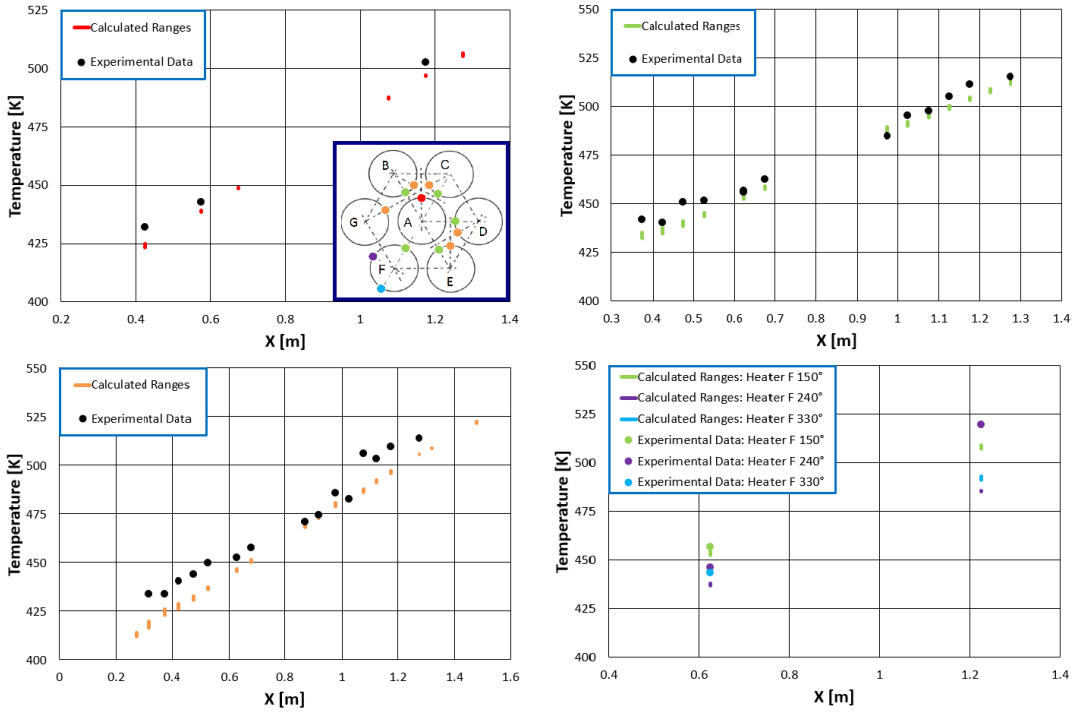

Figure 4. Comparison of the calculated wall temperature values with the experimental data.

In the figure, thermocouples located in nearly equivalent positions are displayed with the same colour. As it can be noted, both the considered models were able to reproduce quite well the experimental data; the measured trend is in fact only slightly underestimated in particular in correspondence of the orange and purple thermocouples. The ranges identified by the two selected models are very narrow as both the models return almost identical results; so, according with the postulated applicability of the Squeeze Theorem, the calculated values were considered plausible enough even before the distribution of the experimental data.
Good predictions, even if with lower quality, were obtained also for case B2; **Figure 5** compares the obtained wall temperature ranges and the measured data. Once again the experimental trend is slightly underestimated by both the models which, in this situation, show larger discrepancies between each other, as the obtained ranges are wider. Problems arise in particular in the final part of the heated section, where the measured values show a stronger heat transfer deterioration than the one predicted by both the models. Anyway, the oscillatory behaviour of the experimental trend in the final part of the test section is a bit strange and the very little differences between the supplied power in the external rods seem to be not sufficient to imply these trends. This may be due to a non-homogeneity in the power supplied within the rods; further analyses changing the power distribution and neglecting the spacer grids were then performed obtaining some interesting results, which will be shown in section 5.

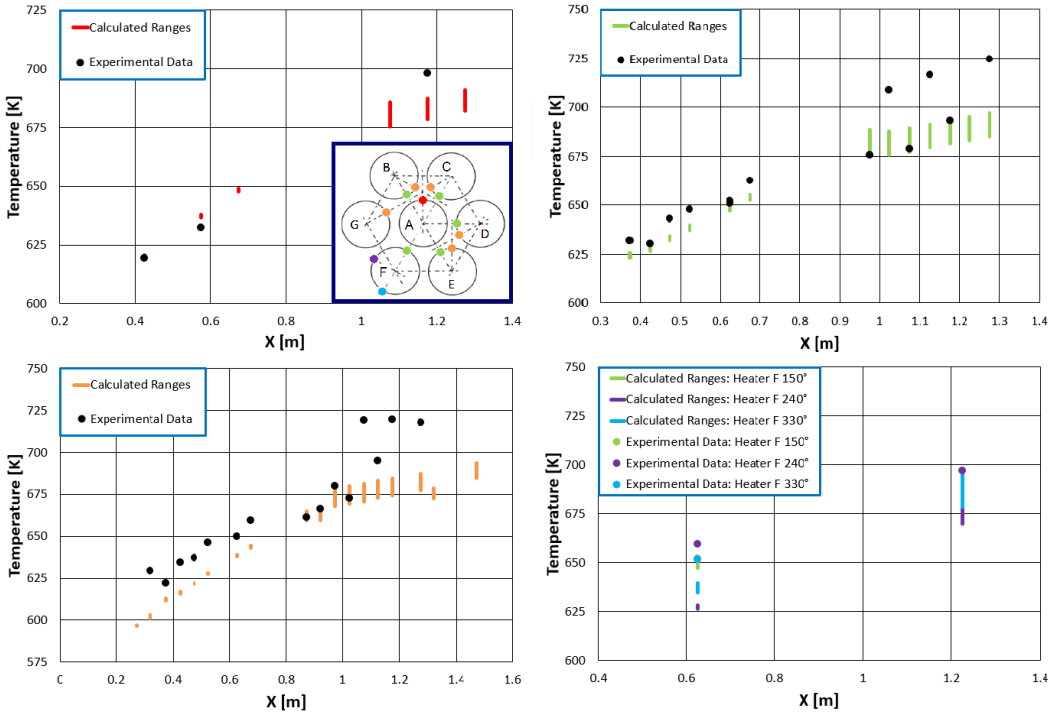

Figure 5 Comparison of the calculated ranges with the experimental data.

The good quality of the predictions obtained in the considered Benchmark cases are probably due to the operating conditions which are very far from the pseudo-critical threshold in particular for Case B1. Concerning the 4-rods bundle considered as further reference, the experimental conditions are instead much more severe and unfortunately, as already pointed out for heat transfer analyses in circular tubes [**9**-**10**-**11**] the considered turbulence models seem not to be able to reproduce the correct trend of the experimental data. **Figure 6** and **Figure 7** report the comparison of the calculated trends and the experimental data for Case 1 when adopting the AKN (1994) and the SST k-ω (1994) model respectively. As it can be easily noticed the quality of the obtained results is poor. When adopting the AKN (1994) model a strong overestimation of the experimental data is obtained in particular at the beginning of the heated section; the

calculated data get closer to the measured ones in the downstream region because of a general improvement of the calculated turbulence conditions, but the measured trend is not reproduced. Slightly better results were obtained when using instead the SST k-ω (1994) model as the strong deterioration predicted by the AKN (1994) model at the beginning of the test section is not present. The model is anyway not able at reproducing the increase of the wall temperature along the pipe since the calculated peaks become smaller progressing in the pipe and the measured trend is generally underestimated. It must be anyway remarked the effect of the six spacers. In fact, they contribute at keeping lower the wall temperature since they imply a periodical remixing of the flow. Results from simulations performed without considering the spacer grids will be shown in section 4, showing that, in cases with operating conditions close to the pseudo-critical ones, accounting for the spacers is fundamental for obtaining more realistic results.

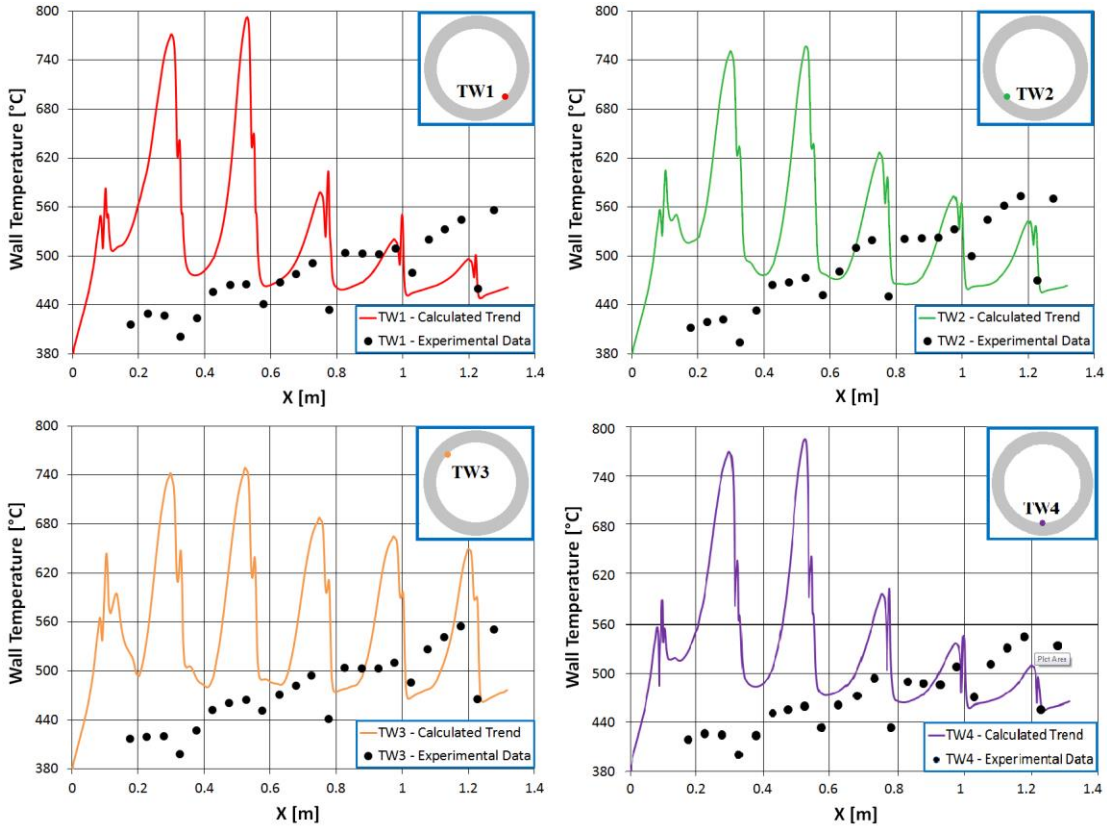

Figure 6. Comparison of the calculated values with the experimental data when adopting the AKN (1994) model for Case 1.

Though still considering trans-pseudo-critical conditions, the results obtained for Case 2 are closer to the experimental data even if their quality is generally insufficient. **Figure 8** and **Figure 9** report the comparison of the calculated trends with the experimental data for Case 2 when adopting the AKN (1994) and the SST k-ω (1994) model respectively. As it can be noticed, both the models underestimate the measured wall temperature trend even if good coherence can be found at the beginning of the heated section in the vicinity of the TW1 and TW2 thermocouples. The two models are not able at reproducing the sharper increase in the wall temperature trend occurring downstream the axial position at 0.8 m. This fact is probably due to the high mass flux characterising this experiment which does not allow the considered models at predicting the evident poorer turbulence conditions and, as a consequence, the strong increase in the wall temperature trend.

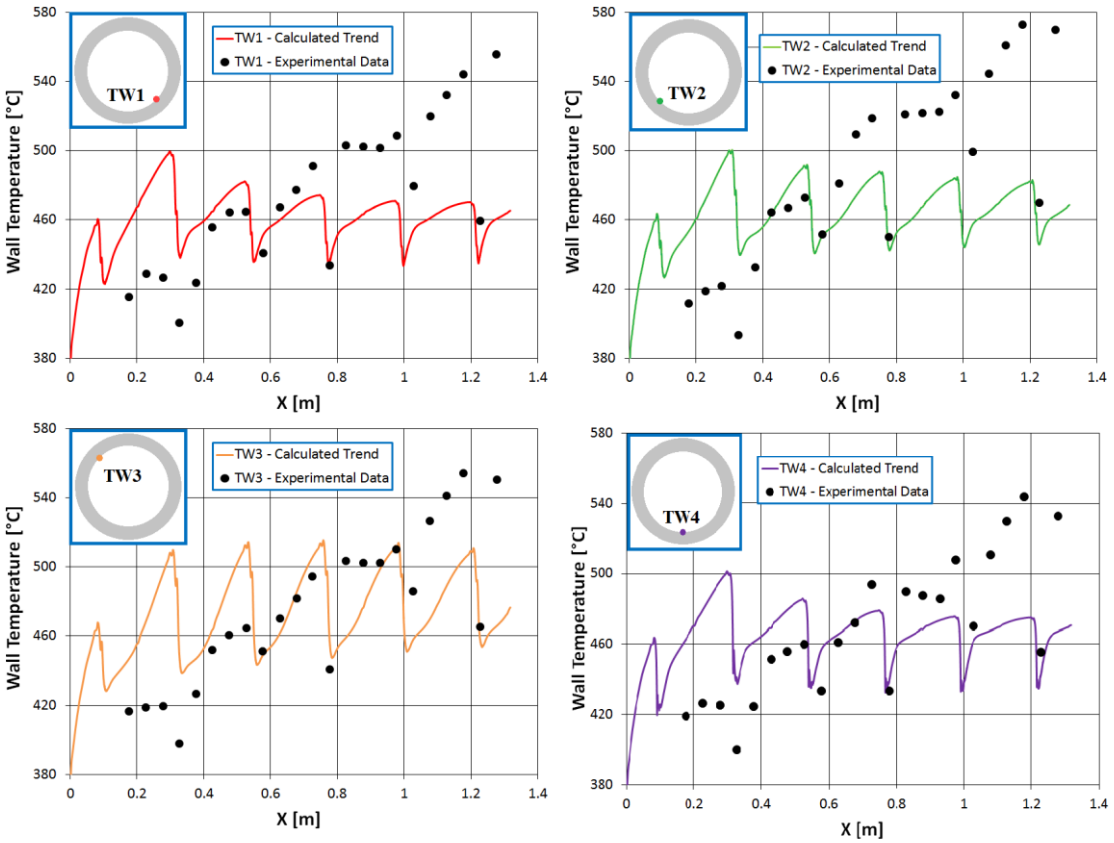

Figure 7. Comparison of the calculated values with the experimental data when adopting the SST k-ω (1994) model for Case 1.

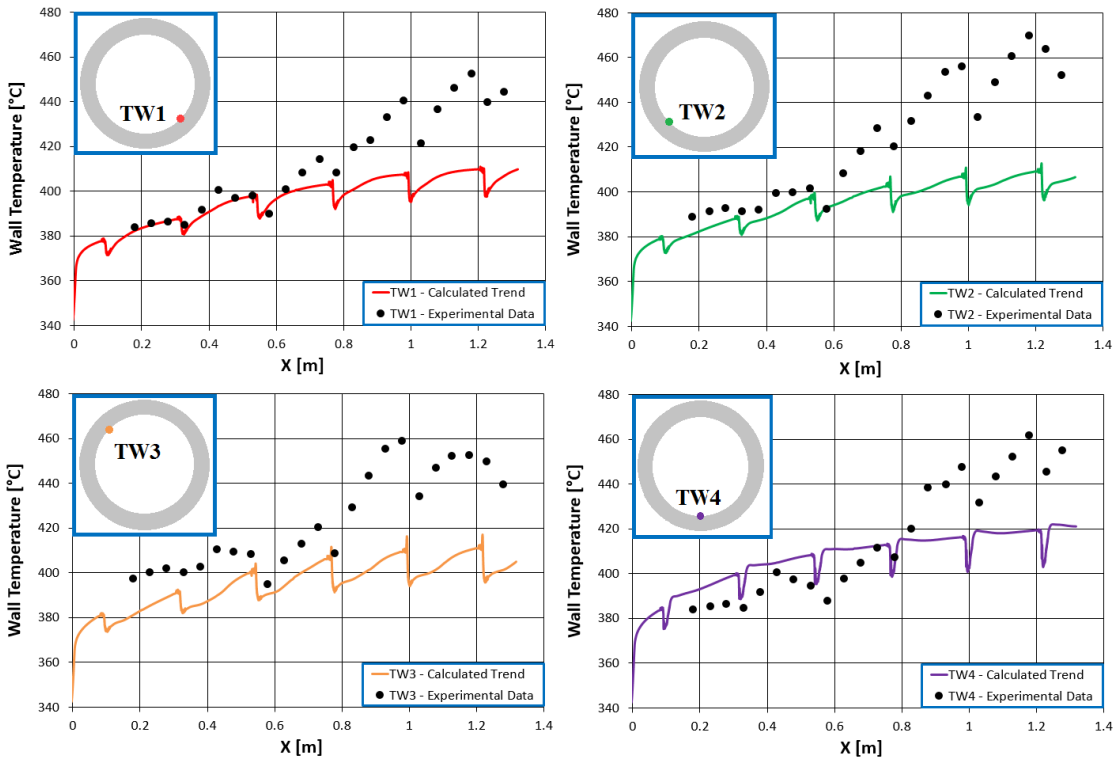

Figure 8. Comparison of the calculated values with the experimental data when adopting the AKN (1994) model for Case 2.

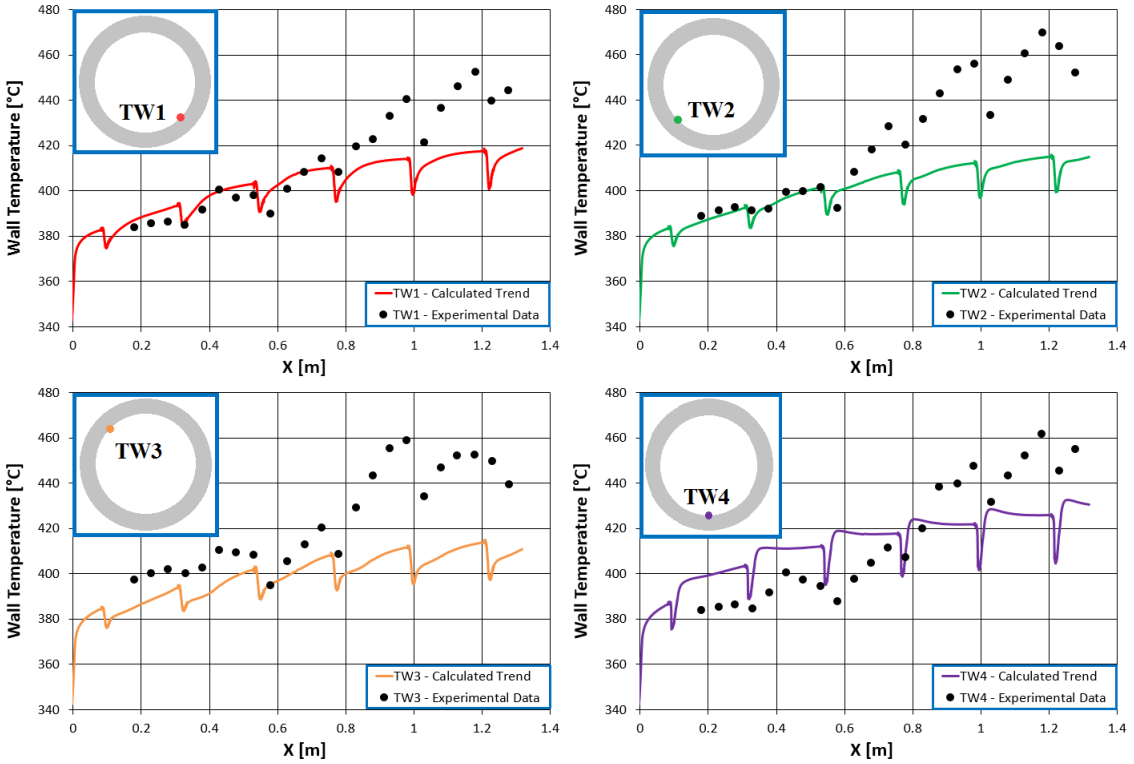

Figure 9. Comparison of the calculated values with the experimental data when adopting the SST k-ω (1994) model for Case 2.

4. Effect of the spacers on the fluid flow and heat transfer

The effect of the spacer on the heat transfer was analysed for both the selected experimental data sets showing a similar impact even if of different magnitude. **Figure 10** and **Figure 11** report the wall temperature trend calculated all around the heating rods for Case B1 of the benchmark considering whether or not the spacer grids respectively. As it can be noticed by comparing the two Figures, in this case the spacer grids only have a local effect. They imply a little enhancement of the heat transfer in correspondence of their location while their effect turns from positive to negative in the downstream region since a little heat transfer deterioration occurs.

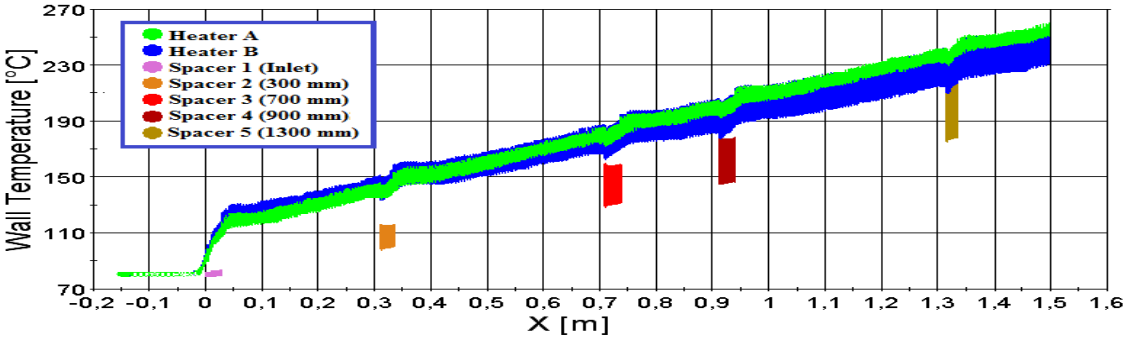

Figure 10. Calculated wall temperature trend for Case B1 when considering the spacer grids and adopting the SST k-ω (1994) model.

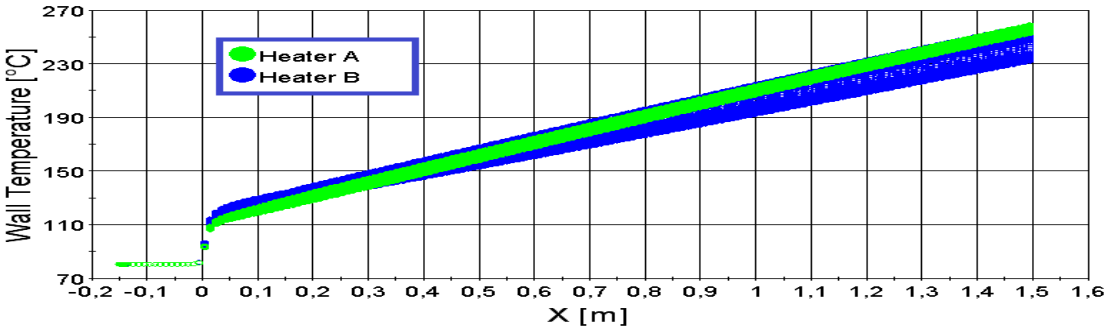

Figure 11. Calculated wall temperature trend for Case B1 when not considering the spacer grids and adopting the SST k-ω (1994) model.

This is due to the changes in the velocity distribution that the flow undergoes when passing through the spacer locations. This can be easily noticed looking at the proposed **Figure 13** to 15 relating to the region straddling the spacer located at 300-325 mm from the beginning of the heated length. The cited Figures relate to the section highlighted in **Figure 12**. **Figure 13** shows the distribution of the axial velocity which improves in correspondence of the spacer grid because of the decrease in the available flow section; as a consequence, also the axial velocity derivatives increase causing a general improvement of the production term of turbulence due to shearing as shown in **Figure 14**. As a final result, as reported in **Figure 15** , the turbulent kinetic energy increases in the region in correspondence of the spacer implying the heat transfer enhancement while it is lower than in the upstream region in the zone immediately downstream the spacer grids causing the little heat transfer deterioration noticed in Figure 10. Different analyses were performed and it turned out that in these cases the spacer grids affect the flow and heat transfer for about 150 mm downstream their axial location; their effect is anyway local and their absence would not undermine the quality of the simulations.

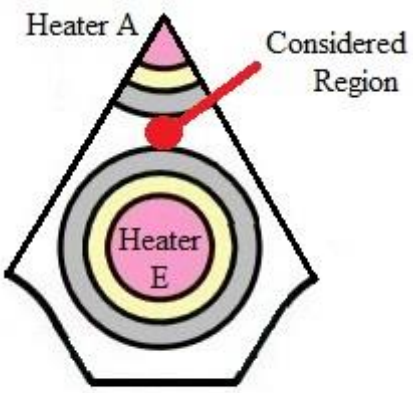

Figure 12. Considered section for the analyses of the spacer effect.

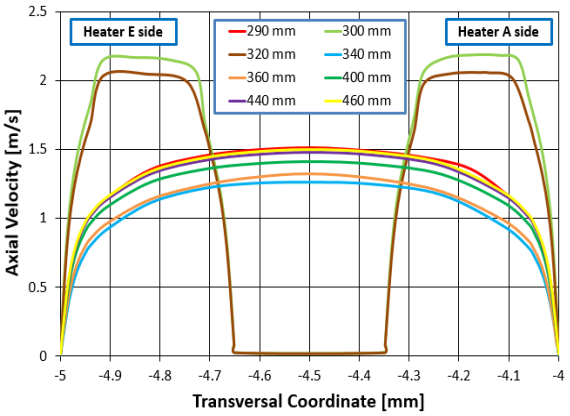

Figure 13. Calculated Axial Velocity Distribution for Case B1 adopting the SST k-ω (1994) model in the region straddling the spacer at 300 mm.

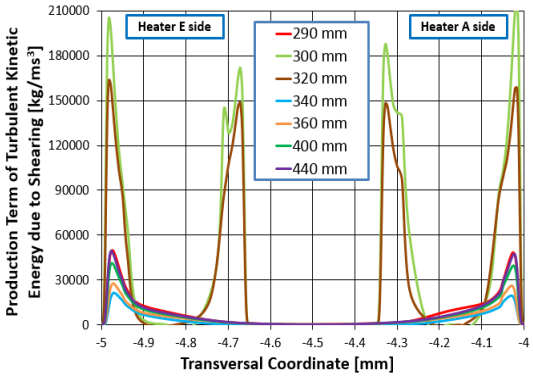

Figure 14. Calculated Production term of turbulent kinetic energy for Case B1 adopting the SST k-ω (1994) model in the region straddling the spacer at 300 mm.

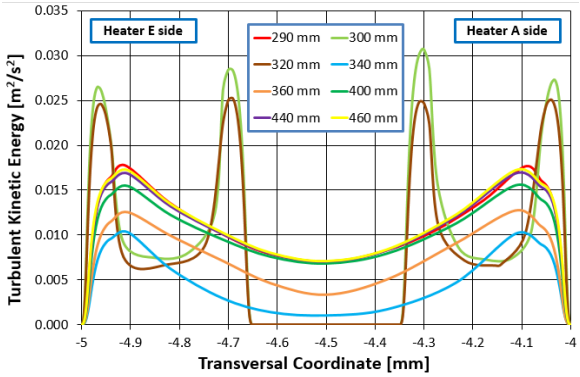

Figure 15. Calculated distribution of turbulent kinetic energy for Case B1 adopting the SST k-ω (1994) model in the region straddling the spacer at 300 mm.

The spacers are instead crucial for trying at obtaining more realistic predictions when considering the cases selected from the 4-rod bundle data sets. **Figure 16** and **Figure 17** show the wall temperature trends obtained adopting the AKN (1994) model for Case 1 when considering or not the spacers respectively. As it can be noticed, by neglecting the spacer grids, the flow undergoes to a strong heat transfer deterioration at the beginning of the heated length and only at the end of the test section returns to temperature values close to the ones measured during the experiments. Even if the quality of the simulations is definitively insufficient, the presence of the spacer grids contributes at keeping lower the temperature; in fact, in trans-pseudo-critical conditions, the spacers imply a periodical mixing between the gas-like fluid near the wall and the liquid like one in the bulk region generally improving the heat transfer. Therefore, since in trans-pseudocritical conditions, as the ones analysed here, the obtained results when considering the spacers are completely different from the ones obtained when neglecting them, a very accurate discretization of the domain is required when performing the simulations. The effect of the spacers is less important in the experiments at higher mass flux (Case 2); the distribution of the turbulent kinetic energy is in fact already improved by the large production term due to shearing and the spacers only introduce secondary effects.

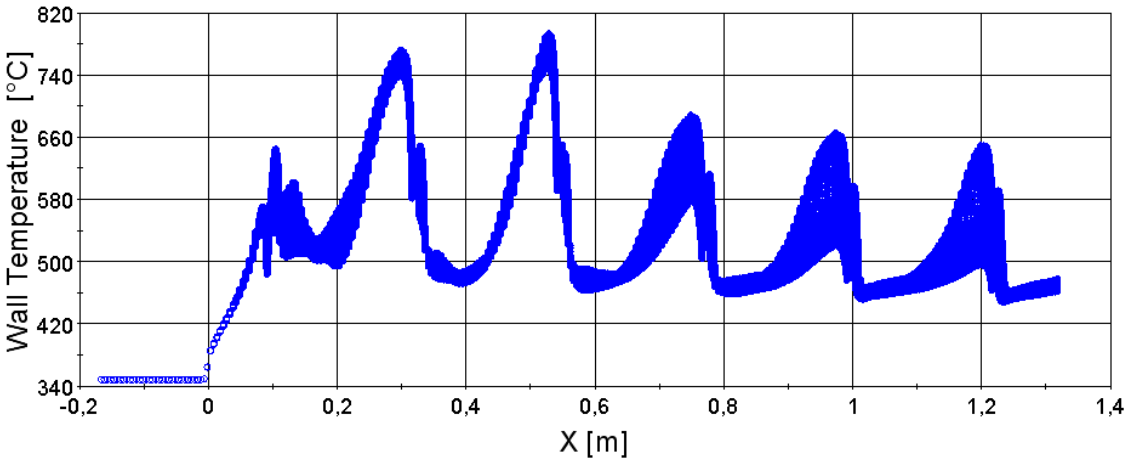

Figure 16. Calculated wall temperature trend for Case 1 when considering the spacer grids and adopting the AKN (1994) model.

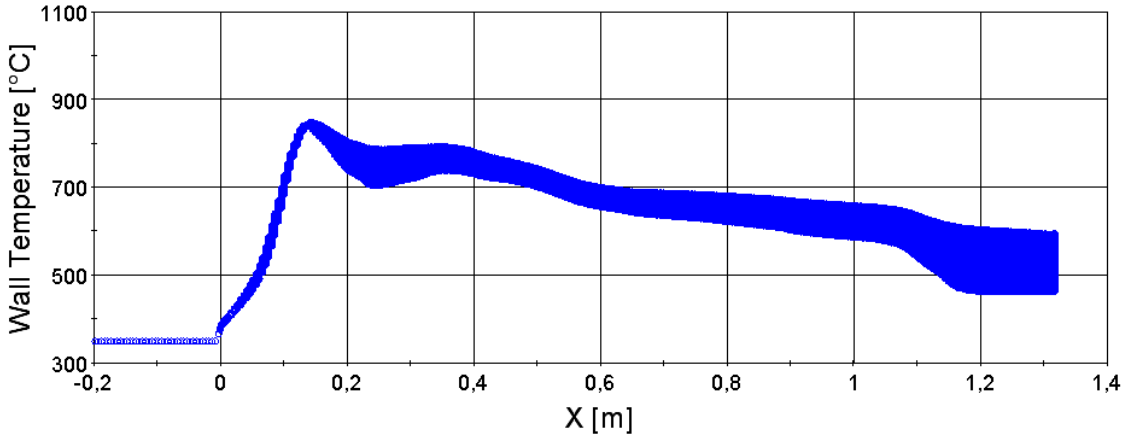

Figure 17. Calculated wall temperature trend for Case 1 when not considering the spacer grids and adopting the AKN (1994) model

5. Effect of improved boundary conditions

As already discussed in section 3 when analysing the results for Case B2, the considered homogenous power generation inside the rods may not be accurate enough for obtaining good coherence between the experimental data and the obtained results.

Unfortunately no clear information is available about the internal structure of the heating rods; the Benchmark organizers suggested to use a homogeneous power generation inside the rods but the situation may be closer to the one obtained considering an internal wrapped electric wire. The introduction of the wire was suggested by the sketch provided by the organizers for the internal structure of the rods and returned some interesting results. The idea at the basis of these further analyses was that a higher temperature may be measured if the thermocouple lays close to the electric wire and a lower one if the thermocouple is instead on the opposite side. The effect of the wire was simulated by assuming the presence of a helical region inside the rods where the power is supplied and a uniform heat generation was assumed in it. The results obtained without considering the spacer grids when adopting the AKN (1994) model in case B2 for two different classes of thermocouples are reported in **Figure 18** compared with the ones obtained considering a homogeneous power generation inside the heating rods. At each axial position the whole range of values must be considered as there is no clear information about the real positioning of the electric wire in the experimental facility.

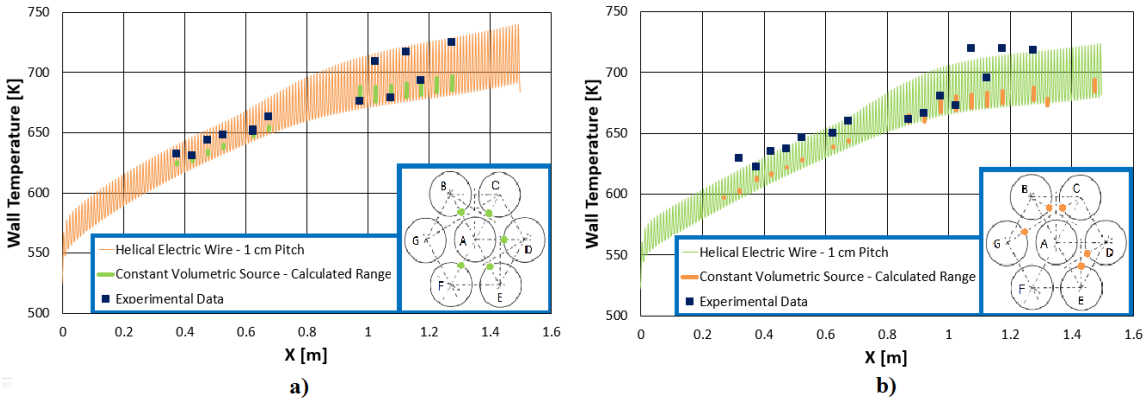

Figure 18: a) Calculated wall temperature trend for the regions in the vicinity of the green thermocouples highlighted in the corresponding sketch; **b)** Calculated wall temperature trend for the regions in the vicinity of the orange thermocouples highlighted in the corresponding sketch

As it can be noticed in **Figure 18** a) the introduction of the electric wire really improves the obtained results which now are able at predicting also the fluctuations in the measured wall temperature trend. Improvements were obtained also for the region analysed in **Figure 18**b) even if some problems still appear. The purpose of this analysis was anyway merely qualitative as no clear information was provided on the actual geometry; the pitch of the helical wire was in fact arbitrarily assumed equal to 1 cm with no sure connection with the experimental reality. The application of the electric heating wire of 1 cm pitch returned good results also for Case B1 (not shown here) in which almost all the measured values lay within the predicted ranges.

6. Conclusions

The analysis of four selected experimental conditions regarding supercritical flow in rod bundles was performed using available k-ε and k-ω turbulence models. Good coherence between the obtained results and the experimental data was found for the operating conditions at relatively low temperature, but problems still hold for the ones close to the pseudo-critical temperature. Concerning these operating conditions, as already pointed out in previous works considering supercritical flow in circular tubes, the k-ε models show some difficulties in managing the passage through the pseudo-critical threshold implying too strong increases in the wall temperature trend; on the other hand the k-ω models show smaller temperature increases but their predictions are often insufficient too.

The effect of the spacer grids was investigated. Generally speaking, this effect can be considered favourable since it improves the heat transfer in correspondence of the spacer locations even if little heat transfer deterioration may occur in the downstream region. The results turned out that the spacer may be neglected for operating conditions far from the pseudo-critical temperature, but they are instead crucial for obtaining more realistic results at higher temperature as occurred in Case 1. An accurate evaluation of the positioning of the spacer grids should be recommended during the design phase of the SCWR core as they could help improving the turbulence conditions and increasing the safety of the plant by reducing the chance of strong heat transfer deterioration phenomena.

A good coherence between the imposed boundary conditions and the real operating conditions is also very important as shown in section 5. Potential non-homogeneity in the power distribution within the rods, in fact, may generate more complicated wall temperature trends which could not be predicted by applying a uniform power generation. In this regard in the future works more realistic axial distributions of the supplied power will be considered. In particular it is expected that in the frame of the forthcoming new Coordinated Research Project (CRP) of IAEA on SCWRs new data on cosine axial power distributions will be provided so that the capabilities of the presently available turbulence models may be evaluated.

Acknowledgements

The kind help in providing us further information about the geometry of their experimental facility by the Authors of a referenced paper Zhao, M., Li, H., Yang, J., Gu, H., Cheng, X., is acknowledged. Partial support to this work by the European Commission through the THINS Project (Grant Agreement No.: 249337) is also acknowledged.

References

1. Jackson,J.D. and Hall,W.B., 1979a. Forced convection heat transfer to fluids at supercritical pressure. In Turbulence forced convection in Channels and Bundles. Manchester: Hemisphere Publishing Corporation. pp.563-611.

2. Jackson,J.D. and Hall,W.B., 1979b. Influences of buoyancy on heat transfer to fluids flowing in vertical tubes under turbulent conditions. In Turbulence forced convection in channel and bundles. Hemisphere Publishing Corporation. pp.613-40.
3. Jackson,J.D., 2009a. The supercritical pressure water heat transfer study at Manchester with natural circulation test facility. IAEA Coordinated Research Programme (CRP). University of Manchester.
4. Watts,M.J., 1980. Heat transfer to supercritical pressure water – Mixed convection with upflow and downflow in a vertical tube. PhD Thesis. University of Manchester.
5. Pioro,R.B. and Duffey,I.L., 2007. Heat transfer and hydraulic resistance at supercritical pressure in power-engineering applications. ASME Press.
6. Pis'mennyy,E.N., Razumovskiy,V.G. and Maevskiy,E.M., 2005. Experimental study on temperature regimes to supercritical water flowing in vertical tubes at low mass fluxes. In Proceedings of the International Conference GLOBAL-2005 "Nuclear Energy System for Future Generation and Global Sustainability". Tsukuba, Japan, 2005
7. Kim, D.E., Kim, M.H., 2010, Experimental investigation of heat transfer in vertical upward and downward supercritical CO2 flow in a circular tube, International Journal of Heat and Fluid Flow 32 (2011) 176–191.
8. Sharabi, M., Ambrosini,W., Forgione,N., He,S. 2007. Prediction of experimental data on heat to supercritical water with two-equation turbulence models. 3rd Int. Symposium on SCWR-Design and Technology. March 12-15, 2007, Shangai, China.
9. Sharabi,M., 2008. CFD Analyses of Heat Transfer and Flow Instability Phenomena Relevant to Fuel Bundles in Supercritical Water Reactors. Tesi di Dottorato di Ricerca. Pisa: Dipartimento di Ingegneria Meccanica, Nucleare e della Produzione, Università di Pisa.
10. Badiali,S., 2011. Numerical investigation using CFD codes of heat transfer with fluids at supercritical pressure. BSc Thesis. Pisa, Italy: Dipartimento di Ingegneria Meccanica, Nucleare e della Produzione, Università di Pisa.
11. De Rosa M., Computational Fluid-Dynamic Analysis of Experimental Data on Heat Transfer Deterioration with Supercritical water, MSc thesis, Department of Mechanical Engineering and Nuclear, University of Pisa, Italy, 2010.
12. Pucciarelli, A.,Borroni,I., Sharabi,M., Ambrosini,W., 2015. Results of 4-equation turbulence models in the prediction of heat transfer to supercritical pressure fluids Nuclear Engineering and Design Nuclear Engineering and DesignVolume 281, January 2015, 5–14
13. Zhao,M., Li,H., Yang,J., Gu,H., Cheng,X., 2013. Experimental Study on Heat Transfer to Supercritical Water Flowing through Circle Tubes and 2x2 Rod Bundles. The 6th International Symposium on Supercritical Water-Cooled Reactors (ISSCWR-6), Shenzhen, Guangdong, China, March 03-07 2013
14. Misawa,T., Nakatsuka,T., Yoshida,H., Takase,K., Ezato,K., Seki,Y., Dairaku,M., Suzuki,S., Enoeda,M., 2009. Heat transfer experiments and numerical analysis of supercritical pressure water in seven-rod test bundle, in: Proc. 13th Int. Topl. Mtg. Nuclear Reactor Thermal Hydraulics (NURETH-13), Kanazawa, Japan, 2009.
15. Rhode,M., Peeters, J. W. R. , Pucciarelli, A. , Kiss, A., Rao,Y., Onder, E. N., Mühlbauer, P., Batta, A., Hartig, M., Chatoorgoon, V., Thiele, R., Chang, D., Tavoularis, S., Novog, D., McClure, D., Gradecka, M., and Takase, K. 2015. A Blind, Numerical Benchmark Study on Supercritical Water Heat Transfer Experiments in a 7-Rod Bundle. The 7th International Symposium on Supercritical Water-Cooled Reactors (ISSCWR-7), Helsinki, Finland, March 15-18 2015
16. Documentation distributed by the Benchmark proposing organisation in March 2013
17. CD-adapco, 2012. USER GUIDE STAR-CCM+ Version 7.04.006.
18. Sharabi, M.B., Ambrosini, W., 2009. Discussion of heat transfer phenomena in fluids at supercritical pressure with the aid of CFD models, Annals of Nuclear Energy, 36 (2009) 60–71.
19. Abe, K., Kondoh, T., and Nagano, Y. 1994. A new turbulence model for predicting fluid flow and heat transfer in separating and reattaching flows 1. Flow field calculations, Int. J. Heat Mass Transfer, 37, pp. 139-151.
20. Menter, F.R. 1994. Two-equation eddy-viscosity turbulence modelling for engineering applications, AIAA Journal 32(8) pp. 1598-1605.

ISSCWR7-#2012

Combined effect of irradiation, temperature, and water coolant flow on corrosion of Zr–, Ni–Cr-, and Fe–Cr-based alloys

O.S. Bakai
NSC KIPT of NAS of Ukraine
1, Akademichna St., 61108, Kharkiv, Ukraine
bakai@kipt.kharkov.ua

D.A. Guzonas
CNL, Chalk River Laboratories
Chalk River, Ontario K0J 1J0, Canada
david.guzonas@cnl.ca

V.M. Boriskin
NSC KIPT
boriskin@kipt.kharkov.ua

A.M. Dovbnya
NSC KIPT
dovbnya@kipt.kharkov.ua

S.V. Dyuldya
NSC KIPT
sdul@kipt.kharkov.ua

Abstract

Investigation of the role of irradiation on the corrosion resistance of structural alloys is of vital importance for selection of Supercritical Water-Cooled Reactor (SCWR) materials. Gamma heating under SCWR conditions, which induces enhancement of radiolysis and corrosion kinetics at interfaces, can be efficiently simulated by electron beam irradiation over a wide range of deposited dose and temperature. The NSC KIPT-sited Canada-Ukraine Electron Irradiation Test Facility (CU-EITF) still remains the only operating facility capable of *in-situ* irradiation of specimens in a supercritical water (SCW) natural circulation loop. This paper reports the results of post-irradiation studies of Zr–1%Nb and Ni–Cr Inconel 690/52MSS alloys after a ~500 hour long exposure in the CU-EITF in the near-critical (23.5 MPa/360-385 °C) regime. Results of Scanning Electron Microscopy (SEM) studies of the sample microstructure are presented along with those of the *e*-irradiated loop piping, SS X18H10T. The results of corrosion tests under *e*-irradiation are correlated to the calculated 3D fields of absorbed dose and temperature and to the reference data obtained in-pile for topical materials. We also discuss the prospects for the use of the CU-EITF facility within a co-operative SCWR programme and present an outlook of the facility development including upgrading of the LPE-10 linac, operation of the SCW loop in the forced convection regime, and development of an enhanced target irradiation cell particularly suitable for investigation of irradiation-assisted stress corrosion cracking (IASCC) of specimens.

1. Introduction

The synergistic effects of supercritical water (SCW) flow, temperature, stress, and coupled neutron-gamma irradiation is a major limiting factor of Generation IV SCWR in-core materials performance [1]. A database of oxidation, corrosion and stress corrosion cracking data for candidate alloys under irradiation must be developed to assess their feasibility for use as the fuel cladding and core internals in an SCWR.

This assessment is hampered due to the lack of appropriate irradiation test facilities. In the EU, a substantial effort is currently focused on establishment of the large-scale R&D infrastructure for in-pile SCW testing of materials under reactor irradiation [2]. Since 2009, a complementary, cost-effective technique was developed [3] at the National Science Center “Kharkiv Institute for Physics and Technology” (NSC KIPT) in cooperation with Atomic Energy of Canada Limited (AECL), now Canadian Nuclear Laboratories (CNL).

A dedicated facility, CU-EITF, is available for simulated irradiation experiments utilizing an electron linac coupled to a SCW natural circulation loop with an irradiation cell (IC) for *in-situ* irradiation of coupons. The facility has been operating since 2012. A pilot 497 h long irradiation of Zr–1%Nb and Ni–Cr-based candidate alloys was completed in the summer of 2012. Sixteen coupons were irradiated by a 9.76 MeV/6.23 kW_e scanning electron beam in the vicinity of the pseudocritical point T_{pc} = 379.5 °C at 23.5 MPa coolant pressure.

The irradiation procedure, the results of the water chemistry analysis and weight gain data for the alloys were reported at ISSCWR6 [4], and are only briefly outlined here. In this paper we present the results of the post-irradiation characterization of the microstructure and hardness of oxidized surface layers of selected specimens including data obtained for a highly irradiated (up to ~10^{21} electrons/cm^2 fluence and ≈16 keV/atom specific deposited energy E_{dep}) specimen of the austenitic stainless steel (SS) 12X18H10T cut from the IC piping.

This is only a very limited subset of the irradiation experiment outputs. Coupons have been irradiated to very different doses (0.2–25 keV/at) over a wide temperature range (360–385 °C) below, near and slightly above the critical point where corrosion is sensitive [5] to turbulent density fluctuations [6]. Not all specimens have been examined to date. As operators of the irradiation facility, we do not attempt to make final conclusions about the mechanisms of the observed combined effects of irradiation, temperature, and water flow. The goal of this communication is to present the currently available results for discussion in order to develop a strategy for subsequent analysis and further irradiations at CU-EITF.

2. Experimental

The experimental setup of the CU-EITF irradiation [4] is sketched in Figure 1. The nomenclature of the IC tubes and alloy samples is also identified in this figure to be referenced hereinafter.

The 1.2 mm thick 50 mm high N5 series of Inconel coupons consisted of the base Alloy 690 ($NiCr_{32.4}Fe_{9.55}Ti_{0.35}C_{0.14\%at}$) welded, in the ≈15 mm high midportion, with the In52MSS alloy $NiCr_{29.6}Fe_8Mo_{1.8}Nb_{1.5}Mn_{0.18}Si_{0.31}Ti_{0.17}C_{0.1\%at}$. The welds facing toward the side of irradiation are noticeable in Figure 1(h) of the Inconel filled IC tube #I. The 0.5 mm thick 40 mm high Zr–1%Nb alloy coupons of the N4 series filled IC tube #III. The IC frontal tube #II and the rear tube #IV held alternating sequences of both kinds of samples.

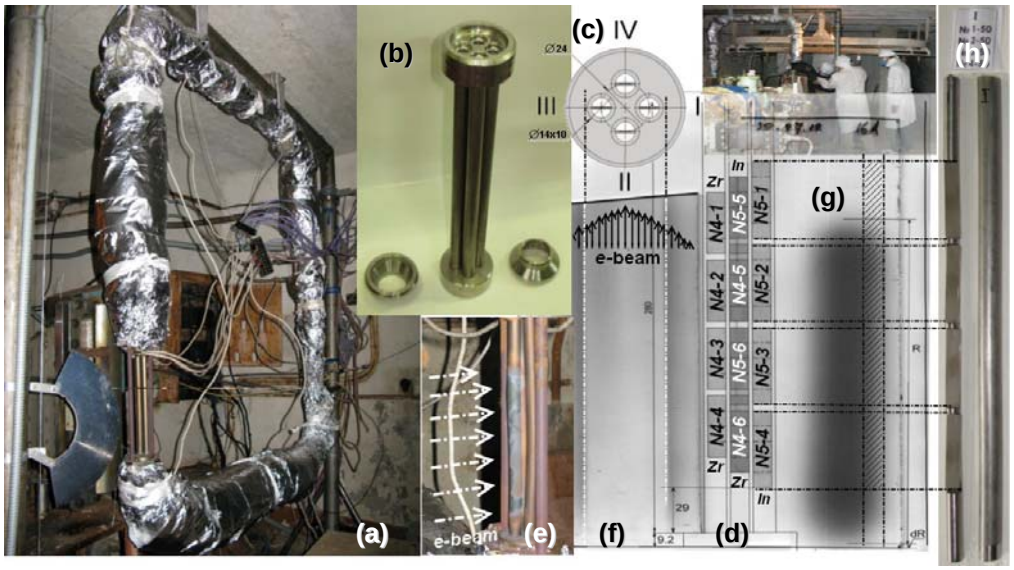

Figure 1. The CU-EITF circulation loop mounted in the KIPT LPE-10 electron linac shelter (a), general (b) and top/front (c/d) sectional views of the coupons-holding four-pipe IC before (b) and after (e) the irradiation session. Scanning *e*-beam glass plate monitor images behind IC (f) and in front of it (g) outline the electron fluence spatial distribution over the irradiated samples, as shown in (g) for the IC tube #I internal cassette filled with Inconel coupons (h).

The specific objective of the experiment was to examine the sensitivity of corrosion to changes in parameters in the vicinity of the super-critical transition. The loop water chemistry was controlled oxygen (<20 ppb, pH ~5–6) and low impurity concentrations, excluding corrosion products released from the materials during the tests. The local corrosion rate was expected to depend on spatial variations of temperature, absorbed dose of *e*-irradiation (which efficiently activates the corrosion kinetics), and electrochemical potential at close couples of different materials. Due to the rather short range (~1 cm) of ~10 MeV electrons in dense structural materials and the lateral shaping of the scanning flux, the irradiation generated large gradients of energy deposited in the coupons. This resulted in different amounts of heating of coupons in different areas. To separate the combined effects of temperature and irradiation (and also electrochemical and stress parameters), the spatial variation of these quantities had to be measured and/or modeled with the appropriate accuracy. This was considered as an essential constituent of the CU-EITF experimental technique. Monte Carlo (MC) simulated 3D maps of energy absorption in the irradiated zone (the IC tubes, coupons, and coolant) were based on actual records of the linac operation (*e*-beam spatial and energy distributions) and coupled to Finite Element Method (FEM) calculations of thermal fields consistent with the System Thermal-Hydraulic (STH) characterization of the coolant natural convection, which agreed with temperature measurements at several points of the loop piping [3,4].

The mean temperature of water inside the IC piping evaluated using STH/MC/FEM ranged from 360 °C (bottom inlet) to 368 °C (top outlet) at the ≈80 g/s mass flow rate during steady-state circulation. This is generally below T_{pc}. However, the temperature T at 50 μm thick coupon-to-water interfaces was higher by 10–15 K. It exceeded T_{pc} for Inconel coupons N5-5 and N5-6 which actually corroded in SCW. In ref. [4], we correlated this to their specific weight gains.

Weight gains of all coupons were measured in KIPT to ~1% accuracy by means of a Class 2 (±0.15 mg) analytical laboratory equal-arm balance VLR-200 just after completion of the irradiation session. The results were published in ref. [4] and are briefly discussed in the next section.

Further tests began about 6 month later when the photonuclear reaction-induced residual activity of certain samples of irradiated materials decreased sufficiently to meet radiation safety regulations. Generally, an order of magnitude higher activation of zirconium samples was observed systematically in comparison with that of Ni–Cr and Fe–Cr alloys and steel. This restricted the selection of samples acceptable for the post-irradiation studies reported here, which have been undertaken in several laboratories in Ukraine and Canada.

Optical metallography (LECO Olympus GX-51 microscope with IA-32 image analyzer) was used to study the macroscopic structural changes. Hardness tester LECO LM-700 was applied to test mechanical properties. Microstructure was studied by means of high resolution (HR) scanning (SEM), scanning-transmission (STEM) electron and focused ion beam (FIB) microscopy coupled to energy dispersive X-ray (EDS) and Auger electron (AES) spectroscopy of corrosion chemistry. Different instruments were used in different labs: JEOL JSM-7001F HR field emission (FE) SEM and JEM-2100 STEM, ZEISS EVO-50XVP SEM with Oxford Instruments INCA-450 EDS analyzer, JEOL JAMP-9500F FE Auger Microprobe with INCA-350 EDS and Ar^+ ion gun for high speed sputter etching as well as the FEI Helios NanoLab™ DualBeam™ FIB / XHR STEM extra-high resolution machine.

3. Results and Discussion

3.1 Zirconium-based alloy Zr–1%Nb

To date, only general corrosion test data are available for the Zr–1%Nb alloy coupons. The measured specific weight gains $\delta m/S$ can be found in Figure 13(a) of ref. [4]. The data are rather scattered (0.27 mg/cm^2 mean $\langle \delta m/S \rangle$ with 0.22 mg/cm^2 r.m.s. deviation), which may be due to the substantially different dose and temperature conditions of the irradiation of the different coupons. No correlation of $\delta m/S$ with the MC calculated absorbed dose of *e*-irradiation was found. However, an increase of $\delta m/S$ with increasing interfacial temperature was observed.

The weight gain of coupon *N4-5*, $\delta m/S$ = 0.75 mg/cm^2, was about triple that of the mean value as its temperature approached T_{pc}.

According to KIPT evaluation [7] of the Zr–1%Nb alloy oxidation chemistry, $\delta m/S$ of 1 mg/cm^2 corresponds to a 6.85 μm oxide film thickness H. This predicts a 1–5 μm thick oxide for our ~500 h exposure in a low-oxygen near-critical (~370 °C) regime under *e*-irradiation.

In a 16.5 MPa/350 °C water environment, and without irradiation, this alloy's corrosion kinetics was shown [7] to obey an empirical equation $\delta m/S(t) = (0.0675\times\cdot^{t}/_{1\,h}])^{1/3.03}\times$mg/cm^2 at exposure times t < 5000 h. This scaling law yields $\delta m/S$ = 0.146 mg/cm^2 and H = 1 μm for t = 500 h.

Our measurements show generally 2–5 times greater values. This may be due to the synergistic effects of *e*-irradiation and temperature variations.

Further investigations of microstructure are definitely required to confirm or deny these speculations. However, it is worth noting that the literature data on in-pile performance of the comparable Zr–2.5%Nb alloy in CANDU reactor pressure tubes (see citations in Table 1 of ref. [4]) report $\delta m/S$ ~ 1–4 mg/cm^2 only for t = 10–16 FPY of exposure at 10 MPa/290 °C. The difference may be the result of water radiolysis in the SCW loop test, which will result in more oxidizing conditions than in a CANDU reactor core; hydrogen gas is added to the coolant in a CANDU reactor to suppress the net radiolytic production of oxidizing species in the core.

3.2 Ni–Cr-based Alloy 690 / In52MSS weld joint

High specific weight gains of the *e*-irradiated Alloy 690 / In52MSS weld joined coupons were obtained (0.2–1.5 mg/cm^2, see Figure 13(b) of ref. [4]). Applying the factor 5.45 μm·cm^2·mg^{-1} derived from the measurements of ref. [8] for *as received* (AR) Alloy 690, we estimated the oxide film thickness H = 1–8 μm of different coupons. It looks abnormally high, and uncommon for this class of SCWR candidate materials which are usually more corrosion resistant than Fe–Cr steels and Zr-based alloys [1]. The mean $\langle\delta m/S\rangle$ = 0.58 mg/cm^2 is more than an order of magnitude greater than $\delta m/S$ ~ 0.01–0.05 mg/cm^2 typically observed at ~$10^{2–3}$ h long exposures of Ni–Cr-based alloys to 500–600 °C low-oxygen SCW without irradiation [1,8].

Probable reason is the generally subcritical regime of exposure in our pilot experiment. The tendency of Ni–Cr-based alloys to retain oxides at $T < T_{pc}$ is known. It was observed at 1024 h long 360 °C water exposure of Alloy 625 (see Figure 25 of ref. [1]). Other possible reasons may be due to irradiation effects which enhance the oxidation kinetics, in particular the highly oxidizing conditions created by water radiolysis. To assess the general corrosion test data, investigations of the microstructure of the irradiated samples of the Ni–Cr-based alloy were initiated. The initial results obtained for the N5-2 coupon shown in Figures 1(d) and 2.

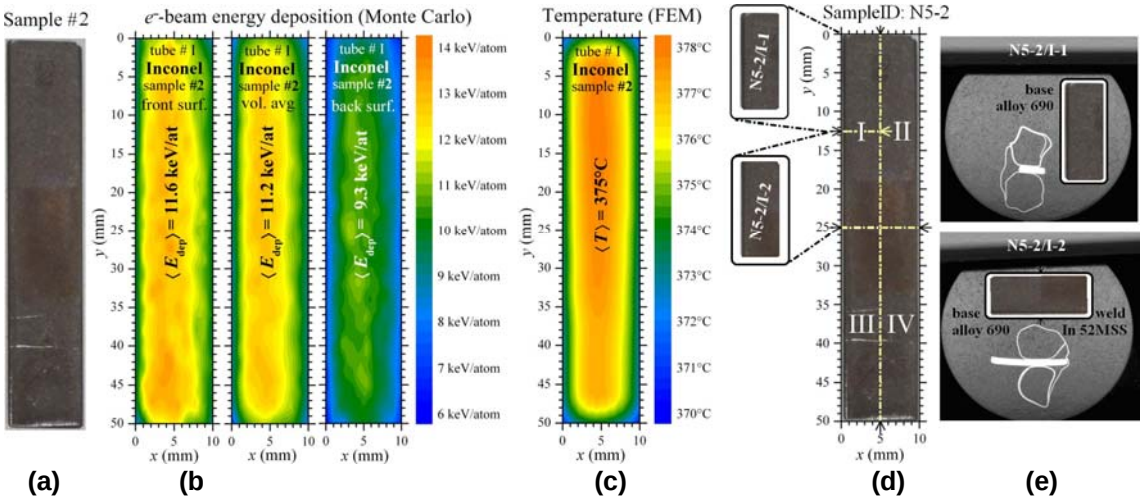

Figure 2. [*color print*] The irradiated Alloy 690/52MSS coupon N5-2 (a), the MC/FEM calculated spatial maps of the specific *e*-beam deposited energy E_{dep} (b) and temperature (c) of this coupon, and the scheme of its cutting and preparation for analysis (d,e).

This is the only Inconel coupon which showed a weight loss of 0.173 mg/cm^2. Thus, its microstructure and oxidation were of special interest. The coupon was irradiated to ≈11 keV/atom (see Figure 2(b)) in the IC tube #I aside the scanning *e*-beam midplane. The surface dose distribution was uniform except for the edge effects of the *e*-beam leakage off the target. The coupon temperature was about 5 K below T_{pc}.

Two specimens, N5-2/I-1 and N5-2/I-2, were prepared from quadrant I as shown in Figure 2(d). The former is pure Alloy 690; the latter contains its weld with the In52MSS alloy as shown in low-magnification (60x) micrographs of Figure 3. At such a scale, the EDS analysis data generally follow the nominal chemistry of these alloys. Low-*Z* elements (C, O, Mg, Al originating from the water exposure and the specimen preparation procedure) were found in quantities up to several %at.

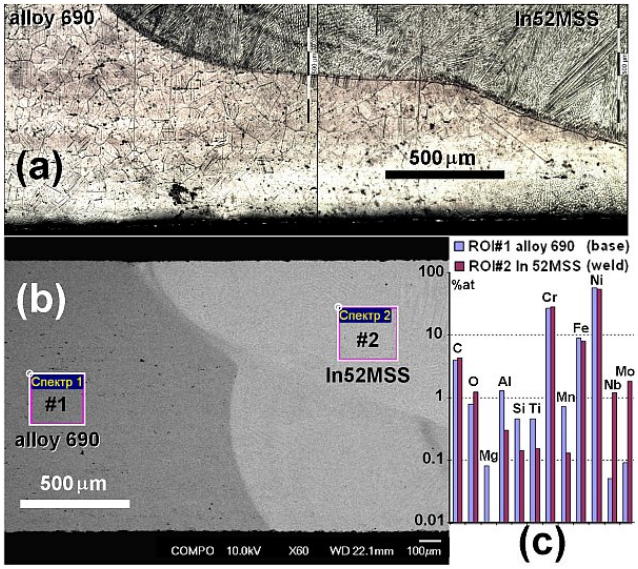

Figure 3. Optical metallographic (a) and backscattered electron (b) images and chemistry (c) of the Inconel base-to-weld sectional area of the specimen N5-2/I-2.

The higher magnification x-section and top morphological views of both specimens are shown in Figure 4. The light microscopy color contrast of Figure 4(a) pointed to the ≈1.5 μm thick corrosion film on the Alloy 690 surface exposed to water. This agrees well with the 11,000x SEM (see (b)) which also reveals the high roughness of the corroded layer. The surface of the In52MSS coupon (see (c.d)) is less rough and exhibits thinner (0.5–1.0 μm) corrosion layer. The surfaces (c,f) still retain the machining marks and are covered with 2–8 μm faceted particles, possibly metal oxides, that appear to have been deposited on the surface.

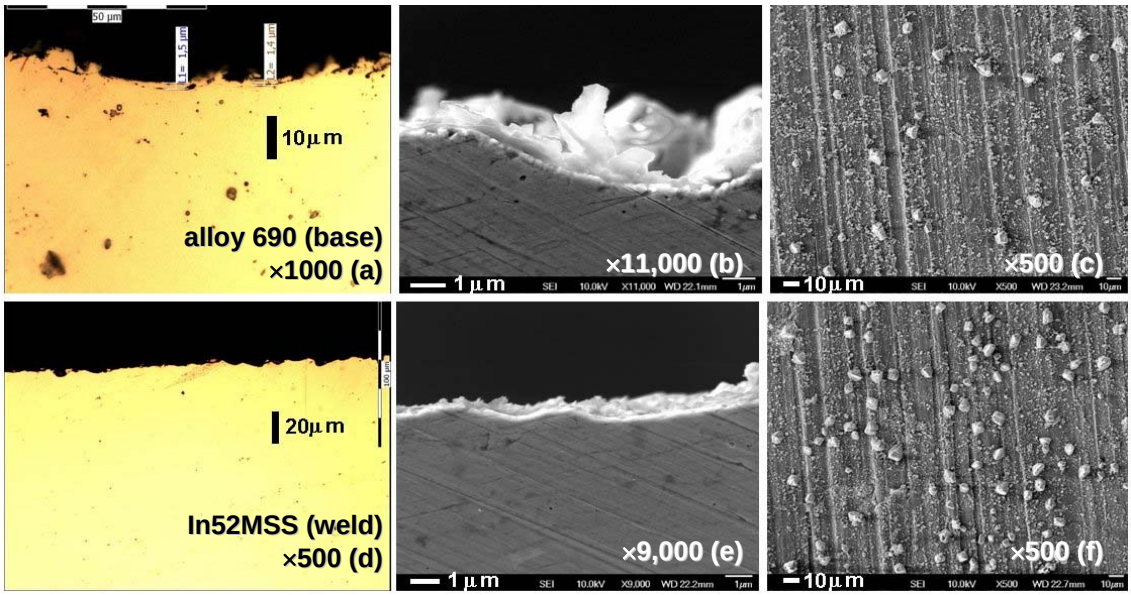

Figure 4. Optical (a,d) and SEM (b,c,e,f) micrographs of the cross-section (a,b,d,e) and surface (c,f) of the Inconel specimens N5-2/I-1 (top row) and N5-2/I-2 (bottom row) after 500 h long exposure to 23.5 MPa/375 °C water under *e*-irradiation to 11 keV/atom energy deposition.

3.2.1 Metallography

Metallography of the electrochemically etched cross-section surfaces of the base and welded alloys specimens is illustrated in Figures 3(a) and 5.

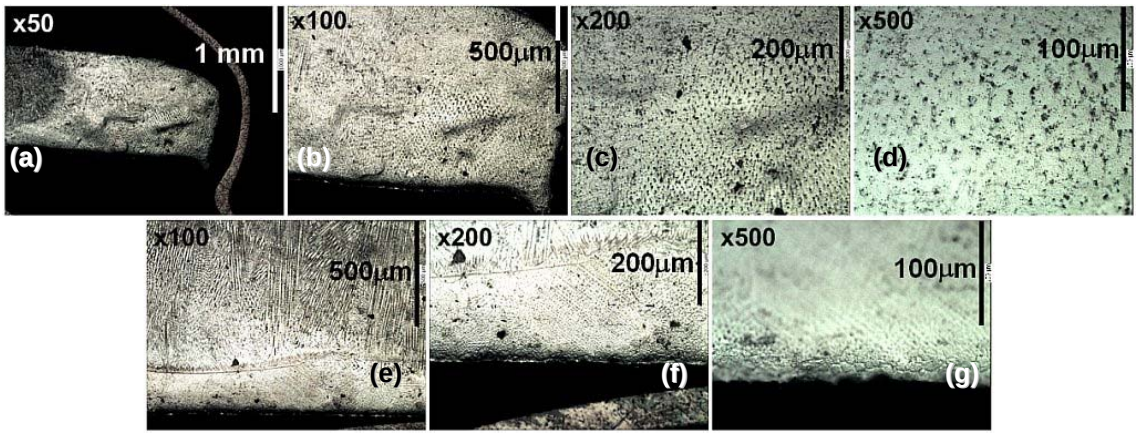

Figure 5. Light microscopy images of the N5-2/I-1 Alloy 690 specimen (top row) and the specimen N5-2/I-2 in the area of welded alloy In52MSS (bottom row) at different magnifications.

Far from the weld, the base Alloy 690 has the predominantly equiaxed cast structure of ~100 μm grains. Slip bands and deformation twins are also present. Grains become fused in the area of the flashing weld joint with the In52MSS alloy. At high magnifications (200x, 500x), small (<10 μm) precipitates are observed inside the grain bodies in Figure 5(c,d,g).

These features most likely result from the metallurgy of the source materials and the thermal treatment of the welded coupon preparation rather than from the water exposure or irradiation. However, the chipping of grains is clearly seen in Figure 5(f,g) at the outer edge of the coupon exposed to water and irradiation in the area of the thinnest (100–200 μm) layer of the weld joint. Cracks are spread along the boundaries of the observable meshwork of the structure and thus can be attributed to the inter-granular (*stress?*) corrosion cracking (IGSCC). This may be the result of residual stress accumulated in the vicinity of the weld joint. The In52MSS alloy's long dendrites contrast with the small-meshed structure of the base Alloy 690 (both are seen in Figures 3(a) and 5(e)). This indicates that, after welding, the base alloy cooled down considerably faster, which could inhibit internal stress relaxation and activate IGSCC.

3.2.2 Oxidation Microstructure and Chemistry

HREM studies focused on the morphology and composition of the corrosion surfaces and layers, and the refinement of the oxide film thickness estimation.

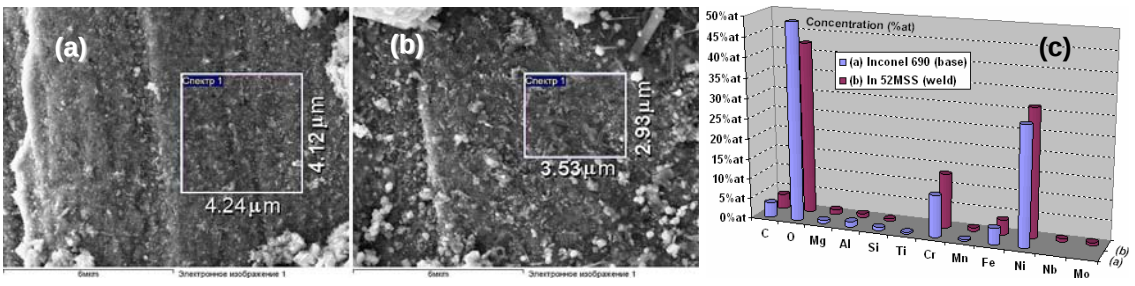

Figure 6. SEM images of the surfaces of oxidized Alloy 690 (a) and In52MSS (b) and the chemistry of the oxide film obtained by EDS (c) in the indicated areas, which were selected to be free of large-scale particles.

Figure 6 shows that general corrosion of both base and welded alloys occur to similar degrees. The randomly dispersed agglomerates of deposited material were found to have a higher oxygen content and contain Ca, Mg, P, W and S as well as Fe, Ni and Cr corrosion products (see Figure 7). Precipitation in the vicinity of the critical point is expected due to the decrease in the dielectric content of water [9]. Some fraction of the deposits likely formed due to the accidental local boiling of water during transients of loop operation. This issue will require special attention in future irradiations.

SEM/EDS results of the oxide film cross-section analysis are shown in Figure 8. The trend of Cr, Ni and Fe depletion in the oxide film is easily observed in these, in other respects scattered, data which also include signals (C, Ca, P) from the surface deposits.

In Figures 9 and 10, the chemistry of the depletion zone and the oxide film thickness are quantified with the cross-section composition profiles. EDS line scans of Figure 9(a–d) show a 1–3 μm thick oxidation layer which is thinner and less spread on the scans (b,d) made away from the deposited surface contaminants. For the same material, the finer scan of Figure 9(e) finds oxygen only up to 1 μm. It is peaked at 100 nm and has a FWHM of ≈400 nm. This is fairly consistent with the much higher resolution Auger Microprobe data of Figure 10(d) measured in the weld joint area over the ~(20×15) μm field of the SEM specimen sputter etching.

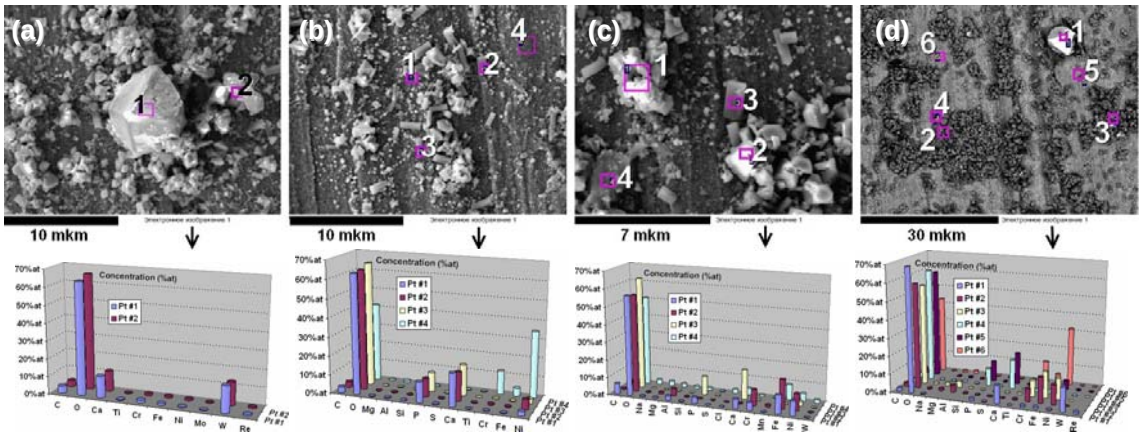

Figure 7. SEM micrographs and the spot EDS derived chemistry of the oxide particles on the corrosion surface in the areas of base Alloy 690 (a,b) and the weld joint with In52MSS (c,d).

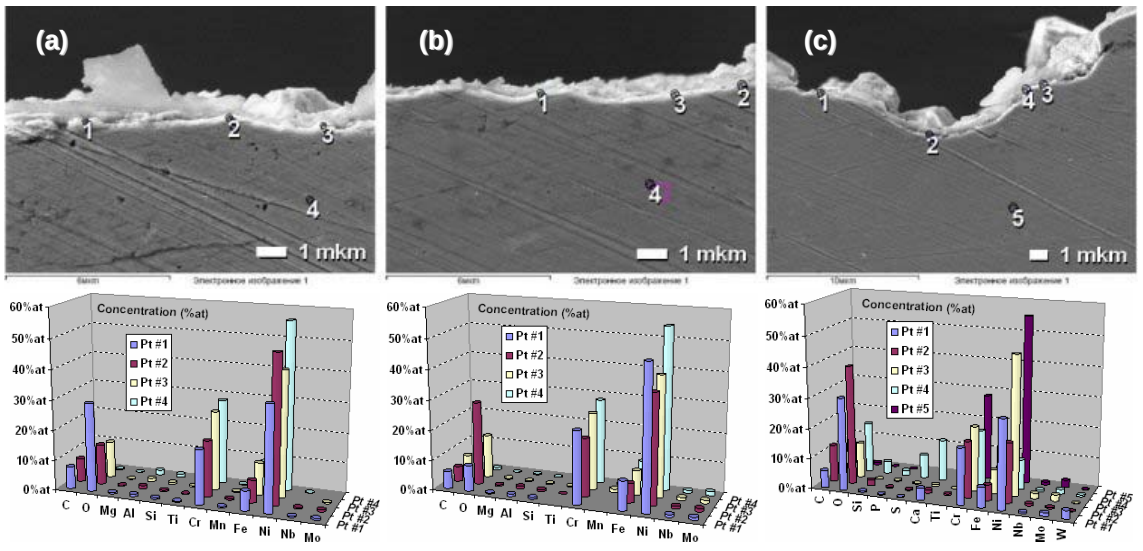

Figure 8. Cross-section SEM images of the oxide film morphology (top) and the location-resolved EDS chemistry (bottom) in the base (a) and weld (b,c) areas of the specimen N5-2/I-2.

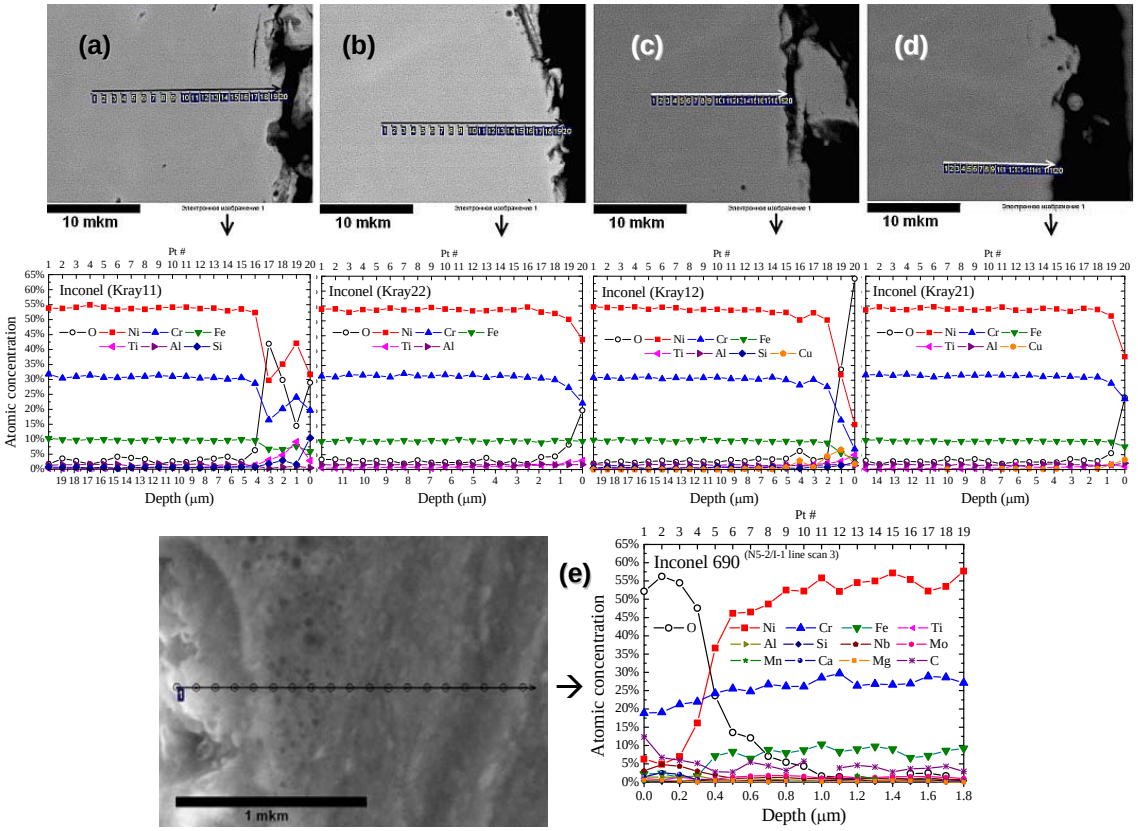

Figure 9. STEM EDS line scans and cross-section composition profiles of the slices scanned from the front (a,b) and rear (c,d) to *e*-irradiation surfaces of the Alloy 690 specimen N5-2/I-1. Higher resolution data are shown in (e) for the same material.

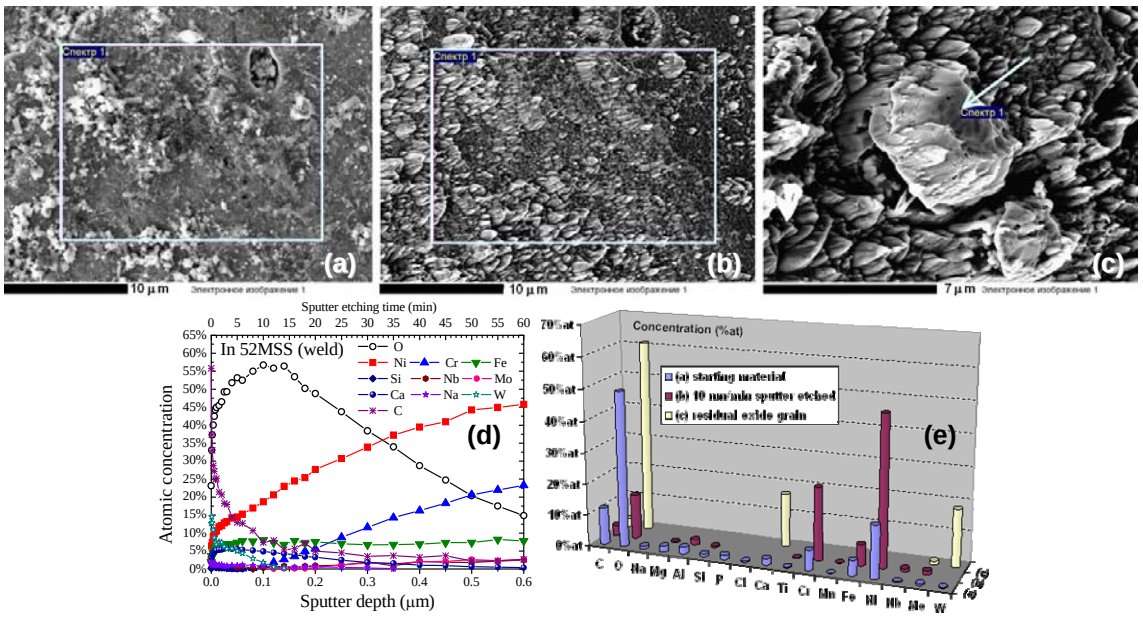

Figure 10. SEM micrographs before (a) and after (b) 60 min of 100 nm/min Ar^+ ion gun sputter etching of the Alloy 690/In52MSS weld area of the specimen N5-2/I-2. The correspondent AES microprobe composition profile is shown in (d). The chemistry of the indicated area of the source (a) and sputter etched material is shown in (e) together with that of the low-sputtered grain (c) of the surface agglomerate of oxide particles.

These data are comparable with those obtained for Alloy 690 over a 8 to 10 week exposure to 500 °C SCW (see ref. [8] Table 4 data for 'rough' regions of oxides). Since our irradiation lasted only 3 weeks, the combined impact of temperature and irradiation is likely.

On the other hand, the observed morphology of the oxides demands careful handling of general corrosion test data [4] of other coupons having abnormally high $\delta m/S$. Direct correlation of the weight gain to the oxide film thickness is absent for the studied sample of Ni–Cr alloy. Therefore, the estimate [4] of the film thickness from the weight gain can be rather overrated.

3.3 Fe-Cr Stainless Steel 12X18H10T

The corrosion behaviour of the material of the circulation loop piping and sample holder tubes, SS 12X18H10T, is also of great interest. As shown in Figure 11(a), two annular samples were prepared from the top and bottom parts of the 0.5 mm thick internal pipes of the IC tube #II holder cassette close to the large IC flanges. At the circulation loop irradiation experiment, the IIB/4 denoted top sample was outside the *e*-beam irradiated zone. Its temperature was circularly uniform and close to the coolant outlet temperature, ~370 °C. The bottom one, IIB/1/0, was highly and non-uniformly irradiated and heated up to 460 °C, see Figure 11(b).

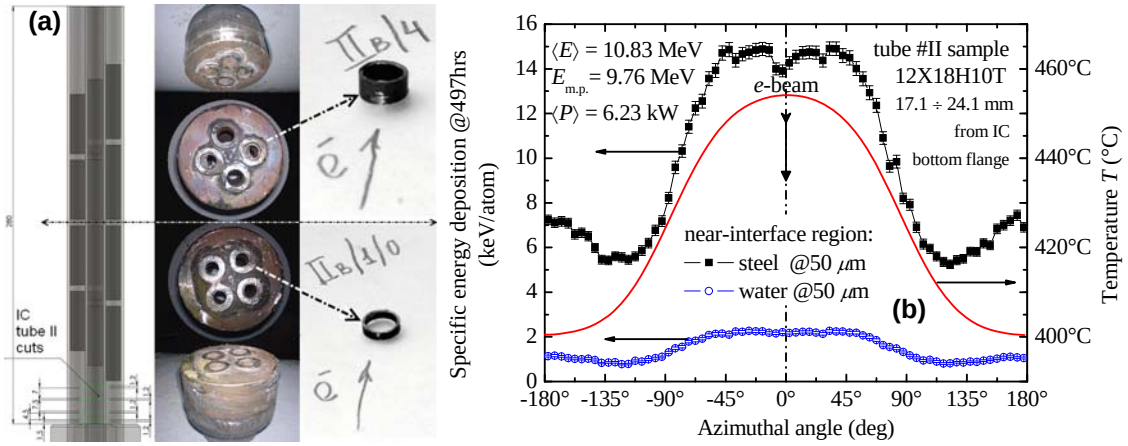

Figure 11. The drawing and photos of the 12X18H10T samples cut out from the IC tube #II (a) and the MC/FEM calculated distribution diagram of the *e*-beam specific energy deposition and temperature in the 100 μm thick interface layer of the bottom sample IIB/1/0 with coolant (b).

3.3.1 Metallography and Microhardness

Polished metallographic sections of both samples were examined without etching. As seen in Figure 12(a), no visible damage of their external surfaces was found, though one might expect to observe the effects of confined corrosion at higher resolutions.

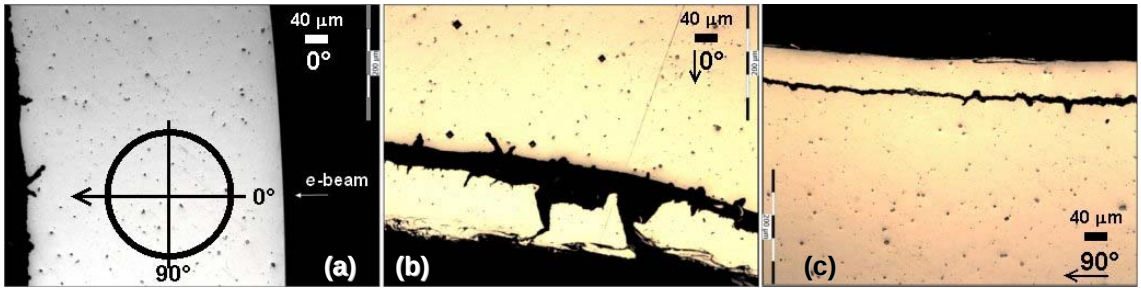

Figure 12. Light microscopy images of the SS 12X18H10T IIB/1/0 highly irradiated sample metallographic section. The *e*-irradiation direction is indicated with arrows.

Crevice corrosion damage at the internal surfaces that contacted the water was found for both samples. Whereas it is insignificant for the sample IIB/4, the irradiated sample IIB/1/0 exhibits severe corrosion cracking, spallation, and exfoliation shown in Figure 12(b,c). Cracking and crevice corrosion also occur behind the delaminated layer.

Damage rate variations were revealed subject to the observation point azimuthal location with respect to *e*-beam. Since cracking can be stress enhanced, it should be correlated with the thermal-elastic stress due to the large irradiation-induced temperature gradients (see Figure 11(b)). FEM stress calculations are in progress.

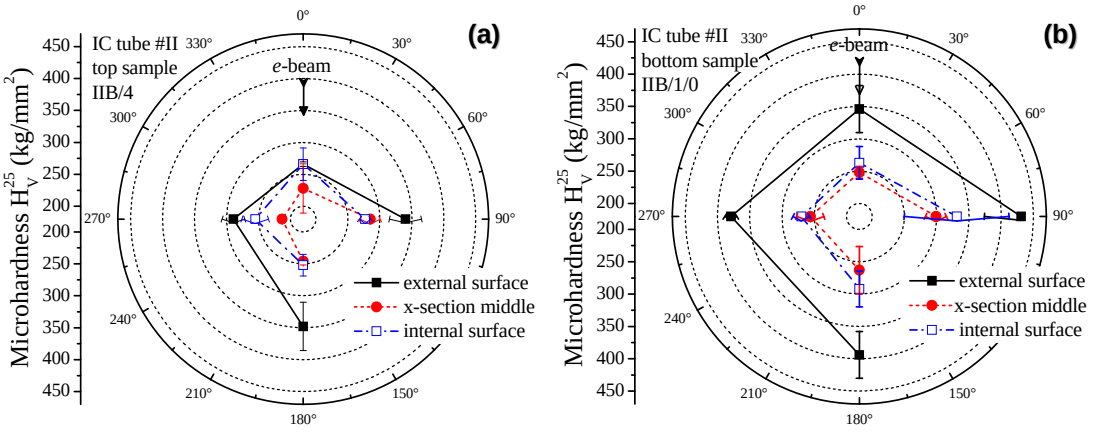

Figure 13. Azimuthal distribution diagrams of the microhardness of unirradiated IIB/4 (a) and *e*-irradiated IIB/1/0 (b) samples of SS 12X18H10T after 500 h long 23.5 MPa 370 °C (a) and 400–450 °C (b) exposure to water flow under electron irradiation.

The Vickers microhardness of the samples was measured across the metallographic section with a 25 gm load. The results are shown in Figure 13.

The hardness generally decreased on approaching the corroded, water-interfaced internal surface of both samples. The outer layer of the highly irradiated bottom sample IIB/1/0 is hardened up to 30% (~100 kg/mm^2, see Figure 13(b)) as compared to that of the IIB/4 sample exposed to a much softer environment (370 °C, no irradiation). The reason is not clear; it is possibly a complex combination of temperature and irradiation effects.

3.3.2 Microstructure and Oxidation

SEM and TEM specimens were prepared from different sectors of the sample IIB/I/0 by means of ion slicing and FIB techniques to study the corroded layers at a microscopic level.

In Figure 14 TEM, the damaged layer is rough, 7–11 μm thick, and oxidized up to 50–60%at.

SEM micrographs of the corrosion surface are shown in Figure 15(a–c). The chaotic agglomeration of 2–5 μm size particles (grains, flakes) of corrosion products and deposits is evident to a much greater extent that observed for the Ni–Cr alloy. No 'flat' area is visible.

The estimates of Figure 15(d) result in 8.74 to 14.51 μm thickness of the corroded layer. This agrees well with the Figure 14 data obtained for another SS 12X18H10T specimen of the sample material using another machine.

The EDS data of Figure 15(e) identifies the oxide chemistry of the corrosion layer. The cracks developed in the bulk material are also easily observed in Figure 15(d,e). This is consistent with the metallography data of Figure 12.

A more refined description of the sample oxidation chemistry was obtained by means of FIB preparation of a thin STEM specimen as shown in Figures 16 and 17. In Figure 16(a), oxygen is identified by the corrosion surface SEM/X-ray spectroscopy. Calcium is present as well; the reasons were discussed above in section 3.2.2. At depths >15 μm the chemistry points to the bulk material (SS) with a minor addition of gallium ions used in FIB technique.

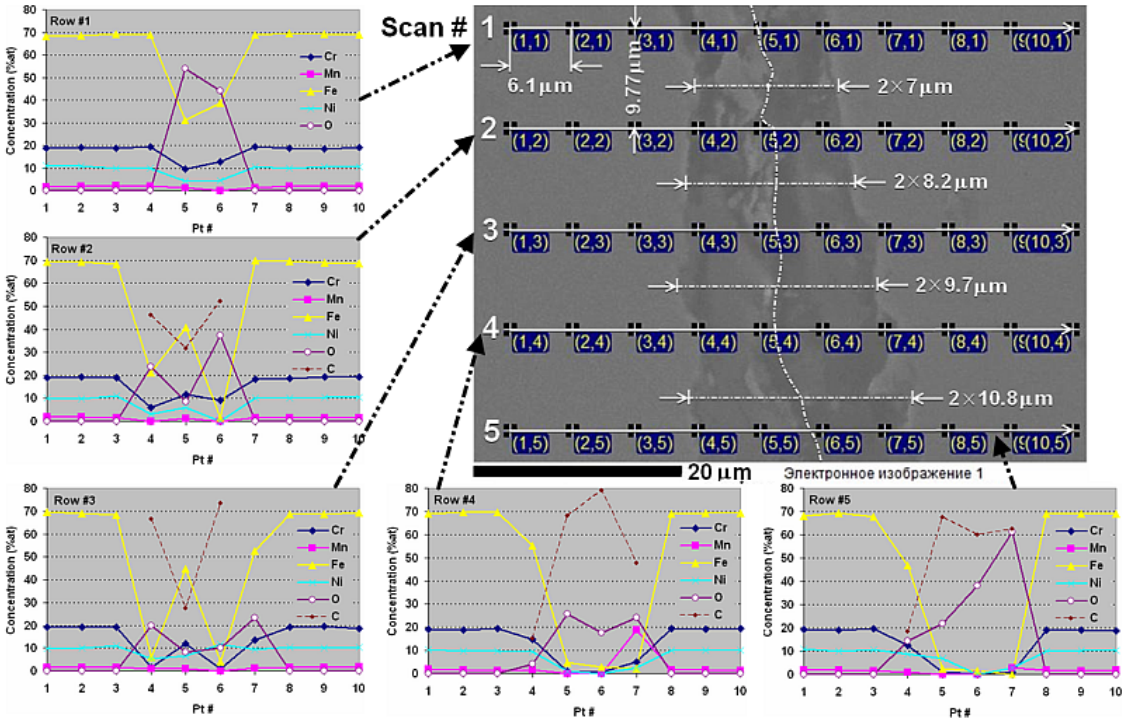

Figure 14. TEM image with cross-section line scans indicated and the EDS atomic composition profiles of the closely coupled sectors of the SS 12X18H10T sample IIB/I/0 internal surface.

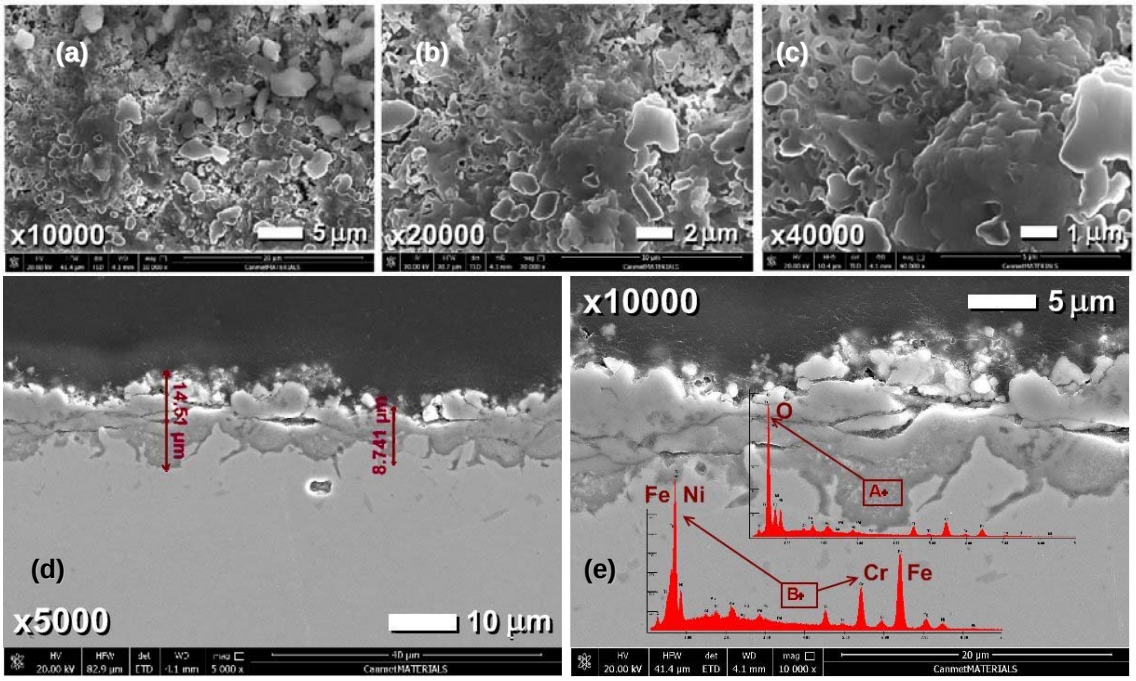

Figure 15. Top-view planar (top row) and cross-section (bottom row) SEM images of the SS 12X18H10T specimen corrosion surface (a–c) and layer (d,e) at different magnifications. The EDS X-ray spectra measured at locations A (oxides) and B (bulk) are shown in (e).

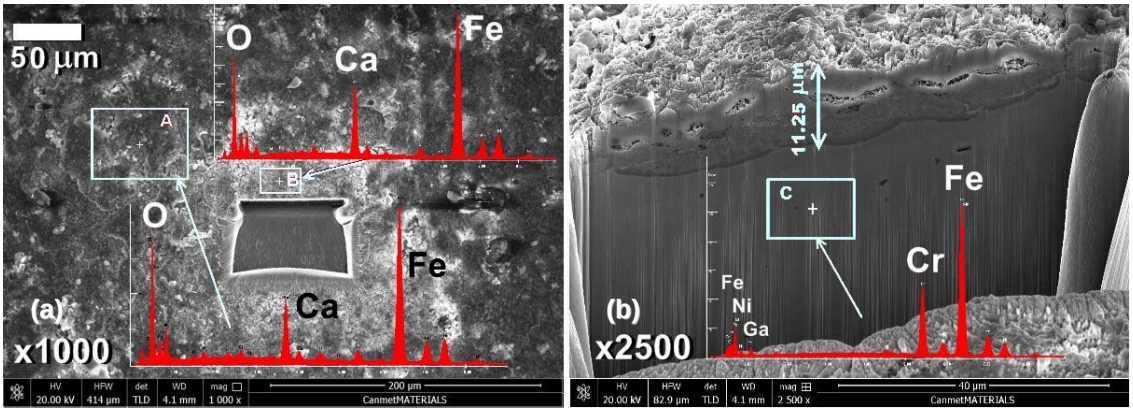

Figure 16. FIB/SEM images and the EDS derived chemistry of the corrosion surface (a) and cross-section (b) in the vicinity of the FIB produced template for STEM.

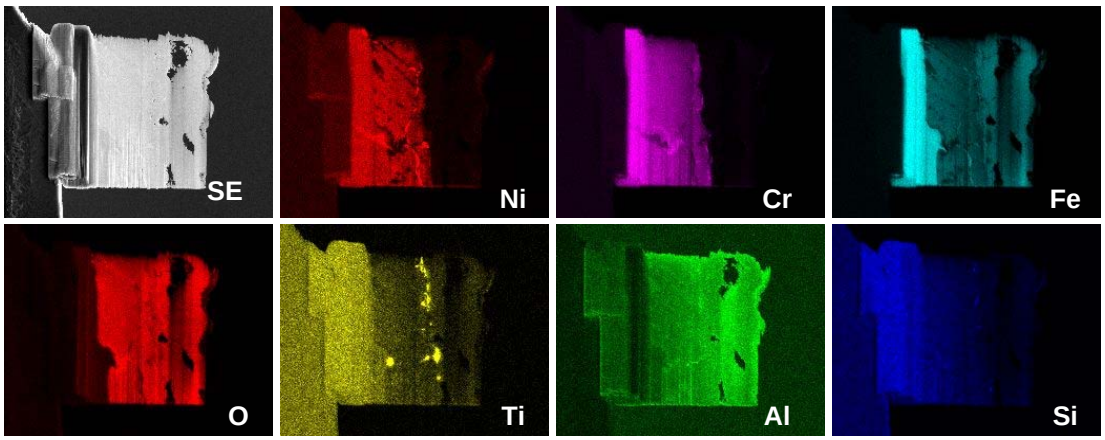

Figure 17. [*color print*] STEM EDS maps of the FIB prepared specimen (shown, in secondary electrons, in the top-left image; see also Figure 16) of the austenitic SS 12X18H10T after the ≈500 h long exposure to 23.5 MPa/~430 °C SCW (see Figure 11(b)) under electron irradiation.

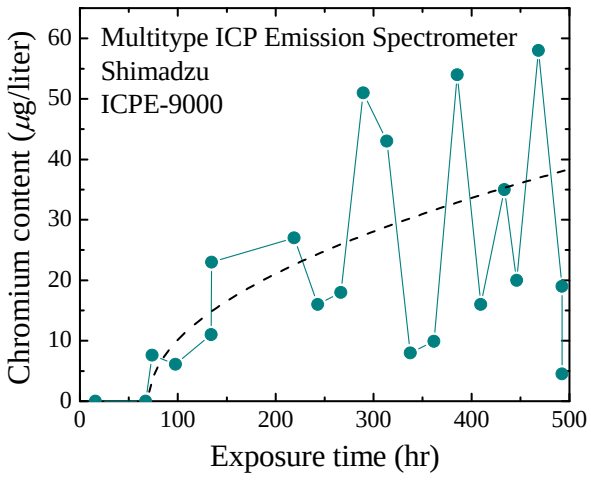

Figure 18. Exposure time dependence of the Cr content in the circulation loop water coolant under *e*-irradiation.

The STEM/EDS 6,500x 2D mapping of the specimen chemistry (see Figure 17) has shown that oxidation is accompanied by substantial depletion of Cr and Ni in the ~10–15 μm thick surface layer. Iron, titanium, and (possibly adventitious) aluminum are observed in this layer, probably in the form of oxides. The decoration of the depletion zone with Ti precipitate is also evident.

Chromium was systematically observed by water chemistry monitoring of the circulating loop coolant during the irradiation experiment (see Figure 18). Though the measured data scatter, they generally follow parabolic ($\propto t^{1/2}$) kinetics of Cr accumulation. The post-irradiation microanalysis definitely points to its principal source, namely corrosion of the base loop material, the Fe–Cr(12 wt.%) austenitic steel.

4. Conclusions and Outlook

- The NSC KIPT novel irradiation facility has shown its capability for investigation of the corrosion and oxidation behaviour of different classes of relevant candidate materials for in-core use in and SCWR in the immediate vicinity of the critical point under *e*-irradiation.
- Post-irradiation characterizations show that both Zr- and Ni–Cr-based alloys exhibit a trend of enhancement of the corrosion and oxidation rate under irradiation.
- Sporadic stress corrosion cracking occurs in the irradiated piping of the irradiation cell and welded coupons of different Ni-Cr alloys due to thermal-elastic stress under irradiation-induced thermal load and the residual internal stress in the vicinity of the weld joint.

The first lessons learned from the pilot irradiation experiment as well as the first results of the post-irradiation characterizations have defined the main tasks for further development of the CU–EITF. These are: (i) better water conditioning, (ii) better control of coolant circulation flow, and (iii) the capability to investigate SCC under irradiation in more controllable conditions. These are the objectives of the facility R&D Phase II timed to the substantial upgrade of the LPE-10 linac toward the improvement of the *e*-beam stability, control and diagnostics for longer exposure irradiations.

We plan the implementation of a more predictable forced convection regime for the facility loop operation at elevated temperatures by application of NSC KIPT-manufactured circulation pump and flow meters. Another controlled parameter, the specimen bending stress, compression and tension, is provided by a new design of the irradiation cell capable of irradiation of bent coupons for SCC and even more complicated fatigue corrosion tests. STH and FEM calculations are in progress as needed for the experimental setup optimization.

We also have seen that the post-irradiation stage of the SCWR candidate materials testing take ~90% of time (as compared to 1–3 weeks under *e*-beam plus 3–6 months of sample deactivation) and expenses. A large database of irradiated coupons of Zr- and Ni–Cr-based alloys now exists and is available for characterization of microstructure and chemistry to improve the statistics and to refine the results presented in this report. Therefore, and in complement to the long-lasting support from CNL, we are open to participation in the EU-sponsored SCWR programme (Karlsruhe, Petten, Řež, VTI) to synchronize our simulation irradiations with future in-pile experiments and to make greater progress in materials screening taking into account irradiation-specific effects.

Acknowledgments

Authors are very grateful to Ninel Rybalchenko, Viktor Bryk and Vira Bovda (NSC KIPT), Vasyl Tkach (Bakul Institute for Superhard Materials), Leonid Kapitanchuk (Paton Institute of Electric Welding), Wenyue Zheng (MTL-NRCan) and Mrs. Pei Liu (CANMET-MTL) for their valuable support in the implementation of post-irradiation analytical researches.

The work was partially supported by Science&Technology Center in Ukraine project #4841.

References

1. T. Allen, Y. Chen, D. Guzonas, X. Ren, K. Sridharan, L. Tan, G. Was, E. West, “Material performance in supercritical water”, Comprehensive Nuclear Materials, **5**, 279, 2012.

2. M. Zychová, A. Vojáček, M. Růžičková, R. Fukač, E. Křečanová. “New research infrastructure for SCWR in Centrum Výzkumu Řež”, Proc. of the 6th Int. Symposium on Supercritical Water-Cooled Reactors (ISSCWR), Shenzhen, Guangdong, China, paper #13031, 2013.

3. A. S. Bakai, V. N. Boriskin, A. N. Dovbnya, S. V. Dyuldya and D. Guzonas, “Supercritical Water Convection Loop (NSC KIPT) for materials assessment for the next generation reactors”, Proc. of the 5th ISSCWR, Vancouver, Canada, paper #51, 2011.

4. A. S. Bakai, V. N. Boriskin, A. N. Dovbnya, S. V. Dyuldya and D. Guzonas, “Supercritical water convection loop for SCWR materials corrosion tests under electron irradiation: First results and lessons learned”, Proc. of the 6th ISSCWR, Shenzhen, Guangdong, China, paper #13062, 2013.

5. D. Guzonas, K. Bissonette, L. Deschenes, H. Dole, W. Cook, “Mechanistic aspects of corrosion in a Supercritical Water-cooled Reactor”, Proc. of the 6th ISSCWR, Shenzhen, Guangdong, China, paper #13086, 2013.

6. A.S. Bakai, “Theory of the heterophase fluctuations in the vicinity of gas-liquid critical point”, Proc. of the 5th ISSCWR, Vancouver, Canada, paper #52, 2011.

7. I. A. Petelguzov, “Study of the corrosion kinetics of calcium-thermal Zr+1%Nb alloy fuel elements piping in a 400–500°C water steam”, Problems of Atomic Sci. and Tech., Ser.: Rad. Damage Phys. and Rad. Mat. Sci., 6(82), 88, 2002, (*in Russian*).

8. P. Xu, L. Y. Zhao, K. Sridharan, T. R. Allen, “Oxidation behaviour of grain boundary engineered alloy 690 in supercritical water environment”, J. Nucl. Mat., **422**, 1–3, 143, 2012.

9. D. Guzonas, P. Tremaine, F. Brosseau, J. Meesungnoen, J.-P. Jay-Gerin, “Key Water Chemistry Issues in a Supercritical-water-cooled Pressure-tube Reactor”, Nucl. Technology, **179,** 205, 2012.

ISSCWR7-2014

HPLWR Fine Mesh Core Analysis

Emese Temesvári, Csaba Maráczy, György Hegyi, Gábor Hordósy, Attila Molnár
Centre for Energy Research,
Hungarian Academy of Sciences
1525 Budapest 114., P.O. Box 49., Hungary
+3613922222, emese.temesvari@energia.mta.hu

Abstract

The European version of Supercritical Water Reactors (SCWR), the High Performance Light Water Reactor (HPLWR) operates in the thermodynamically supercritical region of water. Our basic objective was to elaborate a stationary coupled neutronic-thermohydraulic code capable for the calculation of the actual 3-pass core design with fuel assembly clusters. The calculations covered the neutronic transport calculations of HPLWR fuel assemblies, the coupled neutronic-thermohydraulic global calculations and the pin-wise analysis. Applying conservative assumptions, the relation to the linear heat rate and maximum cladding temperature limits was checked for the equilibrium cycle of HPLWR with this new code system.

1. Introduction

The European version of SCWRs, the HPLWR operates in the thermodynamically supercritical region of water. Our basic objective was to elaborate a stationary coupled neutronic-thermohydraulic code capable for the calculation of the actual 3-pass core design with fuel assembly clusters [1]. In the one loop reactor the water is heated up without change of phase under supercritical pressure. The high outlet temperature results in 44% thermal efficiency. The potential advantages of the HPLWR are the low construction costs because of size reduction of components and buildings compared to current LWR and the low electricity production costs due to high efficiency. The calculations covered the neutronic transport calculations of HPLWR fuel assemblies, the coupled neutronic-thermohydraulic global calculations and the pin-wise analysis.

2. The structure of the HPLWR core

The layout of fuel assemblies can be seen in Figure 1. The basic structure is the fuel assembly with 40 fuel rods and assembly wall. Inside the assembly a water box can be found to provide sufficient moderation. 3x3 fuel assemblies are joined to form a fuel cluster with common foot and head pieces. 156 fuel clusters form the core with reflector regions.

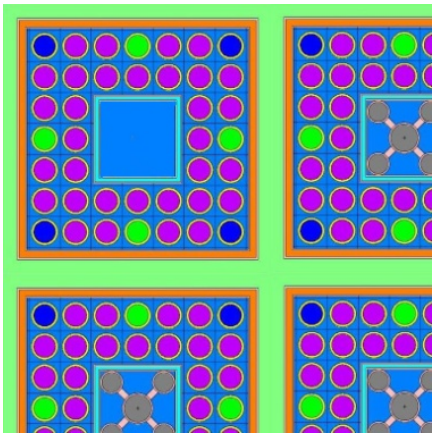

Figure 1: One quarter of the fuel cluster with absorber rods (gray), integrated Gd burnable poison (green).The corner rods (dark blue) have lower enrichment.

The thermal power of HPLWR is 2300 MW, the inlet pressure of the core is 25 MPa. The total mass flow of cooling water is 1160 kg/s with 280 °C inlet temperature, the outlet temperature is 500 °C in the 4.2 m high core.

The core of HPLWR differs from that of the usual light water reactors for the following reasons:

- The outlet water density is one eighth of the inlet water density, so to reach sufficient moderation for the tight lattice fuel the contribution of water gaps between assemblies and the moderator box is important.
- The average enthalpy rise of coolant is nearly 2000 kJ/kg, which exceeds the value in pressurized water reactors by more than a factor of 10. The high enthalpy rise in the hot channels would result in such high cladding temperatures at a usual one pass core arrangement what is beyond any reasonable limit of potential materials. In the three-pass core arrangement [2] the hot spots can be potentially eliminated by multiple flow of coolant through the active core with mixing after each passing (See Figure 2).

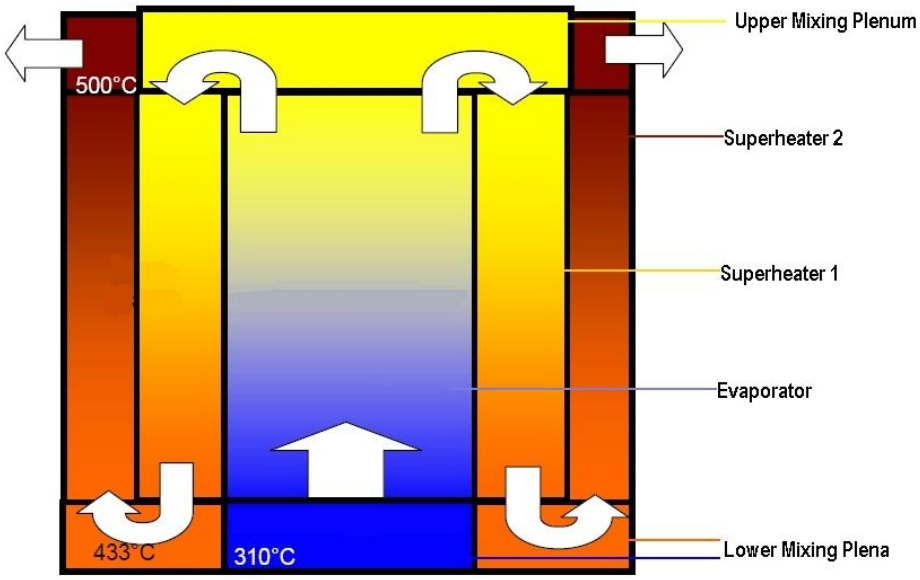

Figure 2: HPLWR 3-pass core concept. (Karlsruhe Institute of Technology)

3. Fine mesh core analysis of the equilibrium cycle

To control the maximum cladding temperatures cluster orifices were applied to tune the mass flow distributions in the three flow regions of the core. As a consequence of the application of burnable absorbers considerable power distribution change can be observed in the HPLWR core which results in the mass flow redistribution among the assemblies affecting the cladding temperatures. Starting from the first loading of the HPLWR, equilibrium cycle was reached, which contains assemblies with Gd integrated poison. On the basis of previous calculations with flat axial enrichment distribution resulting in bottom peaked power, axial enrichment profile has been introduced in the supercritical KARATE nodal code. 7% maximum fuel pin enrichment was applied in the cluster types used in the equilibrium cycle [3]. The main characteristics of the clusters used in the fresh and equilibrium cycles can be seen in Table 1. After three year core residence time on the average the average discharge burnup reached 33.5 MWd/kgU.

Table 1. The main characteristics of the clusters

Cluster type	Axial segment [cm]	^{235}U enrichment [w/o]			Number of Gd rods	Gd_2O_3 content [w/o]
		Basic	Corner	Gd rod		
1	000.00-420.00	4.0	3.0	-	-	-
2	000.00-420.00	5.0	4.0	-	-	-
3	000.00-420.00	6.0	5.0	5.5	4	2.0
4	000.00-204.61	6.0	5.0	5.5	4	2.0
	204.61-420.00	7.0	6.0	6.5	4	2.0
5	000.00-420.00	3.0	2.0	-	-	-
6	000.00-204.61	6.5	5.5	6.0	4	3.0
	204.61-420.00	7.0	6.0	6.5	4	3.0

The following main considerations were taken into account in the equilibrium cycle design from the viewpoint of safety at normal operation conditions:

- Keeping the linear power limit of 390 W/cm
- Keeping the fuel centerline temperature well below the melting point of UO_2 (≈3100 K)
- Keeping the maximum cladding temperature below 903 K

For checking the limits of fuel rods the DIF3D [4] fine mesh diffusion code applicable to pin power distribution calculation was applied. The interface of DIF3D with the supercritical coupled KARATE code was elaborated and the code system was applied for the equilibrium cycle. The main steps of the calculations were the followings:

- Best estimate cycle calculations with the supercritical KARATE 3D nodal code, storing the nodal neutronic, thermohydraulic results for further use.

- On the basis of 2D neutronic transport calculations the evaluation and parametrization of 2-group diffusion type fine mesh cross sections. The parameters taken into account:
  - Burnup
  - ^{235}U concentration
  - ^{238}U concentration
  - ^{239}Pu concentration
  - ^{135}Xe concentration
  - ^{149}Sm concentration
  - Fuel temperature

- Absorber cluster insertion factor
- Coolant density
- Moderator box water density
- Gap water density

- Generating 2-group reflector cross sections with 1D neutronic transport calculations. The reflector structure and the neighboring fuel zone are modeled.

- Application of 2D (x-y) full core fine mesh calculations to derive power peakings inside the assemblies on the basis of the thermohydraulic data and axial bucklings of the KARATE 3D nodal code. The calculated domain in 39 axial levels includes the reflector regions. Calculation of the isotopic concentrations of pins in case of burnup steps. Handling the fuel shuffling.

- Using the results of the best estimate KARATE nodal calculations performing assembly-wise conservative thermohydraulic calculations in which the assembly power is increased by the uncertainty of the k_q radial power peaking factor, the inlet temperature is increased according to the inlet enthalpy uncertainty arising from the non perfect mixing in mixing plena and the assembly flow rate is decreased according to the k_q - relative flow rate curves of flow regions (see Figure 3). (In the HPLWR reactor the assembly flow rates (G) strongly depend on the assembly power owing to the high heatup of coolant and the relatively low hydraulic resistance of orifices.)

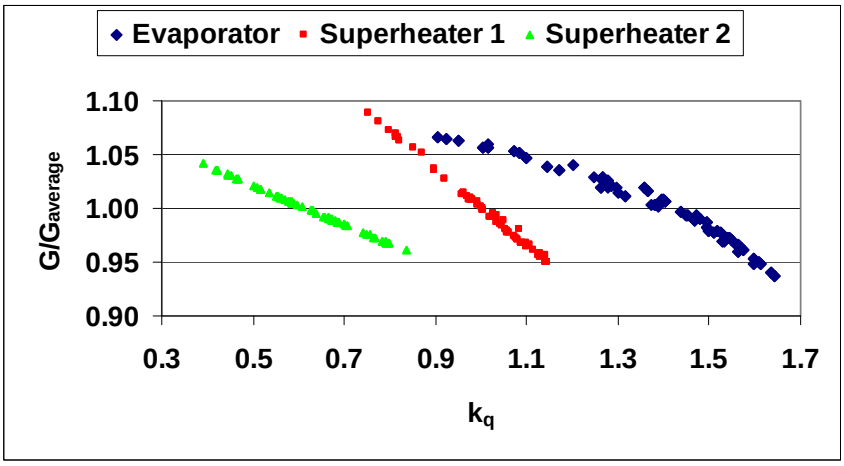

Figure 3: Assembly-wise k_q - relative flow rate curves of flow regions, $g=G/G_{average}$, $g=a+b*k_q$

Table 2. Flow rate coefficients for the different flow regions

Flow region	a	b
Evaporator	1.276	-0.200
Superheater 1	1.337	-0.338
Superheater 2	1.105	-0.173

- Performing conservative pin-wise calculations: The pin-wise radial peaking factors (k_k) are calculated from the pin section powers of DIF3D, the maximum k_k multiplied by the engineering factor corresponding to the pin power calculation uncertainty provides a conservative value. This value is used in the correlation developed in the HPLWR

Phase 2 project for the calculation of the hot channel enthalpy rise peaking factor (k_h). $k_h(k_k) = 0.780+0.235k_k$ [6]. The correlation valid for HPLWR fuel assemblies shows the good mixing between subchannels resulting from the application of helical wire spacers. The maximum cladding and fuel centerline temperature was calculated with a simplified fuel rod model applying the Watt correlation [7] on the surface of cladding. The pin-wise hot channel calculations were performed both for the pin with maximum linear power and for the pin with maximum power. The conservative assembly-wise ($\mathbf{f_{kq}}$) and pin-wise ($\mathbf{f_{kk}}$) engineering factors of power are presented in Table 3.

Table 3: Engineering factors for the 3 flow regions

Flow region	$\mathbf{f_{kq}}$	$\mathbf{f_{kk}}$
Evaporator	1.040	1.072
Superheater 1	1.110	1.072
Superheater 2	1.120	1.072

For the determination of engineering factors results of the KARATE, DIF3D and the reference MCNP calculations of a number core configurations were used.

The best estimate fuel rod linear power distribution at the beginning of the cycle, at the most loaded irradiation time and at the end of cycle in the most loaded axial level can be seen in Figures 4-6. The central evaporator, the first superheater and the peripheral second superheater flow regions are separated by black lines. Considerable axial and radial power redistribution can be observed.

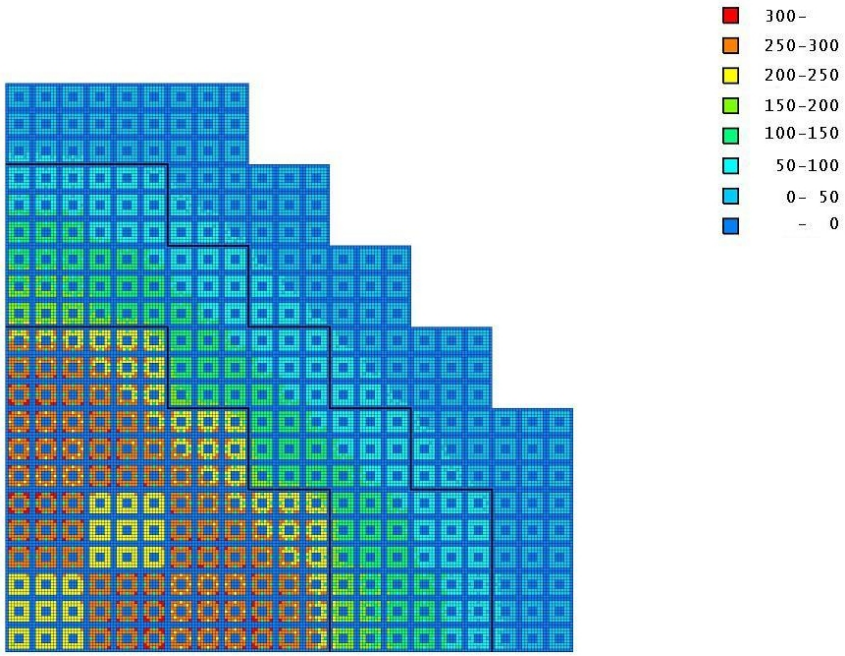

Figure 4: Fuel rod linear power distribution on the 0th day of the equilibrium cycle in the most loaded 22nd level. [W/cm]

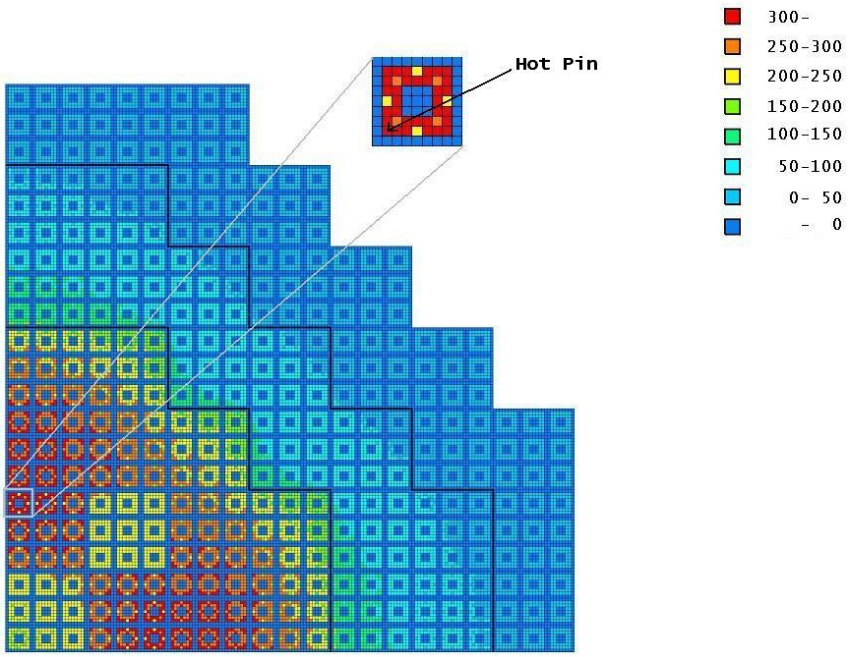

Figure 5: Fuel rod linear power distribution on the 105th day of the equilibrium cycle in the most loaded 8th level. [W/cm]

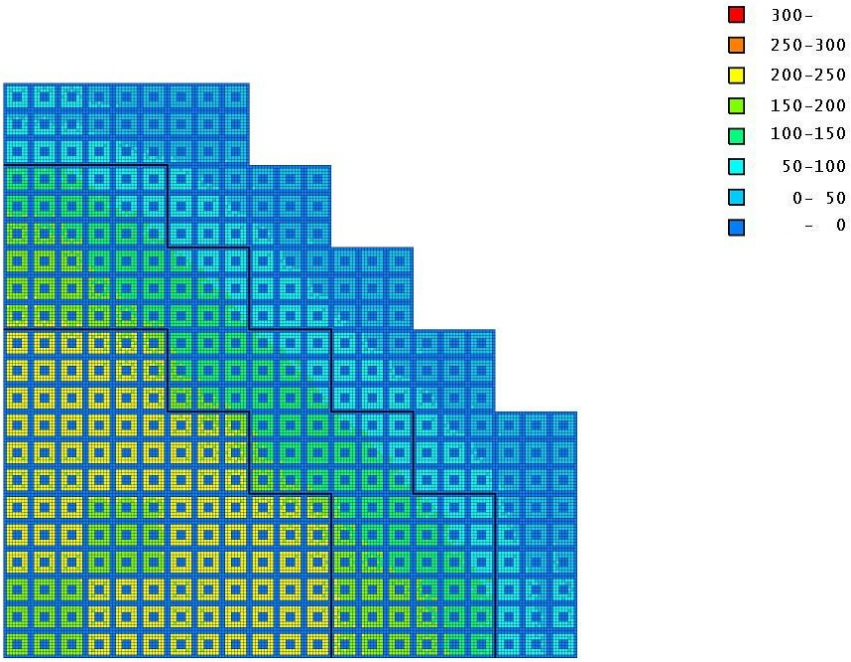

Figure 6: Fuel rod linear power distribution on the 355th day of the equilibrium cycle in the most loaded 32nd level. [W/cm]

The maximum of linear power multiplied by the engineering factors during the equilibrium cycle can be seen in Figure 7. The highest value was achieved at the 105th effective day of the equilibrium cycle. The 390 W/cm limit just can be kept.

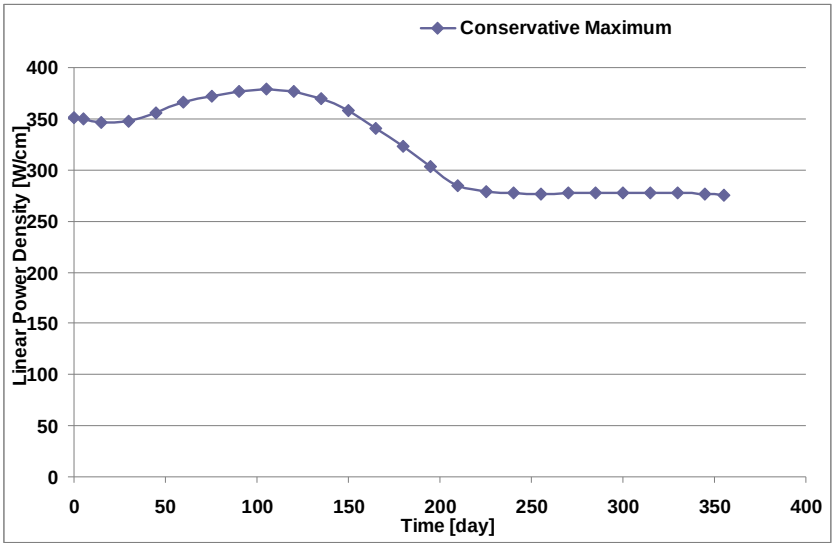

Figure 7: The conservative maximum of the pin-wise linear power during the equilibrium cycle.

The conservative maximum of the pin-wise linear power can be seen in Table 4. The numeration of the assemblies and rods can be found in Figures 8 and 9.

Table 4. The conservative maximum of the pin-wise linear power

Time	Linear power	Assembly	Rod	Level
[day]	[W/m]	[-]	[-]	[-]
0	35153.4	6	40	22
5	35062.9	6	40	22
15	34622.8	6	40	21
30	34735.1	106	1	10
45	35671.0	106	1	10
60	36609.8	106	1	9
75	37272.5	106	1	9
90	37724.6	106	1	8
105	37920.3	106	1	8
120	37732.5	106	1	8
135	37054.9	106	1	8
150	35827.0	106	1	7
165	34130.0	10	34	8
180	32321.9	10	34	8
195	30375.6	10	34	8
210	28592.2	10	34	7
225	27913.6	10	40	22
240	27730.8	10	40	24
255	27692.1	10	40	28
270	27754.7	10	40	29
285	27808.3	10	40	30
300	27826.2	10	40	31
315	27835.2	10	40	31
330	27755.7	10	40	32
345	27681.2	10	40	32
355	27594.7	10	40	32

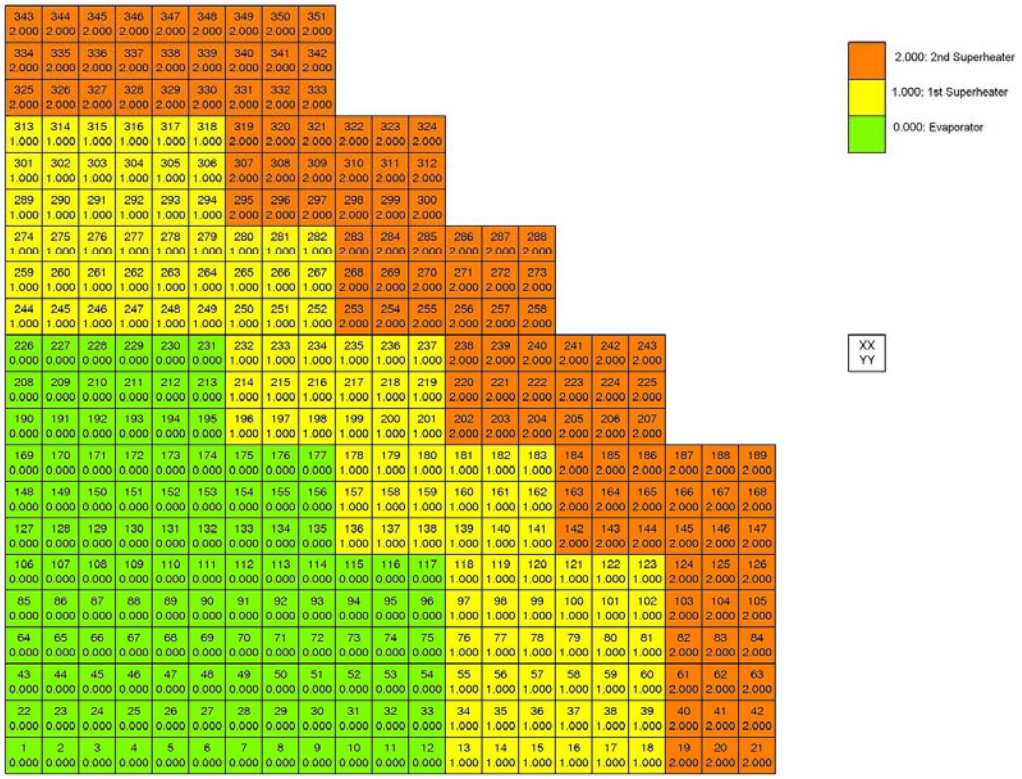

Figure 8. The numeration of the HPLWR assemblies and the flow regions.

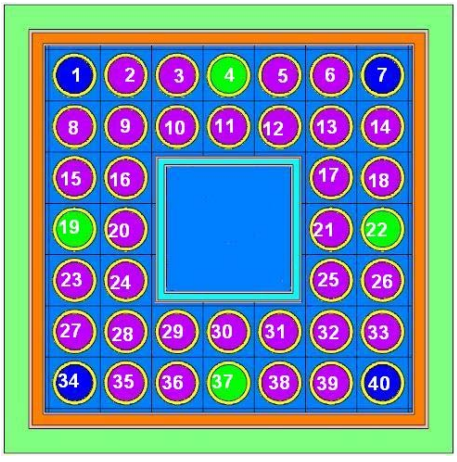

Figure 9. The numeration of the HPLWR rods in the assemblies.

The conservative maximum of the fuel centerline temperature shows similar behavior as the conservative maximum of the pin-wise linear power. It is below the melting point of uranium-dioxide (see Figure 10 and Table 5).

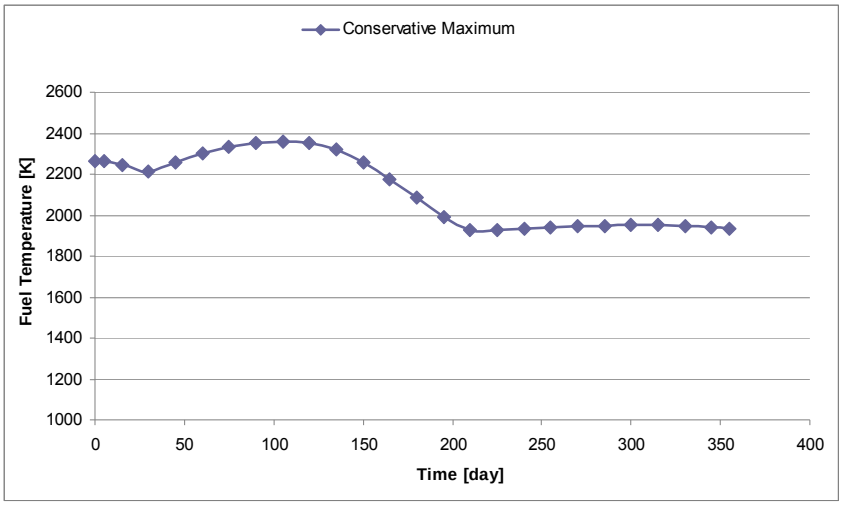

Figure 10: The conservative maximum of the pin-wise fuel centerline temperature during the equilibrium cycle.

Table 5. The conservative maximum of the pin-wise fuel centerline temperature during the equilibrium cycle.

Time	Fuel temperature	Assembly	Rod	Level
[day]	[K]	[-]	[-]	[-]
0	2266.3	106	1	23
5	2264.4	6	40	22
15	2242.9	6	40	22
30	2214.4	6	40	22
45	2259.4	106	1	10
60	2300.5	106	1	9
75	2334.3	106	1	9
90	2352.9	106	1	9
105	2361.0	106	1	8
120	2352.5	106	1	8
135	2319.4	106	1	8
150	2258.1	106	1	8
165	2172.1	10	34	8
180	2085.3	190	34	8
195	1991.9	190	34	8
210	1930.6	10	34	24
225	1928.7	190	34	27
240	1934.7	10	34	29
255	1941.7	190	34	30
270	1944.8	190	1	30
285	1949.5	10	40	31
300	1950.4	10	40	31
315	1950.9	190	1	32
330	1947.3	10	40	32
345	1940.0	190	1	33
355	1936.2	10	40	33

The maximum of the conservative clad surface temperature always exceeds the goal temperature of 903 K during the equilibrium cycle (see Figure 11 and Table 6).

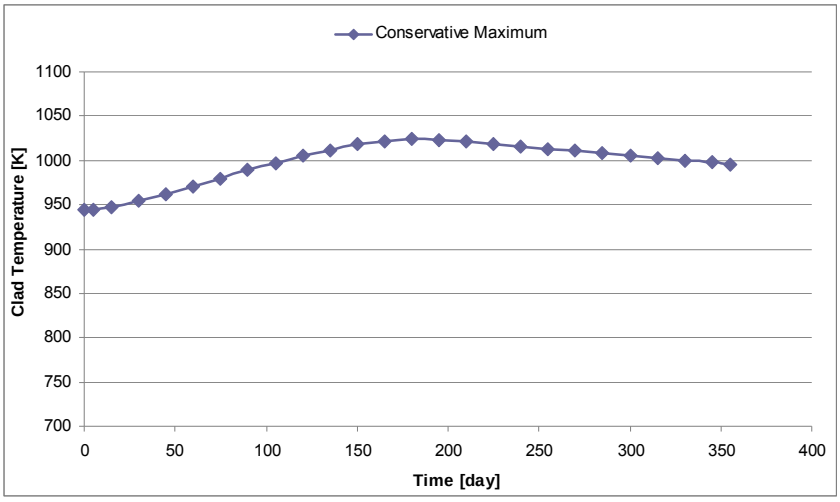

Figure 11: The conservative maximum of the pin-wise cladding temperature during the equilibrium cycle.

Table 6. The conservative maximum of the pin-wise cladding temperature during the equilibrium cycle.

Time	Cladding temperature	Assembly	Rod	Level
[day]	[K]	[-]	[-]	[-]
0	944.4	244	34	7
5	944.9	244	34	7
15	947.2	244	34	7
30	954.3	244	34	7
45	962.7	244	34	7
60	971.5	244	34	7
75	980.4	244	34	7
90	989.2	244	34	7
105	997.7	244	34	7
120	1005.7	244	34	7
135	1012.9	244	34	7
150	1018.7	244	34	6
165	1022.8	244	34	6
180	1024.3	244	34	6
195	1023.7	244	34	6
210	1021.7	244	34	6
225	1019.0	244	34	6
240	1016.5	244	34	5
255	1013.9	244	34	5
270	1011.3	244	34	5
285	1008.6	244	34	5
300	1005.9	244	34	5
315	1003.1	13	34	5
330	1000.4	244	34	5
345	998.2	244	34	4
355	996.8	244	34	4

4. Conclusions

The maximum of the pin-wise cladding temperature was always found in an assembly of the first superheater which is next to the evaporator. As in the evaporator region the maximum linear power is close to the limit, the further direction of optimization is the partial rebalance of power from superheater 1 to superheater 2 where none of the limits are jeopardized. An obstacle of the optimization by shuffle scheme is the 3x3 cluster structure of the assemblies and the cluster-wise orifices. The possibility of assembly wise shuffling and orifices would ease the situation considerably.

5. Acknowledgments

The authors would like to thank the European Commission and the Hungarian National Development Agency for their financial support of projects HPLWR Phase 2 and Nukenerg.

References

1. Schulenberg T, Maraczy Cs, Heinecke J and Bernnat W: *Design and Analysis of a Thermal Core for a High Performance Light Water Reactor*, Nuclear Engineering and Design, 241, pp. 4420–4426 (2011)

2. T. Schulenberg, J. Starflinger, J. Heinecke: *Three pass core design proposal for a high performance light water reactor*, Progress in Nuclear Energy 50, pp.526-531 (2008)

3. Cs. Maráczy, Gy. Hegyi, G. Hordósy, E. Temesvári: *HPLWR equilibrium core design with the KARATE code system*, Progress in Nuclear Energy 53, pp. 267-277 (2011)

4. K.L.Derstine: *DIF3D: A Code to Solve One-, Two, and Three-Dimensional Finite-Difference Diffusion Theory Problems*, ANL-82-64, Argonne National Laboratory, USA (1984)

5. Keresztúri, A., Hegyi, Gy., Korpás, L., Maráczy, Cs., Makai, M. and Telbisz, M.: *General features and validation of the recent KARATE-440 code system*, Int. J. Nuclear Energy Science and Technology, Vol. 5, No. 3, pp.207–238 (2010)

6. T. Schulenberg, J. Heinecke, Köhly, C. Kunik, A. Miotto, L. Monti, X. Tiret, A. Wank, Cs. Maráczy, Gy. Hegyi, E. Temesvári, W. Bernnat: *Thermal Core Design for the HPLWR – Year 3*, HPLWR Phase 2 Project (2009)

7. Watts, M.J., Chou, C.T.: *Mixed convection heat transfer to supercritical pressure water*. In: Proceedings of the 7th IHTC, Munchen, Germany, pp. 495–500 (1982)

ISSCWR7-#2015

Prediction of response of the Canadian super critical water reactor to potential loss of forced flow scenarios

Yang Wu
University of Tokyo
Asano Campus University of Tokyo, Faculty of Engineering Bildg.12 Annex 1, 7-3-1 Hongo, Bunkyo, Tokyo, Japan
Tel:+81-080-7716-7179, Email: wu@vis.t.u-tokyo.ac.jp

D.R.Novog
McMaster University
1280 Main St. West, Hamilton, ON, Canada
Email: novog@mcmaster.ca

Abstract

The Canadian SCWR Design represents an evolutionary concept in safety known as the no core melt concept. Using a combination of active and passive safety features the SCWR achieves a major improvement in Core Damage Frequency and well as system resiliency. This paper presents the accident analysis for a Loss of Offsite Power under various conditions. The first condition assumes availability to the emergency gas turbine generators and hence availability of the main residual heat removal systems is assumed within a short time after the loss of power. The second condition involves a failure of the gas turbine generators where isolation condenser safety systems are assumed available with a single failure criterion leading to a loss of 50% of the isolation condenser heat exchangers, and demonstrates that fuel sheath temperatures have significant margin to the safety limits. The third case involves a complete failure of the gas turbine generators and isolation condenser system and relies solely on the passive moderator heat sink. This case involves interesting thermalhydraulic phenomena wherein flows in the core initially go to very small values but then recover somewhat due to natural circulation phenomena inside the core. The natural circulation flows predicted are on the order of 5%, which represents a significant contribution to cooling during the initial phases of the transient and greatly act to reduce the maximum sheath temperature in the core. Even for cases where all natural circulation driven heat transfer is neglected, and only radiation heat transfer is used to pass heat to the passive moderator system sheath temperature predictions remain within the safety acceptance criteria.

1. Introduction

The pressure tube type Super Critical Water Reactor (SCWR) is a Gen IV reactor concept which is currently being developed by Canada. The Canadian SCWR operates at high temperature and pressure (the coolant temperature and pressure at the reactor core outlet is 625 ^{o}C and 25MPa respectively) with a direct once-through cycle [1]. The moderator system is equipped with passive heat removal driven by buoyancy flow that can remove decay heat power levels. The unique feature of the distributed channel core may allow the reactor to obtain “no-core-

melt" under station blackout conditions by passive radiation heat transfer from the fuel elements to the pressure tubes and subsequently the moderator system during the Loss of Flow Accident.

Since 2005, thermal-hydraulic, reactor physics and material studies have been carried out to evaluate and optimize the thermal performance of Canadian SCWR following the LOCA/ LOECC and LOFA scenarios. The Canadian SCWR fuel design has been modified significantly throughout the past ten years.

In this study, a CATHENA idealization of the most resent 64-element fuel design has been developed including the effects of radiation. Under normal operation heat removal is performed through a number of active systems. During accident conditions the reactor is equipped with gas turbine generators (GTG) which can power a number of independent systems capabale of cooling the core. In a total station blackout (SBO) it is postulated that all power sources are unavailable and in such an event the passive Isolation Condenser System (ICS) will operate based on buoyancy driven flow. In the event of multiple failures from a common mode event such as those encountered in the Fukushima accident, the complete failure of all active systems and ICS is postulated. The Canadian design is unique in that an additional defence in depth barrier is in place which can remove heat from the fuel in such an event. This passive moderator cooling system (PMCS) relies on radiation heat transfer from the fuel to the pressure tube and ultimately to the buoyancy driven moderator cooling system. The PMCS is in service at all times and does not require changes in valve position or any other operator actions. LOFA transients involving failure of emergency power and failure of isolation condensers have been performed in order to study the heat transfer behaviors under the degraded cooling conditions and the behaviour of the PMCS. In addition, the quality of the CATHENA predictions under supercritical pressure conditions and the unique phenomena which occur under these conditions has also been evaluated in this study.

2. System and Model Description

2.1 System Description

The pre-conceptual Canadian SCWR design, which is illustrated in Figure 1 was used in this study.

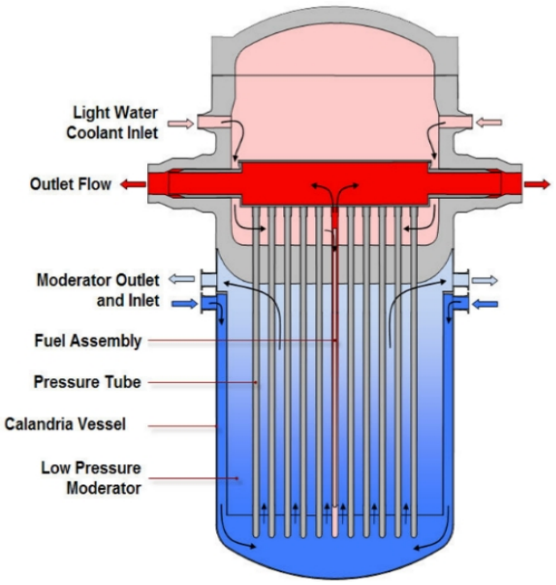

Figure 1. Current Design of the Canadian Pressure-tube Type SCWR[2]

As is shown on the diagram, the high-temperature, high-pressure light water coolant is separated from the low-temperature, low-pressure heavy water moderator by the pressure tubes. The coolant at 25.8MPa and 350 ^{o}C enters the inlet plenum and is then distributed into the center flow tube of each fuel channel. The coolant then flows downwards along the center flow tubes. After exiting the center flow tubes, the coolant changes flow direction (at this time, the coolant temperature is 371 ^{o}C, which is lower than the pseudo-critical temperature of 385 ^{o}C) and starts to flow upwards along the fuel assemblies and absorbs the heat generated as a result of fission. Outlet flows are collected in the outlet plenum (the coolant temperature and pressure are 625 ^{o}C and 25MPa respectively at the exit of the outlet plenum) and then are directly fed to the high-pressure turbines through the hot-leg piping.

The pressure tubes are surrounded by the low-pressure, low-temperature heavy water moderator contained in the calandria vessel. The proposed moderator system operates under normal conditions using a combination of active and passive systems. The active system supplements the continuously operational passive system so that boiling is precluded in the moderator during normal operation. The active system also helps to assure that two-phase natural circulation instabilities are avoided during start-up and shutdown of the reactor. The passive components of the moderator system consist of a two-phase flashing riser which provides a heat sink pathway to heat exchanges which reject heat to the environment. The passive system is in operation at all times and hence requires no power or changes in valve positions. Under emergency or accident conditions the passive moderator cooling system is designed to provide sufficient heat sink capabilities so as to preclude fuel melting. Key parameters regarding the Canadian SCWR concept are summarized in Table A1.

2.2 Fuel Channel Description

The fuel channel design referred as High Efficiency Re-Entrant Channel (HERC) is implemented in the Canadian SCWR concept. Figure 2 shows the configuration of the Canadian SCWR fuel bundle. As is shown in Figure 2(a), the center flow tube is a physical barrier separating the low-temperature coolant which is flowing downwards and the high-temperature coolant which is flowing upwards. Sixty-four fuel rods are assembled into two concentric fuel rings referred as to the inner ring and outer ring. Both rings consist of 32 identical fuel pins with the outer ring elements slightly larger in diameter. The outmost layer of the HERC is the Excel alloy pressure tube which is designed to withstand the high reactor operation pressure. The Zirconia isolator (Yitria-stabilized Zirconia ceramic) located between the fuel assemblies and the pressure tubes isolates the pressure tube from the high-temperature coolant and thus keeps the pressure tube temperature close to the moderator temperature. The inner and outer surfaces of the isolator are cladded with zirconium-modified stainless steel and Excel alloy which is referred as the Liner Tube and Outer Liner. The presence of the liners minimizes the potential mechanical damage to the isolators from both sides. The specifications and materials for the fuel assemblies are provided in Table A2 and Table A3.

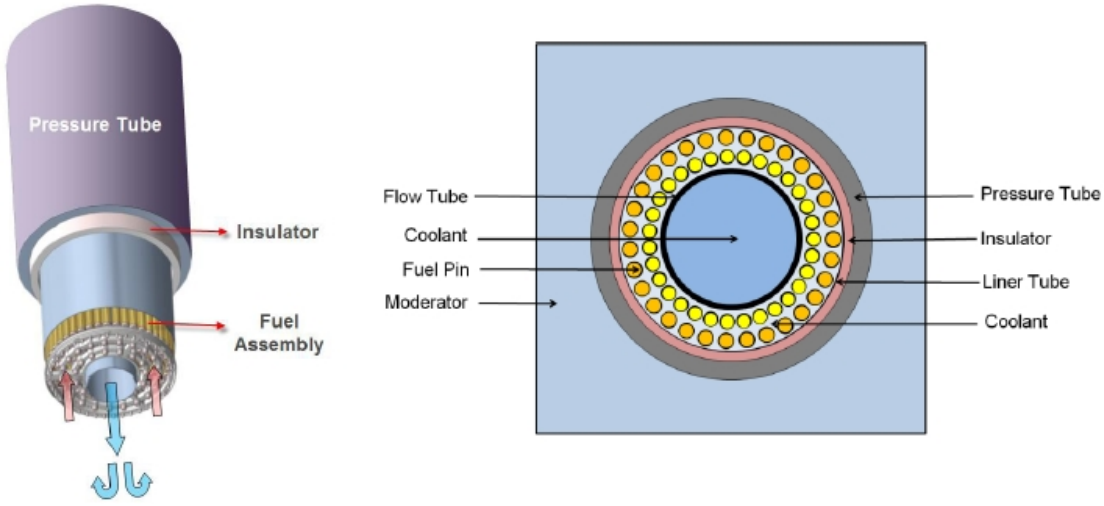

(a) Fuel Channel (b) Cross-section View of Fuel Channel

Figure 2. Canadian SCWR (a) Fuel Channel and (b) Cross-section View of Fuel Channel[3]

2.3 Model Description

The layout of the CATHENA idealization is shown in Figure 3. The model starts from Cold Leg Boundary Condition (CLEGBC) which is a reservoir component simulated as the inlet pressure boundary. Coolant from CLEGBC flows through the main feed water line (i.e., the cold leg, CLEG1 and CLEG2) and enters the inlet plenum. From the inlet plenum (IPLENUM), the coolant is distributed into the 7 fuel channel groups (for steady state normal operation case). In order to obtain the correct total massflow rate, each fuel channel is represented as a number of parallel pipes (the number of parallel pipes in each group is listed in Table A4, column 4). All fuel channels consist of a centre flow tube entrance section (CCH11 and CCH12), the 5-meter-long centre flow tube (CCH2), the 180 degree bending section (CCH3 and CH3), the 5 meter-long fuel region (CH2), the fuel channel exit section (CH11 and CH12, with the numbering selected so that it matches the centre flow tube entrance section) and the outlet end fitting assembly (EF1 and EF2). Coolant from the fuel channels is collected in the outlet plenum (OPLENUM) and fed to the high pressure turbine through the main steam line (HLEG1, HLEG2 and HLEG3). The high pressure turbine is presented as the outlet pressure boundary (denoted as the Hot Leg Boundary Condition, i.e. HLEGBC) in the CATHENA idealization. For each fuel bundle, the 64 fuel pins are modelled by two independent rings with 32 identical cylinders located at the inner concentric ring and 32 cylindrical fuel pins located at the outer concentric ring. The power distribution between inner ring fuel pins and outer ring fuel pins is 48.6% and 51.4% respectively. In the axial direction, the 5-meter long fuel models are divided into 10 sections of equal length. The axial power distribution of beginning of cycle (BOC), middle of cycle (MOC) and end of cycle (EOC) are plotted in appendix (Figure A1).

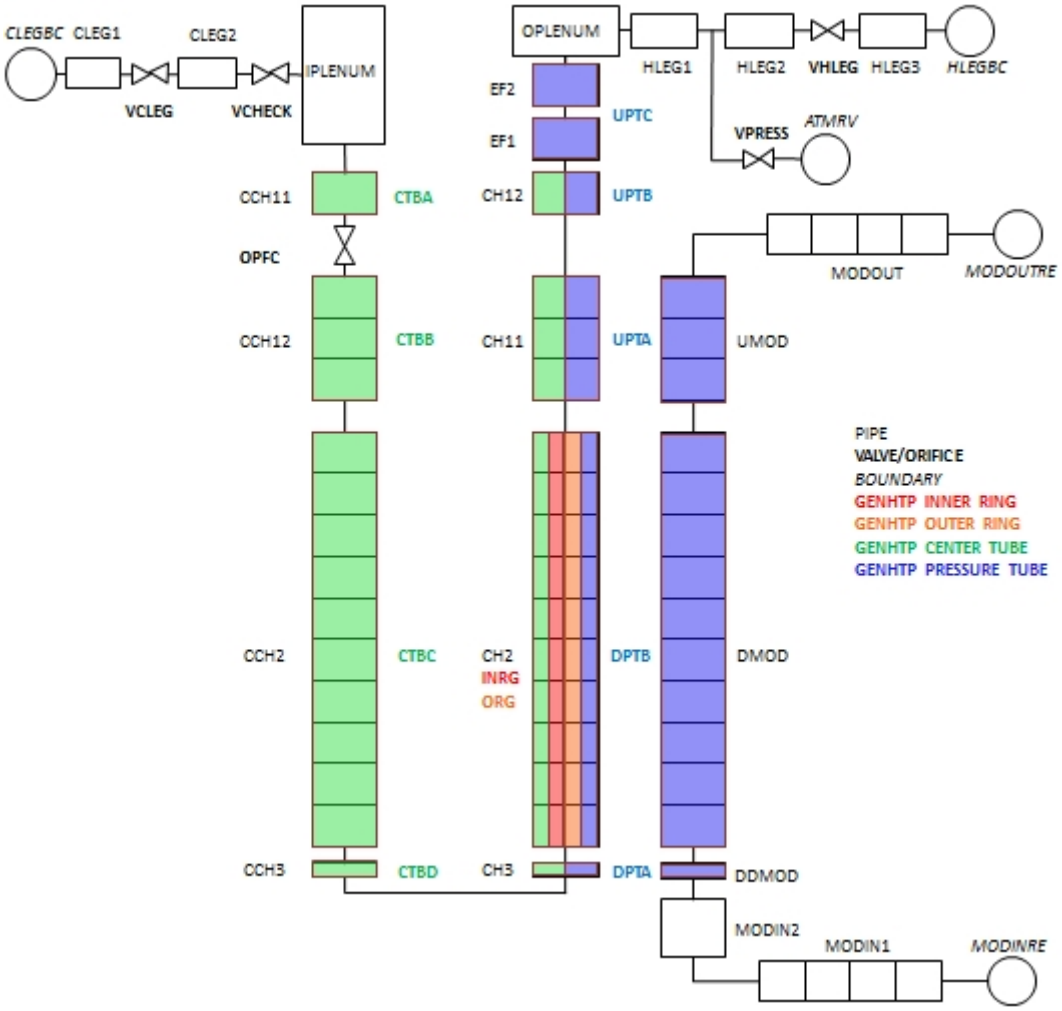

Figure 3. CATHENA Idealization for Canadian SCWR

For the scenario simulated in this thesis the moderator flow and heat transfer would be a function of the power-to-moderator at each point in time since the buoyancy driven flow will be proportional to the power-to-moderator. Again to simplify the analysis we assume a constant and low value for the moderator flow. The sensitivity to these assumptions are not specifically addressed in this work, however since the maximum clad temperatures typically occur in the first 10s of seconds, the moderator bulk flow is not expected to change significantly during this period.

The main controller used to establish the steady state is the Proportional-Integral (PI) controller, which is applied to the orifices denoted as “OPFC”. The PI controller is used to determine the orifice size/mass flow rate in all 84 fuel channel such that a uniformed temperature field of 625 ^{o}C at the exit of the outlet plenum could be achieved. It’s is found out that the orifice size is linear to the channel power. Hence, the orifice sizes of the seven channel groups are determined according to the average channel power in each group. According to the BOC, MOC and EOC power, three sets of orifice size data have been calculated. The MOC orifice sizes are selected for the steady state and transient simulations since they represent the channel powers for a large fraction of time during the batch cycle.

For steady state simulations, fuel channels in the first quarter of the core are divided into 7 groups based on their power. In addition, as channel power evolves over the batch cycles, the power at the beginning-of-cycle (i.e. 0 days), the middle-of-cycle (i.e. 210 days) and the end-of-cycle (1.e. 420 days) are all considered in the grouping. A single power group is used to model

the “hot” channels in order to calculate the upper limited of key parameters such as maximum fuel cladding temperature. The steady state grouping scheme is presented in Table A4. The transient simulations are performed using two different channel grouping schemes. In the first grouping scheme the 336 channels are divided into two groups, with the highest power channel in Group 2 and the remaining 335 channels in Group 1. By studying the LOFA transient in this way, an understanding of the behaviour of heat transfer inside the high efficiency channel is obtained and by assuming a single averaged channel recirculation flows are largely precluded and hence an upper bound estimate of the temperature can be determined. In the second grouping scheme, the core is divided into 4 groups. Again, the highest power channel is placed in a separate group and the rest 335 channels are divided into three groups with approximately equal number of channel in each group. By applying this grouping scheme, the natural circulation established among various channels groups is examined. The 2-channel groups grouping scheme and 4-channel groups grouping scheme are listed in Table A5 and Table A6.

2.4 LOFA Transient Conditions

LOFA transients simulated in this study involve failure of normal and emergency power and failure of isolation condensers. A sufficiently long zero-change transient was performed prior to the LOFA such that CATHENA had reached a steady-state. Two isolation valves located at the main feed-water line and main steam line are closed from 0s to 1s simultaneously, effectively causing a complete loss of driving flow within 1s, and additional flows from pump rundown are conservatively neglected. Reactor shut down is credited at 0.29s due to the low flow trip (with an actuation set-point of 90% of steady state flow), and power reduction from rapid insertion of the shutdown system is credited. As a result of safety system action, the power in the simulations is ramped to decay heat in approximately 2 seconds. The opening and closing set point for the safety relief valves are 26.00MPa and 25.25MPa respectively. The sequences of events are summarized in Table 1.

Table 1. Sequences of Events for LOFA Transients

Time (s)	Events
0.0	Isolation Valves started to close leading to loss of main feedwater
0.29	Reactor shutdown signal triggered (90% of the steady state flow), control rods inserted into reactor core (with a rate between 0.1s and 2s depending on the simulation).
1.0	Isolation Valves were completely closed

3. Result and Discussion

3.1 Steady State Normal Operation

The calculated axial temperature profiles for the coolant, fuel center line and fuel sheath of the maximum power channel (i.e. group7) are plotted in Figure A2, Figure A3 and Figure A4 respectively. For the maximum channel power group, the maximum sheath temperatures predicted by CATHENA for the BOC, MOC and EOC are 816.4^{o}C, 778.0 ^{o}C and 768.2 ^{o}C respectively. These changes in the steady state fuel sheath temperatures are the result of the large swings in channel power that occur with fuel burnup for the pre-conceptual design assessed in this study. For all simulations the orifice sizes corresponding to those determine at the MOC are used with a total core flow of approximately 1256 kg/s. The individual channel

flows from approximately 3.07kg/s for the channels in the low power group to 4.78kg/s for the channels in the maximum power group.

3.2 LOFA Transients for 2-Channel Group Scheme

The simulation results show that the transient developed very fast during the first 20s. For the 2-Group scheme, the maximum cladding temperature reaches 1045 ^{o}C at 14.0s (Fuel sheath temperature is shown in Figure 4 for the average channel – Group 1 and for the high power channel – Group 2). Radiation heat transfer dominants the cooling process during this period of time, however there is a significant contribution from convection in the maximum power channel (shown in Figure 5). One potential explanation for the early phase convection (i.e. massflow) was pseudo-critical transitions of components in the fuel channel. In particular the large amount of high density coolant in the central flow tube is heated and expands which in turn drives flow through the channel.

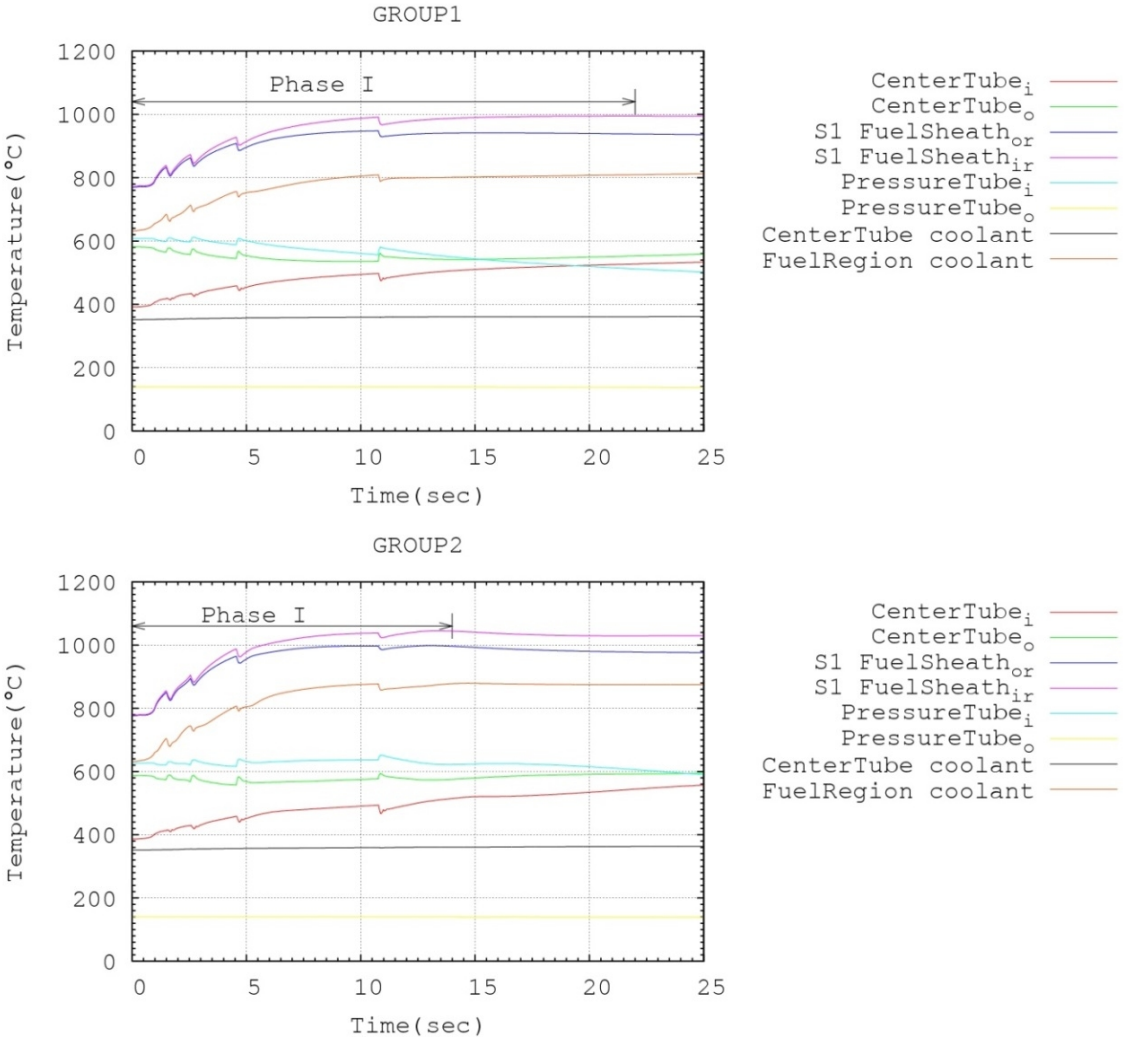

Figure 4. Temperature of Various Components at the Top of Fuel Region

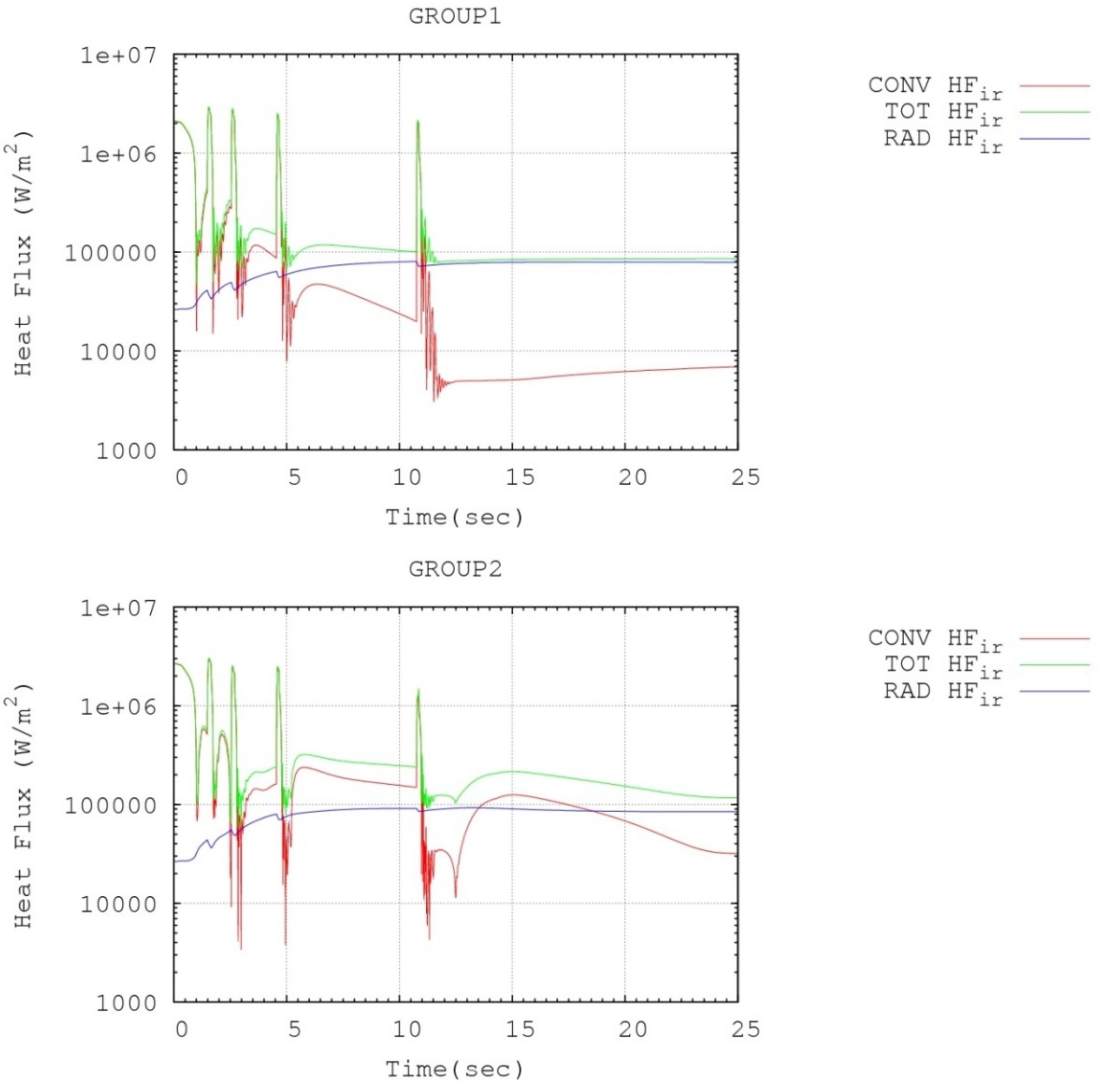

Figure 5. Heat Flux at Fuel Cladding of CH2(10)

Upon reaching the maximum values, the fuel cladding temperature started to decrease as the heat removed from the fuel rods by radiation and convective heat transfer exceeds the decay heat generated in the fuel. After which an accelerated cooling phase has been observed. The reason of it can be explained by the coolant massflow rate which is shown in Figure 10. The narrow spikes on the massflow plot are caused by SRV actions. As shown on the plot these high frequency massflow spikes appear from 120s to 200s corresponding to the times when coolant in the centre flow tubes goes through pseudo-critical transitions. During pseudo-critical transitions, the volume of the coolant inside centre flow tube has expanded approximately 4 times. This would sharply increase the core pressure in addition to that from decay heat accumulation and lead to high frequency SRV actions. In addition, the coolant volume expansion in these components also improve the convective cooling in the core by increasing the massflow rate. This is consistent with the “mass flow effect” noted by Oka in the Japanese SCWR design where the moderator flow boxes provide flow to the fuel regions even with total inlet flow stoppages [**Error! Bookmark not defined.**].

While the simulations above show interesting behaviour and adequate fuel cooling during these initial phases the results are preliminary because of limitations within the CATHENA codes. The default convective heat transfer correlation used in CATHENA under supercritical pressure is Dittus-Boelter correlation which can significantly over-predicted the convective heat transfer

component during pseudo-critical transition. While the fuel to coolant convection is well past the pseudo-critical transition and hence is not largely affected by the correlation limits, te large volumes of coolant in the central flow tube do undergo transitions during the transient. If the Dittus-Boelter correlation overestimates heat transfer in these components then int is likely that CATHENA will over predicted the associated flows generated in the core. Consequently, even though the reactor core would likely still exhibit transition driven flows, it would not as fast as CATHENA predicted. Later the system is largely stabilized with heat transfer from radiation balancing the heat generated in the fuel and the fuel cladding temperature starts to decrease according to the decay curve.

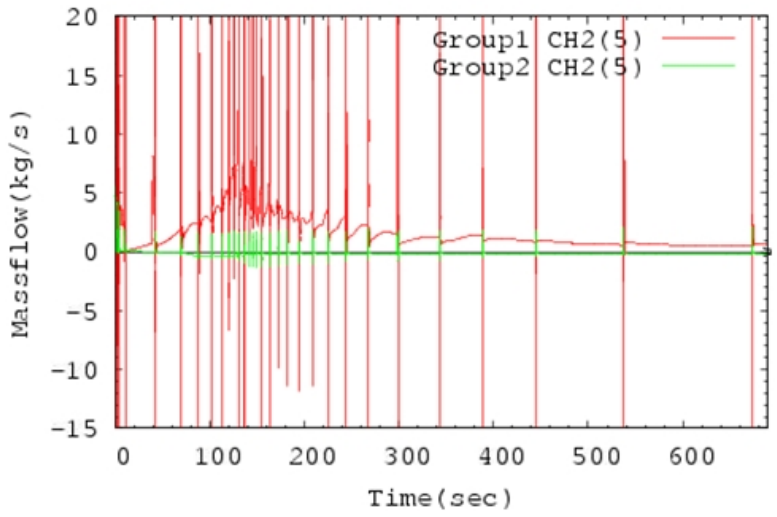

Figure 6. Coolant Massflow Rate per Group for 2-Channel Grouping Scheme

3.3 LOFA Transients for 4-Channel Group Scheme

The simulation results for the 4-group transient are summarized in Table A7. As shown in the table, the highest cladding temperature of 1059 ^{o}C is predicted for the pins of the Inner Ring which is lower than the melting point of the Zr-modified Stainless Steel fuel cladding [4]. Forward flow is mainly found in the medium power group (Group2) and high power group (Group 3) whilst reversed flow is found in the low power group (Group1) and maximum power group (Group4). The direction for these circulation pathways is not obvious and was highly sensitive to channel grouping, orifice size and channel power assumptions. The CATHENA developers have stated that under such low driving force conditions the code may be extremely sensitive to the small differences in orifice size, power level, axial fuel and pressure tube temperature etc…., and even possibly the order in which the matrices are solved within the code. Hence while the directions of flow may not be adequately predicted for the channel grouping concept used here, the end result is a relatively large amount of mass redistribution in the system, leading to higher convection and eventual core-cooldown.

The simulation results of the 4-group scheme share many similarities with those of 2-group's. Accordingly, most of the analyses made for the 2-group simulation are also valid here. A significant difference is observed in the 4-channel group case as compared to the 2-channel group case discussed previously is that the system cooldown rate proceeds much faster in the 4-group case. This is the results from the increased internal convection heat transfer to the pressure tube (and ultimately moderator) caused by much larger recirculation flows. Figure 7 shows the coolant massflow for 4-channel group LOFA transient.

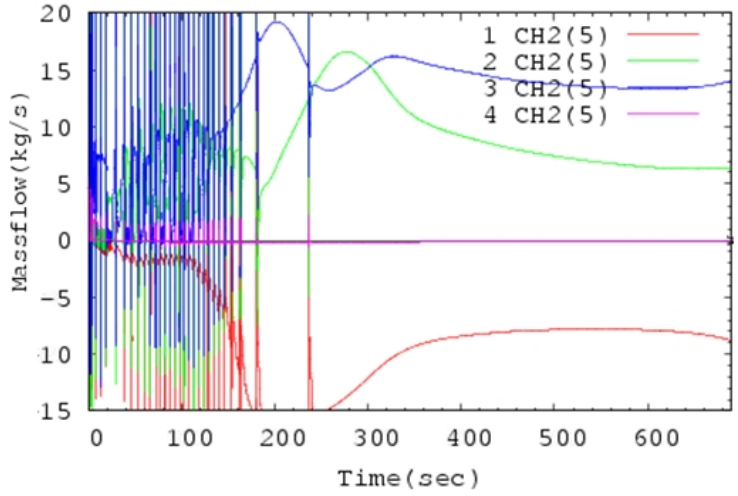

Figure 7. Coolant Massflow per Group for 4-Channel Group Scheme

Another phenomenon associated with natural circulation is mass redistribution in the system. As mentioned earlier net mass flow is found flowing from the inlet plenum to the outlet plenum of which the magnitude related to the mass flow rate of natural circulation. This is also verified by the coolant inventory plot (Figure 8).

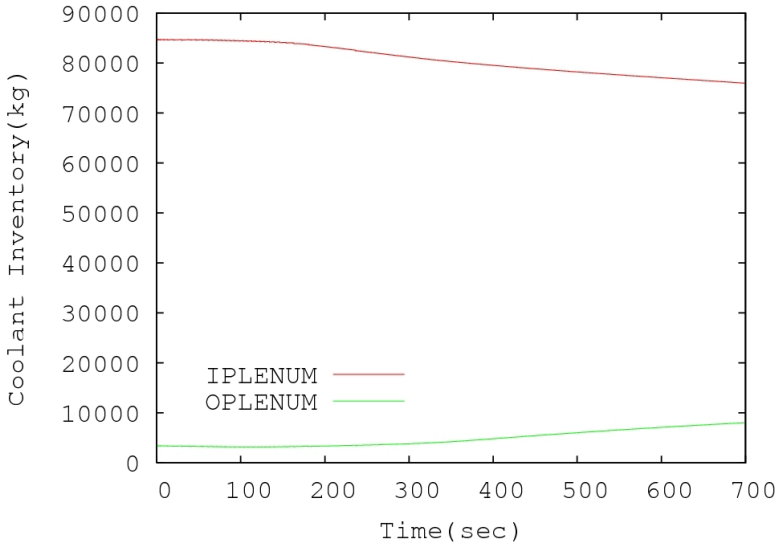

Figure 8. Coolant Inventory at Inlet and Outlet Plenum

The 4-channel group simulation result shows that the maximum fuel sheath temperature is sensitive to the function of flow rundown and reactor SCRAM characteristics. However, as the transient progressed, convective heat transfer dominates the cooling procedure as natural circulation is developed and established in the core. This is a unique feature of the SCWR in that the high density differences between the inlet and outlet plena and the pseudo critical transitions in some core components both act as driving forces for recirculation flows within the core. This convective cooling mode acts to greatly reduce the cladding temperatures in the intermediate phases of the accident. As the densities equalize the natural circulation is reduced but by this point the reactor decay heat is such that the system cooldown and depressurization are self-induced. The direction and intensity of the natural circulation flows is also sensitive to channel grouping assumptions used in the analysis.

Figure 9 illustrates the pressure variation of the inlet plenum and outlet plenum as a function of time. As shown in the plot, at approximately 700s, the core pressure is at 22.07MPa, which is the lower limit of the CATHENA supercritical pressure region. As the system transients through the supercritical to subcritical pressure, a significant discontinuity in core pressure is found at 780s. This means for this specific case CATHENA cannot be applied through trans-critical pressures and therefore all the simulation results after 700s are unreliable and hence are not shown.

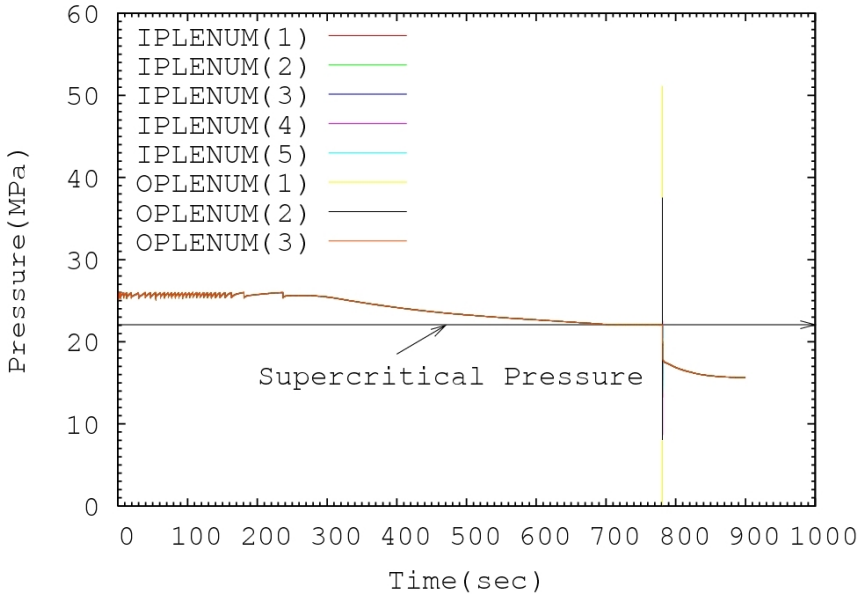

Figure 9. Pressure at Inlet and Outlet Plenum

3.4 Sensitivity Analysis

The prediction of maximum fuel sheath temperature is largely governed by the massflow rate, the power level and the efficiency of radiation heat transfer. Sensitivity analysis of these key parameters and one additional analytical model are performed to demonstrate how the predicted temperature is affected by reactor trip time, power ramping time, emissivity and the convective heat transfer at fuel surfaces during the early stage of transient. Note that all the sensitivity analyses are applied to the 2-group CATHENA idealization, as the 2-group model and 4-group model provide similar predictions on the fuel cladding temperatures before natural circulation initiates.

The simulation results for reactor low-flow trip time are summarized in Table A8. Five additional runs are performed with trip time corresponding to 70%, 50%, 30%, 10%, 0% of the steady state main feed water flow (In the 0% case, the trip time is delayed until the maximum fuel sheath temperature excess the melting point of the cladding material.). The results show that the perditions of maximum fuel sheath temperature are dependent on the time required for the core to reach decay heat. By delaying the trip time from 0.15s to 4.40s, the predicted maximum sheath temperatures are increased by approximately 355 ^{o}C. The upper bound low-flow trip time that ensures the acceptance criteria are met is 4.4s.

The simulation results for safety system SCRAM are summarized in Table A9. Various shutdown system rates from 0.1s to 3s are selected for the sensitivity study. As shown in the table, the ramping time does not have as large impact on the fuel cladding temperature prediction as the reactor trip time. For instance, if the power ramps down within 1 to 2s (which is

a typical value for CANDU reactor) the maximum sheath temperature would be 1077 which is 32 ^{o}C than the reference case.

The predicted maximum fuel cladding temperature using different emissivity is plotted in Figure 10 and summarized in Table A10. By reducing the emissivity value from 1 to 0, the maximum fuel sheath temperatures for the inner and outer rings are increased by 118 ^{o}C and 112 ^{o}C respectively. Also note that in the case where $\varepsilon = 0$ (i.e. radiation heat exchange between fuel cladding and surroundings is not simulated), the maximum fuel cladding temperature is 1151 ^{o}C, which is still lower than the melting point of the cladding material. One potential explanation is that natural circulation is strongly coupled with radiation heat transfer. For the cases of low emissivity, higher fuel cladding temperature leads to stronger recirculation flows within the core, which offests the decreases in radiation. As a result, the coolant density in the fuel region decreased at faster rate. The driven force for natural circulation (i.e. the density difference between the fuel channel inlet and outlet) could be established at earier phase. As natural circlation initiated the fuel cladding can be efficienty cooled.

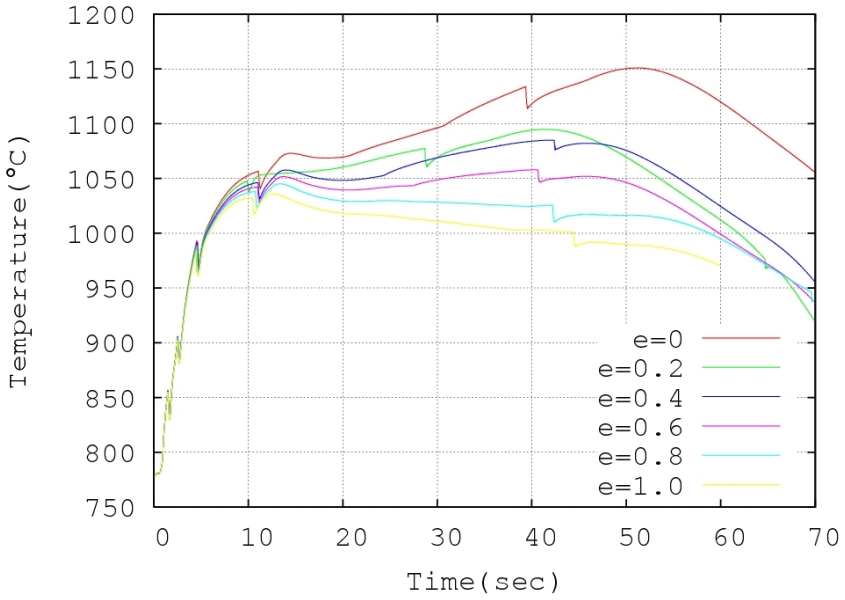

Figure 10. The Prediction of Maximum Fuel Sheath Temperature Using Different Emissivity

To examine how convective heat transfer effects the temperature prediction a LOFA transient is performed with the convective heat transfer coefficient set to zero. Figure 11 shows the variation of the Inner and Outer Ring temperatures as a function of time. By eliminating convective heat transfer coefficient the maximum fuel sheath temperature is increased by 200 ^{o}C for the reference case.

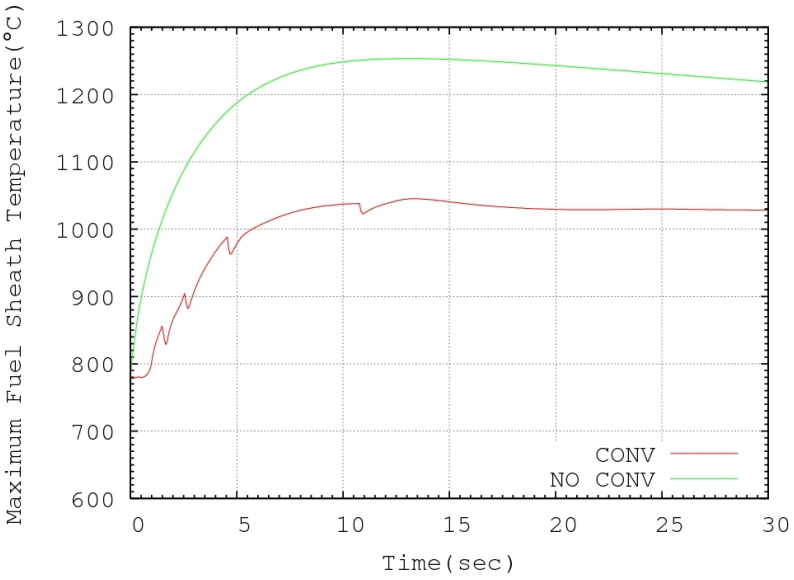

Figure 11. Maximum Fuel Sheath Temperature of Inner Ring With or Without Convection

4. Future Work

Further studies should be focused on determining the orifices sizes at the fuel channel inlets, as they are important in the prediction of maximum sheath temperature in both steady state and LOFA transient, and they may play a role in the magnitude of the recirculation flows that develop in the intermediate stages of the transient. In particular orifice sizing is sensitive to the channel power variations as a function of burnup, and hence the power control system of the reactor should be such as to minimize the channel power swings over a fuel cycle. Also, enhancement and modification should be applied to the CATHENA code to improve its performance in subcritical to supercritical pressure transition (for cases that show depressurization due to overcooling) as well as the heat transfer calculation near the pseudo-critical temperature (since in many cases the induced flow was sensitive to the convective heat transfer assumptions and it is known that near the pseudo critical transition the CATHENA correlations are inaccurate). Since the natural circulation flows are sensitive to the grouping assumptions, a model with no channel grouping should be employed so the best possible picture of recirculation flows can be determined.

5. Summary

The objective of this study was to assess the Canadian pre-conceptual SCWR design for Loss of Flow events leading to degraded cooling conditions. A CATHENA idealization based on the Canadian SCWR has been developed. The simulations are performed using various channel grouping schemes. The steady state simulations are performed with a seven branch (i.e., group) CATHENA model. The LOFA transients are simulated using a 2-channel groups model and a 4-channel groups branch model separately.

Simulation results shows that for steady state normal operation the maximum fuel sheath temperatures at BOC, MOC and EOC are 829.2 ^{o}C ,778.0 ^{o}C and 795.6^{o}C respectively.

For LOFA transient, the transient developed very fast during the first 20s. The maximum fuel cladding temperature of the 4-branch case is predicted to take place at approximately 18.2s at 1059 ^{o}C which is lower than the melting point of the fuel cladding material. Radiation heat transfer dominants the cooling process during this period of time. The early phase convection was driven by pseudo-critical transitions of coolant in the fuel channel. In the later transient, natural circulation has been observed in fuel channels and convective heat transfer dominates the cooling procedures. An important finding is related to the interdependence of convection and radiation in the design. For sensitivity cases where convection is reduced or set to zero, fuel temperatures increase and improved radiation heat transfer is observed, thus compensating for the reduction in convective cooling. Similarly for cases where radiation is reduced, higher sheath temperatures drives larger recirculation flows in the core improving convection. In all cases where reactor trip is credited before approximately 4s the fuel sheath temepratures remain below the acceptance criteria due to the combination of robust design and heat rejection to the moderator.

References

1. D.F. Wang, S.Wang, “A CATHENA Model of Canadian SCWR Concept for Safety Analysis” ISSCWR-6, March, 2013.

2. L. K. Leung, "Thermalhydraulics and Safety-Related Experiments in support of the Canadian SCWR Concept Development," in *Canada-China Conference on Advanced Reactor Development*, Niagara Falls, Canada, 2014.

3. Yetisir M, Gaudet M, Rhodes D. “Development and Integration of Canadian SCWR Concept with Counter-flow Fuel Assembly”. ISSCWR-6, March, 2013.

4. Stainless Steels[M]. ASM international, 1994.

5. Oka Y, Koshizuka S, Ishiwatari Y, et al,” Super Light Water Reactors and Superfast Reactors”, Springer, New York/Dordrecht/Heidelberg/London, 2010.

Appendix

Table A1. Key Parameters of the Canadian SCWR Concept

Parameter	Value
Thermal Power	2540 MW
Electric Power	1200 MW
Coolant	Light water
Moderator	Heavy water
Inlet/ Outlet Temperatures	350 ^{o}C/625 ^{o}C
Inlet/ Outlet Pressures	26MPa/25MPa
Channels	336
Fuel Assembly Length	500 cm
Fuel Batches	3
Core Radius (including radial reflector region)	355 cm
Core Height (including axial D2O reflector regions)	650 cm

Table A2. Specifications and Materials for the Fuel

	Inner Ring	**Outer Ring**
Number of Rods	32	32
Pitch Circle Radius (cm)	5.4	6.575
Radius of Fuel Pins (cm)	0.435	0.460
Thickness of Fuel Cladding (cm)	0.06	0.06
Materials of Fuel Pins	15 wt% PuO2/ThO2	12 wt% PuO2/ThO2
Materials of Fuel Cladding	Zr-mod SS	Zr-mod SS

Table A3. Specifications and materials for the HERC

Component	Dimension (cm)	Material
Flow Tube Inner Cladding	3.60 radius 0.05 cm thick	Zr-modified 310 Stainless Steel (Zr-mod SS)
Center Flow Tube	3.65cm IR 1.00 cm thick	Zirconium Hydride
Flow Tube Outer Cladding	4.65 cm IR 0.05cm thick	Zr-mod SS
Liner Tube	7.20cm IR 0.05cm thick	Zr-mod SS
Insulator	7.25cm IR 0.55cm thick	Yttria Stabilized Zirconia
Outer Liner	7.80cm IR 0.05cm thick	Excel (Zirconium Alloy)
Pressure Tube	7.85cm IR 1.2cm thick	Excel (Zirconium Alloy)

Table A4. Steady State Grouping Scheme

Group Label	Channel Label	Number of Channels (1/4 core)	Total Number of Parallel Pipes
LLL[1] (Group1)	D003, C004, E003, C005, J001, A009, E010, K005, F009, J006, H006, F008, G010, K007, G007, D008, H004,J009	18	72
LMM (Group2)	G008, H007, H010, K008, H009, J008, K009, J010, K010, H008	10	40
MLL (Group3)	B010, K002, B008, H002, C009, J003 C007, G003, E005, A007, G001	11	44
MMM (Group4)	F006, B006, F002, J004 D009, J005, E009, E004, D005, D010, K004, D007, G004, C003	14	56
HMM (Group5)	D006, F004, B005, E002, A008, H001	6	24
HHH (Group6)	A010, K001, B009, J002, B007, G002, F010, K006, C008, H003, C006, F003, E008, H005, F007, G006, C010, K003, G009, J007, D004, E007, G005	23	92
HHH'[2] (Group7)	E006, F005	2	8

[1] L represents low power level, M represents medium level power and H represents high power level. The first letter of the label indicated the power level at beginning of cycle (BOC), the second letter of the label indicated the power level at middle of cycle (MOC), the third letter of the label indicated the power level at the end of the cycle.
[2] HHH' represent the maximum power channel group.

Table A5. 2-Channel Groups Grouping Scheme

	Type of Channel	Number of Channels	Single Channel Power (MW)	Normalized Power Distribution (MW)	Initial Massflow per Channel (kg/s)	Initial Total Massflow per Group (kg/s)
Group1	Average Power	335	7.55	0.99624	3.524	1250.929
Group2	Maximum Power	1	9.56	0.00376	4.758	4.758
The Total Power of All 336 Channels is 2540MW						

Table A6. 4-Channel Groups Grouping Scheme

	Type of Channel	Number of Channels	Single Channel Power (MW)	Total Channel Power (MW)	Normalized Power Distribution
Group1	Low Power	112	6.35	711.20	0.28008
Group2	Medium Power	112	7.59	850.08	0.33447
Group3	High Power	111	8.74	970.14	0.38169
Group4	Maximum Power	1	9.56	9.56	0.00376
The Total Power of all 336 Channels is 2540MW					

Table A7. Simulation Results for the 4-Group LOFA Transient

Parameter	Unit	Group1	Group2	Group3	Group4
Maximum Fuel Cladding Temperature	^{o}C	938	990	1021	1059
Time when MCST approached	s	19.5	19.5	12.7	18.2
Total Massflow at 700s	kg/s	-8.77	6.37	13.84	-0.10
Massflow per channel at 800s	kg/s	-0.0783	0.0574	0.1240	-0.10
Parameter	**Unit**	**Group1**	**Group2**	**Group3**	**Group4**
Maximum Fuel Cladding Temperature	^{o}C	938	990	1021	1059
Time when MCST approached	s	19.5	19.5	12.7	18.2
Total Massflow at 700s	kg/s	-8.77	6.37	13.84	-0.10
Massflow per channel at 800s	kg/s	-0.0783	0.0574	0.1240	-0.10

Table A8. Sensitivity Analysis of Power Ramping Time on the Prediction of Maximum Fuel Sheath Temperature

Trip time (s)	**Flow Ratio ($\frac{\dot{m}_{tr}}{\dot{m}}$)**	**Maximum Sheath Temperature for Inner Ring (^{o}C)**	**Maximum Sheath Temperature for Outer Ring(^{o}C)**
0.29	**90%**	**1045**	**1043**
0.57	70%	1063	1061
0.73	50%	1077	1075
0.84	30%	1087	1084
0.93	10%	1093	1091
4.40	-	1400	1398

Table A9. Sensitivity Analysis of Power Ramping Time on the Prediction of Maximum Fuel Sheath Temperature

Ramping Time (s)	Maximum Sheath Temperature for Inner Ring (^{o}C)	Maximum Sheath Temperature for Outer Ring(^{o}C)
0.1	**1045**	**1043**
0.2	1046	1041
0.5	1059	1057
1.0	1077	1074
1.5	1100	1097
2.0	1121	1119
3.0	1164	1161

Table A10. Sensitivity Analysis of Emissivity on the Prediction of Maximum Fuel Sheath Temperatures

Emissivity	**Maximum Sheath Temperature for Inner Ring (^{o}C)**	**Maximum Sheath Temperature for Outer Ring(^{o}C)**	**Time (s)**
1.0	1033	1032	10.45
0.8	**1045**	**1043**	**14.0**
0.6	1065	1060	36.7
0.4	1082	1079	46.1
0.2	1095	1090	41.6
0.0	1151	1144	51.2

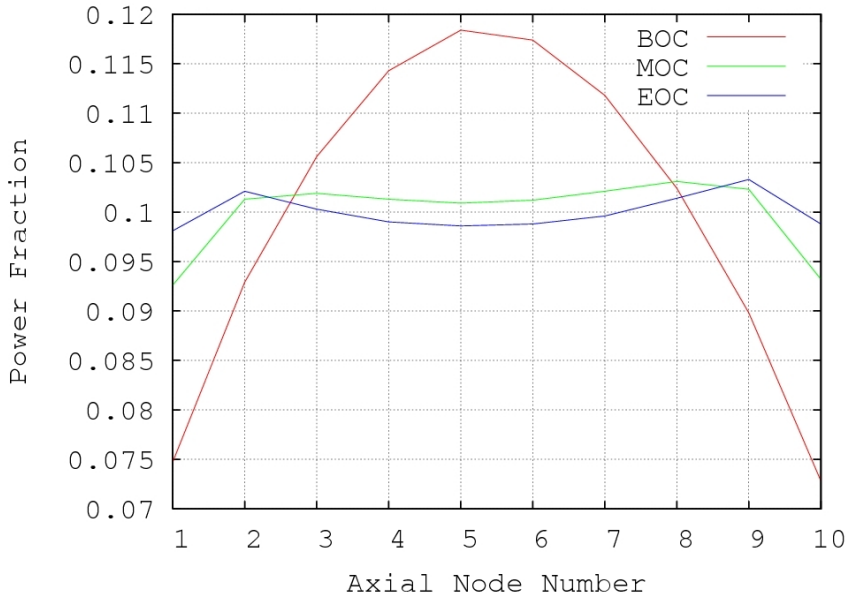

Figure A1. Axial Power Distributions of BOC, MOC and EOC (Power for Given Node Divided by Total Power for all 10 Axial Nodes)

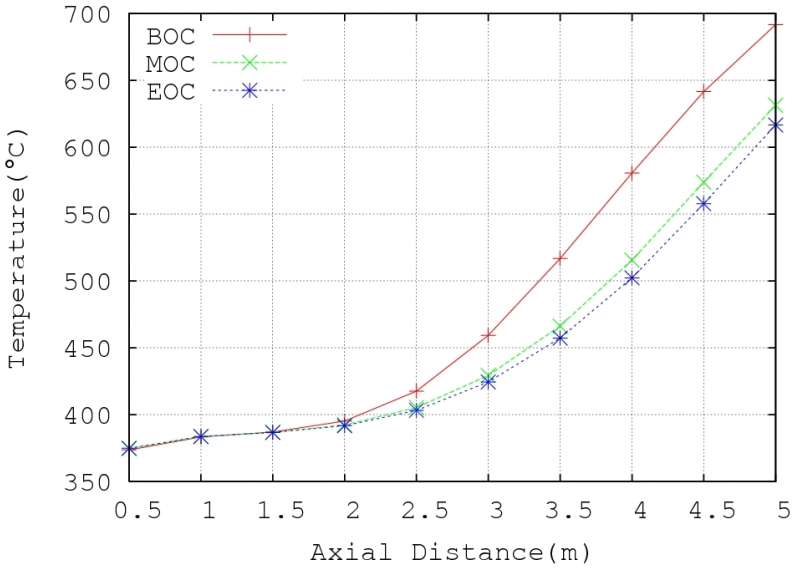

Figure A2. Axial Coolant Temperature Profile for the Maximum Power Channel

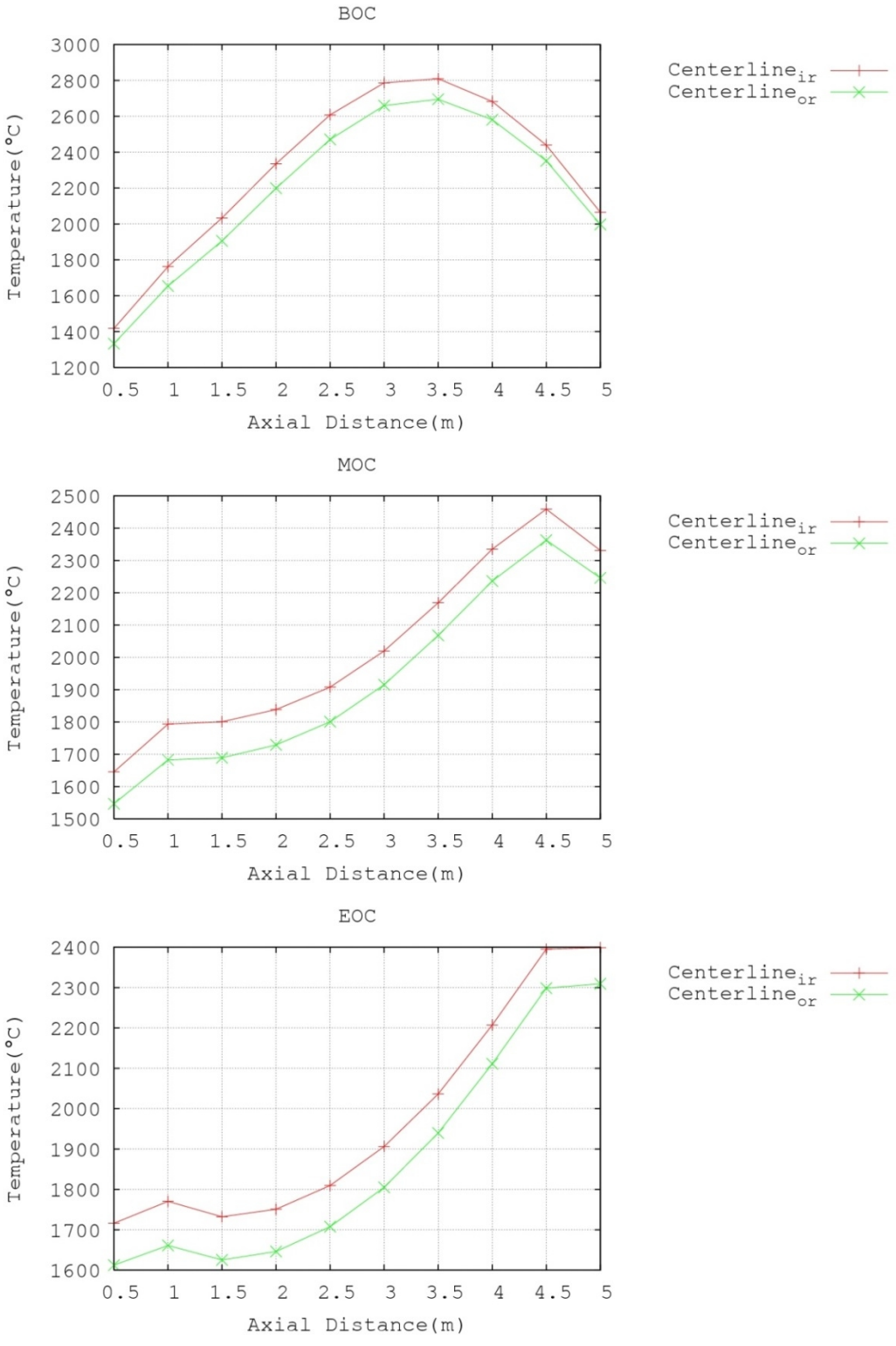

Figure A3. Axial Fuel Centerline Temperature Profile for the Maximum Power Channel

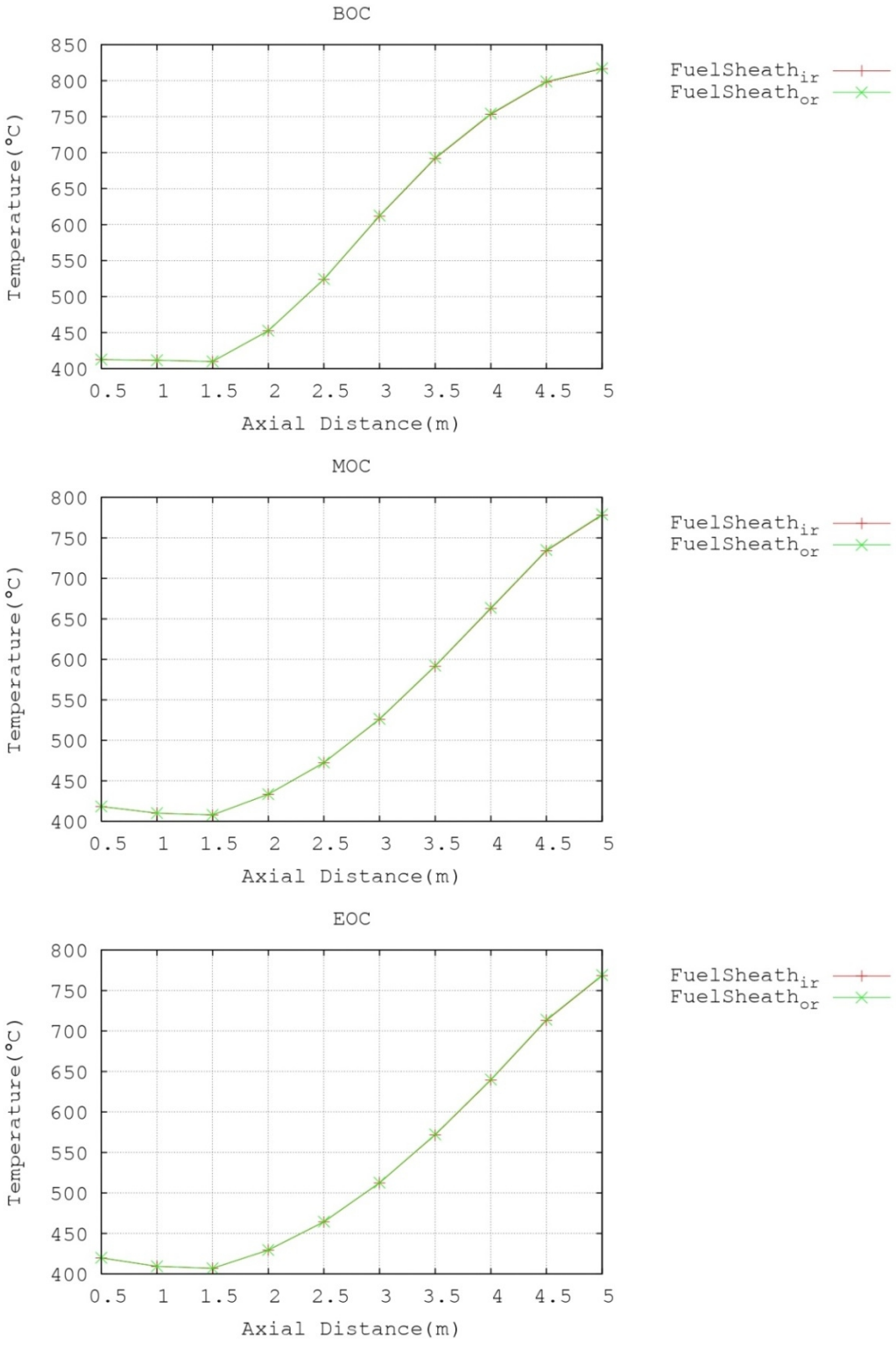

Figure A4. Axial Fuel Sheath Temperature Profile for the Maximum Power Channel

ISSCWR7-2016

Hydrogen Release Rate and Corrosion Measurements on Alloy 800H and Stainless Steel 316 in Supercritical Water Conditions

Kashif I. Choudhry, Dimitrios T. Kallikragas and Igor M. Svishchev
Trent University, Department of Chemistry
1600 West Bank Drive, Peterborough, Ontario, K9J 7B8, Canada
+1-705-748-1011 Ext 7163, kchoudhry@trentu.ca, isvishchev@trentu.ca

Abstract

The interaction of water with iron based alloys at high temperatures leads to the formation of a magnetite-rich surface layer with the release of a significant amount of hydrogen gas. From a viewpoint of a nuclear reactor chemistry control strategy, hydrogen generated in the heat transport system may have a potentially vital role as an oxygen scavenger, effectively removing the corrosive radiolytic products from both the in-core and out-of-core regions. This paper describes the effects of the metal surface, temperature and pressure on the rate of hydrogen evolution during the corrosion process. These experiments were conducted in a flow-through reactor using stainless steel 316 and Alloy 800H tubing, at temperatures and pressures ranging from 650 to 750°C and 5 to 25 MPa.

The effects of pH and oxygenation level on corrosion have also been investigated. Apparent corrosion rates were determined by analyzing dissolved metals concentration (Fe, Ni and Cr) in the reactor's effluent using voltammetry methods. The oxides formed on the metal surfaces were examined by Scanning Electron Microscopy coupled with Energy Dispersive Spectrometry (SEM-EDS) and X-ray diffraction (XRD).

Keywords: Supercritical water, apparent corrosion rate, hydrogen production, dissolved gas analysis, surface oxide analysis.

1. Introduction

Worldwide awareness of climate change, global warming and the sustainability of resources has led to international efforts to develop the GEN-IV nuclear reactors, including the Supercritical Water-Cooled Reactor (SCWR). The Canadian SCWR will operate at a pressure of 25 MPa, with a core inlet temperature of about 350 °C and core outlet temperature of 625 °C [1], which is much greater than those of existing pressurized water reactors (PWRs). To achieve this, the peak cladding temperature can be as high as 800 °C [2]. Therefore engineering materials used in the design of SCWR will be subject to higher levels of stresses over a longer period of time than materials in currently operating reactors [3].

In nuclear power systems, such as the SCWR, the oxidizing potential of the water coolant is significantly increased in the presence of high concentrations of hydrogen peroxide and dissolved oxygen, both being products of the radiolytic breakdown of water in the reactor core. This can increase the corrosion of reactor components, as well as have an effect on the

transport and deposition of corrosion products [4]. In order to mitigate corrosion and corrosion product transport, oxygen scavenging species such as hydrogen gas and hydrazine [5] are added to the coolant, as well as lithium hydroxide (LiOH) [6] for alkalinity control ($pH_{25} \approx 10$). It is well known that at high temperatures, significant amounts of hydrogen gas can be released during the oxidation of a metal surface in the formation of a corrosion layer, and hydrogen is also a product of the radiolytic breakdown of water in the reactor core. The concentrations of dissolved O_2 and H_2 in the coolant, as well as pH, are all crucial parameters affecting the speciation and solubility of the passivation layer formed by the metal oxides and hydroxides that accumulate on the inner surfaces of the SCW bearing components. Supercritical water poses some serious challenges towards materials development, in terms of chemistry control strategies to minimize corrosion and corrosion product transport. As there will be no phase separation in the SCW coolant, the corrosion products that are formed in the reactor core will have the potential to be carried out-of-core with the supercritical coolant.

This study focuses on the corrosion behaviour of stainless steel 316 and Alloy 800H under continuous SCW flow conditions. This research describes the effects that the flow-through reactor temperature has on the rate of hydrogen evolution on both fresh and oxidized stainless steel 316 and Alloy 800H surfaces. The apparent corrosion rate at SCWR flow conditions was also estimated, through the determination of metal loss to the effluent. Oxides formed on the stainless steel 316 and Alloy 800H surfaces are examined by scanning electron microscopy coupled with energy dispersive spectrometry (SEM-EDS) and x-ray diffraction (XRD).

2. Experimental

A flow-through reactor made of stainless steel 316 or Alloy 800H tubing was used to estimate the hydrogen evolution rate from the reactor surface during the formation of a corrosion layer on both fresh and oxidized surfaces at temperatures relevant to the SCWR. A schematic diagram of the experimental set-up is shown in Figure 1. All connections consisted of SS316 capillary tubing (OD = 1.59 mm, ID = 0.75 mm) and zero dead volume unions (Valco®) excluding the reactor tube inside the furnace, which is made of either stainless steel 316 or Alloy 800H. The feed line was connected to three glass bottles, each containing oxygenated (~ 20 ppm, or mg L^{-1}, of oxygen) water, hydrogen saturated or deoxygenated water, with an O_2 concentration of less than 10 ppb (µg L^{-1}). This was achieved by continuous sparging with oxygen gas, hydrogen gas and helium gas (Praxair high purity gases, UHP 5.0), respectively. Low pressure check valves (anti-backflow, Valco®) were installed on the gas sparging lines just outside the bottles to prevent water backflow from the bottles into the gas lines. The volumetric flow rate of the water was continuously monitored by weighing a collected volume of water over a set time period. Three separate HPLC pumps (Waters® 590) were used for control of the volumetric flow rates. Pump 1 and 2 were used to control the flow rate of oxygenated water, and hydrogen saturated water, respectively. Pump 3 was used to control the flow rate of the deoxygenated water. All three flow channels were combined by using a zero dead volume cross (Valco®) and were connected to a switch. The effluent exiting the reactor was cooled and depressurized prior to analysis, and the gas composition was measured using a gas chromatograph (SRI Instruments®-8610C). The dissolved oxygen concentration and pH of the effluent were also monitored, using a NeoFox system (Ocean Optics) equipped with a FOSPOR oxygen probe and Orion 5 Star meter (Thermo Scientific) respectively. The effluent was continuously collected at the exit of the gas analyzer, and was monitored for the dissolved metal concentrations of nickel, chromium, and iron using adsorptive striping voltammetry (797 VA Computrace – Metrohm AG). At the end of each experimental run, the system was first depressurized and then cooled down to room temperature. Reactor tubes were then removed from the furnace and kept in a desiccator (Secador® mini with gas ports) under argon gas to prevent further oxidation until the samples were prepared for surface analysis.

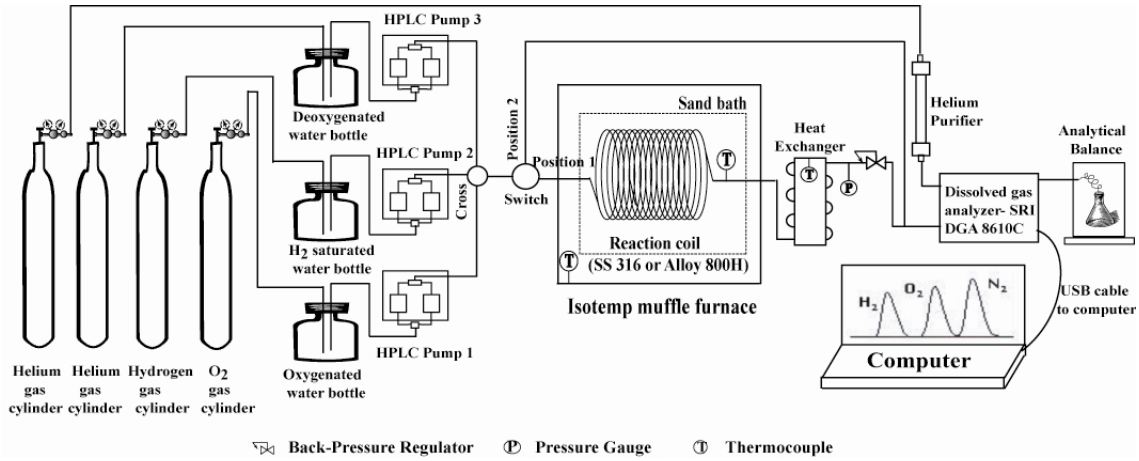

Figure 1. Schematic diagram of the experimental set-up.

3. Results

The hydrogen evolution rate was studied in a flow-through reactor, at conditions relevant to the operation of the SCWR. Here, we explicitly show the experimental data for Alloy 800H reactor tube with a surface-to-volume ratio of 18.53 cm^{-1}. The residence time of the deoxygenated water in the reactor is 138.46 seconds. The measured hydrogen gas concentrations in the effluent at the exit of the reactor as a function of time at a constant temperature of 650 °C, pressure of 25 MPa and an at-pump flow rate of 0.1 mL min^{-1} is presented in Figure 2. The measured hydrogen gas concentration in the depressurized effluent was normalized by the density of water at 650 °C and 25 MPa to give the actual dissolved hydrogen concentrations, in moles per litre of supercritical water, at the exit of the reactor tube.

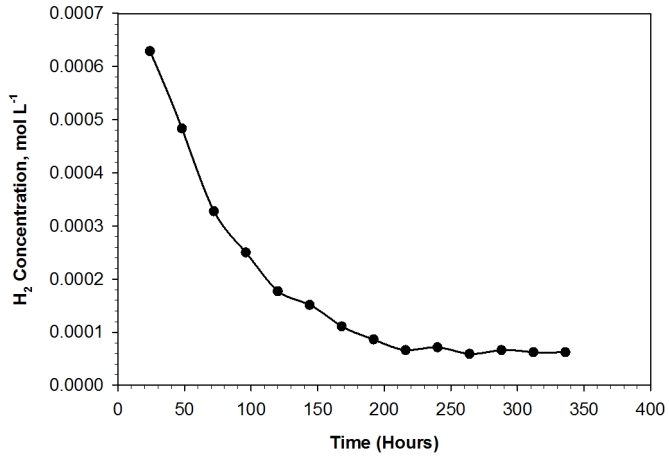

Figure 2. Hydrogen evolution from the Alloy 800H surface in the reactor versus exposure time. Temperature, pressure and flow rate were held constant at 650 °C, 25 MPa and 0.1 mL min^{-1}.

Figure 2 shows a trend of exponential-like decrease with exposure time in hydrogen evolution from the metal surface, and it takes around a week to reach a steady state. A similar trend has

been observed for stainless steel 316, but with a much higher hydrogen evolution rate than seen here for Alloy 800H [7]. Steady state hydrogen evolution rate from the Alloy 800H oxidized surface is 6.47×10^{-5} mol L^{-1}, for the reactor surface area of 66 cm^2. The initial drop in hydrogen evolution can be presumably attributed to a decrease of bare metal available for the reaction with water, as the reactor surface develops an oxide layer over time, resulting in a subsequently lower hydrogen evolution rate. The initial hydrogen concentrations evolved from the bare fresh metal surface was also estimated at the exit of the reactor by extrapolating the concentration to t = 0, and was found to be 8.94×10^{-4} mol L^{-1}, at a constant reactor temperatures of 650 °C and pressure of 25 MPa. The effect of the flow rate, and hence residence time of degassed water in the reactor tube, on hydrogen evolution was investigated with volumetric flow rates ranging from 0.1 to 1.5 ml min^{-1} at a constant reactor temperature of 650°C and pressure of 25 MPa. Experimental results show a linear relationship between the residence time of degassed water in the reactor tube and the steady state hydrogen concentration in the effluent at the exit of the reactor. An increase in the hydrogen concentration with an increase in the residence time could be explained by a larger contact time between degassed water and the reactor surface.

The effective rate constants for hydrogen evolution from stainless steel 316 and Alloy 800H surfaces at temperature of 650°C and pressure of 25 MPa were determined. The effective rate constant k_{eff}, in mol cm^{-2} s^{-1}, was calculated using Equation 1:

$$k_{eff} = \left[\frac{10^{-3} C_M}{\tau\left(\frac{S}{V}\right)}\right]. \quad (1)$$

Here, C_M is the molarity, or mol L^{-1}, of the dissolved hydrogen in the effluent at the exit of the reactor, S/V is the surface area-to-volume ratio of the reactor tube in cm^{-1}, and τ is the residence time in seconds. A value of 1.58×10^{-10} and 2.52×10^{-11} mol cm^{-2} s^{-1}, was obtained as an effective rate constant for steady state hydrogen gas evolution from stainless steel 316 and Alloy 800H surfaces, respectively, at a constant reactor temperature of 650 °C and pressure of 25 MPa. The effect of pressure on steady state hydrogen evolution from the SS316 surface was also studied in the range of 5-25 MPa at a constant reactor temperature of 650 °C. Hydrogen concentration increased at the exit of reactor with a decrease in the pressure, yielding effective rate constants of 1.66×10^{-10} mol cm^{-2} s^{-1} at 15 MPa and 1.83×10^{-10} mol cm^{-2} s^{-1} at 5 MPa.

The influence of temperature in the range of 650 to 750°C on hydrogen production was also investigated at the pressure of 25 MPa and degassed water flow rate of 0.1 ml min^{-1}. Results show that the increase in the reactor temperature increases the amount of hydrogen produced. This was expected since the reaction rate increases with temperature. Figure 3 shows the effects of reactor temperature has on the effective rate constants for stainless steel 316 and Alloy 800H. It can be seen that as the temperature of the reactor increased from 650 to 750 °C, the steady state hydrogen gas concentration at the exit of reactor increased, yielding effective rate constants of 2.52×10^{-11}, 2.88×10^{-11}, and 4.30×10^{-11} mol cm^{-2} s^{-1} for Alloy 800H, and 1.58×10^{-10}, 3.25×10^{-10} and 6.08×10^{-10} mol cm^{-2} s^{-1} for stainless steel 316, for the reactor temperatures of 650, 700 and 750 °C, respectively. Results demonstrate (Figure 3) that the effective rate constants for steady state hydrogen gas evolution from the oxidized Alloy 800H surfaces are much smaller than for stainless steel 316. It is estimated that the increase in hydrogen evolution from the oxidized reactor surfaces with increasing temperature follows the Arrhenius equation. The activation energy for hydrogen evolution from an oxidized Alloy 800H and stainless steel 316 surfaces, were found to be 41.7 and 105.9 kJ/mol, respectively.

Experiments were also performed using oxygenated water to estimate the effect of oxygen in the feed water, on surface oxide layer formation, and on the apparent corrosion rate from total metal loss to the effluent. The apparent corrosion rate, measured by total metal loss to the

effluent was calculated according to the method described by Svishchev et al. [6]. Effluent water samples were analysed for dissolved metal (Fe, Ni and Cr) concentrations to estimate the apparent corrosion rate. The daily dissolved metal concentrations show that it takes about one week to reach a steady state in the metal release rate and matches the time required to achieve a steady state of hydrogen evolution at the exit of reactor tube. Based on these observations, the first week of data was discarded in the calculation of the apparent corrosion rate through loss of metals to the solution.

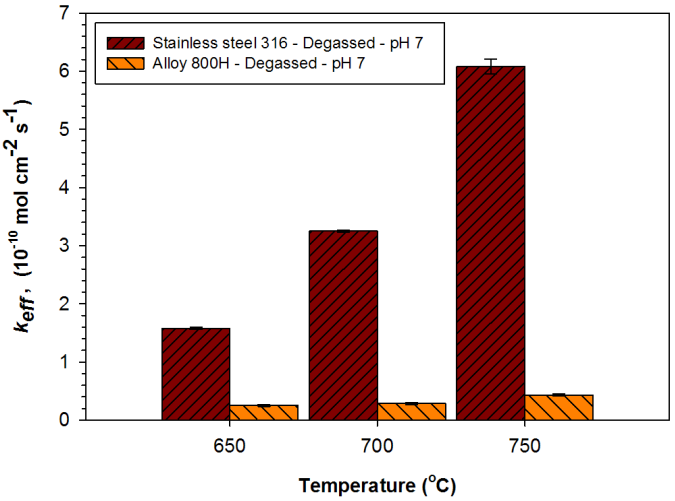

Figure 3. Effect of the temperature on the effective rate constants for Alloy 800H and stainless steel 316 at a constant pressure of 25 MPa, and degassed water flow rate of 0.1 mL min^{-1}.

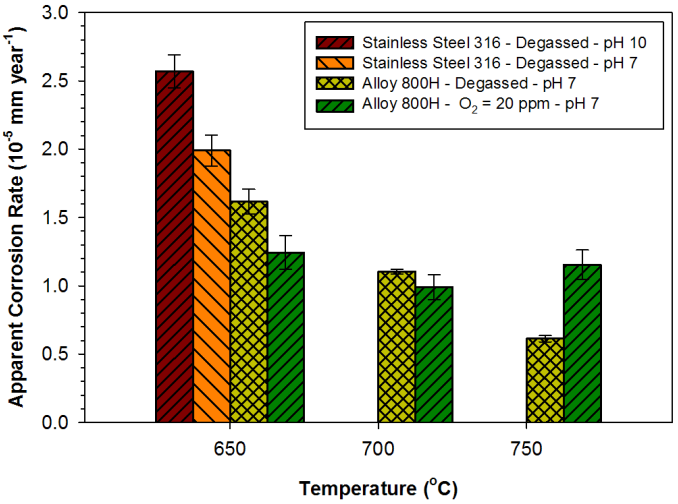

Figure 4. Apparent corrosion rate in mm year^{-1} at a constant pressure of 25 MPa and water flow rate of 0.1 mL min^{-1}.Temperature was varied from 650 to 750 °C.

Figure 4 demonstrates the apparent corrosion rate for stainless steel 316 and Alloy 800H for the temperature range of 650 to 750 $^{\circ}$C at a constant pressure of 25 MPa and water flow rate of 0.1 mL min^{-1}. The concentration of lithium hydroxide (LiOH) in the milli-Q water at alkaline pH 10

was 1.1×10^{-4} mol kg^{-1}, with a concentration of dissolved oxygen less than 10 ppb. Figure 4 shows the evidence that the highest apparent corrosion rate was achieved when the stainless steel 316 tubing exposed to degassed water at 650 °C and pH 10. Results demonstrate that the apparent corrosion rate for stainless steel 316, 2.0×10^{-5} mm $year^{-1}$, is much larger than Alloy 800H at conditions relevant to SCWR using degassed water. This shows that increasing the nickel content in the reactor tubing (Alloy 800H vs. SS316) reduces both the surface-induced hydrothermal hydrogen evolution, as well as the apparent corrosion rate. It can also be seen that increasing the oxygen concentration in the feed water decreased the metal loss from the Alloy 800H surface to the effluent for temperatures between 650 to 700 °C, , but increased at 750 °C, as compared to the deoxygenated water. This increase in the apparent corrosion rate of Alloy 800H at 750 °C is likely caused by an increase in the diffusion of oxygen to the surface at higher temperatures (and higher oxidation rate of a metal).

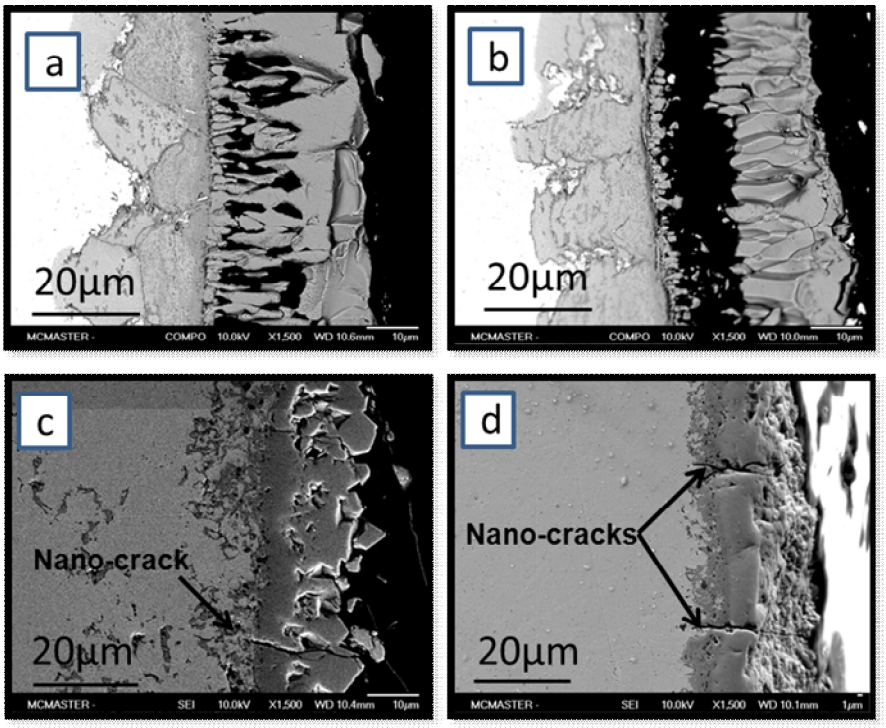

Figure 5. Cross-sectional view of the oxide layer formed on the alloys tubing in SCW (at constant pressure of 25 MPa): (a) SS316 - degassed water - 650°C - 300 hours, (b) oxygenated water (40 ppm) - 650°C - 300 hours, (c) Alloy 800H - degassed water - 750°C - 650 hours, (b) Alloy 800H - oxygenated water (20 ppm) - 750°C - 650 hours.

Oxide scales formed on SS 316 and Alloy 800H exposed in supercritical water under continuous flow conditions were characterized using SEM-EDS and XRD analysis. Figure 5 shows the cross-section of the oxide layers formed on stainless steel at 650 °C and 25 MPa. The total thickness of the oxide scale formed on the SS 316 tubing surface during the exposure time of 300 hours in deoxygenated feed water feed water with pH 7 (Figure 5a) was estimated to be 50 µm but it is reduced to 40 µm when oxygenated water (Figure 5b) was used at similar conditions. Results show that the outer layer contains more pores when SS 316 is treated with oxygenated water but at a longer exposure time of 775 hours, an extensive spallation of the oxide layer from the SS 316 surface was observed. XRD analysis results reveal that the oxide scale formed on the SS 316 surface has a layered structure consisting of an outer magnetite (Fe_3O_4) layer, with the presence of elemental iron and nickel on top of the oxide surface, and an

inner mixed (Fe, Cr, Ni, Mo)$_3O_4$ spinel layer. Doubled oxide layers were also formed on the surface of Alloy 800H exposed to both oxygenated and deoxygenated SCW (Figure 5c and d). The total thickness of the oxide layers formed on the surface was about 20 µm and 15 µm for degassed and oxygenated water, respectively. Nanocracks were observed running through oxide layers, through to the metal substrate in both the deoxygenated and oxygenated conditions. Results of the XRD analysis for Alloy 800H sample exposed to degassed SCW for 650 hours show that outer layer is composed of magnetite with an Cr-rich inner layer comprised of (Cr, Fe, Mn)$_3O_4$ and trace amount of Cr_2O_3. Whereas the XRD analysis of the oxide scale formed on Alloy 800H exposed in SCW with 20 ppm of dissolved oxygen at 650°C and 25 MPa shows that the outer oxide layer is composed of both magnetite and hematite with a very fine iron-enriched (Fe, Mn)$_3O_4$ layer underneath, and a Cr-rich inner layer (Cr, Ni, Mn)$_3O_4$. The surface of the oxide layer is decorated with aluminium and manganese particles.

4. Conclusion

The hydrogen evolution during the corrosion of SS 316 and Alloy 800H in SCW was investigated using a flow-through reactor at temperatures and pressures of 650 to 750 °C and 5 to 25 MPa, respectively. Effective rate constants for hydrogen evolution from the surface during the formation of the corrosion layer and apparent corrosion rates were determined. Results indicate that increasing the nickel content in the reactor tubing (Alloy 800H vs. SS 316) at conditions relevant to the SCWR, both reduces the dissolved hydrogen level and the apparent corrosion rate, as characterized by the release of metals in to the flow. Results show that Alloy 800H is more resistant to surface oxidation, forming a thinner and more stable oxide scale than SS 316, at higher temperatures.

References

1. D. Guzonas, R. Novotny, Supercritical water-cooled reactor materials – Summary of research and open issues, Prog. Nucl. Energ., 77 (2014) 361-372.

2. Jian Li, Pei Liu, Renata Zavadil, Tom Malis, Sami Penttilä, Effect of surface modification on candidate Alloys for Canadian SCWR fuel cladding, J. Miner. Mater. Charact. Eng., 2 (2014) 129-134.

3. S. Baindur, Material challenges for the supercritical water-cooled reactor (SCWR), Bull. Can. Nucl. Soc., 29 (2008) 32-38.

4. I.M. Svishchev, D. Guzonas, Particle Nucleation: Implications for Water Chemistry Control in a GEN IV Supercritical Water-cooled Nuclear Reactor, J. Supercrit. Fluids, 60 (2011) 121-126.

5. D. Guzonas, F. Brosseau, P. Tremaine, J. Meesungnoen, J.-P. Jay-Gerin, Water chemistry in a supercritical water-cooled pressure tube reactor, Nucl. Technol., 179 (2012) 205-219.

6. I.M. Svishchev, R.A. Carvajal-Ortiz, K.I. Choudhry, D.A. Guzonas, Corrosion behavior of stainless steel 316 in sub- and supercritical aqueous environments: Effect of LiOH additions, Corros. Sci., 72 (2013) 20-25

7. K.I. Choudhry, R.A. Carvajal-Ortiz, D.T. Kallikragas, I.M. Svishchev, Hydrogen evolution rate during the corrosion of stainless steel in supercritical water, Corros. Sci., 83 (2014) 226-233.

ISSCWR7-2017

Temperature distribution inside fresh-fuel pins of pressure-tube SCWR

V.Kovaltchouk, E.Nichita and E.Saltanov
Faculty of Energy Systems and Nuclear Science
University of Ontario Institute of Technology
2000 Simcoe Street North, Oshawa, ON
Canada, L1H 7K4
Vitali.Kovaltchouk@UOIT.ca

Abstract

The radial temperature profile for ThO_2-PuO_2 fuel pins of the Pressure-Tube Super-Critical Water-Cooled Reactor is simulated for two different radial distributions of the ThO_2 and PuO_2, one whereby the ThO_2 and PuO_2 are mixed together in a single, homogeneous region, and another one whereby ThO_2 and PuO_2 occupy separate radial regions inside the pin with the ThO_2 occupying the inner region. The radial power density in each fuel pin is calculated from a lattice-level transport calculation using the lattice code DRAGON and is used together with the temperature-dependent fuel thermal conductivity to analytically solve the heat conduction equation and thus calculate the temperature profile inside the fuel pin. Results indicate that the fuel centreline temperature is much lower for a two-region pin than for a single-region pin and thus the risk of fuel melting is greatly reduced for the two-region fuel compared to the single-region fuel.

1. Introduction

The Pressure-Tube Super-Critical Water-cooled Reactor (PT-SCWR) is a Generation IV Power reactor being developed in Canada. It is anticipated to have a total efficiency in excess of 50% with 2.5 GW anticipated fission power. The PT-SCWR reactor is one of the six Generation IV reactor concepts being developed in the world. It uses heavy water as a moderator and light water as coolant. The inlet coolant temperature and pressure exceed those for the critical point of light water, namely 647.096 K and 22.06 MPa, respectively. The operating coolant pressure is 25 MPa, with the inlet and outlet temperatures being 625 K and 900 K, respectively [1].

A diagram of the PT-SCWR reactor [1,2] is shown in Figure 1. The reactor vessel is filled with heavy-water moderator at low temperature and pressure and contains a rectangular array of 336 parallel re-entrant fuel channels oriented vertically. Each re-entrant fuel channel consists of a pressure tube lined by a ceramic thermal insulator, and a central inner flow-tube. The 5 m-long fuel assembly is located in the space between the ceramic insulator and the central flow tube and consists of two 32-rod concentric annuli.

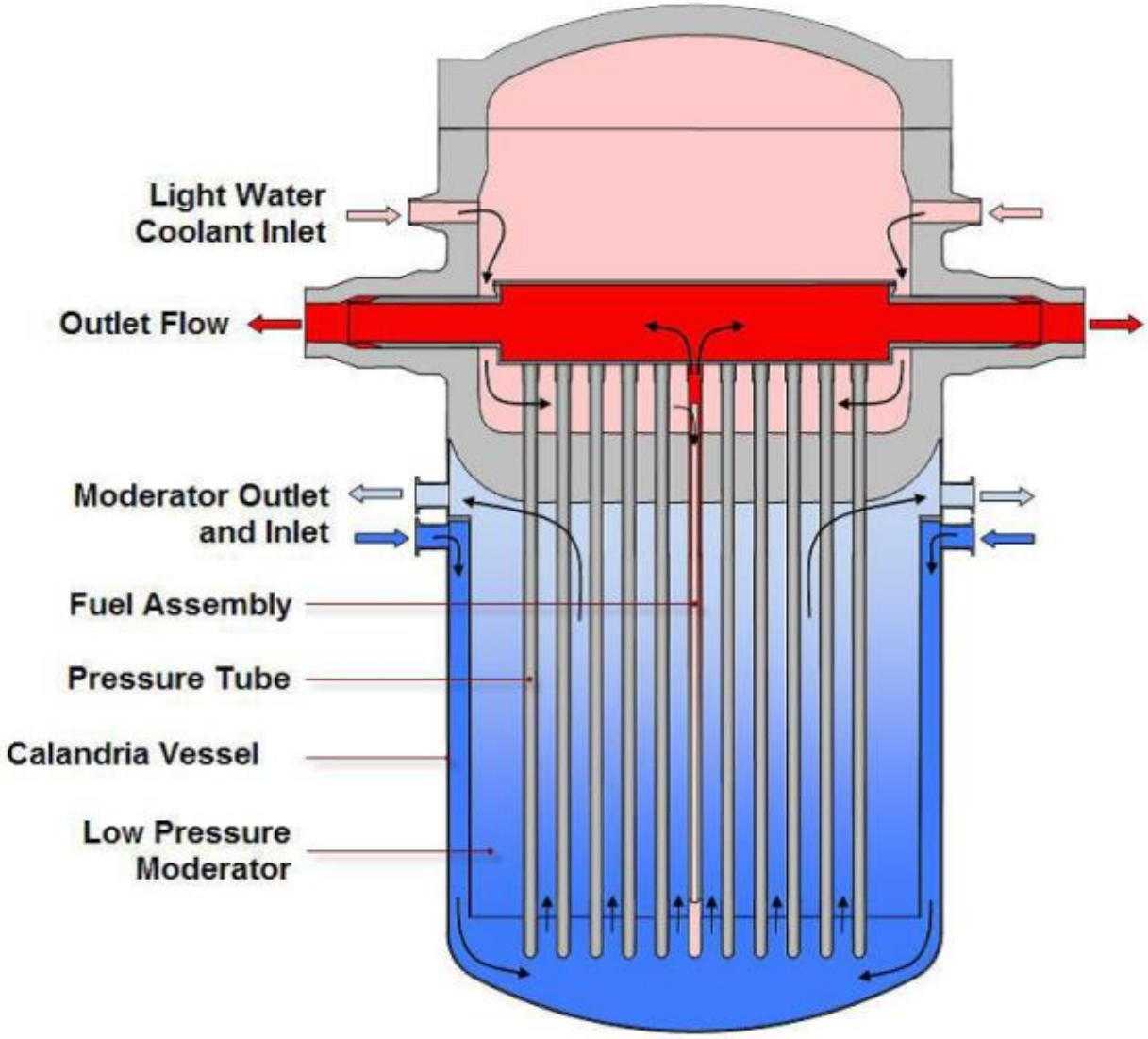

Figure1. Schematic diagram of the Canadian PT-SCWR conceptual design [1].

The coolant inside the flow-tube flows downwards, whereas the coolant between the flow tube and the thermal insulator flows upwards and is heated through contact with the fuel rods. The distance between channels (lattice pitch) is 25 cm. The fuel is a combination of Th-Pu oxide, with Pu representing 13 % by heavy-element weight in the inner fuel ring and 11% in the outer fuel ring. The main characteristics of the re-entrant PT-SCWR fuel [3] are presented in Table 1.

Finding the radial fuel temperature profile is important both for ensuring that no fuel melting occurs and because the radial temperature gradient determines the heat transfer from the fuel pin to the coolant. The present work presents results for the fuel temperature profile for fresh PuO_2-ThO_2 fuel and analyzes the advantage of separating the ThO_2 and PuO_2 into different radial regions for reducing the fuel centerline temperature.

2. Temperature distribution simulation

The simulation of temperature distribution inside fuel pins is done in two steps. First, the radial distribution of the fission power density inside the fuel rod is obtained from neutronics simulations performed using the lattice code DRAGON [4]. The radial fuel temperature profile is subsequently obtained by solving the one-dimensional (radial) heat conduction equation inside the fuel pin analytically, accounting for the temperature dependence of the thermal conductivity and for the radial distribution of the fission power density. Two fuel distributions are studied: one whereby the ThO_2 and PuO_2 are uniformly mixed in the fuel and another one whereby the ThO_2 occupies the central region of the fuel pins and the PuO_2 occupies the outer region of the fuel pins, as shown in Figure 4.

Table 1. PT-SCWR Fuel Characteristics.

Component	Dimension	Material	Composition, wt%	Density(g /cm^3)
Central Coolant (inside fl. tube)	4.60 cm radius	Light Water	100% H_2O	variable
Flow Tube	4.60 cm inner radius (IR) 0.1 cm thick	Zr-modified 310 Stainless Steel (Zr-mod SS)	C:0.034; Si:0.51; Mn:0.74; P:0.016; S:0.0020; Ni:20.82; Cr:25.04; Fe:51.738; Mo:0.51; Zr:0.59	7.90
Inner Pins (32)	0.415 cm radius 5.4 cm pitch circle radius	15 wt% PuO_2/ThO_2	Pu:13.23; Th:74.70; O:12.07	9.91
Outer Pins (32)	0.440 cm radius 6.575 cm pitch circle radius	12 wt% PuO_2/ThO_2	Pu:10.59; Th:77.34; O:12.08	9.87
Cladding	0.06 cm thick	Zr-mod SS	As above	7.90
Coolant	n/a	Light Water	100% H_2O	variable
Liner Tube	7.20 cm IR 0.05 cm thick	Zr-mod SS	As above	7.90
Insulator	7.25 cm IR 0.55 cm thick	Zirconia (ZrO_2)	Zr:66.63; Y:7.87; O:25.5	5.83
Outer Liner	7.80 cm IR 0.05 cm thick	Excel (Zirconium Alloy)	Sn:3.5; Mo:0.8; Nb:0.8; Zr:94.9	6.52
Pressure Tube	7.85 cm IR 1.2 cm thick	Excel (Zirconium Alloy)	Sn:3.5; Mo:0.8; Nb:0.8; Zr:94.9	6.52
Moderator	25 cm square lattice pitch	D_2O	99.833 D_2O; 0.167 H_2O	variable (1.0851, nominal)

2.1. Neutronics simulations

The radial distribution of the power density inside each fuel pin is found from a two-dimensional transport calculation using a detailed lattice cell geometry and reflective boundary conditions. The lattice pitch is 25

cm. The code DRAGON is used to solve the multigroup transport equation using the collision probabilities method and 69 energy groups. The DRAGON code also performs resonance self – shielding calculations. The geometry and material data used in the DRAGON model are listed in Table 1. For computational purposes, each fuel pin is split into ten concentric annular regions. The DRAGON geometrical model is shown in Figure 2. Pin powers are calculated for an average channel power at the axial location corresponding to the maximum channel linear power density, assuming a total reactor thermal power of 2.5 GW. Figure 3 shows the typical axial power distribution along one channel of the PT-SCWR reactor obtained using coupled neutronics-thermal-hydraulic calculations performed using the core diffusion code DONJON [5] and an in-house one-dimensional heat transfer single-channel thermo-hydraulic code [6]. Values in Figure 3 are normalized to an average channel linear power of one. The simulated axial power distribution has an asymmetric shape, resembling a cosine shape skewed towards the inlet. The power production per cell is varied between the maximum and minimum values equal to approximately 1.5 and 0.1 values of the average power density, respectively.

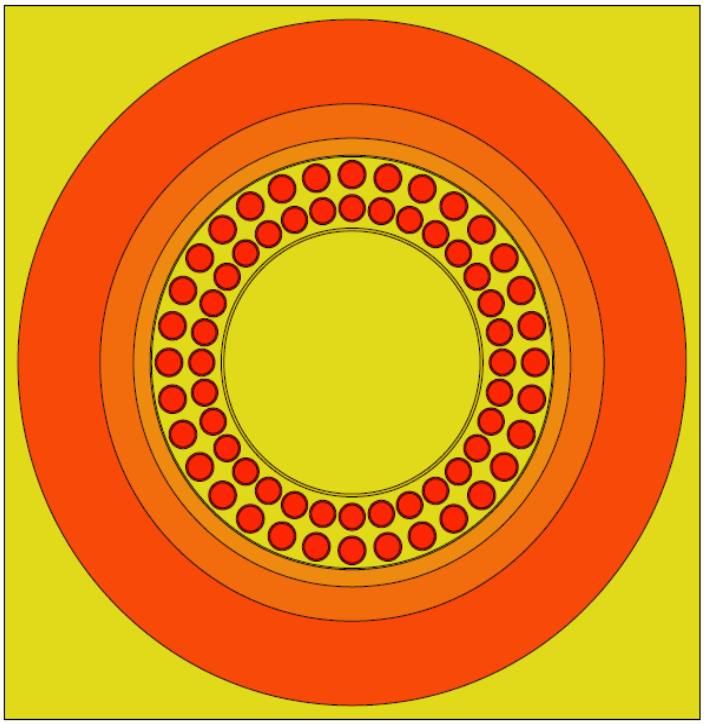

Figure 2. Single-Cell DRAGON Geometry.

2.2. Radial heat conduction in fuel pins

Heat conduction is described by Fourier's law [7]. When ignoring heat conduction in the axial direction, as well as azimuthal dependence, the differential equation governing the variation of temperature with radius in a cylindrical fuel element is:

$$\frac{1}{r}\frac{\partial}{\partial r}\left(r \cdot k \frac{\partial T}{\partial r}\right) + e = \rho \cdot c_p \frac{\partial T}{\partial t} \qquad (1)$$

where:

r – distance to the cylinder center line ;

k – thermal conductivity (temperature dependent);

e – volumetric power density;

c_p – specific heat;

t – time;

T – local temperature;

ρ – local material density.

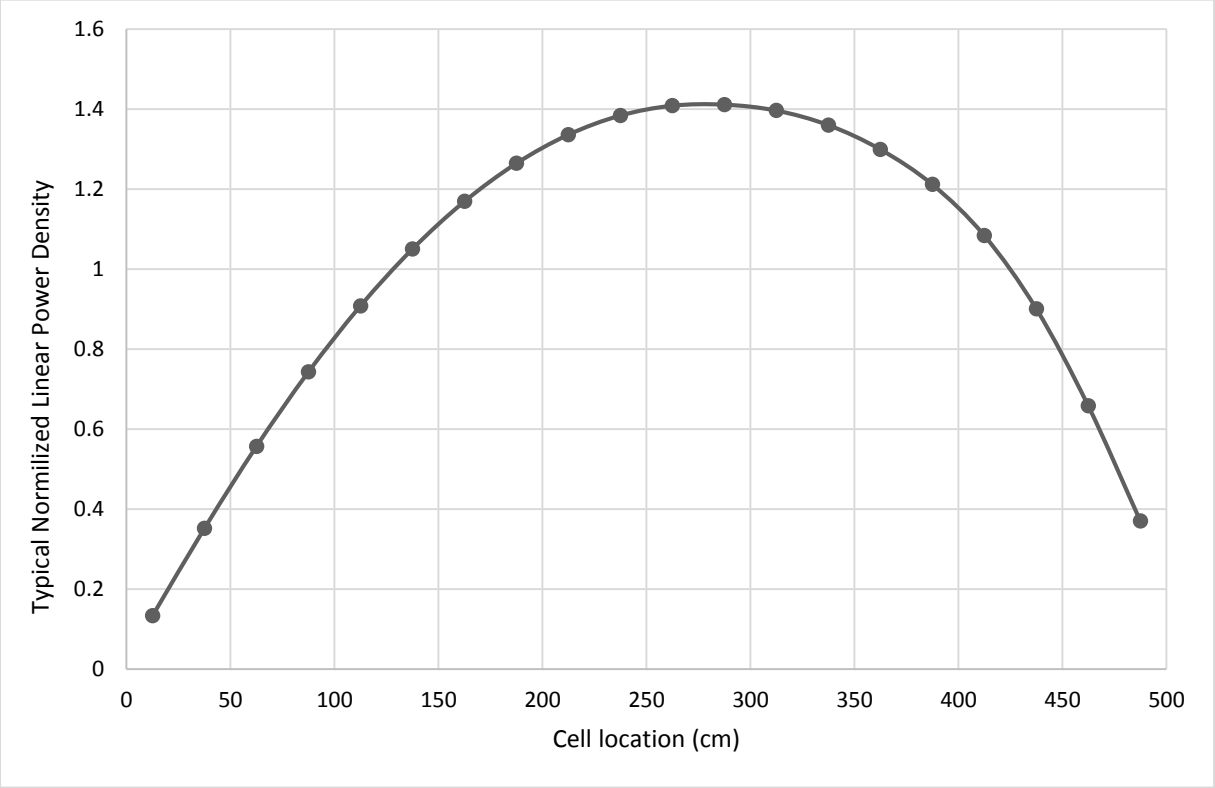

Figure 3. Power production distribution across the PT-SCWR reactor obtained from neutronics simulation in one cell approximation

The differential equation is simplified for a steady-state process where $\frac{\partial T}{\partial t} = 0$ and can be solved analytically if the expressions for the temperature dependence of the thermal conductivity and radial dependence of the power density are available.

The thermal conductivity dependence on temperature can be represented by the following equation [8]:

$$k = \frac{1}{A + B \cdot T} \qquad (2)$$

where “A” corresponds to the density of phonon scattering centres and “B’ to the phonon-phonon interaction process. Constants A and B can be obtained from existing experimental data.

Table 2. The main characteristics of original and modified fuel pins.

Pin location	Config.	Material	Radius, cm	Power, %	Power Density (average), W/m^3
Inner	homo*	(Pu-Th)O	0.415	49.74	4.27E+08
	mod**	ThO_2	0.38	0.48	4.91E+06
	mod	PuO_2	0.38-0.41	50.82	3.17E+09
Outer	homo	(Pu-Th)O	0.44	50.26	3.84E+08
	mod	ThO_2	0.41	0.5	4.52E+06
	mod	PuO_2	0.41-0.43	48.2	3.68E+09

homo* –the original fuel composition;
mod** – the modified fuel composition.

After substituting equation (2) into equation (1) and integrating with respect to r, from the center to the current position, the temperature dependence as a function of distance from the pin centerline is:

$$T(r) = \frac{1}{B} \cdot \exp\left[- B \cdot \int_0^r \frac{f(r)}{r} dr + C \cdot B \right] - \frac{A}{B} \qquad (3)$$

where:

$$C = \frac{1}{B} \cdot \ln\left[A + B \cdot T(R)\right] + \int_0^R \frac{f(r)}{r} dr \qquad (4)$$

$f(r) = \int_0^r x \cdot e(x) dx;$

$T(R)$ - the fuel temperature on the fuel pin surface (boundary condition);

$e(r) = a_0 + a_1 \cdot r + a_2 \cdot r^2 + ... a_5 \cdot r^5$ - the volumetric power density distribution (interpolated by a 5th order polynomial).

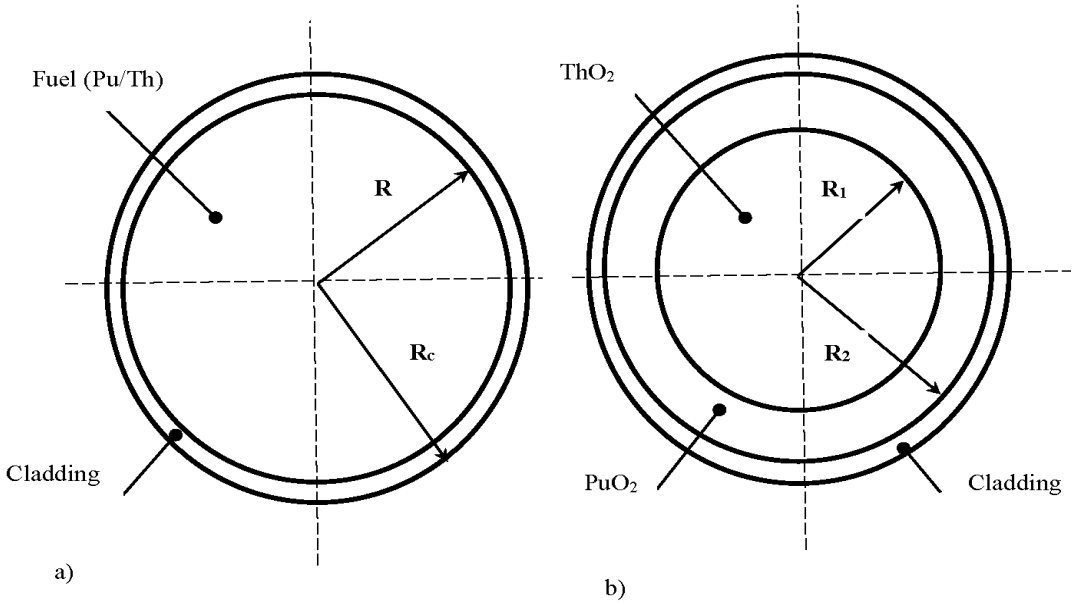

Figure 4. Fuel pin compositions ("a" – homogeneous mixture of ThO_2 and PuO_2, "b" –separate regions of ThO_2 and PuO_2).

Equation (3) is valid both for fuel with a single radial region and for fuel with multiple radial regions. Figure 3 shows the case of a single, homogeneous region together with the case of two regions. If the fuel has a single radial region, as shown in Figure 4(a) equation (3) is applied directly. If the fuel has more than one radial region, equation (3) can be applied separately for each region. For example, when the fuel pin has two radial regions as shown in Figure 4 (b) the temperature distribution inside the inner region can be simulated according to the equation (3), where T(R) will represent the temperature on the boundary between two fuel shells. For the outer shell, the temperature distribution versus distance is:

$$T_2(r) = \frac{A_2 + B_2 \cdot T_2(R_2)}{B_2} \exp\left[F(r)\right] - \frac{A_2}{B_2} \qquad (4)$$

where:

$$F(r) = B_2 \cdot \left[-\frac{e_2}{4}(r^2 - R_2^2) + \frac{e_2 \cdot R_1^2}{2} \ln\left(\frac{r}{R_2}\right) - \frac{e_1 \cdot R_1}{2}\left(r - R_2\right) \right];$$

A_2 and B_2 are the corresponding constants for thermal conductivity for the outer shell;

e_1 and e_2 are the power densities for the inner and outer shell, respectively.

Parameter "r" is varied between R_1 and R_2 representing radii for the inner region and outer shell, respectively.

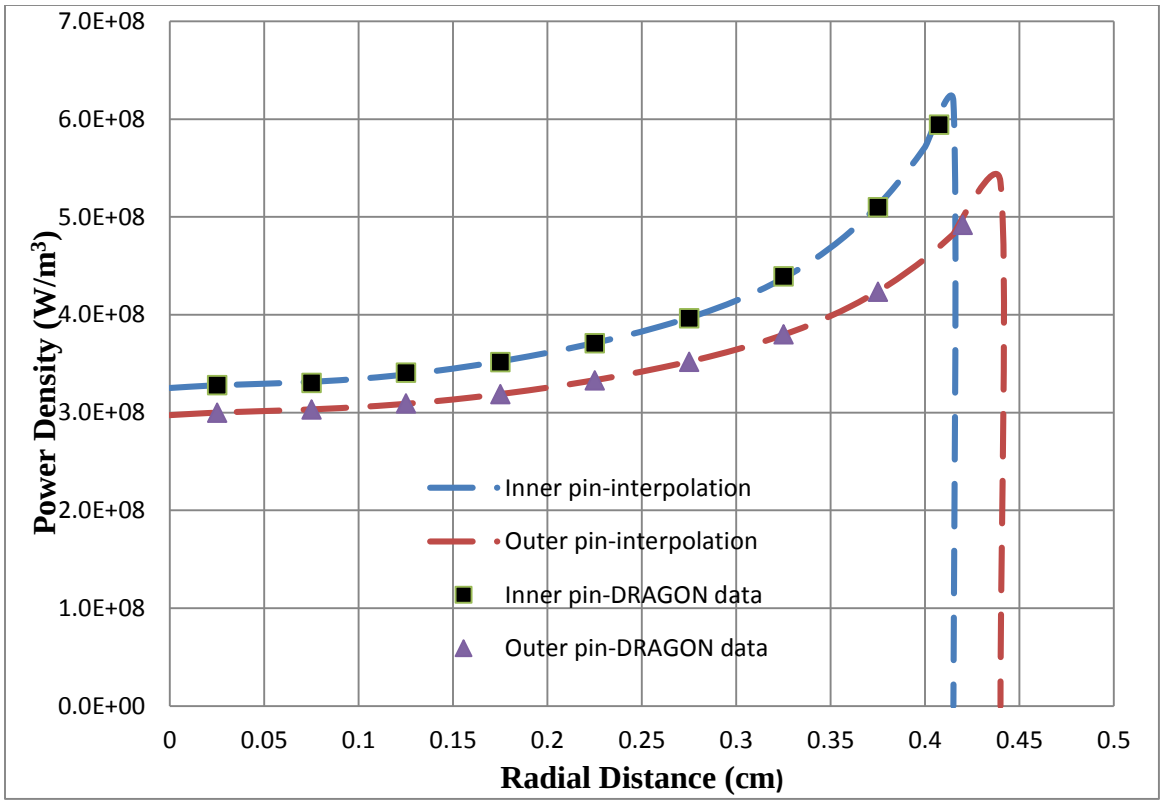

Figure 4. Simulated power density distributions inside the fuel pins for the inner and outer rings.

3. Results and discussion

The temperature distributions were simulated for two fuel compositions: homogeneous mixture of Pu-Th oxide material and modified composition with separation of plutonium dioxide and thorium dioxide inside the fuel pin as they are presented in Figure 3. For the modified composition, the thorium oxide was located inside the inner shell and plutonium dioxide in outer with total mass fractions equal to the original composition.

3.1. Homogeneous Pu-Th fuel

Power density distributions for inner- and outer-ring fuel rods have been simulated with the DRAGON code for fresh fuel. The results of simulations are presented in Figure 4, where points correspond to the simulated data and dashed lines represent interpolated power densities. The interpolation was done as 5^{th} order polynomial (blue and red lines correspond to inner and outer pin location, respectively). According to the simulations, the power density for the fresh fuel is going up with the distance from the pin center line and reaches the maximum value on the fuel surface. Ratio of power densities between the fuel surface and center line are 2.2 and 1.8 for inner and outer pins, respectively. The total power productions for outer and inner pins are practically identical each other (difference is about 1%). However, since the inner pin has smaller radius, the power density inside the outer pin is about 15 % higher than in inner for the same distance relative to the center line. Data for power density for different pins are presented in Table 2. The average power densities were obtained in approximation of homogeneous power density distribution across the 5 m fuel rod with consideration of the total numbers of inner (32 pins) and outer (32 pins) pins inside the cell, the cell number (336) and anticipated total fission power production (2.5 GW).

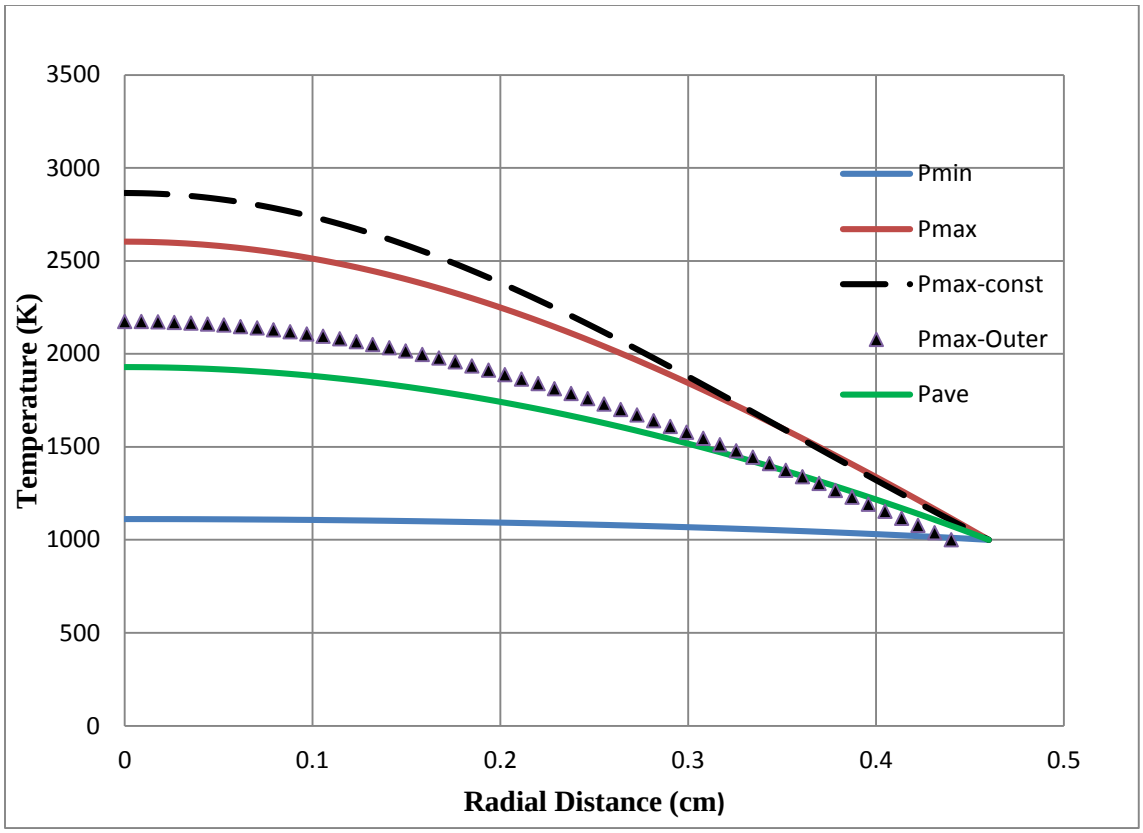

Figure 6. Temperature distributions inside the fuel pins with homogeneous Pu-Th composition.

According to the equation (3) with consideration of the power density distributions inside a pin (as presented in Figure 4), the temperature distributions for the fresh homogeneous Pu-Th fuel pins have been simulated. The results are presented in Figure 6. The temperature on the pin surface was chosen to be 1000 K for all simulations what is inside of region for anticipated temperature variation for cladding surface [9]. The simulations have been done for different average power densities and for the inner and outer pins, separately. Solid lines correspond to temperature distributions inside the inner fuel pin for minimal (3.67E+7 W/m^3, blue line), maximal (6.41E+8 W/m^3, red line) and average (4.27RE+8 W/m^3, green line) values of power densities. The dotted line represents temperature distribution inside the outer fuel pin with maximal (5.73E+8 W/m^3) power density, and the dashed line is temperature distribution for the inner fuel pin with maximal (6.41E+8 W/m^3) but constant in radial direction power density.

According to the simulations, difference in temperatures between the fuel surface and center line can reach few thousand degrees of Kelvin and significantly depends on the fuel thermal conductivity and power production. Moreover, the shape of power density distribution inside the fuel pin can significantly influence the center line fuel temperature. Comparison between two temperature distributions corresponding to constant (dashed line) and anticipated for fresh fuel (red line) power density distributions indicates that in case of constant power density the center line temperature reaches higher value.

3.2. Modified fuel composition

Neutronics simulations for the modified fuel composition have been done in the same way as for homogeneous composition, except that geometry configuration was corrected according to the new fuel design as presented in Figure 3. Results of neutronics simulations show that the power production in inner and outer fuel rods for modified composition are practically identical (difference inside one percent), as it

was for homogeneous fuel composition. On the other hand, there is a big difference in power production between inner and outer shells. The most fission energy is released in PuO_2 material, located in outer shell, and about 1% in ThO_2, occupying the center line volume. Uncertainty of neutronics simulations did not allow to get analytical expression for power density distribution inside the fuel materials. For that reason, the volumetric power density assumed to be constant in each material. The simulated power densities for modified fuel pin composition are presented in Table 2.

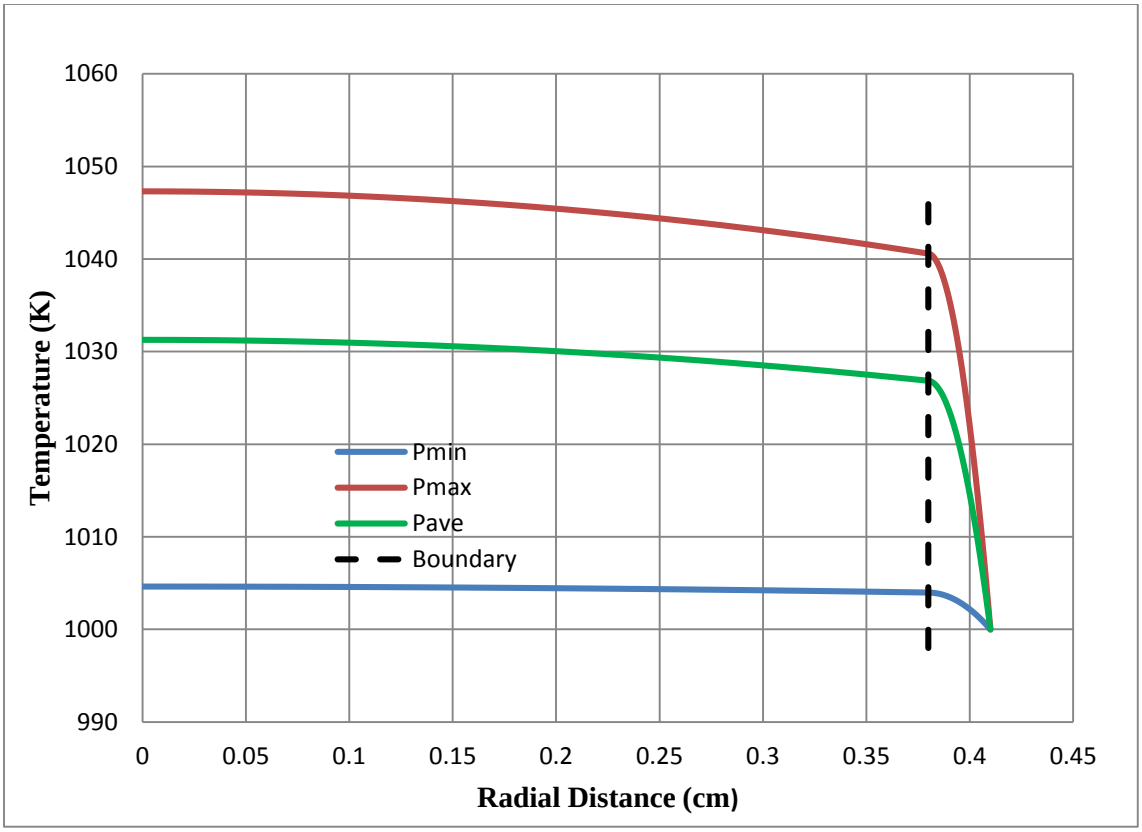

Figure 7. Temperature distributions inside the fuel pins with modified composition. The dashed line corresponds to location of boundary between PuO_2 and ThO_2 fuel materials.

Equations (3) and (4) have been used to get the temperature distribution inside the ThO_2 and PuO_2 fuel materials of modified pins, respectively. The same temperature (1000 K) for the fuel pin surface was applied. For modified composition, it corresponds to the PuO_2 outer surface temperature, where the fuel is touching to cladding material.

Results of simulation for temperature distributions inside the PuO_2 and ThO_2 materials are presented in Figure 7. The simulations have been done for three different values of power densities corresponding to minimum, maximum and average values of fission power in the cell and presented as blue, red and green lines, respectively. The absolute values for power densities were the same as for homogeneous composition. Sharp increase of temperature is observed within the outer shell, where the main value of reactor power is produced. Inside the inner cylinder, the temperature distribution has a flat shape and there is no big difference between the fuel center line and shell boundary temperatures (shell boundary is marked as dashed line in Figure 7 and corresponds to boundary between two materials). The total rise of temperature (difference between the center line and cladding) does not reach even 100 degrees, what is significantly lower in comparison to the homogeneous fuel composition for the same power production.

4. Conclusion

The fuel temperature is one of the main characteristics for any reactor and is a crucial parameter for safe operation of nuclear power plants. The temperature distributions inside the fresh fuel pins of PT-SCWR reactor have been simulated for different power production values. It was found that the center line temperature for homogeneous Pu-Th fuel composition can reach melting point. The fuel composition having significantly smaller value of temperature drop between the fuel center line and pin surface is proposed. The new composition consists of two enclosed shells with different material compositions, where PuO_2 and ThO_2 are located in inner and outer shells, respectively. Results indicate that for the same fission power production, the two-region fuel-material distribution has significantly lower centre line temperature, and the melting point is not reached.

Acknowledgements

Funding to the Canada Gen-IV National Program was provided by Natural Resources Canada through the Office of Energy Research and Development, Atomic Energy of Canada Limited, and Natural Sciences and Engineering Research Council of Canada

References

1. M. Yetsir, M. Gaudet and D. Rhodes, “Development and Integration of Canadian SCWR Concept with Counter-Flow Fuel Assembly”, Proceedings of the 6th International Symposium on Supercritical Water-Cooled Reactors, March 3-7, 2013, Shenzhen, Guangdong, China.

2. E.Nichita, “Kinetic parameters of a Th-Pu re-entrant channel pressure-tube SCWR”, Proceeding of ANS National Meeting, November 10-14, 2013, Washington, DC, USA.

3. J.Pencer at all., “Reactor core and plant design concepts of the Canadian supercritical water-cooled reactor”, Proceeding of Canada-China Conference on advanced reactor development, April 2014, Niagra Falls, ON, Canada.

4. G. Marleau, A Hebert and R. Roy, A Used Guide for DRAGON, Version GRAGON_000331 Release 3.04, Report IGE-174 Rev.5, Institute de genie nucleaire, Ecole Polythechnique de Montreal, Quebec (2000).

5. E. Varin, A.Hebert, R.Roy and J.Koclac, A User Guide for DONJON, Version 3.01, Technical report IGE-208, Rev. 4, Ecole Polythechnique de Montreal, Quebec (2005).

6. V.Kovaltchouk, E.Nichita and E.Saltanov, “Axial power and coolant-temperature profiles for a non-re-entrant PT-SCWR fuel channel”. Proceeding of the 7th International Symposium on Supercritical Water-Cooled Reactors. ISSCWR-7,15-18 March, 2015, Helsinki, Finland.

7. Y.A.Cengel, Heat and Mass Transfer: A Practical Approach. Third Edition (2007).

8. Cozzo, C., Staicu, D., Somers, J., Fernandez, A. and Konings, R.J.M., 2011. Thermal Diffusivity and Conductivity of Thorium-Plutonium Mixed Oxides. *Journal of Nuclear Materials*, 416, pp. 135–141.

9. D.Lokuliyana,”Simulating SCWR thermal-hydraulics with the modified COBRA-TF subchannel code”, Master‘s Degree Thesis, McMaster University, Canada, 2014.

The 7th International Symposium on Supercritical Water-Cooled Reactors
ISSCWR-7
15-18 March 2015, Helsinki, Finland

ISSCWR7-2018

Axial power and coolant-temperature profiles for a non-re-entrant PT-SCWR fuel channel

V. Kovaltchouk, E. Nichita and E. Saltanov
Faculty of Energy Systems and Nuclear Science
University of Ontario Institute of Technology
2000 Simcoe Street North, Oshawa, ON
Canada, L1H 7K4
Vitali.Kovaltchouk@UOIT.ca

Abstract

The axial power and coolant-temperature distributions in a fuel channel of the Generation IV Pressure-Tube Super-Critical Water-cooled Reactor (PT-SCWR) are found using coupled neutronics-thermal-hydraulics calculations. The simulations are performed for a channel loaded with a fresh, 78-element Th-Pu fuel assembly. Neutronics calculations are performed using the DONJON diffusion code using two-group homogenized cross sections produced using the lattice code DRAGON. The axial coolant temperature profile corresponding to a certain axial linear heat generation rate is found using a code developed in-house at UOIT. The effect of coolant density, coolant temperature and fuel temperature variation along the channel is accounted for by generating macroscopic cross sections at several axial positions. Fixed-point iterations are performed between neutronics and thermal-hydraulics calculations. Neutronics calculations include the generation of two-group macroscopic cross sections at several axial positions taking into account local parameters such as coolant temperature and density and average fuel temperature. The coolant flow rate is adjusted so that the outlet temperature of coolant corresponds to the SCWR technical specifications. The converged axial power distribution is found to be asymmetric, resembling a cosine shape skewed towards the inlet (reactor top).

1. Introduction

The Pressure-Tube Super-Critical Water-cooled Reactor or PT-SCWR is the next generation (Generation IV) innovative water cooled reactor concept being developed in Canada. The reactor uses pressurised water above its thermodynamic critical pressure as the reactor coolant. This concept offers high thermal efficiency in comparison to existing nuclear power plants.

The full-core neutronics and thermo-hydraulic characteristics of the PT-SCWR reactor are key components in reactor design. At the same time, there is a direct influence of thermo-hydraulic characteristics on results of neutronics simulations, and vice versa. For example, an axial power production directly affects axial fuel temperature and coolant density distributions which, in turn, affect macroscopic neutron cross section data used in neutronics simulations.

Coupled neutronics and thermal-hydraulic simulations have been presented by different authors [1-6] and still represents an important and challenging task. For the present work, a coupling of full core neutronics and thermo-hydraulic simulations is performed for 78-element non-re-entrant PT-SCWR fuel channels with Th-Pu fuel [7]. Parameters such as coolant temperature, coolant density and fuel temperature are calculated based on axial power

production with corresponding corrections applied to the macroscopic neutron cross section data used in iteration process.

2. Coupled neutronics and thermal-hydraulics code

2.1 Iteration scheme

A block diagram of the coupled neutronics-thermal-hydraulics simulations for non-re-entrant fuel channel of a PT-SCWR reactor is presented in Figure 1. The main components of the iterative process are neutronics simulations and thermal-hydraulics simulations.

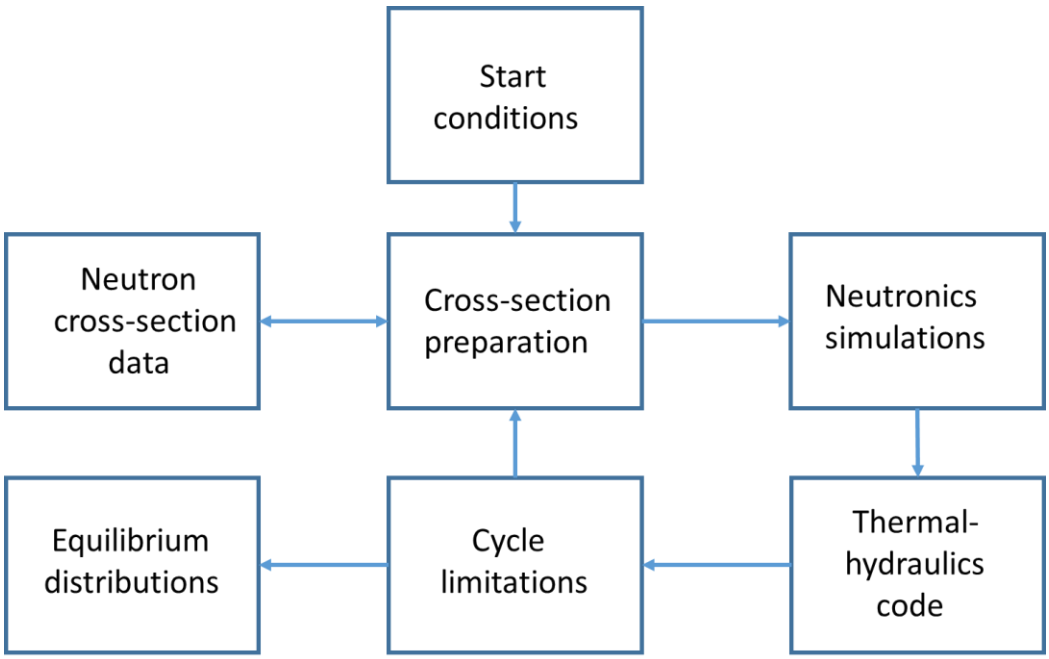

Figure 1. Block diagram of the coupled calculations

The iteration process starts with preparing lattice-level macroscopic cross sections for initial values of the fuel temperature, coolant temperature and coolant density that are uniform across all locations in the reactor.

Based on the generated cross section data, a full-core neutronics simulation is performed, and thus the axial power distributions for all fuel rods are obtained. The newly-calculated axial fission power distribution is used to determine the distribution of the fuel temperature, coolant density and coolant temperature throughout the core. A new set of space-dependent macroscopic cross sections is then generated based on the new temperature and density distributions.

Iterations are continued until convergence, that is until variation in power production between two cycles becomes smaller than a pre-set limit.

2.2 Neutronics simulations

Full-core neutronics calculations are performed in two-group diffusion theory using the DONJON (Ver. 3.0) program package [8] developed at Ecole Polytechnique de Montreal which is capable of solving the multigroup diffusion equation using several separate numerical methods and is applicable to several types of reactors including PT-SCWR and Advanced CANDU reactors. A 25-cm Cartesian mesh (equal to the lattice pitch) is used for the diffusion

calculations in all three directions. Vacuum (zero incoming current) boundary conditions are imposed on all boundaries. For this preliminary work, no reactivity devices are simulated.

The DONJON program is divided into several modules which help define the multi-group macroscopic cross sections, geometry and material distribution. Additional modules solve the diffusion equations using a method chosen by the user.

Lattice macroscopic cross sections are calculated using the lattice code DRAGON [9] for a pre-defined set of values of the fuel burnup, fuel temperature, coolant temperature and coolant density and arranged in a table. The lattice macroscopic cross sections at each iteration step for any given position in the reactor are then calculated by liner interpolation in the table of lattice cross sections.

2.3 Thermal-hydraulics code

A thermal-hydraulics code was developed in FORTRAN to model axial bulk-fluid and wall temperature profiles, as well as axial and radial fuel temperature profiles. Linear heat flux was obtained by using natural cubic spline interpolation of the power profile obtained from the DONJON program. The heat flux was kept at a constant value (first term in the spline interpolation) from the inlet to the channel's to the first node. The following assumptions were made for the heat-transfer model:

1. Steady-state operating conditions;
2. One-dimensional heat-transfer for the bulk fluid;
3. Negligible axial heat-transfer in the fuel and cladding;
4. Negligible contact resistance between the inner surface of the cladding of a fuel element and outer surface of fuel.
5. Uniform volumetric heat generation in fuel;
6. The pressure drop along the fuel channel has no influence on the heat transfer from the fuel to the coolant;

The mass-flow rate was calculated for each fuel channels to ensure that the outlet temperature would be 898 K. Cladding wall temperature and heat-transfer coefficients were calculated using the correlation developed by Mokry et al. [10].

$$\mathbf{Nu_b} = 0.0061\,\mathbf{Re_b}^{0.904}\,\overline{\mathbf{Pr_b}}^{0.684}\left(\frac{\rho_w}{\rho_b}\right)^{0.564} \tag{1}$$

where dimensionless constants were calculated from their definitions as follows:

$$\mathbf{Nu_b} = \frac{htc \cdot D_{hy}}{k};\ \mathbf{Re_b} = \frac{4\dot{m}}{\mu \cdot \pi D_{hy}};\quad \overline{\mathbf{Pr_b}} = \frac{\mu}{k}\cdot\underbrace{\frac{h_w - h_b}{T_w - T_b}}_{c_p} \tag{2}$$

where:
htc – heat transfer coefficient, W/m^{2}K;
D_{hy} – hydraulic diameter, m;
k_b – thermal conductivity calculated at bulk-fluid temperature (T_b), W/m·K;
$\dot{m}$ – mass flow-rate, kg/s;
μ_b – dynamic viscosity calculated at T_b, Pa·s;
h_w – specific enthalpy of the fluid calculated at wall temperature (T_w), J/kg·K; and
h_b – specific enthalpy of the fluid calculated at T_b.

The Mokry et al. [10] correlation was chosen based on a recent research by Zahlan et al. [11]. which showed that the correlation expressed by Eq. (1) has the best agreement with the data in the supercritical region.
The fuel centerline temperature was calculated by dividing fuel pellet radius into 10 ring elements and calculating the temperature increase across each successive ring towards the

center. Expression for the radial steady-state temperature distribution in a cylindrical configuration with uniform internal heat generation rate was used. By denoting volumetric heat generation rate as q''', the temperature at inner surface of a ring element of radius *r* and having thickness Δ*r* may be expressed by follows:

$$T(r-\Delta r) = T(r) + \frac{q'''}{4k_f}(r^2 - (r-\Delta r)^2) \tag{3}$$

where k_f is the thermal conductivity of fuel.

Fuel composition having 13% wt. PuO_2 + 87% wt. ThO_2 fuel was considered. Thermal conductivity of this fuel as a function of weight fraction *y* of PuO_2 was calculated using equation proposed by Cozzo et al. [12]:

$$k\ \ y\ = \frac{1}{6.071\cdot 10^{-3} + 5.72\cdot 10^{-1} y - 5.937\cdot 10^{-1} y^2 + 2.4\cdot 10^{-4} T}, \tag{4}$$

where *T* is in K.

Axial distributions of bulk-fluid temperature, density, and volume-average fuel temperature values for each fuel channel were output by the developed heat-transfer code and used for macroscopic neutron cross-section preparation. Heat-transfer calculations were performed for each channel of a PT-SCWR reactor.

3. Simulation of PT-SCWR reactor with non-re-entrant fuel channel

3.1 PT-SCWR reactor model

The PT-SCWR reactor [7] consists of a low pressure calandria vessel with 336 vertically oriented pressure tubes housing the Th-Pu fuel and light water coolant. An axial dimension of the pressure tubes with fuel is 5 m. The pressure tubes are set on 25 pitch square lattice with 25 cm dimension. The preliminary concept of PT-SCWR reactor is shown in Figure 2.

Table 1. Main characteristics of the fuel channel and 78-element bundle.

Parameters	Unit	Value
Heated fuel-channel length	m	5.0
Inlet pressure	MPa	25.0
Inlet/outlet temperature	°C	350/625
Cladding for all pins	cm	0.06
Cladding material	–	Zr-modified 310 stainless steel
Centre pin radius	cm	2.82
Inner pin radius (15 pins)	cm	0.62
Intermediate pin radius (21 pins)	cm	0.62
Outer pin radius (42)	cm	0.35
Fuel	–	13% wt. PuO_2 + 87% wt. ThO_2
Liner tube (solid) inner radius	cm	6.89

The space between pressure tubes in the calandria is occupied by the heavy water moderator. The moderator has relatively low temperature (around 300 K) and near-atmospheric pressure. The modeled version had a single fuel assembly with 78 fuel elements or pins, and had a

central element made from ZrO_2. The fuel assemblies are separated from the high pressure tubes by a ceramic insulator having 10 mm thickness and made from yttrium stabilized zirconia which has low neutron absorption. Cross-sectional view of the 78-element PT-SCWR fuel assembly obtained from DRAGON program is presented in Figure 3. The pressure tube provides the pressure boundary at close to the moderator temperature, which is confident for its mechanical properties. A thickness and outer diameter of the pressure tube are 1.2 cm and 18.14 cm, respectively. The characteristics of the channel and the fuel bundle are listed in Table 1. Calibrated orifices at each channel inlet are used to adjust the channel flow so that the coolant outlet temperature as approximately the same for all channels.

For neutronics simulations, the modeled SCWR reactor was “sliced” into 26 layers in vertical direction, where 25 layers corresponded to 5 m length of fuel channel, one layer on the top represented the light water. The layer thickness was 25 cm (each layer). In a horizontal plane, the reactor was modeled as an orthogonal lattice structure with 25 cm side dimension, where the fuel channels with coolant were located in the centre of orthogonal net. Cells with fuel were surrounded by cells with heavy water. Total number of cells was 676 cells per one layer. If cell was located outside the reactor volume, it was presented as an empty cell.

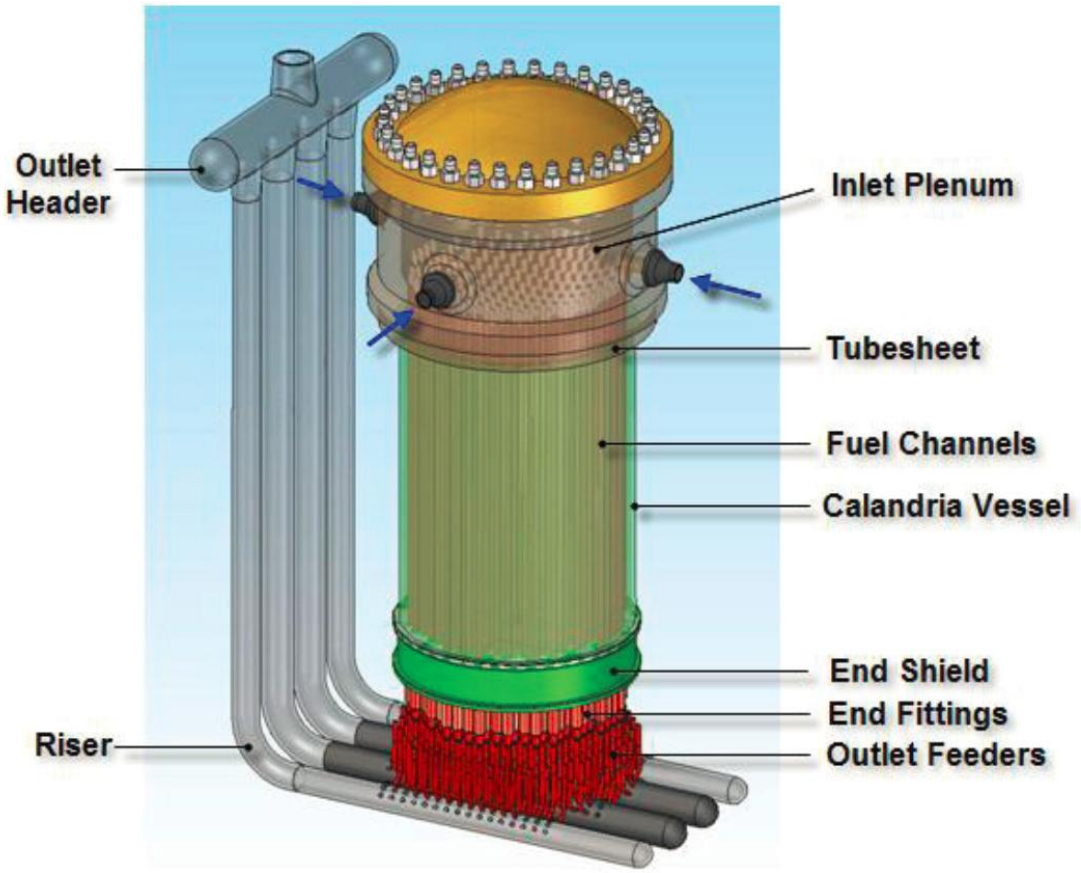

Figure 2. Preliminary Concept of the PT-SCWR.

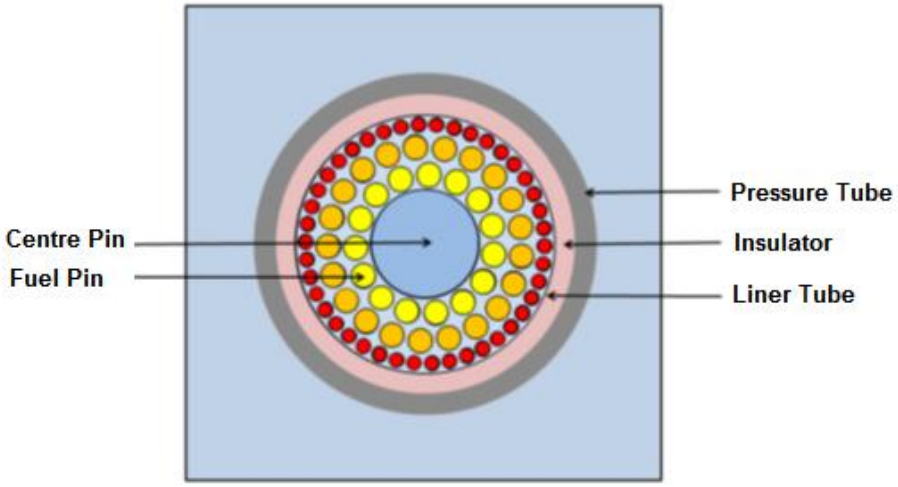

Figure 3. Cross-sectional view of 78 elements PT-SCWR fuel assembly with non-re-entrant fuel channel.

3.2 Iteration process

The iteration process presented in Figure 1 is started from reference conditions, where the fuel temperature, coolant density and coolant temperature have fixed values for any location inside the reactor and are equal to 1650 K, 400 kg/m^3 and 750 K, respectively. The total fission power production was 2.5 GW for all iterations.

The output of full-core neutronics simulation was axial power production in each of the reactor cell with fuel, and it was used as input data set for the thermal-hydraulics code. By considering the reactor parameters (input/output coolant fluid temperature), the axial distribution of fuel temperature and coolant temperature/density were obtained from the thermo-hydraulic program developed at UOIT. Obtained data were used for macroscopic cross-section correction and the next iteration run of the neutronics simulations.

A special module for iteration limitation named “Cycle limitations” was incorporated into the cycle. The module provides limitation for fuel temperature variation between two iterations. When the temperature limitation is too high or is absent the iteration process is not stable. A small value for temperature variation significantly increases the total number of iterations. Variable fuel temperature drop was chosen in a way that for the first ten cycles it allowed few hundred degrees variation with a decrease to a few degrees after a few hundred iterations. The cycle module also limits the total number of iterations and stops the cycle when the difference in cell power production between two cycles is lower than a predefined value.

4. Results and discussion

As a result of iteration process the following distributions were obtained: axial power production, fuel temperature, coolant temperature and coolant density. They are presented in Figure 4 – 6, where the axis is directed across a fuel rod from reactor top (inlet) to bottom.

The axial fission power production distribution across a fuel channel is presented in Figure 4 as a solid line. The power distribution is normalized to anticipated 2.5 GW total power production from PT-SCWR reactor. A dashed line represents average over all cells power production. The converged axial power distribution is asymmetric, resembling a cosine shape skewed towards the reactor inlet.

A typical axial temperature distributions for fuel and coolant for the same fuel rod are presented in Figure 5 as blue and red lines, respectively. The fuel temperature data are averaged over the fuel volume inside the cell. The coolant temperature is raised from inlet

location to outlet and the input/output values are determined from the PT-SCWR reactor requirements. A coolant mass flow rate was corrected to keep the coolant temperature inside the limits. The maximal value of fuel temperature depends from power production presented in Figure 5 data correspond to average power production.

Figure 6 shows an axial coolant density distribution across the fuel channel. The coolant density distributions from different channels have small variation. The absolute value of density drops significantly (from 605 kg/m^3 to 68 kg/m^3) as coolant fluid is moving from reactor inlet to outlet location.

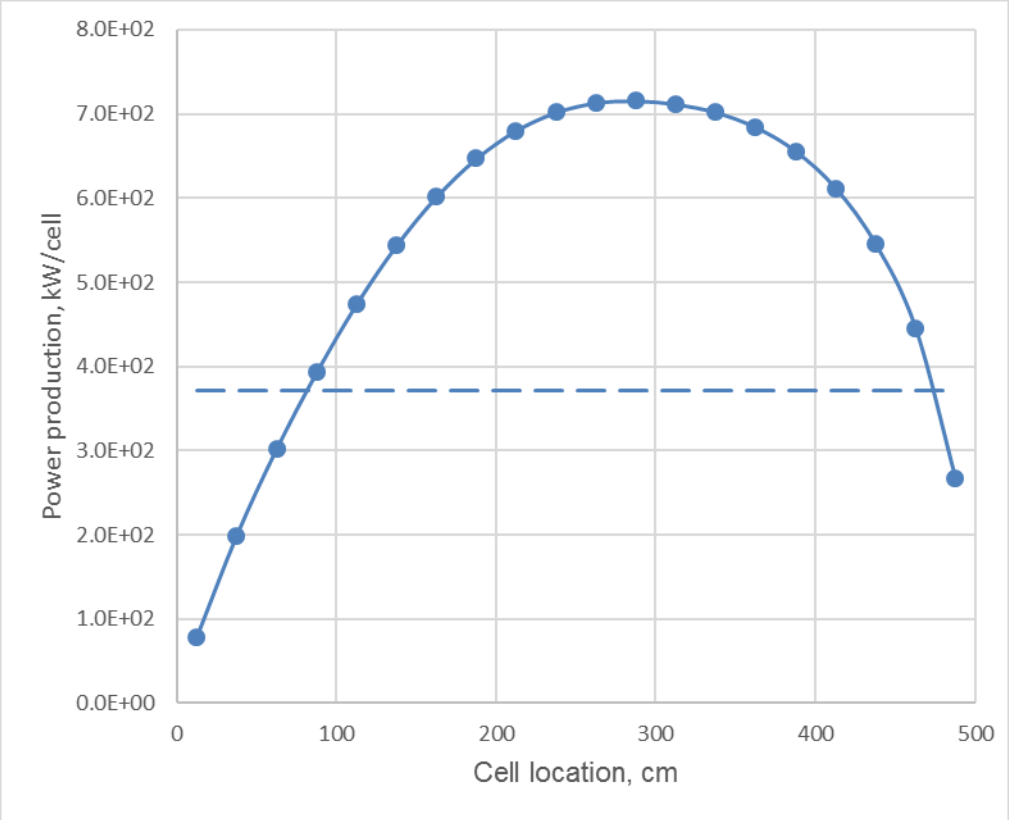

Figure 4. The axial power production.

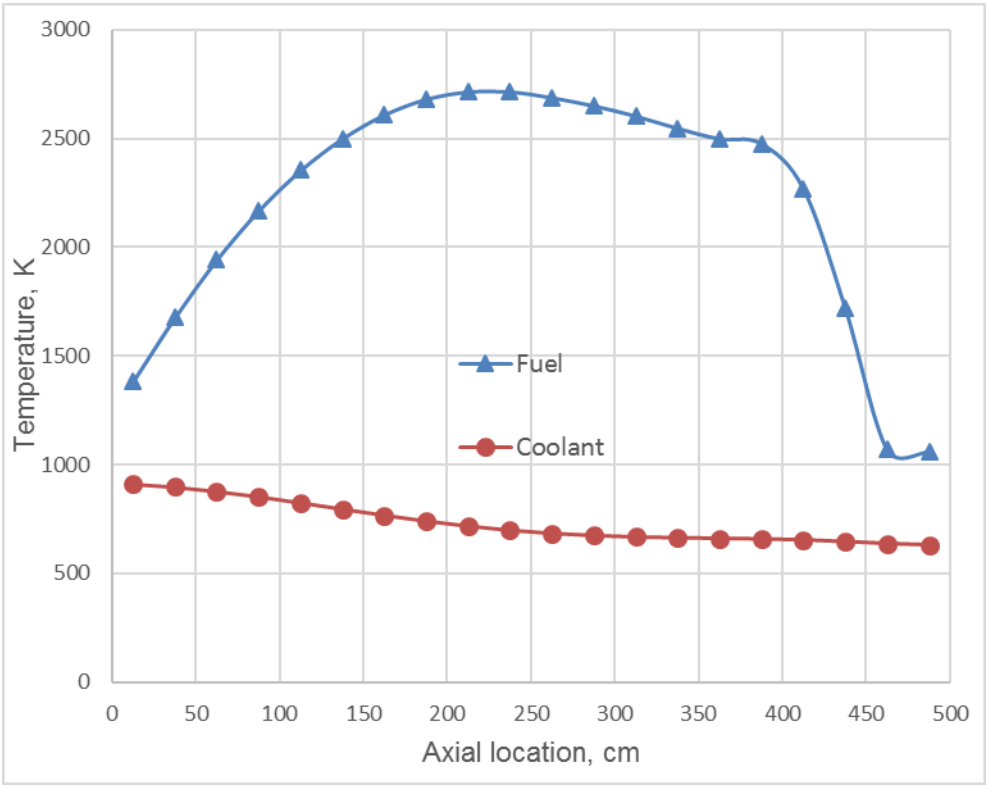

Figure 5. The axial temperature distributions for fuel (blue line) and coolant (red line).

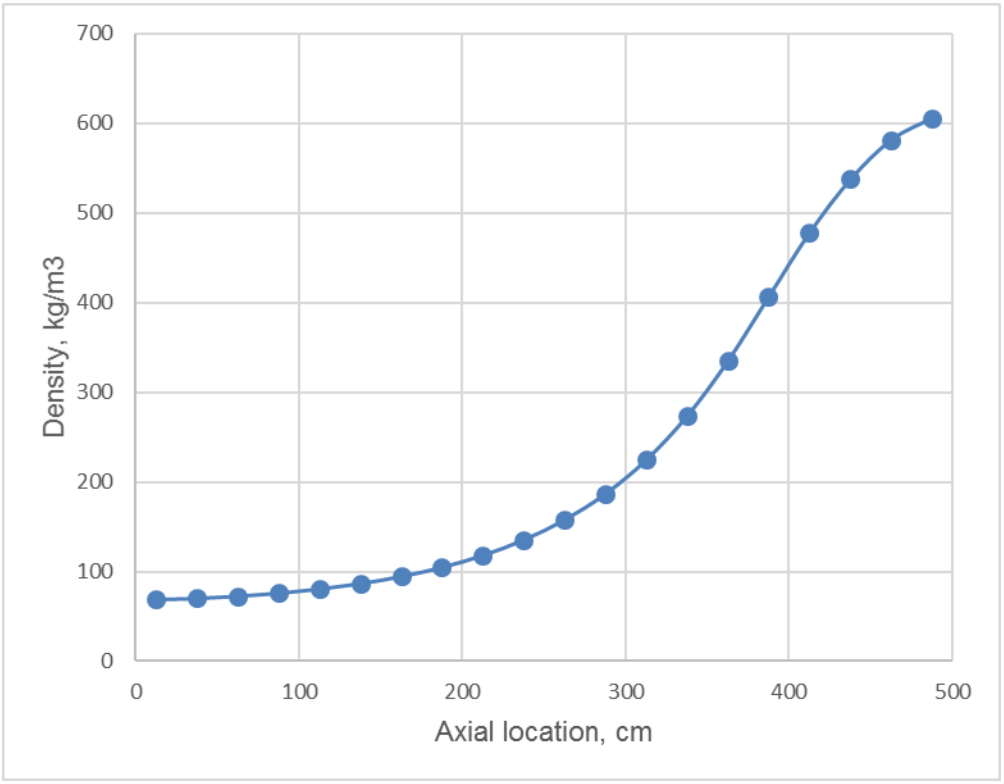

Figure 6. The axial distribution of coolant density.

5. Conclusion

In this paper the in-house developed at UOIT code for coupled neutronics and thermal-hydraulics simulations is presented. The simulations have been done for 78 fuel elements PT-SCWR reactor with non-re-entrant channel configuration. Such characteristics as axial fuel temperature, coolant temperature/density and power production distributions were obtained and analysed for fresh Th-Pu fuel composition.

Acknowledgements

Funding to the Canada Gen-IV National Program is provided by Natural Resources Canada through the Office of Energy Research and Development, Atomic Energy of Canada Limited, and Natural Sciences and Engineering Research Council of Canada.

References

1. C.Hughes, D Schubring, K.Jordan and D.Ratz, ”Coupled computational heat transfer and reactor physics for SCWR”, Proceeding of the ASME 2013 Heat Transfer Summer Conference HT 2013, July 14-19, Minneapolis, MN, USA.

2. W.Peiman, E.Saltanov, L.Grande, I.Pioro, R.Rouben and K.Gabriel, “Power distribution and fuel centerline temperature in a Pressure-Tube Supercritical Water-Cooled Reactor (PT-SCWR)”, Proceeding of the 2012 20th International Conference on Nuclear Engineering collocated with the ASME 2012 Power Conference, ICONE20-POWER212, July 30 – August 3, 2012, Anaheim, California, USA.

3. A.Abdala,”Sensitivity analysis of fuel centerline temperature in SuperCritical Water-cooled Reactors’, Master‘s Degree Thesis, University of Ontario Institute of Technology, Canada, 2012.

4. D.Lokuliyana,”Simulating SCWR thermal-hydraulics with the modified COBRA-TF subchannel code”, Master‘s Degree Thesis, McMaster University, Canada, 2014.

5. K.Jareteg, “Development of an integrated deterministic/thermal-hydraulics model using a CFD solver”, Master‘s Degree Thesis, Chalmers University of Technology, Sweden, 2012.

6. P.Adouki, “Neutronics-thermalhydraulics coupling in a CANDU SCWR”, Master ‘s Degree Thesis, Ecole Polytechnique de Montreal, Canada, 2012.

7. M. Yetsir, M. Gaudet and D. Rhodes, “Development and Integration of Canadian SCWR Concept with Counter-Flow Fuel Assembly”, Proceedings of the 6th International Symposium on Supercritical Water-Cooled Reactors, March 3-7, 2013, Shenzhen, Guangdong, China.

8. E. Varin, A.Hebert, R.Roy and J.Koclac, A User Guide for DONJON, Version 3.01, Technical report IGE-208, Rev. 4, Ecole Polythechnique de Montreal, Quebec (2005).

9. G. Marleau, A Hebert and R. Roy, A Used Guide for DRAGON, Version DRAGON_000331 Release 3.04, Report IGE-174 Rev.5, Institute de genie nucleaire, Ecole Polythechnique de Montreal, Quebec (2000).

10. Mokry, S., Gospodinov, Ye., Pioro, I. and Kirillov, P., 2009. Supercritical Water Heat-Transfer Correlation for Vertical Bare Tubes, Proceedings of the 17th International Conference on Nuclear Engineering (ICONE-17), Brussels, Belgium, July 12-16, Paper#76010, 8 pages.

11. Zahlan, H., Groeneveld, D. and Tavoularis, S., 2010. Look-Up Table for Trans-Critical Heat Transfer, Proc. 2nd Canada-China Joint Workshop on Supercritical Water-Cooled Reactors (CCSC-2010), Toronto, Ontario, Canada: Canadian Nuclear Society, April 25-28.

12. Cozzo, C., Staicu, D., Somers, J., Fernandez, A. and Konings, R.J.M., 2011. Thermal Diffusivity and Conductivity of Thorium-Plutonium Mixed Oxides. *Journal of Nuclear Materials*, 416, pp. 135–141.

ISSCWR7-2019

Control Rod Withdrawal Analysis of the SCWR-FQT Facility in the LVR-15 Research Reactor

Csaba Maráczy, György Hegyi, István Trosztel, Emese Temesvári
Centre for Energy Research, Hungarian Academy of Sciences
1525 Budapest 114., P.O. Box 49., Hungary
+3613922222, csaba.maraczy@energia.mta.hu

Abstract

The aim of the Supercritical Water Reactor - Fuel Qualification Test (SCWR-FQT) Euratom-China collaborative project is to design an experimental facility for qualification of fuel for the supercritical water-cooled reactor. The facility is intended to be operated in the LVR-15 research reactor in the Czech Republic. The pressure tube of the FQT facility encloses four fuel rods which will operate in similar conditions to the evaporator of the HPLWR reactor. The paper deals with the 3D coupled neutronic-thermohydraulic steady state and transient analysis of LVR-15 with the fuelled loop. Conservatively calculated enveloping parameters (e.g. reactivity coefficients) were determined for the safety analysis. The control rod withdrawal analysis of the FQT facility with and without reactor scram was carried out with the KIKO3D-ATHLET coupled dynamic code.

1. Introduction

The FQT experimental facility for qualification of fuel for the supercritical water-cooled reactor is intended to be operated in the LVR-15 research reactor in the Czech Republic [1,2]. This reactor enables to replace one of its assemblies with a pressure tube containing a four rod fuel bundle, which shall be connected with coolant pumps, safety and auxiliary systems to simulate a supercritical water environment. The in-pile test section of the FQT loop has three main parts: the active height with 4 fuel rods, the recuperator and the cooler section with U-tube heat exchangers. To provide temperature conditions similar to the evaporator of the HPLWR reactor a complicated zig-zag type flow path was introduced with four coolant channels with downward, upward, downward, and upward flow directions from the inlet to the outlet of the in-pile test section. The cross section of the FQT loop at the active height can be seen in Figure 1.

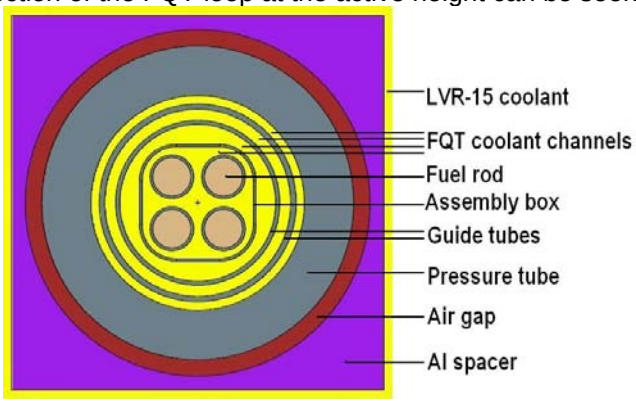

Figure 1. MCNP model of the FQT test section.

Figure 2 shows the LVR-15 core with the FQT test section. The LVR-15 will use low enriched uranium IRT-4M quadratic plate type fuel assemblies at the time of experiments.

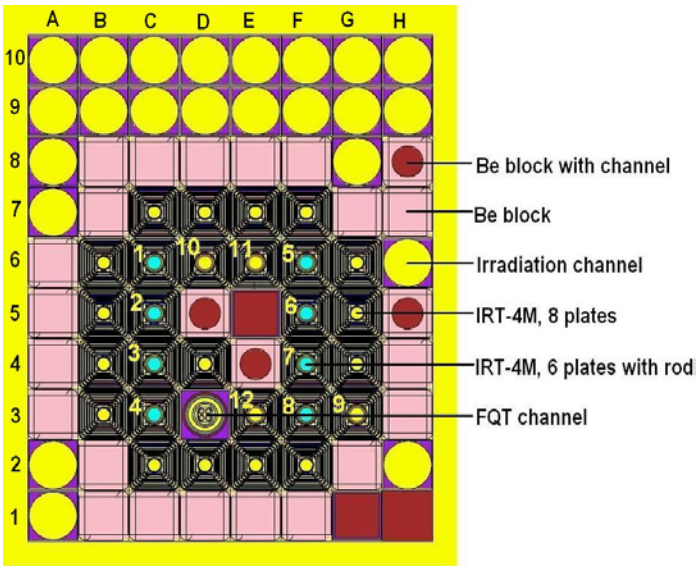

Figure 2. MCNP model of the LVR-15 core with numbered core arrangement:
control rods (1-8), automatic rod (9) and safety rods (10-12).

All necessary documents required for licensing of the FQT facility by the Czech regulator shall be the outcome of this project. The Center for Energy Research participated in the 3D steady state and transient analysis of LVR-15 with the fuelled loop. The Reactivity Initiated Accident (RIA) analyses were carried out with the KIKO3D-ATHLET coupled neutronic-thermohydraulic dynamic code.

2. Steady State Analysis

For the analysis of the Fuel Qualification Test Section in LVR-15 during normal operation the calculation of power profiles is indispensable. A calculation sequence was elaborated for this purpose which can also be applied for the calculation of bounding parameters to be used in safety analysis.

The applied calculation types and tools are the following:

- 1D and 2D calculations with the MULTICELL [3] 70 group neutronic transport code for cross section (XS) generation.
- Full core calculations with the KARATE-SC [4] coupled nodal neutronic-thermalhydraulic code.

The parameters for the cross section calculations covered the normal operation(NO) and anticipated operational occurence (AOO) states. The verification of the MULTICELL transport code and the KARATE-SC coupled code was presented in [5].

Neutronic calculations were performed for the LVR-15 core configuration shown in Figure 2. As the actual core loading plan during irradiation of the test-section is not known a priori, a 'reference core' with 30% burnt research reactor fuel assemblies and unburnt fuel in the FQT section was defined.This simplified reference core served as the first basis for the neutronic analysis and conclusions on the power behaviour of the FQT section under normal operating conditions.

The power profile of the fuel in the test-section changes with irradiation time. To assess the possibilities of core arrangements a series of burnup calculations has been performed with the

GLOBUS code taking into account all feedback phenomena in the LVR core and in the FQT section. To check the reality of the reference core in terms of reactivity a cold zero power state was calculated with no xenon, control rods inserted, safety rods in upper position and the automatic rod in halfway position. The reactor is just subcritical with sufficient margin according to the calculations. Starting from the reference core a full power critical state was searched at equilibrium xenon, then the core was burned up. The corresponding arbitrarily supposed control rod positions are illustrated in Figure 3 (the safety rods were in the upmost position, the automatic rod was in a halfway position). The FQT power profiles are depicted in Figure 4.

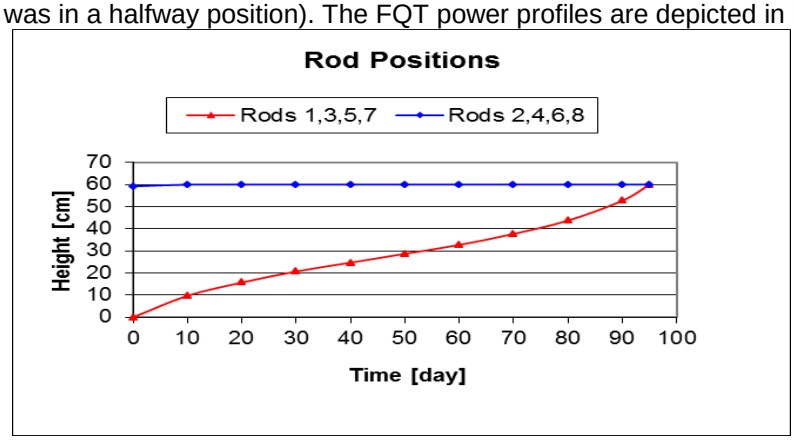

Figure 3. GLOBUS burn-up calculation for the LVR-15 reference core with 30% burnt IRT-4M assemblies next to the FQT section. Critical control rod positions in the LVR-15 core.

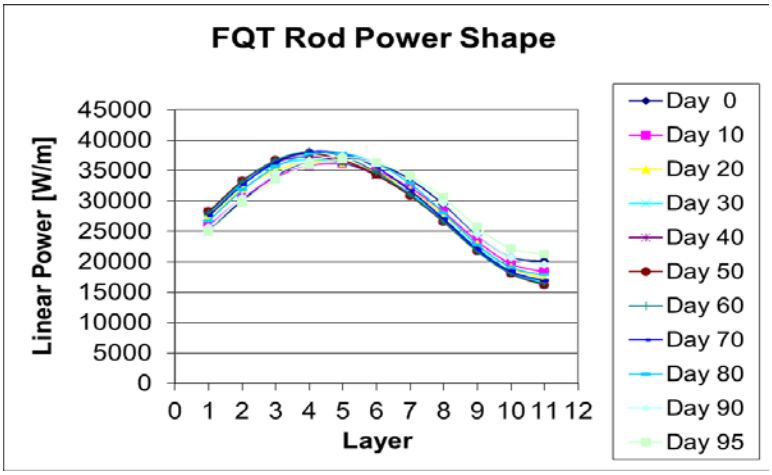

Figure 4. Predicted power profile in the FQT test-section. GLOBUS burn-up calculation for the LVR-15 reference core with 30% burnt IRT-4M assemblies next to the FQT section.

The power profile does not show very significant change, but the maximum values are reached during the irradiation. With proper actual core arrangement e.g. more burnt IRT-4M assemblies near FQT the power might be reduced. Therefore, two more burn-up calculations with roughly 40% and 50% burnt IRT-4M assemblies next to the FQT section were performed. The resulting power profiles for the different core arrangements are compared in Figure 5 and show that the power becomes somewhat lower, but not sufficiently. The lower power of the more burnt IRT-4M assemblies is almost compensated by the more thermal spectrum of these driver assemblies. Figure 5 clearly shows that more power reduction can be achieved with the insertion of rod 4, which is in the C3 position next to the FQT test-section.

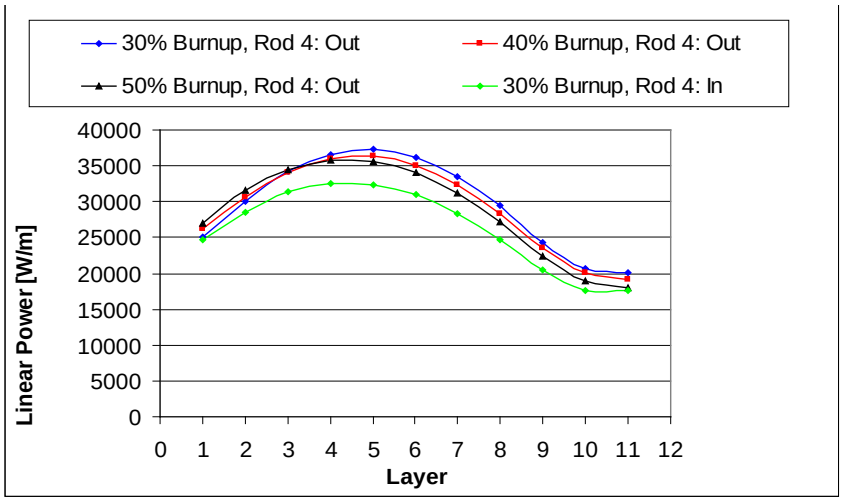

Figure 5. Power profile calculated with GLOBUS for the LVR-15 reference core at different core arrangements.

Besides the calculation of power profiles of the FQT section in LVR-15 at normal operation conditions the calculation of bounding parameters to be used in conservative safety analysis is necessary.
The conservative approach for the dynamic calculations means:

- Using bounding parameters which cover the possible situations. (Reactivity coefficients, control rod worth etc.)
- Always the worst case parameter is used in the calculations.
- The bounding parameters must cover the core loadings, technological and calculational uncertainties.

The bounding parameters were intended for the dynamic calculations with the KIKO3D-ATHLET [6,7] coupled nodal neutronic-thermalhydraulic code. With KIKO3D-ATHLET the Reactivity Initiated Accident analyses of the test section fuel bundle were carried out.The bounding parameter calculations were presented in [5].

3. Reactivity excursion events

The reactivity excursion events were calculated by the KIKO3D-ATHLET coupled neutronic-thermohydraulic code with conservative assumptions. The conservative tuning of reactivity coefficients, rod worths etc. to bounding parameters was achieved by the special tuning features applied in KIKO3D. The calculation of reactivity excursion events with KIKO3D-ATHLET was carried out for several configurations.

3.1 Inadvertent control rod withdrawal with SCRAM

The KIKO3D-ATHLET coupled code was successfully applied to both the safety calculations of the pool type Budapest Research Reactor and the inadvertent control rod withdrawal calculations of the High Performance Light Water Reactor. The KIKO3D code modeling the neutronic behavior of the LVR-15 core and the FQT active channel uses the same 2 group diffusion cross section libraries as the GLOBUS code. The ATHLET code models the thermohydraulic phenomena of both the LVR-15 pool with IRT-4M fuel assemblies and the FQT loop with the heat exchanger in supercritical conditions.

For transients with SCRAM the single failure of one safety rod out of three in stuck condition was used. The rod having the highest rod worth from safety rods was selected as the stuck rod. The rod worths of the two remaining safety rods were tuned to the conservatively low value.

For the case of inadvertent control rod withdrawal with SCRAM (Anticipated Operational Occurence) the following main considerations were found to be the most conservative ones[5]:

- The reactor period signal limit of SCRAM should not be reached
- The 120% power signal limit should initiate SCRAM
- Maximum β_{eff}
- Minimum worth of withdrawn rod
- Strong feedback parameters
- Minimum worth of safety rods
- FQT power tuned to higher value

The FQT fuel rod maximum linear power was tuned to reach 390 W/cm conservatively. When the FQT test section will be placed into the actual LVR-15 core configuration it will be necessary to prove by steady state calculation that the best estimate linear power of the fuel rods plus the uncertainty is less than 390 W/cm. The fuel clad surface temperatures and the fuel centerline temperatures with mild rise are depicted in Figures 6-7. (Here the node numbering differs by one compared to the steady state results.)

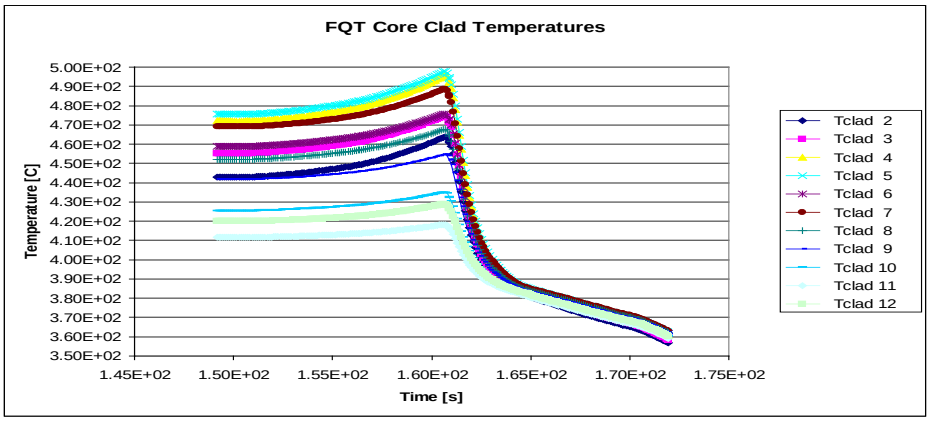

Figure 6. Clad surface temperatures of the FQT fuel pins in 11 layers (2-12).

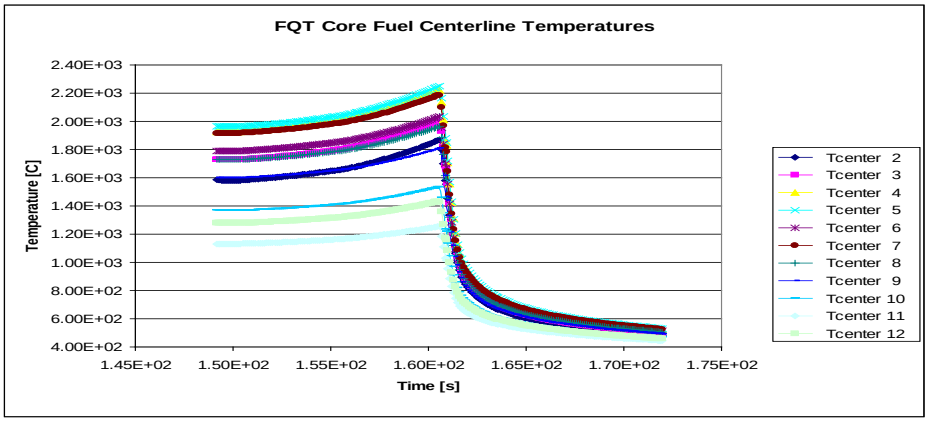

Figure 7. Fuel centerline temperatures of the FQT fuel pins in 11 layers (2-12).

3.2 Inadvertent control rod withdrawal without SCRAM

As the LVR-15 research reactor is operated at ambient pressure, a control rod ejection accident can be excluded. For the inadvertent control rod withdrawal without SCRAM (Postulated Accident) the following considerations were taken:
Despite the evident differences between the LVR-15 Research Reactor and the Budapest Research Reactor, the two reactors are similar in basic terms (e.g. power, fuel enrichment, heat flux, flow direction, coolant velocity, temperatures...). Therefore, using total power curves from

the safety analysis of BRR [8] is meaningful to carry out a parametric study. The power of FQT was found to be roughly proportional to the total power of LVR-15. In the following calculations, the steady state power profile of FQT calculated by the KIKO3D-ATHLET code was multiplied by a factor to reach the conservative 390 W/cm linear heat rate. Then the power profile was multiplied with the time dependent relative power change of the BRR reactor. This approach is slightly conservative because at higher coolant temperatures, and thus less moderation, the power rise in FQT would be slower. The calculations were carried out by the standalone ATHLET code. Five different power rise histories (Case 1-5) were studied which correspond to different reactivity insertions in case of Anticipated Transients Without SCRAM (ATWS). The transients were calculated both for constant mass flow rates and for constant volumetric flow rates in the FQT primary loop. The calculations were carried out to demonstrate the effectiveness of the spring loaded pressure relief valve opening at 26. MPa. In the following, the results for the mildest power increase (Case 1) with constant volumetric flow are presented. The calculations are presented up to 200 s after the beginning of the transient without the actuation of the emergency coolant injection system, which is a conservative approach from the point of view of overpressure. The system would be started and the automatic depressurization system ADS2 would be opened in this transient if

- The coolant temperature at the outlet of the test section exceeds 500°C, or if
- The coolant temperature at the inlet of the primary pump MPP exceeds 350°C

Figure 8 shows the power increase of the FQT test section.

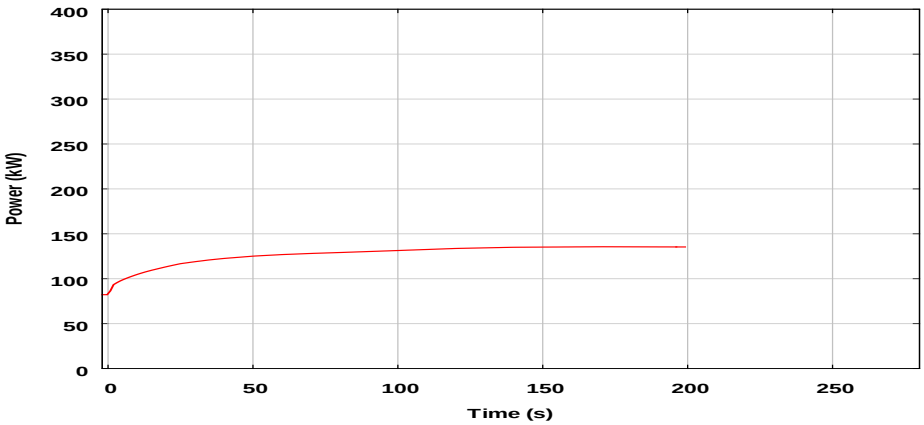

Figure 8. Power curve of the FQT test section.

As a result of the power increase, the temperatures are rising according to Figure 9.

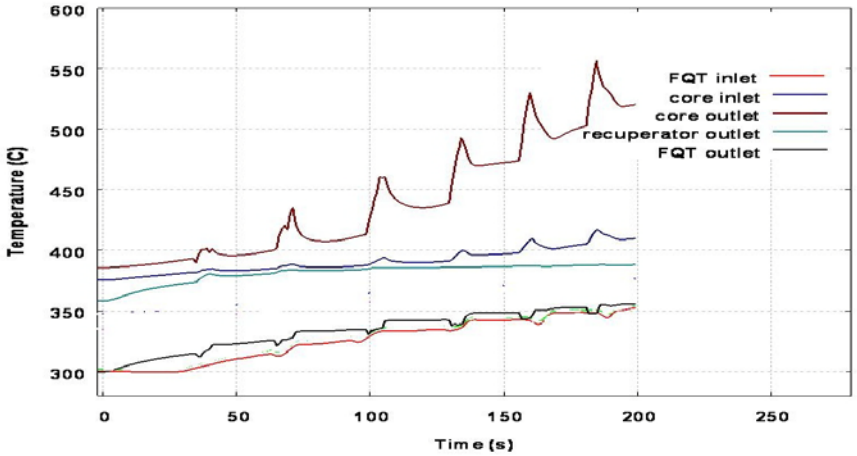

Figure 9. Coolant temperatures in the FQT primary loop.

The pressure in the cold leg (CL), in the core outlet and in the pressurizer(PRZ) can be seen in Figure 10.

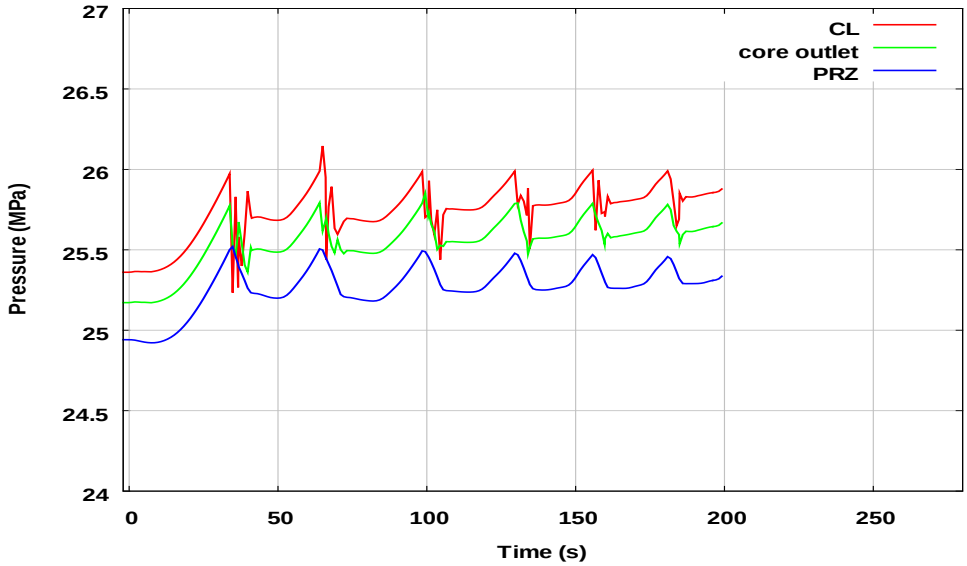

Figure 10. Coolant pressures in the FQT primary loop.

At 26. MPa pressure, the pressure relife valve opens in 0.5 s and closes again. The mass flow rate of the spring loaded pressure reliefe valve reaches 0.12 kg/s. The cladding and fuel centerline temperature evolution of the test fuel rods can be seen in Figures 11 and 12.

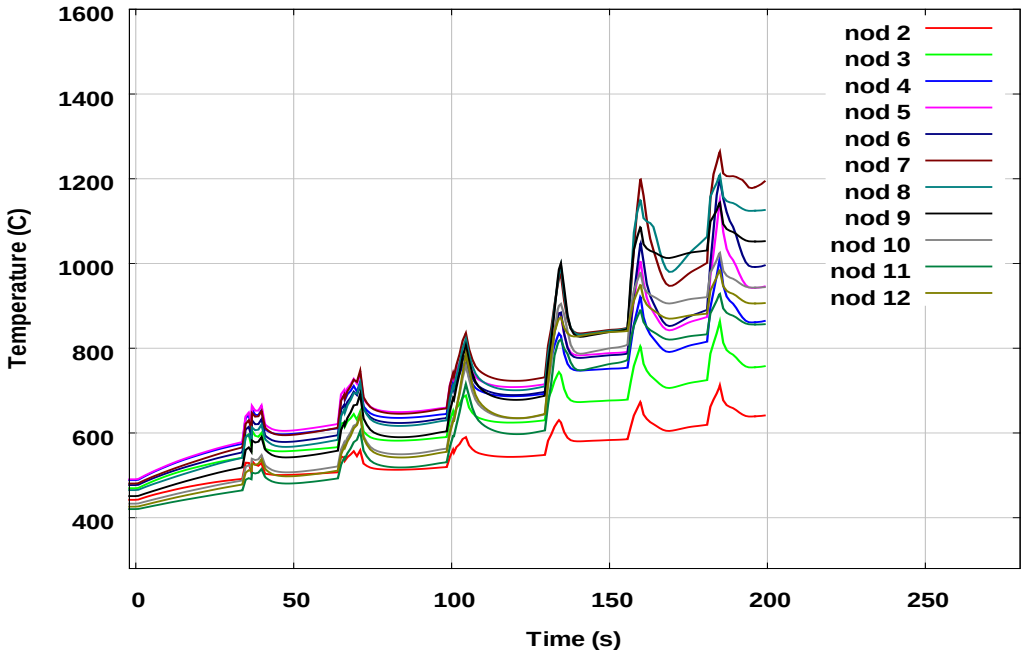

Figure 11. Clad surface temperatures of the FQT fuel pins in 11 layers (2-12).

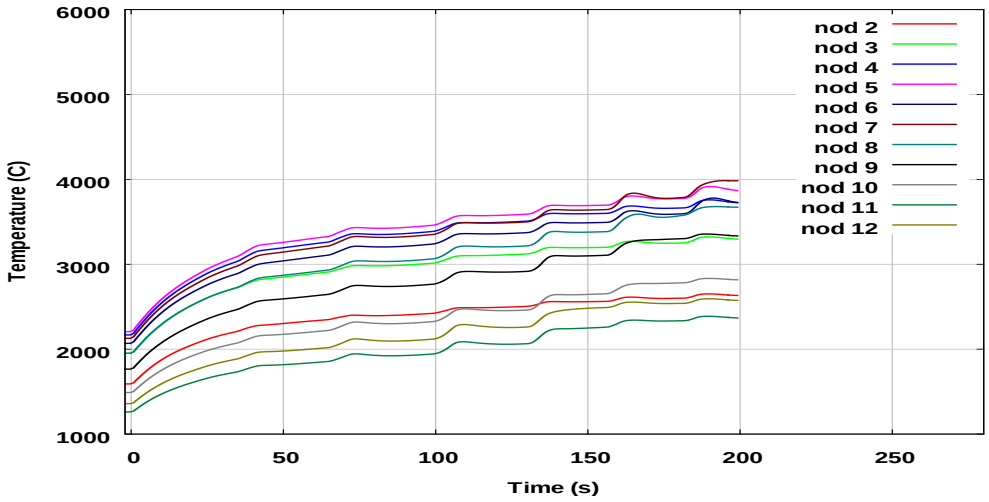

Figure 12. Fuel centerline temperatures of the FQT fuel pins in 11 layers (2-12).

The fuel cladding temperature limit of 1260 C for postulated accidents is exceeded at 183. s while the fuel melting temperature of 2865 C is reached in the centerline very soon at 19. s. For all the 5 power cases considered in the parametric study the fuel centerline temperature is limiting. The maximum calculated pressure of 26.8 MPa is far from the design pressure of 30. MPa.
The fuel integrity in the time sequence is jeopardized by the fuel centerline temperature in the first place. To try to avoid fuel melting in ATWS transients, the results of the coupled KIKO3D-ATHLET calculations can be used.
The main considerations in the ATWS calculations:

- The reactor period signal limit of SCRAM has no effect.
- The 120% power signal limit of SCRAM has no effect.
- The maximum insertable reactivity limit is observed by the operator.
- Minimum β_{eff}
- The inserted reactivity by the withdrawn rod is subject to parametric studies
- Weak feedback parameters
- FQT power tuned to higher value

Three calculations were carried out with reactivity insertion of 2.7, 5.9 and 10. ¢.
The reactivity curves and the total power of LVR-15 can be seen in Figures 13 and 14 The resulting fuel centerline temperatures in the FQT test section are depicted in Figure 15.

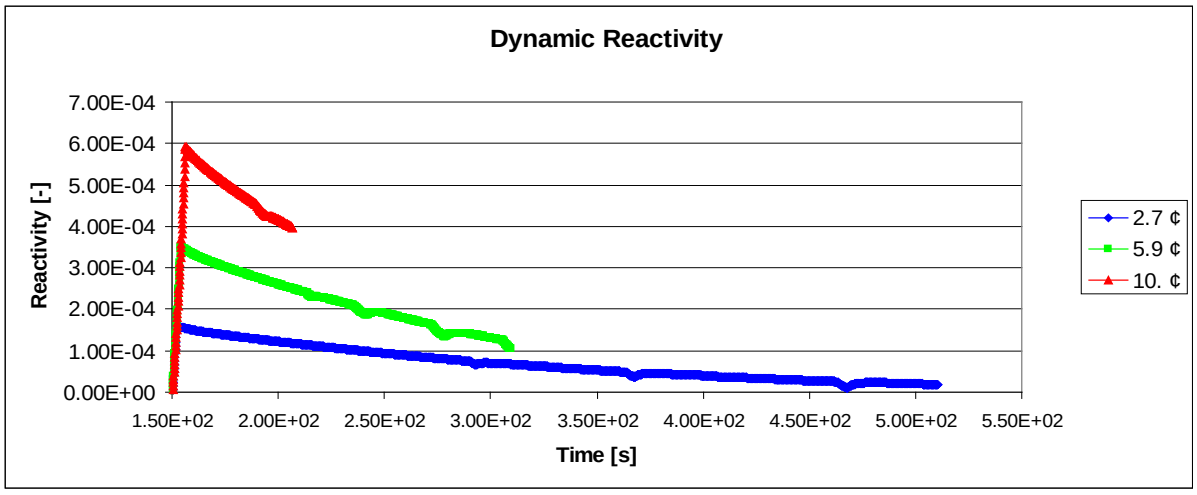

Figure 13. Reactivity of the LVR-15 research reactor during ATWS.

.

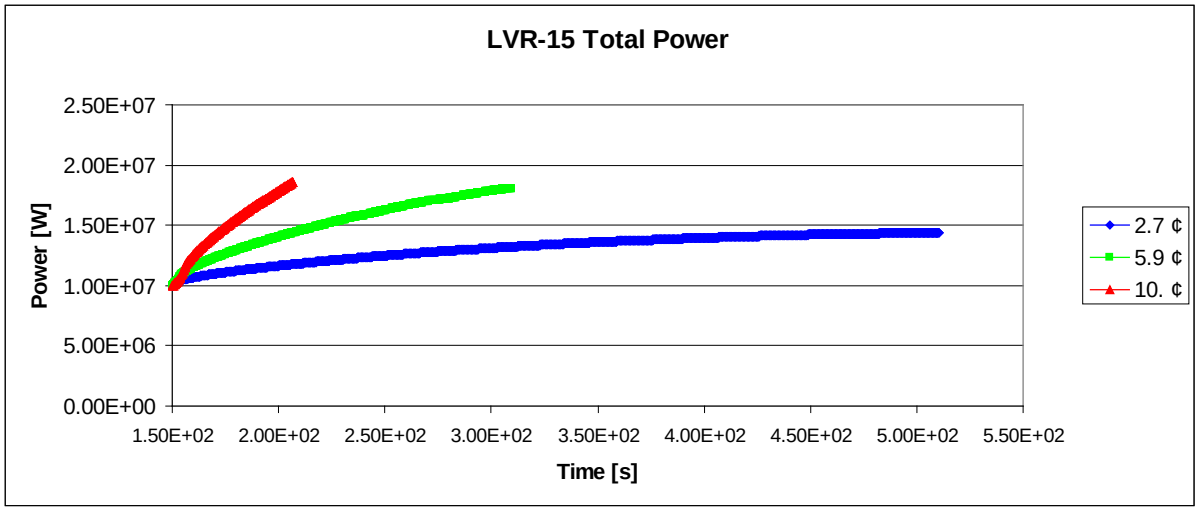

Figure 14. The total power of the LVR-15 research reactor during ATWS.

.

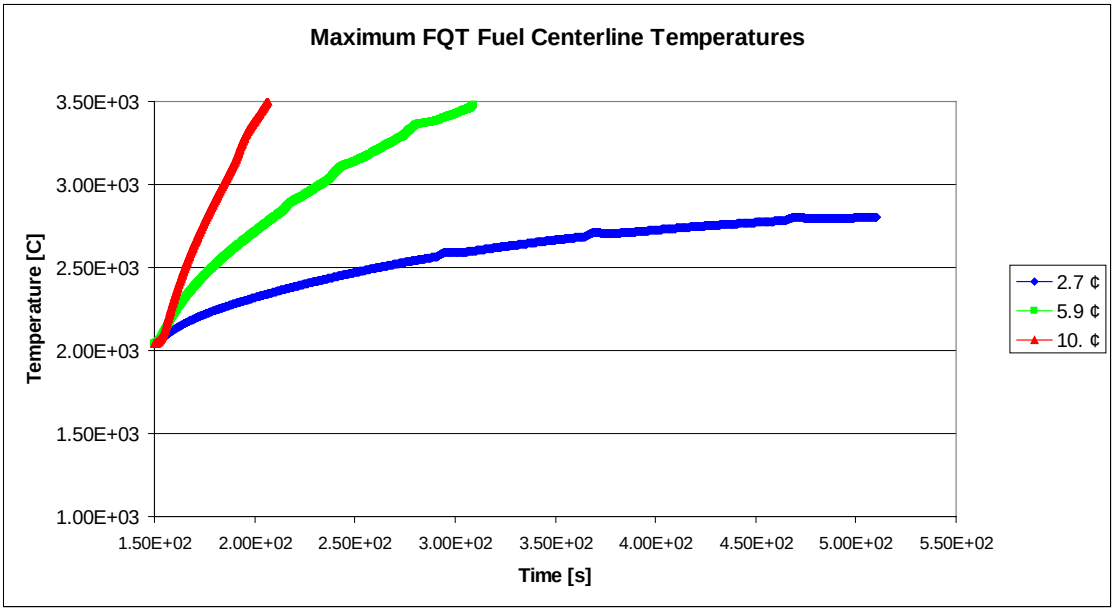

Figure 15. Maximum fuel centerline temperatures of the FQT fuel pins during ATWS.

The available time for operator intervention after the 110% power warning level for reactivity insertions of 2.7, 5.9 and 10. ¢. are >339, 61 and 24 s respectively. The operator can insert the control rods manually. In case of the 2.7 ¢ reactivity insertion the melting temperature was not reached during the calculation, but the operator intervention is necessary even in this case, as the increased burn-up of Xe-135 at elevated power results in reactivity insertion and further power increase.

4. Conclusion

In case of the unadvertent control rod withdrawal with SCRAM (Anticipated Operational Occurence) the 120% power limit for SCRAM in LVR-15 limits the power of FQT fuel rods. As the test section is operated at coolant temperatures below the pseudo-critical point, the coolant temperature rise is minimal during the rod withdrawal, the clad and fuel centerline temperatures are far from AOO limits of 850 C for clad and melting temperature for UO2. The pressure rise is mild during the transient.
In case of the unadvertent control rod withdrawal without SCRAM, the pressure relief valve effectively controls the pressure increase in the FQT loop as described in the parametric study. However, the fuel integrity is jeopardized by the fuel centerline temperature. To avoid FQT fuel melting during ATWS transients, LVR-15 operator intervention times were calculated for a number of inserted reactivity values.

5. Acknowledgement

This work has been funded by the European Commission under SCWR-FQT project, contract number 269908.

References

1. M. Ruzickova, T. Schulenberg, D.C. Visser, R. Novotny, A. Kiss, C. Maraczy, A. Toivonen Overview and progress in the European project: “Supercritical Water Reactor - Fuel Qualification Test” Progress in Nuclear Energy, 77, pp. 381-389 (2014)

2. M. Ruzickova, A. Vojacek, T. Schulenberg, D.C. Visser, R. Novotny, A. Kiss, C. Maraczy, A. Toivonen European Project “Supercritical Water Reactor – Fuel Qualification Test” (SCWR-FQT): Overview, Results, Lessons Learnt and Future Outlook , ISSCWR-7 Proceedings, 15-18 March 2015, Helsinki, Finland, Paper ISSCWR7-1054.

3. A. Keresztúri, Gy.Hegyi, L. Korpás, Cs. Maráczy, M. Makai and M. Telbisz, “General features and validation of the recent KARATE-440 code system”, Int. J. Nuclear Energy Science and Technology, Vol. 5, No. 3, pp. 207–238. (2010).

4. Cs. Hegedűs, Gy. Hegyi, G. Hordósy, A. Keresztúri, M. Makai, Cs. Maráczy, F. Telbisz, E. Temesvári, P. Vértes, “The KARATE Program System”, PHYSOR 2002, Seoul, Korea, October 7-10 (2002)

5. Cs. Maráczy, Gy. Hegyi, I. Trosztel, G. Hordósy, Á. Brolly "RIA Analysis of the SCWR-FQT Facility in the LVR-15 Research Reactor" The 19th Pacific Basin Nuclear Conference (PBNC 2014), Vancouver, Canada, August 24-28, (2014).

6. A. Keresztúri, Gy. Hegyi, Cs. Maráczy, I. Panka, M. Telbisz, I. Trosztel and Cs. Hegedűs, “Development and validation of the three-dimensional dynamic code - KIKO3D”, Annals of Nuclear Energy, Vol. 30, No.1, pp. 93-120. (2003).

7. Cs. Maráczy, A. Keresztúri, I. Trosztel and Gy. Hegyi, ”Safety analysis of reactivity initiated accidents in a HPLWR reactor by the coupled ATHLET-KIKO3D code”, Progress in Nuclear Energy, Vol. 52, pp. 190-196. (2010).

8. A. Keresztúri, Cs. Maráczy, Gy. Hegyi, I. Trosztel and I. Pataki, "Safety Analyses of Reactivity Initiated Accidents (RIA) and Anticipated Transients Without SCRAM (ATWS) of the Budapest Research Reactor", RRFM 2008 Transactions, March 2-5, 2008, Hamburg, Germany, ISBN 978-92-95064-04-1, pp. 122-132., (2008).

ISSCWR7-2020

A new correlation of a heat transfer coefficient in supercritical water

A.N. Churkin
OKB «GIDROPRESS»
st. Ordzhonikidze, 21, Podolsk, Moscow reg., 142103, Russian Federation
+ 7-4967-65-26-01, churkin@grpress.podolsk.ru

V.I. Deev, V.S. Kharitonov
National Research Nuclear University "MEPhI"
Kashirskoe sh., 31, Moscow, 115409, Russian Federation
+ 7-495-324-73-28, videev@mephi.ru, vskharitonov@mephi.ru

Abstract

The paper presents the results of the development of a new empirical correlation for normal heat transfer in the flow of supercritical water in vertical heated pipes. When deriving this correlation the task was to get enough simple relationship which would predict the heat transfer coefficient with an acceptable degree of accuracy. Another requirement was to ensure the asymptotic transition to well-known relationships for heat transfer of a single-phase coolant away from pseudocritical temperature where thermal properties can be considered permanent. The new correlation bases on the processing of more than 3,000 experimental points for water from 12 primary sources. The comparison with several other correlations conducted with more than 4,000 experimental points from 20 works carried out in different years in Russia and other countries has shown that the new equation provides better convergence of computational and experimental data in a wide range of parameters. In the comparative analysis of different correlations the wall temperature, measured in the experiments, was not used in the calculations. The heat transfer coefficient and the wall temperature were determined by the iteration. Also the results of a numerical study are presented, the purpose of which was to establish the areas of the ambiguity that arises in the calculation of the heated wall temperature using the new correlation.

1. Introduction

Currently under the development in different countries, the concepts of supercritical water-cooled reactors (SCWR) have several potential advantages compared with conventional boiling reactors or pressurized water reactors [1]. They are distinguished, first of all, by high-energy conversion efficiency (high efficiency) and relatively low capital construction costs. Russian version of SCWR (VVER-SCP) [2, 3], as well as the concept of Japanese project Super Fast Reactor [4] also provide a significant tightening of the neutron spectrum in the core, that allows to increase the breeding ratio of nuclear fuel.

When creating such a new and high technology, which is used in SCWR, the international cooperation is highly desirable. Therefore, a part of work is coordinated by the IAEA and the International Forum "Generation IV".

One of the most urgent tasks for SCWR is to provide acceptable fuel cladding temperature during normal operation, transients and design accidents. Therefore, an extremely important

factor is the ability to predict the temperature of the fuel claddings. For this purpose, system and subchannel thermal-hydraulic codes, as well as the methods of computational hydrodynamics (CFD) are used.

The use of methods of computational hydrodynamics faces a number of difficulties, which were reflected in a series of papers (see, for example, [5-8]).

Thermal-hydraulic system codes with one-dimensional hydrodynamics are applied to analyse transients and design accidents. The correct prediction of the temperature of fuel claddings requires special correlations suitable for the calculation of the heat transfer coefficient in the bundles of fuel rods. Unfortunately, so far very little experiments with bundles have been done, and now significant efforts are made to obtain the missed experimental data (see., for example, [9, 10]).

In subchannel thermal-hydraulic codes for the analysis of both steady-state and transient conditions the correlations obtained for the pipes are commonly used, and numbers of similarity based on the hydraulic or heat diameter of the channels are applied.

By now a great amount of experimental data on heat transfer to water moving in the pipes at pressure above the critical value is accumulated. In the supercritical pressure (SCP), in the ranges typical of concepts SCWR, and within temperatures close to critical or pseudocritical temperature, there is a strong change in thermophysical properties of water. It leads to very significant features of flow and heat transfer processes that were found in earlier experiments [11 - 26], which were carried out to study heat transfer in the steam-generating pipes of boilers designed for supercritical steam parameters.

The analysis of the obtained results has shown that heat transfer in pipes with SCP water can have different character. According to the classification proposed by Petukhov [27], all conditions of heat transfer in the coolant with supercritical parameters, should be divided into three main types: normal conditions, deteriorated and improved heat transfer. In the conditions with normal heat transfer the temperature of heat-release wall varies smoothly along the pipe. The observed regularities can be roughly described on the basis of known representations of the effect on turbulent transport processes of variability of physical properties of the liquid. At small temperature differences, when the fluid properties in the flow vary slightly, these conditions do not have any specific characteristics, heat transfer in them is described by the usual relationships for constant properties. In the conditions of deteriorated heat transfer due to the reduction of the local heat transfer coefficient, the wall temperature of some sections of the pipe may initially increase sharply and then decrease again. In general case the possibility of the occurrence and the nature of the manifestation of deteriorated heat transfer depend strongly on the orientation of the pipe in the gravitational field, its diameter, flow parameters (pressure, mass velocity and enthalpy of water at the input of the pipe, heat flux density at the wall). The nonmonotonic wall temperature distribution (maximums or "peaks" of temperature) may occur near the entrance to the pipe as well as in those of its sections where the flow enthalpy reaches a value corresponding to the area of pseudophase transition.

In the 60-80s of the last century, different authors attempted to obtain generalized correlations describing heat transfer in water and in other media at supercritical pressures. Among the formulas developed by Russian scientists, for example, the relationships proposed by Miropolskii and Shitsman [28], Krasnoshchokov and Protopopov [29], Petukhov et al. [30] are well known. Among the specialists generalized correlations obtained in other countries - Bishop equation [12], Svensson equation [13] Jackson equation [31] and some others have become widely known. A detailed analysis of the results of the early stage of studies conducted in different countries, was made in 1978 by Hall and Jackson [31] in the review lecture given at the 6th International Conference on Heat Transfer. A fairly complete review of a number of relationships and their comparison with the existing experimental data is contained in the extensive monograph by Pioro and Duffy [32] as well as in some other reviews, for example in [33 - 35].

The analysis of numerous materials on this subject led to the general conclusion that none of the proposed equations still can not satisfactorily describe the effect of a kind of change of water thermal properties in supercritical pressures on heat transfer in a wide range of governing parameters. Recently, it has been also suggested [33, 35], that the revision of the value of previously proposed computational recommendations for amending them is required. The ground is the introduction in 1997 of a new standard of water properties IAWPS-97, which

substantially clarified the standard dependecies of viscosity, thermal conductivity and Prandtl number on temperature and pressure near the critical point [36].

In recent years new experimental data on heat transfer in SCP water have been published [37 - 40]. The prospects for the use of SCP water in nuclear power, taking into account specific requirements for the reliability of the cooling of reactor cores have caused an increased interest in researches on the improvement and the development of new methods for the calculation of heat transfer in supercritical water. The results of the latest achievements in this problem were the subject of a number of published papers and scientific papers at the international conferences and symposiums.A particular attention is paid to the prediction and the description of the conditions of deteriorated heat transfer, which are dangerous for the fuel elements of a nuclear reactor and therefore should be completely excluded. However, as before an urgent task remains the creation of well-founded relationhips for normal conditions, where there is no significant effect of buoyancy forces and thermal acceleration [35]. Obviously, these relationships must be carefully designed and validated by a great number of experimental data.

This paper presents the results of a new empirical correlation for the flow of supercritical water in vertical heated pipes. When deriving this correlation the task was to get enough simple relationship which would predict the normal heat transfer coefficient with an acceptable degree of accuracy. Another requirement is to ensure the asymptotic transition to well-known equations for heat transfer of single-phase coolant away from pseudocritical temperature where thermal properties can be considered permanent. On the basis of the published experimental data, a comparative analysis of the correlation developed by the authors and some other generalized correlations of the greatest interest to the design practice is conducted. The areas of ambiguity that arises in the calculations of the heated wall temperature using the new correlation are identified.

2. The description of the proposed equation

A new generalized correlation was obtained in our previous paper [41]. It allows the calculation of heat transfer to supercritical water forced flow in vertical pipes. The selection of the structure of the calculation equation is based on the experience of generalization of experimental data of heat transfer to different media at supercritical pressures. In particular, the method applied in paper [42] was used, where generalized heat transfer correlation was obtained for the case of natural convection of various fluids (helium, carbon dioxide and water) in the supercritical state. The formula for heat transfer in the developed turbulent flow, commonly known as Dittus–Boelter correlation [43], is used as a basis for new equation of forced flow

$$\mathrm{Nu}_0 = 0.023\,\mathrm{Re}_b^{0.8}\,\mathrm{Pr}_b^{0.4}. \qquad (1)$$

In formula (1) the values of Nusselt number Nu_0, Reynolds number Re_b and Prandtl number Pr_b contain the fluid properties at a given pressure p and bulk coolant temperature t_b in the calculated channel cross-section.

Two correction factors are introduced into the equation to account for the dependence of thermophysical water parameters on temperature and pressure. The first of them is the ratio of water density at wall temperature ρ_w and bulk fluid temperature ρ_b, the second – a ratio of average integral heat capacity along the channel cross-section at constant pressure $\overline{c_p}$ to the same parameter at bulk temperature $c_{p\,b}$. Thus, the final equation is

$$\mathrm{Nu}_b = \mathrm{Nu}_0 \left(\frac{\rho_w}{\rho_b}\right)^m \left(\frac{\overline{c_p}}{c_{p\,b}}\right)^n, \qquad (2)$$

where the average integral heat capacity is expressed, as usual, by the ratio of the corresponding differences of water enthalpies h and temperatures t and it is found as $\overline{c_p} = (h_w - h_b)/(t_w - t_b)$.

In paper [41] to determine the values m and n in the equation (2) the experimental results obtained in the normal heat transfer regimes in SCP, water upflow and downflow in vertical pipes of different diameters d and length L were used. We considered not only the data of early works but also the results of the recent studies which were not used in the preparation of the generalized calculated correlations. A list of these works with a brief description of the test sections and studied ranges of operating parameters (pressure p, mass velocity G, heat flux density q on the wall and fluid enthalpy in the pipe h_b) is shown in Table 1.

Table 1. Characteristics of experimental data used in the work [41] in the derivation of equation (3)

Authors, year [number of reference], number of experimental points	Test section			Ranges of operating parameters			
	d, mm	L, m	Flow direction	p, MPa	G, kg/(m^2 s)	q, kW/m^2	h_b, kJ/kg
Shitsman, 1963 [11], 196	8	1.5	Upflow	22.6; 23.5; 24.5	323 – 1500	233 – 1083	262 – 2477
Bishop et al., 1964 [12], 397	2.54; 5.08	0.6; 2; 3	Upflow	22.9 – 27.8	662 – 3600	320 – 3460	1187 – 3263
Swenson et al., 1965 [13], 166	9.42	1.83	Upflow	22.8; 31.0	2153	791; 1745	551 – 2910
Vikhrev et al., 1967 [14], 354	20.4	6	Upflow	26.5	495; 1400	362 – 930	275 – 2565
Ackerman, 1970 [17], 248	9.4; 18.5; 24.4	1.83; 2.74	Upflow	22.8; 24.8; 31	406; 541; 677; 1218	158 – 1260	391 – 2546
Belyakov et al., 1971 [18], 12	20	6.5 – 7.5	Upflow	24.5	1150	669	627 – 2926
Yamagata et al., 1972 [21], 152	7.5	1.5	Upflow	24.5	1260	233 – 930	1515 – 2650
Krasyakova et al., 1977 [25], 246	20	3.5	Downflow	24.5	300 – 1000	270 – 900	855 – 2510
Kirillov et al., 2005 [37], 867	10	4	Upflow	24	1000; 1500	388 – 884	1449 – 2709
Pis'menny et al., 2005 [38], 62	9.5	0.6	Upflow Downflow	23.5	509 248	101 – 515	437 – 905
Yongliang et al., 2011 [39], 97	6	3	Upflow	23; 24; 25	649 – 1207	600 – 860	1225 – 2765
Hong-bo et al., 2013 [40], 395	7.6	2.64	Upflow	23; 25; 26	448 – 1215	189 – 1150	1231 – 2653

The analysis of the experimental data showed that the value m in the formula (2) is the best to choose to be 0.25. The results of processing of the experimental data of works presented in Table 1 are shown in Figure 1 with coordinates corresponding to this formula. Two regularities are clearly seen from the figure: in the region $\overline{c_p} / c_{p\,b} \geq 1$ the experimental data are described by the equation (2) with the index n = 0.4, and at $\overline{c_p} / c_{p\,b} < 1$ with n = 0.6.

As a result, a new generalized correlation proposed in paper [41] can be written as

$$Nu_b = 0.023\,Re_b^{0.8}\,Pr_b^{0.4}\left(\frac{\rho_w}{\rho_b}\right)^{0.25}\left(\frac{\overline{c_p}}{c_{p\,b}}\right)^{n},\ n=\begin{cases}0.4 & \text{at} \quad \overline{c_p}/c_{p\,b}\geq 1\\ 0.6 & \text{at} \quad \overline{c_p}/c_{p\,b}<1\end{cases}. \tag{3}$$

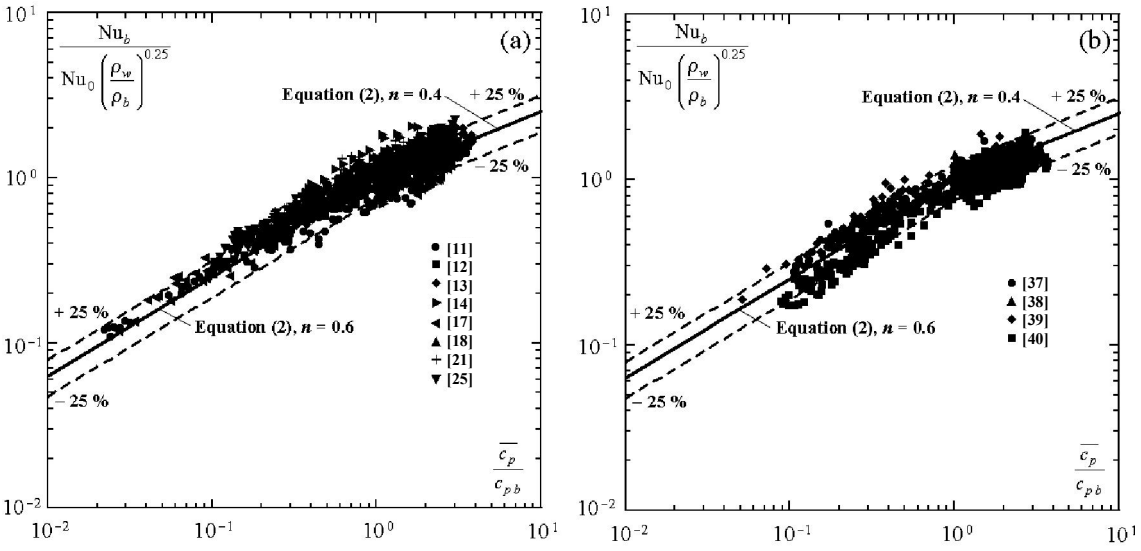

Figure 1. Processing of the experimental data by the equation (2): (a) – early works; (b) – works since 2005.

It should be noted that unlike a well-known method of Krasnoshchekov–Protopopov [29][1], where it is necessary to distinguish three regions of state defined by two parameters (T_b/T_m and T_w/T_m), it is sufficient to consider only two regions delimited by the value $\overline{c_p}/c_{p\,b}$ = 1 in method [41]. Obviously, this circumstance quite significantly simplifies the calculations of heat transfer coefficient, particularly, in cases when the wall temperature is unknown in advance.

All experimental results used in the derivation of the expression (3), originally consisted of a little more than 3000 experimental points for water of 12 original works. The wall temperatures measured in the experiments were used in the calculation of the corrections to Dittus–Boelter formula (the so-called T-method [35]). In this case, as it is evident from Figure 1, the dispersion of the experimental data near the calculated values mainly does not exceed ± 25%.

3. Comparative assessment of the correlations

For comparative assessment of the correlations of heat transfer features in normal SCP regimes except the equation (3), the correlations recently obtained by Cheng et al. [44], Mokry et al. [45] were chosen, as well as one of the variants of the generalized correlation proposed recently by Kurganov et al. [35]. The final goal of the analysis was to compare the relative deviations of heat transfer coefficients found from the equations of the above-mentioned papers from experimental data.

The equation system of Cheng et al. [44]

$$\mathrm{Nu}_b = 0.023\,\mathrm{Re}_b^{0.8}\,\mathrm{Pr}_b^{1/3}\,F(\pi_A),\quad F = \min\,(F1, F2), \tag{4}$$

where $F_1 = 0.85 + 0.776(\pi_A\cdot 10^3)^{2.4}$, $F_2 = 0.48/(\pi_{A\,m}\cdot 10^3)^{1.55} + 1.21(1 - \pi_A/\pi_{A\,m})$, is the new correlation structure which does not contain the wall surface temperature that is unknown in advance. The bulk water temperature in the given cross-section of the channel determines all coolant properties necessary to calculate the local heat transfer coefficient. The correction

[1] The similar method is also used in Jackson's paper [18].

function $F(\pi_A)$, which takes into account the deviation of the experimental data from the calculation results obtained by the heat transfer equation for constant properties, includes only one dimensionless value $\pi_A = \beta_b q/(c_{p\,b} G)$ – "acceleration number", where β_b is a coefficient of thermal expansion of the fluid. The authors [44] used the data from 6 sources (data of Bishop, Swenson, Herkenrath, Yamagata, Griem, Xu) to compare the calculated values with the experimental results. According to [44] the relative deviations of all considered experimental data from the values of heat transfer coefficient that have been determined using the equation (4) were $\sigma_a = -0.07$, $\sigma_{st} = 0.306$.

The correlation developed by Mokry et al. [45] for SCP water

$$\mathrm{Nu}_b = 0.0061 \mathrm{Re}_b^{0.904} \overline{\mathrm{Pr}}_b^{0.684} \left(\frac{\rho_w}{\rho_b} \right)^{0.564} \tag{5}$$

was mainly established basing on the experimental results performed in IPPE [37]. The experimental data from some other sources were involved in work in addition. On the whole, the experimental data spread along the proposed correlation was of $\pm$ 25% for the heat transfer coefficient values and of $\pm$ 15% for the wall temperatures. The authors [46] recommend to use the equation (5) in the following ranges of operating parameters: pressure p = (22.8 – 29.4) MPa; heat flux density q = (70 – 1250) kW/m^2; mass fluid velocity G = (200 – 1500) kg/(m^2 s); pipe inner diameter d = (3 – 38) mm. Mokry et al. formula includes average Prandtl number $\overline{\mathrm{Pr}}_b = \mu_b \overline{c_p} / \lambda_b = \mathrm{Pr}_b \overline{c_p} / c_{pb}$.

The detailed comparative analysis of the existing recommendations for calculation of heat transfer in SCP water was performed in paper [47]. In all, 12 generalized correlations proposed by various authors during the period 1964 – 2010 were considered (including the equation (4) and (5)). The comparison with the extensive bank of the experimental data showed that Mokry et al. equation (5) predicted the heat transfer coefficient best in all studied ranges of parameters determining heat transfer at supercritical pressures [47].

On the basis of the extended Reynolds analogy between heat transfer and friction in turbulent flow, the authors [35] proposed several modifications of the generalized correlation for calculating normal heat transfer in SCP water.[2] The Stanton number $\mathrm{St} = q/[G(h_w - h_b)]$ has been used in the heat transfer equation as a dimensionless characteristic defined by the difference of water enthalpies at wall temperature t_w and bulk temperature t_b. In the variant analyzed further, the calculated Kurganov et al. equation is as follows:

$$\mathrm{St} = \frac{\xi/8}{1 + \dfrac{900}{\mathrm{Re}_b} + 12.7 \sqrt{\xi/8}\, (\overline{\mathrm{Pr}}_{b\text{-}w}^{2/3} - 1)}, \tag{6}$$

where the friction coefficient ξ is determined from the expression $\xi = (1.82 \log \mathrm{Re}_b - 1.64)^{-2} (\rho_w/\rho_b)^{1/3} (\mu_w/\mu_b)^{1/5}$, containing two correction factors to allow for change the density and viscosity of water along the pipe cross-section. Here the average integral Prandtl number is defined as $\overline{\mathrm{Pr}}_{b\text{-}w} = \dfrac{\overline{c_p}}{\overline{(\lambda/\mu)}}$, where $\overline{(\lambda/\mu)} = \dfrac{1}{t_w - t_b} \int_{t_b}^{t_w} \dfrac{\lambda}{\mu} \mathrm{d}t$, so when calculating by formula (6) not only specific heat capacity but also the ratio of thermal conductivity to the viscosity coefficient are subjected to averaging within temperatures t_w, t_b.

It should be emphasized that formulas (3) (5) and (6), however, like many other well-known generalized correlations, contain unknown wall temperature in advance. When using the expressions of this structure to determine the calculated value of heat transfer coefficient the value t_w must be a solution of the corresponding nonlinear equation (Q-method [35]) that requires the iterative procedures. It is important to consider when comparing the computational and experimental data, otherwise, as it is fairly pointed out in [35], the results of such analysis cannot be considered representative. It will also be mind that the non-linearity of the original

[2] Kurganov et al. correlations [35] were not considered in paper [47].

equations can cause the ambiguity of calculated wall temperature [48, 49], and in some ranges of operating parameters the solution of the nonlinear heat transfer equation may be absent altogether.

The results of another 8 experimental studies (Table 2) were subjected to the processing in order to the comparative assessment in addition to the data from the sources listed in Table 1. The experimental data obtained in deteriorated heat transfer regimes (regimes with sharp maximum, or "peaks" of wall temperature along the pipe) were excluded in all calculations. On the whole, the set of the examined data was more than 4000 experimental points. It covers the following range of geometrical and operational parameters: pipe inner diameter d = (2.5 – 32) mm; pressure p = (22.5 – 39.2) MPa; mass velocity and enthalpy of fluid flow respectively G = (193 – 3600) kg/(m^2 s), h_b = (120 – 3263) kJ/kg; heat flux density on a pipe wall surface q = (101 – 3460) kW/m^2.

Table 2. Characteristic of additional experimental data for the comparative assessment

Authors, year [number of reference], number of experimental points	**Test section**			**Ranges of operating parameters**			
	d, mm	L, m	Flow direction	p, MPa	G, kg/(m^2 s)	q, kW/m^2	h_b, kJ/kg
Shitsman, 1968 [15], 100	8; 16	1.6; 3.2	Downflow	24.5	354 – 577	300 – 580	510 – 2629
Alferov et al., 1969 [16], 162	20	1.88; 2	Upflow	24.5; 26.5; 29.4	328; 342	351 – 521	263 – 1122
Ornatsky et al., 1971 [19], 79	3	0.75	Upflow Downflow	25.5	850 – 1530	395 – 1810	120 – 1500
Glushchenko et al., 1972 [20], 56	4; 6; 8	0.35 – 1.0	Upflow	22.5	750; 1000	1050 – 1770	150 – 2710
Alferov et al., 1975 [22], 32	20	3.7	Downflow	26.5	447	480	345 – 1065
Alekseev et al., 1976 [23], 168	10.4	0.5; 0.75	Upflow	24.5	380; 650	270 – 560	443 – 1710
Ishigai et al., 1976 [24], 365	3.92	0.625	Upflow	24.5; 39.2	500; 1000	140 – 826	949 – 3051
Watts and Chou, 1982 [26], 80	25.4; 32.2	2	Upflow Downflow	25	193 – 617	175; 250	629 – 905

Table 3 illustrates the comparison of the results of the calculation of heat transfer coefficient using the equation (3) and the formulas (1), (4) – (6) with the experimental data presented in Tables 1 and 2. The wall surface temperature when calculating the corrections for the change of thermophysical water properties in all appropriate cases was determined by the iteration.

Relative arithmetic mean σ_a and root-mean-square σ_{sq} deviations of the computational data from the experimental data were calculated according to the formulas

$$\sigma_a = \frac{1}{N}\sum_{i=1}^{N}(x_i - 1);$$

$$\sigma_{sq} = \frac{1}{\sqrt{N-1}}\sqrt{\sum_{i=1}^{N}(x_i - 1)^2},$$

where N – the number of data subjected to the statistical processing; $x = \alpha_{calc}/\alpha_{exp}$ – the ratio of the calculated heat transfer coefficient to the experimental value.

Table 3. Deviation of computational and experimental data

Authors, year [number of reference], number of experimental points	**Dittus–Boelter, equation (1)**		**Deev et al., equation (3)**		**Cheng et al., equation (4)**		**Mokry et al., equation (5)**		**Kurganov et al., equation (6)**	
	σ_a	σ_{sq}	σ_a	σ_{sq}	σ_a	σ_{sq}	σ_a	σ_{sq}	σ_a	σ_{sq}
Shitsman, 1963 [1], 196	0.911	2.178	–0.048	0.168	0.004	0.344	–0.191	0.301	0.130	0.373
Bishop, 1964 [2], 397	0.949	1.426	0.020	0.218	–0.049	0.208	–0.279	0.341	0.100	0.239
Swenson, 1965 [3], 166	0.226	0.429	–0.010	0.144	–0.008	0.229	0.009	0.119	0.041	0.105
Vikhrev, 1967 [4], 354	0.273	0.539	–0.041	0.241	–0.073	0.180	–0.112	0.209	–0.025	0.153
Shitsman, 1968 [5], 100	0.795	1.356	0.192	0.250	0.038	0.187	–0.263	0.347	0.215	0.350
Alferov, 1969 [6], 162	0.330	0.359	0.305	0.337	0.199	0.255	–0.039	0.211	0.120	0.177
Ackerman, 1970 [7], 248	0.709	2.012	0.105	0.188	0.063	0.342	–0.031	0.198	0.158	0.315
Belyakov, 1971 [8], 12	0.139	0.467	–0.219	0.267	–0.163	0.200	–0.227	0.252	–0.154	0.184
Ornatskiy, 1971 [9], 79	0.233	0.295	0.224	0.288	0.056	0.166	–0.028	0.215	0.132	0.225
Glushchenko, 1972 [10], 56	0.697	2.259	0.043	0.169	0.019	0.263	–0.225	0.294	–0.150	0.357
Yamagata, 1972 [11], 152	0.149	0.406	–0.201	0.281	–0.100	0.246	–0.118	0.244	–0.042	0.125
Alferov, 1975 [12], 32	–0.101	0.138	–0.116	0.150	–0.211	0.241	–0.287	0.295	–0.228	0.243
Alekseev, 1976 [13], 168	0.178	0.248	0.189	0.255	0.081	0.191	–0.221	0.294	0.073	0.169
Ishigai, 1976 [14], 365	0.009	0.445	–0.173	0.308	–0.225	0.305	–0.349	0.382	–0.149	0.278
Krasyakova, 1977 [15], 246	0.444	0.970	–0.205	0.267	–0.236	0.289	–0.438	0.494	–0.184	0.243
Watts, Chou, 1982 [16], 80	–0.103	0.199	–0.108	0.203	–0.233	0.273	–0.255	0.314	–0.175	0.242
Kirillov, 2005 [27], 867	0.712	1.115	–0,092	0,218	0.045	0.232	–0,031	0,175	0.156	0.241
Pis'menny, 2005 [28], 62	–0.055	0.104	–0.066	0.113	–0.183	0.202	–0.221	0.274	–0.134	0.182
Yongliang, 2011 [29], 97	0.659	0.957	–0.108	0.261	–0.064	0.186	–0.239	0.268	0.059	0.183
Hong-bo, 2013 [30], 395	0.427	0.992	0.077	0.181	–0.060	0.185	–0.170	0.307	0.116	0.260
All data 4234	0.486	1.132	–0.022	0.233	–0.038	0.244	–0.164	0.286	0.049	0.244

Table 3 shows that calculations by formula (3) give the best agreement with the considered set of experimental results. Heat transfer description in supercritical water can also be quite satisfactory obtained by using formulas (4) and (6) in the calculations. As a whole, the first of them gives a little understated values of heat transfer coefficients, and the second, on the contrary, overstated. The most considerable differences between the computational and experimental data are observed when using Dittus–Boelter formula (1). It is not surprising, and once again demonstrates the unfitness of this formula at supercritical pressures.

In PWR-type reactors, including SCWR, the temperature of fuel element claddings is one of the main parameters which limit the thermal power of the core. Therefore it is important to assess how correctly this or that formula determines the calculated value of the heated wall temperature. Figures 2 – 9 show some examples where the results of wall temperature calculations t_w by formulas (1) – (6) are compared with the experimental data from papers [12, 13, 15, 25, 37 – 40]. This figure also shows the calculated wall temperature with a few additional well-known from published sources correlations [50 – 53]. It is evident that the equation proposed by the authors (3) describes quite satisfactory the features of the wall temperature changes with the enthalpy increase of water along the channel.

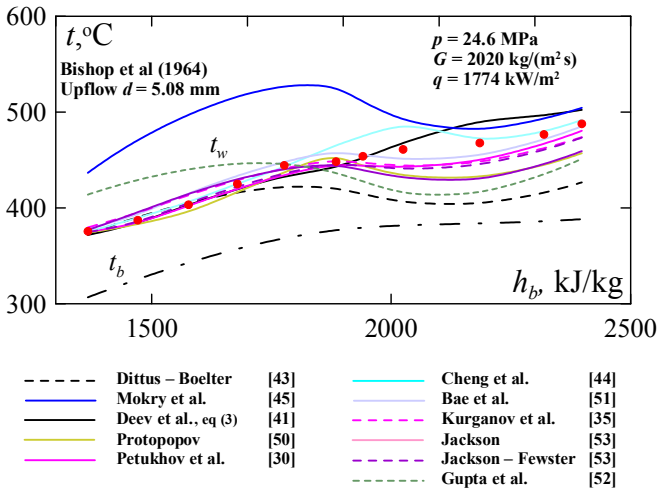

Figure 2. Comparison of calculated and experimental [12] values of the wall temperature

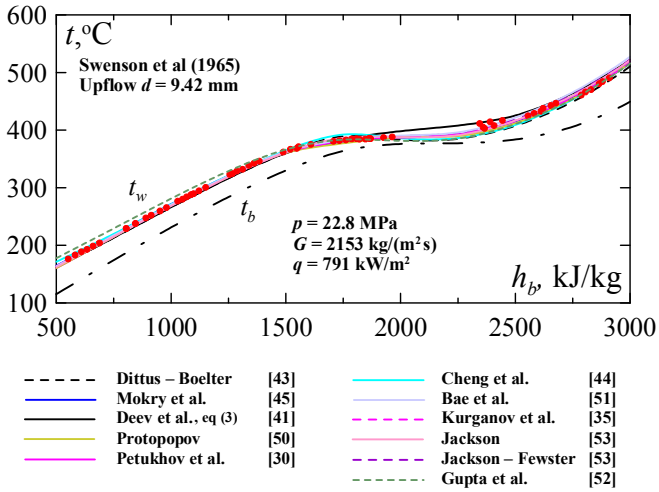

Figure 3. Comparison of calculated and experimental [13] values of the wall temperature

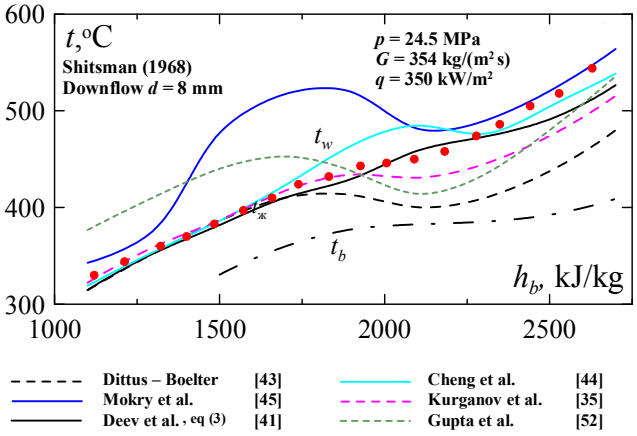

Figure 4. Comparison of calculated and experimental [15] values of the wall temperature

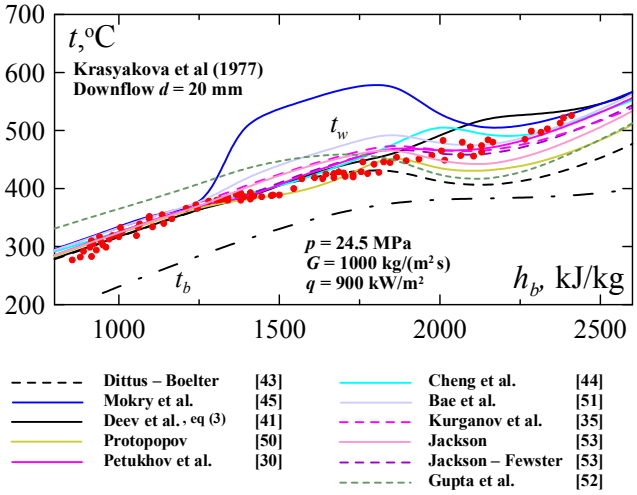

Figure 5. Comparison of calculated and experimental [25] values of the wall temperature

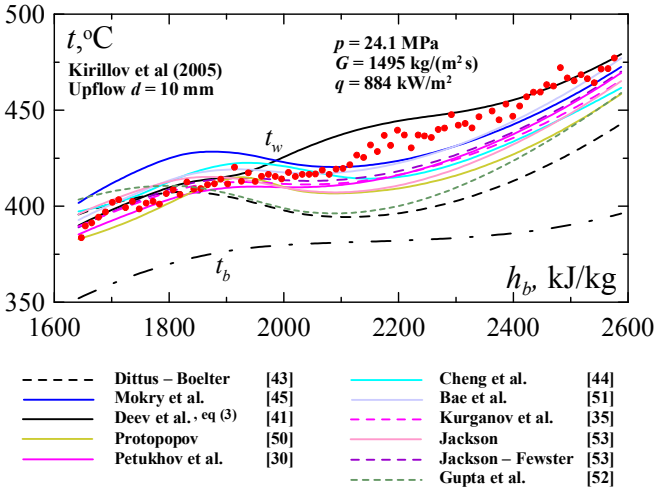

Figure 6. Comparison of calculated and experimental [37] values of the wall temperature

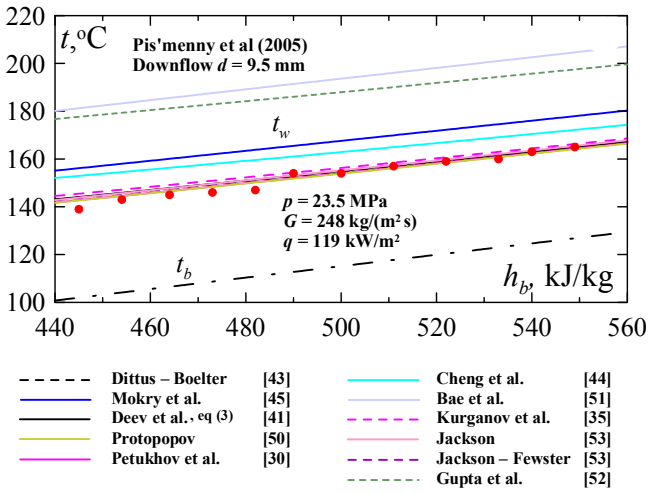

Figure 7. Comparison of calculated and experimental [38] values of the wall temperature

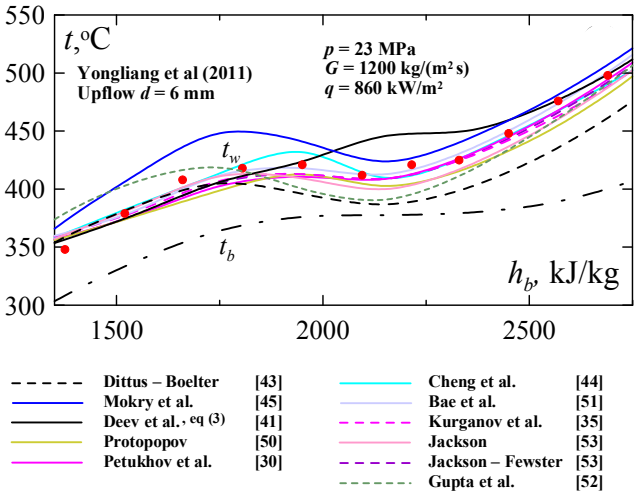

Figure 8. Comparison of calculated and experimental [39] values of the wall temperature

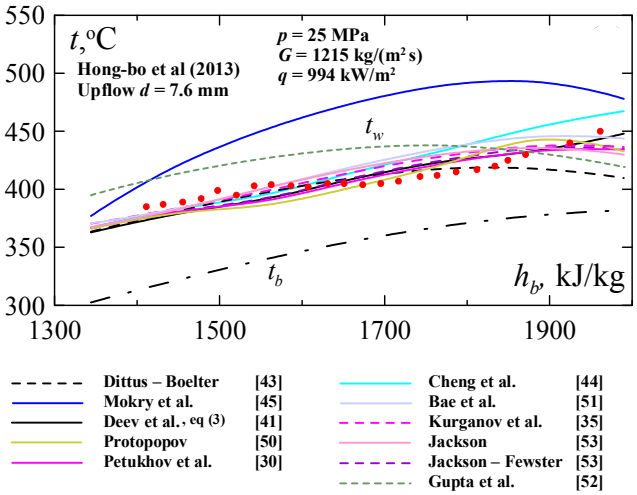

Figure 9. Comparison of calculated and experimental [40] values of the wall temperature

4. Ambiguity regions

Earlier, in [48] it was demonstrated that in the calculation of the temperature of heated wall on empirical correlations for the heat transfer coefficient to supercritical fluid, for certain values of regime parameters, there are several solutions of the equation. The work [49] presents the results of a numerical study to determine the region of ambiguity when using three correlations: Jackson–Fewster [53], Mokry et al. [42] and Swenson et al. [13].

The reason of the ambiguity is nonlinear equations for the wall temperature caused by the use of correlations with the thermo-physical properties at the wall temperature and sharp changes of these properties near pseudocritical temperature. It is shown that the ambiguity region has some threshold bulk fluid temperature t_{bTh}, above which there is no ambiguity of the wall temperature.

The ambiguity region of the new correlation (3) proposed by the authors was also defined. However, instead of the parameter **B**, defined by the expression

$$\mathrm{B} = \frac{q \cdot 10^3}{G\,(h_{cr} - h_b)}\,. \tag{7}$$

proposed to use the parameter $\mathbf{B}_m$

$$\mathrm{B}_m = \frac{q \cdot 10^3}{G\,(h_m - h_b)}\,, \tag{8}$$

since in this case the region of ambiguity is less dependent on the pressure (see Figure 10).

Figure 11 shows a comparison of ambiguity regions of the wall temperature equation for different correlations.

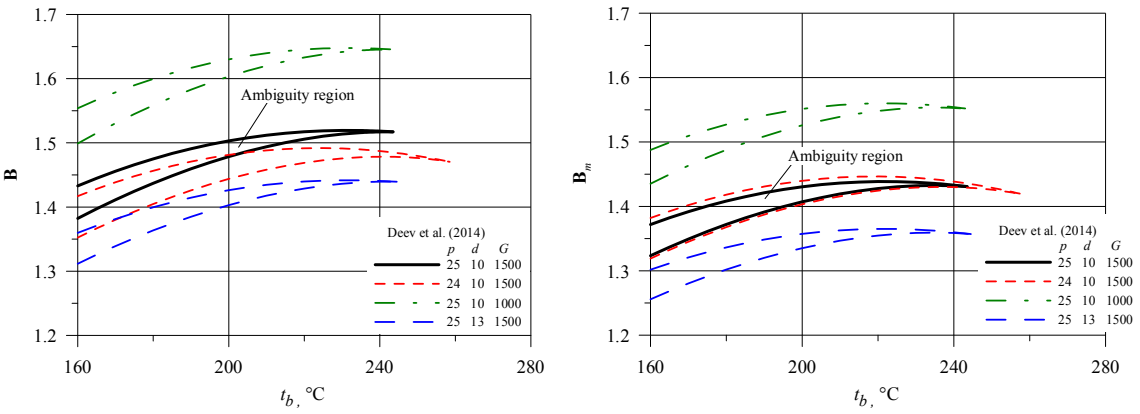

Figure 10. Ambiguity regions of the wall temperature equation with correlation (3) at the various operating parameters

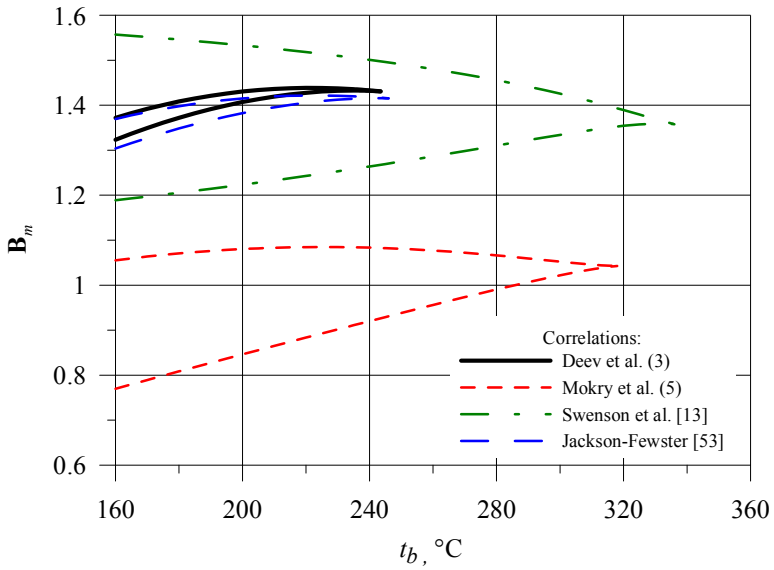

Figure 11. The comparison of ambiguity regions of the wall temperature equation for different correlations (p = 25 MPa; G = 1500 kg/(m^2·s); d = 10 mm).

It is necessary to consider the ambiguity region of calculated temperature of heated wall when using subchannel and system thermal-hydraulic codes, which apply empirical correlations for heat transfer coefficient to avoid possible mistakes in calculations.

5. Conclusions

Based on the comparison with a set of experimental data (more than 4000 experimental points of 20 original works) it is determined that a new generalized correlation (3) used in the calculations provides a satisfactory agreement with the experimental results obtained in the study of normal heat transfer to supercritical water in vertical pipes. A similar conclusion can be drawn with respect to the equations of Cheng et al. (4) and Kurganov et al. (6). The first one is more attractive because of its simplicity.

Ambiguity regions of the wall temperature equation with a new generalized correlation (3) were defined. The found ambiguity region lies outside the range of operating parameters of the experimental points considered in this paper.

Nomenclature

c_p	isobaric specific heat capacity
$\overline{c_p}$	average integral heat capacity
G	mass velocity
d	pipe inner diameter
h	specific enthalpy
L	pipe length
m, n	indexes in the equation (2)
Nu	Nusselt number
p	pressure
p_{cr}	critical pressure
Pr	Prandtl number
q	heat flux density

Re	Reynolds number
St	Stanton number
t	temperature, °C
T	temperature, K
T_m	pseudocritical temperature, K

Greek letters

α	heat transfer coefficient
β	thermal expansion coefficient
λ	thermal conductivity
μ	dynamic viscosity
ξ	friction coefficient
π_A	acceleration number in the equation (4)
ρ	density
σ	relative deviation

Subscripts

a	arithmetical mean value
b	value at bulk temperature
calc	calculated value
cr	value at critical point
exp	experimental value
m	value at pseudocritical temperature
sq	mean-square value
st	standard value
w	value at wall temperature

References

1. P.L. Kirillov, Supercritical water cooled reactors, Thermal Engineering 55 (5) (2008) 365-371.
2. S.B. Ryzhov, P.L. Kirillov, V.A. Mohov, M.P. Nikitenko, A.E. Chetverikov, V.M. Makhin, A.P. Glebov, A.N. Churkin, Concept of a single-circuit RP with vessel type supercritical water-cooled reactor, Proceedings of the 5th International Symposium on Supercritical Water-Cooled Reactors (ISSCWR-5), Vancouver, British Columbia, Canada, March 13–16, 2011. Paper P076.
3. V.A. Mokhov, I.N. Vasilchenko, M.P. Nikitenko, S.N. Kobelev, A.V. Lapin, V.M. Makhin, A.E. Chetverikov, A.N. Churkin, S.V. Shmelev, Core problems of VVER-SCP vessel-type reactor, Proceedings of the 4th International Symposium on Supercritical Water-Cooled Reactors (ISSCWR-4), Heidelberg, Germany, March 8–11, 2009. Paper 42.
4. Y. Oka, S. Koshizuka, Y. Ishiwatari, A. Yamaji, Super Light Water Reactors and Super Fast Reactors. Supercritical-Pressure Light Water Cooled Reactors. Springer, 2010. 416 p.
5. J. Yang, Y. Oka, Y. Ishiwatari, J. Liu, J. Yoo, Numerical investigation of heat transfer in upward flows of supercritical water in circular tubes and tight fuel rod bundles, Nuclear Engineering and Design 237 (2007) 420–430.
6. X. Cheng, B. Kuang, Y.H. Yang, Numerical analysis of heat transfer in supercritical water cooled flow channels, Nuclear Engineering and Design 237 (2007) 240–252.

7. A. Kiss, A. Aszódi, Summary for three different validation cases of coolant flow in supercritical water test sections with the CFD code ANSYS CFX 11.0, Nuclear Technology 170 (1) (2010) 40–53.
8. A. Churkin, S. Bilbao, Y. León, K. Yamada, Analysis of the IAEA benchmark exercise on steady state flow in a heated pipe with supercritical water, Proceedings of the International Congress on Advances in Nuclear Power Plants (ICAPP), Nice, France, May 2–5, 2011. Paper 11367.
9. H. Wang, Q. Bi, L. Wang, H. Lu, L.K.H. Leung, Experimental investigation of heat transfer from a 2×2 rod bundle to supercritical pressure water, Nuclear Engineering and Design 275 (2014) 205–218.
10. H. Li, M. Zhao, H. Gu, D. Lu, F. Wang, J. Zhang, Y. Zhang, J. Yang, Heat transfer research on supercritical water flow in 2×2 bundles, Proceedings of the 6th International Symposium on Supercritical Water-Cooled Reactors (ISSCWR-6), Shenzhen, Guangdong, China, 03-07 March 2013. Paper 13055.
11. M.E. Shitsman, Impairment of the heat transmission at supercritical pressures, High Temperature 1 (2) (1963) 237–244.
12. A.A. Bishop, R.G. Sandberg, L.S. Tong, Forced convection heat transfer to water at near-critical temperatures and supercritical pressures, Report WCAP-2056 Part IV, Westinghouse Electric Corporation, Atomic Power Division, Pittsburgh, Pennsylvania, USA, November 1964.
13. H.S. Swenson, J.R. Carver, C.R. Kakarala, Heat transfer to supercritical water in smooth-bore tubes, Journal of Heat Transfer, Transactions of the ASME, Series C 87 (4) (1965) 477–483.
14. Yu.V. Vikhrev, Yu.D. Barulin, A.S. Kon'kov, A study of heat transfer in vertical tubes at supercritical pressures, Thermal Engineering 14 (9) (1967) 116–119.
15. M.E. Shitsman, Temperature conditions in tubes at supercritical pressures, Thermal Engineering 15 (5) (1968) 72–77.
16. N.S. Alferov, R.A. Rybin, B.F. Balunov, Heat transfer with turbulent water flow in a vertical tube under conditions of appreciable influence of free convection, Thermal Engineering 16 (12) (1969) 90–95.
17. J.W. Ackerman, Pseudoboiling heat transfer to supercritical pressure water in smooth and ribbed tubes, Journal of Heat Transfer, Transactions of the ASME 92 (3) (1970) 490-498.
18. I.I. Belyakov, L.Yu. Krasyakova, A.V. Zhukovskii, N.D. Fefelova, Heat transfer in vertical risers and horizontal tubes at supercritical pressure, Thermal Engineering 18 (11) (1971) 55–59.
19. A.P. Ornatskiy, L.F. Glushchenko, S.I. Kalachev, Heat transfer with rising and falling flows of water in tubes of small diameter at supercritical pressures, Thermal Engineering 18 (5) (1971) 137–141.
20. L.F. Glushchenko, S.I. Kalachev, O.F. Gandzyuk, Determining the conditions of existence of deteriorated heat transfer at supercritical pressures of the medium, Thermal Engineering 19 (2) (1972) 107–111.
21. K. Yamagata, K. Nishikawa, S. Hasegawa, T. Fudjii, S. Yoshida, Forced convective heat transfer to supercritical water flowing in tubes, International Journal of Heat and Mass Transfer 15 (12) (1972) 2575-2593.
22. N.S. Alferov, B.F. Balunov, R.A. Rybin, Calculating heat transfer with mixed convection, Thermal Engineering 22 (6) (1975) 96–100.
23. G.V. Alekseev, V.A. Silin, A.M. Smirnov, V.I. Subbotin, Study of the thermal conditions on the wall of a pipe during the removal of heat by water at a supercritical pressure, High Temperature 14 (4) (1976) 683–687.

24. S. Ishigai, M. Kadgi, M. Nakamoto, Heat transfer and friction for water flow in tubes at supercritical pressures, Proceedings of the 5th All-Union Conference on Heat Mass Transfer, Minsk, Belarus', May 1976. Heat-Mass-Transfer-V, Minsk, 1976, vol. 1, part 1, p. 261–269 (in Russian).

25. L.Yu. Krasyakova, I.I. Belyakov, N.D. Fefelova, Heat transfer with a downward flow of water at supercritical pressure, Thermal Engineering 24 (1) (1977) 9–14.

26. M.J. Watts, C.T. Chou, Mixed convection heat transfer to supercritical pressure water, Proceedings of the 7th International Heat Transfer Conference, München, Germany, 6-10 September 1982. Hemisphere, Wahington, 1982, vol. 3, p. 495–500. Paper MC16.

27. B.S. Petukhov, Heat transfer in a single-phase medium under supercritical conditions (survey), High Temperature 6 (4) (1968) 696–709.

28. Z.L. Miropol'skiy, M.E. Shitsman, Heat transfer to water and steam with variable specific heat (at near-critical region), Journal of Technical Physics 27 (10) (1957) 2359–2372 (in Russian).

29. E.A. Krasnoshchekov, V.S. Protopopov, Experimental study of heat exchange in carbon dioxide in the supercritical range at high temperature drops, High Temperature 4 (3) (1966) 375–382.

30. B.S. Petukhov, V.A. Kurganov, V.B. Ankudinov, Heat transfer and flow resistance in the turbulent pipe flow of a fluid with near-critical state parameters, High Temperature 21 (1) (1983) 81–89.

31. W.B. Hall, J.D. Jackson, Heat transfer near the critical point, Proceedings of the 6th International Heat Transfer Conference, Toronto, Ontario, Canada, 7–11 August 1978. Ottawa, 1978, vol. 6, p. 377-392. Keynote lecture KS-27.

32. I.L. Pioro, R.B. Duffey, Heat Transfer and Hydraulic Resistance at Supercritical Pressures in Power Engineering Applications, ASME Press, New York, 2007. 334 p.

33. V.A. Kurganov, Yu.A. Zeigarnik, I.V. Maslakova, Heat transfer and hydraulic resistance of supercritical-pressure coolants. Part I: Specifics of thermophysical properties of supercritical pressure fluids and turbulent heat transfer under heating conditions in round tubes (state of the art), International Journal of Heat and Mass Transfer 55 (2012) 3061 3075.

34. V.A. Kurganov, Yu.A. Zeigarnik, I.V. Maslakova, Heat transfer and hydraulic resistance of supercritical-pressure coolants. Part II: Experimental data on hydraulic resistance and averaged turbulent flow structure of supercritical pressure fluids during heating in round tubes under normal and deteriorated heat transfer conditions, International Journal of Heat and Mass Transfer 58 (2013) 152-167.

35. V.A. Kurganov, Yu.A. Zeigarnik, I.V. Maslakova, Heat transfer and hydraulic resistance of supercritical pressure coolants. Part III: Generalized description of SCP fluids normal heat transfer, empirical calculating correlations, integral method of theoretical calculations, International Journal of Heat and Mass Transfer 67 (2013) 535-547.

36. A.A. Aleksandrov, B.A. Grigor'ev, Tables of Thermophysical Properties of Water and Steam, second ed., MEI Publishing House, Moscow, 2006. 168 p. (in Russian).

37. P. Kirillov, R. Pomet'ko, A. Smirnov, V. Grabezhnaia, I. Pioro, R. Duffey, H. Khartabil, Experimental study on heat transfer to supercritical water flowing in 1- and 4-m-long vertical tubes, Proceedings of the International Conference GLOBAL-2005 "Nuclear Energy Systems for Future Generation and Global Sustainability", Tsukuba, Japan, 9–13 October 2005. Paper 518.

38. E. Pis'menny, V. Razumovskiy, E. Maevskiy. A. Koloskov, I. Pioro, R. Duffey, Experimental study on temperature regimes to supercritical water flowing in vertical tubes at significant impact of free convection, Proceedings of the International Conference GLOBAL-2005 "Nuclear Energy Systems for Future Generation and Global Sustainability", Tsukuba, Japan, 9–13 October 2005. Paper 519.

39. Li Yongliang, Huang Zhigang, Zeng Xiaokang, Yan Xiao, Huang Yangping, Xiao Zejun, Experimental research on heat transfer of supercritical water upflowing in vertical tube, Proceedings of the 5th International Symposium on Supercritical Water-Cooled Reactors (ISSCWR-5), Vancouver, British Columbia, Canada, 13-16 March 2011. Paper 21.

40. Li Hong-bo, Yang Jue, Fu Xian-gang, Lu Dong-hua, Wang Fei, Zhang Jian-min, Zhang Yong, Research and development of supercritical water-cooled reactor in CGNPC, Proceedings of the 6th International Symposium on Supercritical Water-Cooled Reactors (ISSCWR-6), Shenzhen, Guangdong, China, 03-07 March 2013. Paper 13078.

41. V.I. Deev, V.S. Kharitonov, A.N. Churkin, V.V. Arhipov, Allowance for variability of thermophysical properties of a fluid in the heat transfer to a forced water flow at supercritical pressure, Vestnik of the National Research Nuclear University “MEPhI” 3 (3) (2014) 353-361 (in Russian).

42. V.I. Deev, K.V. Kutsenko, A.A. Lavrukhin, M.Yu. Ternovykh, G.V. Tikhomirov, Modeling heat transfer to water of supercritical pressure by using other fluids, Atomnaya Energiya 115 (4) (2013) 217–222 (in Russian).

43. W.H. McAdams, Heat Transmission, third ed., McGraw-Hill, New York, 1954. 532 p.

44. X. Cheng, Y.H. Yang, S.F. Huang, A simplified method for heat transfer prediction of supercritical fluids in circular tubes, Annals of Nuclear Energy 36 (2009) 1120–1128.

45. S. Mokry, I. Pioro, A. Farah, K. King, S. Gupta, W. Peiman, P. Kirillov, Development of supercritical water heat-transfer correlation for vertical bare tubes, Nuclear Engineering and Design 241 (2011) 1126-1136.

46. S. Mokry, A. Farah, K. King, I. Pioro, Updated heat-transfer correlations for supercritical water-cooled reactor applications, Proceedings of the 5th International Symposium on Supercritical Water-Cooled Reactors (ISSCWR-5), Vancouver, British Columbia, Canada, 13-16 March 2011. Paper 92.

47. H. Zahlan, D.C. Groeneveld, S. Tavoularis, S. Mokry, I. Pioro, Assessment of supercritical heat transfer prediction methods, Proceedings of the 5th International Symposium on Supercritical Water-Cooled Reactors (ISSCWR-5), Vancouver, British Columbia, Canada, 13-16 March 2011. Paper 8.

48. A.N. Churkin, Temperature ambiguity of heated wall in the fluid flow at supercritical pressure, Scientific and Technical Collection of Articles “Issues of Nuclear Science and Engineering”, Series: “Safety Assurance of NPP”, vol. 30, p. 122-126, 2011 (in Russian).

49. A.N. Churkin, V.I. Deev, Ambiguity of calculation results of heat transfer to water using empirical correlations in the region of supercritical pressure, Proceedings of the 6th International Symposium on Supercritical Water-Cooled Reactors (ISSCWR-6), Shenzhen, Guangdong, China, 03-07 March 2013. Paper 13057.

50. V.S. Protopopov, Generalizing relations for the local heat-transfer coefficients in turbulent flows of water and carbon dioxide at supercritical pressure in a uniformly heated circular tubes, High Temperature15 (4) (1977) 687–692.

51. Y.Y. Bae, H.Y. Kim, Convective heat transfer to CO_2 at a supercritical pressure flowing vertically upward in tubes and an annular channel, Experimental Thermal and Fluid Science 33 (2009) 329–339.

52. S. Gupta, S. Mokry, I. Pioro, Developing a heat-transfer correlation for supercritical-water flowing in vertical tubes and its application in SCWR, Proceedings of the ICONE-19, Makuhari, Japan, May 16–19, 2011. Paper 43503.

53. J.D. Jackson, Fluid flow and heat transfer at supercritical pressure, Proceedings of the 14th International Topical Meeting on Nuclear Reactor Thermal Hydraulics (NURETH 14). Toronto, Ontario, Canada, September 25–29, 20011. Paper 574.

ISSCWR7-2021

Heat Transfer of Supercritical Water Flowing in Vertical Annuli with Spacer Effect

M. Zhao[1], H.Y. Gu[1], H.B. Li[2], X. Cheng[1,3] ,J. Yang[2]
(1.Shanghai Jiao Tong University, Shanghai 200240, China;
2. China Nuclear Power Technology Research Institute, Shenzhen 518026, China;
3. Karlsruhe Institute of Technologies, Karlsruhe 76131, Germany)

Abstract

Experimental studies on heat transfer to supercritical water flowing in a concentric annulus channel are carried out at the SWAMUP test facility. The vertical annuli contain a heated inner tube of 8mm OD and a non-heated outer tube of 15.3mm ID with spacers without mixing-vane. Totally more than 500 test data were obtained with the following test conditions: pressure from 23.0 MPa to 26.0 MPa, mass flux from 450 kg/m^{2}s to 1500 kg/m^{2}s, heat flux from 0.45 MW/m^2 to 1.4 MW/m^2 and bulk temperature from 340^{O}C to 390^{O}C. Test data are compared with those obtained in tubes of similar hydraulic diameter. Comparison indicates that spacers enhance heat transfer significantly. Without spacers heat transfer in concentric annuli is slightly lower than that in tubes of similar hydraulic diameters and under comparable thermal-hydraulic conditions.

1. Introduction

Due to several advantages like higher thermal efficiency and a more simplified system, supercritical water cooled reactor (SCWR) was selected as one of the six Generation IV reactors proposed by GIF. However, there are still many technical problems, especially in the field of thermal hydraulics. In the vicinity of pseudo-critical point, the thermo-physical properties of supercritical water show strong variations. These strong variations, combined with different heat flux and mass flux, may lead to large buoyancy effect and flow pattern changes in near wall region and finally result in abnormal behavior such as heat transfer enhancement or heat transfer deterioration (Cheng and Schulenberg 2001).

Heat transfer at supercritical pressures has been investigated since 1950s. These studies have been well reviewed by Cheng and Schulenberg (2001) and Pioro and Duffy (2005). Understanding of heat transfer characteristics of supercritical water flowing in fuel rod bundles or geometries relevant to nuclear reactors is of great importance. In most SCWR design concepts, spacer grids or wires are proposed to keep the fuel pins in fixed position. Besides keeping position, spacers are also believed to improve heat transfer due to disturbance of thermal boundary layer and increase in turbulence. Even though the importance of the space effect, studies on the effect of spacers are very limited, especially in supercritical conditions.

McAdams et al. (1950) conducted experiments with an upward flow of water in a vertical annulus with internal heating with pressure ranging from 0.8 to 24 MPa and bulk temperatures ranging from 221°C -538°C. The experiments showed that with a certain Reynolds and Prandtl numbers, local Nusselt number always decreases as the value of L /Dh increases. It is believed that in supercritical conditions the entrance effect is reduced as flow redevelops.

Bae et al (2011) carried out heat transfer experiments of supercritical CO_2 flowing through annuli with a helical space wire. They founded out that space wire enhances heat transfer several times. They also investigated the parameter effect such as heat flux, mass flux and pressure on heat transfer.

Wang et al (2012) investigated heat transfer characteristics of supercritical water flowing in annuli with space wire. They found that the affected distance of spacer depends strongly on flow condition and spiral spacer has a positive effect on reducing heat transfer deterioration which may occurred at high ratios of heat flux to mass flux.

Yang et al (2013) firstly preformed heat transfer experiment of supercritical water in annuli, using two space grids to positioning internal heating rod and external none-heating tube. They observed heat transfer enhancement downstream of spacer grids.

Literature review reveals that there is still big deficiency in the investigation of heat transfer characteristics of supercritical water flowing in annuli with spacer grids. This paper presents experimental studies on heat transfer of supercritical water flowing upward in annuli with spacer grids. The geometric parameters, e.g. hydraulic diameter, of the test section correspond to those of SCWR design, i.e. the diameter of the inner heated rod is 8 mm, diameter of the outer unheated tube is 15.3, resulting in a hydraulic diameter of 7.3 mm. Four spacer grids with interval distance ranging from 400 mm to 600 mm are applied. These distances are sufficiently large for the redevelopment of flow and heat transfer downstream the spacers, so that heat transfer coefficients with negligibly small effect of spacers can also be obtained.

2. Experimental facility and test section

2.1 SWAMUP test facility

The SWAMUP test facility, shown in Figure 1, is used to perform heat transfer tests in supercritical water. The facility consists of the main test loop, a cooling water loop, a water purification loop, and I&C system. The main test loop, consisting of a circulating pump, pre-heater, mixing chamber, two heat exchangers, accumulator and test sections, is constructed for pressure up to 30 MPa, temperature up to 550°C, mass flow rate up to 1.3 kg/s and electrical power up to 1.2 MW.

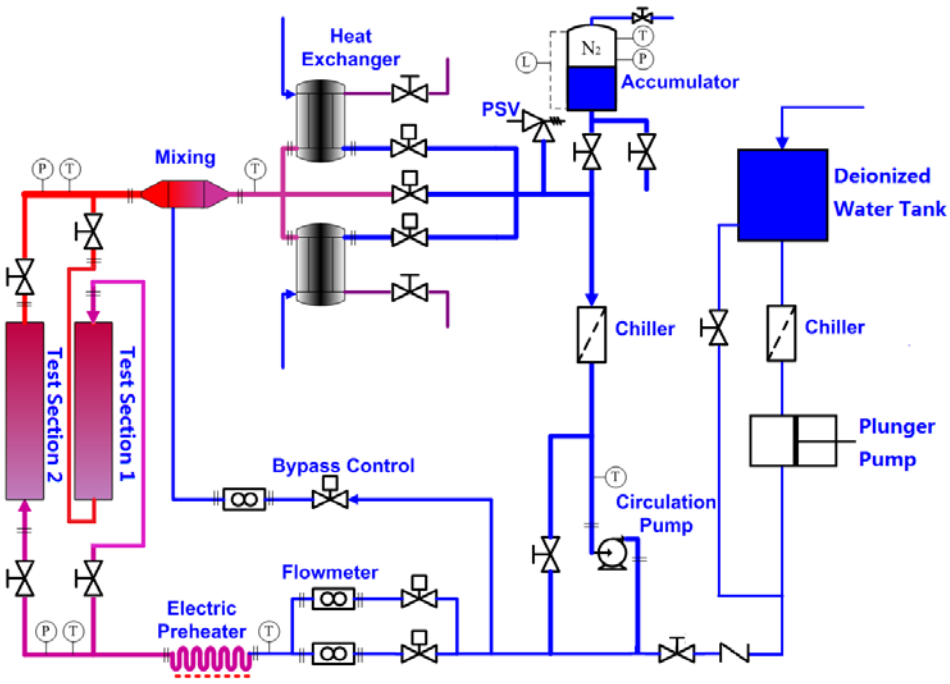

Fig.1: Scheme of the SWAMUP test facility

In the test loop, part of water flow is not heated and flows through the bypass line which is designed for rough adjustment of the flow rate through the test section. The rest portion of flow first passes the pre-heater, where water flow is heated up to a pre-defined test inlet temperature. In the test section water can be heated to 550°C. Both parts merge in the mixing chamber before goes to heat exchangers. The two parallel heat exchangers are used to further cool down the water flow before it enters the pump. Two flow meters with different measurement ranges are installed in parallel in the main flow path, to measure the mass flow rate entering the test section. The main technical parameters are listed in Table 1:

Table 1: Ranges of SWAMUP technical parameters

Parameters	**Values**	**Units**
Design pressure	30	MPa
Design temperature	550	°C
DC power for test section	0.9	MW
Heating power for pre-heater	0.3	MW
Heat exchanger capacity	1.2	MW
Max. flow rate	5.0	t/h
Pump head at maximum flow rate	80	m

2.2 Test section

The test section, as shown in Figure 2, is consisted in an Inconel 718 heated rod (8mm OD and 1.5mm thickness) and a 304 stainless non-heated tube (15.3mm ID and 8.4mm thickness), forming a gap of 3.65mm and a hydraulics diameter of 7.3mm. The heated length of the annular channels is 2032mm and is separated by 4 space grids. The inside of heated rod is installed with a sliding thermal couple to measure the inside wall temperature, while the area between the thermal couple and inside wall is covered with thermal isolation ceramic. The outer tube is non-heated and covered with fiberglass insulation to protect from heating loss.

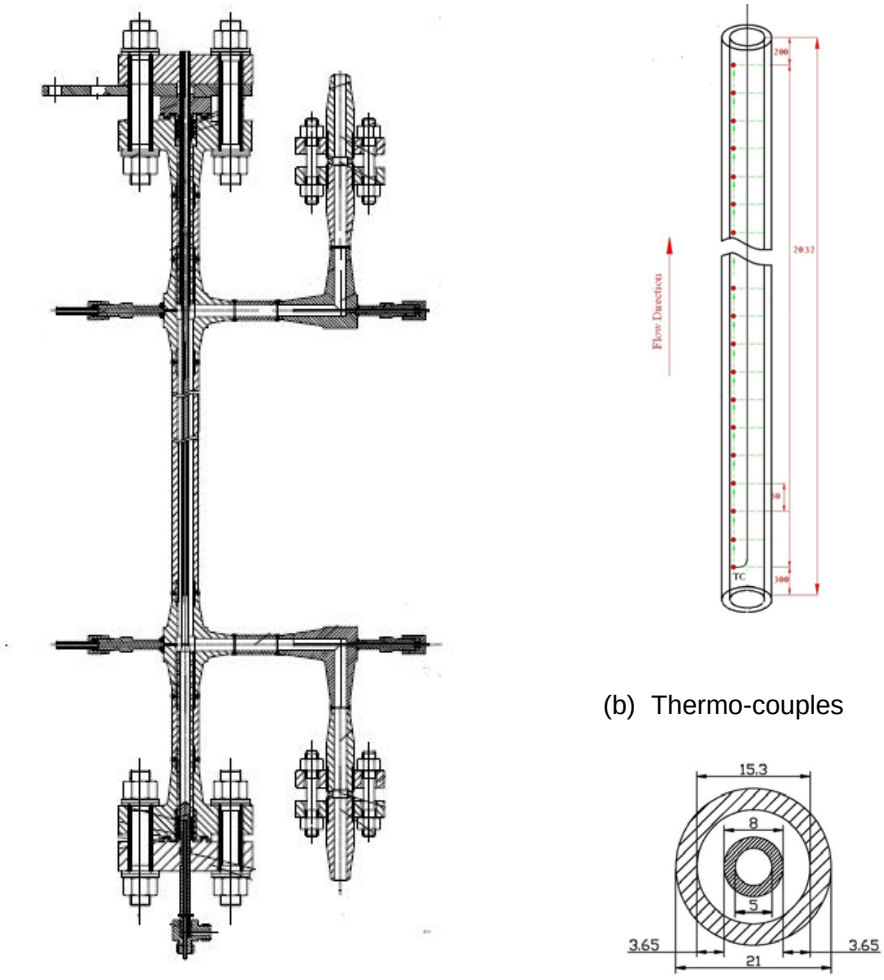

(a) Sketch of the test section design

(b) Thermo-couples

(c)Flow channel

Fig. 2 Annuli section and the arrangement of sliding thermal couples

In order to investigate the effect of spacers of different blockage ratios, two different spacer grids with different blockage ratio ε are used, shown in Fig.3. Both of them are electrically insulated by thermal spraying ceramic powder in grids surface. The four spacer grids were located in the position of 400 mm, 800 mm, 1200 mm and 1600 mm from the test section entrance.

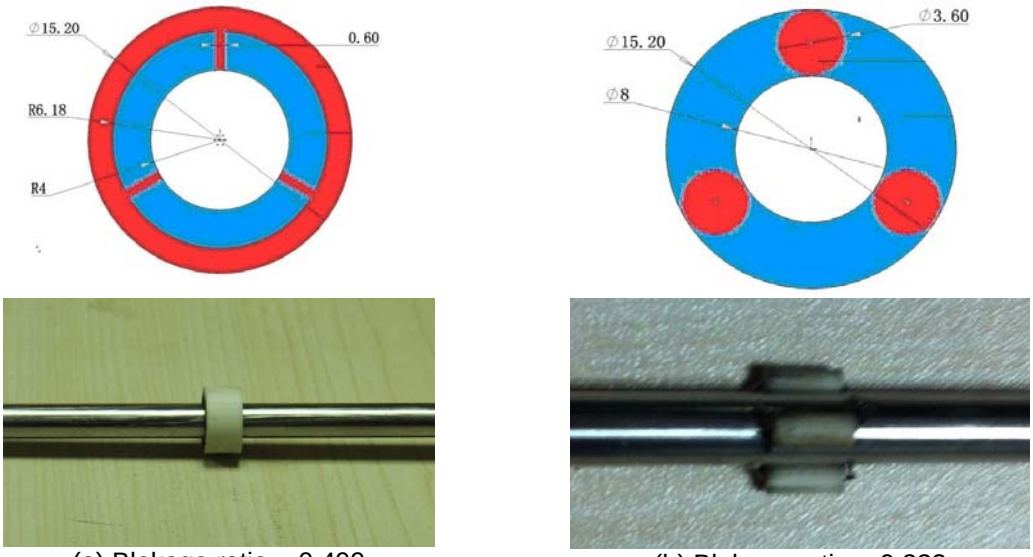

(a) Blokage ratio = 0.499 (b) Blokage ratio = 0.233

Fig.3: Design of two space grids of different blockage ratios

2.3 Test data reduction and error analysis

Experiments were carried out with test parameters shown in Table 2. Totally 520 measurement points were recorded. Temperatures on heating tube outside surface were calculated from the inner surface temperatures of the hated tube. It was assumed that the volumetric power density in the tube is uniform. Neglecting the axial heat conduction, one-dimensional heat conduction equation is numerically solved, so that outer wall temperatures were obtained. In the calculation, the temperature dependence of tube wall thermal conductivity was considered. The uncertainties of every parameter were shown in Table 3.

Table 2 Ranges of Test parameters

Parameters	Values	Units
Pressure	15.5,23, 24, 25, 26	MPa
Mass flux rate	500-1600	kg/m^2s
Heat flux	0.45-1.40	MW/m^2
Bulk temperature	310-390	C

Table 3 Uncertainties of primary parameters

Parameters	Maximum uncertainty
Pressure	± 0.2%
Mass flow rate	± 0.4%
Fluid temperature	$\pm 1.5^{O}C$

DC current	± 1.0%
DC voltage	± 1.0%
Heated tube diameter	± 0.04mm
Heated tube thickness	± 0.02mm
None-heated tube diameter	± 0.10mm
TC axial measurement position	± 0.05mm

The uncertainty of measuring instruments was determined by the manufacture's specifications and the calibration results. The fluctuation magnitude of measured parameters was obtained by analyzing the test data recorded. Heat loss to environment was examined by energy balance at various bulk temperature levels. For the present analysis, the uncertainty of thermal-physical properties was neglected.

The total error of each parameter consists of two parts: systematic and statistic error. Under the assumption that an evaluated parameter is dependent on other input parameters and their relationship can be expressed as follows

$$Z = f\left(Z_1, Z_2, \cdots, Z_n\right), \tag{1}$$

The systematic error of the evaluated parameter was calculated from the systematic error of the input parameters

$$e_s = \sum_{i=1}^{n} \left| \frac{\partial f}{\partial Z_i} e_{s,i} \right| \tag{2}$$

Under the assumption that the statistic errors of the input parameters obey the Gauss-distribution and are independent of each other, the statistic error of the evaluated parameter obeys also a Gauss-distribution with a standard deviation:

$$\sigma = \sqrt{\sum_{i=1}^{n} \left(\frac{\partial f}{\partial Z_i} \sigma_i \right)^2} \tag{3}$$

With the 2σ-criterion (95% criterion) the total error of the evaluated parameter was determined by

$$e = e_s \pm 2\sigma \tag{4}$$

Table 4 gives an example of error analysis results. Regarding the Nusselt number, more than 90% of the experiment data fall into the error range smaller than 10%.

Table 4: Example of error analysis

Parameters	**P** **MPa**	**G** **kg/m^{2}s**	**T_B** **°C**	**T_w** **°C**	**q** **kW/m^2**	**HTC** **kW/m^{2}K**	**Nu** **-**
Values	24.97	789.7	370.3	451.5	610.7	7514.6	132.4
Errors, %	0.20	0.99	0.98	0.64	1.22	5.6	5.9

3 Results and Discussing

Figure 4 shows the measured heat transfer coefficient versus the distance from the test section entrance for the test condition: P=25 MPa, G=800 kg/m2s and q=0.6 MW/m2. Fig.4a presents the HTC distribution over the entire heated length, whereas Fig.4b shows the distribution of HTC in the axial position between 0.4 and 0.8 m with only one spacer located in the range from 0.40 to 0.408m. It is seen that just after the spacer grids, heat transfer coefficient increases strongly. With the increase in the downstream distance from the spacer, heat transfer coefficient decreases at first sharply and then smoothly. Far away from the upstream spacer, e.g. 40 times of the hydraulic diameter (Fig.4b), heat transfer coefficient approaches to a constant value. It can be concluded that at distance of more than 40 times hydraulic diameter, the effect of spacer on heat transfer coefficient is negligibly small. This conclusion is valid for all test conditions.

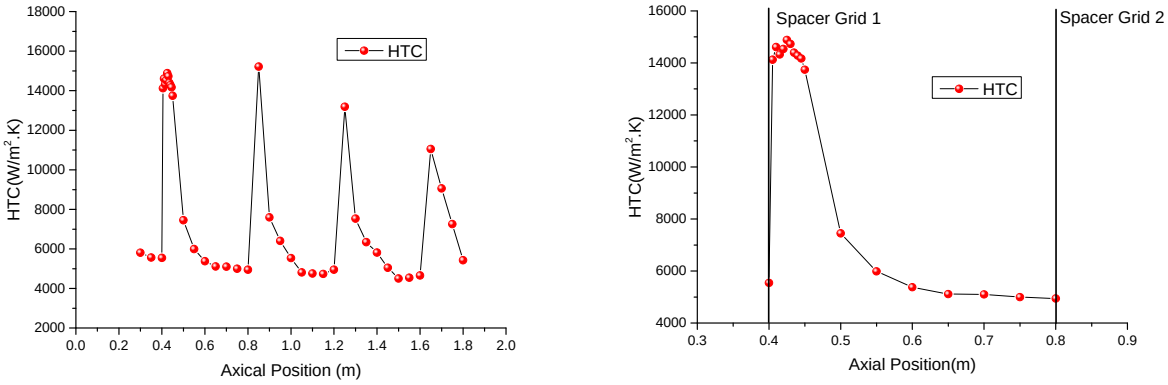

(a) Total heated length

(b) Between two spacers

Figure 4: Measured heat transfer coefficient along axial position (P=25 MPa, G=800 kg/m^{2}s and q=0.6 MW/m^2)

3.1 Comparison with test data in tubes

Fig.5 shows compares the test datsa inannuli with those in tubes (Zhao et al. 2014) of similar hydraulic diameter and thermal-hydraulic parameters (P=25 MPa, 450kg/m2.s,Q=0.6MW/m2). It can be seen that spacer grids enhances HTC in annuli several times just downstream the spacer grid, much stronger than the enhancement due to entrance effect in tubes. Far away from the upstream spacer, where flow is considered to be fully redeveloped and the spacer effect is negligibly small, HTC in annuli is about 15%-20% lower than those in tubes.

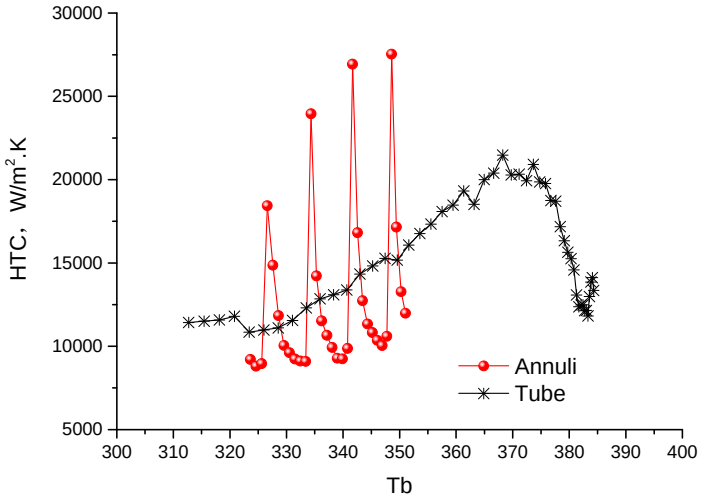

Figure 5 HTC of annuli and tube versus bulk temperature at P=25MPa, G=450kg/m^2.s,Q=0.6MW/m^2

Figure 6 compares the heat transfer coefficients in annuli without spacer effect with test data in circular tubes of similar hydraulic diameter (Zhao et al. 2014). The test conditions are: P=25MPa, G=1000kg/m2s, q=1.0MW/m2. It is clearly seen that tendency of HTC variation in annuli is similar to that in tubes. Near the pseudo-critical point, HTC in annuli is about 10% - 20% lower than that in tubes.

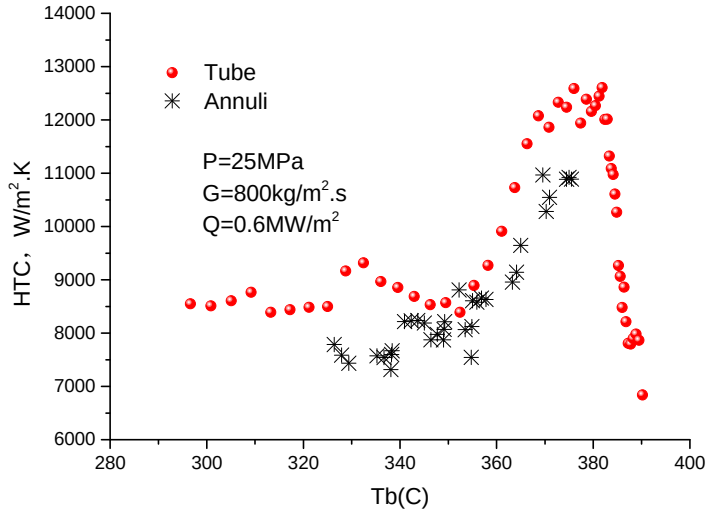

Figure 6: Comparison of HTC in annuli with that in tubes

3.2 Effect of the spacer grids

Enhancement of single phase convection heat transfer downstream of spacer grids in fuel rod bundles has been widely investigated in subcritical conditions. Kidd and Hoffman (1968) measured temperature profile and heat transfer characteristics in the vicinity of spacer grids in rod bundles under subcritical conditions. They found that heat transfer enhancement induced by spacer grids is similar to that due to entrance effect in tube.

Based on results in a 3-rod bundle using air as coolant and spacer grids with blockage ratios varying from 0.25 to 0.35 Marek and Rehme (1975) developed a correlation predicting heat transfer as function of blockage ratio,. They found out that the behavior of heat transfer enhancement caused by spacer grids is similar to that of pressure drop.
Yao et al. (1982) developed a correlation to describe the heat transfer enhancement and its decay behavior downstream of spacer grids.

$$\frac{Nu}{Nu_\infty} = 1 + A\varepsilon^2 \exp(-B\frac{x}{D_h}) \tag{5}$$

where ε is blockage ratio, x the downstream distance from the spacer grids, A and B constants and equal to 5.55 and 0.13, respectively.
According to Yao's correlation, heat transfer enhancement just behind the spacer grids depends only on blockage ratio, whereas the axial decay behavior obeys exponential function of distance from the spacer grid. Both terms are independent of Reynolds number. From the physical mechanism point of view, spacer grids affect fluid flow structure and disturb thermal boundary layer, which is redeveloped downstream of the spacer. The redevelopment procedure takes several tens of hydraulic diameters.

Miller et al (2013) conducted experiments of heat transfer in 7x7-rod bundle under subcritical conditions. They founded that heat transfer enhancement reaches highest level just at the exit of the spacer and the heat transfer enhancement downstream the spacer decays along with distance. Both the maximum heat transfer enhancement and the decay procedure depend on Reynolds number. The following correlation was proposed:

$$\frac{Nu}{Nu_\infty} = 1 + 4.65(\frac{\mathrm{Re}}{10^4})^{-0.5}\varepsilon^2 \exp(-0.291(\frac{\mathrm{Re}}{10^4})^{1.15}\frac{x}{D_h}) \tag{6}$$

Moon et al (2013) conducted heat transfer experiments in a 6x6-rod bundle of single-phase steam flow. Heat transfer enhancement was found in both upstream and downstream of spacer grids. In the downstream of the spacer, heat transfer enhancement decays exponentially with the distance from the spacer grid. Their experimental data also showed that the Reynolds number affects the heat transfer enhancement only at low Reynolds number range., At high Reynolds number, i.e. greater than 104, heat transfer enhancement by spacer grids has been treated to be independent of Reynolds number.

In order to assess and to evaluate the existing correlations, present test data at both subcritical and supercritical conditions in annuli were selected, as shown in Table 5.
Figures 7 and 8 shows the ratio Nu_x / Nu_∞ versus the dimensionless distance downstream from the spacer x/Dh. Nu_x represents the local Nu number and Nu_∞ is defined as the Nu number without spacer effect. Both correlations of Yao (1982) and Miller et al (2013), which were developed based on subcritical test data, show an accurate prediction for the subcritical cases. Near the spacer zone, correlation of Miller shows only 5% deviation from the experimental results. However, due to the strongly property variation near the pseudo-critical point, both correlations of Yao et al (1982) and Miller et al (2013) give a significant under-prediction of the spacer effect, as shown in Fig.7. It can be seen that near the spacer zone, the predicted Nusselt number ratio is only half of the experimental values. Improvement of prediction is thus required.

Table 5 Test cases

Case	Blockage Ratio(-)	Pressure (MPa)	Mass Flux (kg/m^{2}s)	Heat Flux (kw/m^2)	Inlet temperatere (°C)
Case1	0.233	15.5	966	605	182
Case2	0.233	25.1	1432	1224	341

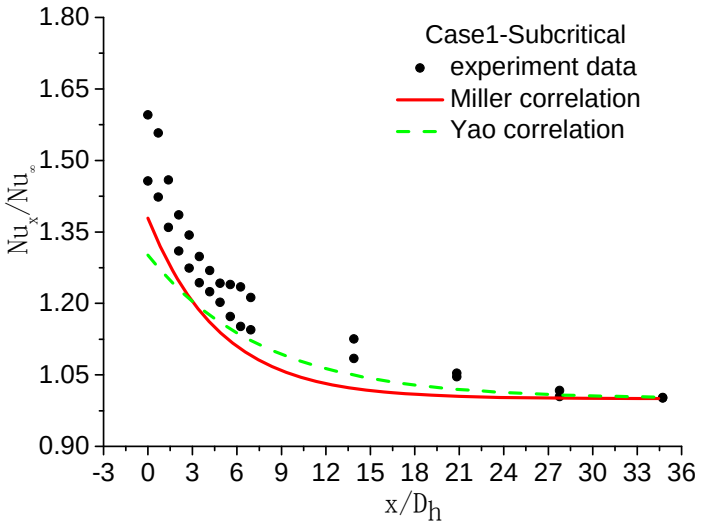

Figure 7: Ratio of measured to calculated Nu versus distance from the spacers at subcritical conditions (case 1)

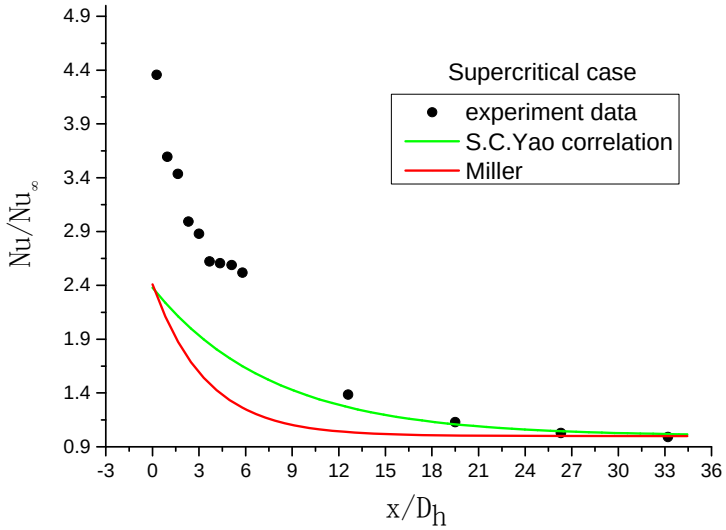

Figure 8: Ratio of measured to calculated Nu versus distance from the spacer at supercritical conditions (case 2)

4. Conclusion.

Heat transfer experiment of supercritical water flowing in annuli with space grids were performed at the SWAMUP test facility of SJTU within the following conditions: Dh=7.3mm, pressure from 23MPa to 26MPa, mass flux from 450-1500 kg/m^{2}s, heat flux from 450-1400 kW/m^2 and bulk temperature from 340 to 390 ^{O}C. The following conclusions can be obtained.

a) Heat transfer coefficient in annuli with negligible small effect of spacer is slightly lower than that in circular tubes of similar hydraulic diameters.
b) The strongest enhancement HT due to space grid occurs directly at the exit of the spacer grid. The HT enhancement effect occurs within the range of x/Dh ≤ 40.

c) The selected correlation of Yao et al (1982) and Miller (2013) can give reasonable prediction of the heat transfer enhancement in subcritical conditions and shows, however, significant deviation in supercritical conditions.
d) More detail studies with focus on spacer effect and the decay behavior of heat transfer enhancement need to be carried out.

Acknowledgment

The authors would like to thank China Nuclear Power Technology Research Institute and Karlsruhe Institute of Technology for providing financial and scientific support for this study.

References

1. Bae, Y.Y., Kim, H.Y., Yoo, T.H., 2011. Effect of helical wire on mixed convection heat transfer to carbon dioxide in a vertical circle tube at supercritical pressures. Int. Journal of Heat and Fluid Flow, 32, 340-351

2. Bishop, A.A., Sandberg, L.O., Tong, L.S., 1964. Forced convection heat transfer to water at near critical temperatures and supercritical pressures, WCAP-2056-P, Part-III-B.

3. Cheng, X., Schulenberg, T., 2001. Heat transfer at supercritical pressures-Literature review and application to a HPLWR. Forschungszentrum Karlsruhe, Technik und Umwelt, Wissenschaftliche Berichte, FZKA 6609, Institute fur Kernund Energietechnik, 2001.

4. Cheng, X., Liu, X.J., Yang, Y.H., 2008. A mixed core for supercritical water-cooled reactor. Nucl. Eng. and Technol., 40, 117-126.

5. Kidd, G.J., Hoffman, H.W., 1968. The Temperature Structure and Heat Transfer Characteristics of an Electrically Heated Model of a Seven-Rod Cluster Fuel Element. ASME Paper 68-WA/HT-33.

6. Kondrat'ev, N.S., 1969. Heat transfer and hydraulic resistance with supercritical water flowing in tubes. Thermal Eng., 16 (8), 73–77.

7. Marek, J., Rehme, K., 1975. Experimentelle untersuchungen der tempera-tureverteilung unter Abstandshaltern in glatten und rauhen Stabbuendeln.Gesellschaft fuer Kernforschung mbH, KFK 2128, Karlsruhe (in German).

8. McAdams, W.H., Kennel, W.E., Addoms, J.N., 1950. Heat transfer to superheated steam at high pressures. Trans. ASME 72 (4), 421–428.

9. Miller, D.J., Cheung, F.B., Bajorek, S.M., 2013. On the development of a grid-enhanced single-phase convective heat transfer correlation. Nuclear Engineering and Design 264, 56-60.

10. Moon, S. K., Cho, S., Kim J., Kim B. J., Park, J. K., Yun, Y.-J. Enhancement of single-phase convective heat transfer in rod bundles near spacer grids. The 15th International Topical Meeting on Nuclear Reactor Thermal - Hydraulics, NURETH-15 NURETH15-505, Pisa, Italy, May 12-17, 2013

11. Oka Y., Koshizuka S., 2000. Design concept of one-through cycle supercritical pressure light water cooled reactor, in: Proc. of SCR-2000, Nol.6-8, Tokyo, Japan, 1-22.

12. Pioro, I.L., Duffey, R.B., 2005. Experimental heat transfer in supercritical water flowing inside channels (Survey). Nucl. Eng. Des. 235,.2407–2430

13. Schulenberg, T., Starflinger, J., Heneche, J., 2008. Three pass core design proposal for a high performance light water reactor. Prog. Nucl. Energy, 50, 526-531.

14. Wang, H., Bi, Q.C., Yang, Z.D., Gang., W., Hu., R., 2012. Experimental and numerical study on the enhanced effect of spiral spacer to heat transfer of supercritical pressure water in vertical annular channels. Applied Thermal Engineering, 48, 436-445.

15. Yang, Z.D., Bi, Q.C., Wang, H., Wu, G., Hu, R., 2012. Experiment of Heat Transfer to Supercritical Water Flowing in Vertical Annular Channels. J. Heat Transfer 135(4), 042504.

16. Yao, S., Hochreiter, L., Leech, W., 1982. Heat transfer augmentation in rod bundles near grid spacers. J. Heat Transfer 104, 76–81.
Miller, D.J., Cheung, F.B., Bajorek, S.M., 2013. On the development of a grid-enhanced single-phase convective heat transfer correlation. Nuclear Engineering and Design 264, 56-60.

17. Zhao, M., Gu, H.Y., Cheng, X., 2014. Experimental study on heat transfer of supercritical water flowing downward in circle tubes. Annals of Nuclear Energy, 63, 339-349.

The 7th International Symposium on Supercritical Water-Cooled Reactors
ISSCWR-7
15-18 March 2015, Helsinki, Finland

ISSCWR7-#2022

A low diffusion numerical scheme for the stability analysis of natural circulation loops containing fluids at supercritical pressure

Andrea Coppedè and Walter Ambrosini
Università di Pisa, Dipartimento di Ingegneria Civile e Industriale
Largo Lucio Lazzarino 2, Pisa, Italy
Tel. +39-050-2218073, Email: walter.ambrosini@ing.unipi.it, andr.cpp@gmail.com

Abstract

This paper reports the latest results of a research concerning the development of a computer programme aimed to be a tool based on 1D balance equations for the linear and the nonlinear stability analysis of natural circulation loops, with main attention to those equipped with fluids at supercritical pressure. With respect to available models, the programme has the useful feature to make use of a brute force numerical linearization of transient equations, aiming at setting up stability maps of loops with realistic features, something going beyond the state of the art of present 1D system codes, while providing data with similar accuracy. Moreover, unlike what is normally found in the literature for the analysis of stability of natural circulation with supercritical pressure fluids, allowance for the presence of heating structures is made, pointing out the strong effect that wall heat capacitance has on stability in the conditions addressed in many previous works.

The further step reported herein addresses in particular the inclusion in the computer programme of a low diffusion numerical scheme that is capable to rule out most of the truncation error effects experienced with similar codes. As in earlier works related to single-phase natural circulation, a second order upwind scheme has been adapted in a “donor cell” form to the case of supercritical pressure fluids, to be included in the conservation law form of the discretised energy balance equations, thus achieving a very low impact of numerical diffusion even with relatively coarse nodalizations. The resulting programme has been applied with success to relevant available data, from both theoretical and experimental analyses. Owing to this step, the programme can be now used as a tool for discussing the important issues of the selection of the most appropriate correlations for heat transfer and friction in natural circulation conditions with supercritical pressure fluids, allowing for excluding a priori a too large effect of the numerical effects on the obtained results.

1. Introduction

The proposed nuclear power plants operating with supercritical water (SCWR) are a possible option among fourth generation systems identified by GIF (Generation IV International Forum). The purposes of fourth generation reactors are obviously related with improvement of technical, economically and safety aspects compared to third generation system [1].

SCWR reactors are conceived to allow for new features to be exploited (see e.g., [2]): the thermal cycle is direct so that it is possible to eliminate the intermediate components existing in PWR plants (greater simplicity); the achievement of high temperatures in thermodynamic cycle allows to increase significantly the thermal efficiency and alternative processes, like cogeneration, can be even envisaged.

In the supercritical state, water has an interesting behaviour in relation to some thermodynamic and thermophysical proprieties, as density, specific heat, thermal conductivity and dynamic viscosity. High density gradients are observed in increasing temperature fields, making very peculiar the behaviour of this fluid; large density differences make also possible large driving forces for natural circulation, being an important physical phenomenon in nuclear technology [3]. Natural circulation with supercritical pressure fluids is presently given increasing attention in research work.

A specific research area attracting strong attention in this frame is related to the stability of the fluid flow and the heat transfer, addressed in several works from both the computational and the experimental points of view (see e.g., [4-14]). Natural circulation phenomena can show a complex dynamics and may result very sensitive to initial and boundary conditions; so, it is necessary to develop and qualify effective tools for its simulation.

NCLoop is a program set up for the stability analysis of natural circulation in closed loops with supercritical fluids and already applied with success in previous analyses [15] making use of a semi-implicit numerical scheme, based on staggered meshes and a first order upwind treatment of the energy equation. The aim of the present work has been to modify the previous version of the programme by implementing in it a new discretization scheme adopted for the energy equation, thus substantially decreasing the effect of numerical diffusion on obtained results. Following the experience gained in the case of single phase thermosyphon loops [16], in the supercritical fluid case it was necessary to adapt the formulation adopted for balance equations including a specifically designed low diffusion scheme. The modified program allows choosing the numerical scheme (first or second order upwind) for both linear analysis (NCLine program, generating stability maps) and non-linear analysis (NCLtran program, evaluating the transient behaviour) in order to address particular operating conditions.

In previous analyses [9, 15], the effect of the volumetric thermal capacitance of active and passive structures on stability predictions was highlighted, showing its stabilising effect. The introduction of the low diffusion numerical scheme allows now to include a further element of realism in the analysis, by ruling out almost completely the effects of numerical discretisation on the stability prediction.

2. The NCLoop program and its numerical scheme

The purpose of the NCLoop program is to simulate the behavior of closed thermo-hydraulic loops in natural circulation with supercritical pressure fluids. The loop is assumed to be composed of ‘segments’ which are characterized by uniform hydraulic, geometrical and physical characteristics each one. The program can operate in two modes: a) linear analysis, highlighting the stability boundaries of system; b) non–linear analysis, simulating the transient of all the relevant variables involved in the simulation. The balance equation of mass, energy and momentum are discretized by the finite–volume method and a classical ‘staggered mesh’ scheme is used: in the centers of the nodes, scalar quantities are defined, while the vector ones variables (velocities and flow rates) are defined at the junctions. The original code had been written using a first upwind order scheme for the discretization of balance equations; so, the program has been modified implementing the Warming-Beam second order diffusion scheme [17], while keeping the ‘staggered mesh’ approach (**Figure 1**).

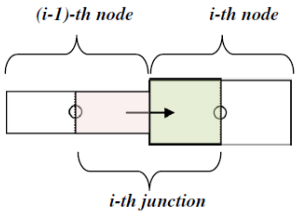

Figure 1 - Sketch of node and junction “staggered mesh” arrangement

2.1 Balance equations

The balance equations are written in one-dimensional form; the variables are averaged on the cross section of pipe. The balance equation of mass is written as

$$\left(\frac{\partial \varrho A}{\partial t}\right)_i + \left(\frac{\partial W}{\partial s}\right)_i = 0 \tag{1}$$

whose discretisation in finite volume form is

$$\varrho_{f,i}^{n+1} = \varrho_{f,i}^{n} + (W_i^{n+1} - W_{i+1}^{n+1})\frac{\Delta t}{V_i} \tag{2}$$

The thermal energy balance equation is written neglecting the dissipation and 'flow work' terms

$$\left(\frac{\partial \rho h_f}{\partial t}\right)_i + \frac{1}{A_i}\left(\frac{\partial W h_f}{\partial s}\right)_i = \frac{1}{A_i}\Pi_{w,i}^{in}\hat{h}_{w,i}^{in}(T_{w,i} - T_{f,i}) \tag{3}$$

leading to the dsicretised form

$$\varrho_{f,i}^{n+1}h_{f,i}^{n+1} = \varrho_{f,i}^{n}h_{f,i}^{n} + \left(W_i^{n+1}\,h_{f,i}^{\cdot n} - W_{i+1}^{n+1}h_{f,i+1}^{n\cdot}\right)\frac{\Delta t}{V_i} + A_{w,i}^{in}\hat{h}_{w,i}^{in}\,(T_{w,i}^{n} - T_{f,i}^{n})\frac{\Delta t}{V_i} \tag{4}$$

Considering the general case with nodes of different transverse sections, momentum equation is written evaluating the separate contribution from left and right segment of '(i)-th' junction (**Figure 1**). The space-discretised formulation of momentum equation is written:

$$\left[\frac{\Delta s_{i-1}}{2A_{i-1}} + \frac{\Delta s_i}{2A_i}\right]\frac{dW_i}{dt} = \frac{\overline{W}_{i-1}^2}{\varrho_{f,i-1}A_{i-1}^2} - \frac{W_i^2}{2\dot{\varrho}_{f,i}A_{i-1}^2} + \frac{W_i^2}{2\dot{\varrho}_{f,i}A_i^2} - \frac{\overline{W}_i^2}{\varrho_{f,i}A_i^2}$$

$$-\left[\frac{\Pi_{f,i-1}^{frict}}{A_{i-1}}\frac{\Delta s_{i-1}}{2}\,f_{fann,i-1}\frac{1}{2\varrho_{f,i-1}A_{i-1}^2} + \frac{\Pi_{f,i}^{frict}}{A_i}\frac{\Delta s_i}{2}f_{fann,i}\frac{1}{2\varrho_{f,i}A_i^2} + K_i\frac{1}{2\dot{\varrho}_{f,i}\left(A_i^{jun}\right)^2}\right]|W_i|W_i \tag{5}$$

$$+p_{i-1} - p_i + \varrho_{f,i-1}g_{i-1}\frac{\Delta s_{i-1}}{2} + \varrho_{f,i}g_i\frac{\Delta s_i}{2}$$

The pressure variations across junctions due to sudden area change are evaluated by the Bernoulli theorem, while the wall-friction contribution is calculated with a Fanning factor evaluated from a from Darcy-Weisbach factor correlation obtained by the Churchill [18] approximation. The walls of the loop are assumed with sufficiently small Biot number, so to justify a lumped parameter treatment of the transient behavior:

$$\frac{dT_{w,i}}{dt} = \frac{q_{w,i}'''}{\varrho_{w,i}C_{pw,i}} + \frac{\hat{h}_{w,i}^{out}\Pi_{w,i}^{out}}{A_{w,i}\varrho_{w,i}C_{pw,i}}(T_{f,i}^{out} - T_{w,i}) - \frac{\hat{h}_{w,i}^{in}\Pi_{w,i}^{in}}{A_{w,i}\varrho_{w,i}C_{pw,i}}(T_{w,i} - T_{f,i}) \tag{6}$$

The fluid-to-wall heat transfer coefficient can be assigned in input or evaluated with the classical Colburn law for forced convection in circular pipes, to be considered as a first guess to be replaced by more appropriate correlations for supercritical fluids in a further phase.

2.2 Steady-state calculation and linear stability analysis

Steady-state conditions are needed as starting point for any perturbation to be included in the analysis in the purpose of evaluating stability. The distribution of fluid temperature in the loop (having an arbitrary composition of heat sources and sinks) must be periodical and the mass flow rate must be such that an appropriate balance between friction and buoyancy forces is achieved. In order to reach, these conditions an iterative algorithm is written with the following steps:

- a first guess of mass flow rate is assigned

$$W_i = W^{ss} \qquad (i=1,...,N) \tag{7}$$

- enthalpy is initialized in the first node $h_1 = h_1^{ss}$,thus evaluating the corresponding distribution along the loop by the energy balance:

$$\dot{h}_{f,i+1}^{ss} = \dot{h}_{f,i}^{ss} + \frac{A_w^{in}\hat{h}_{w,i}^{in}}{W^{ss}}\left[T_{w,i}^{ss} - T_{f,i}^{ss}\right] \tag{8}$$

  owing to nonlinearities, the above expression is solved making use of a Newton iterative method;
- after convergence on fluid temperature, the properties are updated and a new mass flow value is calculated by momentum equation

$$\sum_{i=1}^{N}(GRAV_i) - \sum_{i=1}^{n}(FRICT_i)\, W^{ss}\, W^{ss} = 0$$

  where the $GRAV_i$ and $FRICT_i$ terms express the effects of gravitational and friction forces.

The process is repeated until convergence.

The variables calculated from the steady-state analysis (enthalpies, temperatures, pressures and mass flow rates at junctions) are then separately perturbed by a small quantity and then their evolution in a single time-step is used to establish if they are damped or amplified. The purpose of this process is to perform the linear stability analysis around the selected fixed point.

In particular, a matrix '**A**' is built, representing the linear dynamics of the system; in fact, by representing with $(\delta y)^{n+1}$ and $(\delta y)^n$ the vectors containing the perturbed variables at the previous and the next time step it is, '**A**' satisfies the relation:

$$(\delta y)^{n+1} = \mathbf{A}(\delta y)^n \tag{9}$$

The system is then stable when the matrix **A** is convergent, i.e. has a spectral radius lower than unity. The eigenvalues analysis, as reported in previous publications (see e.g., [16]) leads to the following definitions:

$$\rho(\mathbf{A}) = \max_i |\lambda_i| = e^{Z_R \Delta t} \tag{10}$$

$$Z_R = \frac{1}{\Delta t}\ln[\rho(\mathbf{A})] \tag{11}$$

Z_R gives the possibility to generate stability maps in the form of contour plots as a function of relevant boundary conditions: if $Z_R < 0$ *the system is stable,* while if $Z_R > 0$ it is unstable.

2.3 Numerical diffusion

As known, the numerical solution of partial differential equations brings about a truncation error whose effect may change the mathematical character of the equation itself. For advection dominated problems, the presence of second order derivatives in the expression of the truncation error leads to the introduction of a diffusive behavior that is generally unwanted. This is typical of the first order upwind scheme formulation initially adopted in NCLoop, which suggested its replacement with a second order numerical scheme, adapted from an original Warming-Beam formulation [17] and rewritten in a finite volume formulation with 'donor cell' rule (see e.g., [16]). The resulting form of the energy equation is similar to that obtained with the upwind first order scheme, but the 'donored' enthalpies have different values; this allows to improve the accuracy in the calculation though maintaining a form similar to the one of the first order scheme.

In particular, it is:

a) upwind first order scheme

$$\dot{h}_{i+1} = h_i \qquad (W_{i+1} > 0) \qquad (i = 1,\ldots,N) \tag{12}$$

$$\dot{h}_{i+1} = h_{i+1} \qquad (W_{i+1} < 0) \qquad (i = 1,\ldots N) \tag{13}$$

b) upwind low diffusion scheme

$$\dot{h}_{f,i+1} = \left[1 - \xi_{w,i+1}(W_{i+1})\right] h^n_{f,i} + \xi_{w,i+1}(W_{i+1}) h^n_{f,i-1} + D_i \qquad (W_{i+1} > 0) \quad i = (1,\ldots,N) \tag{14}$$

$$\dot{h}_{f,i+1} = \left[1 - \xi_{w,i+1}(W_{i+1})\right] h^n_{f,i+1} + \xi_{w,i+1}(W_{i+1}) h^n_{f,i+2} + D_{i+1} \qquad (W_{i+1} < 0) \quad i = (1,\ldots,N) \tag{15}$$

In the above formulations, ξ represents a weighting function coherent with an interpretation of the Warming-Beam numerical scheme in terms of the fraction of node masses crossing the junctions during a time step.

$$\xi^n_{w,i+1}(W^n_{i+1}) = \frac{W^n_{i+1}\Delta t - \varrho_{f,i} V_i}{\varrho_{f,i} V_i + \varrho_{f,i-1} V_{i-1}} \tag{16}$$

Junction enthalpies are evaluated on its basis making use of a linear interpolation. The term D_i, appearing in the formulation of the donored enthalpy (Eqs. 14 and 15), is then calculated taking into account the presence of the heating sources in the nodes joined by the junction. This term is needed in order to make transient calculations performed with constant boundary conditions to be coherent with the steady state ones at any value of the adopted time-step. It has the form:

$$D_i = \left(\alpha^n_i\, \xi_{w,i+1}(W_{i+1}) + (1 - \alpha^n_i)\right)\left(\dot{h}_{fi+1} - \dot{h}^n_{f,i}\right) + \xi_{w,i+1}(W_{i+1})(1 - \alpha^n_{i-1})\left(\dot{h}^n_{f,i} - \dot{h}^n_{f,i-1}\right) \tag{17}$$

The constants α^n_i appearing in this relationship relates the donored fluid enthalpies at junctions with the average fluid enthalpy in the node and are evaluated by exponential functions depending on flow rate and heat transfer coefficients at the wall. Their expression is omitted here.

3. Results from preliminary case studies

The calculation cases reported hereafter address idealised loops having adiabatic pipes or walls with decreased heat capacity in the conducting structures. In fact, the presence of heating structures is likely to mask the effects due to numerical diffusion, something that was avoided in these first analyses, in order to show the improvements obtained by the new implemented numerical scheme.

3.1 Welander's loop

A first application to the stability analysis of natural circulation refers to Welander's loop [19]. Though the problem is conceived for subcritical single-phase flow, it was here reconsidered at a supercritical pressure, with a cold, liquid-like fluid just to prove the functionality of the program and the low numerical diffusion of the new numerical scheme. As known, Welander's loop is an elementary thermosyphon loop (**Figure 2**) with two adiabatic legs joined by very short horizontal pipes equipped with relatively large heat transfer surfaces at imposed temperatures.

Welander, in his analysis, identified the conditions for the onset of flow and temperature oscillations. Trying to give an explanation to these phenomena, he introduced the 'hot pocket' idea. The 'hot pockets' are small thermal perturbations (which are formed in the heater/cooler) whose passage through pipes can create instability. Detailed descriptions of the 'hot pockets' mechanism is provided by Vijayan, et al. (1995) [20]. Originally the loop was described in dimensionless terms, but herein a particular numerical realization used by Ambrosini and Ferreri (2003) [16] is considered: two vertical adiabatic legs have a length of 10 m and a diameter of 0.1 m, the horizontal pipes have the same diameter and a length of 0.1 m. These dimensions have been utilized in the simulation NCLoop.

Figure 2. Sketch of Welander's loop (1967) [19]

Other simulation parameters are the internal heat transfer coefficients for heater and cooler, imposed to 20000 $W/(m^2K)$; the temperatures for these elements, respectively maintained at 30 °C e 20 °C by imposing an external heat transfer coefficient of 10^{10} $W/(m^2K)$. The structures were simulated with a very low volumetric heat capacity and high conductivity, to make immaterial their role. The working fluid is chosen to be water at 23 MPa which, at the mentioned temperature, is a relatively heavy liquid-like fluid possessing enough thermal expansion capability to trigger natural circulation. In this respect, the problem is very similar to the one proposed by Welander, though the fluid pressure is much higher; this situation was selected to test the numerical scheme on a problem very close to a well-known one. Linear stability maps were generated as a function of the value of the source temperature and of the internal heat transfer coefficient of source and sink. **Figure 3** reports the results obtained by the first order upwind scheme based on donor-cell rule, when 30 nodes are adopted to discretize the 10 m

long legs; the heater and the cooler, instead, are discretized with only a single node. The map shows a large region where the system is stable but, as reported in the following figures, this is clearly an effect of truncation error. In fact, using the second order scheme and maintaining the same node size, as reported in **Figure 4**, a much smaller stability region is obtained. By reducing the size of the nodes by using 90 nodes per leg, the lower numerical diffusion of the second order scheme for smaller meshes is observed (**Figure 5**), while the low diffusion scheme returns nearly the same results (**Figure 6**), showing the better level of convergence reached with only 30 nodes per leg.

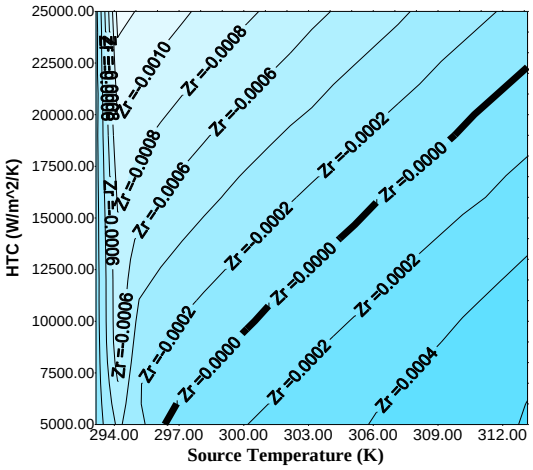

Figure 3. Welander's problem : stability map obtained with the first order upwind scheme (30 nodes per leg, Δt =0.5 s)

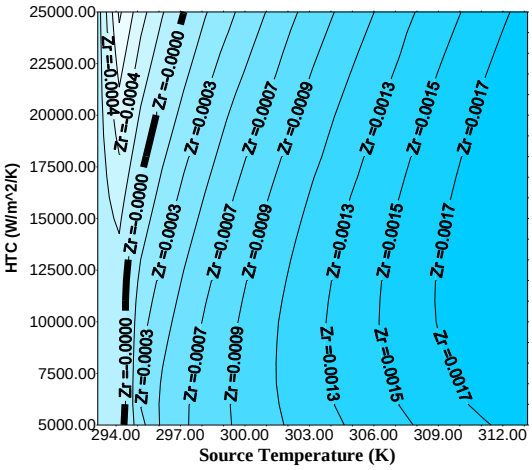

Figure 4. Welander's problem: stability map obtained with the low diffusion scheme (30 nodes per leg, Δt = 0.5 s)

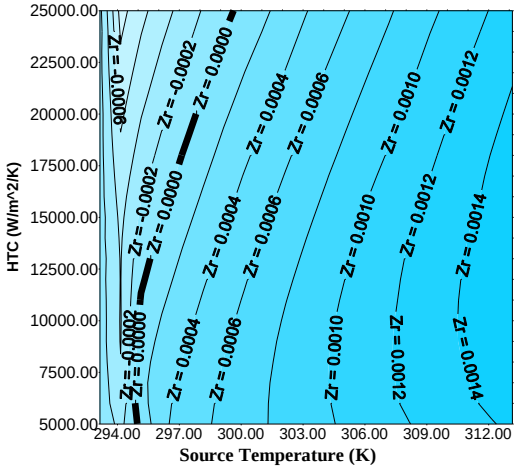

Figure 5. Welander's problem: stability map obtained with the first order upwind scheme (90 nodes per leg ,Δt =0.5 s)

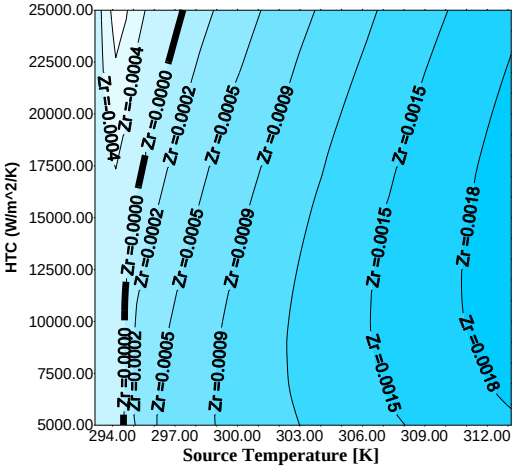

Figure 6. Welander's problem: stability map obtained with the low diffusion scheme (90 nodes per leg, Δt =0.5 s)

3.2 BARC loop

The Bhabha Atomic Research Center (BARC) designed and run an experimental loop for the analysis of stability of natural circulation with supercritical fluids [11]. The loop can operate at multiple operating pressures either with water or with carbon dioxide in the supercritical state. From the geometrical point of view, the loop is rectangular (**Figure 7**), the internal diameter is 13.88 mm while the outer diameter is 21.34 mm. The horizontal elements have a width of 3.01 m, the vertical ones have a height of 4.1 m. As reported in **Figure 7** the loop includes two

heaters and two coolers arranged in different positions in order to allow for the possibility to perform experiments in multiple configurations. The cooler is a tube-in-tube heat exchanger, with an internal diameter of 77.9 10^{-3} m and the cooling can be obtained by water or air as cooling fluids.

The vertical branches of the loop are thermally isolated with ceramic material. In the simulation, the loop is divided into twelve elements, three per each section. The outer heat transfer coefficient for the cooler is imposed equal 335 W/(m^2K) for the case in which water circulates and 850 W/(m^2K) for the circulation of carbon dioxide. The thermal conductivity for all elements is imposed at 16 W/(mK), a typical value for stainless steels. In these analyses, it was necessary to decrease the thermal capacity of the heating structures in order to highlight the effects of numerical diffusion: as previously mentioned, the heat capacity of the wall can lead to the stabilizing effects which were not wanted in this case. The simulations reported were generated as a function of heater power and outer heat transfer coefficient; the fluids used in the analysis were water and carbon dioxide respectively at 23 MPa and 8 MPa.

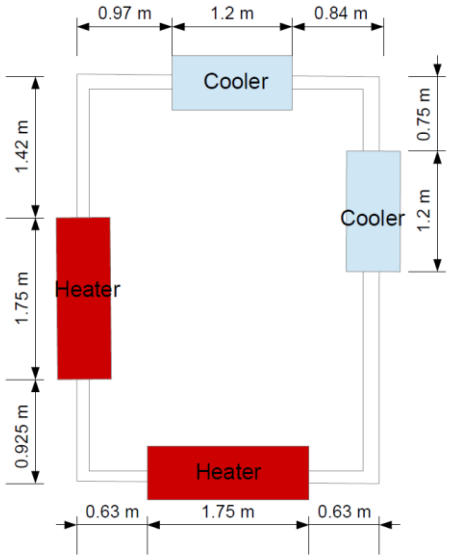

Figure 7. Simplified scheme of BARC loop (Sharma, et al., 2013)

3.2.1 Simulation with water (HHHC configuration)

Figure 8 shows the stability map obtained with the first order upwind scheme using a relatively 'coarse' nodalization (76 nodes): the stability threshold of the system is reached for a heating power between 3000 W and 5500 W, depending on the value of the outer HTC. Using a 'finer' nodalization (353 nodes) the numerical diffusion effects disappear and the system results unstable for any value of power, as shown in the **Figure 9**. The map, reported in **Figure 10** refers to the Warming-Beam scheme with the coarser nodalisation (76 nodes); as it can be noted the obtained results are quite similar to those provided by the finer nodalization and the first order numerical scheme (**Figure 9**), showing the superior behaviour of the low diffusion numerical scheme for stability applications.

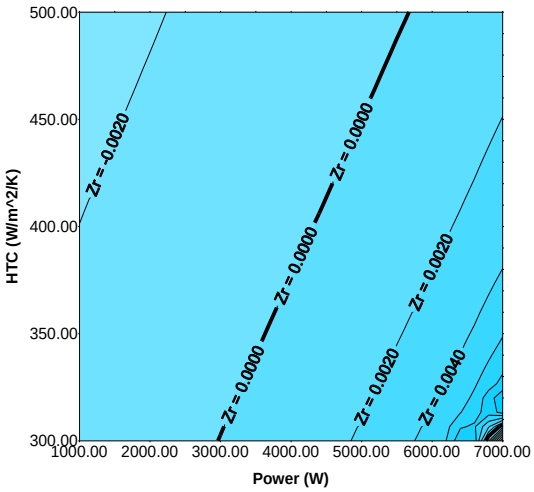

Figure 8. BARC loop : stability map obtained with the first order upwind scheme (76 nodes, Δt = 0.1 s, reduced pipe heat capacity)

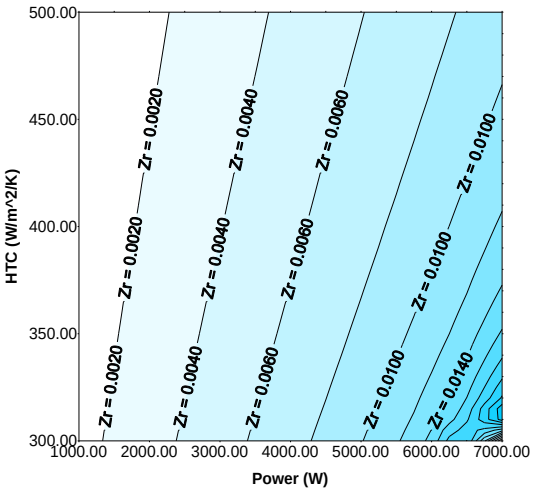

Figure 9. BARC loop: stability map obtained with the first order upwind scheme (353 nodes, Δt = 0.1 s, reduced pipe heat capacity)

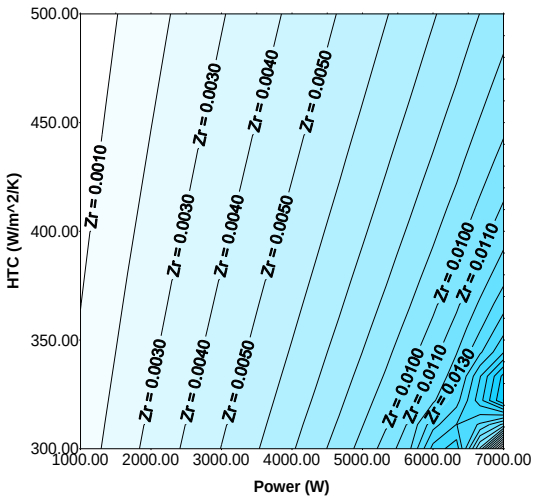

Figure 10. BARC loop: stability map obtained with the low diffusion scheme (76 nodes, Δt = 0.1 s, reduced pipe heat capacity)

3.2.2 Simulation with carbon dioxide (HHHC configuration)

In the simulations performed with carbon dioxide, the same of geometrical parameters as in the previous cases were used. Calculations are again performed with the first order numerical scheme with a 'coarse' nodalization of the computational domain, obtaining the results reported in **Figure 11**. It is possible to see a little area where the system is unstable, in particular for power values between 300 W and 1000 W, as a function of the outer HTC. **Figure 12** shows the simulation obtained with the low diffusion scheme: the map is similar to the one in the previous figure but the zone where system is predicted unstable is much larger. On the other hand, a 'fine' nodalization of the loop with the first order upwind scheme leads to a map (**Figure 13**) very similar to map in the **Figure 12**.

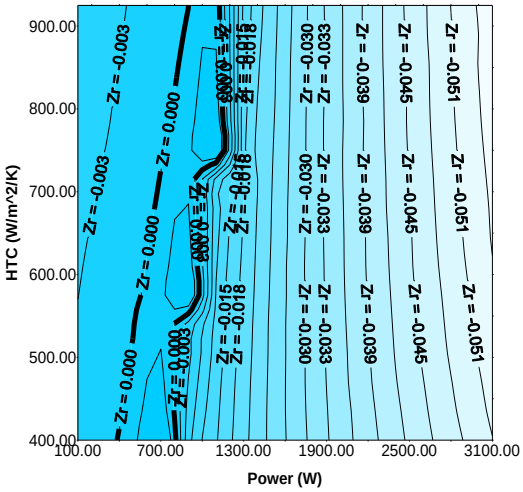

Figure 11. BARC loop : stability map obtained with the first order upwind scheme (89 nodes, Δt = 0.1 s reduced pipe heat capacity)

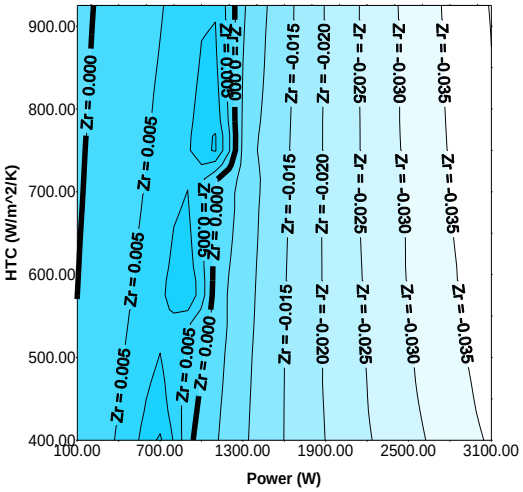

Figure 12. BARC loop : stability map obtained with the low diffusion scheme (89 nodes, Δt = 0.1 s, reduced pipe heat capacity)

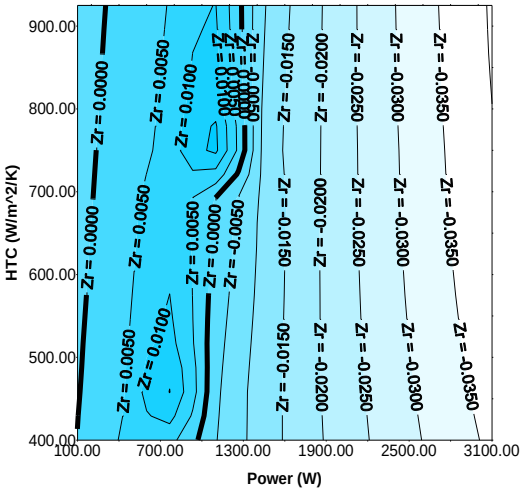

Figure 13. BARC loop: stability map obtained with the first order upwind scheme (190 nodes, Δt = 0.1 s, reduced pipe heat capacity)

Simulations have been performed also considering values of the pipe heat capacity corresponding to real conditions. In such cases, the greater stability induced by the pipe walls masks the benefits of the low diffusion numerical scheme, being the focus of this paper. A discussion of the effectiveness of the computer program in simulating real conditions is also conditioned to the adoption of appropriate closure laws, capable to represent friction and heat transfer phenomena with supercritical fluids.

4. Conclusions

After the advancements performed in recent times by developing a new program for the transient and linear stability analysis of natural circulation loops with fluids at supercritical pressure [15], in this work a low diffusion numerical scheme has been developed and included in the program in order to allow for a more reliable analysis of loop dynamic conditions.

The results of the checks performed in this work on the capabilities of the numerical scheme are quite encouraging. Having eliminated the most important effects of numerical discretisation, the program is now ready to be used as a useful simulation tool to analyse observed experimental data, thus discussing the effectiveness of the most appropriate physical laws to represent friction and heat transfer without the possible bias brought about by truncation error.

References

1. Kelly, J., 2014. Generation IV International Forum: A decade of progress through international cooperation. Progress in Nuclear Energy 77 , 240-246

2. Pioro, I.L., Duffey, R.B., 2007. Heat Transfer and Hydraulic Resistance at Supercritical Pressure in Power Engineering Applications. ASME Press, New York.

3. IAEA, 2005. Natural circulation in water cooled nuclear power plants. IAEA TECDOC 1474

4. Ambrosini, W., 2013. A model for linear and non-Linear stability analysis of general natural circulation loops with supercritical pressure fluids. Università di Pisa, dipartimento di Ingegneria Civile e Industriale, DICI RL12

5. Chatoorgoon, V., 2001. Stability of supercritical fluid flow in a single-channel natural-convection loop. International Journal of Heat and Mass Transfer 44, 1963–1972.

6. Chatoorgoon, V., Voodi, A., Fraser, D., 2005a. The stability boundary for supercritical flow in natural convection loops, Part I: H2O studies. Nuclear Engineering and Design 235, 2570–2580.

7. Chatoorgoon, V., Voodi, A., Upadhye, P., 2005b. The stability boundary for supercritical flow in natural convection loops, Part II: CO 2 and H2 studies. Nuclear Engineering and Design 235, 2581–2593.

8. Chen, L., Dheng, B., Jiang, B., Zhang, X., 2013.Thermal and hydrodynamic characteristics of supercritical CO2 natural circulation in closed loops. Nuclear Engineering and Design 257 , 21– 30

9. Debrah, S.K., Ambrosini, W., Chen, Y., 2013. Discussion on the stability of natural circulation loops with supercritical pressure fluids. Annals of Nuclear Energy 54, 47-57

10. Lomperski, S., Cho, D., Jain, R., Corradini, M.L., 2004. Stability of a Natural Circulation Loop with a Fluid Heated Through the Thermodynamic Pseudo-critical Point. In: Proceedings of ICAPP'04, Pittsburgh, PA, USA, June 13–17, Paper 4268.

11. Sharma, M., Pilkhwal , D.S., Vijayan, P.K., Saha, D., Sinha, R.K., 2010. Steady state and linear stability analysis of a supercritical water natural. Nuclear Engineering and Design 240 , 588–597

12. Sharma, M., Vijayan, P.K., Pilkhwal , D.S., Asako , Y., 2013. Steady state and stability characteristics of natural circulation loops operating with carbon dioxide at supercritical pressures for open and closed loop boundary conditions. Nuclear Engineering and Design 265 , 737– 754

13. Sharma, M., Vijayan, P.K., Pilkhwal , D.S., Asako , Y., 2014. Natural convective flow and heat transfer studies for supercritical water in a rectangular circulation loop. Nuclear Engineering and Design 273, 304–320

14. Swapnalee, B.T. , Vijayan ,P.K. , Sharma, M. , Pilkhwal, D.S., 2012. Steady state flow and static instability of supercritical natural circulation loops. Nuclear Engineering and Design 245, 99– 112

15. Debrah, S.K., Ambrosini, W., Chen, Y., 2013, Assessment of a new model for the linear and nonlinear stability analysis of natural circulation loops with supercritical fluids, Annals of Nuclear Energy 58 , 272–285.

16. Ambrosini, W., Ferreri, J.C., 2003. Prediction of stability of one-dimensional natural circulation with a low diffusion numerical scheme. Annals of Nuclear Energy 30 , 1505–1537

17. Warming, R.F., Beam, R.M., 1976. Upwind second-order difference schemes and applications in unsteady aerodynamic flows. AIAA J. 14 , no. 9, 1241–1249.

18. Churchill, S.W., 1977. Friction equation spans all fluid flow regimes. Chemical Engineering 84 (24), 91-92

19. Welander, P., 1967. On the oscillatory instability of a differentially heated fluid loop. Journal of Fluid Mechanics 29 , 17- 30.

20. Vijayan, P.K., Austregesilo, H., Teschendorff, V., 1995. Simulation of the unstable behavior of single-phase natural circulation with repetitive flow reversal in a rectangular loop using the computer code ATHLET. Nuclear Engineering and Design 155, 623-641

Nomenclature

Roman letters

A	area [m^2]
A	matrix representing linear dynamics
C_p	specific heat [J/(kgK)]
D_i	factor representing source term in energy equation
$f_{fanning}$	fanning friction factor
$FRICT_i$	friction term coefficient
g	gravity [m/s^2]
$GRAVM_i$	gravitational term coefficient
h	specific enthalpy [J/(kg)]
$\dot{h}$	'donored' specific enthalpy [J/(kg)]
$\widehat{h}$	heat transfer conductance [$W/(m^2K)$]
K	singular press drop coefficient
N	number of nodes
p	pressure [Pa]
q'''	volumetric heat power [W/m^3]
s	axial coordinate along the loop [m]
T	temperature [K]
t	time [s]
V	volume [m^3]
W	mass flow rate [kg/s]
Z_R	real part of the exponent z in time evolution

Greek letters

α_i^n	weighting constant
δy	vector containing the perturbed variables
λ	eigenvalue
ξ	numerical weighting function
Π	Perimeter [m]
ϱ	density [kg/m^3]
$\rho(\mathbf{A})$	spectral radius of matrix **A**

Subscripts

f	fluid
i	node or junction index
w	wall

Superscripts

frict	friction
in	inner
jun	juncton
n,n+1	time level
out	outer
ss	steady state
$\bar{\sigma}$	average value

ISSCWR7-2023

Insight from simple heat transfer models

Donald M. McEligot[1,2] and Eckart Laurien[2]
1) Mechanical Engineering Dept., U. Idaho, Idaho Falls, Ida. 83402, USA
2) Institut für Kernenergetik und Energiesysteme (IKE), Uni. Stuttgart, D-70569 Stuttgart, Deutschland
49-(711)-685-62138, Donald.McEligot@ike.uni-stuttgart.de

Abstract

Heat transfer to supercritical-pressure fluids flowing turbulently in ducts is a lovely, complicated situation. Considerable research has been devoted to it for decades --- and is continuing. We now have computational thermal fluid dynamics (CTFD) predictions, direct numerical simulation (DNS) results and scads of correlations to address the problem. The present study takes a different tack. Quasi-developed turbulent flow in a duct is simplified in order to develop semi-analytic treatments of dominant phenomena in the pseudocritical region. Via approximations and basic assumptions, the model is developed to provide a closed-form relation accounting for extreme property variations with wall and/or core temperatures in the pseudocritical region. Typical predictions are compared to results of DNS to evaluate levels of confidence that might be warranted. Consequences of reference property selection are considered. The analyses can provide approximate predictions and foundations of more generalized treatments.

1. Introductory comments

Enhancement and deterioration are in the minds of beholders. For heat transfer to flowing supercritical-pressure fluids in the vicinity of the pseudocritical region, a set of data can give heat transfer parameters which are considered to represent enhancement to one observer and deterioration to another. For example, Figure 1 shows data from an experiment by Ornatskii, Glushchenko and Kalachev [1971] for heat transfer to supercritical water compared to a correlation of Humble, Lowdermilk and Desmon [eq. 14, 1951] for heat transfer to gases with strong property variation with 0.023 as the coefficient. The pseudocritical temperature T_{pc} and the region around it are indicated by the curve of specific heat, $c_p\{T_w\}$. In this case, one sees unexpected reasonable agreement in the "liquid-like" region then, as T_w crosses the pseudocritical region, the Nusselt number based on wall thermal conductivity (Nu_w) begins to increase relative to the correlation; we could call the heat transfer "enhanced" on this basis while other investigators find it "deteriorated" based on other comparisons. .

In the present paper we consider heat transfer to supercritical-pressure fluids flowing steadily through smooth ducts. Behavior beyond the influence of the duct entrance is treated; this region is expected to become "quasi-developed" [McEligot, Smith and Bankston, 1970; Laurien, 2012] thereby reducing the complexity of the analysis. The core flow is turbulent and the extreme fluid property variation through the pseudocritical region is included. Buoyancy forces are neglected. Heat transfer

from the wall to the fluid is studied; while parts of the analysis are reasonable for cooling, some of the assumptions we use would not be valid.

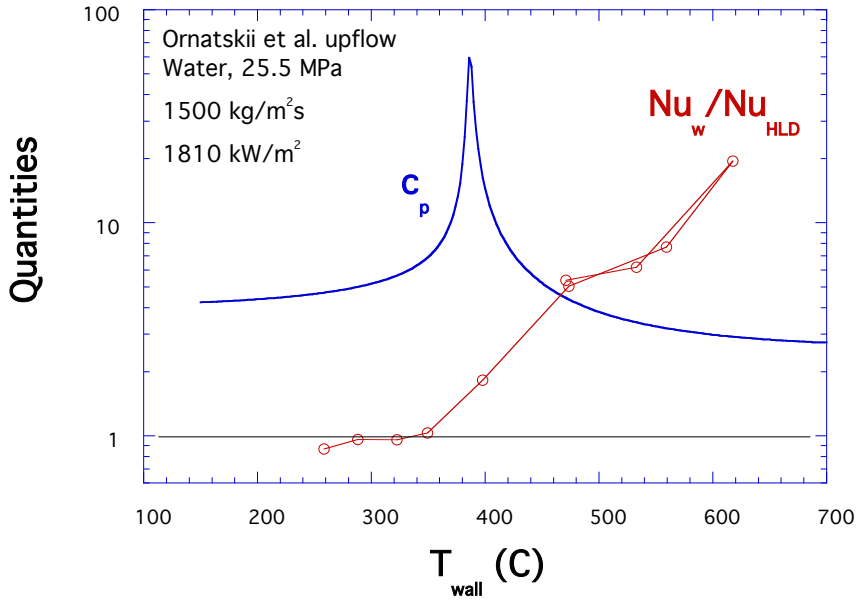

Figure 1. Comparison of data from Ornatskii, Glushchenko and Kalachev [1971] for heat transfer to supercritical water to the empirical correlation of Humble, Lowdermilk and Desmon [1951] for heat transfer to gases with large temperature differences.

For decades, investigators have had difficulties in predicting heat transfer parameters in supercritical fluid flows, particularly when the pseudocritical region is involved. (Readers are referred to articles by Ambrosini [2011], Pioro and Duffey [2007], Yoo [2013] and many others where the variations of the various pertinent properties are displayed graphically.) The "pseudocritical" temperature T_{pc} is defined as the temperature at which the specific heat c_p shows a maximum at a given pressure and the pseudocritical region is the range around it where properties vary severely from those of a liquid to those of a common gas. Heat transfer behavior in the liquid-like and gas-like extremes is reasonably predictable with standard correlations which include treatment of moderate transverse property variation (e.g., McEligot, Magee and Leppert [1965]). Difficulties occur when there is large property variation across the wall layer --- as when the turbulent core flow is below T_{pc} and the wall temperature T_w is above.

For insight into some key effects, one can use a thermal resistance analogy for heat transfer from the heated wall to the denser turbulent core flow. As suggested by McEligot [1967] in considering quasi-developed gas flows with property variation, the convective heat flux can be expressed as $(T_w - T_c) = q_w" \Sigma R_i$ where the thermal resistances R_i represent the individual thermal resistances of two, three or maybe four successive layers. The old text by Knudsen and Katz [1958] gives useful explanations of several of the analogies at the time in terms of approximate fluid layers. For clarity (and convenience) we will employ an extension of the two-layer Prandtl [1910] analogy.

In this paper we will first describe the simple two-layer model for fluids with significant property variation, in particular as when the pseudocritical region is involved, and will demonstrate some justification for our assumptions with results

from direct numerical simulations (DNS). The resulting relation for heat flux will be evaluated employing the temperature of the turbulent core as a reference. Then the wall temperature will be used instead to show effects of this choice. Subsequently, our predictions will be compared to those of a direct numerical simulation to give an idea what level of confidence is warranted in the simple analysis. We finish with some concluding remarks and discussion of logical extensions to the analytical approach.

2. Two-layer model

As in the Prandtl analogy [1910], two layers are considered: (1) a layer near the wall where molecular transport dominates and turbulent transport is ignored and (2) a denser, well-mixed turbulent core where the molecular transport is ignored. The "non-slip" smooth wall is impermeable. Buoyancy and fluid acceleration are neglected. The wall layer thickness is taken as sufficiently thin that wall curvature, if present, can also be neglected so rectangular coordinates are used for this layer. Boundary layer approximations are assumed and, following Prandtl and the text by Kays [1966], q"{y} is taken as equal to q_w" in this layer – a constant heat flux approximation. These assumptions and approximations reduce determination of the transverse temperature distribution to integrating Fourier's Law,

$$q"\{y\} = - k\{T\} (\partial T/\partial y) \approx q_w" \qquad (1)$$

from y = 0 to y within this wall layer. The definite integral can be written as

$$q_w" \, y \approx \int_{Tref}^{Tw} k\{T\} \, dT - \int_{Tref}^{Ty} k\{T\} \, dT \qquad (2)$$

Then this equation can be evaluated for T_l at y_l, the edge of this wall layer.

The integral of the thermal conductivity, a property, can be considered a property itself and can be tabulated as such in tables of properties. So we define it as

$$\omega\{T\} = \int_{Tref}^{T} k\{T\} \, dT \qquad (3)$$

and tabulate it with our table of properties for the specific supercritical pressure of interest. Thus, equation (2) can be streamlined to $q_w" \, y_l \approx \omega_w - \omega_l$ where ω_l is the value at temperature T_l at y_l.

The ideas that the turbulent core is denser, is well-mixed and has higher effective thermal conductivity lead one to expect that its thermal resistance is small relative to that of the wall layer (and can be approximated as negligible). If this situation is the case, the central temperature would be approximately the same as the fluid bulk temperature. One can examine this possibility with temperature profiles from the DNS of J. H. Bae, Yoo and Choi [2005; McEligot et al., 2005].

Case A by Bae treats pure forced convection with a constant wall heat flux applied to flowing carbon dioxide at a supercritical pressure of 8.0 MPa. The entering temperature is 28 C, which is below T_{pc} but already essentially in the pseudocritical region. The heated circular tube length is 30 D. Figure 2 provides the mean temperature profile at x ≈ 29 D where the conditions appear quasi-developed and Re_b ≈ 6560. In this semi-logarithmic presentation the approximately-parabolic shape corresponds to dominant molecular transport, i.e., the wall layer. An approximately straight line from $(y/R_w) \approx 0.1$ to unity represents the turbulent core. The extensions of

these curves to their intersection at $(y/R_w) \approx 0.055$ defines the thickness y_l of the idealized wall layer. One can see, from the magnitudes on the ordinate, that the thermal resistance of the turbulent core is only about ten per cent of the total. Further, T_b is within about five per cent of T_c and about seven per cent of T_l (in terms of $[T_w - T\{y\}]/[T_w - T_b]$).

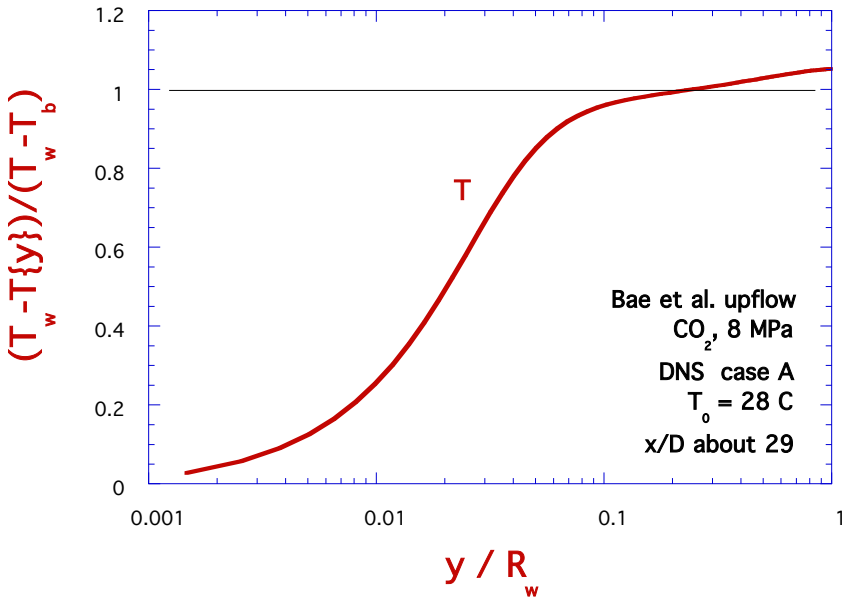

Figure 2. Predicted temperature profile from direct numerical simulation of heat transfer with constant wall heat flux to supercritical flow of carbon dioxide in downstream quasi-developed region without buoyancy effects [Bae, Yoo and Choi, 2005], $Re_b\{x\} \approx 6560$.

Based on this examination of the DNS temperature prediction, we simplify the analysis further by neglecting the thermal resistance of the turbulent core and taking T_c and T_l approximately equal to T_b. Thus, the simplified analysis is further reduced to approximation as

$$q_w'' \, y_l \approx \omega_w - \omega_c \approx \omega_w - \omega_b \qquad (4)$$

The convective heat transfer coefficient is then predicted to be $h \approx (1/y_l)(\omega_w - \omega_b)/(T_w - T_b)$ and the Nusselt number depends on the temperature chosen to evaluate the thermal conductivity. *For demonstration purposes*, we employ the correlation of Drew, Koo and McAdams [1932] to estimate y_l in sections 2.1 and 2.2 below; we recognize that it is not necessarily the best for this situation [Pioro and Duffey, 2007].

2.1 Predictions based on core (bulk) properties

Most, but not all, correlations for heat transfer to supercritical fluids are based on the fluid bulk temperature [Pioro and Duffey, 2007], probably because it can be predicted easily via an energy balance when the wall heat flux distribution is known. The fluid properties needed are evaluated at T_b. The correlations of Dittus and Bölter [1930] and Gnielinski [1975] are popular examples. For the present analysis we need the thickness of the wall layer y_l in equation (4) to predict the wall temperature T_w or the

wall heat flux. In this section we base its estimate on bulk properties after assuming that $y^+_{l,b} \approx 10$ is a reasonable value (guess) in wall coordinates.

From the definitions, y_l can be estimated as

$$(y_{l,b}/D) = y^+_{l,b} / (Re_b (f_b/2)^{½}) \quad (5)$$

where Re_b is defined as $GD/\mu\{T_b\}$ and the bulk friction factor is $(2\,\tau_w)/(\rho_b V_b^2)$. In our calculations we used the correlation by Drew, Koo and McAdams [1932] with Re_b for the friction factor in the present section (i.e., based on core/bulk properties). Alternatively, one could employ the Blasius correlation [Schlichting, 1968] or other popular ones as desired. The core or bulk Nusselt number is then $hD/k\{T_b\}$.

Figure 3 presents results for one example. In this case, the fluid is CO_2 and its pressure is 8.0 MPa, giving $T_{pc} \approx 34.6$ C ≈ 307.8 K, and $T_c \approx T_b$ is taken as 28 C. In our calculations fluid properties are obtained from the NIST REFPROP package [Lemmon, Huber and McLinden, 2010]. The bulk Reynolds number Re_b is chosen to be 10,000. Diameter D is 2 mm. The core temperature was held constant while predictions were calculated as T_w was varied. The dashed green line shows the prediction of the Dittus-Bölter correlation evaluated at $T_c \approx T_b$ which is held constant and, therefore, the predicted $Nu_{DB,c}$ is independent of T_w. The prediction from the simple analysis is shown by the solid blue line denoted Nu_c which remains approximately steady at first as T_w is increased but then decreases significantly passing through the pseudocritical region and begins increasing as T_w increases approaching gas-like behavior. In comparison to the Dittus-Bölter prediction one could say the heat transfer is "deteriorated." Also included is the prediction in terms of the wall Nusselt number, $hD/k\{T_w\}$, (dashed red curve) which is seen to differ significantly since the thermal conductivity at the wall becomes much less than in the core.

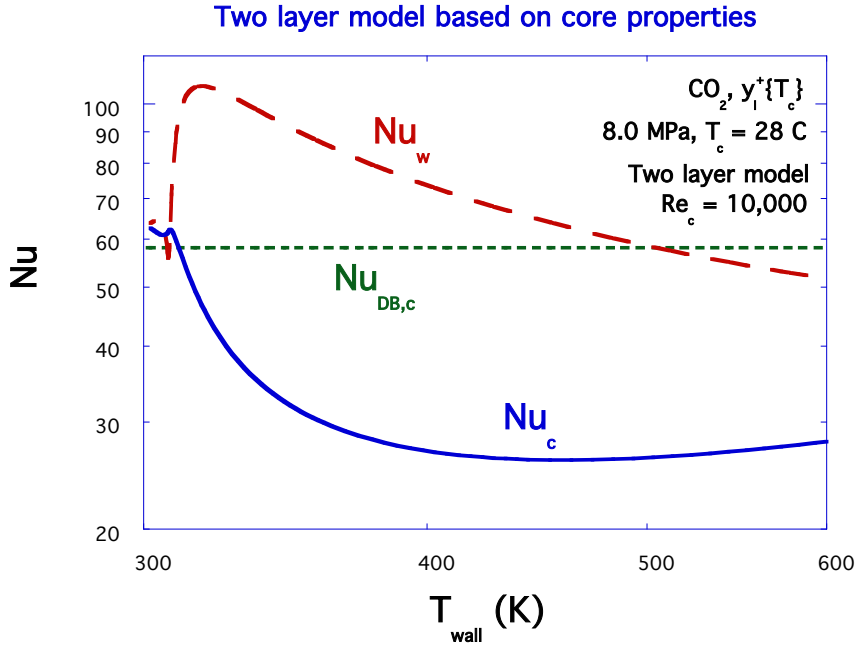

Figure 3. Forced convective heat transfer to supercritical flow of carbon dioxide as predicted by simple model with wall layer thickness based on properties of turbulent core flow. $Nu_{DB,c}$ is value forecast with Dittus- Bölter correlation [1930] using core (≈ bulk) properties.

2.2 Predictions based on wall properties

Since the main thermal resistance is provided by the wall layer, some investigators feel it could be best to predict the heat transfer behavior using the fluid properties in the wall region. This section applies the simple analysis to do so. Specifically, the wall layer thickness is estimated by employing wall properties including an appropriate correlation for evaluating the friction factor (friction velocity u_τ). The non-dimensional thickness is again taken as ten in wall coordinates but they are defined in terms of wall properties rather than core properties. We keep T_c at 28 C and start from Re_b = 10,000 again then vary T_w through the pseudocritical region (indicated approximately by variation of $Nu_{HLD,w}$ in Figure 4) into the gas-like region.

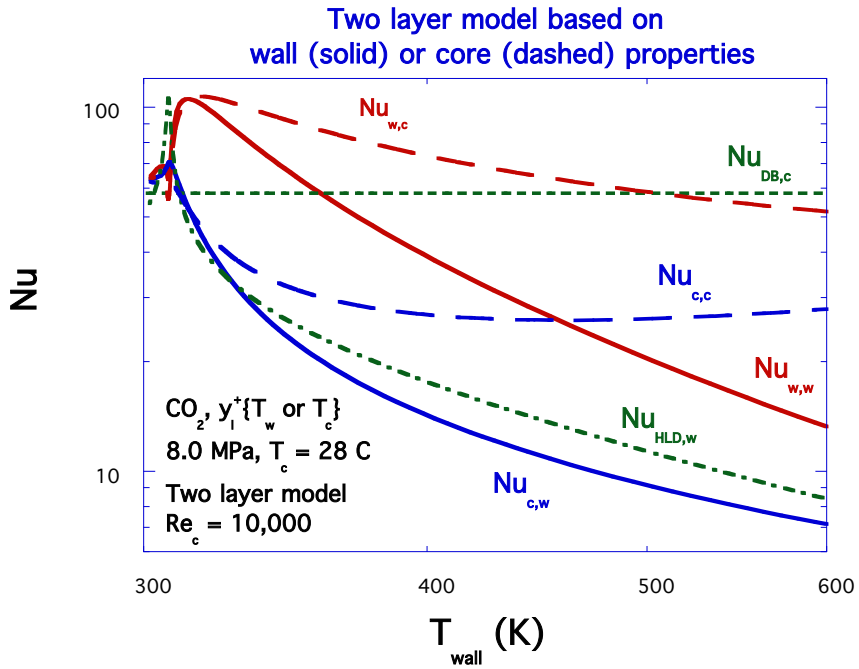

Figure 4. Forced convective heat transfer to supercritical flow of carbon dioxide as predicted by the simple model. Solid lines represent predictions with wall layer thickness based on wall properties while dashed are for thickness estimate based on core (bulk) properties. $Nu_{HLD,w}$ is the empirical correlation of Humble, Lowdermilk and Desmon [1951] employing wall properties.

There are several ways to apply wall properties in this analysis. For this example, we estimated the friction factor by evaluating the correlation of Drew, Koo and McAdams with the wall modified Reynolds number (= $V_bD/\nu\{T_w\}$) as

$$f_w \approx 0.0014 + 0.125\, Re_{w,m}^{(-0.32)} \qquad (6)$$

with the friction factor defined in terms of the wall density. For a given wall temperature, $Re_{w,m}$ is related to Re_b by the ratio of their kinematic viscosities, ν_b/ν_w. With the friction velocity defined here as $(\tau_w/\rho_w)^{1/2}$ and $y^+_{l,w}$ also based on wall properties, one can calculate the specified wall layer thickness as

$$(y_{l,w}/D) = y^+_{l,w} / (Re_{w,m}\,(f_w\{Re_{w,m}\}/2)^{1/2}) \qquad (7)$$

Taylor [1967] examined a wide range of experiments with strong gas property variation and found they could be represented by the correlation of Drew, Koo and McAdams with a temperature ratio. His correlation would introduce a factor of $(T_w/T_b)^{0.25}$ into the relation above (and into the Nusselt number relation in the present analysis).

Results are presented in Figure 4 where comparisons to the above predictions based on T_c are also included. Those using wall properties for estimating y_l are shown with the solid curves while the dashed curves reproduce the predictions of the previous section where the core properties were employed. In addition to the Dittus-Bölter prediction, the correlation by Humble, Lowdermilk and Desmon [1951] with a coefficient of 0.021 is shown as $Nu_{HLD,w}$; it is based on wall properties and was developed for heat transfer to gases with large temperature variations across the flow (as in the case of heat transfer to supercritical fluids).

Using wall properties, one finds increases in the Nusselt number initially as the wall temperature is increased through the pseudocritical region and then the Nusselt number dives. So initially the heat transfer can be considered to be enhanced relative to the Dittus-Bölter correlation and at a bit higher wall temperature then becomes "enhanced" relative to that of Humble, Lowdermilk and Desmon. When based on wall temperature, the predicted Nusselt number remains above $Nu_{HLD,w}$ as the temperature increases whereas Nu_c becomes lower ("deteriorated") as T_w increases. In our case, predicted Nusselt numbers generally are lower when the wall layer thickness is based on wall properties than on core properties.

2.3 Comparison to direct numerical simulation

To see whether any level of confidence in this analysis is justified, this two-layer model *based on wall properties* is compared to the temperature profile predicted via the DNS of Bae, Yoo and Choi [2005], their Case A, at x ≈ 29 D in Figure 5. The fluid is CO_2 at 8.0 MPa again. (The fluid properties differ slightly since Bae employed those from PROPATH [1999].) Tube diameter D is one mm. The heat flux and T_w were taken from the results of Bae. These choices allow deducing T{y} from ω{T} and equation (2) as q_w“ y ≈ $\omega_w - \omega_y$ for its position, y. At this streamwise position, the DNS predictions give $Re_b \approx 6560$, $f_b \approx 0.004729$, $T_{cl} \approx 30.1$ C, $T_b \approx 32.0$ C and $T_w \approx$ 69.3 C yielding $(y_{10,w}/R_w) \approx 0.049$ for a wall layer thickness.

One sees close agreement in the layer modeled from the wall to $(y/R_w) \approx 0.049$ here. And the predicted $T_l \approx 31$ C is close to Bae's T_c in accordance with the approximation that the thermal resistance of the core can be treated as negligible. Our values give $Nu_w \approx 56.8$, differing from Bae's DNS results by about four per cent; this value is probably fortuitous since the arbitrary choice of $y^+_{l,w}$ was primarily for demonstration purposes. These results seem reasonably good, particularly considering the lack of sophistication of our analysis.

3. Concluding remarks

In order to examine the effects of some phenomena believed to be dominant in heat transfer to supercritical fluids, a simplified analysis has been applied. We considered heat transfer from a smooth wall to the fluid; the core flow is turbulent and the extreme fluid property variation through the pseudocritical region is included. Key assumptions / approximations are quasi-developed flow, a well-mixed dense turbulent core, constant q”{y} across the wall layer and dominant forced convection. The idea that the thermal resistance of the near-laminar wall layer dominates is supported by the DNS of Bae, Yoo and Choi [2005]. Evaluation of the behavior in the wall layer is eased by considering the integral of the thermal conductivity as a property and adding

it to our tables of properties. It is demonstrated that use of wall and core (~bulk) properties gives significantly different Nusselt numbers. Predictions agree reasonably with the DNS.

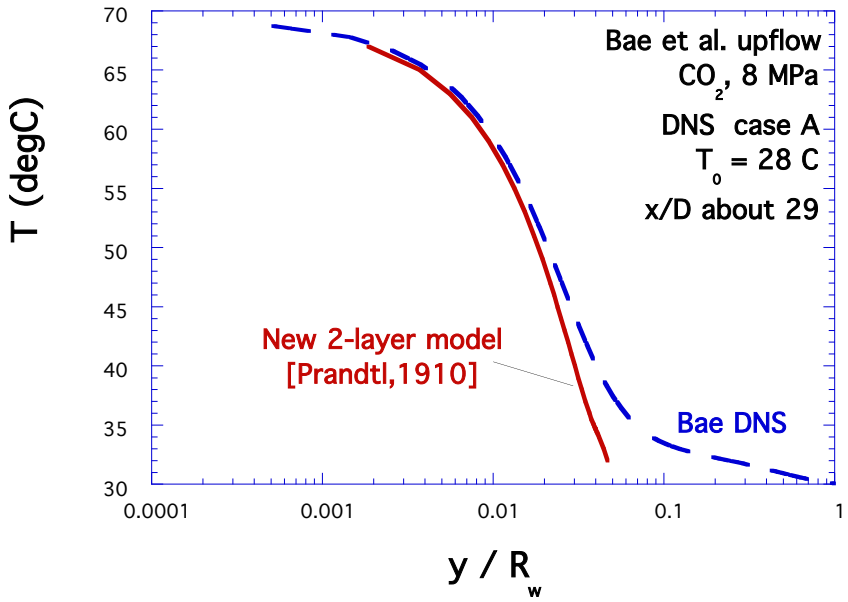

Figure 5. Comparison of temperature profile predicted from the simple model (solid curve) to profile from direct numerical simulation (dashed) by J. H. Bae, Yoo and Choi [2005] in quasi-developed downstream region of supercritical pipe flow. .

Further studies using the model are envisioned to examine effects of varying the assumed thickness of the wall layer modeled and incorporating an approximation of the thermal resistance of a turbulent core flow. We consider this analysis to give a first approximation to the thermal behavior for heating of a supercritical fluid in situations where there is a significant difference between the core properties (e.g., denser) and those at the wall as when $T_c < T_{pc} < T_w$. Our choices of y_{lw}^+ and friction factor correlation were for demonstration purposes; for extended conditions these choices should be revised appropriately. Provided the prediction of friction factor is good and the choice of $y^+_{l,w}$ is reasonable, it is expected that the Nusselt number relation will provide predictions that may be five to fifteen per cent high for this situation, due to neglect of core thermal resistance; this error is possibly less than for some of the existing empirical correlations. Users considering this analysis for a specific application should check the order-of-magnitude of their buoyancy and acceleration parameters [McEligot and Jackson, 2004] to see that the flow is not likely to be significantly affected by either of these phenomena.

Acknowledgements

The first author particularly appreciates the assistance of Dr. J. H. Bae and Profs. J. Y. Yoo and S. He in kindly providing tabulations of the DNS results. He is likewise grateful for the gracious hospitality and guidance of Profs. Eckart Laurien and Jörg Starflinger and their colleagues during his visit to IKE for direct interactions. The study has been partly supported by funds from Julie McEligot's checkbook.

References cited

Ambrosini, W., 2011. Discussion of similarity principles for fluid-to-fluid scaling of heat transfer behaviour at supercritical pressures. *Nuc. Eng. Design*, 241, pp. 5149-5173.

Bae, J. H., J. Y. Yoo and H. Choi, 2005. Direct numerical simulation of turbulent supercritical flows with heat transfer. *Phys. Fluids*, 17, pp. 1-24.

Dittus, F. W., and L. M. K. Bölter, 1930. Heat transfer in automobile radiators of the tubular type. *Publications in Eng.*, U. California, 2, pp. 443-461.

Drew, T. B., E. C. Koo and W. H. McAdams, 1932. The friction factor for clean round pipes. *Trans., AIChE*, 28, pp. 56-72.

Gnielinski, V., 1975. Neue Gleichungen für den Wärme- und den Stoffübergang in turbulenten durchströmten Rohren und Kanälen. *Forsch. Ingen.*, 41 (1), pp. 8-16.

Humble, L. V., W. H. Lowdermilk and L. G. Desmon, 1951. Measurements of average heat-transfer coefficients for subsonic flow of air in smooth tubes at high surface and fluid temperatures. NACA report 1020.

Kays, W. M., 1966. *Convective heat and mass transfer*. New York: McGraw-Hill.

Knudsen, J. G., and D. L. Katz, 1958. *Fluid dynamics and heat transfer*. New York: McGraw-Hill.

Laurien, E., 2012. Semi-analytical prediction of hydraulic resistance and heat transfer for pipe and channel flows of water at supercritical pressures. ICAPP'12 paper 12114.

Lemmon, E.W., M. L. Huber and M. O. McLinden, 2010. NIST Standard Reference Database 23: Reference Fluid Thermodynamic and Transport Properties-REFPROP, Version 9.0. National Institute of Standards and Technology, Standard Reference Data Program, Gaithersburg, November.

McEligot, D. M., 1967. Internal gas flow heat transfer with slight property variation. *Bull., Mech. Engr. Ed.*, 6, pp. 251-263.

McEligot, D. M., and J. D. Jackson, 2004. "Deterioration" criteria for convective heat transfer in gas flow through non-circular ducts. *Nuc. Engr. Design,* 232, pp. 327-333.

McEligot, D. M., P. M. Magee and G. Leppert, 1965. Effect of large temperature gradients on convective heat transfer: The downstream region. *J. Heat Transfer,* 87, pp. 67-76.

McEligot, D. M., S. B. Smith and C. A. Bankston, 1970. Quasi-developed turbulent pipe flow with heat transfer. *J. Heat Transfer,* 92, pp. 641-650.

McEligot, D. M., and fourteen others, 2005. Advanced computational thermal fluid physics (CTFP) and its assessment for light water reactors and supercritical reactors. Idaho National Laboratory, final tech. rpt. INL/EXT-05-00901, 31 October.

Ornatskii, A. P., L. F. Glushchenko and S. I. Kalachev, 1971. Heat transfer with rising and falling flows of water in tubes of small diameter at supercritical pressures. *Teploenergetika*, 18 (5), pp. 91-93.

Pioro, I., and R. Duffey, 2007. *Heat transfer and hydraulic resistance at supercritical pressure in power engineering applications*. New York: ASME Press.

Prandtl, L., 1910. Eine Beziehung zwischen Wärmeaustausch und Strömungswiderstand der Flüssigkeit. *Physik. Z.,* 11, pp.1072-1078.

PROPATH Group, 1999. PROPATH: A program package for thermophysical properties of fluids, Ver. 11.1. Int. Assn. Prop. Water and Steam (IAPWS).

Schlichting, H., 1968. *Boundary layer theory, 6th ed*. New York: McGraw-Hill.

Taylor, M. F., 1967. Correlation of friction coefficients for laminar and turbulent flow with ratios of surface to bulk temperature from 0.35 to 7.35. NASA TR R-267, September.

Yoo, J. Y., 2013. The turbulent flows of supercritical fluids with heat transfer. *Ann. Rev. Fluid Mech.,* 45, pp. 495-525.

ISSCWR7-2024

An improved approach for screening experimental data on heat transfer to fluids at supercritical pressure for influences of buoyancy

J. Derek Jackson
Emeritus Professor of the University of Manchester, UK
jdjackson@manchester.ac.uk

Abstract

A simple criterion for screening experimental data on turbulent heat transfer in vertical tubes to determine whether the influence of buoyancy was negligible was proposed by the author many years ago and found to work quite well for water at normal pressure. However, it was recognised even then that the ideas on which the criterion was based were too simplistic to be suitable for use the case of fluids at supercritical pressure. With the passage of time and the tremendous advancement in data processing capability using present-day computers, it is now possible to contemplate using a refined approach designed to be suitable for such fluids. The present paper describes a semi-empirical model of buoyancy-influenced heat transfer to fluids at supercritical pressure which takes careful account of non-uniformity of fluid properties. It leads to a new criterion for screening data for buoyancy influences which should be much better than those available hitherto. A valuable outcome of the present work is that the very extensive databases on heat transfer in tubes to fluids at supercritical pressure which have been compiled in recent times can be used in conjunction with the new model to re-evaluate the many forced convection correlation equations which have been proposed for such fluids. These mostly relate Nusselt number to Reynolds number, Prandtl number and simple property ratio correction terms. Thus they should only be evaluated using experimental data which are definitely not influenced by buoyancy. A further outcome of the present work is that it might now prove possible to correlate the buoyancy-influenced data in the databases and fit the equation for mixed convection heat transfer yielded by the present model to the data. If this can be done it will represent a major advance in terms of providing thermal analysts with a valuable new tool.

1. Introduction

1.1 Turbulent forced convection in heated tubes with fluids at supercritical pressure

The particular feature of supercritical pressure fluids which makes them of special interest is that they change from being liquid-like to gaseous with increase of temperature in a continuous manner without the discontinuous behaviour encountered as phase change occurs in fluids at sub-critical pressure. However, when heat transfer takes place with fluids at supercritical pressure, extreme non-uniformities of physical and transport properties can be present and lead to very important effects (see Jackson, 2013).

The task of developing correlation equations for turbulent forced convection in heated tubes with fluids at supercritical pressure was clearly a formidable one. However, even in the 1970's quite a number of such equations had been proposed and some success achieved in correlating data. The equations were mostly of the form

$$Nu_{b_o} = K_2 \, Re_b^{m_2} \, Pr_b^{0.4} \, F_{VP_o} \qquad (1)$$

The effect of the non-uniformity of fluid properties on heat transfer was accounted for by the factor F_{VP_o}.

In 1975 the present author reported an evaluation study of sixteen published correlation equations using available heat transfer data for approximately 2000 different experimental conditions. About 75% were from experiments using water and the remainder were from experiments using carbon dioxide.

A feature of the study was that all the data used in the evaluation exercise had been carefully screened using simple criteria to exclude any in which the influence of buoyancy might have been significant. The approach employed to do this was based on the idea that the effect of buoyancy in modifying local normalised shear stress in the turbulent buffer layer region should be small. The recognition that such stress modification constituted an appropriate indicator of buoyancy influence was pointed out in the paper of Hall, Jackson and Watson, 1968 and the idea was used in the detailed report on heat transfer to fluids at supercritical pressure, Jackson, et al, 1975, to specify a criterion in terms of a buoyancy parameter. This involved Grashof number, Reynolds number and Prandtl number combined together in the form $\overline{Gr}_b / (Re_b^{2.7} \, Pr_b^{0.4})$. In this, the Grashof number $\overline{Gr}_b$ was defined as $gD^3(\rho_b - \rho_{av})/(\rho_b v_b^2)$, where ρ_{av} is an average density of the fluid in the buoyant layer within the flow.

In the evaluation study the discrepancies between calculated and experimental values were tabulated for each data point. The results showed that the variable forced convection property correction factor F_{VP_o} of Krasnoschekov and Protopopov, 1966, was clearly the most effective one. This took the form

$$F_{VP_o} = (\rho_w / \rho_b)^{0.3} (\overline{c}_p / c_{p_b})^n \qquad (2)$$

in which $\overline{c}_p$ is a mean value of specific heat integrated with respect to temperature over the range from T_b to T_w. The index n depends on the values of T_w and T_b in relation to the pseudo-critical temperature T_{pc} and is specified using simple equations. For many experimental conditions it takes a value of about 0.4.

1.2 Buoyancy-influenced heat transfer in fluids at supercritical pressure

Buoyancy is a physical influence experienced by fluids as a result of the combined effect of non-uniformity of density and the action of gravity. The effects on heat transfer are surprisingly complicated, even for conventional fluids such as water or air at normal pressure (see Jackson et al, 1989). For upward turbulent flow in a vertical tube, impairment of heat transfer effectiveness develops gradually with onset of buoyancy influence. However, beyond a particular strength of buoyancy influence the effectiveness recovers. With downward flow in a heated tube the behaviour is very different. A systematic improvement in the effectiveness of heat transfer occurs with increase of buoyancy influence.

A model of buoyancy-influenced turbulent flow and heat transfer in vertical tubes suitable for use with conventional fluids such as water and air at normal pressure was developed by the present author in the nineteen eighties. It was based on the following simple physical ideas. Fluid of reduced density within the near-wall thermal layer of a heated flow experiences an upward force due to buoyancy which causes the gradient of shear stress across that region to be modified and this affects the production of turbulence.

For upward flow in a heated tube, the shear stress at the outer edge of the near-wall region of the boundary layer is lower with onset of buoyancy influence than it otherwise would be. Hence, the production of turbulence is reduced, turbulent diffusion is less effective and the flow has the heat transfer effectiveness of an ‘equivalent one’ without buoyancy at some lower value of flow rate. With further increase of buoyancy influence the shear stress becomes negative in part of the near wall region and at some stage the flow becomes unstable and turbulence

production is renewed (but in this case by a rather different mechanism). For downward flow in a heated tube the shear stress at the outer edge of the wall layer is higher, turbulence production is increased, enhancement of heat transfer occurs and the flow exhibits the heat transfer characteristics of an 'equivalent one' without buoyancy at some higher value of flow rate. A very detailed review of buoyancy-influenced heat transfer to liquids and gases flowing through vertical passages can be found in Jackson, 2006.

In the case of heat transfer to fluids at supercritical pressure the strong dependence of density on temperature, can lead to very significant influences of buoyancy and some important effects on turbulence and the turbulent diffusion of heat. As early as 1963 very striking localized deterioration of heat transfer was reported in experiments with upward flow of water at supercritical pressure. This phenomenon was eventually shown to be due to rapid buoyancy-induced lamainarisation of the flow followed by sudden recovery of heat transfer due to renewed turbulence production, see Hall and Jackson, 1970. Interestingly, non-uniformity of heat transfer was not found with downward flow. In this case turbulence production increased as a result of the influence of buoyancy and the effectiveness of heat transfer was systematically improved.

2. A physically-based semi-empirical model of buoyancy-influenced flow and heat transfer in supercritical pressure fluids

2.1 Background

In the course of the recent IAEA Coordinated Research Programme on 'Heat transfer behaviour and thermo-hydraulics code testing for supercritical water-cooled reactors', efforts were made by the present author to develop a semi-empirical model of buoyancy-influenced heat transfer in vertical tubes which accounted in a reliable manner for the effects of the very strong non-uniformity of properties which can present with fluids at supercritical pressure.

2.2 The structure of fully developed turbulent flow in a tube

Normal fully developed turbulent flow in a tube can be thought of as being made up of a turbulent core, where the velocity profile is relatively uniform and a turbulent boundary layer across which the fluid velocity increases from zero at the wall up to the bulk value.

Adjacent to the wall is the viscous-turbulent 'buffer' layer region where the total diffusivity of momentum increases from zero up to a value an order of magnitude greater than the molecular diffusivity. If the symbol δ_t is used to characterize the distance from the wall to the location within the buffer layer where maximum production of turbulence occurs in a normal buoyancy-free turbulent flow, its magnitude can be specified by assigning $\delta_t \sqrt{\tau_w \rho} / \mu$ a value of about 20. In the absence of any buoyancy influence, the variation of shear stress across this near-wall region of a turbulent boundary layer will be very small.

2.3 Modification of the shear stress distribution due to buoyancy in vertical heated tubes

Under conditions where the influence of buoyancy in a heated flow is significant, the shear stress in the region $0 < y < \delta_t$ will be changed (being reduced for upward flow and increased for downward flow) with the turbulence production being modified accordingly. The effect of buoyancy on the shear stress can be determined under conditions where its effect is large compared that those of inertia using a simplified equation of motion. On integrating this, with

respect to y term by term across the entire flow and then across the near-wall layer of the thickness δ_t and re-organizing the resulting equations we obtain.

$$\tau_w - \tau_{\delta_t} = \pm\delta_t(\rho_b - \rho_{av})g \tag{3}$$

in which the average density integrated with respect to distance across the near-wall layer, is given by $\rho_{av} = \frac{1}{\delta_t}\int_0^{\delta_t} \rho \, dy$.

Here, we make use of the idea presented earlier (in sub-section 1.2 of this paper) that the effect of buoyancy in modifying the near-wall distribution of shear stress enables such a flow to be thought of as an equivalent one which is not affected by buoyancy but is flowing at some different value of bulk velocity (lower or higher than the actual one depending with the motion is upward or downward). For the 'equivalent buoyancy-free flow', the shear stress at the wall is assumed to be τ_{δ_t} and the dimensionless near-wall turbulent layer thickness δ_t^+ is defined as $\delta_t\sqrt{\tau_{\delta_t}\rho_{av}}/\mu_{av}$, in which $\mu_{av} = \frac{1}{\delta_t}\int_o^{\delta_t} \mu dy$.

Thus,

$$\tau_w - \tau_{\delta_t} = \pm\delta_t^+\mu_{av}(\rho_b - \rho_{av})g/\sqrt{\tau_{\delta_t}\rho_{ax}} \tag{4}$$

Equation 4 can be re-organised to give

$$\frac{\tau_{\delta_t}}{\tau_w} = 1 \pm \frac{\delta_t^+\mu_{av}(\rho_b - \rho_{av})g}{\tau_w^{3/2}\rho_{av}^{1/2}}\left(\frac{\tau_{\delta_t}}{\tau_w}\right)^{-1/2} \tag{5}$$

The negative sign applies for the buoyancy-aided case (upward flow in heated tube) and the positive one applies for the buoyancy-opposed case (downward flow in a heated tube).

If the wall shear stress τ_w is related to ρ_b, u_b and $f_{b_o}(=\tau_w/\frac{1}{2}\rho_b u_b^2)$, and the latter is expressed in terms of Reynolds number $Re_b(=\rho_b u_b D/\mu_b)$ using a relationship of the form $f_{b_o} = K_1, Re_b^{-m_1}$, we obtain

$$\frac{\tau_{\delta_t}}{\tau_w} = 1 \pm 2\sqrt{2}\delta_t^+ K_1^{-3/2}\left[\frac{gD^3(\rho_b - \rho_{av})}{\rho_b\nu_b^2}\right]\left(\frac{\mu_b}{\rho_b u_b D}\right)^{3-3m_1/2}\left(\frac{\mu_{av}}{\mu_b}\right)\left(\frac{\rho_{av}}{\rho_b}\right)^{-1/2}\left(\frac{\tau_{\delta_t}}{\tau_w}\right)^{-1/2} \tag{6}$$

2.4 A relationship between heat transfer and shear stress

Here, we again make use of the idea that the effect of buoyancy in modifying the near-wall distribution of shear stress enables such a flow to thought of as an 'equivalent one' which is not affected by buoyancy but is flowing at some different value of bulk velocity. This enables the ratio of the Nusselt number for mixed convection, to that for variable property forced convection, Nu_b/Nu_{b_o}, to be related to τ_{δ_t}/τ_w. Thus, assuming that f_{b_o} is proportional to $Re_b^{-m_1}$ and that Nu_{b_o} is proportional to $Re_b^{m_2}$, the relationship between heat transfer and shear stress is found to be

$$\frac{Nu_b}{Nu_{b_o}} = \left(\frac{\tau_{\delta_t}}{\tau_w}\right)^{m_3} \tag{7}$$

in which $m_3=m_2/(2-m_1)$.

2.5 A model of buoyancy-influenced heat transfer in vertical tubes

On combining Equation 6 with Equation 7 so as to eliminate τ_{δ_t} / τ_w, the following equation is obtained for the effect of buoyancy on heat transfer

$$\frac{Nu_b}{Nu_{b_o}} = \left[\left| 1 \mp C_B F_{VP} \frac{Gr_b}{Re_b^{m_5}} \left(\frac{Nu_b}{Nu_{b_o}} \right)^{-m_4} \right| \right]^{m_3} \tag{8}$$

in which, $C_B = 2\sqrt{2}\delta_t^+ K_1^{-3/2}$, $F_{VP} = ((\rho_b - \rho_{av})/(\rho_b - \rho_w))(\mu_{av} - \mu_b)(\rho_{av}\rho_b)^{-1/2}$ and $Gr_b = gD^3(\rho_b - \rho_{av})/(\rho_b \nu_b^2)$, where $\rho_{av} = \frac{1}{\delta_t}\int_0^{\delta_t} \rho \, dy$ and $\mu_{av} = \frac{1}{\delta_t}\int_o^{\delta_t} \mu dy$.

The indices m_4 and m_5 in Equation 8 are given by $m_4=1/(2m_2)$ and $m_5=3(1-m_1/2)$. The negative sign applies for the buoyancy-aided case (upward flow) and the positive one for the buoyancy-opposed case (downward flow).

2.6 Empirical coefficients and indices

The buoyancy-influenced heat transfer model (Equation 8) involves the coefficient K_1 and indices m_3 and m_4, all of which need to be specified.

Different combinations of the coefficient K_1 and the index m_1 have been used in simple power law forms of empirical friction factor – Reynolds number relationships for flow in 'smooth' tubes, examples being $K_1=0.079$ in conjunction with $m_1=0.25$ and $K_1=0.046$ with $m_1=0.20$. In spite of the big differences between the values of K_1 and m_1 in these two particular combinations, rather similar values of friction factor are obtained using them. We will use $K_1=0.046$ with $m_1=0.20$. The Dittus-Boelter form of Nusselt number–Reynolds number relationship for turbulent forced convection heat transfer in tubes, uses values of K_2 and m_2 which are 0.023 and 0.80, respectively. It is found that if the index m_1 is assigned either the value 0.25 or 0.2, and the index m_2 is assigned the value 0.8, very similar values of the index m_3 are obtained, about 0.45. Using $m_3=0.45$ we find that $m_4=1.1$. Finally, using $m_1=0.2$ we find that $m_3=2.7$.

2.7 Specific form of the model equation

With K_1 assigned the value 0.046, m_1 the value 0.2 and m_2 the value 0.8, we obtain the following specific form of an equation for buoyancy-influenced heat transfer,

$$\frac{Nu_b}{Nu_{b_o}} = \left[\left| 1 \mp C_B Bo_b F_{VP} \left(\frac{Nu_b}{Nu_{b_o}} \right)^{-1.1} \right| \right]^{0.45} \tag{9}$$

in which the buoyancy parameter Bo_b is $Gr_b / Re_b^{2.7}$, where $Gr = gD^3(\rho_b - \rho_w)/(\rho_b \nu_b^2)$ and the variable property factor $F_{VP} = ((\rho_b - \rho_{av})/(\rho_b - \rho_w))(\mu_{av} - \mu_b)(\rho_{av}\rho_b)^{-1/2}$, where $\rho_{av} = \frac{1}{\delta_t}\int_0^{\delta_t} \rho \, dy$ and $\mu_{av} = \frac{1}{\delta_t}\int_0^{\delta_t} \mu dy$.

In this model of buoyancy-influenced heat transfer to fluids at supercritical pressure the approach of defining the 'universal' coordinate y^+ using the modified shear stress τ_{δ_t} instead of the wall value τ_w has been adopted with the result that the scaling factor $(Nu_b/Nu_{b_0})^{-1.1}$ appears on the right hand side of Equation 9. A very similar result would have been arrived by defining the universal coordinate y^+ using τ_w and accounting for the buoyancy-induced modification of the thickness of the near-wall region by simply incorporating a scaling factor $(Nu_b/Nu_{b_0})^{-1}$ on the right hand side of Equation 8 directly.

If it is assumed that the modified dimensionless near-wall layer thickness δ_t^+ takes the value 20, the estimated coefficient $C_B(=2\sqrt{2}\delta_t^+ K_1^{-3/2})$ is about 5700.

Figure 1 shows the predicted variation of Nu_b/Nu_{b_o} with the parameter $C_B Bo_b F_{VP}$.

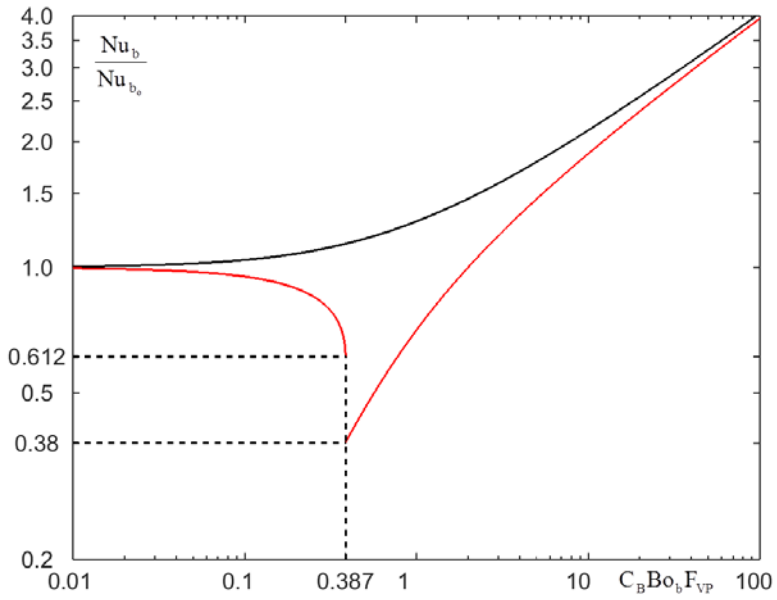

Figure 1. Effect of buoyancy on heat transfer predicted by the model

It is apparent from Figure 1 that the model does capture the well-established trends of buoyancy on heat transfer described earlier. Furthermore, it provides a simple means of screening experimental data to establish under what conditions influences of buoyancy are likely to be negligibly small. As can be seen, if the parameter $C_B Bo_b F_{VP}$ is less than about 0.04 the values of Nu_b for upward and downward flow are very similar, the influence of buoyancy is negligibly small (less than about 2%) and the mode of heat transfer is variable property turbulent forced convection. Thus, a criterion for this to be so is that $Bo_b F_{VP}$ should be less than about 8×10^{-6}. It is of interest to note that if the parameter $C_B Bo_b F_{VP}$ is greater than about 40, very strongly buoyancy-influenced conditions, then flow direction again has only a small effect on heat transfer. In this case the mode of heat transfer is, effectively, one of turbulent free convection. Between these two extremes the mode of heat transfer is mixed, forced and free, convection.

2.8 Determination of the integrated mean values of viscosity and density

Equation 9 involves an integrated average density ρ_{av} and an integrated average viscosity μ_{av}. In order to determine them it is necessary to specify the variation of temperature in the near-wall region $0 < y < \delta_t$. To do this we firstly evaluate the thermal layer thickness δ_T. This is defined as the distance from the wall to the location where the fluid temperature falls to the bulk mean value T_b. It is important not to confuse the thermal layer thickness δ_T with the near-wall turbulent layer thickness δ_t defined earlier and used in the formulation of the model. Based on observed turbulent heat transfer behaviour in tubes, δ_T can be related to the tube radius using the approximate expression $\delta_T = a/\overline{Pr}^{0.4}$, in which the symobol 'a' is the tube radius (=D/2) and $\overline{Pr}$ is defined as $\mu_b \overline{c}_p / k_b$, in which $\overline{c}_p = \dfrac{1}{(T_w - T_b)} \int_{T_b}^{T_w} c_p dT$.

The next step is to determine the dimensionless thermal layer thickness $\delta_T^+ (= \delta_T \sqrt{\tau_{\delta_t} \rho_b} / \mu_b)$. In doing this we again make use of the idea that buoyancy-influenced flow in a tube can be thought of as an 'equivalent one' not influenced by buoyancy but with a bulk velocity which is different from the actual one. So, the wall shear stress in this 'equivalent buoyancy-free flow' will be assumed to be the modified, shear stress τ_{δ_t} at the near-wall location $y = \delta_t$. This approach leads to the result.

$$\frac{\delta_T \sqrt{\tau_{\delta_t} \rho_b}}{\mu_b} = 0.076 \frac{Re_b^{0.9}}{\overline{Pr}_b^{0.4}} \left(\frac{Nu_b}{Nu_{b_o}} \right) \tag{10}$$

The variation of fluid temperature T with distance from the wall y across the thermal layer $0 \le y \le \delta_T$ will be specified using the following second order polynomial equation

$$\left(\frac{T_w - T}{T_w - T_b} \right) = \frac{q_w \delta_T}{k_w (T_w - T_b)} \left(\frac{y}{\delta_T} \right) - \left(\frac{q_w \delta_T}{k_w (T_w - T_b)} - 1 \right) \left(\frac{y}{\delta_T} \right)^2 \tag{11}$$

This satisfies the thermal boundary conditions at the wall, $T=T_w$ when y=0, and $\frac{dT}{dy} = -\frac{q_w}{k_w}$ when y=0. It also satisfies the condition $T=T_b$ when $y = \delta_T$. It is designed to provide a reliable description of the temperature variation across the near-wall region $0 \le y \le \delta_t$ for use in evaluating the average density $\rho_{av} \left(= \frac{1}{\delta_t} \int_0^{\delta_t} \rho dy \right)$ and the average viscosity $\mu_{av} \left(= \frac{1}{\delta_t} \int_0^{\delta_t} \mu dy \right)$.

2.9 A re-cast version of the model with Grashof number defined in terms of the imposed wall heat flux

The semi-empirical model presented here is aimed at providing an equation which describes the effectiveness of heat transfer in a vertical tube of given diameter D, for prescribed values of fluid pressure, local fluid bulk temperature, mass flowrate and imposed wall heat flux. Thus it could be argued that it is appropriate to re-cast Equation 9 in terms of a Grashof number Gr_b^* defined in terms of the wall heat flux q_w by $Gr_b^* = g \beta_b q_w D^4 / (k_b \nu_b^2)$. Grashof number is usually defined in this manner when correlating experimental data in the case free convection heat transfer in systems where the thermal boundary condition is one of imposed heat flux.

The recasting process can be done without changing the model in any way, noting that

$$\frac{g \beta_b q_w D^4}{k_b \nu_b^2} = \frac{g D^3 (\rho_b - \rho_{av})}{\rho_b \nu_b^2} \frac{q_w D}{k_b (T_w - T_b)} \frac{\rho_b \beta_b (T_w - T_b)}{(\rho_b - \rho_{av})} \tag{12}$$

and, therefore, that

$$Gr_b = \frac{Gr_b^*}{Nu_{b_o}} \frac{(\rho_b - \rho_{av})}{(T_w - T_b)} \frac{1}{\rho_b \beta_b} \left(\frac{Nu_b}{Nu_{b_o}} \right)^{-1} \tag{13}$$

in which $Nu_{b_o} = K_2 Re_b^{0.8} \overline{Pr}_b^{0.4} F_{VP_o}$.

Hence, if we define a modified buoyancy parameter $Bo_b^* = \frac{Gr_b^*}{Re_b^{3.5} \overline{Pr}_b^{0.4}}$, and assign the term $\frac{1}{F_{VP_o}} \frac{1}{\beta_b \rho_b} \frac{(\rho_b - \rho_{av})}{(T_w - T_b)} \left(\frac{\mu_{av}}{\mu_b} \right) \left(\frac{\rho_{av}}{\rho_b} \right)^{-1/2}$ the symbol F_{VP}^*, we can re-write Equation 9 as

$$\frac{Nu_b}{Nu_{b_o}} = \left[1 \mp C_B^* B_b^* F_{VP}^* \left(\frac{Nu_b}{Nu_{b_o}} \right)^{-2.1} \right]^{0.45} \qquad (14)$$

in which $C_B^* = C_B / K_2$. $Bo_b^* = Gr_b^* / Re_b^{3.5}\, \overline{Pr}_b^{0.4}$, where $\overline{Pr}_b = \mu_b \overline{c}_p / k_b$, and F_{VP}^* is as defined above.

With C_B assigned the estimated value 5700 and K_2=0.023, the coefficient C_B^* has an estimated value of about 2x10^5.

The relationship between Nu_b / Nu_{b_o} and $C_B^* Bo_b^* F_{VP}^*$ can be readily determined in a direct manner using a similar approach to that described earlier, just before Figure 1. The variation of Nu_b / Nu_{b_o} with $C_B^* Bo_b^* F_{VP}^*$ given by Equation 14 is as shown on Figure 2.

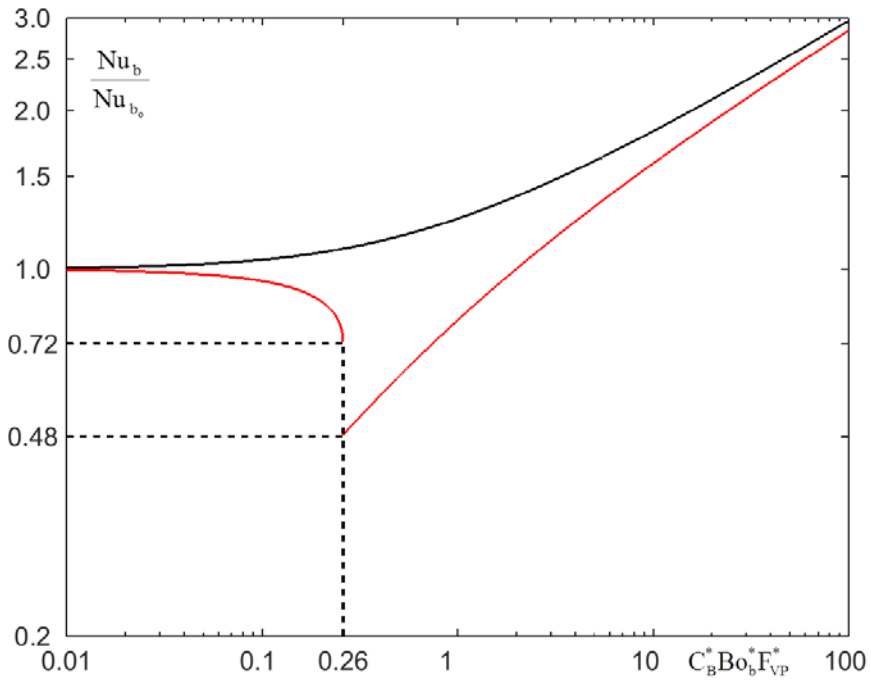

Figure 2, Turbulent mixed convection in vertical tubes
in terms of the parameters of the re-cast model

Expressed in terms of the parameters of the recast version of the model, the criterion for the effect of buoyancy influence to be less than about 2% is $C_B^* Bo_b^* F_{VP}^* \le 0.04$. This can be shown to be completely consistent with the buoyancy-free criterion specified earlier (under Figure 1).

It is of interest to consider an experiment with upward flow in a tube where the imposed heat flux is gradually increased from a low value, with all the other controllable conditions being kept constant. According to the model this would cause Bo_b^* to increase and the operating point on the curve for upward flow shown on Figure 2 to move gradually along it with Nu_b / Nu_{b_o} falling. As this happens a stage will eventually be reached where the increase of wall to bulk temperature difference will become so large with increase of imposed heat flux that the operating condition suddenly moves onto the other upward flow curve shown on Figure 2, with the effectiveness of heat transfer then being reduced even more.

When this transition from the first distribution to the second one occurs, the variation of shear stress with y is will change in a discontinuous manner from one where the stress at the edge of the near-wall layer is positive (but significantly lower than the wall shear stress) to one where it is negative. Thus, at this stage the velocity profile in the core region has become inverted. Any further increase of heat flux will lead to gradual recovery of heat transfer as the operating point moves up the second curve and, eventually to enhanced heat transfer in relation to that for buoyancy-free heat transfer. Under such conditions turbulence can be as readity produced a result of the flow being unstable in the region of the point of inflexion on the velocity profile.

In practice, the changeover described above cannot be discontinuous due to the inertia of the fluid. However, since the inertia terms were omitted in the equation of motion this is not accounted for in the model.

It is also of interest to consider what would happen if, after the changeover the heat flux was then to be gradually reduced keeping all the other controllable conditions fixed. At some stage a transition back onto the other curve for upward flow would have to take place. So, there are some interesting matters that need to be considered in the light of the picture of buoyancy-influenced heat transfer provided by the semi-empirical model presented here.

In contrast to the complex behaviour predicted above for upward flow, systematic enhancement of heat transfer is predicted with increase of buoyancy influence in case of downward flow.

3. Using the model for screening and correlating experimental data

3.1 Separating buoyancy-free and buoyancy-influenced data

As indicated earlier, the model presented here can be used to provide a means of screening experimental data to identify those which are free of any buoyancy influence. According to Equation 9, if $C_B(Gr_b / Re_b^{2.7})((\rho_b - \rho_{av})/(\rho_b - \rho_w))(\mu_{av}/\mu_b)(\rho_{av}/\rho_b)^{-1/2}$ is less than about 0.04, then the effect of buoyancy on heat transfer should be less than about 2%. So, the following criterion for negligible influence of buoyancy is proposed

$$\frac{gD^3(\rho_b - \rho_w)}{\rho_b \nu_b^2}\left(\frac{\rho_b u_b D}{\mu_b}\right)^{-2.7}\left(\frac{\rho_b - \rho_{av}}{\rho_b - \rho_w}\right)\left(\frac{\mu_{av}}{\mu_b}\right)\left(\frac{\rho_{av}}{\rho_b}\right)^{-1/2} \le 6.6\times10^{-6} \qquad (15)$$

3.2 Correlating and fitting the buoyancy-free data

Equation 15 can be used for screening the very large database now available on heat transfer to supercritical pressure water and carbon dioxide in order to identify data not significantly influenced by buoyancy. Then, the various correlation equations which have been proposed over the years for variable property forced convection (buoyancy-free) heat transfer in a tube can be re-evaluated. Many of these equations are of the form indicated earlier in Section 1 (see Equation 1). In particular, the present author is interested in re-evaluating variable property correction factor of Krasnoshchekov and Protopopov, 1966, referred to in that section (see Equation 2). In this case, the well-established value of 0.8 will be used for the index m_2. The coefficient K_1 will initially be assigned the widely used value 0.023 but this will be adjusted later if necessary in order to optimise the fit of Equation 1 to the correlated buoyancy-free data. So, that data will be compared with values of Nusselt number Nu_{b_o} calculated using the equation

$$Nu_{b_o} = 0.023\, Re_b^{0.8}\, Pr_b^{0.4}(\rho_w/\rho_b)^{0.3}(\bar{c}_p/c_{p_b})^n \qquad (16)$$

In order to determine Nu_{b_o} using Equation 16, knowing values of the fluid bulk temperature, the mass flux and wall heat flux, it will be necessary to perform an iterative calculation to obtain T_{wo} starting with an estimated value $T_{wo}^{(1)}$. This will enable an improved value of wall temperature $T_{wo}^{(2)}$ to be determined and then the procedure will be repeated until convergence is achieved and the required values for T_{w_o}, F_{VP_o} and Nu_{b_o} are obtained. Of course, all the other correlation equations which have been proposed to date will also be re-evaluated using the buoyancy-free data.

It should be borne in mind that some of the experimental data in the databases might possibly be affected by the phenomenon of thermally-induced bulk flow acceleration. This could be significant in the case strongly heated flow tubes of small diameter. A model of heat transfer

with bulk flow acceleration which takes account of both thermal expansion and compressibility has been reported by the present author at an earlier ISSCWR meeting, see Jackson, 2013. An updated version of that model incorporating some of the ideas used in the development of the present one, will be reported in the near future.

3.3 Correlation of the buoyancy-influenced heat transfer data

The model of buoyancy-influenced heat transfer to fluids at supercritical pressure presented here provides an indication of the dimensionless parameters which should be used to try to correlate such experimental data. As can be seen from Equation 9, the ratio $\mathrm{Nu}_b / \mathrm{Nu}_{b_o}$ should be plotted against the parameter $\mathrm{Bo}_b((\rho_b - \rho_{av})/(\rho_b - \rho_w))(\mu_{av}/\mu_b)(\rho_{av}/\rho_b)^{-1/2}$. Thus, the entire data set (buoyancy-free and buoyancy-influenced conditions) should be presented in terms of these parameters, to see whether a correlation can be achieved. If the data do correlate on this basis, the estimated value of the coefficient C_B can then be adjusted, so as to optimise the extent to which Equation 9 actually fits the correlated data.

4. Overview and concluding remarks

The physically-based, semi-empirical model of buoyancy-influenced convective heat transfer to fluids at supercritical pressure flowing in smooth vertical tubes presented in this paper has been designed to take proper account the extreme non-uniformity of fluid properties which can be encountered with such fluids.

In developing the model, attention has been concentrated on the modification by buoyancy of the shear stress distribution in the near-wall region. There, the production of turbulence is either impaired or enhanced which depending on the experimental conditions and also the flow direction.

Consequently, it has been necessary to develop an approach which enables the variation of density and viscosity in the near-wall region to be reliably specified. This can only be done by making a reliable estimate of the fluid temperature distribution in that using the known thermal boundary conditions at the wall (temperature and heat flux) and the temperature of the bulk fluid.

The resulting model provides a description of buoyancy-influenced heat transfer with upward and downward turbulent flow in heated tubes which is closely consistent with observed behaviour in the case of both conventional fluids and also fluids at supercritical pressure.

With increase heat flux or reduction of flow rate, onset of buoyancy influence can develop. This leads to the mode of heat transfer changing from forced convection to combined forced and free convection, (with onset of impairment of heat transfer developing for upward flow and enhancement of for downward flow).

A criterion for the influence of buoyancy to be negligibly small can be readily obtained using the model and this should provide reliable means of screening experimental data to ensure that only those which are not significantly influenced by buoyancy are used for the purpose of establishing correlation equations for variable property forced convection heat transfer.

The present model also provides guidance concerning the parameters which should be used for correlating mixed convection heat transfer data. If it proves possible to correlate buoyancy-influenced data using this approach, the model equations could provide a valuable framework for describing mixed convection heat transfer to fluids at supercritical pressure.

Nomenclature

a Tube radius, m(=D/2)

Bo_b Buoyancy parameter $(= \mathrm{Gr}_b / Re_b^{2.7})$

Bo_b^* Buoyancy parameter in the re-cast version of the model $(= \mathrm{Gr}_b^* / Re_b^{3.5}\, \overline{P}r_b^{0.4})$

c_p Specific heat at constant pressure, kJ/kgK

c_{p_b} Specific heat evaluated at the fluid bulk temperature, T_b, kJ/kgK

$\bar{c}_p$ Specific heat integrated between T_b and T_w $(=h_w-h_b)/(T_w-T_b)$), kJ/kgK

C_B Buoyancy coefficient

C_B^* Buoyancy coefficient in the re-cast version of the model

D Tube inside diameter, m

f_b Friction factor $(=\tau_w/(\frac{1}{2}\rho u_b^2))$

F_{VP_o} Variable property correction factor for forced convection in Equation 1

F_{VP} Variable property factor in Equation 8 $\left(=\left(\frac{\rho_b-\rho_{av}}{\rho_b-\rho_w}\right)\left(\frac{\mu_{av}}{\mu_b}\right)\left(\frac{\rho_{av}}{\rho_b}\right)^{-1/2}\right)$

F_{VP}^* Variable property factor in the re-cast version of the model

$\left\{=\frac{1}{F_{VP_o}}\frac{1}{\beta_b\rho_b}\frac{(\rho_b-\rho_{av})}{(T_w-T_b)}\left(\frac{\mu_{av}}{\mu_b}\right)\left(\frac{\rho_{av}}{\rho_b}\right)^{-1/2}\right\}$

g Acceleration due to gravity, m/s^2

Gr_b Grashof number based on $\rho_b-\rho_w$ $(=gD^3(\rho_b-\rho_w)/(\rho_b\nu_b^2))$

Gr_b^* Grashof number based on wall heat flux $(=g\beta_b q_w D^4/(k_b\nu_b^2))$

h Fluid enthalphy, kJ/kg

h_b Enthalphy evaluated at the fluid bulk temperature, KJ/kg

h_w Fluid enthalphy evaluated at the tube wall temperature, KJ/kg g

k Fluid thermal conductivity, W/m^{2}K

k_b Thermal conductivity evaluated at the fluid bulk temperature, W/m^{2}K

k_w Fluid thermal conductivity evaluated at the wall temperature, W/m^{2}K

K_1 Coefficient in the friction factor equation shown above Equation 6

K_2 Coefficient in Equation 1

m_1 Reynolds number index in the friction factor equation above Equation 6

m_2 Reynolds number index in Equation 1

m_3 Index defined below Equation 7 $(=m_2/(2-m_1))$

m_4 Index defined below Equation 8 $(=1/(2m_2))$

m_5 Index defined below Equation 8 (=3(1-m1/2))

$\dot{m}$ Mass flow rate, kg/s $(=\rho_b u_b(\pi D^2/4/\mu_b))$

Nu_b Nusselt number for buoyancy-influenced heat transfer $(=q_w D/(k_b(T_w-T_b)))$

Nu_{b_o} Nusselt number for buoyancy-free, variable property forced convection $(=q_w D/(k_b(T_{w_o}-T_b)))$

Pr Prandtl number $(=\mu c_p/k)$

Pr_b Prandtl number evaluated at the fluid bulk temperature $(=\mu_b c_{p_b}/k_b)$

$\bar{Pr}_b$ Prandtl number defined using a mean specific heat $\bar{c}_p$ $(=\mu_b\bar{c}_p/k_b)$

q_w Wall heat flux, kW/m^2

Re_b Reynolds number $(=\rho_b u_b D/\mu_b)$

T_b Local bulk mixed mean temperature of the fluid, ^{o}C or K

T_t Fluid temperature at the location $y=\delta_t$, ^{o}C or K

T_w Local wall temperature, ^{o}C or K

T_{w_o} Local wall temperature for variable property forced convection, ^{o}C or K

u_b Local bulk velocity, m/s

x Axial coordinate measured from start of heating, m

y Transverse coordinate (measured inward into the fluid from the tube wall), m

Greek symbols

β Thermal expansion coefficient, $\mathrm{K}^{-1}\left(-\frac{1}{\rho}\left(\frac{\partial\rho}{\partial \mathrm{T}}\right)_{\mathrm{p}}\right)$

β_{b} Thermal expansion coefficient evaluated at the fluid bulk temperate T_b

δ_{t}^{+} Dimensionless thickness of the near-wall layer $\delta_{\mathrm{t}}\sqrt{\tau_{\delta_{\mathrm{t}}}\rho_{\mathrm{w}}}/\mu_{\mathrm{w}}$

δ_{t} Thickness of near-wall turbulent layer, m

δ_{T} Thermal layer thickness, m

ν Kinematic viscosity, m^2/s (= μ/ρ)

ν_{b} Kinematic viscosity evaluated at the fluid bulk temperature, m^2/s (= μ_b/ρ_b)

μ Fluid viscosity, kg/ms

μ_{av} Integrated average viscosity across the region $0 \le \mathrm{y} \le \delta_{\mathrm{t}}$, kg/ms $\left(=\frac{1}{\delta_{\mathrm{t}}}\int_{\mathrm{o}}^{\delta_{\mathrm{t}}}\mu\,\mathrm{dy}\right)$

ρ Fluid density, kg/m^3

ρ_{w} Fluid density evaluated at the wall temperature T_w, kg/m^3

ρ_{b} Fluid density evaluated at the bulk temperature T_b, kg/m^3

ρ_{av} Integrated average density across the region $0 \le \mathrm{y} \le \delta_{\mathrm{t}}$, kg/m^3 $\left(=\frac{1}{\delta_{\mathrm{t}}}\int_{\mathrm{o}}^{\delta_{\mathrm{t}}}\rho\,\mathrm{dy}\right)$

τ_{w} Wall shear stress, N/m^2

$\tau_{\delta_{\mathrm{t}}}$ Shear stress at the location of maximum turbulence production, $\mathrm{y}=\delta_{\mathrm{t}}$ within the turbulent buffer layer, N/m^2

References

1. Jackson,J.D., Flow and convective heat transfer with fluids at supercritical pressure, Journal of Nuclear Engineering and Design, Volume 264, pp24-40, November 2013.
2. Hall, W.B., Watson, A. and Jackson,J.D., A review of forced convection heat transfer to fluids at supercritical pressure, Paper 3, I.Mech.E. Symposium on Heat Transfer and Fluid Dynamics of Near Critical Pressure Fluids, Bristol, UK, 27th – 29th March,1968
3. Jackson, J.D., Hall, W.B., Fewster, J., Watson, A. And Watts, M.J., Review of heat transfer to supercritical pressure fluids, UKAEA, H.T.F.S. Design Report No. 34, A.E.R.E. Harwell, UK, 1975
4. Krasnoshchekov, E.A. and Protopopov, V.S., Experimental study of heat exchange in carbon dioxide in the supercritical range at high temperature drops, Teplofizika Vysokikh Temperatur, 4(3), 1966.
5. Jackson, J.D., Cotton, M.A. and Axcell,B.P. , Studies of mixed convection in vertical tubes - A review, International Journal of Heat and Fluid Flow, Vol. 10, No. 1, pp 2-15, 1989
6. Jackson, J.D., Studies of buoyancy-influenced turbulent flow and heat transfer in vertical passages, Invited Keynote lecture, Proc. 13th International Heat Transfer Conference, Sydney, Australia, 2006.
7. Hall, W.B. and Jackson, J.D., Laminarisation of a turbulent pipe flow by buoyancy forces. Paper 69-HT55, ASME AIChE National Heat Transfer Conference, Minneapolis, Minnesota, 1970
8. Jackson, J.D., On the deterioration of forced convection heat transfer in tubes to fluids at supercritical pressure caused by bulk flow acceleration, Paper No. 098, Proceedings of ISSCWR-6, Shenzhen, Guangdong, China, March 2013.

ISSCWR7-#2025

INFLUENCE OF CHANGES IN THE PHYSICOCHEMICAL PROPERTIES OF SUPERCRITICAL WATER IN THE SUSCEPTIBILITY TO STRESS CORROSION CRACKING OF A 316L AUSTENITIC STAINLESS STEEL

A. Sáez-Maderuelo, D. Gómez-Briceño, C. Maffiotte
Structural Materials Division, CIEMAT
Avda. Complutense 40, Madrid 28040, Spain
+34913466607, alberto.saez@ciemat.es

Abstract

The Supercritical Water Reactor (SCWR) is one of the Generation IV designs. The SCWR is characterized by its high efficiency, low waste production and simple design. Despite the good properties of supercritical water as coolant, its physicochemical properties change sharply with pressure and temperature in the supercritical region. For this reason, there are many doubts about how changes in these variables affect the behavior of the materials to some degradation processes like Stress Corrosion Cracking (SCC). Austenitic stainless steels are candidate materials to build the SCWR due to their good behavior in the Light Water Reactors (LWR). Nevertheless, their behavior under the SCWR conditions is not well known.
In this work, an austenitic stainless steel 316 type L was tested in deaerated supercritical water at 673 K/25 MPa and 30 MPa and 773 K/25 MPa to determine how variations in properties of water influence its behavior to SCC and to make progress in the understanding of mechanisms involved in SCC processes in this environment. In addition to this, a selected oxide layer formed at 673 K/30 MPa/< 10 ppb O_2 was analyzed to gain some insight into these processes.

1. Introduction

The aim of the next generation of nuclear power plants (Gen IV) is to improve the efficiency and safety of the Light Water Reactors (LWR) which are currently in use. One of the designs of the Gen IV is the Supercritical Water Reactor (SCWR) that has an analogous design and uses the same coolant than the LWR. The main difference between the LWR and the SCWR is the water phase, while in the first one the water exists as liquid (or a mixture of water and steam in the Boiling Water Reactors (BWR)), in the SCWR water is into the supercritical region which appears above the critical point (648 K, 22.1 MPa). The special properties of water inside the supercritical region (it is in only one phase and it has a high thermal enthalpy (1)) and the similarities with the LWR turn the SCWR into one of the most promising designs of the Gen IV.

In spite of their special properties, it is known that physicochemical properties of water change sharply with pressure and temperature into the supercritical region (2). According to some authors (3), these changes in the physicochemical properties of water could be related with changes in the behavior of water into the supercritical region so that water behaves like a liquid when the pressure increases and like a gas when the temperature increases. Despite the relevance of these considerations, there are few works in the literature about this topic. For instance, Imre (3) tried to define the subzones inside the supercritical region where the supercritical water behaves more like a gas or like a liquid and Guzonas *et al.* (4) who, based

on previous works (5), tried to define the conditions where the oxidation mechanism changes from electrochemical to chemical oxidation in supercritical water. In spite of these works, the behavior of the supercritical water with pressure and temperature into the supercritical region is not well known yet.

The austenitic stainless steels, that have shown a good behavior under LWR conditions, are one of the candidate materials to build the supercritical water reactor (SCWR) due to their good mechanical properties at high temperature, their high corrosion resistance and high strength at high temperature. Nevertheless, their behavior to one of the major degenerative processes that occur in the LWR, the stress corrosion cracking (SCC) (6), in a complex environment like the supercritical water is not well known.

In this work an austenitic stainless steel 316 type L will be tested in SCW at different pressures and temperatures in order to study how changes in these variables into the supercritical region influences its behavior to SCC and to gain some insight into the influence of pressure and temperature on the SCC mechanisms in this environment. This study will be completed with the analysis of an oxide layer formed under selected test conditions (673 K/30 MPa/< 10 ppb O_2) in supercritical water.

2. Experimental

The material used in this test was an austenitic stainless steel 316 L. Its composition is listed in Table 1.

Table 1. Chemical composition of the tested alloy (%wt)

Material	C	Co	Cr	Fe	Mn	Mo	N	Ni	P	S	Si
316 L	0.020	0.14	17.39	Bal.	1.28	2.20	0.020	11.49	0.032	0.001	0.45

Specimens were obtained from a plate that was previously solution heat-treated at 1336 K for 30 min. and then water quenched. After the thermal treatment, specimens were machined from the plate by Electro Discharge Machining (EDM). The surface of the oxidation specimens was polished by SiC abrasive paper up to 600 grit. The surface of the SCC specimens was polished up to silica and alumina. After surface preparation, a selected SCC sample was studied by Electron Back Scattered Diffraction (EBSD) in order to classify the different grain boundaries and to identify where cracks occur. Moreover, the oxidation samples were measured and weighed. Afterward, oxidation and SCC specimens were cleaned ultrasonically using ethanol and acetone and fixed in the autoclave.

Oxidation and SCC tests were carried out in a supercritical water loop with a refreshed autoclave of a 4 L volume made of alloy 625 at two different temperatures: 673 K and 773 K and two different pressures: 25 MPa and 30 MPa (properties of water at testing conditions are shown in Table 2). The dissolved oxygen was controlled below 10 ppb (deaerated) by injection of Ar into a water conditioning tank. The conductivity of water during the tests was around 0.1 μS/cm.

Table 2. Properties of water at testing conditions

Temperature (ºC)	Pressure (MPa)	Density (g/cm^3)	Dielectric constant
400	25 30	0.17 0.35	2.4 5.9
500	25 30	0.09 0.12	1.5 1.7
350	25	0.63	14.85

The susceptibility of the alloy 316 L to SCC was assessed by means Constant Extension Rate Tensile (CERT) tests. Samples were strained up to different percentages of elongation (table 3) at a strain rate of $1x10^{-7}$ s^{-1} which is low enough to investigate SCC susceptibility of ferrous steels (7).

Table 3. Conditions of the CERT tests in supercritical water

MATERIAL	Test Conditions	Final elongation
316 L	673 K/25 MPa/deaerated	up to Failure
316 L	673 K/30 MPa/deaerated	19%
316 L	773 K/25 MPa/deaerated	20 %/up to Failure*

* This sample was studied by EBSD before the test in supercritical water.

After the tests, oxidation samples were weighed and the oxides were studied by scanning electron microscope (SEM). The chemical composition of these oxides was studied by Auger spectroscopy. Furthermore, the side surface and selected fracture surfaces of the SCC samples were studied by scanning electron microscope (SEM)

3. Results and discussion

3.1 Results from CERT tests in supercritical water

The stress-strain curves of the specimens after CERT tests are shown in Fig. 1:

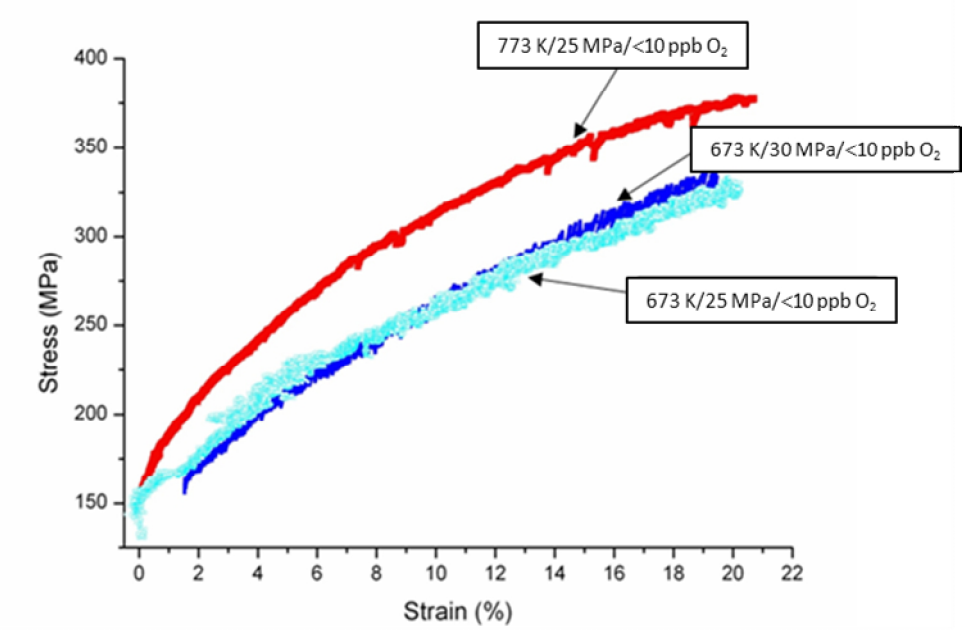

Figure 1 Stress-Strain curves for specimens tested in supercritical water at different pressures and temperatures

Curves of specimens tested in supercritical water at 673 K and 25 MPa and 30 MPa show a similar behaviour without significant differences between them so the effect of pressure, in case it exists, could not be seen in the stress-strain curves. Nevertheless, the curve of the sample tested at 773 K and 25 MPa shows a higher hardening during the test than the samples tested at 673 K. This behaviour may be due to the existence of Dynamic Strain Ageing (DSA) processes which could modify the shape of the curve at certain temperatures. Nevertheless, this is a complex mechanism and more work is needed to understand the processes involved.

In Fig. 2, stress-strain curves of samples tested in supercritical water at 673 K and 773 K and strained up to failure are shown. In this case, the elongation of the curve tested at 773 K was reduced around 13 % by increasing the temperature. These observations suggest changes in the behaviour of water with increasing temperature. Nevertheless, the information can be obtained from this kind of curves is limited.

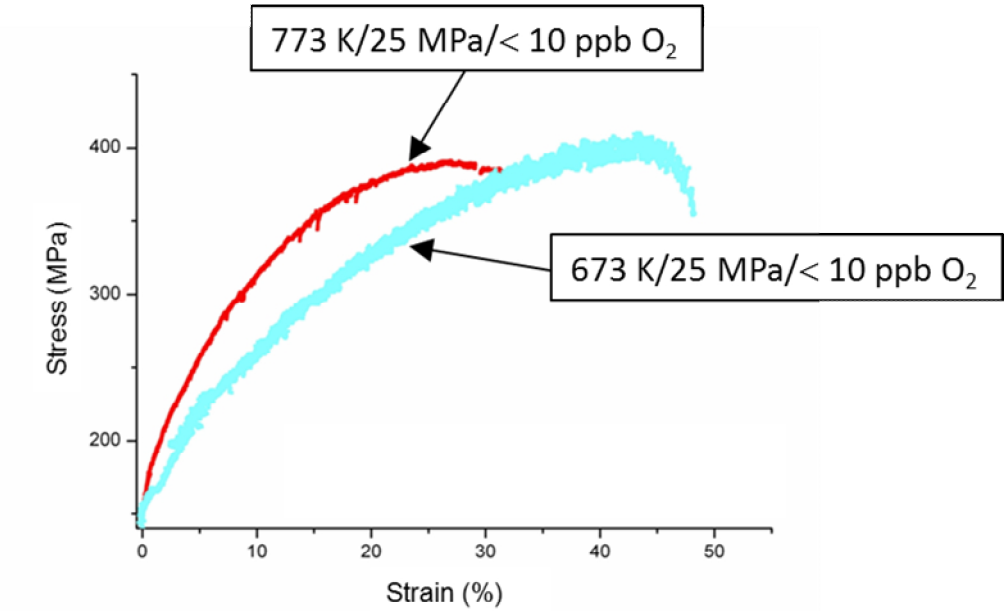

Figure 2 Stress-strain curves for specimens strained in supercritical water up to failure at 673 K and 773 K/ 25 MPa/<10 ppb O_2

After the tests, the oxide layers were removed from the SCC samples and the clean surface was studied by SEM. The density and average size of the cracks were studied in order to assess the susceptibility of the alloy 316 L to SCC in supercritical water. Results from this study are shown in table 4:

Table 4. Results from the study of the surface of the specimens after CERT tests in supercritical water.

MATERIAL	Test Conditions	% Elongation	Crack Density (nº/mm^2)	Average Size (μm)
316 L	673 K/25 MPa	Failure (48)	53	36
316 L	673 K/30 MPa	19	21	~25
316 L	773 K/25 MPa	20	Isolated cracks	~25
316 L	773 K/25 MPa	Failure (35)	61	65

According to the results shown in the previous table, when temperature increases at constant pressure the crack density and the average size of the cracks increase. On the other hand, the fracture surface of the sample tested in supercritical water at 500 ºC/25 MPa (Fig 3 a) shows small areas of SCC (highlighted with red boxes) that initiates in the surface of the sample. The morphology of these areas, a mixture between an intergranular crack and a transgranular crack, is called granulated by some authors (8). This morphology may be caused by a slightly high rate during the test (9). Nevertheless, the surface of the sample tested in supercritical water at 400ºC/25 MPa (Fig. 3 b) shows only a ductile fracture so the study of the fracture surfaces support the above results i.e., the susceptibility of the material to SCC in supercritical water increases with temperature.

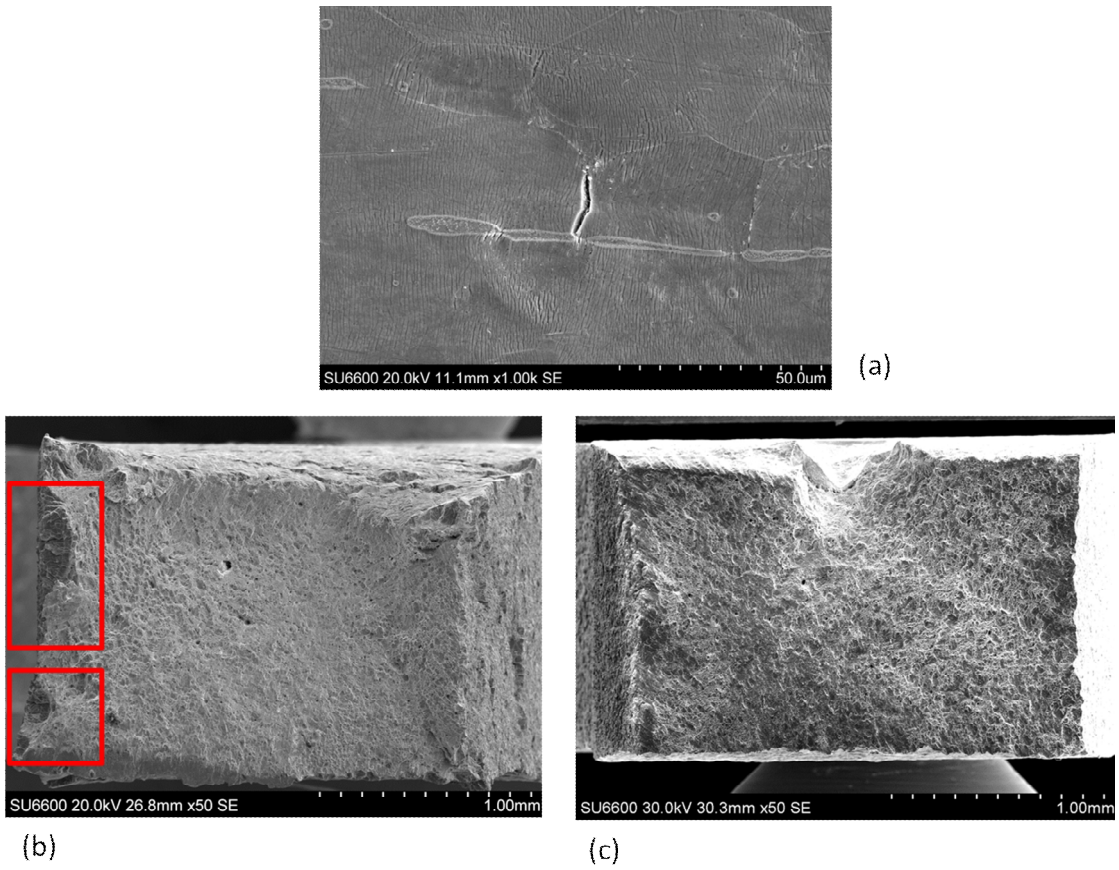

Figure 3 (a) An example of a crack found in the surface of a specimens tested in supercritical water (673 K/30 MPa/<10 ppb O_2); (b) Fracture surface of the specimen tested in supercritical water at 773 K/25 MPa/<10 ppb O_2, granulated cracks are boxed in red; (c) Fracture surface of the specimen tested in supercritical water at 673 K/25 MPa/<10 ppb O_2

On the other hand, when pressure and temperature increase for the same elongation, the effect of pressure seems to prevail over the effect of temperature. In this case, the pressure increases mainly the crack density in the material.

In all cases, the average size of the cracks is small, for this reason it could be more appropriate call them crack precursors instead of cracks. Comparing the surface of the sample tested at 773 K/25 MPa with the EBSD map obtained before the test (Fig. 4) it is possible to affirm that, at least, some of the cracks observed are intergranular and they appear preferentially in the random grain boundaries:

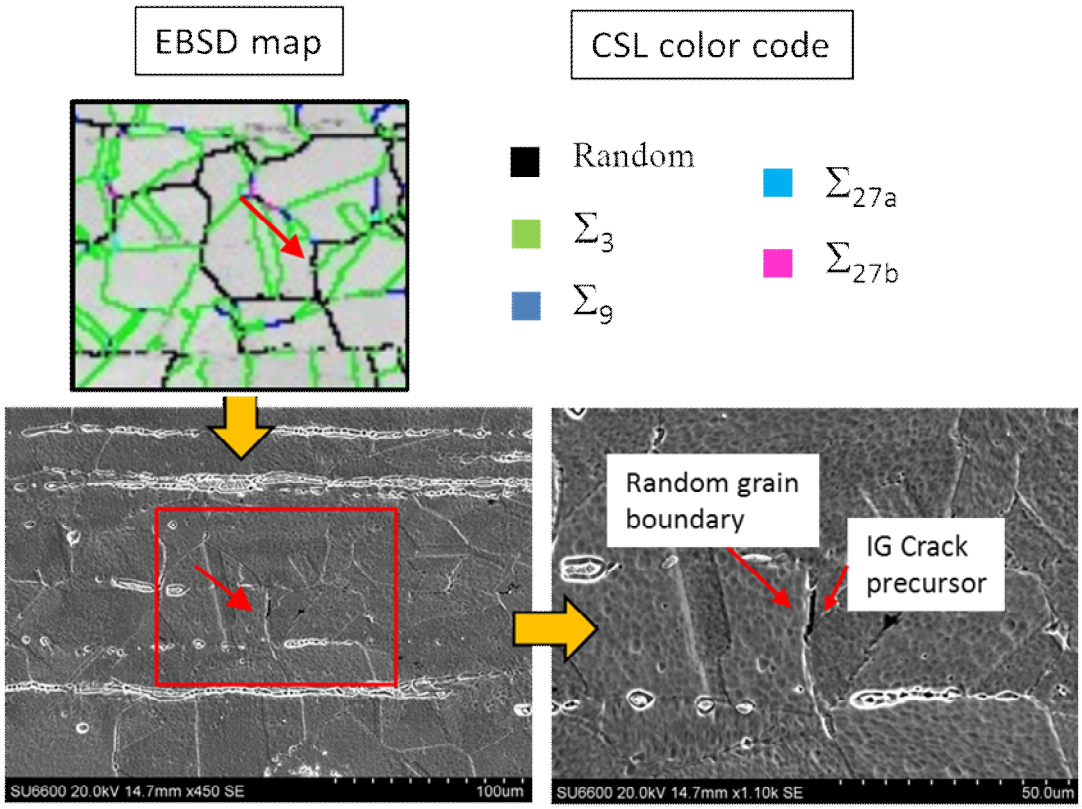

Figure 4 Comparison between the microstructure obtained by EBSD before the test and the same surface after the test in supercritical water at 773 K/25 MPa//<10 ppb O_2.

3.2 Results from oxidation tests in supercritical water

The oxide layer plays a key role in the behavior of an austenitic stainless steel to SCC since it isolates the material from the aggressive environment. In spite of the importance of this topic, the relationship between the susceptibility of the material and the properties of the oxide layers is not well understood, even less if the layer is formed in a not well known environment like the supercritical water. For this reason, the aim of this work is to get some insight into this problem.

In a previous work (10), evidence of changes in the behavior of the supercritical water when pressure increases were shown. In this work, the oxide layers formed in an austenitic stainless steel 316 L tested in supercritical water at different temperatures (673 K and 773 K) and different pressures (25 MPa and 30 MPa) for an oxygen concentration of 8 ppm were analyzed. Studying these results, it was found that only in the sample tested at 400 ºC and 30 MPa the chromium is not incorporated to the external oxide layer. This behavior could be due to changes in the behaviour of supercritical water which seems to be closer to the behavior of liquid water when the pressure increases.

Considering these results and results from CERT test at 673 K/30 MPa/O_2<10 ppb, it seems appropriate to study the oxidation behavior of the alloy 316 L in deaerated water in order to gain some insight into the oxidation mechanisms and the behavior of supercritical water.

Sample tested in supercritical water at 673 K/30 MPa/ <10 ppb of O_2 528 h and sample tested at 673 K/30 MPa/8 ppm of O_2 260 h both gained 2 mg/dm^2. This weight gain keeps constant after 760 h for the sample tested with 8 ppm of oxygen (Fig 5 a).

In Fig. 5 b the surface of the sample tested 528 h in supercritical water at 673 K/30 MPa/8 ppb of O_2 is showed:

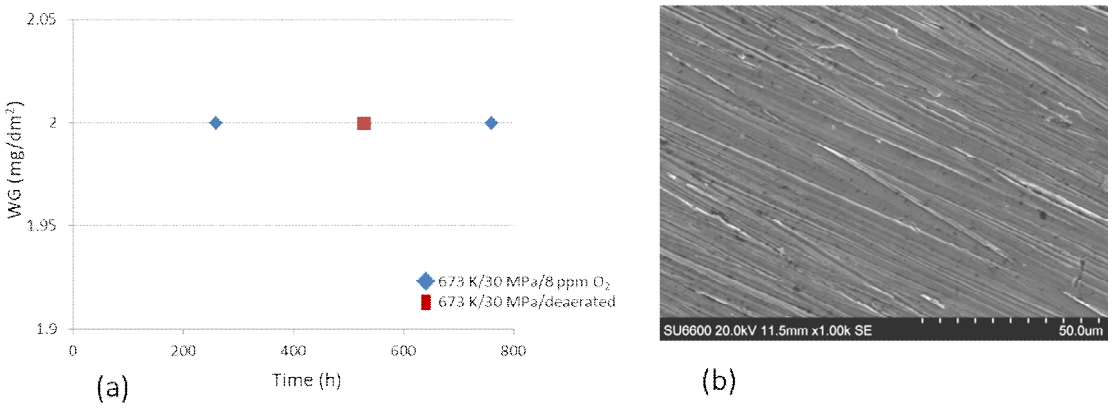

Figure 5 (a) Weight gains as a function of exposure time for the alloy 316 L at 673 K/30 MPa with 8 ppm O_2 and at 673 K in deaerated supercritical water. (b) Scanning Electro Microscope image of the surface of the specimen tested in supercritical water at 673 K /30 MPa/< 10 ppb O_2.

As it can be seen in Fig. 5 (b), the specimen was covered by a very thin oxide layer and the surface grinding marks were still visible. For these reasons, it could be said that low oxygen concentration does not promote the formation of oxide layers in supercritical water, as it was expected.

The oxide layer characterization was carried out by Auger spectroscopy. Results are shown and compared with results from the previous work (10) in Fig. 6:

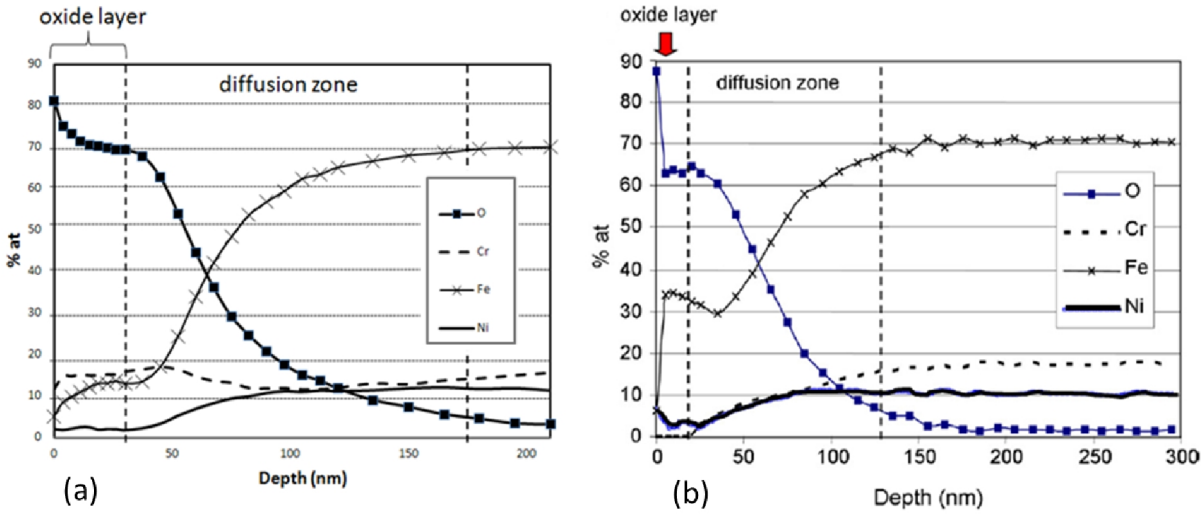

Figure 6 Elemental composition profiles of oxide layers formed on the alloy 316 L at (a) 673K/30 MPa/< 10 ppb O_2 (528 h) and at (b) 673K/30 MPa/ 8 ppm O_2 (760 h).

Comparing Auger profiles showed in Fig. 6 that were obtained from the sample tested in deaerated supercritical water at 673 K/ 30 MPa (a) and from the sample tested in supercritical water at 673 K/30 MPa with 8 ppm of oxygen dissolved (b) it was found that the chromium is incorporated to the external oxide layer when the oxygen concentration decreases. This behavior could be due to a decrease of the electrochemical potential of the system as a result of a reduction in the oxygen concentration. In addition to this, changes in the oxygen concentration modifies the iron concentration and the thickness of the oxide layer.

As it was found in the previous work, when temperature increases from 673 K to 773 K at 30 MPa, chromium is incorporated to the external oxide layer. This could be due to changes in the behavior of the supercritical water related to changes in the physicochemical properties of supercritical water with pressure and temperature. To complete this observation, results from the previous work performed at 773 K/25 MPa (among all tests conditions this is where supercritical water seems to behave more like gas) and 8 ppm of oxygen will be compared with results coming from an unpublished work of the Structural Materials Division of Ciemat. In this case an austenitic stainless steel 316 L was tested in deaerated supercritical water at 500 ºC/25 MPa for 125 h. It should be pointed out that the specimen was polished with diamond paste. Although it is known the surface finishing could modify the response of the material in this environment (11), it can be assumed there are not big differences between these two surface finishes that could modify the behaviour of the material. In Fig. 7 Auger analysis from these specimens are shown:

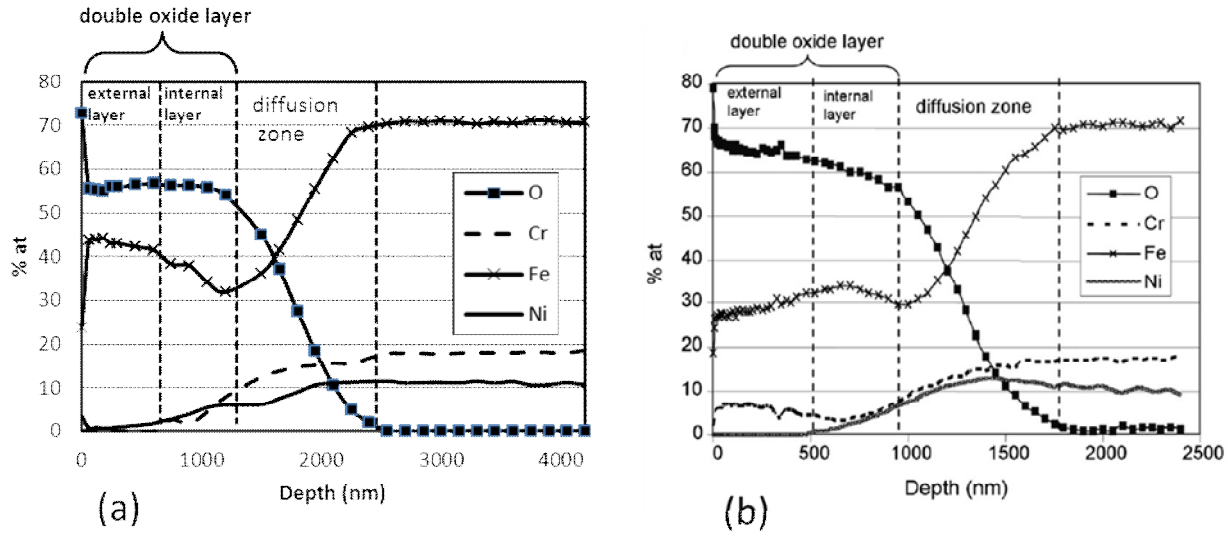

Figure 7 Elemental composition profiles of oxide layers formed on the alloy 316 L at (a) 773K/25 MPa/< 10 ppb O_2 (125 h) and at (b) 773K/25 MPa/ 8 ppm O_2 (750 h).

As can be seen in Fig. 7, when oxygen decreases chromium disappear from the outer oxide layer. This behavior is opposite to that observed in the samples tested at 400 ºC. This may be another clue of changes in the behaviour of supercritical water related to changes in the physicochemical properties with pressure and temperature.

4. Conclusions

The susceptibility of the austenitic stainless steel 316 L to SCC in deaerated supercritical water was studied at different temperatures (773 K and 673 K) and different pressures (25 MPa and 30 MPa). In addition to this, an oxidation test was performed in deaerated supercritical water at 673 K/30 MPa. This result was compared with results from a previous work of the group.

The alloy 316 L showed susceptibility to SCC in supercritical water. Small intergranular cracks (called precursors) were found in all specimens. Nevertheless, the susceptibility of this material seems to increase with the temperature and with the pressure, although the effect of pressure seems to prevail over the effect of temperature. The effect of temperature was supported by the study of the fracture surface of the specimens.

A previous work showed that at 673 K/30 MPa/8 ppm O_2 the chromium is not incorporated to the external oxide layer maybe due to changes in the behaviour of the supercritical water that seems to be water-like when pressure increases. Taking this result into account and to gain some insight into this kind of processes, the oxide layer formed in deaerated supercritical water at 673 K/30 MPa was studied. In this case, the chromium is incorporated to the outer oxide layer maybe due to a decrease of the electrochemical potential of the system as a result of a reduction in the oxygen concentration. Nevertheless, at 773K/25 MPa (where supercritical water seems to be more gas-like) the opposite effect is observed when the oxygen concentration decreases. Observation that can be interpreted as another indication of changes in the behavior of supercritical water with pressure and temperature.

5. References

[1] Pioro, I. and Mokry, S.: "Thermophysical Properties at Critical and Supercritical Conditions" *Heat Transfer-Theoretical Analysis, Experimental Investigations and Industrial Systems*,22 InTech. pp. 654.

[2] Kritzer, P.: "*Corrosion in high-temperature and supercritical water and aqueous solutions: a review*". Journal of Supercritical Fluids, Vol. 29, nº. 1-2, (2004), pp. 1-29.

[3] Imre, A.R., Deiters, U.K., et al.: "*The pseudocritical regions for supercritical water*". Nuclear Engineering and Design, Vol. 252, (2012), pp. 179-183.

[4] Guzonas, D.A. and Cook, W.G.: "*Cycle chemistry and its effect on materials in a supercritical water-cooled reactor: A synthesis of current understanding*". Corrosion Science, Vol. 65, (2012), pp. 48-66.

[5] Macdonald, D.D. and Guan, X. "*Volume of activation for the corrosion of UNS 304000 in high subcritical and supercritical aqueous sysytems*". NACE, Paper 07407 (2007)

[6] Couvant, T. "*Investigations on the mechanisms of PWSCC of strain hardened Austenitic Stainless Steels*". 13th International Conference on Environmental Degradation on Materials in Nuclear Power System Water Reactors. British Columbia. (2007).

[7] ASM. "ASM Handbook Corrosion", Vol. 13. ASM International

[8] Solomon, H.D.: "*Transgranular, Granulated and Intergranular Stress Corrosion Cracking in AISI 304 SS*". National Association of Corrosion Engineers, Vol. 40, (1984), pp. 493-505.

[9] Novotny, R., Hahner, P., et al.: "*Stress corrosion cracking susceptibility of austenitic stainless steels in supercritical water conditions*". Journal of Nuclear Materials, Vol. 409, nº. 2, (2011), pp. 117-123.

[10] Gómez-Briceño, D., Blázquez, F., et al.: "*Oxidation of austenitic and ferritic/martensitic alloys in supercritical water*". Journal of Nuclear Materials, Vol. 78, (2013), pp. 103-113.

[11] Penttilä, S., Toivonen, A., et al.: "*Effect of surface modification on the corrosion resistance of austenitic stainless steel 316L in supercritical water conditions*". The Journal of Supercritical Fluids, Vol. 81, (2013), pp. 157-163.

ISSCWR7-2026

The effect of thermo-mechanical processing on the oxidation behaviour of Incoloy 800H/HT in Supercritical water

Hamed Akhiani[1], Majid Nezakat[1], Sami Pentilla[2], Jerzy Szpunar[1]
[1]Department of Mechanical Engineering, University of Saskatchewan, Saskatoon, Canada
[2] VTT Technical Research Centre of Finland
+1 (306)370 0320, hamed.akhiani@usask.ca

Abstract

Incoloy 800H/HT is one of the promising candidates for the fuel cladding materials in supercritical water-cooled rectors. In the present study, with the help of a specific thermo-mechanical processing, we studied the effects of grain size and grain boundary character distribution on the oxidation behavior of Incoloy 800H/HT in supercritical water (SCW). The processed samples were exposed to supercritical water at 600 ºC and 25 MPa for 100, 300 and 1000 hours. The results showed that grain size and grain boundaries are important factors that affect the oxidation behaviour of Incoloy 800H/HT in supercritical water. We also found that the thermo-mechanical processing improves the adhesion and integrity of oxide scale.

Keywords: Incoloy 800H/HT, Supercritical water, Oxidation, Grain boundary character distribution.

1. Introduction

Due to unique thermo-physical properties, supercritical water (SCW) is considered to serve as cooling and heat transfer medium for one of the Gen IV nuclear reactors [1,2]. One of the major challenges for implementing the supercritical water-cooled reactors (SCWR) is to find the reactor structural materials such as fuel cladding. Conventional zirconium alloys used in Gen II and III nuclear reactors are no longer appropriate choices for Gen IV-SCWR due to their higher corrosion rate and cladding peak temperature in SCW [3,4]. Nickel and iron base superalloys, due to their superior high temperature properties (e.g. oxidation, creep) would be proper choices. However, their neutron transparency are respectively about 14 and 24 times lower than zirconium [5]. Indeed, change in the fuel assembly design e.g. reduce wall thickness, more fuel enrichment might mitigate the neutron transparency issue. Consequently, despite the excellent high temperature properties of nickel alloys, their higher neutron absorption coupled with swelling and embrittlement make Ni base alloys less favorable as fuel cladding material [6].

Among iron based super-alloys, Incoloy 800H receives more attention due to its superior high temperature properties for the Canadian SCWR [4,7,8]. The Incoloy 800H is an austenitic Fe-Ni superalloy which has been used in fossil fuel plants for decades. The alloy exhibits high temperature strength, due to solution hardening and precipitation hardening with Ti and Cr carbides, as well as high oxidation resistance and other types of high temperature degradation

(e.g. creep). Based on these properties, Incoloy 800H has been selected as a potential fuel cladding material for SCWR by the Generation IV International Forum (GIF) [4,6]. Nevertheless, to serve as a nuclear structural material in the Gen IV reactors, some modifications to Incoloy 800H structure need to be considered [9,10]. The few available publications on SCW oxidation of austenitic stainless steels reported that Incoloy 800H alloys family, generally exhibit a lower oxidation rate and weight gain compared to other iron based/stainless steel alloys [7,11]. However, in most of these studies Incoloy 800H shows oxide scale exfoliation and spallation particularly above 500˚C [11–14]. There are some efforts to alleviate the corrosion of these kind of super alloys e.g. CrN coating [15]. It is worthy to mention that most of these studies have been done using a static autoclave which often leads to lower oxidation and less spallation than dynamic/recirculating autoclaves. Nevertheless, a few studies stated the oxide scale spallation can be effectively mitigated by altering the grain boundary characteristics [12,16,17].

In this study, we implement a specific Thermo-mechanical processing (TMP) to improve the oxidation resistance of Incoloy 800H/HT in SCW. In our previous papers, we described the evolution of the deformation/annealing textures, grain boundary character distribution (GBCD) as well as the recrystallization behaviour of Incoloy 800H/HT during the proposed TMP, in detail [18,19]. In the present study, we assess the SCW oxidation behaviour of the thermo-mechanically processed Incoloy 800H with the same TMP procedure as we reported before [19]. Evaluating the oxidation behavior of TMP samples would help us to decipher the role of grain structure and GBCD in SCW oxidation of Incoloy 800H/HT. This could significantly contribute to tailor the optimize structure for enhancing the oxidation resistance of Incoloy 800H/HT in SCW. Based on the cladding tube manufacturing route i.e. extrusion or pilgering, this thermo-mechanical processing can be modified for each specific process.

2. Experimental procedure

Table 1 shows the chemical composition of the Incoloy 800H/HT used in this study. The As-received alloy was fully annealed at 1420˚C and water quenched. TMP was performed on the as-received sample by a series of unidirectional cold rolling (UDR) with 10, 30, 50, 70 and 90% reductions in thickness, followed by annealing at 1050˚C. The annealed samples were labled according to the rolling method and the reduction percentage e.g. 50UDR (50% reduction with UDR). The detail procedure for the thermo-mechanical processing was reported previously [18].

Table 1. Chemical composition (wt%) of Incoloy 800H/HT

Fe	Ni	Cr	Mn	Al	Ti	Mo	Cu	Si	Co	P	C	S
45.41	30.19	20.5	0.98	0.55	0.54	0.42	0.4	0.32	0.3	0.22	0.07	0.0001

Prior to SCW exposure, the samples were polished up to 1200 grade SiC paper. The supercritical water exposure tests were conducted at 600 ºC and 25 MPa for 100, 300, and 1000 hours in an dynamic recirculating autoclave as illustrated in the reference [20]. The SCW parameters such as temperature, pressure, oxygen content and flow rate were controlled as stated in Table 2. To avoid electrochemical reactions, the samples were electrically insulated from the sample holding rack and the autoclave body. The weight of specimens were measured before and after each exposure period (100, 300 and 1000 hours) in order to calculate the weight changes per unit area using an electronic balance with a ±0.01 mg precision.

We used a Hitachi SU6600 Field Emission Gun Scanning Electron Microscope (SEM) equipped with Oxford EDS and Electron Back-Scattered Diffraction (EBSD) in order to investigate the oxide structure. We prepared the samples using typical metallographic

procedure to a mirror like surface followed by the final polishing step with 40 nm colloidal silica on a Beuhler Vibromet^{TM} 2 vibrating polisher. We operated the SEM at 20 kV with the automatic EBSD scan on the TD plane (oxide cross section) of the samples. We utilized HKL AzTec software to acquire and analyze the EBSD data. The annealed samples were labled according to the rolling method and the reduction percentage e.g. UDR70: 70% reduction with UDR.

Table 2. Targeted and recorded values for the supercritical water test environment

Parameter	Target value / range	Notes/ values (recorded mean ± standard deviation)
Temperature	600 ºC	599 ± 1.0 ºC
Pressure	250 bar	250 ± 0.9 bar
Inlet conductivity	0.1-0.5 µS/cm	0.053 ± 0.001 µS/cm
Outlet conductivity	1.0-3.0 µS/cm	0.29 ± 0.11 µS/cm
Inlet dissolved O_2	150 ppb	150 ± 0.5 ppb
pH of the inlet water	7.0	(Pure water)
Flow rate	~5 ml/min	Full renewal about every 2 h

3. Results

3.1 Weight change

The weight change of the starting and processed samples after 100, 300 and 1000 hours exposure to SCW are illustrated in Figure 1. Some of the samples show a negative weight change. Figure 2 shows the images of the samples after SCW exposure, which can validate the oxide spallation and exfoliation in the samples pointed out by black arrows. Mostly the low to medium deformation samples (0, 10, 30 and 50%) exhibit the oxide spallation to some extent, while highly deformed samples (70 and 90%) pose a more integrated oxide layer with less spallation. The spallation of As-received, 10UDR and 10CR samples even after 100 hours exposure to SCW is observable in Figure 2 (indicated by arrows). This is in agreement with their negative weight change in Figure 1.

3.2 Oxide structure

All samples were characterized in terms of oxide appearance, surface morphology, oxide scale thickness, and oxide microstructure at the cross-section. For the ease of comparison and to avoid repetition, we report the important features and differences. Figure 2 shows the images of the As-received and the SCW exposed samples. The As-received sample exhibits a strong discoloration due to oxidation even after 100 hours. Upon increasing the exposure time, the oxide scale exfoliation and spallation are clearly visible in these samples. In the contrast, the 70 and 90 % processed samples show less discoloration and the oxide scale is more integrated.

As for oxide morphology, all the SCW exposed samples exhibit similar typical features including (Fe,Cr,Mn) spinel and iron oxide islands. Figure 3 illustrates these features with their associated elemental EDS maps. The presence of Ti beneath the iron oxide island implies that the titanium carbides might play a role in the formation of these islands. The cross section of a typical island with the associated phase, inverse pole figure (IPF) and EDS maps is presented in Figure 4. The EDS maps suggest the presence of (Cr,Mn) spinel phase beneath the surface. Nevertheless, EBSD technique was not able to detect it due to the small grain size of this oxide. Furthermore, the similarity between the Mn and Cr map suggest the formation of $MnCr_2O_4$ spinel.

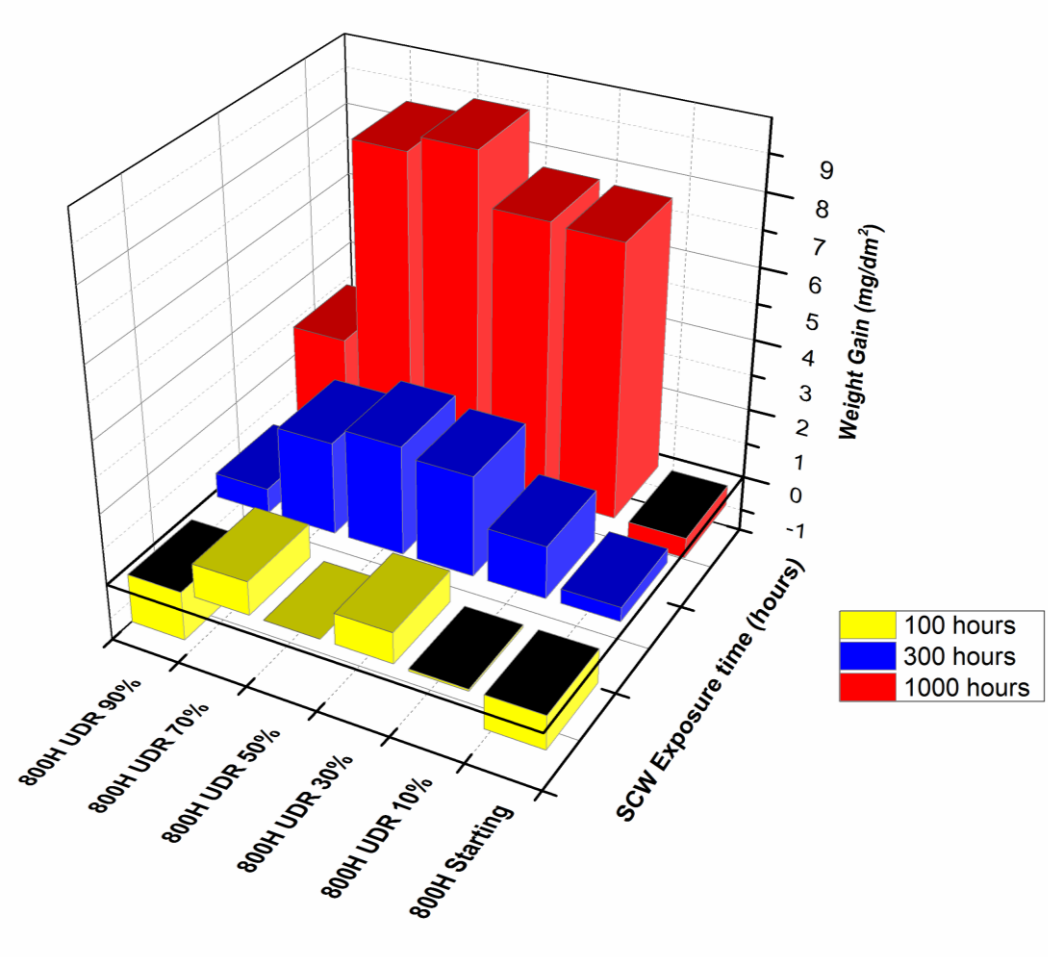

Figure 1. Weight change of the starting and processed Incoloy 800H/HT samples at 100, 300 and 1000 hours of SCW exposure.

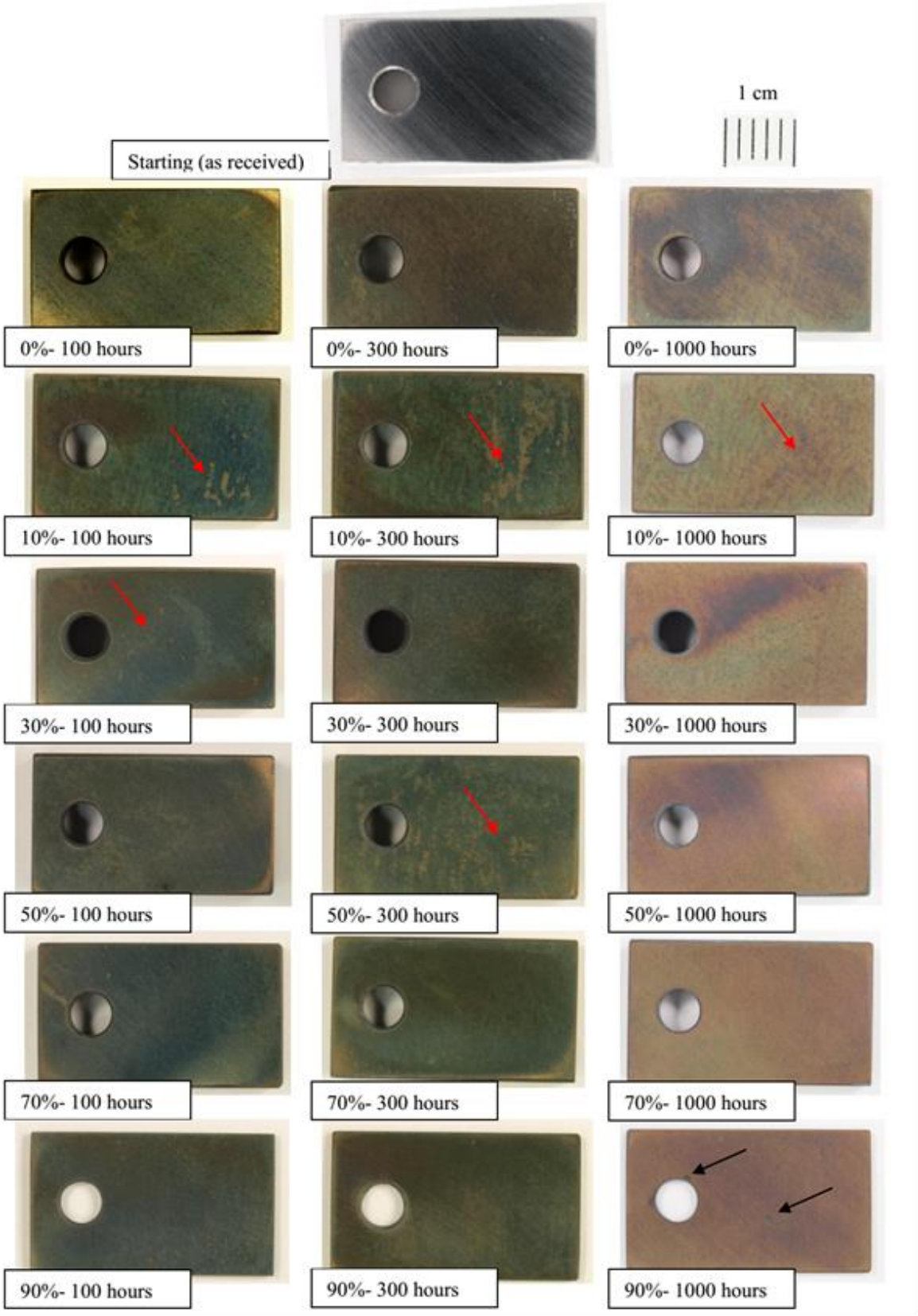

Figure 2. Images of the starting coupon (as received, before exposure), starting and processed samples after 100, 300 and 1000 hours of SCW exposure.

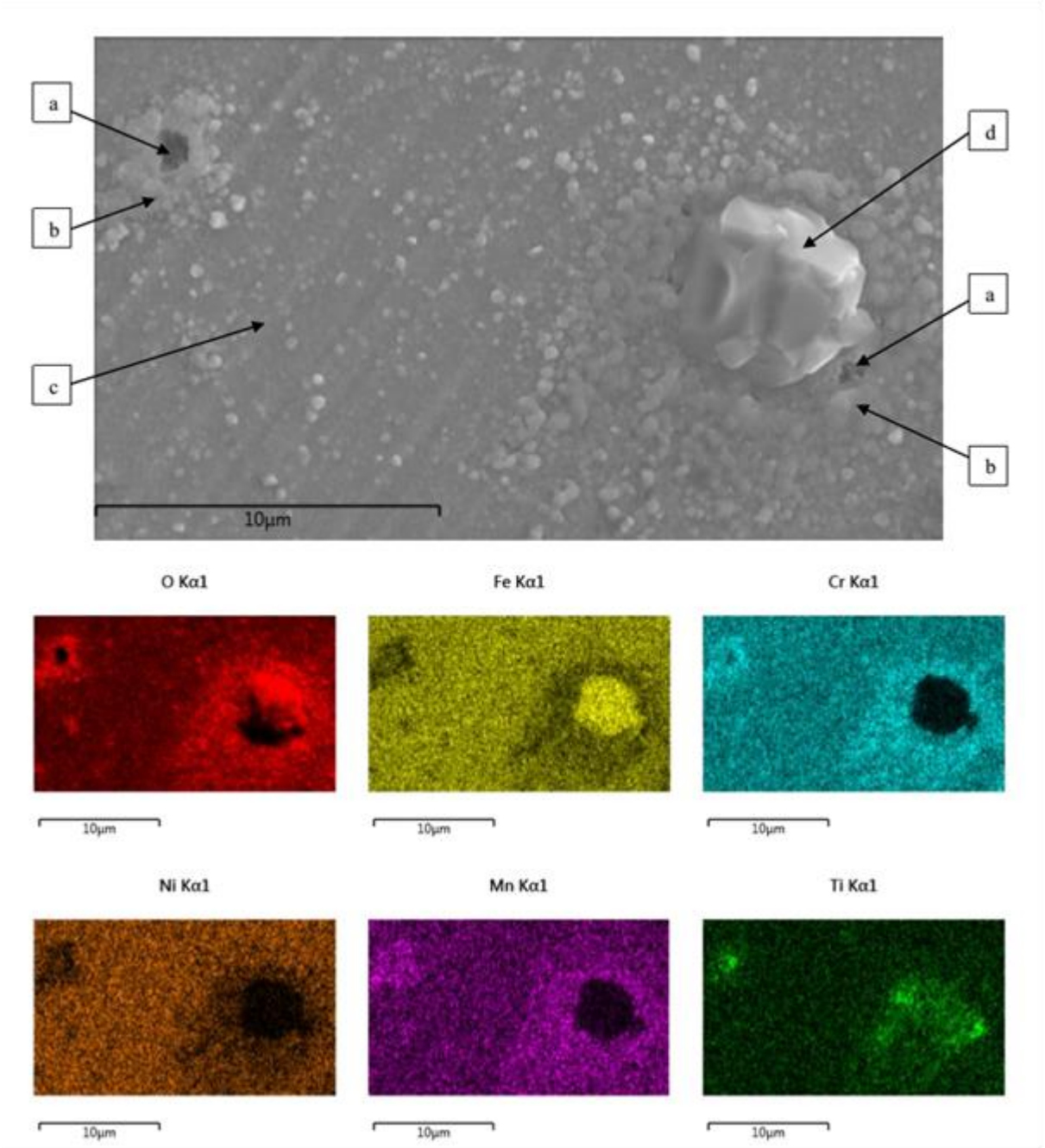

Figure 3. SEM image with EDS maps showing different regions which formed upon oxidation of Incoloy 800H/HT in SCW: (a) titanium carbide precipitate, (b) enrich chromium oxide, (c) Fe, Cr, Ni spinel, (d) Fe oxide island.

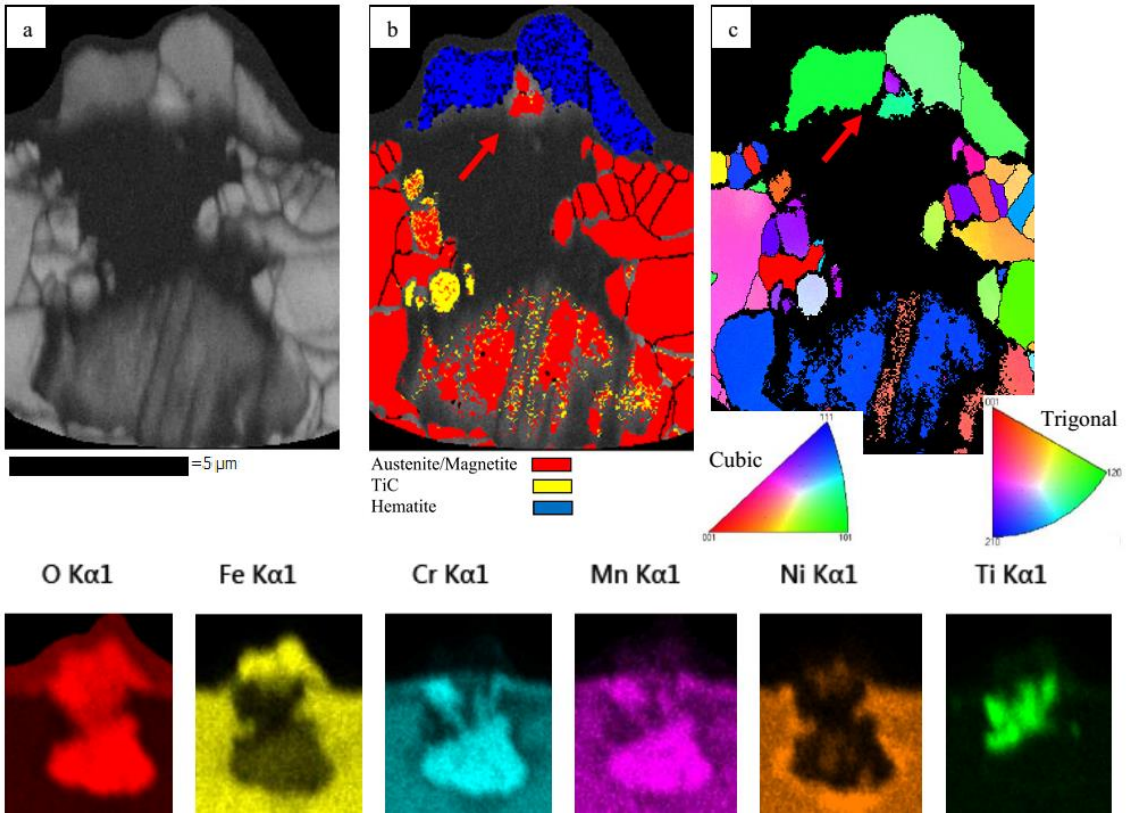

Figure 4. EBSD (a) band contrast, (b) phase map, (c): IPF Z, and EDS maps of iron oxide islands on the cross-section.

4. Discussion

The effects of microstructural parameters (carbides, grain size and GBCD) on the oxidation behaviour of Incoloy 800H/HT in supercritical water are elaborated as follows:

4.1. Effect of carbides

The oxidation behaviour of Incoloy 800 alloy family in SCW was reported in a few studies and the heterogeneous oxide surface morphology including iron oxide islands has been observed in most of them [7,8,14,21]. However no clear explanation was provided for the formation of these islands. In pursuance of island formation origin, we analysed various areas on the cross-section of the exposed samples' oxide scale to investigate the islands formation. Figure 4 represents the most observed cross section of the islands in our study. The presence of titanium precipitates between the $MnCr_2O_4$ spinel and iron oxides (Fe_2O_3 and Fe_3O_4) are clearly visible in the EDS maps of Figure 4. In addition, EBSD phase map (Figure. 4b) also depicts some of the titanium carbides grains. We have studied several cross-sections of these islands areas; the most frequent case is where a relatively high Ti concentration adjacent to $MnCr_2O_4$ in the sub surface of the iron oxides (Fe_2O_3 and Fe_3O_4) scales is present (Figure 4). However, there were a few cases that we found internal mushroom-shaped islands of chromium oxide beneath the external iron oxide island. Indeed, Ti was still observed in the latter case but its quantity is much lower than in the former case. The presence of titanium and chromium carbides together is rational since the larger carbides can act as nucleation site for other carbides in their forming

stages [22,23]. Tan et al.[8], Fulger et al.[7,14] and Mahboubi et al.[21] reported the same mushroom-shaped oxide islands upon oxidation in SCW; however none of them addressed the origin of these islands. Fulger et al.[7] reported that there are no such islands at 450˚C; but by increasing the SCW temperature to 500˚C, 550˚C and 600˚C, the islands begin to form and grow, i.e. the higher the temperature, the larger the islands. Their observation denotes that most likely the diffusion of the oxide forming elements (iron, chromium and oxygen) controls the formation of these islands. Yet, they were unable to predict the islands location. As the islands are formed on the surface and they grow larger with temperature, there should be a fast diffusion path for the species i.e. O, Cr, and Fe around the formed islands. The observation of higher concentration of Ti and Cr close to the islands would suggest that Ti and Cr have a key role in the formation of $MnCr_2O_4$ spinel and iron oxide islands.

Solution hardening and precipitation hardening with Cr and Ti carbides are the main strengthening mechanism in Incoloy 800H/HT [23,24]. Carbides can strongly affect the oxidation behaviour of alloys [22,25–30]. Near surface carbides can be oxidized by the inward diffusion of oxygen [22]. Indeed, carbides oxidation depends on the thermodynamics of their oxidation reaction at the oxidation media temperature, oxygen partial pressure and relative carbides position to the oxidation front [28,31]. Upon oxidation of these carbides usually a volume expansion (e.g. TiO_2/TiC = 1.28) may happen, which leads to impose the expansion to the carbides surrounding [22]. As a result, surface protective layer (Cr_2O_3 and spinel) may crack and fast diffusion path for species will be provided. The schematic of this scenario is illustrated in Figure 5.

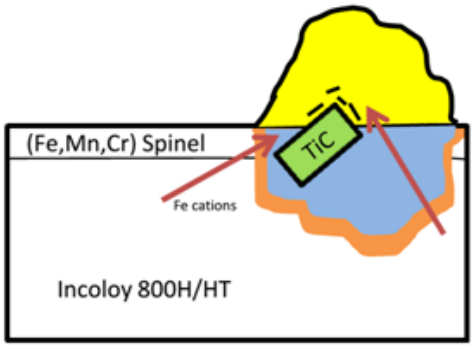

Figure 5. Schematic figure showing the iron oxide islands cross-section.

4.2. Effect of grain size

Figure 6 shows the grain size evolution upon the proposed thermo-mechanical processing. Grain boundaries are fast diffusion paths for species ions in the oxidation process. Therefore, the oxidation mechanism and kinetics strongly depend on the grain boundaries. Smaller grain size has larger grain boundary surface fraction which leads to the easier diffusion of oxide forming elements in compare to a larger grain size structure. Indeed, lowering the grain size could affect the oxidation in two offsetting ways; smaller grains allow faster diffusion of Cr and Mn to form the protective layer. At the same time, oxygen can also diffuse through these fast paths and enter the bulk metal to form internal oxides, which is not desirable. Typically, the amount of protective oxide-forming elements (e.g. Cr) in the bulk metal determines whether smaller grains are beneficial to mitigate oxidation or not. According to Incoloy 800H/HT

composition, the Cr concentration is above the critical value of 17-20% to form a protective oxide layer [26]. Thus, the former effect is more plausible.

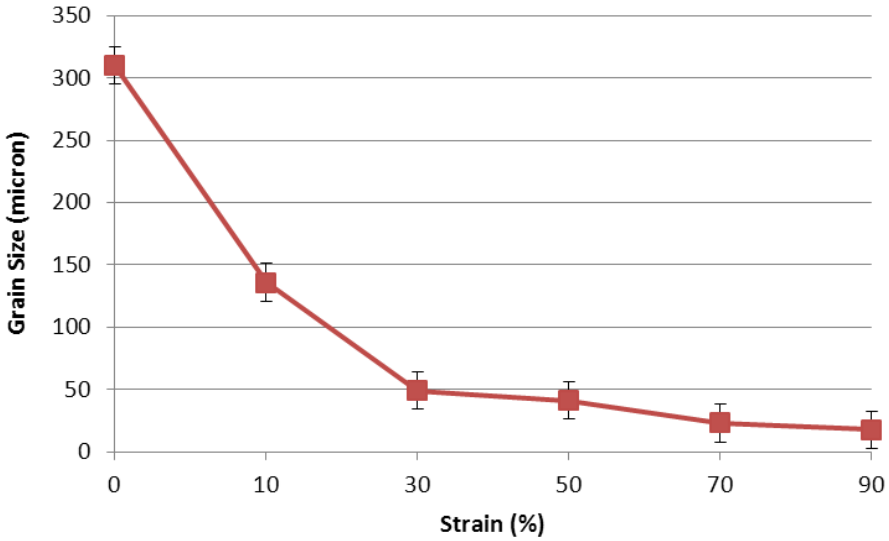

Figure 6. Grain size of the processed samples as a function of rolling modes for various reductions

4.3. Effect of grain boundary character distribution

Figure 7 illustrates the GBCD of the As-received and processed samples. The GBCD evolution upon the proposed TMP was discussed in detail elsewhere. 50UDR sample has the optimum GBCD and it shows the potential of grain boundary engineering (GBE) in this alloy. However, the main concern of coincident site lattice (CSL) effectiveness on the nuclear materials properties is their stability at the reactors service condition e.g. SCW. These boundaries might be changed due to the enhanced atomic migration and diffusion at elevated temperatures. We have previously reported the CSL evolution of this alloy upon the specific TMP.

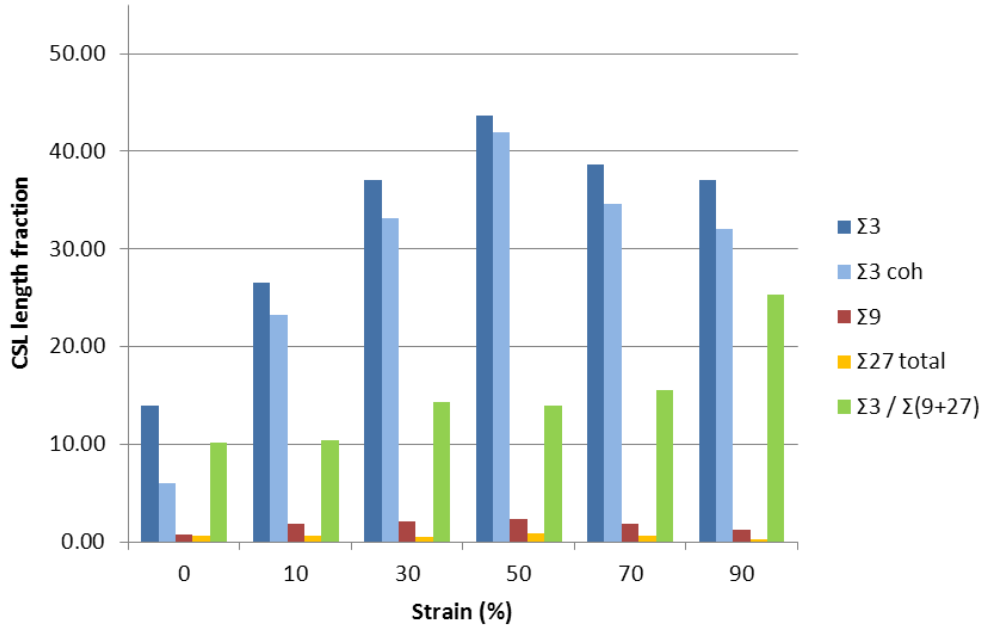

Figure 7. CSL fraction of the starting and processed (annealed) samples versus reduction pct.

To decipher the role of CSL boundaries and their stability in the supercritical water oxidation of Incoloy 800H/HT, we focused on the GBCD of 50UDR sample after SCW exposure at some regions far from the oxidation front. Interestingly, we found that the CSL boundaries, which resulted from the TMP, are reasonably stable after even 1000 hours exposure. Figure 8 shows the grain boundary/CSL maps of the 50UDR sample after 100 and 1000 hours SCW exposure. High Angle Grain Boundaries (HAGB: $\delta>15$), Low Angle Grain Boundaries (LAGB: $5<\delta<15$) and CSL boundaries: Σ3, Σ9, and Σ27 are respectively shown in black, grey, violet, blue and green lines. To clarify their stability, we have characterized and quantified the GBCD of the exposed samples with the same methodology that we used for the samples before exposure. As illustrated in Figure 7, the CSL fractions of the samples after exposure to SCW up to 1000 hours have not changed significantly. This indicates that the resulted GBCD from the proposed TMP is almost stable at the SCW service condition. In addition to temperature, irradiation in nuclear reactors might also affect the GBCD of the processed samples; therefore we plan to study the irradiation effects on GBCD in the near future.

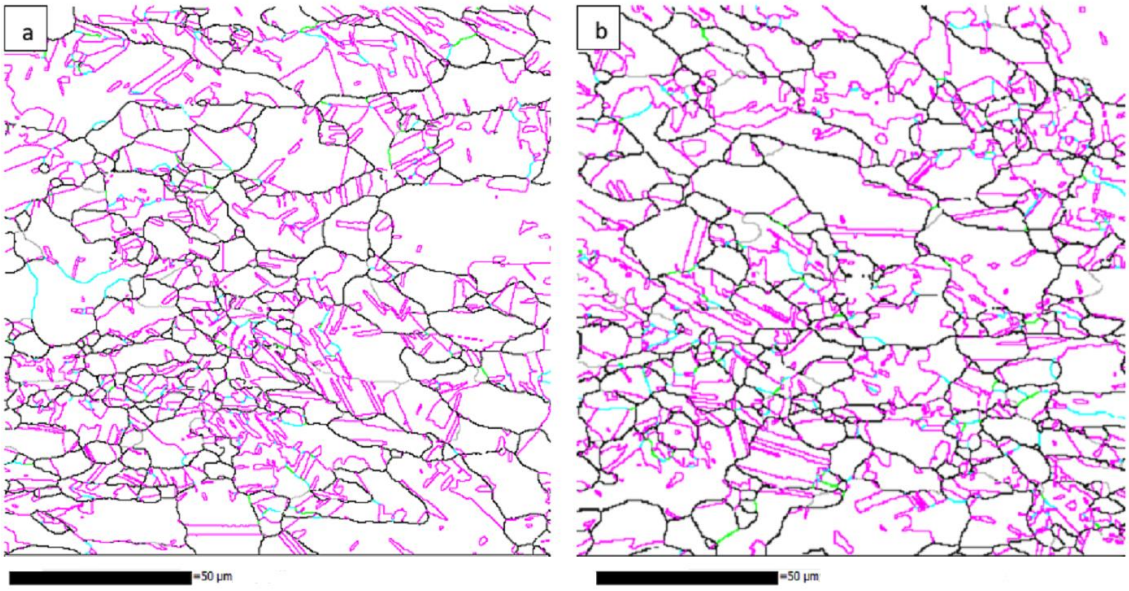

Figure 8. The CSL/GB maps of the 50UDR sample after: a)100 and b)1000 hours of SCW exposure. HAGB: black, LAGB: grey, Σ3: violet, Σ9: blue, and Σ27: green

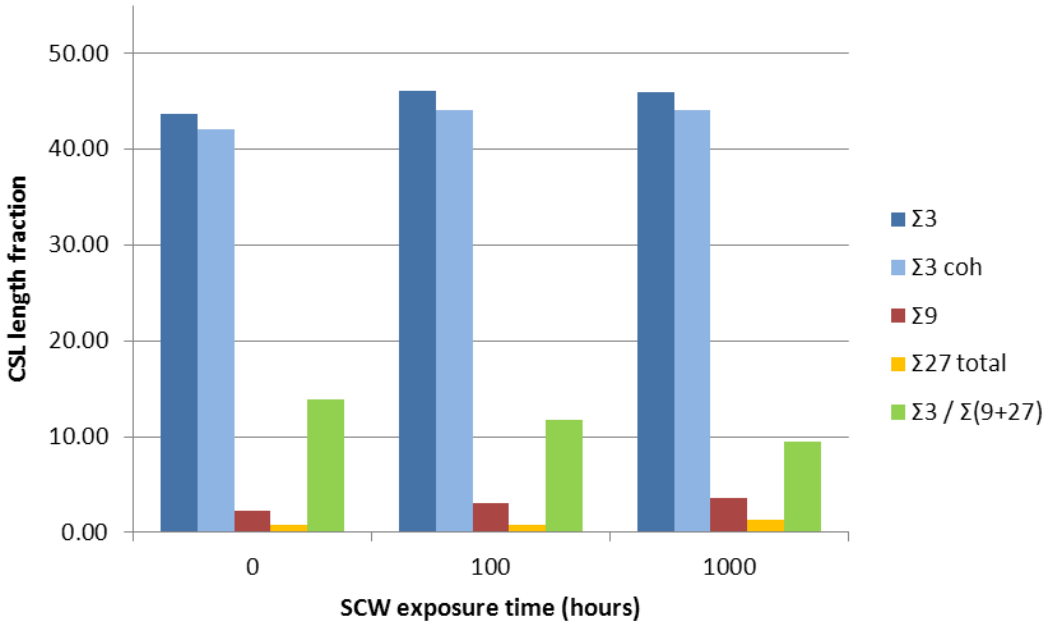

Figure 9. The CSL fraction of the 50UDR sample after: 0, 100 and 1000 hours of SCW exposure.

To study the effect of GBCD on the oxidation of Incoloy 800H/HT in SCW, we focused on some regions far from the oxidation front, due to the fact that oxidation could thicken the grain boundaries and manipulate the GBCD measurement. Figure 10 illustrates a crack which has been formed after 1000 hours SCW exposure in the As-received sample. Focusing on the crack propagation path, we can observe that it is an intergranular crack as it passes along the HAGB. Furthermore, it seems that some cracks are initiated from the incoherent titanium carbides

interfaces. Interestingly, we can observe that there are some points at which the crack has been arrested by a secure triple junction[1] which has two CSL boundaries. This is clearer in the 50UDR sample (Figure 10) with more visible titanium carbides. The secure triple junctions are indicated by arrows. Although not all the junctions could be indexed due to oxidation and grain boundary coarsening, still the number of these junctions in the 50UDR sample is significantly higher than the As-received one.

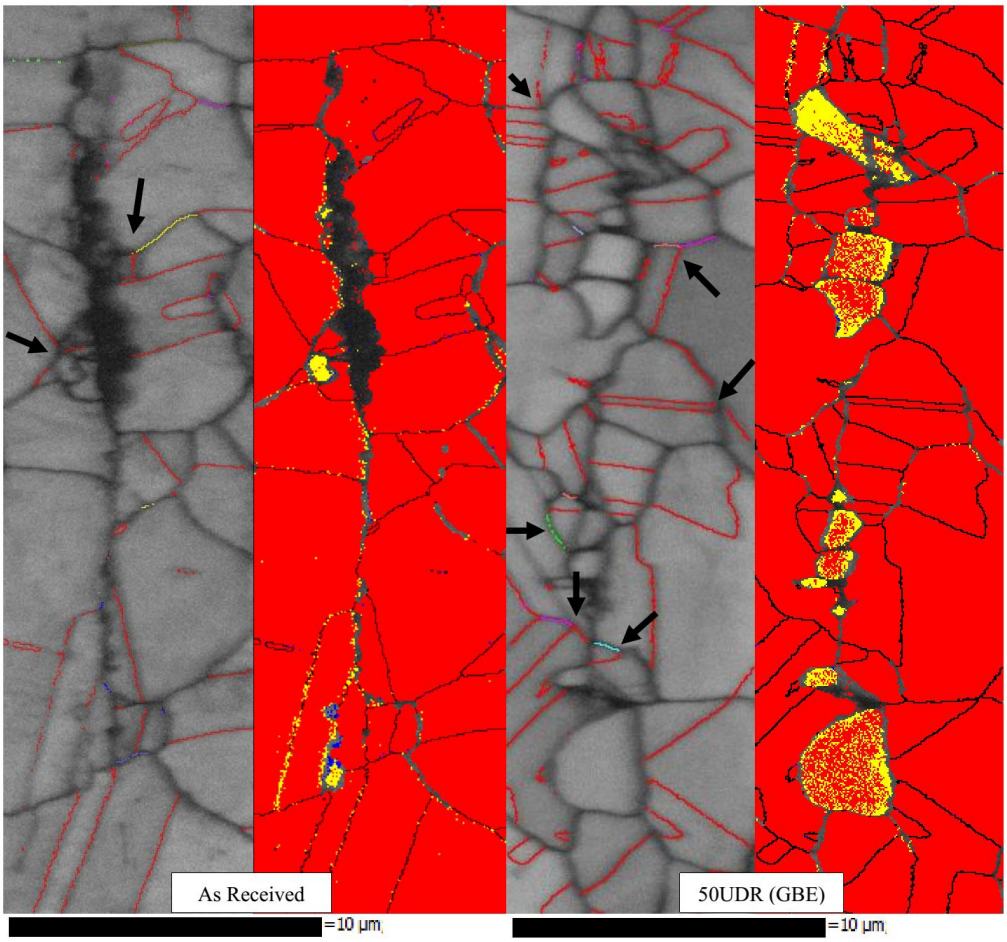

Figure 10. EBSD band contrast with CSL and phase maps of Incoloy 800H/HT: starting (as-received) and 50UDR samples after 1000 hours SCW exposure. Σ3:red, Σ7:blue, Σ9:violet, Σ11:yellow, Σ27:green.

[1] A secure triple junction is a triple junction which resist against further propagation of a crack. In this type of junction, two of the three connected boundaries should be low energy (e.g. CSL) boundaries. When a crack reaches a secure junction, further crack propagation would be arrested by the other two CSL boundaries, regardless to the type of the third boundary [32].

5. Conclusion

The oxidation behavior of thermo-mechanically processed Incoloy 800H/HT in SCW was studied in detail and the following conclusions can be driven:

- The oxidation resistance in SCW has been improved by the thermo-mechanical processing.
- Altering the GBCD was found to be effective in improving the oxidation resistance of Incoloy 800H/HT in SCW, particularly at the incoherent interfaces of carbides on the oxide scale. These interfaces appear to be susceptible to crack propagation. Increasing the CSL boundaries along with secure triple junctions would supress the crack propagation and could enhance the oxidation resistance.
- Decreasing the grain size also improved the oxidation resistance of Incoloy 800H/HT in SCW. Smaller grain size provides faster diffusion path for Cr cations which enables them to reach the surface and form the protective Cr_2O_3. Moreover, the smaller grain size would encourage the formation of Fe_2O_3.

References

[1] C. Sun, R. Hui, W. Qu, S. Yick, Progress in corrosion resistant materials for supercritical water reactors, Corros. Sci. 51 (2009) 2508–2523. doi:10.1016/j.corsci.2009.07.007.

[2] P. Kritzer, Corrosion in high-temperature and supercritical water and aqueous solutions: a review, J. Supercrit. Fluids. 29 (2004) 1–29. doi:10.1016/S0896-8446(03)00031-7.

[3] L. Zhang, Y. Bao, R. Tang, Selection and corrosion evaluation tests of candidate SCWR fuel cladding materials, Nucl. Eng. Des. 249 (2012) 180–187. doi:10.1016/j.nucengdes.2011.08.086.

[4] U.S. DOE Nuclear Energy Research Advisory Committee and the Generation IV International Forum, A Technology Roadmap for Generation IV Nuclear Energy Systems, 2002.

[5] C.R.F. Azevedo, Selection of fuel cladding material for nuclear fission reactors, Eng. Fail. Anal. 18 (2011) 1943–1962. doi:10.1016/j.engfailanal.2011.06.010.

[6] The OECD Nuclear Energy Agency for the Gen IV International Forum, Technology Roadmap Update for Generation IV Nuclear Energy Systems, 2014.

[7] M. Fulger, M. Mihalache, D. Ohai, S. Fulger, S.C. Valeca, Analyses of oxide films grown on AISI 304L stainless steel and Incoloy 800HT exposed to supercritical water environment, J. Nucl. Mater. 415 (2011) 147–157. doi:10.1016/j.jnucmat.2011.05.007.

[8] L. Tan, T.R. Allen, Y. Yang, Corrosion behavior of alloy 800H (Fe–21Cr–32Ni) in supercritical water, Corros. Sci. 53 (2011) 703–711. doi:10.1016/j.corsci.2010.10.021.

[9] W. Ren, R. Swindeman, A review of alloy 800H for applications in the Gen IV nuclear energy systems, in: Proc. ASME 2010 Press. Vessel. Pip. Div., Bellevue, Washington, 2010.

[10] A.K. Roy, V. Virupaksha, Performance of alloy 800H for high-temperature heat exchanger applications, Mater. Sci. Eng. A. 452-453 (2007) 665–672. doi:10.1016/j.msea.2006.11.082.

[11] G.S. Was, P. Ampornrat, G. Gupta, S. Teysseyre, E. a. West, T.R. Allen, et al., Corrosion and stress corrosion cracking in supercritical water, J. Nucl. Mater. 371 (2007) 176–201. doi:10.1016/j.jnucmat.2007.05.017.

[12] L. Tan, K. Sridharan, T.R. Allen, The effect of grain boundary engineering on the oxidation behavior of INCOLOY alloy 800H in supercritical water, J. Nucl. Mater. 348 (2006) 263–271. doi:10.1016/j.jnucmat.2005.09.023.

[13] L. Tan, X. Ren, K. Sridharan, T.R. Allen, Effect of shot-peening on the oxidation of alloy 800H exposed to supercritical water and cyclic oxidation, Corros. Sci. 50 (2008) 2040–2046. doi:10.1016/j.corsci.2008.04.008.

[14] M. Fulger, D. Ohai, M. Mihalache, M. Pantiru, V. Malinovschi, Oxidation behavior of Incoloy 800 under simulated supercritical water conditions, J. Nucl. Mater. 385 (2009) 288–293. doi:10.1016/j.jnucmat.2008.12.004.

[15] R. Van Nieuwenhove, J. Balak, A. Toivonen, S. Pentiilä, U. Ehrnsten, Investigation of coatings , applied by PVD , for the corrosion protection of materials in supercritical water, in: 6th Int. Symp. Supercrit. Water-Cooled React., Shenzhen, China, 2007.

[16] L. Tan, T.R. Allen, J.T. Busby, Grain boundary engineering for structure materials of nuclear reactors, J. Nucl. Mater. 441 (2013) 661–666. doi:10.1016/j.jnucmat.2013.03.050.

[17] F.J. Humphreys, M. Hatherly, Recrystallization and Related Annealing Phenomena, Elsevier, Oxford, 2004.

[18] H. Akhiani, M. Nezakat, A. Sonboli, J. Szpunar, The origin of annealing texture in a cold-rolled Incoloy 800H/HT after different strain paths, Mater. Sci. Eng. A. 619 (2014) 334–344. doi:10.1016/j.msea.2014.09.093.

[19] H. Akhiani, M. Nezakat, J.A. Szpunar, Evolution of deformation and annealing textures in Incoloy 800H/HT via different rolling paths and strains, Mater. Sci. Eng. A. 614 (2014) 250–263.

[20] S. Penttilä, a. Toivonen, J. Li, W. Zheng, R. Novotny, Effect of surface modification on the corrosion resistance of austenitic stainless steel 316L in supercritical water conditions, J. Supercrit. Fluids. 81 (2013) 157–163. doi:10.1016/j.supflu.2013.05.002.

[21] S. Mahboubi, G.A. Button, J. Kish, Oxide scales formed on austinitic Fe-Cr-Ni alloys exposed to supercritical water: role of alloying elements, in: 19th Pacific Basin Nucl. Conf., Vancouver, 2014.

[22] J. Litz, a. Rahmel, M. Schorr, Selective carbide oxidation and internal nitridation of the Ni-base superalloys IN 738 LC and IN 939 in air, Oxid. Met. 30 (1988) 95–105. doi:10.1007/BF00656646.

[23] L. Tan, L. Rakotojaona, T.R. Allen, R.K. Nanstad, J.T. Busby, Microstructure optimization of austenitic Alloy 800H (Fe–21Cr–32Ni), Mater. Sci. Eng. A. 528 (2011) 2755–2761. doi:10.1016/j.msea.2010.12.052.

[24] Special Metals Corporation, INCOLOY alloy 800H & 800HT, 2004. www.specialmetals.com.

[25] N. Birks, G. H.Meier, F.S. Pettit, High-Temprature Oxidation of Metals, 2nd ed., Cambridge University Press, 2006.

[26] U. Krupp, H. Christ, Selective Oxidation and Internal Nitridation during High-Temperature Exposure of Single-Crystalline Nickel-Base Superalloys, Metall. Mater. Trans. A. 31 (2000) 47–56.

[27] R.N. Durham, B. Gleeson, D.J. Young, Factors Affecting Chromium Carbide Precipitate Dissolution During Alloy Oxidation, Oxid. Met. 50 (1998).

[28] C. Ostwald, H.J. Grabke, Initial oxidation and chromium diffusion. I. Effects of surface working on 9–20% Cr steels, Corros. Sci. 46 (2004) 1113–1127. doi:10.1016/j.corsci.2003.09.004.

[29] J. Favergeon, C.Valot, T. Montesin, G. Bertrand, Texture effects on Zircaloy oxidation: Experiment and simulation, Mater. Sci. Forum. 408-412 (2002) 999–1006.

[30] P. Berthod, Influence of Chromium Carbides on the High Temperature Oxidation Behavior and on Chromium Diffusion in Nickel-Base Alloys, Oxid. Met. 68 (2007) 77–96. doi:10.1007/s11085-007-9062-1.

[31] W.F. Chu, A. Rahmel, The Conversion of Chromium Oxide to Chromium Carbide Cr203, Oxid. Met. 15 (1980) 331–337.

[32] C.B. Thomson, V. Randle, The effects of strain annealing on grain boundaries and secure triple junctions in nickel 200, J. Mater. Sci. 32 (1997) 1909–1914.

ISSCWR7-2027

SCC susceptibility of candidate cladding materials for SCWR

Lefu ZHANG, Zhao SHEN
Shanghai Jiao Tong University
A332 School of Mechanical Eng. No.800 Dongchuan Road, Shanghai 200240, P. R. China
+86-21-34205099, lfzhang@sjtu.edu.cn

Rui TANG, Qiang ZHANG
Nuclear Power Institute of China
No.28 Yihuan Road, Chengdu, P. R. China

Abstract

Austenitic stainless steels such as 316Ti and 310S, are short listed as the candidate material for supercritical water cooled reactor. However, it has been confirmed that most of the austenitic stainless steel are susceptible to stress corrosion cracking in subcritical water, especially in oxygenated water. And the stress corrosion cracking (SCC) behaviours of these materials in supercritical water environment arouses great concern. For a quick evaluation of the stress corrosion cracking susceptibility in supercritical water, slow strain rate tensile tests were carried out with 316Ti, HR3C, 310S and 310-ODS steels. High purity Argon was chosen as the comparative blank test environment. The effect of dissolved oxygen on SCC susceptibility was also investigated. The results show obvious SCC susceptibility of 316Ti and HR3C materials at temperature below 550°C. Intergranular cracking was found on both fracture surface and gage surfaces on these specimens. Oxide dispersion strengthening is effective in promoting the strength of 310S base metal while less SCC susceptibility of 310-ODS steels was observed.

Keywords: stress corrosion cracking, susceptibility, fuel cladding, supercritical water cooled reactor

1. Introduction

Austenitic stainless steels have been widely used as the major structural materials for advanced nuclear power reactors. They are also considered for application as nuclear fuel cladding material in supercritical water systems due to their excellent combination of mechanical properties and corrosion resistance in high temperature and pressure water comparing with ferritic/martensitic steels [1,4,5].

Austenitic stainless steel type 316Ti is qualified for making fuel cladding tubes for fast breeder reactors. Scientists have gathered abundant data related to its mechanical properties and irradiation performances. 316Ti is also short listed in the candidate materials for SCWR fuel cladding. General corrosion of these materials has been evaluated in supercritical water (SCW) at temperatures up to 650°C [7]. Its susceptibility to SCC has been studied in supercritical water with different concentration of dissolved oxygen by Shen and Zhang et al [6], showing SCC susceptibility at temperatures below 600°C in oxygenated water.

Austenitic stainless steel type 310 showed very low general corrosion rate in supercritical water. It is also proposed by many researchers to be a candidate material for making SCWR nuclear fuel claddings. However, 310 stainless steel has less application in nuclear system.

Since the corrosive nature of supercritical water, general corrosion of candidate materials for SCWR have been studied intensively and the corrosion mechanisms under supercritical water conditions are quite clear up to present [4-5]. But scientists still have less understanding about localized corrosion, especially SCC, in supercritical water [4].

It is known that austenitic stainless steels are prone to be susceptible to SCC in high temperature and pressure water environment, especially if the materials is cold worked or the water contains oxygen. The wall thickness of fuel cladding tube is usually about 0.5mm and the allowance for the penetration of a corrosion crack is very limited. Clarifying the SCC behaviours of the candidate materials arouses the interests of scientists and many tests have been done up to the present [2,3,6].

SCC of austenitic stainless steels has been studied intensively in subcritical water, and SCC susceptibility is known to be influenced by water chemistry, temperature, chemical compositions, and load, etc. Was et al [1] studied SCC susceptibility of ferritic/martensitic (F/M) steels, austenitic stainless steels and nickel base alloys in supercritical water and concluded that F/M steel generally have best SCC resistance but suffer worst oxidation. Austenitic stainless steels and nickel base alloys show lower general corrosion rate, but are susceptible to SCC in SCW. R. Novotny et al [3] studied SCC susceptibility of 316L stainless steels provided by various suppliers carefully under supercritical water conditions with various level of dissolved oxygen, and found that SCC susceptibility of 316L is related to testing conditions. A phenomenological map describing the SCC regime of SSRT test parameters was proposed.

Oxide dispersion strengthening is a good method to promote the high temperature mechanical strength of metallic materials. And it is a trend for SCWR to use ODS materials for making the fuel cladding tubes. Hwanil Je and Akihiko Kimura [2] studied SCC susceptibility of ferritic 15Cr–4Al–2W ODS steels in supercritical water and the effect of dissolved hydrogen (DH) and dissolved oxygen (DO) on SCC. All the specimens exhibit ductile fracture mode, regardless of the strain rate. The effect of DH and DO on the fracture behaviour is negligible. Small cracks were observed at necking region but most of the cracks were identified as “corrosion layer cracking” by cross-sectional observation. The ODS ferritic steel shows no susceptibility to SCC in SCW at this experimental conditions. However, there is still less data related to ODS austenitic stainless steels.

Slow strain rate tensile (SSRT) test is an effective method to conduct the preliminary evaluation of the SCC susceptibilities of materials at given environment. In this work, slow strain rate test were carried out on 316Ti, HR3C, 310S and 310-ODS steels in SCW, and the effects of DO and temperature on their susceptibility to SCC were studied.

2. Experimental

2.1 Testing materials

Three austenitic stainless steels, 316Ti, HR3C, 310S, and an ODS austenitic stainless steel 310-ODS based on 310S matrix were tested by using SSRT. 316Ti and HR3C were supplied from China Nuclear Power Research Institute, 310S was supplied from Bao Steel Corporation in the as-received condition, 310-ODS steel was prepared by University of Science and Technology Beijing. Chemical compositions of these materials were analysed by X-ray fluorescence spectroscopy (XRF), and are listed in Table 1.

The dimensions of the testing specimens are shown in Fig. 1. Specimens were cut by wire cutting and all surfaces were machined by grinding in workshop to remove about 0.2 mm from each side, so that all the heat affected layer by electric sparkle disappear. Before testing, the specimens were mechanically polished using SiC emery paper from grit 400 up to 1200 to remove the surface cold worked effect due to grinding, and were ultrasonically cleaned with acetone and de-ionized water to prevent from contaminations.

Table 1. Chemical compositions of the testing materials (wt%).

Alloys	C	Si	Mn	S	P	Cr	N	Fe	Ni	Mo	Cu	Nb	Ti
316Ti	0.032	0.40	1.50	0.008	0.014	17	-	Bal.	12.10	2.0	-	-	0.47
HR3C	0.07	0.41	0.40	0.008	0.016	24.80	0.18	Bal.	19.70	-	-	0.4	-
310S	0.06	0.65	1.42	0.005	0.008	25.20	-	Bal	20.40	-	-	0.10	0.12
310-ODS	0.05	0.38	1.26	0.003	0.006	25.01	-	Bal.	19.98	1.99	W 0.14	Y_2O_3 0.35	0.20

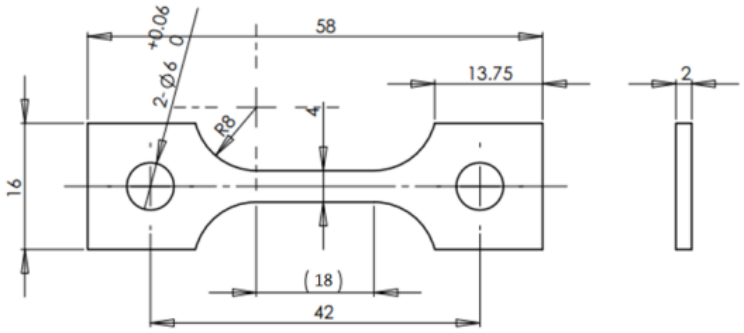

Figure 1. Dimensions of SSRT test specimens.

2.2 Testing method

The parameters that can reflect SCC response of a material include crack initiation time, crack growth rate and stress intensity factor threshold K_{1SCC} that cause the initiation of corrosion crack in the specified environmental condition. Stainless steels and nickel base alloys used in nuclear power industry have excellent corrosion resistant performances, and therefore, the time before a SCC crack initiates in these materials is some times as long as several decades. Therefore, measuring the crack initiation time seems quite un-realistic at the moment for selection of materials.

For more than 30 years, Peter L. Andresen has been improving the direct current potential drop (DCPD) method for measuring SCC crack length in high temperature and pressure water environments. And now, it is possible to detect SCC crack growth rate as low as to the order of 1×10^{-12} mm/s. In this situation, DCPD becomes a powerful tool for scientists to study SCC behaviours, especially the crack growth rate of materials with very low SCC susceptibility and to determine K_{1SCC} with acceptable accuracy. If without a good method for crack growth rate test, K_{1SCC} can not be evaluated accurately. Scientists has realized the importance of SCC crack growth rate measurement, but it needs patient and time to wait for the result to be published. One SCC crack growth rate testing system has been built in our laboratory and started to test CT specimens made of 310S stainless steel in SCW. We expect to obtain reliable SCC crack growth rate data in the near future.

It is difficult but necessary to evaluate the susceptibility to SCC of a material in supercritical water. At high temperature water environments, cracking of a metallic material is caused by combination of corrosion cracking and creep cracking. For a well-defined SCC test, it is expected to separate the portion of cracking induced by corrosion from the portion by creep. However, stress corrosion cracking is usually a slow process involving corrosion reactions that are accelerated by tensile stress. The corrosion process occurs at the specimen surface, while creep cracking mostly occurs in bulk material. Both SCC and creep fracture are usually intergranular cracking, separation between SCC cracking and creep cracking is sometimes of

great difficulty. Fortunately, SCC cracks usually start from surfaces of the specimen, and they grow much faster than creep cracks at specified temperature ranges. The effect of creep on fracture can be evaluated by conducting a comparison test in inert gas or vacuum in which there is no effect of corrosion. Therefore, it is possible to study the SCC susceptibility by slow strain rate tensile tests.

Slow strain rate test is a faster way to evaluate SCC susceptibility of materials in supercritical water at this stage, and it was applied to study the SCC susceptibility of testing materials in this work. In order to separate the effect of creep on fracture of the specimens, the SCC susceptibility of a testing material is characterized by comparison of plastic elongation in supercritical water to that in inert gas at the equivalent temperature. Fracture morphologies were also observed and applied as complementary data for analysing SCC susceptibility of the materials.

2.3 Testing system

The SSRT testing system used for this work includes an electric-mechanical slow strain rate loading servo machine and an autoclave connected to a water chemistry control loop that can provide high pressure water with controlled dissolved oxygen or hydrogen, pH, or impurities such as Cl^-. The autoclave system is schematically shown in Fig.2. It can operate up to the temperature of 650°C and pressure of 31MPa.

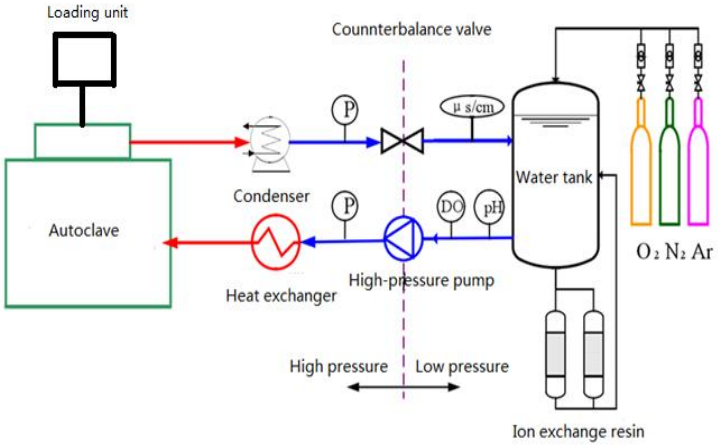

Figure 2. Schematic diagram of the SSRT testing system with water chemistry controlling loop.

2.4 Testing conditions

For 316Ti and HR3C specimens, SSRT tests were performed in SCW at temperature of 550，600 and 650°C, under pressure of 25MPa to investigate their tensile behaviours. For 310S, tests were done to study the SCC susceptibility at near critical points, with temperature from 350 up to 450°C. For 310-ODS steels, the greatest interest is to obtain its mechanical performance at temperature up to 650°C and to evaluate the strengthening effect of dispersed oxide particles.

The conductivity of Inlet water to the autoclave was controlled to below 0.1μS/cm and the dissolve oxygen concentration was controlled by bubbling high purity argon, or argon gas mixed with oxygen for a level of dissolved oxygen. After each test, strain-stress curves, fracture surfaces and the gage surfaces near the fracture were analysed to identify the mechanical properties and SCC morphology. SCC susceptibility was evaluated by comparing the stress-strain curves and portion of intergranular cracking between strained in supercritical water and argon gas.

3. Results and discussions

3.1 SSRT Stress-strain curves

Stress-strain curves of each test are given in Figure 3.Figure (a) and (b) show the tensile stress strain curves of 316Ti and HR3C in SCW at temperatures of 550, 600 and 650°C. It can be clearly seen that 316Ti loses strength from temperature of 600°C, while HR3C loses strength from 650°C.

As known, the strengthening mechanism of 316Ti is by high concentration of alloying elements and slightly by hard particles of Ti(C,N) precipitated in grain interior and $Cr_{23}C_6$ particles precipitated along grain boundaries. The maximum operation temperature of 316Ti is not recommended to exceed 550 °C, in order to avoid failure due to loss of strength during long term of operation.

HR3C is a 310 type heat resistant stainless steel with strengthening of Nb and nitrogen. After HR3C is heated at high temperature for more than 10 hours, $M_{23}C_6$, Z-phase (NbCrN) and Nb(C,N) precipitate at grain boundaries and matrix metal [9], increasing the tensile strength. $M_{23}C_6$ type carbides prefer to precipitate at grain boundaries. Although these carbides play important roles in strengthening the material, they also reduces the corrosion resistance of the grain boundaries, causing intergranular corrosion, and hence increase SCC susceptibility. It is not surprise to see the quick drop of HR3C at temperature of 650°C, which may principally due to the sensitization of this material. From the stress-strain curves of this work, HR3C should be used below 600°C

The stress-strain curves in Figure 3 (c) clearly show the dynamic strain aging effects of 310S when straining at temperature range near to critical temperature. The deformation mechanism is driven by thermal activation [10]. Comparing the stress-strain curves strained in Ar gas and water containing 500 ppb DO at 400°C, the plastic elongation is slightly less in water than in Ar gas, showing the slight SCC susceptibility at this condition. Comparing the stress strain curves strained in SCW containing 500 ppb DO at 400 and 450 °C, it can be seen that the susceptibility to SCC is higher at 450 °C. Intensive study of SCC susceptibility at 450 °C is necessary in the following SCC crack growth rate tests.

Comparison test results of HR3C and 310S in argon gas at 620°C are also shown in Figure 3 (c). The results again demonstrate the loss of strength at temperature above 600°C. The results also show the stronger nature of HR3C than 310S at higher temperatures. Strengthening of these materials is necessary for promoting them to be used for making nuclear fuel cladding tubes for SCWR.

The maximum fuel cladding hot spot temperature at normal operating conditions of a typical pressure vessel type SCWR with outlet coolant temperature of 500 to 510°C is usually above 600°C [4,11]. Oxide dispersion strengthening is potentially an applicable method to increase the high temperature strength of the candidate materials for SCWR, especially up to 650°C, Figure 3 (d) showed the stress-strain curves of an oxide dispersion strengthened steel 310-ODS base on 310S matrix material. The small amount (0.35wt%) of Y_2O_3 can promote the yield strength of 310S base metal up to over 400 MPa at temperature up to 650°C, twice as strong as its base metal, although the elongation decreased remarkably. At temperature of 600°C, 310-ODS showed excellent SCC resistance, without much loss of elongation in SCW with various dissolved oxygen level, comparing with the curve strained in argon gas.

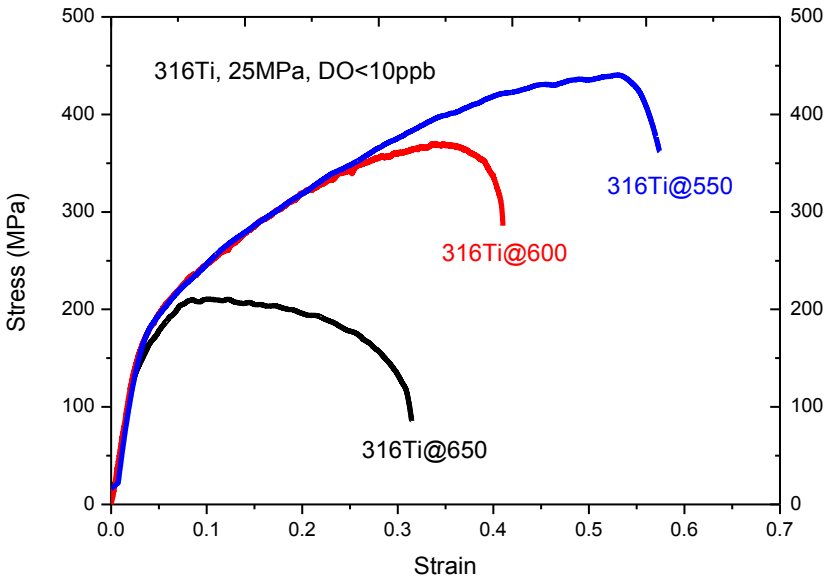

(a) 316Ti

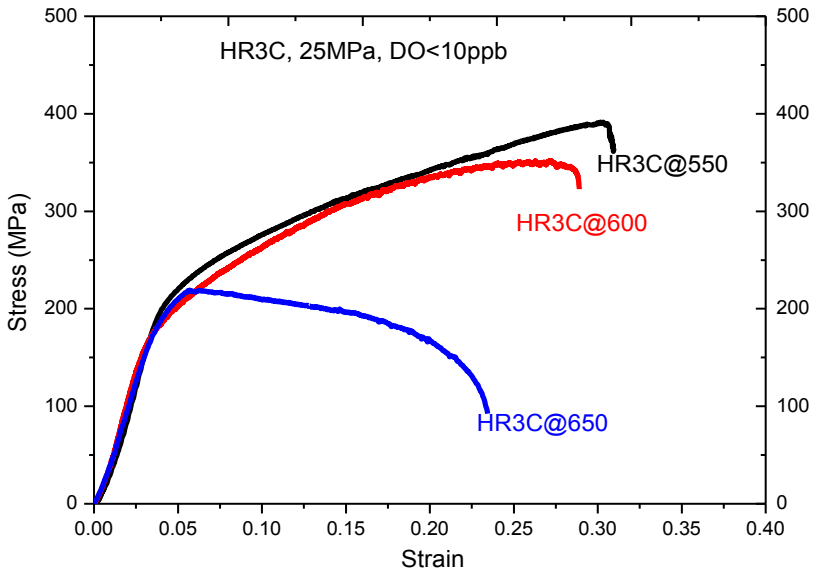

(b) HR3C

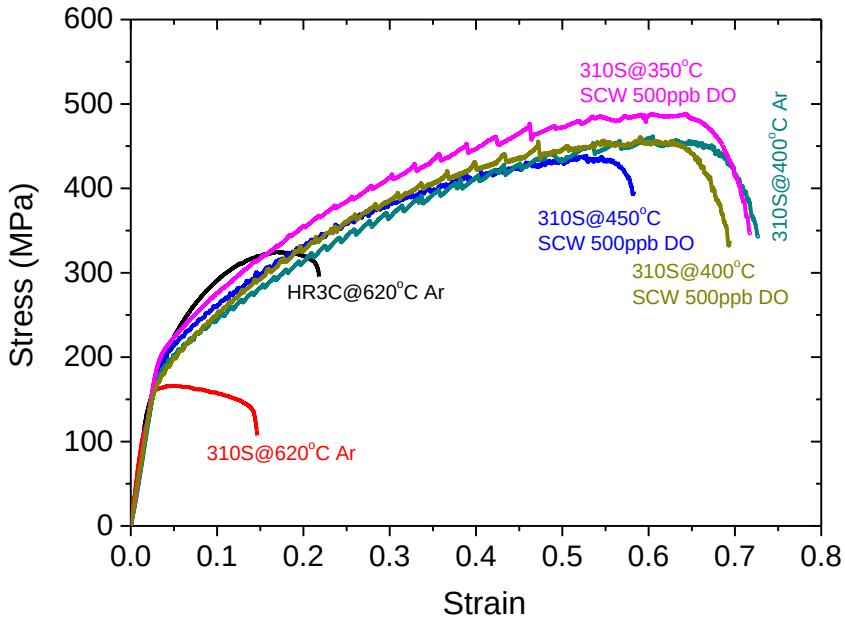

(c) 310S

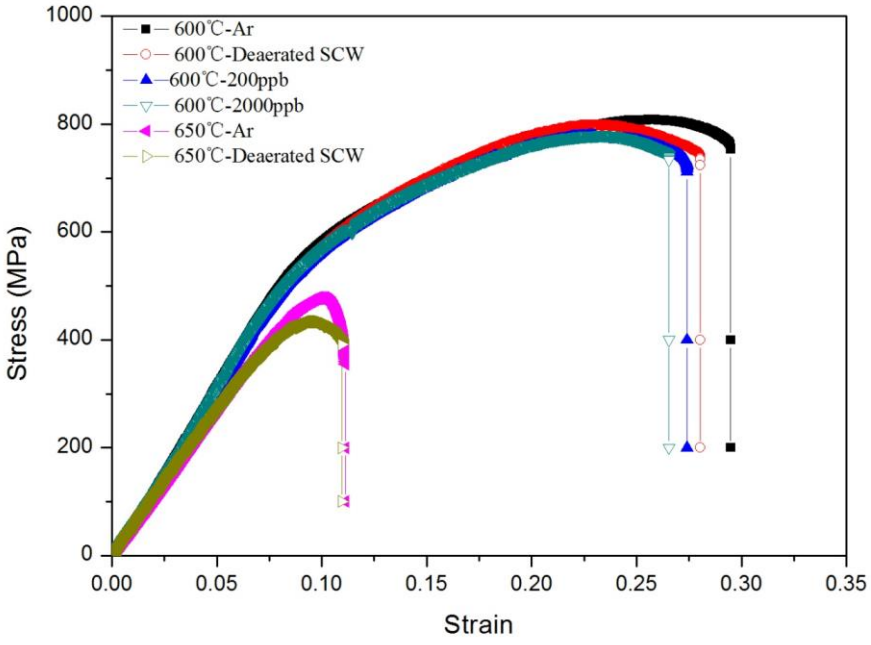

(d) 310-ODS steel

Figure 3. Stress-strain curves of each testing material.

3.2 Microstructure observation of fractured specimens

After SSRT tests, the fracture morphologies of specimens were observed using SEM. The results are shown in Figures 4 to 8.

At temperatures of 550°C, both 316Ti and HR3C show deep intergranular cracks at the gage surfaces. SCC susceptibilities of these two materials may be relatively high. The factors that cause their SCC susceptibilities may probably due to the precipitation of carbides that causes sensitization and weakening of the grain boundaries, while the matrix metal still keep high strength at this temperature.

At temperatures above 600°C, 316Ti loses strength quickly, and it SCC susceptibility decreases, showing shallow intergranular cracks or transgranular cracks at gage surfaces, as shown in Figures 5(a) and 6(a). HR3C still shows deep intergranular cracks at 600°C, as shown in Figure 5(b), and the intergranular cracks change partly to transgranular cracks at 650°C as in Figure 6(b). SCC susceptibility of HR3C decreases with increasing temperature, and it can be concluded that its SCC susceptibility is negligible at temperature up to 650°C.

SCC susceptibility due to sensitization at grain boundaries of HR3C should be considered after long terms of service at high temperature. SCC tests of specimens after aging for some time are proposed for future study. Figure 9 gives a SEM micro-graph that show the interganular crack surface morphology of HR3C after SSRT test at 600°C, it is quite similar to the typical morphology of SCC fracture surfaces obtained from a sensitized austenitic stainless steel.

The fracture surface analysis of 310-ODS specimens at 600 and 650°C show less SCC susceptibilities. Intergranular cracks are hard to be observed either at gage surfaces or at fracture surfaces. Further microstructural observation to clarify the effects of nano-sized fine Y_2O_3 oxide particles on corrosion resistance should be placed for future analysis.

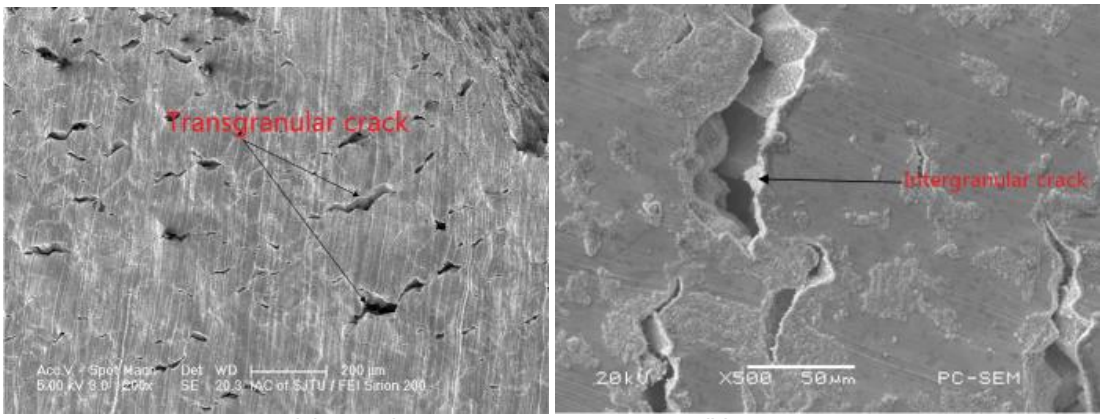

(a) 316Ti (b) HR3C

Figure 4. SEM images of the fracture surface of testing materials in deaerated SCW at 550°C.

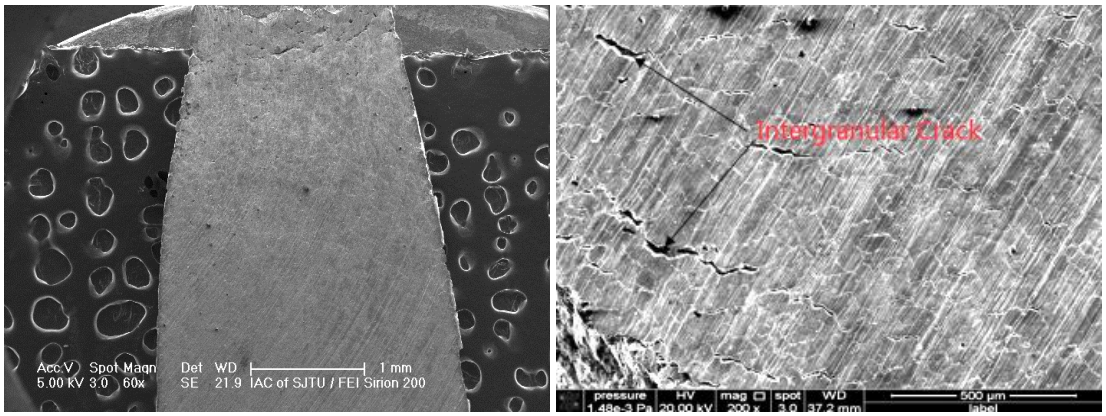

(a) 316Ti (b) HR3C

Figure 5. SEM images of the fracture surface of testing materials in deaerated SCW at 600°C.

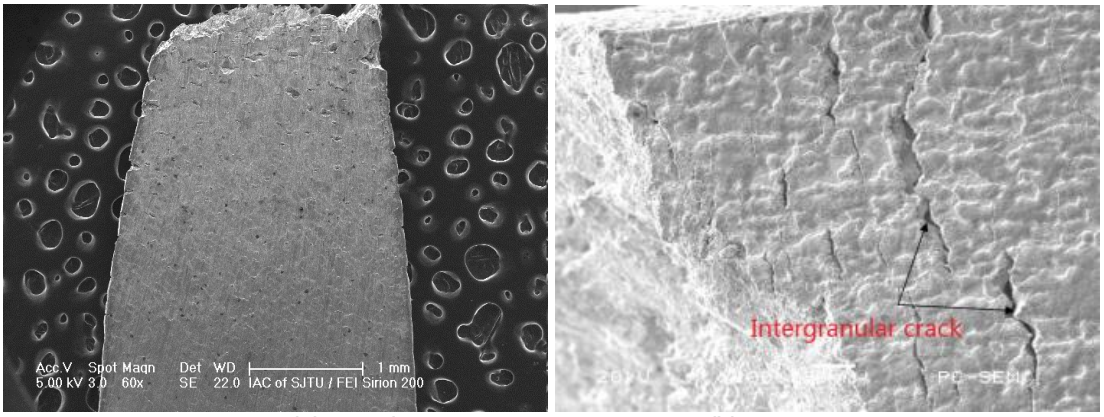

(a) 316Ti (b) HR3C

Figure 6. SEM images of the fracture surface of testing materials in deaerated SCW at 650°C.

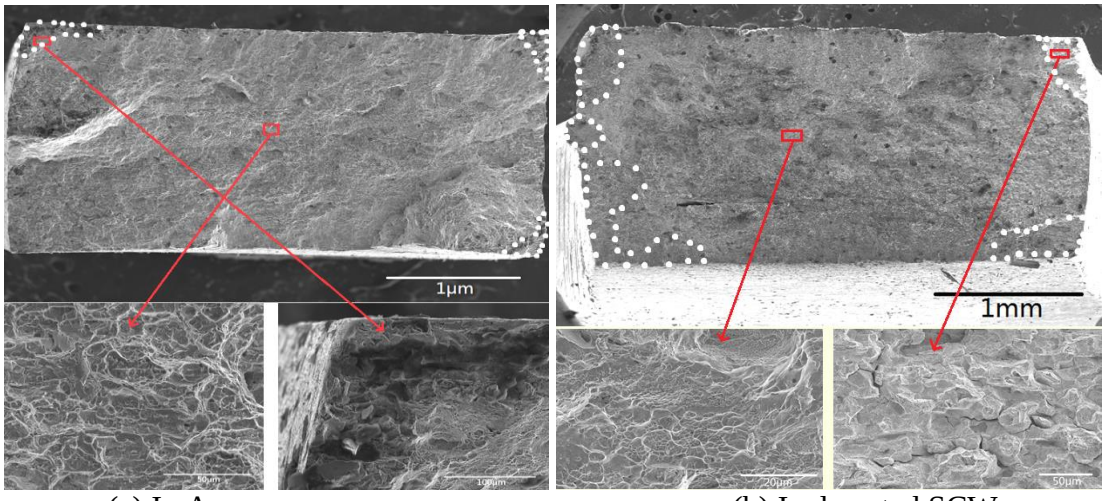

(a) In Ar (b) In dearated SCW

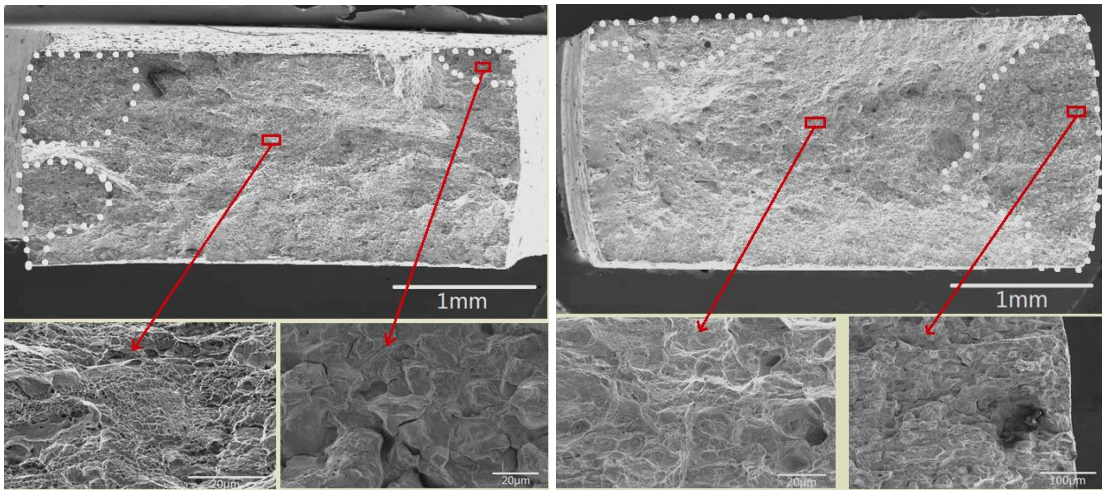

(c) in SCW 200ppd DO (d) in SCW 2000ppb DO

Figure 7. SEM images of the fracture surface of 310-ODS in SCW at 600°C.

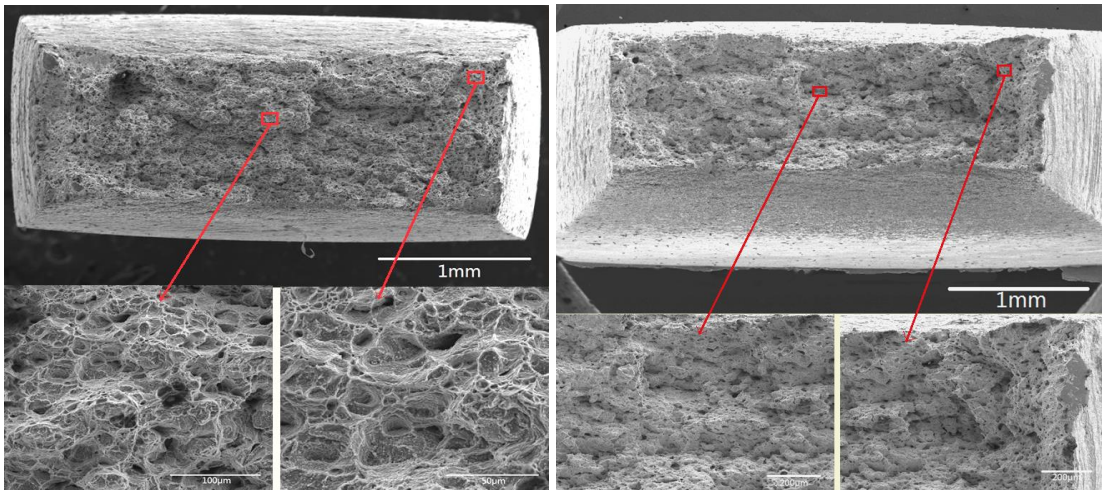

(a) in Ar (b) in dearated SCW

Figure 8. SEM images of the fracture surface of 310-ODS in SCW at 650°C.

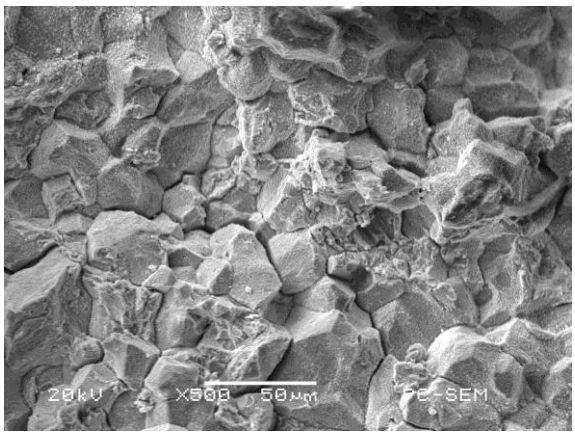

Figure 9. Schematic diagram showing the typical IG fracture morphology.

4. Conclusions

SCC susceptibility of austenitic stainless steels 316Ti, HR3C, 310S and 310-ODS were studied by slow strain rate tensile tests. The following conclusions can be drawn from the results:

(1) 316Ti loses strength when temperature increases up to 600°C, its long term service temperature is suggested be kept below 550°C. It is susceptible to SCC at temperatures up to 550°C.
(2) HR3C keeps strength up to 600°C, while exhibit relatively high SCC susceptibility than 316Ti. Sensitization at grain boundaries may be the major factor that causes SCC.
(3) Straining of 310S at temperatures near to critical temperature show strong effect of dynamic strain hardening which need intense study in the future tests.
(4) Oxide dispersion strengthening method is effective in promoting the strength of 310S while no SCC susceptibility occur in 310-ODS steel. The result is useful for future development of novel materials for SCWR fuel cladding.

Acknowledgement

This work is financially supported by “National Basic Research Program of China” (No. 2007CB209800) and by the SCWR project managed by Nuclear Power Institute of China. Thanks to the Instrumental Analysis Center of SJTU for providing help in SEM observation.

References

1. G. S. Was, P. Ampornrat, G. Gupta, S. Teysseyre, E. A. West, T. R. Allen, K. Sridharan, L. Tan, Y. Chen, X. Ren, and C. Pister. Corrosion and stress corrosion cracking in supercritical water. Journal of Nuclear Materials 371 (1-3):176-201, 2007.

2. Hwanil Je and Akihiko Kimura. Stress corrosion cracking susceptibility of oxide dispersion strengthened ferritic steel in supercritical pressurized water dissolved with different hydrogen and oxygen contents. Corrosion Science 78:193-199, 2014.

3. R. Novotny, P. Hahner, J. Siegl, P. Hausild, S. Ripplinger, S. Penttila, and A. Toivonen. Stress corrosion cracking susceptibility of austenitic stainless steels in supercritical water conditions. *Journal of Nuclear Materials* 409 (2):117-123, 2011.

4. D. Guzonas and R. Novotny. Supercritical water-cooled reactor materials - Summary of research and open issues. Progress in Nuclear Energy 77:361-372, 2014.

5. Lefu Zhang, Yichen Bao, and Rui Tang. Selection and corrosion evaluation tests of candidate SCWR fuel cladding materials. Nuclear Engineering and Design 249:180-187, 2012.

6. Zhao Shen, Lefu Zhang, Rui Tang, and Qiang Zhang. SCC susceptibility of type 316Ti stainless steel in supercritical water. Journal of Nuclear Materials 458:206-215, 2015.

7. S. Penttila, A. Toivonen, J. Li, W. Zheng, and R. Novotny. Effect of surface modification on the corrosion resistance of austenitic stainless steel 316L in supercritical water conditions. The Journal of Supercritical Fluids 81:157-163, 2013.

8. Jian Li, W. Zheng, S. Penttila, P. Liu, O. T. Woo, and D. Guzonas. Microstructure stability of candidate stainless steels for Gen-IV SCWR fuel cladding application. Journal of Nuclear Materials 454 (1-3):7-11, 2014.

9. Bin WANG, Zheng chong LIU, Shi chang CHENG, Chun ming LIU, and Jing zhong WANG. Microstructure Evolution and Mechanical Properties of HR3C Steel during Long-term Aging at High Temperature. Journal of Iron and Steel Research, International 21 (8):765-773, 2014.

10. L. Shi and D. O. Northwood. The mechanical behavior of an aisi type 310 stainless steel. Acta Metallurgica et Materialia 43 (2):453-460, 1995.

11. Thomas Schulenberg, Laurence K. H. Leung, and Yoshiaki Oka. Review of R&D for supercritical water cooled reactors. Progress in Nuclear Energy 77:282-299, 2014.

ISSCWR7-2028

Code to Code Comparison of the Predicted Response of the Canadian SCWR to a Loss of Flow Accident

Mengmeng Lou ,David Novog,
McMaster University
1280 Main St. W., Hamilton, Ontario, Canada
(905) 525-9140 ext. 26128, loum4@mcmaster.ca

Abstract

An SCTRAN model has been created for the Canadian Supercritical Water-Cooled Reactor (SCWR) to assess the reactor's response to a Loss of Forced Flow Accident (LOFA) with Station Black Out (SBO) under the conservative assumption that the primary (shutdown cooling system powered by Gas Turbine Generators) and emergency heat sinks (the passive Isolation Cooling System) become unavailable. The Automatic Depressurization System (ADS) is also conservatively assumed to be delayed such that no blowdown cooling is credited. The event progression assumes isolation valves on the hot and cold legs close shortly after reactor trip. With the loss of forced flow there is a flow-power mismatch and sheath temperatures increase rapidly in the early phases. The Safety Relief Valves (SRV) open at their set pressure to ensure overpressure is limited. The relief valve action cause intense and short duration flow pulses in the core which partially reduces the rate of sheath temperature. Radiation through the fuel channel to the moderator also acts to limit the fuel sheath temperature rise. In the intermediate term internal recirculation in the core provides some additional convection cooling which acts to reduce the fuel sheath temperatures. At this point the heat removal exceeds the decay heat in the core so the temepratures begin to decrease and as a result the core pressure decreases to below the SRV setpoint and relief action is terminated. Further temperature decreases cause natural core depressurization to pressures below the critical pressure. The entire supercritical to subcritical pressure transition is continuously simulated by SCTRAN. Comparison of calculation results between SCTRAN and CATHENA models for the early and intermediate stages of the transient shows good agreement.

1. Introduction

The SCWR is one of the six Gen-IV advanced reactors included in the Generation IV International Forum (GIF). Two types of SCWR are developed internationally, one using a pressure vessel and the other using pressure tubes. The Canadian GENIV design is based on the pressure tube type SCWR concept building upon the successful experiences with CANDU reactors. The Canadian SCWR uses supercritical light water as coolant and a separate heavy water as moderator, achieving the design goals of enhanced safety, economy and high efficiency in various ways. First, the direct once-through design simplifies the steam supply system as well as enhances the economy by reducing equipment (e.g. – a steam generator is not required). Second, higher outlet coolant temperature gives a much higher thermal efficiency than existing nuclear power plants. Third, the pressure tube separates high pressure coolant from low pressure moderator, precluding some typical pressure vessel design accidents such as control rod ejection. Finally, some specific safety facilities such as passive moderator cooling

system and isolation condenser system provide higher safety margins and increased defence-in-depth measures [1].

The pressure tube type SCWR has undergone extensive research and development to improve the conceptual design. The simulation of LOFA transient with CATHENA has shown that even without active cooling systems, the decay heat can be transferred through radiation and convection by which the cladding surface temperature stays under the design criteria [2]. In this paper a further study of flow behavior in LOFA transient is conducted by simulation with SCTRAN, a thermal-hydraulic code developed by Xi'an Jiao Tong University based on RETRAN-02. Due to lack of experimental data, verification of SCTRAN was performed previously through code-to-code comparison with widely used and acceptable thermal-hydraulic codes such as RELAP5-3D and APROS, which will be discussed in Section 2. Further comparisons to CATHENA for the supercritical pressure portion of a LOFA transient are also performed in this work. Section 3 describes the SCTRAN model of the SCWR and the simulation results and analysis, including mass flow rate and maximum cladding sheath temperature (MCST). Finally, major conclusions found in this study are stated in section 4.

2. Verification of SCTRAN

SCTRAN is a Homogeneous Equilibrium Model (HEM) two-phase thermal-hydraulic code based on RETRAN. It has previously been extended by XJTU to simulate accidents at supercritical as well as subcritical pressure. Since experimental data are sparse, the verification of SCTRAN was performed by code-to-code comparisons with APROS for blowdown phenomena [3]. For supercritical fluids a pseudo two-phase method is adopted in SCTRAN by introducing artificial latent enthalpy at pseudo-critical temperature to avoid discontinuity in numerical calculation, as suggested in the system code ATHLET-SC [9]. The latest version of SCTRAN has the ability to simulate radiant heat transfer between high temperature component surfaces, which was verified by modelling a 64-element SCWR fuel channel and comparing the results to CATHENA [4]. Additionally, LOFA and LOCA transient simulations of the US SCWR were conducted by SCTRAN in comparison with RELAP5-3D. All of the verifications above indicate that SCTRAN has the capability to analyse SCWR transients, although direct validation against experimental data is still recommended in the future.

As part of this research paper additional verification test were conducted to demonstrate the acceptability of SCTRAN through comparisons with CATHENA. The first comparison is on the steady-state flow in several channels using SCTRAN and CATHENA, based on simulation results in reference [2]. The 336 channels in SCWR are split into 7 groups according to their power levels through a life cycle in reactor, including beginning, middle and end-of-cycle (BOC, MOC and EOC). The power and channel grouping scheme for each group in MOC are representatively shown in Table 1a. The resultant predictions of the channel flows, clad temperature and centerline temperatures are shown in Table 1b. The maximum errors for each of the three parameters are 0.18%, 1.71%, 2.48%, respectively. The second comparison between SCTRAN and CATHENA is for a LOFA transient and is documented in Section 3.2.

Table 1(a). 7-group channels grouping scheme

	Group1	**Group 2**	**Group 3**	**Group 4**	**Group 5**	**Group 6**	**Group 7**
Number of channels	72	40	44	56	24	92	8
MOC power [MW]	448.56	309.60	292.60	415.52	193.2	805.92	75.04

Table 1(b). 7-group steady state calculation results compared with CATHENA

		Group 1	Group 2	Group 3	Group 4	Group 5	Group 6	Group 7
Mass flow rate [kg/s]	SCTRAN	220.3	156.54	143.2	204	94.2	400	38.1
	CATHENA	220.7	156.4	143	204	94.3	399.8	38.1
	ERROR (%)	0.18	0.09	0.14	0	0.11	0.05	0
MCST [C]	SCTRAN	779.8	785.5	780.9	783.6	785.9	788.3	791.3
	CATHENA	767.1	773.2	769.1	771.4	773.4	775.2	778
	ERROR (%)	1.65	1.59	1.53	1.58	1.61	1.69	1.71
MCT [C]	SCTRAN	1668.4	2008.8	1741.9	1895.6	2021.8	2205.7	2398
	CATHENA	1693.	2050.4	1769.4	1932.3	2058.3	2252.3	2459
	ERROR (%)	1.45	2.03	1.55	1.90	1.77	1.98	2.48

MCST: Maximum Cladding Sheath Temperature
MCT: Maximum Centreline Temperature

3. Analysis of LOFA with SBO

The postulated LOFA transient is performed here and station blackout is assumed where both grid power and emergency power are not available, thus the primary heat sink (driven by unit or grid power), the backup heat sink (driven by on-site emergency generators) are unavailable. In the Canadian SCWR design there are two independent passive heat removal systems capable of removing decay heat in this event: isolation condenser system (ICS) and passive moderator cooling system (PMCS). The isolation condensers provide the planned emergency heat sink for SBO events. However, given the reliability of the ICS the PT-SCWR has the Passive Moderator Cooling System (PMCS) as an additional passive defence-in-depth measure capable of removing heat in the unlikely scenario of a SBO with failure of ICS. The purpose of this paper is to investigate the fuel cooling and flow behaviour to see how effective the SCWR designed cooling system under a postulated SBO scenario with the ICS system unavailable.

3.1 SCTRAN model of Canadian SCWR

The overall schematic of SCTRAN idealization for simulation of LOFA is illustrated in Figure 1. The 336 fuel channels cannot be simulated individually due to code limitations in the present software version. A reasonable approximation is to divide the core into groups according to operational powers of different channels since many parameters in LOFA transients are strongly related to the power levels. The highest power channel should be considered as an individual group for it would reveal the upper limit of many parameters such as maximum cladding sheath temperature (MSCT) and maximum centreline temperature. The other 335 channels are split up into another three groups each with 112,112 and 111 channels and denoted as low, medium and high power group, respectively. Table 2 shows important parameters of different groups for the transient analysis. The group structure was selected to be consistent with the reference CATHENA simulations so as to facilitate comparisons.

Table 2. 4-group channels grouping scheme

	Type of group	Number of channels	Average power per channel [MW]	Normalized power distribution
Group 1	Low power	112	6.35	0.28008
Group 2	Medium power	112	7.59	0.33447
Group 3	High power	111	8.74	0.38169
Group 4	Highest power	1	9.56	0.00376

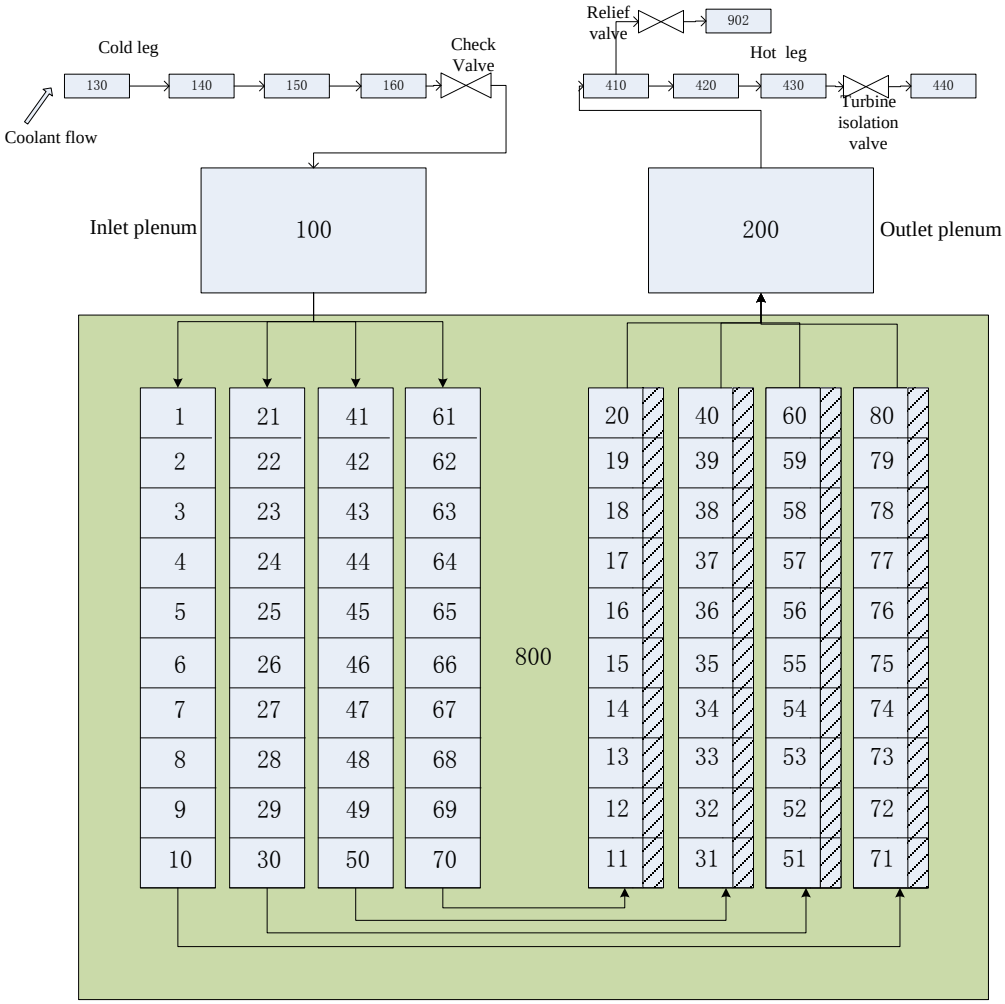

Figure 1. Schematic of SCTRAN idealization for Canadian SCWR

The downward and upward legs of the re-entrant fuel channel in each group (centre flow tube and fuel channel region) are modelled separately with 10 control volumes in each leg. As shown in Figure 1, volumes 1-20 denote low power group; volumes 21-40 denote medium power group; volumes 41-60 denote high power group and volumes 61-80 denote highest power group. The inlet plenum and outlet plenum are modelled as control volumes 100 and 200. Control volumes 130-160 denote the cold leg connecting to inlet plenum and control volumes 410-440 denote hot leg connecting to outlet plenum. A fill model is used at volume 130 which acts as the flow inlet

boundary condition (coolant mass flow rate of 1254.014 kg/s and temperature of 350 ºC). It also acts as cold leg isolation valve during transients by adjusting the inlet mass flow rate as a function of time. The outlet boundary condition is simulated by a time dependent volume acting on volume 440 (outlet coolant temperature of 625 ºC and pressure of 25.0 MPa). A safety relief valve located between volume 410 and 902 (model of containment) is designed to open to depressurize the core when pressure is higher than the threshold opening value and then reset to closing state as pressure approaching a certain value[i]. A steam isolation valve connecting the hot leg and outlet boundary condition is set to close when the actuation setpoint is reached[1]. A check valve between cold leg and inlet plenum is designed to prevent reverse flow from inlet plenum during accident transients[2]. Junction flow resistances from inlet plenum to center flow tube of each group are adjusted during the initial steady-state simulations so that an uniform coolant temperature is achieved to the outlet plenum.

As suggested by the code developer, a single control volume (i.e., 800) is used to simulate the moderator heat sink instead of a detailed model of the passive moderator cooling system, as is treated in CATHENA model in reference [2]. The reason is that the current version of SCTRAN cannot calculate convective heat transfer between the pressure tube and a flowing moderator system. Hence, the moderator heat sink is modelled using a temperature of 80 ºC and convective heat transfer coefficient of 1000 W/m^2-K as recommended in reference [5].

Four types of solid conductor components are used in this model to simulate the centre flow tube, fuel pins of inner and outer rings, and the liners/ceramic insulator/pressure tube. Among these the inner ring and outer ring fuel pins are power production elements and follow the same power distribution as previously studied in the CATHENA models. Convection from the fuel is calculated based on local conditions and the conduction is limited to the radial direction. To calculate the radiant heat transfer between those components a view factor matrix among them is calculated by a code GEOFAC, which is developed by Atomic Energy of Canada Limited (AECL) [6]. Figure 2 illustrates the layout of view factor matrix.

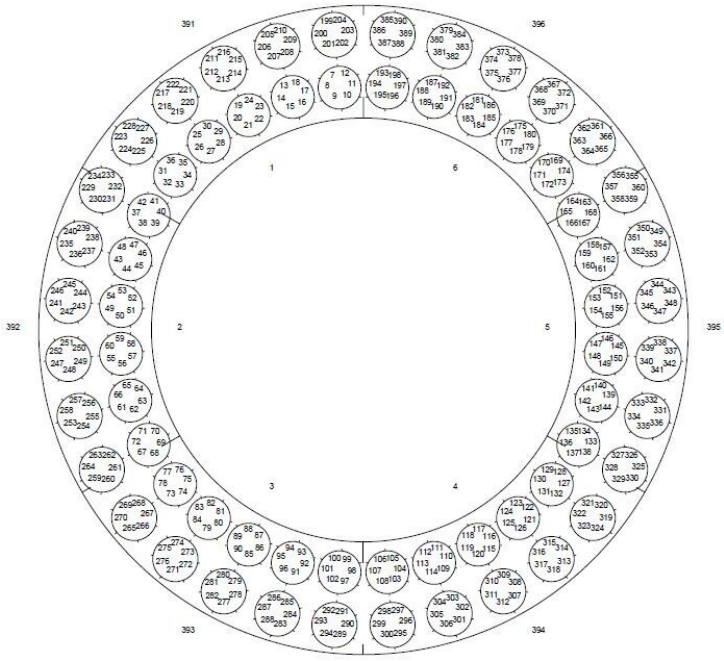

Figure 2. View factor matrix for SCTRAN radiation heat transfer model

[1] Based on a low flow signal measured on the cold leg piping

[2] While check valve leakage may occur it is assumed that an active isolation valve on the cold leg will ensure core isolation is achieved.

3.2 The boundary conditions for the model consist of time dependent volumes and time dependent junction to simulate the loss of flow and initial conditions are established based on a zero-change transient performed at 100% full power. Simulation results

To simulate the LOFA transient the inlet coolant is reduced from normal flow rate to zero linearly within the first second through a user designed time table for mass flow rate in the inlet fill model. A Low Flow Trip is initiated when the mass flow rate is decreased to 90% of full flow and control rods drops into core with a time delay of 0.1 s. The same decay heat curve is adopted as core power changing with time in this SCTRAN model as in reference [2].The steam isolation valve is credited to close at 1.0 s after the loss of flow signal is detected. The event sequence is shown in Table 3.

Table 3. Event sequence of LOFA

Time [s]	Events
0	Loss of main feed water, linearly reduced to zero within 1 s
0.1	Reactor shutdown signal trigged, control rods inserted into reactor with a 0.1 s delay
1.0	Steam isolation valves closed
1000	Calculation terminated

Figure 3 shows the core pressure and discharge rate through the SRV during the transient. After loss of forced flow and subsequent reactor trip the relatively high decay heat of fuel pins cannot be removed effectively due to poor convective heat transfer. Thus, the fuel elements and coolant heat up rapidly and the pressure increases quickly to the level of SRV set-point. Once opened, a large amount of coolant is discharged from the outlet plenum through the relief valve and the core pressure drops until SRV closing setpoint reaches. The high frequency opening and closing actions of SRV in the early stages of the transient introduces several short bursts of flow through the core, which helps to enhance the convective heat transfer and prevent cladding temperature going too high. As is shown in subsequent figures natural circulation is established amongst the fuel channels in intermediate stage of transient, which removes decay heat effectively and depressurize the reactor through coolant shrinkage and SRV action is terminated. The pressure continues to drop until transition from supercritical to subcritical occurs at around 621 s. Following this transition, the pressure decreases continually to the end of calculation without discontinuity. The time from supercritical to subcritical pressure transition is comparable with that of CATHENA which predicts 680s, however SCTRAN is capable of continuing the transient whereas CATHENA numeric prevents the continuous simulation through trans-critical pressure.

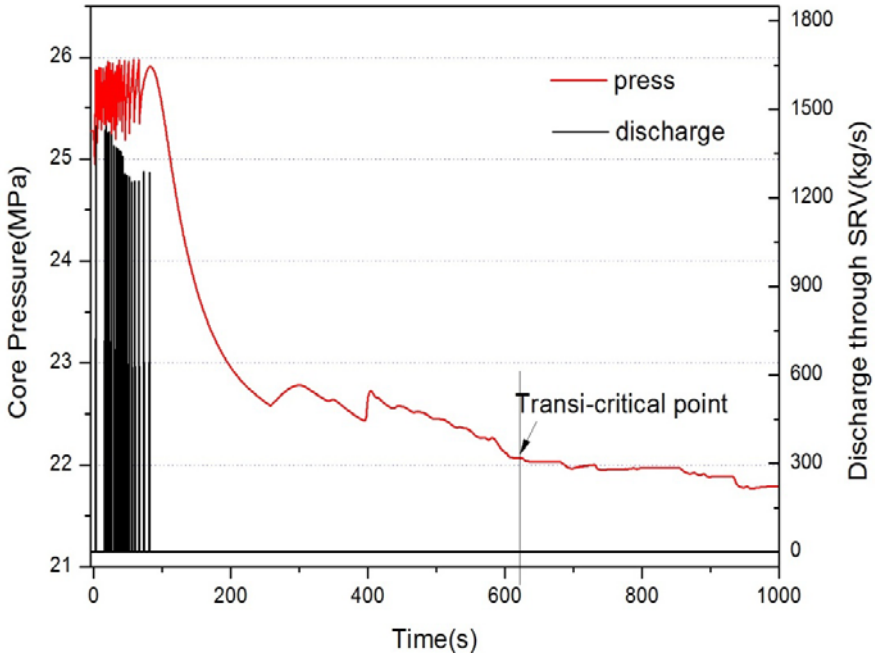

Figure 3. Reactor pressure variation and SRV discharge during transient

Figure 4 illustrates the maximum cladding sheath temperatures (MCST), decay heat generation and heat transferred into moderator as a function of time. The peak MSCT for all groups occur within the first 30 seconds. The peak MCST and corresponding time are presented in Table 4 and compared with results from CATHENA for identical channel grouping and event progression [2]. The maximum MCST obtained in highest power group is 1096.8 ºC which is lower than the acceptance criterion of 1260 ºC by a large margin. The level of agreement between the codes is in general plus or minus 50 ºC and largely results from the difference in convective heat transfer coefficient employed in each code. SCTRAN uses Jackson correlation for supercritical pressure convective heat transfer which is specifically derived for these conditions whereas CATHENA uses Dittus-Boelter correlation. As is shown in Table 4, the time when peak MCST occurs in CATHENA is slightly later than SCTRAN. It's likely caused by artificially higher heat transfer coefficient given by Dittus-Boelter correlation in CATHENA, which predicts more effective convective heat transfer and thus decreases the rate of temperature rise. After reaching the peak temperatures the cladding surface temperatures then dropped quickly below 400 ºC at 100 s for Groups 2, 3, 4 and at around 235 s for Group 1 as a result of radiant and convective heat transfer. The mechanism of coolant flow which enhances convection during the transient will be discussed in detail below.

Table 4. The peak MCST and occurrence time predicted in different groups.

	SCTRAN		CATHENA	
	Time [s]	**Temperature [ºC]**	**Time [s]**	**Temperature [ºC]**
G1	11.0	983.3	19.5	938
G2	11.0	1066.4	19.5	990
G3	7.5	1059.2	12.7	1021
G4	7.5	1096.8	18.2	1059

As seen from Figure 4, the fuel cladding temperature in Group 1 (low power group) becomes higher than those in other groups after approximately 75s. This results from the reversed flow in

Group 1 where hotter coolant from the outlet plenum travels through the channel to the inlet plenum giving rise to elevated coolant temperatures relative to forward flow channels which receive cooler coolant from the central flow tubes and inlet plenum. The channel group flow directions are dictated by the channel power and hence it is expected that higher power groups will have a higher tendency to maintain forward flow. It's claimed in reference [2] that the flow directions of different groups can be strongly sensitive to grouping scheme and orifice sizes in CATHENA, which has the same function as junction resistance in SCTRAN model.

The moderator represents the only long term heat sink available during this postulated accident (i.e., failure of all normal and emergency power sources coupled with failure of the isolation condenser system). Decay heat generation and heat transferred to moderator is illustrated in Figure 4. At around 300 seconds, heat transferred to moderator exceeds decay heat generation which indicates that the current design of Canadian SCWR has inherent self-cooling capability even without a functional isolation condenser system.

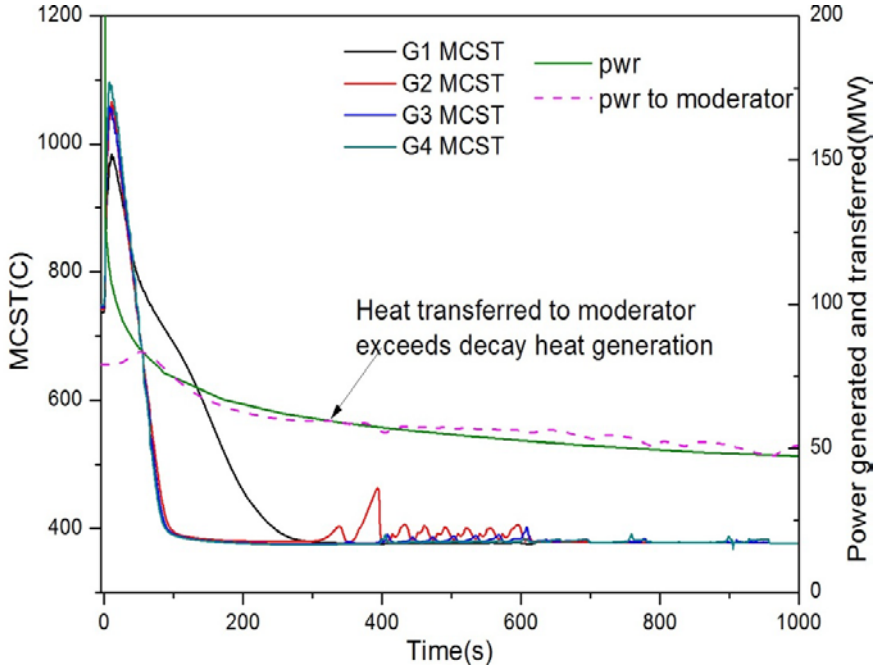

Figure 4(a). MCST in four groups and decay heat compared to heat transferred to moderator

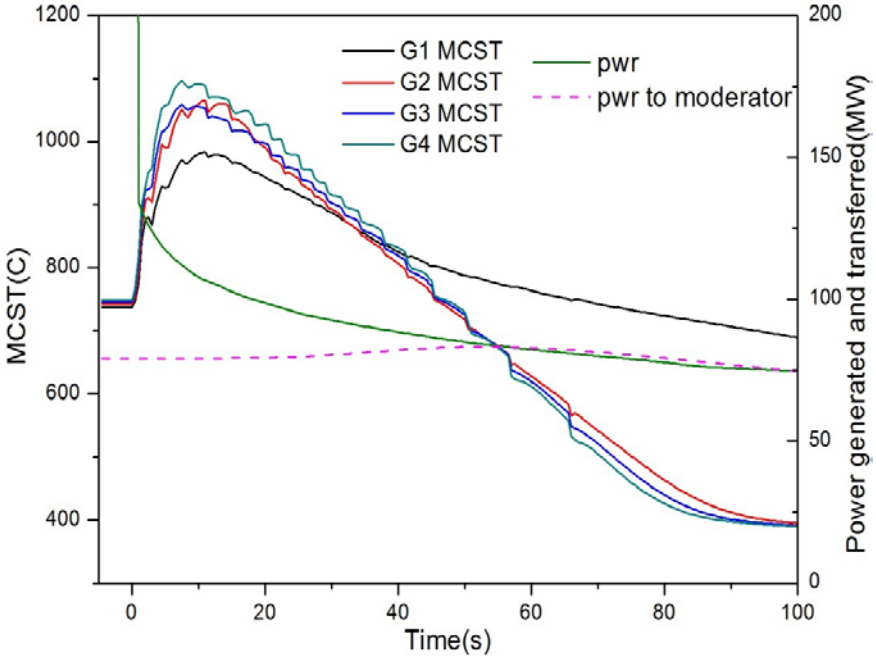

Figure 4(b). MCST of four groups and decay heat compared to heat transferred to moderator zoomed in first 100 seconds

Figure 5 shows the relative mass flow rate in different groups during the transient. The ratios are obtained by mass flow rate of each group divided by their steady state flow. The transient can be divided into five phases according to the flow behaviour, which are Phase 1 (0-30s), Phase 2 (30-100s), Phase 3 (100-300s), Phase 4 (300-621s) and Phase 5 (621-1000s). The flow mechanisms for each phase are discussed in the next several paragraphs.

In Phase 1 the cladding temperature rises sharply due to sudden flow rundown and relatively high decay heat generation, as can be seen from Figure 4. The mass flow rate is nearly zero except for some flow bursts introduced by frequent SRV actions. Radiant heat transfer between high temperature component surfaces dominates over convective heat transfer in this phase.

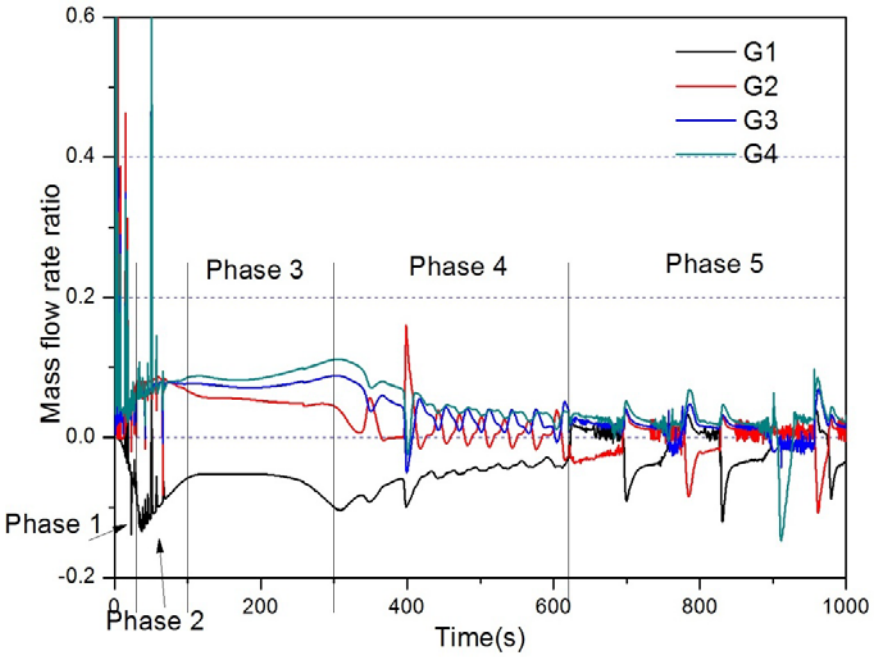

Figure 5(a). Mass flow ratio of four groups during the transient

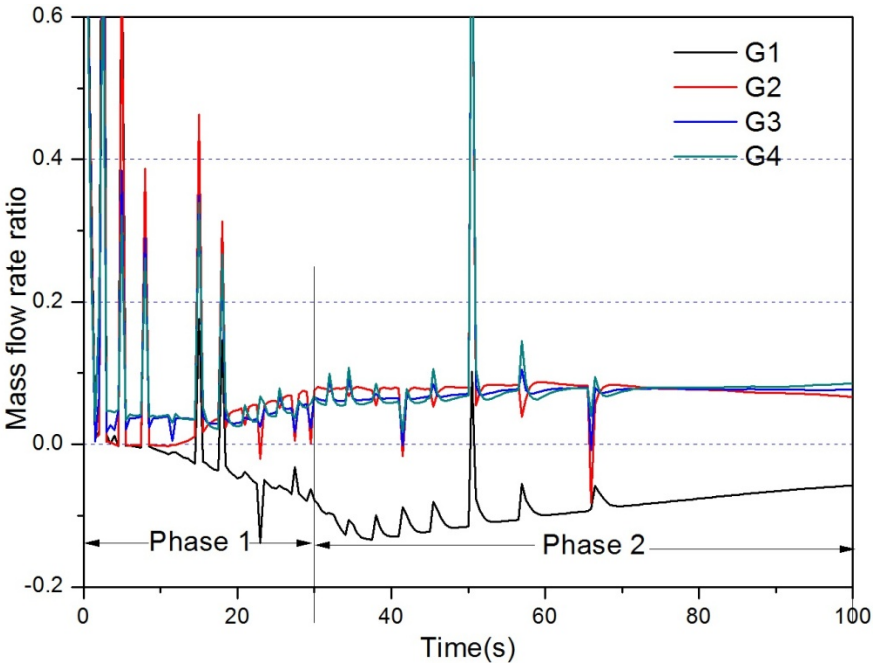

Figure 5(b). Mass flow ratio of four groups during phase 1 and phase 2 of the transient

Phase 2 occurred from 30 s to 100 s and Figure 4(b) shows that the cladding surface temperature decreases sharply for two reasons. The first is the decrease in decay heat generation and the second is enhanced convective heat transfer caused by a combination of:

- SRV actions which initiate the temporary blowdown cooling during each cyclic opening of the valve,
- Pseudo-critical transition driven flow wherein coolant in centre flow tube and fuel pins region expands as its properties cross the pseudo-critical transition.

Figure 6 illustrates the density variations of coolant in centre flow tube and fuel region of different groups and SRV discharge during Phase 2. The pseudo-critical transition of coolant in Group 1 occurred at beginning of Phase 2 while other groups transitioned at alter times in the phase.

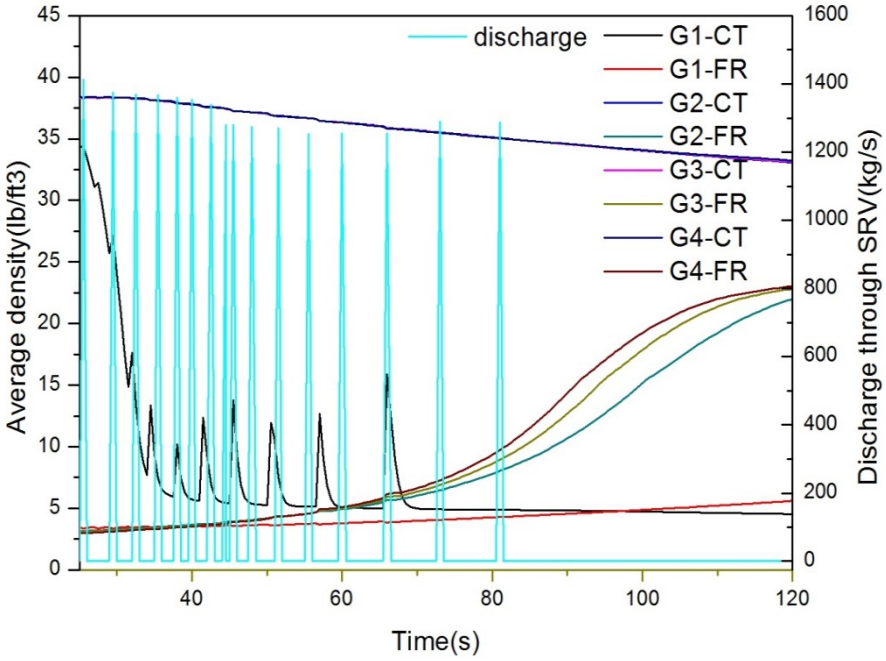

Figure 6. Coolant density variation and SRV discharge

Significant natural circulation is established in Phase 3 wherein all four groups have almost stable mass flow rate. The natural circulation flow rate depends on the balance of driving force, which is fluid density difference, and flow resistance. The total pressure drop through the flow path is a combination of gravity, friction pressure drop, minor resistance pressure drop and acceleration pressure drop. In Figure 7 the pressure drop between first volume and last volume in each group as well as coolant inventory of inlet plenum and outlet plenum is illustrated. The coolant from the inlet plenum flows steadily to outlet plenum through the majority of channels and provides stable driving force for the natural circulation. Also shown in Figure 7 is that Phase 3 ends when the density differences between the plena become similar (at approximately 300s) and the natural circulation flows become less steady. This phenomenon implies the important role of coolant inventory in inlet and outlet plenums during Phase 3.

In Phase 4 the reduction in the density and pressure difference results in less stable flows than in Phase 3. Mass flow rate oscillations occur because the driving force for natural circulation became the slight local density difference along the plena and fuel channels instead of bulk coolant density difference between the plena in phase 2.

Phase 5 starts from 621.s and continues till the calculation is terminated. The effective convective heat transfer in previous phases helps cooling the reactor to relatively low temperature and the decay heat is around 2%. Mass flow rate in four groups resembles behaviour in Phase 4: the flow oscillation still exists and the overall flow rate is decreased. However because the decay heat is reduced considerably relative to previous phases the fuel remains well cooled. The heat sink to the moderator is sufficient to remove the decay heat and the system cooldown/natural depressurization continues.

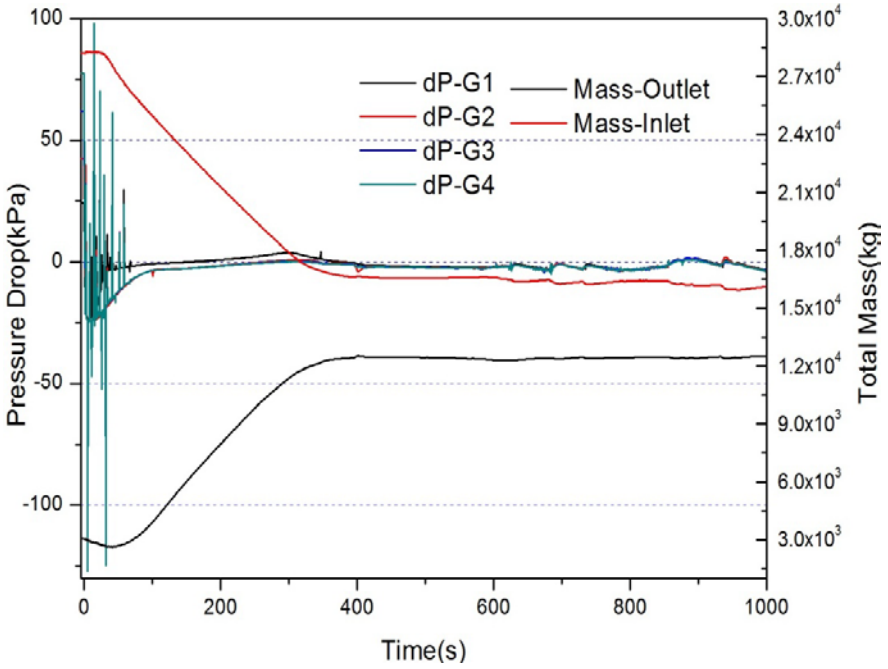

Figure 7. Pressure drop between inlet and outlet of flow path and mass inventory of inlet and outlet plenums

4. Conclusions

A SCTRAN code model has been built for LOFA analysis for Canadian SCWR. The comparison with CATHENA at both steady state and transient simulation indicates a good level of agreement. A 4-group scheme was adopted for LOFA transient and the simulation ran for 1000 s after the accident occurred. The radiation and convection effectively transferred decay heat to the moderator which is the only long term heat sink for conservative assumption. All the analysis above indicates that the reactor is designed with inherent cooling capability during loss of forced flow accident with only moderator cooling systems available.

- The maximum cladding surface temperature during LOFA transient is 1096.8 ºC, which is lower than the thermal-hydraulic criterion of 1260 ºC. The radiant heat transfer at first stage of accident ensures that the temperature does not exceed this limit.
- Natural circulation is established at about 100 s, providing enough convective heat transfer to cool down and depressurize the reactor through coolant shrinkage. SRVs action is terminated early in the transient (phase 2) as a result of the inherent cooling features of the reactor.
- The steady natural circulation ends at around 300 s when the constant mass flow from inlet plenum to outlet plenum terminated. This phenomenon reveals the importance of coolant inventory of inlet and outlet plenum. The larger inventory difference the longer the constant mass flow in fuel channels can last.
- SCTRAN is capable of continuous calculation when the pressure drops from supercritical to subcritical, which makes it a potential effective tool to deal with safety analysis when pressure transient across critical point, such as LOCA.

References

[1] Huang, X.,et al., Analysis of passive residual heat removal systems for the Canadian Supercritical Water Cooled Reactor. Canadian-China Conference on Advanced Reactor Development,CCCARD-2014,April 27-30 2014.Ontario, Canada.

[2] Wu, Y., et al., Prediction of the response of the Canadian Super Critical Water reactor to potential Loss of Forced Flow Scenarios. McMaster University, 2014

[3] Wu, P., et al., Safety analysis code SCTRAN development for SCWR and its application to CGNPC SCWR. Annuals of Nuclear Energy 56(2013)122-135.

[4] Wu, P., et al., Preliminary no core melt assessment for Canadian SCWR with modified SCTRAN, Canadian-China Conference on Advanced Reactor Development,CCCARD-2014,April 27-30 2014.Ontario, Canada.

[5] Feng, J., et al., Preliminary LOFA Analysis of 62-element Bundle Pressure Tube SCWR in the Absence of Safety System. Initial report submitted to AECL, June 25th 2013. Xi'an Jiang Tong University, China.

[6] Nuclear Platform Research and Development, Thermal-hydraulic Branch. GEOFAC User's Manual. May 2007, Atomic Energy of Canada limited, Canada.

[7] Wang, D. F., A preliminary CATHENA thermalhydraulic model of the Canadian SCWR for Safety analysis, AECL Nuclear Review, 2013,3(01):9-16.

[8] RETRAN-02 Code Development and Validation Team, 1981. A Program for Transient Thermal-Hydraulic Analysis of Complex Fluid Flow Systems, Volume 3: User's Manual. Energy Incorporated.

[9] X.J, Liu, et al., LOCA analysis of SCWR-M with passive safety system, Nuclear Engineering and Design 259(2013) 187-197.

[i] In reality the SRV discharge is directed to a suppression pool so as to avoid containment pressurization.

The 7th International Symposium on Supercritical Water-Cooled Reactors

ISSCWR-7-#2029

15-18 March 2015, Helsinki, Finland

Intergranular Corrosion Resistance of Thermally-Treated Type 310S Stainless Steel

Y. Jiao & J. Kish
Department of Materials Science & Engineering, McMaster University
1280 Main Street West, Hamilton, Ontario, Canada L8S 4L7
jiaoyn@mcmaster.ca; kishjr@mcmaster.ca

W. Zheng
CanmetMATERIALS, Natural Resources Canada
183 Longwood Road South, Hamilton, Ontario, Canada L8P 0A5
Wenyue.Zheng@NRCan-RNCan.gc.ca

D. Guzonas
Canadian Nuclear Laboratories
Chalk River Laboratories, Ontario, Canada K0J 1J0
David.Guzonas@cnl.ca

ABSTRACT

The goal of this study was to develop a methodology to quantify the degree of grain boundary sensitization (DOS) in thermally-treated Type 310S stainless steel to be used as a predictive 'signature' of the intergranular stress corrosion cracking (IGSCC) susceptibility when exposed in supercritical water (SCW). Samples of Type 310S stainless steel were solution-annealed (1060°C for 1 h + water quench), sensitized (650 °C for 100 h) to precipitate grain boundary carbides and thermally-treated (800 °C for 1000 h) to precipitate intra-grain and grain boundary carbides and sigma (σ) phase. The intergranular corrosion susceptibility of the thermally-treated material was evaluated using several well-established techniques: X-ray energy dispersive spectroscopy (EDS) coupled with scanning transmission electron microscopy (STEM Huey immersion testing (ASTM A262 Practice C), and double-loop electrochemical potentio-kinetic reactivation (DL-EPR) testing. The sensitized material is predicted likely to be the most susceptible to IGSCC when exposed in SCW assuming the chemical properties across the grain boundary control the IGSCC process. The thermally-treated material is predicted to have a significantly reduced susceptibility to IGSCC, which is attractive from an in-service performance perspective. Confirmation of these results through slow strain rate tests is under way.

1. Introduction

Austenitic stainless steels have received significant attention as candidate fuel cladding materials for various supercritical water-cooled reactor (SCWR) concepts due to their favorable corrosion and irradiation resistance [1-4]. Type 310S stainless steel has been short-listed as a candidate material for the fuel cladding in the Canadian SCWR design [5]. Type 310S stainless steel exhibits relatively good general corrosion and SCC resistance in 550 °C 25 MPa SCW [4]. The Japanese researchers have identified Zr-modified versions of Type 310S stainless steels as their primary fuel cladding materials for their pressure-vessel SCWR concept, which has a maximum fuel cladding material temperature of 700 °C [4]. Despite this promising performance, the expected precipitation of intermetallic phases within the grains and on grain boundaries [6-8] resulting from the prolonged exposure at the predicted range of operating temperatures of the

Canadian SCWR concept (peak cladding temperatures up to 800 °C) is a concern. Along with Cr-rich carbide formation, the relatively high Cr content (about 25 wt.%) also promotes the formation of the intermetallic sigma (σ) phase during prolonged exposure at elevated temperatures [7-8,10-11]. Li et al. reported formation of σ phase in Type 310S stainless steel after relatively short-term exposure to proposed Canadian SCWR operating conditions [21]. Formation of the σ phase is particular detrimental to the mechanical integrity at elevated temperatures as it significantly increases the hardness of the material [7,10-11].

SCC has long been a problem affecting 300-series austenitic stainless steels utilized as core components in light water reactors (BWRs, PWRs) [1,14]. Variations in the chemical properties across grain boundaries due to radiation-induced segregation (RIS) remains a significant factor that is believed to contribute to IASCC [14]. The formation of Cr-rich carbides ($M_{23}C_6$ carbides) on the grain boundaries and associated adjacent Cr depletion zones (sensitization) from this thermal ageing can be accentuated by combined irradiation effects to significantly increase the susceptibility to irradiation-assisted stress corrosion cracking (IASCC) [14-15]. Without the accompanying Cr depletion across the grain boundaries, the formation of Cr-rich carbides or other intermetallic phases on the grain boundaries has been reported to have decreased the susceptibility to IASCC [14,16-17]. Thermal treatment-induced sensitization zone (Cr-depletion along grain boundaries) is the primary means of determing of SCC susceptibility of 300-series stainless steels in an aqueous environment at room temperature [6]. Structures of thermal induced sensitization were observed highly susceptible to cracking under LWR incore environments [14]. This sensitivity could be magnified by irradiation, and increase the IASCC susceptibility of austenitic stainless steels [14-15]. Sensitized 300-series stainless steels usually exhibit higher SCC crack growth rates, suggesting passivation of the Cr-depleted region may not be possible and grain boundaries may become even more susceptible to corrosion and SCC. In supercritical water (SCW), however, the dielectric constant of the water is too low to allow for significant dissociation into ions, and mechanisms that depend invoke electrochemical reactions occurring at distinct cathodic and anodic sites will not apply [18]. The onset of IGSCC could occur by an oxide scale rupture mechanism [19]: the oxide scale ruptures under external stress and exposes fresh metal, then the fresh metal is oxidized and ruptured again by external stress. As a result, sensitization may result in increased SCC susceptibility in SCW even through GB carbides may enhance GB oxidation resistance [22].

Relating the degree of sensitization (DOS) to the susceptibility of austenitic stainless steels to intergranular corrosion (including SCC) has proven particularly effective in identifying the critical factors that drive this damage mechanism. Three most widely used methods to determine the DOS in thermally-treated stainless steel include: (i) transmission electron microscopy (TEM) and associated techniques to measure the extent of Cr-depletion across the grain boundaries [6], (ii) standardized immersion testing to record the weight loss after exposure in a specific boiling solution for a specific time [6, 13], and (iii) double loop electrochemical potentiokinetic reactivation (DL-EPR) testing to record the reactivation/activation current density ratio [6-7, 13]. The susceptibility of Type 310S stainless steel to sensitization and, thus to intergranular corrosion has not received much attention. Tavares et al. [7] proposed optimum test solution for Type 310S stainless steel in DL-EPR test, but there have been no attempts to correlate the DL-EPR test results with those from microscopy characterization and immersion tests.

The goal of this study was to develop a methodology to quantify the DOS in thermally-treated Type 310S stainless steel to be used as a predictive ‘chemical signature’ of the intergranular stress corrosion cracking (IGSCC) susceptibility when exposed in SCW. The intergranular corrosion susceptibility of the thermally-treated material was evaluated using: X-ray energy dispersive spectroscopy (EDS) coupled with scanning transmission electron microscopy (STEM), Huey immersion testing (ASTM A262 practice C) and DL-EPR testing.

2. Experimental Methods

Rectangular test samples were prepared from a commercial Type 310S stainless steel plate provided in the mill-annealed (MA) condition. The chemical composition was analyzed using inductively coupled plasma optical emission spectroscopy (ICP-OES) (Varian Spectrometer) and combustion analysis (LECO CS230). The results are shown in Table 1.

Table 1. Chemical composition (wt.%) of the Type 310S material used in this work.

Cr	Ni	Mo	Mn	Si	P	S	C	Fe
24.3	19.56	0.29	0.96	0.76	0.04	0.04	0.06	Bal.

Three heat-treated conditions were tested: solution-annealed (SA), sensitized (S) and thermally-treated (TT). The SA material was achieved by exposing a set of samples at 1050 °C for 1 h followed by water-quenching to room temperature. A subset of the SA samples was exposed at 650 °C for 100 h followed by air-cooling to room temperature to acquire the S material [7]. A subset of the samples in the MA state were sealed in a nitrogen gas-purged quartz tube and exposed at 800 °C for 1000 h to precipitate the major intermetallic phases ($M_{23}C_6$ and σ) to acquire the TT material. The temperature was selected to be as close to the maximum fuel cladding temperature of 800 °C expected in the Canadian SCWR [5], but still allowing for the sequential formation of the $M_{23}C_6$ and σ intermetallic phase precipitates [8]. Upon removal from the furnace, the TT samples were air-cooled to room temperature while still sealed in the nitrogen gas-purged quartz tube.

The microstructures of the SA, S and TT material were examined in cross-section using light optical microscopy (LOM), scanning electron microscopy (SEM), and TEM: the latter two techniques were coupled with X-ray energy dispersive spectroscopy (EDS). Precipitates (carbide and σ intermetallic phase) were characterized by both EDS and SAD (Selected Area Diffraction). A single SA, S and TT sample for LOM and SEM was cold-mounted (the length of the sample corresponds to the rolling direction) and polished to a 1-μm finish using standard metallographic techniques. Chemical etching was conducted by immersing the polished surface with an acetic acid-glycerine mixture for 40 s. The SEM examination was performed using a JEOL JSM-7000F microscope equipped with a Schottky Field Emission Gun (FEG) filament and an integrated Oxford Synergy system with INCA EDS micro-analysis using an accelerating voltage of 10 kV and a working distance of 10 mm. The TEM examination was performed using JEOL 2010F TEM/STEM equipped with an Oxford Instruments EDS analyser using an accelerating voltage of 200 kV. The thin foil of each material required for TEM was prepared by mechanically-abrading samples to a thickness of 80 μm using SiC paper and H_2O as a lubricant. A small round foil was then punched out from the mechanically-abraded sample and subsequently electrochemically polished in a $HClO_4$ (10%)-methanol (90%) solution at -50 °C to create a small hole.

X-ray diffraction (XRD) after a bulk extraction was also used to help identify the intermetallic precipitates that were present in the TT material. The bulk extraction was carried out by immersing a TT sample in a HCl (10%)-methanol (90%) solution for 4 h at room temperature. An X-ray diffraction pattern of the extracted powder residue was acquired using an X-ray powder diffractometer (Bruker 8D Advanced) operated with a Cu k1 radiation source. A similar analysis was not conducted on a SA and S sample because of the very low expected precipitate content.

Huey immersion testing (ASTM A262 Practice C) was performed to quantify the DOS in the SA, S and TT material. A set of SA, S and TT samples (3 for each set) were cut into small cylinders (2.5 cm in diameter and 1 cm in height) and then cut along the midline of the cylinder. The resulting sample had a surface area of around 12 cm^2. All of surfaces including edges were polished with 120 grit SiC paper with H_2O as a lubricant. The test consisted of five sequential 48

h exposures in replenished boiling (about 120 °C) 65 wt.% reagent grade HNO3 (about 600 cm3). A glass cradle was used to support the specimens in the flask fully immersed at all times during the test. An allihn condenser was placed in the neck of the flask and water was circulated through thee condenser to keep the solution from boiling away. After each test period, the samples were rinsed with water to remove acid. Then the samples were cleaned with soap and in an ultrasonic bath. Upon removal from the bath, the samples were cleaned by rinsing with water and then ethanol.

The DL-EPR testing was conducted in a three-electrode cell with a saturated calomel electrode (SCE) as the reference electrode and a pair of graphite counter electrodes. The test solution was 2 M H_2SO_4 + 0.01 M KSCN, which has been shown to be successful for this purpose [6]. Working electrodes of the SA, S and TT material were prepared by attaching a Cu wire to the back faces of rectangular samples and then embedding the samples in epoxy resin with only the front faces exposed. These working surfaces were mechanically-abraded to a 600 grit surface finish using SiC abrasive paper and H_2O as a lubricant and cleaned by rinsing with ethanol. Working electrodes were conditioned at the open circuit potential for 5 minutes prior to the start of the DL-EPR measurement. The measurement involved sweeping the potential in the anodic direction at a rate of 1 mV/s to +0.3 V_{SCE} then sweeping the potential in the cathodic direction past the corrosion potential (E_{corr}). The DOS was determined by the current density ratio (i_r/i_a), where i_a is the activation peak current density of the forward anodic sweep and i_r is the reactivation peak current density in the reverse cathodic sweep. The DL-EPR test was repeated 10 times for each of the SA, S and TT materials.

3. Results

Figure 1 shows the cross-section microstructure of the MA, SA, S and TT material, as revealed using light optical microscopy. There were large black particles decorating the GBs of MA material. Although not characterized by microscopy, these particles most likely are carbides formed during the milling-annealing process. The SA material exhibited $M_{23}C_6$ type carbides (verified by TEM-SAD) formed on the grain boundaries. No carbides were observed inside the grains (verified by SEM-EDS & TEM-EDS). Solution annealing at 1050 °C for 1 h did not fully dissolve grain boundary carbides. The S material exhibited similar features as the SA material: $M_{23}C_6$ type carbides (verified by TEM-SAD) were observed on the grain boundaries. The major difference between SA and S materials was the population and distribution of the $M_{23}C_6$ precipitates. The $M_{23}C_6$ precipitates in the S material tended to have a higher coverage of the grain boundaries and were also observed inside the grains (verified by SEM-EDS as this is difficult to see by light optical microscopy). The size of $M_{23}C_6$ precipitates in both cases was less than 1 μm. The TT material exhibited distinct differences relative to the SA and S materials. A continuous σ phase (verified by TEM-EDS & TEM-SAD) formed both within the grains and on grain boundaries. The σ phase formed along the GB showed growth as long as 10 μm whereas the σ phase formed within the grain tend to have a needle-like structure. All materials had a similar average grain size number (ASTM E1382): 7.2 for the SA material, 7.5 for S material and 7.0 for TT material, which indicated no significant grain growth had occurred.

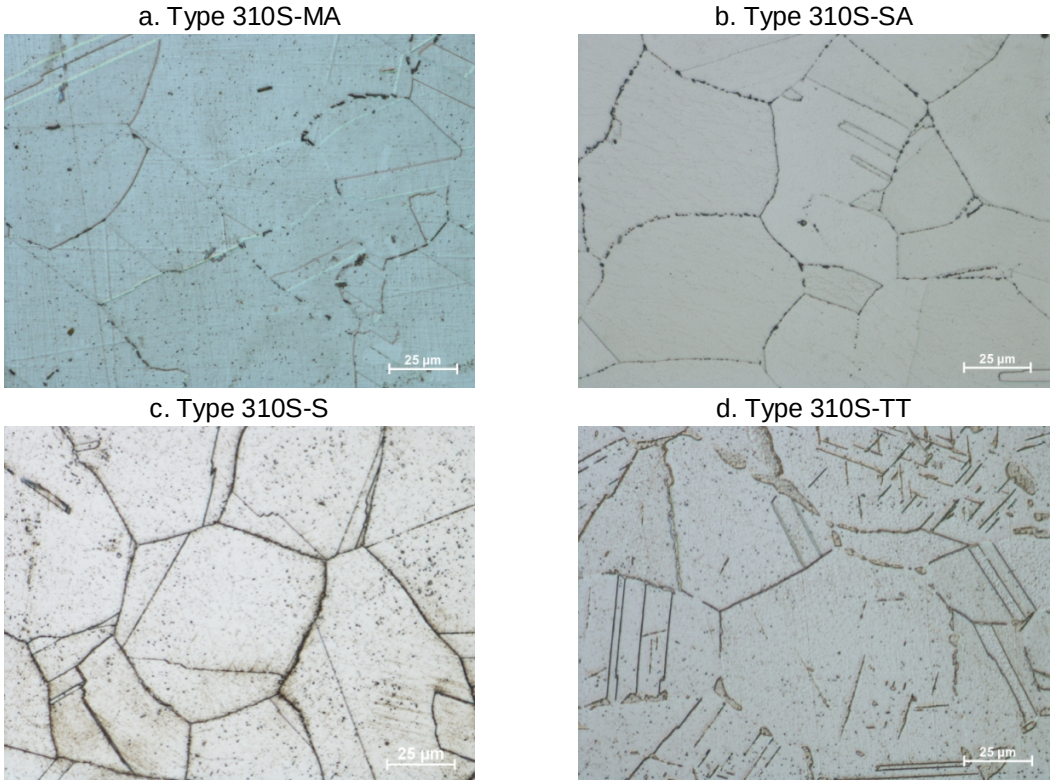

Figure 1. Light optical image showing typical appearance of the microstructure of the (a) MA material, (b) SA material, (c) S material and (d) TT material.

Figure 2 shows TEM-EDS line scans conducted on (a) GB carbide of SA material, (b) GB of SA material, (c) GB carbide of S materials, (d) GB of S material and (e) GB σ phase of TT material. Usually the Cr-depleted zone is characterized by the Cr-depleted width (on each side of the GB) and the minimum Cr concentration [6]. Sensitization to IGC occurs when the Cr content at the GB reaches a critical value close to 12 wt.% or 13 at.% [6]. Thus, the DOS could be represented by the width of sensitized zone [6]. No obvious segregation or depletion of major alloying elements was observed in SA materials as shown in Figure 2a. The S material, however, exhibits obvious Cr depletion around grain carbide as shown in Figure 2b. The sensitization treatment created about 200 nm Cr depleted zone (Cr content below 24 wt.%) in which about 50 nm were sensitized (Cr content below 12 wt.%) on both side of carbide. The GB of the S material also exhibits Cr enrichment a Cr depletion zone adjacent to GBs whether the carbides are present or not. The minimum Cr content is about 8 wt.%. The line analysis clearly revealed that no obvious Cr-depletion was present adjacent to the σ phase in the TT material shown in Figure 2c, and GB of TT material is fully covered by σ phase.

a. Type 310S-SA GB carbide

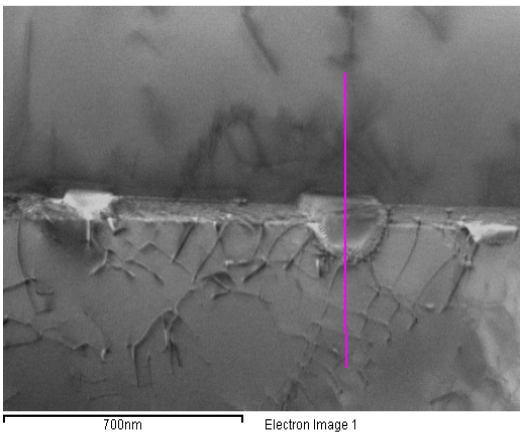

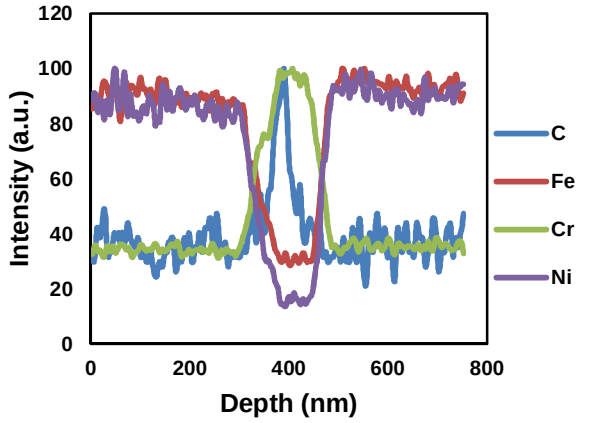

b. Type 310S-S GB carbide

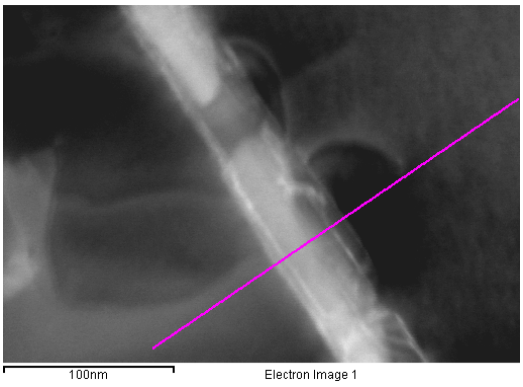

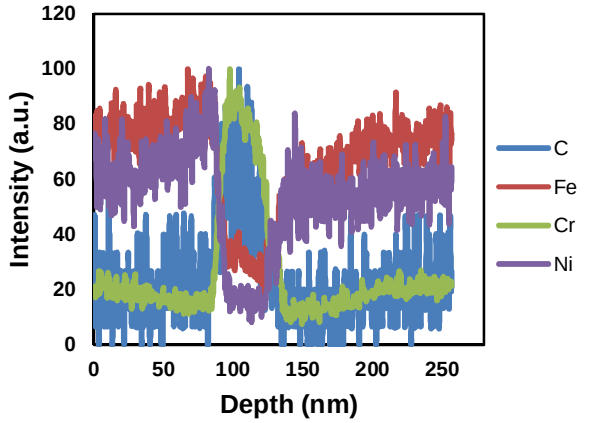

c. Type 310S-TT GB σ phase

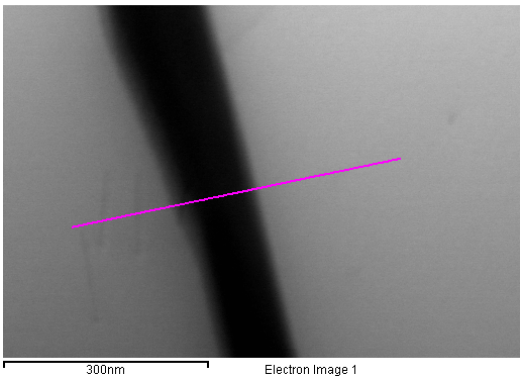

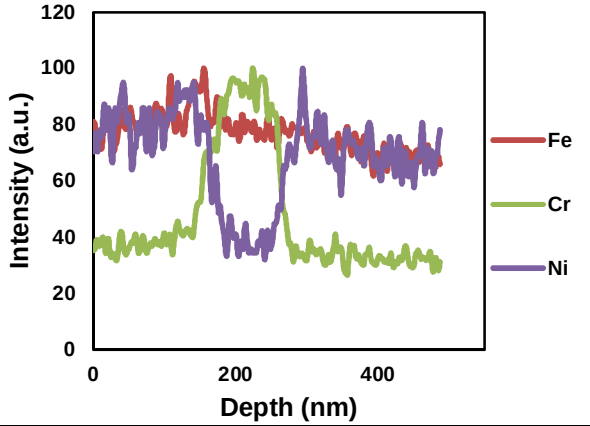

Figure 2. Bright-field STEM image and corresponding STEM/EDS line analysis conducted to identify the various precipitates present within the grains and on grain boundaries in the: (a) Type 310S-SA GB carbide, (b) Type 310S-S GB carbide and (c) Type 310S-TT.

Figure 3 shows the average corrosion rate determined for the set of exposed SA, S and TT samples by Huey immersion testing. The error bars superimposed onto the bar chart demark the highest and lowest values recorded for each set of four samples, indicating the spread in the data. There was no significant difference between the SA material and TT material. The S material exhibited a significantly higher corrosion rate relative to that exhibited by the SA and TT material.

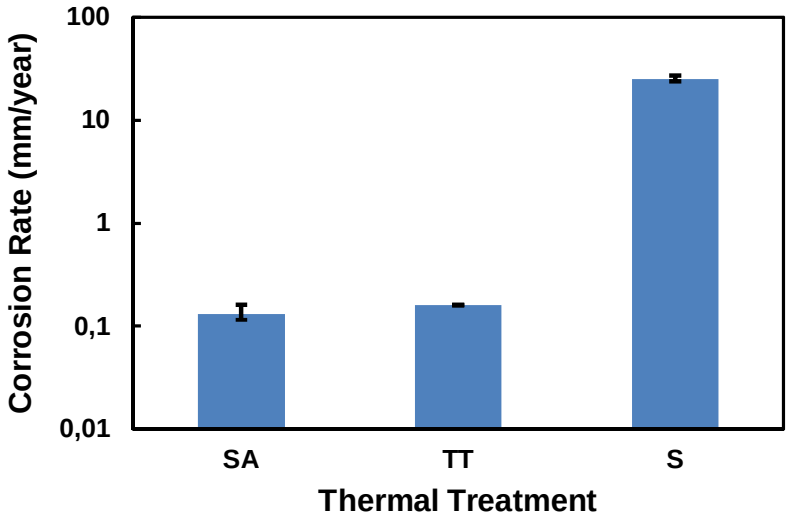

Figure 3. Corrosion rate comparison after Huey immersion testing.

Figure 4 shows a set of plan-view and cross-section view SEM images of the SA, S and TT material that document the mode and extent of corrosion that occurred during the Huey immersion test. The SA material did not show any preferential attack (Figure 4a & 4b). The grain boundaries were slightly outlined on the exposed surface and there was no evidence of any other localized attack (Figure 4a). When viewed in cross-section (Figure 4b) the exposed surface appeared flat and smooth, consistent with there being no preferential attack during the immersion. Thus, the corrosion rates documented in Figure 3 likely corresponded to a uniform corrosion mode. Significant corrosion of the grain boundaries as well as twin boundaries of the S material was observed (Figure 4c). It is noted that the corroded grain boundaries were very narrow (Figure 4d), suggesting that only the Cr depleted zones were dissolved during the immersion. The TT material had the same corrosion rate as the SA material but showed different morphology after the corrosion test. The plan-view image of the TT material (Figure 4e) shows pitting corrosion likely occurred inside grains whereas GBs tended to form ‘crevice’-like structures. When viewed in cross-section (Figure 4f), the exposed surface exhibited shallow pitting. By comparing the LOM images shown in Figure 1d, it seems that the crevice-like structure and pit-like structures were originally occupied by σ phase. Therefore there may be some micro-galvanic effects at the interface of the two phases.

a. Type 310S-SA (Plan-View)

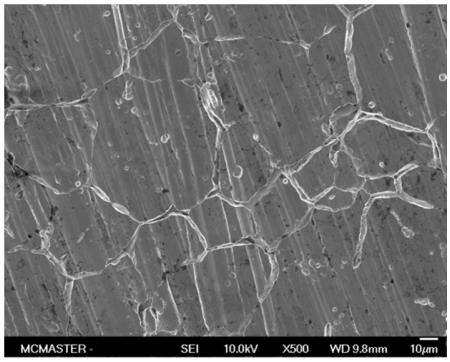

b. Type 310S-SA (Cross-Section)

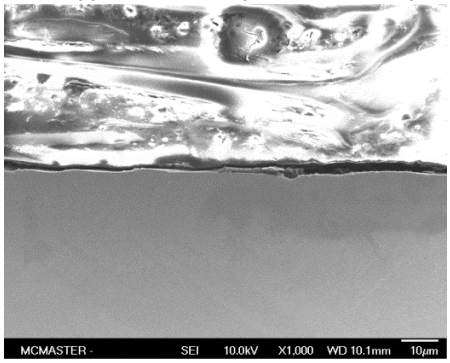

c. Type 310S-S (Plan-View)

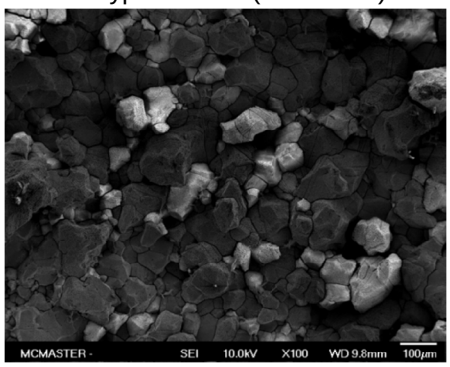

d. Type 310S-S (Cross-Section)

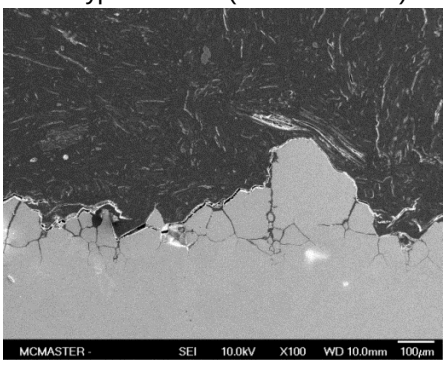

e. Type 310S-TT (Plan-View)

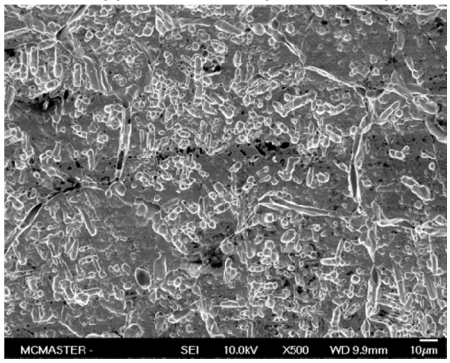

f. Type 310S-TT (Cross-Section)

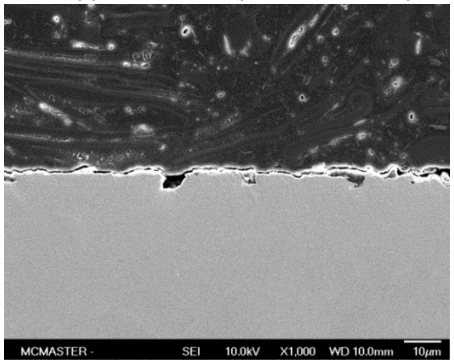

Figure 4. SEM plan-view images of the (a) SA (c) S and (e) TT material and cross-section images of the (b) SA, (d) S and (f) TT material showing the mode and extent of corrosion that occurred during the Huey immersion test.

The typical E-I curves for each material are shown in Figure 5. The forward scan starts from E_{corr} to 0.3 (vs. E_{SCE}). The current density increases with potential until the passivation zone. The current peak of the forward scan (blue line) from E_{corr} to 0.3 (vs. E_{SCE}) corresponds to i_a. The current density drops to a low value due to formation of a protective oxide layer on the sample surface. The current density decreases initially as a result of the decrease in potential during the backward scan. Then the current density begins to continuously increase when the sample is sensitized as the GBs arecontinuously dissolved into the solution. In the case of unsensitized materials, on the other hand, the increase of current density is less obvious due to the uniformly distributed Cr along the GBs. The current peak of the backward scan (red line) corresponds to i_r. The ratio of i_r/i_a is proportional to DOS.

Figure 6 compares the values of the i_r/i_a ratio determined for the SA, S and TT materials after DL-EPR testing. The errors bars represent the 95% confidence interval. The SA material exhibited the lowest apparent DOS, as measured by the i_r/i_a ratio. The TT material showed a significantly the i_r/i_a ratio (apparent DOS) relative to the SA material. Not surprisingly, the S material exhibited the highest i_r/i_a ratio (apparent DOS). All materials have small error bars suggesting good reproducibility for both materials tested by the DL-EPR method.

a. Type 310S-SA

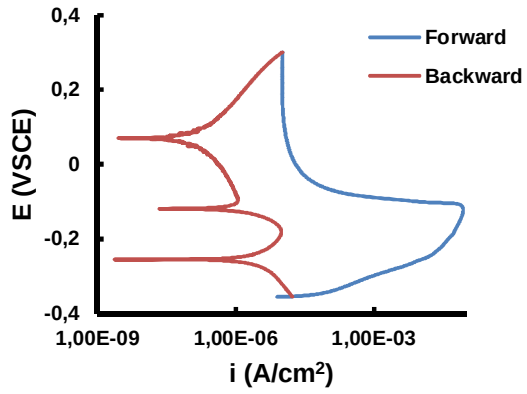

b. Type 310S-S

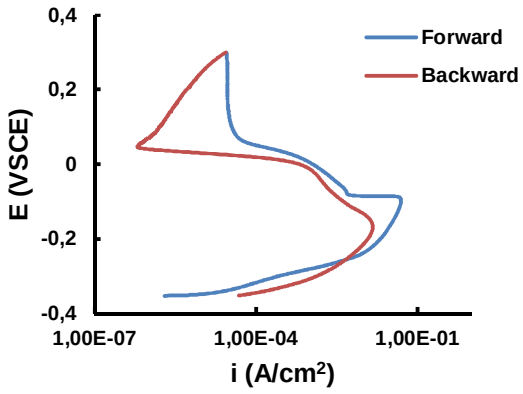

c. Type 310S-TT

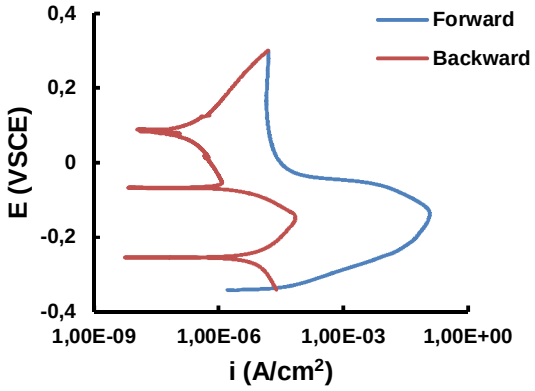

Figure 5. Typical DL-EPR curves measured for the (a) SA, (b) S and (c) TT materials.

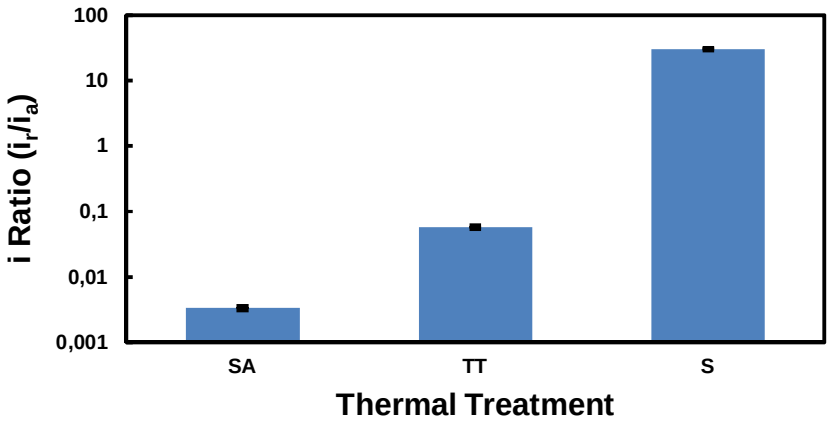

Figure 6. Comparison of i_r/i_a ratios measured for the SA, S and TT materials, as determined from DL-EPR testing.

Figure 7 shows a set of plan-view and cross-section view SEM images of the exposed SA, S and TT surfaces that document the mode and extent of corrosion that occurred during the DL-EPR test. Once again, the SA material showed very little grain boundary attack: slightly outlined in the plan-view image (Figure 7a) and no indications in the cross-section view (Figure 7b). The plan-view image of S material (Figure 7c) exhibited significant grain boundary attack. Twin boundaries were also attacked, but to a much lower extent. Corrosion pits were observed to be uniformly distributed on the surface of the grains. The cross-section image (Figure 7d) revealed that the grain boundaries were attacked to a maximum depth of 10 μm. The widths of the attacked grain boundaries varied from the nanometer scale to the micron scale. The TT material showed distinctly different features compared with those observed after the Huey immersion tests. The plan-view image of the TT material (Figure 7e) revealed that the σ phase was standing proud on the alloy surface after DL-EPR testing, whereas the alloy matrix was preferentially dissolved. The cross-section image (Figure 7f) also clearly showed the σ phase was standing proud on a uniformly corroded matrix.

a. Type 310S-SA (Plan-View)

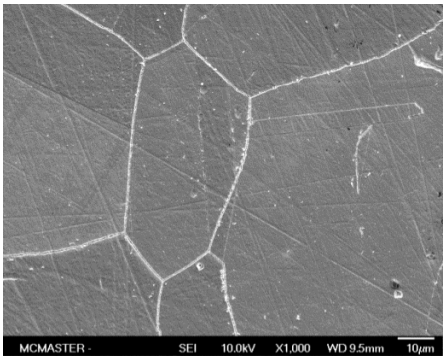

b. Type 310S-SA (Cross-Section)

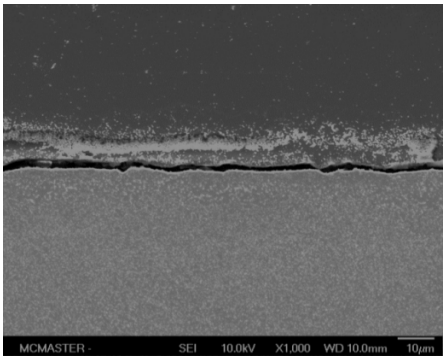

c. Type 310S-S (Plan-View)

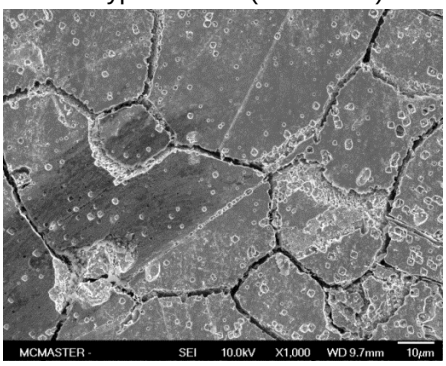

d. Type 310S-S (Cross-Section)

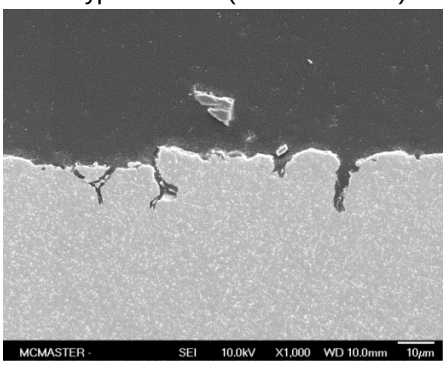

e. Type 310S-TT (Plan-View)

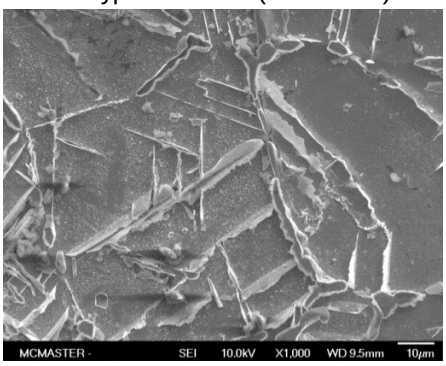

f. Type 310S-TT (Cross-Section)

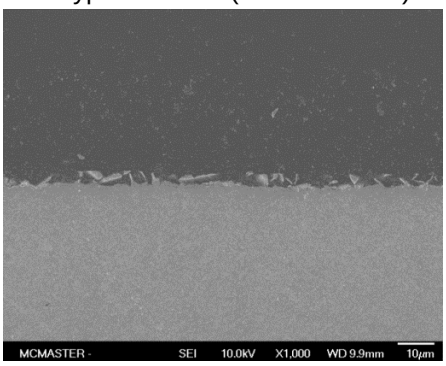

Figure 7. SEM plan-view image of the (a) SA (c) S and (e) TT material and cross-section image of the (b) SA, (d) S and (f) TT material showing the mode and extent of corrosion that occurred during the DL-EPR test.

4. Discussion

Thermal treatments were designed to produce materials with distinct GB chemistry. Despite formation of fine grain size carbides, no segregation/depletion of major alloying elements was observed in the SA material. The formation of GB carbides may be attributed to the high content of C and Cr in the alloy. The solubility of carbon in austenite, with regard to $M_{23}C_6$, can be described empirically as:

$$\log[C]\ (ppm)=7.71-6272/T$$

where C is the carbon concentration and T is the temperature. The solubility of C in austenite also decreases with Cr content [10]. This suggests that the designed solution annealing temperature may not high enough to dissolve C. C preferentially segregates along the GBs, and $M_{23}C_6$ type carbides nucleated during the subsequent water quenching process causing formation of $M_{23}C_6$ type carbides. The S material has a significantly higher content of carbides than the SA material. Growth of carbide was observed both along the GBs and inside the grains. A Cr depleted zone of up to 200 nm was found along the GBs and around grain carbides. The bulk extracted method suggests the total weight of carbides and σ phase is about 5 wt.%. Carbides usually account for only a small amount of weight in the bulk extracted particles due to their fine grain size [6-7]. It is reasonable to assume that the weight fraction of the σ phase in the bulk material is 5 wt.% after 1000 h thermal treatment at 800 ºC and the Cr content in bulk material is about 21.5 wt.%. Despite the fact that carbides were observed on the GBs of the SA material, no Cr depletion was detected by EDS line scan. Similarly, there was no Cr depletion in the TT material although Cr was observed to segregate along the GBs forming σ phase. As a result, the DOS of the SA and TT materials should be regarded as zero. The DOS of the S material is about 50 nm (width of Cr sensitization) on each side of GB whether carbide is present or not. The Cr concentration profile is shown in Figure 8. The SA material exhibit no Cr depletion along the GB and the Cr concentration of bulk material is about 24 wt.%. The TT material has a lower content of Cr in the matrix as a result of σ phase precipitation. The SA and TT materials did not show sensitization. The S material, however, exhibited a Cr depleted zone of about 200 nm width, and a sensitized zone of about 50 nm in width.

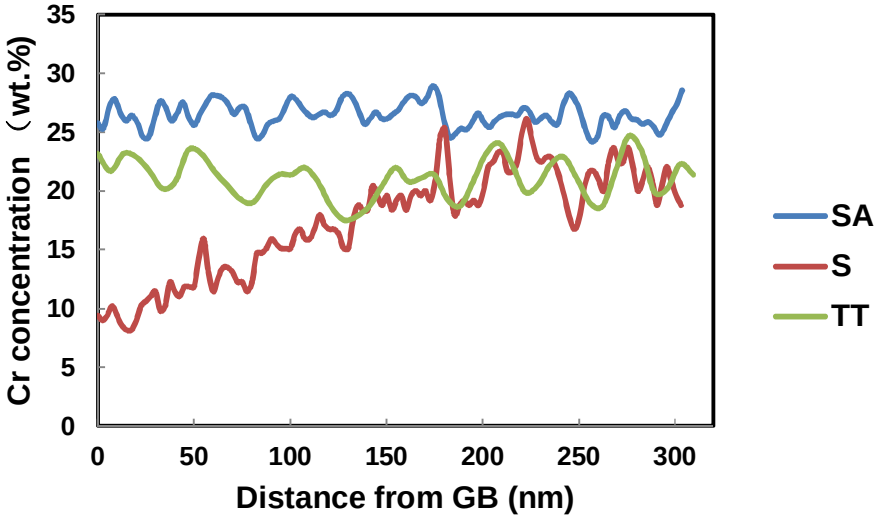

Figure 8. Effect of thermal treatment on the Cr compositional profile near the grain boundaries.

The bulk material is dissolved in the boiling solution during the immersion tests, and the Cr-depleted zone will be preferentially dissolved. The degree of sensitivity is represented by the rate of metal dissolution into the solution. Based on the results of the Huey tests, the SA materials exhibited the lowest corrosion rate, corresponding to the lowest Cr sensitivity. This suggests that there is no Cr depletion after solution annealing. The lack of distinct grain boundary attack is consistent with the lack of any measurable Cr depletion across the GB region as shown in Figure 2a. As a result, the bulk material uniformly dissolved to the solution and there was no preferentially attacked region as shown in Figure 4a and b. The S material exhibited the highest corrosion rate, indicating that it was the most seriously sensitized. The GBs of the S material had an attack width up to micron dimensions, although the dissolving tip was usually limited to the nanometer scale. This suggests that, during the immersion tests, the boiling HNO_3 preferentially dissolved the sensitized zone where the average Cr content is lower than 12 to 13 at. %. The area with higher Cr content (above 12 to 13 at. %) promotes the formation of a more protective oxide layer, which dissolves more slowly during immersion test. It should be noted that only sensitized (i.e., Cr content lower than 12 to 13 at. %) GBs and twin boundaries were dissolved by the boiling HNO_3. Once the GBs were dissolved, the individual alloy grains fell away from the bulk material into the solution. Thus, the corrosion rate/GB sensitivity of the S materials suggested by this technique was exaggerated. The TT material showed a low corrosion rate (comparable with that of the SA material) suggesting that Type 310S steel did not sensitize after thermal treatment despite the Cr segregation along the GB. This also consistent with the lack of measurable Cr depletion across the grain boundary region, as shown in Figure 2c. However, the plan view of the immersion-tested TT materials showed large amounts of pit-like structures, as shown in Figure 4e, and the cross-sectional view (Figure 4f) shows that some of these “pits” could be on the micron scale. A comparison of the TT material in Figure 1d and Figure 4e suggests it is possible that the thermally-induced σ phase could dissolve in boiling HNO_3 during the Huey test despite its high Cr (about 50 wt.%). In summary, the immersion test results correlate well with the DOS as predicted by TEM-EDS.

The DL-EPR tests give similar results as the Huey test with respect to the degree of GB sensitivity. Again, the SA material exhibited the lowest corrosion rate and EPR- tested SA material showed features similar to those observed in the immersion tested material. The S material had the highest sensitivity and the GBs were preferentially attacked during the EPR test. The EPR-tested S material had a large number of pits as shown in Figure 7c. This may be attributed to the growth of grain carbides (Figure 1c). The growth of grain carbides depleted the Cr from the region adjacent to them and dissolved to solution during the DL-EPR test. The attacked GBs of the S material varied from the nanometer scale to the micron scale as shown in Figure 7f. This is most likely affected by the size of carbide and the sensitized zone (Cr concentration lower than the critical value of12 to 13 at.%). The immersion-tested and DL-EPR tested TT materials shown very distinct features. The pit-like structures observed on theimmersion-tested TT material is assumed to have been previously occupied by thermally-induced σ phase. In this case, formation of the σ phase likely decreased IGSCC resistance (at least did not enhance it). Whereas σ phase was outlined after the EPR test as shown in Figure 7e and f, it should be noted that the TT material should still be regarded as nonsensitized due to its low current ratio (below 1%). The higher current ratio of the TT material may attributed to the lower Cr content in the bulk austenitic phase compared with the SA material. However, no GBs were attacked after the DL-EPR test (Figure 7) due to the absence of a Cr depleted zone. To sum up, the DL-EPR test results give the same DOS as that predicted by TEM, and the current ratio value accompanied with examination of the microstructure could reveal minor Cr difference between SA and TT materials.

The results of both sensitization test techniques correlate well with the TEM results and have a very small errors (Figure 3 and Figure 6) implying that both methods are reliable for detecting GB

sensitivity. However, the DL-EPR test should be regarded as a more reliable chemical signature in predicting the IGSCC susceptibility of Type 310S stainless steel in SCW. It provides relatively more acurate results of seriously sensitized material (immersion testing usually gives an exaggerated corrosion rate when the material is heavily sensitized). The EPR test suggests that GB properties could be improved by the presence of σ phase. This correlates well with corrosion results that suggest that intermetallic precipitates could enhance corrosion resistance locally [20], whereas the immersion test indicate that presence of σ phase may increase IGSCC susceptibility. Based on the the IGSCC prediction of DL-EPR method, it is reasonable to suggest formation of σ phase during service will likely increase the IGSCC resistance. In the absence of Cr depletion, formation of carbide will not likely induce increased IGSCC susceptibility.

GB chemistry has a significant effect on crack propagation of austenitic stainless steels in na SCW environment; the onset of SCC/IASCC, however, is actually controlled by the mechanical properties [14]. Thus, a mechanical signature is also necessary to predict IGSCC susceptibility of austenitic stainless steels in an SCW environment. The proposed IASCC mechanisms [14] under LWR environment includes: the slip oxidation model, RIS, irradiation hardening and localized deformation. RIS could be characterized by the DL-EPR method as discussed above. The rest of these mechanisms are closely related to the microstructure of material. Thus, micro- or nano-hardness measurements could be applied to elucidate the mechanical signature predicting SCC initiation. This work is in progress.

The SCC susceptibility of the alloys in the S, SA and TT conditions is being evaluated using slow strain rate tests at Canmet.

5. Conclusion

$M_{23}C_6$ type carbide was observed on the GBs of SA material due to the high Cr and C content of Type 310S austenitic stainless steel.

The DOS of the SA and TT materials is zero due to the absence of Cr depletion, while the DOS of the S materials is about 25 nm whether carbide is present or not.

Both Huey immersion test and DL-EPR test were found correlate well with the DOS of pretreated materials as predicted by microscopy examination. The DL-EPR method is regarded as a better method for predicting IGSCC due to its higher accuracy and ability to capture minor microstructural difference between SA and TT materials.

6. Acknowledgements

Funding to Canada Gen-IV National Program was provided by Natural Resources Canada through the Office of Energy Research and Development, Atomic Energy of Canada Limited, and Natural Sciences and Engineering Research Council of Canada. The expertise provided by the technical staff at CanmetMATERIALS and the Canadian Centre for Electron Microscopy at McMaster University is greatly appreciated for assisting with the SCW corrosion testing and sample characterization respectively.

References

1. G.S. Was, S. Teysseyre, Challenges and recent progress in corrosion and stress corrosion cracking of alloys for supercritical water reactor core components, in: T.R. Allen, P.J. King, L.

Nelson (Eds.), 12th Environmental Degradation Conference of Materials in Nuclear Power Systems - Water Reactors, TMS, Warrendale, PA, 2005, pp.1343-1357.
2. T.R. Allen, Y. Chen, L. Tan, X. Ren, K. Sridharan, S. Ukai, Corrosion of candidate materials for supercritical water-cooled reactors, in: T.R. Allen, P.J. King, L. Nelson (Eds.), 12th Environmental Degradation Conference of Materials in Nuclear Power Systems - Water Reactors, TMS, Warrendale, PA, 2005, pp.1397-1407.
3. T. Allen, Y. Chen, D. Guzonas, X. Ren, K. Sridharan, L. Tan, G. Was, E. West, Material Performance in Supercritical Water, in: R. Konings (Ed.), Comprehensive Nuclear Materials, Elsevier, 2012.
4. J. Kaneda, S. Kasahara, F. Kano, N. Saito, T. Shikama, H. Matsui, Material development for supercritical water-cooled reactor, in: Proceedings of 5th International Symposium on Supercritical Water-Cooled Reactors (ISSCWR-5), Vancouver, BC, Canada, 2011, pp. 13-16.
5. D. Guzonas, R. Novotny, Progress in Nuclear Energy, v 77, p 361-372.
6. H. Sidhom, T. Amadou, H. Sahlaoui and C. Braham. Metallurgical and Materials Transactions A. Vol. 38 (2007) 1269-1280.
7. S.S.M. Tavares, V. Moura, V.C. da Costa, M.L.R. Ferreira, J.M. Pardal. Materials Characterization 60 (2009) 573-578.
8. W.E. White and I. Le May. Metallography. 3 (1970) 35-50.
9. M. Deighton. J. Iron Steel Inst., 1970, 208, 1012-1014.
10. T. Sourmail. Materials Science and Technology Vol. 17, 1-14.
11. B. Weiss and R. Stickler. Metallurgical Transactions 3 (1972) 851-866.
12. F.R. Bechitt and B.R. Clarck. Acta Metall., 1967, 15, 113-129.
13. R. Lackner, G. Mori, R. Egger and F. Winter. Correlation between streicher and EPR test. In: CORROSION/14, NACE International, Houston, TX, 2014, Paper 3946.
14. G. Was, Y. Ahida and P. Andresen. Corros. Rev. 29 (2011) 7-49.
15. R. Katsura, Y. Ishiyama, N. Yokota, T. Kato, K. Nakata, K. Fukuya, H. Sakamoto and K. Asano. Post-irradiation annealing effects of austenitic stainless steels in IASCC. In: CORROSION/98, NACE International, Houston, TX, 1998, Paper 132.
16. K. Arioka, T. Yamada, T. Terachi and G. Chiba. Corrosion, Vol. 62, No. 7, pp 568-575.
17. J.S. Janssen, M.M. Morra and D.J. Lewis. Corrosion, Vol. 65, No. 2, pp 67-78.
18. D.A. Guzonas and W.G. Cook. Cycle chemistry and its effect on materials in a supercritical water-cooled reactor: A synthesis of current understanding. Corrosion Science 65 (2012) 48-66.
19. S. Teysseyre and G.S. Was. Corrosion, vol. 62, pp1100.
20. Y. Jiao, J. Kish, W. Zheng, D. Guzonas, W. Cook, Effect of thermal ageing on the corrosion resistance of stainless steel Type 316L exposed in supercritical water, in: 2014 Canada-China Conference on Advanced Reactor Development (CCCARD-2014), Niagara Falls, ON, Canada, April 27-30, 2014, Paper 027.
21. J. Li, W. Zheng, S. Penttila, P. Liu, O.T. Woo, D. Guzonas. Journal of Nuclear Materials 454 (2014) 7-11.
22. S. Y. Persaud, A. Korinek, J. Huang, G.A. Botton, R.C. Newman. Corrosion Science 84 (2014) 108-122.

ISSCWR7-2030

Experimental Investigation of the Basic Characteristics of Supercritical Carbon Dioxide Natural Circulation in a Rectangular Loop

Guangxu Liu, Yanping Huang*, Junfeng Wang
Nuclear Power Institute of China
NO.25 South third section 1st Ring Road Chengdu, Sichuan Province, P.R. China
00862885908156(O), hyanping007@163.com

Abstract

Experiments were carried out to study the basic characteristics of supercritical carbon dioxide natural circulation in a rectangular loop. A preliminary comparison has been made with results of other investigators. With the increase of heating power, the mass flow rate increased quickly at the beginning, then reached a peak, and finally decreased slowly. The peak of mass flow rate was obtained at a heating section outlet temperature much higher than the pseudo-critical temperature. The system stability of supercritical carbon dioxide natural circulation seems to be better than that of supercritical water, and no flow instabilities were found in experiments. Geometric structure and experimental operation had vital effect on steady-state and stability characteristics of supercritical carbon dioxide natural circulation and more in-depth research should be conducted.

1. Introduction

As safety is a key issue in the design of new nuclear reactor systems, considerable emphasis has been placed on the passive safety system to improve the safety of nuclear reactor. Natural circulation, an essential way to improve the passive safety of nuclear reactor, can be used to remove decay heat passively, which would effectively improve the safety of nuclear reactor. The characteristics of natural circulation are of interest in new nuclear reactor design.

The working medium can affect the system characteristics and safety greatly. Compared with subcritical fluids, supercritical fluids have unique thermal properties variation rules. One distinctive feature of supercritical fluid is the large change in thermal properties, such as density and dynamic viscosity, as the fluid passes through the critical (or pseudo-critical) point. Figure 1 shows the variation of density, specific heat capacity, dynamic viscosity and thermal conductivity versus temperature for carbon dioxide at p=7.5 MPa. As shown in figure 1, density change of carbon dioxide passing through pseudo-critical region can be as much as 500 kg/m^3. The large change in density across the critical (or pseudo-critical) point would generate a substantial driving head in natural circulation, which is favorable to the effective derivation of decay heat in accidental condition. However, due to the particular behaviors of supercritical fluids near the critical (or pseudo-critical) point, the steady-state and stability characteristics of supercritical fluids natural circulation might be distinctly different from those of subcritical fluids natural circulation. Hence, supercritical fluids natural circulation is of interest for many researchers. Researchers usually use water, carbon dioxide and Freon as working medium in supercritical fluids natural circulation. Carbon dioxide, a fluid with relatively low critical point (T_c=30.98 ℃, p_c=7.38 MPa) and relatively high specific heat capacity, is being considered as reactor core coolant and power conversion medium in some advanced nuclear reactor designs

on account of its potential to offer enhancement of reactor passive safety, compact size and high thermal efficiency. Consequently, supercritical carbon dioxide natural circulation has attracted much attention.

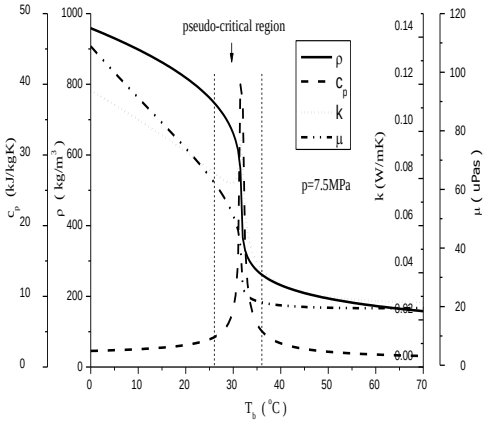

Figure 1 Thermal physical properties of carbon dioxide near pseudo-critical point

The literature reveals that only very few experimental studies on the characteristics of supercritical fluids natural circulation have been performed. Harden and Boggs [1] investigated the characteristics of supercritical fluids natural circulation using Freon 114 as working medium. Results showed that flow oscillations occurred when the outlet temperature of heating section approached the pseudo-critical temperature. A test apparatus called DeLigt was constructed in Holand as a simulating test apparatus of HPLWR (High Performance Light Water Reactor). T'Joen and Rohde [2] conducted experiments on DeLigt using Freon 23 as working medium. They found that for a single inlet temperature the system underwent two transitions as the power increased. At low power the system was stable and became unstable as the power was increased, but further increasing the power the system stabilized. Lv [3] performed experimental investigation on supercritical water natural circulation in a 4000-mm-high rectangular loop, with the pressure of 10 and 21.1~24.8 MPa. Results showed that the maximum mass flow rate of supercritical water circulation was higher than that of subcritical water natural circulation. Distinct oscillations of mass flow rate, pressure and outlet temperature were observed when outlet temperature of heating section got close to pseudo-critical temperature. Adelt and Mikielewicz [4] conducted experiment on a 4000-mm-high loop with supercritical carbon dioxide as working medium. As the fluid was heated over the pseudo-critical temperature, pressure oscillations were observed on part of experimental conditions. Lomperski et al. [5] performed studies on supercritical carbon dioxide in a 2000-mm-high natural circulation loop. The loop was operated in a base case configuration without orifice in the hot leg and in a second case configuration with an orifice in the hot leg. No flow instabilities were observed in all tests. Syouichirou et al. [6] studied the steady-state performance on a natural circulation system for supercritical carbon dioxide. Performance of the system was determined by measuring average flow velocities of carbon dioxide. Results showed that flow rates achieved in the system could be correlated in terms of Grashof number, Prandtl number and effective density difference. Besides, one-dimensional finite-difference simulation could predict the velocities at most conditions to within 35%. In order to demonstrate the potential capability of supercritical carbon dioxide as a passive heat removal medium, a small rectangular natural circulation loop was constructed in KAPL. Milone [7] conducted fundamental experimental studies on the loop using supercritical carbon dioxide and subcritical water as working medium. A detailed comparison between the results of carbon dioxide natural circulation and those of water natural circulation was made. Results showed that supercritical carbon dioxide can passively remove heat at a lower loop-averaged temperature than water, provided the loop-averaged temperature was near the pseudo-critical temperature. Beyond this temperature, supercritical carbon dioxide failed to provide high heat removal capability and behaved more like an ideal gas. Yu et al. [8]

constructed a test loop to predict the region of instability of supercritical fluids natural circulation in Tsinghua University. They performed preliminarily experimental investigations on the loop and no flow ledinegg instability occurring at supercritical pressure in the loop. But it is worthwhile to note that their experimental pressure was 25 MPa (supercritical pressure) and the heating section outlet temperature was much lower than pseudo-critical temperature. Sharma et al. [9-10] experimentally and theoretically investigated the steady-state and stability behavior of supercritical carbon dioxide natural circulation. The authors theoretically studied the effect of orientation, pressure, inlet temperature and diameter on steady-state behavior of supercritical carbon dioxide natural circulation. They gained curves of mass flow rate versus power, and on part of experimental conditions flow instabilities were observed.

In this work, experimental investigation on the basic characteristics of supercritical carbon dioxide natural circulation in a rectangular loop was conducted. A preliminary comparison was made with results of supercritical water natural circulation and supercritical carbon dioxide natural circulation in published literatures

2. Experimental setup

2.1 Test apparatus

The characteristics of supercritical carbon dioxide natural circulation were measured in a rectangular natural circulation loop in Nuclear Power Institute of China (NPIC). A schematic diagram of the test loop is given in figure 2. The major parameters controlled and measured were system pressure, the mass flow rate of the working medium, fluid temperature at the inlet and outlet of the heating section and cooling section, the outside wall temperature of the heat section, and the wall heat flux provided to the working fluid. In this section, more detailed information about the experimental equipment will be given.

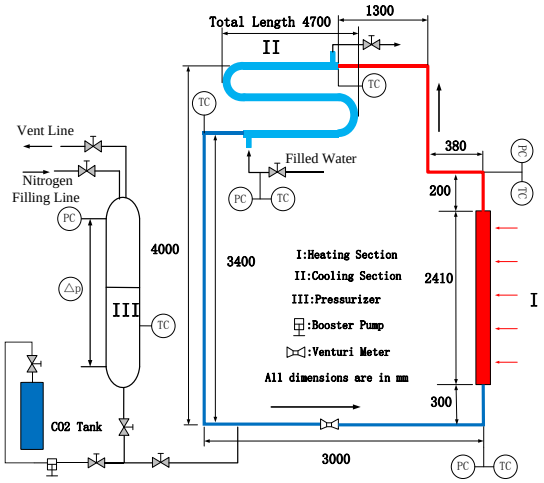

Figure 2 Schematic diagram of supercritical natural circulation loop

The design pressure and temperature of the test facility was 30 MPa and 500 ℃, respectively. In this study, the operating pressure was 8.2-10.2 MPa and the inlet carbon dioxide temperature was 27-30 ℃. The total height and width of the loop was 4000 mm and 3000 mm respectively. The heating section of the loop was constructed from a commercially available INCONEL 625 stainless steel with an inner diameter of 6mm and a thickness of 2.5mm. The total length of the heating section was 2410 mm. The cooling section was constructed from type 316 stainless steel and the total length was 4700 mm. The cooling section was tube-in-tube type with carbon dioxide flowing in the inner tube (6 mm ID and 10 mm OD) and cooling water flowing in the outer tube (23 mm ID). The hot section and the cold section of the loop were made of type 316

stainless steel with an inner diameter of 10mm and a thickness of 3mm. The entire loop was insulated against heat loss using ceramic wool.

For supercritical experiments with supercritical carbon dioxide, the loop should be pressurized above the critical pressure of carbon dioxide (7.38MPa). An air-driven gas booster pump connected to the carbon dioxide tank was used to fill carbon dioxide into the test loop and to increase the pressure of the test loop. The purity of carbon dioxide used in experiments was 99.95%.

The inlet and outlet temperature of the heating section were measured by platinum resistance thermometers with the accuracy of ±0.15℃. Other primary fluid temperatures and secondary fluid temperatures were measured by N-type thermocouples with the accuracy of ±0.4% reading. A total of 30 type-N thermocouples (1mm diameter) were brazed on the outer surface along the heating section to measure the outside wall temperatures. Wall temperature at each location was measured as the average value indicated by two thermocouples inserted inserted diametrically opposite on the outside wall. The mass flow rate was measured by Venturi meter, which has a measure range from 0.00278 to 0.0278 kg/s, an accuracy of ±0.5% (of full scale). The pressure of the loop (including the inlet and outlet pressure of heating section, the pressure of pressurizer) was measured with the help of ST3000 type pressure transmitters, which have a range from 0.1-20.7MPa and accuracy of ±0.1% (of full scale). The pressure drop across the heating section and the pressurizer was measured by ST3000 type differential pressure transmitters of range 0-0.1MPa with accuracy of ±0.0375% (of full scale). The heating section was heated electrically using a DC power supply (20 V, 1000 A, 20 kW) to provide a uniform heat generation rate.

2.2 Test procedure

Before operation with supercritical carbon dioxide, the loop was evacuated by a vacuum pump at first. Then carbon dioxide at low pressure was filled into the loop to flush the loop repeatedly, including all vent lines. The booster pump was used to increase the pressure of the test loop. Finally, nitrogen was filled on the top of the pressurizer to achieve the desired operating pressure. Due to large density difference between carbon dioxide and nitrogen, *i.e.*, 781.8 kg/m^3 and 92.7 kg/m^3, respectively, at 25 ℃/8.2 MPa, the two gases are not expected to mix and a level will be formed in the pressurizer. Once the desired operating pressure was achieved, the cooling section was supplied with cooling water and heating section power was switched on and adjusted to required value. By adjusting the mass flow rate of cooling water of the cooling section, the inlet carbon dioxide temperature of the heating section was adjusted to required value. And at a certain system pressure, the inlet carbon dioxide temperature was fixed by adjusting the mass flow rate of cooling water. Sufficient time was allowed to achieve the steady state.

3. Results and discussion

3.1 Characteristics of natural circulation

Steady-state characteristics of natural circulation are the major concerns of natural circulation research. Curves of mass flow rate versus power were obtained in experiments. In figure 3, the pressure and inlet carbon dioxide temperature were 8.2 MPa and 27 ℃ respectively. With the increase of power, the mass flow rate increased quickly at the beginning, then reached a peak, and finally decreased slowly. Experimental results showed that the peak of mass flow rate was not strictly related to the point where the outlet carbon dioxide temperature was in the vicinity of the pseudo-critical temperature. In figure 3, the peak was obtained at a heating section outlet carbon dioxide temperature (about 60 ℃) much higher than the pseudo-critical temperature (T_{pc}=35.8 ℃ at p=8.2 MPa). It is worthwhile to note that no flow instabilities were observed in all experiments, which suggested that the stability of supercritical carbon dioxide natural circulation in present test loop may be satisfactory.

Mass flow rate variation is the result of common-effect of buoyancy force and frictional resistance. The buoyancy force is related to fluid density difference (△ ρ) between the hot section and the cold section, and the frictional resistance is related to the inverse of fluid density (1/ρ). So the buoyancy force and frictional resistance can be approximately replaced by △ ρ and 1/ρ respectively (shown in figure 4). With the initial increase in power, the mass flow rate increased quickly due to the increase in buoyancy force, caused by the increase of density difference between the cold section and the hot section, was faster than the increase in frictional resistance. When outlet carbon dioxide temperature exceeded the pseudo-critical temperature, the density difference increased became slower, while the inverse of fluid density increases quickly. As a result, the increase in frictional resistance gradually exceeded that of buoyancy force. So the mass flow rate increased quickly at the beginning, then reached a peak and finally decreased, as explained by figure 4.

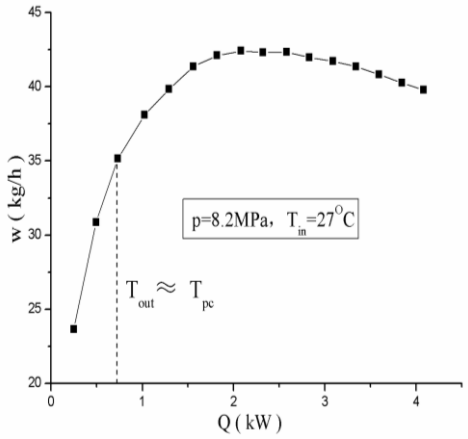

Figure 3 Effect of heating power on mass flow rate

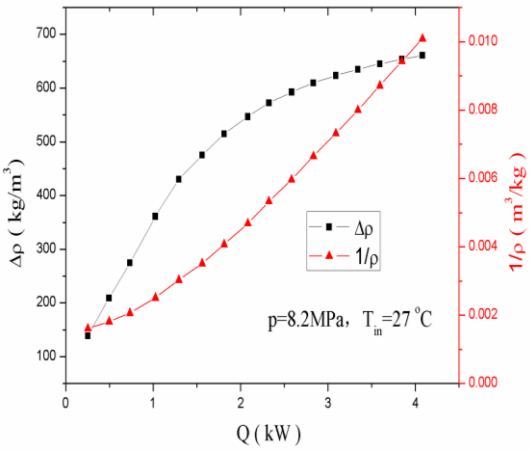

Figure 4 Effect of heating power on △ ρ and 1/ρ

As to the variation of fluid temperature (shown in figure 5), inlet carbon dioxide temperature in present experiments was approximately constant by adjusting the mass flow rate of cooling water in the second side of cooling section and outlet carbon dioxide temperature increased with power. When outlet carbon dioxide temperature got close to the pseudo-critical temperature, fluid temperature increases very slowly duo to high specific heat capacity of supercritical fluid. When the fluid temperature exceeded the pseudo-critical temperature, the specific heat capacity of the fluid decreased so fast that the outlet carbon dioxide temperature of the heating section increased quickly.

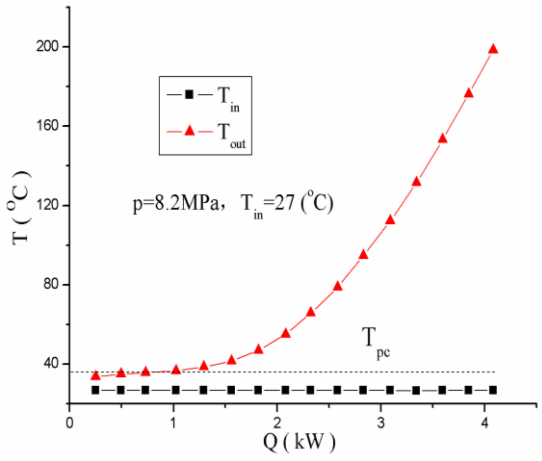

Figure 5 Effect of heating power on inlet and outlet temperature

3.2 Comparison with literature results

The loading fluids and geometric structure of test loop are key factors influencing the characteristics of natural circulation. The present experiment results were compared with experimental results in published literatures using supercritical water or carbon dioxide as working medium.

Lv [3] studied the steady-state and instability behaviors of supercritical water natural circulation in the same natural circulation loop as the present study. The system pressure was 21.1-24.8 MPa and the heating section inlet temperature was 20-50 ℃. The results showed that the natural circulation instability occured when the outlet temperature of the heating section got close to the pseudo-critical temperature. As shown in figure 6, the instability behavior of supercritical water natural circulation showed the fluctuations of the mass flow rate, outlet water temperature of the heating section and pressure et al. However, no flow instabilities were found in present study using supercritical carbon dioxide as working medium. The stability of superitical water natural circulation and that of supercritical carbon dioxide in the same test loop were different. It may be caused by the more dramatic changes of thermal properties of water, as shown in figure 7. More in-depth research should be conducted to study the stablities of supercritical water and carbon dioxide natural circulation.

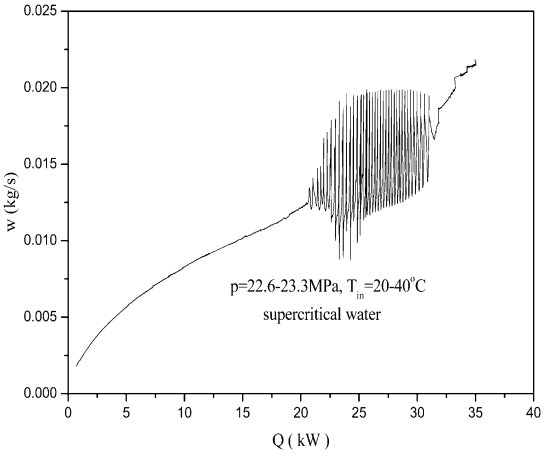

Figure 6 General trends of supercritical water natural circulation instabilities [3]

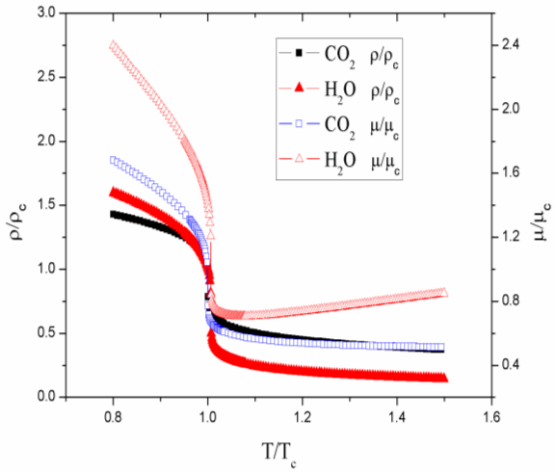

Figure 7 Comparison of supercritical water and carbon dioxide thermal properties

Geometric structure of test loop is a key factor influencing the characteristics of natural circulation. Different orientations of heating section and cooling section (*e.g.*, Horizontal Heating Section Horizontal Cooling section (HHHC), Horizontal Heating Section Vertical Cooling section (HHVC), Vertical Heating Section Horizontal Cooling section (VHHC), Vertical Heating Section Vertical Cooling section (VHVC)) could affect the height difference between the heat source center and cold source center, as well as the length of supercritical region in the national circulation loop. As a result, the characteristics of natural circulation would be changed. Sharma et al. [9] experimentally investigated the steady-state and stability behavior of supercritical carbon dioxide natural circulation in a rectangular loop in which both the heating section and cooling section were horizontal placed (HHHC). More details about the natural circulation loop could be found in literature [9].

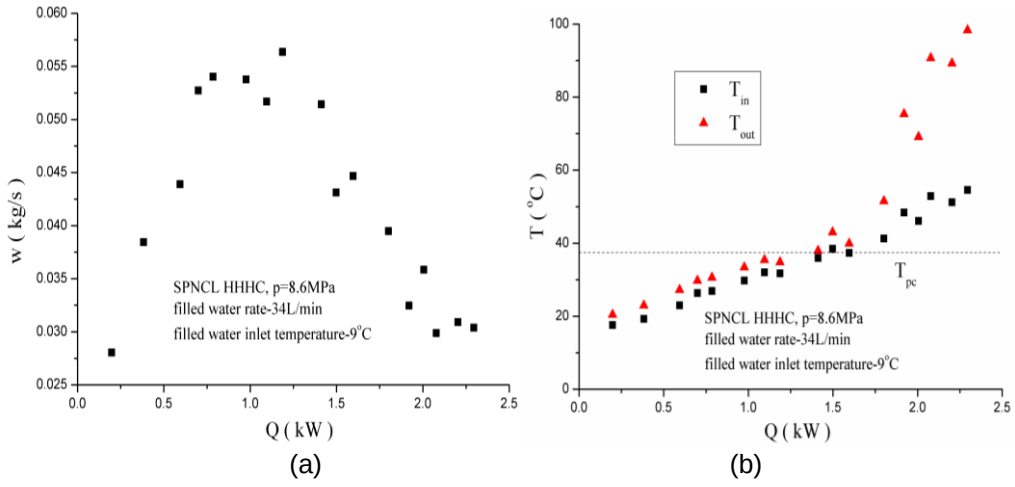

Figure 8 Effect of heating power on mass flow rate, inlet and outlet temperature [9]

In these tests the inlet temperature and mass flow rate of cooling water in the second side of the cooling section were fixed and inlet carbon dioixde temperature of the heating section was not constant, and it was increasing with power. Typical results were shown in figure 8. Researchers found that the steady-state mass flow rate increased untill the outlet carbon dioxide temperatre of the heating section was in the vicinity of the pseudo-critical temperature.

After that there was a sharp reduction in the mass flow rate. The instability was observed in a narrow power region (600-1000W) . The mass flow rate and outlet carbon dioxide temperature of the heating section oscillated periodically. By comparing the results of the present paper with those in literature [9], two important differences are worthwhile to note. The first, in present experiments the peak of mass flow rate was obtained at a heating section outlet carbon dioxide temperature significantly higher than the pseudo-critical temperature and mass flow rate decreased slowly with the increase of power in the descending branch of the curve of w-Q. However, the peak of mass flow rate was obtained at a heating section outlet temperature near pseudo-critical temperature, and in the descending branch of the curve of w-Q, mass flow rate decreased sharply with the increasing of power in literature [9]. The second, no flow instability was found in present study, while noticeable fluctuations of mass flow rate and outlet carbon dioxide temperature of the heating section were found under some experimental conditions in literature [9].

These differences are mainly caused by the difference in geometric structure and experimental operation. The inlet temperature and mass flow rate of cooling water in the second side of the cooling section were fixed and the inlet carbon dioxide temperature of the heating section was increased with power so that the change of mass flow rate in figure 8 was affected by power and inlet carbon dioxide temperature of the heating section simultaneously. But the inlet carbon dioxide temperature was constant in present experiments. So the peak of mass flow rate was obtained at different outlet carbon dioxide temperature in different experiments. As the inlet temperature exceeded the pseudo-critical temperature, both hot and cold section became supercritical and the frictional resistance increased sharply so that there was a sharp reduction in flow rate in literature [9]. `The heating section in the test loop of literature [9] was placed horizontally and the flow direction can be clockwise or counterclockwise. However, the heating section in present experimental loop was vertically placed and the flow direction was invariable. When the frictional resistance increased sharply, fluctuation appeared easily in the loop of literature [9]

4. Conclusions

To study the basic characteristics of supercritical carbon dioxide natural circulation, experiments were conducted in a rectangular loop in which the heating section was vertically placed and the cooling section was horizontally placed. Curves of mass flow rate and inlet (outlet) temperature versus power were obtained. Experimental results were compared with supercritical water natural circulation and supercritical carbon dioxide natural circulation in published literature. The main conclusions obtained are as follows:

(1) With the increase of power, the mass flow rate increased quickly at the beginning, then reached a peak, and finally decreased slowly. The peak was obtained at a heating section outlet carbon dioxide temperature much higher than the pseudo-critical temperature.
(2) No instability was found in present study. The intensity of changes of the thermal properties in pseudo-critical region had vital influence on the stability of natural circulation system.
(3) Geometric structure and experimental operation apparently affect the steady-state and stability behavior of natural circulation system, and more in-depth research should be conducted to study the influence of geometric structure on stability behavior of natural circulation system.

Acknowledgement

The authors are grateful to the National Science Fund for Distinguished Young Scholars (No.11325526) and International Science & Technology Cooperation of China (No.2012DFG61030) for providing financial support for this study.

Nomenclature

c_p	specific heat capacity(kJ/kg/K)
HH	heating section placed horizontally
VH	heating section placed vertically
HC	cooling section placed horizontally
VC	cooling section placed vertically
k	thermal conductivity(W/m/K)
ID	internal diameter(mm)
OD	external diameter(mm)
p	system pressure(MPa)
Q	heating power(kW)
T	temperature (℃)
w	mass flow rate(kg/s)

Greek sysbols

ρ	density of fluid(kg/m^3)
μ	dynamic viscosity(uPa·s)
∆	difference value

subscripts

c	critical point
pc	pseudo-critical point
in	inlet
out	outlet

References

1. D.G. Harden, J.H Boggs, 1964. Transient flow characteristics of a natural circulation loop operated in the critical region. Proceedings of the 1964 heat transfer and fluid mechanics institute. Stanford University Press, 38-50.

2. C. T'Joen, M. Rohde. 2012. Experimental study of the coupled thermo-hydraulic-neutronic stability of a natural circulation HPLWR. Nuclear engineering and design 242, 221-232.

3. F. Lv, Y.P. Huang, Y.L. Wang, X. Yan, 2013. Experimental observation of the general trends of the steady state and instability behaviour of supercritical water natural circulation. Proceedings of the 21st international conference on nuclear engineering, Chengdu, China ,July 29-August2, paper 16504.

4. M. Adelt, J. Mikielewicz, 1981. Heat transfer in a channel at supercritical pressure. International journal of heat mass transfer 24(10), 1667-1674.

5. S. Lomperski, D. Cho, R. Jain, M.L. Corradini, 2004. Stability of a natural circulation loop with a fluid heated through the thermodynamic pseudo-critical point, Proceedings of ICAPP'04, Pittsburgh, PA USA, June 13-17, Paper 4268.

6. S. Yoshikawa, R.L. Smith Jr., H. Inomata, Y. Matsumura, K. Arai, 2005. Performance of a natural convection circulation system for supercritical fluids. Journal of supercritical fluids 36, 70-80.

7. D.V. Milone. Computational model and experimental data on the natural circulation on supercritical carbon dioxide. Proceedings of S-CO2 power cycle symposium 2009.

8. J.Y. Yu, S.W. Che, R. Li, B.X. Qi, 2011. Analysis of ledinegg flow instability in natural circulation at supercritical pressure. Progress in Nuclear Energy 53, 775-779.

9. M. Sharma , P.K. Vijayan, D.S. Pilkhwal, Y. Asako,2013. Steady state and stability characteristics of natural circulation loops operating with carbon dioxide at supercritical pressures for open and closed loop boundary conditions, Nuclear engineering and design 265, 737-754.

10. M. Sharma , P.K. Vijayan, D.S. Pilkhwal, Yutaka Asako,2012. Steady-state behavior of natural circulation loops operating with supercritical fluids for open and close loop boundary conditions. Heat transfer engineering 33(9), 809-820.

11. S. Gupta, D. McGillivray, P. Surendran, L. Trevani, I. Pioro, 2012. Developing heat-transfer correlations for supercritical CO_2 flowing in vertical bare tubes. Proceedings o the 2012 20th International Conference on Nuclear Engineering, Anaheim, California, USA, July 30 – August 3, paper 54626.

The 7th International Symposium on Supercritical Water-Cooled Reactors
ISSCWR-7
15-18 March 2015, Helsinki, Finland

ISSCWR7-2031

A Strategy in Developing Heat-Transfer Correlation for Fuel Assembly of the Canadian Super-Critical Water-cooled Reactor[1]

Laurence Leung and Yanfei Rao
Canadian Nuclear Laboratories
Chalk River, Ontario Canada K0J 1J0
++1-613-584-3311, Laurence.Leung@cnl.ca, Yanfei.Rao@cnl.ca

Abstract

Experimental data and correlations are not available for the fuel-assembly concept of the Canadian SCWR. To facilitate the safety analyses, a strategy for developing a heat-transfer correlation has been established for the fuel–assembly concept at supercritical pressure conditions. It is based on an analytical approach using the computational fluid dynamic tool and the ASSERT subchannel code to establish the heat transfer in supercritical pressure flow. Prior to the application, the computational fluid dynamic tool has been assessed against experimental heat transfer data at the pseudo-critical region obtained with bundle subassemblies to identify the appropriate turbulence model for use. Beyond the pseudo-critical region where the normal heat transfer behaviour is anticipated, the ASSERT subchannel code has also been assessed with appropriate closure relationships. Detailed information on the supporting experiments and preliminary assessment results of the ASSERT subchannel code are presented.

1. Introduction

Safety analyses are required to ensure safe operation during normal operation and abnormal operational occurrences for the Super-Critical Water-cooled Reactor (SCWR) concept. These analyses are the basis for designing or improving the safety system. System codes, such as CATHENA [1] or SCTRAN [2], are applied in safety analyses using the one-dimensional approach. These codes rely on supercritical heat-transfer correlations to predict the wall-to-coolant heat-transfer coefficient. As the calculation is one-dimensional, cross-sectional average flow conditions in the fuel assembly are applied. The calculation focuses on predicting the maximum cladding temperature, based on the minimum heat-transfer coefficient across the fuel assembly.

Since all current SCWR developments are still in the conceptual phase, it is pre-mature to perform full-scale experiments for the fuel assembly concepts (which will evolve through the engineering and final design phases for further enhancement and manufacturing feasibility). Tube-data-based correlations, such as the Dittus-Boelter correlation [3], have been applied in support of the development of the reactor core and safety system concepts. One of the major issues of this approach is the assumption that the supercritical heat transfer in fuel assemblies behaves the same as that in tubes at similar cross-sectional flow conditions and heat fluxes. In many cases, the assumption was shown inadequate (i.e., the supercritical heat transfer in a fuel assembly behaves differently from that in tubes). For example: the deteriorated heat transfer phenomena in tubes have not been observed in bundle subassemblies with

[1] CNL Internal Document #CW-120000-CONF-011 (Unrestricted)

spacing devices at similar flow conditions [4]. Based on the observations, the deteriorated heat transfer phenomena were not considered in fuel assembly analyses.

A fuel-assembly concept has been established for the Canadian SCWR concept. As discussed previously, experimental data on supercritical heat transfer are not available for this concept. A strategy has been established in developing the heat-transfer correlation for predicting the minimum heat transfer coefficient in the Canadian SCWR fuel-assembly concept. This paper presents the strategy, supporting experiments and preliminary assessment results of the ASSERT subchannel code.

2. Canadian SCWR Fuel Assembly Concept

The Canadian SCWR fuel assembly concept is a flask-like structure consisting of 64 fuel rods distributed in two rings around a central flow tube of 94-mm in outer diameter. Each fuel rod has an Alloy 800H clad containing mixed plutonium and thorium pellets over an active length of 5 metres. It is equipped with a large plenum to contain the fission gas and withstand any internal pressure increase. The outer diameter is 9.5 mm for fuel rods in the inner ring and is 10 mm for those in the outer ring. Spacing between fuel rods is maintained with wire-wrapped spacers, constructed with Alloy 800H. Figure 1 illustrates schematically the Canadian SCWR fuel assembly concept inside the fuel channel.

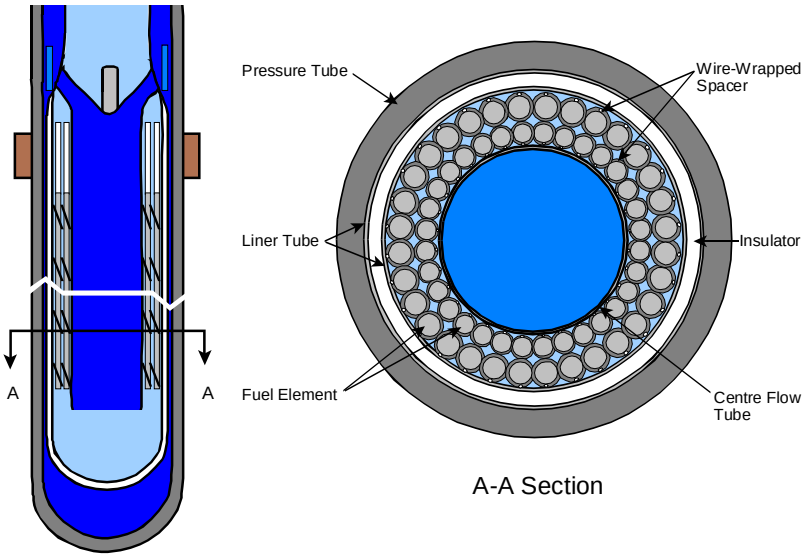

Figure 1: Schematic Diagram of the Canadian SCWR Fuel Assembly Concept inside the Fuel Channel.

The outer shell of the flask consists of a double wall containing an insulator, which is made of yttria stabilized zirconia. During normal operations, a small gap is present between the pressure tube and the external wall of the flask. Nevertheless, a small amount of heat loss (~2%) is anticipated from the coolant to the moderator through the insulator and the pressure tube. With raised temperature inside the flask during accident scenarios, the flask would expand closing the gap and could transfer substantial amount of heat from the fuel to the moderator (through the complex heat-transfer mechanism of radiation from the fuel to the inner wall of the flask, conduction from the inner wall to outer wall through the insulator, conduction from the outer wall through the pressure tube, and convection from the pressure tube to the moderator). The continuous heat transfer between the fuel assembly and the moderator would maintain the cladding temperature below the melting point and preserve the cladding integrity [5].

The top of the central flow tube consists of four nozzles guiding the inlet flow to enter the central flow tube from the pressure tube extension, which has a number of slot openings acting as orifices to control the amount of flow entering into each fuel channel. High-temperature coolant leaving the fuel bundle would travel across the nozzles and discharge into the outlet header.

The prediction of the maximum cladding temperature focuses mainly on the fuel-bundle region (see A-A section in Figure 1). It accounts mainly the clad-to-coolant heat transfer and does not include heat transfer from the coolant to the moderator, which is calculated separately.

3. Approach in Developing a Super-Critical Heat-Transfer Correlation for Canadian SCWR Fuel Assembly Concept

Owing to the fact that experimental data are unavailable for the Canadian SCWR fuel assembly concept, an analytical approach is applied to establish the minimum heat transfer coefficient for predicting the maximum cladding temperature in safety analyses. It is mainly based on predictions of the ASSERT subchannel code for the fuel-assembly concept. The Star CCM+ computational fluid dynamics (CFD) tool is applied to determine whether deteriorated heat transfer is present at the vicinity of the pseudo-critical point at flow conditions of interest.

Figure 2 illustrates the rod and subchannel numbering systems adopted in the ASSERT subchannel code. The central flow tube is considered as an unfuelled rod with no heat generation (gamma heating is anticipated to be small and hence is not included in the calculation). That is why the rod numbering system starts from “2” for a rod in the inner ring and ends at “65” for the rod in the outer ring. Furthermore, there is no heat transfer between the coolant in the fuel bundle and that in the flow tube. The flow area of the fuel assembly concept is subdivided into 96 subchannels. Local subchannel flow conditions (i.e., pressure, mass flux, and enthalpy or bulk fluid temperature) and heat flux are calculated and applied in determining the cladding temperature.

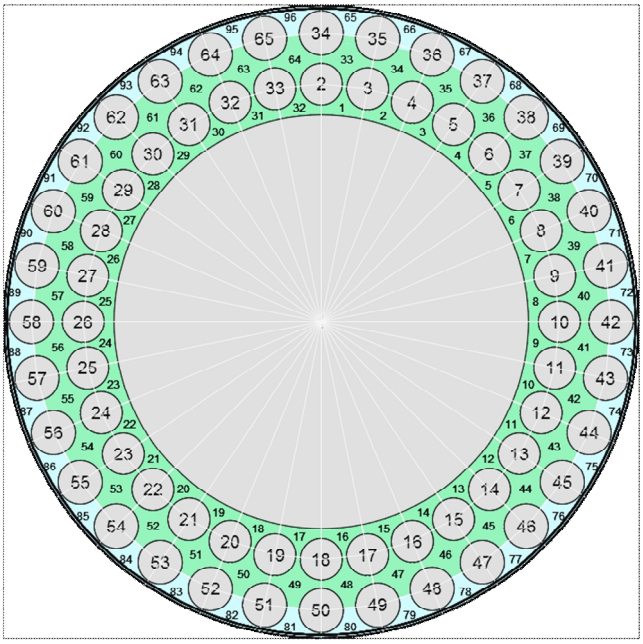

Figure 2: Rod and Subchannel Numbering Systems for ASSERT Subchannel Code Applications.

Prior to applying the analytical tools, the ASSERT subchannel code and Star-CCM+ CFD tool have been assessed against experimental heat transfer data obtained with bundle subassemblies. The ASSERT subchannel code is assessed for its applicability at the normal heat-transfer regimes. Improved subchannel turbulence-mixing models and correlations for subchannel heat-transfer coefficient have been implemented into the ASSERT subchannel code in support of the analysis. The Star-CCM+ CFD tool is

assessed for its applicability in capturing the deteriorated heat transfer phenomena at the vicinity of the pseudo-critical temperature. Sensitivity analyses of turbulence model are performed to identify the appropriate model for use.

4. Supercritical Heat Transfer Experiments

Heat-transfer experiments were performed with supercritical water through a 2×2 bundle to provide circumferential wall-temperature measurements around the heated rods. These experiments consisted of two phases: the first phase focused on the bundle configuration with no spacing device (i.e., bare bundle) [6] and the second phase on the bundle configuration with the wrapped-wire spacers. Figure 3 illustrates the overall configuration of the test section geometry. The test section in the heated region consisted of an outer unheated stainless steel tube with an internal diameter (ID) of 30 mm, which served as the pressure boundary. Insulation was attached to the outer tube to minimize heat loss to the environment. A ceramic insulator having a square internal flow area of 20.32×20.32 mm^2 was installed inside the outer tube to isolate electrically the heated bundle. Corners of the square flow area were rounded to maintain uniform gap sizes with the heated rods. The 2×2 rod bundle consisted of four stainless-steel (SS-304) tubes, each having an outer diameter (OD) of 8 mm and a wall thickness of 1.5 mm. Each end of the four tubes was plated with a silver coating for electric conduction; the middle region of the tube was not plated resulting in a heated section of 600 mm. The gap between adjacent heated rods was maintained at 1.44 mm, and the gap between the heated rod and the rounded corners of the ceramic insulator was also maintained at 1.44 mm. Two grid spacers, having the same outer dimensions as the ceramic insulator, were installed just outside the heated section of the bundle to maintain the gap size between the heated rod and the ceramic insulator.

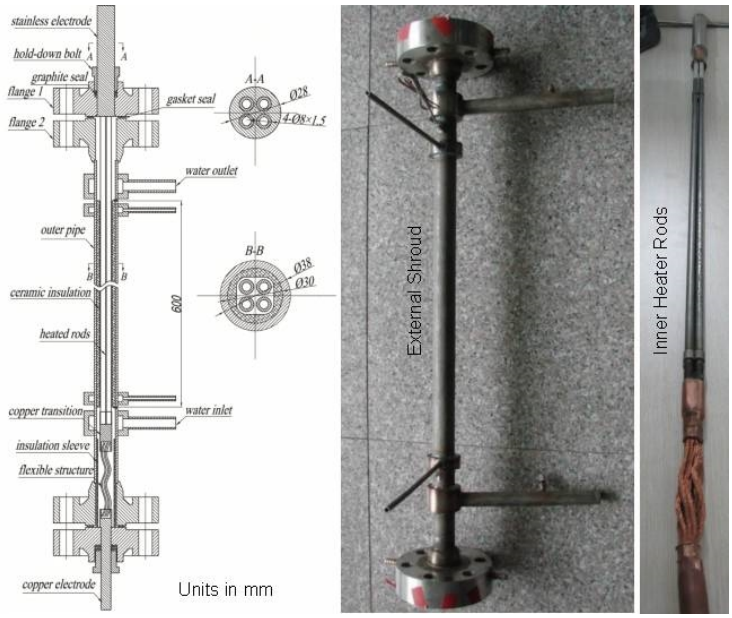

Figure 3: 2x2 Bundle Test-Section Configuration

In the Phase-I test, no spacer was installed over the heated section, but the tubes were spot-welded together at two locations to eliminate vibration when applying the AC current (see Figure 4 for the weld locations). The welds were smooth and small and hence have little interferences to the flow and the wall temperature measurements. In Phase-II test, stainless-steel (SS-304) wire-wrapped spacers of 1.2-mm outer diameter were attached to the outer surface of the heated rods at a pitch of 200 mm.

Wall-temperature measurements were obtained on two of the four heated tubes in the Phase-I test and on all four heated tubes in the Phase-II test. Moveable thermocouples were inserted inside Rod 1 in the Phase-I test and Rod 1 and Rod 3 in the Phase-II test. Fixed thermocouples were installed inside Rod 2 in the Phase-I test and Rod 2 and Rod 4 in the Phase-II test. Figure 4 identifies the five locations (100-mm apart) covered by the moveable thermocouples along the heated tube. The moveable-thermocouples unit consisted of a probe carrying four standard NiCr-NiSi thermocouples (each wire with a 0.2-mm OD) with a circumferential interval of 90°. It was connected to a drive-assembly unit, which could move the probe axially and rotate the probe circumferentially inside the heated tube. At each location, the probe was rotated four times at an interval of 22.5° to measure the inner-wall temperatures (i.e., sixteen wall-temperature measurements along the circumference but only eight angular positions at 45° interval are shown for one rod in the figure). Four fixed thermocouples were attached in a plane at 90° apart and inserted inside the other heated tube at the last measuring point (i.e., mp-5) covered by the moveable thermocouples (see Figure 4). These fixed thermocouples provided confirmatory measurements to the moveable thermocouples ensuring relatively consistent readings for all heated tubes.

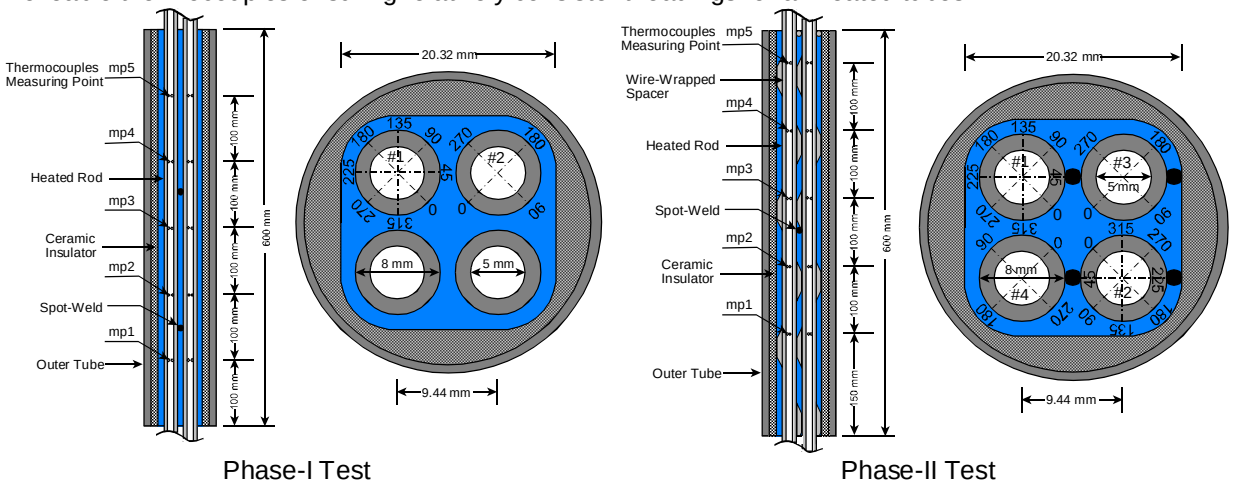

Figure 4: Thermocouple Measuring Points and Cross-Sectional Geometry of Flow Channel

Figure 5 illustrates the circumferential wall-temperature distributions around the heated tubes obtained from the Phase-I test at the pressure (P) of 25 MPa, mass flux (G) of 1000 kg/m^{2}s, surface heat flux (q) of 400 kW/m^2, and inlet-fluid temperature (t_{in}) of 417 °C (well beyond the pseudo-critical point). The presented wall temperatures correspond to the outer-surface values calculated from the inner-surface measurements obtained at the fifth thermocouple measuring point (mp-5). Wall temperatures at the corner region (around 180°) are higher than those at other regions. The increase in wall temperature at the corner region is attributed to the small gap with low flows and high enthalpies lowering the heat-transfer coefficient. The temperature gradient between the corner and the centre subchannel (where the lowest temperature is observed) regions is about 9 °C. This signifies that the wall temperature at the corner region increases more rapidly than that at the centre subchannel region. Overall, the temperature variations from 0°-180° and from 180°-360° are relatively symmetrical. This signifies no tilting or bowing on the heated rod at this location. Measurements are similar between moveable and fixed thermocouples.

Figure 6 illustrates the circumferential wall-temperature distributions around the heated tube obtained from the Phase-I test at the pressure (P) of 25 MPa, mass flux (G) of 1000 kg/m^{2}s, surface heat flux (q) of 600 kW/m^2, and inlet-fluid temperature (t_{in}) of 397 °C (beyond the pseudo-critical point). Wall temperatures at the corner region (around 180°) of Rod 1 remain higher than those at other regions. On the other hand, the peak temperature of Rod 2 was observed at 225°, where the wire-wrapped spacer was located at the axial location. The temperature at round 225° could be attributed to the effect of the wire-wrap that significantly reduces flow at that particular location or a detached wire-wrap there, as the worst case scenario. Similarly, an increase in wall temperature was observed at locations of the wire-

wrapped spacer in Rod 1 and Rod 2 (at 45°). As a result, the circumferential wall temperature distributions are asymmetrical at regions before and beyond the 180° narrow gap. Compared to measurements obtained with the no-wire bundle, the wall temperatures are generally lower in the wire-wrapped bundle than in the no-wire bundle, except at the wire locations where the wall temperature of the wire-wrapped bundle can be higher than that of the no-wire bundle. The peak temperature for the no-wire bundle, however, remains higher than that for the wire-wrapped bundle.

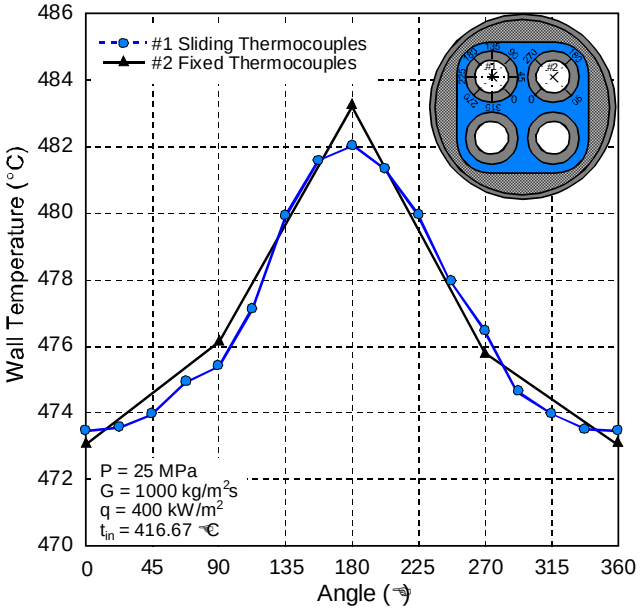

Figure 5: Circumferential Wall-Temperature Distributions obtained from the Phase-I Test

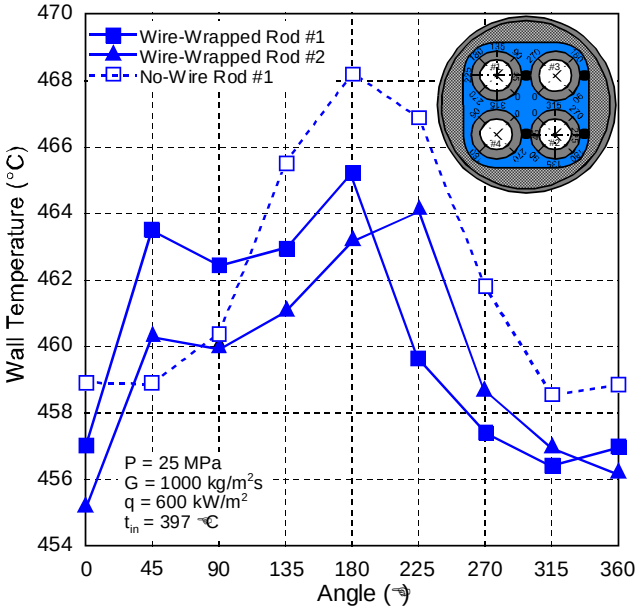

Figure 6: Circumferential Wall-Temperature Distributions obtained from the Phase-II Test

5. Assessment of ASSERT Subchannel Code in Predicting Wall-Temperature Distributions in the 2x2 Bundle

As indicated above, the prediction capability of the ASSERT subchannel code was assessed against the experimental wall-temperature distributions obtained with the 2x2 bundle. The subchannel code ASSERT-PV v3r1m2, applied in this assessment, is an extended ASSERT-PV version [7]-[9] specifically developed for modelling subchannel flow and heat transfer in fuel bundles under steady-state supercritical conditions.

Table 1 lists the models and correlations used in the subchannel analysis. Many friction-factor correlations were suggested for supercritical pressure flow [10]. However, most of these correlations do not take into account roughness effects and hence may only be valid for the specific test section (or roughness). None of these correlations have been assessed against recent experimental data and hence their applicability remains uncertain. The Colebrook-White equation, which takes into the account of the roughness effect, was selected in the analysis. In most cases, the differences in friction factor predictions are relatively small between various correlations.

Table 1: ASSERT-PV v3r1m2 Model Options

Model	Description
Fluid	Water at supercritical conditions
Gravity term	Include gravity terms
Wall friction	Colebrook-White formula for turbulent friction.
Turbulent mixing	Rheme correlation of inter-subchannel turbulent mixing as recommended in [9].
Element-to-coolant heat transfer	Jackson correlation for supercritical pressure conditions.
Appendages/Spacers	Bare bundle, no appendages or wire wrap modeled.

The cross-flow mixing correlation has been recommended for fuel-bundle analyses at subcritical pressures [11]. Zhang et al. [12] developed mixing correlations for various subchannel configurations at supercritical pressures using the FLUENT computational fluid dynamics tool. These correlations have not yet been assessed against experimental data and hence have not been implemented.

Zahlan et al. [13] assessed a large number of heat-transfer correlations against the experimental databank for supercritical-pressure water flow in vertical tubes. They observed good overall prediction accuracy for the correlation developed by Mokry et al. [14]. However, the correlation by Mokry et al. [14] tends to underestimate the heat-transfer coefficients for small-diameter (less than 10 mm) tubes, which are similar to the hydraulics diameters of subchannels in the fuel-bundle concept. The correlation developed by Jackson [15], on the other hand, provides reasonable predictions of heat-transfer coefficient for small-diameter tubes. It has also been shown applicable for annuli of 4 and 6 mm hydraulic diameters [16]. Therefore, the correlation developed by Jackson [15] has been applied in the current analysis.

At this point, the ASSERT code is not equipped with a prediction method for the enhancement effect of the wire-wrapped spacer on supercritical heat transfer. Therefore, the analysis considered only the bundle without the wire-wrapped spacers (i.e., bare rods). Previous experimental and analytical studies showed enhancement of heat transfer at supercritical flow conditions for channels equipped with wire-wrapped spacers [17]-[19]. However, the magnitude of the enhancement depends on the channel configuration and the wire geometry and pitch.

The geometry of the 2x2 bundle does not resemble closely the 64-rod fuel assembly for the Canadian SCWR concept. However, it is similar to the 1/16 symmetry of the fuel assembly (i.e., considering only

Rods 2, 3, 34 and 35 in Figure 2). Therefore, these data are relevant for assessing the prediction capability of the ASSERT subchannel code.

Figure 7 compares the ASSERT preliminary predictions of wall temperature against the measurements at the same flow conditions as listed in Figure 5. The bulk-fluid temperature at the measuring point is about 431 °C, which corresponds to the supercritical region (above the pseudo-critical point). The ASSERT code captures the wall temperature distribution but overpredicts the wall temperature at the narrow-gap region (i.e., 180°) and underpredicts the wall temperature by about 2 °C at the subchannel region (i.e., 0°). The differences are partly attributed to the neglect of the conduction heat transfer through the heated wall. Including the conduction heat transfer around the circumference of the heated wall would lower the wall temperature prediction at the narrow-gap region and raise the wall temperature predictions at subchannels of the 90° and 270° positions.

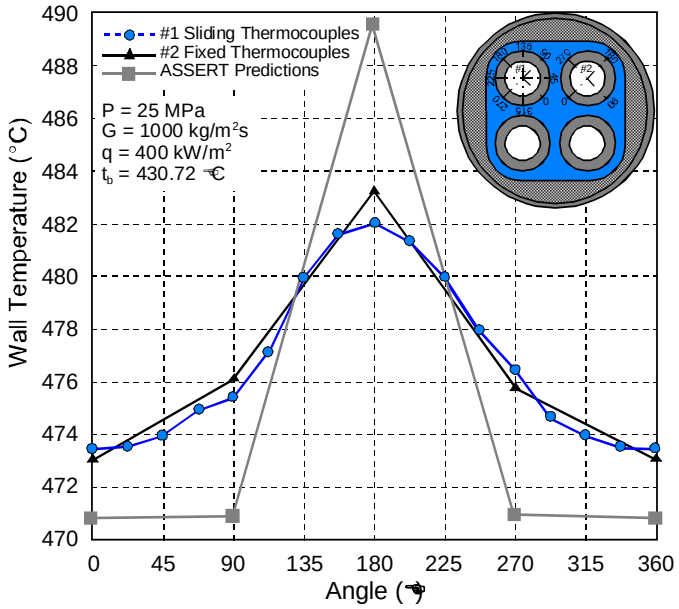

Figure 7: ASSERT Predictions of Circumferential Wall-Temperature Distributions at Supercritical Temperature

Figure 8 compares the ASSERT preliminary predictions of wall temperature against the measurements at the same pressure, mass flux and heat flux but the bulk-fluid temperature at the measuring point is about 384 °C, which is near the pseudo-critical temperature. The ASSERT code predicts the wall temperature at the central subchannel accurately, but underpredicts the wall temperatures at other locations. However, the difference is small (about 1.5 °C only). The temperature gradient between the narrow gap and central subchannel regions is about 5 °C. The impact of neglecting the conduction heat transfer around the heated wall is relatively small for this small temperature difference.

Figure 9 compares the ASSERT preliminary predictions of wall temperature against the measurements at the subcritical bulk-fluid temperature (about 241 °C). Similar to the supercritical temperature case, the ASSERT code overpredicts the wall temperature by about 1 °C at the narrow-gap region and underpredicts the wall temperature at the subchannel region. The temperature gradient between the narrow gap and central subchannel regions is about 9 °C. The impact of neglecting the conduction heat transfer around the heated wall would be significant on the wall temperature predictions.

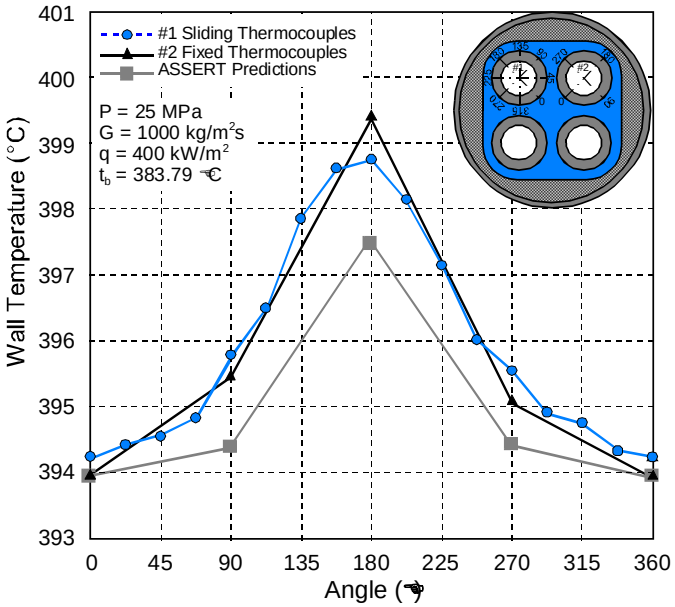

Figure 8: ASSERT Predictions of Circumferential Wall-Temperature Distributions near Pseudo-Critical Temperature

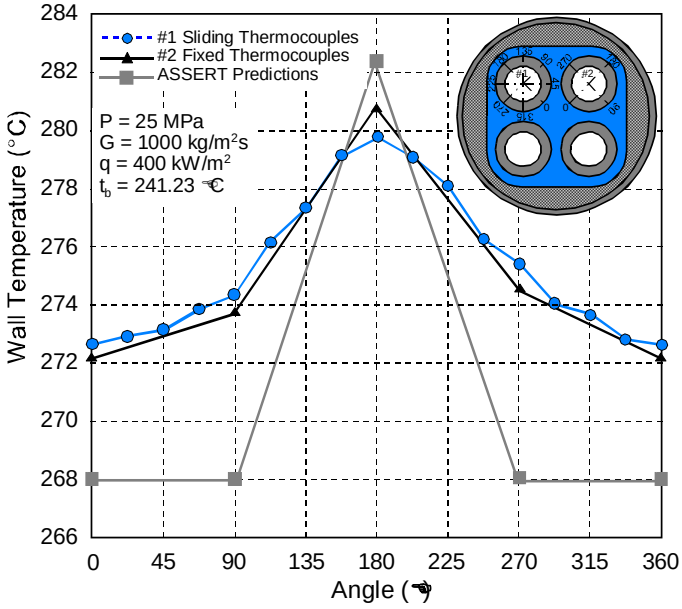

Figure 9: ASSERT Predictions of Circumferential Wall-Temperature Distributions at Subcritical Temperature

6. Conclusions

- A strategy has been established in developing a correlation for predicting the minimum heat-transfer coefficient in the Canadian SCWR fuel assembly concept. It is based on the analytical approach using the ASSERT subchannel code coupled with the Star-CCM+ CFD tool in determining the deteriorated heat-transfer regime.
- Prior to applying the analytical tools to calculate the heat-transfer coefficient in the fuel assembly concept, the prediction capability of the analytical tools were assessed against wall-temperature measurements obtained with a 2x2 bundle in supercritical water flow.
- Wall-temperature measurements obtained with the bare bundle exhibited a symmetrical variation before and beyond the narrow-gap region, where the peak temperature was observed. Those obtained with the wire-wrapped bundle exhibited asymmetrical variation before and beyond the narrow-gap region, and is attributed to the presence of the wire-wrapped spacer, which exhibits a temperature increase under the wire. Overall, the peak wall temperature measurements for the wire-wrapped bundle are lower than those for the bare bundle.
- Preliminary ASSERT predictions of wall temperature were compared against the measurements. The ASSERT captured the trend of the measurements, but tend to overpredict the temperature at the narrow-gap region and underpredict the temperature at the subchannel regions. This is attributed to the neglect of the conduction heat transfer around the heated wall. Improvement in prediction accuracy is anticipated after incorporating the conduction heat transfer model.

7. References

[1] D.F. Wang and S. Wang, “A CATHENA Model of the Canadian SCWR Concept for Safety Analysis”, Proc. 6th International Symposium on Supercritical Water-Cooled Reactors (ISSCWR-6), Shenzhen, Guangdong, China, March 3-7, 2013.

[2] P. Wu, J. Gou, J. Shan, Y. Jiang, J. Yang and B. Zhang, “Safety analysis code SCTRAN development for SCWR and its application to CGNPC SCWR”, Annals of Nuclear Energy, Vol. 56, pp. 122-135, 2013.

[3] F.W. Dittus and L.M.K. Boelter, “Heat transfer in automobile radiators of the tubular type”, University of California - Publications in Engineering, Vol. 2, No. 13, pp. 443-461, 1930.

[4] H. Mori, T. Kaida, M. Ohno, et al., “Heat transfer to a supercritical pressure fluid flowing in sub-bundle channels”, Journal of Nuclear Science and Technology, Vol. 49, pp. 373-383, 2012.

[5] J. Licht and R. Xu, “Preliminary No-core Melt Assessment for the High Efficiency Channel Preconceptual Design”, Proc. 3rd China-Canada Joint Workshop on Supercritical-Water-Cooled Reactors (CCSC-2012), Xi'an, China, April 18-20, 2012.

[6] Wang, H., Bi, Q., Wang, L., Lv, H., and Leung, L.K.H., “Experimental Investigation of Heat Transfer from a 2×2 Rod Bundle to Supercritical Pressure Water”, Nuclear Engineering Design, Vol. 275, pp. 205–218, (2014).

[7] M.B. Carver, J.C. Kiteley, A. Tahir, A.O. Banas and D.S. Rowe, “Simulation of Flow and Phase Distribution in Vertical and Horizontal Bundles using the ASSERT Subchannel Code”, Nuclear Engineering and Design, Vol. 122, pp. 413-424, 1990.

[8] Y.F. Rao and N. Hammouda, “Recent Development in ASSERT-PV Code for Subchannel Thermalhydraulics”, Proc. 8th CNS Int. Conf. on CANDU Fuel, Honey Harbor, Ontario, 2003.

[9] Y.F. Rao, Z. Cheng, G.M. Waddington and A. Nava-Dominguez, “ASSERT-PV 3.2: Advanced Subchannel Thermalhydraulics Code for CANDU Fuel Bundles”, Nuclear Engineering and Design, Vol. 275, pp. 69-79, 2014.

[10] I.L. Pioro and R.B. Duffey, “Heat Transfer and Hydraulic Resistance at Supercritical Pressures in Power Engineering Applications” ASME Press, New York, USA, Chapter 4 and 9, 2007.

[11] L.N. Carlucci, N. Hammouda and D.S. Rowe, “Two-Phase Turbulent Mixing and Buoyancy Drift in Rod Bundles,” Nuclear Engineering and Design, Vol. 227, pp. 65-84, 2004.

[12] B. Zhang, J. Shan and J. Jiang, “Turbulent Mixing Model Applicable To Supercritical Condition”, Proc. 5th International Symposium of Super-Critical Water-cooled Reactors (ISSCWR-5), Paper P43, Vancouver, British Columbia, Canada, March 13-16, 2011.

[13] H. Zahlan, D.C. Groeneveld, S. Tavoularis, S. Mokry and I. Pioro, “Assessment of Supercritical Heat Transfer Prediction Methods”, Proc. 5th International Symposium of Super-Critical Water-cooled Reactors (ISSCWR-5), Paper P8, Vancouver, British Columbia, Canada, March 13-16, 2011.

[14] S. Mokry, Ye. Gospodinov, I. Pioro and P. Kirillov, “Supercritical water heat-transfer correlation for vertical bare tubes”, Proc. 17th International Conference on Nuclear Engineering (ICONE-17), Brussels, Belgium, July 12-16, Paper # 76010, 2009.

[15] J. D. Jackson, “Consideration of the heat transfer properties of supercritical pressure water in connection with the cooling of advanced nuclear reactors”, Proc. 13th Pacific Basin Nuclear Conference, Shenzhen, China, 2002.

[16] G. Wu, Q. Bi, Z. Yang, H. Wang, X. Zhu, H. Hao and L.K.H. Leung, “Experimental Investigation of Heat Transfer for Supercritical Pressure Water Flowing in Vertical Annular Channels”, Nuclear Engineering Design, Vol. 241, Issue 9, pp. 4045-4054, 2011.

[17] Y.-Y. Bae, H.-Y. Kim and T.-H. Yoo, “Effect of a helical wire on mixed convection heat transfer to carbon dioxide in a vertical circular tube at supercritical pressures”, International Journal of Heat and Fluid Flow, Vol. 32, No., 1, pp. 340-351, 2011.

[18] H. Wang, Q. Bi, L. Wang, H. Lv and L.K.H. Leung, “Experimental Investigation of Heat Transfer from a 2×2 Rod Bundle to Supercritical Pressure Water”, Nuclear Engineering and Design, Vol. 275, pp. 205–218, 2014.

[19] K. Podila and Y.F. Rao, “Assessment of CFD for the Canadian SCWR Bundle with Wire Wraps”, Progress in Nuclear Energy, Vol. 77, pp. 373-380, 2014.

ISSCWR7-2032

Experimental study of choking water flow across sharp edged orifices at supercritical pressures

Alberto Teyssedou, Altan Muftuoglu and Akila Hidouche
Polytechnique Montréal / Department of Engineering Physics
2500, chemin de Polytechnique, Montreal University Campus,
Québec, H3T 1J4, Canada
1 514 3404711 x 4522, alberto.teyssedou@polymtl.ca

Abstract

Supercritical Water Cooled Nuclear Reactors (SCWR) will operate at coolant conditions close to 25 *MPa* and outlet temperatures ranging from 500 to 625°*C.* Using pressures higher than critical values limits the occurrence of Critical Heat Flux (CHF.) Furthermore, the higher outlet flow enthalpy will increase the overall plant efficiency by up to 18 points of percentage. However, the thermal-hydraulic behavior of supercritical water are not fully known, i.e. pressure drop, the deterioration of forced convection heat transfer, critical (choked) and blow down flow rate. In particular, the knowledge of critical discharge of supercritical fluids is mandatory to perform future nuclear reactor safety analyses. Nevertheless, existing choked flow data have been collected from experiments at atmospheric discharge pressure conditions and in most cases using fluids different than water. Therefore, a supercritical water test facility has been built at Polytechnique Montreal. This equipment is used to collect choking flow data with 1.0 mm and 1.395 mm diameter sharp edged orifices. The critical mass flux is presented as a function of the temperature difference between the pseudo critical value and the bulk fluid temperature. This representation allows us to compare similar experiments performed not only with different orifices but also using fluids different than water. For both type of orifices, the data show that choking flow occurs above a given fluid temperature. Furthermore, at choking flow conditions the mass flux seems to be independent of the orifice size. This provides indications that at supercritical conditions the mass velocity is thermodynamically self-determined.

1. Introduction

Future SCWRs will operate at a coolant pressure close to 25 MPa and at outlet temperatures ranging from 500° C to 625° C, i.e. above the critical pressure and temperature of the water (22.06 MPa and 373.95° C, respectively.) [1] Using coolant pressures higher than critical values avoid boiling and eventual occurrence of CHF. Among other advantages such as fuel economy and plant engineering simplifications, it is estimated that the future SCWR technology must also permit overall nuclear plant efficiencies of around 48 % to be achieved. Furthermore, for a given thermal power the coolant mass flow rate decreases with increasing the outlet enthalpy; consequently, the water inventory of SCWRs will be low and will require less pump power as compared to actual power reactors. The reactor operation above critical water pressure conditions will eliminate water-steam phase change, which should simplify reactor's design (e.g. remove steam generators and moisture separators.)

Besides the aforementioned advantages of SCWRs, some fundamental aspects must be further studied to completely fulfil necessary technical requirements. For instance, the thermal-hydraulic behavior of future nuclear fuel channels can be very sensitive to both the coolant pressure drop and the heat transfer along fuel bundles. In fact, very limited information exists in the open literature concerning supercritical water frictional pressure drop; therefore, additional experiments are mandatory. Moreover, due to the fast change in fluid properties occurring around pseudo-critical conditions, most of the existing correlations are not able to satisfactorily reproduce the experimental trends. It has been observed that a significant decrease on fluid thermal capacity occurring beyond the critical point causes deterioration on forced convective heat transfer conditions. [2] Consequently, for high heat fluxes, such a situation may compromise the integrity of the nuclear fuel.

In particular, since SCWRs will use reduced coolant inventories, the prediction of flow behavior during a loss of coolant accident becomes fundamental for the correct estimation of core depressurization during transients. It is obvious that understanding the physics behind these problems is crucial to perform reactor safety analyses and to design hydraulic components and safety relief mechanisms. Therefore, from a safety view point, experimental and analytical studies are still necessary to estimate the discharge of supercritical water during an anticipated transient event and during the eventual occurrence of pipe breaks. Up to now, existing discharge flow data have been collected from experiments at atmospheric discharge pressure conditions and in some cases by using working fluids different than water. [3-4] It must be pointed out that keeping the discharge pressure at a unique value (i.e. close to the atmospheric pressure) makes it very difficult to determine whether or not the flow reaches the speed of sound. To overcome some of these drawbacks, herewith we present choking flow experiments performed with water at supercritical conditions and for different constant values of the discharge pressures. The results obtained with two test sections having different orifice sizes are discussed in detail and the data are compared with the predictions of both the Homogeneous Equilibrium Model (HEQ) and the Modified-Homogeneous Equilibrium Model (M-HEM) proposed by Chen et al.[5]

2. The Experimental Facility

To determine whether or not the flow reaches choking conditions (i.e. the speed of sound), it is necessary to change the discharge pressure while maintaining all other flow variables constant. [6,7] Thus, the experimental facility used to this purpose consists of a supercritical water loop connected in parallel with a medium-pressure steam-water loop via a test section. The proposed hydraulic arrangement is schematically illustrated in Fig. 1a and the flow diagram of the supercritical water branch is shown in Fig. 1b. As indicated in these figures, the medium-pressure loop has a thermal power capacity of 200 kW, which is necessary to produce the amount of steam required to obtain a desired value of the discharge pressure (downstream of the test section.) Hence, this loop allows us to control this pressure at will within the range of 0.1 to up to 4 MPa. The supercritical portion of the facility (Fig. 1b) permits supercritical water conditions to be achieved and carefully controlled. It consists of heat exchangers, a water filter, a six piston reciprocating pump, a pulsating damper, a heater element where supercritical water

conditions are achieved, a calming chamber, a test section and a quenching chamber. Other components are used to measure and control the desired flow operation conditions such as pneumatic valves, pressure transducers, thermocouples, flow meters, etc. It is important to mention that both systems share the same working fluid, i.e. distilled and demineralized water without chemical treatment.

The discharge pressure, which can be adjusted between 0.1 MPa to 4.0 MPa, is controlled by the medium-pressure steam-water loop; therefore, the water temperature at the inlet of the reciprocating pump can be much higher than the maximum allowable value of 65^{o}C, as recommended by the pump manufacturer. Therefore, a set of dual tube heat exchangers are used to bring the inlet coolant temperature below the recommended value.

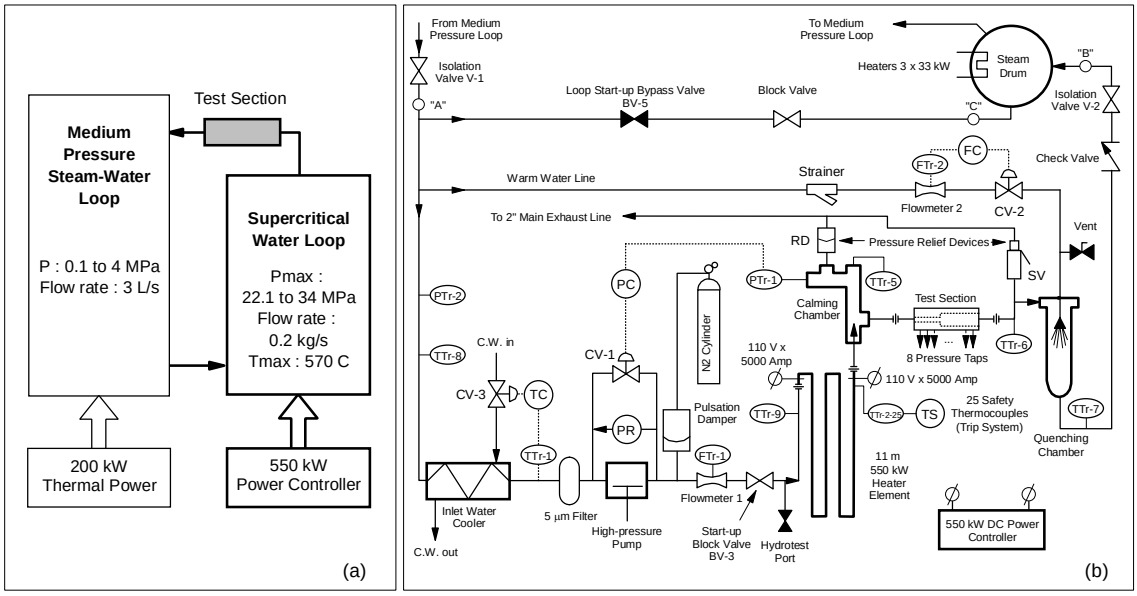

Figure 1. a) Schematic of the parallel hydraulic arrangement; b) Flow diagram of the supercritical-water system.

In order to protect the system from the presence of solid particles bigger than 5 μm dispersed in the water, a glass fiber filter is installed at the inlet of the high-pressure pump. Furthermore, it is well known that positive displacement pumps tend to produce flow and pressure fluctuations. To damp eventual pressure oscillations and to avoid possible harmful effects during the experiments, a pulsation damper (Flowguard bladder style HG Series®) is installed at the outlet of the pump. The damper uses a counter balance nitrogen pressure of about 80% of the working pressure (Fig. 1b.) The results of the commissioning tests performed at different flow temperature conditions without and with the damper installed in the loop are given in: Muftuoglu & Teyssedou.[8] Hence, we have shown that the use of a damper for this kind of experiments is essential; it reduces the pressure pulsations below ±1 % of the pump absolute discharge pressure. Just after the pulsation damper, the water passes through a “Flow Technology” turbine-type flow meter. The accuracy of the flow measurement system, i.e. the flow meter, a frequency-to-current converter, an electronic linearizer and the data acquisition system, is better than 0.1 % of the readings. As shown in Fig. 1b, supercritical water conditions are reached in an 11.2 m long Hastelloy C-276 tubular heater element heated by Joule effect using a 550 kW DC power supply. The branches of the heater element are connected electrically in parallel and the electrical potential is applied to the end of each tube by using 5000 A nickel plated copper clamps and 0.01 mm thick 99.9% silver foils. The electrical connections are arranged in such a way that both inlet and outlet ends of the heater are at ground electrical potential. The applied thermal power is determined by measuring the electrical potential and the electrical current using three separate instruments, i.e. a 5000 A class 0.5 electrical shunt (Simpson®, 5000 A – 50 MV), a Hall effect 5000-LEM® unit and four 1500 A – 50 MV shunts, one for each branch. The heater is instrumented with 25 type-K, 0.8 mm ungrounded thermocouples that are spot welded at different axial and angular locations on the external wall of the tubes. Six additional thermocouples are installed at radial and axial locations

inside the thermal isolation jacket to estimate the heat losses. The instrumentation of the heater element is connected to the data acquisition and control system via galvanic isolation amplifiers. All thermocouples, including their entire electronics are calibrated with a precision of +/-0.5^{o} C of the reading, by using a calibration block from Thermoelectric® (TK Series Dry Block.)

Since supercritical fluids tend to stratify and form agglomerations [9,10], a calming chamber (Fig. 1b) is installed just upstream of the test section. Thus, inside the calming chamber the supercritical fluid is previously stirred before entering into the test section. This process avoids flow stratification and permits correct values of the mean fluid temperature and pressure to be measured (TTr-5 and PTr-1, respectively shown in Fig. 1b.) Before starting the experiments, the calibrations of all pressure transducers are verified using a pressure cell from Druck (DPI 602)®; in all the cases their accuracy is better than 0.1 % of the readings. All measurement and control devices are connected to a stand-alone NI CompactRIO® data acquisition system with an internal sampling time of 8 μs.

The experiments are carried out using two test section having a sharp edged orifice with internal diameters of 1.0 and 1.395 mm, respectively and the same thickness of 3.175 mm. The Fig. 2 shows the schematic of the test sections manufactured from a solid Hastelloy C-276 cylinder using the electro discharge method. The orifices are carefully measured before and after finishing the experiments with a precision higher than +/- 0.001 mm. As shown in this figure, both test sections are instrumented with three pressure taps located upstream and five located downstream of the orifice plate. To determine flow pressure profiles upstream and downstream of the orifice, the pressure taps are connected to four “Sensotec” 0.1 % full scale accuracy absolute pressure transducers. It must be pointed out that the measurement of the downstream pressure is mandatory to determine whether or not choking flow conditions are achieved during the experiments.

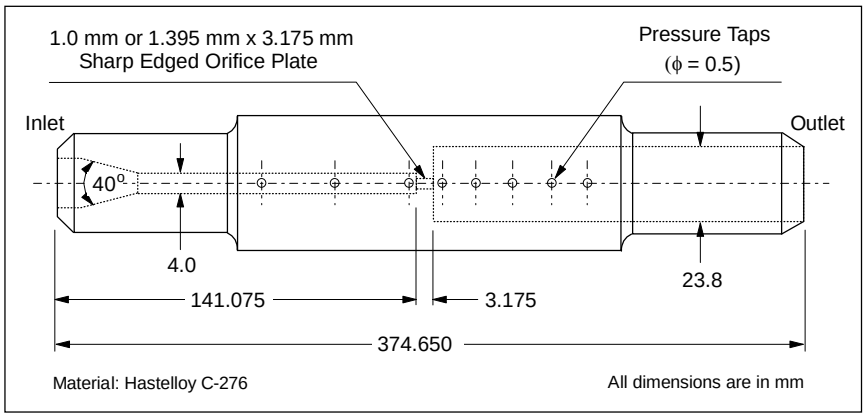

Figure 2. Schematic of the test sections used to perform the experiments.

The test sections are connected to both the supercritical and the medium-pressure loops using high-pressure Hastelloy C-276 Autoclave unions manufactured by Autoclave Engineering®. Before starting the experiments, the complete set-up, i.e. the test sections with their unions, are hydrostatically tested using oil at room temperature, but at a maximum pressure of 62 MPa.

3. Experimental Conditions and Procedures

Experiments were performed for a wide range of flow pressures and temperatures; Table 1 summarizes the experimental matrix covered during the collection of the data presented in this document. As shown in this table, at supercritical pressures, we are able to study a wide range of subcritical and supercritical flow temperatures. In particular, subcritical values can be very useful for designing nuclear safety components. As mentioned in the previous section, the medium-pressure steam-water loop is used as a low pressure-controlled reservoir in such a way that the discharge pressure can be changed and maintained constant at will, independently of the flow pressure prevailing upstream of the orifice. Therefore, most of the experiments included

in the Table 1, are repeated by changing the discharge pressure while maintaining all other flow parameters constant in the supercritical branch. Furthermore, in order to avoid corrosion due to the eventual presence of Oxygen in the loops, after each experiment they are shut-down and filled with compressed nitrogen. Consequently, before starting the experiments, the medium-pressure loop is run for a period of two to three hours at a pressure of 0.6 MPa. At this set-point, a degassing valve opens to the atmosphere to release non-condensable gases. Only after completing this process, the medium-pressure loop is controlled to a desired value of the discharge pressure. This procedure is also mandatory to eliminate, as much as possible, all detrimental loop pressure fluctuations.

Table 1. Experimental matrix covered using both test sections.

Collected Data Points	Upstream Pressure (MPa)	Upstream Temperature (^{o} C)	Discharge Pressure (MPa)
306	22.1 – 23.0	52 – 491	0.1 – 3.6
659	23.0 – 26.0	52 – 502	0.1 – 3.6
93	26.0 – 32.1	52 – 490	0.7 – 3.6

Subsequently, the experiments are performed by increasing slowly the pressure upstream of the orifice. The pressure in the calming chamber (Fig. 1b) is initially increased beyond the critical value before applying the thermal power to the heater element. This methodology is necessary to avoid the occurrence of CHF. For a given fluid pressure, a gradual increase of the power applied to the heater element permits its temperature to be increased at will. The use of two loops, allows the discharge pressure to be varied in small steps and thus, check whether or not the flow is choked. Hence, flow measurements permit us to establish the maximum allowable flow discharge which can be reached for a particular set of supercritical inlet water conditions.

During each experiment, the flow conditions both upstream and downstream of the orifice are maintained constant for several seconds before collecting the data. At subcritical temperature and supercritical pressure conditions, the upstream flow pressure is controlled within a band of ±0.01 MPa. However, for supercritical flow temperatures and pressures the control of the loop is very complex. [8] In turn, the discharge pressure is always controlled within a band of ±0.005 MPa for the entire range of subcritical and supercritical experimental conditions. Each experiment is systematically repeated three times; each record contains 100 measurements at 100 ms per reading. In addition, due to the complexity of this kind of experiments several video cameras are installed around the facility. This system permits us to survey the access to the laboratory as well as the correct operation of key mechanical components of the loops. This safety installation is connected to its own computer that is able to record any event, automatically triggered by a moving detector algorithm. [11]

4. Experimental Results

As shown in the Table 1, the data base contains 1058 points that have been collected using water flows at supercritical pressures and two test sections having different size orifices. As a common practice, the difference between the pseudo-critical temperature with respect to the fluid mean value (i.e. $\Delta T_{pc} = T_{pc} - T_f$) is used to treat the data. In this work, however, a new relationship proposed to estimate the pseudo-critical temperature, is given as: [8]

$$\begin{aligned} T_{pc} &= 3.719 \times P + 291.92 \quad 22.1 \le P < 26.0\ MPa \\ T_{pc} &= 3.306 \times P + 302.68 \quad 26.0 \le P < 31.1\ MPa \end{aligned} \tag{1}$$

It must be pointed out that this equation differs from a similar one proposed earlier by Lee & Swinnerton [12] and used by Chen et al. [5] In fact, it is observed that their correlation does not satisfy the definition of the pseudo-critical temperature. [2] Before using Equation 1 to treat the data, it was validated with values determined using the NIST Standard Reference Database 23. [13] The data presented in the Fig. 3 were collected for flow pressures ranging from 22.1 MPa to up to 32.1 MPa using the two test sections presented in Section 2. As indicated in the Table 1, for all these cases the discharge pressure was changed, step by step, from 0.1 MPa to up to 3.6 MPa. This figure shows the effect of the upstream flow pressure and temperature, as well as the size of the orifice on the mass flux. In particular, for flow temperatures lower than the pseudo-critical value and for both orifice sizes, choking flow seems to be triggered within a very limited region. Note that for the 1.395 mm orifice, the maximum design pressure of the supercritical water loop limits us to collect data above $\Delta T_{pc} > 100^{o}$ C. In the same figure we compare our experimental results with those presented by Chen et al. [5] for a 1.41 mm sharp nozzle very similar to our test sections.

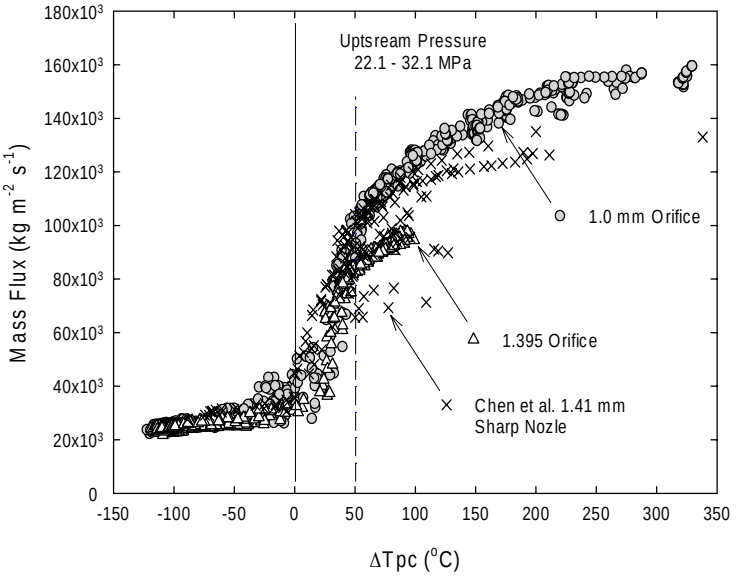

Figure 3. Supercritical water data collected using two orifice sizes.

As shown in this figure, close to the pseudo-critical temperature ($\Delta T_{pc} \approx 0$), our experiments provide data in a region where up to now, are very scarce. This lack of information can be explained by the fact that collecting data close to the pseudo-critical conditions is not an easy task. Approaching the pseudo-critical state with $\Delta T_{pc} > 0$ the heat capacity at constant pressure increases very rapidly while the mass density decreases. Consequently, in this region, the convective heat transfer increases very fast even though the mass flow rate decreases. Subsequently, when pseudo-critical conditions are reached, the difference between the inner wall temperature of the heater element and the fluid bulk temperature decreases in a very noticeably way. This increase in the heat transfer results in a quite fast increase in the fluid temperature, which triggers an unstable condition because the fluid density decreases with increasing the temperature and thus, the flow pressure increases quite rapidly. In particular, around these flow conditions, a voluntary reduction in the mass flow rate (i.e. by controlling the speed of the HP pump shown in Fig. 1) is not able to compensate the increase in the flow pressure. This particular transient behavior is clearly shown by the typical time record presented in Fig. 4. Over passing the pseudo-critical temperature ($\Delta T_{pc} < 0$), the heat capacity at constant pressure starts decreasing quite fast, which triggers a noticeably decrease in the convective heat transfer. Therefore, in this region, the critical mass flux continues to decrease while the temperature difference between the wall and the fluid increases, which increases the fluid density and decreases the flow pressure. The complex interaction between these thermal-hydraulic phenomena, makes the control of the desired fluid pressure to be extremely awkward. In parallel, for safety reasons, the maximum allowable wall temperature of Hastelloy C-276 tubing must also be respected along this process. This is clearly indicated by the reduction of the thermal power

shown in the Fig. 4. Therefore, due to the extreme difficulty of controlling the flow conditions close to the pseudo-critical state, the measured fluid pressures and temperatures may shift by about 0.5 % with respect to the desired values. This is the reason that explain the high dispersion of the data observed close to the pseudo critical thermodynamic state.

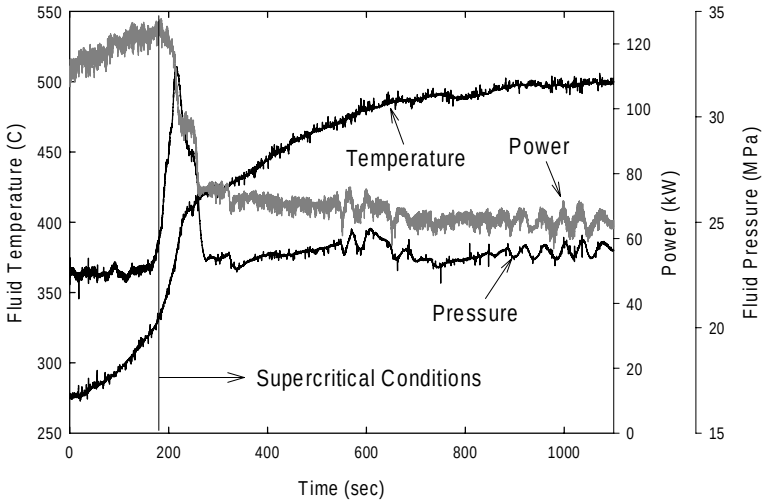

Figure 4. Typical time record of an experiment carried out with a 1 mm orifice.

The experimental results presented in Fig. 3 also show that for both orifice sizes, the mass flux decreases monotonically with increasing the fluid temperature. Similar observations were also reported in the literature for both subcritical and supercritical flow conditions. [3-5,12] It is interesting to note that for $\Delta T_{pc} \leq 50^{o}$ C the data collected with both test sections tend to overlap. This observation does not only provide a strong comprehension about the flow conditions that bring about choking flow, but also indicates that at supercritical conditions the mass velocity seems to be thermodynamically self-determined. Nevertheless, for a 1 mm orifice we have already determined that choking flow seems to occurs before this temperature difference, i.e. for $\Delta T_{pc} \leq 67^{o}$ C. [8] Starting from these values, i.e. $\Delta T_{pc} \leq 50^{o}$ C for a 1.395 mm orifice and $\Delta T_{pc} \leq 67^{o}$ C for a 1.0 mm orifice, the fluid velocity reaches quite rapidly the speed of sound. Since both, the fluid density and the speed of sound decrease with temperature explains the rapid decrease on the mass flux observed in this region (Fig. 3.) Instead, for $\Delta T_{pc} \leq 0^{o}$ C the speed of sound starts increasing at a much lower pace while the fluid density continues to decrease very slowly with increasing the fluid temperature. Thus, when choking flow conditions are well established; this thermodynamic behavior explains the experimental trend shown in the Fig. 3.

Within this framework, most experimental data given in the open literature, have been obtained from blow-down tests at a single atmospheric discharge pressure; therefore, it is difficult to determine whether or not they satisfy choking conditions. In our case, the flow is discharged inside a very long 25.4 mm ID straight pipe (Fig. 1) under different discharge pressure conditions (Table 1.) Thus, for different discharge pressures, Fig. 5 shows the pressure distributions and the mass fluxes obtained for typical supercritical water experiments performed with the 1 mm ID orifice. For each flow conditions several data values are collected at different time intervals; they appear superimposed in the Fig. 5a. Upstream from the orifice a very small pressure drop occurs; however, its slight value makes it very difficult to be observed in the figure. Even though a scattering of about +/- 0.4 MPa is perceived in the data, the aforementioned decrease in pressure occurs systematically, but it is not affected by the discharge flow conditions. Downstream of the orifice a systematic increase in the pressure profiles occurs. It is quite possible that these changes are due to a partial recovery of the reversible component of the pressure drop in this region. Furthermore, Fig. 5b shows the mass fluxes obtained by maintaining the upstream flow conditions constant and by increasing the discharge pressure. It must be pointed out that for each discharge pressure there are several points that appear completely overlapped in the figure. Moreover, we were unable to find any particular correlation between the flow conditions and the scattering of the data observed around a discharge pressure of

1.5 MPa. Therefore, from these results it is apparent that increasing the discharge pressure does not affect the mass flux. This provides a good indication that under the specified flow conditions choking flows are achieved. It must be pointed out that the same behavior is also observed for the data collected with a 1.395 mm sharp edged orifice.

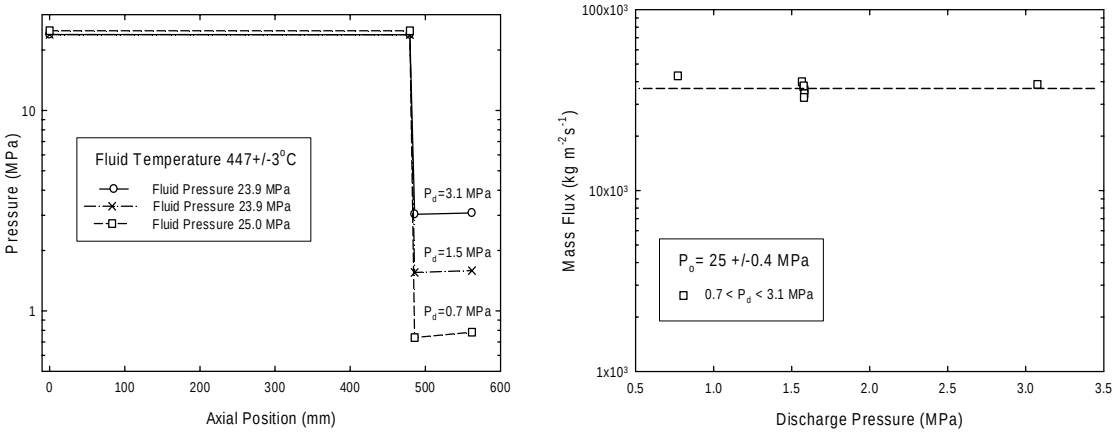

Figure 5. a) Pressure distribution upstream from a 1 mm sharp edged orifice;
b) Mass flux vs. the downstream pressure.

4.1 Experimental Error Analyses

The accuracy of the instrumentation used to perform the experiments has been discussed in Section 2. Due to the number of data points and the complex nature of the supercritical water phenomena, the error analyses are not easy to be carried out. Therefore, to simplify this task the data presented in the Fig. 3 have been subdivided into three distinct regions: Region I for $\Delta T_{pc} <$ -50° C, Region II for -50° C $\leq \Delta T_{pc} \leq$ 50° C and Region III for 50° C $> \Delta T_{pc}$. Within each of these regions the statistical analyses of the measurements for the mean fluid temperature, pressure and mass flux, as well as for the applied power are summarized in the Table 2.

Table 2. Precision of the measurements in three different experimental regions.

Flow Variable	Standard Deviation σ (95% of confidence)		
	Region I $\Delta T_{pc} <$ -50° C	Region II -50° C $\leq \Delta T_{pc} \leq$ 50° C	Region III 50° C $> \Delta T_{pc}$
Temperature (° C)	0.63	2.15	1.14
Pressure (MPa)	0.04	0.30	0.08
Mass Flux (x 10^3 kg $m^{-2}s^{-1}$)	1.52	4.42	2.42
Thermal Power (kW)	0.80	1.75	1.30

As shown in this table, the precision is higher in Regions I and III. In fact as already discussed, for flow conditions corresponding to Region II the control of the system is very cumbersome. As shown in Fig. 4, in this region the coupling between fluid properties as a function of the temperature and the pressure is very strong, which provokes an unstable behavior of the system. Hence, small changes of the control loop variables considerably affect the mass flux. Nevertheless, the behavior shown in Fig. 5 is observed for the entire data set; this confirm that the present methodology permits high quality choking flow data to be obtained at supercritical water flow conditions. In particular, it is important to note that the scattering on the values of

choking mass fluxes is relatively low, which is not obvious the case for similar results obtained with a 1.41 mm sharp nozzle [5] as shown in Fig. 3.

5. Comparison of Model Predictions with Data

The predictions obtained from the Homogeneous Equilibrium Model (HEM) and the Modified Homogeneous Equilibrium Model (M-HEM) proposed by Chen et al. [5] are compared with the experimental data presented in the Section 4. According to this reference, the HEM is written as:

$$G_{cr} = \frac{\left[2\left(h_o - (1-x_E)h_{lE} - x_E h_{gE}\right)\right]^{1/2}}{(1-x_E)v_{lE} + x_E v_{gE}}, \tag{2}$$

and the M-HEM is expressed by:

$$G_{cr} = \left[\frac{2\left(h_0 - (1-x_E)h_{lE} - x_E h_{gE}\right)}{\frac{C}{\overline{\rho}^2} + \left((1-x_E)v_{lE} + x_E v_{gE}\right)^2}\right]^{1/2}. \tag{3}$$

Where C is a local flow resistant factor, h_{o} is the inlet stagnation enthalpy, h_{lE} is the equilibrium liquid enthalpy, h_{gE} is the equilibrium vapour enthalpy, v_{lE} is the equilibrium liquid volumetric mass, v_{gE} is the equilibrium vapour volumetric mass and x_{E} is the equilibrium quality. According the Chen et al., the equilibrium flow properties are calculated at the plane where choking flow occurs. Since this location is *a priori* not known, Equations 2 and 3 are solved by gradually decreasing the discharge pressure until obtaining the maximum value of mass flux (i.e. dG/dP=0.) Furthermore, for each discharge pressure, the equilibrium quality is calculated from the stagnation and the corresponding specific saturation entropies, and the average density is determined at the inlet flow conditions. In particular, Chen et al. have tested Equation 3 and for a sharp nozzle similar to our test sections, they have recommended a value of C = 0.6. The Fig. 6 shows the comparison between the values obtained from Equations 2 and 3 with our experimental data obtained with both test sections.

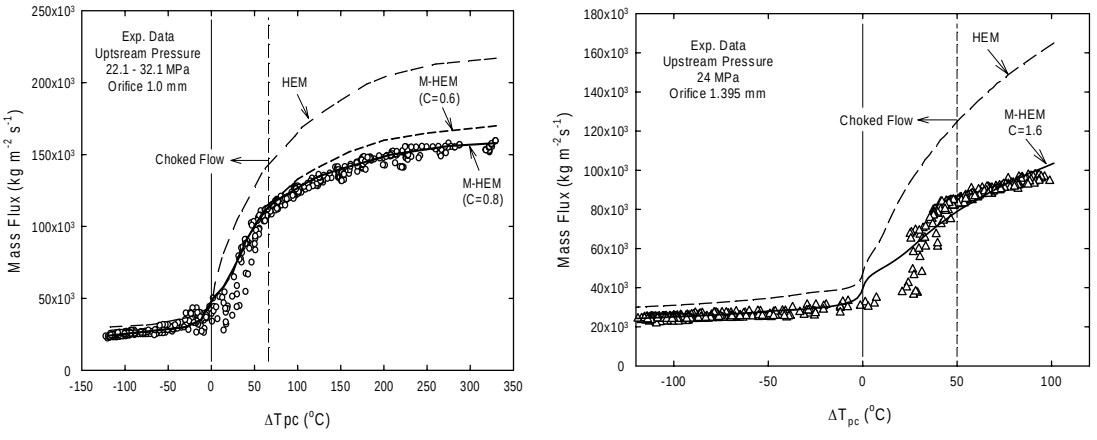

Figure 6. Comparison of the prediction obtained with the HEM and M-HEM with data a) 1.0 mm orifice; b) 1.395 mm orifice.

The calculations are performed using Matlab® (The MathWorks Inc.) and the XSteam water library. [14] Previous to use XSteam, at supercritical water conditions, it was carefully validated [1] against the Schmidt steam table. [15] For the 1 mm orifice, Fig. 6a shows that below the pseudo critical state both models are able to predict the data; however, it can be observed that the HEM model slightly over predicts the experimental trends. Nevertheless, in this regions the predictions are inside the experimental confidence error limit (Region I in Table 2; error bars are not shown in Fig. 6 because they appear overwhelmed by the graphical dimension of the data points.) As was mentioned in Section 4, for a 1 mm orifice test section we have already determined that choking flow takes place for $\Delta T_{pc} \leq 67^{o}$ C [8]; in this region Fig. 6a clearly shows that the HEM considerably diverge from the experimental data. In turn, the M-HEM for two different values of the local flow resistant factor (C in Eq. 3) is able to do a reasonable good job; in particular if we take into account the larger error band that characterizes the data in this zone (i.e. Region II in Table 2.) For $\Delta T_{pc} > 67^{o}$ C, the behavior of the HEM is far away from the experimental trends. In this region, the M-HEM with $C = 0.6$, as recommended by Chen et al. [5], slightly over predicts the data. Under these flow conditions the effect of the nozzle geometry on the phase transition is expected to be quite complex; which can considerably invalidate the assumption of an isentropic expansion, necessary to write-down the Equations 2 and 3. [6,7] In fact, we have already observed that the expansion is neither isentropic nor completely isenthalpic. [8] Therefore, we have used the local flow resistant factor, C, as an additional degree of freedom to fit the predictions of the M-HEM to our data. Thus, Equation 3 with $C = 0.8$ is able to provide the lowest RMS value. It is interesting to note that with this value the M-HEM is able to produce excellent results within the entire experimental range covered by the data.

Figure 6b shows similar comparisons with the data collected with the second test section (i.e. 1.395 mm orifice); for flow temperatures below the pseudo critical value the HEM provides the right behavior but it over predicts the data. For this test section the M-HEM with $C = 0.6$, as suggested by Chen et al. is not able to produce satisfactory results; therefore, only the predictions using $C = 1.6$ in Equation 3 are shown in the figure. This value of the local flow resistant factor is also determined by minimizing the RMS between the calculations and the data. As mentioned in Section 4, we have strong evidences that for this type of test section choking flow occurs for $\Delta T_{pc} \leq 50^{o}$ C; nevertheless, within 0^{o} C $\leq \Delta T_{pc} \leq 50^{o}$ C the M-HEM with $C = 1.6$ is unable to represent entirely the experimental trend. In fact, the predictions follow a complex pattern that is almost in the opposite direction to the behavior shown by the experiments. To this aim, it is important to remark that the same trend, but less noticeable, also occurs for the 1 mm orifice (see Fig. 6a.) In the region $\Delta T_{pc} > 50^{o}$ C the M-HEM with $C = 1.6$, even though it satisfies the minimum RMS value, it is unable to provide appropriate results. It is obvious that this drawback is principally due to the difficulty encountered by the model when choking flow start occurring (i.e. the knee observed in the data just below this temperature difference.)

The comparison presented in Fig. 6 provides indications that the M-HEM is very sensitive to the value of the local flow resistant factor. Moreover, it seems that the value required by this factor increases with increasing the inside diameter of the nozzle. It is obvious that the geometry of the nozzle must affect the flow structure within the expansion region. However, stablishing the appropriate physical ground that should control the resistant factor is not necessarily obvious. The fact that when the flow becomes choked, the critical mass flux seems to be thermodynamically self-determined, as is indicated by the overlapping of the data collected with different orifices (see Fig. 3), provides indications that C must essentially depend on a pure geometrical variable. To this purpose, we tried to correlate C as function of the L/D ratio; however, the amount of available data is not enough to determine an appropriate and definite relation. In particular, this becomes quite difficult because when the flow is choked, the M-HEM seems to be insensitive to the value of C, at least for both 1.41 and 1 mm orifice type nozzles (see Fig. 6a.) In turn, since in this region two different values of C predict the same critical mass flux, for different inlet flow conditions, it is expected that the flow resistance factor should be better correlated using L/D^2 (i.e. as function of the mass flow rate.) The Table 3 summarized these results for the three test section geometries used to collect the data included in Fig. 3. It is apparent that additional experimental information for test sections having different geometries is required to determine unambiguously an appropriate correlation. It is however curious that C increases with increasing the diameter of the orifice. To this aim, the assumption of an isentropic expansion used to determine the equilibrium quality required by both the HEM

and M-HEM is probably inappropriate. In fact, from local flow pressure and temperature measurements, we have a solid evidence that the expansion is more close to a constant enthalpy process than to an isentropic one. [8] From this view point, it is obvious that for some inlet flow conditions such hypothesis does not hold; therefore, the use of the equilibrium quality becomes an inappropriate physical variable. [16] Therefore, for these cases neither the formulation of the HEM nor that of the M-HEM are physically possible.

Table 3. Local flow resistant factor vs geometrical parameters of the test section.

Local flow resistant, C (Eq. 3)	D (mm)	L (mm)	L/D	L/D^2 (mm^{-1})
0.6 (Chen et al.)	1.410	4.350	3.0851	2.1880
0.8	1.000	3.175	3.1750	3.1750
1.6	1.395	3.175	2.2760	1.6316

The aforementioned results show that it is still necessary to provide better modelling approaches to satisfy the real behavior of the sudden discharge of supercritical water through orifices. In particular, to develop an appropriate theoretical background that will be able to take into account the inherently strong irreversible nature of choking flows. [6,7] Nevertheless, as an outcome of the present work we can recommend the use of the M-HEM with an appropriate value of the local flow resistance factor C, as required by the Equation 3.

6. Conclusion

This document presents a novel procedure to control and determine supercritical flow conditions that bring about the occurrence of choking flow. To this aim two loops interconnected in parallel across a test section and sharing the same working fluid (i.e. distilled, demineralized water without chemical treatment) is proposed. The implemented experimental methodology permits us to collect high quality supercritical water data by carefully controlling all key flow parameters. Thus, a new data set containing information in a region where experiments are relatively rare, is included in this paper. This lack of material can be explained by the complex thermal-hydraulic behavior that occurs when the fluid approaches pseudo critical flow conditions.

For two test sections (i.e. 1 mm and 1.395 mm sharp edged orifices) it is observed that once choking flow conditions are well established, the critical mass velocity is not affected by the geometry. However, there is a temperature threshold required to achieve choking flows which seems to depend on the orifice size. Our data is also compared with similar ones, collected by using a 1.41 mm sharp nozzle. [5] Even though this data set presents huge scattering, under super critical flow conditions they have the same flow behavior as our results.

The entire data set is also compared with predictions given by the HEM and the M-HEM. In general, it is observed that for the entire experimental rage, the HEM is not able to follow the experimental trends. For the M-HEM, the proposed local flow resistant factor is used to fit the data. Thus, it is observed that the value suggested by Chen et al. [5] is not appropriate for covering the whole range of experimental conditions. Therefore, for the 1 mm orifice, we suggest to use C=0.8; hence, the M-HEM gives excellent results. Instead, for the 1.395 mm orifice the use of a value C=1.6, which minimizes the RMS, does not produce acceptable results. In particular, it is observed that the M-HEM is unable to follow the experiments immediately after choking flow occurs.

The fact that at supercritical conditions the data do not show any perceivable geometrical effect, provide us indications that the flow resistant factor should be correlated by some geometrical parameter. Due to the lack of experimental information we are unable to find a reliable relationship. However, it must be pointed out that previous observations indicate that the flow expansion follows an inherently irreversible process [6-8]; therefore, the use of the

equilibrium quality in both the HEM and the M-HEM is a problematic issue that should be solved.

References

1. Lizon-A-Lugrin, L., Teyssedou, A. & I. Pioro. (2012) "Appropriate thermodynamic cycles to be used in future pressure-channel supercritical water-cooled nuclear power plants," Nucl. Eng. Design, 246, pp. 2-11.
2. Pioro, I. & R.B. Duffey. (2007) "Heat transfer and hydraulic resistance at supercritical pressures in power engineering applications," ASME, Three Park Av., NY.
3. Mignot, G., Anderson, M. & M. Corradini. (2008) "Critical flow experiment and analysis for supercritical fluid," Nucl. Eng. Technol. 40 (2), pp. 133–138.
4. Mignot, G., Anderson, M. & M. Corradini. (2009) "Measurement of supercritical CO_2 critical flow: effects of L/D and surface roughness," Nucl. Eng. Design, 239 (5), pp. 949–955.
5. Chen, Y., Zhao, M., Yang, C., Bi, K., Du, K. & S. Zhang. (2012) "Research on critical flow of water under supercritical pressures in nozzles," Journal of Energy and Power Eng., 6, pp. 201-208.
6. Olekhnovitch, A., Teyssedou, A., Tye, P. & P. Champagne. (2001) "Critical heat flux under choking flow conditions: Part I – Outlet pressure fluctuations," Nucl. Eng. Design, 205, pp. 159 –173.
7. Olekhnovitch, A., Teyssedou, A. & P. Tye. (2001) "Critical heat flux under choking flow conditions: Part II – Maximum values of flow parameters attained under choking flow conditions," Nucl. Eng. Design, 205, pp. 175–190.
8. Muftuoglu, A. & A. Teyssedou. (2014) "Experimental study of abrupt discharge of water at supercritical conditions," Exp. Therm. Fluid Science, 55, pp. 12–20.
9. Sakurai, K, Ko, H.S., Okamoto, K. & H. Madarame. (2001) "Visualization study for pseudo boiling in supercritical carbon dioxide under forced convection in rectangular channel," Japan School Eng., Univ. Tokyo, 48, pp. 49 – 57.
10. Ota, K., Okamoto, K., Sakurai, K & H. Madarame. (2002) "Measurement of Transient supercritical fluid velocity using infrared pulse laser with high-speed camera," 11th Int. Symp. App. Laser Tech. Fluid Mech., Lisbon, Portugal.
11. Teyssedou, A., Muftuoglu, A. & C. Koclas. (2012) "Choking flow in supercritical fluids – Preliminary commissioning experiments," Submitted to: NSERC/NRCan/AECL, Report IGE-334-R1, Polytechnique Montréal.
12. Lee, D.H. & D. Swinnerton. (1983) "Evaluation of critical flow for supercritical steam-water," Report NP-3086.
13. Lemmon, E.W., Huber, M.L. & M.O. McLinden. (2010) "NIST Reference fluid thermodynamic and transport properties – REFPROP: Version 9.0 user's guide."
14. Holmgren, M. (2006) "X-Steam for Matlab, Edition."
15. Schmidt, E. (1982) "Properties of water and steam in SI - units," 3th edition, Springer-Verlag, Berlin.
16. Muftuoglu, A. (2014) "Experimental study of choking flow of water at supercritical conditions," Ph.D. Thesis, Department of engineering physics, Polytechnique Montréal.

ISSCWR7-2033

Expected Safety Performance of the SCWR Fuel Qualification Test

Thomas Schulenberg, Manuel Raqué, Tobias Zeiger
Karlsruhe Institute of Technology
Karlsruhe, Germany
Tel. +49 721 608 23450, thomas.schulenberg@kit.edu

Abstract

The SCWR fuel qualification test is an in-pile test of a 4 rod fuel assembly at supercritical pressure inside a research reactor, which is operated at atmospheric pressure. The risk of radioactive release from this new test facility should not exceed the accepted risk of the existing research reactor. A large number of safety analyses have been performed to assess this risk, which are summarized in this paper. Among them are studies of design basis accidents, assuming different failure modes of the high-pressure system, as well as an assessment of consequences of postulated accidents beyond the design basis. Results show that the safety objectives can be met.

1. Introduction

As nuclear reactors cooled with supercritical water had never been built in the past, a prototype reactor could not be designed without gaining first experience with such challenging operation conditions. Therefore, a small-scale fuel assembly has been planned as a fuel qualification test inside a nuclear reactor with comparable design features and at similar operation conditions as fuel assemblies of the HPLWR evaporator concept [1]. The pool type research reactor LVR 15 in Řež, Czech Republic, is offering a core position for a pressure tube with 52 mm outer diameter, replacing an ordinary fuel assembly, as described by Ruzickova et al. [2]. Here, a small fuel assembly of 4 fuel rods can be tested with supercritical water at a pressure of 25 MPa. The UO_2 fuel needs to be enriched to almost 20% to provide a total rod power of 63.6 kW over an active length of 60 cm, consisting of 61.2 kW fissile power and 2.4 kW gamma power, which is released inside the fuel. In addition, the γ-radiation of the reactor is causing a power of 9.8 kW in the metal structures of the fuel element, primarily in the thick walled pressure tube.

A cross section of this pressure tube is shown in Fig. 1. The bottom part of the pressure tube (Fig. 1, left) contains the heated test section, where four fuel rods with a wire wrap are housed in an assembly box like in the HPLWR. Two concentric guide tubes around this assembly provide a coolant flow along the inside of the pressure tube, keeping its temperature below a limit of 400°C, and through a recuperator above the heated section (Fig. 1, right). The coolant is thus preheated to 364°C at the inlet of the heated section, which is close to the pseudo-critical temperature of 384°C at 25 MPa. From the test section outlet, the coolant exchanges heat inside the recuperator tubes and it is finally cooled down to 300°C in a U-tube cooler in the top part of the pressure tube. With a peak heat flux of 1500 kW/m^2 at a mass flux of 1380 kg/m^{2}s, the design conditions in the heated section are close to the envisaged peak conditions in the

HPLWR evaporator. The pressure tube is thermally insulated from the reactor pool by an aluminum displacer tube and by an air gap between both parts.

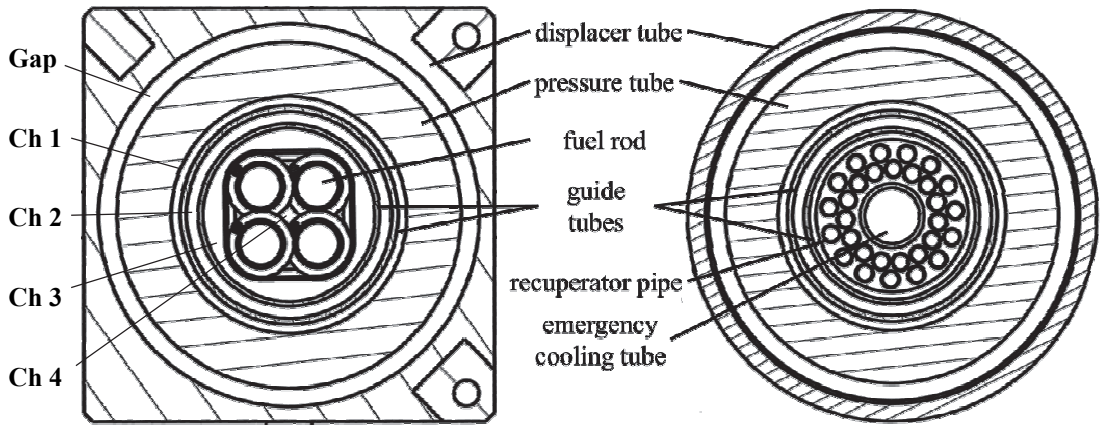

Figure 1. Cross sections of the pressure tube for the fuel qualification test; left: heated test section, right: recuperator section.

A hermetically sealed recirculation pump in a separate room next to the reactor hall is driving the required coolant flow of 0.25 kg/s at 300°C through the supercritical pressure loop, using a feed line and a return line inside a shielded duct to the reactor. This separate room contains also the secondary cooling loop, safety systems and residual heat removal systems. An independent third coolant line is an emergency cooling line which may feed the central emergency tube shown in Fig. 1 in case of a loss of coolant. It ends on top of the heated section and thus may cool the test section, if needed, with a reverse flow.

A safety system, as sketched in Fig. 2, has been designed for this test facility to control and mitigate a number of design basis accidents (additional sampling systems for water chemistry control and purification systems are not shown). The primary system with its pressure tube, the main recirculation pump HCC and a check valve CV1 are shown in red. The coolant for this primary system is supplied from a tank DN and the pressure is built up with the boost pump VC. A bladder type compensator KO1 is minimizing pressure fluctuations due to density variations in the loop. The fissile and γ-power from the test section are removed by the secondary cooling system, shown in blue. Its recirculation pump CS is controlled by the outlet temperature of the primary system from the pressure tube, keeping it at 300°C. The secondary system is equipped with a cooler CH1 and a heater EO1 such that it can also heat up the primary system before the reactor is started.

In case of a loss of coolant from the primary system, the reactor is scrammed and two passive, bladder type accumulators TZ1 and TZ2 are adding their cold coolant inventory of 30 liters each to the feed line L1 of the primary loop and to the emergency cooling line L3, respectively. Their high coolant flow rates are quenching the test section during depressurization, avoiding a temporary boiling crisis or at least minimizing its consequences to acceptable peak cladding temperatures. Afterwards, the residual heat is removed either by a feed line coolant injection system FLCI (shown in orange) or by an emergency coolant injection system ELCI (shown in cyan). Both systems are taking the required coolant from an emergency coolant reservoir HN1. As the exact position of the break can hardly be detected during such an accident, the decision criteria for activation of each system are based on pressures, temperatures and mass flow only. A system pressure of less than 22.5 MPa, measured in the feed line L1, or a coolant mass flow of less than 0.15 kg/s, measured with an orifice downstream of pump HCC, are automatically activating the FLCI system. A negative pressure difference between the feed line L1 and the emergency cooling line L3, or a coolant

temperature of more than 500°C at the outlet of the test section are activating the ELCI system. In case of conflict, the ELCI system is the dominant system.

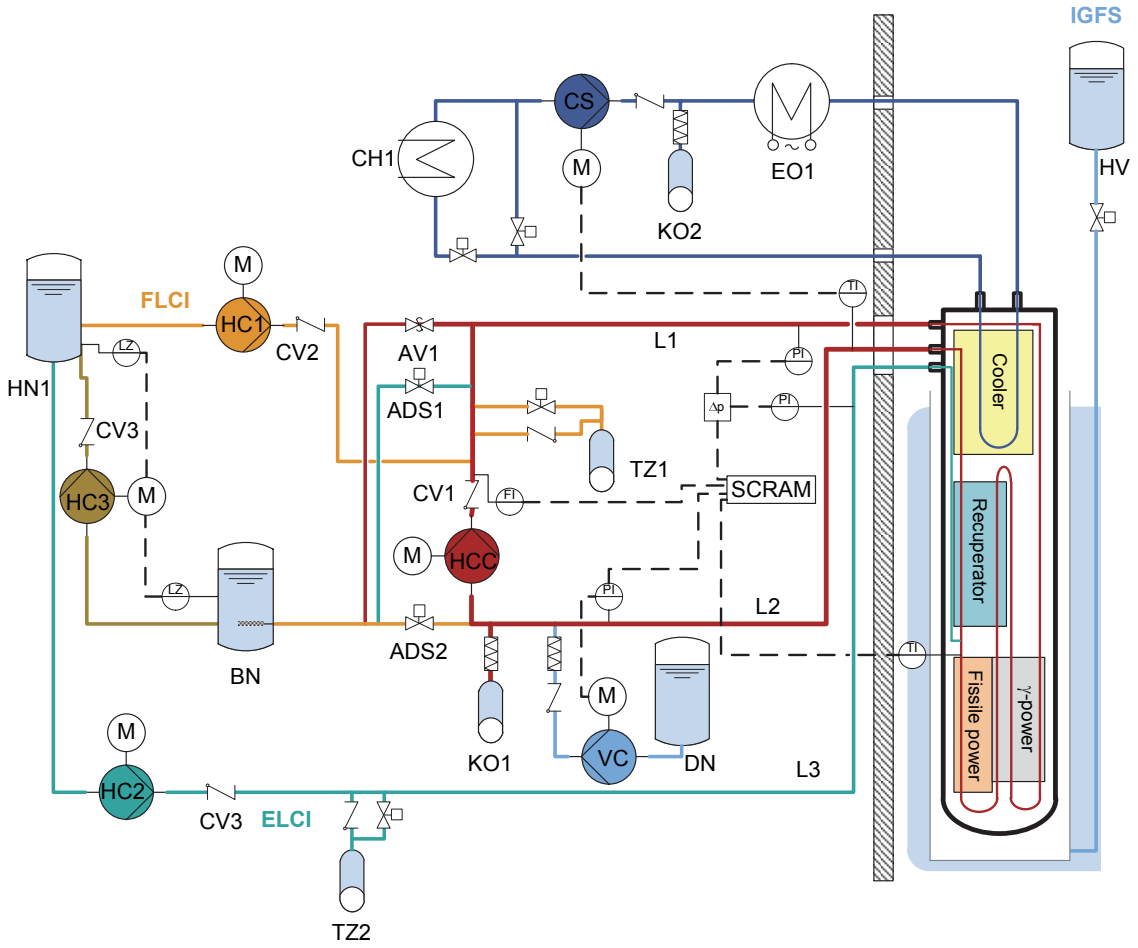

ADS – Automatic depress. system	DN – Refilling tank	HN1 – Emergency coolant reservoir
AV – Pressure relief valve	HC – Emergency pump	HV – Reservoir
BN – Pressure suppression tank	HC2 – Emergency pump 2	KO – Pressurizer
CV – Check valve	HC3 – Refilling pump	TZ – Pressure accumulator
EO1 – Electrical heater	HCC – Recirculation pump	VC – Boost pump

Figure 2. Sketch of the fuel qualification test loop and its safety systems [3].

In case of a loss of flow, caused e.g. by a trip of pump HCC, by a flow blockage or by a shortcut of the coolant, thus bypassing the test section, the reactor is scrammed and the automatic depressurization valves ADS1 or ADS2 are opened with a delay of 1 s. The choice between both valves is based on the decision criteria given above: valve ADS2 is opened together with activation of the FLCI system and valve ADS1 is opened together with the ELCI system, causing a reversed flow. Opening of any ADS valve is first causing a release of coolant from both accumulators TZ1 and TZ2. Once the pressure dropped to sub-critical conditions, pump HC1 of the FLCI system or pump HC2 of the ELCI system provide the required coolant flow rate to remove the residual heat.

Both ADS valves dump the coolant to the pressure suppression tank BN, which will increase its water level, while the one of the emergency coolant reservoir HN1 will decrease. A coolant

pump HC3 between both tanks will refill coolant back into tank HN1 once the water level in tank BN has reached an upper limit.

In case of loss of the heat sink, e.g. in case of failure of the secondary cooling loop, the reactor is scrammed as well, the system is depressurized by valve ADS2 after a delay of 1 s, and the FLCI system removes the residual heat to tank BN and from there to tank HN1 via pump HC3. As an independent heat sink, the residual heat can be removed to the reactor pool simply by flooding the insulation gap between the pressure tube and the aluminum displacer around it, using water from tank HV. Moreover, using this passive insulation gap flooding system IGFS, an active coolant flow would not be needed anymore after 12 days as heat can be removed just by natural convection then.

In case of loss of off-site power, these safety systems are powered by batteries and by a diesel generator.

2. Analyses of design basis accidents

The performance of this safety system has been analyzed with the system code APROS, as described by Raqué [3]. The reactor shut-down rods are released within 0.06 s after a scram signal has been given, and a driving time of 1 s is needed to fully insert them into the reactor core. The automatic depressurization valve, either ADS1 or ADS2, is assumed to open within 0.5 s, but a delay of 1 s between the scram signal and the signal for this valve to open is provided to reduce the fissile power while the pressure is still supercritical. All pumps have been modelled with a run-up or coast down time of 2 s.

The acceptance criteria for transient accident analyses, demonstrating the integrity of the fuel cladding as the second barrier, is the maximum cladding surface temperature. The maximum cladding surface temperature of 550°C, applied for steady state analyses, may be exceeded temporarily since creep and oxidation or corrosion are negligible during temperature peaks of a few seconds duration. Instead, we require simply that the yield strength may not be exceeded such that plastic deformations and thus ballooning of fuel rods can be excluded. For stainless steels like SS 316L, this limits the maximum cladding temperature to 816°C during seldom, short-term events.

2.1 Loss of coolant accidents

As an example for a loss-of-coolant-accident, let us consider a sudden, guillotine break of the emergency cooling line L3, Fig. 2. The APROS result, Fig. 3 (left), shows that this break will cause a rapid depressurization, immediately followed by scram of the reactor once the system pressure is less than 22.5 MPa. The accumulator TZ1 increases the initial, steady-state coolant mass flow of 0.25 kg/s to more than 1 kg/s, which reduces effectively the coolant temperature in the test section as shown in Fig. 3 (right). The other accumulator TZ2 is just feeding into the break. The small contribution of the pressurizer KO1 is negligible. Within 30 s after the break occurred, both accumulators will be empty. In the meantime, pump HC1 of the FLCI system is started and it continues to remove the residual heat with a small mass flow. Change over to the active system causes a short but small increase of the coolant temperature again, but the test section remains well cooled throughout the entire transient. Within 4.5 hours after the break happened, the coolant reservoirs BN and HN1 will be empty and missing water needs to be replaced then.

As a second example, we consider a sudden break of the feed line L1, at a location close to the headpiece of the pressure tube. Fig. 4 shows that the pressure in the broken line L1 will drop much faster than the pressure in line L3, which causes a negative pressure difference

Δp(L1-L3), exceeding the given threshold at -0.3 MPa. Now, during the depressurization phase, the coolant inventory of accumulator TZ2 is quenching the test section with a reverse flow, while accumulator TZ1 will just feed into the break. The negative Δp signal is activating the ELCI system, and pump HC2 is started accordingly. It continues to remove the residual heat of the test section after 30 s, when accumulator TZ2 will be empty.

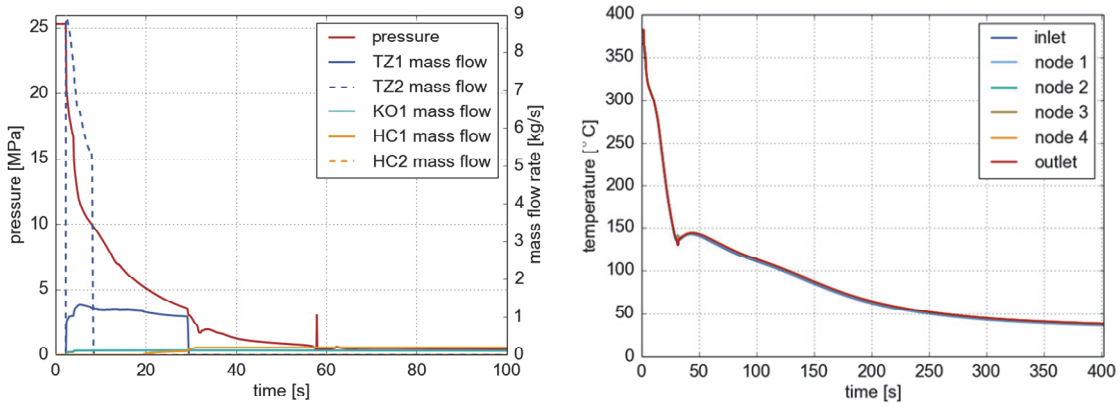

Figure 3. Coolant pressure, mass flows and temperatures in the test section after a sudden break of the emergency cooling line L3 [3].

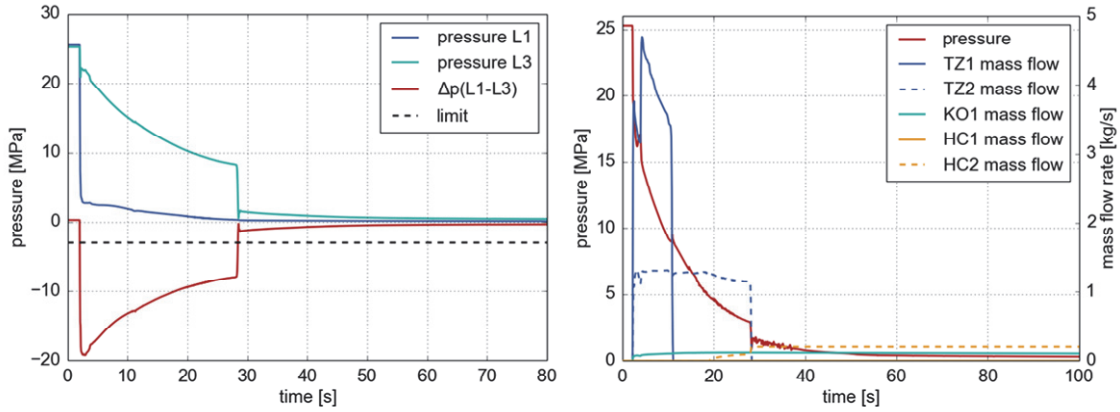

Figure 4. Coolant pressure (left), mass flows in supply lines of the safety system and pressure in the test section (right) after a sudden break of the feed line L1, close to the headpiece of the pressure tube [3].

2.2 Loss of flow accidents

As an example for a loss-of-flow-accident, let us consider a trip of recirculation pump HCC. As indicated in Fig. 5, the pump trip is assumed to occur at time 2 s. Its initial, steady-state mass flow of 0.25 kg/s is reducing within a coast down time of 2 s, but the safety instrumentation is already causing a scram of the reactor once the mass flow is less than 0.15 kg/s. The shutdown rods are inserted within 1 s, and the power is assumed to decrease linearly to the decay heat. Opening of the automatic depressurization valve ADS2 is activated with 1 s delay, and the pressure starts to drop at 4.7 s. Coolant from accumulator TZ1 is increasing the mass flow to ~0.6 kg/s again, and the coolant temperature in the test section is falling rapidly. Opening of valve ADS2 is simultaneously activating the FLCI system, and pump HC1 continues to cool the test section once accumulator TZ1 will be empty.

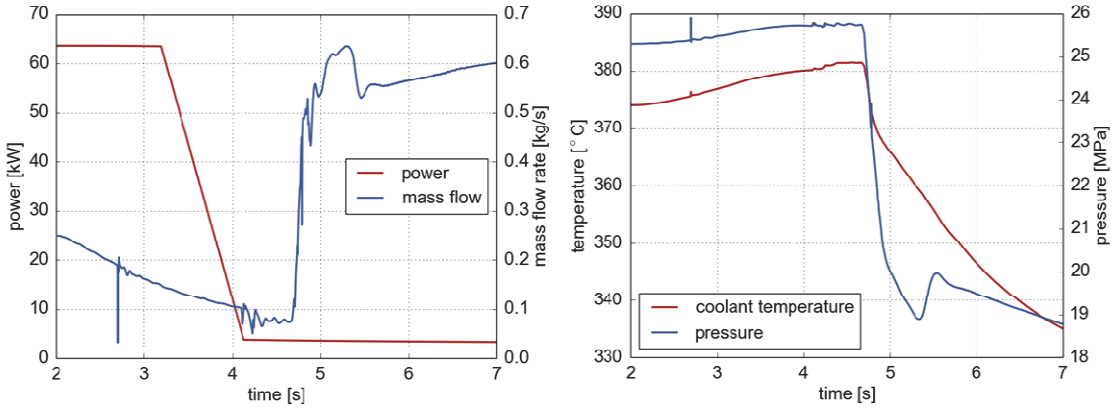

Figure 5. Power, mass flow, pressure and coolant temperature in the test section after a trip of the recirculation pump HCC [3].

2.3 Loss of heat sink

This simulation assumes a trip of the recirculation pump CS of the secondary loop, which means a loss of heat sink. In this case, the reactor is scrammed and the feed-water line injection system (FLCI) is activated by the loss of flow signal of the cooler circuit. This results in a depressurization of the loop via valve ADS2, one second after the reactor shut-down has been initiated. Accumulator TZ1 automatically injects coolant for the first period until emergency pump HC1 takes over for active residual heat removal. During this time, the residual heat released by the fuel rods is dumped in the depressurization tank BN. The IGFS system has been assumed to be activated around 200 s after the pump trip so that the insulation gap surrounding the pressure tube gets flooded. Thus, the reactor pool can be used as a heat sink, keeping the coolant temperature in the primary circuit below saturation. The 50 l water inventory of tank HV is depleted 1000 s later and the flow inside the gap comes to a halt. From now on, the residual heat is transferred to the reactor pool by conduction through the water filled gap. The left hand side of Fig.6 shows the progression of the coolant temperatures inside the depressurization tank BN and inside the emergency reservoir HN1 during the first 10 hours of the accident sequence, as well as the mass flow through the connecting pump HC3.

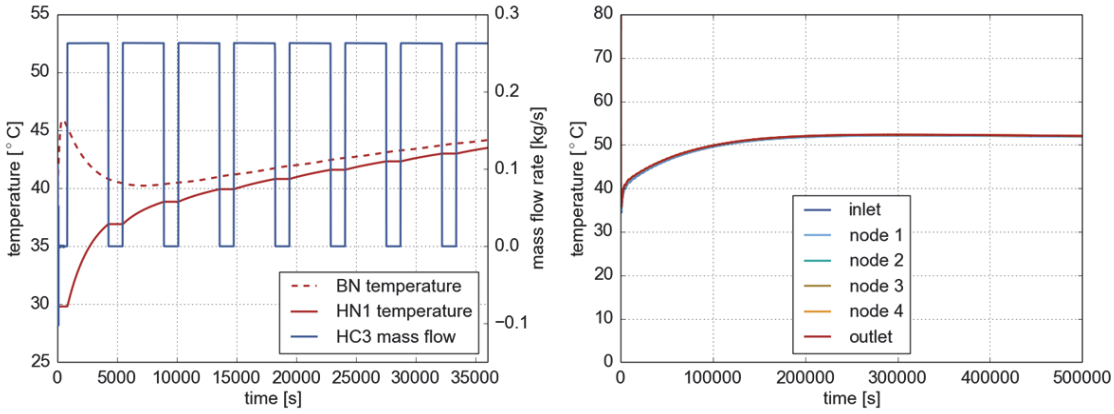

Figure 6. Water temperatures inside depressurization tank BN and inside emergency reservoir HN1 as well as flow rate through pump HC3 (left). Coolant temperatures along the fuel rods over the total simulation period of 500000 s (right) [3].

Within the first 500 s, the heat which had been stored in the coolant and in the piping of the primary loop, which is now released into tank BN, raises the water temperature from 30 to 46 °C. In the following, the temperature decreases again as the coolant coming from emergency reservoir HN1 gets only slightly heated up due to the substantially decreased residual power of the fuel pins. By recirculating and reusing the coolant, its temperature slowly increases again, until it reaches 50 °C after 104000 s (~29 hours), which is the assumed temperature of the reactor pool. After 500000 s, the system is near steady-state conditions with a maximum coolant temperature of 52 °C at the outlet of the test section, which can be seen on the right hand side of Fig. 6. This means that the forced convection in combination with the heat bridge to the reactor pool manages to cool the fuel rods efficiently thanks to the flooded insulation gap. Thus, the reactor pool serves as a redundant heat sink.

2.4 Loss of off-site power

In case of a loss of off-site power, the safety systems are powered by batteries and by an emergency diesel generator. Both recirculation pumps HCC and CS of the primary and secondary system, respectively, may be stopped to minimize the power consumption. The reactor will be scrammed by the loss of power signal, causing valve ADS2 to open with 1 s delay and the FLCI system to start. During the first 30 s, both accumulators TZ1 and TZ2 will inject their coolant inventory into the test section, and pump HC1 will continue to supply coolant from the coolant reservoir HN1 afterwards. The IGFS system needs to fill the insulation gap around the pressure tube to provide a heat sink, and the refilling pump HC3 needs to transport water from the depressurization tank BN to the reservoir HN1 once the latter one has been filled up.

This active system must be operated for around 12 days, but all pumps may be stopped then. Afterwards, the residual heat may be removed passively from the fuel rods to the reactor pool just by radial conduction through the flooded insulation gap. Raqué et al. [4] showed with a CFD analysis that the coolant will not reach the saturation temperature anymore in these cases.

2.5 Conclusions from analyses of design basis accidents

These examples of design basis accidents demonstrate how the safety system of the fuel qualification test loop is designed and how it is intended to work. More examples are discussed by Schulenberg and Raqué [5]. The action taken after reactor scram is always depressurization of the primary system, either caused by a break which might happen at any position of the loop or, actively, by opening the automatic depressurization system. Immediate quenching of the hot test section is always provided by passive coolant injection from accumulators, of which two ones are needed to cover all kinds of accidents and break positions. Afterwards, two active pumps provide the required residual heat removal, which are designed for a small mass flow only to minimize the size of the required coolant reservoirs. These two pumps are not redundant but cover two different kinds of accidents. The large reactor pool can be used as an independent heat sink simply by flooding the insulation gap between the pressure tube and the pool.

A sensitivity analysis with longer scram delay time, longer ADS delay time and larger accumulator volumes has been performed by Zhou et al. [12]. They show that a scram delay of 2 s would already exceed the design criterion of the cladding surface temperature, no matter how large the accumulator volume will be designed. Cladding temperatures in case of depressurization without scram have been predicted by Schulenberg et al. [13]. Even at a moderate power of 25 kW, the boiling crisis at sub-critical pressure would overheat the claddings beyond the temperature limit of 816°C. Therefore, the reactor is scrammed before depressurization, and the ADS valves open with 1 s delay after scram.

3. Analyses of design extension conditions

What happens, however, if these safety systems did not perform as planned, e.g. because two or more failures occurred simultaneously, which is a very unlikely event, or because of any unforeseen event. The consequences of such “design extension conditions” need to be identified to assess the risk of such accidents and to prepare mitigation actions as far as possible.

We differ between potential mechanical consequences and potential radiological consequences. The mechanical consequences of a rupture of the primary system have been studied only for the pressure tube inside the reactor. Having a high pressure component inside a nuclear reactor core could become a severe problem if parts of this pressure tube or the pressure tube as a whole are driven around in the reactor pool in case of an accident, hindering either the control rods from shutting down the reactor or the coolant from cooling the other, ordinary fuel elements. If such cases occur, the rupture of the pressure tube would cause a severe secondary damage.

3.1 Mechanical consequences of a pressure tube rupture

A ductile failure of the pressure tube at design pressure could happen in case of low cycle fatigue, thermal fatigue or creep of the pressure tube, including its welds, causing a steam jet which drives the pressure tube by its thrust. The aluminum displacer around the pressure tube, Fig. 1, will most likely survive this accident without secondary failure, but the pressure tube would be pushed upwards then. Similarly, a ductile rupture near the head piece could drive the pressure tube radially, with the risk of hindering or even blocking the control rods of the reactor. As a consequence, the top attachment of the pressure tube, Fig. 7 (left,) has been checked by Zeiger et al. [6] such that the pressure tube is kept in place under such accident scenarios. Pressures and mass flows inside the break have been determined with APROS, assuming different break size and location. The reaction force acting on the pressure tube equals the momentum of the jet at the break location. As a result, the original upper attachment of the pressure tube, Fig. 7 (left), appeared to be too weak, and an enforced attachment Fig. 7 (right), had to be designed to withstand these forces, keeping the pressure tube in place.

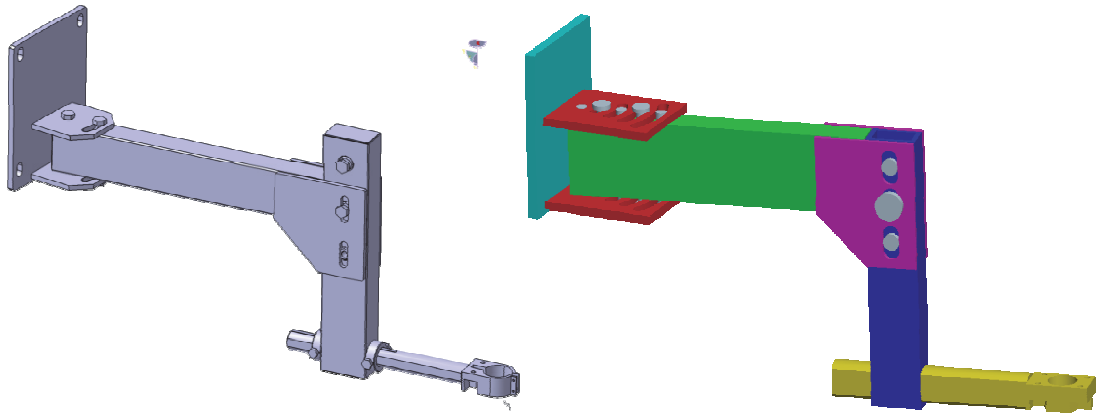

Figure 7. Original (left) and modified attachment (right) of the pressure tube [6].

A brittle failure of the pressure tube at design pressure is unlikely to occur, as the tube material 08Ch18N10T is expected to remain sufficiently ductile during the test runs. Embrittlement of the pressure tube is to be expected only with high dose rates after long term exposure, which can easily be excluded, or in case of hydrogen embrittlement. Even in these

unlikely cases, however, the aluminum displacer can be designed as an effective fragment protection, as will be discussed next.

Fragments of different size and shape have been assumed by Zeiger [7] to be broken out of the pressure tube, accelerated by the coolant jet, which has been modelled with APROS again. For simulation of fragment impact, a short section (up to 300 mm of the total length of 4.7 m) of pressure tube, displacer and outside water environment has been modelled with ANSYS. The pressure tube was held rigidly in two points at each end while the displacer was free to move except for two points at one end to prevent movement along the geometry's rotational axis. The fragment was cut off from the pressure tube and accelerated from rest by the predicted pressure history for an opening of similar size.

Simulations of larger fragments and longer sections of the geometry gave similar results: plastic deformation of the displacer tube, damage and eventual failure are depending on accelerating pressure, relative sizes of fragment and total geometry as well as distance from the end of the geometry. As shown in Fig. 8, a 30 mm square fragment, impacting centrally, is stopped without damage by a dry displacer when the total length reaches approximately 70 mm. Surrounding the displacer with water has an additional effect leading to the conclusion that the displacer holds the fragment by its mechanical strength but inertia contributes considerably in stopping the fragment's motion.

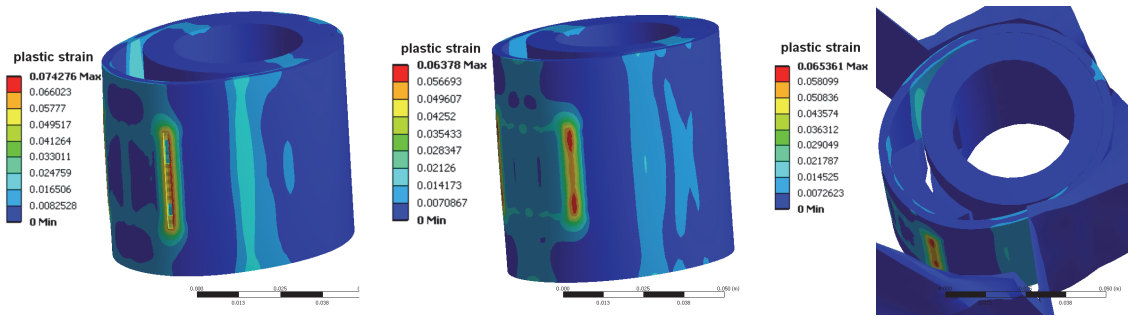

Figure 8. Simulation of a 30 mm square fragment, total length 60 mm (dry), 70 mm (dry) and 60 mm (surrounded by water). Color indicates plastic strain [6].

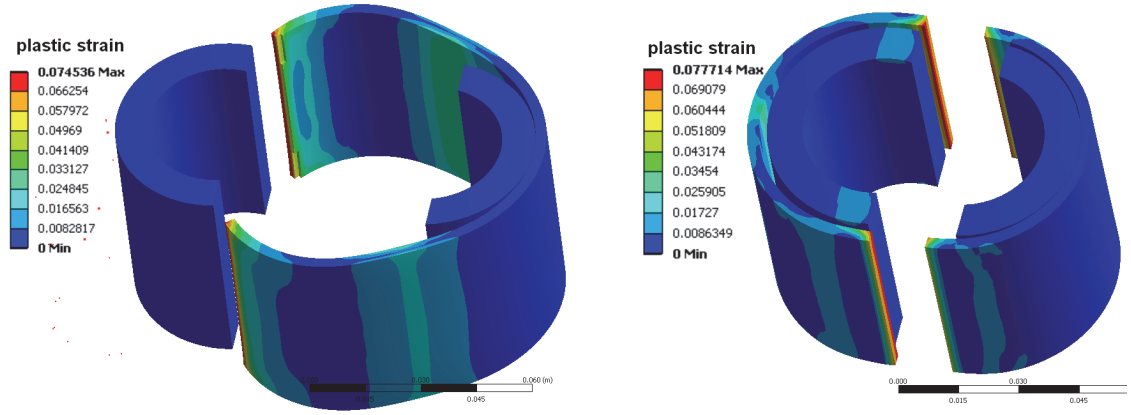

Figure 9. Lengthwise split of the pressure tube, dry (left) and surrounded by water (right, water invisible). Color indicates plastic strain [6].

The most extreme example of a large fragment is the complete split of the pressure tube in two halves, as shown in Fig. 9. In this case, the water does not prevent failure but rather shifts the location of maximum deformation and consequently failure from being opposed to the center of impact to the region close to the fragment's edges. However, this simulation was assuming a pressure transient of a larger hole, while in reality one would expect an even faster drop to a lower pressure in this case, leading to a reduced load on the displacer.

As a conclusion, the surrounding aluminum displacer can potentially stop fragments resulting from a brittle failure of the pressure tube under typical, but not necessarily conservative assumptions. In general, the surrounding water contributes significantly to the resistance of the aluminum displacer: The impact effects are considerably reduced by backing the impact region with mass which is not load-bearing in itself but assisting the energy absorption required to slow the fragment down. However, uncertainties in shape and size of the fragments made it difficult to conclude that the displacer can retain the fragment in any case.

A higher safety margin for the retention of brittle fragments could be obtained, if the displacer material has a higher ductility, even if it has a reduced strength then. An alternative displacer material could be aluminum 5154-0. Due to the higher ductility, such aluminum would dissipate more kinetic energy from the fragments by its larger plastic deformations. Numerical simulations have been performed with square fragments of 30 mm side length and with a lengthwise split of the pressure tube, which turned out to be the most damaging fracture modes in the simulations above. The axial simulation length was varied between 30 and 400 mm, which has some influence on the results. Results of Zeiger [7] show that the maximum peak strain in the aluminum displacer got now a safety margin of 2 or more from the ultimate strain.

3.2 Radiological consequences in case of failure of all active safety systems

The investigated accidental scenario beyond the design basis, which may possess a very low probability of occurrence, is a double-ended guillotine rupture of the feed line L1, Fig. 2. All coolant lines are confined inside a shielded duct between the reactor and the separate experimental hall, so that the reactor hall would not be contaminated, but leaking fluids would be free to enter the experimental hall, which is operated at 20 Pa sub-atmospheric pressure. The volume of this hermetically sealed room is 1762 m^3. It is equipped with a filtering system, which is capable to remove 17620 m^3/h and which keeps the pressure sub-atmospheric even in case of loss-of-coolant accidents. Thus, the reactor, the shielded duct and the experimental hall form a containment.

The initiating event is assumed to be further aggravated by a station black-out in combination with failure of all onsite emergency power supply systems. This would prevent the start-up of the emergency pumps and would stop the flow of the secondary circuit. However, for the first 25s after the accident initiation, cooling of the rods is ensured by the passive pressure accumulator TZ1. After this period, heat is removed solely by conduction over the flooded insulation gap.

The accident scenario was modelled by Raqué [3] with APROS. For the first 25 s of the accident scenario, he predicted a similar coolant temperature progression as for a break of the feed line, section 2.1. As long as accumulator TZ1 injects coolant into the system, the temperatures in the test section decrease rapidly. Different from these simulations, however, no subsequent active cooling was assumed to be available. Therefore, the stagnant water inside the assembly box would be heated up by the residual power of the fuel until it reaches saturation temperature at t = 80 s. Since the coolant inventory of the test section is small, the complete coolant inventory of the assembly box is evaporated already after approximately 400s, causing to a rapid temperature increase, as shown in Fig 10 (left). Short-term failure of the

stainless steel claddings must be expected due to ballooning or rupture at a temperature of more than 816 °C. The peak cladding temperature, predicted by the Dittus-Boelter correlation for superheated steam, is almost reaching the melting point of the claddings (even though the integrity of the claddings will certainly be lost, it was assumed in this analysis that the fuel rod geometry is still unchanged). From that moment on, the shielding and retention capacity of the cooling system would be lost and airborne radioactive material would be free to enter the pressure tube. As the pressure tube would mostly be voided then, the radioactive material would enter the experimental hall without filtering. The cladding temperature progression at different heights of the fuel rods is shown on the right hand side of Fig. 10 for the entire simulation time of approximately 200 minutes. After reaching a maximum temperature of 1400 °C, the temperatures decreases slowly due to decreasing decay power as plotted on the left hand side of Fig. 11. Fuel rod centerline temperatures have been predicted with a heat conduction model of the pellets, assuming three radial segments of the heated pellets and a He gap of 0.5 mm. According to the progression of cladding and fuel centerline temperatures, damage of the core and failure of the claddings must be expected. However, melting of the UO_2 pellets (T_{melt} = 2865 °C) and failure of the pressure tube are unlikely.

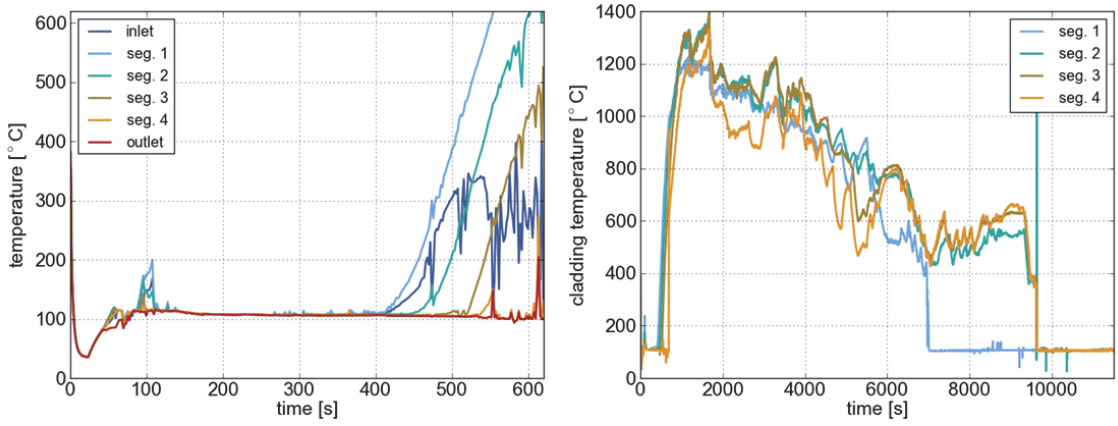

Figure 10. Coolant temperatures along the fuel rods for the first 600 s (left) and cladding temperatures during the total simulation time of 200 minutes (right). Inlet and outlet denote the lower and upper end of the assembly box. Segments 1 to 4 are in between. [3]

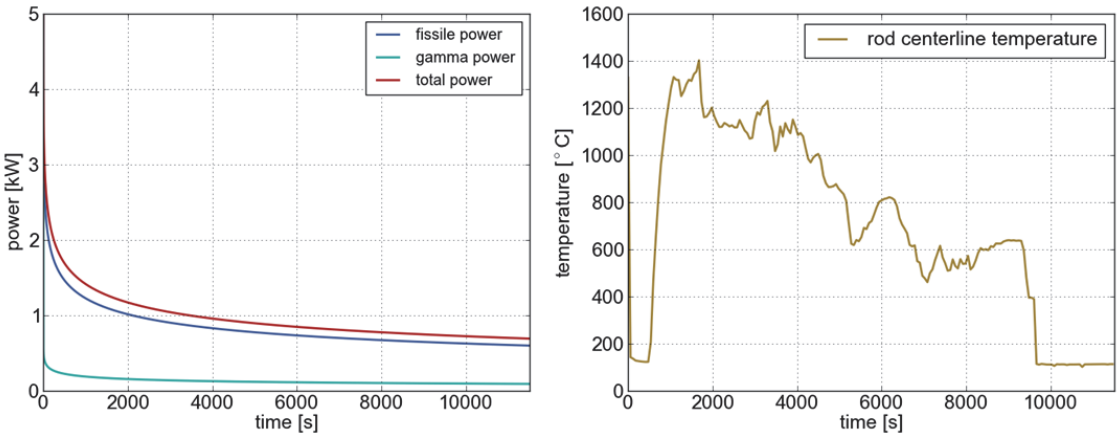

Figure 11. Progression of heating power (left) and rod centerline temperature (right) used as basis for the source term evaluation (right). [3]

The progression of the maximum fuel pin centerline temperature, depicted on the right hand side of Fig. 11, was used to determine the resulting radiological source term for the postulated accident scenario. The methodology applied to determine the transient radiological release followed the recommendations proposed by Lorenz and Osborne [8]. Their fractional release rate model CORSOR-O, a stand-alone model, is geometry independent and should be applicable here. It is based on the fission product release tests performed at the Oak Ridge National Laboratory between 1975 and 1993. A fission product inventory of the test fuel rods has been assumed which corresponds to 115 operation days at full power. For evaluation of the source term, the elements Kr, Sr, Zr, Mo, Ru, Ag, Sb, Te, I, Xe, Cs, Ba, La, Ce, Eu, and Pu were taken into respect.

As an example, release rates of I-131, predicted by Raqué [3], are shown in Fig. 12. The release per time step (Δt = 20 s) is displayed graphically with blue bars. We see that most of the radioactive release would occur within the first 1000 s after the claddings had failed, when the highest fuel temperatures must be expected. As illustrated on the left hand side of Fig. 11, the residual power decreases to 1.4 kW within 1000s after scram. The cyan curve illustrates the integral released activity over time in Bq, as well as the converted effective dose in Sv. The total amount of released I-131 is 2.74×10^{11} Bq, corresponding to 0.5 % of the initial inventory. After conversion, this comes up to an effective dose of 5500 Sv. The total effective dose, including all relevant isotopes, was predicted as 13300 Sv.

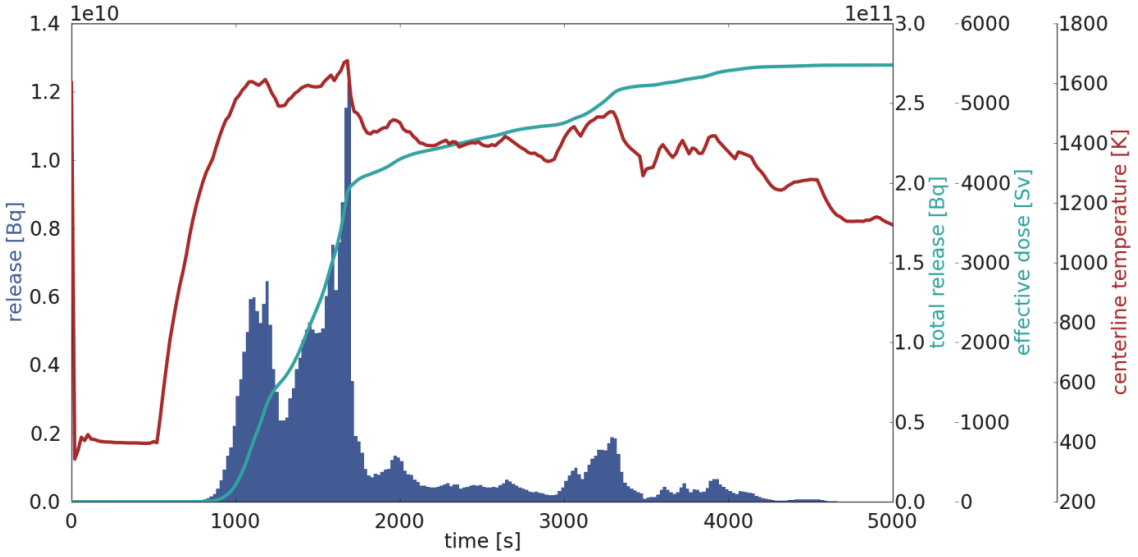

Figure 12. Source term of iodine-131: fuel rod centerline temperature (red) and I-131 release per time step (blue), total release with converted effective dose (both cyan). [3]

It is clear from these predictions that a closed containment around the test facility is mandatory to avoid radioactive release under such worst case assumptions.

3.3 Hydrogen source term in case of failure of all active safety systems

The high temperature exposure to steam, Fig. 10, does not only damage the fuel claddings. According to high temperature oxidation tests of Ishida et al. [9] with stainless steel 304 in steam, we have to assume a total oxide thickness of 250µm, which is half the cladding thickness, within 1000 s at 1300 °C. At 1100 °C, the corrosion rate is already significantly less,

but we still get another 70 µm within 2000 s. As the cladding would be severely damaged at these temperatures, we have to assume oxidation from outside and from inside, so that the entire heated length of all four claddings would have been oxidized.

Oxidation of iron is producing hydrogen according to the reaction equation

$$Fe + H_2O \rightarrow FeO + H_2$$

Taking the simplified assumption that the claddings of these 4 fuel rods would react as Fe according to this equation, we would produce 8.1 g of hydrogen during the accident from cladding oxidation. The wire wrapped around the fuel rods is rather at steam temperature, which is ~100 °C colder than the cladding, as plotted in Fig. 13. An exposure to steam at 1200 °C during 1000 s would cause an oxidation thickness of 70 µm. This produces another 0.2 g of hydrogen.

The assembly box between channel 3 and channel 4 (see Fig. 1) is at an average temperature of these two steam temperatures. Therefore, according to Fig. 13, we can expect an exposure at ~800 °C during 1000 s and at ~700 °C for another 2000 s. The oxidation rate at these temperatures is negligible compared with the cladding and wire oxidation.

The total hydrogen source term predicted for the accident postulated in section 3.2 is thus about 8.3 g. This hydrogen cannot ignite inside the primary system, since air is missing there. However, it can leave the primary system through the postulated break into the containment, where it can ignite if mixed with air as long as the hydrogen concentration is greater than 4 vol%. This constraint limits the air volume to less than 2.8 m^3 for a flammable hydrogen-air mixture.

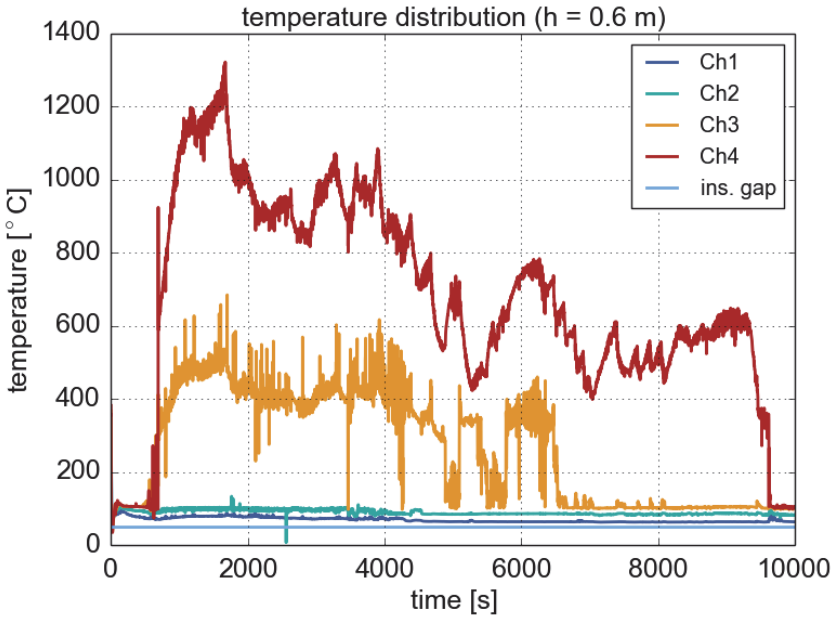

Figure 13. Steam temperature predicted for the accident postulated in section 3.2. Channel numbers refer to Fig. 1.

The experiments of Friedrich et al. [10] give an impression about the potential consequences of a deflagration of 5 to 15 g of hydrogen inside a cabinet at atmospheric pressure. With 6 g of hydrogen, a pressure peak of 10 kPa was measured, which would cause minor structural damage and a low risk of eardrum rupture for personnel in the room. With 15 g of hydrogen, a

pressure peak of 100 kPa was measured and some major structural damage was already observed; an eardrum rupture would be most likely then. Therefore, the release and ignition of 8.3 g of hydrogen is not expected to damage the massive containment structures.

3.4 Conclusions from analyses of design extension accidents

These and other, similar analyses of unlikely accident scenarios demonstrated that a secondary failure of the research reactor can be excluded. They indicated, however, that the use of active fuel inside a high pressure test loop requires a closed containment around the loop and its supply systems to avoid radioactive release to the environment under worst case assumptions. Moreover, diverse and redundant safety injection systems are advisable to minimize the risk of failure of all active safety systems, as postulated here. The SCWR fuel qualification test has been designed accordingly with a closed confinement around the entire test facility, which is strong enough to withstand even a postulated explosion of hydrogen being produced during such postulated severe accidents. The fuel qualification test facility is thus expected to meet the Czech requirements for nuclear safety on nuclear research facilities [11].

Acknowledgement

This work has been funded by the European Commission as part of their project SCWR-FQT, contract number 269908.

References

1. T. Schulenberg, J. Starflinger, High Performance Light Water Reactor – design and analyses, KIT Scientific Publishing, ISBN 978-3-86644-817-9, Karlsruhe, 2012

2. M. Ruzickova, T. Schulenberg, D. Visser, C. Maraczy, A. Toivonen, A. Kiss, R. Novotny, Overview and progress in the European project “Supercritical Water Reactor – Fuel Qualification Test”, Progress in Nuclear Energy 77, 381-389 (2014)

3. M. Raqué, Safety analyses for a fuel qualification test with supercritical water, Dissertation, Karlsruhe Institute of Technology, 2014

4. M. Raqué, O. Frybort, A. Vojacek, T. Schulenberg, Passive residual heat removal system for the SCWR fuel qualification test, NURETH15-112, Pisa, Italy, May 12-15, 2013

5. T. Schulenberg, M. Raqué, Safety analyses for an in-pile SCWR fuel qualification test loop, PBNC 2014-106, Vancouver, Canada, August 24-28, 2014

6. T. Zeiger, M. Raqué, T. Schulenberg, Study of consequences of a pressure tube failure for an SCWR in-pile fuel assembly test, NURETH15-207, Pisa, Italy, May 12-15, 2013

7. T. Zeiger, Auswirkungen eines postulierten Druckrohrversagens während des SCWR Fuel Qualification Tests, Dissertation, Karlsruhe Institute of Technology, 2014

8. R. A. Lorenz and M. F. Osborne, A summary of ORNL fission product release tests with recommended release rates and diffusion coefficients, Oak Ridge National Laboratory, NUREG/CR-6261, 1995

9. T. Ishida, Y. Harayama, S. Yaguchi, Oxidation of 304 stainless steel in high temperature steam, Journal of Nuclear Materials 140, 74-84, 1986

10. A. A. Friedrich, A. Veser, G. Stern, N. Kotchourko, Hyper experiment on catastrophic hydrogen releases inside a fuel cell enclosure, Int. Journal of Hydrogen Energy, Vol. 36, 3, p. 2678-2687, 2011

11. K. Matějka et al., Requirements of the State Office for Nuclear Safety on Nuclear Research Facilities with Respect to Nuclear Safety, Radiation Protection, Physical Protection and Emergency Preparedness, Prague, April 2004

12. C. Zhou, Y. Yang, X. Cheng, Feasibility analysis of the modified ATHLET code for supercritical water cooled systems, Nuclear Engineering and Design 250, pp. 600-612, 2012

13. T. Schulenberg, M. Raqué, K. Arheidt, Prediction of heat transfer during depressurization from supercritical pressure, NURETH15-139, Pisa, Italy, May 12-15, 2013

The 7th International Symposium on Supercritical Water-Cooled Reactors
ISSCWR-7-2034
15-18 March 2015, Helsinki, Finland

Effect of Thermal Treatment on Stainless Steel Corrosion in Flowing Supercritical Water

Y. Jiao & J. Kish
Department of Materials Science & Engineering, McMaster University
1280 Main Street West, Hamilton, Ontario, Canada L8S 4L7
jiaoyn@mcmaster.ca; kishjr@mcmaster.ca

W. Cook & G. Steeves
Department of Chemical Engineering, University of New Brunswick
15 Dineen Drive, Fredericton, New Brunswick, Canada, E3B 5A3
wcook@unb.ca; graham.steeves@unb.ca

W. Zheng
CanmetMATERIALS, Natural Resources Canada
183 Longwood Road South, Hamilton, Ontario, Canada L8P 0A5
Wenyue.Zheng@NRCan-RNCan.gc.ca

D. Guzonas
Canadian Nuclear Laboratories
Chalk River Laboratories, Ontario, Canada K0J 1J0
David.Guzonas@cnl.ca

Abstract

The effect of high temperature microstructure degradation (thermal ageing) on the corrosion resistance of austenitic stainless steels in supercritical water (SCW) was evaluated in this study. Mill-annealed (MA) and thermally-treated (TT) samples of Type 316L and Type 310S stainless steel were exposed in 25 MPa SCW at 550 °C with 8 ppm dissolved oxygen in a flowing autoclave testing loop. The thermal treatments applied to Type 316L (815 °C for 1000 h + water quench) and Type 310S (800 °C for 1000 h + air cool) were successful in precipitating the expected intermetallic phases in each alloy, both within the grains and on grain boundaries. It was found that a prolonged time at the relatively high temperature was sufficient to suppress significant compositional variation across the various intermetallic phase boundaries. This paper presents the results of the gravimetric analysis and oxide scale characterization using scanning electron microscopy (SEM) coupled with X-ray energy dispersive spectroscopy (EDS). The role played by the fine precipitate structure on formation of the oxide scale, and thus corrosion resistance, is discussed. The combined role of dissolved oxygen and flow (revealed by examining the differences between Type 316L samples exposed in a static autoclave and in the flowing autoclave loop) is also addressed. It was concluded that formation of intermetallic phase precipitates during high temperature exposure is not likely to have a major effect on the apparent corrosion resistance because of the discontinuous nature of the precipitation.

1. Introduction

There has been a significant corrosion research effort dedicated to screening candidate materials for use as a fuel cladding for supercritical water-cooled reactor (SCWR) concepts [1-6]. Austenitic stainless steels have received significant attention due to their relatively good corrosion resistance in supercritical water (SCW). Despite the current state of knowledge, a key gap exists: the effect on the corrosion resistance of the slow microstructural evolution due to thermal ageing. For the most part, studies reporting the corrosion resistance of austenitic stainless steels exposed in SCW have been conducted using as-received (typically mill-annealed) material, without much consideration of the microstructural changes that have occurred during testing at high temperatures. This is of particular significant to the Canadian SCWR concept, because of the higher core outlet temperature; the peak cladding temperature may be as high as 800 °C and the in-service life of the cladding is roughly 30,000 h.

Short term thermal ageing or treatment is well known to "sensitize" the microstructure of 300 series stainless steels in which Cr-rich carbide (such as $M_{23}C_6$) precipitates form on the grain boundaries, rendering the grain boundary region more susceptible [7-8]. Other intermetallic precipitates such as the chi (χ), laves (η) and sigma (σ) phases take longer times to form [9-13]. Only very recently have thermal ageing effects on the corrosion and stress corrosion cracking resistance of austenitic stainless steels in SCW been given consideration [14-16]. We reported on the effect of thermal ageing on the short-term (500 h) corrosion resistance of Type 316L stainless steel in 25 MPa SCW at 550 °C using a static autoclave with no attempt to maintain the initial 8 ppm dissolved oxygen content [14]. It was found that although relatively large intermetallic precipitates located at the scale/alloy interface locally affected oxide scale formation, their discontinuous formation did not affect the short-term overall apparent corrosion resistance.

The current study was conducted to evaluate the effect of prior thermal treatment on the short-term (500 h) corrosion resistance of Type 316L and Type 310S stainless steel exposed in 25 MPa SCW at 550 °C using a closed flow loop autoclave testing facility to maintain the dissolved oxygen concentration at 8 ppm. This was achieved by comparing the weight gain and oxide scale structure and composition formed on exposed mill-annealed/solution-annealed material and on thermally-treated material: the latter designed to precipitate the expected intermetallic phases in each alloy. The intermetallic phases formed in each alloy were characterized using transmission electron microscopy (TEM) and associated techniques. The mode and extent of corrosion that occurred was characterized using scanning electron microscopy (SEM) coupled with X-ray energy dispersive spectroscopy (EDS).

2. Experimental Methods

Rectangular (20×10×1 mm) samples were prepared from commercial Type 316L and Type 310S stainless steel rod product provided in the mill-annealed condition. The chemical composition was analysed using ICP-OES (Varian Spectrometer) and combustion analysis (LECO CS230). The results are shown in Table 1. A small (2 mm diameter) hole was drilled into each sample near the top to facilitate mounting on a coupon tree. Type 316L samples were exposed in the mill-annealed (MA) state and a thermally-treated (TT) state. The MA state was evaluated to permit a comparison with our prior test results using a static autoclave [14]. The TT state was achieved by thermal ageing at 815 °C in nitrogen for 1000 h followed by air-cooling to room temperature to precipitate all of the expected intermetallic $M_{23}C_6$, χ, η and σ phases [17]. In contrast, Type 310S samples were exposed in a solution-annealed (SA) state along with a TT state. The SA state was achieved by thermal treating samples at 1050 °C for 1 h followed by water-quenching to room temperature. The TT state was achieved by thermal treating samples at 800 °C for 1000 h followed by air-cooling to room temperature to precipitate the expected intermetallic $M_{23}C_6$ and σ

phases [18]. The treatment temperature was selected to be as close as possible to the maximum fuel cladding temperature of 800 °C expected in the Canadian SCWR concept [6], while still allowing for the sequential formation of each major intermetallic precipitate type. All heat treatments were conducted by sealing the in a quartz tube that was purged with high purity nitrogen gas. Upon removal from the furnace, samples were cooled to room temperature while sealed in the nitrogen gas-purged quartz tube. A set of four samples in each state were mechanically abraded to a 800 grit surface finish using SiC abrasive papers and water as a lubricant, rinsed in acetone in an ultrasonic bath, dried using absorbent wipes and weighed prior to testing.

Table 1. Chemical composition (wt.%) of the commercial stainless steels studied.

Alloy	Cr	Ni	Mo	Mn	Si	P	S	C	Fe
316L	16.3	10.2	2.1	1.6	0.24	0.04	0.03	0.02	Bal.
310S	24.3	19.6	0.3	1.0	0.76	0.04	0.03	0.06	Bal.

The closed flow loop autoclave testing facility available at the University of New Brunswick was used to expose the samples in SCW. Specific details regarding the design of this facility are published elsewhere [4]. Testing was conducted in flowing (200 mL/min.) 25 MPa SCW with a 8 ppm dissolved oxygen concentration at 550 °C for 500 h. The sample sets (four samples of each material) were suspended on a coupon tree that was placed inside the autoclave. The flow loop testing was interrupted at the 100 h and 250 h exposure times so that samples could be removed from the autoclave and weighed. One sample was kept for characterization during each interruption. The relatively short exposure time of 500 h was selected to prevent additional intermetallic precipitates from forming *in-situ* in the Type 316L-MA and Type 310S-SA materials.

The microstructure of the starting material was examined in cross-section using light optical microscopy, SEM, and TEM; the latter two techniques were coupled with EDS. Samples were cold-mounted in cross-section using standard metallographic techniques and polished to a 1 μm surface finish. Chemical etching was conducted by contacting the polished surfaces with an acetic acid-glycerine mixture for 40 s. The SEM examination was performed using a JEOL JSM-7000F microscope equipped with a Schottky field emission gun (FEG) filament and an integrated Oxford Synergy system with INCA EDS X-ray micro-analysis using an accelerating voltage of 10 kV and a working distance of 10 mm. The TEM examination was performed using a JEOL 2010F TEM/STEM equipped with an Oxford Instruments EDS analyser using an accelerating voltage of 200 kV. TEM samples were prepared by mechanically-abrading samples to a thickness of 80 μm using SiC paper and water as a lubricant. Small foils were then punched out of the thinned samples and subsequently electrochemically polished in a perchloric acid (10%)-methanol (90%) solution at −50 ºC to create a small hole in the thin foil. Randomly selected intermetallic precipitates were identified by comparing the elemental composition determined by EDS in both SEM and TEM mode with those published using the same techniques [10-13]. Selected area diffraction (SAD) in TEM mode was used on those phases that were large enough to minimize the diffraction from the austenite matrix. X-ray diffraction (XRD) after a bulk extraction was also used to help identify the intermetallic precipitates that were present after thermal treating. The bulk extraction was carried out in a hydrochloric acid (10%)-methanol (90%) solution. X-ray diffraction patterns of the extracted powder were collected using an X-ray powder diffractometer (Bruker 8D Advanced) operated with a Cu $k_{\alpha 1}$ radiation source.

After the 500 h exposure, the sample sets were photographed and then re-weighed. One sample from each set was selected for a more detailed examination using SEM-EDS of the oxide scale formed. A plan-view examination of the oxide scale was conducted first using SEM (JEOL JSM-7000F) operated with an accelerating voltage of 10 kV and a working distance of 10 mm. The sample was subsequently cold-mounted in cross-section using standard metallographic techniques and polished to a 1 μm finish. SEM-EDS (JEOL JSM-7000F) operated with an

accelerating voltage of 10 kV and a working distance of 10 mm was then used again to examine the oxide scale in cross-section.

3. Results

Figure 1 shows the starting microstructures as revealed using light optical microscopy. The Type 316L-MA material (Figure 1a) exhibited a coarse-grained structure with some twinning and MnS inclusions (verified by SEM-EDS). The Type 316L-TT material (Figure 1b) exhibited similar features as the MA material, but with significant intermetallic precipitation both within the grains and on the grain boundaries. The precipitation was discontinuous in both cases. The Type 310S-SA material (Figure 1c) exhibited a coarse-grained structure with twinning. The most striking feature was the $M_{23}C_6$ grain boundary precipitation (verified by TEM-SAD) that remained after applying the SA treatment. The Type 310S-TT material (Figure 1d) exhibited similar features as the SA material, but with significant intermetallic phase precipitation within the grains and on the grain boundaries to an increased extent. No surprise that majority GB carbides were dissolved after 1000 h thermal treatment as a result of nucleation of intermetallic precipitates [10]. The precipitation was discontinuous in both cases. The average grain size of each material was measured using the commercial software NIS-Elements D with ASTM E1382 procedure. The Type 316L material and Type 310S material had similar grain sizes: 9.0 and 9.5 for the Type 316L MA and TT material respectively, and 7.2 and 7.0 for the Type 310S SA and TT material respectively. Thus, the prolonged thermal treatment did not induce any significant grain growth.

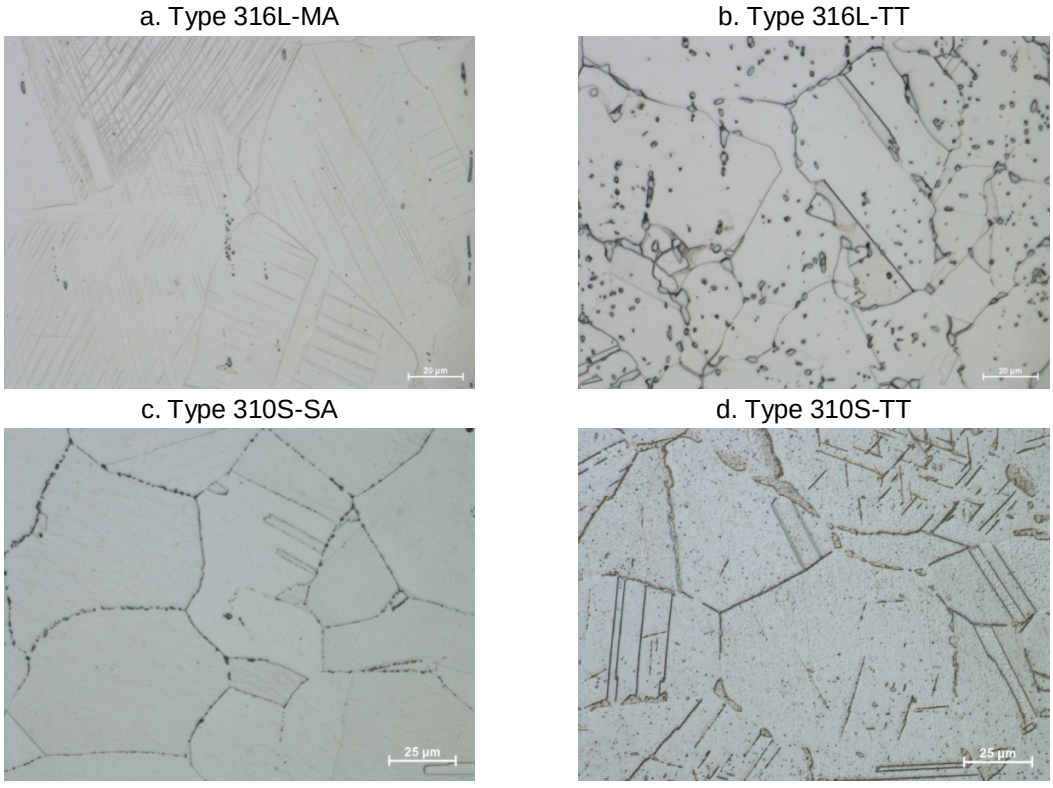

Figure 1. Light optical image of the (a) Type 316L-MA material, (b) Type 316L-TT material, (c) Type 310S-SA material, and (d) Type 310S-TT material.

Figure 2 shows a typical result of the intermetallic phase precipitate characterization conducted using TEM-EDS. Cr-depletion was not detected in any of the intermetallic phase precipitates analyzed in either TT material. This finding implied that the extent of Cr diffusion during the prolonged exposure time (1000 h) at the high temperature (800-815 ºC) was sufficient to replenish any depletion that occurred during the nucleation and initial growth of the Cr-rich intermetallic phase precipitates.

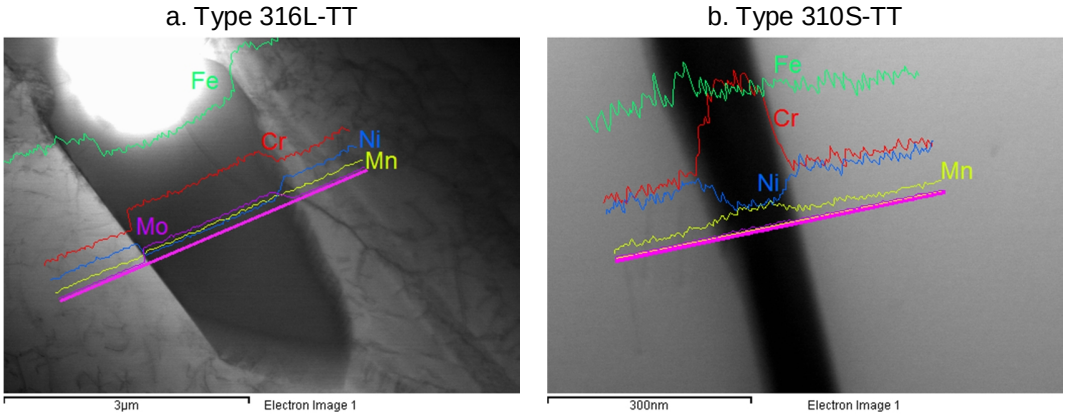

Figure 2. STEM bright-field image and corresponding EDS line analysis conducted to identify the various intermetallic precipitates present within the grains and on grain boundaries in the (a) Type 316-TT material and (b) Type 310S-TT material.

A summary of the intermetallic precipitates identified within the MA and TT material using TEM-SAD, STEM-EDS and XRD techniques is provided in Table 2. A relatively low population of $M_{23}C_6$ type carbides was observed within the grains and on grain boundaries in both the Type 316L-MA and Type 310S-SA material using TEM/STEM. The thermal treatment applied resulted in the precipitation of the χ and σ phases and the σ phase within the grains and on the grain boundaries of Type 316L and Type 310S respectively. Interestingly, $M_{23}C_6$ type carbide precipitates were no longer detected either within the grains or on the grain boundaries of the Type 316L-TT material and on the grain boundaries in the Type 310S-TT material. This indicates that significant dissolution of these precipitates occurred. The detection of this phase by XRD inboth TT materials indicates that complete dissolution did not occur. In summary, the thermal treatment was successful in precipitating the expected phases for both alloys: $M_{23}C_6$ + χ + η + σ for Type 316L [17] and $M_{23}C_6$ + σ for Type 310S [18].

Table 2. Summary of precipitates detected.

Material	TEM-SAD & STEM-EDS		XRD
	Grain	Boundary	
Type 316L-MA	$M_{23}C_6$	$M_{23}C_6$	Not Analysed
Type 316L-TT	χ + σ	χ + σ	$M_{23}C_6$ + χ + η + σ
Type 310S-SA	$M_{23}C_6$	$M_{23}C_6$	Not Analysed
Type 310S-TT	$M_{23}C_6$ + σ	σ	$M_{23}C_6$ + σ

The XRD diffraction patterns of bulk extracted intermetallic phase precipitates acquired from each TT material are shown in Figure 3. Distinct peaks of the $M_{23}C_6$, χ, η and σ were observed in Type 316L-TT material (Figure 3a), and distinct peaks of $M_{23}C_6$ and σ were observed in the Type 310S-TT material (Figure 3b). The peak at 46° for the Type 316L-TT material is inherent to both the η and σ phases. The peak at 47° is inherent to the σ phase only. There were no peaks

inherent to any other phases within the range of 2θ range plotted. If the entire bulk extracted particles mass was the σ phase, then the intensity of the 47° peak would be higher than the intensity of the 46° peak. However, Figure 3 shows that these two peaks (46° and 47°) had similar intensities. The higher than expected intensity of the 46° indicated that the η phase was likely included in bulk extracted precipitate mass. Similarly, the peaks at 37.5° and 50.5° are mainly contributed by $M_{23}C_6$ carbides due to low intensity of χ phase and η phase. However, the location of the η phase (within grains and/or on grain boundaries) was not known.

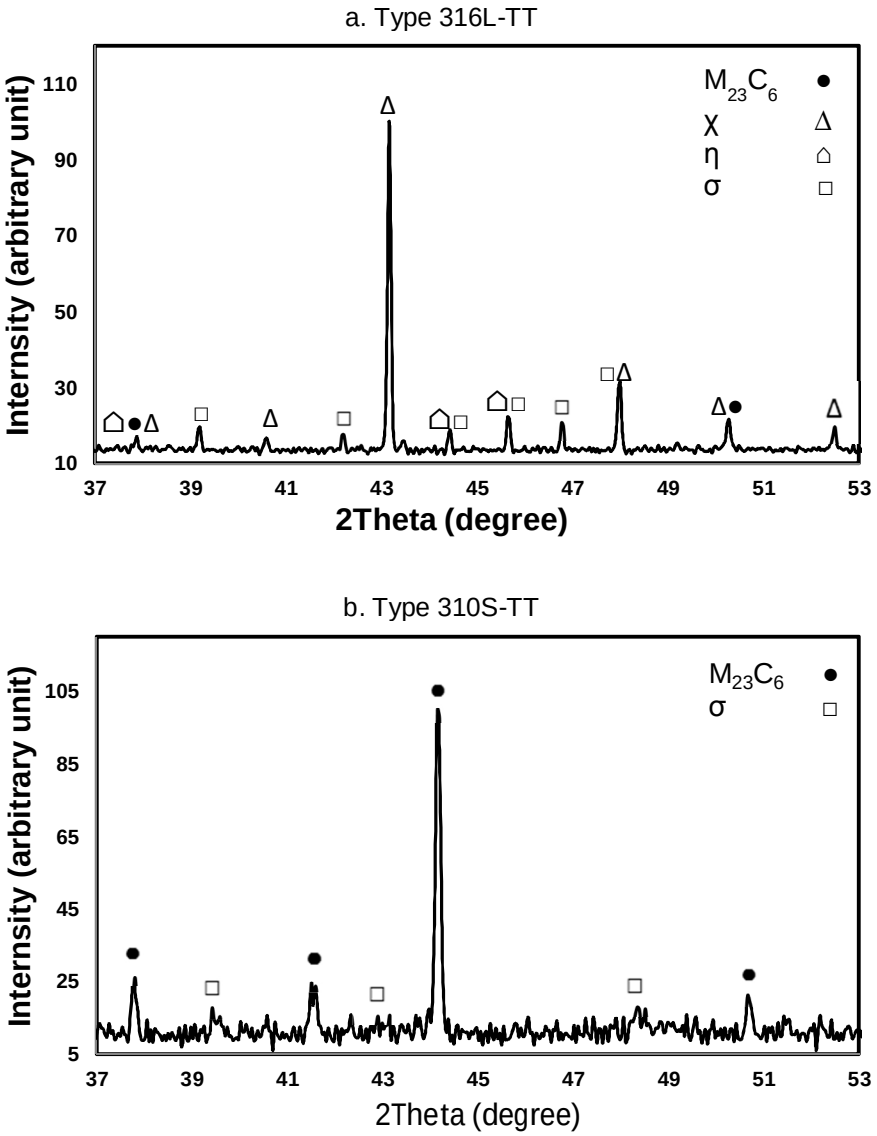

Figure 3. Powder XRD pattern of intermetallic precipitates bulk extracted from the TT material: (a) Type 316L-TT and (b) Type 310S-TT.

Figure 4 compares the average weight change exhibited by each sample set after exposure in flowing 25 MPa SCW at 550 °C with 8 ppm dissolved oxygen for 500 h. The bars superimposed onto the chart mark the highest and lowest values recorded for each sample set, indicating the spread in the data. All four weight average change values were positive, indicating a significant

portion of the oxide scale formed remained intact upon removal from the autoclave. The average weight gain exhibited by the TT material was higher than that of the MA material for Type 316L and the SA material for Type 310S. The difference was outside of the spread of the data for Type 316L, but was within the spread of the data for Type 310S. It was clear that alloy composition had a more significant effect than thermal treatment on the short-term corrosion resistance as shown by weight change measurements.

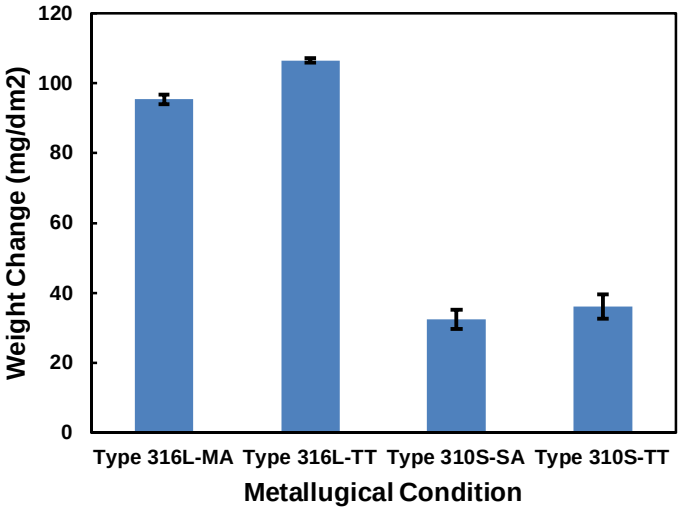

Figure 4. Bar chart comparing weight change data of the sample sets exposed in flowing 25 MPa SCW with 8 ppm dissolved oxygen at 550 ºC after 500 h.

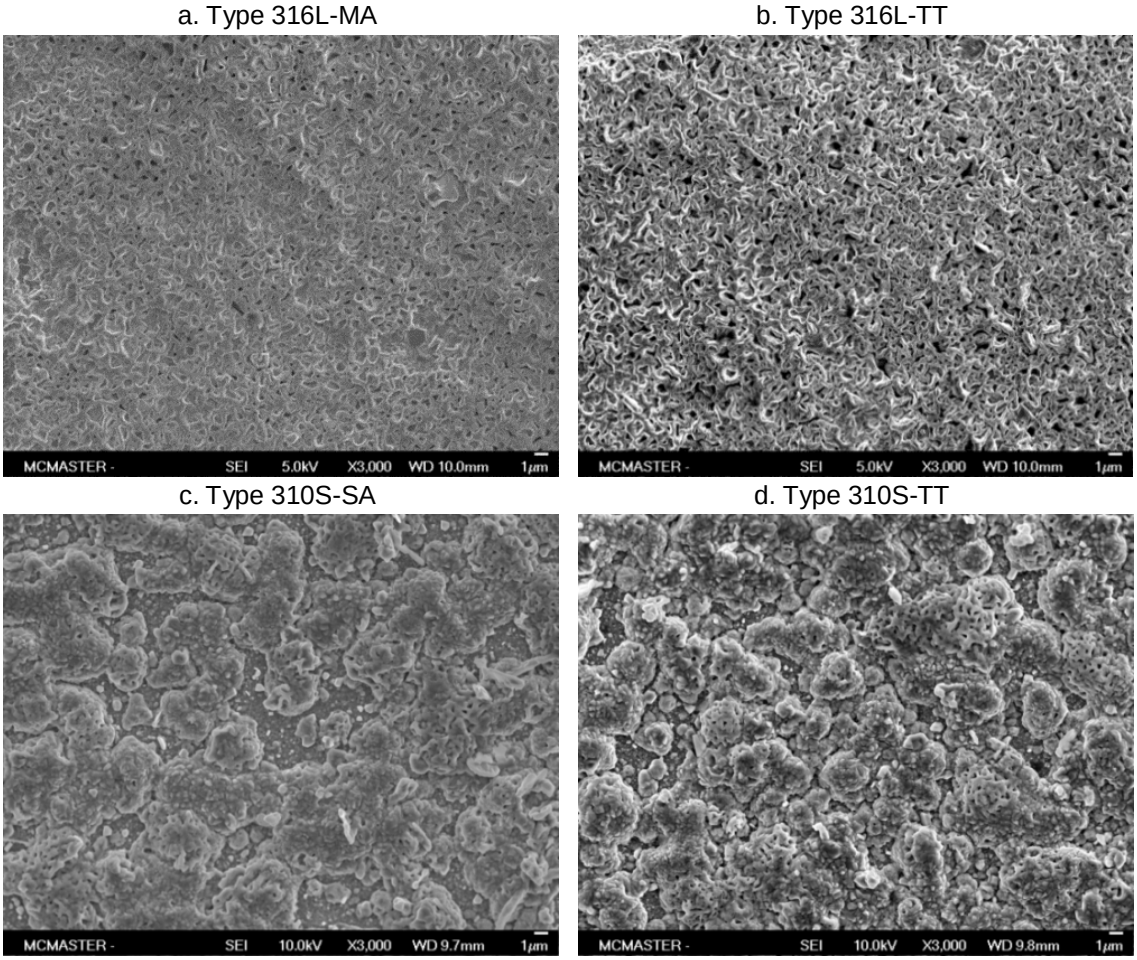

Figure 5. Secondary electron images (plan-view) showing the typical morphology of the oxide scale formed on the (a) Type 316L-MA material, (b) Type 316L-TT material, (c) Type 310S-SA material and (d) Type 310S-TT material after exposure in flowing 25 MPa SCW with 8 ppm dissolved oxygen at 550 ºC after 500 h.

Figure 5 shows a secondary electron image (plan-view) of the oxide scale formed on each material. The surface of both Type 316L materials exhibited a similar morphology, consisting of an adherent interconnecting network of fine platelets. Localized areas of apparent oxide exfoliation were observed on both surfaces to a similar extent. The surface of both Type 310S materials also exhibited a similar morphology, consisting of an adherent discontinuous network of coarse nodules residing on top of a more compact inner layer. No evidence of any significant cracking or spallation was found.

Figure 6 shows a backscattered electron image (cross-section) of the oxide scale formed on both Type 316L materials along with an elemental composition profile measured using EDS across the alloy/scale interface. The horizontal line superimposed on each backscattered electron image identifies the location of the EDS line profile, whereas the vertical lines identify the location of the interfaces between distinct phases as deduced from the EDS line profile. The oxide scale formed on both the MA and TT material consisted of three distinct oxidized layers: a Cr-rich inner

layer, a Fe-rich middle layer and a mixed Cr-Fe outer layer. The discontinuous morphology of the inner layer was consistent with internal oxidation, whereas the more continuous morphology of the middle layer was consistent with external oxidation. Porosity was observed both at the inner layer/middle layer interface and within the outer layer. The EDS line scan were conducted on representative regions and the average thickness of oxide have no significant difference.

a. Type 316L-MA (BSE Image)

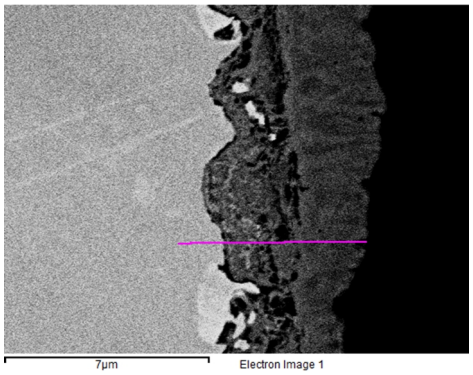

b. Type 316L-MA (EDS)

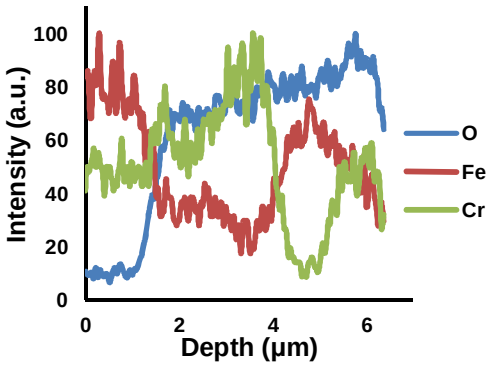

c. Type 316L-TT (BSE Image)

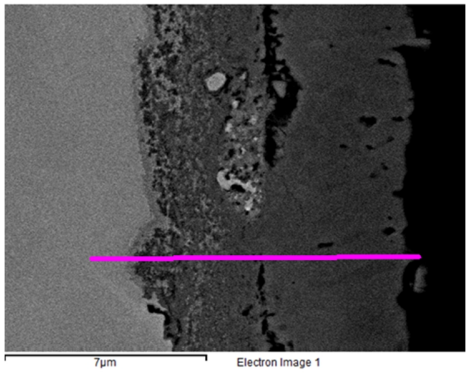

d. Type 316L-TT (EDS)

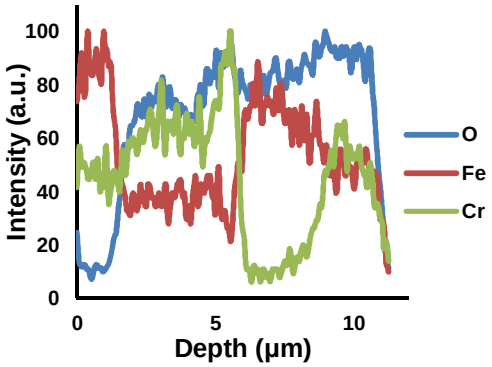

Figure 6. Back scattered electron image (cross-section) of oxide scale formed on the (a) Type 316L-MA material and (b) Type 316L-TT material. EDS line scans across alloy/scale interface of the (b) Type 316L-MA material and (d) Type 316L-TT material.

Figure 7 shows a back scattered electron image (cross-section) of the oxide scale formed on both Type 310S materials along with an elemental composition profile measured using EDS across the alloy/scale interface. Although two distinct oxidized layers were observed on both materials, they appeared to have a different composition. The oxidized scale on the MA material consisted of a Cr-rich inner layer underneath a Fe-rich outer layer, whereas it consisted of a Cr-rich inner layer underneath a mixed Cr-Fe outer layer on the TT material. The discontinuous morphology of the inner layer was consistent with internal oxidation. Porosity was also observed at the inner layer/outer layer interface, but to a lesser extent than observed on the Type 316L material.

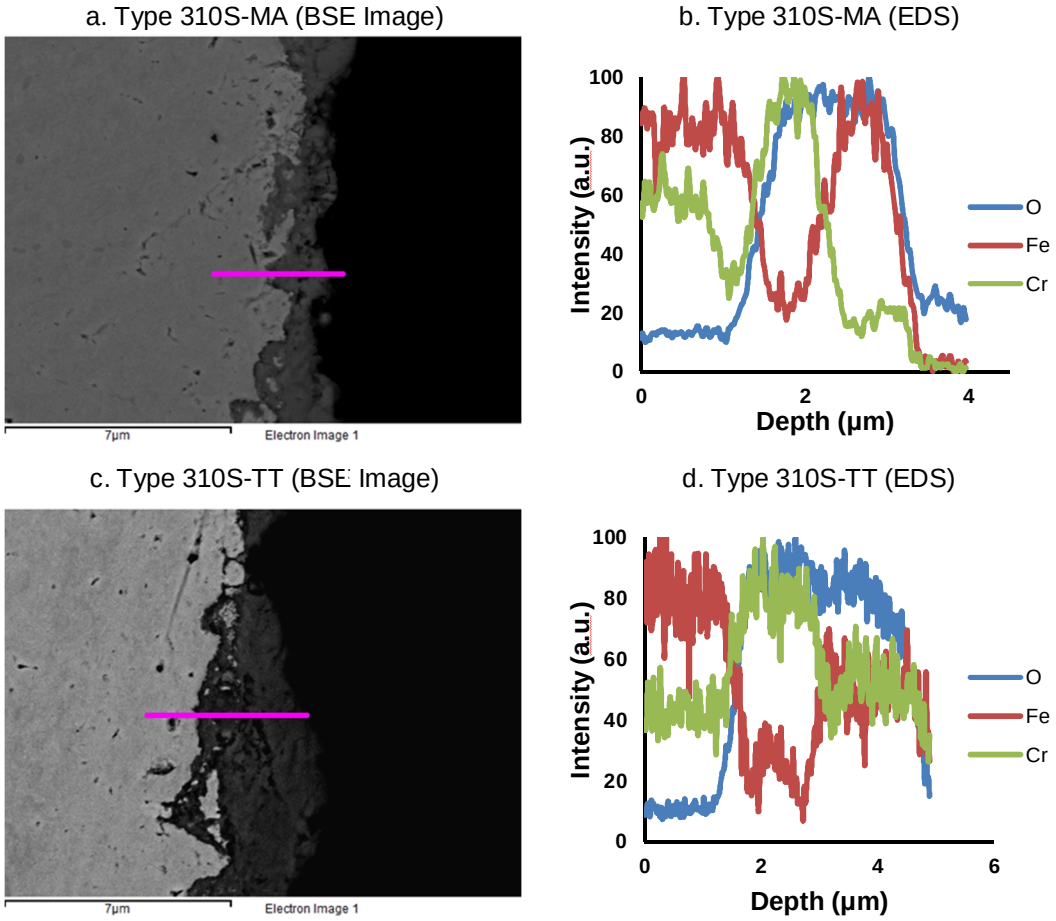

Figure 7. Back scattered electron image (cross-section) of oxide scale formed on the (a) Type 310S-SA material and (c) Type 310S-TT material. EDS line scans across alloy/scale interface of the (b) Type 310S-SA material and (d) Type 310S-TT material.

4. Discussion

The effect of thermal treatment on the corrosion resistance was found to be different for the two stainless steels. The TT material exhibited a statistically higher weight change than the MA material for Type 316L stainless steel, whereas there was no statistically significant difference in the weight changes for the TT and SA Type 310S stainless steel. The difference in the oxide scale thickness was consistent with this finding, being thicker on the TT material than on the MA material for Type 316L, but having similar thicknesses on the TT and SA material for Type 310S. However, as discussed in more detail later, comparing the Type 316L weight change data with published data for a similar exposure suggests that if there was an effect of intermetallic phase precipitates on the apparent (surface area normalized) corrosion resistance, then it was minor at best. The discontinuous network of Cr-binding intermetallic phase precipitates both within the grains and on the grain boundaries is believed to be responsible for the absence of any apparent

major effect. The corrosion resistance relies on the formation of a protective oxide scale, which has been reported to be comprised of a combination of a less-protective magnetite (Fe_3O_4) layer residing on top of a more-protective inner Fe-Cr spinel-structure oxide [$(Fe,Cr)_3O_4$] layer for Type 316L stainless steel [19-26] and of a chromia (Cr_2O_3) layer for Type 310 stainless steel [15,27]. Modifying the near surface grain structure through cold working, as first reported many years ago [28], has a significant beneficial influence on the corrosion resistance of stainless steel in SCW [4,26,29]. This is believed to result from enhanced Cr diffusion to the alloy/scale interface along the increased density of grain boundaries and dislocations promoting the formation of a more-protective, continuous inner oxide layer enriched in Cr (relative to that formed on a stress-relieved grain structure). Thus, the formation of intermetallic phase precipitates during thermal treatment has the potential to dramatically affect scale formation in two ways: (i) binding alloyed Cr and (ii) physically blocking diffusion along the short-circuit grain boundary paths. It seems plausible that a detrimental effect can only be realized if there is a continuous network of intermetallic phase precipitates formed on the short-circuit grain boundary diffusion paths. As shown in the set of images presented, this clearly was not the case in the current study. The formation of a continuous network with stainless steel is also unlikely over the in service life of the fuel cladding (about 30,000 h) based on published predictions of intermetallic phase precipitate volume fractions formed in Type 316L stainless steel after prolonged exposure times (up to 100,000 h at 700 ºC) [9]. A parallel study on the effects of Cr-rich precipitates [31], in the TT samples, at the grain boundaries on the SCC susceptibility is being conducted. Although the Cr-rich precipitates did not show significant effects on general corrosion, their effects on SCC could be very different.

The oxide scale formed on both stainless steels exposed in the closed flow loop autoclave exhibited a different structure relative to what has been published in the literature [1-2,17]. The major difference is the presence of the Cr rich outer layer: forming a tri-layer oxide scale on Type 316L and a bi-layer oxide scale on Type 310S. The inner layers on both alloys were most likely formed by solid state diffusion [1-6,19-27], whereas the mixed Cr-Fe oxide outer layer on both alloys was most likely formed by precipitation from a supersaturated SCW layer adjacent to the scale/SCW interface [4,30]. The combined effect of flow and the constant high dissolved oxygen content likely resulted in the uptake of dissolved metal ions released from the corrosion of upstream loop components in the hot sub-critical water. These loop corrosion products plus those produced by the dissolution of the sparingly soluble oxide corrosion products in SCW [4] produce a supersaturated SCW layer adjacent to the oxide/SCW interface. Both Cr and/or Fe corrosion products have been found to deposit onto/incorporate into the protective oxide formed on metallic coupons exposed in SCW [30]. It is unclear at this time to what extent the precipitation of the mixed Cr-Fe outer layer had on the impeding the oxidation process. Regardless, the effect would have been consistent for each material tested and thus, relative comparisons in weight gain are meaningful.

Figure 8 compares weight gain data for Type 316L materials exposed in the closed flow loop autoclave (reported herein) and a static autoclave (reported elsewhere [16]). Also included in the plot is the weight gain value reported by Was et al. [19] for electropolished Type 316L-SA material exposed in deaerated 25 MPa SCW at 550 °C for 500 h in a closed flow loop autoclave (10-50 mL/min.). Electropolished surfaces have been found to result in reduced corrosion resistance compare to abraded surfaces [4], due to the higher dislocation density in the latter [32]. Two observations were extracted from the comparison presented. First, the average weight gain of the MA and TT material from our testing was higher in the closed flow loop autoclave relative to the static autoclave. However, the apparent increased weight change of the MA material was within the spread of the data set (error bars). Second, the weight gain or our entire set of samples (MA and TT in both autoclave tests) was lower than that reported by Was et al. [19] for SA material. These surface finish effects may account for the slightly higher corrosion resistance observed in the current work compared with the corrosion results reported by Was et al.. Both observations suggest that thermal treatment has a minor second-order effect on the short-term corrosion resistance of stainless steel in SCW. Testing of thermally-aged stainless steel material at both longer exposure times and higher temperature is in progress to validate this initial claim.

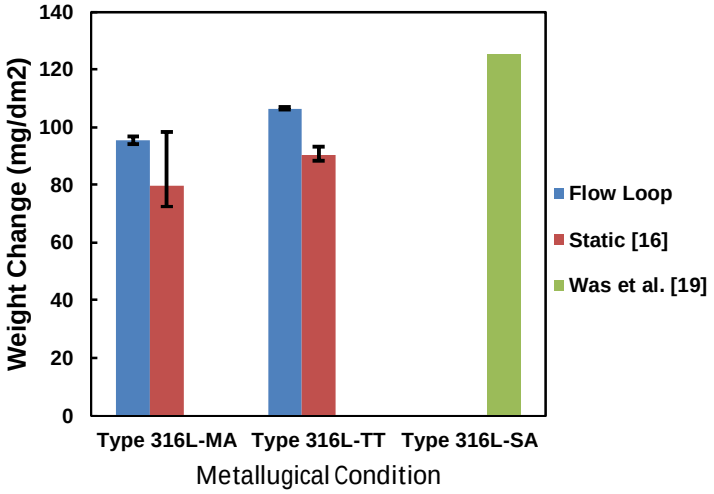

Figure 8. Weight change data obtained for: mechanically-abraded (MA) Type 316L stainless steel exposed in 25 MPa SCW at 550 °C for 500 h using a closed flow loop autoclave (8 ppm dissolved oxygen and 200 mL/min) and a static autoclave (dearated) [16] Also included is the weight gain value reported by Was et al. [19] for electropolished Type 316L-SA (solution-annealed) material exposed in 25 MPa SCW at 550 °C for 500 h in a closed flow loop autoclave (deaerated and 10-50 mL/min.).

5. Conclusion

The effect of high temperature microstructure degradation (thermal ageing) on the short-term corrosion resistance of Types 316L and Type 310S austenitic stainless steel exposed in SCW was evaluated in this study. It was concluded that the formation of intermetallic phase precipitates during exposure to high temperatures for prolonged times (thermal ageing) did not have a major effect on the corrosion resistance. The likely reason for this was the discontinuous nature of the precipitates observed within the grains and on the grain boundaries. Of the test parameters under study, alloying was found to have the more pronounced effect on the corrosion resistance than the combined effect of dissolved oxygen and flow. The higher corrosion resistance of 310S, in comparison with 316L, is associated with the presence of a more protective chromia inner layer in the oxide film.

6. Acknowledgements

Funding to Canada Gen-IV National Program was provided by Natural Resources Canada through the Office of Energy Research and Development, Atomic Energy of Canada Limited, and Natural Sciences and Engineering Research Council of Canada. The expertise provided by the technical staff at CanmetMATERIALS and the Canadian Centre for Electron Microscopy at McMaster University is greatly appreciated for assisting with the SCW corrosion testing and sample characterization respectively.

References

1. G.S. Was, P. Ampornrat, G. Gupta, S. Teysseyre, E.A. West, T.R. Allen, K. Sridharan, L. Tan, Y. Chen, X. Ren, C. Pister, *J. Nucl. Mater.,* 371 (2007), 176-201.
2. J. Kaneda, S. Kasahara, F. Kano, N. Saito, T. Shikama, H. Matsui, "Material Development for Supercritical Water-Cooled Reactor," 5th International Symposium on Supercritical Water-Cooled Reactors, Vancouver, BC, Canada, 2011, March 13-16.
3. T.R. Allen, Y. Chen, X. Ren, K. Sridharan, L. Tan, G.S. Was, E. West, D. Guzonas, Material Performance in Supercritical Water," Comprehensive Nuclear Materials, Volume 5: Material Performance and Corrosion/Waste Materials, R.J.M. Konings (Ed.), Elsevier, Amsterdam, The Netherlands, 2012, pp. 279-326.
4. D.A. Guzonas, W.G. Cook, *Corros. Sci.*, 65, 2012, 48-66.
5. S. Penttila, A. Toivonen, L. Rissanen, L. Heikinheimo, *J. Disaster Res.*, 5 (2010), 469-477.
6. D. Guzonas, R. Novotny, *Prog. Nucl. Energy*, 77 (2014), 361-372.
7. R.A. Mulford, E.L. Hall, C.L. Briant, *Corrosion*, 39 (1983), 132-143.
8. S.S.M. Tavares, V. Moura, V.C. da Costa, M.L.R. Ferreira, J.M. Pardal, *Mater. Charact.,* 60 (2009), 573-578.
9. T. Sourmail, H.K.D.H. Bhadeshia, *Calphad*, 27 (2003), 169-175.
10. B. Weiss, R. Stickler, *Metall. Trans.*, 3, (1972), 851-866.
11. J.E. Spruiell, J.A. Scott, C.S. Ary, R.L. Hardin, Metall. Trans., 4 (1973), 1533-1544.
12. J.K.L. Lai, *Mater. Sci. Eng.*, 58 (1983). 195-209.
13. T. Sourmail, *Mater. Sci. Technol.*, 17 (2011), 1-14.
14. S. Mahboubi, G.A. Botton, J.R. Kish, "Oxide Scales Formed on Austenitic Fe-Cr-Ni Alloys Exposed to Supercritical Water (SCW): Role of Alloying Elements," 19th Pacific Basin Nuclear Conference, Vancouver, BC, Canada, 2014, August 24-28.
15. J. Li, W. Zheng, S. Penttilä, P. Liu, O.T. Woo, D. Guzonas, *J. Nucl. Mater*, 454 (2014), 7-11.
16. Y. Jiao, J. Kish, W. Zheng, D. Guzonas, W. Cook, "Effect of Thermal Ageing on the Corrosion Resistance of Stainless Steel Type 316L Exposed in Supercritical Water," 2014 Canada-China Conference on Advanced Reactor Development (CCCARD-2014), Niagara Falls, ON, Canada, 2014, April 27-30.
17. C A. Kriaa, N. Hamdi, H. Sidhom, *Prot. Met.*, 44 (2008), 506-513.
18. W.E. White, I. Le May, *Metallography*, 3 (1970), 35-50.
19. G.S. Was, S. Teysseyre, Z. Jiao, *Corrosion*, 62 (2006), 989-1005.
20. X. Gao, X. Wu, Z. Zhang, H. Guan, E.H. Han, *J. Supercrit. Fluids* 42 (2007), 157-163.
21. X. Luo, R. Tang, C. Long, Z. Miao, Q. Peng, C. Li, *Nucl. Eng. Technol.*, 40 (2008), 147-154.
22. M. Sun, X. Wu, Z. Zhang, E.H. Han, *Corros. Sci.*, 51 (2009), 1069-1072.
23. M. Fulger, M. Mihalache, D. Ohai, S. Fulger, S.C. Valeca, *J. Nucl. Mater.*, 415 (2011), 147-157.
24. I.M. Svishchev, R.A. Carvajal-Ortiz, K.I. Choudhry, D.A. Guzonas, *Corros. Sci.*, 72 (2013), 20-25.
25. M. Sun, X. Wu, E.H. Han, J. Rao, *Scripta Mater.*, 61 (2009), 996-999.
26. S. Penttilä, A. Toivonen, J. Li, W. Zheng, R. Novotny, *J. Supercrit. Fluids,* 81 (2013), 157-163.
27. H. Abe, S.M. Hong, Y. Watanabe, *Nucl. Eng.Design*, 280 (2014), 652–660.
28. W.E. Ruther, R.R. Schlueter, R.H. Lee, R.K. Hart, *Corrosion*, 22 (1966), 147-155.
29. Y. Tsuchiya, F. Kano, N. Saito, M. Ookawa, J. Kaneda, N. Hara, Corrosion and SCC Properties of Fine Grain Stainless Steel in Subcritical and Supercritical Pure Water," CORROSION/07, Nashville, TN, 2007, March 11-15.
30. Y. Daigo, Y. Watanabe and K. Sue. Corrosion, 63 (2007) 277-284.
31. S.Y. Persuad, A. Korinek, J. Huang, G.A. Botton, R.C. Newman, Corrosion Science 86 (2014) 108-122.

32. T. Maekawa, M. Kagawa and N. Nakajima. Transactions of the Japan Institute of Metals. 9 (1968) 130-136.

ISSCWR7-2035

Low-LET radiolysis of supercritical water at 400 ℃ : A sensitivity study of the density dependence of the yield of hydrated electrons on the (e^-_{aq} + e^-_{aq}) reaction rate constant

Sunuchakan Sanguanmith,[1] Jintana Meesungnoen,[1] David A. Guzonas,[2] Craig R. Stuart,[2] and Jean-Paul Jay-Gerin[1,*]
[1]Université de Sherbrooke, 3001, 12e Avenue Nord, Sherbrooke, Québec, Canada J1H 5N4
Tel: 1-819-821-8000 ext.74682, Email: jean-paul.jay-gerin@USherbrooke.ca
[2]Canadian Nuclear Laboratories, Chalk River, Ontario, Canada

Abstract

The temperature dependence of the rate constant (k) of the bimolecular reaction of two hydrated electrons (e^-_{aq}) measured in *alkaline* water exhibits an abrupt drop between 150 and 200 ℃; above 250 ℃, it is too small to be measure d reliably. Although this result is well established, the applicability of this sudden drop in $k(e^-_{aq} + e^-_{aq})$ above ~150 ℃ to *neutral* or *slightly acidic* solution, as recommended by Bartels and co-workers, still remains uncertain. Recent work by Hatomoto *et al.* combined ultrashort pulse radiolysis experiments with spur diffusion kinetic model simulations; this work suggested that in near-neutral water the abrupt change in k above ~150 ℃ does not occur and that k should increase, rather than decrease, at temperatures greater than 150 ℃ with roughly the s ame Arrhenius dependence of the data below 150 ℃. In view of this uncertainty of k, Monte Carlo simulations were used in this study to examine the sensitivity of the density dependence of the yield of e^-_{aq} in the low linear energy transfer (LET) radiolysis of supercritical water (H_2O) at 400 ℃ on variations in the temperature dependence of k. Two different values of the e^-_{aq} self-reaction rate constant at 400 ℃ were used: one based on the temperature dependence of k above 150 ℃ as measured in alkaline water (4.2×10^8 M^{-1} s^{-1}) and the other based on an Arrhenius extrapolation of the values below 150 ℃ as initially proposed by Elliot (2.5×10^{11} M^{-1} s^{-1}). In both cases, the density dependences of our calculated e^-_{aq} yields at ~60 ps and 1 ns were found to compare fairly well with the available picosecond pulse radiolysis experimental data (for D_2O) for the entire water density range studied (~0.15-0.6 g/cm^3). Only a small effect of k on the variation of $G(e^-_{aq})$ as a function of density at 60 ps and 1 ns could be observed. In conclusion, our present calculations did not allow us to unambiguously confirm (or deny) the applicability of the predicted sudden drop of $k(e^-_{aq} + e^-_{aq})$ at ~150 ℃ in near-neutral water.

1. Introduction

The Generation IV supercritical water-cooled reactor (SCWR) is an advanced reactor, which would operate with core inlet and outlet temperatures of ~350 and 625 ℃, respectively, at a pressure of 25 MPa. It is an extremely energy-efficient system; its thermodynamic cycle efficiency is greater than ~45% vs. 28-32% for current conventional pressurized water reactors. By generating lower-cost electricity, SCWRs offer considerable economic advantages.[1-7]

Supercritical water (SCW) refers to water above its thermodynamic critical point: for H_2O, t_c = 373.95 ℃ and P_c = 22.06 MPa or 217.7 atm; and for D_2O, t_c = 370.74 ℃ and P_c = 21.67 MPa or 213.9 atm.[8] A quantitative understanding of the radiation chemistry of SCW is required in the design and operation of Generation IV SCWRs, particularly to specify chemical control strategies. It is important to minimize the corrosion and degradation of reactor components resulting from the radiolytic formation of oxidizing species at high concentrations, such as $^{\bullet}OH$, H_2O_2, O_2, and $O_2^{\bullet-}$ (or its protonated form $HO_2^{\bullet}$, depending on the pH).[4,5,7,9,10] The water in reactor cores, however, is subject not only to extreme conditions of high temperature and pressure but also to the action of intense fluxes of ionizing radiation: fast neutrons, γ-rays, recoil protons and heavy ions. They are the main source of oxidizing products, but radiolysis is difficult to determine experimentally.

Direct observations or measurements at very high temperatures and pressures and in mixed radiation fields are difficult to perform. In addition, Generation IV SCWRs are still at the conceptual design stage. For these two reasons, chemical models and computer simulations are an important route of investigation for predicting the detailed radiation chemistry in SCWRs and the consequences for materials.[5,7,11-14] A key parameter to assess the chemical effects of ionizing radiation is the radiation-chemical yield or *G* value of each radiolytic species. The *G* value is defined as the number of species formed or consumed per 100 eV of absorbed energy. Another key parameter is the rate constant for each of the chemical reactions involving these species (and any other chemicals present in the system).

Experimental data on the radiation chemistry and reaction kinetics of transients under proposed SCWR operating conditions are very limited, and there are significant gaps.[15] Some data are still controversial. Certain preliminary studies suggest markedly different behavior for the effects of radiation under supercritical conditions compared to what would be predicted from simplistic extrapolations of values originally measured at lower temperatures. Here we examine one of these controversies regarding the temperature dependence of the rate constant (*k*) for the bimolecular reaction of two hydrated electrons (e^-_{aq}):[16]

$$e^-_{aq} + e^-_{aq} (+ 2H_2O) \rightarrow H_2 + 2OH^- . \quad (1)$$

In *alkaline* water, *k* exhibits a “catastrophic” drop between 150 and 200 ℃; above 250 ℃, it is too small to be measured reliably (Figure 1).[17-20] The mechanism behind this non-Arrhenius behavior above 150 ℃ is not well understood, but it is generally thought to involve the formation of some transient intermediate, such as a hydrated electron dimer (or “dielectron”, $e_2^{2-}{}_{aq}$) sharing the same solvent cavity, a hydride ion (H^-), or yet an “incompletely relaxed” localized electron (e^-_{ir}).[17,20-22] The controversy here concerns the applicability of this drop in *k* above 150 ℃ to *neutral* or *slightly acidic* solution, which has been questioned because it could be a function of the pH of the solution.[18] Up to now, an Arrhenius extrapolation procedure of the values below 150 ℃, previously proposed by Elliot [18] and Stuart *et al.*,[19] has been used in most computer models of the radiolysis of water at high temperatures in neutral solution (Figure 1). This procedure assumes that such an abrupt change in *k* does *not* occur and that reaction (1) is diffusion controlled at temperatures greater than 150 ℃. This assumption was justified by the good agreement obtained between the model and experiments.[23-25]

Recently, Hatomoto *et al.*[26] directly measured the time dependence of $G(e^-_{aq})$ in pure deaerated neutral water by using picosecond and nanosecond pulse radiolysis in the temperature range from room temperature to 250 ℃. The results were analyzed using a spur diffusion kinetic simulation model. Their findings suggest that $k(e^-_{aq} + e^-_{aq})$ under neutral conditions increases monotonically at high temperature; no abrupt drop was observed at temperatures higher than 150 ℃.

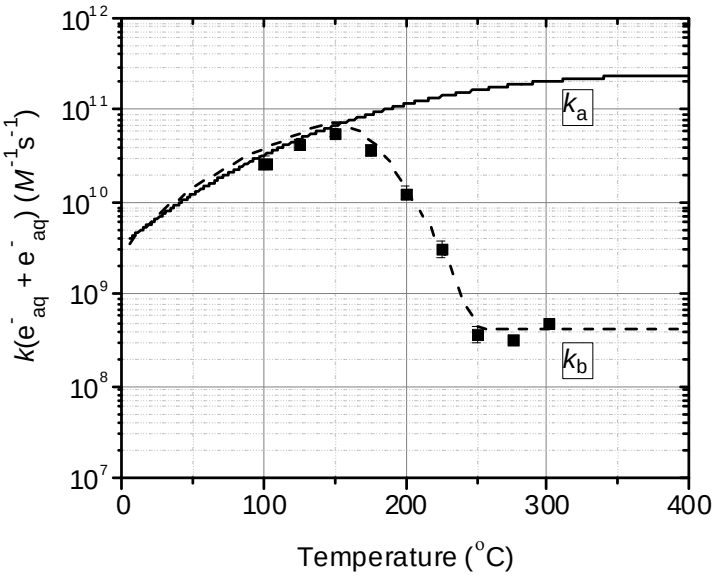

Figure 1. Rate constant for the self-reaction of two hydrated electrons as a function of temperature. The solid line (denoted k_a) shows the (e^-_{aq} + e^-_{aq}) reaction rate constant that was obtained by using an Arrhenius extrapolation procedure above 150 ℃ as proposed by Elliot (ref. 18), Stuart *et al*. (ref. 19) and Hatomoto *et al*. (ref. 26). The dashed line (denoted k_b) shows the (e^-_{aq} + e^-_{aq}) reaction rate constant that was measured by Bartels and coworkers (■, refs. 20 and 27) under alkaline conditions. Note that k_b was assumed to remain constant between 275 and 400 ℃.

The present work aims to examine the impact of the (e^-_{aq} + e^-_{aq}) reaction rate constant on the hydrated electron yield at 400 ℃ as a function of water density in the range of ~0.15-0.6 g/cm^3. To show the sensitivity of $G(e^-_{aq})$ to $k(e^-_{aq}$ + $e^-_{aq})$ in our simulations, we used two distinct temperature dependences for k above 150 ℃ (Figure 1): one extrapolated from the values below 150 ℃ following an Arrhenius procedure initi ally proposed by Elliot[18] (k_a) and the other extrapolated from the last three data points measured between 250 and 300 ℃ by Marin et al. [27] in alkaline solution (k_b). In the results and discussion section, we compare our calculated density dependence for $G(e^-_{aq})$ in irradiated SCW (H_2O) at 400 ℃ with the available experimental data obtained from time-resolved picosecond pulse radiolysis measurements in supercritical D_2O.[28,29]

2. Monte Carlo simulations

Supercritical water conditions have several specific features; we have developed an extended version of our Monte Carlo track chemistry simulation code, called IONLYS-IRT, for liquid water at ambient and elevated temperatures and which simulates irradiation by high-energy protons or heavier ions.

This IONLYS-IRT program simulates, in a three-dimensional geometrical environment, the initial production of various radiolytic species and the subsequent track expansion during which these species diffuse randomly and react with one another or with dissolved solutes (if any) present at the time of irradiation. A detailed description of the code has been given previously.[13,24,30,31] Briefly, the IONLYS step-by-step simulation program is used to cover the early *physical* and *physicochemical* stages[32] of track development. It models all the physical interactions (energy deposition) and the subsequent establishment of thermal equilibrium in the system (conversion of the physical products created locally after completion of the physical

stage into the various "initial" free radicals and molecular products of the radiolysis). The complex, highly nonhomogeneous spatial distribution of reactants at the end of the physicochemical stage (~10^{-12} s; we assume that this time also marks the beginning of diffusion), which is provided as an output of the IONLYS program, is then used directly as the starting point for the subsequent *nonhomogeneous chemical* stage.[32] This third stage, which consists of diffusion and reactions of the reactive species during track expansion until all track processes are complete, is modeled by our IRT program. This program employs the "independent reaction times" (IRT) method,[33-35] a computer-efficient stochastic simulation technique used to simulate reaction times without having to follow the trajectories of the diffusing species. The IRT method relies on the approximation that the reaction time of each pair of reactants is independent of the presence of other reactants in the system. Within the framework of this approach, the competition between the reactions is simply described via a sorting out of the stochastically sampled reaction times of each potentially reactive pair. The implementation of this program has been previously described in detail;[35,36] its ability to give accurate, time-dependent chemical yields has been well validated by comparison with full random flight (or step-by-step) Monte Carlo simulations, which do follow the reactant trajectories in detail.[37,38] This IRT program can also be used to efficiently describe the reactions that occur in the bulk solution during the *homogeneous chemical* stage,[32] *i.e.*, in the time domain typically beyond a few microseconds.

In the current version of IONLYS-IRT, several updates and modifications have been made, as fully described in refs. 13, 28, and 31. In particular, we used the self-consistent radiolysis database, including rate constants, diffusion coefficients, reaction mechanisms and *G* values, recently compiled by Elliot and Bartels.[27] This new database provides recommendations for the best values to use in high-temperature modeling of light water radiolysis over the range of 20-350 °C. These data were simply extrapolated above their experimentally studied temperature range to obtain the rate constants of the various reactions involved in the radiolysis of SCW at 400 °C, as well as the diffusion coefficients of the intervening reactive species. In some cases, we also used the kinetic data of Ghandi and Percival[39] and of Alcorn *et al.*[40] inferred from muon spin spectroscopy measurements in SCW (up to 450 °C). In the absence of any other information, we chose to neglect any dependence of the reaction rate constants on water density for the 400 °C isotherm of interest.[13,14] In the ~0.15-0.6 g/cm^3 density range studied here, this approximation seems reasonable, judging from the relatively slowly varying reaction rate values for the few reactions whose rates have been measured as a function of water density.[40-42] The recent re-evaluation of the temperature dependence of certain key parameters involved in the early physicochemical stage of radiolysis (*e.g.*, the thermalization distance of subexcitation electrons, the dissociative electron attachment, and the branching ratios of the different excited water molecule decay channels) has also been incorporated in the simulations.[28,31] Finally, we included in the simulations a prompt geminate electron-cation ($H_2O^{\bullet+}$) recombination (*i.e.*, prior thermalization of the electron) that decreased in irradiated SCW at 400 °C as the water density decreased from ~ 0.6 to 0.15 g/cm^3.[13]

The density (pressure) dependence of the self-diffusion coefficient of compressed SCW at 400 °C was taken from the measurements of Lamb *et al.*[43] in the region from 0.1 to 0.7 g/cm^3. For the diffusion coefficients of the radiolytic species $^{\bullet}OH$, $H^{\bullet}$, H_2O_2, and H_2, which have been explicitly determined only at 25 °C but are essentially unknown at 400 °C, we have assumed here that they scale proportionally to the self-diffusion of water above room temperature.[24,30,43] The diffusion coefficients of e^-_{aq}, H^+, and OH^- were estimated as previously described.[30] For the hydrated electron, we extrapolated the data of Schmidt *et al.*[44] (up to 90 °C) and of Marin *et al.*[20] (at 300 °C). For the proton and the hydroxide ion, we extrapolated the data reported by Elliot and Bartels[27] over the 20-350 °C temperature range. The density dependences of the viscosity, static dielectric constant and molar concentration of SCW at 400 °C used in this work were taken from the NIST Chemistry WebBook.[8] The values for the ionic product of water (K_w) were obtained from Bandura and Lvov.[45]

We have ignored the heterogeneous molecular structure of SCW originating from the existence of large local density fluctuations (or water "clustering") that are fundamentally connected to the high compressibility of water in the vicinity of the critical point.[46-49] In our simulations, we assumed that the overall instantaneous picture of SCW could simply be viewed as a *homogeneous* medium with a *mean* density equal to the density of bulk water. This approximation was shown to be reasonable in determining the radiation chemistry of SCW at 400 ℃ at the water densities considered in this study.[12,30,50]

To mimic ^{60}Co γ-ray or fast electron irradiation, we used short (typically ~100 μm) track segments of ~300-MeV incident protons for which the average *linear energy transfer* (LET) obtained in the simulations was essentially constant and equal to ~0.3 keV/μm at 25 ℃. Such model calculations thus gave "track segment" yields at a well-defined LET.[51] The number of proton histories (usually ~500) was chosen so as to ensure only small statistical fluctuations when calculating average yields, while keeping acceptable computer time limits.

3. Results and discussion

Figure 2 displays our calculated e^-_{aq} yields at 60 ps and 1 ns after the ionizing event, for the low-LET radiolysis of pure, deaerated SCW (H_2O) at 400 ℃ as a function of water density over the range of ~0.15 to 0.6 g/cm^3, using 300-MeV incident protons. To show the sensitivity of $G(e^-_{aq})$ to $k(e^-_{aq} + e^-_{aq})$, our simulations were carried out for two different values of k at 400 ℃, namely, 2.5×10^{11} M^{-1} s^{-1} (based on the Arrhenius extrapolation of the values below 150 ℃; represented by the solid line k_a in Figure 1)[18,19,26] and 4.2×10^8 M^{-1} s^{-1} (based on the temperature dependence of k above 150 ℃ observed in alkaline water; represented by the dashed line k_b in Figure 1).[20,27] Available e^-_{aq} yields obtained from time-resolved picosecond pulse radiolysis experiments in supercritical D_2O at 400 ℃, for both times considered (*i.e.*, ~60 ps, the rise time of the signal of e^-_{aq}, and 1 ns),[28,29] are also included in the figure for comparison.

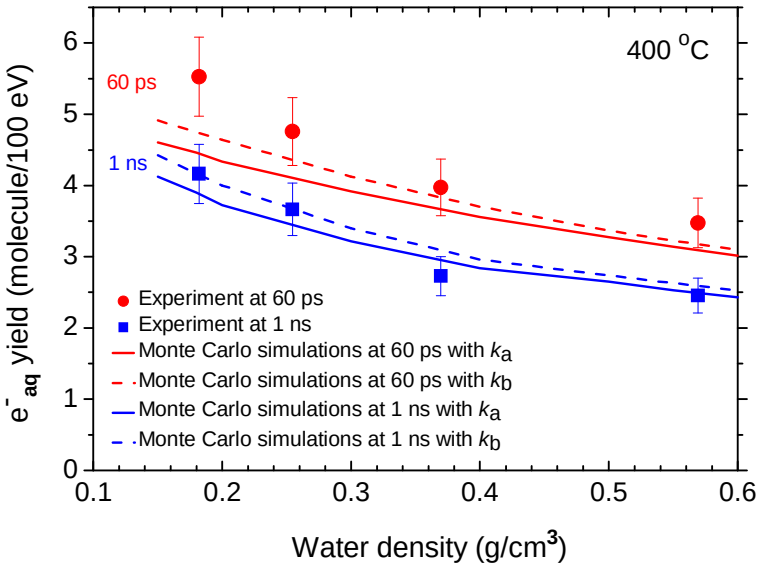

Figure 2. Density dependence of $G(e^-_{aq})$ (in molecule per 100 eV) in SCW at 400 ℃ measured directly by picosecond pulse radiolysis experiments (in D_2O) (refs. 28 and 29) at ~60 ps (●) and 1 ns (■) (estimated uncertainty of ±10%). The solid red and blue lines show our Monte Carlo simulated results in supercritical H_2O when $k(e^-_{aq} + e^-_{aq}) = 2.5 \times 10^{11}$ M^{-1} s^{-1} was used at ~60 ps and 1 ns, respectively. The dashed red and blue lines show our corresponding calculated e^-_{aq}

yields when $k(e^-_{aq} + e^-_{aq}) = 4.2 \times 10^8\ M^{-1}\ s^{-1}$ was used at ~60 ps and 1 ns, respectively. For conversion into SI units (mol/J), 1 molecule per 100 eV ≈ 0.10364 μmol/J.

A very good agreement is found between our calculations and the experimental data at 1 ns for the entire density range studied. At ~60 ps, there is also a good agreement between experiment and theory at the highest densities plotted, but at low density our calculated yields slightly deviate from the experimental data. It can be seen that, at the water density of ~0.18 g/cm^3, our calculated e^-_{aq} yield is about 1 *G*-unit lower than the experimental value. The origin of these deviations at short times has been previously discussed.[13] One reason that could explain this difference is that we compare our calculated yields of e^-_{aq} for H_2O with values obtained experimentally for D_2O. As for the radiolysis of D_2O, it is worth pointing out that Bartels *et al*.[52] predicted that the "initial" yield of e^-_{aq} in D_2O should be ~7% larger than in H_2O (due to the greater distance of secondary electron travel in heavy water). Based on this result, our e^-_{aq} yields calculated at ~60 ps would agree very well with the experimental data.[53] Another reason that could explain the deviations observed at ~60 ps in the low-density region near ~0.2 g/cm^3 is a possible increase in the *electron thermalization distance* (r_{th}) (recall here that r_{th} was kept constant in the present calculations and equal to ~3 nm, a value that we determined at 350 ℃ from an analysis of the spur decay kinetics of e^-_{aq} at elevated temperatures).[28] Such an increase would slightly augment the yields of e^-_{aq} at ~60 ps and thus our simulated values would be closer to the experimental data.

Figure 2 also shows that $G(e^-_{aq})$ is relatively little affected by the choice of $k(e^-_{aq} + e^-_{aq})$ at 400 ℃ at both times considered (~60 ps and 1 ns). The calculated e^-_{aq} yields are only *slightly* lower when the value of $2.5 \times 10^{11}\ M^{-1}\ s^{-1}$ (k_a) is used in the simulations. Indeed, decreasing the value of *k* to $4.2 \times 10^8\ M^{-1}\ s^{-1}$ (k_b), *i.e.*, by roughly three orders of magnitude, leads to an increase of $G(e^-_{aq})$ of at most ~7% at the water density of ~0.18 g/cm^3, at both ~60 ps and 1 ns. Given the relative insensitivity of $G(e^-_{aq})$ to the value of the $(e^-_{aq} + e^-_{aq})$ reaction rate constant, we cannot favor either of the *k* values used over the other. Based on the present results, we are therefore unable to unambiguously confirm or deny the applicability of the sudden drop of $k(e^-_{aq} + e^-_{aq})$ at 150 ℃ in *near-neutral water*, as recommended by Bartels and coworkers.[20,27]

4. Conclusion

Monte Carlo simulations have been used to study the effect of the temperature dependence of $k(e^-_{aq} + e^-_{aq})$ up to 400 ℃ on the hydrated electron yield in the low-LET radiolysis of supercritical water (H_2O) at 400 ℃ over the density range of ~0.15 to 0.6 g/cm^3. Two different values of *k* were used: one ($2.5 \times 10^{11}\ M^{-1}\ s^{-1}$) was based on an Arrhenius extrapolation procedure of the values below 150 ℃ (k_a) and the other ($4.2 \times 10^8\ M^{-1}\ s^{-1}$) was based on the temperature dependence of *k* observed above 150 ℃ in alkaline water (k_b). In both cases, the density dependences of our calculated e^-_{aq} yields at ~60 ps and 1 ns compared well with the available picosecond pulse radiolysis experimental data in supercritical D_2O for the entire water density range studied.

Decreasing *k* by about three orders of magnitude increased $G(e^-_{aq})$ by a factor of at most ~7% at low water densities, at both ~60 ps and 1 ns. Such a small effect of $k(e^-_{aq} + e^-_{aq})$ on the variation of $G(e^-_{aq})$ as a function of density prevented us from unambiguously confirming or denying the applicability of the predicted sudden drop of *k* at ~150 ℃ in neutral water or slightly acidic solution.

Considering the importance of the self-reaction of e^-_{aq} as a main source of molecular hydrogen in high-temperature water radiolysis, further measurements of its rate constant in pure water are obviously highly desirable. These measurements, which would be extremely beneficial to the aqueous radiation chemistry modeling community, would generate valuable insight for better understanding and predicting reactor coolant water chemistry in SCWRs.

Acknowledgments

Financial support from the Natural Sciences and Engineering Research Council of Canada (NSERC), Natural Resources Canada (NRCan), and Atomic Energy of Canada Limited (AECL) through Canada's National Program on Generation IV Energy Technologies is gratefully acknowledged. Special thanks go to Professor Yusa Muroya for his close collaboration, constant encouragement, and important experimental input for the re-evaluation of our Monte Carlo simulation code for the radiolysis of water at high temperatures.

References

1. R. Viswanathan, A.F. Armor, and G. Booras, *Power* **148**, 42-49 (2004).

2. Y. Oka and S. Koshizuka, *Prog. Nucl. Energy* **32**, 163-177 (1998).

3. H.F. Khartabil, R.B. Duffey, N. Spinks, and W. Diamond, Proceedings of the International Congress on Advances in Nuclear Power Plants, Seoul, Korea, May 15-19, 2005. Paper 5564.

4. Y. Katsumura, in: *Charged Particle and Photon Interactions with Matter: Chemical, Physical, and Biological Consequences with Applications* (A. Mozumder and Y. Hatano, eds.), Marcel Dekker, New York, 2004, p. 697-727.

5. D.M. Bartels, M. Anderson, P. Wilson, T. Allen, and K. Sridharan, *Supercritical water radiolysis chemistry. Supercritical water corrosion*. Idaho National Laboratory, Idaho Falls, 2006 (http://nuclear.inl.gov/deliverables/docs/uwnd_scw_level_ii_sep_2006_v3.pdf).

6. M. Růžičková, P. Hájek, Š. Šmida, R. Všolák, J. Petr, and J. Kysela, *Nucl. Eng. Technol.* **40**, 127-132 (2008).

7. D. Guzonas, P. Tremaine, and J.-P. Jay-Gerin, *PowerPlant Chem.* **11**, 284-291 (2009); D. Guzonas, F. Brosseau, P. Tremaine, J. Meesungnoen, and J.-P. Jay-Gerin, *Nucl. Technol.* **179**, 205-219 (2012).

8. *NIST Chemistry WebBook*, NIST Standard Reference Database No. 69 (P.J. Linstrom and W.G. Mallard, eds.), National Institute of Standards and Technology, Gaithersburg, MD, 2005 (http://www.webbook.nist.gov).

9. D.A. Guzonas and W.G. Cook, *Corrosion Sci.* **65**, 48-66 (2012).

10. G.S. Was, P. Ampornrat, G. Gupta, S. Teysseyre, E.A. West, T.R. Allen, K. Sridharan, L. Tan, Y. Chen, X. Ren, and C. Pister, *J. Nucl. Mater.* **371**, 176-201 (2007).

11. K. Kanjana, K.S. Haygarth, W. Wu, and D.M. Bartels, *Radiat. Phys. Chem.* **82**, 25-34 (2013).

12. S. Sanguanmith, J. Meesungnoen, and J.-P. Jay-Gerin, *Phys. Chem. Chem. Phys.* **14**, 11277-11280 (2012).

13. J. Meesungnoen, S. Sanguanmith, and J.-P. Jay-Gerin, *Phys. Chem. Chem. Phys.* **15**, 16450-16455 (2013).

14. S.L. Butarbutar, J. Meesungnoen, D.A. Guzonas, C.R. Stuart, and J.-P. Jay-Gerin, *Radiat. Res.* **182**, 695-704 (2014).

15. D.A. Guzonas, C.R. Stuart, J.-P. Jay-Gerin, and J. Meesungnoen, *Testing requirements for SCWR radiolysis*, Report AECL No. 153-127160-REPT-001, Atomic Energy of Canada Limited, Mississauga, Ontario, Canada, 2010.

16. S.L. Butarbutar, Y. Muroya, L. Mirsaleh Kohan, S. Sanguanmith, J. Meesungnoen, and J.-P. Jay-Gerin, *Atom Indonesia* **39**, 51-56 (2013).

17. H. Christensen and K. Sehested, *J. Phys. Chem.* **90**, 186-190 (1986).

18. A.J. Elliot, *Rate constants and g-values for the simulation of the radiolysis of light water over the range 0-300* ℃, Report AECL-11073, Atomic Energy of Canada Limited, Chalk River, Ontario, Canada, 1994.

19. C.R. Stuart, D.C. Ouellette, and A.J. Elliot, *Pulse radiolysis studies of liquid heavy water at temperatures up to 250* ℃, Report AECL-12107, Atomic Energy of Canada Limited, Chalk River, Ontario, Canada, 2002.

20. T.W. Marin, K. Takahashi, C.D. Jonah, S.D. Chemerisov, and D.M. Bartels, *J. Phys. Chem. A* **111**, 11540-11551 (2007).

21. C. Ferradini and J.-P. Jay-Gerin, *Radiat. Phys. Chem.* **41**, 487-490 (1993).

22. K.H. Schmidt and D.M. Bartels, *Chem. Phys.* **190**, 145-152 (1995).

23. D. Swiatla-Wojcik and G.V. Buxton, *J. Phys. Chem.* **99**, 11464-11471 (1995).

24. M.-A. Hervé du Penhoat, T. Goulet, Y. Frongillo, M.-J. Fraser, Ph. Bernat, and J.-P. Jay-Gerin, *J. Phys. Chem. A* **104**, 11757-11770 (2000).

25. T. Tippayamontri, S. Sanguanmith, J. Meesungnoen, G.R. Sunaryo, and J.-P. Jay-Gerin, *Recent Res. Devel. Physical Chem.* **10**, 143-211 (2009).

26. D. Hatomoto, Y. Muroya, Y. Katsumura, S. Yamashita, and T. Kozawa, Book of Abstracts, 5th Asia-Pacific Symposium on Radiation Chemistry, The University of Tokyo, Tokyo, Japan, 8-11 September 2014, Paper P08, p. 140.

27. A.J. Elliot and D.M. Bartels, *The reaction set, rate constants and g-values for the simulation of the radiolysis of light water over the range 20 to 350* ℃ *based on information available in 2008*, Report AECL No. 153-127160-450-001, Atomic Energy of Canada Limited, Mississauga, Ontario, Canada, 2009.

28. Y. Muroya, S. Sanguanmith, J. Meesungnoen, M. Lin, Y. Yan, Y. Katsumura, and J.-P. Jay-Gerin, Phys. Chem. Chem. Phys. **14**, 14325-14333 (2012).

29. Y. Muroya, M. Lin, V. de Waele, Y. Hatano, Y. Katsumura, and M. Mostafavi, *J. Phys. Chem. Lett.* **1**, 331-335 (2010).

30. J. Meesungnoen, D.A. Guzonas, and J.-P. Jay-Gerin, *Can. J. Chem.* **88**, 646-653 (2010).

31. S. Sanguanmith, Y. Muroya, J. Meesungnoen, M. Lin, Y. Katsumura, L. Mirsaleh Kohan, D.A. Guzonas, C.R. Stuart, and J.-P. Jay-Gerin, *Chem. Phys. Lett.* **508**, 224-230 (2011).

32. R.L. Platzman, in: *Radiation Biology and Medicine. Selected Reviews in the Life Sciences* (W.D. Claus, ed.), Addison-Wesley, Reading, MA, 1958, p. 15-72.

33. S.M. Pimblott, M.J. Pilling, and N.J.B. Green, *Radiat. Phys. Chem.* **37**, 377-388 (1991).

34. M. Tachiya, *Radiat. Phys. Chem.* **21**, 167-175 (1983).

35. Y. Frongillo, T. Goulet, M.-J. Fraser, V. Cobut, J.P. Patau, and J.-P. Jay-Gerin, *Radiat. Phys. Chem.* **51**, 245-254 (1998).

36. J. Meesungnoen and J.-P. Jay-Gerin, in: *Charged Particle and Photon Interactions with Matter: Recent Advances, Applications, and Interfaces* (Y. Hatano, Y. Katsumura, and A. Mozumder, eds.), Taylor & Francis, Boca Raton, Florida, 2011, p. 355-400.

37. T. Goulet, M.-J. Fraser, Y. Frongillo, and J.-P. Jay-Gerin, *Radiat. Phys. Chem.* **51**, 85-91 (1998).

38. I. Plante, Ph.D. Thesis, Université de Sherbrooke, Sherbrooke, Québec, Canada, 2009.

39. K. Ghandi and P.W. Percival, *J. Phys. Chem. A* **107**, 3005-3008 (2003).

40. C.D. Alcorn, J.-C. Brodovitch, P.W. Percival, M. Smith, and K. Ghandi, *Chem. Phys.* **435**, 29-39 (2014).

41. M. Lin and K. Katsumura, in: *Charged Particle and Photon Interactions with Matter: Recent Advances, Applications, and Interfaces* (Y. Hatano, Y. Katsumura, and A. Mozumder, eds.), Taylor & Francis, Boca Raton, Florida, 2011, p. 401-424.

42. J. Cline, K. Takahashi, T.W. Marin, C.D. Jonah, and D.M. Bartels, *J. Phys. Chem. A* **106**, 12260-12269 (2002).

43. W.J. Lamb, G.A. Hoffman, and J. Jonas, *J. Chem. Phys.* **74**, 6875-6880 (1981).

44. K.H. Schmidt, P. Han, and D.M. Bartels, *J. Phys. Chem.* **99**, 10530-10539 (1995).

45. A.V. Bandura and S.N. Lvov, *J. Phys. Chem. Ref. Data* **35**, 15-30 (2006).

46. N. Akiya and P.E. Savage, *Chem. Rev.* **102**, 2725-2750 (2002).

47. H. Ohtaki, T. Radnai, and T. Yamaguchi, *Chem. Soc. Rev.* **26**, 41-51 (1997).

48. N. Metatla, J.-P. Jay-Gerin, and A. Soldera, Proceedings of the 5th International Symposium on Supercritical-Water-Cooled Reactors, Vancouver, British Columbia, Canada, 13-16 March 2011. Paper P101.

49. J.-P. Jay-Gerin, M. Lin, Y. Katsumura, H. He, Y. Muroya, and J. Meesungnoen, *J. Chem. Phys.* **129**, 114511 (2008).

50. S. Sanguanmith, J. Meesungnoen, D.A. Guzonas, C.R. Stuart, and J.-P. Jay-Gerin, *Recent Res. Devel. Physical Chem.* **11**, 1-14 (2014).

51. J.A. LaVerne, *Radiat. Res.* **153**, 487-496 (2000).

52. D.M. Bartels, D. Gosztola, and C.D. Jonah, *J. Phys. Chem. A* **105**, 8069-8072 (2001).

53. Measurements of $G(e^-_{aq})$ using time-resolved picosecond pulse radiolysis of supercritical H_2O conducted at 400 ℃ at diverse water densities are currently being undertaken at

Osaka University and the University of Tokyo in Japan (Y. Muroya, personal communication).

ISSCWR7-2036

Irradiation capabilities at the Halden reactor and testing possibilities under supercritical water conditions

Rudi Van Nieuwenhove
Institute for Energy Technology (IFE), Halden Reactor Project
P.B. 173, NO-1751, Halden, Norway
Email: rudivn@hrp.no

Abstract

Different types of instruments have been developed both for in-pile fuel and materials studies at the Halden Reactor Project. Over the last years, several of the standard instruments have been upgraded to be able to tolerate much higher temperatures. In particular, several instruments are now able to operate up to 650 ºC and 250 bar, thus in the range suitable for supercritical water (SCW) studies. In addition, a feasibility study for an in-pile supercritical water loop has been carried out which shows that such a loop can be realized in the Halden reactor, allowing for all the instrumentation possibilities which are presently carried out in PWR and BWR conditions. Another, and cheaper alternative, is to perform corrosion experiments inside a small capsule in which supercritical water is maintained by means of gamma heating and external pressure lines. The conceptual designs of the SCW loop and SCW capsule will be highlighted.

Keywords: Supercritical water, corrosion, fuel, instrumentation

1. Introduction

The Halden Boiling Water Reactor (HBWR) started operation in 1958, being originally built in order to demonstrate the usefulness of nuclear power as an energy source for the process industry. The Halden Project is a joint undertaking of national organizations in 18 countries sponsoring a jointly financed program under the auspices of the OECD - Nuclear Energy Agency. An important part of this project is related to the study of nuclear fuel and the behavior of materials under nuclear radiation. Over the past 15 years, increasing emphasis has been placed on testing fuel and materials in the HBWR under thermal-hydraulic and water chemistry conditions representative of commercial nuclear power plants. These conditions are achieved by housing test rigs in pressure flasks connected to dedicated water loops. Eleven water loops are currently in operation in which boiling water reactor (BWR), pressurized water reactor (PWR) and CANDU reactor conditions are being simulated.
Different types of instruments have been developed both for fuel and materials studies [1]. Many of these were already developed in the period 1966-1974, but have been continuously improved and refined since then. For materials studies, the following types of on-line in-pile measurements are presently possible; crack growth measurements, creep, stress relaxation and crack initiation. In addition, in-core reference electrodes have been developed for measuring the electrochemical corrosion potential (ECP).
For fuel studies, various in-pile measurements are possible (see Table 1).

Table 1: Possible measurements on fuel rods

Quantity	Related to the following properties
Fuel center temperature	Fuel thermal conductivity, fuel cladding gap conductance
Fuel elongation	Fuel densification and swelling
Cladding elongation	Fuel pellet cladding interaction, oxide and crud deposition on cladding
Fuel rod internal pressure	Fission gas release, fuel stack densification and swelling
Fuel rod diameter	Cladding creep, pellet cladding interaction, fuel swelling

The heart of many of our in-core instruments is the Linear Variable Displacement Transducer (LVDT). The LVDT (see Figure 1) is a versatile instrument used to transform a mechanical movement into an electrical signal. The primary coil is activated by a 400 Hz constant-current generator and the position of the magnetic core in relation to the coils affects the balance of the signal from the secondary coils. Thus any mechanical movement changes the position of the magnetic core, and the corresponding signal can be measured. The LVDTs were originally designed to operate under PWR conditions (350 °C and 150 bar).

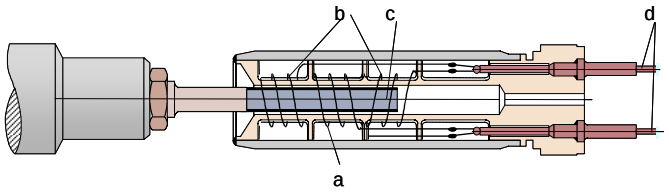

Figure 1: Principle of the LVDT (a: primary coil, b: secondary coil, c: ferritic core, d: signal cables)

The figure above shows the principle design of our LVDT. The LVDTs are made in many different sizes at customers request, but the most used size is the “type 5” LVDT. This LVDT has a linear range of ± 2.5 mm, hence the “type 5” designation referring to the linear range of the LVDT. The size of this LVDT is Ø 11.5 mm and a length of 55 mm. The signal cables used are 2-wire mineral insulated (Al_2O_3) cables with Inconel 600 sheath. The outer diameter of the cables is 1.0 mm.

Since the Halden Reactor Project started making in-core measurements, more than 2200 Linear Voltage Differential Transformers of different types have been installed in test rigs in the Halden Boiling Water Reactor. A failure rate of less than 10% after 5 year operation is expected for LVDTs.

2. Extension of instrumentation to SCW

When designing a SCW reactor (SCWR), there is a need for studying physical properties of SCW (such as heat transfer), materials behavior as well as fuel behavior [2]. In fact, all the types of measurements which are presently performed on fuels and materials for Gen II and Gen III reactors will also be needed for Gen IV type of reactors, such as the SCWR. Therefore, there is a need to extend the present instrumentation capabilities to higher temperatures and more aggressive chemical conditions. Since the LVDT is the basic instrument for most of these

measurements, a high temperature version has been developed, capable of operation up to 700 °C [3]. This was accomplished by using a different type of wire for the coils and a different way for connecting these wires to the signal cables. Stable operation for 2000 hours has been achieved at a temperature of 550 °C. In addition, such LVDTs were also tested in supercritical water at 650 °C and 250 bar. Such LVDTs were also tested in the Halden reactor, albeit at a lower temperature (300 °C) for a period of almost three years. This means that all the measurements which were described in the previous paragraph are now also possible in SCW conditions (and in the core of a reactor).

The crack growth measurement on Compact Tension (CT) specimens by means of the potential drop technique can already be applied in SCW, without major modifications. The set-up is shown in Figure 2. The CT is loaded by means of a miniature metallic bellows, coupled to an external pressure line and coaxial signal capable (radiation resistant) are coupled to extension arms to apply the DC current and measure the potential drops.

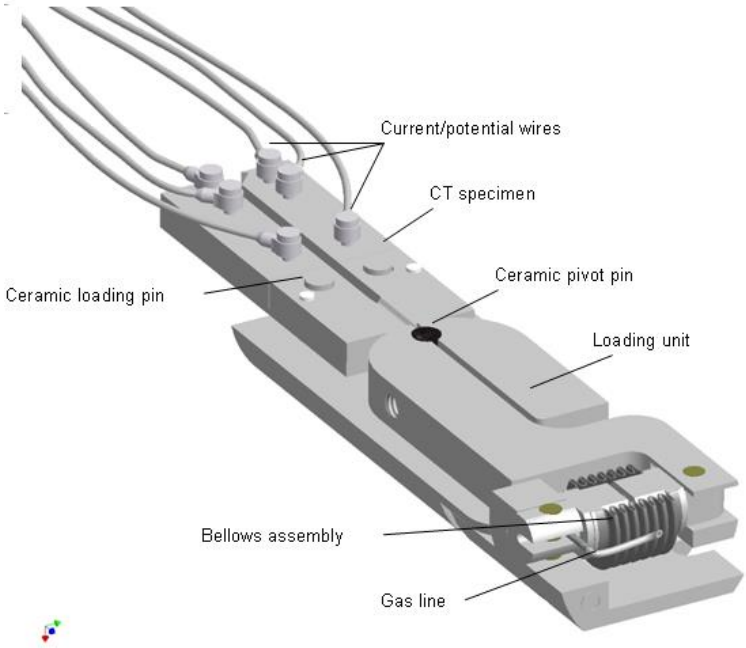

Figure 2: Compact tension specimen for crack growth measurements.

Reference electrodes, for measuring the ECP, have also been developed at the Halden Reactor Project [1,3]. A picture of such an electrode is shown in Figure 3.

Figure 3: Picture of a reference electrode for use in SCW.

This electrode consists of a ceramic tube made of Yttrium Stabilized Zirconium oxide (YSZ), and filled with a mixture of an iron and iron oxide powder which surrounds a Fe conductor. The zirconium oxide body becomes an ionic conductor of oxygen ions at high temperature while being impermeable to other gases or water. These oxygen ions take part in the electrochemical reactions at the ceramic/water and at the ceramic/ iron oxide interface and thereby determine the potential of the inner Fe conductor. By measuring the potential difference between a working electrode (for instance a stainless steel sample) and this iron/iron oxide electrode, it thus becomes possible to measure its corrosion potential. Such an electrode has been successfully used in a SCW loop at JRC, in the Netherlands [4].

In case sufficient hydrogen is dissolved into the SCW, it is also possible to use a so-called Platinum electrode. This type of electrode can be used as reference electrode under so-called reducing conditions, which is normally defined as being when the molar ratio of hydrogen to oxygen is greater than 2. In this case, the platinum functions as a hydrogen electrode. The standard Halden Pt electrode (see Figure 4) is based on a mechanical seal between the ceramic (Mg stabilized Zirconium oxide or Mg PSZ) tube and the metal parts and is therefore relatively bulky. The outer diameter of the Pt tip is 13 mm. The diameter of the signal cable is 1 mm.

Figure 4: Picture of the Pt-reference electrode

Such an electrode has also been tested successfully at a SCW loop at VTT, Finland.
Since the instruments will also be subject to corrosion, it is envisaged to apply a CrN coating (applied by PVD) to the most vulnerable parts. It has been shown [6] that such a coating provides perfect corrosion protection in supercritical water. It has also been tested on samples and fuel rod claddings in the Halden reactor in BWR and PWR conditions, showing excellent radiation and chemical resistance [5].

3. Supercritical water loop possibility

A feasibility study has shown that it is possible to install an instrumented supercritical water loop into the Halden reactor for materials and fuel studies. The external loop system will be similar to a PWR-loop system and with possibility for hydrogen addition. For materials studies, a flow rate of 0.1 kg/s is sufficient, while for fuel irradiations a flow rate of 0.35 kg/s is required. The

useable inner diameter of the in-pile section will be 35 mm (Fuel Flask Assembly) or 43 mm (Instrumented Loop System). The pressure flask will be made out of Inconel 718. Another tube surrounds the pressure flask in order to provide a thermally insulating gas gap (2 - 4 mm Ar or Xe). The heat exchanger represents the most challenging part of the whole SCW loop. The transition between subcritical and supercritical water occurs within the heat exchanger. The heat exchanger and the required electrical heaters and coolers will be located outside of the rig. A schematic drawing of the SCW loop system is shown in Figure 5.

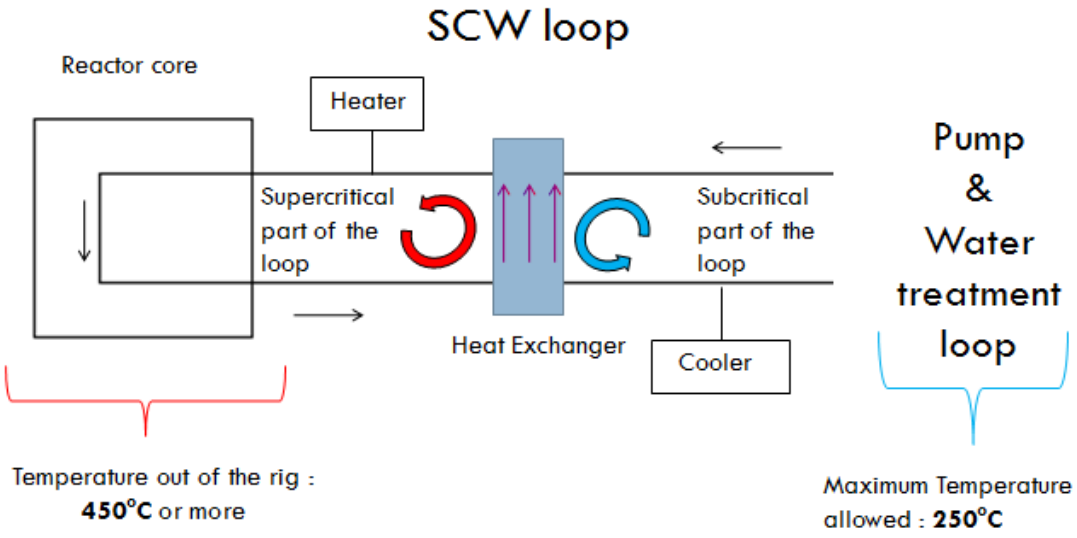

Figure 5: Schematic drawing of the SCW loop in the Halden reactor

The heat exchanger considered is of the counter-flow type [7], consisting of a bundle of many parallel thin pipes, where the flow inside these thin pipes is opposite to the flow outside these pipes. For the case of a mass flow of 0.1 kg/s (materials testing loop), calculations show that one would need about 60 parallel tubes (outer diameter 3 mm, inner diameter 2 mm) with length of about 8.4 meter, while for the high mass flow rate of 0.35 kg/s, one would need about 90 tubes (outer diameter 4 mm, inner diameter 3 mm) with a length of about 8.4 meter. In these designs, the total pressure drop over the heat exchanger can be kept below 1 bar.
Such a SCW loop would allow making all the in-pile measurements on fuels and materials which are presently carried out at the Halden reactor. Due to lack of financing, such a loop could however not be realized.

4. Supercritical water capsule

A cheaper alternative to an SCW-loop is a capsule which can be loaded into an existing Pressurized Water Reactor (PWR) rig (in the Halden reactor), connected to a PWR loop. Inside the capsule, the temperature required to obtain SCW is provided by gamma heating of the material sample within. Thermal insulation is provided by means of a thin xenon gas gap.
The advantage of locating such a capsule inside a PWR loop is two-fold: 1) One starts with a higher outer temperature (320 °C) such that the required extra temperature increase can easily be achieved, and 2) The PWR pressure flask provides an extra barrier in case something goes wrong with the SCW capsule.
The capsule can be equipped with thermocouples and external hydraulic pressure tubes (outer diameter 1 mm) allow continuous (but slow) refreshment of the water inside. For this purpose, it is envisaged to use a HPLC pump which can refresh the inner content several times a minute.

In addition, the pressure lines allow to regulate the pressure inside the capsule and to avoid the accumulation of hydrogen within the capsule. Dimensions of a possible design are shown in Table 2 and a drawing of the proposed capsule is shown in Figure 6. The assumed gamma heating is 0.8 W/g (typical for the core of the Halden reactor) and for simplicity, the material of the sample has been chosen to be Inconel 600. The sample should be placed near the middle (axially) of the reactor core region in order to minimize the neutron heat flux gradient. A separate capsule can be envisaged to pre-heat the water before it enters the main capsule.

Table 2: Characteristics of a SCW capsule

Item	**Dimensions (mm)**
Outer (thermal insulation) tube	19/17 (outer/inner diameter)
Width of the xenon gas gap	0.5
Inner (pressure) tube	16/12 (outer/inner diameter)
Sample diameter	6
Sample length	80
Total length of capsule	140

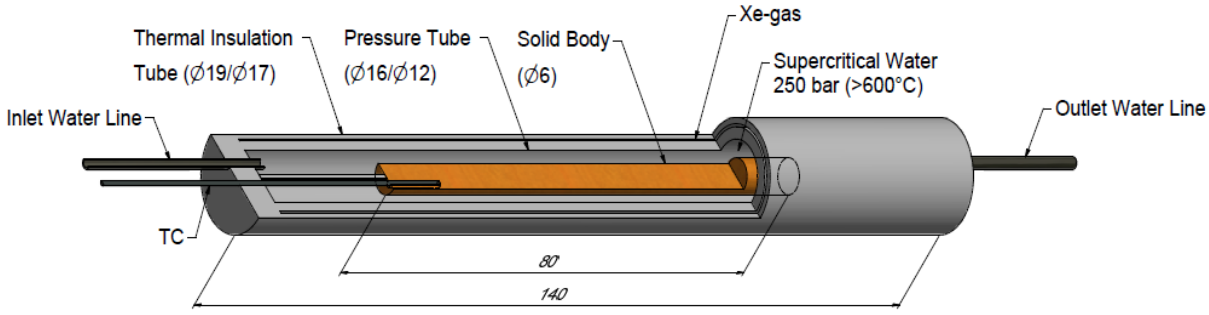

Figure 6: Drawing (cut-open view) of the proposed capsule for materials testing in supercritical water in the core of the Halden reactor.

The temperature distribution within the capsule (finite element method) is shown in Figure 7. The temperature along the surface of the cylindrical sample is shown in Figure 8.

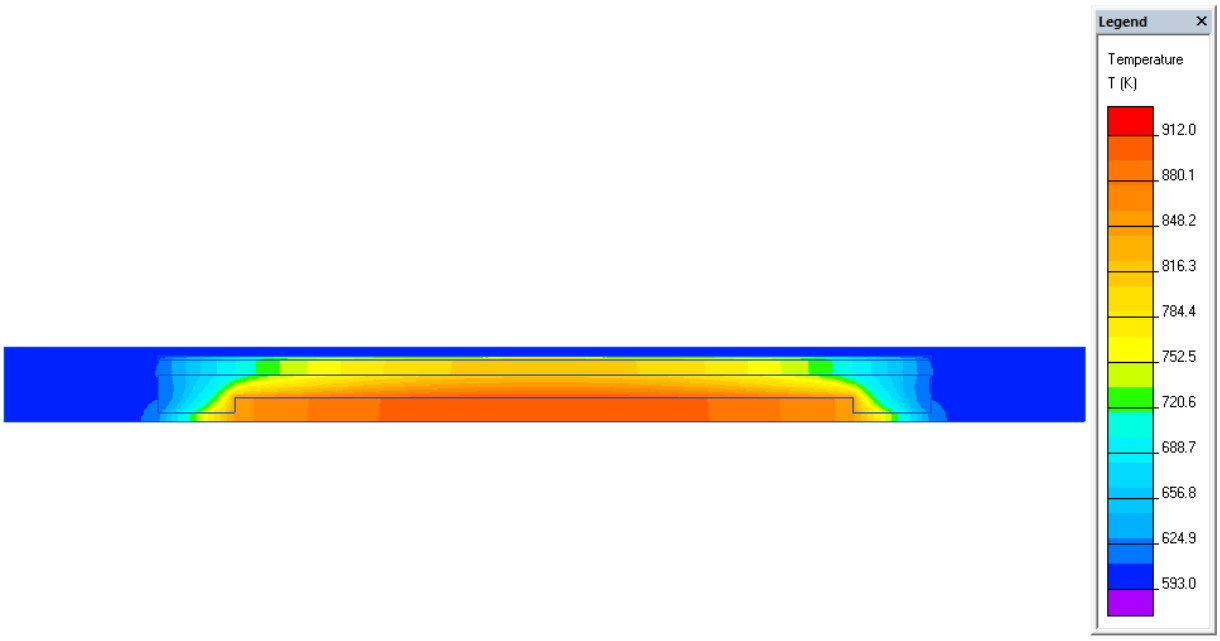

Figure 7: Temperature distribution within the SCW capsule.

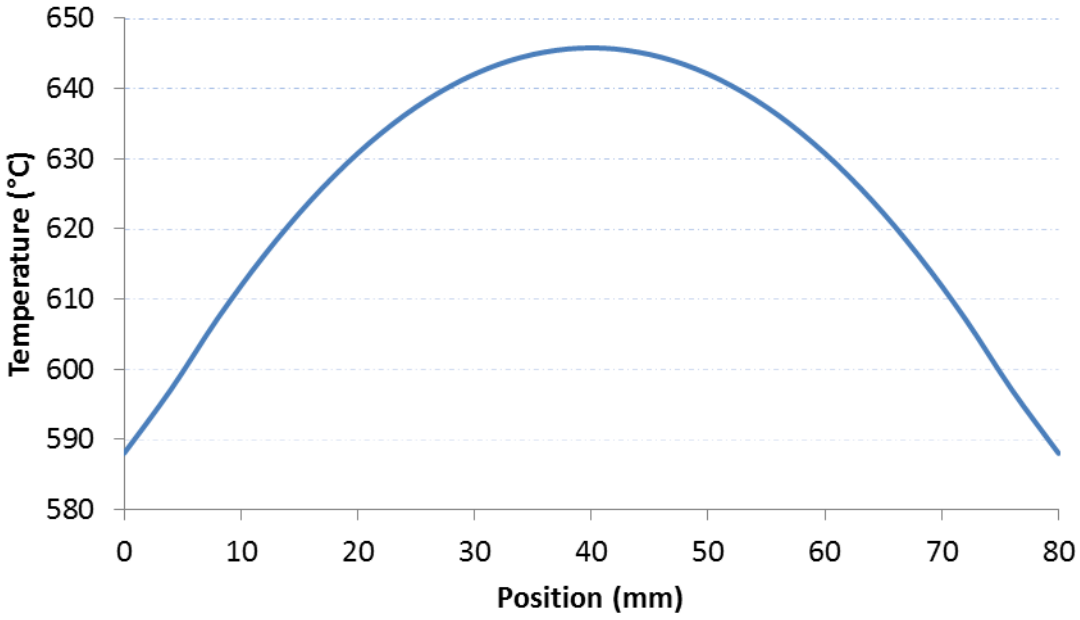

Figure 8: Temperature distribution along the surface of the cylindrical sample.

Instead of one sample, one can of course also consider different samples (in different materials), stacked together. To remove the samples (for surface analysis and weight measurements), the capsule needs to be cut open in a hot cell.

5. Conclusions

Various instruments have been developed at the Halden Reactor Project for the on-line and in-pile study of fuels and materials under SCW conditions. It has been shown that it is technically feasible to realize an in-pile SCW-loop in the Halden reactor. For limited in-pile corrosion studies on materials in SCW, it has been shown that one could achieve this by means of a small capsule located within an existing PWR loop.

References

1. R. Van Nieuwenhove, S. Solstad, IEEE Transactions on Nuclear Science, Vol. 57, Issue 5, (2010), 2683-2688.

2. T. Schulenberg, H. Matsui, L. Leung, A. Sedov, Super-Critical Water-cooled Reactors (SCWRs), GIF-INPRO Meeting, Vienna, Feb. 28 to March 1, 2013.

3. R. Van Nieuwenhove, Proceedings of a IAEA Technical Meeting held in Halden, Norway, 21-24 August 2012, In-pile Testing and Instrumentation for Development of Generation-IV Fuels and Materials, Session 1 (Instrumentation Development), Development and testing of instruments for Generation-IV materials research at the Halden reactor project, IAEA TECDOC-CD-1726, http://www-pub.iaea.org/MTCD/Publications/PDF/TE-CD-1726/PDF/IAEA-TECDOC-CD-1726.pdf

4. K. Turba, R. Novotny, K.-F. Nilsson, P. Hähner, Progress in the qualification of candidate materials for Generation IV nuclear systems at the European Commission Joint Research Centre (JRC-IET), Nordic Forum for Generation IV Reactors, Status and activities in 2012, Nordic Nuclear Safety Research (NKS), 2012, (NKS-270).

5. R. Van Nieuwenhove, “IFA-774: the first in-pile test with coated fuel rods”, Enlarged Halden Program Group Meeting, Røros, HWR-1106, 7-12 September, 2014

6. R. Van Nieuwenhove, J. Balak, A. Toivonen, S. Pentiilä, U. Ehrnsten, Investigation of coatings, applied by PVD, for the corrosion protection of materials in supercritical water, The 6th International Symposium on Supercritical Water-Cooled Reactors, ISSCWR-6, March 03-07, 2013, Shenzhen, Guangdon, China.

7. P. Vierstraete, R. Van Nieuwenhove, B. Lauritzen, NOMAGE4 activities 2011, Part II, Supercritical water loop, Nordic Nuclear Safety Research (NKS), 2012, (NKS-255).

ISSCWR7-2037

Numerical Study of Fluid-Structure Interaction with Heat Transfer at Supercritical Pressure in a Fuel Rod Assembly

Maximilian Hartig, Abdalla Batta, Thomas Schulenberg
Institute for Nuclear and Energy Technologies, Karlsruhe Institute for Technology
Hermann-von-Helmholtz-Platz 1, D - 76344, Eggenstein-Leopoldshafen, Germany
Phone +49 721 608 22888, maximilian.hartig@kit.edu

Abstract

Bending of reactor fuel rods occurs due to thermal stresses caused by non-symmetric temperature profiles. The bending implicates an intensification of the temperature profile inside the fuel rod assembly and causes the phenomenon to be self-amplifying. Due to difficulties in implementing this phenomenon, it is usually neglected in CFD analyses. The thermo-elastic instability effect has been modelled in this study by simplifying the overall problem on the fluid-dynamical side, but its impact on the fuel rod temperatures has been taken into account. The fluid-structure analysis has been performed for a 7 rod test fuel assembly, using the ANSYS Academical software suite version 15.0. The spacer geometry was simplified for the structural as well as for the fluid-dynamical side of the problem. The k−ε turbulence model was used for calculations including structural deformation. A coarse mesh was used to reduce the calculation time, ensuring convergence regardless of mesh deformation. The near wall y^+ was 160 at maximum. Conjugate heat transfer (CHT) and fluid-structure interaction (FSI) were considered simultaneously. As a reference case, a pure CFD analysis has been conducted employing a finer mesh with a maximum y^+ of 2.5, using the k−ω –SST turbulence model. Conclusions are drawn regarding the future implementation of fluid-structure interaction in analysis of heat transfer problems in reactor geometries.

1. Introduction

Heat transfer and pressure drop of supercritical water has been a continuous subject of research since the 1930ies [1], but prediction of heat transfer in supercritical media still presents a challenge. Available prediction methods still lack of satisfactory accuracy or are applicable only for a small parameter range. Especially for geometries surpassing the complexity of circular tubes, information is sparse. This presents a problem when confronted with the task of developing a reactor core and evaluating risks connected to the design. In light of this, the Japanese Atomic Energy Association (JAEA) has conducted experiments evaluating surface temperatures in a test assembly of fuel rods. The experimental setup consists of seven electrically heated rods cooled by water at 25*MPa* absolute pressure.

In the context of those experiments, the JAEA proposed a blind benchmark [2]. Research institutes were invited to conduct numerical analysis of the experimental setup. Results of the numerical studies were compared to the experimental data. The goal of the participants was to predict the temperatures at predefined points as exact as possible. Measured data were unavailable prior to the conduction of the numerical studies. Objective of the endeavour was to give an overview regarding the performance of state of the art numerical codes and their

suitability for the analysis of heat transfer in supercritical water. The present study was conducted in the context of this blind benchmark.

The irregular temperature profile inside a reactor vessel leads to deflection of the rod cladding enclosing the nuclear fuel. Those deformations influence the sub-channel geometry around. Flow conditions inside the sub-channel are changing as a result. Consequentially, shape and intensity of the temperature profile are influenced. It is crucial, however, to have exact knowledge of temperatures of fuel claddings, and the maximum arising cladding temperature is one of the most important criteria for design validation. In order to check if this criteria is met, the bending of the rods has also to be considered.

A number of numerical codes are available for the analysis either of the fluid or of the structural side of the problem. Each by itself has made it possible to gather an increasing amount of information on fuel rod performance. Together, however, they have the potential to predict fuel rod behaviour with a new degree of detail. It is the aim of this work to investigate the feasibility of a fluid structure interaction analysis by making use of existing code infrastructure regarding both sides of the problem. With the resulting setup, the impact of rod bending on the temperature profile is analysed. Focus lies on the analysis of both thermal-hydraulic and structural side of the problem. Both domains stand in interaction, which is considered during the analysis. The idea is to approach both problem sides with advanced numerical codes and to resolve three-dimensional phenomena. The ANSYS software package, version 15.0, offers both kinds of analyses and may include their interaction.

1.1 Experimental Conditions

The experimental setup consists of seven electrically heated, vertical rods, with an outer diameter of 8 mm and a pitch of 9 mm, inside a flow channel, shown in Figure 1. The channel wall is thermally insulated. Water at an inlet pressure of 25 *MPa* is flowing upwards through the assembly.

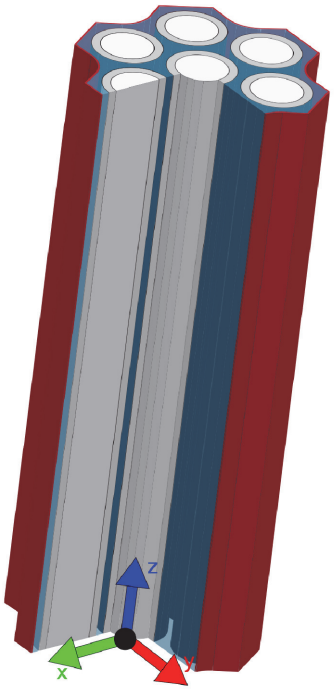

Figure 1: Flow Channel

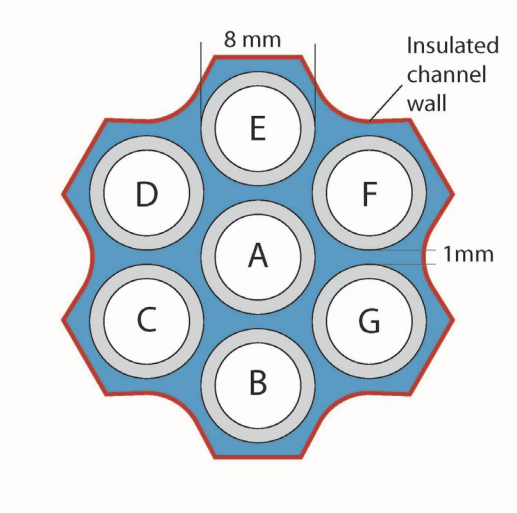

Figure 2: Cross sectional view of the flow channel

The heated section has a length of 1.5 m, starting 150 mm downstream of the channel inlet. A cavity with a horizontal inlet is mounted upstream of the channel inlet.

The rods are controlled in three groups with individually adjustable heating power as illustrated in Figure 2. Rod A is controlled separately while B, D, F, respectively C, E, G are grouped together. Cladding material of the heating rods is the nickel based alloy *Inconel 600*. The tubes have an outer diameter of 8 mm and a wall thickness of 1 mm. Heat is generated by heating wires inside the rods. The remaining space inside the rods is filled with boron nitride. Figure 3 shows a cross sectional view of a single heating rod.

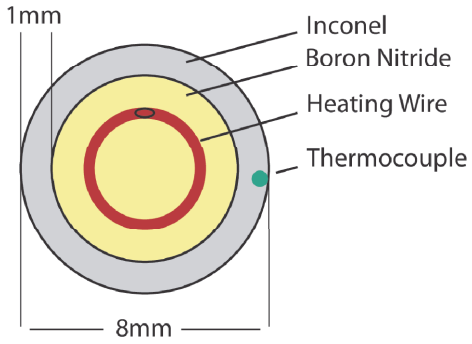

Figure 3: Cross sectional view of a heating rod

In order to minimise lateral displacement of the heating rods, six spacers are placed throughout the length of the channel at -200, 0, 300, 700, 900, and 1300 mm, measured from the beginning of the heated section. The distance between two spacers varies thus over the length of the assembly. The first spacer is outside the flow channel, just keeping the fuel bundle together. All spacers are metal sheet constructions in honeycomb form. The spacers are clamped onto the rods. The length of one spacer is 25 *mm* and the thickness of the metal sheet is 0.3 mm. Altogether, about 24 % of the cross sectional flow area is blocked by each spacer.

Temperatures inside the channel are measured by 42 thermocouples in total. They are located at different circumferential positions of all rods and distributed throughout the entire length of the heated section. All are embedded inside the rod cladding. The surface temperatures, used for evaluating the results of the numerical studies, have been extrapolated to the cladding surface.

Two pressure tabs are included in the experimental setup to evaluate the pressure drop over the channel length. Both are located inside the heated section.

Mass flux G and inlet temperature of the water as well as the heating power of the rods are varied throughout the experiment. Three configurations are part of the blind benchmark (see Table 1).

For the configuration of case B1, the temperature remains sub-cooled at all positions inside the channel. For case B2, the bulk outlet temperature is close to the pseudo-critical temperature corresponding to 25 *MPa* absolute pressure. Wall temperatures can be expected to exceed the pseudo-critical temperature. In the context of this work, only case B2 was investigated. Exhibiting temperatures in the pseudo-critical region, this case is the most relevant one.

Table 1: Experiment conditions for the respective cases in the blind benchmark.

Case	$T_{in}[K]$	$p_{in}[MPa]$	$\dot{m}\left[\frac{kg}{s}\right]$	$G\left[\frac{kg}{m^2 s}\right]$	Heater A [kW]	Heaters B,D,F [kW]	Heaters C,E,G [kW]
A1	297.35	25.0	26.33	2283.44	0	0	0
B1	353.58	24.98	16.69	1447.56	19.67	22.51	22.52
B2	519.58	25.03	16.52	1432.97	34.14	34.08	34.13

2. Previous studies

Non-uniform surface temperature distributions must be expected in any tight rod bundle. The non-uniform temperature of the fuel rods causes their bending due to thermal expansion. If the deflection of the rods changes significantly the cross section of its surrounding sub-channels, the fluid temperature around the fuel rods is getting non-uniform, and the fuel rod is bending further to the hotter side, amplifying the initial temperature non-uniformity. This effect is known as *thermo-elastic instability*.

The phenomenon was investigated by *Heinecke and Weber* [3] in 1991 for a sodium cooled fast reactor, making use of an adapted sub-channel code. It was found that the positions of the spacers as well as clearances at the contact areas with fuel pins had significant impact on shape and amplitude of the bending line. The phenomenon of thermo-elastic instabilities was discovered as pins showed inexplicable wear. Cause for the abrasion was found to be oscillations of the fuel pin caused by a changing temperature field inside the rod bundle. The oscillations had a frequency in the order of 1 Hz. A stable solution could be reached by increasing the stiffness of the spacers.

Numerous papers are available in literature on the subject of heat transfer in supercritical fluids. However, most of the research was focused on fluids inside a flow tube with a circular cross section being imposed to a heat flux from the outside in the context of fossil fired power plants operated a supercritical conditions. Available data for more complex, such as annular flow geometries is much sparser [4], [5].

Yang et al. [5] performed an analysis of upwards flow in a flow tube as well as a heated fuel rod bundle assembly in 2006. The high-Re $k-\varepsilon$ turbulence model was attested to have acceptable prediction capabilities. For bulk temperatures outside the critical range, the results correlated well with the experimental data. They found a strong circumferential temperature gradient to occur at the rod walls.

In 2012, *Kunik* [6] evaluated the performance of different turbulence models in a RANS analysis of heat transfer in supercritical carbon dioxide. Results from the respective analysis were compared with those of a DNS analysis conducted by *Kim* and *Moin* [7] for supercritical CO_2. He found that damping functions for the near-wall region, which depend on fluid properties, tend to significantly overestimate wall temperatures.

In 2013, *Jaromin et al.* [8] conducted a numerical analysis making use of the $k-\omega$–SST turbulence model and resolving the boundary layer with a near wall mesh size of $y^+<1$. They found the results to be coherent to experimental data. A significant sensitivity of the results to a change in the turbulent Prandtl number was found.

All numerical analysis agreed that there is no way around resolving the boundary layer in order to obtain quantitatively accurate results. The $k-\omega$ –SST model showed an overall good performance. On the other hand, the $k-\varepsilon$ model tends to predict wall temperatures that are lower than reference values from experimental data [9].

3. Modelling and Simulation

Only $^1/_6$ of the channel geometry was numerically analysed (Figure 4). Symmetry was assumed at the radial faces of this sub channel.

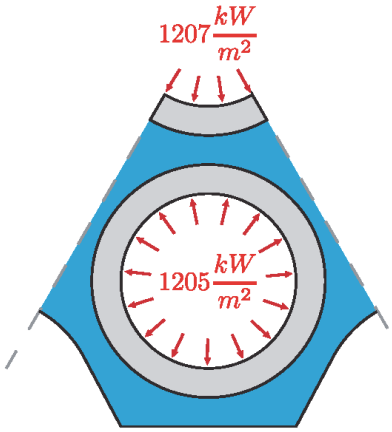

Figure 4: Cross sectional view of the reduced geometry for the detailed analysis

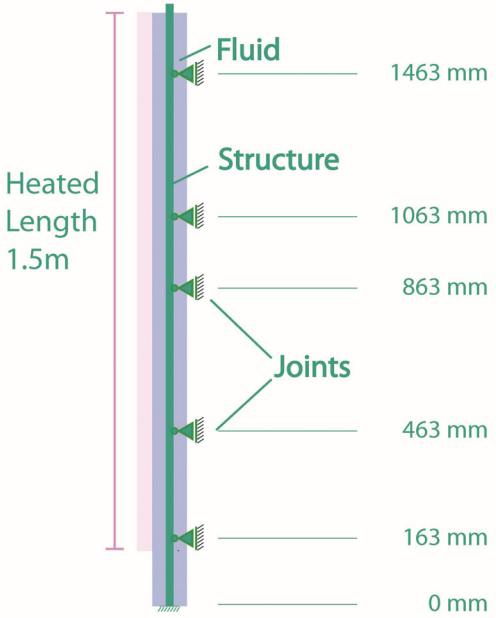

Figure 5: Positions of the modelled spacers in the reduced geometry

In reactor geometries and sub-assemblies such as the present one, secondary flows cause mixing between sub-channels. They can either be directed to lower static pressures or turbulent diffusive. When limiting the analysis to a few sub-channels, this behaviour cannot be modelled in its entire detail. Among the rods, the heating power varies by 0.2% in respect to the central rod. By restricting the computational domain in the way it is done here, a small error is introduced due to the slight asymmetry of the configuration. The error, however, is expected to be negligible.

The spacers present rather complex geometries compared to the rest of the flow channel. Their implementation in the numerical model would call for a dense mesh in the respective region. In the fluid domain, this would be necessary to resolve the small scale effects introduced by the spacers. Sharp edges and small wires forming the contact areas require a dense mesh in the structural domain as well. Non-linear contacts between spacer, rod and outer channel wall would have to be created, significantly increasing complexity and computational cost for the structural side of the problem. Spacer geometries are therefore neglected in structural and fluid domain. This permits a significant reduction of the mesh size in both domains and therefore in calculation time. In addition, the solver becomes more stable. This might partially compensate the instabilities and the augmented complexity introduced by the implementation of fluid structure interaction.

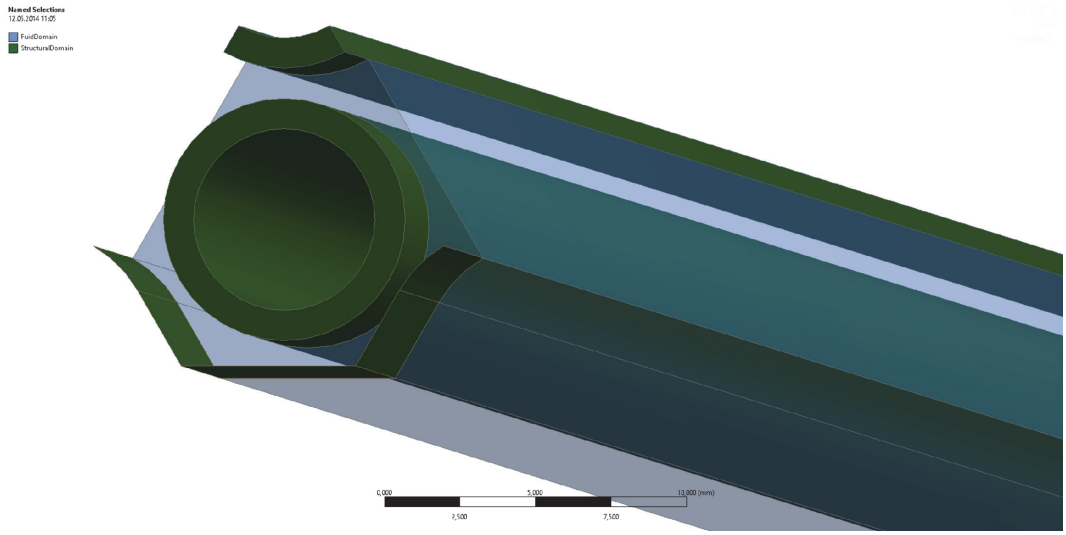

Figure 6: Reduced geometry of the numerical analysis of the problem. Parts in green belong to the structural domain; the fluid domain is in light blue.

A zero displacement condition in the horizontal X-Y- plane is considered to replace the spacer geometries on the structural side. It is imposed to the nodes at the contact points of the spacers.

The interior of the rod cladding is not represented in the numerical model. The boron nitride inside the rods is a loose filling. Its influence on the stiffness of the structure is therefore negligible. Heat generation is modelled by a uniform heat flux imposed to the inner walls of the rod cladding. Upper and lower end of the heating rod are modelled as adiabatic surfaces.

3.1 Consequences from the Neglect of the Spacer Geometries

The neglect of spacer geometries represents a significant change from the experimental configuration. With a length of 25 mm each, they occupy about 8% of the total channel length.

The drag induced by the spacer geometries will cause a drop in absolute pressure. This has an influence on fluid properties. To give an estimation, we assume a combined pressure drop of 0.5 *bar* caused by the sum of all spacers as a conservative value. For temperatures far from the pseudo-critical line, the introduced error is negligible. 5 *K* above and below the pseudo-critical temperature however, the difference becomes significantly stronger with a maximum error of the specific heat of 6.3%.

The flow is accelerated in the passage between spacer and rods, leading to a higher degree of turbulence and an enhancement of convective transport. Over the actual height of the spacer and for some distance downstream, the temperature is therefore expected to become more uniform.

The abrupt change of the channel cross section by about 24% imposed by the spacer geometry can cause flow separation on downstream positions. In the resulting recirculation regions, the wall temperature will rise.

It can be concluded that the wall circumferential temperature profile will experience an overall flattening in proximity to the spacer. The mean wall temperature will decrease slightly over the spacer height directly followed by a sudden increase due to flow separation. The circumferential temperature profile will then resume the characteristic shape it had before passing the spacer. None of those effects, however, is expected to have a significant effect on rod bending and will thus not be represented by the numerical model.

The real spacer geometries permit lateral movement to a certain degree as a consequence of their finite stiffness and manufacturing tolerances. With the assumed infinite stiffness, the joints

on the model restrict movement of the rods to a higher degree than is the case in reality. The smaller the permitted horizontal movement at the fixation points is, the less pronounced becomes the bending line of the rods [3].

We can conclude that the neglect of spacers has two consequences on the shape of the bending line. First, by neglecting the homogenisation of the circumferential temperature profile in proximity of the spacers, the potential for bending tends to be overestimated. Second, by restricting the rod movement to a higher degree than is the case in reality, the deflection resulting from a certain temperature profile is underestimated. Both effects act thus in opposite direction, but we cannot say for sure that they will balance out.

3.2 Fluid Models

A single phase fluid model is used in this study. The Jackson and Hall criterion [10] for the importance of buoyancy effects is not satisfied. Buoyancy effects are therefore neglected in this study.

For analyses featuring conjugate heat transfer and deformation, the $k-\varepsilon$ turbulence model is chosen. Mesh deformation effects and the strongly non-linear fluid behaviour tend to cause divergence of the solver. The $k-\varepsilon$ model is able to provide a solution regardless of poor mesh quality and non-linearity of the problem. Also, a more aggressive time step can be chosen for the solver leading to a lower number of total iterations and less computing time.

Boundary layer phenomena are the driving force in convective heat transfer problems. For a near wall mesh size y^+ in the order of 100 the boundary layer is not resolved. Instead, wall functions are applied to model the fluid's behaviour near the wall. The boundary layer is accurately resolved for y^+ in the order of 1 permitting the avoidance of wall functions. The corresponding low Re applied here is the $k-\omega-$ SST model.

To sum up, high Re calculations employ the standard $k-\varepsilon$ model while low Re calculations feature the $k-\omega-$ SST model according to Menter [11].

3.3 Boundary Conditions

At the channel inlet, the fluid has a normal velocity of 1.7366m/s. This corresponds to the mass flux given in benchmark case B2. The absolute pressure in the domain is 25 *MPa*. The outlet is assigned to a relative pressure of 0 *Pa*.

Symmetry is imposed to the related radial faces. For the rods, displacement in the lateral plane is set to zero at the respective contact points of the spacers. Rotational degrees of freedom as well as displacement in axial direction remain unrestricted. At the lower end of the rods, no movement of any kind is permitted in the centre point of the rod bundle. Expansion in radial direction remains possible for the rest of the inlet surface. The upper end of the rods is free to move in any direction.

The symmetry faces of rod A are assigned a *frictionless support*. This type of boundary condition prevents deformation in normal face direction. The assumption of circumferential symmetry suppresses a number of other possible bending modes in respect to the original configuration.

A heat flux is imposed to the inner rod wall. Upper and lower faces of the rods are considered adiabatic, as well as the outer channel walls.

Communication between structural and fluid dynamical solver is set up at the fluid-solid interface. Surface temperatures along the outer rod walls are sent from the fluid flow- to the structural solver and imposed to the corresponding nodes by means of interpolation. The fluid solver itself receives information regarding heat flow and displacement of the rod surface. For the first iteration, initial conditions are set.

3.4 Mesh

The mesh is generated separately for fluid and solid domain. In the structural domain, meshing parameters are assigned to the lower face of the fuel rods. The surface mesh is then extruded along the length of the rods. Expecting a close to linear behaviour of the radial temperature profile, at least two elements are used in the corresponding direction. The circumferential temperature distribution is expected to show strong variations being the origin of thermal stresses and deformation. The outer surface of rod B is therefore mapped with 110 equally distributed nodes. Respectively the correspondent smaller number on the partially present centre rod. The cell height in axial direction is 10 mm.

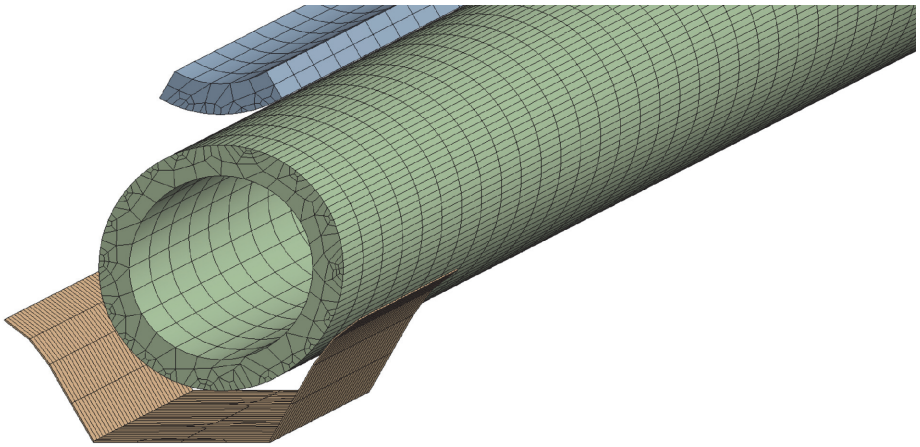

Figure 7: Mesh for the structural domain

Two different grids for the fluid domain are used. Calculations featuring the $k-\varepsilon$ model are all carried out with a rather high y^+ value on a coarse mesh (Figure 8). As it is impossible to resolve flow and temperature boundary layers with such a mesh, those regions are modelled by wall functions. This method is less accurate than completely resolving the effects inside the boundary layer region. With low y^+ values problems arise regarding the mesh deformation. Heavy distortions of cells as well as the creation of negative volume elements do occur. These effects cause a destabilisation of the solver and might lead to its complete shutdown. Avoiding these effects comes at the cost of a reduced accuracy of the results.

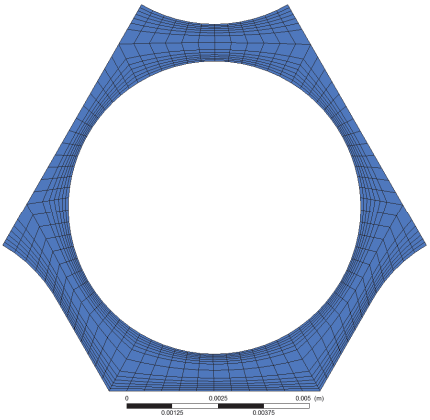

Figure 8: Mesh used for the k-ε analysis

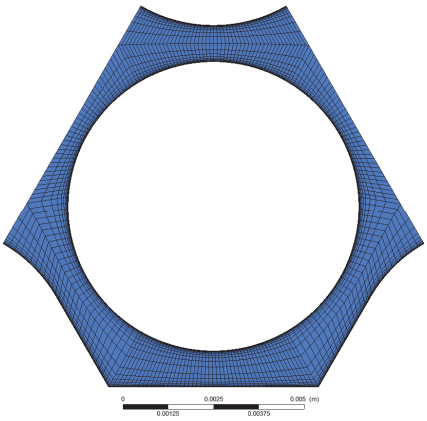

Figure 9: Mesh for the k-ω SST analysis

The heat transfer mechanism is strongly dependent on processes inside the boundary layer. Since for the fluid-structure-interaction analysis the mesh density in the near wall region is not dense enough to do so, a reference case with a higher mesh density is considered. A y^+ in the order of 1 for the first node is necessary for a satisfactory representation of the heat transfer phenomena in supercritical water. The height of the first element of the refined mesh is $6\times10^{-7}m$.

3.5 Performed Analyses

In order to determine the impact of conjugate heat transfer and heating rod deformation, three detailed analyses with a coarse mesh are performed using the $k-\varepsilon$ turbulence model. It was discussed in chapter 2 that the $k-\omega-$ SST model is more adapt to analyse heat transfer problems in supercritical media. To evaluate the error introduced by application of the $k-\varepsilon$ turbulence model and the corresponding high y^+ values, a reference analysis is performed. It implements the $k-\omega-$ SST model according to *Menter* [11] and makes use of a finer mesh. Conjugate heat transfer (CHT) and fluid-structure-interaction (FSI) analyses featuring the $k-\omega$-SST model are not covered in this paper. Table 2 gives an overview of the calculations performed in the context of this work.

Table 2: Overview of the performed detailed analyses. The mesh size is relating to the fluid domain mesh only.

Case	Turbulence Model	Software	$y^{+,max}$	Mesh Size	CHT	FSI
1	$k-\varepsilon$	ANSYS	160	0.5 million	No	No
2	$k-\varepsilon$	ANSYS	160	0.5 million	Yes	No
3	$k-\varepsilon$	ANSYS	160	0.5 million	Yes	Yes
4	$k-\omega$ –SST	ANSYS	2.5	3.2 million	No	No

4. Results and Discussion

4.1 Temperature Profile

Aim of the detailed analysis is to provide information regarding the temperature distribution inside the assembly. To obtain an idea on the profile, temperatures are evaluated at different positions throughout the model. The emphasis hereby lies on the surface temperatures of rod B according to Figure 2.

Over the entire channel length, temperatures at the respective positions of thermocouples in the experimental setup are analysed. As only $^1/_6$ of the entire cross section is implemented in the numerical model, all measuring points are mapped to the existing extract. Figure 10 shows their horizontal positions.

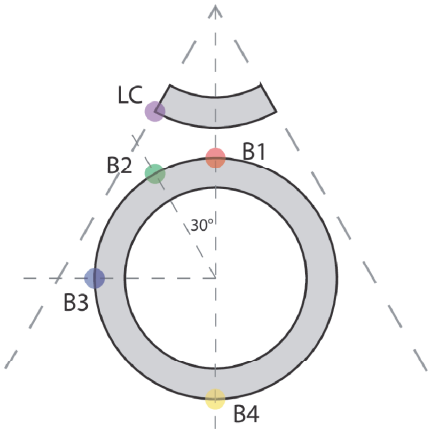

Figure 10: Positions of the monitor lines in the numerical model geometry.

As a first step, the fluid-dynamical part of the problem (*Case 1* according to Table 2) is examined exclusively. Neither CHT nor FSI are considered. The temperatures at the monitor point positions over the channel length are presented in Figure 11. It becomes quickly apparent that temperature curves B2 and LC display close to coherent behaviour. Near the pseudo-critical line, between 650 and 670 *K,* all temperature curves display a stagnating behaviour, because the specific heat capacity has its maximum there.

Line *B1* exhibits the highest temperature over the entire channel length. At this position on rod B, the fluid gap is small and heated from two sides. Approaching the pseudo-critical line, the curves converge in the channel section between 1 m and 1.4 m. Here, the circumferential range of temperatures is reduced and the circumferential temperature profile is flattened.

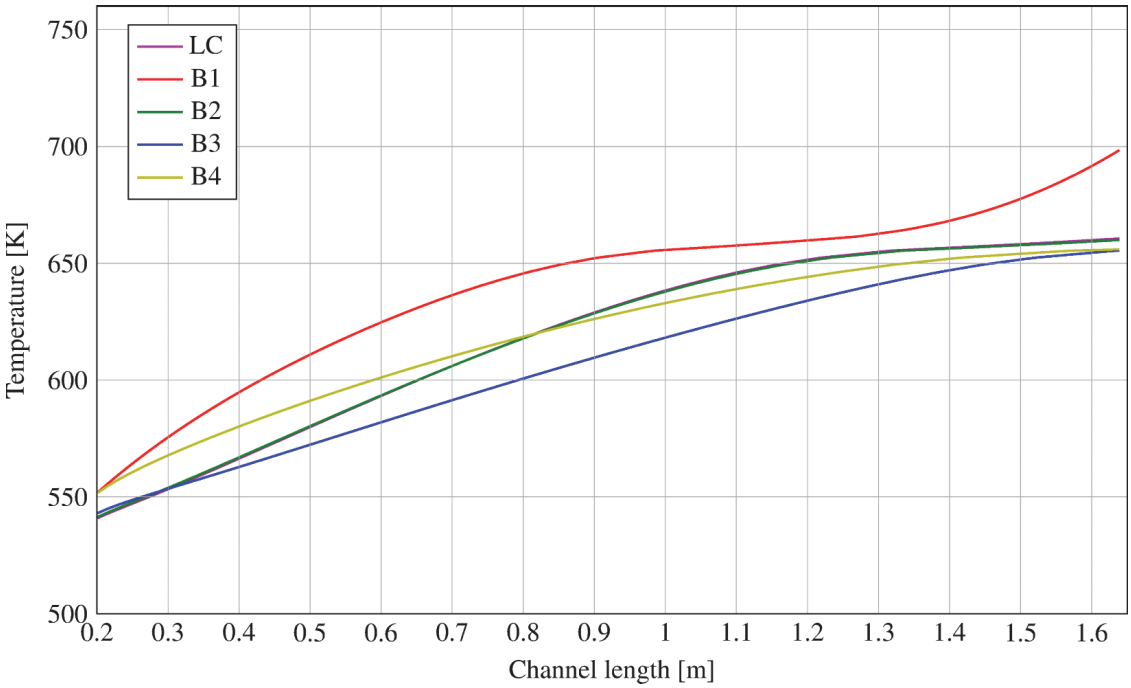

Figure 11: Development of temperatures over channel length at monitor point positions for the analysis without consideration CHT or FSI, case 1.

The circumferential temperature profile is visualised at two representative axial positions. Figure 12 and Figure 13 show the temperatures of rod B in dependence of the circumferential position at heights 1325 mm and 1625 mm, respectively. These specific axial positions were chosen because thermocouples are mounted there in the experimental setup. The first plane lies in the region where enhanced heat transfer is suspected at line B1. The second plane is positioned close to the outlet where the temperature on B1 exhibits an upwards trend. At both axial positions, the temperatures on the centre-oriented half of the rod wall between 0 ° and 180° are higher than on the opposite half. It is easy to locate the elevated temperature at B1 in Figure 13. The peak is pronounced and the elevated temperature is limited to a small area. Figure 12 shows a similar effect at 1325 mm, although the peak is less pronounced there. Small secondary peaks occur at 220 ° and 310 ° respectively. These are not captured by the monitor points.

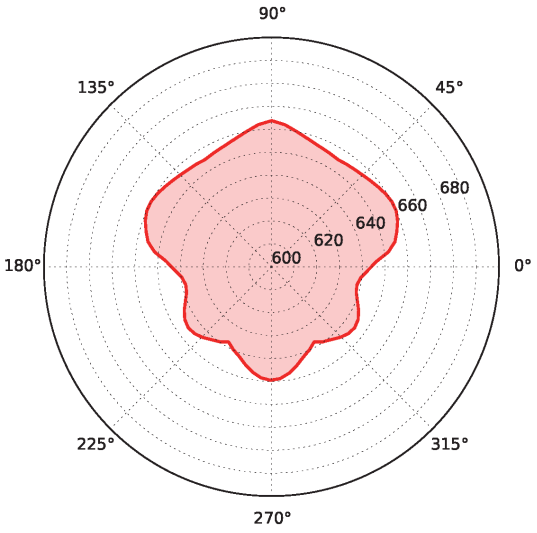

Figure 12: Outer wall temperature on rod B in K over the circumference for case 1 at 1325mm axial position.

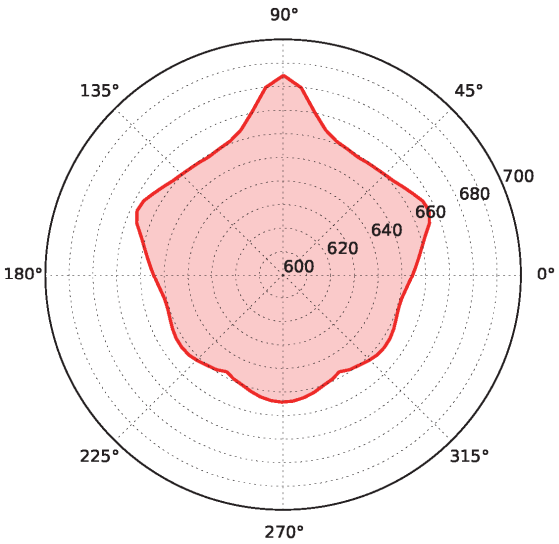

Figure 13: Outer wall temperature on rod B in K over the circumference for case 1 at 1625mm axial position.

To investigate the development of the temperature profile along the channel, a three dimensional visualisation is the most suitable. Figure 14 shows the areas of increased temperature where neighbouring rods find themselves in direct proximity to rod *B*. Towards the central heating rod, the peak is most distinct, while peaks in the direction of the circumferentially neighbouring rods do not exhibit the same intensity. The areas of elevated temperatures are sustained and are present over the entire heated length.

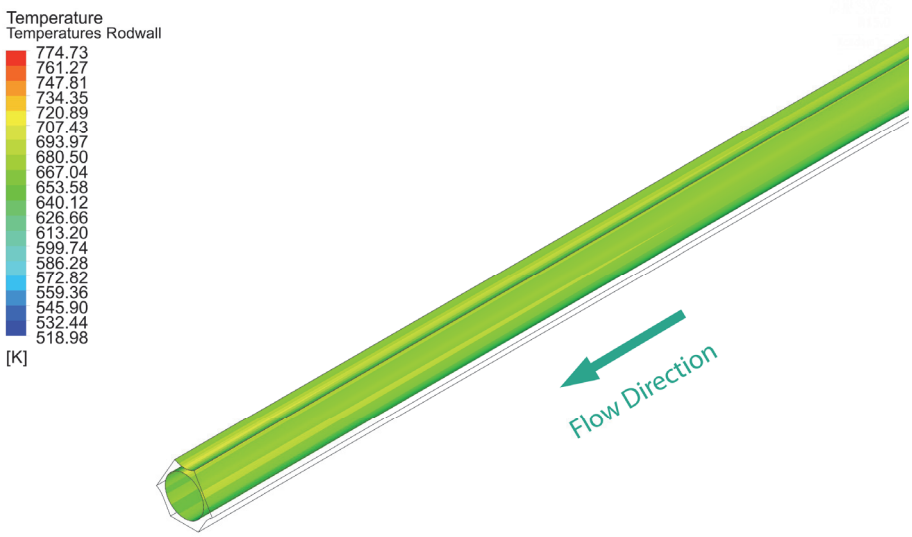

Figure 14: Surface temperatures of the heating rods in the computational domain.

Although the circumferential temperature profile varies among the channel length, the centre-oriented half of rod B always shows an overall higher temperature than the opposing side. Throughout the heated zone, the potential for rod deflection is hence present. Inside the

structural domain, conductive heat transfer mechanisms have a homogenising effect on the circumferential temperature profile. This effect will be analysed next.

Figure 15 shows the temperatures at the monitor point positions with heat conduction taken into account (Case 2). In general, we observe an analogue behaviour to Case 1. The upwards trend of the temperature slope at line B1 towards the outlet however is less pronounced. We observe an overall reduced range of the circumferential temperatures regarding case 1. The centre-oriented wall of rod B still displays higher overall temperatures than the outward facing one.

The contrast between both cases becomes more evident when examining the temperature differences on the rod wall. Figure 16 shows the quantitative difference in surface temperatures. A negative value designates that in the respective region, case 2 exhibits lower temperatures than case 1. At the circumferential positions, where elevated temperatures could be observed in case 1, the results for case 2 are distinctively colder. Especially where rods A and B find themselves in direct proximity, the surface temperatures are reduced in respect to case 1.

The circumferential temperature profiles at both representative axial positions underline this. Figure 17 and Figure 18 show the profiles for both cases at the corresponding channel heights. Especially in Figure 18, it becomes evident that the distinct peak at B1 is flattened by conductive heat transfer inside the rod wall. Figure 17 shows that also the secondary variances at 220° and 320° are flattened out. Over the channel length, the circumferential temperature profile is smoother for case 2 than for case 1.

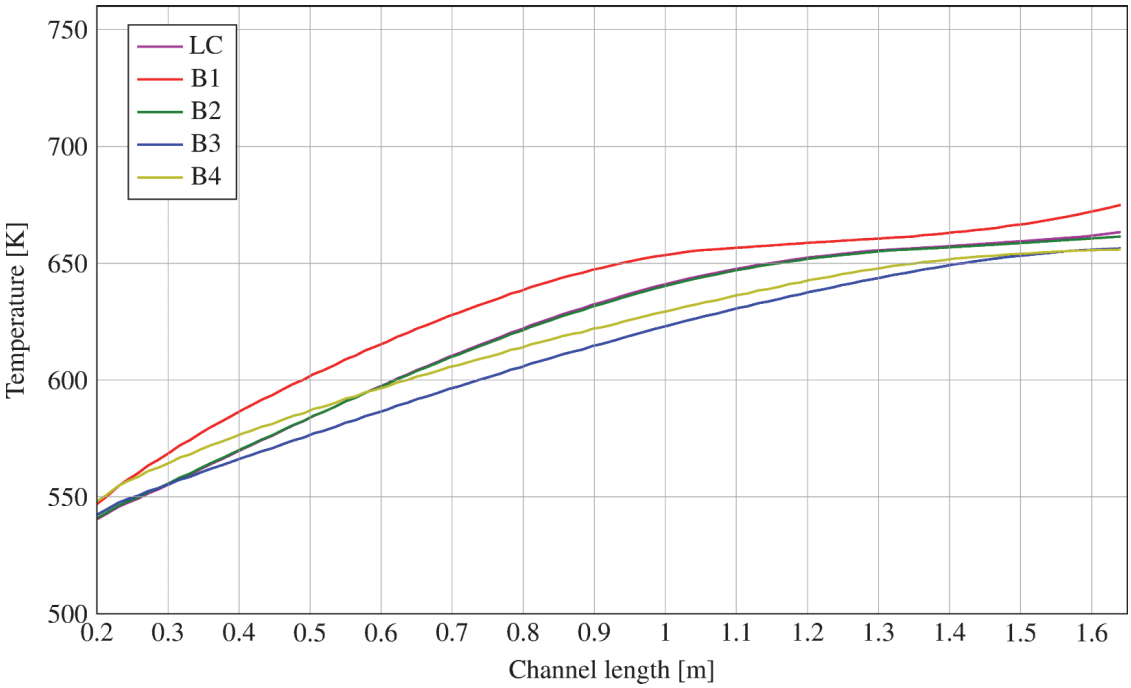

Figure 15: Development of temperatures over channel length at monitor point positions for the analysis including conjugate heat transfer, case 2.

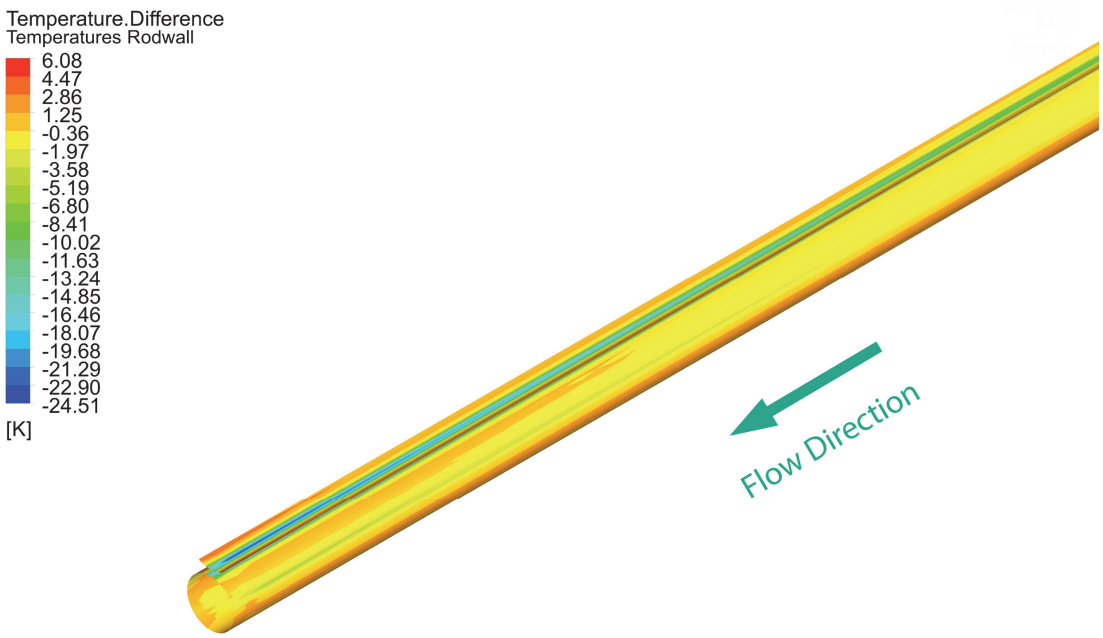

Figure 16: Temperature difference between case 2 and case 1. Negative values designate lower temperatures for case 2 in respect to case 1.

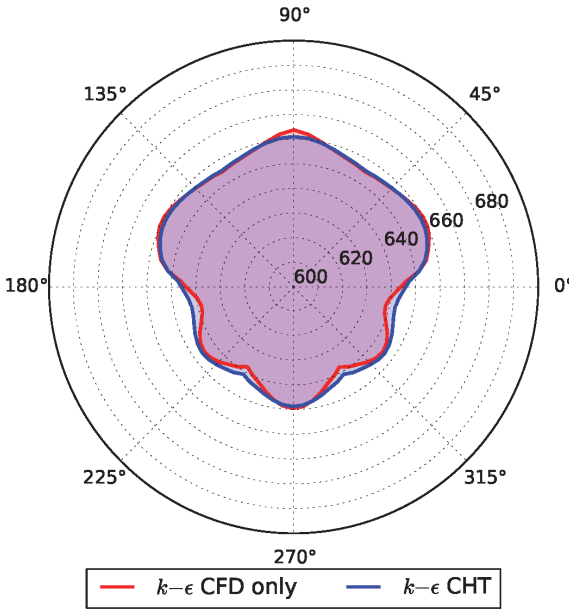

Figure 17: Outer wall temperatures on rod B in K over the circumference for cases 1 and 2 at an axial position of 1325mm.

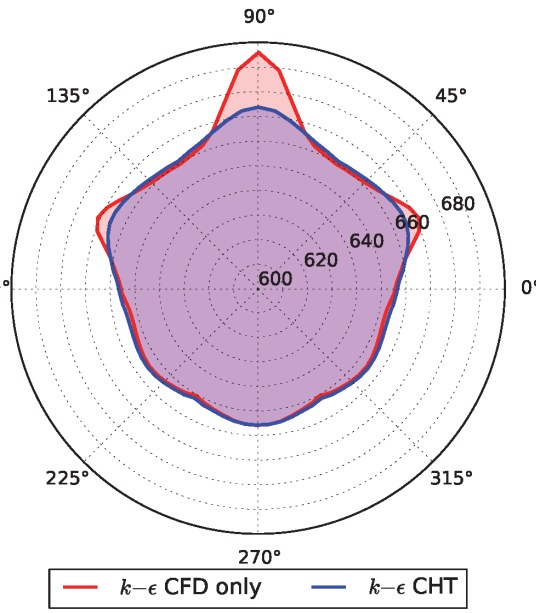

Figure 18: Outer wall temperatures on rod B in K over the circumference for cases 1 and 2 at an axial position of 1625mm.

To check the temperature distribution in fluid and structure, the cross sectional profile at 1625 mm as a representative position is evaluated (Figure 19). It can be observed that the temperatures inside rod B augment towards the channel centre. This is the case throughout the thickness of the rod wall. On the inner rod surface, temperatures vary by about 25*K*. A potential

for thermally induced bending is hence still present after considering the equalising effect of heat conduction inside the rod wall.

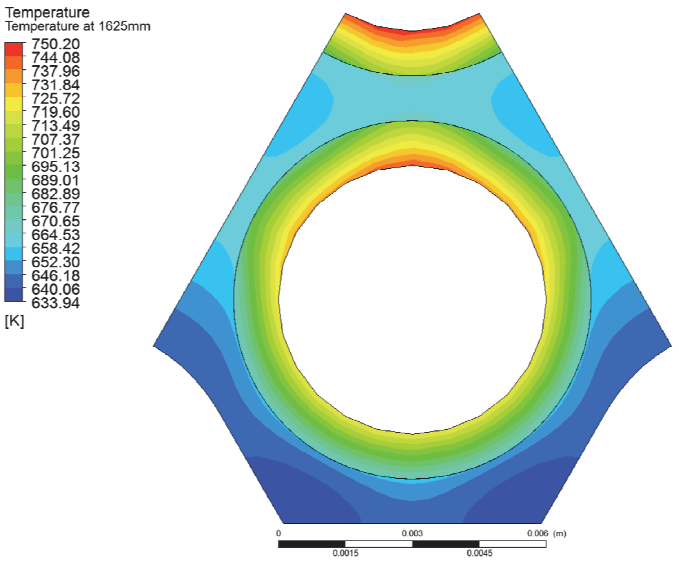

Figure 19: Cross sectional temperature profile for analysis including conjugate heat transfer at 1625 mm.

Before analysing the temperature distribution of case 3, it is reasonable to investigate the deformed geometry of rod B. Due to the thermal stresses, the heating rod is bent as shown in Figure 20. For a better visualisation, the deflection is amplified by a factor of 20. Bending in the first two thirds of the channel is minimal. In the outlet region, rod *B* is deflected towards the outer channel wall, leaving a distance of 0.45 mm towards the channel wall. Between the last spacer and the previous, rod *B* curves towards the centre rod. This leaves a distance of 0.9 mm between both rods at the narrowest point.

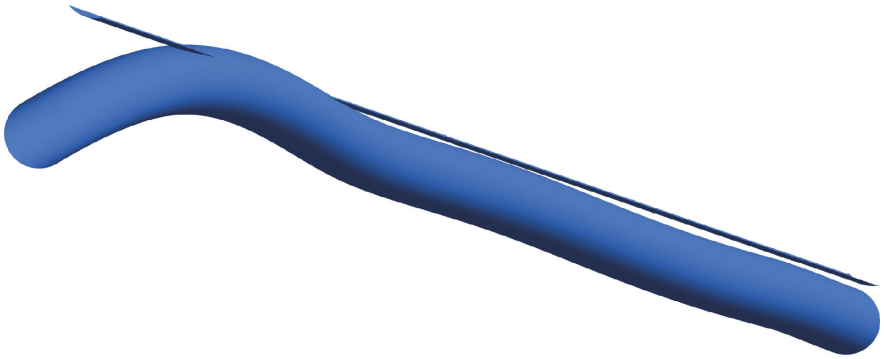

Figure 20: Deformation of the heating rod B scaled by a factor of 20, assuming temperatures of case 2.

The bending line is changing the flow structure and thus heat transfer, which is studied in case 3. Figure 21 shows the temperatures on the monitor point positions for case 3. Differences between cases 2 and 3 are most pronounced in the last third of the heated section where the deformation is the strongest. The upwards trend of the temperature at monitor line B1 towards the outlet is no longer present. Line B4 shows a slight upwards trend there now. In the outlet

region, this point approximates the adiabatic channel wall due to the deflection of rod B. Lines B2 and LC are still close to coherent behaviour except in direct proximity to the outlet. The temperature at line B2 shows a downwards trend at the outlet while the slope of LC remains its linear increase. On point B3, the temperature decreases slightly between 1.4 m and 1.6 m.

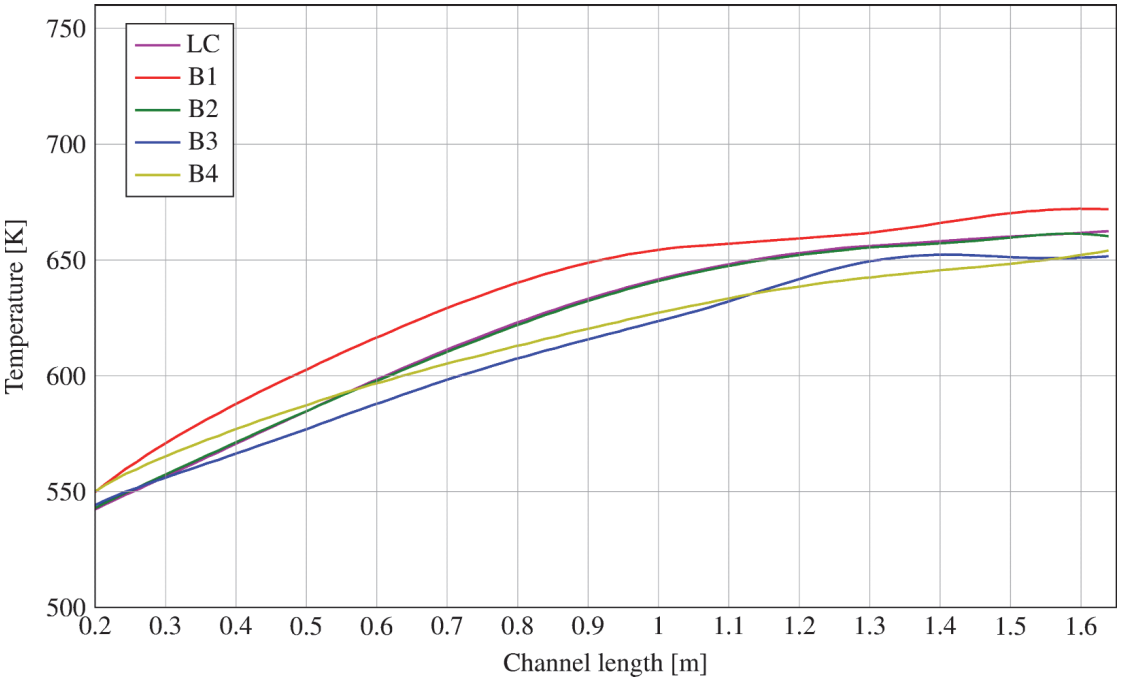

Figure 21: Development of temperatures over channel length at monitor point positions for the analysis including deflection of the rods, case 3. Line LC is overlapping with line B1.

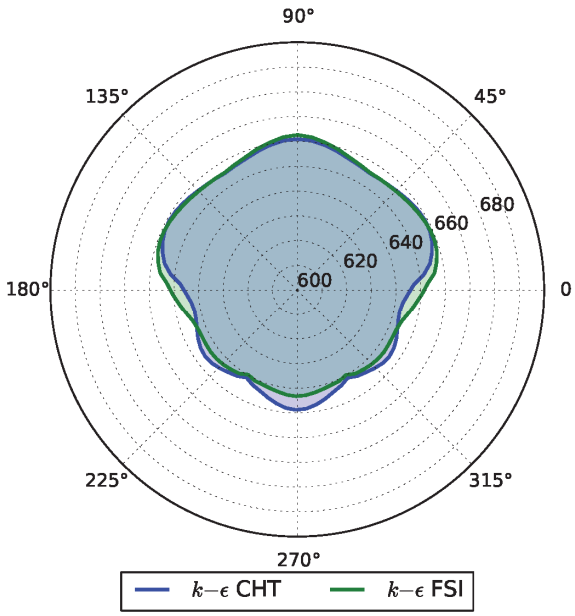

Figure 22: Outer wall temperature on rod B in K over the circumferential position for cases 2 and 3 at an axial position of 1325mm.

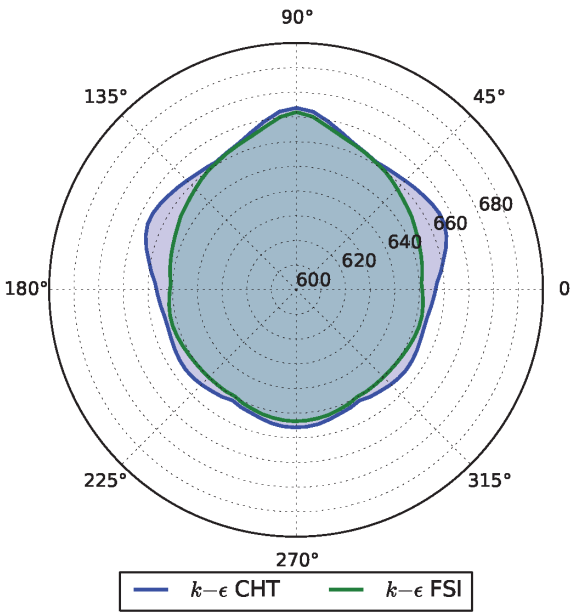

Figure 23: Outer wall temperature on rod B in K over the circumferential position for cases 2 and 3 at an axial position of 1625mm.

To better understand this behaviour, the circumferential temperature profiles are investigated (Figure 22 and Figure 23). The overall wall temperature is slightly decreased regarding both, cases 1 and 2 at 1625 mm (Figure 23). The 90° axis is pointing towards the flow channel centre. Especially both peaks oriented towards the circumferentially neighbouring rods show a lower maximum value and are hardly distinguishable any more. The profile at 1325 mm shows different behaviour (Figure 22). The secondary peaks formerly at 30° and 150° are now expanded towards the outer channel wall.

To further investigate, the three dimensional visualisation is considered (Figure 24). The temperature profile on the rod walls shows the characteristic areas of elevated temperature. Their shape however differs from those in the precedent analysis. While in cases 1 and 2 the hot areas were perfectly straight, they show in case 3 an orientation towards the channel centre in the last section. The origin for this behaviour lies in the deformation of rod B.

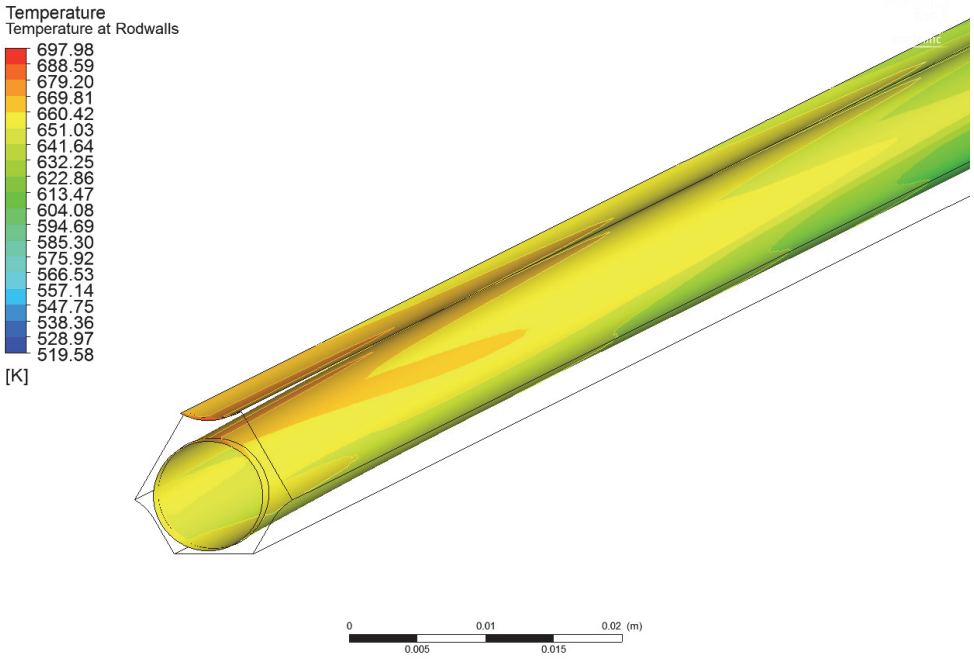

Figure 24: Wall temperatures on rod A and B for case 3. View on the outlet section.

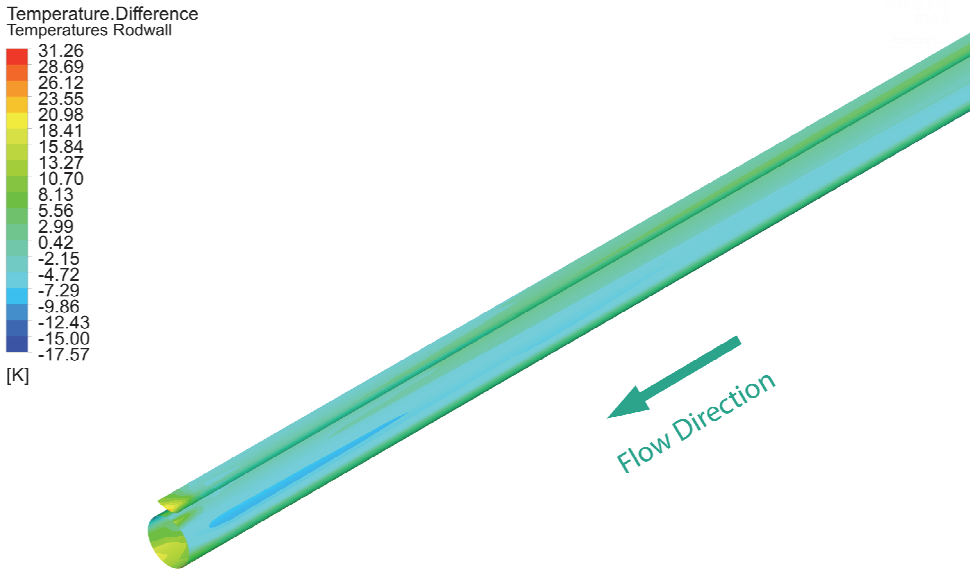

Figure 25: Differences in wall temperatures between cases 2 and 3. Negative values designate a lower temperature of case 3 in respect to case 2

For case 4, a larger circumferential temperature spectrum can be observed over the entire channel length. The general trend of the curves resembles that for case 1. At position B1, although still present, the flattening is less pronounced and occurs at a temperature that lies beyond the pseudo critical value. The upwards trend on B1 towards the channel outlet is more pronounced.

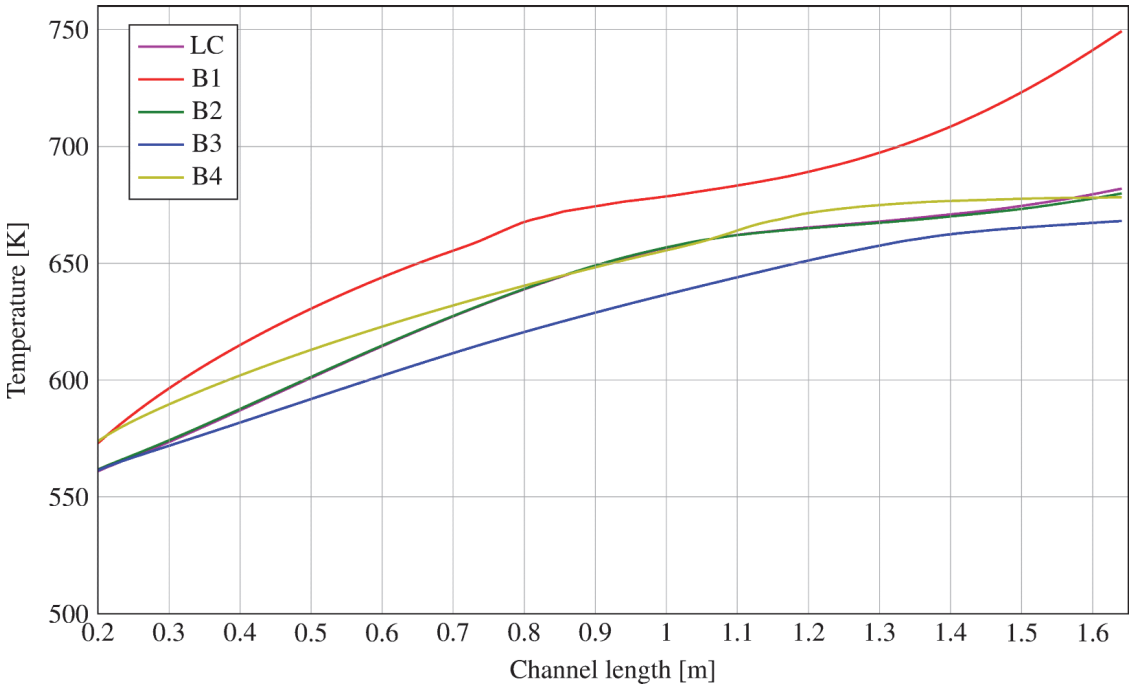

Figure 26: Development of temperatures over channel length at monitor point positions for the k−ω –SST analysis, case 4.

For a better visualisation, the circumferential temperature profiles are considered (Figures 27 and 28). It becomes evident that case 4 yields an overall higher wall temperature. The circumferential temperature profile at rod B shows the same characteristic shape as observed for cases 1 and 2. Temperature peaks are even more pronounced than for case 1. Their circumferential positions however remain the same as for cases 1 and 2.

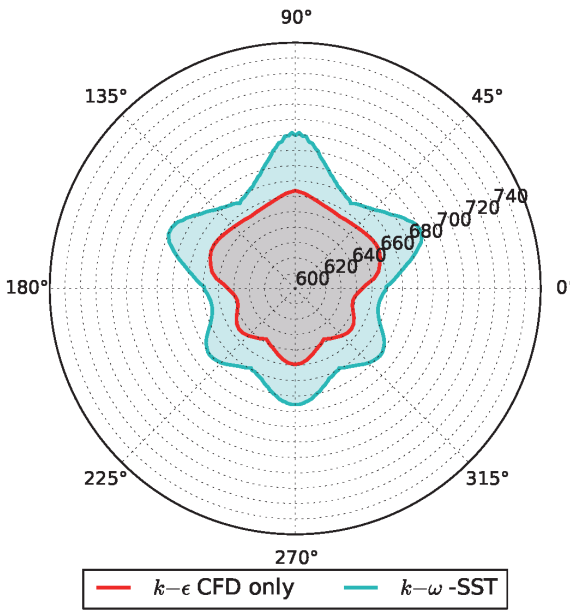

Figure 27: Outer wall temperature on rod B in K over the circumferential position for cases 1 and 4 at an axial position of 1325mm.

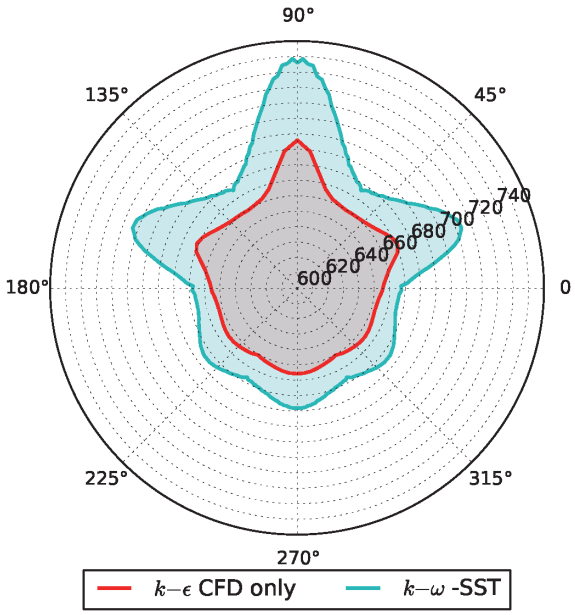

Figure 28: Outer wall temperature on rod B in K over the circumferential position for cases 1 and 4 at an axial position of 1625mm.

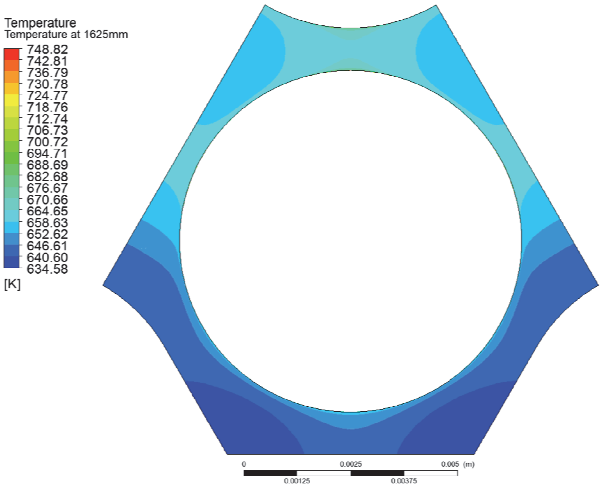

Figure 29: Cross sectional temperature profile for the k−ω –SST analysis at 1625mm.

5. Discussion of Results

5.1 Impact of Mesh Size and Turbulence Model

As discussed in chapter 2, the $k-\varepsilon$ model tends to underestimate wall temperatures. Furthermore, larger cells work to the advantage of numerical diffusion. For cases 1 to 3, mesh density in the near wall region is so coarse that the boundary layer cannot be resolved and the fluid flow behaviour is modelled by a wall function. Especially for supercritical conditions, this setup is known to underestimate the wall temperature. The strongly non-linear fluid behaviour cannot be adequately modelled by the wall functions. Furthermore, as the fluid temperature is evaluated as the mean value of the cell, a coarser mesh flattens the pronounced temperature gradients that are to be expected in the near-wall region.

5.2 Impact of Conjugate Heat Transfer

The results for case 2 show an overall flattened circumferential temperature profile as was to be expected. The circumferential temperature gradient implies the existence of homogenising conductive heat flows in the structural domain. This leads to a more even temperature distribution on the outer rod wall. In the experimental setup, the boron nitride filling of the rods is expected to further flatten the temperature profile as well, if only by a relatively small factor. This can be concluded from the presence of a circumferential variance in temperature at the inner rod wall. By flattening the temperature profile of the rod, the potential for thermal stresses and hence rod deflection is reduced by the boron nitride. The boron nitride, however, is expected to have a small effect on the bending line of rod B.

5.3 Impact of Rod Deflection

The differences in shape and intensity of the temperature profiles for cases 2 and 3 result from the differing incident flow on the rods in the upper channel section. The inclined outer rod wall in case 3 presents an increased surface of attack for the flow increasing the heat transfer coefficient in that area. The occurrence of pronounced secondary flows is able to explain the differences in the temperature profiles.

A transient solution of the problem cannot be excluded. A strong hint in that direction is that, depending on the initial conditions, the initial displacement of rod B's end varied in orientation. When choosing a uniform temperature distribution inside the fluid as initial condition, the end of rod B approached the central rod. The orientation of the bending line changed after some iterations and the rod end came in contact with the outer channel wall. The mesh displacement solver was incapable of coping with that kind of behaviour so that it could not be further investigated. Choosing the converged solution of case 2 as initial conditions, the end of rod B immediately moved towards the perimeter of the channel and stayed there until the solution reached convergence. For further analysis it might be interesting to approach the problem with a transient solver.

5.3.1 Errors Entailed by Mesh Deformation

Due to thermal expansion, the heating rods are elongated and, on their upper end, pushed out of the fluid computational domain. This causes a risk that a small part of the outer rod surface does not participate in the exchange of variables for the coupling. The conservative interpolation mapping guarantees that the net heat flow over the interface remains the same. Nonetheless, we can see a sudden rise in the mean wall temperature at the outlet for the case where the deformation was implemented. It is reasonable to assume that this represents an artefact introduced by the decrease in mesh quality at the outlet. Further away from the outlet, the error can be assumed to be negligible due to the choice of an upwind convection scheme.

6. Conclusions

Ideally, the full rod bundle should have been modelled without symmetry constraints, using the k-ω-SST turbulence model with a fine resolution of the boundary layer ($y^+<1$) including CHT and FSI. This ideal case has not been feasible yet with ANSYS. Nevertheless, this study can show trends and the sensitivity of different simplifications which were assumed.

The deflection of rod B causes a change in the wall temperature profile towards the outlet. Origin is the occurrence of secondary flows in the upper channel section induced by the bending. The mean wall temperature is reduced where strong deflections arise. In this particular case, the influence of rod deflection on the temperature profile is small in comparison to that of turbulence model and mesh density. This might change when the heat flux is increased.

The choice of turbulence model and the y^+ values of the mesh have a strong impact on the surface temperatures. The $k-\omega$ –SST model in combination with small y^+ values proved to deliver a more pronounced temperature profile than the $k-\varepsilon$ model on the coarse mesh. Wall temperatures were highest for case 4. The effects of heat conduction and rod deflection on the temperature profile can be expected to be more pronounced when considered in combination with a fine mesh and the $k-\omega$–SST model. More reliable results can be obtained by conducting an FSI analysis with a finer mesh primarily; secondarily with a more adapt turbulence model.

The mesh density in the near wall region has to be increased in order to obtain more accurate results, regardless which kind of turbulence model is implemented in future analysis. The initial shape of the mesh does however have a significant influence on the stability of the solver for the mesh displacement. A finer mesh in proximity of the wall might call for a readjustment of the mesh displacement solving parameters such as mesh stiffness and relaxation factor. The problem presented by deformation of the first cell layer at the outlet in normal direction becomes increasingly important for smaller cell heights and aspect ratios. Distortions of this kind are more likely to cause mesh folding for small cell heights in normal wall direction.

For a higher mesh density further away from the wall, another difficulty arises. Especially the lack of cells with large radial extent in the gap between rod B and other boundaries might prove to be problematic. The mesh displacement solver has to find a solution that prevents the creation of negative volume elements. Having cells with large extend in the respective direction facilitates this. The difficulty of the task is increased when more cells are placed in the gap which is reduced in size due to deformation.

References

1. I. L. Pioro, R. B. Duffey. Experimental heat transfer in supercritical water flowing inside channels (survey). *Nuclear Engineering and Design*, 235(22):2407–2430, 2005.

2. M.Rhode J.W.R. Peeters et. Al. A blind, numerical benchmark study on supercritical water heat transfer experiments in a 7-rod bundle. *The 7th International Symposium on Supercritical Water-Cooled Reactors*, 2015

3. J. Heinecke, G. Weber. Thermoelastic instabilities of fast reactor fuel pins. *IMechE*, C416/027:343–348, 1991.

4. J, Licht, M, Anderson, M. Corradini. Heat transfer to water at supercritical pressures in a circular and square annular flow geometry. *International Journal of Heat and Fluid Flow*, 29(1):156 – 166, 2008.

5. J. Yang, Y. Oka, Y. Ishiwatari, J. Liu, J. Yoo. Numerical investigation of heat transfer in upward flows of supercritical water in circular tubes and tight fuel rod bundles. *Nuclear Engineering and Design*, 237(4):420–430, 2007.

6. C. Kunik. *CFD-Simulationen turbulenter konvektiver Strömungen bei überkritischen Drücken*. PhD thesis, Karlsruher Institut für Technologie (KIT), 2012.

7. J. Kim, P. Moin. Transport of passive scalars in a turbulent channel flow. In *Turbulent Shear Flows 6*, pages 85–96. Springer, 1989.

8. M. Jaromin, R. Thiele, H. Anglart. CFD prediction of heat transfer to supercritical water. *THINS cluster workshop 2*, February 2013.

9. X.Cheng, B.Kuang, Y. Yang. Numerical analysis of heat transfer in supercritical water cooled flow channels. *Nuclear Engineering and Design.* 237(3): 240-252, 2007.

10. J.D. Jackson, M.A. Cotton, and B.P. Axcell. Studies of mixed convection in vertical tubes. *International Journal of Heat and Fluid Flow*, 10(1):2–15, 198

11. F. R. Menter. Two-equation eddy-viscosity turbulence models for engineering applications. *AIAA journal*, 32(8):1598–1605, 1994.

ISSCWR7-2038

Thermal hydraulic and safety analysis of the supercritical water cooled fuel qualification test bundle

X. J. Liu, C. Zhou, Z.D. Wang, T. Yang, X. Cheng
School of Nuclear Science and Engineering, Shanghai Jiao Tong University
800 Dong Chuan Road, Shanghai, 200240, China
Phone: +86-21-34207121 Fax: +86-21-34205182
Email: xiaojingliu@sjtu.edu.cn

Abstract

In 2012, China and European Union issued one joint project for the R&D work of supercritical water cooled reactor (SCWR). This joint project is called Supercritical Water Reactor -Fuel Qualification Test (SCWR-FQT) in Europe, and Super-Critical Reactor In Pipe Test Preparation (SCRIPT) in China. The main subject of this joint project is design and licensing of a small scale fuel assembly including the required coolant loop with supercritical water and its safety and auxiliary systems. One of the most important tasks in SCRIPT project is to perform thermal hydraulic and safety analysis of the FQT loop. To this end, both sub-channel code COBRA-SC and system code ATHLET-SC are developed for transient analysis of SCWR. Validation and verification work for these two codes are carried out using the current supercritical water data. Several accidents such as Loss of coolant due to break, fuel bundle local blockage, are analyzed by the new developed codes. During the safety analysis, the whole system behavior including safety system characteristic is analyzed by system code ATHLET-SC, whereas the local thermal-hydraulic parameters are predicted by the sub-channel code COBRA-SC. Sensitivity analysis are carried out to identify the appropriate models for description of the transient phenomenon in the test loop. Some measures to mitigate the accident consequence are also trialed to demonstrate their effectiveness.

The results indicate that the new developed codes has good feasibility to transient analysis of supercritical water-cooled test. And the peak cladding temperature in the fuel assembly can be reduced effectively by the safety measures of SCWR-FQT.

Keywords

Supercritical water reactor-fuel qualification test (SCWR-FQT), sub-channel code, system code, coupling analysis

1. INTRODUCTION

The SCWR (Supercritical Water-Cooled Reactor) is selected as one of the six Generation IV reactors proposed by Generation IV International Forum (GIF). In the last few years, SCWR R&D activities are ongoing worldwide and great effort is made on both experimental and theoretical investigation on SCWR safety related phenomena [1].The steering committee of the SCWR system in GIF has prepared a system research plan which outlines the necessary research and development steps to enable a small SCWR prototype of a kind to be constructed and operated in the 2020s [2].

As the next step, this system research plan proposes to test a small scale fuel assembly under typical prototype conditions in a research reactor. Design and licensing of such a small scale fuel assembly including the required coolant loop with supercritical water and its safety and auxiliary systems is subject of the project Supercritical Water Reactor -Fuel Qualification Test (SCWR-FQT) [3]. Among the task list of SCWR-FQT project, to determine the detailed thermal-hydraulic behavior in the bundle region at blockage condition is one of the key problems needed to be investigated and solved. Therefore, the sub-channel simulation for the SCWR-FQT fuel bundle is required within this project [4].

However, the boundary condition of the sub-channel code, e.g. mass flow, inlet temperature, needs to derive from the system code results. Considering the interaction between the system code and sub-channel code, the effect of one code on the other, i.e. the coupled effect should be included to predict a reasonable behaviors. Thus, it is better to couple these two codes by data transfer and adaptation at the interface of the system and the active core.

In this paper, a coupled sub-channel and system code system is developed to simulate the system and local behavior of the SCWR-FQT system. Some measures to mitigate the accident consequence are derived from sub-channel calculation and trialed in the coupled code to demonstrate their effectiveness.

2. THE SCWR-FQT SYSTEM AND ITS ACTIVE CORE

2.1 System Description

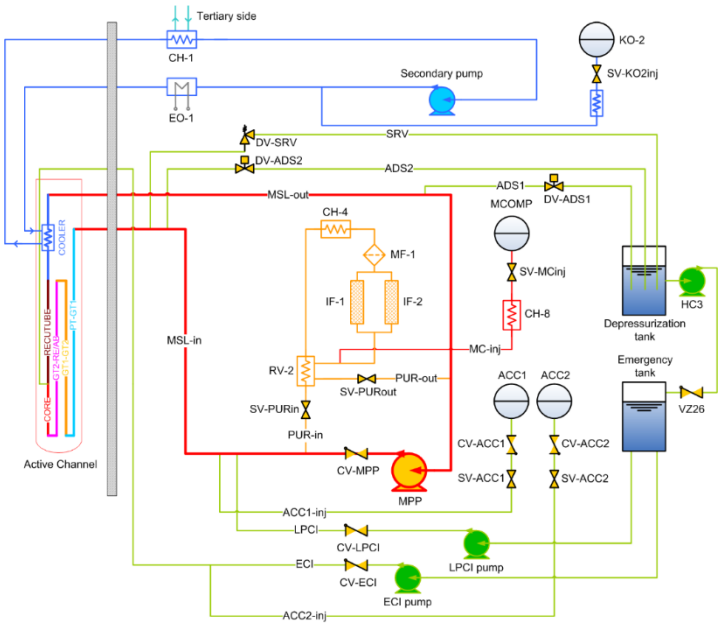

Fig.1 Scheme of the SCWR-FQT test loop [3]

The SCWR-FQT test loop consists of the primary loop and the safety system. Fig.1 shows the SCWR-FQT test loop. As shown in Fig. 1, the primary loop is connected to the fuel assembly (active channel). The primary pump (MPP) feeds cold water of 300°C into the active channel, and after it there is a check valve (CV-MPP) which avoids reverse flow. The coolant is then heated up along the internal flow paths inside the active channel to about 383°C, and it is cooled down again to 300°C afterwards before it exits the active channel. MSL-in is the pipe before the inlet of the active channel and MSL-out is the one after the outlet of the active channel. A compensator (Mcomp) is connected to the primary loop via the purification system. It acts as a pressurizer which compensates pressure fluctuation and keeps the pressure in the loop at constant value of about 25 MPa. Water volume in the compensator is 30 L.

The safety system includes two accumulators (ACC1 and ACC2), a low pressure cooling injection system (LPCI), an emergency cooling injection (ECI) system and an automatic depressurization system (ADS). The automatic depressurization line on MSL-out (ADS1) is used to induce the coolant flow during depressurization and to keep the coolant outlet open during cooling by LPCI. Table 1 and table 2 summarize the settings of the safety signals and the countermeasures for difference signals.

Table 1: safety signal settings and scram signals

General settings	
SCRAM delay (s)*	2.0
SCRAM rod insertion time (s)*	2.0
ADS valve driving time (s)	0.5
Pump run up and shut down time (s)	2
Pressure relief valve activation (MPa)	26
SCRAM signals	
Mass flow in primary system (kg/s)	0.15
Fluid temperature (test section outlet) (°C)	500
Pressure in primary system (MPa)	22.5
Pressure difference cross the fuel: MSLin-ECI (MPa)	-1.5

*This value is updated recently, the delay time is 0.06s, and insertion time is 1.0s.

Table 2: countermeasures for difference signals

Signal	**Actions**	**Device**
System pressure p < pmin (22.5 MPa) Low mass flow G < Gmin (150 g/s)	Reactor SCRAM ADS2 opens HC1 pump starts HCC pump stops	LPCI
System pressure p > pmax (26 MPa)	PRV opens (spring loaded)	_
Coolant temperature in test section T > Tmax Heated section Tcoolant > 500 °C Inlet temperature of HCC pump > 350 °C Pressure difference inversion over fuel element	Reactor SCRAM ADS1 opens HCC pump starts HCC pump stops	ECI

2.2 Active Core Description

This water cooled reactor with a core height of 60 cm enables to replace one of its assemblies with a pressure tube containing a four rods fuel bundle, to simulate a supercritical water environment at the fuel assembly. The cross-section of the core is illustrated in Fig. 3. The primary system pressure keeps at 25 MPa, and the fissile power is 63kW. In normal condition, the circulation flow in the active channel is 0.25kg/s. Due to the heat generation in the fuel rod as well as the heat transfer between active channel and the assembly box, the coolant

temperature at the bundle inlet and outlet are about 370°C and 384°C respectively[3]. Wire wrap spacer is adopted in SCWR-FQT fuel bundle to enhance the coolant mixing flow between sub-channels and to maintain the cooling geometry by prevention the fuel rod contacting adjacent rods. However, the utilization of the wire wrap may bring some severe problems, e.g. the detachment of the wire wrap, causing local flow path blockage inside the test section. This phenomenon is importance because the local coolant and cladding temperature will increase significantly at the downstream of the blockage position. Thus, the integrity of the fuel clad can be threatened when the blockage is formed in the flow path of SCWR-FQT bundle.

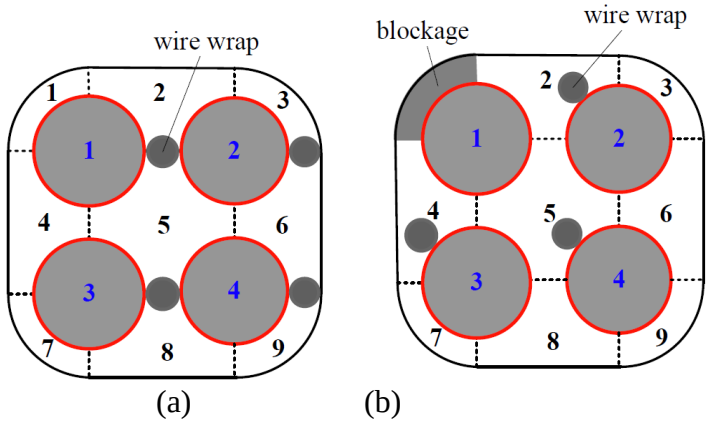

Fig.3 Scheme of sub-channel and fuel rod in SCWR-FQT fuel assembly

Table3 summaries the geometry data and the normal operation conditions of the fuel bundle. The sub-channel and fuel rod distribution is shown in Fig. 3(a). An illustration of blockage case is also presented in Fig. 3(b), i.e. detached wire wrap block sub-channel 1. Due to the geometry of the wire and the sub-channel 1, this will cause a total blockage of SC1. The boundary condition parameter, e.g. the inlet mass flow, inlet fluid temperature, outlet pressure is derived from design requirement of SCWR-FQT project. Fig. 4 presents the normalized axial power profile vs. the axial position for fuel rod. The radial power distribution of the fuel rod is uniform.

Table 3 design parameters of the active core

Rod diameter (mm)	8.0
Pitch (mm)	9.44
Duct of the wall (mm)	1.44
Pitch of the wire (mm)	216.67
Diameter of the wire (mm)	1.44
Heating length (mm)	600.0
Radial power factor (-)	1.0
Total Power (kW)	63.6
Mass flow (kg/s)	0.25
Outlet pressure of the bundle (MPa)	25.00
Inlet temperature of bundle (°C)	370.0

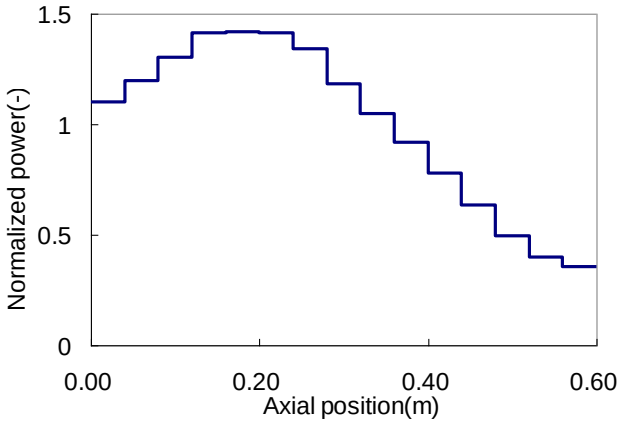

Fig. 4 Normalized power distribution

3. ADAPTION OF THE CURRENT CODES

It is well known that at subcritical pressure, there is a saturated region for water, where vapor and liquid simultaneously exist. With the transition between vapor and liquid in this region, the fluid temperature keeps as constant and void fraction varies between 0 and 1. But when the pressure is above the critical pressure (over 22.06MPa), the fluid has only single-phase state, so there is no phase change in the supercritical region. Therefore the change in void fraction is not continuous when the pressure undergoes across the critical point. This discontinuous change of void fraction will directly affect the numerical calculation, cause severe errors, and result in the termination of the calculation.

In order to avoid discontinuity of void fraction during the trans-critical process, a pseudo two-phase method is introduced both in system code ATHLET-SC and sub-channel code COBRA-SC with a virtual region of saturation at pseudo-critical temperatures (heat capacity c_p has maximum value at this temperature). This virtual saturated region is based on the detachment of the pseudo-critical line, which is an extension of the saturation curve to the supercritical pressure region, to get a narrow band of the pseudo two phase region.

3.1 System Code ATHLET-SC

The system code ATHLET-SC, which is developed with pseudo two-phase method on the basis of ATHLET 2.1, is utilized to simulate the trans-critical transients, i.e. the pressure from the supercritical condition decrease to subcritical condition. As indicated by Fig. 5, the pseudo two-phase method is proposed by introducing a fictitious region of latent heat (enthalpy of vaporization h_{fg}*) at pseudo-critical temperatures. Consequently, a smooth transition of void fraction can be realized by using liquid-field conservation equations at temperatures lower than the pseudo-critical temperature, and vapor-field conservation equations at temperatures higher than the pseudo-critical temperature. Detailed description and validation work about the code ATHLET-SC can be found in paper of Fu et al. [5].

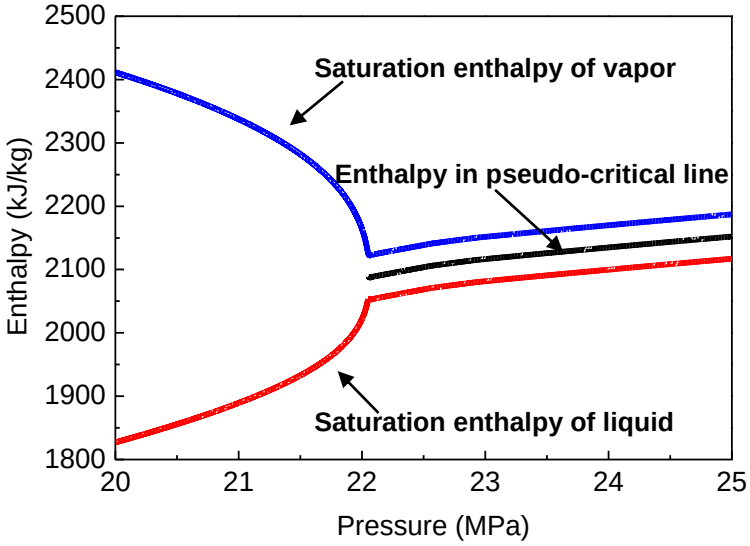

Fig. 5 Illustration of pseudo two-phase method in ATHLET-SC

3.2 Subchannel Code COBRA-SC

By utilization of this method, the supercritical condition in COBRA-SC code is similar to the sub-critical condition. As a result, a smooth transition of void fraction can be realized. Then the discontinuity of void fraction will not occur during the trans-critical transient.

During the trans-critical transient, the occurrence of boiling crisis during depressurization transients should be considered in COBRA-SC, since the critical heat flux (CHF) is close to zero right underneath the critical pressure. Therefore, several CHF correlations valid near critical pressure are chosen and added in COBRA-SC code.

The heat transfer correlation selection criterion is expressed by equation (1) to (4). In the region of right underneath the critical pressure, if the cladding heat flux exceeds the critical heat flux q''_{cr} developed by Zuber [6] or the cladding surface temperature is over the minimum film boiling temperature T_{MFB} defined by Groeneveld [7], it assumed that the boiling crisis takes place and the corresponding CHF heat transfer correlation then is applied in the code. There are three new added heat transfer correlations can be used in COBRA-SC, described in equation (5-7).

$$q''_{cr} = 0.13 \cdot H_{fg}\rho_v \left[\frac{\sigma(\rho_l - \rho_v)g}{\rho_v^2}\right]^{1/4} \quad (1)$$

$$T_{MFB} = T'_{MFB} - \frac{x \cdot 10^4}{(2.82 + 1.22 \cdot p)} \quad (2)$$

where x is the subcooled quality, p is the pressure in MPa.
For pressure≤9Mpa

$$T'_{MFB} = 284.7 + 44.1 \cdot p - 3.72 \cdot p^2 \quad (3)$$

For pressure>9MPa

$$T'_{MFB} = T_{MFB}(9MPa) - T_{Sat}(9MPa) \cdot \frac{p_{cr} - p}{p_{cr} - 9} + T_{Sat} \quad (4)$$

For the high vapour quality region (x≥0.03), e.g. the liquid-deficient region, the Bishop equation [8] is used:

$$Nu_f = 0.0193 \cdot \mathrm{Re}_f^{0.8} \cdot \mathrm{Pr}_f^{1.23} \cdot \left(\frac{\rho_g}{\rho_l}\right)^{0.068} \cdot \left[\alpha + \frac{\rho_l}{\rho_g}(1-\alpha)\right]^{-0.68} \quad (5)$$

For the low vapour quality region (x<0.03), such as inverted annular flow region, the Berenson correlation [9] is applied:

$$h_{fb} = 0.425 \cdot \left[\frac{H_{fg} \cdot \rho_v \cdot g(\rho_l - \rho_v)\lambda_v^3}{\mu_v \cdot \sqrt{\frac{\sigma}{g \cdot (\rho_l - \rho_v)}} \cdot (T_W - T_v)}\right]^{0.25} \quad (6)$$

When the heat flux and cladding temperature fail to meet the criteria from equation (1) to (4), the Griem heat transfer correlation at the region of near critical point (20-22.06MPa), defined by equation (7) will be applied. When the pressure departs from the high pressure region, the normal heat transfer correlation in COBRA-IV will be applied.
Griem correlation [10] (1996), the more definition of subscript in equation (7) can be found in [10]:

$$Nu = 0.0169 \cdot \mathrm{Re}^{0.8356} \cdot \mathrm{Pr}^{0.432} \cdot \left(\frac{\rho_W}{\rho_B}\right)^{0.231} \cdot F \quad (7)$$

where, $\lambda = 0.5 \cdot (\lambda_B + \lambda_W)$, $\mu = \mu_B$, $C_P = \frac{1}{3} \cdot \left\{\sum_{i=1}^{5} C_{P,i} - C_{P,\max} - C_{P,2,\max}\right\}$

$$F = \min\left\{\begin{matrix}1.0, \\ \max\left[\begin{matrix}0.82, \\ 0.82 + 9 \cdot 10^{-7}\left(H - 1.54 \cdot 10^6\right)\end{matrix}\right]\end{matrix}\right\}$$

It is supposed that the heat transfer behavior near the critical pressure can be well simulated by the new implemented correlations and CHF judgment logic in COBRA-SC. And this has been confirmed by the validation work performed in paper [11].

Table 4 summarizes the conclusions achieved in the previous work [11] and gives the recommendation of the thermal-hydraulic models in COBRA-SC code for the simulation of SCWR-FQT bundle. In the following steady state and transient calculation the models listed in table 4 will be applied.

Table 4 Recommend models for analysis [11]

Thermal-hydraulic model	Recommend model
Heat transfer	Bishop
Friction	Cheng & Todeas
Turbulence mixing	Jeong
Axial node number	60

4. CODE COUPLING METHOD

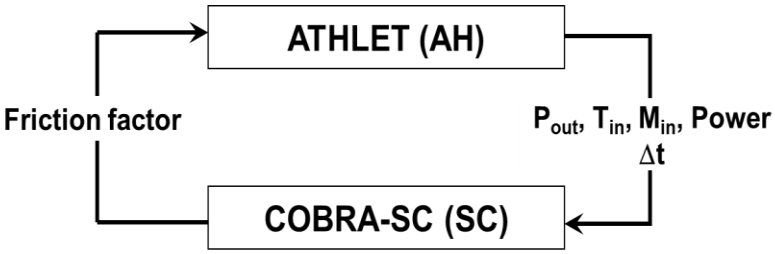

Fig. 6 Coupled methodology for ATHLET and COBRA codes

As shown in Fig. 6, the two modified codes, i.e. ATHLET and COBRA-SC are coupled by the interface at the active core. ATHLET, performing the whole system simulation, provides the pressure at the core outlet (P_{out}), coolant temperature at the core inlet (T_{in}), coolant mass flow rate at the core inlet (M_{in}), and heat generated in the active core as the boundary conditions for COBRA-SC code. These parameters are calculated or transferred from the ATHLET results as followed:

P_{out}= PRESS (outlet-CV)
T_{in} = TDOM (inlet-CV)
M_{in}= GJ (inlet-junction)
Power= (rod power generation)-(heat loss from active channel to other channels)

The sub-channel code will provide the pressure frication coefficient to ATHLET calculation as an input geometry parameter. This parameter can be calculated by:
Frication factor: $ALAMO_{(New)} = \Delta P_f(SC)/ \Delta P_f(AH) \times ALAMO_{(old)}$.

Therefore, the spatial coupling is fixed in this study. The sub-channel code will re-calculate the active core in detail and give the feedback to the system code, in which the active core is also simulated in a very coarse modeling.

For the temporal control of the coupled system, the time step from ATHLET dominates the whole calculation and to be used as the time step of COBRA-SC. The time control methodology are shown in Fig. 7. The COBRA is first called for input initialization, and then ATHLET input initialization and zero-transient calculation. Then ATHLET is performed for real transient calculation from t_0 to t_1 and provide the boundary conditions (power, mass flow, pressure and so on) to COBRA-SC. With these parameters, COBRA calculation is carried out from t_0 to t_1 with the same time step, and give the estimated friction factor of the core to ATHLET. And the ATHLET start another time step calculation at t_1. It should be pointed out that during the transient, ATHLET time step dominates the whole calculation. In this way, the restart calculation of ATHLET is flexible to start the coupling simulation with COBRA-SC code.

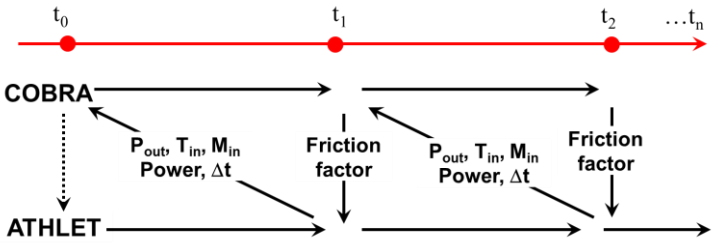

Fig. 7 Time step control methodology

5. RESULTS AND DISCUSSION

Using the coupled code system, calculation is performed to achieve steady-state firstly, and then the transient simulation starts. In this paper, the accident of local flow path blockage inside the test section, caused by the detachment of the wire wrap, is analyzed.

5.1 Steady-State Results

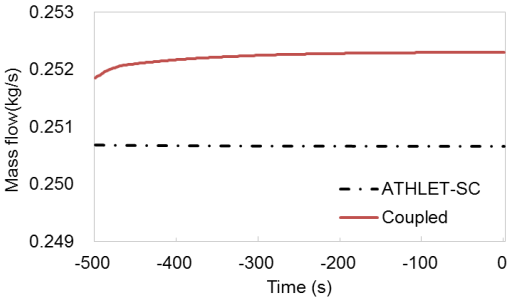

(a) Mass flow rate

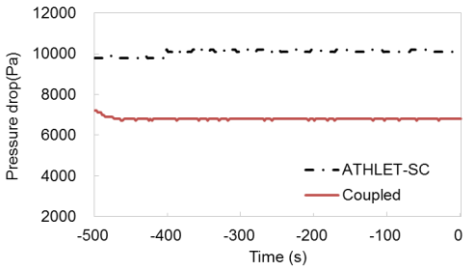

(b) Pressure difference across the core

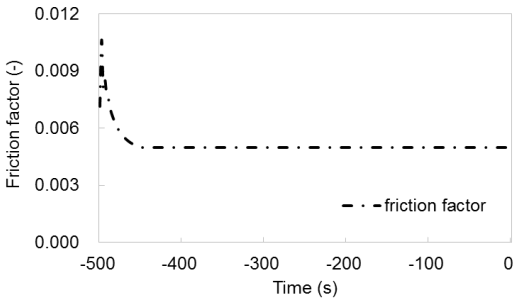

(c) Friction factor adapted by the coupled code

Fig. 8 Steady state results from coupling simulation

It can be found that most of the coupled results is very close to the single ATHLET calculation, except the parameters shown in Fig. 8. ATHELT predict a lower mass flow in the active bundle due to its higher friction data in the input. As a results, the coupled code gives a much lower pressure drop in the active core (as shown in Fig.8 (b)). It is general accepted that the sub-channel code shows a better modelling capability for bundle geometry. Therefore, it can be assumed that the pressure drop calculated by COBRA-SC is reasonable comparing to the single ATHLET calculation. The adaptation of the friction factor can be clearly seen in Fig.8 (C).

5.2 Transient Results

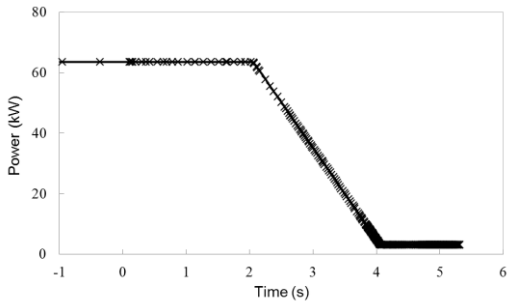

Fig. 9 core power

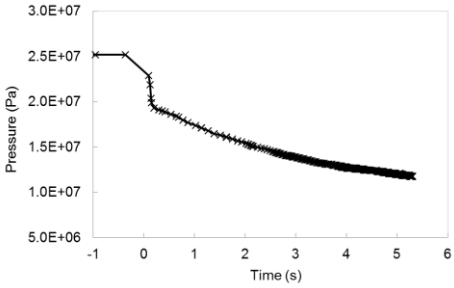

Fig. 10 transient pressure at the core outlet

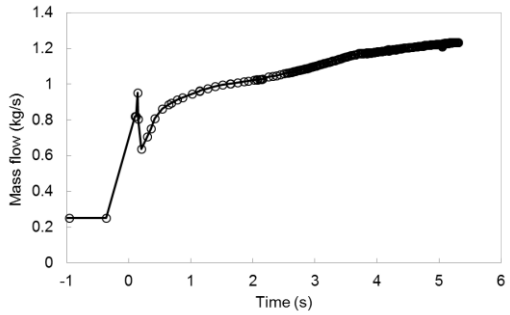

Fig. 11 mass flow rate at the core outlet

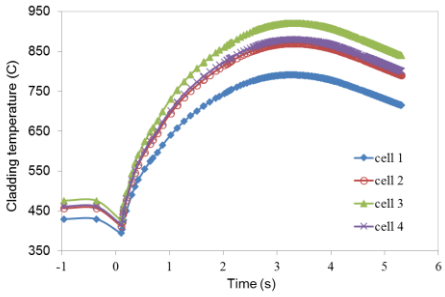

Fig. 12 peak cladding temperature from system code

Fig.9-Fig.12 show the results of the coupled simulation. Due to the occurrence of the blockage (at 2050s), high cladding temperature at the blockage position causes the scram of the core power. Afterwards, the ADS at the outlet opens, pressure in the primary system decreases, the mass flow in the core increases from 0.25kg/s to 1.2kg/s. The cladding temperature drops a little at beginning (around 2050s) and then increases to 900°C during 0.2-3.0 s. This is due to the occurrence of the boiling crisis phenomenon when the system pressure drops to the region right underneath the critical point. The transient results indicate that by the aid of the safety measures of the SCWR-FQT system, the accident consequence by local blockage in the fuel bundle can be mitigated effectively. This effect can be easily found in Fig. 12 and Fig. 13, where the cladding temperature are reduced significantly.

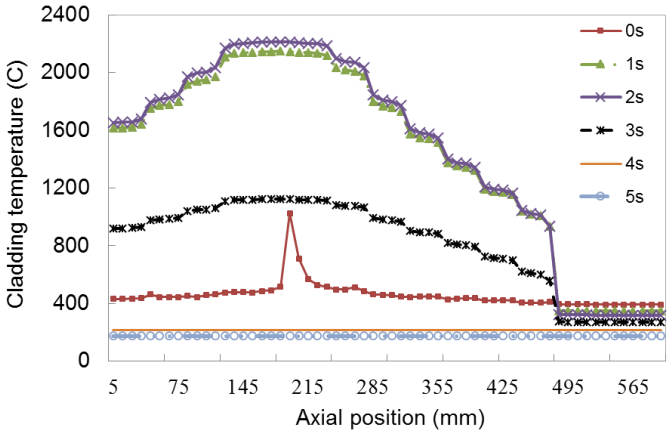

Fig. 13 peak cladding temperature from sub-channel code

Fig. 13 shows the transient peak cladding temperature from the sub-channel code. It can be clear that at 0s (corresponding to 2050s in ATHLET simulation) the blockage occurs, the decrease of the system pressure causes the peak cladding temperature increase to 2200°C. With the core power keeps at high level, the cladding temperature remains at a high value. It have to be pointed out that when the core power decrease to a low value, the cladding temperature reduce to a low value around 200°C. The modelling of subchannel code is in detail and it can predict the local phenomenon. Therefore, the subchannel code shows a higher cladding temperature caused by blockage comparing to the ATHLET code.

6. CONCLUSIONS

In this paper, ATHLET-SC and COBRA-SC are coupled together to simulate the transient behavior of the supercritical water reactor-fuel qualification test (SCWR-FQT). The system and local performance of SCWR-FQT loop are predicted by the system code and sub-channel code respectively. The steady and transient results indicate that the new developed code shows good

feasibility to transient analysis of supercritical water-cooled test. Some measures to mitigate the blockage accident consequence are also trialed to demonstrate their effectiveness..

7. ACKNOWLEDGMENTS

This work is supported by National Natural Science Foundation of China (51106097).

8. REFERENCES

1. Y. Oka. 2000. “Review of high temperature water and steam cooled reactor concepts”. *Proc. of SCR-2000*, Tokyo, pp. 37-57(2000).
2. Gen IV Roadmap, “US DOE Nuclear Energy Research Advisory Commit-tee and the Generation IV International Forum. A Technology Roadmap for Generation IV Nuclear Energy Systems. GIF002-00, December 2002. http://gif.inel.gov/roadmap/
3. C. Zhou, Y.H. Yang, X. Cheng. “Feasibility analysis of the modified ATHLET code for supercritical water cooled systems", *Nucl. Eng. Des.* **250**,pp 600-612(2012)
4. M. Raqué, A. Vojecek, P. Hajek, P., T. Schulenberg, “Design and 1D analysis of the safety systems for the SCWR fuel qualification test”. *In: Proceedings of the 9th International Topical Meeting on Nuclear Reactor Thermal Hydraulics, Operation and Safety*, Kaohsiung, Taiwan, September 9-13, 2012.
5. S.W. Fu, X.J. Liu, C. Zhou et al. “Modification and application of the system analysis code ATHLET to trans-critical simulations”, *Annals of Nuclear Energy*, **44**, pp 40-49(2012)
6. N. Zuber, “Hydrodynamic aspects of boiling heat transfer”, *AECU-4439*, USAEC.(1959)
7. D. C. Groeneveld, J. C.Stewart “The minimum film boiling temperature for water during film boiling collapse”, *Proc. 7th Int. Heat Transfer Conf*., 4, 393-398, Munich, Germany.(1982)
8. A.A. Bishop, R.O. Sandberg, L.S. Tong, “Forced convection heat transfer to water at near critical temperatures and supercritical pressures”. *WCAP-2056-P, Part-III-B.*(1964)
9. P.J. Berenson, “Film boiling heat transfer from a horizontal surface”. *J. Heat Transfer* **83**, pp 351-357(1961)
10. H. Griem “A new procedure for the prediction of forced convection heat transfer at near- and supercritical pressure”, *Heat and Mass Transfer* **31**, 301-305.(1996)
11. X.J. Liu, T. Yang, X. Cheng, “Thermal-hydraulic analysis of flow blockage in a supercritical 4water-cooled fuel bundle with sub-channel code”, *Annals of Nuclear Energy* **59**, pp 194-203, (2013).

ISSCWR7-2039

Oxidation of 800H/HT and AISI316L alloys in air and supercritical water

Majid Nezakat[1], Hamed Akhiani[1], Sami Penttilä[2], Seyed Morteza Sabet[3] Jerzy Szpunar[1]
[1] Department of Mechanical Engineering, University of Saskatchewan
57 Campus Drive, Saskatoon, SK, S7N 5A9, Canada
[2] VTT Technical Research Center of Finland, Materials for Power Engineering
P.O. Box 1000, FI-02044 VTT, Finland
[3]Department of Ocean and Mechanical Engineering, Florida Atlantic University
Boca Raton, FL 33431, USA
Telephone: +1 (306) 966-5374, Email address: majid.nezakat@usask.ca

Abstract

In this study, we evaluated the oxidation resistance of two Fe-Ni-Cr based alloys (stainless steel 316L and incoloy 800H/HT) in air and supercritical water at 600 ºC. Results indicate that Incoloy 800H/HT shows considerably better oxidation resistance in supercritical water, compared to stainless steel 316L, and therefore it is a better candidate as a structural material for SCWR. The difference in chemical composition of the alloys was found to be the main reason for better oxidation resistance of incoloy 800H/HT as it has higher amount of chromium and nickel and, on the contrary, lower amount of iron. This resulted in the formation of a protective layer on the surface which significantly retarded the oxidation in supercritical water environment.

1. Introduction

Water at pressure and temperature more than 22.1 MPa and 374.15 ºC, respectively, exhibits significant changes in its properties, such as higher thermal conductivity and reactivity. These changes in properties can be utilized for a large number of applications, including destruction of hazardous chemicals by oxidation [1,2] or implementing as a cooling and heat transfer medium [3,4]. In view of that, the latter application was employed to increase the thermal efficiency of future generation of nuclear reactors in a unique design called supercritical water reactor (SCWR) [5,6]. However, since SCW environment is highly corrosive and there is a higher fuel cladding temperature due to higher fuel burn up, one of the major challenges upon bringing this concept reactor to a practical use is to find the reactor structural materials such as fuel cladding. As a result, Generation IV International Forum (GIF) was started a quest to find the appropriate materials which can resist the harsh environment inside SCWR core [5]. Among the proposed materials, Fe-Ni-Cr based alloys such as austenitic stainless steel 316L and incoloy 800H/HT, which are used as structural materials in conventional nuclear reactors [7,8], drew a lot of attentions due to their superior properties including oxidation and creep resistance [5,9–16]. Few available literature on SCW oxidation of Fe-Ni-Cr based alloys reported that incoloy 800H alloys family generally exhibit a lower oxidation rate and weight gain, compared to stainless steel alloys [13,17]. However, most of these studies have been done using a static autoclave which often leads to lower oxidation and less spallation than dynamic/recirculating autoclaves. In this study, we evaluated the performance of stainless steel 316L and incoloy 800H/HT in

supercritical water (at 600 ºC) using a dynamic/recirculating autoclaves. For comparison, air oxidation at the same temperature and atmospheric pressure was conducted.

2. Materials and methods

As-received hot rolled stainless steel 316L and incoloy 800H/HT billets, used in this study, were fully annealed at 1420 ℃ and water quenched. The chemical composition of the alloys is shown in Table 1. Specimens with dimensions of 24 mm × 14 mm × 0.6 mm (L×W×T) were cut from the as-received billets and mechanically abraded on all surfaces with abrasive paper up to grit number 2000 (10 µm SiC particles).

The specimens were oxidized in supercritical water at 600 ºC and 25 MPa for 100, 300 and 1000 h in an autoclave connected to a recirculation water loop, as illustrated in Figure 1. The values of temperature, pressure, inlet and outlet water conductivity, oxygen content and flow rate, which were monitored and controlled, are listed in Table 2.

Bruker D8 Discover X-ray diffraction (XRD) system with Cr Kα radiation was used to identify the present phases in the oxide scale. In addition, to characterize the oxide structure, the samples were mounted in a conductive edge retention resin (Struers Polyfast®) and then grinded with abrasive paper up to grit number 2000 (10 µm SiC particles). Polishing was performed using a water based diamond suspensions up to 1 µm diamond particle size (Struers DiaPro®) at polishing wheel speed lower than 150 rpm to avoid breakdown of the fragile oxide layer. Final stage of polishing was done using 0.04 µm colloidal silica suspension (Struers OP-S®) on a Vibratory Polisher (Buehler VibroMetTM 2) for 24 h. The cross-section of all samples was then analyzed using FEG-SEM at 20 kV equipped with EBSD and energy dispersive spectroscopy (Oxford X-Max Silicon Drift EDS) detectors.

Table 1. Chemical Composition (wt%) of stainless steel 316L and incoloy 800H/HT

Alloy	C	Mn	Al	Ti	P	S	Si	Cr	Ni	Co	Cu	Mo	Fe
316L	0.016	1.33	-	-	0.03	0.001	0.54	17.32	10.07	0.21	0.35	2.02	68.11
800H/HT	0.07	0.98	0.55	0.54	0.22	0.0001	0.32	20.5	30.19	0.3	0.4	0.42	45.41

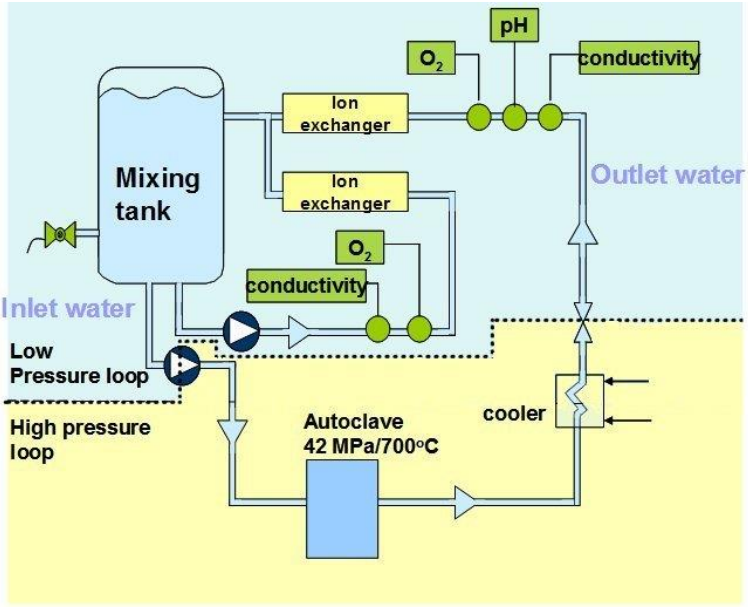

Figure 1. The supercritical autoclave system at VTT.

Table 2. Targeted and realized values for the supercritical water test environment

Quantity	Target value / range	Notes/realized values (mean ± SD)
Temperature	600 ºC	Recorded mean 599 ± 1.0 ºC
Pressure	250 bar	Recorded mean 250 ± 0.9 bar
Inlet conductivity	0.1-0.5 µS/cm	Recorded mean 0.053 ± 0.001 µS/cm
Outlet conductivity	1.0-3.0 µS/cm	Recorded mean 0.29 ± 0.11 µS/cm
Inlet dissolved O2	150 ppb	Recorded mean 150 ± 0.5 ppb
pH of the inlet water	7.0	(Pure water)
Flow rate	~5 ml/min	Full renewal about every 2 h

3. Results

3.1 Weight change

Figure 2 shows the weight change of the austenitic stainless steel 316L after oxidation in air and supercritical water at 600 ºC for 100, 300, and 1000 h. In general, the alloy shows a better oxidation resistance in air than that in supercritical water. As seen, after 100 h of oxidation in air, stainless steel 316L has a weight gain about 0.2 mg/cm^2. This remains almost constant up to 1000 h of oxidation. The weight change trend is different in supercritical water. As observed, the weight gain is about 0.6 mg/cm^2 after 100 h of exposure to supercritical water and it increases to 1.8 mg/cm^2 after 300 h of oxidation. It seems that weight change is increasing by oxidation time in supercritical water, however, a weight loss is observed after 1000 h. Results also indicate that stainless steel 316L does not show a good performance in supercritical water compared to air at 600 ºC.

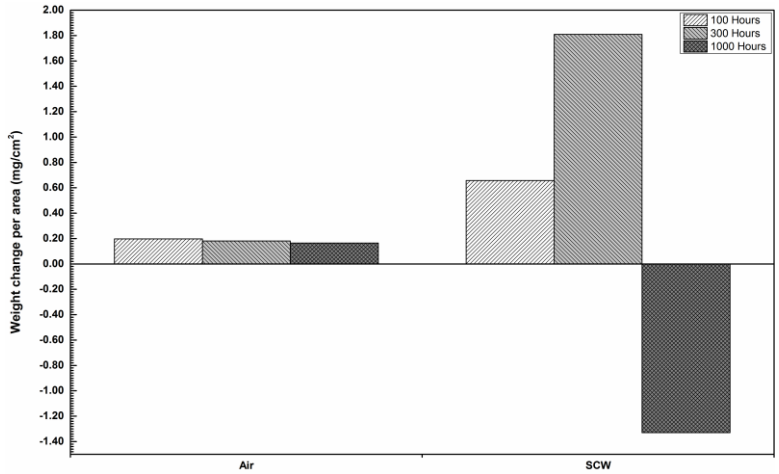

Figure 2. Weight change of austenitic stainless steel 316L in air and supercritical water.

Figure 3 illustrates the weight change of incoloy 800H/HT after exposure to air and supercritical water at 600 ºC for 100, 300, and 1000 h. Upon 100 h of air oxidation, weigh change reaches almost a constant value. In comparison to austenitic stainless steel, incoloy 800H/HT shows at least a hundred times less weight gain. Similarly, this alloy also shows a worse oxidation resistance in supercritical water compared to air oxidation. In addition, weight loss happened after 100 h of exposure to supercritical water. This is also the case after 1000 h of oxidation. In total, in comparison to stainless steel 316L, the difference in weight change after 1000 h of oxidation in both air and supercritical water is not significant in incoloy 800H/HT.

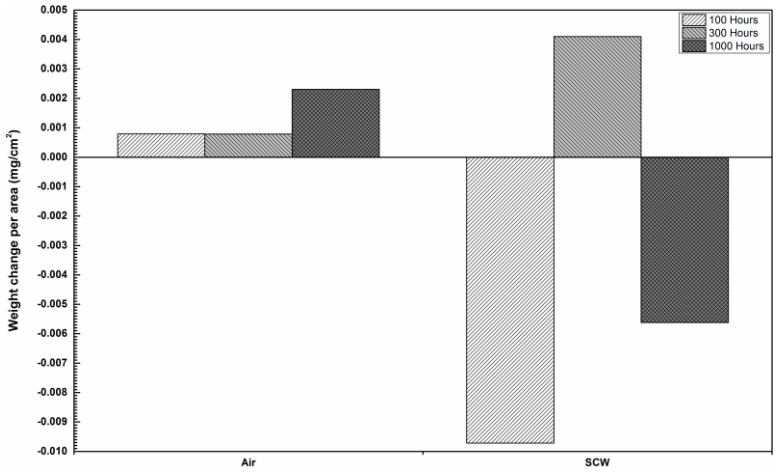

Figure 3. Weight change of incoloy 800H/HT in air and supercritical water.

3.2 Phase identification

Figure 4 depicts the x-ray diffraction pattern of austenitic stainless steel 316L after oxidation in supercritical water at 600 ºC and 25 MPa for 1000 h. The oxidation mechanism of the alloy was studied in our previous work [18]. As seen, the peaks of three different phases including austenite, magnetite (Fe_3O_4) and $FeCr_2O_4$ spinel phase are present.

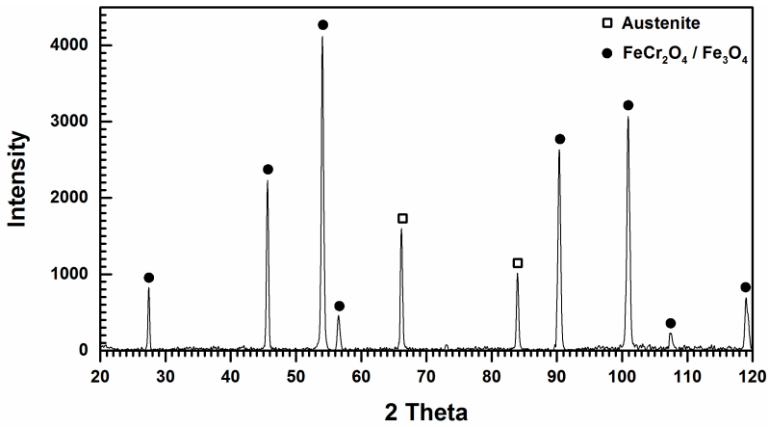

Figure 4. X-ray diffraction patterns of stainless steel 316L after exposure to supercritical water at 600 ºC and 25 MPa for 1000 h.

X-ray diffraction pattern of incoloy 800H/HT oxidized in supercritical water at 600 ºC and 25 MPa for 1000 h is illustrated in Figure 5. As it can be seen, the peaks of austenite phase are visible in the pattern. However, there are other peaks present in the pattern which are only visible at higher magnifications due to their low intensities. These peaks belong to four different oxides including iron-chromium spinel ($FeCr_2O_4$), magnetite (F_3O_4), hematite (Fe_2O_3), and chromium oxide (Cr_2O_3).

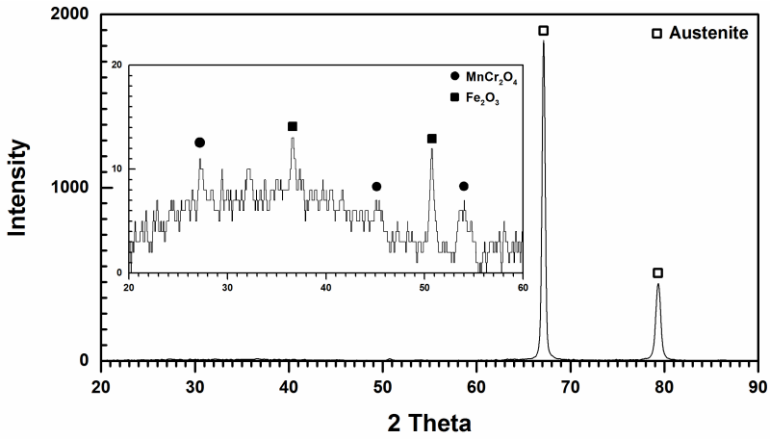

Figure 5. X-ray diffraction patterns of incoloy 800H/HT after exposure to supercritical water at 600 ºC and 25 MPa for 1000 h.

To complement the XRD results, the cross-section of samples were studied using EBSD. Figure 6 illustrates the EBSD band contrast and EDS elemental composition maps on the cross-section of stainless steel 316L after 1000 h of oxidation. Due to very low concentration of chromium and nickel, compared to oxygen and iron, the EDS maps were not normalized. According to Figure 6, three different regions are present. Iron and oxygen are the only two elements present in the top layer (external oxide) and therefore, based on the XRD results and EBSD observations, it is composed of magnetite. The second layer (internal oxide), which is right beneath of the surface, is consisted of chromium, iron, and oxygen. The internal oxide layer has a similar thickness to that of the external one. According to XRD pattern, this layer is identified as $FeCr_2O_4$ spinel phase with a crystal structure similar to magnetite.

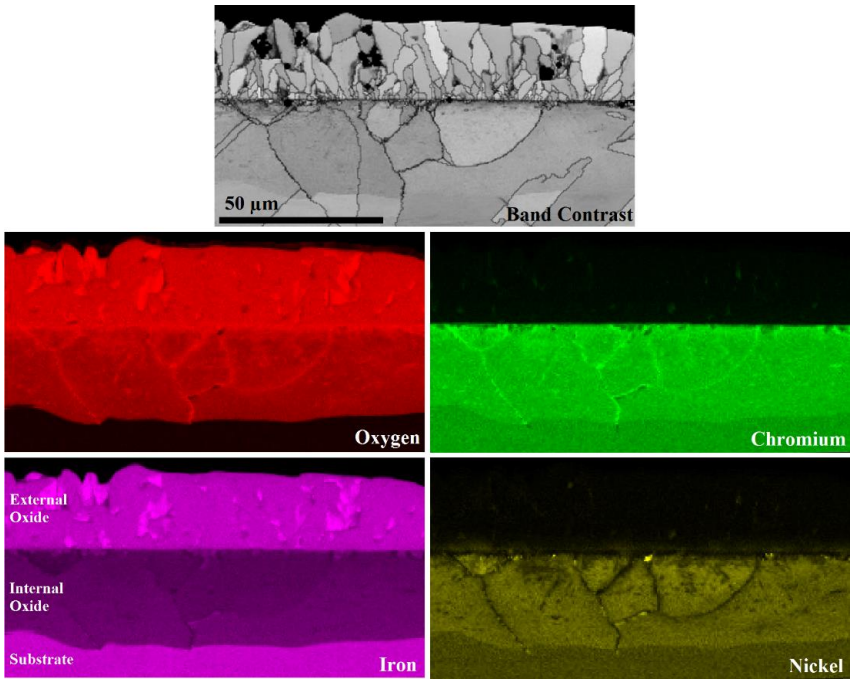

Figure 6. EBSD band contrast and EDS elemental composition of stainless steel 316L after exposure to supercritical water at 600 ºC and 25 MPa for 1000 h.

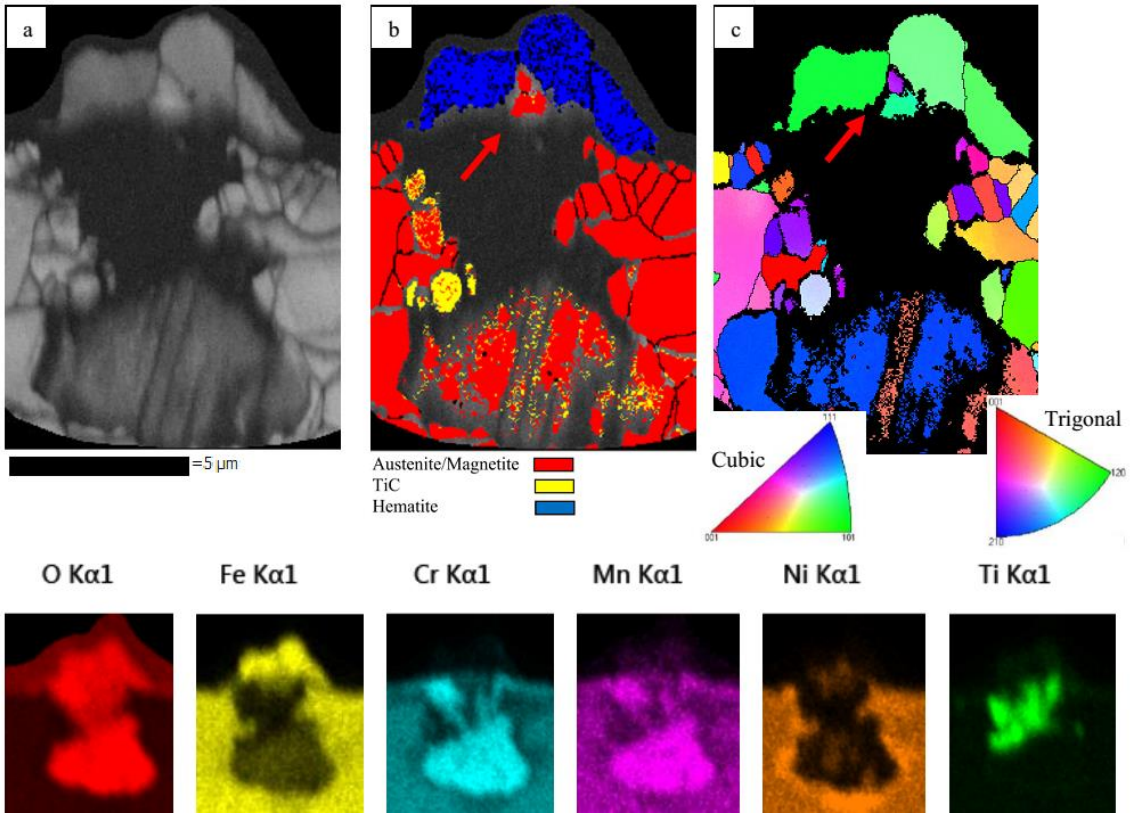

Figure 7. EBSD (a) band contrast, (b) phase map, (c): IPF Z, and EDS maps of iron oxide islands on the cross-section.

EBSD band contrast, EBSD phase map, EBSD inverse pole figure, and EDS elemental composition maps on the cross-section of incoloy 800H/HT after exposure to supercritical water are shown in Figure 7. In our previous study it was found that the surface of incoloy 800H/HT is covered by thin layer of $MnCr_2O_4$ spinel phase as well as small islands of iron oxides [19]. As it can be seen, hematite (Fe_2O_3) is the first layer at the top of the oxide island. In addition, there are small magnetite (Fe_3O_4) grains right below the hematite. According to phase map, these grains are indexed as austenite due to the similar structure of magnetite and austenite. However, EDS maps revealed that they are iron oxide. The next layer is composed of titanium carbide and titanium oxide. Due to small grain size of titanium oxide, the EBSD phase map was not enable to detect it. Finally, $MnCr_2O_4$ spinel is the last phase present at the bottom of the oxide island.

4. Discussion

Figure 2 shows the weight change of stainless steel 316L after oxidation in air and supercritical water at 600 ºC for 100, 300, and 1000 h. As seen, the weight change of the alloy after oxidation in air is almost constant. This can be due to the presence of protective chromium oxide (Cr_2O_3) layer which is formed and still present at this temperature. Figure 8 shows the EDS elemental maps and EDS elemental line scan on the surface of stainless steel 316L after 1000 h of oxidation in air. As seen, two different phases are present on the surface of the alloy. The first, which covers the entire surface, is chromium oxide (Cr_2O_3), and the latter is $MnCr_2O_4$

spinel. This indicates that the formation of the protective layer hinders further oxidation of the alloy.

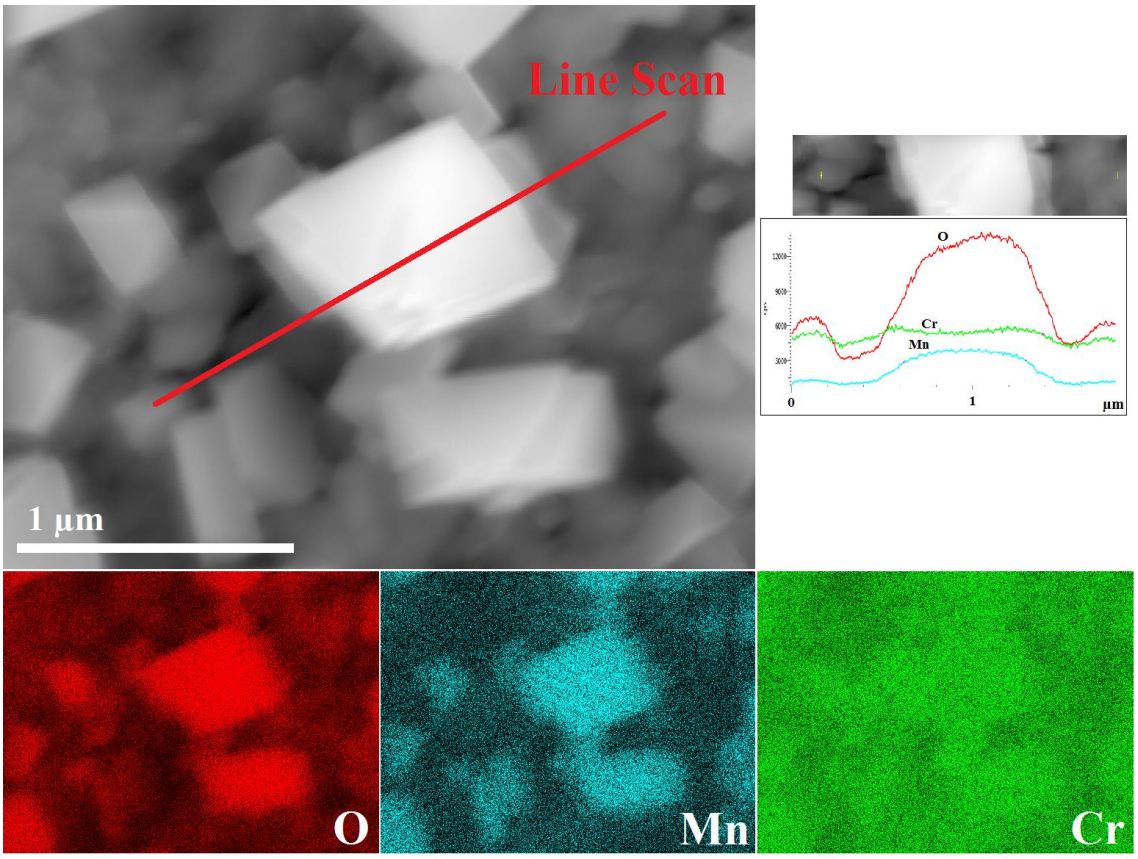

Figure 8. EDS elemental composition of stainless steel 316L after 1000 h of oxidation in air at 600 ºC.

According to XRD results (Figure 4) and EDS observations (Figure 6), the protective layer is absent on the surface of the alloy when oxidation takes place in supercritical water. As seen, both internal and external oxidation took place in supercritical water. First, iron diffuses to the surface of the alloy to interact with oxygen and form magnetite. At the same time, oxygen diffuses inside the substrate and interacts with chromium and iron to form the internal spinel phase ($FeCr_2O_4$). As a result, since there is no barrier to retard or stop the inward and outward diffusion processes, oxidation will continue and thickness of the oxide layer would increase by time. However, as illustrated in Figure 2, oxide exfoliation would happen after 1000 h of oxidation. This could be due to the increase in strain energy with thickness of the oxide layer [20–22]. As a result, the oxide layer could crack and exfoliation would happen when layer thickness exceed a critical value.

Figure 3 depicts the weight change of incoloy 800H/HT after exposure to air and supercritical water at 600 ºC for 100, 300, and 1000 h. Similar to stainless steel 316L, oxidation in air was retarded on this alloy as the weight change is constant after 100, 300 and 1000 h of oxidation. This is also because of formation of the protective chromium oxide (Cr_2O_3) at this temperature. On the other hand, based on XRD results (Figure 5) and EDS observations (Figure 7), although chromium oxide (Cr_2O_3) is not present on the surface of the alloy, a thin layer of $MnCr_2O_4$ spinel phase exist. This layer would also act as a barrier to retard the diffusion of elements through the surface. However, islands of iron oxide are present on the surface which increases the weigh change to some extent. The formation mechanism of these islands were studied in our previous work [19]. It was found that iron oxide islands would form where there is a titanium carbide (TiC). When titanium carbide (TiC) oxidizes to titanium oxide (TiO_2), usually a volume expansion (e.g.

TiO_2/TiC = 1.28) may happen, which leads to impose the expansion to the carbides surrounding [23]. As a result, surface protective layer may crack and fast diffusion path for iron will be provided, and finally iron oxide islands would form. On the other hand, oxide exfoliation happened at much earlier stages of oxidation, i.e. 100 h, in this alloy, compared to stainless steel 316L. Since the protective layer on the surface of the incoloy 800H/HT is very thin, the strain energy of the oxide scale may not play a significant role in the oxide exfoliation. The cause could lie in the formation of the cracks as a result of the aforementioned volume expansion right beneath the surface. These cracks could remove a part of the oxide scale each time an expansion results in a crack. As a result, the weight change of incoloy 800H/HT could decrease with increase in the oxidation time.

Moreover, in comparison to stainless steel 316L, incoloy 800H/HT does not show considerable differences in weight change after oxidation in air and supercritical water at 600 ºC. This could be related to the difference in the chemical composition of both alloys. It is believed that higher amount of chromium could increase the probability of formation of the chromium oxide (Cr_2O_3) protective layer on the surface upon oxidation. However, since chromium is a ferrite stabilizer, the amount of nickel, as an austenite stabilizer, should be increased with increase in chromium concentration. On the other hand, less amount of iron in the composition could decrease the possibility of formation of iron oxides. Therefore, as listed in Table 1, since incoloy 800H/HT has higher amount of chromium and nickel and less amount of iron, formation of the protective layer on the surface of the incoloy 800H/HT is more plausible.

5. Conclusion

The oxidation resistance of two Fe-Ni-Cr based alloys including stainless steel 316L and incoloy 800H/HT in air and supercritical water at 600 ºC was studied and the followings were concluded:

1. Stainless steel 316L does not show a good oxidation resistance in supercritical water compared to air at 600 ºC.
2. Incoloy 800H/HT does not show considerable differences in weight change after oxidation in air and supercritical water at 600 ºC.
3. Incoloy 800H/HT is a better candidate as a structural material for SCWR compared to stainless steel 316L as it shows considerably better oxidation resistance in supercritical water.
4. Higher amount of chromium and nickel and, on the contrary, lower amount of iron in incoloy 800H/HT alloy compared to stainless steel 316L resulted in formation of a protective layer on the surface which retarded the oxidation significantly.
5. Oxide exfoliation in stainless steel 316L was related to the strain energy of the oxide scale which is proportional to the thickness. As a result, if the oxide thickness, i.e. strain energy, exceeds a critical value, oxide exfoliation may happen. On the other hand, oxide exfoliation of the incoloy 800H/HT was found to be due to the cracks as the result of a volume expansion right beneath the surface. The expansion caused by oxidation of titanium carbide (TiC) to titanium oxide (TiO_2).

Acknowledgements

The authors would like to express their gratitude to The Natural Sciences and Engineering Research Council of Canada (NSERC) and Academy of Finland for funding this project. Valuable discussions with Dr. Hamed Asgari is appreciated.

References

[1] X. Gao, X. Wu, Z. Zhang, H. Guan, E. Han, Characterization of oxide films grown on 316L stainless steel exposed to H2O2-containing supercritical water, J. Supercrit. Fluids. 42 (2007) 157–163.

[2] E. Asselin, A. Alfantazi, S. Rogak, Corrosion of nickel–chromium alloys, stainless steel and niobium at supercritical water oxidation conditions, Corros. Sci. 52 (2010) 118–124.

[3] C. Sun, R. Hui, W. Qu, S. Yick, Progress in corrosion resistant materials for supercritical water reactors, Corros. Sci. 51 (2009) 2508–2523.

[4] P. Kritzer, Corrosion in high-temperature and supercritical water and aqueous solutions: a review, J. Supercrit. Fluids. 29 (2004) 1–29.

[5] U. DoE, A technology roadmap for generation IV nuclear energy systems, Nucl. Energy Res. Advis. Comm. …. (2002).

[6] P. Today, E. Needs, Technology Roadmap Update for Generation IV Nuclear Energy Systems, (n.d.).

[7] T.R. Allen, F. Balbaud-Celerier, T. Asayama, M. Pouchon, J.T. Busby, S. Maloy, et al., Status Report on Structural Materialsfor Advanced Nuclear Systems, 2013.

[8] X.I.N. Luo, R.U.I. Tang, C. Long, Z.H.I. Miao, Q. Peng, C. Li, CORROSION BEHAVIOR OF AUSTENITIC AND FERRITIC STEELS IN SUPERCRITICAL WATER, 40 (2007).

[9] S. Penttilä, A. Toivonen, J. Li, Effect of surface modification on the corrosion resistance of austenitic stainless steel 316L in supercritical water conditions, … J. Supercrit. …. 81 (2013) 157–163.

[10] T.M. Hayward, I.M. Svishchev, R.C. Makhija, Stainless steel flow reactor for supercritical water oxidation: corrosion tests, J. Supercrit. Fluids. 27 (2003) 275–281.

[11] M. Sun, X. Wu, Z. Zhang, E. Han, Oxidation of 316 stainless steel in supercritical water, Corros. Sci. 51 (2009) 1069–1072.

[12] M. Sekine, N. Sakaguchi, M. Endo, H. Kinoshita, S. Watanabe, H. Kokawa, et al., Grain boundary engineering of austenitic steel PNC316 for use in nuclear reactors, J. Nucl. Mater. 414 (2011) 232–236.

[13] M. Fulger, M. Mihalache, D. Ohai, S. Fulger, S.C. Valeca, Analyses of oxide films grown on AISI 304L stainless steel and Incoloy 800HT exposed to supercritical water environment, J. Nucl. Mater. 415 (2011) 147–157.

[14] I. Betova, M. Bojinov, P. Kinnunen, S. Penttilä, T. Saario, Surface film electrochemistry of austenitic stainless steel and its main constituents in supercritical water, J. Supercrit. Fluids. 43 (2007) 333–340.

[15] D. Gómez-Briceño, F. Blázquez, a. Sáez-Maderuelo, Oxidation of austenitic and ferritic/martensitic alloys in supercritical water, J. Supercrit. Fluids. 78 (2013) 103–113.

[16] L. Tan, T.R. Allen, Y. Yang, Corrosion behavior of alloy 800H (Fe–21Cr–32Ni) in supercritical water, Corros. Sci. 53 (2011) 703–711.

[17] G.S. Was, P. Ampornrat, G. Gupta, S. Teysseyre, E. a. West, T.R. Allen, et al., Corrosion and stress corrosion cracking in supercritical water, J. Nucl. Mater. 371 (2007) 176–201.

[18] M. Nezakat, H. Akhiani, S. Penttilä, M. Sabet, J. Szpunar, Effect of thermo-mechanical processing on oxidation of austenitic stainless steel 316L in supercritical water, Corros. Sci. (2015).

[19] H.Akhiani, M. Nezakat, S. Penttilä, J.A. Szpunar, The oxidation resistance of thermo-mechanically processed Incoloy 800H/HT in supercritical water, J. Supercrit. Fluids. (2015).

[20] J. Pelleg, L.Z. Zevin, S. Lungo, N. Croitoru, Reactive-sputter-deposited TiN films on glass substrates, Thin Solid Films. 197 (1991) 117–128.

[21] U.C. Oh, J.H. Je, Effects of strain energy on the preferred orientation of TiN thin films, J. Appl. Phys. 74 (1993) 1692.

[22] L. Hultman, Low-energy (~100 eV) ion irradiation during growth of TiN deposited by reactive magnetron sputtering: Effects of ion flux on film microstructure, J. Vac. Sci. Technol. A Vacuum, Surfaces, Film. 9 (1991) 434.

[23] J. Litz, a. Rahmel, M. Schorr, Selective carbide oxidation and internal nitridation of the Ni-base superalloys IN 738 LC and IN 939 in air, Oxid. Met. 30 (1988) 95–105.

ISSCWR7-41

Methodology to Design Simulated Irradiated Fuel by Maximizing Integral Indices (c_k,E,G)

Jason R. Sharpe[1], A. Buijs[1], J. Pencer[1,2]
[1] McMaster University, Hamilton, Ontario, Canada
(905-975-5122, Sharpejr@mcmaster.ca)
[2] Canadian Nuclear Laboratories, Chalk River, Ontario, Canada

Abstract

Critical experiments are used for validation of reactor physics codes, in particular to determine the biases and uncertainties in code predictions. To reflect all conditions present in operating reactors, plans for such experiments often require tests involving irradiated fuel. However, it is impractical to use actual irradiated fuel in critical experiments due to hazards associated with handling and transporting the fuel. To overcome this limitation a simulated irradiated fuel (SIMFUEL), whose composition mimics the neutronic behavior of the actual irradiated fuel (TRUFUEL), can be used in a critical experiment. Here we present an optimization method in which the composition of SIMFUEL for the Canadian Supercritical Water-cooled Reactor (SCWR) concept at midburnup (20.1 MWd/kg[IHM]) is varied until the integral indices c_k, E, and G are maximized between the TRUFUEL and SIMFUEL. In the optimization, the SIMFUEL composition is simplified so that only the major actinides (^{233}U, $^{238\text{-}242}$Pu and ^{232}Th) remain, while the absorbing fission products are replaced by dysprosia and zirconia. In this method the integral indices, c_k, E and G are maximized while the buckling, k_{inf} and the relative pin-ring fission powers are constrained, within a certain tolerance, to their reference lattice values. Using this method, we obtained maximized integral similarity indices of c_k = 0.967, E = 0.992, and G = 0.891.

1. Introduction

Determination of simulation biases and uncertainties is becoming increasingly important in the conceptualization, design, and licensing of new critical assemblies as well as in the continuing operation of existing facilities. For that reason, an understanding of fuel performance at midburnup (or any burnup) is needed; however, difficulties associated with using irradiated fuel, due to restrictions placed by international treaties, transportation issues and handling hazards, motivate the use of simulated fuel (SIMFUEL) that neutronically mimics the truly irradiated fuel (TRUFUEL) instead.

When mimicking the TRUFUEL a number of neutronic responses can be used to describe the similarity of two fuels, i.e.: the multiplication constant (k_{inf}), flux spectra, fission powers, buckling (B^2), nuclear data sensitivities ($S_{k,\alpha}$), reactivity coefficients, and others. Although no SIMFUEL exactly matches a corresponding TRUFUEL without having all the original isotopes included at their respective number densities, we can approximate the neutronic responses by replacing the built-in absorbing fission products with a small number of absorbing (or moderating) isotopes. By using gradually more isotopes, the SIMFUEL and TRUFUEL's neutronic responses will become increasingly similar. However, the availability of certain isotopes limits the isotopic options; also, by increasing the complexity of the SIMFUEL

(i.e. adding more isotopes), finding optimal solutions becomes more computationally expensive, because the optimizing algorithm has a larger parameter space to cover.

Although much research exists in designing SIMFUEL for investigating its chemical properties, there is little literature in the way of designing SIMFUEL for neutronic purposes, most likely because the existing experimental knowledge is derived from privately funded experiments and is therefore proprietary. In this study a method is introduced to design a SIMFUEL's isotopic composition. Since the main purpose of this study is to select a SIMFUEL for nuclear data adjustment and bias calculation, the similarity of the global integral indices c_k, E and G are maximized – meanwhile, certain lattice parameters: B^2, inner and outer fuel ring relative fission powers (P_i and P_o respectively) and k_{inf} are constrained to mimic the TRUFUEL's neutronic behaviour.

1.1 Sensitivity, Uncertainty and Similarity

To determine the three global integral indices, c_k, E and G (defined below), a lattice cell-based calculation to find the cell's nuclear data sensitivities is first required. The Scale 6.1 simulation suite [1], developed at Oak Ridge National Laboratories, includes the SAMS (Sensitivity Analysis Module for Scale) [2] module which calculates the system's nuclear data sensitivities using the adjoint-based perturbation method [3,4]. The adjoint-based method calls for the cell's forward and adjoint fluxes which is accomplished using the deterministic neutron transport code NEWT [5] (also included in Scale 6.1).

SAMS produces explicit sensitivities, which represent the sensitivity of k to the perturbation of resonance self-shielded multigroup nuclear data:

$$S_{k,\alpha} = (\alpha / k)(dk / d\alpha) \quad (1)$$

where k is the multiplication constant and α is a nuclear data component (i.e. energy-, reaction- and nuclide-specific cross sections (Σ_j), fission spectra (χ), and (ν) the number of neutrons emitted per fission). SAMS also produces implicit sensitivities, which arise from changes in k coming from the effect of perturbing one resonance-shielded cross section on another. The explicit and implicit sensitivities are then added to make the complete sensitivity. The complete sensitivity vector, $\mathbf{S_k}$, is of length M, where M is the number of energy groups multiplied by the number of reactions, multiplied by the number of nuclides (refer to [6,7,8] for a complete discussion and derivation of sensitivities.). This sensitivity vector is then combined with a 44 energy group nuclear data covariance matrix, $\mathbf{C_{\alpha\alpha}}$, to produce the system variance σ^2 (refer to [9] for information on the covariance matrix):

$$\sigma^2 = \mathbf{S_k}\, \mathbf{C_{\alpha\alpha}}\, \mathbf{S^T_k} \quad (2)$$

where $\mathbf{S^T_k}$ is the transpose of $\mathbf{S_k}$. Individual group-wise, nuclide- and reaction-specific variances can also be found by performing element-wise multiplication.

The integral similarity index c_k between systems can then be found by computing the sensitivity vectors for each system, then treating $\mathbf{S_k}$ as an I×M matrix where I is the number of systems and multiplying as in equation (2) [10,11]. The elements of that matrix give the c_k between systems *i* and *j*:

$$c_k = \sigma^2_{ij} / (\sigma_i\, \sigma_j) \quad (3)$$

This similarity index represents the overlap in the contribution to the total system uncertainty from the group (j), reaction (x) and nuclide (n) specific nuclear data. Physically, c_k can be thought of as the overlap in uncertainty contributions, on the multiplication constant, between two systems.

Another integral index, E, representing a direct comparison of how similar the sensitivity vectors are between two systems, is calculated as [10]:

$$E = (\mathbf{S^T_a}\, \mathbf{S_e}) / (|\mathbf{S_a}||\mathbf{S_e}|) \quad (4)$$

where $\mathbf{S_a}$ and $\mathbf{S_e}$ are the application and the experiment's sensitivities, in this case the TRUFUEL and SIMFUEL, respectively. Physically this index can be viewed as a projection of the application's sensitivity vector onto the experiment's sensitivity vector. This is analogous to two directional vectors pointing in the same direction (i.e. all group (j), reaction (x) and nuclide (n) specific sensitivities in two systems are equal) have their dot product equal to 1, or if the vectors are perpendicular (i.e. j,x,n specific sensitivities in one system have their matching j,x,n in another system equal to zero), the dot product is equal to zero.

The final integral index, G, also known as the coverage, is a measure of how much one system's sensitivities are covered by another system's sensitivities, for all the nuclides' reactions, in all energy groups. G is calculated as follows [10,12]:

$$G = 1 - \sum_{nxj} (S^{a}_{nxj} - S^{e'}_{nxj}) \,/\, \sum_{nxj} (S^{a}_{nxj}) \qquad (4)$$

Where $S^{e'}$ is S^{e} if: $|S^{a}| \geq |S^{e}|$, or S^{a} if: $|S^{a}| < |S^{e}|$ and 0 if the sign of S^{e} and S^{a} are different. It is important to have adequate coverage for performing bias calculations; otherwise a large adjustment of nuclear data adjustment would be needed to match the experiments k.

2. Methodology

Before any transport or depletion calculations could be performed, Dancoff factors were needed to properly account for resonance self-shielding effects. Contrary to boiling water and pressurized water reactor designs, which feature a regular geometry of repeating cells [13], the more complicated structure of the SCWR fuel lattice cell (as shown in figure 1) is not repeating, nor uniform, thus a 3-D Monte Carlo approach was needed to determine the Dancoff factors at midburnup. This was performed using the MCDancoff module [14] within Scale 6.1. For each new calculation within this methodology, new Dancoff factors were found.

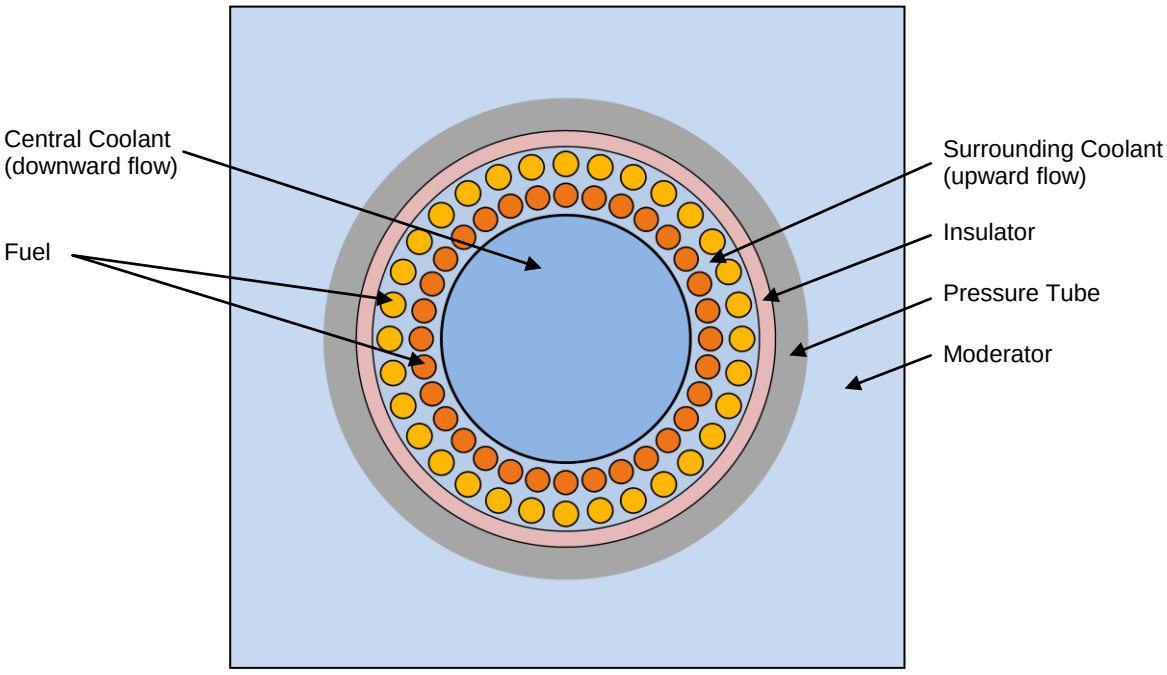

Figure 1. Cross-sectional view of the 64-element Canadian PT-SCWR fuel bundle concept, channel and lattice cell.

The deterministic neutron transport code NEWT was used to model the most recent layout of the Canadian PT-SCWR fuel lattice cell and perform a depletion calculation. A midburnup of 20.1 MWd/kg[IHM] was chosen to respresent a typical midburnup value within a cell. At each burnup step, NEWT reported the number densities of 388 isotopes, including major and minor

actinides, light isotopes and fission products. A one-eighth-cell model was used because of the symmetry of the PT-SCWR lattice as shown in Figure 2 below. Also shown in Figure 2 is the cartesian and radial meshing used to find the forward and adjoint fluxes.

As the TSUNAMI-2D sequence cannot accept an input of 388 isotopes, the list was systematically reduced to adhere to TSUNAMI's constraints: any isotope with a number density below 10^{-9} nuclides/cm*barn was excluded, resulting in a reduction in the number of isotopes in the inner and outer fuel rings to 192, each. This reduced-reference case of TSUNAMI-2D was compared to the NEWT calculation (using 388 isotopes) to ensure the removed isotopes did not contribute significantly to important lattice parameters.

In order to design the SIMFUEL, a number of assumptions were made:

- ^{232}Th would be available,
- ^{233}U would be available by extracting it from irradiated ^{232}Th,
- Only reactor-grade Pu would available. ^{239}Pu was matched to the number density found in the TRUFUEL, while ^{238,240,241,242}Pu were matched to the appropriate weight percentages relative to the ^{239}Pu,
- All other actinides would not be available due to difficulties in shipping and handling, and
- All fission products would be represented by a mixture of dysprosia (Dy_2O_3) and zirconia (ZrO_2).

The SIMFUEL would therefore be composed of ^{232}Th, ^{233}U, reactor grade Pu and a mixture of dysprosia (Dy_2O_3) and zirconia. The amounts of ^{232}Th and ^{233}U are set to equal those of the TRUFUEL, with the amount of reactor grade Pu defined as above. After accounting for these assumptions, a "missing mass" was found by matching the SIMFUEL's density to that of the TRUFUEL's density. This missing mass was then replaced by varying amounts of dysprosia (Dy_2O_3) and zirconia (ZrO_2) that maxmized the integral indices c_k, E and G while constraining B^2, P_i, and P_o to within ±10% and and k_{inf} to within ±2 mk of thier reference values.

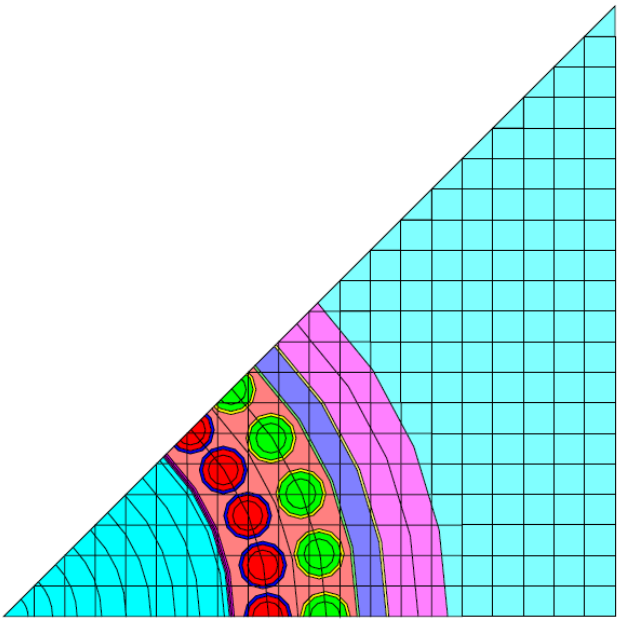

Figure 2. Radial and Cartesian meshing used in the one-eighth fuel cell modelled with NEWT.

2.1 Optimization

A multi-objective genetic algorithm [15,16] was used to find the appropriate concentrations of dysprosia and zirconia in both the inner and outer fuel rings in order to maximize the integral indices while obeying the constraints. The genetic algorithm is included in the computer code Dakota [16] which is an analysis driver code that can interface with any third party software (in this case TSUNAMI-2D and TSUNAMI-IP). The steps followed in the execution of Dakota were:

1. An initial population of data points (using various concentrations of dysprosia and zirconia) was generated and evaluated (to find the integral indices and constraints).
2. Some points were chosen as parents then crossover and mutation operations were performed on these parent points (this is considered the selection operator).
    a. Crossover: A set of parents was chosen to create new individuals (new data points) at some point in space between sets of parents (old data points).
    b. Mutation: From the cross-overed individuals, some were mutated. A random number was chosen to be added to each of the cross-overed dimensions (i.e. dysprosia and zirconia content) - still within the constraints of the phase space. These random numbers got progressively smaller as a solution was approached, so that initially the mutated individuals could be created over the whole phase space, but near the end of the analysis, they were created near the solution. This functionality was to see if other maxima existed near the solution, and to allow for multiple solutions along a Pareto front. The cross-overed and mutated individuals were evaluated.
3. The best individuals were kept for the next generation.
4. Steps 2 through 5 were repeated until solutions were found. A solution was found if there was less than a 0.05% change in function evaluation, over 10 generations.

3. Results

3.1 Verification

Table 1 shows the verification of the reduced set of isotopes and a comparison between NEWT and TSUNAMI-2D. Although TSUNAMI-2D uses NEWT to solve the 2D transport problem, the TSUNAMI-2D sequence uses BONAMIST for the unresolved resonance region and NITAWLST for the resolved resonances to process the resonant self-shielded multigroup cross-section information, where NEWT uses BONAMI and NITAWL. One difference is that BONAMIST and NITAWLST generate explicit and implicit sensitivity data for the sensitivity and uncertainty analysis whereas BONAMI and NITAWL do not. Additionally, when introducing Dancoff factors into the self-shielding calculations, TSUNAMI-2D does not accept the “dan2pitch” parameter, which is accepted into the CENTRM module in NEWT. Instead, NEWT provides an adjusted lattice pitch to account for the effect of the Dancoff factors, which is then used in TSUNAMI-2D. The adjusted lattice pitch approach, or the Dancoff approach, will both provide the same set of resonance self-shielded cross-sections.

Table 1 shows small deviations from the reference case from various responses using the reduced list of isotopes in NEWT, the reduced list of isotopes in TSUNAMI-2D and the optimized SIMFUEL responses from Dakota using TSUNAMI-2D and TSUNAMI-IP. Notice all constraints of 2 mk and ±10% have been met in the optimization. Table 2 shows the maximized integral indices.

Table 1. Verification results for the numerous steps in this evaluation.
[a] Reference case of 388 isotopes.
[b] The reduced list of 192 isotopes.
[c] Optimized SIMFUEL results from Dakota's multiobjective genetic algorithm.
[d] Average relative fission power per fuel ring.

	Scale 6.1 Sequence				
Response	**T-Depl (450 Days)**	**T-Newt Ref. [a]**	**T-Newt Reduced [b]**	**TSUNAMI-2D Reduced [b]**	**Dakota Optimized [c]**
k_{inf}	1.14810	1.14833 (0.18 mk)	1.14833 (~0.00 mk)	1.14832 (-0.01 mk)	1.14900 (-0.51 mk)
Crit. B^2 (10^{-3})	-	1.0301	1.0300 (-0.01%)	1.0301 (~0.00%)	1.0285 (-0.16%)
In. Ring[d]	-	0.5095	0.5095 (0.00%)	0.5095 (0.00%)	0.5218 (2.41%)
Out. Ring[d]	-	0.4905	0.4905 (0.00%)	0.4905 (0.00%)	0.4782 (-2.51%)

3.2 Integral Indices

Table 2 shows the values of the integral indexes that were maximized during the optimization process performed by Dakota (the corresponding k_{inf}, critical B^2, P_i and P_o are found in the last column of Table 1).

Table 2. List of maximized integral indices.

Integral Index	Value
c_k	0.967
E	0.992
G	0.891

The results found in Table 2 were obtained using a number density of dysprosia of n_i = 0.0226 nuclides/cm*barn in the inner ring and n_o = 0.0583 nuclides/cm*barn in the outer ring.

4. Discussion

This work puts an upper limit on the similarity indices under the prescribed constraints. Thus, by solely replacing fission products and a number of actinides with dysprosia and zirconia, maximum achievable values are found, as reported in Table 2. However, other isotopes may be added in the optimization process to better match the TRUFUEL – this will likely lead to higher similarities and tighter constraints, and will be investigated in future work.

In addition, the thermalhydraulic conditions presented here use supercritical water (~625 K, 22 MPa) as a coolant, which likely is not an achievable condition in available test reactors. Deviating from the Canadian SCWR's nominal operating conditions will likely lead to a decrease in integral index; due to changes in the absorption and moderation of the neutron population by the supercritical water (i.e., changes in its density) which affects the flux spectra and in turn would change the sensitivities, these considerations should be included in the optimization phase.

Another major factor that would influence the integral indices is the availability of actinides, such as ^{233}U, reactor grade Pu and ^{241}Am (an important absorber that builds up in plutonium

stockpiles). Again, these considerations can be accounted for in the optimization process described above.

An additional constraint that could be included in the optimization could be the infinite lattice coolant void reactivity. By the same argument as above, this would likely lead to lower integral indices due to changes in the flux's energy spectrum; however, it would provide further critical experiments for data adjustment procedures.

5. Conclusion

This study has demonstrated the use of a new methodology to design simulated fuel using the sensitivity and uncertainty analysis methods included in the Scale 6.1 simulation suite and the Dakota analysis suite.

High similarity (c_k and E) and coverage (G) integral indices, as shown in Table 2, have been found after absorbing fission products were replaced with dysprosia and zirconia in the inner and outer fuel rings (separately) of the Canadian PT-SCWR lattice fuel cell. The high similarity index of $c_k = 0.967$ indicates that many of the contributors to the uncertainty in k_{inf} are shared between the TRUFUEL and SIMFUEL. Additionally, the high similarity index of E = 0.992 demonstrates a close match of the nuclear data sensitivity vectors between the two fuels – showing the neutronic characteristics and responses will be similar. Finally, the high coverage index of G = 0.891 confirms that the TRUFUEL can be included in a data adjustment and simulation bias determination.

Acknowledgements

The author (J. Sharpe) expressed his thanks to Dr. Alex Trottier of CNL for introducing him to the Dakota analysis software, which was heavily relied upon in this work. The work described in this paper was supported in part by the National Science and Engineering Research Council (NSERC) of Canada, under grant number 125519967 and by the NSERC/NRCan/AECL Generation IV Energy Technologies Program

References

1. Radiation Safety Information Computational Center. https://rsicc.ornl.gov, 2013.

2. B. T. Rearden et al., "SAMS: Sensitivity analysis module for SCALE," Tech. Rep. ORNL/TM-2005/39 Version 6.1 Sect. F22, Oak Ridge National Laboratory, June 2011.

3. E. M. Oblow, "Sensitivity Theory from a Differential Viewpoint," *Nucl. Sci. Eng.,* **59**, 187 (1976).

4. A. Gandini, "A Generalized Perturbation Method for Bilinear Functionals of the Real and Adjoint Neutron Fluxes," *J. Nucl. Energy,* **21**, 755 (1967).

5. M. A. Jessee and M. D. DeHart, "NEWT: A New Transport Algorithm for Two-Dimensional Discrete-Ordinates Analysis in Non-Orthogonal Geometries," Tech. Rep. ORNL/TM-2005/39 Version 6.1 Sect. F21, Oak Ridge National Laboratory, June 2011.

6. C. R. Weisbin *et al*., *Application of FORSS Sensitivity and Uncertainty Methodology to Fast Reactor Benchmark Analysis*, ORNL/TM-5563, Union Carbide Corp., Oak Ridge National Laboratory (1976).

7. M. L. Williams, B. L. Broadhead, and C. V. Parks, "Eigenvalue Sensitivity Theory for Resonance-Shielded Cross Sections," *Nucl. Sci. Eng.,* **138**, 177–191 (2001).

8. M. L. Williams, “Perturbation Theory for Reactor Analysis,” *CRC Handbook of Nuclear Reactors Calculations*, Vol. 3, pp. 63–188, CRC Press, 1986.

9. M. E. Dunn, *PUFF-III: A Code for Processing ENDF Uncertainty Data Into Multigroup Covariance Matrices*, ORNL/TM-1999/235 (NUREG/CR-6650), U.S. Nuclear Regulatory Commission, Oak Ridge National Laboratory (2000).

10. B. T. Rearden and M. A. Jessee, “TSUNAMI utility modules,” Tech. Rep. ORNL/TM-2005/39 Version 6.1 Sect. M18, Oak Ridge National Laboratory, June 2011.

11. B. L. Broadhead, B. T. Rearden, C. M. Hopper, J. J. Wagschal, and C. V. Parks, “Sensitivity- and Uncertainty-Based Criticality Safety Validation Techniques,” *Nucl. Sci. Eng.*, **146**, 340–366 (2004).

12. S. Golouglu, C. M. Hopper, and B. T. Rearden, “Extended Interpretation of Sensitivity Data for Benchmark Areas of Applicability,” *Trans. Am. Nuc. Soc.*, **88**, 77–79 (2003).

13. N. M. Greene, “BONAMI, Resonance Self-Shielding by the Bondarenko Method,” Tech. Rep. ORNL/TM-2005/39 Version 6.1 Sect. F1, Oak Ridge National Laboratory, June 2011.

14. L. M. Petrie and B. T. Rearden, “MCDANCOFF Data Guide,” Tech. Rep. ORNL/TM-2005/39 Version 6.1 Sect. M24, Oak Ridge National Laboratory, June 2011.

15. J. L. C. Chapot, F. C. D. Silva and M. R. Schirru, “A New Approach to the use of Genetic Algorithms to Solve the Pressurized Water Reactor’s Fuel Management Optimization Problem,” *Ann. Nucl. Energy*, **26**, 641-655 (1999).

16. The Dakota Project, Sandia National Laboratories. http://dakota.sandia.gov, 2014.

ISSCWR7-2042

Effect of Oxidation Chemistry of SCW on Stress Corrosion Cracking of Austenitic Steels

Bin Gong, E Jiang, Yanping Huang, Yongfu Zhao, Weiwei Liu, Zhiru Zhou
Nuclear Power Institute of China
Third section of huafu road, huayang town, shuangliu country chengdu, China
Telephone: +0086-028-8590-8156, Email: gongbin_npic@163.com

Abstract

Austenitic steel is a candidate material for Supercritical Water-Cooled Reactor. This study is to investigate stress corrosion cracking behavior of HR3C under effect of supercritical water chemistry. A transition phenomenon of water parameters was monitored during a pseudo critical region by water quality experiments at 650 °C and 30 MPa. The stress-strain curves and fracture time of HR3C were obtained by slow strain rate tensile tests in supercritical water at 620 °C and 25 MPa. The concentration of dissolved oxygen was 200-1000 μg/kg and the strain rate was 7.5×10^{-7} /s. Recent results showed the failure mode was dominated by intergranular brittle fracture. The relations of oxygen concentration and fracture time were nonlinear. 200-500 μg/kg of oxygen accelerated the cracking but a longer fracture time was measured when oxygen concentration was increased to 1000 μg/kg. Chromium depletion occurred in the oxide layer at the tip of cracks. Grain size increased and chain precipitated phases was observed in the fractured specimens. These characteristics were considered to be contributive to the intergranular stress corrosion cracking.

1. Introduction

As one of advanced reactor concepts for Generation IV nuclear energy systems, Supercritical Water-Cooled Reactor (SCWR) is under development based on the direct cycle nuclear power plant technologies. SCWR adopts water as core coolant media and operates above the critical point (374.096 °C, 22.064 MPa). SCWR has significant benefits due to great thermal efficient realized by a smaller and simpler system. For these advantages, various research organizations joined SCWR development project under the Generation IV International Forum (GIF) Program.

The system layout and design for SCWR depends on the following issues: materials, water chemistry, thermal hydraulic, physics and safety etc. The problems of materials and water chemistry are interrelated. The extremely corrosive super critical water (SCW) increases the difficulty of screening materials. Restricted requirements on materials properties limit the water chemistry specifications. Since corrosion of materials can be inhibited into relative safety level by controlling water chemistry, it is necessary to establish adequate water chemistry operation methods for maintaining the structure integrity of the reactor, extending the service life and decreasing the irradiation dosage. For safe and effective application of water chemistry method, the compatibility with materials should be evaluated by out-of-core and in-pile tests.

SCWR has a good linkage to the current light water reactors (LWR) technologies in China and will be of benefit for the great electrical demands in this country. A project to develop million kilowatts SCWR (CSR1000) has been initiated by NPIC in 2009. In the martials field, more than 20 kinds of materials, including T91, T92, 316NG, 304, AL-6XN [1], C276 [2], 625, X750, etc.,

have been tested for the mechanical properties and the corrosion properties. Several kinds of materials were selected for the cladding manufacture, typical 310S and modified austenitic stainless steel. For the further research on water chemistry technologies, a project of "SCC behavior under the effect of SCW chemistry", funded by the National Natural Science Foundation of China, was started in 2012. The project objective is to understand the characteristics and the corrosion effects of the chemistry environments in the SCWR. The relationship of the water chemistry parameters and the SCC behavior is being tested, including the effects of dissolved oxygen (DO), dissolved hydrogen (DH) and pH. The "pH" in this paper means the feed water quality is controlled to be alkaline by addition of ammonia or similar alkalizing agent, referring the experience of the supercritical fossil plants. The influence of temperature will be also investigated. Those tests are scheduled into several stages and listed in Table 1. The tests results will be used to establish a database to investigate SCC sensitivities and screen out water chemistry specifications that benefit for the control of SCC.

Table 1. Project schedule - SCC behavior under effect of SCW chemistry

Tasks	2013	2014	2015	2016	2017
Construction of SCW-SCC Test Loop					
Corrosion tests under effect of DO, 0-2000 μg/kg					
Corrosion tests under effect of DH, 0-1000 μg/kg					
Corrosion tests under effect of temperature, 350 °C-650 °C					
Corrosion tests under alkaline condition					

For hydrogen chemistry, previous research [3] identified SCC growth rate was a function of the critical hydrogen concentration for the nickel/nickel oxide transition. The critical hydrogen concentration increases with temperature and may be out of the specification of the current LWR plants when temperatures reach critical point. The inhibition of low hydrogen concentration on the SCC is scheduled to be qualified at the present stage. For higher concentration greater than 1000 μg/kg, its effect on corrosion and mechanical properties will be considered in the later stage.

2. Experiments

3. Technologies

For SCC tests in SCW, the Water chemistry laboratory of NPIC has developed a facility named SCW-SCC Test Loop. The flow chart of the SCW-SCC Test Loop is shown in Figure 1. The loop consists of the following parts:

- A 2.5 liter autoclave made from Hastelloy C 276 with the maximum testing temperature of 650 °C at 30MPa.
- Monitoring & control system for water chemistry parameters including DO, DH, pH, oxidation-reduction potential (ORP), and conductivity of inlet and outlet water, shown in Figure 2a.
- Loading system for slow strain rate tensile test (SSRT), constant load test and low cyclic fatigue tests, shown in Figure 2b.
- Components for control and stability of pressure in subcritical and supercritical range.
- Pump and pipe system with the maximum flow rate of 15 L/h.

Standard tensile specimens of plate, round bar and tube can be tested in the SCW-SCC Test Loop, including compact tension specimen and post-irradiated specimen, shown in Figure 3.

For observation of water parameters transition from subcritical to supercritical condition, the SCW-SCC Test Loop has been operating at 650 °C and 30 MPa in short term tests. The

autoclave was treated as a specimen in pure water with 0-50 μg/kg of dissolved oxygen (DO). Figure 4 shows operation parameters of SCW-SCC Test Loop. The variation of flow and pressure can be observed during heating up and cool down. The peak values of flow occurred in 420-450 °C where water experienced a dramatic transition of density near critical point (Figure 4a).

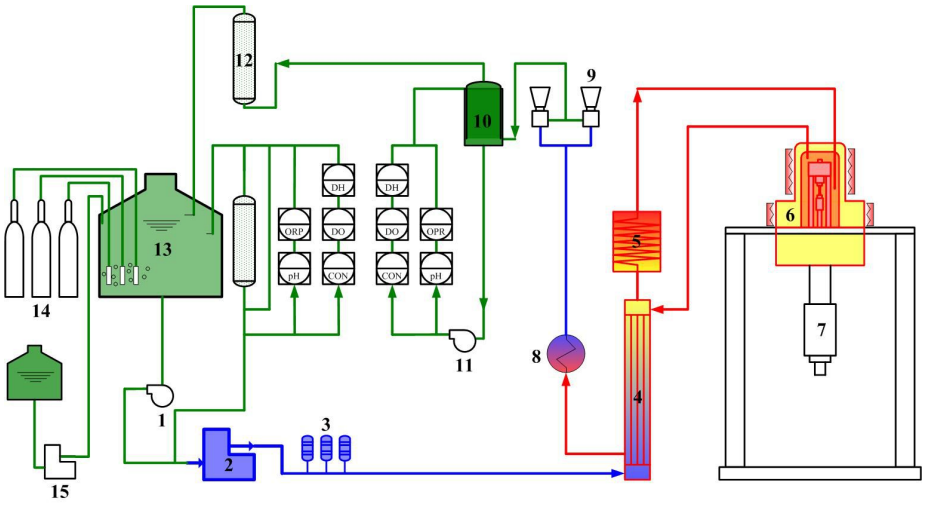

Figure 1. Flow chart of the SCW-SCC Test Loop. 1-feeding pump, 2-high pressure pump, 3-pressure storage, 4-heat exchanger, 5-preheater, 6-test cell, 7-loading system, 8-cooler, 9-pressure regulator, 10-outlet water storage, 11-measure pump, 12-purify column, 13-test solution storage, 14-gas cylinders, 15-chemicals feeding pump

Figure 2. SCW-SCC Test Loop. a) water chemistry system, b) Loading system

Figure 3. Types of specimen for SCC tests

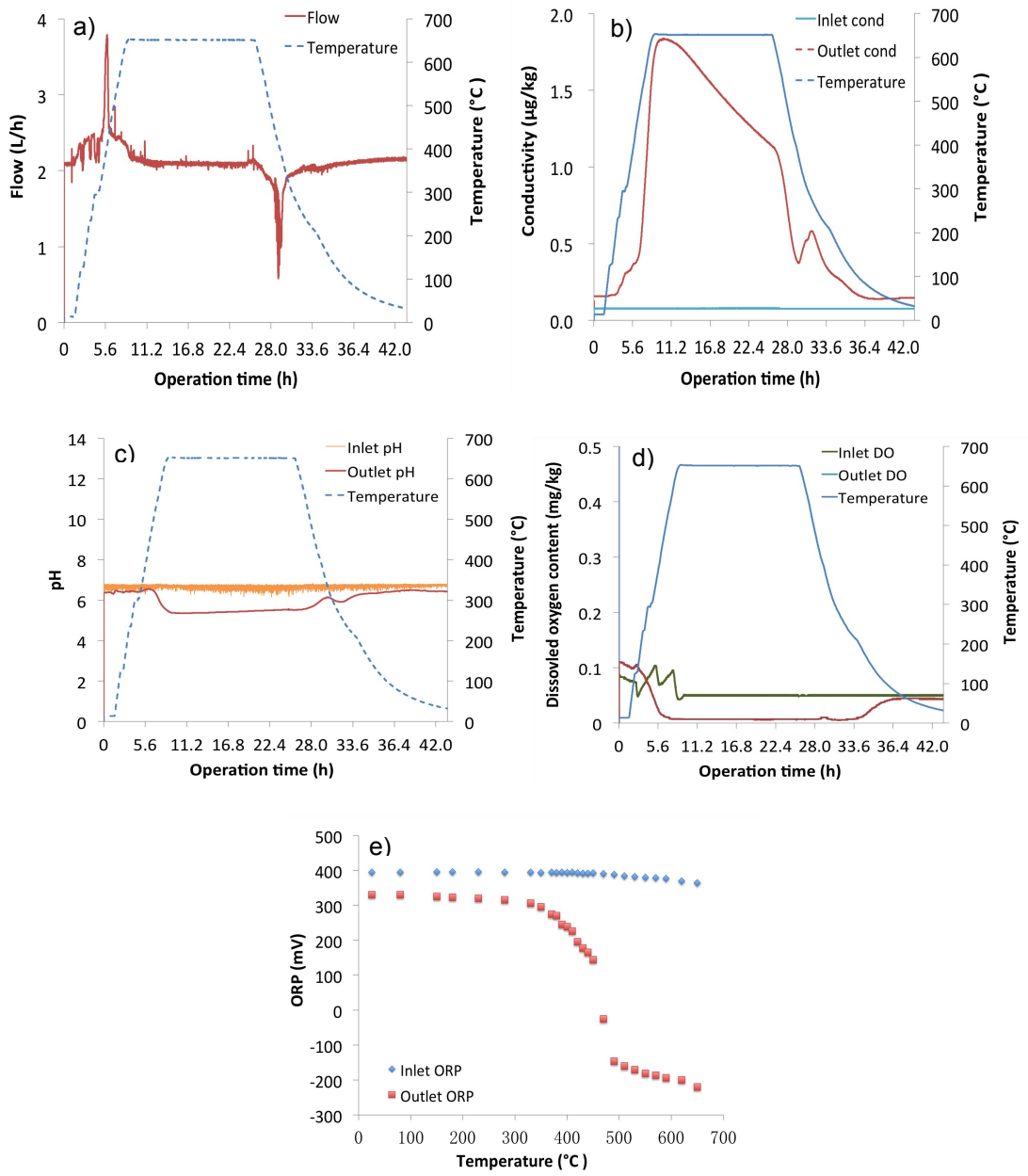

Figure 4. Operation parameters of SCW-SCC Test Loop at 650 °C and 30 MPa. a) flow rate ~ temperature, b) conductivity ~ temperature, c) pH ~ temperature, d) DO ~ temperature, e) ORP ~ temperature

Apparent variations of the outlet water parameters were monitored. The conductivity of the outlet water increased during the heating up and reached to a maximum value of 1.8 μs/cm at 650 °C (Figure 4b). Outlet pH decreased to a weak acidic range (Figure 4c) .The corrosion of autoclave may cause the shifting of outlet water parameters; however, this phenomenon occurred only during the heating up and cooling process. The solubilities of impurities experience significant changes near 400 °C and also lead to a fluctuation of the conductivity. The chloride ion concentration of the outlet water decreased from 56.8 μg/kg at 300°C to 0.7 μg/kg at 450°C. This phenomenon may indicate chloride deposition or chemical "hideout" [4] near the pseudo critical points. Previous research [5] revealed the severe SCC induced by the chloride ion under supercritical water conditions. To avoid the heavy deposition of chloride, the fluid was purified continuously during the SCC tests and the chloride concentration of the feed

water was maintained below 0.1 mg/kg. The total carbon concentration (TOC) of the outlet water reached to ~ 1 mg/kg at the beginning of the test and contributed to the decrease of the outlet pH. The outlet DO decreased to ~ 0 μg/kg when temperatures were above 400 °C and returned to the same level as the inlet water when temperatures were below 400 °C (Figure 4d). The outlet ORP experienced a sharp decline near the critical point (Figure 4e). It is not easy to make the outlet DO keep same as the inlet DO because oxygen is exhausted quickly by the chemistry reactions in the supercritical region. The test flow was ~3 L/h at 25MPa and the solution in the test cell was refreshed per hour. The initial results showed that the oxygen content achieves a steady value quickly and the SCC tests can be started within 24 h. In the later stages of the test, the release of corrosion products slowed down due to the formation of the passive oxide film. The water samples from the outlet indicated a decrease of total iron concentration from the initial value of 12.9 μg/kg to 2.2 μg/kg at the end of test.

4. SCC Tests under Effect of Dissolved Oxygen

The work is progressing to investigate the effect of dissolved oxygen in SCW on SCC susceptibility. HR3C was selected for tests, a kind of austenitic heat resistant steel developed from TP310 by addition of Nb and N. HR3C exhibits improved oxidation resistance and creep strength at high temperature and has been used for super-heater pipes in ultra-supercritical fossil fuel plants. HR3C is under testing as a candidate structural material for SCWR. The material specification is listed in Table 2.

Table 2. Material specification of HR3C

Chemistry composition (wt%)										
C	Mn	Si	P	S	Cr	Ni	Fe	Nb	N	Cu
0.060	1.200	0.225	0.017	0.003	24.92	21.00	Bal.	0.500	0.230	0.040
Mechanical properties										
Yieth Strength (MPa)			Tensile Strength (MPa)					Elongation (%)		
360/355			815/810					60/58		

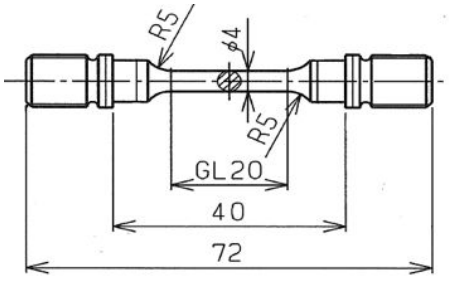

Figure 5. Drawing of specimen for SCC tests by SSRT

SSRT tests are used to evaluate the SCC sensitivity at the present stage. The specimen was dynamically loaded with a strain rate of 7.5×10^{-7} /S in pure water at 620 °C and 25 MPa. The DO concentration was controlled from 0-1000 μg/kg. The round bar specimen for SSRT is shown in Figure 5.The Stress-Strain curves are shown in Figure 6 and results are listed in Table 3. A slight reduction of mechanical properties can be observed when DO was increased to 500 μg/kg. Compared with the data measured in deaerated SCW, the failure time was shortened by 7 hours and tensile strength decreased by ~ 2.3 % and Yield Strength increased by ~ 2.6 % at 500 μg/kg. The data may suggest an increased SCC susceptibility with higher concentration of DO. However, the longest time of failure was measured at 1000 μg/kg. This result indicated non-linear relationship between SCC sensitivity and DO. A hypothesis was proposed that

oxygen played a role of accelerating SCC at very low concentration and acted as a passivator at higher concentration that inhibited crack propagation. To verify this hypothesis, the data is being collected for the possible functions between DO and SCC in SCW.

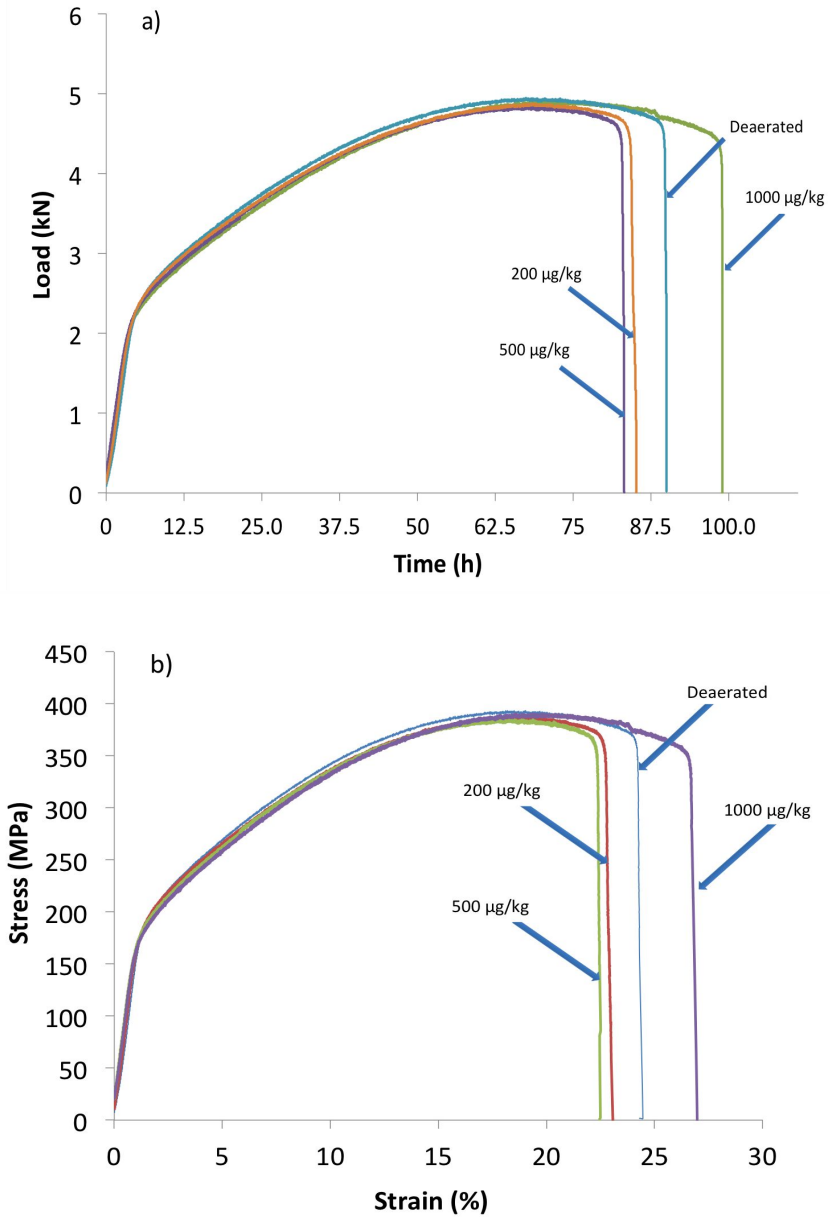

Figure 6. Comparison of a) Load ~ time, b) stress ~ strain, obtained by SSRT tests on HR3C in SCW with 0-1000 µg/kg DO at 620 °C and 25 MPa

The specimens fractured in the SCW containing 200 µg/kg DO were examined with a reference specimen fractured in the deaerated SCW. A darker oxide film formed on the specimen and indicates the higher degree of oxidation, shown in Figure 7. Almost no necking occurred at the fracture section. Small cracks were found in the gage section, shown in Figure 8. The metallographic images show that the cracks initiate from the surface and propagate into the base metal along the grain boundaries (Figure 9). Some micro-cracks can be observed in the matrix and originate from the grain boundaries.

The fractured specimens were analyzed by scanning electron microscope (SEM). As shown in Figure 10, 200 μg/kg of DO did not cause obvious changes of the fractography excepted in the thicker oxide layer. Intergranular facets appeared in most areas of the fractured surface (Figure 11). Cleavage river patterns as the evidences for the brittle fracture were observed at the edge of the fracture surface, showed in the rectangle of Figure 12a. Cracks are distributed along the grains boundary, as shown in Figure 12b. The fractography indicates that the failure mode is dominated by the intergranular brittle fracture.Micro-cracks with the length of 10-50 μm were observed on the gage section exposed to both test conditions. In contrast to the 0 μg/kg case, the micro-cracks of the specimen following exposure in 200 μg/kg of DO were surrounded by oxide particles (Figure 13). The energy dispersive spectrometer (EDS) analysis indicated a depletion of Cr and Mn at the crack tips (Figure 14). Cr is known for improving the corrosion resistance of the oxide film and Mn for improving the ductility of the metal. Cracks prefer to start from the area where these elements are depleted. Micro-cracks are distributed along the grain boundaries, which seems to be caused by a synergistic effect of the stress and the sensitization. HR3C was immune to the intergranular corrosion in a boiling CuSO4/H2SO4 solution after sensitizing treatment at 650 °C for 2 h, a preliminary retest of austenitic steel according to ASTM A262-10. The possible reason for the sensitization behavior in the SCW was considered to be aging at the SSRT test temperature. As shown in Figure 15, a notable grain growth and chain precipitated phases had occurred after SSRT test and may cause a decrease of the grain boundary strength.

The EDS analysis also indicated about 7wt% enrichment of carbon in the oxide film. Since the test fluid was deaerated, the carbon is considered as the contaminations of the organic compound indicated by a high level of TOC, which affects water quality and may be contributive to IGSCC.

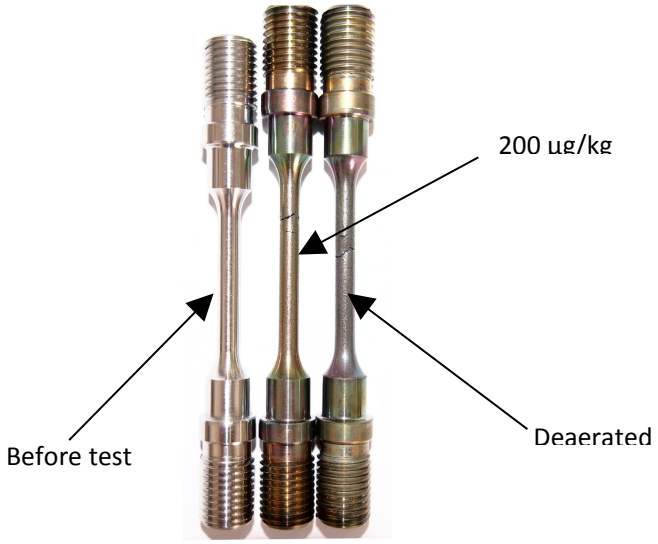

Figure 7. View of fractured specimens

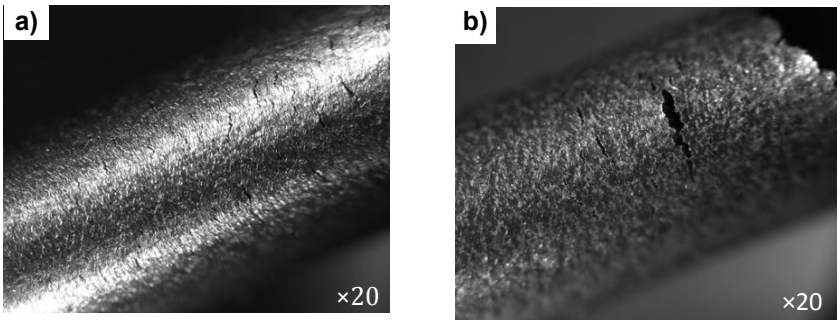

Figure 8. Stereo microscope morphology of gage surface of specimens following exposure at 620 °C and 25 MPa in a) deaerated SCW, b) SCW with 200 μg/kg DO

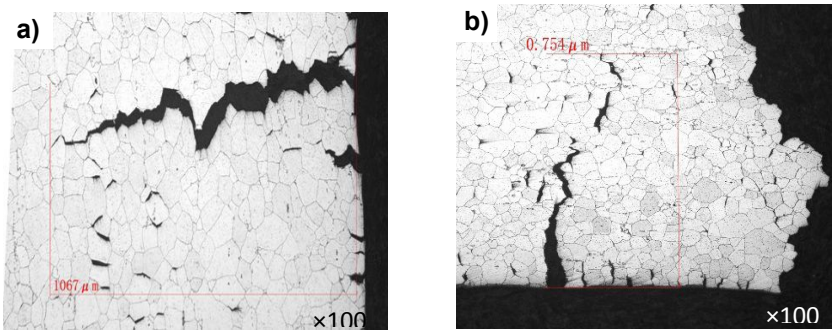

Figure 9. Cracks metallographic of gage section of specimens following exposure at 620 °C and 25 MPa in a) deaerated SCW, b) SCW with 200 μg/kg DO

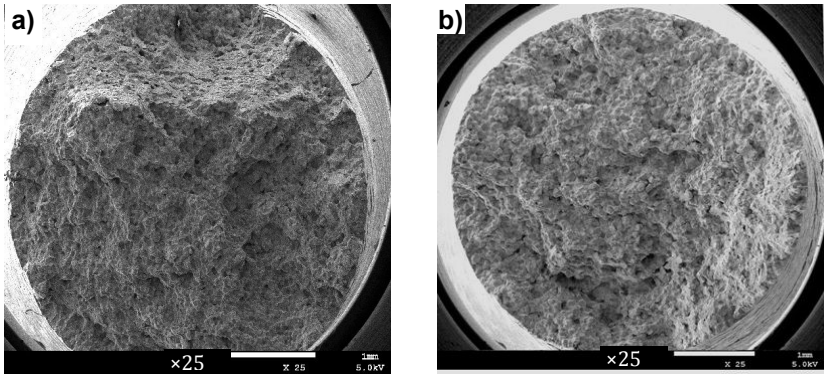

Figure 10. SEM fractography of specimens following exposure at 620 °C and 25 MPa in a) deaerated SCW, b) SCW with 200 μg/kg DO

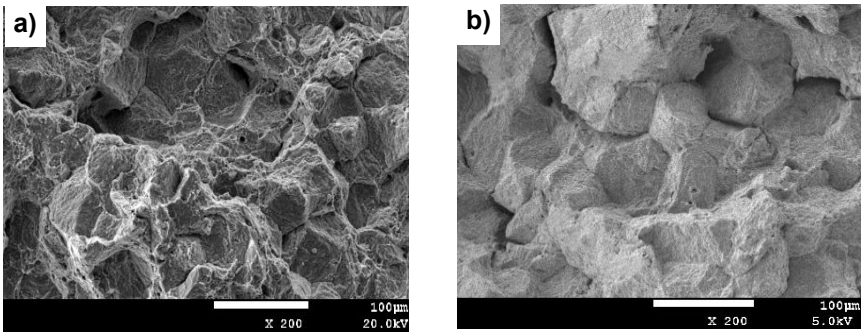

Figure 11. Intergranular facets in the central of fracture surface at 620 °C and 25 MPa in a) deaerated SCW, b) SCW with 200 μg/kg DO

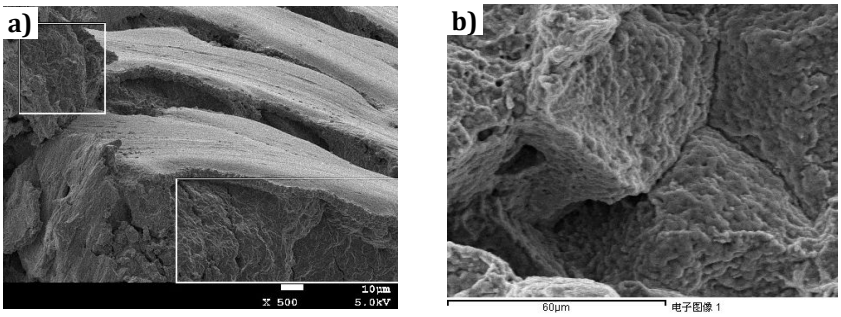

Figure 12. SEM of specimens showing a) River pattern at the edge of fracture surface, b) grain boundary cracks following SSRT at 620 °C and 25 MPa in SCW with 200 μg/kg DO

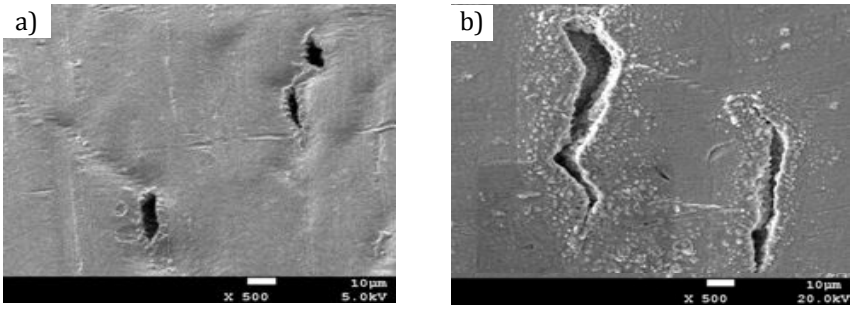

Figure 13. Micro-cracks on the gage section of specimens tested at 620 °C and 25 MPa in a) deaerated SCW, b) SCW with 200 μg/kg DO

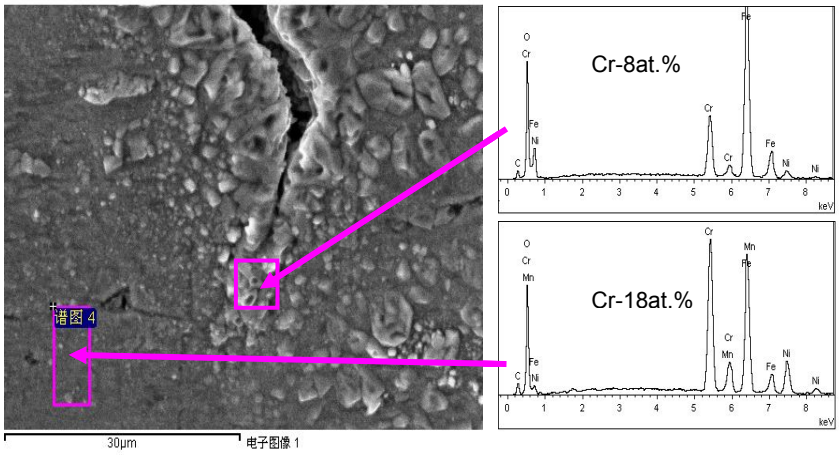

Figure 14. Comparison of chromium content by EDS analysis at the tip of micro-cracks of specimens tested at 620 °C and 25 MPa in SCW with 200 μg/kg DO

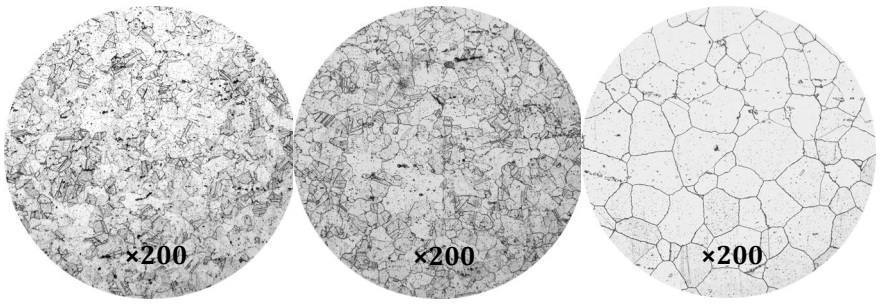

Figure 15. Comparison of metallurgical structure. a) Before test, b) sensitized at 650 °C for 2 h, c) after SSRT test at 620 °C and 25 MPa for 90 h

5. Conclusion

Ongoing research of the SCW chemistry effect on the SCC of HR3C is introduced in this technical brief. Current test results lead to the following conclusions: The transition of the water parameters has been observed near the critical point that may be caused by the conversion of the corrosion behavior and the solubility of impurities. HR3C exhibited an intergranular cracking tendency in the SCW at 620 °C and 25 MPa. 200-500 μg/kg of DO shortened the failure time and caused a slight decrease of the elongation and the strength. The longest failure time was

measured at 1000 μg/kg and indicated a non-linear relationship between the SCC sensitivity and the oxygen concentration. The failure mode of HR3C in the SCW is dominated by the intergranular brittle fracture. Depletion of Cr at the crack tips indicated the initiation of cracks. Microstructure transformation due to the aging at sensitive temperature may cause a decrease of the grain boundary strength and provide the path for the crack propagation. Comparison tests in the inert environment at the same temperature are required to discriminate between the effect of the microstructure transformation and the water chemistry factors.

Acknowledgment

The work presented in this paper was supported by the National Natural Science Foundation of China (NFSC) under Grant No. 51271171 and China National Funds for Distinguished Young Scientists under Grant No.11325526. Any opinions, findings and conclusions or recommendations expressed in this publication are those of the authors and do not necessarily reflect the views of the foundation.

References

1. Shen, Z., Zhang, L., Tang, R., and Zhang, Q., 2014, "The effect of temperature on the SSRT behavior of austenitic stainless steels in SCW," Journal of Nuclear Materials, 454(1–3), pp. 274-282

2. Zhang, Q., Tang, R., Yin, K., Luo, X., and Zhang, L., 2009, "Corrosion behavior of Hastelloy C-276 in supercritical water," Corrosion Science, 51(9), pp. 2092-2097.

3. Steven, A. A., and David, S. M., 2003, "Measurement of the nickel/nickel oxide transition in Ni-Cr-Fe alloys and updated data and correlations to quantify the effect of aqueous hydrogen on primary water SCC," Technical Report No. LM-03K049; TRN: US200411%%203, Lockheed Martin Corporation, Schenectady, NY 12301 (US).

4. Guzonas, D., Tremaine, P., and Jay-Gerin, J.-P., 2009, "Chemistry Control challenges in a supercritical water-cooled reactor," PowerPlant Chemistry, **11(5)**, pp.284-291.

5. Fujisawa, R., Nishimura, K., Nishida, T., Sakaihara, M., Kurata, Y., and Watanabe, Y., "Cracking Susceptibility of Ni Base Alloys and 316 Stainless Steel in Less Oxidizing or Reducing SCW," Corrosion 2005, NACE International, Houston, Texas, Paper No. 05395.

ISSCWR7-2043

Channel Optimization for a Pressure-Tube SCWR

Ammar Ahmad
Xi'an Jiaotong University, Xi'an, China
ammar_nustian@hotmail.com

Liangzhi Cao
Xi'an Jiaotong University, Xi'an, China
caolz@mail.xjtu.edu.cn

Hongchun Wu
Xi'an Jiaotong University, Xi'an, China
hongchun@mail.xjtu.edu.cn

Chuanqi Zhao
Xi'an Jiaotong University, Xi'an, China
necpzhaolegend@gmail.com

Abstract

Supercritical water reactor is the only concept under GEN IV International forum utilizing water as coolant or moderator. Pressure tube SCWR is a kind of SCWRs having distributed pressure tubes or channels containing fuel bundles, similar to conventional CANDU and RBMK nuclear reactors. In this research, a recently presented pressure tube SCWR design has been further optimized on the basis of coupled neutronics and thermal hydraulics calculations. A 3D fine mesh diffusion theory code was used for neutronics analysis while single channel model was used for thermal hydraulics analysis. A link code was used to couple these two codes by using external coupling technique. Moreover as a second step, sub-channel analysis was also performed by selecting the hottest assembly from the core. Results show that the maximum cladding surface temperature (MCST) for proposed channel design is under design limits i.e. less than 850^{o}C.

1. Introduction

One of the most promising concepts under the generation-IV nuclear reactors forum is supercritical water reactor (SCWR). SCWR is a high temperature, high pressure water cooled and moderated reactor that operates above the thermodynamic critical point (374^{o}C, 22.1 MPa) of water. Because of its simplicity, high thermal efficiency, and fifty years of industrial experience from coal-fired power plants, SCWR is considered as the next evolutionary step for water cooled reactors. Pressure vessel and pressure tube concepts are the two main categories of SCWRs [1].

Many design aspects of SCWRs have been under considerations for the past few years. One of the important design aspect is preconceptual core design. In recent past years, many assembly and core designs have been proposed by the scientists and reseachers for both pressure vessel [2] and pressure tube type [3, 4] SCWRs.

In Pressure tube SCWRs, a number of pressurized channels are distributed through out the core instead of a large pressure vessel. In this kind of SCWR, light water is used as coolant while moderator is heavy water. In ongoing research for pressure tube SCWRs many assembly and core designs have been proposed and optimized to fulfill the criteria of maximum cladding surface temeratrue (MCST) i.e. < 850^{o}C.

The thermal and physical properties of water vary strongly above supercritical condition (374^{o}C and 22.1MPa). There is a large drop in the coolant density from inlet to outlet for SCWRs. The coolant density distribution in the core directly affects the moderation and the absorption of neutrons, power distribution is also affected by this change of neutron spectrum. Coolant

density distribution in the core is then affected by this power distribution. A coupling neutronics and thermal hydraulics analysis is therefore an essential requirement for design studies of SCWRs, because of this strong interaction between the power distribution and the coolant water density [5].
In the present research, the design presented in reference [3] is taken as the reference design and further optimization has been done on this design because of its high MCST (854^{o}C). Neutronics and thermal hydraulics coupled system has been used for the optimization of the assembly design. A 3D fine mesh diffusion theory code was used for neutronics analysis and a single channel model was used for thermal hydraulics calculations. Some improvements for the design have been proposed on the basis of these coupled calculations.
Moreover, a subchannel analysis was also performed for the channel concept presented in [3] to check the feasiblity of the design, as the proposed design in [3] was only assessed on the basis of single channel model. For this subchannel analysis, hottest assembly was selected from the core analysed by the coupled neutronics and single channel thermal hydraulics system and subchannel analysis was performed on that hottest assembly. An in-house code SUBSC was used for this analysis. SUBSC is an inherrently developed code for supercritical flow applications.

2. Coupling calculations using single channel model

2.1 Design Tools and Methodology

A transport theory code DRAGON [6] based on 69-group cross section library was used for two dimensional lattice calculations. For burnup calculations, macroscopic burnup dependent coss-sections were generated for assembly by considering all anticipated water densities in the core and given as input to a 3D fine mesh diffusion theory code CITATION [7] for whole core calculations. As there is no fucntion for whole core burnup calcuations in CITATION, a supporting code was developed for core depletion calculations [9]. The calculations were based on four energy groups macroscopic cross-sections obtained from assembly burnup. Quarter core symmetry was used for whole core calculations.
For thermal hydraulics calcualtions, the single channel model was used. There are two typical single channels for each assembly, hot channel with maximum power and average channel with average power. 3D power profile for the core calculated by the CITATION is then given to the thermal hydraulics code. Maximum power and MCST criterion was first used to search flow rate for each assembly. Then coolant density distribution was calculated by using this flow rate and average power profile for each assembly. This coolant density distribution was then fed back as input to the neutronics code and the process was repeated until the convergence criteria for both the burn up and thermal calculations were met. Dittus-Boelter [8] correlations were used for heat transfer coefficient calculations. Although, Dittus-Boelter correlation tends to be optimistic for super critical water. Since the heat transfer correlations of supercritical water is a very challenging topic and there is still no widely accepted correlation up to now. The main purpose of this paper is the concept core design analysis, so Dittus-Boelter correlation is just employed because it has high accuracy as compared to other correlations for single-phase flows like super critical water as claimed by Kamei et al., in the reference [12]. A link code was used to exchange required data between neutroniucs and thermal hydraulics code The input for one code was prepared from the output of the second code with the help of a link code. Further details of calculation methodology can be seen in references [3] and [4].

2.2 Channel and Core Geometry

Cross-sectional view of the channel design presented in [3] is shown in Fig. 1. It consists of two rings of fuel rods, each ring having 32 fuel pins. There is a central flow tube made up of zirconium modified stainless steel. Coolant first flows down from the flow tube and then flows

upwards carrying the heat from fuel pins. Some of the geometrical specifications for the assembly is shown in Table 1. The reactor core has thermal power of 2540MW and electric power of 1250MW and has three batch of fuel. Each fuel assembly is 500cm long and fuel assemblies are arranged in 25cm square lattice pitch. There is 50cm heavy water reflector both at bottom and top which make total core height of 600cm. Core loading pattern for quarter core is shown in Fig. 2.

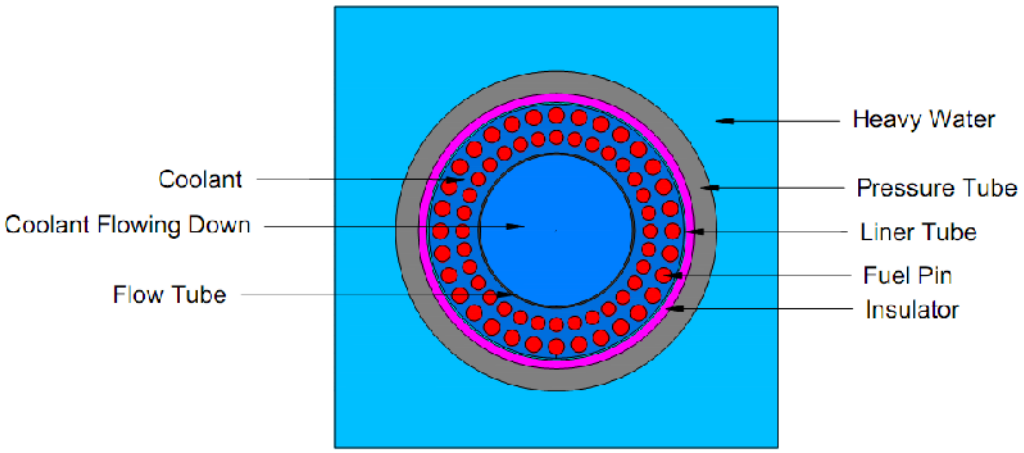

Fig. 1 Cross-sectional View of Assembly design

Table 1 Geometerical Specification for Assembly

Component	**Dimensions**
Central Coolant	4.65 cm Radius
Flow Tube	4.65 cm inner Radius(IR), 0.1 cm Thick
Inner Pins (32)	0.415 cm radius, 5.30 cm circle radius
Outer Pins (32)	0.465 cm radius, 6.55cm circle radius
Cladding	0.06 cm thick
Liner tube	7.20 cm (IR), 0.05 cm thick
Insulator	7.25 cm IR, 0.55 cm thick
Outer Liner	7.80 cm IR, 0.05 cm thick
Pressure Tube	7.85 cm IR, 1.02cm thick
Fuel Bundle Heated Length	500 cm

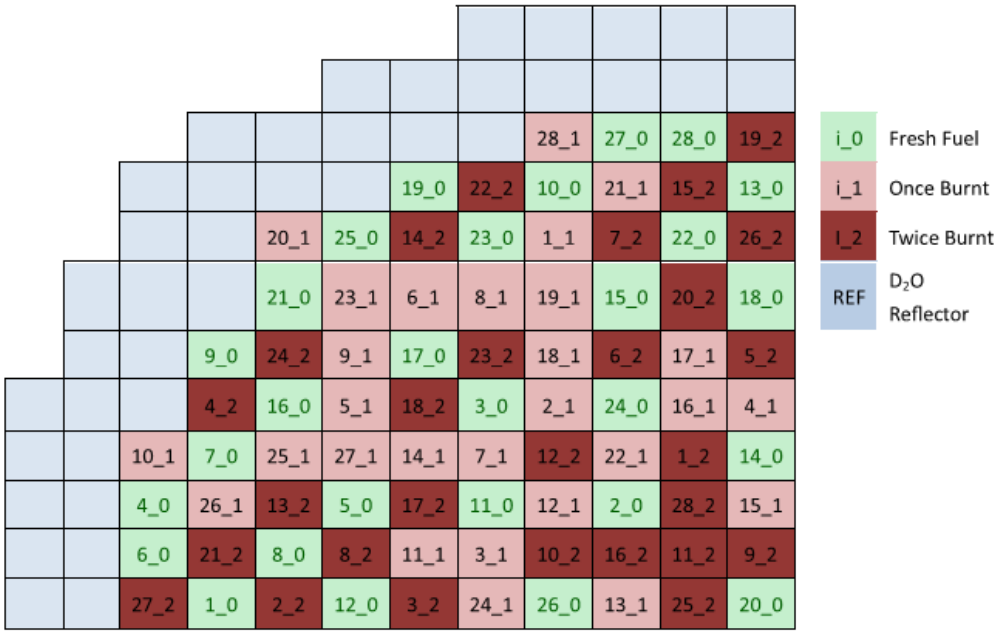

Fig. 2 Core Loading Pattern [3]

2.3 Optimization of Channel Design

In reference [3], several design options for assembly design were investigated by varying flow tube inner diameter, thickness, fuel pin dimensions and number of fuel pins etc. In the present study, all the other design parameters are kept constant except number of fuel pins because most of the design parameters have already been optimized to the maximum possible value keeping in view the mechanical and manufacturing constraints. For example, flow tube inner diameter cannot be increased further as it was optimized to its maximum diameter to have enough clearance between flow tube and fuel pins in the first ring. Number of fuel pins can be further optimized, as design option of different number of pins in two rings was not investigated before. So various options for number of fuel pins are investigated in the present study and a sensitivity of MCST is examined to a number of fuel pins in two rings. Average outlet temperature for all the cases is kept constant at 625^{o}C. Fuel loading pattern for the sensitivity analysis is same as shown in Fig. 2. The results for the sensitivity analysis are shown in Table 2. Number of pins in ring 1 cannot be further increased from 32 because further increase in number of fuel rod will reduce the clearance between fuel pins i.e. less than 1mm which will be a challenge from manufacturing view point. From Table 2 it can be seen that when number of fuel pins in ring 2 is increased from 31 to 34 while keeping number of fuel pins in ring1 constant, MCST both at BOC and EOC is decreased. This is due to the fact that increased number of pins are causing hydraulics diameter to decrease and with this decrease of hydraulic diameter the heat transfer coefficient between cladding and coolant will increase and as a result MCST will decrease. In Table 2, for case 4 and 5, MCSTs are close to each other, this is because the total number of pins in the assembly is same i.e. 66, so hydraulic diameter is almost same for these two cases. Pin configuration for case number 4 is selected for the present design and detailed results for this configuration are described in next section.

Table 2 Sensitivity analysis for number of fuel pins

Number of fuel Pins per ring			MCST BOC/EOC (^{o}C)
Case #	**Ring1**	**Ring2**	
1	32	31	851/863
2	32	32	844/854
3	32	33	838/849
4	32	34	826/844
5	31	35	826/841

2.4 Results for equilibrium core

Design parameters for proposed channel design is shown in Table 3. The coolant flow rate distribution for quarter core is shown in Fig. 3. The numbers shown in Fig. 3 are the ratios of the flow rate of each assembly to the average flow rate for all assemblies. Axially averaged radial power distribution both at BOC and EOC is shown in Fig. 4. Radial Power peaking factors at BOC and EOC are 1.22 and 1.15. Fig. 5 shows core average axial power distribution. Axial power peaking factors at BOC and EOC are 1.18 and 1.05 respectively. At BOC the power peaking factor is located at 300cm from the bottom of the core. The axial power distribution becomes flat and symmetric at EOC with power peaks located at 100cm and 450cm from the bottom of the core.

Table 3 Dimensions for proposed Assembly Design

Component	**Dimensions**
Central Coolant	4.65 cm Radius
Flow Tube	4.65 cm inner Radius, 0.1 cm Thick
Inner Pins (32)	0.415 cm radius, 5.30 cm circle radius
Outer Pins (34)	0.465 cm radius, 6.55cm circle radius
Cladding	0.06 cm thick
Liner tube	7.20 cm (IR), 0.05 cm thick
Insulator	7.25 cm IR, 0.55 cm thick
Outer Liner	7.80 cm IR, 0.05 cm thick
Pressure Tube	7.85 cm IR, 1.02cm thick
Fuel Bundle Heated Length	500 cm

						1.15	1.21	1.21	1.18
				1.37	1.07	0.96	0.87	0.94	0.94
		1.27	1.34	0.98	1.02	0.93	1.00	1.00	0.84
		1.18	0.93	0.94	0.94	1.03	1.03	1.00	1.02
	1.42	0.90	1.03	1.05	0.87	0.95	0.93	0.92	0.87
	0.96	1.03	0.93	1.05	1.06	1.05	1.05	0.94	1.05
1.22	0.98	0.95	0.95	0.96	0.97	0.95	0.95	1.02	1.06
1.10	0.88	1.03	1.03	1.04	1.05	1.01	1.01	0.88	1.00
1.10	0.97	1.01	0.91	0.92	0.92	0.85	0.79	0.74	0.78
0.87	0.96	1.00	1.00	0.89	0.94	1.05	0.92	0.94	1.01

Fig. 3 Flow Rate Distribution for quarter core

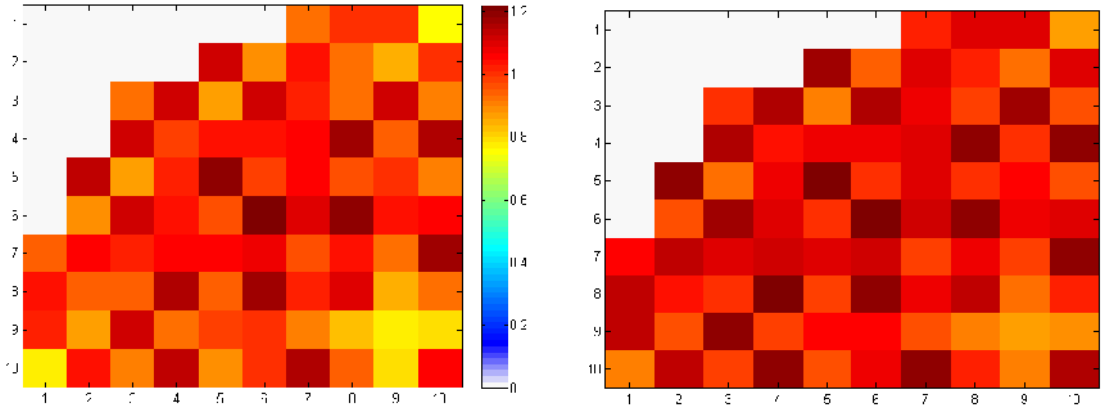

BOC EOC

Fig. 4 Radial Power Distribution

The coolant outlet temperature distribution at BOC and EOC for quarter core is shown in Fig. 6. The average coolant outlet temperature is 625^{o}C. At BOC, coolant temperature ranges from 471^{o}C to 732^{o}C and it is higher towards the center of the core. At the end of cycle the outlet temperatures ranges from 450^{o}C to 710^{o}C. Fig. 7 shows MSCT distribution for the quarter core. The MCST at BOC is 826^{o}C and at EOC is 844^{o}C. MCST through out the burnup cycle, is below the design criterion for pressure tube SCWRs i.e < 850^{o}C.

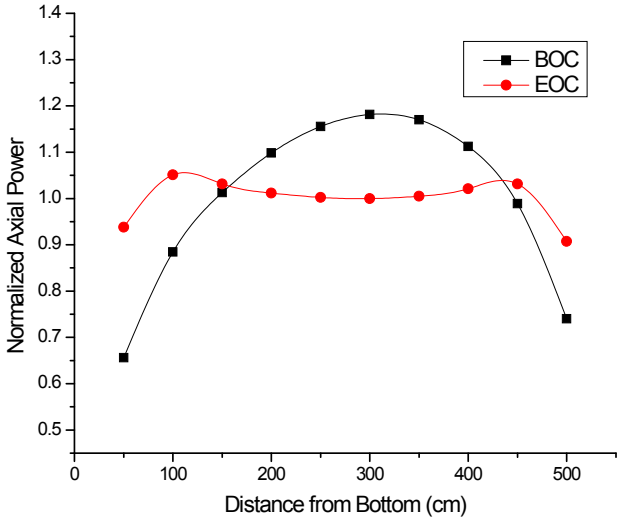

Fig. 5 Axial Power Distribution

	1	2	3	4	5	6	7	8	9	10	
A							509	524	516	434	BOC
							526	536	531	450	EOC
B					514	515	684	669	556	682	
					504	520	689	696	576	698	
C			471	518	547	686	687	571	708	682	
			474	509	547	671	689	573	697	687	
D			586	660	686	703	643	721	596	714	
			576	662	680	692	630	691	586	688	
E		503	598	621	722	708	705	657	694	659	
		497	602	617	687	682	680	635	680	648	
F		575	683	701	576	732	650	724	697	625	
		587	674	695	557	684	622	681	681	613	
G	494	675	681	702	691	707	634	688	564	700	
	515	687	691	698	676	682	613	674	558	674	
H	586	665	568	713	567	715	635	680	601	582	
	608	701	578	696	558	684	628	670	618	599	
I	578	556	701	639	680	686	674	653	653	635	
	605	584	705	643	685	686	680	677	696	676	
J	563	675	567	717	625	669	691	635	532	658	
	612	703	581	710	632	675	681	663	564	679	

Fig. 6 Coolant outlet Temperature Distribution

	1	2	3	4	5	6	7	8	9	10	
A							803	804	803	804	BOC
							834	841	841	836	EOC
B					826	789	801	780	807	807	
					812	815	816	820	830	830	
C			821	821	808	807	788	815	815	791	
			811	811	803	800	798	808	808	799	
D			816	787	789	792	815	815	819	815	
			814	797	793	792	790	790	806	792	
E		822	784	811	819	799	798	792	792	796	
		813	803	793	788	782	781	787	787	781	
F		799	800	789	819	819	817	816	790	815	
		815	802	793	785	779	780	780	786	781	
G	774	796	781	783	795	796	793	793	808	809	
	826	827	800	796	783	780	783	782	787	787	
H	793	772	802	803	810	810	803	802	773	800	
	843	821	803	797	786	783	789	789	797	790	
I	792	797	803	782	781	781	778	769	759	767	
	844	828	813	803	793	789	788	795	806	798	
J	788	795	805	804	774	775	795	765	778	785	
	844	834	818	812	797	794	794	801	818	816	

Fig. 7 MCST Distribution

3. Sub-Channel Analysis

A sub-channel analysis has been performed on the channel design (Fig. 2) presented in [3]. Hottest assembly at BOC from the core; analysed by the coupled neutronics and thermal hydraulics system was selected and its power distribution for the fuel rod pins were used for this analysis.

3.1 Design Tool and Methodology

An indigenously developed code SUBSC [11] is used for the analysis. It is based on fundamental theory of sub-channel analysis like conventional sub-channel code COBRA [10]. SUBSC has a feature to cater supercritical flow applications. Basic equations for conservation of mass, energy and momentum are solved numerically in the code to obtain necessary thermal hydraulics parameters. These basic four equaitons are given below.
Mass continuity Equation:

$$\frac{\partial}{\partial z}(\rho_i u_i A_i) + \sum_j (\rho' v_{ij}) S_{ij} = 0 \qquad (1)$$

Axial momentum and conservation equation:

$$\frac{\partial}{\partial z}(\rho_i u_i^2 A_i) + \sum_j (\rho' u' v_{ij}) S_{ij} = -A_i \frac{\partial P_i}{\partial z} - \frac{1}{2}\left(\frac{f}{D_h} + \frac{k}{\Delta z}\right)(\rho_i u_i^2) A_i - A_i \rho_i g \cos\theta - \sum_j C_t w'_{ij}(u_i - u_j) \quad (2)$$

Transverse Momentum conservation Equaiton:

$$\frac{\partial}{\partial z}(\rho_i u' v_{ij} S_{ij}) + C_s \sum_k \frac{\rho' v_k^2}{l_{ij}} \cos\beta_k S_{ij} = \frac{P_i - P_j}{l_{ij}} S_{ij} - \frac{1}{2} K_g \frac{\rho' v_{ij}^2}{l_{ij}} S_{ij} - \rho_i g \sin\theta \cos\gamma S_{ij} \quad (3)$$

Energy Conservation Equaiton:

$$\frac{\partial}{\partial z}(\rho_i u_i h_i A_i) + \sum_j (\rho' h' v_{ij}) S_{ij} = \sum_i q' p_h \Delta z + \frac{\partial}{\partial z}\left(A_i k \frac{\partial T}{\partial z}\right) - \sum_j Ck \frac{T_i - T_j}{l_{ij}} - \sum_j w'_{ij}(h_i - h_j) \quad (4)$$

SUBSC can employ number of heat transfer co-relations, frictional models and flow distribution model. Dittus-Boelter [8] heat transfer co-relation is used for present calculations. For flow distribution model, pressure drop for all open channel is considered as same and total flow rate is given in the input and the flow rate for the water rod is also specified in input. Flow rate calculated by the single channel model coupling calulations for the particular assembly is used here. Moreover code has the feature to divide fuel pins angularly in number of regions and thermal hydraulics parameters for each angular division can be calculated. For present study pins are divided into four angular divisions (0^o, 95^o, 180^o, 264^o, 360^o) depending upon the geometry of subchannels arround a pin. Fig. 8 gives the sub-channel divisions and fuel pin numbers for the assembly design presented in reference [3]. Fig. 8 has the central water rod through which water flows down. There are three type of sub-channels (SC) in Fig. 8, type 1 includes the SC from 1 to 32, type 2 includes the SC from 33 to 64 and type 3 includes the SC from 65 to 96. All SC in one type have same flow areas. The geometrical specifications of the assembly are described in Table 1. Power profile calculated by the neutronics/thermal hydraulics coupling system for the hottest assembly at BOC is used for the subchannel analysis. The pin-power reconstruction calculation is performed to obtain the pin power used for sub-channel analysis. The reconstruction is based on the shape factors obtained from the lattice transport calculation and the assembly power obtained from the core calculation.

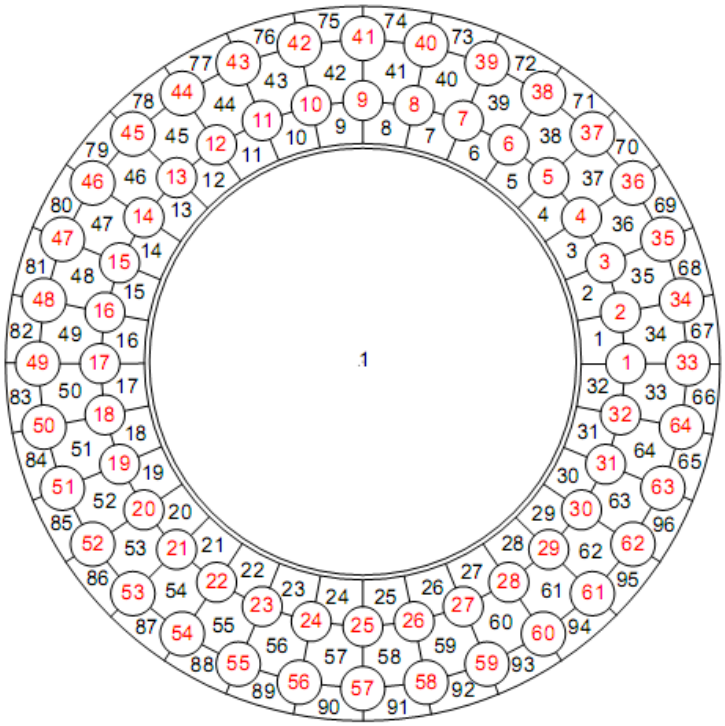

Fig. 8 Sub-channel divisions for assembly

3.2 Results and Discussion

MCST distribution for each fuel pin and outlet temperature for each sub-channel is shown in Fig. 9. Hottest pin in Fig. 9 is pin number 3 having MCST 822^{o}C. This MCST is well below the design criterion i.e. 850^{o}C. Average outlet temperature for all channels is 500^{o}C. The highest coolant temperature is 676^{o}C which is at sub-channel number 35 and 36 in the vicinity of fuel pin number 3. Lowest outlet coolant temperature is 413^{o}C, which is at sub-channel number 44 and 59. Most of the rods in ring 1 have more MCSTs than corresponding rods in ring 2. The reason is the difference of coolant flow area, flow area of coolant channels around rods of ring 1 is less than the flow area of coolant channels around rods of ring 2. Axial distribution of MCST for some of the fuel pins (3, 19, 41, and 57) is shown in Fig. 10. For each axial position there are four angular divisions of pins so there would be four cladding surface temperatures for each axial level, maximum of these four temperatures is plotted in Fig 10 for each axial level. Pin number 3 is the hottest pin having MCST at about 450 cm from the bottom of the assembly. Other pins are randomly selected to observe the axial trend of MCST. Axial coolant temperature distribution in some of the SC (2, 18, 35, 51, 74 and 91) is shown in Fig. 11. SC number 35 has the highest temperature because it is near to the hottest pin.

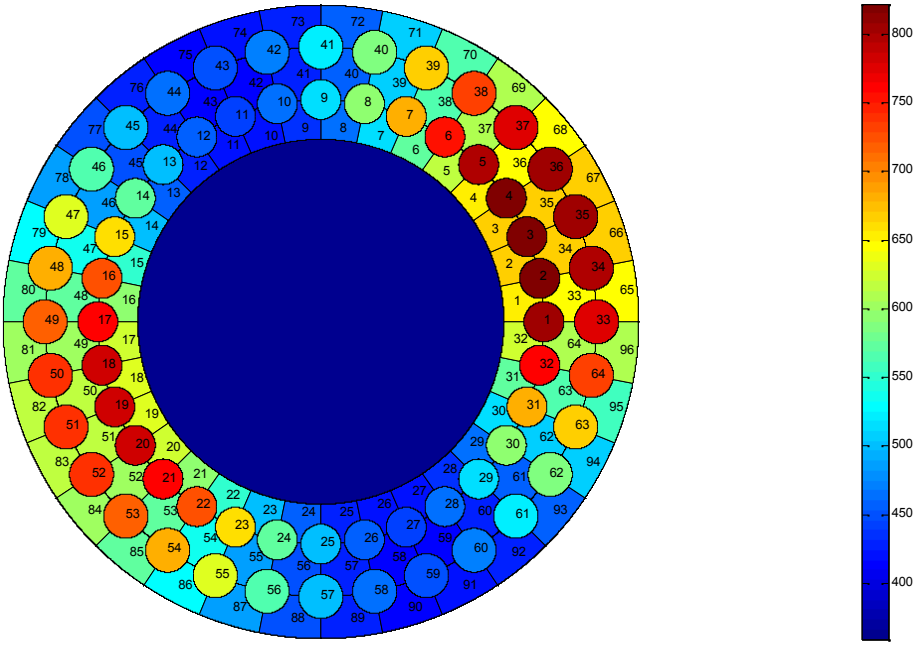

Fig. 9 MCST and outlet temperature distribution

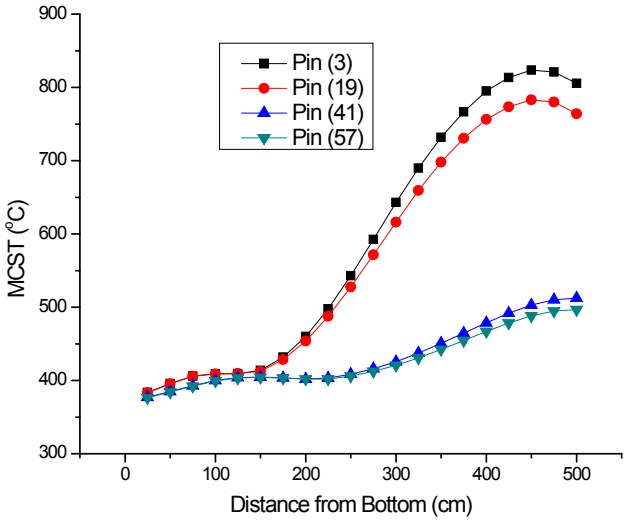

Fig. 10 MCST for Axial Intervals

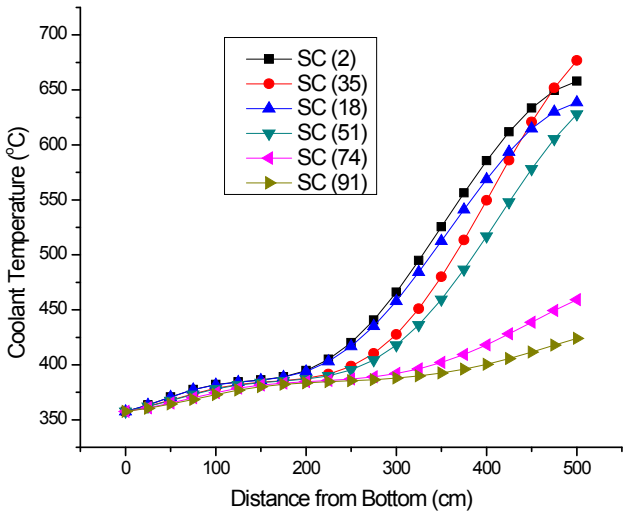

Fig. 11 Axial Coolant Temperature Distribution

On the basis of sub-channel analysis, the design presented in reference [3] is feasible as its MCST is well below the design criteria. But for the present study, this sub-channel analysis is performed at BOC only. MCST at EOC also needs to be evaluated which will be done in future. Moreover the optimized assembly design presented in this paper in section 2.3 needs to be assessed on the basis of sub-channel calculations which will be performed in future.

4. Conclusion

A channel design for pressure tube SCWRs has been optimized on the basis of neutronics and thermal hydraulics coupling. For these coupling calculations, single channel model was used for thermal hydraulics calculations. The sensitivity analysis for number of fuel pins inside assembly has been performed and number of fuel pins is optimized. The proposed and optimized design has MCSTs of 826^{o}C and 844^{o}C at BOC and EOC respectively. Therefore, contrary to the original design presented in reference [3] having MCST 854^{o}C, this design has MCST of 844^{o}C and it is fulfilling the criterion for MCST (i.e. < 850^{o}C). Moreover as a second step, a sub-channel analysis has also been performed on the channel design presented in [3], by selecting the hottest assembly from the core. MCST for this design on the basis of sub-channel analysis is found to be 822^{o}C which is satisfying the MCST criterion. Sub-channel analysis at EOC for the design presented in [3] and for the optimized design presented in section 2.3 of this paper will be considered for future work.

Acknowledgement

This work was financially supported by the National Science Foundation of China (approved number 91226106).

References

[1]. Shan, J., Chen, W., Rhee, B.W., et al., 2010. Coupled neutronics/thermal–hydraulics analysis of CANDU–SCWR fuel channel. Annals of Nuclear Energy 37, 58-65.

[2]. Zhao, C., Cao, L., Wu, H., et al., 2013. Conceptual design of a supercritical water reactor with double-row-rod assembly. Progress in Nuclear Energy 63, 86-95.

[3]. Ammar, A., Cao, L., Wu, H., 2014. Coupled analysis and improvements for Canadian-SCWR core design. Nuclear Engineering and Design 268, 104-112.

[4]. Ammar, A., Cao, L., Wu, H., et al., 2014. Conceptual design of pressure-tube super critical water reactor with inverted geometry. Nuclear Engineering and Design 278, 618-626.

[5]. Feng, J., Zhang, B., Shan, J., et al., 2014. Optimization of 54-element pressure tube SCWR bundle through neutronics/thermalhydraulics coupling analysis. Progress in Nuclear Energy 73, 1-10.

[6]. Marleau, G., Hébert, A., Roy, R., 2010. A User's Guide for DRAGON Version 4. Institut de génie nucléaire, Département de génie mécanique, École Polytechnique de Montsréal.

[7]. Fowler, T.B., Vondy, D.R., 1971. Nuclear Reactor Core Analysis Code CITATION. ORNLTM-2496. Oak Ridge National Laboratory.

[8]. Dittus, F.W., Boelter, L.M.K., 1930. Heat Transfer in Automobile Radiators of the Tubular Type, vol. 2. Univ. of California Publ., English, Berkeley, pp. 443–461.

[9]. Yang, P., Cao, L., Wu, H., et al., 2011. Core design study on CANDU-SCWR with 3D neutronics/thermal hydraulics coupling. Nuclear Engineering and Design 241, 4714-4719.

[10]. Basile, D., Beghi, M., Chierici, R., Salina, E., Brega, E., 1987. COBRA-EN: Code System for Thermal-Hydraulic Transient Analysis of Light Water Reactor Fuel Assemblies and Cores.

[11]. Zhao, C., 2014. Neutronics/Thermal Hydraulics Coupling Method and Conceptual Design of Supercritical Water Reactor with Annular Fuel. Xi'an Jioatong University, Xi'an, China.

[12]. Kamei, K., Yamaji, A., Ishiwatari, Y., et al., 2005. Fuel and core design of super light water reactor with low leakage fuel loading pattern. Journal of Nuclear Science and Technology, 43 (2), 129–139.

A Blind, Numerical Benchmark Study on Supercritical Water Heat Transfer Experiments in a 7-Rod Bundle

M. Rohde*[,1], J. W. R. Peeters[1], A. Pucciarelli[2], A. Kiss[3], Y. F. Rao[4], E. N. Onder[4], P. Mühlbauer[5], A. Batta[6], M. Hartig[6], V. Chatoorgoon[7], R. Thiele[8], D. Chang[9], S. Tavoularis[9], D. Novog[10], D. McClure[10], M. Gradecka[11] and K. Takase[12]

[1]Delft University of Technology, [2]University of Pisa, [3]BME NTI, [4]CNL, [5]Research Centre Rez Ltd., [6]KIT-IKET, [7]University of Manitoba, [8]KTH Royal Institute of Technology, [9]University of Ottawa, [10]McMaster University, [11]Warsaw University of Technology, [12]Japan Atomic Energy Agency

*Corresponding author: e-mail: m.rohde@tudelft.nl, tel.: +31 15 2786962

Abstract

Heat transfer in supercritical water reactors (SCWR) shows a complex behavior, especially when the temperatures of the water are near the pseudo-critical value. For example, a significant deterioration of heat transfer may occur, resulting in unacceptably high cladding temperatures. The underlying physics and thermodynamics behind this behavior is not well understood yet. To assist the worldwide development in SCWRs, it is therefore of paramount importance to assess the limits and capabilities of currently available models, despite the fact that most of these models were not meant to describe supercritical heat transfer. For this reason, the Gen-IV International Forum initiated the present blind, numerical benchmark, primarily aiming to show the *predictive ability* of currently available models when applied to a real-life application with flow conditions that resemble those of an SCWR. This paper describes the outcomes of ten independent numerical investigations and their comparison with wall temperatures measured at different positions in a seven-rod bundle with spacer grids in a supercritical water test facility at JAEA. The wall temperatures were not known beforehand to guarantee the blindness of the study. A number of models have been used, ranging from a 1D, analytical approach with heat transfer correlations to a RANS simulation with the SST turbulence model on a mesh consisting of 62 million cells. None of the numerical simulations accurately predicted the wall temperature for the test case in which deterioration of heat transfer occurred. Furthermore, the predictive capabilities of the subchannel analysis were found to be comparable to those of more laborious approaches. It has been concluded that predictions of supercritical heat transfer in rod bundles with the help of currently available numerical tools and models should be treated with caution.

1 Introduction

One of the most pressing issues to be investigated for the development of SCWR's is the possible occurrence of strong deterioration and enhancement of heat transfer of fluids at supercritical pressures. The accurate prediction of this "abnormal" behavior remains an unsolved and challenging problem. As fluid temperature increases past the pseudo-critical value, fluid density, viscosity, specific heat and other thermophysical properties drastically change. As a result, small changes in the flow conditions may cause a strong impairment

of turbulence production, leading to undesirably high wall temperatures that can damage the fuel elements in the SCWR core.

Currently available methods to predict supercritical heat transfer (SCHT) are mostly based on empirical heat transfer correlations fitted to local bulk and wall temperature measurements (see the extensive review of Pioro *et al.* [1] and references therein and recent work by e.g. Jackson [2, 3]). Such correlations have the advantage that they are suitable for use in subchannel codes, but have only been validated for specific channel geometries (mainly circular tubes) and limited ranges of conditions. Moreover, empirical correlations cannot provide insight into the complex SCHT mechanisms and are generally inapplicable to conditions under which heat transfer deterioration occurs. An alternative, more fundamental, approach would be to numerically solve the flow and energy equations in a computational domain that would be a realistic model of the SCWR fuel channel. Ideally, such approaches should use models of turbulence and other properties that would be applicable to supercritical conditions [4, 5, 6, 7] and would, therefore, be suitable for wide ranges of applications. However, as we know from turbulence modeling in general, such models would be very difficult and time consuming to develop and would also need suitable experimental databases for their validation under conditions relevant to SCWR operation and safety analysis. Before proceeding in this direction, it is therefore worthwhile to investigate the capability of currently available models to predict SCHT. Several comparative studies of empirical correlations and CFD analyses using turbulence models are already available (see, for example, Refs. [1, 8, 9, 10, 11]).

The aim of this work is to contribute to the testing of available methods by comparing results of independently conducted numerical simulations with experimental results obtained in a rod bundle under conditions that approximated those in an SCWR. The experimental conditions included practical effects, such as inlet effects and possible rod deformations, which would be present in an operating SCWR.

The measurements, which were not released to the participants until the end of the exercise, consisted of wall temperatures at different axial, radial and azimuthal positions on the rods. By being parts of a blind benchmark exercise, participants had no opportunity to fine-tune the models to improve the outcome.

This paper first describes the experimental facility and conditions and summarizes the experimental data. Then, it outlines the numerical approach of each participant. Finally, it compares all predictions with each other and with the measurements and expresses some useful conclusions and recommendations.

2 Description of the Experiments

2.1 Facility

The experiments were performed in a supercritical water test facility at JAEA, which consists of seven hexagonally arranged heating rods. A detailed description of the facility and measurement equipment, such as thermocouples and pressure sensors, can be found in Misawa *et al.* [12]. A cross-sectional image of the bundle is shown in Figure 1a. The rods have a heated length of 1500 mm and are uniformly heated by a Ni-Cr alloy heating element with a diameter of 4.2 mm that is embedded in Boron nitride. The thickness of the cladding amounts to 1 mm. The spacing of 1 mm between the heating rods is assured by five honeycomb-shaped spacers with an axial length of 25 mm. See Figure 1b for a detailed schematic of these spacers. The cross-sectional area of the bundle amounts to 192.2 mm^2. The distance between the inlet and the start of the heated section is 350 mm, which is approximately 120 times the hydraulic diameter of the rod bundle ($D_h = 2.757$ mm).

The wall temperature of each rod can be measured at six locations at different axial and azimuthal positions. The axial locations of the thermocouples, which are welded inside a 0.5 mm deep groove, are given in Figure 2. The pressure drop Δp can be measured with the help of pressure sensors located at positions 144 mm and 1360 mm from the inlet of the heated region. The pressures in the facility are around the typical value of 25 MPa in an SCWR.

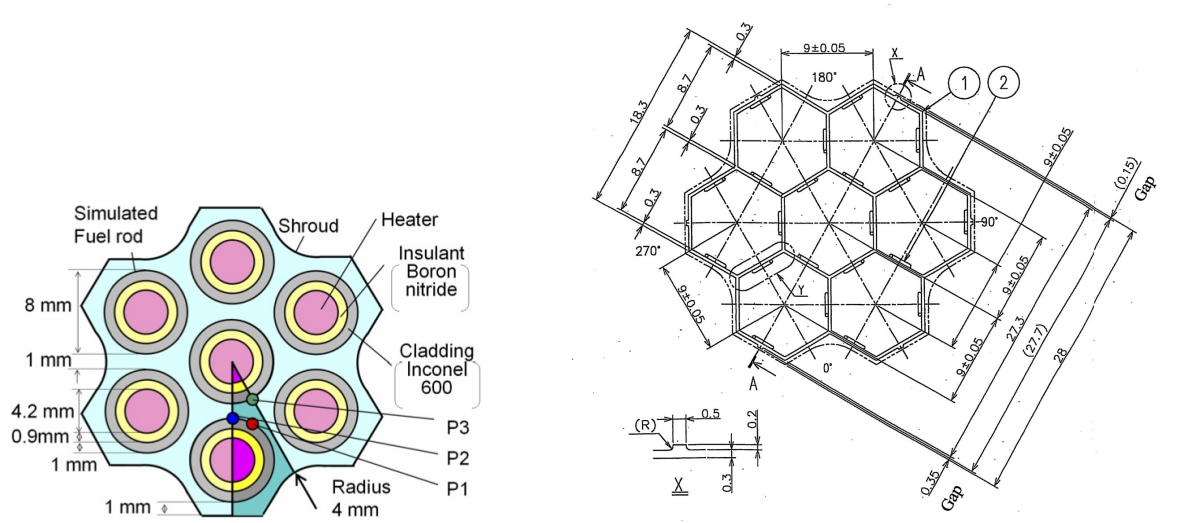

(a) Cross-sectional image of the 7-rod bundle. Picture taken from Misawa *et al.* [12].

(b) Spacer that holds the seven rods apart. Note the small, skew wires (indicated by Y) that keep the rods apart from the honeycomb structure.

Figure 1: Top-down view of the rod bundle geometry and its spacer configuration.

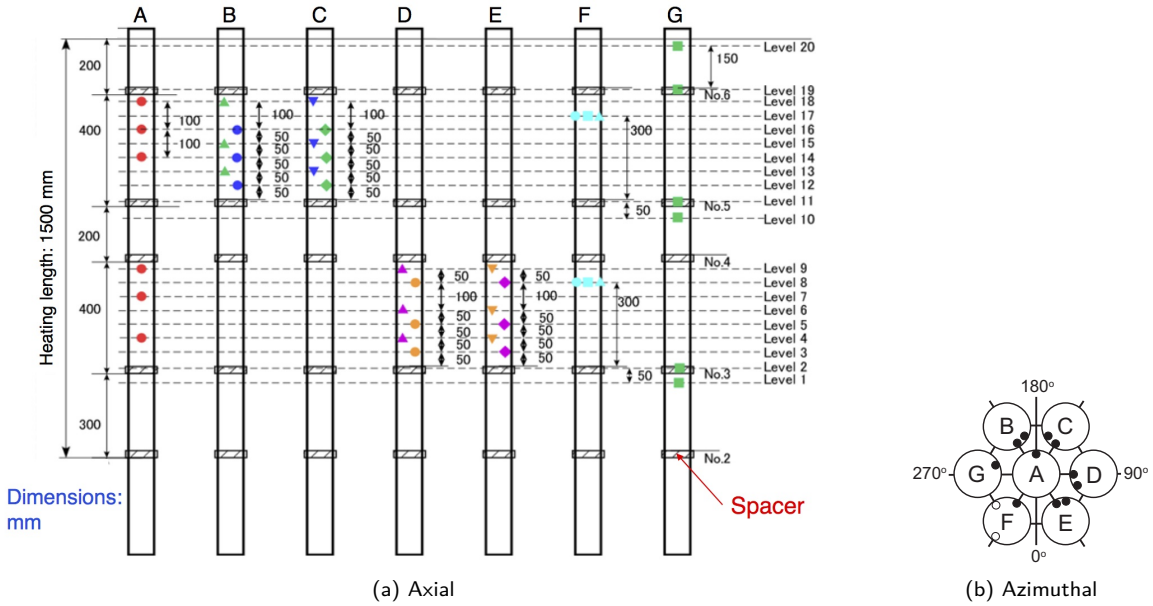

(a) Axial

(b) Azimuthal

Figure 2: Locations of the thermocouples on each separate heating rod. The open circles on rod F in (b) indicate the ones that are not used in this study.

There are a few uncertainties in this experimental setup that cannot be quantified nor verified at this stage, but possibly could have a significant effect on the local temperature measurements. These are

1. Rod bending may take place caused by lateral and azimuthal variations in the rod cladding temperature.

2. The heating element may not be entirely centered inside the rods, resulting in an azimuthally dependent heat flux.

3. Entrance effects may play a role because the inlet of the test section is perpendicular to the rod bundle. Such a configuration results in complex flow patterns at the entrance (such as a lateral swirl) that may require a longer development length than the well-known rule of a thumb $z/D_h > 30$ predicts. Zhu *et al.* [13], for example, show that spacer grids with small mixing vanes locally disturb the lateral flow such that relative development lengths of $z/D_h \approx 50$ exist. In the current experiment, the entire flow enters the bundle in a lateral way, possibly taking an even longer length before settling to an axially developed flow.

2.2 Studied Cases

Three cases have been used for this benchmark study and are shown in Table 1. In case A1, being the simplest one, no heat is applied to the rods. For this reason, the outcome does not depend on the complex behavior supercritical fluids show as the temperature of the water is the same throughout the entire bundle. In case B1, a relatively low inlet temperature and power are applied. Despite the fact that heat transfer comes into play, the water temperatures remain far below the pseudo-critical temperature (i.e. the temperature where the specific heat capacity shows its maximum at 25 MPa). Note that the power of the central rod is 13% lower than the outer rods. In case B2, the inlet temperature and power are sufficiently large to bring the water temperatures close to the surface of the heating elements beyond the pseudo-critical temperature, resulting in strong variations in the fluid properties such as the density and specific heat capacity. For this reason, it is to be expected that this case will reveal the largest deviations between experiments and calculations and amongst the calculations.

Table 1: Overview of the experimental cases studied for water at $p = 25$MPa.

Case	T_{in} (K)	$\dot{m}$(kg/s)	G (kg/m^{2}s)	Q_A (kW)	$Q_{B,D,F}$ (kW)	$Q_{C,E,G}$ (kW)	Δp (kPa)
A1	297.4	0.4388	2283	n/a	n/a	n/a	58.1
B1	353.6	0.2782	1448	19.67	22.51	22.52	n/a
B2	519.6	0.2753	1433	34.14	34.08	34.13	n/a

The measured rod surface temperatures can be found in Figure 3. A distinction has been made between thermocouples located in the gap region (i.e. the narrow region between two sub-channels) and the ones facing the center region of the sub-channel, because wall temperatures may be very different due to strong lateral variations in local velocities. Another distinction has been made between thermocouples facing inwards and the ones facing outwards (i.e. two thermocouples on rod F, Fig. 2b). In this study, only the inwards facing thermocouples have been considered.

Rod surface temperatures, measured in the same region and at the same height, are the same in a perfect experiment. To a certain extent, such behavior is found for case B1, because temperatures are similar with the largest difference being 10 K. These differences are caused by the aforementioned uncertainties in Section 2.1, but are of small influence in case B1 as fluid properties do not vary significantly. Case B2, on the other hand, shows large variations up to 40 K, especially at larger heights where the rod surface temperatures reaches beyond the pseudo-critical temperature of 658 K. In this case, rod bending, eccentric heating elements and entrance effects seem to induce significant azimuthal variations in heat transfer. One of the most striking examples is given by the two gap-facing thermocouples on rods B ($\theta = 30°$) and C ($\theta =$

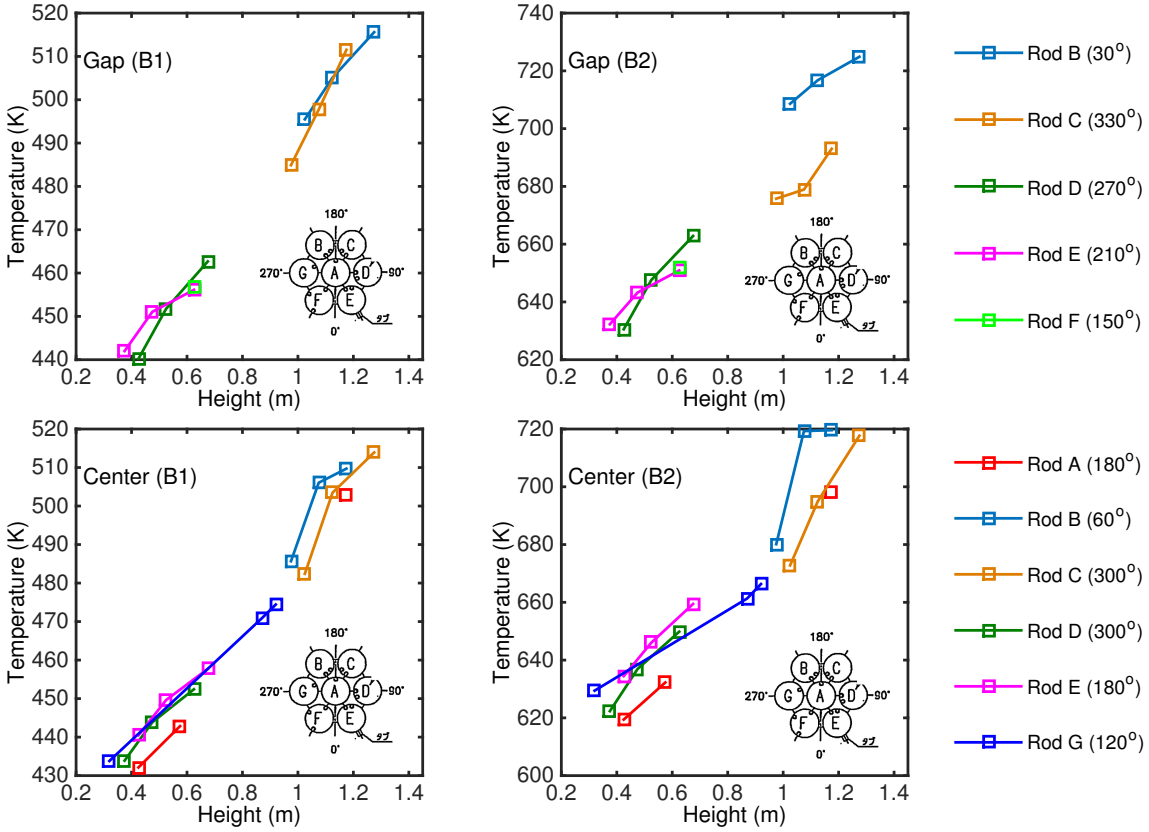

Figure 3: Experimentally obtained rod surface temperatures located at the gap and center regions. The left figures represent case B1, the right ones case B2. The angles indicate the angular location of the thermocouple with respect to the rod.

330°) in Figure 3, which are located at exactly the same radial and azimuthal position. Both thermocouples show the same rod surface temperatures in case B1, but differ by ~35 K in case B2.

3 Numerical Approaches

This section briefly describes the numerical approaches of the ten participants. Each of them independently made a choice with respect to the code (in-house or commercial), the number of dimensions, the turbulence models, the definition of the grid, the inclusion of fluid-structure interaction and conjugated heat transfer and the database for the water properties.

3.1 Delft University of Technology (TUD)

A very simple approximation of the 7-rod bundle geometry is to regard it as a duct with a single heat source. The advantage of making such a simplification, together with using heat transfer correlations, is that heat transfer results are obtained very quickly. The disadvantage is that such calculations only yield average rod wall temperatures. For a duct with a single heat source, the enthalpy transport equation can be reduced

to:

$$h_b = h_{b0} + \left(\frac{q''_w}{G}\right)\left(\frac{P}{A}\right)(z - z_0),$$

in which h_{b0} is the bulk enthalpy at the inlet, P the total perimeter of the rods, A the flow cross-sectional area and z_0 the vertical position of the inlet. The bulk temperature can be calculated as a function of the bulk enthalpy. This is done with the help of third order spline interpolations and a look-up table, which lists the fluid properties and the temperature vs. the enthalpy. Because many heat transfer correlations are implicit functions (see Ref. [1]), an iterative solver in fortran was used to calculate the Nusselt number at the vertical position z of each thermo-couple. The calculated Nusselt numbers, along with the calculated bulk temperature yields an estimation for the average wall temperature. Four different heat transfer correlations were used: the Dittus-Boelter correlation (valid in sub-critical pressure circumstances), a correlation by Dyadyakin and Popov [14](developed for a rod bundle), one by Jackson [15] and one by Mokry *et al.* [16] (two of the more recent correlations).

3.2 University of Pisa (UPisa)

The CD-Adapco's STAR-CCM+ code version 7.04.006 was used for performing all the simulations; two-equation turbulence models with the Low y^+ approach were considered, since a good experience in their application was gained during the past works at the University of Pisa [17, 18]. Generally speaking, these models can be divided into the two families of the $k-\epsilon$ and the $k-\omega$ ones. When approaching the study of heat transfer to supercritical fluids, models from each family, though obviously showing differences among each other, tend to behave in a similar way: in particular, the $k-\epsilon$ models usually overestimate the measured wall temperature trend, predicting strong heat transfer deterioration phenomena, while the $k-\omega$ ones underestimate it [8]. This feature was exploited for performing the blind calculations. Borrowing the concept at the basis of the Squeeze Theorem (or Sandwich Theorem) regarding the limit of a function, it was supposed that the measured data could lie between the results obtained using a $k-\omega$ model (lower bound) and a $k-\epsilon$ one (upper bound). So, if the models of the two kinds return similar results, the calculations could be possibly assumed reliable.

As a final comment, it must be remarked that because of problems related to the computational effort, the simulations could not be performed in a single run. The difficulties were bypassed by subdividing axially the computational domain into five parts, one for each spacer. After the simulation of the inlet part of the test section converged, its conditions in the vicinity of the outlet were used at the inlet of the downstream section and so on for the other parts. This approach obviously adds further uncertainties on the quality of the results. Anyway, at least in this application, the spacer grids have only a local effect and the good level of coherence obtained in the region far from them between the simulations performed considering with or without spacers is a valid indication of the fact that the adopted technique should be reliable.

3.3 BME NTI

The CFD models of BME NTI represent a single phase, steady-state, turbulent, buoyant flow and an isotropic, Newtonian, compressible and dissipative (viscous and heat conducting) fluid (supercritical water) based on the past experience of BME NTI [19, 20]. The Finite Volume Method (FVM) has been applied to discretize the RANS equations by the ANSYS CFX 14.5 commercial CFD program package. Block structured, hexahedral, 3 dimensional numerical grids have been generated by ANSYS ICEM CFD 14.5 program. The convective, diffusive and turbulent terms have been approximated by second order accurate numerical schemes. The BSL Reynolds stress and SAS-SST turbulence models were used for the final calculations.

The CFD investigation of BME NTI consists of three coupled steps. Downstream to the inlet of the CFD models an entrance part was used to generate developed inflow profile. To avoid the possible disturbance effect of a closely located outlet boundary condition on the results of heated section a discharge part was

included upstream to the outlet. In the first step, a grid sensitivity study have been performed on full heated length and 1/12 perimeter with simplified spacer geometry. The outcome of grid sensitivity study was the needed resolution of the grid in the radial, peripheral, axial directions and in the near wall region. The second step was about a geometry sensitivity study on 1/5 heated length and 1/6 perimeter with three differently detailed spacer geometries. The outcome of geometry sensitivity study was that the spacer geometry with full details has to be used in order to avoid modeling errors by geometry simplification of spacer grids [21]. In the third step, the final CFD calculations with conjugated heat transfer (CHT) model have been performed for the three experimental cases (A1, B1 and B2) on the full heated length and 1/3 perimeter with fully detailed spacer geometry. The effect of buoyancy on the production and dissipation of turbulence has been modeled at the final calculations.

3.4 Canadian Nuclear Laboratories (CNL)

CNL used the Canadian subchannel code ASSERT-PV in this benchmark. ASSERT-PV has been developed and qualified for predictions of flow and enthalpy distributions, critical heat flux, and post-dryout cladding temperatures for CANDU bundles [22]. The code has been designed to be general enough to accommodate other bundle geometries and flow orientations. For applications in support of the Canadian SCWR bundle design [23], the code has been updated with supercritical fluid properties and supercritical heat transfer correlations, resulting in a prototype version of the code ASSERT-PV(SCWR) for the prediction of flow and enthalpy distributions and cladding temperatures under supercritical flow conditions. In modeling the benchmark geometry, 1/6 symmetry is assumed (i.e., same rod power distribution for all outer rods), resulting in a total of three rods or partial rods (R1: centre, R2 and R3: outer rods), and four subchannels (S1: inner, S2 to S4: outer subchannels). Since the two outer subchannels (S2 and S4) are identical by symmetry, there are only four wall temperatures as independent output at any axial location: R1-S1, R2-S1, R2-S3, R2-S2. For submission to the blind-test benchmark, the Jackson correlation [15] is used for wall-to-coolant heat transfer coefficient calculation as was used in applications for the Canadian SCWR bundle design [23]. For other phenomenon models including frictional and form-loss coefficients, and inter-subchannel turbulent mixing, the recommended (or default) model options [22] are used. The fuel model in ASSERT-PV, required for including conjugated heat transfer (CHT), is not used in this study.

3.5 Research Center Rez Ltd (CVREZ)

Validation computations performed with ANSYS FLUENT 12 computer code based on experiments Pismenny *et al.* [24], run 1, provided us with basic knowledge on suitable mesh and model of turbulence. Limitations of available hardware and prescribed power in the individual heated rods led to decision to analyze one-twelfth of the rod bundle cross-section. The computational domain comprised a 200 mm long unheated bare rod bundle, a 1500 mm long heated rod bundle with spacers, and 30 mm long unheated part. Mass flow rate, temperature, turbulence intensity and viscosity ratio were prescribed at the inlet. Pressure at the outlet, no-slip condition at solid walls and symmetry on the remaining boundaries were set. Turbulence was modeled with the $k-\omega$ SST model with low-Re correction. A mesh sensitivity study was conducted using three meshes with 2M, 4M and 5.6M of mainly hexahedral computational cells. Difference in pressure drop between the last two meshes was lower than 1.5%. Fine mesh with $y^+ \approx 0.1$ (wall distance as low as 0.001 mm) was used near the heated walls where large changes of temperature and therefore, large changes in fluid properties can be assumed. Fluid properties were obtained from the National Institute of Standard and Technology (NIST) Refrigerants and Refrigerant Mixture Database (REFPROP) Real Gas Model, which is available in ANSYS FLUENT 12. SIMPLE scheme for $p-v$ coupling and QUICK discretization scheme were used.

3.6 KIT-IKET

Among possible approaches that can be followed for the benchmark considering analysis of heat transfer in supercritical water the KIT has applied the Fluid Structure Interaction (FSI), where the structural and

Table 2: Overview of the analyzed cases by KIT-IKET. Mesh size relating to the fluid domain mesh only.

Case	Turbulence Model	Mesh Size	y^+	CHT	FSI
1	$k-\epsilon$	0.5 M	160	No	No
2	$k-\epsilon$	0.5 M	160	Yes	No
3	$k-\epsilon$	0.5 M	160	Yes	Yes
4	$k-\omega$ (SST)	3.2 M	2.5	No	No

Table 3: Meshes used for the grid independence study of UMan.

Mesh	BSP-1	BSP-2	BSP-3	BSP-4
Cases	A1	A1, B1, B2	B1,B2	B2
Total (% increase)	32M	49M (+52%)	55M (+13%)	63M (+14%)
In z direction	1,483	1,582	1,769	1,777
Fluid	21M	31M	35M	39M
Cladding (coarse/fine)	0.27M/1.8M	0.39M/2.5M	0.43M/2.8M	0.75M/4.8M
Heater (coarse/fine)	0.38M/5.5M	0.62M/9.7M	0.70M/11M	0.82M/12M
Insulator (coarse/fine)	0.15M/1.0M	0.22M/1.4M	0.25M/1.6M	0.37M/2.4M
Spacer	1.7M	2.9M	3.0M	3.1M

fluid side of the problem are considered. Details of the considered studies is given in Ref. [25]. Ansys-CFX and Ansys-Structure codes were used. In order to determine the impact of conjugate heat transfer (CHT) and heating rod deformation, three detailed analysis with a coarse mesh are conducted by considering the $k-\epsilon$ turbulence model. To evaluate the error introduced by application of the $k-\epsilon$ turbulence model and the corresponding high y^+ values, a reference analysis is conducted. It implements the $k-\omega$ SST model and makes use of a finer mesh. Table 2 gives an overview of the calculations executed in the context of this work. Due to the geometrical complications it is hard to keep constant y^+ values. The tabulated y^+ values denotes the maximum computed values.

3.7 University of Manitoba (UMan)

A $^1/_{12}$ th section of the benchmark 7-rod bundle was modeled. Symmetry was assumed on both section planes. The Ni-Cr heating elements with their C-shaped cross sections were modeled as solid rods of the same outside diameter as the C-shape. To simplify modeling of the spacers, only the main frame of the spacer that wrapped around the perimeter of the heater rods was modeled.

A grid independence study was performed for cases A1, B1 and B2, using the $k-\omega$ SST turbulence model. Four meshes were generated that included a 0.3 m unheated inlet, 0.03 m unheated outlet, 1.5 m heated section, and 6 spacers, each of which were 0.025 m long. The runs and the corresponding meshes for each run are summarized in Table 3. Table 3 shows two meshes were used for cases A1 and B1, and three meshes were used for case B2. In summary, the meshes BSP-2, BSP-3, and BSP-4 give mesh independent results and grid independence was achieved. For cases A1, B1 and B2, final results were taken from runs in which the mesh with the greatest number of nodes was used.

3.8 Royal Institute of Technology (KTH)

In this benchmark study KTH used the ANSYS CFX version 15 code as computational code of choice. The full domain of all 7 rods and an additional inlet section are modelled. The inlet section before the first spacer develops the flow towards the inlet of the first section of the benchmark domain. A two equation $k-\omega$ SST RANS approach is used with a constant turbulent Prandtl number of 0.9. From [9] it is known that a constant turbulent Prandtl number will introduce errors, however, the suggested ways of varying the turbulent Prandtl number, are not feasible in such a complicated geometry as the one at hand. In order to

capture the near wall behaviour in case of deteriorated or enhanced heat transfer in the heated cases B1 and B2, a low Reynolds number approach was used as suggested by [9]. This means that y^+ is kept below 1 in most of the domain, and the maximum value on the heated walls around the spacers is around 10. Automatic wall scaling is applied in regions where y^+ is above 1. This requirement results in a mesh of about 28 M cells, of which the majority are tetrahedral cells within the spacers' vicinity. The sections between the spacers use a purely hexahedral mesh. All wall boundary conditions are no-slip smooth boundaries. A heat flux is applied along the heated rods and all other wall boundaries are perfectly adiabatic. The fluid properties are based on the IAPWS-IF97 properties provided by the ANSYS software.

3.9 University of Ottawa (UOttawa)

The University of Ottawa team used ANSYS FLUENT 15 for all computations. The computational domain comprised an upstream subdomain that was a 200 mm long unheated bare rod bundle and a downstream subdomain that was a 1500 mm long heated rod bundle with spacers. The cross-section of the domain was a 60° sector of the rod bundle cross-section. The mesh with 62M cells consisted of hexahedral cells, except near the grid spacers, where tetrahedral cells were used. The dimensionless wall distance was $y^+ < 0.1$ in most of the computational domain, except near the spacers, where $y^+ \approx 5$. The supercritical water thermodynamic properties were obtained from the National Institute of Standard and Technology (NIST) Refrigerants and Refrigerant Mixture Database (REFPROP) Real Gas Model version 7. The mass flow boundary condition was used at the inlet plane, while the static pressure boundary condition was employed at the outlet plane. The turbulent Prandtl number was set to be 0.9. Rotationally periodic boundary conditions were applied on the two plane boundaries of the domain. The adiabatic boundary condition was applied to the outer shroud, whereas, for the heated cases, heat flux values were imposed on the rod surfaces. Two kinds of simulations were performed: unsteady Reynolds-averaged Navier-Stokes (RANS) simulations with the Scale Adaptive Simulations (SAS) turbulence model for the high heat flux case (B2) and RANS simulations with the Shear Stress Transport (SST) turbulence model for all other cases. The second-order upwind scheme was used for spatial discretization in the RANS simulations with SST. For the unsteady simulations with SAS, the bounded central differencing scheme and the second-order implicit Euler scheme were used for spatial and temporal discretization, respectively. The Semi-Implicit Pressure Linked Equations – Consistent (SIMPLEC) algorithm was used for pressure-velocity coupling of the incompressible flow equations. The time step size was set as 0.00025 sec, which corresponded to values of the Courant number less than one.

3.10 McMaster University (McMU)

McMaster University carried out simulations using STAR-CCM+ 9.02.005 with the SST $k-\omega$ turbulence model. A near wall treatment that ensured a $y^+ < 0.53$ was applied to the isothermal case A1 while a $y^+ < 0.09$ was applied to the heated cases B1 and B2. The thermodynamic properties of the supercritical water were obtained from the NIST database using the REFPROP 9 application. The choice of turbulence model and computational grid were determined through a separate effects study and mesh sensitivity study that are both detailed in Ref. [26].

The computational domain consisted of a 1/3 cut of the rod-bundle cross section. Rotationally periodic boundary conditions were applied in order to exploit this reduced geometry. This domain was divided axially into five subdomains with each subdomain containing a grid spacer. The division of the domain was done for practical reasons that allowed for simplified troubleshooting and analysis. The grid spacer geometry was simplified to maintain the integrity of the computational grid. A constant mass flow boundary condition was used at the inlet plane of the furthest upstream section. The inlets of successive sections were then defined by the velocity vector, temperature, turbulent kinetic energy and specific dissipation rate of a plane near the outlet of the previous section. A constant heat flux was applied to the inner side of the cladding and conduction within the cladding was explicitly modeled. A constant turbulent Prandtl number of 0.9 was used. The entire domain consisted of hexahedral cells.

Table 4: Overview of the numerical approaches. FSI = Fluid Structure Interaction, CHT = Conjugated Heat Transfer

	CFD package	Description	Modeling	Grid size	Circumferential domain	FSI	CHT	Analyzed spacers	Fluid Properties
TUD	in-house	1D channel analytical solver	Range of correlations for heat transfer, basic correlations for wall friction	n/a (analytic)	entire	no	no	no	REFPROP 9
UPisa	STAR-CCM+ 7.06	Multipurpose CFD package	$k-\omega$ SST, AKN $k-\epsilon$	1.4M(no spacers), 24M	1/12	no	yes	yes	REFPROP 7
BME NTI	ANSYS CFX v14.5	Multipurpose CFD package	SAS, $k-\omega$ SST	5M(1/12), 3.5M(1/6), 14M(1/3)	1/12,1/6,1/3	no	yes	yes	IAPWS-IF97
CNL	ASSERT-PV	Models regions within the bundle as parallel, intermixing sub-channels	Jackson [15] for heat transfer, basic correlations for wall friction	axial: 60, radial: 4	1/6	no	no	yes	HLWP 1.0
CVREZ	FLUENT 12	Multipurpose CFD package	$k-\omega$ SST	A1: 3.4M B1+B2: 1.4M, 2M, 4M, 5.6M	1/12	no	yes	yes	REFPROP 7
KIT-IKET	Ansys-CFX and Ansys-Structure	Multipurpose CFD package and package to study FSI and CHT	$k-\omega$ SST, $k-\epsilon$	B2: 0.5M, 3.2M	1/6	yes ($k-\epsilon$)	yes ($k-\epsilon$)	no	IAPWS-IF97
UMan	ANSYS CFX v14.5	Multipurpose CFD package	$k-\omega$ SST, $k-\epsilon$, SSG	A1: 32M, 49M B1+B2: 49M, 55M B2: 63M	1/12	no	yes	yes	IAPWS-IF97
KTH	ANSYS CFX v. 15	Multipurpose CFD package	$k-\omega$ SST	28M	entire	no	no	yes	IAPWS-IF97
UOttawa	ANSYS FLUENT 15	Multipurpose CFD package	SAS, $k-\omega$ SST	62M	1/6	no	no	yes	REFPROP 7
McMU	STAR-CCM+ v9.02	Multipurpose CFD package	$k-\omega$ SST	A1: 17M, B1: 54M, B2: 37M	1/3	no	no	yes	REFPROP 9

Table 5: Pressure drops between $z = 144$ mm and $z = 1360$ mm of case A1, according to the experiments and calculations.

Contribution	Pressure drop (kPa)
Experimental	**58.1**
TUD	not determined
UPisa	72.2 (+24%)
BME NTI	68.1 (+17%)
CNL	56.6 (-3%)
CVREZ	69.2 (+19%)
KIT-IKET	not determined
UMan	67.5 (+16%)
KTH	67.6 (+16%)
UOttawa	139.4 (+140%)
McMU	53.7 (-7%)

3.11 Overview of Contributions

An overview of the contributions is given in Table 4.

4 Results and Discussion

The results presented and discussed here comprise the cases A1, B1 and B2 as indicated in Table 1. Numerical results are referred to by using the name of the organization and the case in question in parentheses, e.g. TUD(B2).

Case A1: Pressure drop over the unheated bundle

Table 5 shows the pressure drops obtained from the simulations. Most calculations give an acceptable overestimation of the pressure drop in the range of +10 to +20%. In contrast, UOttawa(A1) over-predicted this pressure drop by 140%; this discrepancy is attributed to high values of artificial viscosity across the used mesh interfaces between adjacent bare rod subdomains and spacer grid subdomains and could be alleviated by mesh redistribution. CNL(A1), being the result of a subchannel approach, shows the best estimate for the pressure drop.

Overall performance of the simulations

The overall performance of the calculations can be found in Figure 4 and Figure 5. Figure 4 indicates that, even though the average of the calculations coincides rather well with the experiments, the scatter in wall temperatures is rather large. Even for case B1, calculations significantly differ by 30 K (at the beginning of the bundle) to 60 K (at the end of the bundle). Figure 5 indeed shows that the relative average error of the calculations, defined as

$$\epsilon\left(T_w\right) \equiv \frac{1}{N}\sum_{i=1}^{N}\frac{\left|T_{w,i}^{exp} - T_{w,i}^{num}\right|}{T_{w,i}^{exp} - T_{bulk,i}},$$

is roughly 20%. Note that the denominator is the local temperature difference between the wall and the bulk, being a relevant parameter to normalize the absolute error with. Again, CNL(B1) shows the smallest error, being 11% by ASSERT-PV. Most analytical solutions, TUD(B1), except for the case with Mokry's model, show the largest error of approximately 30 to 40%.

None of the simulations could capture the high wall temperatures found above $z = 1$ m for case B2. Figure 4 clearly shows that, on average, the simulations (except CVREZ(B2)) give too low wall temperatures

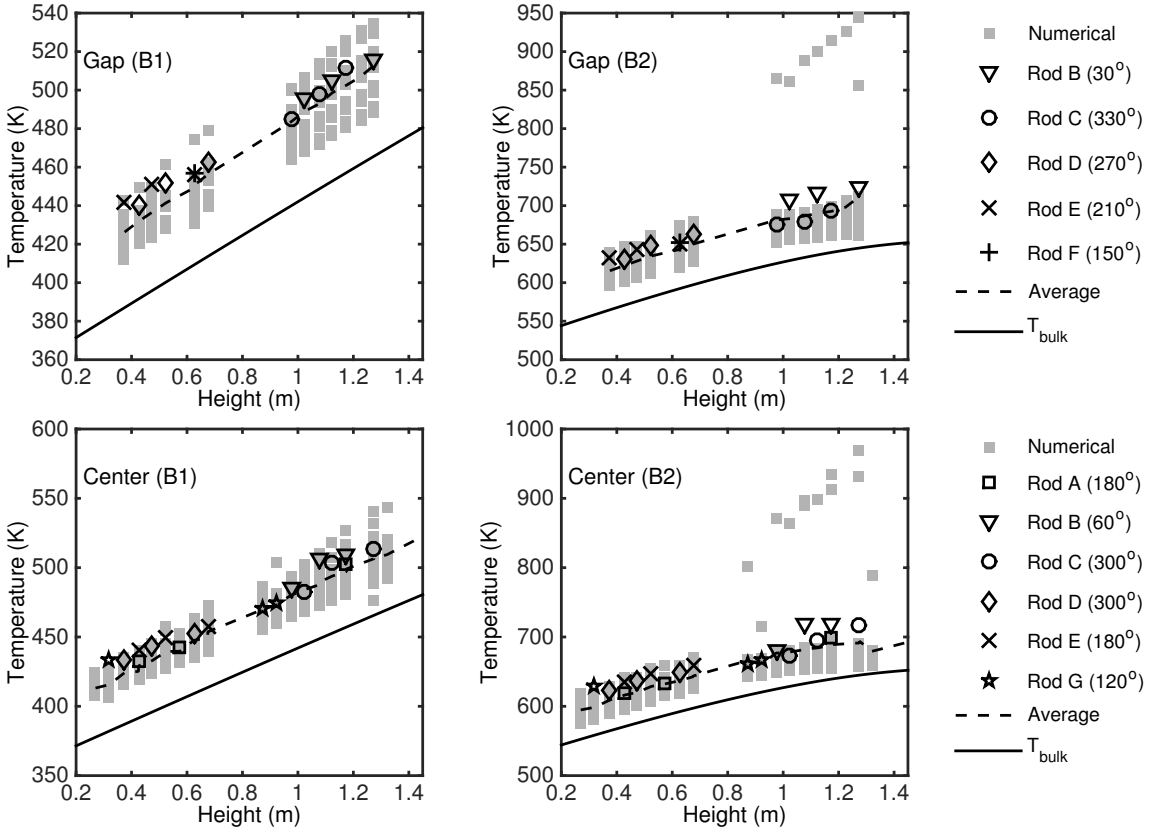

Figure 4: Rod surface temperatures located at the gap and center regions. The left figures represent case B1, the right ones case B2. The gray squares show all numerical results for all gap facing locations, the other symbols indicate measured wall temperatures. The dashed line is a polynomial fit of the numerical results.

for $z = 1$ m and higher. Moreover, the scatter in this case is even higher, ranging from 50 K at the beginning of the bundle to 70 K at the end (or 300K when CVREZ(B2) is included). The relative average error of the calculations is around 40%, and the differences are larger than in case B1. UPisa(B2) and McMu(B2) show the smallest average errors (20%, both being RANS calculations) and CNL(B2) has a relatively small error as well (23%). Hence, the relatively simple subchannel approach performs as well as the more complex and computationally expensive RANS approach. Despite these small errors, however, the typical deterioration of heat transfer in supercritical flows is not captured.

Effect of the grid size

The range of number of grid nodes in this study is large, i.e. from 240 (CNL) to 63M (Uman). The domain, however, needs to be taken in to account as well. For this reason, the grid size for the entire domain is considered. E.g. KIT-IKET(B2) comprises 3.2M nodes on a 1/6 th domain, hence the entire domain would take $3.2 \times 6 = 19.2$M nodes. Figure 6 shows the results of case B2 for RANS simulations on large, medium and small grids. The results clearly show that a larger grid (i.e. a more refined mesh) does not assure better results. The simulation performed on the smallest grid (KIT-IKET(B2)) performs even *better* in the gap region than the other calculations. There is no obvious explanation for these findings, although one

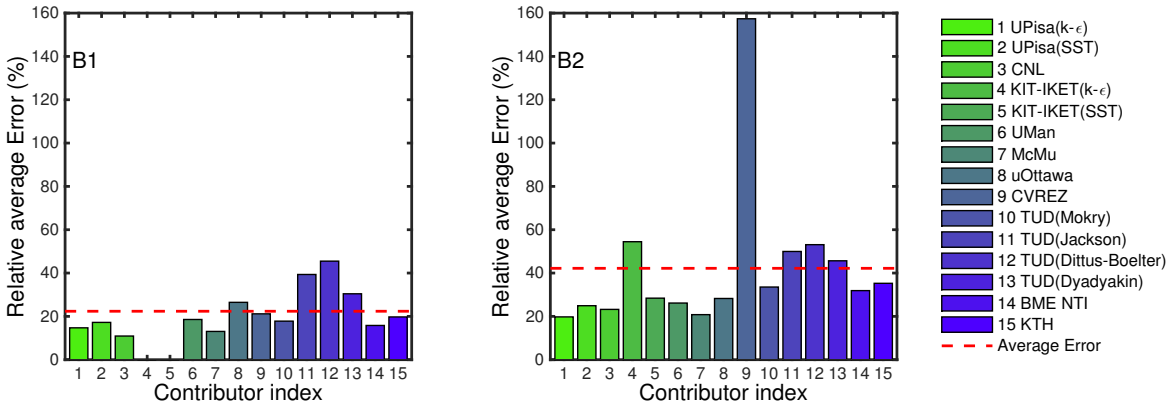

Figure 5: Relative average errors with respect to the experiments. The error is normalized by the difference between the calculated local wall temperature and local bulk temperature. The dashed line indicates the average error of all numerical contributions. Note that KIT-IKET did not perform calculations on case B1.

could argue that the localities of grid refinement may be of importance as well. As the grid sizes in Figure 6 mutually differ orders of magnitude, however, it is not expected that differences in local grid refinement could explain the aforementioned findings.

RANS versus 1D and subchannel approaches

Figure 7 reveals the effect of using the computationally intensive RANS calculations compared to the fast 1D and subchannel approaches. In the gap region, the RANS approach clearly performs better than the analytical approach of TUD, even though the high temperatures at the end of the bundle are not captured. The wall temperatures obtained from UMan(B2) and uOttawa(B2) are closer to the experimental values. Temperatures in the gap region are expected to be higher than at locations facing the center region because of the lower streamwise velocity there. As the 1D analytical approach is not capable of calculating these local effects, the temperatures are estimated too low. For wall temperatures at locations facing the center region, it is found that the analytical approach performs slightly better than in the gap region, but wall temperatures are still too low. The RANS simulations are relatively close to the measured values (as expected), as well as the subchannel approach CNL(B2).

Difference between RANS $k-\epsilon$ and RANS $k-\omega$

According to Sharabi and Ambrosini [8], the $k-\epsilon$ models usually overestimate the measured wall temperature, while the $k-\omega$ models underestimate them. Figure 8, however, shows that this finding is in correspondence with UPisa(B2), but not with KIT-IKET(B2): the wall temperatures from KIT-IKET($k-\epsilon$)(B2) are *lower* than those from KIT-IKET($k-\omega$)(B2). At this stage, no obvious reason can be given for these trends. The results from KIT-IKET($k-\epsilon$)(B2) are too low at both the gap and the center facing locations. Interestingly, UPisa($k-\epsilon$)(B2) and, to a lesser extent UPisa($k-\omega$)(B2), yield high wall temperatures at axial locations that coincide with the locations where deteriorated heat transfer is found in the experimental facility (center facing locations). Why this trend is not found for the gap region cannot be derived from the current data.

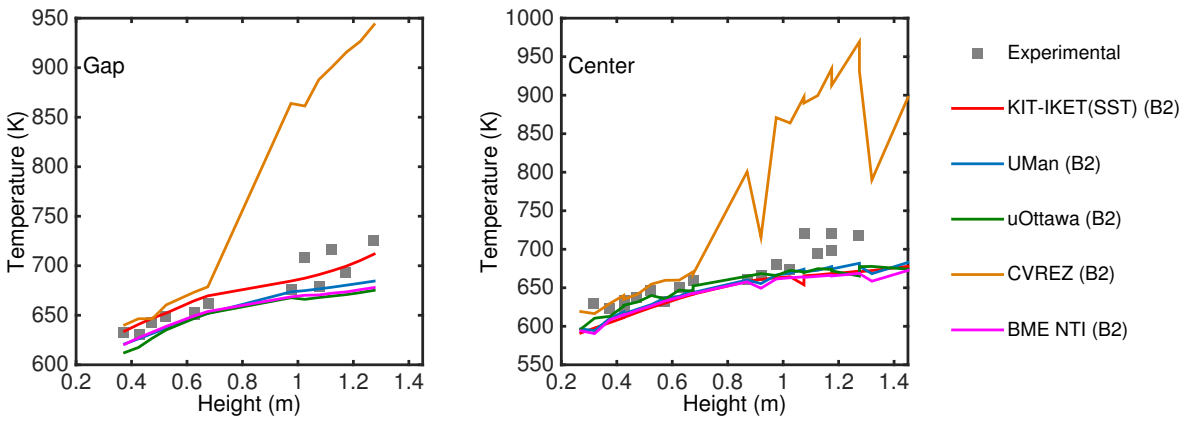

Figure 6: Comparison of rod surface temperatures for case B2 obtained by RANS calculations with large grids (UMan: 756M, uOttawa: 372M), medium grids (CVREZ: 67M, BME NTI: 42M) and a small grid (KIT-IKET: 18M). These grid sizes are adjusted to the entire circumferential domain. The gray squares indicate the experimental data in the regions concerned.

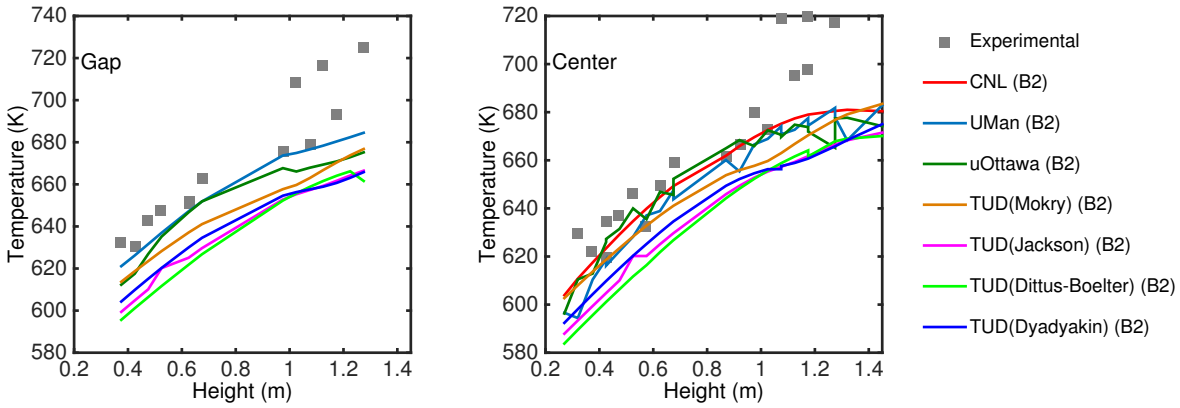

Figure 7: Comparison of rod surface temperatures obtained by a 1D approach (CNL, TUD) and RANS calculations with large grids (UMan, uOttawa: 62M). Note that the lateral discretization by CNL into four subchannels results in wall temperatures facing the center only (right figure). The gray squares indicate the experimental data in the regions concerned.

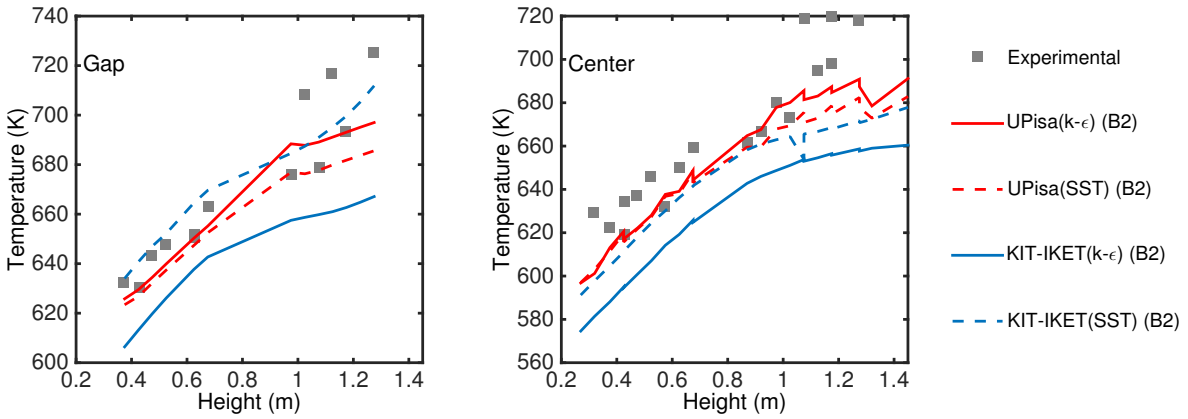

Figure 8: Comparison of rod surface temperatures obtained by RANS $k-\epsilon$ and RANS $k-\omega$ calculations. Two organizations (KIT-IKET and UPisa) applied both models and are therefore most suitable for comparison. Note that UPisa applied a much larger grid than KIT-IKET. The gray squares indicate the experimental data in the regions concerned.

Effect of the inclusion of Conjugated Heat Transfer (CHT)

Although not confirmed by the experiments, the wall temperatures in a perfectly symmetrical system should be circumferentially evened out by CHT due to thermal conduction in the cladding of the heating elements. This presumption is confirmed by KIT-IKET($k-\epsilon$)(B2) as indicated in Figure 9a, where the wall temperatures in the gap region are significantly reduced by 15 K at the bundle exit. A comparison of BME NTI(B2) (with CHT) and KTH(B2) (without CHT) is shown in Figure 9b. Both simulations are performed at approximately the same average grid resolution and make use of the $k-\omega$ model. These calculations show similar profiles at the gap region except for a notably high temperature for KTH(B2) at $z > 1.2$ m, possibly confirming the effect of neglecting thermal conduction in the cladding. More work, however, is required to affirm that this peak can be attributed to local heat transfer deterioration; other numerical differences may play a role, such as the local structure of the grid and in the inlet conditions applied.

Effect of the inclusion of Fluid Structure Interaction (FSI)

Investigation of the effect of FSI can be done by comparing numerical simulations only because it is not known to what extent rod bending has occurred in the experimental facility. To this purpose, the cases 2 and 3 of KIT-IKET ($k-\epsilon$)(B2) can be used. In case 3, rod bending resulted in rod G bending away from rod A near the outlet of the bundle, thereby locally creating a larger gap between both rods. The circumferential wall temperatures at the outlet of the bundle are shown in Figure 4. In this particular case, rod bending seems to even out the temperatures even more, especially at the center-facing positions where the temperature drops by approximately 5 K. Note that this finding does not mean that rod bending is favorable at all times, but shows that bending can be of importance in supercritical flows.

5 Conclusions

The primary aim of this blind, numerical benchmark study was to show the *predictive ability* of currently available models when applied to a real-life application with flow conditions that resemble those of an

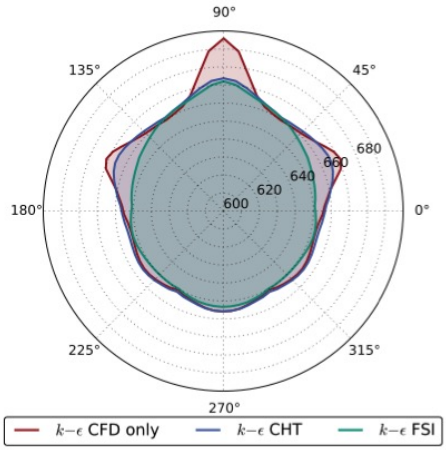

(a) Circumferential temperature profile (in K) of rod G for case 1 (w/o CHT and FSI), case 2 (with CHT and w/o FSI) and case 3 (with CHT and FSI) at the outlet of the domain. The three cases refer to KIT-IKET($(k-\epsilon)$)(B2). The azimuthal coordinate corresponds with Figure 3, hence rod G is facing rod A at $\theta = 90°$.

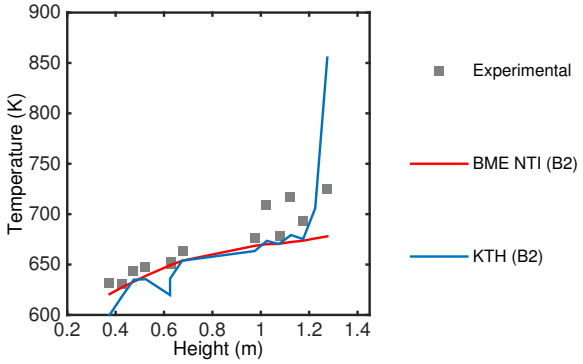

(b) Comparison of rod surface temperatures in the gap region, obtained by RANS $k-\omega$ calculations with CHT (BME NTI) and without CHT (KTH). The average grid resolution is roughly comparable, i.e. BME NTI applied 14M cells in a 1/3 domain, KTH applied 28M cells in the entire domain. The gray squares indicate the experimental data in the regions concerned.

Figure 9: The effect of CHT and FSI

SCWR. The term 'real-life' refers to the fact that a physical setup was considered that is subject to practical unknowns and uncertainties that one typically encounters during the design of a reactor core.

First, it can be concluded that none of the calculations was able to convincingly capture the typical heat transfer behavior close to the pseudo-critical point. Second, there was no evidence that the RANS approaches performed better than the method based on subchannel modeling. It should be noted, however, that only RANS (or other CFD modeling) can provide detailed circumferential cladding temperature profiles by its ability to capture the different turbulence structures in the gap region and the center region.

The analytical 1D approach showed the least correspondence with the experiments. Third, a comparison between different grid resolutions, turbulence models and CFD codes did not reveal any explicit trend in differences between experimental and numerical data. Finally, all simulations show a significant dispersion in all three cases, i.e. the pressure drop in case A1 and the wall temperatures in cases B1 and B2. Hence, overall, it can be concluded that predictions of supercritical heat transfer with the help of currently available numerical tools and models should be treated with caution. Currently, an *a posteriori* investigation is being performed i) to interpret the inability of the numerical approaches in this work to predict the increased wall temperatures near the outlet of the bundle, ii) to clarify the dispersion of the numerical results and iii) to find ways to improve the application of currently available modeling.

6 Acknowledgment

This work has been carried out as part of the program of work of the SCWR "Thermal-hydraulics and Safety" Project Arrangement of the Generation-IV International Forum, `www.gen-4.org`, involving Canada, the European Union and Japan.

References

[1] I. L. Pioro, H. F. Khartabil, R. B. Duffey, Heat transfer to supercritical fluids flowing in channels - empirical correlations (survey), Nuclear Engineering and Design 230 (1-3) (2004) 69 – 91, 11th

International Conference on Nuclear Energy. doi:http://dx.doi.org/10.1016/j.nucengdes.2003.10.010.
URL http://www.sciencedirect.com/science/article/pii/S0029549303003856

[2] D. Jackson, Fluid flow and heat transfer at supercritical pressure, in: Proc. 14th Int. Topl. Mtg. Nuclear Reactor Thermal Hydraulics (NURETH-14), Toronto, Canada, 2011.

[3] D. Jackson, Ideas for an improved semi-empirical model of turbulent mixed convection heat transfer to fluids at supercritical pressure, in: Proc. 15th Int. Topl. Mtg. Nuclear Reactor Thermal Hydraulics (NURETH-15), Pisa, Italy, 2013.

[4] M. Mohseni, M. Bazargan, Modification of low reynolds number k-ϵ turbulence models for applications in supercritical fluid flows, International Journal of Thermal Sciences 51 (2012) 51–62.

[5] Y.-F. Mao, B.-F. Bai, L.-J. Guo, A novel model of turbulent convective heat transfer in round tubes at supercritical pressures, Heat Transfer Engineering 32 (11-12) (2011) 1082–1092.

[6] E. Laurien, Semi-analytical prediction of hydraulic resistance and heat transfer for pipe and channel flows of water at supercritical pressure, in: Proceedings of the 2012 International Congress on Advances in Nuclear Power Plants-ICAPP'12, 2012.

[7] J. W. R. Peeters, R. Pecnik, B.-J. Boersma, M. Rohde, T. H. J. J. Van der Hagen, Direct numerical simulation of heat transfer to co_2 in an annulus at supercritical pressure, in: Proceedings of ETMM-10, Marbella, Spain, 2014.

[8] M. Sharabi, W. Ambrosini, Discussion of heat transfer phenomena in fluids at supercritical pressure with the aid of CFD models, Annals of Nuclear Energy 36 (1) (2009) 60–71.

[9] M. Jaromin, H. Anglart, A numerical study of heat transfer to supercritical water flowing upward in vertical tubes under normal and deteriorated conditions, Nuclear Engineering and Design 264 (2013) 61–70.

[10] S. He, W. S. Kim, J. H. Bae, Assessment of performance of turbulence models in predicting supercritical pressure heat transfer in a vertical tube, International Journal of Heat and Mass Transfer 51 (19) (2008) 4659–4675.

[11] B. Ničeno, M. Sharabi, Large eddy simulation of turbulent heat transfer at supercritical pressures, Nuclear Engineering and Design 261 (2013) 44–55.

[12] T. Misawa, T. Nakatsuka, H. Yoshida, K. Takase, K. Ezato, Y. Seki, M. Dairaku, S. Suzuki, M. Enoeda, Heat transfer experiments and numerical analysis of supercritical pressure water in seven-rod test bundle, in: Proc. 13th Int. Topl. Mtg. Nuclear Reactor Thermal Hydraulics (NURETH-13), Kanazawa, Japan, 2009.

[13] X. Zhu, S. Morooka, Y. Oka, Numerical investigation of grid spacer effect on heat transfer of supercritical water flows in a tight rod bundle, International Journal of Thermal Sciences 76 (0) (2014) 245 – 257. doi:http://dx.doi.org/10.1016/j.ijthermalsci.2013.10.003.
URL http://www.sciencedirect.com/science/article/pii/S1290072913002391

[14] B. V. Dyadyakin, A. S. Popov, Heat transfer and thermal resistance of tight seven-rod bundle, cooled with water flow at supercritical pressures (in russian), Trans. All-Union Heat Eng. Inst. 11 (1977) 244–253.

[15] D. Jackson, Consideration of the heat transfer properties of supercritical pressure water in connection with the cooling of advanced nuclear reactors, in: The 13th pacific basin nuclear conference. Abstracts, 2002.

[16] S. Mokry, I. Pioro, A. Farah, K. King, S. Gupta, W. Peiman, P. Kirillov, Development of supercritical water heat-transfer correlation for vertical bare tubes, Nuclear Engineering and Design 241 (4) (2011) 1126–1136.

[17] M. Sharabi, CFD analyses of heat transfer and flow instability phenomena relevant to fuel bundles in supercritical water reactors, Ph.D. thesis, University of Pisa (2008).

[18] A. Pucciarelli, Analysis of heat transfer phenomena with supercritical fluids by four equation turbulence models, Master's thesis, University of Pisa (2013).

[19] A. Kiss, A. Aszodi, Summary for three different validation cases of coolant flow in supercritical water test sections with the CFD code ANSYS CFX 11.0, Nuclear technology 170 (1) (2010) 40–53.

[20] A. Kiss, A. Aszodi, Numerical investigation on the physical background of deteriorated heat transfer mode in supercritical pressure water, in: Proc. 6th International Symposium on SCWRs (ISSCWR-6), Shenzhen, China, 2013.
[21] B. Mervay, CFD calculations in SCWR relevant geometries – the GIF 7 rods benchmark, Master's thesis, BME NTI (2014).
[22] Y. F. Rao, Z. Cheng, G. M. Waddington, A. Nava-Dominguez, ASSERT-PV 3.2: Advanced subchannel thermalhydraulics code for CANDU fuel bundles, Nuclear Engineering and Design 275 (2014) 69–79.
[23] E. N. Onder, Y. F. Rao, J. Pencer, Assessment of ASSERT subchannel code for the canadian SCWR bundle at supercritical conditions, in: Proceedings of the 3rd China-Canada Joint Workshop on Supercritical Water Cooled Reactors, no. 12041, 2012.
[24] E. N. Pis'menny, V. G. Razumovskiy, E. M. Maevskiy, A. E. Koloskov, I. L. Pioro, Heat transfer to supercritical water in gaseous state or affected by mixed convection in vertical tubes, in: 14th International Conference on Nuclear Engineering, American Society of Mechanical Engineers, 2006, pp. 523–530.
[25] M. Hartig, Numerical analysis of fluid-structure interaction with heat transfer at supercritical pressure in a rod test assembly, Master's thesis, KIT (2014).
[26] D. McClure, A computational benchmark study of forced convective heat transfer to water at supercritical pressure flowing within a 7 rod bundle, Master's thesis, McMaster University (2014).

Nomenclature

D_h	Hydraulic diameter
ϵ	Relative average error of the calculations w.r.t. the experiment
h_b	Bulk enthalpy
$\dot{m}$, G	Mass flow rate, mass flux
Δp	Pressure drop over the heated section
$q''_{w,i}$, Q_i	Wall heat flux, power of rod i
T_b, T_w, T_{in}	Bulk, wall, inlet temperature
$T_{w,j}$	Wall temperature at position j
θ	Azimuthal position, see Fig. 3
y^+	Distance to the rod surface in wall units
z	Stream wise position
$A - G$	Rod index number
CHT	Conjugated heat transfer
FSI	Fluid structure interaction
SCHT	Supercritical heat transfer

ISSCWR7-2045

The numerical simulation of peak cladding temperature in small-scale wire-wrapped 4-rod fuel assembly

Jinguang Zang, Yongliang Li, Xiaokang Zeng, Xiao Yan, Yanping Huang
（Nuclear Power Institute of China, Chengdu, Sichuan, China）

Abstract

Abstract

The SCWR-FQT-SCRIPT project aims at licensing of a small scale fuel assembly with four wire-wrapped fuel pins under supercritical conditions. The active assembly composed of four wire-wrapped fuel rods is cooled by the forced flow of supercritical water. In this paper, the cladding temperature of the fuel rods was analyzed with CFD code. Because of the difficulty of the mesh generation in the tangential contact region between the wire wrap and the fuel rod, three kinds of geometries with various space locations were compared to find the effect of local gap size on the cladding temperature. The SST turbulence model was selected to solve the Reynolds average equations. The heat conduction took place through the fuel cladding and the wire wrap, which impaired the peak cladding temperature and should be considered in the simulation. It was found that the local hot spot easily occurred near the contact region of wire wrap and fuel cladding at the high heat flux place. The stagnant flow and the boundary layer separation behind the wire wrap decreased the heat transfer ability.

1. Introduction

The SCWR-FQT-SCRIPT project is a Europe and China cooperation program aiming at licensing of a small scale fuel assembly with four wire-wrapped fuel pins under supercritical conditions. The fuel qualification loop is planned to be built at the Czech research reactor [1]. In order to verify the loop design, some steady analysis should be performed to clarify the boundary condition and check cladding temperature within the limit. Since there is no CHF or DNB criterion for supercritical water, the maximum cladding temperature could be considered as one of the important safety instructions. The CFD tools were used in this paper to predict the peak cladding temperature of the small fuel rod bundle to provide support for the design work.

In this paper, the CFD simulation method would first be discussed, such as the geometry simplification, the mesh generation and calculation setup. Secondly, the mesh independent analysis was performed after a big effort in mesh generation. At last the distribution of temperature profiles would be described. The effect of the wire-wrap contact with cladding was discussed on the influence of peak temperature.

2. CFD Method Introduction

2.1 The Model Geometry

The FQT-SCRIPT test loop is a closed forced circulation loop operating at supercritical conditions [1]. The fuel rod bundle is placed inside a pressure tube which could withstand the pressure of 25 MPa. The coolant comes into the pressure tube from the top head and flows down and up twice before gets out of the pressure tube. The fuel rod bundle is placed at the bottom of the pressure tube, including the fuel rods, wire wraps, upper spacer and bottom spacer. There are four fuel rods, 2×2 square arranged. Each rod has the diameter of 8 mm. The distance between two adjacent rods is 9.44mm. Each rod is wound by a wire wrap with the diameter of 1.44 mm which means that the wire wrap is in tangential contact with its neighbour rods. The wire wrap pitch is 200 mmm. The width of the fuel assembly box is 20.32mm. The upper and bottom spacers were designed to keep the fuel rods fixed. Geometry optimization has been made to the bottom spacer to minimize the instability caused by possible inlet fluid eddies.

The geometry file has much information than it is needed in CFD simulation. For example, the spring disk of the upper spacer in the geometry file aims to compensate the thermal expansion of the wire wrap and rod cladding; however, it is at downstream of the active region and has no big influence on the cladding temperature profile. Another example is the inner structure of the fuel rod. Since our calculation focuses on the outer cladding temperature, the heat flux is imposed on the inner side of the cladding. The inner fuel is removed in the simulation. Besides this, some geometry details need to be modified for mesh generation. For example, the tangential contact of the wire wrap and fuel rod makes it difficult to generate mesh in such extreme small angle region. At first step, radius of rotation for the wire wrap is scaled down to make extra 0.1mm space with the adjacent rod. In the next step, other geometry versions would be considered to see their effect on the cladding temperature.
The geometry files were first repaired and modified with NX UG software and exported to CATIA V4 file format to be imported by ANSYS ICEM CFD for mesh generation. Although the ANSYS ICEM CFD supports many kinds of geometry types, such as stp, iges files, the CATIA V4 format is preferred after test and comparison in the author's opinion.

2.2 Mesh generation

The mesh generation is a tough part for such kind of geometry. The main tough reason is the tangential contact of the wire wrap with the fuel rod. Even though the tangential contact is avoided through decreasing the rotation radius of the wire wrap, the small gap thus obtained is still very thin and narrow in comparison with the large size of the length of the whole domain. In the small gap, the prism mesh needs to be generated to resolve the boundary layer. Besides, in order to predict the cladding temperature, the solid part of the fuel cladding should be included for thermal coupled calculation through preliminary work. Considering these aspects, the mesh generation for the fluid part and solid part were made separately.
For the fluid part, the unstructured mesh method was applied. For the prism layer, the size of first grid near the wall is set to 0.1 mm with three layers to avoid mesh overlapping. The increasing ratio is 1.05, below than 1.1.
The global mesh size is set 0.5mm, and minimal size is 0.1mm. The wire wrap diameter is far less than the fuel rod diameter, so the maximum size is set 0.2 mm instead with 0.05mm of minimal size. In the mesh independent analysis, the global scaling factor was adjusted to generate various mesh numbers.

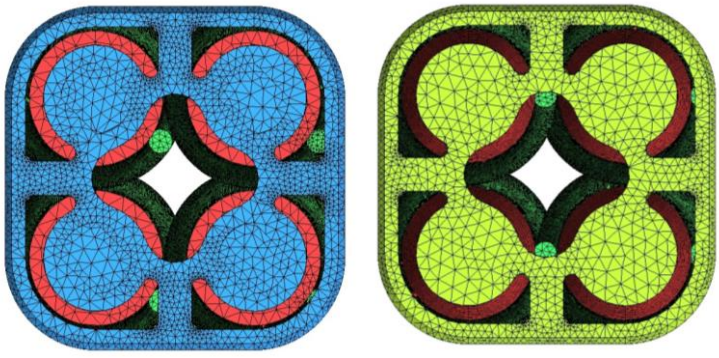

Figure 1 The scheme picture for the fluid mesh

For the solid part, the wire wrap and cladding were combined into a union. The wire wrap winds the cladding for several turns and it is a rotational periodic geometry. This leads to the possible mesh generation with structure grid. The bottom-up mesh generation strategy was applied. First, the two dimensional mesh was generated with just a slice of the cladding and wire wrap. Then the two dimensional mesh was extruded and rotated according to specified relationship, so that the mesh could conform to the geometry in a good way. Using this method, the mesh number could be decreased with good mesh quality.

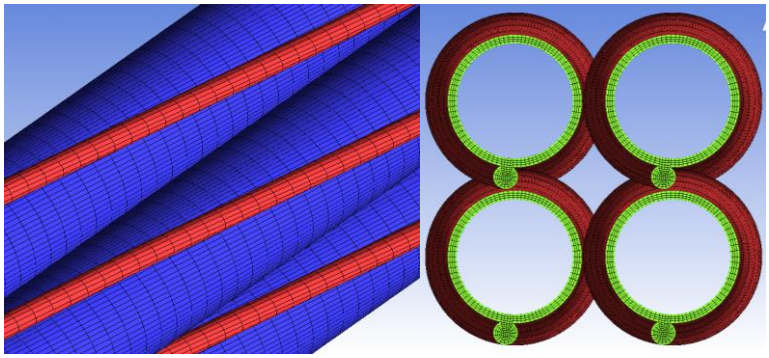

Figure 2 The scheme picture for the solid mesh

The fluid part is unstructured mesh, while the sold part is structured mesh. Each method accounted for the geometry characteristics of each region. These two mesh files were connected in ANSYS CFX by the General Grid Interface (GGI) [2]. The GGI method allows for the flexible mesh type at the interface, without strict agreement of the two meshes. The GGI method could automatically sets up the relationship at the interface and keeps mass, momentum and energy conservative without losing the accuracy and robust.

2.3 Computation setup

The ANSYS CFX 13.0 was used as the simulation software. The SST k-w model was selected for the turbulence model. The operating pressure is 25.34MPa and mass flow rate 0.25kg/s, inlet temperature 366℃. Total power is 63.6kW with axial variation (FIGURE 3) calculated by MCNP code. The material type for the cladding is SS36L. The IAPWS IF97 library imbedded in ANSYS CFX was used to calculate the physical properties of supercritical water. The maximum point number was set to 1000 for interpolation refinement.
The detailed calculations were summarized in TABLE 1.

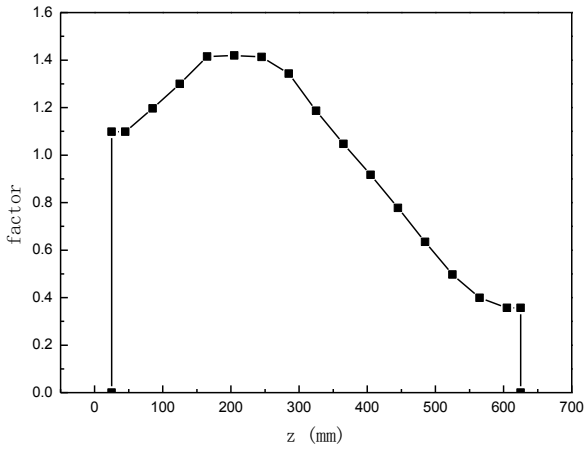

Figure 3 The axial power profile of the fuel rod bundle

Table 1 Computation setup

Simulation platform	ANSYS CFX 13.0
Turbulence model	SST $k-\omega$
Geometry parameters	Rod pitch = 9.44mm Rod inner /outer diameter = 7/8mm Wire wrap diameter = 1.44mm
Materials	Solid: SS316L Fluid: Supercritical water, using the IAPWS IF97 water library
Operating conditions	Pressure P=25.34MPa Mass flow rate m=0.25kg/s Total power 63.6kW, with axial profile Inlet temperature Tin=366℃

3. Results and Analysis

3.1 Mesh independent analysis

The mesh is an important part in CFD simulation. The mesh could affect the simulation results if the mesh is not generated in a proper way. The simulation results should be independent of the mesh numbers. In order to check this, two mesh files were generated through adjusting the global scale factors. The maximum size is 0.5mm and minimal size 0.1mm for the whole part. The maximum size is 0.2 mm and minimal 0.05 mm for the wire wrap. These two meshes correspond to the global scaling factor 1.0 and 2.0. FIGURE 4 shows the picture of these two meshes. The first mesh has about 11.2million tetrahedron elements and 2.8 million prism elements, while the second mesh has about 5 million tetrahedron elements and 1.6 million prism elements. TABLE 2 listed the information for these two meshes and their results for comparison. For the inner and outer cladding surfaces (FIGURE 5), the wire wrap and assembly box (FIGURE 6), the maximum temperature difference is about 3℃, and average temperature difference is only 1℃. So the results have low dependency on mesh numbers. The first mesh was selected for further analysis.

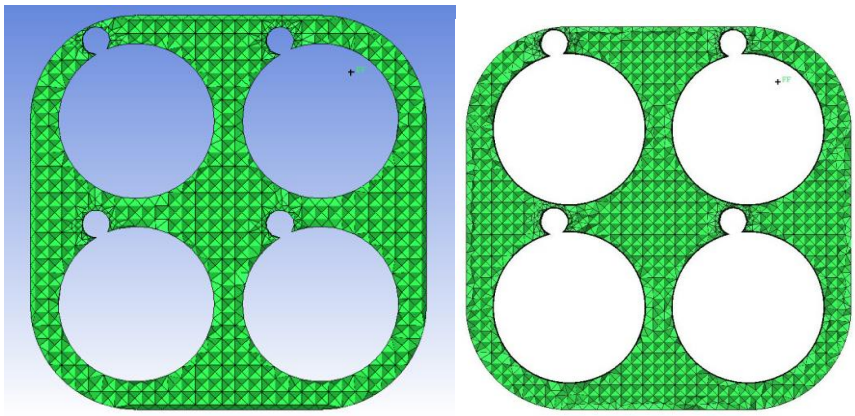

(a) scale=1.0 mesh (b) scale=2.0 mesh

Figure 4 The two generated mesh for dependent analysis

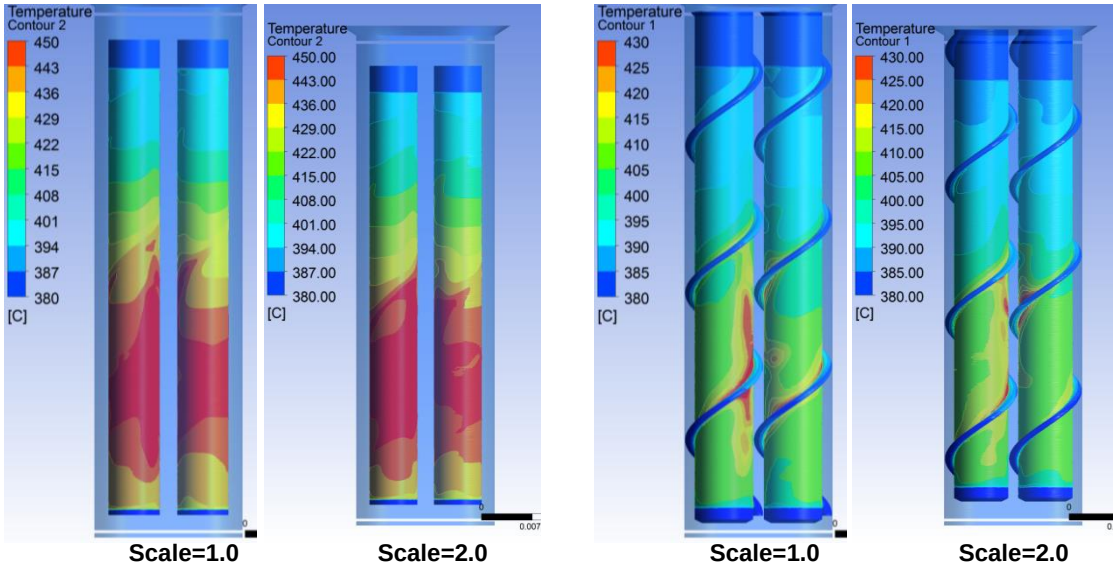

Scale=1.0 **Scale=2.0** **Scale=1.0** **Scale=2.0**

(a) Inner cladding surface (b) Outer cladding surface

Figure 5 The temperature contours comparison for mesh dependent analysis

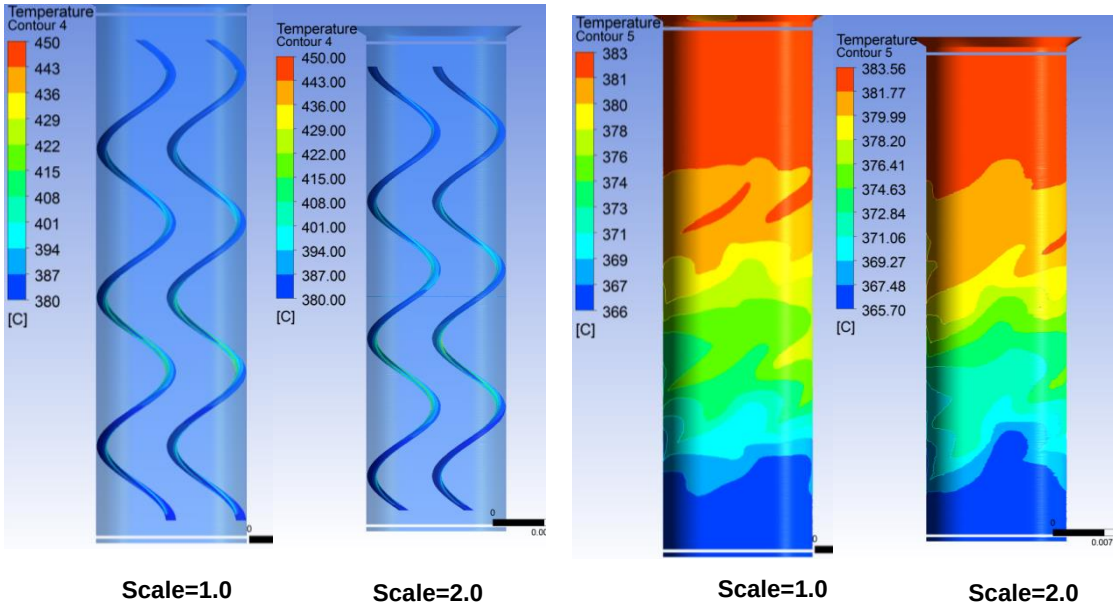

Figure 6 The temperature contours of the wire wrap and assembly box

Table 2 Mesh independent analysis comparison

	scale=1.0		scale=2.0	
Tetrahedron elements	11165937		5024287	
Prism elements	2826606		1627224	
	Ave.Tw(℃)	Max.Tw(℃)	Ave.Tw(℃)	Max.Tw(℃)
Outer cladding surface	403	457	402	455
Wire wrap	387	436	388	435
Inner cladding surface	431	496	430	493
Assembly box	376	383	376	384

3.2 Cladding temperature distribution

The fuel cladding temperature is an important parameter in evaluating the safety and feasibility of the loop design. The CFD tools may have some uncertainty in simulation accuracy in complex structure flow at supercritical pressures, especially in the pseudocritical region where large variation of fluid properties may change the turbulence fluctuation characteristics. The experimental data is needed for further verification. Some experimental studies are ongoing and expected to provide the data bank. At present, the CFD results are analyzed with respect to the local flow and temperature filed information to provide reference for fuel structure design.

The wall temperature is tightly related to the heat flux profile (shown in FIGURE 3). From the core physical calculation, the heat flux reaches its maximum point at the lower part of the fuel rod and decreases as the distance is getting far. After normalization with average heat flux, the maximum value is about 1.4 and the minimal value is 0.36. The non-uniformity of heat flux profile leads directly to the non-uniformity of the wall temperature. FIGURE 7 presents the temperature distribution for the wire wrap, inner and outer cladding surface, the assembly box. The region

with high heat flux tends to have high wall temperature and the region with low heat flux tends to have relatively low temperature from the global perspective. At the inner cladding, the maximum temperature reaches up to 496℃ in the high heat flux region. At the outer cladding, the maximum temperature the maximum temperature reaches up to 457℃ in the high heat flux region near the stagnation place caused by the intersection of the wire wrap and fuel cladding. In this place, the wire wrap may block the flow. The heat transfer ability becomes weak. In addition with the high heat flux, the maximum temperature easily occurs.

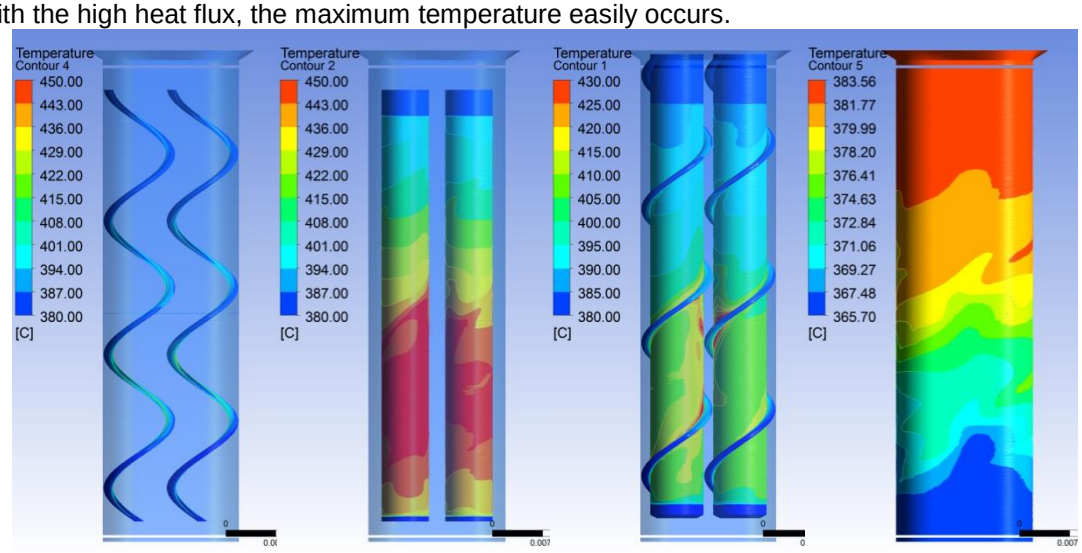

Figure 7 The temperature contours of the wire wrap and assembly box

3.3 The effect of geometry contact between wire wrap and rod

In the original geometry file, the wire wrap diameter is 1.44mm and is in tangential contact with two adjacent rods. At the tangential contact place, the wire wrap surface is tangent to the cladding surface and brings about large difficulty in mesh generation. In order to get over this problem, the wire wrap was artificially modified into three versions, shown in TABLE 3 and FIGURE 8. The aforementioned results correspond to geometry version 1.

Table 3 Geometry parameters for these three geometry versions

Name	Rod pitch(mm)	Rod diameter(mm)	Wire wrap diameter (mm)	Gap with master rod (mm)	Gap with neighbor rod (mm)
Version 1	9.44	8	1.44	-0.1	0.1
Version 2	9.44	8	1.24	0.1	0.1
Version 3	9.44	8	1.64	-0.1	-0.1

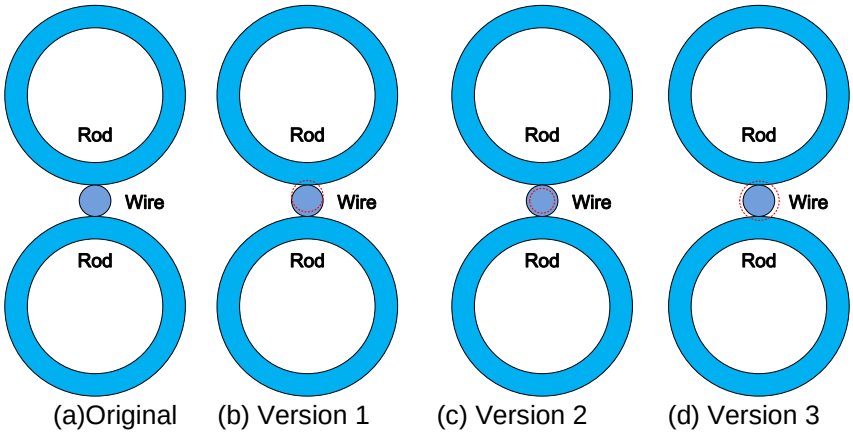

Figure 8 The scheme picture of three geometry versions

For version 1, the wire wrap diameter is fixed and the turning radius is decreased down by 0.1mm, so the wire wrap will insect with its master rod and leave 0.1mm space for the neighbor rod. For version 2, the wire wrap diameter is scaled down to 1.24mm, so that it will make room of 0.1mm for both the master rod and the neighbor rod. For version 3, the wire wrap diameter is enlarged to 1.64mm, so that it will insect with both the master rod and neighbor rod. These three versions of geometry tend to provide insight on how the local tangent region affects the cladding temperature.

FIGURE 9~FIGURE 10 presents the inner and outer cladding temperature comparisons for these three geometry versions. The global temperature distribution is similar with high temperature region at the lower part and relatively lower temperature region at the upper part. The occurring place for local heat spot is also similar, near the wire wrap. TABLE 4 lists the average and maximum temperature for them. The average temperatures among them are very close, no more than 3℃, while the maximum temperatures seem to have big difference. For the maximum outer cladding temperature, the version 1 is 457℃, version 2 489℃ and version 3 539℃. In correspondence, the maximum inner cladding temperatures are 496℃, 520℃ and 573℃, respectively.

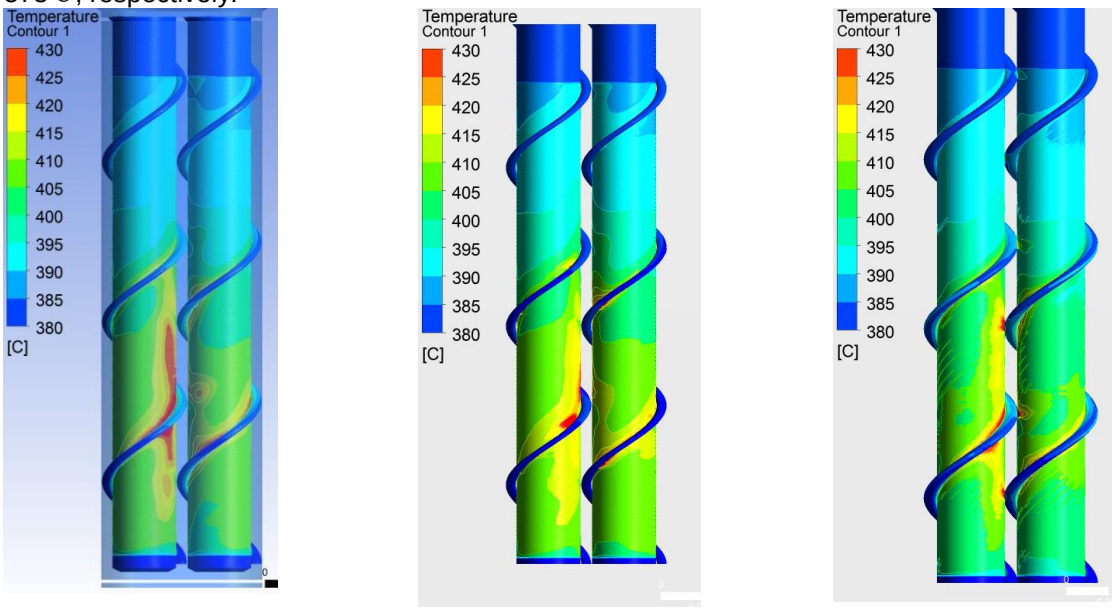

Figure 9 The outer cladding temperature comparisons for these three geometry versions

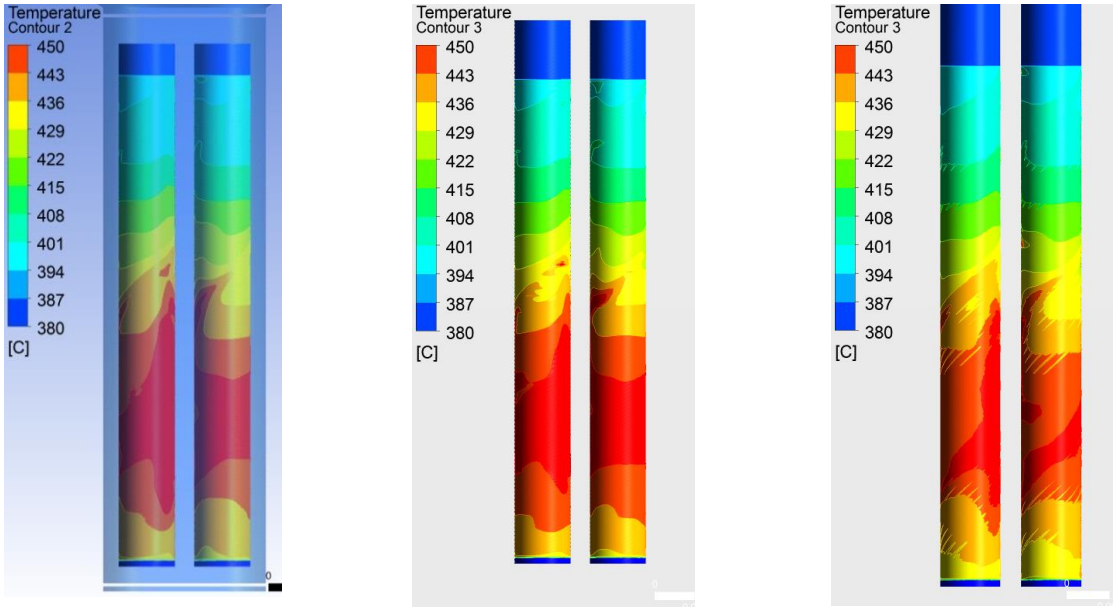

Figure 10 The inner cladding temperature comparisons for these three geometry versions

Table 4 The calculation results for these three geometry versions

	version 1		version 2		version 3	
	Ave.Tw (℃)	Max.Tw (℃)	Ave.Tw (℃)	Max.Tw (℃)	Ave.Tw (℃)	Max.Tw (℃)
Outer cladding	403	457	401	489	400	530
Wire wrap	387	436	379	385	386	431
Inner cladding	431	496	428	520	426	555
Assembly box	376	383	376	384	376	383

Next, we are going to analyze the reason that the version 3 has the highest cladding temperature. FIGURE 11 presents the outer cladding temperature and corresponding heat flux for Version 3. From the contour picture, the hot spots are located at the high heat flux region and at the back of the wire wrap. FIGURE 12 shows the details of temperature distribution. At the gap between two adjacent rods, the flow resistance is large and the mass flux is small. When the wire wrap is wound to the gap place, it will deteriorate the heat transfer performance and cause the local heat spots.

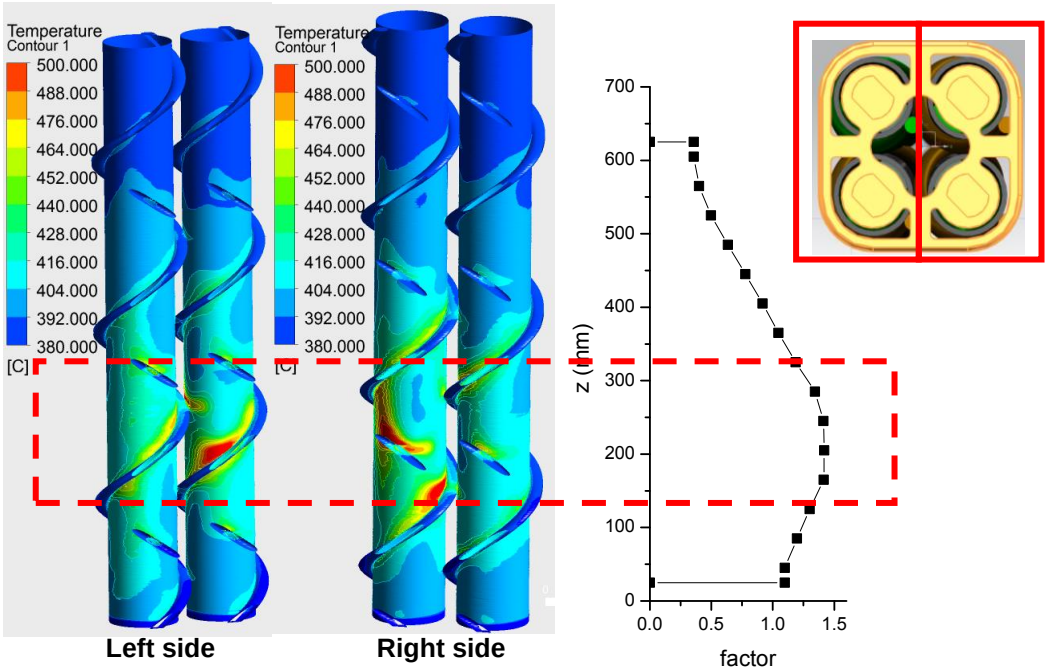

Figure 11 The outer cladding temperature for geometry version 3

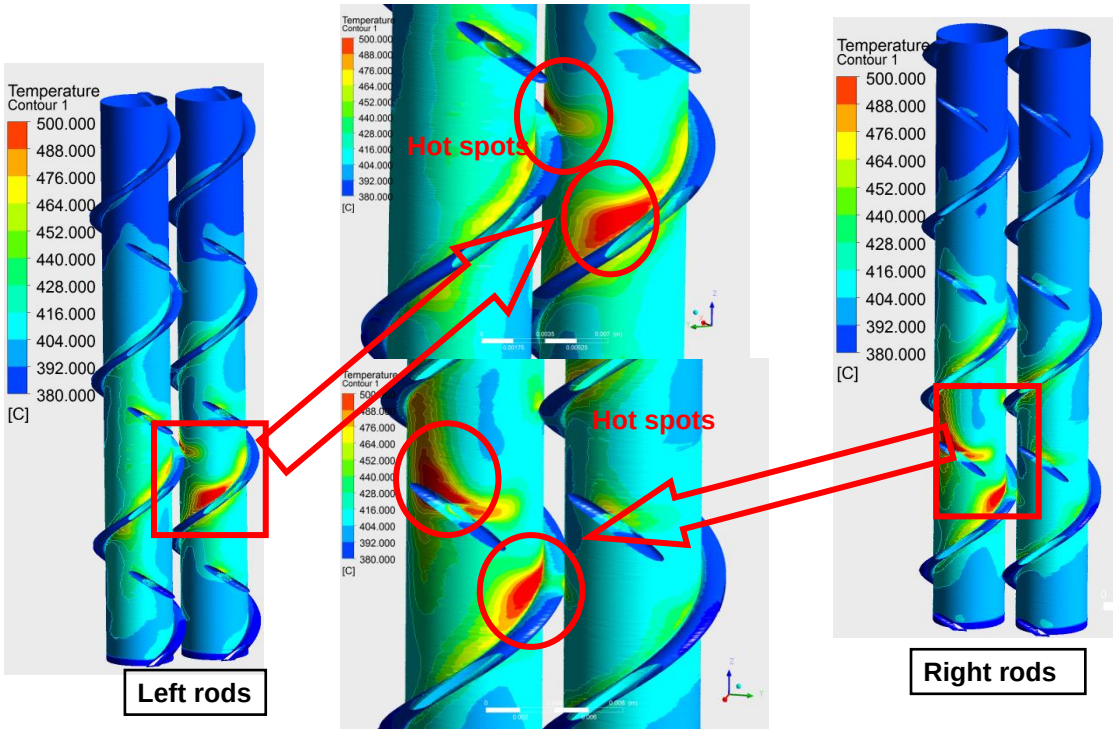

Figure 12 The local heat spots on the outer cladding for geometry version 3

FIGURE 13 shows the temperature contour pictures at different places. The wire wrap is wound counter-clockwise along the flow direction. For the first four places, the hot spot occurs at the lower right rod, behind the wire wrap. The blocking of the wire wrap caused the flow separation, led to the heat transfer deterioration. As the wire wrap is approaching the gap, a new heat spot

appears at the lower left rod. When the wire wrap is just right at the gap, it will insect with the two adjacent rods because the wire wrap has increased diameter. The wire wrap can transfer part of the heat through conduction, so the heat spot doesn't appear underneath of the wire wrap. As the wire wrap is wound further, a stiff gap still exists while the heat conduction effect disappears. Because of the large flow resistance in the gap, the flow may become laminar and lead to the heat spot shown in FIGURE 14. Just because the hot spots are easy to occur at the gap region where mesh generation is very hard, the mesh quality may have big influence on the maximum cladding temperature.

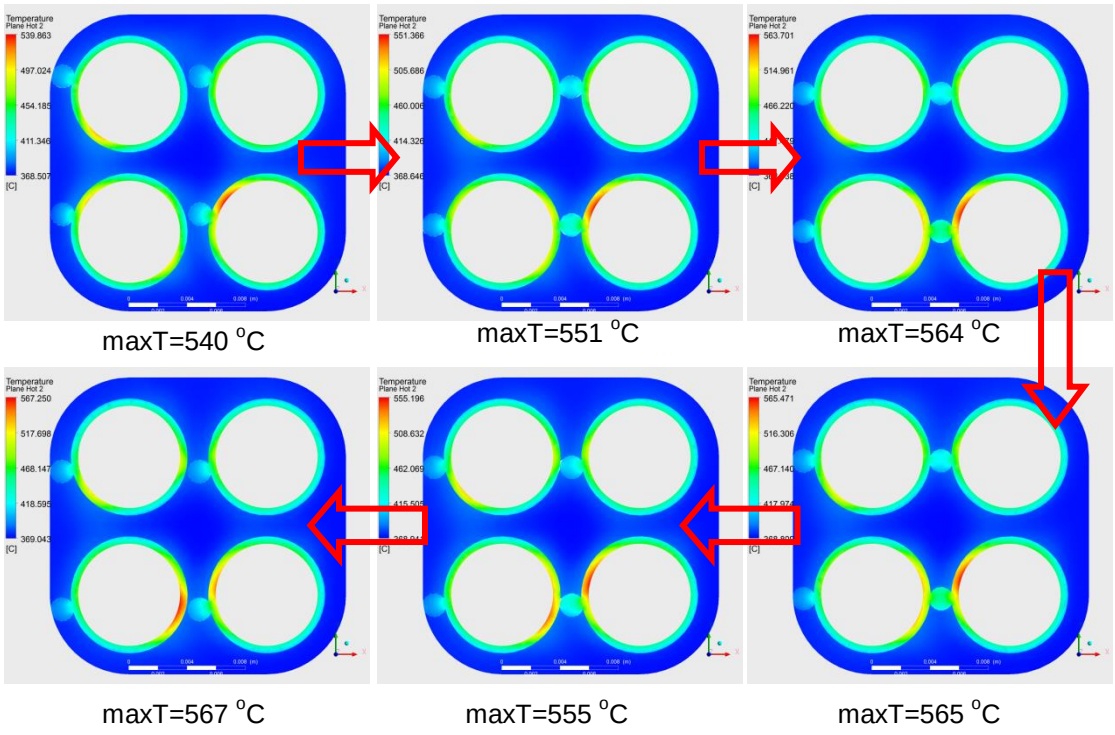

Figure 13 The development of hot spots along the flow direction for version 3

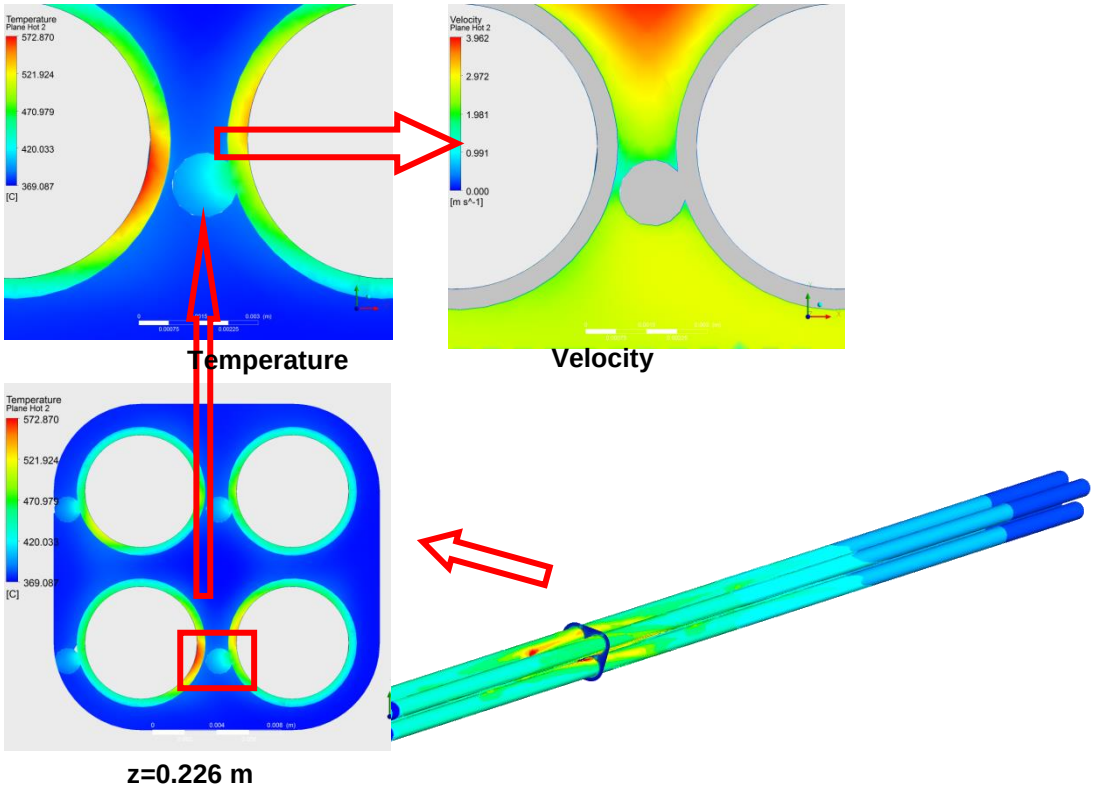

Figure 14 The local temperature and velocity files near the wire wrap

4. Conclusions

In this paper, the CFD simulations have been performed on a small scale fuel assembly to predict the cladding temperature. The main conclusions are listed below:

1) The investigated fuel assembly has very complex structures and some details may not be essential for CFD simulation. Some geometry simplification has been done, such as ignoring some details, adjusting the wire wrap. The mesh were generated separately for the fluid part and solid part and then connected into a union. Such method could reduce the mesh number without losing the mesh quality.
2) The CFD simulation results show that the flow structure is very complex in the fuel assembly because of the presence of the wire which has changed the flow paths a lot. The hot spots are easy to occur at the high heat flux region and near the wire wrap.
3) Three kinds of geometry files were analyzed to investigate the wire wrap contact relationship with fuel cladding on the maximum temperature. The average temperatures are very close for these three geometry versions and the maximum temperatures differ a lot. The version 3 geometry has the highest maximum temperature. The reason is believed to be the blocking effect of the wire wrap as it is located in the fuel rod gap.

REFERENCE

[1]. A.Vojacek, DELIVERABLE E1.1, WP1 Interim report after year 1, 2012.

[2]. ANSYS, ANSYS CFX User Guide.

The 7th International Symposium on Supercritical Water-Cooled Reactors
ISSCWR-7
15-18 March 2015, Helsinki, Finland

ISSCWR7-2046

Experimental Study on Heat Transfer of Supercritical Water in 2×2 Rod Bundle

Li Yongliang, Huang Zhigang, Zang Jinguang, Zhu haiyan, Zeng Xiaokang, Yan Xiao, Huang Yanping, Xiao Zejun
（Nuclear Power Institute of China, Chengdu, Sichuan, China）

ABSTRACT

Heat transfer experiments of supercritical water in 2×2 rod bundle were carried out, which were abstracted as an important flow channel to represent the thermal hydraulic characteristics of Chinese Supercritical Water Cooled Reactor (CSR1000) fuel assembly design. A peak of heat transfer coefficient in pseudo-critical area was found at the same mass flux and pressure condition, which would be decreased with increasing heat flux. The heat transfer coefficient at the same bulk fluid enthalpy would be increased with increasing mass flux when the heat flux and pressure of the fluid kept the same respectively. The heat transfer coefficient of 2×2 rod bundles increased slightly in the pseudo-critical area with increasing pressure from 23MPa to 25MPa when the heat flux and mass flux of the fluid remained unchanged respectively.

KEYWORDS: 2×2 rod bundles; supercritical water; heat transfer; experimental study.

1. Introduction

The Supercritical Water Cooled Reactor (SCWR) belongs to the six nuclear reactor types currently being investigated within the framework of the Generation IV International Forum, which are expected to exceed the current nuclear reactors in reliability, safety, electricity generation costs and proliferation resistance[1]. The most visible advantages of the SCWR are the low construction costs because of size reduction of components and buildings compared to current PWR and low electricity production costs due to high system thermal efficiency (approaching 44%)[2-3]. In China, SCWR is competitive and promising in Generation IV nuclear reactor system not only for the low construction costs and the low electricity production costs, but also for successive technology of Chinese PWR roadmap and technology base of current supercritical-water-cooled fossil-fired power plants.

Nuclear Power Institute of China (NPIC) started SCWR technology research supported by Chinese Government in 2009, which aimed at the design and construction of the Chinese Supercritical Water Cooled Reactor (CSR1000)[4-5]. One of the important SCWR technologies is thermal hydraulic performance of the reactor system, which influences the safety and economics of SCWR significantly [6]. However, the supercritical water environment is unique and the thermal

hydraulic performance of supercritical water flowing in fuel assembly at high heat flux is really complicated. Moreover, the practicability of out-of-pile thermal hydraulic experiment with water flowing in full-scale simulate rod bundle of the real fuel assembly is low and difficult because of expensive costs and several problems with experimental techniques. As a result, the thermal hydraulic performance of SCW is still not grasped deeply and data are missing on the thermal hydraulic performance of water in complicated geometries at near-critical and pseudo-critical conditions [7].

A 2×2 rod bundle is abstracted as an important flow channel to represent the thermal hydraulic characteristics of the CSR1000 fuel assembly, which is also the simplest bundle of the CSR1000 reactor core with square fuel assembly design. Compared with tests in round tubes or in annuli, the thermal hydraulic experiment with SCW flowing in 2×2 rod bundles does not only contain more sub-channels of the CSR1000 fuel assembly, but also provides the transfer and conversion behavior of mass, momentum and energy between different sub-channels. It is the technical basis for further experiments in more complicated rod bundles.

This paper is devoted to the experimental research on heat transfer of Supercritical Water in a 2×2 rod bundle with a heated length of 2.5m and a rod outer diameter of 9.5mm, which were performed in the Large scale Supercritical Water Thermal-hydraulic (LSWT) test loop. The experimental conditions covered pressures of 23, 24 and 25MPa, mass fluxes of 680 to 1200 kg/(m^2•s), and heat fluxes of 174 to 968 kW/m^2.

2. Test Loop and experimental conditions

2.1 Description of the LSWT test Loop

The LSWT test Loop was designed and constructed at NPIC for experimental research on SCW flow resistance, heat transfer, flow stability etc. with various complicated flow channels, especially rod bundles. The test loop does not only support the supercritical water thermal-hydraulic test and technology research, but also meets the R&D demand of the CSR1000 in next decade.

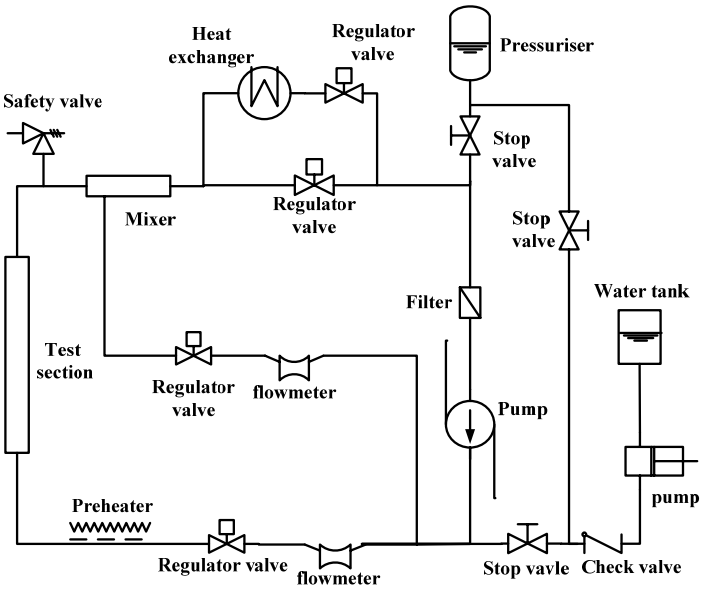

Fig.1 Schematic diagram of LSWT test loop

The schematic diagram of LSWT test Loop is shown in Fig.1. Distilled and deionized water was driven through a filter by a high pressure centrifugal pump which had a capacity of operating at up to 32MPa and mass flow rate supply up to 20t/h, then flowed into the test line and the bypass line. The mass flow rate of test section was controlled and measured by control valves and flow meters in the test line and bypass line. Before flowing into the test section, the water was preheated to the demanded temperature in the preheater, which was heated directly by a 800 kVA AC power supply. The heat flux of the test section was controlled by a 5.0 MW DC power supply. The water from the test section outlet with high temperature up to 550℃ was mixed with the water from the bypass line with much lower temperature in the mixer, and then the mixed water flowed back to the centrifugal pump. On the way back to the pump, part of the water was firstly cooled down by the heat exchanger with circulating cooling water and then mixed with the other part of the water, so that the temperature of the water flowing into the pump could be controlled by control valves in the lines. The test loop was controlled and measured by a control and data acquisition system, for which NI Company provided the hardware.

2.2 Test section

A detailed structure of the 2×2 rod bundles test section is shown in Fig.2a. Four heating rods were arranged in a square with a pitch of 10.5mm in a 21×21 mm square flow channel, as shown in Fig.2b. Each heating rod was made of Inconel 625, with outer diameter of 9.5mm and effective heating length of 250cm. Besides 2 N-type thermocouples to measure the temperature of the test section at inlet and outlet, there were another 4 N-type thermocouples to measure the wall temperature of different positions along each heating rod, as shown in Fig.2c. Also there were 2 pressure transmitters to measure the pressure of the test section at inlet and outlet. Tab.1 shows the uncertainties of main measured parameters in this experiment.

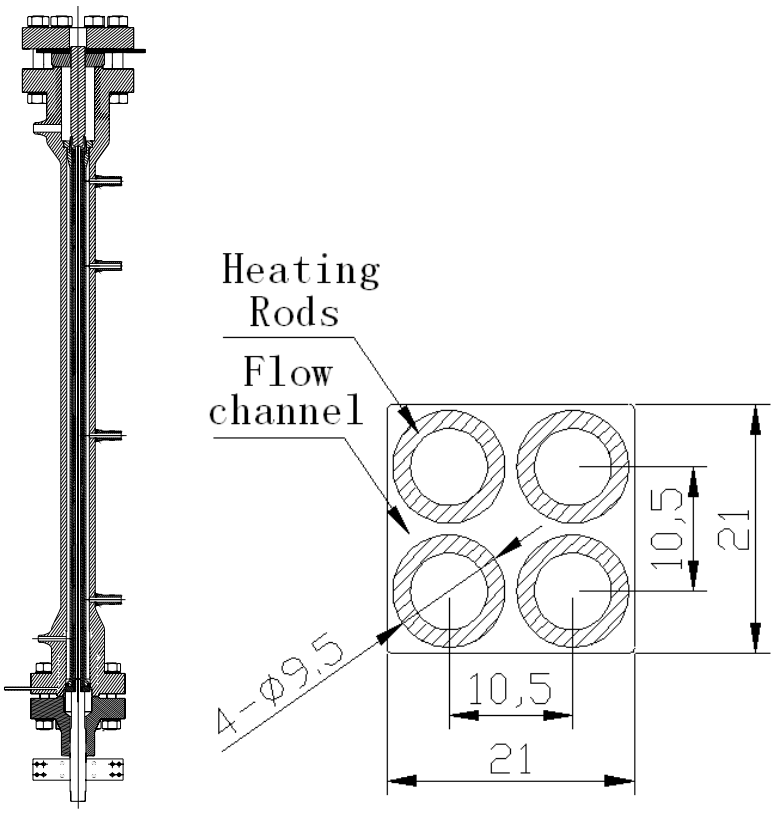

(a) Section view of the test section (b) Cross section of the flow channel

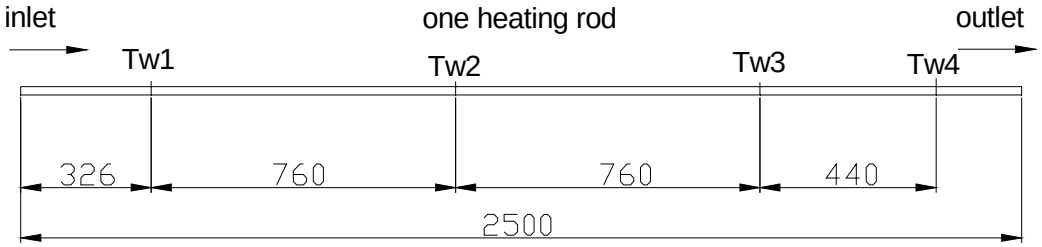

(c) distribution of wall temperature measuring points along each heating rod

Fig.2 Schematic diagram of test section

Tab.1 Uncertainties of measured parameters

Parameter	Maximum uncertainties
Temperature	±1.1℃
Mass flowrate	±0.97%
Pressure	±0.50%
Pressure difference	±0.75%
Heated power	±1.1%

2.3 Experimental condition

Experiments were completed by changing the pressure and heat flux at given mass flow rate. The selected pressures were 23, 24 and 25MPa, the mass flux changed from 680 kg/(m^2•s) to 1400 kg/(m^2•s), and the heat flux ranged from 174kW/m^2 to 968kW/m^2. The detailed parameters of the experiment conditions are shown in Tab.2.

Tab.2 Parameter range of the experimental conditions

Parameter	Range
Pressure(MPa)	23, 24, 25
Mass flux (kg/m^2•s)	680～1400
Heat flux(kW/m^2)	174～968

3. Results and discussion

3.1 Effect of heat flux

The heat transfer experimental data at 25MPa, 1040 kg/(m^2•s) and different heat flux are shown as Fig.3. It can be seen from the data in Fig.3(a) and 3(b) that there is a peak of heat transfer coefficient in the pseudo-critical area at different heat fluxes and the peak will decrease obviously when the heat flux increases. The pseudo-critical enthalpy is at 2151 kJ/kg. However, the heat

transfer coefficients far away from the pseudo-critical enthalpy at different heat fluxes are similar at equal specific enthalpies. The wall temperature varies gradually at near critical enthalpies at different heat fluxes as the specific enthalpy increases, but the wall temperature rises rapidly with increasing specific enthalpy, when the bulk temperature is beyond the pseudo-critical temperature, and the wall temperature increases at the same specific enthalpy when the heat flux increases.

Maybe different heat fluxes change the thermal physical parameters of the boundary layer, which influence the heat transfer characteristic of SCW directly. As shown in Fig.3(c) and 3(d), the ratio of constant-pressure specific heat capacity in average to that calculated by bulk temperature, and the ratio of density calculated by wall temperature to bulk temperature, will decrease at the same specific enthalpy when the heat flux increases, which is due to differences of thermal physical parameters between the boundary layer and bulk fluid becoming larger when the heat flux increases. As a result, the heat transfer performance decreases when the heat flux increases.

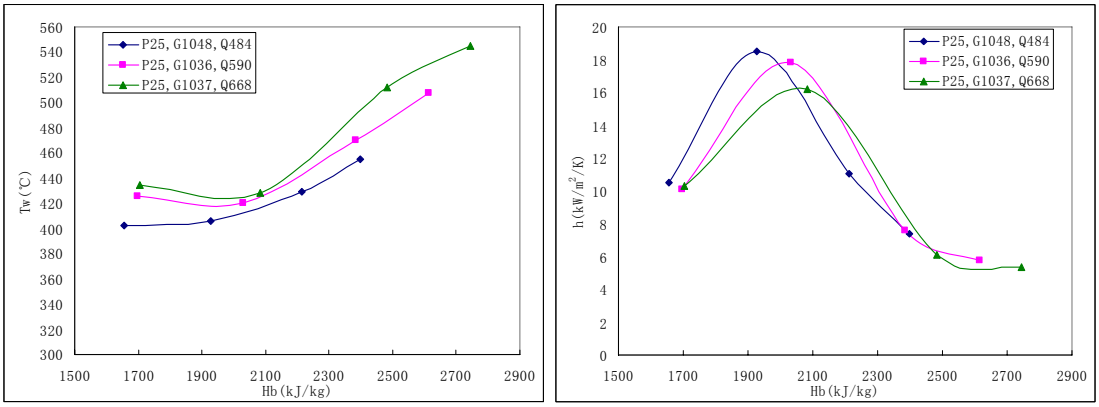

(a) wall temperature (b) heat transfer coefficient

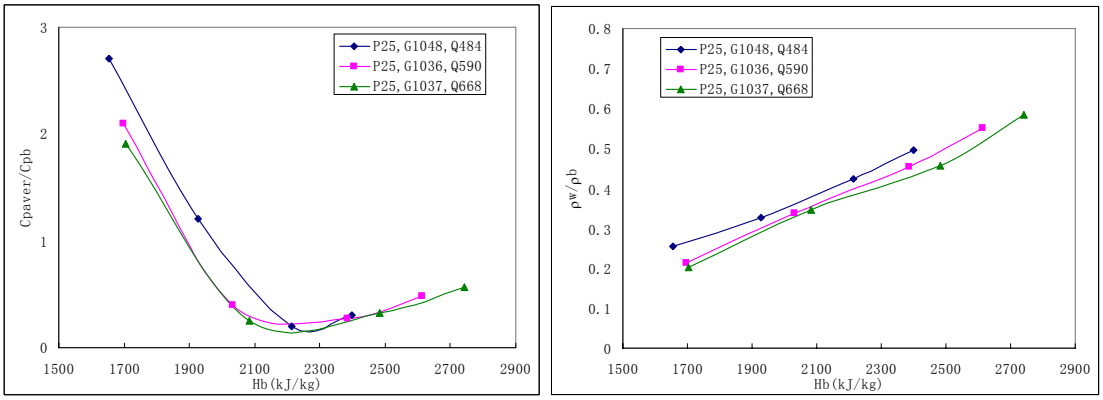

(c) (d)

(c) ratio of constant-pressure specific heat capacity in average to calculated by bulk temperature

(d) ratio of density calculated by wall temperature to bulk temperature

Fig.3 experimental data at 25MPa, 1040 kg/(m^2•s) and different heat fluxes

3.2 Effect of mass flux

The heat transfer experimental data at 530kW/m^2, 24MPa and different mass fluxes are shown as Fig.4. It can be seen from the data in Fig.4(a) and 3(b) that the peak of heat transfer coefficient will

increase obviously when the mass flux increases and the heat transfer coefficients at the same specific enthalpy will also increase as the mass flux increases. Meanwhile, the wall temperature will decrease at the same specific enthalpy when the mass flux increases.

Differences of thermal physical parameters between the boundary layer and bulk fluid become smaller as the mass flux increases as shown in Fig.4(c) and 4(d). Maybe increasing mass fluxes change the Reynolds number of the fluid which influences the turbulent fluctuation intensities of SCW directly. As a result, the heat transfer performance increases.

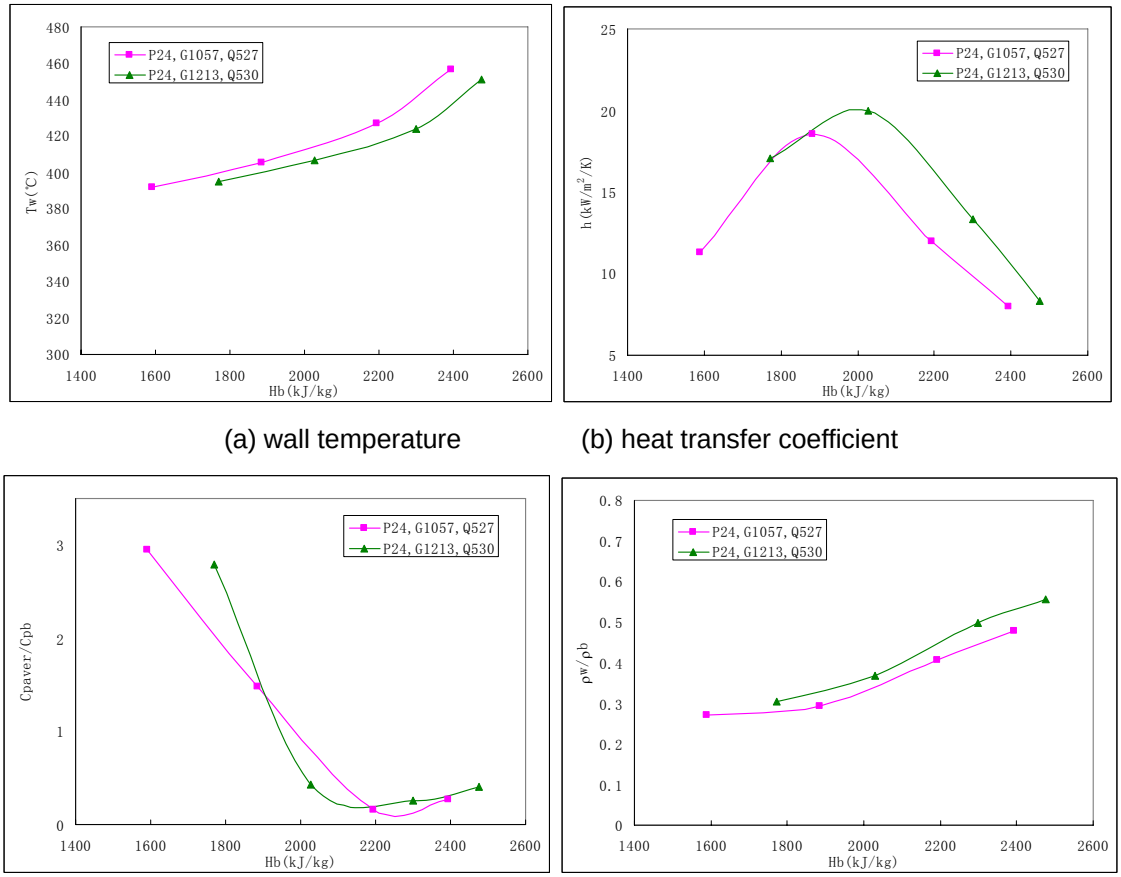

(a) wall temperature (b) heat transfer coefficient

(c) (d)

(c) ratio of constant-pressure specific heat capacity in average to calculated by bulk temperature

(d) ratio of density calculated by wall temperature to bulk temperature

Fig.4 experimental data at 530kW/m^2, 24MPa and different mass fluxes

3.3 Effect of pressure

The heat transfer experimental data at 400kW/m^2, 700 kg/(m^2•s) and different pressures are shown in Fig.5. It can be seen from the data in Fig.5(a), 5(b) and 5(c) that the heat transfer coefficient at the same specific enthalpy will slightly increase when the pressure increases. Meanwhile, the wall temperature and the average constant pressure specific heat capacity from near-wall fluid to bulk fluid will vary a little at the same specific enthalpy when the pressure increases.

The thermal physical parameters of SCW in the pseudo-critical area vary more significantly and rapidly when the pressure decreases as shown in Fig. 6, resulting in stronger non-uniform distribution of thermal physical parameters, mass flux, momentum and energy in different sub-channels of the 2×2 rod bundle and a decrease of the whole heat transfer performance of the 2×2 rod bundle channel in pseudo-critical area.

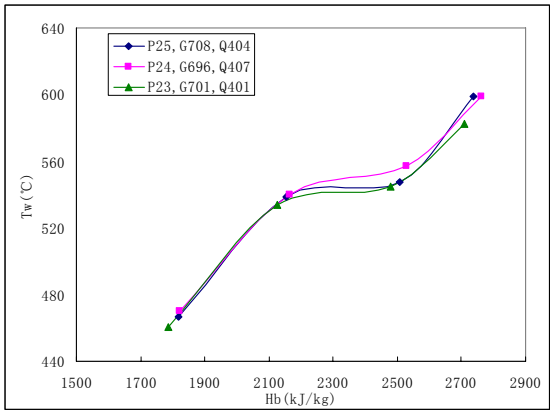

(a) wall temperature

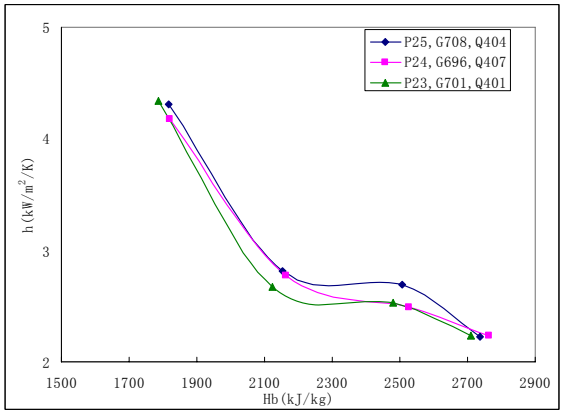

(b) heat transfer coefficient

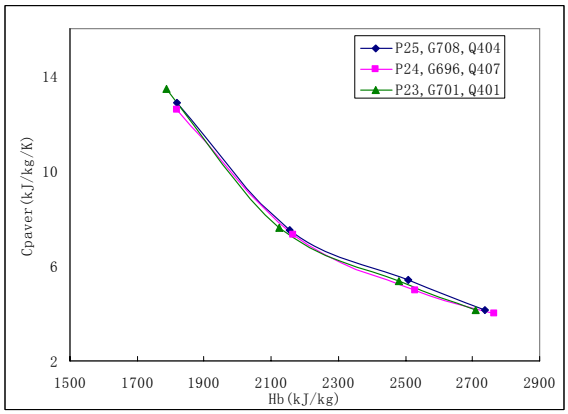

(c) average constant-pressure specific heat capacity

Fig.5 experimental data at 400kW/m^2, 700 kg/(m^2•s) and different pressures

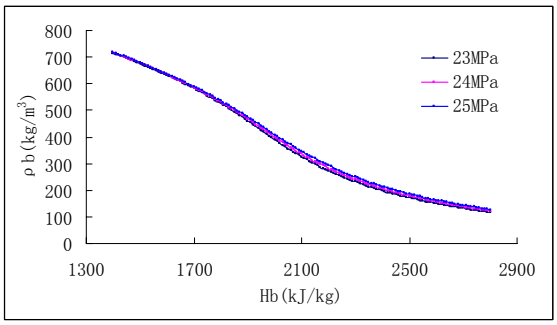

（a）density

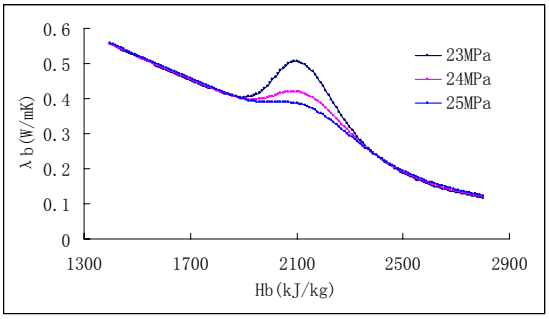

（b）thermal conductivity

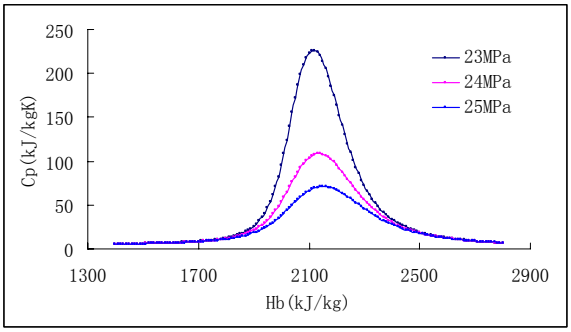

（c）constant-pressure specific heat capacity

Fig.6 thermal physical parameters of SCW at different pressures in pseudo-critical area

4. Conclusions

Heat transfer experiment of SCW upward flowing in 2×2 rod bundles was carried out in LSWT test Loop of NPIC. A peak of heat transfer coefficient in pseudo-critical area was found at the same mass flux and pressure condition, which would be decreased with increasing heat flux. The heat transfer coefficient at the same bulk fluid enthalpy would be increased with increasing mass flux when the heat flux and pressure of the fluid kept the same respectively. The heat transfer coefficient of 2×2 rod bundles increased slightly in the pseudo-critical area with increasing pressure from 23MPa to 25Mpa when the heat flux and mass flux of the fluid remained unchanged respectively.

Acknowledgement

The authors are grateful to National Natural Science Foundation of China (No.11325526) and International Science & Technology Cooperation of China (No.2012DFG61030) for providing financial support for this study.

References

[1] Subcommittee on Generation IV Technology Planning, A Technology Roadmap for Generation IV Nuclear Energy Systems. 2003.

[2] Tami Mukohara, Sei-Ichi Koshizuka, Yoshiaki Oka. Core design of a high-temperature fast reactor cooled by supercritical light water. Annals of Nuclear Energy 26 (1999) 1423-1436.

[3] Jacopo Buongiorno, Philip E. MacDonald. Progress Report for the FY-03 Generation-IV R&D Activities for the Development of the SCWR in the U.S. 2003.

[4] Xiaoyan Tian, Wenxi Tian, Dahuan Zhu, Suizheng Qiu , Guanghui Su, Bangyang Xia. Flow instability analysis of supercritical water-cooled reactor CSR1000 based on frequency domain. Annals of Nuclear Energy. Volume 49, November 2012, Pages 70–80.

[5] Pan Wu, Junli Gou, Jianqiang Shan, Bo Zhang, Xiang Li. Preliminary safety evaluation for CSR1000 with passive safety system. Annals of Nuclear Energy. Volume 6549,

March 2014, Pages 390–401.

[6] S.S. Penner, R. Seiser, K.R. Schultz. Steps toward passively safe, proliferation resistant nuclear power. Progress in Energy and Combustion Science, 34 (2008) 275–287.

[7] Y. Oka, S. Koshizuka, T. Jevremovic and Y. Okano. Supercritical-pressure, light-water-cooled reactors for improving economy, safety, plutonium utilization and environment. Progress in Nuclear Energy, Vol. 29 (Supplement), pp. 431-438, 1995.

ISSCWR7-2047

Numerical Study of Supercritical Heat Transfer in a Seven-rod Bundle

Dongil Chang and Stavros Tavoularis
University of Ottawa
Ottawa, Canada
Corresponding author: stavros.tavoularis@uottawa.ca

Abstract

This work reports the results of CFD simulations performed after those submitted in the framework of an international benchmark exercise to assess the accuracy of different CFD approaches in simulating supercritical water flow in a seven-rod bundle with spacer grids. For the reported simulations, we removed an existing discontinuity of the computational mesh, enlarged the computational domain from a 60° sector to a 120° sector and tested different turbulence models and turbulent Prandtl numbers. We found that the best agreement of predictions with the experimental results was when the v^2-f turbulence model was chosen and the turbulent Prandtl number was set to 0.85.

1. Introduction

The supercritical water-cooled reactor (SCWR) is one of six next-generation nuclear energy generation reactors developed by the multilateral international research program through the Generation IV International Forum (GIF). SCWR has many advantages compared to conventional pressurized water reactors (PWR), most importantly, an increased thermal efficiency and a simpler design achieved by eliminating the steam generators and other components [1]. An increased thermal efficiency introduces the possibility of using lower mass flow rates, which in turn allows the use of compact rod bundle designs. The simplified reactor design would also result in lower overall operational and capital costs [1]. Despite these advantages, several challenges need to be overcome to ensure safe operation of SCWR. One of these challenges, which is of interest in the present study, is the prediction of turbulent convective heat transfer at temperatures near the pseudo-critical value. Strong variations in the fluid properties are observed near this point and, under certain conditions, heat transfer deterioration may be induced either by flow acceleration or by buoyancy [1]. Although CFD simulations can provide detailed information about supercritical flows, they can only be used if their predictions are thoroughly validated, because no computational methods have consistently provided satisfactory predictions of supercritical heat transfer [1]. Numerous experimental studies of heat transfer in supercritical water flow have been performed, however, most of these studies used circular tubes and very few were conducted using rod bundle configurations relevant to nuclear applications [2]. This is significant because the geometrical configuration has a strong effect on supercritical heat transfer characteristics. For example, Silin et al. [3] noted that, under similar conditions, heat-transfer deterioration could occur in a tube but not in a rod bundle.

In an effort to assess the capabilities of presently available CFD approaches in the analysis of supercritical heat transfer, the thermal-hydraulic and safety project management board (PMB) of

GIF organized an international CFD benchmark exercise during the period between January 2013 and June 2014. Experimental data used for comparison with the submitted simulation results were provided by the Japan Atomic Energy Agency (JAEA), from experiments in a seven-rod bundle with spacer grids, conducted in the JAEA supercritical water facility. Provided measurements included pressure drop for an isothermal flow case and temperature variations for two cases with imposed heat fluxes. As part of this benchmark exercise, a series of CFD simulations were performed at the University of Ottawa Computational Fluid Mechanics Laboratory. The simulations included Reynolds-Averaged Navier-Stokes (RANS) simulations for all three cases and scale adaptive simulations (SAS) for the high heat flux case. Predictions of the rod wall temperature for the high heat flux case were within 7% of the measured values, with larger differences occurring near the exit of the rod bundle. To gain insight into these discrepancies, we performed additional simulations, henceforth referred to as the post-benchmark simulations, to investigate the effects of the turbulence model and the turbulent Prandtl number. The findings of our benchmark simulations, together with results by other participants, are reported in a separate article [4]. This article summarises the findings of our post-benchmark simulations.

2. Experimental conditions

The experiments were performed in a channel containing a seven-rod bundle with spacer grids (Figure 1) in the JAEA supercritical water test facility. The rod diameter was D = 8.0 mm and the gap width was δ = 1.0 mm, while the heated length was L = 1.5 m. The spacer grids, each with a length of 25 mm, were inserted in the rod bundle at the axial locations z = 0, 300, 700, 900 and 1300 mm. Thermocouples were embedded on the surface of each rod to measure the wall temperature at locations specified by the axial location z and the angle φ, defined separately for each rod as shown by example in Fig. 1(a). The experimental conditions for the three benchmark cases are summarized in Table 1; additional details about the experiments have been presented by Rohde et al. [4]. In this paper, we will focus on two of the benchmark cases: the isothermal flow case (A1) and the high heat flux case (B2), for which large discrepancies between the measurements and the benchmark simulations were observed.

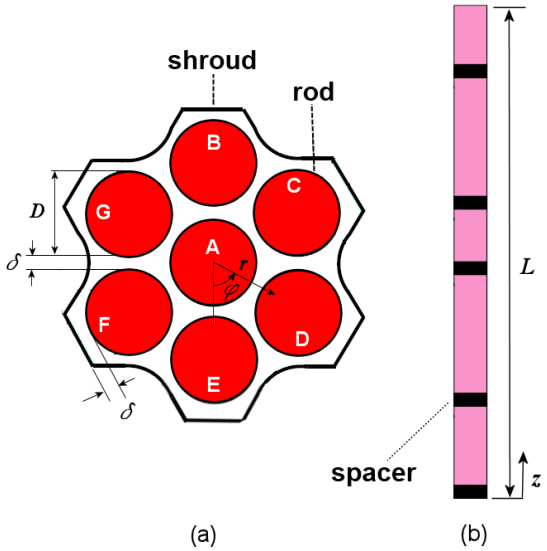

Figure 1. (a) Cross-section of the seven-rod bundle; (b) schematic side view of the rod bundle, also indicating the locations of spacer grids.

Table 1. Experimental conditions for the benchmark cases.

Case	Inlet temperature (K)	Inlet pressure (MPa)	Mass flow rate (kg/min)	Heat rate rod A (kW)	Heat rate rods B,D,F (kW)	Heat rate rods C,E,G (kW)
A1	297.35	25.00	26.33	-	-	-
B1	353.58	24.98	16.69	19.67	22.51	22.52
B2	519.58	25.03	16.52	34.14	34.08	34.13

3. CFD methodology

3.1 Governing equations

In view of the strong density variations in the present flows, we used the Favre averaged formulation of the Navier-Stokes equation. The governing equations are as follows.

Continuity equation:

$$\frac{\partial \overline{\rho}}{\partial t} + \frac{\partial (\overline{\rho} \widetilde{U}_i)}{\partial x_i} = 0 \tag{1}$$

where the density-weighted time-averaged velocity (the Favre averaged velocity) is $\widetilde{U}_i = \frac{\overline{\rho U_i}}{\overline{\rho}}$

Momentum equation:

$$\frac{\partial (\overline{\rho} \widetilde{U}_i)}{\partial t} + \frac{\partial (\overline{\rho} \widetilde{U}_j \widetilde{U}_i)}{\partial x_j} = -\frac{\partial \overline{P}}{\partial x_i} + \overline{\mu} \frac{\partial^2 \widetilde{U}_i}{\partial x_j \partial x_j} + \frac{\partial (-\overline{\rho} \overline{u_i u_j})}{\partial x_j} + \overline{\rho} g_i \tag{2}$$

where and the gravitational acceleration vector is g_i (it is noted that the axial component of the latter would be negative becasue the flow was upward). To provide closure, the turbulent shear stress was modelled as $-\overline{\rho} \overline{u_i u_j} = \mu_t \frac{\partial \widetilde{U}_i}{\partial x_j}$ and the turbulent viscosity was modelled as

$$\mu_t = \overline{\rho} C_\mu f_\mu \frac{\widetilde{k}^2}{\widetilde{\varepsilon}} \tag{3}$$

where C_μ is a constant and f_μ is a damping function that accounts for near-wall effects. The turbulent kinetic energy $\widetilde{k}$ and the turbulent dissipation $\widetilde{\varepsilon}$ in Eq. 3 were determined with the use of turbulence models.

Energy equation:

$$\frac{\partial (\overline{\rho} \widetilde{H})}{\partial t} + \frac{\partial \left(\overline{\rho} \widetilde{U}_j \widetilde{H}\right)}{\partial x_j} = \frac{\partial}{\partial x_j} \left(\frac{\overline{\mu}}{\overline{\mathrm{Pr}}} \frac{\partial \widetilde{T}}{\partial x_j} \right) + \frac{\partial (-\overline{\rho} \overline{C_p u_j h})}{\partial x_j} \tag{4}$$

The turbulent heat flux in the last term of the right side of Eq. 4 was defined using the gradient diffusion hypothesis (SGDH) as

$$-\overline{\rho} \overline{C_p} \overline{u_j h} = \frac{\partial}{\partial x_j} \left(\frac{\mu_t}{\mathrm{Pr}_t} \frac{\partial \widetilde{T}}{\partial x_j} \right) \tag{5}$$

The turbulent Prandtl number Pr_t was taken to be a constant.

Turbulence models:
Five turbulence models were tested in the present study, including three k-ε models and two k-ω models. The k-ε models include the AKN (Abe-Kondon-Nagano) linear eddy viscosity model [5] and two non-linear eddy viscosity models, v^2-f [6][7] and k-ε-v^2/k [8], while the k-ω models include the SST (shear stress transport) model [9] and SAS (scale-adaptive simulation) [10]. The unsteady terms in the governing equations and the turbulence model equations were only included in the SAS simulations.

3.2 Computational procedure

For the present simulations, we used a 120° sector of the rod bundle cross-section as the computational domain instead of the 60° sector that we used for the benchmark simulations (Figure 2). This change reduced the restrictions imposed on the flow in the gap region and also permitted us to apply different heat fluxes on the two outer rods. The computational domain comprised a 200 mm long unheated bare rod bundle and a 1500 mm long heated rod bundle with spacers. In order to reduce the computational resources needed for mesh generation, the domain for the benchmark simulations was divided into six bare-rod bundle subdomains and five spacer grid subdomains, while the domain for the post-benchmark simulations was split into one unheated bare-rod bundle subdomain and five subdomains, each containing a bare-rod bundle section and one spacer grid. The mesh used in the benchmark simulations consisted of hexahedral elements, except near the spacer grids, where tetrahedral elements were used. On the other hand, the mesh for the post-benchmark simulations was composed of polyhedral elements. The size of the mesh elements near the walls for the benchmark simulations was selected such that the dimensionless distance from the wall was $y^+ < 0.1$ in most of the computational domain, except near the spacers, where $y^+ \approx 5$. For the post-benchmark simulations, the dimensionless distance from the walls was in the range of $0.6 < y^+ < 1.0$ for most of the domain, except near the spacers where $y^+ \approx 10$. A mesh sensitivity study was conducted using three meshes for the benchmark simulations, having 17M, 36M and 62M elements; the differences in velocity magnitudes calculated using the 62M and 36M meshes were less than 5%, while the differences between the 17M and 36M meshes were about 14%. The 62M element mesh was chosen as the standard mesh for the benchmark simulations. A separate mesh dependence study was not performed for the post-benchmark simulations and a 57M element mesh was used for those simulations.

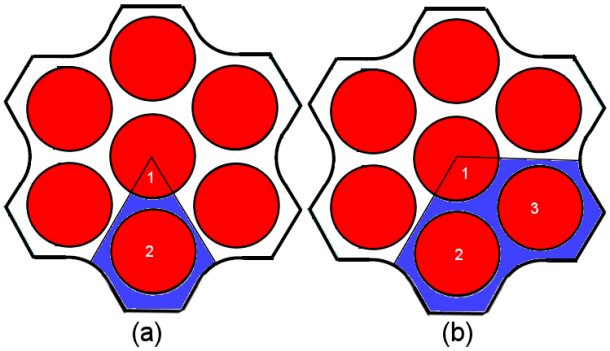

Figure 2. Computational domains (marked in blue colour) used for the benchmark simulations (a) and the post-benchmark simulations (b).

The thermodynamic properties of supercritical water, including the viscosity, density, thermal conductivity and specific heat at constant pressure, were obtained from the National Institute of Standard and Technology (NIST) Refrigerants and Refrigerant Mixture Database (REFPROP) Real Gas Model version 7 for the benchmark simulations. Although STAR-CCM+ has in-built supercritical water property models based on the International Association for the Properties of Water and Steam (IAPWS-IF97) database, numerous problems were encountered when using these models for the post-benchmark simulations. Therefore, it was decided to model the

specific heat and the density using piecewise polynomial equations, while the thermal conductivity and dynamic viscosity were tabulated and specific values were calculated using linear interpolation.

The mass flow rate, turbulence intensity, and hydraulic diameter were specified at the inlet plane, while static pressure was specified at the outlet plane. The turbulent Prandtl number was assumed to be equal to 0.9 for the benchmark simulations, while different values were used for the post-benchmark simulations to evaluate the effect of the turbulent Prandtl number. No-slip conditions were applied at all solid walls, whereas rotationally periodic boundary conditions were applied on the two plane boundaries of the domain. For the heat flux cases, heat flux values were imposed on the rod surfaces, whereas adiabatic conditions were applied to the outer shroud. For the benchmark simulations, the shell conduction approach was adopted for solid parts of the grids and spacers, whereas the solid parts of the grids and spacers of the post-benchmark simulations were fully meshed for conjugate heat transfer analysis.

The benchmark simulations include the unsteady RANS simulations with the SAS turbulence model for the high heated-rod case (B2) and RANS simulations with the SST turbulence model for all cases. The post-benchmark simulations employed RANS simulations with different turbulence models to examine the effect of turbulence model. For the unsteady simulations with SAS, the bounded central differencing scheme and the second-order implicit Euler scheme were used for spatial and temporal discretization, respectively. The second-order upwind scheme was used for spatial discretization in the RANS simulations for both benchmark and post-benchmark simulations. For the benchmark simulations, the Semi-Implicit Pressure Linked Equations – Consistent (SIMPLEC) algorithm was used for pressure-velocity coupling of the incompressible flow equations, while the SIMPLE algorithm was chosen for the post-benchmark simulations. The time step size for the unsteady benchmark simulations was set as 0.00025 s, which corresponded to values of the Courant number less than one. Two commercial CFD software packages were used in this study: ANSYS FLUENT 15 for the benchmark simulations and Star-CCM+ 9.04 for the post-benchmark simulations. The simulations were run on 64-bit Linux servers with six Quad CPU processors. A summary of the different simulations performed in the present study is presented in Table 2.

Table 2. Summary of the numerical simulations.

CFD case	Benchmark case	Turbulence model	Turbulent Prandtl number
Benchmark_1	A1	SST	0.90
Benchmark_2	B2	SST	0.90
Benchmark_3	B2	SAS	0.90
Post-benchmark_1	A1	SST	0.90
Post-benchmark_2	A1	v^2-f	0.90
Post-benchmark_3	B2	SST	0.90
Post-benchmark_4	B2	AKN k-ε	0.90
Post-benchmark_5	B2	v^2-f	0.90
Post-benchmark_6	B2	k-ε-v^2/k	0.90
Post-benchmark_7	B2	v^2-f	0.80
Post-benchmark_8	B2	v^2-f	0.85

4. Post evaluation of our benchmark simulations

In view of the tight deadline for the submission of benchmark results, we had insufficient time to evaluate their accuracy. We have subsequently examined carefully the pressure, mean velocity and turbulence distributions in these simulations and found them to be unrealistic. For example, the predicted pressure drop exceeded the measured value by about 140% and the turbulent kinetic energy level was larger than conventional values in tightly packed rod bundles by at least one order of magnitude. We attributed these discrepancies to discontinuities in the computational mesh at the interfaces between adjacent heated bare rod subdomains and spacer grid subdomains, which were used in order to keep the number of mesh elements as low as possible during pre-processing. These discontinuities introduced high values of artificial viscosity near the Interfaces and distorted grossly the simulation results. To avoid these problems, we eliminated these discontinuities in the post-benchmark simulations by combining all subdomains into a single computational domain.

5. Results

5.1 Pressure drop prediction

For the isothermal flow case (A1), JAEA provided the measured pressure drop between the axial locations z = 0.144 m and 1.340 m. The present predictions of pressure drop were in good agreement with the experimental value; the lowest difference from the experimental value was 6.5%; this was obtained with the v^2-f model.

Table 3. Comparison of predicted pressure drop values.

Case	Pressure drop (kPa)	Percent difference from measurement
Experiment (A1)	58.1	-
Post-benchmark_1	67.5	16.2
Post-benchmark_2	61.9	6.5

5.2 Effect of turbulence model

The effect of turbulence model on the solution accuracy was examined by conducting RANS simulations with four different turbulence models, namely, the SST, AKN k-ε, v^2-f, and k-ε-v^2/k models. The first two turbulence models are low Reynolds number eddy-viscosity models, while the latter two are low Reynolds number non-linear eddy-viscosity models, which account for the near-wall turbulence anisotropy as well as non-local pressure-strain effects. In the v^2-f turbulence model, the near-wall turbulence anisotropy is modelled through the elliptic relation function f. The velocity scale v^2 can be regarded as a wall normal velocity fluctuation to provide the scaling information for the turbulent damping near the walls. However, the v^2-f turbulence model suffers from numerical instability, especially for separated flows. In order to reduce the chance for instability, the k-ε-v^2/k model was proposed; this variant uses the normalized wall-normal velocity scale v^2/k instead of v^2. Figure 3 shows the axial variation of wall temperature in the gaps predicted using different turbulence models. It was found that the v^2-f model had the best agreement with the measurements, especially near the exit of the test section. Consequently, the v^2-f model was chosen for the study of the turbulent Prandtl number effect.

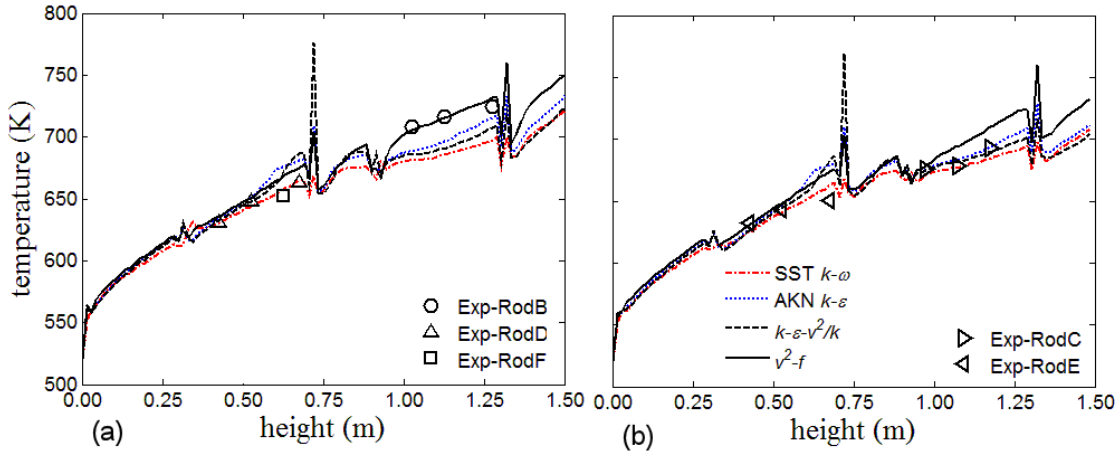

Figure 3. Axial variations of the wall temperature computed with the use of different turbulence models: (a) predictions for rod 3 and measurements for rods B, D, and F; (b) predictions for rod 2 and measurements for rods C and E.

5.3 Effect of turbulent Prandtl number

In this section, the effect of turbulent Prandtl number on the solution accuracy was studied, using the v^2-f turbulence model. Three values were considered, namely, 0.80, 0.85 and 0.90. Figure 4 shows the axial variations of the wall temperature in the gaps. It is evident that the predicted wall temperature increased with an increase in the turbulent Prandtl number. The best agreement was obtained when using a turbulent Prandtl number equal to 0.85.

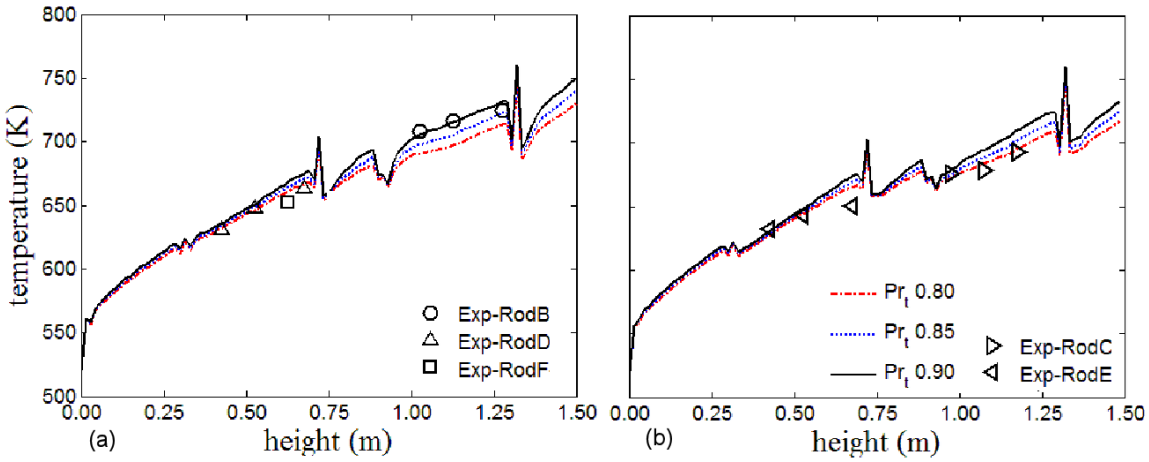

Figure 4. Axial wall temperature distributions in the gap between two outer rods, computed with different values of the turbulent Prandtl number: (a) predictions for rod 3 and measurements for rods B, D, and F; (b) predictions for rod 2 and measurements for rods C and E.

6. Conclusions

As part of this benchmark exercise, a series of CFD simulations was performed. Simulations include solutions of the RANS equations with SST model for all three cases and SAS for the high heat case. Predictions of the absolute wall temperature for the high heat flux case were within 7% of the measured values, with higher differences occurring near the exit of the rod bundle. To gain insight into these discrepancies, we performed additional simulations to investigate the effects of the turbulence model and the turbulent Prandtl number value. We

found that the best predictions were obtained when using the v^2-f turbulence model and a turbulent Prandtl number equal to 0.85.

Nomenclature

C_p	specific heat capacity
D	rod diameter
g_i	gravitational acceleration
H	enthalpy
h	enthalpy fluctuation
k	turbulent kinetic energy per unit mass
L	streamwise length of the rod bundle, the turbulent length scale
P	pressure
Pr	Prandtl number
$\mathrm{Pr_t}$	turbulent Prandtl number
r	radial coordinate
T	temperature
t	time
U_i	velocity
u_i	velocity fluctuation
v^2	turbulent normal velocity scale
x_i	coordinate axes
y	distance from the nearest walls
z	streamwise coordinate

Greek symbols

δ	gap size
ε	local turbulent kinetic energy dissipation rate
μ	dynamic viscosity
μ_t	turbulent viscosity
ρ	density
φ	azimuthal coordinate, the normalized turbulent normal scale
ω	specific turbulent kinetic energy dissipation rate

Superscripts

+	quantity non-dimensionalized by wall scales

Other notation

$(\overline{a})$	time average
$(\widetilde{a})$	Favre average

References

[1] Yoo, J.Y., 2013. The turbulent flows of supercritical fluids with heat transfer, Annual Review of Fluid Mechanics 45, 495–525.

[2] Pioro, L., and Duffey, R.B., 2005. Experimental heat transfer in supercritical water flowing inside channels (survey), Nuclear Engineering and Design 235, 2407–2430.

[3] Silin, V.A., Vozneskensky, V.A., and Afrov, A.M., 1993. The light water integral reactor with natural circulation of the coolant at supercritical pressure B-500 SKDI, Nuclear Engineering and Design 144, 327–336.

[4] Rohde, M., Peeters, J.W.R., Pucciarelli, A., Kiss, A., Rao, Y., Onder, E.N., Mühlbauer, P., Batta, A., Hartig, M., Chatoorgoon, V., Thiele, R., Chang, D., Tavoularis, S., Novog, D., McClure, D., Gradecka, M., and Takase, K., 2015. A blind, numerical benchmark study on supercritical water heat transfer experiments in a 7–rod bundle, 7th International Symposium on Supercritical Water-Cooled Reactors (ISSCWR-7), Helsinki, Finland, March 15 –18.

[5] Abe K., Kondoh T., Nagano Y., 1994. A new turbulence model for predicting fluid flow and heat transfer in separating and reattaching flows – 1. Flow field calculations, International Journal of Heat and Mass Transfer 37, 138–151.

[6] Durbin, P.A., 1996. On the k–3 stagnation point anomaly, International Journal of Heat and Fluid Flow 17, 89–90.

[7] Davidson, L., Nielsen, P.V., and Sveningsson, A., 2003. Modifications of the v^2 – f model for computing the flow in a 3D wall jet, Turbulence, Heat and Mass Transfer 4, 577–584.

[8] Billard, F., and Laurence, D., 2012. A Robust k–ε–v^2/k elliptic blending turbulence model applied to near-wall, separated and buoyant flows, International Journal of Heat and Fluid Flow 33, 45–58.

[9] Menter, F.R. 1994. Two-equation eddy-viscosity turbulence modeling for engineering applications, AIAA Journal 32, 1598–1605.

[10] Menter, F.R., Egorov, Y., 2010. The scale-adaptive simulation method for unsteady turbulent flow predictions Part 1: Theory and model description, Flow Turbulence Combustion 85, 113–138.

The 7th International Symposium on Supercritical Water-Cooled Reactors
ISSCWR-7
15-18 March 2015, Helsinki, Finland

ISSCWR7-2048

Numerical Simulation of Supercritical Water Flow and Heat Transfer in 4-rod Bundle

Siqi He
State Nuclear Power Software Development Center
Beijing, China
+86 010-56681572, hesiqi@snptc.com.cn

Siyu Zhang
School of Nuclear Science and Engineering,
Shanghai Jiao Tong University,
Shanghai, China
+86 021-34202944, sjtuzhsy@gmail.com

Xiaoliang Fu
State Nuclear Power Software Development Center
Beijing, China
+86 010-56681571, fuxiaoliang@snptc.com.cn

Yanhua Yang
State Nuclear Power Software Development Center
Beijing, China
+86 010-56681105,
yangyanhua@snptc.com.cn

Abstract

Investigation on the thermal-hydraulic behavior in the SCWR fuel bundles is a very significant content of SCWR research. However, there is still a lack of understanding to predict the heat transfer behavior of supercritical fluid. In this paper, the heat transfer behavior of supercritical fluid in a 4-rod bundle with spacers is simulated with the computational fluid dynamics (CFD) code. The effect of grid structure on the flow and heat transfer is discussed. The numerical simulation using the Reynolds stress model SSG gives a reasonable prediction compared with the experimental results. The calculation shows that the spacer significantly changes the velocity profile in the downstream of channel, and enhances turbulent mixing and heat transfer. Consequently, the rod wall temperature drops sharply downstream of the spacer grid and the wall temperature appears more uniform in the circumferential direction. At the same time the peak wall temperature spot is also shifted by the spacer.

Nomenclature

λ	thermal conductivity	π	PI
T	Fahrenheit degrees	$\overline{uu}$	normalized Reynolds stress
t	Celsius degrees	u_τ	shear velocity
θ	angle	τ_ω	wall shear stress
$\overline{\lvert \varepsilon \rvert}$	average amplitude of the velocity fluctuation	W	mean flow velocity across adjacent sub-channels
$\overline{\varepsilon}$	average Reynolds stress	w	axial mean flow velocity
f	friction factor	β	mixing coefficient
Re	Reynolds number	ρ	density

1. Introduction

Investigations on supercritical water-cooled reactor (SCWR) have attracted more attention since the capability of achieving much higher power conversion efficiency and compact system structure. However, because of the limited experimental technique and costs, data in bundle experiments was very little to understand thermal-hydraulic behavior of supercritical fluid. Recently, numerical analysis has been conducted to investigate thermal-hydraulic behavior in rod bundles. Cheng et al. studied heat transfer behavior in sub-channels using the computational fluid dynamics (CFD) code CFX [1]. The turbulent model SSG showed the best result. CFD analysis was also carried out by SCWR research group at the University of Tokyo to investigate thermal-hydraulic behavior of supercritical fluids in sub-channels [2]. However, mostly numerical research is for simple geometrical flow channel such as circular channel or for local sub-channel in bundles. And research which is for bundle channel investigates primarily the effects of pitch-to-diameter ratios, rod arrangements and thermal boundary conditions. The effect of spacer on the flow and heat transfer is neglected. In this paper, the heat transfer experiment of supercritical water in a 4-rod bundle with spacers was simulated with the computational fluid dynamics (CFD) code CFX.

2. Experimental data used

The heat transfer experiment of supercritical water in a 4-rod bundle has been conducted in Shanghai Jiao Tong University. Fig. 1a shows the cross-section of the test bundle. The heated length is 1300 mm. The width of the square channel is 23.2 mm and the outer diameter of rod is 8 mm. The pitch of the rods is 2.4 mm which is same with the rod-to-wall gap. There are 6 spacer grids for support. Then the distances between spacer grids and bundle inlet are 100 mm, 325 mm, 550 mm, 775 mm, 1000 mm and 1225 mm, respectively. Each rod is made by Inconel718 and the thickness was 1 mm. The rods are heated by a direct current power supply. Four sliding thermocouples are attached to the inner wall of rod, and they measure the temperature of the wall of heated rod. The location of thermocouples is showed in Fig. 1a.

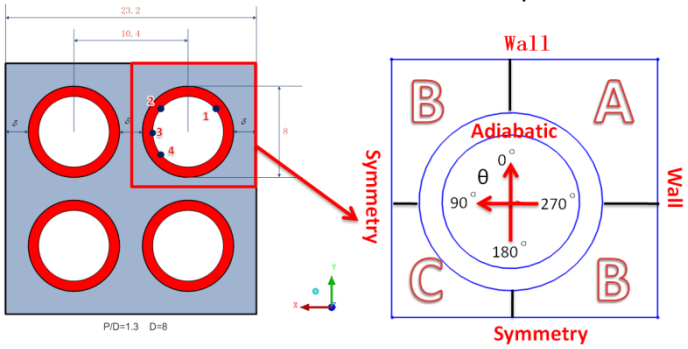

a—Cross-section of the 4-rod bundle; b—computational domain

Figure 1. Cross-section of 4-rod bundle and computational domain

3. Numerical model and grid generation

Considering of the symmetry of the 4-rod bundle, the computational domain is defined as 1/4 of the bundle. There are three kinds of sub-channels in the computational domain which are shown in Fig.1 b. Region A, B, C represent corner sub-channel, edge sub-channel and center sub-channel, respectively. Fig.1 b defines the angle θ of the heated rod for description. The thermal conductivity of the heated rod is calculated by Eq. (1).

$$\lambda(T) = 11.03703 + 0.01601t \tag{1}$$

The thermal physical properties of supercritical water are applied in CFX12. Boundary conditions are as stated below:

1) Mass flux, fluid temperature, turbulent kinetic energy (5% inlet kinetic energy) and turbulent dissipation are uniform at the inlet.
2) Constant pressure boundary condition is applied at the outlet.
3) Adiabatic boundary condition is applied on inner surfaces of the heated rods.
4) Symmetry boundary condition is applied on symmetry surfaces.The heated rods are uniform volume heat sources.

The structured body-fitted mesh is used to fit the complex geometries and the y+ values are below 10. Fig. 2 and Fig. 3 show the cross-section of computational mesh. For the axial direction of heated rod, there are 700 nodes and the total number of mesh nodes is 4.65 millions. The convergence criterion for normalized residual of each individual equation is set to be less than 10^{-7}. The sensitivity of calculation results is carefully checked and the grid independent solutions are obtained. The Reynolds stress model of Speziale (SSG) which is capable of simulating the anisotropic behavior of turbulence is selected in this study.

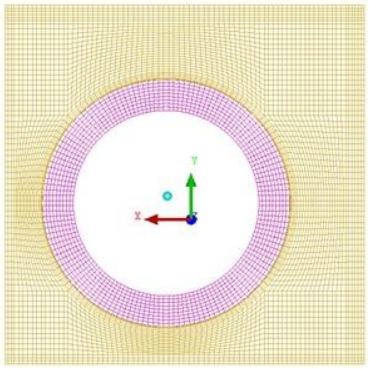

Fig. 2 Mesh structure for CFD analysis

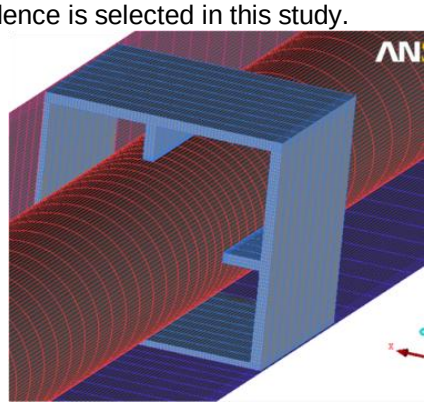

Fig. 3 Example of mesh structure for space grid

For discussing the effect of grid structure, four planes which are close to the third spacer grid are selected to be analyzed. Fig. 4 shows the locations of the selected planes. The first plane is located 10 mm upstream of the spacer grid. The second, third and fourth surfaces are located 10 mm, 90 mm and 150 mm downstream of the grid structure, respectively.

The specific experimental condition simulated in this study is summarized in Table 1.

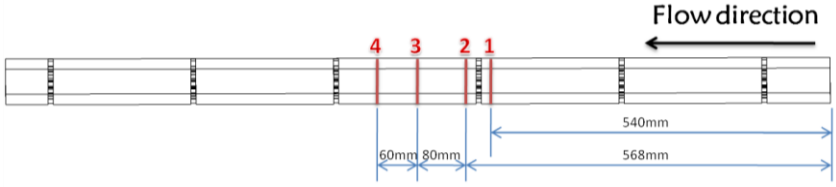

Fig. 4 Analysis section of the 4-rod bundle

Table 1. Simulation cases

Parameter	Value
Pressure/Pa	$23*10^6$
Inlet Temperature/℃	334.9
Outlet Temperature/℃	372.5
Mass Flux/(kg/m^2·s)	932.4
Volume Heat Flux/(kW/m^3)	901257.1
Surface Heat Flux/(kW/m^2)	788.6

4. Results and discussion

4.1 Effects on cladding temperature

Fig. 5 shows the comparison between the predictions and measurement of heated rod inner wall temperature on the axial line θ = 90° and θ = 315°. In the condition without spacer grids, the temperature increased smoothly along the flow direction. In the condition with spacer grids, the rod wall temperature droped sharply downstream of the spacer grids. The simulation predicted the wall temperature distribution well.

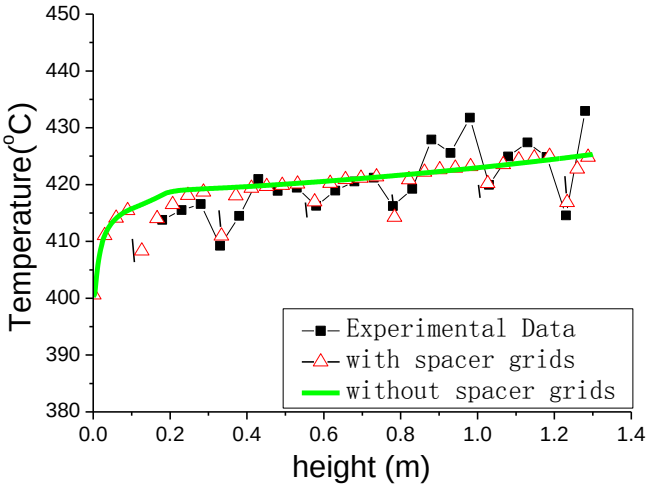

θ = 90°

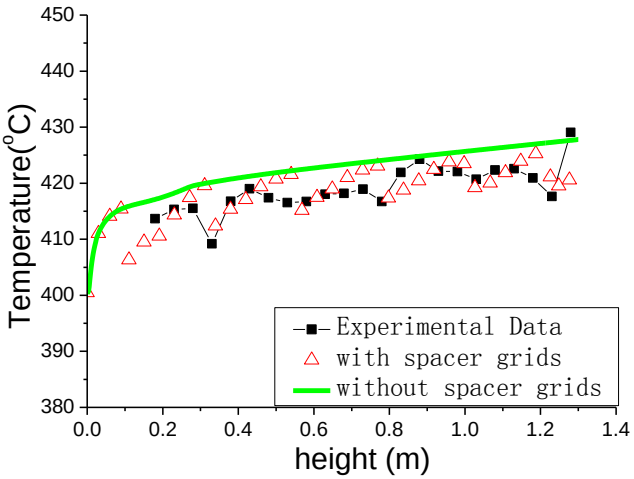

θ = 315°

Fig. 5 Temperature profile at cladding surface at gap region

Fig. 6 and Fig. 7 shows circumferential temperature distributions of the heated rod outer wall at section 2, section 3 and section 4. At each section, the temperature in the condition without spacer grids was higher than the temperature in the condition with spacer grids. At section 2, the temperature difference was 8 ℃ while the maximum temperature difference at section 4 was below 2 ℃. The phenomena show that the effect of spacer grids was negligible at section 4. Furthermore, the maximum temperature appeared near θ = 90° and θ = 180° in the condition with spacer grids. However, in the condition without spacer grids the maximum wall temperature appeared in the corner sub-channel (270°<θ<360°). When the downstream flow improved by the spacer grids, the temperature of outer heated rod decreased due to the enhanced heat

transfer. As this phenomena exhibited significantly in the corner sub-channel, the wall temperature appeared more uniform in the circumferential direction and the peak wall temperature spot was also shifted by the spacer.

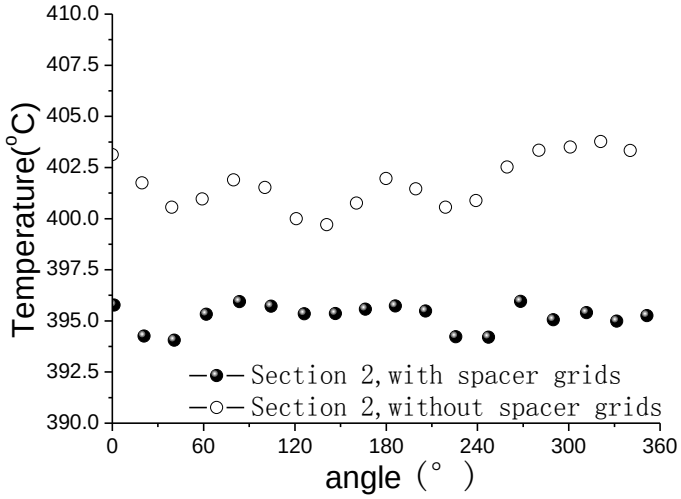

Fig. 6 Temperature profiles at Section 2

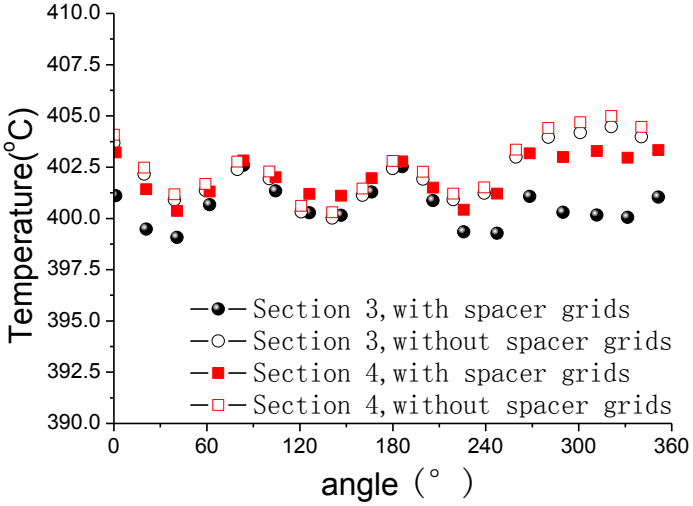

Fig. 7 Temperature profiles at Section 3 and Section 4

4.2 Effects on downstream flow

Fig. 8 gives average mass flux in sub-channels and it shows that the effect of spacer grids was negligible. The mass flux in edge sub-channel was nearly the same along the flow direction, while the mass flux in corner sub-channel decreased and the mass flux in center sub-channel increased gradually. Besides, the average mass flux difference in three sub-channels decreased due to the spacer grids. In the condition without spacer grids, the mass flux in center sub-channel at the outlet was about 930 kg/（m^2·s）, and in the corner sub-channel the mass flux at the outlet was only about 780 kg/（m^2·s）, therefore the mass flux difference was 270 kg/（m^2·s）. However, in the condition with spacer grids, the mass flux in center sub-channel was about 970 kg/（m^2·s）, while the value in corner sub-channel was about 870 kg/（m^2·s）, so the difference was only 100 kg/（m^2·s）. Fig. 9 and Fig. 10 shows velocity contours in two conditions at section 2. The velocity profile difference of three sub-channels was significant in

the condition without the spacer grids. But in the condition with spacer grids, the fluid at gap region and near spacer grids flowed to edge sub-channel, therefore the velocity profiled uniformly.

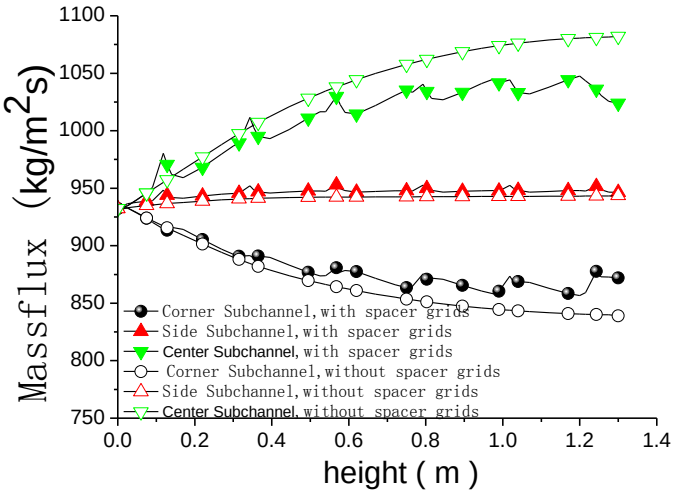

Fig. 8 Massflux profile in sub-channels

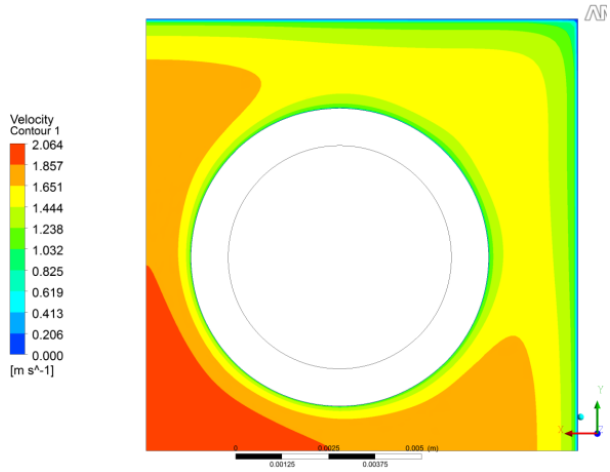

Fig. 9 Velocity profile at section 2 without spacer grids

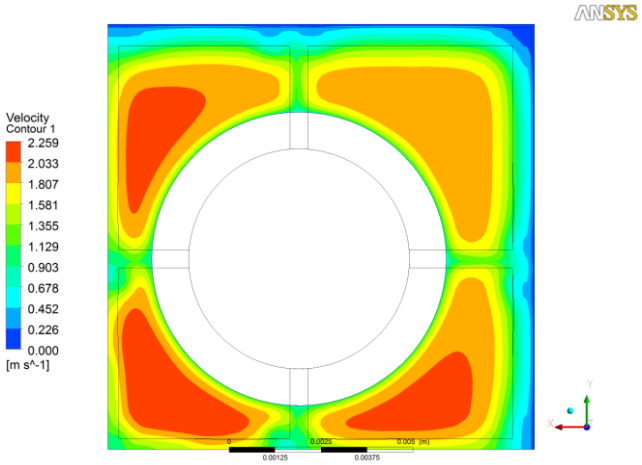

Fig. 10 Velocity profile at section 2 with spacer grids

Fig. 11 shows the average temperature of sub-channels along the flow direction. As it showed, the effect of spacer grids on average temperature of sub-channels was negligible. In the three sub-channels, the maximum temperature was in center sub-channel, while the minimum temperature was in corner sub-channel. Fig. 12 and Fig. 13 shows the fluid temperature contours in the section 2. The temperature at gap region decreased, therefore the local maximum temperature at gap region was reduced because of the spacer grids.

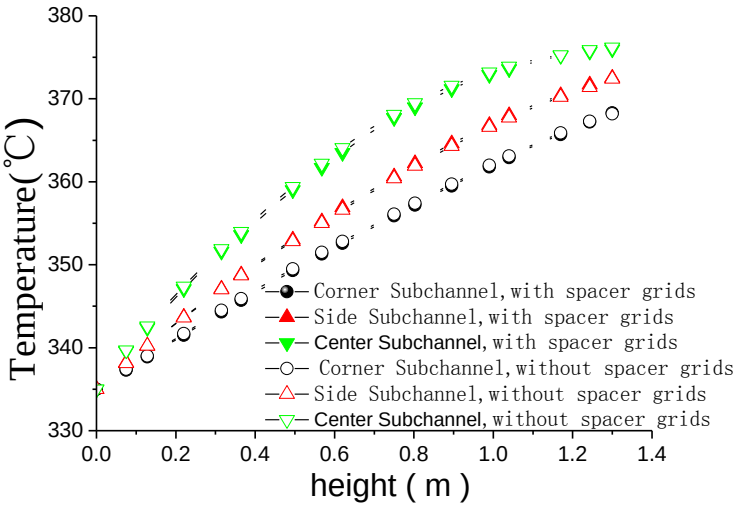

Fig. 11 Temperature profile at sub-channels

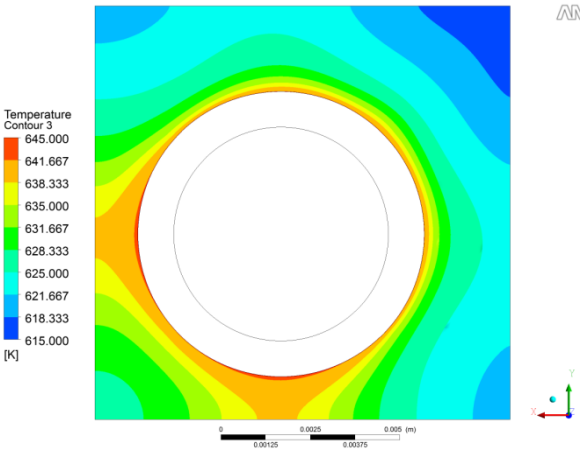

Fig. 12 Temperature profile at section 2 without spacer grids

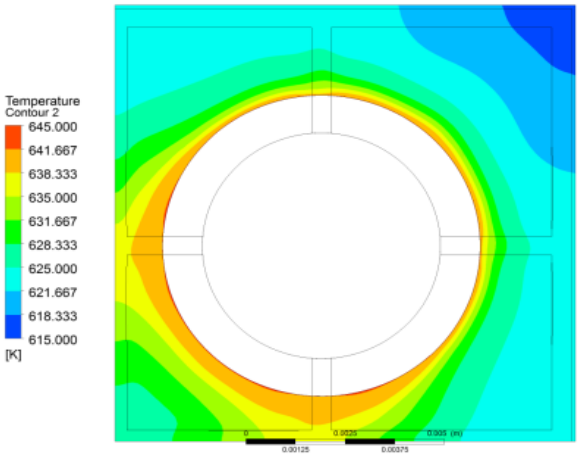

Fig. 13 Temperature profile at section 2 with spacer grids

4.3 Effects on turbulent mixing coefficient

To study the effect of spacer grids on turbulent mixing in flow channel, the normalized velocity fluctuation across gap and turbulent mixing coefficient were compared in conditions with or without spacer grids. Fig. 14 shows the position of gap and the length of gap was normalized. The location of "0" represents heated rod outer wall while the location of "1" represents the axis of symmetry of rod-to-rod gap.

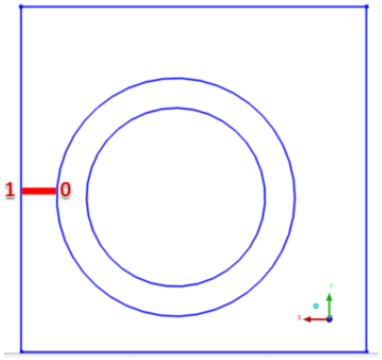

Fig. 14 Position of gap

Eq. (2) is used in the present study to derive the average amplitude of the velocity fluctuation across the gap from the Reynolds stress, which is obtained from the CFD analysis [3].

$$\overline{|\varepsilon|} = \frac{\sqrt{\overline{\varepsilon\varepsilon}}}{\sqrt{\pi}} \tag{2}$$

The Reynolds stress can be calculated by Eq. (3).

$$\overline{\varepsilon\varepsilon} = \overline{uu} \tag{3}$$

The average amplitude of the velocity fluctuation across the gap is normalized by the shear velocity.

$$u_t = \sqrt{\frac{\tau_w}{\rho}} = \sqrt{\frac{f}{8}}w \tag{4}$$

$$f = \frac{0.3164}{\mathrm{Re}^{0.25}} \tag{5}$$

Fig. 15 shows the average amplitude of the velocity fluctuation across the gap normalized by the shear velocity in the condition without spacer grids. The results show that in all four analysis sections, the difference in the normalized velocity fluctuation across the gap is negligibly small. The average amplitude of the velocity fluctuation across the gap has its maximum close to the wall. It decreases with the distance to the wall. The ratio of maximum value to minimum value is 1.6.

Fig. 16 shows the average amplitude of the velocity fluctuation across the gap normalized by the shear velocity in the condition with spacer grids. The average amplitude of the velocity fluctuation across the gap has its maximum close to the downstream of spacer grids. It decreases with the distance to the spacer grids. At section 2, the upstream of the spacer grid form strong turbulence mixing, therefore the tendency of velocity fluctuation across the gap is contrary to the tendency in the condition without spacer grids. The average amplitude of the velocity fluctuation across the gap has its minimum close to the wall. It increases with the distance to the wall. The ratio of maximum value to minimum value is about 1.5.

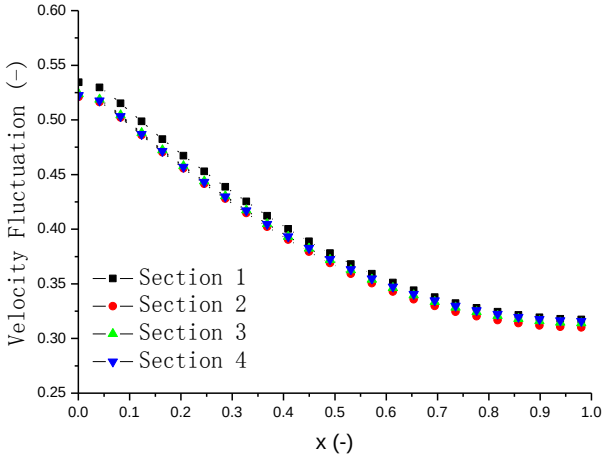

Fig. 15 Normalized velocity fluctuation across gap without spacer grids

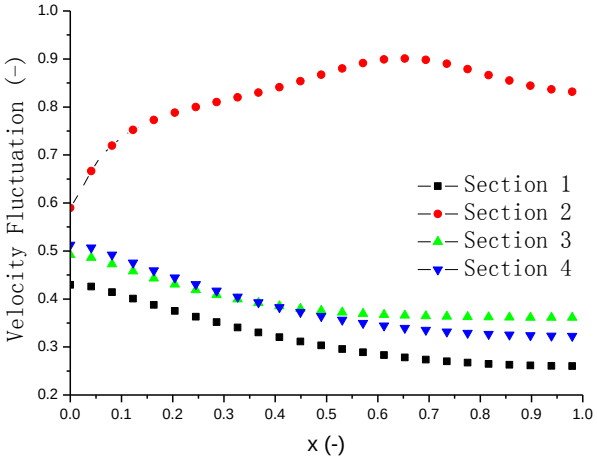

Fig. 16 Normalized velocity fluctuation across gap with spacer grids

According to the definition of the so-called turbulent mixing coefficient widely used in sub-channel analysis codes, the mixing coefficient [4] can be derived as

$$\beta = \frac{\overline{|\varepsilon|}}{W} \qquad (6)$$

Fig. 17 shows the turbulent mixing coefficient at four sections. In the condition without spacer grids, the difference in the four sections is negligibly small and the value is about 0.017. However, the turbulent mixing coefficient at section 1 in the condition with spacer grids is about 0.0167 smaller than the value in the condition without spacer grids. At section 2, the turbulent mixing coefficient increased significantly to the value about 0.036 and 112% higher than the

value in the condition without spacer grids. The turbulent mixing coefficient at section 3 and section 4 are similar with the value in the condition without spacer grids, therefore the effect on turbulent mixing can be neglected.

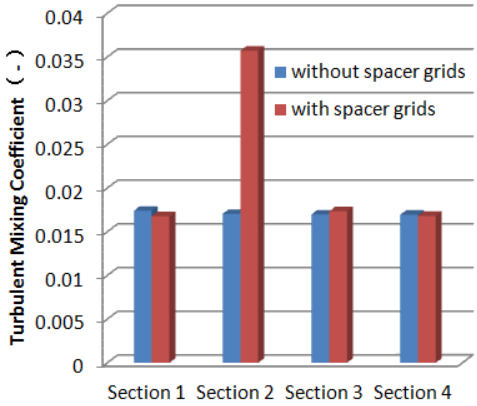

Fig. 17 Turbulent mixing coefficient profile

5. Conclusion

Heat transfer of supercritical water has been investigated in a 4-rod bundle using the computational fluid dynamics code CFX-12. The effect of the spacer grids was investigated. Some main conclusions achieved are summarized below.

1. Based on a comparison of the numerical results in SSG turbulent model with experimental data, the accuracy and applicability of the computational fluid dynamics (CFD) code are assessed.
2. The spacer significantly changes the velocity profile in the downstream of channel, and the massflux in different sub-channels appears more uniform.
3. The heated rod wall temperature appears more uniform in the circumferential direction. The peak wall temperature spot is also shifted from corner sub-channel to the gap region by the spacer.
4. The spacer enhances turbulent mixing and heat transfer in the downstream of spacer grids.

References

1. CHENG X, KUANG B, YANG Y H. Numerical analysis of heat transfer in supercritical water-cooled flow channels[J]. Nuclear Engineering and Design, 2007, 237(3): 240-252.
2. YANG J, OKA Y, ISHIWATARI Y, et al. Numerical investigation of heat transfer in upward flown of supercritical water in circular tubes and tight fuel rod bundles[J]. Nuclear Engineering and Design, 2007, 237(4): 420-430.
3. CHENG X, TAK N I. CFD analysis of thermal-hydraulic behavior of heavy liquid metals in sub-channels[J]. Nuclear Engineering and Design, 2006, 236(18): 1 874-1 885.
4. STEWART C W. COBRA-IV: The models and the methods, BNWL-2214[R]. Richland: Battelle Pacific Northwest Laboratories, 1977.Reference Text

ISSCWR-2052

Experimental studies on heat transfer to supercritical water in 2×2 rod bundle

H.Y. Gu[1], H.B.Li[2], Z.X.Hu[1], X. Cheng[1]

1. School of Nuclear Science and Engineering, Shanghai Jiao Tong University, Dongchuan Road 800, 200240 Shanghai, China. Email: guhanyang@sjtu.edu.cn
2. China Nuclear Power Technology Research Institute, Shenzhen, China. Email: lihongbo@cgnpc.com.cn

Abstract:
Experimental study on heat transfer to supercritical water flowing in a 2x2 rod bundle test section with two passes is carried out at Shanghai JiaoTong University. The bundle consists of four heated rods of 10 mm O.D. and its pitch-to-diameter ratio is 1.18. The 2X2 rod bundle is inserted into a square assembly box with rounded corners by which the test section is separated into two passes. Water flows downward in the first pass between the pressure tube and the assembly box and then turns upward in the second pass inside the assembly box to cool the 4 heated rods, which are directly heated by DC. The experimental conditions are as follows: pressure ranging from 23 to 26MPa, mass flux from 400 to 1200 kg/m^{2}s, heat flux among 300 and 1000kW/m^2, bulk fluid temperature from 200 to 480^{o}C. The heat transfer through the assembly box is strongly affected by the temperature difference between the two passes. The minimum fluid enthalpy increase in the first pass appears near in the pseudo-critical temperature region. Effects of various parameters on heat transfer behavior inside the 2x2 rod bundle are similar to those observed in tubes. Six developed correlations are compared with the test data. The correlation of Jackson and Bishop gives the best prediction of the test data among the selected correlations.

Keywords:
Heat transfer; Supercritical water; Rod bundle; Empirical correlation

Highlights:
Heat transfer to supercritical water in a 4 rod bundle with two passes are tested.
Effects of mass flux, heat flux and pressure on heat transfer in rod bundle are analyzed.
Heat transfer correlations are assessed against the experiment data.

Nomenclature

C_p	specific heat at constant pressure (J/(kg ^{o}C))
D	diameter (m)
e	error (-)
F	correction factor (-)

G	mass flux (kg/(m^2 s))
g	gravity acceleration (m/s^2)
H	specific enthalpy (J/kg)
I	current (A)
L	length (m)
N	total number of data points (-)
Nu	Nusselt number (-)
P	pressure (Pa)
Pr	Prandtl number (-)
Q	heat (W/m) (From Eq.8)
q	heat flux (W/m^2)
q_v	volumetric heat source (W/m^3)
R	radius(m)
Re	Reynolds number (-)
S	Perimeter(m)
T	temperature (^{o}C)
U	voltage (V)
W	Power (W)
x	axial locaiton along the heated length(m)
z	axial location (m)

Greek symbols

α	heat transfer coefficient (W /(m^2 ^{o}C))
β	volumetric expansion coefficient (/^{o}C)
δ	thickness(m)
λ	thermal conductivity (W/(m ^{o}C))
μ	dynamic viscosity (kg /(m s)), average deviation (-)
π_A	acceleration parameter proposed by Cheng (-)
π_B	buoyancy parameter proposed by Cheng (-)
π_C	specific heat ratio proposed by Cheng (-)
ρ	density (kg/m^3)
σ	standard deviation (-)

Subscripts and superscripts

b	bulk
bo	bottom
c	calculated value
j	index
e	experiment data
in	inlet
out	outlet
pc	pseudo-critical
v	volume
w	wall

Acronyms

HTC	heat transfer coefficient
SCWR	supercritical water-cooled reactor

1. Introduction

The supercritical water-cooled reactor (SCWR) is selected as one of six candidates of Generation IV nuclear reactors recommended for further development. The design of the SCWR is considered as a promising development of conventional light water reactor technology and

the supercritical fossil power plant experience, with the capability of achieving much higher power conversion efficiency and compact system structure (Oka et al.(2001)). However, in the vicinity of the pseudo-critical temperature, the thermal-physical properties such as density, specific heat, viscosity and thermal conductivity experience sharp variations which will lead to strong coupling between flow field and temperature field. Very strong non-uniform buoyancy force is created and it affects both the mean flow parameters and turbulence structure (Jackson and Hall (1979)). This phenomenon results in surprising heat transfer characteristics compared with fluids at sub-critical pressures.

Research on the heat transfer of fluids at supercritical pressures has attracted attentions worldwide. Detailed literature reviews on the heat transfer behavior of supercritical fluids were reported by Cheng et al. (2001) and Pioro et al. (2005). Most experimental work was performed for round tubes while experiments on simulated fuel bundles are very limited in open literature. Dyadyakin and Popov (1977) conducted experiments on heat transfer of supercritical water in a tight-lattice 7-rod bundle. They observed significant pressure oscillations at large mass fluxes and high heat fluxes. The heat transfer coefficient (HTC) was measured with a movable thermocouple installed inside the central rod .However, the data reduction, in terms of the HTC, was based on heat transfer through the rod wall without taking into account internal heat generation. Sillin et al. (1993) reported a large database for water flowing in large bundles at supercritical pressures. They reported that the experimental heat transfer data can be satisfactorily described by correlations obtained for water flow in tubes for the normal heat transfer regime at supercritical pressures. Zhao et al. (2013) carried out the experiment on the heat transfer of supercritical water in 2X2 rod bundle. A strong effect of grid spacer on heat transfer and non-uniform circumferential wall temperature distribution was observed. More recently, Wang et al. (2014) performed the heat transfer experiments with supercritical pressure water flowing upward in 2X2 rod bundle. The inner wall temperatures were measured by a movable thermocouple. A non-uniformity of circumferential wall temperature distribution was observed in the experiment. They assessed eight selected correlations against the experimental data, and found that the correlations of Jaskson (2002) and Ornatsky et al (1970) provide the best prediction accuracy. Mori et al.(2012) performed experiments on heat transfer of supercritical Freon R22 flowing vertically upward and downward in 3-rod and 7-rod bundles. They found that heat transfer was enhanced downstream of grid spacer in upward flow, but not in the downward flow. The degree of heat transfer deterioration in bundle was smaller than that in tubes. Richards et al.(2013) performed the experiment on heat transfer of Freon R12 flowing in a vertical 7-rod bundle at supercritical pressure. Three heat transfer regimes including normal heat transfer, deteriorated heat transfer and enhanced heat transfer were observed. The strong effect of spacer grid on the heat transfer was also observed.

Schulenberg et al.(2008) presented a novel core concept for a nuclear reactor cooled by

supercritical water. The core is also called three-pass core, in which the coolant is heated in four steps. A fuel qualification test based on the three-pass core concept is planned. A fuel bundle is going to be irradiated at supercritical pressure conditions inside the LVR-15 research reactor in Rez, Czech Republic. In support of the fuel qualification testing, the heat transfer of supercritical water in 2x2 rod bundle with two passes are carried out at Shanghai Jiao Tong University. In this paper, the heat transfer between the two passes and heat transfer in 2x2 rod bundle are presented. Seven correlations are assessed against the experimental data, and the best correlations to predict the heat transfer of supercritical water in bundle are recommended.

2. Experimental techniques

2.1 Experimental facility

The SWAMUP-II test facility at Shanghai Jiao Tong University, shown in Fig.1, is used to perform the heat transfer tests in supercritical water. It consists of a main loop, a cooling loop, a purification loop, and I&C system. The main loop has a plunger pump, a pre-heater, a re-heater, a mixing chamber, a heat exchanger and the test section. This loop is designed for pressure up to 35 MPa, temperature up to 550 °C, mass flow rate up to 2.8 kg/s. The distilled and de-ionized feed water in the water tank is driven by the plunger pump. Main flow goes through the re-heater to absorb the heat of the hot fluid coming from the test section. It passes the pre-heater where it is heated up to a pre-defined temperature and enters the test section. It exits the test section with high temperature up to 550°C. The pre-heater is directly heated by AC power supplies with maximum heating capabilities of 600 kW. The test section is heated by DC power with maximum heating capacities of 900kW. Another part is led through the bypass. Both parts merge in the mixing chamber. The water temperature is reduced, before it enters the heat exchangers. Water exiting the heat exchangers goes back to the water tank. Two venturi flow meters with different ranges are installed in parallel in the main flow path, to measure the mass flow rate of water entering the test sections. The pressure at the inlet of the test section is controlled by adjusting the pressure regulator valve at the exit of the main loop. The pressure at the inlet of test section is measured by a Yokogawa EJA-150A capacitance-type pressure transducer, the pressure drop over the test section is obtained a Yokogawa EJA-130A capacitance-type differential pressure transducer. Fluid temperatures at the inlet and the outlet of the test section are measured by two ungrounded N-type thermocouples with a sheath outer diameter of 0.5 mm. All data are collected and recorded using a National Instrument data acquisition system.

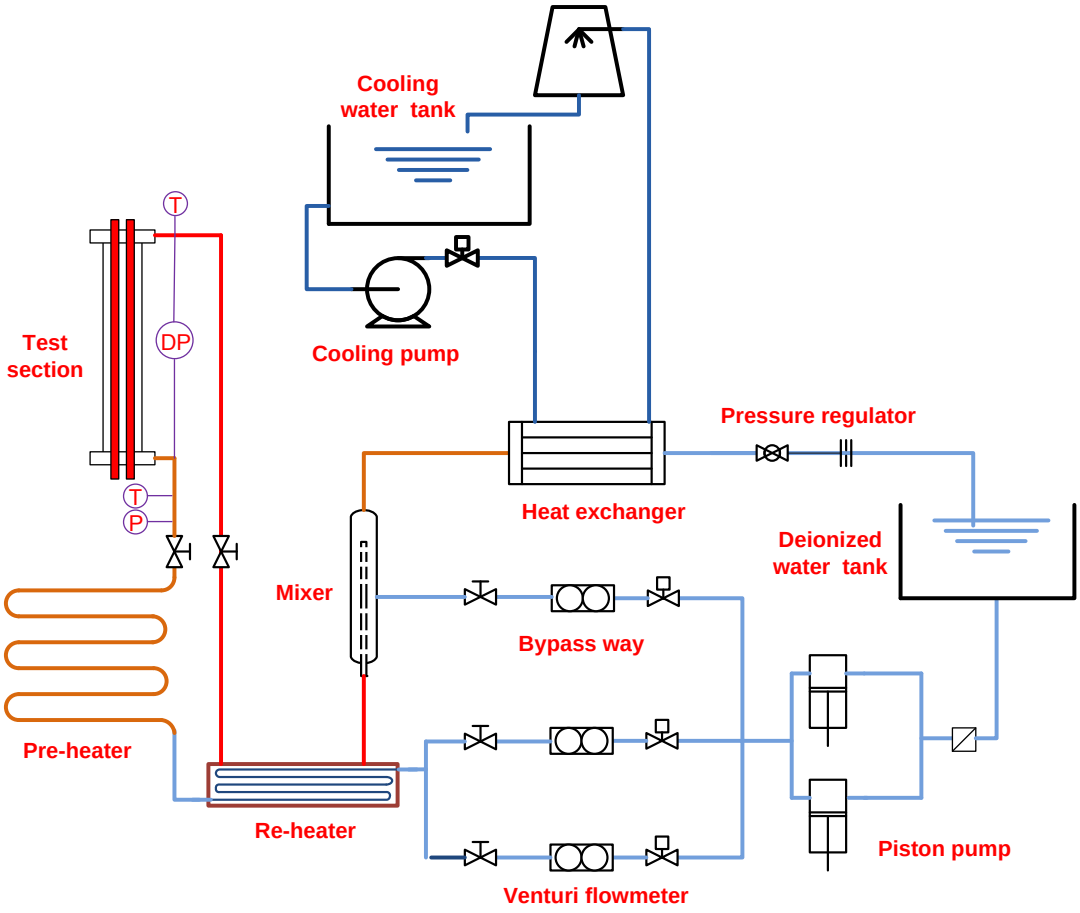

Fig. 1: Scheme of the SWAMUP-II test facility

2.2Test section

Figure 2 and Fig.3 show the configuration of the test section used in the experiment. A stainless tube with 38mm in inner diameter is served as the pressure vessel. There are two passes in the test section. They are separated by a square assembly box. with round corners. The first pass is between the pressure vessel and the assembly box. The second pass is inside the assembly box. The water entering the test section goes the first pass downward. It is mixed in the mixing chamber at the bottom of the test section. Then it turns to the pass of the second pass and goes upward. Inside the assembly box, four rods are installed and fixed by spacer grid. These rods are directly heated by DC electricity. Water in the first pass absorbs the heat transferred from the assembly box due to the fluid temperature difference between two passes.

The 2X2 rod bundle shown in Fig.2 is consisted of four stainless-steel (SS-304) tubes with inner diameter 6.0 mm and outer diameter 10.0 mm. Each end of the tube is connected to a copper electrode. The heater rods are uniformly heated by DC electricity directly. The length of the

heated section is 833mm. The pitch of the rod array is 11.8mm. To support the heater rods, two grid spacers are installed at the inlet and outlet of the box, respectively, as depicted in Fig.2. Each spacer grid is painted with a ceramic coating for electric isolation between the assembly box and heater rods. Detailed parameters of the rod bundle are listed in Table 1.

As shown in Fig.3, there are 16 thermocouples (0.5mm OD, sheath N-type) fixed in the inner wall of the rods at the horizontal plane which is 600mm from the bottom of the test section. Every rod has four thermocouples. For the four thermocouples in the same rod, they have a circumferential interval of 90^{o}. The distribution of the thermocouples differs from rod to rod. The details can be seen in Fig.3. The inlet and outlet fluid temperatures are measured by the sheath thermocouples at the inlet and outlet of the test section, respectively. Moreover, fluid temperature at the inlet of second pass is measured by sheath thermocouple in the mixing chamber at the bottom of test section.

Table 1 Test section parameters

Parameters	**Values**
Heater rod outer diameter(mm)	10.0
Wall thickness of rod(mm)	2.0
Rod pitch(mm)	11.8
Heating length of rod(mm)	833.0
Inner width of assembly box (mm)	25.4
Wall thickness of assembly box(mm)	2.0
Radius of round corner in assembly box(mm)	6.8
Length of assembly box(mm)	820.0
Inner diameter of pressure vessel(mm)	38.0
Hydrualic diameter of the first pass(mm)	6.06
Hydrualic diameter of the second pass (mm)	5.40
Material of rods	SS304
Material of assembly box	SS304

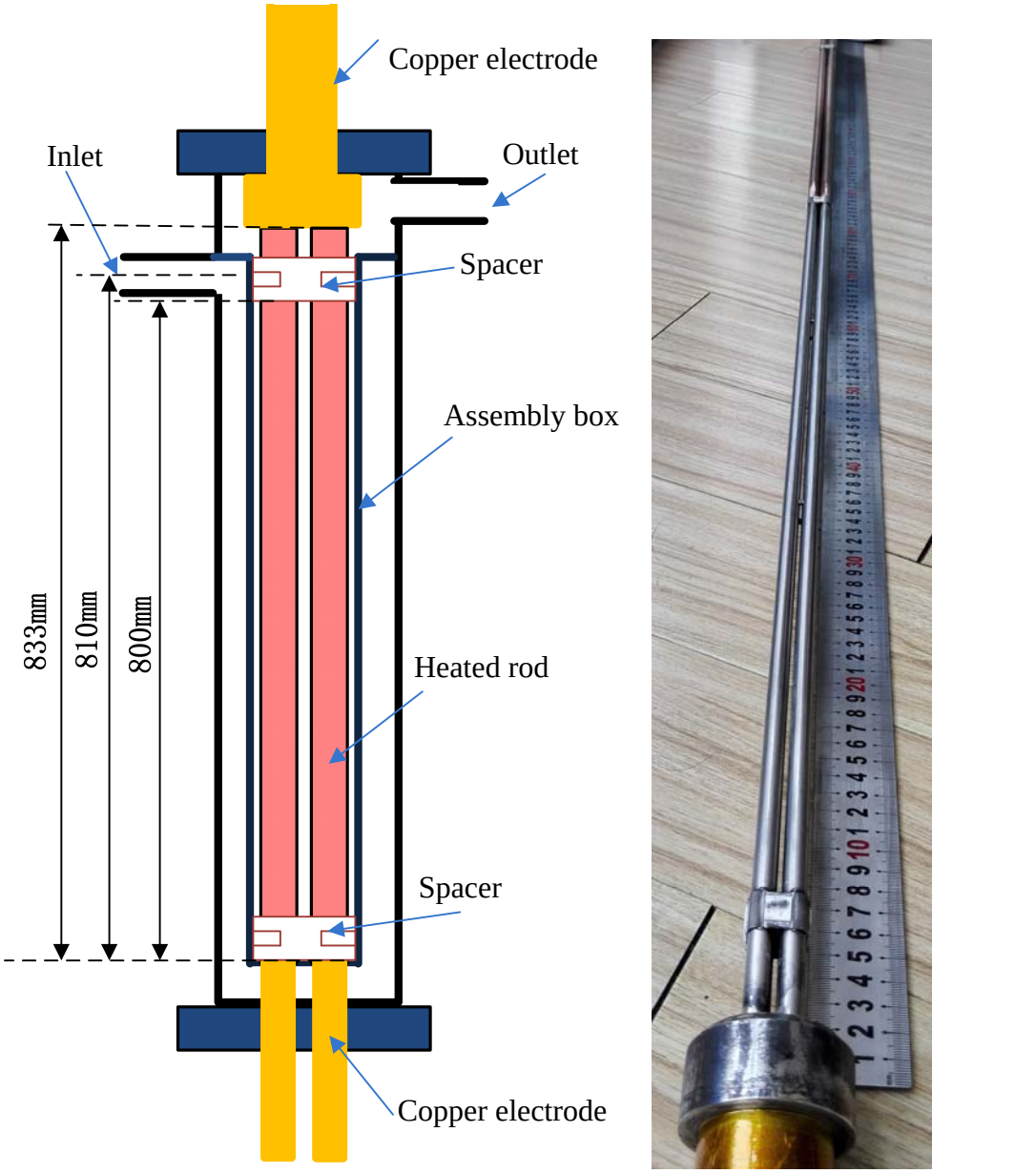

(a) Schematic of test section (b) photograph of the heated rods

Fig. 2 Configuration of test section

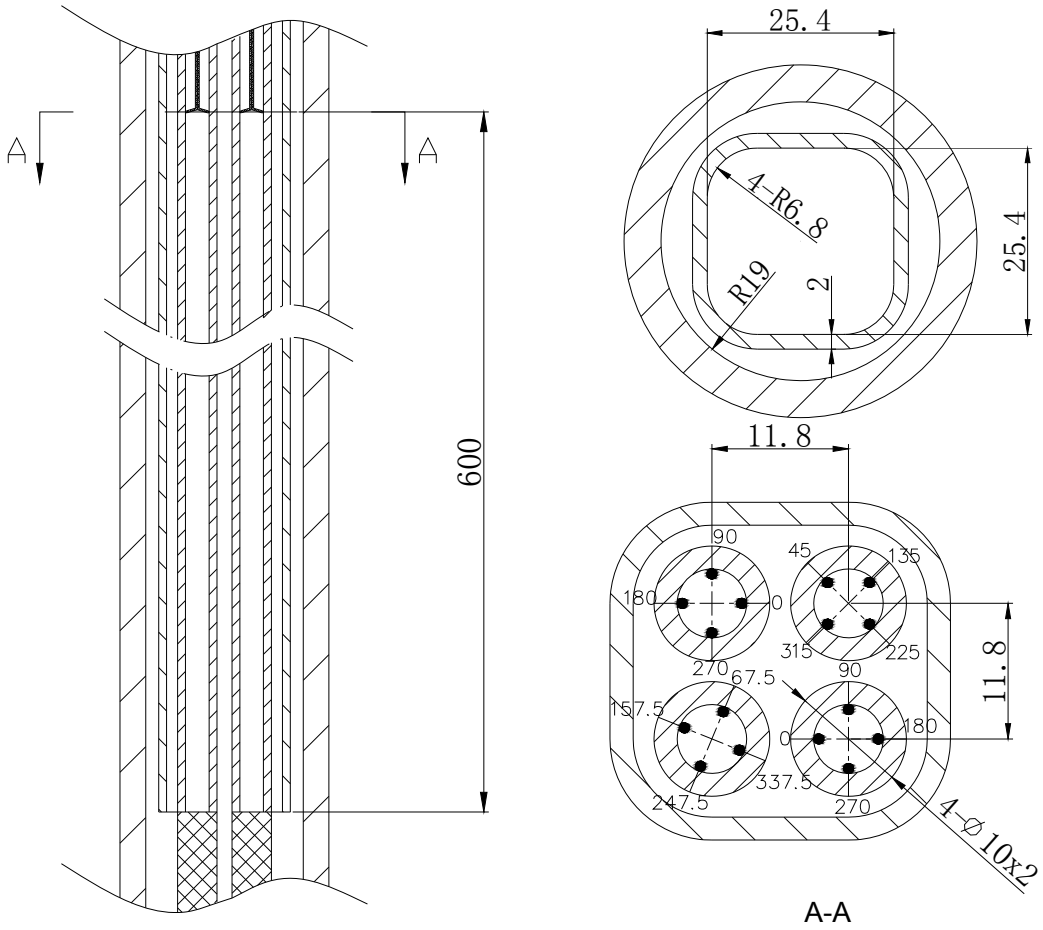

Fig. 3 Configuration of thermocouples positons and cross-sectional view of test section

2.3 Test parameters

Table 2 Ranges of test parameters

Parameters	Values	Units
Pressure	23, 25, 26	MPa
Mass flux	400~1200	kg/(m^2 s)
Heat flux	300~1000	kW/m^2
Inlet temperature	200~420	^{o}C
Outlet temperature	350~500	^{o}C

The range of each parameter of the test is summarized in Table 2. The experiments are conducted at three pressures, i.e., 23, 25 and 26 MPa. The mass flux varies from 400 to 1200 kg/m^2 s and heat flux is up to 1000 kW/m^2. The inlet temperature varies from 200 ^{o}C to 420 ^{o}C , and leads to the variation of the outlet temperature from 350 ^{o}C to 500 ^{o}C. The temperature range covers the pseudo-critical value, where unusual heat transfer behavior is expected.

2.4 Test procedure

The pressure in the test loop is set up by controlling the pressure regulator valve at the outlet of loop after the the piston pump is put into operation. The mass flow rate is adjusted by the control valves in the bypass loop. The power heating of rods is increased step by step to the expected value. Experiments are performed by holding the pressure, mass flow rate constant and power on heater rods constant for each run. While the fluid temperature at the inlet of the test section is increased gradually by controlling the heating power of the pre-heater. After the steady state condition is reached, data including pressure at inlet,mass flow rate, power to the heated rods, fluid temperature and inner wall temperaute are recorded at each step . The test is terminated when wall temperature at any location exceeds 580^{o}C or when the inlet temperature is higher than 420^{o}C.

2.5 Data reduction

The enthaply increase of water in the first pass due to the heat tranfer between the two passes is evaluated by

$$H_1 = H(T_{in}) - H(T_{bo}) \tag{1}$$

where H(T_{in}) and H(T_{bo}) are determined by fluid temperatures at the inlet and the mixing chamber of the test section. The efficiency of heat transfer throug the assembly box η is defined as the ratio of the increased fluid enthaply in the first pass to the power for the rods .

$$\eta = \frac{H_1 M}{W} \tag{2}$$

where the power W is product of electricity voltage and current of the fuel rods.

$$W = UI \tag{3}$$

Analyses on the heat transfer behavior in the heated rods is based on the cross-secitonal average parameter in the second passes.The local heat transfer coefficent is defined as the ratio of the heat flux to the temperature difference between the outside wall and the fluid.

$$\alpha(z) = \frac{q}{T_{w,o} - T_b} \tag{4}$$

The heat flux q can be determined by dividing the power by the heated area.

$$q = \frac{W}{4\pi D_o L} \tag{5}$$

The temperature of the tube outer wall is calculated from the heat flux and inner wall temperature, as shown by Eq.(6). The volumetric heat source of the tube wall is assumed to be uniform. The dependence of the wall thermal conductivity on temperature is taken into account. The inner wall temperature is obtained by solving the one-dimensional heat conduction equation (Eq.(7)).

$$T_{w,o}(z) = T_{w,i}(z) + \sum \left(T_{w,j}(z) - T_{w,j-1}(z) \right) \tag{6}$$

$$T_{w,j}(z)-T_{w,j-1}(z)=\frac{q_v}{4\lambda_{w,j}}\left[\left(\frac{D_{j-1}}{2}\right)^2-\left(\frac{D_j}{2}\right)^2\right]-\frac{q_v D_j^2}{8\lambda_{w,j}}\ln\frac{D_{j-1}}{D_j} \quad (7)$$

In the second pass, the average bulk fluid temperature T_b at the cross section whose elevation is the same as the inner wall tempertuare measured can not be meansured directly. It is evaluated from the heat exchange between two passes and heat balance. The heat transfer between two passes is calculated by Eq.(8).

$$Q(z)=\frac{\left(T_{b,2}(z)-T_{b,1}(z)\right)}{\frac{1}{\alpha_1 S_1}+\frac{1}{\alpha_2 S_2}+\frac{1}{\frac{2\pi\lambda}{\ln(R_1/R_2)}+\frac{\lambda}{\delta S_3}}} \quad (8)$$

where, α_1, α_2 are heat transfer coefficients of the outer wall and inner wall of the assembly box, respectively.S1, S2 are the perimeters of the outer and inner walls of the assembly box, respectively. S3 is the width of the inside wall in the assembly box for heat conduction . δ is the thickness of the assembly box. R1, R2 are the outer and inner radius of corner in the assembly box. λ is the heat conductivity of the box.

In recent decades, several heat transfer correlations for supercritical water are put forward by many researchers(Pioro et al.,2004). To predict the heat transfer coefficients α_1, α_2 in formula (8) and heat transfer coefficient on outside walls of the rods, seven empirical correlations are selected and compared.

- Jackson and Fewster (1975) correlation:

$$\mathrm{Nu}_b=0.0183\cdot\mathrm{Re}_b^{0.82}\,\mathrm{Pr}_b^{0.5}\left(\frac{\rho_w}{\rho_b}\right)^{0.3} \quad (9)$$

- Shitsman et al.(1975) correlation:

$$\mathrm{Nu}_b=0.023\cdot\mathrm{Re}_b^{0.8}\,\mathrm{Pr}_{\min}^{0.8} \quad (10)$$

where Pr_{min} is the minimum value of Pr_b or Pr_w

- Ornatsky et al.(1970) correlation:

$$\mathrm{Nu}_b=0.023\cdot\mathrm{Re}_b^{0.8}\,\mathrm{Pr}_{\min}^{0.8}\left(\frac{\rho_w}{\rho_b}\right)^{0.3} \quad (11)$$

- Swenson et al.(1965) correlation:

$$\mathrm{Nu}_w=0.00459\cdot\mathrm{Re}_w^{0.923}\,\overline{\mathrm{Pr}}_{\mathrm{w}}^{0.613}\left(\frac{\rho_w}{\rho_b}\right)^{0.231} \quad (12)$$

where $\overline{\mathrm{Pr}}_{\mathrm{w}}=\frac{\mu_w}{k_w}\frac{H_w-H_b}{T_w-T_b}$

- Bishop et al.(1964) correlation:

$$\mathrm{Nu}_x = 0.0069 \cdot \mathrm{Re}_x^{0.9}\, \overline{\mathrm{Pr}}_x^{0.66} \left(\frac{\rho_w}{\rho_b}\right)_x^{0.43} (1+2.4\frac{D}{x}) \tag{13}$$

where x is the axial locaiton along the heated length.

- Cheng et al.(2009) correlation:

$$\mathrm{Nu}_b = 0.023 \cdot \mathrm{Re}_b^{0.8}\, \mathrm{Pr}_b^{1/3} \cdot F \tag{14}$$

$$F = \min\left(F_1, F_2\right) \tag{15}$$

$$F_1 = 0.85 + 0.776 \cdot \left(\pi_A \cdot 10^3\right)^{2.4} \tag{16}$$

$$F_2 = \frac{0.48}{\left(\pi_{A,pc} \cdot 10^3\right)^{1.55}} + 1.21 \cdot \left|\left(1 - \frac{\pi_A}{\pi_{A,pc}}\right)\right| \tag{17}$$

where π_A is acceleration parameter.

The result calculated by the conventional Dittus-Boelter (1930) correlation is also plotted for reference.

$$\mathrm{Nu}_b = 0.023\, \mathrm{Re}_b^{0.8}\, \mathrm{Pr}_b^{0.4} \tag{18}$$

The cross-section average bulk fluid enthalpy in the first pass, $H_1(z)$, is evaluated from the heat balance:

$$H_1(z) = H_{in} + \int_{z_{in}}^{z} \frac{Q(z)}{M} dz \tag{19}$$

where H_{in} is the inlet fluid enthalpy and z is the axial distance at the locaiton of interest from the top of the first pass. The cross-section average bulk fluid enthalpy in the second pass, $H_2(z)$, is evaluated from the heat balance:

$$H_2(z) = H_{bo} - \int_{z_{bo}}^{z} \left(\frac{4\pi D_o q - Q(z)}{M}\right) dz \tag{20}$$

where H_{bo} is the fluid enthalpy at the mixing chamber and z is the axial distance at the locaiton of interest from the start of the second pass. The cross seciton average bulk fluid temperature in the second pass t_b is evaluated from the calculated fluid enthalpy $H(z)$ and the measured pressure. The physical properties of water are calculated by NIST vesion8.0 (Lemmon et al., 2007).

The pressures are measured by pressure transmitters with accuracy of $\pm$0.2 %. The flow rate is measured by venturi flow meter with accuracy of $\pm$0.5%. The inlet and outlet fluid temperatures are measured by sheath thermocouples at the inlet, outlet, and the mixing chambers with accuracy of $\pm$0.2 °C. and the inner-wall temperatures of the heated tube are measured by 16 sheath thermocouples with accuracy of $\pm$0.2 °C . The DC power applied to the test section is measured by a voltmeter shunt with accuracy of $\pm$0.1 % and a current shunt with accuracy of

±0.2 %. The accuracy of various parameters is summarized in Table 3.Uncertainty of Nusselt numbert is analyzed based on the method reported in reference(Zhang et al., 2013). 87.7 % of the Nu deducted by experimental data fall into the error range smaller than 5 %, and 95.1 % fall into the error range smaller than 10 %.

Table 3 Uncertainties of primary parameters

Parameters	**Maximum uncertainties**
Pressure	±0.2 %
Mass flow rate	±0.5 %
Inlet temperature	±0.2 °C
Wall temperature	±0.2 °C
Voltage	±0.1 %
Current	±0.2 %
Tube diameter	±0.03 mm
Tube thickness	±0.02 mm

3. Results and discussion

3.1 Heat transfer between flow passes

Fig. 4 shows cross-section average bulk fluid temperature profiles in the two passes with different fluid inlet temperature. The working pressure is 25MPa. The mass flux is 800kg/m^{2}s and heat flux is 600kW/m^2. Jackson and Fewster (1975) correlation is adopted to calculate the hear transfer coefficients on the inside and outside walls of the assembly box. The water temperature in the first pass increases gradually by absorbing heat from the assembly box when water flows downward. The water flow turns to upward in the second pass after it arrives at the bottom of the test section. Then the water temperature continually increases due to the heat transfer from the four heated rods until the water flows to the outlet.The fluid temperature difference between the two passes is small when the water temperature at the inlet is in the vicinity of the pseudo-critical point where the sepcific heat is large. The predicted fluid temperature at the bottom of the test section agrees well with experimental result as shown in Fig.4. For example, the predicted and measured fluid temperatures at the end of first pass are 304.9°C and 304.7 °C respectively when the inelt fluid temperature is 300°C.

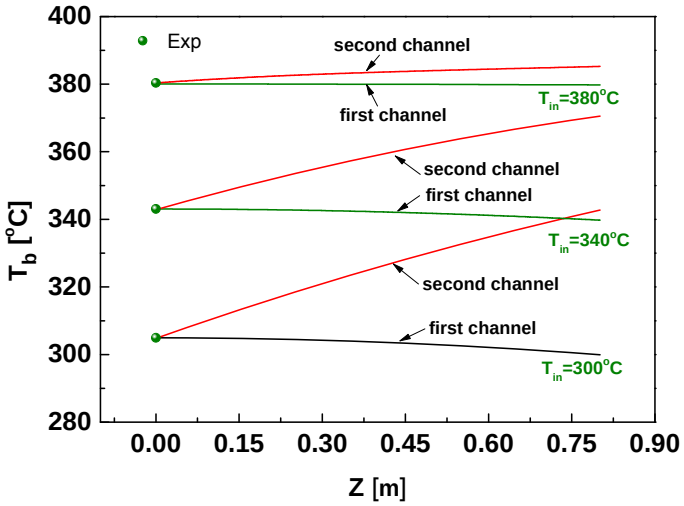

Fig. 4 Bulk fluid temperature distributon along the axial length in the two passes (P=25MPa, G=800kg/m^{2}s, q=600kw/m^2)

Figure 5 shows the fluid temperature at the end the first pass, T_{bo}, with the increase of inlet fluid temperature, T_{in}. It's found that the water temperature predicted by four different correlations agrees well with the experimental data. The fluid temperature difference between T_{bo} and T_{in} decreases gradually as the fluid temperature approachs the vicinity of the pseudo-critical point. The percentage of absorbed heat by the water in the first pass, η, is depicted in Fig.6. The heat transfer between the two passes reduces with the increase of inlet temperature, and minimizes in the vicinity of the pseudo-critical point. This is caused by the small temperature difference between the two passes when the fluid temperature at the inlet is in the vicinity of the pseudo-critical temperature. The predicted η by Bishop correlation is sligtly lower than those predicted by other correlations. Generally, the predicted results by correlations fit well with the experimental data. The heat transfer from the second pass to the first pass is lower than 15% under the test conditon.

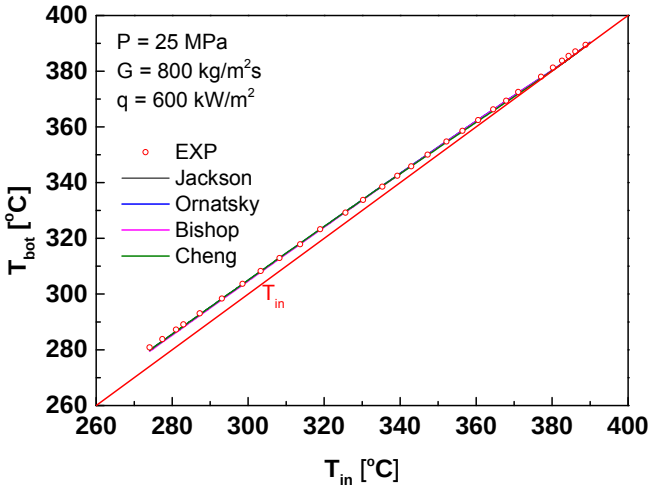

Fig. 5 Bulk fluid temperature at the bottom of the test section

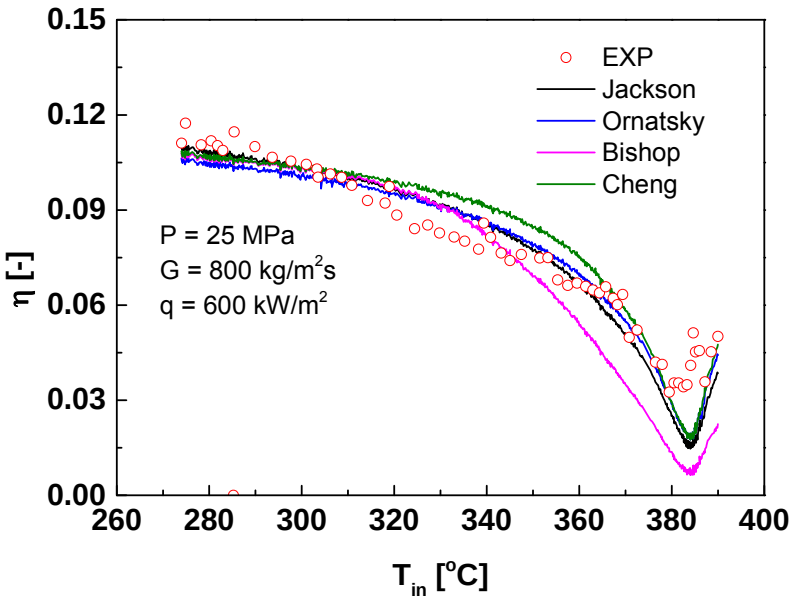

Fig. 6 Heat transfer from second pass to first pass

Fig. 7 gives the predicted average fluid temperature at the cross section where the inside wall temperature of rods is measured in the second pass. Since the cross-section average fluid temperature in two passs can not be measured directly, Jackson and Fewster(1975) correlation is selected to predict the heat transfer coefficients on the inside and outside wall of the assembly box when calculating the cross-section average fluid temperature in the paper. The temperature difference predicted by different heat transfer correlations is negligible. This is because the location where the wall temperature is measured is near the outlet and the effect of heat transfer between the two passes on the average fluid temperature is small.

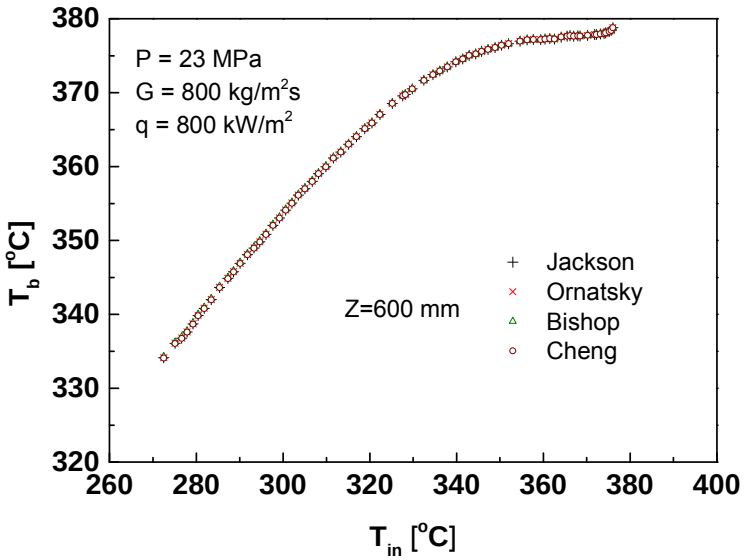

Fig. 7 Bulk fluid temperature at the location where wall temperature of heated rods measured in the second channel

3.2 Heat transfer in the rods

Analyses of heat transfer in the rods are based on the mean wall temperatures at the 16 measuring points and the cross-section average water temperature in the second pass. The effects of heat flux,mass flux and pressure are discussed.

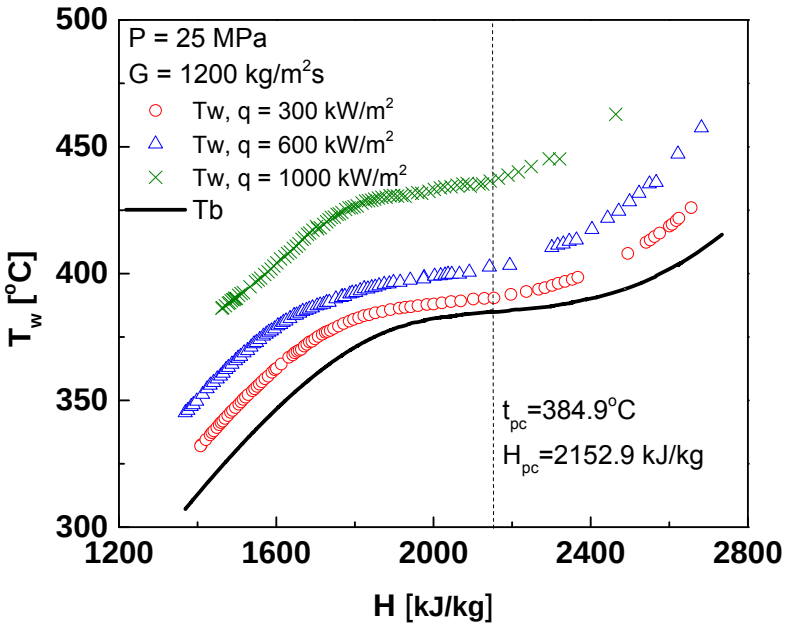

(a) Wall temperature

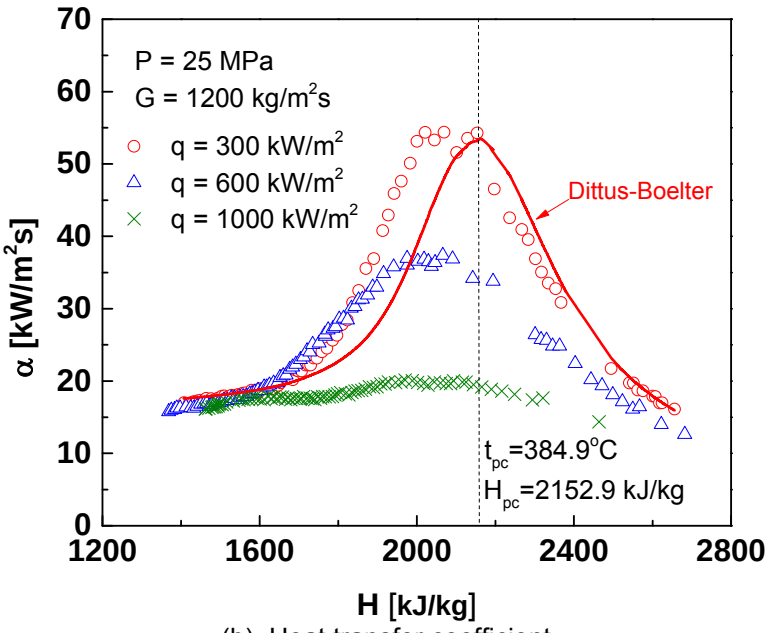

(b) Heat transfer coefficient

Fig. 8 Effect of heat flux on the variation of (a) wall temperature and (b) HTC

Figure 8 (a) and (b)show the variations of the mean wall temperature and heat transfer coefficient(HTC) at various heat fluxes. The working pressure is 25 MPa and mass flux is 1200

kg/m^{2}s. The black solid line in Fig. 8(a) represents the corresponding bulk fluid temperature. The vertical dashed line in each figure indicates the specific enthalpy at the pseudo-critical temperature . In general, as the heat flux increases, the heat transfer coefficient decreases. When the heat flux is 300 or 600kW/m^2, the heat transfer shows a normal behavior. The heat transfer coefficient increases monotonously with the increase of enthalpy until it reaches a maximum value at a specific enthalpy slightly lower than the pseudo-critical value. As the heat flux increases to 1000 kW/m^2, the variance of heat transfer coefficient at the region with a low enthalpy is similar to that of 600 kW/m^2. However, in the pseudo-critical region the rise of HTC is mild compared to that of 600 kW/m^2. The experimental heat transfer coefficient is much lower than that predicted by Dittus-Boelter heat transfer correlation at the heat flux 1000 kW/m^2. The heat transfer coefficient ratio of the experimtal data to the prediction by Dittus-Boelter correlation is smallest at the pseudo-critical specific enthalpy.

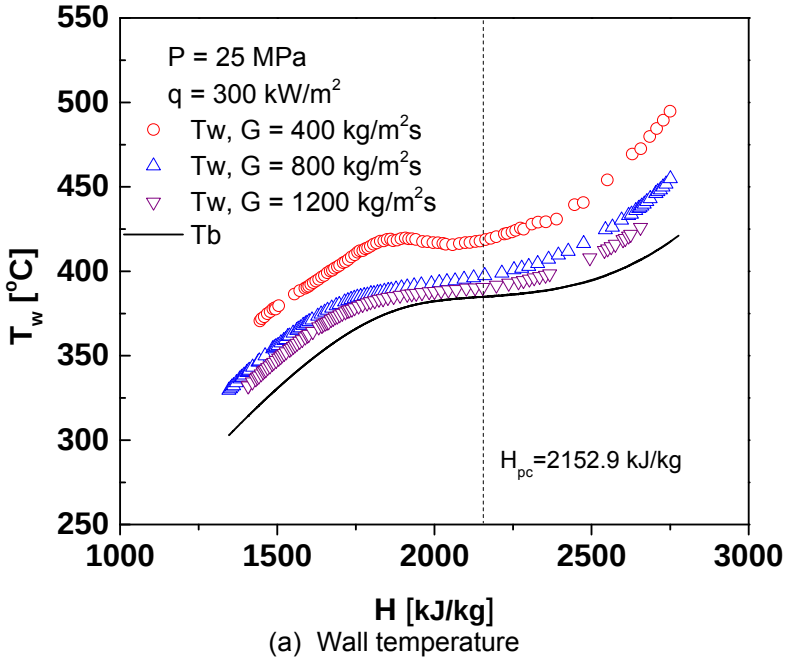

(a) Wall temperature

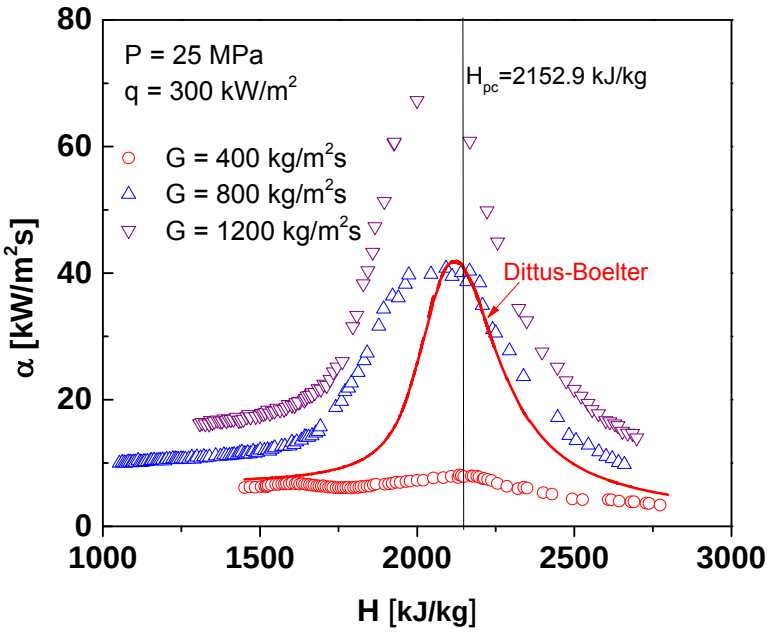

(b) Heat transfer coefficient

Fig. 9 Effect of mass flux on the variation of (a) wall temperature and (b) HTC

Figure. 9 (a) and (b) show the variations of mean wall temperature and heat transfer coefficient (HTC) at various mass fluxes. The working pressure is 25 MPa and heat flux is 300 kW/m^2. As the mass flux increases, the wall temperaures decrease and the heat transfer coefficients increase. At a large mass flux of 1200 kg/(m^2 s) and a medium mass flux of 800 kg/(m^{2}s), the variation of heat transfer coefficient is similar to each other. The wall temperature does not show any irregular behavoir and it increases almost in parallel with the bulk temperature. When the mass flux is 400 kg/(m^{2}s), the wall temperature shows a mild peak and the heat transfer coefficient is much lower than that predicted by Dittus-Boelter correlation in the pseudo-critical temperature region.

Figure10 shows the wall temperature and heat transfer coefficient(HTC)for two diffent pressures, i.e., 23 and 25MPa. The heat flux and mass flux are kept constant at 300kW/m^2 and 800kg/m^{2}s, respectively.The results show that the general shape of the wall temperature and HTC profile remains the same under different pressures.The effect of the pressure becomes outstanding as the fluid temperature approaches to the critical point, especially in the vicinity of the critical temperature due to the steep variation of the physical properties. In general, the heat transfer characteristics of supercritical water flowing outside the rod bundle is similar to those observed in the tubes or annular pass.

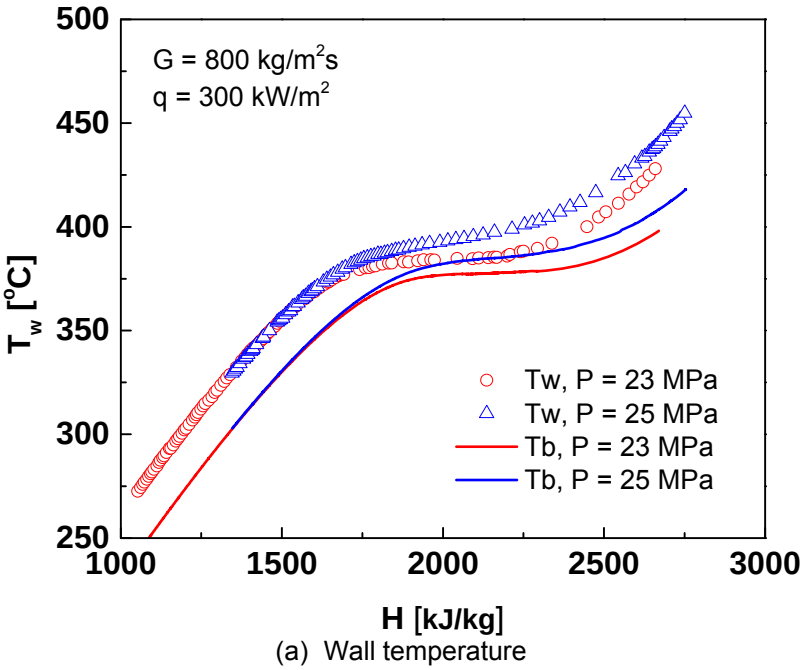

(a) Wall temperature

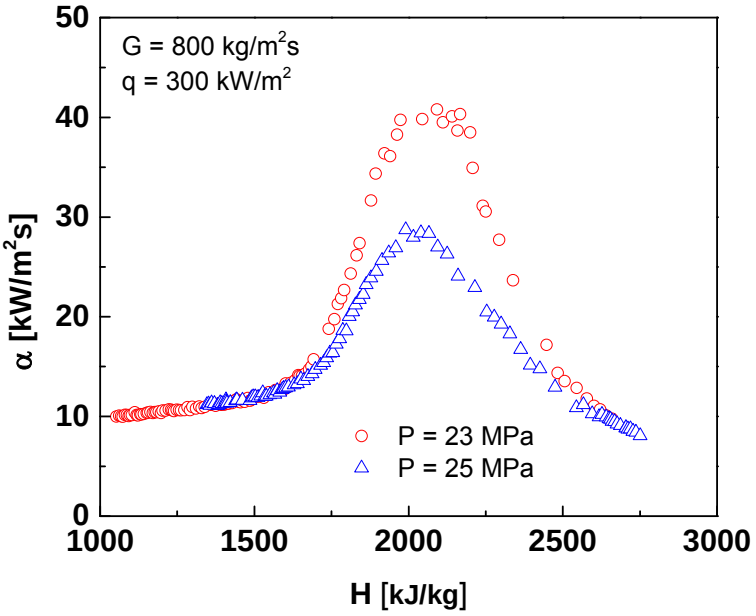

(b) Heat transfer coefficient

Fig. 10 Effect of pressure on the variation of (a) wall temperature and (b) HTC

3.3 Comparison with correlations

Figure 11 compared the results predicted by the correlations of Shitsman,Jackson, Ornatsky, Swenson, Bishop and Cheng with measured data. The Dittus-Bolter correlation is also plotted for reference. In the condition of low heat flux as shown in Fig11(a), all the correlations show good agreement at the temperature much lower or higher than pseudo-critical temperature. As the fluid temperature approaching to the pseudo-critical value, all the correlations can capture the trend of the expermental heat transfer coefficients. But both correlation of Shitsman and that

of Ornatsky significantly overpredict the heat transfer coefficient. Cheng correlation underestimates the heat transfer coeffcient.

For the high heat flux condition, the heat transfer coefficient decreases significantly. Difference between the predicted heat transfer coefficients and experimental results is large. The trend of the heat transfer coefficient is not well predicted by correlations. Among these correlations, Jackson correlation and Bishop correlation predict the results mostly close to the experimental heat transfer coefficient as shown in Fig.11(b).

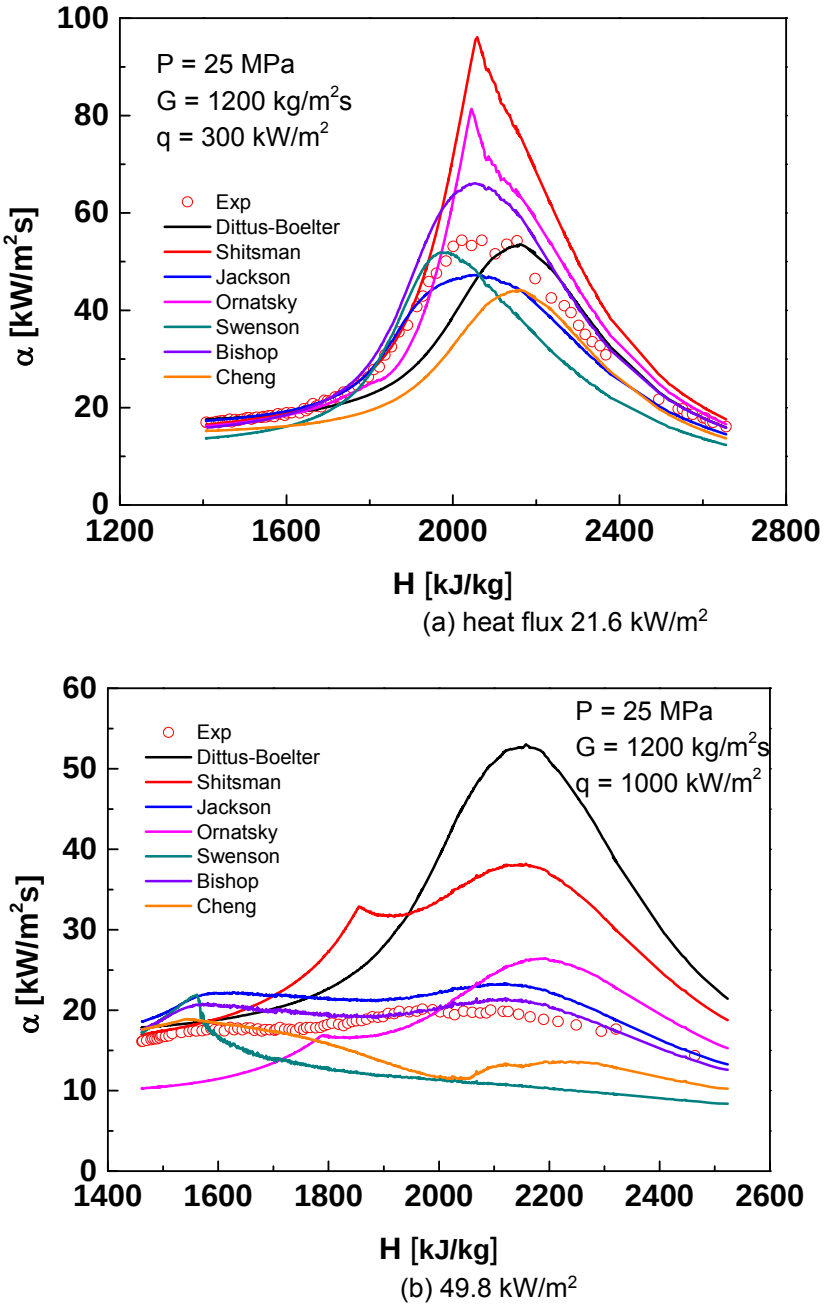

Fig. 11 Comparison of correlations with test data at (a) heat flux 300 kW/m^2, and (b) heat flux of 1200 kW/m^2

To achieve quantitative conclusion, statistic evaluation of the deviation is done is done with 8,582 experimental data points. The deviation for each data point is defined as:

$$e_i = \frac{2 \cdot (\alpha_C - \alpha_e)_i}{(\alpha_C + \alpha_e)_i} \tag{21}$$

The average deviation and standard deviation of the data are computed as following:

$$\mu = \frac{1}{N} \sum_{i=1}^{N} e_i \tag{22}$$

$$\sigma = \sqrt{\frac{1}{N-1} \sum_{i=1}^{N} (e_i - \mu)^2} \tag{23}$$

Table 4 Comparison of test data with correlations

Correlations	**Data points**	**μ**	**σ**
Dittus-Boelter (1930)	8582	0.26	0.36
Shitsman (1975)	8582	0.25	0.28
Jackson (1975)	8582	0.14	0.19
Ornatsky (1970)	8582	-0.06	0.31
Swenson(1965)	8582	-0.24	0.29
Bishop(1964)	8582	-0.07	0.17
Cheng (2009)	8582	-0.10	0.26

Table 4 summarizes the deviation and Fig. 12 shows the details of the comparison of the Nusselt number. The standard deviation of Dittus-Bolter correlation is much larger than those of other correlations. Bishop correlation and Jackson correlation show best agreement with the test data among all the seven correlations. Cheng correlation is independent on fluid bulk temperature. Thus it has the advantage of being explicit and does not need to do the iteration like other correlations. Although the average deviation is relatively large, the result of Cheng correlation shows good symmetry. The development of a new explicit correlation like Cheng correlation based on the experimental data is encouraged.

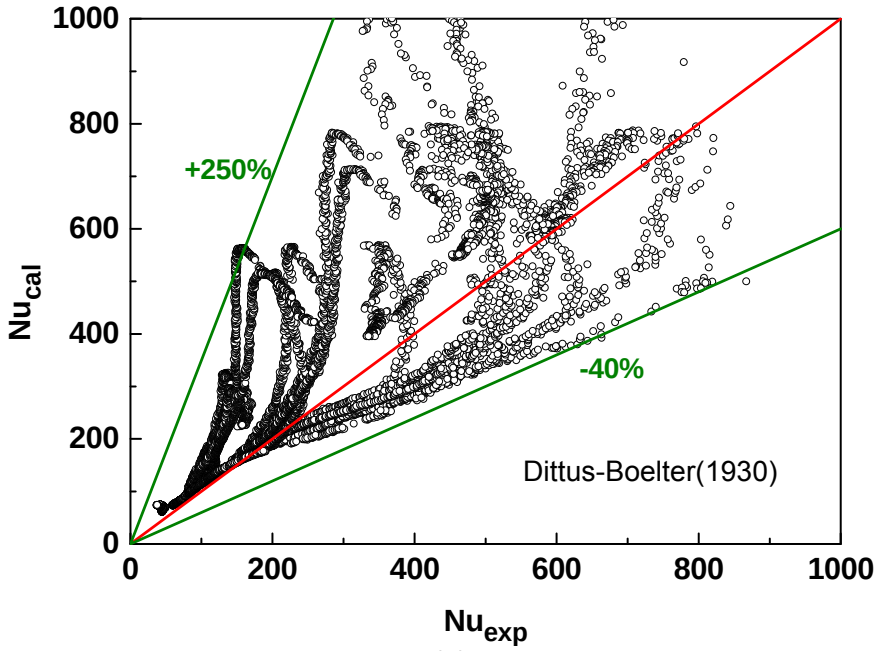
1000
800
600
400
200
0
0
200
400
600
800
1000
+250%
-40%
Dittus-Boelter(1930)
Nu_cal
Nu_exp

(a)

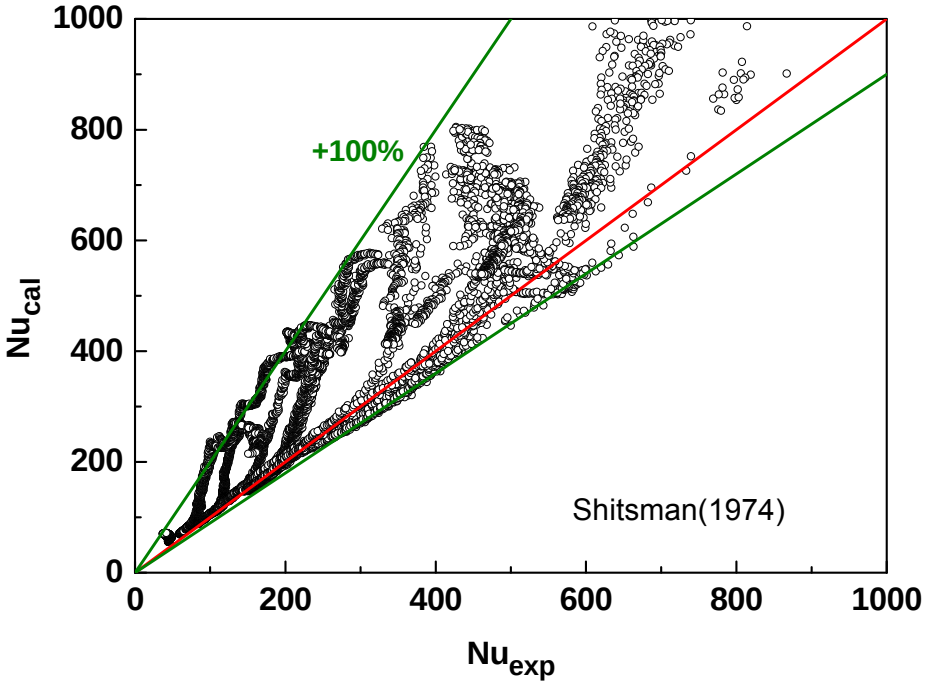
1000
800
600
400
200
0
0
200
400
600
800
1000
+100%
Shitsman(1974)
Nu_cal
Nu_exp

(b)

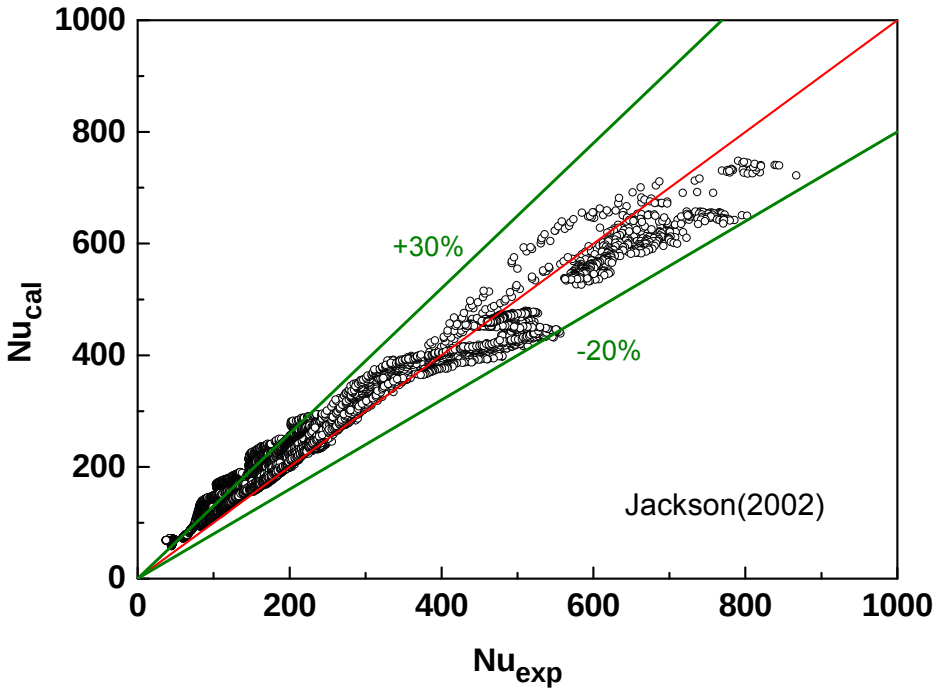
1000
800
600
400
200
0
0
200
400
600
800
1000
Nu_cal
Nu_exp
+30%
-20%
Jackson(2002)

(c)

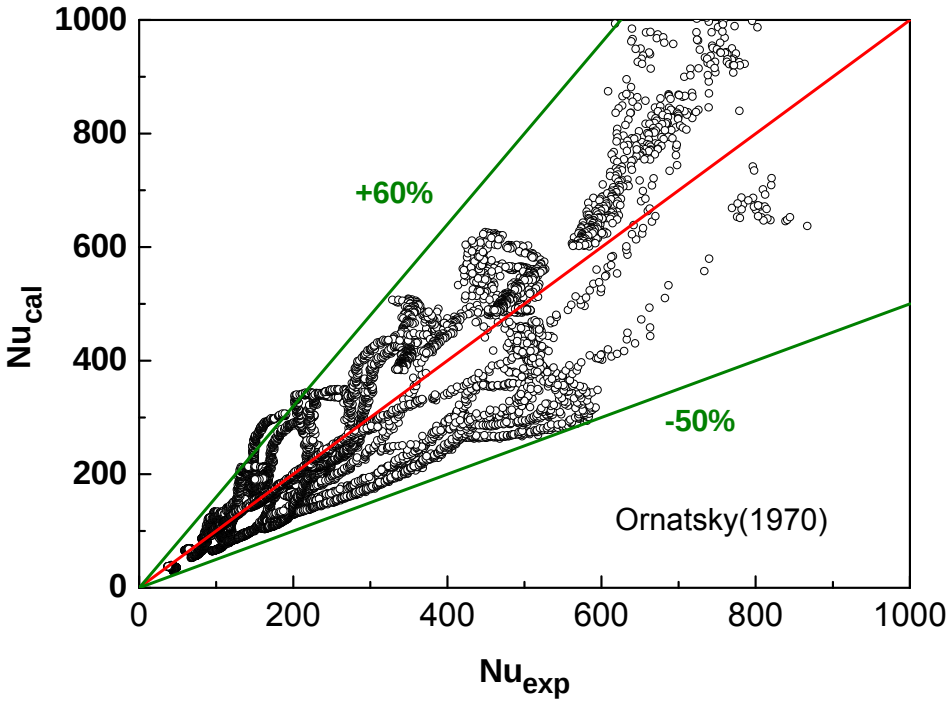
1000
800
600
400
200
0
0
200
400
600
800
1000
Nu_cal
Nu_exp
+60%
-50%
Ornatsky(1970)

(d)

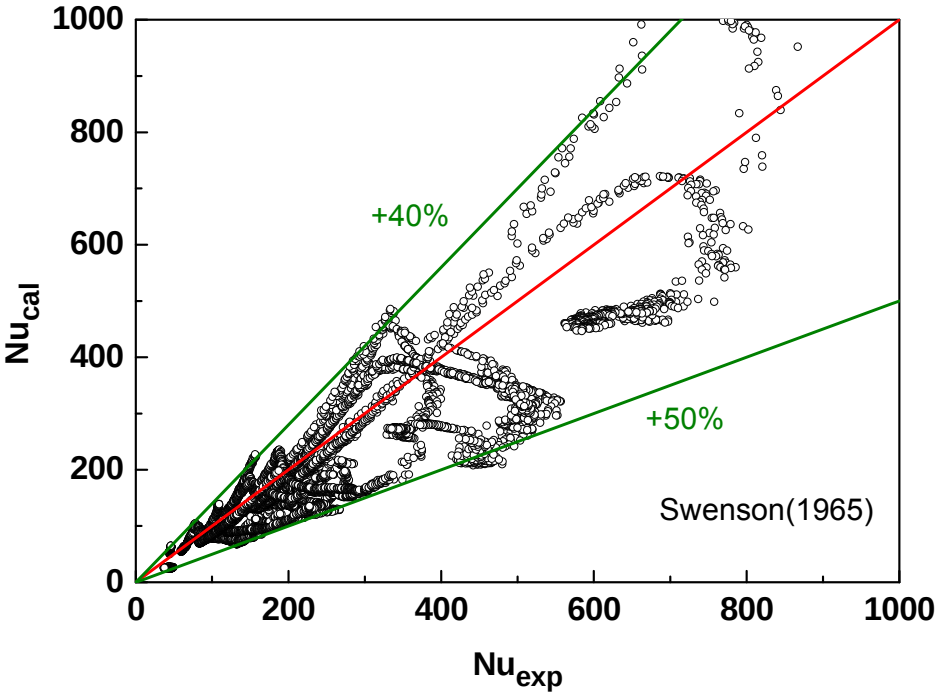
1000
800
600
400
200
0
0
200
400
600
800
1000
Nu_cal
Nu_exp
+40%
+50%
Swenson(1965)

(e)

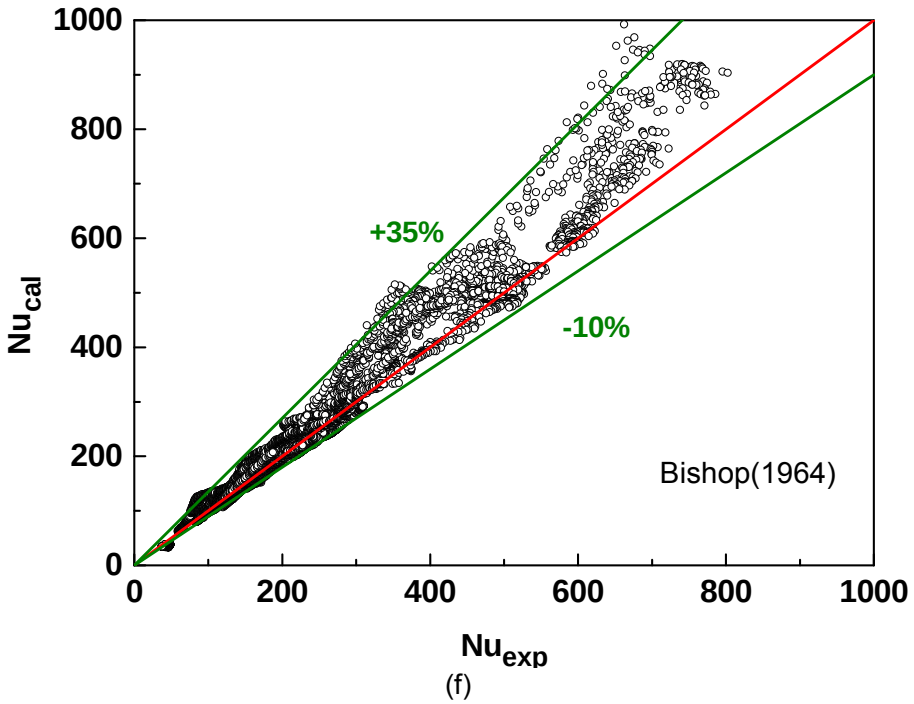
1000
800
600
400
200
0
0
200
400
600
800
1000
Nu_cal
Nu_exp
+35%
-10%
Bishop(1964)

(f)

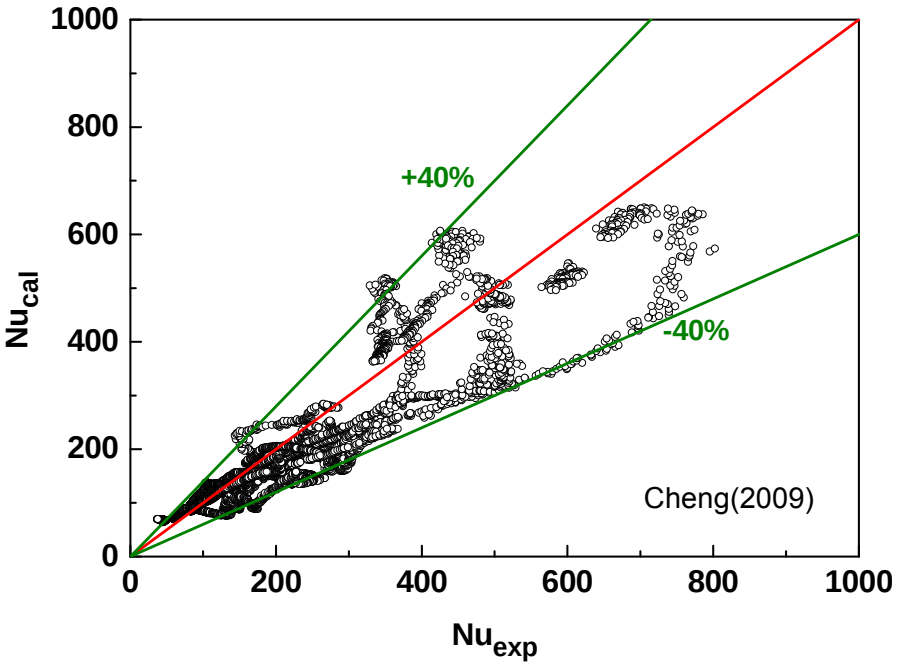

(g)

Fig. 12 Comparison of correlation and measured data for the Nusselt number.
(a) Dittus-Boelter, (b) Shitsman, (c) Jackson, (d) Ornatsky (e) Swenson,(f) Bishop,(g)Cheng

4. Conclusion

In the frame of the development of supercritical water cooled reactors, experiments are performed at the SWAMUP-II test facility at Shanghai Jiao Tong University to study the heat transfer to supercritical water flowing upward in 2X2 rod bundle with two flow passes.

The fraction of heat transfer from the second pass to the first pass is lower than 15% under the test conditons. It reduces with the increase of inlet temperature and reaches the lowest value when the inlet temperature is in the vicinity of the pseudo-critical point.

The effects of systerm parameters including heat flux,mass flux and pressure on the heat transfer of supercritical water in the bundle are similar to those observed in tubes or annuli. High heat flux leads to low heat transfer coefficient in the vicinity of the pseudo-critical point. Inceasing mass flux resusts in the enhancement in heat transfer. The effect of pressure is weak when bulk temperature is beyond the pseudo-critical point.

Seven correlations developed for supercritical heat transfer are compared with the test data.The scatter degree is high when the heat flux is high. Generally speaking, the correlation of Jackson et al.(1975) and Bishop et al.(1964) show best prediction accuraccy.

Acknowledgement

Finacial supports from the China General Nuclear Power Group (CGN) are gratefully acknowledged.

References

Bishop, A.A., Sandberg, L.O., Tong, L.S., 1964. Forced convection heat transfer to water at near critical temperatures and supercritical pressures. WCAP-2056-P, Part-III-B, Westinghouse Electric Cooperation.

Cheng, X., Schulenberg, T., 2001. Heat transfer at supercritical pressures: literature review and application to an HPLWR. Wissenschaftliche Berichte, FZKA 6609, Forschungszentrum Karlsruhe.

Cheng, X., Yang, Y.H., Huang, S.F., 2009. A simplified method for heat transfer prediction of supercritical fluids in circular tubes. Ann. Nucl. Energy 36, 1120–1128.

Dittus, F.W., Boelter, L.M.K., 1930. Heat transfer in automobile radiators of the tubular type. Univ. Calif. Publ. Eng. 2 , 443–461.

Jackson, J., Hall, W., Influences of buoyancy on heat transfer to fluids flowing in vertical tubes under turbulent conditions, in: Turbulent Forced Convection in Passs and Bundles, Vol.2, Hemisphere, New York, 1979, pp. 613-640.

Jackson, J.D., 2002. Consideration of the heat transfer properties of supercriticalpressure water in connection with the cooling of advanced nuclear reactors.In: Proceedings of the 13th Pacific Basin Nuclear Conference, Shenzhen, China,October 21–25, 2002.

Jackson, J.D., Fewster, J., 1975. Forced Convection Data for Supercritical Pressure Fluids, HTFS 21540.

Lemmon, E.W., Huber,M.L., Mclinden,M.O., 2007. Reference fluid thermodynamic and transport properties,NIST Standard Reference Database 23,Ver.8.0,NIST.

Mori, H., Kaida, T., Ohno, M., Yoshida, S., Hamamoto, Y., 2012. Heat transfer to a supercritical pressure fluid flowing in sub-bundle passs. J. Nucl. Sci. Technol. 49, 373-383.

Ornatsky, A.P., Glushchenko, L.P., Siomin, E.T., 1970. The research of temperatureconditions of small diameter parallel tubes cooled by water under supercriticalpressures. In: Proceedings of the 4th International Heat Transfer Conference,Paris-Versailles, France. Elsevier, Amsterdam.

Oka, Y., Koshizuka, S., 2001.Supercritical-pressure, Once-through Cycle Light Water Cooled Reactor Concept., J. Nucl. Sci. Technol. 38,1081–1089.

Pioro, I.L., Duffey, R.B., 2005. Experimental heat transfer in supercritical water flowing inside passs (survey). Nucl. Eng. Des. 235, 2407–2430.

Pioro, I.L., Khartabil, H.F., Duffey, R.B., 2004. Heat transfer to supercritical fluids flowing in passs - empirical correlations (survey). Nucl. Eng. Des. 230, 69-91.

Richards, G., Harvel, G.D., Pioro, I.L.,et al., 2013. Heat transfer profiles of a vertical, bare, 7-element bundle cooled with supercritical Freon R-12. Nucl. Eng. Des. 264, 246–256.

Shitsman, M.E., 1968. Temperature conditions in tubes at supercritical pressures. Therm. Eng. 15, 72.

Silin, V.A., Voznesensky, V.A., Afrov, A.M., 1993.The light water integral reactor with natural circulation of the coolant at supercritical pressure B-500 SKDI, Nucl. Eng. Des. 144,327–336.

Swenson, H.S., Caever, J.R., Kakarala, C.R., 1965. Heat transfer to supercritical water in smooth-bore tube. J. Heat Transfer 477–484.

Schelenberg,T., Straflinger,J., Heinecke,J., 2008. Three pass core design proposal for a high performance light water reactor, Pro.Nucl.Energ.50,526-531

Wang, H., Bi,Q.C., Wang, L.C., et al.,2014. Experimental investigation of heat transfer from a 2X2 rod bundle to supercitical pressure water. Nucl. Eng. Des. 280, 205-218.

Zhao,M., Li,H.B., Yang,J., et al., 2013. Experimental study on heat transfer tosupercritical water flowing through circular tubes and 2X2 rod bundles. In:Proceeding of the 6th International Symposium on Supercritical Water-cooledReactors, Shenzhen, China, March 3–7, 2013.

Zhang,S.Y., Gu,H.Y., Cheng,X.,et al., 2014. Experimental study on heat transfer of supercritical Freon flowing in a circular tube. Nucl. Eng. Des. 280, 305-315.

ISSCWR7-2053

Conceptual proposals on the test reactor of VVER-SCP

V.A.Mokhov, V.Ya.Berkovich, M.P.Nikitenko, A.N.Churkin, V.M.Makhin
OKB «GIDROPRESS»
st. Ordzhonikidze, 21, Podolsk, Moscow reg., 142103, Russian Federation
+ 7-4967-65-26-01, makhin@grpress.podolsk.ru

P.L.Kirillov, Yu.D.Baranaev, A.P.Glebov
SSC RF – IPPE
Obninsk, 249033, Russian Federation
kirillov@ippe.ru

Abstract

A necessity was demonstrated of creation of a prototype of a power reactor plant with supercritical parameters of coolant (small test reactor) for experimental justification of technical solutions and optimization of selection of the design and parameters of operation of VVER-SCP (SCWR) and meeting the requirements of the basic regulatory document “General provisions of ensuring safety of nuclear power plants” (OPB-88/97, i.1.2.5) concerning use of justified and experience-based technical solutions in nuclear engineering.

The main technical requirements and conceptual solutions are proposed for the test reactor of reactor VVER SCP as well as proposals on a research program and a long-term economically beneficial use of this facility.

1. Introduction

In 2008-2011, after a long period of inactivity, the Russian research and design organizations resumed elaborations of water-cooled nuclear reactors with supercritical parameters of coolant (innovative Super-VVER). Three conceptual proposals on NPP design were prepared [1]. The main system requirements were established, which the Unit must meet, as well as target indices on capital expenditures, improvement of fuel use and operational characteristics [1, 2]. The approaches for GIF (Generation-4) plants, accepted internationally, experience in elaboration of VVER technologies, as well as extensive positive experience of creation and operation of turbine-steam facilities with supercritical parameters in heat and power engineering, were taken into account in the work [3, 4]. The report covers the main “key” technical problems, along with a number of expected positive qualities and advantages in respect to NPP with active VVER – improvement of technical and economical characteristics due to 5-10% increase in efficiency and decrease in specific steel intensity of the Unit main equipment, as well as improvement of fuel use (for reactors with fast or fast-resonance neutron spectrum). The problems are determined by sufficient increase in coolant parameters (temperature to 600 ^{o}C, pressure 25 MPa) and peculiarities of its thermal-physical properties in the considered field and can be solved by creation of structural materials with increased thermal and radiation stability and elaboration of special design solutions, ensuring thermal and technical stability and safety of the reactor.

The interconnected complicated character of neutron-physical and thermal-hydraulic processes, stipulated by a considerable change in the water physical properties near critical

temperature, is aggravated by the necessity of consideration of the scale factor, i.e. consideration of the design and dimensions of the core and internals [4-6].

One will remember that in thermal power engineering insufficiency of knowledge of the processes near critical temperature led to decrease in design parameters of commissioned SCWR Units when supercritical parameters were introduced (namely, the steam temperature in typical Units was decreased to 540 ^{o}C, which is 50-60 ^{o}C lower than in pilot Units) and, as a result, it led to decrease in real efficiency of the Unit in respect to estimated theoretical values (according to academician L.A. Melentiev) [7]. It took time to specify knowledge regarding such phenomena as “degraded” or “deteriorated” heat exchange for specific structures of direct-flow heated tubes to substantiate operability of materials and create new materials with improved mechanical characteristics at temperature of ~600 ^{o}C, to elaborate new norms and requirements for Units with super critical parameters of water and to improve the design and technology of manufacturing and operation of Units to reach increased efficiency [7]. The following steam parameters have been mastered in thermal engineering by now: temperature - 590-600 ^{o}C and pressure - 24-30 MPa, the field of supercritical steam parameters is being studied (pressure to 35 MPa, temperature to 650 ^{o}C; in the European Union code TERMI – 37.5 MPa and 700 ^{o}C [3]). So, application of supercritical parameters of coolant and increase in efficiency of Units achieved in thermal engineering make it possible to implement the strategy aimed at fuel saving and decrease in the load on environment by decrease of harmful emissions.

Important conclusions are made in the article on the basis of the analysis of the experience of development of thermal and nuclear engineering:

- elaboration of the Unit with reactor plant with supercritical coolant parameters is a promising direction of nuclear engineering development;
- it is reasonable to develop supercritical coolant parameters in nuclear engineering on a stage-by-stage basis, beginning from creation of a pilot prototype of reactor plant (test reactor) with thermal power to 100 MW for experimental justification of the basic technical solutions and optimization of selection of the design and parameters of operation of VVER-SCP;
- development and operation of a prototype of VVER-SCP reactor plant will make it possible to ensure meeting the requirements of the basic regulatory document “General provisions of ensuring safety of nuclear power plants” (OPB-88/97) on application of justified and tested technical solutions and materials in nuclear engineering.

The main technical requirements and conceptual solutions are proposed on the pilot prototype of VVER-SCP reactor, as well as considerations on the research work program and economically profitable application of this plant for a long time.

2. The main results of the stage of conceptual elaboration of SCWR reactors

Reactors with supercritical coolant parameters have been elaborated since the 1950’s (USA) and 1960’s (USSR). In 21 century elaborations were resumed as studies of one out of six selected promising directions of program Generation-4 - Super Critical Water Reactor (SCWR). International symposiums were systematically held between 2000 and 2013 (ISSCWR-1, …, ISSCWR-6) with reviews of the results of elaboration of SCWR in different countries: Canada, China, European Union, Japan, Republic of Korea, Russia, USA, etc. Some target characteristics of elaborated SCWR were specified [2, 4]. It is proposed to increase the following parameters in comparison with modern VVER and PWR: coolant pressure from 16 to 25 MPa, temperature at the reactor outlet – from 320 ^{o}C to 500 – 625 ^{o}C, Unit efficiency – from 35% to 40-45%. The level of the above-mentioned coolant parameters in SCWR is close to the level reached in thermal engineering [3]. In Russian designs increase in the coefficient of nuclear fuel conversion from 0,4 (active VVER) to the value close to 1 is assumed as the basic system requirement for VVER-SCP reactors, in order to ensure effective use of VVER-SCP in the structure of future nuclear engineering, assuming extension of resources due to introduction into the fuel cycle ^{238}U [1].

There are at least 15 elaborations of SCWR reactor. Characteristics of some SCWR, made abroad, are given in Table 1 [2,4]. The following elaborations were performed in Russia in 21 century: a two-circuit fast neutron reactor, cooled by steam-water mixture VVER- SCWR; single-circuit VVER- SCP with dual-lead scheme of coolant circulation in the core; a two-circuit fast reactor with a supercritical steam coolant in the primary circuit; and elaboration of a two-circuit integral VVER-ISCWR with natural coolant circulation was performed at the end of 20 century [1]. The variety of versions is largely stipulated by the possibility of the supercritical water to act as coolant and moderator, allowing one to implement a varied spectrum of neutrons in the core (thermal, fast, fast-resonance), to use various schemes of coolant circulation in the core (single, double and multiple) and various versions of design and layout of fuel rods (for example, "tight" fuel rod grids, fuel rods with spacing ribs, spherical fuel rods on the basis of micro fuel rods with different coatings etc.). Coolant with reactor outlet temperature of 270-290 ^{o}C and 350-388 ^{o}C and pressure 25 MPa (see Table 1 and [1]) is used in the conceptual designs. So, the conceptual elaboration stage is mostly over and selection of the version or versions is required for more detailed elaboration and justification of the main technical solutions.

"General provisions of safety assurance of nuclear power plants" ("OPB - 88/97" i. 1.2.5) specify that technical and organizational measures accepted for safety assurance shall be proven by the former experience or *tests, studies, operational feedback of prototypes*. "Nuclear safety regulations of reactor plants of nuclear power plants" ("NP - 082-07" i. 2.1.4 also proclaims the necessity of tests and specify their end use (study of new FA designs and verification at perfection of systems important to safety). Thus, considering novelty of the trend, except studies of insufficiently investigated physical, thermohydraulic, science of materials and other processes and phenomena within the considered interval and other operating conditions (the stage of pre-design studies), the stage of creation of the test prototype of VVER-SCP reactor and the results of its operation are necessary. Special-purpose of the test reactor - prototype or test reactor – experimental verification of the basic provisions that are applied at the stage of conceptual design and can influence quality of development of industrial power reactors as well as obtaining the design characteristics.

Table 1. Comparative characteristics of foreign designs of water-cooled reactors with SCP coolant

Characteristic	SCWR-R Korea	SCLWR Japan	SCWR USA	Ultra-CANDU^{+} Canada	SCWR HPLWR Europe	SCWR China	SCFR Japan
Thermal power, MW	3989	2273	3570	2540	2188	2284	3832
Electric power, MW	1739	950	1600	1220	1000	1000	1698
EFFICIENCY, %	43,7	42	44,8	48	44	43	44,3
Temperature of feedwater, °C	350	280	280	350	280	280	280
Temperature of live steam, °C	510	508	500	625	508	500	523
Pressure of live steam, MPa	25	25	25	25	25	25	25
Spectrum of neutrons	T	T	T	T	T	T	F
Flowrate of feedwater, kg/s	2518	1816	1843	1312	1113	1177	1897
T – thermal, F - fast							

3. Background of nuclear power engineering

Experience of nuclear power engineering development calls for necessity of creation of small-power prototypes in support of preliminary studies, study of possibilities and verification of a series of high-power units. Three consecutive stages in development of each type of reactor plants (three stage scheme) is possible to pick out:

- conceptual study of power reactors (power units) and elaboration of the basic requirements and target indices of power units with assessments of possibility of creation of power lines of nuclear power plants with various power. If necessary calculation - experimental studies of the so-called "key" problems are provided [4, 8];
- creation of experimental reactors - prototypes of the future power reactors (test reactor - prototype, test reactor) for corroboration of basic provisions in practice and for verification of industrial power units;
- development of the reactor - prototype based on operational feedback and implementation of power reactors, for example, some power units with various power.

Each of thee stages is characterized by implementation of research engineering and accumulation of deficient knowledge of the physical phenomena, necessary for verification of design solutions.

While creation of BN reactors - essentially new trend in nuclear power engineering - development and operation of a series of experimental reactors - prototypes - "small" reactors with various liquid-metal coolant (mercury, sodium - potassium, sodium , etc.) and various fuel (metal, oxide, carbide and nitride) was required. Among this series of reactors BOR - 60 (thermal power - 60 MW) and MBIR (150 MW) reactors are expedient to note in terms of their great demand at this stage, namely - for verification of a series of power reactors and for creation of large-scale nuclear power engineering.

While creation of VVER and PWR this series involved less number of stages for the coolant (water) well studied and used in thermal power engineering was applied and changes of physical properties of the coolant, fuel and other materials were less significant and, therefore, their study acquired short-term period. As a consequence, characteristics of new reactors of the given trend are highly predictable.

In power vessel boiling reactors (BWR and VK) in comparison with VVER and PWR changes of density are significant that demanded to take into account interrelation of the core neutronics and thermohydraulic processes in more detail, and also to solve the problem on stability of operational conditions. At the initial stage small power reactors with natural coolant circulation were used, for example, Humbold Bay, Dodewaard and etc. [9]. Because of more complex physics of boiling reactors, the number of modifications (generations) of the power reactors developed is essentially more and changes in boiling reactor design are significant at increase in their power. In developing industrial power reactors BWR with thermal power from 600 up to 4200 MW there are the following design features to provide coolant recirculation in the vessel and heat transfer enhancement in the core (the initial stage of development), and also for simplification of the reactor plant design (at present):

- arrangement of ex-vessel special circuits and in-vessel jet pump to increase coolant velocity in the core (reactors BWR-1 … BWR-6, were commissioned in 1955-1972);
- application of the built - in pumps in the lower vessel part for arrangement of recirculation in the vessel (ABWR, 1996).

In near-term outlook conditions of the coolant developed natural circulation in vessel (designs SBWR and ESBWR, the stage of licensing in the USA has passed) will be realized in practice.

In the USSR reactor VK-50 with coolant natural circulation in the vessel (Dimitrovgrad, 1965) was created “for studying problems of steam boiling and superheating” [10]. Research of conditions with superheating steam in the core was planned. The article [11] specifies its destination –verification of reliability of the assumed process scheme for obtaining steam and its various components under operational conditions. Reactor design enabled to study also different cores ("small" and "large" cores). At the first stage the "small" core for obtaining saturated steam (diameter – 1.8 m, height - 2 m) was used. The basic outcome of the first stage studies was verification of controllability of the reactor within the wide interval of parameters and determination of area of parameters with possible significant power fluctuations (resonance instability) [12].

So, expediency of the a.m. three-stage pattern of development and implementation of power reactors is corroborated in practice. In reactors SCWR under development, like in reactors BWR and VK, change of coolant density in the core is significant, therefore, consideration of the interrelated neutronics and thermohydraulic processes is necessary. By analogy with

development of BWR and VK, the stage of creation of the reactor - prototype of power reactor and realization of studies in this reactor are important in creating SCWR.

4. The basic phenomena and the processes being subject to studies for SCWR verification

Since in the world practice SCP water has never been used as NPP coolant, there are numerous technical challenges that must be evaluated during the SCWR development.

In comparison with VVER at transition to reactor SCWR coolant parameters change considerably: pressure (P=25МПа MPa) and temperature (at the outlet up to 600-650 ^{o}C). In connection with new conditions it is necessary to provide the calculational-experimental support of adequacy of materials and serviceability of the products a well as selection and verification of water chemistry in whose modes operability of the core, vessel, internals, pipelines, valves and instrumentation is realized. Studies are necessary also for meeting the above-stated requirements of regulatory documents OPB - 88/97 and NP 082-07.

It is necessary to note also the specific studies caused by application of coolant at supercritical parameters. Change of physical properties of water is significant in the field of critical temperature. Pressure increase brings about smoother change of parameters at higher temperature of inflection point. Inflection point corresponds to pseudo-critical temperature that is characterized by the maximum of heat capacity (at 25 MPa the pseudo-critical temperature is ~385 ^{o}C). In the field of temperature 350-400 ^{o}C at pressure 25 MPa the density changes 3 times more from 625 kg/m^3 to 166 kg/m^3; enthalpy - from 1626 to 2583 kJ/kg. Also changes of ductility and other properties are significant. The specified changes can influence neutronics and other characteristics of the reactor.

Therefore, for reactor SCWR, like for reactors BWR, interrelation of neutronics and thermal-hydraulic processes in the core shall be taken into account. It is necessary to verify controllability of the given processes and availability of the area of reactor forgiving feature to provide stability of conditions of its operation. analysis of reactor stability under transient and accident conditions

The specified and significant change of physical properties can also result in the phenomenon of the “deteriorated” heat transfer [5,6,8,13,14]. The given phenomenon is investigated as applied to thermal power engineering, i.e. at application of experimental sections in the form of tubes with diameter about 10 mm or experimental once-through boiler. Necessity of other consideration of “scale” effect is stated than in analysis of heat transfer at sub-critical parameters [14]. The first test results of the bundles similar to fragments of FA of Chinese reactor being designed corroborate possibility of occurrence of deteriorated heat transfer also in the bundles of fuel rods [13]. So, for the core being designed it is necessary to determine the area of permissible parameters where “deteriorated” heat transfer does not occur at all.

Extremely important for practice study of start-up and transient conditions. As thermal-hydraulic tests of bundles of fuel rods with " swirling " of the coolant and mixing of its "hot" and "cold" jets have shown, significant oscillations of pressure and other parameters (tests of Dyadyakin B.V. and Popov A.S. [14]) are possible. It is necessary, as at development of reactors BWR and VK-50, to determine additional requirements for operating conditions of power reactors of the given type, for example, for the permissible amplitude and frequency of oscillations of neutron flux [15,16].

Carried out experiments shall be applied not only to verification and support of design development, but also for verification of software that is necessary for designing large-power reactor plants. Therefore, its creation shall be agreed with development of software and first of all for the coupled thermal-hydraulic and neutroncs calculations of reactors SCWR. Pretest calculations are important not only for verification of software, but also for forecasting non-stationary conditions of operation of the reactor - prototype.

As operational feedback of the reactor plant VK–50 demonstrates, verification of water chemistry and water chemistry optimization are necessary to refer to the objectives of studies [17].

With a number of the conceptual studies of SCWR specified in section 1, tests of various cores, different schemes of cooling and designs of reactor internals and other changes are expedient for selection of applicable version for a power reactor. Therefore, the requirement for universality of the approach is considered, namely - as to the reactor rig with possibility to change its core and internals. Therefore, it is necessary to provide possibility for conducting similar tests (for example, pools for arrangement of the used large-sized equipment, transport-technological equipment with the extended range of operations, etc.).

The key areas of R&D related with the SCWR reactor core design are:

• development and verification of best estimate computer codes for coupled calculations of neutron physics and thermohydraulics including heat transfer to SCP water flow in the core fuel assemblies and throughout the reactor;
• design engineering of fuel elements and fuel assemblies, substantiation of their operational capability;
• analysis of reactor stability under transient and accident conditions;
• selection of heat-resistant structural materials for fuel pins and FA characterized by high resistance to corrosion and corrosion cracking;
• justification and development of optimal water chemistry.

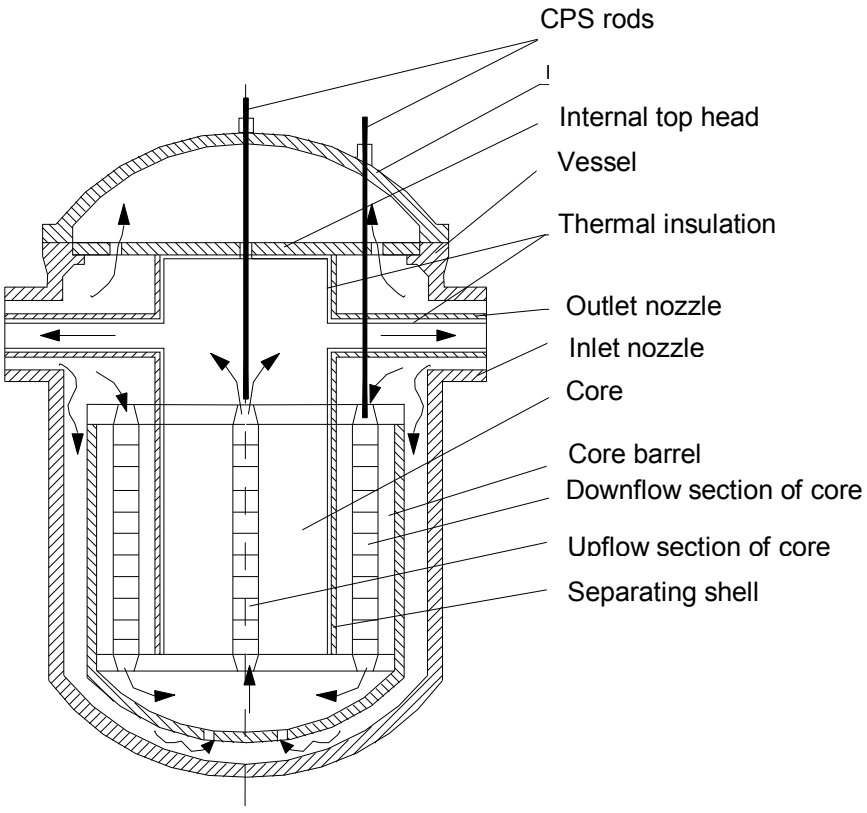

Figure. General diagram of the reactor of the stand – prototype [18]

As operational feedback of similar plants (VK-50, BOR-60 and others) demonstrates it is expedient to use them also for other problems including production of heat and the electric power. It extends the program of studies and improves economic indices of the reactor plant.

5. Proposals on specific version of the stand – prototype

The stand - prototype consists of permanent units and components (vessel, pipelines with valves, water purification system, a turbine generator, etc.) and a replaceable part (a core, possibly, the units and components for its cooling, control and protection system). The replaceable part shall meet, in terms of its design, the requirements of the prototype of power reactor, for example, out of the versions considered in [1].

As an example, calculation results of the core of the stand - prototype are considered and its basic characteristics are compared with characteristics of power reactor VVER-SCP. Similar assessments and studies can be provided for any other version from [1].

Figure gives the general view of the reactor of stand - prototype VVER-SCP. Tables 2 and 3 represent the results of calculations of power reactor and the stand [18].

The most important characteristics are fast neutron flux and neutron flux of all types of energy. Values of neutron flux in the core center are as follows: $5.18 \cdot 10^{14}$ neutr./cm^2·s (E ≥ 0.11 MeV) and $8.85 \cdot 10^{14}$ neutr./cm^2·s (E ≥ 4 eV) [18].

For comparison neutron fluxes in reactor VVER-SCP are given: $6.14 \cdot 10^{14}$ neutr./cm^2·s (E ≥ 0.11 MeV) and $12.0 \cdot 10^{14}$ neutr./cm^2·s (E ≥ 4 eV) [18]. Hence, rates of accumulation of damaging dose in power reactor and reactor of the stand - prototype are close (difference up to 20 % of value fast neutron flux). Thus, in terms of rate of accumulation of damaging dose tests of the core components are representative. Studies can be the basis for designing a stand–prototype.

Table 2. The basic physical characteristics of power reactor VVER-SCP (conceptual studies of one of versions of Russian SCWR) [18]

Name	Value (Importance) [1)]
Nominal reactor thermal power, MW	3830
Coolant flowrate through the reactor under the nominal conditions, kg/s	1890
Coolant pressure at the reactor outlet, absolute, MPa	24.5
Coolant temperature at the reactor inlet, °C	270-290
Coolant temperature at the reactor outlet, nominal, °C	540
Design temperature of the reactor vessel, °C	350
Calculated pressure of the reactor vessel, MPa	27
Design temperature of internals, °C	600
The assigned service life of reactor, years	60
Overall dimensions reactor, m: height / highest diameter	21.1 / 5.32
Number of FA in the core, pcs.	241
Space between FA (nominal), mm	207
Width-across-flats of FA jacket, mm	205
Jacket thickness, mm	2,25
Fuel rod cladding dimension (steel ChS-68), mm	10.7×0.55
Space of fuel rod triangular grid, mm	12
Average specific fuel rate of the core, kW/l	115
Average linear heat rate of fuel rod, W/cm	156
Fuel height in cold state, m: single-pass / double-pass	4.05 / 3.76
Breeding ratio	0.94
Fuel burn-up, MWD/kg U	40 – 60
Maximum damage dose in fuel pin cladding, dpa	50
FA service life in reactor, years	5
Refuelling interval, mnth.	12

[1)] Values of parameters can be specified in further designing

Table 3. Physical characteristics of versions of the stand - prototype core [18]

Name	Value		
Reactor thermal power, MW	30		
Coolant flowrate through the reactor, kg/s	14.7		
Coolant pressure at the reactor inlet, MPa	25		
Coolant temperature at the reactor inlet/outlet, °C	290/540		
Fuel types	UO_2	$(U + Pu)O_2$	$(U + Pu)O_2$
Core dimensions as regards fuel equivalent diameter[2)] / height, cm	74/85	66/70	66/70
Number of FAs in the core, CA/PA, pcs.	91/90	73/72	73/72
Space between FA, cm	5.23	5.23	5.23
Number of fuel rods in FA, CA/PA, pcs.	19/18	19/18	19/18
Space of arrangement of fuel rods, mm	12	12	12
Diameter / thickness of fuel rod cladding, mm	10.7/0.55	10.7/0.55	10.7/0.55
Load of fuel/fissionable isotopes into the reactor, kg/kg	1728/345	1139/256	1159/236
Average specific fuel rate of the core, W/cm^3	82.4	125	125
Average linear heat rate of fuel rod, W/cm	105	160	160

[2)] In calculations of equivalent diameter the volume of separating shell is not taken into account (Figure). CA and PA – central area and peripheral area (Figure).

6. Conclusion

Now three-stage pattern of development of power reactors is assumed:
- conceptual study of power reactors;
- development and providing tests at test reactor;
- creation of power reactors of various power.

Analysis of conceptual development of reactors SCWR shows necessity of transition to the stage of test reactor creation for experimental corroboration of basic design features of power reactor. Similar test reactor- prototype of a power reactor is provided by regulatory documents, for example, OPB-88/97.

The basic features of power reactor of the given trend and the phenomena that are expedient to study in the test reactor are considered . Possibility of creation of experimental low power reactor has been shown for representative reactor tests of fuel and mock-ups of reactor internals (close values of the rate of accumulation of damage dose in the rig and power reactor).

On the basis of analysis of application of similar plants of prototypes (BOR-60 for verification of BN-reactors, VK-50 for verification of boiling vessel reactors of type VK-300) the conclusion is made on expediency of use of the universal reactor rig with thermal power to 100 MW (it is specified in designing) with possibility for the core, reactor internals and other components and units to be replaced. To improve economic characteristics during long-term operation of the rig, generation of additional electric energy and heat is useful.

Test reactor is expedient to be used by the specialists of other entities and also of different countries. Therefore, the organizational structure of providing studies shall be similar to that provided in Team Centers, i.e. epy similar is being planned for the facility MBIR. It does not only improve economic indices, but also enhances quality of outcomes of the studies.

Acronyms

BN – Fast Reactors
BOR – Fast Experimental Reactor (in Russia, Dimitrovgrad)
BWR – Boiling Water Reactor
CA − Central Area
ChS-68 – Stainless Steel
CPS – Control Power System
FA − Fuel Assembly
GIF − Generation IV International Forum
ISSCWR – International Symposium on SCWR
MBIR –Fast Experimental Reactor (construct in Russia, Dimitrovgrad)
NPP − Nuclear Power Plant
PZ − Peripheral Zone
R & D − Research and Development
SCP − Supercritical Pressure
SCWR − Supercritical Water Reactor
VK – Water Boiling
VVER – water-cooled water-moderated energy reactor

References

1. Сидоренко В.А., Асмолов В.Г., Семченков Ю.М. ВВЭР: задание на завтра. Облик АЭС с легководными реакторами следующего поколения, РОСЭНЕРГОАТОМ, №6, стр.3-10, 2010.

2. Duffy R.B., Pioro I.L. Supercritical water-cooled nuclear reactors: revief and status, “Nuclear Energy Materials and Reactors”Vol.II, Encyclopedia jf Life Support Systerm (EOLSS)

3. Основы современной энергетики, т.1 Современная теплоэнергетика, под редакцией А.Д.Трухния, М.: МЭИ, 2008, -472 с.

4. Makhin V.M., Mokhov V.A., Vasilchenko I.N., Nikitenko M.P. Core problems of VVER-SCP vessel-type reactor. Paper No. 42. 4th International Symposium on Supercritical Water-Cooled Reactors. March 8-11, 2009, Heidelberg,

5. Кириллов П.Л., Пометько Р.С., Смирнов А.М., Грабежная В.А. Исследование теплообмена при сверхкритических давлениях воды в трубах и пучках стержней, препринт ФЭИ-3051, Обнинск, 2005, 51 стр.

6. Кириллов П.Л., Ложкин В.В., Смирнов А.М. Исследование границ ухудшенных режимов теплообмена в каналах при сверхкритическом давлении / Препринт ФЭИ-2988.–Обнинск: ГНЦ РФ –ФЭИ, 2003, 20 стр.

7. Мелентьев Л.А. Очерки истории отечественной энергетики: Развитие науч. - техн. мысли - М.: Наука, 1987, 280 стр.

8. Шицман М.Е. Ухудшенные режимы теплоотдачи при закритических давлениях, «Теплофизика высоких температур», т.1, №2, 1963, стр.267-275.

9. Ragheb M. Boiling Water Reactors, chapter 3, 04.09.2011, multimedia_fukushima_data_General Documents_uiuc.edu_Boiling Water Reactors.

10. Соколов И.Н. и др. Опытный реактор корпусного типа для изучения вопросов кипения и перегрева пара, доклад P/306 СССР, Zeneva III,сборник трудов, 1984, стр. 237-247.

11. Соколов И.Н. и др. Опытный реактор корпусного типа и некоторые результаты его энергопуска, Теплоэнергетика, №5, 1968, стр.63-67.

12. Nayak A. K. and . Vijayan P. K Flow Instabilities in Boiling Two-Phase Natural Circulation Systems: A Review(Review Article), Science and Technology of Nuclear Installations,Volume 2008 (2008), Article ID 573192, 15 pages http://dx.doi.org/10.1155/2008/573192

13. Li H., ZhanM., Cu H. et al Heat Transfer Research on Supercritical Water Flow in 2x2 Bundles, report ISCWR-2013, China, Shenzhen March, 2013.

14. I. L. Pioro, R. B. Duffey, “Heat transfer and gidraulic resistance at supercritical pressures in power-engineering applications”, ACME; New York, 2006.

15. Семидоцкий И.И. и др. О взаимосвязи теплогидравлических и нейтронно-физических характеристик легководного корпусного реактора с переменной плотностью теплоносителя в активной зоне реактора (на примере режимов РУ ВК-50). «Обеспечение безопасности АЭС с ВВЭР».Материалы конференции, ОКБ «Гидропресс», 28-31 мая 2013, Подольск
http://www.gidropress.podolsk.ru/files/proceedings/mntk2013/autorun/article141-ru.htm

16. Семидоцкий И.И., Махин В.М. Влияние пространственной гидродинамики и стохастических эффектов на устойчивость расчетной модели корпусного кипящего реактора ВК-50 на основе теплогидравлического кода RELAP5/MOD3.3.— ВАНТ. Сер. Обеспечение безопасности АЭС, 2007, вып.19, с. 111 — 122.

17. Забелин А.И. и др. Особенности водного режима АЭС ВК-50, Симпозиум «Водные режимы водо-водяных реакторов, радиационный контроль теплоносителей и средства снижения радиационной опасности теплоносителей», ГДР Гера, 10-16 ноября 1968 г., стр.72-78.

18. Baranaev Y.D., Glebov A.P., Kirillov P.L., Neutronic Characteristics of a 30 MWt SCW Experimental Reactor: From Water-Cooled Power Reactor Technology to a Direct Cyclr Nuclear Reactor with Supercritical Water Parameters and Fast Neutron Spectrum, report ISCWR-2013, China, Shenzhen March, 2013.

ISSCWR7-2054

European Project "Supercritical Water Reactor – Fuel Qualification Test" (SCWR-FQT): Overview, Results, Lessons Learnt and Future Outlook

M. Ruzickova[1], A. Vojacek[1], T. Schulenberg[2], D.C. Visser[3], R. Novotny[4], A. Kiss[5], C. Maraczy[6], A. Toivonen[7]
[1]Centrum vyzkumu Rez, s.r.o., Hlavni 130, 25068 Rez, Czech Republic,
Mariana.Ruzickova@cvrez.cz
[2]KIT, Hermann-vomHelmholtz-Platz 1, 76344 Eggenstein-Leopoldshafen, Germany
[3]NRG, Westerduinweg 3, 1755 ZG Petten, The Netherlands
[4]JRC-IET, Westerduinveg 3, 1755 LE Petten, The Netherlands
[5]BME, Muegyetem rkp. 9, 1111 Budapest, Hungary
[6]MTA EK, Konkoly Thege Miklos Ut 29-33, 1525 Budapest, Hungary
[7]VTT, Kemistintie 3, 02044 VTT Espoo, Finland

Abstract

The Supercritical Water Reactor (SCWR) is one of the six reactor concepts being investigated under the framework of the Generation IV International Forum (GIF). One of the major challenges in the development of a SCWR is to develop materials for the fuel and core structures that will be sufficiently corrosion-resistant to withstand supercritical water conditions, as well as to gain thermal-hydraulic experimental data that could be used for further improvement of heat transfer predictions in the supercritical region by numerical codes. Previously, core, reactor and plant design concept of the European High Performance Light Water Reactor (HPLWR) have been worked out in substantial detail. As the next step, it has been proposed to carry out a fuel qualification test of a small scale fuel assembly in a research reactor under typical prototype conditions. Design and licensing of an experimental facility for the fuel qualification test, including the small scale fuel assembly, the required coolant loop with supercritical water and safety and auxiliary systems, was the scope of the recently concluded project "Supercritical Water Reactor – Fuel Qualification Test" (SCWR-FQT) described here. This project was a collaborative project co-funded by the European Commission, which took advantage of a Chinese – European collaboration, in which China offered an electrically heated out-of-pile loop for testing of fuel bundles. The design of the facility, and especially of the test section with the fuel assembly, as well as the most important results of steady-state and safety analyses are presented. Material test results of the stainless steels considered for the fuel cladding are briefly summarized. Finally, important outcomes and lessons learnt in the "Education & Training" and "Management" work packages are presented.

1. Introduction

The Supercritical Water Reactor (SCWR) is a Light Water Reactor (LWR), which operates above the thermodynamic critical point of water (374°C, 22.1 MPa). The Generation IV International Forum (GIF) Technology Roadmap has identified several of the key technical advantages of the SCWR compared to conventional water technologies that make it attractive for consideration as a Generation IV system. The main advantages are improved economics because of the higher thermal efficiency, plant simplification as a result of single-phase coolant

directly coupled to the energy conversion equipment and therefore no need for steam generators, steam separators, dryers or coolant recirculation pump. The reference system is operated at a pressure of 25 MPa and at a reactor outlet temperature of 500°C or more, and the reference fuel is uranium dioxide.

As the system uses existing light water technology, there is already extensive worldwide experience in constructing and operating such sort of reactor. The containment design and safety systems may be based on latest boiling water reactor design, and most of the steam cycle components have widely been used in fossil fired power plants operating at supercritical conditions. However, a major challenge for the SCWR is to develop a viable core design, accurately estimate the heat transfer coefficient and develop materials for the fuel and core structures. Significant progress has been achieved in recent years in these areas, and core, reactor and plant design concepts have been worked out in substantial detail, such as the European High Performance Light Water Reactor (HPLWR) concept [1] or the Japanese Super light water reactor or the Super fast reactor [2]. As the next step, the GIF SCWR system research plan proposes to test a small scale fuel assembly under typical prototype conditions in a research reactor. Design and licensing of such a small scale fuel assembly including the required loop and safety systems is subject of the European project described here.

2. “SCWR-FQT”

SCWR-FQT project constituted the European contribution to the collaborative EU-China project, where the Chinese contribution was through the project called Supercritical water cooled In-Pile Test (SCRIPT). The SCWR-FQT project aimed at achieving significant progress towards the design, analyses and licensing of a fuel assembly cooled with supercritical water in a research reactor. The European consortium consisted of seven partners: six research centers and one university. All partners have in the past contributed to the development of the European HPLWR, whether through participating in previous Framework Programme based projects, or as active contributors without project funding from the European Commission.

The Chinese consortium carrying out the parallel project SCRIPT, which was complementary to the European project SCWR-FQT, comprised 9 partners – universities, national research centers and 2 partners from industry, who have previously joined in a national project funded by the Chinese Ministry of Science and Technology.

The project SCWR-FQT started in January 2011 and was executed during a total of 48 months until December 2014, and was co-funded by the European Commission under the Grant Agreement number 269908. The consortium consisted of 7 partners from Europe:

- Centrum výzkumu Řež (CVR)
- Karlsruhe Institute of Technology (KIT)
- Nuclear Research and Consultancy Group (NRG)
- Magyar Tudományos Akadémia Energiatudományi Kutatóközpont (MTA EK)
- VTT Technical Research Centre of Finland (VTT)
- Budapesti Muszaki es Gazdasagtudomanyi Egyetem (BME)
- Joint Research Centre – Institute for Energy and Transport (JRC-IET)

and 9 partners from China:

- Shanghai Jiao Tong University (SJTU)
- Tsinghua University (THU)
- North China Electric Power University (NCEPU)
- University of Science and Technology Beijing (USTB)
- Nuclear Power Institute of China (NPIC)
- China Institute of Atomic Energy (CIAE)
- China Guangdong Nuclear Power Group (CGNPG)
- State Nuclear Power Technology Corporation (SNPTC)
- Xi’an Jiaotong University (XJTU)

3. OBJECTIVES

The High Performance Light Water Reactor (HPLWR), the European SCWR concept [3], has been developed to significant extent since 2006. In the “HPLWR – Phase 2” project (2006-2010), documented by Schulenberg and Starflinger [1], neutronic, mechanical, thermal-hydraulic and safety analyses have been performed to assess the feasibility of this innovative core design. It has been supported by a numerical CFD study on coolant heat transfer inside the fuel assemblies. While heat transfer in supercritical water inside the tubes or around single fuel rods can be predicted with reasonable accuracy, major uncertainties are still expected in rod bundles of the first heat-up step, called the “evaporator”, where the coolant properties change from subcritical to supercritical conditions. Regions of high heat flux are causing cladding temperature peaks which can only be resolved with an ultra-fine resolution of the boundary layer, none of which have ever been confirmed experimentally.

Cladding materials have been tested in autoclaves up to 650°C and stainless steels turned out to be among the most promising candidates [4]. A significant positive influence of cold work, machining, plane milling or shot peening of the cladding surface on the corrosion resistance has been observed, however, rather few experimental data or lack of standardization of certain surface treatments still leave major uncertainties. In-pile tests with coupons at prototypical temperatures and pressures up to 600°C and 25 MPa, respectively, are planned to be performed in a supercritical water loop in the LVR-15 research reactor in Rez, Czech Republic [5]. First tests shall be performed in order to measure the effect of radiolysis and water chemistry on corrosion of cladding materials. These tests will cover typical superheater conditions such as expected in HPLWR fuel assemblies close to core outlet, where the coolant temperature is hottest, but the heat flux is lowest. A test of fuel assemblies under evaporator conditions is addressed with the Fuel Qualification Test (FQT), to be performed in the experimental facility designed within this project.

Hence, the objectives of the proposed project were to make significant progress towards the design, analysis and licensing of a fuel assembly cooled with supercritical water in a research reactor, which include:

- to design a test section, a supercritical water loop and all safety and auxiliary systems required for safe operation of such a fuel assembly test;
- to analyze this test equipment under normal and accidental conditions to demonstrate safe operation;
- to build and operate with supercritical water an out-of-pile test assembly having the same test section geometry, but heated electrically;
- to validate codes for thermal-hydraulic predictions of the flow structure in SCWR fuel assemblies, using the above mentioned out-of-pile test results;
- to focus the material research on those in-core materials which could be licensed in near future and to prepare a qualified, reliable material data base;
- to complete the required licensing documents for this fuel qualification test and thus to find out if a nuclear facility operated at supercritical pressure can be licensed or, otherwise, to identify challenges associated with it;
- to teach and train young scientists in licensing procedures of nuclear facilities including the required quality management methods.

European partners contributed with the design of the facility, as well as most of the analyses, and autoclave tests of the potential cladding materials. The Chinese partners contributed by sharing certain analyses and material tests with the European partners, and especially by constructing the out-of-pile, electrically heated test section designated for the pre-qualification test of the fuel assembly.

4. WORK PACKAGE DESCRIPTION

The SCWR-FQT project consisted of six work packages: WP1: “Design”, WP2: “Analyses of normal operation”, WP3: “Safety analyses”, WP4: “Pre-qualification”, WP5: “Education and Training”, and WP6: “Management”; the technical and research activities are contained in the first 4 work packages. The SCRIPT project was structured similarly in order to complement the

SCWR-FQT project and to profit as much as possible from the European – Chinese collaboration.

5. RESULTS ACHIEVED IN "SCWR-FQT" AND "SCRIPT"

By the end of the project in December 2014, the design of the facility and the necessary analyses had been completed. General corrosion tests as well as mechanical tests of the cladding materials have been performed. The out-of-pile test section is being manufactured and the test is foreseen to be carried out in 2014. The following sections describe some of the results achieved within each work package.

5.1 WP1: "Design"

Design of the Fuel Qualification Test (FQT) facility, including the test section containing fuel rods and all necessary auxiliary circuits, is the purpose of WP1. The initial boundary conditions, especially the size of the test section and the maximum number of the fuel rods are given by the possibilities and constraints of the LVR-15 research reactor. Preliminary design of the active channel with the test section and the necessary loop and auxiliary systems has been available at the start of the project. This pre-design with its operational and safety conditions has been used as input for analyses in WP2 and WP3. The design has been continuously refined according to the results from the aforementioned work packages.

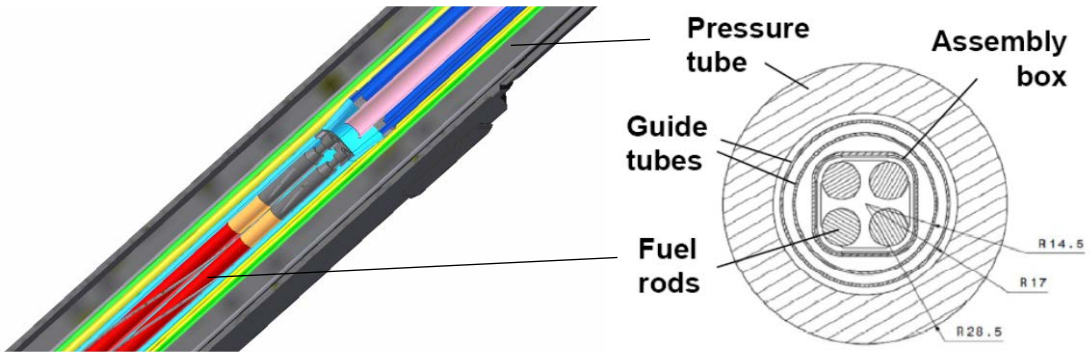

Figure 1. Design details of the test section inside the pressure tube (left) and the cross-section of the test section with the fuel assembly (right).

The test section is placed in the lower part of the active channel constituting of the pressure tube with 57 mm outer diameter and 9 mm wall thickness and positioned in a single cell of the reactor core grid. The pressure tube is fixed in the grid by an aluminium displacer, which simultaneously provides for insulation from the cold reactor water by means of an air gap. It contains 4 fuel rods with 8 mm diameter and 9.44 mm pitch, like the HPLWR assembly concept, inside a square assembly box. The rod total length is 709 mm, which includes the fission gas plenum, thermal compensation mechanism and end caps. The actual fuel height is limited to 600 mm to match with the core height of the reactor. With a ^{235}U enrichment of 19.7%, the 4 rods reach a fissile power of 64 kW. The fuel rods are constrained axially by spacers and radially by wire wraps. A set of disk springs on top of the rods allows for compensation of the different thermal expansion of wire and cladding. The cross-section of the test section with the fuel assembly and its position in the active channel are pictured in Figure 1.

Supercritical water at 25 MPa pressure enters the pressure tube at an inlet temperature of 300°C, as sketched in Figure 2. It is first driven by the outer guide tube along the pressure tube wall (Ch-1, blue), keeping its peak temperature well below 400°C, and heated up then in a recuperator (Ch-3, orange) and by the gamma power released in the structural material to

almost 370°C before entering the test section at height ~0 (Ch-4, red). Before leaving the pressure tube, a U-tube cooler in the upper part of the pressure tube (Ch-4, red) reduces the coolant temperature back to 300°C. The design details of the recuperator and cooler inside the active channel are illustrated in Figure 3.

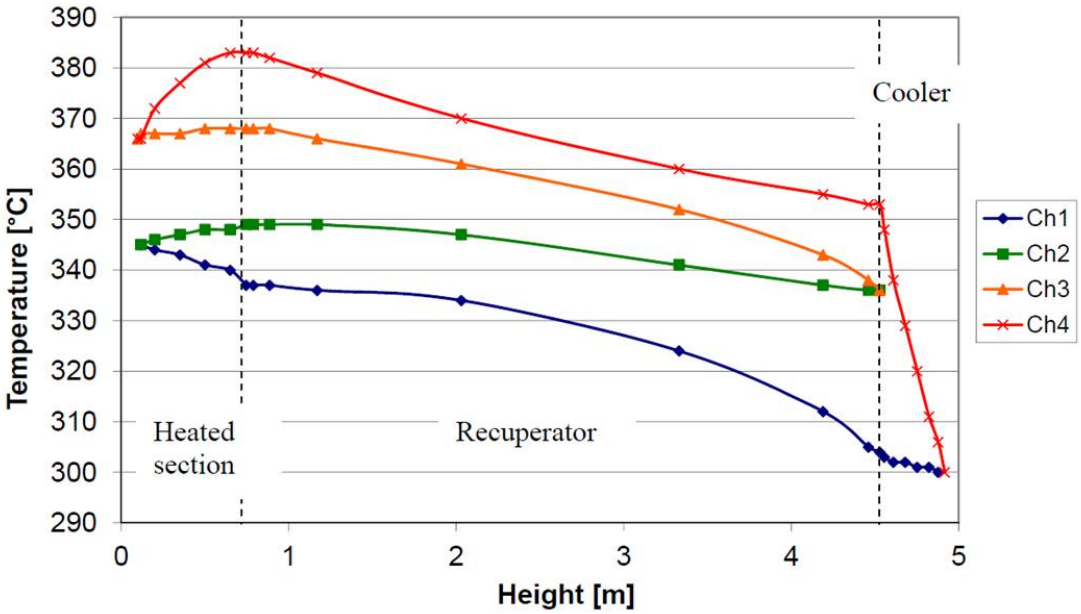

Figure 2. Steady state temperature distribution inside the pressure tube [7].

The fuel assembly dimensions together with key operating parameters are summarized in Table 1.

Table 1. Summary of key operating parameters and fuel assembly dimensions

Parameter	Value
Rod diameter (4 rods)	8 mm
Pitch	9.44 mm
Total rod height	709 mm
Fuel height	600 mm
Fissile power	63.6 kW
γ-heat power	9.8 kW
Nominal operating pressure	25 MPa
Nominal operating temperature at inlet of active channel	300°C
Nominal operating temperature at outlet active channel	300°C
Inlet temperature in the test section (fuel assembly)	366°C
Outlet temperature from the test section (fuel assembly)	386°C
Nominal flow rate in active channel	900 $kg.h^{-1}$
Total volume of water in primary circuit	57 dm^3
Coolant velocity around fuel rods	3÷4 $m.s^{-1}$

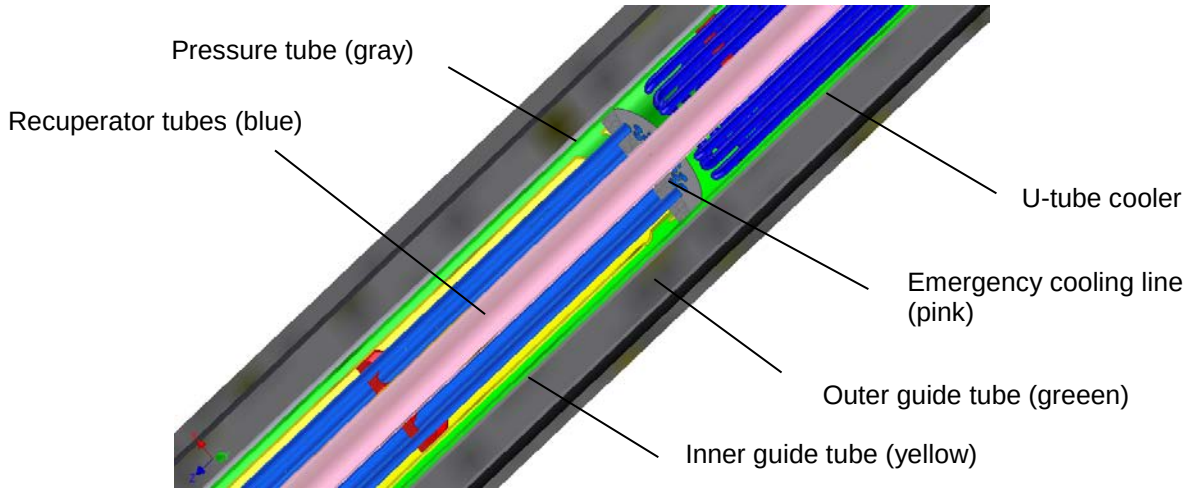

Figure 3. Design details of the recuperator and the U-tube cooler inside the pressure tube.

These test conditions represent the most challenging part of the evaporator in which the bulk temperature of the coolant is slightly below the pseudo-critical temperature of 384°C at 25 MPa, but the cladding temperature is higher than the pseudo-critical temperature, such that a deterioration of heat transfer is challenged [6]. The peak linear heat rate of the fuel rods corresponds with a peak heat flux of 1500 kW/m^2, and the design mass flow corresponds with a coolant mass flux of 1380 kg/m^{2}s. For the first test series to be performed, the available stainless steel 316L, qualified for reactor applications, shall be used for fuel claddings, which implies that the peak cladding temperature must be kept below 550°C under normal operating conditions.

Mechanical parts of the FQT loop are assembled in 2 blocks placed on top of each other on a platform and installed in the adjacent building (currently under construction) to the existing reactor hall. Inlet and outlet lines of the primary system are lead through a shielded duct from the primary block into the reactor hall and through the reactor shielding into the reactor, where they are connected to the active channel. The active channel with the test section is inserted into the reactor. The overall model of the facility (the upper block with auxiliary systems is not shown) is shown in Figure 4.

All active parts of the loop are situated in the lower block, listed as follows:

- Primary circuit;
- Safety system (including depressurization system);
- H_2 treatment system;
- Purification system of primary circuit;
- Measurement system of primary circuit up to mechanical filter MF-2;
- Hot part of the sampling system.

Systems situated in the lower block:

- Secondary circuit;
- Tertiary circuit;
- Water chemistry system and dosing system of primary coolant;
- Cold part of the measurement system of primary circuit;
- Cold part of the sampling system;
- Main parts of the draining system.

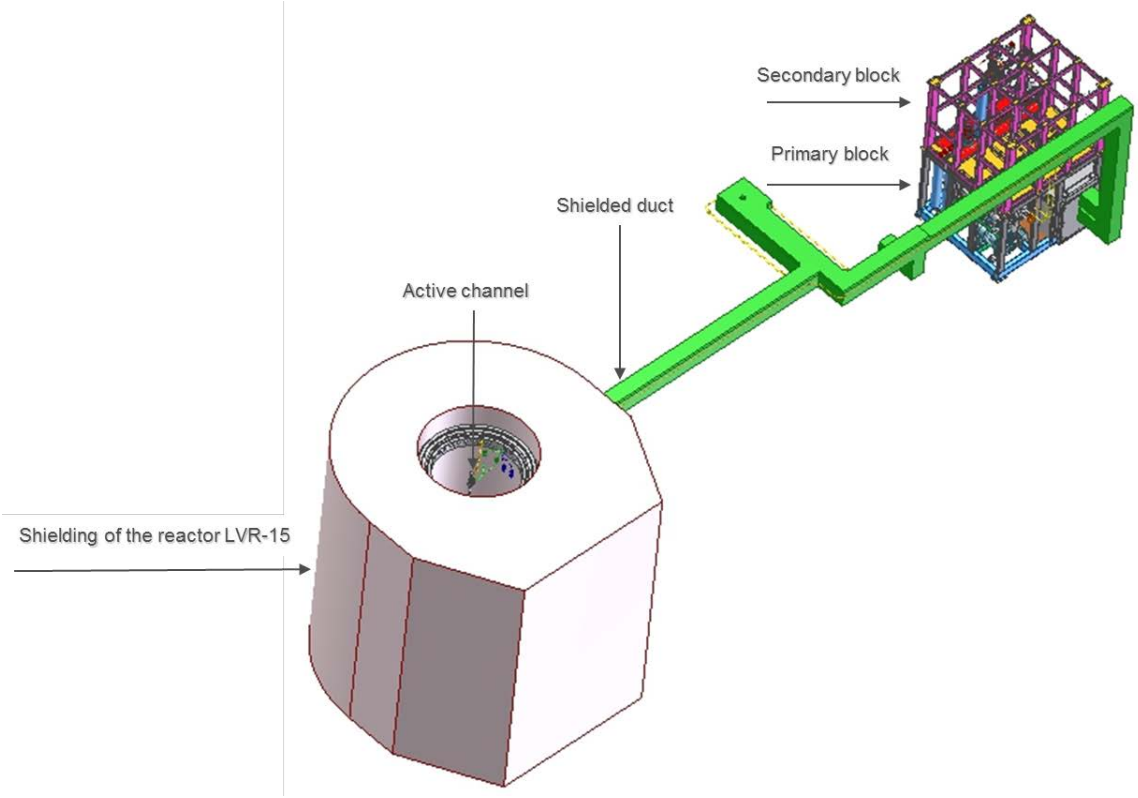

Figure 4. Overall model of the FQT facility.

The FQT facility shall be the first experimental facility for testing of nuclear fuel in the LVR-15 research reactor, and therefore, a fuel handling system has been designed that shall enable dismantling the active channel and removing the test section. A model of the fuel handling system is shown in Figure 5. This fuel handling system shall be used in the case of a failed experiment during which radiological release into the coolant water may be expected; a successful experiment that will end without failure of the test section may be dismantled using standard dismantling procedures available at the reactor. The dismantling procedure shall start with disconnecting the inlet and outlet coolant lines from the pressure tube by freezing the headpiece and the connected lines with liquid nitrogen, disconnecting the lines and finally blinding the openings. In the next step, the system will enable the extraction of the internals together with the test section from the pressure tube. Finally, the internals placed in a shielded container may be transported to the hot cells. The handling system and the chosen dismantling procedure shall thus enable to contain all the fission products released during failure inside the loop.

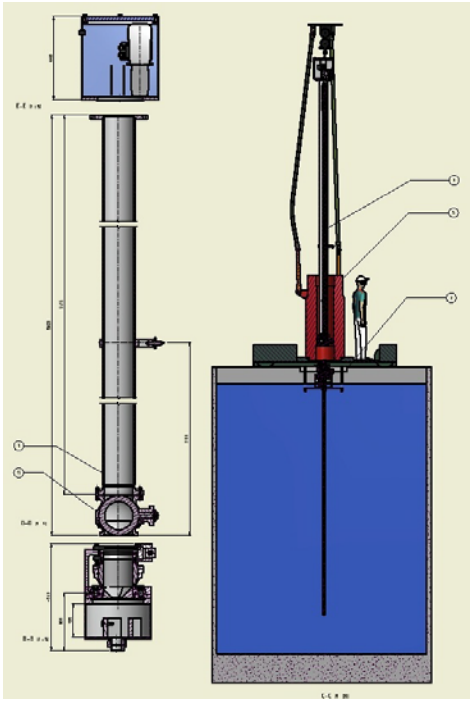

Figure 5. Model of the fuel handling system.

5.2 WP2: “Analyses of normal operation”

The objective of WP2 “Analyses of normal operation” is to ensure the integrity of the in-pile test section including the wire-wrapped fuel rods under normal steady-state operation, as well as during start-up and shut-down, by means of flow and heat transfer analyses, structural analyses and neutronic analyses. Continuous exchange of information with WP1 is necessary to integrate the results from WP2 into the design of the FQT loop.

One of the important tasks in WP2 is to analyze the flow and heat transfer in the 4-rod fuel assembly with Computational Fluid Dynamics (CFD) codes. In Europe, flow and heat transfer analyses for the conceptual design of the fuel assembly have been performed with the widely used commercial CFD code Fluent 6.3. The updated design of the fuel assembly, modified during the project, has been analyzed with the code STAR-CCM+ 7.06 [7]. In parallel, thermal-hydraulic analyses have also been performed in China, using the code ANSYS CFX. Figure 6 shows the comparison between the predicted temperature distribution on the inner surface of the fuel rod; final design of the fuel assembly has been assumed. For better visualization the assembly is scaled by a factor of 1/10 in axial direction. In both cases, a hot spot appeared in the wake of the fuel rod bearing near the inlet. Small differences in results between the two codes may be observed: 12°C in mean surface temperature and 50°C in peak surface temperature. Nevertheless, both codes resulted in cladding temperatures that were well below the acceptable peak cladding temperature limit of 550°C. More details on the CFD calculations of the fuel assembly have been published elsewhere [8].

In the next step, bending of the fuel rods due to thermal stresses has been assessed.

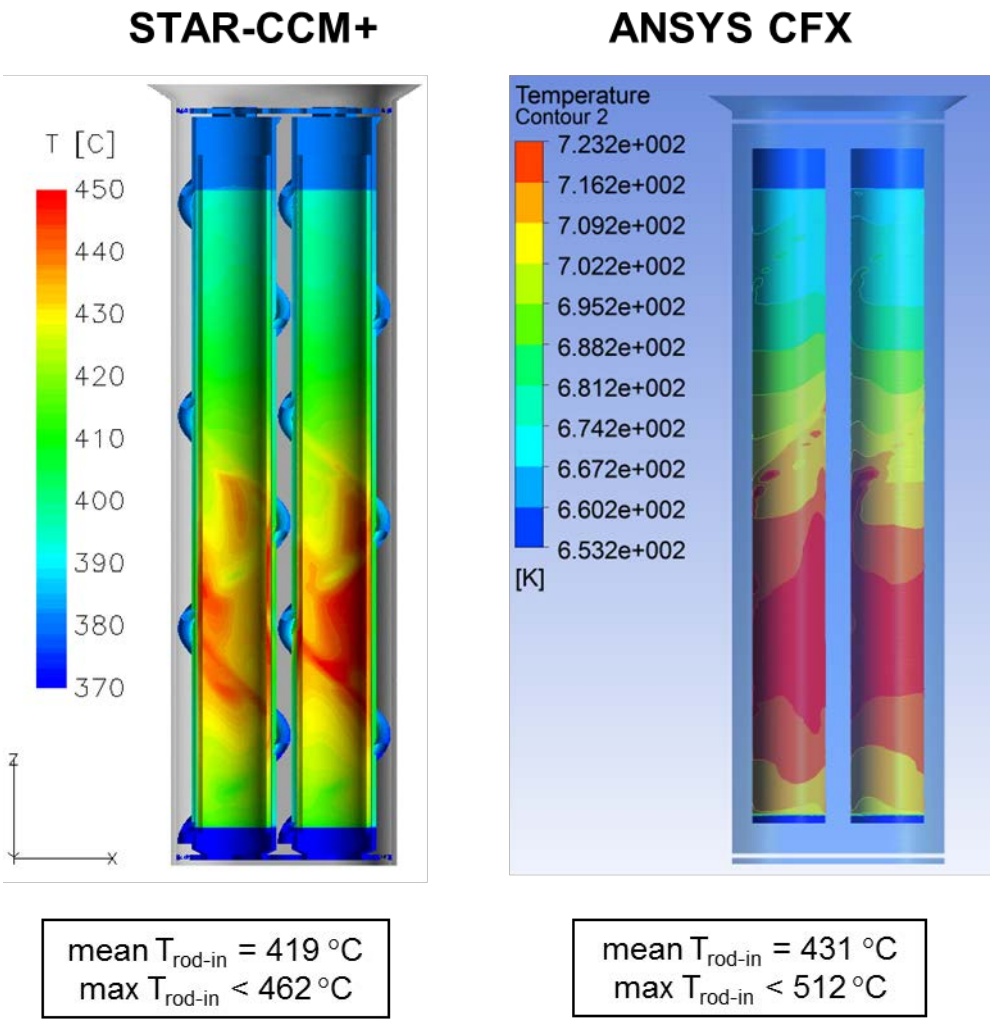

Figure 6. Predicted temperature distribution for the wire wrapped 4-rod fuel assembly.

Analyses of flow distribution at inlet and outlet of the test section have been performed in ANSYS CFX 13.1 that provided results indicating that changes of the fuel assembly design are necessary. Analyses showed a large vortex near the inlet into the fuel assembly, and stagnant areas generating a hot spot behind the foot piece situated a little further down the flow path. These results have led to redesigning the bottom closure of the fuel assembly as well as the foot piece. The new designs of the fuel assembly components have sufficiently eliminated the undesirable phenomena [9]. Figure 7 on the left shows the large vortex found in the flow direction changing chamber situated at inlet into the fuel assembly with a disk bottom closure (conceptual design), and on the right a stabilized velocity field when an improved design of the bottom closure is used (updated design). Figure 8 on the left shows the stagnant areas found in the conceptual design in corners between the fuel rods and the square assembly box situated directly downstream of the foot piece, and on the right the same situation for the updated design with an improved foot piece. Low velocity zones appear directly behind the stagnant areas which could cause heating deficiencies at the beginning of the heated length, especially in the corner sub-channels. The foot piece used for the updated design almost fully eliminates the low velocity zones due to its optimized shape [9].

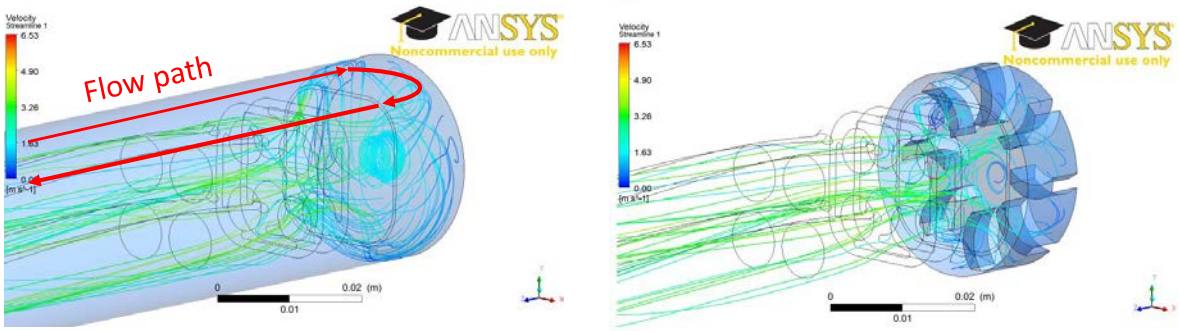

Figure 7. Flow distribution in the flow direction changing chamber for the conceptual design (left) and updated design (right) of the fuel assembly.

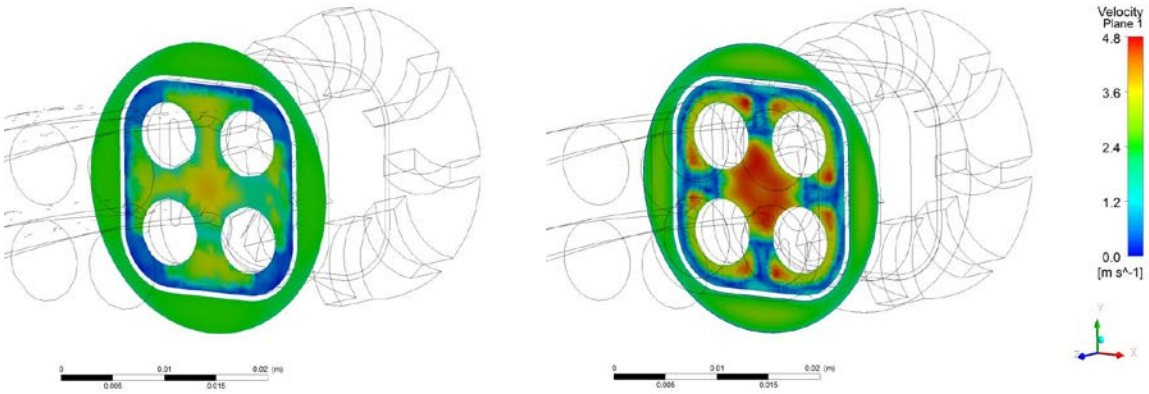

Figure 8. Time averaged velocity distribution for the conceptual (left) and updated (right) foot piece designs on horizontal cross section directly downstream of the foot piece (0.025 m above the bottom closure).

Fuel power and shielding calculations have been performed with neutronics codes for a configuration of the LVR-15 core that reflects (as much as possible) the situation 5+ years ahead. Figure 9 shows the MCNP model of the FQT test section and the entire LVR-15 core configuration.

The total power and power profile of the fuel in the test-section is required as input for the structural and thermal-hydraulic analyses. Table 2 compares the calculated fission and gamma power of the fuel rods in the FQT test-section for the different codes (MCNP/GLOBUS) and code-users (CVR/MTA EK). The results are all close to each other and very close to the maximum linear power limit of 39 kW/m applied in the HPLWR project. Taking into account the uncertainty in the calculations, this limit may be exceeded for the reference core. The actual power of FQT section at the time of irradiation can be tuned by the actual shuffle scheme.

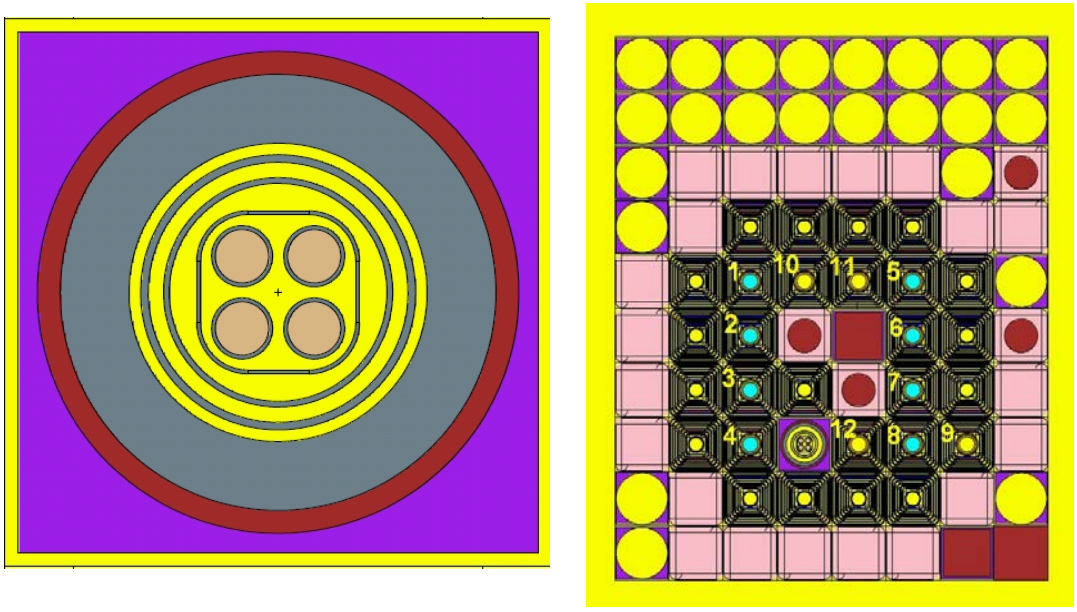

Figure 9. MCNP model of the FQT test-section (left) and LVR-15 core (right) with numbered core arrangement; control rods (1-8), automatic rod (9) and safety rods (10-12).

Table 2. Overall fission and gamma power of the fuel rods in the FQT test section.

Code	Fission power [kW]	Gamma power [kW]	Total power from fuel rods [kW]	Maximum linear power per fuel rod [kW/m]
MCNP (CVR)	61.2	2.4	63.6	37.6
MCNP (MTA EK)	n.a.	n.a.	64.5	38.1
GLOBUS (MTA EK)	n.a.	n.a.	65.9	38.7

5.3 WP3 “Safety analyses”

The Fuel Qualification Test loop is planned to be the first nuclear facility in the world which shall be operated with supercritical water. Like with conventional water cooled reactors, its safety systems shall follow a defense in depth strategy. The fuel matrix is considered as the first barrier against release of radioactive material. The closed fuel claddings form the second barrier. A third barrier is the primary system, which is at supercritical pressure under normal test conditions, formed by the pressure tube, the coolant inlet and outlet lines, the recirculation pump, and the emergency cooling systems. In case this barrier should fail, the reactor, the experimental hall and the bridge between them are designed as a containment, kept under reduced pressure and are thus available as a fourth barrier.

The integrity of the fuel claddings under normal operation shall be ensured by using a qualified stainless steel, by qualification tests of an assembly mock-up with end caps and welds of the wrapped wire, and by a design and operation which keeps the claddings within the stress and temperature limits. Thus, the purpose of the tests shall be to qualify the fuel assembly for typical HPLWR operation conditions, but the test program should not aim at running the tests until the cladding will fail. Material qualification tests of the assembly have been performed in an autoclave at JRC-IET in Petten, using a small mock-up of a single fuel rod and running it at nominal conditions, during a simulated LOCA and the loss of internal pressure inside the rod. A

confirmation of the predicted cladding surface temperatures, and thus a validation of thermal-hydraulic codes, is expected from an out-of-pile test of the fuel assembly in an electrically heated, supercritical water loop at Shanghai Jiao Tong University. Both of the tests mentioned above shall be performed within the scope of WP4 “Pre-qualification”, described in the next chapter.

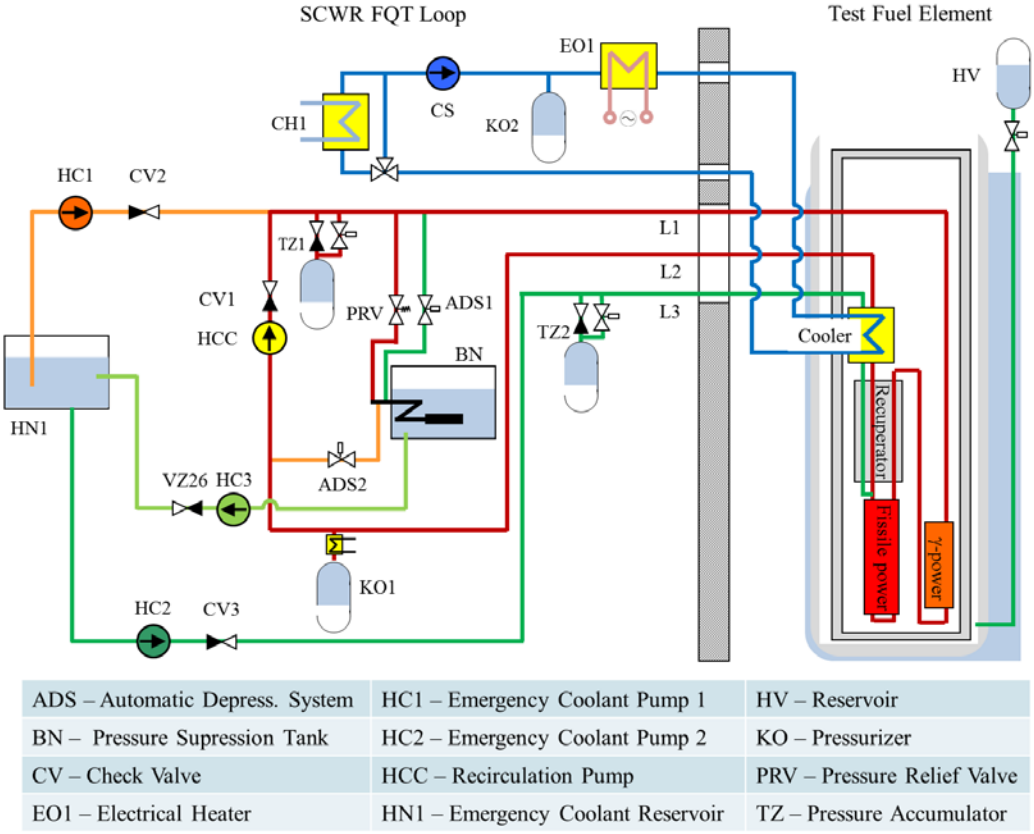

ADS – Automatic Depress. System	HC1 – Emergency Coolant Pump 1	HV – Reservoir
BN – Pressure Supression Tank	HC2 – Emergency Coolant Pump 2	KO – Pressurizer
CV – Check Valve	HCC – Recirculation Pump	PRV – Pressure Relief Valve
EO1 – Electrical Heater	HN1 – Emergency Coolant Reservoir	TZ – Pressure Accumulator

Figure 10. Schematic illustration of the FQT loop. FLCI in orange, ELCI in dark green.

Important safety systems ensuring a loop operation within the design limits include:

- A spring loaded pressure relief valve in the primary system opening passively at high pressure,
- 3 thermocouples measuring the coolant temperature inside the test section, causing a warning first, and a reactor scram if the local coolant temperature exceeds 500°C or if two of these thermocouples fail,
- 2 pressure sensors causing first a warning at high or low pressure, and a reactor scram as soon as the loop pressure is lower than 23 MPa, which will avoid a boiling crisis during depressurization while the reactor is still operating,
- two thermocouples at the inlet of the recirculation pump, causing first a warning at 350°C, and a reactor scram if the coolant temperature exceeds 370°C, avoiding steam like conditions outside the pressure tube,
- monitoring of the pump speed, causing a warning at minimum speed which is required to meet the cladding temperature limit, and a reactor scram if the speed is getting lower than 90% of the minimum speed,
- permanent hydrogen removal in the coolant make-up system to avoid increased hydrogen concentrations in the loop.

Outside normal operation, two emergency coolant injection systems and two automatic depressurization systems are foreseen to mitigate the following risks:

- Loss of coolant due to break of any coolant supply line.
- Trip of the recirculation pump in the primary system.

- Loss of electricity supply for the loop.
- Blockage of the coolant flow path.
- Detachment of the wire wrap of the fuel assembly, causing local blockage inside the test section.
- Fatigue or buckling collapse of the internal structures of the pressure tube.
- Coolant bypassing the test sections, e.g. due to a break of the internal structures of the pressure tube.
- Thermal fatigue of the pressure tube by local thermal stresses due to coolant temperature differences.
- Creep rupture of the pressure tube due to a merely un-cooled test section.
- Spontaneous rupture of the pressure tube due to a sudden, violent steam generation,
    a) Caused by a reactivity excursion of the core and thus a power excursion of the test fuel rods;
    b) Caused by re-wetting of overheated test fuel rods.
- Failure of the pressure tube by hydrogen formation and its detonation.

Safety systems are sketched in Figure 10. Details of these safety systems are shown and discussed by Raqué et al. [10]. The feedwater line coolant injection (FLCI) system supplies coolant to the high pressure side of the supercritical water loop. It is activated if the system pressure drops below 23 MPa which is interpreted as a loss of coolant caused by any leakage of the primary system. Simultaneously, the reactor is scrammed and a depressurization valve on the low pressure side of the loop is opening, causing an accumulator to supply passively 30 liters of cold water to the test section until the FLCI pump has been started. This system is also activated in case of a trip of the recirculation pump. Results of the safety analyses performed so far have been published elsewhere, e.g.: performed safety analyses have been summarized in [11], pressure tube failure and its consequences for the adjacent reactor structures has been described in [12]. Modification of the system code ATHLET for supercritical water application and first validation of the modified code by performing LOCA analysis of the FQT facility have been performed and described in [13].

As discussed above, safety systems have been designed to mitigate design basis accidents, covering a number of anticipated, single-component failures. These systems shall reliably detect accidental conditions, scram the reactor and initiate the emergency cooling systems through the best injection line in each case, including the depressurization of the loop. Therefore, the radiological source term is zero during such design basis accidents. Additionally to these analyses, beyond design basis accidents and their radiological consequences have been studied. The aim was to determine an in-containment source term, which allows the evaluation of radiological hazards for the facility operators in case of an unlikely, severe, multi-component failure. In a first step, a hypothetical accident scenario for the unlikely case of a combined failure of barriers 1 to 3 has been simulated with APROS to obtain a worst case fuel centerline temperature. This temperature sequence has then been used in a second step to determine the radiological source term of the overheated fuel, which is assumed then to propagate without any further filtering to the experimental hall. For this purpose, the CORSOR-O fractional release rate model of Lorenz and Osborne (1995), developed at the Oak Ridge National Laboratory, has been applied. The results of these analyses are described in detail in [14].

5.4 WP4: “Pre-qualification”

The first objective of WP4 was to select candidate materials for the fuel cladding and subject them to testing in autoclaves. The candidate materials for the cladding are commercially available stainless steels of nuclear grade: 347H, 316L, 08Ch18N10T, 316Ti. As a next step, autoclave test of a mock-up of a single fuel rod have been performed. The second objective of WP4 was to construct a similar test section, but electrically heated, and test it out-of-pile at identical operating conditions in a supercritical water loop, which is available at SJTU, China. This test is intended as pre-qualification test before actual testing with fuel.

Material tests have been performed at temperatures of 500°C and 550°C due to the maximum peak cladding temperature being 530°C. Samples were exposed in pure supercritical

water with low oxygen content (150ppb) as well as high oxygen content (2000 ppb). While high oxygen content has a negative impact on general corrosion performance of the materials, no significant effect of oxygen levels on the mechanical properties is observed. Based on the results of general corrosion tests as well as SSRT (Slow Strain Rate Test), stainless steel 316L has been chosen as the most appropriate cladding material for the envisaged fuel qualification test; maximum reasonable duration of the test is foreseen around 6 months. Figure 11 shows the results of weight gain measurements after exposure for both low as well as high oxygen levels. Figure 12 shows the stress-elongation curves of the tested materials in supercritical water at 550°C and 25 MPa, with oxygen concentrations 2000 ppb and 100 ppb; several results in air, which was used as reference environment, are shown as well.

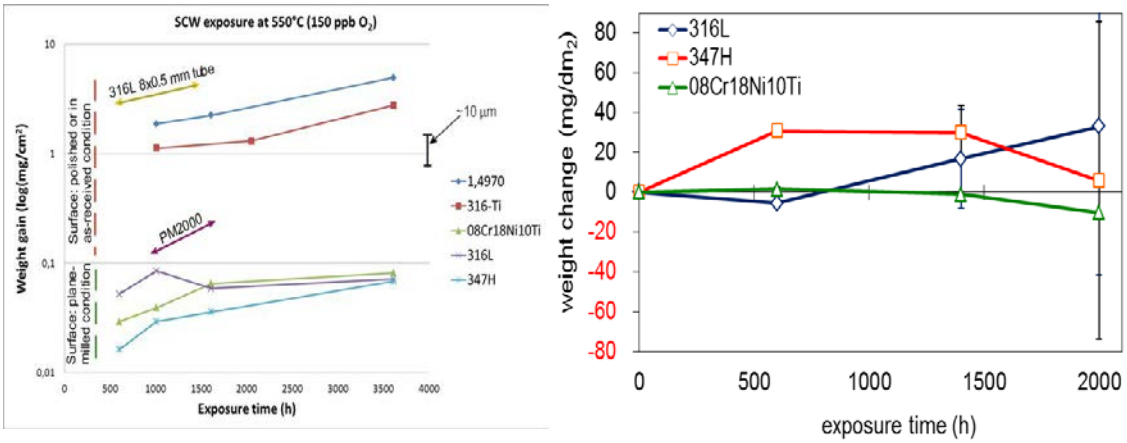

Figure 11. Weight gain of specimens after exposure in supercritical water at 550°C in low oxygen (150 ppb) – left – and in high oxygen (2000 ppm) – right.

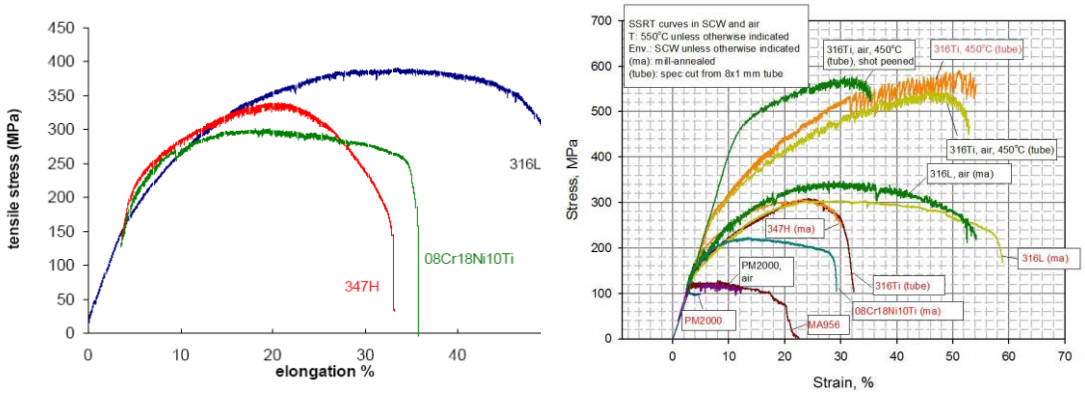

Figure 12. Stress-elongation curves of the indicated materials exposed in supercritical water at 550°C, 25 MPa, 2000 ppb O_2 (left), and in supercritical water at 550°C (SS 316Ti at 450°C), 25 MPa, 100 ppb O_2 and air (right).

Due to a significant delay in the start of the counterpart project SCRIPT in China, the design and construction work on the electrically heated out-of-pile fuel assembly to be tested in China has started after a delay of 18 months. The test section has been scaled by a factor of 1.25 based on current manufacturing capabilities in China. Scaling of the geometry will have no effect on the data expected from the test. In order to obtain as much data as possible, thermocouple positions have been elaborated in detail. The tests will be performed in an existing facility available at Shanghai Jiao Tong University, called SWAMUP pictured in Figure 13; the facility has been slightly adjusted to accommodate the test section. The planned tests

include steady-state operation as well as a number of depressurization transients where experimental data, needed for code validations, are lacking. At present, the tests are in progress and the results are expected to be available at the beginning of 2015.

Figure 13. The SWAMUP thermal-hydraulic test facility at SJTU.

5.5 WP5 “Education and training”

The project has attracted a good number of young scientists contributing to design and analyses with master and doctorate theses or other project work. Two workshops have been organized so far within the project: workshop on Quality Management has been held in September 2012 and workshop on Codes and Experimental Methods to Analyze SCWRs has been held a year later.

5.6 WP6 “Management”

From the management point of view, the project has faced several challenges that were brought about by the preparation, evaluation and approval of the counterpart project SCRIPT in China, as well as by the lengthy process of creating the Coordination Agreement between the European and Chinese consortiums. The Coordination Agreement is equivalent to the Consortium Agreement, a mandatory agreement signed by European consortiums prior to every project. The above mentioned challenges caused that the SCRIPT project started with a delay of 18 months. This delay was partially compensated by extending the SCWR-FQT project by 12 months to a total of 4 years. Valuable comparison of a number of analyses have been performed between results obtained in Europe and in China, whether it was between different codes or to verify the used model of the facility and the reactor core. Moreover, the out-of-pile qualification of the test section and the acquired data obtained from experiments in China will be of great importance for the subsequent in-pile operation with fuel as well as for validation of codes for supercritical water conditions. Therefore, the European – Chinese collaboration may be considered successful, and a valuable experience with such larger collaborations.

Following the end of the SCWR-FQT and SCRIPT projects, the results will be used for building the facility and for the pre-operational safety report needed for the licensing process. Building of the facility will be financed by the SUSEN Project CZ.1.05/2.1.00/03.0108 realized in the framework of the European Regional Development Fund (ERDF).

6. CONCLUSIONS

The SCWR-FQT project has been executed over 4 years starting in January 2011 and ending in December 2014. A detailed design of the facility has been produced, all the foreseen analyses have been performed, results of which were used for the refinement of the design, and material tests for general corrosion and mechanical properties of candidate fuel cladding

materials have been carried out and evaluated. The results will be documented as part of the licensing documentation of the facility required by the Czech nuclear safety authority. Experimental data expected from the out-of-pile test in China needed for validation of CFD and system codes will be available beyond the lifetime of the project in 2015.

Another important goal is to sign the Project Arrangement in Generation IV International Forum (GIF) for a project of the same name, where results of the European project are Euratom's contribution to GIF. China has signed the SCWR System Arrangement in 2014, and a representative has been present at the first Fuel Qualification Test Project Management Board meeting in October 2014.

Acknowledgments

The authors like to thank the European Commission for their financial support of the SCWR-FQT project under the grant agreement n° 269908.

References

1. T. Schulenberg, J. Starflinger, "High Performance Light Water Reactor, design and analyses", KIT Scientific Publishing, ISBN 978-3-86644-817-9, Karlsruhe, 2012.

2. Y. Oka, S. Koshizuka, Y. Ishiwatari, A. Yamaji, Super light water reactors and Super fast reactors, Springer, New York (2010), ISBN 978-1-4419-6034-4.

3. T. Schulenberg, J. Starflinger, P. Marsault, D. Bittermann, C. Maráczy, E. Laurien, J.A. Lycklama à Nijeholt, H. Anglart, M. Andreani, M. Ruzickova, A. Toivonen, "European supercritical water cooled reactor", Nucl. Eng. Design 241 (2011) 3505-3513.

4. K. Ehrlich, J. Konys, L. Heikinheimo: "Materials for High Performance Light Water Reactors", Journal of Nuclear Materials 327 (2004) 140-147.

5. M. Ruzickova, R. Vsolak, P. Hajek, M. Zychova, R. Fukac: "The Supercritical Water Loop for In-Pile Materials Testing." Proc. ISSCWR-5, Vancouver, British Columbia, Canada, March 13-16, 2011.

6. J.D. Jackson: Fluid flow and convective heat transfer to fluids at supercritical pressure, Nuclear Engineering and Design 264 (2013) 24-40.

7. STAR-CCM+, User Manual, CD Adapco, London, 2012.

8. A. Shams, M.S. Loginov, D.C. Visser, F. Roelofs: "CFD Analysis of Flow and Heat Transfer in a Wired Rod-Bundle Cooled with Supercritical Water." Proc. NUTHOS-9, Paper N9P0201, Kaohsiung, Taiwan, September 9-13, 2012.

9. T. Vágó, A. Kiss, S. Tóth and A. Aszódi, "Numerical Investigation on the Inlet and Outlet Effect of Heated Test Section of SCWR Fuel Qualification Test Design", Proc. NURETH-15, Paper 499, Pisa, Italy, May 12-15, 2013.

10. M. Raqué. A. Vojacek, P. Hajek, T. Schulenberg, "Design and 1D analyses of the safety systems for the SCWR fuel qualification test", Proc. NUTHOS-9, Kaohsiung, Taiwan, September 9-13, 2012, Paper N9P0124.

11. T. Schulenberg, A. Vojacek, T. Zeiger, M. Raqué: "Risks and Safety Analyses of an SCWR Fuel Qualification Test Loop", Proc. ISSCWR-6, Paper 13014, Shenzhen, Guangdong, China, March 3-7, 2013.

12. T. Zeiger, M. Raqué, T. Schulenberg: “Study of Consequences of a Pressure Tube Failure for an SCWR In-Pile Fuel Assembly Test“, Proc. NURETH-15, Paper 207, Pisa, Italy, May 12-15, 2013.

13. Ch. Zhou, Y. Yang, X. Cheng: “Feasibility analysis of the modified ATHLET code for supercritical cooled systems“, Nuclear Engineering and Design 250 (2012) 600-612.

14. T. Schulenberg: “Expected Safety Performance of the SCWR Fuel Qualification Test”, ISSCWR-7 Proceedings, 15-18 March 2015, Helsinki, Finland, Paper ISSCWR7-1033.

ISSCWR7-#2055

Conceptual Proposals on Reactor VVER-SCW Developed on the Basis of Technologies of VVER and Steam-Turbine Installations at Supercritical Parameters

Pavel Alekseev, Yurij Semchenkov, Aleksei Sedov, Viktor Sidorenko, Vladimir Silin,
National Research Center "Kurchatov Institute"
Kurchatov sq., 1, Moscow 123182, RF
Tel:+7(499)196-7142, Email: Sedov_AA@nrcki.ru

Viktor Mokhov, Mikhail Nikitenko, Valentin Makhin, Andrey Churkin
OKB “GIDROPRESS”
Ordzonikidze Str., 21, Podolsk 142103, RF
Tel:+7(495)502-7910, Email: Nikit@grpress.podolsk.ru

Abstract

One of principal condition of ensuring sustainment development is creation of Nuclear Power System (NPS) with next-generation reactors, operated in closed fuel cycle. In such an improved NPS the even heavy isotopes of thorium-232 and uranium-238 should be effectively involved in production of secondary nuclear fuel. Utilization of these isotopes for breeding in vessel-type LWRs will require considerable upgrade of this kind of reactors. One of possible innovation ways of advancement of LWRs relates with the use of light-water coolant of supercritical parameters. This allows both enhancing efficiency of energy conversion system of Nuclear Power Installation and getting the fast neutron spectrum in the core, improving visibly reproduction of secondary nuclear fuel in reactor.
During 2008-2011 yrs. a number of Russian research and design organizations were developing conceptual studies for three variants of innovative VVER with supercritical water coolant (VVER-SCW). Conducted elaborations and studies based on achievements of technologies of VVERs and super-critical steam-turbine installations of the fossil-fuel plants. In the result the main requirements for VVER-SCW and the main system objectives on the cost indexes and fuel consumption characteristics has been formulated. Two-circuit nuclear installation with indirect power conversion has been chosen as basic variant for further development. A matrix of problems has been compiled to be solved and a R&D program has been elaborated for the key technologies in support of this reactor designing. A road map of the works to be done up to construction of a demonstration pilot and commercial power plant has been developed, and the plan of RF contribution in international collaboration on SCWR in the framework of the Generation-4 has been worked out as well.
In this paper the considered variants of the VVER-SCW concepts are briefly described, and their main technical features and characteristics are indicated. The key problems for R&D in support of design of VVER-SCW are specified.

1. Introduction

Analysis of a current state of the primary nuclear fuel market shows that recent decrease of a prises for nature uranium has been mainly related with abrupt reduction of the demand in Japan right after Fukushima disaster and excessive quotation of uranium due to Russian supply in the frame of US-RF treatment "Megatons to Megawatts". As well, a fast growth of shale gas and oil

production has contributed for decrease of all energy resources' prices. To-day scopes and forecasts made by WNA, UxC and other organizations show that current misbalance between market offer and demand for nature uranium will start to reveal even in 2015. Further trend of uranium prices growth with annual rate of 4-5% they relates with a rapid commissioning of now-abuilding Chinese and Indian NPPs as well as restart of a certain part of Japanese NPPs. Besides, OECD analysis of dynamics of uranium mining at the leading world mining sites shows stable tendency for shortening of quantity of relatively inexpensive uranium with a price lower \$80/kg U_3O_8 and growth of share of poorer ores, which give uranium prices more \$130 and (what is a main current resource now) more \$260. A rise of demand for the primary nuclear fuel will result in increase of the prises for uranium enrichment. Simultaneously, the expenditures will grow related with storing of permanently accumulating radwastes and spent fuel.

In this situation, together with necessity of improving economy effectiveness of NPPs, the actual task becomes a wide-scale implementation of the secondary nuclear fuel resources, related with closing the fuel cycle and reprocessing of stored spent fuel. This task will require realization of enlarged breeding of plutonium and ^{233}U from even isotopes of ^{238}U and ^{232}Th in cores and blankets of nuclear reactors. For solution of this task, an introduction of reactors, effectively breeding the secondary fuel, into the system of Nuclear Power as well as considerable upgrade of light-water reactors become necessary.

In prospective, the vessel-type reactor technologies, using high-pressure light water, could enforce possibilities of fuel consumption effectiveness due to enhance the reactor coolant thermodynamic parameters up to supercritical state and realization of fast neutron spectrum in reactor core. Such reactors could both utilize the secondary nuclear fuel and work in regime of self-supplying, producing as much the secondary fuel as it has burnt in them. Note, use of the supercritical water coolant will require upgrade of existing light-water industrial infrastructure, but not creating a new one, as in the case of utilization of liquid-metal coolants for fast breeder reactors.

Resolving the problems of new materials for reactor core, vessel and structures opens a way of stage-by-stage implementation of higher pressures and temperatures of water coolant in reactor installations that could result in rise of NPP net efficiency from 40% at 25 MPa / 500 ^{0}C up to 52% at 30 MPa /650 ^{0}C and allow step-by-step decreasing the equipment and construction blocks sizes, volumes and their metal and concrete consumptiveness.

2. Conceptual studies for SCW reactors made in RF during 2008 - 2011

In period of 2008 – 2011 a few RF organization, NRC "Kurchatov Institute", OKB "GIDROPRESS", SSC RF-IPPE and JSC "Atomenergoproekt", supported by Rosenergoatom Concern OJSC, were conducting R&D for elaboration of innovative VVER with supercritical pressure of water coolant – VVER-SCP. These studies and developments were directed for solution of three main problems: 1) enhancing of Nuclear Installation safety up to the level of avoiding of necessity of evacuation of population even in the sequence of beyond design severe accident; 2) decrease of specific costs for NPP construction and operation; 3) decrease of expenditures for fabrication, handling, transport, storing and reprocessing of used nuclear fuel.

Two-circuit Nuclear Power Installation with indirect power conversion has been chosen for further development. In the result of the work the matrix of problem to be solved for VVER-SCP and R&D Program on key technologies have been developed, a Road Map on designing and construction of a pilot demonstration and commercial power block has been elaborated. A part of R&D works has been defined for collaboration with SCWR research groups in the frame of International Forum Generation-4.

The main G-4 system requirements were demanded to the developed reactor concepts: sustainment development, economical efficiency, safety and reliability, non-proliferation and physical protection. Besides, additional specific requirements were formulated for VVERs-SCP:

- Adaptability to requirements of the Nuclear Power System with the closed nuclear fuel cycle (utilization of U-Pu and Th fuel of different isotopic content), maximum decrease of nature uranium consumption;
- Maximum possible utilization of mature technologies of light-water reactors with account of tendencies of their advancement;
- Multi-functionality: enlargement of power series, enhancing of market adaptability, extended power maneuvering, possibility of multi- coproduction (district heat, water demineralization, chemistry and so on).
- Industrial construction and fabrication with account of leading world experience in reactor and other technologies.

The main challenge for VVER-SCP was called a creation of commercial power block with high thermodynamic efficiency and operation in closed fuel cycle with self-supplying by secondary fuel. The following goal characteristics were formulated for VVER-SCP:

- Effective utilization of fissile and fertile materials: getting the ratio of the loaded/unloaded fissile heavy atoms up to ~ 1.0 – 1.05;
- Increase of NPP net efficiency up to 40 - 42 %;
- Appropriate capital and O&M costs (as in requirements of G-4);
- Appropriate level of safety, protection and non-proliferation (as in requirements of G-4).

In the result of conducted in 2008-2011 R&D works the technical proposals has been developed to the design of the following three variants of VVER-SCP:

- VVER-SCP 1700: one-circuit two-loop Nuclear Power Installation with direct power conversion, one- or two- coolant pass through the reactor core, fast-resonant neutron spectrum in the core, fed by subcooled SCP water and producing an overheated steam for a turbine.
- V-670 SCPI: Two-circuit Nuclear Power Installation with indirect power conversion, having integral lay-out of primary circuit equipment inside reactor vessel with natural circulation of the primary coolant, epithermal-to-resonant neutron spectrum. In-vessel steam generator produces a subcritical-pressure lightly-overheated steam for turbine.
- SPCS-600: Two-circuit two-loop Nuclear Power Installation with indirect power conversion, with pseudo-vapor supercritical primary coolant, fast neutron spectrum in the core. Steam generator produces supercritical overheated steam for turbine.

R&D of 2008-2011 concerned to the following circle of questions:

- Research of different variants of fuel cycles for the different variants of VVER-SCP;
- Investigation of the problems of SCP water hydrodynamics and heat exchange;
- Studying of thermal hydraulic and neutron - thermal hydraulic instabilities.
- Development of principle technical solutions for the reactor and core;
- Analysis of phenomena of mass exchange and transport, processes of corrosion, analysis of candidate structure materials and appropriate coolant chemical regime;
- Calculation simulation of predefined accident scenarios;
- Technical-economical assessments for the different variants of VVER-SCP;
- Elaboration of the Program for development of complex mathematics models and codes, development of V&V procedures with verification matrices for the codes for VVER-SCP.

3. Reactor concepts considered in 2008 – 2011 R&D

3.1 One-circuit Nuclear Power Installation VVER-SCP 1700

Up to the moment, OKB "GIDROPRESS" has developed at the conceptual level the reactor design, reactor internals and several versions of hexahedral ducted FAs for a core with a single-pass and double-pass coolant flow diagrams (see Figure 1). Reactor Installation design has been considered for a power unit of 1700 MW (el.). The main characteristics of the reactor are given in Table 1.

A balance-of-plant of VVER-SCP 1700 is based upon utilization of two modified turbine K-800-240-5 used in fossil-plant supercritical power units. In this turbine balance-of-plant scheme the eight-stage system of feed water heating is foreseen, which consist of 4 low-pressure

heaters (LPH), deaerator and 3 high-pressure heaters (HPH). LPH 1 and LPH2 are the vertical mixing-type heaters. Main condensate goes to LPH1 and then is pumped into the LPH2. Going then through LPH3 and LPH4 the water coolant comes to deaerator (D). Three HPHs switched sequentially after deaerator can heat up to 105% of nominal flow rate of feed water. turbine K-800-240-5 has two intermediate steam reheaters between high-pressure cylinder (HPC) and mid-pressure cylinder (MPC) as well as between MPC and low-pressure cylinder (LPC). On the contrary, the modified turbine installation of VVER-SCP 1700 has no steam reheating in reactor and uses proven scheme with indirect reheating of the steam after MCP by part of hot steam going from reactor (see Figure 2).

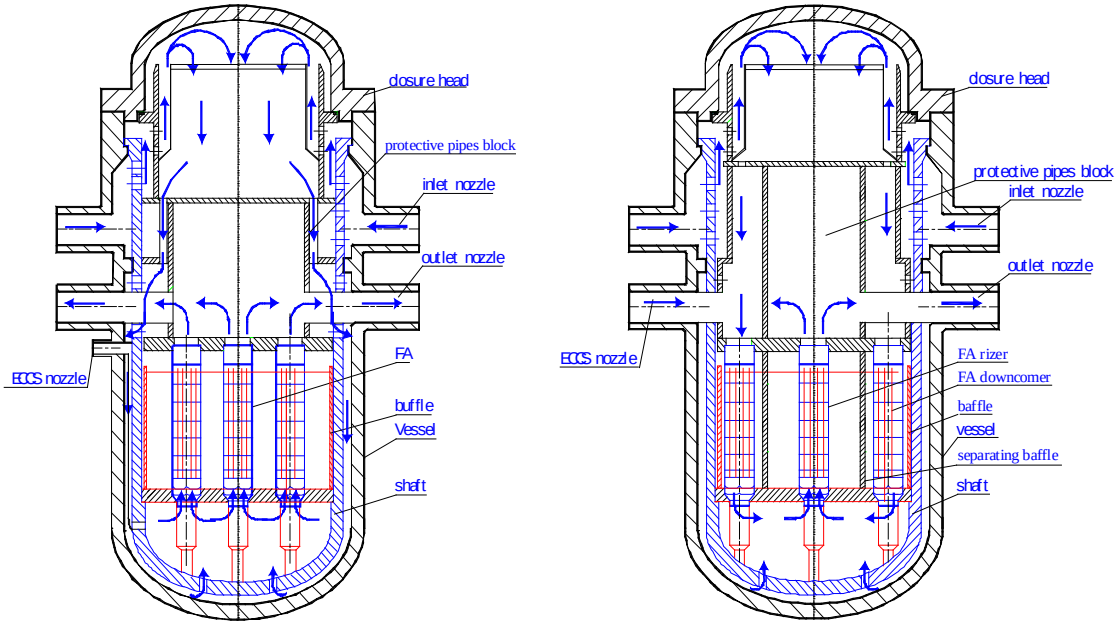

a) b)

Figure 1. Diagram of flows in reactor for the variants of one (a) and two (b) coolant passes through the reactor core.

Table 1. Main design characteristics of VVER-SCP 1700.

Name of characteristics	Value
Power of reactor thermal / electric, MW	3830 / 1700
Flowrate of the reactor coolant, kg/s	1890
Pressure of the coolant at the reactor outlet nominal / disign-limited, MPa	24,5 / 27
Temparature of the coolant at the reactor inlet/outlet, °C	290 / 540
Temperature of the vessel (disign upper limit), °C	350
Temperature of the in-vessel structures (disign upper limit), °C	600
Life-time of the reactor, years	60
Reactor overall sizes, m: - height - maximum outer diameter	 21.1 5.32

Number of Fuel Assemblies in the core	241
Volumetric power load (core-averaged), kW/l - one-pass core - two-pass core	 107 115
Height of fuel stack, m: - one-pass core - two-pass core	 4.05 3.76
Diameter of the core (equivalent), mm	3380
Start load of weapon-grade Pu into the core, tones - one-pass core - two-pass core	 15.68 9.47
Annual load / unload of fissiles (235U, 239Pu, 241Pu), tonnes/year - one-pass core - two-pass core	 2.65/2.48 2.34/2.18
Burn-up (fuel-averaged), MW-days/kg h.a. - one-pass core - two-pass core	 33.1 39.8
FE cladding damage doze maxixmum, dpa	50
Number of Fuel Assemblies reloads in the fuel campaign	5
Interval between fuel reloads, days - one-pass core - two-pass core	 250 300
Void reactivity effect at the start / end of equilibrium microcampaign, % - one-pass core - two-pass core	 -0,2/0,562 -5,88/-3,64

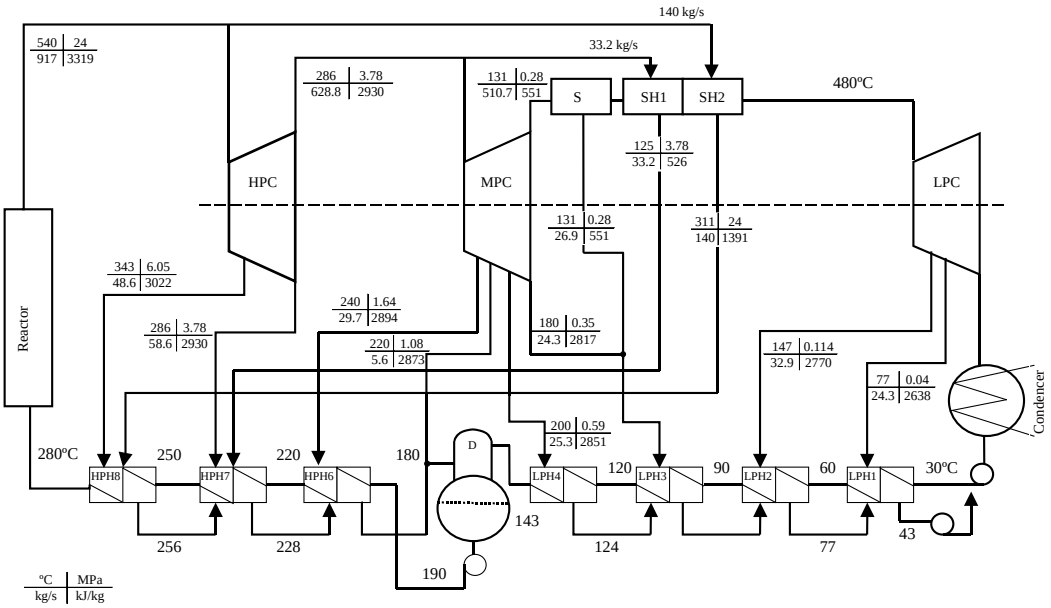

Figure 2. Balance-of-plant scheme of Turbine Installation of VVER-SCP 1700.

The basic diagram of a single-circuit Reactor Installation VVER-SCP 1700 within the containment is shown in Figure 3. Only one coolant circulation loop is shown in the Figure, one channel from each safety system is also shown performing the following functions : containment

isolation (MSIV); passive residual heat removal from the core (PHRS); emergency core cooling system and reactor makeup (PCFS accumulators and tanks, ECCS pumps); prevention of pressure increase in the containment (PPDS, spray system); heat removal from the containment (CECS). The function of limitation of the coolant pressure in reactor executes PORV system, which drops a steam of excessive pressure through a prevention check valve into the relief tank, filled with cold water. BRU system drops excessive pressure in emergency to the big-volume PCFS tank.

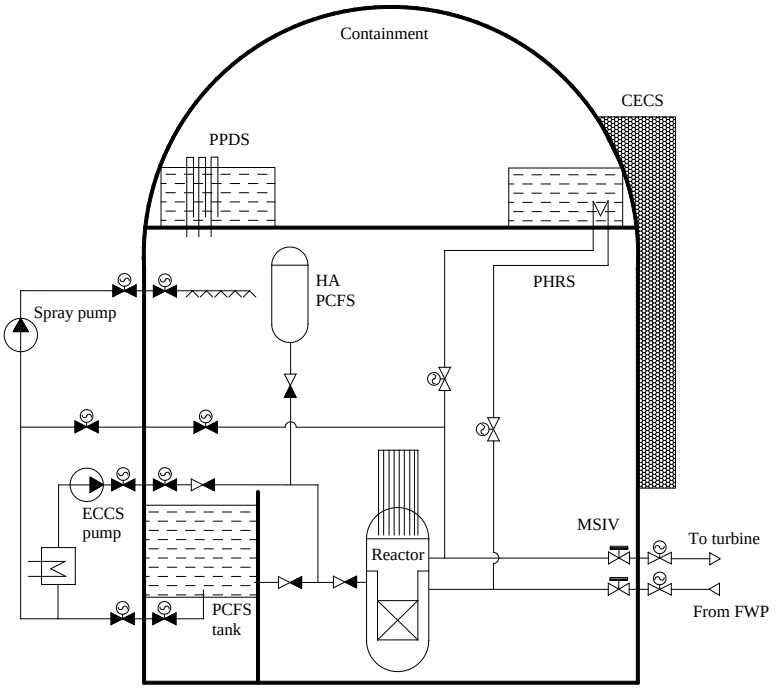

Figure 3. VVER-SCP 1700 safety systems fulfilling the following functions: 1 – containment isolation (MSIV on steam line and feed water pipeline); 2 – passive residual heat removal from the core (PHRS); 3 – emergency core cooling and reactor make-up (PCFS accumulators and tanks, ECCS pumps); 4 – overpressure protection in the containment (PPDS, sprinkler system); 5 – heat removal from the containment (CECS)

3.2 V-670-SCPI: two-circuit VVER-SCP with integral layout of the primary circuit and natural circulation of reactor coolant

In two-circuit Nuclear Power Installation of V-670 SCPI the core, steam generators, in-reactor structures are integrated within a monoblock reactor vessel. Distinguished peculiarity of reactor is a natural circulation of SCP-water coolant inside reactor, which goes up through the core and goes down through the modular steam generators. The other one specificity of the reactor is utilization of compensation of burn-up reactivity margin by control of the core-averaged coolant density. This method of reactivity control in the course of the campaign allows shifting the neutron spectrum, making its softer during burn-up following the gradual decrease of the feed-water temperature. This gives a possibility to avoid the following reactivity-initiated accidents:

- Insertion of big positive reactivity (more than β_{eff}) in the result of unforeseen control rods withdrawal, because of there are not big-weight control rods in the core;
- Insertion of big positive reactivity (more than β_{eff}) in the result of boron-less water ingress into the core, because of no boron is added to the primary water coolant in normal operation.

Besides, procedure of spectrum shifting prevents events with quick reactor power growth in all regimes. Compactness of the integral Reactor Installation makes it possible to use an

additional metallic protective housing, which becomes additional barrier of reactor safety (see Figure 4). Main characteristics of V-670 SCPI are listed in the Table 2.

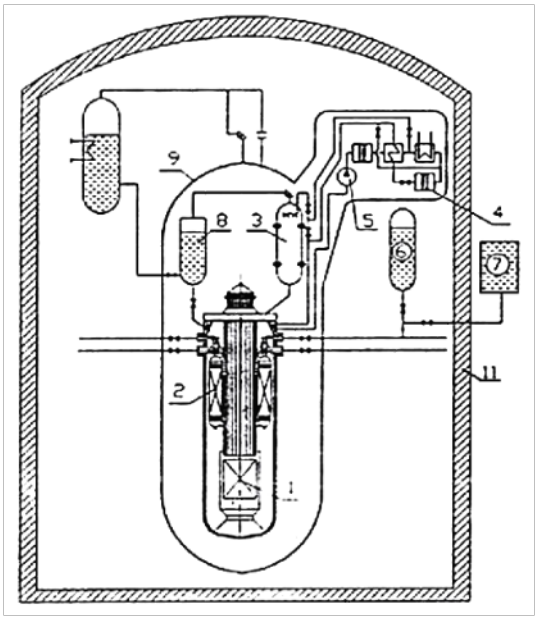

Figure 4. Scheme of primary systems of V-670 SCPI: 1 – reactor; 2 – steam generator; 3 – pressurizer; 4 – coolant purification system; 5 – pump; 6, 7, 8 – borated water tanks of emergency core cooling system; 9 – protective housing surrounding reactor; 10 – bubbler; 11 –reactor building.

High level of safety of integral Reactor Installation V-670 SCPI bases on inherent safety features, active and passive means. Integral layout comparatively loop one provides the flowing advantages:

- Significant shortening of primary circuit lengths, volumes and, therefore, stored energy;
- Preventing of quick drying of the core by the barrier of safety housing;
- Prevention of accidents, related with abrupt decrease of reactor flow rate due to natural circulation of reactor coolant;
- Decrease of probability of the leakage from primary to the secondary circuit due to steam generator's tubes work under the impact of compressive stresses;
- Self-adjustment of the Fuel Assembly flow rates due to big part of driving buoyancy forces;
- Decrease of neutron fluence for the reactor vessel due to big water down comer;
- Decrease of radioactive emissions in normal operation and in the result of the accidents due to additional safety housing barrier.

Emergency core cooling system of V-670 SCPI consists of two independent sub-systems: the primary ECCS and secondary one. Primary ECCS has active and passive parts, secondary ESSC consists of only passive mechanisms. Active part of primary ECCS has 3 independent channels, including pumps of high- and low- level pressure, responding for the emergency feeding the borated water into the core. The passive part of the primary ECCS consists of two independent channels, having hydro-accumulator and big-volume pool with water inventory.

In the case of loss of the primary circuit integrity, the primary coolant leaves reactor vessel and fills safety housing, increasing the pressure in it. Borated water from the hydro-accumulators goes through the check-valves into the reactor and steam-water mix from the volume of the safety housing goes to big-volume water pool and condenses there. Cooling of the latest is provided by water going from a water tank outside the reactor building.

Table 2. Main characteristics of reactor V-670 SCPI.

Name of characteristic	Value
Nuclear Power Installation mains Power conversion system Primary circuit layout Circulation of primary coolant	 Inderect 2-circuit Integral Natural
Reactor power thermal / electric, MW	1635 / 670
Overall reactor sizes, мм Height Maximum outer diameter Thickness	 23500 4780 330
Characteristics of the primary circuit Reactor pressure nominal / design-limited, MPa Coolant temperature, °C At the core inlet (BOL / EOL) At the core outlet (BOL / EOL) Reactor coolant flowrate (BOL / EOL), kg/s	 23.6 / 26 377 / 361 395 / 381 2252 / 2720
Core characteristics Equivalent diameter, mm Height, mm Fuel Pu content in the feeding fuel, % Number of Fas in the core Volumetric power load (core-averaged), kW/l Void effect of reactivity (BOL / EOL), %	 2610 4200 U-Pu MOX 18.5 163 72 - 4.6 / - 23.8
Characteristics of the fuel cycle Load of heavy atoms in the core, kg Time of the fuel life, days Fuel campaign duration, days Averaged core fuel burn-up, MW-days / kg h.a. Loaded / unloaded fissile atoms ratio	 55040 1368 342 42.7 0.82
Characteristics of Turbine Installation Pressure of steam for the turbine, MPa Temperature of steam for the turbine (BOL / EOL), °C Turbine Installation efficiency, %	 14.7 380/370 39 – 40

Secondary ECCS has a function of removal of decay core heat through the secondary circuit systems. It consists of 2 independent channels having hydro-accumulators and low-pressure water tank located in the Reactor Building. When the feed-water pumps stop the hydro-accumulators begins to feed the steam generators with their water. The accumulators is fed by the condensate of steam going from steam generator through the emergency heat exchanger, where the heat is removed by the intermediate circuit and discharged into the ambient air.

In the case of a sever accident it is foreseen that reactor vessel will be cooled by the water, fed to the safety housing. Calculation simulation showed that in the case of core melting the decay heat can be discharged into the water between reactor vessel and safety housing without destruction of the vessel.

3.3 SPCS-600: Two-circuit VVER-SCP with supercritical pseudo-vapor primary coolant

One of the three considered options of VVER-SCP was a concept of NPP with two-circuit indirect power conversion Nuclear Power Installation, having a fast reactor, cooled by supercritical pseudo-vapour coolant – SCPS-600. The core of this reactor has a tight fuel lattice and pseudo-vapour coolant of 24.5 MPa entering with temperature of 390 ^{0}C and leaving the core with averaged temperature of 500 ^{0}C. Reactor is characterized by fast neutron spectrum and moderate volumetric power load. The secondary circuit has a Turbine Installation with supercritical steam at the entrance of 23.5 MPa and 480 ^{0}C. Layout of the SCPS-600 Reactor Installation is shown in Figure 5, and balance-of-plant scheme is presented in Figure 6. Main characteristics of reactor installation are given in Table 3.

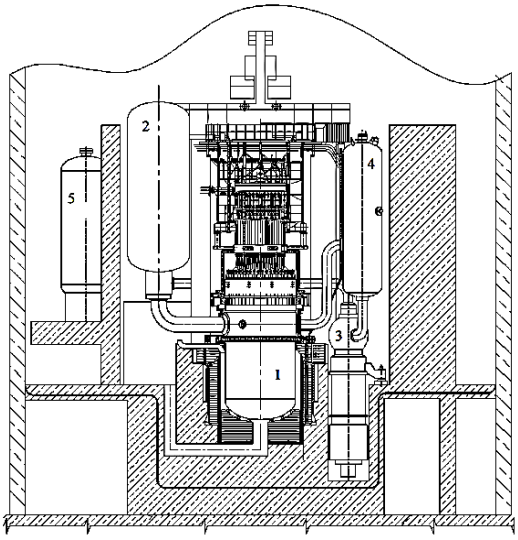

Figure 5. Layout of SCPS-600 Reactor Installation: 1 – Reactor; 2 – Steam generator; 3 – MCP; 4 – Buffer tank-pressuriser; 5 – ECCS hydro-accumulators.

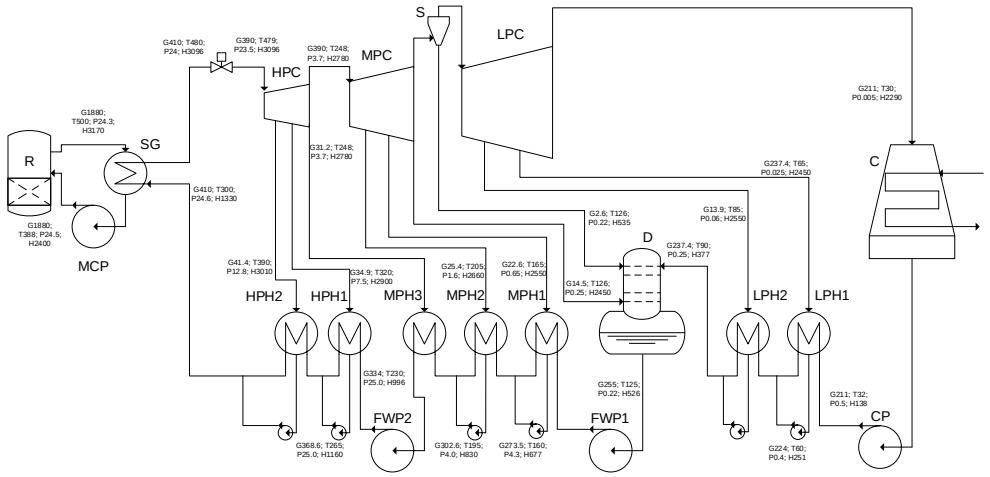

Figure 6. Balance-of-plant scheme of SCPS-600 Nuclear Power Installation: R – reactor; SG – steam generator; MCP – main circulation pump; C – condenser; LPH – low-pressure heaters; D – deaerator; MPH – mid-pressure heaters; HPH – high-pressure heaters; CP – condensate pump; FWP – feed-water pumps; HPC, MPC and LPC – high-pressure, mid-pressure and low-pressure turbine cylinders; S – separator.

Table 3. Main characteristics of SCPS-600 reactor.

Name of characteristic	Value
Type of reactor	Vessel-type
Thermal / electric reactor power, MW	1430 / 600
Net NPP efficiency	40.2%
Primary coolant	Light-water supercritical pseudo vapour
Primary equipment layout	Block-loop
Number of the primary loops	2
Neutron spectrum in the core	Fast
Type of the primary coolant circulation	Forced
Nominal primary coolant flow rate, kg/s	1880
Nominal / design-limited primary coolant pressure, MPa	24.8 / 27
Coolant temperature at the reactor inlet / outlet, °C	388 / 500
Overall reactor sizes, mm (outer diameter / height / thickness)	4535 / 7500 / 320
Number of Fuel Assemblies in the core	349
Numbers of FA of side blanket	72
Core height (without butt blankets), mm	1700
Axial thickness of blankets (central / upper / lower), mm:	300 / 150 / 150
Equivalent core diameter, mm (without side blanket / with side blanket)	3000 /3200
Core-averaged volumetric power load, kW / l	160
Core-averaged linear power load, W / cm	150
Reactor life time, years	60

There are three groups of Fuel Assemblies with different content of PuO_2 in them: 16, 18.5 and 24 % (weight) respectively. The isotopic vector of this Pu corresponds to the self-supply of the reactor in the closed fuel cycle. Depleted uranium with content of ^{235}U equalled to 0.2 % (weight) is located in the butt and side blankets. In the central part of the core there is a central blanket with ThO_2 fuel in it. It serves for breeding the ^{233}U and for lowering the void reactivity effect. In the Table 4 the characteristics of equilibrium reactor fuel cycle are listed.

Table 4. Characteristics of SCPS-600 equilibrium fuel cycle

Name of characteristic	Value
Duration of the fuel micro-campaign, days	330
Fuel load in the core, tones of h.a.	32.3
Averaged / maximum burn-up in unloaded fuel, MW-days/kg h.a.	54.2 / 74.7
Fluence of neutrons of E > 100 keV for 40 years, n/cm^2	$4.6*10^{19}$
Annual fuel consumption, tonnes h.a./year	8.08
Reactivity margin for burn-up, %	1.5
Fissile load / unload ratio	1.02

Reactor Installation of SCPS-600 has the following safety systems:

- Decay heat removal system;
- Emergency high pressure water supply to the core;
- Emergency passive core cooling system;
- Emergency heat removal from steam generator system;
- Emergency feed water supply system.

4. Current state and planning of further R&D for VVER-SCP in the frame of collaboration with G-4

On July 18 2011, RF signed the System Arrangement for the International Research and Development of The Supercritical Water-Cooled Reactor Nuclear Energy System.

At the SSC (System Steering Committee) SCWR G-4 meeting held in Paris on September 28, 2012 RF presented a “Draft RF Plan of Research and Development works in elaboration of Concept Project of Demonstration Reactor Installation with light - water coolant of supercritical parameters for collaboration in the frame of Generation 4 International Forum." It was implyed to join to the SCWR Project Arrangements on differnt directions listed in Table 5.

At the SSC meeting in Petten on September 11, 2013 RF presented 4-year plan of the works as contribution in Project Plan on “Thermal Hydraulics and Safety” of SCWRs. Given proposals are listed in Table 6.

In September 2014 Rosenergoatom Concern OJSC has approved a Program of R&D in support of designing of evolutionary advancing VVERs and international collaboration on reactor direction VVER-SCP in the framework of SCWR G-4. Now, in accord with this Program a contract is prepare with a 3-year work plan up to the end of 2017. In the result of execution of this plan, the new experimental data on heat transfer to SC water in figured channels and more precise neutron data for complex transition neutron spectra typical VVER-SCP cores to be got, the number of thermal hydraulics and neutron-physics benchmarks to be conducted, proposals for SC-coolant chemistry regimes to be elaborated, design and economical analysis of safety and economic efficiency potentials of VVER-SCP to be estimated.

Table 5. RF proposals on collaboration in the frame of SCWR G-4 Project Arrangements

№	Name of task
1	Thermal Hydraulics and Safety
1.1	Development and V&V of computational fluid dynamics codes
1.2	Experimental investigation of SCW hydrodynamics and heat transfer:
1.3	Development, Upgrade and V&V of Neutron-Physics codes for SCW Reactors’ Cores
1.4	Experimental investigation of neutron-physical characteristics for different configurations of SCWR’s Cores under normal and accidental condition at critical assemblies
1.5	Calculations of Thermal Hydraulics, Neutron Physics and Thermal Mechanics in support of designing the projects of experimental facilities, loops, and reactors
1.6	Investigation of thermal hydraulic and neutron - thermal hydraulic instabilities
1.7	Development of Concept of Safety of Vessel-type Reactor with SC light-water coolant
2	Materials and Chemistry
2.1	Selection of candidate structure materials for Reactor and Core
2.2	Development and V&V of analytical model and code for simulation of processes of corrosion, coolant impurities’ transport, activation and deposition at circuit surfaces
3	Fuel qualification, Fuel Element modeling
3.1	Irradiation of fuel, structure material candidates and model fuel elements under condition of different neutron spectrum in Ampules and Test Channel of in-pile SCW loop of experimental reactor at NIIAR
3.2	Upgrade, development and V&V of thermomechanics codes for modeling the Stress-Strain State of fuel elements under normal and accident condition

4	System Integration and Assessment
4.1	Presentation of different conceptual solutions of vessel-type reactors with SC light-water coolant
4.2	Development of Concept and Designing of Low-Power Experimental Reactor with SC light-water coolant

Table 6. RF proposals on contribution in Project “Thermal Hydraulics and Safety”

TH&S Task #	Name of the Task	Comments
WP 2.1 Experimental Heat Transfer Studies		
2.1.1	Heat transfer to water at supercritical pressure in tubes	OKB ”GIDROPRESS” plans to design, mount and operate small SCW rig (MUV) for simulation of SCW heat transfer for flows in tube, annular channel with FE-simulator in tube, 2-3 FE-simulators in figure-carved channel
2.1.2	Heat transfer to water at supercritical pressure in annuli	
2.1.3	Heat transfer to water at supercritical pressure in bundles	
2.1.10	Heat transfer at subcritical pressure	Heat transfer for system pressure of 18-22 MPa can be conducted at MUV rig
2.1.12	Development and validation of best-estimate heat transfer correlations	The new (or renewed) correlation will be developed against the RF tests for heat transfer of SCW in tubes
2.1.14	Preparation of data bank for SCW tubes	Such kind of work goes on now in a few RF institutions
2.1.16	Test of fuel rod cladding ballooning during LOCA	For SCWR candidate structure materials it is planned to conduct series of tests with simulating of behavior of FE claddings on LOCA scenario: fall of the system pressure, decrease of flow rate and following rise of wall temperature
2.1.17	Experimental measurement of pressure loss in the heated / cooled SCW fluid, flowing in the vertical channel	It is planned to conduct experimental measurements of pressure loss in the heated and cooled SCW fluid (with special accuracy in the area of pseudo-critical transition) at MUV rig
WP 2.2 Critical Flow		
2.2.2	Condensation of high-temperature steam in the subcooled water	Phenomena accompanying mixing of superheated vapor with subcooled water is planned to be explored at MUV rig
WP 2.3 Safety Requirements and Evaluation		
2.3.1	Definition of reactor safety requirements and limits	
2.3.2	Conceptual design of reactor protection system	
2.3.3	Conceptual design of diversified shut-down systems	
2.3.4	Conceptual design of emergency core cooling systems	
2.3.5	Conceptual design of residual heat removal systems	
2.3.6	Over-pressurization protection systems	
2.3.7	Development of severe accident management strategies	
2.3.8	Conceptual design of severe accident mitigation systems	
WP 2.4 Stability		
2.4.1	Development of simplified analytical models	An open and closed system (loop) with vertical heated channel will be modeled with account of SCW singular compressibility in pseudo-critical transition region

2.4.4	Supporting experiments	Instability regimes onset limits as well as oscillations of pressure and SCW flowrate are planned to be investigated at MUV rig
WP 2.7 CFD modeling of Flows with Supercritical Water		
2.7.1	Numerical simulations of deteriorated heat transfer	RF conducts now elaboration of new fluid-dynamics model basing on kinetic equations (Boltzmann, etc.). At first stage the simple equation of SCW state (Peng-Robinson) is used
2.7.3	CFD code validation against supercritical heat transfer data or DNS results	CFD code validation together with search of reliable (reproducible) experiments and estimation of experimental methodical and statistical errors
2.7.4	Getting the dependencies of inter-subchannel exchange with the use of CFD analysis of rod bundles' flows.	The dependencies of inter-subchannel exchange (by mass, momentum, energy) will be defined from the results of CFD calculations for the flows in the rod bundles
WP 2.8 Subchannel Analysis		
2.8.1	Subchannel code development/modification for the SCW conditions	Subchannel code TEMPA-SC is now under ongoing development for simulation SCW flows in rod bundles. SCW properties as well as RF heat-transfer correlations are incorporated to the code. Subchannel exchange correlations are planned to be got from CFD analysis
2.8.2	Subchannel code-to-code benchmark	
2.8.3	Subchannel code validation	

5. Conclusion

Technologies of reactors cooled by the light-water of supercritical pressure (SCWR) have been developing since 1960-ths years. In the beginning of the 21st century these elaborations have been recognized as prospective and caused appearing of SCWR direction in the International Forum Generation-4. The case-study works being done in 2008-2011 in Russia resulted in Technical Proposals for designing of NPP having reactor VVER-SCP with supercritical water coolant on three variants of reactor concept:

- VVER-SCP 1700: one-circuit two-loop Nuclear Power Installation with direct power conversion, one- or two- coolant pass through the reactor core, fast-resonant neutron spectrum in the core, fed by subcooled SCP water and producing an overheated steam for a turbine.
- V-670 SCPI: Two-circuit Nuclear Power Installation with indirect power conversion, having integral lay-out of primary circuit equipment inside reactor vessel with natural circulation of the primary coolant, epithermal-to-resonant neutron spectrum. In-vessel steam generator produces a subcritical-pressure lightly-overheated steam for turbine.
- SPCS-600: Two-circuit two-loop Nuclear Power Installation with indirect power conversion, with pseudo-vapor supercritical primary coolant, fast neutron spectrum in the core. Steam generator produces supercritical overheated steam for turbine.

Every of the listed installations have a number of desirable qualities which are required from Generation-4 SCWR reactors. But taking into account the goals of getting the high-effective fuel consumption and reproduction of the secondary fuel with a ratio of unloaded / loaded fissile atoms of 1 – 1.05 together with high NPP net efficiency (not less than 40%) the concept of double-circuit loop-type reactor SPCS-600 with the fast neutron spectrum has been chosen as a basic variant for the following more detailed development.

The R&D program in support of development of design of reactor installation VVER-SCP has been elaborated and the part of these works has been determined for the collaboration in the framework of G-4.

ISSCWR7-2056

Supercritical oxidation of boiler tube materials

Satu Tuurna, Sanni Yli-Olli, Sami Penttilä, Pertti Auerkari, Xiao Huang[1]
Technical Research Centre of Finland Ltd
PL 1000, 02044 VTT FINLAND
+358 40 566 8179, satu.tuurna@vtt.fi
[1]Dept. of Mechanical and Aerospace Engineering, Carleton University, Canada

Abstract

The advantage of using supercritical water (SCW) systems for power generation is based on the increased thermodynamic efficiency when operating at higher temperature and pressure. This has been realised for many years in medium to large size supercritical fossil plants. High efficiency in power generation is not only desirable because of economical reasons but also for enhanced environmental performance meaning reduced quantity of forming ash and emitted pollutants including CO_2. Steam oxidation has become an important issue for steam power plants as operating temperatures increase from current to 650°C and even higher. To achieve these higher steam values new materials are needed. This paper presents results of the oxidation performance of potential new alloys (FeCrAlY, NiCrAl and Sanicro 25) in a supercritical water autoclave environment at 650°C/250 bar, with 150 ppb dissolved oxygen.

1. Introduction

The main target behind the material development for advanced power plant concepts, both conventional and nuclear, is to extend the limits set on the technical and economic performance and operability of the energy production units. The demands on safety, efficiency and reduced environmental impact are the driving forces that guide the development.

The efficiency of conventional power plants is elevated by increasing steam temperature and pressure. In modern medium to large size power plants, improvements require supercritical steam values meaning increasing material temperatures. Increasing temperatures will promote the growth rate of nearly all damage mechanisms. Increasing service temperature accelerates the steamside oxidation rate that will also continuously increase with the growth of the insulating oxide layer, when an approximately constant heat flow is extracted through the heat transfer surfaces. The loss of load-bearing wall thickness and the temperature increase resulting from decreased heat transfer due to forming oxides may lead to creep failures. Spallation of oxides can cause tube blockages leading to possible creep failures due to local overheating and steam flow disturbances, and erosion damage in the turbines [1-4].

The austenitic steels are one of the material options available for superheaters and re-heaters in power plants, the hottest part of the ultrasupercritical (USC) boilers operating at 620°C or the intermediate temperature components for the future 700°C boilers. For alloys with about 18%Cr, the evolution has first seen added Ti (type 321) or Nb (type 347) to reduce sensitisation or loss of available protective Cr by chromium carbide precipitation, for example, due to welding. Relatively high carbon content (e.g. 347H) increases creep strength, and added niobium and surface processing have been used to reduce grain size (347HFG) and to minimise spalling of the internal oxide. For further improvement in the corrosion and oxidation resistance, chromium content has been increased to 22-27%, with corresponding increase in austenitising elements such as Ni, Mn, Cu and N. One of the materials considered for USC boilers is the quite newly developed austenitic steel Sanicro 25 [5-7].

In addition, different coating solutions on high temperature steels are a tempting option for corrosion protection, because the development load bearing tube components is a very slow and expensive process. The utilization of corrosion resistant coatings on high temperature steels (in-core) or nickel-based alloys (out-of-core) has emerged as a possible answer to address the required corrosion resistance of these materials. The ability to tailor the properties of the base material and coating combination, as has been done in the gas and steam turbine industries for many years, offers a means to achieve the mechanical and corrosion resistance needed for the construction of different type of SCWR concepts.

Corrosion resistant coatings for gas and steam turbines are primarily based on MCrAlY (M = Ni, Fe, NiCo, or CoNi) overlay and aluminide (β-Ni(Fe)Al) coatings. These coatings rely on the formation of dense, adherent, and renewable alumina/chromia layers, via selective oxidation of aluminium and chromium to provide high temperature oxidation and corrosion resistance [8,9]. The MCrAlY coatings, composed of β or γ' aluminide embedded in more ductile γ-Ni(Fe,Co) solid solution, are more ductile than aluminide diffusional coatings. They can be deposited by either thermal spray or electron beam physical vapour deposition techniques. The aluminium content in commercial MCrAlY coatings typically varies between 5 and 12 wt%. When Al is combined with Cr, a synergistic effect can result in less Al being required to form a dense Al_2O_3 layer. This is particularly important when considering long term high temperature exposure where Al inward diffusion will take place, leading to the depletion of Al in the coating surface. Addition of Y to the coating alloy enhances alumina scale adhesion and has been observed to prolong coating life [10]; 0.6% Y was included in the FeCrAlY alloy of this study.

Previous tests of two model alloys, Ni-20Cr-5Al and Fe-22Cr-6Al-Y, in SCW at 500°C yielded extremely low and stable weight change over other commercial alloys [11,12], as shown in Figure 1. However, the behaviour of these two alloys at higher temperature in supercritical water or steam is unknown.

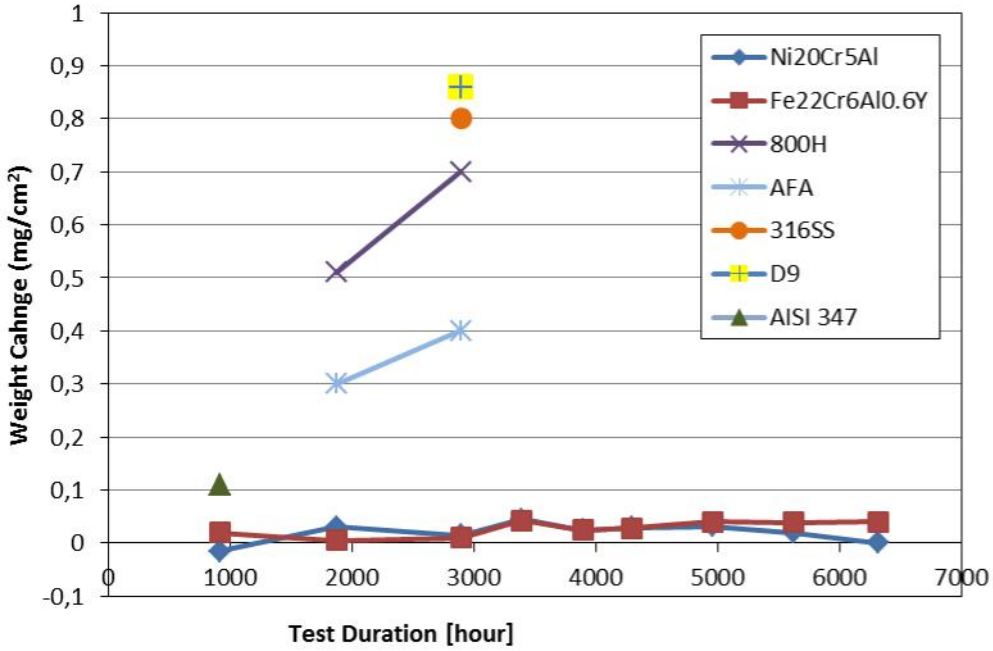

Figure 1. Comparison of weight changes of selected alloys (800H=Fe-32Ni-20Cr-0.76Mn-0.57Ti-0.5Al-0.42Cu, AFA=Fe-20Ni-14Cr-3Al-0.6Nb-0.1Ti, 316=Fe-17Cr-10Ni-2Mn-2Mo-0.65Si, D9=Fe-16Ni-14Cr-2Mn-2Mo-0.6Si-0.3Ti, AISI-347=Fe-11Ni-17.6Cr-2Mn-0.56Nb-0.29Si) with FeCrAlY and NiCrAl [13-17].

Water vapour accelerates the oxidation of most technical steels compared to dry air or oxygen [18-19]. The initial formation of a protective chromium-rich oxide can be followed by

breakaway oxidation in the presence of water vapour due to the formation of a non-protective porous, multiphase and iron-rich scale [20,21]. The above presented results suggest that the oxides formed on both FeCrAlY and NiCrAl are more stable and adherent.

Oxidation rate depends on many variables; service conditions, surface treatment, alloy composition and microstructure [11,23]. The present paper describes the steam oxidation behaviour of FeCrAlY, NiCrAl and Sanicro 25 alloys during the exposure in a supercritical water autoclave environment at 650°C and 250 bar up to 1000 h. In this investigation, the main emphasis was on the oxide scale formation inbeneath forming oxide layer and weight change.

2. Materials and Methods

Steam oxidation test was conducted to three alloys, FeCrAlY, NiCrAl and Sanicro 25. Table 1 shows the nominal compositions of the alloys. Bar stocks of Fe-22wt%Cr-6wt%-0.6wt%Y Al and Ni-20Cr-5Al were cast by Sophisticated Alloys Inc. (PA, USA) using vacuum casting. Sanicro 25 was machined from a tube sample. Specimen geometries varied due to the available material batches, Figure 2. The samples were ground with SiC paper (P1200), washed with deionized water and ultrasonically degreased in ethanol. Exposure testing was carried out in a supercritical water autoclave at 650°C and 250 bar with 150 ppb dissolved oxygen in the inlet flow and a pH of 7 (measured at room temperature in the low pressure part of the recirculation loop). The test duration was up to 1000 h. The autoclave is connected to a recirculation water loop, Figure 3. The high pressure loop consisted of a high pressure pump, a heat exchanger and a preheater. The flow rate during the exposure was around ~5 ml/min resulting in refresh time of the autoclave roughly every 2 hours. Specimens were hung up on the specimen holder rack using electrically insulating ZrO_2 rings.

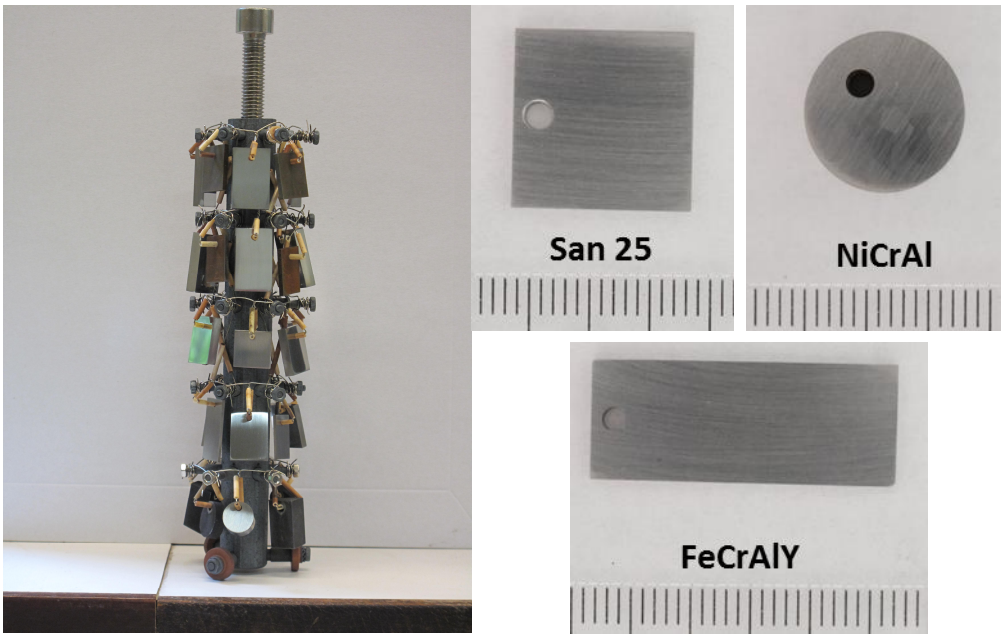

Figure 2. Specimen rack and the samples before exposure to supercritical water (scale in mm)

Table 1. Nominal compositions of studied alloys (wt-%)

Alloy	C	Si	Mn	Cr	Ni	Co	W	Nb	Cu	Fe	Al	Y
FeCrAlY				22						69	6	1
NiCrAl				20	75						5	
Sanicro 25	0.1	0.2	0.5	22.5	25.0	1.5	3.6	0.5	3.0	bal		

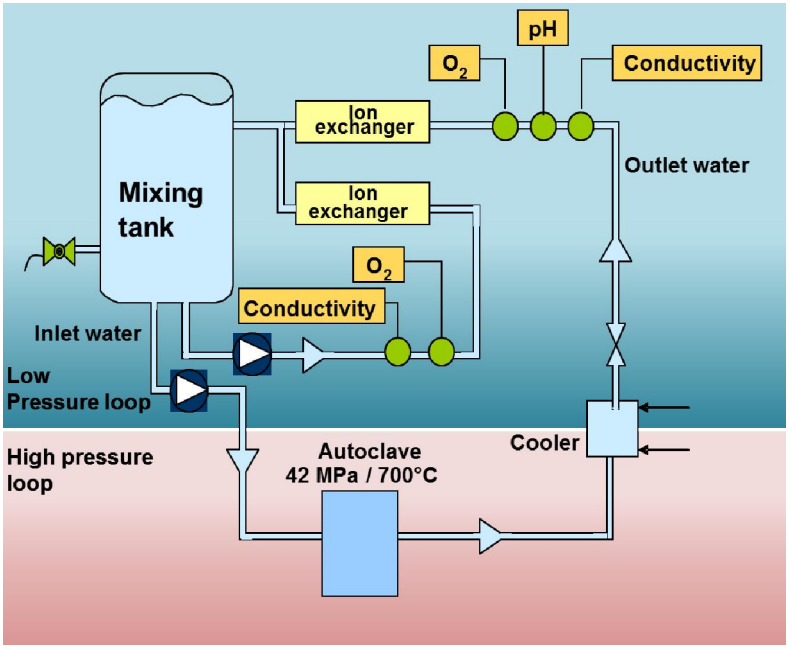

Figure 3. A schematic presentation of the SCW autoclave system with water recirculation loops

The specimens were weighed before and after the exposure with a Mettler AT261 balance to calculate the weight change per unit area. After autoclave exposure, surface appearance, oxide thickness and microstructure were characterised with 3D profilometry (pLy-Confocal Imaging Profiler), light optical microscopy (LOM, Leica MEF4M) and scanning electron microscopy (SEM, Zeiss ULTRA Plus). Surface oxides and compositional changes beneath oxide scale were studied with energy dispersive X-ray spectroscopy (EDX).

3. Results

3.1. 3D surface profiles

Figures 4-6 present 3D surface profiles of the specimens after 300 and 1000 h exposure at 650°C. Figure 3 shows the oxide growth on the FeCrAlY surface during the exposure. After 300 h some higher peaks are already seen on the 3D profile corresponding to the incipient oxide formation. After 1000 h, a continuous oxide network has formed on the surface. The characteristics of the ground surfaces are still visible on the surfaces of NiCrAl and Sanicro 25, Figures 5 and 6, suggesting slower oxide growth rate.

a)

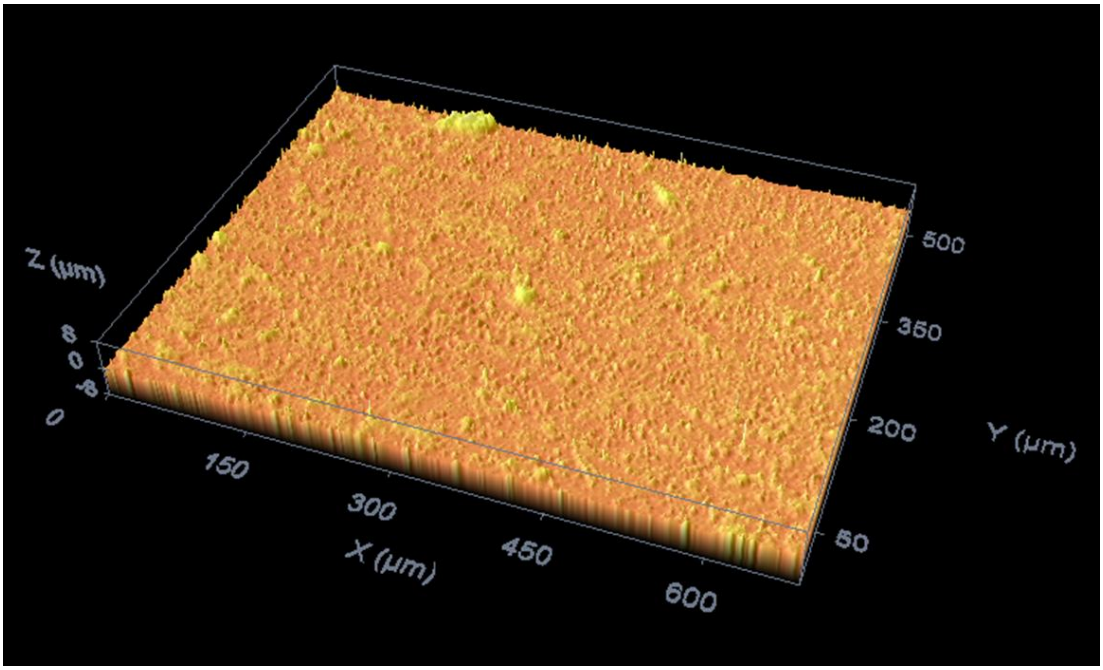

b)

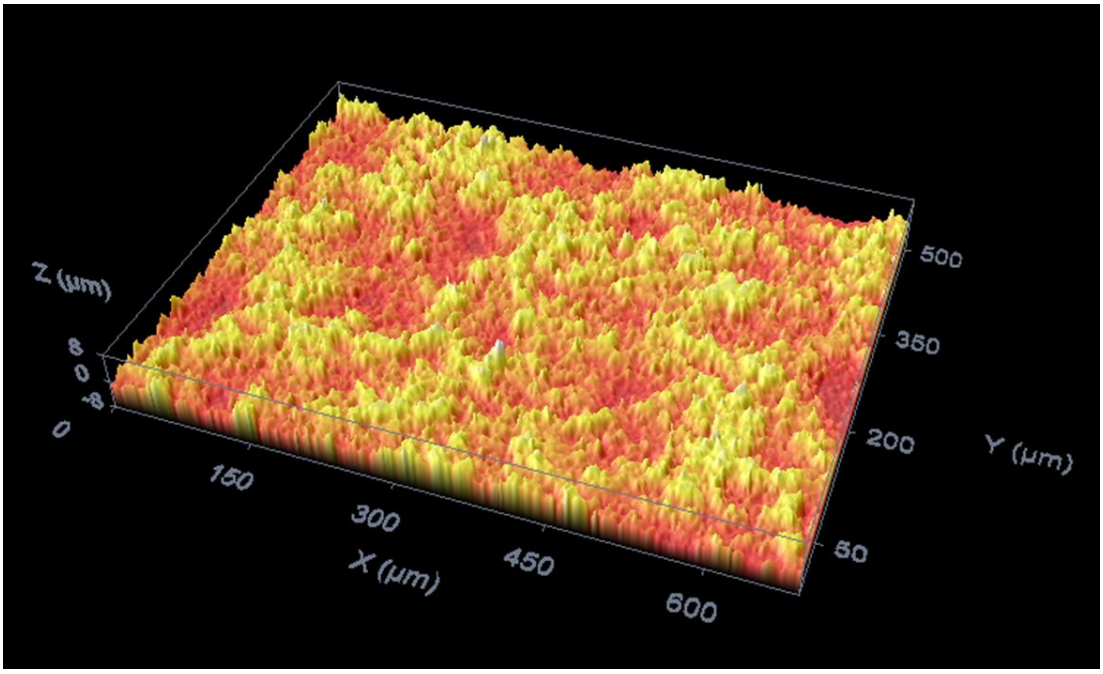

Figure 4. 3D surface profiles of FeCrAlY after a) 300 h and b) 1000 h exposure

a)

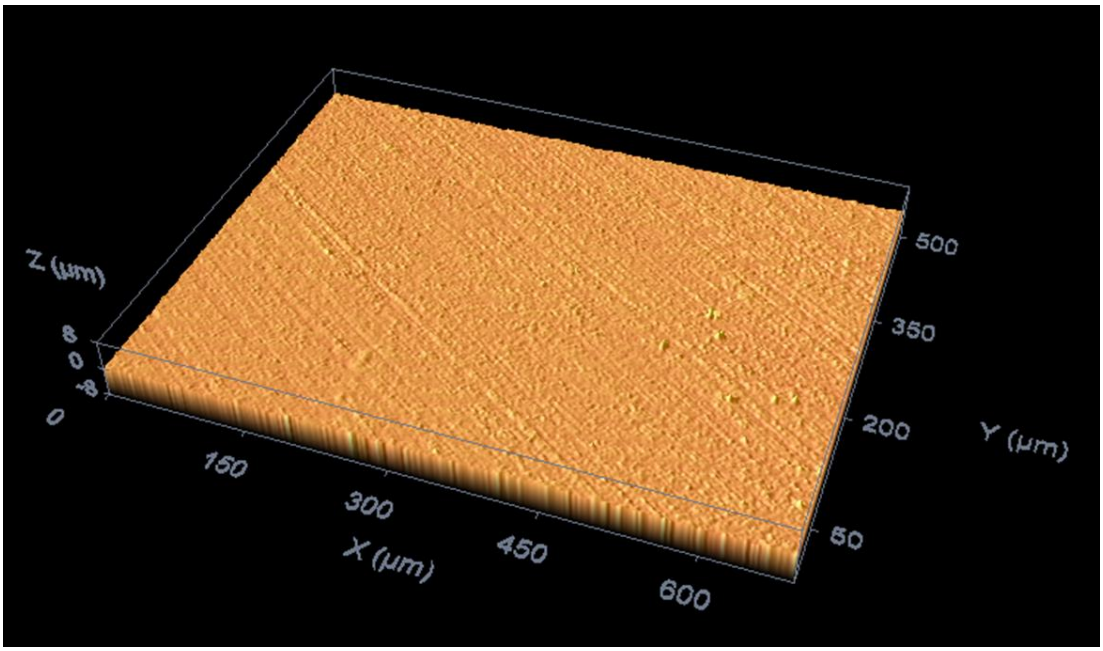

b)

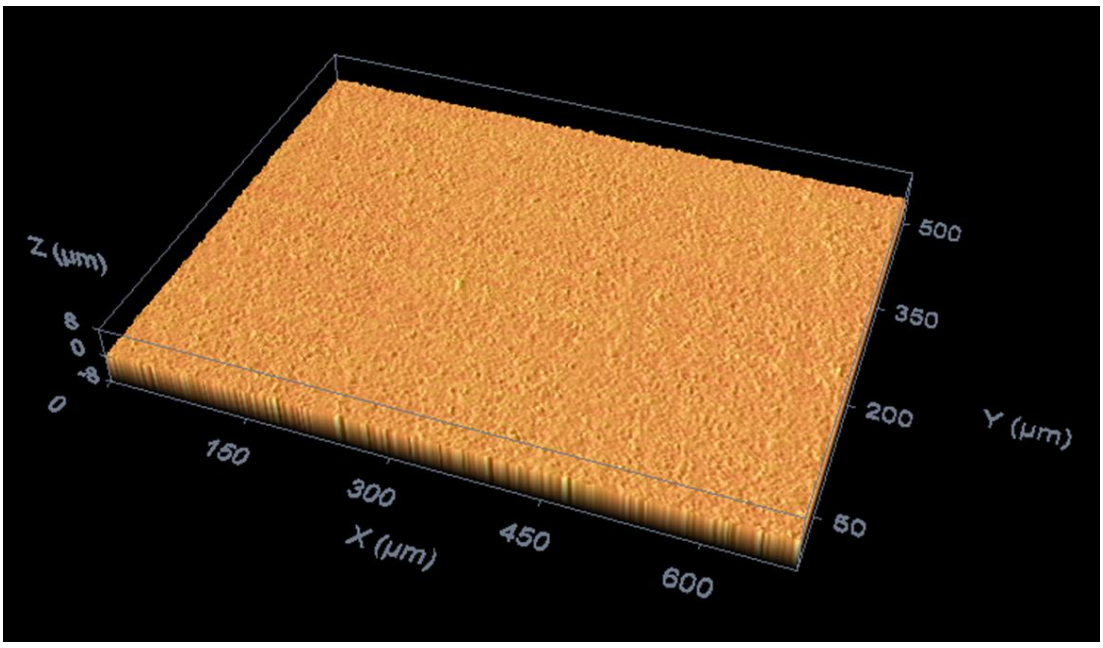

Figure 5. 3D surface profiles of NiCrAl after a) 300 h and b) 1000 h exposure

a)

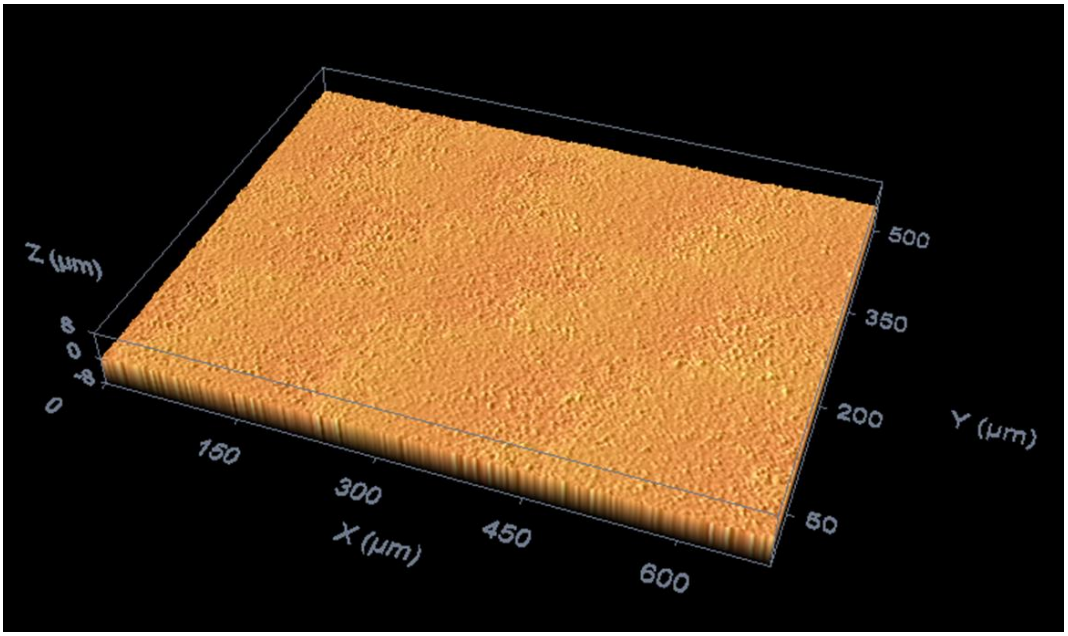

b)

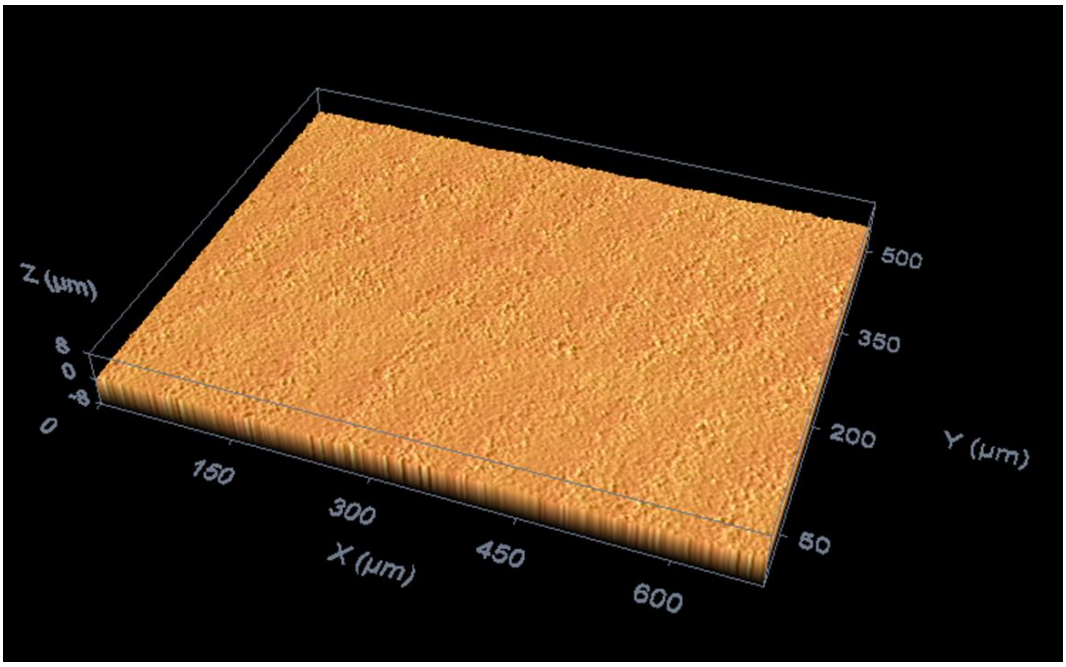

Figure 6. 3D surface profiles of Sanicro 25 after a) 300 h and b) 1000 h exposure

3.2. Surface and cross-sectional studies with SEM

Figure 7 shows the surface morphology of FeCrAlY specimen after 1000 h supercritical water exposure. The whole surface was covered with iron-containing oxide, at the smoother areas (marked “1”), somewhat lower amount of chromium was observed with the EDX. Figures 8-10 shows the cross-sectional view of three specimens after 1000 h exposure at 650°C. A layered oxide with a thickness of ~8-15 µm was observed on the surface of FeCrAlY specimen. This oxide composed of an outward growing iron rich oxide and inward growing layer of spinel oxide containing chromium, iron and aluminium, Figure 11. Aluminium oxide particles were observed on the interface between these two oxide layers. The oxide of FeCrAlY was uneven, relatively

thin bridges (probably smoother areas shown in Figure 7) between thicker areas, suggesting formation via dominating growth of oxide nodules. Very thin (< 1µm) and dense oxide layer was observed on NiCrAl and Sanicro 25 (Figures 9 and 10). This layer is more uneven in NiCrAl, apparently due to partial oxide spallation mainly at sites of small nodules.

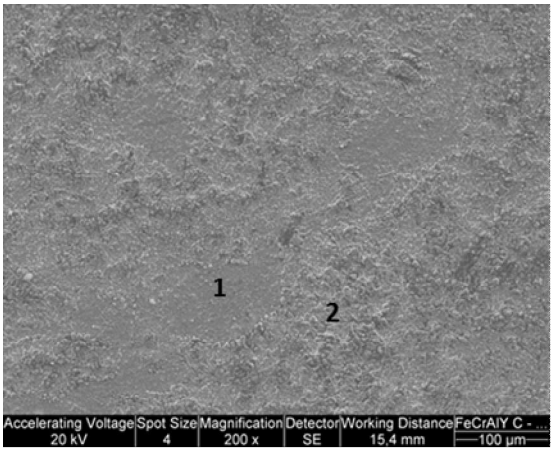

Element	1	2
O K	33.7	26.7
Fe K	63.4	59.6
Cr K	1.6	12.6
Al K	1.1	1.6
Si K	0.2	

Figure 7. Microstructure and EDX analysis results of FeCrAlY surface after 1000 h exposure

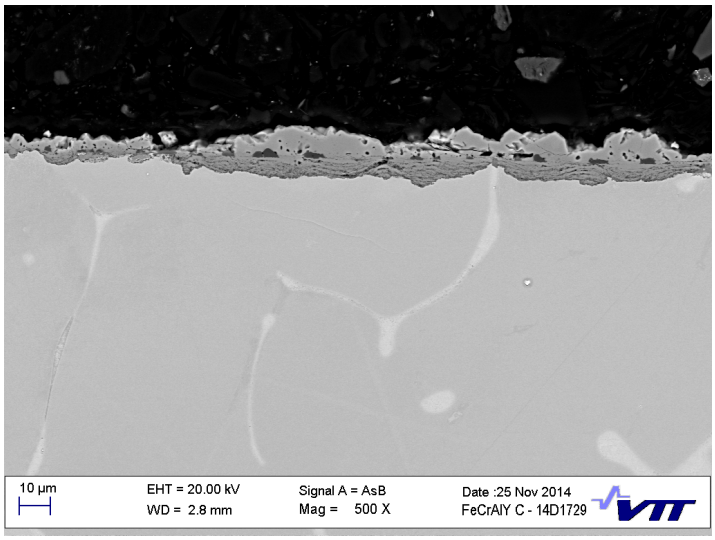

Figure 8. Oxides grown on FeCrAlY after 1000 h exposure

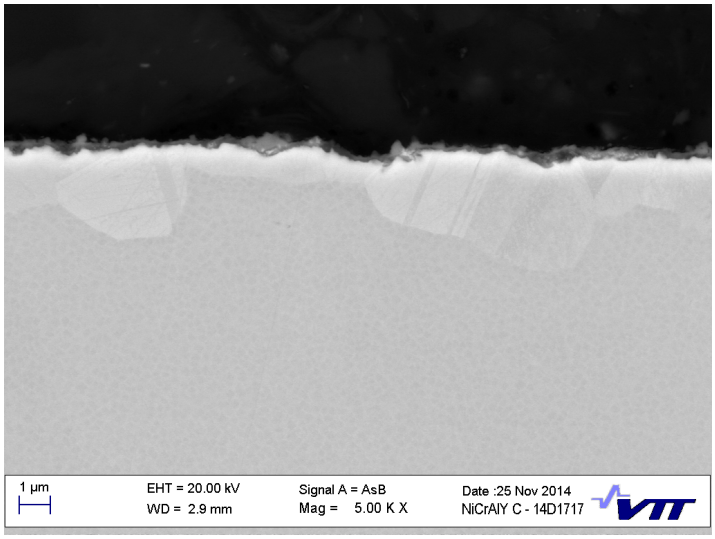

Figure 9. Oxides grown on NiCrAl after 1000 h exposure

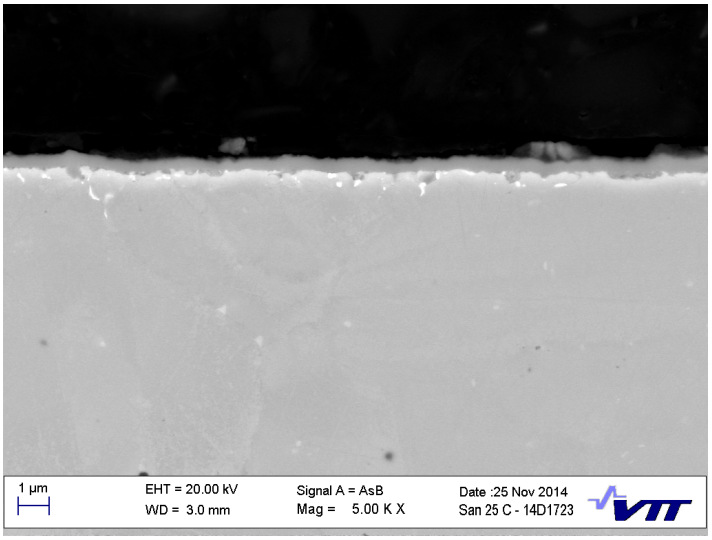

Figure 10. Oxides grown on Sanicro 25 after 1000 h exposure

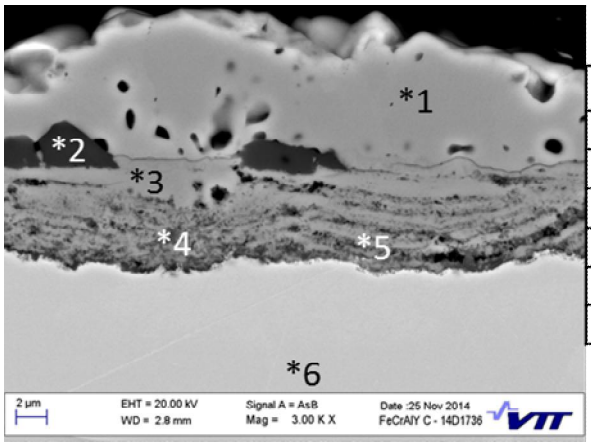

	O-K	Al-K	Ti-K	Cr-K	Fe-K
pt1	34.6	1.0		1.4	63.0
pt2	49.8	40.8	0.2	2.7	6.4
pt3	36.3	1.4		40.8	21.5
pt4	40.2	18.5		28.8	12.5
pt5	37.9	9.6		32.3	20.2
pt6		6.0		23.2	70.8

Figure 11. EDX analyses (wt%) of the oxide formed on the surface of FeCrAlY after 1000 h

Figures 12 and 13 present the surface views of NiCrAl and Sanicro 25 specimens. Some grinding grooves from specimen preparation were still visible after 1000 h exposure. Small spherical oxide particles were observed on the NiCrAl surface, Figure 12. On the Sanicro 25 specimen surface some blocky-shaped iron oxide particles were visible locally, Figure 13. Otherwise the surface layer was mainly mixed oxide containing iron, chromium and nickel. A protective chromia layer is usually observed to form at 650°C on the cromia formers; at higher temperatures the rate of chromium evaporation increases due to the formation of metal hydroxides, resulting in mass loss and reduced protection against oxidation [e.g. 22]. However, it has also been shown that the high steam pressure accelerates the evaporation already at lower temperatures [23].

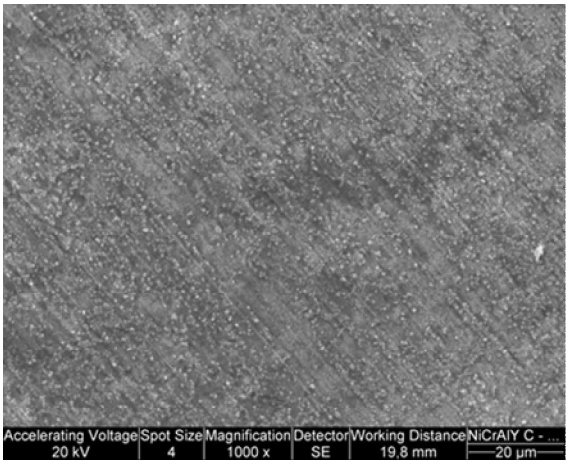

Element	
O K	23.9
Ni K	46.5
Cr K	18.8
Al K	10.8

Figure 12. Microstructure and EDX analysis (wt%) of NiCrAl surface after 1000 h exposure

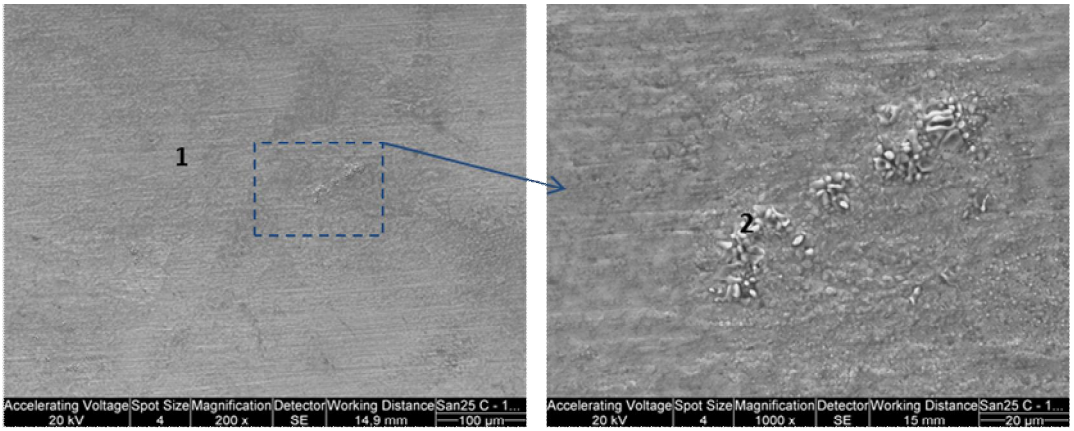

	O K	Fe K	Cr K	Ni K	Cu K	Al K	Si K	Ti K
1	22.4	30.2	31.3	12.7	2.0	0.5	0.9	
2	31.6	60.8	3.4	1.8		0.6		1.8

Figure 13. Microstructure and EDX analysis (wt%) of Sanicro 25 surface after 1000 h exposure

3.4. Oxide thickness and mass change

Figure 14 shows the weight change per unit surface area after exposure testing. The oxidation rate of FeCrAlY alloy accelerated heavily during the 1000 h testing compared to NiCrAl and Sanicro 25 alloys. Table 2 summarises the weight gain and oxide thickness measurement results for FeCrAlY, NiCrAl and Sanicro 25 materials. For FeCrAlY, the average thickness of inward grown oxide is also shown.

Unlike in previous SCW tests at 500°C where NiCrAl and FeCrAlY exhibited similarly low weight change (Figure 1), FeCrAlY had much higher oxidation rate than NiCrAl, despite the higher Al content (than NiCrAl) and Y addition. The evaporation of cromia in steam may have led to the formation of less protective oxides at 650°C, and thus the oxidation of iron based alloy has accelerated compared to the nickel alloy. The Ni substrate and Al addition in NiCrAl seem to reduce the oxidation rate/weight gain when comparing it to Sanicro 25 with higher Cr content. However, the difference between NiCrAl and Sanicro 25 is small and partly compensated by oxide spalling in NiCrAl (Figure 10), resulting in decreasing weight gain in time (Figure 14).

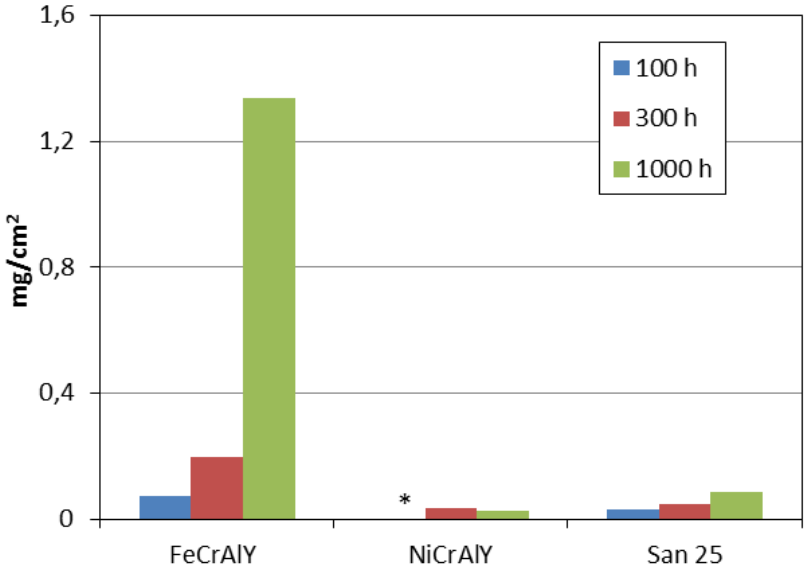

Figure 14. Weight gain (mg/cm^2) for tested materials after exposure at 650°C/250 bar. *100 h specimen not available

Table 2. Weight gain and oxide thickness results after exposure at 650°C/250 bar. * spallation of outer layer of oxide scale

	Weight gain [mg/cm^2]			**Oxide thickness [µm]**
	100 h	**300 h**	**1000 h**	**1000 h**
FeCrAlY	0.07	0.20	1.34	11.6 ± 4.1 (inward grown oxide 5.9 ± 1.8)
NiCrAl	-	0.04	0.02	0.20* ± 0.02
Sanicro 25	0.03	0.05	0.08	0.48 ± 0.08

4. Summary

All three materials showed relatively good initial SCW oxidation resistance at 650°C/250 bar, but after 100 hours the oxidation rate of FeCrAlY increased rapidly. In comparison, Sanicro 25 showed steady and much lower rate of oxide growth and weight gain. The rate of oxidation and weight gain was also low for NiCrAl, but by 1000 h exposure this included some oxide spalling and associated mass loss.

The oxide growth on the FeCrAlY surface started with formation of oxide nodules, resulting in a continuous network of nodules so that after 1000 h the whole surface was covered with a layered oxide scale. The outer oxide layer was composed of iron oxide and the inner layer of mixed iron-chromium-aluminium oxides. Aluminium oxide particles were observed at the interface between these two layers. The nickel rich oxide (with Cr and Al) of NiCrAl shows a low growth rate but also some oxide spalling after 1000 h exposure, when the mean oxide thickness was about 0.2 µm. On the surface of Sanicro 25, a more evenly thin (~0.5 µm) spinel oxide was observed along with occasional patches of iron oxide.

5. Acknowledgements

The authors would like to acknowledge the financial support from SA IDEA project. The authors would also like to acknowledge the skilful assistance of P. Väisänen, J. Lukin and J Metsäjoki.

References

1. Sarver J.M., Tanzosh, J.M. Effect of temperature, alloy composition and surface treatment on the steamside oxidation / oxide exfoliation behavior of candidate A-USC boiler materials, 7th International Conference on Advances in Materials Technology for Fossil Power Plants, October 22-25, 2013, Hawaii, USA.

2. Ennis, P.J., Quadakkers, W.J., Implications of steam oxidation for the service life of high-strength martensitic steel components in high-temperature plant, Pressure Vessels and Piping, Vol 84, p. 82 (2007).

3. Lukaszewicz, M., Dudziak, T., Nicholls, J.R., Simms, N.J., Steam oxidation of superheater / reheater alloys: Impact of steam flow rates and specimen geometries, EUROCORR 2011–Proceedings, p. 1788 (2011).

4. Wright, I.G., Dooley, R.B. A review of the oxidation behaviour of structural alloys in steam, International Materials Reviews, Vol 55, p. 129 (2010).

5. Barnard, P.M., Buchanan, L.W., Barrie, M. Material developments fro supercritical boilers and pipework – Bridging the gap? 9th Liege Conference: Materials for Advanced Power Engineering 2010, 27-29.9.2010, p. 39.

6. Abe F., Kern T-U., Viswanathan R. Creep-resistant steels, Woodhead Publishing 2008, 678 p

7. Chai, G., Kjellström, P., Boström, M. Creep and fracture behaviors of an advanced heat resistant austenitic stainless steel for A-USC power plant. 13th International Conference on Fracture, 16–21.6.2013, Beijing, China

8. Aguero, A., Muelas, R., Gonzalez, V. HVOF Coatings for Steam Oxidation Protection, Materials and Corrosion, Vol. 59 (5), pp. 393-401 (2008).

9. Saunders, S. R. J., MacCartney, N.L. The oxidation behaviour of metals and alloys at high temperatures in atmospheres containing water vapour: A review. Materials Science Forum 522–523, p. 119 (2006).

10. Allam, I., Whittle, D., Stringer, J. The Oxidation Behavior of CoCrAl Systems Containing Active Element Additions, Oxidation of Metals, Vol. 12 (1), p.35-67 (1978).

11. Huang, X., Guzonas, D., Li., J. Characterisation of Fe–20Cr–6Al–Y model alloy in supercritical water. Corrosion Engineering, Science and Technology (2014). http://dx.doi.org/10.1179/1743278214Y.0000000210

12. Huang, X., Guzonas, D. Characterization of Ni–20Cr–5Al model alloy in supercritical water. Journal of Nuclear Materials, Vol. 445, p. 298 (2014)

13. Xu, P., Zhao, L., Sridharan K., Allen, T. Oxidation Behaviour of Grain Boundary Engineered Alloy 690 in Supercritical Water Environment, J. of Nuclear Engineering, Vol. 422, p. 143-151 (2012).

14. Bischoff, J., Motta, A., Eichfeld, C., Comstock, R., Cao, G., Allen, T. Corrosion of Ferritic-Martensitic Steels in Steam and Supercritical Water, J. of Nuclear Materials, 2012, in press.

15. Allen, T., Sridharan, K., Chen, Y. , Tan, L., Ren, X., Kruizenga, A. Research and Development on Materials Corrosion Issues in Supercritical Water Environment, ICPWS XV, Berlin, Sept. 8-11, 2008.

16. Nie, S. H., Chen, Y., Ren, X., Sridharan, K., Allen, T.R. Corrosion of Alumina-forming Austenitic Steel Fe-20Ni-14Cr-3Al-0.6Nb-0.1Ti, Journal of Nuclear Materials, Vol. 399, p. 231-235 (2010).

17. Penttila, S. Materials for the SCWR Concept, GEN4FIN Seminar, Lappeenranta, Oct. 2-3, 2008.

18. P. Kofstad, High Temperature Corrosion (Elsevier Applied Science Publishers Ltd, London and New York, 1988).

19. Asteman, H., Svensson, J.E., Johansson, L.-G. Evidence for chromium evaporation influencing the oxidation of 304L: The effect of temperature and flow rate. Oxidation of Metals, Vol. 57, p. 193 (2002).

20. Wright, I. G., Pint, B.A. An Assessment of the High-Temperature Oxidation Behavior of Fe-Cr Steels in Water Vapor and Steam, NACE Paper 02-377, NACE Corrosion 2002, Denver, CO, USA, 8–11.4.2002.

21. Ehlers,J., Young, D. J., Smaardijk, E.J., Tyagi, A.K., Penkalla, H.J., Singheiser, L, Quadakkers, W.J. Enhanced oxidation of the 9%Cr steel P91 in water vapour containing environments. Corrosion Science 48, p. 3428 (2006).

22. Tuurna, S, Pohjanne, P, Yli-Olli, S, Coda Zabetta, E, Vänskä, K. Fireside corrosion and carburization of superheater materials in simulated oxyfuel combustion conditions. 7th International Conference on Advances in Materials Technology for Fossil Power Plants; Waikoloa, HI, United States, 22 - 25 October 2013 Proceedings. EPRI (2014), p. 881 - 891

23. Holcomb, G.R. Steam oxidation and cromia evaporation in ultrasupercritical steam boilers and turbines. Journal of the Electrochemical Society 156, p. C292-C297 (2009).

ISSCWR7-2057

Oxidation performance coatings for future supercritical power plants

Maria Oksa, Satu Tuurna, Jarkko Metsäjoki, Sami Penttilä
VTT Technical Research Centre of Finland
PL 1000, 02044 VTT FINLAND
+358 50 536 5844, maria.oksa@vtt.fi

Abstract

For improved efficiency and reduced emissions, the future power plants need to operate at high temperatures and pressures, which however are limited by the durability of conventional materials such as ferritic steels. Steam oxidation of a number of coatings (Al slurries, thermal spraying, CVD siliconizing and nickel plating) has demonstrated the feasibility of coatings to improve the oxidation resistance. Al slurry coatings combine good high temperature oxidation resistance through the growth of an Al_2O_3 layer and the possibility to apply the coating on an industrial scale at moderate cost. This work aimed to test the oxidation performance of coatings and reference alloys in ultrasupercritical (USC, 650˚C / 250 bar) water. The tested materials included Al slurry coating on ferritic 9%Cr steel and nickel-base A263 substrates, and bulk P92, MARBN and A263 alloys as reference specimens. Oxidation resistance was tested by exposure to flowing supercritical water (SCW) with 125 ppb dissolved oxygen at 650˚C/250 bar up to 1000 h.

1. Introduction

Designs of advanced combustion systems that utilize coal as a feedstock must include improved thermal efficiency and significant reduction in release of sulfur oxides, nitrogen oxides and carbon dioxide [1]. Advanced ultrasupercritical power plants that are planned to operate up to 750...800 °C and 34.5 MPa will face materials challenges [2]. In the planned boilers both fireside corrosion and steam side oxidation may bring out problems that have not been experienced before. Attaining adequate creep strength, fireside corrosion resistance and steamside corrosion resistance is therefore a serious challenge [1]. Presently applied and potential new materials have to be tested in the planned conditions in order to validate their resistance against planned conditions.

Steam oxidation damage to heat transfer surfaces has strong influence on the service life of the components. The reduction in rupture life due to material loss can be significant after comparatively short exposure times already at 600 °C [3]. Potentially a more serious consequence can be thermal insulation effect of the porous, thick oxide scales, which can cause overheating of the heat exchanger tubes. Long steam oxidation behaviour of ferritic Cr steels depends on the chromium content [3]. Steels with 9-10 % Cr form typically thick oxide scales consisting mainly of magnetite Fe_3O_4. Steels with 10-12 % Cr show variable steam oxidation behaviour and steels with more than 12.5 % Cr have high steam oxidation resistance. According to steam oxidation testing at 550-650 °C, some of the 10-12 % Cr ferritic steels formed a very thin and protective oxide scale at higher temperatures whereas at lower temperature a rapidly growing, less-protective oxides were formed [4]. This “kinetics inversion”

behaviour is related to two parallel processes during temperature increase. Enhanced in-scale diffusion and surface reaction kinetics leads to an increase in the oxidation rate and enhanced incorporation of chromium in the scale results in a decrease of the oxidation rate [4]. Unfortunately, the steels that possess the highest rupture strengths at 600-650 °C show the poorer steam oxidation resistance. Schematic of typical scale formation in the steam oxidation conditions at temperature range 600-700 °C in the presence of water vapour is presented in **Figure 1**. Three clearly defined oxide layers consisting of innermost layer of $(Fe,Cr)_3O_4$ spinel, intermediate layer of porous magnetite Fe_3O_4 and outermost compact thinner layer of hematite Fe_2O_3 form under isothermal conditions [5], following parabolic kinetics at 575-650 °C. Under cyclic steam oxidation conditions, oxide scales formed as irregular and cracked in the temperature range of 575-700 °C [5].

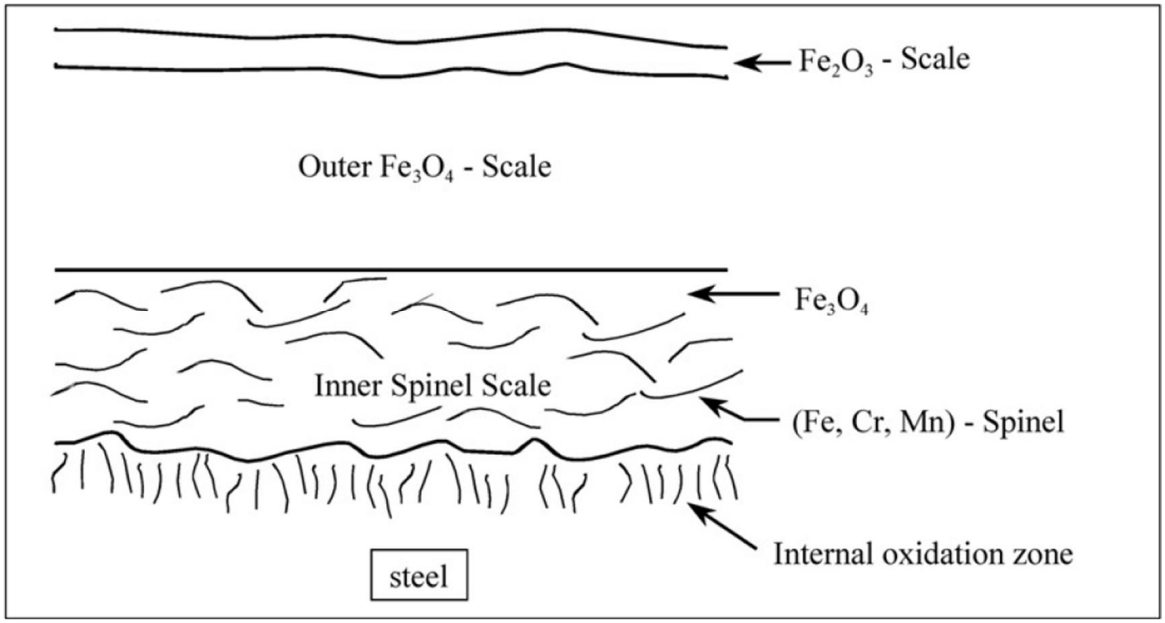

Figure 1. Schematic of typical oxide scale formation on P91 steel in the presence of water vapour at 600-700 °C presenting external oxide scales and internal oxidation zone [6].

Previous steam oxidation testing of iron-base alloys with high chromium content at 725 °C for up to 1850 hours by Natesan et al. [1] showed that weight change of the materials had a sharp increase initially (about 200 h) due to formation of an oxide film. The overall corrosion rates were negligible for the tested materials. However, significant internal oxidation had occurred in the steam oxidation conditions (0.03…0.66 mm/y).

In this study, corrosion protection by aluminium slurry diffusion coating on 9 % Cr steel and nickel-base alloy was tested in steam oxidation exposure with increased pressure. The performance of the coated materials was compared to uncoated base alloys.

2. Experimental

Diffusion aluminised ferritic steel T92 and nickel-base super alloy A263 and uncoated base alloys P92 and A263 were exposed to high temperature and high pressure supercritical water conditions to study the behaviour and corrosion protection ability of the applied coatings.

2.1 Materials

The tested coating materials were aluminium slurry coated ferritic 9%Cr T92 steel and nickel-base alloy A263. Bulk materials P92 and A263 were applied as reference specimens. 9Cr-3W-3Co-VBN steel, a martensitic steel strengthened by boron and nitrides (MARBN) developed for long term creep and oxidation for USC power plants at 650 °C, was also tested in the same conditions. Chemical composition of the bulk materials is presented in **Table 1**. The slurry coating was an aluminium organic diffusion coating LR2054 by Indestructible Paint Ltd, Birmingham, UK. The slurry coating was applied on ground (600/1200 grit) specimens and the samples were heat treated at 700 °C for 10 hours in a vacuum furnace (10^{-4} mbar). The slurry coated specimens before and after the heat treatment are presented in **Figure 2**. Detailed information on properties of T/P92 material is presented by Vaillant et al. [7] and of A263 by Pohja et al. [8].

Table 1. Chemical composition of the tested materials [w.%]. * [ppm]

Material	Ni	Fe	Cr	Mo	Co	W	Ti	V	Mn	Si	Al	B *	N *
T/P92	0.3	Bal.	9	0.3	…	2	…	0.2	0.5	0.2	0.2	…	…
A263	Bal.	0.5	20	5.7	20	…	2.1	…	0.4	0.2	0.7	…	…
MARBN	0.2	Bal.	9	0.1	2.6	2.6	…	0.2	0.6	0.3	0.2	120-150	60-90

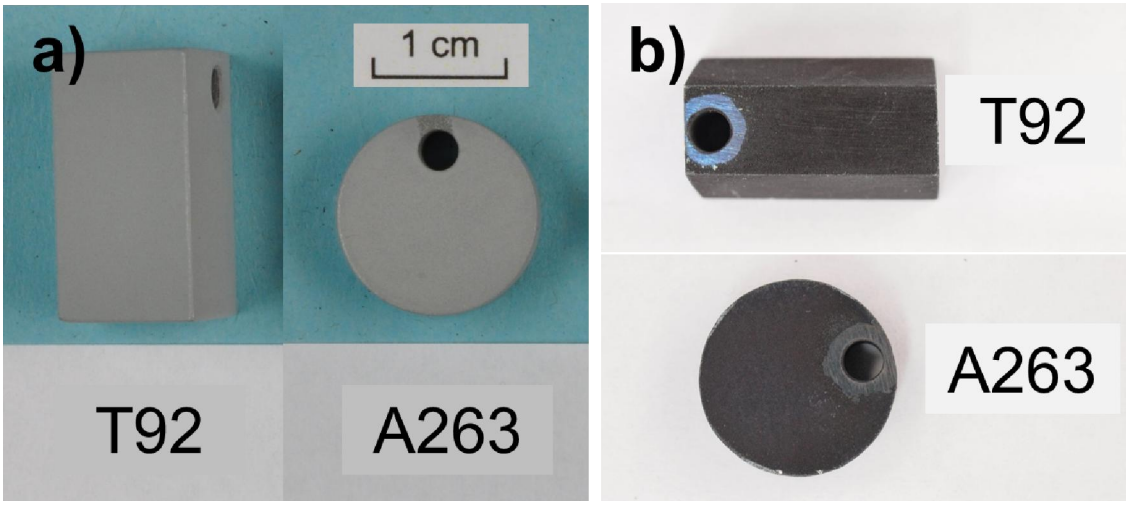

Figure 2. Test specimens T92 and A263 a) after applying the slurry coating and b) after heat treatment.

2.2 Test procedure

The oxidation test was performed under high temperature and high pressure conditions. The specimens were exposed to supercritical water (SCW) at temperature of 650 °C and pressure of 250 bar in the autoclave environment with 125 ppb dissolved oxygen in the inlet flow. The autoclave system is described in detail in [9]. The schematic of the test system is presented in **Figure 3**. Exposure times for the coated specimens were 300 h and 1000h and for the reference materials 100 h, 300 h and 1000 hours.

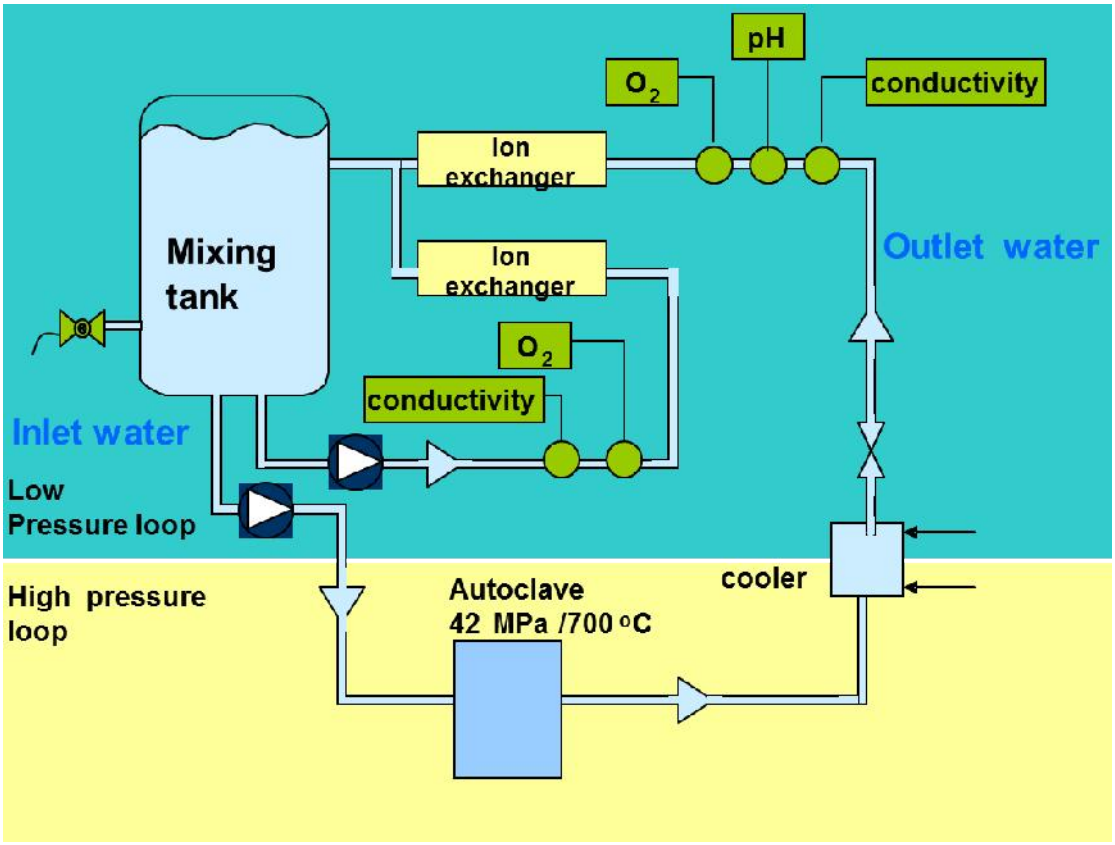

Figure 3. Schematic diagram of VTT's high pressure steam oxidation facility: the supercritical autoclave and the associated water recirculation loop.

2.3 Characterization

Metallographic sample preparation before and after the exposure was performed by cutting the samples with a diamond cutter, mounting the samples into resin and grinding and polishing the samples to 1 µm diamond paste fineness. After the slurry coating, the cross-sections of the heat treated specimens were inspected by optical microscopy. Surface analysis of the specimens was performed with scanning electron microscopy (SEM) and energy-dispersive X-ray spectroscopy (EDX).The cross-sections of the exposed specimens were analysed with SEM.

3. Results

3.1 Al slurry coated samples

The ferritic steel T92 and nickel-base alloy A263 were diffusion deposited with the aluminium slurry coating. The thickness of the diffusion layer varied between 9 to 39 µm with T92 steel and 22-82 µm with A263. The diffusion layer of T92 contained pores and vertical cracks. The diffusion coating on A263 was thicker and denser, showing a layered structure. Examples of the cross-sections of the diffusion coated samples are presented in **Figure 4**. According to EDX analysis from the surface of the specimen, the chemical composition of the slurry coating on T92 after the 10 h heat treatment included 39.2 % iron, 41.8 % aluminium, 13.8 % oxygen, 4.4 % chromium and 0.9 % silicon. The oxygen in the surface originates probably from the oxidation of the slurry coating prior the heat treatment.

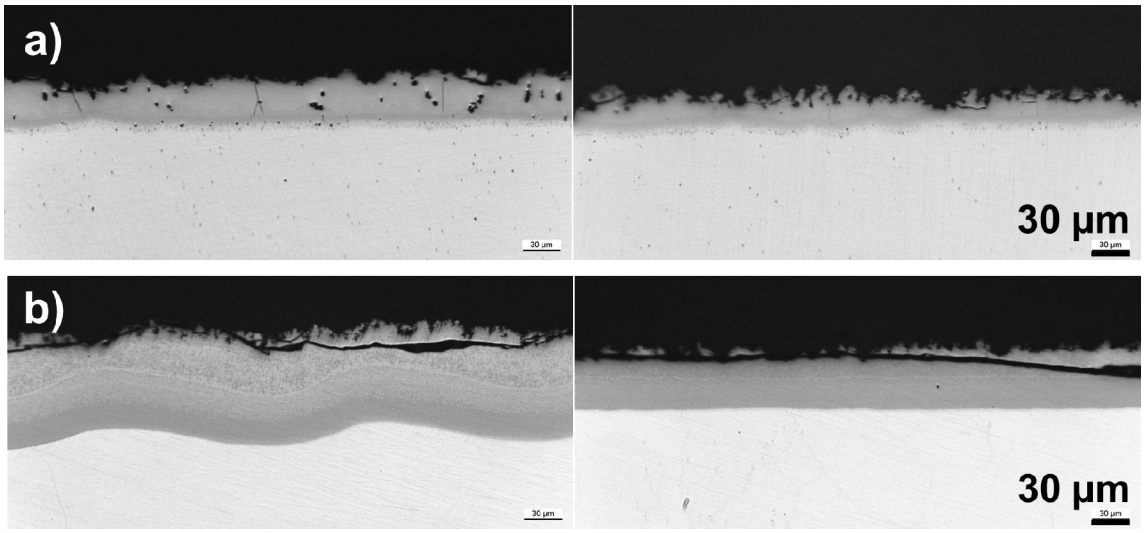

Figure 4. Optical images of the cross-sections of the Al diffusion coated specimens after the 10 h heat treatment: a) T92 and b) A263.

3.2 Oxidation of coatings in supercritical water exposure

The Al slurry coated specimens T92 and A263 were exposed to flowing supercritical water with 125 ppb dissolved oxygen at 650˚C/250 bar for 300 h and 1000 h. The diffusion layer on the steel T92 had failed in the tests, whereas the diffusion coating on the nickel-base alloy A263 had formed a protective layer on the substrate material. Deep cavities had formed during the exposure on the T92 material, as presented in **Figure 5**. The diffusion coating on A263 had reacted in the test conditions and a reaction layer was formed in the surface of the coating. The thickness of the outermost reaction layer was higher in the 300 h exposure compared to the 1000 h. However, in the longer exposure, some horizontal cracking was detected in the diffusion coating layer. The appearance of the A263 Al slurry coated specimens after the exposure is presented in **Figure 6**. Detailed images of the outer surface of the exposed slurry coated samples are presented in **Figure 7**. The outermost reaction layer on the T92 steel is thicker than on A263 probably due to high amount of iron in the coating. The reaction layer reaches also deeper due to vertical cracks in the coating. The layer thicknesses of the coated test specimens are presented in **Table 2**.

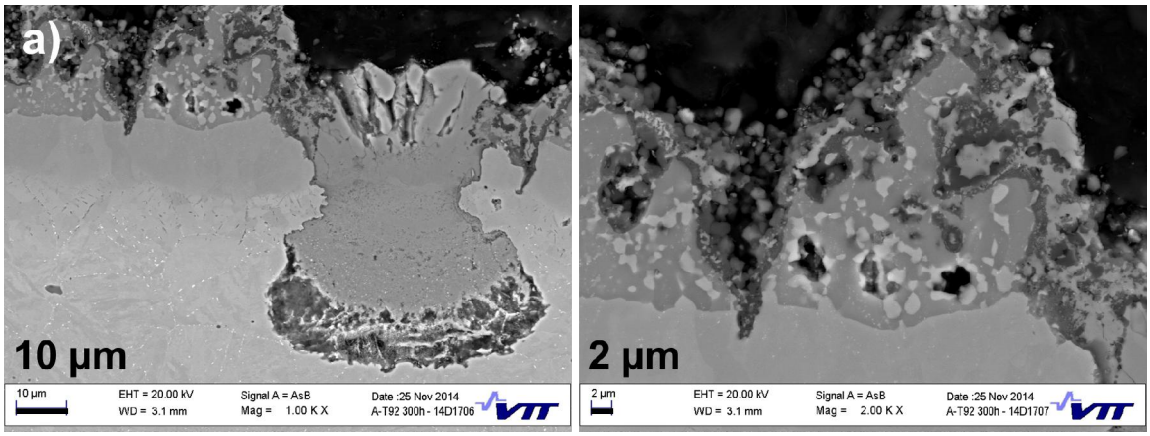

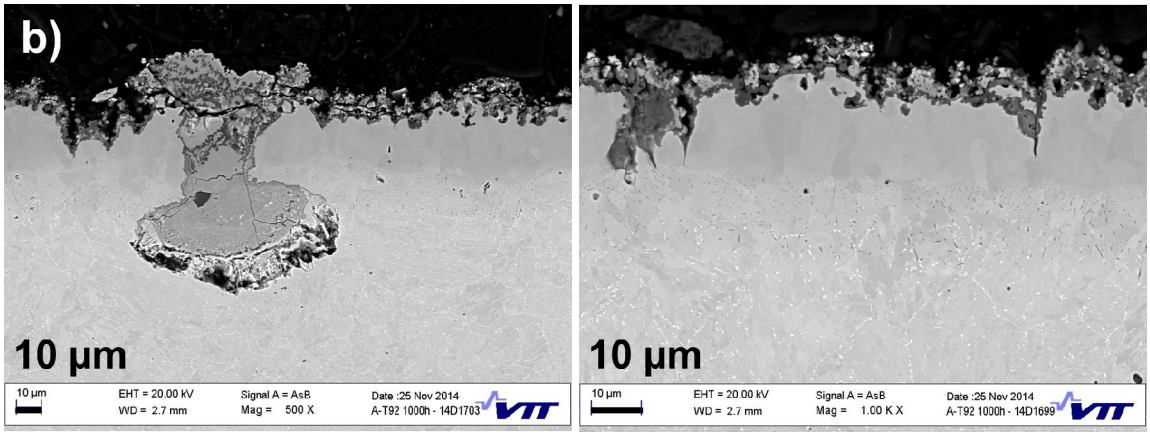

Figure 5. Al slurry coated T92 steel specimens after the exposure: a) 300 h and b) 1000 h.

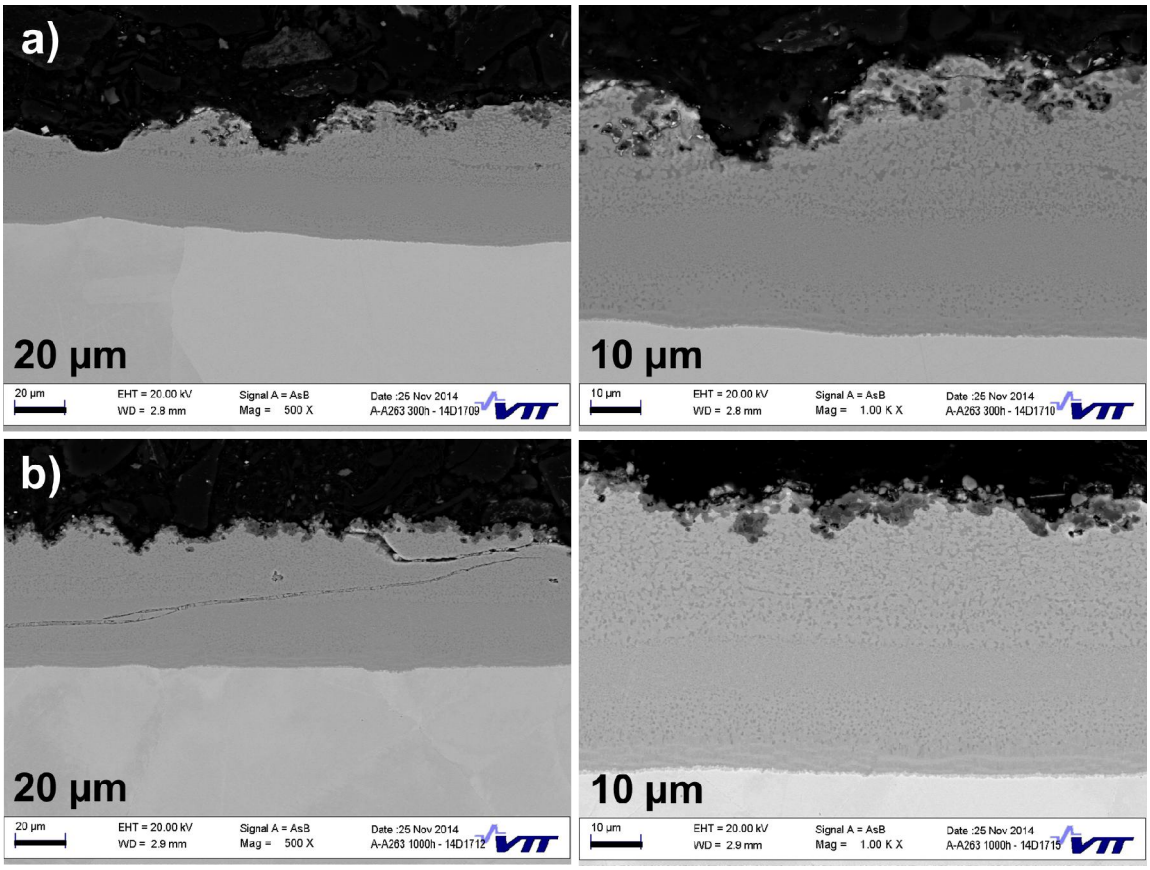

Figure 6. Al slurry coated A263 nickel-base alloy specimens after the exposure: a) 300 h and b) 1000h.

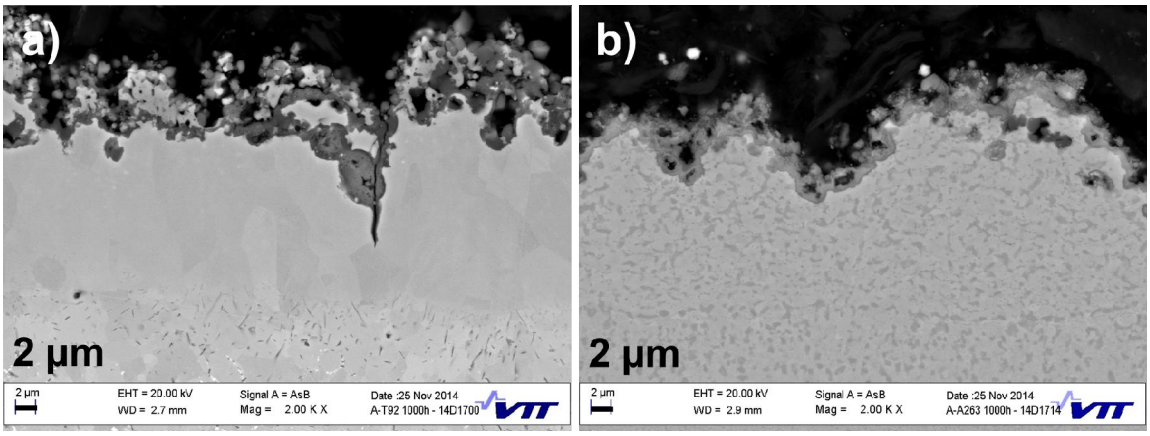

Figure 7. Outer surface of the diffusion coating on a) T92 steel and b) A263 nickel-base alloy after the exposure of 1000h.

Table 2. Thickness measurement of the tested Al slurry coated specimens T92 and A263 after the coating and after the exposures for 300 h and 1000h.

State	Thickness [µm]	T92_C	A263_C
Original	Diffusion layer	9…39	22…82
300 h	Diffusion layer	0…17	22…56
	Reaction layer (max.)	35	24
	Internal reaction layer (max.)	40	-
1000 h	Diffusion layer	0…27	22…59
	Reaction layer (max.)	50	9
	Internal reaction layer (max.)	46	-

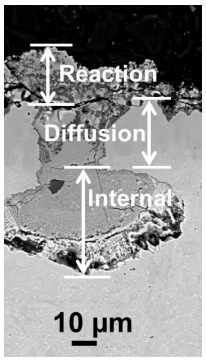

3.3 Oxidation of bulk materials in supercritical water exposure

Nickel-base alloy A263 and martensitic MARBN steel were tested in the same conditions for 300 h and 1000 h. The thickness of oxide layer on A263 alloy was about 0.5 µm maximum after the 1000 h exposure. Internal attack down to 0.6 µm was detected on the nickel alloy. For MARBN, the external oxide layer thicknesses were 44-72 µm after the 1000 h exposure. Thickness of the internal oxidation layer on MARBN was even higher, approximately 79 µm at maximum. SEM images of the cross-sections of the exposed bulk material specimens are presented in **Figure 8**. **Figure 9** presents EDX mapping of the MARBN steel after the 1000h exposure. Previous SCW oxidation testing of P92 steel has given following weight changes at 650°C / 25 MPa with O_2 125 ppb: after 100 h exposure 9.64 mg/cm^2 and after 578 h exposure 15.33 mg/cm^2. Maximum oxide thickness was measured 119.5 µm after the 578 h of exposure by SEM analysis. Weight changes for the tested coated and uncoated materials are presented in **Figure 10**.

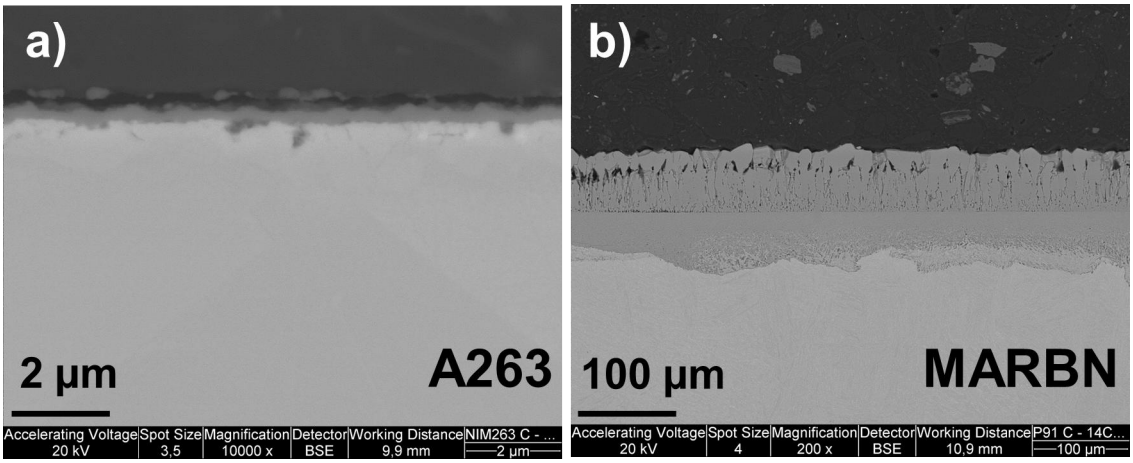

Figure 8. SEM images of a) A263 nickel-base alloy and b) MARBN steel after the SCW oxidation exposure of 1000 h.

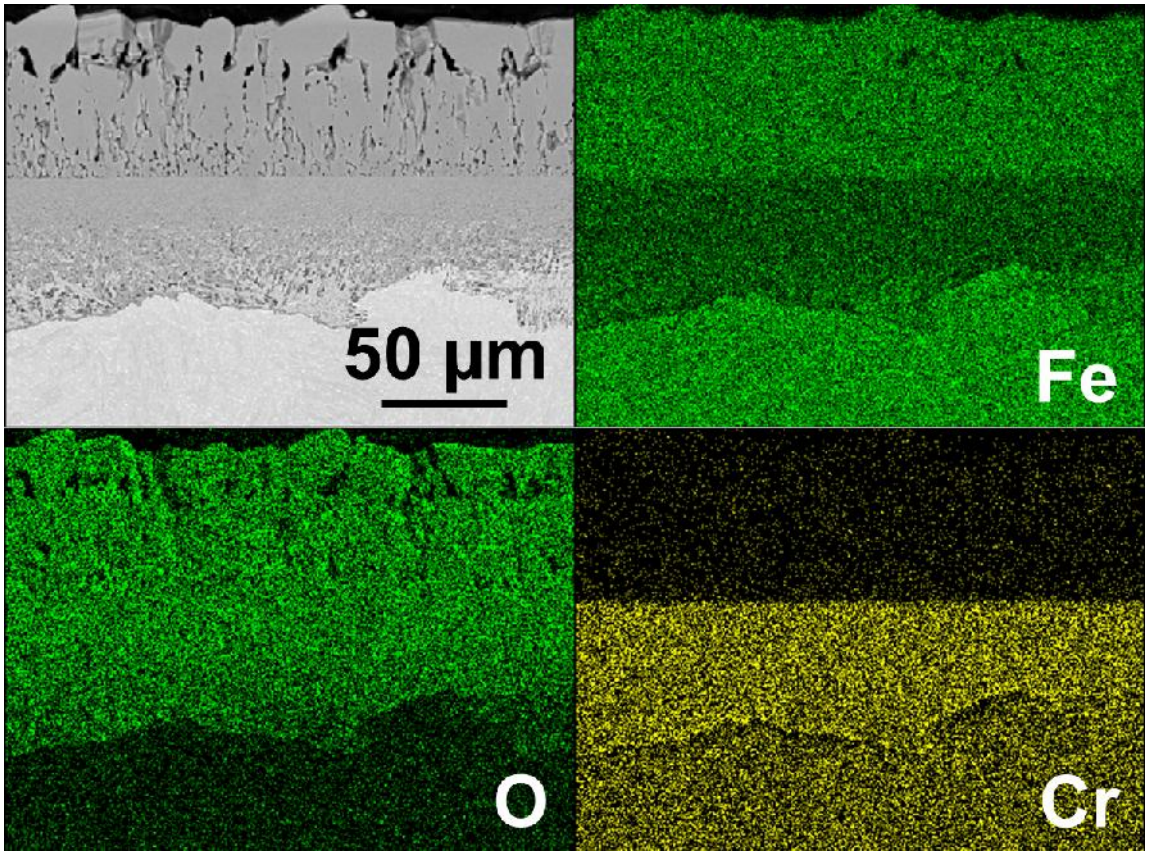

Figure 9. EDX mapping of MARBN steel after the SCW oxidation exposure of 1000 h presenting distribution of iron, oxygen and chromium in the oxide layers and the subsurface.

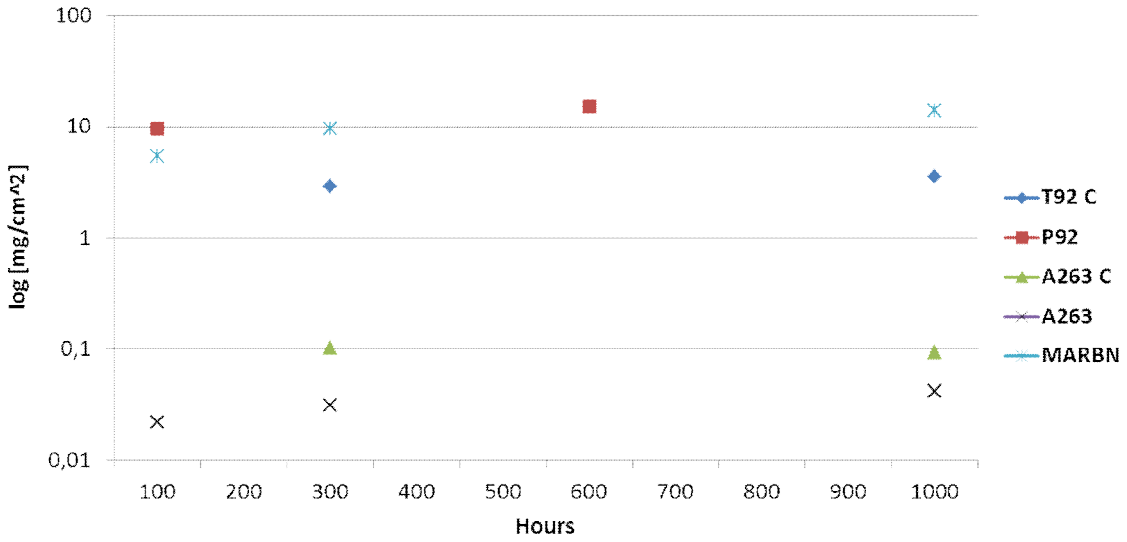

Figure 10. Weight change [log mg/cm^2] of the coated T92_C and A263_C specimens and uncoated P92, MARBN and A263 materials during the SCW oxidation exposure at 650 °C / 250 bar up to 1000 hours.

4. Conclusions

The oxidation resistance of Al slurry coated ferritic steel T92 and nickel-base superalloy A263 were tested in an autoclave system, exposed to supercritical water at 650 °C and 250 bar, with 125 ppb dissolved oxygen in the inlet flow. The diffusion coating was thicker and denser on A263 alloy before the testing and the coating performed better compared to the coating on the T92 steel. Coating on A263 protected the substrate material from oxidation, even though horizontal cracking had occurred in the coating. On T92, the original diffusion coating was uneven and rather thin in places. After the exposure, corrosion/oxidation damage was detected both in the diffusion layer and in the substrate material T92. Deep cavities down to 75 µm were detected in the steel.

In comparison, the uncoated P92 and MARBN steels had experienced high oxidation rate during the exposure. Both tested steels had high weight change compared to the coated T92 material. A263 nickel-base alloy was almost intact after the 1000 h testing with only a very thin (0.5 µm) external oxide layer and a thin internal attack layer.

Based on the results of the SCW oxidation test, nickel-base material A263 had highest corrosion resistance and Al slurry coating should not be applied on the material. For lower alloyed 9 % steel, the Al slurry coating was beneficial against the steam oxidation, which confirms previous results performed by Agüero et al. [10]. However, the quality of the coating, as sufficient density and thickness, is essential to offer protection.

Acknowledgements

This work has been funded by EU FP7 project NextGenPower - Meeting the Materials and Manufacturing Challenge for Ultra High Efficiency PF Power Plants with CCS (2010-2014) and Academy of Finland project IDEA (Interactive modelling of fuel cladding degradation mechanisms).

References

1. Natesan, J.H. Park, Fireside and steamside corrosion of alloys for USC plants. International Journal of Hydrogen Energy 32 (2007) 3689 – 3697

2. R Viswanathan, R Purgert, P Rawls, 'Coal-Fired Power Materials', Advanced Materials & Processes (August 2008) 47-49

3. P.J. Ennis, W.J. Quadakkers, Implications of steam oxidation for the service life of high-strength martensitic steel components in high-temperature plant. International Journal of Pressure Vessels and Piping 84 (2007) 82–87

4. J. Zurek, E. Wessel, L. Niewolak, F. Schmitz, T.-U. Kern, L. Singheiser, and W.J.Quadakkers, "Anomalous temperature-dependence of oxidation kinetics during steam oxidation of ferritic steels in the temperature range 550–650°C", Corrosion Science, 46 (9) (2004) 2301–2317

5. D. Laverde, T. Gomez-Acebo, F. Castro, Continuous and cyclic oxidation of T91 ferritic steel under steam. Corrosion Science 46 (2004) 613-631

6. J. Ehlers, D.J. Young, E.J. Smaardijk, A.K. Tyagi, H.J. Penkalla, L. Singheiser, W.J. Quadakkers, Enhanced oxidation of the 9%Cr steel P91 in water vapour containing environments. Corrosion Science 48 (2006) 3428–3454

7. J.C. Vaillanta, B. Vandenberghe, B. Hahn, H. Heuser, C. Jochum, T/P23, 24, 911 and 92: New grades for advanced coal-fired power plants—Properties and experience. International Journal of Pressure Vessels and Piping 85 (2008) 38–46

8. R. Pohja, S. Holmström, A. Nurmela, P. Moilanen, A study of creep-fatigue interaction in the nickel-base superalloy 263. 10th Liege Conference : Materials for Advanced Power Engineering 2014 edited by J. Lecomte-Beckers, O. Dedry, J. Oakey and B. Kuhn (2014) 678-687

9. A. Toivonen, S. Penttilä, General corrosion and SCC tests on ODS steels in supercritical water, Baltica IX. International Conference on Life Management and Maintenance for Power Plants, Espoo, Finland (2013)174 – 193

10. A. Agüero, R. Muelas, A. Pastor, S. Osgerby, Long exposure steam oxidation testing and mechanical properties of slurry aluminide coatings for steam turbine components. Surface & Coatings Technology 200 (2005) 1219 – 1224

ISSCWR7-2058

Sensitivity Studies of SST Turbulence Model Parameters on the Prediction of 7-Rod Bundle Benchmark Experiments

C. Bergmann, S. Ormiston, V. Chatoorgoon
University of Manitoba, Mechanical Engineering
Winnipeg, Manitoba, Canada
umbergm5@myumanitoba.ca, scott.ormiston@umanitoba.ca, vijay.chatoorgoon@umanitoba.ca

Abstract

This paper reports the findings of a sensitivity study of parameters in the SST turbulence model in a commercial CFD code to predict an experiment from the GIF SCWR 2013-2014 7-rod sub-channel benchmark exercise. This study was motivated by the result of the benchmark that all the CFD codes gave similar results to a sub-channel code, which does not possess any sophisticated turbulence modelling. Initial findings were that the CFD codes generally under-predicted the wall temperatures on the B2 case in the region where the flow was supercritical.

Therefore, it was decided to examine the effect of various turbulence model parameters to determine if a CFD code using the SST turbulence model could do a better job overall in predicting the wall temperatures of the benchmark experiments. A sensitivity study of seven parameters was done and changes to two parameters were found to make an improvement.

1. Introduction

This paper presents numerical analysis of the supercritical water 7-rod bundle experiment carried out by The Japan Atomic Energy Agency (JAEA) for the benchmark exercise, organised by The Generation IV International Forum (GIF) Project Management board. Numerical results were obtained from ANSYS CFX v14.5 for the 7-rod bundle experiment for cases A1, B1, and B2 using the SST (Shear Stress Transport) turbulence model. The resulting cladding surface temperatures of cases B1 and B2, and the pressure drop of case A1 were presented at a conference on June 25 and 26, 2014 in Delft, Netherlands. Water temperatures above the pseudocritical temperature were found in only one of the benchmark cases: case B2.

This benchmark was created to help gain insight into the current state of numerical analysis for predicting supercritical water heat transfer. The JAEA carried out three experiments involving supercritical pressure water in a 7-rod bundle, with water flowing vertically upwards. The experiment was meant to simulate the core of a Generation IV Supercritical-water-cooled reactor. The heater rods emulate fuel rods in a nuclear reactor. Participants from around the world carried out blind numerical simulations on the bundle. Values of inlet temperature, inlet pressure, inlet flow rate, heat rate, and geometry of the bundle setup were supplied to all participants of the benchmark. The outlet pressure and thermocouple temperatures were kept secret and had to be determined by the participants. The numerical results of all participants were presented and compared to the experimental results at a conference in Delft, Netherlands on June 25 and 26, 2014, to determine the numerical method that produced the most accurate results.

2. Experimental Setup

The experimental setup consists of 7 heater rods, orientated in a hexagonal arrangement, enclosed in a shroud to create a sub channel. The heaters rods are labelled A through G. Six spacers that are 25 [mm] long position the rods inside the shroud, and position the rods relative to one another. The heater rods consist of a C-shaped Nichrome element, encased in a boron nitride insulator, all of which is encased in a protective Inconel 600 cladding. Pressure taps are placed at 144 [mm] and 1340 [mm] from the start of the heated section. A total of 42 thermocouples are embedded into the cladding at various locations along the heater rods, to measure the cladding surface temperature. The conditions of the benchmark are given in Table 1 below.

Table 1. Experimental conditions of benchmark experiments.

Case	Inlet Temperature [K]	Inlet Pressure [MPa]	Flow Rate [kg/min]	Mass Flux [kg/m²s]	Heater A [kW]	Heater B, D, F [kW]	Heater C, E, G [kW]
A1	297.35	25.0	26.33	2283.44	0	0	0
B1	353.58	24.98	16.69	1447.56	19.67	22.51	22.52
B2	519.58	25.03	16.52	1432.97	34.14	34.08	34.13

Numerical analysis of the benchmark was performed using ANSYS CFX v14.5, and the meshes were generated using ANSYS ICEM CFD v14.5. Selection of the correct turbulence model was important, hence, three different turbulence models were used in this study: k-ε, SST (Shear Stress Transport), and SSG (Speziale-Sarkar-Gatski) Reynolds Stress. After analysis of the results, the SST model was selected as the model that we believed would provide reasonable results in a reasonable amount of computational time. The SST model requires the fluid domain mesh have a very fine mesh close to the solid walls, specifically: $y^+ \leq 1$ for the first mesh elements adjacent to the walls.

3. Governing Equations

The following governing equations are given in Cartesian coordinates, using summation notation where appropriate, and were taken from CFX digital reference documentation [1]. The governing equations consist of continuity, momentum, thermal energy, and turbulence quantities. Steady state versions of the equations are presented.

3.1 Continuity, Momentum, and Energy

The continuity equation is:

$$\frac{\partial(\rho U_i)}{\partial x_i} = 0 \qquad (1)$$

The conservation of momentum equation is:

$$\frac{\partial(\rho U_i U_j)}{\partial x_j} = -\frac{\partial P}{\partial x_i} + \frac{\partial}{\partial x_j}\left[\mu\left(\frac{\partial U_i}{\partial x_j} + \frac{\partial U_j}{\partial x_i}\right)\right] - \frac{\partial}{\partial x_j}\left(\rho\overline{u_i u_j}\right) + S_{M,buoy} \qquad (2)$$

Where $\rho\overline{u_i u_j}$ are the Reynolds stresses and $S_{M,buoy}$ is the momentum source term due to buoyancy. The eddy-viscosity assumption is used to approximate the Reynolds stresses ($\rho\overline{u_i u_j}$). This eddy-viscosity assumption is:

$$-\rho\overline{u_i u_j} = \mu_t\left(\frac{\partial U_i}{\partial x_j}+\frac{\partial U_j}{\partial x_i}\right)-\frac{2}{3}\delta_{ij}\left(\rho k+\mu_t\frac{\partial U_k}{\partial x_k}\right) \quad (3)$$

Where μ_t is the eddy viscosity, k is the turbulence kinetic energy, δ_{ij} is the Kronecker delta function, and the $\frac{\partial U_k}{\partial x_k}$ term is ignored in CFX because it is insignificant for incompressible flows. Using the above eddy-viscosity assumption, the conservation of momentum equations for use with two equation turbulence models become:

$$\frac{\partial\left(\rho U_i U_j\right)}{\partial x_j} = -\frac{\partial P'}{\partial x_i}+\frac{\partial}{\partial x_j}\left[(\mu+\mu_t)\left(\frac{\partial U_i}{\partial x_j}+\frac{\partial U_j}{\partial x_i}\right)\right]+S_{M,buoy} \quad (4)$$

Where P' is the modified pressure and $S_{M,buoy}$ is the momentum source term due to buoyancy. Using the full buoyancy model in CFX, the momentum source term due to buoyancy is:

$$S_{M,buoy} = g_i\left(\rho-\rho_{ref}\right) \quad (5)$$

The reference density (ρ_{ref}) is defined as the average density over the entire fluid domain. For the z axis aligned with the upward flow direction the acceleration due to gravity (g_z) is -9.81 [m/s^2] and 0 in the x and y directions (g_x and g_y).

The modified pressure is defined using the pressure (P) and turbulence kinetic energy (k) as follows:

$$P' = P+\frac{2}{3}\rho k \quad (6)$$

Since the full buoyancy model is enabled in CFX, the absolute pressure includes the pressure (P) and the hydrostatic pressure due to the reference density (ρ_{ref}):

$$P_{abs} = P_{ref}+P+\rho_{ref}\vec{g}\left(\vec{r}-\vec{r}_{ref}\right) \quad (7)$$

Where $\vec{g}$ is the acceleration of gravity, and $\vec{r}_{ref}$ is the buoyancy reference location, specified at the centroid of a pressure defined boundary. In this case the outlet is the pressure defined boundary. The absolute pressure and the temperature are used to define fluid properties.

Since all flows under consideration are incompressible (the Mach number is less than 0.3) the thermal energy equation is used:

$$\frac{\partial(\rho U_j h)}{\partial x_j} = \frac{\partial}{\partial x_j}\left(\lambda\frac{\partial T}{\partial x_j}+\frac{\mu_t}{Pr_t}\frac{\partial h}{\partial x_j}\right)+\frac{\partial}{\partial x_j}\left[U_i\left(\tau_{ij}-\rho\overline{u_i u_j}\right)\right]+S_E \quad (8)$$

Where Pr_t is the turbulent Prandtl number, S_E is the energy source term, and $\frac{\partial}{\partial x_j}\left[U_i\left(\tau_{ij} - \rho\overline{u_\iota u_j}\right)\right]$ is the viscous work term. When two equation turbulence models are used the Reynolds Stress term ($\rho\overline{u_\iota u_j}$) is approximated using the eddy viscosity hypothesis.

3.2 Turbulence

The following Shear Stress Transport (SST) model is the Menter SST model [2]. The SST turbulence model effectively uses the k-ε turbulence model of Sharma [3] in the free stream and the k-ω model of Wilcox [4] in the near wall region, with a blending function to merge the two models between the free stream and the near wall region.

The eddy viscosity is calculated using the following equation:

$$\mu_t = \frac{a_1 k\rho}{max(a_1\omega, SF_2)} \quad (9)$$

Where a_1 is 0.31, F_2 is a blending function, and S is the magnitude of the strain rate tensor S_{ij}:

$$S_{ij} = \frac{1}{2}\left(\frac{\partial U_i}{\partial x_j} + \frac{\partial U_j}{\partial x_i}\right) \quad (10)$$

$$S = \sqrt{2S_{ij}S_{ij}} \quad (11)$$

The blending function F_2 is:

$$F_2 = tanh(arg_2^2) \quad (12)$$

Where arg_2 is:

$$arg_2 = max\left(\frac{2\sqrt{k}}{\beta'\omega y}, \frac{500\nu}{y^2\omega}\right) \quad (13)$$

Where β' is 0.09.

The turbulence kinetic energy (k) and specific turbulence dissipation (ω) of the SST model result from solving the following transport equations:

$$\frac{\partial}{\partial x_j}\left(\rho U_j k\right) = \frac{\partial}{\partial x_j}\left[\left(\mu + \frac{\mu_t}{\sigma_{k3}}\right)\frac{\partial k}{\partial x_j}\right] + P_k - \beta'\rho k\omega + P_{kb} \quad (14)$$

$$\frac{\partial}{\partial x_j}\left(\rho U_j \omega\right) = \frac{\partial}{\partial x_j}\left[\left(\mu + \frac{\mu_t}{\sigma_{\omega 3}}\right)\frac{\partial \omega}{\partial x_j}\right] + (1 - F_1)\, 2\rho\frac{1}{\sigma_{\omega 2}\omega}\frac{\partial k}{\partial x_j}\frac{\partial \omega}{\partial x_j} + \alpha_3\frac{\omega}{k}P_k - \beta_3\rho\omega^2 + P_{\omega b} \quad (15)$$

Where P_k is the production of turbulence due to viscous forces, P_{kb} is the turbulence production due to buoyancy, $P_{\omega b}$is the turbulence dissipation due to buoyancy, and F_1 is a blending function. σ_{k3}, $\sigma_{\omega 3}$, α_3, and β_3 are constants that result from the following blending function:

$$\phi_3 = F_1\phi_1 + (1 - F_1)\phi_2 \quad (16)$$

Where ϕ is σ_k, σ_ω, α, or β. The constants used in equation (16) are: σ_{k1} = 1.17647, σ_{k2} = 1.0, $\sigma_{\omega 1}$ = 2.0, $\sigma_{\omega 2}$ = 1.16822, α_1 = 0.553167, α_2 = 0.440355, β_1 = 0.075, and β_2 = 0.0828.

The blending function F_1 is:

$$F_1 = tanh(arg_1^4) \quad (17)$$

Where arg_1 is:

$$arg_1 = min\left(max\left(\frac{\sqrt{k}}{\beta'\omega y}, \frac{500\nu}{y^2\omega}\right), \frac{4\rho k}{CD_{k\omega}\sigma_{\omega 2}y^2}\right) \quad (18)$$

$$CD_{k\omega} = max\left(2\rho\frac{1}{\sigma_{\omega 2}\omega}\frac{\partial k}{\partial x_j}\frac{\partial \omega}{\partial x_j}, 10^{-10}\right) \quad (19)$$

And y is the distance to the closest wall.
The turbulence production due to viscous forces is:

$$P_k = \mu_t\left(\frac{\partial U_i}{\partial x_j} + \frac{\partial U_j}{\partial x_i}\right)\frac{\partial U_i}{\partial x_j} - \frac{2}{3}\frac{\partial U_k}{\partial x_k}\left(3\mu_t\frac{\partial U_k}{\partial x_k} + \rho k\right) \quad (20)$$

The turbulence dissipation due to buoyancy is:

$$P_{\omega b} = \frac{\omega}{k}\left((\alpha_3 + 1)C_3 max(P_{kb}, 0) - P_{kb}\right) \quad (21)$$

Where C_3 is 1.0.
The turbulence production due to buoyancy is:

$$P_{kb} = -\frac{\mu_t}{\rho\sigma_\rho}g_i\frac{\partial \rho}{\partial x_i} \quad (22)$$

Where the turbulent Schmidt number, σ_ρ, is 1.0.

3.2.1 Inlet Turbulence

Boundary conditions of the turbulence models must be defined at the inlet. This condition at the inlet is defined using an intensity and eddy viscosity ratio. The turbulence kinetic energy at the inlet is:

$$k_{inlet} = \frac{3}{2}I^2U^2 \quad (23)$$

Where I is the turbulence intensity that is specified, and U is the magnitude of the mean flow velocity.
The turbulence dissipation at the inlet is:

$$\varepsilon_{inlet} = \frac{k_{inlet}^{3/2}}{0.3D_h} \quad (24)$$

Where D_h is the hydraulic diameter.
Since an ω-based turbulence model is used, the turbulence dissipation can be converted to a specific turbulence dissipation using the following equation:

$$\omega = \frac{\varepsilon}{\beta' k} \quad (25)$$

The eddy viscosity is defined at the inlet as a boundary condition by defining an eddy viscosity ratio, μ_t/μ. The molecular visocity is already known, since it is determined from the temperature and pressure of water.

3.3 Supercritical Water Properties

In CFX, properties of water are calculated based on the temperature and pressure of water and steam using the IAPWS-IF97 database, formulated by Wagner et al. [5]. This database provides an accurate equation of state for water and steam properties. The range of validity for this property package as implemented in CFX is as follows:

0 [°C] < T ≤ 800 [°C] for 10 [MPa] ≤ P ≤100 [MPa]
800 [°C] < T < 2000 [°C] for P < 10 [MPa]

3.4 Turbulence Parameters

The coefficients found in the transport equations of turbulence kinetic energy (k) and specific turbulence dissipation (ω) have values assigned to them based on simplifications to the equations and results of experimental data. The values of the coefficients can be different for various types of the same model, for example the original k-ε model of Jones and Launder [6] uses slightly different values for $C_{\varepsilon 1}$ and $C_{\varepsilon 2}$ than the revised k-ε model of Launder and Sharma [3].

The Wilcox k-ω model [4] will be used to explain the origins of the coefficients of the SST model, since the governing equations were based on the k-ω model.

The non-steady turbulence kinetic energy and specific turbulence dissipation transport equations can be simplified for decaying homogeneous, isotropic turbulence as follows:

$$\frac{dk}{dt} = -\beta' \omega k \quad (26)$$

$$\frac{d\omega}{dt} = -\beta \omega^2 \quad (27)$$

The asymptotic solution for turbulence kinetic energy, given in [4] is:

$$k \sim t^{-\beta'/\beta} \quad (28)$$

Experiments of Townsend [7] give a value of 1.25±0.06 for the ratio β'/β. The Wilcox and SST models set the value of this ratio at 6/5 (1.2).

The governing equations of momentum, turbulence kinetic energy, and specific turbulence dissipation can be simplified for an incompressible constant pressure boundary layer in the near wall layer. In this near wall layer, the effects of molecular viscosity are assumed negligible compared to the effects of eddy viscosity. The simplified equations are:

$$0 = \frac{\partial}{\partial y}\left[\nu_t \frac{\partial u}{\partial y}\right] \quad (29)$$

$$0 = \nu_t \left[\frac{\partial u}{\partial y}\right]^2 - \beta' \omega k + \sigma_k \frac{\partial}{\partial y}\left[\nu_t \frac{\partial k}{\partial y}\right] \quad (30)$$

$$0 = \alpha \left[\frac{\partial u}{\partial y}\right]^2 - \beta \omega^2 + \sigma_\omega \frac{\partial}{\partial y}\left[\nu_t \frac{\partial \omega}{\partial y}\right] \quad (31)$$

Note that the σ_k and σ_ω coefficients in the above simplifications are in the numerator, but in the governing equations section of this paper the coefficients are in the denominator. This just results from the fact that Wilcox derived the k-ω model with these coefficients in the denominator. The solution to the above equations for the log law region of the boundary layer is:

$$u = \frac{u_\tau}{\kappa} \ln\left(\frac{u_\tau y}{\nu}\right) \quad (32)$$

$$k = \frac{u_\tau^2}{\sqrt{\beta'}} \quad (33)$$

$$\omega = \frac{u_\tau}{\sqrt{\beta'}\kappa y} \quad (34)$$

Where u_τ is the friction velocity. From the above solution and the governing equations, the following equation must hold, according to Wilcox:

$$\alpha = \frac{\beta}{\beta'} - \frac{\sigma_\omega \kappa^2}{\sqrt{\beta'}} \quad (35)$$

When σ_ω and σ_k are in the denominator of the transport equations of turbulence kinetic energy and specific turbulence dissipation (such as for the SST model), then the above equation become:

$$\alpha = \frac{\beta}{\beta'} - \frac{\kappa^2}{\sigma_\omega \sqrt{\beta'}} \quad (36)$$

The above equation will yield a value for the α coefficient when β, β', and σ_ω are assigned values.

The equation for β' can be derived from the solution for turbulence kinetic energy in the log law region ($k = u_\tau^2/\sqrt{\beta'}$), and the fact that the Reynolds shear stress (τ) is constant in the near wall region and is equal to u_τ^2:

$$\beta' = \left(\frac{\tau}{k}\right)^2 \quad (37)$$

Experiments of Townsend [7] indicate that the ratio of Reynolds shear stress to turbulence kinetic energy (τ/k) is about 3/10 (0.3) in the near wall region. This gives a value of 0.09 for β'.

The values of σ_k and σ_ω come from a detailed analysis of the defect layer and sublayer. The variation of wake strength in the boundary layer to the dimensionless pressure gradient most closely match experimental data when $\sigma_k = \sigma_\omega = 0.5$ [4]. In CFX, these coefficients are actually 1/0.5 (2.0), since these two coefficients are in the denominator of the transport equations for turbulence kinetic energy and specific turbulence dissipation.

The constant $a_1$appearing in the equation for eddy viscosity comes from the shear stress anisotropy:

$$a_1 = 2b_{12} \quad (38)$$

Where the normalized Reynolds stress anisotropy is:

$$b_{ij} = \frac{\overline{u_i u_j}}{\overline{u_i u_i}} - \frac{\delta_{ij}}{3} = \frac{\tau_{ij}}{2k} - \frac{\delta_{ij}}{3} \quad (39)$$

In the constant shear stress log region, the ratio τ/khas been found to be 0.3, as previously stated for the constant β'. For the SST model this ratio is set to 0.31 [2]. This leads to the following equation for b_{12}:

$$b_{12} = \frac{\tau}{2k} \quad (40)$$

Which leads to a value of 0.31 for a_1.

The SST model uses coefficients of the Wilcox k-ω model in the near wall region and the coefficients of the Launder and Sharma k-ε model away from the wall. The exception to this is the coefficient σ_{k1} of the SST model, as it has been recalibrated from Wilcox's σ_k so that the model properly predicts flat plate log law behaviour near the wall [8].

The coefficients of the Launder and Sharma k-ε model have been converted in such a way that they can be used in the SST model as follows [8]. (Coefficients with a subscript of 2 refer to the SST model):

$$\sigma_{k2} = \sigma_k \quad (41)$$

$$\sigma_{\omega 2} = \sigma_\varepsilon \quad (42)$$

$$\beta_2 = C_\mu (C_{\varepsilon 2} - 1) \quad (43)$$

$$\alpha_2 = \frac{\beta_2}{C_\mu} - \frac{\kappa^2}{\sigma_{\omega 2}\sqrt{C_\mu}} = C_{\varepsilon 1} - 1 \quad (44)$$

Where σ_ε is calculated using the folowing formula:

$$\sigma_\varepsilon = \frac{\kappa^2}{\sqrt{C_\mu}(C_{\varepsilon 2} - C_{\varepsilon 1})} \quad (45)$$

3.4.1 Turbulence Production and Dissipation Due to Buoyancy

The turbulence production due to buoyancy term has a single coefficient, a turbulent Schmidt number, σ_ρ. This value is the ratio between rates of turbulent transport of momentum and the turbulent transport of mass. The $\sigma_\rho$term has a value of 1.0 for all turbulence models.

The turbulence dissipation due to buoyancy has the dissipation coefficient C_3 and is equal to 1.0. This coefficient determines the ratio of turbulent production due to buoyancy to turbulence dissipation due to buoyancy.

3.4.2 Turbulent Heat Transfer

The only coefficient appearing in the thermal energy equation is the turbulent Prandtl number, Pr_t. This coefficient is the ratio of eddy viscosity to turbulent thermal diffusivity. Its default value in CFX v14.5 is 0.9.

4. Geometry, Domain Definitions, Boundary Conditions, and Mesh

A 1/12th section of the benchmark 7-rod bundle was modelled, and symmetry was assumed on both section planes. The Nichrome elements with their C-shaped cross sections were modelled as solid rods of the same outside diameter as the C-shape. The hydraulic diameter of the sub channel is 2.84038 [mm]. An x-y cross section of the bundle showing the section that has been modelled is given in Figure 1.

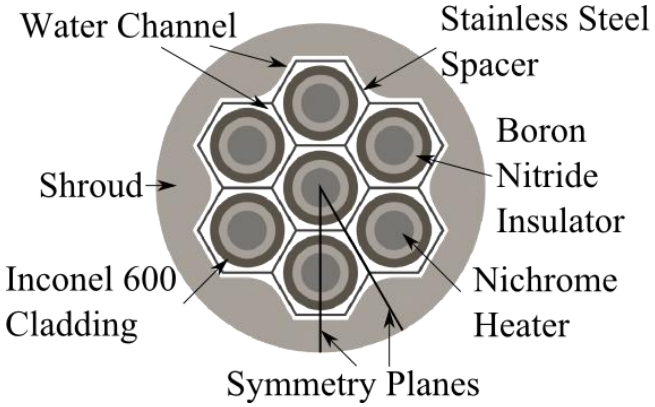

Figure 1. Cross section of 7-rod bundle, showing domain that was modelled in this study, along with the planes of symmetry.

The total length of the domain is 1.83 [m] in the z-direction, which includes a 0.3 [m] inlet section, 1.5 [m] heated section, and a 0.03 [m] outlet section. The six spacers are 0.025 [m] long, and are located at various positions throughout the domain. A y-z cross section, showing the locations of these spacers, as well as the inlet, outlet, heated section, and location of the pressure taps is given in Figure 2.

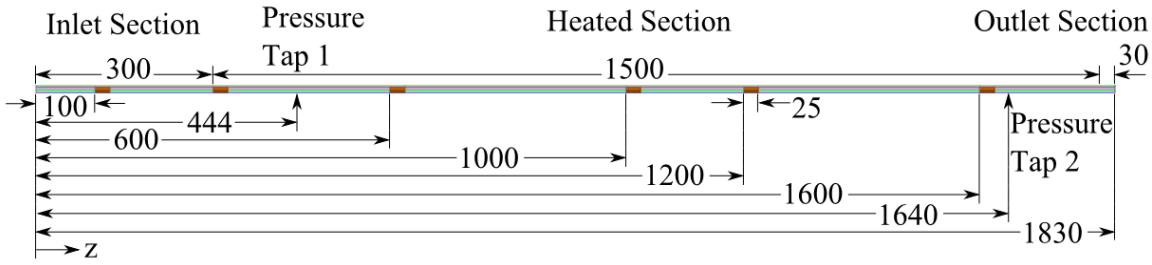

Figure 2. y-z cross section of mesh, showing inlet, heated section, outlet, location of all 6 spacers relative to the inlet, and location of the pressure taps. All spacers are of the same length. Dimensions are in [mm].

The thermocouples are attached to the heater rods at various angles and axial locations. When the entire benchmark domain is simplified to the 1/12th section, the total number of locations of thermocouples on the x-y plane is reduced to 5, because of symmetry. These locations correspond to lines a, b, c, d, and e as shown in Figure 3, which gives more details about the geometry of the computational domain. The thermocouples are located at certain axial locations along lines a, b, c, d, and e.

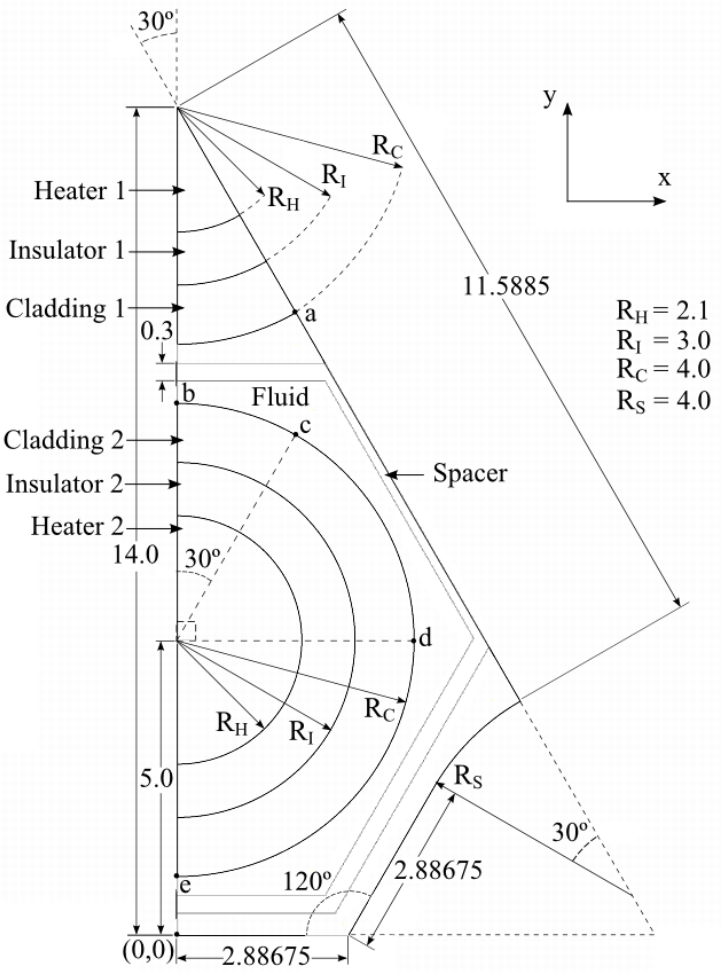

Figure 3. Typical x-y cross section showing fluid and solid domains and locations of thermocouples: lines a, b, c, d, and e. All dimensions in [mm].

Table 2 to Table 5 provide domain definitions and boundary conditions for each of the domains shown in Figure 3.

Table 2. Domain definition and boundary conditions of water domain

Fluid	
Domain, Case B2	Turbulence model: SST Buoyancy Turbulence Production and Dissipation Turbulent Prandtl Number: 0.9 (For Initial Results)
Material Properties	IAPWS-IF97 Database
Inlet, Case B2	Mass Flow Rate: $0.022944444\ [\mathrm{kg\ s^{-1}}]$ Temperature: $519.58\ [\mathrm{K}]$ Turbulence: Low Intensity ($I = 1\%$) and Eddy Viscosity Ratio ($\mu_t/\mu = 1.0$)
Fluid Properties at Inlet, Case B2	velocity $\mathrm{w} = 1.73644\ [\mathrm{m\ s^{-1}}]$ $\rho = 825.735\ [\mathrm{kg\ m^{-3}}]$ $\mu = 1.13316 \cdot 10^{-4}\ [\mathrm{Pa\ s}]$ $\mathrm{c_p} = 4611.90\ [\mathrm{J\ kg^{-1}\ K^{-1}}]$ $\mathrm{k} = 0.649645\ [\mathrm{W\ m^{-1}\ K^{-1}}]$ $Re = 35957.3$
Outlet	Reference Pressure: $0\ [\mathrm{Pa}]$
Wall (Shroud)	Adiabatic, No-Slip Wall

Table 3. Domain definition and boundary conditions of cladding 1 and 2 domains.

Cladding 1 and 2, Inconel 600	
Material Properties	$\rho = -0.3922057147\ [\mathrm{kg\ m^{-3}\ K^{-1}}]\ \mathrm{T} + 8528.0312491363\ [\mathrm{kg\ m^{-3}}]$ $\mathrm{c_p} = 7.524 \cdot 10^{-7}\ [\mathrm{J\ kg^{-1}\ K^{-4}}]\ \mathrm{T^3} - 0.0012939439\ [\mathrm{J\ kg^{-1}\ K^{-3}}]\ \mathrm{T^2}$ $+ 0.9069264845\ [\mathrm{J\ kg^{-1}\ K^{-2}}]\ \mathrm{T} + 262.8297423839\ [\mathrm{J\ kg^{-1}\ K^{-1}}]$ $\mathrm{k} = 0.0160336023\ [\mathrm{W\ m^{-1}\ K^{-2}}]\ \mathrm{T} + 9.6331381197\ [\mathrm{W\ m^{-1}\ K^{-1}}]$
Wall	Adiabatic wall across x-y plane at $\mathrm{z} = 0.0\ [\mathrm{m}]$ and $\mathrm{z} = 1.83\ [\mathrm{m}]$

Table 4. Domain definition and boundary conditions of insulator 1 and 2 domains.

Insulator 1 and 2, Boron Nitride	
Material Properties	$\rho = 2130\ [\mathrm{kg\ m^{-3}}]$ $\mathrm{c_p} = 1265.3[\mathrm{J\ kg^{-1}\ K^{-1}}]$ $\mathrm{k} = 1.792707 \cdot 10^{-4}\ [\mathrm{W\ m^{-1}\ K^{-3}}]\ \mathrm{T^2} - 0.3714505815\ [\mathrm{W\ m^{-1}\ K^{-2}}]\ \mathrm{T}$ $+ 298.4687499009\ [\mathrm{W\ m^{-1}\ K^{-1}}]$
Wall	Adiabatic wall across x-y plane at $\mathrm{z} = 0.0\ [\mathrm{m}]$ and $\mathrm{z} = 1.83\ [\mathrm{m}]$

Table 5. Domain definition and boundary conditions of heater 1 and 2 domains.

Heater 1 and 2, Nichrome (NCH-1)	
Material Properties	$\rho = 8410\ [\mathrm{kg\ m^{-3}}]$ $\mathrm{c_p} = 420\ [\mathrm{J\ kg^{-1}\ K^{-1}}]$ $\mathrm{k} = 0.0179188239\ [\mathrm{W\ m^{-1}\ K^{-2}}]\ \mathrm{T} + 4.5115124321\ [\mathrm{W\ m^{-1}\ K^{-1}}]$
Wall	Adiabatic wall across x-y plane at $\mathrm{z} = 0.0\ [\mathrm{m}]$ and $\mathrm{z} = 1.83\ [\mathrm{m}]$
Heated Section Energy Source Subdomain, Case B2	Heater 1 Energy: $1.642796601 \cdot 10^{9}\ [\mathrm{W\ m^{-3}}]$ (from heat rate of Heater A: 34.14 [kW]) Heater 2 Energy: $1.641112422 \cdot 10^{9}\ [\mathrm{W\ m^{-3}}]$ (from average heat rate of Heaters B, C, D, E, F, and G: 34.105 [kW])

5. Grid Independence Study

A mesh of the 1/12th section of the 7-rod bundle was generated using ANSYS ICEM-CFD, and the spacers were not modelled in order to substantially reduce the total number of nodes. A number of initial meshes were first generated for which solutions were obtained using CFX. A mesh with a large number of nodes was eventually created and a solution was obtained. This mesh is referred to here as the BNSP-1 mesh and it had 18,035,143 nodes. Eight meshes were then generated and solutions were obtained, where the x-y and/or z cross section grid spacing's were increased incrementally for each mesh, so that the total number of nodes was reduced for each newly created mesh. The coarsest mesh had 480,438 nodes. The percent difference in overall pressure drop and difference in cladding surface temperature along each of the lines a, b, c, d, and e between each mesh and the mesh with the greatest number of nodes were compared. The differences in temperature were quantified using a range normalized root mean square parameter, $RMS_{RN,T}$, defined below:

$$\mathrm{RMS}_{\mathrm{RN,T}} = \sqrt{\frac{1}{\mathrm{N}}\sum_{\mathrm{i=1}}^{\mathrm{N}}\left(\frac{T_{\mathrm{i,1}} - T_{\mathrm{i,2}}}{Max(T_1) - Min(T_1)} \cdot 100\right)^2} \quad [\%] \qquad (46)$$

Table 6 lists the meshes that were generated, the total number of nodes, the difference in nodes compared to the previous mesh, and notes on which mesh was modified in order to generate the mesh. These meshes are listed in descending order of total nodes.

Table 6. Mesh properties for grid independence study, listed in descending order of total nodes.

Mesh ID	Notes	Total Nodes	Δ Nodes to Previous Mesh	Δ % Decrease Nodes to Previous Mesh
BNSP-1	Finest Mesh	18,035,143	-	-
BNSP-4	BNSP-3 w/increased z nodes	4,495,768	13,539,375	75.07
BNSP-2	BNSP-1 w/reduced x,y,z nodes	4,389,824	105,944	2.36
BNSP-3	BNSP-2 w/reduced x,y nodes	3,753,688	636,136	14.49
BNSP-5	BNSP-3 w/reduced x,y,z nodes	2,362,572	1,391,116	37.06
BNSP-6	BNSP-5 w/reduced z nodes	2,077,434	285,138	12.07
BNSP-7	BNSP-6 w/reduced x,y nodes	1,510,110	567,324	27.31
BNSP-8	BNSP-7 w/reduced x,y nodes	1,016,226	493,884	32.71
BNSP-9	BNSP-8 w/reduced z nodes	480,438	535,788	52.72

The changes made to each mesh can be described using a cylindrical r-θ coordinate system. Figure 4 shows the equivalent r-θ coordinate system superimposed on the x-y cross section of the mesh. The z cross section has constant spacing.

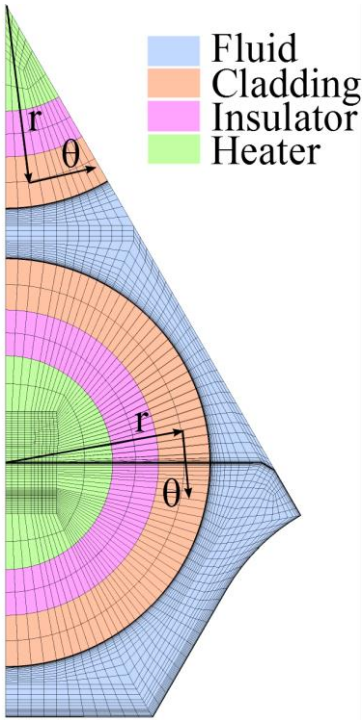

Figure 4. Equivalent r-θ coordinate system for describing mesh modification procedure.

Table 7 lists the geometric parameters of each mesh. The meshes were created by taking the previously created mesh and reducing the number of nodes in the z, r, and/or θ direction, i.e. the BNSP-1 mesh was created first, and then the BNSP-2 mesh was created from the BNSP-1 mesh, and so on. The exception to this is the BNSP-4 mesh: the number of nodes in the z-direction was increased from the previously created mesh. The near wall grid spacing was only modified to maintain y^+~1.

Table 7. Geometric parameters of individual meshes, listed in descending order of date created.

Mesh ID	Maximum z-Spacing [mm]	Maximum θ-Spacing [mm]	Maximum r-Spacing, Fluid [mm]	Near Wall Grid Spacing [mm] / Expansion Ratio Next to Cladding	Near Wall Grid Spacing [mm] / Expansion Ratio Next to Shroud	Solid Domain Nodes in r-Direction: Heater/Insulator/ Cladding
BNSP-1	2.340	0.105	0.074	0.0006/1.3	0.0006/1.3	4/4/7
BNSP-2	3.125	0.210	0.134	0.0006/1.3	0.0006/1.48	4/4/4
BNSP-3	3.125	0.270	0.134	0.0006/1.3	0.0006/1.48	3/3/3
BNSP-4	2.529	0.270	0.134	0.0006/1.3	0.0006/1.48	3/3/3
BNSP-5	3.571	0.270	0.222	0.00055/1.4	0.0007/1.65	3/3/3
BNSP-6	4.167	0.270	0.222	0.00055/1.4	0.0007/1.65	3/3/3
BNSP-7	4.167	0.333	0.206	0.00055/1.6	0.0007/2.0	3/3/3
BNSP-8	4.167	0.472	0.250	0.00055/2.0	0.0007/2.0	3/3/3
BNSP-9	8.774	0.472	0.250	0.00055/2.0	0.0007/2.0	3/3/3

The maximum and minimum y^+ values of the nodes closest to the cladding and shroud domains of each mesh is given in Table 8. As can be seen in the table, the maximum y^+ value was maintained at approximately 1 for all meshes.

Table 8. Maximum and Minimum y^+ values of nodes closest to cladding and shroud domains.

Mesh ID	y^+ Max	y^+ Min
BNSP-1	1.03690	0.13440
BNSP-4	1.03553	0.13461
BNSP-2	1.03597	0.13459
BNSP-3	1.03559	0.13461
BNSP-5	0.95114	0.12385
BNSP-6	0.95107	0.12385
BNSP-7	0.95411	0.12197
BNSP-8	0.96233	0.12411
BNSP-9	0.96629	0.12412

The minimum angle, maximum expansion factor, and maximum aspect ratio between individual elements in the fluid domain are given in Table 9.

Table 9. Minimum angle, maximum expansion factor, and maximum aspect ratio of elements in the fluid domain of each mesh.

Mesh ID	Minimum Angle [º]	Maximum Expansion Factor	Maximum Aspect Ratio
BNSP-1	19.9	6	11,476
BNSP-4	21.7	7	14,616
BNSP-2	21.5	6	15,221
BNSP-3	21.7	6	15,225
BNSP-5	21.9	9	18,982
BNSP-6	21.9	10	22,140
BNSP-7	20.0	10	22,990
BNSP-8	22.6	8	22,047
BNSP-9	22.5	17	46,866

The minimum angle never changed significantly for each mesh, and the maximum expansion factor stayed between 6 and 17. The maximum aspect ratio had a large range, where values ranged between 11,476 and 46,866.

Figure 5 shows the percent difference in total pressure drop between each mesh and the BNSP-1 mesh.

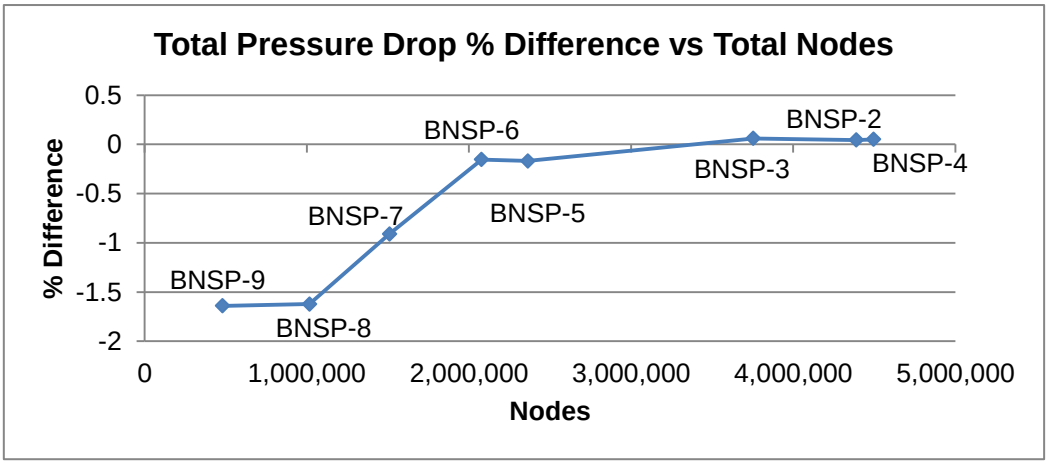

Figure 5. Percent difference in total pressure drop between each mesh and BNSP-1 mesh.

The total pressure drop for all meshes greater than 2,000,000 nodes is effectively the same. Selecting any of the meshes with greater than 2,000,000 nodes will yield a result with a pressure drop that is accurate to within ±1 % of the BNSP-1 mesh.

A plot of the cladding surface temperature $RMS_{RN,T}$ along lines a, b, c, d, and e for each mesh is given in Figure 6.

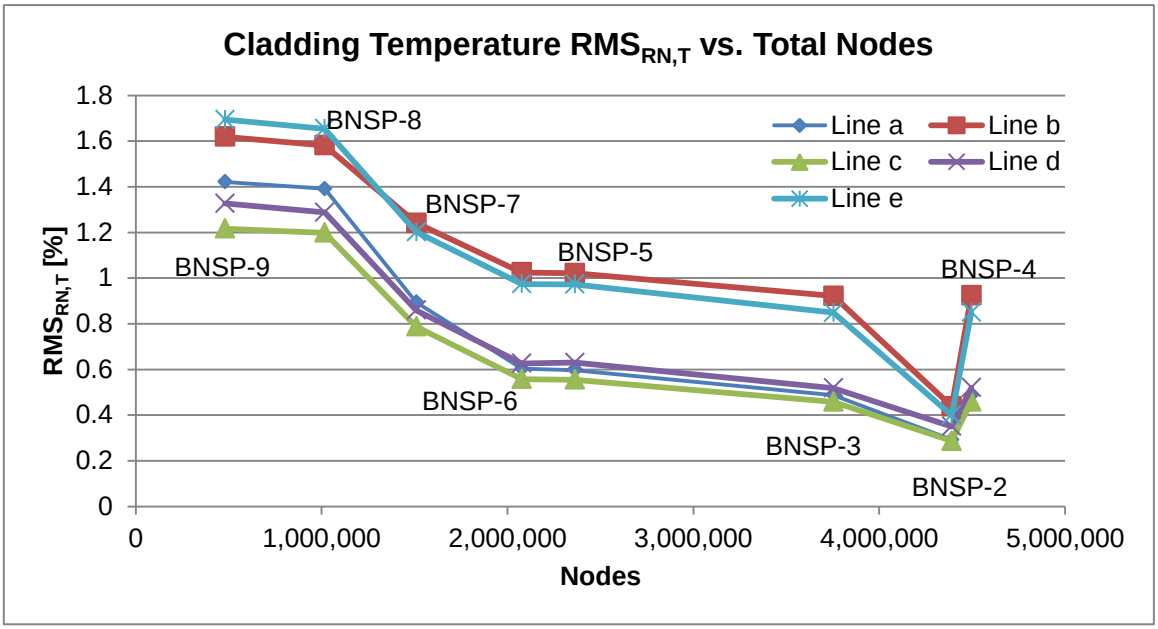

Figure 6. Cladding surface temperature $RMS_{RN,T}$ vs. total nodes.

From Figure 6, it can be seen that as the number of nodes increases, the cladding surface temperature $RMS_{RN,T}$ along each line decreases, with the exception of the mesh with 4,389,824 nodes, BNSP-2. The $RMS_{RN,T}$ are a minimum for this mesh, then increases for the next largest mesh, BNSP-4. The BNSP-4 mesh has identical x-y grid spacing's as the BNSP-3 mesh, but has more nodes in the z-direction. The BNSP-2 mesh has a finer x-y grid than the BNSP-3 (and BNSP-4) mesh, but has fewer nodes in the z-direction than the BNSP-4 mesh. This leads to the BNSP-2 mesh having fewer nodes than the BNSP-4 mesh, yet the finer x-y grid leads to results with a lower cladding surface temperature $RMS_{RN,T}$. Thus, the grid spacing in the z-direction does not significantly affect cladding surface temperature results, but the x-y grid spacing does significantly affect cladding surface temperature results.

The mesh that provided a reasonably low pressure drop percent difference and cladding surface temperature $RMS_{RN,T}$ while having the least possible number of nodes was selected as the optimal mesh.

The final mesh that was selected is BNSP-6. The maximum and minimum y^+ values for this mesh are 0.951072 and 0.123853 respectively. The BNSP-6 mesh gives an overall pressure drop percent difference of -0.15 % and a cladding surface temperature $RMS_{RN,T}$ of 1 % or less. An x-y cross section of the mesh can be seen in Figure 7.

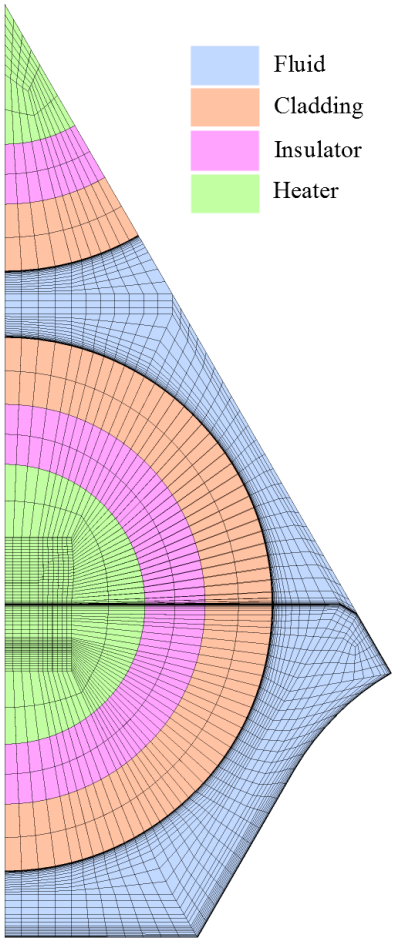

Figure 7. Typical x-y cross section of BNSP-6 mesh.

6. Initial Results

For the benchmark exercise, the default values for all parameters of the SST model were used. Figure 8 shows the cladding surface temperature obtained using CFX compared to the experimental data of case B2. Only experimental and numerical data for line b and line c are reported, since only 3 data points exist for line a thermocouples, 2 data points for line d thermocouples, and 1 data point for line e thermocouples.

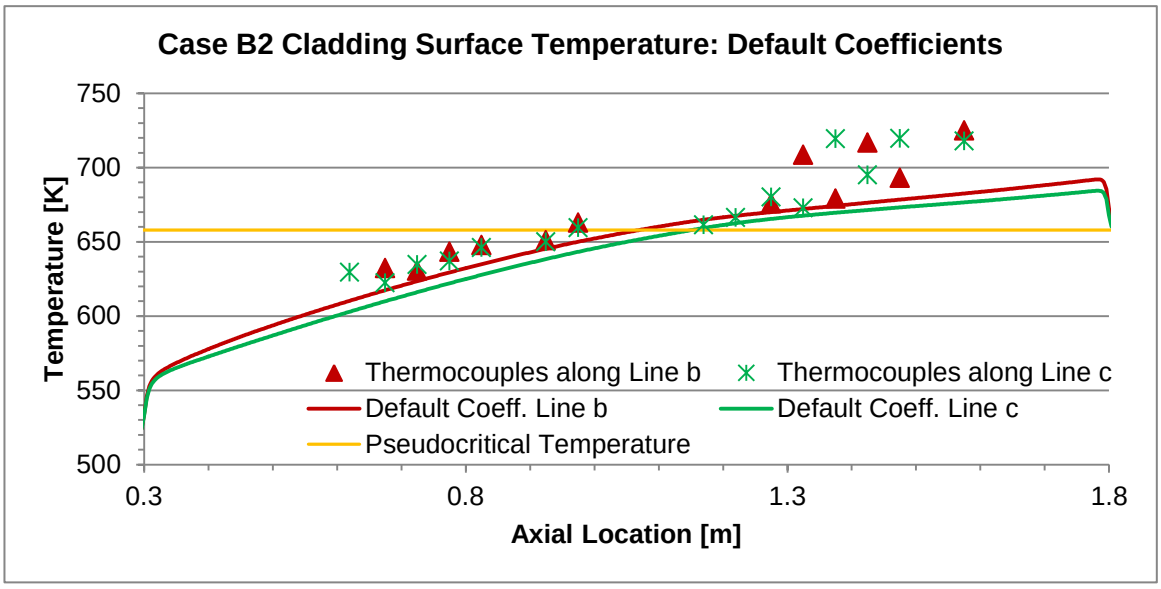

Figure 8. Blind modelling results of cladding surface temperature, compared to case B2 experimental data. Default values for SST coefficients were used.

The numerical results generally under-predicted the experimental data, with this under prediction being more pronounced after the surface temperature exceeded the pseudocritical temperature.

6.1 Initial Results with Spacers Included in Mesh

To determine the effect the spacers had on the cladding surface temperatures, runs were performed on a mesh that included all 6 spacers. In order to maintain $y^+<1$ at the first node from all solid surfaces, the grid spacing was reduced before and after the spacers in the axial, z-direction. This reduction in grid spacing can be seen in a y-z cross section of the mesh, shown below in Figure 9.

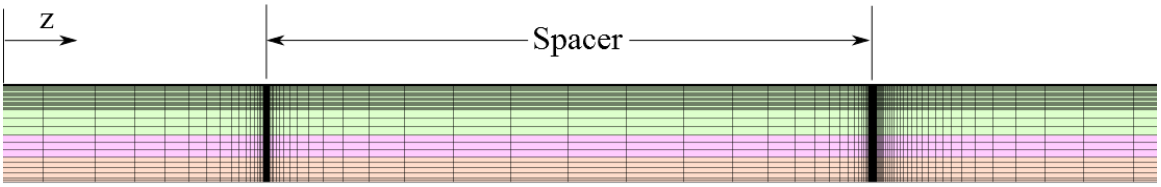

Figure 9. y-z cross section at location of spacer showing reduction in grid spacing in z-direction.

This reduction in grid spacing at all 6 spacers greatly increased the total number of nodes. The total number of nodes of the mesh with spacers included was 62,740,257. The cladding surface temperature is given in Figure 10. Again, only data for line b and line c are reported, since limited experimental exists for line a, d, and e thermocouples.

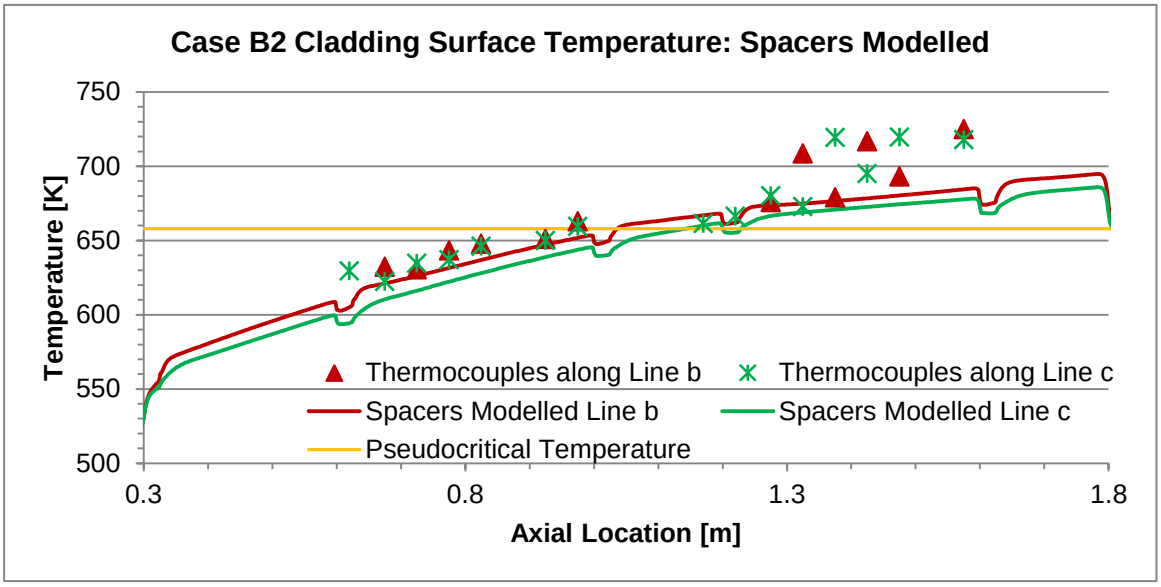

Figure 10. Blind modelling results of cladding surface temperature with spacers modelled, compared to case B2 experimental data. Default values for SST coefficients were used.

The location of each spacer is easily recognizable, as a local drop in temperature occurs at each spacer. The cladding surface temperature drops when the flow encounters a spacer, then increases after passing the spacer. The cladding surface temperature profiles of the mesh with the spacers closely match the temperature profiles from using a mesh without the spacers. The drop in temperature only affects the cladding surface temperatures locally, and do not alter the cladding surface temperature downstream of the spacers.

7. SST Modification

A study was undertaken to determine if modifying the coefficients of the SST turbulence model could lead to better prediction of the case B2 experiment. There are a total of 13 coefficients that can be modified in the SST model: σ_{k1}, σ_{k2}, $\sigma_{\omega1}$, $\sigma_{\omega2}$, β_1, β_2, α_1, α_2, β', a_1, C_3, σ_ρ, and Pr_t. The total number of possible combination of coefficients is enormous. For example, if each coefficient has only 3 possible values: the default value, a minimum, and a maximum, then the total number of possible combinations of values is 3^{13}. Therefore, certain coefficients must be held constant. Additionally the equations given in the previous section will be used to make certain coefficients dependant on other coefficients.

Since heat transfer deterioration occurs near the wall, only the portion of the SST model that is activated near the wall will be modified. The portion of the SST model that is activated in the free stream, away from the wall, will remain unchanged. The coefficients that are activated in the near wall region have a subscript 1 to identify them. These are the inner region coefficients. The coefficients in the free stream region, away from the wall, have a subscript 2 to identify them. These are the outer layer coefficients. The SST default inner layer coefficients are based on the Wilcox k-ω coefficients, while the outer layer coefficients are based on the Launder and Sharma k-ε coefficients.

Because coefficients in the free stream region depend on the value of β' due to equation (45), and the coefficients in this free stream region are to be held constant, the value of β' will be held constant at 0.09. It follows that the constant a_1 will also be held constant, since this value results from the same experimental data as β'. These experimental data are for the ratio of Reynolds shear stress to turbulence kinetic energy (τ/k).

The value of α results from equation (36), and since β' and κ have set values, only $\sigma_{\omega1}$ and β_1 need to be specified in order to obtain a value of α_1. After the ratio of β'/β_1 is specified, the

value of β_1 can be determined, since β' is held constant. The ratio of β'/β_1 will be modified, because this is how the value of β_1 was originally determined in the Wilcox k-ω model. The value of σ_{k1} will also vary. The turbulent Schmidt number, σ_ρ, and the dissipation coefficient, C_3, will vary, since these have effects of turbulence production and dissipation due to buoyancy.The turbulent Prandtl number, Pr_t, will also vary, since this coefficient has an effect of turbulent heat transfer. This results in a total of 6 quantities whose values will be modified: σ_{k1}, $\sigma_{\omega1}$, β'/β_1, C_3, σ_ρ, and Pr_t. The values of β'/β_1 and α_1 are automatically determined from on the other coefficients.

Initial runs will be performed where the value of only one coefficient was modified from the default value. Each coefficient was given a minimum and maximum value. The minimum value was the default value multiplied by 0.5, and the maximum value was the default value multiplied by 2. There are two exceptions to this: the turbulent Prandtl number and $\sigma_{\omega1}$. The turbulent Prandtl number had a maximum value of 1.5, which is less than twice the default value of 0.9. The minimum value of $\sigma_{\omega1}$ was such that the calculated value of α_1 was greater than zero, since α_1 depends on $\sigma_{\omega1}$. A summary of the values of the coefficients that were modified is given in Table 10.

Table 10. Default, minimum, and maximum values of coefficients that were used in the first set of parametric sensitivity studies.

Coefficient	Minimum Value	Default Value	Maximum Value
σ_{k1}	0.588235	1.17647	2.35294
$\sigma_{\omega1}$	1.0	2.0	4.0
β'/β_1	0.6	1.2	2.4
C_3	0.5	1.0	2.0
σ_ρ	0.5	1.0	2.0
Pr_t	0.5	0.9	1.5
β_1	0.0375	0.075	0.15
α_1	0.132917	0.553167	1.3865

The cladding surface temperatures and overall pressure drop of each of these initial runs were compared to the run with all default values. Table 11 summarizes the overall pressure drop of each case, compares the pressure drop to the default case, and gives the range normalized RMS of the temperature difference between each case and the default case.

Table 11. Results of initial modification to SST turbulence model coefficients: overall pressure drop, percent difference between overall pressure drop of each case and default case, and $RMS_{RN,T}$ between each case and default case.

Case	ΔP [Pa]	ΔP Difference [%] from Default Case	$RMS_{RN,T}$ [%] from Default Case
Default	21938.9	-	-
σ_{k1} Min	21306.3	2.883	0.424
$\sigma_{\omega1}$ Min	28309.8	-29.039	4.512
β'/β_1 Min	23044.8	-5.041	2.273
C_3 Min	21942.2	-0.015	0.003
σ_ρ Min	21945.2	-0.029	0.004
Pr_t Min	22981.9	-4.754	6.613
σ_{k1} Max	22052.1	-0.516	0.335
$\sigma_{\omega1}$ Max	16618.1	24.253	8.719
β'/β_1 Max	19275.2	12.141	5.089
C_3 Max	21938.3	0.003	0.009
σ_ρ Max	21946.8	-0.036	0.007
Pr_t Max	20460.4	6.739	8.426

Table 11 shows that decreasing and increasing the values of $\sigma_{\omega 1}$, β'/β_1, and Pr_t leads to a $RMS_{RN,T}$ greater than 2%. Decreasing the value of $\sigma_{\omega 1}$, β'/β_1, and Pr_t leads to an increase in the magnitude of the overall pressure drop greater than 5% compared to the default case. Increasing the values of these coefficients leads to a decrease in overall pressure drop greater than 7%. The value of $\sigma_{\omega 1}$ greatly affects overall pressure drop more than the other coefficients, as evident by the 29% pressure drop difference for using the minimum coefficient value.

For the next set of runs, only the values of β'/β_1 and Pr_t were altered. These coefficents were shown to affect the cladding surface temeprature more than any other coefficient, with the exception of $\sigma_{\omega 1}$. The $\sigma_{\omega 1}$ coefficient affected the cladding surface temperature to the same degree as the β'/β_1 and Pr_t coefficients, but affected the overall pressure drop significantly more than any other coefficient. For this reason, the value of the $\sigma_{\omega 1}$ coefficent was not modified for the next set of runs.

The values of β'/β_1 and Pr_t were each given one of four values: minimum, default, medium, and maximum. Runs were performed using every combination of β'/β_1 and Pr_t except for one: the case of minimum β'/β_1 and minimum Pr_t. The reason for this is that the cases that used similar values gave cladding surface temperature results that were in poor agreement with experimental data. A summary of the values that were used is given in the Table 12.

Table 12. Default, minimum, medium, and maximum values of coefficients that were used for the second set of runs.

Coefficient	Minimum Value	Default Value	Medium Value	Maximum Value
β'/β_1	0.6	1.2	1.8	2.4
β_1	0.0375	0.075	0.05	0.15
α_1	0.1365	0.553167	-	1.3865
Pr_t	0.5	0.9	1.2	1.5

The resulting cladding surface temperature of the runs is compared to the experimental cladding surface temepratures. The pressure cannot be compared, as it was not measured in the experiments. Table 13 gives the range normalised RMS of the temperature difference between the measured thermocouple data and the cases with differing values of β'/β_1 and Pr_t.

Two additional runs were also performed in which the Pr_t coefficient was given a value of 1.0 and the medium and maximum values of β'/β_1 were used.

Table 13. $RMS_{RN,T}$ of experimental cladding surface temepratures and surface termperature from differing values of β'/β_1 and Pr_t.

ΔT,RMS % Difference from Experimental		Pr_t				
		0.5	0.9	1	1.2	1.5
β'/β_1	0.6	-	12.885	-	9.807	6.827
	1.2	15.553	11.129	-	7.913	5.932
	1.8	14.115	9.090	7.937	6.210	7.368
	2.4	12.662	7.182	6.309	6.452	11.815

The default case (β'/β_1 = 1.2, Pr_t = 0.9) gives a $RMS_{RN,T}$ of 11.1% when compared to the experimental data. The values of β'/β_1 and Pr_t. that give results that in the best agreement with experimental data are 1.2 and 1.5, respectively. The values of β'/β_1 and Pr_t. that give results that in the second best agreement with experimental data are 1.8 and 1.2, respectively.

The turbulent Prandtl number, Pr_t, is defined as follows:

$$Pr_t = \frac{\overline{u_i u_j}\frac{\partial T}{\partial y}}{\overline{u_j t}\frac{\partial U_i}{\partial y}} \quad (47)$$

Where the overbar denotes an averaged quantity and lower case indicates the turbulent fluctuating quantities. The values of this turbulent Prandtl number can be determined from direct

numerical simulation (DNS). According to the DNS data from [9], the turbulent Prandtl number of water does not exceed 1.2. Although this conclusion was made for flat duct flow of subcritical water, with a Reynolds number of 11,000. The turbulent Prandtl number also varies with distance from the wall, so the average number would be less than 1.2. With this in mind, the maximum value of turbulent Prandtl number, Pr_t will be limited to 1.2 for these numerical simulations. Therefore, the selected optimal values of β'/β_1 and Pr_t are 1.8 and 1.2, respectively. These values give a more accurate cladding surface temperature for the B2 case of the benchmark than if the default coefficient values were used. A plot showing the cladding surface temperatures resulting from using these modified coefficients is given in Figure 11. Again, only data for line b and line c are reported, since limited experimental exists for line a, d, and e thermocouples. The results indicate that using the modified coefficient values results in a better overall prediction of the cladding surface temperatures.

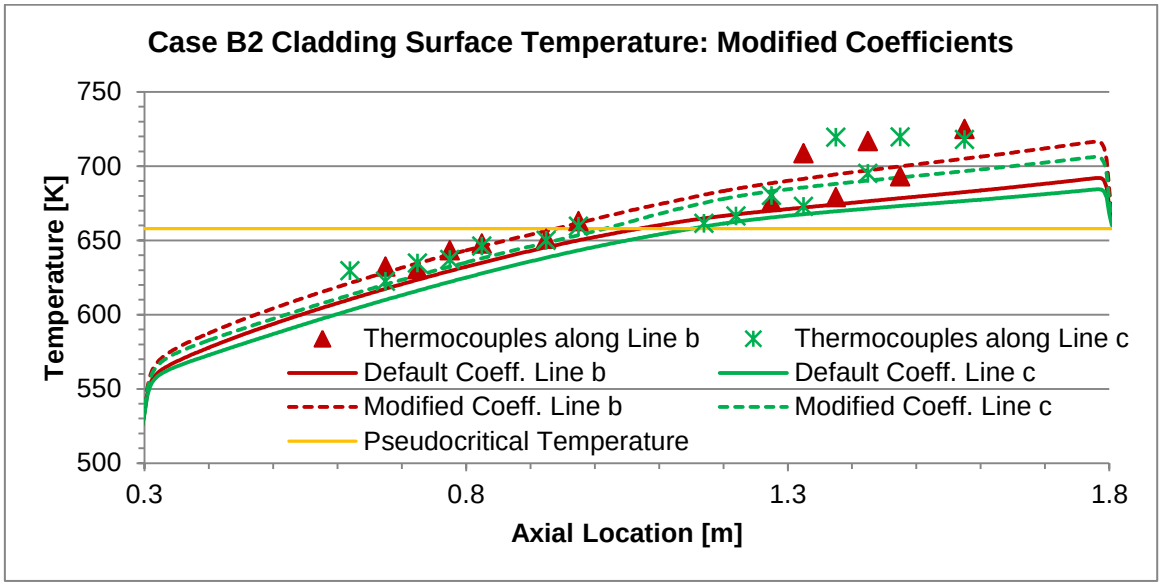

Figure 11. Cladding surface temperature from using optimized SST coefficient values, compared to result from using default SST coefficient values and experimental data.

8. Summary and Conclusions

Numerical analysis of case B2 of the GIF SCWR 2013-2014 7-rod sub-channel benchmark experiments was performed using ANSYS CFX v14.5 and meshes that were generated using ANSYS ICEM CFD v14.5. Initial results using the Shear Stress Transport (SST) model indicated that the cladding surface temperatures were underpredicted, and the $RMS_{RN,T}$ was 11.129 %. A sensitivty study of 7 parameters of the SST model was performed and a new set of coefficient values was found to better predict the cladding surface temperatures. Using these updated coefficient values resulted in a $RMS_{RN,T}$ of 6.210 %. The updated coefficient values are given in Table 14.

Table 14. Updated coefficient values for the SST turbulence model.

Coefficient	Value
β'/β_1	1.8
Pr_t	1.2
β_1	0.05
α_1	0.275389

These coefficient values produce results which are in better agreement with the experimental results of the benchmark B2 case, than if the default coefficient values are used. A limitation to this study is that only one case has been studied and, hence, we cannot recommend this set of modified parameters without further validation against different experiments.

The updated coefficient values were used to predict the surface temperatures of two heated tube experiments with upwards flowing supercritical water: Shitsman [10] and Ornatskii [11]. Initial findings show that using the updated coefficient values results in an over prediction of the surface temperatures, and gives a higher $RMS_{RN,T}$ than if the default values of coefficients are used.

References

[1] SAS IP, Inc, "ANSYS 14.5 Help," 2012.

[2] F. R. Menter, "Two-equation eddy-viscosity turbulence models for engineering applications," *AIAA Journal,* vol. 32, no. 8, pp. 1598-1605, 1994.

[3] B. E. Launder and B. I. Sharma, "Application of the energy-dissipation model of turbulence to the calculation of flow near a spinning disc," *Letters in Heat and Mass Transfer,* vol. 1, pp. 131-138, 1974.

[4] D. C. Wilcox, "Reassessment of the scale-determining equation for advanced turbulence models," *AIAA Journal,* vol. 26, no. 11, pp. 1299-1310, 1988.

[5] W. Wagner, J. R. Cooper, A. Dittman, J. Kijima, H. J. Kretzschmar, A. Kruse, R. Mares, K. Oguchi, H. Sato, I. Stocker, O. Sifner, Y. Takaishi, I. Tanishita, J. Trubenbach and T. Willkommen, "The IAPWS industrial formulation 1997 for the thermodynamic properties of water and steam," *Journal of Engineering for Gas Turbines and Power, Transactions of the ASME,* vol. 122, 2000.

[6] W. P. Jones and B. E. Launder, "The prediction of laminarization with a two-equation model of turbulence," *International Journal of Heat and Mass Transfer,* vol. 15, pp. 301-314, 1972.

[7] A. A. Townsend, The Structure of Turbulent Shear Flow, 2nd ed., Cambridge: Cambridge University Press, 1976.

[8] B. Launder and N. Sandham, Closure Strategies for Turbulent and Transition Flows, Cambridge, UK: Cambridge University Press, 2002.

[9] W. M. Kays, "Turbulent Prandtl number - Where are we?," *Journal of Heat Transfer,* vol. 116, pp. 284-295, 1994.

[10] M. E. Shitsman, "Impairment of the heat transmission at supercritical pressures," *High Temperature,* vol. 1, no. 2, pp. 237-244, 1963.

[11] A. Ornatskii, L. Glushchenko and S. Kalachev, "Heat-transfer with rising and falling flows of water in tubes of small diameter at supercritical pressures," *Thermal Engineering,* vol. 18, no. 5, pp. 137-141, 1971.

ISSCWR7-2059

Corrosion behaviour of 14Cr ODS ferritic steels in a supercritical water

Mengqiang Gong[a], Zhangjian Zhou[a]*, Helong Hu[a], Sami Penttilä[b], Aki Toivonen[b]

[a]School of Materials Science and Engineering, University of Science and Technology Beijing, Beijing 100083, China

[b]VTT Technical Research Centre of Finland, Espoo, 02044, Finland

Tel.: +86 10 62334951 E-mail: zhouzhj@mater.ustb.edu.cn (Zhangjian Zhou)

Abstract

The corrosion behavior and oxide layer structure of two 14Cr ODS (Oxide Dispersion Strenghtened) steels with or without alloying element of Al have been investigated in supercritical water (SCW) at 650℃/25MPa for exposure times of 100h, 300h and 1000h. The oxide structure was studied using scanning electron microscope (SEM), energy dispersion spectroscopy (EDS) and X-ray diffraction (XRD). Both ODS alloys showed a three-layer oxide structure after 1000h of exposure in SCW. The 14Cr-Al samples exhibited a structure with Fe_2O_3 in the outer layer, a mixture of $(Cr, Fe)_3O_4$ and $(Al,Cr)_2O_3$ in the inner layer, and a mixture of metal and oxide grains Al_2O_3 in the diffusion layer. The outer layer of Al-free samples consist of Fe_2O_3, the inner layer and the diffusion layer contain $(Fe, Cr)_3O_4$ and Cr_2O_3, respectively. Cracks, pores and exfoliations could be observed for both alloys after SCW exposure up to 1000h.

1. Introduction

As one of the Generation IV initiative, the supercritical water reactor (SCWR) design is considered for its high thermal efficiency and plant simplification. This reactor is designed to function above the critical point of water (374°C and 22.1 MPa) at a temperature between 500 and 650°C, and a pressure of 25 MPa[1-3]. Water in the supercritical phase exhibits properties significantly different from those of liquid water below the critical point which leads to different corrosion mechanisms for materials used in such an environment. Corrosion resistance is among the key requirements for structural materials to be used in the proposed SCWR [4]. This reactor is designed to function at high outlet temperature, which requires cladding and structural materials that can perform at these elevated temperatures for extended exposures.

As candidate structural material for advanced nuclear energy systems, ODS ferritic steels show good creep strength and neutron irradiation tolerance [5−7].This alloy also exhibits good corrosion resistance, which has been suggested to be caused by the enhanced chromium segregation to form Cr_2O_3 [8-10] due to the fine grain microstructure. Balanced addition of chromium (>13%) and aluminum (≥4.5%) are known to be highly effective in lowering corrosion rate in the SCW [10-11].

Although several studies have been conducted to evaluate the ability of Al-alloying surface treated steels to withstand SCWR corrosion, only a few studies have considered temperatures above 600°C. In addition, long-term corrosion tests are needed to investigate the stability of

surface treatment layers and oxide scales on steel surfaces and the possibility of self-healing after spalling-off of the oxide scale. In this study, corrosion behaviour of 14Cr-ODS ferritic steel with or without Al alloying element have been conducted in SCW with 150 ppb oxygen content at 650°C/25MPa for 1000 h.

2. Experiments

2.1. Materials

Table 1 shows the nominal chemical compositions of two kinds of 14Cr-ODS samples. The nitrogen-gas-atomized pre-alloyed powders with an average particle size of 74μm were mechanical alloyed with nano sized Y_2O_3 powders in a high-energy planetary ball mill under a pure argon atmosphere. The ball-to-powder weight ratio of 10:1 and a rotation speed of 300 rpm were conducted with milling time up to 30 h. Subsequently, the milled powders were consolidated by hot isostatic pressing (HIP) at 1150°C under a pressure of 150 MPa for 2 h.

The as-hipped steels were forged and hot rolled in order to improve density and ductility of the samples. The initial and final forging temperatures were 1250°C and 1150°C respectively with a forging ratio of 3:1.

2.2. Supercritical water exposure tests

For the corrosion tests in a SCW environment, the different materials were tested as the dimensions of 20 x 10 x 2 mm. For each specimen, the edges and the two main faces were mechanically polished with abrasive papers down to 1200 grit. The tests were done in SCW at 650°C. The dissolved oxygen content in the feed water was between 100 and 150 ppb and conductivity was <0.1 μS/cm. The specimens were exposed to SCW at the pressure of 25 MPa in supercritical autoclave connected to a recirculation water loop.

2.3. Post test analysis

The samples were weighed before and after exposure using Mettler AT261 scale with a measuring uncertainty of ± 0.002%. The mass change per unit area was calculated using coupon dimensions measured before testing. Surface oxide phases were identified by an X-ray diffractometer (Rigaku DMAX-RB) with a Cu Ka radiation source. Chemical composition and oxide morphology were characterized with SEM equipped with EDS.

3. Results and discussion

3.1. Weight change

Fig. 1 shows the dependence of weight change on the exposure hours and the influence of alloying element Al on the corrosion resistance of ODS ferritic steels exposed in SCW at 650°C. Obviously, the addition of 4.5 wt.% Al in 14Cr-ODS steel improved its corrosion resistance in SCW significantly. The weight change after 1000h is unexpectedly low for both samples, which should be due to the exfoliating of oxide layer.

3.2. Surface oxide morphology

The surface morphologies of the oxide layer formed on the samples exposed for various hours in SCW are shown in Fig. 2. Loose and fine Al enriched oxide grains are distributed on the surface of 14Cr-Al-ODS sample after 100 h exposure, as shown in Fig 2(a). While dense Fe enriched oxide with large grain size formed on the surface of Al free sample after 100h exposure. The grain size of the oxide layer increased with the increasing of exposure time from 100h to 300h. Partial oxide scale exfoliation could be found for 300h exposure samples. After 1000h exposure, new oxide grains are generated and got together to form a rough oxide surface with round-cornered and cauliflower shaped oxide particles for both samples. Generally, the exfoliation could be ascribed to the thermal mismatch of the outer and inner layer, which decreases the stability of the oxide and adhesion [12,13]. However, in our previous investigation of corrosion behaviour of 14Cr-ODS steel in SCW at 550°C we didn't find the similar

phenomena [14]. Whether the oxide scale exfoliation was due to high testing temperature or some other factors needs further detailed investigation.

The oxide phase structures of the samples exposed for 300 and 1000 h were identified using XRD (as shown in Fig. 3). It is confirmed that the dominant phases in the oxide scale are hematite and magnetite. The amount of hematite increased while the magnetite decreased with the increasing exposure time.

3.3. Cross sectional analysis

Fig. 4 show the cross-section images of the 14Cr-Al samples exposed to the SCW for 1000 h. An EDS line-scan across the oxide scale was also performed. It can be concluded from the SEM image that the layer thicknesses of the samples exposed for 1000 h were about 16 μm. According to the morphology and elemental concentration distribution, the oxide scales developed a typical triple oxide scale that consists of an outer oxide layer, inner oxide layer, and a diffusion layer, labeled 1, 2 and 3 respectively in Fig. 4. The outer oxide layer almost disappeared due to the oxide scale exfoliation. Aluminum and chromium were found to be enriched in the inner layer and depleted in the outer layer, while iron showed the opposite trend. At the interface of the metal substrate and oxide scale, there is a peak in the aluminum content and a sharp drop in that of chromium. Fig. 5 shows the cross-section images of the Al free 14Cr-ODS sample exposed to the SCW for 1000 h. The oxide layer thicknesses was about 60 μ m much thicker than that of 14Cr-Al ODS. Based on the SEM image and EDS line-scan analysis, the oxide scale of the sample can be segmented into triple layers: a Fe-rich outer oxide layer (labeled 1 in Fig. 5), a Fe-Cr-rich inner oxide layer (labeled 2 in Fig. 5) and a Cr-rich diffusion layer (labeled 3 in Fig. 5). The formation of the oxide layers structure was resulted from oxidation of metal irons and diffusion of cations/anions [14]. Pores (labeled 4) and cracks (labeled 5) are observed in Fig. 5.

.

3.4. Oxidation mechanism

There are few surveys of oxidation in SCW for ODS ferritic steels, and the oxidation mechanism for Al alloyed ODS steel is not clear. According to Bischoff et al.,the oxidation models can be classified into three distinct types: the formation of the inner oxide layer by dissociation of the outer layer, the formation of a dual layer due to differences in diffusion rates, and finally the ‘‘available space’’ model [15]. In addition, the oxidation behavior in SCW is similar to that in gaseous environment rather than in liquid conditions. Oxidation in a gaseous environment is dominated by molecular processes and the diffusion rate of anions and cation in the oxide, which are the rate determining step. Moreover the diffusion of oxygen and iron through the inner layer but not the outer layer is the rate determining process [12, 16, 17] . The 14Cr-Al alloy presents a more complex multi-layer oxide film. As it was seen previously, there is an iron-rich outer oxide layer that has been identified as magnetite for 300h and hematite for 1000h. As the exposure time increasing, Fe_3O_4 (magnetite) converted to Fe_2O_3 (hematite) by the reaction (1)[12].

$$4Fe_3O_4+O_2=6Fe_2O_3 \quad (1)$$

An aluminium rich diffusion layer (which should be Al_2O_3 according to the EDS result) and a Cr riched inner layer formed along the exposure time. Oxygen affinity for Al and Cr are larger than Fe. Oxidation occurs more rapidly by reaction with the diffusion oxygen to form Al-rich layer. However until the complete formation of Al oxide, Fe can diffuse outward and react with oxygen to form the Fe-rich outer oxide layer [18]. Al oxides formed first because its formation energy is lower than Cr. Furthermore, the Cr presence may promote the formation of Al_2O_3 oxide [19]. The formation of Al_2O_3 oxide rather than Cr_2O_3 oxide is also reported in previous study [20, 21]. Thus aluminium slows the formation of Cr oxide explaining the presence of the Fe-rich outer layer. The Cr-rich layer may be a spinel oxide $(Cr, Fe)_3O_4$ and $(Al,Cr)_2O_3$. The composition depends on the testing temperature and on the exposure duration [9-10]. The Al-free alloys produce only Cr-rich diffuse layer, which are Cr_2O_3 oxide or a spinel type such as $(Cr, Fe)_3O_4$. Atkinson also noted [22] the diffusion rate of iron is higher than that of chromium, thus, the outer

layer is Fe-rich and Cr-depleted, and contains the phases of Fe_2O_3 and Fe_3O_4. The oxygen partial pressure decreases gradually from outside to inside in the oxide layer. So there are (Fe, Cr)$_3O_4$ and Cr_2O_3 in the inner layer and diffusion layer, respectively [22] .

4. Conclusions

The corrosion properties of 14Cr–Al and Al free 14Cr-ODS ferritic steels were investigated in a SCW environment at 650°C / 25MPa. The oxide film formation in 14Cr-Al samples is controlled by the presence of aluminium. The 14Cr-Al-ODS steel showed better corrosion resistance, compared with 14Cr-ODS steels. The oxide film formed in 14Cr-Al is much thinner than that of 14Cr-ODS alloys, about 16 vs 64 μm after exposure in SCW for 1000h, respectively. For the Al-free alloys, the oxide film is a triple layer composed of Fe_2O_3, (Cr, Fe)$_3O_4$ and Cr_2O_3 that forms by an oxidation process with limited inward oxygen diffusion. For the Al-added alloys, the oxide film is composed of an outer Fe-rich oxide layer identified as magnetite, and a diffusion Al-rich oxide layer identified as Al_2O_3. The interface between the outer and the diffusion layer is Cr-rich and may form (Cr, Fe)$_3O_4$ and (Al,Cr)$_2O_3$. Oxygen affinity with Al is superior to Cr and Fe. The Al oxide formed readily due to inward diffusion of oxygen. Oxide exfoliation and cracks were observed in the outer layer for both samples already after 300h of exposure in SCW.

References

[1] A Technology Roadmap for Generation IV Nuclear Energy Systems, US DOENERAC and Generation IV International Forum GIF-002-00, 2002.

[2] G.S.Was, P. Ampornrat, G. Gupta, S.Teysseyre, E.A.West, T.R.Allen, K.Sridharan, L.Tan, Y.Chen, X.Ren, C.Pister. Corrosion and stress corrosion cracking in supercritical water. Journal of Nuclear Materials. 371(1-3), 176(2007)

[3] Todd R. Allen, Kumar Sridharan, Yun Chen. Research and Development on Materials Corrosion Issues in Supercritical Water Environment. 15th International Conference on the Properties of Water and Steam. Berlin, September 8–11, 2008

[4] Y. Chen, K. Sridharan, S. Ukai, T.R. Allen, J. Nucl. Mater. 371 (2007) 118–128.

[5] A. Alamo a, V. Lambard, X. Averty, M.H. Mathon. Assessment of ODS-14%Cr ferritic alloy for high temperature applications. Journal of Nuclear Materials. 329-333(A),333(2004).

[6] M.B. Toloczko, D.S. Gelles, F.A. Garner. Irradiation creep and swelling from 400 to 600℃ of the oxide dispersion strengthened ferritic alloy MA957. Journal of Nuclear Materials.329–333 (2004) 352–355.

[7] J. Chen, P. Jung, J. Henry. Irradiation creep and microstructural changes of ODS steels of different Cr-contents during helium implantation under stress. Journal of Nuclear Materials 437 (2013) 432–437.

[8] J. Isselin, R. Kasada, A. Kimura. Corrosion behaviour of 16%Cr–4%Al and 16%Cr ODS ferritic steels under different metallurgical conditions in a supercritical water environment. Corrosion Science 52 (2010) 3266–3270.

[9] Tong Liu, Chenxi Wang, Hailong Shen, Wusheng Chou, Noriyuki Y. Iwata, Akihiko Kimura.The effects of Cr and Al concentrations on the oxidation behavior of oxide dispersion strengthened ferritic alloys. Corrosion Science 76 (2013) 310–316.

[10] J.H. Lee, R. Kasada, A. Kimura, T. Okuda, M. Inoue, S. Ukai, S. Ohnuki, T.Fujisawa, F. Abe, Influence of alloy composition and temperature on corrosion behavior of ODS ferritic steels, J. Nucl. Mater. 417 (2011) 1225–1228.

[11] A. Kimura, R. Kasada, N. Iwata, H. Kishimoto, C.H. Zhang, J. Isselin, P. Dou, J.H.Lee, N. Muthukumar, T. Okuda, M. Inoue, S. Ukai, S. Ohnuki, T. Fujisawa, T.F.Abe, Development of Al added high-Cr ODS steels for fuel cladding of next generation nuclear systems, J. Nucl. Mater. 417 (2011) 176–179 .

[12] H. Hu, Z. Zhou, M. Li, L. Zhang, M. Wang, S. Li, C. Ge, Study on the corrosion behaviour of a 18Cr-ODS steel in supercritical water, Corros. Sci. 65 (2012) 209-213.

[13] Y. Chen, K. Sridharan, T.R. Allen, Corrosion behavior of ferritic-martensitic steel T91 in supercritical water, Corros. Sci. 48 (2006) 2843-2854.

[14] H.L. Hu , Z.J. Zhou , L. Liao, etal.Corrosion behavior of a 14Cr-ODS steel in supercritical water, Journal of Nuclear Materials 437 (2013) 196–200.

[15] Jeremy Bischoff, Arthur T. Motta, Oxidation behavior of ferritic–martensitic and ODS steels in supercritical water, Journal of Nuclear Materials 424 (2012) 261–276.

[16] M. Sun, X. Wu, Z. Zhang, E.-H. Han, Corr. Sci. 51 (2009) 1069–1072.

[17] D.D. Macdonald, J. Supercrit. Fluids 30 (2004) 375–382.

[18] S.H. Nie, Y. Chen, X. Ren, K. Sridharan, T.R. Allen, J. Nucl. Mater. 399 (2010) 231–235.

[19] L. Liu, Y. Li, F. Wang, Mater. Lett. 62 (2008) 4081–4084.

[20] H. Asteman, M. Spiegel, Corr. Sci. 50 (2008) 1734–1743.

[21] I.M. Wolff, L.E. Iorio, T. Rumpf, P.V.T. Scheers, J.H. Potgieter, Mater. Sci. Eng. A241 (1998) 264–276.

[22] A. Atkinson, Transport processes during the growth of oxide films at elevated temperature, Rev. Mod. Phys. 57 (1985) 437–470.

Figure captions

Fig. 1. Comparison of weight gain of ODS ferritic steels with minor alloying element Al under SCW condition at 650 ℃.

Fig. 2. SEM images of the surface morphologies of the oxide layer on 14Cr-Al (a,c,e)and 14Cr-ODS (b,d,f) steels exposed to SCW for different times (a) 100 h, (c) 300 h, (e) 1000 h, (b) 100 h, (d) 300 h, and (f) 1000 h.

Fig. 3. XRD analyses of the oxide layer formed on 14Cr–4Al(a) and 14Cr(b) ferritic steels after exposure in a SCW environment for 300 h and 1000h.

Fig. 4. Cross-section images of samples and EDS line-scan image of 14Cr-Al sample exposed for 1000 h

Fig. 5. Cross-section images of samples and EDS line-scan image of 14Cr-ODS sample exposed for 1000 h

Table captions

Table 1.Chemical compositions of the ODS ferritic steels used in the present study (wt%)

Table 1. Nominal chemical compositions of the ODS ferritic steels used in the present study (wt%)

Material	Si	W	Al	Ti	V	Cr	Y_2O_3	Fe
14Cr-Al-ODS	**0.2**	**1**	**4.5**	**0.3**	**0.2**	**14**	**0.35**	**Bal.**
14Cr-ODS	**0.2**	**1**	**-**	**0.3**	**0.2**	**14**	**0.35**	**Bal.**

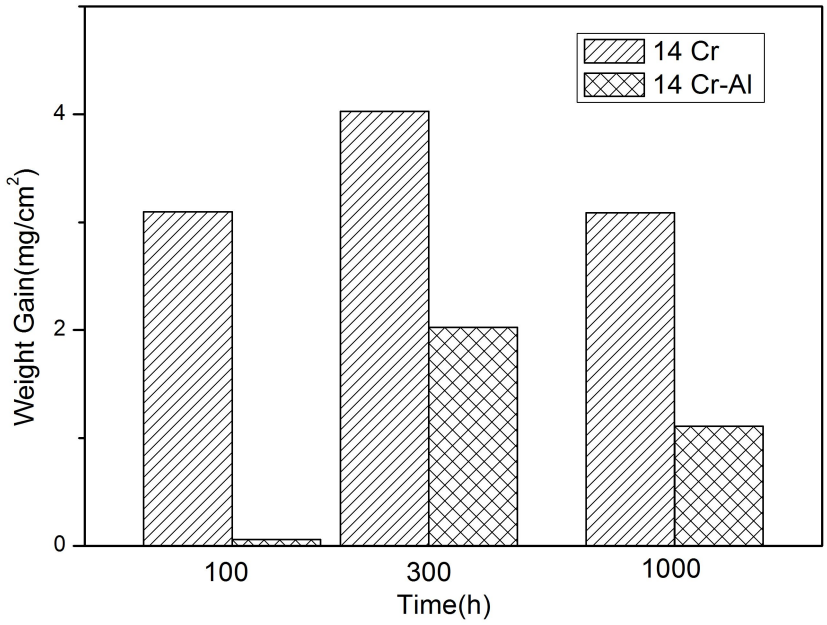

Fig. 1. Comparison of weight gain of ODS ferritic steels with minor alloying element Al under SCW condition at 650 ℃.

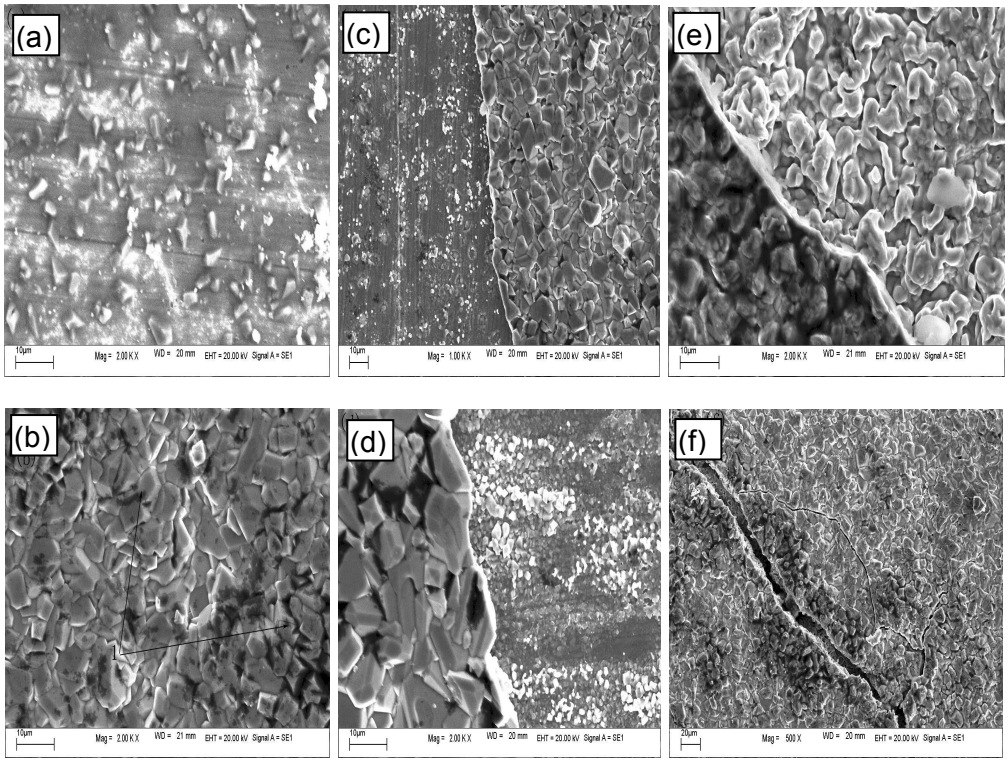

Fig. 2. SEM images of the surface morphologies of the oxide layer on 14Cr-Al (a,c,e)and 14Cr-ODS (b,d,f) steels exposed to SCW for different times (a) 100 h, (c) 300 h, (e) 1000 h, (b) 100 h, (d) 300 h, and (f) 1000 h.

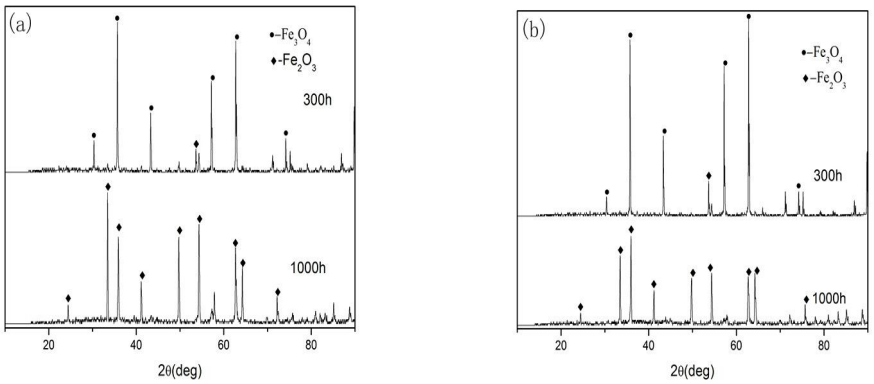

Fig. 3. XRD analyses of the oxide layer formed on 14Cr－4Al(a) and 14Cr(b) ferritic steels after exposure in a SCW environment for 300 h and 1000h.

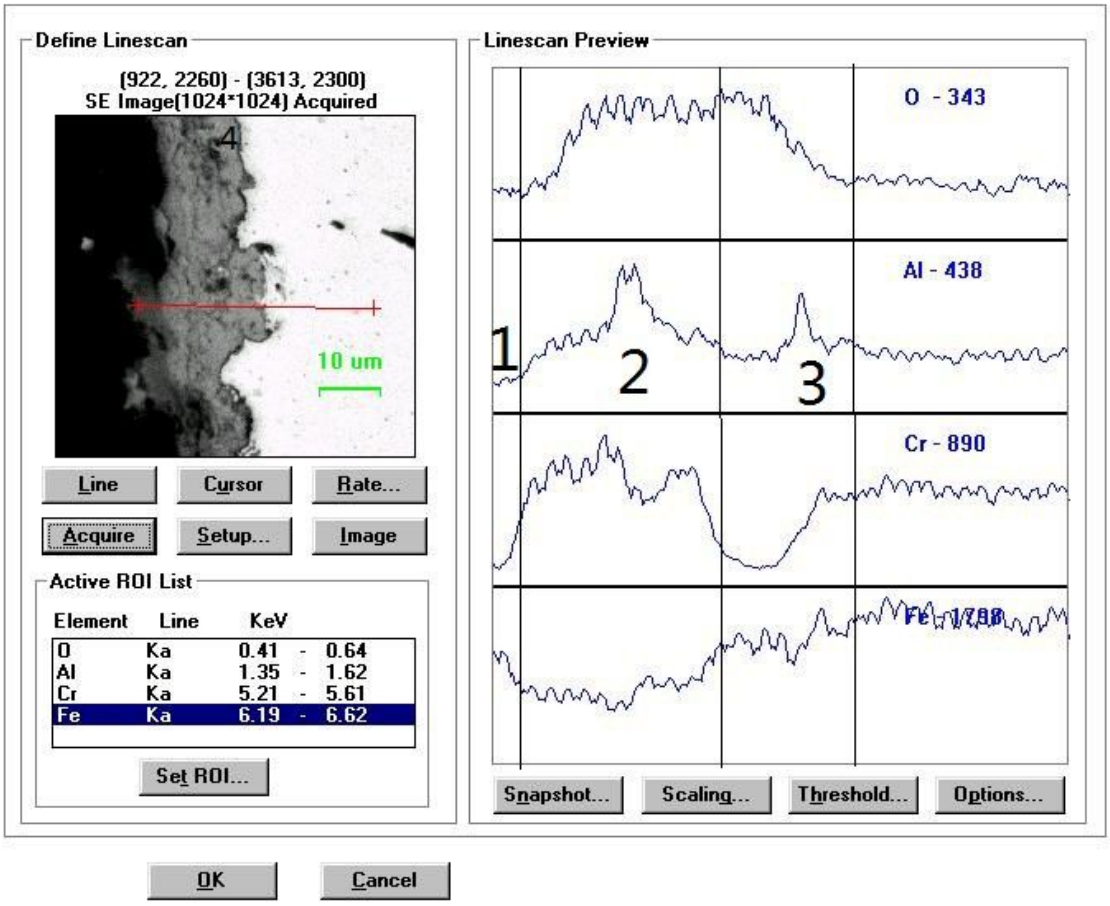

Fig. 4. Cross-section images of samples and EDS line-scan image of 14Cr-Al sample exposed for 1000 h

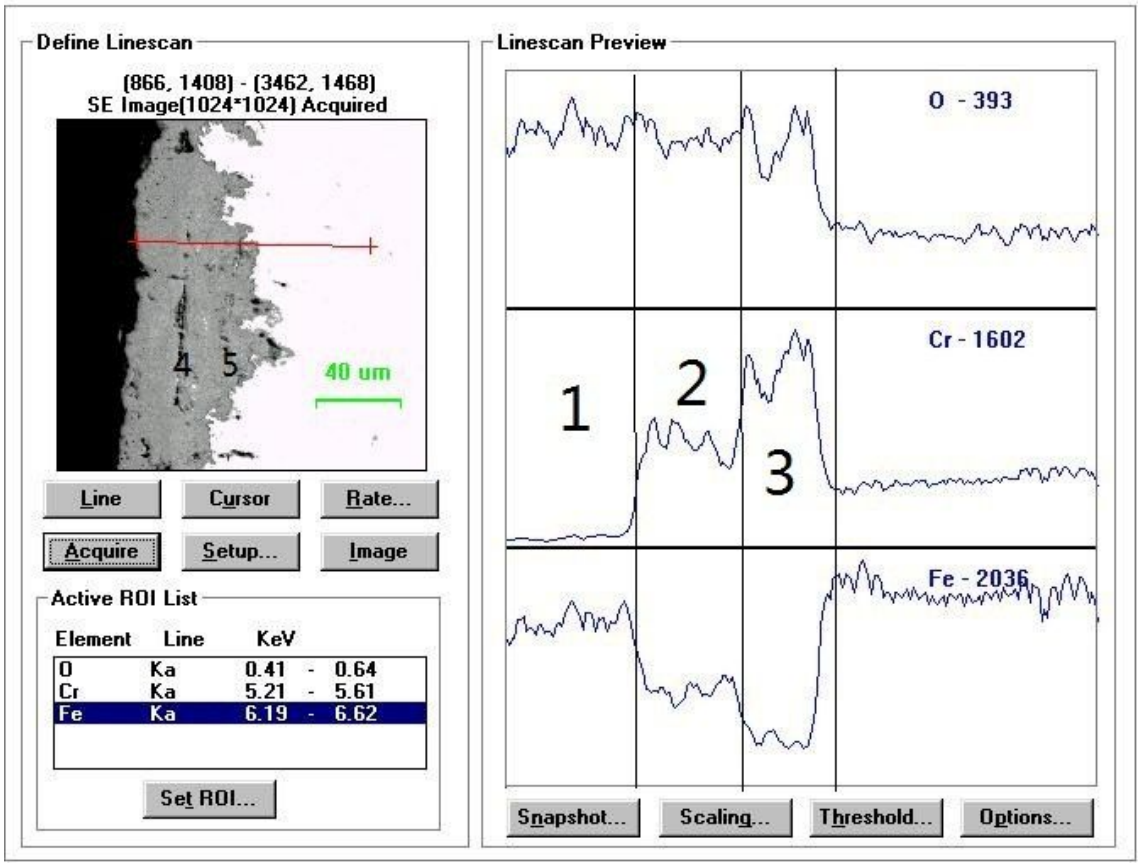

Fig. 5. Cross-section images of samples and EDS line-scan image of 14Cr-ODS sample exposed for 1000 h

ISSCWR7-2060

Experiments of heat transfer to supercritical water in a 2×2 rod bundle with wire-wrapped spacers

Han Wang
Xi'an Jiaotong University
Xi'an Shaanxi, China
han.0506@stu.xjtu.edu.cn

Qincheng Bi
Xi'an Jiaotong University
Xi'an Shaanxi, China
qcbi@mail.xjtu.edu.cn

Zesen Nie
Xi'an Jiaotong University
Xi'an Shaanxi, China
hardstick@stu.xjtu.edu.cn

Haicai Lv
Xi'an Jiaotong University
Xi'an Shaanxi, China
lvhaicai@stu.xjtu.edu.cn

Miao Gui
Xi'an Jiaotong University
Xi'an Shaanxi, China
meloman989715@stu.xjtu.edu.cn

Abstract

Heat transfer experiments of supercritical pressure water in a 2×2 rod bundle with wire-wrapped spacers have been performed at Xi'an Jiaotong University. Particular attention was paid to the heat transfer characteristics of water at supercritical pressures with respect to the R&D of the Supercritical Water-cooled Reactor (SCWR). A fuel-assembly simulator with four heated rods was installed inside a square channel with rounded corners. The outer diameter of each heated rod is 8 mm with an effective heated length of 600 mm. The outer surface of each heated rod was helically-covered by a wrapped wire with an outer diameter of 1.2 mm and an axial pitch of 200 mm. The experiments covered the pressure range of 23-28 MPa, mass flux range of 400-1000 kg/m^{2}s and heat flux range on the rod surface of 200-1000 kW/m^2. Heat transfer characteristics of supercritical pressure water through the bundle were examined with respect to variations heat flux, system pressure, and mass flux. These characteristics were shown to be similar to those previously observed in tubes or annuli. A non-uniform and unsymmetrical wall temperature distribution was observed along the circumferential direction of the heated rod. It was found that the circumferential wall temperature was affected by both of the wrapped wire and the non-uniform flow area. Comparisons of the circumferential wall temperature distribution were made between the wire-wrapped bundle and the bare rod bundle. It was found that the wrapped wire increases the local wall temperature adjacent to the heated surface, but lowers the circumferential nonuniformity in low and high enthalpy regions.

1. Introduction

Research on the Supercritical Water-cooled Reactor (SCWR) began from the 1990s. SCWR is selected as one of the six Generation IV nuclear reactors by the Generation IV International Forum (GIF) in 2002 [1]. A SCWR power plant may have a thermal efficiency of 45% by operating its coolant at a higher temperature (500℃) and pressure (25MPa) compared to the efficiency of current Light Water-cooled Reactor (LWR) power plants of about 33% [2]. Moreover, since the reactor coolant experiences no liquid-vapor transition beyond the critical pressure, a SCWR power plant system becomes more compact by eliminating the coolant recirculation pump, steam generator and steam-water separator, which further lowers the capital cost.

Although there is no phase change at supercritical pressure and the boiling crisis can be eliminated in a SCWR, the thermophysical properties of supercritical water experience strong variations at the vicinity of the pseudo-critical temperature. These drastic variations cause large non-uniformity of buoyancy over the flow channel and result in unusual heat transfer behaviours. This issue is more complicated in fuel assemblies where large imbalances in flow and enthalpy can be encountered. Therefore, a thorough knowledge of heat transfer characteristics of supercritical water in geometries relevant to nuclear reactor, such as annular or bundle channels, is essential for the design of SCWR fuel bundle.

Heat transfer of supercritical fluid has gained much attention since the 1950s and a lot of experimental investigations have been done in this research field. Swenson et al. [3] reported that the heat transfer coefficient shows a peak when the bulk temperature is within the pseudo-critical temperature range, and this peak decreases with the increase of heat flux. Shiralkar and Griffith [4] determined both theoretically and experimentally the limits for safe operation, in terms of maximum heat flux for a particular mass flux. They observed the deteriorated heat transfer at high heat-flux to mass-flux ratios. This phenomenon has also been investigated by other researchers, such as Shitsman [5], Ackerman [6], Yamagata et al. [7], Hall and Jackson [8], and Bazargan [9]. These work showed a reduction in heat transfer due to buoyancy and fluid acceleration impacting the heat transfer boundary layer profile for upward flow. In recent years, heat transfer of supercritical water in annular flow channels have been performed at Xi'an Jiaotong University with the background of SCWR [10-12]. These investigations accumulate considerable experimental data and provide a primary foundation for the thermal-hydraulic analysis in SCWR reactor core.

Experimental investigations on heat transfer to supercritical fluids were reviewed by Pioro and Duffey [13], which showed that the majority of previous experiments were conducted with circular tubes. The heat transfer experiments in rod bundles with the working medium of supercritical water has not been seen in public. For this situation, Xi'an Jiaotong University performed heat transfer experiments at supercritical pressures with a 2×2 rod bundle over a wide range of flow conditions. This paper presents the heat transfer characteristics of supercritical water in the rod bundle flow geometry and provides fundamental data for further analysis.

2. Experimental Facility and Methods

The experiments were carried out in a high-temperature high-pressure steam-water test loop shown schematically in Figure 1. Distilled and de-ionized feed water from the water tank was driven through a filter by a high pressure plunger-type pump with a maximum operating pressure of 40MPa. Part of the water was returned to the water tank through a bypass and the rest part of the water flowed through measuring orifices and adjusting valves into a heat exchanger to absorb the heat of the hot fluid coming from the test section. Then this part of water was heated to the test state by the pre-heater and test section transformer, using electrical AC power supplies with maximum capacities of 760kW and 250kW, respectively. Heat transferred from the test section to the coolant was extracted with a regenerative heat exchanger and a condenser. The feed water was directed back to the water tank and recirculated. The pressure and mass flux in the test section were controlled by adjusting the main valve and bypass valve.

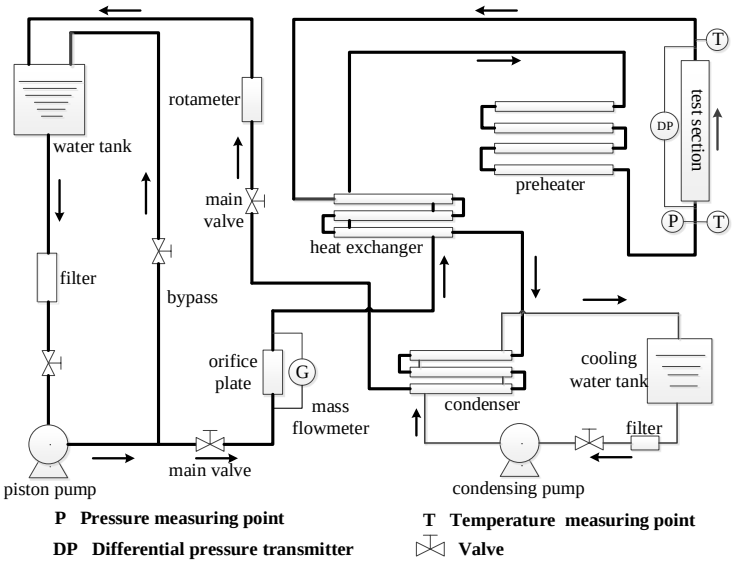

Figure 1. Schematic drawing of the supercritical water test loop.

The 2×2 rod bundles consists of four Φ8×1.5 mm heated rods (stainless steel 304) and a square insulator with round corners, as illustrated in Figure 2. The outer unheated stainless steel tube is used for holding the inner pressure and is thermally insulated to minimize heat loss to the environment. Large AC power is applied on the four rods through the top stainless electrode and the bottom copper electrode, thus heat is generated and then carried away by supercritical water. The inner heated rods are electrically insulated from the outer stainless tube by a ceramic insulator which is arranged between the two parts. The inner shape of the insulator is square with four round corners, leaving a rod-to-corner gap of 1.44 mm which is the same with the gap between neighboring two rods. From the right photograph of Figure 2, it is seen that ach heated rod was helically-covered with a metallic wrapped wire. The axial pitch of the wrapped wire is 200 mm and three pitches were arranged along the effective heated length of 600 mm. The stainless steel wrapped wires, with a diameter of 1.2 mm, were welded on the surface of the heated rods. These wrapped wires not only provide the appropriate spacing between the heated rods, but also disturb the flow and thus, enhance heat transfer.

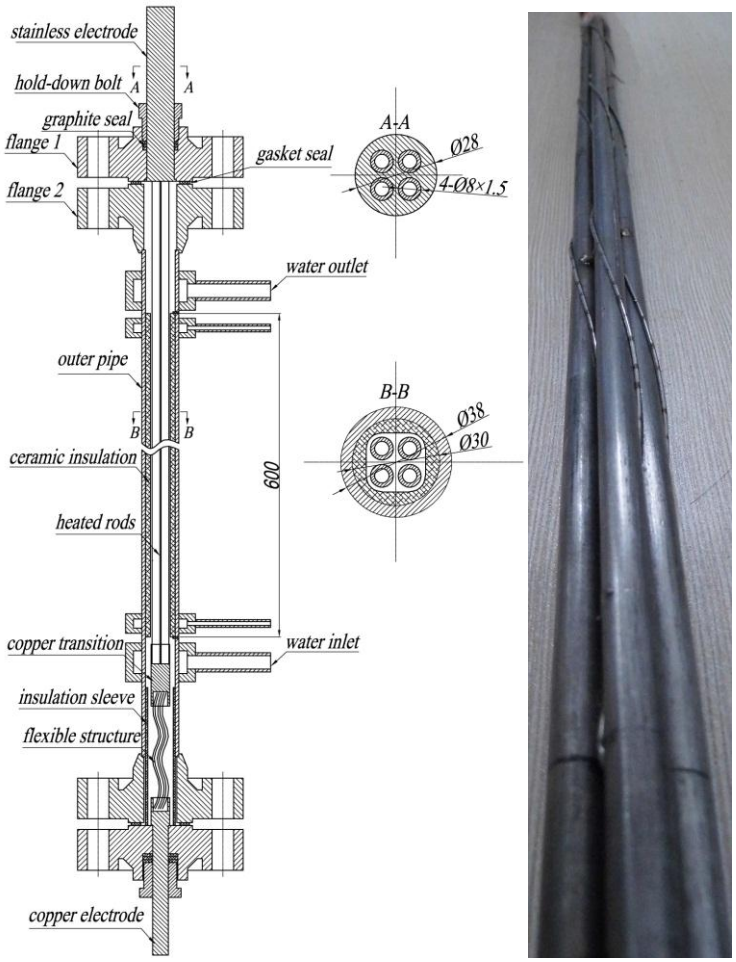

Figure 2. Geometry of the 2×2 rod bundle test section (left) and the photograph of the inner heated tubes (right).

The wall temperature were obtained at each of the four heated tubes. Sliding thermocouples were inserted inside two of the tubes and fixed thermocouples were installed inside the others. Figure 3 identifies the five locations (100-mm apart) covered by the sliding thermocouples along the heated tube. In principle, the sliding thermocouples could scan the inner surface of the entire heated rod. The sliding thermocouples unit consisted of a probe carrying four standard NiCr-NiSi thermocouples (each wire with a 0.2-mm OD) with a circumferential interval of 90°. It was connected to a drive-assembly unit which moved the probe axially and rotated the probe circumferentially inside the heated tube. At each location, the probe was rotated twice at an interval of 45° to measure the inner-wall temperatures. Four fixed thermocouples were attached in a plane at 90° apart and inserted inside the other two heated tubes at the last measuring point covered by the sliding thermocouples. The measured inner wall temperatures were converted into outer wall temperature on the fluid side using two-dimensional heat conduction equations proposed by Taler and Zima [14]. The fluid temperatures were measured by K-type sheathed thermocouples. The fluid pressure at the inlet of the test section was measured by Rosemount 3051 capacitance-type pressure transmitter and the pressure drop of the test section was measured with a Rosemount 3051 capacitance-type differential pressure transducer. The NIST property database [15] is applied in evaluating all fluid properties. All data were collected and recorded by an IMP 3595 data acquisition system. Estimated uncertainties in measured and calculated parameters are summarized in Table 1.

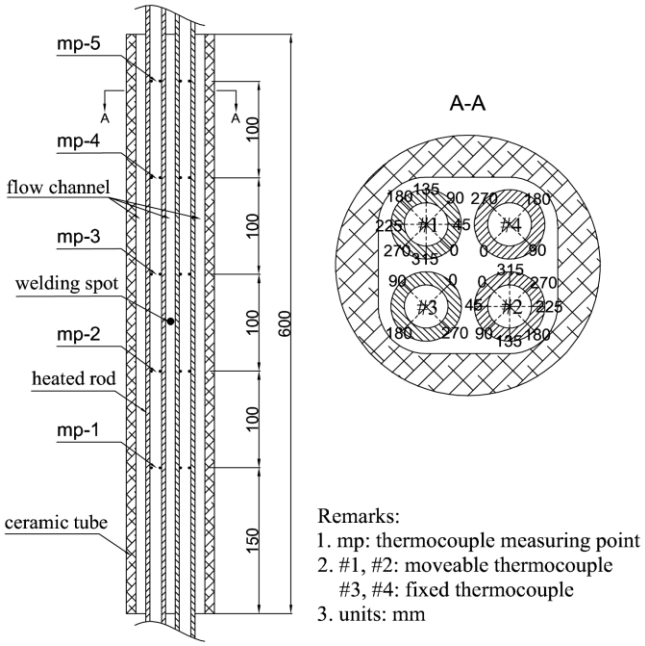

Figure 3. Thermocouple arrangements inside the heated rods.

Table 1. Uncertainties in measured and calculated parameters.

Parameter	Unit	Uncertainty
Pressure	(MPa)	0.44%
Pressure drop	(kPa)	0.52%
Electrically-heated power	(kW)	6.25%
Mass flow rate	(kg/s)	1.02%
Fluid temperature	(℃)	0.4℃
Wall temperature	(℃)	0.16%
Heat transfer coefficient	(kW/m^2K)	8.83%

3. Experimental Results and Discussion

3.1 Circumferential wall temperature distribution

The circumferential wall temperature distributions of the four heated tubes are illustrated in Figure 4 at the pressure of 25 MPa, mass flux of 1000 kg/m^2s, heat flux of 400 kW/m^2 and inlet bulk temperature of 419.3℃. A ±0.16% measuring error of the wall temperature is also plotted in this figure. At mp-5, it is seen that the #1 sliding thermocouple gives unsymmetrical wall temperature distributions. The highest wall temperature emerges at the angle of 180° where the flow area and flow quantity are small compared to others regions. However, it is clear that the wall temperature at the large-flow-area angle of 90° is also pretty high. The reason for this phenomenon may be attributed to the wrapped wire covered on the heated surface at this angle, which blocks the contact between the coolant and the heated surface. A similar phenomenon could also be observed for the #2 sliding thermocouple. The wall temperature at 270° where the tube is covered by the spacer is almost as high as that of 180°. The highest wall temperatures of #3 is also at the angle of 180°, however, the wall temperature at 0° is not the lowest anymore because of the impact of wrapped wire. For the heated tube #4, the wall temperature at 180° is

the highest among the four heated tubes due to the combined actions of small flow area and covering effect of the wire.

At the measuring cross-section of mp-3, only the wall temperatures of the two sliding thermocouples #1 and #2 were collected. Due to the same location of the wire-wrapped spacer, wall temperature distributions at mp-3 are similar to those of mp-5. However, the wall temperatures at 90° of the heated tube #1 is higher than that at 180°, which is not seen in mp-5.

At the cross-section of mp-4, it is also observed that the wall temperature of #1 gives two peaks at the angle of 180° and 270°. For the heated tube #2, the highest wall temperature appears at the spacer-covered angle of 90°, which is about 0.6℃ higher than the wall temperature of 180°. Wall temperature distributions at mp-2 are similar to those at mp-4 due to the same location of the wire.

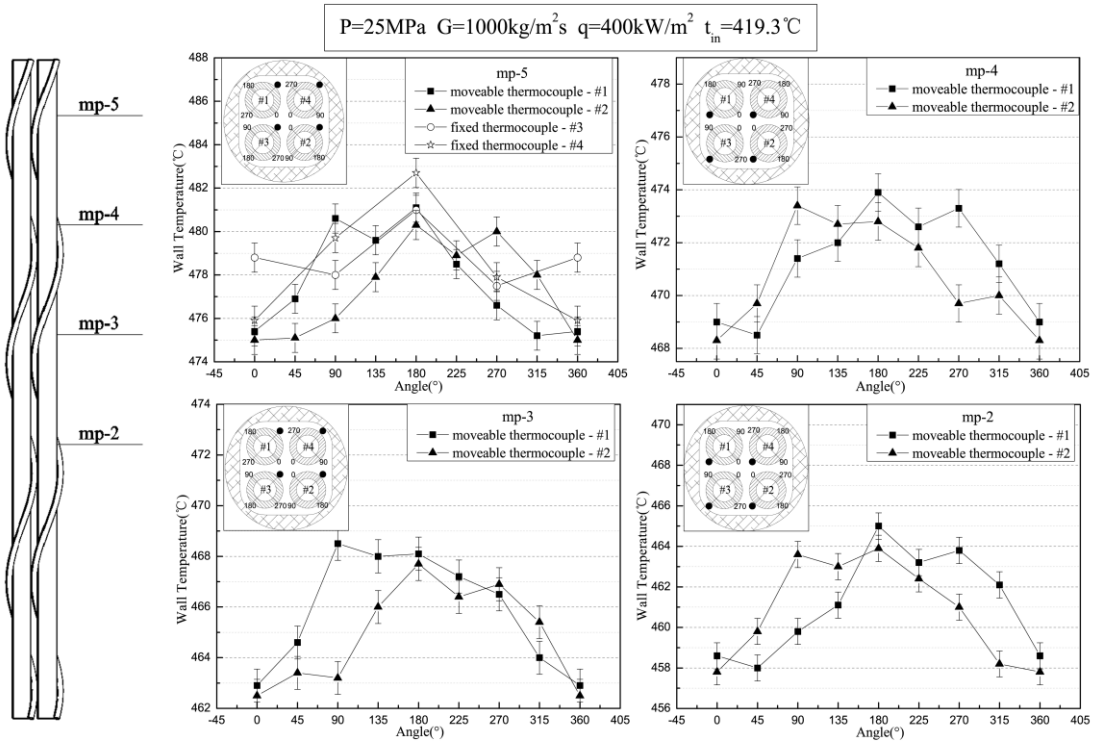

Figure 4. Circumferential wall temperature distributions.

The circumferential wall temperature gradient of the heated tube #1 with cross-sectional average bulk enthalpy and heat flux is displayed in Figure 5 at the pressure of 25 MPa and mass flux of 1000 kg/m^{2}s. The circumferential wall temperature gradient was calculated between the maximum and minimum wall temperature along the circumferential direction. It is seen in Figure 5 that the circumferential wall temperature gradient decreases with increasing bulk enthalpy before the pseudo-critical enthalpy, but increases accordingly after the bulk enthalpy surpasses the pseudo-critical enthalpy. In general, the circumferential wall temperature gradient near the pseudo-critical enthalpy is the lowest, whereas the gradients at low and high enthalpy regions are much higher. Within the whole enthalpy region, the profiles under various heat fluxes are nearly the same, but the temperature gradient is promoted with increasing heat flux.

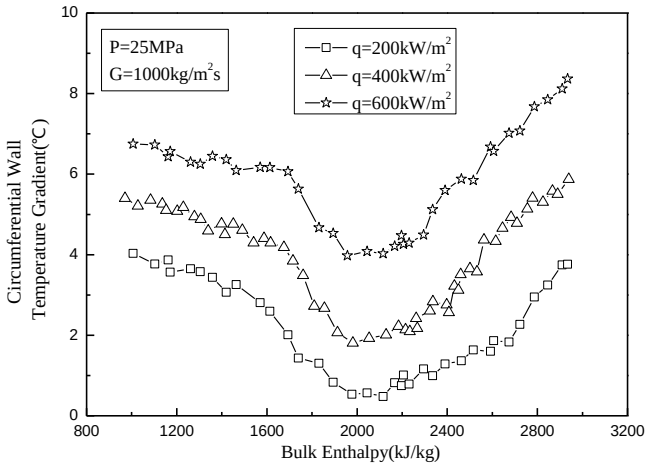

Figure 5. Circumferential wall temperature gradient with bulk enthalpy and heat flux.

At the pressure of 25 MPa and heat flux of 400 kW/m^2, the variations of circumferential wall temperature gradient plotted against cross-sectional average bulk enthalpy and mass flux are shown in Figure 6. In is seen that the effect of mass flux on circumferential wall temperature gradient is obvious. The circumferential wall temperature gradient increases by about 2℃ when the mass flux is reduced from 1000 kg/m^{2}s to 700 kg/m^{2}s. When the mass flux is further decreased to 400 kg/m^{2}s, a significant wall temperature gradient could be observed. In low and high bulk enthalpy regions, the temperature gradient are more than 10℃ while it is still very small near the pseudo-critical enthalpy.

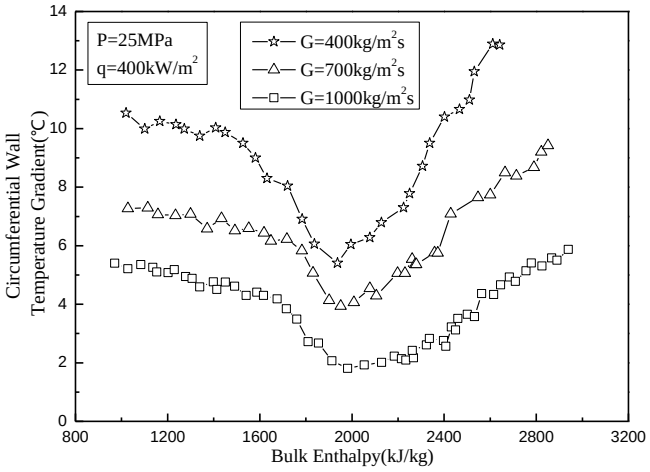

Figure 6. Circumferential wall temperature gradient with bulk enthalpy and mass flux.

3.2 Effects of heat flux on heat transfer

Figures 7 and 8 show the variation of average wall temperature and average heat transfer coefficient of heated tube #1 (mp-5) with bulk enthalpy at various heat fluxes. It is seen in Figure 7 that wall temperature increases consistently with bulk enthalpy and heat flux. These variations exhibit a smooth trend at the vicinity of the pseudo-critical enthalpy at low heat fluxes. With the increase of heat flux, the wall temperature difference between the heated wall and bulk fluid increases accordingly. The wall temperature is expressed in term of the heat transfer coefficient, as shown in Figure 8. The heat transfer coefficient increases with increasing bulk enthalpy when approaching the pseudo-critical point. Beyond the pseudo-critical point, the heat transfer coefficient decreases with increasing bulk. The effect of heat flux on heat transfer coefficient is

relatively small at low and high bulk enthalpies. At the pseudo-critical region, the heat transfer coefficient depends strongly on the heat flux, and decreases with the increase of heat flux.

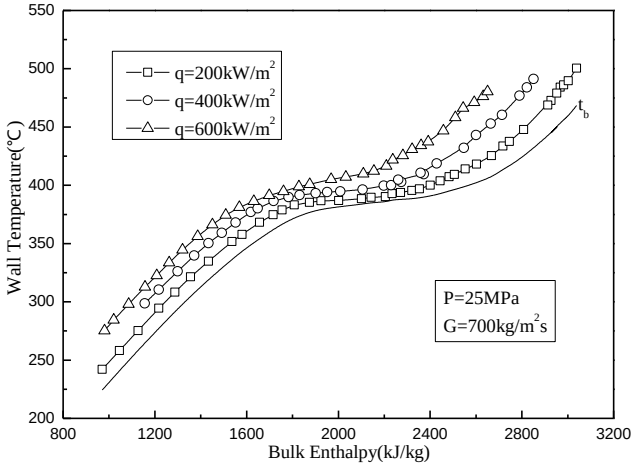

Figure 7. Effects of heat flux on average wall temperature.

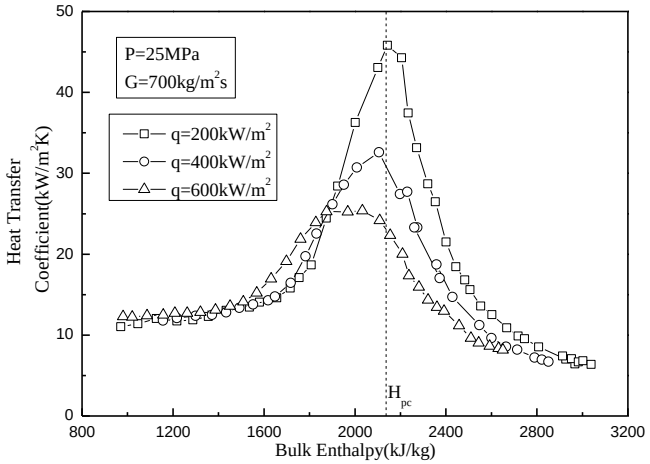

Figure 8. Effects of heat flux on heat transfer coefficient.

3.3 Effects of mass flux on heat transfer

The average wall temperature of heated tube #1 with bulk enthalpy and mass flux at mp-5 are shown in Figure 9. The wall temperature increases with increasing bulk enthalpy but decreases with increasing mass flux. The wall temperature variation is much steeper at low mass flux than high mass flux. A sharp temperature rise is observed when decreasing the mass flux from 700 to 350 kg/m^{2}s. On the other hand, only a small wall temperature rise is observed when the mass flux is decreased from 1000 to 700 kg/m^{2}s. As illustrated in Figure 10, the heat transfer coefficient at different mass fluxes follows the same trend as in Figure 8 with bulk enthalpy. However, the peak heat transfer coefficient does not shift with increasing mass flux. The effect of mass flux is strong on the heat transfer coefficient, which systematically increases with increasing mass flux.

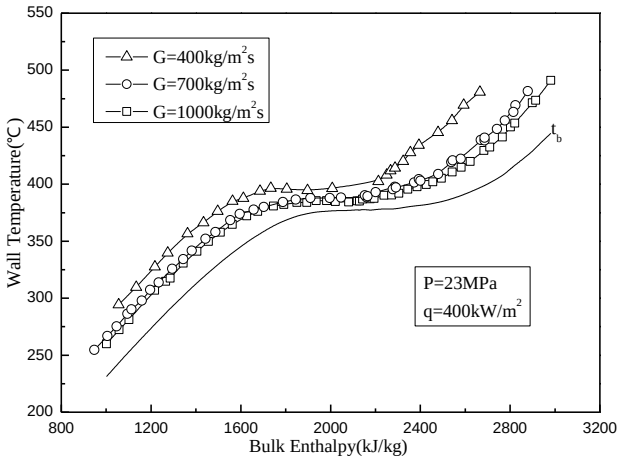

Figure 9. Effects of mass flux on average wall temperature.

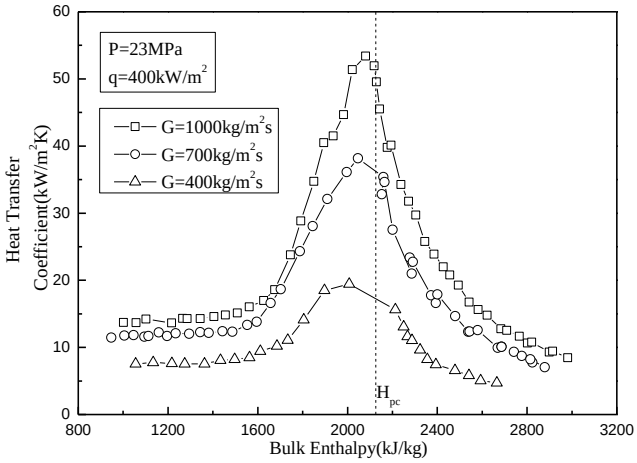

Figure 10. Effects of mass flux on heat transfer coefficient.

3.4 Effects of pressure on heat transfer

Figure 11 displays the variations of average wall temperature at mp-5 with bulk enthalpy and pressure at the heat flux of 400 kW/m^2 and mass flux of 1000 kg/m^{2}s. The effect of pressure on wall temperature becomes notable as the bulk enthalpy increases. The leveling-off wall temperature trend is observed clearly at the pressure of 23 MPa, and diminishes with increasing pressure. The wall temperature is higher at high pressure than low pressure. Beyond the pseudo-critical region, the effect of pressure seems to diminish with increasing enthalpy. The variations of corresponding average heat transfer coefficient with bulk enthalpy and pressure are shown in Figure 12. The heat transfer coefficient is generally lower at high than low pressures. Differences in heat transfer coefficient are small at the low and high enthalpy regions, but become significant at the pseudo-critical region.

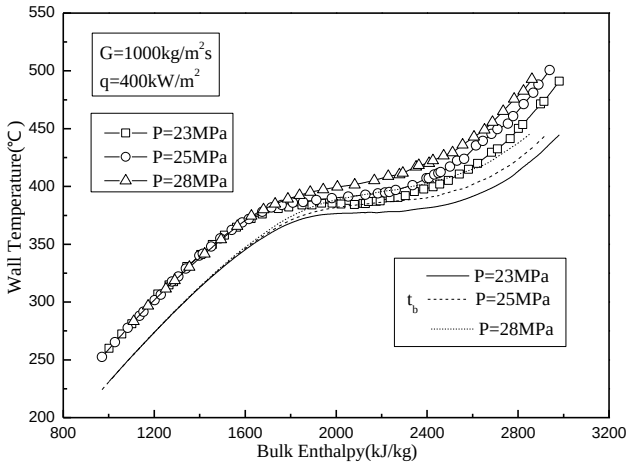

Figure 11. Effects of pressure on average wall temperature.

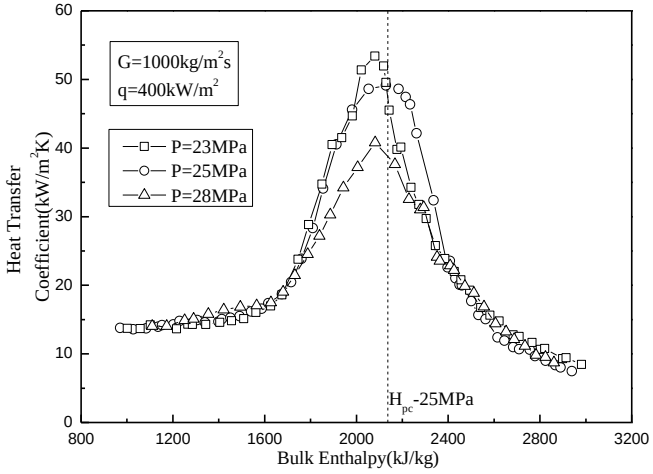

Figure 12. Effects of pressure on heat transfer coefficient.

3.5 Comparisons with 2×2 bare rod bundle

The circumferential wall temperature distributions in the 2×2 bare rod bundle [16] and wire-wrapped bundle are signified in Figure 13 at the pressure of 25 MPa, mass flux of 1000 kg/m^{2}s, heat flux of 600 kW/m^2 and inlet bulk temperature of about 397℃. It is seen that the wall temperature distribution of the bare rod bundle are basically symmetrical between the 0-180° and 180-360°. The highest wall temperature emerges at the angle of 180° which faces the small flow area, and the lowest wall temperature appears at the direction of 0-45°. For the case of using wrapped wires, the circumferential wall temperatures are not symmetrical anymore. The wall temperature profiles show two local peaks along the circumferential direction. The wall temperature facing the angle of 180° is still pretty high due to the small flow area. Moreover, the wall temperatures of the wire-covered surface (45° for heated tube #1 and 225° for heated tube #2) are higher than other directions. It is concluded that the circumferential wall temperature distribution with spacer is affected by both of the wrapped wire and the non-uniform flow area.

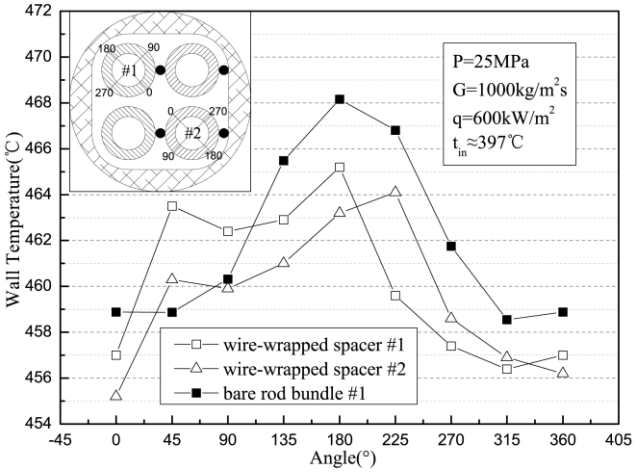

Figure 13. Circumferential wall temperature distributions in the 2×2 bare and wired bundles.

Figure 14 gives the circumferential wall temperature gradient with and without wire-wrapped spacer. At a low heat flux of 200 kW/m^2, the circumferential wall temperature gradients with and without spacers show little difference within the whole bulk enthalpy region. The temperature gradient with wrapped wire is lower than that without spacer only by about 0.4℃ at middle bulk enthalpy range. When the heat flux is increased to 600 kW/m^2, the temperature gradient with and without spacer is quite obvious. In low and high bulk enthalpy regions, the circumferential wall temperature gradient of the bare rod bundle reaches 10℃ and 12℃, respectively. However, the circumferential wall temperature gradient with wrapped wire is lowered to about 7℃. Near the pseudo-critical enthalpy, the difference in temperature gradients with and without spacer is very small. The effect of spacer on circumferential wall temperature gradient becomes weak as the bulk enthalpy approaches the pseudo-critical enthalpy.

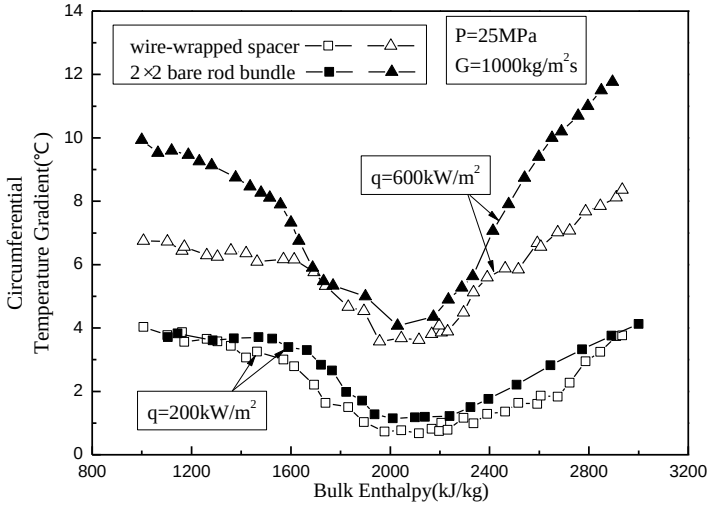

Figure 14. Comparisons in circumferential wall temperature gradient.

4. Conclusions

(1) Circumferential wall temperature distributions of the four heated tubes were obtained in the 2×2 rod bundle with wire-wrapped spacers. The wall temperatures along the circumferential direction are not uniform and unsymmetrical. Generally speaking, the wall temperatures at the corner sub-channel and the location where the heated wall was covered by the wire are higher than other locations.

(2) System parameters have great effects on average heat transfer characteristics. With the increase of heat flux, the wall temperature increases accordingly. The heat transfer coefficient decreases with increasing heat flux in the pseudo-critical region. The increase of mass flux enhances heat transfer within the whole bulk enthalpy region. The effect of pressure on heat transfer is relatively weak and is only notable in the pseudo-critical region.
(3) The circumferential wall temperature distribution and temperature gradient were compared in the 2×2 rod bundle with wrapped wires and the bare rod bundle. It was found that the circumferential wall temperature profiles differ a lot due to the introduction of wire-wrapped spacers. The spacers lower the wall temperature gradient in low and high enthalpy regions, especially at high heat-flux to mass-flux condition.

References

1. U.S. DOE, Nuclear energy research advisory committee and generation IV international forum, a technology roadmap for generation IV nuclear energy systems, 2002.

2. Yo.Oka, S. Koshizuka, Design concept of one-through cycle supercritical-pressure light water cooled reactor, Proc. of the 1st International Symposium on Supercritical Water Cooled Reactor Design and Technology (SCR-2000), Tokyo, Japan, p. 101, 2000.

3. H.S. Swenson, J.R. Carver, C.R. Karakala, Heat transfer to supercritical water in smooth-bore tubes, Journal of Heat Transfer, Trans. ASME, Ser. C, 87 (4), 477-484, 1965.

4. B.S. Shiralkar, P. Griffith, The effect of swirl, inlet conditions, flow direction, and tube diameter on the heat transfer to fluids at supercritical pressure, Journal of Heat Transfer, Trans. ASME, 92 (3), 465-474, 1970.

5. M.E. Shitsman, Impairment of the heat transfer at supercritical pressures and high temperature, (Translated from Teplofzika Vysokikh Temperaur), 1 (2), 267-275, 1963.

6. J.W. Ackerman, Pseudo-boiling heat transfer to supercritical pressure water in smooth and ribbed tubes, Journal of Heat Transfer, Trans. ASME, 92 (3), 490-498, 1970.

7. K. Yamagata, K. Nishikawa, S. Hasegawa et al., Forced convective heat transfer to supercritical water flowing in tubes, International Journal of Heat and Mass Transfer, 15 (12), 2575-2593, 1972.

8. W.B. Hall, J.D. Jackson, Heat transfer near the critical point, Proc. of the 6th International Heat Transfer Conference, vol.6, Toronto, Canada, pp. 377-392, 1978.

9. M. Bazargan, Forced convection heat transfer to turbulent flow of supercritical water in a round horizontal tube, Ph.D. thesis, the University of British Columbia, pp. 60-61, 2001.

10. G. Wu, Q.C. Bi, Z.D. Yang, et al., Experimental investigation of heat transfer for supercritical pressure water flowing in vertical annular channels, Nuclear Engineering and Design, 241, 4045-4054, 2011.

11. Z.D. Yang, Q.C. Bi, H. Wang, et al., Experiment of heat transfer to supercritical water flowing in vertical annular channels, Journal of Heat Transfer 135, 2013.

12. H. Wang, Q.C. Bi, Z.D. Yang, et al., Experimental and numerical study on the enhanced effect of spiral spacer to heat transfer of supercritical pressure water in vertical annular channels, Applied Thermal Engineering, 48, 436-445, 2012.

13. I.L. Pioro and R.B. Duffey, Heat Transfer and Hydraulic Resistance at Supercritical Pressures in Power Engineering Applications, ASME Press, New York, 2007.

14. J. Taler, W. Zima, Solution of inverse heat conduction problem using control volume approach, International Journal of Heat and Mass Transfer, 42, 1123-1140, 1999.

15. E.W. Lemmon, M.O. Mclinden, M.L. Huber, eds., NIST Reference Fluid Thermodynamic and Transport Properties-REFPORP, NIST Standard reference database 23, Ver. 7.0. U.S. Department of Commerce 2002.

16. H. Wang, Q.C. Bi, L.C. Wang, et al., Experimental investigation of heat transfer from a 2×2 rod bundle to supercritical pressure water, Nuclear Engineering and Design 275, 205-218, 2014.

ISSCWR7-2061

Experimental study of heat transfer and flow instabilities in heated channels with supercritical CO_2

Xiaolu Li[1], Ruina Xu[1], Zhen Zhang[2], Peixue Jiang[1,*], Walter Ambrosini[3]

1. Key Laboratory for Thermal Science and Power Engineering of Ministry of Education, Beijing 100084, CHINA;

2. Key Laboratory of Advanced Nuclear Reactor Engineering and Safety of Ministry of Education, Institute of Nuclear and New Energy Technology, Tsinghua University, Beijing 100084, CHINA.

3. Dipartimento di Ingegneria Meccanica Nucleare e della Produzione, Università di Pisa, Via Diotisalvi 2, 56126 Pisa, Italy

Email: jiangpx@mail.tsinghua.edu.cn; Tel / Fax: +86 (10) 62772661

Abstract

Heating and cooling may lead to flow instabilities in systems with single-phase natural circulation loops, two-phase boiling channels and various kinds of channels containing fluids at supercritical pressure. Previous experience and theories developed for two-phase flow instabilities can be used to study the flow excursions and oscillations of supercritical fluids due to the similar basic features, which is more interesting in the supercritical water-cooled reactors. Many numerical models have been developed to simulate heated channels with increased heating power to capture the threshold heating power and the excursion or oscillation effects on the mass flow rates and temperatures. However, very few experimental studies have been found for flow instabilities of supercritical fluids. This paper described a closed experimental system with CO_2 as the working fluid. The system stability with supercritical CO_2 was tested using the constant pressure output mode and the constant mass flow rate output mode of a supercritical pump, with different external characteristics. By programming the input voltage and current on the experimental channel, CO_2 was heated by a linearly or stepwise increasing heating power. The internal characteristic of the heated channel, i.e., the relationship between the pressure drop of the channel and the mass flow rate, was obtained. Flow excursion of a sudden decrease in the mass flow rate, which is called the Ledinegg instability was found in the experiment. The convection heat transfer characteristics and the influence of the buoyancy force and the flow acceleration on the heat transfer were analyzed for condition of the Ledinegg instability

1. Introduction

The development of supercritical water-cooled and CO_2-cooled nuclear reactors, supercritical CO_2-EGS (Enhanced Geothermal System) and supercritical CO_2 solar power systems has focused on the heat transfer characteristic and flow stability of systems with supercritical fluids.

The temperature of the supercritical fluid increases dramatically between the channel inlet and outlet with a high ratio of heating flow and mass flow rate, leading to significant density reductions along the flow direction, especially when crossing the pseudo-critical temperature, which can cause flow instabilities. The excursions or oscillations of the mass flow rate in the channel may lead to mechanical vibrations, break-down of the facilities or burn out the tubing due to the high temperatures. In addition, another type of flow instability, pressure-wave oscillation, may also take place in CO_2 injection wells and CO_2 transport pipelines in CO_2 storage and utilization projects. When an injection well is closed-in or a transport pipeline ruptures, the CO_2 pressure in the well or pipeline will suddenly decline dramatically, leading to potentially pressure-wave oscillations.

Flow instability investigations began in the field of two-phase flows, when Ledinegg found a sudden change in the mass flow rate of a two-phase flow for some conditions, which is called the Ledinegg instability [1]. This instability happens when the slope of the internal channel pressure drop versus mass flow rate curve is negative and steeper than the external (pump, natural circulation or imposed constant) pressure drop versus mass flow rate curve, so there are multiple points of intersection between the internal and external characteristics [2]. When disturbed in this region, the system will undergo a sudden change in the mass flow rate or move back and forth between different mass flow rates. Another type of instability, the density-wave oscillation, can be explained by the propagation time lags and feedback of the density variations along the tube [3-5]. Previous experience and theories developed for two-phase flow instabilities has been used to analyse instabilities in supercritical fluids due to their similar pressure drop versus mass flow rate curves [6-8]. Labuntsov and Mirzoyan developed the basic equation for the density wave instabilities for supercritical helium in heated channels [9]. Ambrosini identified dimensionless parameters for stabilities in heated channels with supercritical fluids with linearly or stepwise increasing heat fluxes and wall temperatures and drew instability maps based on CFD results, which showed the thresholds of the ratio of the heat flow and the mass flow rate for stability with various inlet conditions, local pressure drops, and tube configurations [10-13]. Zhang et al. numerically simulated supercritical CO_2 flow in natural circulation loops and found a periodically reversing flow pattern [14]. They also found a transition heat source temperature for which the system changed from unstable repeatedly reversing flow to stable one-directional flow with the increase of temperature [15].

For experimental investigation, Sharma et al. [16] set up a natural circulation experimental systems with a supercritical fluid and observed oscillations of the pressure drop and temperatures in the heater over a very narrow range of power. Sharma et al. [16] stated that during the experiments, the instability could be missed if the step change in the power was too large, which differs from the simulation results. Zhang et al. [17] experimentally investigated flows in a forced circulation loop with supercritical water and found oscillations of the flow rate and wall temperatures. Xiong et al. [18] observed oscillations for parallel channels with supercritical water and indicated that the flow became more stable with increasing pressure or decreasing inlet temperature. However, there is still limited experimental data for flow instabilities of supercritical fluids. Experimental validation is needed for different classifications of instability (Ledinegg instability, density-wave instability or pressure-wave instability) for various supercritical fluids.

This study used a closed experimental system with CO_2 as the working fluid. The system stability was investigated with different external characteristics using the constant pressure mode and constant mass flow rate mode of the supercritical pump. By programming the input heating power on the channel, CO_2 was heated by a linearly or stepwise increasing heating power. The experiment showed the internal characteristic of the heated channel, i.e., the relationship between the pressure drop of the channel and the mass flow rate. Flow excursion of a sudden mass flow rate decrease, the Ledinegg instability, was found. The experiments also discussed the convection heat transfer characteristics and the influences of buoyancy and flow acceleration on the heat transfer with the Ledinegg instability.

2. Experimental system

2.1 Experimental apparatus

The experimental forced circulation loop shown in Fig. 1 was built with CO_2 as the working fluid. The CO_2 flowed from a container to an accumulator and then to a supercritical CO_2 plunger pump. The pump (Waters P-350, Waters Technologies) pressurized CO_2 to supercritical pressure through the motion of plungers and the effect of check valves. The range of the mass flow rate was 2.1 kg/h to 21 kg/h, and the maximum discharge pressure was 34.5 MPa. The pump was cooled by a circulation of a mixture of water and ethylene glycol at -5 ^oC offered by a separate cooling pump (DLSB-5/-10 ^oC) because only liquid CO_2 can be delivered through this pump. A Coriolis-type mass flowmeter was used to measure the CO_2 mass flow rate with a measurement error of less than 0.1%. The CO_2 flowed from a mixer to the test section and entered a cooler after another mixer. A decompression valve controlled the CO_2 pressure at the test section outlet. There was just CO_2 with a purity of 99.995% flowing in the system without lubricating oil.

The test section was a stainless steel tube (1Cr18Ni9Ti) with a heating length of 196 mm, outer diameter of 2.1 mm, and inner diameter of 0.953 mm. A programmable power source provided the adjustable heating power to the test section. The outer wall temperatures were measured with K-type thermocouples with accuracies of 0.5 ^oC. The uniform inlet and outlet CO_2 temperatures were measured by four-wire platinum resistance (PT-100) with accuracies of 0.08 ^oC. The test section inlet pressure was measured by a pressure transducer with the pressure measurement range of 0-15 MPa and accuracy of 0.12%. The CO_2 pressure drop from the inlet to the outlet of the test section was measured by a differential pressure transmitter with a measurement range of -30 KPa to 30 KPa and accuracy of 0.075%.

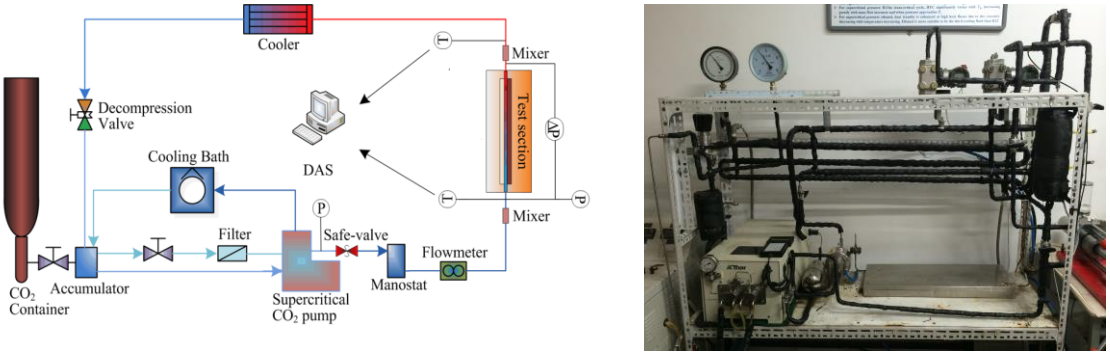

(a) Schematic diagram (b) Photograph

Figure 1. Schematic diagram and photograph of the experimental system.

2.2 Experimental procedure and parameters

The flow instabilities are affected by the external characteristic of the forced circulation loop, such as the supercritical pump and the decompression valve in this system. With the constant opening of the decompression valve during heating of the test section, the test section outlet pressure could be assumed to be constant. The pump had a the constant output mass flow rate mode and a constant output pressure mode which provided two different external characteristics. The ranges of the experimental parameters are shown in Table 1.

Table 1. Experimental parameters.

Parameter	Range
Inlet pressure	7-9 MPa
Inlet temperature	20 °C
Inlet mass flow rate	0-21 kg/h (0-0.0058 kg/s)
Heating power	0-360 W

3. Experimental results and discussion

3.1 Internal characteristic of a channel with supercritical CO_2

The pressure drop from the heating tube inlet to the outlet can be described by:

$$\Delta P = \Delta P_f + \Delta P_a \tag{1}$$

The total frictional pressure drop for CO_2 with variable properties in the test section can be calculated as:

$$\Delta P_f = \int f_x \frac{1}{2d} \rho_x u_x{}^2 dx = \int f_x \frac{G^2 dx}{2\rho_x d} = \frac{G^2}{2d} \int \frac{f_x}{\rho_x} dx \tag{2}$$

The acceleration pressure drop is caused by the density reduction from the heating section inlet to the outlet, which can be described by:

$$\Delta P_a = G^2 \left(\frac{1}{\rho_{out}} - \frac{1}{\rho_{in}}\right) \tag{3}$$

Where f is the friction factor, x is an infinitesimal heating section, d is the tube diameter, ρ is the CO_2 density, u is the velocity, and G is the mass flux.

As shown in Fig. 2 (a), with the constant pump mass flow rate mode, the mass flow rate is relatively stable during the transient heating. Therefore, the pressure drop gradually increases due to the decreasing outlet density and the corresponding increasing acceleration pressure drop. However, when the pump mass flow rate can vary, with an inverse relationship between the inlet pressure and the mass flow rate, the relationship between the pressure difference and the mass flow rate is more complicated (Fig. 2 (b)). When the mass flow rate decreases during transient heating, the pressure difference first drops (100 s to 150 s) because the heating power is less and the density is large. Afterwards, the pressure difference increases greatly (150 s to 225 s) due to the high temperature and low CO_2 density which leads to a dramatic thermal acceleration effect. After the heating is stopped, the inverse relationship between the pressure drop and the mass flow rate can again be seen from 225 s to 240 s in Fig. 2 (b). This non-linear relationship is similar to that in boiling two-phase flow and may leads to the Ledinegg instability as explained in Fig. 3 [2].

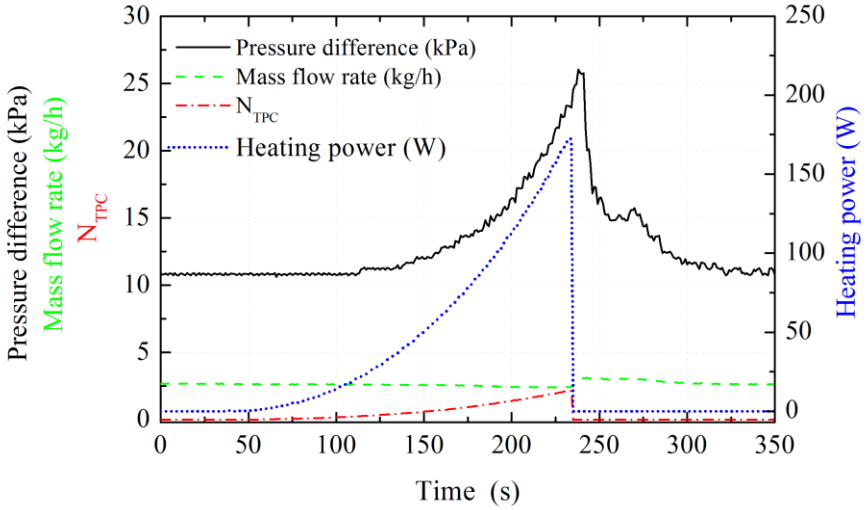

(a) Constant mass flow rate mode (P_{in}=8.1 MPa, T_{in}=20 °C, M_{in}=2.6 kg/h)

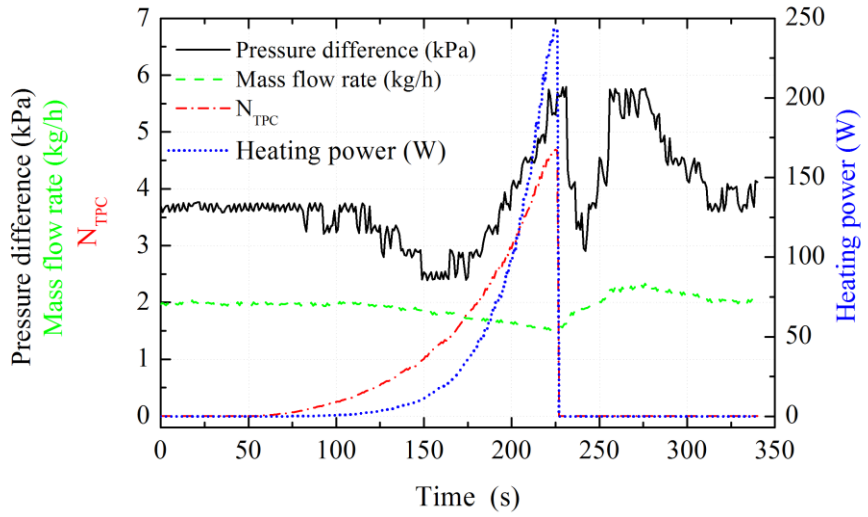

(b) Variable mass flow rate mode (P_{in}=8.1 MPa, T_{in}=20 °C)

Figure 2. Relationship between the pressure difference, mass flow rate and N_{TPC} during transient heating with increasing heating power.

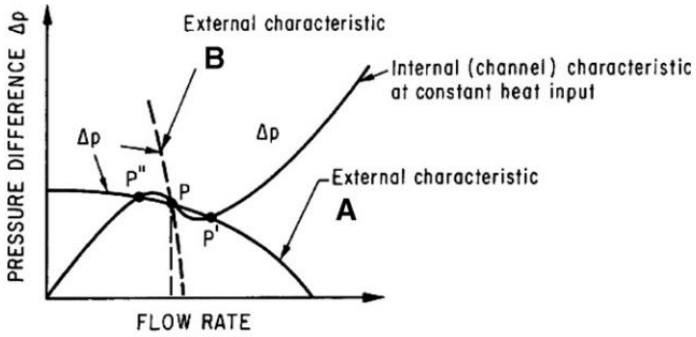

Figure 3. Explanation of the Ledinegg instability in two-phase flow [2].

Ambrosini proposed two dimensionless parameters to describe the inlet conditions and the stability of a heated channel with supercritical fluid [10]:

$$N_{SPC} = \left[h_{pc}(P) - h_{in} \right] \frac{\beta_{pc}(P)}{Cp_{pc}(P)} \tag{4}$$

$$N_{TPC} = \frac{Q}{M} \frac{\beta_{pc}(P)}{Cp_{pc}(P)} \tag{5}$$

Where the subscript pc refers to properties calculated at the pseudo-critical temperature corresponding to the operating pressure, h is the enthalpy, β is the volumetric expansion coefficient, C_p is the specific heat, Q is the heating power, and M is the channel inlet mass flow rate.

With the inlet pressure and temperature in Fig. 2, N_{SPC} is 0.8. The variation of N_{TPC} during transient heating is shown in Fig. 2. Even though N_{TPC} is greater than 4 in Fig. 2 (b), which is the typical threshold for the density wave instability according to the instability map, no obvious periodic oscillations are seen. The reasons might include the specific heat of the tubing wall which stabilizes the system, the rapid rate of increase of the heating power, or the short experimental time. However, the vibrations of pressure difference is still observed, showing an unstable tendency.

3.2 Ledinegg instability with stepwise increasing heating power

In another series of experiments, the heating power to the channel was increased in steps. As shown in Fig. 4, when the heating power was increased suddenly at about 1000 s, the CO_2 outlet temperature suddenly crossed the pseudo-critical temperature (35.8 °C) at a pressure of 8.2 MPa. As a consequence, the dramatic density decrease in the channel lead to strong thermal acceleration, causing a mass flow rate excursion to another intersection of the internal and external characteristics.

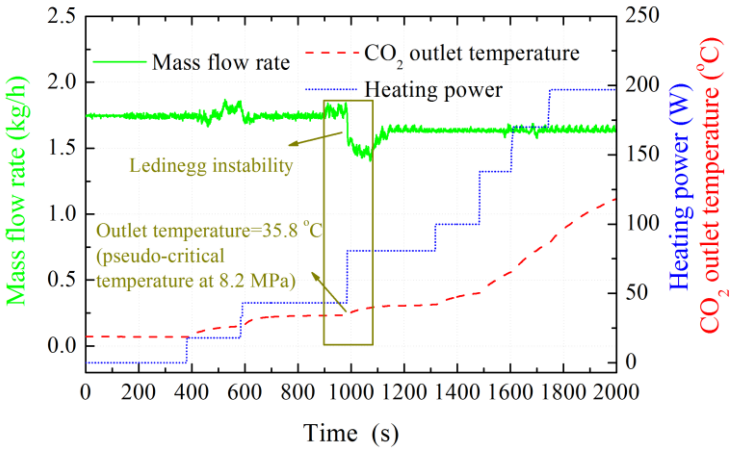

Figure 4. Ledinegg instability observed with stepwise increases in the heating power (P_{in}=8.2 MPa, T_{in}=20 °C).

3.3 Convection heat transfer with the Ledinegg instability

The data also shows the convection heat transfer characteristics and the influence of buoyancy and flow acceleration. The tube wall temperature is given by one-dimensional transient heat conduction with an internal heat source. Therefore, the local inner wall

temperatures, $T_{w,i}(x,\tau)$ at location x and time τ, were calculated from the measured outer wall temperatures, $T_{w,o}(x,\tau)$, as:

$$T_{w,i}(x,\tau) = T_{w,o}(x,\tau) + \frac{q_v(x,\tau)\text{-}\rho_w C_{Pw}\dfrac{\partial T_{w,o}(x,\tau)}{\partial \tau}}{16\lambda_w}\left[d_o^{\,2} - d_i^{\,2}\right] + \frac{q_v(x,\tau)\text{-}\rho_w C_{Pw}\dfrac{\partial T_{w,o}(x,\tau)}{\partial \tau}}{8\lambda_w} d_o^{\,2} ln\frac{d_i}{d_o} \quad (6)$$

Where the density, specific heat and thermal conductivity of the wall are respectively ρ_w =7900 kg/m^3, C_{Pw} =502.4 J/(kgK), and λ_w =16.38 W/(mK), d_o and d_i are the outer and inner tube diameters, and the internal heat source intensity, $q_v(x,\tau)$, was calculated as:

$$q_v(x,\tau) = \frac{16 I_{(\tau)}^{\,2}\rho_{e(T_{w,o(x,\tau)})}}{\pi^2\left(d_o^{\,2} - d_i^{\,2}\right)^2} \quad (7)$$

Where I is the input current, ρ_e is the electrical resistivity of the wall which is influenced by the wall temperature. The local heat transfer coefficients, $h(x,\tau)$, along the axial direction were calculated as:

$$h(x,\tau) = \frac{q_{w,i}(x,\tau)}{T_{w,i}(x,\tau)\text{-}T_f(x,\tau)} \quad (8)$$

Where the local heat flux on the inner wall, $q_{w,i}(x,\tau)$, was calculated as:

$$q_{w,i}(x,\tau) = \frac{(q_v(x,\tau)\text{-}\rho_w C_{Pw}\dfrac{\partial T_{w,o}(x,\tau)}{\partial \tau})\cdot\left(d_o^{\,2} - d_i^{\,2}\right)}{4d_i} \quad (9)$$

$T_f(x,\tau)$, the local fluid temperature, was obtained using the NIST software REFPROP 7.0 referenced from the local fluid enthalpy, $h_f(x,\tau)$, which was calculated from:

$$h_f(x,\tau) = h_{f,b}(0,\tau) + \frac{q_{w,i}(x,\tau)\pi d_i x}{M} \quad (10)$$

The local Nusselt number, $\mathrm{Nu}(x,\tau)$, and Reynolds number, $\mathrm{Re}(x,\tau)$, along the axial direction are:

$$\mathrm{Nu}(x,\tau) = \frac{h(x,\tau)d_i}{\lambda_f(x,\tau)} \quad (11)$$

$$\mathrm{Re}(x,\tau) = \frac{4M}{\pi d_i \mu_f(x,\tau)} \quad (12)$$

Where λ_f and μ_f are the fluid thermal conductivity and the dynamic viscosity.

The buoyancy effect was evaluated by the non-dimensional parameter, Bo*, introduced by Jackson and Hall [17], calculated as:

$$\mathrm{Bo}^* = \mathrm{Gr}^*/(\mathrm{Re}^{3.425}\,\mathrm{Pr}^{0.8}) \quad (13)$$

Where Gr* was calculated as:

$$\mathrm{Gr}^* = g\beta_f d_i^{\,4} q_{w,i}/(\lambda_f \upsilon_f^{\,2}) \quad (14)$$

Where Pr is the Prandtl number, β_f is the volumetric expansion coefficient, and υ_f is the kinematic viscosity of CO_2.

The effect of the flow acceleration was evaluated based on the non-dimensional parameter, Kv:

$$\mathrm{Kv} = \frac{\nu_f}{u_f^2}\frac{du_f}{dx} = \frac{4q_{w,i}d_i\beta_f}{\mathrm{Re}^2\,\mu_f C_{p,f}} + \frac{(-d_i)}{\mathrm{Re}}\cdot\beta_{T,f}\frac{dp}{dx} = \mathrm{Kv_T} + \mathrm{Kv_p} \quad (15)$$

Where Kv_T prposed by McEligot et al. [20] was used to describe the flow acceleration effect due to heating and Kv_p proposed by Jiang et al. [21] was used to describe the flow acceleration effect due to the pressure drop through the test channel.

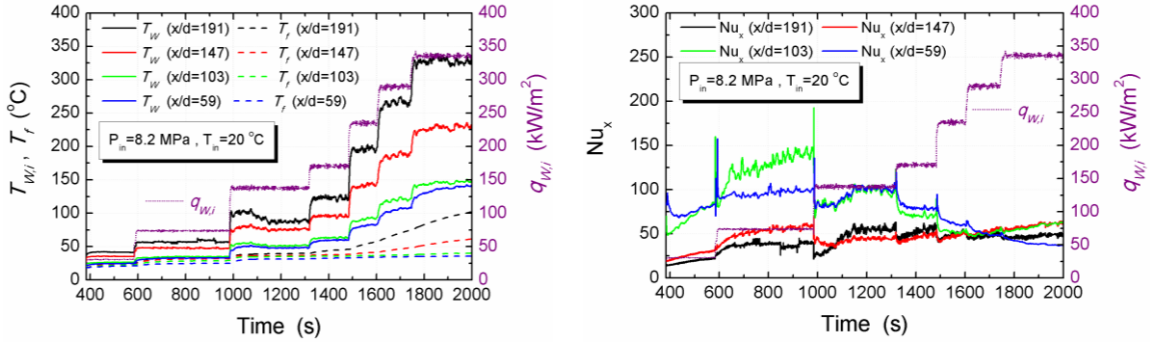

(a) Inner wall and fluid temperatures (b) Local Nusselt number

Figure 5. Variation of the inner wall temperature, fluid temperature and local Nusselt number at different axial locations with stepwise heating (P_{in}=8.2 MPa, T_{in}=20 °C).

As shown in Fig. 5, the inner wall temperatures experience stepwise increases with time with the stepwise increasing heating power. However, the corresponding fluid temperatures increase much more smoothly due to the heat capacities of the tube wall and the fluid. The local Nusselt number is unstable especially just as the heating power increases. In Particular, just before 1000 s when the CO_2 outlet temperature crosses the pseudo-critical temperature at 8.2 MPa (Fig. 4), the Nusselt number increases due to the increasing specific heat of CO_2. After 1000 s, the heat transfer is suppressed because of the decline of the specific heat of CO_2 and the mass flow rate decrease when the Ledinegg instability occurs (Fig. 4).

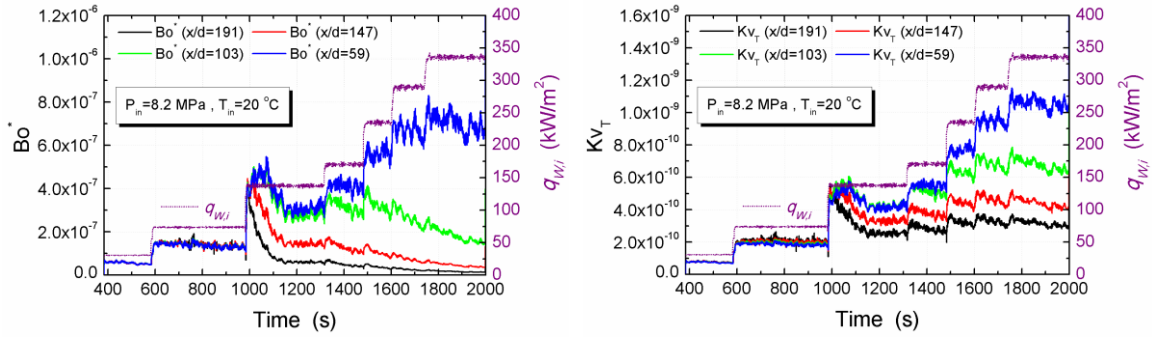

(a) Bo^* (b) Kv_T

Figure 6. Variation of Bo^* and Kv_T at different axial locations with time with stepwise increasing heating power (P_{in}=8.2 MPa, T_{in}=20 °C).

The inlet Reynolds number was around 8000 in this experiment. Jackson and Hall [19] indicated that for turbulent flow the buoyancy significantly influences the heat transfer when $Bo^* \geq 5.6\times10^{-7}$. As shown in Fig. 6, Bo^* at x/d of 59 is larger than 6×10^{-7} when the inner heat flux is greater than 200 kW/m^2, which reduces the heat transfer at this location with the Nusselt number decreasing to 37 at 2000 s as shown in Fig. 5 (b). At the other locations with x/d of 191, 147 and 103, Bo^* has a local peak at 1000 s when the system undergoes the Ledinegg instability and then decreases gradually with time. According to the criterion proposed by McEligot et al. [20] that when $Kv \geq 3\times10^{-6}$ and by Jiang et al. [21] that when $Kv \geq 8\times10^{-7}$, the turbulence is significantly reduced and the heat transfer is deteriorated due to the flow

acceleration. For these experimental conditions studied, Kv_T is less than 1.6×10^{-9}, so the flow acceleration has little effect on the heat transfer.

4. Conclusions

A forced circulation loop was used to investigate the flow and heat transfer with supercritical CO_2. The experiments investigated the internal characteristic of a heated channel, which meant the relationship between the pressure drop and the mass flow rate. When the mass flow rate was held relatively constant, the pressure drop increased during the transient heating, while the pressure drop and the mass flow rate had a non-linear relationship when the mass flow rate varied during the transient heating. The Ledinegg instability was observed during stepwise increasing heating of the channel with a sudden drop of the mass flow rate when the CO_2 outlet temperature crossed the pseudo-critical temperature, at which time the local Nusselt number had a local peak. Heat transfer at x/d of 59 was significantly deteriorated when the inner heat flux exceeded 200 kW/m^2 due to the significant buoyancy effect.

5. Acknowledgements

This program was supported by the International S&T Cooperation Program of China (No. 2012DFG71950), the National Natural Science Foundation of China Science Fund for Creative Research Groups (Grant No. 51321002) and the Tsinghua University Initiative Scientific Research Program.

References

1. Ledinegg M. Instability of flow during natural and forced circulation. Die Warme, 1938, 61(8): 891-898.

2. Kakac S, Bon B. A review of two-phase flow dynamic instabilities in tube boiling systems. International Journal of Heat and Mass Transfer, 2008, 51(3): 399-433.

3. Stenning A H. Instabilities in the flow of a boiling liquid. Journal of Fluids Engineering, 1964, 86(2): 213-217.

4. Stenning A H, Veziroglo T N. Flow oscillation modes in forced convection boiling. Proceedings of the Heat Transfer and Fluid Mechanics Institute, Stanford Univ. Press, 1965, pp. 301–316.

5. Svanholm K. Study of hydrodynamic instability in natural circulation boiling coolant channels by means of graphical computation. Multiphase transport: fundamentals, reactor safety, applications (Proceedings of the Multi-Phase Flow and Heat Transfer Symposium-Workshop), 1979.

6. Zhao J, Saha P, Kazimi M S. Stability of supercritical water-cooled reactor during steady-state and sliding pressure start-up. The 11th International Topical Meeting on Nuclear Reactor Thermal-Hydraulics (NURETH-11). 2005, 106: 2-6.

7. Gómez T O, Class A, Lahey Jr R T. Stability analysis of a uniformly heated channel with supercritical water. Nuclear Engineering and Design, 2008, 238(8): 1930-1939.

8. Ambrosini W. On the analogies in the dynamic behaviour of heated channels with boiling and supercritical fluids. Nuclear Engineering and Design, 2007, 237(11): 1164-1174.

9. Labuntsov D A, Mirzoyan P I. Analysis of the Boundaries of Stability of Motion of Flow of Helium at Supercritical Parameters in Heated Channels. Thermal Engineering, 1983, 30(3): 121-124.

10. Ambrosini W, Sharabi M. Dimensionless parameters in stability analysis of heated channels with fluids at supercritical pressures. Nuclear Engineering and Design, 2008, 238(8): 1917-1929.

11. Ambrosini W. Discussion on the stability of heated channels with different fluids at supercritical pressures. Nuclear Engineering and Design, 2009, 239(12): 2952-2963.

12. Ambrosini W. Assessment of flow stability boundaries in a heated channel with different fluids at supercritical pressure. Annals of Nuclear Energy, 2011, 38(2): 615-627.

13. Sharabi M, Ambrosini W, He S, et al. Transient Three-Dimensional Stability Analysis of Supercritical Water Reactor Rod Bundle Subchannels by a Computatonal Fluid Dynamics Code. Journal of Engineering for Gas Turbines and Power, 2009, 131(2): 022903.

14. Zhang X R, Chen L, Yamaguchi H. Natural convective flow and heat transfer of supercritical CO_2 in a rectangular circulation loop. International Journal of Heat and Mass Transfer, 2010, 53(19): 4112-4122.

15. Chen L, Zhang X R, Yamaguchi H, et al. Effect of heat transfer on the instabilities and transitions of supercritical CO_2 flow in a natural circulation loop. International Journal of Heat and Mass Transfer, 2010, 53(19): 4101-4111.

16. Sharma M, Pilkhwal D S, Vijayan P K, et al. Steady-State Behavior of Natural Circulation Loops Operating With Supercritical Fluids for Open and Closed Loop Boundary Conditions. Heat Transfer Engineering, 2012, 33(9): 809-820.

17. Zhang L, Wang H, Gu H, et al. Experimental investigations on flow instabilities in a forced circulation loop at near-critical and supercritical pressures. 7th International Symposium on Multiphase Flow, Heat Mass Transfer and Energy Conversion. AIP Publishing, 2013, 1547(1): 312-319.

18. Xiong T, Yan X, Xiao Z, et al. Experimental study on flow instability in parallel channels with supercritical water. Annals of Nuclear Energy, 2012, 48: 60-67.

19. Jackson J D, Hall W B. Influences of buoyancy on heat transfer to fluids flowing in vertical tubes under turbulent conditions. Turbulent forced convection in channels and bundles, 1979, 2: 613-640.

20. McEligot D M, Coon C W, Perkins H C. Relaminarization in tubes. International Journal of Heat and Mass Transfer, 1970, 13(2): 431-433.

21. Jiang P X, Liu B, Zhao C R, et al. Convection heat transfer of supercritical pressure carbon dioxide in a vertical micro tube from transition to turbulent flow regime. International Journal of Heat and Mass Transfer, 2013, 56(1): 741-749.

ISSCWR7-2062

Numerical Study of Heat Transfer and Flow Instability of Water at Supercritical Pressure in a Vertical Tube

Zhen Zhang[1,2], Xing-Tuan Yang[1], Pei-Xue Jiang[2,*] Walter Ambrosini[3]

1. Key Laboratory of Advanced Nuclear Reactor Engineering and Safety of Ministry of Education, Institute of Nuclear and New Energy Technology, Tsinghua University, Beijing 100084, China;
2. Key Laboratory of Thermal Science and Power Engineering of Ministry of Educations, Department of Thermal Engineering, Tsinghua University, Beijing, 100084, China
3. Department of Civil and Industrial Engineering, Università di Pisa, Italia

Corresponding author: jiangpx@tsinghua.edu.cn
Tel: +86 10 62772661, Fax: +86 10 62775566

Abstract

The parameters of water in the steam generator of high-temperature gas-cooled reactor could be increased to supercritical then the reactors and the supercritical steam generators can work with the supercritical steam turbine unit considering the high efficiency, no phase change heat transfer at the supercritical pressures, so the heat transfer and the flow instability of water at supercritical pressure is very important and was studied numerically in this paper. The comparison between the numerical results with the experimental data showed that the RNG *k-ε* model with enhanced wall treatment performed well in the steady-state calculation and was also adopted in the transient state calculation. The flow and heat transfer characteristics at various moments, and the effects of fluid inlet enthalpy were then studied. The results show that the flow rates oscillate intensely once the fluid enters the unsteady zone, and the wall temperature can increase dramatically due to the very low flow rate at some moments. The flow rate and the heating power at the unstable initial points decrease as the inlet fluid enthalpy increases, whereas N_{TPC} relatively increases.

Nomenclature

c_p	specific heat at constant pressure ($\mathrm{kJ \cdot kg^{-1} \cdot K^{-1}}$)
ρ	fluid density ($\mathrm{kg \cdot m^{-3}}$)
μ	molecular viscosity ($\mathrm{Pa \cdot s}$)
μ_T	turbulent viscosity ($\mathrm{Pa \cdot s}$)
Pr	Prandtl number
σ_T	turbulent Prandtl number
β	isobaric thermal expansion coefficient (K^{-1})
r	radial coordinate (m)
x	axial coordinate (m)
y^+	non-dimensional length
G	mass flow rate ($\mathrm{kg \cdot m^{-2} \cdot s^{-1}}$)

h_{pc}	pseudo critical specific enthalpy ($J \cdot kg^{-1}$)
h_{in}	inlet enthalpy ($J \cdot kg^{-1}$)
P	pressure (MPa)
T	temperature (^{o}C)
T_{pc}	pseudo critical temperature (^{o}C)
u	axial velocity ($m \cdot s^{-1}$)
v	radial velocity ($m \cdot s^{-1}$)
N_{SPC}	sub- pseudocritical number
N_{TPC}	trans-pseudocritical number

1. Introduction

HTR-PM, which is built by the Institute of Nuclear and New Energy Technology of Tsinghua University in China, is a 200 MW(e) modular high-temperature gas-cooled reactor. Water in the secondary circuit of the steam generator in HTR-PM is at a pressure of about 15 MPa. In the meantime, water pressures in almost all the thermal power plants are supercritical, and the design and fabrication of the supercritical turbine have been already sophisticated in China. The obviously high efficiency of supercritical thermal power plant compared with that of a subcritical one is a significant advantage and the highest efficiency of supercritical thermal power plant has reached up to 49%[1]. Moreover, there is no phase change in the supercritical pressure fluid, and the heat transfer deterioration occurs only in a narrow parameter range and is relatively moderate, which is also good for the steam generator. Therefore, the parameters of water in the steam generator of high-temperature gas-cooled reactor can be increased to supercritical so the reactors and the supercritical steam generators can work with the supercritical steam turbine unit by adapting multiple-reactors-one-unit scheme. Thus, the flow, heat transfer and the flow instability of water at supercritical pressure is of great importance.

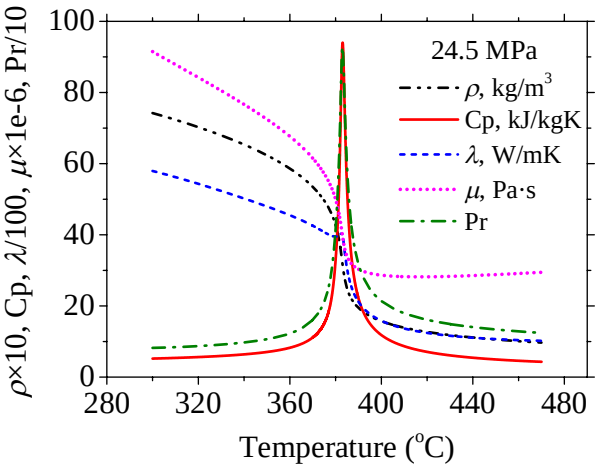

Fig. 1 Water property at a pressure of 24.5 MPa

Figure 1 shows the physical properties of water at a pressure of 24.5 MPa[2]. As can be seen from this figure, the specific heat variation with temperature shows a sharp peak at a specific temperature (approximately 383^{o}C at a pressure of 24.5 MPa) which is defined as the pseudo-critical temperature, T_{pc}. Other properties including the density, thermal conductivity and viscosity vary also significantly within a small range of temperature in the vicinity of T_{pc}. With these thermophysical characteristics, the flow and heat transfer of supercritical pressure water will be strongly influenced and quite different from those fluids with constant thermophysical properties.

There have been many papers published on internal forced and mixed flow and heat transfer of supercritical fluids in tubes. Jackson commenced research on supercritical pressure fluids many years ago and sumarized the fluid flow and convective heat transfer characteristics to fluids at supercritical pressure recently[3]. Jiang et al.[4-5] have done lots of experiments and numerical researches on flow and heat transfer of supercritical pressure fluid such as CO_2, R22 and ethanol in normal size tubes and micro-size tubes, evaluating and analyzing the effects of buoyancy, flow acceleration, and significant variations in thermophysical properties. He et al.[6, 7] used an 'in-house' CFD code named SWIRL to perform simulations of supercritical pressure fluid heat transfer by comparison with DNS results available in the literature, to evaluate the performance of low-Reynolds number turbulence models, especially paying attention to the features which enable them to respond to the modifications of the turbulence field due to influences of flow acceleration and buoyancy. The results show that for strong-buoyancy-influenced cases, most models are able to reproduce turbulence recovery reasonably well but not the improvement on heat transfer, which is attributed to the inability of turbulence models in reproducing turbulent heat flux using a constant turbulent Prandtl number. Pan et al.[8] conducted experiments of water flowing in smooth and rifled tubes at subcritical and supercritical pressure to explore the heat transfer characteristics of the new-type rifled tube at low mass flux. The results exhibited that the rifled tube improves the heat transfer of supercritical water remarkably, especially near the pseudo-critical point. Recently, Yoo[9] presented an overview of the progress made towards understanding the mechanisms of supercritical pressure flows in the pseudo-critical temperature region.

In the field of flow dynamic instabilities, Ruspini et al. [10] presented an updated review of two-phase flow instabilities including experimental and analytical results regarding density-wave and pressure-drop oscillations, as well as Ledinegg excursions, introducing the latest findings about the main mechanisms involved in the occurrence of these phenomena. Besides, Ambrosini and his research group have done lots of work on the numerical study of fluid flow instabilities. They first analyzed the mechanism of density-wave oscillations in a boiling channel with uniform and constant heat flux by linear and nonlinear analytical tools[11]. Then they proposed a unified view of boiling and supercritical fluid instabilities[12], and got dimensionless parameters for the analysis of stability in heated channels with supercritical fluids[13]. Recently they adopted two different turbulence models, the standard k-ε model equipped with non-equilibrium wall functions and a low-Reynolds number model, Yang and Shih model in FLUENT code, to simulate the unstable behavior in a heated channel with water at supercritical pressure, and the results were also compared with those from one-dimensional models[14]. It represents a first attempt to address the transient dynamic and thermal behavior of heated supercritical fluids by CFD. Experimental data on the stability of a supercritical loop is rare in open literature. T'Joen and Rohde [15] explore the stability of a natural circulation High Performance Light Water Reactor considering the thermos-hydraulic–neutronic feedback (driven by the coupling between friction, mass flow rate and power production) experimentally, and found a clear instability zone within the stability plane, which seemed to be similar to that of a BWR.

The primary objective of the current study is to investigate the flow, heat transfer and flow instability of water at supercritical pressure in a vertical tube numerically.

2. Steady-state calculation

The experimental set-up used by Yamagata et al. [16] was applied to verify the simulation method by FLUENT 13.0. The test section was a smooth tube with a diameter of 7.5 mm and a heated length of 1.5 m. The modelled tube was extended at the inlet by 0.5 m to obtain a fully developed flow. Supercritical water flowed upward vertically with a pressure of 24.5 MPa and a flow rate of 1260 kg/m^2s.

The mass flow rate, temperature, turbulence intensity and turbulence length scale were specified at the tube inlet, and it has been found that the selected turbulence quantities had no effect on the fully developed computed flow field downstream. The inlet temperature was varied to cover the range of bulk temperature and bulk enthalpy as presented in Yamagata et al. [16].

The pressure was specified at the tube outlet and the uniform heat fluxes on the tube wall were 233, 465, 698 and 930 kW/m^2.

The flow is assumed to be 2D axisymmetry and the governing equations of the continuity, momentum and energy are as follows:

Continuity equation:

$$\frac{1}{r}\left\{\frac{\partial}{\partial x}(\rho r u)+\frac{\partial}{\partial r}(\rho r v)\right\}=0 \tag{1}$$

Momentum equations:

$$\frac{1}{r}\left\{\frac{\partial}{\partial x}(\rho r u^2)+\frac{\partial}{\partial r}(\rho r v u)\right\}=-\frac{\partial p}{\partial x}+\rho g+\frac{1}{r}\left\{2\frac{\partial}{\partial x}\left[r\mu_e\left(\frac{\partial u}{\partial x}\right)\right]+\frac{\partial}{\partial r}\left[r\mu_e\left(\frac{\partial u}{\partial r}+\frac{\partial v}{\partial x}\right)\right]\right\} \tag{2}$$

$$\frac{1}{r}\left\{\frac{\partial}{\partial x}(\rho r u v)+\frac{\partial}{\partial r}(\rho r v^2)\right\}=-\frac{\partial p}{\partial r}+\frac{1}{r}\left\{\frac{\partial}{\partial x}\left[r\mu_e\left(\frac{\partial u}{\partial r}+\frac{\partial v}{\partial x}\right)\right]+2\frac{\partial}{\partial r}\left[r\mu_e\left(\frac{\partial v}{\partial r}\right)\right]\right\}-2\frac{\mu_e v}{r^2} \tag{3}$$

where μ_e is the effective viscosity defined by $\mu_e=\mu+\mu_T$ and μ_T is the turbulent viscosity defined as $\mu_T=\rho f_\mu C_\mu k^2/\varepsilon$, in which f_μ is a damping function to account for near-wall effects and C_μ is a constant.

Energy equation:

$$\frac{1}{r}\left\{\frac{\partial}{\partial x}(\rho c_p r u T)+\frac{\partial}{\partial r}(\rho c_p r v T)\right\}=\frac{1}{r}\left\{\frac{\partial}{\partial x}\left[rc_p\left(\frac{\mu}{\mathrm{Pr}}+\frac{\mu_T}{\sigma_T}\right)\frac{\partial T}{\partial x}\right]+\frac{\partial}{\partial r}\left[rc_p\left(\frac{\mu}{\mathrm{Pr}}+\frac{\mu_T}{\sigma_T}\right)\frac{\partial T}{\partial r}\right]\right\} \tag{4}$$

where Pr is molecular Prandtl number and σ_T is the turbulent Prandtl number and 0.9 is used in this study.

Turbulent kinetic energy equations:

$$\left[\frac{\partial(\rho u k)}{\partial x}+\frac{1}{r}\frac{\partial(r\rho v k)}{\partial r}\right]=\frac{\partial}{\partial x}\left[\left(\mu+\frac{\mu_T}{\sigma_k}\right)\frac{\partial k}{\partial x}\right]+\frac{1}{r}\frac{\partial}{\partial r}\left[r\left(\mu+\frac{\mu_T}{\sigma_k}\right)\frac{\partial k}{\partial r}\right]+P_k+G_k-\rho\varepsilon+\rho D \tag{5}$$

Turbulence dissipation rate:

$$\left[\frac{\partial(\rho u \varepsilon)}{\partial x}+\frac{1}{r}\frac{\partial(r\rho v \varepsilon)}{\partial r}\right]=\frac{\partial}{\partial x}\left[\left(\mu+\frac{\mu_T}{\sigma_\varepsilon}\right)\frac{\partial \varepsilon}{\partial x}\right]+\frac{1}{r}\frac{\partial}{\partial r}\left[r\left(\mu+\frac{\mu_T}{\sigma_\varepsilon}\right)\frac{\partial \varepsilon}{\partial r}\right] + C_{\varepsilon 1}f_1\frac{\varepsilon}{k}(P_k+G_k)-C_{\varepsilon 2}f_2\frac{\rho\varepsilon^2}{k}+\rho E \tag{6}$$

where

$$P_k=\mu_T\left[2\left\{\left(\frac{\partial u}{\partial x}\right)^2+\left(\frac{\partial v}{\partial r}\right)^2+\left(\frac{v}{r}\right)^2\right\}+\left(\frac{\partial u}{\partial r}+\frac{\partial v}{\partial x}\right)^2\right] \tag{7}$$

$$G_k=-\overline{\rho' u'}g_x=-\frac{\beta\mu_T}{C_{1t}}\left(\frac{k}{\varepsilon}\right)\left(\frac{\partial u}{\partial r}+\frac{\partial v}{\partial x}\right)\left(\frac{\partial T}{\partial r}\right)g_x \tag{8}$$

and $g_x = -g$ for upward flow.

The structured mesh was refined in the radial direction towards the tube wall to assure that the non-dimensional length $y^+<0.2$ at the first node close to the wall when the enhanced wall treatment was used. Grid independence was established by employing various meshes, ranging from 150,000 to 400,000 and a typical mesh of 150,000 (75×2000) was finally used.

The NIST Standard Reference Database 23 (REFPROP) Version 8.0 [2] was used for calculating the temperature and pressure dependent properties of water. The SIMPLEC algorithm was used to couple the pressure and velocity. The second-order upwind scheme was used for discretization of the momentum, energy, turbulent kinetic energy, and turbulent energy dissipation equations. The convergence criteria required a decrease of at least 6 orders of

magnitude for the residuals with no observable change in the surface temperatures for an additional 200 iterations.

RNG *k-ε* model with enhanced wall treatment was used to calculate the flow and heat transfer at the four heat fluxes, 233, 465, 698 and 933 kW/m^2, with the wall temperature and heat transfer coefficient shown in Fig. 2, and the simulated results were in very good agreement with the experimental results. Therefore, RNG *k-ε* model with enhanced wall treatment was adopted to simulate the heat transfer and flow instability of water at supercritical pressure in a vertical tube at transient state.

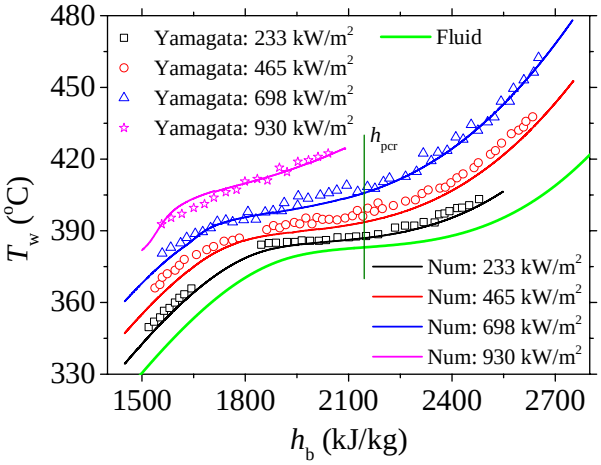

(a) Wall temperature as a function of bulk enthalpy

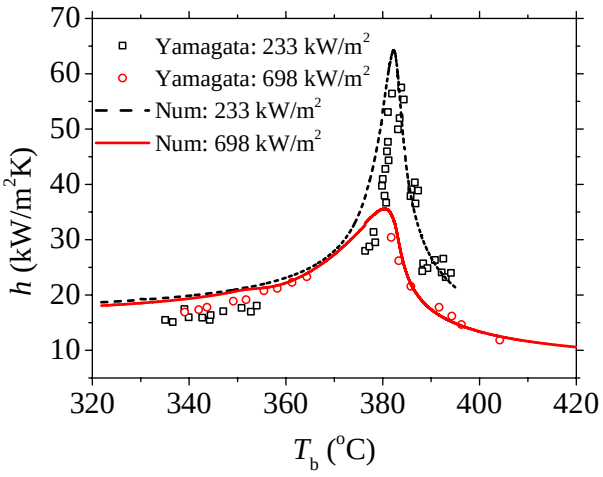

(b) Heat transfer coefficient as a function of bulk temperature

Fig. 2 Comparison of RNG *k-ε* + EWT simulated results and experimental results

3. Transient-state calculation

The unstable behavior in a heated channel with water at supercritical pressure was also studied based on the steady state results. Sharabi and Ambrosini [13] reported that the unstable conditions is only governed by two relevant dimensionless quantities, sub-pseudocritical number, N_{SPC}, and the trans-pseudocritical number, N_{TPC}, once the geometry of the system is defined.

$$N_{\mathrm{SPC}} = \left[h_{\mathrm{pc}}(P) - h_{\mathrm{in}} \right] \frac{\beta_{\mathrm{pc}}(P)}{Cp_{\mathrm{pc}}(P)} \tag{9}$$

$$N_{\mathrm{TPC}} = \frac{Q}{G}\frac{\beta_{\mathrm{pc}}(P)}{Cp_{\mathrm{pc}}(P)} \tag{10}$$

where h_{pc} is the fluid enthalpy at the system operating pressure and the corresponding pseudocritical temperature. Cp_{pc} is the specific heat and β_{pc} is the isobaric thermal expansion coefficient at the system operating pressure and the corresponding pseudocritical temperature. G is the mass flow rate.

Water pressure in this simulation was 24.5 MPa, T_{pc} = 383.07°C, h_{pc} = 2145.4 kJ/kg, Cp_{pc}=94.015 kJ/kgK and β_{pc} = 0.16053 1/K, the inlet enthalpy was set as 1400 kJ/kg, so N_{SPC} = 1.27. The heating power was quite large for the occurrence of unstable behavior, so the heated wall length was extended to 6 m and the total tube length was 6.5 m.

The inlet and outlet pressure drop was evaluated in the steady-state calculations, assuming an initial flow rate in the range of 0.056 kg/s (1260 kg/m^{2}s). The obtained pressure drops were then set in the boundary conditions and kept constant in the transient-state simulations to calculate the mass flow rate. The heating power was increased linearly with time from initial values up to the occurrence of unstable behavior and beyond in the order of 85~130 kW and the corresponding heat fluxes were in the order of 600~920 kW/m^2.

The PISO algorithm was used to couple the pressure and velocity. The second-order upwind scheme was used for discretization of the momentum, energy, turbulent kinetic energy, and turbulent energy dissipation equations. The convergence criteria required a decrease of at least 5 orders of magnitude for the continuity residual and 6 orders of magnitude for the other residuals. A mesh of 32,500 (50×650) was tried considering the enormous computing time in the transient-state calculation. As the heated wall length was extended to 6 m and the total tube length was 6.5 m in the transient-state calculation, a mesh of 10,000 (50×200), which is the same mesh structure with that in the transient-state calculation, was used to simulate in the steady-state calculation case in Section 2 (the total tube length was 2 m) for grid independence study. The results show that the maximum wall temperature difference at the same fluid bulk enthalpy between the mesh 10,000 and mesh 150,000 is less than 2 °C, so the typical mesh of 32,500 was finally selected in the transient-state calculation. The non-dimensional length y^+<0.2 at the first node close to the wall as the enhanced wall treatment was used.

4. Results and discussions

4.1 Flow and heat transfer characteristics at four moments

Four moments have been selected to analyze the flow and heat transfer characteristics when the supercritical fluid enter the unstable region when the inlet fluid enthalpy is 1400 kJ/kg as shown in Fig. 3. Moment A (t = 312.8 s) and moment B (t = 313.9 s) are the inlet and outlet flow rate peaks, moment C (t = 315.0 s) and moment D (t = 315.6 s) are the inlet and outlet flow rate valleys, and moment D happens to be the peak of the inlet flow rate.

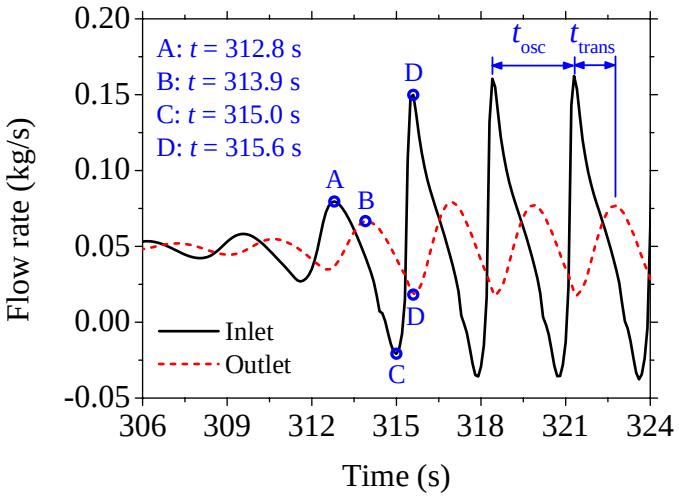

Fig. 3 Schematic diagram of four moments, t_{osc} and t_{trans} (Inlet enthalpy = 1400 kJ/kg, Inlet pressure = 24.5 MPa)

Figure 4 shows the axial profiles of mass flow rate, pressure drop, axial and wall temperature and density when the inlet fluid enthalpy is 1400 kJ/kg. When the inlet flow rate arrives an obvious peak for the first time, namely moment A, the outlet flow rate is approximately half of the inlet flow rate and the pressure drops linearly along the tube. The wall temperature increases rapidly at the tube downstream due to the low flow rate, and moreover, the fluid temperatures pass through T_{pc}, so the fluid density, thermal conductivity and specific heat near the wall are quite low, which impairs the heat transfer between the fluid and the wall as well.

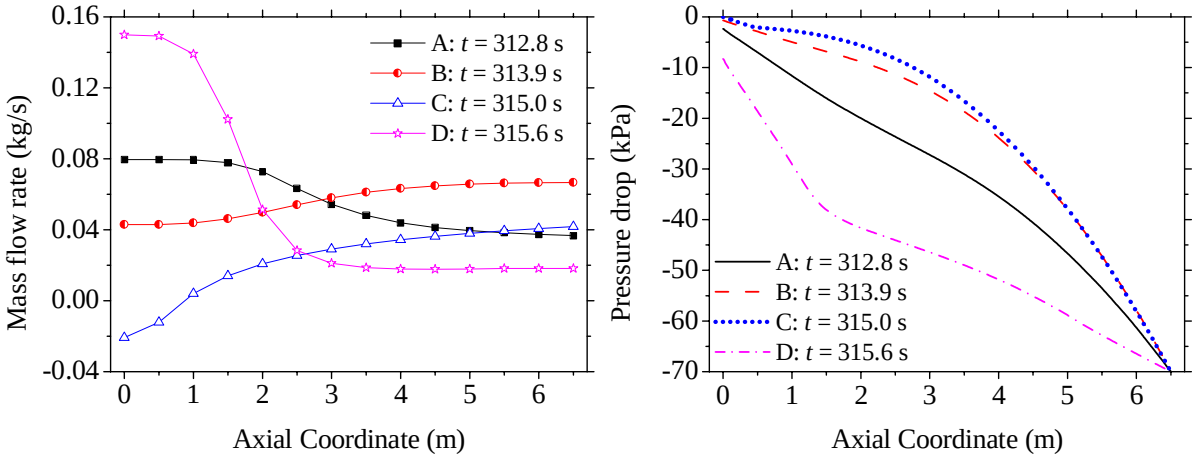

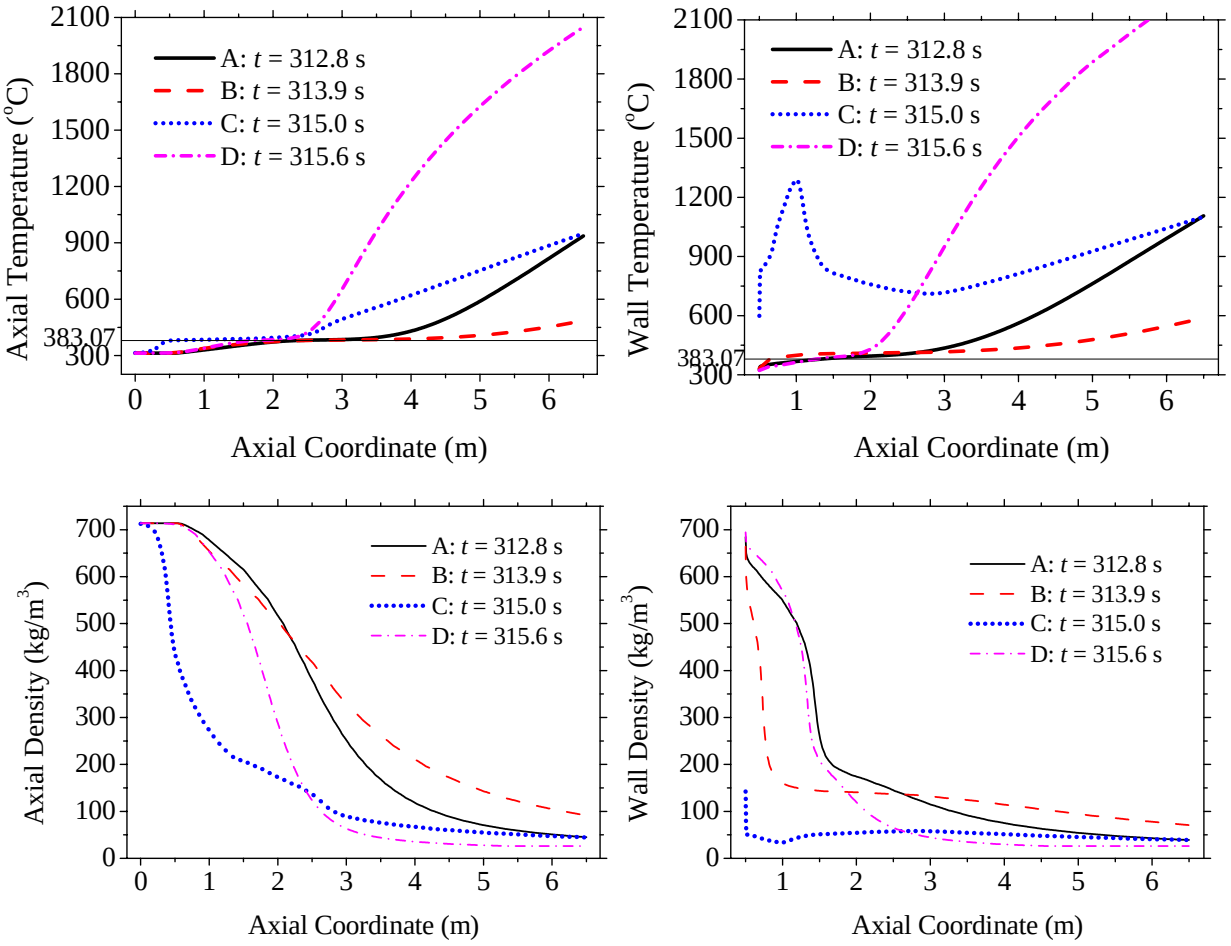

Fig. 4 Axial profiles of mass flow rate, pressure drop, axial and wall temperature and density (Inlet enthalpy = 1400 kJ/kg)

When the peak of the inlet flow rate is delivered to the outlet, namely the outlet flow rate arrives an obvious peak for the first time, moment B, the flow rate along the tube oscillates nearly in counterphase with that at moment A. The pressure drop of the tube former half is much smaller than that of the tube latter half due to the low flow rate, high fluid density and low flow velocity. The wall temperature increases moderately along the pipe because of the high flow rate.

The inlet flow rate is negative at moment C, which means that backflow is observed at the inlet. The wall temperature firstly increases sharply to a local maximum as the axial coordinate, x, is about 1 m, resulting in a strong heat transfer deterioration, then the wall temperature decreases, and increases again along the tube. The pressure drop is similar with that at moment B.

The inlet flow rate reaches a peak again at moment D and the outlet flow rate happens to be a valley. The flow rate at the tube former half is far higher than that at the latter half, which means that the flow rate non-uniform in this tube reaches an extreme at that moment. The flow rate at the tube downstream is too low, and as the fluid temperature increases to far above T_{pc}, the fluid stays in a gas-like state, so the local wall temperature increases and the heat transfer is deteriorated dramatically. The pressure drop of the tube former half is higher due to the high flow rate and fluid flow velocity.

4.2 Effects of inlet fluid enthalpy

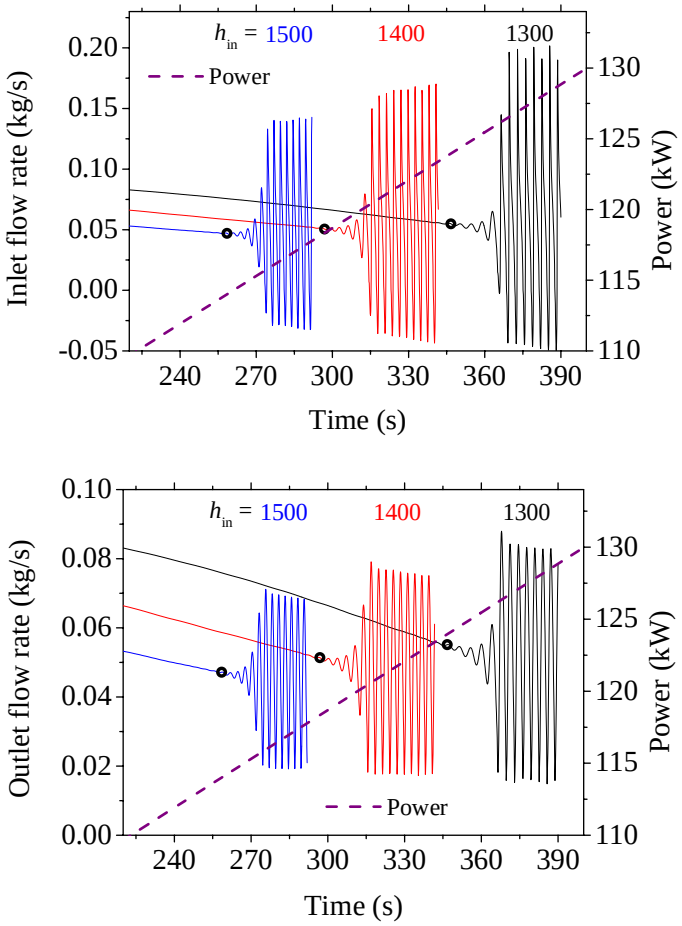

Fig. 5 Inlet and outlet flow rate as a function of time at various inlet enthalpies

(The black circles represent the unstable initial points)

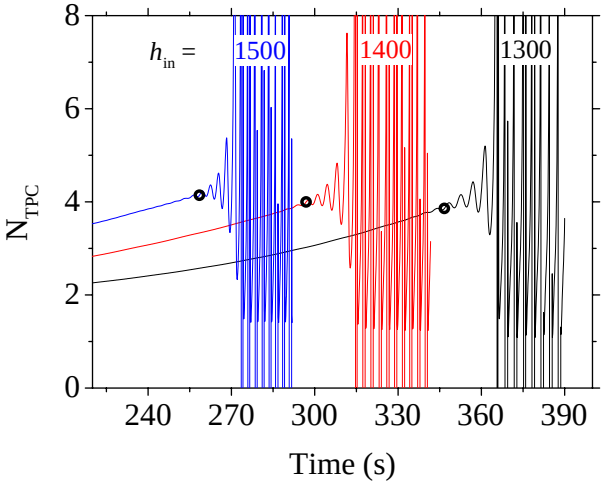

Fig. 6 N_{TPC} as a function of time at various inlet enthalpies

(The black circles represent the unstable initial points)

Table 1 Flow and heat transfer characteristics at unstable initial point

Inlet enthalpy (kJ/kg)	Time (s)	Inlet flow rate (kg/s)	Heating power (kW)	N_{SPC}	N_{TPC}	t_{osc} (s)	t_{trans} (s)	t_{trans}/t_{osc}
1300	346.7	0.055	124.0	1.44	3.86	3.1	1.6	0.50
1400	296.9	0.051	118.3	1.27	4.00	2.8	1.4	0.51
1500	258.5	0.047	114.0	1.10	4.14	2.4	1.3	0.51

The time when the inlet flow rate changes of 0.2% is defined as unstable initial point for analyzing the supercritical fluid flow instability, as shown in the black circles in Figs. 5 and 6. The time difference between two adjacent peaks of the inlet flow rate, t_{osc}, is regarded as the oscillation period, and the time difference between two adjacent peaks of inlet and outlet flow rate, t_{trans}, is regarded as the fluid transit time in the tube as shown in Fig. 3.

Figures 5 and 6 shows that when the inlet fluid enthalpy increases from 1300 kJ/kg to 1500 kJ/kg and the pressure drop across the tube is constant, 70 kPa with the same linearly increasing heating power, the flow rate in the tube decreases when the fluid flows steady. Afterwards, the flow instability phenomena occurs earlier, and the inlet and outlet flow rates and the heating power at the unstable initial points decrease, whereas N_{TPC} relatively increases, from 3.86 to 4.14 as listed in Table 1 when the inlet fluid enthalpy increases. Meanwhile, Table 1 also shows that the oscillation period, t_{osc}, and the fluid transit time, t_{trans}, decreases, meaning that the fluid flow oscillation is fiercer. However, the ratio between the fluid transit time and the oscillation period, t_{trans}/t_{osc}, stays almost constant, approximately 0.5, quite similar with the findings of two-phase flow density-wave oscillations mechanism, which illustrates that it takes around twice the residence time of a fluid particle for a complete set of events to repeat [17].

5. Conclusion

The heat transfer and flow instability of water at supercritical pressure in a vertical smooth tube was studied numerically. The key findings from this study are:

1. The steady-state calculation using RNG k-ε model with enhanced wall treatment was first performed to verify the simulation method by comparing with the experimental data of Yamagata et al.[16], and the results show that the simulation results agreed well with the experimental data and this model was adopted to simulate the heat transfer and flow instability of supercritical water at transient state.
2. The flow rates oscillate intensely once the fluid enters the unsteady zone and even backflow can be observed, the wall temperature can increase dramatically due to the very low flow rate at some moments. Such phenomena is extremely disadvantageous and should be avoided.
3. The flow rate and the heating power at the unstable initial points decrease as the inlet fluid enthalpy increases, whereas N_{TPC} relatively increases. The fluid transit time and the oscillation period decreases, while the ratio between them stays almost constant, approximately 0.5, quite similar with the findings of two-phase flow density-wave oscillations mechanism.

Acknowledgements

This program was supported by the International S&T Cooperation Program of China (No. 2012DFG71950), the National Natural Science Foundation of China Science Fund for Creative Research Groups (Grant No. 51321002) and Tsinghua University Initiative Scientific Research Program.

Reference

[1]. Hu N S, Steam turbine equipment and systems ultra-supercritical power unit, Chapeter 1. 2008, Beijing: Chemical industry press.
[2] Lemmon E W, Huber M L and McLinden M O, Reference fluid thermodynamic and transport properties. NIST Standard Reference Database 23, Version 8.0. 2007.
[3] Jackson J D, Fluid flow and convective heat transfer to fluids at supercritical pressure. Nuclear Engineering and Design, 2013, 264(SI): 24-40.
[4] Jiang P X, Liu B, Zhao C R, Convection heat transfer of supercritical pressure carbon dioxide in a vertical micro tube from transition to turbulent flow regime. International Journal of Heat and Mass Transfer, 2013, 56(1): 741-749.
[5] Jiang P X, Zhao C R, and Liu B, Flow and heat transfer characteristics of r22 and ethanol at supercritical pressures. Journal of Supercritical Fluids, 2012, 70: 75-89.
[6] Kim W S, He S and Jackson J D, Assessment by comparison with DNS data of turbulence models used in simulations of mixed convection. International Journal of Heat and Mass Transfer, 2008, 51(5-6): 1293-1312.
[7] He S, Kim W S and Bae J H, Assessment of performance of turbulence models in predicting supercritical pressure heat transfer in a vertical tube. International Journal of Heat and Mass Transfer, 2008, 51(19-20): 4659-4675.
[8] Pan J, Yang D, Dong Z C, et al., Experimental investigation on heat transfer characteristics of low mass flux rifled tube with upward flow. International Journal of Heat and Mass Transfer, 2011, 54(13-14): 2952-2961.
[9] Yoo J Y, The Turbulent Flows of Supercritical Fluids with Heat Transfer. Annual Review of Fluid Mechanics, 2013, 45: 495-525.
[10] Ruspini L C, Marcel CP, and Clausse A, Two-phase flow instabilities: A review. International Journal of Heat and Mass Transfer, 2014, 71: 521-548.
[11] Ambrosini W, Di Marco P and Ferreri J C, Linear and nonlinear analysis of density wave instability phenomena. International Journal of Heat and Technology, 2000, 18(1): 27-36.
[12] Ambrosini W, On the analogies in the dynamic behaviour of heated channels with boiling and supercritical fluids. Nuclear Engineering and Design, 2007, 237(11): 1164-1174.
[13] Ambrosini W and Sharabi M, Dimensionless parameters in stability analysis of heated channels with fluids at supercritical pressures. Nuclear Engineering and Design, 2008, 238(8): 1917-1929.
[14] Sharabi M B, Ambrosini W and He S, Prediction of unstable behaviour in a heated channel with water at supercritical pressure by CFD models. Annals of Nuclear Energy, 2008, 35(5): 767-782.
[15] T'Joen C, and Rohde M, Experimental study of the coupled thermo-hydraulic–neutronic stability of a natural circulation HPLWR. Nuclear Engineering and Design 2012, 242: 221-232.
[16] Yamagata K, Nishikawa K, Hasegawa S, et al., Forced convective heat transfer to supercritical water flowing in tubes. International Journal of Heat and Mass Transfer, 1972, 15(12): 2575-2593.
[17] Kakac S and Bon B, A Review of two-phase flow dynamic instabilities in tube boiling systems. International Journal of Heat and Mass Transfer, 2008, 51(3-4): 399-433.

ISSCWR7-2063

Prediction of heat transfer of supercritical Freon flowing upward in vertical tubes

Siyu Zhang, Hanyang Gu, Xu Cheng
School of Nuclear Science and Engineering, Shanghai Jiao Tong University
800 Dongchuan Road, Shanghai, China
(+86) 13564666614, sjtuzhsy@gmail.com

Abstract

Experimental investigations of heat transfer to supercritical Freon flowing upward in vertical tubes of 7.6 mm and 10.0 mm diameter have been carried out on the SMOTH test facility. 18 representative correlations are selected and assessed by the experimental data. Correlations of Jackson, Petukhov, Watts-Chou and Bae show satisfactory agreement with the test data. The acceleration parameter π_A shows regular effect on the heat transfer coefficient ratio. A new correlation is developed following the method of the Cheng's correlation.

Nomenclature

Bo	buoyancy parameter proposed by Jackson (-)
c_P	specific heat at constant pressure (J/kgK)
e	error (-)
F	correction factor (-)
G	mass flux (kg/m^{2}s)
Gr	Grashof number (-)
N	total number of data points (-)
Nu	Nusselt number (-)
P	pressure (Pa)
Pr	Prandtl number (-)
q	heat flux (W/m^2)
Re	Reynolds number (-)
T	temperature (℃)
Z	evaluated parameter (-)

Greek symbols

α	heat transfer coefficient (W/m^{2}K)
β	volumetric expansion coefficient (1/K)
Δ	error parameter for least square method (-)
μ	dynamic viscosity (kg/ms), average deviation (-)
π_A	acceleration parameter proposed by Cheng (-)
σ	standard deviation (-)

Subscripts and superscripts

b	bulk
c	calculated
m	measured
s	systematic
w	wall

Acronyms

AD	average deviation
HTC	heat transfer coefficient
MD	mean deviation
SCWR	supercritical water-cooled reactor
SD	standard deviation
SMOTH	supercritical model fluid thermal-hydraulics

1. Introduction

The supercritical water-cooled reactor (SCWR) is selected as one of six candidates of the Generation IV nuclear reactors recommended for further development [1]. To keep the maximum cladding temperature below the design limit, reliable knowledge of heat transfer characteristics and accurate predictions of heat transfer under supercritical pressures is necessary for SCWR design.

The conventional convective heat transfer correlations such as the Dittus–Boelter [2] correlation are no longer applicable to supercritical fluids due to the complex coupling effect between the sharp variation of properties and flow structure in the vicinity of pseudo-critical point. The studies of heat transfer to supercritical fluids in tubes have been performed since 1950s [3-15]. In the framework of the development of SCWR, further efforts have been made to develop prediction methods for heat transfer to supercritical fluids [16-19]. However, although these correlations have been found to predict reasonably well for their original experimental data, deviations cannot be avoided in estimating the heat transfer coefficient for different conditions.

This paper derives a correlation of heat transfer to supercritical fluids based on experimental data of Freon R134a flowing upward in vertical tubes. Based on dimensionless parameters analysis of heat transfer behaviour, a new heat transfer correlation is proposed, which contains a single dimensionless number and excludes the direct dependence of heat transfer coefficient on the wall temperature.

2. Experimental study

2.1 Experimental facility and test sections

Experiments have been carried out at the SMOTH (Supercritical MOdel fluid Thermal-Hydraulics) test facility, which is a forced circulation loop with working fluid of Freon R134a, as shown in Fig. 1. The Freon is circulated in the loop by a circulation pump and is electrically preheated to a required temperature by a preheater before entering the test section. Passing through the test section, the Freon is cooled by a heat exchanger and returns to the pump. The pressure in the loop is kept constant and adjusted by accumulators connected to a high pressure nitrogen gas supply.

In this study, experiments were performed in two test sections, which are Inconel 625 round tube of inner diameter 7.6 and 10.0 mm, respectively. The test sections are uniformly heated by a DC power supply directly. The heated length is 2300 mm. The Freon flows upward through test sections vertically. The inlet and outlet fluid temperatures are measured by sheath thermocouples at the inlet and outlet mixing chambers, and the outer-wall temperatures of the tube are measured by 45 sheath thermocouples distributed uniformly along the axial direction with 50 mm intervals.

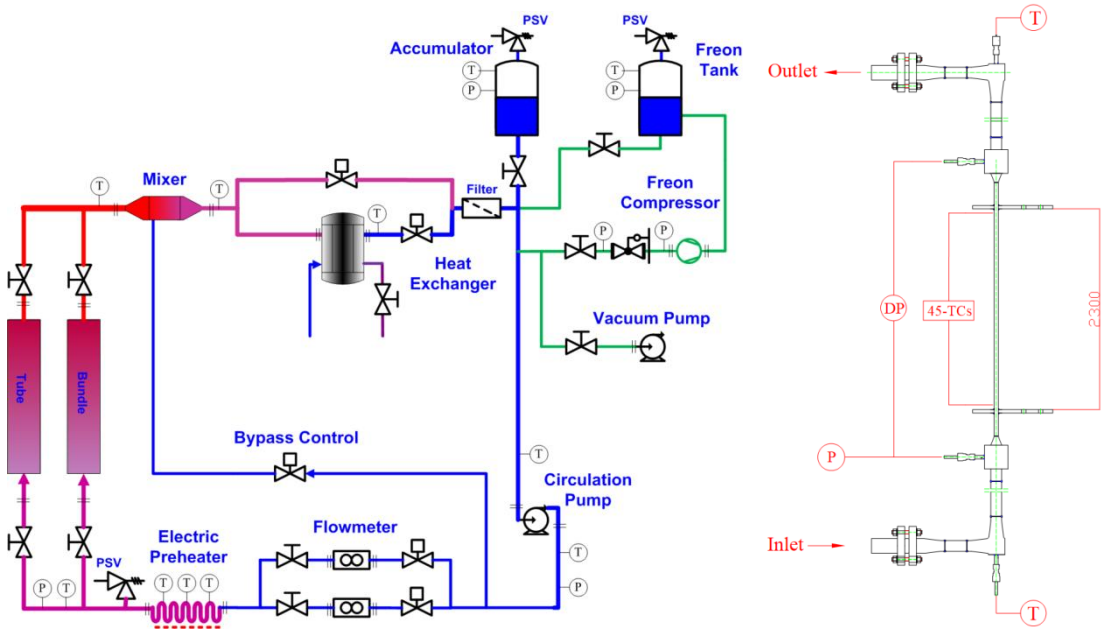

Figure 1. Schematic diagrams of SMOTH test facility and test sections

2.2 Test procedure and conditions

The test parameter ranges of the present experiments are summarized in Table 1. The temperature range covers the pseudo-critical value, where unusual heat transfer behavior is expected.

Table 1. Ranges of test parameters

Parameters	Values	Units
Pressure	4.3, 4.5, 4.7	MPa
Mass flux	400~2500	kg m^{-2} s^{-1}
Heat flux	10~180	kW m^{-2}
Fluid temperature	71~115	℃

Before experiments, the Freon in the main loop is circulated through the purification system until a high purity is obtained. The purification system is kept working during the experiments. The pressure in the test loop is increased stepwise by controlling the bladder accumulator. When the pressure reaches the required level, the pump is put into operation. The required inlet fluid temperature is obtained by adjusting the heating power of the pre-heater. Experiments are performed by holding the pressure, inlet temperature, mass flow rate and heating power constant.

2.3 Measurement accuracy and uncertainty analysis

The measurement accuracy of various parameters is summarized in Table 2. For each data point errors of parameters are analyzed. The total error of each parameter consists of two parts: systematic and statistic error. Assume that an evaluated parameter is dependent on other input parameters and their relationship can be expressed as follows:

$$Z=f\left(Z_1,Z_2,\cdots,Z_n\right) \tag{1}$$

With the 2σ-criterion the total error of the evaluated parameter is determined by

$$e=e_s\pm 2\sigma \tag{2}$$

Well calibration of each instrument and validation experiments under subcritical pressures convince the authors that the systematic error has been eliminated.

$$e=\pm 2\sigma \tag{3}$$

Under the assumption that the statistic errors of the input parameters obey the Gauss-distribution and are independent of each other, the statistic error of the evaluated parameter also obeys the Gauss-distribution with a standard deviation:

$$\sigma=\sqrt{\sum_{i=1}^{n}\left(\frac{\partial f}{\partial Z_i}\sigma_i\right)^2} \tag{4}$$

Table 3 shows one example of the error analysis. Regarding the Nusselt number, 83 % of the 10,155 experimental data points fall into the error range smaller than 5 %, and 98 % fall into the error range smaller than 10 %.

Table 2. Uncertainties of primary parameters

Parameters	Maximum uncertainties
Pressure	± 0.2 %
Mass flow rate	± 0.1 %
Inlet temperature	± 0.2 ℃
Wall temperature	± 0.5 ℃
Voltage	± 0.1 %
Current	± 0.2 %
Tube diameter	± 0.04 mm
Tube thickness	± 0.02 mm

Table 3. Example of error analysis

Parameters (Units)	P (MPa)	G (kg m^{-2} s^{-1})	T_b (℃)	T_w (℃)	q (kW m^{-2})	HTC (W m^{-2} K^{-1})	Nu (-)
Values	4.31	1493	88.4	104.1	61.1	3878	523
Errors (%)	0.14	0.70	0.14	0.32	0.38	2.32	2.32

2.4 Experimental results and analysis

Fig. 2 shows the effects of heat flux and tube diameter on the variation of heat transfer coefficient. At the condition of low heat flux, the heat transfer coefficient increases monotonously and reaches a maximum value at a specific enthalpy slightly lower than the pseudo-critical value. For high heat flux, the heat transfer coefficient shows a significant reduction at low enthalpy region. As the heat flux increases, the heat transfer deterioration is stronger and the heat transfer coefficient is smaller in the region near the pseudo-critical point. The heat transfer coefficient is smaller and the heat transfer deterioration tends to occur in the case of larger diameter test section.

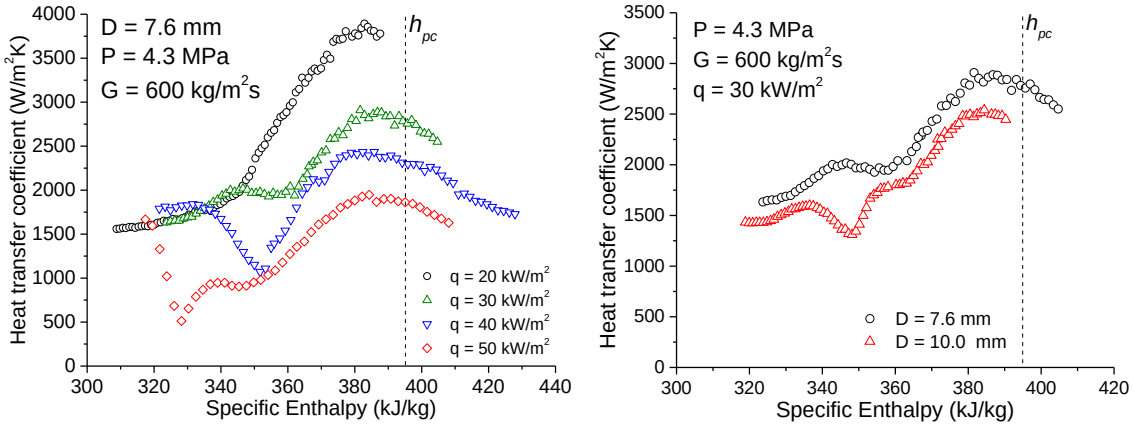

Figure 2. Effects of heat flux and tube diameter on the variation of heat transfer coefficient

3. Correlations validation

3.1 Existing correlations

Various correlations have been developed for heat transfer under supercritical pressures, based on the experimental data of water, carbon dioxide, and the Freon. Through an extensive survey, representative correlations are selected and assessed in this paper.

Griem [3] modified the coefficient and exponents in the Dittus-Bolter correlation. Shitsman [4], Bishop [5], Swenson [6], Jackson [7] and Hu [8] considered correction terms of various property ratios based on the structure of Dittus-Bolter correlation and proposed correlations respectively. Petukhov and Kirillov [9-11]tried to correlate the heat transfer coefficient with friction coefficient. Yamagata [12], Jackson [13] and Krasnoshchekov [14] developed correlations with different partitions, respectively. Watts [15], Bae [16], and Kuang [17] took dimensionless parameters into account to improve the prediction accuracy. Cheng [18] derived a correlation with simple structure and strong connection with physical phenomenon. Zhao [19] modified the Cheng correlation and applied it on downward flow.

3.2 Predicting performance

To achieve quantitative conclusion, statistic evaluation of the deviation between calculated and measured heat transfer coefficient has been done with 7,915 experimental data points. The test data obtained in the region of abrupt heat transfer coefficient reduction is excluded.

The deviation for each point is defined as:

$$e_i = \frac{\left(\alpha_c - \alpha_m\right)_i}{\alpha_{m,i}} \tag{5}$$

The average deviation (AD), mean deviation (MD), and standard deviation (SD) of the data are computed as below:

$$\mathrm{AD} = \mu = \frac{1}{N}\sum_{i=1}^{N} e_i \tag{6}$$

$$\mathrm{MD} = \frac{1}{N}\sum_{i=1}^{N} \left|e_i\right| \tag{7}$$

$$\mathrm{SD} = \sigma = \sqrt{\frac{1}{N-1}\sum_{i=1}^{N}\left(e_i - \mu\right)^2} \tag{8}$$

Fig. 3 shows the heat transfer coefficient deviations of eq. (4) according to each correlation. Table 4 lists average deviation, mean deviation and standard deviation of each correlation. Generally, it is much more difficult to obtain a good prediction for small heat transfer coefficient. Table 4 shows the Jackson (1975), Petukhov (1983), Watt and Bae correlations have better prediction accuracy.

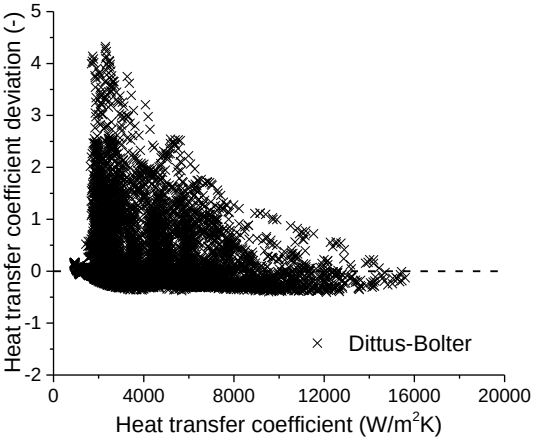
Heat transfer coefficient deviation (-)
Heat transfer coefficient (W/m²K)
Dittus-Bolter

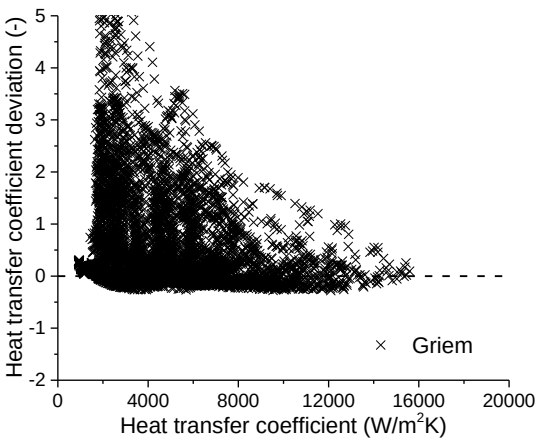
Heat transfer coefficient deviation (-)
Heat transfer coefficient (W/m²K)
Griem

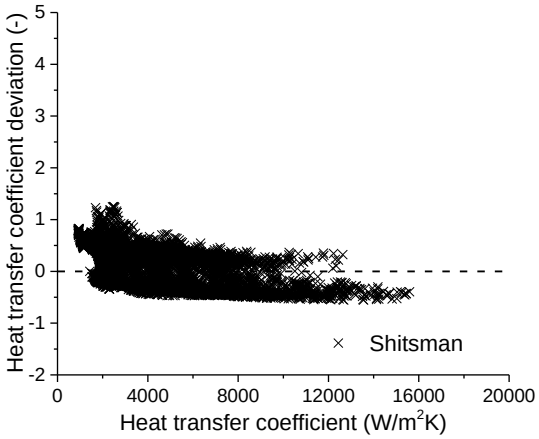
Heat transfer coefficient deviation (-)
Heat transfer coefficient (W/m²K)
Shitsman

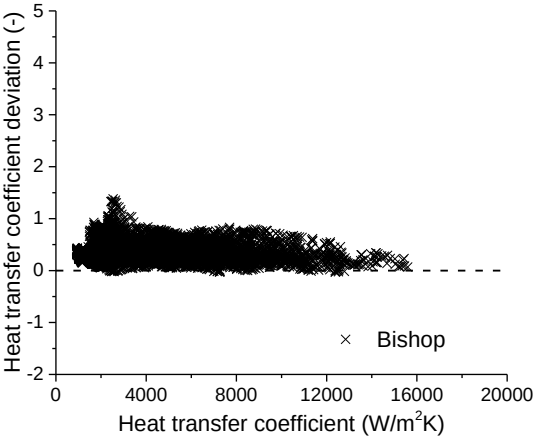
Heat transfer coefficient deviation (-)
Heat transfer coefficient (W/m²K)
Bishop

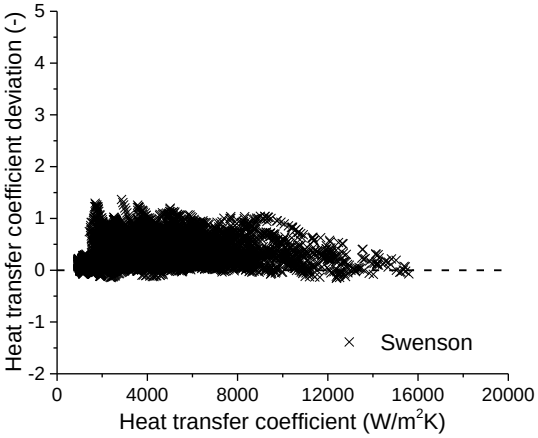
Heat transfer coefficient deviation (-)
Heat transfer coefficient (W/m²K)
Swenson

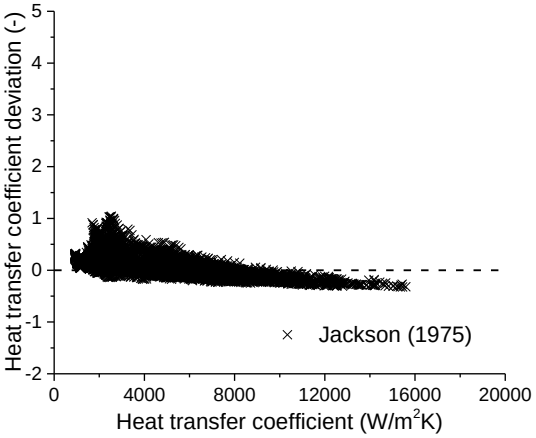
Heat transfer coefficient deviation (-)
Heat transfer coefficient (W/m²K)
Jackson (1975)

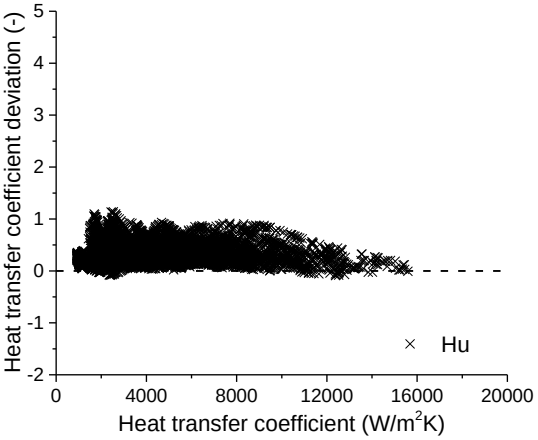
Heat transfer coefficient deviation (-)
Heat transfer coefficient (W/m²K)
Hu

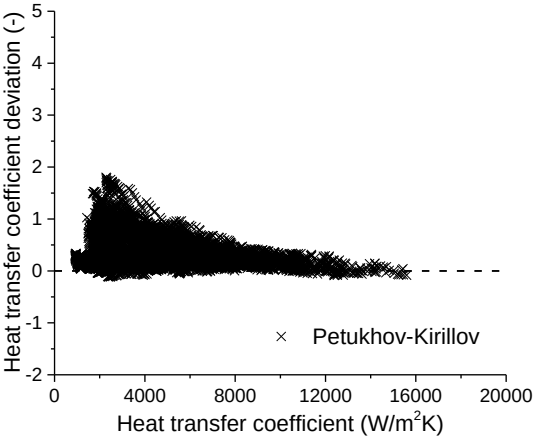
Heat transfer coefficient deviation (-)
Heat transfer coefficient (W/m²K)
Petukhov-Kirillov

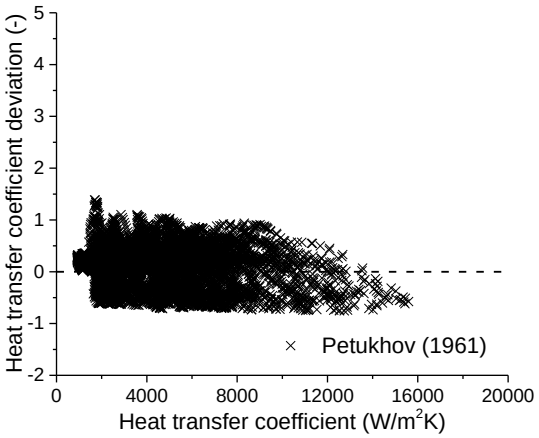
Heat transfer coefficient deviation (-)
Heat transfer coefficient (W/m²K)
Petukhov (1961)

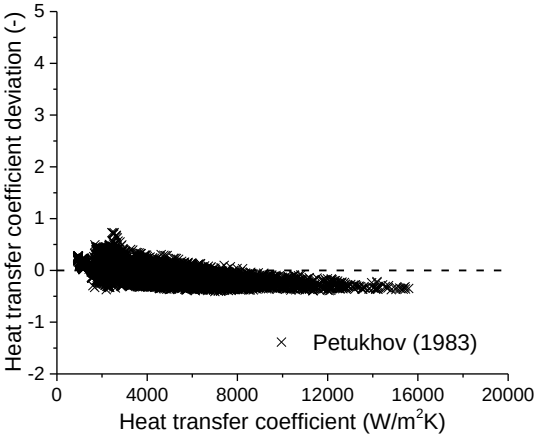
Heat transfer coefficient deviation (-)
Heat transfer coefficient (W/m²K)
Petukhov (1983)

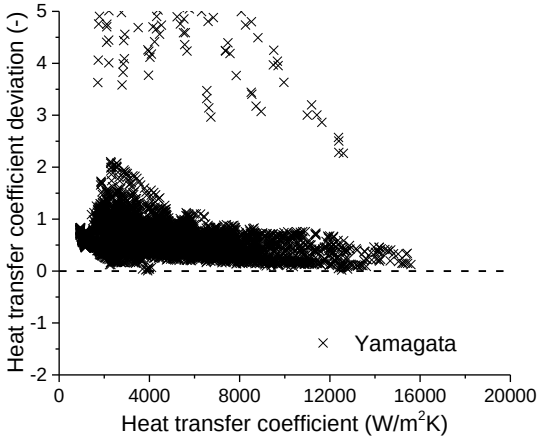
Heat transfer coefficient deviation (-)
Heat transfer coefficient (W/m²K)
Yamagata

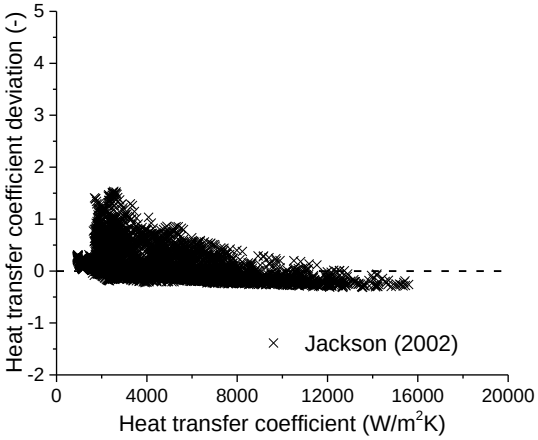
Heat transfer coefficient deviation (-)
Heat transfer coefficient (W/m²K)
Jackson (2002)

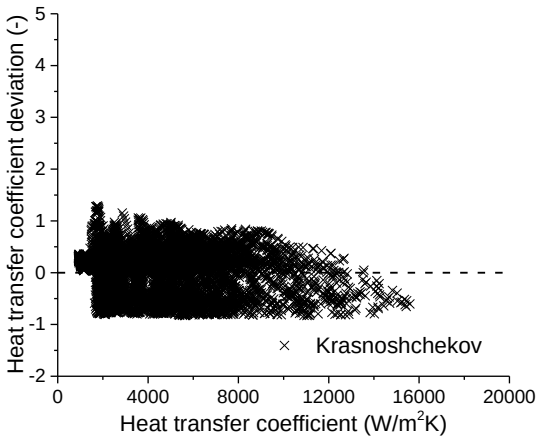
Heat transfer coefficient deviation (-)
Heat transfer coefficient (W/m²K)
Krasnoshchekov

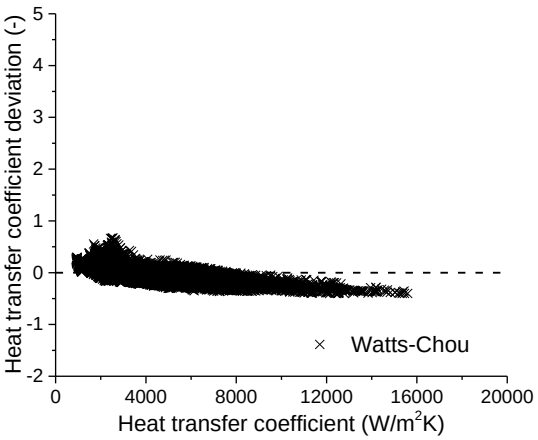
Heat transfer coefficient deviation (-)
Heat transfer coefficient (W/m²K)
Watts-Chou

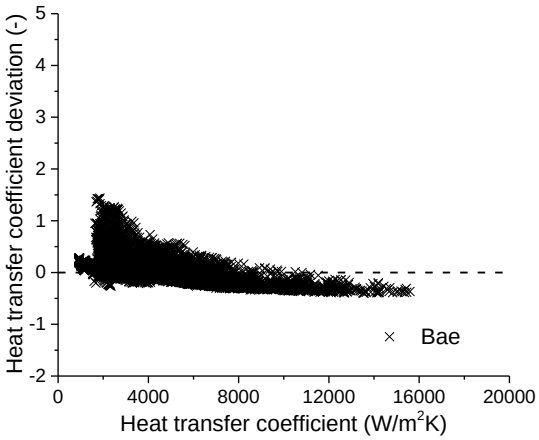
Heat transfer coefficient deviation (-)
Heat transfer coefficient (W/m²K)
Bae

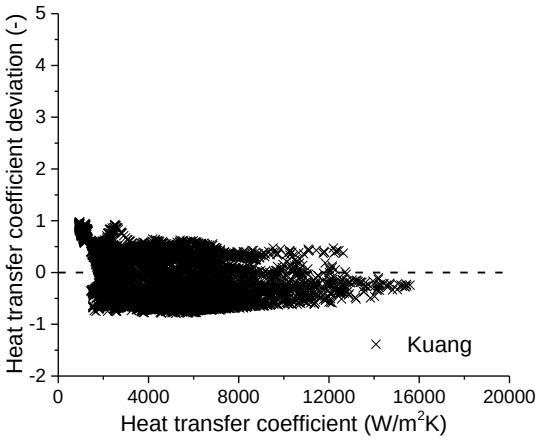
Heat transfer coefficient deviation (-)
Heat transfer coefficient (W/m²K)
Kuang

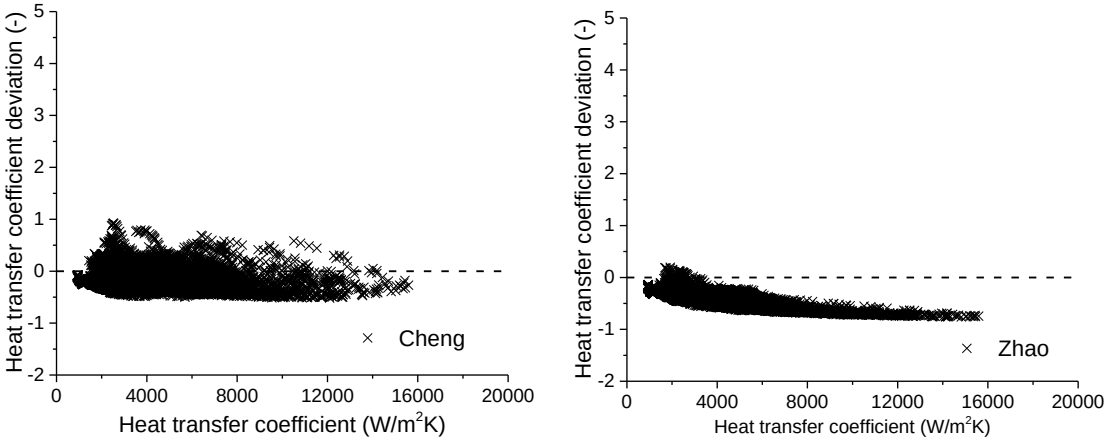

Figure 3. Heat transfer coefficient deviations of calculated and measured values

Table 4. Prediction deviations of all the selected correlations

Correlations	Data points	AD	MD	SD
Dittus-Boelter (1930)	7915	0.084	0.288	0.392
Griem (1996)	7915	0.249	0.302	0.393
Shitsman (1968)	7915	0.051	0.327	0.352
Bishop (1964)	7915	0.292	0.292	0.118
Swenson (1965)	7915	0.289	0.292	0.177
Jackson (1975)	7915	0.056	0.124	0.155
Hu (2001)	7915	0.289	0.289	0.133
Petukhov-Kirillov (1958)	7915	0.297	0.298	0.193
Petukhov(1961)	7915	0.025	0.307	0.381
Petukhov(1983)	7915	-0.093	0.163	0.181
Yamagata (1972)	7915	0.559	0.559	0.401
Jackson (2002)	7915	0.052	0.148	0.205
Krasnoshchekov (1966)	7915	-0.057	0.374	0.480
Watts-Chou (1982)	7915	-0.045	0.131	0.164
Bae (2010)	7915	0.013	0.158	0.215
Kuang (2008)	7915	-0.213	0.483	0.529
Cheng (2009)	7915	-0.212	0.275	0.237
Zhao (2014)	7915	-0.589	0.590	0.266

4. New correlation

4.1 Effect of dimensionless parameters

Watts and Bae correlations achieve good agreement with test data, which contain a dimensionless *Bo* number derived by Jackson [20] to express the effect of buoyancy. The *Bo* number is defined as:

$$Bo = \overline{\mathrm{Gr}}_b \Big/ (\mathrm{Re}_b^{2.7}\ \overline{\mathrm{Pr}}_b^{0.5}) \tag{9}$$

Cheng et al. [18] proposed a dimensionless acceleration parameter π_A to building the correction factor in heat transfer correlation, which is defined as:

$$\pi_A = \beta_b q / (G c_{p,b}) \tag{10}$$

Fig. 4 shows the effects of dimensionless parameters on the heat transfer coefficient ratio of measured value and calculated value by Dittus-Bolter correlation. Although Watts and Bae correlations achieve good prediction relying on the *Bo* number, the *Bo* number does not show clear effect on the heat transfer coefficient ratio. The cooperation of *Bo* number and iteration of wall temperature is indispensable for a good prediction. By contrast, the acceleration parameter π_A shows regular effect on the heat transfer coefficient ratio.

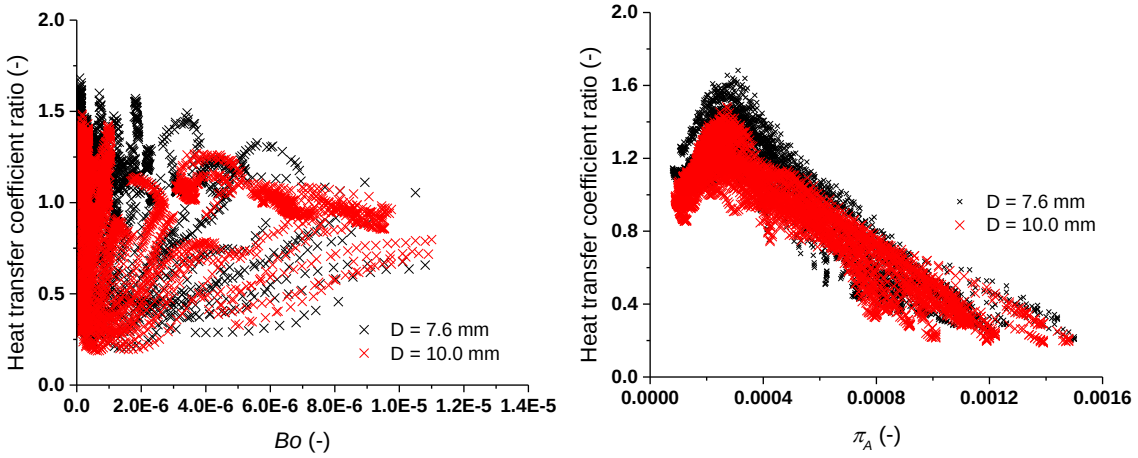

Figure 4. Effect of dimensionless parameters on heat transfer coefficient ratio

4.2 New heat transfer correlation

Clear dependence of the heat transfer coefficient ratio on π_A in two regions is shown in Fig. 4.

In the smaller π_A region, a power function is applied to describe the dependence which has a value of 1 when π_A is 0 to maintain a convergence with the Dittus-Bolter correlation when the acceleration effect is negligible.

$$F_1 = 1.0 + a_1 \cdot {\pi_A}^{b_1} \tag{11}$$

In the larger π_A region, Fig. 5 shows that the heat transfer coefficient ratio has a strong linear dependence on $\ln \pi_A$.

$$F_2 = a_2 + b_2 \cdot \ln \pi_A \tag{12}$$

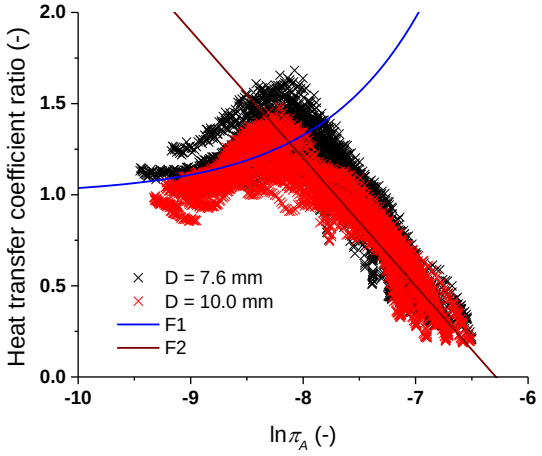

Figure 5. Relationship between heat transfer coefficient ratio and ln π_A

Based on the criterion that the error parameter

$$\Delta = \frac{1}{N}\sum_{i=1}^{N}\left|\frac{\mathrm{Nu}_C}{\mathrm{Nu}_M} - 1\right|_i \tag{13}$$

has its minimum value, coefficients in the new correlation are determined. The derived new correlation is as follows. Due to the experimental data, the valid scope of this correlation is ln π_A < -6.5.

$$\mathrm{Nu}_b = 0.023 \cdot \mathrm{Re}_b^{0.8}\,\mathrm{Pr}_b^{0.4} \cdot F \tag{14}$$

$$F = \min\left(F_1, F_2\right) \tag{15}$$

$$F_1 = 1.0 + 2000 \cdot \pi_A{}^{1.09} \tag{16}$$

$$F_2 = -4.4 - 0.7 \cdot \ln\pi_A \tag{17}$$

Fig. 6 shows the heat transfer coefficient ratio of calculated value by new correlation and measured value. The present correlation predicts well for test data of both tube diameter 7.6 mm and 10.0 mm. Table 5 shows that the deviations of the present correlation are better than all the correlations in the last section.

Due to the close connection of π_A and fluid properties, modification of coefficients is necessary for application of the proposed correlation on other fluid.

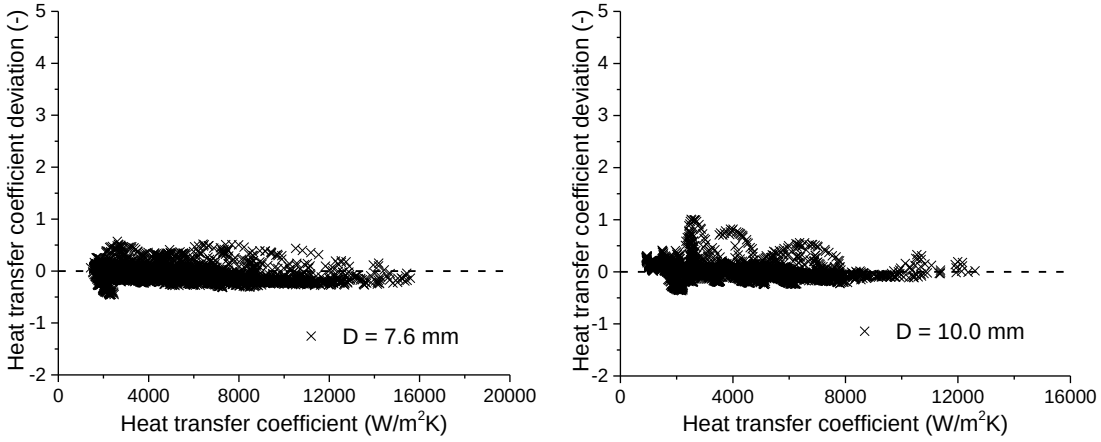

Figure 6. Heat transfer coefficient deviations of calculated value by new correlation and measured value

Table 5. Prediction deviations of the new correlation

Diameter (mm)	Data points	AD	MD	SD

7.6	3763	-0.056	0.124	0.149
10.0	4152	0.017	0.100	0.137
All	7915	-0.017	0.111	0.147

5. Summary

Experimental investigations of heat transfer to supercritical Freon flowing upward in vertical tubes of 7.6 mm and 10.0 mm diameter have been carried out on the SMOTH test facility at Shanghai Jiao Tong University. Through extensive literature survey, 18 representative correlations are selected and assessed by the experimental data. The acceleration parameter π_A shows regular effect on the heat transfer coefficient ratio. A new correlation is developed following the method of the Cheng correlation. The new correlation shows very satisfactory prediction accuracy. The present correlation has a simple and strong connection with the physical phenomenon and gets rid of iteration of wall surface temperature and correction terms of various property ratios.

References

1. U.S. DOE and GIF, 2002. A technology roadmap for Generation IV nuclear energy systems. in: U.S. DOE Nuclear Energy Research Advisory Committee and the Generation IV International Forum.

2. Dittus, F.W., Boelter, L.M.K., 1930. Heat transfer in automobile radiators of the tubular type. Univ. Calif. Publ. Eng. 2 (13), 443–461.

3. Griem, H., 1996. A new procedure for the prediction of forced convection heat transfer at near- and supercritical pressure, Heat and Mass Transfer, 31 (5), 301–305.

4. Shitsman, M.E., 1968. Temperature conditions in tubes at supercritical pressures. Therm. Eng. 15(5), 72.

5. Bishop, A.A., Sandberg, L.O., Tong, L.S., 1964. Forced convection heat transfer to water at near critical temperatures and supercritical pressures. WCAP-2056-P, Part-III-B, Westinghouse Electric Cooperation.

6. Swenson, H.S., Caever, J.R., Kakarala, C.R., 1965. Heat transfer to supercritical water in smooth-bore tube. J. Heat Transfer, 477–484.

7. Jackson, J.D., Fewster, J., 1975. Forced Convection Data for Supercritical Pressure Fluids, HTFS, 21540.

8. Hu Z.H., 2001. Heat transfer characteristics of vertical upflow and inclined tube in the supercritical pressure and near-critical pressure region. Xi'an Jiaotong University (thesis).

9. Petukhov, B.S., Kirillov, P.L., 1958. About heat transfer at turbulent fluid flow in tubes, (In Russian), Thermal Engineering, 4, 63–68.

10. Petukhov, B.S., Krasnoshchekov, E.A., Protopopov, V.S., 1961. An Investigation of Heat transfer to fluids flowing in pipes under supercritical conditions. In: 2nd International Heat Transfer Conference, Boulder, U.S.A.

11. Petukhov, B.S., Kurganov, V.A., Ankudinov, V.B., 1983. Heat transfer and flow resistance in the turbulent pipe flow of a fluid with near-critical state parameters, High Temperatures, 21 (1), 81–89.

12. Yamagata, K., Nishikawa, K., Hasegawa, S., et al., 1972. Forced convective heat transfer to supercritical water flowing in tubes, J. Heat Mass Transfer, 15 (12), 2575–2593

13. Jackson, J.D., 2002. Consideration of the heat transfer properties of supercritical pressure water in connection with the cooling of advanced nuclear reactors. In: Proc. 13th Pac. Basin Nucl. Conf., Shenzhen, China.

14. Krasnoshchekov, E.A., Protopopov, V.S., 1966. Experimental study of heat exchange in carbon dioxide in the supercritical range at high temperature drops. High Temp. 4, 389–398.

15. Watts, M.J., Chou, C.T., 1982. Mixed convection heat transfer to supercritical pressure water. In: Proc. 7th Int. Heat Transfer Conf., Munchen.

16. Bae, Y.Y., Kim, H.Y., Kang, D.J., 2010. Forced and mixed convection heat transfer to supercritical CO_2 vertically flowing in a uniformly-heated circular tube. Exp. Therm. Fluid Sci. 34, 1295–1308.

17. Kuang, B., Zhang, Y., Cheng, X., 2008. A new, wide-ranged heat transfer correlation of water at supercritical pressures in vertical upward ducts. In: 7th International Topical Meeting on Nuclear Reactor Thermal hydraulics, Operation and Safety (NUTHOS-7), Seoul, Korea.

18. Cheng, X., Yang, Y.H., Huang, S.F., 2009. A simplified method for heat transfer prediction of supercritical fluids in circular tubes. Ann. Nucl. Energy 36, 1120–1128.

19. Zhao, M., Gu, H.Y., Cheng, X., 2014. Experimental study on heat transfer of supercritical water flowing downward in circular tubes. Ann. Nucl. Energy 63, 339-349.

20. Jackson, J.D., Hall, W.B., 1979. Influences of buoyancy on heat transfer to fluids flowing in vertical tubes under turbulent conditions. in: Turbulent Forced Convection in Channels and Bundles, Vol.2, 613-640, Hemisphere, New York.

ISSCWR7-2064

Oxidation model for construction materials in supercritical water – estimation of kinetic and transport parameters

Sami Penttilä[1], Iva Betova[2], Martin Bojinov[3], Petri Kinnunen[1], Aki Toivonen[1]

[1]VTT Materials and Building, Technical Research Centre of Finland, P.O. Box 1000, FIN-02044 VTT, Espoo, Finland
[2] Department of Chemistry, Technical University of Sofia, 1000 Sofia, Bulgaria
[3]Department of Physical Chemistry, University of Chemical Technology and Metallurgy, 1756 Sofia, Bulgaria

Abstract

In the present paper, the kinetic and transport parameters of inner and outer layer growth on two ODS (Oxide Dispersion Strengthened) alloys, PM2000 and MA956, is presented. Parameters are estimated using an upgraded model that assumes that the growth of the outer layer is governed by the transport of cations through the inner layer via an interstitialcy mechanism. The updated model is able to reproduce accurately the depth profiles of individual constituent elements in the inner and outer layers, as well as in the diffusion/transition layer of the alloy situated between the inner layer and the bulk substrate. As a result of the calculations, kinetic and transport parameters of inner and outer layer growth are estimated for oxidation times from 600 to 2000 h at 650 °C. The main conclusion that can be drawn from the calculations is that the most of the rate constants and also the diffusion coefficients tend to decrease with time of oxidation at a constant temperature.

1. Introduction

As part of the Generation IV International Forum (GIF), the Supercritical Water Reactor (SCWR) is a promising design operating at high core outlet temperature (between 500 and 650 °C depending on the design) above the critical point of water (374°C, 22.1 MPa). The use of a single phase coolant eliminates the need for components such as steam generators, steam separators, dryers, recirculation and jet pumps, and thus simplifies the design leading to much higher efficiency (ca. 45% vs. 33% of current Light Water Reactors) [1-3]. However, Supercritical Water (SCW) is expected to be more aggressive towards structural materials compared to conventional Light Water Reactors (LWR) and the performance of materials used as thin-walled components in this environment continues to be a challenge [4,5].

ODS (Oxide Dispersion Strengthened) materials are considered for many applications in the nuclear industry. They are potential structural materials for fusion reactors and Gen IV reactor concepts. Due to fact that ODS materials can sustain very high irradiation doses (200 dpa) and can operate at high temperature (up to 900 °C) they are also target material for fuel cladding in an SCWR. ODS F/M (ferritic/martensitic) steels exhibit a very low swelling under irradiation because of their body centered cubic structure but also excellent creep properties due to the nano-oxides present in the matrix. In the longer term, the experimental ODS alloys offer an

even higher potential, whereas high performance nickel-based alloys that are being considered for use in supercritical fossil-fired plants are less favorable for use in SCWR due to their high neutron absorption and associated swelling and embrittlement [6].

The main candidate construction materials considered for the SCWR are austenitic steels and nickel-based alloys, as well as ferritic/martensitic and ODS steels. ODS steels are extensively investigated in view of their resistance to irradiation embrittlement and their high temperature strength [7, 8]. However, data of ODS steels on corrosion resistance properties in SCW are limited. As the most critical issue for the application of ODS steels in SCW is to improve their corrosion resistance, experimental evaluation of such materials is urgently needed [9-12]. Thus in order to achieve lower oxidation rates, further structural material performance data have to be obtained and models need to be developed and validated for more demanding operating conditions.

The overall goal of the present paper is to estimate the parameters of inner and outer layer growth on construction materials exposed to SCW environments using an upgrade of a model used to predict the growth of ferritic and austenitic steels in high-temperature water conditions that has already been proposed and tested [13-18]. As a result of the calculations, kinetics of inner and outer growth and oxide layer restructuring, as well as modifications in the diffusion layer between the bulk substrate and the inner layer will be obtained and the model will be verified and validated for two ODS alloys – PM2000 and MA956.

2. Model description

According to the Mixed Conduction model (MCM) for passive films on construction materials and its adaptations to corrosion layers in high-temperature water environments [13-18], the growth of the inner layer of oxide proceeds via generation of normal cation positions and oxygen vacancies at the interface with the alloy:

$$M_m \xrightarrow{k_2} \frac{1}{3}\left[M_3O_4\right]\left(\frac{4}{3}V_O^{\bullet\bullet}\right)+\frac{8}{3}e' \qquad (1)$$

The Kroger-Vink notation is used throughout the present paper. The oxygen vacancies are then transported by diffusion-migration to the film / electrolyte interface where they are consumed by reaction with oxygen

$$\frac{1}{3}\left[M_3O_4\right]\left(\frac{4}{3}V_O^{\bullet\bullet}\right)+\frac{4}{3}H_2O \xrightarrow{k_4} \frac{1}{3}\left[M_3O_4\right]+\frac{8}{3}H^+ \quad (2)$$

In writing these reactions, it is assumed that the inner layer has a spinel structure. This assumption is verified a posteriori using X-ray diffraction analysis.

In parallel to that reaction, for materials with high chromium content, film growth can proceed via chromium cation transmission through the inner layer, involving generation of cation vacancies at the outer interface, their transport and consumption at the inner interface

$$1.5\mathrm{H_2O} \xrightarrow{k_{3Cr}} \frac{1}{2}\left[M_3O_4\right]\left(V_{Cr}^{'''}\right)+3H^+ \quad (3)$$

$$Cr_m+\frac{1}{2}\left[M_3O_4\right]\left(V_{Cr}^{'''}\right) \xrightarrow{k_{1Cr}} \frac{1}{2}\left[M_3O_4\right]+3e' \quad (4)$$

For alloys containing significant amounts of Al, such as ODS steels, it can be also considered that the growth of the inner layer is mediated by transfer of aluminum ions through the layer via a vacancy mechanism. Since this assumption would require a priori knowledge of the

distribution of chromium and aluminum in the tetrahedral positions of the spinel phase, it is considered somewhat premature at this stage of the modeling.

The other alloy constituents, e.g. Fe, Ni, Mn, Mo, etc., are assumed to be transferred through the inner layer via generation, transport and consumption of interstitial cations exchanged with normal cation sub-lattice sites (the so-called interstitialcy mechanism)

$$Fe \xrightarrow{k_{1Fe}} Fe_i^{\bullet\bullet}(IL) + v_m + 2e' \quad (5)$$

$$3Fe_i^{\bullet\bullet}(IL) + 4\mathrm{H_2O} \xrightarrow{k_{3Fe}} Fe_3O_4(OL) + 8\,\mathrm{H^+} + 2e' \quad (6)$$

where v_m is a vacancy in the metal. In the present treatment, it is assumed that the growth of the outer layer of oxide is due to direct reaction of interstitial cations with water and/or oxygen at the inner layer / outer layer interface layer, as recently proposed by Sloppy et al. [19] for the growth of bi-layer oxides on tantalum at ambient temperature and others [1-5, 13] for SCW oxidation of stainless steels. A simplified picture of the processes described above is presented in Fig. 1.

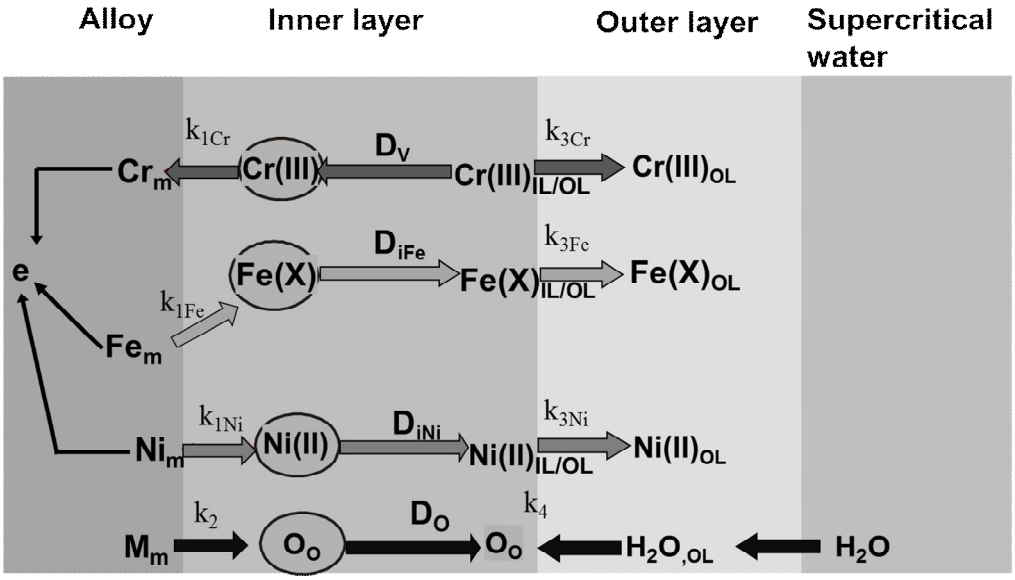

Figure 1 A simplified scheme of the growth of the inner and outer layers of the film formed on an Fe-Cr-Ni alloy according to the proposed approach. For details see text.

In order for film growth to take place under free corrosion conditions, a transfer of electrons through the inner layer to couple the oxidation of metal constituents with the reduction of water and dissolved oxygen is needed. Within the framework of the MCM, it is assumed that ionic point defects play the role of electron donors or acceptors [14], the electronic conduction being coupled to the transport of ionic defects.

During oxidation in the temperature range between 500-700 °C, in analogy to what has been proposed in subcritical LWR coolants at temperatures above 150 °C and also in SCW [14-18], the low-field approximation of the transport equation of Fromhold and Cook [20] is valid

$$J_j(x,t) = -D_{i,j}\frac{\partial c_j(x,t)}{\partial x} - \frac{XF\vec{E}}{RT}D_{i,j}c_j(x,t) \quad (7)$$

The electric field strength in the oxide is considered to be independent on distance within the oxide following previous treatments within the frames of the point defect and mixed-conduction models [14, 21]. The concentration c_j of a metallic oxide constituent j can be expressed as atomic fraction, $y_j = c_j V_{m,MO}$, where $V_{m,MO}$ is the molar volume of the phase in the layer, assumed to be equal to that of a spinel oxide (47 cm^3 mol^{-1}). Then the non-stationary transport

equations for a given component of the film (in this case, Fe, Cr, Ni, Mo, Cu, Si, Al and Mn) acquire the form:

$$\frac{\partial y_{Fe}}{\partial t} = D_O \frac{\partial^2 y_{Fe}}{\partial x^2} + \frac{XF\vec{E}D_O}{RT}\frac{\partial y_{Fe}}{\partial x},\ \frac{\partial y_{Cr}}{\partial t} = D_V \frac{\partial^2 y_{Cr}}{\partial x^2} + \frac{3F\vec{E}D_V}{RT}\frac{\partial y_{Cr}}{\partial x},\ \frac{\partial y_{Ni}}{\partial t} = D_O \frac{\partial^2 y_{Ni}}{\partial x^2} + \frac{2F\vec{E}D_O}{RT}\frac{\partial y_{Ni}}{\partial x},$$
$$\frac{\partial y_{Mn}}{\partial t} = D_O \frac{\partial^2 y_{Mn}}{\partial x^2} + \frac{2F\vec{E}D_O}{RT}\frac{\partial y_{Mn}}{\partial x},\ \frac{\partial y_{Si}}{\partial t} = D_O \frac{\partial^2 y_{Si}}{\partial x^2} + \frac{4F\vec{E}D_O}{RT}\frac{\partial y_{Si}}{\partial x},\ \frac{\partial y_{Mo}}{\partial t} = D_O \frac{\partial^2 y_{Mo}}{\partial x^2} + \frac{4F\vec{E}D_O}{RT}\frac{\partial y_{Mo}}{\partial x} \quad (8)$$
$$\frac{\partial y_{Cu}}{\partial t} = D_O \frac{\partial^2 y_{Cu}}{\partial x^2} + \frac{2F\vec{E}D_O}{RT}\frac{\partial y_{Cu}}{\partial x},\ \frac{\partial y_{Al}}{\partial t} = D_O \frac{\partial^2 y_{Al}}{\partial x^2} + \frac{3F\vec{E}D_O}{RT}\frac{\partial y_{Al}}{\partial x}$$

where *X* stands for the nominal valence of Fe in the oxide (assumed to be 2.67 as in magnetite).

The atomic fractions at the alloy / film interface are taken as initial and boundary conditions

$$y_{Fe}(x,0) = y_{Fe,a}, y_{Cr}(x,0) = y_{Cr,a}, y_{Ni}(x,0) = y_{Ni,a}, y_{Mn}(x,0) = y_{Mn,a},$$
$$y_{Si}(x,0) = y_{\mathrm{Si},a}, y_{Cu}(x,0) = y_{Cu,a}, y_{Mo}(x,0) = y_{Mo,a},\ y_{Al}(x,0) = y_{Al,a}$$
$$y_{Fe}(0,t) = y_{Fe,a}, y_{Cr}(0,t) = y_{Cr,a}, y_{Ni}(0,t) = y_{Ni,a}, y_{Mn}(0,t) = y_{Mn,a}, \quad (9)$$
$$y_{Si}(0,t) = y_{\mathrm{Si},a}, y_{Cu}(0,t) = y_{Cu,a}, y_{Mo}(0,t) = y_{Mo,a},\ y_{Al}(0,t) = y_{Al,a}$$

The boundary conditions at the inner layer / outer layer interface are given by the concentrations of metallic constituents, obtained from the steady-state solution of the transport equations of the type of (7) [15-18]:

$$y_{Fe}(L_i,t) = \frac{k_{1Fe}y_{Fe,a}V_{m,MO}}{k_4},\ y_{Cr}(L_i,t) = 2 - k_{3Cr}V_{m,MO}\left(\frac{1}{k_{1Cr}y_{Cr,a}} + \frac{RT}{3F\vec{E}D_{Cr}}\right)$$
$$y_{Ni}(L_i,t) = \frac{k_{1Ni}y_{Ni,a}V_{m,MO}}{k_4},\ y_{Mn}(L_i,t) = \frac{k_{1Mn}y_{Mn,a}V_{m,MO}}{k_4}, y_{Ti}(L_i,t) = \frac{k_{1Ti}y_{Ti,a}V_{m,MO}}{k_4}, \quad (10)$$
$$y_{Cu}(L_i,t) = \frac{k_{1Cu}y_{Cu,a}V_{m,MO}}{k_4}, y_{Al}(L_i,t) = \frac{k_{1Al}y_{Al,a}V_{m,MO}}{k_4}, y_{Nb}(L_i,t) = \frac{k_{1Nb}y_{Nb,a}V_{m,MO}}{k_4}$$

In the equations labelled (10), x = 0 is located at the alloy / film interface and x = L_i at the inner layer / outer layer interface, L_i being the inner layer thickness. The concentration of chromium cations is determined by subtracting the concentration of chromium cation vacancies at that interface from the maximum occupancy of tetrahedral sites in the cation sub-lattice of a spinel oxide. To obtain the compositional profiles in the inner layer, the system of equations (8) is solved subject to the initial and boundary conditions (9) and (10) using a Crank-Nicholson method [22].

Further, a growth law proposed in both the PDM and MCM [15-17] and previously employed to predict oxide film growth on austenitic materials in nuclear power plant coolants has been adopted for the inner layer:

$$L_i(t) = L_i(t=0) + \frac{1}{b}\ln\left[1 + V_{m,MO}k_2 b e^{-bL_i(t=0)}t\right],\ b = \frac{3\alpha_2 F\vec{E}}{RT} \quad (11)$$

For the outer layer, a new growth law was derived under the assumption that it is formed via the reaction of interstitial cations transported through the inner layer with water. A model for the growth of bi-layer films proposed by Sloppy et al. [19] was used as a starting point and a following result was obtained

$$L_o(t) = \frac{(k_{1,Fe}y_{Fe,a} + k_{1,Ni}y_{Ni,a} + k_{1,Si}y_{Si,a} + k_{1,Mn}y_{\mathrm{Mn},a} + k_{1,\mathrm{Mo}}y_{Mo,a} + k_{1,Cu}y_{\mathrm{Cu},a} + k_{1,Al}y_{Al,a})}{k_2}(L_i(t) - L_i(t=0)) \quad (12)$$

Then in order to calculate the compositional profiles in the outer layer, a system of equations analogous to (10) except for Cr:

$$\frac{\partial y_{Fe}}{\partial t} = D_i\frac{\partial^2 y_{Fe}}{\partial x^2} + \frac{XF\vec{E}D_i}{RT}\frac{\partial y_{Fe}}{\partial x},\ \frac{\partial y_{Cr}}{\partial t} = D_i\frac{\partial^2 y_{Cr}}{\partial x^2} + \frac{3F\vec{E}D_i}{RT}\frac{\partial y_{Cr}}{\partial x},\frac{\partial y_{Ni}}{\partial t} = D_i\frac{\partial^2 y_{Ni}}{\partial x^2} + \frac{2F\vec{E}D_i}{RT}\frac{\partial y_{Ni}}{\partial x},$$
$$\frac{\partial y_{Mn}}{\partial t} = D_i\frac{\partial^2 y_{Mn}}{\partial x^2} + \frac{2F\vec{E}D_i}{RT}\frac{\partial y_{Mn}}{\partial x},\ \frac{\partial y_{Si}}{\partial t} = D_i\frac{\partial^2 y_{Si}}{\partial x^2} + \frac{4F\vec{E}D_i}{RT}\frac{\partial y_{Si}}{\partial x},\ \frac{\partial y_{Mo}}{\partial t} = D_i\frac{\partial^2 y_{Mo}}{\partial x^2} + \frac{4F\vec{E}D_i}{RT}\frac{\partial y_{Mo}}{\partial x},$$
$$\frac{\partial y_{Cu}}{\partial t} = D_i\frac{\partial^2 y_{Cu}}{\partial x^2} + \frac{2F\vec{E}D_i}{RT}\frac{\partial y_{Cu}}{\partial x},\ \frac{\partial y_{Al}}{\partial t} = D_i\frac{\partial^2 y_{Al}}{\partial x^2} + \frac{3F\vec{E}D_i}{RT}\frac{\partial y_{Al}}{\partial x} \quad (13)$$

is solved with the following boundary conditions at the outer layer / water interface

$$y_{Fe}(L_o,t) = \frac{k_{1Fe}y_{Fe,a}V_{m,MO}}{k_{3iFe}},\ y_{Cr}(L_o,t) = \frac{k_{1Cr}y_{\mathrm{Cr},a}}{k_{3iCr}},\ y_{Ni}(L_o,t) = \frac{k_{1Ni}y_{Ni,a}V_{m,MO}}{k_{3iNi}},$$
$$y_{Mn}(L_o,t) = \frac{k_{1Mn}y_{Mn,a}V_{m,MO}}{k_{3iMn}},\ y_{Ti}(L_o,t) = \frac{k_{1Ti}y_{Ti,a}V_{m,MO}}{k_{3iTi}}, y_{Cu}(L_o,t) = \frac{k_{1Cu}y_{Cu,a}V_{m,MO}}{k_{3iCu}}, \quad (14)$$
$$y_{Al}(L_o,t) = \frac{k_{1Al}y_{Al,a}V_{m,MO}}{k_{3iAl}}, y_{Nb}(L_o,t) = \frac{k_{1Nb}y_{Nb,a}V_{m,MO}}{k_{3iNb}}$$

The expression for the concentration of Cr at the outer layer / water interface differs from the others due to the fact that the stoichiometry of reactions (4) and (5) is different. The boundary conditions at the inner interface of the outer layer are identical to those used as outer boundary conditions at the inner layer / electrolyte interface, which ensures the continuity of the composition of the film.

At this stage of the modeling, the effect of the physicochemical and associated electrical properties of the solvent (SCW) is not taken into account. Since these properties may have a significant impact on the rate constants at the inner layer/SCW interface and hence on the structure and composition of the outer layer, as pointed out in a recent review [23], the inclusion of these effects in a refined version of the model is planned as a future step.

Finally, a procedure to estimate the diffusion coefficients in the modified metallic phase adjacent to the inner layer (sometimes called the diffusion or transition layer) is proposed. The transport of individual alloy constituents from the bulk of the alloy to the interface is treated as non-stationary diffusion [24-26]:

$$\frac{\partial y_{Fe,DL}}{\partial t} = D_{v,FeDL}\frac{\partial^2 y_{Fe,DL}}{\partial x^2},\ \frac{\partial y_{Cr,DL}}{\partial t} = D_{\mathrm{v},CrDL}\frac{\partial^2 y_{Cr,DL}}{\partial x^2},\frac{\partial y_{Ni,DL}}{\partial t} = D_{\mathrm{v},NiDL}\frac{\partial^2 y_{Ni,DL}}{\partial x^2},$$
$$\frac{\partial y_{Mn,DL}}{\partial t} = D_{v,MnDL}\frac{\partial^2 y_{Mn,DL}}{\partial x^2},\frac{\partial y_{\mathrm{Si},DL}}{\partial t} = D_{v,SiDL}\frac{\partial^2 y_{Si,DL}}{\partial x^2},\frac{\partial y_{\mathrm{Ti},DL}}{\partial t} = D_{v,\mathrm{TiDL}}\frac{\partial^2 y_{Ti,DL}}{\partial x^2}, \quad (15)$$
$$\frac{\partial y_{\mathrm{Nb},DL}}{\partial t} = D_{\mathrm{v},NbDL}\frac{\partial^2 y_{\mathrm{Nb},DL}}{\partial x^2},\frac{\partial y_{Cu,DL}}{\partial t} = D_{\mathrm{v},CuDL}\frac{\partial^2 y_{\mathrm{Cu},DL}}{\partial x^2},\frac{\partial y_{\mathrm{Al},DL}}{\partial t} = D_{v,\mathrm{AlDL}}\frac{\partial^2 y_{Al,DL}}{\partial x^2}$$

For the sake of simplicity, only a vacancy mechanism of diffusion for the constituents is considered. The boundary conditions are set by the concentrations of respective constituents at the alloy / inner layer interface (the sink interface) $y_{i,a}$ and the concentrations in the bulk alloy, $y_{i,DL}$, as follows:

$$\begin{aligned}
&y_{Fe}(x,0) = y_{Fe,DL}, y_{Cr}(x,0) = y_{Cr,DL}, y_{Ni}(x,0) = y_{Ni,DL}, y_{Mn}(x,0) = y_{Mn,DL},\\
&y_{Si}(x,0) = y_{\mathrm{Si},DL}, y_{Cu}(x,0) = y_{Cu,DL}, y_{Ti}(x,0) = y_{Ti,DL}, y_{Nb}(x,0) = y_{Nb,DL},\\
&y_{Fe}(0,t) = y_{Fe,DL}, y_{Cr}(0,t) = y_{Cr,DL}, y_{Ni}(0,t) = y_{Ni,DL}, y_{Mn}(0,t) = y_{Mn,DL},\\
&y_{Si}(0,t) = y_{\mathrm{Si},DL}, y_{Cu}(0,t) = y_{Cu,DL}, y_{Ti}(0,t) = y_{Ti,DL}, y_{Nb}(0,\mathrm{t}) = y_{Nb,DL},\\
&y_{Fe}(L_D,t) = y_{Fe,a}, y_{Cr}(L_D,t) = y_{Cr,a}, y_{Ni}(L_D,t) = y_{Ni,a}, y_{Mn}(L_D,t) = y_{Mn,a},\\
&y_{Si}(L_D,t) = y_{Si,a}, y_{Cr}(L_D,t) = y_{Cu,a}, y_{Ti}(L_D,t) = y_{\mathrm{Ti},a}, y_{Nb}(L_D,t) = y_{Nb,a},
\end{aligned} \tag{16}$$

In the above notation, L_D is the penetration depth of the diffusion layer that can be deduced from the analytical solution of the diffusion equations in a thin layer limit as

$$L_D = 2\sqrt{\sum_i y_{i,DL} D_{i,DL} t} \tag{17}$$

3. Experimental

The test coupons were first machined (plane-milled) using new cutting tools to the dimensions of 25 x 15 x 5 mm and were left in the as-milled state. The composition of the two materials at a depth of 10 µm as estimated by Glow Discharge Optical Emission Spectroscopy (GDOES) is given in Table 1. The samples were exposed to SCW at 650 °C/25MPa in an autoclave connected to a recirculation water loop. The test conditions that were controlled and monitored included temperature, pressure, inlet and outlet water conductivity, dissolved oxygen content and flow rate. The dissolved oxygen content was maintained at 150 ppb and the inlet conductivity below 0.1 µS cm^{-1}. In general, three coupons per material were initially placed into the autoclave on a holder rack using electrically insulating ZrO_2 washers. One coupon at a time was removed after 600, 1000 and 2000 h of exposure.

Table 1 Actual composition of the studied materials at a depth of 10 µm as estimated by GDOES (wt %).

Material	Fe	C	Mn	Si	Cr	Ni	Mo	Cu	Ti	Al
MA956	74.2	0.009	0.11	0.001	20.7	0.03	0.01	0.03	0.29	4.5
PM2000	70.1	0.010	0.04	0.013	22.2	0.03	0.02	0.03	0.40	7.3

The samples were weighed before and after each test period, using a Mettler AT261 scale with a measuring uncertainty of ± 0.002%. The mass change per unit area was calculated using coupon dimensions measured before testing. Cross-sections of the samples were mechanically polished and inspected using scanning electron microscopy (SEM) to estimate the oxide layer thickness. In-depth composition profiles were obtained by GDOES on an area of about 5 mm^2, using a GDA 750 instrument with a polychromator of 750 mm focal length and a grating of 2400 grooves/mm. Since the measurement area is comparable by order of magnitude to the sample area, the profiles can be considered as average compositions. The spectrometer was calibrated by a sputtering rate corrected calibration method using certified reference materials. For the

simulation of the depth profiles of metallic elements, the respective non-steady state differential equations were solved by using Maple software.

4. Results and discussion

4.1 Composition and thickness of the oxides

In order to compare the experimental data for the studied material to the proposed model outlined in the model description section, the weight percent compositional profiles obtained by GDOES were recalculated to atomic fractions using the respective atomic weights of the constituent elements. The atomic fractions vs. depth for the studied materials are shown in Fig. 2 (2000 h). The differences between the positions of the metal / film interface estimated from sigmoid fits to the oxygen and major metallic constituent profiles were in general smaller than 15%. The respective average positions (or equivalently, oxide layer thicknesses) are also shown in the figures with vertical lines. The layer thicknesses do not increase significantly with time of exposure, in accordance to general kinetic expectations. It is worth mentioning that the circulating water in the autoclave system typically contains corrosion products introduced from the loop surfaces and/or released by test samples. In the studied samples a 0.05-0.1 µm thick contamination layer was typically observed containing impurities such as C, Si etc. In the subsequent comparison with model calculations, the thickness of this layer was subtracted (see below).

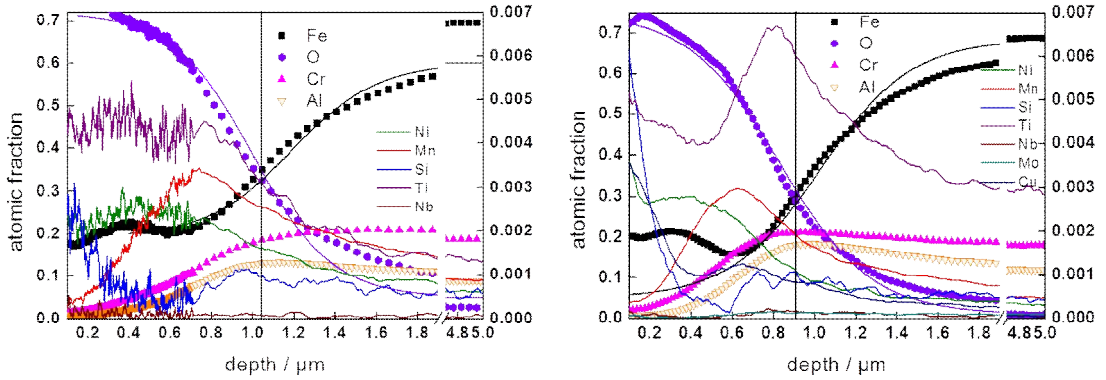

Figure 2 Atomic fractions of oxide constituents vs. depth on MA956 (left) and PM2000 (right) oxidized for 2000 h at 650 °C. Left – major constituents, right – minor constituents. Sigmoid fits to determine the position of the alloy/oxide interface are shown as vertical solid lines.

4.2 Comparison of model calculations with experimental data

In analogy to our previous papers [13-18], the profiles were recalculated to represent the fractions of the metallic constituents normalized to the total concentration of metallic constituents and represented vs. the distance from the alloy / oxide interface as estimated in the previous section. The comparisons between the experimental and calculated profiles as depending on material type and exposure time are presented in Fig. 3.

Since the present calculation method does not make use of a non-linear least square fitting procedure, in order to estimate the confidence intervals of the respective parameters, a sensitivity study was performed for each depth profile in accordance to what has been reported earlier for oxides both in light water reactor coolants [17] and in SCW [13]. For the purpose, the respective values of the kinetic constants and diffusion coefficients found to give best match to the experimental profiles were changed by ± 10% and the resulting profiles were also compared to the experimental data. As an example, the results of such a sensitivity study for the oxide formed on MA956 are shown in Figure 4 and demonstrate that the confidence intervals (or in

other words, the deviations of the values that cause the profile to deviate in a fashion more significant than the experimental error) for the rate constants and diffusion coefficients for the main alloy constituents are close to ±10%. This sensitivity study allowed us to define the parameters which most strongly affect the compositional profiles, namely, the rate constants at the alloy / inner layer interface, the rate constant of generation of chromium vacancies at the inner layer / water interface and the diffusion coefficients of point defects in the inner layer. In what follows, a discussion on the influence of alloy composition and time of exposure on these parameters is presented.

On the overall, the sets of kinetic constants were found to be rather homogeneous, indicating the validity of the model approach for the studied systems. Another point worth noting is that most of the rate constants and also the diffusion coefficients tend to decrease with time of oxidation. This trend is illustrated in Figure 5 for the rate constants and Figure 6 for the diffusion coefficients. The decrease of the rate constant values could indicate that the steady-state is not established at the interfaces even at such comparatively long oxidation times. Another possibility is that not all experimental features are taken into account in the present version of the model, such as the role of Al in the inner layer growth and the effect of solvent on the outer layer growth, as discussed already above.

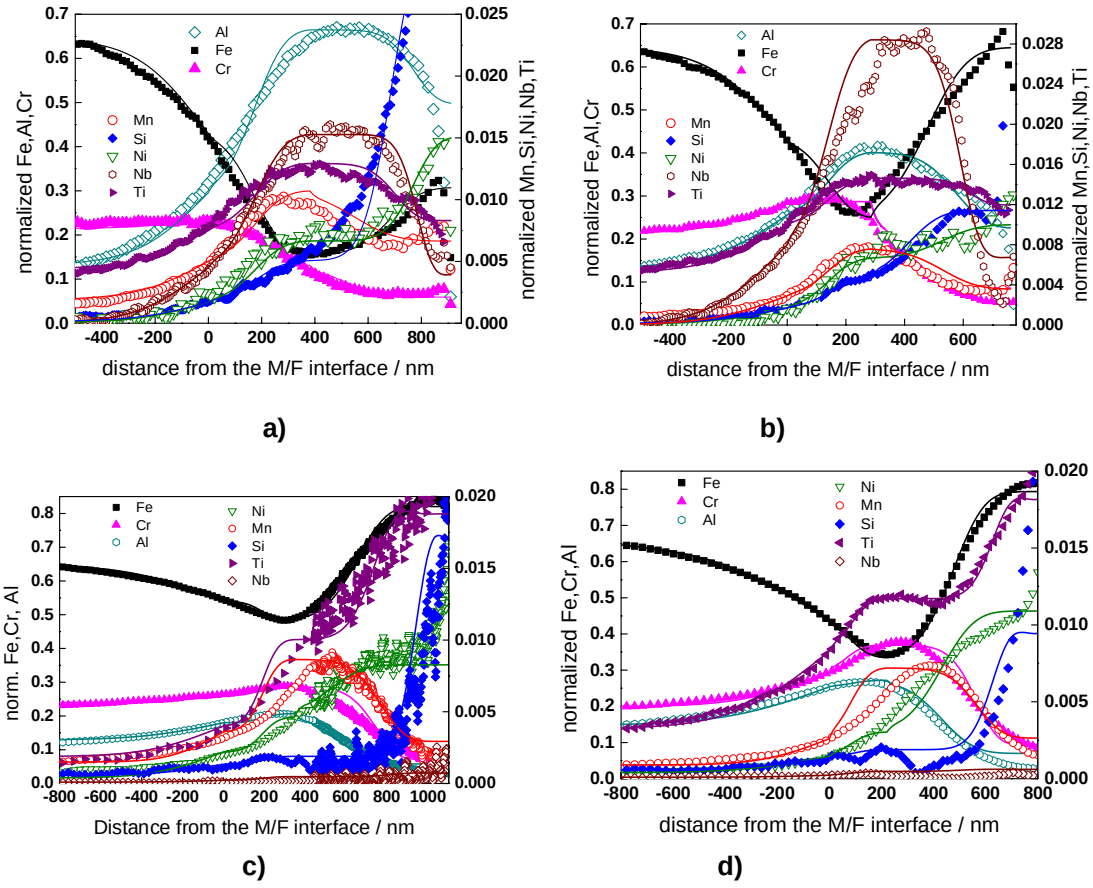

Figure 3 Comparison between the experimental (points) and calculated according to the model procedure (solid lines) fractions of metallic constituents at 650 °C (Fe, Cr, Al, Ni, Mn, Si, Ti and Nb) in the oxide formed on a) MA956 for 600 h, b) PM2000 for 600 h c) MA956 for 2000 h and d) MA956 for 2000 h.

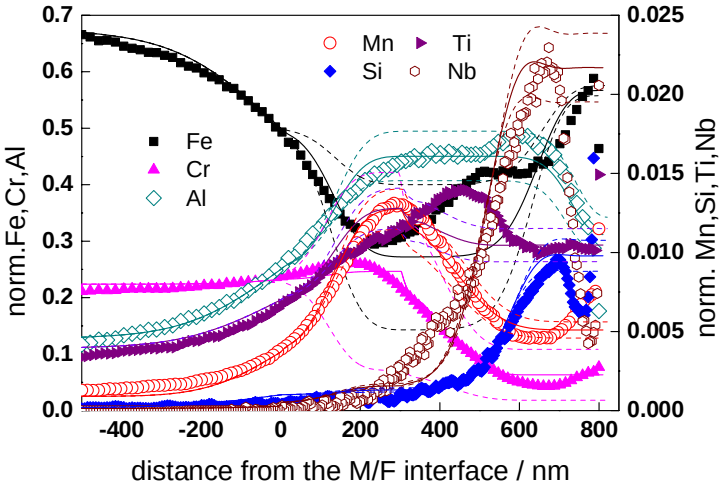

Figure 4 Sensitivity study of the rate constants of oxidation at the alloy/inner layer interface (k_{1Fe}, k_{1Cr}, k_{1Al}, k_{1Mn}, k_{1Si}, k_{1Nb}, k_{1Ti} and k_2) as well as the rate constant of production of trivalent chromium vacancies (k_{3Cr}) for the oxide formed on MA956 for 1000 h. Dashed lines represent variation of the respective parameters with 10%, respectively.

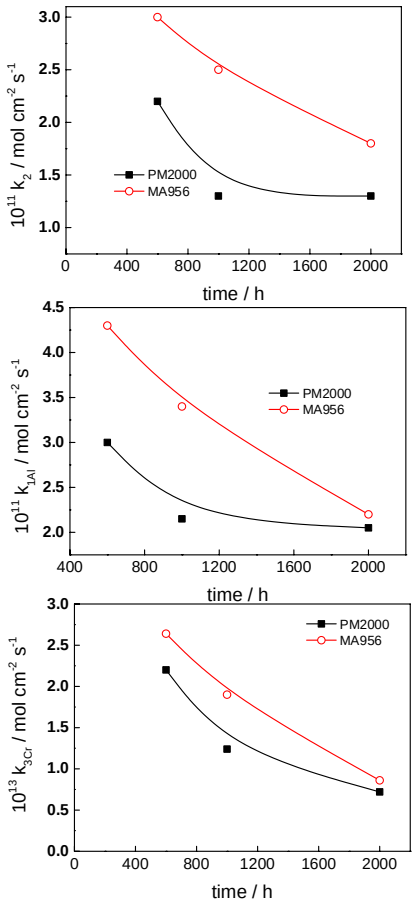

Figure 5 Rate constants of inner layer growth, aluminium oxidation and generation of chromium cation vacancies expressed vs. time of exposure.

Finally, the thicknesses of the oxides calculated by the upgraded model as depending on alloy type and exposure time are compared to the thicknesses estimated from the experimental GDOES depth profiles in Figure 7. The experimental thicknesses were corrected by subtracting 0.05 -0.1 µm of contamination layer. The calculated values obtained for the oxide film thicknesses were in a good agreement with the GDOES analyses results. The good correspondence between the two sets of values furnishes additional proof for the validity of the proposed approach.

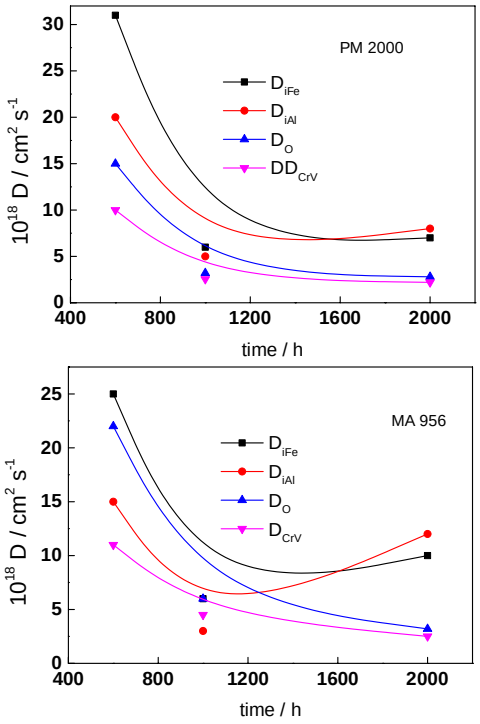

Figure 6 Diffusion coefficients of main constituents of the oxide on PM2000 (top) and MA956 (bottom) expressed vs. time of exposure.

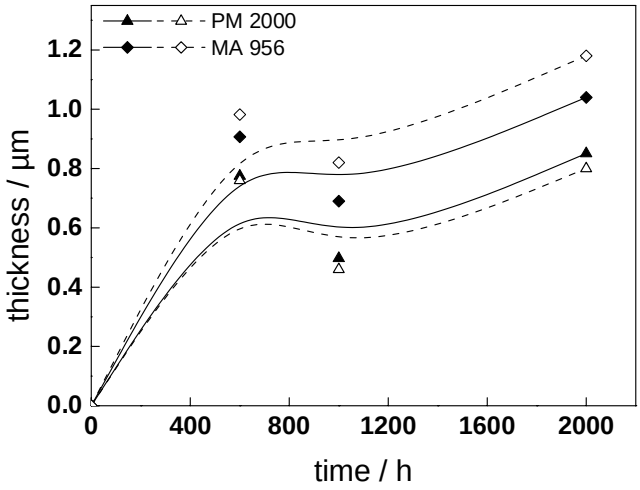

Figure 7 Comparison between the oxide thicknesses calculated from the model (open symbols) and the thicknesses estimated from the experimental GDOES depth profiles (closed symbols). Experimental thicknesses corrected by subtracting 0.05…-0.1 µm of contamination layer.

5. Conclusions

In the present paper, an upgraded model for the growth of bi-layer oxide was successfully employed to reproduce compositional profiles for both major and minor constituents of the corrosion layers on two ODS alloys – MA956 and PM2000 - after 600, 1000 and 2000 h of exposure in supercritical water at 650 °C. Furthermore, the model was able to reproduce also the evolution of the atomic fractions of all constituents in the transition layer situated between the inner layer of oxide and the bulk alloy substrate. The following conclusions can be drawn from the kinetic and transport parameter values obtained as a function of oxidation time.

Most of the rate constants and also the diffusion coefficients tend to decrease with time of oxidation at a constant temperature. Concerning the values of the rate constants, this might be related to the fact that the steady-state approximation that is used for the boundary conditions at the interfaces is not entirely valid for 600 h of oxidation. Another possibility is that not all experimental features are taken into account in the present version of the model, such as the role of Al in the inner layer growth and the effect of solvent on the outer layer. Concerning the diffusion coefficients, in order to explain the effect of film aging on its properties, the effect of microstructure should be considered. Preliminary calculations using a simplified model that aspires to take into account the evolution of the oxide microstructure during growth has been performed and will be published in the near future.

In general, the diffusion coefficients of interstitial cations in the inner layer are the largest, whereas the diffusion coefficients of oxygen and Cr vacancies the smallest, which is in accordance with the fact that the outer layer of oxide grows by the transport of cations through the inner layer most probably via an interstitialcy mechanism. MA956 showed the highest diffusion coefficient of Al after 2000 h of exposure indicating high rate of dissolution of this element from the outer oxide. This could be due to the dissolution of aluminum oxide from the scale at longer oxidation times in SCW.

Acknowledgements –The authors gratefully acknowledge the financial support of this work by the Academy of Finland project IDEA (Interactive modelling of fuel cladding degradation mechanisms).

References

1. T. R. Allen, Y. Chen, X. Ren, K. Sridharan, L. Tan, G.S. Was, E. West, D. Guzonas, Material Performance in Supercritical Water, in Comprehensive Nuclear Materials, Vol. 5, T.R. Allen, R.E. Stoller, S. Yamanaka, Eds., Elsevier, 2012, chapter 5.12, 280-326.
2. G.S. Was, P. Ampornrat, G. Gupta, S. Teysseyre, E.A. West, T.R. Allen, K. Sridharan, L. Tan, Y. Chen, X. Ren, C. Pister, Corrosion and stress corrosion cracking in supercritical water, J. Nucl. Mater. 371 (2007) 176–201.
3. L. Tan, T.R. Allen, Y. Yang, Corrosion behavior of alloy 800H (Fe–21Cr–32Ni) in supercritical water, Corros. Sci. 53 (2) (2011) 703–711.
4. L. Tan, X. Ren, K. Sridharan, T.R. Allen, Corrosion behavior of Ni-base alloys for advanced high temperature water-cooled nuclear plants, Corros. Sci. 50 (2008) 3056–3062.
5. S. Yesodharan, Supercritical water oxidation: an environmentally safe method for the disposal of organic wastes, Curr. Sci. 82 (2002) 1112–1122.
6. Technology Roadmap Update for Generation IV Nuclear Energy Systems, January 2014, Issued by the OECD Nuclear Energy Agency for the Generation IV International Forum, https://www.gen-4.org
7. S. Ukai, M. Harada, H. Okada, M. Inoue, S. Nomura, S. Shikakura, K. Asabe, T.

Nishida, M. Fujiwara, Alloying design of oxide dispersion strengthened ferritic steel for long life FBRs core materials, J. Nucl. Mater. 204 (1993) 65–73.
8. S. Ukai, M. Harada, H. Okada, M. Inoue, S. Nomura, S. Shikakura, T. Nishida, M. Fujiwara, K. Sabe, Tube manufacturing and mechanical properties of oxide dispersion strengthened ferritic steel, J. Nucl. Mater. 204 (1993) 74–80.
9. H.S. Cho, A. Kimura, Corrosion resistance of high-Cr oxide dispersion strengthened ferritic steels in super-critical pressurized water, J. Nucl.Mater. 367–370 (2007) 1180–1184.
10. T. Kaito, T. Narita, S. Ukai, High temperature oxidation behavior of ODS steels, J. Nucl. Mater. 329–333 (2004) 1388–1392.
11. H.S. Cho, H. Ohkubo, N. Iwata, Improvement of compatibility of advanced ferritic steels with super critical pressurized water toward a higher thermally efficient water-cooled blanket system, Fusion Eng. Des. 81 (2006) 1071–1076.
12. H.S. Cho, A. Kimura, S. Ukai, M. Fujiwara, Corrosion properties of oxide dispersion strengthened steels in supercritical water environment, J. Nucl. Mater. 329–333 (2004) 387–391.
13. S. Penttilä, I. Betova, M. Bojinov, P. Kinnunen, A. Toivonen, Estimation of kinetic parameters of the corrosion layer constituents on steels in supercritical water coolant conditions, Corros. Sci. 53 (2011) 4193–4203.
14. M. Bojinov, P. Kinnunen, K. Lundgren, G. Wikmark, A Mixed-Conduction Model for the Oxidation of Stainless Steel in a High-temperature Electrolyte. Estimation of kinetic parameters of oxide layer growth and restructuring, J. Electrochem. Soc. 152 (2005) B250-B261.
15. M. Bojinov, A. Galtayries, P. Kinnunen, A. Machet, P. Marcus, Estimation of the parameters of oxide film growth on nickel-based alloys in high-temperature water electrolytes, Electrochim. Acta 52 (2007) 7475–7483.
16. I. Betova, M. Bojinov, P. Kinnunen, K. Lundgren, T. Saario, Mixed-Conduction Model for Stainless Steel in a High-Temperature Electrolyte: Estimation of Kinetic Parameters of Inner Layer Constituents, J. Electrochem. Soc. 155 (2008) C81-C92.
17. I. Betova, M. Bojinov, P. Kinnunen, K. Lundgren, T. Saario, Influence of Zn on the oxide layer on AISI 316L(NG) stainless steel in simulated pressurized water reactor coolant, Electrochim. Acta 54 (2009)1056-1069.
18. I. Betova, M. Bojinov, V. Karastoyanov, P. Kinnunen, T. Saario, Effect of water chemistry on the oxide film on Alloy 690 during simulated hot functional testing of a pressurised water reactor, Corros. Sci.58 (2012) 20–32.
19. J.D. Sloppy, Z. Lu, E.C. Dickey, D.D. Macdonald, Growth mechanism of anodic tantalum pentoxide formed in phosphoric acid, Electrochim. Acta 87(2013)82-91.
20. A.T. Fromhold Jr., E. L. Cook, Diffusion currents in large electric fields for discrete lattices, J. Appl. Phys. 38 (1967)1546-1551.
21. D.D. Macdonald, The Passive State in Our Reactive Metals-Based Civilization, Arab J. Sci.Eng. 37 (2012) 1143–1185.
22. J. Crank, P. Nicolson, A practical method for numerical evaluation of solutions of partial differential equations of the heat conduction type, Proc. Camb. Phil. Soc. 43 (1947) 50-61.
23. D.A. Guzonas and W.G. Cook, Cycle Chemistry and Its Effect on Materials in a Supercritical Water-Cooled Reactor: A Synthesis of Current Understanding, Corrosion Science, 65 (2012) 48-66.
24. K. Leistner, C. Toulemonde, B. Diawara, A. Seyeux, Oxide Film Growth kinetics on Metals and Alloys Part II, J of The Electrochemical Society 160 (6) (2013) C197-C205.
25. T.R. Allen, J.T. Busby, G.S. Was, E.A. Kenik, On the mechanism of radiation-induced segregation in austenitic Fe–Cr–Ni alloys, J. Nucl. Mater. 255(1998)44-58.
26. K. Fukuya. K. Fujii, A Multicomponent Model of Radiation-induced Segregation for Commercial Stainless Steels, J. Nucl. Sci. Technol. 46(2009)744-752.
27. I. Betova, M. Bojinov, P. Kinnunen, V. Lehtovuori, S. Peltonen, S. Penttilä, T. Saario, Composition, Structure, and Properties of Corrosion Layers on Ferritic and Austenitic Steels in Ultrasupercritical Water, J. Electrochem. Soc. 153 (2006) B464-B473.

28. I. Betova, M. Bojinov, P. Kinnunen, S. Penttilä, T. Saario, Surface film electrochemistry of austenitic stainless steel and its main constituents in supercritical water. J. Supercritical Fluids 43 (2007) 333-340.
29. J.H. Lee, R. Kasada, A. Kimura, T. Okuda, M. Inoue, S. Ukai, S. Ohnuki, T. Fujisawa, F. Abe, Influence of alloy composition and temperature on corrosion behavior of ODS ferritic steels, J. Nucl. Mater. 417 (2011) 1225.

ISSCWR7-2065

Design of an in-pile SCWR fuel qualification test loop

Ales Vojacek[1], Mariana Ruzickova[1], Thomas Schulenberg[2]
[1]Research Centre Rez, Czech Republic
[2]KIT, Germany
ales.vojacek@ujv.cz
mariana.ruzickova@cvrez.cz
schulenberg@kit.edu

Abstract

In the development of the supercritical water cooled reactor (SCWR), an in-pile fuel assembly test loop has been designed within the framework of the joint Chinese-European project, called SCWR-FQT (Fuel Qualification Test). This paper presents basic design of the loop with its auxiliary and safety systems, which has been examined in detail by thermal hydraulic analyses in order to achieve operation of the loop above the thermodynamic critical point of water (374 °C, 22.1 MPa) and checked by stress analyses to assure safe operation.

The designed experimental loop for fuel qualification in supercritical water consists of a closed pressurized water circuit with forced circulation of the coolant through the test section – the active channel which is intended to be installed into the existing research pool type reactor LVR-15.

The active channel will be operated at temperatures and pressures, which are typical for the High Performance Light Water Reactor (HPLWR). A thick-walled pressure tube made from austenitic stainless steel able to withstand the high system pressure, encloses the active channel. It contains four fuel rods with UO_2 (enrichment of 19.7% U235) with a total heating power of ~64 kW and a recuperator in order to achieve hot channel conditions as they are expected to occur in the evaporator of the HPLWR. The internal flow is realized so as to prevent the creep condition of the pressure tube. An internal U-tube cooler serves as heat sink and is connected to the secondary circuit. The entire active channel is isolated from water of the reactor pool by an air gap between the pressure tube and an aluminum displacer. The test section with fuel is connected to a 300°C closed loop and to a primary pump located outside the reactor building as well as safety systems and auxiliary systems such as purification and measurement circuits, which are all connected with the primary circuit.

1. Introduction

The interest in the development of innovative supercritical water cooled reactor (SCWR) is high. This comes mostly from high thermal efficiencies (44-45%), compact containment (no steam generators) and compact turbines (high steam enthalpy drop) which results in a promising competitive nuclear concept of Generation-IV. Apart from Europe, Canada continues to invest in research for the design of a pressure tube SCWR, Japan supports research and development of innovative SCWR designs, and China and the Russian Federation recently joined GIF for SCWR development.

Attractive plant net efficiency > 44% however does not come for free. There are challenges which need to be overcome. One important issue is validation of codes predictions. Several system codes such as APROS and ATHLET are able to simulate fast transients in supercritical

water, e.g. a depressurization from supercritical to sub-critical conditions, but models have not been validated yet. Deteriorated heat transfer, which occurs at a high ratio of heat flux to mass flux, which is typical for the SCWR design concept at conditions near the pseudo-critical line, remains an unresolved issue. All numerical codes fail still to predict temperatures of the heated wall for such conditions. Moreover, there are not sufficient experimental data available for validation. Data for heat transfer in tubes and annuli are available, but reliable data for rod bundles are still required. Thus, conducting new experiments for a complex data library are indispensable for further SCWR development.

Therefore, new information and data are planned to be obtained through a fuel qualification test in a research reactor. The test facility was designed within the 4-year project called "Supercritical Water Reactor Fuel Qualification Test" (SCWR-FQT) executed between 2011 and 2014. The SCWR-FQT project was a joint EU-China project. The European part aimed to work out the design, analyses and a pre-operational safety report of the loop with a small scale fuel assembly built in the LVR-15 research reactor. The Chinese project contributed with out-of-pile experiments with the same test section geometry, but electrically heated. The scope of this paper is to describe the final design of the SCWR-FQT experimental loop.

2. Characteristic of the SCWR-FQT loop

2.1 General description

The designed experimental loop for fuel qualification in supercritical water consists of a closed pressurized water circuit with forced circulation of the coolant through the test section – the active channel which is intended to be inserted into the existing research pool type reactor LVR-15. The initial boundary conditions, especially the size, i.e. the number and dimensions of the fuel rods of the active channel, are given by the possibilities and constraints of the research reactor LVR-15 in Rez, Czech Republic.

The active channel will be operated at temperatures and pressures, which are typical for the High Performance Light Water Reactor (HPLWR) [1]. A thick-walled pressure tube made from austenitic steel 08Ch18N10T, able to withstand the high system pressure, encloses the active channel. It contains four fuel rods with a total heating power of 63 kW and a recuperator in order to achieve hot channel conditions as they are expected to occur in the evaporator of the HPLWR. An internal flow of coolant is preventing creep conditions of the pressure tube. An internal U-tube cooler, which is connected to the secondary circuit, serves as a heat sink. The entire active channel is isolated from water of the reactor pool by an air gap between pressure tube and aluminum displacer. The test section with fuel is connected by a 300°C closed loop with a primary pump located outside the reactor building as well as with safety systems and auxiliary systems such as purification and measurement circuits. In the first phase of the project, a pre-conceptual design of the test facility was carried out.

2.2 Operational conditions

The intended operational conditions and design limits are listed as general design requirements in Table 1. Maximum temperature conditions are a consequence of the selected materials, which must be qualified for such nuclear application and which must be available today. This constraint had sorted out some advanced material options for the first test runs.

The maximum power and the γ-power are a consequence of the chosen enrichment of the test fuel rods and of the available neutron flux in the reactor core. The coolant mass flow is simulating hot channel conditions of an evaporator fuel assembly of the HPLWR.

Table 1. Operational conditions of theSCWR-FQT loop.

a)	Nominal working pressure (measured at inlet to the active channel)	25 MPa
b)	Max. working pressure (at the suction of main circulation pump HCC*)	30 MPa
c)	Max. working cladding temperature of fuel rods during normal operation	450°C
d)	Max. allowed cladding temperature of fuel rods during normal operation	550°C
e)	Nominal working temperature at inlet of the active channel	300°C
f)	Max. working temperature at inlet of the active channel	380°C
g)	Nominal working temperature at outlet of the active channel	300°C
h)	Max. working temperature at outlet of the active channel	380°C
i)	Nominal thermal power of 4 fuel rods	63.6 kW
j)	γ – heat power	9.8 kW
k)	Nominal thermal power of U-tube cooler inside the active channel when inlet temperature of the U-tube cooler ~ 200°C and outlet temperature ~ 235°C and flow rate of the secondary circuit ~1800 kg/h	72 kW
l)	Nominal thermal power of the cooler CH-1 when closed by-pass and inlet temperature of the CH-1 ~ 235°C and outlet temperature ~ 200°C and flow rate of the secondary circuit ~1800 kg/h	72 kW
m)	Nominal flow rate of the active channel	900 kg/h
n)	Coolant of the primary circuit	demineralized water (water chemistry adjustable)
o)	Total mass of coolant in the primary circuit of the SCWR-FQT loop (including approx. 39 dm^3 stored in pressurizer KO-1 and approx. 5 dm^3 in cooling side of the main circulation pump HCC)	65 m^3

* HCC – is a Czech abbreviation of main circulation pump (“Hlavni Cirkulacni Cerpadlo”)

3. Description of main systems

3.1 Loop lay-out

Mechanical parts of the SCWR-FQT loop are assembled in 2 blocks with dimensions 3x3.5x2.5 m. These 2 blocks are placed on top of each other on a platform and are situated in the newly built hall – 211/12. Inlet and outlet lines of the primary system are running inside a shielded duct through the reactor building to the primary block situated in this hall adjacent to the reactor hall. Maintenance and control of the upper block is possible from the platform. The active channel is inserted in the reactor LVR-15. The overall model of SCWR-FQT is shown in **Figure 1**.

All active parts of the loop are situated in the lower block no. 1-“Primary block”, listed as follows:

- Primary circuit
- Safety system (including depressurization system)
- H_2 treatment system
- Purification system of primary circuit
- Measurement system of primary circuit up to mechanical filter MF-2
- Hot part of the sampling system

Systems situated in the lower block n. 2-“Secondary block” include:

- Secondary circuit
- Tertiary circuit
- Water chemistry system and dosing system of primary coolant
- Cold part of the measurement system of primary circuit
- Cold part of the sampling system
- Main parts of the draining system

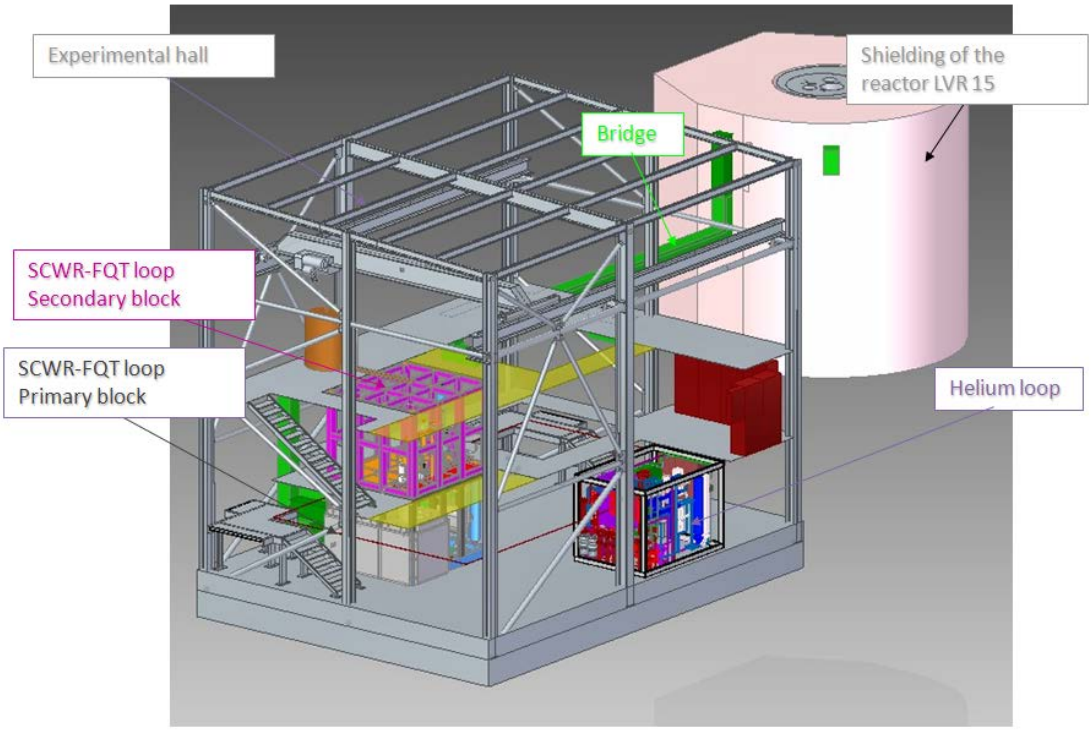

Figure 1. Overall model of SCWR-FQT facility.

3.2 Primary circuit – general description

The technological scheme of the primary circuit is marked in red in **Figure 2**.

The primary circuit ensures that the required thermal physical conditions are achieved around the fuel rods located in the active channel. Hence, temperature, pressure and flow rate of the primary coolant are measured.

The circulation of the coolant in the primary circuit is provided by the main circulation pump HCC with a head of 60 m at a frequency of 50 Hz and a flow rate of 900 kg/h (at 300°C, 25 MPa). The flow is controlled by the change of rotational speed of the pump. An orifice in the primary circuit is measuring the flow rate of the primary coolant.

The design coolant temperature around the fuel rods of the SCWR-FQT loop is 385°C – 450°C. In order to achieve such conditions, while maintaining the temperature entering the active channel during normal operation as low as 300°C to ensure safe operation of the primary circulation pump HCC, a recuperator is installed in the active channel. Temperature of the stainless steel pressure tube at high pressure conditions must be kept below the safety limits of the material, i.e. around 450°C. To achieve it, internal structures guiding the flow are inserted in the active channel. Therefore the first downward flow after the inlet into the active channel provides cooling of the pressure tube from inside.

An internal U-tube cooler is installed in the active channel to keep the outlet temperature at 300°C. In the rest of the primary circuit, connecting the active channel with the main circulation pump HCC, the temperature is kept constant at 300°C. During start-up, and before the reactor LVR – 15 is started, the primary circuit is gradually heated up to ~ 300°C by the U-tube cooler which transfers the heat from the secondary circuit generated by an electric heater EO-1.

The required pressure in the primary circuit is controlled by pressurizers, to compensate thermal expansion of the coolant when heated, and by supply pumps. The pressure in the circuit is kept constant through control of volume changes, which are induced by changes of temperature provided by pressurizers KO-1 and by supply pumps. The pressurizer is a bladder type accumulator, which is filled with nitrogen. The initial filling pressure of nitrogen is ~ 9 MPa at 20°C. The nominal pressure of 25 MPa in the loop is then provided by heating up the loop. Depressurization of the primary circuit is enabled either by on-line discharging through the sampling system or by fast opening of valves, which allows for the coolant to flow to the depressurization tank BN.

Over-pressure protection is ensured by a pressure relief valve with its opening at a pressure of 32 MPa. Discharged coolant flows to the depressurization tank BN, where generated steam condenses. Non-condensable gases are directed from the depressurization tank to the special venting system. All devices and pipes are made of stainless steel.

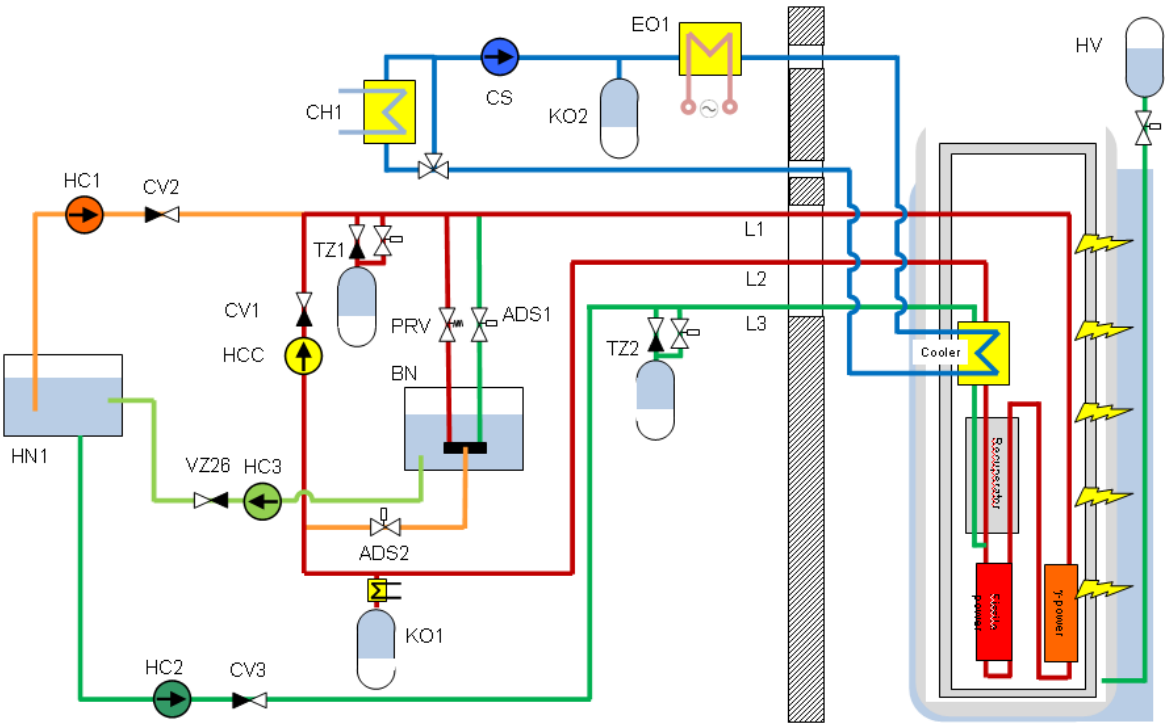

Figure 2. Technological scheme of the SCWR-FQT facility.

3.2.1 The active channel

Design of the active channel is limited by the following constraints:

- Space limitation in the reactor core of LVR-15;
- Material availability for pressure tube certified for nuclear use;
- Thermo-physical properties in pseudo-critical region;
- Nuclear safety.

The active channel is manufactured from stainless steel 08Ch18N10T, for which the temperature limit, if used for pressure boundary tubes, is around 450°C. Nominal temperature

around the fuel elements of the SCWR-FQT loop is 385°C – 450°C. The active channel contains four fuel rods with a total heating power of ~63.8 kW. The fuel rods (see **Figure 3**) will contain pellets of UO_2 (enrichment of 19.7% U235) on a total height of 600 mm inserted in a stainless steel tubing 8x0.5 mm. The cladding shall be filled with helium gas (required pressure approx. 7 MPa) and seal-welded on both ends. A spiral wire of 1.44 mm diameter shall be wrapped along the rod with 200 mm pitch and welded to both end caps. Above the fuel pellets a gas plenum with 40 mm height is situated to maintain space for fission gases generated inside the fuel rod during irradiation. In the gas plenum a spring shall be placed to compensate the temperature induced dilatation of the fuel which is expected to be greater than that of the cladding tube. Thus the plenum height will decrease as the spring will be gradually compressed by the expanding fuel.

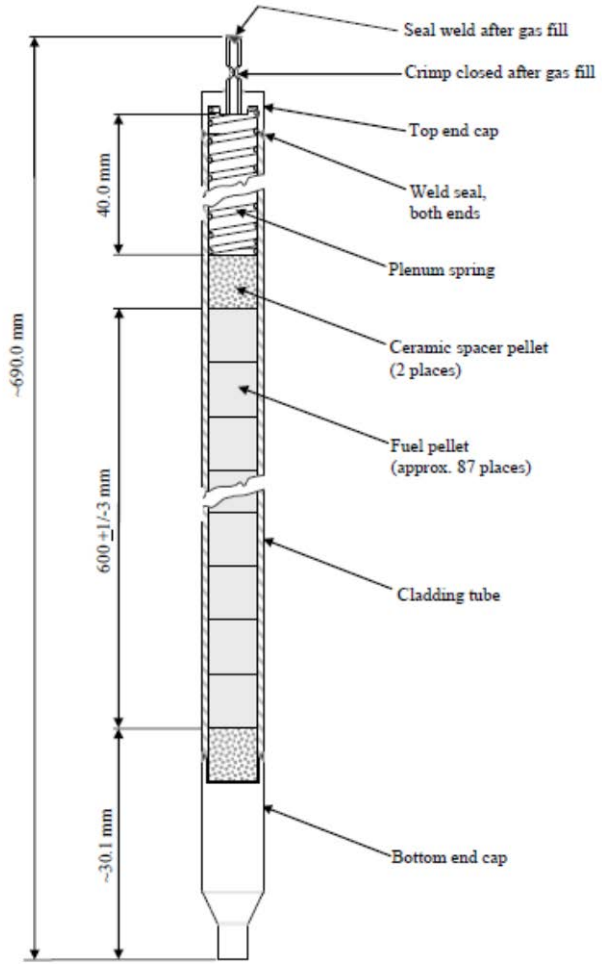

Figure 3. Drawing of the SCWR-FQT fuel rod.

Above the fuel assembly a recuperator is placed to achieve hot channel conditions as they are expected to occur in the evaporator of the HPLWR. The internal flow is preventing creep conditions of the pressure tube, which would occur at around 450°C.

The total mass flow rate at inlet of the active channel is guided down along the pressure tube and cools down the pressure tube, in which γ-heat is generated. After turning around at the bottom of the pressure tube, water flows upwards by passing the internal structures to the top of the active channel. At the top, the flow turns down and enters the shell side of the recuperator. In the core region, the coolant flows around the test section with the fuel rods located at the

bottom of the active channel. Underneath the fuel rods, the flow is turned around at the bottom and enters the test section, cooling the fuel rods.

CFD calculations performed by BME and NRG [2] revealed stagnant areas at the corners of the fuel assembly box right above the bottom support of the fuel rods, causing local hot spots of the fuel claddings. Different geometries of the bottom plate were designed to eliminate these areas. The bottom plate design shown in **Figure 3** could eliminate the large eddies at the inlet of the fuel assembly, which occurred with the initial flat plate design. Therefore, this wing design was finally recommended.
Furthermore, 2 new designs of spacers (supports) of the rods had been proposed; and CFD calculations were repeated at BME with the new fuel assembly geometries. It was found that the design of the spacer with open corners, as shown in **Figure 4**, significantly reduces the temperature peaks of the cladding appearing in the corners behind the spacers. Therefore, this design of the spacer was used in the final design.

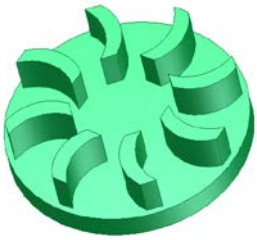

Figure 4. Bottom plate (wing design).

Figure 5. Spacer (support) of the fuel assembly.

The fuel rods are constrained axially by these spacers and radially by wire wraps. To allow for compensation of the different thermal expansion of wire and cladding, 50 disk springs placed on top of each other were designed. In order to place the disk springs in the top part of the fuel rods, the top plug had to be redesigned as shown in **Figure 5**, where the whole expansion mechanism is sketched as well.

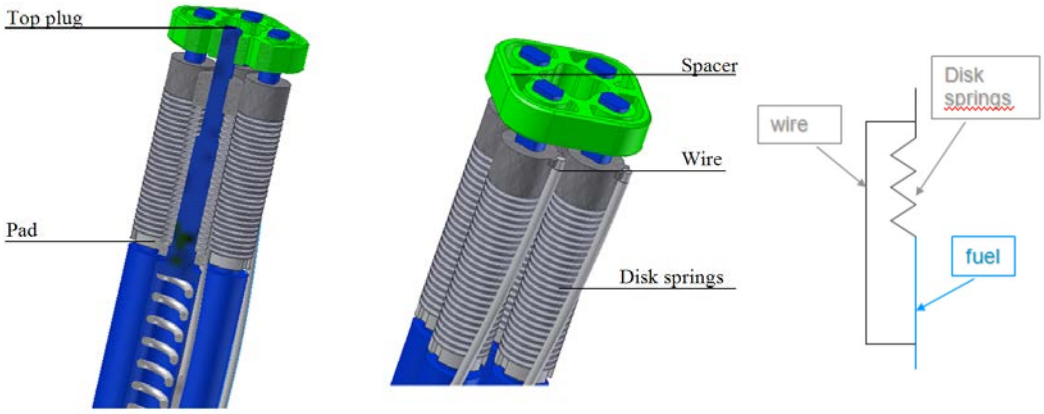

Figure 6. Top part of the fuel assembly with disc springs and sketch of the compensation mechanism (right).

The assembly is designed such that it presses the disk springs during operation when the cladding is hotter than the wire. During manufacturing of the fuel rods, particularly when adding the wire wrap, it is important to install the wire wrap tightly. Therefore, a pad (see **Figure 5**)

enables to adjust the vertical position of the disk springs, ensuring that the wire will be tight before fixing (welding) it to the top endings. A tight wire minimizes the risk of possible fretting of the fuel cladding. For the first test series to be performed, the available stainless steel 316L, qualified for reactor applications, shall be used for fuel claddings, which implies that the peak cladding temperature must be kept below 550°C under normal operating conditions. The material of the disk springs, the end plugs and the wire is from 316L as well to mitigate possible negative interaction.

In the test section, the coolant reaches the required test temperature of 385°C – 450°C. Each fuel rod has its own wire wrap around it and each wire is also in contact with the other two neighbouring rods. Above the fuel assembly, water enters the tube side of the recuperator, where it is cooled down. Above the recuperator, water is further cooled down in the U-tube cooler to outlet temperature which is equivalent to the inlet temperature. The coolant of the primary circuit is on the shell side, and coolant of the secondary circuit is on the tube side. After the U-tube cooler, water leaves the active channel through the headpiece. An emergency tube is placed in the central part of the active channel, passing from the head through the recuperator to the top of the test section. During emergency cases, water is lead from the pressurizers TZ through the emergency tube and cools down the fuel rods. The principle flow distribution in the active channel can be seen in **Figure 6**.

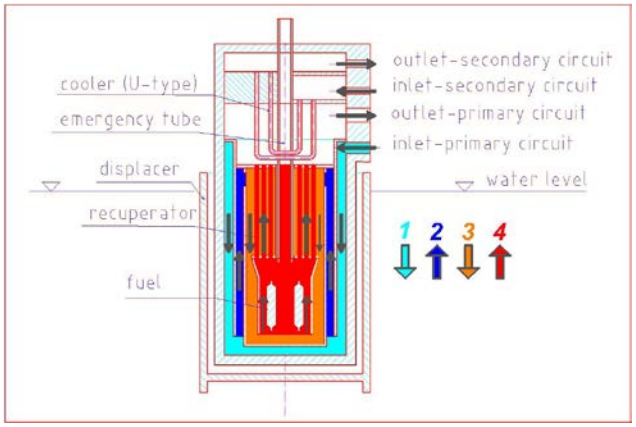

Figure 7. Flow distribution in the active channel.

A spherical bottom piece and a headpiece are welded to the pressure tube. The headpiece consists of 3 head parts, as shown in **Figure 7**. The primary circuit piping is connected to the head part 1 by flanges. The emergency tube, U-tube cooler and instrumentation pass through the head part 1. Finally, it also enables to carry the internal structures.

The active channel occupies one cell of the active zone of the reactor. This determines the actual space limitation for maximum dimensions of the pressure tube. The entire active channel is inserted in an aluminum displacer, which determines its position in the grid of the active zone of the reactor LVR-15. The aluminum displacer assembly consists of an aluminum tube ϕ70x3 mm, to which the actual displacer with a shape identical to an ordinary fuel assembly of the reactor LVR-15 is welded. Grooves are machined at the bottom of the aluminum displacer, which enable the displacer to be placed in its position in the active zone of the reactor. The entire active channel with its wall temperature in the active zone of up to 400°C is isolated from the colder water of the reactor pool with 50°C by an air gap of 3.5 mm between pressure tube and aluminum displacer. The air gap prevents the reactor water from boiling on the outer side of the aluminum displacer.

The length of the active channel with the aluminum displacer is determined by the level of the reactor water, by the height of the reactor lid and by the sufficient space for mounting and dismounting operations. The maximum height from the active core to the bottom of the reactor lid is approximately 5500 mm. From the head part 1 between inlet and outlet of the primary circuit, tube 1 (the most external tube with dimensions ϕ36x1.5 mm) is hanging down, to which all other internal structures including the fuel assembly are fixed. Tube 1 allows for thermal expansion by about 16.5 mm with respect to the pressure tube.

According to fast depressurization analyses performed with APROS [4] as mentioned earlier in the text, high pressure differences across the thin-walled guide tubes may arise during fast depressurization. The most critical of all the guide tubes was Tube 1 inside the cooler section, which faces the highest pressure differences.

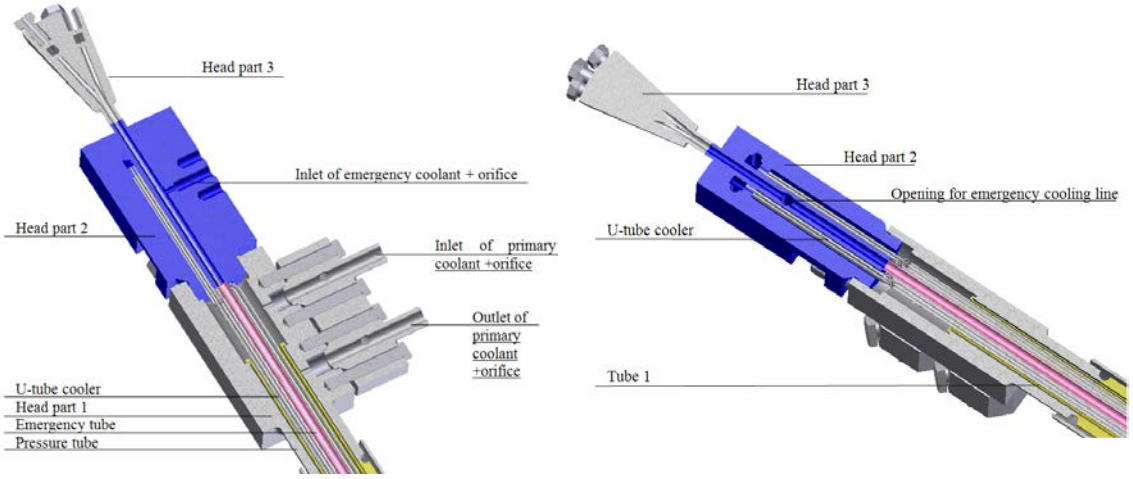

Figure 8. Cross section of the headpiece.

However, the design is such to prevent buckling of internal structures. Tube 2 with dimensions ϕ30x0.75 mm is closed at its bottom to separate the flows from each other. There are 4 openings in Tube 2 in the top section, which enable the flow to enter the shell side of the recuperator. The recuperator consists of 30 ϕ3x0.2 mm tubes closed by the tube sheets on each end and held by 18 spacers, which are distributed equally along the total length of 3.7 m of the recuperator. The segments are mutually turned by 120°. Thus, a spiral flow is created to enhance heat transfer and thermal efficiency.

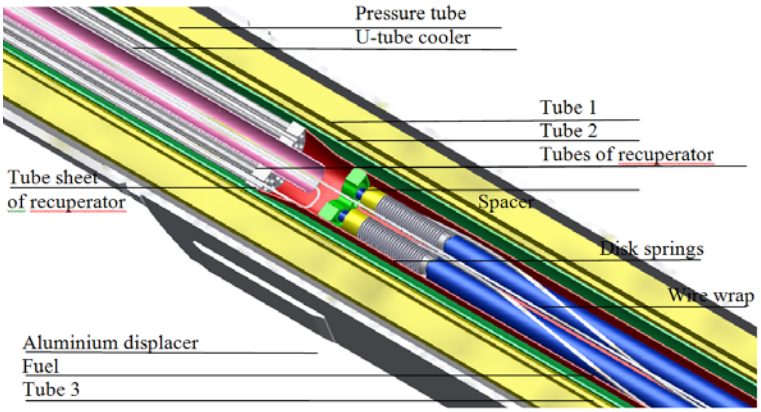

Figure 9. Cross section of the middle part of the active channel.

The emergency tube is terminated right above the fuel assembly so that the fuel assembly can be flooded in case of emergency (see **Figure 8**). Certain tubes of the recuperator will be blinded to serve as guide tubes for thermocouples. Several thermocouples are planned to pass through the emergency tube as well.

The U-tube cooler is placed above the recuperator. Primary water passes on the shell side of the U-tube cooler. The constructional length of the U-tube cooler is approx. 585 mm. However, the effective length of the U-tube cooler, where most of the heat is exchanged, is around 400 mm. Primary water leaves the active channel through the ϕ22 mm opening in the head part 1.

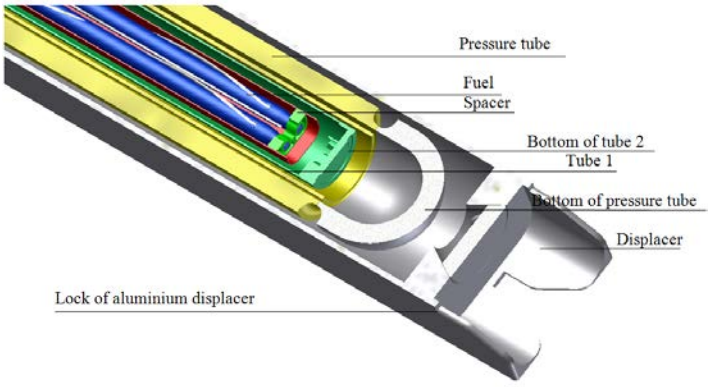

Figure 10. Cross section of the bottom part of the active channel.

3.3 Safety system

The technological scheme of the safety system is marked in dark green, light green and orange in **Figure 2**. Since the SCWR-FQT loop includes nuclear fuel, a safety system of the test loop is unconditionally needed. The elementary principle of nuclear safety is defense-in-depth. Defense-in-depth is in principle multiple, redundant, and independent layers of safety systems. The aim is to reduce the risk that a single failure of a critical system could cause release of radioactive material. The structure of the fuel itself, the fuel claddings and the high pressure system form the first, second and the third barrier, respectively, against release of radioactive material. The reactor building of the LVR-15 test reactor acts as the fourth barrier. In an experimental nuclear facility, the reactor building serves as containment, although it is not constructed as leak tight. Instead, the shielded bridge and the hall with primary block are kept below atmospheric pressure by active ventilation (at -20 Pa). It was checked in [4] that the active ventilation system can keep the pressure inside the experimental hall at sub-atmospheric conditions even during a large break LOCA, so that any activation of the primary coolant prior to the accident will be kept inside the building. Therefore, leakage of activity potentially present in the SCWR-FQT loop to the outside environment is prevented. The safety systems are described in more detail in [3, 4].

3.4 Auxiliary systems

3.4.1 Purification system

The purification system maintains the desired chemical parameters of primary water. Maintaining these parameters at required level is secured by continuous filtration of water, which passes through filters connected by a bypass to HCC and uses a pressure gradient generated by the pump. Recovered water is gradually cooled in economizer RV-2 and cooler CH-4 from 300°C to 40°C; then it passes through mechanical filter MF-1 to 4 ionex filters IF-1 connected in parallel. In case of accidents, there are 2 additional ionex filters parallel to the 2

standard ionex filters used for normal operation. The volume of the filtering medium (monospheric nuclear grade mixbed) is designed as 1 dm^3 (for 1 filter) with a height of 0,85 m. The filtration speed is expected to be 15 m/h for nominal flowrate 30 kg/h.

3.4.2 On-line measurement system

The system provides continuous control of chemical and physical properties of primary water. Depending on the required type of measurement, the system must enable installation of appropriate measuring probes as well as to provide sufficient cooling and pressure reduction for their operation. The measuring probes are installed for measurement of conductivity and H_2 and O_2 concentration. Dissolved gasses, mostly H_2 or O_2, are released from water when the pressure of water declines (behind reduction valve in venting device). From there they are drawn off by an air vent machine to a recombining chamber, where they are diluted by air flow to non-explosive concentration.

3.4.3 Secondary system

The technological scheme of the secondary system is marked in blue in **Figure 2**. The secondary circuit is used for heat removal from the primary circuit. Heat transfer to the secondary circuit is realized in the U-tube cooler situated in the top part of the active channel. Heat transfer from the secondary circuit to the tertiary circuit is realized via cooler CH-1. The system is pressurized to 25 MPa (pressurizer KO-2 similar to KO-1) since it remains on high temperatures (200-235°C) to mitigate boiling. The nominal flow rate is designed for 1800 kg/h and is maintained by a pump CS-1 (similar to primary pump). There is an electric heater EO-1 (maximum power 50kW) which heats up the secondary circuit, which then transfers heat to the primary circuit (during start-up operation). During normal operation the electric heater is switched off. During shut down, the electric heater may be employed to prevent thermal shocks during fast shut down. Normal start-up and shut down of SCWR-FQT loop is described in detail in [5].

4. Conclusion

This paper presents the final design of SCWR-FQT loop. All necessary analyses have been performed. To summarize, 1D thermal hydraulic analysis [5] proved that the loop is capable of safe start-up, shut-down and operation at nominal conditions (25 MPa, 385°C – 450°C around fuel rods). Further, the stress analyses proved that the strength in the primary system of the SCWR-FQT loop and in-pile components for design conditions are kept within the limits for normal operation according to Czech standards for nuclear facilities NTD A.S.I.The safety analyses [4] performed with system codes (APROS, ATHLET) confirmed effective cooling of the fuel rods during design basis accidents. It can be concluded that the analyses demonstrated that the design of SCWR-FQT is safe and robust.

References

1. A. Vojáček. *Design of the Active channel of the SCWR-FQT loop*: Master thesis. Prague: Czech Technical University, 2009.

2. D.C. Visser, A. Shams, A. Kiss, T. Vágó, A. Vojacek, O. Frybort, “WP2 Analyses of normal operation ”, SCWR-FQT, Contract Number: 2669908, Petten, The Netherlands, December 4, 2013.

3. R. Schneider, M. Schlagenhaufer, T. Schulenberg, “Conceptual design of the safety system for a SCWR fuel qualification test”, NUTHOS-08, Shanghai, China, October 10-14, 2010.

4. Thomas Schulenberg, Xu Cheng Xiaojing Liu, Chong Zhou, Manuel Raqué, Tobias Zeiger, Ales Vojacek, “E3.3 - Analysed of design basis accidents“, SCWR-FQT, Contract Number: 2669908, KIT - Karlsruhe, January 1, 2014.

5. A. Vojacek, G. Mazzini, Analysed of the start-up and shut-down of SCWR Fuel qualification test, “*Proceedings of the 22nd International Conference on Nuclear Engineering ICONE22”,* July 7-11, 2014, Prague, Czech Republic.

6. A.Vojacek, “WP1 Interim report after year 1”, SCWR-FQT, Contract Number: 2669908, Prague, Czech Republic, May 28, 2012.

The Multi-peak Phenomenon of Heat Transfer Deterioration At Supercritical Pressure in The Vertical Upward Tubes

Xianliang Lei , Huixiong Li, Weiqiang Zhang, Qian Zhang, Liangxing Li
State Key Laboratory of Multiphase Flow in Power Engineering, Xi'an Jiaotong University
No.28 West Xian-Ning Road, Xi'an 710049, China
xianlianglei@mail.xjtu.edu.cn Tel: +86-29-82665870 Fax: +86-29-82669033

ABSTRACT

Recently, supercritical pressure water-cooled reactors (SCWRs), as one of the six most promising reactor concepts accepted in the Generation IV International Forum (GIF) with high efficiency and its economic advantages, is rapidly developed. Flow and heat transfer of supercritical water becomes more and more important for both the systematic design and operation safety of the related facilities. Heat transfer characteristics are especially significant among all of issues for the SCWRs. It has been found that in the extreme heating conditions or accident cases (i.e. q/G>0.6 for water), the wall temperatures of vertical upward tubes exhibit multi-peak wall temperature phenomenon in regions of $T_b<T_{pc}<T_w$, which can be verified from Shitsman and Jackson's experimental test. However, so far the special multi-peak result has not been pay much attention due to less data and difficulty of experiments. Hence, in the present study, numerical investigation was carried out to investigate the characteristics of HTD multi-peak phenomenon of supercritical pressure water/carbon dioxide at high q/G conditions. The results show that the higher of heat fluxes, the more temperature peaks may appear and the flow stability becomes weak. Besides, the mechanism of multi-peak heat transfer deterioration is given through quantitatively analyzing the distribution of flow parameters and thermophysical properties in the near-wall region.

1 Introduction

Nuclear energy has increasingly been considered as a key power generation technology in recent years, especially China has been formally joined the group of Supercritical-Water-Cooled Reactors (SCWRs) in 2014, which is an most perspective reactor types in the next generation nuclear energy systems at Generation IV International Forum (GIF-IV). SCWRs is the only Gen-IV type using light water as coolant, the concepts is similar to existing power reactor, where the concept of design methods and operation safety can be obtained from the existing water cooled reactors and supercritical fossil fuel plant. SCWRs operates above the thermodynamic critical point of water (22.1MPa, 374 ˚C), make the system significant simplified and promote thermal efficiency exceed 44%, which is better than the current Light Water Reactors (LWRs) with 34% efficiency.

In SCWRs, thermal-hydraulics and safety is always an important issue, especially after the Fukushima accident. Due to the steep variation of thermal-physical properties in pseudocritical point, the heat transfer behaviors are different with it. According to the review of Pioro [1], there are divided into three modes of heat transfer for supercritical fluids according to the discrepancy of heat transfer coefficient, i.e. normal heat transfer, heat transfer enhancement (THE), heat transfer deterioration (HTD). These heat transfer modes are also depicted in the literature of Jackson and Hall[2].

Many studies for heat transfer of supercritical pressures fluid have been conducted since 1950s'.

Comprehensive literature reviews of supercritical water and carbon dioxide are reported by Cheng [3], Pioro and Duffey [1]. In the aspect of experiment, Yamagata et al. [4] studied the heat transfer phenomenon of supercritical water flowing in a circular tube in the broader parameters, and they found that HTE appears when the bulk enthalpy was less than the pseudo-critical bulk enthalpy. Adebiyi et al. [5] investigated the heat transfer of supercritical and subcritical pressure CO_2 flowing through a uniformly heated 22.14 mm I.D. horizontal tube and Song et al. [6] explored the criterion on the similarity of heat transfer of supercritical fluid flow in vertical pipes at different diameters by performing comparative experiments, a similar conclusion are obtained for enhanced heat transfer. Coincidentally, the occurrence condition of HTD is also similar, according to viewpoint of Shiralkar and Griffith [7], Shitsmann [8], that is, at high heat fluxes, deteriorated heat transfer occurred when the bulk fluid temperature was below while the wall temperature was above the pseudo-critical temperature.

From existing literatures, an interesting phenomenon has been observed from the experimental data of Shitsman [8] in a 8 mm diameter tube under the heat flux of 396kg/m^{2}s, mass flux of 449kW/m^2, as shown in Figure 1. In this case, the heat transfer deterioration happened twice, two peaks can be discovered from his experimental data. However, the author has not focus on it and not given more explanation.

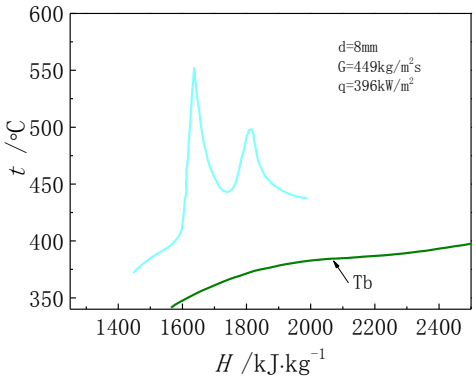

Figure 1 Experimental result of heat transfer deterioration（from Shitsman[8]）

Similarly, the experimental data of carbon dioxide obtained by Jackson also show the interesting results [9-11], as shown in Figure 2. However, scholars are ignored the special two-peak and multi-peak deterioration phenomenon.

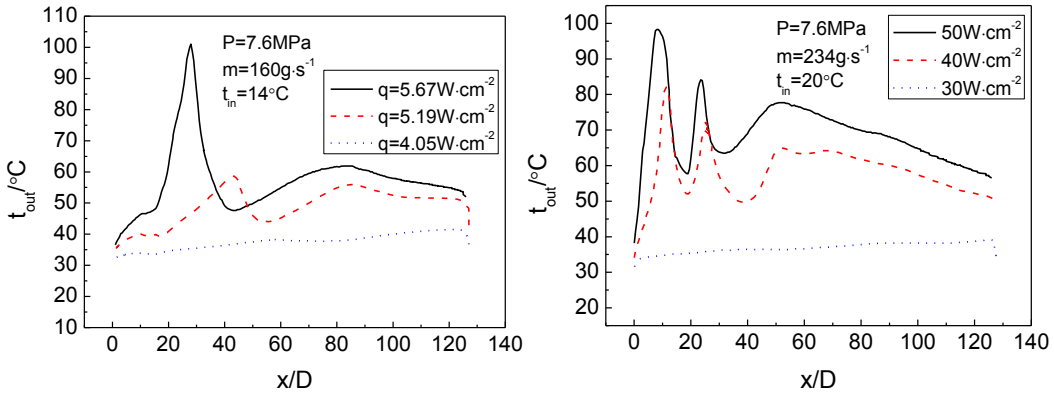

(a) One-peak temperature (b) two-peak temperature

Figure 2 Result of heat transfer deterioration（from Jackson[11]）

Meanwhile, with the rapid development of advancement computer technology, Computational Fluid Dynamics (CFD) increasingly play a key role in the nuclear reactor design and safety analysis, many scholars focus on the thermal-hydraulic behavior of supercritical fluid in reactor coolant system by using CFD tools. Bae et al. [12] studied the effects of large density variation on strongly heated internal air flows, demonstrated that their DNS (Direct Numerical Simulation) for mixed convection showed good agreement with the experimental data for mean velocity, turbulence intensity obtained by Shehata & McEligot. Koshizuka et al. (1995) [13] performed a 2-D numerical analysis on the HTD in a vertical pipe with supercritical water flowing upward with Jones-Launder k-ε turbulence model, and he divided the mechanism of HTD into two parts. At high heat flux, the property variation was employed to explain HTD, while at low mass flux, the buoyancy effect was considered to explain HTD. He et al.[14] performed computational simulations on convective heat transfer to CO2 at a pressure just above the critical value, and found that both V2F () and AKN (Abe, Kondoh and Nagano) turbulence models were able to capture the variation of wall temperature, however the predicted peak wall temperatures with both two turbulence model are much higher than observed experimentally due to overprediction of buoyancy within large-property-variation (LPV) region. Wen [15] numerical investigation of heat transfer deterioration (HTD) in supercritical water flowing through vertical tube is performed by using six low-Reynolds number turbulence models, and considered that SST model is able to quantitatively reproduce the two heat transfer deterioration phenomena. Sharabi et al. [16] carried out numerical studies of heat transfer to supercritical water flowing upward and downward in a circular pipe and found that all the k-ε low-Reynolds number models were able to qualitatively predict the HTD, but over-estimated the peak wall temperatures. Moreover, Kim et al. [17] achieved a success in predicting the experimental data of Yamagata et al. [4] by using the RNG k-ε (Renormalization Group) turbulence model with enhanced wall treatment. Roelof et al. [18] discussed further into the discrepancy of the results predicted by different second order turbulence models, and the effect of the near wall mesh spacing (i.e., Y+) to the accuracy of the computed heat transfer coefficient, and then suggested that Y+ should be lower than 1. Utilizing CFD tools, Shang et al. [19] analyzed the system pressure drop changes in SCWRs according to the variation of buoyancy effect intensity. Zhang et al. [20] and Liao et al. [21] studied forced convection heat transfer of supercritical CO_2 in the horizontal mini/micro channels. Gu et al. [22] studied the thermal-hydraulic behavior of supercritical water flows in sub-channels of a typical SCWRs fuel assembly. Kao et al. [23] concluded that buoyancy effect and Prandtl number play important roles in heat transfer deterioration of supercritical water inside vertical circular tubes. Shang and Chen [24] investigated the diameter effect on heat transfer behaviors. Lei[25] carried out CFD studies of heat transfer to supercritical water flowing horizontal and explained the mechanism of HTD.

For calculation of supercritical fluid, the turbulence model undoubtedly plays a key role in the simulations but the model selection is controversial. Kim et al. [17] believed that the RNG-*k*-ε [26] model was fully capable of modelling the heat transfer of supercritical pressure water, while Palko and Anglart [27] found that the SST k-ω [28] turbulence model was completely capable to model the heat transfer of supercritical fluid even in the deteriorated heat transfer region, and based on his results, Visser et al. [29] recognized that the *k*-ε model performed better at high mass fluxes and SST k-ω seemed to perform better at low mass fluxes. Zhu et al. [30] and Gu et al. [15] also found that the behavior of the SST k-ω model in case of heat transfer deterioration is more superior than that of *k*-*ε* model. However, Farah et al. [31] concluded that the realizable *k*-ε and

SST k-ω [28] model in predicting the deteriorated heat transfer regime are not accurate, which is inconsistent with Zhu et al. [30] and Gu et al. [15]. Therefore, the work of model validation need to be solved firstly, especially for multi-peak HTD phenomenon.

In the present paper, the HTD with multi-peak wall temperature at high heat fluxes of supercritical fluids has been investigated numerically. A comparative study at different heat fluxes was carried out, and then the mechanism of HTD occurrence are also discussed.

2 Numerical modelling

2.1 Physical Model

The difficulty in modelling supercritical flow mainly exists in the modelling of turbulence, particular for the LPV region. Until now there are three available numerical methods in modelling turbulence, including Reynolds-Averaged Navier-Stokes (RANS), Large Eddy Simulation (LES), and Direct Numerical Simulation (DNS). Unfortunately, carrying out DNS and LES studies for high Reynolds numbers and the complex geometry of flow regions corresponding to practical applications is prohibitively expensive and time-consuming. Thus the RANS approach become main method in simulation of engineering flow, which focuses on the mean flow and the effects of turbulence on mean flow properties.

In order to take into consideration the effect of turbulent fluctuations on properties of the mean flow, an approach called time-averaging or Reynolds-Averaging is adopted. The velocity variable u in the N-S equations are replaced by the sum of a mean and fluctuating component

$$u = \bar{u} + u'$$

where the Favre averaging is used, since the flow of supercritical fluids is a variable-property turbulent flow with large density variation. The Favre averaging is defined as follows:

$$\vec{u} = \frac{1}{\bar{\rho}} \lim_{\Delta t \to \infty} \frac{1}{\Delta t} \int_{t}^{t+\Delta t} \rho(\rho, \tau)\, \mathrm{u}(\mathrm{x}, \tau)\, \mathrm{d}\tau$$

This yields the following Reynolds-Averaged Navier-Stokes equations, The governing equations of the continuity, momentum and energy used in the present study are given as follows:

Continuity

$$\frac{\partial \rho}{\partial t} + \nabla \cdot (\rho \vec{u}) = 0$$

Momentum

$$\frac{\partial}{\partial t}(\rho \vec{u}) + \nabla \cdot (\rho \vec{u}\vec{u}) = -\nabla p + \nabla \cdot [\mu(\nabla \vec{u} + \vec{u}^{T})] + \rho \vec{g} + \vec{F}$$

Energy

$$\frac{\partial}{\partial t}(\rho h) + \nabla \cdot (\vec{u}(\rho h + p)) = -\nabla \cdot (k_{eff} \nabla T + (\tau_{eff} \cdot \vec{u})) + S_h$$

Where, the variables detail and assemble term in equations can be seen [32].

For turbulence model, the SST model uses a transformation of the k-ε model into a k-ω model in the near-wall region and the standard k-ε model in the fully turbulent region far from the wall. The Reynolds stress and k-ε equation of SST are identical to that of the standard k-ω model, while the ω-equation is obtained by substituting $\varepsilon = k\omega$ [32]. The Reynolds stress model (RSM) is the most elaborate type of RANS turbulence model. Abandoning the isotropic eddy-viscosity hypothesis, the RSM closes the Reynolds-averaged Navier-Stokes equations by solving transport equations for the Reynolds stresses, together with an equation for the dissipation rate.

In the aspect of wall function, Enhanced Wall Treatment (EWT) for the ε-equation is a near-wall modeling method that combines a two-layer model with so-called enhanced wall functions. If the near-wall mesh is fine enough to be able to resolve the viscous sublayer (typically with the first near-wall node placed at y+≈1). In the fully turbulent region , the k -ε models or the RSM adapt turbulence model. In the viscosity-affected near-wall region (Rey<Rey*), the one-equation model of Wolfstein is employed.

The physical models used in present paper as shown in Figure 3, a 2-D axisymmetric model is built, the test heated section with length of 2000 mm arranged after the adiabatic section with the length of 1000 mm in order to get fully development flow from upstream. Besides, the hydraulic pressure drop in this study is negligible compared to the system pressure.

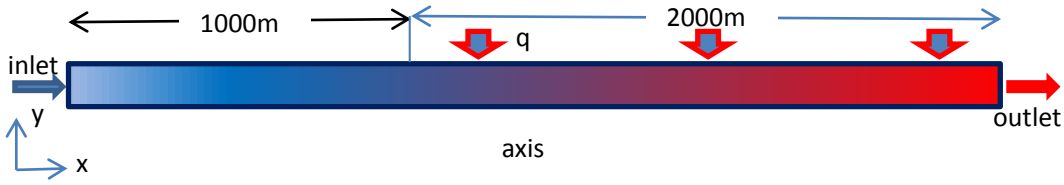

Figure 3 the calculated model

2.2 Mesh

In order to significantly reduces the computational cost, the axisymmetric mesh is used. The structured body-fitted mesh is used in the present study. Finer mesh near the wall is built to ensure property gradients being properly resolved. Resolution of the boundary layer (i.e. mesh spacing near walls), plays a significant role in the accuracy of the computed wall shear stress and heat transfer coefficient and therefore should be carefully adjusted. To fulfill the requirement of the near wall models, it is required that the non-dimensional distance (y^+) values at the wall-adjacent nodes are always less than 1. The primary mesh parameters for both CO_2 study and H_2O study are summarized in Table 1.Figure 4 shows the meshes of present model.

Table 1 the structure and meshes

	Diameter×Length	radial×Axial	Radial Growth Ration	Y+
CO_2	8 mm×3 m	80×3000	1.15	0.14
H_2O	8 mm×3 m	80×3000	1.15	0.22

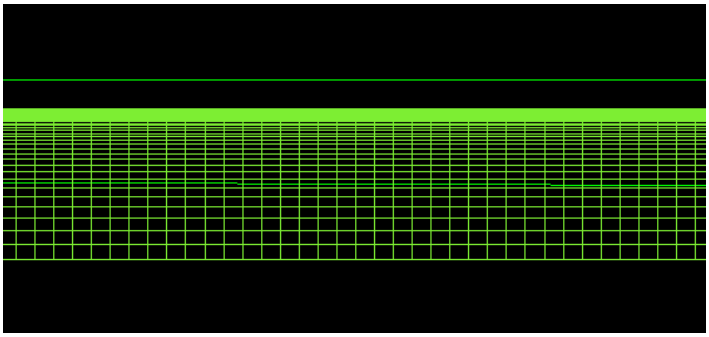

Figure 4 Meshes of Model

2.3 Numerical method

At the inlet of the tube, mass flux, temperature, turbulence intensity, and turbulence length scale are specified. The outlet boundary conditions of the domain are specified as pressure outlet, the wall face is

set as a heat flux boundary.

A finite-volume method [33] was employed and the equations of motion and continuity are integrated over each computational cell. The computations of HTD phenomena had been performed using the well-validated commercial CFD code FLUENT [32]. The coupling between pressure and velocity was implemented by the SIMPLEC algorithm [34]. A Quick upwind scheme was used for the discretization of the equations in the current work, and the discretized equations were then linearized and solved in a segregated manner [33]. Considering that fast and steep variation of the fluids thermo-physical properties in the pseudo-critical region of supercritical waters, precise thermo- physical properties should be given in proper formula. In the present paper, the IAPWS95 program [35] coded by FORTRAN was compiled to UDF (user defined function) and called in the simulation.

In order to obtain an easily-converged solution, the under-relaxation factor for the density is lowered to 0.8 from the default value of 1 to smooth the changes of the temperature and its dependent properties between iterations. The absolute convergence residual for energy equation is less than 10^{-7} and for the other transport equations are less than 10^{-4}.

2.4 Model verification

As mentioned above, the turbulence models need to be checked due to its controversy. A comparison of experimental data with numerical results of the low-Re, SST k-ω, standard k-ε, RNG k-ε, Realizable k-ε and RSM turbulence models have been conducted. The corresponding experiment data under the condition of mass flux 500kg/m^{2}s, pressure 7.5MPa and heat flux 80kW/m^2.

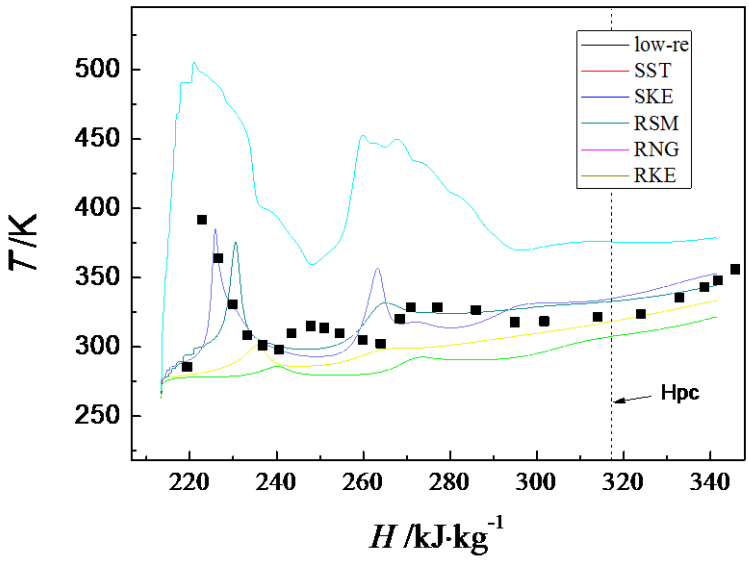

Figure 5 comparison of experimental data with different turbulent model

It is found that the Realizable k-ε, and SST k-ω and RSM can capture two temperature peaks in the whole enthalpy region, but the RNG k-ε and standard k-ε has a bad prediction. Compared with other turbulence model, the SST k-ω is obviously over predicted the wall temperature, which is different with the conclusion of Zhu[30] and Gu [15]. Compared with experiments data, both RSM and RKE in predicting HTD is better than other models. The RSM model is quantitatively better than other turbulence models due to its smooth variation at the second peak point.

3 Results and discussions

A systematic numerical simulations (see Table 2) over a wide range of experimental conditions for CO_2 and H_2O are carried out. In order to gain a deeper insight into the multi-peak heat transfer behavior at supercritical pressures, the distribution of flow parameters and thermophysical properties in the near-wall region are discussed.

Table 2 computing cases used in the present paper

	P/MPa	Tin/ K	q_w/kW·m^{-2}	G/kg·m^{-2}·s^{-1}
CO_2	7.53	273~303	30~200	400,510,600
H_2O	25	580, 600, 630	200~1000	400,449,510

3.1 Effect of turbulent Prandtl number

Kao et al. [23] and Jung[36] point out the turbulent Prandtl number has a significant effect, especially for the case of steep variation thermalphysical properties. Thus the effect of turbulent Prandtl number is finished by comparing the results of different constant Pr_t, i.e. 0.85, 0.9, 0.95, where the default value set as 0.85 in CFD code. Figure 6 shows the comparison result between experimental data and calculation data at different Pr_t at pressure of 7.53MPa, mass flux of 510 kg·m^{-2}·s^{-1} and heat flux of 50kW·m^{-2}.

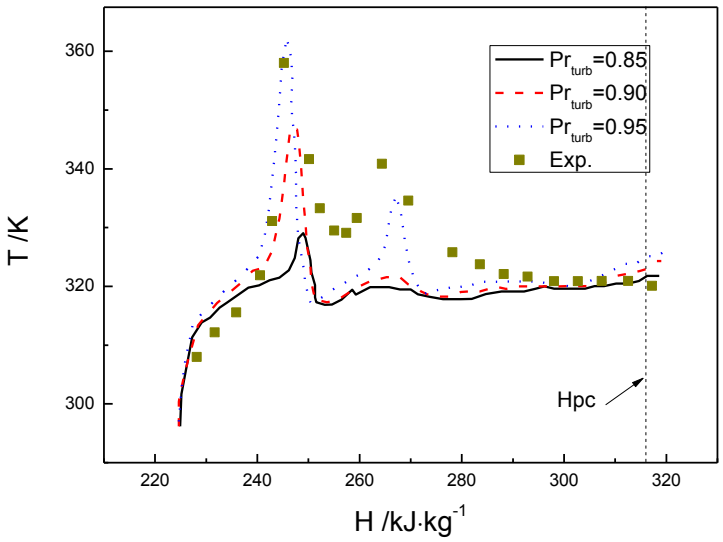

Figure 6 the effect of turb. Prandtl number

It can be seen that the temperature curves at different Pr_t show obvious discrepancies, especially in the region starting from the onset of HTD, the discrepancies enlarge. When the Prt is 0.85, the second peak can not be captured, but when the Prt increased to 0.95, both peaks are present and the second peak also have a good agreement with experimental data. As a whole, the Prt of 0.95 is the best choices. Therefore, the value in the following calculations will be applied.

3.2 Effect of heat fluxes

Figure 7 shows the effect of heat fluxes to wall temperature at the pressure of 25Mpa and mass flux of 510kg/m2s.

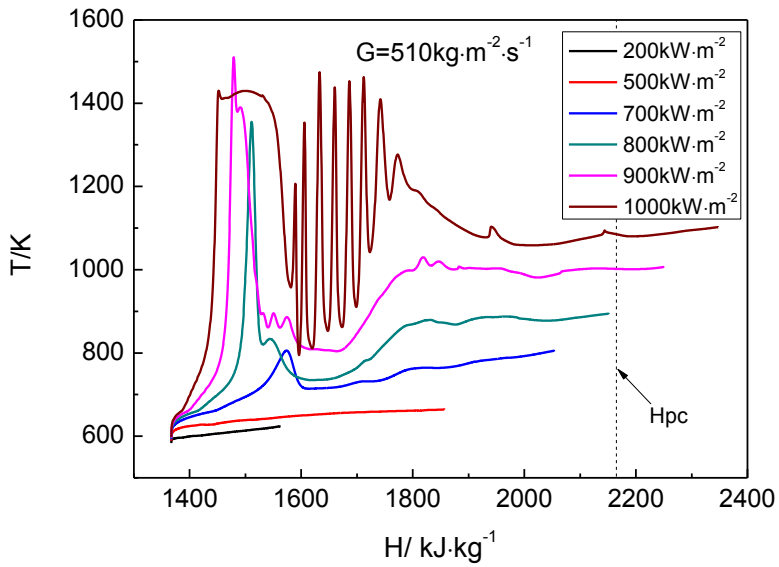

Figure 7 Effect of heat fluxes at the condition of 25MPa, 510kg·m^{-2}·s^{-1}

It is seen from Figure 7 that the peak temperature appeared when the heat fluxes increased to 700kW/m2, below the value, there is no presence of HTD phenomenon. With the heat fluxes increases, the wall temperature peak increased and the bulk enthalpy corresponding to the maximum value are toward to lower value. For example, when the heat flux is 700kW/m2, the maximum temperature is 803K and its enthalpy is 1576kJ/kg, but when the heat flux reached to 800kW/m2, the corresponding value moved to 1355K and corresponding enthalpy is 1511kJ/kg, which indicated that the HTD peak will get higher value and the occurrence of HTD will be in advance. Another intereting phenomonen has been observed, when the heat flux reached to 1000kW/m2, a unstable periodical wall temperature peak present in the LPV region.

3.3 Effect of mass fluxes

The effect of mass fluxes is also analyzed. Figure 8 shows the effect of mass fluxes at the pressure of 25Mpa and heat flux is 700kW/m2.

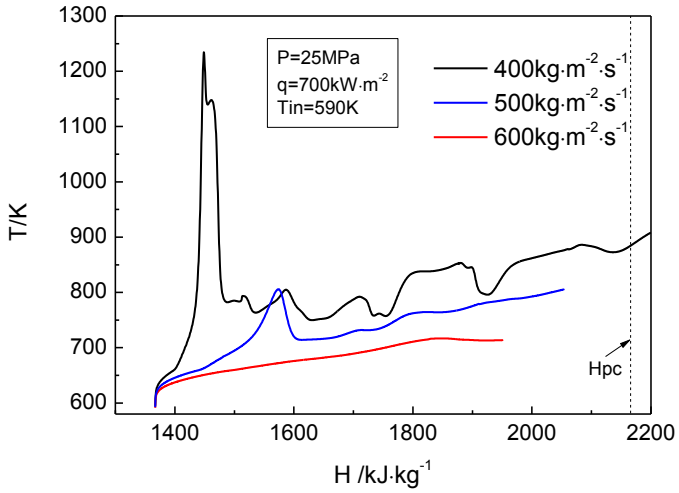

Figure 8 Effect of mass fluxes at the condition of 25MPa, 700kW/m^2

From Figure 8, it is found that when the mass flux equal to 600kg/m2s, there is no HTD happening, the wall temperature presents a flatten curve. But when the heat flux decrease to 500kg/m2s, a wall temperature peak appears due to the HTD happened, the reached maximum value of temperature is 810K. when the mass flux continually decrease to 400kg/m2s, the greatest value become 1243K, a unstable temperature fluctuation appeared following downstream. In short, the higher of mass flux, the probability of HTD occurrence and the temperature peak are lower.

3.4 Mechanism of HTD multi-peak

In order to further get insight into the mechanism of multipeak phenomenon of heat transfer deterioration, a series of cases at different heat fluxes are selected to investigated the multipeak behaviour with mass flux of 400 $kg \cdot m^{-2} \cdot s^{-1}$ and pressure of 25Mpa and the inlet temperature of 600K, the result as seen in Figure 9. Form (a) to (c), the heat flux increases, the wall temperature developed from one-peak to multi-peak.

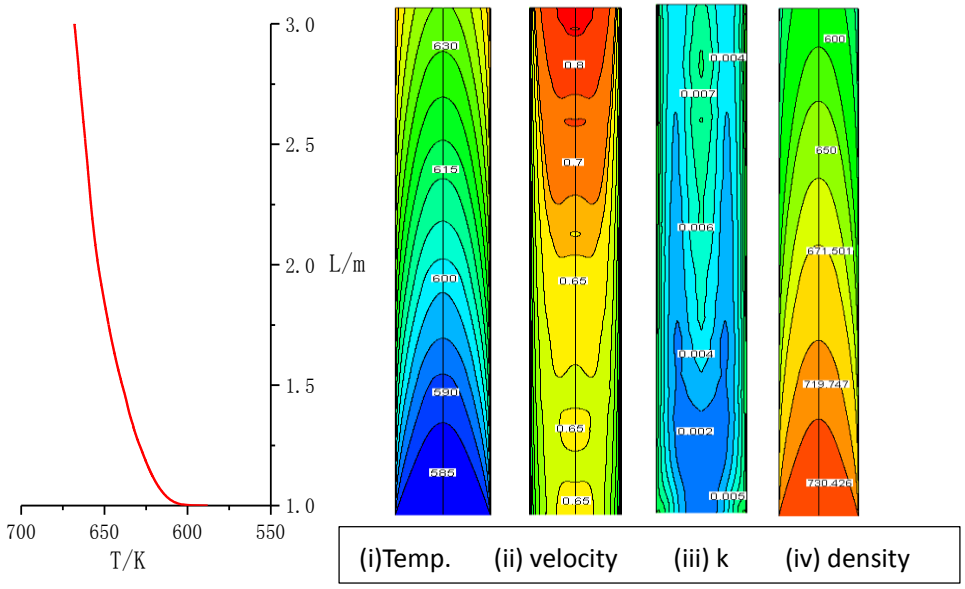

(a) q=100 $kW \cdot m^{-2}$

Obviously, when the heat flux is 100 $kW \cdot m^{-2}$, there is no temperature peak, the contour line of temperature in pipe present parabola shape and changed uniformity, the density as well. But the velocity and k changed dramatically. The velocity contour lines developed to “M” shape with flowing to the downstream due to the thermal acceleration as a result of steep thermal properties in the near-wall region. The turbulent kinetic energy increases near the wall , it indicate that the mixed convection enhances, which will promotes the heat and mass transfer transmit between near wall region and core region.

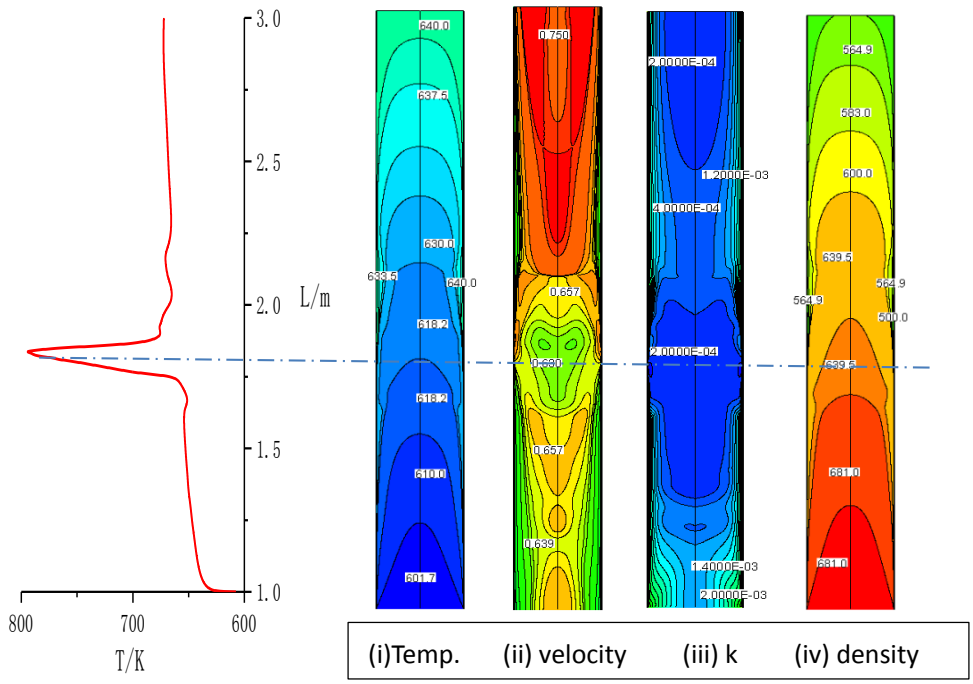

(b) q=250 kW·m^{-2}

From Figure 9(b), it can be found that a wall-temperature peak appeared at heat flux of 250 kW·m^{-2} due to occurrence of HTD, where the maximum wall temperature value reached to 800K. As seen in contours, before the HTD, the temperature and density in the core region changed smoothly, the heat transfer transmission are good to keep the temperature increase slowly, but the local velocity and turbulent kinetic energy become complicated due to the combining effect of buoyancy and thermal accelerations in the near-wall region. Near the peak point, a region coupled with low velocity and low k are embedded in the core region affected by accelerating of fluid in the near wall region. After the maximum value, wall temperature start to recovery, velocity and k begin to recover and the fluid close to near wall have good heat transfer performance with high velocity and kinetic energy again.

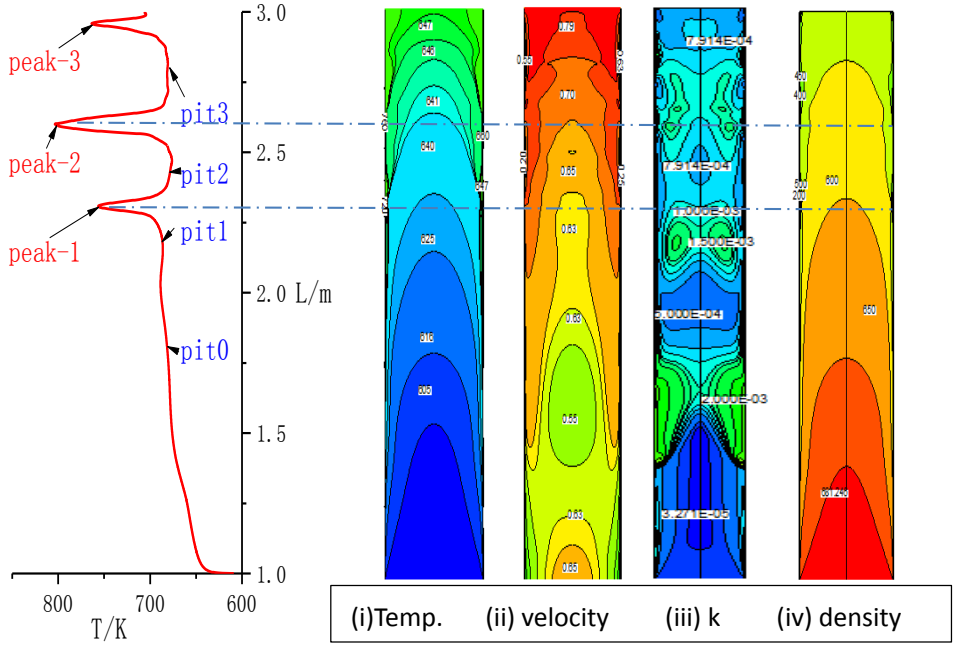

（c）q=300 kW·m^{-2}

Figure 9 Contour of temperature, velocity, turbulent kinetic energy and density

The interesting multi-peak of wall temperature happens when the heat flux increase to 300 kW·m^{-2}, as seen in Figure 9(c)， where three temperature peak can be found at the location of x=2.30, 2.60, 2.96m respectively. Influenced by LPV in the vicinity of the pseudo-critical temperature, the significant non-uniformity of velocity and k between the near-wall region and the core region can be observed, where the deformation of velocity profile k line are more complicated. A pair of vortex is formed close to the each peak point. When the HTD peak appear, there is a low velocity region exist in the near wall region, leading to the heat transfer blocked, the process is similar to the deterioration in subcritical pressure. Moreover, the process is not stable due to detachment of vortex.

Further explanation and more detailed information are given to make the mechanism clearly, the multi-peak case above-mentioned is employed. Figure 10 gives radial distributions of velocity, temperature and turbulence kinetic energy at different location, where the corresponding location of “peak” and “pit” can be known from Figure 9(c).

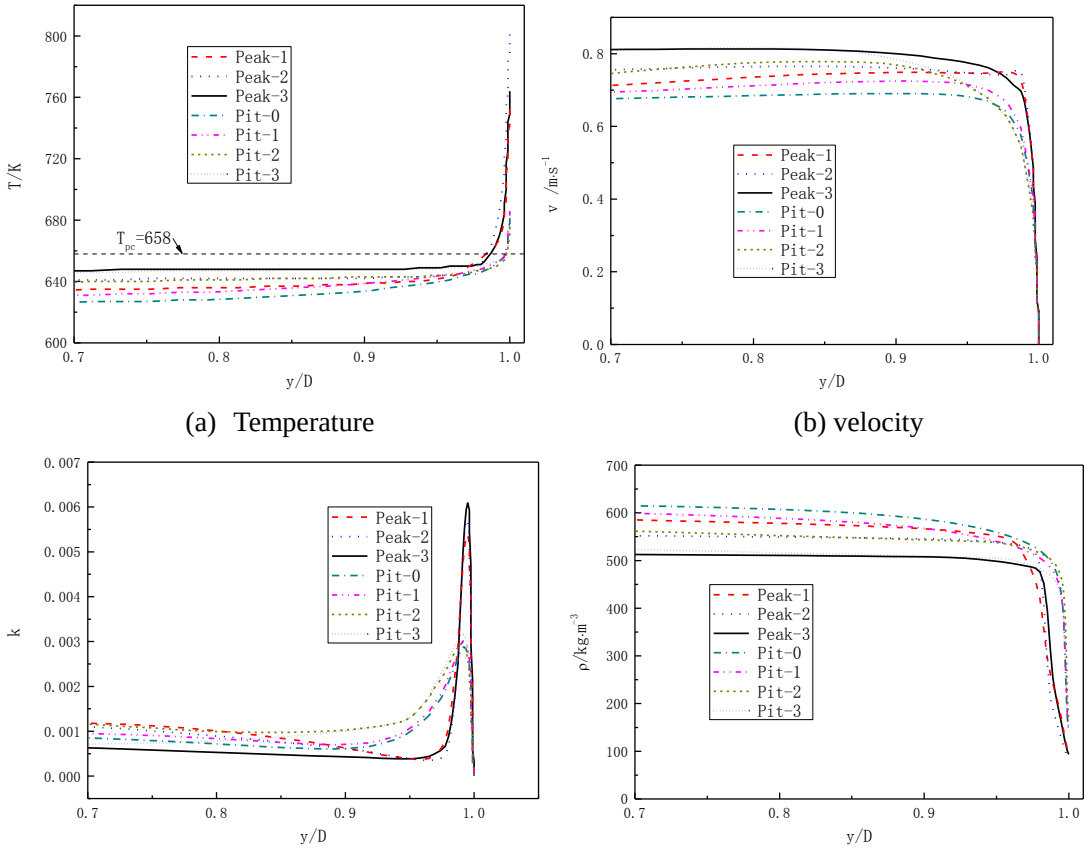

(a) Temperature (b) velocity

(c) Turb. kinetic energy (d) density

Figure 10 Distribution of velocity, temperature and turb. kinetic energy and density at different locations

It can be confirmed from Figure 10(a) that each HTD peak occurs under the condition that the wall temperature is higher than pseudo-critical point temperature (Tpc=658K) while the bulk fluid temperature is lower than Tpc. That is, the occurrence of HTD need contain the LPV region. From

the velocity distribution, as seen in Figure 10(b), it is found that the variation velocity gradient of "Peak" in the region close to 1 is faster than that of "pit" line, which indicated that in this region, thermal acceleration has been intensified and promotes the heat and mass flux exchange between "hot" fluid in the near wall region and "cool" fluid in the core region, the resulting variation of turbulent kinetic energy increase to a higher value. From Figure 10(c), it is found that the curves of k at each peak all reached to a maximum value in Y/D=0.99.

Besides, the buoyancy effect, to some extant, can be depicted by density. Figure 10(d) gives the change of density. It is known that the occupied space close to the wall of low density with "peak" line is broader than that of "pit" line. During the process from "pit" to "peak", the layer of low density get thicker and prompt the buoyancy and acceleration effect enhanced. On the whole, although each peak happened in different locations and have different shape in the core region, the peak or pit curves in the near wall region are almost overlap, that means, one of the occurrence conditions of multipeak phenomenon need to generate thick enough layer in the near wall region, which is easy to reached the requirment at high q/G.

4 Conclusions

Compared with different turbulence models, RSM model shows best prediction in multi-peak heat transfer deterioration of supercritical water among all turbuence models. The turbulent Prandtl number also play a important role in accurate predicting wall temperature, the value of 0.95 presents better result.

A series of numerical simulations at different mass fluxes and heat fluxes have been finished. It is found that with increase of q/G, higher peak temperature and peak amount will obtained.

The contours of temperature, velocity, turbulent kinetic energy and density at different heat fluxes are described. It is found that the contours of velocity and k is complicated at high heat fluxes, low velocity and low k occupied the near wall region when the HTD occurs. A pair of vortex is even observed in contour of turbulent kinetic energy at heat flux of 300kW/m^2.

The distributions of thermal properties and turbulent parameters show that at the peak point, the buoyancy and thermal accerlation reached to a higher value in the radial direction and a thicker low velocity and density layer formed. Once the layer built, it will lead to HTD one or more, and the layer is easy to formed at high q/G.

Acknowledgement

The authors acknowledge the support of the National Basic Research Program of China (973 Program) (Grant No. 2009CB219805), the National Natural Science Foundation of China (Grant No. 50876090) and the Fundamental Research Funds for the Central Universities.

Reference

[1]. Pioro IL, Duffey RB. Experimental heat transfer in supercritical water flowing inside channels (survey)[J]. Nuclear Engineering and Design, 2005, 235 (22): 2407-2430.

[2]. Hall WB, Jackson JD, Watson A. A review of forced convection heat transfer to fluids at supercritical pressures[J]. Proceedings of the Institution of Mechanical Engineers, 1967, 182: 10-22.

[3]. Cheng X, Schulenberg T. Heat Transfer at Supercritical Pressures -Literature Review and

Application to an HPLWR. Institute for Nuclear and Energy Engineering Nuclear Safety Research: Karlsruhe, 2001.

[4]. Yamagata K, Yoshida S, Fujii T, et al. Forced Convective Heat-Transfer to Supercritical Water Flowing in Tubes[J]. International Journal of Heat and Mass Transfer, 1972, 15 (12): 2575-2592.

[5]. Adebiyi GA, Hall WB. Experimental Investigation of Heat-Transfer to Supercritical Pressure Carbon-Dioxide in a Horizontal Pipe[J]. International Journal of Heat and Mass Transfer, 1976, 19 (7): 715-720.

[6]. Song JH, Kim HY, Kim H, et al. Heat transfer characteristics of a supercritical fluid flow in a vertical pipe[J]. Journal of Supercritical Fluids, 2008, 44 (2): 164-171.

[7]. Shiralkar.Bs, Griffith P. Deterioration in Heat Transfer to Fluids at Supercritical Pressure and High Heat Fluxes[J]. ASME J Heat Transfer, 1969, 91 (1): 27-36.

[8]. Shitsman ME. The effect of natural convection on temperature conditions in horizontal tubes at supercritical pressures[J]. Thermal Engineering, 1966, 13 (7): 69-75.

[9]. Jackson JD. Fluid flow and convective heat transfer to fluids at supercritical pressure[J]. Nuclear Engineering and Design, 2013.

[10]. Jackson JD, Lutterodt KE, Weinberg R. Experimental Studies of Buoyancy-influenced Convective Heat Transfer in Heated Vertical Tubes at Pressures Just Above and Just Below the Thermodynamic Critical Value. GENES4/ANP2003: Kyoto, JAPAN, 2003: paper 1177.

[11]. Hall WB, Jackson JD, Watson A. A review of forced convection heat transfer to fluids at supercritical pressures[J]. Proc Instn Mech Engrs, 1967, 182: 10-22.

[12]. Bae JH, Yoo JY, Choi H, et al. Effects of large density variation on strongly heated internal air flows[J]. Phys Fluids, 2006, 18: 075102.

[13]. Koshizuka S, Takano N, Oka Y. Numerical analysis of deterioration phenomena in heat transfer to supercritical water[J]. Int J Heat Mass Transfer, 1995, 38 (16): 3077-3084.

[14]. He S, Kim WS, Jackson JD. A computational study of convective heat transfer to carbon dioxide at a pressure just above the critical value[J]. Applied Thermal Engineering, 2008, 28 (13): 1662-1675.

[15]. Wen QL, Gu HY. Numerical simulation of heat transfer deterioration phenomenon in supercritical water through vertical tube[J]. Annals of Nuclear Energy, 2010, 37 (10): 1272-1280.

[16]. Sharabi MB, Ambrosini W, He S. Prediction of unstable behaviour in a heated channel with water at supercritical pressure by CFD models[J]. Annals of Nuclear Energy, 2008, 35 (5): 767-782.

[17]. Kim SH, Kim YI, Bae YY, et al. Numerical Simulation of the Vertical Upward Flow of Water in a Heated Tube at Supercritical Pressure[C]. Pittsburgh, PA, USA, 2004: 5-10.

[18]. Roelof F. CFD analysis of heat transfer to supercritical water flowing vertically upward in a tube. Under the contract of the Netherlands Ministry of Economic Affairs, 2004.

[19]. Shang Z, Yao YF, Chen S. Numerical investigation of system pressure effect on heat transfer of supercritical water flows in a horizontal round tube[J]. Chemical Engineering Science, 2008, 63 (16): 4150-4158.

[20]. Zhang XR, Yamaguchi H. Forced convection heat transfer of supercritical CO2 in a horizontal circular tube[J]. Journal of Supercritical Fluids, 2007, 41 (3): 412-420.

[21]. Liao SM, Zhao TS. Measurements of heat transfer coefficients from supercritical carbon dioxide flowing in horizontal mini/micro channels[J]. ASME J Heat Transfer, 2002, 124 (3): 413-420.

[22]. Gu HY, Cheng X, Yang YH. CFD analysis of thermal-hydraulic behavior of supercritical water in sub-channels[J]. Nuclear Engineering and Design, 2010, 240 (2): 364-374.

[23]. Kao M, Lee M, Ferng Y, et al. Heat transfer deterioration in a supercritical water channel[J]. Nuclear Engineering and Design, 2010, 240 (10): 3321-3328.

[24]. Shang Z, Chen S. Numerical investigation of diameter effect on heat transfer of supercritical water flows in horizontal round tubes[J]. Applied Thermal Engineering, 2011, 31 (4): 573-581.

[25]. Lei X, Li H, Zhang Y, et al. Effect of buoyancy on the mechanism of heat transfer deterioration of supercritical water in horizontal tubes[J]. Journal of Heat Transfer, 2013, 135 (7).

[26]. Orszag SA, V. Yakhot, Flannery WS, et al. Renormalization Group Modeling and Turbulence Simulations". International Conference on Near-Wall Turbulent Flows: Tempe, Arizona., 1993.

[27]. Palko D, Anglart H. Theoretical and Numerical Study of heat transfer Deterioration in HPLWR. Science and Technology of Nuclear Installations. Hindawi Publishing Corporation, 2008: 5.

[28]. Menter. FR. Two-Equation Eddy-Viscosity Turbulence Models for Engineering Applications[J]. AIAA Journal, 1994, 32 (8): 1598-1605.

[29]. Visser DC, Nijeholt JALa, Roelofs F. CFD Predictions of Heat Transfer in Super Critical Flow Regime[C]. Anaheim, USA, 2008: Paper 8155.

[30]. Zhu Y. Numerical Investigation of the Flow and Heat Transfer within the Core Cooling Channel of a Supercritical Water Reactor[D]: Universität Stuttgart, 2010.

[31]. Farah A, Kinakin M, Harvel G, et al. Numerical Study of Supercritical Water Heat Transfer in Vertical Bare Tubes Using FLUENT CFD Code. 5th Int Sym SCWR (ISSCWR-5): Vancouver, British Columbia, Canada, 2011: 1-14.

[32]. Ansys F. Fluent Ansys. Canonsburg, PA, 2002.

[33]. Tao WQ. Numerical heat transfer. Xi'an Jiaotong University Press: Xi'an, China, 2001: 333-392.

[34]. P vDJ, D RG. Enhancement of the SIMPLE method for predicting incompressible fluid flow[J]. Numer Heat Transfer, 1984, 7: 147-163.

[35]. Wagner W, A.Pruß. The IAPWS Formulation 1995 for the Thermodynamic Properties of Ordinary Water Substance for General and Scientific Use[J]. J Phys Chem Ref Data, 2002, 31 (2): 387-585.

[36]. Yoo JY. The Turbulent Flows of Supercritical Fluids with Heat Transfer[J]. Annu Rev Fluid Mech, 2013, (45): 495-525.

ISSCWR7-2067

Mechanisms of buoyancy effect on heat transfer in a horizontal flow

Wei Wang[1] and Shuisheng He[1*]
[1]Department of Mechanical Engineering, The University of Sheffield,
Mappin building, Mappin Street, Sheffield, S1 3JD, UK
[*]Corresponding author: s.he@sheffield.ac.uk

Abstract

A complex feature of a heated (or cooled) flow of fluids at a supercritical pressure is that it always continually develops in the flow direction due to the very complex property-temperature relationships, which makes the analysis and data correlation very difficult. We have carried out a fundamental study of flow between parallel plates with heating from one surface and cooling from the other using direct numerical simulation. Under such a condition, the flow can reach a fully developed state in the flow direction when the heat input equals to the heat removed from the system. We report investigations into the characteristics of the effects of buoyancy in a stably and an unstably stratified horizontal flow, and comparisons with a forced convection simulation. The stably stratified flow is laminarized due to buoyancy whereas the turbulence is strongly enhanced in the unstably stratified case.

1. Introduction

The heat transfer to water at supercritical pressure has been studied intensively since the supercritical water-cooled reactor (SCWR) was selected as one of the Generation IV nuclear systems due to its high thermal conversion efficiency [1]. SCWR operates above the thermal dynamic critical point of water (P_c=22.1MPa, T_c=647K). **Figure 1** displays the thermal physical properties of water at 23.5MPa, a pressure slightly above its critical value. At this pressure, the pseudocritical temperature T_{pc} is 652.5K, at which the heat capacity C_p reaches its maximum. Within a narrow temperature range across the pseudocritical temperature, thermaldynamic and thermalphyiscal properties of water encounters dramatic variations. Depending on flow development and wall thermal conditions, these large variations of thermal properties can cause significant changes in heat transfer characteristics, among which heat transfer deterioration (HTD) needs to be avoided in SCWR for safety. Fundamental research of turbulence heat transfer for supercritical water is necessary in order to improve plant safety and efficiency.

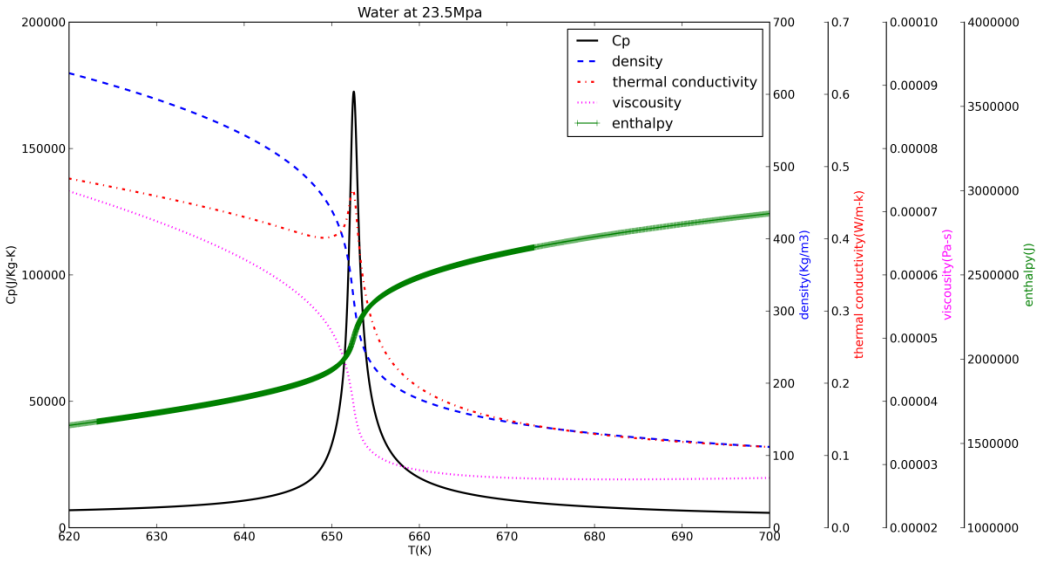

Figure 1 Thermal physical properties of water at 23.5MPa

The two most intensively studied fluids at supercritical pressure are carbon dioxide and water. The critical pressure and temperature of carbon dioxide are much lower than those of water, which makes experiments much easier to be conducted than using water. In addition to experiments, some direct numerical simulations (DNS) of CO2 at supercritical conditions were also performed to study the influences of buoyancy on turbulence statistics, eg. Bea *et al*.[2]. Due to the lack of fluid-to-fluid scaling study, heat transfer characteristics obtained in CO2 cannot be directly used for water. Over the last decade, studies on supercritical water begin to emerge due to its potential application in nuclear reactors. Pis'menny *et al* [3] preformed physical experiments for water at supercritical pressure in a vertical pipe at Reynold's number around 35,000. Niceno and Sharabi [4] validated a large eddy simulation of supercritical water at the same condition as above but replacing the pipe with parallel plates. A number of RANS studies of water at supercritical water were carried out in different geometries, such as circular tubes [5-11], annulus [12-13], rectangular duct [14-15] and bundles [16-17]. DNS study of water at supercritical pressure is limited by Reynolds number. A mass flux around 200Kg/m^2/s with a diameter of 6mm corresponds to a bulk velocity and tube diameter based Reynolds number around 22000 ($Re = D\dot{m}/\mu$). Considering the current computing capacity and with a proper diameter of tube, DNS studies have to be limited to low mass flux cases. Liu *et al* [11] studied the influences of mass flux to HTD for supercritical water in upward annular channel using RANS, and found that HTD at low mass flux is mainly caused by buoyancy effect, while HTD at high flux is due to variation of fluid properties and the acceleration effect. Our DNS study will focus on low mass flux fluid and investigate buoyancy effect on turbulence statistics and heat transfer.

Fluids at supercritical pressure are often accompanied by strong variable thermo-properties, buoyancy-influences and 'abnormal' thermal developments, which may interact with each other and hence makes the understanding of individual effects on turbulence and heat transfer a difficult task. The studies with constant wall heat flux conditions investigated thermal developing flow, involving complex interaction between flow development and heat transfer characteristics. To some extent, these studies mimicked conditions of physical experiments and real applications. On the other hand, for a fundamental study of individual effects of variable property and buoyancy, a simple flow setup which decouples the various effects may be advantageous. In 1960s, Khan [18] designed an experiment on CO2 flowing through a horizontal plane passage with constant but different wall temperatures. Under such a condition,

the final state is a fully developed stably stratified flow with balanced zero net heat input. The statistic temperature distribution in the streamwise direction will be constant after a sufficient distance. As a result, there is no heat advection but only thermal diffusion. Therefore, the effects of variable properties and buoyancy are separated from the intricate effects of the thermal/flow development. However, these conditions were quite difficult to be achieved in real experiments. For example, radiative heat transfer always exists between two walls. In addition, the strong influences of buoyancy also led to ill-defined and non-uniform thermal wall temperatures, as commented by Jackson [19]. With the development of high performance computing, numerical study of supercritical fluids makes above isothermal wall condition feasible. To realize the aim of understanding thermal physics in a fully developed flow, a series of numerical experiments should be performed to study influences to heat transfer characteristics, such as influences of the location of supercritical temperature relative to the wall and wall temperature differences. In this paper, some preliminary research results are reported, which focus on a horizontal stably stratified and an unstable stratified flow with the same temperature differences. The heat transfer characteristics in the two flows are compared with each other.

2. Governing equations

In a supercritical water-cooled reactor, the flow can be considered incompressible. the acoustic interactions and compressibility effects are negligible. The thermal properties may vary significantly with temperature but can be assumed to be independent of the pressure variation. For the equation of energy conservation, heat from viscous dissipation and work done by gravity are also neglected because they are small in comparison with other terms. Based on all these assumptions, an in-house direct numerical simulation code has been developed to study heat transfer to fluids at supercritical pressures.

The governing equations in dimensionless form, including the mass conservation equation, the momentum conservation equation and the energy conservation equation, are listed below, respectively,

$$\frac{\partial \rho}{\partial t} + \frac{\partial \rho u_i}{\partial x_i} = 0 \tag{1}$$

$$\frac{\partial \rho u_i}{\partial t} + \frac{\partial \rho u_i u_j}{\partial x_j} = -\frac{\partial p}{\partial x_i} + \frac{1}{Re} \cdot \frac{\partial \tau_{ij}}{\partial x_j} - \frac{L_0}{v^2} \rho g \cdot \delta_{2i} \tag{2}$$

$$\frac{\partial \rho h}{\partial t} + \frac{\partial \rho u_j h}{\partial x_j} = + \frac{1}{Re \cdot Pr} \cdot \frac{\partial}{\partial x_j} \left(\lambda \frac{\partial T}{\partial x_j} \right) \tag{3}$$

All the flow and thermal variables are normalized by properties at a reference state with the subscript 0. The definitions of dimensionless variables follow those used in [2], which are not repeated here. A negative sign of the gravity stands for a condition when the direction of the gravity force is in opposite direction of coordinate of the system.

Above equations are solved on a staggered mesh with a second order central difference finite-difference method. A pressure-correction method for the incompressible flow is used to enforce the continuity equation. For the temporal discretization, a third order explicit Runge-Kutta scheme is used for the nonlinear terms, and a second order implicit Crank-Nicholson scheme for the linear terms of the momentum equations. Details on the spatial discretization schemes for the momentum and continuity equations were given in [20]. For the energy equation, enthalpy is calculated using an explicit Runge-Kutta method, and the thermal conductivity term takes the form of temperature gradient not enthalpy and C_p. The process to solve the coupled equations in each Runge-Kutta stage is as follows: Firstly, the energy equation is solved to obtain enthalpy; then, temperature, density, viscosity and thermal conductivity are updated based on the new enthalpy. This is done by searching a physical property table generated with the NIST database [21]; next, the momentum equations are solved with updated density and viscosity; finally, the continuity equation is satisfied by a predictor-corrector method via solving the Poisson equation.

3. Computational Configuration

3.1 Geometry and mesh

Direct numerical simulation was carried out for water at a pressure of 23.5 MPa in a channel of the height of $2\delta = 6.28$ mm (δ stands for the half channel height). The Reynolds number based on the channel height is $Re_0 = 5600$ for the isothermal flow. As discussed before, in order to avoid complex interactions between thermo-physical properties and flow-development, we consider a flow in a horizontal channel with the temperatures of its top and bottom walls fixed at constant but different temperatures. When the flow is developed, the heat input from the hotter wall will be balanced by the heat removal from the colder wall and hence there is no advection of heat in the streamwise direction. Considering these features, a periodic boundary condition is applied to streamwise direction of the computational channel domain.

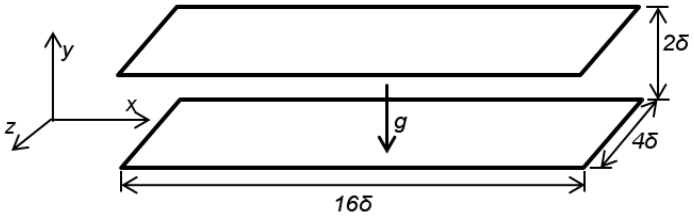

Figure 2 Sketch of the horizontal channel flow

A sketch of the horizontal channel flow is shown in **Figure 2**. The computational domain for the channel flow is chosen to be 16δ, 4δ and 2δ in the streamwise, spanwise and wall-normal directions, respectively. The numbers of grid points in these three directions are 512, 160 and 160, and the corresponding grid resolutions based on wall unit at the isothermal state are $\Delta x^+ \approx 5.6$, $\Delta z^+ \approx 4.5$ and $0.4 < \Delta y^+ < 4.4$. **Figure 3** shows the mean velocity and turbulence intensity for the isothermal flow, comparing with the DNS data of [22]. Both the mean velocity and the turbulence intensity in all the three directions show good agreement with the reference data.

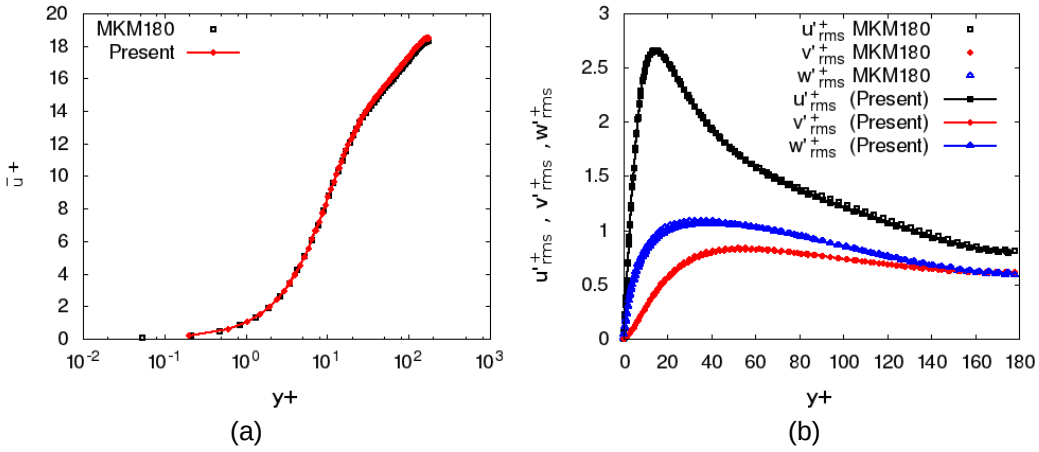

Figure 3 Isothermal flow (a) the mean velocity, (b) root mean square of velocities. The reference data marked as “MKM180” is from [22].

3.2 Initial and boundary conditions

When the horizontal channel has a higher temperature on the top wall and a lower temperature on the bottom wall, a stable thermal stratification is achieved. When the heated/cooled walls are

reversed, the flow is unstably stratified. In this study, initially a DNS of isothermal flow was carried out with dimensionless forms. A reference temperature T_0=648.15K, approximately in the middle of two wall temperatures, is used to initialize turbulence flow. The mass flux is 48.6Kg/m^2-s, which is kept the same for cases studied. The wall temperatures are chosen to be on either sides of the pseudocritical temperature, namely, T_c (cooling) =635K and T_h (heating)=655K. A forced convection case, allowing property variations with temperature without considering buoyancy force, is also studied. A summary of the wall temperatures for the various cases is given in **Table 1**.

Table 1 Constant temperature on the walls

Case	isothermal	Forced	Stably Stratified	Unstably Stratified
$T(y/\delta=-1)$**(K)**	-	635.0	635.0	655.0
$T(y/\delta=+1)$**(K)**	-	655.0	655.0	635.0

The periodic boundary condition is applied in the spanwise and streamwise directions. The no-slip boundary condition is applied on the two channel walls.

4. Results and discussions

Both the Reynolds averaging and the Favre averaging are used to present results. The Reynolds averaging is defined as an average both over time and over homogenous directions (streamwise and spanwise directions), labelled as $\overline{\varphi}$. The Favre averaging is defined as $\tilde{\varphi} = \overline{\rho\varphi}/\bar{\rho}$. The relations between the averaged mean and fluctuations in these two averaging are

$$\varphi' = \varphi - \overline{\varphi} \tag{4}$$

$$\varphi'' = \varphi - \tilde{\varphi} \tag{5}$$

The density of both the supercritical and the subcritical fluids decrease monotonically with increase of temperature, and therefore, generally speaking, the thermal stratification effects with flows of the two types of fluids are similar. General descriptions of flow developments in a stable and an unstable stratification are given below based on studies of the subcritical flow [23-24]. For an unstably stratified flow, when a fluid particle near the heated wall moves upwards towards the core of the channel due to velocity fluctuations, its surrounding (colder) fluids with a higher density provides a buoyancy force in the direction that accelerates its movement. Similarly, when a fluid particle near the core is displaced towards the lower heated wall, the buoyance force is again in the direction that accelerates its movement. Therefore, the buoyancy force in the unstable stratification always enhances turbulence mixing and heat transfer in the wall-normal direction in a horizontal flow. The buoyancy force near a cooled wall in the unstably stratified flow also enhances turbulence mixing due to a similar mechanism as near a heated wall. In a stably stratified flow, when particles near a upward-facing cooled wall moves upwards due to fluctuations, the surrounding (hotter) flows with lower density impedes its movement due to decreased buoyancy force. As a result, the turbulence fluctuations are dampened, and heat transfer decreases. Bearing in mind these general mechanisms of stable/unstable stratification, the thermal stratifications with supercritical fluids will be analysed below.

4.1 Bulk parameters

Table 2 summarizes the bulk parameters, which are defined in the same way as in [2]. An exception is the Grashof number, which in this study is defined as

$$Gr = g\beta\rho^2(T_h - T_c)\cdot(2\delta)^3/\mu^2 \tag{6}$$

This is based on the heated/cooled wall temperatures, rather than the density difference widely used in pipe flow. The Nusselt number is defined as

$$Nu = 2\delta/k_b \cdot q_w/(T_w - T_b) \tag{7}$$

The subscript ‘c’ stands for cooled wall, ‘h’ for heated wall, and ‘b’ for bulk values.

Table 2 Summary of bulk/wall parameters

Case	isothermal	Forced	Stably Stratified	Unstably Stratified
$y+(T_{pc})$	-	3.27	10.28	1.13
$H_b \times 10^6(J)$	-	1.91	1.89	1.92
$q_w(kW/m^2)$	-	29.1	4.5	91.3
$T_b(K)$	-	648.88	648.01	649.27
Re_b	5600	5722	5578	5800
Pr_b	-	3.21	2.77	3.48
$Gr_b/Re_b^{2.7} \times 10^3$	-	0.0	8.0	9.97
Nu_c	-	32.6	5.4	100.0
Nu_h	-	75.9	10.1	249.0
$\tau_{w,c} \times 10^{-3}$	4.0	4.7	1.3	18.2
$\tau_{w,h} \times 10^{-3}$	4.0	2.2	0.6	8.7

As mentioned before, the condition of constant wall temperatures will lead to a fully developed state without net energy input statistically. Even with the same wall temperatures, the mean bulk enthalpy and mean wall heat flux are different in stably/unstably stratified flows due to the buoyancy effect. As shown in **Table 2**, the bulk enthalpy of the unstably stratified flow is slightly higher than that of the forced convection flow, while the stably stratified flow has a slightly lower bulk enthalpy. Consequently, the unstably stratified flow has the highest bulk temperature, but it is still below the pseudo critical temperature. The unstably stratified flow has a larger buoyancy parameter ($Gr_b/Re_b^{2.7}$) than the stably stratified flow. For all three cases, the heated wall has a larger Nusselt number than the cooled wall. Compared with the forced convection flow, heat transfer near both the heated and cooled wall is worsen for the stably stratified flow, and the unstably stratified flow has enhanced heat transfer.

4.2 Mean flow characteristics

After averaging over time and the homogenous directions, the 3D flow degenerates into a 1D y-distribution. To enable a direct comparison, the profiles of the unstably thermal stratified flow are plotted as a function of $(-y/\delta)$, while others are plotted of (y/δ) in the specified coordinate system shown in **Figure 2**. Under such a plotting scheme, the heated/cooled walls for all three cases overlap in the figures, with $y/\delta = 1$ corresponding to the hot wall and $y/\delta = -1$ for cold wall. All variables shown below are normalized by the properties at the reference state.

Figure 4 (a) and (b) show the distributions of the mean temperature and the thermal conductivity. For each case, since the wall heat fluxes on heated and cooled walls are the same, the temperature gradient on the wall is directly correlated with the thermal conductivity ($q_w = -\lambda_w(T_w - T)/\Delta y$). The temperature near the heated wall has a larger gradient than on the cooled wall in all the three cases (see **Figure 4** (a)) because of a smaller wall thermal conductivity on the heated wall. Different from supercritical carbon dioxide whose thermal conductivity decreases linearly with increasing temperature, the thermal conductivity of supercritical water at 23.5MPa has a peak value near the pseudo critical temperature, as shown in **Figure 1**. This property causes dramatic variation in thermal conductivity near the heated wall for all three cases studied, as shown in **Figure 4** (b). For the unstably stratified flow with T_{pc} at $y+\approx1$, a large variation of thermal conductivity around $y+\approx1$distorts the temperature distribution near the wall, which has a rapid reduction followed by a slight recovery near the heated wall as shown in **Figure 4** (a).

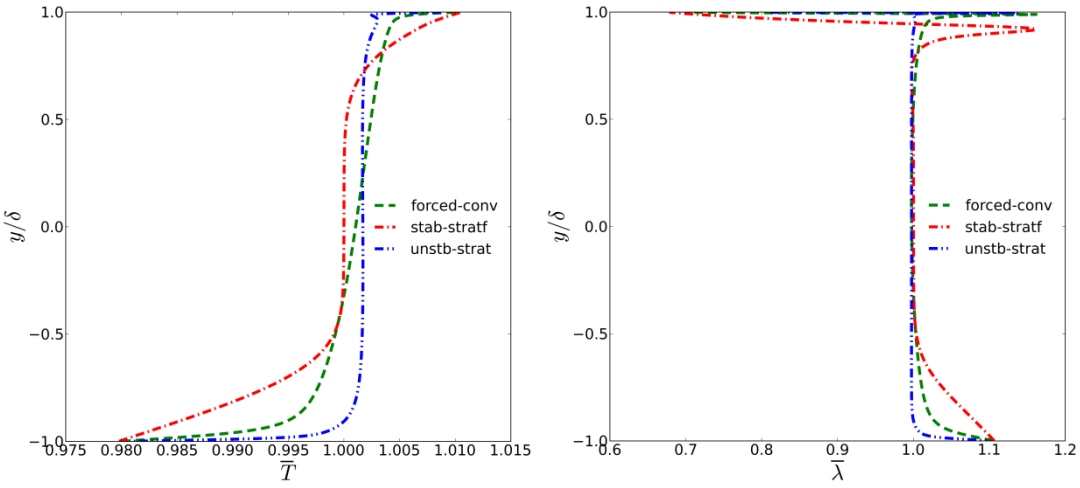

(a) (b)

Figure 4 Mean thermal properties distribution: (a) temperature (T), (b) thermal conductivity (λ)

Figure 5 shows the mean velocity distributions. The velocity profile of the forced convection flow is asymmetrical about the centre y=0, with a slight deceleration near the cooled wall and an obvious acceleration near the heated wall. Without considering the gravity, flow acceleration near the heated wall is due to reduced density (shown in **Figure 6**) and other changes of properties. When the buoyancy effect is considered, the buoyancy force contributes to a source of turbulence in the unstably stratified flow, enhancing turbulence mixing near both heated and cooled walls. The enhanced turbulence mixing, on the one hand, increases momentum transport vertically to lead to accelerated velocity near walls and levelled-off of the central part velocity. On the other hand, it also decreases density variation in the central part of the channel, which alleviates flow acceleration/deceleration due to density variation. Effects of buoyancy and density variation together lead to a higher velocity than that of both the isothermal and forced convection flow near the cooled wall and a smaller velocity than that of the forced convection flow near the heated wall. The buoyancy force works as a sink of turbulence in the stably stratified flow, damping turbulence fluctuations. In the current condition, the stably stratified flow is laminarized due to very strong buoyancy effect. With almost negligible turbulence mixing (will be shown in the next section), the velocity profile recovers to a quasi-laminar Poiseuille profile, and both the temperature and density distributions show more gradual variations, compared to the forced convection and unstably stratification turbulence flow.

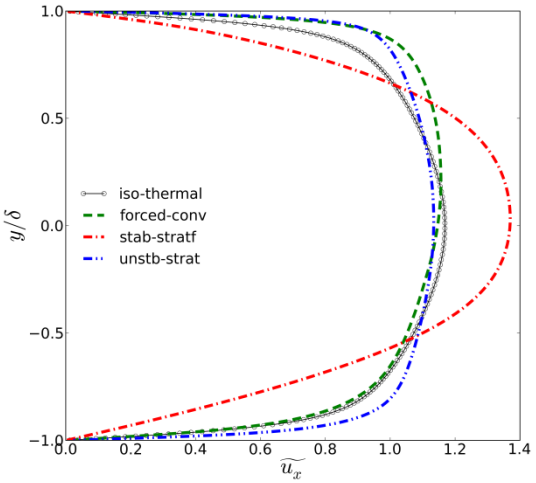

Figure 5 Mean velocity distribution

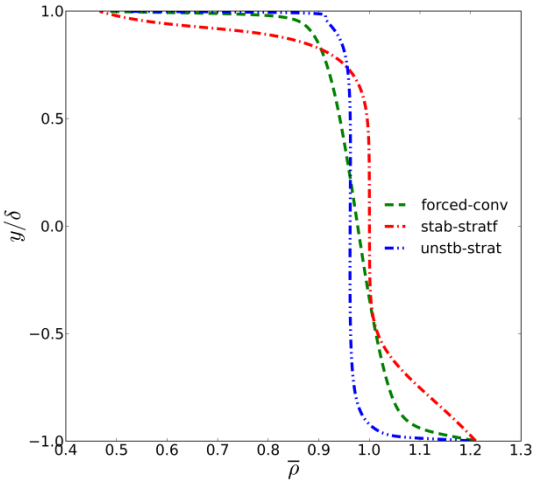

Figure 6 Mean density distribution

4.3 Buoyancy effect on turbulence statistics

The gravity force explicitly contributes to the production of $\overline{\rho u_x'' u_y''}$, $\overline{\rho u_y'' u_y''}$ and $\overline{\rho u_y'' h''}$ through the buoyancy production terms $-\frac{g_0}{\cdot\cdot_2}\overline{\rho' u_x'}$, $-2\frac{g_0}{\cdot\cdot_2}\overline{\rho' u_y'}$ and $-\frac{g_0}{\cdot\cdot_2}\overline{\rho' h'}$, respectively. The remaining production reflects the production purely due to turbulence fluctuation.

Figure 7 displays the distribution of Reynolds normal stress $\overline{\rho u_x'' u_x''}$ and $\overline{\rho u_y'' u_y''}$. It is obvious that the stably stratified flow has nearly zero turbulent fluctuations. Turbulence fluctuations in the forced convection flow are enhanced, compared to the isothermal flow, in both the streamwise and the normal directions due to property variations. In addition, both $\overline{\rho u_x'' u_x''}$ and $\overline{\rho u_y'' u_y''}$ are stronger near the heated wall than those near the cooled wall in the forced convection flow. Different from the forced convection flow, the wall-normal Reynolds stress$\overline{\rho u_y'' u_y''}$. in the unstably stratified flow is stronger than its streamwise stress $\overline{\rho u_x'' u_x''}$ due to buoyancy effect.

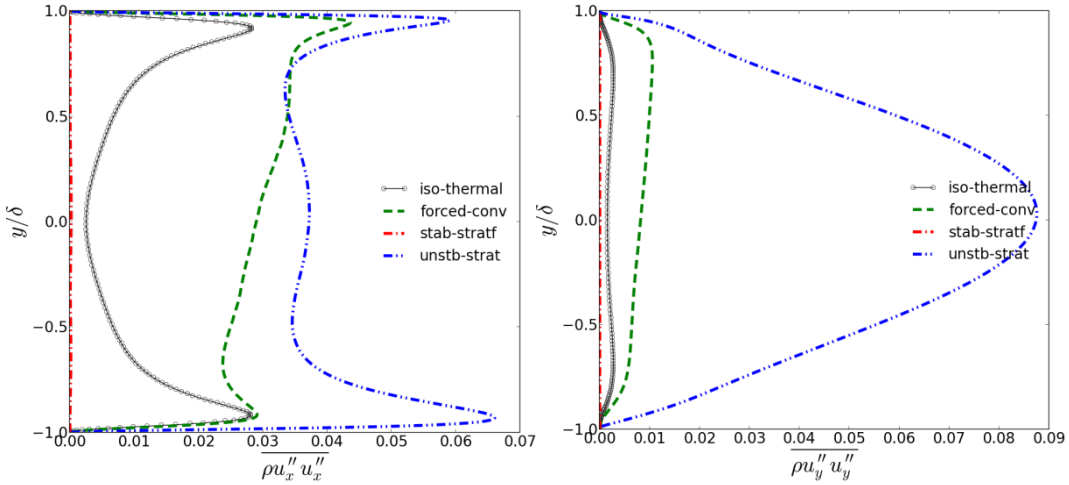

Figure 7 Distribution of normal Reynolds stress (a) $\overline{\rho u_x'' u_x''}$ (b) $\overline{\rho u_y'' u_y''}$

Figure 8 compares the turbulent and viscous shear stresses. As expected, the total Reynolds shear stress in the isothermal flow shows a straight line distribution. The forced convection and unstably stratified flow also shows a linear change in the total shear stress. The relamianarized stably stratified flow has a dominating viscous shear stress across the whole domain, which is higher than that of the turbulence flow, but far less than the total shear stress of forced convection and unstably stratified flow.

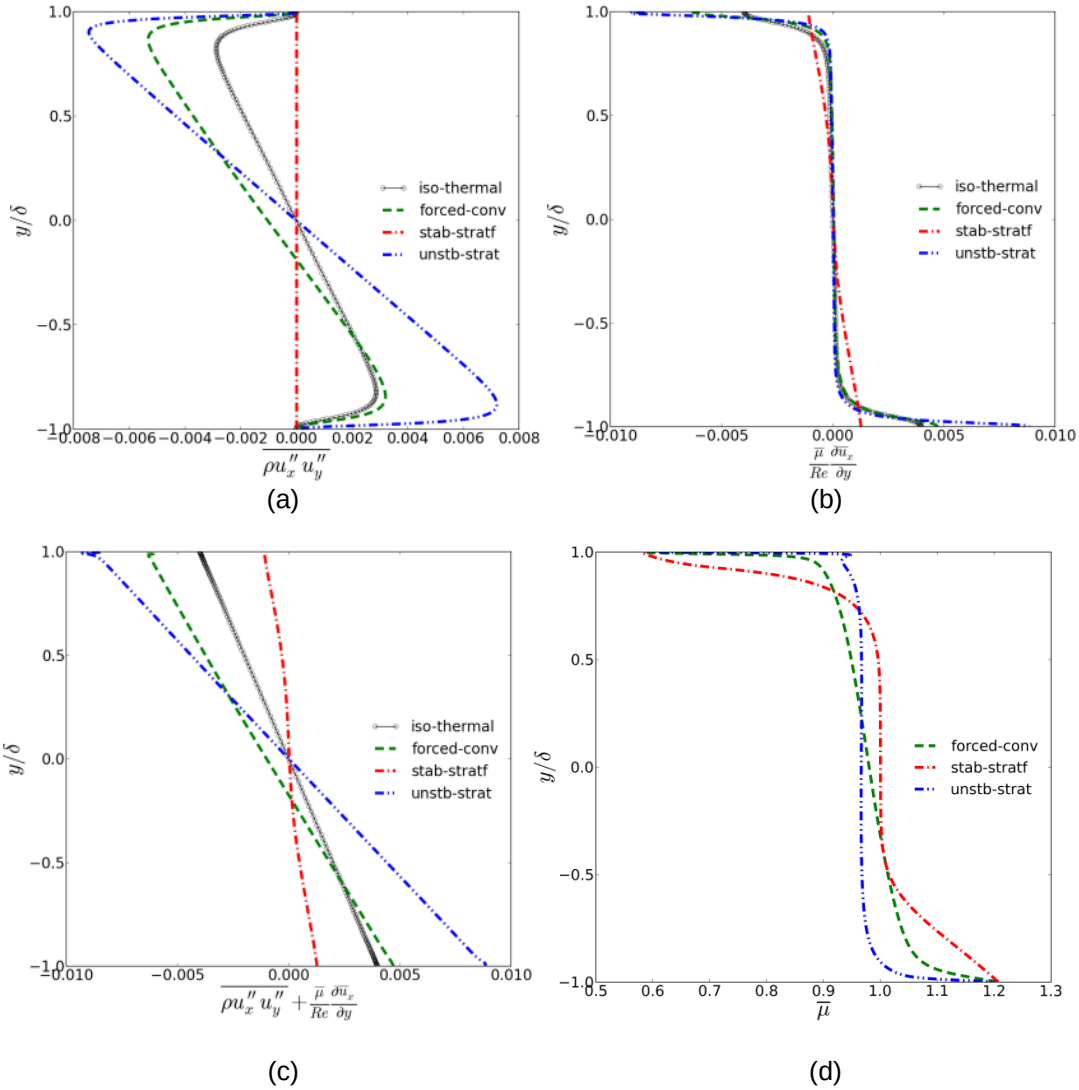

Figure 8 Shear stress distribution: (a) Turbulent shear stress, (b) Viscous shear stress, (c) Total shear stress, (d) Molecular viscosity distribution.

Bea *et al*.[2] discussed the correlation between the buoyancy production term $-g\delta/U_0^2\overline{\rho' u_i'}$ and the turbulent heat flux $\overline{\rho u_i'' h''}$, which usually have the same sign in supercritical CO2 in vertical pipes. Figure 9 shows the buoyancy production of $\overline{\rho u_x'' u_y''}$ and the turbulent heat flux $\overline{\rho u_x'' h''}$ for both the stable and unstable stratification. For the stably stratified flow, the turbulence fluctuation production of the turbulence shear stress $\overline{\rho u_x'' u_y''}$ is almost zero, and the buoyancy production dominates. However, the absolute value is very small and far less than that in the unstably stratified flow. The distributions of the buoyancy production term $-g\delta/U_0^2\overline{\rho' u_x'}$ and the turbulent heat flux $\overline{\rho u_x'' h''}$ are positively correlated in the stably stratified flow, as that in CO2 vertical pipe flow [2]. This implies that a positive/negative buoyancy production term $-g\delta/U_0^2\overline{\rho' u_x'}$ increase/decrease the turbulence mixing in the normal direction and

correspondingly increase/decrease the turbulent heat flux $\overline{\rho u_x'' h''}$ in the streamwise direction. However this positive correlation is not linearly dependent, but also depends on the total turbulence production and local thermal properties. (There is no explicit buoyancy production for the turbulent heat flux $\overline{\rho u_x'' h''}$ in horizontal flow.) **Figure 9** (b) shows that the buoyancy production term for $\overline{\rho u_x'' u_y''}$ is smaller than the turbulence fluctuation production across the whole domain in the unstably stratified flow. At the location of peak $-g\delta/U_0^2\overline{\rho' u_x}'$ near the cooled wall, it accounts for slightly over one third of the total production. Different from the stably stratified flow, the distribution of the turbulent heat flux $\overline{\rho u_x'' h''}$ in the unstable stratification is not always positively correlated with the buoyancy production term across the domain. Actually, for this unstably stratified flow with a stronger vertical turbulence perturbation than the streamwise perturbation, the main contribution to the shear stress production is the vertical fluctuation and the distribution of the turbulent heat flux $\overline{\rho u_x'' h''}$ is more relevant to the total production of Reynolds shear stress than the buoyancy production.

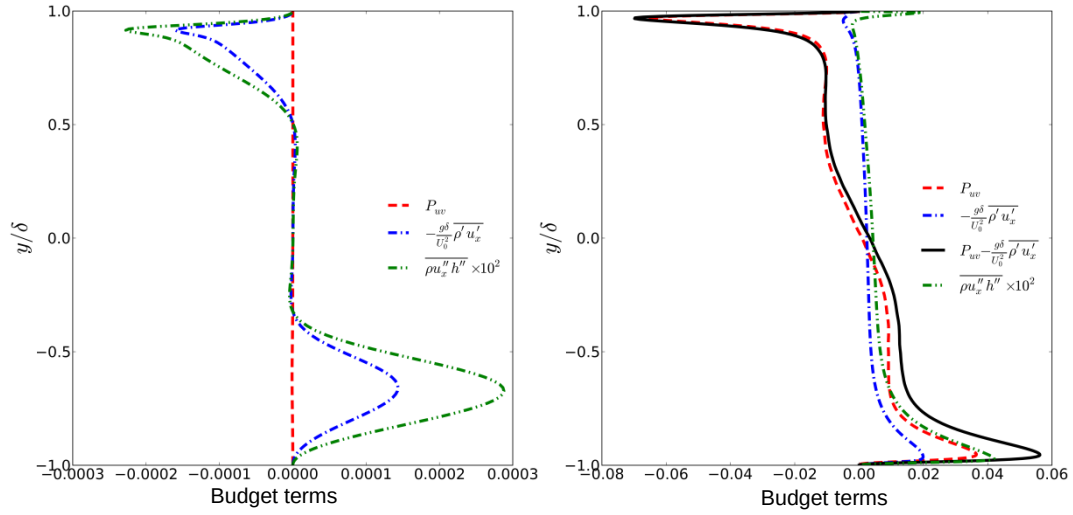

(a) Stable stratification (b) Unstable stratification

Figure 9 Production terms (both buoyancy production term $-\frac{g\delta}{U_0^2}\overline{\rho' u_x'}$ and the stress production term P_{uv}) of turbulence shear stress $\overline{\rho u_x'' u_y''}$, and streamwise turbulent heat flux distribution $\overline{\rho u_x'' h''}$. (a) Stable stratification (b) Unstable stratification

Figure 10 shows the turbulence production for Reynolds wall-normal stress $\overline{\rho u_y'' u_y''}$, including the buoyancy production $-2g\delta/U_0^2\overline{\rho' u_y'}$ and the stress production term P_{vv}, the turbulent heat flux $\overline{\rho u_y'' h''}$ and its buoyancy production $-g\delta/U_0^2\overline{\rho' h'}$ for the unstably stratified flow. Similar to that in an isothermal flow, the stress turbulence production term of $\overline{\rho u_x'' u_y''}$ is nearly zero. The buoyancy generates positive turbulence production for $\overline{\rho u_y'' u_y''}$ in the unstably stratified flow, as expected. The distribution of the buoyancy production $-2g\delta/U_0^2\overline{\rho' u_y'}$ is strongly related to the density variation in the normal direction, and the peak near the heated wall corresponds to the severe change of density shown in Figure 6. Figure 10 also shows that the effect of buoyancy production for the turbulence heat flux $\overline{\rho u_y'' h''}$ is strong near the walls, especially near the heated wall, where both enthalpy and density have large fluctuations. The positive sign of the turbulence heat flux $\overline{\rho u_y'' h''}$ implies the heat is transferred from the heated wall towards the cooled wall.

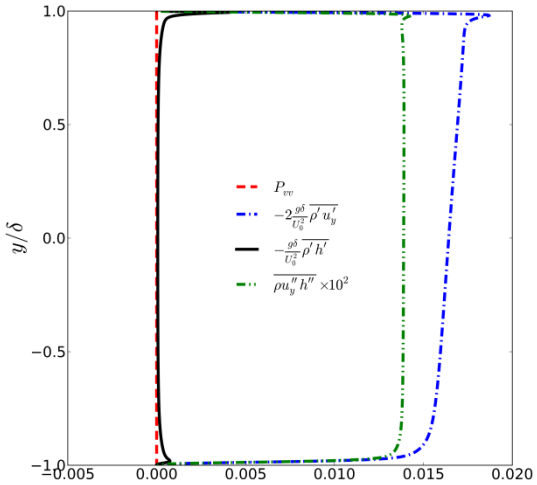

Figure 10 Unstable stratification: Production term of turbulence stress $\overline{\rho u_y'' u_y''}$ (both buoyancy production term $-2g\delta/U_0^2\overline{\rho' u_y'}$ and the stress production term $P_{u_v u_v}$) and vertical turbulent heat flux distribution $\overline{\rho u_y'' h''}$ and its buoyancy production $-\frac{g\delta}{U_0^2}\overline{\rho' h'}$

4.4 Instantaneous flow structures

The instantaneous flow structures are shown to visualize the buoyancy effect on turbulent flow structures. **Figure 11** displays the instantaneous flow structures with the λ_2 criterion [26]. Here, λ_2 is the second largest eigenvalue of the symmetric tensor $S^2 + \Omega^2$ where S and Ω are the symmetric and antisymmetric parts of the velocity gradient tensor, $\nabla \boldsymbol{u}$. In order to show a clear picture, different λ_2 values are used, and usually a smaller magnitude of λ_2 iso-surface shows smaller turbulence structures in one case. **Figure 11** shows that the turbulence structures of the stably stratified flow are significantly damped, consistent with earlier observations when discussion of the velocity and turbulence shear stress distribution was presented. Both the forced convection and the unstably stratified flow shows turbulence enhancement compared with the isothermal flow. For the forced convection flow, motions of turbulence elements near the top heated wall are increased than those near the cooled wall, and no obvious large-scale vertical motions are observed. For the unstably stratified flow, large-scale vertical motions are observed, since turbulence elements near the bottom heated wall tend to move upwards and those near the top cooled wall move downwards, which increase turbulence mixing on both sides.

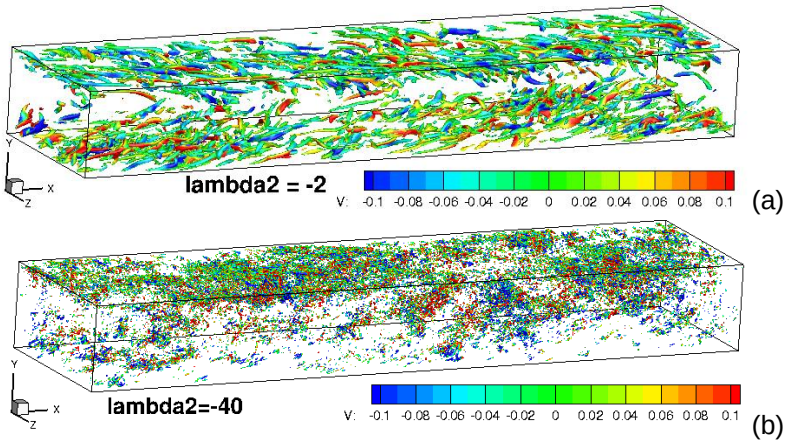

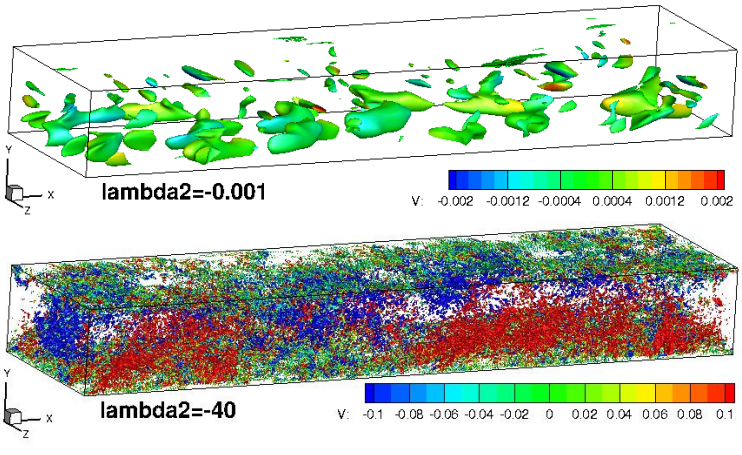

Figure 11 Instantaneous iso-surface of λ_2 criterion, coloured by the normal velocity. The original y direction is used for all cases, which means that for the unstably stratified flow, the bottom wall is heated and the top wall is cooled, while for the forced convection and stably stratified flow, they are opposite. (a) iso-thermal flow, (b) forced convection flow, (c) stably stratified flow, (d) unstably stratified flow

5. Conclusions

This study investigates the characteristics of turbulent heat transfer to supercritical water in a horizontal channel with constant but different wall temperatures using direct numerical simulation. Forced convection flow, stably stratified flow and unstably stratified flow have been numerically studied and turbulence statistics, buoyancy effects and stratification effects on turbulence and heat transfer are discussed.

With the same temperature differences, the stably stratified flow is laminarised, but in the unstably stratified flow, turbulence mixing and heat transfer are enhanced due to the buoyance force working as a source of turbulence. For the stably stratified flow, the buoyancy effect is stronger than the variation effect of thermal properties. The latter effect enhances turbulence mixing in the forced convection flow, but this is not strong enough to compensate the effect of laminarisation due to buoyancy and hence, overall, heat transfer is worsened. For the unstably stratified flow, the buoyancy effect introduces strong vertical fluctuations, higher than the streamwise fluctuations. Such large fluctuations in the unstably stratified flow contribute to a strong Reynolds shear stress. Nevertheless the dominant production term is due to turbulence fluctuations while the buoyancy production mainly functions near the cooled wall.

Acknowledges

This work is supported by the Engineering and Physical Sciences Research Council of the United Kingdom under Grant No. EP/K007777/1. This work made use of the facilities of the N8 HPC, provided and funded by the N8 consortium and EPSRC (Grant No. EP/K000225/1). The Centre is co-ordinated by the Universities of Leeds and Manchester.

References

1. DoE, U. S. "A technology roadmap for generation IV nuclear energy systems." Nuclear Energy Research Advisory Committee and the Generation IV International Forum. (2002).

2. Bae, Joong Hun, Jung Yul Yoo, and Haecheon Choi. "Direct numerical simulation of turbulent supercritical flows with heat transfer." Physics of Fluids (1994-present) 17.10 (2005): 105104.

3. Pis'menny E. N., Razumovskiy V. G., Maevskiy E. M., Koloskov A. E. and Pioro I. L., "Heat Transfer to Supercrtical Water in Gaseous State or Affected by Mixed Convection in Vertical Tubes," in Proceedings of ICONE14, Miami, Florida, USA, (2006)

4. Ničeno, B., and M. Sharabi. "Large eddy simulation of turbulent heat transfer at supercritical pressures." Nuclear Engineering and Design 261 (2013): 44-55.

5. Koshizuka, S., Takano, N., & Oka, Y. Numerical analysis of deterioration phenomena in heat transfer to supercritical water. International Journal of Heat and Mass, 38(16), 1–8. (1995).

6. Lei, X., Li, H., Yu, S., & Chen, T. Numerical investigation on the mixed convection and heat transfer of supercritical water in horizontal tubes in the large specific heat region. Computers & Fluids, 64, 127–140. (2012).

7. Zhang, G., Zhang, H., Gu, H., Yang, Y., & Cheng, X. Experimental and numerical investigation of turbulent convective heat transfer deterioration of supercritical water in vertical tube. Nuclear Engineering and Design, 248, 226–237. (2012)

8. Kao, M.-T., Lee, M., Ferng, Y.-M., & Chieng, C.-C. Heat transfer deterioration in a supercritical water channel. Nuclear Engineering and Design, 240(10), 3321–3328 (2010).

9. Jaromin, M., & Anglart, H. A numerical study of heat transfer to supercritical water flowing upward in vertical tubes under normal and deteriorated conditions. Nuclear Engineering and Design, 264, 61–70. (2013).

10. Bazargan, M., & Mohseni, M. (2009). The significance of the buffer zone of boundary layer on convective heat transfer to a vertical turbulent flow of a supercritical fluid. The Journal of Supercritical Fluids, 51(2), 221–229.

11. Liu, Lei, et al. "Numerical simulation of heat transfer deterioration phenomenon to supercritical water in annular channel." Annals of Nuclear Energy 53 (2013): 170-181.

12. Hassan Zaim, E., & Gandjalikhan Nassab, S. a.. Numerical investigation of laminar forced convection of water upwards in a narrow annulus at supercritical pressure. Energy, 35(10), 4172–4177. (2010)

13. Liu, L., Xiao, Z., Yan, X., Zeng, X., & Huang, Y. Numerical simulation of heat transfer deterioration phenomenon to supercritical water in annular channel. Annals of Nuclear Energy, 53, 170–181. (2013).

14. Lee, S. H. Numerical study of convective heat transfer to supercritical water in rectangular ducts. International Communications in Heat and Mass Transfer, 37(10), 1465–1470. (2010).

15. Baniasad Askari, I., Gandjalikhan Nassab, S. a., & Peymanfard, M.. Numerical Analysis of Convective Heat Transfer in Supercritical Water Flow Channels. Engineering Applications of Computational Fluid Mechanics, 3(3), 408–418. (2014)

16. Cheng, X., Kuang, B., & Yang, Y. H. Numerical analysis of heat transfer in supercritical water cooled flow channels. Nuclear Engineering and Design, 237(3), 240–252. (2007).

17. Yang, Z., Bi, Q., Wang, H., Wu, G., & Hu, R. Experiment of Heat Transfer to Supercritical Water Flowing in Vertical Annular Channels. Journal of Heat Transfer, 135(4), 042504. (2013).

18. Khan, S. A. Heat transfer to carbon dioxide at supercritical pressure'Ph. D. Diss. Thesis University of Manchester, (1965).

19. Jackson, J. D. "Fluid flow and convective heat transfer to fluids at supercritical pressure." Nuclear Engineering and Design 264 (2013): 24-40.

20. He, S., and M. Seddighi. "Turbulence in transient channel flow." Journal of Fluid Mechanics 715 (2013): 60-102.

21. J. A. Manion, R. E. Huie, R. D. Levin, D. R. Burgess Jr., V. L. Orkin, W. Tsang, W. S. McGivern, J. W. Hudgens, V. D. Knyazev, D. B. Atkinson, E. Chai, A. M. Tereza, C.-Y. Lin, T. C. Allison, W. G. Mallard, F. Westley, J. T. Herron, R. F. Hampson, and D. H. Frizzell, NIST Chemical Kinetics Database, NIST Standard Reference Database 17, Version 7.0 (Web Version), Release 1.6.8, Data version 2013.03, National Institute of Standards and Technology, Gaithersburg, Maryland, 20899-8320. Web address: http://kinetics.nist.gov/

22. Kim, John, Parviz Moin, and Robert Moser. "Turbulence statistics in fully developed channel flow at low Reynolds number." Journal of fluid mechanics 177 (1987): 133-166.

23. Iida, O., and N. Kasagi. "Direct numerical simulation of unstably stratified turbulent channel flow." Journal of heat transfer 119.1 (1997): 53-61.

24. Zainali, A., and B. Lessani. "Large-eddy simulation of unstably stratified turbulent channel flow with high temperature differences." International Journal of Heat and Mass Transfer 53.21 (2010): 4865-4875.

25. Jackson, J. D., and W. B. Hall. "Influences of buoyancy on heat transfer to fluids flowing in vertical tubes under turbulent conditions." Turbulent forced convection in channels and bundles 2 (1979): 613-640.

26. Jeong, Jinhee, and Fazle Hussain. "On the identification of a vortex." Journal of fluid mechanics 285 (1995): 69-94.

ISSCWR7-2068

Development of Safety Analysis Code TACOS and Application to FQT Loop

Chaofei Jiang
Xi'an Jiaotong University
No.28, Xianning West Road, Xi'an, Shaanxi, 710049, P.R. China
+86 151 9143 7587, chaofei@stu.xjtu.edu.cn

Wenxi Tian
Xi'an Jiaotong University
No.28, Xianning West Road, Xi'an, Shaanxi, 710049, P.R. China
+86 131 8617 6945, wxtian@mail.xjtu.edu.cn

Suizheng Qiu
Xi'an Jiaotong University
No.28, Xianning West Road, Xi'an, Shaanxi, 710049, P.R. China
+86 131 5241 0318, szqiu@mail.xjtu.edu.cn

Guanghui Su
Xi'an Jiaotong University
No.28, Xianning West Road, Xi'an, Shaanxi, 710049, P.R. China
+86 132 5979 0835, ghsu@mail.xjtu.edu.cn

Abstract

In this study, a transient analysis code of SCWRs (TACOS), with the ability of simulating transients under supercritical and subcritical conditions, has been developed with Fortran 90 language, and simulation has been performed to the European SCWR fuel qualification test (SCWR-FQT) system. The semi-implicit finite difference technique was adopted for the solution of coolant dynamic behaviour in the loop. Furthermore, an illustration of numerical solution for the heat structure model and other models was presented. Therefore, the design basis accidents with the trans-critical transient were investigated for the SCWR-FQT system, and the code was verified by the code ATHLET under the same initial condition and boundary condition. The results by TACOS showed a good agreement with the ones by ATHLET, and indicated that the SCWR-FQT with existing safety system can be cooled effectively under designed basic accidents (DBAs).

1. Introduction

Supercritical water-cooled reactors (SCWRs), the only light water cooled ones in GIF IV generation reactors concept design, have unique advantages in economic and technology. SCWR takes large amount of mature technology over light water cooled reactors (LWRs), including pressure water cooled reactors (PWRs) and boiling water cooled reactors (BWRs), and even supercritical fossil-fired plant technology. Among the R&D of SCWR, the safety analysis is a key issue. Safety analysis codes for other nuclear applications, however, have to be extended for SCWR analysis. Due to the significant difference between supercritical water

and subcritical water, the extensions should include (a) the use of steam tables for supercritical water, (b) the use of heat transfer correlations, (c) the use of pressure drop correlations and (d) the use of critical flow correlations. Up to now, some safety analysis codes, like APROS, ATHLET, and RETRAN, have been modified to simulations transients and accidents of SCWR. As experiment data for SCWR is quite rare, the V&V of these codes are mainly through other codes' results at present.

In this paper, the code TACOS is improved to perform the depressurization transients or accidents of SCWR, and is applied to the European SCWR-FQT loop. The trip of pump accident of FQT loop is simulated, the results is compared with the one by ATHLET, and discussed.

2. Code TACOS development

The earlier version of TACOS has developed [1], and was used to perform the loss of flow accident (LOFA) analysis on SCWR-M. However, due to the simplification on the momentum control equation, the code TACOS is unable to predict the behaviour of SCWR during the depressurization transients or accidents. In the newest version of TACOS, the combined solution of the mass equation, momentum equation, and energy equation of the coolant in a single channel is adopted, and other auxiliary models are updated at the same time.

2.1 Hydrodynamic model and its difference

The supercritical water can be treated to be single phase; on the other hand, the homogenous equilibrium model (HEM) was applied during two phase appears. HEM assumes: (1) that the there is no velocity difference between the two phases (i.e., homogeneous flow); (2) and that the mixture are in thermodynamic equilibrium. For the single phase and the mixture with HEM assuming, the one-dimension mass, momentum, and energy conservation equation can be written as follows. Mention that the parameters discussed below mean the single phase properties or the mixture HEM properties if no specific illustration.

Mass:

$$\frac{\partial}{\partial t}\rho + \frac{\partial}{\partial z}\rho u = 0 \tag{1}$$

Momentum:

$$\frac{\partial}{\partial t}\rho u + \frac{\partial}{\partial z}\rho uu = -\frac{\partial p}{\partial z} - \frac{f\,\rho uu}{2D_e} - \rho g\cos\theta \tag{2}$$

Energy:

$$\frac{\partial}{\partial t}\rho h + \frac{\partial}{\partial z}\rho uh = \frac{q'' P_h}{A} + \frac{\partial p}{\partial t} + u\frac{\partial p}{\partial z} \tag{3}$$

where ρ = the density of coolant; t = the time; u = the velocity of coolant; z = the spatial coordinate; p = the pressure of coolant; f = the coefficient of frictional resistance; D_e = the equivalent hydraulic diameter of flow channel, ρ = the coefficient of gravity; θ = the angle of the z direction with the upward vertical; h = the specific enthalpy of coolant; q'' = the heat flux.

The state equation for coolant is

$$\rho = \rho(p,h) \tag{4}$$

The chain rule may be applied to mass and energy conservation equations to eliminate the density in equation (1) and (3).

$$\frac{\partial\rho(p,h)}{\partial t} = \frac{\partial\rho(p,h)}{\partial h}\frac{\partial h}{\partial t} + \frac{\partial\rho(p,h)}{\partial p}\frac{\partial p}{\partial t} \tag{5}$$

Substituting equation (5) into equation (1) and equation (3) yields

$$\frac{\partial\rho}{\partial h}\frac{\partial h}{\partial t} + \frac{\partial\rho}{\partial p}\frac{\partial p}{\partial t} + \frac{\partial}{\partial z}\rho u = 0 \tag{6}$$

and

$$(h\frac{\partial\rho}{\partial h}+\rho-\frac{p}{\rho}\frac{\partial\rho}{\partial h})\frac{\partial h}{\partial t}+(h\frac{\partial\rho}{\partial p}-1-\frac{p}{\rho}\frac{\partial\rho}{\partial p})\frac{\partial p}{\partial t}+\frac{\partial}{\partial z}\rho hu-\frac{\partial}{\partial z}pu=\frac{q''P_h}{A} \quad (7)$$

The semi-implicit finite difference numerical solution scheme is based on replacing the differential equations with the finite difference equations partially implicit in time. In the paper, the above-mentioned method is adopted as the numerically set of the conservation equations. Also, it should be mentioned that the difference equations are based on the concept of a control volume where mass and energy are conserved by the equating accumulation to the rate of mass and energy in through the volume boundary minus the rate of mass and energy out through the volume boundary plus the source terms. So, the staggered grid is adopted as meshing scheme. In this meshing scheme, the scalar properties (pressure, specific enthalpy) are stored at the center of the volumes, while the vector (velocities) are stored at the boundary of the volumes, as shown in Fig. 1.

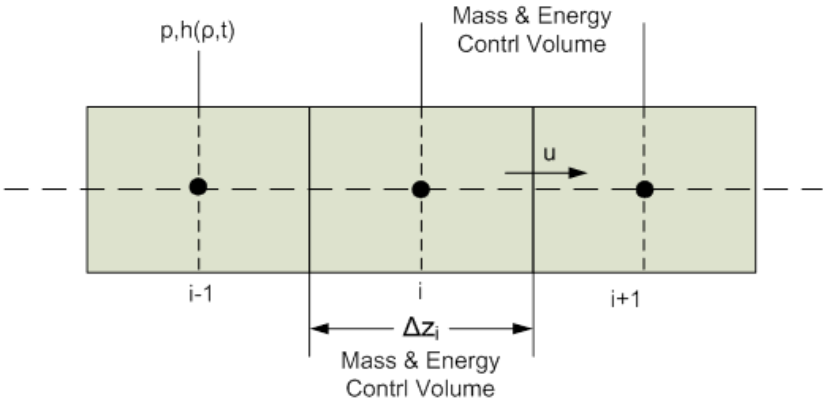

Fig. 1. Staggered grid layout

The momentum equation becomes:

$$\frac{\rho_i^n u_i^{n+1}-\rho_i^n u_i^n}{\Delta t}+\frac{\rho_{i+1/2}^n(u_{i+1/2}^n)^2-\rho_{i-1/2}^n(u_{i-1/2}^n)^2}{\Delta z_{i+1/2}}$$
$$=-\frac{(p_{i+1}^{n+1}-p_i^{n+1})}{\Delta z_{i+1/2}}-\frac{f\rho_{i+1/2}^n(u_{i+1/2}^n)^2}{2D_e}-\rho_{i+1/2}^n g\cos\theta \quad (8)$$

where the superscript *n* represents the old time-step, *n+1* represents the new time step; the subscript *i+1/2* of ρ or Δz represents the boundary between volume i and volume i+1.

The interface velocity can be expressed as in the form of pressures and old-time velocity as:

$$u_{i+1/2}^{n+1}=\alpha_{i+1/2}+\beta_{i+1/2}(\Delta p_{i+1}-\Delta p_i) \quad (9)$$

where $\Delta p=p^{n+1}-p^n$ at a certain volume; α and β are coefficients. With the semi-implicit finite difference method, the equation (6) and equation (7) can be written as:

$$(\frac{\partial\rho}{\partial h})_i^n\frac{h_i^{n+1}-h_i^n}{\Delta t}+(\frac{\partial\rho}{\partial p})_i^n\frac{p_i^{n+1}-p_i^n}{\Delta t}+\frac{\dot\rho_{i+1/2}^n u_{i+1/2}^{n+1}-\rho_{i-1/2}^n u_{i-1/2}^{n+1}}{\Delta z_i}=0 \quad (10)$$

$$\left[(h-\frac{p}{\rho})\frac{\partial\rho}{\partial h}+\rho\right]_i^n\frac{h_i^{n+1}-h_i^n}{\Delta t}+\left[(h-\frac{p}{\rho})\frac{\partial\rho}{\partial p}-1\right]_i^n\frac{p_i^{n+1}-p_i^n}{\Delta t}$$
$$+\frac{\dot\rho_{i+1/2}^n u_{i+1/2}^{n+1}\dot h_{i+1/2}^n-\dot\rho_{i-1/2}^n u_{i-1/2}^{n+1}\dot h_{i-1/2}^n}{\Delta z_i}-\frac{\dot p_{i+1/2}^n u_{i+1/2}^{n+1}-\dot p_{i-1/2}^n u_{i-1/2}^{n+1}}{\Delta z_i}=(\frac{q''P_h}{A})_i^n \quad (11)$$

In the equation (10) and equation (11), the term $(h_i^{n+1} - h_i^n)$ and $(p_i^{n+1} - p_i^n)$ can be expressed by the equation in the terms of $u_{i+1/2}^{n+1}$ and $u_{i-1/2}^{n+1}$ as follows

$$(p_i^{n+1} - p_i^n) = a + bu_{i+1/2}^{n+1} + cu_{i-1/2}^{n+1} \tag{12}$$

Substituting equation (9) into equation (12) gives

$$f_{i-1}\Delta p_{i-1} + f_i\ \Delta p_i\ + f_{i+1}\Delta p_{i+1} = d_i \tag{13}$$

Considering all the volumes of coolant, equation (13) can be extended to be as follows.

$$\begin{cases} f_{1,1}\Delta p_1 + f_{1,2}\Delta p_2 = d_1 \\ f_{2,1}\Delta p_1 + f_{2,2}\Delta p_2 + f_{2,3}\Delta p_3 = d_2 \\ \vdots \\ f_{i,i-1}\Delta p_{i-1} + f_{i,i}\Delta p_i\ + f_{i,i+1}\Delta p_{i+1} = d_i \\ \vdots \\ f_{N-1,N-2}\Delta p_{N-2} + f_{N-1,N-1}\Delta p_{N-1} + f_{N-1,N}\Delta p_N = d_{N-1} \\ f_{N,N-1}\Delta p_{N-1} + f_{N,N}\Delta p_N = d_N \end{cases} \tag{14}$$

Rewrite equation (14) in the form of matrix, and an *N* x *N* type matrix will obtain. *N* is the number of coolant volumes.

$$\begin{bmatrix} f_{1,1} & f_{1,2} & & & & & & \\ f_{2,1} & f_{2,2} & f_{2,3} & & & & & \\ & \ddots & \ddots & \ddots & & & & \\ & & f_{i,i-1} & f_{i,i} & f_{i,i+1} & & & \\ & & & \ddots & \ddots & \ddots & & \\ & & & & f_{N-1,N-2} & f_{N-1,N-1} & f_{N-1,N} & \\ & & & & & f_{N,N-1} & f_{N,N} & \end{bmatrix} \begin{bmatrix} \Delta P_1 \\ \Delta P_2 \\ \vdots \\ \Delta P_i \\ \vdots \\ \Delta P_{N-1} \\ \Delta P_N \end{bmatrix} = \begin{bmatrix} d_1 \\ d_2 \\ \vdots \\ d_i \\ \vdots \\ d_{N-1} \\ d_N \end{bmatrix} \tag{15}$$

The matrix can be solved by the Gaussian elimination method. After solving equation (15), we'll get the new pressures for all volumes. Then through equation (9), we'll update all the velocities. In the third stage, the new enthalpies can be obtained by equation (10). At last, other parameters at new time step, for example ρ , can be updated.

2.2 Heat structure model and its difference

The heat structure model is used to predict the temperature distribution and the heat flux between heat structure and coolant. Its control equation for one-dimension, transient condition is

$$\rho c \frac{\partial T}{\partial t} = \frac{1}{r}\frac{\partial}{\partial r}(r\lambda \frac{\partial T}{\partial r}) + q_V \tag{14}$$

where c = the specific heat capacity of heat structure; T = the temperature of heat structure; r = the radial coordinate; λ = the thermal conductivity of heat structure; q_v = the internal heat source.

The typical mesh scheme for heat structure is shown in Fig. 2. The temperature is stored at the points, such as point P, point E, and point W. And the temperature terms are evaluated implicitly. The difference form of equation (14) becomes

$$a_P T_P + a_E T_E + a_W T_W = a_0 T_0 + b \tag{15}$$

Where

$$a_E = -\frac{\lambda_e r_e}{(\delta r)_e},\ a_W = -\frac{\lambda_w r_w}{(\delta r)_w},\ a_0 = -\frac{(\rho c)_P \Delta V_P}{\Delta t},\ b = \Delta V_P q_V,\ \Delta V_P = 0.5(r_w + r_e)\bullet\Delta r_P,$$

T_0 = the temperature of point P at old time step, the subscript e means the boundary between point W and point P, and the subscript w means the boundary between point P and point E. So, r_e and r_w stand for the radial coordinate of boundary e and boundary w respectively, as shown in Fig. 2. It should be mentioned that the boundary thermal conductivity λ_e, for example, is the harmonic mean of thermal conductivities at point P and point E.

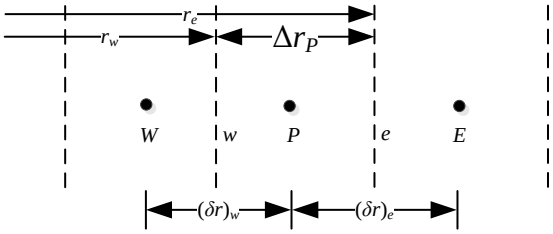

Fig. 2. Mesh scheme for heat structure

For the fuel rod, its boundary conditions involve the second kind and the third kind. In detail, for the centreline of the fuel pellets, the adiabatic condition is suitable; for the surface of the fuel cladding, the convection heat transfer condition is suitable. The mesh scheme for the fuel rods is illustrated in Fig. 3.

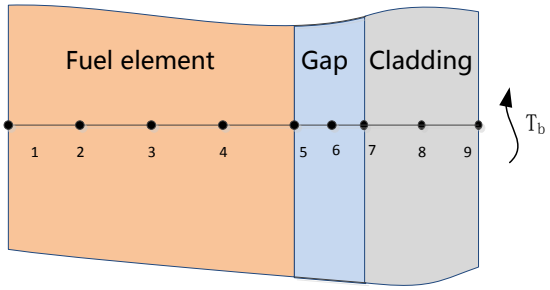

Fig. 3. Mesh scheme for fuel rods

2.3 Critical flow model

For the critical pressure of choking flow is unknown, reduce the back pressure to search the maximum flow, and the maximum flow is corresponding to the critical flow pressure. Chen [2] proposed the estimation of mass flow base on the theoretical analysis and the experimental data. It is realized that with low sub-cool degree the chocking flow might not happen. Hence the mass flow should be predicted by the Bernoulli model. And the method for SCW critical flow is proposed as:

$$G = \min(G_{M-HEM}, G_{Bernoulli}) \tag{16}$$

G_{M-HEM} is critical mass flow rate calculated by modified HEM model,

$$G_{M-HEM} = \sqrt{\frac{2\left[h_0 - (1-x)h_L - xh_V\right]}{\frac{c}{\bar{\rho}^2} + \left[(1-x)v_L + xv_V\right]^2}} \tag{17}$$

where h = the specific enthalpy, h_0 = the stagnation enthalpy, v = the specific heat capacity, subscripts L and V stand for liquid phase and vapour phase respectively, c = coefficient of local resistance, $\bar{\rho}$ = the density of mixture, and the equilibrium quality at the critical plane, x, is calculated by

$$x = \frac{s_0 - s_L}{s_V - s_L} \tag{18}$$

with s = the specific entropy.

$G_{Bernoulli}$ is critical mass fow rate by Bernoulli model,

$$G_{Bernoulli} = 0.61\sqrt{2\rho\left(P_0 - P_b\right)} \tag{19}$$

where P_0 = the stagnation pressure, P_b = the back pressure, and ρ = the mixture density.

2.4 Other auxiliary models

At supercritical pressure, the heat transfer to the supercritical water is calculated with the correlation of Bishop [3], for its balance between conservative calculation principle and accuracy [1].

At supercritical pressure, the correlation of Kirillov [4] is recommended:

$$f = f_o \bullet \left(\frac{\rho_W}{\rho_B}\right)^{0.4} \tag{20}$$

with

$$f_o = \left(1.82\log\left(\mathrm{Re}/8\right)\right)^{-0.2} \tag{21}$$

REFPROP (NIST Reference Fluid Thermodynamic and Transport Properties) version 9.0, with a high quality database for water covering temperature of 273.16K to 2000K and pressure up to 10000 MPa, is selected as the water table for TACOS.

3. Application of the code TACOS

Within the SCWR-FQT project, it is planned to carry out a test of a small scale fuel assembly in a research reactor. Design and licensing of such a small scale fuel assembly with 4 fuel pins including the required loop with its safety and auxiliary system is subject of FQT project. In this paper, the loss of flow accident/transient due to trip of primary pump of SCWR-FQT loop is simulated by the code TACOS, and the safety characters of FQT loop are discussed.

3.1 SCWR-FQT system description

The SCWR-FQT loop consists of the primary circuit, secondary system, safety system and other auxiliary systems, as shown in Fig. 4 [5, 6].

The primary circuit is shown in red in Fig. 4. The coolant of 300°C is drived by the recirculation pump (HCC), and then flows into the active channel through the inlet line (L1). During the steady state, the coolant flows out of the active channel with a temperature of 300°C through the outlet line (L2). As shown in Fig. 5, the active channel can be mainly divided into three part: the cooler, the recuperator, and the test section, and is made up by the pressure tube, two guide tubes, the assembly box, the recuperator tubes and the cooler tubes. Two active safety systems, the feed line coolant injection (FLCI, orange) and the emergency line coolant injection (ELCI, dark green), are designed. Once a DBA happens, water of 30°C may be injected through FLCI or ELCI. The ELCI is the dominant safety system for FQT loop. So, once the ELCI is actuated, the FLCI should be closed to ensure the sufficient cooling of core. Should a critical incident occur, the system has to be depressurized immediately through automatic depressurization system (ADS). Moreover, pressure relief valve (PRV) is used to avoid the

overpressure of FQT loop. More detail description can be seen in [7]. As shown in Table 2.1, the FLCI and the ELCI system are activated by different, independent signals.

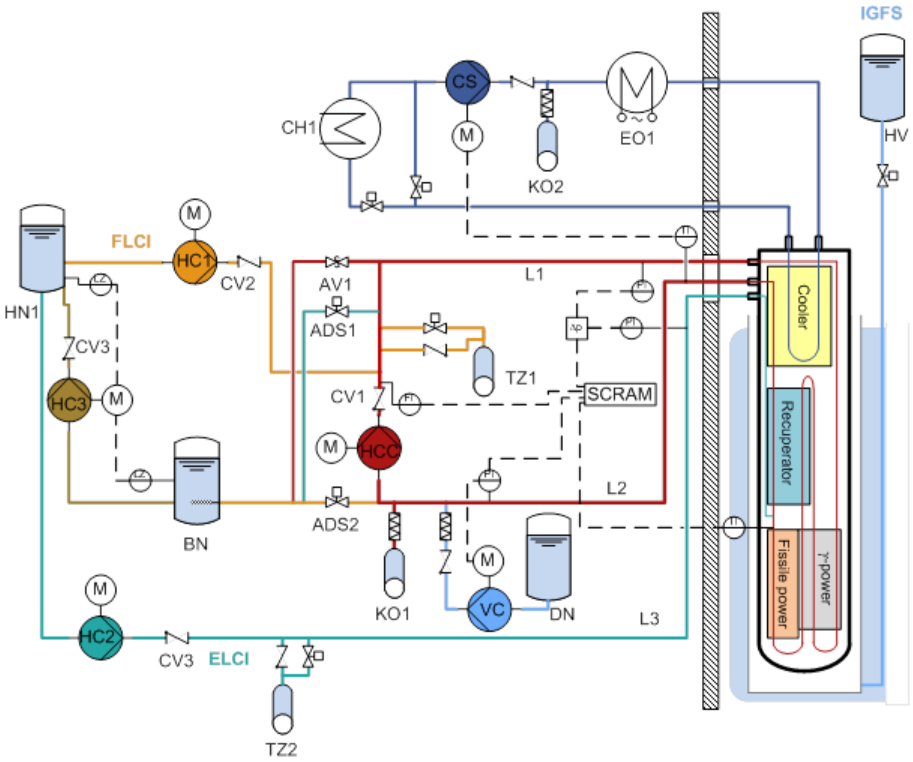

ADS – Automatic depress. system	DN – Refilling tank	HN1 – Emergency coolant reservoir
AV – Pressure relief valve	HC – Emergency pump	HV – Reservoir
BN – Pressure suppression tank	HC2 – Emergency pump 2	KO – Pressurizer
CV – Check valve	HC3 – Refilling pump	TZ – Pressure accumulator
EO1 – Electrical heater	HCC – Recirculation pump	VC – Boost pump

Fig. 4. Sketch of the SCWR-FQT loop, Raqué (2014).

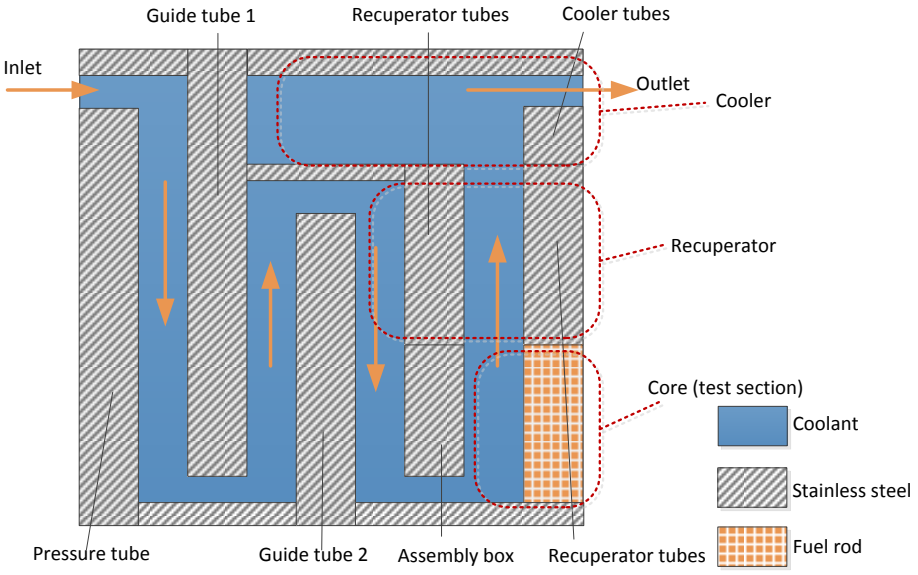

Fig. 5. Schematic diagram of active channel (not in scale)

Table 1. Signals and actions of the safety systems

System	Signal	Scram level	Action
FLCI	System pressure low [MPa] Coolant mass flow low [g/s]	< 22.5 <150	Reactor scram *1 s later:* ADS2 opens HC1 pump starts HCC pump stops IGFS opens
ELCI	Coolant temp. in test section high [°C] Pressure diff. L1-L3 negative [MPa]	> 500 < -3	Reactor scram *1 s later*: ADS1 opens HC2 pump starts HCC pump stops IGFS opens
PRV	System pressure high [MPa]	none	AV1 opens

3.2 Result and analysis

Fig. 6 shows the nodalization of fluid zone in the FQT loop. Nodes 6 to 98 represent the active channel of SCWR-FQT loop. 10 nodes (node 74 to node 83) are meshed in the fluid zone nearby the fuel rods, which is called core in this paper. The fissile power and gamma power are 63.6 kW and 9.8 kW respectively. As shown in Fig. 7, the water at temperature of 300 °C flows into the active channel, and flows downwards through the outer zone heated to temperature of 348 °C. The temperature of water flowing through the gap between guide tube 1 and guide tube 2 decreases gradually to 338 °C. At the inlet of core, the water is at temperature of 373 °C, and then is heated to 384 °C at the outlet of core, which is higher than the critical temperature of water. After passing through the cooler part, the water is cooled to 300 °C at the outlet of active channel.

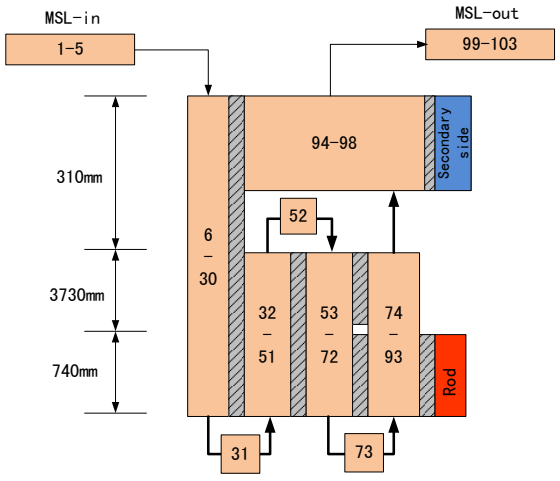

Fig. 6. Nodalization of SCWR-FQT in code TACOS

In this paper, the trip of pump accident, as one the design basic accidents of SCWR-FQT, is simulated by code TACOS. Decay heat is estimated with the correlation:

$$P(t) = A_2 + \frac{A_1 - A_2}{1 + (\frac{t}{t_0})^p} \ [\%] \tag{22}$$

With A_1=7.86259, A_2=-0.0403, t_0=41.97635, and p=0.34749.

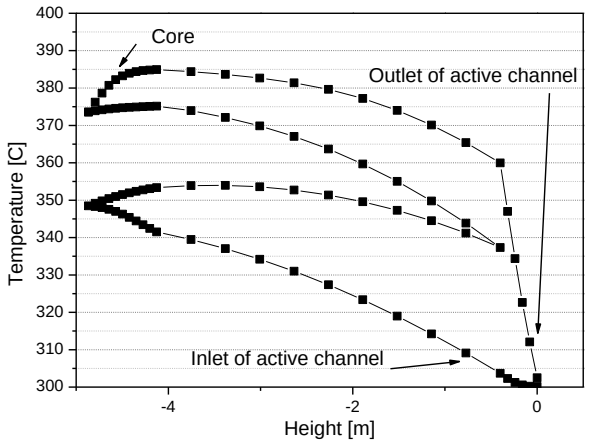

Fig. 7. Fluid temperature distribution in active channel

It is assumed that the main pump of the primary circuit is tripped at 1.0 s during steady state, and then the mass flow of pump outlet decreases to zero in 2.0 s. Low mass flow (<150 g/s) is measured at the active channel inlet at 1.8 s, and then the scram signal is triggered at 1.86 s. Once the scram signal is trigered, the scram starts, and the FLCI signal and ADS2 signal are trigered. The ADS2 begins to open immediately after trigered, and opens at 2.36 s. The TZ2 start injection at 2.40 s from the core outlet, due to the depressurization of the loop. And the TZ1 start injection from the active channel inlet. The time sequence after trip of pump accident is illustrated in Table 2. The mass flow of safety system, including ADS2, TZ1, FLCI, and TZ2, is shown in Fig. 8. The mass flow rates at the inlet and outlet of core decrease firstly after the trip of pump, and then increase more than 1 kg/s, which are much larger than flow rates during steady state. Influenced by the coolant mass flow, the inlet and outlet coolant temperatures increase little after the accident, and the gradually decrease, as shown in Fig. 10. The pressure at the core inlet and out let are shown in Fig. 11. It could be seen that sharp depressurizations appear at 14 s and at 24 s, which is mainly caused by TZ2 and TZ1 empty. Fig. 12 shows the pressure change by ATHLET. The results show that code TACOS shows a good agreement with the one by ATHLET.

During the accident, the maximum temperature of cladding is at the node 4 of cladding (see Fig. 13), and reaches a maximum temperature below 600 °C, which proves the core's safety during accident. The the maximum temperature of cladding by ATHLET is shown in Fig. 14. Though differance exists in max temperature, the change trend is quite the same.

Table 2. Time sequence after trip of pump accident

Time	Event
1.00	Primary pump trip
1.80	Low flow of coolant signal
1.86	Scram Signal FLCI signal Scram start ADS2 actuation
2.36	ADS2 open
2.40	TZ2 injection start
2.86	Scram complete
2.95	TZ1 injection start
13.70	TZ2 empty
22.23	FLCI injection start
23.10	TZ1 empty

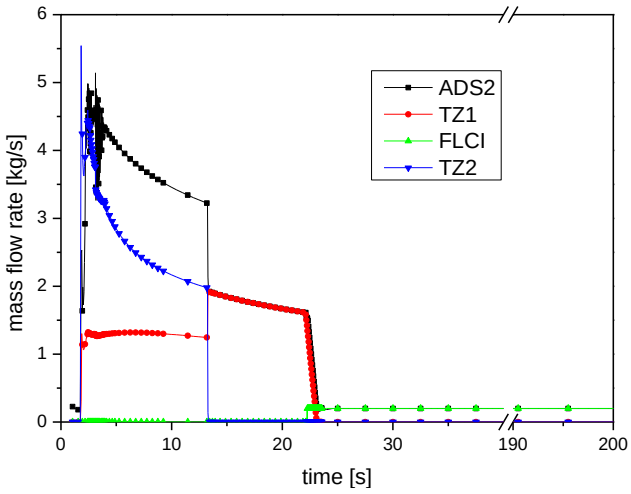

Fig. 8. Mass flow of safety system

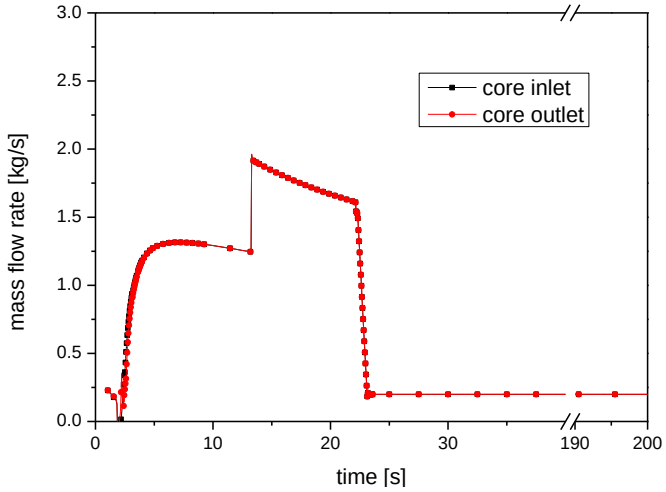

Fig. 9. Mass flow of core inlet and outlet

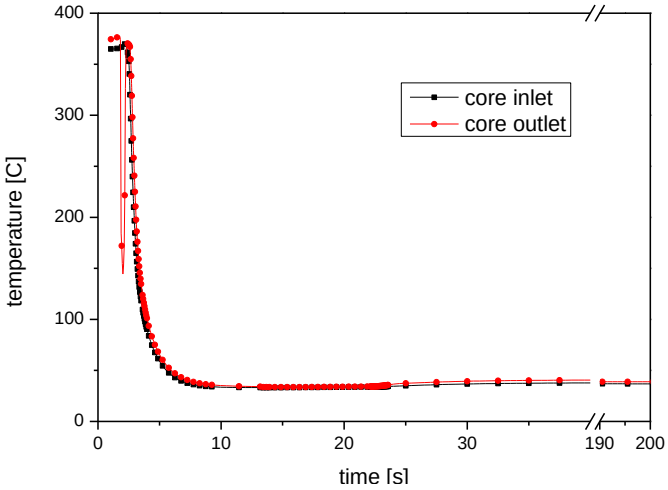

Fig. 10. Temperature of core inlet and outlet

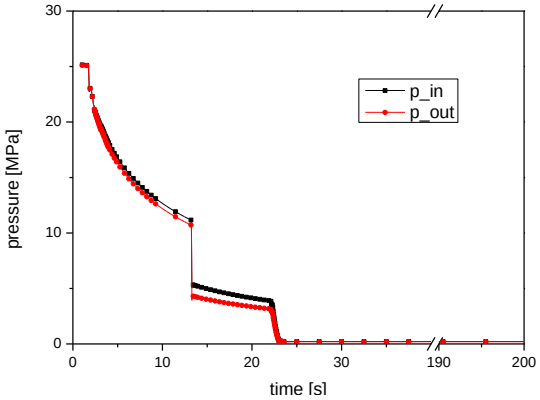

Fig. 11. Pressure at core inlet and outlet

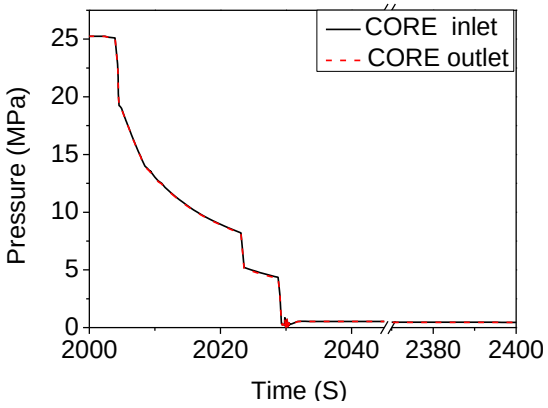

Fig. 12. Pressure at core inlet and outlet by ATHLET

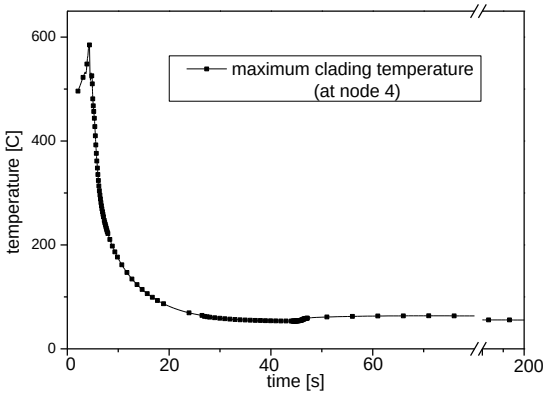

Fig. 13. Maximum cladding temperature (at node 4 of cladding)

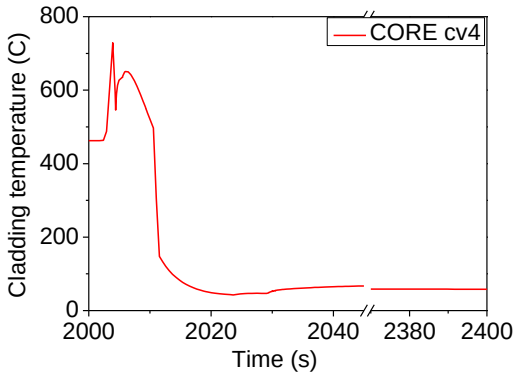

Fig. 14. Maximum cladding temperature (at node 4 of cladding) by ATHLET

Conclusion

In this study, TACOS with the ability of simulating transients under supercritical and subcritical conditions, has been developed and some models are updated and improved, and simulation has been performed to the European SCWR fuel qualification test (SCWR-FQT) system. The results by TACOS showed a good agreement with the ones by ATHLET, and indicated that the SCWR-FQT with existing safety system can be cooled effectively under the trip of pump accident.

References

[1]. D. Zhu, H. Zhao, W. Tian, Y. Su, K. S. Chaudri, G. Su and S. Qiu, “Development of TACOS code for loss of flow accident analysis of SCWR with mixed spectrum core”. Prog. Nuclear Energy 54, 150-161, 2012.

[2]. Chen Y.Z., Yang C.S., Zhao M.F., et al., ”Experimental Studies on Critical Flow and Heat Transfer of Water for Near-critical and Supercritical Pressures”. Proceedings of the IAEA Technical Meeting on Heat Transfer, Thermal-Hydraulics and System Design for Supercritical Water-Cooled Reactors, 2010 [C]. Pisa, Italy, 2010.

[3]. A.A. Bishop, R.O. Sandberg, L.S. Tong, ”Forced convection heat transfer at near critical temperatures and supercritical pressure”, WCAP-2056-P, Part-III_b, 1964

[4]. Kirillov, P.L., Pomet’ko, R.S., Smirnov, et al., ”Experimental study on heat transfer to supercritical water flowing in vertical tubes”. Proceedings of the International Conference GLOBAL-2005 “Nuclear Energy Systems for Future Generation and Global Sustainability,” Tsukuba, Japan, October 9–13, Paper No. 518, 8 pages., 2005.

[5]. R. Schneider, M. Schlagenhaufer, T. Schulenberg, “Conceptual design of the safety system for a SCWR fuel qualification test”. Proceedings of the 8th International Topical Meeting on Nuclear Reactor Thermal Hydraulics, Operation and Safety, Shanghai, China, October 10–14, 2010.

[6]. M. Raqué, A. Wank, T. Schulenberg, P. Hajek, "Thermal analysis of a test fuel element for a reactor with supercritical water", *NUTHOS-8*, Shanghai, China, October 10-14, 2010.

[7]. C. Zhou, Y. Yang, X. Cheng, ”Feasibility analysis of the modified ATHLET code for supercritical water cooled systems”, Nuclear Engineering and Design 250, 600-612, 2012

ISSCWR7-2069

Development of a circumferential heat transfer model in sub-channel code for tight lattice

Ting Yang[1)], X.J. Liu[1)], Xu Cheng[2)]

1) School of Nuclear Science and Engineering, Shanghai Jiao Tong University
800 Dong Chuan Road, Shanghai, 200240, China
Phone: +86 21 34206277 Email: yang-ting@sjtu.edu.cn
2) Institute of Fusion and Reactor Technology, Karlsruhe Institute of Technology, Vincenz-Prieβnitz-Str. 3, 76131 Karlsruhe, Germany

Abstract

Previous CFD and experimental investigations show that obvious non-uniform circumferential distribution of temperature exists in tight lattice, compared to regular rod bundles with larger pitch-to-diameter ratio. Since cladding temperature is one of the key design criteria for some advanced reactor design, it is necessary to carry out study on the behavior of circumferential heat transfer in tight lattice and develop numerical tools to predict circumferential distribution of temperature in the fuel rod.

To investigate the circumferential non-uniformity of heat transfer in rod bundles, this paper firstly establishes mathematical model and make theoretical analysis, based on which influential non-dimensional are summarized. Then a semi-empirical correlation describing this phenomenon is proposed based on theoretical results and CFD sensitivity analysis; finally a three dimensional fuel rod model is introduced in sub-channel code to predict circumferential heat transfer non-uniformity in different geometry and flow conditions. To validate this model some results are compared with experimental data of bundle test of subcritical and supercritical water.

The results of this paper indicate that (i) For fluid of constant property, the distribution local heat transfer coefficient and wall temperature is not uniform, with gap temperature being higher than central region in a sub-channel; (ii) The distribution of local heat transfer is affected strongly by pitch-to-diameter ratio. Because of the flattening effect of cladding, it is also affected by thermal conductivity ratio of cladding to fluid. The non-uniformity gets stronger with the decreasing Prandtl number when the fluid is of very low Prandtl number; (iii) The non-uniform fuel rod model developed for the sub-channel code has the ability to calculate circumferential variation of temperature in the fuel rod, and the results agree well with the existing experimental data.

Key words

heat transfer non-uniformity, Gen IV reactor, fuel model, sub-channel, CFD

1. Introduction

In the past a number of experimental and computational researches are carried out to investigate the flow and heat transfer in rod bundles. Results show that the cladding temperature distribution is not uniform in the circumferential direction, especially in a tight lattice, which is widely applied in the fuel assembly design in order to enhance the fuel utilization and economics. Since the maximal cladding temperature is one of the key design criteria, the circumferential temperature difference should be taken into consideration in the fuel assembly design for tight lattice, for example, of LMFR and SCWR[1, 2].

Some preliminary study has been performed relating to this topic for tight lattice. Liquid metal, as the coolant of LMFR, is often characterized by its high thermal conductivity and small specific heat. From the last 60s, theoretical studies have been done on the temperature distribution in

both triangular and square lattice bundles in LMR. Based on the assumption that the Peclet number is approaching zero for liquid metal, reference [3] gives a semi-theoretical solution of temperature distribution in the fuel, gas gap, cladding and coolant in an infinite bundle. A number of similar solutions in the form of Fourier series were obtained in laminar and turbulent flows [4-7]. Some of the theoretical results were compared with experimental data and good agreements were achieved [8, 9]. Results showed that the temperature distribution in liquid-metal-cooled bundles is dependent on dimensionless numbers of geometry, property and flow conditions. Besides LMFR, some water-cooled reactor designs with tight lattice are proposed in the recent years. A pitch-to-diameter ratio (*p/d*) less than 1.2 is applied in the following conceptual assembly designs to increase the fuel utilization, Advanced Pressurized Water Reactor (APWR) [10], Supercritical Water-Cooled Reactor (SCWR) [11-13], High Performance Light Water Reactor (HPLWR) [14], Reduced Moderation Water Reactor (RMWR) [15], and Innovative Water Reactor for Flexible Fuel Cycle (FLWR) [16].

Experimental results indicate that the circumferential non-uniformity of heat transfer exists on the cladding surface in a rod bundle [17-19]. On the other hand growing analysis using CFD codes are carried out to investigate the turbulent behavior, flow pattern and temperature distribution in tight lattices [17, 20, 21]. The effects of geometry and wall heat flux on the non-uniformity of heat transfer are analyzed in references [22, 23] at different boundary conditions in typical flow channels in SCWR.

Although intensive experimental and numerical investigations on the thermal-hydraulic behavior in tight lattices have been launched, the effect of independent parameters on the heat transfer non-uniformity has not been studied systematically, and the circumferential heat transfer variation is not taken into consideration by sub-channel codes currently.

To consider the non-uniform heat transfer distribution in sub-channel codes, this paper presents an empirical correlation of heat transfer non-uniformity based on CFD analysis. The correlation is applied in the sub-channel code COBRA-SC [24].

2. Theoretical analysis

To study the temperature field in rod bundle, the following assumptions are made at first: (1) infinite bundle at radial direction; (2) fully developed flow; (3) axial thermal conductivity ignored; (4) constant property; (5) secondary flow neglected; (6) isotropic turbulence. Based on the results obtained by previous CFD study, the gas gap between fuel and cladding has very limited influence on circumferential non-uniformity of cladding temperature, so the gas gap is neglected in the following study in this paper. As a result, the computational domain could be simplified as Figure 1, which is 1/8 of a subchannel in the infinite rod bundle, consisting of fuel, cladding and fluid. For square lattice, $0 \le \varphi \le \frac{\pi}{4}$ and $0 \le r \le P/\cos(\varphi)$.

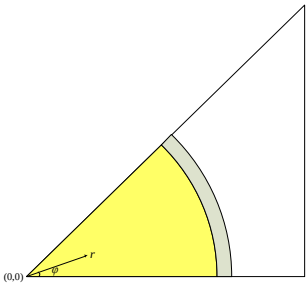

Figure 1 Computational domain

Based on the previous assumptions, the control equations of temperature could be simplified as Eq.(1), for fuel, cladding and fluid respectively.

$$\begin{cases} \dfrac{\partial^2 T_f}{\partial r^2}+\dfrac{1}{r}\dfrac{\partial T_f}{\partial r}+\dfrac{1}{r^2}\dfrac{\partial^2 T_f}{\partial \varphi^2}+\dfrac{q_v}{\lambda_f}=0 & r\in[0,R_f] \\ \dfrac{\partial^2 T_c}{\partial r^2}+\dfrac{1}{r}\dfrac{\partial T_c}{\partial r}+\dfrac{1}{r^2}\dfrac{\partial^2 T_c}{\partial \varphi^2}=0 & r\in[R_f,R_c] \\ \dfrac{1}{r}\dfrac{\partial}{\partial r}\left[r(1+\dfrac{\lambda_t}{\lambda})\dfrac{\partial T}{\partial r}\right]+\dfrac{1}{r^2}\dfrac{\partial}{\partial \varphi}\left[(1+\dfrac{\lambda_t}{\lambda})\dfrac{\partial T}{\partial \varphi}\right]=\dfrac{4\,\overline{q''}}{\lambda D_e}\cdot\dfrac{u}{u_b} & r\in[R_c,R_c+\dfrac{\sqrt{2}}{2}P] \end{cases} \tag{1}$$

By introducing dimensionless temperature $\Theta_{sub}=\dfrac{\lambda\left(T_{sub}-T_b\right)}{R_c\overline{q''}}$, Eq.(1). is non-dimensionalized as Eq.(2), (3) and (4).

$$\frac{\partial^2\Theta_f}{\partial(\frac{r}{R_c})^2}+\frac{1}{\frac{r}{R_c}}\frac{\partial\Theta_f}{\partial(\frac{r}{R_c})}+\frac{1}{(\frac{r}{R_c})^2}\frac{\partial^2\Theta_f}{\partial\varphi^2}+2\frac{\lambda}{\lambda_f}=0 \tag{2}$$

$$\frac{\partial^2\Theta_c}{\partial(\frac{r}{R_c})^2}+\frac{1}{\frac{r}{R_c}}\frac{\partial\Theta_c}{\partial(\frac{r}{R_c})}+\frac{1}{(\frac{r}{R_c})^2}\frac{\partial^2\Theta_c}{\partial\varphi^2}=0 \tag{3}$$

$$\frac{1}{\frac{r}{R_c}}\frac{\partial}{\partial(\frac{r}{R_c})}\left[\frac{r}{R_c}(1+\frac{\lambda_t}{\lambda})\frac{\partial\Theta}{\partial(\frac{r}{R_c})}\right]+\frac{1}{(\frac{r}{R_c})^2}\frac{\partial}{\partial\varphi}\left[(1+\frac{\lambda_t}{\lambda})\frac{\partial\Theta}{\partial\varphi}\right]=\frac{1}{\frac{2}{\pi}\left(p/d\right)^2-\frac{1}{2}}\cdot\frac{u}{u_b} \tag{4}$$

Here λ_t is turbulent thermal conductivity and λ is the thermal conductivity of fluid. The boundary condition for this model are

(1) symmetry boundary

$$\begin{cases} \dfrac{\partial\Theta_{sub}}{\partial\varphi}=0 & \left(\varphi=0,\ 0\le\dfrac{r}{R_c}\le\dfrac{p/d}{\cos\varphi}\right) \\ \dfrac{\partial\Theta_{sub}}{\partial\varphi}=0 & \left(\varphi=\dfrac{\pi}{4},0\le\dfrac{r}{R_c}\le\dfrac{p/d}{\cos\varphi}\right) \\ \dfrac{\partial\Theta}{\partial(r/R_c)}=\dfrac{\sin\varphi}{p/d}\dfrac{\partial\Theta}{\partial\varphi} & \left(0\le\varphi\le\dfrac{\pi}{4},\dfrac{r}{R_c}=\dfrac{p/d}{\cos\varphi}\right) \end{cases} \tag{5}$$

(2) bounded boundary

$$\Theta_f=\text{finite}\quad\left(r/R_f=0\right) \tag{6}$$

(3) continuity boundary

$$\begin{cases} \Theta_f=\Theta_c \\ \dfrac{\lambda_f}{\lambda_c}\dfrac{\partial\Theta_f}{\partial(r/R_c)}=\dfrac{\partial\Theta_c}{\partial(r/R_c)} & \left(\dfrac{r}{R_c}=\dfrac{R_f}{R_c},0\le\varphi\le\dfrac{\pi}{4}\right) \end{cases}$$

$$\begin{cases} \Theta_c=\Theta \\ \dfrac{\lambda_c}{\lambda}\dfrac{\partial\Theta_c}{\partial(r/R_c)}=\dfrac{\partial\Theta}{\partial(r/R_c)} & \left(\dfrac{r}{R_c}=1,0\le\varphi\le\dfrac{\pi}{4}\right) \end{cases} \tag{7}$$

(4) periodicity boundary

$$\Theta_{sub}(r,\varphi)=\Theta_{sub}(r,\varphi+\frac{\pi}{2}) \tag{8}$$

To get solution of the equations above, the key is to model the distribution of turbulent viscosity $\frac{\lambda_t}{\lambda}$ and velocity $\frac{u}{u_b}$ in Eq.(4). The basic assumption of constant turbulence model is that turbulent viscosity is irrelevant to velocity gradient. In some cases, the assumption could be made that turbulent viscosity is constant,

$$\frac{\eta_t}{\eta} = C_1 \cdot Re \tag{9}$$

If we further suppose that turbulent Prandtl number Pr_t is constant, the turbulent thermal conductivity could be expressed by Eq.(10), where C_t is a combination of constants.

$$\frac{\lambda_t}{\lambda} = C_t \cdot Pe \tag{10}$$

In fact the distribution of velocity $\frac{u}{u_b}$ can hardly be obtained since the equation of momentum is coupled with that of energy. Reference [3] gets the expression of $\frac{u}{u_b}$ through experiments. This paper supposes that radial distribution of velocity follow the exponential law and friction factor obeys the form of Blasius correlation, the same as that in round tube. In this situation the distribution of velocity is expressed as Eq.(11).

$$\frac{u}{u_b} = C_2 Re^{C_3} \left(\frac{\gamma - 1}{\frac{p/d}{\cos\varphi} - 1} \right)^n \tag{11}$$

Where is γ is the non-dimensionalized radial coordinate, $\gamma = r/R_c$ and n is the index of exponential law, equaling to 1/7 when $Re = 1.1\times10^5$. Combining Eq.(4) and (11) yields to

$$\frac{\partial^2\Theta}{\partial\gamma^2} + \frac{1}{\gamma}\frac{\partial\Theta}{\partial\gamma} + \frac{1}{\gamma^2}\frac{\partial^2\Theta}{\partial\varphi^2} = f(\gamma,\varphi) \tag{12}$$

In Eq.(12) $f(\gamma,\varphi) = a\frac{(\gamma-1)^n}{\left(\frac{p/d}{\cos\varphi}-1\right)^n}$, where coefficient *a* is a function of *Re*, *Pe*, *p/d* and other constants in the empirical correlations. Combining Eq.(2), (3), (12) and boundary conditions, the simultaneous solution are Eq.(13), (14) and (15) for the temperature field of fuel, cladding and fluid respectively, in which *F* and *q* are defined as

$F(\gamma) = a_0\left[\frac{(\gamma-1)^{n+2}}{(n+2)^2} + \frac{(\gamma-1)^{n+1}}{(n+1)^2(n+2)} - \frac{1}{(n+1)(n+2)}\int_1^\gamma \frac{(\gamma-1)^n}{\gamma}\mathrm{d}\gamma\right]$ and

$q(\gamma) = \frac{2b\,\lambda_f/\lambda}{\sqrt{2}\,p/d-1}(\sqrt{2}\frac{p}{d}\ln\sqrt{2}\frac{p}{d}+1-\sqrt{2}\frac{p}{d}) - \frac{\int_1^\gamma F(\gamma)\mathrm{d}\gamma}{\sqrt{2}\,p/d-1}$.

$$\Theta_f = q(\sqrt{2}\frac{p}{d}) - 2b\frac{\lambda_f}{\lambda_c}\ln\frac{R_f}{R_c} + b - b\left(\frac{r}{R_f}\right)^2 + \sum_{k=1}^{\infty}\frac{2C_k}{1+\lambda_f/\lambda_c}\left(\frac{r}{R_c}\right)^{4k}\cos 4k\varphi \tag{13}$$

$$\Theta_c = q(\sqrt{2}\frac{p}{d}) - 2b\frac{\lambda_f}{\lambda_c}\ln\frac{r}{R_c} + \sum_{k=1}^{\infty}C_k\left[\left(\frac{r}{R_c}\right)^{4k} + \frac{1-\lambda_f/\lambda_c}{1+\lambda_f/\lambda_c}\left(\frac{R_f}{R_c}\right)^{8k}\left(\frac{r}{R_c}\right)^{-4k}\right]\cos 4k\varphi \tag{14}$$

$$\Theta = q(\sqrt{2}\frac{p}{d}) - 2b\frac{\lambda_f}{\lambda}\ln\frac{r}{R_c} + F\left(\frac{r}{R_c}\right) + \sum_{k=1}^{\infty}\left\{\begin{array}{l}\frac{1}{2}\left[\left(1+\frac{\lambda_c}{\lambda}\right)+\left(1-\frac{\lambda_c}{\lambda}\right)\frac{1-\lambda_f/\lambda_c}{1+\lambda_f/\lambda_c}\left(\frac{R_f}{R_c}\right)^{8k}\right]C_k\left(\frac{r}{R_c}\right)^{4k} \\ +\frac{1}{2}\left[\left(1-\frac{\lambda_c}{\lambda}\right)+\left(1+\frac{\lambda_c}{\lambda}\right)\frac{1-\lambda_f/\lambda_c}{1+\lambda_f/\lambda_c}\left(\frac{R_f}{R_c}\right)^{8k}\right]C_k\left(\frac{r}{R_c}\right)^{-4k} + G_k\left(\frac{r}{R_c}\right)\end{array}\right\}\cos 4k\varphi \quad (15)$$

The solution of the temperature field indicates that on the radial direction the temperature distribution is cosine series of angle. Besides, the radial distribution of dimensionless temperature is affected by some dimensionless numbers, and they are (1) dimensionless numbers of geometry, that is, pitch-to-diameter ratio (*p/d*) and radius ratio of fuel to cladding (R_f/R_c), (2) dimensionless numbers of property: thermal conductivity ratio of cladding to coolant ($\lambda_{clad}/\lambda_{coolant}$) and that of cladding to fuel ($\lambda_{clad}/\lambda_{fuel}$) and (3) dimensionless numbers of flow and heat transfer *Re*，*Pr* (or *Re*, *Pe*). However, the prerequisite of this solution is the assumption of constant turbulent viscosity and this will lead to significant increase in circumferential temperature non-uniformity. The analytical method in this section can show what the influencing factors are and how they affect the circumferential temperature non-uniformity qualitatively.

Thus the normalized local heat transfer coefficient htc_N can be expressed as a function of the parameters above,

$$htc_N = \frac{htc_{local}}{\overline{htc}} = f\left(\varphi, Re, Pr, \frac{p}{d}, \frac{R_f}{R_c}, \frac{\lambda_{fuel}}{\lambda_{clad}}, \frac{\lambda_{clad}}{\lambda_{coolant}}\right) \quad (16)$$

where the local and mean heat transfer coefficient are defined as

$$htc_{local} = \frac{q''_{local}}{T_{c,local} - T_b} \quad (17)$$

$$\overline{htc} = \frac{\overline{q''}}{\overline{T_c} - T_b} \quad (18)$$

where T_b is the bulk temperature of the cross section perpendicular to the flow direction. To determine the expression of Eq.(16), CFD studies are performed in the next section. The objective of the simulation is to analyze the effects of different parameters on the local heat transfer coefficient at each angle htc_{local} .

3. CFD analysis

In this paper CFD calculations are carried out on three typical types of sub-channels in a square rod bundle. The computational domains are shown in Figure 2 with the shadow, including fuel, cladding and coolant. The symmetry boundary condition is applied in the cases of central sub-channel due to the symmetric geometry while the wall boundary condition is applied at the assembly box in the cases of wall and corner sub-channels. The physical properties of solid and coolant are assumed to be constant. All the results are achieved on the elevation in fully developed flow. The turbulence model used in this paper is SSG model recommended in reference [17].

Using commercial software, first a number of CFD simulations are performed on 1/8 of a central sub-channel in the square lattice, as shown in Figure1. The present study investigates the effects of geometry, properties, *Re*, *Pr* on the non-uniform distribution of heat transfer coefficient. Some parameters are illustrated in Table 1, covering the range of engineering interest of LMFR and SCWR.

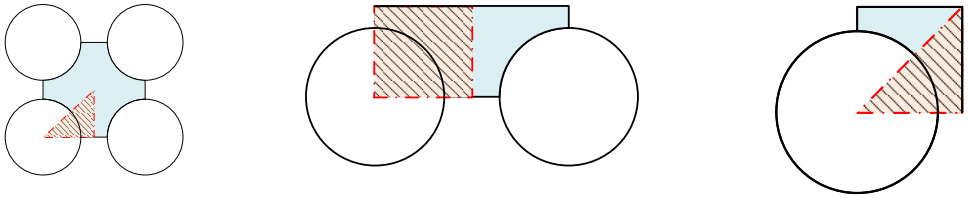

(a) Central channel (b) Wall channel (c) Corner channel

Figure 2 Sub-channel configuration and computational domain

Table 1 Parameters in CFD simulation

	p/d	*Re*	*Pr*	$\lambda_{clad}/\lambda_{coolant}$
Range	1.1-1.4	5×10^4-10^6	0.001-30	0.1-500
Reference	1.1	92197	0.9	36.8

3.1. Effect of angle

Taking the reference case as an example, Figure 3 shows the circumferential distribution of heat transfer coefficient and heat flux on the cladding surface. It is obvious to see that the distribution of local heat transfer coefficient is not uniform, that is, higher near central region and lower near gap region. And the other cases show the same trend, similar to that of analytical result, the cosine series as a function of azimuth.

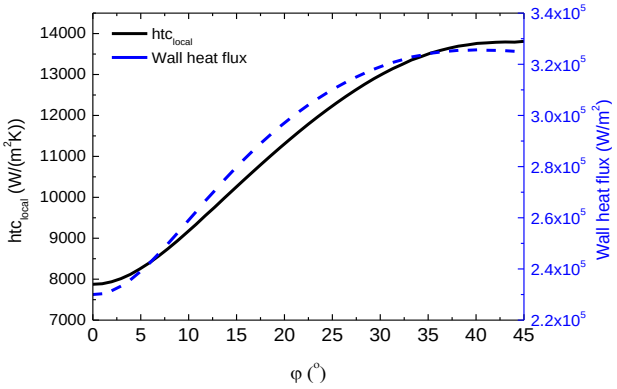

Figure 3 Circumferential distribution of local heat transfer coefficient and heat flux

3.2. Effect of fuel

The effect of thermal conductivity of fuel is presented in Figure 6 and Figure 7. With 10 times increase in λ_{fuel} while keeping other parameters being the same, the distribution of heat flux is more non-uniform at the fuel pellet surface but the change becomes neglectable at the outer surface of cladding. This is because usually the thermal conductivity of the fuel is much smaller than that of cladding, and the circumferential distributions of heat flux and temperature are significantly flattened while the heat is transferred through cladding. This flattening effect is associated with the radial thermal resistance of cladding, which is defined proportional to its thickness and inversely proportional to its thermal conductivity. Comparing to the thermal conductivity and thickness of cladding, the geometry and property inside the cladding have very limited effect on the heat transfer behavior at the cladding surface, which is also implied by ref.[23]. Based on this fact, the effect of λ_{fuel} will be neglected in the following analysis.

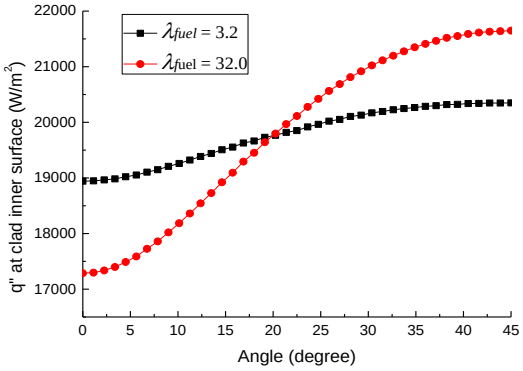

Figure 6 Distribution of heat flux at cladding inner surface

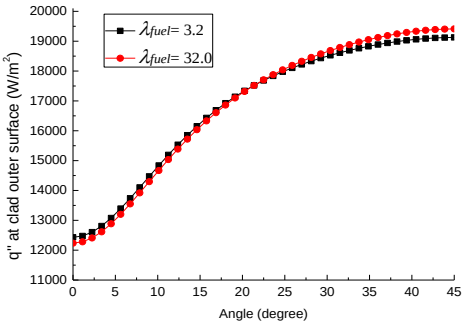

Figure 7 Distribution of wall heat flux under different λ_{fuel}

3.3. Effect of *p/d*

Figure 8 shows the distribution of the normalized local heat transfer coefficient under different *p/d* keeping other parameters the same as the reference case. The non-uniformity increases significantly with the decrease in *p/d* because of the non-uniform geometry. When *p/d* equals to 1.1, the local heat transfer coefficient at $\varphi = 45^{\circ}$ could be 2.6 times as much as that at $\varphi = 0^{\circ}$. It needs to be clarified that in this paper the geometry model is of *p/d* larger than 1.1. When *p/d* goes below 1.1, the CFD models used in this paper are no longer applicable as they may underestimate the gap fluctuation between two sub-channels.

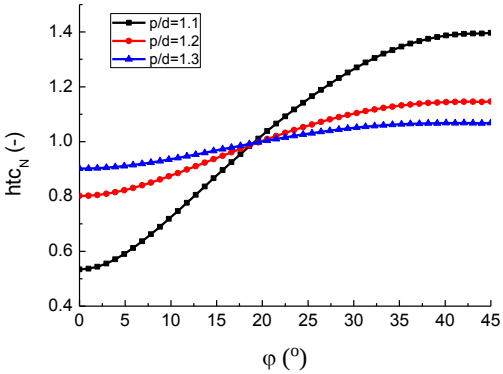

Figure 8 Distribution of normalized htc under different *p/d*

3.4. Effect of cladding thickness

As shown in Figure 9, for cases with the cladding thickness equal to 0.2mm, 0.5mm, 0.8mm and 1.0mm, the distribution of htc_N are very similar. With the increase in the cladding thickness, the heat transfer will be flattened. This is explained by the equivalent thermal resistance of the circumferential and radial heat conduction in ref [23]. Nevertheless, this effect is no longer

significant when the cladding thickness exceeds 0.5mm, which is within the common design range of cladding. Thus $\frac{R_f}{R_c}$, which is related to the cladding thickness, will not be taken into consideration in the future analysis.

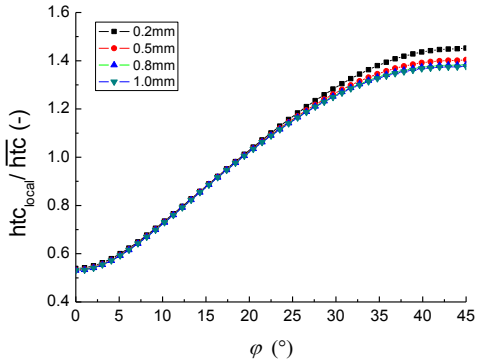

Figure9 Distribution of Normalized *htc* of different clad thickness

3.5. Effect of *Pr* and $\lambda_{clad}/\lambda_{coolant}$

Figure10 shows the circumferential distribution of htc_N under various *Pr* numbers. The non-uniformity is increasing with the decrease in *Pr* number. When p/d equals to 1.15 and *Pr* equals to 0.01, the ratio of the maximal to minimal htc_N can reach 3.1. Similarly the non-uniformity gets stronger with the decreasing thermal conductivity ratio $\frac{\lambda_{clad}}{\lambda_{coolant}}$, as illustrated in Figure11. This implies that with the same p/d , the non-uniformity gets stronger in the lattice cooled by liquid metal, which is usually of much smaller *Pr* and $\frac{\lambda_{clad}}{\lambda_{coolant}}$ than water.

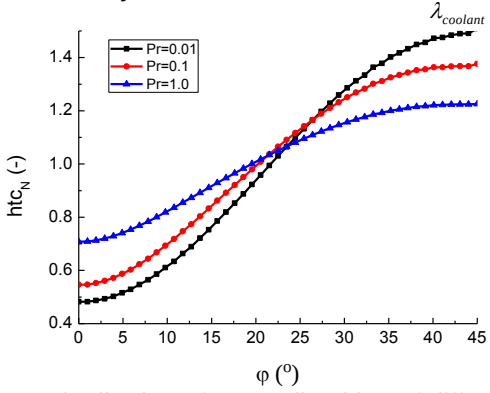

Figure10 Distribution of Normalized htc of different *Pr*

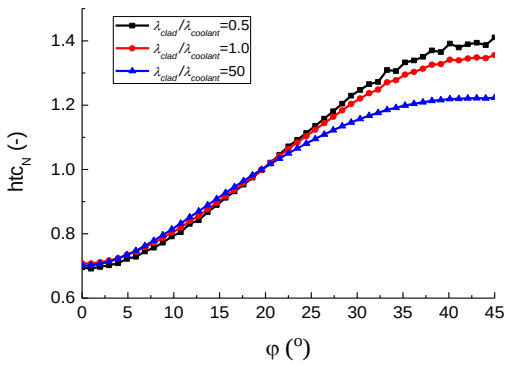

Figure11 Distribution of Normalized htc of different thermal conductivity ratio

3.6. Effect of *Re*

The Normalized heat transfer coefficient at gap ($\varphi = 0^\circ$) has a slight increase with the increasing *Re*, as shown in Figure12. Figure13 shows the normalized heat transfer coefficient at central region ($\varphi = 45^\circ$). Simulation results indicate that *Re* has very limited effect on heat transfer non-uniformity, especially within the *Re* range under normal operating condition. Hence the influence of *Re* is ignored in further analysis.

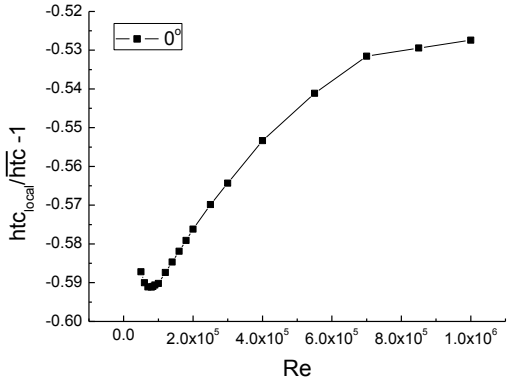

Figure12 Normalized htc at $\varphi = 0^\circ$ under different *Re*

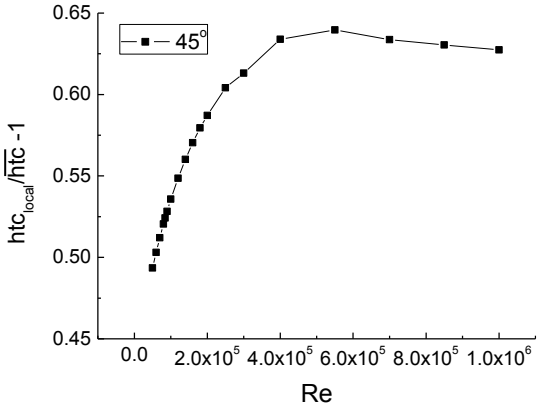

Figure13 Normalized htc at $\varphi = 45^\circ$ under different *Re*

From previous analysis, we can see that the effect of φ, $\frac{p}{d}$, *Pr* and $\frac{\lambda_{clad}}{\lambda_{coolant}}$ are much stronger compared to that of gas gap, $\frac{\lambda_{fuel}}{\lambda_{clad}}$, $\frac{R_f}{R_c}$ and *Re*. Thus only φ, $\frac{p}{d}$, *Pr* and $\frac{\lambda_{clad}}{\lambda_{coolant}}$ are considered to simplify the expression of the correlation discussed in the next part of the paper.

4. Correlation

4.1. Correlation for central sub-channel

The effects of gas gap, $\frac{\lambda_{fuel}}{\lambda_{clad}}$, $\frac{R_f}{R_c}$ and *Re* are ignored, and the distribution of normalized heat transfer coefficient is supposed to be a function of the dominant dimensionless numbers φ, $\frac{p}{d}$, *Pr* and $\frac{\lambda_{clad}}{\lambda_{coolant}}$. Because the semi-analytical solution of the temperature field, htc_{local} and heat flux

contains cosine series of φ in ref.[3], and in Figure3 the curve is approximately a cosine function as illustrated above, this paper keeps the first order cosine term and assumes that the distribution of htc_N could be expressed as Eq.(20). The selection of the exponential form of $\frac{p}{d}$, *Pr* and $\frac{\lambda_{clad}}{\lambda_{coolant}}$ is arbitrary. The product of these exponential terms is in the denominator to ensure that htc_N is always positive when the correlation is extrapolated outside the range of data pool.

$$htc_N = 1 - \frac{\cos(4\varphi)}{1 + c_0 \cdot \left(\frac{p}{d} - 1\right)^{n1} \cdot Pr^{n2} \cdot \left(\frac{\lambda_{clad}}{\lambda_{coolant}}\right)^{n3}} \qquad (19)$$

Within the parameter range listed in Table 1, the data pool for curve fitting is obtained from totally 60 cases, each case 47 points. These data are used to fit curve for Eq.(19), and a correlation Eq.(21) is obtained with RMSE equal to 0.08. At $\varphi = 0^\circ$ and $\varphi = 45^\circ$, the comparison of htc_N value between CFD results and correlation prediction is illustrated in Figure14, Figure15 and Figure16. The agreement is acceptable except that in Figure16, the slope gets much higher when $\lambda_{clad}/\lambda_{coolant}$ approaching zero in the curve as a function of $\lambda_{clad}/\lambda_{coolant}$.

$$htc_N = 1 - \frac{\cos(4\varphi)}{1 + 46.8\left(\frac{p}{d} - 1\right)^{1.873} Pr^{0.244} \left(\frac{\lambda_{clad}}{\lambda_{coolant}}\right)^{0.229}} \qquad (20)$$

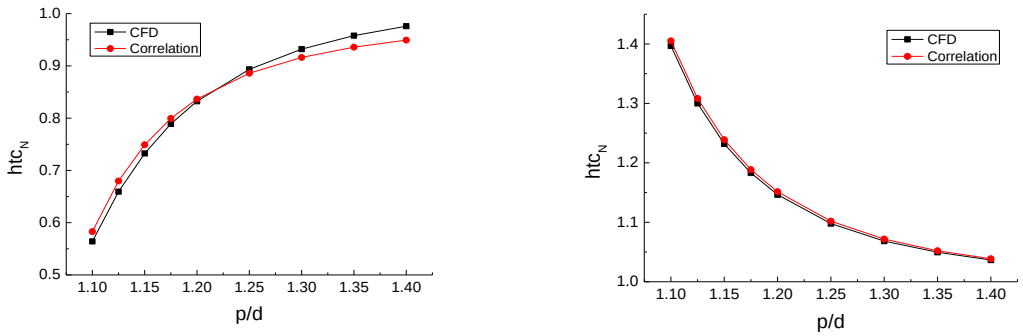

(a) $\varphi = 0^\circ$ (b) $\varphi = 45^\circ$

Figure14 Effect of *p/d* on htc_N distribution

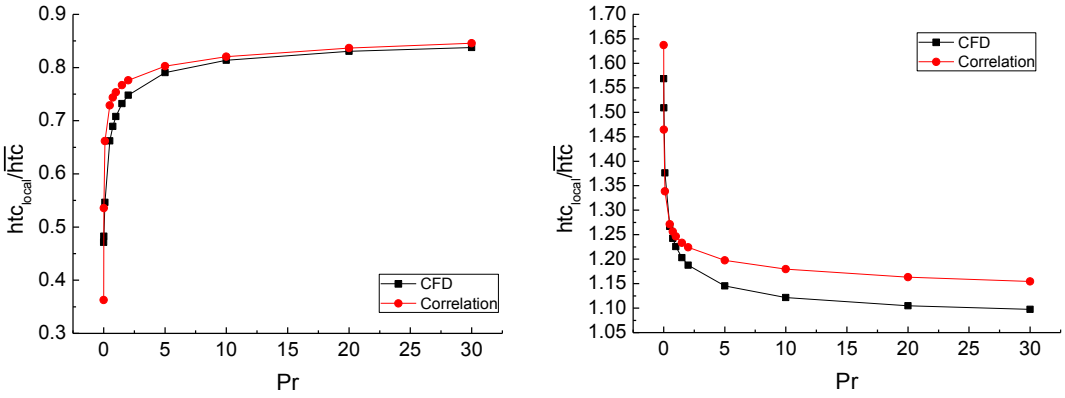

(a) $\varphi = 0^\circ$ (b) $\varphi = 45^\circ$

Figure15 Effect of *Pr* on htc_N distribution

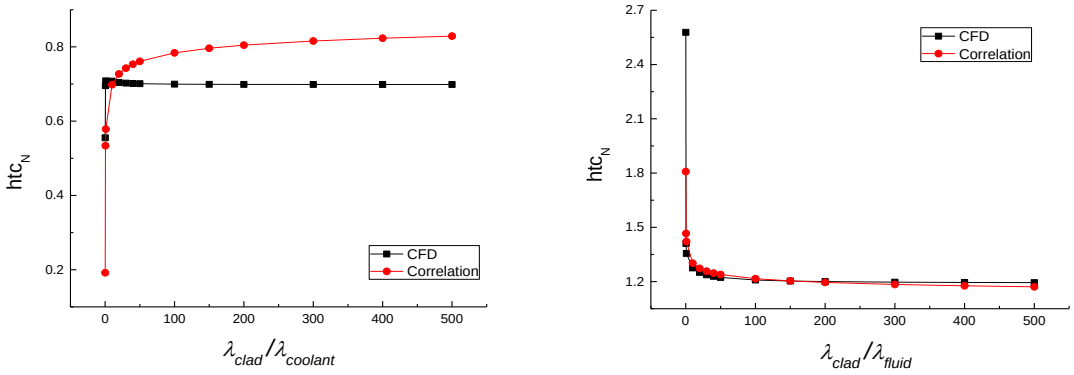

(a) $\varphi = 0^\circ$ (b) $\varphi = 45^\circ$

Figure16 Effect of $\lambda_{clad}/\lambda_{coolant}$ on htc_N distribution

4.2. Correlation for corner and wall sub-channel

Figure17 shows the computational domain of the corner sub-channel together with a contour of velocity. CFD results indicate that the computational domain of wall sub-channel, shown in Figure18, can be treated as two parts. In part I ($0^\circ \sim 45^\circ$), the distribution of htc_N is similar to that in a central sub-channel domain and in part II ($45^\circ \sim 90^\circ$) it is similar to a corner sub-channel. Thus in this paper only the corner sub-channel is studied and it is supposed that the results are applicable to part II in the wall sub-channel.

Figure19 shows the value of htc_N at $\varphi = 45^\circ$ in corner and central sub-channel and it is obvious that under the same p/d , the non-uniformity is stronger in a corner sub-channel. To obtain an empirical correlation of htc_N distribution for corner sub-channel, the idea is to assume that in a corner channel, a line of maximal velocity exits parallel to the assembly box. Within this imaginary symmetry boundary line the flow and heat transfer is similar as that in the central sub-channel, but with a smaller p/d . Suppose that the relation of the gap width bounded by the new symmetry line (marked with asterisk) δ^* and the real gap width δ is expressed by Eq.(22)

$$\frac{\delta^*}{R_c} = c\frac{\delta}{R_c} \quad (21)$$

which yields to

$$\left(\frac{p}{d}-1\right)^* = c\left(\frac{p}{d}-1\right) \quad (22)$$

where $0 < c < 1$. This is equivalent to transform the x coordinate in Figure19. Combining Eq.(22) and Eq.(20) yields to

$$htc_{N,corner} = 1 - \frac{\cos(4\varphi)}{1 + c_0 \cdot \left[c\left(\frac{p}{d}-1\right)\right]^{n1} \cdot Pr^{n2} \cdot \left(\frac{\lambda_{clad}}{\lambda_{coolant}}\right)^{n3}} \quad (23)$$

Assuming that the value of c_0, n_1, n_2 and n_3 are the same for corner and central sub-channels, a best estimated c is obtained by achieving the minimal distance between black line and the red line in Figure19 after coordinate transformation. As a result c is equal to 0.712 based on the data of 5 CFD cases.

From the discussion above, it can be concluded that Eq.(25) is the correlation of htc_N distribution in the square lattice, where $c = 1$ for central sub-channels and part I of wall sub-channels, and $c = 0.712$ for corner sub-channels and part II of wall sub-channels.

$$htc_N = 1 - \frac{\cos(4\varphi)}{1 + 46.8\left[c\left(\frac{p}{d} - 1\right)\right]^{1.873} Pr^{0.244}\left(\frac{\lambda_{clad}}{\lambda_{coolant}}\right)^{0.229}} \quad (24)$$

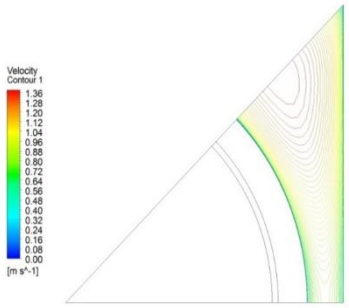

Figure17 Velocity distribution in a corner sub-channel

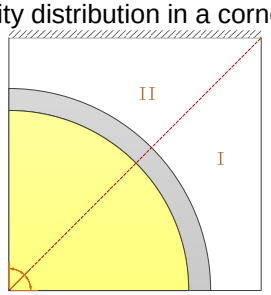

Figure18 Geometry of the wall sub-channel

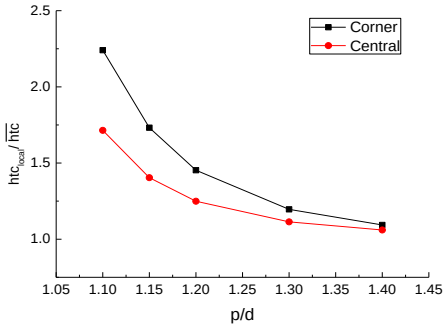

Figure19 Normalized *htc* at $\varphi = 45^\circ$ in corner sub-channel

4.3. Central sub-channel in triangular lattice

All the previous computations are focused on the sub-channels in the square lattice. Similar procedure is performed on the triangular lattice. Assuming that the effect of *Pr* and $\frac{\lambda_{clad}}{\lambda_{coolant}}$ on heat transfer non-uniformity is the same as that in square lattice, only the index of the *p/d* term differs then. Based on CFD results, the correlation for triangular sub-channel is

$$htc_N = 1 - \frac{\cos(6\varphi)}{1 + 46.8\left(\frac{p}{d} - 1\right)^{1.428} Pr^{0.244}\left(\frac{\lambda_{clad}}{\lambda_{coolant}}\right)^{0.229}} \quad (25)$$

For cases of square and triangular central sub-channel respectively, *p/d* equal to 1.1, the curves of CFD data and empirical correlations are compared in Figure20. Here Φ is defined as the normalized angle; for square lattice $\Phi = \frac{\varphi}{\pi/4}$ and for triangular lattice $\Phi = \frac{\varphi}{\pi/6}$. We can

see that the circumferential non-uniformity is stronger in a square lattice than triangular lattice under the same pitch to diameter ratio.

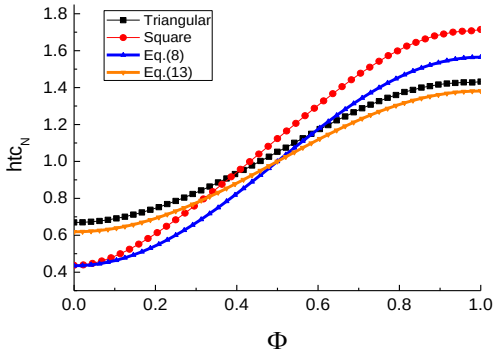

Figure20 Circumferential distribution of normalized htc

5. Application to sub-channel code

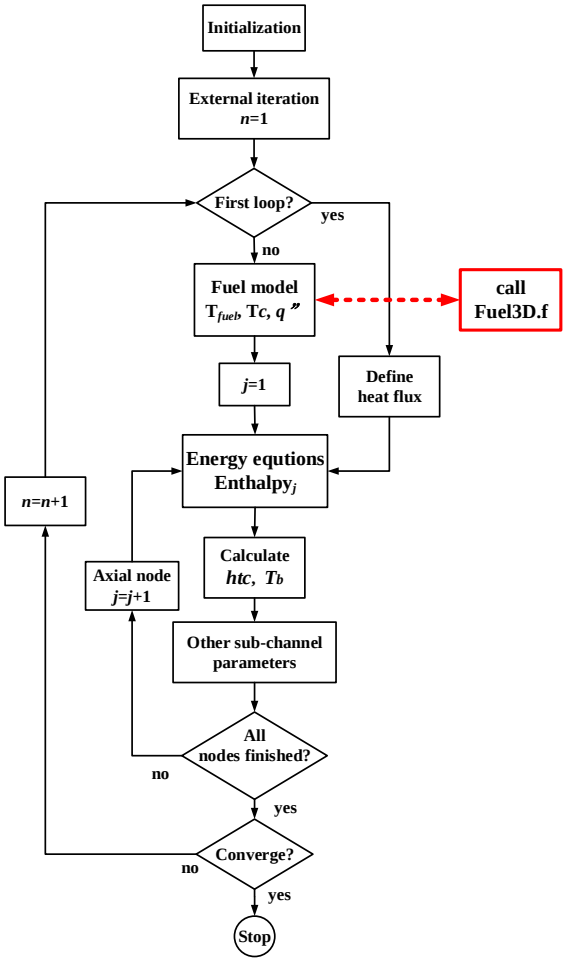

Figure21 Flow chart of modified COBRA-SC

Based on the results achieved above, a three dimensional fuel model is introduced in the sub-channel code COBRA-SC. To keep the energy balance a correction factor c_q is added to Eq.(24), and calculated before every invocation of 3D fuel model, as shown in Eq.(27).

$$\frac{htc_{local}}{\overline{htc}} = c_q \left[1 - \frac{\cos(\pi\Phi)}{1 + c_0 \left[c\left(\frac{p}{d} - 1 \right) \right]^{n1} Pr^{n2} \left(\frac{\lambda_{clad}}{\lambda_{coolant}} \right)^{n3}} \right] \tag{26}$$

$$\left[\lambda \frac{\partial T}{\partial r} \right]_{r=R_c} = - htc_{local} \left(T_c - T_b \right) \tag{27}$$

$$\frac{1}{r}\frac{\partial}{\partial r}\left(\lambda r \frac{\partial T}{\partial r} \right) + \frac{1}{r^2}\frac{\partial}{\partial \varphi}\left(\lambda \frac{\partial T}{\partial \varphi} \right) + \frac{\partial}{\partial x}\left(\lambda \frac{\partial T}{\partial x} \right) + q_v = \rho c_p \frac{\partial T}{\partial \tau} \tag{28}$$

Eq.(26) is used to calculate htc_{local} in Eq.(27), which is taken as the boundary condition of 3D fuel model. This boundary condition is applied on the cladding surface. For fuel rods to be calculated with 3D fuel model, the heat conduction equations Eq.(28) are discretized in central difference scheme in cylindrical coordinate, and here q_v equals to 0 in the cladding region. The axial node length are kept the same with the fluid part, and the radial and azimuthal nodes are user input. The harmonic mean of thermal conductivity is used at the contact of different materials. The equations are solved numerically, combined with the boundary condition, that is, Eq.(27) in discretized form. Thus the 3D temperature distribution could be obtained. Figure21 is a brief flow chart of the modified COBRA-SC for steady state calculation. A subroutine is called to solve the 3D conduction equations instead of the original fuel model in COBRA-SC. The heat flux is feedback to the fluid and therefore the solid and coolant domains are coupled. Suppose that fuel rod *J* faces different sub-channels and it is divided into *I* circumferential nodes on the parameter fraction facing channel *N*, the heat gained by channel *N* from rod *J* is calculated by Eq.(30) at a certain axial position. htc_i is calculated by Eq.(26) and L_i is circumferential mesh length of node *i*.

$$Q_{J \to N} = \sum_{i=1}^{I} htc_i \left(T_{c,i} - T_{b,N} \right) L_i \Delta x \tag{29}$$

First a simple case is simulated using the modified COBRA-SC to verify the 3D fuel model. A 1.6 meter long central sub-channel with only one fuel rod is simulated by CFX and the modified COBRA-SC respectively, with the same boundary conditions. The values of some parameters are listed in Table 2. Figure22 and Figure23 compare the results between different codes of the heat flux and normalized temperature on the cladding surface. For this case the maximal error of the normalized cladding surface temperature between the CFD and sub-channel code is 0.007, lying in the gap.

According to the results obtained so far, the empirical correlation can make a reasonable prediction of the circumferential heat transfer variation. Figure24 shows a 9-rod case whose parameters are listed in Table 3. In this case the coolant is water and Dittus-Boelter correlation is employed for heat transfer. Figure25 is local heat transfer coefficient around Rod 1 calculated by Eq.(26). Figure26 and Figure27 show the circumferential distribution of wall temperature and wall heat flux of Rod 1. It can be found that in this case the maximal cladding surface temperature occurs close to the gap of the corner rod. Comparing to the original code, the modified COBRA-SC with 3D fuel model gives a result of maximal cladding temperature about 15℃ higher in this case, which is more reasonable than the prediction of uniform cladding temperature.

Table 2 Parameters of single channel case

p/d -	*Pr*	$\lambda_{clad}/\lambda_{coolant}$	$\overline{q''}$ kW/m²	*G* kg/(m²s)
1.15	0.25	10.0	292	958

Table 3 Parameters of 9-rod bundle case

p/d -	*elevation* m	T_{inlet} ℃	*pressure* MPa	$\overline{q}$'' kW/m^2	*G* kg/(m^{2}s)
1.15	1.94	395.0	25.0	454.5	1000

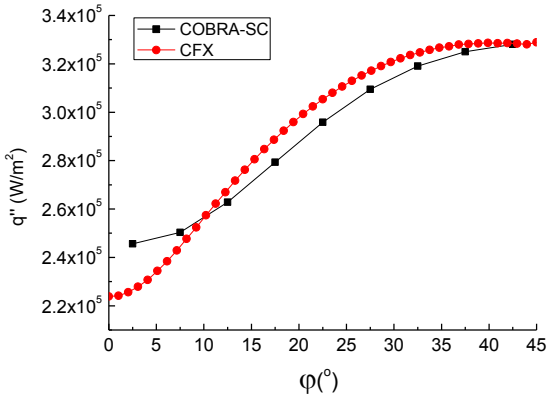

Figure22 Circumferential distribution of heat flux

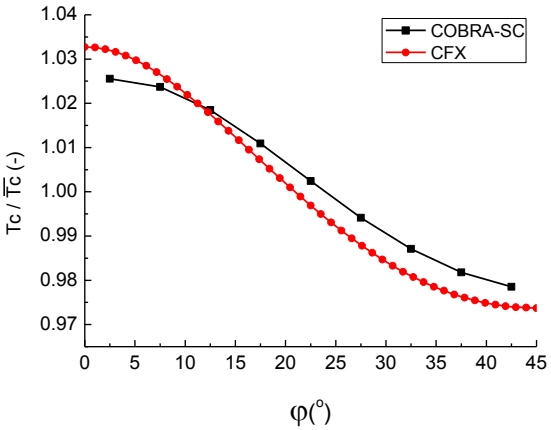

Figure23 Circumferential distribution of normalized wall temperature

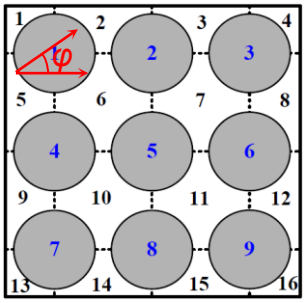

Figure24 Sub-channel configuration

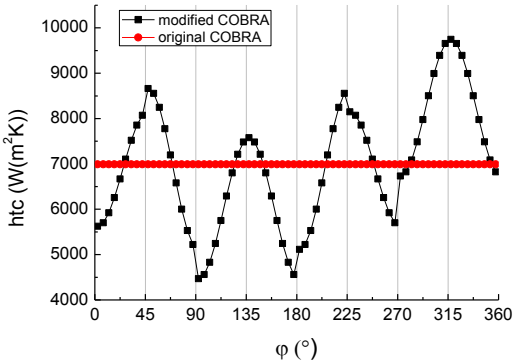

Figure25 Local htc distribution around Rod 1

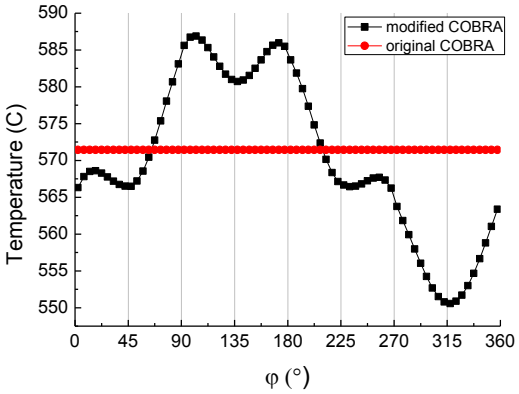

Figure26 Cladding temperature distribution around Rod 1

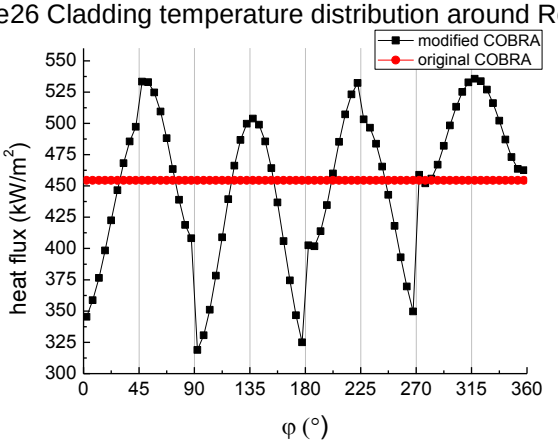

Figure27 Wall heat flux distribution around Rod 1

6. Code validation

Supercritical water multipurpose test loop (SWAMUP) is a test facility in Shanghai Jiao Tong University, on which flow and heat transfer experiments of water can be performed both above and under supercritical pressure. According to [25], Figure28 is the cross section of test section 2×2 rod bundle arranged in square lattice。Four tubes made of Inconel718 are heated by electricity and the temperature of their inner surface is measured by sliding thermal couples. There are one measuring point in every 15º in the shadowed area in Figure28. The heated length is 1328mm，the temperature is measured at the elevation of 500, 600, 700, 800，900, 1000mm.

In this paper two cases are compared between experimental and computational results, whose parameters are listed in Table.4. D-B correlation is employed for heat transfer coefficient prediction. According to the symmetry of test section, all the test points are assumed to be on one rod in Figure29. Results show that non-uniformity exists in circumferential distribution of

cladding inner temperature. The computational results have the similar trend as experimental data, and the maximal temperature appears at the same point at cladding inner surface. The average temperature is different between two curves in both cases. This is probably due to the following reasons: (1) the heat transfer coefficient predicted by D-B correlation is not accurate; (2) the heat source distributes in the fuel pellet in non-uniform fuel model of subchannel code, but the cladding is heated in the experiment. (3) experimental error may exists.

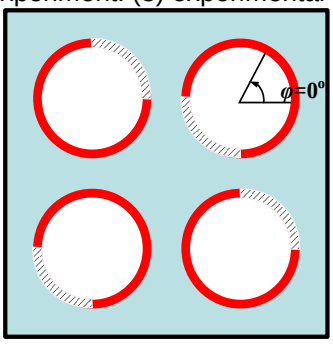

Figure28 Cross section of test assembly

Table 4 Parameters of cases for code validation

	p/d	*p*	*q''*	*G*	T_{in}	*z*	T_b	$T_{w,ave}$
	-	MPa	kW/m^2	kg/s m^2	^{o}C	m	^{o}C	^{o}C
Case1	1.18	7.78	457.8	1248.8	120.1	1.0	163.9	196.8
Case2	1.18	7.76	441.9	862.2	120.9	1.0	184.0	226.1

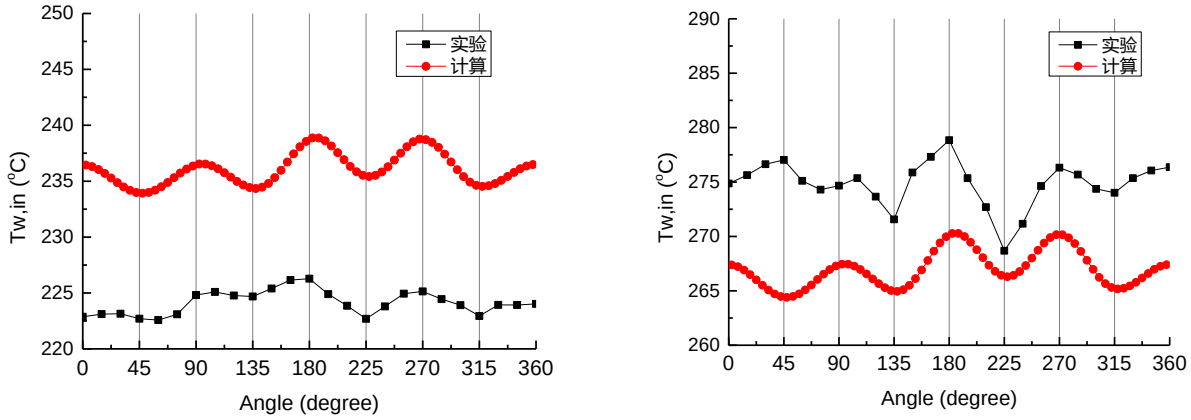

(a) Case1 (b) Case2

Figure29 Comparison between subchannel and experimental results of cladding inner surface

7. Summary

In this paper CFD simulations are carried out to evaluate the heat transfer non-uniformity around the cladding surface, which is an important phenomenon in reactor cores with tight lattice, e.g. LMFR and SCWR. The effects of some dimensionless numbers on the non-uniformity of local heat transfer coefficient are investigated. The dominant dimensionless numbers including angle, $\frac{p}{d}$, *Pr* and $\frac{\lambda_{clad}}{\lambda_{coolant}}$ are identified, based on which an empirical correlation is proposed and the undetermined coefficients are obtained based on the results of CFD simulations in normal operating conditons.

The empirical correlation is incorporated in sub-channel code as a boundary condition to establish a 3D fuel model in COBRA-SC. Results obtained by the modified COBRA-SC show the circumferential temperature variation on the cladding surface, and the peak temperature is higher than that predicted by the original code.
This work is preliminary to incorporate the circumferential non-uniformity effect into the sub-channel code, and more discussion and validation for the computation model is needed. It has to be pointed out that since the constant property assumption is employed in the CFD simulation, Eq.(26) is reasonable for the cases in which fluid property variation is quite small. For the cases with great circumferential property variation, such as water near critical point, the property change and its coupling with heat transfer must be considered. For model validation more experimental work is being carried out. Further investigations on this topic are still ongoing. Application of the modified code to SCWR and LMFR will be carried out in the near future.

ACKNOWLEDGMENTS

This work is financially supported by National Natural Science Foundation of China (51106097)

NOMENCLATURE

d	fuel rod diameter [m]
G	mass flux [kg/m^{2}s]
htc	heat transfer coefficient [W/m^{2}K]
p	pitch [m]
p/d	pitch-to-diameter ratio [-]
Pe	Peclet number [-]
Pr	Prandtl number [-]
Q	heat [w]
q"	heat flux [W/m^2]
q_v	Volumetric heat [W/m^3]
R	radius [m]
r	radial distance [m]
Re	Reynolds number [-]
T	temperature [K]
u	velocity [m/s]
x	axial distance [m]
γ	dimensionless radial distance [-]
Φ	dimensionless angle [-]
φ	angle, circumferential distance [degree]
η	dynamic viscosity [Pa·s]
λ	thermal conductivity [W/m K]
Θ	dimensionless temperature [-]

Subscripts	
0	reference
b	bulk, fluid
c	cladding outer surface
clad	cladding
f	fuel pellet surface
fuel	fuel pellet
local	local value
N	normalized
t	turbulence

REFERENCES

1. Cochran, T.B., Liquid metal fast breeder reactor. An environmental and economic critique. 1974.
2. Kim, T.K. and T.J. Downar, Thorium fuel performance in a tight pitch LWR lattice. Nuclear Technology, 2002. **138**(1): p. 17-29.
3. Nijsing, R. and W. Eifler, Analysis of liquid metal heat transfer in assemblies of closely spaced fuel rods : A theoretical evaluation of two-dimensional temperature- and heatflux distribution for conditions of turbulent axial flow at relatively low Peclet numbers. Nuclear Engineering and Design, 1969. **10**(1): p. 21-54.
4. Dwyer, O.E., H.C. Berry, and P.J. Hlavac, Heat transfer to liquid metals flowing turbulently and longitudinally through closely spaced rod bundles. Part II. Uniform heat flux at the inner surface of the cladding. Nuclear Engineering and Design, 1972. **23**(3): p. 295-308.
5. Ushakov, P.A., Calculation of the Temperature Fields of Bundles of Fuel Elements in Axial Turbulent Flows of Heat - Transfer Media with Vanishingly Small Pradtl Numbers. Teplofizika Vysokikh Temperatur, 1974. **12**(4): p. 775-784.
6. Ushakov, P.A., Calculation of the Hydrodynamic Characteristics of the Longitudinal Flow of a Liquid Around Regular Arrays of Fuel Element Rods. Teplofizika Vysokikh Temperatur, 1974. **12**(1): p. 103-110.
7. Ushakov, P.A., A.V. Zhukov, and N.M. Matyukhin, Azimuthal Temperature Nonuniformity in a Regular Array of Fuel Elements for Turbulent Liquid Metal Flow. High Temperature, 1977. **15**(1): p. 64-71.
8. Kolyaskin, V.I., L.K. Kudryavtseva, and P.A. Ushakov, Investigation of Temperature Fields in the Flow of a Sodium - Potassium Melt in the Cell of a Compact Rod Bundle. Teplofizika Vysokikh Temperatur, 1974. **12**(3): p. 559-564.
9. Subbotin, V.I., P.A. Ushakov, et al., Heat exchange during the flow of mercury and water in a tightly packed rod pile. The Soviet Journal of Atomic Energy, 1961. **9**(6): p. 1001-1009.
10. Oldekop, W., H.D. Berger, and W. Zeggel, General features of advanced pressurized water reactors with improved fuel utilization. Journal Name: Nucl. Technol.; (United States); Journal Volume: 59:2, 1982: p. Medium: X; Size: Pages: 212-227.
11. Oka, Y., T. Jevremovic, and S.-i. Koshizuka, Direct-cycle, supercritical-water-cooled fast breeder reactor. Journal of Nuclear Science and Technology, 1994. **31**(1): p. 83-85.
12. Koshizuka, S. and Y. Oka, Supercritical-pressure, light-water-cooled reactors for economical nuclear power plants. Progress in Nuclear Energy, 1998. **32**(3-4): p. 547-554.
13. Cheng, X., X.J. Liu, and Y.H. Yang, A mixed core for supercritical water-cooled reactors. Nuclear Engineering and Technology, 2008. **40**(2): p. 117-126.

14. Squarer, D., T. Schulenberg, et al., High performance light water reactor. Nuclear Engineering and Design, 2003. **221**(1-3 SPEC.): p. 167-180.
15. Shelley, A., S. Shimada, et al., Optimization of seed-blanket type fuel assembly for reduced-moderation water reactor. Nuclear Engineering and Design, 2003. **224**(3): p. 265-278.
16. Uchikawa, S., T. Okubo, et al., Conceptual design of innovative water reactor for Flexible Fuel Cycle (FLWR) and its recycle characteristics. Journal of Nuclear Science and Technology, 2007. **44**(3): p. 277-284.
17. Cheng, X. and Y.Q. Yu, Local thermal-hydraulic behaviour in tight 7-rod bundles. Nuclear Engineering and Design, 2009. **239**(10): p. 1944-1955.
18. Krauss, T. and L. Meyer, Characteristics of turbulent velocity and temperature in a wall channel of a heated rod bundle. Experimental Thermal and Fluid Science, 1996. **12**(1): p. 75-86.
19. Krauss, T. and L. Meyer, Experimental investigation of turbulent transport of momentum and energy in a heated rod bundle. Nuclear Engineering and Design, 1998. **180**(3): p. 185-206.
20. Cheng, X. and N.I. Tak, CFD analysis of thermal–hydraulic behavior of heavy liquid metals in sub-channels. Nuclear Engineering and Design, 2006. **236**(18): p. 1874-1885.
21. Ninokata, H., E. Merzari, and A. Khakim, Analysis of low Reynolds number turbulent flow phenomena in nuclear fuel pin subassemblies of tight lattice configuration. Nuclear Engineering and Design, 2009. **239**(5): p. 855-866.
22. Yang, J., Y. Oka, et al., Numerical investigation of heat transfer in upward flows of supercritical water in circular tubes and tight fuel rod bundles. Nuclear Engineering and Design, 2007. **237**(4): p. 420-430.
23. Gu, H.Y., X. Cheng, and Y.H. Yang, CFD analysis of thermal-hydraulic behavior in SCWR typical flow channels. Nuclear Engineering and Design, 2008. **238**(12): p. 3348-3359.
24. Liu, X.J. and X. Cheng, Thermal-hydraulic and neutron-physical characteristics of a new SCWR fuel assembly. Annals of Nuclear Energy, 2009. **36**(1): p. 28-36.
25. Zhao, M., H.Y. Gu, and X. Cheng, Experimental study on heat transfer of supercritical water flowing downward in circular tubes. Annals of Nuclear Energy, 2014. **63**(0): p. 339-349.

ISSCWR7-2070

Experiments on Heat Transfer in Rod-bundle Flows of CO_2 at Supercritical Pressures

Ahmad Eter, Dé Groeneveld and Stavros Tavoularis

University of Ottawa

Ottawa, ON, Canada K1N 6N5

Tel: 0016135625800, Ext.-2474, eng.eter@yahoo.com

Abstract

Supercritical heat transfer (SCHT) measurements on a three-rod bundle equipped with wire wrap spacers were obtained at the Supercritical University of Ottawa Loop (SCUOL). The tests were performed using CO_2 as a surrogate fluid for water and conditions equivalent to the nominal operating conditions of the proposed Canadian Super-Critical Water-Cooled Reactor (SCWR). The test section contained three 10-mm OD heated rods and three unheated rod segments with a pitch-to-diameter ratio of 1.14. The detailed heater-surface temperature distributions in the axial and circumferential directions were measured using remotely controlled sliding/rotating thermocouples. The following ranges of test conditions were covered: pressure from 6.6 to 8.36 MPa (equivalent water pressure: 19.7 to 25 MPa); inlet temperature from 11 to 30 °C (equivalent water temperature: 330 to 371°C); mass flux from 330 to 1173 kg/m^{2}s (equivalent water mass flux: 510 to 1819 kg/m^2/s); and wall heat flux from 56 to 175 kW/m^2 (equivalent water heat flux: 590 to 1847 kW/m^2). Equivalent water conditions were calculated using the alternative approach provided by Zahlan *et al.* (2014). The results for a relatively low mass flux suggest the occurrence of mild heat transfer deterioration near the inlet. The average heat transfer coefficient (HTC) in the rod bundle was not very different from that in an 8 mm tube under comparable flow conditions. Heat transfer at super-critical pressures in the three-rod bundle was found to be insensitive to pressure and inlet temperature. The minimum HTC in the three-rod bundle decreased somewhat with increasing heat flux and decreased strongly at a low mass flux. The circumferential and axial variations of wall temperature were quite complex but systematic and reproducible.

1. Introduction

The Super-Critical Water-Cooled Reactor (SCWR) is one of the candidate designs considered by the Generation IV International Forum as an innovative nuclear energy system with increased safety, more compact size, lower cost of energy production and reduced volume of nuclear waste, compared to existing systems. The present research is in support of the Canadian National Program for the development of the SCWR.

The super-critical heat transfer (SCHT) mode has distinct characteristics not present at subcritical pressures. When the fluid pressure and temperature are near their critical values, or when the pressure is supercritical and the temperature is near its pseudo-critical value, small changes in temperature can cause large changes in the thermo-physical properties and the heat transfer may undergo enhancement or deterioration. Of particular importance for the safety of SCWR is the phenomenon of heat transfer deterioration (HTD), during which the supercritical heat transfer coefficient (HTC) drops below the value that would be expected during normal forced convective heat transfer; when HTD occurs, wall temperatures that are higher than normal can be encountered. Heat transfer deterioration is thought to be associated with the suppression of turbulence near the wall.

Heat transfer in channels may be significantly affected by the presence of flow obstructions, including rod spacers in rod bundles. Eter *et al.* (2013) reviewed the literature of the spacer effect on SCHT. Based on the sparse available literature on SCHT in rod bundles, one may speculate that HTD is unlikely to occur in rod-bundle flows. It has been observed that flow obstructions generally enhance heat transfer and that the highest heat transfer enhancement occurred when the flow temperature was near the pseudo-critical value; in such cases, the enhanced heat transfer coefficient was more than twice its value in channels without flow obstructions. Significant heat transfer enhancement was found to occur downstream of grid spacers in upflow; in downflow, however, the effect of grid spacers on heat transfer was less pronounced and it was sometimes absent altogether. Predictions of spacer effects on super-critical heat transfer using CFD codes were found to be in fair agreement with experimental observations for normal heat transfer conditions, but were deemed to be of questionable accuracy for HTD conditions.

The vast majority of previous SCHT experiments have been performed in tubes and, to a lesser degree, in annular channels. Very few experimental studies are available for SC flows in rod bundles, and even fewer have addressed directly the spacer effect on SCHT. For SCWR development and safety analysis, relevant experiments in rod bundles are needed. The objective of the current study is to investigate experimentally SCHT in vertical upflow through a rod-bundle subassembly equipped with wire wrap spacers. Of particular interest in this work is to investigate whether HTD is possible in this device.

2. Experimental facility and instrumentation

The present SCHT investigation was conducted in the University of Ottawa Supercritical CO_2 loop (SCUOL), which was constructed especially for this purpose. Heat transfer

measurements in upward flow through a three-rod bundle with wire-wrap spacers were obtained using a sophisticated thermocouple traversing system. This section describes the test facility, its instrumentation and the test section.

2.1 The flow loop

Figure 1 shows the major components of SCUOL, while Figure 2 shows a schematic diagram of the loop. The maximum operating pressure was 10 MPa. The heat supplied to the test section was provided by a rectified DC power supply having a maximum voltage of 60 V DC and a maximum current of 2833 A. The fluid inlet temperature to the test section was controlled by a 22 kW pre-heater. Cooling of the loop was achieved by passing the operating fluid through four heat exchangers connected in parallel; two of these units used centrally supplied chilled water as a secondary fluid, whereas the other two used ethylene glycol, that was circulated from a tank contained in a freezer room.

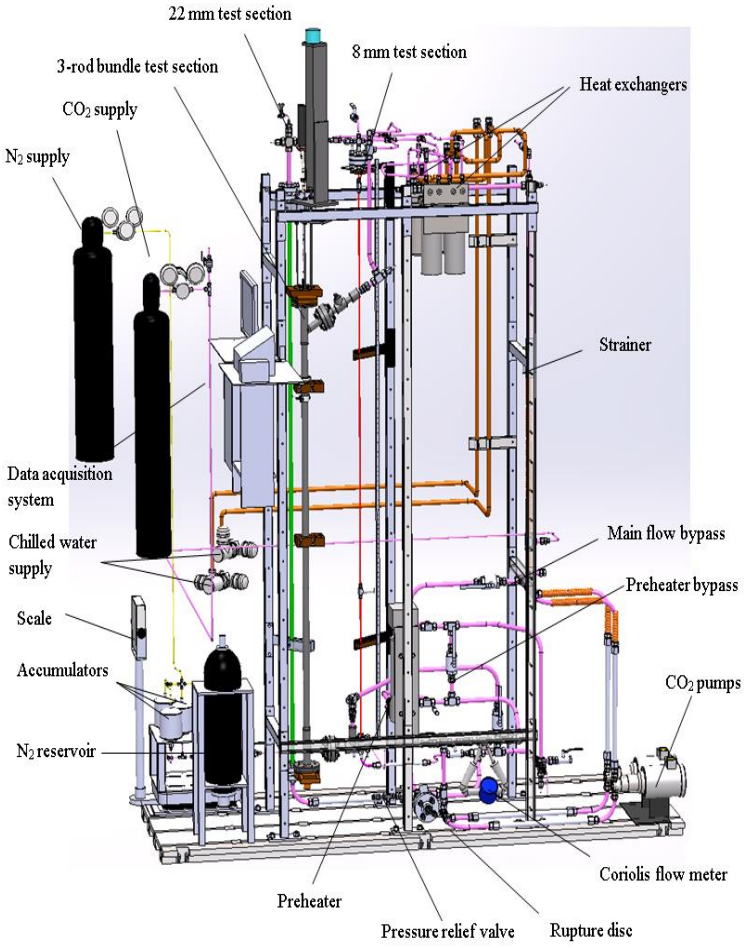

Figure 1. University of Ottawa CO_2 supercritical loop (Jiang, 2014)

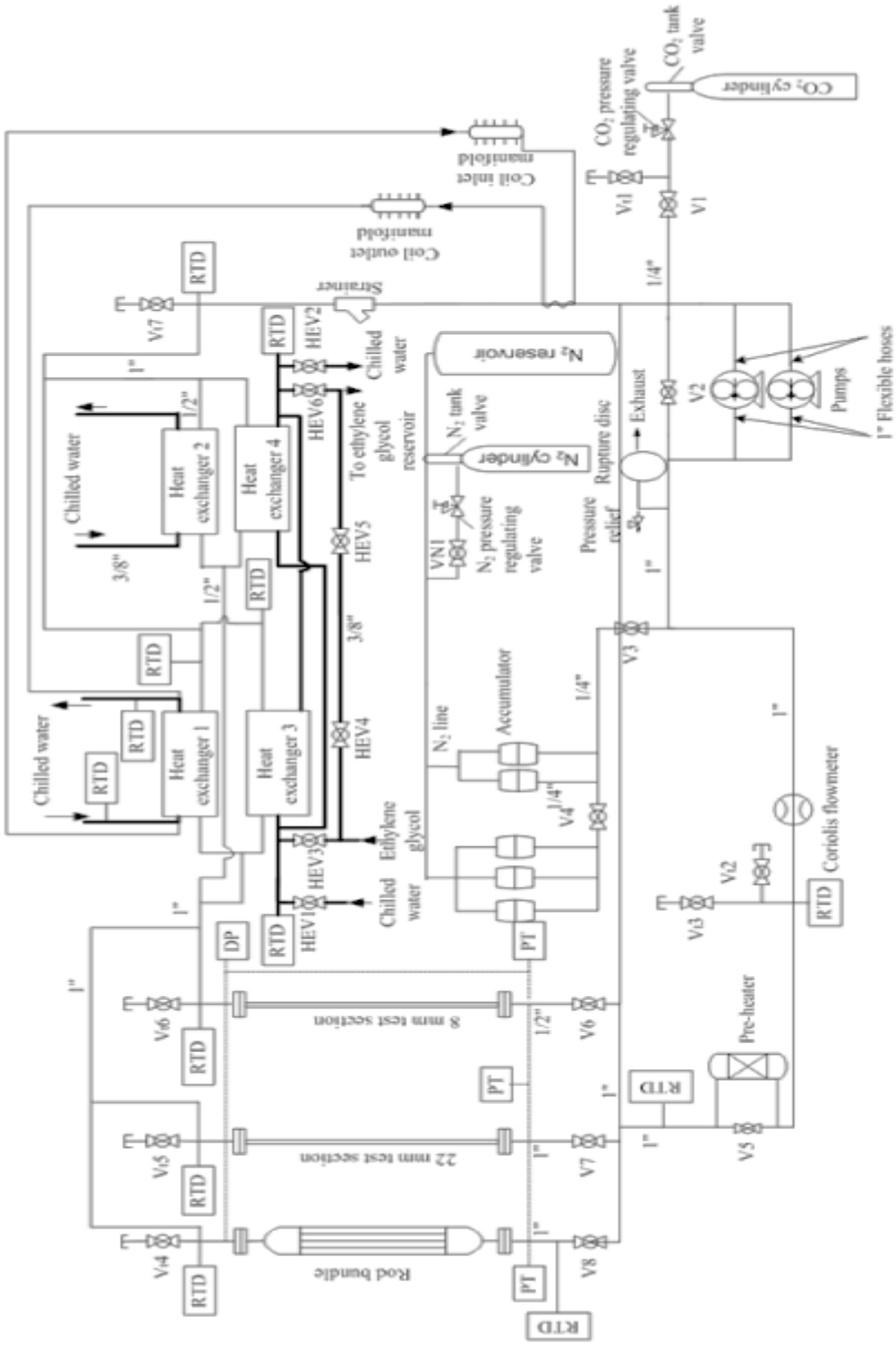

Figure 2. Schematic diagram of the loop and its components

2.2 Rod bundle test section

The rod bundle was mounted vertically and was cooled by pressurised CO_2 flowing upwards. The rod bundle had a total length of 2500 mm and each heated rod was made of Inconel 600 tubing with an outer diameter of 10.0 mm and a length of 1500 mm. Figure 3 shows an overall view of the rod bundle and Figure 4 shows its cross section. The three rods were identified as Rod A, Rod B and Rod C. Circumferential positions around each rod were specified such that positions at 0° were facing the exterior of the rod bundle, positions at 180° were facing the axis of the rod bundle subassembly and positions at 90° and 270° were facing the gaps with the unheated rod fillers, more details about the unheated rod fillers are provided by Jiang (2014). The rods were separated from each other by a wire with a diameter of 1.3 mm that was wrapped around each rod with a pitch of 200 mm. These wires are made from stainless steel T304 and had a resistance of 1.82 Ohm/m, which is much higher than the resistance of the heated rods, which was 0.036 Ohm/m. The rod bundle hydraulic diameter is D_h = 4.08 mm. The test section and the associated piping were insulated by a 2 mm thick layer of fibreglass and a 10 mm thick layer of insulating foam.

2.3 Sliding thermocouple assembly

A unique feature of this apparatus is the use of a sliding thermocouple system, which measured the inside wall temperature distributions of each of the three heated rods in the bundle. Each rod contained five thermocouples, positioned at three axial stations that were separated axially by a distance of 480 mm; two pairs of two thermocouples were placed at diametrically opposite locations at the two upstream stations and a single thermocouple was placed at the downstream station. Each set of five thermocouples was attached to a push rod that could also be rotated over the full 360° range by a step motor. These three step motors were mounted on a traversing system, which was traversed axially by a fourth step motor (Figure 5).

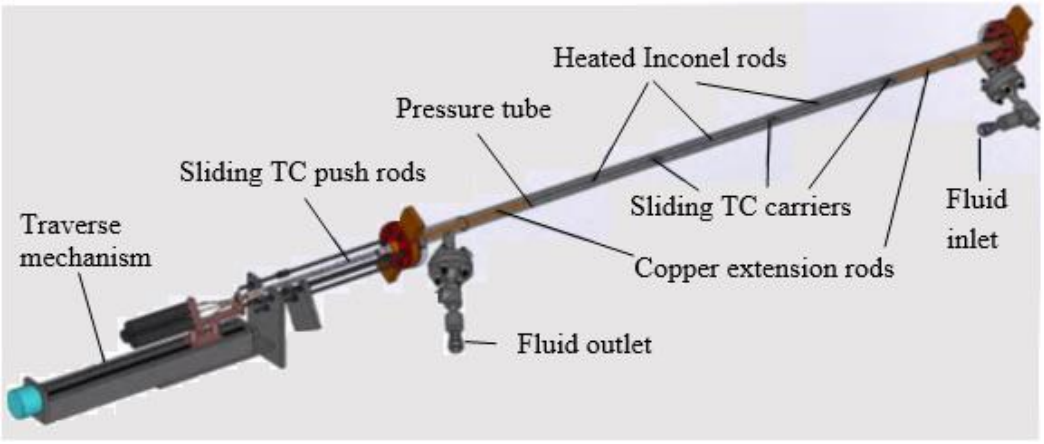

Figure 3. Overall view of the three-rod bundle (Jiang, 2014)

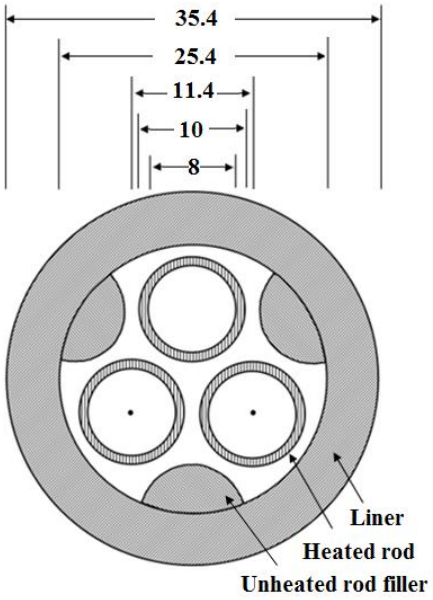

Figure 4. Cross section of the rod bundle

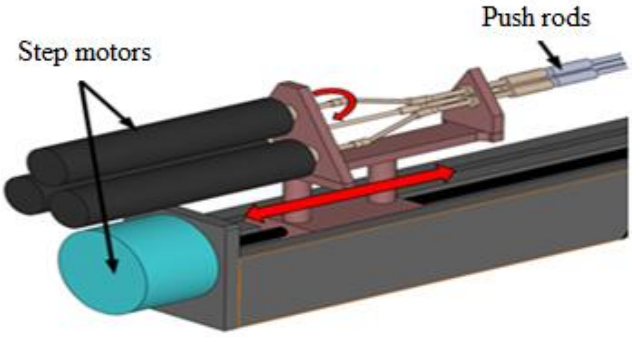

Figure 5. Thermocouple traversing system

2.4 Instrumentation

The bulk fluid temperature at the inlet of the rod bundle, as well as temperatures at different locations of the loop, were measured with in-flow ultra-precise RTD sensors (Omega P-M-1/10-1/8-5-1/2-G-15). The range of these RTD sensors was from 0 to 100 °C and their uncertainty was (0.3 + 0.005 |T|)°C. J-type thermocouples were installed in the sliding thermocouple system; these thermocouples had an uncertainty of 1.0 K at the 95 % confidence level. Potentiometers were used to measure the axial and angular displacements of the thermocouples.; the potentiometer measuring the axial displacement had a linearity of ±0.25% over its full moving range of 0.470 m and the potentiometer measuring the angular displacement had an estimated uncertainty of 5°. The absolute pressure at the inlet of the rod bundle was measured with a pressure transducer (Rosemount, Model 3051T) having an uncertainty of 15.5 kPa. A Coriolis flow meter (Micro Motion® Elite®, Model CFM050M320N0A2E2ZZ) was used to measure the mass flow rate; this device was factory

calibrated and had an uncertainty of 0.05 % within its full measurement range of 0 - 56.7 kg/min. The heating power was calculated from the voltage drop across the rod bundle and the electrical resistance of the test section, which was measured prior to its installation. The voltage drop was measured with an uncertainty of 0.034 V.

3. Test matrix and experimental procedure

Table 1 lists the test matrix of the present tests and the equivalent water values.

Table 1. CO_2 flow conditions and the equivalent water values

H_2O					**CO_2**					
P (MPa)	Pr (-)	G (kg/m^{2}s)	T_{in} (°C)	q (kW/m^2)	P (MPa)	Pr (-)	G (kg/m^{2}s)	T_{in} (°C)	Q (kW/m^2)	Date
25.0	1.13	1156.9	330.0	949.8	8.36	1.13	746	10.8	90.0	2014-02-24
25.0	1.13	1156.9	330.0	1846.9	8.36	1.13	746	10.8	175.0	2014-04-30
25.0	1.13	1550.9	330.0	1319.2	8.36	1.13	1000	10.8	125.0	2014-02-25
25.0	1.13	1819.2	330.0	1319.2	8.36	1.13	1173	10.8	125.0	2014-05-08
25.0	1.13	1142.5	350.0	979.3	8.36	1.13	711	20.2	90.0	2014-05-02
25.0	1.13	1142.5	350.0	1305.7	8.36	1.13	711	20.2	120.0	2014-05-08
25.0	1.13	510.0	330.5	885.0	8.36	1.13	330	11	84.0	2014-09-26
25.0	1.13	558.3	370.8	955.3	8.36	1.13	330	30	84.0	2014-09-25
25.0	1.13	510.0	330.5	590.0	8.36	1.13	330	11	56.0	2014-09-08
25.0	1.13	558.3	370.8	636.8	8.36	1.13	330	30	56.0	2014-09-25
25.0	1.13	680.0	330.5	1159.0	8.36	1.13	440	11	110.0	2014-09-09
25.0	1.13	744.4	370.8	1250.9	8.36	1.13	440	30	110.0	2014-09-22
25.0	1.13	680.0	330.5	772.3	8.36	1.13	440	11	73.3	2014-09-09
25.0	1.13	744.4	370.8	833.6	8.36	1.13	440	30	73.3	2014-09-19
23.0	1.04	510.4	331.1	886.1	7.69	1.04	330	11	84.0	2014-09-03
23.0	1.04	551.6	371.5	944.8	7.69	1.04	330	30	84.0	2014-09-24
23.0	1.04	510.4	331.1	590.7	7.69	1.04	330	11	56.0	2014-09-04
23.0	1.04	551.6	371.5	629.9	7.69	1.04	330	30	56.0	2014-09-24
23.0	1.04	680.5	331.1	1160.3	7.69	1.04	440	11	110.0	2014-09-04
23.0	1.04	735.5	371.5	1237.2	7.69	1.04	440	30	110.0	2014-09-23
23.0	1.04	680.5	331.1	773.2	7.69	1.04	440	11	73.3	2014-09-05
23.0	1.04	735.5	371.5	824.5	7.69	1.04	440	30	73.3	2014-09-23

Data acquisition: All pressure and temperature measurements were acquired at a rate of 10 samples/s. After the operating conditions were stabilized, measurements were recorded

continuously. During recording of the results, the traversing system was programmed to reposition the thermocouples, either axially or circumferentially, every 80 s. During post-processing, each data set was divided into blocks, each of which contained data for a different position of the thermocouple assembly. The data collected during the last 10 s of each block were found to correspond to steady conditions. Data processing was done with the use of a code written in MATLAB. Spurious values in the data were removed. The data values used in the analysis of the results represent time-averages over intervals 10 s long.

Outer wall temperature calculation: The outer wall temperature T_w was calculated from the measured inner wall temperature $T_{w,i}$ as (Incropera et al., 2007)

$$T_w = T_{w,i} - \frac{q^v r_i^{\,2}}{2k} ln\frac{r_i}{r_o} + (r_i^{\,2} - r_o^{\,2})\frac{q^v}{4k} \quad (1)$$

Thermocouple and RTD calibration check: To check the accuracy of the thermocouples, a zero-power test at a high mass flux was performed for every run. Figure 6 shows that all sliding thermocouples measured the same wall temperature within ±0.1 K and were in excellent agreement with the RTD (within 0.1 K), even at the relatively low mass flux of 502 kg/m^2/s.

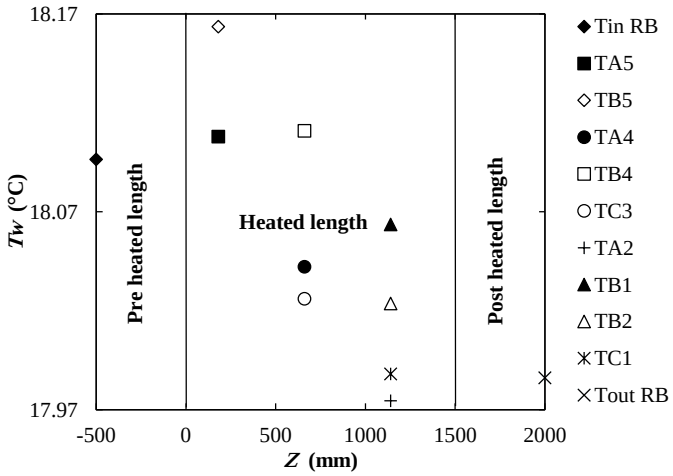

Figure 6. Temperature readings along the unheated rod bundle; G = 502 kg/m^{2}s

Heat balance check: As an overall check of the accuracy of the measured flow rate $\dot{m}$, the inlet and outlet RTD measurements and the NIST code property values, we compared the electrical power N supplied to the test section to the power $\dot{m}(h_{out} - h_{in})$ given to the fluid. The heat balance error was calculated as

$$\Delta N(\%) = 100\frac{N - \dot{m}(h_{out} - h_{in})}{N}\% \quad (2)$$

The specific enthalpies at the inlet h_{in} and the outlet h_{out} of the test section were calculated from the corresponding measured bulk temperatures and the measured pressure at the inlet. The heat balance error for all cases with relatively high power range (7.9 - 15.5 kWe) was

about 3%; however, higher heat balance errors (~5%) were encountered when the outlet temperature was close to the pseudo critical temperature T_{pc}, (36.7 °C and 32.8 °C corresponding to pressure of 8.36 and 7.69 MPa, respectively). This increase in the heat balance error is attributed to the properties variation when T_b approaches T_{pc}.

Repeatability check: We performed two types of repeatability checks, a classical one, in which we compared measurements for nominally the same test conditions at roughly the same time, and a second one, in which we compared corresponding measurements taken after a long period on inactivity or after making changes to the loop. The second type would indicate the appearance of errors in measuring devices due to instrument drift or due to changes made to the loop. Figure 7 shows an example of a test of the first type of repeatability, performed within a time interval of 3 hrs; it can be seen that the wall temperatures were in excellent agreement for the two trials. An example of the second type of test, performed with a time separation of 3 months, is shown in Figure 8; in this case as well, the measurement repeatability was excellent.

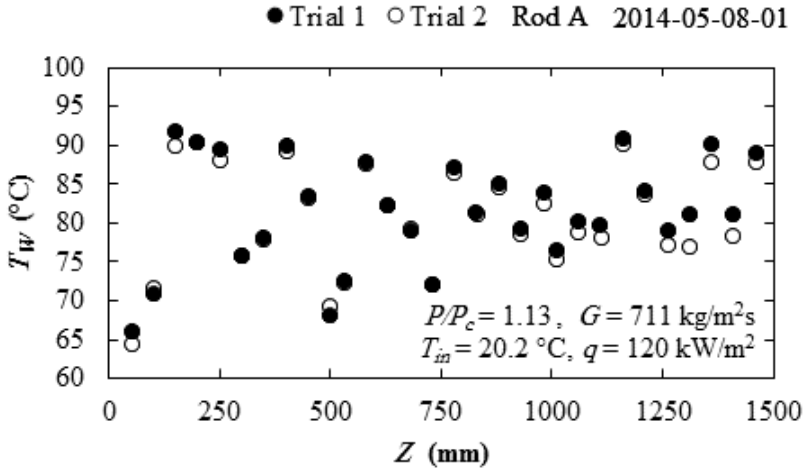

Figure 7. Repeatability check after 3 hrs of operation

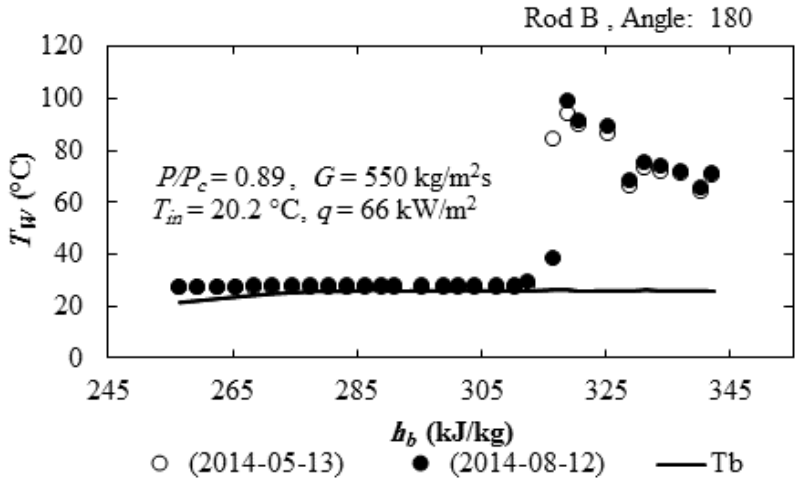

Figure 8. Repeatability check after 3 months of operation

4. Experimental results and discussion

4.1 Variations of wall temperature and HTC along the heated rods

Representative plots of the wall temperature measured at different circumferential and axial positions along one of the three rods, and the corresponding heat transfer coefficient *H*, vs. the local specific bulk enthalpy are presented in Figures 9 and 10. Figure 9 shows that, despite the presence of the wire-wrap spacers wrapped as a grid at the start of the heated length (which enhances turbulence and subchannel flow mixing), HTD appears to occur near the start of the heated section for G = 440 kg/m^{2}s. Because HTD was observed so far only to happen in the first pitch of the wire-wrapped rods, one should not draw a general conclusion that the enhanced mixing introduced by wire-wrap spacers cannot prevent HTD. In contrast, results at higher flow rates shown in Figure 10 seem to be free of HTD and have relatively high local values of wall temperature only at locations that depend on proximity to wire-wraps and the circumferential position on the rod. This figure also shows that the average HTC in the rod bundle was not very different from that in an 8 mm tube under comparable flow conditions.

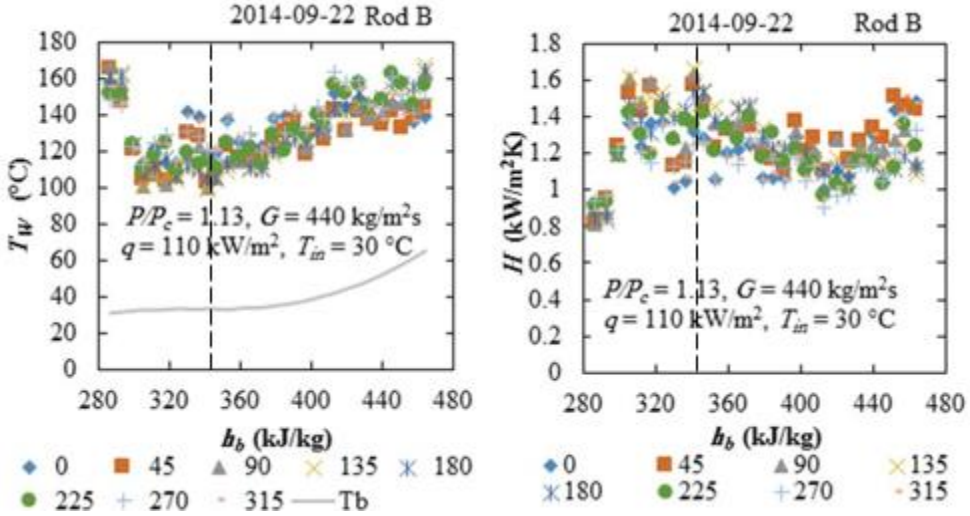

Figure 9. Wall temperature and heat transfer coefficient variation as a function of bulk enthalpy at various circumferential positions along rod B

The results shown in Figures 9 and 10 display a significant spread in temperatures around each rod at each axial location and an irregular axial temperature variation. Although wall temperature and HTC variations may appear to be random to a casual viewer, they were actually found to be systematic and repeatable. The complexity of these variations is such, however, that it is impossible to identify their causes, or connect consistently the specific local temperature values to local geometrical features, including the local wire-wrap patterns. Among the factors that would affect wall temperature and HTC variations would be the distance from the nearest wire-wrap location, and the orientation of the measurement position, namely whether the thermocouple faces an open subchannel, an unheated wall,

or a heated wall. Enthalpy and flow imbalances between the different types of subchannels would also affect the local temperature.

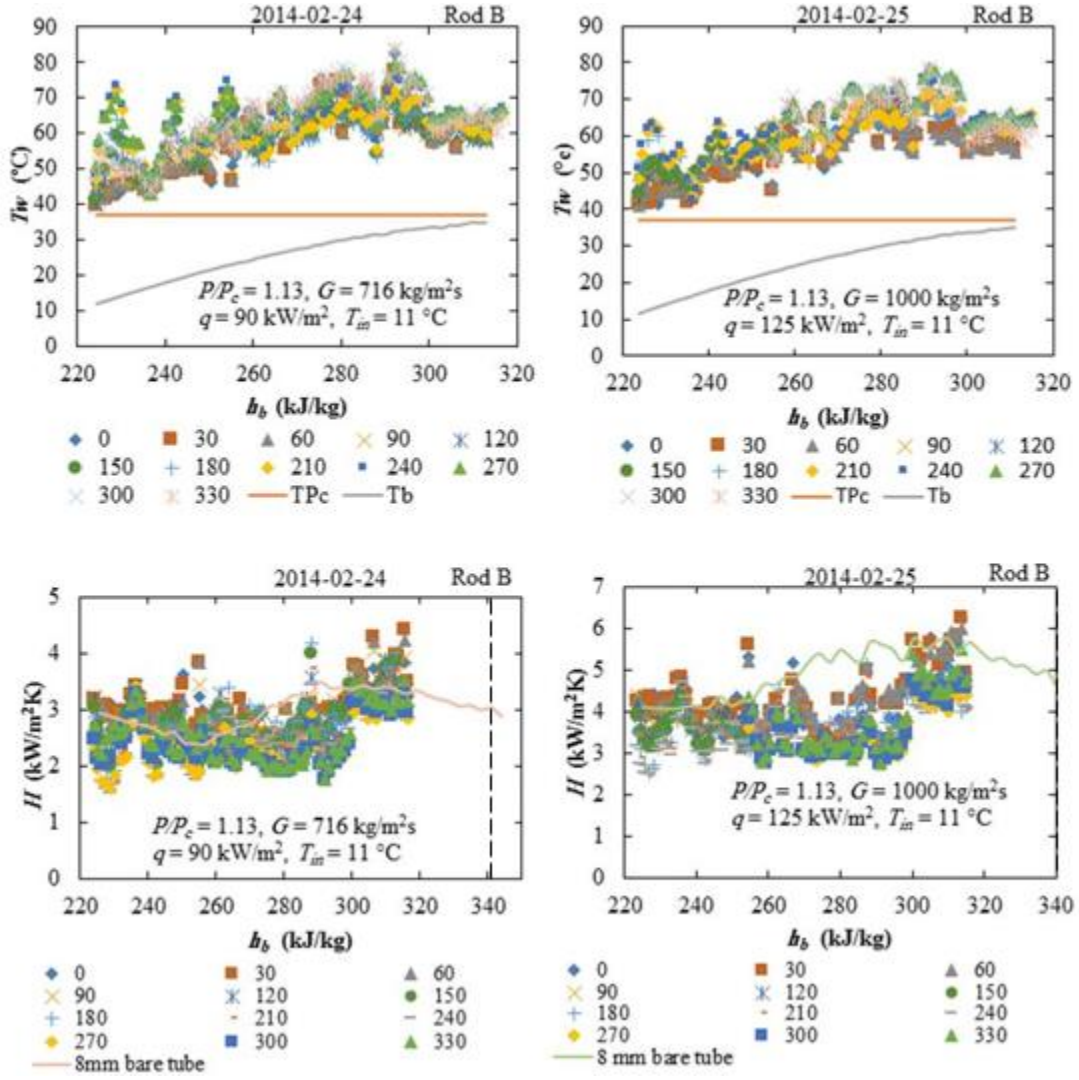

Figure 10. Wall temperature and heat transfer coefficient vs. specific bulk enthalpy at different circumferential positions along Rod B; solid lines in the HTC plots indicate values in an 8 mm tube under comparable conditions

4.2 Parametric trends of maximum wall temperature and minimum HTC

In nuclear reactor safety analyses, it is the maximum wall temperature T_{max} at each axial location that is of primary concern. The values of T_{max}, as well as the corresponding minimum heat transfer coefficients H_{min}, were extracted from the database and will be presented and discussed in this subsection. In particular, we are going to examine the dependence of these extremes upon the values of the imposed heat flux, mass flux, pressure and inlet temperature.

Heat flux effect: Figure 11 shows the axial variations of T_{max} and H_{min} for four representative pairs of runs; each pair had the same pressure, mass flux and inlet temperature but two different heat fluxes. In conformity with the First Law of Thermodynamics, T_{max} increased significantly with increasing heat flux in all cases. In addition, it is interesting to note that H_{min} generally decreased with increasing heat flux, but this dependence was much weaker than the dependence of T_{max}; this trend was also compatible with the expectation that the maximum wall temperature would likely increase more than the local bulk temperature for a given increase in heat flux. The dependence of H_{min} on heat flux was stronger at locations where the bulk temperature approached the pseudo-critical temperature, and where the thermal conductivity of the fluid was very sensitive to temperature.

Mass flux effect: The effect of mass flux on T_{max} and H_{min} for the same values of other flow conditions is shown in Figure 12. In general, T_{max} increased and H_{min} decreased with decreasing mass flux, with the sensitivity of these properties becoming quite strong for the change of mass flux from 1000 to 440 kg/m^{2}s. These trends are compatible with the expectation that the efficiency of convective heat transfer would decrease with decreasing flow rate. These results do not show any clear evidence of HTD, although it seems possible that some mild form of HTD may have occurred near the inlet of the heated section.

Pressure effect: Comparisons of T_{max} and H_{min} in two flows, one at a low SC pressure (P/P_c = 1.04) and another at the nominal operating pressure of the Canadian SCWR (P/P_c = 1.13) are shown in Figure 13. It appears that pressure in this range had little effect on the maximum wall temperature and the minimum heat transfer coefficient. In addition, one can see that the corresponding data points for the two pressures nearly coincided, which provides further proof that the variation of wall temperature was systematic and repeatable.

Inlet temperature effect: The effect of inlet temperature on T_{max} and H_{min} for the same values of other flow conditions is shown in Figure 14. In general, the applied relatively small changes in inlet temperature did not appear to have a significant effect on the values of T_{max} and H_{min} corresponding to the same bulk enthalpy.

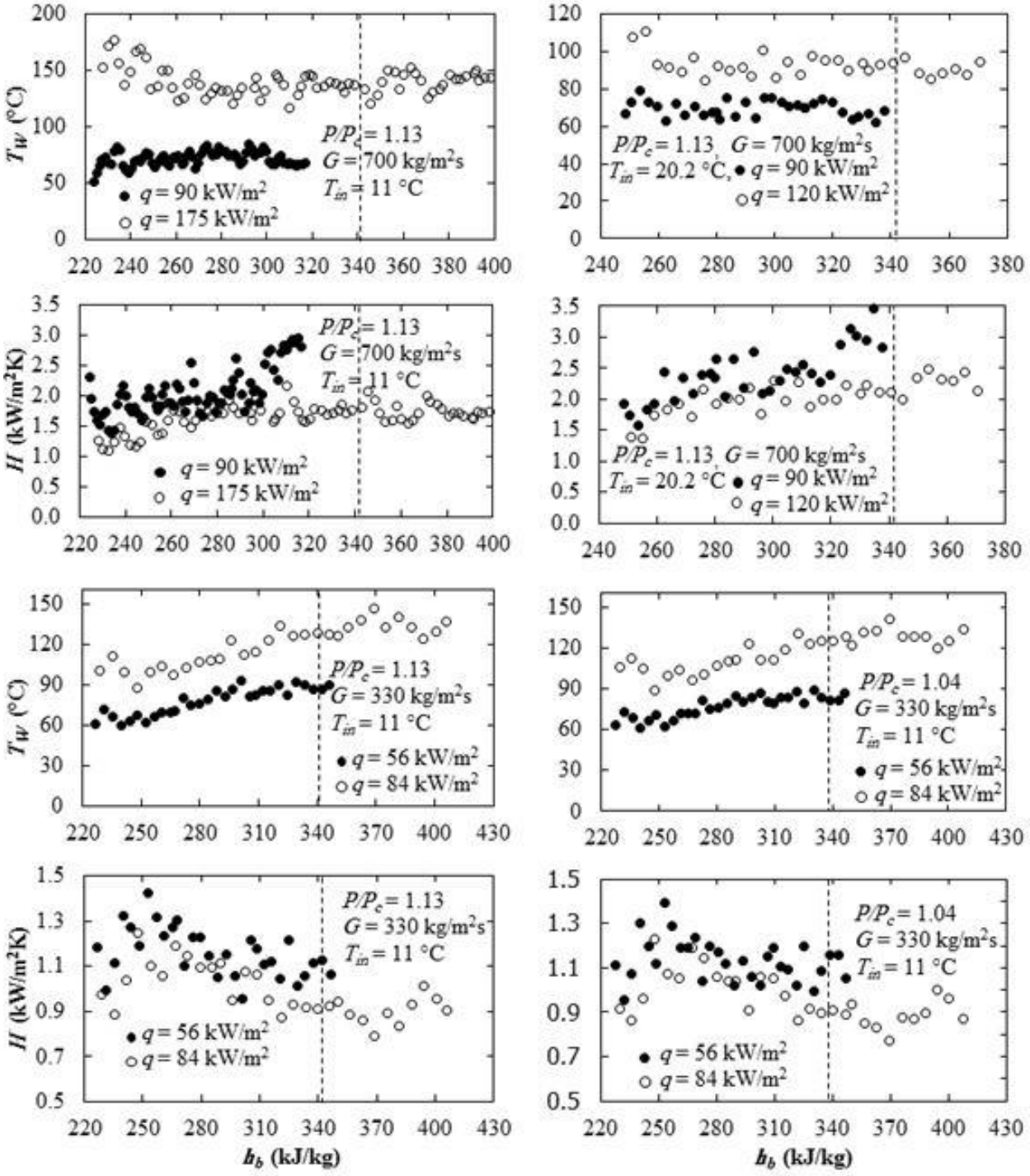

Figure 11. Effect of heat flux on the maximum wall temperature and the minimum heat transfer coefficient; dashed lines represent the pseudo-critical enthalpy

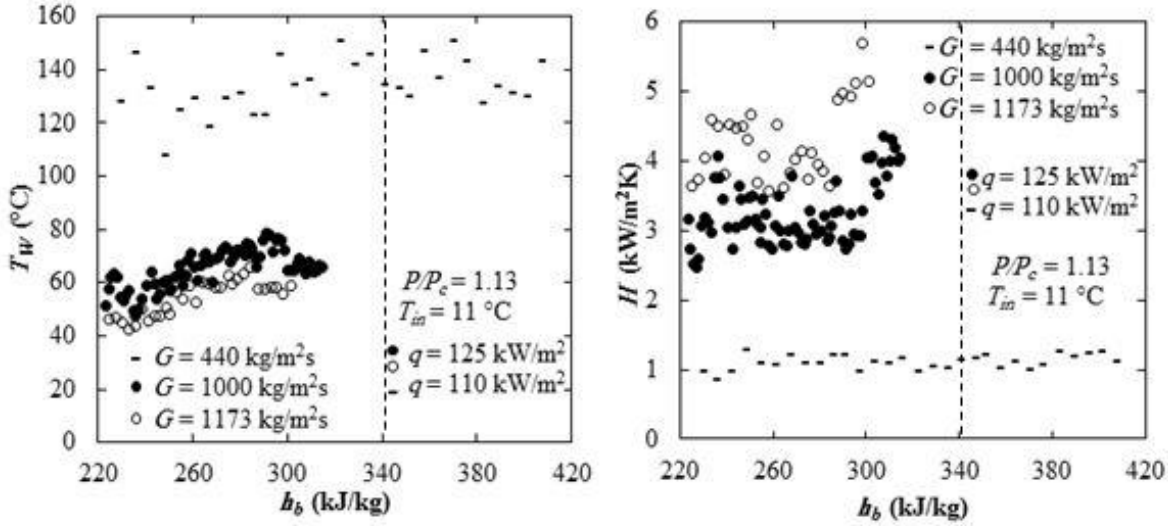

Figure 12. Effect of mass flux on the maximum wall temperature and the minimum heat transfer coefficient

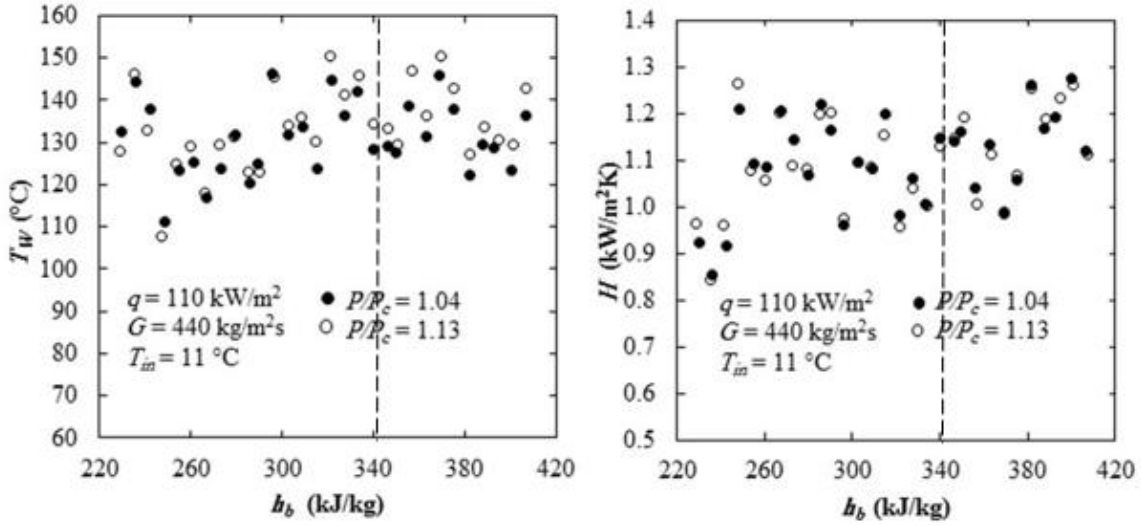

Figure 13. Effect of pressure on the maximum wall temperature and the minimum heat transfer coefficient

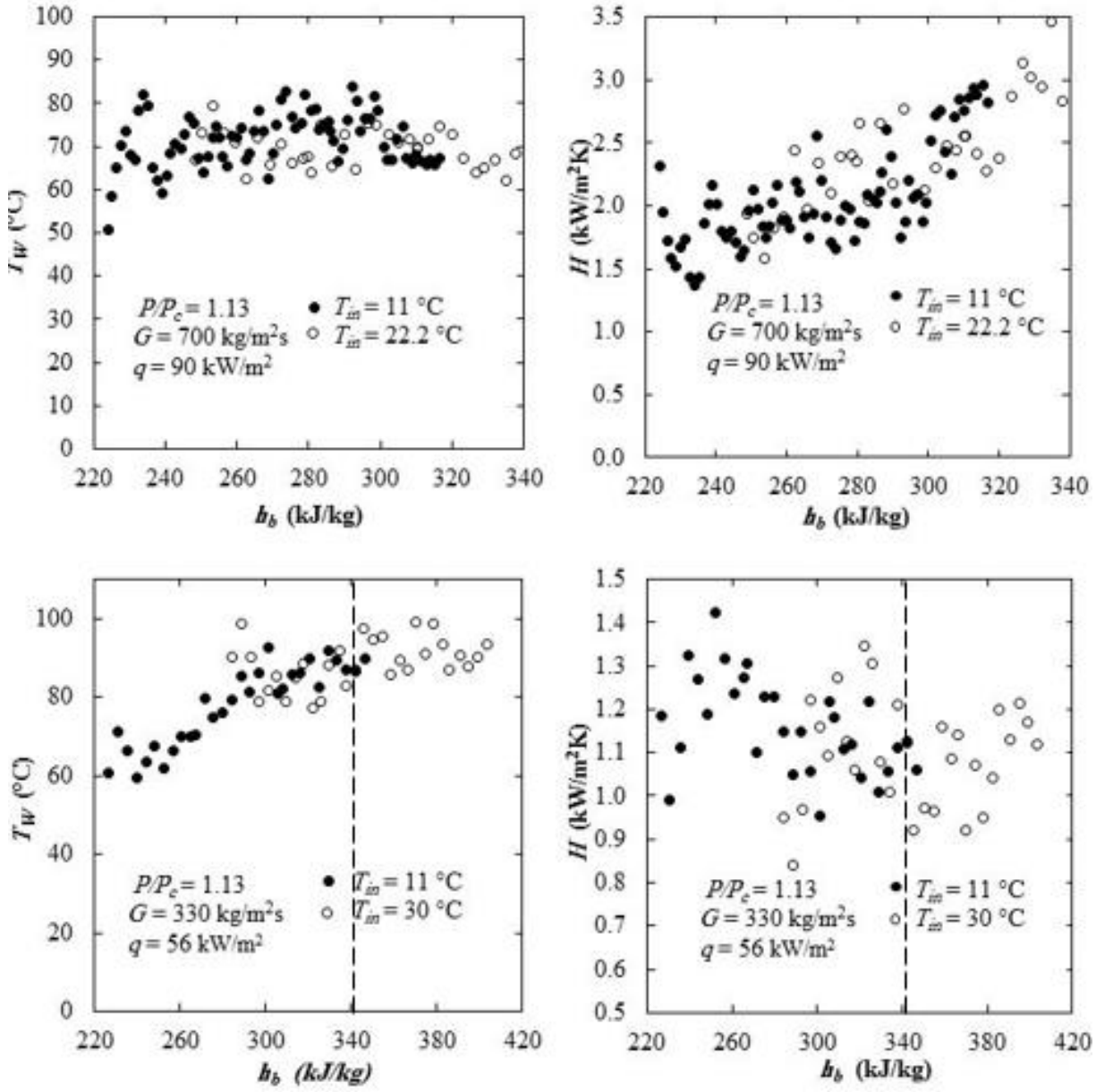

Figure 14. Effect of inlet temperature on the maximum wall temperature and the minimum heat transfer coefficient

4.3 Wire-wrap spacer effects

Wire-wraps spacers were fastened on the rods such that at the start of the heated section they were facing outwards (0º angle), they reached locations facing the rod-bundle axis (180º angle) at an axial distance of 100 mm, and they completed the first pitch at an axial distance of 200 mm. To verify that the wire-wraps maintained their initial positions, while at the same time also examining the effect they had on the local heat transfer, we plotted the axial variations of the three-rod-average wall temperature measured for several runs with thermocouples facing the axis of the central subchannel (Figure 15). These variations are quite complex, but, when all runs are considered together, an overall pattern emerges that the wall temperature at these central circumferential locations tended to have maxima at the locations of the wire-wraps, which appeared with a pitch of 200 mm and coincided with the nominal locations of the wire-wraps during their installation on the rods. Wall temperature minima tended to occur at locations between wire-wraps. This observation is also compatible with the expectation that the flow obstruction by a wire-wrap would increase the turbulence level downstream of it, and would thus enhance local flow mixing and heat transfer rate, which in turn would reduce the local wall temperature (Chandra *et al.*, 2009). Because we have no heat transfer measurements in the same rod-bundle without wire-wrap spacers to compare with, it is not possible to evaluate the overall wire-wrap effect. Moreover, we cannot determine whether wire-wraps are responsible for the generally observed lack or marginalization of heat transfer deterioration. We hope to be able to address these issues in the near future.

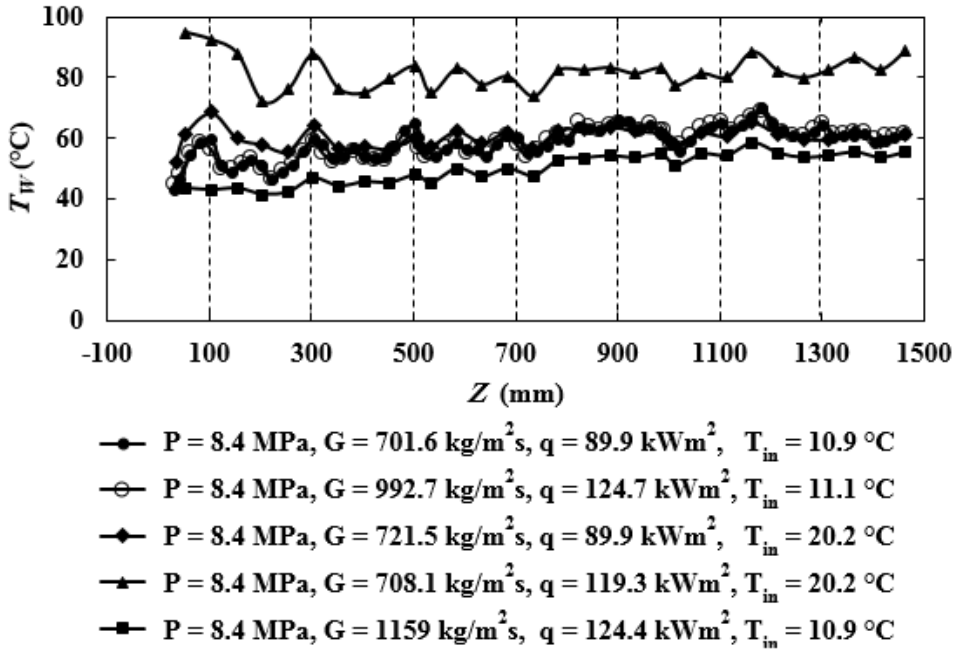

Figure 15. Axial **v**ariation of the three-rod average wall temperature at circumferential locations facing the axis of the rod-bundle subassembly (180° angles); presumed wire-wrap locations are indicated by dashed lines

5. Conclusions

The main conclusions of the present study are as follows.

1. Heat transfer deterioration appears to have occurred in a run with a relatively low mass flux near the start of the heated section of a three-rod bundle subassembly, which was equipped with wire-wrap spacers.
2. Heat transfer at super-critical pressures in the three-rod bundle was found to be insensitive to pressure and inlet temperature.
3. The minimum heat transfer coefficient in the three-rod bundle decreased somewhat with increasing heat flux and decreased strongly at a low mass flux.
4. The circumferential and axial variations of wall temperature were quite complex but systematic and reproducible.

Acknowledgments

This project is part of the Canadian Gen-IV National Program. Funding for this program was provided by Natural Resources Canada through the Office of Energy Research and Development, Atomic Energy of Canada Limited, and Natural Sciences and Engineering Research Council of Canada.

References

Chandra, L., J.A. Lycklama, C.V. Dirk and F. Roelofs, 2009, "CFD analysis on the influence of wire wrap spacers on heat transfer at supercritical conditions", 4th International Symposium on Supercritical Water-Cooled Reactors (ISSCWR-4), March 8-11, Heidelberg, Germany, Paper No. 30.

Eter, A., D. Groeneveld, S. Tavoularis and N. Onder, 2013, "Heat transfer enhancement at supercritical pressures", 12th International Conference on CANDU Fuel, September 15-18, Kingston, Ontario, Canada.

Incropera, F.P., D.P. DeWitt, T.L. Bergman and A.S. Lavine, 2007, "*Fundamentals of Heat and Mass Transfer*", 6th edition, John Wiley and Sons.

Jackson, J.D., 2011, "A model of developing mixed convection heat transfer in vertical tubes to fluids at supercritical pressure", 5th International Symposium on Supercritical Water-Cooled Reactors (ISSCWR-5), March 13-16, Vancouver, British Columbia, Canada.

Jiang, K., 2014, "An experimental facility for studying heat transfer in supercritical fluids", M.Sc. thesis, Department of Mechanical Engineering, University of Ottawa, Ottawa, Canada.

Zahlan, H., D. Groeneveld and S. Tavoularis, 2014, "Fluid-to-fluid scaling for convective heat transfer in tubes at supercritical and high subcritical pressures", International Journal of heat and mass transfer, Volume 73, 274–283.

ISSCWR7-2071

Monte Carlo simulation of inclined reactivity control rod and boron poisoning for the Canadian-SCWR supercell

H. Raouafi and G. Marleau
Institut de génie nucléaire, Département de génie physique, Polytechnique Montréal, Montréal (QC), Canada
haykel.raouafi@polymtl.ca, guy.marleau@polymtl.ca

Abstract

The Canadian-SCWR is a heavy water moderated supercritical light water cooled pressure tube reactor. It is fuelled with CANDU type bundles (62 elements) containing a mixture of thorium and plutonium oxides. Because the reactor is vertical, the upper region of the core is occupied with the pressure tubes inlet and outlet headers making it nearly impossible to insert vertical control rods in the core from the top. Insertion of solid control devices from the bottom of the core is possible, but this option was initially rejected because it was judged impractical. The option that is proposed here is to use inclined control rods that are inserted from the side of the reactor and benefit from the gravitational pull exerted on them.

The objective of this paper is to evaluate the neutronic performance of the proposed inclined control rods. To achieve this goal, we first develop a 3-D supercell model to simulate an inclined rod located between four vertical fuel cells. Simulations are performed with the SERPENT Monte Carlo code at five axial positions in the reactor to evaluate the effect of coolant temperature and density, that varies substantially with core height, on the reactivity worth of the control rods. The effect of modifying the inclination and spatial position of the control rod inside the supercell is then analyzed. Finally we evaluate how boron poisoning of the moderator affects their effectiveness.

Keywords: Canadian-SCWR, Inclined control rod worth, SCWR supercell, Boron poisoning, and SERPENT simulations.

1. Introduction

The Super-Critical Water Reactor (SCWR) concept [1] is designed to operate above the thermodynamic critical point of water reaching a thermodynamic efficiency higher than 40%. This type of reactor is one of six advanced reactor systems chosen by the Generation IV International Forum (GIF) [2] for study within its collaborative research and development program.

Similar to the CANDU6 design [3], the Canadian-SCWR is moderated using heavy water and its fuel bundles reside inside a pressure tube. Likewise, some features of the Canadian-SCWR are similar to that of the BWR, for instance the arrangement of the core is vertical and the coolant density has a strong axial dependence. The coolant is light water at 25 MPa, with an inlet temperature of 350 °C and an outlet temperature of up to 625 °C. The latest concept proposed by Atomic Energy of Canada Limited (AECL) is a High-Efficiency Re-entrant Channel (HERC) fuelled with CANDU type bundles (62 elements) containing a mixture of thorium and plutonium oxides [1].

Many aspects of the Canadian-SCWR are under consideration. Conceptual reactivity control devices and shutdown systems as well as control poison systems are amongst them. The basic

purpose of these systems is to bring the power output up to the desired level and to maintain it at that level as well as to shut the reactor down in the event of potentially unsafe operating conditions.

Because the reactor is vertical, the upper region of the core is occupied by the pressure tubes inlet and outlet headers making it virtually impossible to insert vertical control rods in the core from the top [4]. Furthermore, insertion of solid control devices from the bottom of the core, similar to those used for BWR, was considered but this option was rejected because it was judged impractical. One alternative that has been proposed to solve this problem is a system analogous to that used for the ATUCHA-II reactor [5] where one can still benefit from the gravitational pull exerted on the rods by using reactivity control devices that are inserted diagonally from the side of the reactor.

In this paper, we present a 3-D supercell Canadian-SCWR model to simulate inclined rods located between four vertical fuel cells using SERPENT [7] Monte Carlo code. Because of the large axial variations of the supercritical water temperature and density, neutronic properties vary significantly along the entire length of the channel. In order to evaluate how this impacts the control rod worth, the coolant properties are averaged over five axial positions in the reactor, each corresponding to a representative coolant temperature [6]. This model is then used to compute the effect of coolant density variations, rod rotations and displacements in the supercell and boron poisoning of the moderator on the control rods worth. The impact of the control rods on coolant void reactivity (CVR) is also assessed.

In section 2 of this paper, we present the SCWR supercell features as well as the geometry and composition of the control rods we propose. Then, in section 3, we present our SERPENT model followed in Section 4 by our results. Finally, in Section 5, we conclude.

2. SCWR supercell features

The most recent Canadian-SCWR concept is a re-entrant channel that is fuelled by 62 pins bundle (see Figure 1). The supercell model that is used to simulate control rods consists in a single inclined reactivity device inserted between a two by two array of vertical fuel channels. Because of the lack of symmetry along the y and z axes, the numerical simulation of the supercell involves a 3-D transport calculation. Reflective boundary conditions are applied on the external surfaces in the x, y and z directions.

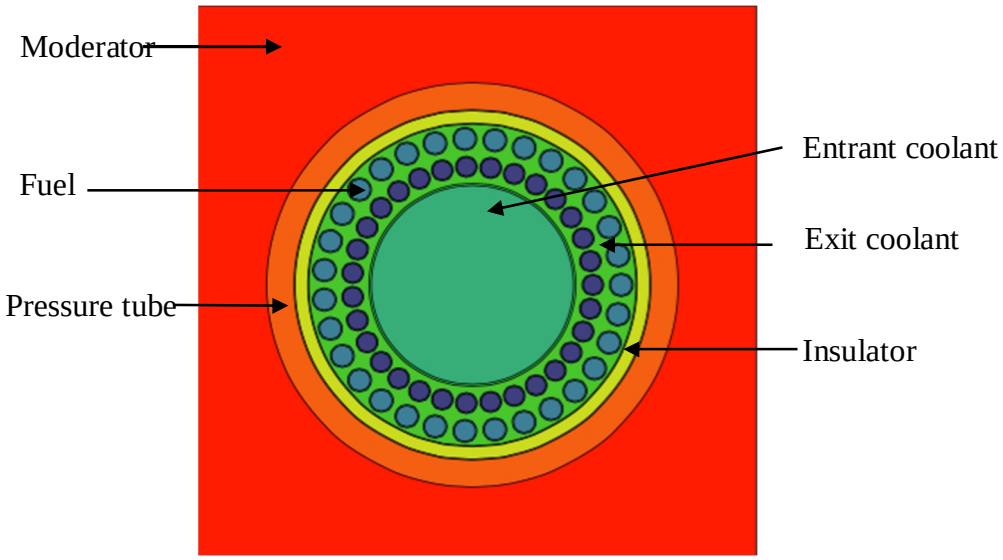

Figure 1. Cross sectional view of the 62-elements Canadian-SCWR fuel cell cluster.

2.1 Fuel bundle design

The central annular region of the fuel bundle is a hollow tube of zirconium-modified 310 stainless steel that is filled with light water at a temperature below super-critical conditions. The fuel pins, cladded in 0.6 mm thick zirconium-modified 310 stainless steel, are organized in two rings. For each ring, 31 identical fuel pins of outer radius 0.415 cm (inner ring) and 0.465 cm (outer ring) are found. The inner and outer fuels are composed of different mixtures of plutonium oxide and thorium oxide. The plutonium is reactor-grade (PuRG) and the isotopic composition and density of these fuels are given in Table 1. The coolant located in the central tube is light water of density 0.59254 $g.cm^{-3}$ whereas the density of coolant between fuel pins can vary from a value of 0.59254 $g.cm^{-3}$ to less than 0.07 $g.cm^{-3}$. The moderator located outside the pressure tube is 99.833 % pure heavy water of density 1.0851 $g.cm^{-3}$. The perforated liner tube surrounding the coolant is made of zirconium-modified 310 stainless steel that is surrounded by a porous cylinder of zirconia (ZrO_2) insulator, an outer liner and a pressure tube.

Table 1. Canadian-SCWR fuel bundle and channel specifications.

Component	Dimension	Material	Composition (wt%)	Density ($g.cm^{-3}$)
Central Coolant	4.45 cm OR	Light water	100 % H_2O	0.59254
Central tube	0.1 cm thick	Zr-modified stainless steel	C:0.034;Si: 0.51; Mn:0.74;P:0.016;S:0.002;Ni:20.82: Cr:25.04;Fe:51.738;Mo:0.51;Zr:0.59	7.9
Inner pins (31)	5.3 cm pitch circle radius	15 wt% PuO_2/ThO_2	Pu:13.23;Th:74.70;O:12.07	9.91
Outer pins (31)	6.55 cm pitch circle radius	12 wt% PuO_2/ThO_2	Pu:10.59;Th:77.34;O:12.08	9.87
Cladding	0.06 cm thick	Zr-modified stainless steel	As above	7.9
Coolant	7.2 cm OR	Light water	100% H_2O	Variable
Liner tube	0.05 cm thick	Zr-modified stainless steel	As above	7.9
Insulator	0.55 cm thick	Zirconia (ZrO_2)	Zr:66.63;Y:7.87;O:25.5	5.83
Outer liner	0.05 cm thick	Zirconium alloy	Sn:3.5;Mo:0.8;Nb:0.8;Zr:94.9	6.52
Pressure tube	1.2 cm thick	Zirconium alloy	Sn:3.5;Mo:0.8;Nb:0.8;Zr:94.9	6.52
Moderator	25 cm square	D_2O	99.833%D_2O;0.167%H_2O	1.0851

2.2 Reactivity control mechanisms

Two types of reactivity control mechanisms are proposed for the Canadian-SCWR: solid control rods and moderator poisoning with Boron.

Control rods are made of neutron absorbing materials and their presence in the core leads to a local depression of the neutron flux distribution. In fact, if a single vertical absorber rod is inserted at the center of a uniform reactor core; the neutron flux distribution will behave as shown qualitatively in Figure 2. It is seen that the flux depression in the control rod region is partially compensated by an equivalent flux increase further out [8].

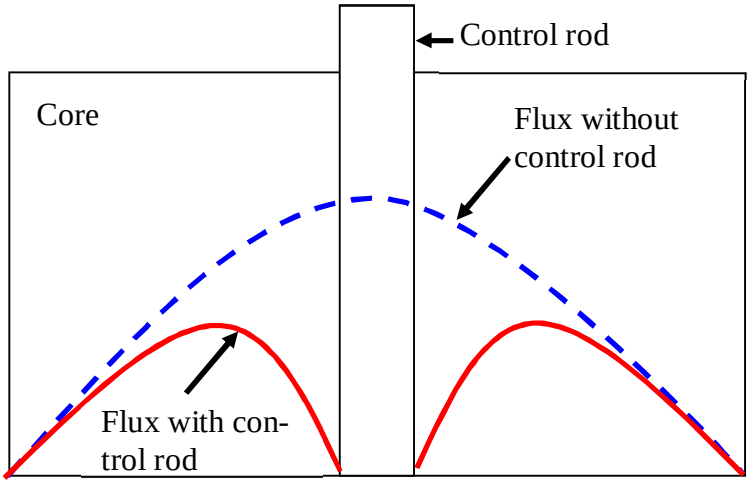

Figure 2. Effect of vertical control rod on radial flux distribution.

A 3-D MCNP [9] model for ATUCHA-II reactor was developed to analyse inclined control rod worth in the core [10]. It can be seen that the neutron flux decreases close to the control rod and that the effect on axial flux is asymmetric (see Figure 3).

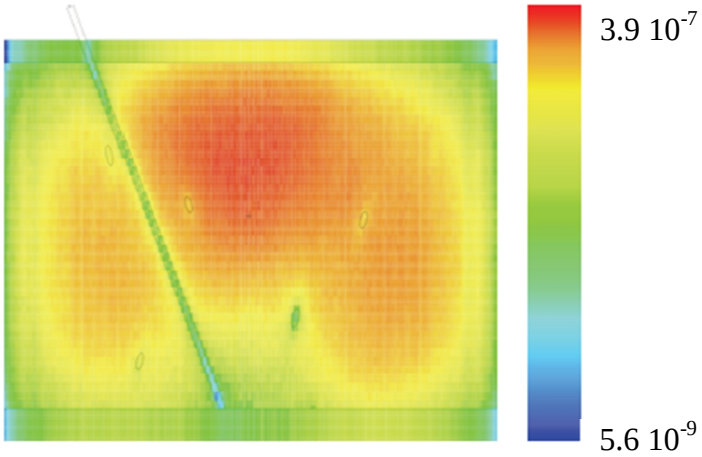

Figure 3. Results from the ATUCHA-II MCNP5 3-D model thermal flux distribution; axial view [9].

Boron poisoning can be used for various reasons including: 1) compensate fresh fuel high excess reactivity, 2) maintain the core for a long period in a guaranteed shutdown state. The actual geometry of the boron injection system is under development. Here, we model boron poisoning by a variation of moderator compositions with imposed boron concentrations.

2.3 Geometry of the SCWR Supercell

The geometric complexity of the Canadian-SCWR supercell (because the control rod will be analysed at a variety of angles and depths) implies the development of a 3-D Monte Carlo transport simulation model.

The supercell is a two by two array of vertical fuel bundles (see Figure 4) of lattice pitch equal to 25 cm and depth equal to 50 cm. The control rod is located halfway between two rows of fuel bundles and inclined in the $y - z$ plane. The explicit geometry of the control rod is illustrated in Figure 5, its material composition being given in Table 2. In addition to the possibility of

choosing different inclinations for the control rod, it can also be displaced along the y and z axes to simulate the situation when it is only partly inserted in the supercell.

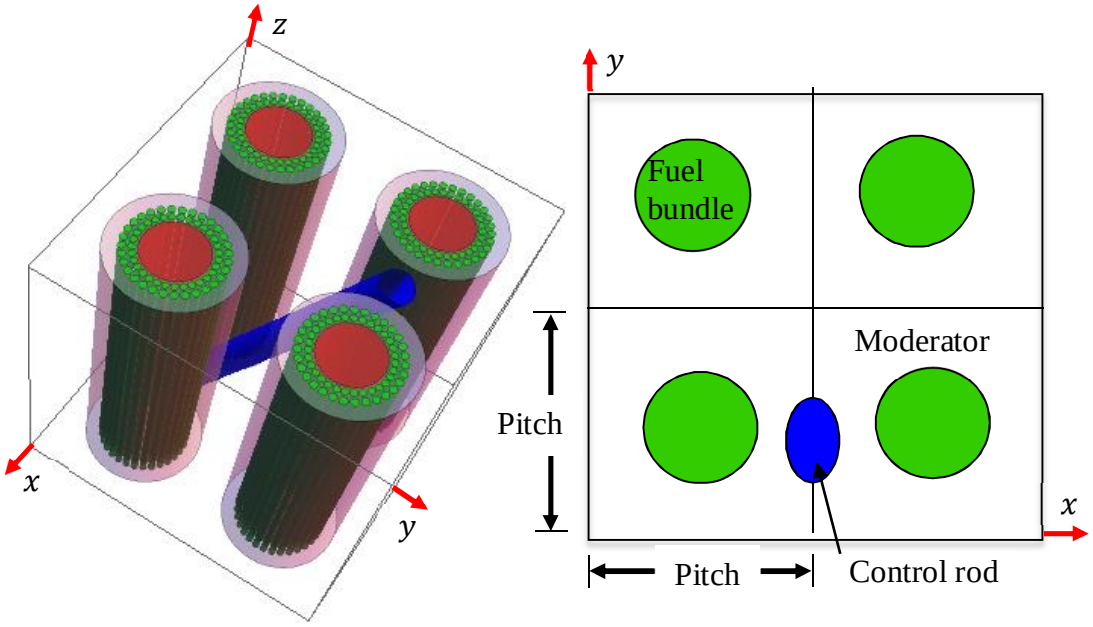

Figure 4. 3-D Canadian-SCWR supercell (left) and a 2-D projection in the $x - y$ plane (right).

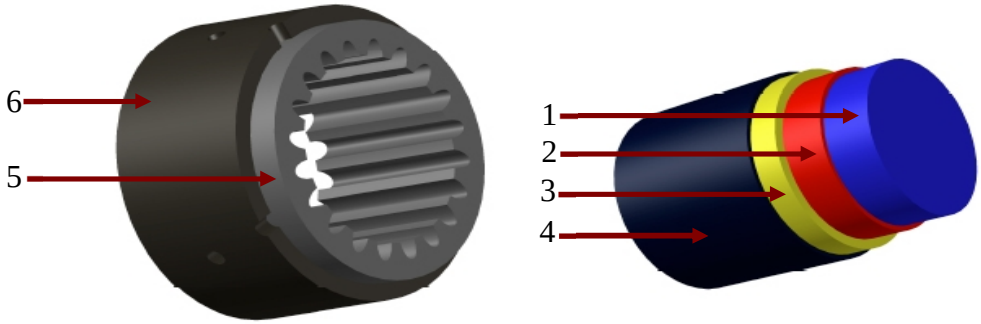

Figure 5. 3-D geometry of control rod (right) and its solid guide tube (left).

Table 2. Isotopic compositions of the moderator, the control rod and its guide tube (mixtures order provided in Figure 5).

Mixture	Radius (cm)	Isotopic compositions	Density ($g.cm^{-3}$)
1. Moderator	1.6	99.833% D_2O and 0.167% H_2O	1.0851
2. Stainless steel	1.7	Cn-nat, Cu-nat, Fe-nat, Mo-nat, Si-nat, Co-nat, Ni-nat, N-nat, Mn-nat, Cr-nat	7.8894
3. Cadmium	1.9	Cd-nat	1.16
4. Zr-modified (Zr2)	2.0	Zr-nat, Fe-nat, Cr-nat, Ni-nat, B10, B11 (IC1)	6.4003
5. Zr-2 perforated to 35.66 %	2.4	IC1	6.4003
6. Zr-2 perforated to 0.5 %	2.5	IC1	6.4003

3. SERPENT modelling of SCWR supercell

SERPENT is a three-dimensional continuous-energy Monte Carlo reactor physics code that uses a stochastic method to solve the neutron transport equation.

Our SERPENT simulations are performed at Hot Full Power (HFP) for the cells containing only fresh fuel. The following control rods configurations are considered:

- Rotation in $y-z$ plane between θ = 0 and $\theta = \pi/2$ with θ the angle between the control rod axis and z −axis.
- Translation along the y −axis.
- Translation along the z −axis.

The effect of coolant density at five axial positions is considered for each case above. The coolant density and temperature (same temperature as liner) for the five axial positions are given in Table 3. The temperature of the central coolant, insulator and pressure tube are fixed at 600 K for the five positions. The temperature of cladding and fuel pins are fixed at 900 K. Finally the temperature of moderator is fixed to 300 K.

SERPENT k_{eff} computations were performed using 10000 initial neutrons located inside the fuel, where the materials cross sections data were taken from a continuous energy ENDF/B-VII library. Calculations are run for 2000 active neutron cycles with 200 inactive cycles.

Table 3. Coolant density and temperature for five axial positions along the Canadian-SCWR fuel channel

Case	Distance from channel inlet (m)	Coolant density ($g.cm^{-3}$)	Coolant temperature (K)
1	0.5	0.59254	600
2	1.5	0.38246	600
3	2.5	0.16092	600
4	3.5	0.08949	900
5	4.5	0.06963	900

4. Result and discussion

In this section, we first evaluate the supercell effective multiplication constant k_{eff} and the coolant void reactivity for the five axial cases presented in Table 3 in three configurations:

- Supercell without control rod nor guide tube (R)
- Supercell with guide tube only (G)
- Supercell with control rod and guide tube (CR)

Then we evaluate the impact of spatial displacement (angular rotation and spatial translation) of the control rod on the supercell reactivity. Finally, we discuss the effect of boron poisoning on the control rod reactivity worth.

4.1 k_{eff} results

Tables 4, 5 and 6 provide the k_{eff} results obtained for a centered rod inclined at 45-degrees. Our SERPENT calculations were performed for two options: supercell with coolant and supercell without coolant. The coolant void reactivity ρ is computed using

$$\rho = 1000 \times \left(\frac{1}{k_{eff}^{C}} - \frac{1}{k_{eff}^{V}} \right) \quad (1)$$

where, k_{eff}^{C} and k_{eff}^{V} are respectively the multiplication constant when the light water coolant is present at its reference density and that when the coolant density is reduced to 0.001 g.cm^{-3}.

The relative stochastic errors obtained on k_{eff} are all below 0.03 mk. From tables 4 and 5, one sees that the contribution of the coolant surrounding the fuel bundles to neutron moderation is relatively large. The k_{eff} increases by about 15 mk when coolant density goes from 0.59254 g.cm^{-3} to 0.06963 g.cm^{-3}. Neutron absorption by the control rod guide tube is very low compared with the effect of control rod. The maximum effect of the guide tube is observed when the coolant has the lowest density.

From table 6, we can conclude that a decrease in coolant density results in an increase in the overall reactivity of the control rod. The presence of the control rod also shifts the CVR further into the negative direction. The ratio of CVR between the cases when control rod is inserted and the cases when it is withdrawn decreases from 4 to 2 when the coolant density goes from 0.59254 g.cm^{-3} to 0.06963 g.cm^{-3}.

Table 4. Effect of control rod and its solid guide inclined at 45-degree on k_{eff}^{C} results.

Case	1	2	3	4	5
k_{eff}^{C} **(R)**	1.28778	1.29103	1.29783	1.29990	1.30263
k_{eff}^{C} **(CR)**	1.23886	1.24002	1.24585	1.24805	1.24991
Δk_{eff}^{C} **(mk)**	48.92	51.01	51.98	51.85	52.72
k_{eff}^{C} **(G)**	1.28707	1.28910	1.29491	1.29886	1.30048
Δk_{eff}^{C} **(mk)**	0.07	0.19	0.29	0.10	0.21

Table 5. Effect of control rod and its solid guide inclined at 45-degree on k_{eff}^{V} results.

Case	1	2	3	4	5
k_{eff}^{V} **(R)**	1.27895	1.27895	1.27895	1.27855	1.27855
k_{eff}^{V} **(CR)**	1.20595	1.20595	1.20595	1.20589	1.20589
Δk_{eff}^{V} **(mk)**	73.00	73.00	73.00	72.66	72.66
k_{eff}^{V} **(G)**	1.27542	1.27542	1.27542	1.27547	1.27547
Δk_{eff}^{V} **(mk)**	3.53	3.53	3.53	3.08	3.08

Table 6. Impact of control rod on supercell CVR.

Case	1	2	3	4	5
ρ **(mk) (R)**	-5.36	-7.32	-11.37	-12.85	-14.46
ρ **(mk) (CR)**	-22.03	-22.78	-26.56	-28.01	-29.21
ρ **(mk) (G)**	-7.10	-8.32	-11.80	-14.12	-15.08

4.2 Effect of inclination on control rod worth

In Figure 6, k_{eff} is plotted as a function of rod inclination. Here we observe that a control rod inclination of 45-degree leads to the maximum neutron absorption in the supercell (Figure 6(a)).

We can observe in Figures 6(b) and 6(c) that the absorption of the control rod increases linearly with an increase in the rod volume in the supercell, except in the interval of inclination [0, 20] where we observe no variation. This can be explained by the fact that in this interval two effects are competing: 1) inclination of the control rod increases the rod volume inside the supercell, leading to an increase in absorption, 2) when the angle between the rod axis and the z −axis increases the neutron absorption in the supercell decreases because the rod is, on the average, further from the fuel.

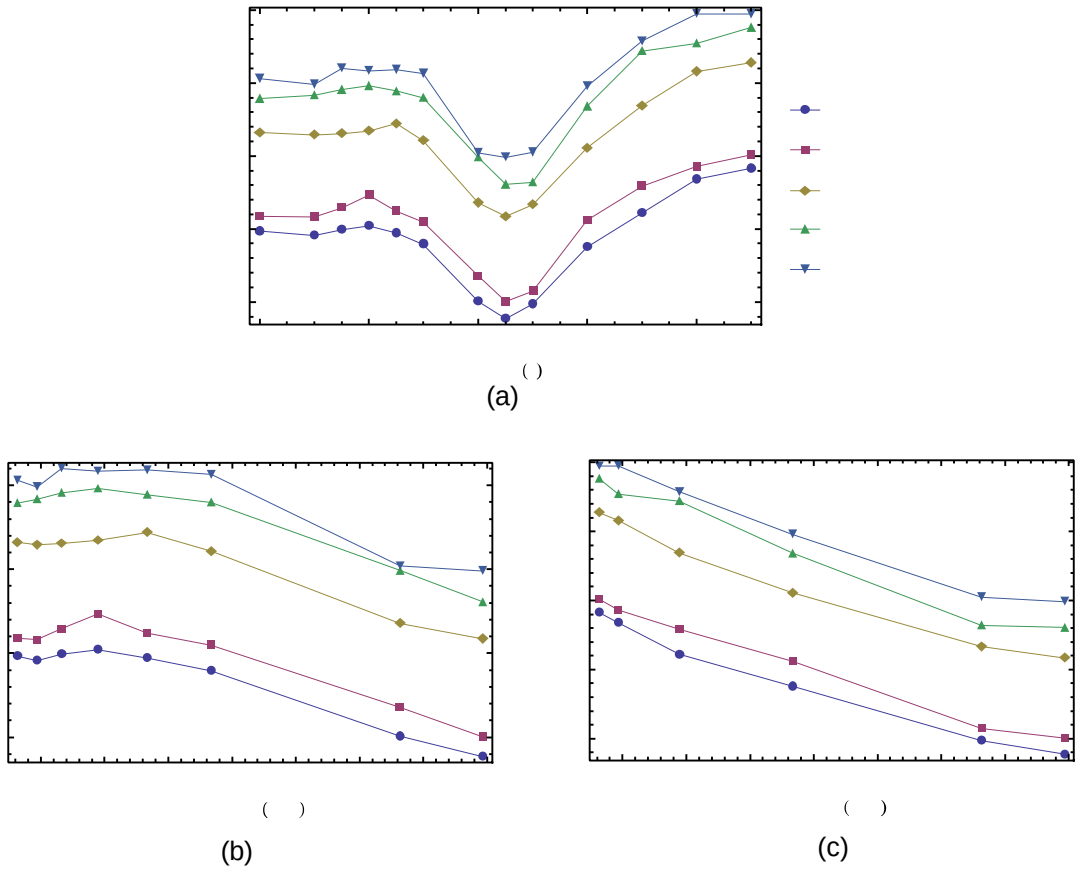

(a) (b) (c)

Figure 6. Effect of inclination of control rod on multiplication factor (k_{eff}): (a) k_{eff} variations with inclination angle; (b) k_{eff} variations with control rod volume (0 to 45-degree inclination); (c) k_{eff} variations with control rod volume (90 to 45-degree inclination).

4.3 Control rod worth dependence on spatial location

In the above section, results show that at an inclination of 45-degree, the control rod produce a significant absorption in the supercell. In this section we perfomed a k_{eff} calculation assuming the following options: 1) the control rod is inclined at 45-degree: 2) the geometric centre of rod is displaced at various locations along the y and z axes.

In Figure 7, k_{eff} is plotted as a function of control rod geometric centre displacement with respect to the center of the cell. In figures 7(a) and 7(b), we observe that the k_{eff} variation is roughly linear with the y displacment of the geometric center. The same observation is also true

for displacement along the z –axis. In fact this observation is explained by the fact that as the control rod moves along these axes, the geometric volume inside the supercell decreases resulting in an equivalent reduction in k_{eff} as seen in Figure 7(c).

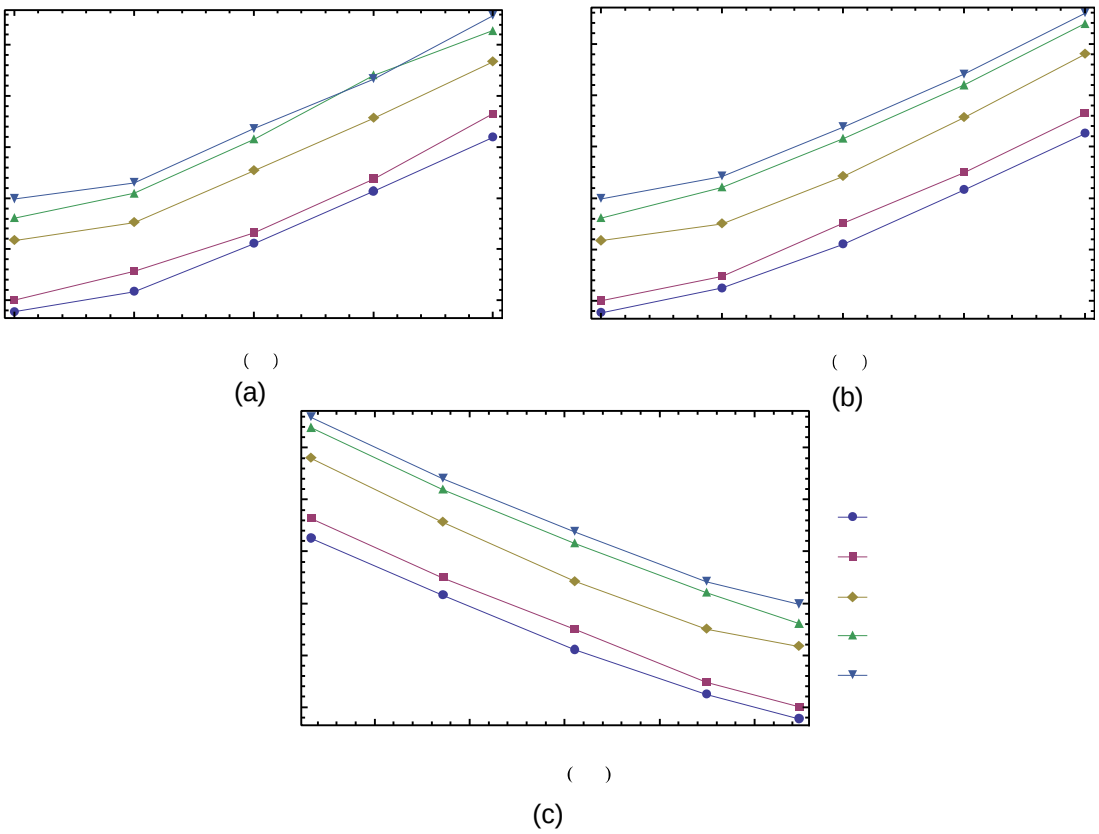

Figure 7. Effect of axial position of control rod on k_{eff}: (a) as a function of displacement along the y –axis; (b) as a function of displacement along the z –axis; (c) as a function of rod volume inside the supercell.

4.4 Effect of boron poisoning on control rod worth

Here, we first need to evaluate the boron concentration in the moderator that is required to make the supercell critical without the control inserted. We therefore performed supercell calculations for several boron concentrations, in the range 30 to 92 ppm, for each of the five axial variations in coolant density. The same calculations are repeated for the situation where one inserts a control rod centrered in the supercell and inclined at an angle of 45 degrees. The results for k_{eff} we obtain for both cases are presented in Figure 8 and Table 7.

Our results show that for fresh fuel, the critical boron concentrations is between 65 and 75 ppm, depending on the axial cell location we considered. As expected, the insertion of a control rod reduces the supercell k_{eff}. The results for the reactivity worth of the control rods are presented in Table 8. We see that Δk_{eff} decreases as the boron concentration increases. The effect is even more striking when Table 8 is compared with Table 4 where the calculations were performed without boron poisoning. A reduction in Δk_{eff} by a factor between 4 and 5 is then observed. This is not surprising since boron strongly shields the control rod by absorbing a large part of the neutrons reaching the moderator.

This means that the reactivity worth of the control rods will vary considerably during a full burnup cycle, if excess core reactivity is controlled by boron poisoning. To avoid this undesirable effect, it is advisable to use a different mean to control the core initial excess reactivity using, for example, burnable fuel poisons.

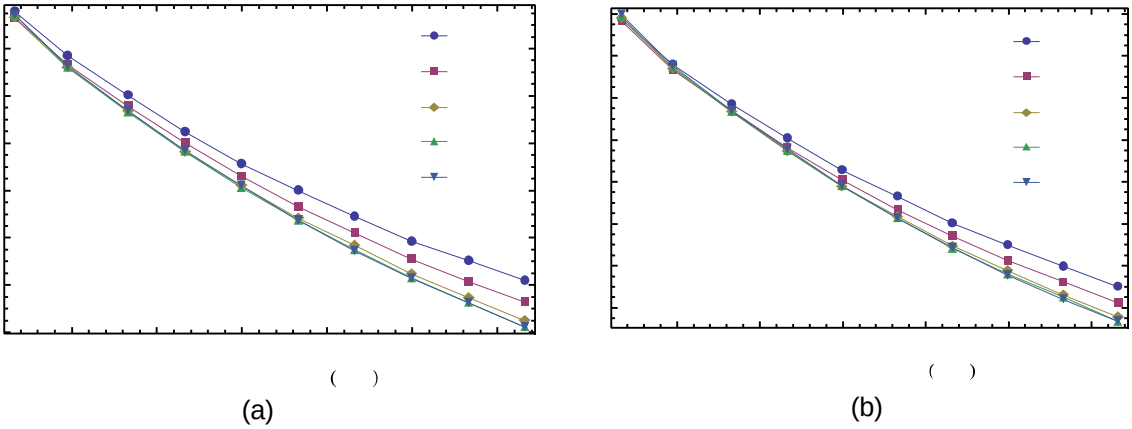

(a) (b)

Figure 8. Effect of boron poisoning on k_{eff} : (a) k_{eff} variation when control rod is inserted; (b) k_{eff} variation when control is withdrawn.

Table 7. Effect of boron poisoning on supercell k_{eff} with and without control rods.

Concentration (ppm)	k_{eff} (case_1)	k_{eff} (case_2)	k_{eff} (case_3)	k_{eff} (case_4)	k_{eff} (case_5)
59.9	1.02557(*)	1.02088	1.01776	1.01801	1.01813
	1.01129(**)	1.00599	1.00209	1.00115	1.00202
66.6	1.01300	1.00658	1.00335	1.00260	1.00262
	0.99999	0.99306	0.98822	0.98745	0.98738
73.2	1.00029	0.99411	0.98934	0.98825	0.98850
	0.98893	0.98200	0.97678	0.97497	0.97444

(*) Configuration R.
(**) Configuration CR.

Table 8. Effect of boron poisoning on control rods worth.

Concentration (ppm)	Δk_{eff} (case_1)	Δk_{eff} (case_2)	Δk_{eff} (case_3)	Δk_{eff} (case_4)	Δk_{eff} (case_5)
59.9	14.3	14.9	15.7	16.9	16.1
66.6	13.0	13.5	15.1	15.1	15.2
73.2	11.4	12.1	12.6	13.3	14.1

5. Conclusion

The models developed in this work were used to evaluate, using the code SERPENT, the impact of inclination and spatial displacement on control rod worth for the Canadian-SCWR supercell. We concluded that a 45-degree inclination of the control rod positioned at the center of the SCWR supercell is the most efficient for the point of view of neutron absoption. The reactivity worth of the control rod depends linearly on the total volume of insertion in the supercell, as evidenced by looking at the effect of displacing the rod in the y and z directions with respect to the supercell center or rotating the rod.

The coolant water of the 62-fuel elements bundle plays a significant role as a moderator with k_{eff} rising when the coolant density decreases. As a result, the control rods reactivity worth increases as the coolant density decreases. Finally, boron moderator poisoning has a large impact on the control rod worth. It decreases by a factor ranging from 4 to 5 with respect to the unborated cases when concentrations between 50 and 60 ppm of boron are used. An alternative option to poisoning the moderator should therefore be considered to compensate excess initial reactivity for a fresh or refueled core.

We are in the process of modelling a full SCWR core to simulate inclined control rods at various positions and inclinations. In future papers, we will present models to estimate the number and positions of control rods in the Canadian-SCWR.

6. Acknowledgements

The authors are grateful to Mission Universitaire de Tunisie en Amérique du Nord (MUTAN), the Natural Science and Engineering Research Council (NSERC) and the NSERC/NRCan/AECL Gen-IV Energy Technologies Program for their support to this work.

7. References

[1] J. Pencer, D. Watts, A. Colton, X. Wang, L. Blomeley, V. Anghel and S. Yue, ‘‘Core neutronics for the Canadian SCWR conceptual design,” in *The 6th international symposium on supercritical water-cooled reactors*, Shenzhen, Guangdong, China, 2013.

[2] The Generation IV International Forum (GIF), URL: https://www.gen-4.org/gif/jcms/-c_9260/public.

[3] L. Ian, “CANDU Design and Equipment Overview,” AECL CANDU supply chain forum Saskatoon, Atomic Energy of Canada Limited, Saskatoon, Canada, 2010.

[4] H. Raouafi, G. Marleau, “A simplified 3D DRAGON simulation of an inclined reactivity control device for the Canadian-SCWR,” in *The 19th Pacific Basin Nuclear Conference*, Vancouver, British Columbia, Canada, 2014.

[5] C. Grant, R. Mollerach, F. Leszczynski, O. Serra, J. Marconi, and J. Fink, “Validation of updated neutronic calculation models proposed for ATUCHA-II PHWR. Part II: Benchmark comparisons of PUMA core parameters with MCNP5 & improvements due to a simple cell heterogeneity correction,” in *The International Conference on Advances in Nuclear Analysis and Simulation*, Vancouver, British Columbia, Canada, 2006.

[6] G. Marleau, G. Harrisson, H. Raouafi, A. Bouchon and T. Benguedouar, *Evaluation of the 2-D benchmark using SERPENT, TRIPOLI and DRAGON*, Technical report IGE-333, École Polytechnique de Montréal, Montréal, Canada, 2012.

[7] J. Leppänen, *PSG2/SERPENT a continous-energy Monte Carlo reactor physics burnup calculation code*, VTT technical research centre of Finland, Finland, 2013.

[8] S. Glasstone, A. Sesonske, *Nuclear reactor engineering: reactor design basics*, Fourth edition, CBS publishers & distributors, New Delhi, 2004.

[9] Briesmeister, J. F. *MCNPTM - A general Monte Carlo N-Particle Transport Code, Version 4C*. Los Alamos National Laboratory, New Mexico, USA, 2000.

[10] M. Pecchia, C. Parisi, F. D’Auria, and O.Mazzantini, “Development and application of MCNP5 and KENO-VI Monte Carlo models for the ATUCHA-2 PHWR analysis,” *Science and Technology of Nuclear Installations*, vol. 2011, Article ID 683147, 2011.

ISSCWR7-2072

Various Design Aspects of the Canadian Supercritical Water-Cooled Reactor Core

M. Yetisir, R. Xu, M. Gaudet, M. Movassat, H. Hamilton, M. Nimrouzi, J. Goldak
Canadian Nuclear Laboratories Limited
Fluid Sealing Technology
Chalk River Laboratories
Chalk River, Ontario, K0J 1J0
metin.yetisir@cnl.ca

Abstract

The Canadian SCWR is a 1200 MW(e) channel-type supercritical water-cooled nuclear reactor (SCWR). The reactor core includes 336 vertical pressurised fuel channels immersed in a low-pressure heavy water moderator and calandria vessel containment. The supercritical water coolant flows into the fuel channels through a common inlet plenum and exits through a common outlet header. One of the main features of the Canadian SCWR concept is the high pressure (25MPa) and high temperature (350ºC at the inlet, 625ºC at the outlet) operating conditions that result in an estimated thermal efficiency of 48%, which is 40% higher than the thermal efficiency of the present light water reactors. This paper presents a description of the Canadian SCWR core design concept, various numerical analyses performed to understand the temperature, flow and stress distributions of various core components and how the analyses results provided input for improved concept development.

1. Introduction

Canada has been developing a channel-type supercritical water-cooled nuclear reactor (SCWR) concept with an objective to meet the goals of the Generation IV International Forum (GIF) for next generation nuclear reactor development [1]. The Canadian SCWR core consists of a high-pressure inlet plenum, a separate low-pressure heavy water moderator contained in a calandria vessel, and 336 fuel channels surrounded by the moderator. The fuel channel includes a pressure tube that is in direct contact with the moderator, a fuel assembly with an integral down-flow coolant channel and ceramic insulator between the fuel assembly and the pressure tube, pressure tube extensions that connect the pressure tube to the outlet header and an outlet header located inside the inlet plenum. The reactor uses supercritical water as a coolant, and a direct steam power conversion cycle. Advanced safety concepts are adopted through the use of passive core cooling, long-term decay heat rejection to environment and fuel melt prevention via passive moderator cooling. These features significantly reduce core damage frequency as compared to existing nuclear reactors.

2. Reactor Core Concept

The reactor core design concept is illustrated in Figure 1. It consists of a pressurized inlet plenum, a low-pressure calandria vessel that contains heavy water moderator and pressure-tube fuel channels that are attached to a common outlet header. The reactor core is oriented vertically for ease of batch refuelling. The supercritical water (SCW) coolant flows into the inlet

plenum, around the outside of the outlet header and then enters the pressure tube extension through a group of slots, into the fuel assembly (see Figure 5) through a cross over piece, down through a flow tube in the centre of the fuel assembly, back up through the fuel elements and then out through the outlet header. A counter-flow fuel channel is adopted to position the inlet and outlet piping above the reactor core so that a complete break of either an inlet pipe or an outlet pipe will not result in an immediate loss of coolant in the fuel channels. This configuration ensures that the fuel channels will not dry out as long as the core flooding system, activated upon low core pressure signal, provides sufficient water to remove residual heat in the fuel.

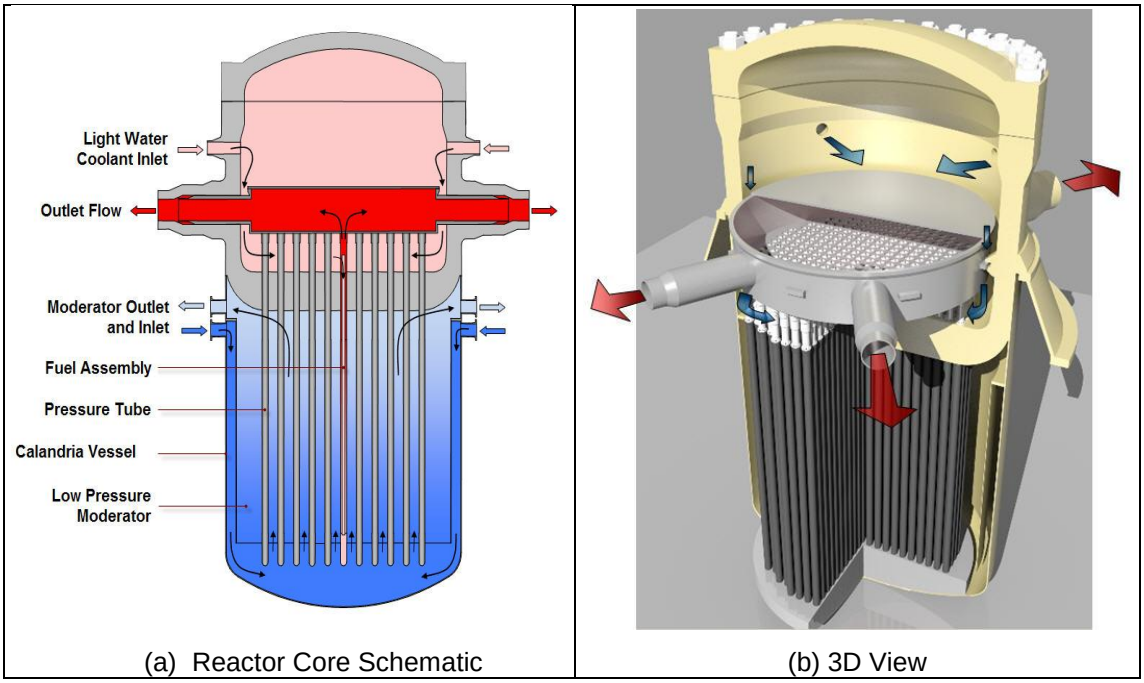

(a) Reactor Core Schematic (b) 3D View

Figure 1. Canadian SCWR Core Concept

The feedwater pipe inlet is situated as high in the inlet plenum as possible so that, in the case of an inlet line break and depressurization, a volume of coolant will remain in the inlet plenum, providing cooling to the fuel. In addition, a vortex fluidic diode is located at the coolant inlet, which allows a low forward flow resistance and a much greater reverse flow resistance. This would limit the rate of depressurization on an inlet line break, allowing a greater time period of forward flow before depletion of coolant inventory in the inlet plenum.

The inlet plenum and inlet/outlet piping are insulated to reduce heat losses to the environment. The outlet header is nested inside the inlet plenum vessel with outlet pipes sealed externally where they penetrate the inlet plenum. It is recognised that the temperature difference between inlet and outlet streams is large and, hence, the resultant thermal stresses can be high in some components. Numerical analyses are being conducted to evaluate thermal stresses and the structural integrity of various components.

2.1 Inlet Plenum, Outlet Header

2.1.1 Inlet Plenum

The inlet plenum is a pressure vessel operating at 25.3 MPa and at 350 °C. It consists of two pieces: the main plenum vessel and the head. They are each built from single forged steel

pieces to avoid welds and, therefore, eliminate inspection requirements associated with the degradation risk of welds. A pressure vessel steel, SA 508 grade 4N, has been selected for both plenum components, which is approved under Section III of the American Society of Mechanical Engineers (ASME) Boiler & Pressure Vessel code for use in nuclear components at metal temperatures of 350 °C. To further inhibit corrosion, the interior surfaces of the vessel could be overlaid with type 308 or 309 stainless steel weld materials. The domed head of the inlet plenum is joined to the rest of the plenum at a bolted flange, which is sealed with a series of concentric metallic O-rings. The four inlet and four outlet extensions, machined out to form nozzles, are connected to the four inlet and four outlet pipes, respectively. The inlet and outlet pipes are sized such that the inlet and outlet flow velocities are smaller than 7 m/s and 30 m/s, respectively. These velocities are selected to avoid excessive flow accelerated corrosion of these components.

The areas of maximum stress in the inlet plenum were computed for one complete start-up/shut down cycle [3] using the VrSuite finite-element software developed at the Carleton University, Ottawa, Canada. Internal pressure and transient thermal loadings were modelled using an elastic-plastic analysis and a material hardening model. High effective stress regions are found to be: top of the head of the plenum (A), inside corner of the head (B), the outer fillet of the outlet nozzle (C), the inner edge of the outlet nozzle (D), and the corner that joins the plenum to the tube sheet (E) as shown in Figure 2. The stresses at the outlet nozzle (C and D) can be reduced by rounding the inner corners of the nozzle and using a thermal sleeve and, hence, are not major concerns. Stresses at other locations (A, B and E) are higher than the yield stress resulting in localised plastic deformations. The maximum effective plastic strains are shown in Figure 3. Localised plastic deformations may be acceptable as long as the plasticity shakes-down, i.e. after repetitive startup/shutdown cycles, plastic zones become elastic as a result of strain hardening and residual stress evolution.

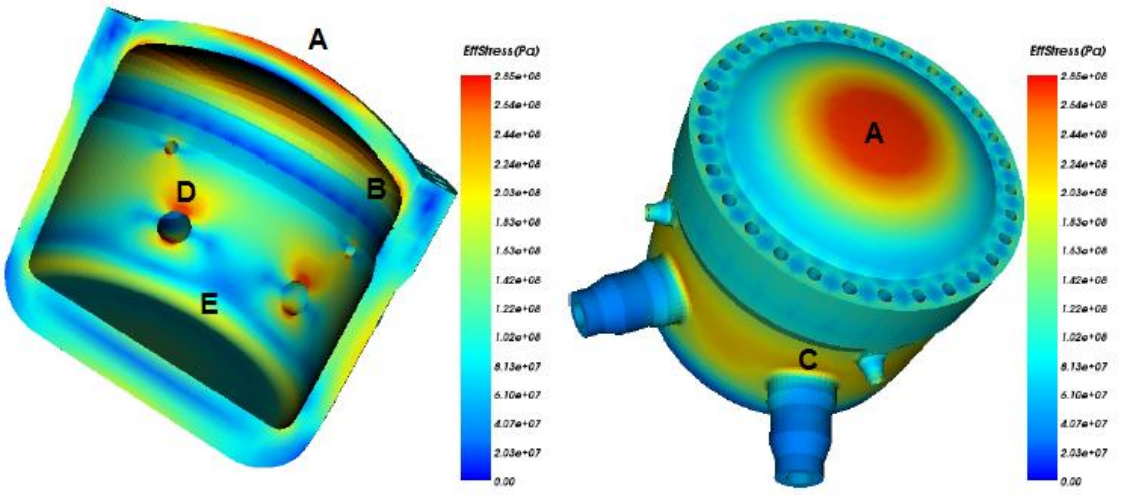

Figure 2. Maximum Effective Stress A) Cut Plane View B) Top View

A shakedown analysis of the inlet plenum was conducted using an assumed startup transient and it was found that the high stress zone E will shake down after 10 cycles, but zones A and B will ratchet, i.e. keep on plastically deforming. Ratcheting is not acceptable as it will eventually lead to the failure of the pressure vessel with repetitive cycling. Fortunately, this is a simple problem to fix by increasing the thickness of the plenum head. Regarding zone E, further work needs to be done to evaluate the structural integrity of this zone as the tubesheet (the bottom of the plenum) perforations needed for fuel channels are not simulated in this model, resulting in a stiffer tubesheet than the actual `perforated` tubesheet.

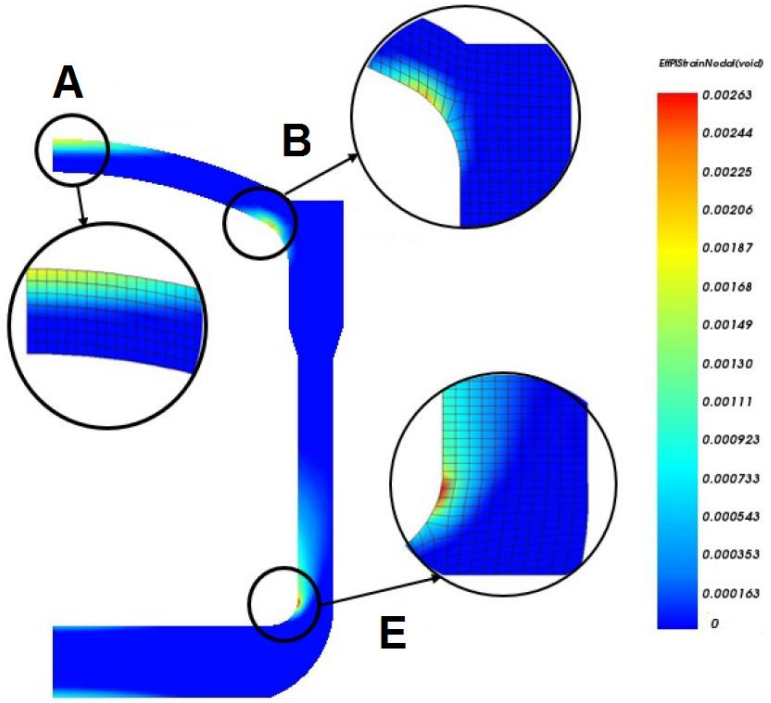

Figure 3. Maximum Effective Plastic Strain

The distributions of temperature, pressure and velocity of the SCW coolant within the inlet plenum were evaluated using a computational fluid dynamics (CFD) simulation program ANSYS-Fluent. Some of the flow features investigated with CFD were: flow distribution amongst the fuel channels, possible flow instabilities within the inlet plenum, and heat transfer from outlet header to inlet plenum. To reduce computing time, fuel channels are simplified while maintaining the basic characteristics of the channels: the length of the channels are shortened, central flow tube (see Section 2.2) and cross-over piece are modelled, fuel assembly is simplified and treated as porous media, all fuel channels are assumed to have the same average channel power, temperature-dependent fluid properties are included using user-defined functions, inlet vessel walls are assumed to be adiabatic, and the channel pressure drop is adjusted to match that of analytical calculations. Predicted temperature and velocity distributions in the inlet plenum are plotted in Figure 4. As the channel pressure drop is significantly higher than the pressure drop inside the inlet plenum, the flow distributes reasonably uniformly across the flow channels. Analysis results showed that the peripheral fuel channels have about 4% higher flow rates than those at central fuel channels resulting in more than 30ºC temperature gradient across the outlet header.

For CFD simulations, the inlet plenum, pressure tubes and outlet plenum are modeled. One quarter of the domain with appropriate symmetry boundary conditions representing the complete geometry is used. ANSYS MESH software is used to discretize the domain into 37 million grids. The simulation is run in parallel on 8 CPUs. Standard k-ε model with standard wall function is used to model the turbulence. First order upwind methods are employed to solve momentum and turbulence equations while energy equation is solved by a second order upwind scheme. The SIMPLE scheme is used to couple velocity and pressure and standard spatial discretization is used for pressure variable. Solution is obtained for steady state with residual convergence criteria of 10^{-6} for energy equation and 10^{-3} for other equations. It was found that the temperature-dependent properties caused oscillations in solution. To stabilize the solution,

properties need to be introduced step by step to the solver which causes longer simulation times.

For an optimal design, channel outlet temperatures should all be the same so that the maximum fuel cladding temperatures (a limiting parameter) in fuel channels will be about the same. Channel-to-channel variation in reactor power introduce further variation in channel flow rate as typically higher power central flow channels will see higher pressure drops and further skew the channel flow distribution. These effects can be mitigated by adjusting the sizes of channel inlet orifices (i.e. making the inlet orifices smaller for the peripheral channels). Changes in channel power as a function of burnup and after fuel shuffling are additional factors influencing channel outlet temperatures that should be considered.

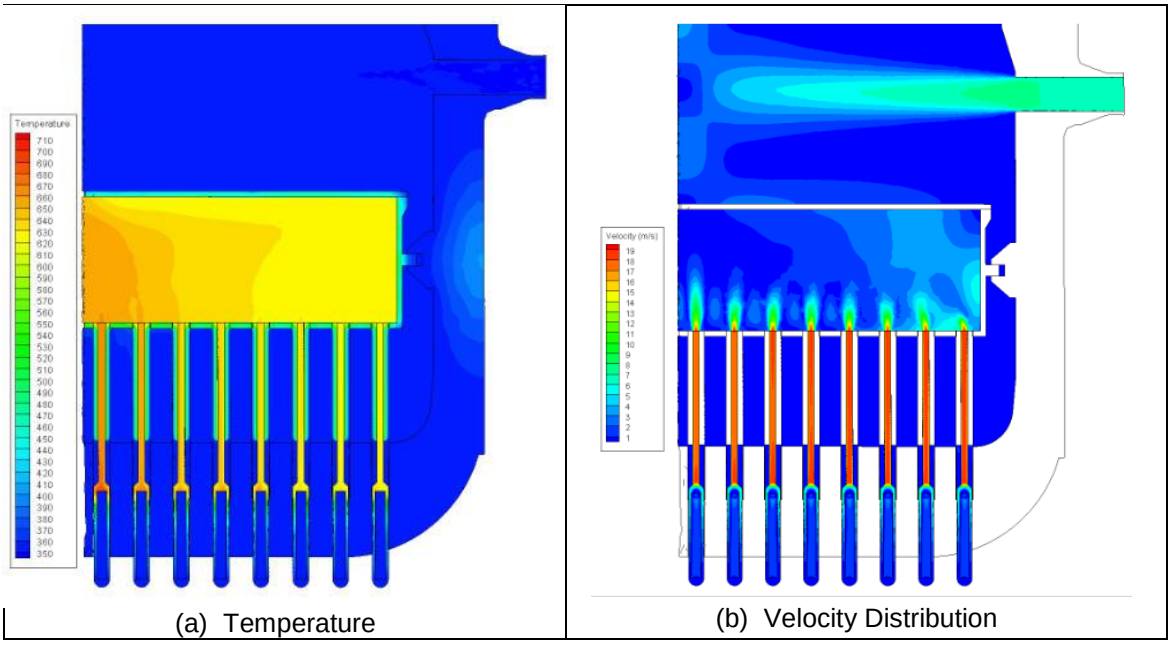

(a) Temperature (b) Velocity Distribution

Figure 4. Temperature and Velocity Distributions predicted by the CFD analysis

No significant flow oscillations are predicted, although some oscillations (as manifested itself in the steady state calculations with CFD solution oscillating from one steady state to another) are observed to occur at the center of the inlet plenum above the outlet header where four inlet streams meet. Such oscillations were considered minor and, if needed, can be mitigated with the use of inlet baffle plates. Heat transfer from outlet header to inlet plenum is estimated to be 8 MW, which is 0.3% of the total thermal power. Although this is not a major issue, some insulation of the outlet header either using a thermal barrier coating or by layering (for example, double-walling) is considered to reduce thermal stresses cased by the large temperature difference across the outlet header walls.

2.2 Fuel Channel

There are 336 fuel channels in the Canadian SCWR core concept. A simplified version of a fuel channel and a fuel assembly is shown in Figure 5. In this figure the length of the channel is greatly shortened and the gap between the pressure tube and the fuel bundle assembly is exaggerated to illustrate the details.

The fuel channel consists of a pressure tube that is connected to the inlet plenum tubesheet in a leak-tight fashion, a guide tube (pressure tube extension) that extends the fuel channel into the

inlet plenum and an expansion bellows (not shown in the figure) that connects the guide tube to the outlet header.

The fuel assembly includes, a central flow tube, a ceramic insulator on the outside, an inner liner tube separating the fuel and the insulator, an outer liner encasing the insulator and a two-ring fuel-element configuration [4]. A cross section of the fuel bundle is shown in Figure 6 as part of the fuel channel cross section.

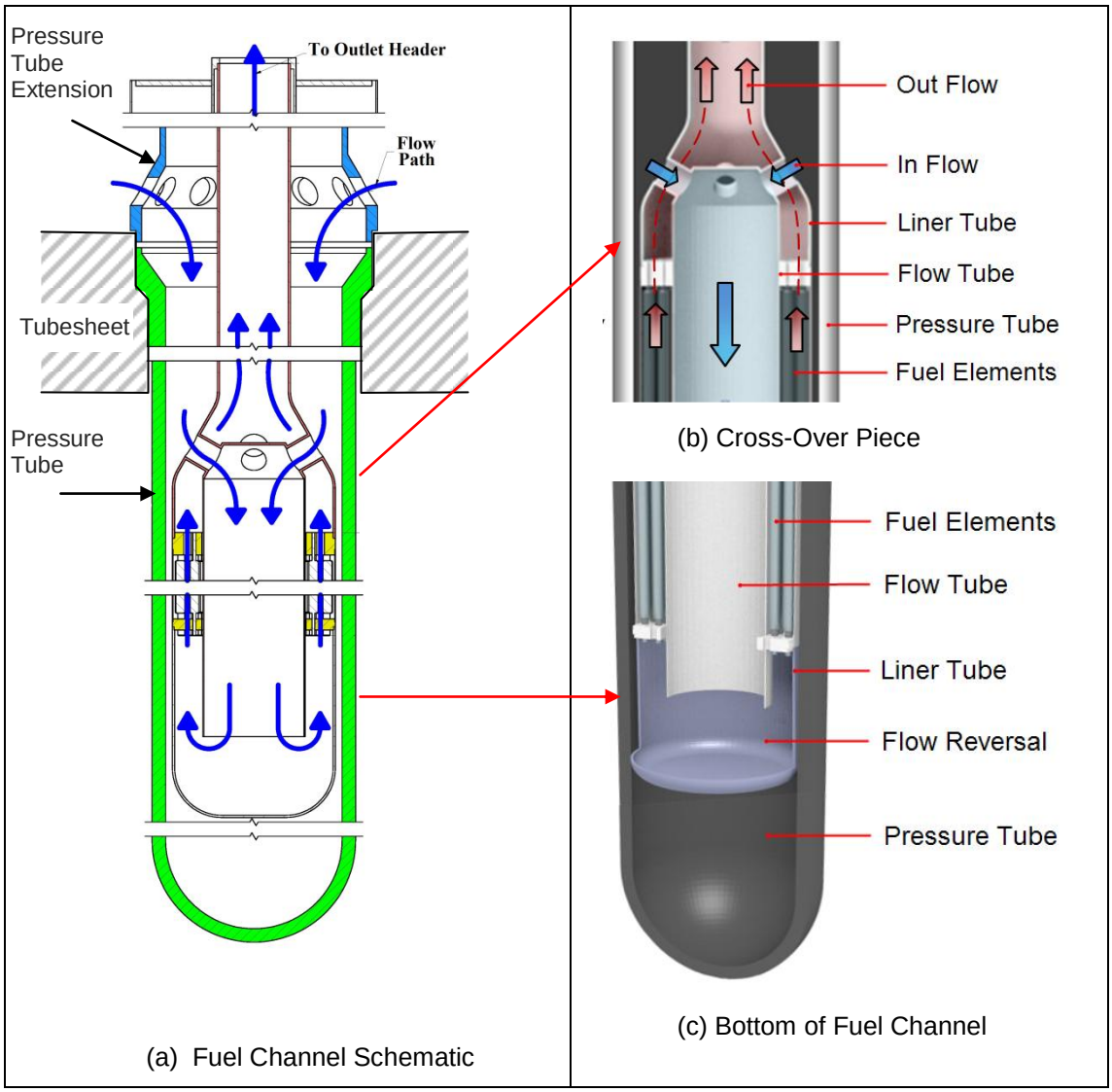

Figure 5. Canadian SCWR Fuel Channel Concept. The fuel channel consists of a pressure tube and a pressure tube extension. All fuel channel internals are part of the fuel assembly and removed after three refuelling cycles.

Due to manufacturing tolerances and to ease fuelling and reshuffling activities, there are gaps between these components (inner liner, insulator, outer liner and pressure tube). These gaps are a critical part of the no-core-melt argument and are optimized to minimize heat transfer resistance during accident conditions so that core decay heat can be transferred to the moderator more effectively. Above the core, the assembly also includes a cross-over piece that admits inlet coolant into the central flow tube. The fuel assembly, as a whole, is moved to a new location or replaced during a fuel shuffling and refuelling activity. As a result, all the components in the fuel assembly are replaced with the fuel.

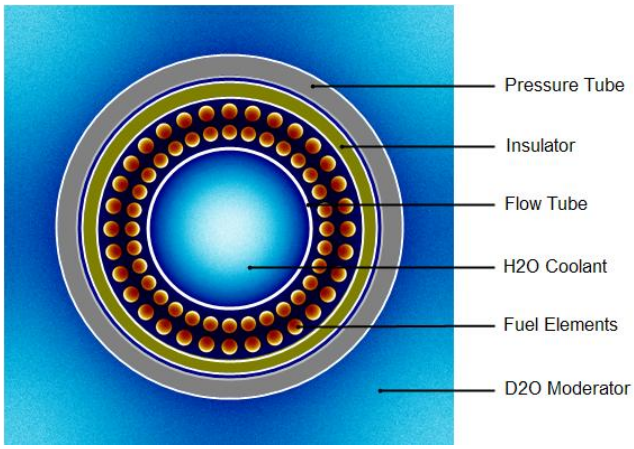

Figure 6. Cross-Section of Fuel Channel and Fuel Assembly

2.2.1 Inlet Cross-Over Component

The inlet flow stream enters the fuel assembly through, first, inlet ports on the pressure tube extension, and then, the cross-over piece as shown in Figure 5(a) and Figure 5(b). Four connecting tubes attach the fuel assembly liner (outer cylindrical structure) to the central flow tube. The cross-over piece directs the inlet flow stream into the central flow tube through these connecting tubes while allowing the hot outlet flow stream to flow in the opposite direction, around the connecting tubes. These connecting tubes see the inlet flow stream at 350 ºC on the inside surface and the outlet flow stream at 625 ºC on the outside surface, and, hence, subject to a considerable thermal stress. To evaluate these thermal stresses, a finite-element analysis of this component was performed using the ANSYS software. Figure 7 shows the results of this analysis. Thermal stresses as high as 214 MPa (von Mises) were calculated. Analysis showed that, in addition to the thermal gradients across component walls, differential thermal expansion of the liner and the central flow tube contributed significantly to the high stresses calculated at the connecting tubes.

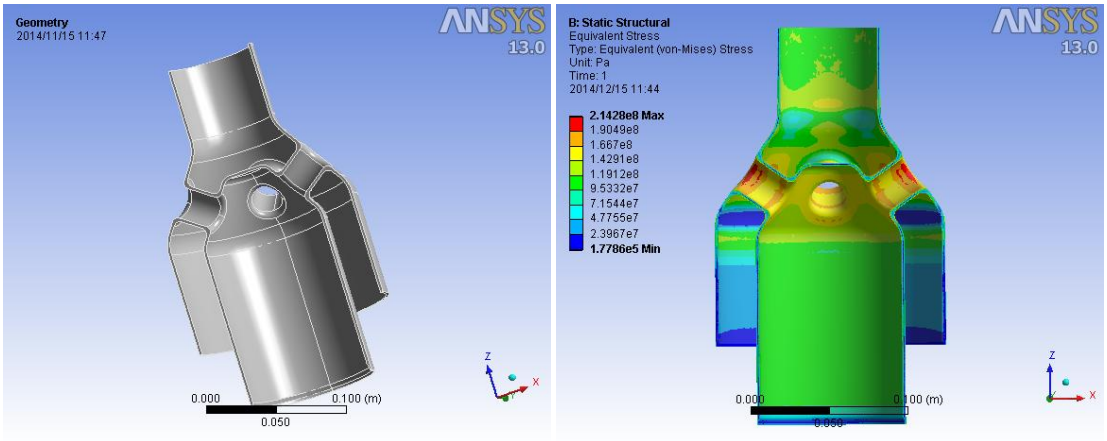

Figure 7. Modeled Geometry of the Cross-Over Piece and Maximum Equivalent Thermal Stress (von Mises Stress)

The analysis further showed that the thermal stresses can be reduced by (i) using more flexible connecting tubes – to accommodate differential thermal expansion of the central flow tube and the liner tube, and (ii) physically separating the inlet and outlet streams.

2.2.2 Collapsible Fuel Cladding

The Canadian SCWR fuel assembly comprises of sixty-four fuel elements in a two-ring configuration of thirty-two fuel elements each arranged circumferentially around the central flow channel. The diameters of the central flow channel, ring and fuel elements are determined through an iterative solution process that couples the physics and thermalhydraulics analyses [5]. The high outlet temperatures of the Canadian SCWR combined with the reduced heat-transfer coefficient of SCW (compared to water) result in high fuel cladding temperatures compared with current typical reactor fuels. Fuel cladding temperatures close to 800 ºC are predicted for the proposed assembly without considering any heat-transfer enhancements, such as wire-wrapped spacers. At this temperature, strengths of materials are significantly reduced from those at the typical cladding temperatures of 400 ºC found in existing water-cooled reactors. Hence, internally pressurised fuel cladding is not a feasible option without a very thick cladding material. However, collapsible fuel cladding, as used in CANDU®[1] reactors, is a possibility.

The CANDU fuel cladding is designed to be collapsible onto the fuel pellet. This feature results in good pellet/clad contact at operating conditions, enhances heat transfer between the pellet and the cladding, and thus lowers the pellet temperatures. A concern with the collapsible cladding is the possibility of ridge formation as shown in Figure 8(a). The thermo-mechanical behaviour of the Canadian SCWR fuel element, specifically the ridge formation, is analysed using the commercial finite-element software ANSYS [6]. In that analysis and subsequent work, all significant parameters affecting ridge formation are investigated. These parameters were cladding material properties, fuel pellet material properties, operating conditions (applied pressure and temperature), cladding geometry (diameter, wall thickness, and ovality), and pellet-to-clad diametral gap. The cladding ridge shown in Figure 8(a) is also called “longitudinal ridge” as it extends in the axial direction of the fuel element. Longitudinal ridging is unacceptable as it results in local plastic deformation of the cladding material in the ridge area and can lead to environmental assisted cracking. Similation result shown in Figure 8(a) demonstrates that ridging can be modelled successfully and the local effects are well-understood. Ridge formation is a highly non-linear phenomenon as illustrated by Figure 9. In this figure, the evolution of ridge formation is illustrated by increasing the external pressure of the Canadian SCWR fuel element for a very thin cladding of 0.2 mm with a large pellet-to-clad radial gap and a candidate cladding material of Inconel 625. The infection point of the curve labelled as “Maximum Gap Location”, indicating the deflection at the initial maximum gap location, illustrates the start of the ridge formation. In order to show the typical non-symmetric ridge formation, an initial oval shape and a slight eccentricity between the cladding and the fuel pallet are introduced.

The simulations showed that, for a given cladding material and operating conditions, the longitudinal ridge formation is more likely to occur with decreasing cladding thickness and increasing pellet-cladding gap size. Figure 10 shows the calculated maximum percent strain as a function of the Canadian SCWR fuel cladding thickness at 25 MPa of coolant pressure and 800 ºC cladding temperature. For this example, the cladding material was assumed to be Inconel 625. A high level of strain is an indication of ridge formation. Figure 10 indicates that with a radial pallet-cladding gap of 0.1 mm, longitudinal ridging can be an issue if the cladding thickness is smaller than 0.4 mm. However, by reducing the radial gap value to 0.05 mm, ridging can be avoided with all practical cladding thicknesses. Fuel pellets can be freely slid into fuel cladding with a radial gap of 0.05 mm, which is possible with currently achievable ovality and straightness tolerances.

[1] CANDU – Canada Deuterium Uranium, a registered trademark of Atomic Energy of Canada Limited (AECL).

(a) A Photo of A Typical Longitudinal Ridge	(b) Deformed Shape of Fuel Element in ANSYS Model
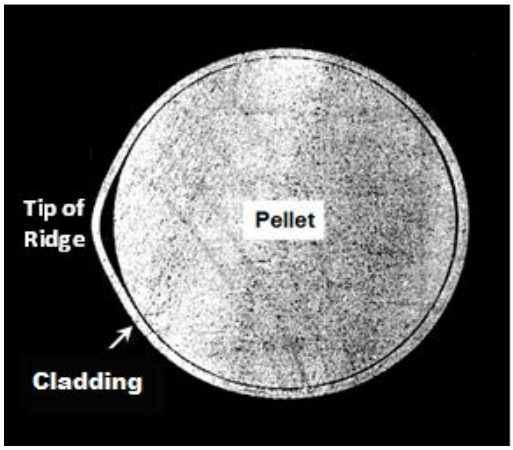	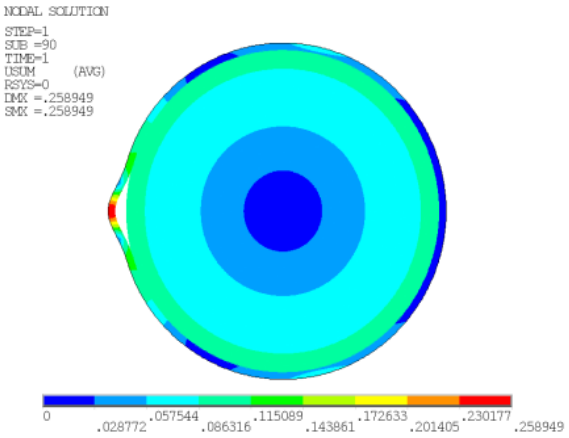

Figure 8 Comparisons of the Simulated Deformed Shape of Fuel Element and a Typical Longitudinal Ridge.

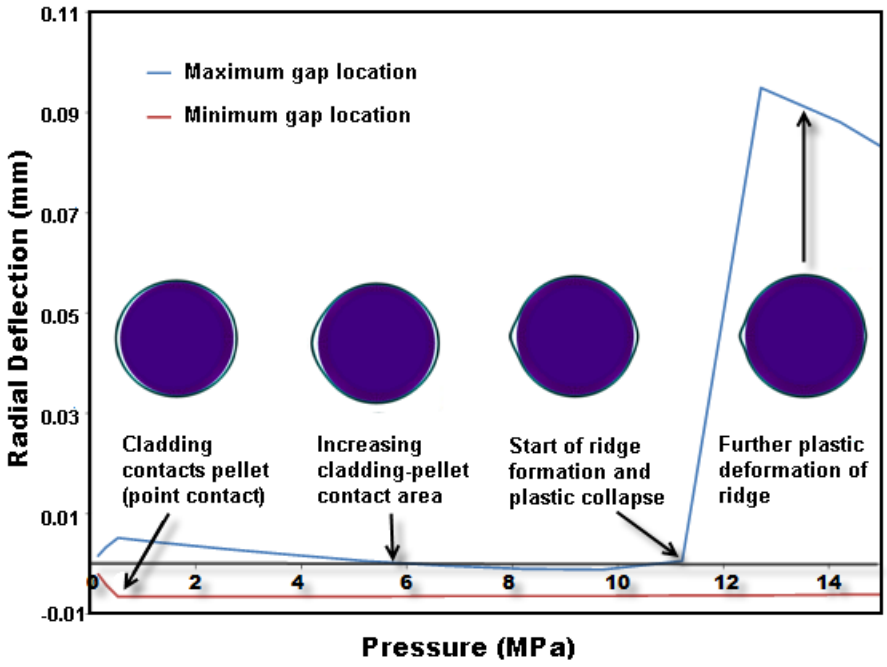

Figure 9 Radial Deflection at the Maximum Gap Location Varied with External Pressure for Canadian SCWR Fuel Sheath with Different Eccentricity (High Sheath Temperature Case, Sheath Thickness = 0.2 mm, Radial Gap = 0.1 mm)

2.2.3 Segmented Insulator

The Canadian SCWR fuel channel uses yttria-stabilized zirconia (YSZ) as an insulator to shield the pressure tube from the high-temperature coolant and reduce heat loss to the moderator. The insulator is mounted in the fuel assembly, separated from the fuel by an inner liner and encapsulated by the outer liner, as shown in Figure 2(a). The fuel bundle, liner tubes and the

insulator are all part of the fuel assembly. They are all replaced or shuffled as a single component during refuelling activities. A concern with the ceramic insulator is the possibility of cracking due to high thermal stresses. Since the coolant temperature can be as high as 625 ºC inside the fuel channel and the moderator temperature is 80 ºC outside the fuel channel, a possibility exists that the insulator may crack due to high thermal stresses. To mitigate this concern, the insulator is segmented both in the axial direction and in the circumferential direction.

Heat transfer analyses are performed for normal and accident conditions to estimate the fuel-to-moderator heat flow [6]. These analyses took into account the effects of the radial gaps between components and the contact resistance when the gaps are closed. It is found that the heat transfer across the fuel channel wall is primarily limited by the contact resistance and the heat transfer resistance of the stagnant fluid in the clearance gaps.

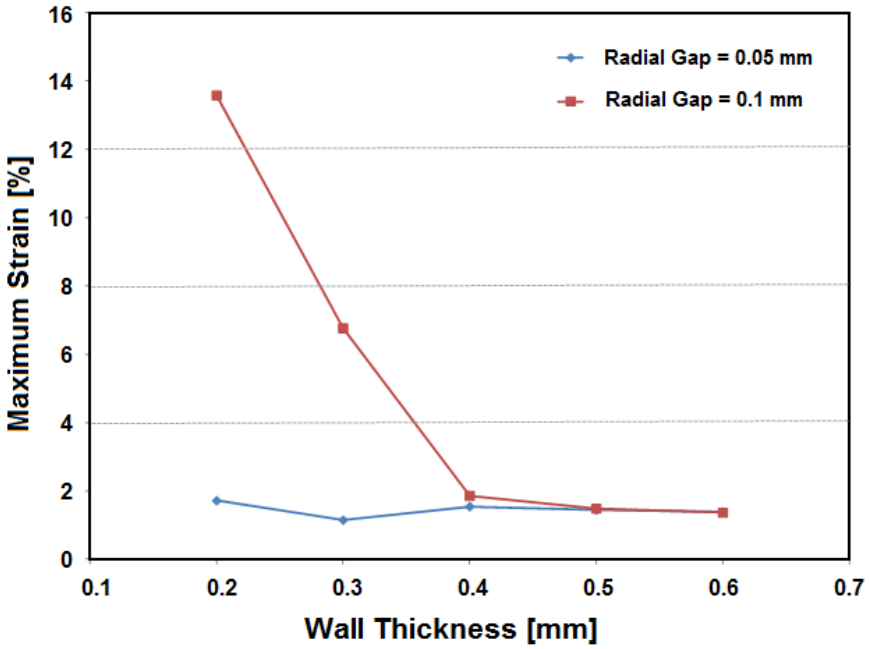

Figure 10 Maximum Strain Variation as a Function of the Sheath Thickness for the Canadian SCWR Fuel Sheath (High Sheath Temperature Case, Pressure = 25 MPa)

Temperature gradient across the insulator is found to be about 130 ºC at normal conditions and about 200 ºC at accident conditions. Hotter inner wall temperatures result in tensile thermal stresses at the outside surface (OD) of the insulator[2], which can be calculated by the formula below [7].

$$\sigma_{OD} = \frac{\Delta T \cdot \alpha \cdot E}{2 \cdot (1-\upsilon) \cdot \ln\left(\frac{R_0}{R_i}\right)} \cdot \left(1 - \frac{2 \cdot R_i^2}{R_i^2 - R_o^2} \cdot \ln\left(\frac{R_o}{R_i}\right)\right)$$

In this formula, ΔT is the temperature difference across the insulator wall, α is the thermal expansion coefficient of YSZ zirconia ($13.5 \cdot 10^{-6}$ 1/ºC), E is the modulus of elasticity ($205 \cdot 10^9$ Pa), υ is Poisson's ratio (0.3), R_O is the outside radius (83 mm) and R_i (78 mm) is the inner radius.

[2] Hoop stress at the inside surface is compressive. Because compressive strength of zirconia is very high (2500 MPa), cracking on the inside surface is not a concern.

For normal (ΔT=130 ºC) and accident (ΔT=200 ºC) conditions, the thermal hoop stress is calculated to be 290 MPa and 390 MPa, respectively. These values are smaller than the tensile strength of solid YSZ zirconia, which may be as high as 800 MPa. Since the tensile strength of zirconia is a strong function of porosity, solid YSZ zirconia is adopted for the Canadian SCWR fuel channel. Also, the insulator is segmented to further reduce stresses. As the tensile strength of zirconia can be affected by the manufacturing process, material specifications must include this high tensile strength requirement.

3. Summary and Conclusions

This paper presented a description of the Canadian SCWR core design concept and some of the challenges introduced by high temperature and pressure operating conditions from a mechanical point-of-view. Various analyses are performed to predict and understand the behaviour of key components. Insights gained from these analyses are used to support design decisions and to make design modifications. In some cases, future work is identified for further study.

References

[1]. L.K.H. Leung, M. Yetisir, W. Diamond, D. Martin, J. Pencer, B. Hyland, H. Hamilton, D. Guzonas, and R. Duffey, "A Next Generation Heavy Water Nuclear Reactor with Supercritical Water as Coolant," Proc. of the Int. Conf. Future of HWRs, Canadian Nuclear Society, Ottawa, Ontario, Canada, Oct. 2-5, 2011.

[2]. E.F. Ibrahim and B.A. Cheadle, 1985, "Development of Zirconium Alloy for Pressure Tubes in CANDU Reactors", Can. Met. Quart., Vol.24, p.273.

[3]. M. Nimrouzi, "A Methodology for Optimal Design of the Canadian SCWR reactor Core", *M.Sc. Thesis*, Carleton University, April 2014.

[4]. J. Pencer, D. Watts, A. Colton, X. Wang, L. Blomeley, V. Anghel, S. Yue, "Core Neutronics for the Canadian SCWR Conceptual Design," The 6th International Symposium on Supercritical Water-Cooled Reactors (ISSCWR-6), Shenzhen, Guangdong, China, 2013 March 3-7.

[5]. A. Nava-Dominguez, N. Onder, J. Pencer and D. Watts, "Canadian SCWR Bundle Optimization for the New Fuel Channel Design", *Proc. 6th International Symposium on Supercritical Water-Cooled Reactors (ISSCWR-6)*, Shenzhen, Guangdong, China, March 3-7, 2013.

[6]. R. Xu, M. Yetisir, H. Hamilton, 2014 April, "Thermal-Mechanical Behaviour of Fuel Element in SCWR Design," 2014 Canada-China Conference on Advanced Reactor Development (CCCARD-2014), Niagara Falls, Ontario, Canada, 2014 April.

[7]. S. P. Timoshenko and J.N. Goodier, Theory of Elasticity, 3rd Edition, McGraw-Hill Book Company, Inc., 1970, pg. 449.

ISSCWR7-2073

Optimization of the PT-SCWR Control Blade Sequence using PARCS and DAKOTA

F. Salaun, J. R. Sharpe, D. W. Hummel, A. Buijs, D. R. Novog
McMaster University
1280 Main Street west, Hamilton, Ontario L8S4L8
salaunf@mcmaster.ca, sharpej@mcmaster.ca, hummeld@mcmaster.ca, buijsa@mcmaster.ca, novog@mcmaster.ca

Abstract

This paper presents a full-core model of the Pressure Tube type Supercritical Water-cooled Reactor (PT-SCWR) concept, including proposed reactivity control devices, created with the diffusion code PARCS. Transport calculations of the lattice cell have been performed with SCALE/TRITON to determine the few-group neutronic parameters as functions of burnup for input in the full-core model (2-group condensed and homogenized cross sections including assembly discontinuity factors). With a three-batch refuelling scheme, an equilibrium core was achieved after several iterations (without control devices). The 110 mk initial excess reactivity, however, needs to be compensated for at the beginning of cycle and adjusted accordingly throughout. 89 cruciform control blades have been implemented in the model to remove part of the excess reactivity and to balance radial core power. The goal of this study is to minimize the channel power ripple over the core throughout the cycle. This was achieved by coupling the diffusion code (PARCS) to a large-scale engineering optimization code (DAKOTA). An automated process has been developed to find a control blade sequence that holds each channel power as close to constant as possible while keeping the core reactivity around the desired value throughout the cycle, while also maintaining acceptable maximum nodal powers.

1. Introduction

Canada is developing a Supercritical Water-cooled Reactor (SCWR) as part of the Generation IV program. This future reactor draws its inspiration from the well-known Canada Deuterium Uranium (CANDU) reactor. The concept uses pressure-tubes for each channel and a low pressure heavy water moderator. The reactor is vertically orientated instead of horizontal like a traditional CANDU [1].

A total of 336 High-Efficiency Re-entrant Channels (HERC) house the fuel and provide the pressure boundary for the heat transport system coolant [2]. As depicted on Figure 1 below, the light water coolant enters the channel at the top at 350°C and 25.8 MPa and travels downward in a central flow tube. At the bottom of the channel the coolant turns around and travels upward around the two fuel rings each made up of 32 PuO_2-ThO_2 fuel pins to remove heat and exit the channel at 625°C and 25 MPa. The low pressure moderator (heavy water) is separated from the hot coolant by a ceramic insulator and a pressure tube [3].

A refuelling scheme has been proposed by Atomic Energy of Canada Limited (AECL) [4] and an equilibrium core can be found after several iterations. However, the design lacks mechanisms to compensate for the initial excess reactivity at beginning of cycle (BOC). Options for reactivity hold-down include carefully selected burnable neutron absorbers or movable control devices, such as control blades. In the case of the latter, as fuel depletes during a cycle the positions of the control blades must be adjusted accordingly to maintain a critical core. The

goal of this work is to demonstrate the use of SCALE/TRITON, PARCS and DAKOTA for optimizing control rod positions during a fueling cycle.

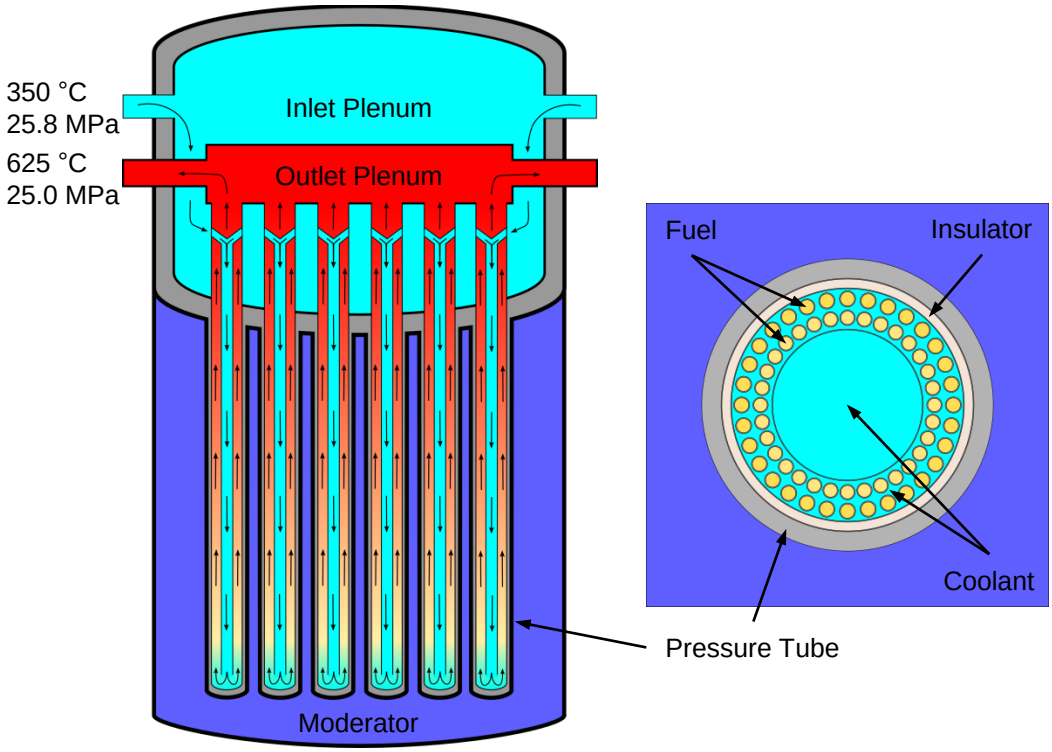

Figure 1. PT-SCWR core and HERC layout

In the current reference design static orifices at each channel inlet will regulate the flow through the channel to be proportional to its reference power to ensure a uniform channel outlet temperature of 625 °C. Without reactivity control devices channel powers change significantly during a cycle and it is not possible to match the flow due to these transients. As a consequence each channel power has to remain constant and matched to the flow rate or the outlet temperature will drift. As of this writing no system has been proposed to keep each channel power constant throughout the cycle. A set of BWR-like cruciform control blades has thus been proposed in this work to address this challenge in addition to holding down the initial excess reactivity. The blades are then analysed and the optimal positions through the fuelling cycle are determined such as to minimize the channel power changes anticipated with burnup.

The design of the control blades and the lattice calculations with the SCALE/TRITON code are first described [6]. Using the homogenized and condensed cross sections from SCALE/TRITON, a full-core SCWR model has been created with the PARCS code [7]. Finally, the DAKOTA optimization software [8], using a genetic algorithm, has been coupled to PARCS to find the control blade insertion levels throughout the cycle that maintains the channel powers as constant as possible while satisfying the desired constraints.

2. PT-SCWR Core Physics Model

2.1 Lattice Calculations: SCALE/TRITON

The SCALE 6.1 package was developed at the Oak Ridge National Laboratory (ORNL) in the United States [6]. Among other capabilities, SCALE can use the TRITON module to solve the multigroup transport equation and create problem-dependent cross sections. Moreover, the ORIGEN module is used to predict the isotopic concentrations when depletion is required. The major output from the SCALE package produces homogenized cross sections for subsequent nodal core calculations.

The 2D infinite lattice cell with a control blade was modelled in TRITON as shown in Figure 2. The transport equation is solved for different stages of fuel burnup and thus generates a set of few-group homogenized cross sections indexed by burnup. All simulations were performed using the included 238 energy group library based on the ENDF/B-VII Release 0.

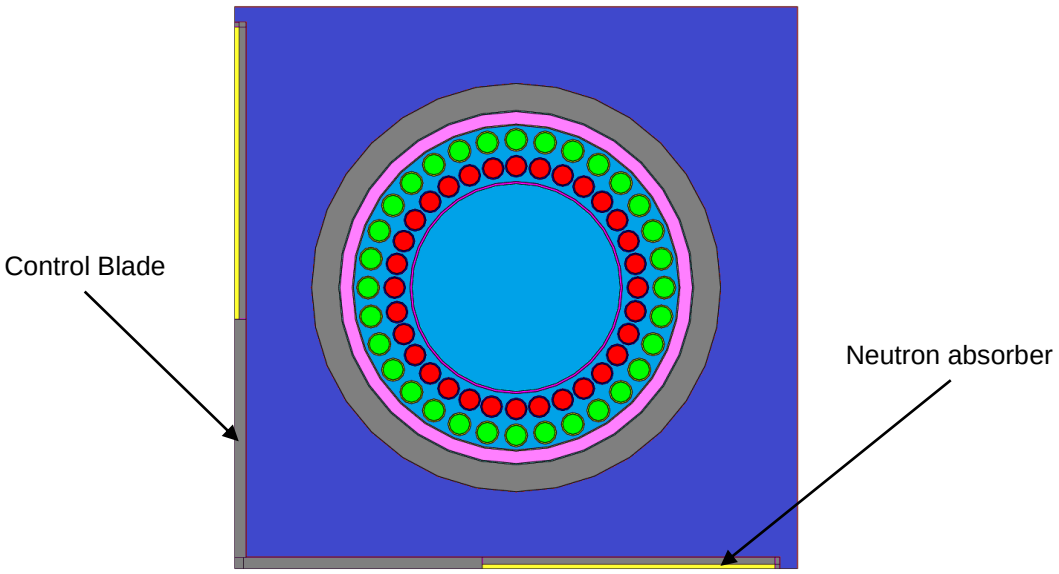

Figure 2. Infinite lattice cell with a control blade inserted

In order to accurately represent the control blades, two types of calculations need to be added to the bladeless infinite lattice cell. First, when a control blade is inserted into the assembly, it changes the flux spectrum in the cell and consequently changes the few-group homogenized cross-sections. However, this impact depends on the fuel burnup. For each burnup step the impact of the control blade is thus evaluated by re-solving the transport equation with the control blades inserted. This is called a branch calculation. Thus far, the fuel has only been burned when the control blade was removed. Consequently, the previous process has to be done again, but the reference cell has a control blade inserted, and, at each burnup step a branch calculation is performed with the control blade removed. This is called a history calculation. The multiplication constant (k_{eff}) for the four sets of cross sections is plotted in Figure 3 below to observe the impact of the blades as a function of burnup.

The specifications of the control blade are given in Table 1 below. As can be seen in Figure 2, the neutron absorbing material is located near the tip of the blades because it tends to reduce the flux (power) tilt in the fuel pins.

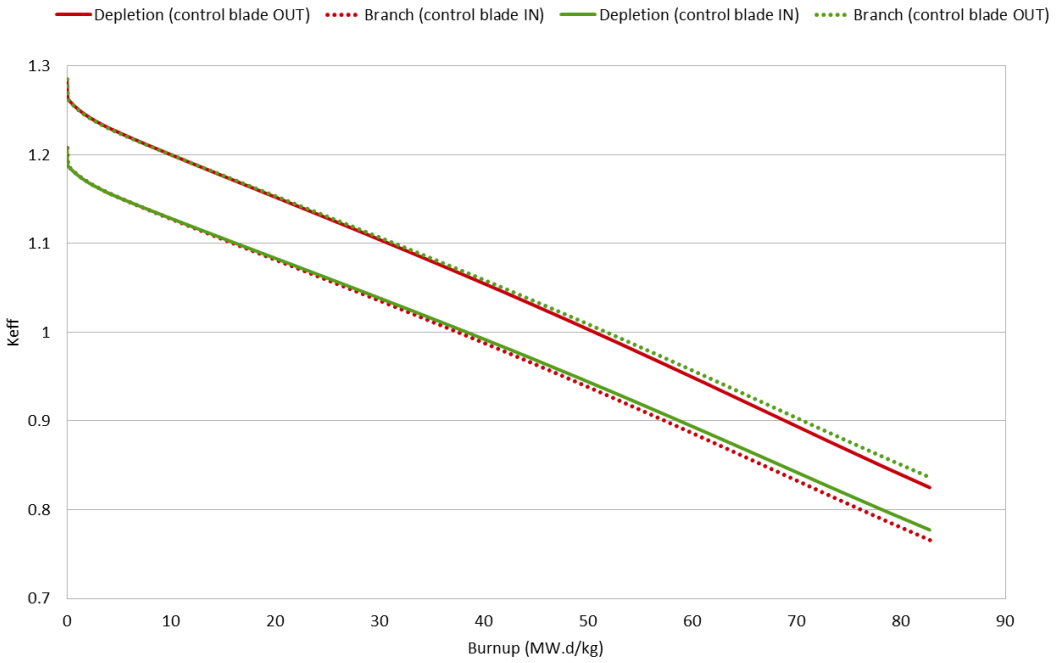

Figure 3. k_{eff} as function of burnup for the four sets of cross sections from the transport calculation

Table 1. Control blade specifications

Half span	24.2 cm
Thickness	1 cm
CB material (wt%)	Sn:3.5; Mo:0.8; Nb:0.8; Zr:94.9
Length of absorber	13 cm
Thickness of absorber	0.4 cm
Absorber material	Stainless Steel 304
Density	7.94 $g \cdot cm^{-3}$

Moreover, as the coolant density considerably changes axially (roughly by a factor 10), the core has been divided into twenty slices to account for the density change's impact on the lattice physics. Therefore, the above sets of condensed and averaged cross sections have been simulated in SCALE/TRITON for those twenty positions using appropriate local averaged temperatures and densities.

Finally, few-group homogenized cross sections for the D_2O reflector were evaluated using a multicell calculation which includes multiple fuel channels near the core periphery.

2.2 Full-Core Model: PARCS

The Purdue Advanced Reactor Core Simulator (PARCS) is a three-dimensional reactor core simulator used by the US Nuclear Regulatory Commission (USNRC) as a reference for BWR and PWR analysis. PARCS solves the few-group neutron diffusion equation for steady-state and time-dependent reactor cores and can also predict dynamic responses to several perturbations. The output files from TRITON need to be converted into the PARCS format which is done by a separate code named GenPMAXS [9]. GenPMAXS constructs the required input for PARCS for the reference case and all branches.

The PT-SCWR core is quarter symmetric; therefore only 84 out of the 336 channels have been simulated in PARCS. Each assembly has been divided into 20 axial positions with the 20 lattice physics properties calculated beforehand. Heavy water radial and axial reflectors have also been included into the model and are 100 cm and 75 cm thick, respectively.

A refuelling scheme without control devices has been proposed Atomic Energy of Canada Limited (AECL) for this core [4]**.** However, with the addition of the control blades, a new refuelling scheme (Figure 4) has been generated but not yet optimized. In a BWR like fashion, 89 control blades are inserted from the bottom of the core into the low pressure moderator. Their location in a quarter of the core is displayed on Figure 5 below.

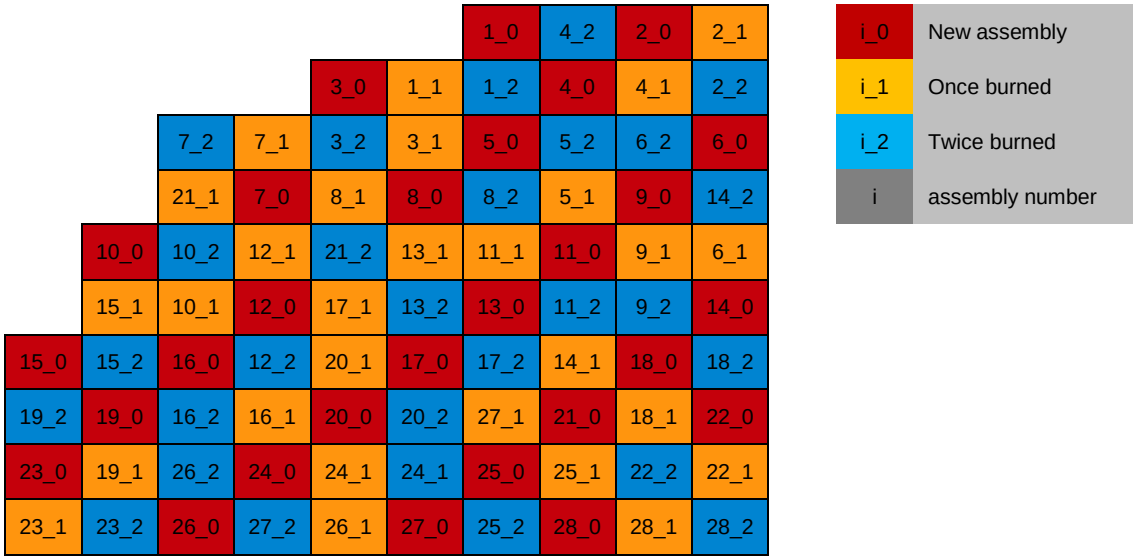

Figure 4. Three-batch refuelling scheme used in the study

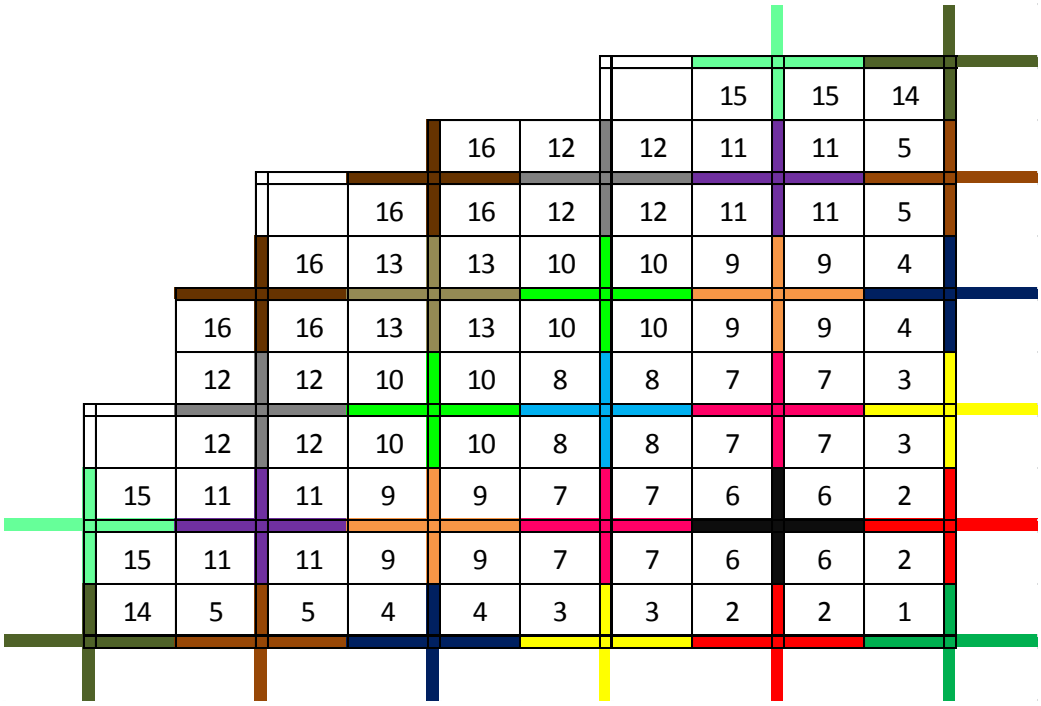

Figure 5. Control blade locations and bank numbers (same color = same bank)

Before including any control devices into the core, a steady-state equilibrium has been calculated using the refuelling scheme in Figure 4. PARCS depletes the core by steps of 5 Full Power Days (FPD) and when the core reactivity is lower than 10 mk, the core is refuelled. A convergence is achieved after roughly 15 iterations. The powers of the 84 channels throughout the cycle are shown in Figure 6. One can observe that the power in each channel is not constant during the cycle with the steepest gradients near the BOC.

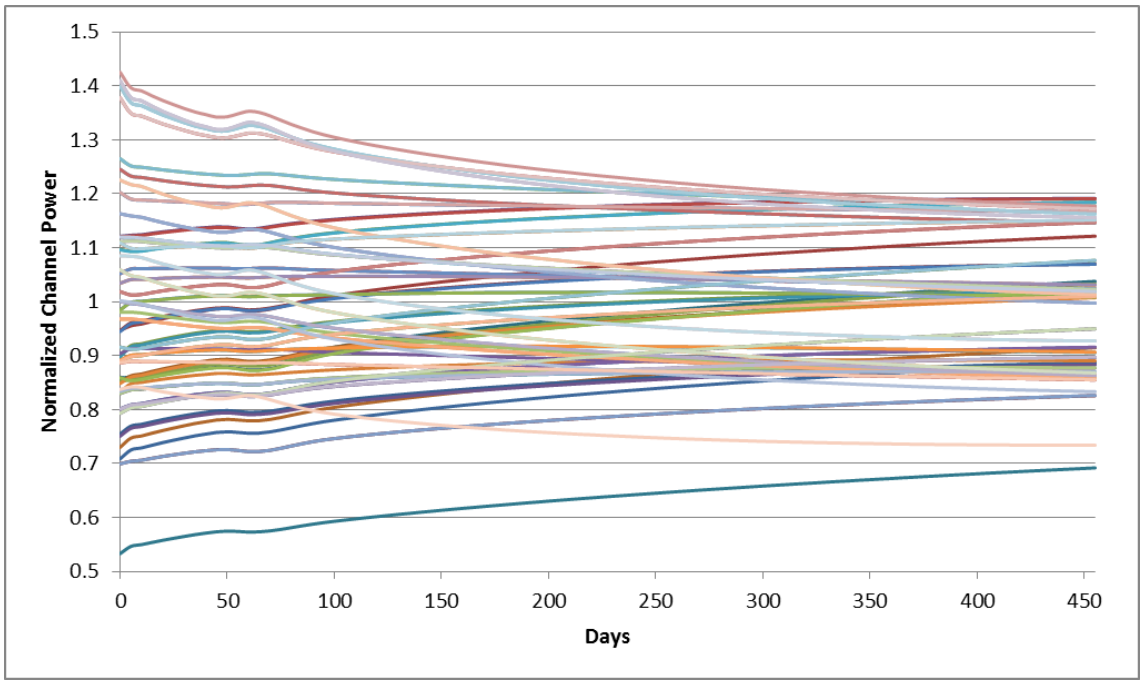

Figure 6. Powers of the 84 channels throughout the cycle without devices

3. Optimization process

The Design Analysis Kit for Optimization and Terascale Applications (DAKOTA), developed at Sandia National Laboratories, is a multilevel parallel object-oriented framework for design optimization, parameter estimation, uncertainty quantification and sensitivity analysis. It is a very general and flexible tool which can be coupled with any simulation code to solve engineering-based problems. Among others, DAKOTA possesses algorithms for optimization with non-gradient based methods which are of particular interest for this study. Control device position optimization during a cycle is a very complex problem since the search space is quite vast and non-linear. This powerful tool was thus chosen to investigate the control blade sequence optimization for the PT-SCWR.

3.1 Evolutionary Algorithm

A brief description of the evolutionary algorithm applied to the optimization of the control blades position is given in order to understand the main concept of the method.

First an initial population is generated. For each individual in this population, a random position is attributed to each control blade within the predefined range. PARCS is then run for each individual in the population and the outputs are collected by DAKOTA. Afterwards, the individuals are classified in terms of their fitness. From this organized population, crossovers and mutations are applied at a fixed probability chosen by the user.

Like in genetics, two individuals can give birth to an offspring by each bringing part of their genetic information. This action tends to choose two relatively good individuals in order to

(ideally) find a better solution. Mutations are then applied to the newly generated individuals. This action allows the method to look for other solutions in the larger phase space.

The fitness of all the individuals generated from crossovers and mutations are now evaluated and added to the initial population. The ones with the lowest fitness are deleted and a new initial population has thus been created. This last process can be seen as evolution since the most fit individuals are more likely to survive.

With the new population, crossover and mutations are applied again and the whole process is repeated until convergence criteria are satisfied or iteration limits are reached. Figure 7 depicts the evolutionary algorithm process.

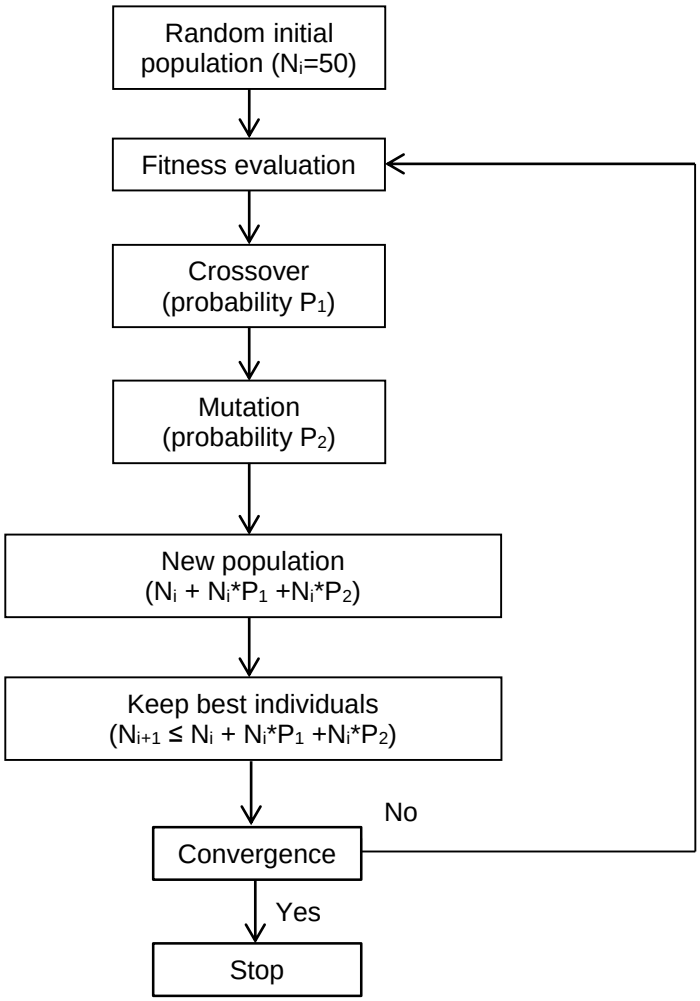

Figure 7. Evolutionary algorithm process

4. PARCS-DAKOTA Coupling Goal

Since the current design of the PT-SCWR includes static inlet orifices for each assembly, the power of each assembly should remain as constant as possible over the cycle in order to ensure uniform coolant outlet temperatures of 625°C in each channel. A control blade sequence has to be found in order to fit as closely as possible a predefined channel power distribution at any time during the cycle. Thus, the goal of this study was to minimize the standard deviation of the 84 channel powers, relative to their desired power.

However, there are constraints to be respected: The initial excess reactivity is 110 mk and has to be compensated at day 0 by the insertion of neutron absorbers (a combination of burnable poison, control blades and a soluble poison). As only control blades are used in this

study, the total initial excess reactivity was not fully compensated but the first constraint made sure to remove as much reactivity as possible.

In the simulation, there are 84 channels, each with 20 axial positions, which gives a total of 1680 nodes. Each node has a certain power and linear element rating (LER) associated to it. The average LER of the PT-SCWR can be evaluated using the following equation:

$$LER = P_{tot}/N_{ch}L_{ch}N_{pins} \quad (1)$$

where P_{tot} is the core total power (2540 MW), N_{ch} is the total number of fuel channels (336), L_{ch} is the length of a fuel channel (5 m), and N_{pins} is the number of pins per channel (64). Therefore, the average LER is equal to 23.6 kW·m^{-1}. A maximum of 40 kW·m^{-1} has been suggested in early studies and has been included as a constraint, thus the power in a given node should not exceed a normalized nodal power of 1.7 [9].

In order to find an acceptable solution while respecting the above constraints, a total of 16 banks of control blades can be inserted into the core with discrete steps of 25 cm. As the core is 5 meters high, 21 positions can be occupied by each blade. Therefore, the space to be searched contains $21^{16} \approx 1.43\text{x}10^{21}$ solutions.

The coupling process won't be described in details but the main features are listed below:

- Core depleted by steps of 5 FPD
- Optimization of the control blades position every 20 FPD
- Only the closest positions from the previous optimization are allowed
- At the BOC, only the closest positions from the previous BOC control blades positions are allowed (except for the first optimization where the entire space is searched)

The results obtained from the optimization process are shown and discussed in the next section.

5. Results and Discussion

In order to evaluate the results achieved, the equilibrium cycle for both the core without control blades and with the optimized control blade sequence are compared.

The power to be reached in each channel for both cores is depicted on Figures 8 and 9. For clarity's sake, the channel power has been normalized to the average channel power of the PT-SCWR. A total of 336 channels are producing 2540 MW which gives an average of 7.56 MW per channel. The channel powers to be reached, without control blades, have been estimated from the equilibrium cycle by calculating the weighted average power over the cycle for each channel. One can notice that the two average channel power distributions are very close.

						0.952	0.778	1.007	0.891
				0.965	0.954	0.878	1.093	0.968	0.865
		0.632	0.848	0.845	1.034	1.152	0.867	0.862	1.13
		0.823	1.056	0.988	1.17	0.912	1.042	1.176	0.872
	0.959	0.841	0.986	0.882	1.013	1.045	1.207	1.061	1.06
	0.952	1.033	1.169	1.013	0.892	1.179	0.902	0.915	1.234
0.951	0.878	1.152	0.913	1.045	1.179	0.909	1.058	1.232	0.933
0.778	1.093	0.868	1.042	1.207	0.903	1.058	1.251	1.085	1.226
1.007	0.968	0.863	1.176	1.061	0.915	1.233	1.085	0.889	0.977
0.891	0.865	1.13	0.873	1.06	1.234	0.933	1.227	0.977	0.766

Figure 8. Average channel powers over the cycle without control blades

						1.012	0.815	1.031	0.936
				0.955	0.996	0.908	1.067	0.949	0.878
		0.633	0.866	0.859	1.069	1.161	0.856	0.852	1.137
		0.841	1.094	1.033	1.165	0.9	1.024	1.17	0.925
	0.952	0.856	1.033	0.921	1.029	1.042	1.175	1.052	1.072
	0.995	1.069	1.165	1.029	0.904	1.179	0.879	0.875	1.152
1.011	0.908	1.161	0.9	1.042	1.179	0.911	1.016	1.144	0.908
0.815	1.067	0.856	1.024	1.175	0.879	1.016	1.186	1.066	1.233
1.031	0.949	0.852	1.17	1.052	0.876	1.144	1.067	0.889	0.98
0.936	0.878	1.137	0.925	1.072	1.152	0.908	1.233	0.98	0.763

Figure 9. Channel powers to be kept constant throughout the cycle with control blades

On Figures 10 and 11, the channel powers (in MW) is given in the grey boxes with below it the standard deviation (in MW) throughout the cycle, with respect to those channel powers. By looking at the two figures, the overall standard deviation is significantly lower for the core with the control blades which means that the channel power ripple is considerably reduced by the use of control device.

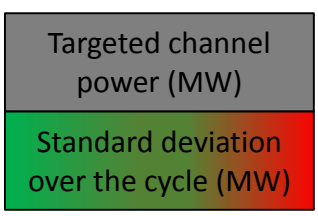

						7.20	5.88	7.61	6.74
						0.38	0.27	0.37	0.32
				7.29	7.21	6.64	8.26	7.32	6.54
				0.39	0.32	0.24	0.31	0.25	0.20
		4.78	6.41	6.39	7.82	8.71	6.56	6.52	8.54
		0.32	0.37	0.26	0.24	0.21	0.09	0.07	0.12
		6.22	7.98	7.47	8.84	6.90	7.87	8.89	6.60
		0.35	0.37	0.22	0.16	0.03	0.04	0.05	0.08
	7.25	6.36	7.45	6.67	7.66	7.90	9.13	8.02	8.01
	0.40	0.26	0.22	0.09	0.04	0.09	0.16	0.20	0.22
	7.20	7.81	8.84	7.66	6.74	8.92	6.82	6.92	9.33
	0.33	0.24	0.16	0.04	0.10	0.19	0.25	0.30	0.39
7.19	6.64	8.71	6.90	7.90	8.92	6.88	8.00	9.32	7.05
0.38	0.24	0.21	0.03	0.09	0.19	0.27	0.36	0.45	0.40
5.89	8.26	6.56	7.88	9.13	6.82	8.00	9.46	8.20	9.27
0.27	0.31	0.09	0.03	0.16	0.25	0.36	0.48	0.45	0.49
7.61	7.32	6.52	8.89	8.02	6.92	9.32	8.20	6.72	7.38
0.37	0.25	0.07	0.05	0.20	0.30	0.45	0.45	0.37	0.36
6.74	6.54	8.54	6.60	8.01	9.33	7.06	9.27	7.38	5.79
0.32	0.20	0.12	0.08	0.22	0.39	0.40	0.49	0.36	0.25

Figure 10. Channel powers (MW) and their standard deviation (in MW) over the cycle without control blades

					7.65	6.16	7.80	7.08
					0.16	0.08	0.08	0.08
			7.22	7.53	6.87	8.07	7.17	6.64
			0.11	0.16	0.18	0.06	0.07	0.05
		4.78	6.54	6.50	8.08	8.78	6.47	6.44	8.59
		0.11	0.05	0.05	0.12	0.08	0.03	0.03	0.10
		6.36	8.27	7.81	8.81	6.81	7.74	8.84	6.99
		0.09	0.08	0.13	0.07	0.03	0.08	0.11	0.06
	7.20	6.47	7.81	6.96	7.78	7.88	8.88	7.95	8.10
	0.12	0.04	0.13	0.11	0.06	0.05	0.14	0.07	0.05
	7.52	8.08	8.80	7.78	6.83	8.92	6.64	6.62	8.71
	0.15	0.11	0.08	0.06	0.06	0.04	0.08	0.08	0.11
7.65	6.87	8.77	6.81	7.88	8.92	6.88	7.68	8.65	6.86
0.15	0.18	0.08	0.03	0.05	0.04	0.09	0.10	0.15	0.05
6.16	8.07	6.47	7.74	8.88	6.64	7.68	8.96	8.06	9.32
0.08	0.06	0.03	0.08	0.14	0.08	0.10	0.21	0.13	0.06
7.80	7.17	6.44	8.84	7.95	6.62	8.65	8.06	6.72	7.41
0.08	0.07	0.03	0.11	0.07	0.08	0.15	0.13	0.05	0.03
7.08	6.64	8.60	7.00	8.10	8.71	6.86	9.32	7.41	5.77
0.08	0.04	0.10	0.06	0.05	0.11	0.05	0.06	0.03	0.07

Figure 11. Channel powers (MW) and their standard deviation (in MW) over the cycle with control blades

To observe the deviation of the channel powers from their target values during the cycle, the standard deviation of the 84 channels has been plotted every 5 FPD during the cycle in Figure 12. The graph explicitly shows that the control blades managed to keep the channel powers closer to their reference values. However, the deviation is higher at BOC and EOC. The discrepancy at EOC could be reduced by a better refuelling scheme that flattens the power distribution and avoids a channel to burn too quickly or slowly. Moreover, all the blades have not been fully removed at EOC because the nodal peak power would become too large; this issue could also be avoided by using a better refuelling scheme. As for the BOC, the use of burnable absorbers in fresh fuel could help in reducing the discrepancy from the onset by flattening the power distribution in the core.

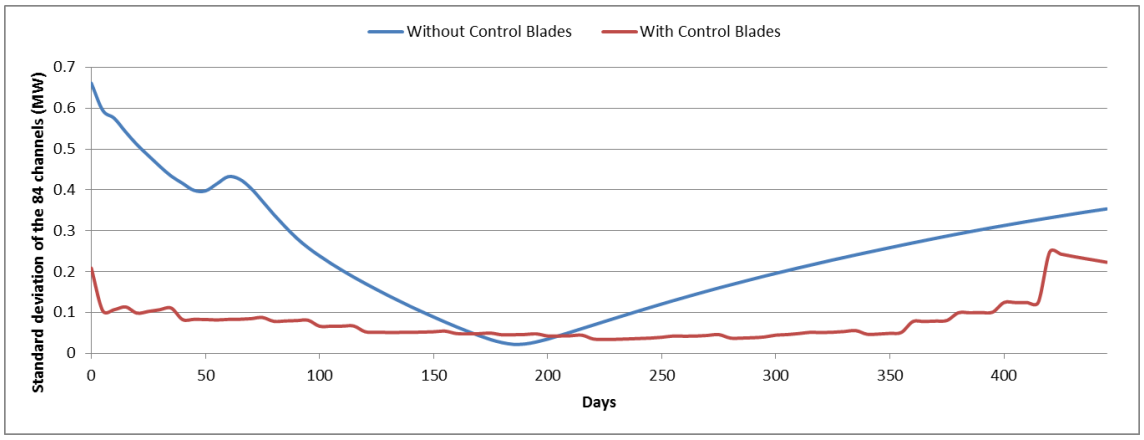

Figure 12. Standard deviation of the 84 channel powers throughout the cycle, with respect to their individual power target

The next two figures (13 and 14) display the multiplication constant (k_{eff}) and the maximum nodal power of the PT-SCWR core during the cycle with and without the use of control blades. By inserting control blades in the core, the initial excess reactivity has been reduced from 110 mk to 77.8 mk but the maximum nodal power is higher over the cycle, especially toward the EOC. This is directly related to use of control blades which deform the flux shape in order to fit our constraints throughout the cycle but could be improved by a better refuelling scheme as well as strategically placed burnable absorbers.

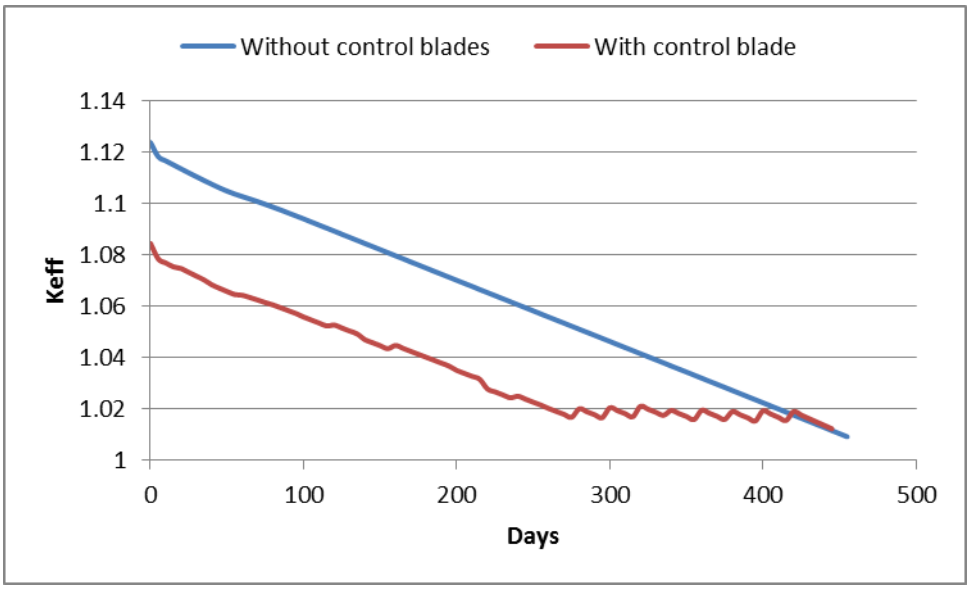

Figure 13. Multiplication constant (k_{eff}) over the cycle with and without the use of control blades

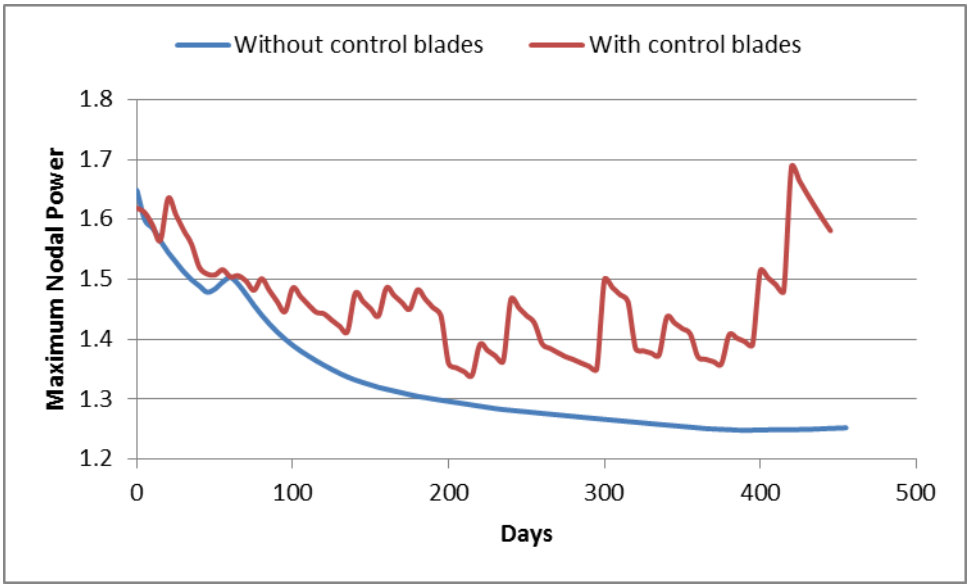

Figure 14. Maximum nodal power during the cycle with and without the use of control blades

6. Conclusions

In this study the use of cruciform control blades inserted from the bottom of the core has been investigated for the PT-SCWR. A coupling process between the diffusion code PARCS and the optimization software DAKOTA has been developed to minimize the power ripple in each channel over the length of the cycle while contraining k_{eff} and the maximum nodal power. In fact, as the PT-SCWR design includes a static orifice at the inlet of each channel , a constant flow rate will be imposed in each channel. Therefore, in order to maintain an outlet coolant temperature of 625°C, the power in the channel should ideally be constant throughout the cycle. The results obtained have been compared to the case without any control devices and the use of control blades has considerably improved the power ripple. The reference fuelling scheme provided by AECL is no longer optimal for cases with control rods and hence it is recommended to redo the fueling scheme as part of a larger core optimization process.

7. Future Work

The work performed for this paper was a preliminary study. As the limiting factor for the PT-SCWR is the sheath temperature, the reactor physics code PARCS will be coupled to the thermal-hydraulic code RELAP5 in order to predict the local sheath temperature and the outlet coolant temperature. The optimization results will also be improved by performing a sensitivity study on several parameters.

Finally an optimized refuelling scheme should be found to improve the power deviations at EOC. The implementation of burnable absorber in fresh fuel might also improve the ripple at BOC while reducing the initial excess reactivity. Ultimately soluble boron in the moderator could also be used to bring the excess reactivity to zero during the first FPD.

References

1. L. K. H. Leung, M. Yetisir, W. Diamond, D. Martin, J. Pencer, B. Hyland, H. Hamilton, D. Guzonas and R. Duffey, “A Next Generation Heavy Water Nuclear Reactor with Supercritical Water as Coolant”, International Conference on Future of Heavy Water Reactors, Ottawa, 2011

2. M. Yetisir, M. Gaudet and D. Rhodes, “Development and Integration of Canadian SCWR Concept With Counter-Flow Fuel Assembly”, The 6th International Symposium on Supercritical Water-Cooled Reactors (ISSCWR-6), Shenzhen, 2013

3. J. Pencer and A. Colton, “ Progression of the Lattice Physics Concept for the Canadian Supercritical Water Reactor”, 34th Annual Conference of the Canadian Nuclear Society, Toronto, 2013

4. J. Pencer, D, Watts, A. Colton, X. Wang, L. Blomeley, V. Anghel and S. Yue, “Core neutronics for the Canadian SCWR Conceptual Design”, The 6th International Symposium on Supercritical Water-Cooled Reactors (ISSCWR-6), Shenzhen, 2013

5. Oak Ridge National Laboratory, SCALE: A comprehensive modelling and simulation suite for nuclear safety analysis and deisgn, ORNL/TM-2005/39 Version 6.1, 2011

6. T. Downar, Y. Xu and V.Seker, PARCS v3.0 U.S.NRC Core Neutronics Simulator, USER MANUAL draft (05/29/2013)

7. Dakota, A Multilevel Parallel Object-Oriented Framework for Design Optimization, Parameter Estimation, Uncertainty Quantification and Sensitivity Analysis, Version 5.4

Reference Manual released December 2009 and updated November 2013, Sandia National Laboratories.

8. A. Ward, Y. Xu and T. Downar, GenPMAXS – v6.1.2dev, Code for Generating the PARCS Cross Section Interface File PMAXS, 2013

9. M. H. McDonald, B. Hyland, H. Hamilton, L. K. H Leung, N. Onder, J. Pencer and R .Xu, “Pre-conceptual Fuel Design Concepts For The Canadian Super Critical Water-cooled Reactor”, The 5th International Symposium on Supercritical Water-Cooled Reactors (ISSCWR-5), Vancouver, 2011

ISSCWR7-2076

Development of Kinetic Models for the Long-term Corrosion Behaviour of Candidate Alloys for the Canadian SCWR

G. Steeves & W. Cook
Department of Chemical Engineering, University of New Brunswick
15 Dineen Drive, Fredericton, New Brunswick, Canada, E3B 5A3
1; graham.steeves@unb.ca

D. Guzonas
Chalk River Laboratories, Atomic Energy of Canada Ltd.
1 Plant Road, Chalk River, Ontario, Canada K0J 1J0
guzonasd@aecl.ca

Abstract

Corrosion behaviour of Inconel 625 and Incoloy 800H, two of the candidate fuel cladding materials for Canadian supercritical water (SCW) reactor designs, were evaluated by exposing the metals to SCW in UNB's SCW flow loop. A series of experiments were conducted over a range of temperatures between 400°C and 600°C and the corrosion rates were evaluated as the weight change of the materials over the exposure time (typical experiments measured the weight change at intervals of 100, 250, and 500 hours, with some longer term exposures included). SEM, EDX, and TEM techniques were used to examine and quantify the oxide films formed during exposure and the corrosion mechanisms occurring on the candidate metals.

Data from in-house experiments were used to create an empirical kinetic equation for each material that was then compared to literature values of weight change. Dissolved oxygen concentrations varied between experimental sets, but for simplicity were ignored since the effect of dissolved oxygen has been demonstrated to be a minor secondary effect. Activation energies for the alloys were determined with Inconel 625 and Incoloy 800H showing a distinct difference between the low-temperature electrochemical corrosion mechanism and direct high-temperature chemical oxidation. The results were modelled using these separate effects showing dependence on the bulk density and dielectric constant of the SCW through the hydrogen ion concentration.

1. Introduction

As the world's demand for energy and environmental stewardship increases, it is important to use power plants that provide reliable base-load power while also minimizing carbon dioxide emissions during operation. The nuclear industry meets these demands, and Canada has a proprietary nuclear design in the CANDU reactor. Research is currently underway to create the next generation of nuclear plants through the Generation IV International Forum (GIF). The emphasis of the research is to create safer, more efficient nuclear designs. Canada has chosen to participate in GIF by investigating one of the most promising designs: the SCWR (Supercritical Water-Cooled Reactor). The Canadian SCWR design is seen as an advancement to existing CANDU reactors. [1] The currently envisaged design for the Canadian SCWR uses a re-entrant fuel channel consisting of a central, single pass flow tube with an annular pass back

through the fuel bundles (Figure 1). Due to the liquid-gas nature of supercritical water, no steam generators or steam separators are necessary. [1] Plant efficiency is greater than existing CANDU reactors as using SCW allows higher operating temperatures as well as avoiding energy loss due to the heat of evaporation. The current design could achieve efficiencies of nearly 48% as compared to the 30-33% in the current fleet of CANDU reactors.

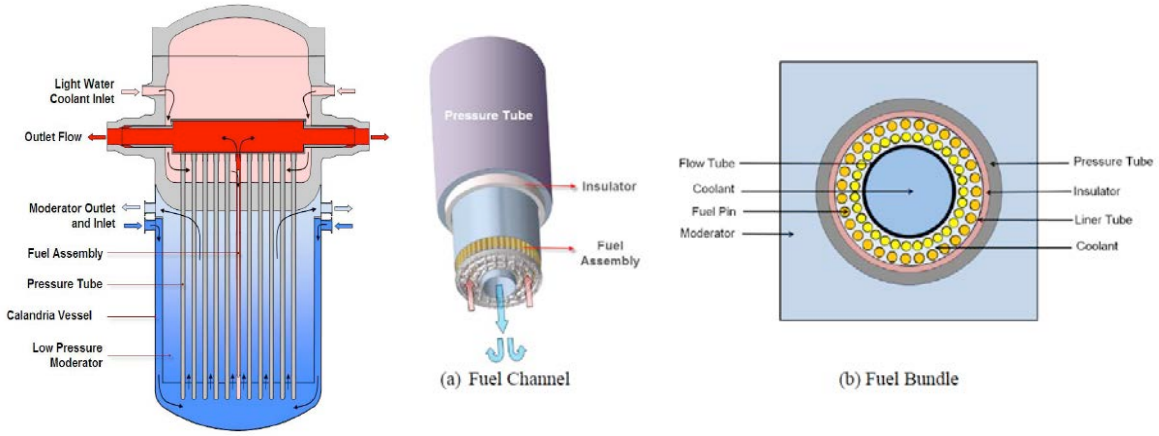

Figure 1. Conceptual design of the Canadian SCWR and re-entrant fuel channel.

One of the key challenges of the Canadian SCWR concept is in material selection. Material concerns include general corrosion at elevated temperatures and pressures and stress corrosion cracking while related effects are associated with water chemistry control, corrosion product transport, and activity transport. General corrosion is of concern and related to the required thickness of materials for operation. General corrosion will also produce thick oxide layers that may limit heat transfer and run the risk of fuel overheating. The proposed design for SCWR plants uses equipment with much smaller tolerances for oxidation such as pressure tubes [2] and fuel cladding as compared to other reactor components. The proposed fuel cladding design for the Canadian SCWR will be collapsible, thus material thickness for pressure retention is not a significant issue. Complicating these requirements is the fact that the temperatures under which the fuel cladding will operate will range from about 350 - 800^{o}C. Allowance for through-wall corrosion is very limited due to the constraints of the reactor design. The minimum thickness of the cladding is 0.4 mm in order to prevent longitudinal ridging and the maximum is 0.6 mm for the purposes of neutron economy. Thus the maximum penetration or corrosion allowance is 0.2 mm. The anticipated lifespan of the cladding is 3.5 years, or 30 600 hours incorporating three passes through the core during refuelling outages.

Oxide growth can be caused by general corrosion or by deposition from saturated solution, and may be a concern for candidate materials. Oxidation can cause the material to expand and exert force on neighbouring sections. The Canadian SCWR fuel assembly is expected to have a gap of 1.240 mm between pins in the outer ring. The gap is not a very tight geometry and thus physical expansion is not a major concern. A more relevant concern is in the oxide layers acting as insulation. Heat transfer through SCW-built oxides is not well known and may act purely as insulation. If the oxide acts as insulation, then the temperature of the metal will be greater and thus the rate of corrosion will increase, potentially leading to fuel failures. Stress corrosion cracking may occur before a material surpasses the mechanical limitations of the material. Once initiated, cracks are expected to propagate quickly due to the high operating temperatures of the system. It is important that the candidate materials are not overly susceptible to SCC, a stipulation that requires specific laboratory tests to identify vulnerability.

Over the past six years, over 20 independent tests have been conducted in the UNB SCW corrosion test loop investigating the oxidation behaviour of over a dozen alloys and potential protective coatings for use in the Canadian SCWR. Recently, the list of candidate materials for use in the Canadian SCWR was shortened to five and includes 310s SS, 347SS, Inconel 625,

Alloy 800H and Haynes 214. Targeted testing at selected temperatures and for extended durations for these materials has been the focus of the experimental work over the past year with the aim of creating a predictive kinetic model of the materials' corrosion rates over the intended lifetime of critical core components including the fuel cladding and core annulus. Reported here are the results obtained when assembling the kinetic model for Inconel 625 and Alloy 800H as compiled from numerous tests conducted at UNB.

2. Test Methods

The test loop at the University of New Brunswick was constructed to simulate the conditions under which the Canadian SCWR is expected to operate. The loop has a total capacity of approximately 65 litres and a maximum flow rate of 500 mL/min – a schematic diagram of the system is shown in Figure 2. A constant displacement pump with a metallic diaphragm (Milton Roy model PL120(145) S(M) 14M 456 VV) maintains a system pressure of 25 MPa in conjunction with a back pressure regulating valve (BPRV) at the cooled end of the test loop. Flow pulses induced by the pump are damped by a nitrogen-based pulsation dampener connected just downstream of the pump discharge. Pure water (typically 18.0 MOhm-cm, produced through a Barnstead, 4-stage water deionising system) is heated using a tube-in-tube heat exchanger, followed by a 15 kW electric heater in order to achieve the desired fluid temperature. System temperature is maintained by a furnace encasing the 2 litre, Hastelloy C-276 autoclave, which houses the metal coupons used for testing. Water leaving the autoclave passes back through the tube-in-tube heat exchanger and is further cooled to ambient temperature by passing through a shell-and-tube cooler, operating with chilled water.

Dissolved oxygen concentration in the loop is measured by an Orbisphere EC oxygen sensor and Chemets colourmetric indicators. Loop oxygen concentration was controlled by bubbling either compressed air or an inert gas through the main water reservoir. System flow rate was measured by a rotamater located in the low temperature, low pressure return line from the test loop to the reservoir. Water conductivity was measured by strategically placed conductivity probes in the loop and confirmed through water samples and a bench-top conductivity probe. System pH was measured by water samples using a bench-top pH probe. Coupons from the same production lot were used in all the supercritical water corrosion testing conducted at UNB.

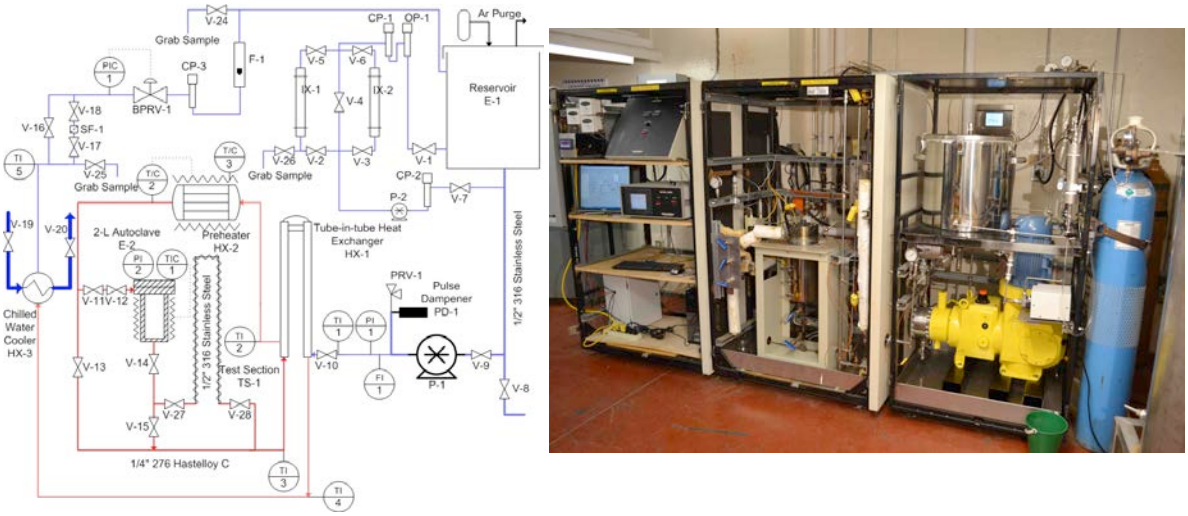

Figure 2. Schematic diagram and photo of UNB' s SCW test loop.

Coupons were progressively polished using 200, 400, and 600-grit silicon carbide paper and were stamped with a unique identifier. Once polishing was complete, all coupons were placed in an ultra-sonic bath with acetone for 20 minutes in order to remove any grease or grit accumulated from the polishing process. Each coupon was approximately 2cm x 1cm x 2mm,

and the precise dimensions for each coupon were measured to an accuracy of 10 microns using digital calipers prior to exposure. Coupons were weighed after dimensioning and cleaning to an accuracy of 0.1 mg or 0.01 mg, and placed onto the coupon tree. The location of each coupon was recorded in order to ensure that mass changes are attributed to the correct metal in the case that the oxide layer completely obscured the stamped label. The coupon tree was placed into the autoclave once the test loop was ready for operation.

The majority of experiments were performed with approximate exposure times of 100, 250, and 500 hours within UNB's SCW loop at temperatures of 370, 400, 500, 550, and 600°C. A few experiments were run with extended durations, up to 1500 hours. The full set of experiments included for the work described in this paper and the conditions under which they were run is given in Table 1.

Coupons were weighed before the start of each experiment and after each exposure time checkpoint. At least one coupon was removed for surface characterisation using SEM, TEM, etc. after each checkpoint. While most samples were eventually descaled to determine the true "corrosion rate", the results presented here are of direct weight change of coupons over time.

Table 1. Experiments included in kinetic model

Experiment	Temperature (°C)	Pressure (MPa)	Flow Rate (mL/min)	DO_2 (ppb)	Date Run
Run E	550	25	200	5	Oct-Nov 2009
Run F	400	25	200	5	Nov-Dec 2009
Run G	500	25	200	5	March 2010
Run J	500	25	200	200	January 2011
Run K	400	25	200	200	Feb 2011
Run P	550	25	200	8000	August 2012
Run Q	600	25	200	8000	January 2013
Run U	370	25	140	8000	Sept-Oct 2014

3. Results & Discussion

The averaged weight change versus time data from each of the experiments is presented in Figure 3 (a – g) below. It is noted that, after an initial rapid increase in mass, results from all the tests reveal a weight loss after the first exposure period for I625; this occurred at approximately the first 100 hours of exposure. Similar data for Alloy 800H exhibited a more or less linear weight gain after the first 100 hours of exposure. For the experiment conducted at 370°C (Run U), the first exposure period lasted 500 hours. In some experiments, particularly the ones conducted at higher temperatures, the weight loss on the I625 material started immediately upon exposure to supercritical water. These results are interesting in that most of the other candidate alloys (310s SS, 347 SS, and 800H) exhibited a continuous weight gain over the exposure time that tended to reach a more-or-less constant rate, or linear oxidation rate after prolonged exposure. The Inconel 625 results reveal a continuous weight loss that is roughly linear at each temperature, and can be readily modelled through a direct linear fit, assuming a first-order time dependence ($\alpha = 1$), as shown in equation 1. For cases where a large initial weight gain was recorded, the short-term data is excluded from the fit as it is considered to be not representative of the longer-term behaviour of the alloy.

$$\Delta W = k\, t^{\alpha} \qquad [1]$$

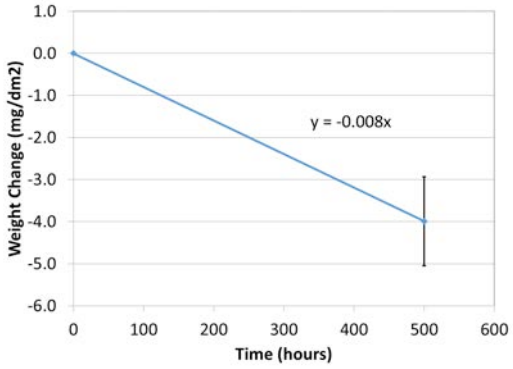

(a) Run U (370°C, 8000 ppb O_2)

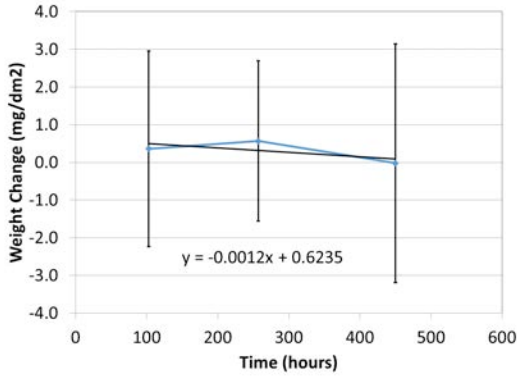

(b) Run F (400°C, 5 ppb O_2)

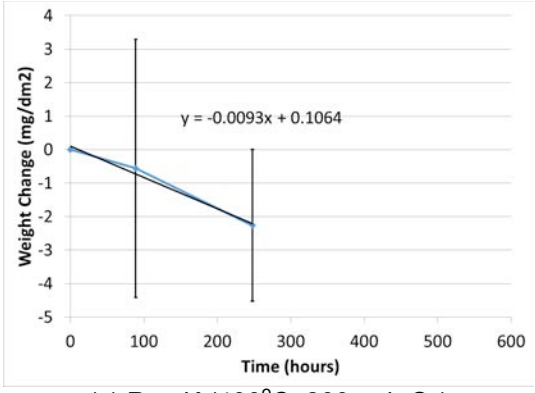

(c) Run K (400°C, 200 ppb O_2)

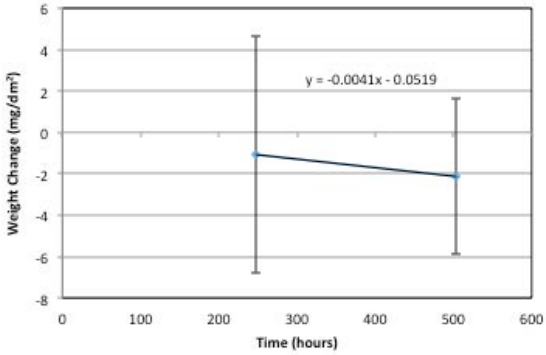

(d) Run G (500°C, 5 ppb O_2)

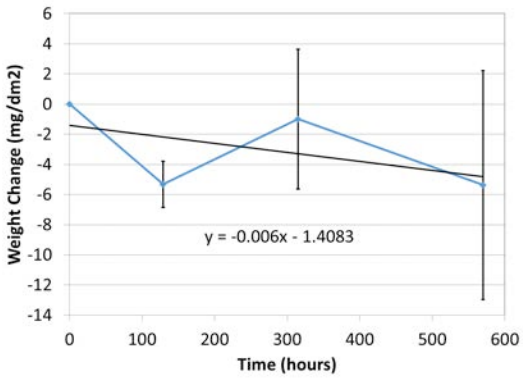

(e) Run E (550°C, 5 ppb O_2)

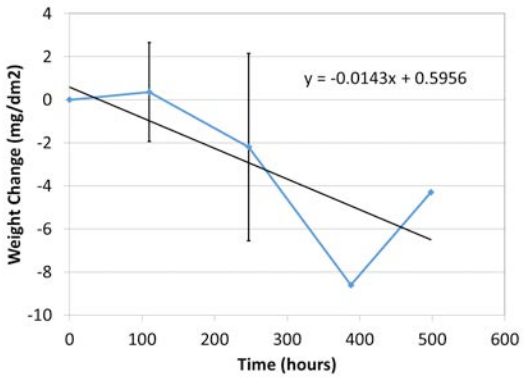

(f) Run P (550°C, 8000 ppb O_2)

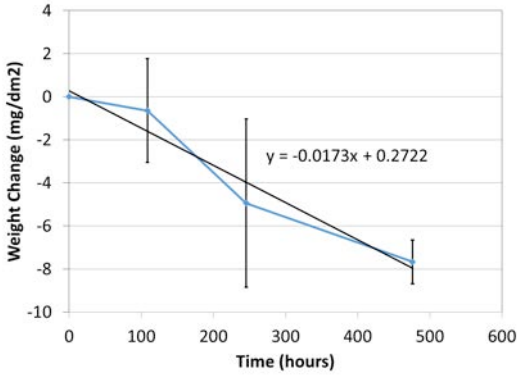

(g) Run Q (600°C, 8000 ppb O_2)

Figure 3 (a–g). I625 experimental data results including the averaged mass change.

SEM pictures were taken from experiments E, F, G and U. Pictures shown in Figures 4 & 5 are arranged in order of increasing temperature:

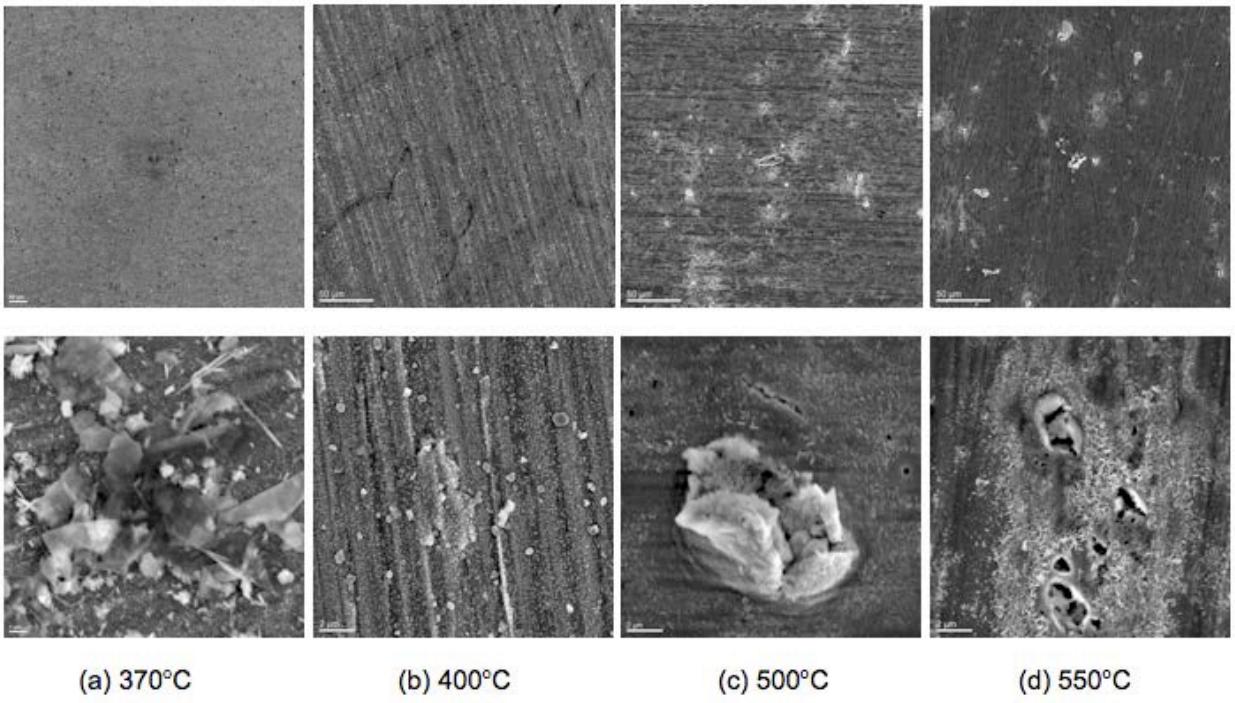

Figure 4. SEM images of I625 at different temperatures.

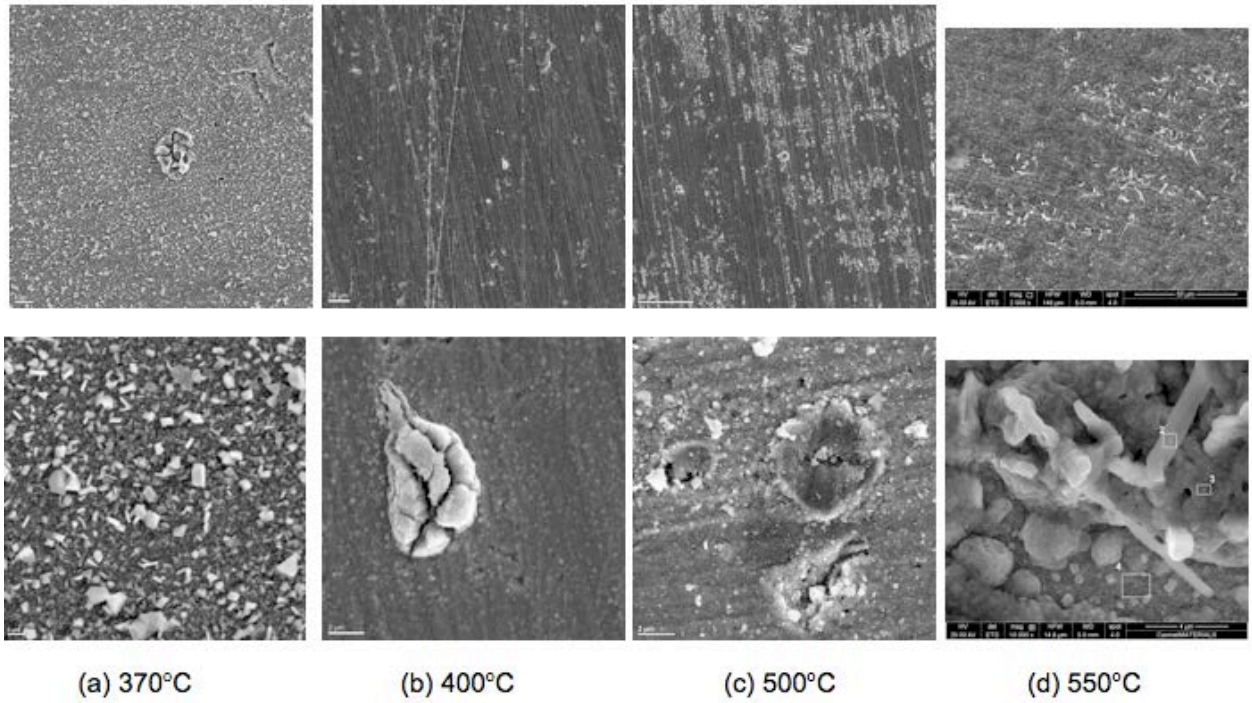

Figure 5. SEM images of A800H at different temperatures.

The SEM images show that in subcritical water, both alloys are covered with a typical dual-oxide film with the outer oxide being precipitated from solution. At supercritical temperatures, the outer oxide layer is not present, except for A800-H at the higher temperatures where the material's oxidation rate is increasing leading to sparse coverings of oxide at 400-500°C with nearly complete coverage at 550°C. I625 shows evidence of pitting with Fe-Cr rich oxide particles surrounding the pits at temperatures above 500°C. Overall, the oxidation rate of I625 was considerably lower than that of A800H at all the temperatures investigated and actually showed continuous weight loss at extended exposure times whereas A800H exhibited a continuous weight gain. Interestingly, the outer oxide films formed at the higher temperatures showed significant chromium content. The majority of these tests were run under air-saturated conditions and it has been demonstrated that the phenomena of "chromia evaporation" can occur in oxygen-containing steam at elevated temperatures [3 – 4]. The chromium observed in these outer films are likely the result of chromium transport from the corrosion of the loop material (HC-276) under the oxygen-containing conditions.

For I625, the averaged weight change over time, determined from the experimental data shown above, was used to create a linear fit, where the slope of the line gives the specific kinetic constant describing the weight change of the alloy at the experimental temperature. Although all experiments were not conducted under the same concentration of dissolved oxygen in the system, the specific kinetic constants for experiments conducted at the same temperature were considered equivalent and averaged to give a value for each temperature, neglecting the effect of dissolved oxygen. The results are summarized in Tables 2 and 3:

Table 2. Experimental kinetic constants for each experiment run.

Experiment	Temperature (°C)	- k (I625)
U	370	0.00798
F	400	0.00119
K	400	0.00932
G	500	0.00413
J	500	0.02756
E	550	0.00597
P	550	0.01125
Q	600	0.01727

The results from Run J indicated an abnormally large kinetic constant for Alloy 625 at 500°C due to the large initial oxidation that was observed, where the coupons underwent an initial weight gain of approximately 15 mg/dm^2. After the initial change in mass the coupons underwent constant weight loss, albeit at a rate far faster than any other run. For the inconsistency with other runs, results from Run J were discarded for the purposes of this analysis. Run G also showed a large initial weight change and oxidation rate, but at the 250-hour mark data the weight changed slowed and was more consistent with the other experiments. The first two data points from Run G were excluded for that reason. Additional data was obtained from literature in order to give a second data point for weight change of Inconel 625 in subcritical water. The weight change was described by a parabolic function that was used to determine the lower-temperature weight change as at 500 hours of exposure [5]. For Alloy 800H data at lower temperature (305°C) were extracted from Alvarez et al. [6]. The kinetic constants used to formulate the models are shown in Table 3:

Table 3. Averaged experimental kinetic constants at each temperature.

Temperature (°C)	Average (- k) (I625)	Average k (800H)
260 / 305	0.00331(Ziemniak)	0.006 (Alverez)
370	0.00798	0.01293
400	0.00525	0.01408
500	0.00413	0.01619
550	0.01011	0.02953
600	0.01727	n/a

The negative, averaged kinetic constants for I625 were used to derive an Arrhenius plot to determine the activation energy and pre-exponential factor for I625 oxidation. The results are shown in Figure 6 below. As shown, a straight line fit is not readily apparent from the data presented as would be expected for a pure chemical process from which the Arrhenius parameters and thus activation energy can be derived. Instead, the results suggest two separate oxidation mechanisms with an inflection point in the corrosion rate just past the pseudo-critical transition. This phenomenon has been described previously in literature [3 & 7]. It is attributed to the differences between the electrochemical corrosion (EC) of the alloy at sub-critical conditions versus the direct chemical oxidation (CO) mechanism at elevated, supercritical temperatures. The direct chemical oxidation resembles high-temperature oxidation processes. For the purpose of analyzing the data presented here, the "apparent" rate constant at each temperature is separated into its EC and CO components and is described by:

$$k_{app} = k_{EC} \exp\left(-\frac{E_{EC}}{RT}\right) C_{H^+} + k_{CO} \exp\left(-\frac{E_{CO}}{RT}\right) \quad [2]$$

where k_{app} is the apparent specific rate as determined through the corrosion experiments presented above (dW/dt), E_{EC} is the low-temperature activation energy (electrochemical) and E_{CO} is the high temperature activation energy (for the direct chemical oxidation term). The terms k_{EC} and k_{CO} are the frequency factors for the EC and CO mechanisms respectively. The term C_{H+} is the concentration of hydrogen ions (mol/kg), which was calculated for neutral conditions from the ionization constant of water [8]. Since the electrochemical corrosion mechanism relies upon distinct redox processes occurring at separate locations on the metal, the C_{H+} term implicitly applies a function of the dielectric nature of the supercritical water and its effect should be diminished to non-existent at supercritical temperatures.

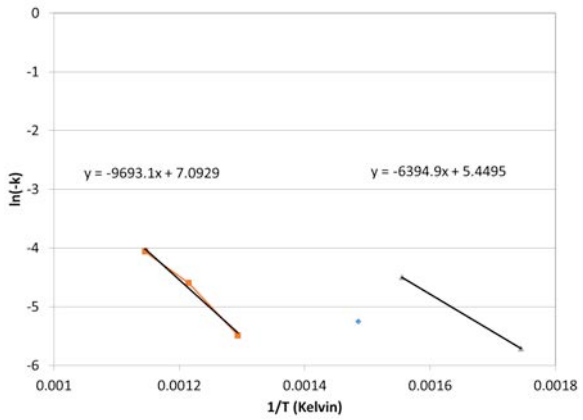

Figure 6. Arrhenius plot of I625 oxidation indicating separate oxidation mechanisms.

The above equation was used with the observed experimentally determined kinetic constants to describe the processes involved. The high temperature activation energy due to direct chemical oxidation was derived through the slope and intercept over the data range of 500-600°C where it is assumed that the electrochemical oxidation term would be negligible. The activation energy and pre-exponential factor for I625 oxidation were determined to be:

E_{CO} = 80.6 kJ/mol
k_{CO} = 1201 mg/dm^2.hr^{-1}

The apparent rate constant at 400°C is likely a combination of the EC and CO terms. In order to separate the electrochemical term from the oxidation term data, results from Ziemniak and Hanson [5] at 260°C were used to estimate the kinetic constant in lower temperature sub-critical water. The resulting parameters were determined for the EC mechanism for I625 oxidation using the data points at 260 and 370°C:

E_{EC} = 51.2 kJ/mol
k_{EC} = 1.151 x 10^8 mg/dm^2 kg/mol hr^{-1}

Formulating these kinetic parameters into the corrosion rate equation results in the following equation describing the weight change of the alloy over time:

$$\Delta W = \left\{ k_{EC} \exp\left(-\frac{E_{EC}}{RT}\right) C_{H^+} + k_{CO} \exp\left(-\frac{E_{CO}}{RT}\right) \right\} \Delta t \quad mg / dm^2 \qquad [3]$$

Figure 7(a) shows the modelled effect of temperature on weight loss of I625 over a period of 500 hours along with the averaged weight loss values derived from the experiments at UNB. A similar approach was taken for the Alloy 800H data set (weight gain kinetic constants shown in Table 3) using lower temperature data from Alvarez and the modelled effect as a function of temperature with the 500 hour data is shown in Figure 7(b).

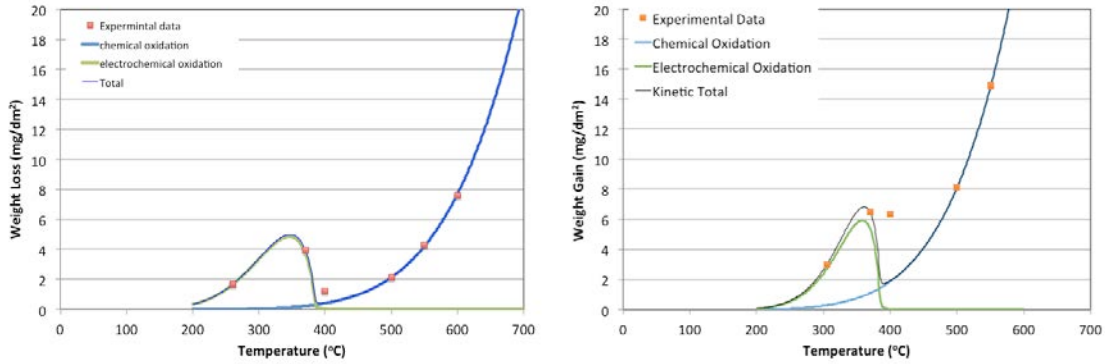

(a) **(b)**

Figure 7. Experimental and modeled corrosion rates of (a) I625 and (b) A800H.

The results of the analysis for Alloy 800H indicated the following activation energies and frequency factors for the CO and EC terms:

E_{CO} = 63.6 kJ/mol
k_{CO} = 321.6 mg/dm^2.hr^{-1}

E_{EC} = 81.0 kJ/mol
k_{EC} = 4.259 x 10^{10} mg/dm^2 kg/mol hr^{-1}

The model fits the experimental values reasonably well and demonstrates the local maximum in oxidation rate around the supercritical point. It must be emphasized that the Alloy 800H exhibited a continuous weight gain over the exposure time whereas I625 exhibited a weight loss. It is interesting to note that a local maximum is observed in both cases. This local maximum has been much reported in the literature, incorrectly, as a maximum in corrosion rate at the critical point. It is clear from the data and the model presented here that is not the case.

The models were applied to estimate the corrosion penetration of I625 and 800H after 30 600 hours at 800^{o}C, representing the hypothetical operating lifetime of a Canadian SCWR fuel element. The models predict penetrations of 0.0506 mm and 0.0986 mm for I625 and A800H respectively over this timeframe, which is well below the 0.2 mm maximum corrosion allowance in the fuel cladding specification. From this result, both of these alloys would appear to meet the design specification for the Canadian SCWR but one must still consider other effects such as propensity for stress-corrosion cracking, helium embrittlement and neutron economy before making a final material selection.

4. Conclusions

Gravimetric data for Inconel 625 and Alloy 800H were collected from experiments performed over multiple years in the UNB SCW corrosion test loop and from compiled literature sources for lower temperature conditions. The data was used to evaluate kinetic parameters for the general corrosion or oxidation of the alloys and Arrhenius plots revealed the separation of oxidation mechanisms – electrochemical oxidation in subcritical temperatures, direct chemical oxidation at supercritical temperatures. The results demonstrated a local maxima in corrosion rate is obtained around the critical point but that the overall alloy corrosion rate increases with increasing temperature, as would be expected. The models developed were used to estimate the expected corrosion penetration after approximately three-years of service at 800^{o}C, the maximum fuel cladding temperature expected in the Canadian SCWR concept. Results demonstrated that the penetration was well within an acceptable margin for both alloys indicating that either could be used as the reactor's fuel cladding.

5. Acknowledgments

The authors are grateful for the funding for this work from the NSERC/NRCan/AECL Generation IV Technologies program, the Canadian Foundation for Innovation and the New Brunswick Innovation Fund. Jamie Miles, Steven Cogswell (UNB) and Jian Li (CANMET) are also thanked for helping to provide the SEM images.

References

[1] R.B. Duffey, "CANDU® and Generation IV System," *Abstracts of the Pacific Basin Nuclear Conference*, pp. 273-277, 2004.

[2] W.T. Diamond, "Development of Out-of-Core Concepts for a Supercritical-Water Pressure-Tube Reactor," *Conference Proceedings: The 2nd Canada-China Joint Workshop on Supercritical Water-Cooled Reactors (CCSC-2010)*, April, 2010.

[3] D.A. Guzonas and W.G. Cook, "Cycle Chemistry and its effect on materials in a supercritical water-cooled reactor: A synthesis of current understanding," *Corrosion Science*, pp. 48-66, 2012.

[4] G.R. Holcomb, "Steam oxidation and chromia evaporation in ultrasupercritical steam boilers and turbines," *Journal of the Electrochemical Society, 156 (2009), pp. C292–C297*, vol. 156, pp. C292-C297, 2009.

[5] Stephen E Ziemniak and Michael Hanson, "Corrosion behavior of NiCrMo Alloy 625," *Corrosion Science*, pp. 1595-1618, 2003.

[6] M. G. Alvarez, A. M. Olmedo, and M. Villegas, "Corrosion behaviour of Alloy 800 in high temperature aqueous solutions: long term autoclave studies," *Journal of Nuclear Materials*, vol. 229, pp. 93-101, 1996.

[7] L. B. Kriksunov and D. D. Macdonald, "Corrosion in supercritical water oxidation systems: a phenomenological analysis," *Journal of the Electrochemical Society*, pp. 4069-4073, 1995.

[8] A. V. Bandura and S. N. Lvov, "The ionization constant of water over wide ranges of temperature and density," *Journal of Physical and Chemical Reference Data*, vol. 35, pp. 15-30, 2006.

ISSCWR7-#2077

European Project "Supercritical Water Reactor – Fuel Qualification Test" (SCWR-FQT): Summary of general corrosion tests

Radek Novotny[1, 4], Přemysl Janík[1], Aki Toivonen[2], Anna Ruiz[1], Zoltan Szaraz[1], Lefu Zhang[3], Jan Siegl[4], Petr Haušild[4], Sami Penttilä[2]

[1] European Commission, Joint Research Centre, Institute for Energy and Transport
Westerduinweg 3, 1755 LE, Petten. Netherlands
+31224565357, Pardubra@gmail.com

[2] VTT Technical Research Centre of Finland, materials Performance in New Energy technologies Finland

[3] Shanghai Jiao Tong University, School of Nuclear Science and Engineering, China

[4] Czech Technical University Prague, Faculty of Nuclear Sciences and Physical Engineering, Czech republic

Abstract

The main target of the EUROATOM FP7 project "Fuel Qualification test for SCWR" is to make significant progress towards the design, analysis and licensing of a fuel assembly cooled with supercritical water in a research reactor. The program of dedicated WP4 - Pre-qualification was focused on evaluation of general corrosion resistance of three pre-selected austenitic stainless steels 08Cr18Ni10Ti, AISI 347H and AISI 316L, which should be pre-qualified for application as a cladding material for fuel qualification tests in supercritical water. Therefore, the experiments in support of WP4 concentrated on 2000 h corrosion exposures in 25 MPa SCW at two different temperatures 550 and 500^{o}C dosed with both 150 and 2000 ppb of dissolved oxygen content. Moreover, water chemistry effect was investigated by conducting tests in 550^{o}C SCW with 1.5 ppm of dissolved hydrogen content. At first, corrosion coupons were exposed for 600, 1400 and 2000 h in JRC IET, VTT and SJTU autoclaves connected to recirculation loop allowing continual water chemistry control during the test. Following examination of the exposed specimens consisted of weight change calculations and detailed macro and microscopic investigation of oxide layers using SEM and EDX. With respect to general corrosion results, all tested steels showed sufficient corrosion resistance in SCW conditions taking into account the conditions foreseen for future fuel qualification test in the research reactor in CVR Rez. When the results of weight change calculations were compared for all three materials, it was found out, that the corrosion resistance increased in the following order: 316L<347H<08Cr18Ni10Ti. Results obtained in hydrogen water chemistry did not indicate any significant beneficial effect compared to tests in SCW with 150 or 2000 ppb dissolved oxygen content. Additional tests were dedicated to investigation of surface finish effect. In these exposures polished, sand-blasted and plane-milled surface finish technique were investigated. Beneficial effect of surface cold work in particular of sand-blasting was clearly demonstrated.

1. Introduction

The Supercritical Water Reactor (SCWR) concept is a Light Water Reactor (LWR), which would be operated above the thermodynamic critical point of water (374 C, 22.1 MPa). In the last 10 years, the European Concept of SCWR – European High Performance Light Water Reactor (HPLWR) have been elaborated in substantial details within EUROATOM FP5 and FP6 projects

[2, 6]. The follow-up project within that a fuel qualification test using small scale assembly in a research reactor under typical prototype conditions would be performed was prepared and proposed as the next step. This project is a collaborative project co-funded by the European Commission, which takes advantage of a Chinese and European collaboration, in which China offers an electrically heated out-of-pile loop for testing of fuel bundles. Design and licensing of an experimental facility for the fuel qualification test, including the small scale fuel assembly, the required coolant loop with supercritical water and safety and auxiliary systems, is the scope of the currently running project "Supercritical Water Reactor - Fuel Qualification Test" (SCWR-FQT). The scope of WP4-Prequalification is pre-qualification of the FQT test section by means of designing, building and operating a similar electrically heated test section, as well as the selection of materials and pre-qualification of all critical components of the FQT test section. The pre-selection of candidate materials was carried out taking into account the following criteria:

1. These materials had to be commercially available in nuclear grade, i.e. these materials have been licensed as nuclear material and utilized in the currently operated LWRs.
2. Evaluated in the previous projects on development of the European HPLWR concept as the promising cladding candidates.

Currently, there is no commercial material available which would sustain long term exposure in SCW at estimated peak cladding temperature reaching up to ~630^{o}C due to synergistic detrimental effect of temperature and supercritical water on mechanical properties (e.g. low Yield Strength (YS) and creep resistance), general corrosion and stress corrosion cracking (SCC) resistance. The worldwide programs to study corrosion in SCW have examined many material classes, including ferritic-martensitic (F/M) steels, austenitic steels, Ni-base alloys, Zr-base alloys, and Ti-base alloys [1]. The studies focused on corrosion of steels and nickel-based alloys in SCW have shown that corrosion rate increased rapidly at temperatures above the critical point of water. For example, autoclave corrosion tests of various austenitic SSs, F/M steels, and ODS steel, in 400, 500, 550 and 600^{o}C SCW, were performed within HPLWR Phase 2 FP6 project [3]. In this study, corrosion rates of all tested austenitic stainless steels increased rather dramatically above 550^{o}C SCW. However, stabilized grades of austenitic stainless steel AISI 321 and 1.4970 exhibited lower increases of oxidation rates with temperature compared to non-stabilized grade such as e.g. AISI 316NG.

The primal objective of WP4 – Pre-qualification and this work was to select a fuel cladding material for future FQT facility after evaluation of their general corrosion resistance and high temperature mechanical properties particularly SCC resistance. However, the portfolio of activities carried out within this project was in reality much broader. It included additional corrosion tests with focus in particular on two aspects: optimization of surface finish procedure and optimization of water chemistry for future fuel qualification test to be performed in CVR Rez.

2. Experimental

2.1 Pre-selected materials

For the purpose of SCWR FQT project WP4 material pre-qualification, three grades of austenitic stainless steels 347H, 08Cr18Ni10Ti and 316L, licensed for light water reactor applications, have been selected. From those, for instance 08Cr18Ni10Ti (Russian production, equivalent to 321) was selected as the construction material for the pressure tube and most loop components of in-pile loop designed and built within of HPLWR Phase 2 project [6, 12]. This steel is utilized in the reactor cores of the type WWER (Russian production of PWR) and RBMK, and also in the fast-neutron reactors BOR-60, BN-350 and BN-600. Generally, steel of 08Cr18Ni10Ti type had extensive application as the material for the cladding and the wrappers of fuel assemblies and control rods [4]. Moreover it should be mentioned that all pre-selected materials or their close equivalents were, except for 08Cr18Ni10Ti, also studied in USA in 1950-1960 within the various programs on development of superheated water nuclear power plant [5, 7]. However, 08Cr18Ni10Ti SS was studied as well at superheated steam in Russia at the Beloyarsk Nuclear

Power Plant (NPP) where channels were operated at superheated steam parameters for several years. The chemical composition for all three studied steels is given in Table 1.

Table 1. Chemical composition of all three pre-selected materials.

Material	C	Si	Mn	S	P	Cr	Ni	Others
316L	0.022	0.65	1.86	0.001	0.03	16.6	10.12	Mo = 2.06
347H	0.048	0.29	1.84	0.013	0.026	17.6	10.7	Nb = $10xC_{min}$
O8Cr18Ni10Ti	0.085	0.45	1.07	0.009		18.0	10.0	Ti = 0.64

While the 316L and 347H austenitic stainless steels were supplied in plates by SOLOMON'S Metalen B.V., 08Cr18Ni10Ti was delivered by OAO Saint-Petersburg, Russia. Generally, 316 is susceptible to sensitization - the formation of grain boundary chromium carbides at temperatures in the range of 900 and 1500°F (425 to 815°C). Generally, one way how to prevent sensitization is to decrease the carbon content in the steels. The low carbon grade 316L is resistant to sensitization; however, extended exposures in the temperature range mentioned above will eventually result in sensitization of even the low carbon grade. Alloying with the elements such as titanium, columbium or niobium that form carbides more preferably than chromium is another way how to stabilize the microstructure against chromium carbide grain boundary precipitation. This process called stabilization is achieved by an intermediate temperature heat treatment, during which the titanium reacts with carbon to form titanium carbides. This significantly reduces susceptibility to sensitization in service by limiting the formation of chromium carbides. Thus, such an alloy can be used for extended periods at elevated temperatures without compromising its corrosion resistance. While Alloy 347 is stabilized by the addition of niobium and tantalum, the 08Cr18Ni10Ti type stainless steel by addition of titanium.

2.2 Test specimens and surface finish

The blocks of materials were cut without any additional heat treatment and the corrosion coupons were manufactured with the final dimensions of 25x15x3 mm for JRC IET (see Figure 1) and respectively 25x15x5 mm (VTT).

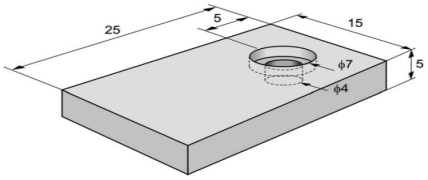

Figure 1. Schematic drawing of the coupon specimens.

The effect of surface finish and pre-treatment on corrosion resistance has long been recognized. For example, Berge [8] listed four factors that should be considered in order to give a complete description of the surface: geometrical factors such as roughness; chemical factors such as compositional differences between bulk and surface; structural factors such as cold working; and mechanical factors such as residual surface stresses. Ruther et al. [9] noted that surface preparation giving a strain free surface resulted in maximum general corrosion in SCW while the surface finish which resulted in severe cold-work reduced general corrosion. Therefore, in addition to standard polished specimens (polished using 1200 grit paper according to ASTM standard G1-03), plane-milled and sand blasted (less than 50μm big sand particles

were shot at the specimen surface. from 100 mm distance for 5min respectively 10 min). While the plane-milling process resulted in average surface roughness (Ra) 3-4 µm, sand-blasted ones had surface roughness lower than 1 µm.

2.3 Test Procedure

The general corrosion tests were conducted according to ASTM standard G1-03 i.e. Long term (up to 3610 h) corrosion tests were performed in Joint Research Centre Institute for Energy and and Transport (JRC IET), VTT Technical Research Centre of Finland (VTT) and Shanghai Jiao Tong University (SJTU) autoclaves in 500°C (JRC IET), 550°C (JRC IET, VTT and SJTU) 25 MPa SCW. Simulated water chemistry included those corresponding to both NWC with high and low dissolved O2 contents (2000 ppb (JRC IET) and 150 ppb (VTT)) and HWC with 2.5 ppm of dissolved H2 content. Always several coupons per material were placed into the autoclave, and then one coupon at a time was removed after each heating sequence, i.e. after 600, 1000, 1200, 1400, 1500, 2000 and 3610 hours. Corrosion coupons were cleaned with ethanol in ultrasonic bath, dried, weighted and following that fixed to a specimen holder rack using electrically insulating ZrO2 (yttrium or magnesium stabilized), Al2O3 washer rings or they were hanged on 316L wires, as it is shown for illustration in Figure 2.

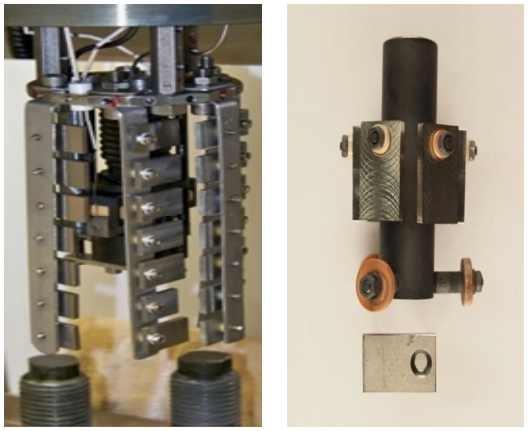

Figure 2. Specimen holder racks with the test coupons were attached to the autoclave lid.

All specimens were exposed to supercritical water in an autoclave connected to a recirculation water loop. The high-pressure parts of the loops consisted in high-pressure pump, heat exchanger, pre-heater and cooler. The autoclave outlet water was lead through a pre-cooler, heat-exchanger and cooler. The autoclaves were pressurized using a diaphragm pumps and back-pressure regulators. The maximum flow rate in the high temperature and pressure part of the loop ranged from 5 to 17 dm3/h. That resulted in the exchange of the autoclave volume up to ten times per hour. The selected dissolved oxygen content was controlled for instance jn JRC IET by using West controller connected to solenoid valves at the autoclave inlet. Conductivity was maintained bellow 0.1 µS/cm by continuous pumping of inlet and outlet water through set of ion exchangers. In each of tests, Temperature and pressure in the autoclave, as well as flow rate and dissolved oxygen content, conductivity and pH at the inlet/outlet of the autoclave were continuously monitored and recorded.

2.4 Evaluation procedure

Specimens were always weighted before and after each heating sequence and the weight change per unit area was calculated. Standard analytical balance system Sartorius with 0.01 mg readability was used by JRC IET, while Mettler AT261 with a measuring uncertainty of

0.002% was used by VTT. The mass change per unit area was calculated using the specimen dimensions measured before testing. Besides that, the selected specimens were studied using scanning electron microscope (SEM) in conjunction with energy dispersive X-ray spectroscopy (EDX). EDX compositional analysis was performed, in order to obtain detailed information on oxide scale morphology and chemical composition. Following that, in order to get information on oxide thickness, its and bulk material microstructure the selected specimens were cross-cut approximately in the middle and sealed in conductive Bakelite resin.

3. Results and discussion

3.1 Effect of temperature and flow rate

Taking into account the extreme requirements given by designers of FQT, with for example the thickness of fuel cladding elements designed well below 1 mm, the current austenitic stainless steels licensed as nuclear materials can be utilized up to maximum 550°C. Understandably, the evaluation of the corrosion resistance of pre-selected alloys became one of the primary objectives within SCWR FQT project. Experimental program included two sets of long term exposures at two different temperatures 500 and 550°C in 25 MPa SCW with either 150 or 2000 ppb of dissolved O2 content. The influence of was found rather straightforward for 316L and 347H plane-milled coupon specimens. The summary of results is given in the plots of weight change respectively maximum oxide thickness versus exposure time in Figure 3.

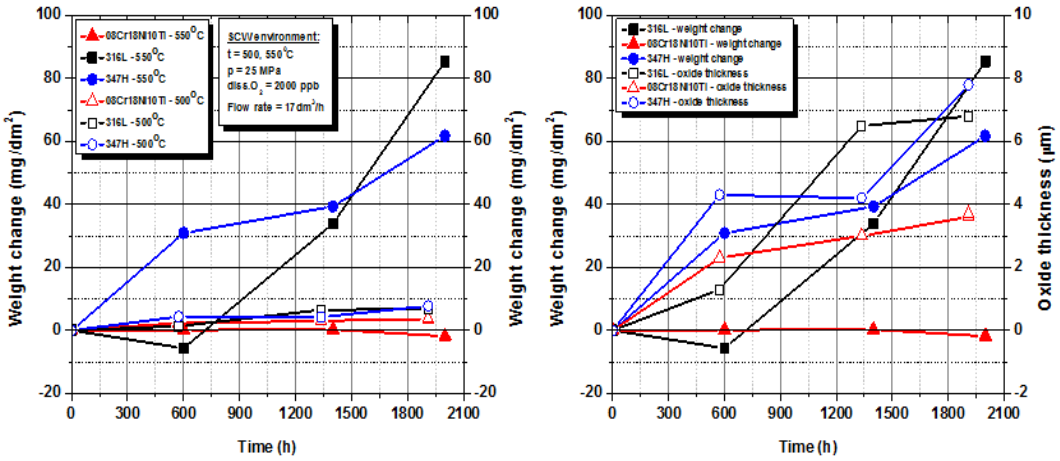

Figure 3. Plot of a) weight change and b) maximum oxide thickness b) as a function of exposure time obtained for 08Cr18Ni10Ti, 316L, and 347H plane-milled specimens after 600, 1400 and 2000 h long exposure to 500 and 550°C a) and 550°C b), 25 MPa SCW.

Obviously, the weight changes measured for 316L and 347H specimens in 500°C 25 MPa SCW were significantly lower than those measured at 550°C. Furthermore, those 316L specimens exposed in 550°C SCW exhibited higher tendency to oxide spallation compared to those of 347H already after first 600h long exposure. However, after second exposure, both stainless steels showed lower susceptibility to oxide spallation since weight gain values closely follows the trend of oxide growth expressed by maximum oxide thickness along the corrosion layer (see Figure 3b). Anyway, despite of that, for both 316L and 347H, the weigh change values very probably underestimated the real corrosion yield. Moreover, results of weight change analysis after the third 2000 h exposure show on rather linear growth of oxide layer with time. On the other hand, also this time weight change results clearly underestimated oxide layer growth expressed by maximum oxide thickness observed by SEM along the oxide layer. The

SEM cross-sectional images for 316L, 347H, and 08Cr18Ni10Ti specimens after 2000h long exposure in 550°C SCW with 2000 ppb of dissolved oxygen are presented in the Figure 4.

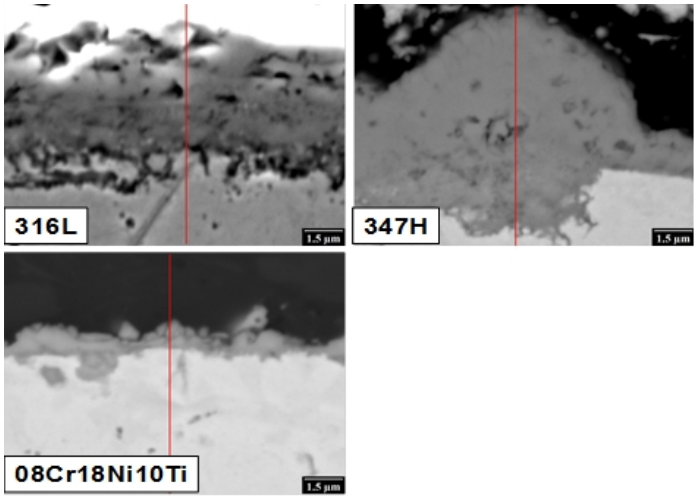

Figure 4. Cross-sectional SEM images of the specimens exposed 2000h in 550°C SCW with 2000 ppb of dissolved O2.

The SEM analysis confirmed that 316L specimens were the least affected by oxide spallation from all three tested materials. While the inner oxide of 316L specimen have already grew into uniform layer and the continuous oxidation followed pre-determined paths along the specimen surface at the inner oxide/base material interface, the layer of 08Cr18Ni10Ti coupons was substantially reduced probably due to spallation of the oxide from the surface. As regards as the 347H specimens, apart from the very compact layer, the sites with big blisters of oxides were observed on the surface. This could finally lead in longer term to oxide spallation and following that initiation of pitting and at the highly stressed sites even e.g. to SCC initiation. Furthermore, EDX line scans were taken for each of material, after every heating sequence i.e., after 600h, 1400 and 2000h exposure, in order to determine the chemical composition across the oxide scales and to identify the interface between outer and inner oxide sub-layers. The example of EDX line scans after 2000h long exposure is for 316L and 347H presented in Figure 5.

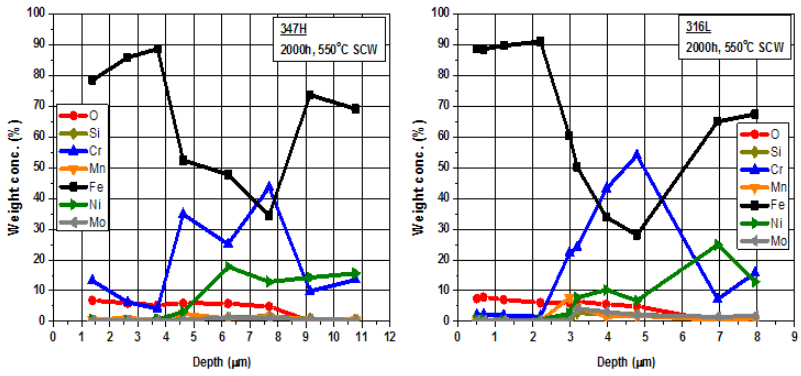

Figure 5. EDX line scans across the oxide layers of a) 347H and b) 316L08Cr18Ni10Ti specimens after 2000h long exposure in 550°C SCW.

For both materials (see Figure 5), EDX revealed double layer oxide approximately 6.5 µm (316L) and 8 µm (347H) thick with the chemical composition typical for Fe-rich outer oxide and

Cr-enriched inner Fe-Cr oxide. The oxide scale grew predominantly due to diffusion of Cr from the base metal into the protective inner Cr-enriched Fe-Cr oxide thus effectively preventing penetration of Fe to the outer layer, which resulted in decrease of corrosion rate. In contrast to 316L specimens, 8 µm large bristles were occasionally found along the surface of the 347H specimen exposed 2000h (see Figure 5). The following examination performed on one of these locations revealed different chemical composition, in particular as regards as the inner oxide, Ni was found to be almost two times enriched in the bristle compared to the locations with uniform film where Ni was enriched at the interface between inner oxide and base material. However, when the EDX line scans, obtained for 08Cr18Ni10Ti specimens after 2000h exposure, were compared to those of 316L and 347H, clearly significantly thinner Cr-enriched inner Fe-Cr oxide was observed in the corresponding EDX spectra. Consequently, the thinner and less protective inner oxide could be one of the reasons why 08Cr18Ni10Ti material seemed to be more sensitive to oxide spallation than the other two austenitic stainless steels. In summary, 316L coupons exhibited the highest resistance to oxide spallation from all three tested stainless steels. In contrast, 08Cr18Ni10Ti specimens showed much lower resistance to oxide spallation than the other two stainless steels since the values of measured weight changes in 550°C SCW remained very close to those measured in 500°C SCW. Nevertheless it must stressed, that for all three tested alloys, weight change values constantly underestimated the real oxide layer growth.

Based on the results of the first sets of tests, in particular in terms of the susceptibility to oxide spallation, further question was raised to what extent flow rate influences general corrosion and oxide spallation and to what extent results obtained by different laboratories are comparable. It is well known that flow rate belongs to major factors affecting attack by a corrosive medium. For example, Ruther [9] observed that at 600°C and 650°C the measured corrosion rate of electropolished annealed type 304 stainless steel decreased with increasing time during 80 day static tests. On the other hand, the corrosion appeared more linear with time in dynamic tests at 650°C. Certainly, the expected flow rates used in the fuel qualification test device will be considerably higher than those simulated in the laboratory conditions. Therefore, general corrosion tests in 550°C 25 MPa SCW at two different flow rates 5 dm3/h respectively 17 dm3/h up to 1200 h respectively 1400 h (see Figure 6) were conducted.

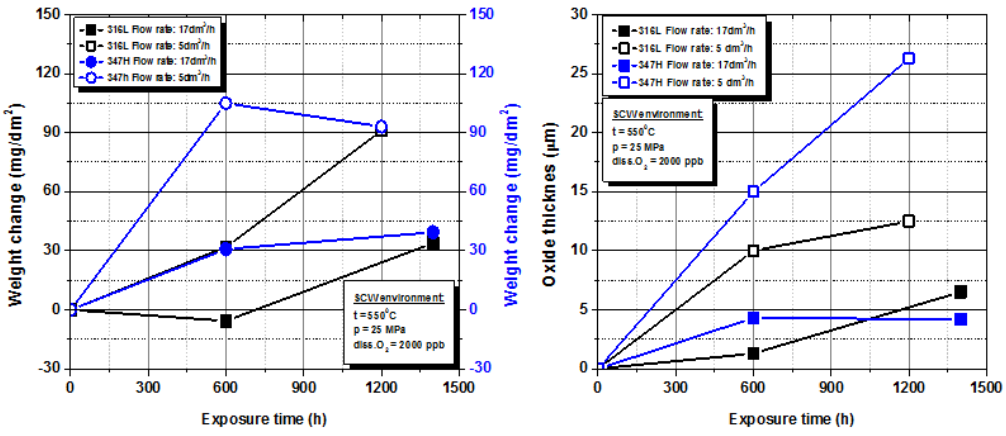

Figure 6. Plot of a) weight gain and b) maximum oxide thickness as a function of exposure time obtained for 316L and 347H plane-milled specimens after 600 and 1200h long exposure to 550°C 25 MPa SCW with 2000 ppb of dissolved oxygen content.

The results of weight change measurement shown in Figure 6 are for both steels rather surprising. These results prove that weight change values measured at higher flow rate 17 dm3/h clearly underestimated, due to mentioned higher tendency to oxide spallation, oxide layer growth. This finding is further confirmed when those results of maximal oxide thickness

were compared in Figure 6b. While 316L consistently exhibited, in line with weight change measurement, almost constant ratio of oxide layer thickness between that measured at higher flow rate and at lower flow rate, 347H showed substantial growth of that ratio at higher flow rate despite the fact that measured weight change values indicated rather weight loss than weight gain after 1200h long exposure. SEM examination revealed, in line with the previous statement, the thicker oxide layers were (approximately 10 µm for 316L respectively 15 µm for 347H) for those specimens exposed in the test with lower flow rate 5 dm3/h despite of shorter exposure time. The SEM cross-sectional images for those 316L and 347 specimens exposed either 1200h in 550°C SCW with flow rate 5 dm3/h are presented in the Figure 7.

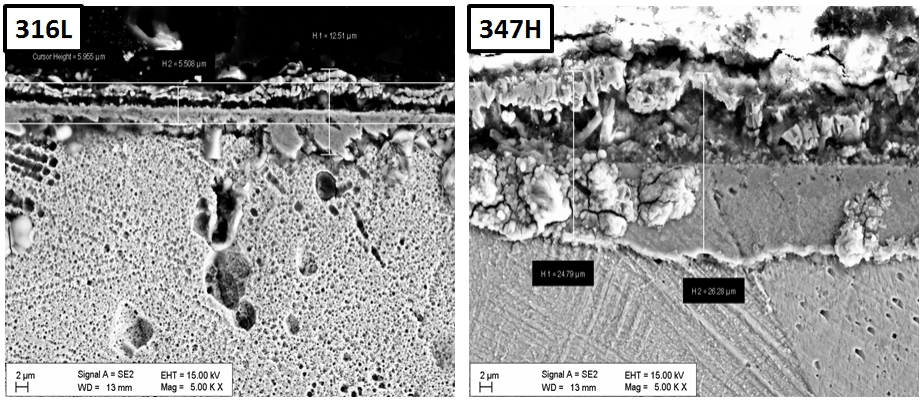

Figure 7. Cross-sectional SEM images of the specimens exposed 1200h in 550°C SCW with 2000 ppb of dissolved O_2 with flow rate equal to 5 dm3/h.

This is another prove that weight change values heavily underestimated the real corrosion rate. Although, it cannot be excluded, also in the test at lower flow rate, weight change values most probably underestimated the real corrosion rates particularly for 347H specimens. On the other hand, SEM examination presented in Figure 7 indicates less homogenous layer rather for 316L than for 347H specimens. The following EDX analysis (see Figure 8) again confirmed double layer oxide with the chemical composition typical for Fe-rich outer oxide and Cr-enriched inner Fe-Cr oxide.

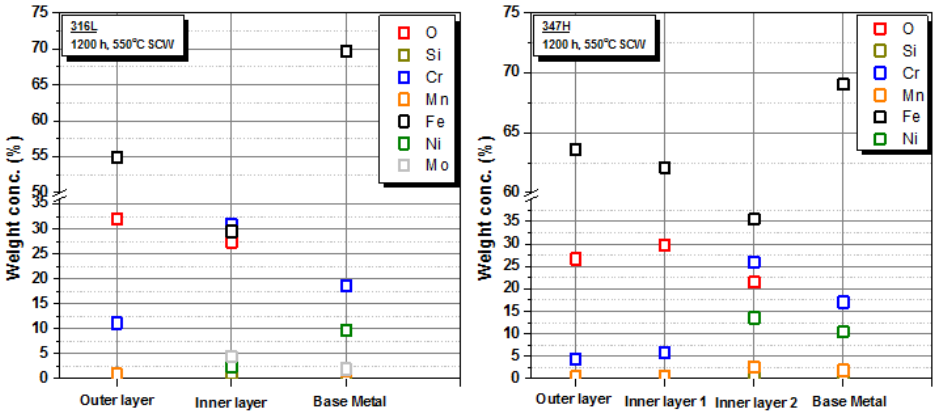

Figure 8. EDX point scans were taken at three different locations across the oxide layers of a) 347H and b) 316L specimens after 1200h long exposure in 550°C SCW.

3.2 Effect of water chemistry

Water chemistry strategy has not been yet determined for any of SCWR concepts. This aspect is becoming more and more important and research in this area intensifies. In general, two strategies are considered based on those applied in current BWRs; Normal water chemistry (NWC) where ultrapure water with up to 300 ppb of dissolved oxygen content is used or hydrogen water chemistry (HWC) where ultrapure water with 25-50 cc/kg is used. Understandably, optimization of water chemistry for fuel qualification test was one of the most important objectives of the SCWR FQT project. Within this task, sets of corrosion exposures were performed in VTT and SJTU in 550^{o}C, 25 MPa SCW but with lower 150 ppb of dissolved O2 content (VTT) respectively with 1.5 ppm of dissolved H2 content (SJTU). It should be mentioned that based on the conclusions made in the previous sub-chapter it must be kept in mind that VTT and SJTU tests were performed at lower flow rate (5 dm^3/h) than that of JRC IET (17 dm^3/h). The plots of weight change versus exposure time are presented in Figure 9.

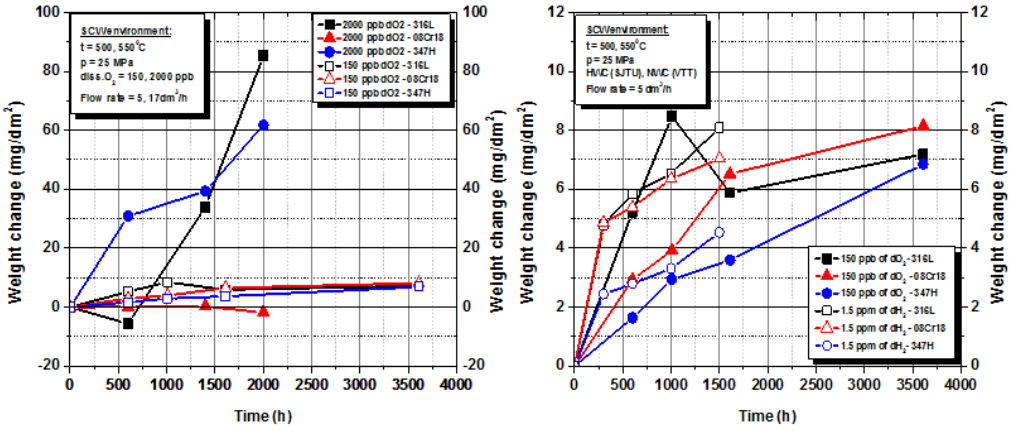

Figure 9. Plots of weight change as a function of exposure time obtained for 08Cr18Ni10Ti, 316L and 347H specimens after exposure to 550^{o}C, 25 MPa SCW with a) 2000 ppb of dissolved O_2 content (JRC IET), a, b) 150 ppb of dissolved O2 content (VTT) and b)1.5 ppm of dissolved H2 content (SJTU).

In summary, if both corrosion tests conducted in 550^{o}C SCW with either higher or lower oxygen content were compared (see Figure 9), the obvious negative effect of high dissolved oxygen content on corrosion resistance could be observed for both 316L and 347H specimens after 2000h (JRC IET), respectively 3610 h (VTT) long exposures. Furthermore, in the test in SCW dosed with 150 ppb of dissolved oxygen content significant decrease of susceptibility of all three tested stainless steels to oxide spallation, even if, in this context, the flow rate effect can't be separated. As illustrated in Figure 9b, for all three stainless steels, weigh change values increased linearly with exposure time. Regarding the test in HWC SCW (1.5 ppm of dissolved H2 content) hydrogen water chemistry did not bring any additional benefit in terms of corrosion rate compared to NWC conditions (see Figure 9b). When those results presented in Figure 9b are analysed, one can observe that not only that similar weight change values were measured in both NWC and HWC conditions but also similar weight change rates were obtained for all three materials. This observation was further confirmed with SEM images, as it is illustrated in Figure 10 (NWC- VTT) respectively in Figure 11 (SJTU-HWC).

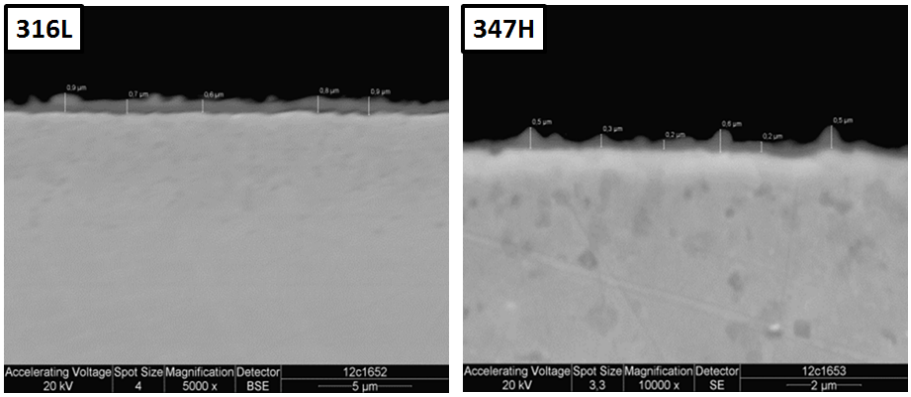

Figure 10. Cross-sectional SEM images of a) 347H and b) 316L specimens after 3610 h exposure to 550ºC/25MPa NWC SCW.

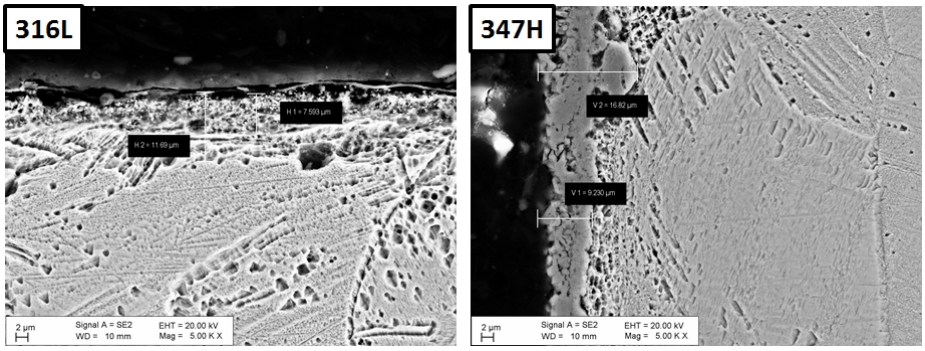

Figure 11. Cross-sectional SEM images of a) 347H and b) 316L specimens after 1500 h exposure to 550ºC/25MPa HWC SCW.

In agreement with low weight change values, SEM images (see Figure 10) for both alloys showed thin (<1 µm) and uniform oxide films 550^{o}C NWC SCW even after much longer exposure time 3610 h compared to that in other sets of tests. In contrast to those specimens tested in SCW with higher 2000 ppb of dissolved oxygen content (see Figure 4), the oxide layers appear uniform without any signs of paths of preferential oxidation penetrating into the materials. As already mentioned above, tests in 550^{o}C HWC SCW conditions did not bring any improvement of corrosion resistance compared to that in NWC SCW. In fact, quite opposite can be observed, when across-sectional SEM images in Figure 10 and 11 were compared. The EDX line scans were again taken through the cross sections of 316L respectively 347h specimens exposed in both NWC and HWC SCW. However, due to the very thin oxide layer, any specific layer structure could not be distinguished by EDX

3.3 Effect of surface finish

The fact that Surface finish has significant effect on corrosion resistance of materials in high temperature applications has long been recognized [8], for instance, electropolishing is recommended to reduce corrosion and activity build-up in the current nuclear power plants. Differences in corrosion rate between specimens that had been electropolished, pickled, or abraded using 400 grit abrasive paper were reported [10], the behavior reversing above and below the critical point. This reversal in behaviour is supported by the work of Ziemniak et al. [11] who reported that in subcritical water at high temperatures, treatments that remove cold work reduce the general corrosion rate. Since optimization of surface finish procedure can have significant effect on corrosion resistance, three surface finish procedures were studied within SCWR FQT project with the main objective to identify the most promising approach: plane-

milling, polishing and sand-blasting. All three surface finish procedures are described in detail in subchapter 2.2. Within SCWR FQT, only limited number of exposures was performed for 316L and 347H specimens as the best performers in the previous tests In total, two 600h long corrosion exposures in 550°C 25 MPa SCW with 2000 ppb of dissolved oxygen content at flow rate equal 5 dm^3/h were performed. The results of weight change analysis are presented in Figure 12.

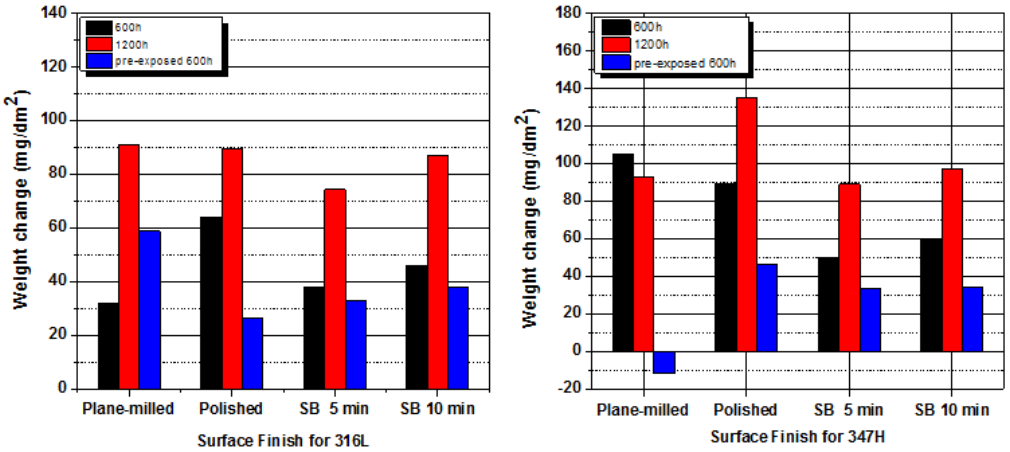

Figure 12. Plots of weight change vs. surface finish procedure after either 600h or 1200h long exposure were obtained in 550° 25 MPa SCW with 2000 ppb of dissolved O2 content for a) 316L and b) 347H austenitic stainless steels coupon specimens.

In total, three types of specimens have been analyzed; those exposed for 600h in the first test, those exposed for 1200h and finally those examined after the first 600h long exposure following that returned back to the autoclave and exposed for additional 600 h in order to investigate the effect of pre-oxidation. Surprisingly, weight gain analysis revealed rather different behaviour for both tested materials. While 316L coupons with plane-milled surface exhibited the lowest weight change values after the first 600h, the 347H coupons with plane-milled surface showed even higher weight change values than those of polished ones. After 1200h, for both materials, plane-milled specimens exhibited either significant increase of weight change values as those of 316L or even weight loss as those of 347H. In contrast, polished specimens of both materials showed decrease of weight change values, however in this case oxide spallation can't be excluded. The sand-blasted specimens exhibited consistently the best corrosion resistance in SCW for both materials even after 1200h exposure to 550°C SCW. It also became obvious, that optimization of the procedure itself will have substantial impact on corrosion resistance of materials in given environment. However, the most important question is whether the selected surface finish can guarantee the sufficiently consistent corrosion resistance in the long term in the range of at least several thousand hours. In conclusion, care must be taken when specifying a surface finish for SCWR core materials. On the top of that, it must be taken into account that the core inlet temperature for all SCWR concepts is below the critical temperature which makes the selection of the best surface finish method even more complex.

4. Conclusions

The presented results indicate that acceptable corrosion resistance is for materials such as 316L and 316Ti with mill-annealed surface finish limited to 500°C. It is obvious that 550°C is too high temperature for mill-annealed austenitic stainless steels with 15-19% of Cr. On the other hand, surface cold work resulting from plane-milling gives an adequate general corrosion

resistance even at high dissolved oxygen content up to 2000h (JRC IET) and at low oxygen content up to 3610h (VTT), respectively. There are several reasons why these results should be treated with care. First of all, with the higher oxygen content, which was further strengthened with the several heating-cooling steps (induction of thermal stresses due to differences in thermal expansion coefficient (CTE) of the metals and oxides), the tendency to oxide spallation became much higher. This can lead to errors in interpretation of measured results i.e., the decrease of weight gain rate and even weight loss is measured rather than increase of weight gain rate. Furthermore, as already mentioned in the previous sub-chapter, corrosion and tendency to oxide spallation in high temperature water or SCW is also affected the velocity of SCW water flow. Therefore, the results of JRC IET could be more affected than those of VTT, due to significantly higher flow rate 17 dm3/h applied in JRC IET corrosion tests compared to that of VTT (5 dm3/h). However, plane-milling is not an applicable method for fuel cladding or other components with sub-millimetre wall thicknesses. In this case, either sand blasting, shot peening or cold work version of 316L austenitic stainless steel that licensed as nuclear material may be acceptable solution. At 500^{o}C, the general corrosion resistance is adequate for both plane-milled (all tested materials) and also with mill-annealed 316L based on currently and previously obtained results. The critical temperature seems to be between 500 and 550^{o}C for mille-annealed austenitic stainless steels at least up to 3610h.

References

1. G. Was, P. Ampornrat, G. Gupta, S. Teysseyre, E. West, T. Allen, K. Sridharan, L. Tan, Y. Chen, X. Ren, and C. Pister, Corrosion and stress corrosion cracking in supercritical water, Journal of Nuclear materials, 371, 176 (2007).

2. T. Schulenberg, J. Starflinger, P. Marsault, D. Bittermann, C. Maráczy, E. Laurien, J.A. Lycklama à Nijeholt, H. Anglart, M. Andreani, M. Ruzickova, A. Toivonen, European supercritical water cooled reactor, Nuclear Engineering and Design 241 (2011) 3505-3513.

3. R. Novotny R., P. Hähner, J. Siegl, P. Hausild, S. Ripplinger, S. Penttilä, A. Toivonen, Stress Corrosion Cracking Susceptibility of Austenitic Stainless Steels in Supercritical Water Conditions, Journal of Nuclear Materials, Vol. 409, No. 2, pp. 117-123

4. V.I. Prokhorov, F.V. Risovanaya, Properties of the 08Cr18Ni10Ti steel as a construction material for nuclear reactors, Russian Federation Agency on Atomic Energy, Federal State Unitary Enterprise, State Scientific Centre of Russian Federation, The Research Institute of Atomic Reactors, 2005.

5. C.N. Spalaris, Finding a corrosion resistant cladding for superheater fuels, Nucleonics, Vol. 21, #9, 1963.

6. Ruzickova M., Hajek P., Smida S., Vsolak R., J. Petr, Kysela J., Supercritical water loop design for corrosion and water chemistry tests under irradiation, Nuclear Engineering and Technology - Special Issue on SCWR, Vol. 40, No. 2, November 15, 2007, pp. 127-132.

7. J. C. Griess, J. M. Martin, A. E. Mravca, R. J. Impara and S. Weems, Task force review on feasibility of bonus reactor stainless steel clad superheater materials, GNEC 257, 1963.

8. P. Berge, Importance of surface preparation for corrosion control in nuclear power stations, Materials Performance 36, 1997, 56-62.

9. W.E. Ruther, R.R. Schlueter, R.H. Lee, R.K. Hart, Corrosion behaviour of steels and nickel alloys in superheated steam, NACE - International Corrosion Conference Series (1965).

10. T. Maekawa, M. Kagawa, N. Nakajima, Corrosion behaviour of stainless steel in high temperature water and superheated steam, Trans. Jpn. Inst. Metals 9 (2), 130-136, (1968 0

11. S.E. Ziemniak, P.A. Guilmette, H.M. Tunison, Oxidative dissolution of nickel metal in hydrogenated hydrothermal solutions, Corrosion Science 50 (2), 449-462

12. S. Penttilä, A. Toivonen, L. Heikinheimo, Corrosion studies of candidate materials for European HPLWR", Nuclear Technology, 170 No. 1, 2010, pp. 261-271.

ISSCWR7-2078

European Project "Supercritical Water Reactor – Fuel Qualification Test" (SCWR-FQT): Results of SCC susceptibility tests

Radek Novotny[1, 3], Přemysl Janík[1], Aki Toivonen[2], Anna Ruiz[1], Zoltan Szaraz[1], Jan Siegl[3], Petr Haušild[3], Sami Penttilä[2]

[1] European Commission, Joint Research Centre, Institute for Energy and Transport
Westerduinweg 3, 1755 LE, Petten. Netherlands
+31224565357, Pardubra@gmail.com
[2] VTT Technical Research Centre of Finland, materials Performance in New Energy technologies Finland
[3]Czech Technical University Prague, Faculty of Nuclear Sciences and Physical Engineering, Czech republic

Abstract

The main target of the HPLWR Phase 2 follow-up FP7 project "Fuel Qualification Test for Super Critical Water Reactor" is to make significant progress towards the design, analysis and licensing of a fuel assembly cooled with supercritical water in a research reactor which also includes the material research on those in-core materials which could be licensed in near future. In frame of WP4 - Pre-qualification, stress corrosion cracking (SCC) resistance of three selected austenitic stainless steels 08Cr18Ni10Ti (equivalent of AISI 321), AISI 347H and AISI 316L was investigated by conducting slow strain rate tensile tests in an autoclave in 550°C supercritical water. SCC susceptibility was evaluated using three criteria: loss of mechanical properties compared to those in inert environment, fractographic analysis of the fracture surfaces and finally analysis of secondary cracks. Obtained results were compared to those available in the literature and utilization of these results is discussed. Based on the results of SSRT tests and following fractographic analysis, 316L was selected as the best performer.

1. Introduction

The scope of WP4 is pre-qualification of the fuel qualification test (FQT) loop test section by means of designing, building and operating a similar electrically heated test section, as well as pre-qualification of all critical components of the FQT loop. For both, the pre-qualification and FQT loop test sections, the critical issue is the cladding material for fuel rods. The selection of candidate materials was carried out taking into account the following criteria; these materials must be commercially available in nuclear grade (Ni-base alloys and austenitic stainless steels) and previously evaluated as promising cladding candidates. Based on the available data from literature several material candidates were pre-selected including Ti-stabilized 08Cr18Ni10Ti (Russian production, equivalent to 321), Nb-stabilized 347H and low carbon 316L austenitic stainless steels.

Stress corrosion cracking (SCC) was identified as one of the degradation mechanisms which potentially could cause unexpected failure of the FQT facility. To date, investigations have in majority of studies focused only on the susceptibility to SCC initiation in supercritical water [1]. According to ASTM standard G129, SCC susceptibility is indicated by a decrease in mechanical

properties (e.g. strain to failure, ultimate tensile strength, and reduction in area) over those observed in an inert environment and, in some cases, the presence of secondary cracking along the gage length of the specimen. A major advantage of slow strain rate tensile (SSRT) technique over constant load or deflection techniques is that the test period is generally shorter with the SSRT technique. SSRT technique also avoids the problem of specifying a test time. For example, if cracking is not observed in a 1000-hour test period with U-bend specimen, would it occur in 1500 hours? With the SSRT technique the specimen is generally strained to failure and the test duration itself provides an indication of cracking susceptibility. The SSRT technique is also much less costly than fracture-mechanics crack propagation since the specimen geometry and test procedures are generally simpler with SSRT technique. While the SSRT technique has been shown to be a useful tool for SCC testing, recent laboratory results may indicate problems with the technique for at least some alloy-environment systems. Specifically, it has been discovered that results from SSRT tests do not display cracking in the environment where SCC is known to occur in field conditions or with other tests methods such as U-bend tests. There are number of possible explanations for the apparent discrepancy between SSRT and constant load and constant strain test results. These include incubation time effects, potential range effects, strain rate effects etc. Unfortunately, the evaluation of SSRT test is not always straightforward. For example, Was et al. [2] investigated SCC susceptibility in SCW for several pre-selected alloys including austenitic stainless steels 304, 316, 316L, 347 and UNS S31266. Was critically reviewed the available SSRT results and he observed two trends depending on how the cracking behaviour was characterised. While the %IG on the fracture surface as a measure of SCC susceptibility was used for instance by Tsuchyia et al. [3], Was et al. [2] used the crack depth and the crack density on the gage surface as an indicator of the IGSCC susceptibility. Unfortunately, these measures were not always in agreement. Consequently, in this study, both approaches were utilized in order to evaluate SCC susceptibility of pre-selected alloys in supercritical water.

2. Materials, test specimens and test procedure

2.1 Materials

Three grades of austenitic stainless steels 347H, 08Cr18Ni10Ti (equivalent 321) and 316L, licensed for light water reactor applications, have been selected for SCC susceptibility SSRT tests. The chemical composition of the studied steels is given in Table 1.

Table 1. Chemical composition of all three pre-selected materials.

Material	**C**	**Si**	**Mn**	**S**	**P**	**Cr**	**Ni**	**Others**
316L	0.022	0.65	1.86	0.001	0.030	16.6	10.12	Mo = 2.06
347H	0.048	0.29	1.84	0.013	0.026	17.6	10.70	Nb = 10xC_{min} to 1.0 max
O8Cr18Ni10Ti	0.085	0.45	1.07	0.009	-	18.0	10.00	Ti = 0.64

The 316L and 347H austenitic stainless steels were supplied in the form of plates by SOLOMON'S Metalen B.V. The Ti-stabilized 08Cr18Ni10Ti type stainless steel (equivalent to 321 SS) was supplied by OAO Saint-Petersburg, Russia, with the average grain diameter in a range from 0.031 to 0.015 mm.

As one of the objectives of SCWR FQT project, the data on high temperature mechanical properties of the pre-selected materials were collected from available material datasheets and literature [4, 5] and excel file containing data on all required physical and mechanical properties was prepared, in order to provide reliable material data for design and analyses (WP1, WP2

and WP3) of the test section. The plots of mechanical properties data - yield strength and ultimate tensile strength, in the range of temperatures up to 650°C are shown in figure 1.

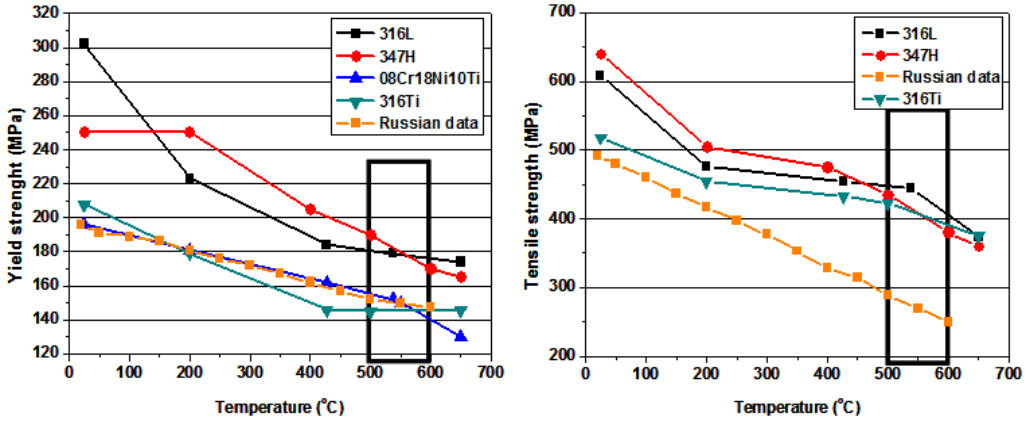

Figure 1. The plots of yield strength values and ultimate tensile strength collected from datasheets for the relevant range of temperatures required for the design of fuel qualification test section of pre-selected austenitic stainless steels. Russian data concerning 08Cr18Ni10Ti in both graphs were collected from [6].

2.2 Specimens and test procedure

Both JRC IET and VTT tensile specimens were manufactured and following that tested according to the standard practice: “Slow strain rate testing to evaluate the susceptibility of metallic material to environmentally assisted cracking” ASTM G129. The schematic drawings of round shape tensile specimen (JRC IET) and flat tensile specimens (VTT) are shown in figure 2.

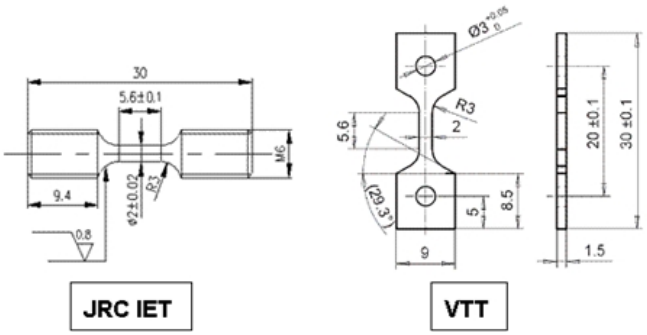

Figure 2. Schematic drawing of the tensile specimens tested in JRC IET and VTT SCW autoclaves.

Both types of tensile specimens were tested in ultra-pure supercritical water solution with an electric conductivity of less than 0.1 µS/cm measured at the autoclave inlet. Flow charts of both JRC IET and VTT SCW loops were previously described in detail for instance in the following articles [7, 8]. In this study, the specimens were tested in as-received condition, i.e. without additional heat treatment prior to the exposure to SCW environment. The specimens, electrically insulated from the loading grips, were first exposed at a constant pre-load 25±5 MPa to SCW environment for 24h. Following that, the specimens were strained with constant elongation rate of $5.2 \cdot 10^{-7}$ 1/s (JRC IET) and five times lower one of $1 \cdot 10^{-7}$ 1/s (VTT) until their failure. SSRT tests were performed in SCW at 500 and 550°C at JRC-IET and at 550°C at VTT.

Dissolved oxygen content in inlet water was continuously set and controlled on 2000 ppb in the tests performed at JRC IET respectively 150 ppb at VTT. Reference tests were conducted at the same temperature either in air (VTT, JRC IET) or in gaseous N_2 (JRC-IET).

2.3 Fractographic analysis

Fractographic analysis of failed specimens was carried out at VTT, JRC IET and at the Department of Materials of Faculty of Nuclear Sciences and Physical Engineering of Czech Technical University in Prague by using a scanning electron microscope (SEM), in order to identify: (i) failure mechanisms taking place during SSRT tests, (ii) influence of different testing conditions (i.e. temperature and oxygen content) on failure mechanism, (iii) evaluation of the ratio of SCC growth to ductile fracture on the failed specimen cross-sections. Fractographic analysis of the specimens exposed to high temperature aqueous environment is rather complicated task since fracture surface is very often, in particular after a long exposure, covered with rather thick oxide layers. Therefore a careful cleaning is needed before the fractographic analysis is carried out. In this project, the cleaning procedure consisted of the ultrasonic cleaning in a solution according to ASTM Standard (HCl + hexamethylenetetramine + water), followed by SEM to verify the efficiency of the cleaning. This procedure was applied in repetitive steps in order to avoid any spurious alterations of the fracture micromorphology.

3. Results and discussion

Overview and summary of the results are for all three alloys pre-selected within SCWR FQT project by both JRC IET and VTT presented in table 2.

Table 2. Summary of SSRT tests conducted in SCW and N_2 in JRC IET Petten and in SCW and air VTT. (* - tests performed by VTT at Lower strain rate: $1e^{-7}$ 1/s).

Specimen input data		Experimental conditions			SSRT tests results			SEM SCC indication	
		Env.	Temp.	Press.	Diss. O_2	time	σ_{max}	ε_{pl}	
Material	**Code**	-	^oC	MPa	ppb	h	MPa	%	
316L	F14-01	SCW	550	25	150	240.0	399	43.16	TG
	F14-02	SCW	550	25	2000	261.4	391	45.90	TG
	F14-05	SCW	500	25	2000	244.0	439	43.54	TG/IG
	F14-07	N_2	550	0.2	-	149.6	392	27.66	IG
	F14-08	N_2	25	0.2	-	359.4	566	67.62	Ductile
	F15-01*	SCW	550	25	150	1637	305	55.2	Ductile
	F15-02*	Air	550	0.1	-	1505	340	49.2	Ductile
347H	F24-01	SCW	550	25	2000	168.2	340	28.06	TG
	F27-09	SCW	550	25	2000	97.5	322	20.92	TG/IG
	F24-02	SCW	500	25	2000	184.0	389	31.55	TG
	F24-05	N_2	550	0.2	-	167.9	368	33.45	IG
	F24-07	N_2	25	0.2	-	376.0	598	70.85	Ductile
	F25-01*	SCW	550	25	150	837	307	24.10	TG
08Cr18	F34-01	SCW	550	25	2000	185.5	302	30.72	TG
	F34-03	SCW	500	25	2000	151.0	340	24.27	TG
	F34-05	SCW	500	25	2000	163.3	335	27.18	TG

	F34-07	N_2	550	0.2	-	108.0	304	19.03	IG
	F34-08	N_2	25	0.2	-	278.1	526	51.60	Ductile
	F35-01*	SCW	550	25	150	812	223	26.80	TG

3.1 SSRT tests in supercritical water

At least two SSRT tests for each of materials were conducted at selected conditions of supercritical water (see table 2). An example of stress–elongation curves measured in 500 and 550°C 25 MPa SCW in JRC autoclaves is presented in figure 3.

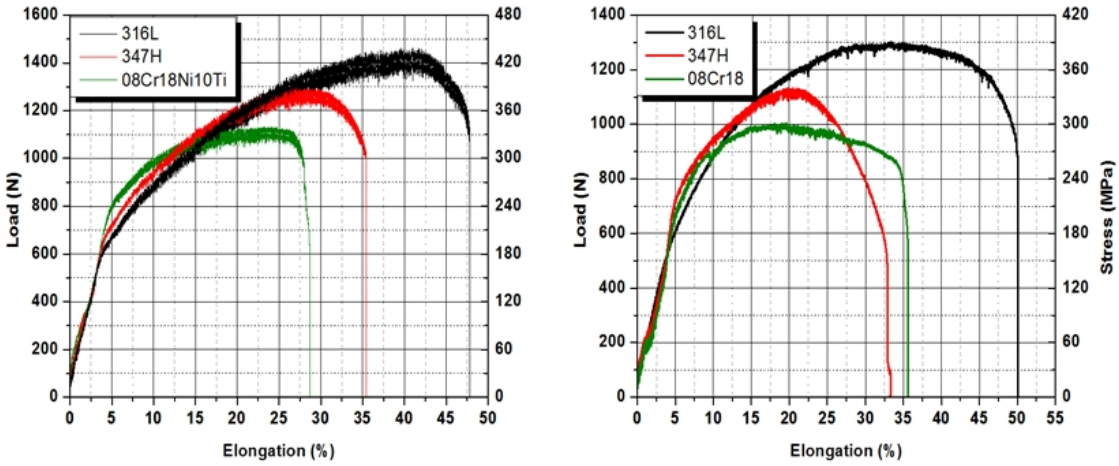

Figure 3. Stress-elongation curves obtained for selected stainless steels exposed in a) 500°C 25 MPa and b) 550°C 25 MPa SCW with 2000 ppb of dissolved O2 content.

As regards as the mechanical properties, the stress-elongation curves (see figure 3) clearly demonstrate the best performance of 316L specimens at both SCW temperatures. Not only that 316L exhibited the highest strain hardening capacity compared to that of 347H and 08Cr18Ni10Ti. Even if tendency to strain hardening was somewhat reduced with increase of temperature (see figure 3b), it still reached around 30-35% of total elongation for 316L specimens in 550°C SCW compared to 20% (347H) respectively 15% (08Cr18Ni10Ti) obtained for other two alloys. Furthermore, 316L specimens also had far the highest ductility at both SCW temperatures. In contrast to 316L, resistance to fracture of 347H specimens was lost rather quickly after reaching the maximum level of tensile stress which resulted in reduction of ductility. On the other hand, in case of 08Cr18Ni10Ti, the increase of SCW temperature caused significant change of behaviour. Although the values of measured elongation to fracture were found even higher (almost 10%) than that obtained in 500°C SCW, typically instead of strain hardening strain softening occurred with the tensile stress reaching its maximum around 15% of total elongation.

When evaluating the susceptibility to SCC, in order to compare the effect of an environment on mechanical properties for various materials, some quantification is required. In this study, parameters such as time to failure, the maximum load or stress and ductility represented by extent of plastic elongation/strain were compared for all alloys and test conditions, because they are either measured during the SSRT test or rather easily determined from test results. The values of time to failure, maximum stress and plastic strain are summarized for all three pre-selected alloys in table 2. As an example, the values of maximum tensile stress and plastic strain are compared for all tested materials in figure 4.

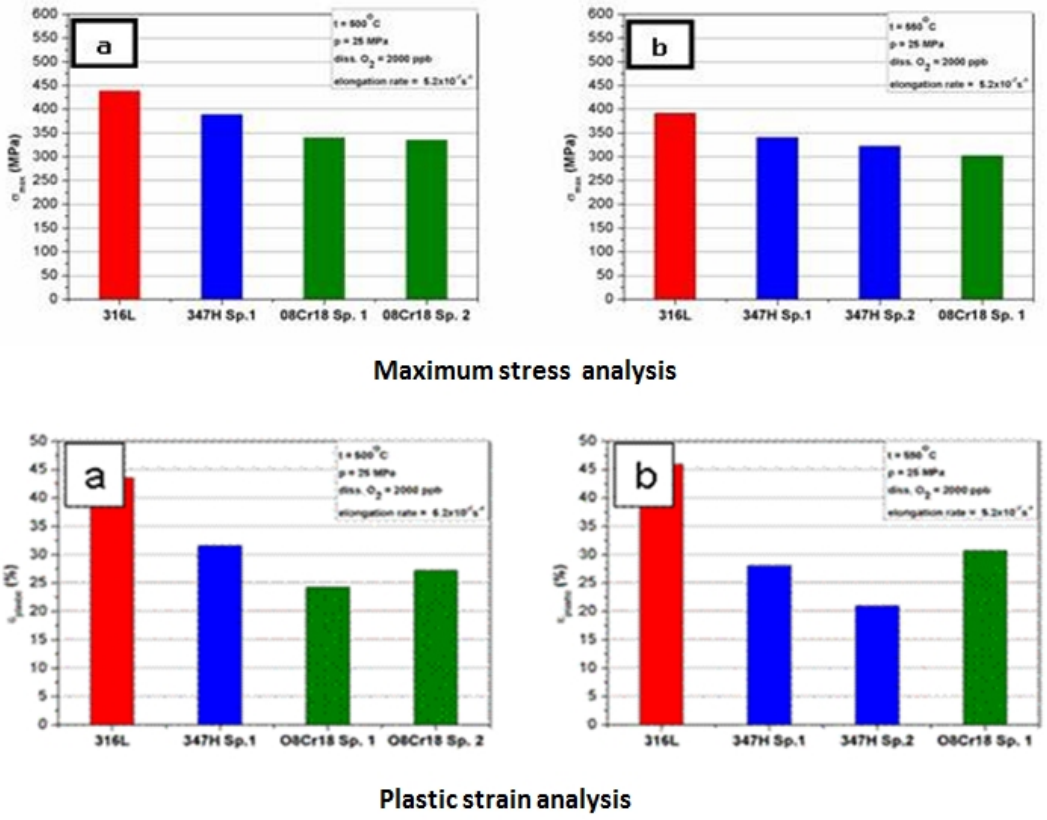

Figure 4. Plots of maximum stress and plastic strain after completion of SSRT tests performed in a) 500 and b) 550°C 25 MPa SCW with 2000 ppb dissolved O_2 content.

In summary, 316L exhibited the highest values of maximum stress in 550°C SCW from all three tested austenitic stainless steels. However, for all alloys, the results in figure 4 indicate further decrease of maximum stress which could be due to exposure in SCW environment. The highest values of plastic strain were calculated for 316L specimens at both SCW temperatures (see figure 4). Moreover, almost the same ductility expressed by plastic strain to fracture values (or percentage of elongation) was observed for 316L specimens after the SCW temperature was increased from 500 to 550°C. On the other hand, 347H specimens reached consistently lower plastic strain values at both SCW temperatures than 316L specimens. The 08Cr18Ni10Ti specimens showed similar properties however significantly lower values of plastic strain to fracture. In conclusion, the results in figure 4 shows that plastic strain for 347H specimens was more affected by the increase of SCW temperature from 500 to 550°C compared to other two materials.

3.1.1 Fractographic analysis

It should be mentioned that cleaning procedure described in the subchapter 2.4 had to be applied since the fracture surfaces were heavily oxidized due to exposure in SCW. Within post-test fractographic SEM examination, both approaches [2] how to evaluate tensile specimens exposed in SSRT tests were utilized, in order to determine the susceptibility of tested alloys to SCC:

1. Analysis of the fracture surface in order to identify a failure mechanism taking place in course of tests.
2. Cross-sectional analysis of the gage section where the occurrence and the length of secondary cracks and their mechanism of in particular initiation is evaluated.

In general, concerning to SCC susceptibility, fracture surfaces showed ductile appearance with “feathery” cleavage facets characteristic for transgranular SCC (TGSCC). However, only a few regions always close to the specimen surface were observed as it is for instance demonstrated in the SEM images in figure 5.

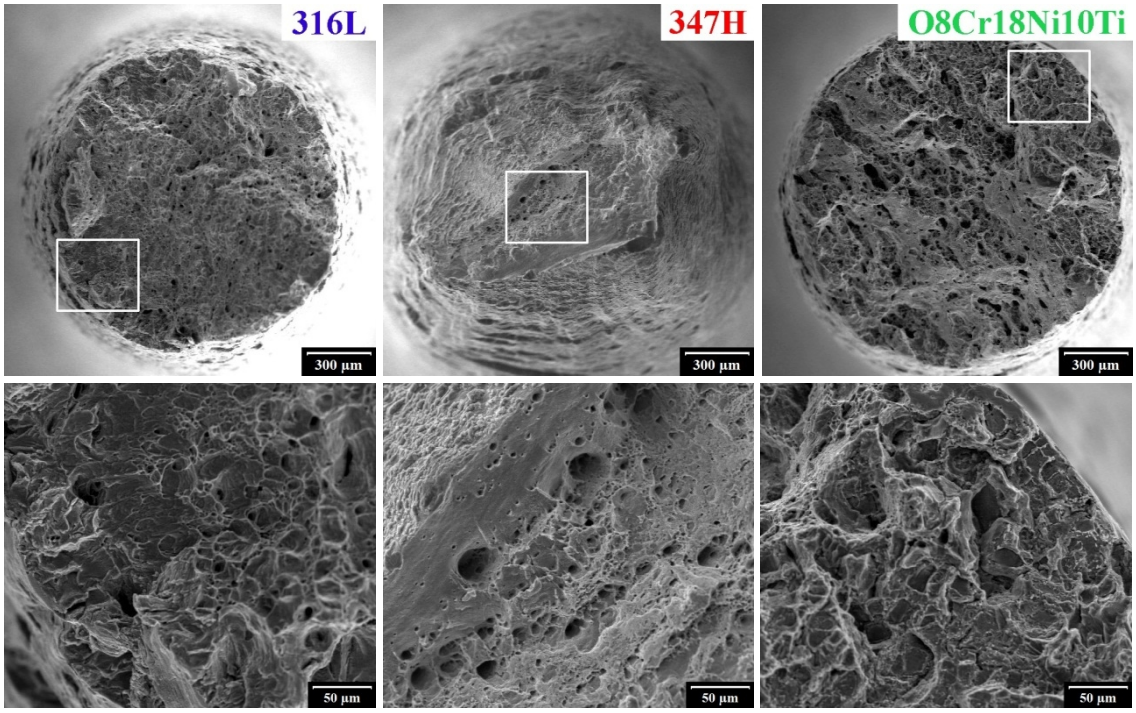

Figure 5. Fracture surfaces of a) 316L b) 347H and c) 08Cr18Ni10Ti specimens after the SSRT tests in 550°C 25 MPa SCW with 2000 ppb dissolved oxygen.

SEM examination showed that the initiated TG cracks grew only a few micrometers deep into the material until they were stopped. At current stage, it is not possible to determine with sufficient certainty why that happened. However, both continuous plastic deformation and fast oxidation at the crack tip are the most probable factors leading to crack blunting. Therefore, in the major part of the fracture surfaces, a dimpled morphology typical for failure by ductile fracture mechanism was observed. Only in few cases (see for example figure 6) also the initiation sites of intergranular SCC (IGSCC) in the range of only a few grains were found at the investigated fracture surfaces.

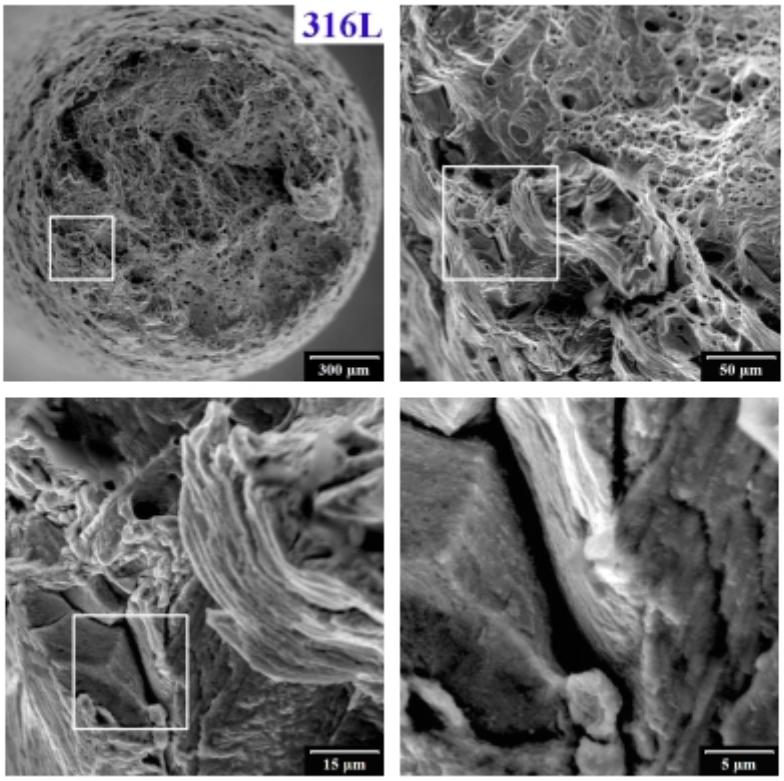

Figure 6. Indication of IGSCC on the fracture surface of 316L exposed to SCW at 500°C with 2000 ppb dissolved oxygen.

The gage sections of specimens 316L and 347H exhibited relatively big contraction, while that of 08Cr18Ni10Ti was nearly zero (see figure 5 and 7). For all three materials, it was observed that the values of the ratio of TG/IG SCC area to that of ductile fracture higher for those specimens exposed 550°C 25MPa SCW. Furthermore, for specimens tested at higher temperature of SCW, the increased susceptibility to SCC was further demonstrated by the localization of increased number of regions at the fracture surface where IGSCC was indicated. Even if the VTT specimens were loaded with five time lower elongation rate, SEM examination did not indicate any increase of areas with TG/IG SCC cracking. Within the second approach consisting of SEM analysis of the gage section, the occurrence and the length of secondary cracks and their mechanism of propagation were evaluated. SEM images including the details of the largest cracks for all three materials exposed in 550^{o}C SCW are shown in figure 7.

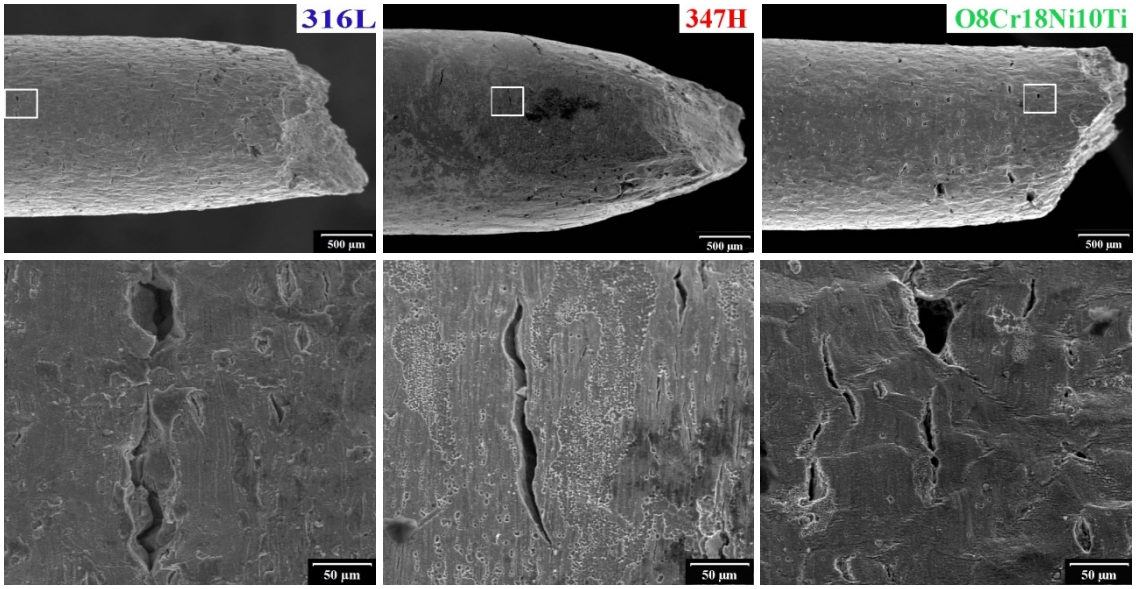

Figure 7. Secondary cracks observed on gage sections of 316L (a), 347H (b) and 08Cr18Ni10Ti (c) after SSRT tests conducted at 550°C in SCW with 2000 ppb of dissolved O2 content.

In this study, only qualitative analysis of secondary cracks was performed, i.e. occurrence of cracks along the specimen surface and their mechanism of growth. Although only few sites of TG/IG SCC initiation were found on the fracture surfaces of those specimens exposed in SCW, significant number of secondary cracks was observed along their gage sections. These cracks can be divided into two groups in dependence on the distance from the area of final fracture. The first group includes those cracks which were located close to the fracture area. Consequently majority of these cracks are TG cracks generated due to continuous loading significantly in extent of yield stress. On the other hand, the further from the fracture area the higher was the number of IG cracks along the gage section. In conclusion, these cracks were most probably initiated by SCC mechanisms.

3.2 SSRT tests in N_2 or in air

As mentioned above reference tests in inert environment were conducted first under 0.2 MPa N_2 overpressure at room temperature and following that at the same maximum temperature 550^{o}C as those tests performed in supercritical water (see figure 8).

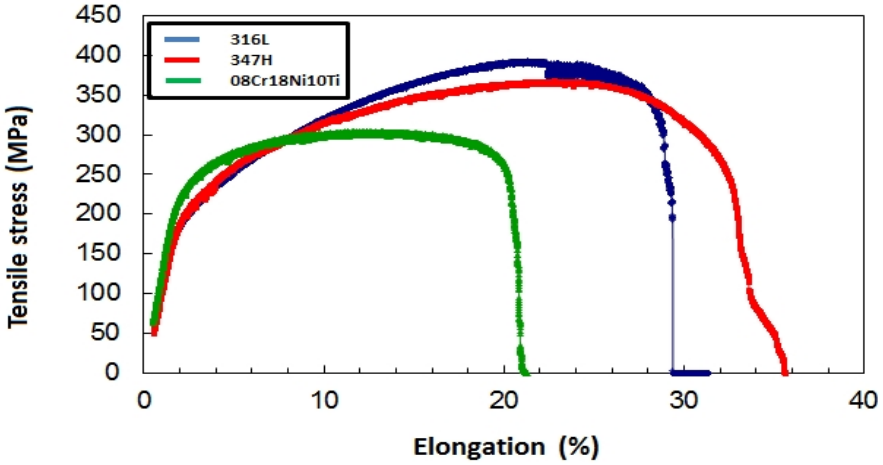

Figure 8. Stress-elongation curves obtained for selected stainless steels exposed in 550°C N2 atmosphere (99.99% pure N_2, 0. 2 MPa N_2 overpressure).

Hardly any detrimental effect of SCW environment was observed when the results of the tests performed at 550°C 25 MPa SCW (see figure 3) were compared to those obtained from tests conducted at the same temperature but under N_2 overpressure. In fact, in particular 316L and 08Cr18Ni10Ti tensile specimens showed rather different behaviour. For instance, in contrast to 347H specimen, both 316L and 08Cr18Ni10Ti exhibited unexpected significant decrease of plastic strain to fracture values in the tests in reference inert environment (see table 2). This surprising behaviour was the main reason why additional reference tests were conducted by both JRC IET and VTT at 550°C but this time in air. The measured stress-elongation curves did not indicate any decrease of resistance to fracture as it is demonstrated for example for 316L in figure 9.

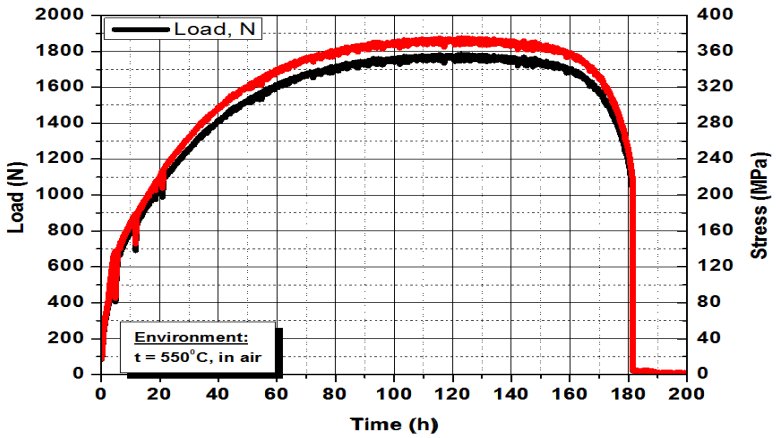

Figure 9. Stress-elongation curves obtained for 316L exposed in 550°C in air in JRC IET.

These findings further confirmed that the results of the previous reference tests in N_2 were affected by the test environment. However, it is not obvious what caused such dramatic change in their microstructure and reduction of mechanical properties. It needs to be mentioned, that very similar stress-elongation curves as that given in figure 9 were measured also in VTT in their tests where specimens were loaded with five times lower elongation rate than those in JRC IET.

3.2.1 Fractographic analysis

The SEM images of gage sections taken for those specimens exposed in 0.2 MPa N_2 overpressure in figure 10 revealed rather surprising findings.

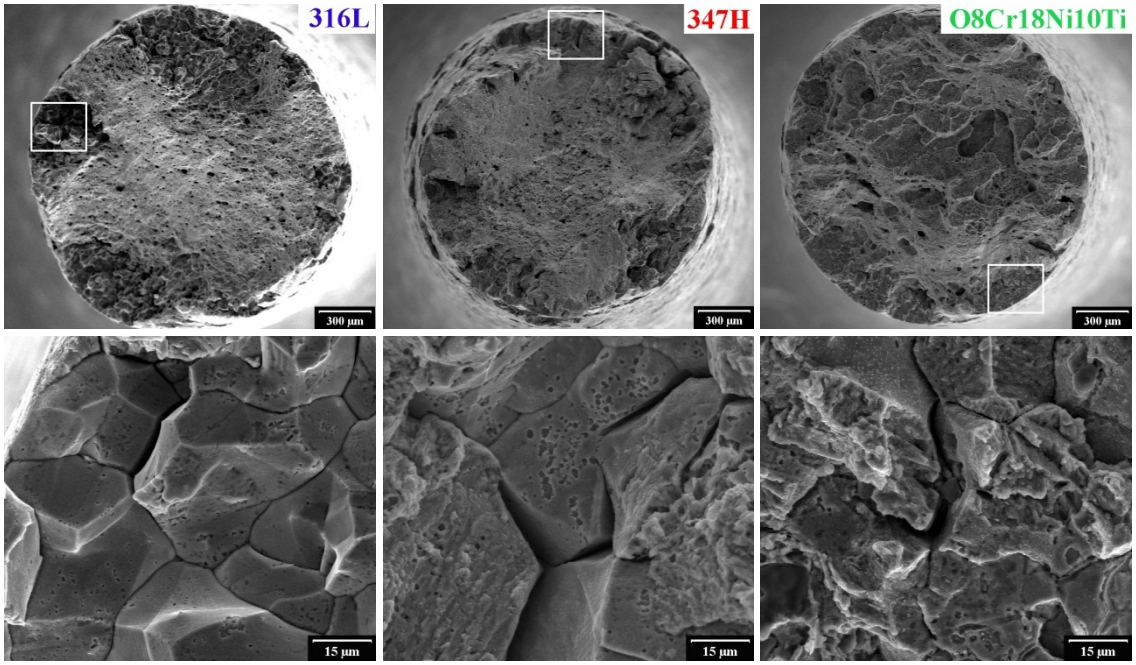

Figure 10. SEM images of fracture surfaces for a) 316L b) 347H and c) 08Cr18Ni10Ti specimens after the SSRT tests at 550°C in 0.2 MPa N_2 overpressure.

Surprisingly, all three specimens exhibited significantly higher susceptibility to IG cracking in the environment of 0.2 MPa N_2 overpressure than the specimens loaded with the same elongation rate in SCW at 550^{o}C 25 MPa with 2000 ppb of dissolved oxygen content. First of all, more regions of either TGSCC or IGSCC initiation were observed along the specimens' surfaces. Moreover, these regions were found to be much larger. The ratio of TG/IG SCC area to total fracture surface were 27% (316L), 21% (347H) respectively 20% (08Cr18Ni10Ti) as shown in figure 11.

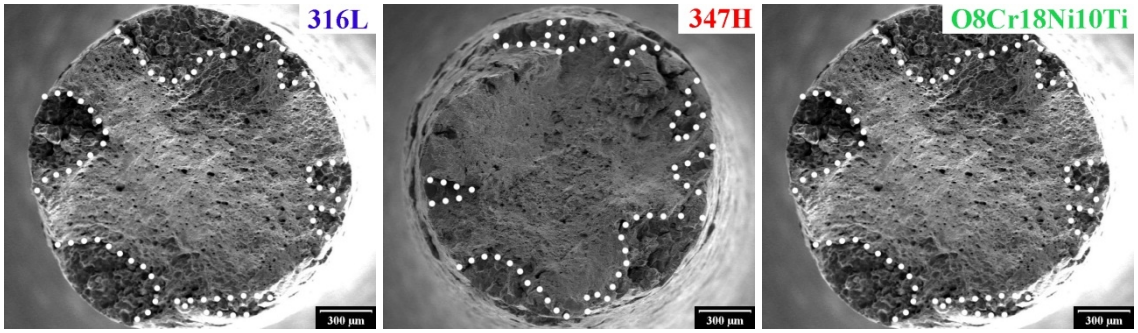

Figure 11. Regions of SCC morphology (outlined with dotted lines) observed on fracture surface of a) 316L b) 347H and c) 08Cr18Ni10Ti specimens after SSRT tests at 550°C in 0.2 MPa N_2 overpressure.

On the top of that, some of these regions exhibited pure IG cracking (see figure 12) considerable larger than those IGSCC regions that were observed on the fracture surfaces of those specimens tested in 550°C 25 MPa SCW (see an example in figure 6).

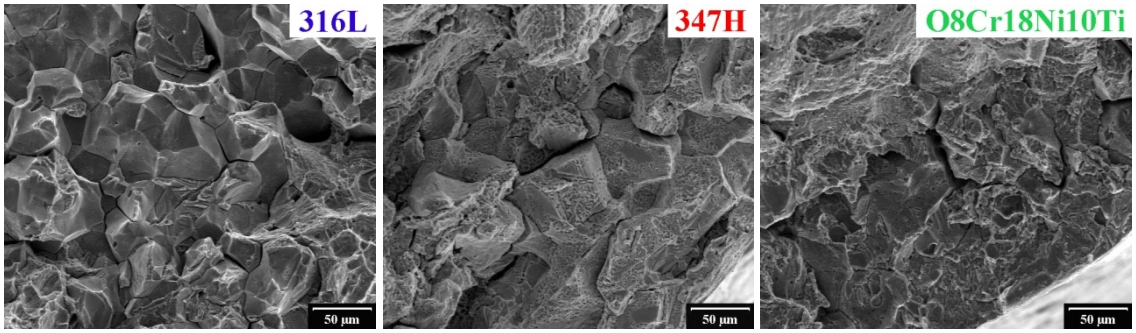

Figure 12. Regions of almost pure IG SCC found on the fracture surface of all three materials after the SSRT tests in N_2 at 550°C.

The gage sections of these specimens exhibited almost zero contraction compared to those exposed in SCW. Relatively big sharew of IG fracture facets was observed on both fracture surfaces (see figure 12) and faces of secondary cracks (see figure 13).

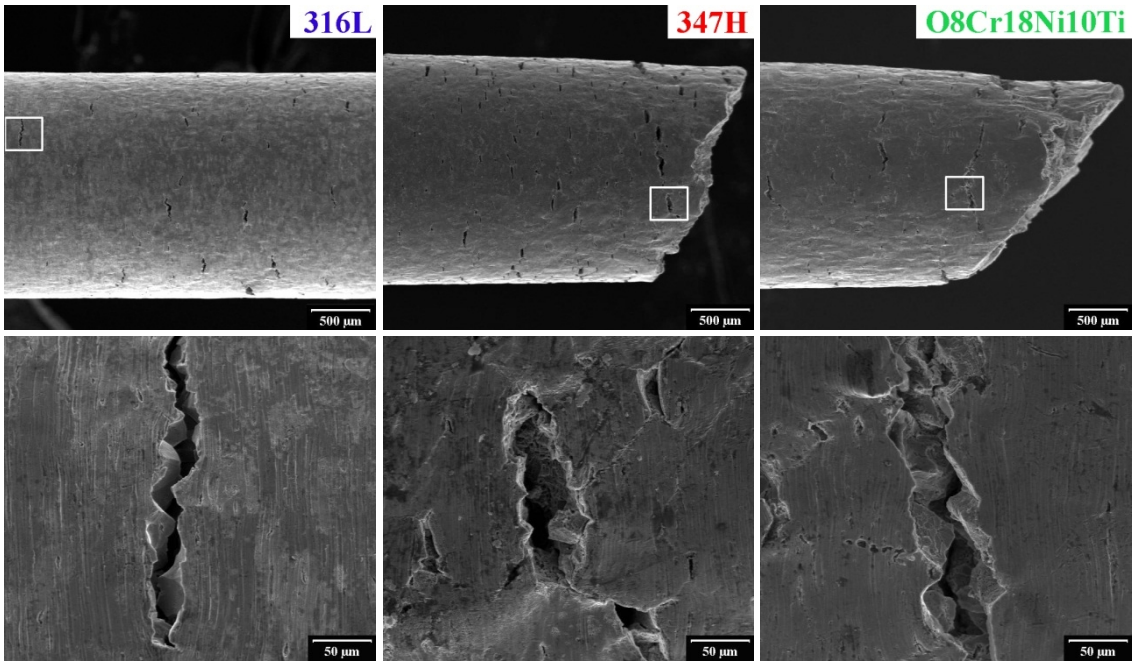

Figure 13. SEM images of gage sections for 316L, 347H and 08Cr18Ni10Ti after SSRT tests conducted at 550°C under 0.2 MPa N_2 overpressure.

Furthermore, the density of secondary cracks on the gage sections of these specimens was found to be significantly higher than on the specimens exposed in SCW environment. On top of that, many of these cracks apparently grew along the grain boundaries into the material similarly as IG cracks located far from the fracture area on the specimens exposed in SCW (see figure 10). This unexpected results obtained in the environment that is generally considered an inert one could be explained several ways. One of the possible explanation is that the used N_2 (6.0 quality) gas contained traces of impurities such as oxygen, carbon dioxide or water. The fact that the tests were conducted in the same autoclave where the SCW tests were performed

gives a possibility that the “inert” atmosphere could be also contaminated with moisture originating from the high pressure part of the loop. On the other hand, SEM images of specimens exposed at the same temperature 550^{o}C in air did not show any indication of IG cracking and only limited local occurrence of TG cracks on the main fracture surface (see figure 14).

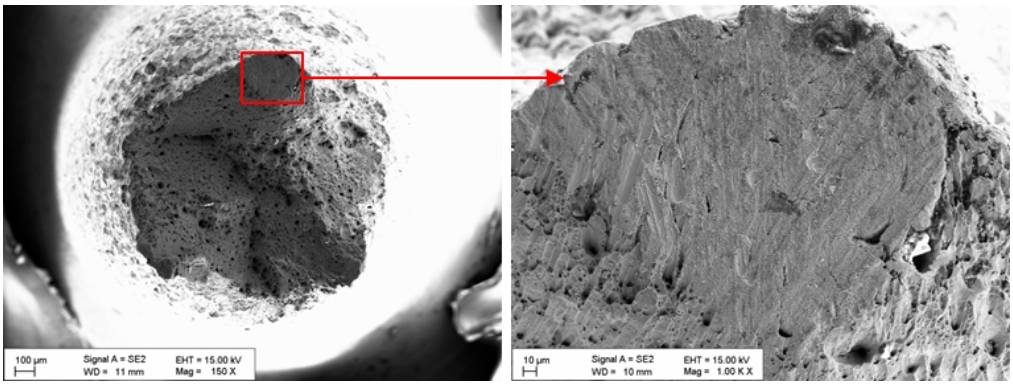

Figure 14. SEM images of fracture surfaces for 316L specimens after the SSRT tests at 550°C in air.

In agreement with our expectations, most of the fracture surface was covered with small dimples, which is typical for ductile fracture. Contrary to the SEM images of gage sections (see figure 13) for those SSRT specimens tested under N_2 atmosphere, SEM images of for instance that of 316L exposed in air at 550^{o}C showed typical cup and cone appearance and almost 50% contraction (see figure 15).

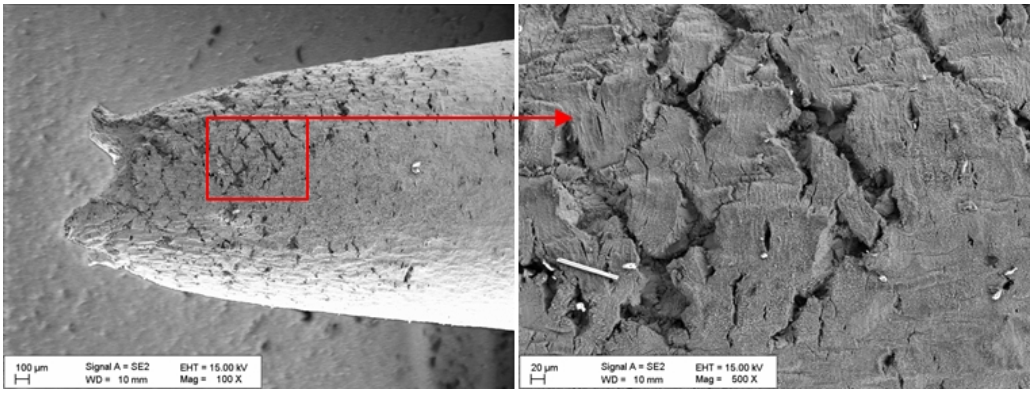

Figure 15. SEM images of gage sections for 316L after SSRT tests conducted at 550°C in air.

As one can see, due to severe oxidation of the specimen surface, it was rather difficult to distinguish what cracks were in fact just cracks in the oxide or what cracks continued propagating into the base material. However majority of these secondary cracks was found in the area of high plastic deformation close to the main fracture thus obviously these cracks initiated due the mechanical loading.

4. Conclusions

Supercritical water at 550 and 500°C temperatures and 25MPa pressure with either 2000 or 150 ppb dissolved oxygen didn't have any significant effect on material behavior in any of the SSRT tests performed using the strain rate of 5.18x10^{-7} s^{-1} respectively 1.0x10^{-7} s^{-1}. Decrease of yield

strength, maximum stress and plastic strain observed in SCW environment was obviously caused by increase of temperature, i.e. we did not observe any additional effect of SCW environment. In conclusion, all three tested austenitic stainless steels 316L, 347H and 08Cr18Ni10Ti proved to have sufficient stress corrosion cracking resistance under the applied conditions. Dissolved oxygen content didn't have any significant influence on the SSRT results either except for somewhat larger areas of IG/TG SCC on the main fracture surfaces and higher occurrence of secondary cracks in the environment having the higher oxygen content. Unexpectedly high susceptibility to SCC was observed for all three materials in N_2 atmosphere that was assumed to be an inert environment. Not only significantly higher area of IG/TG SCC was found on the main fracture surface but also reduction of plastic strain and maximum strength values were measured in high temperature N_2 atmosphere. The most probable reason is that the used N_2 gas contained traces of impurities such as oxygen, carbon dioxide or water or the test environment was contaminated by water vapour originating from the loop components (e.g. tubing of the re-circulation loop) surrounding the materials testing autoclave.
Based on the performed tests and post-test SEM analyses, 316L of the original test materials was concluded to be the best fuel cladding material candidate for the Fuel Qualification Test facility, because it showed the highest ductility and maximum stress levels in SCW environment at both temperatures of interest. In general, thermal sensitization of 316L after long exposure at elevated temperatures should be considered as a potential risk. Resistance of 316L to intergranular stress corrosion cracking should be investigated by SSRT testing with slower strain rates, or on pre-exposed specimens. Variation of plastic elongation and yield strength values measured in SCW resp. in hot gaseous N_2 could be function of cold work on the surface of the tensile specimens. Cold working has, as is the case in LWR plants, apparently high effect on obtained results and relation between the degree of cold work and occurrence of SCC should be investigated deeper.
The last not least it should be stressed that, due to still limited number of data available on 316L SCC behaviour in SCW, it is important that the specific heat of 316L for the fuel cladding would be carefully verified on corrosion, SCC and in general on high temperature cladding coolant interaction in supercritical water before any fuel pins is manufactured.

References

1. W. Zheng, Y. Zeng, J. Luo, R. Novotny, J. Li, B. Shalchi Amirkhiz, D. Guzonas, M. Matchim, J. Collier and L. Yang, Stress-Corrosion Cracking Properties of Candidate Fuel Cladding Alloys for the Canadian SCWR: A Summary of Literature Data and Recent Test Results, The 19th Pacific Basin Nuclear Conference (PBNC 2014), British Columbia, Canada, August 24-28, 2014.
2. G. Was, P. Ampornrat, G. Gupta, S. Teysseyre, E. West, T. Allen, K. Sridharan, L. Tan, Y. Chen, X. Ren, and C. Pister, Corrosion and stress corrosion cracking in supercritical water, Journal of Nuclear materials, 371, 176 (2007).
3. Y. Tsuchiya, F. Kano, N. Saito, A. Shioiri, S. Kasahara, K. Moriya, H. Takahashi, SCC and Irradiation Properties of Metals under Supercritical-water Cooled Power Reactor Conditions, GENES4/ANP2003, Kyoto, Japan (September 15–19, 2003) Paper 1096
4. H. Matsui et al. Overview of materials development for JSCWR, Joint IAEA&JRC Technical Meeting on Materials and Chemistry for SCWR, Petten, The Netherlands, July 18-22, 2011.

5. L. Zhang et al., Selection and corrosion behaviour of materials for SCWR fuel cladding, Joint IAEA&JRC Technical Meeting on Materials and Chemistry for SCWR, Petten, The Netherlands, July 18-22, 2011.
6. V.I. Prokhorov, F.V. Risovanaya, Properties of the 08Cr18Ni10Ti steel as a construction material for nuclear reactors, Russian Federation Agency on Atomic Energy, Federal State Unitary Enterprise, State Scientific Centre of Russian Federation, The Research Institute of Atomic Reactors, 2005.
7. R. Novotny, P. Hähner, J. Siegl, P. Haušild, S. Ripplinger, S. Penttilä, A. Toivonen, Stress corrosion cracking susceptibility of austenitic stainless steels in supercritical water conditions, J. Nucl. Mater., 409 (2) (2011), pp. 117–123.
8. S. Penttilä, A. Toivonen, L. Heikinheimo, R. Novotny, Corrosion studies of candidate materials for European HPLWR, Proceedings of the 2008 International Congress on Advances in Nuclear Power Plants (ICAPP'08), Paper 8163/Special Issue on the 2008 International Congress on Advances in Nuclear Power Plants/Materials for Nuclear Systems, Nuclear Technology, vol. 170(1) (2010), pp. 261–271.

ISSCWR7-2080

European Project "Supercritical Water Reactor – Fuel Qualification Test" (SCWR-FQT): Results of fuel pin mock-up tests

Radek Novotny[1, 4], Theo Timke[1], Alan Van de Sande[1], Dirk Visser[2], Stefan Ripplinger[1], Ales Vojacek[3], Otakar Frybort[3]
[1] European Commission, Joint Research Centre, Institute for Energy and Transport
Westerduinweg 3, 1755 LE, Petten. Netherlands
+31224565357, Pardubra@gmail.com
[2] NRG, Westerduinweg 3, 1755 LE Petten, Netherlands
[3] Research Centre Rez, Husinec-Rez, cp. 130, 25068 Rez, Czech Republic
[4] Czech Technical University Prague, Faculty of Nuclear Sciences and Physical Engineering, Czech Republic

Abstract

The main target of the EUROATOM FP7 project "Fuel Qualification test for SCWR" is to make significant progress towards the design, analysis and licensing of a fuel assembly cooled with supercritical water in a research reactor. On the basis of the experimental results assessment and calculations, fuel rod mock-up was designed and three fuel rod mock-ups were manufactured by CVR. Based on the possible accident scenarios, it was decided to conduct three different types of tests. Simulation of loss of external pressure was the target of the Test1. While the autoclave was depressurized as fast as possible down to p_{Aut} < 1 MPa by opening the close valve located behind the cooling part of the high pressure part of the loop, pressure inside the pin – internal pressure p_{Pin} was hold on constant value of 20 MPa by continual pumping high pressure water via the pin and in parallel separate relief valve connected directly to the pin using filling pressure tube. Similar approach was chosen when the opposite case i.e. loss of internal pressure in the pin was simulated in the Test 2A. Eventually, Test 2A was conducted one more time, but with modified set-up in order to determine the limiting value of p_{Pin} (collapse of the pin due to external overpressure) more accurately. The presented paper summarizes the results of all three performed tests.

1. Introduction

The scope of WP4 of the Euratom FP7 European project: Supercritical Water Reactor Fuel Qualification Test (SCWR FQT) is pre-qualification of the FQT loop test section by means of designing, building and operating a similar electrically heated test section, as well as pre-qualification of all critical components of the FQT loop. The selection of candidate materials was carried out taking into account the following criteria; these materials must be commercially available in nuclear grade (Ni-base alloys and austenitic stainless steels) and previously evaluated as promising cladding candidates. This further narrowed the selection process to austenitic stainless steels. Based on the available data several material candidates were pre-selected including Nb-stabilized 347H, Russian production 08Cr18Ni10Ti (equivalent to Ti stabilized austenitic stainless steel 321) and low carbon 316L austenitic stainless steels. In the first and second phase of this project general corrosion as well as stress corrosion cracking slow strain tensile tests were conducted in supercritical water up to 550^{o}C, i.e. the calculated maximum cladding temperature. Based on the results of these first two phases 316L was

selected for the fuel cladding of the FQT facility. This paper summarizes the work performed in the third phase. The main objective of this phase was to manufacture fuel rod mock-ups based on the final design of the test section and test the structural integrity of the 316L fuel rod cladding with respect to different pressure loads during possible accident scenarios, such as loss of external pressure (i.e. risk of ballooning) and loss of internal pressure (i.e. risk of buckling). The latter test with an underpressure in the pin has been performed twice to verify if the design can fulfil the calculated limits and help to determine the optimal level of pre-pressure in the FQT fuel pin at the beginning of the test.

2. Experimental

2.1 Material

It was already mentioned in the Introduction that fuel cladding material was selected as a result of general corrosion and SSRT SCC susceptibility tests performed within SCWR FQT project. On the base of the performed tests and follow up SEM analysis, 316L has been selected as the best candidate for fuel cladding material in Fuel Qualification Test facility, because it showed not only acceptable general corrosion and SCC resistance, but also the highest ductility and maximum stress levels in SCW environment at the maximum peak cladding temperatures. Due to unavailability of the 316L tubing of the required dimensions in particular wall thickness on the European market, the tubing was ordered from OnlineMetals.com. The chemical composition of the delivered 316L austenitic stainless steel is given in table 1.

Table 1 Chemical composition of the selected austenitic stainless steel 316L [el. %].

Material	C	Si	Mn	S	P	Cr	Ni	Others
316L	0.0022	1	3	0.03	0.045	18	Max. 14	Mo = max. 3

Tubing with the dimensions (Outside Diameter (O.D.) = 0.3125”, wall thickness = 0.02” was purchased from OnlineMetals.com. The dimension had to be at least similar to those of the designed fuel pin.

2.2 Mechanical properties

Input data on high temperature mechanical properties of the selected 316L were collected from available material datasheets and literature [4, 5] and excel file containing all required physical and mechanical properties was prepared, in order to provide reliable material data not only for the design of the fuel pin mock-ups but for an analysis of different accident scenarios. For example, such data were obtained within Japanese R&D project on development of Japanese concept of supercritical fast reactor [1] for some of the pre-selected austenitic stainless steels.

2.3 Design and manufacturing of fuel rod mock-up

Fuel rod mock-up was designed according to the design of future Fuel Qualification Test facility that was completed within WP1: Deliverable E1.2 – Final design of the active channel and the primary loop. The design temperature around the fuel rods of the SCWR-FQT loop is 385°C – 450°C. The active channel contains four fuel rods with a total heating power of ~63.8 kW and a recuperator in order to achieve hot channel conditions as they are expected to occur in the evaporator of the HPLWR where the pseudo-critical region is exceeded. The internal flow is realized so as to prevent the creep condition of the pressure tube, which occurs around 450°C.
The fuel rods are constrained axially by spacers and radially by wire wraps. To allow for compensation of the different thermal expansion of wire and cladding, 50 disk springs placed on

top of each other were designed. The material of the disk springs and of the fuel rod claddings was stainless steel 316L, as well as the end plugs and the wire wrap around it (see figure 1).

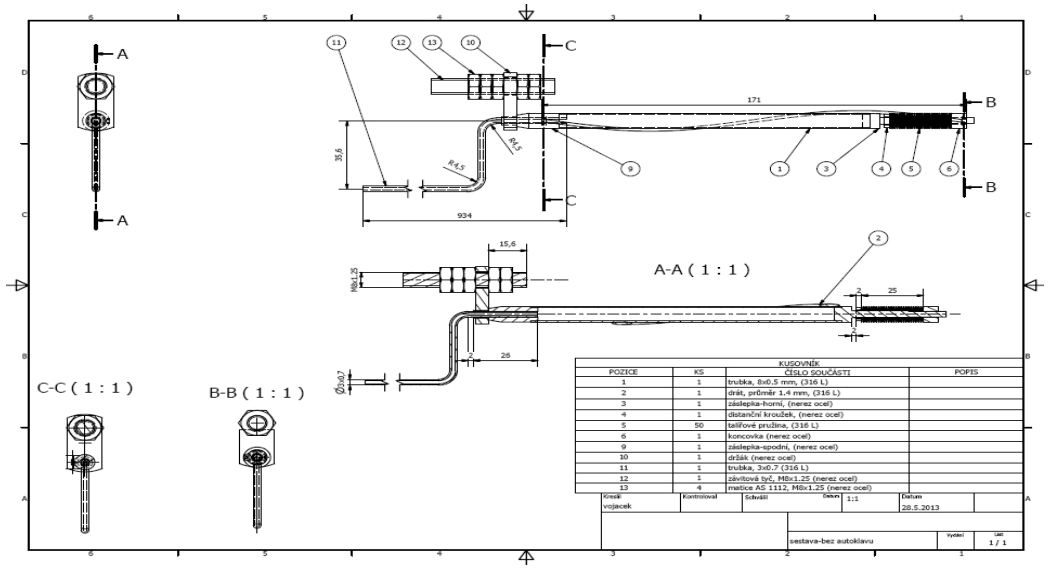

Figure 1. Design technical drawing of the fuel pin mock-ups including the wire wrap.

Design of the fuel rod mock-up including all internal structures for the installation in the autoclave was completed by A. Vojacek and O. Frybort from CVR. The detailed description and design drawings are summarized in the final report of Deliverable 4.3 SCWR FQT project [2]. Summary of all important dimensions is given in table 2.

Table 2. Summary of fuel rod mock-ups dimensions.

Dimension		**[mm]**
Length	L	200
Inner diameter	D_i	7
Outer diameter	D_o	8
Wall thickness	s	0.5

Each of tested fuel pin mock-ups was installed in JRC IET autoclave according to schematic drawing shown in figure 2.

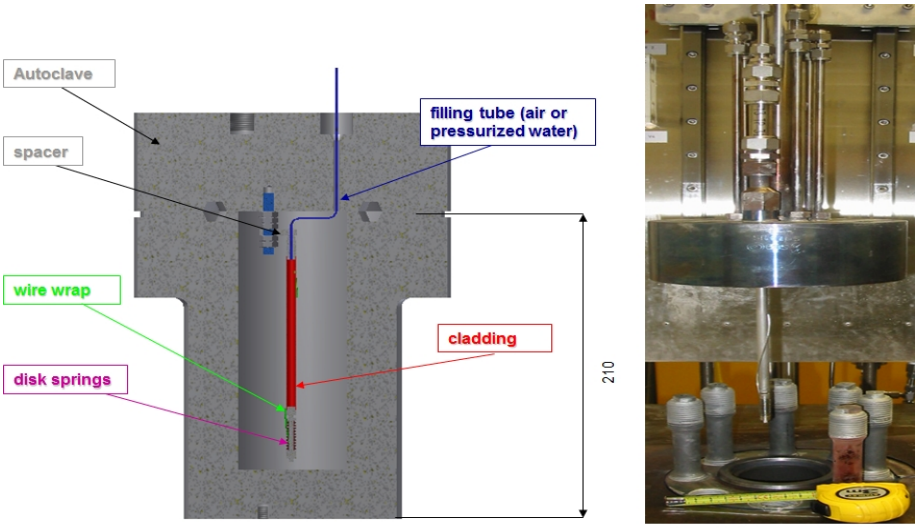

Figure 2. The fuel rod mock-up set-up was adapted in order to fit into one of the JRC IET SCW autoclaves.

Notice, the main purpose of disk springs was to prevent wire wrap failure due to development of additional stresses during cooling or heating stage. 24 disk springs manufactured from 316L plate were installed on the upper plugging cap and fixed in the position using end cap with welded wire wrap. The fuel pin mock-up was attached to the autoclave using the spacer and filing tube. Filling tube (O.D. = 3 mm) was electron beam welded inside the Swagelok 6 mm O.D. tube that was lead through the lid outside of the high temperature zone (see figure 2). Following that were sealed against leakage outside of high temperature zone using Teflon rings which were placed in the Swagelok type of 6 mm connector. Teflon disks were literally smashed when pressed by upper and lower ZrO_2 washer rings. Furthermore, the layout in figure 3 of the configuration used for the Test 2B includes also linear variable differential transducer (LVDT) for in-situ displacement measurement.

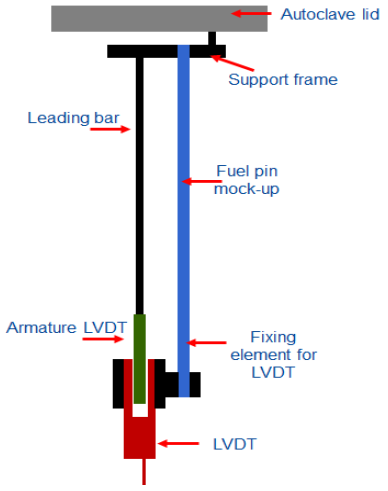

Figure 3. Schematic drawing of the fuel pin mock-up set-up used in the Test 2 and 3 including in situ deflection measurement provided using LVDT.

Notice that to be able to measure deflection along the whole length of the pin the upper and lower support frames with the LVDT holder respectively screwed leading bar with armature were installed on lower plugging cap and upper end cap. LVDT signal was lead outside of the

autoclave in Inconel 625 mineral insulated (MI) cable and sealed in the upper part of the vessel outside of high temperature zone with set of support elements and Teflon rings.

2.4 Test procedure

Originally three different tests were planned to be carried out using all three manufactured fuel pin mock-ups including long term corrosion test. In reality only two tests were performed. The third one Test 2B was in fact modified Test 2A (see table 3).

Table 3. The most important parameters of the performed tests

Test ID	Description	t_{Aut} [^oC]	$p_{Aut - Start}$ [MPa]	$p_{Aut – End}$ [MPa]	$p_{Pin - Start}$ [MPa]	$p_{Pin-End}$ [MPa]
Test 1A, B	LOCA	450	25	< 1	20	20
Test 2A	Loss of internal pressure	450	25	25	15	< 0.2
Test 2B	Loss of internal pressure 2	450	25	25	25	< 0.2

Simplified simulation of LOCA was the target of the Test 1A and 1B. While the autoclave was depressurized as fast as possible down to p_{Aut} < 1 MPa, pressure inside the pin – internal pressure p_{Pin} was held on constant value of pressure 20 MPa. Similar approach was chosen when the opposite case i.e. loss of internal pressure in the pin was simulated in the Test 2A. This time, while the p_{Aut} was hold on constant value 20 MPa, p_{pin} was relieved by simultaneous closing the line from high pressure pump and opening of the relief valve directly connected to the pin reducing thus the p_{pin} down to <1 MPa. Finally, instead of long term corrosion test, it was decided to conduct Test 2A one more time, but with modified set-up in order to determine the limiting value of p_{Pin} (p_{Pin} value when pin collapsed due to external overpressure) more accurately (see Table 3 – Test 2B).

2.5 Pressure control in the autoclave and the fuel-pin mock-up

2.5.1 Water circulating loop

All three pins were exposed in ultra-pure supercritical water solution with an electric conductivity <0.1 µS/cm at the autoclave inlet. Flow chart of the JRC IET water loop is shown in figure 4.

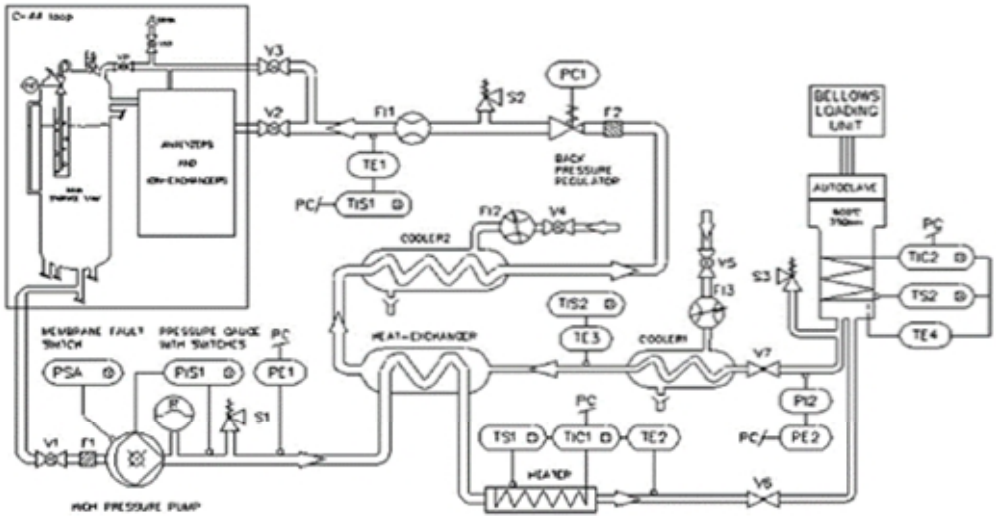

Figure 4. Schematic drawing of supercritical water loop with autoclave installed at JRC-IET.

The high-pressure part of the loop consists in high-pressure pump, heat exchanger, pre-heater and cooler. Water returning from the autoclave flows through a pre-cooler, heat-exchanger and cooler. The high pressure loop is pressurized using a diaphragm pumps and a back-pressure regulators. Maximum flow rate in both high pressure loops is 5 dm^3/h. Chemical parameters pH value, conductivity and dissolved oxygen content were monitored continually in the low-pressure part of the loop, both at the inlet and the outlet of the high-pressure part. Dissolved oxygen content in inlet water was continuously set and controlled on 2000 ppb. Inlet water conductivity was 0.065 µS/cm with flow rate equal 2.2 ± 0.2 l/h. Both dissolved oxygen content and conductivity at the outlet were monitored in regular time intervals.

2.5.2 Fuel pin mock-up – control of internal pressure using water loop by-pass

In this set-up, internal pressure p_{Pin} was controlled by continuous circulation of water via by-pass through fuel pin mock-up as well as in parallel installed relief valve (see schematic drawing in figure 5).

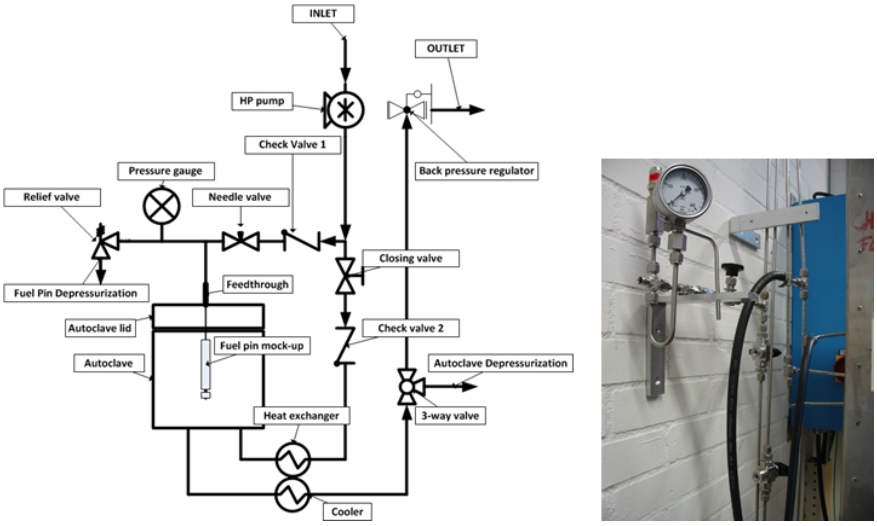

Figure 5. Schematic drawing of internal pressure p_{Pin} control system used in the Test 1A and 1B as well as the Test 2A.

Notice, that check valves 1 and 2 were installed at the inlet into the by-pass respectively into the autoclave in order to be able to adjust both internal pressure p_{Pin} and autoclave pressure p_{Aut} independently on each other. Moreover, in the depressurization tests either p_{Pin} or p_{Aut} were required to stay constant during the test, i.e. whatever happened in one side of the facility could not under any circumstances affect the other side of the testing facility. For example, Autoclave was depressurised by reducing p_{Aut} from 25 MPa to < 1 MPa in the Test 1A and 1B simultaneously disconnecting the autoclave from the water preparation loop by closing the closing valve and switching of 3-way valve to the drain. At the same time, check valve 1 prevented any loss of internal pressure p_{Pin} (kept on constant value 20 MPa) since it allows water flowing only one way – through the pin and relief valve to the drain. Fuel pin mock-up was depressurised using similar procedure: as soon as the needle valve was closed, the relief valve was fully opened with subsequent loss of pressure p_{Pin} from 20 MPa to < 1 MPa. At the same time check valve 2 ensured that autoclave pressure p_{Aut} was not affected and stayed on 25 MPa.

2.5.3 Fuel pin mock-up – control of internal pressure using pressure adjusting loop

In contrast to water by-pass, to complete Test 2B, the pressure adjusting loop where pressurised air is produced by high pressure compressor was used to generate and control pressure p_{Pin}. The basic scheme of the loop is shown in figure 6.

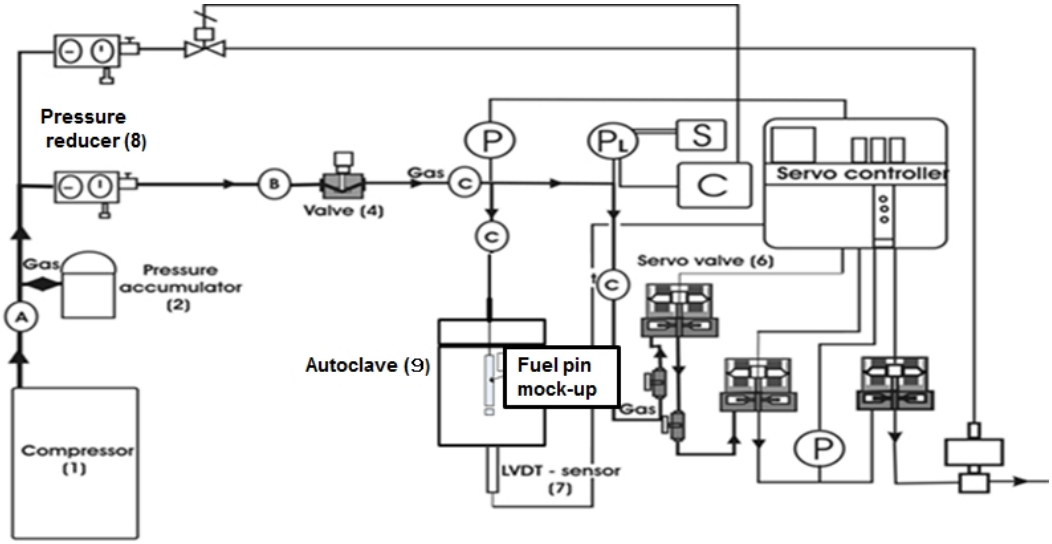

Figure 6.Schematic drawing of the pressure adjusting loop.

As it is presented in figure 6, pressurized air is produced and delivered by a high pressure compressor via the pressure accumulator (Section A) to the pressure-adjusting loop (Sections B and C). Pressure accumulator was incorporated into the loop to increase the volume of pressurized air available for the loop as well as to dampen the oscillation of pressure before the loop inlet. The high pressure reducer (8) and very accurate Tescom flowing valve (4) then forms further elements of the loop which define the pressure range for the test as well as stabilize the air flow to the fuel pin mock-ups and in parallel to servo-valves (6). The pressure in the fuel pin p_{Pin} was controlled by Moog servo-valves (6) with the feedback provided by high precision RDP pressure transducers (P). The operation of the servo valves (6) and thus the internal pressure p_{Pin} was controlled by MOOG servo controller using MOOG MACS software and hardware. The set up shown in figure 6, with two controlling servo-valves as well as buffer one was applied in the Test 2B.

2.6 Fuel rod mock-up stress calculations

Within the FQT project, the possible accident scenarios for the FQT were identified and necessary calculations were performed according to German KTA Safety Standard 3201.2 [3]. The mechanical properties of 316L austenitic stainless steel needed for the stress calculations are summarized in table 4.

Table 4. Summary of mechanical properties for 316L austenitic stainless steel [4].

Variable		[MPa]
Tensile stress at room temperature	R_m	606
Tensile stress at operating temperature (t = 450°C)	R_{mt}	455
Yield stress at room temperature	$R_{p0.2}$	302
Yield stress at operating temperature (t = 450°C)	$R_{p0.2t}$	184

For 316L the allowed stress S_m is equal to the yield stress at operating temperature $R_{p0.2t}$ divided by a safety factor of 1.5. The allowed stress *Sm* at the operating temperature of 450°C was calculated as follows:

$$S_m = \min\left\{\frac{Rp02t}{1.5}, \frac{Rmt}{2.7}, \frac{Rm}{3}\right\} = \frac{Rp02t}{1.5} = \frac{184}{1.5} = 122.7MPa \qquad (1)$$

2.6.1 Allowable over-pressure in fuel pins ($p_{Pin} > p_{Aut}$) – Test 1

In other words, here the target was to determine, according the KTA safety standards, what the maximum of $\Delta p_{max,1}$ (p_{Pin}-p_{Aut}) is the fuel rod mock-up wall can withstand. For D_o/D_i < 1.7 (see table 2) the allowable over-pressure of the FQT fuel pins is calculated as:

$$\Delta p_{\max,1} = \frac{2 \cdot S_m \cdot s}{D_i + s} = 16.4MPa \qquad (2)$$

, where D_i is inner diameter and *s* is the wall thickness of the fuel pin mock-ups.

According the KTA safety standards the fuel pin wall can withstand an over-pressure (p_{Pin} > P_{Aut}) of 16.4 MPa. As long as the safety factor of 1.5 would not be considered, the plastic deformation (ballooning) is expected to start at $\Delta p_{max,1}$ = 1.5 x 16.4 = 24.6 MPa over-pressure inside the fuel pins.

2.6.2 Allowable under-pressure in fuel pins ($p_{Pin} < p_{Aut}$) – Test 2A and 2B

As regards as the Test 2A and 2B, the target was to determine the maximum of $\Delta p_{max,2}$ (p_{Aut}-p_{Pin}, according to KTA safety standards [3]) the fuel rod mock-up wall can withstand as well as to optimize the initial pre-pressure inside the pin for future fuel qualification testing in CVR. For D_o/L < 5 the allowable under-pressure inside the FQT fuel rods is calculated as follows:

$$\Delta P_{\max,2,3} = \frac{2 \cdot S_m}{f_v} \cdot \frac{s}{D_o} \cdot \left(1 + \frac{1.5 \cdot U \cdot D_o \cdot (1 - 0.2 \cdot D_o / L)}{100 \cdot s}\right)^{-1} = 9.4MPa \qquad (3)$$

, where safety factor – f_v = 1.2 and ovality – U = 1.5%

According the KTA safety standards the fuel rod wall can withstand an under-pressure ($p_{Pin} < p_{Aut}$) of 9.4 MPa. As long as the safety factor of 1.5 would not be considered, plastic deformation (buckling) is expected to start at $\Delta p_{max,2}$ = 1.5 x 9.4 = 14.1 MPa under-pressure inside the fuel rods.

2.7 Post-test examination

Post-test analysis consisted of visual inspection, radiographic X-ray examination and X-ray computed tomography of the exposed fuel pin mock-ups.
While Radiographic scan prior and after the test was carried out in order to detect and identify defects along the full length of a fuel rod, CT scans on the other hand helped to detect, characterize and identify defects such as cracks, voids and inclusions in the weld regions. The Radiographic inspection was performed with a Philips 450 kv dual focus X-ray machine.
X-ray tomography was performed using a Phoenix Nanotoms "research edition" Computer Tomography (CT) with 180 kV/15 W nanofocus source. CT analysis focused in particular on those areas of a boundary between autoclave SCW and high pressure water/air inside the pin where welds between the fuel cladding element and lower and upper plugging caps were located. Weld positions are depicted in figure 7.

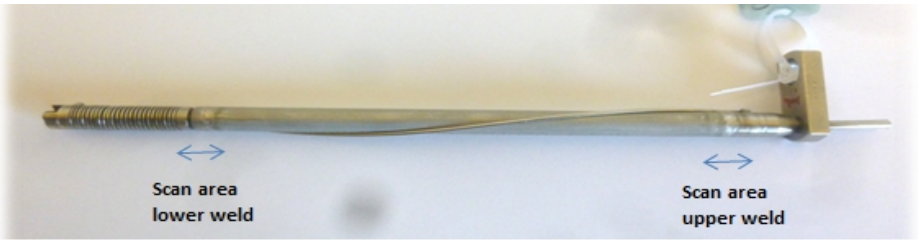

Figure 7. Image of one of the fuel pin mock-ups, CT scan area and weld position.

The most important scan parameters are shown below:

Voltage: 150 kV
Current: 120 µA
Timing: 750 ms
Voxel size: 7.0 µm (fuel pin 1: 10 µm)

Phoenix Datos|x software from GE was used to re-construct the voxel data's.

Metrology software VG Studio Max 2.2 from Volume Graphics, Germany was used for the analysis and visualization of the volume data file. To ensure comparability of the evaluated samples, 3D voxel data's were processed in an identical way. Data sets were filtered using adaptive gauss algorithm (smoothing of 1.2 and edge threshold of 0.040). A standard surface determination was followed by an advanced mode surface determination with a search distance of 4 voxels. The lower weld scan area of the fuel pins represents a height of 9.4 mm. For analysis purpose a Region of Interest (ROI) was introduced with a height of 4.2 mm to reduce the calculation time. The upper weld scan area of the fuel pins represents a height of 7.4 mm whereas the ROI for defect analysis is at a height of 3.5 mm.

3. Results and discussion

3.1 Test 1 – simulation of LOCA

The safety systems of SCWR FQT facility were designed to prevent any severe secondary damage to the fuel claddings including loss of coolant due to break of any coolant supply line. The countermeasures may include scram of the reactor and low pressure coolant injection after depressurization. Evaluation of the performance of designed safety systems was made within SCWR FQT – Deliverable E3.1 [5], a numerical model of the SCWR-FQT loop, as described in this report by Schulenberg, was set up using the one-dimensional system code APROS [5]. For example, the first simulations investigated the behaviour of the emergency systems on a guillotine break of the feed-water line (see figure 8).

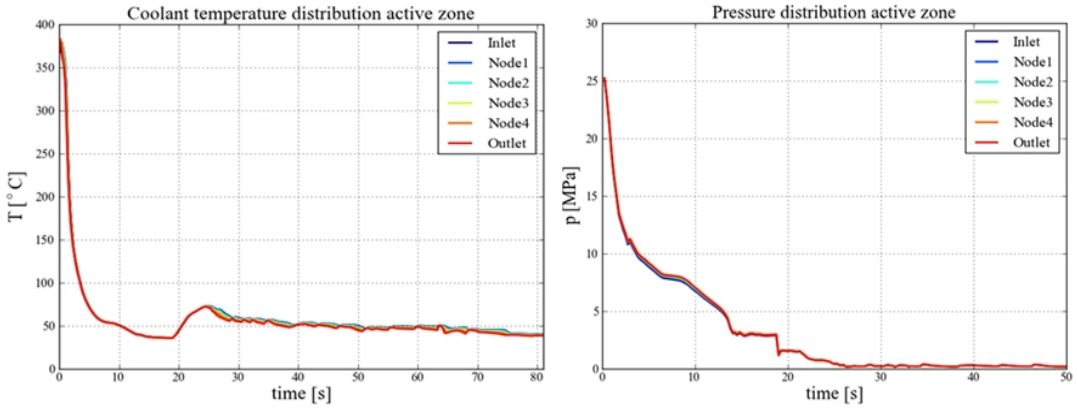

Figure 8. The graph on the left hand depicts the temperature progression in case the pressure surveillance over the fuel element is applied. On the left hand side, the according pressure progress in the active section is shown. As visible, the loop is completely depressurized 25 seconds after the break occurred.

Test 1 was performed with the main purpose to evaluate integrity of the fuel rod mock-up in case of LOCA. Since, the Test 1 as well as all the other tests was conducted on laboratory scale using facility primarily designed for material testing; certain limitations had to be taken into account. These included, significantly lower flow rates thus heat flux due to limitations of the high pressure pump, pre-heater and autoclave heater. Furthermore, during normal operation, achieving the desired temperatures is provided by 4 fuel rods inserted in the active channel and by γ-heat power released in the structural material of the active channel (mostly in the pressure tube) in the active zone of the reactor LVR – 15. Since fuel or any type of internal additional heating source could not be included in the design of the fuel rod mock-up, it was impossible to simulate and measure possible increase of fuel cladding temperature caused due to LOCA.
All these tests, including the Test 1A and 1B, were started by initial simultaneous pressurization of the fuel rod mock-up and autoclave. Both autoclave pressure p_{Aut} = 25 MPa and internal pressure p_{Pin} = 20 MPa was controlled using high pressure pump. Notice, that before the heating was switched on all components including the fuel rod and autoclave itself were carefully examined in order to detect any leakages. Depressurization procedure applied in the Test 1 is graphically presented in figure 9. Autoclave was depressurised from 25 MPa to < 1 MPa by simultaneous disconnecting the autoclave from the water preparation loop by shutting the closing valve and opening the outlet line to the drain via additional cooler by switching 3-way valve (see figure 5). During the depressurization, check valve 1 prevented any loss of internal pressure p_{Pin} (kept on constant value 20 MPa) since it allowed inlet water flowing through the pin as well as relief valve to the drain.

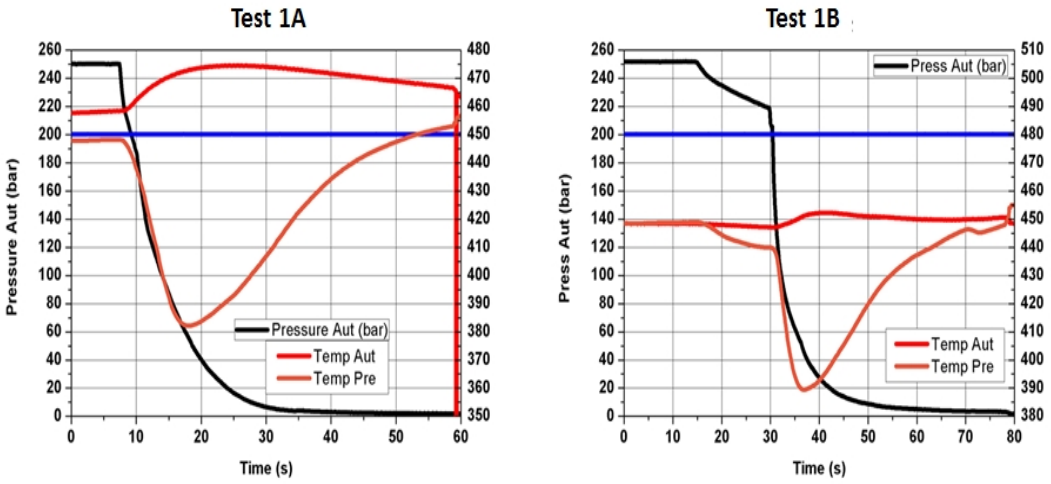

Figure 9. Plots of pressure and temperature recorded within the LOCA simulation a) Test 1A and b) Test 1B.

The APROS simulation performed by Raque [5] (see figure 5) demonstrated that in case of LOCA the total depressurization of the fuel pins from 25 MPa to less than 1 MPa would be completed in approximately 30s. For comparison, in the Test 1A, it took approximately 35s to decrease the autoclave pressure to less than 1 MPa. Notice, that at the beginning of the test in the first 5s, depressurization was accompanied by the drop in temperature in the pre-heater due to steam expansion as well as by rather small rise of autoclave temperature to approximately 465^{o}C. Since no apparent damage caused by depressurization procedure was observed, Test 1A was repeated using the same fuel rod mock-up one more time (see figure 9 – Test 1B). As in the first test, the pressure in the autoclave dropped to pressure lower than 1 MPa in approximately 25s. This time, the rise of autoclave temperature reported in the Test 1A was even more noticeable; temperature increased up to 475^{o}C. Even so the maximum value of overpressure $\Delta p_{\max,1}$ reached almost 20 MPa which was significantly higher compare to that calculated including the safety factors in sub-chapter 2.6.1 (($\Delta p_{\max,1}$=16.4 MPa). Visual observation did not indicate any apparent damage to the tested fuel pin mock-up 1.
The following analysis of the fuel pin mock-up 1 included, just as prior the test, radiographic inspection followed by detailed CT examination with focus; in particular on analysing the structure of the weld regions (see figure 10 and 11).

Figure 10. Radiographic 2D X-Ray image of the fuel rod mock-up 1 taken after the depressurization test.

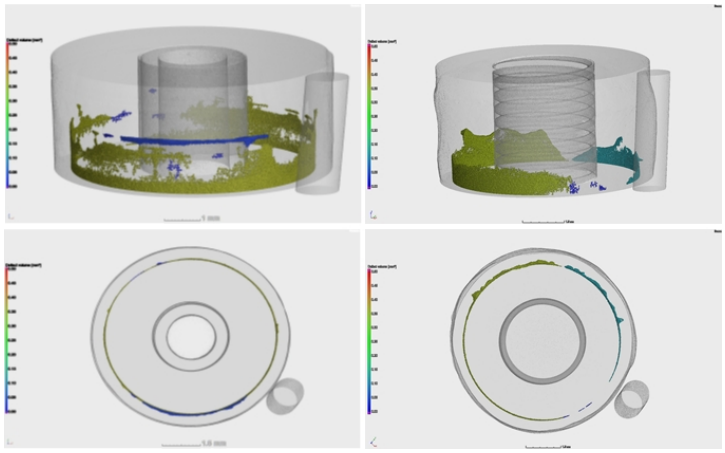

Figure 11. Result of the post-test CT defect analysis using the "Default" algorithm in 3D side- and top view.

Radiographic inspection did not reveal any significant changes in the fuel rod structure after the depressurization test. The processing of 3D voxel data's and defect analysis was equal as those used before the Test 1. In contrast to radiographic inspection, CT scans indicated changes in the both upper and lower weld regions. The volume of detected defects calculated prior and after tests is compared in the Table 5.

Table 5. An overview of the detected defect volumes of fuel rod 1 prior and after testing.

	Defect volume prior testing [mm^3]	**Defect volume after testing [mm^3]**	**Difference of defect volume [mm^3]**	**Difference of defect volume [%]**
Fuel pin 1 lower weld	**0.61**	**0.49**	**-0.12**	**- 19.67**
Fuel pin 1 upper weld	**0.52**	**0.41**	**-0.09**	**- 21.15**

Notice, that volume of defects detected prior the test decreased about 20% in the lower weld region respectively 21% in the upper weld regions. This does not mean that these detected defects would heal some way as results of pressurizing test and exposure to high temperature. In fact, it rather indicates that the gap between the cladding element and plugging caps was partly closed most probably as a result of exposure to high temperature water inside the pin. In agreement with radiographic inspection, CT scans did not reveal any significant generation of new defects due to depressurization. In summary, laboratory simulation of possible LOCA event in JRC IET autoclave proved that integrity of the fuel rod should not be affected if the temperature of the pin would not increase significantly.

3.2 Test 2 – loss of internal pressure

First of all, it should be stressed that event of loss of internal pressure p_{Pin} (see table 3) is not the relevant accident scenario for the FQT since in reality this event could not take place. Obviously, calculations carried out in the sub-chapter 2.6.2 indicate that the fuel rod mock-up wall of current configuration can be according to KTA standards operated at maximum underpressure of $\Delta P_{\max,2}$ = 9.4 MPa (see equation 3). In other words, fuel pin would have to be pre-pressurised at least to p_{Pin} = 15.6 MPa before the installation in the FQT device. On the other hand, at current level of knowledge it is practically impossible to assess how much the internal pressure p_{Pin} would increase due to fission product formation since the fuel [6] will be fundamentally different from that used in the current LWRs. Considering these, it was decided

to check on laboratory scale, whether the fuel pin would sustain the scenario of a fuel pin installed without in the FQT without initial overpressure (Test 2A) as well as to determine as accurately as possible the value of p_{Pin} when the fuel pin mock-up collapses i.e. to optimize the initial pre-pressure in the pin for future fuel qualification testing in CVR.

3.2.1 Test 2A

Similar approach as that in the Test 1A, 1B (see subchapter 2.5.2) was chosen when the opposite case i.e. loss of internal pressure in the pin was simulated in the Test 2A. This time, while the p_{Aut} was hold on constant value 25 MPa by continually circulating water through the autoclave using water circulation loop, however, p_{pin} was relieved by simultaneous closing the line from high pressure pump and opening of the relief valve directly connected to the pin. The p_{pin} was thus reduced from initial pressure of 20 MPa down to less than 0.2 MPa (see figure 12).

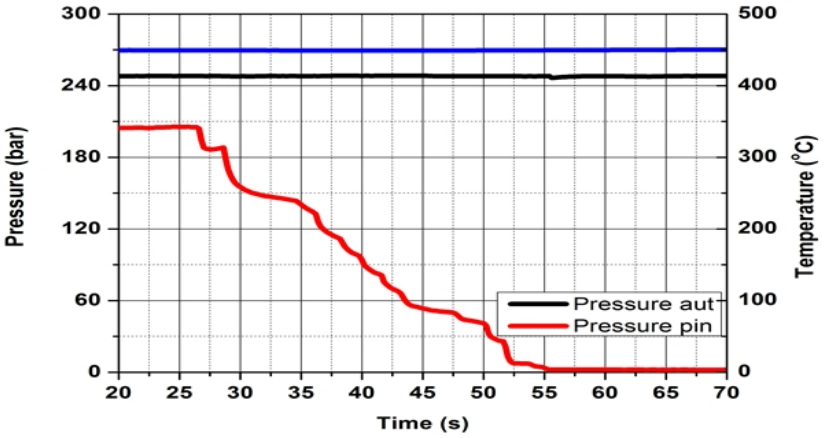

Figure 12. Plot of pressure and temperature recorded within the LOCA simulation a) Test 1A and b) Test 1B.

Both post-test visual and radiographic inspection showed complete collapse of the fuel pin mock-up which is for instance demonstrated by the image of radiographic inspection in figure 13

Figure 13. Radiographic 2D X-Ray image of the fuel rod mock-up 2 taken after completing Test 2A.

It should be mentioned, that the same procedure as that in the Test 2A was applied also for the first fuel pin mock-up 1 which sustained the LOCA simulation in the Test 1A and 1B with the same result i.e. complete collapse of the fuel pin mock-up. . It is not that surprising that fuel pin mock-up failed since even if the safety factor (KTA standards) of 1.5 for the yield stress is excluded plastic deformation (buckling) is expected to start at 1.5 x 9.4 = 14.1 MPa under-pressure inside the fuel pin. In other words, according to calculations, for the current configuration and selected material of the fuel pin mock-up buckling is inevitable at internal pressures p_{Pin} < 10.9 MPa (p_{Aut} = 25 MPa).

3.2.2 Test 2B

Unfortunately, the set-up of the Test 2A did not allow sufficient control and accuracy of pressure drop rate. Therefore, Test 2B was prepared (see table 6) and this time the fuel pin mock-up was connected to one of the pressure adjusting loops. The principle of the pressure adjusting loop operation is described in detail in chapter 2.5.3. Not only that, LVDT sensor was attached to the evaluated fuel pin mock-up 3 according to schematic drawing shown in figure 3, in order to measure and record any indications of plastic deformation of the pin while decreasing the p_{Pin} with the defined pressure drop rate. In the test 2B the internal pressure p_{Pin} was decreased in steps; altogether five steps were applied (see table 6).

Table 6. Summary of the Test 2B.

Step	p_{Pin}/dt [MPa/s]	t_{Aut} [°C]	$p_{Aut\text{-}Start}$ [MPa]	$p_{Aut-End}$ [MPa]	$p_{Pin\text{-}Start}$ [MPa]	$p_{Pin\text{-}End}$ [MPa]
Step 1	0.02	450	25	25	25	15.5
Step 2	0.01	450	25	25	15.5	10.9
Step 3	0.01	450	25	25	10.9	10.6
Step 4	0.01	450	25	25	10.6	5.0
Step 5	0.01	450	25	25	5.0	0.5
Step 6	0.01	450	25	25	0.5	<0.2

For example, in the Step 1 the pin was depressurized to target pressure p_{Pin} = 10.9 MPa in agreement with maximum $\Delta P_{\max,2}$ that was calculated in chapter 2.6.2 including the safety factors. Starting from the Step 2 two times lower pressure drop rate dp_{Pin}/dt was adjusted in order to be able to identify the beginning of plastic deformation more accurately (see figure 13).

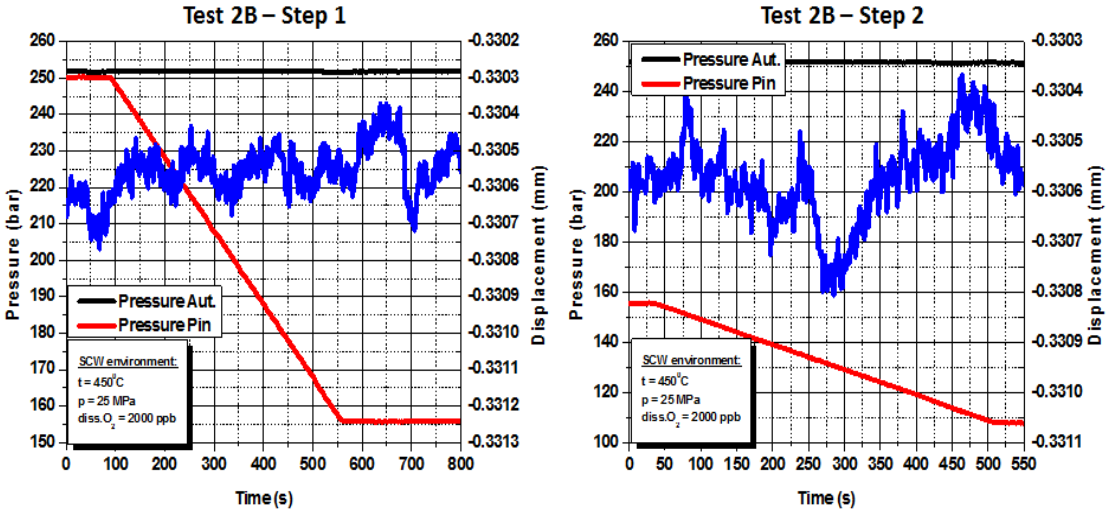

Figure 13. Plots of pressure and displacement recorded within a) Step 1 and b) Step 2 of the Test 2B.

In Step 1 to 4, the record of displacement measurement was rather similar than those presented in the figure 21. In conclusion, it did not indicate any plastic deformation process on the fuel pin

mock-up 3. In this particular case, the noise in the recorded displacement was caused by the intrinsic characteristics of the sensor and by the oscillations of the autoclave pressure. The fuel pin mock-up 3 collapsed during the step 5 as it is demonstrated by the PC record of the Step 5 in figure 14.

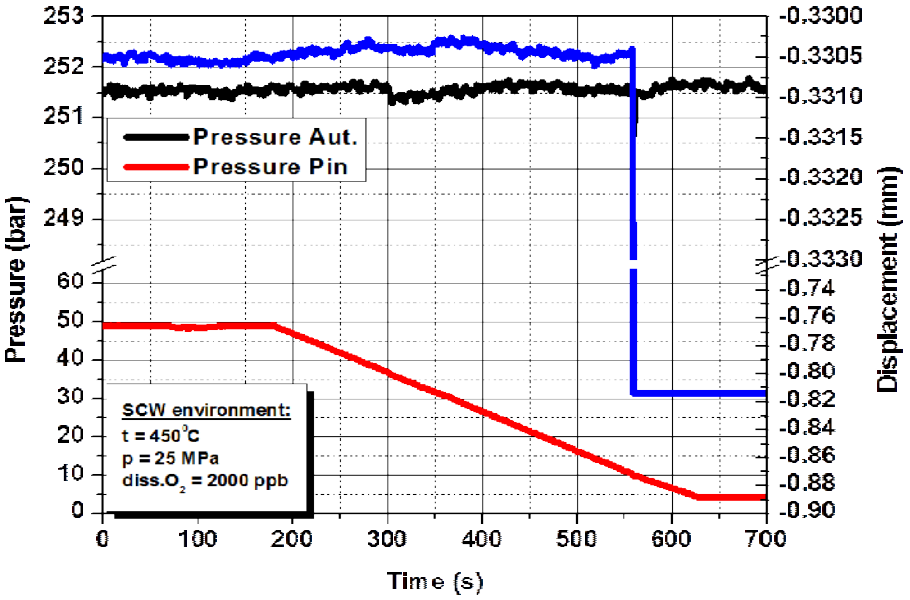

Figure 14. Plots of pressure and displacement recorded within Step 5 of the Test 2B for fuel pin mock-up 3.

Obviously, the collapse of the fuel pin mock-up 3 is indicated by significant almost 0.5 mm drop of displacement which occurred approximately at p_{Pin} = 1 MPa. Furthermore, it seems that this collapse was not preceded by any slowly increasing bending process at least displacement measurement did not show on anything like that. Certainly, the question is if the configuration of the displacement measurement used in the Test 2B (see figure 3) could detect such processes. In any case, according to this measurement, the fuel pin mock-up 3 collapsed at significantly higher underpressure $\Delta P_{\max,2}$ of 24.2 MPa (p_{Aut} = 25.2 MPa) than it was expected based on performed calculations.

4. Conclusions

Within SCWR FQT project, for the future FQT two different accident scenarios of fuel cladding failure including LOCA (ballooning) and loss of internal pressure (buckling) were evaluated both theoretically and experimentally. It must be stressed that these experiments were conducted on laboratory scale using facility primarily designed for material testing; certain limitations have to be taken into account. These included, significantly lower flow rates thus heat flux due to limitations of the high pressure pump, pre-heater and autoclave heater.

Theoretical calculations (according to KTA standard 3201.2) showed that for the case of LOCA the overpressure $\Delta P_{\max,1}$ ($p_{Pin} - p_{Aut}$) inside the fuel pin must not be higher than 16.4 MPa. The similar calculation performed for the second of considered scenario loss of internal pressure (buckling) demonstrated that the underpressure $\Delta P_{\max,2}$ ($p_{Aut} - p_{Pin}$) must not be higher than 9.4 MPa. In conclusions, according to these calculations those fuel pins used for the purpose of FQT will have to pre-pressurized to at least 15.6 MPa. However than the question is how much the pressure p_{Pin} will increase due to fission gas formation during FQT.

Two types of laboratory tests were conducted in support of theoretical calculations using fuel pin mock-ups designed and manufactured in CVR. In the Test 1, loss of coolant accident (LOCA)

case was evaluated. The results showed that fuel pin mock-up 1 did not fail even if the maximum value of overpressure $\Delta p_{\max,1}$ reached almost 20 MPa which was significantly higher compare to that calculated including the safety factors. With regards to Test 2, the results of the Test 2A proved that fuel pin would not sustain and collapsed if it would not be installed without any initial prepressurizing of the pin. On the other hand, as the Test 2A confirmed, the fuel pin mock-up collapsed due to buckling at significantly higher underpressure $\Delta p_{\max,2}$ = 24.2 MPa (p_{Aut} = 25. 2 MPa) compared to the results of theoretical calculations.

References

1. R H. Matsui et al. Overview of materials development for JSCWR, Joint IAEA&JRC Technical Meeting on Materials and Chemistry for SCWR, Petten, The Netherlands, July 18-22, 2011.
2. R. Novotny, P. Janik, T. Timke, A. Van Der Sande, T. Heftrich, D. Visser, A. Vojacek, O. Frybort, SCWR FQT Project (Contract Number: 2669908) , Deliverable (D-N^{o}: E4.3) Report on Fuel Pin Mock-up test, 2015
3. KTA 3201.2, Components of the Reactor Coolant, Pressure Boundary of Light Water Reactors; Part 2: Design and Analysis. Safety Standards of the Nuclear Safety Standards Commission (KTA), June 1996 (incl. rectification from BAnz 129, 13.07.00).
4. 2007 ASME Boiler & Pressure Vessel Code, 2007 Edition. Juli 1, 2007.
5. T. Schulenberg, M. Raque, Ch. Zhou, T. Zeiger, SCWR FQT Project (Contract Number: 2669908) , Deliverable (D-N^{o}: E3.1), WP3 Interim Report after Year 1, 2012.
6. T. Schulenberg, J. Starflinger, P. Marsault, D. Bittermann, C. Maraczy, E. Laurien, J. A. Lycklama à Nijehot, H. Anglart, M. Andreani, M. Ruzickova, A. Toivonen, European supercritical water reactor, Nuclear Engineering and Design 241 (2011) 3505-3513.

ISSCWR7-#2081

Applications of Supercritical Fluids in Power Engineering

I. Pioro, Eu. Saltanov and A. Dragunov

Faculty of Energy Systems and Nuclear Science
University of Ontario Institute of Technology
2000 Simcoe Str. North, Ontario, L1H 7K4, Canada
Tel.: 1-905-721-8668 ext. 5528, Fax: 1-905-721-3046, E-mail: Igor.Pioro@uoit.ca

Abstract

It is well known that electrical-power generation is the key factor for advances in industry, agriculture, technology and the level of living. In general, the electricity in the world is mainly generated with coal (41%), natural gas (21%), large hydro (16%), nuclear (14%) and oil (5.5%). Renewable sources of energy, such as biomass, wind, geothermal, and solar, represents only 2.5% of the total electricity generation in the world. In addition, renewable energy sources, such as wind and solar, are intermittent from depending on Mother Nature.

Despite all advances in thermal-power-plants design and operation worldwide (combined-cycle power plants have reached impressive gross thermal efficiency of 62%), they are still considered as not environmentally friendly due to significant carbon-dioxide emissions and air pollution as a result of the combustion process. In addition, coal-fired power-plants produce also enormous amounts of slag and ash, and other gas emissions may contribute to acid rains.

Although nuclear power is often considered a non-renewable energy source as the fossil fuels, nuclear resources can be used for significantly longer time than fossil fuels. Major advantages of nuclear power are: 1) High capacity factors, often in excess of 90% with long operating cycles; 2) Essentially negligible operating emissions of carbon dioxide into atmosphere compared to alternate thermal-power plants; 3) Relatively small amount of fuel required compared to that of fossil-fueled thermal-power plants. Due to that, this source of energy is considered as the most viable one for electrical generation for the next 50–100 years.

In spite of all current advances in nuclear power, nuclear power plants have the following deficiencies: 1) Generate radioactive wastes; 2) Have relatively low thermal efficiencies (up to 2 times lower than that of modern advanced thermal-power plants), especially, water-cooled nuclear power plants (96% of all power reactors in the world); 3) Risk of radiation release during severe accidents; and 4) Production of nuclear fuel is not an environment-friendly process. Eventually, all these deficiencies should be addressed in Generation IV nuclear-reactor concepts and plants.

Therefore, the current paper addresses some of these issues with the emphasis on application of supercritical fluids (carbon dioxide, helium, and water) in Generation-IV nuclear-reactor concepts and corresponding to that power cycles.

1. Introduction

It is well known that electrical-power generation is the key factor for advances in industry, agriculture, technology and the level of living [1]. In general, the electricity in the world is mainly generated with coal (41%), natural gas (21%), large hydro (16%), nuclear (14%) and oil (5.5%). Renewable sources of energy, such as biomass, wind, geothermal, and solar, represent only 2.5% of the total electricity generation in the world and can be appreciable only in selected countries. In addition, operation of wind and solar power plants, and even large hydro-electric power plants depends on Mother Nature, and due to that these plants have relatively low capacity factors[1] (for details, see Table 1).

Table 1. Average (typical) capacity factors[1] of various power plants [1].

No	Power Plant type	Location	Year	Capacity factor, %
1	Hydroelectric	USA and UK	2011	40
		World (average)	-	44
		World (range)	-	10-99
2	Wind	UK	2011	30
		World	2008	20-40
3	Concentrated-solar thermal	USA California Spain	- -	21 75
4	Photovoltaic (PV) solar	USA Arizona	2008	19
		UK	2011	5-8

Despite all advances in thermal-power-plants design and operation worldwide (combined-cycle power plants have reached impressive gross thermal efficiency[2] of 62%) (for details, see Table 2), they are still considered as not environmentally friendly due to significant carbon-dioxide emissions and air pollution as a result of the combustion process. In addition, coal-fired power-plants produce also enormous amounts of slag and ash, and other gas emissions may contribute to acid rains.

Table 2. Typical ranges of thermal efficiencies (gross[2]) of modern advanced thermal power plants [1].

No	Thermal Power Plant	Gross Eff., %
1	Combined-cycle power plant (combination of Brayton gas-turbine cycle (fuel - natural gas; combustion-products parameters at the gas-turbine inlet: T_{in}≈1650°C) and subcritical-pressure Rankine steam-turbine cycle (steam parameters at the turbine inlet: T_{in}≈620°C (T_{cr}=374°C)).	Up to 62
2	SuperCritical-Pressure (SCP) coal-fired power plant (Rankine-cycle "steam" inlet turbine parameters: P_{in}≈25–38 MPa (P_{cr}=22.064 MPa), T_{in}≈540-625°C (T_{cr}=374°C) and T_{reheat}≈540-625°C).	Up to 55

[1] The net capacity factor of a power plant is the ratio of the actual output of a power plant over a period of time (usually, during a year) and its potential output if it had operated at full nameplate capacity the entire time. To calculate the capacity factor, the total amount of energy a plant produced during a period of time should be divided by the amount of energy the plant would have produced at the full capacity. Capacity factors vary significantly depending on the type of a plant.

[2] Gross thermal efficiency of a unit during a given period of time is the ratio of the gross electrical energy generated by a unit to the thermal energy of a fuel consumed during the same period by the same unit. The difference between gross and net thermal efficiencies includes internal needs for electrical energy of a power plant, which might be not so small (5% or even more).

Therefore, the current paper discusses some of the issues related to the current fleet of Nuclear Power Plants (NPPs) as well as Generation-IV nuclear-reactor concepts with the emphasis on application of SuperCritical Fluids (SCFs), such as carbon dioxide, helium, and water; in Generation-IV nuclear-reactor concepts and corresponding to that power cycles.

2. Current Fleet of NPPs

Although nuclear power is often considered to be a non-renewable energy source as the fossil fuels, like coal, gas and oil, nuclear resources can be used for significantly longer, or even indefinite time, than some fossil fuels, especially, if recycling of unused uranium fuel, thorium-fuel resources and fast reactors are used [1]. Major advantages of nuclear power are:
1) High capacity factors are achievable, often in excess of 90% with long operating cycles, making the units suitable for semi-continuous base-load operation, alongside intermittent windmills backed by coal/gas peaking power plants.
2) Essentially negligible operating emissions of carbon dioxide into atmosphere compared to alternate thermal power plants.
2) Relatively small amount of fuel required (for example, a 500-MW_{el} coal-fired SCP power plant requires 1.8 million tons of coal annually, but a fuel load into 1300-MW_{el} Pressurized Water Reactor (PWR) is 115 t (3.2% enrichment) or 1330-MW_{el} Boiling Water Reactor (BWR) – 170 t (1.9% enrichment)). Therefore, this source of energy is considered as the most viable one for electrical generation for the next 50 – 100 years.

In spite of all current advances in nuclear power, NPPs have the following deficiencies: 1) Generation of radioactive wastes; 2) Relatively low thermal efficiencies, especially, water-cooled NPPs (up to 2 times lower than that of modern advanced thermal power plants (see Tables 2 and 3)); 3) Risk of radiation release during severe accidents; and 4) Production of nuclear fuel is not an environment-friendly process. Therefore, all these deficiencies should be addressed.

Table 3. Typical ranges of thermal efficiencies (gross) of modern NPPs [1]. (simplified T-s diagrams of selected power cycles of current NPPs are shown in Figure 1a-c).

No	Nuclear Power Plant	Gross Eff., %
1	Advanced Gas-cooled Reactor (AGR) (carbon-dioxide-cooled) NPP (Generation-III) (reactor coolant: P=4 MPa & T=290-650°C; steam: P=17 MPa (T_{sat}=352°C) & T_{in}=560°C)	Up to 42
2	Sodium-cooled Fast Reactor (SFR) NPP (Generation-IV) (steam: P=14 MPa (T_{sat}=337°C) & T_{in}=505°C) (for T-s diagram, see Fig. 1c)	Up to 40
3	Pressurized Water Reactor (PWR) NPP (Generation-III+, to be implemented within next 1-10 years) (reactor coolant: P=15.5 MPa & T_{out}=327°C; steam: P=7.8 MPa & T_{in}=293°C) (for T-s diagram, see Fig. 1a)	Up to 38
4	Pressurized Water Reactor (PWR) NPP (Generation-III, current fleet) (reactor coolant: P=15.5 MPa & T_{out}=292-329°C; steam: P=6.9 MPa & T_{in}=285°C)	Up to 36
5	Boiling Water Reactor (BWR) NPP or Advanced BWR (ABWR) NPP (Generation-III or III$^+$, current fleet) (P_{in}=7.2 MPa & T_{in}=288°C) (for T-s diagram, see Fig. 1b)	Up to 34
6	RBMK (boiling, pressure-channel) NPP (Generation-III, current fleet) (P_{in}=6.6 MPa & T_{in}=282°C)	Up to 32

7	Pressurized Heavy Water Reactor (PHWR) NPP (Generation-III, current fleet) (reactor coolant: P=11 MPa & T=260-310°C; steam: P=4.6 MPa & T_{in}=259°C)	Up to 32

Currently, 31 countries in the world have operating nuclear-power reactors [2] (for details see, Table 4). Analysis of these data shows that 15 countries plan to build new reactors; 16 countries do not plan to build new reactors; and 4 countries without reactors (Bangladesh, Belarus, Turkey and United Arab Emirates (UAE) work towards introducing nuclear energy on their soils.

Table 4. Number of nuclear-power reactors in operation and forthcoming as per March 2014 [2] and before the Japan earthquake and tsunami disaster (March 2011) [3].

No	**Reactor type** (Some details on reactors)	**No. of units**		**Installed capacity, GW_{el}**		**Forthcoming units**	
		As of March 2014	**Before March 2011**	**As of March 2014**	**Before March 2011**	**No. of units**	**GW_{el}**
1	**Pressurized Water Reactors (PWRs)** (largest group of nuclear reactors in the world – 63%)	**270** ↑	268	**250** ↑	248	89	93
2	**Boiling Water Reactors (BWRs) or Advanced BWRs** (2nd largest group of reactors in the world – 19%; ABWRs – the only ones Gen-III+ operating reactors)	**81** ↓	92	**76** ↓	84	6	8
3	**Pressurized Heavy Water Reactors (PHWRs)** (3rd largest group of reactors in the world – 11%; mainly CANDU-reactor type)	**48** ↓	50	**24** ↓	25	9	6
4	**Gas Cooled Reactors (GCRs)** (UK, Magnox reactor, only 1 left) and **Advanced Gas-cooled Reactors (AGRs)** (UK, 14 reactors); (all these CO_2-cooled reactors will be shut down in the nearest future and will not be built again)	**15** ↓	18	**8** ↓	9	1	0.2
5	**Light-water, Graphite-moderated Reactors (LGRs)** (Russia, 11 RBMKs and 4 EGPs[3]; these pressure-channel boiling-water-cooled reactors will be shut down in the nearest future and will not be built again)	**15**	15	**10**	10	0	0
6	**Liquid-Metal Fast-Breeder Reactors (LMFBRs)** (Russia, SFR – BN-600; the only one Gen-IV operating reactor)	**1**	1	**0.6**	0.6	5	1.6
	In total	**430** ↓	**444**	**369** ↓	**378**	**110**	**109**

[3] EGP – Power Heterogeneous Loop reactor (in Russian abbreviations), channel-type, graphite-moderated, light-water coolant, boiling reactor with natural circulation.

Explanations to Table 4:
Data in Table 4 include 48 reactors from Japan, which are currently not in operation.
Arrows mean decrease or increase in a number of reactors.
Forthcoming GCR is a helium-cooled reactor.

Analysis of the data in Table 4 shows that the vast majority of all nuclear-power reactors in the world (96%) is actually water-cooled reactors. Moreover, this trend will stay for quite long time, because the largest number of oncoming reactors is PWRs (in total 89). However, we have reached the maximum gross thermal efficiency of water-cooled NPPs, which will stay at about 36-38% for oncoming Generation III$^+$ PWRs. Of course, we need to have bright future for this largest group of nuclear reactors in terms of thermal efficiency and competiveness with advanced thermal power plants.

3. Application of Supercritical Fluids (SCFs) and SCPs in Generation-IV NPPs

The three key challenges to new nuclear energy today [1] are:

(a) competing with lower costs generating options, especially, natural gas and subsidized wind/solar power;
(b) improving safety, so that even the threat of uncontrolled releases and consequent public fear and evacuation is avoided; and
(c) ensuring more sustainable fuel cycles, to make better use of existing natural resources, and reduced waste streams.

The demand for clean, non-fossil-based electricity is growing. Therefore, the world needs to develop new nuclear reactors with inherent safety and higher thermal efficiencies in order to increase electricity generation per kg of fuel and decrease detrimental effects on the environment. The current fleet of NPPs is classified as Generation-II and III (just a limited number of Generation-III$^+$ reactors (mainly, Advanced Boiling Water Reactors (ABWRs)) operate in some countries). However, all these designs (here we are talking only about water-cooled power reactors) are not as energy efficient as they should be, because their operating temperatures are relatively low, i.e., below 350°C for a reactor coolant and even lower for steam in the power-conversion cycle (see Table 3).

Currently, a group of countries, including Argentina, Brazil, Canada, China, France, Japan, the Republic of Korea, the Russian Federation, South Africa, Switzerland, the United Kingdom and the United States have initiated an international collaboration to develop the next generation nuclear reactors (Generation-IV reactors) [1]. Having been started in recognition of the need for international collaboration at the pre-commercial phase, this collaboration is intended for market deployment over a longer time frame, after planned cooperative development. The ultimate goal of developing such reactors is to meet the three challenges, with an increase in thermal efficiencies of NPPs from 30 - 36% to 40 - 50% and even higher (see Table 5). This increase in thermal efficiency would result in a higher generation of electricity compared to current Light-Water-Reactor (LWR) technologies per 1 kg of uranium.

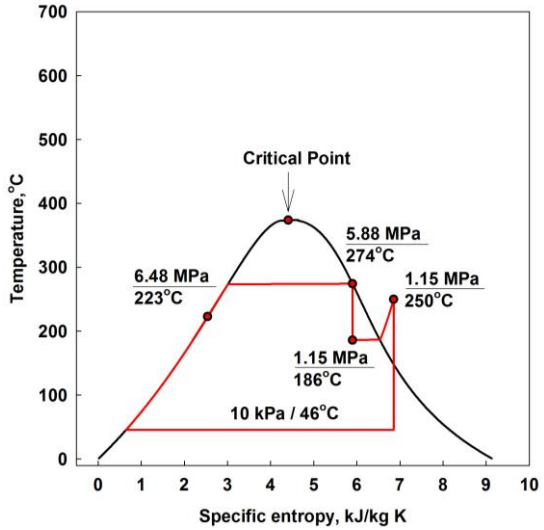

(a) 1000-MW_{el} VVER-1000 PWR NPP [4]

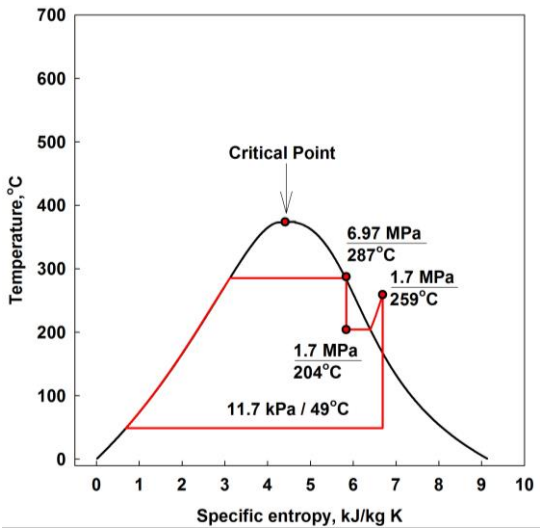

(b) ABWR NPP [4]

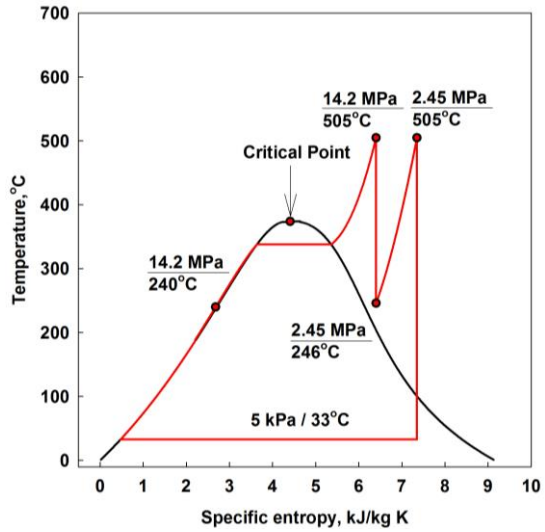

(c) 600-MW_{el} BN-600 SFR NPP [4]

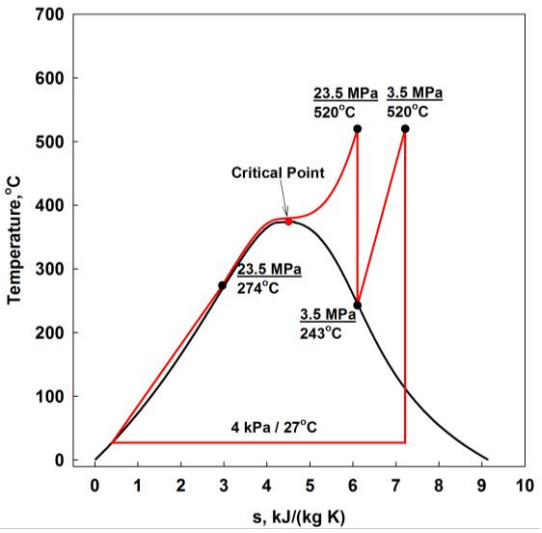

(d) 1200-MW_{el} LFR NPP (based on data for Brest-1200 and corresponding Russian turbine K-1200-240)

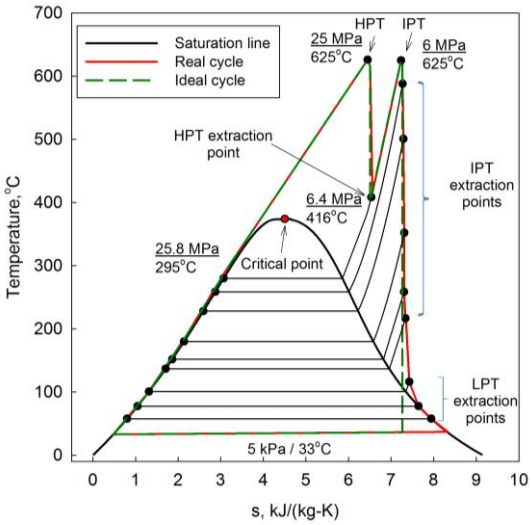

(e) 1200-MW_{el} SCWR NPP (for thermal layout, see Figure 2)

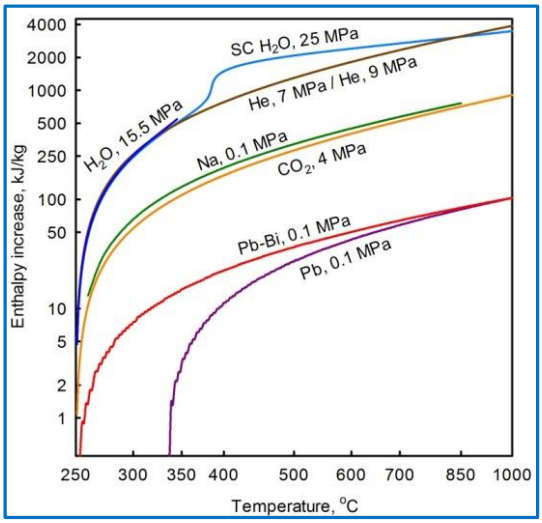

(f) Specific enthalpy rise vs. temperature [5]

Figure 1. Simplified T-s diagrams of selected Generation III (a), III+ (b) and IV (c-e) NPPs and specific enthalpy rise vs. temperature for various reactor coolants.

Table 5. Estimated ranges of thermal efficiencies (gross) of Generation-IV NPP concepts (critical parameters of carbon dioxide, helium and water are listed in Table 6) [1].

No	Nuclear Power Plant	Gross Eff., %
1	Very High Temperature Reactor (VHTR) NPP (reactor coolant – SuperCritical (SC) helium: P=7 MPa and T_{in}/T_{out}=640/1000°C; primary power cycle – direct SCP Brayton gas-turbine cycle; possible back-up – indirect subcritical-pressure Rankine steam cycle[1]; there is a possibility that indirect SCP carbon-dioxide Brayton gas-turbine cycle can be used).	≥55
2	Gas-cooled Fast Reactor (GFR) or High Temperature Reactor (HTR) NPP (reactor coolant – SC helium: P=9 MPa and T_{in}/T_{out}=490/850°C; primary power cycle – direct SCP Brayton gas-turbine cycle; possible back-up – indirect subcritical-pressure Rankine steam cycle[1]; there is a possibility that indirect SCP carbon-dioxide Brayton gas-turbine cycle can be used).	≥50
3	SuperCritical Water-cooled Reactor (SCWR) NPP (one of Canadian concepts; reactor coolant – light water: P=25 MPa (P_{cr}=22.064 MPa) and T_{in}/T_{out}=350/625°C (T_{cr}=374°C); direct or indirect SCP Rankine "steam" cycle[2] with single secondary-steam superheat (up to 625°C)) (for T-s diagram, see Fig. 1e, and for thermal layout – Figure 2).	45-50
4	Molten Salt Reactor (MSR) NPP (reactor coolant – sodium-fluoride salt with dissolved uranium fuel: T_{out}=700 - 800°C; primary power cycle – indirect SCP carbon-dioxide Brayton gas-turbine cycle; possible back-up – indirect subcritical-pressure Rankine steam cycle[1]).	~50%

No	Nuclear Power Plant	Gross Eff., %
5	Lead-cooled Fast Reactor (LFR) NPP (Russian design Brest-300: reactor coolant – liquid lead: P≈0.1 MPa and T_{in}/T_{out}=420/540°C; primary power cycle – indirect SCP Rankine "steam" cycle[2]: P_{in}≈24.5 MPa (P_{cr}=22.064 MPa) and T_{in}/T_{out}=340/520°C (T_{cr}=374°C) (for T-s diagram, see Fig. 1d); with single secondary-steam superheat (possible back-up in some other countries – indirect SCP carbon-dioxide Brayton gas-turbine cycle)).	~43
6	Sodium-cooled Fast Reactor (SFR) NPP (Russian design BN-600: reactor coolant – liquid sodium (primary circuit): P≈0.1 MPa and T_{in}/T_{out} =380/550°C; liquid sodium (secondary circuit): T_{in}/T_{out} =320/520°C; primary power cycle – indirect subcritical-pressure Rankine steam cycle[1]: P_{in}≈14.2 MPa (T_{sat}≈337°C) and $T_{in\ max}$=505°C (T_{cr}=374°C); with single secondary-steam superheat: P≈2.45 MPa and T_{in}/T_{out}=246/505°C (for T-s diagram, see Fig. 1c); possible back-up in some other countries - indirect SCP carbon-dioxide Brayton gas-turbine cycle).	~40

[1, 2] Subcritical-pressure and SCP Rankine steam cycles are the only power cycles proven and used in power industry for many years. All other cycles: SCP helium and carbon-dioxide Brayton gas-turbine cycles have not been proved in industry yet.

Table 6. Basic properties of selected reactor and power-cycle fluids [6].

No	Gas	Molar mass	Triple point T	Normal boiling T	T_{cr}	P_{cr}	ρ
		kg/kmol	°C	°C	°C	MPa	kg/m^3
1	Carbon dioxide, CO_2	44.01	-56.56	-78.46	30.98	7.377	467.6
2	Helium, He	4.00	-270.97	-268.93	-267.95	0.228	72.6
3	Water, H_2O	18.02	0.01	99.97	373.95	22.064	322.0

The Generation-IV International Forum (GIF) Program has narrowed design options of nuclear reactors to six concepts [1]. These concepts are:
1) Very High Temperature Reactor (VHTR),
2) Gas-cooled Fast Reactor (GFR) or just High Temperature Reactor (HTR),
3) SuperCritical Water-cooled Reactor (SCWR) [7-11],
4) Molten Salt Reactor (MSR),
5) Lead-cooled Fast Reactor (LFR), and
6) Sodium-cooled Fast Reactor (SFR).

Currently, from all six concepts of Generation-IV reactors only an SFR is in operation in Russia (BN-600). Next concepts, which will be possibly put into operation, are: 1) LFR (Brest-300) in Russia, and 2) helium-cooled HTR in China. In general, as it was mentioned before, we need to have bright future for the most "popular" reactors, i.e., water-cooled ones. Therefore, an SCWR concept [7-11] looks quite attractive as the Generation-IV water-cooled reactor with high thermal efficiency (see Table 5). This concept is based on materials and technology and direct-cycle turbines already developed and deployed worldwide at SCP coal-fired power plants, which have extended their efficiencies using higher temperatures and pressures in order to improve costs and reduce specific emissions. However, more research is required, especially, in material science to define candidate materials for reactor-core elements, which will be subjected to very aggressive medium such as SuperCritical Water (SCW), high pressures and temperatures, and high neutron flux.

The intent of all the newer concepts is to have a recyclable fuel, and often to extend the resource use to include thorium-based cycles.

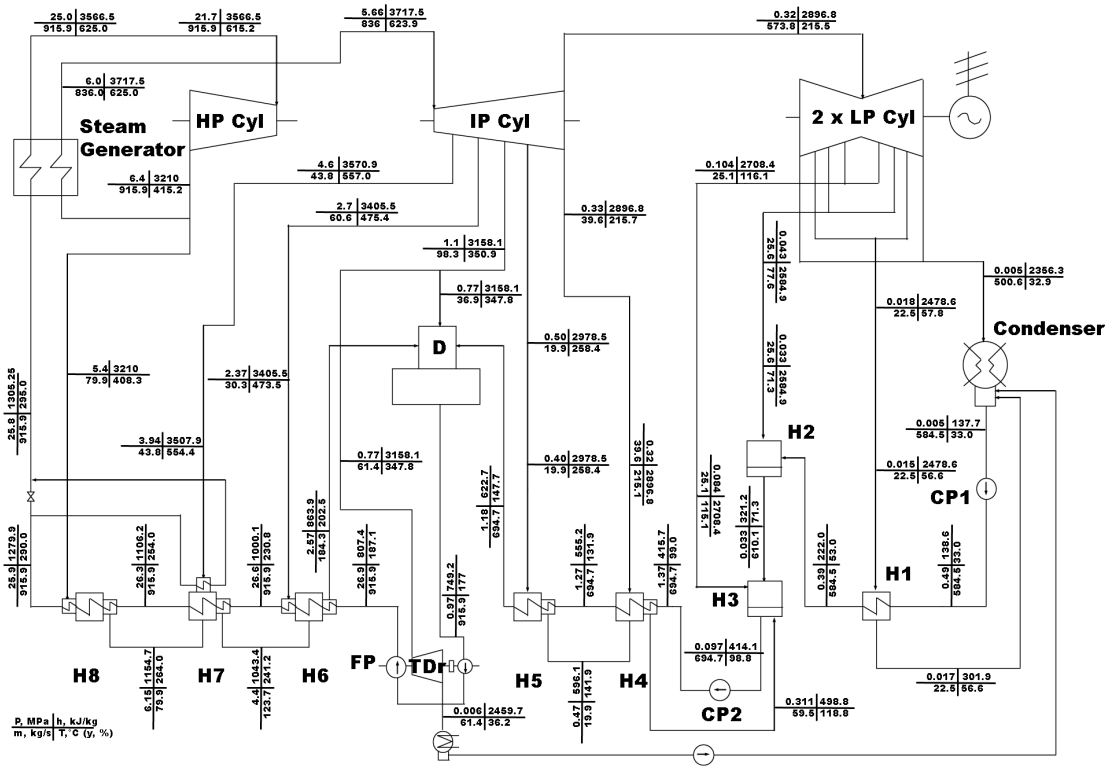

Figure 2. Thermal layout of 1200-MW_{el} SCWR (direct-cycle option) (for T-s diagram, see Fig. 1e) [12]. This thermal layout is based on single-reheat-cycle 660-MW_{el} Tom'-Usinsk thermal power plant (Russia): HP- High Pressure; Cyl – Cylinder; IP – Intermediate Pressure; LP – Low Pressure; D – Deaerator; H – Heat exchanger (feedwater heater); FP - Feedwater Pump; CP – Condenser Pump; and TDr – Turbine Drive.

4. Conclusions

The basis for nuclear energy for future electric-power generation must take into account the key influences of the global, political, financial and social pressures in the evolving energy marketplace. The competitive pressures and political factors are likely to dominate the future usage and deployment, including national attitudes to, and international issues arising from energy security and climate change.

1. Major sources for electrical-energy production in the world today are: 1) thermal - primary coal (41%) and secondary natural gas (21%) (also, oil is used (5.5%)); 2)"large" hydro (16%); and 3) nuclear (14%). Other energy sources have visible impact just in some countries, especially, where there are government incentives for wind- and solar-power portfolios with electricity prices guaranteed by legislation and power-purchase contracts.
2. In spite of advances in combined-cycle and coal-fired power-plants design and operation worldwide they are still considered as not particularly environmental friendly due to producing gaseous carbon-dioxide emissions as a result of combustion process, plus coal-fired power-plants have significant tailings of slag and ash.

3. In general, the major driving force for all advances in thermal and nuclear power plants is thermal efficiency and generating costs. Ranges of gross thermal efficiencies of modern power plants are as the following: 1) Combined-cycle thermal power plants – up to 62%; 2) Supercritical-pressure coal-fired thermal power plants – up to 55%; 3) Carbon-dioxide-cooled reactor NPPs – up to 42%; 4) Sodium-cooled fast reactor NPP – up to 40%; 5) Modern water-cooled NPPs (the largest group of power reactors – 96% of the total number of 430) – 30 – 36%. Therefore, this group of reactors must have bright future to be competitive with modern thermal power plants.
4. Nuclear power is, in general, a non-renewable source as the fossil fuels unless fuel recycling is adopted, which means that nuclear resources can be used significantly longer than some fossil fuels, plus nuclear power does not emit carbon dioxide into atmosphere. Currently, this source of energy is considered as the most viable one for base-load electrical generation for the next 50 – 100 years.
5. The major advantages of nuclear power are well known, including cheap reliable base-load power, high capacity factor and low emissions and minor environmental impact. But these factors are offset today by a competitive disadvantage with natural gas, the occurrence of three significant nuclear accidents (Fukushima, Chernobyl and Three Mile Island), which caused significant social disruption and high capital costs.
6. All current Generation-II and III and oncoming Generation-III$^+$ NPPs are not very competitive with modern thermal power plants in terms of thermal efficiency, the difference in values of thermal efficiencies of thermal and nuclear power plants can be up to 50% with NPPs having higher generating cost and construction times than that of thermal power plants.
7. Therefore, enhancements are needed beyond the current builds. New generation (Generation-IV) NPPs must have thermal efficiencies close to those of modern thermal power plants, i.e., within a range of at least 40 – 50%, and improved safety measures and designs in order to be built in the nearest future.
8. All six concepts of Generation-IV reactors are high-temperature reactors. Generation-IV NPPs will have higher thermal efficiencies starting from 40% (SFR) and going beyond 45-50% for VHTR, HTR, MSR and SCWR concepts.
9. SCWR concept is considered as the conventional way for increasing thermal efficiency of a water-cooled NPP as it was done in supercritical-pressure coal-fired power plants more than 50 years ago. The major advantages of SCWR NPP is high thermal efficiencies and proven in power industry for more than 50 years SCP Rankine “steam”-turbine cycle with the corresponding equipment and layout. However, the major problem in SCWR design is reliability of in-core materials at SCPs, high heat fluxes and neutron fluxes, and aggressive reactor coolant – SCW. In addition, in comparison with other five Generation-IV nuclear-reactor concepts no one SCWR has been tested as an experimental, transport or any other kind prototype reactor.
10. Analysis of Generation-IV nuclear-reactor concepts and corresponding power cycles shows that three concepts: VHTR, HTR and SCWR; will use supercritical fluids as reactor coolants (helium (first two concepts) and water (the third one)). Also, the following three SCP power cycles can be used: 1) direct SCP-helium Brayton gas-turbine cycle as the primary choice in VHTR and HTR; 2) SCP Rankine “steam”-turbine cycle as the only option for SCWR (direct or indirect cycle); and as the current option for LFR (Breat-300, Russian design, indirect cycle); and 3) indirect SCP-carbon-dioxide Brayton gas-turbine cycle as primary or back-up option for SFR, MSR, LFR and even VHTR and HTR.

5. Acknowledgements

This research is related to the IAEA Coordinated Research Project (CRP) on Understanding and Prediction of Thermal-Hydraulics Phenomena Relevant to SCWRs.

6. Nomenclature

P	pressure, MPa
s	specific entropy, J/kg K
T	temperature, ºC

Greek Symbols

ρ	density, kg/m^3

Subscripts

cr	critical
el	electrical
in	inlet
out	outlet
reheat	reheat
sat	saturation

Abbreviations:

ABWR	Advanced Boiling Water Reactor
AGR	Advanced Gas-cooled Reactor
BN	Fast Neutrons (reactor) (in Russian abbreviation)
BWR	Boiling Water Reactor
eff.	efficiency
GCR	Gas-Cooled Reactor
GFR	Gas-cooled Fast Reactor
GIF	Generation IV International Forum
HTR	High Temperature Reactor
LFR	Lead-cooled Fast Reactor
LGR	Light-water Graphite-moderated Reactor
LMFBR	Liquid-Metal Fast-Breeder Reactor
LWR	Light-Water Reactor
MSR	Molten Salt Reactor
NPP	Nuclear Power Plant
PHWR	Pressurized Heavy-Water Reactor
PWR	Pressurized Water Reactor
RBMK	Reactor of Large Capacity Channel type (in Russian abbreviations)
SCF	SuperCritical Fluid
SCP	SuperCritical Pressure
SCW	SuperCritical Water
SCWR	SuperCritical Water Reactor
SFR	Sodium Fast Reactor
VHTR	Very High Temperature Reactor
VVER	Water-Water Power Reactor (in Russian abbreviation)

7. References

[1] Pioro, I. and Duffey, R., 2015. Nuclear Power as a Basis for Future Electricity Generation, ASME Journal of Nuclear Engineering and Radiation Science, Vol. 1, No. 1, 19 pages.
[2] Nuclear News, 2014, March, Publication of American Nuclear Society (ANS), pp. 45-78.
[3] Nuclear News, 2011, March, Publication of American Nuclear Society (ANS), pp. 45-78.
[4] Dragunov, A., Saltanov, Eu., Pioro, I., et al., 2015. Power Cycles of Generation III and III+ Nuclear Power Plants, ASME Journal of Nuclear Engineering and Radiation Science, Vol. 1, No. 1.
[5] Dragunov, A., Saltanov, Eu., Pioro, I., et al., 2013. Investigation of Thermophysical and Nuclear Properties of Prospective Coolants for Generation-IV Nuclear Reactors, Proc. 21st Int. Conf. On Nuclear Engineering (ICONE-21), July 29-August 2, Chengdu, China, Paper #16020, 11 pages.
[6] National Institute of Standards Technology, NIST Reference Fluid Thermodynamic and Transport Properties-REFPROP: NIST Standard Reference Database 23, Ver. 9.0, Department of Commerce, Boulder, CO, USA, 2010.
[7] Pioro, I., 2011. The Potential Use of Supercritical Water-Cooling in Nuclear Reactors. Chapter in Nuclear Energy Encyclopedia: Science, Technology, & Applications, Editors: S. Krivit, J. Lehr and Th. Kingery, J. Wiley & Sons, Hoboken, NJ, USA, pp. 309-347 pages.
[8] Pioro, I.L. and Duffey, R.B., 2007. Heat Transfer and Hydraulic Resistance at Supercritical Pressures in Power Engineering Applications, ASME Press, New York, NY, USA, 328 pages.
[9] Oka, Yo., Koshizuka, S., Ishiwatari, Y. and Yamaji, A., 2010. Super Light Water Reactors and Super Fast Reactors, Springer, Germany, 416 pages.
[10] Schulenberg, Th. and Starflinger, J., Editors, 2012. High Performance Light Water Reactor. Design and Analyses, KIT Scientific Publishing, Germany, 241 pages.
[11] Heat Transfer Behaviour and Thermohydraulics Code Testing for SCWRs, IAEA TECDOC Series, IAEA-TECDOC-1746, 2014, September, Vienna, Austria, 496 pages.
[12] Saltanov, Eu., Peiman, W., Draper, Sh. and Pioro, I., 2011. Heat-Transfer Analysis of Supercritical-Water and Superheated-Steam-Cooled Channels of SCWR, Proc. 5th Int. Symp. on SCWR (ISSCWR-5), Vancouver, BC, Canada, March 13-16, Paper P65, 11 pages.

ISSCWR7-2083

Steady-State Radiolysis of Supercritical Water: Model Development, Predictions and Validation

V. Subramanian[1], J.M. Joseph[1], H. Subramanian[1], J.J. Noël[1], D.A. Guzonas[2], J.C. Wren[1]
[1] Department of Chemistry, the University of Western Ontario, London, Ontario, Canada N6A 5B7
[2] Canadian Nuclear Laboratories, Chalk River, Ontario, Canada K0J 1J0
Telephone: 519 661 2111 Ex 86339, jcwren@uwo.ca

Abstract

Chemical kinetic models are being developed for the γ-radiolysis of subcritical and supercritical water (SCW) to estimate the concentrations of radiolytically-produced oxidants. Many of the physical properties of water change sharply at the critical point. These properties control the chemical stability and transport behaviour of the ions and radicals generated by the radiolysis of SCW. The effects of changes in the solvent properties of water on primary radiolytic processes and the subsequent aqueous reaction kinetics can be quite complicated and are not yet well understood.

The approach used in this work was to adapt an existing liquid water radiolysis model (LRM) that has already been validated for lower temperatures and a water vapour radiolysis model (VRM) validated for higher temperatures, but for lower pressures, to calculate radiolysis product speciation under conditions approaching the supercritical state. The results were then extrapolated to the supercritical regime by doing critical analysis of the input parameters. This exercise found that the vapour-like and liquid-like models make similar predictions under some conditions.

This paper presents and discusses the LRM and VRM predictions for the concentrations of molecular radiolysis products, H_2, O_2 and H_2O_2 at two different irradiation times, 1 s and 1 h, as a function of temperature ranging from 25 °C to 400 °C. The model simulation results are then compared with the concentrations of H_2, O_2 and H_2O_2 measured as a function of γ-irradiation time at 250 °C. Model predictions on the effect of H_2 addition on the radiolysis product concentrations at 400 °C are presented and compared with the experimental results from the Beloyarsk Nuclear Power Plant (NPP).

1. Introduction

Supercritical water (SCW) is an attractive candidate as a coolant in nuclear reactors owing to its increased thermal efficiency compared to subcritical water. The Canadian SCW reactor (SCWR) is a pressure tube concept which would operate with a core outlet temperature of 625 °C and a thermal efficiency of ~48%. One of the main challenges in the use of SCW as a reactor coolant is corrosion of in-core materials, and predicting the corrosion rate of candidate materials requires an understanding the effects of the oxidizing products of water radiolysis [1,2].

Exposed to ionizing radiation, liquid water and water vapour decompose to form a number of chemically reactive species, as shown in reaction schemes (1) and (2) respectively [3]. The primary radiolysis yields per absorbed energy at 25 °C are given in brackets (G-values in units of $\mu mol \cdot J^{-1}$):

$$H_2O\ (-0.41) \xrightarrow{\gamma} \bullet OH(0.27),\ \bullet e_{aq}^-(0.26),\ \bullet H(0.06),\ H_2(0.04),\ H_2O_2(0.07),\ H^+(0.26) \quad (1)$$

$$H_2O\ (-0.74) \xrightarrow{\gamma} \bullet OH(0.63), \bullet H(0.74), H_2(0.055), \bullet O(0.11) \quad (2)$$

These primary radiolysis species also react to form secondary products such O_2 and $\bullet O_2^-$. One major difference between the radiolysis of liquid water and water vapour is the absence of ionic products for vapour radiolysis. As well, H_2O_2 is formed as a primary product during the radiolysis of liquid water while it is formed as a secondary product during the radiolysis of water vapour.

In the presence of a constant radiation source, water decomposition products are continuously produced at a constant rate. As the concentrations of the radiolysis products accumulate, the reaction rates to remove the radiolysis products increase, eventually matching their radiolytic production rates. The system reaches a pseudo-steady state on a time scale on the order of milliseconds. It then more slowly approaches a true steady state over a longer period of time which is controlled by the rates of slower processes, such as surface reactions and interfacial transport [4,5]. In the proposed SCWR concept the coolant resides in the core for a few seconds. This time scale may not be long enough for the coolant radiolysis system to reach a true steady state but will be long enough to reach a pseudo-steady state. The pseudo steady-state concentrations, not the primary radiolysis yields, of important oxidizing species (such as •OH, H_2O_2, and O_2) in the water phase are crucial in determining the corrosion behaviour of in-core materials [6-8]. Thus, it is important to understand the radiolysis behaviour of SCW in a steady-state radiation field.

The critical point of water is 374 ºC and 22 MPa. Many of the physical properties of water, such as density and water dissociation constant, change drastically with temperature in the vicinity of the critical point. These properties control the chemical stability and transport behaviour of the ions and radicals generated by radiolysis [9,10]. However, the effect of changes in the solvent properties of water on the primary radiolysis yields and the subsequent aqueous reaction kinetics in the sub- and supercritical water regimes are not well established, due to the difficulty in performing experiments at very high temperature and pressure [11,12]. The situation is somewhat better for the primary radiolysis yields, but some discrepancies in the measured primary radiolysis yields have been reported which could have risen due to scavenging experiments having been performed at different time scales [13,14]. Monte Carlo simulations of low linear energy transfer (LET) radiation interactions with water have also been used to predict the yields and lifetimes of species in a radiation spur for SCW at 400 °C [15]. These can provide valuable information regarding the temperature and density dependence of primary radiolysis yields. The experimental situation is worse for chemical reaction rate constants. In the supercritical state, wide ranges of densities are possible for water [11], making its behavior gas- or liquid-like. The effects of solvent properties at SCW temperatures and pressures on chemical reaction kinetics are not understood well. The rate constant of a diffusion-limited reaction (such as $H_2 + \bullet OH \rightarrow H_2O + \bullet H$) is particularly sensitive to the solvent properties and can increase by more than an order of magnitude for the reaction in the gas phase to that in the liquid phase, at a given temperature. At high temperatures many chemical reactions also become diffusion limited in the respective solvent environments.

As a consequence, we cannot yet construct a fully validated predictive analysis tool for SCW radiolysis. The accuracy of a radiolysis model depends on the proper choice of G values, reaction rate constants and the set of chemical reaction rate equations that it includes. Given the challenges, as an interim approach, we chose to construct two different SCW radiolysis models based on existing liquid-water [4,5,16] and water-vapour [17] radiolysis models. The intent was to explore the differences in predictions of water radiolysis behaviour by the two models as the temperature moves from the sub-critical regime to above the critical temperature. The model predictions would provide bounding limits for key radiolytically-produced oxidants, namely, H_2O_2 and O_2, as a function of fluid density in SCW. We can also use these models to explore suppression of the net formation of oxidizing radiolysis products by H_2 addition, a technique commonly used in water-cooled reactors. Hence, we have developed two chemical kinetics models for the continuous radiolysis of sub-critical and supercritical water: (1) a liquid radiolysis model (LRM) and (2) a vapour radiolysis model (VRM).

In this paper we present and discuss the LRM and VRM predictions for the concentrations of molecular radiolysis products, H_2, O_2 and H_2O_2 at two different irradiation times, 1 s and 1 h, as a function of temperature ranging from 25 °C to 400 °C. The model simulation results are then compared with the

concentrations of H_2, O_2 and H_2O_2 measured as a function of γ-irradiation time at 250 °C. We also present model predictions on the effect of H_2 addition on the radiolysis product concentrations at 400 °C and compare the predicted O_2 concentration as a function of the concentration of added H_2 with the results obtained from the experiments performed at the Beloyarsk Nuclear Power Plant (NPP) [18,19].

2. Experimental

The high-temperature experiments were performed using a 300 ml Type 316 stainless steel autoclave (the test cell) equipped with an online sampling assembly. All experiments were performed using a 0.01 M borate buffer solution at pH 10.6 to minimize the release of corrosion products from the autoclave cell. All experiments were performed with deaerated solutions purged with Ar and covered with Ar gas in the test cells. The test cells had a gas to liquid volume (V_g:V_{aq}) ratio of 9:1 and an liquid-gas interfacial area of 28.3 cm^2 (i.e. the cross-sectional area of the test cell). The presence of a cover gas allowed us to measure the concentrations of radiolytically-produced H_2 and O_2 that migrated to the gas phase.

Irradiation was carried out for 5 h in a ^{60}Co gamma-cell (MDS Nordion), which provided an irradiation chamber with a uniform absorbed dose rate of 3.3 $kGy \cdot h^{-1}$, determined using Fricke dosimetry [3]. The autoclave was heated to the desired temperature prior to irradiation, and the temperature was maintained constant during the irradiation time. After irradiation, samples of the gaseous and aqueous phases were extracted using the online sampling assembly. The sampling assembly consisted of a feed line drawing samples from the autoclave headspace in the gamma-cell, a sampling tube with cooling jacket and isolation valves, and provision for gas sampling from the tube. The sampling procedure was standardized by optimising the sampling duration and repeating the measurements. The gas samples were extracted using a gas-tight syringe with a Luer lock (Agilent Technologies) and analyzed for H_2 and O_2 using gas chromatography (GC-6580, Agilent Technologies). The condensed liquid samples were analyzed for H_2O_2 using the Ghormley tri-iodide method [20]. At 250 °C, the liquid sample also was analysed for H_2O_2.

The detection limit for the gaseous concentrations [H_2] and [O_2] were found to be 4.0×10^{-7} $mol \cdot dm^{-3}$ and 4.0×10^{-5} $mol \cdot dm^{-3}$, respectively. The H_2O_2 analysis in the condensed liquid phase was performed within 2 minutes of sampling to minimize thermal decomposition. The Ghormley tri-iodide method gave a detection limit for [H_2O_2] of 3×10^{-6} $mol \cdot dm^{-3}$.

3. Models and Model Results on Temperature Dependence

3.1 The models

Each of the radiolysis models consists of a set of primary radiolysis processes (reactions 1 and 2) and a set of elementary reactions in the respective water phase. In these models the radiolysis processes that occur prior to the attainment of homogeneous yields (typically occurring in less than 1 μs) are not modelled in detail. Instead, the model uses G-values and the absorbed radiation dose rate to determine the radiolysis production rate. The rates of the elementary chemical reactions follow classical chemical reaction rate equations:

$$\frac{\mathrm{d[i]}}{\mathrm{dt}} = (10^{-6} \cdot G_i) \cdot \rho_{H_2O} \cdot D_R + \sum_{l,m \to i} k_{lm} \cdot [l] \cdot [m] \cdot - \sum_j k_{ij} \cdot [i] \cdot [j] \qquad \text{(Eq. 1)}$$

Here G_i is the G-value for production of species i ($\mu mol \cdot J^{-1}$), D_R is the absorbed radiation dose rate ($Gy \cdot s^{-1}$ or $J \cdot kg^{-1} \cdot s^{-1}$), ρ_{H2O} is the density of water ($kg \cdot dm^{-3}$), and k_{lm} and k_{ij} are 2nd order rate constants for the reactions of species l with m, and i with j, respectively ($dm^3 \cdot mol^{-1} \cdot s^{-1}$).

The LRM consists of the reaction set used in an existing model that was developed and validated for the radiolysis of liquid water at ambient temperatures [16,4,5]. The temperature dependences of the rate parameters, the G-values and the chemical reaction rate constants in the LRM are those established for solution reactions up to 350 °C [16]. The LRM does not take into account the effect of changes in the water solvent properties near the critical point. The VRM consists of the reaction set developed by Arkhipov et al. [17] for water vapour radiolysis at high temperatures (900 K). His model was developed for much lower pressures (10^4 to 10^6 Pa) and lower vapour densities ($0.25 \times 10^{-3} - 1 \times 10^{-3}$ g·cm^{-3}) than those of SCW. The G-values for water vapour radiolysis do not change with temperature [3] and hence are assumed to be constant with temperature in the VRM. The temperature dependences of the chemical reaction rate constants are those established for vapour phase reactions [17].

The LRM and VRM calculations were performed at a dose rate of 1000 kGy·h^{-1}, simulating SCWR core conditions. Figure 1 shows the concentrations of molecular radiolysis products as a function of temperature predicted by the LRM and VRM after 1 s and 1 h irradiation periods. In each graph the left hand curves are the predictions of the LRM and the right hand curves are the predictions of the VRM. The bar at the top of the graphs indicates the nature of the fluid being modelled. The left hand panels show the concentrations in M (mol·dm^{-3}), whereas the right hand panels show the concentrations in g·kg^{-1} (or weight fraction), the units typically used by nuclear station chemists.

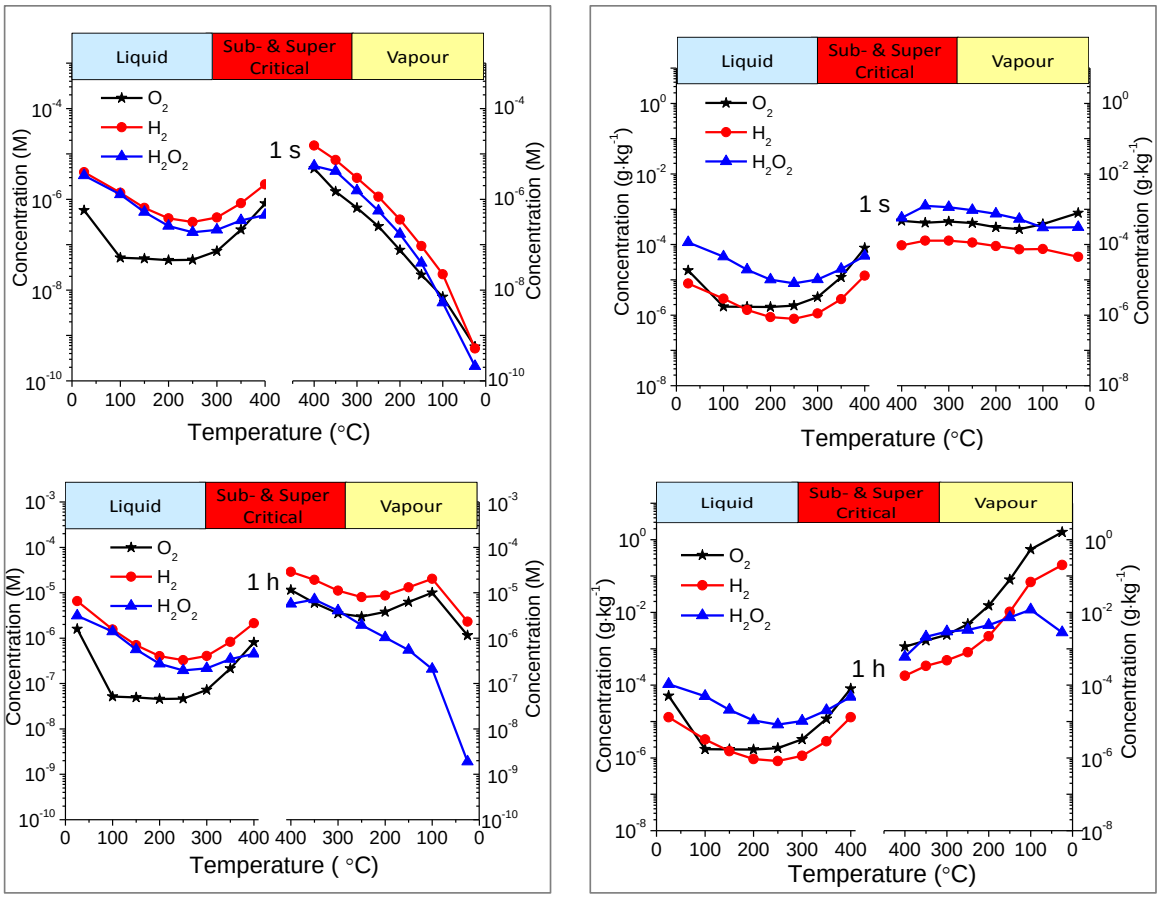

Figure 1. Radiolysis product concentrations as a function of temperature predicted by the LRM and VRM after 1 s and 1 h irradiation at a dose rate of 1000 kGy·h^{-1}. The left hand panels show the concentrations in M (mol·dm^{-3}), whereas the right hand panels show the concentrations in units of g·kg^{-1}.

The density of water used in the model calculations was that of liquid water for the LRM and that of water vapour at saturation pressure for the VRM, Table 1 [21]. It should be noted that in the model, for 400 °C, a density of 0.322 was chosen; this corresponds to a pressure of 29.2 MPa. Over the temperature range studied, the change in the density of liquid water is small while the saturation water vapour density increases very rapidly with temperature. At a given temperature, the LRM predicts that the concentrations of the primary radiolysis products, H_2 and H_2O_2, are similar at both 1 s and 1 h. This indicates that their concentrations reach near steady state very rapidly, particularly at T > 100 °C. The concentrations of these species decrease by about 1.5 orders of magnitude with increasing temperature, but then rise again. The concentration of the secondary product O_2 shows the fastest decrease with increasing temperature, but then remains constant with temperature in the range 100 °C to 250 °C and rises at T > 250 °C. The faster attainment of the pseudo steady-state concentrations at T > 100 °C can be attributed to the increased rates of chemical reactions (the last term in Eq. 1). The increases in the concentrations of the radiolysis products with temperature above 250 °C can be attributed to the changes in the density and other solvent properties of water in this regime and the effect of these changes on the G-values and the rate constants.

Table 1. Densities of liquid water and water vapour as a function of temperature.

Temp (°C)	Saturation Pressure (MPa)	Liquid Density ($g \cdot cm^{-3}$)	Vapour Density ($g \cdot cm^{-3}$)
25	0.003	0.997	2.31×10^{-5}
100	0.101	0.958	59.8×10^{-5}
150	0.476	0.917	2.55×10^{-3}
200	1.555	0.865	7.86×10^{-3}
250	3.976	0.799	19.96×10^{-3}
300	8.588	0.712	46.2×10^{-3}
350	16.529	0.575	0.114
374	22.064	0.322	0.322
400(SCW)	29.2	0.322	0.322

The VRM predicts that the molar concentrations of the radiolysis products at 1 s increase very rapidly with increasing temperature, while the molal ($g \cdot kg^{-1}$) concentrations show negligible temperature dependence. The results are mostly due to the increase in the saturation water vapour density used in the calculations. The increased density increases the rate of radiation energy absorption per unit volume ($(\rho(T) \cdot D_R)$ in Eq. 1) and hence the rates of primary radiolysis species production. Note that in water vapour O_2 and H_2O_2 are secondary radiolysis products formed from the reactions of radicals such as •O and •OH. At longer times the slower reactions of the molecular species become important. The rates of removal of the molecular products increase faster with increasing temperature than the rates of their production. The net effect is that the molal concentrations of the molecular species increase with irradiation time at a given temperature but the increases are smaller at higher temperature. At 400 °C the molal concentrations at 1 h are similar to those reached at 1 s, indicating that the radiolysis system also reaches steady state in 1 s in the vapour phase.

It is encouraging that the LRM and VRM predictions converge as the temperature increases. This shows that the two different approaches for extrapolating the rate constants used in the VRM and LRM are useful and can provide bounding values for the chemical consequences of irradiation of SCW.

4. Model Simulation Results

4.1 Model predictions versus experimental data at 250 °C

We are performing γ-radiolysis experiments as a function of temperature to validate the models. This paper mainly discusses the validation of the LRM and VRM at 250 °C. The radiolysis experiments were performed in test cells partially filled with water (leaving a headspace above) and the radiolysis kinetics were followed by measuring the amounts of H_2, O_2 and H_2O_2 formed in the headspace after irradiation for a desired period of time. In the presence of a headspace, the volatile species (H_2 and O_2) that are formed by radiolysis in the liquid phase will transfer to the gas phase and establish phase equilibria [4]. For the VRM there is only one phase and such mass transfer does not occur.

The LRM and VRM predictions are compared with experimentally measured concentrations of H_2 in vapour phase (Figure 2(a)) and H_2O_2 in liquid phase (Figure 2(b)) at 250 °C. Note that thermal decomposition of H_2O_2 has been taken into account for both LRM [16] and VRM [17]. For these calculations the water in the radiolysis cell was assumed to be present only as saturated steam for the VRM and as liquid water for the LRM. For the LRM the predictions are given with and without inclusion of an interfacial mass transfer process. The experimental data are in very good agreement with the VRM predictions for both [H_2] and [H_2O_2]. Note that the amounts of H_2O_2 measured in the liquid phase match well with those predicted by the VRM. This observation suggests that H_2O_2 formed in the vapour phase tends to dissolve in the aqueous phase. The LRM with interfacial mass transfer predicts [H_2] reasonably well but underestimates [H_2O_2] by more than two orders of magnitude.

In our experiments [O_2] was below the detection limit of the GC. The VRM and the LRM with and without interfacial mass transfer all predict [O_2] below our detection limit, see Figure 3.

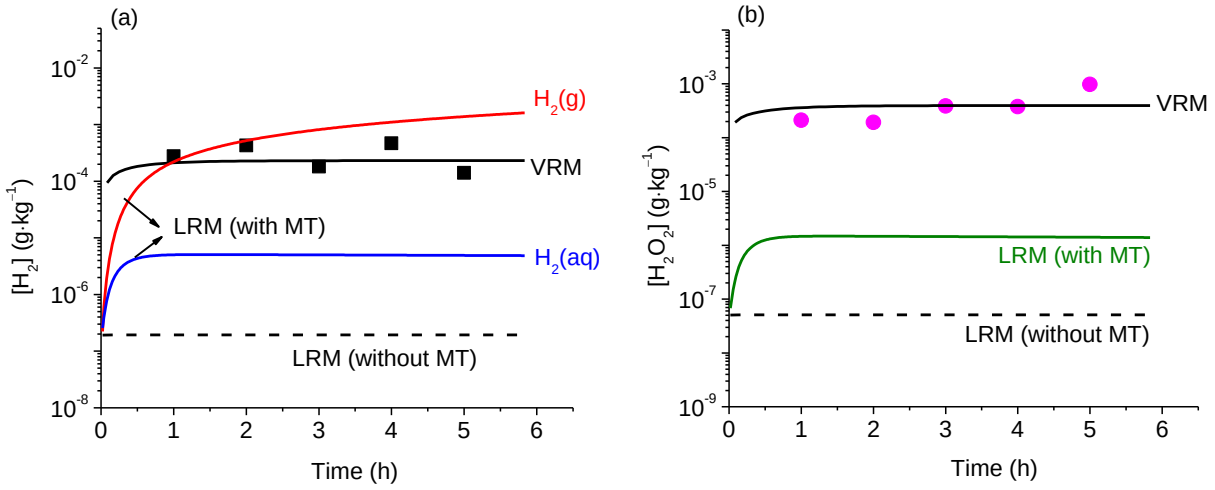

Figure 2. (a) Concentrations of H_2 in the vapour phase and (b) H_2O_2 in liquid phase measured as a function of irradiation time at 250 °C. The symbols represent the experimental data and the lines represent the predictions by the VRM, the LRM without interfacial mass transfer (without MT), and the LRM with the mass transfer (with MT).

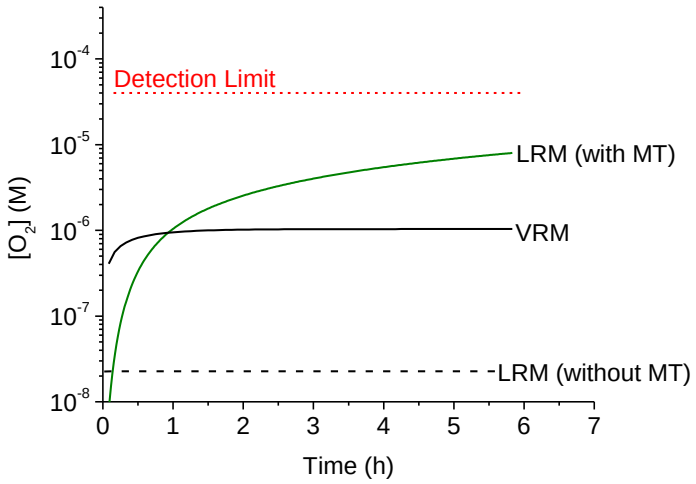

Figure 3. The O_2 concentration predicted by the models at 250 °C. In the experiments, $[O_2]$ was below the detection limit, which is indicated as a dotted line.

The model simulation results indicate that radiolysis of water vapour is more effective (per unit mass) in producing the molecular species, H_2, O_2 and H_2O_2 at 250 °C. With partitioning into the gas phase taken into account the production of the molecular species by liquid water radiolysis increases but the change is more effective for H_2 than for H_2O_2.

The higher production of H_2O_2 from the radiolysis of water vapour than the radiolysis of liquid water was unexpected since H_2O_2 is not a primary radiolysis product for water vapour. In vapour radiolysis H_2O_2 is formed by the combination of two •OH radicals and O_2 is formed by combination of two •O radicals. The G-values for these radicals are higher in water vapour than in liquid water (see reactions 1 and 2). The G-values for •OH, •O and H_2O_2 at 250 °C are 0.63, 0.11 and 0 $\mu mol \cdot J^{-1}$ in water vapour [17] and 0.51, 0 and 0.035 $\mu mol \cdot J^{-1}$ in liquid water [16], respectively. The absence of ionic radiolysis products in water vapour eliminates some of the removal pathways for these radicals seen in the liquid water phase (e.g., the reaction of $\bullet e_{aq}^-$ with •OH to form OH^-), leaving •OH free to combine to form H_2O_2:

$$\bullet OH + \bullet OH \rightarrow H_2O_2 \quad (3)$$

In the radiolysis of liquid water the combination of two •OH radicals forming H_2O_2 is much slower because of many more effective competing reaction pathways for •OH:

$$\bullet e_{aq}^- + \bullet OH \rightarrow OH^- \quad (4)$$

In addition, there are more decomposition pathways available for H_2O_2 during radiolysis of liquid water than radiolysis of water vapour. In addition to thermal decomposition, as H_2O_2 accumulates, it reacts with •OH in both liquid water and water vapour. However, in liquid water H_2O_2 can also decompose via reaction with $\bullet e_{aq}^-$:

$$H_2O_2 + \bullet OH \rightarrow H_2O + \bullet HO_2 \quad (5)$$
$$H_2O_2 + \bullet e_{aq}^- \rightarrow \bullet OH + OH^- \quad (6)$$

The ion-molecule reaction (6) can be very fast in liquid water and this results in a very low steady-state concentration of H_2O_2 as predicted by LRM.

Similarly for H_2 the rates of production and removal are different for vapour and liquid radiolysis. During radiolysis of liquid water, the main production path of H_2 is the primary radiolysis (reaction 1) while the main removal path is its reaction with •OH:

$$H_2 + \bullet OH \rightarrow H_2O + \bullet H \quad (7)$$

The steady-state concentration of H_2 can then be approximated as:

$$[H_2] \approx \frac{10^{-6} \cdot G_{H2} \cdot \rho_{H2O} \cdot D_R}{k_7 \cdot [\bullet OH]} \quad \text{(Eq. 2)}$$

where k_7 is the 2nd order rate constant for reaction (7).

During radiolysis of water vapour, the main production path for H_2 is also primary radiolysis (reaction scheme 2) and its removal occurs mainly via reaction with •O:

$$\bullet O + H_2 \rightarrow \bullet OH + \bullet H \quad (8)$$

Reaction of H_2 with •OH also occurs, but it is slower. Although the G-value for •OH is higher than the G-value for •O (reaction 2), the steady state concentration of •OH is about an order of magnitude lower than that of •O. Therefore, the steady state concentration of H_2 can be approximated by:

$$[H_2] \approx \frac{10^{-6} \cdot G_{H2} \cdot \rho_{H2O} \cdot D_R}{k_8 \cdot [\bullet O]} \quad \text{(Eq. 3)}$$

where k_8 is the 2nd order rate constant for reaction (8).

4.2 Suppression of water radiolysis by H_2 addition

Suppression of the net production of oxidizing radiolysis species by H_2 addition is a common practice in pressurized light and heavy water reactors [22] and, to a lesser extent, in boiling water reactors [23]. The H_2 produced by radiolysis is not sufficient to achieve this; in order to be effective, the concentration of H_2 must be initially high enough to react with the primary radiolysis products (•O and •OH) as they are formed. This prevents them from reacting with each other to form O_2 and H_2O_2. A key question in the development of a water chemistry strategy for the SCWR is whether H_2 addition can be used to control the concentrations of oxidizing species in SCW [6].

The effect of H_2 addition on the radiolysis of SCW (29.2 MPa, 0.322 g·cm^{-3}) at 400 °C predicted by the VRM and LRM is shown in Figure 4. For this figure, the units typically used by station chemists are used, $[H_2]$ in mL·kg^{-1} (STP) and $[O_2]$ in g·kg^{-1}. Since the liquid water radiolysis system reaches steady state early (< 1 s) the LRM predicts the same concentrations of molecular products at 1 s and 1 h at all $[H_2]_0$ studied. The LRM predicts that H_2 addition could reduce (but not suppress)[1] the radiolytic production of O_2; $[O_2]$ at both 1 s and 1 h are below 1×10^{-11} g·kg^{-1} when $[H_2]_0$ > 10 mL·kg^{-1} is added. However, the addition of H_2 is less effective at reducing the formation of H_2O_2. The addition of $[H_2]_0$ < 10 mL·kg^{-1} decreases $[H_2O_2]$ by about two orders of magnitude but further increases in $[H_2]_0$ do not affect the $[H_2O_2]$, which remains relatively high at ~0.5×10^{-6} g·kg^{-1} even at a $[H_2]_0$ of 2000 mL·kg^{-1}, the highest concentration studied.

The VRM predicts different concentrations of O_2 at different times. The shaded area between the two solid lines envelops the range of $[O_2]$ predicted by the VRM as a function of time (t > 1 s) until steady state is achieved (typically less than 1 h). The VRM predicts that addition of any reasonable amount of H_2 will not be effective in suppressing the production of either O_2 or H_2O_2; addition of 200 mL·kg^{-1} H_2 would reduce $[O_2]$ by an order of magnitude but result in negligible reduction of $[H_2O_2]$.

[1] Suppression of net radiolysis means undetectable concentrations of oxidants at the core outlet.

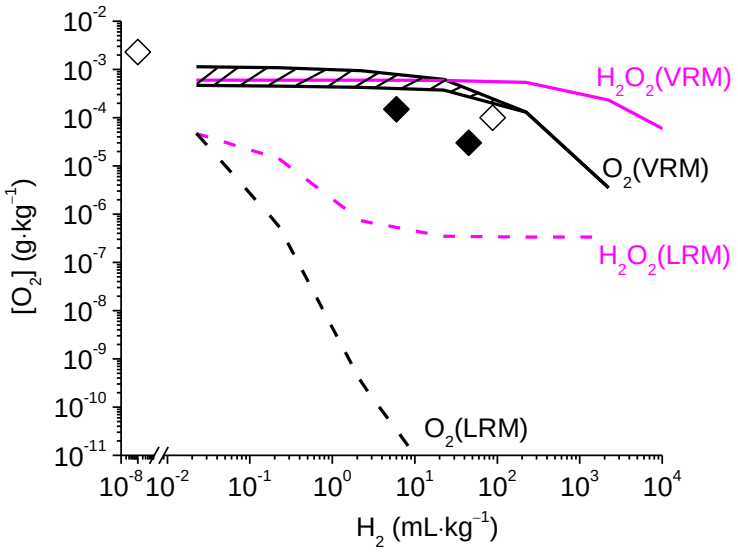

Figure 4. Effect of H_2 addition on suppression of radiolytic production of O_2 and H_2O_2 predicted by the VRM (solid lines) and the LRM (broken lines). The shaded area enveloped by solid lines represents the range of values over different irradiation periods predicted by the VRM and symbols represent plant data from Beloyarsk NPP unit-1(◆ - direct H_2 addition and ◇ - NH_3 addition).

The suppression of net radiolysis under high temperature steam conditions was studied at the Beloyarsk Nuclear Power Plant (NPP) [18,19]. Initially, Unit 1 used ammonia alone to control pH and reduce the production of oxidizing species by radiolysis using hydrogen produced by partial decomposition of the ammonia. The hydrogen concentration in the steam entering the superheating channels was 45-88 mL·kg^{-1} (at NTP) and the oxygen concentration in the superheated steam was 2.3 mg·kg^{-1} at the beginning of the test and then decreased to 0.1 mg·kg^{-1}. Unit 1 also tested direct hydrogen injection to reduce the production of oxidizing species by radiolysis in the superheating channels. Hydrogen injection to maintain steam hydrogen concentrations at 1.2-6.2 mL·kg^{-1} reduced but did not suppress the production of oxygen by radiolysis, resulting in an oxygen concentration of less than 0.15 mg·kg^{-1} in the superheated steam; ammonia was not added to the feedwater during these tests. It was found that the oxygen concentration in the superheated steam could be maintained below 0.03 mg·kg^{-1} with a steam hydrogen concentration greater than 45 mL·kg^{-1}. These experimentally observed points are plotted along with the VRM predictions in Figure 4. The addition of ammonia and H_2 produces similar reductions of radiolysis in steam as indicated by the O_2 concentrations.

The VRM predictions are comparable with the observed effect of H_2 addition on the radiolytic production of O_2 in tests performed with superheated steam. The VRM predicts slightly higher $[O_2]$, but within an order of magnitude of measured concentrations. It also predicts that addition of H_2 at $[H_2]_0$ > 20 mL·kg^{-1} will reduce the production of O_2. Hydrogen peroxide is more difficult to detect but it may be a more important oxidant for corrosion of metals and alloys than O_2. The VRM predictions on the effect of H_2 addition on $[H_2O_2]$ are also shown in Figure 4. It shows that $[H_2]_0$ > 200 mL·kg^{-1} is required for any observable reduction in $[H_2O_2]$.

5. Conclusions

To model the radiolysis of supercritical water, a two-way approach has been used. This was achieved by adapting an existing liquid water radiolysis model (LRM) that has already been validated for lower temperatures and a water vapour radiolysis model (VRM) validated for higher temperatures, but for lower

pressures. The models were then extrapolated to the supercritical regime using a critical analysis of the existing input parameters. Despite the model differences and uncertainties in the model parameters, the predictions of the two models converge as the temperature approaches supercritical levels. These results indicate that both modelling approaches may work reasonably well for the radiolysis of SCW particularly at higher temperatures. However, steady-state radiolysis experiments are easier to perform for water vapour than liquid water or SCW at high temperatures. Validation of the VRM against experimental data as a function of temperature was thus performed. The VRM predictions matched well with the experimental data for the radiolysis of water vapour at subcritical temperatures. The VRM was also able to predict the observed reduction of the concentration of O_2 in superheated steam (at > 400 °C) in a nuclear power plant by addition of H_2. Modest H_2 addition was predicted by the VRM to be ineffective in suppressing H_2O_2, a reactive oxidant which is more important as far as the corrosion of materials is concerned.

Acknowledgments

This research was funded by a Natural Science and Engineering Council of Canada (NSERC), Natural Resources of Canada (NRCan) and Atomic Energy of Canada Limited (AECL) Collaborative Research and Development (CRD) grant in The Canadian National Program on Generation IV Energy Technologies.

References

1. M. Yetisir, M. Gaudet, D. Rhodes, Development and integration of Canadian SCWR concept with counter-flow fuel assembly, in Proceedings of 6th International Symposium on Supercritical Water-Cooled Reactors (ISSCWR-6), Shenzhen, Guangdong, China, March 3-7, 2013, Paper ISSCWR6-13059.
2. D.A. Guzonas, SCWR materials and chemistry status of ongoing research, in Proceedings of the GIF Symposium, Paris, France, September 9-10, 2009, pp. 163-171.
3. J.W.T. Spinks, R.J. Woods, An Introduction to Radiation Chemistry, 3rd ed., Wiley-Interscience, New York, 1990.
4. P.A. Yakabuskie, J.M. Joseph, J.C. Wren, The effect of interfacial mass transfer on steady-state water radiolysis, Radiat. Phys. Chem., 79 (2010) 777-785.
5. J.C. Wren, G.A. Glowa, A simplified kinetic model for the degradation of 2-butanone in aerated aqueous solutions under steady state gamma-radiolysis, Radiat. Phys. Chem., 58 (2000) 341-356.
6. D.A. Guzonas, F. Brosseau, P. Tremaine, J. Meesungnoen, J.-P. Jay-Gerin, Water chemistry in a supercritical water-cooled pressure tube reactor, Nuclear Technology, 179 (2012) 205-219.
7. D.A. Guzonas, P. Tremaine, J.-P. Jay-Gerin, Chemistry control challenges in a supercritical water - cooled reactor, Power Plant Chem., 11 (2009) 284-291.
8. P. Kritzer, Corrosion in high-temperature and supercritical water and aqueous solutions: A review, J. Supercrit. Fluids, 29 (2004) 1-29.
9. H. Ohtaki, T. Radnai, T. Yamaguchi, Structure of water under subcritical and supercritical conditions studied by solution X-ray diffraction, Chemical Society Reviews, 26 (1997) 41-51.
10. A.A. Galkin, V.V. Lunin, Subcritical and supercritical water: A universal medium for chemical reactions, Russ. Chem. Rev., 74 (2005) 21-35.
11. M. Lin, Y. Katsumura, Y. Muroya, H. He, G. Wu, Z. Han, T. Miyazaki, H. Kudo, Pulse radiolysis study on the estimation of radiolytic yields of water decomposition products in high-temperature and supercritical water: Use of methyl viologen as a scavenger, J. Phys. Chem. A, 108 (2004) 8287-8295.
12. P. Causey, C.R. Stuart, Test plan for pulse radiolysis studies of water at high temperature and pressure, AECL Report 217-127160-TP-001, Chalk River Laboratories, Chalk River, Ontario, Canada, 2011.
13. K. Haygarth, D.M. Bartels, Neutron and β/γ radiolysis of water up to supercritical conditions. 2. SF_6 as a scavenger for hydrated electron, J. Phys. Chem. A, 114 (2010) 7479-7484.

14. M. Lin, Y. Katsumura, H. He, Y. Muroya, Z. Han, T. Miyazaki, H. Kudo, Pulse radiolysis of 4,4'-bipyridyl aqueous solutions at elevated temperatures: Spectral changes and reaction kinetics up to 400 °C, J. Phys. Chem. A, 109 (2005) 2847-2854.
15. J. Meesungnoen, D.A. Guzonas, J.-P. Jay-Gerin, Radiolysis of supercritical water at 400 °C and liquid-like densities near 0.5 g/cm^3 — A Monte Carlo calculation, Can. J. Chem., 88 (2010) 646-653.
16. A.J. Elliot, D.M. Bartels, The reaction set, rate constants and g-values for the simulation of the radiolysis of light water over the range 20°C to 350°C based on information available in 2008, AECL Report 153-127160-450-001, Chalk River Laboratories, Chalk River, Ontario, Canada, 2009.
17. O.P. Arkhipov, A.O. Verkhovskaya, S.A. Kabakchi, A.N. Ermakov, Development and verification of a mathematical model of the radiolysis of water vapor, Atomic Energy, 103 (2007) 870-874.
18. V.A. Yurmanov, V.N. Belous, V.N. Vasina and E.V. Yurmanov, Chemistry and corrosion issues in supercritical water reactors, in Proceedings of the Nuclear Plant Chemistry Conference 2010, Quebec City, Canada, October 3-8, 2010, Paper 11.02.
19. N.I. Gruzdev, G.A. Shchapov, S.A. Tipikin and V.B. Boguslavskii, Investigating the water conditions in the second unit at Beloyarsk nuclear power station, Therm. Eng., 17 (1970) 20-22 [Translated from Russian, Teploenergetika 17 (1970) 20-22].
20. C.J, Hochanadel, Effect of cobalt gamma-radiation on water and aqueous solutions, J. Phys. Chem., 56 (1952) 587-594.
21. The International Association for the Properties of Water and Steam Revised Release on the IAPWS Industrial Formulation 1997 for the Thermodynamic Properties of Water and Steam, 2007.
22. I. de Curieres, The evolution of chemistry in PWR nuclear power plants: Overview and safety perspectives, Nuclear Plant Chemistry Conference 2014, October 26–31, 2014, Sapporo, Japan.
23. D.D. Macdonald, Viability of hydrogen water chemistry for protecting in-vessel components of boiling water reactors, Corrosion, 48, (1992) 194-205.

ISSCWR7-2084

Adhesion of Oxides Grown in Supercritical Water on Selected Austenitic Alloys.

D. Artymowicz, C. Bradley, R. C. Newman
Department of Chemical Engineering and Applied Chemistry, University of Toronto
200 College Street, Toronto, ON, M5S 3E5 Canada
c.bradley@mail.utoronto.ca

Abstract

A series of austenitic alloys (800H, H214, I625, 310S and 347) were exposed to supercritical water at 550 ºC and 25 MPa for 260 h and 450 h in a static autoclave with an initial level of dissolved oxygen of 8 ppm. Cross sections of oxidized samples were imaged with SEM and analysed with EDS for the composition of the oxide layer(s). Indentation with a hardness indenter was used for assessment of oxide adhesion. Mass loss was obtained through descaling. Two surface finishes were applied – a coarse grinding with 120 grit abrasive (applied by the manufacturer) or polishing with either 1200 grit, 1 µm diamond or 0.05 µm alumina suspension. The only sample which delaminated during indentation was polished H214 (both alumina and 1 µm).

1. Introduction

The global energy demand is rapidly increasing, with some predictions of up to a 70% increase by 2035 [1]. Burning fossil fuels for energy production has become untenable due to environmental side effects. A focus on developing new, carbon neutral technologies is crucial to maintaining this balancing act between a healthy environment and quality of life for future generations. Many carbon neutral technologies are in development, such as solar or wind, but nuclear energy remains the most reliable and mature solution. Currently, 15% of Canada's electricity is produced with nuclear power plants [2]. It is expected that nuclear power will play a key role in the energy mix of the future.

The supercritical water reactor (SCWR) design is the focus of Canada's contribution to the development of Generation IV nuclear technology. It is expected to benefit from a huge jump in thermal efficiency, up to 45% from current technology outputs of 33% for light water reactors or 35% for CANDU-6 reactors [3]. Along with this efficiency increase, the SCWR is also attractive compared to current systems because of its simpler "once-through" design; eliminating the need for costly pieces of equipment such as steam generators. The higher heat capacity of supercritical water translates into a smaller required flow rate and reduced coolant tube size along with other equipment reductions [4].

There are many challenges that must be overcome before the application of SCWR technology, especially from a materials perspective. Of key interest is the integrity of the interface between the protective corrosion layer and substrate of the proposed material in supercritical water environments. As materials corrode, it is desirable to have a protective oxide layer develop on the surface of the material which acts to inhibit further corrosion [5]. It is important that this layer not only exists at equilibrium but is also mechanically stable on the surface. Significant spallation due to stresses within the oxide is potentially catastrophic, resulting in greatly increased corrosion rate. Spallation may be induced by: residual stress from the growth of oxide due to differences in density between oxide and substrate, thermal cycling and the difference in between the coefficient of thermal expansion of the scale and substrate, or even an external load. This challenge is being explored in the second phase of Canada's SCWR materials research project.

The Rockwell indentation method is a technique for measuring the interface toughness of brittle films on ductile substrates using common laboratory equipment. A Rockwell indenter with a Brale indenter tip (120º diamond, conical) can be used to induce delamination of the brittle film on the sample. By modelling the elastic-plastic response due to the indent, it is possible to relate the interface toughness of the coating to the radius of delamination caused by the indent. The test is more likely to be effective when the residual stress in the coating is compressive and applies to coatings with thicknesses on the order of 10 µm. [6]

The five shortlisted materials being evaluated for the Gen IV program were obtained from Atomic Energy of Canada Limited (AECL) as rolled plates with a 120 grit surface finish. The elemental composition of each material is shown in Table 1. H214 and I625 are high strength austenitic nickel based alloys designed for superior high-temperature oxidation resistance, H214 also has a significant aluminium component [7] [8]. Incoloy 800H is an iron-nickel-chromium alloy designed for high-temperature applications, the "H" refers to the carbon content which lies in the upper range of the 800 series requirements for improved creep properties [9]. 310S is low carbon version of the 310 series known for ease of fabrication with high-temperature oxidation resistance while 347 is a niobium stabilized stainless steel with good oxidation properties and resistance to intergranular corrosion in the chromium carbide precipitation temperature range [10] [11].

Table 1. Candidate alloy composition.

Alloy	Fe	Ni	Cr	C	Si	Mn	Mo	Al	Ti	N	P	S
H214	3.58	bal	16.24	0.04	0.05	0.21	<0.1	4.15	<0.0027	-	0.002	<0.002
347	bal	9.08	17.24	0.05	0.61	1.71	0.47	-	-	-	0.028	0.0001
I625	4.07	61.1	22.04	0.04	0.20	0.18	8.35	0.19	0.21	-	0.008	0.0001
800H	46.3	31.0	20.0	0.07	0.30	0.80	-	0.44	0.52	0.01	0.012	0.001
310S	bal	19-22	24-26	0.08	0.75	2.0	-	-	-	0.11	0.045	0.015

2. Experimental

In order to investigate the oxide integrity of these candidate alloys after exposure in supercritical water conditions, the static-autoclave facilities at CanmetMATERIALS were used. Two exposures have been done to date with durations of 260 h and 450 h at 25 MPa and 550 ºC with an initial O_2 concentration of 8 ppm. There will be two more exposures with durations of 250 h and 125 h in this project.

Coupons were cut from the supplied sheets to the nominal dimensions of 20x20x2 mm with a 2 mm diameter hole drilled near one edge for mounting. For the 450 h exposure, half of the samples were prepared with a 0.05 µm alumina polish while the other half were left with the as received finish of 120 grit. A set of finer surface finishes were chosen for the 260 h exposure, samples were prepared with 1200 grit as well as 1 µm polishes.

The mass of each coupon was measured immediately before and after exposure for weight gain results using an analytical balance of ±0.001 mg precision. The exact dimensions of each sample were measured using a pair of digital callipers with a precision of ±0.01 mm.

At minimum there were 2 coupons corresponding to a given material and surface finish in each exposure. Of this pair, one coupon was destined for oxide integrity analysis via the Rockwell indentation method as well as descaling for a weight loss measurement, while the other remained for surface and cross-section imaging.

The oxide integrity measured by the Rockwell indentation method was done using the indenter in the Materials Science and Engineering Department at the University of Toronto. A 120º diamond conical indenter (Brale) was employed. Indents with loadings of 60 kgf, 100 kgf and 150 kgf were performed on each exposed sample of a given material and surface finish type. The extent of delamination was then determined on these indented samples from SEM micrographs. Since the delamination was not of uniform radius from the centre of the indent, the area of the delamination was measured and then an equivalent disc radius determined, see Figure 1.

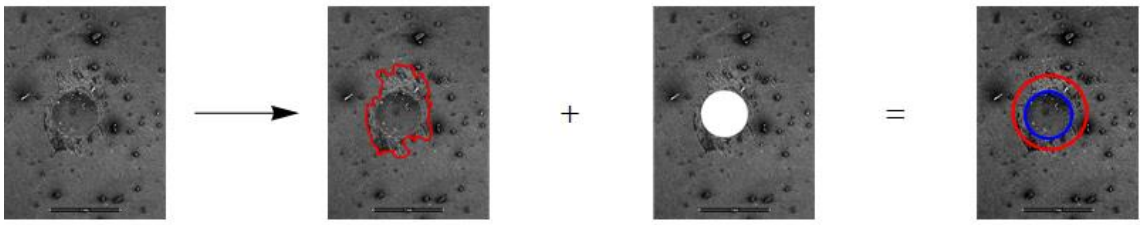

Figure 1. Example of the extent of delamination determination, Fe-13Cr-1.5Si ferritic/martensitic alloy.

After determining the extent of delamination on the indented samples, a descaling procedure was performed to remove the oxide from the surface of the coupons to measure the total weight lost due to corrosion. This corrosion indicator is considered preferable to simple weight gain because it circumvents fluctuations due to deposition and exfoliation.

The descaling procedure consists of submerging the samples in one of two solutions at 90 ºC for 30 or 60 minutes at a time until the oxide has been completely removed. Solution compositions can be found in Table 2. Between each submersion the coupons are sonicated in methanol for 15 minutes and weighed using a balance with ±0.01 mg of precision. An unexposed coupon of each material type is included in the descaling procedure to act as a blank; the descaling is complete once the weight lost between submersions for a coupon approaches that of the corresponding blank. Including the blank allows for a correction to be applied to the result, which compensates for the amount of bulk alloy dissolved into solution as a consequence of the descaling procedure. Initially the samples being descaled are submerged in solution (a) for 60 minutes. Next they are submerged in solution (b) for 60 minutes. Then the samples are submerged in solution (a) for 30 minutes at a time until completion.

Table 2. Descaling solutions.

Solution (a)		Solution (b)	
2.0%	Citric Acid	10.0%	Potasium Permanganate
5.0%	Dibasic Ammonium Citrate	4.0%	Caustic Soda
0.5%	Disodium EDTA		

In order to maintain the outer edge of the oxide, the cut coupons destined for cross-section imaging were electroplated with a layer of nickel 5 µm thick before being mounted in epoxy and polished to a 0.05 µm alumina finish followed by ion-milling to reduce the impact of mechanical damage.

3. Results and Discussion

In Phase 1 of the Gen IV project several ferritic/martensitic (F/M) alloys were produced to explore the effect of alloying elements on corrosion rate and oxide morphology. The samples were exposed at 500 ºC, 25 MPa, for 500 h in the flow-through supercritical water loop at the University of New Brunswick with oxygen concentration maintained relatively low at 200 ppb. The oxides produced on these F/M alloys had a thickness on the order of 10 µm. The elemental composition of these alloys is shown in Table 3.

Table 3. Ferritic/Martensitic alloy composition.

Nominal	Cr	C	Si	Mn	Al	V	Ti	N	O	P	S
Fe-9Cr-1.5Al	9.33	0.09	<0.20	0.2	1.25	<0.01	0.01	0.09	0.031	0.005	0.002
Fe-9Cr-1.5Si	9.65	0.1	1.22	<0.05	0.12	<0.01	0.01	0.06	0.127	0.007	0.002
Fe-9Cr	8.65	0.14	<0.20	<0.05	<0.01	<0.01	-	0.04	n/a	0.002	0.004
Fe-13Cr-1.5Si	14.15	0.09	1.49	<0.05	<0.01	<0.01	0	0.09	0.058	0.005	0.002
Fe-9Cr-1.5V	8.68	0.17	<0.19	<0.05	<0.01	1.71	0.01	0.11	2.492	<0.009	0.003
Fe-13Cr	13.9	0.13	<0.20	<0.05	<0.01	<0.01	0	0.17	0.21	0.007	0.002

The F/M alloys were submitted to the Rockwell indentation method for measuring oxide integrity as a test of the methods applicability to this project. The extent of delamination resulting from these tests is shown in Figure 1, *r* is the radius of delamination and *R* is the radius of the plastic region of the indent.

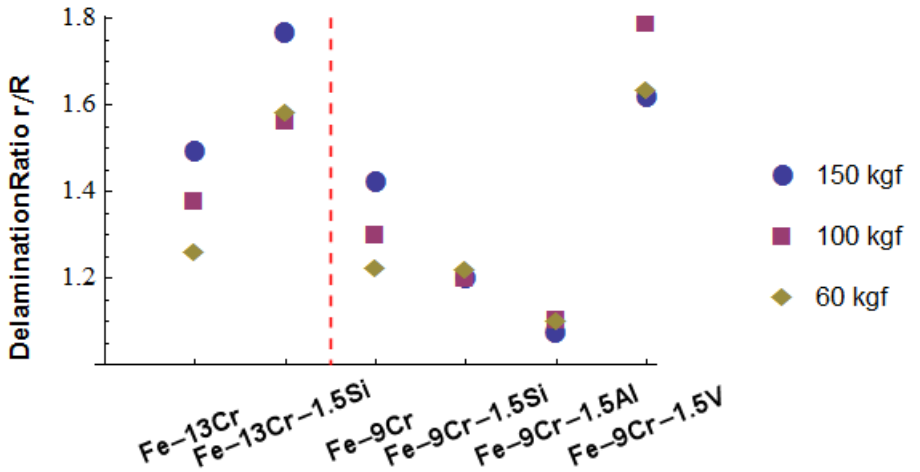

Figure 2. Extent of delamination of ferritic/martensitic alloys from Phase 1 (dashed line separates 9% Cr from 13% Cr alloys)

The threshold delamination ratio for the applicability of a quantified measurement of interface toughness as calculated by the Rockwell indentation method is 2.0 [6]. None of the F/M alloys had a delamination ratio exceeding the threshold, thus only the minimum interface toughness can be calculated for the oxide grown on these materials. Using this method, the minimum interface toughness for these oxide-metal pairs was estimated to be 170 J/m^2. A relative interface toughness can still be inferred from the results of the indentation tests; however, it is important to note that the mode with which the oxide delaminates differs between materials and different modes of delamination are expected to have an impact on the protection from further corrosion provided by the delaminated region.

The morphology of the oxides grown on these materials typically shows a bi-layer structure with the original metal surface acting as the interface between the inner and outer oxides [12]. Examining the delaminated regions with SEM shows that in some cases only the outer oxide layer is removed, leaving the inner layer to offer some protection from further general corrosion. This behaviour is shown in Figure 3.

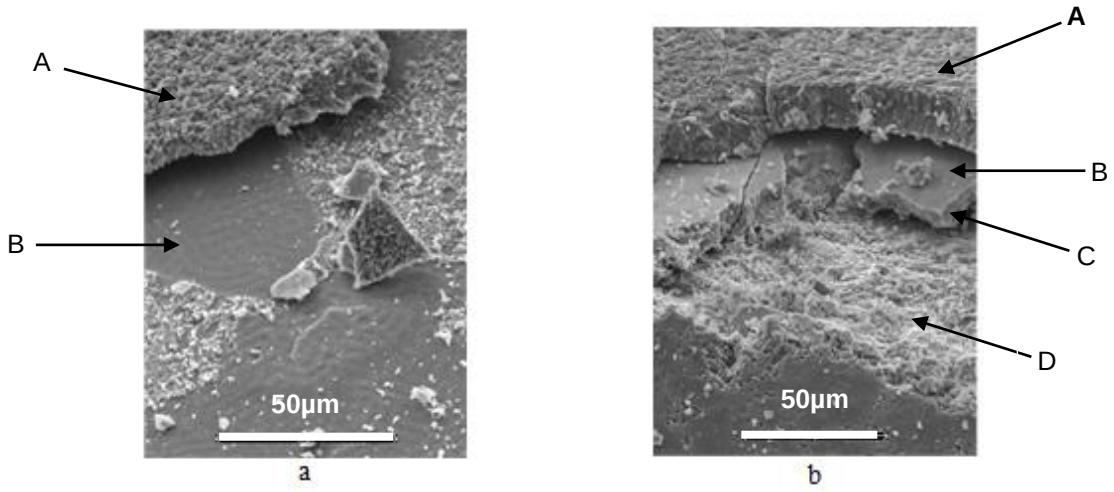

Figure 3. Two delamination modes observed in a) Fe-13Cr-1.5Si and b) Fe-9Cr.

The F/M alloy with a nominal composition of Fe-13Cr-1.5Si (a) had only the outer oxide layer delaminate while the Fe-9Cr (b) sample showed delamination progressing along oxide/oxide as

well as metal/oxide interfaces. The latter mode of delamination was observed in all but Fe-13Cr-1.5Si samples. The capital letters designate: A, the outer oxide (magnetite); B, outer/inner oxide interface (this is the original surface of the coupon); C, the inner mixed oxide $(FeCr)_3O_4$; and D, inner oxide/metal interface.

The Fe-13Cr-1.5Si sample showed one of the highest extents of delamination but this may be misleading since it was only the outer oxide layer which delaminated.

Each of the candidate alloys have been chosen because of their corrosion resistance at high temperatures, thus it comes as no surprise that the amount of general corrosion experienced by these alloys is much less compared to the F/M alloys. The thicknesses of the oxide layer for these materials are on the order of 1 µm, compared to 10 µm for the F/M alloys. The weight gain associated with this corrosion can be seen in Figure 4.

In addition to the standard weight gain measurement, some of the samples were descaled for a more accurate measurement of corrosion, unaffected by exfoliation or oxide composition. Simple weight gain includes the measurement of additional material from the environment, such as oxygen, that contribute to the final mass of the sample; whereas the before and after weight measurements of the bulk alloy in the descaling procedure are independent of the composition of the oxide formed during exposure. By comparing the two measurements we can make statements about the oxides integrity with respect to the amount of material lost to the environment. The descaling results are shown as red dots on Figure 4 and represent the amount of bulk material lost due to corrosion.

A measurement of the weight gain is expected to be greater in magnitude compared with the descaled measurement. Assuming no exfoliation takes place during the exposure, weight gain is generally about 20% greater than descaled weight loss.

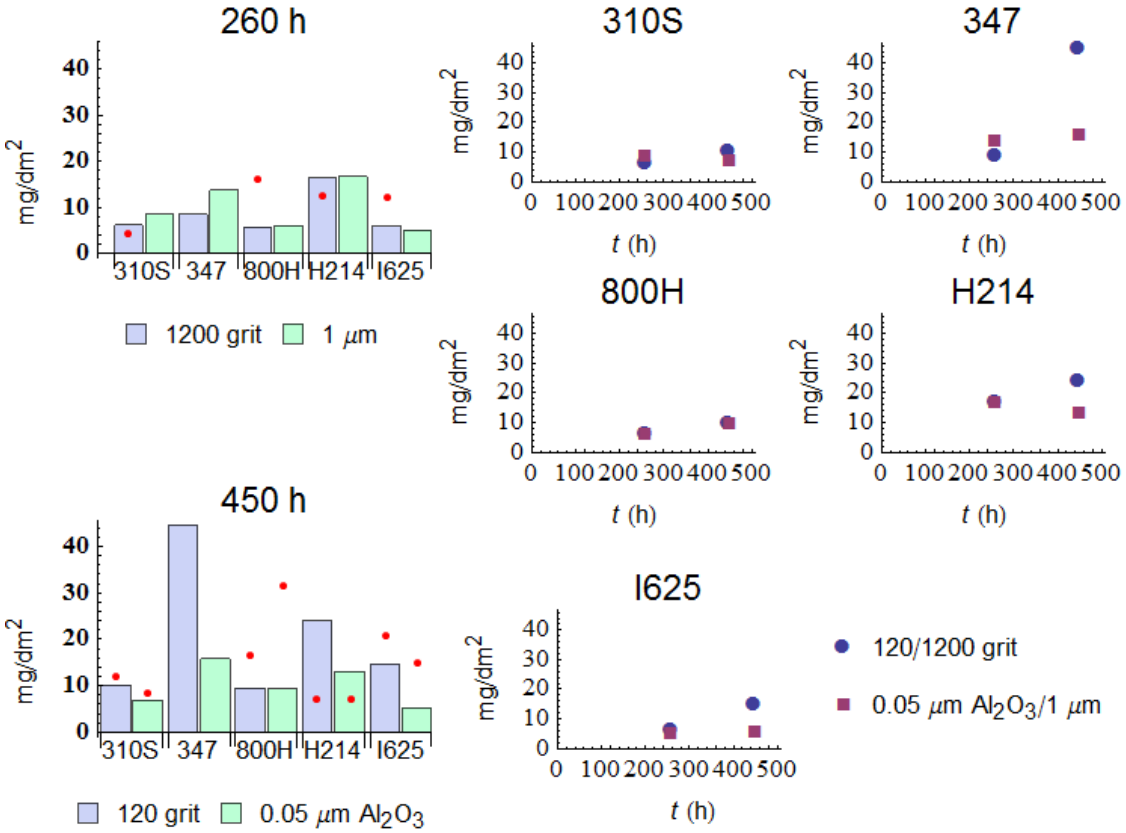

Figure 4. Weight gain results for candidate alloys. Red dots represent descaled weight loss measurement. Some silver contamination was found on the 347, 120 grit sample believed to have arisen from an electroplated seal on the autoclave.

The materials 310S and H214 appear to have a relatively stable oxide since the weight loss and weight gain results show the expected relationship. On the other hand, 800H and I625 seem to have lost quite a bit of material to the environment.

Some silver nodules found on the 347, 120 grit sample suggest some contamination from an electroplated seal on the autoclave. This artificially inflated the weight gain of that sample.

All austenitic candidate alloys except for 347, which had been dropped as a candidate by that point, were subjected to the Rockwell indentation test to measure oxide integrity. The candidate alloys from the 450 h exposure showed almost zero delamination for every material and surface finish combination with the exception of the alumina polished H214 sample, which had a delamination ratio of just under 2.0. Unlike with the F/M alloys, it was not even possible to extract relative oxide integrity from the indentation results and a more sensitive evaluation of oxide integrity will be needed to differentiate the oxide integrity of the candidate materials.

A closer inspection of the surface of the 310S sample after indentation showed cracks extending radially from the indent but no delamination of the oxide from the surface, as seen in Figure 5. This indicates that the interface between the oxide and substrate was stronger than the oxide itself.

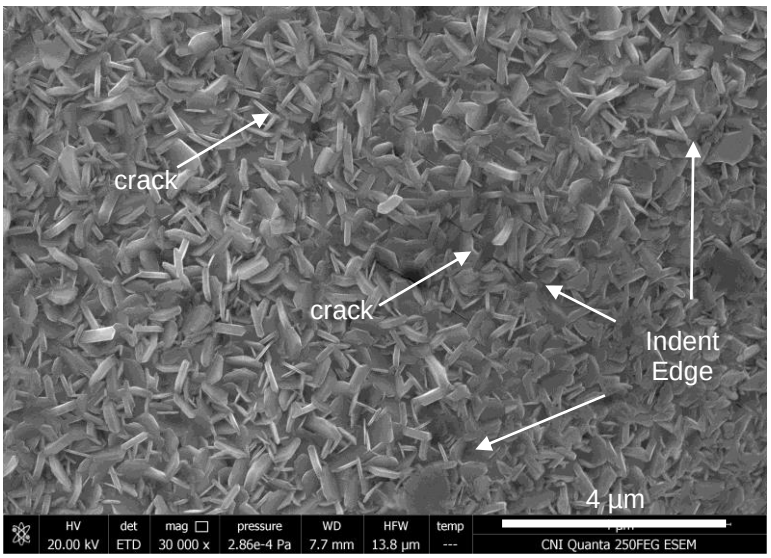

Figure 5. Indented 310S sample showing cracks without delamination.

Alloys 800H, I625 and 310S contain enough Cr (20%, 22%, 24-26% respectively) to form a Cr_2O_3 layer without extensive diffusion of Cr from the bulk toward the surface. Alloy H214 relies on both Cr and Al in smaller amounts to form a protective scale, the expected phase sequence being Cr_2O_3-Al_2O_3-Metal. The Al content of H214 is low and requires some diffusion from the bulk towards the surface. This is facilitated by the cold work leftover from the 120 grit polishing. The H214 alumina polished samples do not have the surface cold work region and as a result the Al does not diffuse as readily. This pushes the Al_2O_3 phase deeper into the alloy where inward diffusing oxygen finally meets outward diffusing Al. As a result, there is a layer of bulk alloy between the outer Cr_2O_3 layer and the inner Al_2O_3.

The difference in the structure of the H214 oxides between the rough 120 grit surface finish and the smoother alumina polished samples can be seen in the micrographs in Figure 5. With both surface finishes a thin, sub-micron Cr_2O_3 layer (A) with needle structures protruding from the flat surface constitutes the outer most layer. The alumina polished samples exhibit a network of mixed aluminium-chromium oxide (B) penetrating several microns into the metal leaving islands of bulk metal (C). Finally, an alumina layer (D) acts as the interface between the bulk alloy and the surface structure.

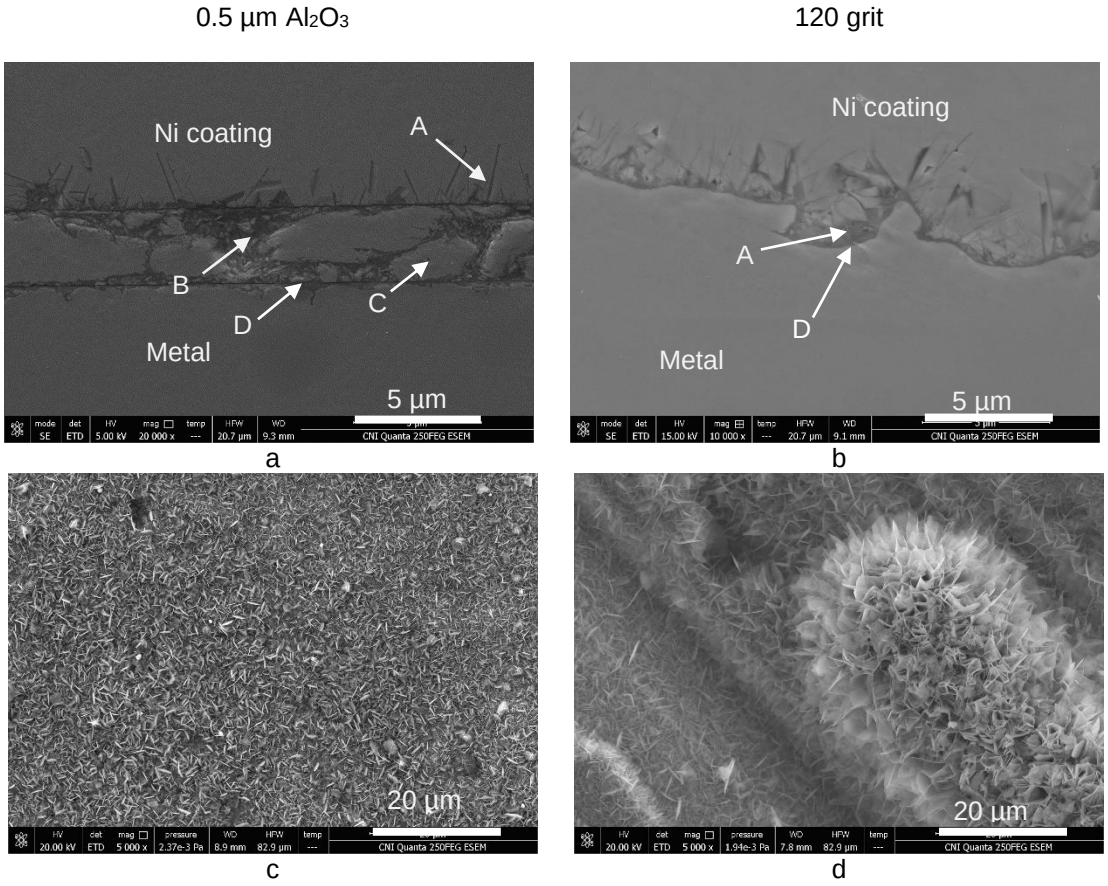

Figure 6. Cross-section (a, b) and planar view (c, d) images of H214 after 450 h at 550 ºC.

The depth of the alumina layer in the more polished H214 sample amplifies the thickness of the surface structure to more than would be expected given the amount of weight gain or descaled weight change. This could be part of the reason why we only see delamination in this sample when applying the indentation test; however, the delamination appears to take place at the Cr_2O_3-metal interface when looking at partially delaminated pieces of oxide in planar view, see Figure 7. This partially delaminated piece has peeled up and rotated about 90ºC out of the plane of the page. The Cr_2O_3 needles can be seen toward the bottom of the delaminated piece with the flat interface section toward the top, nearest to the gap left behind in the outer oxide layer. This mode of delamination is similar to that seen in the Fe-13Cr-1.5Si F/M alloy, leaving the inner layer intact and able to provide some protection while the outer layer is removed.

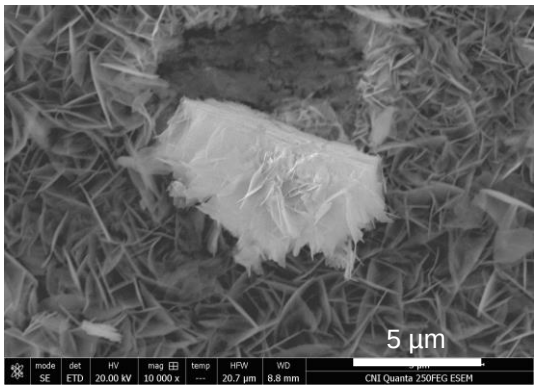

Figure 7. Partially delaminated oxide on indented H214 alumina polished.

4. Conclusions

Comparing the weight gain and descaled weight loss results of the candidate alloys suggests that 310S and H214 form oxides that remain relatively stable during an autoclave exposure, while the 800H and I625 samples experienced a significant loss of oxide to the environment.

The SCWR candidate alloys show stronger oxide adhesion as measured by the Rockwell indentation test compared to the F/M alloys investigated in Phase 1 of the project. The exception being the H214 with an alumina polished surface finish which performed about the same as the F/M alloys. 310S showed radial cracks around the indent but no delamination of the oxide, which suggest that the interface between the oxide and substrate is tougher than the oxide itself in this case. A more sensitive adhesion test should be performed on the candidate alloys to determine their relative oxide integrity.

Surface finish had an impact on the oxide structure of the H214 samples particularly. The lack of a cold worked region near the surface of the alumina polished H214 alloy hindered the formation of an effective Al_2O_3 scale.

References

[1] International Energy Agency, “World Energy Outlook 2012 Factsheet,” 2012. [Online]. Available: http://www.worldenegyoutlook.org/media/weowebsite. [Accessed 4 April 2013].

[2] Goverment of Canada, “Table 127-0002 Electric power generation by class of electricity producer,” March 2013. [Online]. Available: http://www5.statcan.gc.ca/cansim/pick-choisir?lang=eng&p2=33&id=1270002. [Accessed 8 April 2013].

[3] E. Parent, Nuclear Fuel Cycles for Mid-Century Deployment, Boston: Massachusetts Institute of Technology, 2000.

[4] J. Wolf, “Supercritical water reactor,” in *Nuclear Energy Encyclopedia*, Hoboken, Wiley, 2011, pp. 305-308.

[5] M. G. Fontana, Corrosion Engineering, new York: McGraw-Hill, 1986.

[6] M. D. Drory and J. W. Hutchinson, “Measurement of the adhesion of a brittle film on a ductile substrate by indentaion.,” *Mathematical, Physical and Engineering Sciences,* vol. 452, no. 1953, pp. 2319-2341, 1996.

[7] Special Metals, “Inconel alloy 625,” Special Metals, 2013.

[8] HAYNES International, “HAYNES 214 Alloy,” HAYNES International, Kokomo, 2008.

[9] Special Metals, “INCOLOY alloy 800,” Special Metals, 2004.

[10] Allegheny ludlum Corporation, “Stainless Steels Types 321, 347 and 348,” Allegheny ludlum Corporation, Pittsburgh.

[11] Atlas Steels, “Grade Data Sheet 310 310S 310H,” Atlas Steels, Melbourne, 2011.

[12] W. Li, Oxidation Resistance and Nanoscale Oxidation Mechanisms in Model Binary and Ternary Alloys Exposed to Supercritical Water, Toronto: University of Toronto, 2012.

The 7th International Symposium on Supercritical Water-Cooled Reactors
ISSCWR-7
15-18 March 2015, Helsinki, Finland

ISSCWR7-2088

Validation of Constant Load C-Ring Apex Stresses for SCC Testing in Supercritical Water

R. Swift, W. Cook
Department of Chemical Engineering, University of New Brunswick
15 Dineen Drive, Fredericton, New Brunswick, Canada, E3B 5A3
rogan.swift@unb.ca; wcook@unb.ca

Colin Bradley, R.C. Newman
Department of Chemical Engineering, University of Toronto

W. Zheng
CanmetMATERIALS, Natural Resources Canada
183 Longwood Road South, Hamilton, Ontario, Canada L8P 0A5
Wenyue.Zheng@NRCan-RNCan.gc.ca

Abstract

In selecting the materials for the Canadian SCWR, it is important to consider the effects and extent of stress corrosion cracking under various operational conditions. Several methods of stressing a corroding material are available and each have their perceived benefits and drawbacks; for simplicity of the experimental set-up, at UNB a constant load C-ring assembly has been used with Inconel 718 Belleville washers acting as a spring to deliver a near-constant load to the sample. To predict the stress at the apex of the C-ring, a mechanistic model has been developed to determine the force applied by the spring due to the thermal expansion of each component constrained within a fixed length.

In an attempt to validate the mechanistic model, trials to measure the force applied by the washers as they thermally expanded were performed using an Instron machine and an environmental chamber. Accounting for the thermal expansion of the pull rods, the force was measured as temperature was increased while maintaining a constant displacement between the platens holding the C-ring. Results showed the initial model to be insufficient, as it could not predict the force measured through this simple experiment. The revised model presented here considers the thermal expansion of the C-ring and all the components of the testing apparatus including the tree, backing washers and Belleville washers. Further validation using the finite element code ABAQUS is presented, as are preliminary results from the use of the apparatus to study the SCC of a zirconium-modified 310s SS exposed to supercritical water.

1. Introduction

With the interests of improving nuclear reactor designs for a fourth generation of nuclear reactor systems, the Generation IV International Forum (GIF) has proposed a number of higher-efficiency designs which are characterized by higher temperatures and pressures. One of the tasks in GenIV reactor development is to experimentally determine which alloys are capable of withstanding the harsh design conditions the higher temperatures and pressures present. Alloys are considered based on resistance to mechanical failure (strength and durability), resistance to all types of corrosion, resistance to nuclear effects, and cost.

One source of failure which presents itself at these conditions is stress-corrosion cracking, a hybrid of the corrosion, fracture mechanics and metallurgy disciplines. Occurrences of stress-corrosion cracking are heavily dependent on the combination of metal, environment, stress intensity, and time under stress, and thus can only (presently) be determined experimentally. As a result of this, failures by stress-corrosion cracking in industry are almost always unexpected and dangerous. [1] Stress-corrosion cracking resistance is often represented as the stress at which a given alloy sample would undergo stress corrosion cracking in a given environment after an unlimited amount of time.

Many methods to test stress-corrosion cracking exist. Constant-strain tests have a C-ring or O-ring fixed between a hard surface and a tightening nut; as the C-ring or O-ring expands, it presses against the tightening nut and is constrained within a fixed distance, the constant strain. Constant-load tests have a C-ring or O-ring and a set of springs fixed within a hard surface and a tightening nut; the C-ring or O-ring expands into the springs, reducing the stress increase from expansion. Constant Extension Rate Tensile (CERT) testing have a metal rod or bar stretched at a constant rate; rates that are too high will mechanically fracture and rates that are too low will chemically corrode, so there often exists a rate in between at which stress-corrosion cracking occurs. Each method has pros and cons and correct applications, but no method maintains a constant stress throughout the experiment if the sample undergoes stress corrosion cracking. An issue which complicates the testing is temperature and pressure: a testing apparatus must either fit entirely in a vessel which can maintain the desired experimental conditions or the apparatus must fit partially in the vessel and allow movement through the sealed vessel wall to allow for applied strain. For this reason, apparatuses are small, expensive or both.

For simplicity of the experimental set-up, at UNB a constant load C-ring assembly has been used with Inconel 718 Belleville washers acting as a spring to deliver a near-constant load to the sample. To determine the stress at the apex of the C-ring, Raoul prepared a testing apparatus for use in a 300 mL Inconel 625 static autoclave. Raoul then created a mechanistic model and attempted to validate it with a finite-element method using the commercial program ABAQUS.

2. Experimental Setup

2.1 UNB SCW Autoclave Tests

To improve our ability to characterize stress corrosion cracking, it is important to improve the reliability of the available methods and to estimate the magnitude of the applied stress. For a constant-load setup, this means deriving a model to determine the stress at the apex of a C-ring accurately and fabricating an experimental setup and procedure that can control that stress reliably and precisely. The model depends upon the setup and process just as the setup and process will be limited by the ability of the model.

A standard constant-load C-ring test involves loading a C-ring onto a sample tree. The sample is constrained by a tightening nut on one side and the tree trunk on the other. As the C-ring thermally expands when the temperature in the autoclave is raised, adjacent disc springs cushion the C-ring and limit the increase in force. Additionally, ceramic washers insulate the C-ring from the setup on either side, to limit galvanic coupling effects, and metal backing washers protect the ceramic from the curved surfaces that apply very localized pressure. For the ceramic washers to properly insulate the C-ring, the C-ring must be suspended above the tree branch by an initial force. A complete loaded tree branch is shown below in Figure 1.

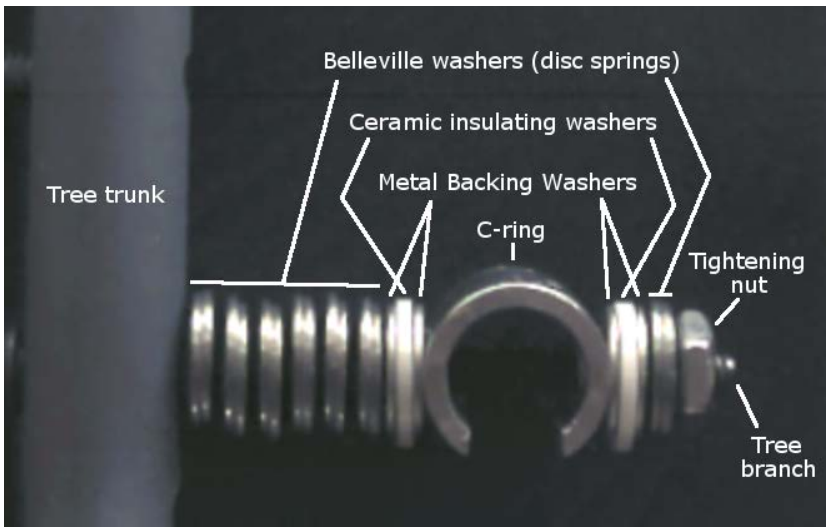

Figure 1: Constant-Load C-ring Setup

The tightening nut is set to an initial distance from or into the disc springs, relative to the surface of the unstressed disc springs. This distance is called the “initial deflection” and is the determining factor for the final stress of the C-ring. Results presented below indicate that this distance must be precise within 0.01 mm for the final stress to be within 5% of the desired stress for a given number of disc springs. Using more disc springs decreases the precision required, but also increases the space that the setup occupies, which is limited in a relatively small autoclave.

Once loaded with 12 samples, the tree is placed into the autoclave and heated to 600 ^{o}C. The pressure is set by placing a calculated quantity of water into the autoclave with the samples before heating. At the end of each trial, samples are cooled down, dried with nitrogen and stored in a desiccator until they are set in epoxy for polishing and examination. Polishing takes place using 400 grit SiC paper progressively to 0.3 μm diamond polish. All samples are polished a few millimetres down to remove the effect of any stresses from sample preparation at low grit, then polished to mirror finish in stages. SEM pictures are taken of the polished samples.

2.2 Instron Validation Experiment

In an attempt to experimentally validate the model, an Instron machine equipped with an environmental chamber was used. To perform the test, all of the parts of an autoclave trial (C-ring, metal backing washers, ceramic washers, disc springs) except the tightening nut are loaded onto a vertical metal rod, which is attached to the bottom platen and pull rod.

An appropriate number of washers and disc springs were then loaded on top of the c-ring and the force was applied by the upper platen in which a cavity was machined to accept the

positioning rod and disc springs (Figure 2). The Instron would measure the distance travelled between the two arms and the force applied could be precisely controlled; for this reason, it was thought that this set up would be very well suited to determining force to deflection curves (spring constants, for example) at constant temperature.

A correction to the pull-rod positions, to account for the thermal expansion within the environmental chamber, was developed as follows: without any sample between the platens, the arms are pressed together with an arm separation distance such that the force was 50 Newtons at room temperature. As temperature is increased to the operating temperature, the separation distance is changed to keep the applied force at 50 Newtons. If done sufficiently slowly (pseudo-steady-state), this generates a calibration curve relating the temperature to the arm separation distance which causes no change in the real distance between the arms.

For the actual tests, the Instron was loaded with the C-ring and disc springs as described above and given an initial deflection as recommended by the model discussed in the next section. As the temperature is increased, the arm separation distance is controlled based on the calibration curve ensuring that the distance between the two arms is always the initial distance minus the initial deflection. This process should give a precise measurement of the force in the setup as a function of temperature.

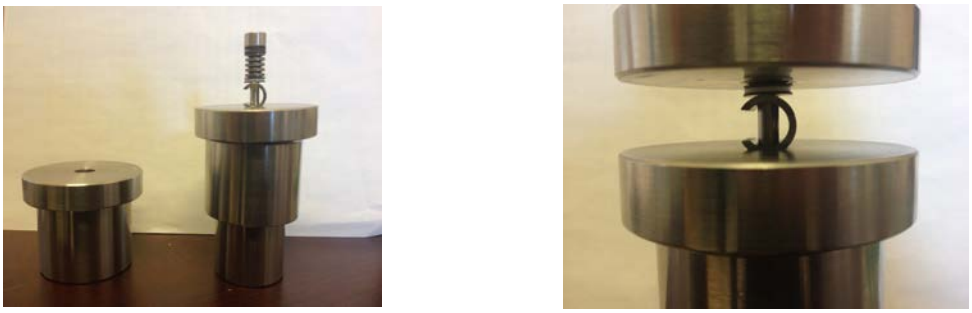

Figure 2: Picture of upper and lower platens and c-ring installation for Instron validation experiment.

2.3 Mechanistic and FE models

The mechanistic model developed by Raoul [2] determines the stress as experienced at the apex of a C-ring in a constant load setup, where ceramic washers galvanically isolate the C-ring and metal backing washers protect the ceramics. As the C-ring thermally expands, Belleville washers (disc springs) maintain the force applied to the C-ring, leading to an applied force which causes the desired apex stress at operating temperature and pressure (typically taken as 0.2% offset Yield stress as per ASTM G38-01.) [3]

The initial model assumed the following:

- only the C-ring and metal backing washers thermally expand as heated
- only the Belleville washers compress due to force
- radial thermal expansion and deflection are negligible
- “The theory of arches relies on the assumption that plane cross sections remain plane, stress is proportional to strain, rotations and translations are small, and the thickness of the bar must be small in comparison to the curvature” [4]
- The normal stress applied is constant over the cross-section
- The C-ring can be considered a pressure-vessel
- Thermal expansion and elastic compression occur only along the axis
- No creep or stress relaxation

- The tightening nut does not move with respect to the tree branch
- Steady-state conditions (No cracking/weakening/corrosion of materials over time)

These assumptions give rise to the following deflection balance [5](note: a list of nomenclature is provided in Section 5):

$$TE_{C-ring} + TE_{BackingWashers} - \#_{\text{Springs}} * EC_{One\ Spring} + d_{Initial} = 0 \quad (1)$$

The stress experienced at the apex of the C-ring is related to the force applied to either side of the C-ring by the following equation, derived by Raoul and Cook: [4]

$$Stress = \frac{Force}{A}\left(\frac{R}{r_{outer}} * \frac{A_m * r_{outer} - A}{A_m * R - A} - 1\right) - P_{op} \quad (2)$$

As the C-ring and metal backing washers thermally expand, they compress the Belleville washers. This increases the force applied by the Belleville washers onto the C-ring according to equation 3 below. The equation is given as follows [6]:

$$Force = 4 * E * \frac{t^3 * D_{PerSpring}}{(1-\mu) * K * D_{out}} * \left[\left(\frac{h}{t} - \frac{D_{PerSpring}}{t}\right) * \left(\frac{h}{t} - \frac{D_{PerSpring}}{2*t}\right) + 1\right] \quad (3)$$

To implement this model, Raoul prepared a MATLAB code in which Equations 2 and 3 are applied to determine the deflection of each disc spring. The known total thermal expansion is divided by this number to give the required number of springs, according to Equation 1, rounded down since the number of springs must be a whole number. This rounding means the stress caused by thermal expansion must be lower than the desired stress. To correct for this, the system is given an initial deflection by tightening a nut before the heating occurs. This initial deflection is determined assuming that the initial-deflection-induced stress is the difference between desired apex stress and expansion-induced apex stress. Finally, the actual final stress is calculated by adding the initial deflection and the thermal expansion and using this total deflection with Equations 2 and 3.

This process is represented more clearly by Figure 3 below, where the calculation path is the presented via the hallow arrows:

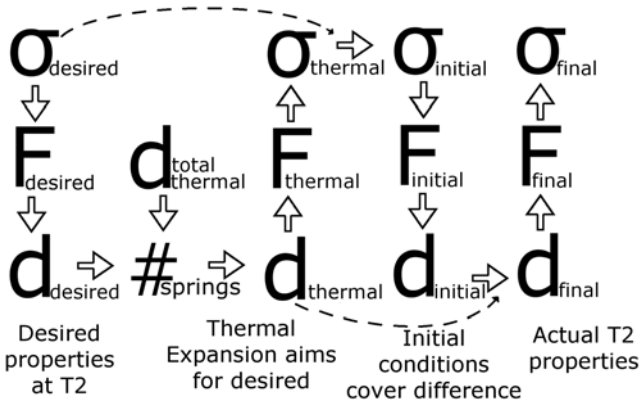

Figure 3: Flow Chart of Calculation Methodology

In order to confirm the above implementation, the C-ring assembly has been modelled in ABAQUS, a commercial finite-element calculation package, using the initial displacement/force as determined from the numerical calculation.

3. Results

3.1 Instron Validation

To validate the above model for the apex stress of a constant-load C-ring, a series of tests were performed at CANMET using an Instron machine equipped with an environmental chamber in order to determine deflection to force curves; thus, the goal of the test was to validate Equations 1 and 3 in the previous section.

Five tests were performed where, in each, one C-ring sample and all of the required backing, ceramic and Belleville washers were loaded on a vertical pole. The setup was displacement-constrained by a surface at the bottom and a movable bar at the top and the distance between platens determined by the position of the Instron pull arms (effectively reproducing the space that would be from the tree trunk to the tightening nut). As the temperature was increased at atmospheric pressure, the distance between the surface and the bar was kept constant, accounting for the thermal expansion of the Instron pull arms themselves with a calibration curve between temperature and displacement. Measurements of temperature and force were taken at regular intervals and continued after the operating temperature was reached for approximately an hour.

The thermal expansion of the C-ring and metal backing washers was calculated by the model, then all deflections (initial deflection applied by the Instron machine and thermal expansion) were normalized to units of deflection per Belleville washer, as Equation 1 only applies to a single Belleville washer. As well, a metal spacer was required to ensure the upper platen was pushing the springs, not the centring rod; this metal spacer was counted as an equivalent length of metal backing washers in the model.

Shown below in Figure 4 is a plot of the forces and deflections at the end of the Instron test (individual points) and the model predictions (solid lines):

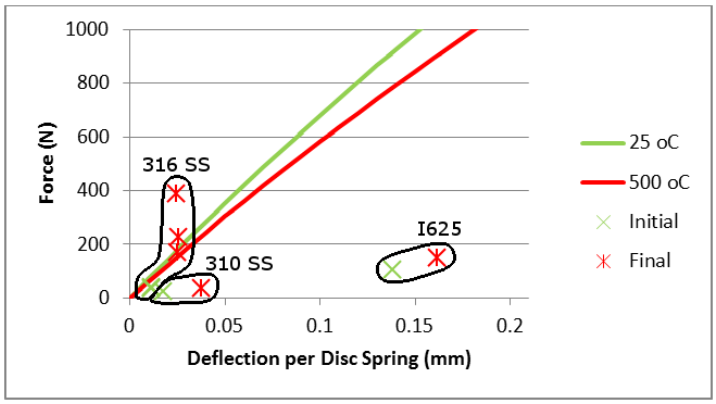

Figure 4: Results of Instron Testing

From this plot, it is clear that, while each trial increased in force as the temperature was increased, no trial produced the results expected. Even the three trials of 316 SS with identical initial conditions had a range of final forces. Most interesting is the Inconel 625 trial, which was given an initial deflection many times higher than the others and still had low initial and final forces. From these results it is clear that something went wrong with the implementation of the validation experiment. More useful results would have been produced if a direct measurement of the pull rod / platen positions within the environment chamber could have been made with high temperature extensometers instead of relying upon the calibration for thermal expansion.

3.2 Mechanistic model

3.2.1 Revisions to the model

The model revised for the work reported here removes the assumptions that only the C-ring and metal backing washers thermally expand; only the Belleville washers compress due to force; and radial thermal expansion and deflection are negligible by performing a deflection balance on the system as described by equation 4:

$$\sum \mathrm{TE}\,(\mathrm{material}, \mathrm{T}) - \sum \mathrm{EC}\,(\mathrm{material}, \mathrm{shape(T)}, \mathbf{Force}) - \mathrm{TE\ Branch(T)} - \mathrm{ET\ Branch(T}, \mathbf{Force}) + \mathbf{D_{Initial}} = 0 \quad (4)$$

The above equation simplifies to the following, for ease of use:

$$d_{NotSprings} + \#_{Springs} * d_{PerSpring} + d_{initial} = 0 \quad (5)$$

where $d_{PerSpring}$ covers the thermal expansion and elastic compression of a single Belleville washer and $d_{NotSprings}$ covers the thermal expansion and elastic compression of all other components.

Given the desired stress (0.2% offset Yield stress at temperature, for example) and the number of Belleville washers, equation 4 calculates the required force from the stress, then Equation 5 is solved for the required initial deflection at room temperature as follows:

$$d_{Initial} = -d_{NotSprings} - d_{PerSpring} * \#_{Springs} \quad (6)$$

Given the desired stress and the initial deflection, Equation 2 is used to calculate the force from the stress and Equation 5 is solved for the number of disc springs required below:

$$\#_{Springs} = (-d_{initial} - d_{NotSPrings})/d_{PerSpring} \quad (7)$$

The actual number of springs must be an integer, so the value is rounded up to the nearest integer and the initial deflection required is re-calculated via Equation 6. If the number of springs is less than zero, zero springs is taken as the number. If neither the initial deflection nor the number of springs are given, this method is used assuming an initial deflection of 0.1 mm.

Given an initial deflection and a number of Belleville washers, the Newton method is applied as a root-finding technique to set the left hand side of Equation 4 to zero by changing the force. Equation 2 is then applied to calculate the actual stress from the force. While the two other methods of using the implementation recommend experimental setup parameters, this method predicts the actual stress given actual experimental setup parameters, which might not be those predicted. As shown later in this section, this method can be used to generate sensitivity curves, to show the apex stress as the sample heats up or to compare different versions of the implementation at the same conditions.

In the implementation, $d_{NotSprings}$ is calculated from the list of components by summing the difference of thermal expansion and elastic compression for each component. The thermal expansion of each component follows the following equation, where α is the thermal expansion coefficient of the material, integrated from room temperature to operating temperature:

$$d_{thermal} = L * (\exp(\alpha) - 1) \quad (8)$$

For the C-ring, L is the outer diameter. For the ceramic washers and metal backing washers, L is the thickness. For the tightening nut, L is half of the thickness, since it is assumed the

center of the nut does not move with respect to the tree branch. For the tree trunk, L is the radius. For the tree branch, L is the length from the tree trunk (exclusive) to the tightening nut (inclusive), which is the total initial length of all other components; for this reason, the tree branch must be calculated last, once all other components have been considered.

The elastic compression of each component differs depending on the shape of the component. The equations of all components are given below, where Discs represents the ceramic washers, metal backing washers, tightening nut, and tree branch.

For the C-ring, the following equation describes the force to deflection curve [4]:

$$d_{C-ring} = \frac{-\pi * Force * R^3 * 6}{E * width * thick^3} \tag{9}$$

For the ceramic insulating washers, metal backing washers and tightening nut, the definition of Young's modulus can be re-arranged to give the following force to deflection curve:

$$d_{discs} = \frac{-4 * Force * thick}{\pi * E * (D_{out}^2 - D_{in}^2)} \tag{10}$$

For the tree trunk, the following equation describes the force to deflection curve [7]:

$$d_{trunk} = \frac{Force}{2 * a} * (V_1 + V_2)(1 + \ln\left(\frac{4 * a}{(V_1 + V_2) * Force * D}\right)) \tag{11}$$

where 2a is the contact area between the trunk and a backing washer and

$$V_i = \frac{1 - \mu_i^2}{\pi * E_i} \tag{12}$$

Furthermore, in the implementation, $D_{PerSpring}$ is calculated using Equation 3, a cubic equation in deflection, solved for deflection using equations by Cardano [8], as implemented by Raoul [2].

Additional features of the model include adding or removing setup components in the function call (no modification of the code is necessary); an optional output of the initial length, thermal expansion and elastic compression of each setup component; and the option to revert the results to earlier versions of the implementation, including the original implementation. As the model is implemented in Visual Basic for Microsoft Excel, all of Excel's many features are also available, such as drag-and-drop calculations.

3.2.2 Modelling Results

The model has been used to generate sensitivity data for constant-load and constant-strain experiments. The main consideration in precision is the initial position of the tightening nut, as small deviations in position cause large changes in the final stress. This sensitivity to initial position can be mitigated by adding more Belleville washers; as the determining factor in force is deflection in each component, adding more components reduces the offset per component. This effect is shown in Figure 5 below, where steeper lines indicate greater sensitivity to errors in initial deflection.

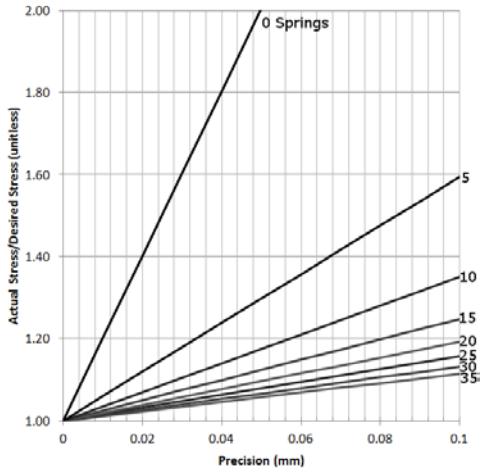

Figure 5: Sensitivity of Final Stress Due to Initial Deflection

The highest sensitivity found in experiment is for a constant-strain scenario, where no Belleville washers are used. For reference, the edge of readability for a pair of standard vernier callipers is about 0.02 millimetres. If using vernier callipers to check initial deflection, a constant-strain test operator using all of the same parts as those found in UNB's setup could expect a final stress no more precise than ±40%. A constant-load experiment with 14 disc springs, as is being performed at UNB, could give a final stress no more precise than ±5%. Using strain gauges or larger samples than used in this implementation (cut from 0.5" tubing), more precise results can be obtained.

Additionally, it has been found that, for many materials of the C-ring, the stress at the apex of the C-ring exceeds the 0.2% offset yield stress as the sample heats up. In these cases, the sample may plastically deform before exposure to the desired testing conditions. Under the default settings and dimensions of the implementation**,** this effect is experienced with C-ring samples made of Inconel 625 (UNS N06625), 310 stainless steel (UNS S31008) with more than 6 disc springs, Hastelloy C (UNS N10002), Hastelloy C-276 (UNS N10276), 347 stainless steel (UNS S34700) with more than 2 disc springs, and Haynes 214 (UNS N07214). The effect is not experienced with 316 stainless steel (UNS S31600) and Alloy 800HT (UNS N08811).

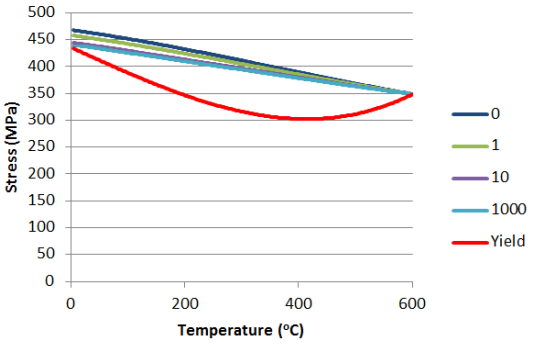

Figure 6a: Heating Curves (Inconel 625)

Technique is not appropriate.

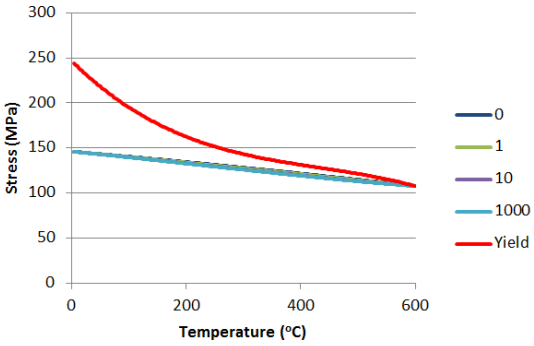

Figure 6b: Heating Curves (316 Stainless Steel)

Technique is appropriate.

3.3 ABAQUS model

3.3.1 Preliminary Setup

As progress towards a complete model of the whole setup, the C-ring was modelled as bounded by two metal backing washers (Figure 7a). To speed computations, the model was simplified further to gather preliminary comparative data. The simplification involved replacing the two metal backing washers with flat nubs protruding from the C-ring horizontally. (Figure 7b) With this change, no surface contact needed to be modelled, but the area effect of the washer on applying force is retained.

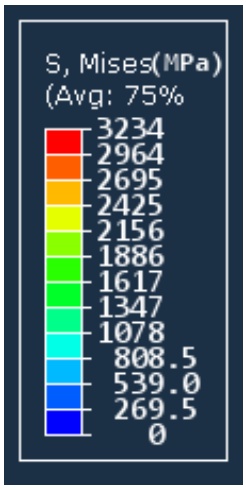

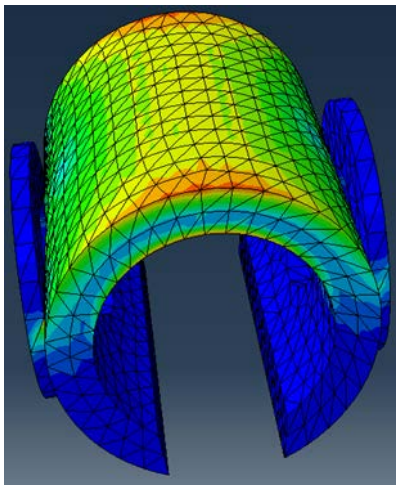

Figure 7a: Preliminary Abaqus Model

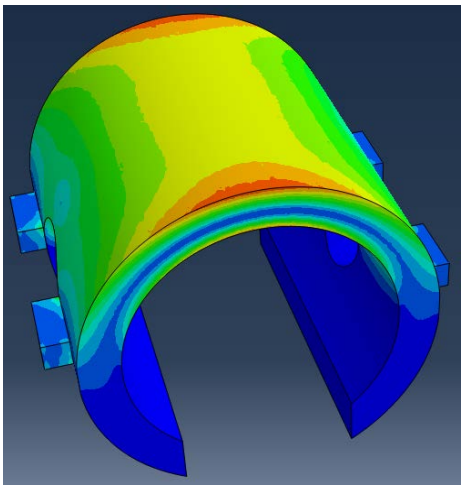

Figure 7b: Modified Preliminary Abaqus Model

A force in the ballpark of the force calculated by the mechanistic model is applied to the washers, stressing the C-ring. The results gathered from repeated applications of the above Abaqus model are plotted below as Figures 8 and 9. These graphs serve to verify equations 9 and 2, which are plotted as solid lines for comparison.

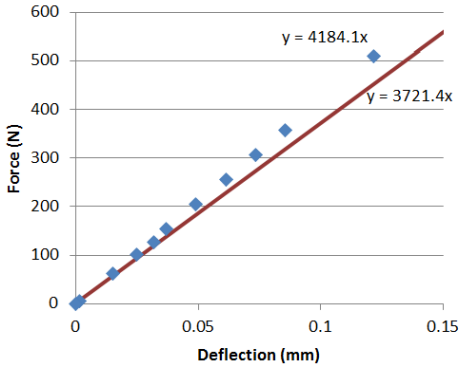

Figure 8: C-ring Deflection to Force Curve

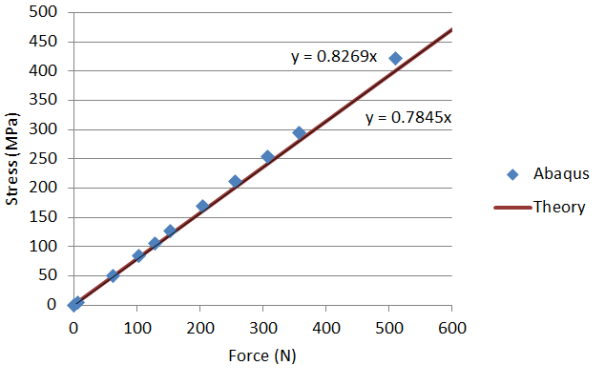

Figure 9: C-ring Force to Stress Curve

For the conditions of the model (room-temperature properties, only one piece with force applied laterally), both models indicates a straight line fit for both deflection-force and force-stress curves with intercepts at the origin, as expected. However, the slope of each Abaqus-calculated line deviates slightly from the theoretical line.

It is expected that the deviations in Figures 8 and 9 are due to the two major differences between the Abaqus model and the equation: the knobs on either end of the Abaqus model and the point-application of force in the theoretical equation are both unrealistic. Further tests with the bounding washers (Figure 7a) will likely generate more realistic curves for use in the mechanistic model.

3.4 Autoclave tests on modified 310 SS

Three separate tests in the static autoclave were conducted on the modified 310s SS material frabricated at CANMET at the conditions shown in Table 1. Only preliminary analyses have yet been performed to identify the extent or mode of cracking or fracture for the specimens. It was expected that by conducting the testing with samples at various initial deflections, information could be gathered about the stress-to-SCC behaviour of the materials. Further autoclave and loop tests are proceeding but preliminary findings have indicated that the spring-loaded technique, accounting for thermal expansion, can indeed cause brittle fracture of the samples as evidenced by the most stressed samples in experiment FX.SC. An example of sample F11.SC, stressed to the point where the treaded rod began to bend, is shown in Figure 12. It is impossible to try and estimate the actual magnitude of the stress applied since the equations developed here assume that the material is still in the elastic region. The mode of failure is obviously brittle fracture but there is evidence of oxidation along the crack surfaces.

Table 1. Experimental test conditions for the C-ring static autoclave exposures.

Experiment	Specimen	Percent of Yield (%)	No. of Specimens	Loading (MPa)	Initial Deflection (mm)	Temp (°C)	Pressure (MPa)	Duration (Hours)
FX.SC	310s SS (Zr)	100	4	200	0.315	600	25	600
	310s SS (Zr)	200	2	400	0.635			
	310s SS (Zr)	400	2	790	1.256			
	310s SS (Zr)	>500	3	??	??			
GX.SC	310s SS(Zr)	100	2	200	0.315	600	25	720
	310s SS(Zr)	75	1	150	0.265			
	310s SS(Zr),	0	1	0	0			
IX.SC	310s SS (Zr)	50	3	100	0.222	600	25	ongoing
	310s SS (Zr)	100	3	200	0.657			
	310s SS (Zr)	150	3	300	0.977			
	310s SS (Zr)	200	2	400	1.356			

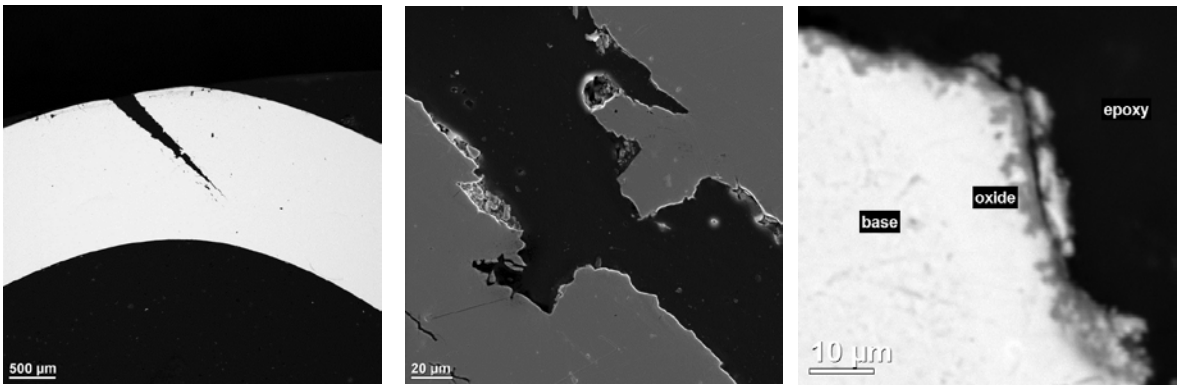

Figure 12. Evidence of brittle fracture and subsequent oxidation within a crack on 310s SS.

4. Conclusions

In an attempt to simplify the experimental setup for conducting SCC testing in SCW, the UNB SCW Group have been developing a technique using constant load C-ring samples along with a model validation of the technique. Results of the revised modelling have indicated that only certain alloys are conducive to the constant load technique relying upon thermal expansion to induce the force on the samples. Suitable materials include 316SS and A800. Several autoclave tests have been conducted on a Zr-modified 310s SS and results, once analysed will provide input for materials selection for the Canadian SCWR.

5. Nomenclature

$\#_{Springs}$	The number of Belleville washers in the setup.
α	The coefficient of thermal expansion for the material in question.
σ	See Stress.
μ	The poisson ratio of the part in question.
π	The ratio of the circumference of a circle to its diameter.
a	Half of the contact area between the tree trunk and the adjacent backing washer.
A	The cross-sectional area of the C-ring as cut from along the apex to the centre of curvature. 21.209 mm^2, for our setup.
A_m	The area divided by the radius of the neutral axis. 3.875 mm, for our setup.
d	Deflection. $D_{Initial}$ is the initial deflection applied by the tightening nut. $d_{PerSpring}$ is the thermal expansion and elastic compression of a single Belleville washer. $d_{NotSprings}$ is the thermal expansion and elastic compression of all other components.
D_{in}	The inner diameter of the circular part in question.
D_{out}	The outer diameter of the circular part in question.
$D_{PerSpring}$	The elastic compression of each spring.
E	Young's Modulus of Elasticity as a function of temperature.
EC	Elastic Compression, calculated using the appropriate equation for whichever part is being compressed. Disc springs - Eqn. 3; C-ring – Eqn. 9; Tightening nut, ceramics, backing washers, tree branch – Eqn. 10; Tree trunk – Eqns. 11 and 12.
F	See Force.
Force	The force applied to and by each part in the setup.
h	The difference between the height of the disc spring and its thickness. 1.2192 mm, for our setup.
K	A calculation coefficient equivalent to the following:

$$K = \frac{1}{\pi} * \frac{\left(\frac{\frac{D_{out}}{D_{in}} - 1}{\frac{D_{out}}{D_{in}}}\right)^2}{\frac{\frac{D_{out}}{D_{in}} + 1}{\frac{D_{out}}{D_{in}} - 1} - \frac{2}{Log\left(\frac{D_{out}}{D_{in}}\right)}} \quad (13)$$

L	The length of the part in question along the same axis as the tree branch.
Mesh	The average side length of an element in an Abaqus model.
P_{op}	The operating pressure. 25 MPa = 25 N/mm^2, for our setup.
r_{outer}	The radius of the outer surface of the C-ring. 6.35 mm, for our setup.

R	Halfway between the inner and outer radii of the C-ring. 5.515 mm, for our setup.
Stress	The stress at the apex of the C-ring, the point of highest tensile stress.
t	The thickness of the part in question.
T	Thermal Expansion, calculated using Equation 8.
V	A calculation coefficient defined in Equation 12.

6. Acknowledgements

The authors acknowledge the financial support for the project through the NRCan/NSERC/AECL Generation IV Technologies program. Bryce Raoul, Adon Briggs and Keith Rollins are thanked for their work toward the initial development of the model and constant load technique and for their fantastic machining work in fabricating the test samples and tree branch assembly.

7. References

[1] National Physical Laboratory, “Stress Corrosion Cracking - Guides to Good Practice in Corrosion Control,” 2007. [Online]. Available: http://www.npl.co.uk/upload/pdf/stress.pdf.

[2] B. Raoul, “Evaluation of Stress-Corrosion Cracking of Materials in Supercritical Water using a Novel Spring-Loaded C-ring Technique (Masters Thesis),” University Of New Brunswick, Fredericton, 2014.

[3] ASTM, “ASTM G38-01: Standard Practice for Making and Using C-Ring Stress-Corrosion Test Specimens,” 2013. [Online]. Available: http://compass.astm.org/EDIT/html_annot.cgi?G38+01(2013). [Accessed 2015].

[4] Pilkey, Formulas for Stress, Strain and Structural Matrices (p811, example 8), NY: John Wiley & Sons, 1994.

[5] E. Gutierrez-Miravete, “Rensselaer - Education for Working Professionals,” 7 September 2008. [Online]. Available: http://www.ewp.rpi.edu/hartford/~ernesto/F2008/MEF2/Z-Links/Papers/Intro_Termoelast.pdf.

[6] DIN, DIN 2092: Disc Springs - Calculation, Berlin: DIN Deutsches Institut für Normung, 1992.

[7] M. Puttock and E. Thwaite, “Elastic Compression of Spheres and Cylinders at Point and Line Contact,” 1969. [Online]. Available: http://emtoolbox.nist.gov/publications/nationalstandardslaboratorytechnicalpaperno25.pdf.

[8] K. Ward, “Ken Ward's Mathematics Pages,” Trans4Mind, 20 October 2012. [Online]. Available: http://www.trans4mind.com/personal_development/mathematics/polynomials/cardanoMethodExamples.htm. [Accessed 10 March 2015].

[9] Nuclear Energy Agency, “The Generation IV International Forum,” 3 September 2010. [Online]. Available: http://gen-4.org/. [Accessed 20 November 2013].

[10] J. C. Scully, “The Theory of Stress Corrosion Cracking in Alloys,” *Anti-Corrosion,* vol. September, pp. 5-10, 1972.

ISSCWR7-2089

Water Chemistry Specifications for the Canadian Supercritical Water-Cooled Reactor Concept

D. Guzonas
Chalk River Laboratories, AECL
Chalk River, Ontario, Canada K0J 1J0
guzonasd@aecl.ca

W. Cook
Department of Chemical Engineering, University of New Brunswick
15 Dineen Drive, Fredericton, New Brunswick, Canada, E3B 5A3
wcook@unb.ca

Abstract

Canada is developing a Supercritical Water-cooled Reactor (SCWR) concept that has operating conditions compatible with the advanced high-pressure turbines designed for supercritical water (SCW) fossil power plants (i.e., turbine inlet pressure of 25 MPa and temperature of 625 °C). Before long-term qualification testing of candidate alloys can be performed, the water chemistries expected in various parts of the plant must be specified. These specifications must include proposed ranges for key parameters such as pH, concentrations of dissolved oxygen and hydrogen, and the concentrations of additives and important impurities such as chloride and sulfate. It was recognized that there were significant gaps in the available experimental data and in the mechanistic understanding of both corrosion product transport and water radiolysis in SCW that precluded the development of predictive models of these phenomena. To address these gaps, Canada initiated an SCWR Water Chemistry Project whose high level goals are to predict and mitigate corrosion product and activity transport and to predict in-core chemistry conditions, in particular the effects of water radiolysis. Information generated by this project is being used to provide interim water chemistry specifications to groups doing materials testing in support of the Canadian SCWR concept, especially the testing of candidate fuel cladding alloys.

Canada has now proposed its preliminary water chemistry specifications for the Canadian SCWR concept. This paper presents these specifications and outlines their technical rationale.

1. Introduction

Canada is developing a Super-Critical Water-cooled Reactor (SCWR) concept with operating conditions compatible with the advanced high-pressure turbines designed for SCW fossil power plants (i.e., turbine-inlet pressure of 25 MPa and temperature of 625 °C). It is a pressure-tube concept [1] with a light water coolant and a separate, low-pressure heavy-water moderator. Final selection and qualification testing of candidate alloys requires long-term testing under water chemistry conditions representative of those expected in an SCWR. The proposed water chemistry regimes in various parts of the plant must be fully specified, including the expected ranges for key parameters (i.e., pH and the concentrations of dissolved oxygen and hydrogen, other additives, and deleterious impurities). Ultimately, these candidate chemistries must be assessed using in-reactor loop tests to determine their effects on water radiolysis and corrosion product and activity transport.

The key water chemistry issues for SCWR concepts have been summarized [2, 3, 4]. Yurmanov et al. [4] discussed chemistry and corrosion issues in SCWRs with a focus on the extensive Russian experience with the operation of nuclear superheated steam channels in the pressure-tube boiling water reactors (BWRs) at the Beloyarsk Nuclear Power Plant (NPP); nuclear superheated steam plants operate at temperatures above the critical point of water, but at subcritical pressures. Guzonas and Cook [5] have recently emphasized that, at temperatures above about 500 °C, corrosion issues in superheated steam[1] and SCW are very similar.

The coolant system of a typical SCWR concept consists of:

1. The feedtrain, which takes condensate from the turbines, purifies it to remove impurities, and then reheats it to the core inlet temperature through a series of low- and high-pressure heaters;
2. The reactor core, which heats the feedwater through the pseudo-critical point by passing it over the nuclear fuel; and
3. The main steam line, turbines and generator, which convert the thermal energy of the coolant into electrical energy.

Figure 1 illustrates the major processes that define the chemistry control requirements in an SCWR. Corrosion product transport from the feedtrain into the core is controlled by the feedtrain chemistry control strategy. The in-core chemistry environment is defined by the feedtrain chemistry plus any adjustments made at the core inlet (e.g., hydrogen addition) and the effects of water radiolysis. Corrosion product and activity transport from the core will affect the downstream piping and turbines.

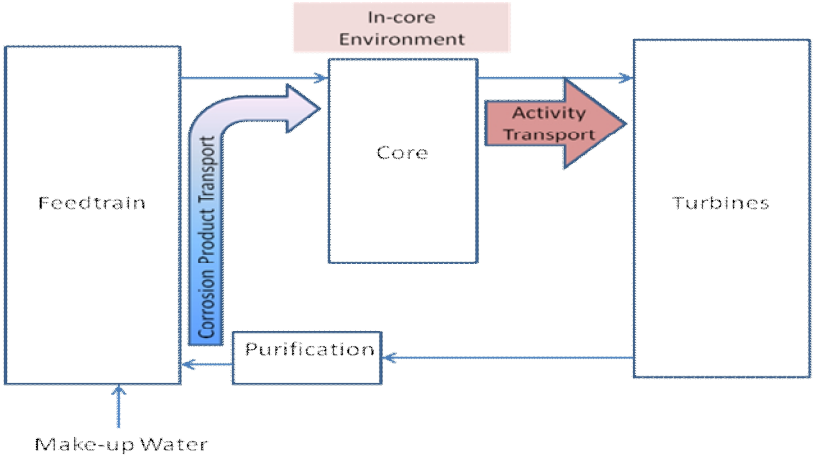

Figure 1: Simplified schematic of an SCWR water cycle showing the three key chemistry control phenomena important for defining a chemistry control strategy.

This paper summarizes the current knowledge on water chemistry control for the Canadian SWCR concept.

2. Water chemistry control for the Canadian SCWR concept

All fluids exhibit a critical point in the P-V-T diagram, defined by T_c, P_c and V_c, above which it is not possible to liquefy the gas by the application of pressure. In the supercritical region there is no phase segregation leading to liquid and vapour co-existence (i.e., in the case of water, wet steam) and hence, no boiling. With reference to Figure 2, a simple way to visualize a supercritical fluid is that above the critical temperature the average thermal energy of the fluid molecules (k_BT) is larger than the interaction energies between the molecules ($\Delta\varepsilon$), i.e., a

[1] Superheated steam is steam at temperatures above the saturation temperature.

persistent liquid phase cannot be formed when T> Δε/k. Instead, short-lived molecular clusters form and disappear, so that SCW consists of regions of high-density clusters of aggregated water molecules and low-density regions of individual water molecules. This inhomogeneity in molecular distribution is one of the characteristic properties of supercritical fluids. While the term supercritical water is typically restricted to the area of the T-P phase diagram where both $T > T_c$ and $P > P_c$ are satisfied, it is more instructive to consider the entire region where $T > T_c$ as SCW. This highlights the close connection between corrosion in superheated steam at temperatures above T_c and corrosion in SCW at higher pressures (e.g., 25 MPa).

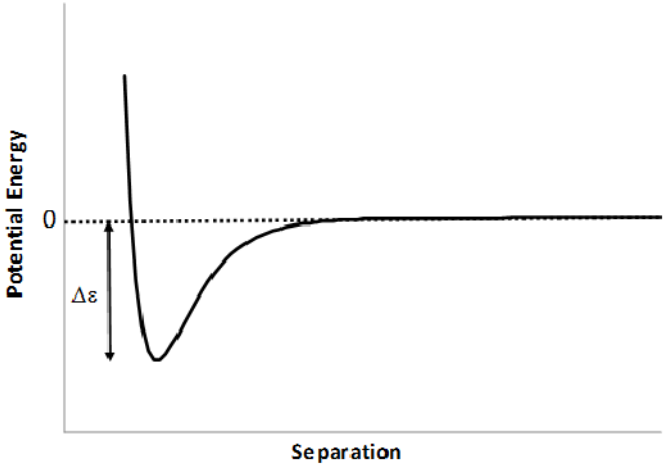

Figure 2: Simplified schematic of the dependence of potential vs separation distance for two interacting molecules in the liquid state. When the thermal energy kT exceeds Δε, the molecules will always escape from the potential well and no permanent liquid phase can form.

Extensive experimental and modeling studies have shown that SCW is a "mixture" of regions of lower density and higher density giving an average bulk density that correlates with thermochemical datasets. Macroscopically, at the higher bulk fluid density at the SCWR core inlet, the properties of SCW are more "liquid-like", while at the lower bulk fluid density at the core outlet, SCW is more "gas-like". As the SCW density decreases, the water structure at a solid surface will change an electrical double layer to one in which only clusters of adsorbed water exist. As a result, the corrosion mechanism must change [5].

2.1 Feedtrain Chemistry Control

2.1.1 Corrosion Product Transport

Feedtrain water chemistry must be carefully controlled to minimize degradation of feedtrain components; the optimum practices are now well-established in the BWR and SCFP power cycles. However, the SCWR poses additional challenges: in 1960, Marchaterre and Petrick [6] noted that "The major gap in supercritical water technology pertaining to a reactor system is the lack of information on the magnitude of the problems of deposition of radioactivity in the external system and of the buildup of internal crud under irradiation." Burrill [7] highlighted the possibility that corrosion product deposition could be significant in an SCWR core in the region of the critical transition. High concentrations of corrosion products transported into the core can result in: a) increased corrosion product deposition on fuel cladding surfaces leading to reduced heat transfer and the possibility of fuel failures, and b) increased production of radioactive species by neutron activation, leading to increased out-of-core radiation fields and worker dose. The effects of corrosion product layers on thermalhydraulics in an SCWR core have not been assessed in significant detail, although Pencer et al. [8] have modeled the effects of in-core deposits on core physics and Cook and Olive [9] modeled the potential reduction in flow area across a fuel channel using a corrosion product transport and deposition model.

As there have been no laboratory measurements of corrosion product deposition under SCWR conditions, modeling provides the only means of assessing corrosion product deposition. Cook and Olive [9, 10] and Olive [11] recently modeled iron and nickel deposition in the Canadian SCWR core concept for coolant saturated and unsaturated in the metal species of interest at the core inlet. The Canadian SCWR core concept uses a fuel channel in which the coolant enters the core and flows downward in a flow tube that passes through the centre of the fuel, then turns and flows upward through the fuel. Modeling performed with this configuration showed that the deposition profile within the reactor core is highly dependent upon the concentration of corrosion product entering the reactor from the feedtrain [10]. Figure 3 shows the modeled deposit profiles for an insulated flow tube and demonstrates that deposition will follow the transition through the pseudo-critical point of the coolant.

The deposition rate constant in SCW has not been reported. Cook and Olive [9, 10] used a value of 0.05 m/s based upon published deposit profiles from SCFPs that had shown significant deposition in superheater tubes at temperatures around the critical point [12]. Olive [11] compared deposition rate constants of 0.01 and 0.001 m/s to 0.05 m/s, finding that, for unsaturated coolant at a dissolved iron concentration of 1 $\mu g \cdot kg^{-1}$ at the core inlet, peak magnetite thickness could be anywhere between 10 and 65 µm/a over one year of operation depending on the deposition rate constant and corrosion rate. Experimental measurements of deposition under proposed SCWR conditions are needed to better predict corrosion product deposition. Extrapolation of the predictions of Cook and Olive [9] suggests that for optimized feedtrain design, materials and chemistry, such that the dissolved Fe concentration at the core inlet is 0.1 $\mu g \cdot kg^{-1}$, the deposit thickness[2] after one fuel cycle (~425 d) would be about 15 µm, not significantly higher than the average oxide thickness of 5.4 µm reported for PWR spent fuel [13]. In-core deposition in an SCWR could be managed if feedtrain materials and chemistry are optimized such that the core inlet dissolved iron concentration is below 0.1 $\mu g \cdot kg^{-1}$. A key design consideration is cascading of feedwater heater drains back to the turbine condenser; plants with this design have the lowest final feedwater concentrations (0.1-0.5 $\mu g \cdot kg^{-1}$) [14].

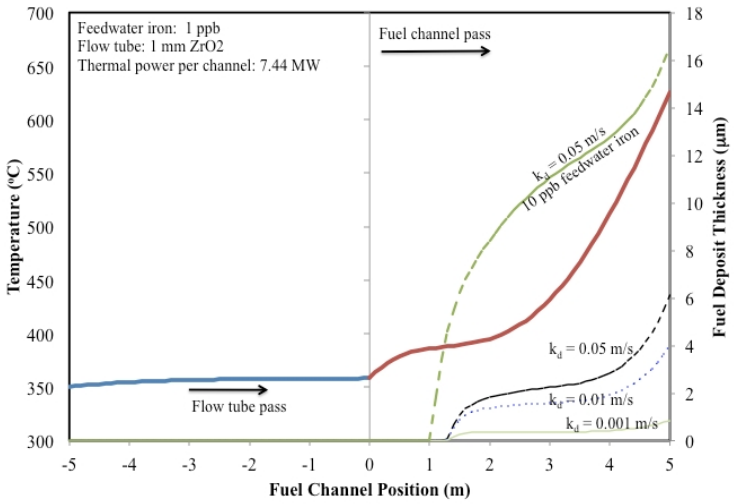

Figure 3: Deposit profiles for insulated flow tubes in the re-entrant fuel channel design over one-year of operation [10]. k_d is the dissolution rate constant.

In direct cycle NPPs impurity ingress can expose reactor core components to species that can enhance corrosion rates or lead to SCC. Ru and Staehle [15] noted that materials testing during the US nuclear superheated steam development program in the 1960s found chloride deposition eventually led to failure by SCC, even with the best available water purification. A study of chloride deposition in the BONUS[3] reactor showed that wet steam containing chloride

[2] This is the deposit thickness due to deposition of corrosion products from out-of-core, and does not include the thickness of the oxide formed on surfaces by corrosion of the base metal.

[3] BOiling NUclear Superheater, a nuclear steam reheat test reactor developed in the United States that started operation in 1964.

and oxygen caused chloride-induced SCC failure of Type 304 and Type 347 stainless steels. Tests showed that the stainless steel (1Kh18N10T) used for the channel elements at Beloyarsk NPP cracked due to SCC after 144-1100 h of temperature and pressure cycling in an environment containing chloride [16]. No tests with representative concentrations of chloride or other impurities known to promote SCC have been carried out in recent SCWR materials tests. BWRs operate with feedwater chloride concentrations as low as 0.25 $\mu g \cdot kg^{-1}$ (typically the method detection limit) and sulphate concentrations as low as 2 $\mu g \cdot kg^{-1}$ [14].

The reported solubility data [17, 18] for NaCl in high temperature water as a function of water density (ρ) are reasonably well described by $\log(S) \propto \log(\rho)$ (Figure 4), while the temperature dependence is relatively weak. NaCl solubility is an order of magnitude higher at 850 °C and 25 MPa (~20 $mg \cdot kg^{-1}$) than at 8.8 MPa (Beloyarsk NPP) and more than an order of magnitude higher than at 6 MPa, the pressure used in the chloride deposition tests [19, 20]. Since there is no phase change in the SCWR core, the solubility of NaCl should be sufficiently high under in-core conditions that operation with a feedwater chloride concentration of 0.25 $\mu g \cdot kg^{-1}$ should result in low chloride deposition. However, molecular dynamics simulations [21] suggest that chloride atoms will tend to associate with the higher density surface water, suggesting that chloride could concentrate in the oxide layers on fuel cladding surfaces leading to SCC.

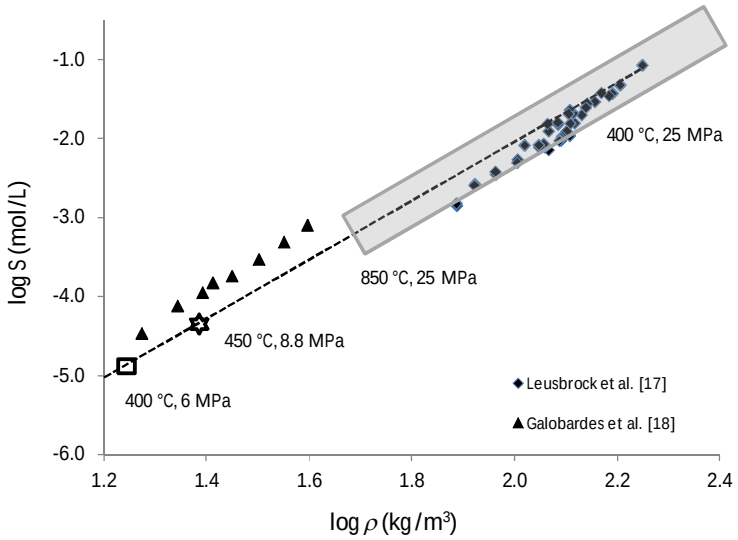

Figure 4: Logarithm of the solubility of NaCl as a function of the logarithm of water density at 400 °C. The shaded area indicates the range of SCW densities expected in a 25 MPa SCWR core, up to a peak cladding temperature of 850 °C. The open star indicates the operating density of the Beloyarsk NPP, and the open square indicates the lowest density studied in the corrosion tests of Bevilacqua and Brown [19].

2.2 Chemistry Control In-Core

The water chemistries used in SCFPs are primarily feedtrain chemistries, and corrosion testing for the various SCWR concepts has been carried out in low conductivity, neutral pH_{25C} water with various concentrations of dissolved oxygen. These test conditions appear to be based on a generally unstated assumption that the feedwater chemistry would be the Oxygenated Treatment commonly used in SCFPs and BWRs. However, with the exception of the Combined Mode (100 $\mu g \cdot kg^{-1}$ dissolved oxygen, pH adjusted to 8.2 using ammonia), the measured weight gain and descaled weight loss data for 304 SS coupons after exposure to a number of common water chemistries at 450 °C SCW in static autoclaves for 340 h were about the same within the experimental uncertainties, suggesting no significant effect of these feedtrain additives on in-core corrosion [5]. Figure 5 shows the metal release data from 316 stainless steel at temperatures from 350 to 650 °C at neutral (pH=7±0.3) and alkaline (pH=10±0.3) pH_{25}, pH adjusted using LiOH [22], plotted as apparent corrosion rate (calculated from the metal release) versus temperature. The data show that above about 500 °C, pH control in the core is not

possible due to the very low dissociation of potential pH control agents. As the portion of the fuel assembly exposed to the highest temperatures is above 500 °C, the use of a pH control agent for ***in-core*** chemistry control is not recommended.

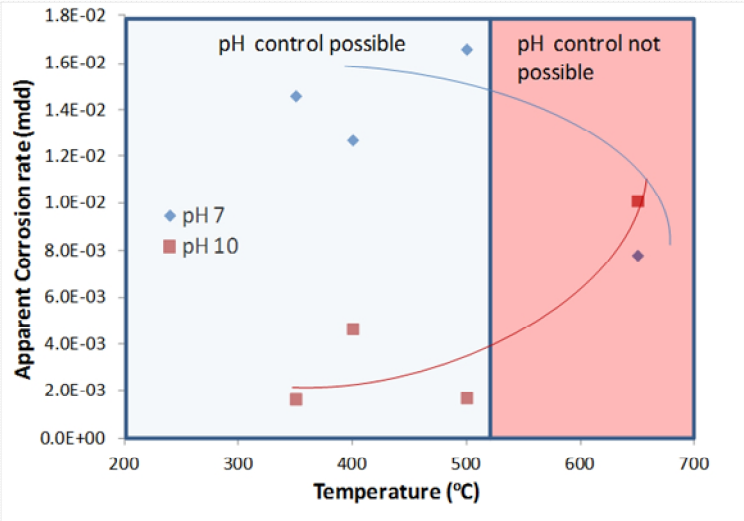

Figure 5: Metal release from 316 SS as a function of temperature (adapted from [22]). The plot has been divided into two regions based on the apparent effectiveness of LiOH (pH) for reducing metal release. The division between 'pH control possible' and 'pH control not possible' is based on mechanistic discussions presented in Guzonas and Cook [5] and reflects a change in the corrosion mechanism.

2.3 Water Radiolysis

Ionization of the SCWR coolant by the intense radiation field in the reactor core forms a number of primary species: hydrated electrons, hydroxide radicals, hydrogen atoms, molecular hydrogen, hydrogen peroxide, superoxide radicals, and protons [23, 24]. The exact species formed will depend upon whether the coolant is liquid-like or gas-like in density. For liquid water, the process is as follows:

$$H_2O + \gamma, \text{fast neutron radiation} \rightarrow e_{aq}^-, H, OH, HO_2/O_2^-, H_2, H_2O_2 \qquad \text{Equation 1}$$

These primary species undergo additional reactions as they diffuse away from the initial ionization centre to form the stable end-species hydrogen, oxygen and hydrogen peroxide:

$$e_{aq}^-, H, OH, HO_2/O_2^-, H_2, H_2O_2 \rightarrow H_2, O_2, H_2O_2 \qquad \text{Equation 2}$$

In water vapour, the breakdown of water into H_2 and •O becomes an important reaction [23].

Chromium oxide dissolution under oxidizing conditions due to the formation of soluble Cr(VI) species is of particular concern, as these oxides form the barrier films on almost all alloys proposed for in-core use in an SCWR (e.g., austenitic stainless steels). Chromium oxide dissolution as H_2CrO_4 (transpassive dissolution) is observed in BWRs that operate with normal water chemistry because of the high concentrations of oxidizing species produced by water radiolysis, and similar behaviour is expected in an SCWR if water radiolysis cannot be controlled [2, 25, 26]. Initial ~500 h tests [27] at temperatures in the vicinity of the critical point under electron irradiation using an SCW convection loop with an irradiation cell coupled to a 10 MeV, 10 kW linear electron accelerator [28] provide clear evidence for chromium oxide dissolution. Samples of the outlet water contained at least 3-5 $\mu g \cdot kg^{-1}$ of oxygen, and elemental analysis using Inductively-Coupled Plasma Optical Emission Spectrometry indicated the presence of chromium at concentrations up to 54 $\mu g \cdot L^{-1}$ in the water; there was no detectable chromium in the water before exposure to the electron beam.

In the absence of in-reactor SCW test facilities, and because of difficulties in making measurements close to the reactor core, modeling becomes the only avenue for predicting the

effects of water radiolysis in an SCWR. Modeling the effect of radiation on water at elevated temperature requires knowledge of the temperature dependencies of the chemical yields of oxidizing (•OH, H_2O_2,·HO_2/O_2^-) and reducing (e^-_{aq}, H•, H_2) radiolytic products and of the rate constants for the reactions taking place in spurs and tracks that result in these primary yields [2]. The *g*-values for the primary yields formed by using low-linear energy transfer (gamma or fast electrons) radiation at temperatures from ambient up to ~350 °C have been measured by several groups. In general the measured temperature dependencies of these rate constants do not follow an Arrhenius relationship at high temperatures, and their values in SCW cannot therefore be predicted by simple extrapolations of existing sub-critical water data. The temperature dependences for many relevant reactions are non-Arrhenius and show a local minimum (for both light and heavy water) near the critical point; specifically, at thermodynamic conditions where the compressibility[4] of the fluid is a maximum [29, 30, 31, 32, 33].

Changes in the relative stabilities of ionic and radical species in solution with changes in temperature may change the relative importance of various pathways (e.g., diffusion versus recombination). The dependencies of water radiolysis rate constants on the relative stabilities of ionic and radical species, which in turn depend on solvent properties, suggest that water radiolysis will be of greatest concern in an SCWR at temperatures around the critical point.

Monte Carlo simulations offer a promising avenue to quantitatively describe the temperature and pressure (density) effects on SCW radiolysis, to identify key parameters, and also to help elucidate mechanisms by which radiation interacts with water in its supercritical regime [34]. Molecular dynamics simulations provide a better microscopic understanding of SCW and the precise role of its molecular structure in SCW radiolysis for a wide range of densities.

Perhaps the most important reaction in water-cooled reactors is the reaction between •OH and dissolved hydrogen (Equation 3):

$$\bullet OH + H_2 \rightleftarrows H\bullet + H_2O \qquad \text{Equation 3}$$

This is a key reaction in the suppression of net water radiolysis by addition of molecular hydrogen to the coolant of water-cooled reactors, because it removes the oxidizing •OH radical. •OH recombines to form H_2O_2, which can then decompose to give molecular oxygen. The relative concentrations of reactants and products in Equation 3 can be altered by adjusting the H_2 concentration, and since it is the only reaction in the set of radiolysis reactions that removes H_2 [24], it is common practice to inject molecular hydrogen into PWR and PHWR coolant systems. This addition exploits the reaction between the hydroxide radical and hydrogen to produce hydrogen atoms and water, adding a high concentration of hydrogen to drive the reaction in Equation 3 to the right, converting the oxidizing •OH radical into the reducing •H radical before the •OH radical can oxidize another species. When a sufficient quantity of excess hydrogen is added to the coolant in PWRs, the *net* production of hydrogen, oxygen and hydrogen peroxide becomes essentially zero. However, it is not possible to add sufficient hydrogen to the boiling portion of a BWR core to achieve this suppression.

The suppression of net radiolysis under high temperature steam conditions was studied at the Beloyarsk NPP [4; 35]. Initially, Unit 1 used ammonia alone to control pH and suppress net radiolysis indirectly through the radiolysis of ammonia to produce hydrogen. Despite a hydrogen concentration of 45-88 mL·kg^{-1} (at NTP) in the steam entering the superheat channels, the oxygen concentration in the superheated steam was still 2.3 mg·kg^{-1}. Unit 1 tested hydrogen injection to suppress net radiolysis in the superheat channels, discontinuing ammonia feedwater treatment during the studies. Hydrogen injection was successful in maintaining steam hydrogen concentrations at 1.2-6.2 mL·kg^{-1}, which resulted in an oxygen concentration of less than 0.15 mg·kg^{-1} in the superheated steam. Further testing showed that

[4] Compressibility is a measure of the relative volume change of a fluid or solid as a response to a pressure (or mean stress) change,

$$\beta = -\frac{1}{V}\frac{\partial V}{\partial p}$$

where V is volume and p is pressure.

the oxygen concentration in the superheated steam could be maintained below 0.03 mg·kg^{-1} with a steam hydrogen concentration greater than 45 mL·kg^{-1}.

Subramanian et al. [36] have developed preliminary steady-state models for the radiation chemistry of water near the critical point that take into account some of the influences of the changing water properties in this region. A liquid-like radiolysis model (LRM) was constructed using a reaction set similar to that used in an existing radiolysis model developed and validated for liquid water at ambient temperatures [37, 38, 39, 40]. A vapour-like radiolysis model (VRM) uses the reaction set developed for water vapour radiolysis [41], applied to water vapour chemistry at high temperatures (900 K), but at much lower pressures (0.01 to 1 MPa) and lower vapour densities (0.25-1 kg m^{-3}) than those that will be used in an SCWR.

The LRM predicts that H_2 addition could reduce (but not suppress)[5] radiolytic production of O_2; $[O_2]$ at 1 s is below 10^{-11} g·kg^{-1} when $[H_2]_0$ > 10 mL·kg^{-1} is added. However, H_2 is less effective at reducing production of H_2O_2; $[H_2O_2]$ at 1 s remains at ~10^{-7} g·kg^{-1} even at $[H_2]_0$ > 100 mL·kg^{-1}. The VRM predicts that addition of any reasonable amount of H_2 will not suppress production of either O_2 or H_2O_2 (Figure 6). The experimental data from the test performed in Beloyarsk NPP Unit 1 are also plotted in Figure 6. The VRM predictions are comparable to the Beloyarsk data, predicting slightly higher $[O_2]$, but still within an order of magnitude of the measured concentrations. The VRM predicts that addition of H_2 at $[H_2]_0$ > 20 mL·kg^{-1} should reduce production of O_2, but that $[H_2]_0$ > 200 mL·kg^{-1} is required for any observable reduction in $[H_2O_2]$. These results suggest that H_2 addition to the SCWR coolant at concentrations similar to those currently used in PWRs may reduce (but not suppress) the net radiolytic production of O_2, but is unlikely to reduce the production of H_2O_2, a potentially more important oxidant.

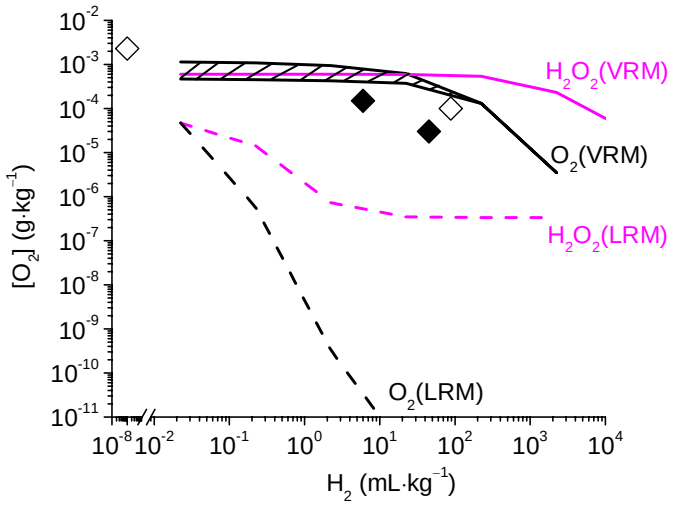

Figure 6: Radiolysis product concentrations as a function of initial H_2 addition predicted by the LRM and VRM at 1 s irradiation at 400 °C and 1000 kGy·h^{-1}. The shaded area envelops the predicted range of $[O_2]$ as a function of time (t > 1 s) until steady state is achieved. The oxygen concentrations measured in the tests performed in Unit 1 of the Beloyarsk NPP are also shown: (◇) - ammonia addition; (◆) - direct H_2 addition.

2.4 Activity Transport and Release

There are three source terms for activity that must be considered in an SCWR (Figure 7) [42]:

1. Corrosion products transported to the core, activated and then released;
2. Release of activated elements by corrosion of in-core materials; and
3. Fission products and actinides released from failed fuel.

[5] Suppression of net radiolysis is defined as having undetectable concentrations of oxidants at the core outlet.

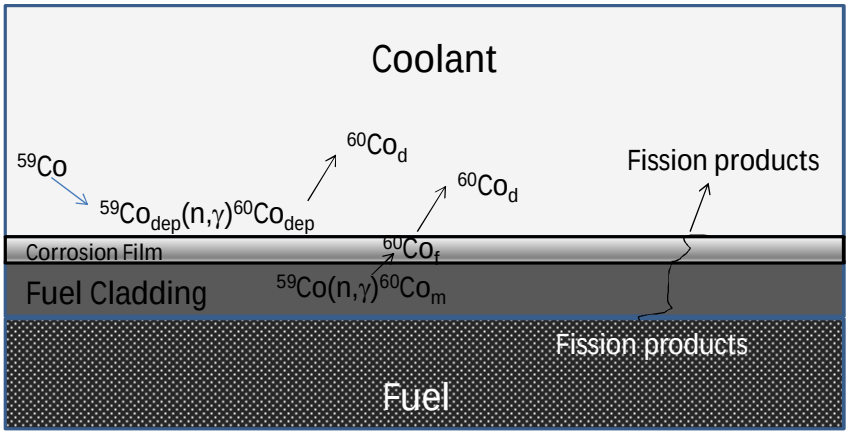

Figure 7: The three source terms for activity transport in an SCWR. From left to right the processes are: 1) deposition of corrosion products (in this example ^{59}Co) released by corrosion in the feedtrain, neutron activation and then release of ^{60}Co to the coolant; 2) neutron activation of ^{59}Co in the alloy, and subsequent diffusion of ^{60}Co into the corrosion film and release into the coolant, and 3) release of fission products into the coolant through a fuel defect. Subscripts indicate location: "dep" for within deposit, "d" for dissolved in the coolant, "m" for within the metal, and "f" for within the film.

Corrosion products on in-core surfaces can originate from base metal corrosion and from deposition of corrosion products transported to the core from the feedtrain. The relative importance of these two terms may change across the core since the two phenomena have different temperature dependences. Corrosion rates typically increase with increasing temperature, while metal oxide solubilities typically decrease with increasing temperature. Thus, naively one expects that corrosion product deposition will dominate at the core inlet while base metal corrosion will dominate at the core outlet. Calculations of in-core deposition for the Canadian SCWR concept [9, 10] predict that deposition continues along the entire length of the core under all conditions studied, i.e., the coolant is always saturated in dissolved metals in the core, and the surface oxides never become soluble. Therefore, during normal operation, release of activity by iron and nickel oxide ***dissolution*** is not expected, but dynamic exchange of active and inactive species at the oxide-solution interface is possible[6].

Activity release is also possible during shutdown/start-up and other system transients. The solubilities of most metal oxides of interest increase by several orders of magnitude as the temperature decreases below the critical temperature. Oxide spalling (exfoliation) is also a concern due to the different thermal expansion characteristics of the oxide and alloy [43]. Other possible release mechanisms during normal operation are mechanical wear (e.g., due to vibration of the fuel rods) and erosion by the flowing coolant.

While corrosion products transported from out-of-core sources are typically deposited and released over relatively short periods, in-core materials reside in the core for long periods. During this time they are subjected to nearly continuous irradiation, leading to production of radionuclides by nuclear reactions. Some of these radionuclides can then be released into the coolant by corrosion or abrasion. There have been few studies of metal release into the coolant in SCW. Guzonas and Cook [5] reported data on the release of iron, manganese, nickel and chromium from 403 stainless steel in static autoclaves, and on the release of various elements into SCW from Hastelloy C and Alloy 625 autoclaves. Han and Muroya [44] quantified release of ^{60}Co radiotracer from irradiated 304 SS samples as a function of time and temperature in SCW. The temperature dependence of the release decreased between 300 and 550 °C, reflecting the change in solubility of ionic species through the critical point, both directly by lowering the solubility of cobalt in water, and indirectly because, as the solubility of the iron oxides decrease, the thickness of the corrosion film on the surface increases, slowing diffusion of cobalt from the bulk metal to the solution interface.

[6] The exchange of isotopes of an element in the coolant with those in the oxide.

The metal release data of Carvajal-Ortiz et al. [22] can be used to estimate the ^{60}Co activity release from the stainless steel fuel cladding. Data [45] on activation of 304 SS fuel cladding suggests that the amount of ^{60}Co activity in the cladding will be about 2 MBq·mg^{-1}, and a reasonable estimate for the ^{60}Co release rate AR (in MBq·d^{-1}) can be obtained (Equation 4):

$$AR = 2\ MBq \cdot mg^{-1}\ metal \times S_{ac} \times R \qquad \text{Equation 4}$$

where S_{ac} is the surface area of the cladding and R is the metal release rate from the surface. The value of the release rate, R, will vary with location in the core, as it depends on corrosion rate and on the solubility of the surface oxide film; the latter depends on the SCW density [46], which changes with distance through the core. In the two limiting cases, namely at the core inlet (high oxide solubility) and core outlet (low oxide solubility), the predicted peak ^{60}Co release rates are about 25000 MBq (0.7 Ci) per day and 5000 MBq (0.14 Ci) per day, respectively. This corresponds to coolant ^{60}Co concentrations of about 175 Bq/kg (~4.7 nCi·kg^{-1}), on the same order as the coolant concentration of ^{60}Co found in current generation PWRs and pressurized heavy water reactors. The Co concentration is ~10^{-13} mol·kg^{-1}, well within the range of metal oxide solubilities at 600 °C (as low as 10^{-15} mol kg^{-1} for NiO to as high as 10^{-8} mol·kg^{-1} for Cr_2O_3 [5]). Therefore in spite of the reduced solubilities of metal oxides in SCW, significant activity transport to out-of-core surfaces is possible as dissolved species. Note that in the more realistic case that the concentration of metal species in the coolant is non-zero, the dissolution of the oxide film may be very low if the coolant is already saturated with the relevant dissolved metal species. Thus the presence of a **very low** concentration of dissolved metal species in the coolant at the core inlet is not necessarily detrimental from an activity transport perspective.

Essentially the only data on the transport of activation products at supercritical temperatures comes from the Beloyarsk NPP. ^{51}Cr, ^{54}Mn, ^{58}Co, ^{60}Co, ^{65}Zn, and ^{124}Sb were reported in deposits and coolant samples [47, 48, 49]. These are the same activation products found in other WCRs. In general, the data on radioactive corrosion product deposition from Beloyarsk agree well with data reported for corrosion product deposition in fossil-fired SCW power plants.

There is a significant amount of data on the behaviour of noble gases and iodines in superheated steam from the US nuclear steam superheat program carried out in the 1960s. Because gases are infinitely soluble in SCW, data on noble gas transport obtained at lower pressures are directly relevant to their transport in an SCWR. Several fuel defects occurred during the experimental program at the Superheat Advanced Demonstration Experiment Vallecitos Experimental Superheat Reactor, which was deliberately operated for several months with a grossly defected fuel bundle to determine the effects [50]. Fission product release was highly dependent upon the reactor power and reactor exit steam temperature. Operation at the fuel full-rated temperature led to deposition of tellurium and other fission products on the steam piping, resulting in surface dose rates of up to 300 mR/h on piping external to the containment building and up to 5 R/h on one valve in the reactor pipe gallery. The radiation levels decreased with a 78-h half-life following reactor shutdown. Based on the large amount of data available from the US nuclear steam superheat program, the behaviour of noble gases and iodines released from a fuel defect in an SCWR is not considered a major knowledge gap.

No data could be found on the release of so-called depositing fission products. To address this knowledge gap, leaching tests of SIMFUEL in SCW were performed to identify those fission product species capable of dissolving from the fuel matrix, as well as to determine the risk that the fuel itself might dissolve in SCW [51]. Only Sr and Ba were detected in all tests at significant concentrations. At 400 °C, Zr, Ru, Rh, Pd, Ag, and Sn were detected in one or more tests, and at 500 °C, Rh, Ce, La and Nd were detected in one or more tests, in both cases at close to the Method Detection Limit of Inductively-Coupled Plasma Mass Spectrometry. This suggests that these elements have low solubilities under SCWR conditions. A measurable concentration of U in solution was reported in two tests: at 400 °C a value of 0.031 µg·kg^{-1} ($\log_{10}$([U]/[mol/kg]) = -9.9 mol·kg^{-1}) was reported, and at 500 °C a value of 0.069 µg·kg^{-1} ($\log_{10}$([U]/[mol/kg]) = -9.5 mol·kg^{-1}) was obtained. These values are in reasonable agreement with literature values. Sunder [52] showed that uranium in a matrix of thorium oxide will be less easily oxidized, and therefore the dissolution of uranium from such materials will be significantly lower than for pure UO_2 under similar conditions. A crude solubility measurement of thoria powder (5.5 g placed in 78 mL water in an autoclave) was performed for 216 h at

400 °C and a pressure of 25 MPa. Analysis of the test solution after cooling and filtering gave a thorium concentration in solution of less than 0.2 $\mu g \cdot L^{-1}$, or $K_{sp} \approx 8.6 \times 10^{-10}$ $mol \cdot kg^{-1}$, which gives $\log_{10}Ksp = -9.1$, very close to the value for UO_2 ($\log_{10}(S/[mol/kg]) = -9.0 \pm 0.5$ $mol \cdot kg^{-1}$).

3. Conclusions

Significant progress has been made in both the fundamental understanding of the key phenomena underlying chemistry control in an SCWR and in predicting the potential impact of these phenomena in a future SCWR plant. It is possible that the in-core deposition of impurities and corrosion products can be minimized in an SCWR by adopting the best practices for feedtrain materials selection and chemistry control from the SCFP and BWR industries. The available data suggest that an oxygenated feedwater chemistry will be the best option.

Based on the available data and recent modeling, it does not appear that the production of oxygen and hydrogen peroxide by water radiolysis can be 'suppressed' by the addition of hydrogen at the core inlet, but it appears that their concentrations can be reduced. Therefore it is recommended that hydrogen be added, but no specification for this can be recommended at this time. The possibility that an explosive mixture of hydrogen and oxygen could exist in the SCW exiting the core will need to be considered during the design stage of any SCWR.

A review of available data on activity transport and the results of preliminary calculations suggest that activity transport in the Canadian SCWR will be of a similar magnitude as in current water-cooled reactors. However, it must be emphasized that, unlike BWRs where the phase change results in little activity transport out of the core in the steam, the solubilities of most metals in SCW, while low, is non-zero; the single-phase coolant can also easily transport particulates.

Based on the discussion presented above, preliminary chemistry specifications for the Canadian SCWR can be proposed (Table 1).

Table 1
Proposed Chemistry Specifications for the Canadian SCWR

Parameter	Value	Comments
Chloride	0.25 $\mu g \cdot kg^{-1}$	Measured at core inlet
Sulphate	2.0 $\mu g \cdot kg^{-1}$	Measured at core inlet
Iron	0.1 $\mu g \cdot kg^{-1}$	Measured at core inlet
Initial Feedwater Dissolved Oxygen	200 $\mu g \cdot kg^{-1}$	Measure at injection point
Final Feedwater Dissolved Oxygen	50 $\mu g \cdot kg^{-1}$	Measured at core inlet
Hydrogen	To be determined	Added at the core inlet
pH	7.0	Measured as per best industry practices
Conductivity	8 $\mu S \cdot m^{-1}$	Measured on-line as per best industry practices
Silica	300 $\mu g \cdot kg^{-1}$	Measured at core inlet

4. Acknowledgements

The authors thank L. Qiu, S. Livingstone, M.K. Edwards, C.R. Stuart (CNL) for data and valuable discussions, and M.K. Edwards and C.R. Stuart (CNL) for their careful review of the report. The authors acknowledge the significant contributions of the university professors and students through the NSERC/NRCan/AECL Generation IV Energy Technologies Program.

5. References

[1] Yetisir,M.; Gaudet, M.; Rhodes, D. (2013) “Development and Integration of Canadian SCWR Concept with Counter-flow Fuel Assembly”, ISSCWR-6, March 3-7, 2013, Shenzhen, China.

[2] Guzonas, D.; Tremaine, P.; Brosseau, F.; Meesungnoen, J.; Jay-Gerin, J.-P. (2012) “Key Water Chemistry Issues in a Supercritical-water-cooled Pressure-tube Reactor”, Nucl. Technology, **179** , 205.

[3] Kysela, J.; Růžičková, M.; Petr, J. (2009) “Water Chemistry Specification for Supercritical Water Cooled Reactors – Possible Options”, 4th International Symposium on Supercritical Water-Cooled Reactors, Heidelberg, Germany, 2009, March 8-11. Paper No. 68.

[4] Yurmanov, V.A.; Belous, V.N.; Vasina, V.N.; Yurmanov, E.V. (2010) “Chemistry and Corrosion Issues in Supercritical Water Reactors”, Proceedings of the Nuclear Plant Chemistry Conference 2010 (NPC 2010), October 3-8, 2010, Quebec City, Canada, Paper 11.02.

[5] Guzonas, D.A.; Cook, W.G. (2012) “Cycle Chemistry and its Effect on Materials in a Supercritical Water-cooled Reactor: A Synthesis of Current Understanding”, Corrosion Science, **65,** 48.

[6] Marchaterre, J.F.; Petrick, M. (1960) “Review of the Status of Supercritical Water Reactor Technology”, Argonne National Laboratory Report ANL-6202.

[7] Burrill, K.A. (2000) “Water Chemistries and Corrosion Product Transport in Supercritical Water in Reactor Heat Transport Systems”, in: Proceedings of the 8th BNES Conference on Water Chemistry of Nuclear Reactor Systems, Bournemouth, UK, 2000, p 357.

[8] Pencer, J.; Edwards, M.K.; Guzonas, D.; Edwards, G.W.R.; Hyland, B. (2011) **“**Impact of Corrosion Product Deposition on CANDU-SCWR Lattice Physics”, The 5th Int. Sym. SCWR (ISSCWR-5) Vancouver, British Columbia, Canada, March 13-16, 2011.

[9] Cook, W.G; Olive R.P. (2012), “Corrosion Product Deposition on Two Possible Fuel Geometries in the Canadian-SCWR Concept”, 3rd China-Canada Joint Workshop on Supercritical-Water-Cooled Reactors, Paper 12064, Xi’an, China, April 18-20, 2012.

[10] Cook, W.G.; Olive, R.P. (2013) “Corrosion Product Transport and Deposition in the Canadian Supercritical Water-Cooled Reactor”, Proceedings ICPWS16, Greenwich, UK, paper 123, September 2013.

[11] Olive, R.P. (2012) “Pourbaix Diagrams, Solubility Predictions and Corrosion-product Deposition Modelling for the Supercritical Water-cooled Reactor”, PhD Thesis, University of New Brunswick, Department of Chemical Engineering.

[12] Vasilenko, G.V. (1976) “The Effect of the pH of the Feedwater on Corrosion of the Low Pressure Heaters of Supercritical Power Generating Units", Thermal Eng., **23**, 51.

[13] Hazelton, R.F. (1987)“Characteristics of Fuel Crud and its Impact on Storage, Handling and Shipment of Spent Fuel”, Pacific Northwest Laboratory, PNL-6273.

[14] Stellwag, B.; Landner, A.; Weiss, S.; Huttner F. (2011) “Water Chemistry Control Practices and Data of the European BWR Fleet”, PowerPlant Chemistry, **13**, 167.

[15] Ru, X.; Staehle R.W. (2013) “PART I– Review: Historical Experience Providing Bases for Predicting Corrosion and Stress Corrosion in Emerging Supercritical Water Nuclear Technology”, Corrosion, **69**(3), 211-229.

[16] Emel’yanov, Ya.; Shatkaya, O.A.; Rivkin, E.Yu.; Nikolenko, N.Ya. (1972) “Strength of Construction Elements in the Fuel Channels of the Beloyarsk Power Station Reactors”, Atomnaya Energiya, **33**,729.

[17] Leusbrock, I.; Metz, S.J.; Rexwinkel, G.; Versteeg G.F. (2008) “Quantitative Approaches for the Description of Solubilites of Inorganic Compounds in Near-critical and Supercritical Water”, J. Supercritical Fluids, **47**, 117.

[18] Galobardes, J.F.; Van Hare, D.R.; Rogers, L.B. (1981) “Solubility of Sodium Chloride in Dry Steam”, J. Chem. Eng. Data, **26**, 363.

[19] Bevilacqua, F.; Brown, G.M. (1963a), “Chloride Deposition from Steam onto Superheater Fuel Clad Materials”, General Nuclear Engineering Corporation Report GNEC 295.

[20] Bevilacqua, F.; Brown, G.M. (1963b) “Chloride Corrosion Effects on BONUS Superheater Materials”, Terminal Report under Job No. 66-14, Chloride Corrosion Program, USAEC Report GNEC 257.

[21] Kallikragas, D.T.; Plugatyr, A. Yu.; Guzonas, D.A.; Svishchev, I.M. (2015) “Effect of Confinement on the Hydration and Diffusion of Chloride at High Temperatures”, J. Supercritical Fluids **97**, 22–30.

[22] Carvajal-Ortiz, R.A.; Choudhry, K.I.; Svishchev, I.M.; Guzonas, D.A. (2012) “Chemical Species Influences under Flow Conditions Relevant to PWR and SCWR”, Nuclear Plant Chemistry Conference (NPC 2012), Paris, France 2012 September 23-28.

[23] Spinks, J.W.T.; Woods, R.J. (1990) “An Introduction to Radiation Chemistry”, 3rd ed., Wiley: New York.

[24] Elliott A. J.; Bartels, D.M. (2009) "The Reaction Set, Rate Constants and g-Values for the Simulation of the Radiolysis of Light Water over the Range 20 to 350 °C Based on Information Available in 2008", Atomic Energy of Canada Ltd., Chalk River, ON (2009).

[25] Karasawa, H.; Fuse, M.; Kiuchi, K.; Katsumura, Y. (2004) “Radiolysis of Supercritical Water”, 5th Int. Workshop on LWR Coolant Water Radiolysis and Electrochemistry, San Francisco, USA, 2004 October 15.

[26] Fujiwara, K.; Watanabe, K.; Domae, M.; Katsumura, Y. (2007) “Stability of Chromium Oxide Film formed by Metal Organic Chemical Vapor Deposition in High Temperature Water up to Supercritical Region”, Corrosion 2007, Nashville, Tennessee, March 11-15, 2007.

[27] Bakai, A.S.; Guzonas, D.A.; Boriskin, V.N.; Dovbnya, A.N.; Dyuldya, S.V. (2013) “Supercritical Water Convection Loop for SCWR Materials Corrosion Tests under Electron Irradiation: First Results and Lessons Learned”, 6th International Symposium on Supercritical Water-Cooled Reactors March 03-07, 2013, Shenzhen, Guangdong, China.

[28] Bakai, A.S.; Boriskin, V.N.; Dovbnya, A.N.; Dyuldya S.V.; Guzonas, D. (2011) “Supercritical Water Convection Loop (NSC KIPT) for Materials Assessment for the Next Generation Reactors”, Proc. of the 5th Int. Symposium on Supercritical Water-Cooled Reactors, Vancouver, Canada, 2011.

[29] Ghandi, K.; Addison-Jones, B.; Brodovitch, J.-C.; McKenzie, I.; Percival, P.W. (2002) “Near-diffusion-controlled Reactions of Muonium in Sub- and Supercritical Water”, Phys. Chem. Chem. Phys., **4**, 586-595.

[30] Percival, P.W.; Brodovitch, J.-C.; Ghandi, K.; McCollum, B.M.; McKenzie, I. (2007) “H Atom Kinetics in Superheated Water Studied by Muon Spin Spectroscopy”, Rad. Phys. Chem., **76**, 1231-1235.

[31] Ghandi, K.; Addison-Jones, B.; Brodovitch, J.-C.; Kecman, S.; McKenzie, I.; Percival, P.W. (2003) “Muonium Kinetics in Sub- and Supercritical Water”, Physica B, **326** (1-4), 55-60.

[32] Marin, T.W.; Jonah, C.D.; Bartels, D.M. (2005) “Reaction of Hydrogen Atoms with Hydroxide Ions in High-Temperature and High-Pressure Water”, J. Phys. Chem. A, **109**(9), 1843-1848.

[33] Bonin, J.; Janik, I.; Janik, D.; Bartels, D.M. (2007) “Reaction of the Hydroxyl Radical with Phenol in Water up to Supercritical Conditions”, J. Phys. Chem. A, **111**(10), 1869-1878.

[34] Meesungnoen, J.; Sanguanmith, S.; Jay-Gerin, J.-P. (2013) “Density Dependence of the Yield of Hydrated Electrons in the low-LET Radiolysis of Supercritical Water at 400 °C: Influence of the Geminate Recombination of Subexcitation-energy Electrons prior to Thermalization”, Phys.Chem. Chem. Phys., **15**, 16450.

[35] Gruzdev, N.I.; Shchapov, G.A.; Tipikin, S.A.; Boguslavskii V.B. (1970) “Investigating the Water Conditions in the Second Unit at Beloyarsk”, Therm. Eng., **17** (12), 22-25.

[36] Subramanian, V.; Joseph, J.M.; Subramanian, H.; Noël, J.J.; Guzonas, D.A.; Wren J.C. (2015) “Steady-State Radiolysis of Supercritical Water: Model Development, Predictions and Validation”, 7th Int. Symposium on Supercritical Water-Cooled Reactors (ISSCWR-7), 15-18 March 2015, Helsinki, Finland.

[37] Wren, J.C.; Glowa, G.A. (2000) “A Simplified Kinetic Model for the Degradation of 2-butanone in Aerated Aqueous Solutions under Steady-state Gamma-radiolysis”, Radiat. Phys. Chem., **58**, 341–356.

[38] Wren, J.C.; Ball, J.M. (2001) “LIRIC 3.2 An Updated Model for Iodine Behaviour in the Presence of Organic Impurities”, Radiat. Phys. Chem., **60**, 577–596.

[39] Yakabuskie, P.A.; Joseph, J.M.; Wren, J.C. (2010) “The Effect of Interfacial Mass Transfer on Steady-state Water Radiolysis”, Radiat. Phys. Chem., **79**, 777–785.

[40] Yakabuskie, P.A.; Joseph, J.M.; Stuart, C.R.; Wren, J.C. (2011) “Long-term γ-radiolysis Kinetics of NO3(-) and NO2(-) Solutions”, J. Phys. Chem. A., **115**, 4270–4278.

[41] Arkhipov, O.P.; Verkhovskaya, A.O.; Kabakchi, S.A.; Ermakov, A.N. (2007) “Development and Verification of a Mathematical Model of the Radiolysis of Water Vapor”, Atomic Energy **103**(5), 870-874. DOI: 10.1007/s10512-007-0138-4.

[42] Guzonas, D.A.; Qiu, L. (2013), “Activity Transport in a Supercritical Water-cooled Reactor”, 6th International Symposium on Supercritical Water-Cooled Reactors, March 03-07, 2013, Shenzhen, Guangdong, China.

[43] Wright, I.G.; Tortorelli, P.F.; Schutze, M. (2007) “Program on Technology Innovation: Oxide Growth and Exfoliation on Alloys Exposed to Steam”, EPRI Report 1013666.

[44] Han, Z.; Muroya, Y. (2009) “Development of a New Method to Study Elution Properties of Stainless Materials in Subcritical and Supercritical Water”, 4th Int. Symp. on Supercritical Water-cooled Reactors, 2009.

[45] Cohen, P. (1985) “Water Coolant Technology of Power Reactors”, American Nuclear Society.

[46] Guzonas, D.; Bissonette, K.; Deschenes, L.; Dole, H.; Cook, W (2013) “Mechanistic Aspects of Corrosion in a Supercritical Water-cooled Reactor”, 6th Int. Symp. on Supercritical Water-cooled Reactors, Shenzhen, Guangdong, China, 2013 March 03-07.

[47] Dollezhal, N.A.; Aleshchenkov, P.I.; Evdokimov, Yu.V.; Emel'yanov, I.Ya.; Ivanov, B.G.; Kochetkov, L.A.; Minashin, M.E.; Mityaev, Yu.I.; Nevskii, V.P.; Shasharin, G.A., Sharapov, V.N.; Orlov, K.K. (1969), “Operating Experience with the Beloyarsk Nuclear Power Station”, Atomnaya Energiya, **27**, 379.

[48] Aleksandrova, V.N.; Veselkin, A.P.; Levich, A.A.; Lyutov, M.A.; Sklyarov, V.P.; Khandamirov, Yu.E.; Shchapov, G.A. (1968), “Investigation of the Radioactivity of Long-Lived Isotopes in the Coolant of the I.V. Kurchatov Nuclear Power Station at Beloyarsk”, Atomnaya Energiya **24**, 222.

[49] Veselkin, A.P.; Lyutov, M.A.; Khandamirov, Yu.E. (1968) “Radioactive Deposits on the Surfaces of the Technological Equipment of the I.V. Kurchatov Nuclear Power Station at Beloyarsk”, Atomnaya Energiya, **24**, 219.

[50] Murray, J.L. (1965) “EVESR-Nuclear Superheat Fuel Development Project Thirteenth Quarterly Report”, General Electric Report GEAP-4941.

[51] Guzonas, D.; Qiu, L.; Livingstone, S.; Rousseau, S. ”Fission Product Release under Supercritical Water cooled Reactor Conditions”, 7th International Symposium on Supercritical Water-Cooled Reactors (ISSCWR-7), 15-18 March 2015, Helsinki, Finland.

[52] Sunder, S. (1999) “Corrosion Resistance of (Th,U)O2 Fuel in Water”, In Proceedings of the 6th International CNS CANDU Fuel Conference, Niagara Falls, September 26 - 30, 1999.

ISSCWR7-2090

Assessment of Candidate Fuel Cladding Alloys for the Canadian Supercritical Water-cooled Reactor Concept

D. Guzonas, M. Edwards
Chalk River Laboratories, Canadian Nuclear Laboratories
Chalk River, Ontario, Canada K0J 1J0
David.Guzonas@cnl.ca

W. Zheng
CanmetMATERIALS, Natural Resources Canada
183 Longwood Road South, Hamilton, Ontario, Canada L8P 0A5
Wenyue.Zheng@NRCan-RNCan.gc.ca

Abstract

Selecting and qualifying a fuel cladding material for the Canadian Super-Critical Water-cooled Reactor (SCWR) concept remains the most significant materials challenge to be overcome. The peak cladding temperature in the Canadian SCWR concept is predicted to be as high as 800 °C, and therefore zirconium-based alloys cannot be used for this application. While advanced materials such as oxide dispersion-strengthened ferritic-martensitic steels show promise for future deployment, at this time, the best options available are austenitic stainless steels and nickel-based alloys. Many of these alloys were extensively studied for use as fuel cladding materials in the 1960s, as part of programs to develop nuclear superheated steam reactors.

After an extensive initial round of out-of-pile testing and consideration of the existing data, five alloys, 347 SS, 310 SS, Alloy 800H, Alloy 625 and Alloy 214, were selected for a further, more detailed assessment using a combination of literature surveys and targeted testing to fill in major knowledge gaps. Where possible, performance criteria were developed for key materials properties. This paper summarizes the methodology used for the assessment and presents the key results, which show that 310 SS, Alloy 800H and Alloy 625 would all be expected to give acceptable performance in the Canadian SCWR concept.

1. Introduction

The use of supercritical water (SCW) as the coolant in a nuclear reactor is the logical evolution of the current generation of water-cooled reactors (WCRs), which generate almost all of the electricity produced by nuclear power worldwide. Using SCW as the coolant in nuclear reactors allows a much higher core exit temperature, which increases the efficiency over that of currently operating nuclear power plants, decreases capital and operational costs, and decreases electricity costs. Water is a familiar and relatively safe heat transfer medium, and many power utilities already operate both nuclear power plants (NPPs) and fossil-fired SCW power plants (FFSPs).

The move to supercritical temperatures and pressures was considered by many countries during the development of the first commercial water-cooled reactors [1]. The idea of using

SCW as the coolant in a WCR dates back to the 1950s and 1960s [2,3,4,5,6]. Although reactors operating at supercritical temperatures and sub-critical pressures (superheated steam) were tested, no reactor operating with a coolant above the thermodynamic critical point of water (373 °C and 24 MPa) was ever built. The Russians developed significant experience with the operation of nuclear superheated steam channels in the pressure-tube boiling water reactors (BWRs) at the Beloyarsk NPP, which operated for almost three decades at 500 ºC and 8 MPa. The combination of operating experience, decades of research, and advances in technology bring the SCWR concept to reality.

In the Canadian SCWR concept, water at a pressure of 25 MPa enters the core at 350 ºC and exits at 625 ºC, challenging the limits of material strength and corrosion resistance. To meet these challenges, the Canadian SCWR concept employs several design features which minimize the requirement for high-temperature strength. The zirconium alloy pressure tubes are in contact with the 100 ºC moderator, and at that temperature, zirconium alloys possess considerable strength. Each pressure tube contains a fuel assembly, as illustrated in **Figure 1**. The outermost component of the fuel assembly is an encapsulated zirconia insulator, which separates the pressure tube from the high-temperature coolant. Adjacent to the insulator are two rings of fuel elements, each clad with a collapsible fuel cladding. The collapsible cladding experiences very little stress during normal operation. At the centre of the fuel assembly is the flow tube, which conveys the 350 ºC inlet coolant to the bottom of the core and surrounds a central rod (not shown), which supports the fuel assembly. The entire fuel assembly is to be replaced every three fuel cycles (approx. 3.5 years).

Of all the in-core components, the fuel cladding poses the greatest challenge for material selection. It will experience the highest temperature and the highest irradiation dose, and its failure comes with grave consequences. Failure to select an alloy that will survive the harsh conditions for three fuel cycles would lead to fuel cladding failure, forced outages, and shortened fuel cycles, jeopardizing the economics of plant operation. For these reasons, much of the Canadian SCWR materials program has focussed on fuel cladding R&D. This paper describes the approach Canada has used to assess the performance of fuel cladding alloys, using the corrosion assessment as an example.

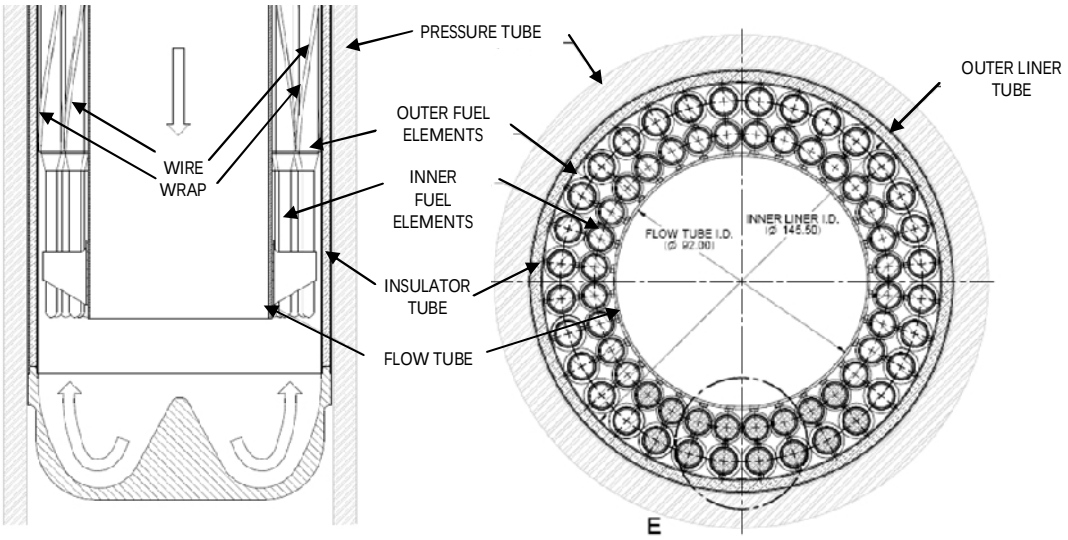

Figure 1. Canadian SCWR fuel channel horizontal cross-section (left) and vertical cross section (right), showing central flow tube, fuel elements, wire wrap, inner liner tube, insulator tube, outer liner tube and pressure tube.

2. Candidate Alloy Selection

One of Canada's earliest efforts to assess candidate fuel cladding alloys was to compile a database of performance data from the literature [7]. Today it includes data spanning 60 years of research on many material classes including Zr-base alloys, Ti-base alloys, ferritic-martensitic steels, oxide-dispersion strengthened (ODS) alloys, austenitic stainless steels and Ni-base alloys. The literature used to populate it include nuclear superheated steam studies from the 1960s, tests on zirconium alloys from the 1970s, the extensive body of work on materials for FFSPs including more recent studies for ultrasupercritical FFSPs, on-going research into SCWO systems, and the growing body of literature from Generation IV SCWR programs in Canada and across the world.

Many classes of alloys can be eliminated because their measured corrosion rates in SCW are unacceptable. Among the classes of alloys available, only some austenitic stainless steels, Ni-base alloys and ODS alloys can be shown to possess the corrosion resistance needed. While considerable operating experience exists on the use of stainless steel fuel cladding in BWRs and PWRs [8], and the stainless steels Kh18Ni10T and EI-847[1] were used at Beloyarsk NPP [9], ODS alloys are a new class of alloy, and may take decades to become qualified for nuclear applications. Selecting from among the two remaining classes of alloys, Canada chose five candidate alloys spanning the range of Cr and Ni that either had great promise or had been examined for similar applications: 347 SS, 310S SS, Alloy 800H, Alloy 625, and Alloy 214. The EU examined 347H SS for their SCWR concept, as well as 1.4970 and 316 [10]. Japan focussed on modified versions of 310 SS for their SCWR concept, and proposed a Zr-modified 310 SS as their primary fuel cladding candidate [11]. The American nuclear superheated steam program extensively evaluated many austenitic stainless steels and Ni-base alloys for fuel cladding, including Alloy 800 and Alloy 625 [12, 13]. Alloy 214 showed up in a few studies for ultrasupercritical FFSPs [14, 15], and was chosen as a candidate by Canada because it is one of the few alloys to produce an aluminium oxide layer.

3. Assessment Approach

The goal of the assessment was not to demonstrate that any one of the five candidate alloys examined would work as the fuel cladding in the Canadian SCWR, but to demonstrate that the Canadian SCWR concept is viable by showing that one or more of them could work. It is recognized that significant gaps remain in our knowledge of these materials and of the performance criteria they must meet.

Performance criteria were developed from the high-level requirement that the fuel cladding cannot fail. Failure could occur by:

1. Through-wall penetration by general corrosion;
2. Oxide build-up that can impede heat transfer;
3. Stress corrosion cracking (SCC);
4. Stress exceeding the yield limits of the material caused by:
    a. Reduced yield limits as the material ages and is irradiated, which includes changes in strength caused by creep and swelling, as well as microstructural changes leading to fatigue and embrittlement, and
    b. Increased stress as the material is irradiated, which includes internal pressurization due to fission gas release, as well as swelling within a constrained geometry.

[1] Composition of Kh18Ni10T: C max 0.1; Si max 0.8; Mn(1 – 2); Ni(10 – 11); S max 0.02; P max 0.035; Cr (17 – 19); 5(C - 0.02) < Ti < 0.6. This is very similar to the composition of 321 Stainless Steel. Composition of EI-847: C(0.04-0.06); Mn(0.4-0.8); Si≤0.4; S≤0.010; P≤0.015; Cr(15.0-16.0); Ni(15.0-16.0); Mo(2.7- 3.2); Nb≤0.9; N≤0.025; B≤0.001; Co≤0.02; Cu≤0.05; Bi≤0.01; Pb≤0.001; Ti≤0.05.

The remainder of the paper illustrates the overall assessment strategy using general corrosion and oxide build-up on Alloy 800H as an example. Similar approaches were taken for the SCC and material strength assessments.

3.1 Performance Criteria

3.1.1 Corrosion Allowance

The collapsible cladding must have a minimum thickness of 0.4 mm to prevent longitudinal ridging of fresh fuel, based on finite-element calculations. (Irradiated fuel cladding would have higher tensile strength and would be less prone to ridging.) However, it is also undesirable to have a cladding much thicker than 0.6 mm for reasons of neutron economy. Therefore, the maximum metal loss (penetration) is:

$$\text{Penetration} = 600\ \mu\text{m} - 400\ \mu\text{m} = 200\ \mu\text{m} \quad (1)$$

This number must provide for corrosion penetration, including average oxide penetration along grain boundaries, for the in-service lifetime of the cladding, 30,600 h (3.5 y).

3.1.2 Oxide Thickness

Oxide build-up can occur both through oxidation of the cladding and through deposition of corrosion products originating in the feedtrain and carried to the core by the coolant. This oxide build-up can have a number of consequences. Oxide growth in tight geometries, such as between fuel pins, can exert force on members leading to tensile stresses sufficient to cause structural failure. The closest distance between fuel pins in the Canadian SCWR fuel assembly is 1240 µm, between pins of the inner ring. Although small, this is not a tight geometry from the perspective of oxide thickness.

A more immediate concern is that the oxide could act as an insulator, leading to overheating of the cladding, accelerated corrosion and accelerated creep. With a constant heat flux, the exterior of the oxide at any given location has a constant temperature, regardless of thickness. Heat conduction through the oxide governs the cladding temperature. Very little is known about the nature of heat conduction through an oxide layer formed in SCW. In PWRs, pores in the oxide layer create a phenomenon known as wick boiling that enhances heat transfer through the oxide layer by adding a convective component [16]. It is not known, however, if a similar mechanism would exist in an SCWR. At present, it is conservative to assume a purely conductive mechanism of heat transfer.

The calculated maximum (bare) cladding temperature for the Canadian SCWR is 800 ºC. If a 25 µm-thick oxide layer is present, the cladding temperature would be approximately 830 ºC, depending on the porosity and again assuming purely conductive heat transfer. Although arbitrary, this was chosen as a prudent cut-off point. A thicker oxide would give a hotter fuel cladding, and a hotter fuel cladding would accelerate the rate of oxide growth. The maximum tolerable oxide thickness, t_{oxide} is therefore:

$$t_{oxide} \leq 25\ \mu\text{m at } 830\ ^\circ\text{C} \quad (2)$$

This value must provide for oxide growth over one fuel cycle, 10,200 h (425 d). One fuel cycle was chosen as the fuel can be ultrasonically cleaned during a refuelling outage to remove thick deposits if required.

3.2 Corrosion Rate Laws

To date, most corrosion tests performed in Canada and internationally in support of recently-proposed SCWR concepts have been relatively short in duration (typically 500-1000 h). In

order to predict fuel cladding corrosion in the proposed Canadian SCWR concept over the expected in-core residence time (~30,600 h) it is necessary to extrapolate data obtained from these relatively short-duration tests to the in-service lifetime by assuming a particular model for the corrosion kinetics. While this approach can be used to rule out proposed candidate alloys, longer tests are necessary to obtain the data needed to validate the extrapolations.

It is often assumed that the corrosion rate has the following functional form

$$CR = k \cdot \exp\left(-\frac{E_a}{RT}\right) \cdot t^x \tag{3}$$

with x being 0.5. Measuring the time and temperature dependencies in independent experiments gives values for E_a and k, which can then be used to perform a double extrapolation (time and temperature) to obtain the corrosion penetration at the cladding design lifetime. Because of the limited dataset used to perform the extrapolation, there is a considerable uncertainty associated with this extrapolation. While such a double extrapolation is reasonable, it requires that the parameters E_a, k, and x be determined and the functional form in Equation (3) be validated. For instance, parabolic behavior cannot always be assumed.

There is a significant amount of data that suggests that Alloy 800H corrosion in superheated steam follows linear kinetics, e.g., Pearl et al. [12]. The corrosion model developed by Brush [17] to describe the kinetics took the form of Equation (4), with a constant term and a linear term.

$$\Delta W = k_0 \cdot T \cdot \exp\left(-\frac{A}{T}\right) + k_1 \cdot T \cdot \exp\left(-\frac{B}{T}\right) \cdot t \tag{4}$$

A change from an electrochemical to a gas-phase corrosion mechanism is expected as the density changes above the critical temperature [18,19]. A mechanism involving separated cathodic and anodic sites, denoted electrochemical oxidation (EO) transitions to a mechanism involving direct chemical reaction between the metal surface and reactive species, denoted chemical oxidation (CO). This leads to a **local** maximum corrosion rate in the vicinity of the critical point. Well above the critical point, the corrosion rate again exhibits Arrhenius behaviour with increasing temperature. Recently, Steeves et al. [20] developed a model that includes both mechanisms and validated it using data for the corrosion of Alloy 625 measured over several years in the SCW loop at the University of New Brunswick (UNB). Below a density of 100 kg/m^3, the CO mechanism is expected to dominate and the differences between corrosion in supercritical water and superheated steam become small. As the activation energies of the rate-determining step may not be the same for the EO and CO mechanisms[2], care must be taken when extracting activation energies from experimental data. In the context of the current assessment, only data obtained at temperatures above 500 °C were used to derive the activation energies.

3.3 Factors Affecting Corrosion Rates

Guzonas [21] rated the factors affecting general corrosion rates in SCW in terms of their relative contributions as:

Temperature ≈ Surface Finish > Water Chemistry > SCW Density

[2] Each oxidant, in fact, would be involved in a different (electro)chemical reaction having a different activation energy, and care must also be taken to compare experiments with similar concentrations of oxidants.

Work on the effect of grain size [22, 23] suggests that grain size is at least as important a factor as temperature and surface finish:

Temperature ≈ Surface Finish ≈ Grain Size > Water Chemistry > SCW Density

While it is obvious that temperature would have a large effect, what this scale conveys is that the same alloy can experience a largely different corrosion rate at the same temperature if it has been ground, polished, or electropolished or if it has been heat treated, annealed or mechanically processed in a different way. Ruther et al. [24] noted that, in SCW, surface preparations that gave a strain-free surface resulted in maximum general corrosion while the surface finishes that resulted in severe cold-work reduced general corrosion.

Most of the available data suggest that water chemistry has only a second-order effect on corrosion rate. Most recent testing in support of SCWR development has been performed with low (25 ppb) or high (8000 ppb) dissolved oxygen concentrations. In general, increasing the concentration of dissolved oxygen increases the general corrosion rate, but the effect is not large. This is not surprising as water itself can act as the oxidant in SCW.

Water density also has a second-order effect, which has important implications. Bischoff [25], Motta et al. [26] and Guzonas and Cook [27] have highlighted the similarity between corrosion in SCW at 25 MPa and in steam at T>>Tc (i.e., low-density SCW), the weight gain being only slightly higher at the higher pressure. This suggests that a reasonable assessment of materials behaviour under SCWR conditions (above 500 °C) can be obtained using measurements in low pressure steam; these experiments can be much simpler than those using SCW above the critical pressure. This is particularly important for the Canadian SCWR program, because the peak fuel cladding temperature may be as high as 800 °C; there are currently no autoclave or loop facilities that can operate at this temperature at 25 MPa. The ability to use the steam data also allows the significant body of data on materials performance acquired in support of the American and Russian nuclear superheated steam programs in the 1960s and 1970s to be used.

To assess the suitability of superheated steam as a surrogate for SCW, tests at 625 °C and three pressures (steam test rig at 0.1 MPa, static autoclave at 29 and 8 MPa) were performed. Four alloys were tested; A286, 304 SS, 310 SS and Alloy 625. The dependence of weight change on density is shown in **Figure 2**. The behavior of the two groups of alloys was significantly different, the former showing a roughly one order of magnitude higher weight gain than the latter in the two static autoclave tests. In addition, the weight changes for 310 SS and Alloy 625 were similar under all three conditions studied, whereas the weight change for A286 at 1000 h exposure time was much higher at 8 MPa and at 29 MPa than it was at 0.1 MPa. Many studies have shown that the corrosion resistance of austenitic steels in SCW is much better when the Cr content is greater than roughly 19 wt.% [15, 28]. Figure 2 suggests that a similar dividing line for the pressure dependence, with the two alloys with greater than 20 wt.% Cr showing little pressure dependence. This suggests that corrosion measurements in superheated steam should be a reasonable substitute for corrosion measurements at 25 MPa for the candidate alloys with more than 19-29 wt.% Cr, namely 310 SS, 800H, Alloy 625. This may not be the case for 347 SS, which contains a similar amount of Cr as 304 SS.

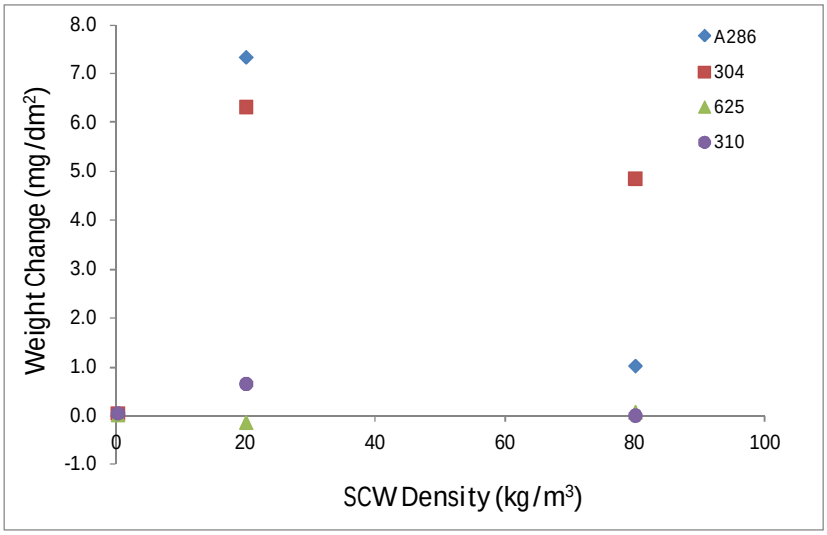

Figure 2. Weight change as a function of density for A286, 304 SS, 310 SS and Alloy 625 exposed to 600 °C SCW for 1000 h.

3.4 Approach to Data Analysis

To begin the assessment, all available data from tests performed in SCW and in superheated steam at temperatures above 500 °C were compiled. Pressure and dissolved oxygen concentration were assumed to have only second order effects, but surface finish was considered.

The data reported by various research groups was in the form of either weight change (difference in weight between the coupon before and after the corrosion exposure) or descaled weight loss (difference in weight between the coupon before exposure and after exposure after the removal of the surface oxides by chemical or electrochemical methods), necessitating a conversion into a common form. As most of the data obtained in recent experiments performed in support of SCWR development have been reported as weight gain, all the weight loss data were converted into weight gain assuming that the surface oxide was magnetite (Fe_3O_4). Since the molecular masses of Fe, Cr and Ni are similar, the assumption that the oxide is magnetite rather than a specific Fe-Cr spinel introduces only a small error. Weight gain data, on the other hand, do not contain information about the mass of oxide lost by dissolution or spalling, and their use to estimate oxide thickness and penetration can introduce significant and unquantifiable uncertainty if there is oxide loss.

The weight gain data at each temperature were plotted as a function of exposure time to obtain the rate constant. In general, for the austenitic steels the rate law changed with time, becoming linear for long exposures. As a linear rate law predicts a higher mass gain than a parabolic rate law when fit to the same data set, the assumption of a linear rate law is more conservative.

The linear rate constants were then plotted as ln(k) vs 1/T to obtain an activation energy from which the temperature dependence could be predicted; when necessary, a model for the short-term (<500 – 1000 h) behavior was also developed to model the short-term behavior if required. The rate law and temperature dependencies were then combined into a “master equation” that could be used to predict the weight gain at end-of-life, taken as 30,600 h at 830 °C. The inclusion of data measured in steam tests increased the amount of data available at higher temperatures (including 800 °C), so that only the extrapolations with time had significant uncertainties.

The weight gain equations obtained typically had the form:

$$WG(t,T) = a \cdot T + b \cdot \exp\left(\frac{-c}{RT}\right) \cdot t \tag{5}$$

where R is the gas constant and a, b, and c were empirically determined constants. The weight gain for the candidate alloys at 30,600 h and 830 °C was calculated using this expression. The weight gain was then converted to metal penetration using:

$$Penetration\ (\mu m) = WG \times \left(\frac{1 - f_{o/ox}}{f_{o/ox}}\right) \cdot \frac{1}{\rho_{alloy}} \cong WG\ (mg/dm^2) \cdot 0.033 \tag{6}$$

where $f_{o/ox}$ is the weight fraction of oxygen in Fe_3O_4 (i.e., 0.276) and ρ_{alloy} is the density of the alloy. This approximation applies only when oxide loss is negligible. For any alloy with a density around 8 g/cm^3, the multiplication factor is approximately 0.033.

4. Assessment of Alloy 800H

Alloy 800H is an iron-nickel-chromium alloy having the same basic composition as Alloy 800 but with significantly higher creep rupture strength [29]. Alloy 800H contains a higher concentration of carbon (0.05 to 0.1 wt.%) and has a larger grain size (>ASTM 5) to optimize stress rupture properties. Although there was a distinction between Grade 1 and Grade 2 Alloy 800 from 1963, the designation "800H" was first applied in 1971. During the period when most of the testing for the US nuclear reheat program was performed, only Alloy 800 existed as an alloy designation, and the composition and grain size could vary from test to test. Nonetheless, the designation "800H" is used in the remainder of this paper to clearly define the alloy being considered.

Alloy 800H was identified as a potential alloy for the fuel cladding of the various nuclear superheated steam reactors assessed during the late 1950s and early 1960s in the United States. Ru and Staehle [30] have summarized much of the material testing data from these tests. Clark et al. [31] summarized the results of tests at 649, 732 and 816 °C for a number of alloys including Alloy 800H, including measurements of tensile properties, impact toughness, hardness and metallography. The specimens were tested in a commercial power station for 18 months as 50.8 mm diameter x 1066.8 mm long tubes with a 12.70 mm wall thickness at a steam flow rate of 188 kg/h and operating pressures between 0.08 and 0.1 MPa. No failures occurred over the 18 month exposure at 649 or 732 °C but the Alloy 800H tubes were removed from the 816 °C test after about 6 months (~4300 h) due to excessive bulging.

Spalaris [32] tested Alloy 800 along with other alloys in the exit steam from a superheater. These experiments lasted between two to four months. While most stainless steels tested were found to fail by SCC due to the accumulation of chlorides on the hot surfaces, Spalaris [32] showed that in boiling and superheated water containing suitable impurities, materials with higher nickel content such as Alloy 800H, Alloy 600 and Hastelloy X did not crack. Comprelli et al. [33] summarized the results of these extensive tests. They reported that all the specimens were sensitized throughout and the degree of sensitization increased with exposure time. Ruther and Greenberg [34] showed that Alloy 800 performed well in isothermal testing at 650 °C in flowing oxygenated steam.

The corrosion of Alloy 800H was studied in detail in experiments by Pearl et al. [12]. They developed a quantitative rate law to predict (descaled) metal weight loss as a function of exposure time:

$$WL(t,T) = 48.43 \cdot T \cdot \exp\left(\frac{-5\,230}{T}\right) + 3409 \cdot T \cdot \exp\left(\frac{-10\,388}{T}\right) \cdot t \tag{7}$$

where WL is in mg/dm^2, T is in K and t is the exposure time in **months**. Notably, Pearl et al. [12] also reported the metal lost from the corrosion coupons into the steam, noting that at least one-half of the corrosion products from Alloy 800H would be carried downstream from the core at cladding temperatures of 649 -704 °C.

Fulger and co-workers measured the weight change and the oxide thicknesses for both Alloy 800 [35] and Alloy 800HT [36]. The weight gains for Alloy 800 were larger than those measured for Alloy 800HT. For Alloy 800, the measured weight gain data at 450 °C indicated cubic corrosion kinetics whereas at 500, 550 and 600 °C the kinetics were parabolic. For Alloy 800HT the weight gain data at 450 °C indicated linear corrosion kinetics whereas at 500, 550 and 600 °C a power law behaviour was observed. They concluded that processes other than solid state diffusion were affecting the oxidation rate.

Pentilla [37] reported almost negligible weight gain for Alloy 800H exposed to SCW for 600 h at 400 and 500 °C and a dissolved oxygen concentration of 0 - 150 ppb, but a weight loss when exposed at the same temperatures under hydrogen water chemistry conditions (30 cc/kg H_2).

4.1 Corrosion Assessment

The data from various studies (**Table 1**) at temperatures above 500 °C were evaluated, with an emphasis on data from long-term tests.

Three data sets at 500 °C were located in the literature. Claudson and Pessl [38] reported only one value, after 100 days of exposure. The coupons used in the experiments of Fulgar et al. [36] and Tan et al. [39] were polished to a 1 µm finish, which might be expected to give an increase in corrosion rate. The effect of surface finish depends on corrosion mechanism (EO versus CO), but data suggest that at 500 °C the effect is not large. All three data sets were combined for the analysis, and are shown in **Figure 3**.

A large number of data sets at 550 °C were located in the literature. The data from McCoy and McNabb [41] were excluded because the tests contained ammonia to raise the pH, and the data from Mahboubi [42] were excluded because of the short test duration. It was found that the master model greatly overpredicted the measured weight change at this temperature.

There was considerable variation between the results of the various tests at 600 °C. The datasets of Wozadlo and Pearl [40] and Leistikow [43] (pickled dataset for comparison with the data of Wozadlo and Pearl) were used for the fit. The data of Tan et al. [39] are also plotted but were not included in the fit.

Three data sets at 750 °C were located in the literature. The data of Ruther et al. [24] were excluded because the specimens were electropolished; this surface treatment is known to give higher corrosion rates in steam and SCW than surfaces that have been ground.

Measurements in superheated steam at 800 °C were performed at Carleton University [46]. Abe and Yoshida [47] reported the results of corrosion tests of Alloy 800H in superheated steam at 800 °C; the data are plotted in Figure 3 but were not included in the fit. The master model developed for 800H significantly overpredicts the weight gain for the data obtained in these tests.

Table 1. Summary of corrosion studies of Alloy 800H in SCW and steam at temperatures above 500 ºC.

Exposure Time (h)	Pressure (MPa)	Surface Finish	Reference
500 °C			
2400	34.5		Claudson and Pessl [38]
1200	25	1 µm polish	Fulger et al. [36]
3162	25	1 µm polish	Tan et al. [39]
550 °C			
10143	6.9	Machined, pickled in 20 % HNO_3 for 20 minutes at 54 °C	Wozadlo and Pearl [40]
2400	20.7		Claudson and Pessl [38]
19000	24.2		McCoy and McNabb [41]
500	25	800 grit	Mahboubi et al. [42]
965	6.9	Machined and pickled in 20 % HNO_3 for 20 minutes at 54 °C	Brush [17]
600 °C			
9898	6.9	Machined and pickled in 20% HNO_3 for 20 minutes at 54 °C	Wozadlo and Pearl [40]
5000	0.1	Pickled	Leistikow [43]
4500	0.1	Ground	Leistikow [43]
873	25	1 µm polish	Fulger et al. [36]
1026	25	1 µm polish	Tan et al. [39]
650 °C			
4078	6.9	Machined and pickled in 20 % HNO_3 for 20 minutes at 54 °C	Brush [17]
1344	4.1	Various	Ruther et al. [24]
700 °C			
2500	24.13	Grinding with 180 grit	Cowen et al. [44]
750 °C			
1200	4.1	Electropolished	Ruther et al. [24]
3000	0.1		Sarver [45]
2039	6.9	Machined and pickled in 20 % HNO_3 for 20 minutes at 54 °C	Brush [17]
800 °C			
3000	0.1	600 grit then oven dried at 200 °C for 2 h	Huang [46]
3000	4.0	1 µm polish	Abe and Yoshida [47]

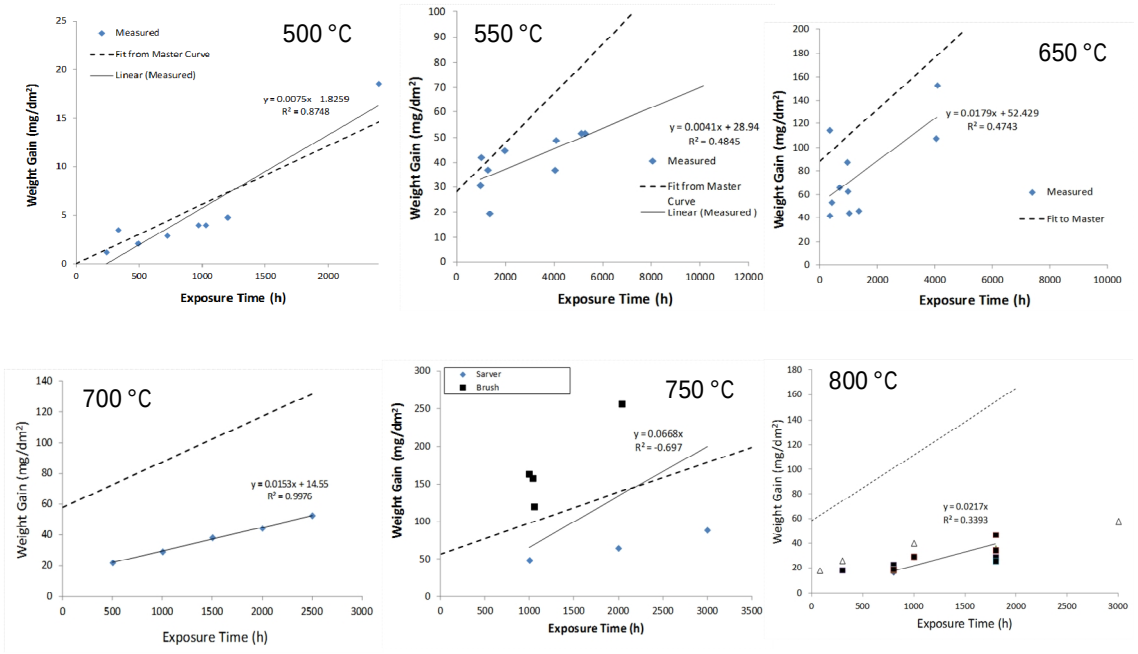

Figure 3. Weight gain as a function of exposure time data for Alloy 800H exposed to SCW at 500 °C. The solid line is a linear least squares fit to the data; the dashed line is the predicted weight gain based on Equation (8).

4.1.1 Corrosion Model

The rate constants were plotted as ln(k) versus 1/T to obtain the activation energy for the corrosion reaction. The rate constant data for the linear portion of the reaction are given in **Table 2** and plotted in **Figure 4**.

Table 2. Rate constant data for the linear portion of the reaction.

T (K)	1/T (K^{-1})	k	-ln(k)
500	0.001293	0.0073	4.92
550	0.001215	0.0068	4.99
600	0.001145	0.0066	5.02
650	0.001083	0.0179	4.02
730	0.000997	0.0668	2.71
750	0.000977	0.0202	3.90
800	0.000932	0.0592	2.83

A good linear fit was obtained to the ln(k) versus T^{-1} data, and the following master equation for weight gain at any given temperature was developed:

$$WG(t,T) = \left(0.6 \cdot T - 302\right) + 17 \cdot \exp\left(\frac{-51\,000\ \text{J/mol}}{RT}\right) \cdot t \qquad (8)$$

Using this equation and converting to metal penetration gives about 78 µm after 30,600 h at 830 °C, which is within the acceptance criteria.

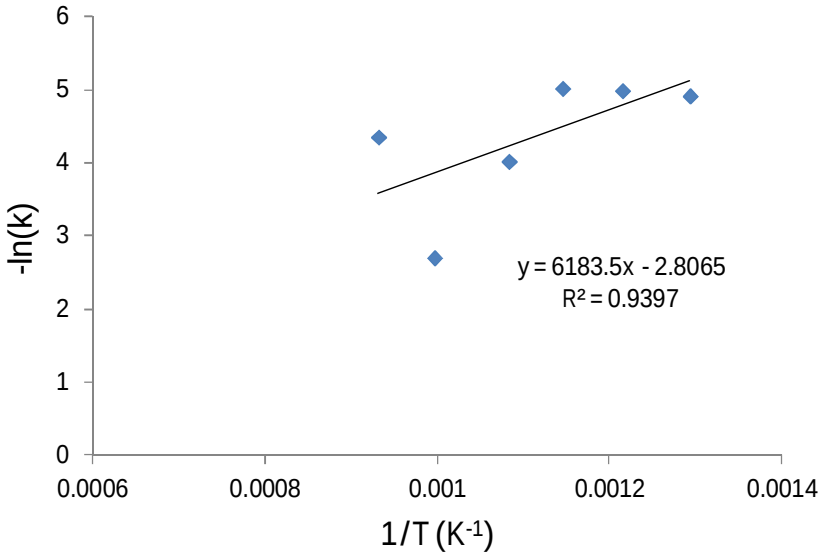

Figure 4. Arrhenius plot for Alloy 800H for the linear (long term) portion of the weight change data.

5. Summary

Five alloys were chosen as candidates for the Canadian SCWR fuel cladding and were assessed in detail against performance criteria related to possible routes of failure, including through-wall corrosion, SCC, and mechanical failure. This paper has summarized the assessment of Alloy 800H against the corrosion-related performance criteria to illustrate the methodology used. Similar approaches were taken for the SCC and material strength assessments. A summary of the complete assessment of the candidate alloys is presented as a scorecard in **Table 3**. While significant gaps remain in our knowledge base, the assessment demonstrated that several of the candidates could meet the performance criteria.

Table 3. Scorecard of candidate cladding materials.

Alloy	Property							
	Corrosion	Oxide Thickness	SCC (un-irradiated)	IASCC	Creep	Void Swelling	Ductility (4% elongation)	Strength
800H								
310S								
625								
347								
214								

GREEN – Available data suggest that this alloy meets the performance criteria under all conditions expected in the core
YELLOW – Some (or all) available data suggest that this alloy may not meet the performance criteria under some conditions expected in the core
RED - Some (or all) available data suggest that this alloy will not meet the performance criteria under some conditions expected in the core
GREY – There are insufficient data to make even an informed guess as to the behavior in an SCWR core

References

1. Cohen, K.; Zebroski E., Operation Sunrise, Nucleonics **17** (1959) 63.

2. Dollezhal, N.A.; Krasin A.K.; Aleshchenkov, P.I.; Galanin, A.N.; Grigoryants, A.N.; Emelyanov, I.Ya.; Kugushev, N.M.; Minashin, M.E.; Mityaev, U.I.; Florinsky, B.V.; Sharpov, N.N. (1958) Uranium-Graphite Reactor with Superheated High Pressure Steam, Proc. 2nd Int. Conf. on the Peaceful Uses of Atomic Energy, 8, 398, UN, Geneva, 1958.

3. Wright, J.H.; Paterson, J.F. (1966) Status and Application of Supercritical-Water Reactor Coolant, Proc. Am. Power Conf. 1966, XXVIII, 139-149.

4. Moore, R.V.; Barker, A.; Bishop, J.F.W.; Bradle,y N.; Iliffe, C.E.; Nichols, R.W.; Thorn, J.D., Tyzack, C.; Walker, V. (1964) The Utilization of Supercritical Steam in Nuclear Power Reactors, Final report of the Supercritical Steam Panel, United Kingdom Atomic Energy Authority, TRG Report 776, 1964.

5. Kornbichler, H. (1958) Superheat Reactor Development in the Federal Republic of Germany, Proc. 2nd Int. Conf. on the Peaceful Uses of Atomic Energy, 8, UN, Geneva, 1958, p 266.

6. Margen, P.H.; Leine, L.; Nilson, R. (1958) The Design of the Marviken Boiling Heavy-Water Reactor with Nuclear Superheat, Proc. 2nd Int. Conf. on the Peaceful Uses of Atomic Energy, 8, UN, Geneva, 277 (1958).

7. Gu, G.P.; Zheng, W.; Guzonas, D. (2010) Corrosion Database For SCWR Development. 2nd Canada-China Joint Workshop on Supercritical Water-Cooled Reactors (CCSC-2010) Toronto, Ontario, Canada, April 25-28, 2010.

8. Strasser, A.; Santucci, J.; Lindquist, K.; Yario, W.; Stern, G.; Goldstein, L.; Joseph, L.; Stoller, S.M. (1982) An Evaluation of Stainless Steel Cladding for Use in Current Design LWRs. EPRI Report NP 2642, 1982.

9. Emel'yanov, I.; Shatskaya, O.A.; Rivkin, E.Yu.; Nikolenko, N.Ya. (1972) Strength of Construction Elements in the Fuel Channels of the Beloyarsk Power Station Reactors. Atomnaya Energiya, Vol. 33, No. 3, 1972, pp. 729-733 [in Russian] (Translated in Soviet Atomic Energy Vol. 33, No.3, 1972, pp. 842-847).

10. Schulenberg, T. (2011) Material Requirements of the High Performance Light Water Reactor. IAEA Technical Meeting on Materials and Chemistry for Supercritical Water Cooled Reactors, TM-41430, Petten, the Netherlands, June 18-22, 2011.

11. Higuchi, S.; Sakurai, S.; Yamada, K.; Ishiwatari, Y. (2011) Feasibility Study for Design of Fuel Rod in JSCWR. Proceedings of the 5th Int. Symp. SCWR, Paper 025, Vancouver, Canada, March 13-16, 2011.

12. Pearl, W.L.; Brush, E.G.; Gaul, G.G.; Wozadlo, G.P. (1965) General Corrosion of Incoloy-800 in Simulated Superheat Reactor Environment. Nuclear Applications, Vol. 1, pp. 235.

13. Pearl, W.L.; Brush, E.G.; Gaul, G.G.; Leistikow, S. (1967) General Corrosion of Inconel Alloy 625® in Simulated Superheat Reactor Environment. Nuclear Applications, Vol. 3, pp. 418.

14. Viswanathan, R.; Henry, J.F.; Tanzosh, T.; Stanko, G.; Shingledecker, J.; Vitalis, B.; Purgert, R. (2005) U.S. Program on Materials Technology for Ultra-Supercritical Coal Power Plants. Journal of Materials Engineering and Performance, Vol. 14, No. 3, pp. 281.

15. Sarver, J.M.; Tanzosh, J.M. (2013) Effect of Temperature, Alloy Composition and Surface Treatment on the Steamside Oxidation/Oxide Exfoliation Behavior of Candidate A-USC Boiler Materials. Babcock & Wilcox Technical Paper BR-1898. Presented at the Seventh International Conference on Advances in Materials Technology for Fossil Power Plants, Waikoloa, Hawaii, USA, October 22-25, 2013.

16. Cinosi, N.; Haq, I.; Bluck, M.; Walker, S.P. (2011) The Effective Thermal Conductivity of Crud and Heat Transfer from Crud-coated PWR Fuel. Nuclear Engineering and Design, Vol. 241, 2011, pp. 792-798.

17. Brush, E.G. (1965) Corrosion Rate Law Considerations in Superheated Steam. Nuclear Applications, Vol. 1, pp. 246.

18. Yi, Y.; Watanabe, Y.; Kondo, T.; Kimura, H.; Sato, M. (2001) Oxidation Rate of Advanced Heat-resistant Steels for Ultra-supercritical Boilers in Pressurized Superheated Steam. Journal of Pressure Vessel Technology, Vol. 123, 2001, pp. 391-397.

19. Betova, I.; Bojinov, M.; Kinnunen, P.; Penttilä, S.; Saario, T. (2007) Surface Film Electrochemistry of Austenitic Stainless Steel and its Main Constituents in Supercritical Water. Journal of Supercritical Fluids, Vol. 43, 2007, pp. 333-340.

20. Steeves, G.; Cook, W.; Guzonas, D. (2015) Development of Kinetic Models for the Corrosion Behaviour of Candidate Alloys for the Canadian SCWR. Accepted for presentation at the 7th International Symposium on Supercritical Water-Cooled Reactors, ISSCWR-7, 15-18 March 2015, Helsinki, Finland.

21. Guzonas, D.A. (2011) Materials and Chemistry for a Supercritical Water-Cooled Reactor - Progress and Challenges. 5th International Symposium on SCWR (ISSCWR-5), Vancouver, British Columbia, Canada, March 13-16, 2011, Paper K005.

22. Li, J.; Penttila, S.; Zheng, W. (2012) Effects of Surface Modifications on SCW Corrosion Resistance. Proceedings of the 2012 TMS Annual Meeting & Exhibition, TMS. 2012.

23. Tsuchiya, Y.; Saito, N.; Kano, F.; Ookawa, M.; Kaneda, J.; Hara, N. (2007) Corrosion and SCC Properties of Fine Grain Stainless Steel in Subcritical and Supercritical Pure Water. Corrosion 2007, Paper 07415, NACE, Houston.

24. Ruther, W.E.; Schlueter, R.R.; Lee, R.H.; Hart, R.K. (1966) Corrosion Behavior of Steels and Nickel Alloys in Superheated Steam. Corrosion, Vol. 22, No. 5, 1966, pp. 147-155. Presented at 21st Conference, National Association of Corrosion Engineers, St. Louis, Missouri, USA, 1965 March 15-19.

25. Bichoff, J. (2011) Oxidation Behavior of Ferritic-Martensitic and ODS Steels in Supercritical Water. PhD Dissertation, Pennsylvania State University.

26. Motta, A.T.; Yilmazbayhan, A.; Gomes da Silva, M.J.; Comstock, R.J.; Was, G.S.; Busby, J.T.; Gartner, E.; Peng, Q.; Jeong, Y.H.; Park, J.Y. (2007) Zirconium Alloys for Supercritical Water Reactor Applications: Challenges and Possibilities. Journal of Nuclear Materials, Vol. 371, Nos. 1-3, 2007, pp. 61-75.

27. Guzonas, D.A.; Cook, W.G. (2012) Cycle Chemistry and its Effect on Materials in a Supercritical Water-cooled Reactor: A Synthesis of Current Understanding. Corrosion Science, Vol. 65, pp. 48-66.

28. Wright, I.G.; Dooley, R.B. (2010) A Review of the Oxidation Behavior of Structural Alloys in Steam. Int. Materials Reviews, Vol. 55, No.3, 2010, pp. 129-167.

29. INCOLOY® Alloy 800H & 800HT information sheet. (2004) Special Metals Corp., www.specialmetals.com.

30. Ru, X.; Staehle, R.W. Historical Experience Providing Bases for Predicting Corrosion and Stress Corrosion in Emerging Supercritical Water Nuclear Technology: Part 1–Review. Corrosion, Vol. 69, No. 3, 2013, pp. 211-229.

31. Clark, C.L.; Rutherford, J.J.B.; Wilder, A.B.; Cordovi, M.A. (1962) Metallurgical Evaluation of Superheater Tube Alloys after 12 and 18 Months Exposure to Steam at 1200, 1350 and 1500 °F. Transactions of the ASME.

32. Spalaris, C.N. (1963) Finding a Corrosion Resistant Cladding for Superheater Fuels. Nucleonics, Vol. 21, 1963.

33. Comprelli, F.A.; MacMillan, D.F.; Spalaris, C.N. (1963) Materials for Superheated Fuel Sheaths: Relative Performance of Alloys in Superheated Steam Environments. General Electric Company Report GEAP-4351.

34. Ruther, W.E.; Greenberg, S. (1964) Corrosion of Steels and Nickel Alloys in Superheated Steam. Journal of the Electrochemical Society, Vol. 111, pp. 1116.

35. Fulger, M.; Ohai, D.; Mihalache, M.; Pantiru, M.; Malinovschi, V. (2009) Oxidation Behavior of Incoloy 800 under Simulated Supercritical Water Conditions. Journal of Nuclear Materials, Vol. 385, pp. 288–293.

36. Fulger, M.; Mihalache, M.; Ohai, D.; Fulger, S.; Constantin Valeca, S. (2011) Analyses of Oxide Films Grown on AISI 304L Stainless Steel and Incoloy 800HT Exposed to Supercritical Water Environment. Journal of Nuclear Materials, Vol. 415, pp. 147-157.

37. Pentilla, S. (2008) Materials for the SCWR Concept. Slides from the GEN4FIN Seminar, Lappeenranta, Finland, October 2-3, 2008.

38. Claudson, T.T.; Pessl, H.J. (1965) Evaluation of Iron- and Nickel-base Alloys for Medium and High Temperature Reactor Applications: Part II. Pacific Northwest Laboratory Report BNWL-154, 1965.

39. Tan, L.; Allen, T.R.; Yang, Y. (2010) Corrosion Behavior of Alloy 800H (Fe-21Cr-32Ni) in Supercritical Water. Corrosion Science, Vol. 53, No. 2, pp. 703.

40. Wozadlo, G.P.; Pearl, W.L. (1965) General Corrosion of Stainless Steels and Nickel Base Alloys Exposed Isothermally in Superheated Steam. Corrosion, Vol. 21, No. 11, 1965, pp. 355-369.

41. McCoy, H.E.; McNabb, B. (1977) Corrosion of Several Metals in Supercritical Steam at 538°C. Oak Ridge National Laboratory Report ORNL/TM-5781, 1977.

42. Mahboubi, S.; Botton, G.; Kish, J. (2014) Microstructural Characterization of Oxide Scales Grown on Austenitic Fe-Cr-Ni Alloys Exposed to Supercritical Water (SCW). 2014 Canada-

China Conference on Advanced Reactor Development (CCCARD-2014), Niagara Falls, Canada, April 27-30, 2014.

43. Leistikow, S. (1972) Isothermal Steam Corrosion of Commercial Grade Austenitic Stainless Steels and Nickel Base Alloys in Two Technical Surface Conditions. Proceedings of the Fourth International Congress on Metallic Corrosion, Amsterdam, Netherlands, 1969 September 7-14. Houston, TX: National Association of Corrosion Engineers, 1972, pp.278-290.

44. Cowen, H.C.; Longton, P.B.; Hand, K. (1966) Corrosion of Stainless Steels and Nickel-Base Alloys in Supercritical Steam, UK Atomic Energy Authority Report TRG Memorandum 3399 (C).

45. Sarver, J.M. (2009) The Oxidation Behavior of Candidate Materials for Advanced Energy Systems in Steam at Temperatures Between 650°C and 800°C, 14th Int. Conf. on Env. Degradation of Materials in Nuclear Power Systems, Virginia Beach, 2009 August 23-27.

46. Huang, X. (2014) Unpublished data.

47. Abe, F.; Yoshida, H. (1985) Corrosion Behaviors of Heat-resisting Alloys in Steam. Zeitschrift fur Metllkunde, Vol. 76, pp. 219-225.t

ISSCWR7-2091

Fission Product Release under Supercritical Water-cooled Reactor Conditions

D. Guzonas, L. Qiu, S. Livingstone, S. Rousseau
Chalk River Laboratories, CNL
Chalk River, Ontario, Canada K0J 1J0
David.Guzonas@cnl.ca

Abstract

Most Super-Critical Water-cooled Reactor (SCWR) concepts being considered as part of the Generation IV initiative are direct cycle. In the event of a fuel defect, the SCW coolant will contact the fuel pellet, potentially releasing fission products and actinides into the coolant and transporting them to the turbines. The release of gaseous fission products into superheated steam at temperatures as high as 700 °C was extensively studied in the 1960s as part of programs to develop nuclear superheated steam reactors. However, at the higher pressure (25 MPa) in an SCWR, the coolant does not undergo a phase change as it passes through the critical temperature in the core, and there is the potential for non-gaseous species to also be transported out of the core and subsequently deposited on out-of-core components, leading to increased worker dose. It is therefore important to identify species with a high risk of release, and develop models of their transport and deposition behavior.

This paper presents the results of preliminary leaching tests in SCW of U-Th simulated fuel pellets prepared from natural U and Th and containing representative concentrations of the (inactive) oxides of fission products corresponding to a fuel burn-up of 60 GWd/tonne. The results show that Sr and Ba are released at relatively high concentrations at 400 and 500 °C. The implications for the SCWR and the upcoming Fuel Qualification Testing are discussed.

1. Introduction

Guzonas and Qiu [1] listed three source terms for activity that must be considered in a supercritical water-cooled reactor (SCWR):

1. Corrosion products transported to the core, activated and then released;
2. Release of activated elements by corrosion of in-core materials; and
3. Fission products and actinides released from failed fuel.

A fuel defect is a breach in the fuel cladding that allows the primary coolant to enter the fuel-to-sheath gap and allows fuel particles and fission products to escape. Defected fuel phenomena in Water-cooled Reactors are reasonably well understood, and various detection, location, diagnostic and management techniques have been developed [2]. Less is known about the consequences of a fuel defect in an SCWR, and the interaction of supercritical water (SCW) and fuel needs to be investigated, along with the solubility and transport of fuel contaminants in SCW. Furthermore, the interaction between the SCW and the inside of the fuel sheath will be important in determining defect degradation behaviour (e.g., internal sheath oxidation). For example, in defected Zircaloy-clad fuel, the surface heat flux determines the post-defect residence time before massive secondary hydriding of the sheath results in significant fuel degradation [3].

This paper briefly summarizes available data on fission product and actinide behavior in SCW, and presents the results of recent leaching tests of simulated fission products from a U-Th based SIMFUEL.

2. Fission Gases

There is a significant amount of data on the behaviour of noble gases and iodines in superheated steam from the US nuclear steam superheat program carried out in the 1960s. Because gases are infinitely soluble in SCW, data on gas transport obtained at similar temperatures but lower pressures are directly relevant to the transport of these gases in the coolant of an SCWR.

The Superheat Advanced Demonstration Experiment (SADE) test loop was initially placed in operation in the Vallicitos Boiling Water Reactor (VBWR) in 1959 May to test fuel elements and equipment for the nuclear superheat development program undertaken by the General Electric Company [4]. The loop was later enlarged to irradiate nine fuel elements simultaneously, and designated the ESADE (Expanded-SADE) loop, which was placed into operation in 1962 June. Chemistry monitoring in the ESADE-VBWR test program was aimed primarily at detecting the failure of fuel cladding and measuring fission product released rates. Radiochemistry measurements during the ESH-1 irradiation did not indicate the presence of defective fuel, although a small defect was later found by sipping and subsequent metallographic sectioning. However, it was noted that the sensitivity of the measurements was severely limited because there was a known defect in the VBWR [5].

Several fuel defects occurred during the experimental program at the ESADE-Vallecitos Experimental Superheat Reactor (EVESR), performed primarily with Alloy 800 fuel cladding. EVESR was deliberately operated for several months with a grossly defected fuel bundle (KB-41) to determine the effects [6]. The KB-41 bundle was found to be defective about 3 h after the reactor power was increased from 15 MW(t) to 17 MW(t), as indicated by an increase in the plant off-gas noble gas monitor from 1.5 to 15 $mR \cdot h^{-1}$ over a 15 minute period [7]. It was found that the release of fission products was highly dependent upon the reactor power and the reactor exit steam temperature. Operation at the fuel full-rated temperature led to the deposition of tellurium and other fission products on the superheat steam piping, resulting in contact dose rates of up to 300 mR/h on piping external to the containment building and up to 5 R/h on one valve in the reactor pipe gallery. Radiation levels were highest close to the reactor and at piping irregularities such as fittings or valves. The radiation levels decreased with a 78-h half-life following reactor shutdown.

Figure 1 shows the noble gas and iodine release from EVESR superheat fuel rod KB-40 [8] after it failed, plotted as release rate versus radionuclide decay constant. The slope obtained from this plot was interpreted as indicating a long delay between the fission events producing the radionuclide and their release, i.e., hold-up of the fission products in the fuel rod. Similar data were also obtained for the KB-41 defect. Detailed discussions of these data can be found in the original reports.

A test (KB-41-2) was performed with a purposely defected fuel rod; the defect was a 0.005-0.013 inch wide by 1 inch long slit in the cladding (0.016 inch thick Alloy 800). The purpose of the test was to place a known defect in a known position in the core to study the release of fission products and the consequences of such operation on a steam superheat system. The release of 13 noble gas and five iodine isotopes was measured [9].

Based on the large amount of data available from the US nuclear steam superheat program, the behaviour of noble gases and iodines released from a fuel defect in an SCWR is not considered a major knowledge gap.

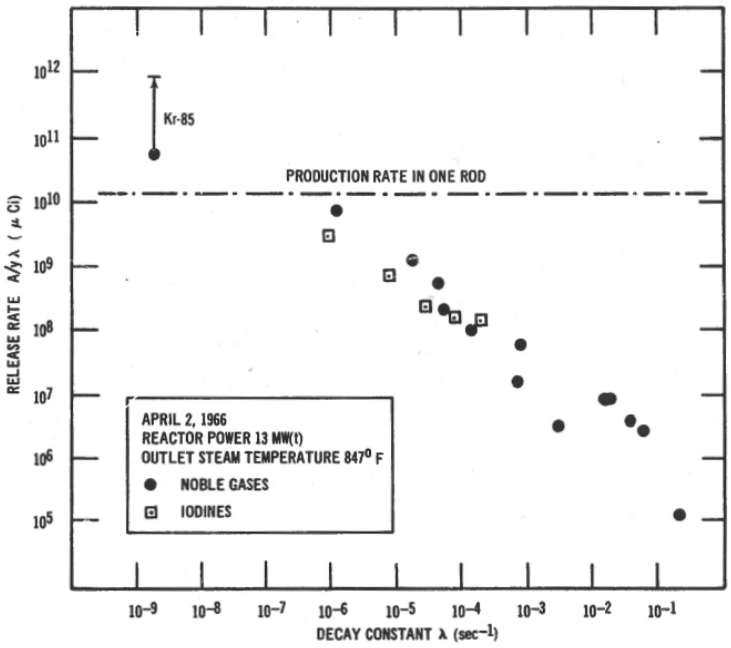

Figure 1: Noble gas and iodine release from EVESR superheat fuel rod KB-40 [8]. The peak cladding temperature at the time of failure was estimated to be 777 °C

3. SIMFUEL Leaching Tests

In contrast to the large amount of data on fission gases and iodines available from the US nuclear steam superheat program, no data could be found on the transport of so-called depositing fission products. No data on fission product transport appeared to be available from Beloyarsk Nuclear Power Plant [10]. To address this knowledge gap, leaching tests of SIMFUEL in SCW were performed to identify those fission product species capable of dissolving from the fuel matrix, as well as to determine the risk that the fuel itself might dissolve in SCW.

3.1 Experimental

The composition of the current Canadian SCWR reference fuel is 13 wt.% PuO_2 in ThO_2 [11]. The radiotoxicity of plutonium complicates the handling of fresh fuel with this composition, and irradiated fuel presents additional challenges. Simulated Extended Burnup Fuel (SIMFUEL) containing natural UO_2 as a surrogate for PuO_2 and non-radioactive additives to simulate the fission products present in irradiated fuel can be used to estimate the thermal, mechanical, and chemical characteristics of fresh and irradiated Canadian SCWR fuel. This avoids the complications of handling plutonium and irradiated fuels. A 60 GWd·tonne^{-1} SIMFUEL (Table 1) was chosen for the leaching tests because it contains the highest concentrations of fission product surrogates, which improves their detection in solution. It should be noted that the SIMFUEL samples did not contain any Cs, which has a high solubility in subcritical water.

Two SIMFUEL pellets (13 mm long, 11.5 mm diameter, ~ 9.2 g·cm^{-3}, ~ 25 g total) were cut into 5 slices, creating six 2 mm slices and four 2.5 mm slices (10 slices in total). One 2.5 mm slice was used for Scanning Electron Microscopy examination of surface morphology and phases (and archiving) with the remainder used for the leaching tests. The 2.5 mm slices were taken from the pellet centre area to guarantee that both sides were cut faces.

Table 1: Mass of Additives in the 60 GWd·tonne^{-1} Burn-up SIMFUEL used in the Leaching Tests. The shaded rows indicated species for which some relevant solubility data exist.

Actinide/Fission Product	Representative Element	Additive	Mass Added (g)	Percent of Total Mass
Ag	Ag	Ag	0.0443	0.03
Ba	Ba	$BaCO_3$	0.5026	0.34
Ce/Np	Ce	CeO_2	0.7197	0.48
La	La	La_2O_3	0.3310	0.22
Mo/Nb	Mo	MoO_3	1.0835	0.72
Nd/Pr/Pm/Sm/Gd/Tb/Eu/Ho/Er	Nd	Nd_2O_3	1.5887	1.06
Pd	Pd	PdO	0.6492	0.43
Rh	Rh	Rh_2O_3	0.1962	0.13
Ru	Ru	RuO_2	1.1195	0.75
Sn	Sn	SnO_2	0.0221	0.015
Sr	Sr	SrO	0.1675	0.11
Th	Th	ThO_2	128.33	85.55
U/Pu/Am/Pa/Cm	U	UO_2	14.293	9.53
Y	Y	Y_2O_3	0.0924	0.06
Zr	Zr	ZrO_2	0.8640	0.58
Total			**150.00**	

The leaching tests were performed in SCW in a Parr 250 mL autoclave at temperatures of 400 and 500 ºC and a pressure of 25 MPa. A temperature of 400 ºC was chosen because the solubilities of most of the SIMFUEL constituents are expected to be relatively high at this temperature. Metal oxide solubility tends to decrease as the SCW density decreases at temperatures well above the critical temperature (374 °C), although the oxides of some fission products, such as Mo, show the opposite behavior [12, 13]. At the same time, this temperature is sufficiently far above the critical temperature that temperature and pressure control of the autoclave was relatively straightforward. The second test was performed at 500 ºC, which was the maximum temperature at which the autoclave could be operated.

Each of the three tests at 400 °C included two ~ 2 mm pellet slices (at least one 2 mm pellet had a non-cut surface) and one ~ 2.5 mm pellet slice. The same pellets were used for the tests at 500 °C.

Due to the potential radiological hazard, particularly in the event of overpressurization and failure of a rupture disk, the tests were performed in a large ventilated cabinet in a laboratory designed to handle radioisotopes. Pellet cleaning, weighing, and loading into the autoclave was performed consecutively and as quickly as possible. Each pellet slice was cleaned by rinsing in water, then acetone, followed by methanol and then drying with argon. Each slice was then weighed and its weight and exact location on the sample hanger recorded; one 2 mm slice with a non-cut surface had its orientation recorded to ensure the non-cut surface could be identified post-test.

Test solutions were not de-aerated; however, in a non-refreshed static autoclave the reaction of oxygen with the walls of the autoclave is rapid and it is expected that the actual oxygen concentration in the autoclave was low. The tests had durations of 1, 3 and 7 days to determine the time required for ‘equilibrium’ to be reached. Once the autoclave exposure was complete, the samples were removed (and not rinsed) and placed immediately into a desiccator to cool. Once cool, pellet slices were re-weighed on the same scale. All the solution remaining in the autoclave was withdrawn using a syringe and split into two aliquots. One was filtered through a 0.1 µm filter, and the filtrate and filter retained for analysis; the other was unfiltered. Both liquid samples were acidified to prevent precipitation and sent for analysis.

3.2 Results

The SIMFUEL pellets all increased in weight after exposure to SCW at 400 °C (Figure 2), with the exception of Sample 9; a small fragment of this sample appeared to have broken off. Significant releases of corrosion products (Fe, Ni, Cr, Mo) from the autoclave were detected in the water removed from the autoclave after the tests (Figure 3). Of the simulated fission products, only Sr and Ba were detected in all tests at significant concentrations (Figure 4). It appears that both species have relatively high solubilities under the test conditions. It should be noted that the data may not represent equilibrium solubility values as dissolution may be limited by diffusion of these elements, present in the SIMFUEL matrix at concentrations of less than 1%, through the sintered SIMFUEL pellets.

Zimmerman et al. [14] recently reported preliminary results of an experimental study to determine the association constants of strontium with hydroxide and chloride ions at temperatures up to 350 °C, using high-pressure flow AC conductance. The systems [$Sr(OH)_2 + H_2O$] and [$SrCl_2 + H_2O$] were chosen because of their importance to modeling fission product transport in SCWRs, and because they are soluble in near-critical water and so may be used as model systems for other M^{2+} species. Under SCWR conditions, the formation of $SrOH^+$ and $Sr(OH)_2^0$ ion-pairs was established to be greater than $SrCl^+$ and $SrCl_2^0$ ion pairs, so that hydroxy complexes will be the dominant strontium species in solution. Neutral species were found to be substantial at 350 ºC for concentrations above 10^{-3} mol·kg^{-1}, for both salts. The Sr concentration at 350 °C was predicted to be 6.5 x 10^{-3} M (570 mg·kg^{-1}) [15]; as it is expected that the solubility will be lower at 400 °C, the value of 200 mg·kg^{-1} obtained in the leaching tests is consistent with the data measured at lower temperatures.

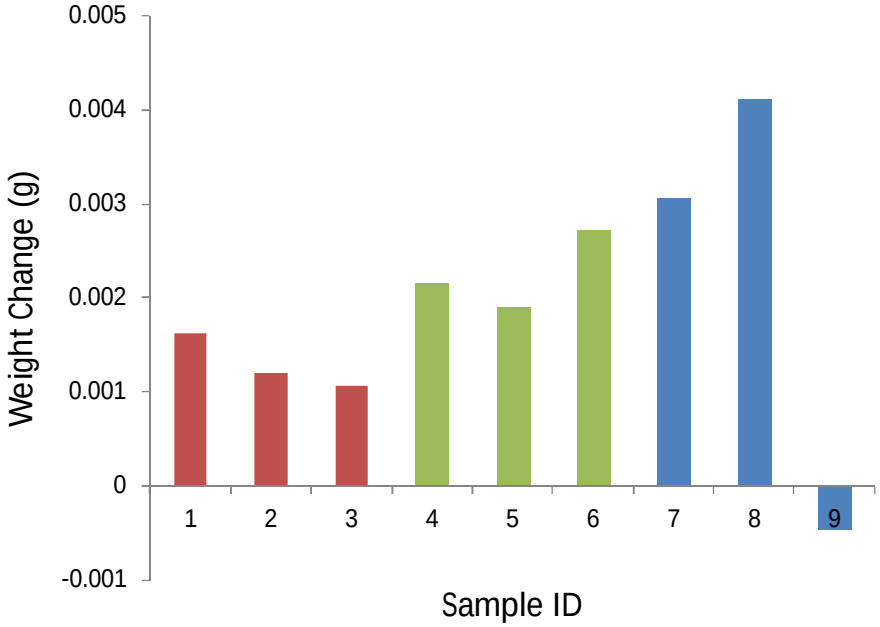

Figure 2: Weight change for the SIMFUEL samples tested at 400 °C and 25 MPa at different exposure times. Samples 1, 2 and 3 were exposed for 1 day, Samples 4, 5 and 6 for 3 days, and Samples 7, 8 and 9 for 7 days

A significant concentration of Mo was detected in the test solutions. However, Mo release from SIMFUEL could not be quantified in these tests because Mo is a major constituent (16 wt.%) of the Hastelloy C autoclave used for testing. The wetted surface area of the autoclave is much higher than that of the test specimens, so that Mo release due to autoclave corrosion masks release from the samples.

At 400 °C, Zr, Ru, Rh, Pd, Ag, and Sn were detected in one or more tests at close to the Method Detection Limit of Inductively-Coupled Plasma Mass Spectrometry, suggesting these elements have low solubilities under SCWR conditions. The data are listed in Table 2.

Similar results were obtained at 500 °C (Figure 4). With the exception of the first data point measured for Ba, the concentrations measured were not significantly higher than those measured at 400 °C. At 500 °C, Rh, Ce, La and Nd were detected in one or more tests at close to the Method Detection Limit of Inductively-Coupled Plasma Mass Spectrometry. The data are listed in Table 2.

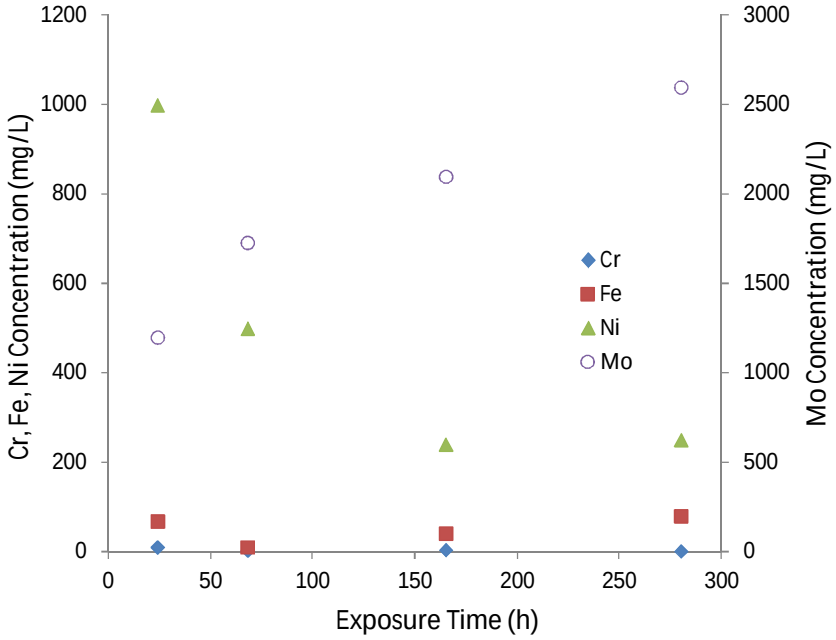

Figure 3: Concentrations of Autoclave Corrosion Products in the Test Solution as a Function of Exposure Time at 400 °C and 25 MPa

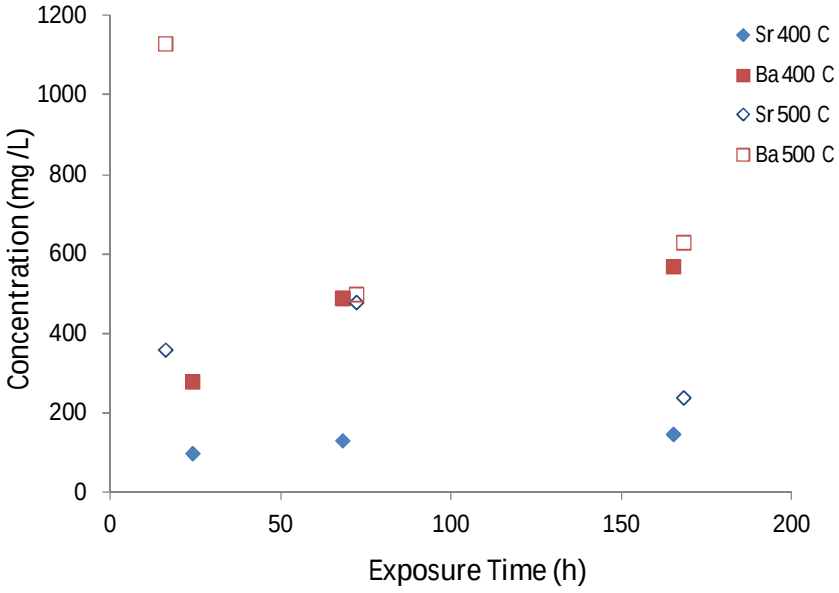

Figure 4: Concentrations of Sr and Ba in the Test Solution as a Function of Exposure Time at 400 °C and 500 °C, 25 MPa

Table 2: Concentrations of Elements (other than Sr, Ba, U and Th) Detected in the Test Solution in One or More Leaching Tests

Element	Concentration ($ug \cdot kg^{-1}$) [M in brackets]	
	400 °C	500 °C
Zr	0.12 [1.32×10^{-9}]	-
Ru	0.04 [4.0×10^{-10}]	-
Rh	0.10 [9.7×10^{-10}]	0.019 [1.8×10^{-10}]
Pd	0.085 [8.0×10^{-10}]	-
Ag	0.35 [3.2×10^{-9}]	-
Sn	0.23 [1.93×10^{-9}]	-
La	-	0.058 [4.2×10^{-10}]
Ce	-	0.039 [2.7×10^{-10}]
Nd	-	0.033 [2.29×10^{-10}]

The solubility of ZrO_2(c) in alkaline and acidic supercritical solutions was studied by Korzhinskaya [16] and Ryzhenko et al. [17]. Their results show that the solubility of ZrO_2 in weakly acidic and alkaline solutions is 1.28×10^{-5} mol/kg at 400 °C and 100 MPa and is independent of pH. The concentration of Zr detected in the current work was much lower. Rhodium was the only element detected at both 400 and 500 °C. The concentration at 500 °C was about one order of magnitude lower than the value measured at 400 °C.

3.2.1 Actinides

Th and U were detected in the test solution in one or more of the tests at close to the Method Detection Limit of Inductively-Coupled Plasma Mass Spectrometry, suggesting low solubilities under SCWR conditions. In the final experiment, a simple solubility measurement of thoria powder (5.5 g placed in 78 mL water in the autoclave) was performed for 216 h at 400 °C and a pressure of 25 MPa. It should be noted that the data for U may not represent an equilibrium solubility value as dissolution may be limited by diffusion through the (mainly thoria) sintered SIMFUEL pellets.

The solubility of UO_2 has been studied by many groups [18, 19] because of its importance as a nuclear fuel. Differences in the measured solubility of UO_2 can be as large as four orders of magnitude due to the morphology of the UO_2 sample (crystalline or amorphous), redox conditions and equilibration time. The solubility values for amorphous UO_2 ($UO_2 \cdot nH_2O$) reported by Rai et al. [20] at room temperature and pH values between 2 and 12 were four orders of magnitude lower than those reported earlier [21, 22]. It was recognized that dissolved O_2 in the test solutions can oxidize U(IV) to the more soluble U(VI) oxide [20]. Above pH 4, the solubility of UO_2 is almost independent of pH; $U(OH)_4^0$ becomes the dominant species and further hydroxylation is not favoured thermodynamically (Figure 5). Experimental measurements found similar solubilities for microcrystalline and amorphous UO_2 at pH>4 [23, 18], although theoretical calculations suggest that crystalline UO_2(c) should have a much lower solubility. The similar values measured experimentally is largely due to the hydration of crystalline UO_2, resulting in the formation of an amorphous surface phase. Amorphous UO_2 can also partially re-crystallize to form a microcrystalline phase during the dissolution process.

In neutral water, most measured values for the solubility of UO_2 range from 10^{-7} to 10^{-9} $mol \cdot kg^{-1}$ at 25 ºC, which can be assumed to be the concentration of the neutral species $U(OH)_4^o$. Ollila [18] reported that UO_2(am) had a solubility of $(2.6 \pm 0.6) \times 10^{-10}$ $mol \cdot kg^{-1}$ in neutral water at 25 ºC, similar to that of Parks and Pohl [24]. Neck and Kim [23] and Fanghänel et al. [25] critically reviewed the solubility data of UO_2: based on these data the calculated solubilities of amorphous and crystalline UO_2 are 3.16×10^{-9} and 1.38×10^{-15} $mol \cdot kg^{-1}$, respectively, in neutral water at 25 ºC.

The solubility of crystalline UO_2(c) at temperatures from 100 to 300 ºC and pH values from 1 to 10 was studied by Parks and Pohl [24] at 50 MPa under reducing aqueous solutions. At pH values above 2, the only important dissolved species is $U(OH)_4^o$:

$$UO_2(c) + 2\ H_2O = U(OH)_4^o \qquad \text{Equation 1}$$

They determined that $\log_{10}K_{sp}$ = -9.47±0.3, equal to a concentration of $U(OH)_4^o$ of 3.39×10^{-10} mol·kg^{-1}. Their results showed that the temperature effect on the solubility of UO_2 at pH> 4 was insignificant, which agrees with the results of Tremaine et al. [26].

Red'kin et al. [27, 28] studied the solubility of crystalline UO_2 in SCW at temperatures from 300 to 600 ^{o}C at a pressure of 1 kbar at different pHs. The solubility of UO_2 in pure water was found to be independent of temperature and buffer (Ni/NiO and Fe_2O_3/Fe_3O_4) within experimental uncertainty with an average of $\log_{10}$([U]/[mol/kg]) = -9.0±0.5 mol·kg^{-1}. Their value is similar to that of Parks and Pohl [24] measured under sub-critical conditions.

In the current work, a measurable concentration of U in solution was reported in two tests; in one test at 400 °C a value of 0.031 µg·kg^{-1} ($\log_{10}$([U]/[mol/kg]) = -9.9 mol·kg^{-1}) was reported and in one test at 500 °C a value of 0.069 µg·kg^{-1} ($\log_{10}$([U]/[mol/kg]) = -9.5 mol·kg^{-1}). These values are in reasonable agreement with the literature values. Sunder [29] showed that uranium in a matrix of thorium oxide will be less easily oxidized, and therefore the dissolution of uranium from such materials will be significantly lower than for pure UO_2 under similar conditions.

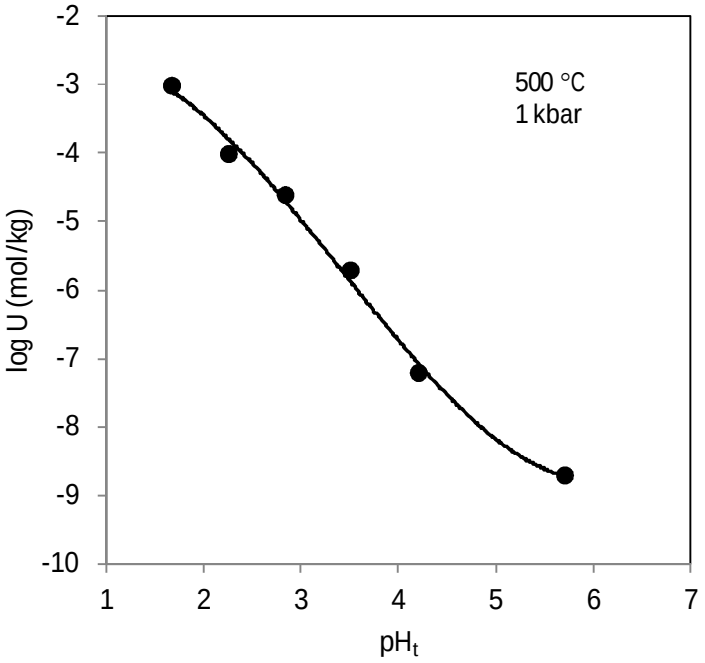

Figure 5: Solubility of UO_2(c) at 500 ºC as a function of pH using a Ni-NiO buffer. Adapted from Red'kin et al. [27]

3.2.1.1 ThO_2

Rand et al. [30] and Neck and Kim [23] recently reviewed the solubility data for ThO_2; a detailed discussion of the solubility of Th under conditions relevant to the SCWR can be found in [12, 13]. As with UO_2, factors such as morphology, pH, formation of colloid particles, and experimental methods lead to differences of 3 to 4 orders of magnitude between values reported by different authors. Figure 6 compares the solubility of ThO_2 with different morphologies and illustrates the differences encountered between data measured at similar ionic strengths.

In neutral and alkaline solutions, the solubility of ThO_2 is independent of pH over the range pH 6 to pH 14. Although crystalline ThO_2(c) has a lower solubility than amorphous ThO_2(am) or $Th(OH)_4$(s), as with UO_2 the measured solubility of these two phases usually has the same value because of the formation of an amorphous layer of ThO_2 on the surface of the bulk material. The dissolution reaction in this region can be expressed as

$$ThO_2(am) + 2\ H_2O = Th(OH)_4^o \qquad \text{Equation 2}$$

or

$$Th(OH)_4(s) = Th(OH)_4^o(aq) \qquad \text{Equation 3}$$

The equilibrium constant of the reactions in Equations (2) and (3) has a value of $K°_{s14} = -8.5 \pm 1.0$ at 25 ºC after ultracentrifugation (90000 rpm) or ultrafiltration at a filter pore size less than 2 nm to exclude colloidal particles [30, 23]. The value of $K°_{s14}$ can be assumed to be the concentration of $Th(OH)_4^o$, 3.16×10^{-9} mol·kg^{-1} for the purposes of calculating the solubility of ThO_2(am). However, the value probably also includes the concentration of neutral polynuclear species with particle sizes less than 2 nm [30].

The Gibbs energies of formation of the dissolved species of ThO_2 [30] can be used to calculate the solubility of ThO_2 at 25 ºC; the calculated solubilities are shown in Figure 6.

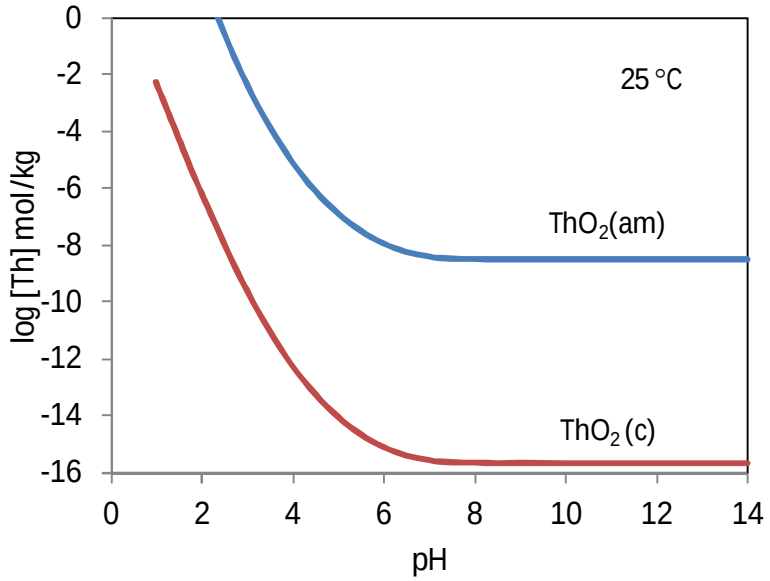

Figure 6: Thermodynamically calculated solubility of ThO_2 at 25 ºC as a function of pH

Rai et al. [31] measured the solubility of crystalline ThO_2(c) at 90 ºC in acidic solutions and determined the solubility constant of Equation 12 to be $\log_{10}K°_{sp} = -51.4 \pm 0.2$ or $\log_{10}K°_{sp} = -1.94$ for Equation 11. The concentration of dissolved Th^{4+} decreased as the temperature increased.

There are no solubility data available in neutral and alkaline solutions and a complete solubility profile of ThO_2(c) as a function of pH and temperature cannot be prepared at this time. Considering the similarities in the dissolution behaviour between UO_2 and ThO_2 and their similar solubilities at room temperature, it is possible that the solubility of ThO_2(c) shows only a weak dependence on temperature in neutral and alkaline solutions and the value in SCW may be close to that of UO_2.

As part of the current work, a crude solubility measurement of thoria powder (5.5 g placed in 78 mL water in an autoclave) was performed for 216 h at 400 °C and a pressure of 25 MPa. Analysis of the test solution after cooling and filtering gave a thorium concentration in solution of less than 0.2 µg·L^{-1}, or $K_{sp} \approx 8.6 \times 10^{-10}$ mol· kg^{-1}, which gives $\log_{10}$Ksp = -9.1. This value is very close to the value for UO_2 ($\log_{10}$(S/[mol/kg]) = -9.0±0.5 mol·kg^{-1}).

4. Conclusions

A good understanding of the release and transport of fission products and actinides in the coolant of an SCWR after a fuel defect is required to determine the radiological hazards that will exist on downstream piping and the high pressure turbines. These data will also be useful in preparation for future fuel qualification tests.

Leaching tests of these species from specimens cut from a pellet of U-Th SIMFUEL have shown that only Sr and Ba are released from the SIMFUEL at 400 and 500 °C in quantities well above their method detection limits. Only limited dissolution of the other simulated fission products and of the U and Th of the pellet matrix was observed. With the exception of Zr, the concentrations of the released species were in reasonable agreement with the very limited amount of data available on the solubilities of these species in neutral SCW.

References

[1] Guzonas, D.; Qiu, L. “Activity Transport in a Supercritical Water-cooled Reactor, 6th International Symposium on Supercritical Water-cooled Reactors”, ISSCWR-6, March 03-07, 2013, Shenzhen, Guangdong, China

[2] IAEA (2002) “Fuel Failure in Water Reactors: Causes and Mitigation”, Proceedings of a Technical Meeting held in Bratislava, Slovakia, IAEA-TECDOC-1345, June 2002.

[3] Locke, D.H. (1972) "The Behaviour of Defective Reactor Fuel," Nuclear Engineering and Design, **21**, 318.

[4] Cohen, K.; Zebroski, E. (1959), “Operation Sunrise”, Nucleonics, **17**, 63.

[5] Hazel, V.E.; Boyle, R.F.; Busboom, H.J.; Murdock, T.B.; Skarpelos, J.M.; Spalaris, C.N. (1965), “Fuel Irradiations in the ESADE-VBWR Nuclear Superheat Loop”, General Electric Report GEAP-4775.

[6] Murray, J.L. (1965), “EVESR-Nuclear Superheat Fuel Development Project Thirteenth Quarterly Report”, General Electric Report GEAP-4941.

[7] Busboom, H.J.; Boyle, R.F.; Harling, G.; Hazel, V.E. (1966), “Post-irradiation Examination of EVESR Mark III Superheat Fuel (0.008 Inch Cladding Failure)”, General Electric Report GEAP-5135.

[8] Rabin, S.A.; Atraz, B.G.; Bader, M.B.; Busboom, H.J.; Hazel, V.E. (1967), “Examination and Evaluation of Rupture in EVESR Superheat Fuel Rod with 0.012-inch-thick Incoloy-800 Cladding”, General Electric Report GEAP-5416.

[9] Roof, R.R. (1966), “EVESR-Nuclear Superheat Fuel Development Project Seventeenth Quarterly Report”, General Electric Report GEAP-5269.

[10] Yurmanov, V.A.; Belous, V.N.; Vasina, V.N.; Yurmanov, E.V. (2010), “Chemistry and Corrosion Issues in Supercritical Water Reactors”, Proceedings of the Nuclear Plant Chemistry Conference 2010 (NPC 2010), October 3-8, 2010, Quebec City, Canada, Paper 11.02.

[11] Bergeron, A.; Hamilton, H. (2013), “Fabrication and Characterization of Canadian SCWR SIMFUEL”, 6th International Symposium on Supercritical Water-cooled Reactors (ISSCWR-6), March 03-07, 2013, Shenzhen, Guangdong, China.

[12] Qiu, L.; Guzonas, D.A. (2010), “An Overview of Corrosion Products Solubilities in Subcritical and Supercritical Water”, 2nd Canada-China Joint Workshop on Supercritical Water-Cooled Reactors (CCSC-2010), Toronto, Ontario, Canada, April 25-28, 2010.

[13] Qiu, L. (2014) “Solubilities of Fission Products under Supercritical Water-cooled Reactor Conditions”, 2014 Canada-China Conference on Advanced Reactor Development (CCCARD-2014), Niagara Falls, Ontario Canada, April 27-30, 2014.

[14] Zimmerman, G.H.; Arcis, H.; Tremaine, P. (2011) “Ion-pair Formation in Strontium Chloride and Strontium Hydroxide Solutions under Supercritical Water Reactor Operating Conditions”, in proceedings of the 5th Int. Symp. SCWR (ISSCWR-5), Vancouver, Canada, March 13-16, 2011.

[15] Tremaine, P. (2014) Personal Communication.

[16] Korzhinskaya, V.S. (1999) “Solubility of Baddeleyite (ZrO_2) and Zircon ($ZrSiO_4$) in Aqueous Hydrochloric Solutions at Elevated T and P Parameters”, Experimental Geoscience, **8** (1), 9-18.

[17] Ryzhenko, B.N.; Kovalenko, N.I.; Prisyagina, N.I.; Starshinova N. P.; Krupskaya V.V. (2008) “Experimental Determination of Zirconium Speciation in Hydrothermal Solutions”, Geochemistry International, **46** (4), 328-339.

[18] Ollila, K. (2008) “Solubility of UO_2 in the High pH Range in 0.01 and 0.1 M NaCl Solution under Reducing Conditions”, POSIVA working report 2008-75, Finland.

[19] Casas, I.; Pablo, J.D.; Gimenez, J.; Torrero, M.E.; Bruno, J.; Cera, E.; Finch, R.J.; Ewing, R.C. (1998) “The Role of pe, pH and Carbonate on the Solubility of UO_2 and Uraninite under Nominally Reducing Conditions”, Geochimica et Cosmochimica Acta, **62**, 2223.

[20] Rai, D.; Felmy, A.R.; Ryan, J.L. (1990) “Uranium(IV) Hydrolysis Constants and Solubility Product of $UO_2 \cdot xH_2O$(am)”, Inorganic Chemistry, **29**, 260.

[21] Gayer, K.H.; Leider, H. (1957) “The Solubility of Uranium(IV) Hydroxide in Solutions of Sodium Hydroxide and Perchloric Acid at 25 ^{o}C”, Canadian Journal of Chemistry, **35**, 5.

[22] Bruno, J.; Casas, I.; Lagerman, B.; Munoz, M. (1987) “The Determination of the Solubility of Amorphous UO_2(s) and the Mononuclear Hydrolysis Constants of Uranium(IV) at 25 °C”. In: Scientific Basis for Nuclear Waste Management X (Eds. J.K. Bates and W.B. Seefeldt), Pittsburgh, Pennsylvania, USA: Mat. Res. Soc. Symp. Proc. **84**, 153.

[23] Neck, V.; Kim J.I. (2001) “Solubility and Hydrolysis of Tetravalent Actinides”, Radiochimica Acta, **89**, 1.

[24] Parks, G.A.; Pohl, D.C. (1988) “Hydrothermal Solubility of Uraninite”, Geochimica et Cosmochimica Acta, **52**, 863.

[25] Fanghänel, T.; Neck, V.; Fuger, J.; Palmer, D.A.; Crenthe, I.; Rand, M.H. (2003) “Update on the Chemical Thermodynamics of Uranium, Neptunium, Plutonium, Americium, and Technetium”, Nuclear Energy Agency, Organization for Economic Co-operation and Development.

[26] Tremaine, P.R.; Chen, J.D.; Wallace, G.J.; Boivin, W.A. (1981) “Solubility of Uranium (IV) Oxides in Alkaline Aqueous Solutions to 300 °C”, Journal of Solution Chemistry, **10 (**3), 221-230.

[27] Red'kin, A.F.; Savel'yeva, N.I.; Sergeyeva, E.I.; Omel'yaneko, B.I.; Invanov, I.P.; Khodakovsky, I.L. (1990) Experiment 89, Informative Volume, Moscow, Nauka, p79.

[28] Red’kin, A.F.; Savelyeva, N.I.; Sergeyeva, E.I.; Omel’yanenko, B.I.; Ivanov, I.P.; Khodakovsky, I.L. (1989) “Investigation of Uraninite UO_2(c) Solubility under Hydrothermal Conditions”, Sciences Géologiques Bulletin, **42,** 329.

[29] Sunder, S. (1999) ”Corrosion Resistance of (Th,U)O_2 Fuel in Water”, Proceedings of the 6th International CNS CANDU Fuel Conference, Niagara Falls, September 26 - 30,1999.

[30] Rand, M.; Fuger, J.; Grenthe, I.; Neck, V.; Rai, D. (2007) “Chemical Thermodynamics of Thorium”, OECD Nuclear Energy Agency.

[31] Rai, D.; Moore, D.A.; Oakes, C.S.; Yui, M. (2000) “Thermodynamic Model for the Solubility of Thorium Dioxide in the Na^+-Cl^- - OH^- -H_2O System at 23 and 90 $^{\circ}$C”, Radiochimica Acta, **88**, 297.

Paper ID: 2092

Effect of temperature and dissolved oxygen on the SCC behavior of 316Ti in supercritical water

ZHANG Qiang[1]*, TANG Rui[1], XIONG Ru[1] , ZHANG Lefu[2]

(1 Science and Technology on Reactor Fuel and Materials Laboratory, Nuclear Power Institute of China, Chendu 610213, P. R. China

2 Institute of Nuclear Science and Engineering, Shanghai Jiaotong University, Shanghai 200240, P. R. China)

Abstract: As one of the Generation IV reactor concepts, the supercritical water reactor (SCWR) is characterized by simplified design, smaller volume, and higher thermal efficiency compared with the light water reactor (LWR). Since the physical and chemical properties of the coolant will undergo great changes crossing the critical point, a systematic study of the SCC behavior of candidate materials is required for the safe operation of the SCWR.

In this study, 316Ti coupons were tested in supercritical water at 450℃, 550℃ and 650℃ through SSRT mode, with various dissolved oxygen (DO) concentration (deaerated, 200ppb and 2ppm). The SCC sensitivity index of this material was calculated based on the Stress-Strain curve and relevant mechanical data. By various analytical methods (SEM/EDS, XRD and TEM), the fracture and crack morphology of the SSRT specimen were observed, while the oxide (formed on both the stable and deformed areas) composition and microstructure were analyzed. In 450℃ supercritical water, 316Ti shows moderate SCC sensitivity, which increased with higher DO. In 550℃ supercritical water, 316Ti shows severe SCC sensitivity, which decreased with higher DO. In 650℃ supercritical water, 316Ti shows no SCC sensitivity along with rather high uniform deformation rate, which was attributed to anneal softening. The SCC sensitivity in all cases is related to the Ni content in the oxide film near the crack tip.

Key words: temperature, dissolved oxygen, SCC behavior, 316Ti, supercritical water

***Corresponding author: zhangqiang0726@sina.com**

1. Introduction

The Supercritical water reactor (SCWR) has been selected as one of the Generation IV reactor concepts[1-4], due to its simplified design, smaller volume, and higher thermal efficiency (~ 44 %) compared with conventional light water reactors (LWRs). Based on the current design by NPIC, the fuel cladding and internal components in the SCWR experience much higher temperatures (>500 ℃) and neutron irradiation ($\geq 10^{23}$ n/cm^2) than in a PWR. Therefore a systematic study of the Stress corrosion cracking (SCC)behavior of candidate materials is required for the safe operation of the SCWR[5-16]. Austenitic stainless steels are widely used in the LWR and have become candidate materials for the SCWR, because of their excellent corrosion resistance and good high temperature strength under the relevant working conditions.

In this work, 316Ti coupons were tested in supercritical water (SCW) at 450−650 ℃ through Slow strain rate test (SSRT) mode. The SCC sensitivity index of this material was calculated based on the Stress-Strain curve and relevant mechanical data. Fracture morphology and surface oxide were observed by SEM/EDS, XRD and TEM. Effect of temperature and dissolved oxygen (DO) concentration (deaerated, 200ppb and 2ppm) on the SCC behavior of 316Ti in supercritical water have been investigated.

2. Experimental

The tested material is ANSI 316Ti with an average grain size of 50μm, whose chemical composition is shown in table 1. SSRT with a strain rate of 1×10^{-6}/s was conducted in a SCW tensile loop with a circulation capacity of 2L/h. The test temperature was set as 450℃, 550℃ and 650℃ with the pressure as 25 MPa, and three dissolved oxygen concentration were studies at each test temperature, namely <10 ppb (marked 0 ppb in figures and tables), 200 ppb and 2 ppm. In order to get the SCC sensitivity index at each test condition, SSRT in Ar at the three temperatures was also performed. Single axis tensile specimen with a thickness of 2 mm were used in this research, as illustrated in figure 2. The specimen was machined according to GB/T 15970 and the gauge surface was polished to a mirror finish with 1 μm diamond paste. Before the SSRT, the specimen was ultrasonically cleaned in acetone for 10 min and deionized water for 5 min. After the SSRT, the strain-stress curve was drawn by Origin7.5 for each test condition and the relevant mechanical property (yield strength, ultimate tensile strength, elongation rate and rupture energy) was calculated accordingly. In this paper, the SCC sensitivity index (I_e) was determined by the rupture energy ratio of the specimen tested in SCW and Ar, as shown in equation 1:

$$I_e = 1 - A_w/A_a \quad (1)$$

Where A_w and A_a represented the rupture energy ratio tested in (SCW and Ar respectively. The fracture surface of the specimen was observed by Scanning electron microscope (SEM) to get a clearer understanding of the severity of SCC sensitivity in a certain environment. Oxide scales on the gauge surface (near the fracture) and fracture surface (near the edge) were analyzed by Glancing Incidence X-ray Diffration (GIXRD), Energy Dispersive Spectroscope (EDS)and Transmission electron microscope (TEM) in order to characterize the relationship between the oxide and SCC sensitivity. Since the oxide scale was rather thin and brittle, Focused Ion Beam (FIB) was used for TEM sample preparation.

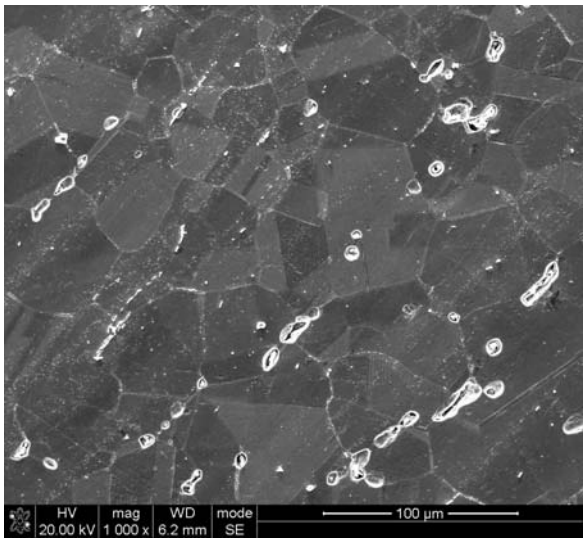

Figure 1. Microstructure of the tested 316Ti

Table 1. Chemical composition of the tested 316Ti (wt.%)

Element	C	Mn	Si	Ni	Cr	Ti	Mo	Fe
Content	0.02	1.5	0.4	12.1	17.0	0.47	2.1	Bal.

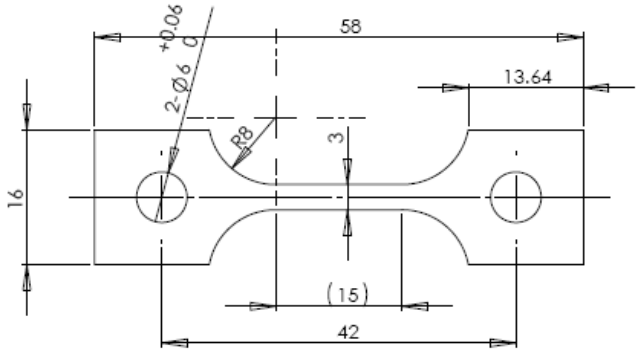

Figure 2. Illustration of the SSRT specimen (mm)

3. Results

3.1 Test at **450℃**

The strain-stress curves of 316Ti in 450℃ SCW and Ar are shown in figure 3 and the relevant mechanical properties in table 2. In 450℃ Ar, the specimen undergoes elastic deformation at the beginning and experience plastic deformation (together with strain strengthening) beyond the stress of 180 MPa. The stress declines suddenly after the peak level of 473 MPa, as the specimen undergoes necking and rupture simultaneously. In 450℃ SCW, the specimen shows the same deformation trend but apparently lower mechanical properties. Addition of dissolved oxygen into the SCW induces deteriorated mechanical properties and much higher SCC sensitivity.

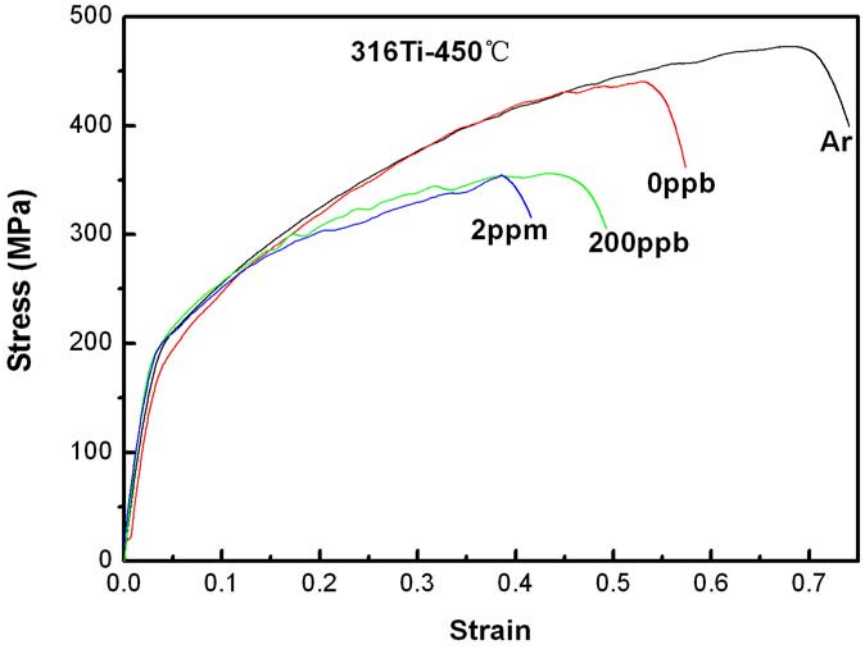

Figure 3. Strain-stress curve of 316Ti tested in 450 ℃ SCW and Ar

The fracture morphology of 316Ti tested in 450 ℃ SCW and Ar is shown in figure 4. For the specimen tested in Ar, the whole fracture surface is covered by microvoids with a size of 2 -10 μm. For the specimen tested in deaerated SCW, microvoids still prevail on the fracture surface but take on a much smaller size and depth. For the specimen tested in low DO SCW, minor evidence of

brittle fracture appears. For the specimen tested in high DO SCW, the fracture surface is a mixture of brittle and ductile features, appearing as rock candy and microvoids respectively, an indication of Intergranular Stress corrosion cracking (IGSCC). Combining the strain-stress curve with the fracture observation, 316Ti shows slight SCC sensitivity in 450℃ SCW and addition of dissolved oxygen will greatly increase its SCC sensitivity.

Table 2. Mechanical properties of 316Ti tested in 450 ℃ SCW and Ar

Dissolved oxygen（ppb）	Ultimate tensile strength（MPa）	Elongation rate（%）	Reduction Area（%）	Rupture energy（J）	I_g
Ar	473	74	45	24.75	—
0	441	57	52	17.55	0.29
200	356	49	46	13.14	0.47
2000	354	42	36	10.71	0.57

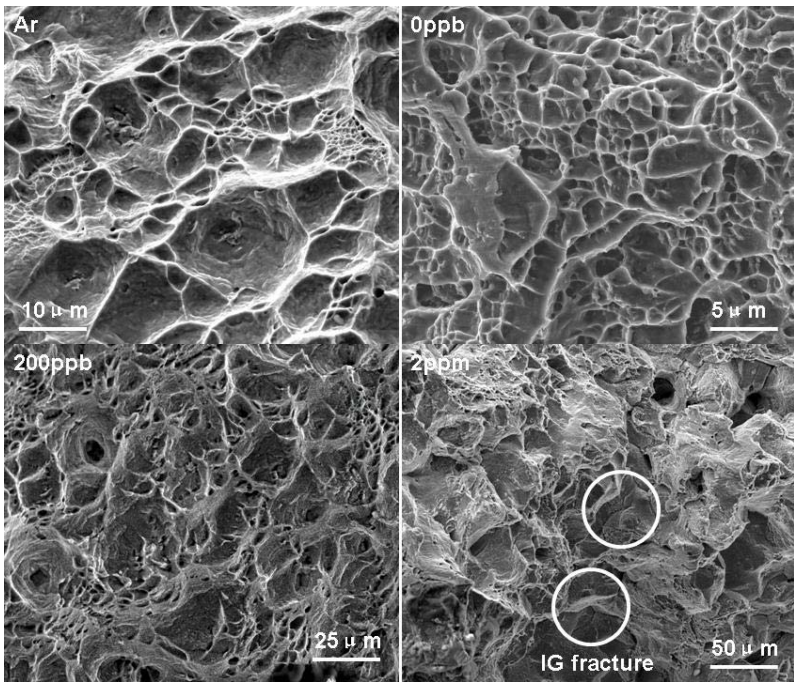

Figure 4. Fracture morphology of 316Ti tested in 450 ℃ SCW and Ar

The gauge surface oxide of 316Ti tested in 450℃ SCW displays a varied morphology. The oxide scale formed in low DO SCW features uniform polygonal crystals. In deaerated and high DO SCW, the oxide scale is a mixture of nano- and micropolygonal crystals. The most distinct of the high DO oxide scale is enrichment of Fe and depletion of Ni, Cr and Mo. The phase structures of the oxide scales are quite different for the specimens tested at different DO concentrations. In deaerated SCW, the oxide scale is mainly composed of Fe_2O_3 (card 33-0664), Fe_3O_4 (card 19-0629) and $FeCr_2O_4$ (card 34-0140). In low DO SCW, the peak of the matrix is prominent due to the rather thin oxide scale, and $Ni(OH)_2$ (card 14-0117) is observed at high concentrations. In high DO SCW, the XRD pattern looks similarly to the case in deaerated SCW. But due to enrichment of Fe and depletion of Cr, the oxide scale must be mainly composed of Fe_3O_4 and

Fe_2O_3 rather than $FeCr_2O_4$.

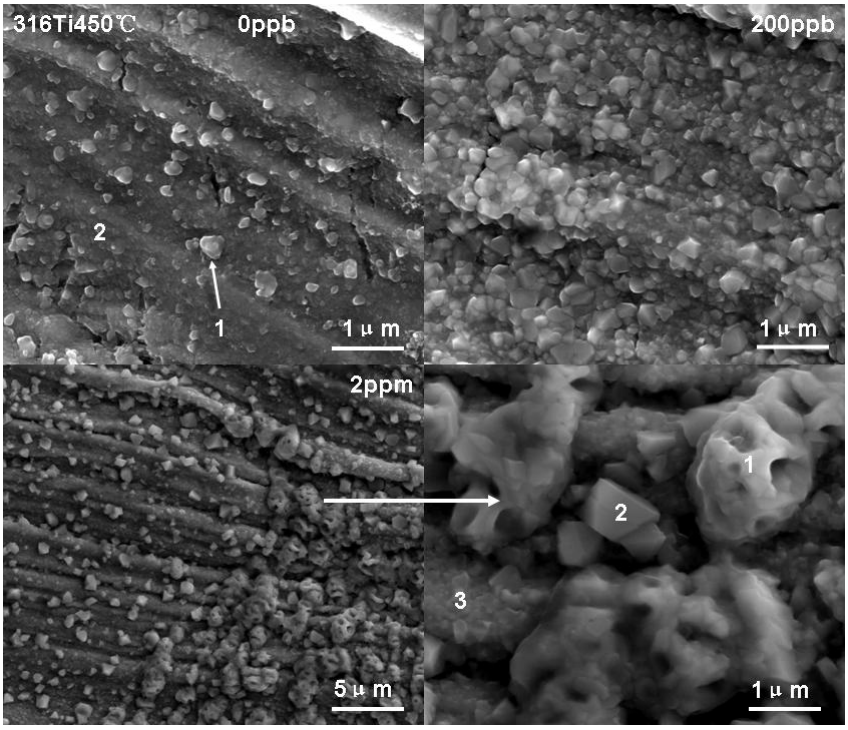

Figure 5. Gauge surface oxide morphology of 316Ti specimen tested in 450 ℃SCW

Table 3 Gauge surface oxide composition of 316Ti specimen tested in 450 ℃SCW (wt.%)

DO(ppb)	O	Si	Ti	Cr	Mn	Fe	Ni	Mo
0	11.37	1.08	0.34	20.84	1.90	56.07	7.76	0.64
200	18.38	1.09	0.35	19.81	2.03	51.48	6.12	0.76
2000	30.40	—	—	5.17	0.61	63.83	—	—

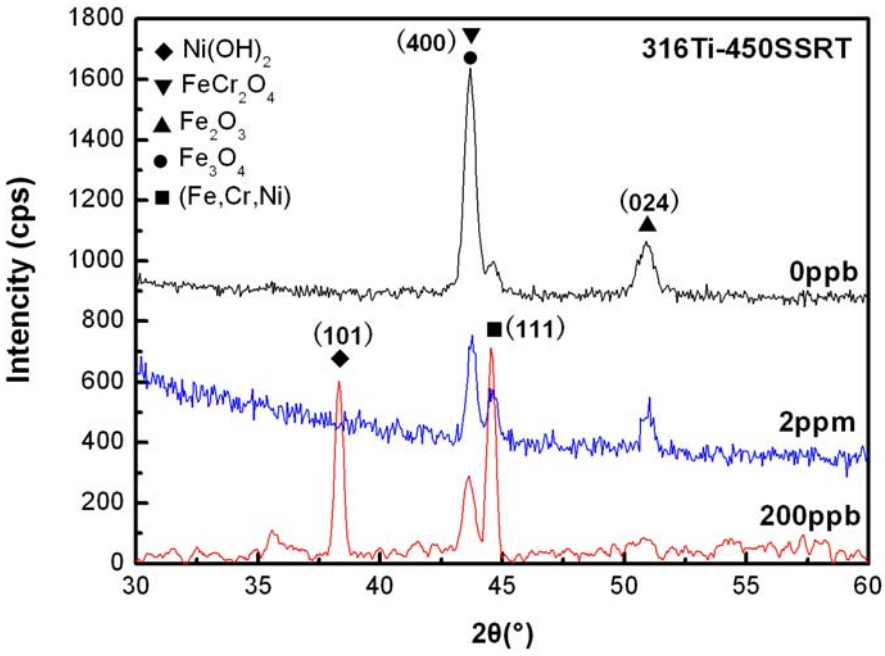

Figure 6. GIXRD pattern of 316Ti specimen tested in 450℃SCW

3.2 Test at **550℃**

The strain-stress curve of 316Ti in 550℃ SCW and Ar is shown in figure 7 and the relevant mechanical properties in table 4. In 550℃ Ar, the specimen undergoes elastic deformation at the beginning and experiences plastic deformation (together with strain strengthening) beyond the stress of 125 MPa. The stress declines suddenly after the peak level of 370 MPa, as the specimen undergoes necking and rupture simultaneously. In 550℃ SCW, the specimen shows the same deformation trend but apparently lower mechanical properties. In deaerated SCW, 316Ti shows severe SCC sensitivity with an I_g of 0.34. However, addition of dissolved oxygen into the SCW decreases the SCC sensitivity to a large extent. In SCW containing 200 ppb DO, the resulting Ig is only 0.08.

The fracture morphologies of 316Ti tested in 450 ℃ SCW and Ar are shown in figure 8. For the specimen tested in Ar, the whole fracture surface seems to exhibit ductile features. For the specimen tested in deaerated SCW, a brittle fracture surface prevails with a rock candy appearance, an indication of IGSCC. For the specimen tested in low DO SCW, the fracture surface is mainly composed of microvoids, evidence of ductile failure. For the specimen tested in high DO SCW, the fracture surface is a mixture of rock candy and microvoid features. Combining the strain-stress curvse with the fracture observations, 316Ti shows moderate SCC sensitivity in 550℃ SCW and addition of dissolved oxygen will greatly mitigate its SCC sensitivity.

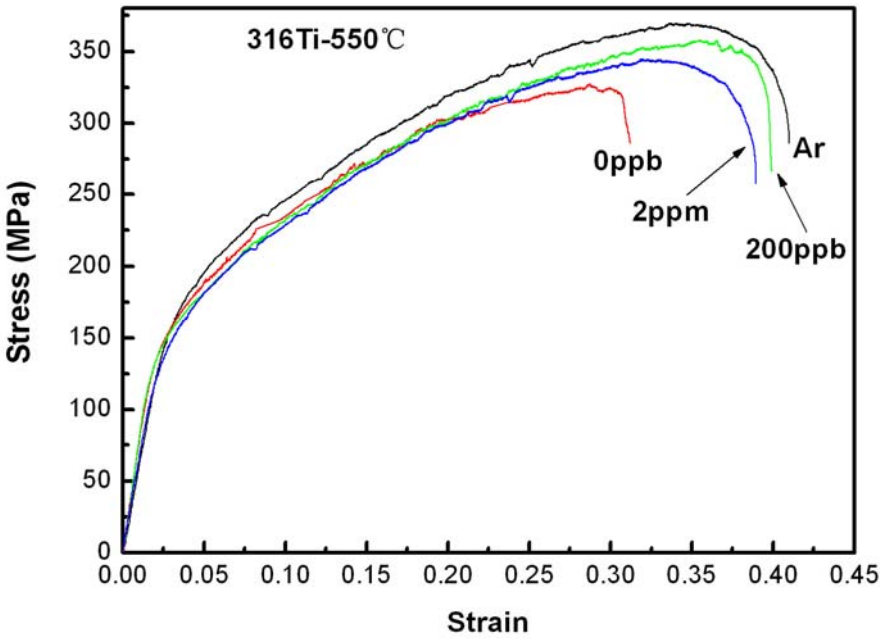

Figure 7. Strain-stress curves of 316Ti in 550 ℃ SCW and Ar

Table 4. Mechanical properties of 316Ti tested in 550 ℃ SCW and Ar

Dissolved oxygen（ppb）	Ultimate tensile strength（MPa）	Elongation rate（%）	Reduction Area（%）	Rupture energy（J）	I_g

Ar	370	41	21	10.8	—
0	327	31	32	7.11	0.34
200	358	40	18	9.99	0.08
2000	345	39	40	9.45	0.13

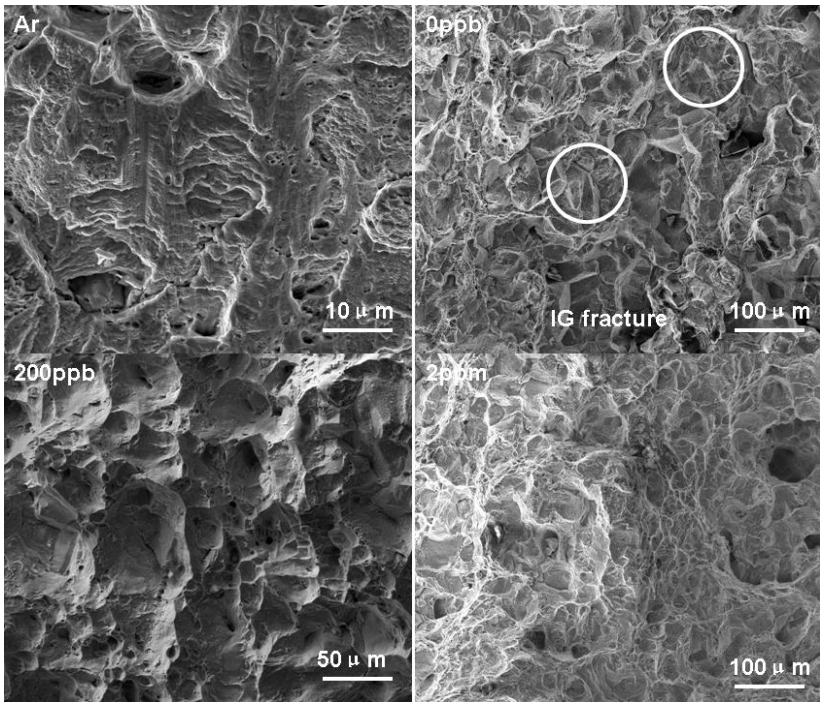

Figure 8. Fracture morphologies of 316Ti tested in 550℃ SCW and Ar

The gauge surface oxides of 316Ti tested in 550℃ SCW display similar morphologies but varied compositions. In deaerated SCW, the oxide scale is depleted in Cr compared with other two test conditions. The phase structures of the oxide scales are quite different for the specimens tested at various DO concentrations , In deaerated and low DO SCW, the peak of the matrix is prominent due to the rather thin oxide scale, and there is a high concentration of $Ni(OH)_2$. Addition of 200 ppb DO will induce a little Fe_2O_3 in the oxide scale. In high DO SCW, the oxide scale is mainly composed of $FeCr_2O_4$, Fe_3O_4 and Fe_2O_3.

Table 5. Gauge surface oxide composition of 316Ti tested in 550℃SCW (wt.%)

DO(ppb)	O	Si	Cr	Mn	Fe	Ni	Mo
0	25.96	1.18	12.21	3.17	55.17	1.74	0.57
200	18.27	1.86	26.31	3.95	44.92	4.69	—
2000	30.38	0.30	26.23	12.75	29.21	1.14	—

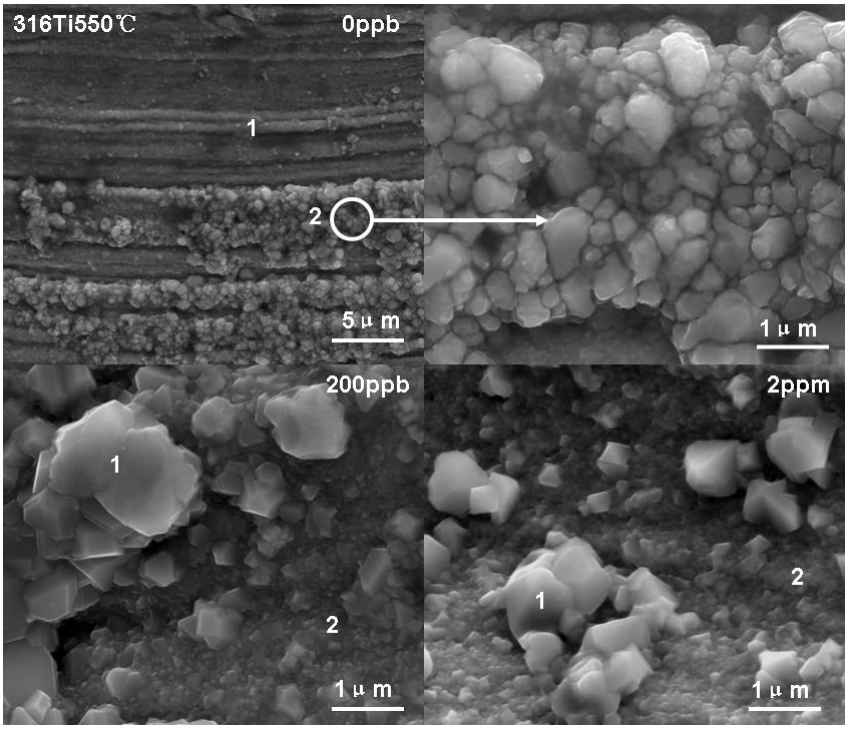

Figure 9. Gauge surface oxide morphology of 316Ti tested in 550 ℃ SCW

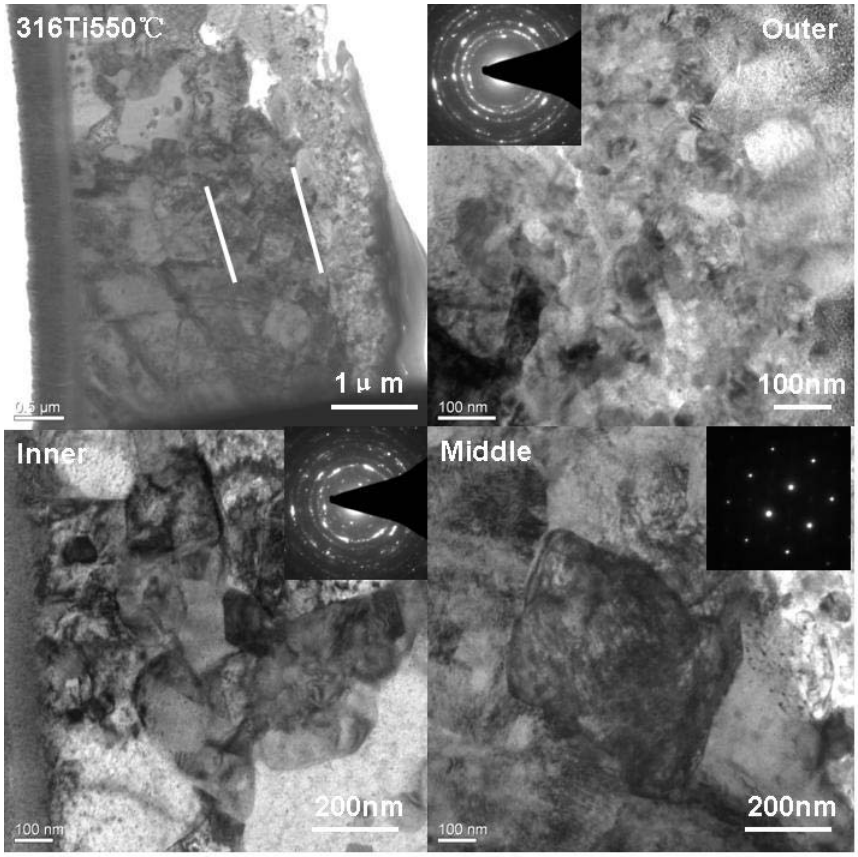

Figure 10. Gauge surface oxide image of 316Ti tested in 550 ℃ deaerated SCW

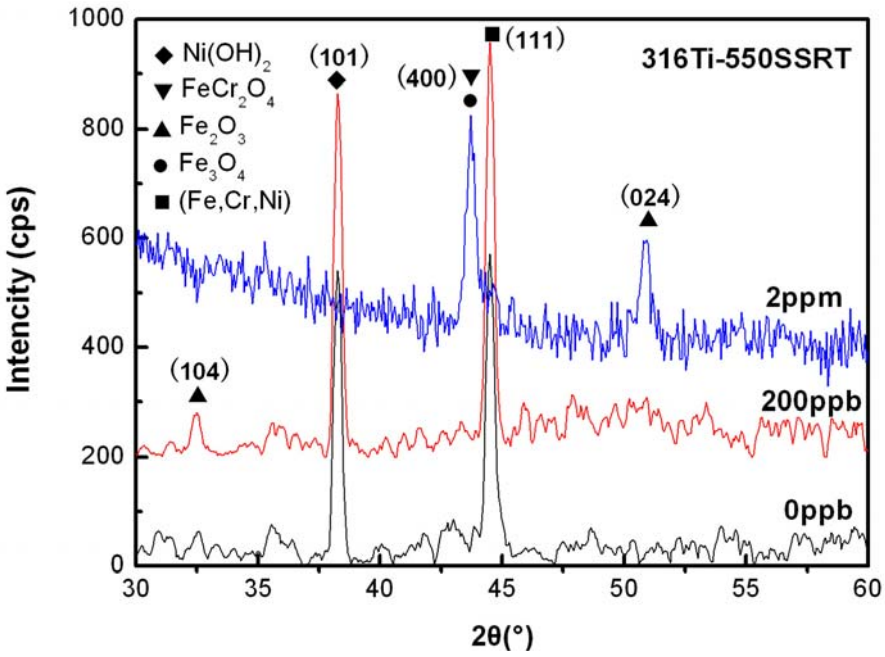

Figure 11. GIXRD pattern of 316Ti tested in 550 ℃ SCW

3.3 Test at **650℃**

The strain-stress curves of 316Ti in 650℃ SCW and Ar are shown in figure 12 and the relevant mechanical properties in table 6. Under all the conditions, the specimen undergoes the same deformation processes; elastic deformation at the beginning and plastic deformation (together with strain strengthening) beyond the stress of 110 MPa. The stress decline gradually after the peak level of 200 MPa, inducing a yield platform in the strain-stress curve. Since all the mechanical properties in SCW and Ar are similar, 316Ti shows little SCC sensitivity in 650℃ SCW.

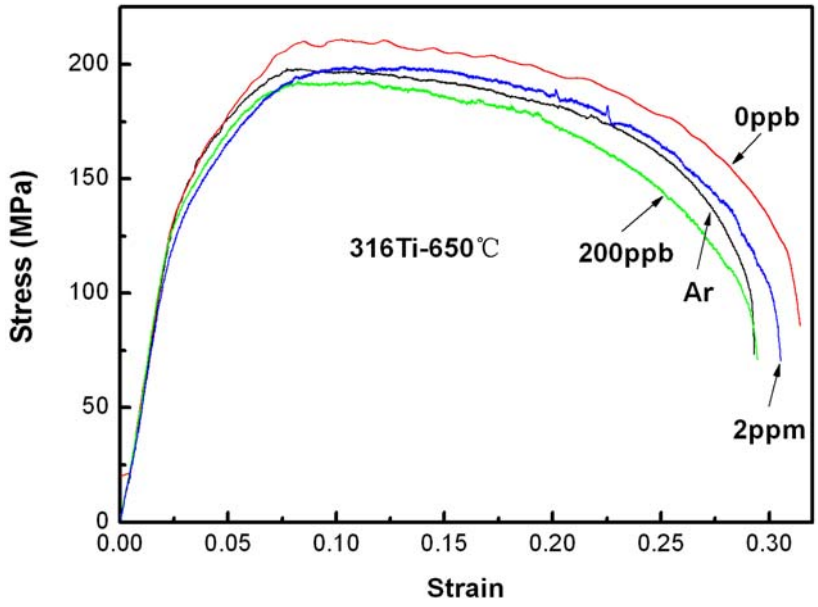

Figure 12. Strain-stress curves of 316Ti in 650 ℃ SCW and Ar

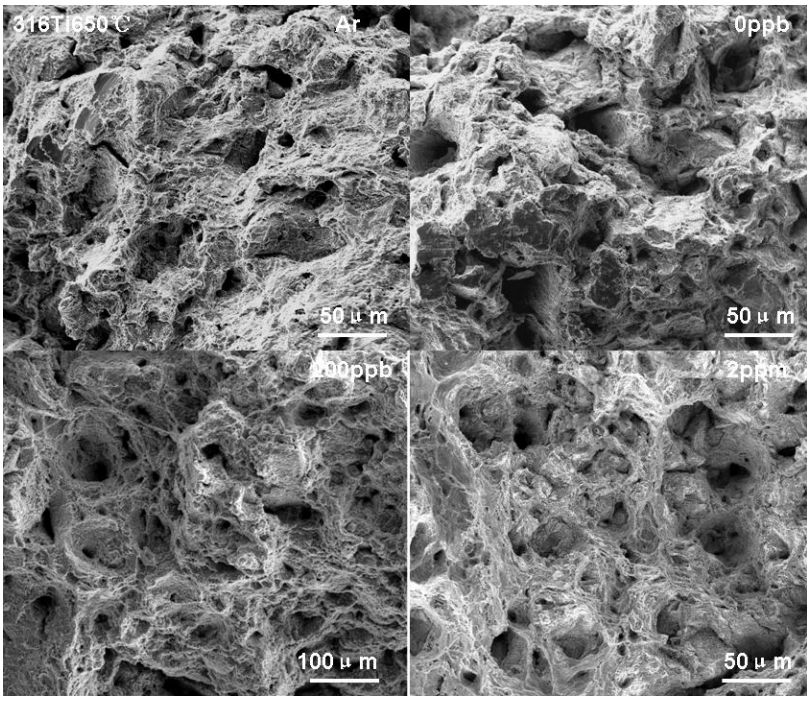

Figure 13. Fracture morphologies of 316Ti tested in 650℃ SCW and Ar

Table 6. Mechanical properties of 316Ti tested in 650 ℃ SCW and Ar

Dissolved oxygen（ppb）	Ultimate tensile strength（MPa）	Elongation rate（%）	Reduction Area（%）	Rupture energy（J）
Ar	198	29	55	4.41
0	211	31	57	4.95
200	193	29	59	4.23
2000	200	31	61	4.68

4. Conclusion

In this paper, 316Ti coupons were tested in SCW at 450−650 ℃ using Slow Strain Rate Test (SSRT). The SCC sensitivity index of this material was calculated based on the Stress-Strain curve and relevant mechanical data. The fracture morphologies and surface oxides were observed by SEM/EDS, XRD and TEM. The main conclusions are as follows:

1. 316Ti shows slight SCC sensitivity in 450 ℃ SCW and addition of dissolved oxygen will greatly increase its SCC sensitivity.

2. 316Ti shows moderate SCC sensitivity in 550 ℃ SCW and addition of dissolved oxygen will greatly mitigate its SCC sensitivity.

3. 316Ti shows little SCC sensitivity in 650 ℃ SCW due to annealing softening. The specimen displays a rather high elongation rate and reduction area.

Reference

[1] G.S. Was, S. Teysseyre. CHALLENGES AND RECENT PROGRESS IN CORROSION

AND STRESS COROSION CRACKING OF ALLOYS FOR SUPERCRITICAL WATER REACTOR CORE COMPONENTS. Proceedings of the 12th International Conference on Environmental Degradation of Materials in Nuclear Power System-Water Reactors, 2005.

[2] G. S. Was, P. Ampornrat, G. Gupta, et al. Corrosion and stress corrosion cracking in supercritical water. J. Nucl. Mater., 2007, 371: 176-201

[3] W Zheng, Gordon Gu, Dave Guzonas, et al. Assessment of corrosion and stress corrosion cracking results for SCWR development: Gaps and Needs, The 2nd Canada-China Joint Workshop on Supercritical Water-Cooled Reactors (CCSC-2010), 2010, Toronto, Ontario, Canada

[4] Y. Tsuchiya, F. Kano, N. Saito, A. Shioiri, S. Kasahara, K. Moriya, H. Takahashi. SCC and Irradiation Properties of Metals under Supercritical-water Cooled Power Reactor Conditions. GENES4/ANP2003, Paper 1096, Kyoto, Japan, September 2003

[5] S. Teysseyre, G.S. Was. Stress Corrosion Cracking of Austenitic Alloys in Supercritical Water. CORROSION, 2006, 62(12): 1100-1116

[6] R. Novotny, P. Haner, J. Siegl. Stress corrosion cracking susceptibility of austenitic stainless steels in supercritical water conditions. Journal of Nuclear Materials, 2011, 409: 117-123

[7] Y. Watanabe, H. Abe, Y. Diago and T. Nishida. Corrosion Resistance and Cracking Susceptibility of 316L Stainless Steel in Sulfuric Acid-Containing Supercritical Water. Corrosion2004, NACE International, New Orleans, TX, Paper 04493, 2004

[8] C. Bosch and D. Delafosse. Stress Corrosion Cracking of Ni-Based and Fe-Based Alloys in Supercritical Water. Corrosion2005, NACE International, Houston, TX, Paper 05396, 2005

[9] L. Fournier, D. Delafosse, C. Bosch, Th. Magnin. Stress Corrosion Cracking of Nickel Base Superalloys in Aerated Supercritical Water. Corrosion 2001, Paper No. 01361, NACE, Houston, TX, 2001

[10] R. Fujisawa, et al.. Cracking Susceptibility of Ni Base Alloys and 316 Stainless Steel in Less Oxidizing or Reducing SCW. Corrosion2005, NACE International, Houston, TX, Paper 05395, 2005

[11] Rongsheng Zhou, Elaine A. West, Zhijie Jiao, et al. Irradiation-assisted stress corrosion cracking of austenitic alloys in supercritical water. Journal of Nuclear Materials, 2009, 395: 11-22

[12] S. Teysseyre, Z. Jiao, E. West, et al. Effect of irradiation on stress corrosion cracking in supercritical water. Journal of Nuclear Materials, 2007, 371: 107–117

[13] E.A. West, G.S. Was. IGSCC of grain boundary engineered 316L and 690 in supercritical water. Journal of Nuclear Materials, 2009, 392: 264-271

[14] G. Gupta, P. Ampornrat, X. Ren, et al. Role of grain boundary engineering in the SCC behavior of ferritic–martensitic alloy HT-9. Journal of Nuclear Materials, 2007, 361: 160-173

[15] Pantip Ampornrat, Gaurav Gupta, Gary S. Was. Tensile and stress corrosion cracking behavior of ferritic-martensitic steels in supercritical water. Journal of Nuclear Materials, 2009, 395: 30–36

[16] N. Muthukumar, J.H. Lee, A. Kimura. SCC behavior of austenitic and martensitic steels in supercritical pressurized water. Journal of Nuclear Materials, 2011, 417: 1221-1224

ISSCWR7-2093

The Stress Corrosion Cracking (SCC) Behavior of Type 310S Stainless Steel in Supercritical Water (SCW)

XIONG Ru, ZHANG Qiang, ZHAO Yu-xiang, TANG Rui, XIAO Zejun

Nuclear Power Institute of China (NPIC), Reactor Fuel and Materials Key Laboratory, Chengdu, 610041, China

+86 28 85903839, littlexiongru@126.com

Abstract

Abstract

Stress corrosion cracking（SCC） is an vital behavior of nuclear materials for PWR, BWR as well as SCWR. Study the SCC behavior of 310S stainless steel is very necessary because it is the prosperous material and selected as fuel cladding as well as internal structural material for SCWR for its neutron economy and good comprehensive properties. Two types of experiments including U-shape tests and SSRT(Slow Strain Rate Test) tests have been done to reveal the sensitivity of SCC for 310S in supercritical water in this paper. The results of U-shape tests in water at 290℃, 380℃, 550℃, 650℃ indicates that the time-to-crack of 310S is longer at least than 2000h, the oxide film of 310S is consists of two layers, the inner layer composed of Cr-contain oxides is compact and have resistance to SCC, while the outer layer is mainly iron oxides and its valence will be affected by temperature, when temperature is 380℃, the large particles of Fe_3O_4 in the loose outer layer then will drop not only for volume expansion coefficient difference between it and inner layer, but also for the stress during the formation of film. Additional, the existing of Nb will lead to the film drops or pittings which would accelerate or be original of SCC in the local surface film both at 380℃ and 550℃, especially in the latter it was the sole reason now. There is no pitting after 650℃ immersion, but the brittlement tendency occurred, the micro-structures such as second phase of carbide changed and changed properties such as the hardness, which means the increase of potential SCC sensitivity. The SSRT results at 550℃, 650℃ indicates that with the increasing of the temperature, the intensity of SCC increased, the surface cracks increased, the fracture morphornogy turns from ductility to fragility with thick oxides, this is coinsicide with the result at 650℃ in U-shape test. Engineering design should pay attention to such ageing phenomenon and degradation avenues at temperature up to 650℃.

1. Introduction

The purpose of this research was to assess the behavior of UNSS310S00 (Type 310S) at surface temperatures of fuel elements, which are utilized in supercritical water reactor environments (SCWR). This alloy is more attractive at the higher surface temperatures of the SCWR than the lower alloy stainless steels used in light water reactors (LWR). The surface temperatures of SCWRs are higher obviously than that in LWRs. In the design of SCWR by NPIC(nuclear power institute of China) which is named CSR1000 with 1000MWt power, the maxium outside surface temperature of fuel cladding is determined now to be 650℃ with the corresponding outlet temperature being about 500 ℃, choosing materials for the SCWR applications should recognize that at such environment with high temperatures water of 25MPa, metallurgical creep would be the main mode of failure, SCC then follows closely. This present research considers two main modes of failure: (a) creep and (b) stress corrosion cracking.

Other modes of damage such as surface oxidation and pitting are included, where useful, in the studies.

In SCWRs, the higher temperatures and pressures together with the change of designs, compared with LWRs accelerate the degradation of components and especially accelerate corrosion including SCC. These conditions also accelerate creep deformation.

In general, Alloy 310S is an important engineering material for a variety of applications. Now, it is a popular candidate for fuel cladding of SCWRs due to its good corrosion resistance and good mechanical properties. Alloy 310Shas been utilized since the 1940s in the fossil power industry, has been used as fuel cladding material for AGRs (advanced gas reactor), because the higher temperatures above 400°C in the AGRs have exceeded the application limits for both zirconium alloys and Alloy 316 which once were used in fast reactors. 310S has been approved by the ASME Boiler and Pressure Vessel Committee. Its experience in fossil power industry and nuclear power industry provides good bases for the selection of Alloy 310S as an SCWR material.

In this research experiments have been conducted to assess the sensitivity of Alloy 310S for SCC in deaerated sub-critical water, pesudo-critical water and supercritical water at four temperatures respectively: 290℃、380℃、550℃、and 650℃. The experimental conditions (temperature, time and testing methods) as well as the microstsructures of Alloy 310S were then analyzed to assess the influence to the SCC behavior.

2. EXPERIMENTAL PROCEDURES

2.1 Material and Specimen

The chemical composition of the Alloy 310S, which is used in this study, is shown in Table 1 and is compared with ASME SA240 and GB5310S-2009. “S” means that the C concentration in Type 310 stainless steel is less than 0.08 wt%. Because there is N and Nb in this steel, it was also named HR3C commercially（20Cr-25Ni-Nb-N, ASMECC2115, or SA-213TP310SHCNb） Alloy 310S has a lower Ni content or lower thermal neutron cross section relative to the high nickel alloys. The wrought material was annealed at 1150℃-1200℃ for 20min-25min and quenched in water.

The microstructure of specimens is characterized using optical microscopy(OM), as shown in Figure 1. Darker phases are austenite with equilateral grains; brighter phases are carbides containing Nb. Most of carbides are formed inside the austenite grains, with few formed at grain boundaries.

U-bend specimens for SCC testing were utilized; their dimensions are 75x15x2mm. They were cut and mechanically and ground with 2000 grit silicon carbide (SiC) emery paper. The surfaces of the specimens were then electrochemically polished in oxalic acid ($H_2C_2O_4$) , ultrasonically cleaned in acetone (CH_3COCH_3), and washed with deionized water before starting the corrosion experiments. The U-bend was fabricated with a R20 tool. A ceramic electrical isolation material was placed between the coupon and fastening holders.

The dimensions of the slow strain rate testing (SSRT) specimen is 58x16x2mm as show in Figure 2. Gauge dimensions of 15x3x2mm were cut, and sections were mechanically ground by 800 and 1200 grit SiC emery paper. The surfaces were then polished with diamond paste to a mirror finish(1μm); the surfaces were then cleaned in acetone(CH_3COCH_3) for 10 min and washed with deionized water before being dried for 80℃×24h.

Table 1. Chemical composition（wt.%）of Alloy 310S.

Element	C	Si	Mn	P	S	Cr	Ni	Nb	N	Fe
Standard	0.04-0.10	≤1.00	≤2.00	≤0.03	≤0.03	24.0-26.0	19.0-22.0	0.20-0.60	0.15-0.25	-
310S	0.07	0.2	0.4	0.016	0.008	24.8	19.7	0.40	0.18	Bal.

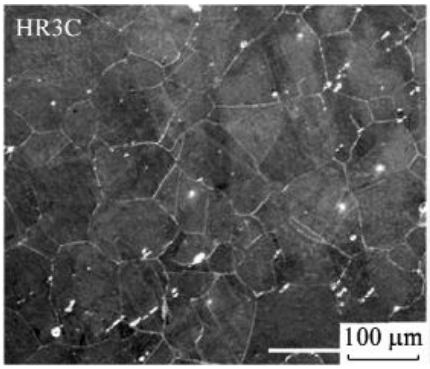

Figure 1. Microstructure of experimental specimen.

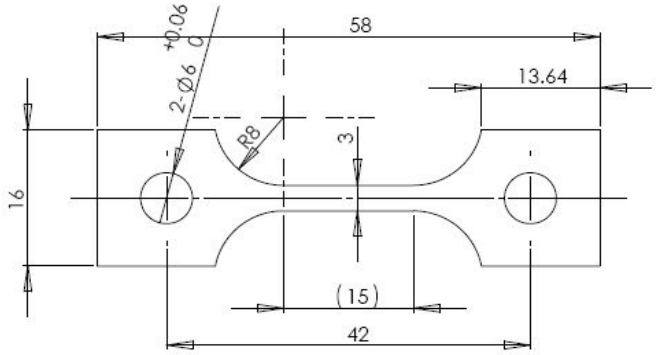

Figure 2. Schematic view of SSRT specimen (dimensions in mm)

2.2 Experimental Methods

Two types of testing were utilized: (a) constant strain testing with U-bend specimens were utilized for initiation considerations and time-to-cracking measurements; (b) SSRT was used for the integration of initition, propagation and fracture. Test parameters are given in Table 2. Since water chemistry, especially the dissolved oxygen concentration (DO), influences substaintially the corrosion potential and subsquently the SCC behavior of stainless steel, the DO in the highly purified deionized water was controlled to less than 20ppb by utilizing pure N_2.

The system used with U-bend specimen is shown in Figure3, with a small loop for dynamic supercritical water. This system consists of an autoclave and water chemistry system; the DO concentration, electrical conductivity, and pH were continuously monitored on line. A system integrated with autoclaves for the SSRT is shown in Figure 4.

After testing, the morphology and microstructure of the specimens were characterized with optical microscopy (OM), scanning electron microscopy (SEM), transmission electron microscopy (TEM), X-ray photoelectron spectroscopy (XPS) , electron probe micro analyzer (EPMA), and energy-dispersive x-ray spectroscopy(EDS).

Table 2. Methods and parameters in stress corrosion experiments

Methods	Temperature（℃）	Pressure（MPa）	Parameter	Water chemistry
Constant strain test	290	More than saturated pressure	2000h total，400h each cycle	pH: 6.5~7.5；electric conductivity ≤0.2 μs/cm；DO≤10ppb
	380	25MPa		
	550	25MPa		
	650	25MPa		
SSRT	550	25MPa	Strain rate: $10^{-6/s}$	
	650	25MPa		

Figure 3. Test equipment for stress corrosion cracking with U-bend specimens

Figure 4. Test loop for SSRT in dynamic SCW

3. RESULTS AND DISCUSSIONS

3.1 Results of U-bend Tests

3.1.1 Results

All the U-bend specimens exhibited no cracks after immersion in water at 290℃, 380℃, 550℃, 650℃ for 2000h as shown in Table 3 and also shown in Figure 5. Such results indicate that the time-to-crack of Alloy 310S is longer at least than 2000h under these conditions. The influence of temperature on SCC could not be determined, even at 650°C, from such experiments periods. However, these temperatures influence the surface oxide films with dark and thick layers at 290℃, 380℃, dark and a thin layer at 550℃, and a brown and thin layer at 650℃. These results indicate significant changes in the nature of the oxidation. These effects should be evaluated in subsequent experiments.

Table 3. SCC test results with U-bend specimen

Temperature（℃）	Pressure(MPa)	Total time（h）	Conditions after cycling
290	15MPa	2000	No cracking
380	25MPa	2000	No cracking
550	25MPa	2000	No cracking
650	25MPa	2000	No cracking

Figure 5. Surface morphology of U-bend specimen after exposure at 290℃, 380℃, 550℃, 650℃ respectively for 2000h (from left to right)

3.1.2 Oxide Layer

The structures of the oxide layers of the corroded specimens are characterized by OM and TEM shown in Fig.6, the oxides on all the samples exhibited a dual-layer structure with the thicknesses less than 2μm. The inner oxide layer on all samples was compact without evident pores after SCW exposures; while the outer layers were not continuous. The oxide scale during the exposure time remains thin. The interface between the inner oxide layers and the base material is not so sharp as the interface between the outer and inner oxide layers. The increased mixing that occurred at the interface may contribute to stronger adhesion between the inner oxide layer and matrix and thus minimize extensive oxide spallation which could produce pittings or would provide faciliate for SCC. The material substrate retains a single austenitic phase. The inner oxide layer exhibits a multi-crystaline structure; the outer oxide layer is a single phase which is mainly magnetite (Fe_3O_4) at 380℃ and 550℃, mainly hematite (Fe_2O_3) at 650℃.

XPS with Ar ion sputter were used to evaluate the valence of element as shown in Figure 7, the oxides were also determined by XRD jointly. The valence of Cr, Fe, Ni were mainly existing as +3(Cr_2O_3), +2 and +3(Fe_3O_4), +2(Ni), after sputtered for about 30min to 40min, it turned from cation state in surface film to the atomic state in the substrate of Alloy 310S, the multi-crystal structures in the inner oxide layer is a mixture of magnetite (Fe_3O_4)/ Cr_2O_3 and spinel($FeCr_2O_4$). Other oxides such as NiO exist in small amounts because Ni is more passive than Cr and Fe. Cr is the most active both in diffusivity and thermodynamically and has the highest diffusion coefficient in this Alloy 310S. The main mechanism of corrosion behavior of Alloy 310S presents to be oxidation, Cr could first form Cr-rich oxides such as Cr_2O_3 and $FeCr_2O_4$ in Alloy 310S, these Cr oxides will improve not only the oxidation resistance but also the resistance to oxide exfoliation; this step will then improve the SCC resistance. With increasing temperature, the Cr flux will increase via lattice and grain boundaries and will maintain a stable and integrated surface film to improve the SCC resistance.

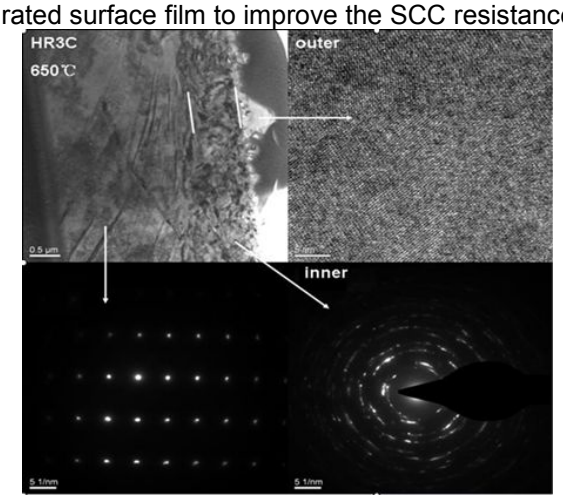

Figure 6. TEM analysis of 310S after exposed in water at 650℃

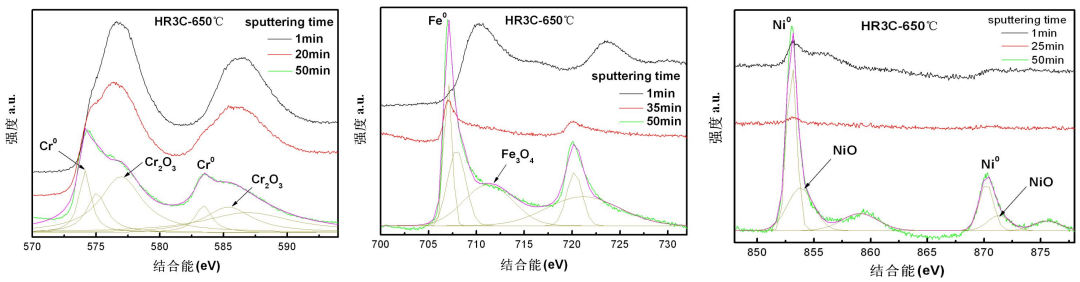

Figure 7. Valence analysis of Cr, Fe, Ni by XPS from surface film to matrix of 310S after exposed in SCW at 550℃

3.2.3 Pitting in Surface Layer

No obvious extensive oxide spallation were observed on these specimens, while some pittings was observed on the surfaces after exposures in SCW at 380℃ and 550℃ as shown in Figure 8, with no pittings at 650℃. The number of pittings decreased from 380 ℃ to 550℃, the size of the pittings increased with the increasing exposure time both at 380 ℃ and 550℃, the maxium depth of the pittings is less than 1μm. This phenomenon of pittings is generally caused by stress in the oxide scale, such stress generally including 3 types, in addition to loading stress. there are usually two types of stresses in oxide scales: growth stress (also called “intrinsic stress”), which develops during the oxidation process, and thermal stress, which develops during cooling due to the different thermal expansions between the oxide scale and the metal substrate.

According to the oxides analysis in the previous chapter, this former stress is likely to be negligible because the substrate has the same face centered cubic (FCC) structure and a similar oxide/metal volume ratio (Pilling-Bedworth ratio) as that of spinel and magnetite as well as hematite.

The thermal stress becomes the critical factor, which produces pitting in the surface oxides. This stress is produced by the significant difference of the thermal expansion coefficients between magnetite(Fe_3O_4) and either spinel($FeCr_2O_4$), or Cr_2O_3 and substrate; these differences lead to a strain accumulation at these interfaces. The spinel and substrate or Cr_2O_3 have similar thermal expansion coefficients, which is about 2.0×10^{-5}/K; these are much less than that of magnetite (7.0×10^{-5}/K) at temperature to 550℃. Then, the outer layer with magnetite formed in SCW at 380℃ and 550℃ is prone to produce pitting with the spallation of Fe_3O_4. The outer layer mianly with hematite (Fe_2O_3) in SCW at 650℃ does not easily sustain pitting because of the smaller mismatch resulting from the smaller thermal expansion; also the smaller hematite grain size may alleviate the increase of growth stress and thus the spallation resistance. The EDS analysis also shows that the reason for the pitting in 380℃ and 550℃ SCW lies in the presence of Nb which produces the same mismatch of expansion coefficient and galvanic-corrosion between the Nb-rich phase and the substrate. Such results suggest that the pitting could be mitigated by preventing the formation of magnetite on the specimen surface or produce alloy chemistry without Nb precipitations. Attention should be given to pitting, since it could produce stress corrosion cracks.

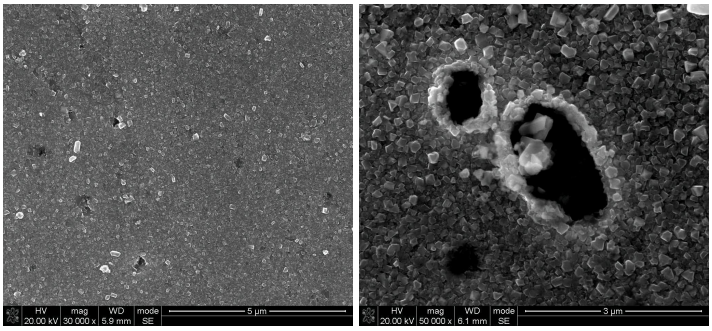

a 380℃×400h b 380℃×1200h

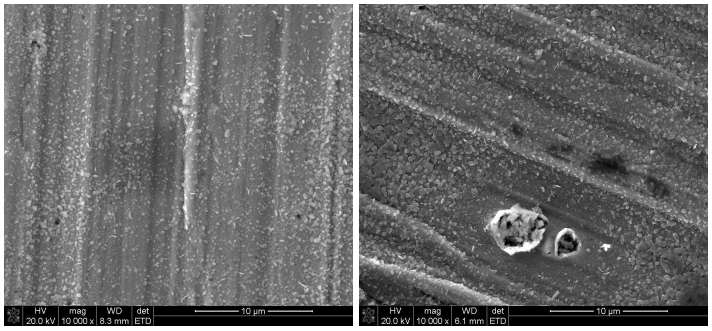

c 550℃×600h d 550℃×1800h

Figure 8. Oxide film morphology with pitting after exposure in SCW at 380℃and 550℃

3.2.4 Microsture

Figure 9 shows the microstructure of the U-bend specimen after exposure under constant strain by TEM. Here, slip occurred under tensile stress(Fig.9a); higher density dislocations formed closer to U-bend area(Fig.9b). Dislocations accumulated inside bundles or formed into walls. Oxide-filled corrosion tunnels developed along the bundles(Fig.9c), while some dislocations formed into dislocation cells(Fig.9d). Also, as shown in Figure 6, when there was a stacking fault or slip band with the mouth open to the surface, it was oxidized to fine oxides, become passive and avoided the new metal exposing to the environment again, thereby stopped the typical SCC process. The main mechanism for SCC of Alloy 310S should related to the corrosion resistance of oxidation film in U-bend specimens.

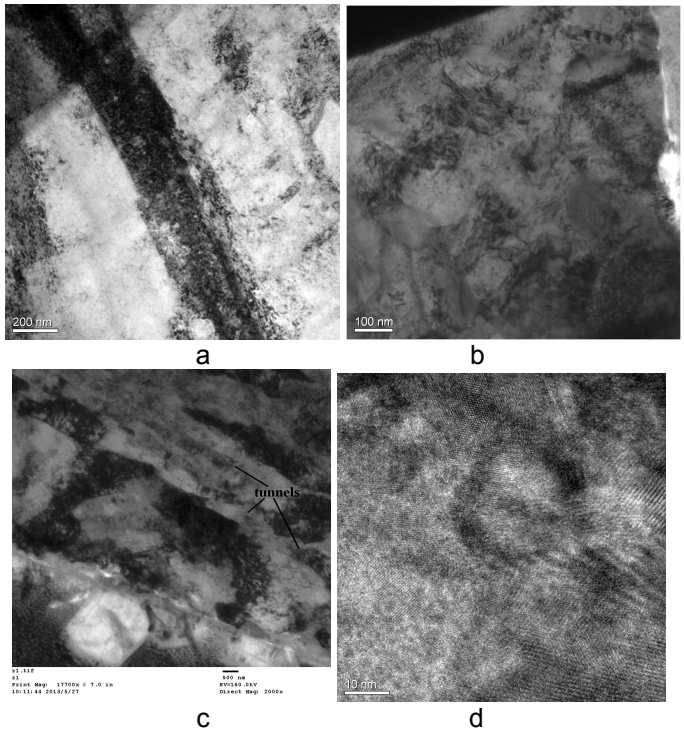

a b

c d

Figure 9. TEM images of specimen after immersion in SCW

3.2.5 Structure Stability

Figure 10 shows the change of hardness of specimens before and after exposure in SCW at 380℃, 550℃ and 650℃ for 2000h and 3000h. The hardness of the specimen after exposure at 650℃ changed more than the other two temperatures. As it has been well known, SCC increases generally with increasing hardness. This mechanical change

indicates that there is some microstructural change in the specimen after long time at high temperature in SCW. Such a change is characterized by OM as show in Figure 11; the size of grain boundaries seems broader and the extent of the second phase seems increased when exposed at 650℃ for a long time.

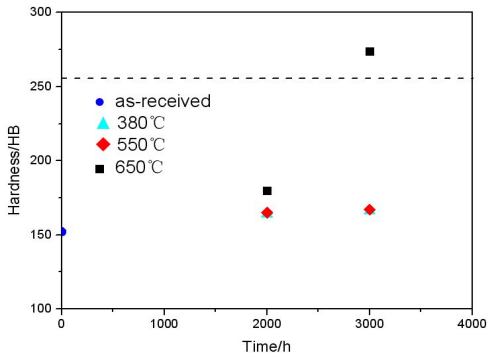

Figure 10. Hardness vs. time in corrosion test at various temperatures

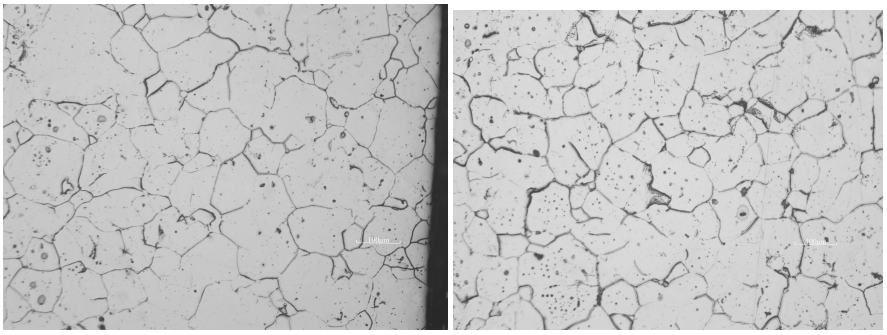

a-550℃ b-650℃

Figure 11. The micro-structure of 310S after exposed in supercritical water at 550℃ and 650℃

Figure 12 shows TEM images of second phases such as NbC precipitates in grains or along grain boundaries. The interaction of the second phase with dislocations will increase the resistance to slip and then improve the mechanical strength or hardness of the metal. However, the interface between such precipitates and substrate would also provide sources of cracks when the loading stresses increases If such interfaces are near the surface they will promote SCC. Figure 13 shows the planar distributions of Fe, Cr, Ni, and Nb. Here the distribution of Nb is not uniform, and mainly forms precipitates， such precipitates could promote pitting easily when it close to the surface or facilitate SCC directly.

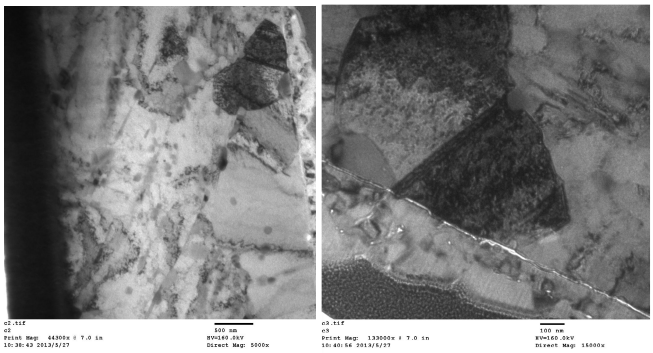

Figure 12. TEM images of 310S SS after immersion in SCW

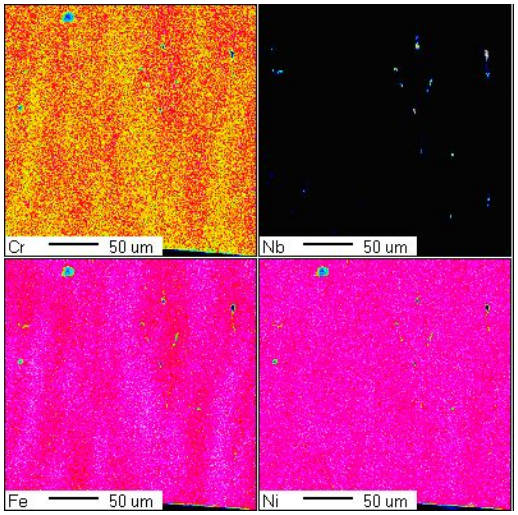

Figure 13. Planar distribution of Fe, Cr, Ni, Nb of 310S

3.2 SSRT Results

3.2.1 Strain-stress Curves

To illustrate the overall behavior of SCC, SSRT was performed in Ar, air, and SCW at comparable temperatures. Figure 14 shows the stress-strain curves of 310S specimens in SCW and in Ar at 550℃ and 650℃. These results together with the results of the tensile data of 310S specimens in SCW and air at 550℃ and 650℃ show that, with the increase of temperature, the decrease in maximum stress of SSRT in SCW is comparable to that of tensile testa in air and Ar, i.e. softened at elevated temperature. With the increase of temperature, the elongation ratio of 310S in SCW decreased, which presents the opposite tendency in air, i.e. embrittlement at elevated temperature. Such embrittlement coincides with the hardness tendency in U-bend experiments. i.e. the hardness or embrittlement increases the potential sensitivity of SCC. These results indicate that the sensitivity of 310S specimen to SCC increases from 550℃ to 650℃. Such susceptibility of 310S was calculated and characterized by elongation, elongation ratio and profile contraction percentage.

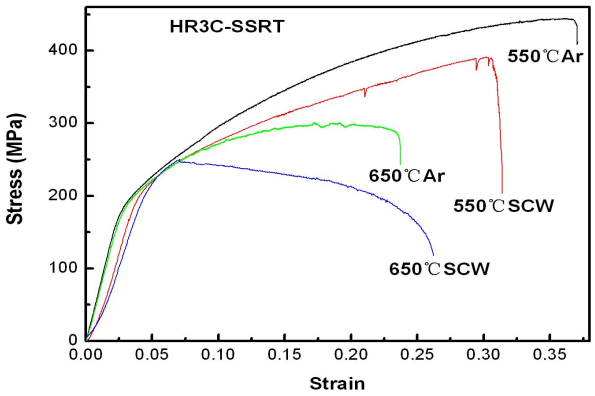

Figure 14. Stress vs. strain of alloy 310S(HR3C) for temperatures and two environments.

3.2.2 Fracture Morphologies

The fracture morphologies were examined by SEM as shown in Figure 15 to Figure 16. Figure 15 is the side surface of the SSRT specimen in SCW at 550℃ and 650℃; no side cracks were observed at 550℃, while but there were plenty of side cracks at 650℃, and the micro-cracks occurred not only on the side surface but also inside of cross-section after

SSRT at 650℃. Such side cracks occurred also in Ar and air at 650℃. Such side cracks could be SCC or creep cracks, because creep damage was found in the previous creep project by authors in air at 800℃ after about 500h with similar side cracks, these results suggests the side-cracks, which occurred in Figure 15b, were caused by creep deformation probably.

The fracture morphology of 310S after SSRT at 550℃ presents typical dimples as shown in Figure 16a; this observation indicates that there is no stress corrosion cracking after SSRT. The 310S specimen fractured with ductility is similar to that of a tensile specimen in air. However, in Figure 16b the fracture morphology presents shallower and less dimples with obvious oxides; between dimples there is some inter-granular (IG) stress corrosion cracking, with almost no faceting which indicates trans-granular (TG) type of cracks. The IG cracks were covered by oxide films, indicating that SCC is a corrosion process during the machanical process. In addition, the IG cracks is more obvious on the site of the surface corner which relates to higher stress or on the location of the interface between Nb carbides and the substrate.

location of the interface between Nb carbides and the substrate.

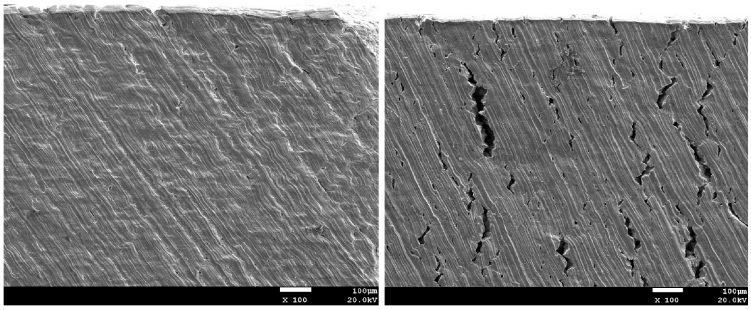

a-550℃ b-650℃

Figure 15. Side surface after SSRT at 550℃ and 650℃

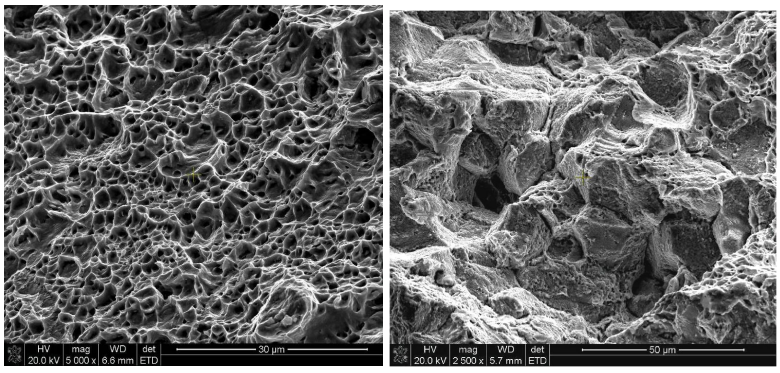

a-550℃ b-650℃

Figure 16. Fracture morphology of 310S after SSRT at 550℃ and 650℃

4. CONCLUSIONS

(1) Two kinds of tests were performed: U-bends and SSRT.
(2) U-bend specimens exhibited no SCC in 2000h after exposure in SCW at 290℃, 380℃, 550℃ and 650℃.
(3) The oxide film of U-bend specimens after testing consists of two layers; the inner layer is composed of Cr-containing oxides and is compact and resists SCC up to 650°C. Pitting occurs

at 380℃ and 550℃, the drop of Fe_3O_4 in the loose outer layer is the reason for the pitting at 380℃, while the existing of Nb is the main reason for the pitting at 550℃. There was no pitting at 650℃;, but the hardness increased with the change of micro-structures, which suggests the potential increase of susceptibility to SCC.
(4) With the increase of temperature from 550℃ to 650℃ in the SSRT, the sensitivity of SCC for 310S increased with decreasing of tensile elongation. The fracture characteristics changed from dimples at 550℃ to IG SCC at 650℃ indicates Alloy 310S has some SCC sensitivity in SCW at 650℃.

5. ACKNOWLEDGMENTS

The authors appreciate the financial support from the project “Technology Research and Development for SCWR (First Stage)” funded by State Science, Technology and Industry for National Defence. We appreciate also the project “Applicational Technology Research of Fuel Cladding Material for SCWR NPP” funded by Science & Technology Department of Sichuan Province.

References

1. Ru X， Staehle R W. Historical Experience Providing Bases for Predicting Corrosion and Stress Corrosion in Emerging Supercritical Water Nuclear Technology: Part 1-review [J]. Corrosion, 2013, 69(03): 211-229.

2. Ru X， Staehle R W. Historical Experience Providing Bases for Predicting Corrosion and Stress Corrosion in Emerging Supercritical Water Nuclear Technology-part 2: Review [J]. Corrosion, 2013, 69(04): 319-334.

3. Xiong Ru，Staehle R W. Historical experience providing bases for predicting corrosion and stress corrosion in emerging supercritical water nuclear technology：part 3-Review[J]. Corrosion, 2013, 69(05): 423-447.

4. Ru Xiong，Yingjie Qiao and Guiliang Liu, Stress Corrosion Cracking(SCC) of Nickel-base Weld Metals in PWR Primary Water[J]. Materials Science Forum, Vols. 747-748(2013) pp723-732.

5. G.S. Was and T.R. Allen, “Time, temperature, and dissolved oxygen dependence of oxidation of austenitic and ferritic-martensitic alloys in supercritical water,” Proceedings of ICAPP ‘05. Seoul, Korea, May 15-19, 2005, Paper 5690.

6. G.S. Was, S. Teysseyre, and Z. Jiao, “Corrosion of Austenitic Alloys in Supercritical Water,” Corrosion, Vol. 62, No. 11, November 2006, p. 989-1005.

7. P.L. Andresen, “Emerging Issues and Fundamental Processes in Environmental Cracking in Hot Water”, Proc. Research Topical Symposium on Environmental Cracking, Corrosion/07, NACE, 2007.

8. R.W. Staehle, “Serious Concerns and Actions for Mitigating Future Degradation in Modern Steam Generators,” Proceedings of the 5th CNS International Steam Generator Conference, Canadian Nuclear Society, Toronto, Ontario, Canada, November 26-29, 2006.

The 7th International Symposium on Supercritical Water-Cooled Reactors
ISSCWR-7
15-18 March 2015, Helsinki, Finland

ISSCWR7-#2095

SPECIFICS OF HEAT TRANSFER TO SUPERCRITICAL WATER FLOWING UPWARD IN ANNULAR CHANNEL AND 3-ROD BUNDLE

V.G. Razumovskiy, Eu.N. Pis'mennyi, K. Sidawi*, I.L. Pioro*, E.M. Maevskiy, and A.Eu. Koloskov

National Technological University of Ukraine "KPI",
Thermal-Power Engineering Department, Prospect Peremogy, 37, Kyiv 03056, Ukraine
Tel.: (044) 236-1034; Fax: (044) 241-7587; E-mail: vgrazum@yandex.ru

** Faculty of Energy Systems and Nuclear Sciences*
University of Ontario Institute of Technology
2000 Simcoe Street North Oshawa, Ontario L1H 7K4 Canada
Phone: 905-721-8668 ext. 2880 Fax: 905-721-3046, E-mail: igor.pioro@uoit.ca

Abstract

SuperCritical Water-cooled Reactor (SCWR) is one of the six Generation-IV concepts under development worldwide. SCWR concept is considered as the conventional way for increasing thermal efficiency of water-cooled Nuclear Power Plants (NPPs) as it was done in SuperCritical-Pressure (SCP) coal-fired power plants more than 50 years ago. Major advantages of an SCW NPP is high thermal efficiencies and proven in power industry for more than 50 years SCP Rankine "steam"-turbine cycle with the corresponding equipment and layout. However, the major problem in an SCWR design is reliability of in-core materials at SCPs, high heat fluxes and neutron fluxes, aggressive reactor coolant – SCW, and unknown heat-transfer characteristics of SCW-cooled bundles. In addition, in comparison with other five Generation-IV nuclear-reactor concepts no one SCWR has been tested as an experimental, transport or any other kind prototype reactor.

There have been relatively few publications detailing heat transfer to SCW flowing through a bundle geometry or just through an annular channel with a single heated rod, as compared to SCW heat transfer in bare tubes. Therefore, in the present paper, results of heat transfer to SCW flowing upward in an annular channel with a heated rod equipped with 4 helical ribs and a 3-rod bundle (rods are also equipped with 4 helical ribs) are discussed. The experimental results contain bulk-fluid-temperature, wall-temperature and heat-transfer-coefficient profiles along the heated length (485 mm) of the mentioned above flow geometries. The data resulted from the study could be applicable as a reference estimation of heat transfer in future fuel-bundle designs.

1. Introduction

SuperCritical-Water-cooled-Reactor (SCWR) concepts aim to increase thermal efficiency by operating the primary-side coolant at SuperCritical Pressures (SCPs), i.e., a coolant pressure of about 25 MPa, inlet temperatures between 300 − 350°C, and outlet temperatures between 550 − 625°C [1-6]. Since the

pseudocritical point[1] of water lies within the operating temperature range ($T_{pc@25MPa}$ = 384.9°C), significant changes occur in thermophysical properties of water (and thus, heat-transfer regimes) along the heated length [6-9]. SuperCritical Water (SCW) heated to temperatures above the pseudocritical temperature is considered to be in a "gas-like" state; whereas, SCW at temperatures below the pseudocritical point is considered to be in a "liquid-like" state, as shown in Figures 1 and 2.

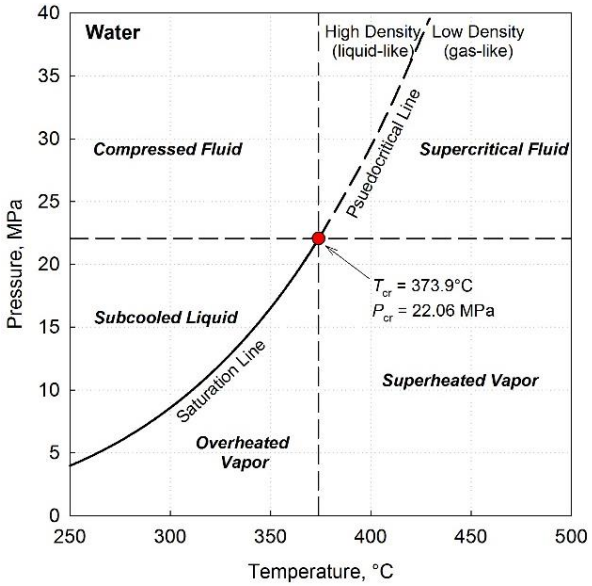

Figure 1. *P-T* diagram of water.

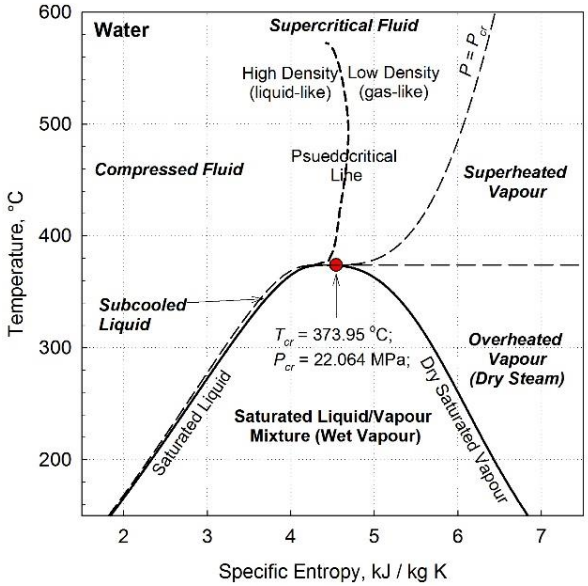

Figure 2. *T-s* diagram of water.

The vast majority of publications have been dedicated to heat transfer in bare tubes cooled with SCW [6, 10-13]. Very few publications are related to heat transfer in other flow geometries, such as annular channels with a single heated rod [14-16] and bundles [17-19], especially, cooled with SCW [20-25]. Due to that more experiments in various bundle geometries cooled with SCW as the primary choice and other modelling fluids (carbon dioxide, refrigerants) as the secondary choice are urgently required. Also, experiments in annular channels with a single heated rod can be of interest as a simplified model of a bundle geometry.

Therefore, the current paper is our first step towards estimation of various phenomena and heat-transfer characteristics in an annular channel with a heated rod equipped with 4 helical ribs and a 3-rod bundle (rods are also equipped with 4 helical ribs). This work is based on our previous studies published in the following papers: [12, 13, 22-24]. All experiments have been performed in a SCW loop at the National Technical University of Ukraine "Kiev Polytechnic Institute".

2. Supercritical-Water Test Facility

2.1 SCW Experimental Setup

The SCW experimental setup is an "open" stainless-steel loop operating at pressures up to 28 MPa and at temperatures up to 700°C. Chemically desalinated water (pH = 7.5 and an average hardness of 0.2-μg-eqv./kg) was used as a coolant. Test sections were installed vertically with an upward flow of SCW and were directly heated with a 90-kW AC power supply, as shown in Figure 3.

[1] The pseudocritical point is a point at a supercritical pressure ($P > P_{cr}$), and at a temperature ($T > T_{cr}$) corresponding to the maximum value of specific heat at that particular pressure [6-9].

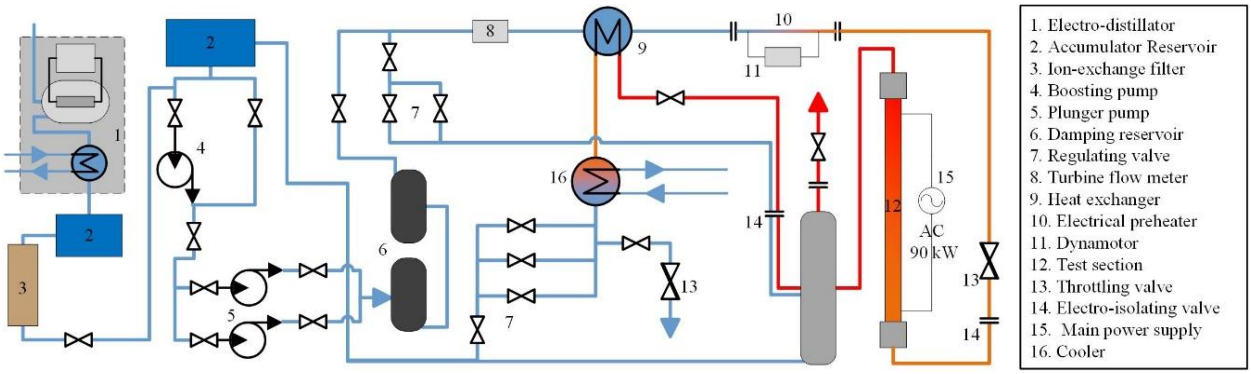

Figure 3. General schematic of SCW experimental setup.

2.2 Test-Section Design

Heated elements in each flow geometry consist of a 485-mm heated-length cylindrical rod (actually, it is a tube) with four helical ribs wound over a 400-mm pitch, as shown in Figures 4 & 5. The gap between a heated rod and a cylindrical flow tube (displacer) in an annular channel allowed the formation of just a peripheral subchannel, whereas the flow geometry of the 3-rod bundle allows the formation of central and peripheral subchannels, as shown in Figure 6. Rods were heated by a direct heating with an AC current going through the tube (rod) wall(s).

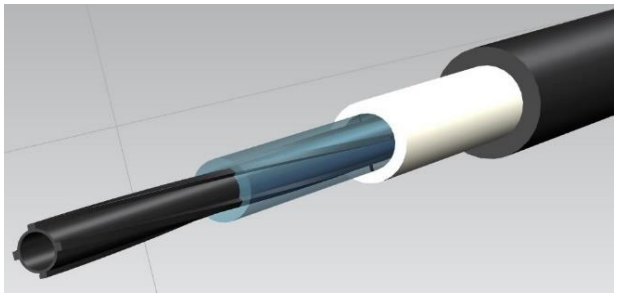

Figure 4. 3-D image of heated-central-rod annular channel.

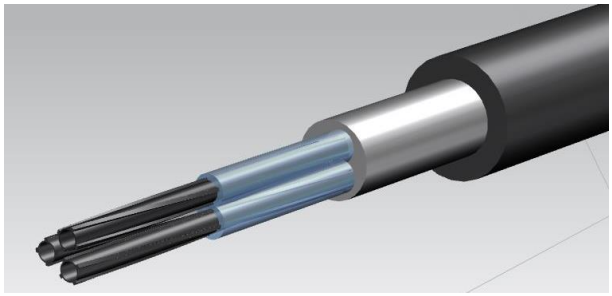

Figure 5. 3-D image of 3-rod bundle.

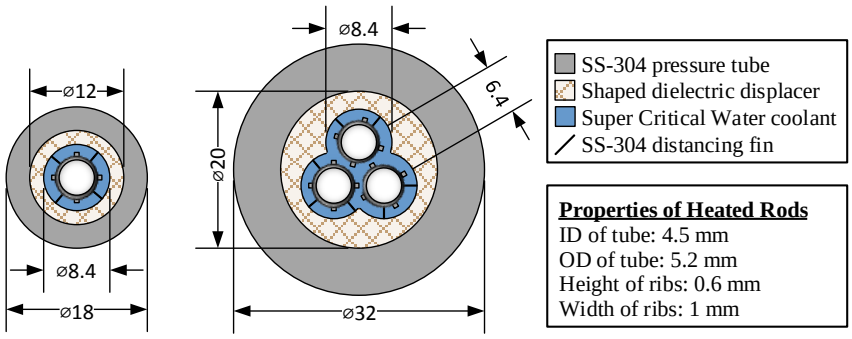

Figure 6. Radial cross-sections of annular channel and 3-rod bundle (note: actually, a Ukrainian stainless steel has been used, but by content and other parameters this steel is very close to SS-304).

Calibrated stainless-steel fins of 0.1-mm thickness were welded to the rods providing a 1-mm gap between the rod ribs and a shaped dielectric displacer, as shown in Figure 6. The displacers were inserted into pressure tubes of 18/12-mm and 32/20-mm OD/ID diameters, respectively. A hydraulic-equivalent diameter, D_{hy}, was determined to be 2.67-mm for the annular channel, and 2.4-mm for the 3-rod bundle.

$$D_{hy} = \frac{4 \cdot A_{fl}}{P_{wet}} \quad (1)$$

Wall temperatures in the test sections were measured using 7 thermocouples installed along the heated length on the inner surface of the heated rod (tube) at: 95, 195, 255, 315, 375, 415, and 475 mm from the entrance (the first thermocouple is located beyond the entrance region (L/D > 25)). Each thermocouple was tightly engraved into a copper plug of a diameter equal to the inner diameter of the rod (tube). The plugs were covered with heat-resistant silicone resin that provided electrical insulation. Good contact and high thermal conductivity of the copper plugs allowed measurement of an averaged temperature in each cross-section with a good response time. This was verified by isothermal tests.

Bulk-fluid temperatures were measured by using chromel-alumel ungrounded sheathed thermocouples of 0.2-mm diameter (wire) inserted into the fluid flow inside mixing chambers. These chambers were used to minimize non-uniformity in the cross-sectional-temperature distribution and to damp pressure pulsations within the test sections. The inlet and outlet sections of hydrodynamic stabilization were provided.

2.3 Instrumentation and Test Matrix

The following test-section parameters were measured or calculated in the experiments:

- Test-section current and voltage. These parameters were used to calculate the power.
- Pressure at the test-section inlet.
- Bulk-fluid temperatures at the test-section inlet and outlet.
- Thermocouples were calibrated within the temperature range of 20 to 450°C.
- Internal-wall temperatures of the heated rod(s) (tube(s)) by using the probe with 7 thermocouples.

The instrumentation used to measure the loop parameters was thoroughly checked and calibrated. The maximum uncertainties of primary parameters are listed in Table 1.

Table 1. Maximum uncertainties of measured and calculated parameters.

-	**Parameters**	**Maximum Uncertainty**
Measured Parameters	Inlet pressure	±0.2%
	Bulk-fluid temperatures	±3.4%
	Wall temperature	±3.2%
Calculated Parameters	Mass-flow rate	±2.3%
	Heat flux	±3.5%
	HTC	±12.7%
	Heat loss	≤3.4%

Experimental data were recorded using a Data Acquisition System (DAS) when the required power level and flow conditions have been reached and stabilized (steady-state conditions). Increases in power was limited with the maximum wall temperature; power trip was set up at a wall temperature of 620°C. The heat-loss characteristics of the test sections were determined prior to performing experiments, as shown in Table 1.

3. Determination of Experimental Heat Transfer Coefficient (HTC)

By applying a heat balance to the test section, the axial step increase (dx set to 1 mm) of the coolant's specific enthalpy as a bulk fluid can be determined.

$$h_{b(i+1)} = h_{b(i)} + \frac{q_{(i)} \cdot dx \cdot p_h}{A_{fl} \cdot G} \quad (2)$$

The outer-wall temperature of the heated rod(s) was determined by using a general solution for the temperature distribution in a tube with the uniform volumetric heat generation [26]. Steady-state conditions and one-dimensional radial heat conduction were assumed.

$$T_{w_o} = T_{w_i} + \frac{q_v}{4k}(r_o^2 - r_i^2) - \frac{q_v}{2k} r_o^2 \, ln\left(\frac{r_o}{r_i}\right) \quad (3)$$

From the bulk-fluid-enthalpy profile and the calculated outer-wall-temperature points (at 7 points across the heated length), experimental HTCs were determined.

$$HTC_{(i)} = \frac{q_{(i)}}{T_{w_{o(i)}} - T_{b_{calc}(i)}} \quad (4)$$

Thermophysical properties of water at each axial position were calculated according to the inlet pressure and local bulk-fluid temperature using NIST REFPROP [9]. Pressure losses were considered to be negligible along the heated length.

4. Experimental Results and Analysis

Figures 7–11 show bulk-fluid-temperature, wall-temperature and HTC profiles at a pressure of 22.6 MPa (for SCW: P_{cr}=22.064 MPa), mass flux of 2000 kg/m^{2}s, inlet temperatures within the range of 205-210°C and various heat fluxes (1.543-2.547 MW/m^2) in the annular channel. In general, this range of heat fluxes is higher than those applied in long bare tubes (1-6 m). Accounting, that we are dealing with quite short heated-length test section (only 485 mm), in all cases bulk-fluid temperature is well below the pseudocritical temperature in spite of high heat fluxes. Also, wall temperatures were below the pseudocritical temperature within the range of heat fluxes up to 2.244 MW/m^2. And only at a heat flux of 2.547 MW/m^2 the wall temperature at the outlet of the test section is above the pseudocritical temperature. Therefore, only at these operating conditions the Deteriorated-Heat-Transfer (DHT) regime was noticed (see Figure 11). Temperature profiles were stable, close to linear and easily reproducible within a wide range of mass and heat fluxes.

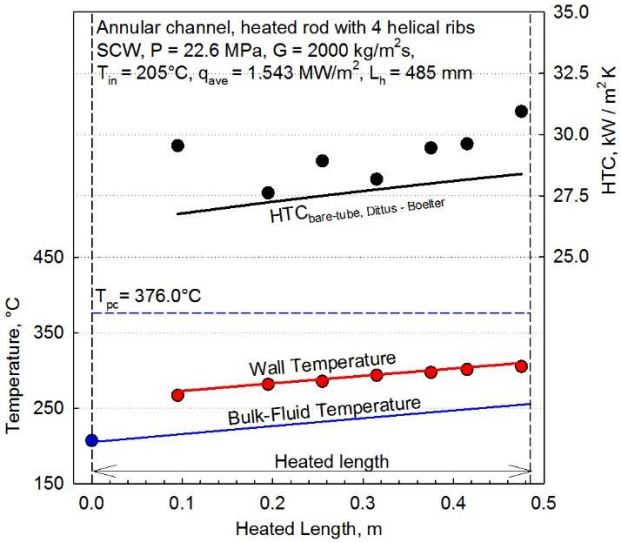

Figure 7. Bulk-fluid-temperature, wall-temperature and HTC profiles along heated length of annular channel: Symbols – experimental data; Lines – calculated profiles; Heat flux - 1.543 MW/m^2.

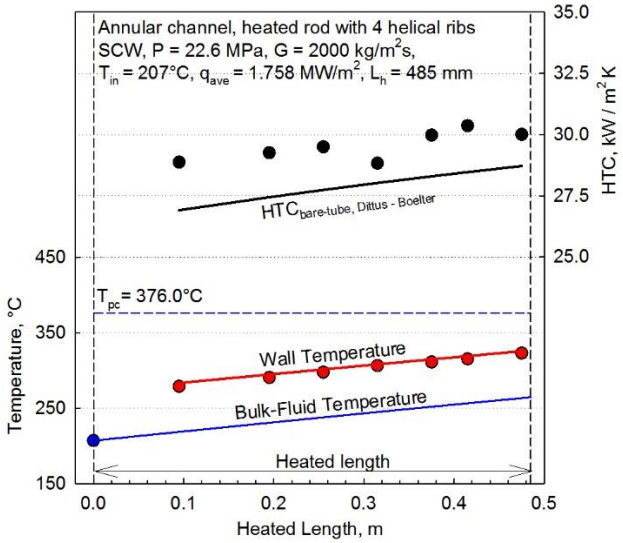

Figure 8. Bulk-fluid-temperature, wall-temperature and HTC profiles along heated length of annular channel: Symbols – experimental data; Lines – calculated profiles; Heat flux - 1.758 MW/m^2.

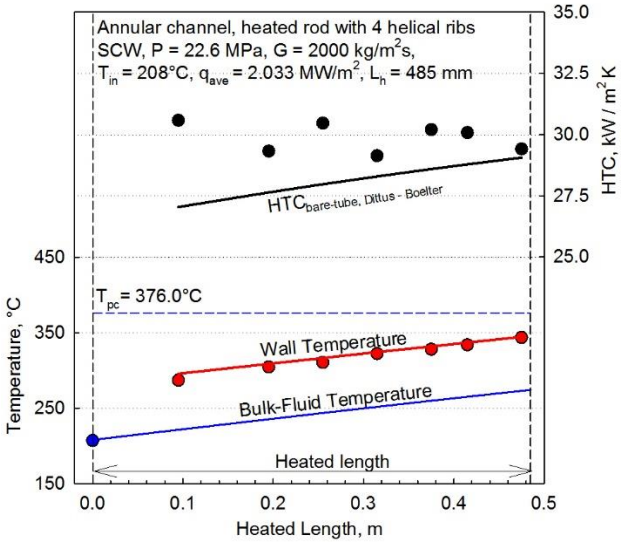

Figure 9. Bulk-fluid-temperature, wall-temperature and HTC profiles along heated length of annular channel: Symbols – experimental data; Lines – calculated profiles; Heat flux - 2.033 MW/m^2.

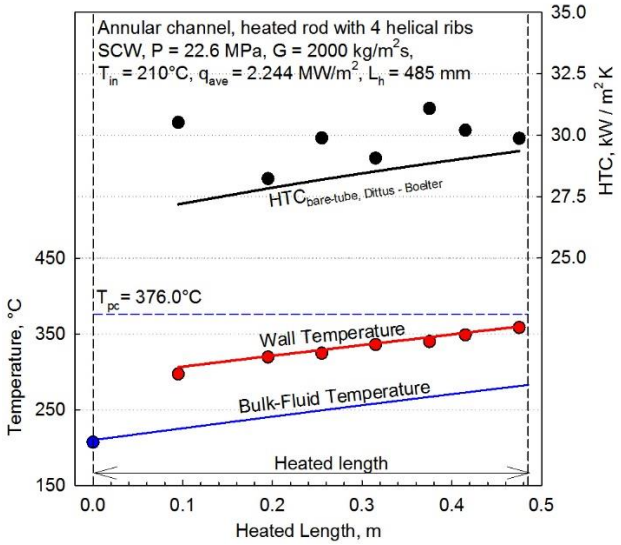

Figure 10. Bulk-fluid-temperature, wall-temperature and HTC profiles along heated length of annular channel: Symbols – experimental data; Lines – calculated profiles; Heat flux - 2.244 MW/m^2.

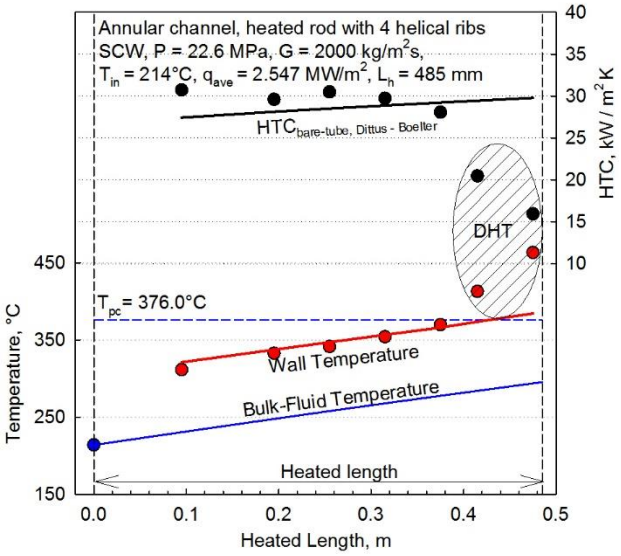

Figure 11. Bulk-fluid-temperature, wall-temperature and HTC profiles along heated length of annular channel: Symbols – experimental data; Heat flux - 2.547 MW/m^2.

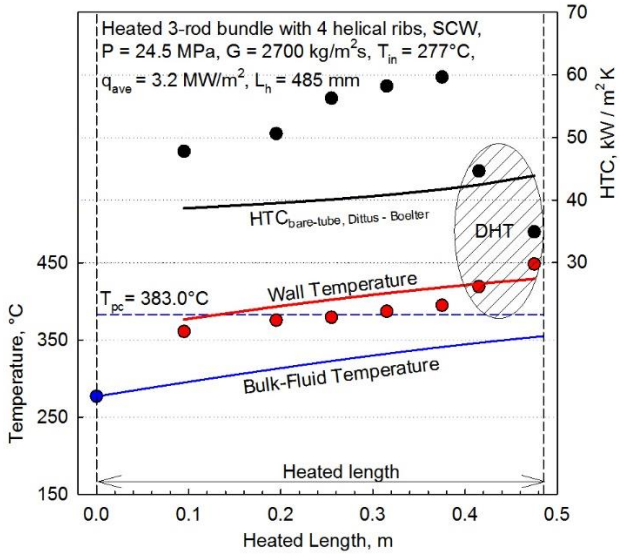

Figure 12. Bulk-fluid-temperature, wall-temperature and HTC profiles along heated length of 3-rod bundle: Symbols – experimental data; Heat flux - 3.2 MW/m^2.

Just for reference purposes, calculated HTC values, based on the Dittus-Boelter correlation [27] as it was introduced by McAdams [28]:

$$\mathbf{Nu} = 0.0243\mathbf{Re}^{0.8}\mathbf{Pr}^{0.4} \quad (5)$$

were added to Figures 7-14. Basic ideas behind using this correlation are as the following:

1. This correlation showed quite good results outside a pseudocritical region [6, 11].
2. This correlation is not affected by heat flux.
3. This correlation is valid within the following ranges: $0.6 \le \mathbf{Pr} \le 160$; $\mathbf{Re}_D \ge 10{,}000$ and $L/D \ge 10$, which correspond to those in Figures 7-14. And
4. In general, SCW bare-tube correlations have been obtained at lower heat fluxes [6, 11].

As a result, the Dittus-Boelter correlation predicts experimental HTC values with offset of about 5% (see Figures 7-11), which is actually within the uncertainties of experimental HTCs. The DHT regime shown in Figure 11 cannot be predicted with the Dittus-Boelter correlation.

Figures 12–14 show bulk-fluid-temperature, wall-temperature and HTC profiles in the 3-rod bundle test section at various operating conditions, but at approximately the same heat flux – 3.1-3.2 MW/m^2. It looks that all three HT regimes: 1) normal, 2) DHT and 3) Improved HT (IHT); can be identified in Figures 12-14. Due to high heat flux wall temperatures in Figures 12-14 are below, equal to and above pseudocritical temperatures, but bulk-fluid temperatures are still below pseudocritical temperatures. Therefore, the Dittus-Boelter-correlation predictions of the HTC values obtained in the 3-rod bundle are not so close as in the annular channel. The reasons for that can be extra heat-transfer enhancement in the bundle geometry and/or IHT regimes noticed at these operating conditions.

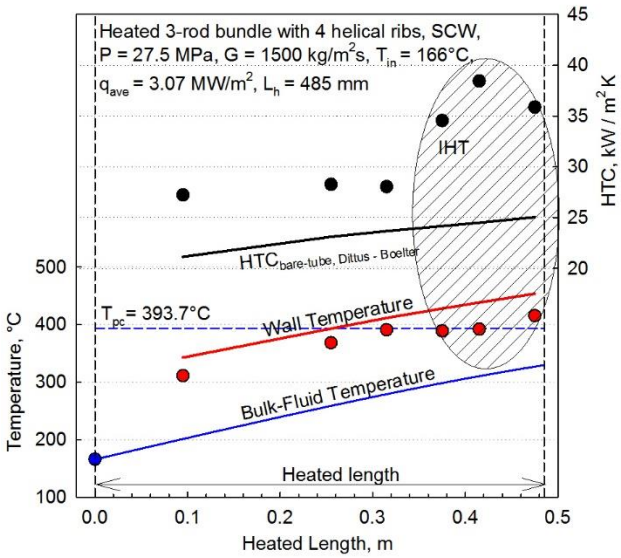

Figure 13. Bulk-fluid-temperature, wall-temperature and HTC profiles along heated length of 3-rod bundle: Heat flux - 3.070 MW/m^2 and inlet temperature - 166°C.

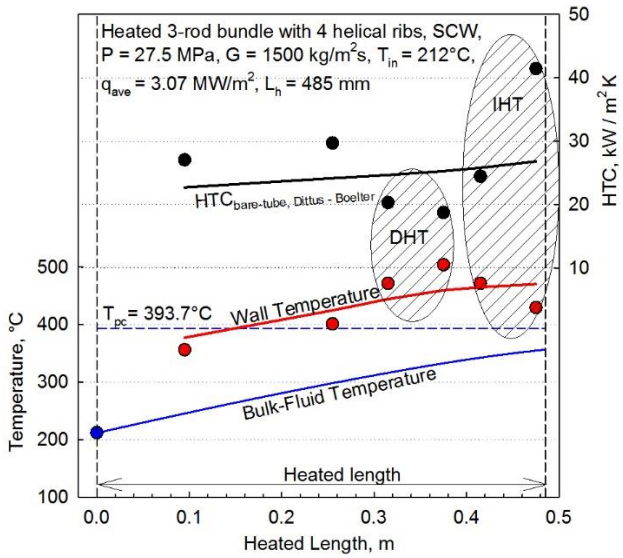

Figure 14. Bulk-fluid-temperature, wall-temperature and HTC profiles along heated length of 3-rod bundle: Heat flux - 3.070 MW/m^2 and inlet temperature - 212°C.

The DHT regime is usually defined by a sharp decrease in heat transfer compared to normal heat-transfer regime. Usually, heat-transfer correlations cannot predict accurately the DHT regime even in bare tubes. However, there are some simplified correlations, which can predict a heat flux at which the DHT starts. As such, Mokry et al. [11] proposed an approximate empirical correlation for calculating the minimum heat flux at which the DHT in bare tubes appeared:

$$q_{DHT} = -58.97 + 0.745\ G, \left(\frac{kW}{m^2}\right) \qquad (6)$$

Table 2 lists q_{DHT} in bare tubes (calculated values) and q_{DHT} in the annular test section and 3-rod bundle (experimental values).

Table 2. Comparison between onset of DHT between bare-tube, annular channel, and 3-rod bundle.

	Test section	Operating Conditions	q_{DHT}, kW/m^2
1	Bare-tube	P = 24.1 MPa and G = 2000 kg / m^2 s	1.43
2	Single-rod annulus	P = 22.6 MPa and G = 2000 kg / m^2 s	2.55
3	Bare-tube	P = 24.1 MPa and G = 2700 kg / m^2 s	1.95
4	3-rod bundle	P = 22.6 MPa and G = 2700 kg / m^2 s	3.20

Analysis of the data in Table 2 shows that q_{DHT} values in bare tubes are significantly lower (up to 1.8 times) than those in the single-rod annulus and 3-rod bundle. This difference can be due to three reasons:

1. We have three different flow geometries;
2. We have rods equipped with helical ribs (which can be considered as an enhanced HT surface) compared to bare-tube flow geometry;
3. We have relatively short test sections in which even at high heat fluxes bulk-fluid temperature is always below a pseudocritical one. However, when the wall temperature crossing a pseudocritical temperature we can notice the DHT regime in both test sections with rods.

Also, this analysis shows that such simple function as q_{DHT} vs. G might not be enough to cover various flow geometries and different heated lengths.

In general, we need to analyze more experimental data, obtained in the single-rod annular and 3-rod bundle flow geometries, to make wide-range "solid" conclusions.

5. Conclusions

The following preliminary conclusions can be made:

1. A limited set of experimental data, obtained in the annular channel with a heated rod equipped with 4 helical ribs and a 3-rod bundle (rods are also equipped with 4 helical ribs) cooled with upward flow of SCW, has been processed and analyzed. The experimental results contain bulk-fluid-temperature, wall-temperature and heat-transfer-coefficient profiles along the heated length (485 mm) of the corresponding flow geometry. The data were obtained within the following operating ranges: at three values of pressure above the critical point (22.6, 24.5, and 27.5 MPa), mass fluxes within 1500 - 2700 kg/m^{2}s, inlet temperatures within 166 - 277°C and heat fluxes up to 3.2 MW/m^2.

2. Analysis of the data obtained in the single-rod annular channel showed that in spite of existence of helical ribs over heated rod, which can be considered as an enhanced HT surface compared to that of a bare tube, there is no significant enhancement in HTC values compared to those calculated according to the Dittus-Boelter correlation. The Dittus-Boelter correlation was applied here just for reference purposes, because this correlation showed quite good results outside a pseudocritical region, which is the case for the studied flow geometries. Also, this correlation is not affected by heat flux. In general, SCW bare-tube correlations have been obtained at lower heat fluxes compared to those studied here.

3. Normal and DHT regimes have been identified in the single-rod annular channel. However, all three HT regimes (Normal, DHT and IHT) can be identified in the 3-rod bundle.

4. Analysis of the data on q_{DHT} values shows that these values in bare tubes are significantly lower (up to 1.8 times) than those in the single-rod annulus and 3-rod bundle. This difference is possibly due to the relatively short test sections in which even at high heat fluxes bulk-fluid temperature is always below a pseudocritical one. However, when the wall temperature crossing a pseudocritical temperature the DHT regime was noticed in both test sections with rods.

5. In general, we need to analyze more experimental data, obtained in the single-rod annular and 3-rod bundle flow geometries, to make wide-range "solid" conclusions.

6. Acknowledgement

This research is related to the IAEA Coordinated Research Project (CRP) on Understanding and Prediction of Thermal-Hydraulics Phenomena Relevant to SCWRs.

7. Nomenclature

A	area, m^2
c_p	specific heat, $\mathrm{J/kg \cdot K}$
D_{hy}	hydraulic-equivalent diameter, m $\left(\frac{4\,A_{fl}}{p_{wet}}\right)$
dx	step axial length change, m
G	mass flux, $\mathrm{kg/m^2 s}$ $\left(\frac{\dot{m}}{A_{fl}}\right)$
HTC	Heat Transfer Coefficient, $\mathrm{W/m^2 K}$
h	specific enthalpy, $\mathrm{J/kg}$
i	axial step position, m
k	thermal conductivity, $\mathrm{W/m \cdot K}$
L	heated length, m
$\dot{m}$	mass flow rate, $\mathrm{kg/s}$
P	pressure, Pa
p	perimeter, m
q	heat flux, $\mathrm{W/m^2}$
q_v	volumetric heat flux, $\mathrm{W/m^3}$
r	radius, m
s	specific entropy, $\mathrm{kJ/kg \cdot K}$
T	temperature, $\mathrm{°C}$
V	volume, $\mathrm{m^3}$
x	axial position, m

Greek Letters

μ	dynamic viscosity, $\mathrm{Pa \cdot s}$
ρ	density, $\mathrm{kg/m^3}$

Non-dimensional Numbers

Nu	Nusselt number $\left(\frac{HTC \cdot D_{hy}}{k}\right)$
Pr	Prandtl number $\left(\frac{\mu \cdot c_p}{k}\right)$
Re	Reynolds number $\left(\frac{G D_{hy}}{\mu_b}\right)$

Subscripts

b	bulk-fluid
calc	calculated
cr	critical point
exp	experimental
fl	flow
h	heated
i	inner
o	outer
pc	pseudocritical point
w	wall
wet	wetted

Abbreviations and Acronyms

AC	Alternative Current
DHT	Deteriorated Heat Transfer
ID	Inside Diameter
IHT	Improved Heat-Transfer
HTC	Heat Transfer Coefficient
OD	Outside Diameter
SCP	SuperCritical-Pressure
SCW	SuperCritical Water
SCWR	SuperCritical Water Reactor

References

[1] Pioro, I. and Duffey, R., 2015. Nuclear Power as a Basis for Future Electricity Generation, ASME Journal of Nuclear Engineering and Radiation Science, Vol. 1, No. 1, 19 pages.

[2] Pioro, I., Saltanov, Eu., and Dragunov, A., 2015. Applications of Supercritical Fluids in Power Engineering, Proceedings of the International Symposium of SCWR (ISSCWR-7), Helsinki, Finland, Paper #2081, 11 pages.

[3] *Heat Transfer Behaviour and Thermohydraulics Code Testing for SCWRs*, IAEA TECDOC Series, IAEA-TECDOC-1746, 2014, September, Vienna, Austria, 496 pages. Free download from:

http://www-pub.iaea.org/books/IAEABooks/10731/Heat-Transfer-Behaviour-and-Thermohydraulics-Code-Testing-for-Supercritical-Water-Cooled-Reactors-SCWRs.

[4] Pioro, I. and Kirillov, P., 2013. Generation IV Nuclear Reactors as a Basis for Future Electricity Production in the World, Chapter in the book: Materials and Processes for Energy: Communicating Current Research and Technological Developments, Energy Book Series #1, Editor: A. Méndez-Vilas, Publisher: Formatex Research Center, Spain, pp. 818-830. Free download from: http://www.formatex.info/energymaterialsbook/book/818-830.pdf.

[5] Pioro, I., 2011. The Potential Use of Supercritical Water-Cooling in Nuclear Reactors. Chapter in Nuclear Energy Encyclopedia: Science, Technology, and Applications, Editors: S.B. Krivit, J.H. Lehr and Th.B. Kingery, J. Wiley & Sons, Hoboken, NJ, USA, pp. 309-347.

[6] Pioro, I.L. and Duffey, R.B., 2007. *Heat Transfer and Hydraulic Resistance at Supercritical Pressures in Power Engineering Applications*, ASME Press, New York, NY, USA, 334 pages.

[7] Pioro, I. and Mokry, S., 2011. Thermophysical Properties at Critical and Supercritical Conditions, Chapter in book "Heat Transfer. Theoretical Analysis, Experimental Investigations and Industrial Systems", Editor: A. Belmiloudi, INTECH, Rijeka, Croatia, pp. 573-592. Free download from: http://www.intechopen.com/books/heat-transfer-theoretical-analysis-experimental-investigations-and-industrial-systems/thermophysical-properties-at-critical-and-supercritical-pressures.

[8] Pioro, I., Mokry, S. and Draper, Sh., 2011. Specifics of Thermophysical Properties and Forced-Convective Heat Transfer at Critical and Supercritical Pressures, Reviews in Chemical Engineering, Vol. 27, Issue 3-4, pp. 191–214.

[9] National Institute of Standards Technology, NIST Reference Fluid Thermodynamic and Transport Properties-REFPROP: NIST Standard Reference Database 23, Ver. 9.0, Department of Commerce, Boulder, CO, USA, 2010.

[10] Pioro, I. and Mokry, S., 2011. Heat Transfer to Fluids at Supercritical Pressures, Chapter in book "Heat Transfer. Theoretical Analysis, Experimental Investigations and Industrial Systems", Editor: A. Belmiloudi, INTECH, Rijeka, Croatia, pp. 481-504. Free download from: http://www.intechopen.com/books/heat-transfer-theoretical-analysis-experimental-investigations-and-industrial-systems/heat-transfer-to-supercritical-fluids.

[11] Mokry, S., Pioro, I.L., Farah, A., King, K., Gupta, S., Peiman, W. and Kirillov, P., 2011. Development of Supercritical Water Heat-Transfer Correlation for Vertical Bare Tubes, Nuclear Engineering and Design, Vol. 241, pp. 1126-1136.

[12] Pis'menny, E.N., Razumovskiy, V.G., Mayevskiy, E.M., Koloskov, A.E. and Pioro, I.L., 2006. Heat Transfer to Supercritical Water in Gaseous State or Affected by Mixed Convection in Vertical Tubes, Proc. of the 14th Int. Conf. on Nuclear Engineering (ICONE-14), July 17-20, Miami, Florida, USA, Paper #89483, 8 pages.

[13] Pis'mennyy, E.N., Razumovskiy, V.G., Maevskiy, E.M., Koloskov, A.E., Pioro, I.L. and Duffey, R.B., 2005. Experimental Study on Temperature Regimes to Supercritical Water Flowing in Vertical Tubes at Low Mass Fluxes, Proc. of the Int. Conf. GLOBAL-2005 "Nuclear Energy Systems for Future Generation and Global Sustainability, Tsukuba, Japan, October 9–13, Paper #519, 9 pages.

[14] Wu, G., Bi, Q., Zhu, X., Yang, Z., Wang, H., 2011. Experimental Investigation on Heat Transfer of Supercritical Pressure Water in Annular Flow Geometry, Proceedings of the 5th International Symposium on SCWR (ISSCWR-5), Vancouver, BC, Canada, March 13–16.

[15] Wu, G., Bi, Q., Yang, Z., and Li, M., 2010. Experimental Investigation on Heat Transfer of Supercritical Pressure Water in Annular Channel, Proceedings of the 2nd Canada-China Joint Workshop on SCWR, Toronto, ON, Canada, April 25–29.

[16] Bae, Y.Y. and Kim, H.Y., 2009. Convective Heat Transfer to CO_2 at a Supercritical Pressure Flowing Vertically Upward in Tubes and an Annular Channel, Exp. Therm. Fluid Sci., **33** (2), pp. 329–339.

[17] Richards, G., Harvel, G.D., Pioro, I.L., Shelegov, A.S. and Kirillov, P.L., 2013. Heat Transfer Profiles of a Vertical, Bare, 7-Element Bundle Cooled with Supercritical Freon R-12, Nuclear Engineering and Design, Vol. 264, pp. 246-256.

[18] Mori, H., Kaida, T., Ohno, M., Yoshida, S., and Hamamoto, Y., 2012. Heat Transfer to a Supercritical Pressure Fluid Flowing in Sub-Bundle Passes. J. Nucl. Sci. Technol., Vol. 49, pp. 373-383.

[19] Chun, S.Y., Hong, S.D., and Shin, C.H., 2005. Heat Transfer Characteristics of 5×5 Heater Bundle Cooled with Refrigerant HFC-134a Near the Critical Pressures, PaRTSEE-5, Auckland, New Zealand, April 28–29.

[20] Wang, H., Bi, Q.C., Wang, L.C., et al., 2014. Experimental Investigation of Heat Transfer from a 2×2 Rod Bundle to Supercritical Pressure Water, Nuclear Engineering and Design, Vol. 280, pp. 205-218.

[21] Zhao, M., Li, H.B., Yang, J., et al., 2013. Experimental Study on Heat Transfer to Supercritical Water Flowing through Circular Tubes and 2×2 Rod Bundles, Proceeding of the 6th International Symposium on Supercritical Water-cooled Reactors, Shenzhen, China, March 3–7.

[22] Razumovskiy, V.G., Mayevskiy, E.M., Koloskov, A.E., Pis'mennyi, E.N. and Pioro, I.L., 2013. Heat Transfer to Water at Supercritical Parameters in Vertical Tubes, Annular Channels, 3- and 7-Rod Bundles, Proceedings of the 21st International Conference on Nuclear Engineering (ICONE-21), July 29-August 2, Chengdu, China, Paper #16442, 8 pages.

[23] Razumovskiy, V.G., Pis'mennyy, Eu.N., Koloskov, A.Eu., and Pioro, I.L., 2009. Heat Transfer to Supercritical Water in Vertical Annular Channel and 3-rod Bundle, Proceedings of the 17th International Conference On Nuclear Engineering (ICONE-17), Brussels, Belgium, July 12-16, Paper #75212, 6 pages.

[24] Razumovskiy, V.G., Pis'menny, E.N., Koloskov, A.E. and Pioro, I.L., 2008. Heat Transfer to Supercritical Water in Vertical 7-Rod Bundle, Proceedings of the 16th International Conference on Nuclear Engineering (ICONE-16), Orlando, Florida, USA, May 11–15, Paper #48954, 6 pages.

[25] Dyadyakin, B.V. and Popov, A.S., 1977. Heat transfer and thermal resistance of tight seven-rod bundle, cooled with water flow at supercritical pressures, (In Russian), Transactions of VTI (Труды ВТИ), No. 11, pp. 244–253.

[26] Bergman, Th.L., Lavine, A.S., Incropera, F.P., and Dewitt, D.P., 2011. *Fundemantals of Heat and Mass Transfer*, 7th edition, John Wiley & Sons, Danvers, MA, USA, 1048 pages.

[27] Dittus, F.W. and Boelter, L.M.K., 1930. Heat Transfer in Automobile Radiators of the Tubular Type, University of California, Berkeley, Publications on Engineering, **2** (13), pp. 443–461.

[28] McAdams, W.H., 1942. *Heat Transmission*, 2nd edition, McGraw-Hill, New York, NY, USA, 459 pages.

ISSCWR7-2096

Coupled 3D Neutron Kinetics and Thermalhydraulic Characteristics of the Canadian SCWR

D. W. Hummel and D. R. Novog
McMaster University
1280 Main Street West, Hamilton, Ontario, Canada L8S 4L8
hummeld@mcmaster.ca, novog@mcmaster.ca

Abstract

The Canadian SuperCritical Water-cooled Reactor concept, as an evolution of the CANada Deuterium Uranium (CANDU) reactor, includes both pressure tubes and a low temperature heavy water moderator. The current Pressure Tube type SCWR (PT-SCWR) concept features a 64-element fuel assembly containing a recycled plutonium and thorium fuel mixture (336 such assemblies comprising the core). These assemblies are placed within High Efficiency Re-entrant Channels (HERCs) that connect to core inlet and outlet plena. The features of the PT-SCWR have been modelled with the neutron transport code DRAGON to create a database of homogenized and condensed cross-sections and thermalhydraulic feedback coefficients. These are used as input to a quarter-core (84 channel) neutron diffusion model created with the code DONJON. The features of the primary heat transport system are modelled with the thermalhydraulic system code CATHENA. A procedure has been developed to couple the outputs of DONJON and CATHENA, facilitating 3D spatial neutron kinetics and coupled thermalhydraulic analysis of the PT-SCWR core. This paper presents the coupled simulation results of several postulated transients that are initiated by changes to the PT-SCWR core inlet and outlet boundary conditions.

1. Introduction

Canada Nuclear Laboratories (formerly Atomic Energy of Canada Limited), in collaboration with Natural Resources Canada and the National Sciences and Engineering Research Council, has developed a conceptual Supercritical Water-Cooled Reactor (SCWR) design that is an evolution of the CANada Deuterium Uranium (CANDU) reactor, featuring both pressure tubes and a low temperature heavy water moderator. This Pressure Tube type SCWR (PT-SCWR), unlike a typical CANDU or Pressurized Heavy Water Reactor (PHWR), contains vertical fuel channels, light water coolant, and uses batch refuelling [1].

In the PT-SCWR concept, coolant travels in a once-recirculating path through the core in what is referred to as the High Efficiency Re-Entrant Channel (HERC) [2]. Figure 1 shows how coolant at 350 °C and 25.8 MPa enters an inlet plenum and then travels downward through a centre flow tube in each fuel channel. The coolant then reverses at the bottom of the channels before flowing upwards around the fuel pins towards the outlet plenum, where it exits at 625 °C. Thermal isolation between the supercritical light water coolant and the low temperature and pressure heavy water moderator is provided by a ceramic insulator within the pressure tube. The fuel is a PuO_2-ThO_2 mixture in two concentric rings of 32 elements (averaging 13 weight per cent PuO_2) with a 5 m active length and zirconium modified stainless steel cladding [3].

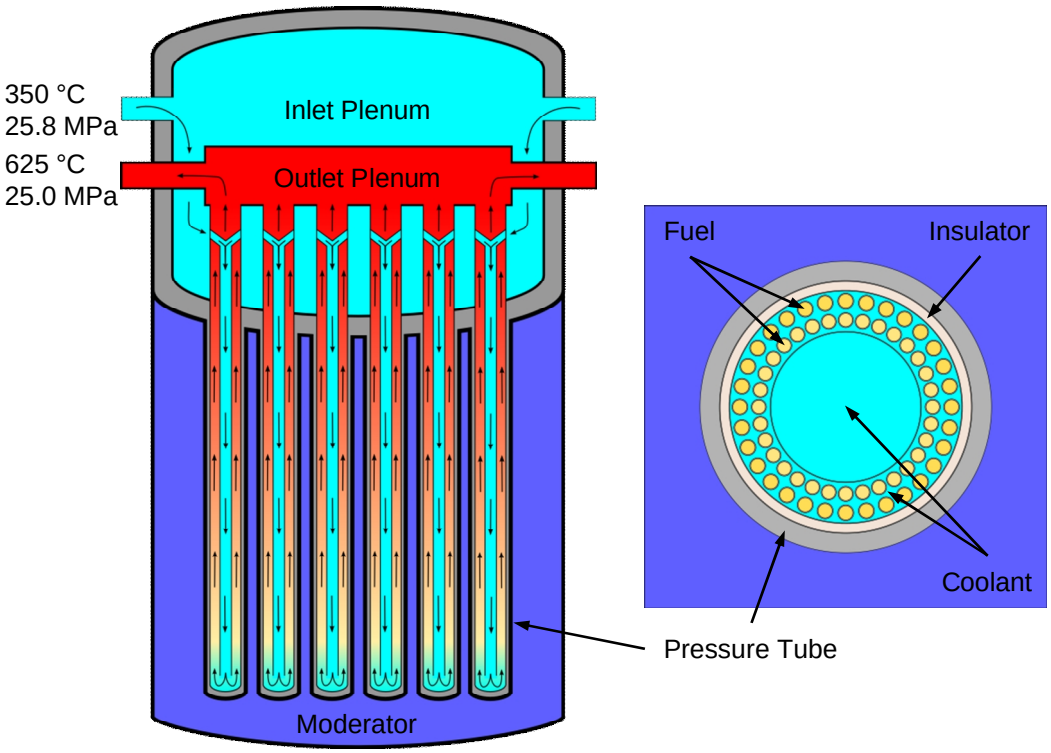

Figure 1. PT-SCWR HERC concept with 64-element fuel assembly.

One of the stated design goals for the PT-SCWR concept was to have a negative Coolant Void Reactivity (CVR). “Coolant Void” typically refers to the case where there is no coolant in the channels without distinguishing between the downward (flow tube) and upward (fuel region) flow directions. This does not necessarily imply that coolant void exclusively in the flow tube *or* fuel region must both have negative reactivity worths. In fact, lattice level calculations have shown that while the reactivity is negative when voiding the flow tube or the entire channel, the reactivity is positive when voiding the fuel region only. Several quick transients can be postulated where the coolant density around the fuel decreases before changes propagate to the centre flow tube. These density changes have corresponding reactivity feedbacks that will affect the reactor power and in turn the heat being delivered to the fluid, feeding back to the fluid density. The objective of this study was to model several postulated coupled neutronic-thermalhydraulic transients and establish if there are any significant safety implications for the current PT-SCWR concept.

2. Methodology

The complex multiphysics of coupled neutron kinetics and thermalhydraulic transients typically require dedicated computational solvers which are coupled externally. In this work the PT-SCWR was modelled at the core level through the coupling of the DONJON and CATHENA codes. Both of these models and the coupling procedure are described in turn.

2.1 Core Neutronics: DRAGON/DONJON

DRAGON is a freely available code developed at École Polytechnique de Montréal that is capable of solving the neutron transport equation with burnup in two and three dimensions [4]. In this study DRAGON was used to generate homogenized cross-sections and a thermalhydraulic feedback database for input to DONJON. Like DRAGON, DONJON is a freely available code developed at École Polytechnique de Montréal [5]. It is capable of solving the

neutron diffusion and spatial kinetics equations in three dimensions, and is used in this work to calculate the steady-state and transient power distribution in the PT-SCWR core.

2.1.1 DRAGON Lattice Cell Calculations

The large reduction in coolant density along the PT-SCWR channel (from 615 $kg \cdot m^{-3}$ to 68 $kg \cdot m^{-3}$, mostly in the fuel region) has a significant impact on the lattice physics and has been the subject of much previous study. To capture this effect in two-dimensional lattice calculations, the typical approach has been to model several lattice cells with different local conditions (i.e. fluid densities and material temperatures) [6,7] This approach was used in this work as well. Each lattice cell is evaluated with a set of 20 different local conditions, corresponding to 25 cm increments from channel inlet to outlet.

According to each channel's position in the core and its proximity to the D_2O reflector, the approximation of a single cell within an infinite lattice of identical cells is not always valid. Previous study has shown that this heterogeneity can be captured with additional "multicell" models for channels on the "corner" (with other channels on two sides) and "side" (with other channels on three sides) of the core [8]. Figure 2 shows how the cell geometries were modelled with DRAGON. Each was evaluated at the aforementioned 20 local thermalhydraulic conditions, resulting in 60 sets of homogenized cross-sections (20 each for the infinite lattice, side, and corner cells). These calculations were performed with DRAGON 3.06K using the International Atomic Energy Agency's 172 group nuclear data library [9].

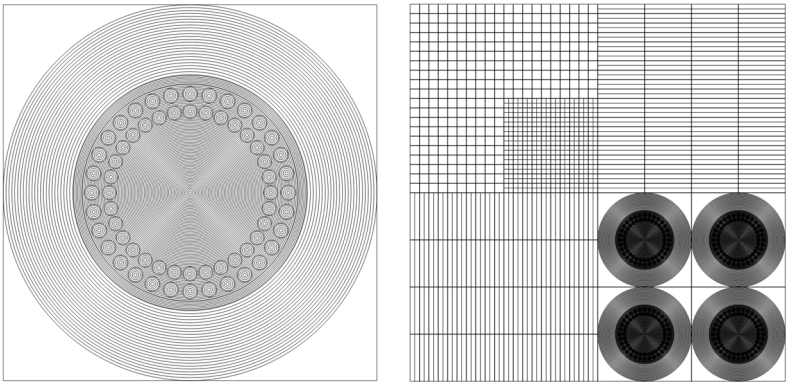

Figure 2. DRAGON spatial mesh for the infinite lattice (left) and reflector multicell (right)

Due to the high plutonium content in the PT-SCWR fuel, it's expected that a two-group energy condensation would not accurately capture the effect of the low energy resonances in the homogenized cross-sections. An eight-group structure was thus selected based on previous studies of high plutonium content mixed-oxide fuel [10]. The homogenized eight-group cross-sections, as functions of burnup, are used to create fuel tables for the steady-state DONJON calculation.

DRAGON was also used to create the thermalhydraulic feedback database. For this calculation the reference thermalhydraulic parameters are perturbed at each of the 20 axial locations at each burnup step and new sets of homogenized and condensed cross-section are generated. DRAGON's CFC module then takes these homogenized cross-sections and creates a database of first and second order coefficients that describe how each homogenized value changes with the thermalhydraulic parameters. Note that it's assumed the fuel depletes only at the reference conditions (i.e. there are no history effects for burning the fuel at different local conditions aside from that provided by simulating 20 axial locations, effectively creating 20 independent databases). The database (contained within the FBM data structure), along the with reference condition cross-sections, are used to create the core-level 3D model with DONJON.

2.1.2 DONJON Quarter-Core Calculations

The batch fuelling scheme of the PT-SCWR is quarter symmetric, so it was only necessary to include one quarter of the 336 fuel channels to model the core [11]. The 84 channels were modelled with 20 axial nodes, each corresponding to a single reference lattice cell calculation as described previously. 84 5 m channels, each split in to 20 axial nodes, combined with the 25 cm lattice spacing, results in the core being modelled with 1,680 cubic nodes. A 100 cm radial reflector and 75 cm axial reflector (both D_2O) were also included in the model with an additional 1,820 equally sized nodes. The three-batch refuelling scheme (relating the position of first, second and third cycle fuel assemblies) was implemented as shown in Figure 3.

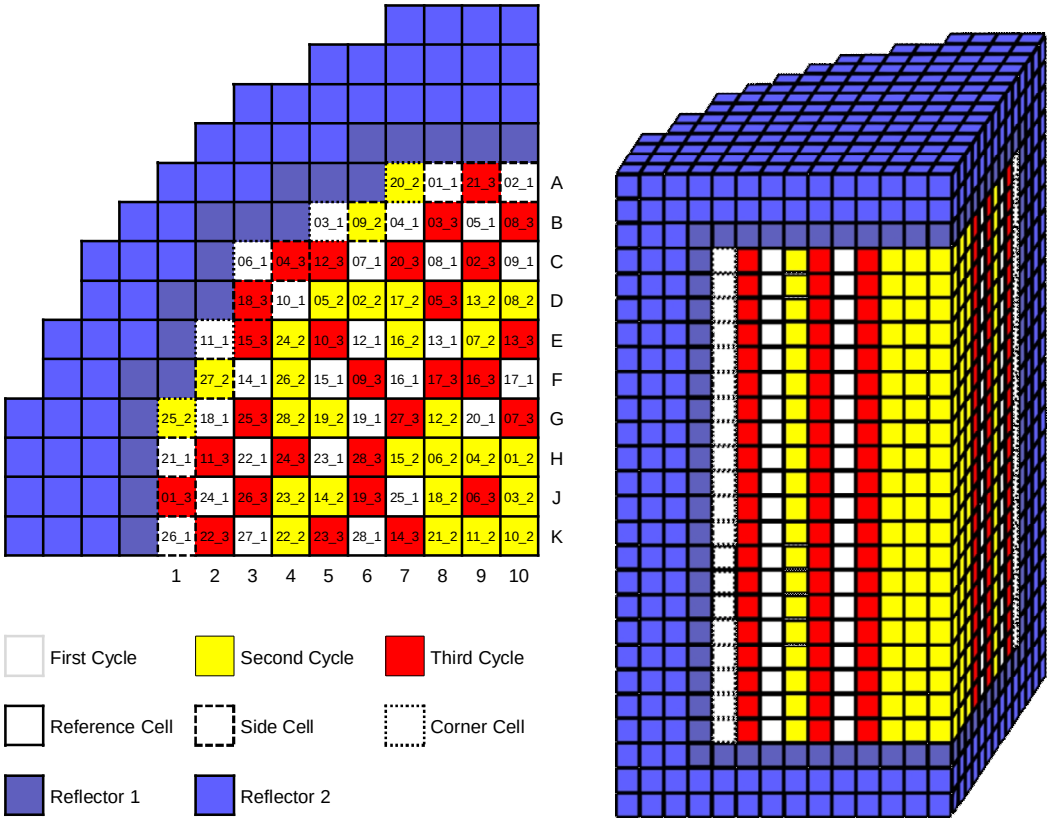

Figure 3. PT-SCWR core modelled in DONJON

The channel power distribution will be a function of the burnup distribution in the core. It's expected that each assembly will age differently depending on its position during each cycle. Further, it's expected that after many identical refuelling cycles the channel power history in each location will be the same from one cycle to the next. Even with the refuelling scheme in Figure 3, whatever initial guess that is made for the burnup distribution is not likely to be the same as this "equilibrium" distribution. The modelling strategy was thus to start with an informed guess for the final burnup distribution and then step forward in time, modelling several refuelling cycles until equilibrium was achieved.

The DONJON model thus calculates the core flux and power distribution at an instant in time (a core "snapshot") and then uses that power distribution to age the fuel over a time step where the power is assumed to be constant. This process is repeated until the end-of-cycle criterion is reached. At this point the fuel assemblies are removed, shuffled, and added to the core according to the scheme, and the process is repeated for the next cycle. This work used time steps of 1.0 Full Power Days (FPD) and an end-of-cycle criterion of core k_{eff} < 1.010. One hundred batch cycles were ran, although it was observed that the individual node powers converged and equilibrium was achieved in less than 30. The two equilibrium channel power

distributions shown in Figure 4 were selected as the initial conditions for the transients in this study.

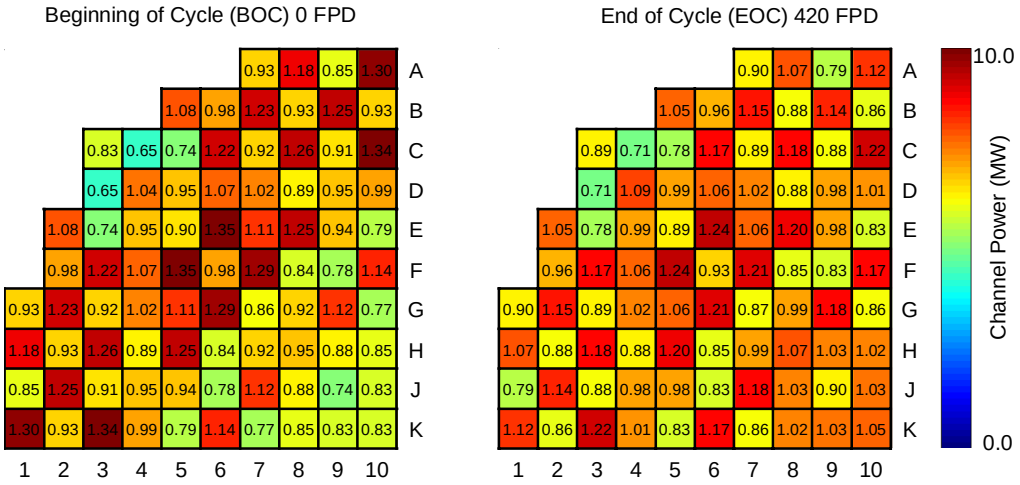

Figure 4. PT-SCWR channel power distributions used as initial conditions

Note that the DONJON model in Figure 3 contains no control devices or other neutron absorbers for reactivity hold-down during the batch cycle. No such devices were part of the reference PT-SCWR conceptual design while this work was being performed. Since burnup was evaluated in the reference DRAGON cells with a single reference set of thermalhydraulic parameters, it's inherently assumed in the steady-state DONJON model that each channel possess the same axial temperature and density distributions. All else being equal, this is contrary to the channel power evolution shown in Figure 4, i.e. different channel powers should provide different axial fuel temperature and coolant profiles. Without channel power shaping provided by movable control devices, this work assumed that variable orifices at the inlet of each channel were capable of matching the channel flow to channel power, thus maintaining axial thermalhydraulic profiles close to the reference. More details on these orifices are provided in the following section.

2.2 Core Thermalhydraulic: CATHENA

CATHENA (Canadian Algorithm for THErmalhydraulic Network Analysis) is a thermalhydraulics code developed by AECL primarily for Loss of Coolant Accident (LOCA) analyses of CANDU reactors [12]. It uses a one-dimensional, two-fluid representation to calculate transient flows in piping networks. The included GENeralized Heat Transfer Package (GENHTP) allows calculation of convective heat transfer from surfaces to the fluid, as well as conduction within walls. The code has recently been enhanced to function in supercritical flow regimes with an expanded set of fluid properties, although it currently has no wall friction or heat transfer correlations specific to supercritical water [13]. This study used CATHENA MOD-3.5d/Rev 3 to model the thermalhydraulics of the PT-SCWR heat transport system.

The PT-SCWR has been modelled as in Figure 1 with pressure and temperature boundary conditions for simplicity, omitting the coolant pumps, turbine, and other elements that are expected to be part of the primary circuit. Each of the 84 channels in the quarter-core is represented as four identical parallel pipes, thus giving the correct total flow for the entire core. Component dimensions are consistent with previous models of the PT-SCWR where available [13].

Heat transfer is modelled across the pipe wall separating the centre flow tube and fuel channel, as well as through the pressure tube to a constant temperature boundary condition representing the moderator. The inner and outer rings of fuel elements are modelled separately,

including conduction within the elements and convective heat transfer to the coolant (using the simple Dittus-Boelter correlation for supercritical water). To be congruent with the DONJON model, each channel (also including the flow tube and all heat transfer elements) is modelled with 20 axial nodes. The power distribution output from DONJON can thus loaded directly in to the CATHENA input. A simplified schematic of the CATHENA model is shown in Figure 5. The quarter-core CATHENA model shown in the figure consists of 1,014 individual components, including 4,124 hydraulic volumes, 420 GENHTP models and 84 control connections (the valve controllers).

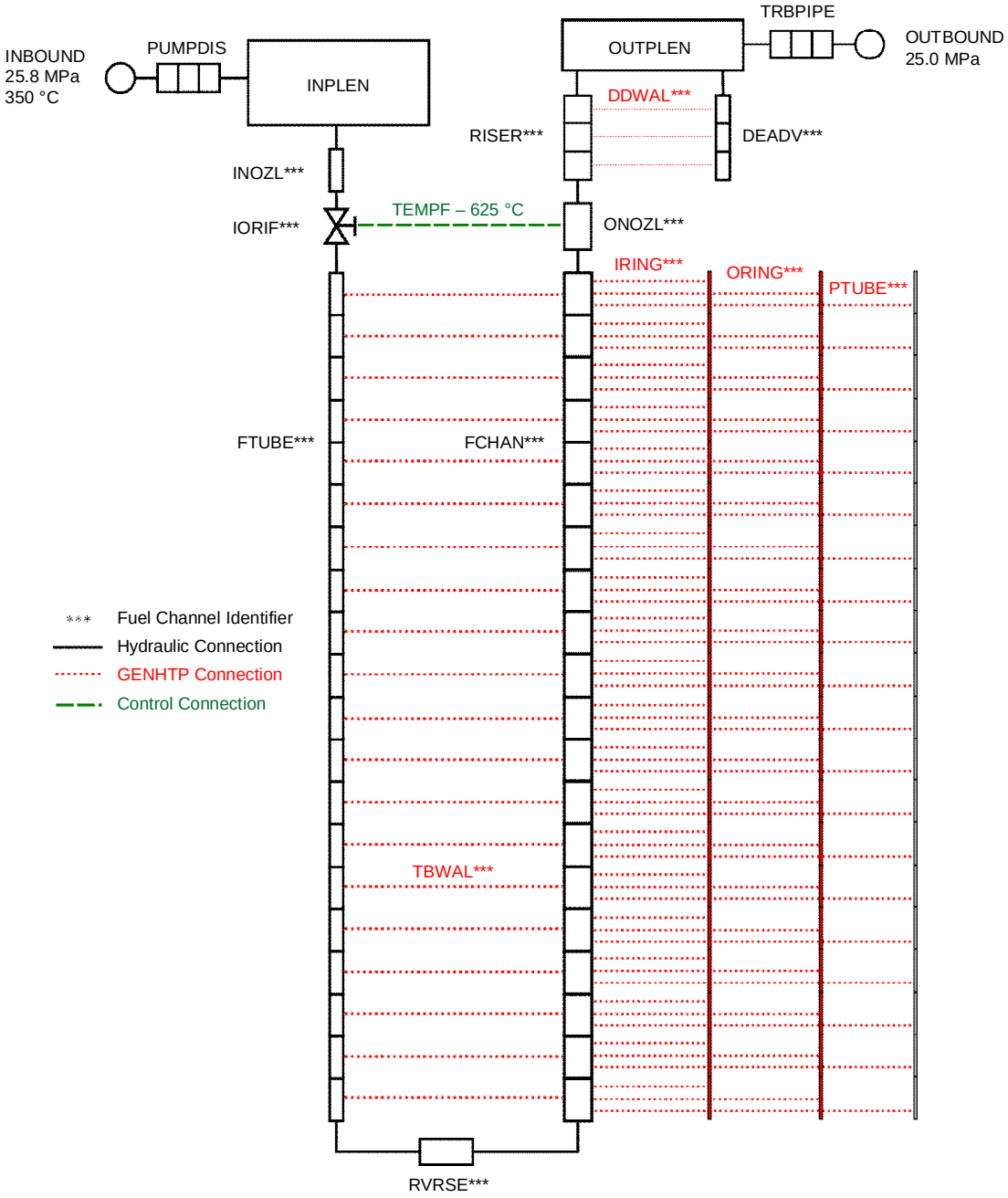

Figure 5. CATHENA idealization of the PT-SCWR

Valve type components, located at the junction of the inlet nozzle and centre flow tube in each channel, are used as flow-limiting orifices that match each channel's flow to its power, ensuring

a uniform coolant outlet temperature of 625 °C. A PI (Propotional-Integral) controller is used to find a unique open fraction for each channel for each discrete core state (e.g. BOC or EOC). The requirements for these flow-limiting orifices were studied previously and it was concluded that no static open fraction could ensure acceptable temperature drift during a cycle without a reactivity control system shaping the channel power distribution [14]. Nevertheless, realistic initial conditions (i.e. close to the reference conceptual design specifications) are necessary for simulating relevant transients. The valve controllers are thus used exclusively in generating steady-state initial conditions and are disabled (thereby assuming static values corresponding to the initial channel powers) when simulating coupled transients.

2.3 Neutronics-Thermalhydraulics Coupling and Transient Simulation Procedures

DONJON uses the Improved Quasi-Static (IQS) method to model spatial kinetics [5]. The IQS module requires the initial forward and adjoint flux distributions (determined by the 3D neutron diffusion calculation), the perturbation in macroscopic cross-sections, neutron kinetic data (delayed group fractions and precursor half-lives), and the time step over which to evaluate the transient. The single set of kinetics parameters were evaluated for fuel near the core mid-plane (2.375 m). Other studies have shown that these parameters are only weekly dependent on the local thermalhydraulic conditions, so this should be a valid approximation [15].

The macroscopic cross-sections for the transient are provided by the AFM module. This module accesses the FeedBack Matrix (FBM) of thermalhydraulic feedbacks (created by DRAGON) and, given the values of thermalhydraulic parameters in each node, generates complete cross-sections corresponding to the current conditions in the core. The differences in cross-sections from the previous step are input to IQS. This process is summarized in Figure 6.

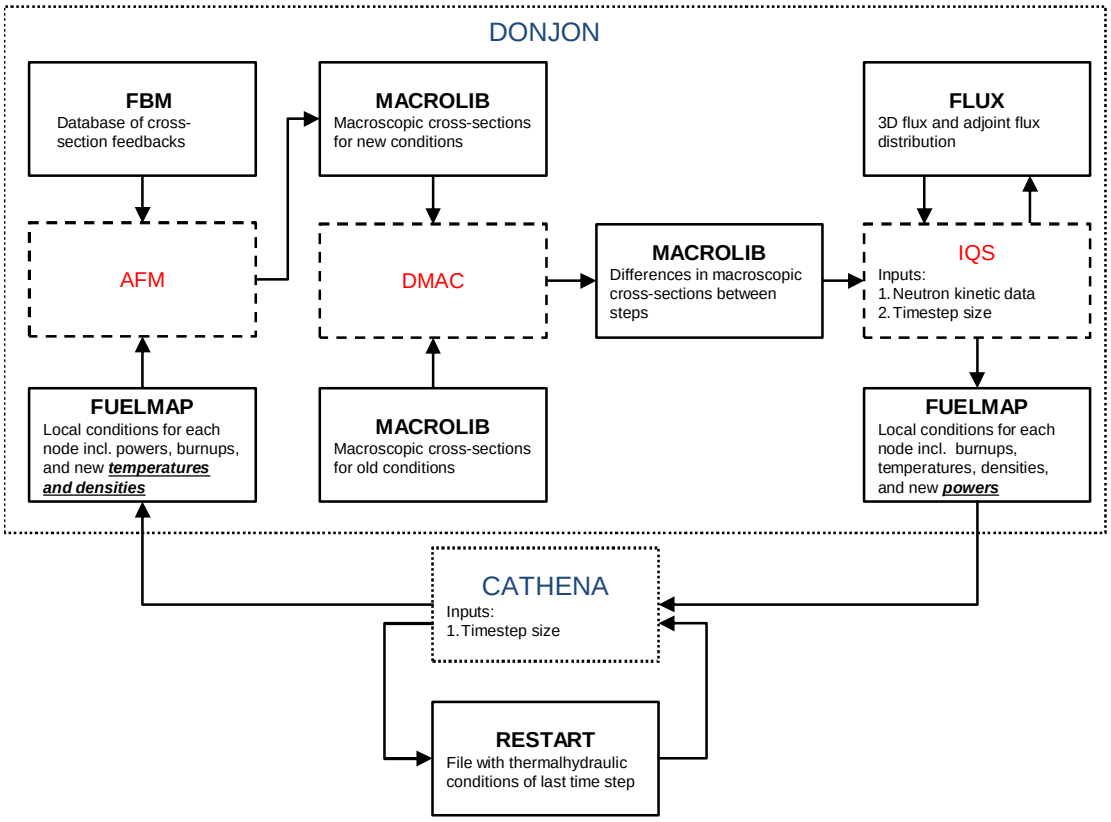

Figure 6. Transient coupling procedure used for DONJON and CATHENA

The FUELMAP data structure read by AFM contains the current conditions for each node in the core, including power, burnup, coolant density and temperature in the centre flow tube, coolant density and temperature in the fuel region, and fuel temperature. This FUELMAP, saved as a file after every step, facilitates the coupling between DONJON and CATHENA. The coupling script reads the power data written in the FUELMAP and creates new CATHENA input using the new power distribution. CATHENA is then executed, continuing immediately from the previous calculation, to generate new distributions of densities and temperatures. The coupling script parses the CATHENA output and writes the new thermalhydraulic conditions to the FUELMAP file to be read by AFM.

The IQS module in DONJON and the CATHENA calculation both use the same time step size. In the coupling algorithm shown in Figure 6, DONJON "leads" the transient over a step and CATHENA "catches up". The size of the step is determined dynamically by the coupling algorithm based on the maximum power rate of change in each node. If the maximum difference in node power from the previous step exceeds 0.5 per cent, the current step is reattempted with a smaller step size. Similarly, if the criterion is satisfied for multiple consecutive steps the size is increased. This work used minimum and maximum time steps of 0.0005 s and 0.5 s respectively.

3. Simulation Results

Without reactivity devices included in the model, the easiest way to initiate transients in the PT-SCWR core is to modify the thermalhydraulic boundary conditions. These boundary conditions are shown in the CATHENA nodalization (Figure 5) attached to the pump discharge (the inlet boundary) and the turbine (the outlet boundary). This study focussed on inlet temperature and pressure transients.

Generally no changes in the core radial power shape were observed in these transients. Since each channel equally experiences changes to the boundary conditions (i.e. there is no flow distribution modelled within the inlet and outlet plena) and each channel's inlet orifice was artificially matched to its initial power, this result is not surprising. The focus of the analysis will instead be directed towards the axial shape variation.

3.1 Temperature Perturbations

Figures 7 through 10 show the transient results of a relatively modest 5 °C reduction to the coolant inlet temperature.

Figure 7 shows the evolution of the core-wide parameters following the step temperature decrease at 5 s. The reactor gradually reaches a new steady power at approximately 95 per cent of the initial value. There is a small but noticeable delay between the temperature change and the beginning of the power transient. The large fluid volume in the inlet plenum likely dampens and delays the effects of coolant inlet temperature variations. At 300 s the inlet temperature is stepped back to the initial value of 350 °C and the core power follows a similar trajectory in returning to its initial steady-state value.

The values shown in Figure 8 are averaged by plane (i.e. each point is the average of all 84 channels in the quarter-core) and correspond to the 20 axial nodes used to model the channels. While the model includes coolant temperature feedbacks, generally the magnitude is smaller than for the coolant density so the temperature profiles are omitted. There are two clearly defined axial profiles corresponding to each of the steady power levels achieved in Figure 7, and the variation in axial properties is equally slow as the integral parameters (10 s after the perturbation the new profiles are indistinguishable).

Figures 9 and 10 show the same transient executed at the EOC core state. Similar trends are observed, but the magnitude of the power transient is much larger (in this case decreasing to approximately 85 per cent of full power). The thermalhydraulic feedbacks are seen to be much larger with burnt fuel.

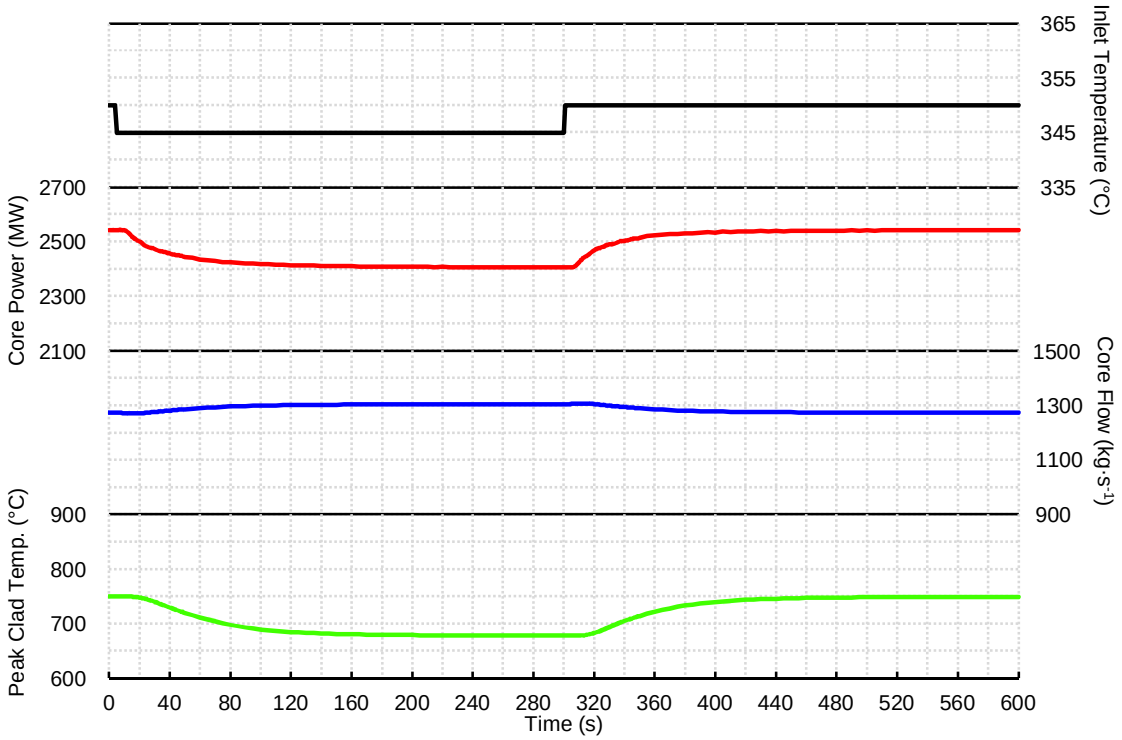

Figure 7. Integral core parameters for inlet temperature step change at BOC

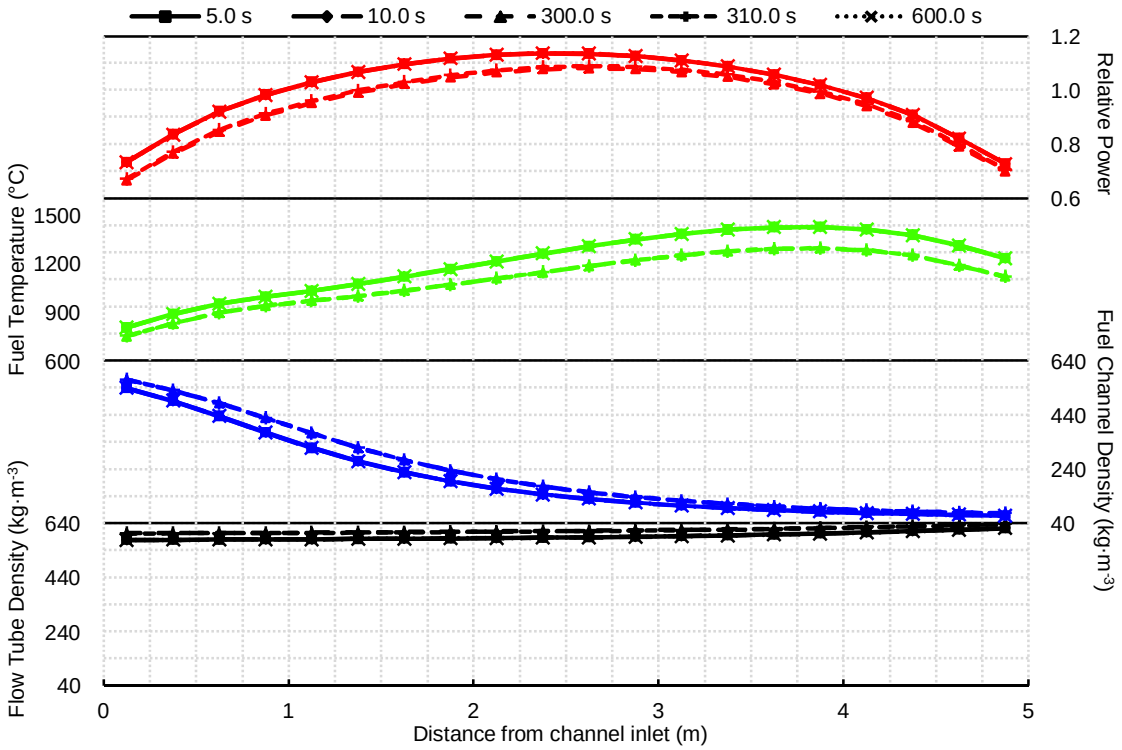

Figure 8. Plane-averaged axial properties for inlet temperature step change at BOC

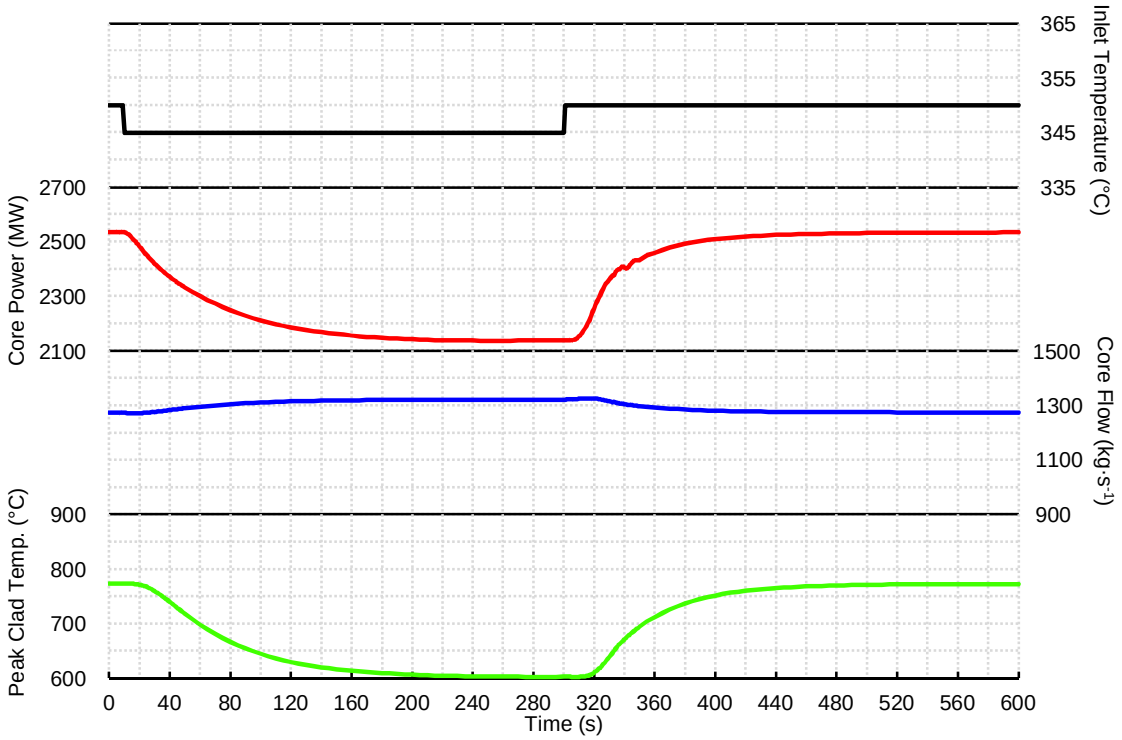

Figure 9. Integral core parameters for inlet temperature step change at EOC

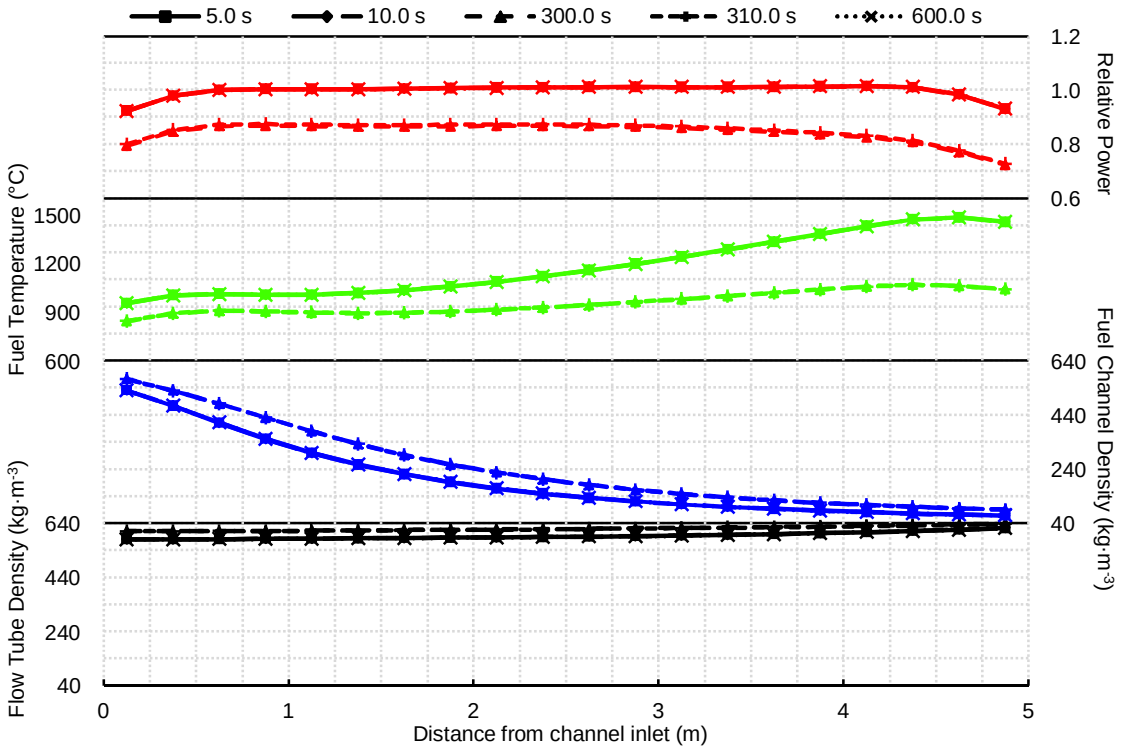

Figure 10. Plane-averaged axial properties for inlet temperature step change at EOC

An interesting observation is that the axial power profile does not shift the same way for BOC and EOC core states from the same coolant temperature perturbation. Figure 8 shows that at BOC the power is more depressed at the inlet, but at EOC the greater depression is at the outlet. This is likely due to the large differences in the initial fuel temperature, power, and burnup profiles between the core states since the initial fluid property distributions are largely determined by the inlet orifices.

3.2 Pressure and Flow Perturbations

The pressure boundary conditions are used to initiate flow transients in the PT-SCWR core. Some care must be given when interpreting the results of these simulations given the artificial nature of specifying pressures at the core inlet and outlet. The exact pressure transients imposed for this work may not be possible in the real system. Nevertheless, since the objective of this study was to examine how the coupled system responds, controlling the boundary conditions in this way is a straight forward means of achieving the desired conditions.

Figures 11 and 12 show a transient where the inlet pressure falls from 25.8 MPa to 25.4 MPa and then quickly recovers. The result is a momentary drop in the core flow which in turn causes the coolant density in the fuel region to decrease as heat continues to be removed from the fuel. The positive reactivity worth of the density reduction causes a power increase, but since the flow quickly recovers the density increases and the power rise is arrested. The core quickly returns to the initial steady conditions.

Figures 13 and 14 show a “flow rundown” transient where the inlet pressure exponentially decays to match the outlet pressure. This is similar to a postulated primary heat transport pump rundown without reactor SCRAM. The decreasing coolant density in the fuel region again causes a power increase, but in this case the pulse is arrested by the density decrease in the centre flow tube. The negative reactivity worth of the centre flow tube density decrease is sufficient enough that the reactor power is approaching zero within 25 seconds of initiating the transient. The peak cladding temperature in the core is very high in spite of the low power due to the flow stagnation that has occurred in the channels.

Figures 15 and 16 show a “flow reversal” transient where the inlet pressure rapidly drops below the outlet pressure, causing fluid to flow backwards from the outlet plenum to the inlet plenum. This can be interpreted as a large LOCA following an inlet pipe break, but there’s an important caveat in the way this was implemented. The version of CATHENA used in this work was unable to model transition over the supercritical/subcritical boundary at 22.1 MPa. The inlet pressure transient was limited to 23.0 MPa to ensure that no hydraulic volume neared the boundary, but the transient was allowed to continue to examine the behaviour of the system in reverse flow. The depicted transient is thus not a realistic simulation of a LOCA, but was nevertheless successful in achieving the desired flow reversal.

Figure 15 shows that the core undergoes a complicated flow transient as a result of the inlet pressure falling so suddenly. Three seconds after initializing the transient the flow has relatively stabilized at a small negative value. Reverse flow means that low density fluid is coming back in to the channel from the outlet plenum, and this causes a large power increase (> 210 per cent full power) that’s terminated once the low density fluid reaches the centre flow tube. The duration of the pulse is approximately four seconds, after which the core rapidly shuts down due to the loss of coolant in the centre flow tube.

Figure 16 also shows a notable shift of the axial power profile towards the nominal channel outlet during the power pulse. This is consistent with the progression of the low density fluid during the flow reversal. The coolant density in the fuel region will first decrease nearest to the outlet, but the flow tube density at the same axial position will be the last to decrease since the fluid has to twice travel the length of the channel.

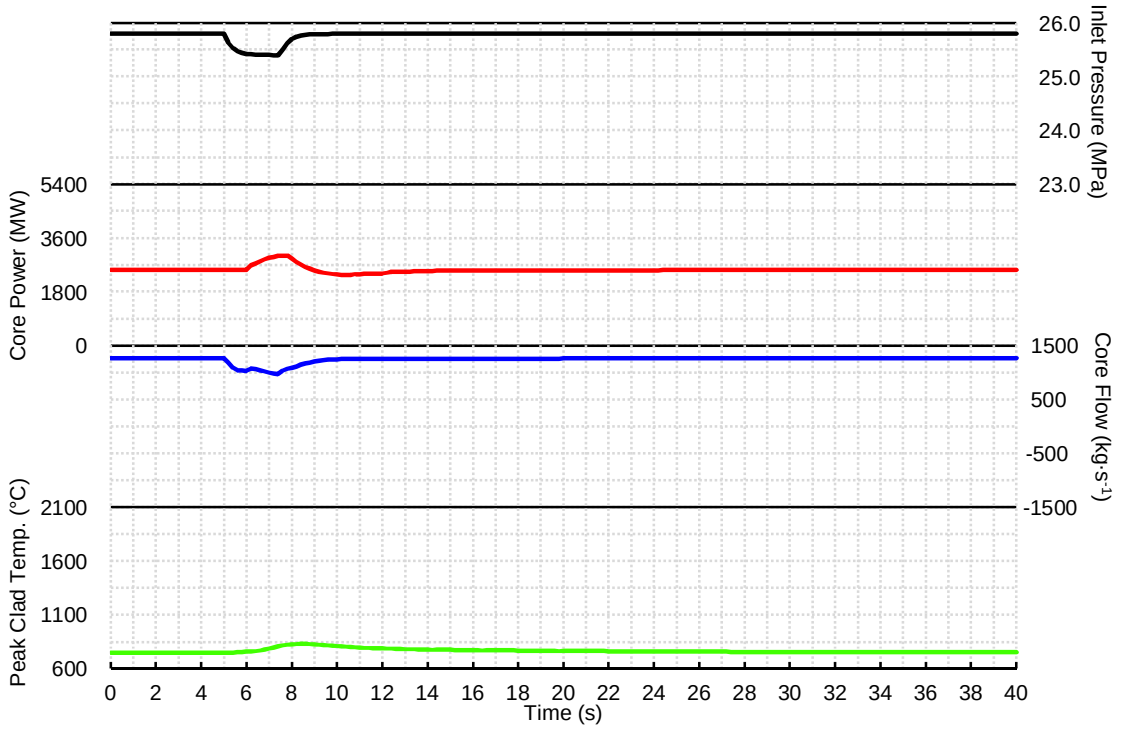

Figure 11. Integral core parameters for inlet pressure perturbation at BOC

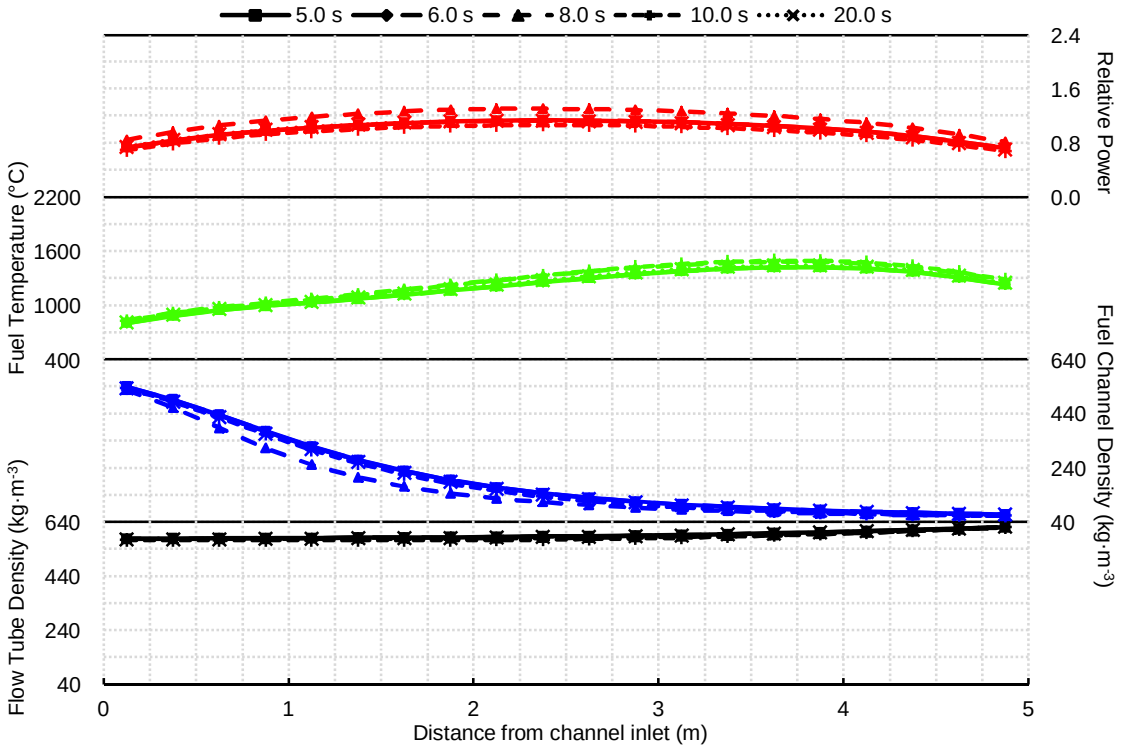

Figure 12. Plane-averaged axial properties for inlet pressure perturbation at BOC

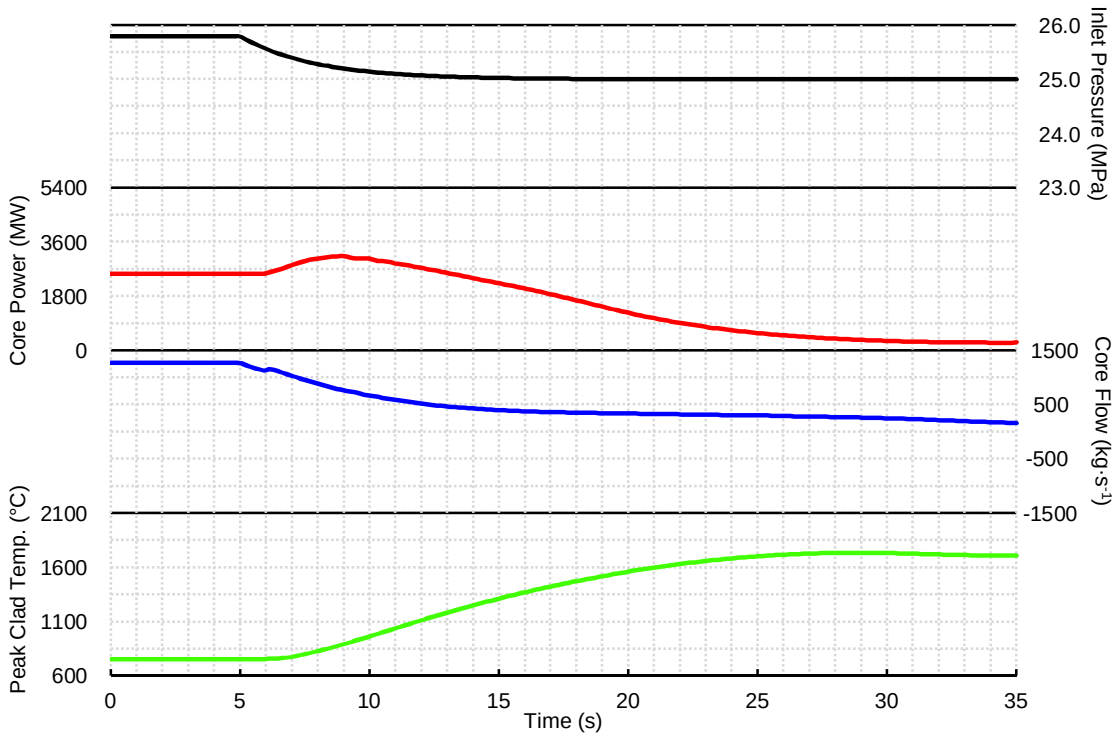

Figure 13. Integral core parameters for inlet pressure rundown at BOC

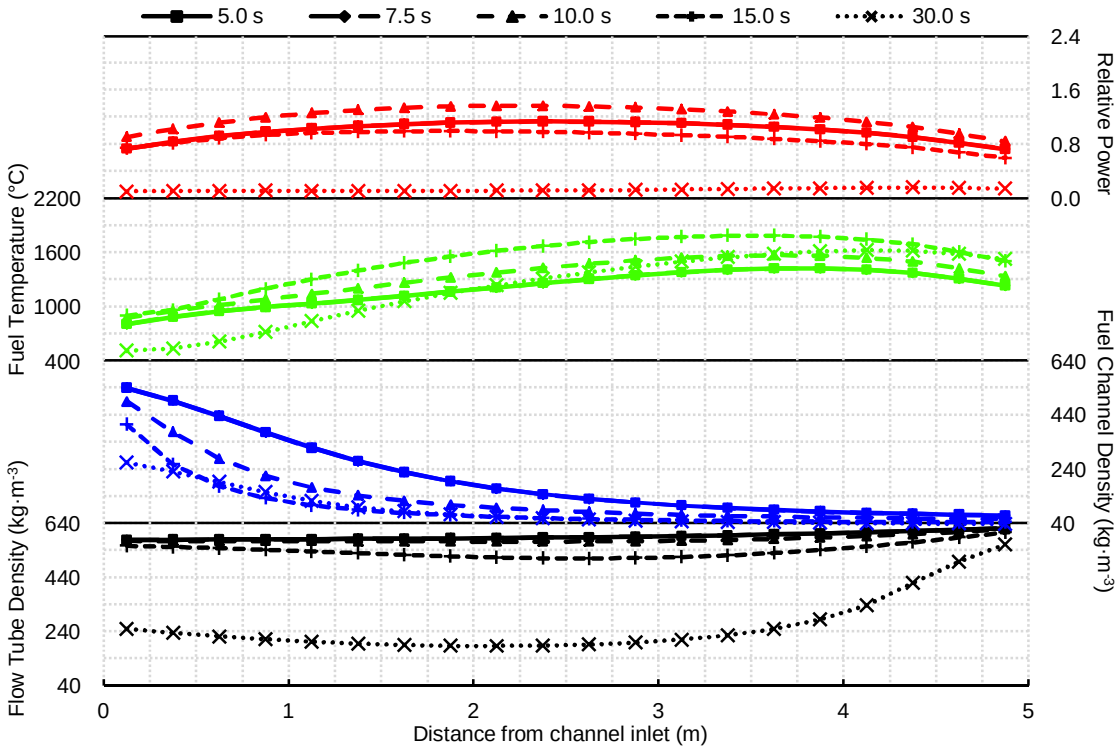

Figure 14. Plane-averaged axial properties for inlet pressure rundown at BOC

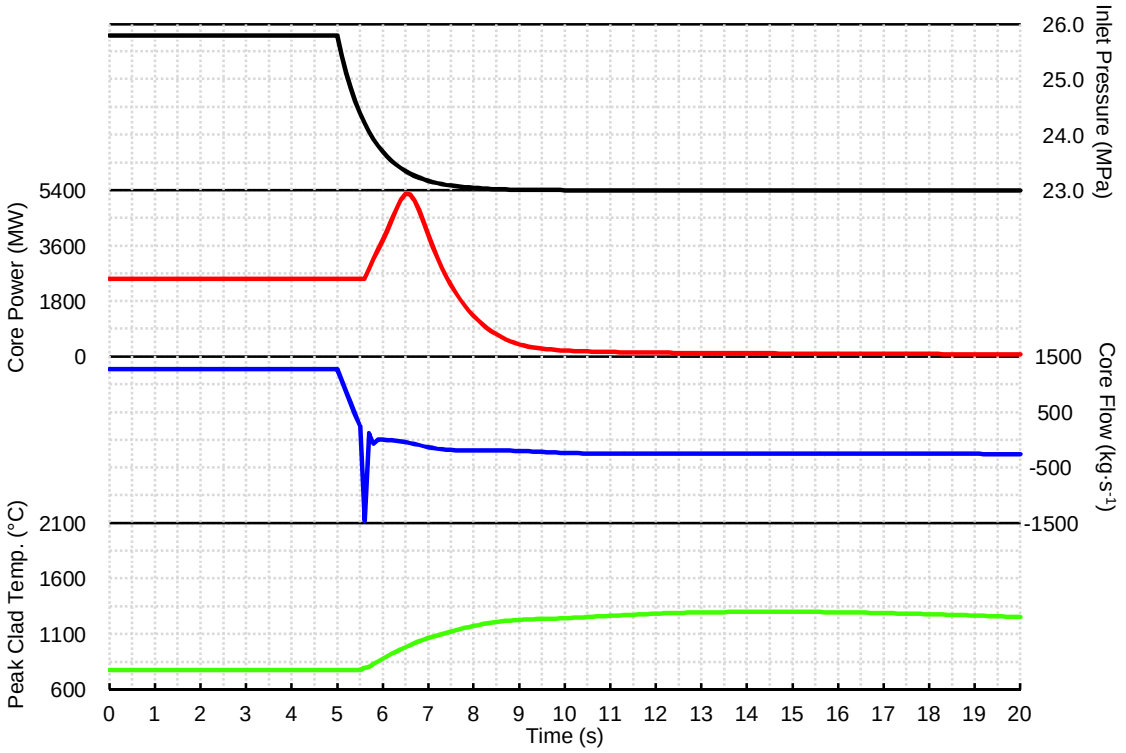

Figure 15. Integral core parameters for flow reversal transient at EOC

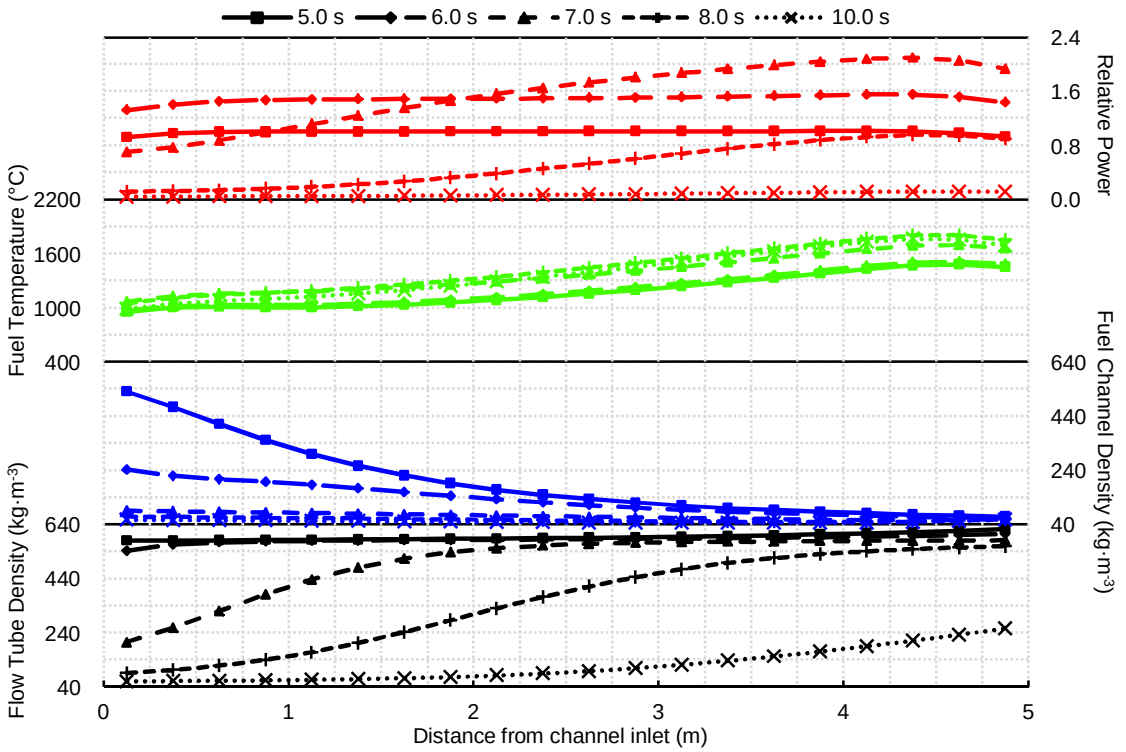

Figure 16. Plane-averaged axial properties for flow reversal transient at EOC

4. Conclusions

A 3D coupled thermalhydraulics and spatial kinetics model of the PT-SCWR conceptual design has been created. This model has been used to model several postulated transients initiated by changes to the core boundary conditions. From analysis of these transients it's possible to make several conclusions regarding the PT-SCWR conceptual design:

- In general, power transients with higher burnup fuel (i.e. end-of-cycle as compared to beginning-of-cycle) will be larger in magnitude;
- The reactor will reach a unique steady power as a function of the coolant inlet temperature (observed changes were 1-3 per cent full-power per degree Celsius);
- The core will return to its original operating conditions after brief perturbations to the coolant flow or temperature without oscillations;
- A sudden reduction or reversal in core flow is likely to cause a small power pulse.

It will be useful to expand this analysis by including reactivity control devices in the core model, which will eliminate the need for approximating variable flow-limiting orifices at the inlet of each channel and will allow reactivity-initiated transients to be simulated.

5. Acknowledgements

Funding to the Canada Gen-IV National Program was provided by Natural Resources Canada through the office of Energy Research and Development, Chalk River National Labs, and the Natural Sciences and Engineering Research Council of Canada.

The authors would also like to thank Professor Guy Marleau at École Polytechnique de Montréal for his help implementing the thermalhydraulic feedback model in DRAGON and DONJON.

References

1. L. K. H. Leung, M. Yetisir, W. Diamond, D. Martin, J. Pencer, B. Hyland, H. Hamilton, D. Guzonas, and R. Duffey, "A Next Generation Heavy Water Nuclear Reactor with Supercritical Water as Coolant," in *International Conference on Future of Heavy Water Reactors*, Ottawa, 2011.

2. M. Yetisir, M. Gaudet, and D. Rhodes, "Development and Integration of Canadian SCWR Concept with Counter-Flow Fuel Assembly", in *The 6th International Symposium on Supercritical Water-Cooled Reactors (ISSCWR-7)*, Shenzhen, 2013.

3. J. Pencer and A. Colton, "Progression of the Lattice Physics Concept for the Canadian Supercritical Water Reactor" in *34th Annual Conference of the Canadian Nuclear Society*, Toronto, 2013.

4. G. Marleau, A. Hébert, and R. Roy, "A User Guide for DRAGON 3.06", Montréal, 2008.

5. E. Varin, A. Hébert, R. Roy, and J. Koclas, "A User Guide for DONJON Version 3.01," Montréal, 2005.

6. D. W. Hummel, S. E. Langton, M. R. Ball, D. R. Novog, and A. Buijs, "Description and Preliminary Results of a Two-Dimensional Lattice Physics Code Benchmark for the Canadian Pressure Tube Supercritical Water-cooled Reactor (PT-SCWR)," in *The 6th International Symposium on Supercritical Water-Cooled Reactors (ISSCWR-6)*, Shenzhen, 2013.

7. G. Harrison and G. Marleau, “Simulation Strategy for the Evaluation of Neutronic Properties of a Canadian SCWR Fuel Channel,” in *Science and Technology of Nuclear Installations*, 2013.

8. F. Salaun, D. W. Hummel, and D. R. Novog, “The Impact of the Radial Reflector on the 8-Group Cell-Averaged Cross-Sections for the SCWR 62-element Lattice Cell,” in *2014 Canada-China Conference on Advanced Reactor Development (CCCARD-2014)*, Niagara Falls, 2014.

9. International Atomic Energy Agency, “WIMS Library Update Project,” 28 January 2008. [Online]. Available: http://www-nds.iaea.org/wimsd. [Accessed 29 October 2012].

10. T. Kozlowski and T. J. Downar, “Pressurized Water Reactor MOX/UO2 Core Transient Benchmark – Final Report,” Paris, 2006.

11. J. Pencer, D. Watts, A. Colton, X. Wang, L. Blomely, V. Anghel, and S. Yue, “Core Neutronics for the Canadian SCWR Conceptual Design,” in *The 6th International Symposium on Supercritical Water-Cooled Reactors (ISSCWR-6)*, Shenzhen, 2013.

12. B. N. Hanna, “CATHENA: A thermalhydraulic code for CANDU analysis,” *Nuclear Engineering and Design*, vol. 180, pp.113-131, 1998.

13. D. F. Wang and S. Wang, “A CATHENA Model of the Canadian SCWR concept for Safety Analysis,” in *The 6th International Symposium on Supercritical Water-Cooled Reactors (ISSCWR-6)*, Shenzhen, 2013.

14. D. W. Hummel and D. R. Novog, “Optimized Channel Inlet Orifice Sizing for the Pressure Tube type Supercritical Water Cooled Reactor,” in *The 19th Pacific Basin Nuclear Conference (PBNC 2014)*, Vancouver, 2014.

15. J. Pencer, M. McDonald, and V. Anghel, “Parameters for Transient Response Modelling for the Canadian SCWR,” in *The 19th Pacific Basin Nuclear Conference (PBNC 2014)*, Vancouver, 2014.

The 7th International Symposium on Supercritical-Water-Cooled Reactors, ISSCWR-7-#2097
Hotel Radisson Blu Royal, Helsinki, Finland, March 15-18, 2015

Fuel Assembly Design for Supercritical Water-Cooled Reactor

Feng Linna，Zhu Fawen，Pang Hua，Li Xiang，Li Qing
(Nuclear Power Institute of China, Chengdu of Sichuan Province, 610041, China)

Abstract

The supercritical water-cooled reactor has been selected as one of the most promising reactors for Generation Ⅳ nuclear reactors due to its higher thermal efficiency and more simplified structure compared to state-of-the-art LWRs. However, there are a large number of potential problems needed to be dealt with, particularly the fuel assembly design of supercritical water-cooled reactor. SCWRs are a kind of high-temperature, high-pressure, water-cooled reactors that operate above the thermo-dynamic critical point of water (374℃, 22.1 MPa). Corrosion and degradation of materials used in supercritical water environments are determined by several environment and material dependent factors. In particular, irradiation-induced changes in microstructure and microchemistry are major concerns in a nuclear reactor. Many structural materials including alloys and ceramics have been proposed for use as SCWR components or materials for applying protective coatings in SCWRs. In this paper, the present status of supercritical fuel assembly design at home and abroad is studied. According to the special requirements of supercritical core design, a kind of configuration design of fuel assembly with two-flow core and using SiC as cladding material is proposed. The analysis results have shown that, the design basically meets the requirements of fuel assembly design, which has good feasibility and performance.

Introduction

The Supercritical Water-cooled Reactor (SCWR) is one of the six concepts of the Generation IV International Forum, which has an operating pressure of 25MPa and a core outlet temperature of over 500℃. SCWR is a promising advanced nuclear system because of its high thermal efficiency (about 45% vs. about 33% efficiency for current Light Water Reactors, LWRs) and more simplified structure.

However, the high outlet temperature and high enthalpy in the core cause many challenges to fuel assembly design of SCWR. The high outlet temperature increases the complexity of core design and the temperature difference between inlet and outlet temperature is up to 220℃, which results in much change of coolant density and low neutron moderation, so single-pass core no longer meets the requirements of SCWR. In order to solve the temperature difference issue, it is necessary to design a core arrangement with two-pass or three-pass. In this paper, the research development of SCWR fuel assembly at home and abroad is studied and a new design of fuel assembly with two-pass core arrangement is proposed.

The use of SiC in commercial nuclear reactors, particularly as cladding for advanced fuels, could provide substantial safety and economic benefits. Zirconium alloy cladding materials that are presently used in light water reactors present limitations in heat ratings and overall fuel burn-up due to their loss of strength during reactor flow transients and during other overheating accidents, surface oxidation at high burn-up, and their potential for exothermic metal water reactions at design base loss of coolant accident conditions. On the other hand, SiC possesses excellent high-

temperature mechanical properties, and it has been shown to be stable under superior high-temperature and neutron irradiation [1, 2]. Considering its safety and economics, in this paper, SiC is chosen as the clad material.

1. Development status

So far, many countries have participated in the development of SCWR technology, and most thermal SCWR concepts can be generalized in the following manner. The assemblies are of square or hexagonal type with water rods or solid pins (mostly zirconium-hydride) as extra moderator. The high enthalpy rise in the core enables the use of two- and three-pass cores, which reduce the maximum cladding temperature, but increase the complexity of core design [3]. Among all conceptual designs of SCWR fuel assemblies, the Japanese and European concepts are the most typical, although the complicated water flow path sets new challenges. The main typical conceptual designs of fuel assembly are introduced as follows.

1.1 Japanese design

In Japan, the SCWR concept was first named SCLWR-H, which is called Super LWR later. A two-pass core with 121 fuel assembly boxes is adopted by Japan [4]. Each fuel assembly box comprises 300 fuel rods, 36 square water rods and 24 periphery rectangle water rods. Instrumentation tube is located at the center of whole fuel assembly, and guide tubes are located at the center of 16 water rod boxes. The cross-section of SCLWR-H fuel assembly is shown in Fig.1.

In Fig.1, the outer diameter of fuel rods is 10.2 mm, with a cladding thickness of 0.63 mm and a fuel rod pitch of 11.2 mm. The thickness of water rod boxes is 0.2 mm, while the wall thickness of fuel assembly boxes is among 2.5~3.0 mm. An active core height of 4200 mm and a fuel assembly pitch of 292.4 mm are adopted. All structural and cladding materials are nickel-base alloy.

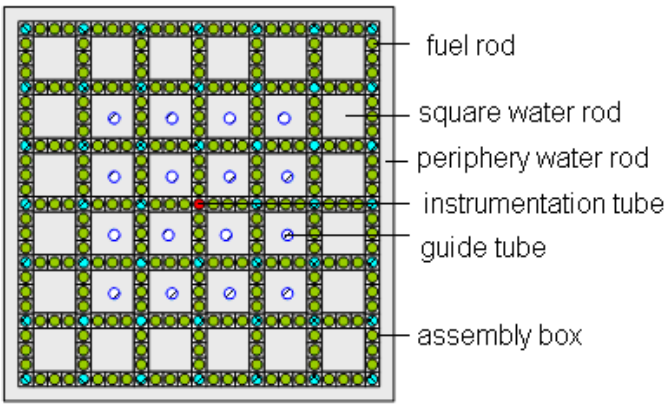

Fig.1 SCLWR-H fuel assembly of Japan

1.2 European design

In Europe, investigations on SCWR have been integrated into a joint research project, called High Performance Light Water Reactor (HPLWR) [5]. In order to achieve the high outlet temperature of over 500℃, a core with a three-pass arrangement is proposed to keep local cladding temperatures within current material limits. A fuel assembly cluster consisting of nine subassemblies and with a gap of 10 mm between the boxes is shown in Fig.2.

In Fig.2, A total number of 40 fuel rods in each subassembly with 8 mm outer cladding diameter at a pitch of 9.44 mm is housed within a stainless steel box of 2.5 mm wall thickness and 72.5 mm outer size. A single wire of 1.34 mm diameter is wrapped around each fuel rod, leaving a tolerance of 0.1 mm between the wire and the fuel rods or the box walls, respectively. The inner moderator box made by stainless steel has an outer size of 26.9 mm and a wall thickness of 0.8 mm. The cladding thickness is 0.5 mm. The active length is 4200 mm, resulting in a fuel rod length of more than 4700 mm [6]. The clad material is 316L.

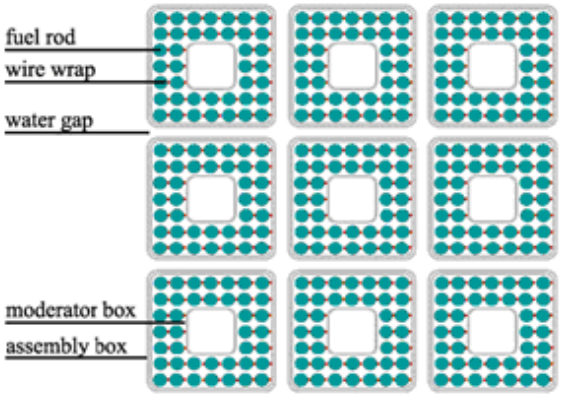

Fig.2 HPLWR fuel assembly of Europe

1.3 American design

American SCWR concept has been developed by INEEL, ANL, ORNL, Westinghouse, BREI and MIT. Its concept is similar with SCLWR-H and HPLWR. The fuel assembly box comprises fuel rods, square water rods and periphery rectangle water rods. Instrumentation tube is located at the center of whole fuel assembly, and guide tubes are located at the center of water rod boxes.

E. Barringer et al. have investigated the behavior of SiC in deoxygenated supercritical water at 500℃ [7]. The research results show that High-purity CVD (Chemical Vapor Deposition) b-SiC present relatively low corrosion rates in deoxygenated supercritical water at 500℃. Few about SiC as clad in supercritical water has been reported in the open literature and the existing database is limited.

1.4 Canada design

Canada ’s CANDU-SCWR concept has been developed by AECL. The fuel assembly of CANDU-SCWR (shown in Fig.3) keeps on the pressure tube (PT) / Calandria tube (CT) design developing from CANDU and the moderator adopts heavy-water. PT operates at coolant temperature and the moderator operating at low temperature/pressure flows around CTs. Compared with CANDU, CANDU-SCWR fuel enhances passive safety, because the insulator provides controlled heat rejection to moderator and the insulator thickness is optimized to obtain usual heat loss by conduction/convection to the moderator under normal operation and sufficient heat rejection by radiation/conduction/convection under accident conditions [8].

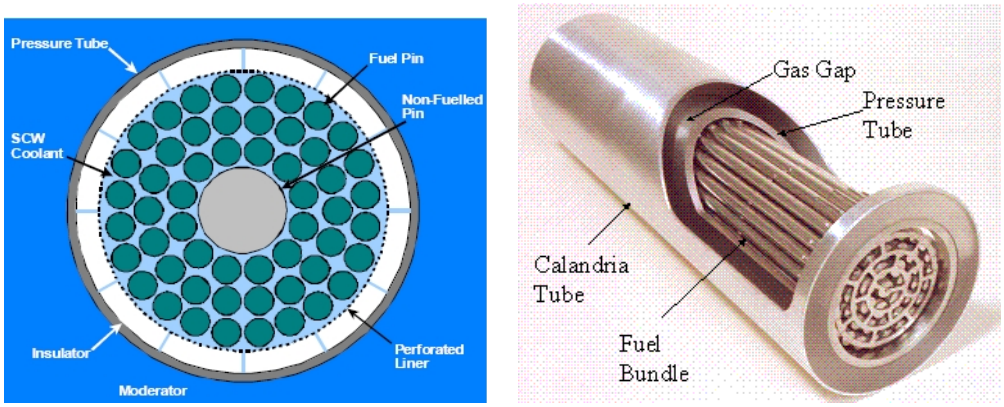

Fig.3 CANDU-SCWR fuel assembly of Canada

2. The design of fuel assembly

The difficulty of SCWR fuel assembly design embodies mainly two aspects: one is supplying sufficient and even neutron moderation for each fuel rod. The other is that, the design of fuel assembly should be relatively simplified and easy to be manufactured.

2.1 Materials

Many structural materials including alloys and ceramics have been proposed for use as SCWR components or materials for applying protective coatings in SCWRs. Various surface modification processes are also explored to change the chemical composition and microstructure of the near surface regions. Zirconium alloy cladding materials that are presently used in light water reactors present limitations in heat ratings and overall fuel burn-up due to their loss of strength during reactor flow transients and during other overheating accidents, surface oxidation at high burn-up, and their potential for exothermic metal water reactions at design base loss of coolant accident conditions.
SiC has been studied extensively for use in fuels because of its superior high-temperature tolerance and reasonable stability under neutron irradiation. Advantages also suggest that SiC has a high potential for use as a fuel cladding materials for light water reactors (LWRs) in the pursuit of power up rates with improved safety. Particularly after the Fukushima Dai-ichi nuclear power plant accident, which showed that the current Zr alloy claddings do not have sufficient accident tolerance to guarantee fuel safety in the case of beyond-design-basis accidents, the research efforts to use SiC as fuel claddings are significantly increasing. The manufacturing technology for SiC cladding has been improved over the last decade to fulfill the requirements of LWR fuels. One of the proposed designs for SiC cladding has a triplex structure that consists of an inner monolith layer for fission-gas retention, a fiber-reinforced matrix composite middle layer for superior mechanical performance, and an outer coating layer for oxidation resistance [9, 10]. So SiC can be considered as the candidate materials of SCWR fuel clad.
However, there are still many hurdles to be overcome before SiC claddings can be used for fuel clad:1) A variety of SiC performances must be evaluated over a wide range of operation conditions, including normal operation and a severe accident. 2) The pellet-clad gap should be designed appropriately to solve the swell induced by irradiation because the plasticity of SiC is not quite well. 3) the sealing technology of SiC clad should be researched further.

2.2 Assembly style

A systematic design study shows that a square fuel assembly with two rows of fuel rods and a central moderator box is best to minimize the structural material, to optimize the moderator to fuel ratio and to reduce differences of fuel rod power [11]. According to the design basis of SCWR fuel assembly at home and abroad, as well as synthetically considering the manufactural realization, a new design of fuel assembly with a gap of 21 mm between the assembly boxes is proposed, as shown in Fig.4.

In Fig.4, the 2 × 2 fuel assembly cluster consisting of four subassemblies has 224 fuel rods, 4 square moderator boxes and 4 guide thimbles. A 9 × 9 square arrangement for fuel rods in each subassembly is adopted, while central moderator box takes up 5 × 5 fuel rod cells. The outer diameter of fuel rod is 9.5 mm, with a cladding thickness of 0.57 mm and a rod pitch of 10.5 mm. A dual wire with 0.45 mm diameter is wrapped around each fuel rod, leaving a clearance of 0.1 mm between the wire and the fuel rods or 0.05 mm between the wire and the box walls, respectively. The outer length of inner moderator box is 52.5 mm, with a wall thickness of 0.8 mm; while the assembly box has an outer size of 98.5 mm and a wall thickness of 0.5mm with ZrO_2 filling whose thickness is 1.0mm. The cluster side length is 218 mm, which is close to a PWR size, which is convenient during a refueling process. The boxes and cladding materials both are 310S stainless steel, which shows good performance under supercritical water condition.

The cross rod with a width of 8mm is located at the center of 4 moderator box, which is inserted into the cross channel from the top of assembly.

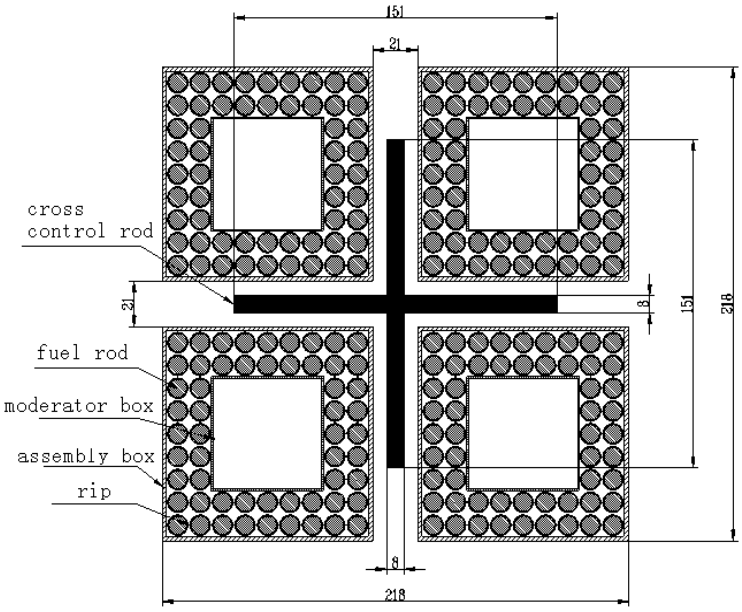

Fig. 4 2×2 assembly cluster of China

2.3 Core flow distribution

As is shown in Fig.5, a two-pass core arrangement is presented and there are 157 fuel assemblies in the core, 57of which are located in the center, signed as “Ⅰ” style fuel assembly; the rest lie in periphery of the core, marked as “Ⅱ” style fuel assembly.

In Fig.5, the flow (100%) entering the core is divided into five parts: 1) 38% coolant flowing downward into “Ⅰ” style fuel assemblies; 2) 6.5% moderator water entering downward moderator boxes of “Ⅰ” style fuel assemblies; 3) 13.7% moderator water entering downward moderator boxes of “Ⅱ” style fuel assemblies; 4) 6% coolant through the downcomer; 5) 35.8% moderator water flowing downward in the gaps between assemblies. All the coolant and moderator water needs to be mixed homogeneously at the core bottom, regarding as the coolant of “Ⅱ” style fuel assemblies rising upward out of the core.

According to the flow distribution data above, the average coolant flow speed of “Ⅰ” style fuel assemblies is 3.1 m/s, while for “Ⅱ” style fuel assemblies, the value is up to 19.3 m/s, which is far beyond the water flow speed of PWR.

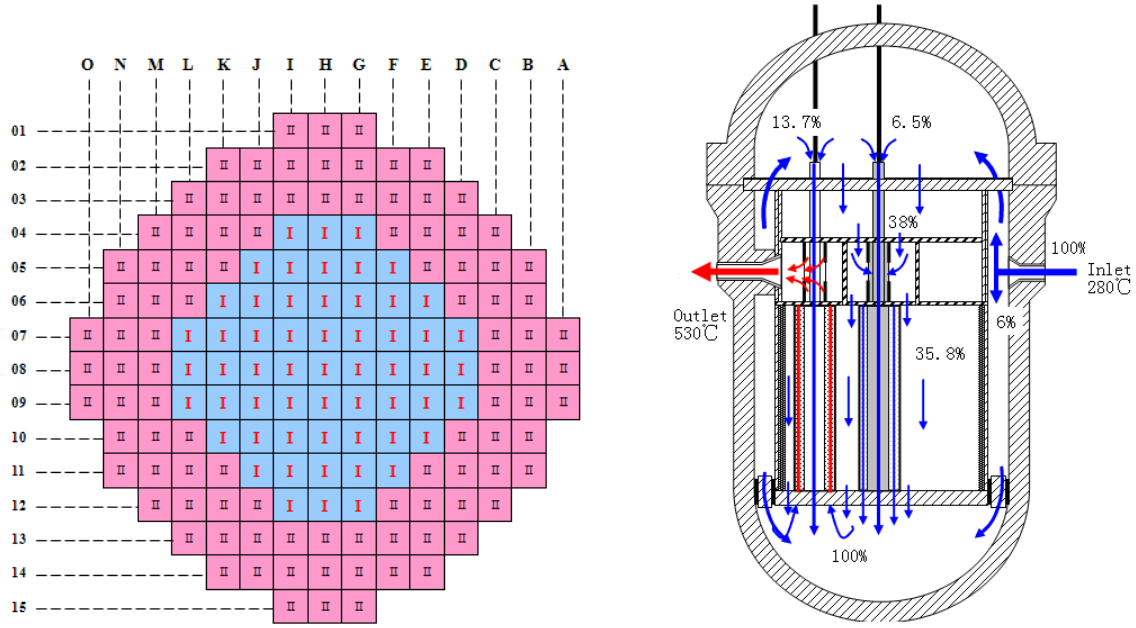

Fig. 5 Two-pass core design and core flow distribution

2.4 Mechanical design

In order to meet refueling requirement, the structure of “Ⅰ” style fuel assemblies must be the same as that of “Ⅱ” style fuel assemblies. Considering two-pass core arrangement, moderator water passage and coolant passage must be separated from each other. In addition, moderator water and coolant should have enough flow area, and there is no interference with structure among the different components of fuel assembly.

According to the requirements above, a kind of fuel assembly cluster designed for SCWR is proposed (see Fig.6(a)). The fuel assembly cluster has a total length of 5.9 m, which is composed by fuel rods, top/bottom nozzle, guide thimbles, adaptor plates, assembly boxes, nozzle connectors, structural grids, moderator boxes, moderator tubes and instrumentation tube. In order to strengthen the laterally support and connect subassemblies into a cluster, 2 grids with a height of 30 mm is

designed. Combining four small assemblies into a common assembly cluster allows reducing the number of individual control rod drives to similar numbers as in a PWR.

2.4.1 Fuel rod design

A preliminary choice of mature fuel design on PWRs is adopted, with a diameter of 9.5 mm and a wall thickness of 0.57 mm, as shown in Fig.6 (b). In order to accommodate more fission gas and reduce the central temperature of fuel pellets, a kind of annular fuel pellet is used, with an outer diameter of 8.192 mm and a central hole of 2.0 mm. The total length of fuel rod is about 4.6 m, of which the active length is 4.2 m.

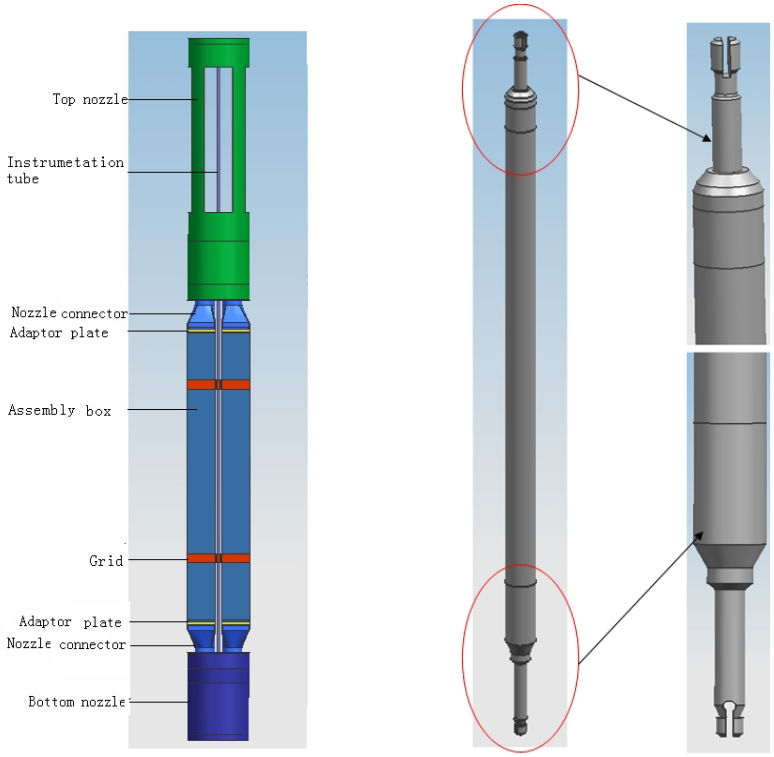

(a) (b)

Fig. 6 The illustration of fuel assembly cluster (a) and fuel rod (b)

The position illustration of fuel rod is shown in Fig.6. Ligaments are welded to adaptor plate at slot position by spot welding, and then top end plug is inserted into the ligament to restrict fuel rod rotary movement, see Fig.7 (a). Fig.7 (b) shows that the position of bottom end plug. The bottom end with a notch is inserted into the adaptor plate and then put the lamellas to the opposite side for realizing the lower position of fuel rod.

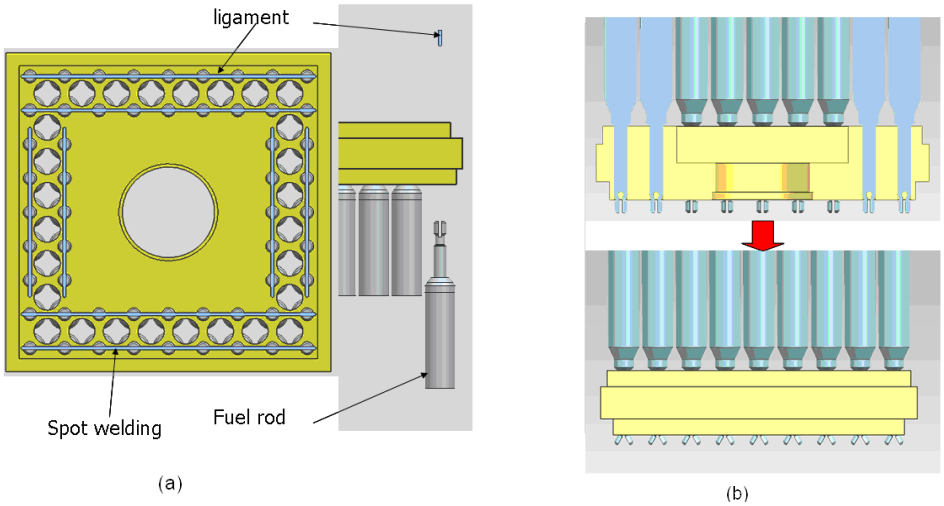

Fig. 7 The position illustration of fuel rod (a) upper position (b) lower position

2.4.2 Head piece

The head piece of fuel assembly cluster is composed by top nozzle, nozzle connectors, base plate, assembly boxes and moderator tubes, as shown in Fig. 8. First, the four assembly boxes shall be welded into the base plate through nozzle connectors and adaptor plates. Then, the top nozzle shall be welded into the base plate. Finally, the moderator tubes shall be welded into the top of the top nozzle. The cross groove is designed for the top nozzle, which supply the cross channel for the cross control rod.

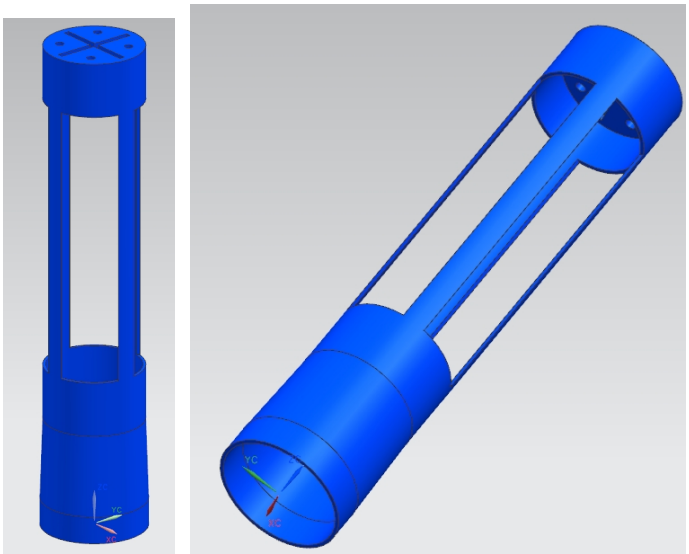

Fig. 8 the top nozzle

2.4.3 Foot piece

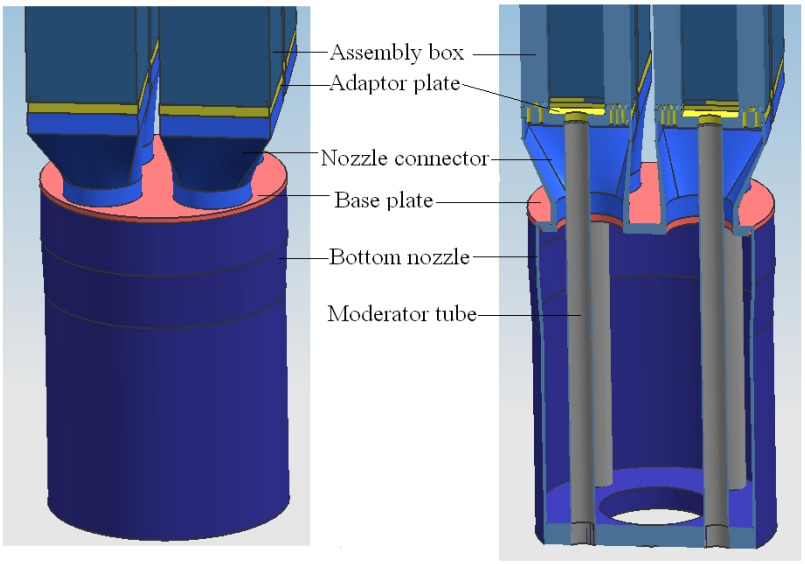

Fig. 9 Foot piece of fuel assembly cluster

The foot piece of fuel assembly cluster is composed by bottom nozzle, nozzle connectors, base plate, assembly boxes and moderator tubes, as shown in Fig. 9. First, the four assembly boxes shall be welded into the base plate through nozzle connectors and adaptor plates. Then, the bottom nozzle shall be welded into the base plate. Finally, the moderator tubes shall be welded into the bottom of the bottom nozzle.

3. Conclusion

A new design of fuel assembly with two-pass core arrangement is proposed in this paper. The results have shown that, the mechanical design basically meets the requirements of fuel assembly design, which has good feasibility and performance.

SiC possesses excellent high-temperature mechanical properties, and it has been shown to be stable under superior high-temperature and neutron irradiation. Considering its safety and economics, SiC is chosen as the clad material.

4. References

[1] E. E. Bloom, ‘ ‘ The Challenge of Developing Structural Materials for Fusion Power Systems, J. Nuclear Mater., 263 [Part A] 7–17 (1998).

[2] D. J. Senor, G. E. Youngblood, C. E. Moore, D. J. Trimble, G. A. Newsome, and J. J. Woods, Effects of Neutron Irradiation on Thermal Conductivity of SiC-Based Composites and Monolithic Ceramics, Fusion Technol., 30 [3 Part 2A] 943–55 (1996).

[3] T.Reiss, Gy.Csom, S.Feher, et al. The simplified Supercritical Water-Cooled Reactor(SSCWR), a new SCWR design, progress in Nuclear Energy 52, 2010, 177-189.

[4] A. YAMAJI, K.Kamai, Y. Oka and S. Koshizuka, Improved Core Design of the High Temperature Supercritical-Pressure Light Water Reactor. Annals of Nuclear Energy, Vol. 32, p.651-670, 2005

[5] T. Schulenberg, J. Starflinger, P. Marsault, et al. European supercritical water cooled reactor, Nuclear Engineering and Design 241, 2011, 3505-3513.

[6] K. Fischer, T. Schulenberg, E. Laurien. Design of a supercritical water-cooled reactor with a three-pass core arrangement, Nuclear Engineering and Design 239, 2009, 800-812.

[7] E. Barringer,w Z. Faiztompkins, and H. Feinroth, Corrosion of CVD Silicon Carbide in 500℃ Supercritical Water, J. Am. Ceram. Soc., 90 [1] 315–318 (2007).

[8] Daniel Brady, Jessica Poupore,Laurence Leung, Generation IV International Forum and Canada's Gen IV National Program, CNSC January 14, 2011

[9] K. Yueh, D. Carpenter, H. Feinroth, Nucl. Eng. Int. (January 2010) 14.

[10] W.J. Kim, D.J. Kim, J.Y. Park, Nucl. Eng. Tec. 45 (2013) 565.

[11] J. Hofmeister, C. Waata, J. Starflinger, et al. Fuel assembly design study for a reactor with supercritical water, Nuclear Engineering and Design 237, 2007, 1513-1521.

ISSCWR7-2098

The influence of the start-up procedure on the corrosion behavior of selected stainless steels in supercritical water

Markéta Kryková[1], Jan Macák[2], Petr Sajdl[2], Zuzana Skoumalová[3], Tomáš Popela[1]
[1]Centrum výzkumu Řež, Hlavní 130, 250 68 Husinec - Řež, Czech Republic, +420720733180,
marketa.krykova@cvrez.cz
[2]Institute of Chemical Technology Prague, Czech Republic
[3]UJV a.s., Czech Republic

Keywords: supercritical water, martensitic stainless steel, austenitic stainless steel

In order to enhance overall efficiency of today's fossil-fuelled power plants the working parameters of the working media – water – are increased substantially. Currently the energy industry is focused on units operating up to 600 °C and 27 MPa the conditions under which water is supercritical. There are many advantages in operating such supercritical unit but several drawbacks as well. One of the biggest negative of supercritical water is its high corrosiveness towards commonly used constructional steels. The corrosion resistance of these materials in supercritical water is given by the quality of oxide layer which forms a barrier between the metal surface and the corrosive media and therefore hinders further corrosion of material. In this paper we studied and evaluated the corrosion behaviour of selected both martensitic the austenitic stainless steels in supercritical water. We modified default boiler start-up procedure and observed whether it has an impact on corrosion behaviour of studied stainless steels. The structure and quality of formed oxide layers were examined by SEM-WDS, electrochemical impedance measurements and Mott-Shottky analyses.

1. Introduction

To increase the thermal efficiency of the power plant installations, the trend is to increase the operational parameters. The parameters of the current power plants are up to 600°C and 27MPa. The properties of the supercritical water (SCW) (above 374 °C and 22MPa) are unique, the high parameters increase the efficiency of the plants, but on the other hand, the SCW is a very corrosive environment and proposes a challenge for the constructional materials.
The usual materials for SCW power plants installations are ferritic-martensitic steels (such as P92, VM-12SHC) and austenitic stainless steels (as Super-304H and HR3C). The P92 steel was developed in Japan in 90´s to increase the creep resistance of the steel P91 [1]. This steel is alloyed by W to increase the strength of the material. It also contains borides it stabilizes chromates as $Cr_{23}C_6$ and decrease the coarsening [2]. The VM-12SHC was developed to increase the creep resistance even more than P92 (and contains up to 13% of Chromium) [3]. The goal of this work was to study the corrosion behaviour of steels P92, VM12-SHC, HR3C and Super 304H.

2. Results and discussion

2.1 Experimental facilities

Two types of experiments were performed. First focused on the corrosion behaviour at operational parameters – the exposition at full parameters (600°C, 25MPa, 1000 hours, pH 9,8 adjusted by ammonia). The water was degassed to D(O_2) concentration ≤ 20 ug/l). The second

type of experiments was focused on the study of the start-up regime influence (same chemical parameters). Three regimes were studied (the parameters are summarized in the chapter below):
Echem – oxide generated by electrochemical repasivation
Ar-SCW – oxide generated only at supercritical conditions of water (580-600°C, 25MPa), the start-up procedure was in argon (18 MPa) atmosphere and then the system was filled pressurized by supercritical water.
SubC-SCW – oxide created only by water environment (580-600°C, 25MPa), the transition from sub-to supercritical conditions is involved.

2.1.1 Supercritical water loop

The primary objective of Supercritical water loop (SCWL) is testing of materials for cladding and in-core structures at operational conditions of the high-performance light-water reactor. The SCWL in Řež is therefore designed for material and water chemistry experiments. The loop itself consists of two main parts, irradiation (active) channel and auxiliary circuits. The operational parameters (600 °C and 25 MPa) are reached in the irradiation channel, which is also designed geometrically to fit into one rig of the research reactor LVR-15. The auxiliary circuits provide the inlet parameters to the channel, sampling, and regulation, chemicals dosing, filtering, purifying and other. Currently, the loop is used out-of-pile for fossil-fuelled supercritical water-cooled power plants material research.

Figure 1: SCWL

2.1.2 Supercritical water autoclave I

In order to perform additional experiments in supercritical water the supercritical water autoclave (SWAc) (Figures 6 and 7) operates in the Centrum výzkumu Řež. It can reach parameters of 600 °C and 25 MPa. The deaerated and demineralized water serves as the medium. The flow rate is 3 ml.min^{-1}. The medium is pressurized up to required pressure by a HPLC pump. The autoclave itself is placed in a 1500 W electrical furnace.
The on-line analysis and monitoring of conductivity of the media in the SCWAc is possible. Other analyses (gas content, water composition, pH) needs to be measured off-line. For this reason, a sampling outlet is installed on the autoclave loop.
In near future a complete upgrade of SCWAc is planned. The new autoclave will allow performing various on-line analyses and will be more reliable (installation of backup pumps etc.).

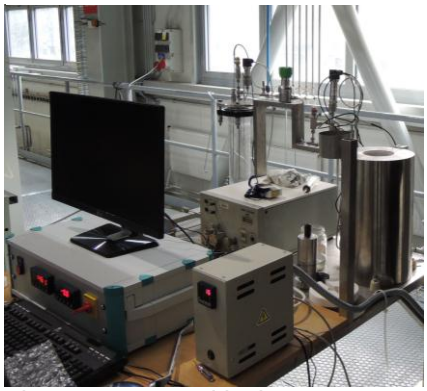

Figure 2: Supercritical Water Autoclave SWAc

2.1.3 Supercritical water autoclave II

The facility supercritical water autoclave placed at University of chemical technology (UCT) is designed and was adjusted to perform the tests focused on the various ways of start-up operation. Experiments were carried out in continuous-flow apparatus without recirculation (Fig. 3). Experimental set-up was composed of a low-volume tube autoclave (20 cm^3) equipped with electrical heating, storage vessel and high-pressure pump.

Demineralised and deaerated (<20ppb of O2) supercritical water (25 MPa and 580 °C) and alkalized by ammonia (pH=9.8) was used. Flow rate of SCW through autoclave was adjusted to 1 ml/min. The size of steel samples (Super 304H, HR3C, VM12-SHC, P92) was approximately 5x8 mm. The samples were polished by emery papers up to 4000 grit. These were exposed in tube autoclave for 12 and 50 hours. Exposures were performed in containing ammonia to pH control (pH 9,8) at 580°C and 25 MPa.

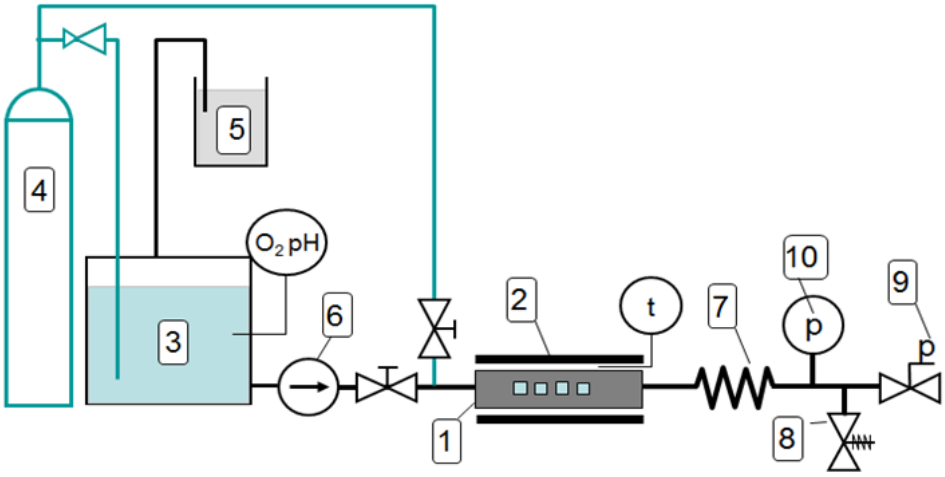

Figure 3: Supercritical water autoclave UCT, 1-Autoclave, 2- heater, 3- tank, 4- Ar supply, 5 – water cap, 6- pump, 7- air cooler, 8- safety valve, 9- regulation valve, 10- pressure sensor

In a part of experiments pre-heating in an inert atmosphere (Ar) was used. This experiment was performed with the aim to assess the influence of the heating up period. During the heating –up, which took approximately 2-3 hours the samples are part of the heating up time exposed to water at subcritical temperature. This may have some influence on oxide chemical and transfer properties. To avoid exposure of samples in sub-critical (t) water during heating up period, the system of autoclave and intake armatures was carefully flushed by argon (99.996%, O_2 content<5ppm) for 30 minutes to ensure the ousting of air. Then the autoclave was pressurized by argon to 18 MPa. The system was heated up to 580 °C in argon atmosphere and after that argon was slowly displaced by water pre-heated to 580°C and pressurized to 25 MPa. In this way the samples were exposed only in supercritical water.

2.2 Studied materials

This study was focused on the materials, which are currently used in circuits of fossil-fuelled supercritical water cooled power plants. Also the surface preparation remain “as received” to simulate the behaviour of real systems. Four materials were tested: P92 ferritic/martensitic steel, Super304H and HR3C austenitic stainless steels. The chemical composition of the materials is summarized in Table 1.

Table 1: Chemical composition of the studied materials (comparison between declared and measured composition)[1]

Material	Chem. Comp.	C	Si	Mn	P	S	Cr	Ni	Mo	Cu	Nb	N	Al	V	W	B	Co
Super 304H		0,07	max	max	max	max	17	7,5		2,5	0,3	0,05					
	Declared	0,13	0,3	1	0,04	0,01	19	10,5	-	3,5	0,6	0,12					
	Measured	0,09	0,23	0,8	0,03	0,009	18,1	8,4	-	2,9	0,4						
HR3C		0,04	Max	Max.	Max.	Max.	24	17	-		0,2	0,15					
	Declared	0,1	0,75	2	0,03	0,03	26	23			0,6	0,35					
	Measured	0,05	0,46	1	0,03	0,001	25,9	20	-		0,25						
VM12-SHC		0,08	0,2	0,1	Max.	Max.	10	Max.	Max		0,03	0,03	Max.	0,18	1	0,001	0,5
	Declared	0,18	0,6	0,8	0,02	0,01	13	0,6	0,8	-	0,06	0,09	0,04	0,3	1,8	0,01	2
	Measured	0,13	0,27	0,19	0,018	0,015	11,6	0	0,17		0,055			0,27			
P92		0,07	max	0,3	max	max	8,5	max	0,3		0,04	0,003	max	0,15	1,5	0,001	
	Declared	0,13	0,5	0,6	0,020	0,010	9,5	0,4	0,6	-	0,09	0,006	0,04	0,25	2	0,006	-
	Measured	0,12	0,22	0,47	0,019	0,02	8,7	0,33	0,24		0,096			0,24			

[1] Declared= declared by producer

2.2.1 SEM analyses

P92

T/P9 grade steels were developed for high-temperature applications. The creep resistance is increased by vanadium and niobium alloying to stabilize the carbonitrides [4]. The P92 steel was developed in Japan and to the alloy P91 the tungsten was added to increase strength, as well as boron to stabilized carbides [5] .

Microstructure of the P92 steel is imaged on the . The structure is composed of tempered martensite. There is a well-developed magnetite oxide layer ($Fe^{3+}Fe^{2+}$) $Fe^{3+}O_4$ (Figure 5). The chemical composition analysed on layers is summarized in Table 2.

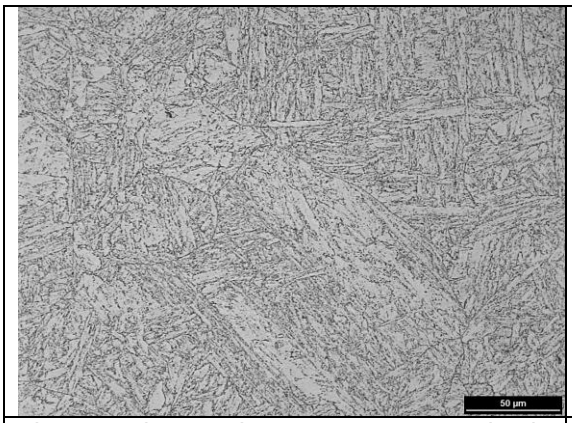

Figure 4: a) P92,microstructure, as received

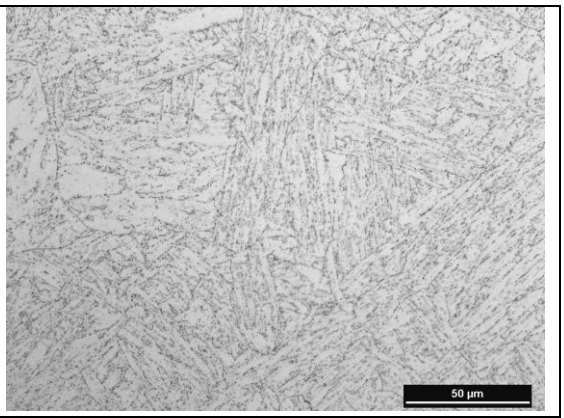

b) P92, after exposition, 600°C, 25 MPa, 1000 hours, microstructure

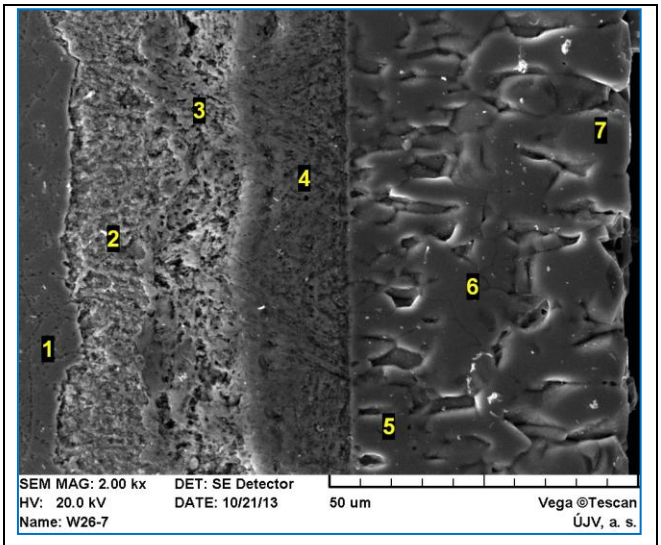

Figure 5: P92, after exposition, 600°C, 25 MPa, 1000 hours, surface layers cross section

Table 2: Chemical composition mapping, P92

Analýza	O	Si	V	Cr	Mn	Fe	Ni	W
1	0,00	0,41	0,12	7,71	0,45	89,45	0,64	1,23
2	0,31	0,43	0,08	3,10	0,30	91,58	1,12	3,09
3	20,27	0,29	0,25	4,36	0,45	68,32	0,29	5,78
4	19,42	0,35	0,33	7,62	0,43	69,05	0,26	2,54
5	24,17	0,05	0,04	0,69	0,20	74,81	0,03	0,01
6	23,08	0,02	0,04	0,15	0,20	76,46	0,05	0,00
7	22,31	0,02	0,05	0,03	0,72	76,78	0,09	0,00

Super304H

Microstructure of the base material is composed of the austenitic polyendric grain, lined by the gentle carbide precipitates (see Figure 6). Microstructure of the base material is composed of polyendric austenitic grain. Due to the exposition in the SCW the carbides on the grain boundaries precipitates more intensively (most probably Cr23C6). Chemical composition of the surface layers after exposition is summarized in Table 1.

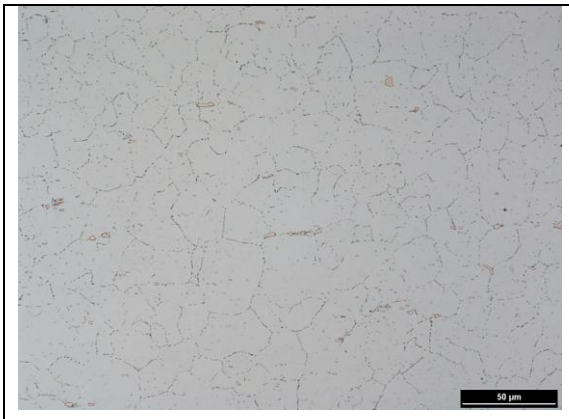

Figure 6: a) Super304H microstructure- as received

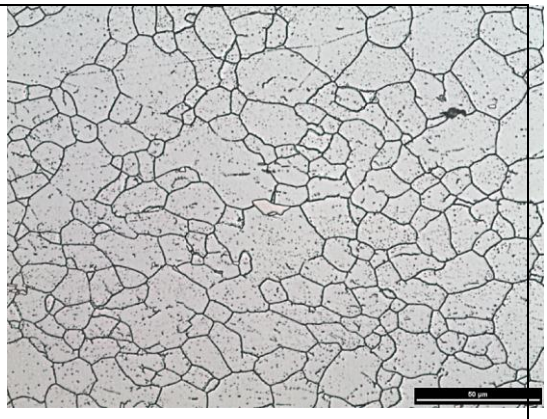

b) Super304H microstructure, after exposition, 600°C, 25 MPa, 1000 hours

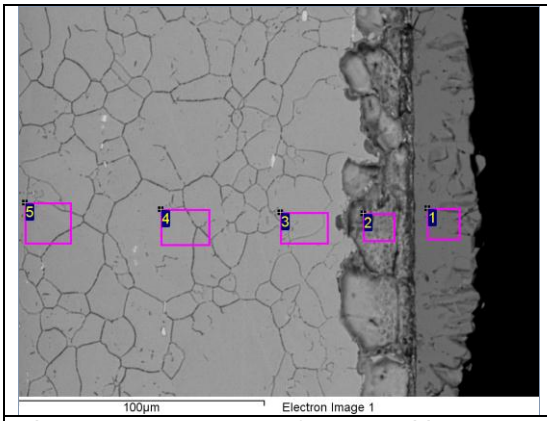

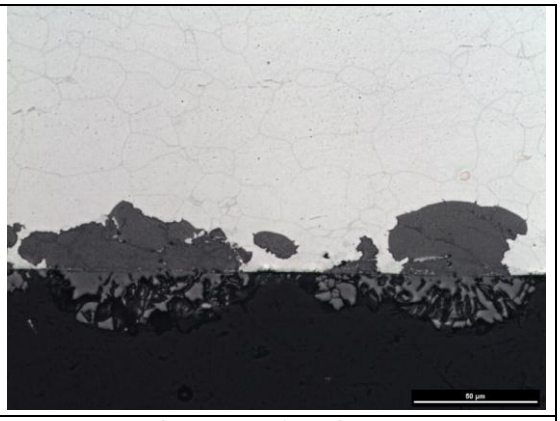

Figure 7: Super304H, after exposition, 600°C, 25 MPa, 1000 hours, surface layers cross section left – compact layer, b) locally deteriorated layer

Table 3: Chemical compostion mapping Super 304 H

Analyses	O	Si	Cr	Mn	Fe	Ni	Cu	Nb
1	28,27	0,04	0,57	0,28	70,42	0,37	0,00	0,05
2	10,96	0,49	20,61	1,04	34,49	27,03	4,74	0,64
3	0,43	0,42	19,46	0,69	67,72	8,81	2,47	0,00
4		0,48	19,19	0,97	67,69	8,24	3,05	0,38
5		0,31	18,88	1,01	68,43	8,07	2,68	0,62

VM12SHC

The VM12-SHC was developed as steam oxidation resistant material with sufficient creep resistance, comparable with P/T9 grade F/M steels. As received martensitic steel structure was tempered trough the exposition (Figure 8). On the specimen after exposition, there is continual layer 20 ± 3 µm thick composed by magnetite grains (Figure 9). Under this layer is layer of corroded material 25 ± 2,5 (max. 40µm) deep. The layer is compact and covers whole surface. The chemical composition of the surface layers is summarized in Table 4.

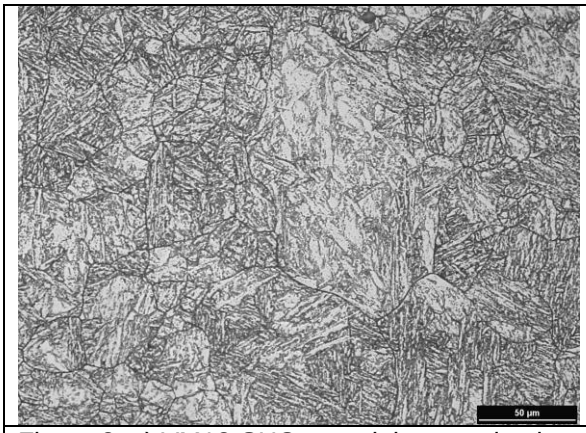

Figure 8: a) VM12-SHC material as received

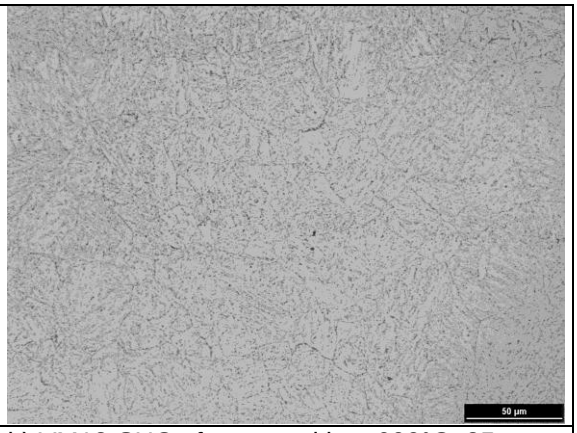

b) VM12-SHC after exposition, 600°C, 25 MPa, 1000 HRS, microstructure

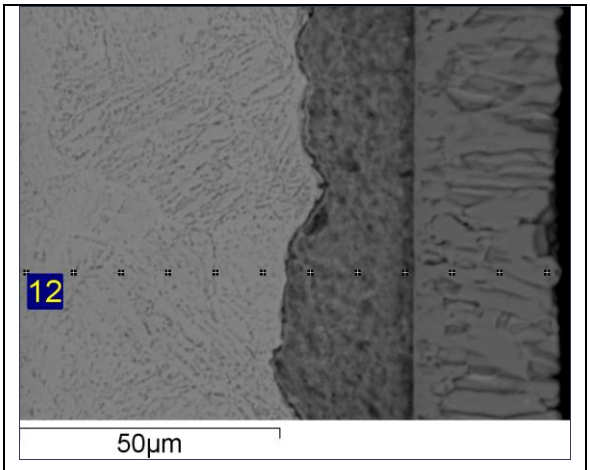

Figure 9: VM12-SHC after exposition, 600°C, 25 MPa, 1000 HRS, surface layers

Table 4: Chemical compostion mapping VM12-SHC

Analýza	O	Si	V	Cr	Mn	Fe	W
1	27,13			0,18	0,74	71,62	0,33
2	28,47	0,02		0,27	0,42	70,73	0,09
3	26,88	0,10		0,60	0,34	71,82	0,26
4	19,12	0,83	0,47	13,72	0,27	63,34	2,24
5	24,11	0,66	0,04	8,54	0,35	62,64	3,66
6	28,52	1,56	0,34	15,57	0,26	49,09	4,67
7		0,27	0,23	11,71	0,50	85,09	2,20
8		0,29	0,46	10,93	0,69	85,92	1,72
9		0,30	0,33	11,79	0,54	85,10	1,94
10		0,33	0,18	12,06	0,58	84,80	2,06
11		0,42	0,29	11,77	0,64	85,62	1,26
12		0,32	0,22	12,33	0,53	84,75	1,85

HR3C

HR3C steel was developed on the basis of steel 310 and contain high cromium and nickel content. Due to the exposition in SCW, the gentle carbide precipitates of carbides, creating the net copying the net of grain boundaries (most probably Cr23C6), see Figure 10. The specimen was free of any oxide layers. On the surface is not corroded but modified layer approx. 15 *μm* thick with similar composition as base material, enriched by Fe and Ni with lower concentration of Cr (see Figure 11 and Table 5).

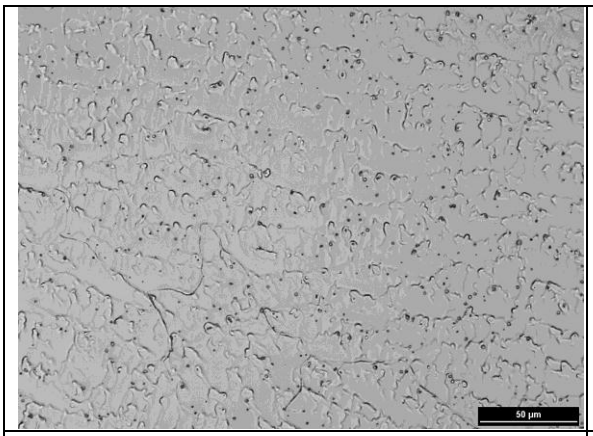

Figure 10: a) HR3C material as received

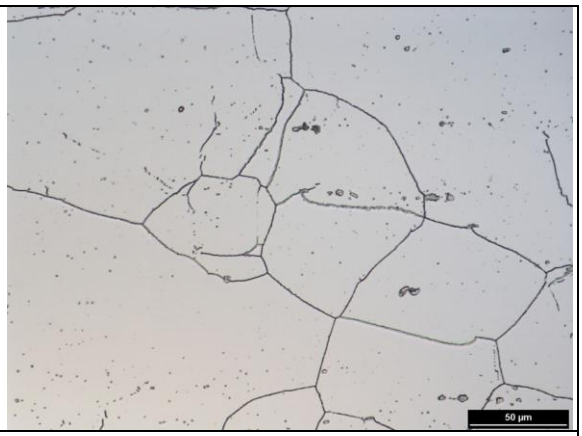

b) HR3C, after exposition, 600°C, 25 MPa, 1000 HRS, microstructure

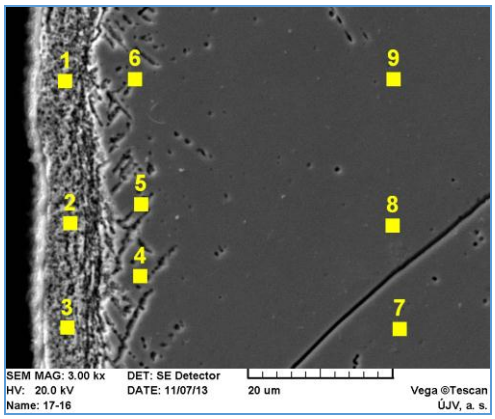

Figure 11: HR3C, after exposition, 600°C, 25 MPa, 1000 HRS, surface layers

Table 5: Chemical composition mapping, HR3C

Analýza	O	Cr	Mn	Fe	Ni	Nb
1	0,00	18,90	1,03	57,33	22,51	0,23
2	0,00	19,15	0,70	57,10	22,68	0,38
3	0,00	19,42	1,08	57,18	22,51	0,00
4	0,00	26,37	1,27	51,05	21,17	0,14
5	0,00	25,50	1,49	51,71	20,98	0,32
6	0,00	26,14	1,66	50,64	21,12	0,44

2.2.2 Electrochemical measurements

2.2.2.1 Impedance spectroscopy

The oxide layers were characterized by impedance spectrometry and other electrochemical methods to study their behaviour and predict the stability at long-term operation. Impedance measurements were performed ex-situ in borate buffer (pH=9,3) in a three electrode arrangement. As the working electrode the pre-exposed samples were used, as reference and counter electrodes a saturated kalomel electrode (SCE) and a platinum mesh were used respectively. In part of the experiments samples of steels covered with oxide formed by anodic oxidation (borate buffer, pH=9.3, E=0.8 V vs SCE, t=2hours) were used as working electrodes. Impedance was measured typically in the range.

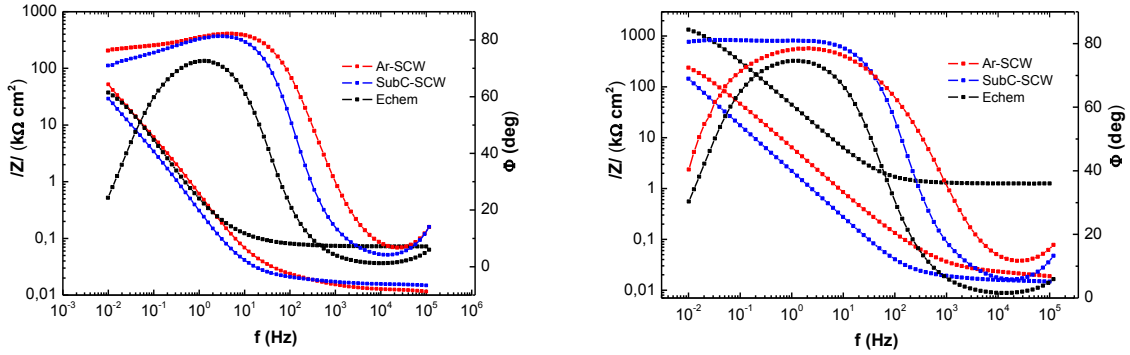

Figure 12Impedance spectry by P92 (left) and Super304H (right), Ar-SCW – Ar-water expostion, SubC-SCW – water exposition, Echem – electrochemical anodisation at laboratory conditions.

The spectra of electrochemically generated oxides exhibits lower level of frequency dispersion. According the expectations, the oxide generated by electrochemical way is in all cases compact and presence of single time constant indicates the unified behaviour in the charge transfer point of view. Thermally generated oxide exhibits at all studied conditions higher dispersion rate, generally higher in the subcritical area. Even after 50 hours of exposition the spectra indicates two time constants due to the duplex character of the oxide layer. Presence of outer crystallic and porous oxide layer causes higher degree of surface roughness and as consequence higher dispersion of electrode impedance. Previous studies have shown, that less dispersive spectra were obtained after removing the loosely adherent outer oxide [6]. More significant difference is in the case of 1000 hours exposition.
This results implies, that at the beginning of the exposition, the inner, thinner and more compact layer is growing. It has topotactic character than slower-growing outer epitactic layer, with more gentle oxide grains . More significant differences in the impedance spectra measured after different exposure times were observed in the case of ferritic-martensitic steels (P92, VM12-SHC), where the creation of the outer oxide layer is faster than on the austenitic stainless steels (Super 304H, HR3C).

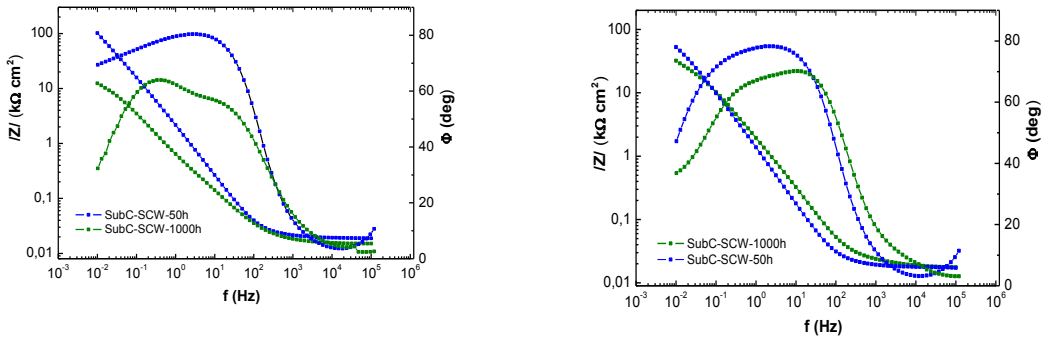

Figure 13: Impedance spectra of VM12SHC (left) and HR3C (right) (50 and 1000 hours expositions are compared

Impedance spectra were evaluated by the experimental data approximation by so called equivalent circuits (see Figure 14).

Figure 14: Equivalent circuits – compact oxide layer (left) and duplex layer (right)

In the results assessment, the impedance polarisation resistance Rp (low frequency impedance limit) was evaluated. In the case of complex layer (Figure 14 left) is Rp equal to R1, in the second (Figure 14 right) is Rp equalled to the arithmetic sum of R1 and R2. In the real electrochemical systems is the dispersion limit implied by constant phase element (CPE), where is valid:

$$Z_{CPE} = \frac{1}{\sigma}(j\omega)^{-n}$$

where σ is elements coefficient and n is CPE´s exponent (value is 0-1) and specifies the deviation from the ideally smooth surface (when n=1, than CPE behaves as ideal condenser).

All the exposed specimens had the same surface treatment, so the assumption is, that deviations in the dispersion level are relevant to the rate of macroscopic outer oxide deposition. It characterize the charge transfer on the oxide/electrolyte boundary. Values of polarization resistance and CPE exponent are on Figure 15 (left and right respectively).

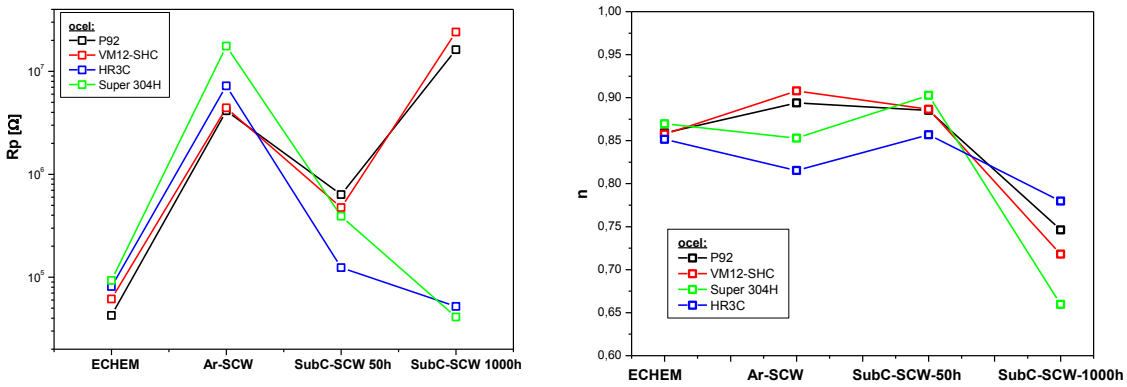

Figure 15: Values of polarization resistance and CPE exponent are on Figure 15 (left and right, respectively).

Oxide created by electrochemical repasivation is thin and it´s charge-transport properties are similar at all tested steel types. It has low impedance dispersion rate (oxide creates one homogenic layer). High values of the polarization resistance indicates the very compact oxide layer on the specimens without subcritical-supercritical transition and is comparable on all tested steels. Low value of the n for austenitic steels is hard to explain – most probably is it determined by the morphology of austenite (grain bulk – grain boundaries). The specimens, which were exposed same exposure time and passed the sub- to supercritical transition indicates more than ten times higher values of resistance, austenite lower than F/M. This phenomena is more significant with longer exposition. In the case of martensitic steels is resistance in tens of MΩ, and in case of austenitic steels is Rp 2,5 orders of magnitude lower In all cases the value of n significantly decreased for 1000h exposed specimens. Martensitic steels creates very thick oxide layer (few micrometres), containing thick layer of epitactic sublayer with microcrystalic character with higher dispersion rate. The charge transfer is deteriorated and it increases the polarisation resistance.

2.2.2.2 Mott-Schottky analyses

Protective properties of oxide films are determined by the electron or ion transfer through the oxide layer. Oxides on iron, chromium, nickel and many other metals and alloys are of semiconductive nature and some of their electronic characteristics, as doping concentrations, were closely linked to the oxide protective properties [6,7]. In case of the semiconductive behavior, concentration of dopants can be investigated by measuring capacitance dependence on electrode potential. In case that capacitance can be interpreted as space charge capacitance, doping density can be estimated from the linear slope of C^{-2} vs E plot:

$$\frac{1}{C_{sc}^2} = \frac{2}{\varepsilon_o \varepsilon_r e_o r^2 N}\left(\left|E - E_{fb}\right| - \frac{kT}{e_o}\right)$$

where C_{sc} is the space charge layer capacitance, U the applied potential, U_{fb} the flat-band potential, k the Boltzmann constant, T the temperature and q is the electronic charge.

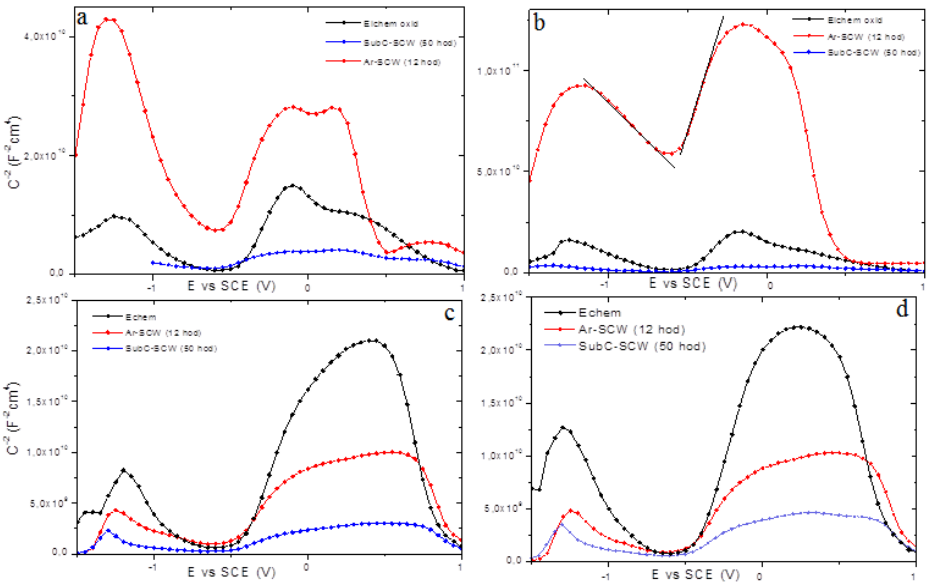

Figure 16: Mott-Schottky plots, ***red*** - exposition Ar-SCW, ***black*** – Echem oxid, ***blue*** – SubC-SCW; steel: **a** - Super 304H, **b** - HR3C , **c** - P92, **d** - VM12-SHC

Mott-Schottky plots measured on oxides formed different steels samples are given in Figure 16 a)-d). Two linear slopes are visible, one with positive slope in the range of -0,4 to -0.2 V and the second with negative slope in more negative potentials (approx. -0.75 to -1.25 V). This capacitance behavior seems to correspond to the generally accepted duplex structure of the oxide films formed on chromium alloyed steels. The capacitance behavior at higher potentials corresponds to the epitaxially grown outer layer, usually rich with iron. Capacitance behavior at lower potentials then is attributed to the inner (topotactically grown) layer, which is rich with chromium. Evaluation of doping densities of the oxides formed both in Ar-SCW and SubC-SCW experiments shown very different behavior (table 1). Thermally grown oxides are also compared with oxides formed by electrochemical anodisation:

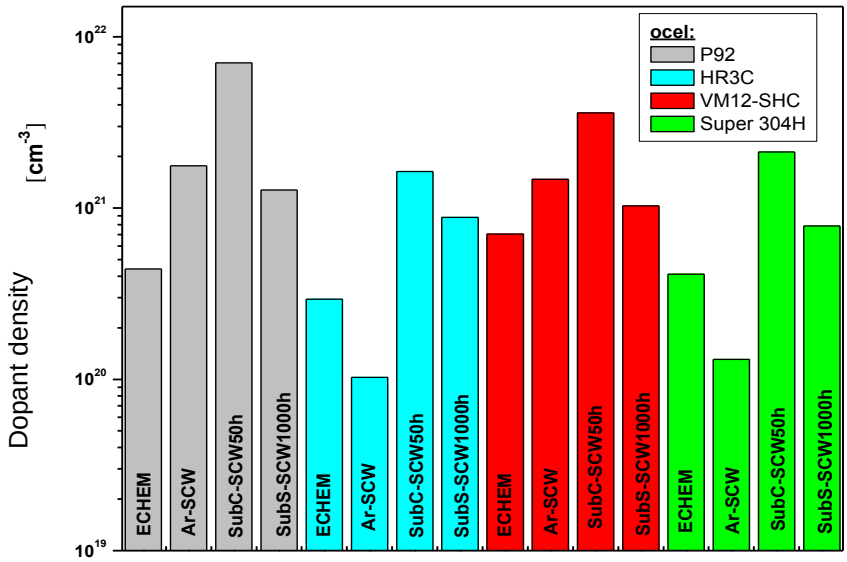

Figure 17: Dopants density in oxidic layers

2.2.2.3 Potentiokinetic repasivation

The sensitisation of the steels was determined by the potentiokinetic repasivation method. The steels with content of chromium higher than 15 % (and passivating) are potentially predisposed to sensitization. When heated in critical area (450-900°C) the carbon atoms move to the grain boundaries and create the Cr23C6 than the areas with lower (less than 12%) chromium content are created at and near the grain boundaries and the passivation effect is deteriorated. In aggressive environment the grain boundaries are attacked preferably. Electrochemical reactivation with double loop (EPR-DL) tests were performed according to the ASTM G-108 standard in the mixture of 0,5 M H_2SO_4 and 0,01M KSCN. Steel samples were polished using emery paper (up to 4000 grid). After keeping it for 20 minutes at native oxide reduction potential (-0,8 V vs SCE). The rate of potential scan was 1mV/s .

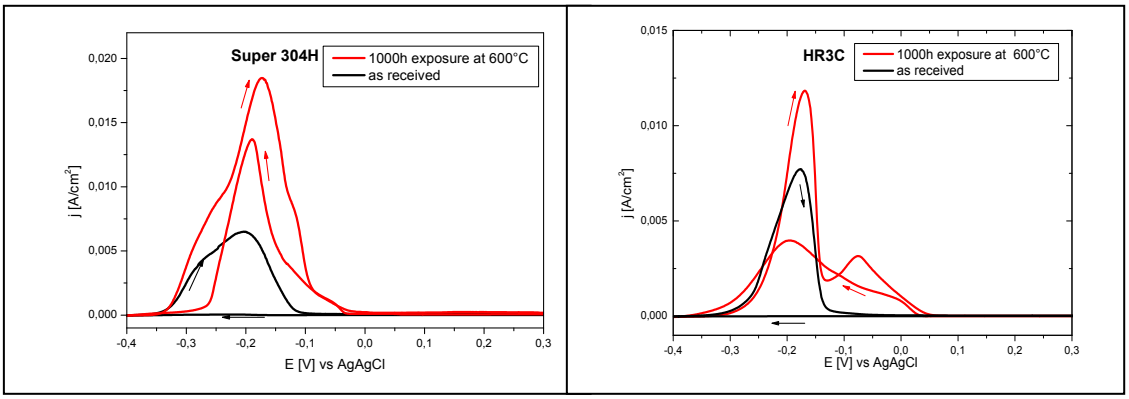

Figure 18 The potentiokinetic reactivation curves for HR3C (left) and Super 304H (right), green – as received, red – 1000 hrs exposition in SCW.

For comparison the same measurements were performed for the “as received” status of specimens. The results are in Figure 18 for both tested austenitic stainless steels.
The sensitisation rate was determined as ratio of critical reactivation current density (current maximum on the back polarization curve) and density of passivation current (current maximum on the anodic polarization curve).
Evidently, some degree of sensitization occured in both steels during 1000h exposure in SCW. In Super304H case due to the lower Cr the sensitisation rate is about 85-100%, in case of HR3C it is about 30 %. This fact explains the impedance decrease after longer exposure in the case of both austenitic stainless steels. The specimens were evaluated by optical microscopy (after reactivation experiment). The grains of sensitized materials are clearly visible, deteriorated and even the precipitated carbides are visible.
The Raman spectra were recorded using dispersive spectrometer The Thermo Scientific DXR Raman Microscope which is equipped with confocal optical microscope (based on a confocal optical microscope). A diode Nd:YAG laser was used as the excitation source with 532 nm wavelength and the input power 10 mW. A typical spectrum was obtained with 5-10 mW of lase power, during 30 s and 10-20 accumulation of spectrum. Grating with 400 grooves/mm and aperture 50 µm slit were used. Detection was achieved with multichannel thermoelectrically cooled CCD camera. Samples were measured using magnification 50x with measuring spot approximately 1 µm.
XPS measurements were performed on ESCA Probe P instrument (Omicron Nanotechnology Ltd.) using Al Kα monochromatic X-ray source with energy 1486,6 eV in high vacuum conditions. The energy of the emitted photoelectrons was analysed with a hemispherical electron analyser. Analysed region covers approximately 1 mm2 with a depth about 5 nm. Typical example of XPS concentration profiles measured after Ar-SCW and SubC-SCW experiments on Super 304H steel are presented on Figure 19.

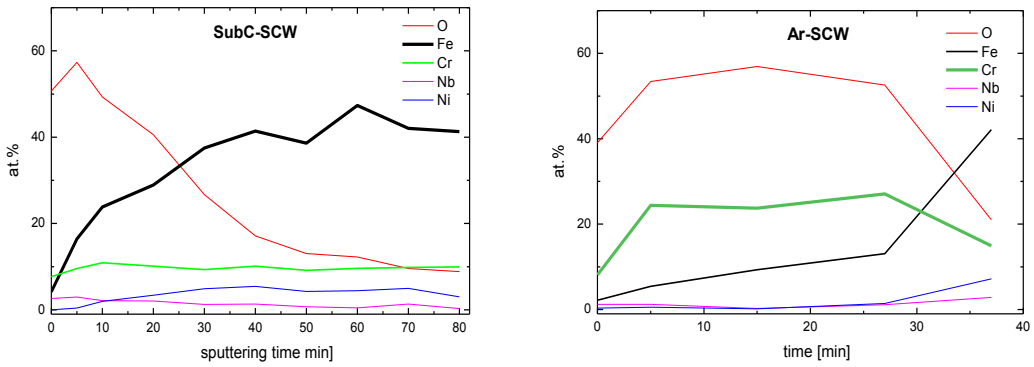

Figure 19**:** XPS concentration profiles of the oxides formed on Super 304H steel during SubC-SCW and Ar-SCW

Raman spectroscopy performed on outer oxide layer found high intensity band at 558 cm^{-1} corresponding to Cr_2O_3 in case of austenitic steels exposed in Ar-SCW experiment. This peak was completely missing in oxides exposed in SubC-SCW (Figure 20) at short exposures. Other bands correspond to chromium-iron spinel $Fe_xCr_yO_4$. Main components of the oxide found in samples from SubC-SCW were chromium – iron spinel and magnetite Fe_3O_4.
Outer oxide layer formed on ferritic-martensitic steels was composed mostly of magnetite.

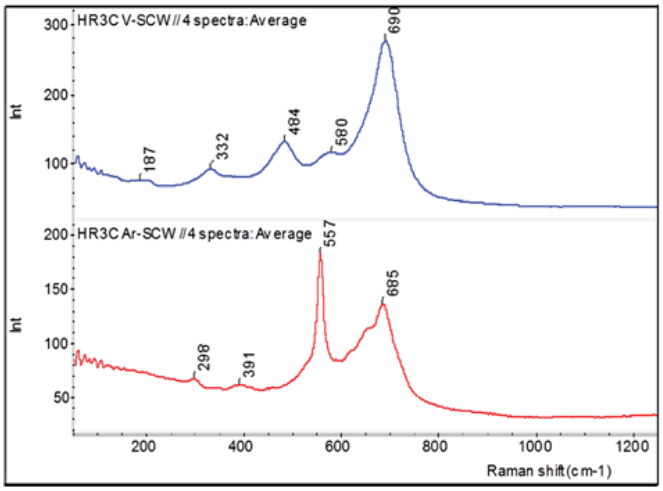

Figure 20: Raman spectra of oxide formed on HR3C steel under SubC-SCW (blue) and Ar-SCW (red) conditions.

3. Summary

Significant differences between the oxides formed during short-term experiments with subcritical-supercritical water transition and those with heat-up in argon were found. In the former case higher iron content was found and typical constituent was magnetite (F-M steels) or magnetite and chromium-iron spinel (austenitic steels). In the latter case no significant difference was found for F-M steels (magnetite, high iron content), while for austenitic steels higher content of chromium was found in the concentration profile. The layer consisted of chromia Cr_2O_3 and chromium-iron spinel $Fe_xCr_yO_4$. Moreover, oxide formed in the latter case

(Ar-SCW) exhibited relatively lower density of dopants and, as consequence, lower density charge carriers.
This could be discussed in the view of different corrosion mechanisms in subcritical and supercritical water. In case of partial exposure under subcritical conditions, formation of chromia-based oxide is limited due to its slow nucleation rate [8] moreover, due to higher diffusivity of iron, ionic transport of dissolved iron outwards through the oxide is enabled, contrary to SCW conditions. In the outer layer magnetite is formed. In case of heat up in argon, chromia-based oxide is formed, possibly due to oxidation by traces of oxygen beneath primarily formed spinel oxide.

4. Acknowledgement

This work has been supported by the SUSEN Project CZ.1.05/2.1.00/03.0108, realized in the framework of the European Regional Development Fund (ERDF), and by PRAMEK project no. TA02021406 supported by Technological Agency of Czech Republic.

5. References

1. YIN, Kaiju, Shaoyu QIU, Rui TANG, Qiang ZHANG a Lefu ZHANG. Corrosion behavior of ferritic/martensitic steel P92 in supercritical water. *The Journal of Supercritical Fluids*. 2009, č. 50, 235–239.
2. Výrostková, V. Homolová, J. Pecha, M. Svoboda, “Phase evolution in P92 and E911 weld metals during ageing, ” Mater. Sci. Eng. A. 480 (2008), pp. 289–298. doi:10.1016/j.msea.2007.07.036.
3. K. Yin, S. Qiu, R. Tang, Q. Zhang, L. Zhang, “Corrosion behavior of ferritic/martensitic steel P92 in supercritical water, ” J. Supercrit. Fluids. 50 (2009), pp. 235–239. doi:10.1016/j.supflu.2009.06.019.
4. S. Maleki, Y. Zhang, K. Nikbin, Prediction of creep crack growth properties of P91 parent and welded steel using remaining failure strain criteria, Eng. Fract. Mech. 77 (2010) 3035–3042. doi:10.1016/j.engfracmech.2010.04.022.
5. M. Svobodová, L. Horváth, J. Čmakal, Aplikační omezení žáropevné oceli P92, All Power. (2009)
5. M. Łomozik, M. Zeman, J. Brózda, “Modern martensitic steels for power industry, Arch. Civ. Mech. Eng. 12 (2012), pp. 49–59. doi:10.1016/j.acme.2012.03.010.
6. Macák J., Sajdl P., Kučera P., Novotný R., In-situ and ex-situ study of steel corrosion in high temperature water, Presentation at Eurocorr 2006, European Corrosion Federation Congress, Maastricht, 25-28.9., (2006)
7. Z. Szklarska-Smialowska: Corros.Sci. 44 (2002), p. 1143
8. P. Schmuki, H. Böhni: Electrochim.Acta 40 (1995), p. 775
9. J. Robertson, Corros.Sci. 32 (1991), p. 443

ISSCWR7-2099

Performance of high temperature materials for efficient power plant: the water side challenge

Pertti Auerkari, Sanni Yli-Olli, Sami Penttilä, Satu Tuurna, Rami Pohja
Technical Research Centre of Finland
PL 1000, 02044 VTT FINLAND
+ 358 50 566 6850, pertti.auerkari@vtt.fi

Abstract

Improved steam plant efficiency via elevated temperature and pressure levels can be justified if it is more than compensated by the return on investment and other benefits like reduced emissions. The balance is a moving target with simultaneous shifts in relative cost, availability and acceptability of fuels, process development, regulation and operating modes, but technical limits are partly set by the performance of materials in some critical high temperature components of the plant. For optimal material solutions, one limiting factor is the water side oxidation resistance at highest operating temperatures and pressures that extend to the supercritical (SC) range. In this paper, selected materials and modelling options are compared for components where waterside oxidation can contribute by limiting the service life. The implications are discussed for future service thermal plants that increasingly need to accommodate cyclic service, fast ramping and reduced minimum loads.

The results from recent materials development programs have not been able to circumvent all consequences from counteracting features in materials properties, so that the overall progress towards higher maximum temperatures has been slow, and the improvements in oxidation or corrosion resistance tend to be associated with significant direct and indirect alloying cost. The constraints from fluctuating demand in plant operation are likely to grow in importance, and the design codes and other guidelines include only partial solutions and tools to account for such trend. For example, the life-limiting contributions of high temperature oxidation and corrosion via lost load-bearing wall thickness is more easily accommodated than impact from increased growth rates of cracks and defects. The solutions are however likely to be only partly directly related to the materials that define the life-limiting boundaries for a given component and its process environment.

1. Introduction

To improve the benefit-cost ratio in provision and use of energy in the service of the society, one can for example try to save energy, shift to lower cost base in production, or reduce the inefficiencies of the energy systems. The historical development of production in thermal power plants demonstrates the systematic improvement by elevating the maximum temperature and pressure of the process, although the relative benefit is somewhat diminishing (Figure 1).

Because the limits in temperature, stress and chemical environment are set by materials, there is an incentive to develop and apply new materials that could survive at ever tougher environments. New material variants are only accepted and introduced to routine operation after

proven to perform, and this can be slow for example for the regulated structural materials of pressure equipment.

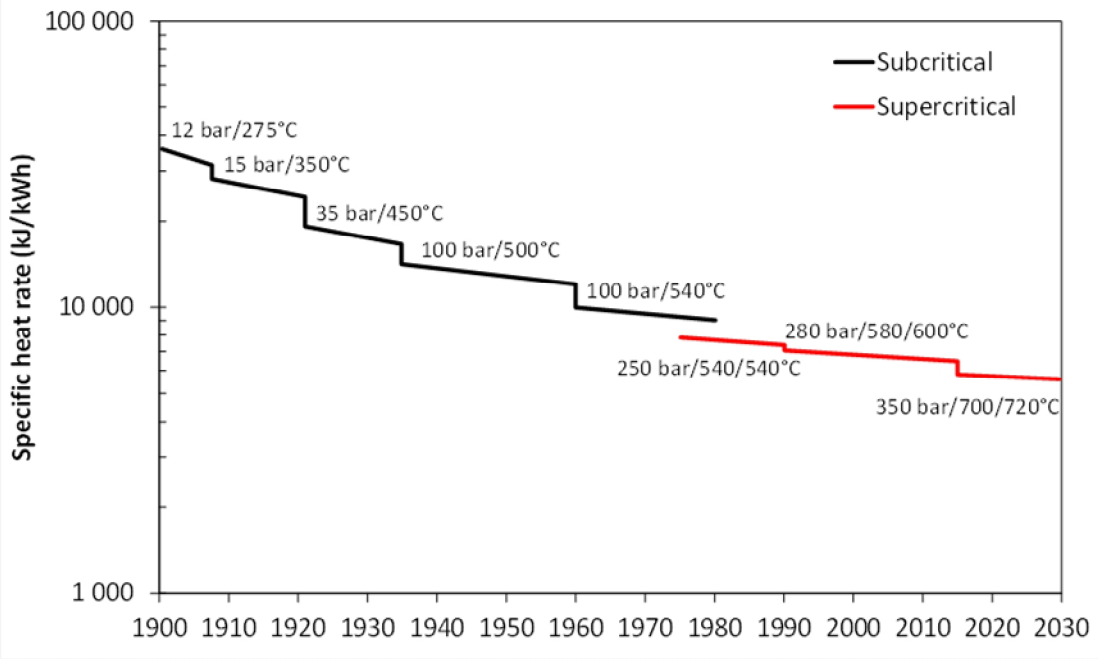

Figure 1. Development of the heat rate of the best thermal power plants; data from [1,2]

In the material (and other) development for the future thermal plant, at least three challenges stand out. One arises from fuels: major cost and emission issues are at stake, but a given plant is designed for a constrained range of fuels, for which the future cost, availability and acceptability are unlikely to remain equal to those assumed at the time of the original design and investment decisions. Flexibility is also needed for another challenging aspect: an increasing share of (subsidised) wind and solar production in Europe and elsewhere, with regulated priority to supply and no sensitivity to demand, requires the remaining mostly hydro and thermal capacity to cover the remaining fluctuating part of supply (Figure 2). The third challenge is doing all this while continuing to improve the plant performance and productivity, for example by reducing the specific cost and emissions of operation. Nevertheless, regardless of the selected solutions, one underlying trend is to aim for high efficiency by maximising the top temperatures and pressures in the Carnot cycle of a steam plant. This also applies to a supercritical plant where these process values are already high, for new supercritical (SC) plants up to about 600-620°C/30 MPa.

To successfully introduce a new material for a given component, the candidate solution must fulfil a range of criteria on properties related to cost, fabrication and service, and then show sufficient improvement to earn acceptance, in spite of added (often alloying related) investment to recover. Although the criteria may be clear and competition from the existing solutions well defined, it can be challenging to achieve significant improvement, for example because improving some property may require disproportionately high level of additional expensive alloying, or because of conflicting trends in simultaneously required properties: for example it would be good for corrosion and oxidation resistance to have at least 12% chromium in weldable ferritic/martensitic steels, but so far the best creep strength is seen at or slightly below 9% Cr, like in the steels P/T91 and P/T92. In this case increasing Cr content improves corrosion and oxidation resistance but via precipitation of unwanted secondary phases (soft ferrite, Z-phase) can also compromise mechanical strength and/or ductility.

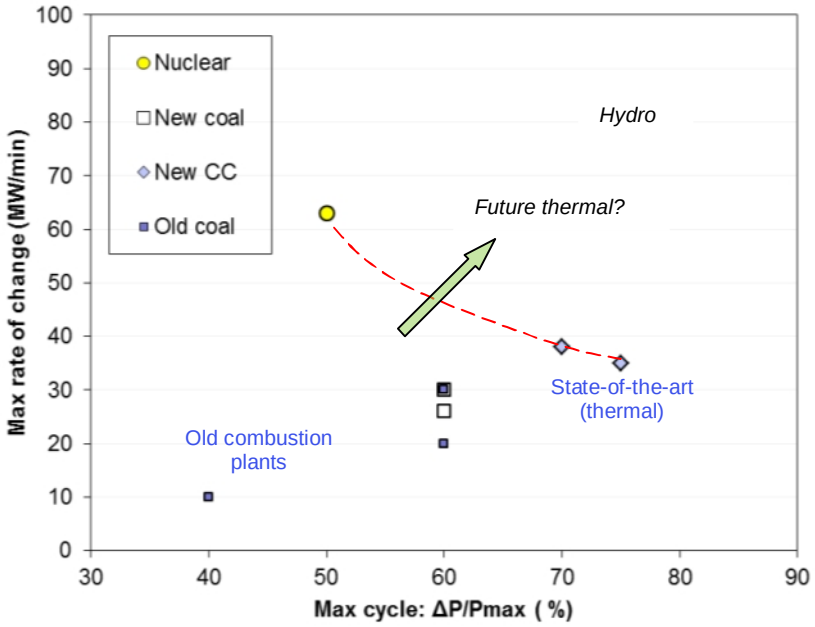

Figure 2. Flexibility for cycling and ramping of thermal plants; data from [3-5]

The optimal material solutions for a given component depend on multiple factors, but towards the upper limits of the operating temperatures in a steam plant, one typical limiting factor is the resistance to waterside oxidation. In this paper, selected materials and modelling options are compared for components where waterside oxidation can contribute by limiting the service life. The implications are discussed for future service thermal plants that increasingly need to accommodate more cyclic service, fast ramping and low minimum loads.

2. Waterside oxidation: predicting the layer thickness

Using classical deterministic approach of fitted kinetic parameters (see [6]) for mean parabolic inner oxide growth on 9%Cr and 11% Cr steels gives the predicted evolution of approximate oxide thickness as shown in Figure 3. It is seen that one can expect relatively thick oxide on 9%Cr steels up to likely spalling perhaps before 10000 h at 650^{0}C, but for 11%Cr steel up to an order of magnitude later in time. Dropping the temperature to 580^{0}C, which is close to the upper limit of the actual common application range, gives expected spalling of 9%Cr steel well before 100000 h of service but not for 11% Cr steels. This is fairly well in agreement with the experience in using X20, the 11%Cr steel of choice for e.g. superheaters and headers since 1960's (Figure 4a), and also with the experiments on newer 9%Cr steels (Figure 4b). In many applications the principal uncertainty to the observed high temperature performance arises from the assumed temperature, because of the temperature sensitivity of the rate of progression of many damage mechanisms, including that of high temperature corrosion and oxidation. To demonstrate the impact of uncertainty in temperature, the same oxidation model that was used in Figure 3 can be applied with a Monte-Carlo assessment of this uncertainty. For this purpose, Figure 5 shows the resulting range of predicted oxide thickness for 11%Cr steel (X20) after 100000 h of service, when the assumed uncertainty in the actual service temperature is for simplicity taken as normally distributed with a mean of 580°C and standard deviation (SD) of 3.8°C; this would translate to a typical temperature range of about ±10^{0}C, which is not considered unreasonable for e.g. a given location in an end section superheater.

The classical approach used above is not taking into account the variation of composition such as chromium content that is allowed to vary within the standard (or sometimes tighter)

limits. To accommodate the effect of such variation, another Monte Carlo simulation was conducted for 100000 h of exposure, assuming that the Cr content is normally distributed with a mean of 11.25% and SD of 0.45%; this would approximately correspond to the allowed range from 10% to 12.5% in the standard EN 10216-2 for X20CrMoV11-1. The results are shown in Figure 6 for mean temperature of 580C ± 3.8ºC, and more generally for the mean behaviour in Figure 7a. The modelling is here based on the concept of Cr and Ni equivalents, modified for to include the contribution of the concentration of individual elements [12].

The third predictive approach oxidation (Figure 7b) can be based on more detailed modelling of the reaction rates producing the inner (mixed oxide) and outer (largely magnetite) layers in contact with high temperature water [11]. Such models are more complex and more demanding to build, but also promise more fundamental understanding of the details, also for new materials and service environments.

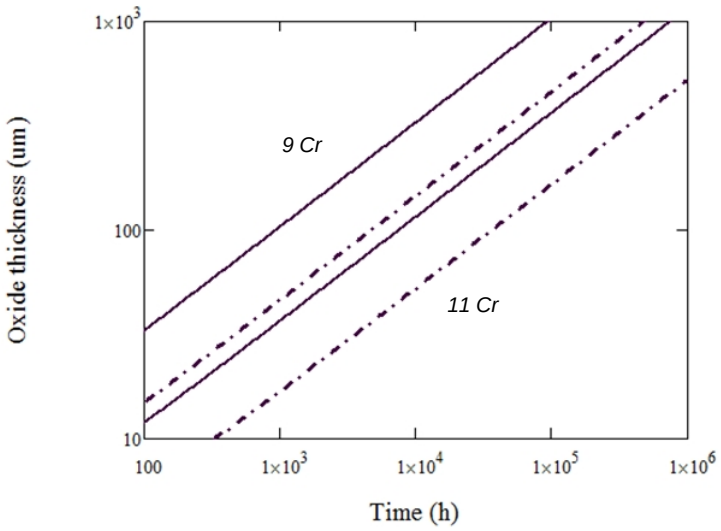

Figure 3. Predicted (parabolic) inner oxide growth for 9%Cr (solid lines) and 11% Cr steels (dashed lines) at 580°C (lower line) and 650°C (upper line of the pairs)

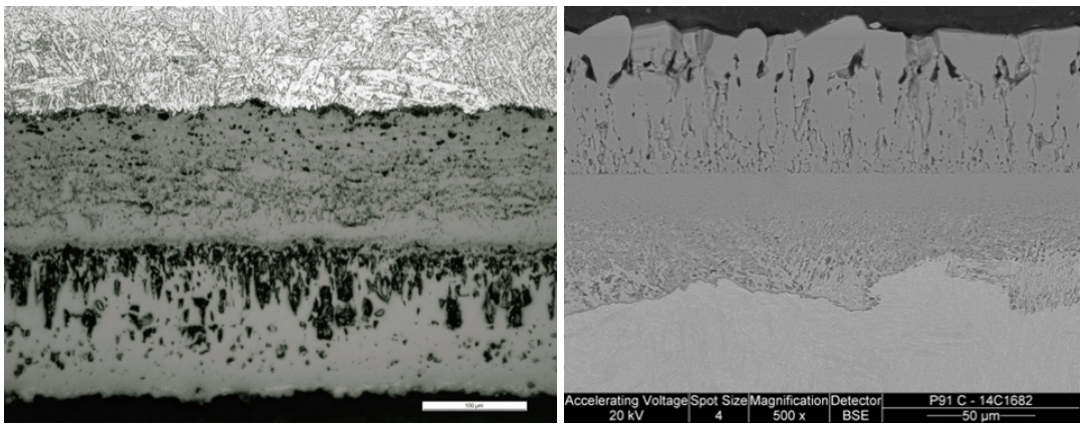

a) b)

Figure 4. a) Internal oxide of a X20 superheater tube after more than 100000 h in service; b) oxide on 9%Cr steel (MARBN), grown in supercritical water for 1000 h at 650°C/25 MPa

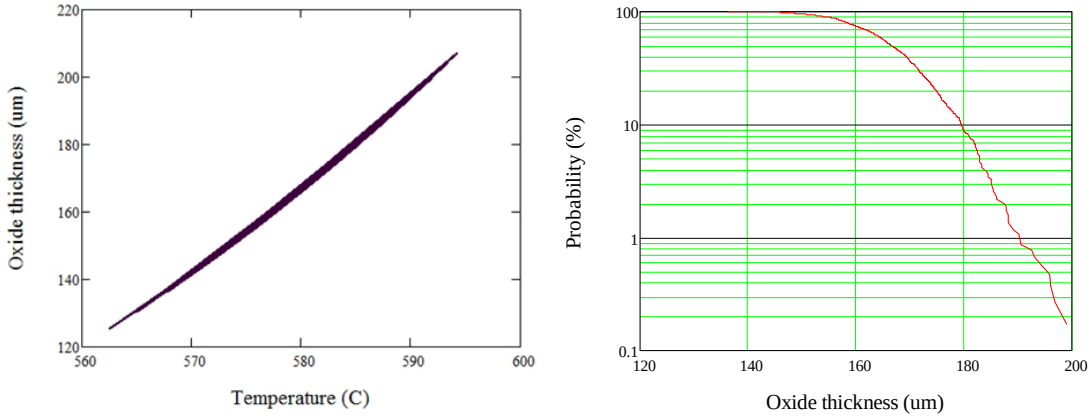

a) b)

Figure 5. a) Predicted range of X20 oxide thickness at 580°C ± 3.8°C (mean ± SD); b) corresponding exceedance probability for oxide thickness

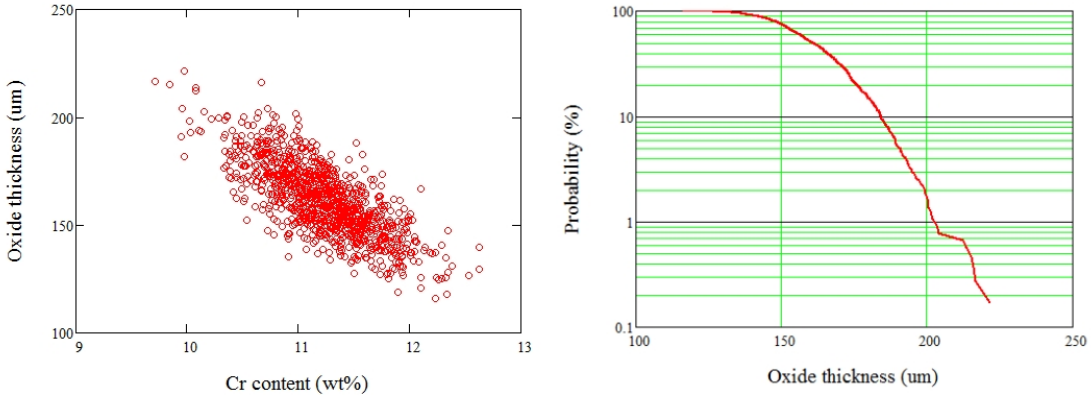

a) b)

Figure 6. a) Predicted oxide thickness for 11.25 ± 0.45% Cr (mean ± SD) in X20 at material temperature of 580 ± 3.8°C; b) corresponding exceedance probability for oxide thickness

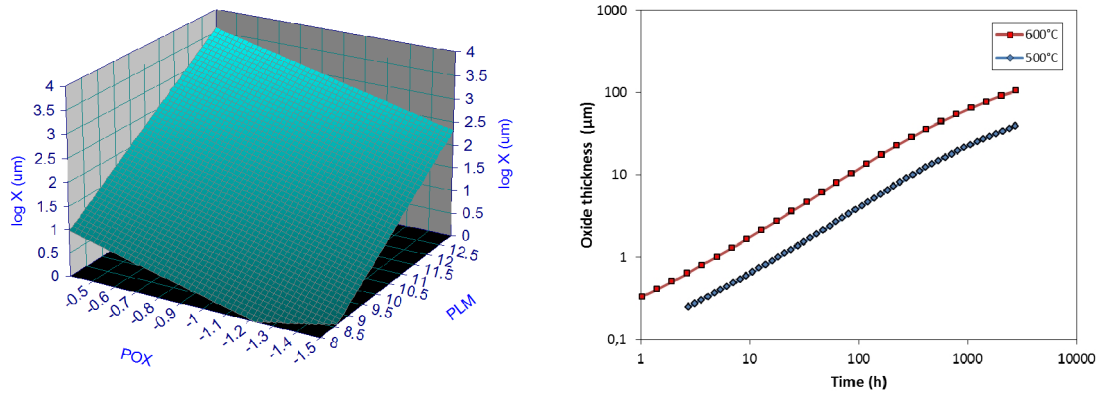

a) b)

Figure 7. a) Predicted oxide thickness as a function time and temperature (PLM) and modified Cr and Ni equivalents (POX) for ferritic Cr steels; b) predicted oxidation of 9% Cr steels [11]

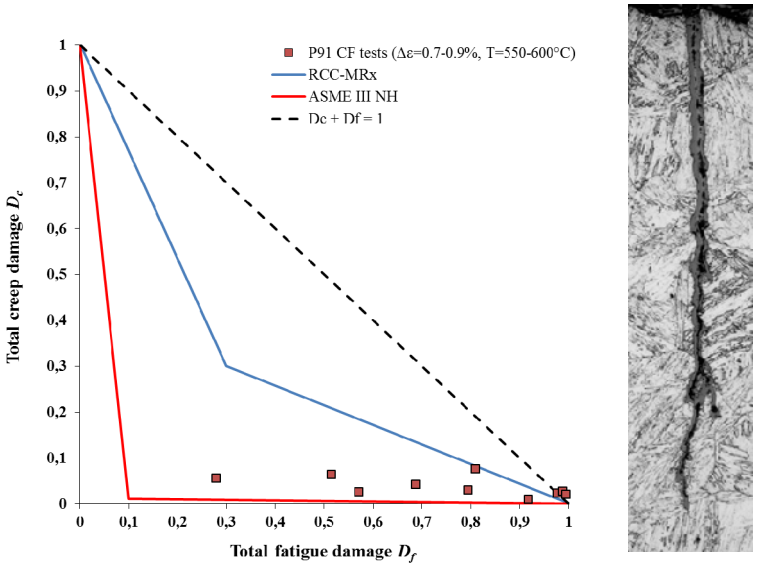

a) b)

Figure 8. a) Design/lifing limits for creep and fatigue life assessment with to creep-fatigue (CF) test results of P91; b) high temperature oxidation promoting crack growth

In plant oxidation or corrosion at high temperature is not necessarily acting alone but in combination, e.g. with mechanical loading (Figure 8). The combined impact on the component life can be approximately additive, but can also be drastically accelerated by true interaction of the mechanisms. An example of dealing with combined mechanisms can be seen in the assessment of creep, fatigue or creep-fatigue life according to design/lifing standards or guidelines like ASME III, RCC-MRx and EN 12952-4 (Figure 8a). For design this is applied to nominally intact material where oxidation and corrosion are taken to cause wall thinning, without need to consider growth of defects since these are disregarded as long as they are smaller than the indication limit for acceptance in QA. The assessment is less straightforward for growing cracks where oxide wedging or other mechanisms can promote the growth of e.g. fatigue cracks or other defects (Figure 8b). Such combined effects are also likely to become more common with increasing plant cycling and ramping.

3. Discussion and conclusions

It remains a challenge to improve the water oxidation resistance of structural steels in ways that do not conflict with optimising other properties like resistance to creep or thermal fatigue. In particular, for reasons of cost and compatibility to cyclic and ramping service, the available ferritic/martensitic steels like 9-11% Cr steels have attractive features but are lacking in water/steam oxidation resistance when taken to service temperatures above 600-620°C. While the current standard steel grades apparently can be improved for higher creep strength, less obvious routes are available to reduce the rates of high temperature oxidation. Protective coatings can work in principle but may require new concepts to provide satisfactory performance for example at welds or repair sites of the internal surfaces. Some austenitic grades show better resistance to creep and high temperature oxidation/corrosion, and therefore are widely used in relatively flexible or thin walled components like superheaters, where their higher thermal expansion and reduced thermal conductivity do not produce undue levels of thermal stress. However, such flexible components can also suffer in cyclic and ramping service: the oxide of austenitic steels can spall away at much lower thickness than the oxide on ferritic steels, and more often by buckling under compression [9,10].

As was shown above and is well known, for known common material types the waterside oxide growth can be approximately predicted from the temperature and time of exposure by fitting experimental data to conventional oxidation models. However, the details in chemical composition and surface condition, as well as exposure environment, can also impose significant effects and are not generally included in such models. For the ferritic 9% Cr steels it is not only the Cr content that will be important: for example the added tungsten in P/T92 steel, in comparison to P/T91, appears to increase the oxidation rate, and silicon may be helpful to some extent [8]. Nevertheless, Cr content is of major importance for these steels, as can be seen from the relative oxidation advantage of 11%Cr steels like X20 (Figure 3), and also in the relatively clear difference in the expected oxidation rates between batches of X20 that happen to be close to the lower and upper standard limits of the Cr content. For applications like superheaters both fireside corrosion and internal oxidation can be reduced in principle by specifying steel composition with higher than standard minimum for Cr content of X20. For some cases the temperatures are still higher and the material performance is insufficient. Then austenitic steels such as 347 or 310 are widely used up to about 650°C in superheaters and reheaters, and again an increasing temperature or otherwise more demanding environment requires more alloying. Then chromium no more dominates and nickel (or a Ni equivalent together with a Cr equivalent) is important for corrosion and oxidation resistance. Unfortunately the high coefficient of thermal expansion of austenitic steels partly compensates for the higher protective capability (and higher strength), resulting in spalling of thinner oxide layers than in ferritic steels [7-10]. In the extreme, even more resistant Ni and Co alloys (like in gas turbines) could be adopted up to temperatures of 700-800°C or higher, if the added cost can be justified for a steam plant.

The expected further increase in cycling and ramping service will impose an important constraint to future design and operation of thermal plants. The design codes and other guidelines include tools to account for such trend, for example for combined creep and fatigue. High temperature oxidation and corrosion can be important contributing factors to reduced component life, not only through reduced load-bearing wall thickness or increasing metal temperature (internally insulated cooling water flow), but also via increased growth rates of crack and defects. To improve the process efficiency by increasing the operational temperatures and pressures tends to increase the section thickness and material alloying in the high temperature end of the plant, thus increasing the challenge from abrupt start-ups, shutdowns and changes in operating loads. The accommodating solutions are likely to be only partly in the materials that define the life-limiting boundaries for any section of the plant structure and its process environment.

References

1. Mayer K-H, Masuyama F. The development of creep-resistant steels. In: Creep resistant steels (ed. F Abe, T-U Kern, R Viswanathan). Woodhead Publishing, Cambridge 2008, p. 15-77.

2. Auerkari P, Holmström S. Material and component requirements in existing and new power plants. Presentation in VDI Alloys seminar, June 2012, Berlin.

3. Timpf W, Fuchs M. Lastwechselfähigkeiten von Kernkraftwerken, VGB Powertech 92 (2012) 30-34.

4. Jeschke R, B. Henning B, Schreier W. Flexibility through highly-efficient technology. VBG Powertech 92 (2012) 64-68.

5. Fübi M, Krull FF, Ladwig M. Increase in flexibility with latest technologies. VGB Powertech 92 (2012) 30-34.

6. Viswanathan R, Foulds JR, Roberts DI. Methods for estimating the temperature of reheater and superheater tubes in fossil boilers. In: Conference Proceedings, Boiler Tube Failures in Fossil Plants. EPRI CS-5500-SR, EPRI, Palo Alto 1988, p. 3-35…3-53.

7. Holcomb GR. Steam Oxidation in steam boiler and turbine environments. In: Power plant life management and performance improvement (ed. J.E. Oakey), Woodhead Publishing, 2011, p. 453-489.

8. Ennis PJ, Quadakkers WJ. Mechanisms of oxidation and the influence of steam oxidation on service life of steam power plant components. In: Creep resistant steels (ed. F Abe, T-U Kern, R Viswanathan). Woodhead Publishing, Cambridge 2008, p. 519-535.

9. Fry A, Osgerby S, Wright M. Oxidation of alloys in steam environments – a review. NPL Report MATC(A)90, Teddington.

10. Wright IG, Dooley RB. A review of the oxidation behaviour of structural alloys in steam. International Materials Reviews 55 (2010) 129-167.

11. Penttilä S, Betova I, Bojinov M, Kinnunen P, Toivonen A. Estimation of kinetic parameters of the corrosion layer constituents on steel in supercritical water coolant conditions. Corrosion Science 53 (2011) 4193-4203.

12. Yli-Olli S, Holmström S, Auerkari P, Penttilä S**.** New model for steam oxidation of power plant steels. Baltica IX Conference on life management and maintenance for power plants, Helsinki-Stockholm 2013. VTT Technology 106, Espoo, p. 647-655.

Series title and number
VTT Technology 216

Title	**ISSCWR-7 2015 – 7th International Symposium on Supercritical Water-Cooled Reactors** **15th–18th March 2015, Radisson Blu Royal Hotel, Helsinki, Finland**
Author(s)	Penttilä, Sami (Ed.)
Abstract	The 7th International Symposium on Supercritical Water-Cooled Reactors was held in Helsinki, Finland, March 15th – 18th, 2015. The Symposium provided an updated review on the current status of international R&D work on SCWR concepts. ISSCWR7 focused on new issues and recent experiences in different national and international research programs including topics such as reactor core, neutronics, fuel designs, material issues, water chemistry and corrosion as well as thermal-hydraulics and safety analysis, and balance of plant.
ISBN, ISSN	ISBN 978-951-38-8289-1 (USB flash drive) ISBN 978-951-38-8290-7 (URL: http://www.vttresearch.com/impact/publications) ISSN-L 2242-1211 ISSN 2242-122X (Online)
Date	March 2015
Language	English
Pages	
Name of the project	
Commissioned by	
Keywords	SCWR, Reactor core, neutronics, fuel designs, materials, water chemistry, corrosion, thermal-hydraulics, safety analysis, balance of plant
Publisher	VTT Technical Research Centre of Finland Ltd P.O. Box 1000, FI-02044 VTT, Finland, Tel. +358 20 722 111

ISSCWR-7 2015

ISBN 978-951-38-8289-1 (USB flash drive)
ISBN 978-951-38-8290-7 (URL: http://www.vttresearch.com/impact/publications)
ISSN-L 2242-1211
ISSN 2242-122X (Online)

VTT TECHNOLOGY 216

ISSCWR-7 2015